Global COE Program

International Urban Earthquake Engineering Center

for Mitigating Seismic Mega Risk

Sixth International Conference on Urban Earthquake Engineering

Center for Urban Earthquake Engineering

Tokyo Institute of Technology

Tokyo Tech

CUEE

Global COE Program

International Urban Earthquake Engineering Center
for Mitigating Seismic Mega Risk

Sixth International Conference on Urban Earthquake Engineering

Center for Urban Earthquake Engineering
Tokyo Institute of Technology

Tokyo Tech
CUEE

PREFACE

I am delighted to convene our 6th International Conference on Urban Earthquake Engineering here in Tokyo on March 3rd and 4th, 2009, welcoming numerous distinguished experts and guests from around the world. The conference has been held annually since fiscal year 2003, under two consecutive Center of Excellence (COE) programs headquartered at the **Center for Urban Earthquake Engineering (CUEE)** at Tokyo Tech. These are the original 21st Century COE agenda for the "Evolution of Urban Earthquake Engineering" (FY 2003- 2007) and the recently established current Global COE program entitled **"International Urban Earthquake Engineering Center for Mitigating Seismic Mega Risk"** launched in FY 2008.

This new G-COE program aims not only to promote research to mitigate the seismic mega risk that confronts vast modern cities in earthquake-prone counties throughout the world. It also proposes to establish a uniquely original center devoted both to research and the education of the next generation, who, it is our hope, will develop new strategies, practices, and technologies to deal with this risk. Our program will continue to promote intensive information dissemination and technology transfer based on research results and outcomes in the field. We shall also seek to further and maintain the international network oriented toward younger researchers and to sustain its goals by international collaborative effort as well as frequent professional gatherings. With these aims in mind, we have recently concluded several collaborative agreements with Pacific Earthquake Engineering Research Center (PEER), starting with a joint one-day Young Researchers Workshop on the day preceding the Conference. We are committed to extending the scope of like activities to other organizations worldwide.

In the decisive renewal of these aims, the Sixth Conference, in March, together with our Young Researchers Workshop, offers a strong immediate platform for the sharing of common interests, new information, and recently developed technologies in Urban Earthquake Engineering. In addition, we shall strive to communicate research and educational outcomes in the interest of a greatly strengthened active worldwide network serving the overall field. This year's Conference promises seven state-of-the-art keynote lectures as well as over 135 oral and poster presentations on themes of the utmost relevance to Urban Earthquake Engineering, with the participation of scientists, engineers, researchers, and planners of divers generations, inclusive of graduate students. We shall greatly appreciate your kind participation, contributions, and discussions during the upcoming Conference. Our hope is that the Sixth Conference will prove a rich and stimulating opportunity for all of us dedicated to Urban Earthquake Engineering.

Kohji Tokimatsu
Global COE Program Leader and
Director of CUEE at Tokyo Tech

Global COE program entitled **"International Urban Earthquake Engineering Center for Mitigating Seismic Mega Risk"**

Center for Urban Earthquake Engineering (CUEE), Tokyo Institute of Technology
CUEE O-okayama Office TEL/FAX: +81-(0) 3-5734-3200
CUEE Suzukakedai Office TEL/FAX: +81-(0) 45-924-5576/5199
URL: http://www.cuee.titech.ac.jp

TABLE OF CONTENTS

Concrete Structures

Risk Management

Design & Standards

Base Isolation/Vibration Control

Geotechnical Earthquake Engineering

Bridge Structures

Steel Structures

Human Behavior

Tsunami

Sixth International Conference on Urban Earthquake Engineering
March 3-4, 2009, Tokyo Institute of Technology, Tokyo, Japan

OUTLINE OF OUR GLOBAL COE PROGRAM: INTERNATIONAL URBAN EARTHQUAKE ENGINEERING CENTER FOR MITIGATING SEISMIC MEGA RISK

Kohji Tokimatsu[1)]

1) Professor and Director, Center for Urban Earthquake Engineering, Tokyo Institute of Technology, Japan
kohji@o.cc.titech.ac.jp

Abstract: The background of our Global COE program entitled "International Urban Earthquake Engineering Center for Mitigating Seismic Mega Risk", launched in 2008 and headquartered at the Center for Urban Earthquake Engineering (CUEE) at Tokyo Institute of Technology, is presented in outline. Also introduced briefly are the major themes of implementation in both Research and Education proposed under the terms of the program, as well as the scope of its international collaborative effort.

BACKGROUND OF THE G-COE PROGRAM

Major cities in seismically active regions of the world are confronted with a substantial seismic risk of catastrophic damage to complex urban functions, that have resulted from an excessive concentration over time of population, economic activities and other significant developments ("seismic mega risk"). Moreover, recent earthquakes in Japan have revealed new problems such as effects of long period ground motion on large structures, as well as consequential impacts of the shutdown of critical facilities such as the Kashiwazaki-Kariwa nuclear power plant. In order to reduce such seismic mega risk and build a safe society, advanced research activities in the field of Urban Earthquake Engineering that seek out and emphasize earthquake resistance technology relevant to urban development, regeneration, and reconstruction, and stress their integration into a single framework, are urgent. Naturally, any such consideration must include the formation of researchers, educators, disaster management engineers, and other earthquake professionals. These individuals should be qualified to develop new strategies and put into practice appropriate technology for mitigating all such mega risks in a global framework.

This **Global COE (G-COE)** program entitled "International Urban Earthquake Engineering Center for

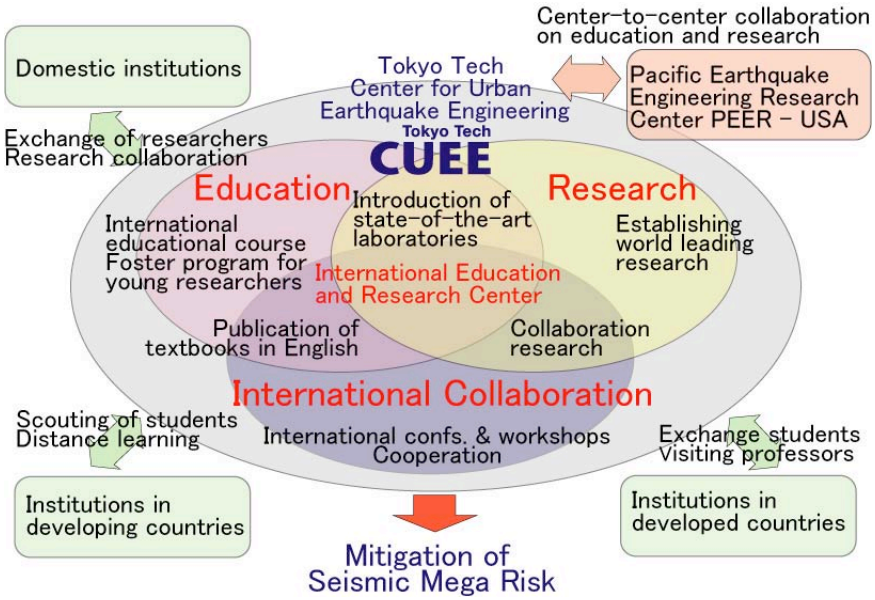

Figure 1. Schematic drawing of our G-COE program

Mitigating Seismic Mega Risk" is headquartered at the **Center of Urban Earthquake Engineering (CUEE)**, at **Tokyo Institute of Technology**. It aims not only to promote research to mitigate the seismic mega risk confronting vast modern cities in earthquake regions all over the world but also to strengthen graduate and post-doctoral educational programs, as well as to disseminate the fruits of research and its outcomes worldwide via an international collaborative effort.

The CUEE, established on September 1, 2003, to carry out the preceding COE program now provides the wherewithal to implement this updated program under a renewed and continued sponsorship extended by the Japan Ministry of Education, Culture, Sports, Science and Technology (MEXT).

G-COE IMPLEMENTATION

1. Research to Mitigate Seismic Mega Risk

Urban Earthquake Engineering research to mitigate seismic mega risk can be advanced only by integrating technologies for the creation, renovation, and eventual disaster recovery of an ideally earthquake-proof society. Our areas of research are to include the following:

(1) Innovation technology for earthquake disaster mitigation, applicable in the solution of emerging problems liable to simulate or increase seismic mega risk, such as advanced technology for precise seismic and tsunami hazard simulations, high-performance seismic response reduction, high-performance design of soil-foundation-superstructure systems and remote-sensing earthquake damage information systems;

(2) Renovation technology for urban earthquake resilience, effective in reducing divers seismic hazards in existing mega-cities and other metropolises, namely, seismic evaluation technology, the retrofit and reinforcement of existing buildings, the reinforcement of underground infrastructures, seismic improvements in non-structural components and interiors, emergency traffic-flow control during and after seismic events, regional evacuation planning, and overall design measures for the accommodation of handicapped individuals; and

(3) **Management technology for urban disaster mitigation**, effective in restoring functions of urban facilities and/ or minimizing secondary disasters after the occurrence of a catastrophic earthquake. Such technology includes comprehensive research and development into seismic performance improvement for urban complexes taking into consideration social and business risks, effective temporary accommodation measures for the public after an earthquake, education to increase disaster awareness, performance-based design strategies for business continuity plans (BCP) and divers social strategies for eventual community post-disaster restoration.

2. Educational Program to Foster International Specialists

The "**International Graduate Program in Urban Earthquake Engineering**" has been established by combining the existing master and doctoral programs in a new Integrated Doctoral Education Program (IDEP) for producing international specialists on earthquake disaster

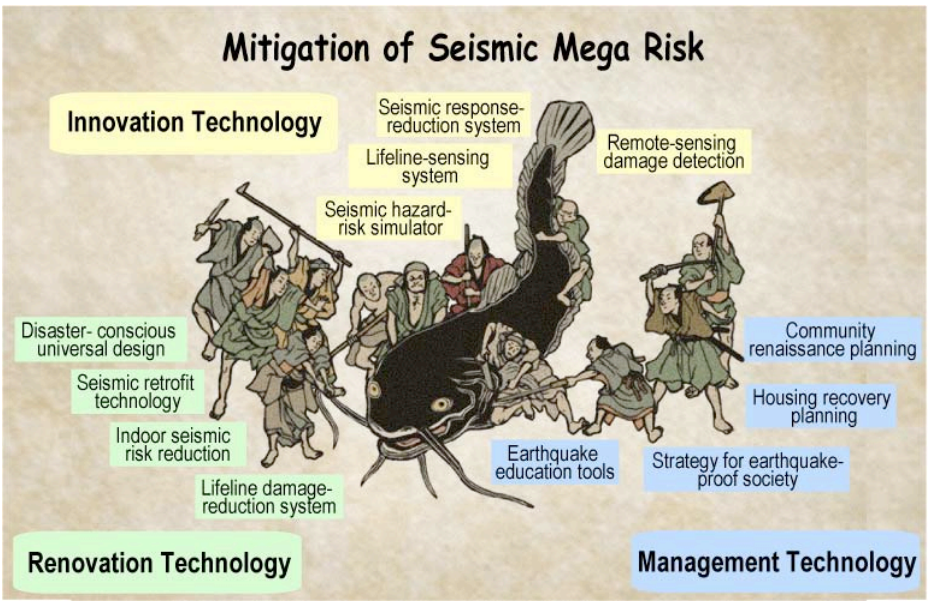

Figure 2. Our thrust research areas to mitigate seismic mega risk

mitigation.

This **International Graduate Program** is intended to diversify our educational mission for Japanese students, international students, and related professionals, through graduate courses, research supervision, and participation in international workshops and research collaboration with other domestic and international entities. All courses and lectures in this program are in English. In addition to basic and specialized topics on urban earthquake engineering studies, the three-step international approach conceived under this program is intended to develop skills and promote leadership in the field of Urban Earthquake Engineering.

We are continually implementing measures to create an environment enabling graduate students and other young researchers to build creative minds and to grow academically. Individual financial support includes:

(1) **Japanese government scholarships** (approx. JPY 170,000/mo.), including waiver of admission and tuition fees at Tokyo Institute of Technology: Five Japanese Government Scholarships are available for international students enrolling in the Integrated Doctoral Education Program (IDEP) on Urban Earthquake Engineering.

(2) **Research Assistantships and Teaching Assistant-ships**: Full-time doctoral students can apply for the position of Research Assistant (RA) (JPY 100,000-200,000/mo.). These grants include Teaching Assistantships. Each doctoral student should work as a Teaching Assistant (TA) for at least one semester.

(3) **Postdoctoral Fellowships**: Outstanding postgraduate students can apply for the position of Postdoctoral Fellow (PD).

(4) **Support for International Activities and Internship**: Study awards for domestic or overseas internships and participation in international conferences and workshops, and

(5) **Research Awards (**up to JPY 1,500,000/ year**)** for young researchers including doctoral students to conduct independent research.

3. International Collaboration and Dissemination of Research and Educational Outcomes

In collaboration with the Pacific Earthquake Engineering Research Center (PEER) as well as other leading educational and research centers in the Americas, Europe and elsewhere in Asia and Japan, our **G-COE Program** looks to the following strategies to achieve an eventual mitigation of seismic mega risk worldwide:

(1) Exchange of students and researchers, notably postgraduate students, to conduct research, pursue coursework, and promote integration with related academic activities at collaborating institutions.

(2) Organization of academic meetings, symposia, and workshops bringing students, as well as professionals and researchers, together in order to exchange knowledge and research findings.

(3) Carrying out joint research in areas of mutual interest with collaborating institutions, including the coordination of earthquake reconnaissance.

The G-COE program will further promote intensive information dissemination and technology transfer, as well as the establishment of an international network for young researchers in the field. These activities are enabled not only by the above efforts at international collaboration but

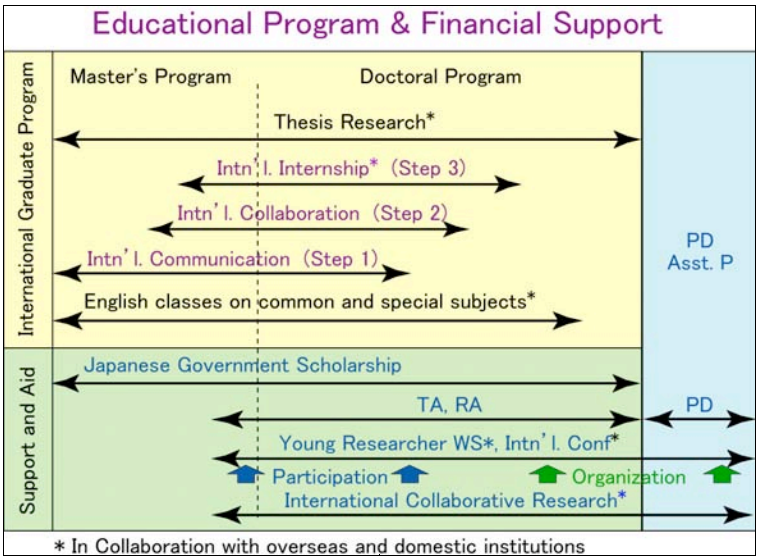

Figure 3. Our international program and financial support

will also be sustained by international conferences held every year and publication of English-language books and other texts of proceedings and research outcomes. In order to publicize our research outcomes to practicing engineers, public servants, and ordinary citizens, it is also planned to conduct seminars; and open courses on Urban Earthquake Engineering will also be conducted on a regular basis.

IN CONCLUSION

The *ukiyo-e* style portrayal of a concentrated group of individuals wielding arms of all sorts in attacking a catfish (Figure 2; in Japanese lore this creature is considered to be the source of earthquakes) suggests our center's multifaceted and collaborative approach to mitigating seismic mega risk. Beneficial reduction of the potentially huge damage and loss caused by a catastrophic earthquake cannot be attained by strengthening single buildings and/ or infrastructure alone, or by the efforts of a small number of people. Integrated and collaborative effort is decisively called for, where various professions and technologies in divers disciplines worldwide must join together. We, therefore, wish to solicit each of you for continued advice, guidance, contributions, and collaboration, towards achieving this profound mutual objective that is our goal.

Sixth International Conference on Urban Earthquake Engineering
March 3-4, 2009, Tokyo Institute of Technology, Tokyo, Japan

NEXT GENERATION ATTENUATION (NGA) PROJECT: EMPIRICAL GROUND MOTION PREDICTION EQUATIONS FOR ACTIVE TECTONIC REGIONS

K. Campbell[1], N. Abrahamson[2], M. Power[3], B. Chiou[4], Y. Bozorgnia[5], T. Shantz[6], and C. Roblee[7]

1) Vice President, ABS Consulting (EQECAT) Inc., Oakland, California, USA
2) Engineering Seismologist, Pacific Gas & Electric Company, San Francisco, California, USA
3) Principal Engineer, AMEC Geomatrix Consultants Inc., Oakland, California, USA
4) Senior Seismologist, California Department of Transportation, Sacramento, California, USA
5) Associate Director, Pacific Earthquake Engineering Research Center, University of California, Berkeley, California, USA
6) Senior Research Engineer, California Department of Transportation, Sacramento, California, USA
7) Senior Research Engineer, California Department of Transportation, Sacramento, California, USA
kcampbell@eqecat.com, mpower@geomatrix.com, brian.chiou@dot.ca.gov, naa3@earthlink.net, yousef@berkeley.edu, tom.shantz@dot.ca.gov, cliff.roblee@ dot.ca.gov,

Abstract: The "Next Generation Attenuation" (NGA) Project was a partnered research program conducted by the Pacific Earthquake Engineering Research Center-Lifelines Program (PEER-LL), U.S. Geological Survey (USGS), and Southern California Earthquake Center (SCEC). The project had the objective of developing updated ground motion prediction equations (attenuation relationships) for the western U.S. and other worldwide active shallow tectonic regions through a comprehensive and highly interactive research program. Five sets of updated attenuation relationships were developed by teams working independently but interacting throughout the development process. An overview of the NGA project components, process, and products developed by the project is presented in this paper.

1. INTRODUCTION

The objective of the "Next Generation Attenuation" (NGA) Project was to develop updated ground motion prediction equations (attenuation relationships) for shallow crustal earthquakes in the western U.S. (WUS) through a comprehensive and highly interactive research program that involved the following components: (1) development of separate sets of attenuation relationships by five teams (the "Developers"); (2) development of an updated and expanded PEER strong motion database to provide the recorded ground motion data and the supporting metadata on the causative earthquakes, source-to-site travel paths, and local site conditions needed by the Developers for their empirical model development; (3) a number of supporting research projects, including theoretical simulations of rock motions, soil site response and basin response, to provide an improved scientific basis for evaluating the functional forms of and constraints on the attenuation relationships; and (4) a series of workshops, working group meetings, Developer meetings, and external review that provided input into and review of the project results by both the scientific research community and the engineering user community. These project components are briefly described in subsequent sections of this paper. A more detailed overview of the NGA project is given in Power et al. (2008).

2. MODEL DEVELOPMENT

Developers of five pre-existing and widely used attenuation relationships participated in the concurrent development of the NGA models. The Developers are listed below with references to their updated attenuation relationships shown in parentheses: Norman Abrahamson and Walter Silva (Abrahamson and Silva 2008), David Boore and Gail Atkinson (Atkinson and Boore 2008), Kenneth Campbell and Yousef Bozorgnia (Campbell and Bozorgnia 2008); Brian Chiou and Robert Youngs (Chiou and Youngs, 2008), I.M. Idriss (Idriss 2008). These models are referred to as AS08, BA08, CB08, CY08, and I08, respectively, in the remainder of this paper. The NGA models and supporting studies have been fully documented in a special issue of *Earthquake Spectra* (Vol. 24, No. 1, February 2008) entitled "Special Issue on the Next Generation Attenuation Project" edited by Jon Stewart, Ralph Archuleta, and Maury Power.

To meet the needs of the engineering seismology and earthquake engineering communities, all of the NGA models were required to be applicable to (1) ground motion parameters of peak ground acceleration, velocity, and displacement (PGA, PGV, PGD), and 5%-damped linear elastic response spectral acceleration (S_a) in the period range of 0.01 to 10 sec, (2) average horizontal motion, defined as

the orientation-independent geometric mean horizontal component, GMRotI50 (Boore et al. 2006), (3) shallow crustal earthquakes with strike slip, reverse, and normal fault mechanisms in the WUS, (4) moment magnitudes ranging from 5 to 8.5, (5) fault distances ranging from 0 to 200 km, and (6) commonly used site classification schemes, including the NEHRP classification scheme. In regards to this latter requirement, all of the NGA models, except I08, used the time-averaged shear-wave velocity in the top 30 m of the site (V_{S30}) to model site conditions.

2.1 Data Selection

To provide a common database of recorded ground motions and supporting metadata for the Developers, the NGA Project conducted an extensive update and expansion of the PEER strong motion database (Chiou et al. 2008). Although the NGA developers all started with the same database of 3551 recordings from 173 earthquakes (Fig. 1), the selected data sets used to develop the models had significant differences. The number of selected earthquakes and recordings are summarized in Table 1. A key difference in the data sets is the treatment of aftershocks. The AS08 and CY08 data sets included aftershocks, resulting in a much larger number of earthquakes than the BA08 and CB08 data sets. The I08 data set included aftershocks, but had the smallest number of recordings, because it only included rock sites ($450 < V_{S30} < 900$ m/s). The specific earthquakes and number of recordings selected by each Developer are listed in Abrahamson et al. 2008.

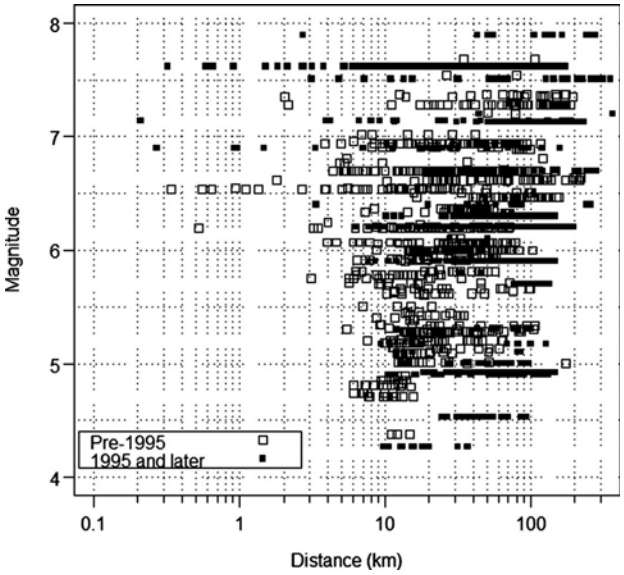

Figure 1 Distribution of Recordings Included in the NGA Strong Motion Database

An important issue in the selection of the earthquakes was the applicability of the well-recorded large-magnitude earthquakes from outside of the WUS (e.g., 1999 Chi-Chi and 1999 Kocaeli) to the prediction of ground motions in the WUS. All of the Developers considered both the Chi-Chi and Kocaeli data to be applicable to the WUS. Furthermore, comparisons of the NGA models with European data have shown that the NGA models are applicable to this region as well (Stafford et al. 2008). Similar preliminary studies in Iran, Taiwan, New Zealand, and South America suggest that the NGA models might be generally applicable to shallow crustal earthquakes in active tectonic regions worldwide.

Table 1 Summary of Data Sets Used by NGA Developers

Data	AB08	BA08	CB08	CY08	I08
No. Eqs.	135	58	64	125	72
No. Recs.	2754	1574	1561	1950	942

2.2 Functional Forms

The main features of the functional forms of the five NGA models are summarized in Table 2 (Abrahamson et al. 2008). Saturation at short distances is a feature of ground motion models that leads to weaker magnitude scaling at short distances as compared to larger distances. This is not the same as including a quadratic magnitude scaling that applies at all distances. In ground motion studies, a model is said to have "full saturation" if there is no magnitude scaling of the median ground motion at zero distance. A model is said to have over-saturation if the median ground motion decreases with increasing magnitude at zero distance. All of the NGA models include some form of saturation of the short-period ground motion at short distances through either a magnitude-dependent distance decay (AS08, BA08, CB08, I08) or a magnitude-dependent fictitious depth (CY08). In several cases, the selected data sets would have lead to over-saturation of the short-period ground motion at short distances had the regression not been constrained, but none of the Developers allowed over-saturation in their models.

Table 2 Effects Modeled by the NGA Models

Term	AB08	BA08	CB08	CY08	I08
Saturation Effects	X	X	X	X	X
Fault Mechanism	X	X	X	X	X
Rupture Depth	X		X	X	
Hanging-Wall Effects	X		X	X	
Nonlinear Site Effects	X	X	X	X	
Sediment Depth	X		X	X	
Magnitude effect on σ_T	X			X	X
Nonlinear Effect on σ_T	X		X	X	

As indicated in Table 2, besides saturation at short distances, other effects modeled by the functional forms of one or more of the NGA models include: (1) style-of-faulting and fault mechanism, (2) depth to the top of the rupture plane, (3) hanging-wall effects, (4) nonlinear site amplification, (5) sediment depth, (6) magnitude-dependent standard deviation (σ_T), and (7) nonlinear site-dependent σ_T.

2.3 Model Parameters

The model parameters used by each Developer are summarized below. I08, which is only for rock sites, has the simplest parameterization (magnitude, distance, and style-of-faulting). BA08 has the next simplest parameterization; in addition to magnitude, distance, and style-of-faulting, it has the added parameters of V_{S30} and rock outcrop motion to model nonlinear site response. AS08, CB08, and CY08 have the most complex parameterizations. In addition to the above parameters, these models include additional parameters to model hanging-wall effects, rupture-depth effects, and sediment-depth effects.

A complete list of the parameters used in the NGA models is as follows:

M	Moment magnitude
R_{RUP}	Closest distance to rupture plane
R_{JB}	Closest horizontal distance to rupture plane
R_X	Closest horizontal distance to top of rupture plane
Z_{TOR}	Depth to top of rupture plane
F_{RV}	Indicator variable for reverse faulting
F	Indicator variable for reverse faulting (I08)
RS	Indicator variable for reverse faulting (BA08)
F_{NM}	Indicator variable for normal faulting
NS	Indicator variable for normal faulting (BA08)
SS	Indicator variable for strike-slip faulting (BA08)
US	Indicator variable for unspecified faulting (BA08)
F_{AS}	Indicator variable for aftershocks (AS08)
AS	Indicator variable for aftershocks (CY08)
δ	Dip of rupture plane
W	Down-dip width of rupture plane
F_{HW}	Indicator variable for site on hanging wall
V_{S30}	Time-averaged S-wave velocity in top 30 m
$Z_{1.0}$	Depth to 1000 m/s S-wave velocity horizon
$Z_{2.5}$	Depth to 2500 m/s S-wave velocity horizon
PGA_{1100}	Median estimate of PGA on rock (AS08)
PGA4NL	Median estimate of PGA on rock (BA08)
Y_{REF}	Median estimate of S_a on rock (CY08)
τ, σ, σ_T	Inter-event, Intra-event, and total std. deviation

All five models are based on moment magnitude and all five models include a style-of-faulting (fault mechanism) term, although I08 does not distinguish between strike-slip and normal earthquakes. For the three models that include rupture-depth effects (AS08, CB08, and CY08), the rupture depth is parameterized by the depth to the top of the rupture plane. Of the three models that include aftershocks (AS08, CY08, and I08), AS08 and CY08 account for differences between the median ground motion for aftershocks and mainshocks, with aftershocks having smaller ground motions than mainshocks.

There are two primary distance measures used in the NGA models. BA08 uses the closest horizontal distance to the surface projection of the rupture plane, R_{JB}. The other four models use the closest distance to the rupture plane, R_{RUP}. For the hanging-wall (HW) term, AS08, CB08, and CY08 use additional distance measures to smooth this term. All three models use the R_{JB} distance measure in their HW scaling. AS08 and CY08 also use a third distance measure, R_X. This distance measure is defined as the horizontal distance from the top edge of the rupture plane, measured perpendicular to the fault strike (R_X is positive over the hanging wall and negative over the footwall).

All of the models except for I08 use the time-averaged S-wave velocity in the top 30 m of a site, V_{S30}, as the primary site parameter. In addition, all four models that model site response incorporate nonlinear site effects. Two different measures for the strength of the shaking are used to quantify nonlinear site response effects. AS08, BA08, and CB08 use the median estimate of PGA on a reference rock outcrop in the nonlinear site response term. CY08 uses the median estimate of spectral acceleration on a reference rock outcrop at the period of interest. BA08 defines reference rock as having V_{S30} = 760 m/s, CY08 defines it as having V_{S30} = 1130 m/s, and AB08 and CB08 define it as having V_{S30} = 1100 m/s. As mentioned previously, I08 is valid only for a reference rock outcrop with V_{S30} = 450-900 m/s. In all cases, a rock outcrop is assumed to have linear site response. Three models include sediment depth as an additional site parameter to model basin effects and other long-period site effects not modeled by V_{S30}. AS08 and CY08 use the depth to the 1000 m/s S-wave velocity horizon, $Z_{1.0}$, and CB08 uses the depth to the 2500 m/s velocity horizon, $Z_{2.5}$, to capture these additional effects.

3. MODEL COMPARISONS

The NGA models use different source parameters and distance measures. Some of the models include the depth to top of rupture as a source parameter. To compare with the NGA models that do not include this parameter, a median estimate of Z_{TOR} derived from the NGA data base was used as follows: 6 km for **M** = 5, 3 km for **M** = 6, 1 km for **M** = 7, and 0 for **M** = 8.0. To address the different distance measures used by the NGA models, the ground motions were computed for specified source-site geometries.

There is also an issue of an appropriate sediment depth to use in the comparisons. AS08 and CY08 give recommended values of $Z_{1.0}$ to use if the sediment depth is not known. However, the relations for the median estimate of $Z_{1.0}$ for a given value of V_{S30} are not consistent between these two models. For the general comparisons presented in this paper, the recommended median $Z_{1.0}$ values were used for each model. For CB08, which uses $Z_{2.5}$ as the sediment-depth parameter, the recommendation is to estimate $Z_{2.5}$ from the value of $Z_{1.0}$. For the comparisons, the value of $Z_{2.5}$ is estimated using the AS08 estimates of $Z_{1.0}$.

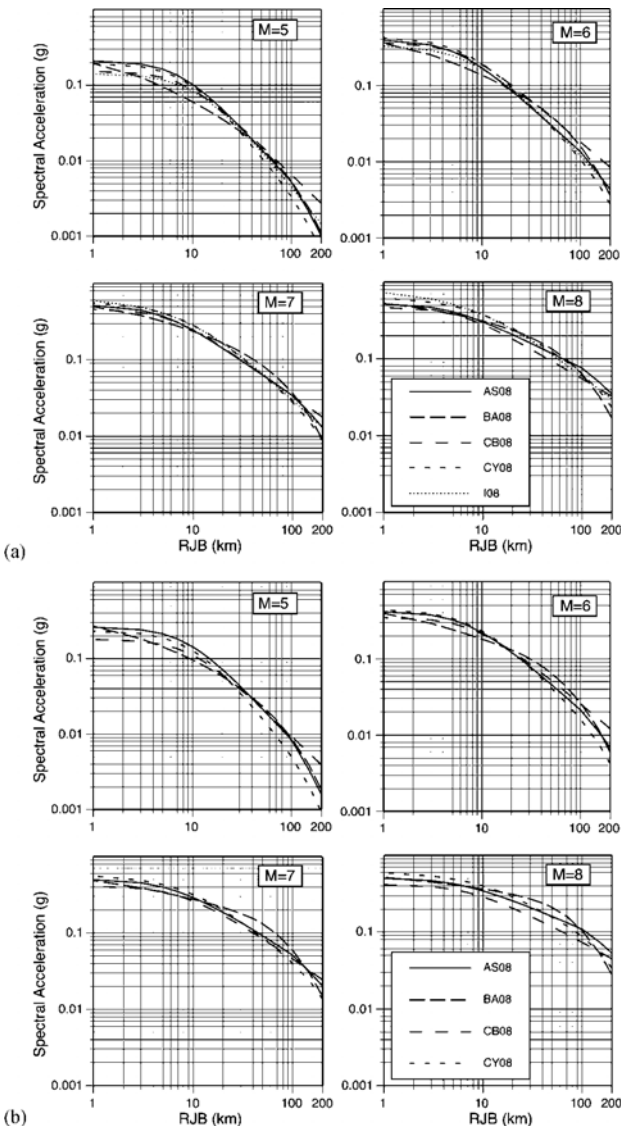

Figure 2 Predicted Distance Scaling for Strike-Slip Earthquakes and V_{S30} = 760 m/s: (a) PGA, (b) S_a at T = 1 s.

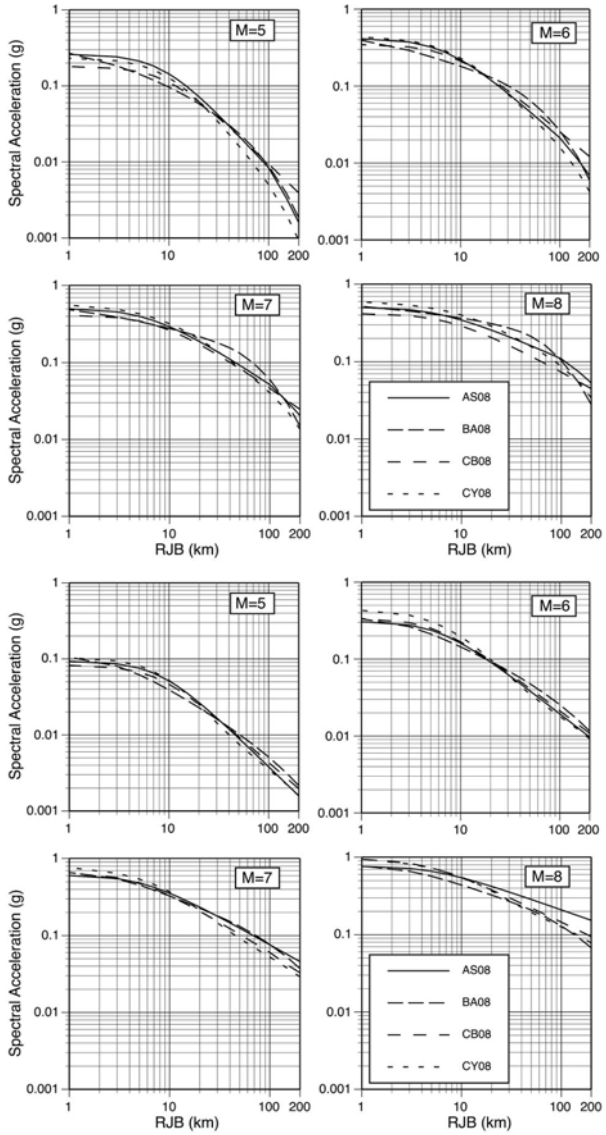

Figure 3. Predicted Distance Scaling for Strike-Slip Earthquakes and V_{S30} = 270 m/s: (a) PGA, (b) S_a at T = 1 s.

3.1 Attenuation Effects

The distance effects (attenuation) predicted by the NGA median models for vertical strike-slip faults and firm-rock site conditions (V_{S30} = 760 m/s, $Z_{1.0}$ = 340 m for AS08, $Z_{1.0}$ = 240 m for CY08, $Z_{2.5}$ = 640 m for CB08) is shown in Figures 1a and 1b for PGA and S_a at T = 1 s, respectively. For **M** = 6 and 7 earthquakes, the five NGA models lead to similar ground motions (within a range of a factor of 1.5). At **M** = 5 and 8, the differences between the NGA models become larger (up to a factor of 2) due to the smaller amount of strong motion data from earthquakes of these magnitudes. The distance scaling for soil sites is shown in Figures 2a and 2b for PGA and S_a at T = 1 s, respectively. The range of the soil ground motions for the four NGA models that are applicable to soil sites are similar to the range of ground motions for rock sites, indicating that the prediction of nonlinear site response in each of these models is similar, even though their nonlinear site response terms are different.

3.2 Magnitude Effects

The magnitude effects predicted by the NGA median models for vertical strike-slip faults and firm-rock site conditions is compared in Figure 4 for R_{JB} = 30 km. Overall, the magnitude scaling for the five NGA models is very similar. For short spectral periods, the median ground motions are within a factor of 1.5. At long periods, the range increases to a factor of 2 at **M** = 5 and 8. These plots clearly show the weaker magnitude scaling (saturation) at short periods predicted by all of the NGA models.

3.3 Rupture-Depth Effects

The rupture-depth effects predicted by the NGA median models vary with each model. For BA08, there is no dependence on depth, since this model uses R_{JB} as the distance measure. For I08, there is a systematic decrease in the median ground motion with increasing depth because

this model uses R_{RUP} without including a rupture-depth term. AS08 and CY08 include a rupture-depth term for both strike-slip and reverse earthquakes in which the buried ruptures have stronger shaking than surface ruptures at the same distance. As a result of this depth scaling, these two models predict an increase in the median ground motion as the rupture depth increases. CY08 has a smooth increase from 0 to 7 km depth and then becomes almost constant, similar to the R_{JB} scaling of BA08. AS08 has a strong scaling with depth with a limit on the depth scaling of 10 km. This causes the AS08 model to have a peak in the scaling at a depth of 10 km. CB08 includes a rupture-depth term for reverse earthquakes only for depths greater than 1 km. As a result, CB08 predicts a systematic decrease in the PGA with increasing depth for strike-slip earthquakes and an increase from surface rupture to 1 km depth (buried rupture) for reverse earthquakes, followed by a smooth decrease.

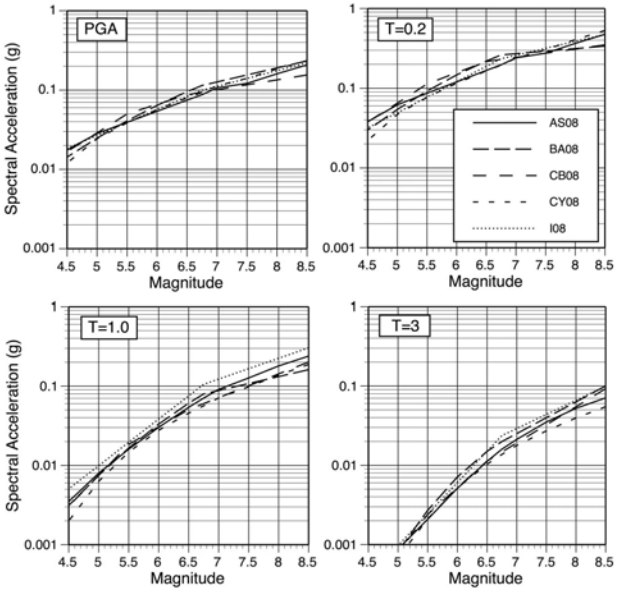

Figure 4 Predicted Magnitude Scaling for Strike-Slip Earthquakes, V_{S30} = 760 m/s, and R_{JB} = 30 km.

3.3 Effect of Site Conditions

The effect of site conditions (V_{S30}) predicted by the median NGA models is shown in Figures 5a and 5b for **M** = 7 strike-slip earthquakes and R_{RUP} = 100 and 10 km, respectively. For the 100 km case, the site response is nearly linear and the four models all show similar scaling. The 10 km case shows significant nonlinear site effects at short periods. There are two limits to V_{S30} scaling. First, there is a limit beyond which the amplification becomes constant. For AS08 this limit is period-dependent, whereas for CB08 and CY08 it is period-independent at V_{S30} = 1100 m/s. For BA08, this limit is not included as part of the model. The second limit is the maximum value of V_{S30} for which the models are considered to be applicable. The largest V_{S30} values recommended by the Developers are 1300 m/s for BA08, 1500 m/s for CB08 and CY08, and 2000 m/s for AS08.

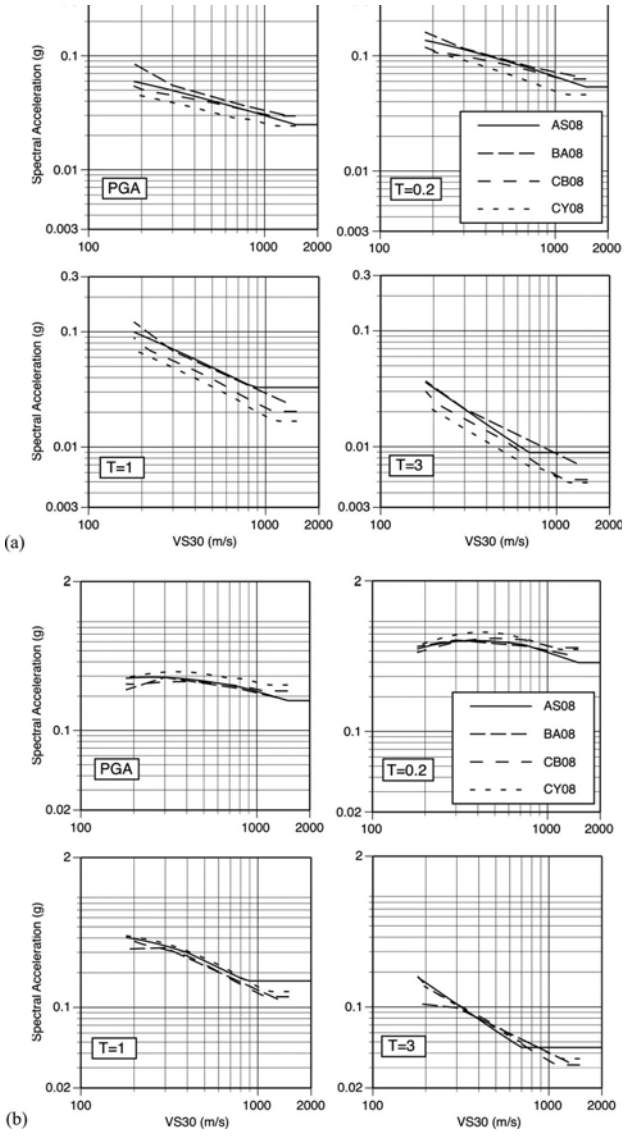

Figure 5 Predicted V_{S30} Scaling for **M** = 7 Strike-Slip Earthquakes: (a) R_{RUP} = 100 km, (b) R_{RUP} = 10 km.

3.4 Hanging-Wall Effects

The HW effects predicted by the median NGA models is shown in Figure 6 for reverse and normal **M** = 6.7 earthquakes with surface and buried rupture. For this example, the top of rupture for the buried case is at 6 km. AS08, CB08, and CY08 include explicit HW effects. BA08 implicitly includes HW effects through the use of the R_{JB} distance measure, which leads to constant ground motion for sites located over the rupture plane (R_{JB} = 0). I08 does not include HW effects so this model attenuates smoothly as a function of R_{RUP}. The buried rupture case leads to the largest difference in the models with a range of a factor of 2.5 for sites located over the hanging wall. CY08 has the strongest HW scaling for surface rupture and AS08 has the strongest HW scaling for buried rupture.

3.5 Response Spectra

The response spectra predicted by the NGA median models for **M** = 5, 6, 7, and 8, strike-slip earthquakes and firm-rock site conditions are shown in Figure 7. For **M** = 6 and 7, the spectra for the five models are similar (within a factor of 1.5). At **M** = 5 and 8, the range increases to a factor of 2.

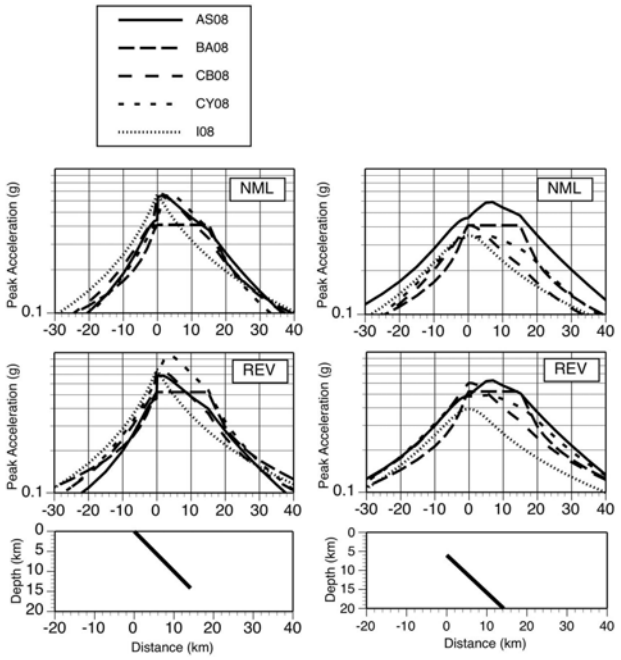

Figure 6 Predicted HW Effects on PGA for 45°-Dipping **M** = 6.7 Earthquakes and V_{S30} = 760 m/s: (left) Surface Rupture, (right) Buried Rupture (Z_{TOR} = 6 km).

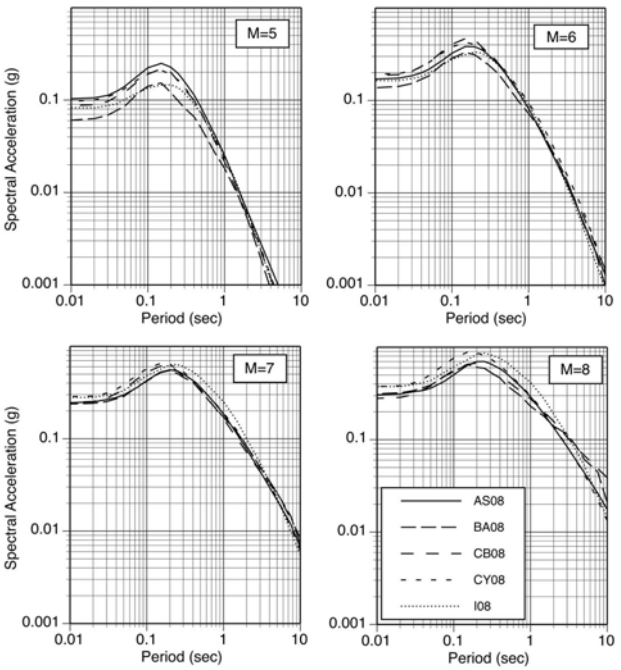

Figure 7 Predicted 5% Damped Response Spectra for Strike-Slip Earthquakes, V_{S30} = 760 m/s, and R_{JB} = 10 km.

The response spectra predicted by the NGA median models for **M** = 7 strike-slip earthquakes at R_{JB} = 10 km for different sediment depths is shown in Figure 8. Soil sites (V_{S30} = 270 m/s) are evaluated for sediment depths defined as shallow ($Z_{1.0}$ = 100 m, $Z_{2.5}$ = 900 m), average ($Z_{1.0}$ = 500 m, $Z_{2.5}$ = 2.3 km), and deep ($Z_{1.0}$ = 1.2 km, $Z_{2.5}$ = 4.8 km). Firm-rock sites are evaluated as before. I08 does not have a soil model and is not shown. BA08 does not include sediment depth as a parameter. For average depth conditions, the four models have very similar spectra (within a factor of 1.3). AS08, CB08, and CY08 all show a large increase in the long-period motion as compared to the BA08 model that does not include sediment depth as a parameter.

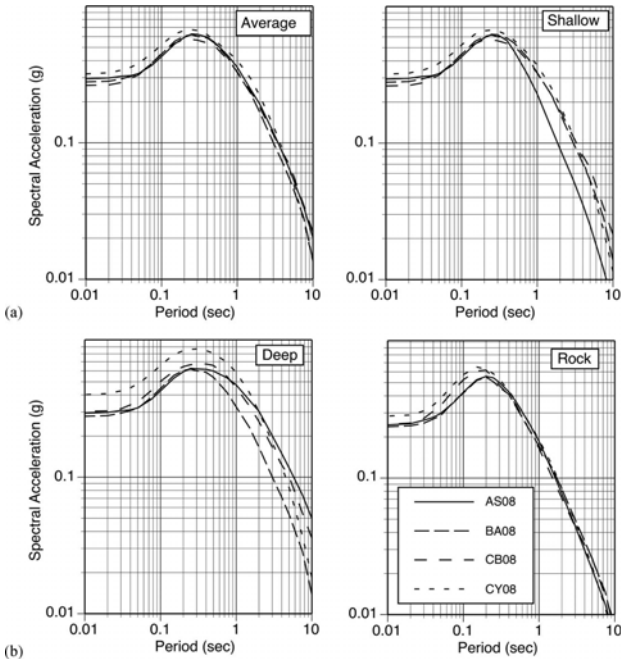

Figure 8 Predicted 5% Damped Response Spectra for Strike-Slip Earthquakes and R_{JB} = 10 km. Soil Sites (V_{S30} = 270 m/s) are Evaluated for Shallow, Average, and Deep Sediments (See Text). Firm-Rock Sites are Evaluated as in Figure 7.

3.6 Standard Deviations (Aleatory Variability)

The period dependence of the total standard deviation, σ_T, for **M** = 5 and 7 earthquakes is shown in Figure 9. For **M** = 7, the five models have similar standard deviations. However, for **M** = 5, there is a large difference in the standard deviations, with the three magnitude-dependent models exhibiting much larger standard deviations than the magnitude-independent models. The magnitude-dependence of the standard deviation is shown in Figure 10 for PGA and S_a at T = 1 s, respectively. The three models that include a magnitude-dependent standard deviation (AS08, CY08 and I08) all included aftershocks, whereas the two models that used a magnitude-independent standard deviation (BA08 and CB08) excluded them. Including aftershocks greatly increases the number of small-magnitude earthquakes, but there is a trade-off of significantly larger variability in predicted ground motions than if only large-magnitude mainshocks are used.

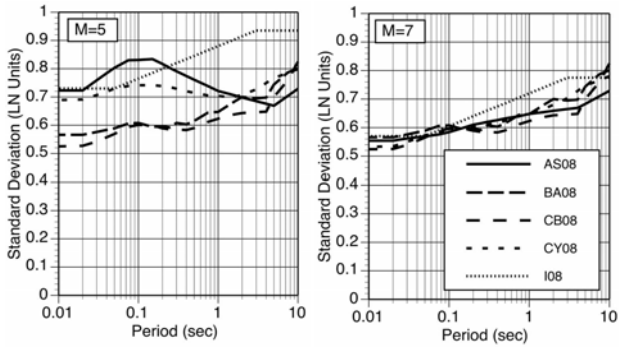

Figure 9 Period-Dependence of Standard Deviation (σ_T) for Strike-Slip Earthquakes, V_{S30} = 760 m/s, and R_{JB} = 30 km: (left) **M** = 5, (right) **M** = 7.

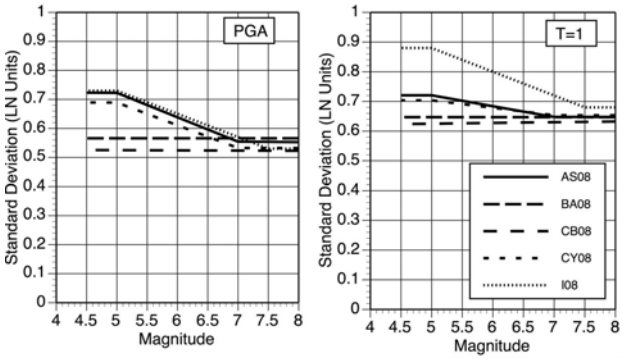

Figure 10 Magnitude-Dependence of Standard Deviation (σ_T) for Strike-Slip Earthquakes, V_{S30} = 760 m/s, and R_{JB} = 30 km: (left) PGA, (right) S_a (T = 1 s).

All four models that include nonlinear site effects on the median site amplification also include these effects on the standard deviation. AS08 and CY08 include the impacts on both τ and σ (inter-event and intra-event standard deviations). CB08 only includes the impact on σ. BA08 does not include the impact on either τ and σ. When nonlinear site effects are included, the standard deviations for the short-period ground motions are reduced as shown in Figure 11. At short distances (large ground motions), nonlinear effects lead to a σ_T reduction of 0.1 to 0.15 natural log units.

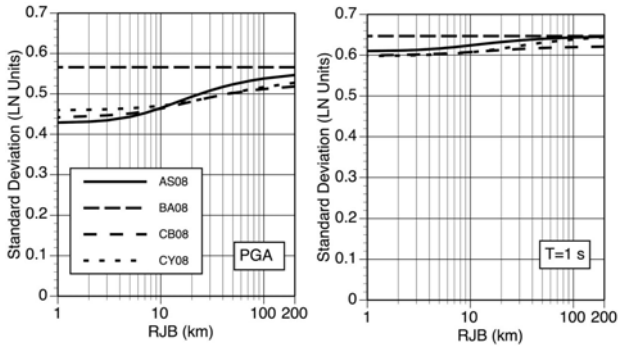

Figure 11 Distance-Dependence of Standard Deviation (σ_T) for **M** = 7 Strike-Slip Earthquakes: (left) PGA, (right) S_a (T = 1 s). This Dependence Shows the Strong Impact of Nonlinear Site Response on the Standard Deviation for Soil Sites (V_{S30} = 270 m/s).

4. CONCLUSIONS

The NGA project serves as an example of how a consistent and reliable set of attenuation relationships can be developed. Overall, the NGA models predict similar median values (within a factor of 1.5) for vertical strike-slip earthquakes with 5.5 < **M** < 7.5. The largest differences are for small magnitudes (**M** = 5), very large magnitudes (**M** = 8), and sites located over the hanging wall. The standard deviations are similar for **M** > 6.5 and firm-rock sites. The largest differences in the standard deviations are for small magnitudes (due to inclusion or exclusion of aftershocks) and for soil sites at short distances (due to inclusion or exclusion of nonlinear site effects on the standard deviation).

Acknowledgements:

This study was sponsored by the Pacific Earthquake Engineering Research Center's (PEER's) Program of Applied Earthquake Engineering Research of Lifelines Systems supported by the California Department of Transportation, the California Energy Commission, and the Pacific Gas and Electric Company. This work made use of the Earthquake Engineering Research Centers Shared Facilities supported by the National Science Foundation, under award number EEC-9701568 through PEER. Any opinions, findings, and conclusions or recommendations expressed in this material are those of the authors and do not necessarily reflect those of the National Science Foundation.

References:

Abrahamson, N.A. and Silva, W.J. (2008). "Summary of the Abrahamson & Silva NGA Ground-Motion Relations," *Earthq. Spectra* **24**, 67-97.

Abrahamson, N., Atkinson, G., Boore, D., Bozorgnia, Y., Campbell, K., Chiou, B., Idriss, I.M., Silva, W., and Youngs, R. (2008). "Comparison of the NGA Ground Motion Relations," *Earthq. Spectra* **24**, 45-66.

Boore, D.M. and Atkinson, G.M. (2008). "Ground-Motion Prediction Equations for the Average Horizontal Component of PGA, PGV, and 5%-Damped PSA at Spectral Periods Between 0.01 s and 10.0 s," *Earthq. Spectra* **24**, 99-138.

Boore, D.M., Watson-Lamprey, J., and Abrahamson, N.A. (2006). "GMRotD and GMRotI: Orientation-Independent Measures of Ground Motion," *Bull. Seismol. Soc. Am.* **96**, 1502-1511.

Campbell, K.W. and Bozorgnia, Y. (2008). "NGA Ground Motion Model for the Geometric Mean Horizontal Component of PGA, PGV, PGD and 5% Damped Linear Elastic Response Spectra for Periods Ranging from 0.01 to 10 s," *Earthq. Spectra* **24**, 139-171.

Chiou, B.S.J. and Youngs, R.R. (2008). "An NGA Model for the Average Horizontal Component of Peak Ground Motion and Response Spectra," *Earthq. Spectra* **24**, 173-215.

Chiou, B., Darragh, R., Gregor, N., and Silva, W. (2008). "NGA Project Strong-Motion Database," *Earthq. Spectra* **24**, 23-44.

Idriss, I.M. (2008). "An NGA Empirical Model for Estimating the Horizontal Spectral Values Generated by Shallow Crustal Earthquakes," *Earthq. Spectra* **24**, 217-242.

Power, M., Chiou, B., Abrahamson, N., Bozorgnia, Y., Shantz, T., and Roblee, C. (2008). "An Overview of the NGA Project," *Earthq. Spectra* **24**, 3-21.

Stafford, P.J., Strasser, F.O., and Bommer, J.J. (2008). "An Evaluation of the Applicability of the NGA Models to Ground-Motion Prediction in the Euro-Mediterranean Region," *Bull. Earthq. Eng.* **6**, 144-177.

Sixth International Conference on Urban Earthquake Engineering
March 3-4, 2009, Tokyo Institute of Technology, Tokyo, Japan

THE NORTHERN TOKYO BAY EARTHQUAKE AS MEGA-DISASTER AND STRATEGIC STUDIES FOR MITIGATION AND RECOVERY

Itsuki Nakabayashi[1)]

1) Professor, Dept. of Urban System Science, Graduate School of Urban Environmental Sciences, Tokyo Metropolitan University, Japan,
nakabasi@comp.metro-u.ac.jp

Abstract: The probability of the next Tokyo Earthquake which will occur beneath the capital region as Tokyo metropolis in next three decades is estimated 70 % by Central disaster management council. As damage estimation researches of the next various Tokyo Earthquakes, the Northern Tokyo Bay Earthquake which occurs in an evening of winter with strong winds is the severest case as a mega-disaster. Approximately two hundred thousands of houses are collapsed by shake and six and half hundred thousands of houses are burnt down by fires after the shake. One and half million household lose their dwelling houses by shake and fires. If the earthquake occurs in noon of weekday, approximately six and half millions persons of long way to home who are unable to return home easily by walk. Many millions people have to evacuate from fires. The recovery and restoration from these mega-damages is very hard works Nobody have experienced such mega-disaster yet. In this paper, the result of damage estimation is introduced and the strategic studies for mitigation and recovery from the mega-disaster are presented, from focus on the response activities issues such as return home problem, numerous refugees and shortage of shelter capacities, and on the urban reconstruction issues from the mega-damage as eight times as the 1995 Kobe Earthquake.

1. INTRODUCTION

Even if the next Tokyo Earthquake is a mega-disaster, damage caused by natural disaster is able to be mitigated through three stages of countermeasures; pre-disaster measures of damage reduction, post-disaster measures of emergency responses and of recovery and restoration. The emergency response activities are able to stop the expanding of direct damages through preparedness measures which established in pre-disaster period. Therefore, various response drills such as a rescue, fire fighting, relief, evacuating and so on are implemented. The effective recovery and restoration from disaster is also determined by the pre-establishment of recovery and restoration measures in pre-disaster period. In Tokyo, community-based restoration exercises are implemented by residents, local government and professionals.

On the other hand, we learned from the 1995 Kobe Earthquake that these measures of not only pre-disaster period but post-disaster period are able to be implemented effectively only by total activities of government, community and individual resident. Especially in case of mega-disaster, the individual activity is basically important, because huge scale damage is unable to be reduced by governmental activities but by every individual. In addition it is important to carry out the community-based urban improvement in the vulnerable districts with crowded wooden houses along narrow streets, because huge scale of damage caused by shaking and fires shall be concentrated in these districts.

In this paper, the damage estimation of the Northern Tokyo Bay Earthquake as mega-disaster is introduced. The characteristic features of mega-disaster damage are explained and the strategic studies for effective mitigation of them, the more satisfiable restoration from enormous losses and urban reconstruction from the vulnerable district with crowed wooden houses to the safer district are presented.

2. ESTIMATED DAMAGE OF THE NORTHERN TOKYO BAY EARTHQUAKE

2.1 Result of Damage Estimation by Central Disaster Management Council

The most important feature of the next Tokyo Earthquake is not only huge scale of direct damages such as collapse and burnt-down of houses but also high level of functional damage such as capital and central functions. In case of the Tokyo Earthquake, the central government cannot avoid the earthquake disaster. The Northern Tokyo Bay Earthquake causes the most severe damage to the central Tokyo where the central government facilities are located and the central economic activities are concentrated.

The Central Disaster Management Council (CDMC) conducted the damage estimation research of the next Tokyo Earthquake not only for local government's preparedness but for central government's preparedness. CDMC sets eighteen earthquakes of three kinds. Main items of estimated damage

and their damages are shown in Table 1 as the severest case. It is the case of Northern Tokyo Bay Earthquake of magnitude 7.3 as same as the 1995 Kobe Earthquake, which occurs in the evening of weekday in winter blowing strong winds of 15 meters per second.

Table 1. Damage Estimation of the Northern Tokyo Bay Earthquake by CDMC(2005)

Items	Unit	Estimation
Severely damaged houses	buildings	850,000
Collapsed by shaking	buildings	150,000
Collapsed by liquefaction	buildings	33,000
Collapsed by landslide	buildings	12,000
Burnt-down by fires	buildings	650,000
Killed persons *	persons	13,000*
Killed by collapsed buildings	persons	4.500
Killed by fires	persons	8,000
(Disabled and Elderly)	(persons)	(4,100)
Casualties*	Persons	240,000
Closed in collapsed buildings	persons	43,000
Persons of long way to home	persons	6,500,000
Refugee in shelter in next day	persons	4,600,000
Refugees after one month	persons	2,700,000
Sufferers who lost homes	households	1,500,000
Suspension of water supply (Recovered period)	units (days)	11,000,000 (30)
Destruction of drainage service (Recovered period)	units (days)	450,000 (30)
Power failure (Recovered period)	units (days)	1,600,000 (7)
Suspension of telephone service (Recovered period)	units (days)	1,100,000 (14)
Suspension of piped gas supply (Recovered period)	units (days)	1,200,000 (90)
Debris of buildings & facilities	million ton	83 ~96
Total economic losses	trillion yen	112
Cost for urban reconstruction of buildings & facilities.	trillion yen	67
Loss by suspension of economic activities & productivities.	trillion yen	45

* In the case of Western Central Tokyo Earthquake, in which is the severest case of the killed and Casualties, because this earthquake hits the densest population areas in the western part of central Tokyo.

In case of the 1995 Kobe Earthquake, approximately one hundred and five thousands of houses were collapsed and seven thousands of houses were burnt down. Five thousands and five hundreds of persons were killed by collapsed houses and fires. The volume of debris was approximately twenty million ton. Economic loss was estimated as approximately ten trillion yen.

In comparison with the 1995 Kobe Earthquake, the Northern Tokyo Bay Earthquake causes huge damage of buildings as eight times as it and also causes economic loss as ten times as it.

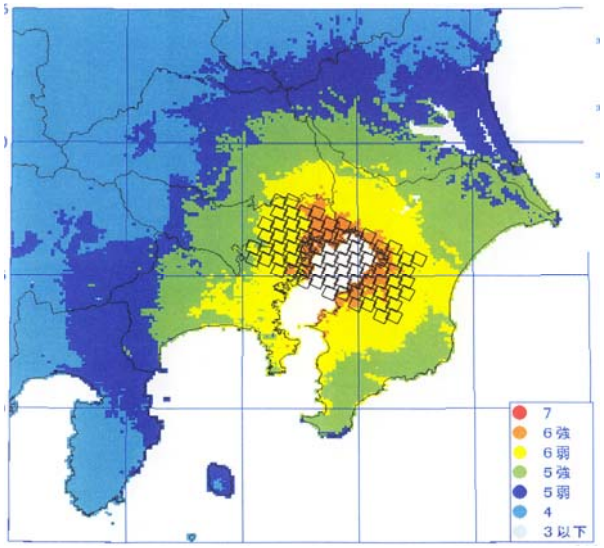

Fig.1 Distribution of estimated seismic intensity of Northern Tokyo Bay Earthquake (CDMC 2005)

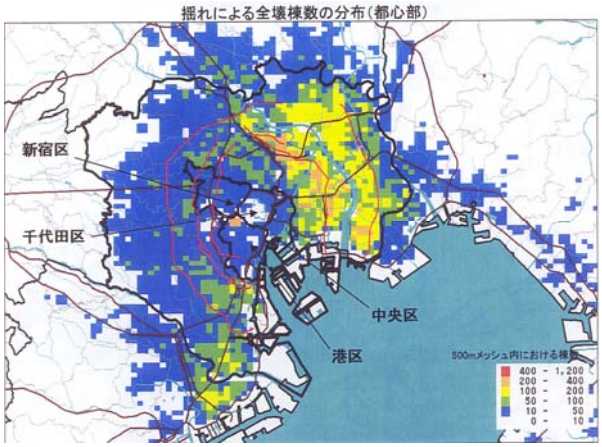

Fig.2 Distribution of collapsed buildings in Northern Tokyo Bay Earthquake (CDMC 2005)

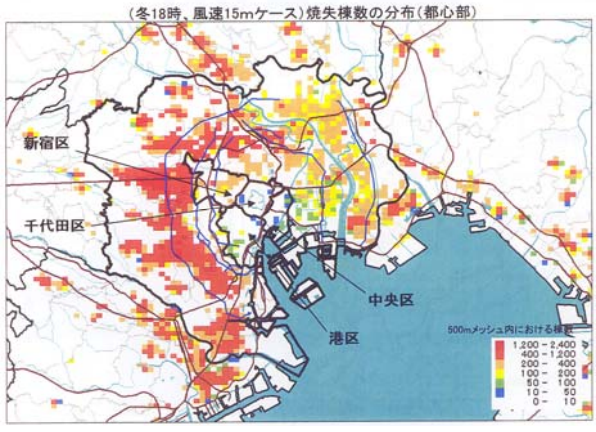

Fig.3 Distribution of Burnt-down houses in Northern Tokyo Bay Earthquake (CDMC 2005)

2.2 Damage Estimation of Northern Tokyo Bay Earthquake by Tokyo Metropolitan Government

Tokyo Metropolitan Government (TMG) conducted the more detailed damage estimation because the damage

estimation of CDMC can be identified not in each local government area but in every prefecture area. If every local government as city and special ward can identify the damage of each local area, they can revise their earthquake mitigation measures.

Table 2 Damage Estimation of the Northern Tokyo Bay Earthquake by TMG(2006)

Estimated items	Unit	Estimation
Severely damaged houses	buildings	472,000
Collapsed by shaking	buildings	127,000
Collapsed by fire	buildings	345,000
Killed persons *	Persons	6,000
Killed by collapsed buildings	Persons	2.500
Killed by fires	Persons	3,500
Persons of long way to home	persons	3,920,000
Refugee in shelter in next day	Persons	3,990,000
Suspension of water supply (Recovered period)	percentage (days)	34.8 % (30)
Destruction of drainage service (Recovered period)	percentage (days)	22.3 % (30)
Power failure (Recovered period)	percentage (days)	16.9 % (7)
Suspension of telephone service (Recovered period)	percentage (days)	10.1 % (14)
Suspension of piped gas supply (Recovered period)	percentage (days)	17.9 % (90)

The volume of damage in TMG shares approximately two thirds of the whole damage in case of Northern Tokyo Bay Earthquake. It is as 5 times as in the Kobe Earthquake. The huge volume of direct damage and the amount of economic loss make us to recognize the next Tokyo Earthquake as typical mega-disaster, which nobody have experienced yet.

We have to recognize mega-disaster as imaginably as possible and to find strategic issues for mitigation of mega-disaster. There are various issues to be resolved and various countermeasures to be developed. In order to mitigate the mega-disaster effectively, we have to organize the academic issues to be approached originally. Because the mitigation measures of mega-disaster must be produced from new way of thinking.

3. STRATEGIC STUDIES FOR MITIGSATION OF MEGA-DISASTER

3.1 Strategic Study on Resolution of Return Home Problem: How are ten million persons able to return home without chaos and riot?

I defined that the “person of long way to home” means “persons difficult to return home” in 1980s (Nakabayashi1985).as follows; 1) the persons who have to walk more than 20km to return home are difficult to return home, 2)in case of the persons who have to walk more than 10 km to return homes are located, each ten percentage of persons are difficult to return home in each one kilo meter longer way to home, 3) in reverse, each ten percentage of the persons whose homes are located in the distance of less than 20km are able to return home by walk, in each one kilo meter shorter than 20km, and 4) all persons whose homes are located less than 10 km are able to return home by walk.

If the next Tokyo Earthquake occurs in noon of weekday, approximately twenty-one million persons are hit in the various spaces outside of their home and twelve and half million persons are hit inside of their home in Tokyo metropolitan region. Two thirds of population has to return home by walk after earthquake. It is estimated that the six and half million persons in the twenty-one million persons are very difficult to return home by walk because their homes are located far away from their offices, schools and various places where they are.

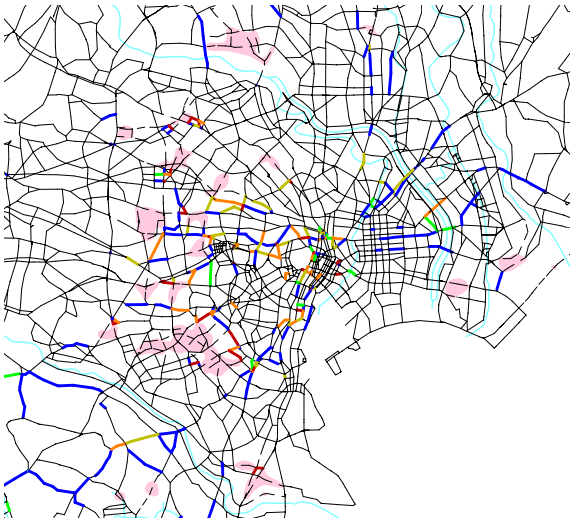

Fig. 4 Simulated congestion of walkers to home in three hours after earthquake; in case of all persons who begin to walk to home with no information of street situation and safety of family.

Fig. 5 Simulated congestion of walkers to home in three hours after earthquake; in case of the half persons begin to walk in next day half persons begin to walk to home just after earthquake with information of street situation and safety of their family.

In Fig.4 and Fig.5, pink-colored zones mean fire zones. These fire zones make congestion of walkers to home from CBD to suburbs residential district. The pink lines mean the severe congestion of more than six persons per square meters as same congestion as in the train of rash hour in Tokyo. In this situation, people can walk 400m per one hour.

Fig. 4 clarifies that there are many congested streets near the fire zones, if all persons begin to walk to home just after earthquake. However, Fig.5 shows that there are few congested streets of walkers, if half persons stay in their offices one night and start to walk to home in the next day, with information of every street situation and of safety of their family. Specifically, if the persons of long way to home can stay in their offices, the congestion of walkers to home is reduced dramatically. It is capable, because the seismic intensity of their homes is maybe the degree of 5strong or weaker than in the central Tokyo. Their homes are located more than 20km far from CBD of Tokyo in Japanese seismic intensity 6 strong. Their homes are not damaged severely and their family may not be suffered.

However, it is necessary to develop and to revise new technologies such as a distribution system of street situation information to every walker, an information system of safety inquiry among each family of more than tens million individuals, and so on. In same time, it is clarified that the community-based urban improvement in crowded wooden houses districts is very important not only for reduction of damage but also for reduction of street congestion in the period of disaster responses such as rescue, relief, fire-fighting, evacuation, delivery of emergency foods and waters, walking to home and the others.

3.2 Strategic Study on Preparedness of recovery and reconstruction measures: How can Tokyo be recovered and reconstructed satisfyingly?

Tokyo is most important city to be recovered as quickly as possible, because the functional failure of Tokyo as capital city causes the severe damages not only of national wide but also of world wide both directly and indirectly. Even if the volume of damage is as eight times as in the 1995 Kobe Earthquake according to the damage estimation, Tokyo have to be recovered as speedily as in the 1995 Kobe Earthquake. The recovery periods of life-line facilities in Fig.1 and Fig.2 are as same as in the Kobe Earthquake. However, the recovery and restoration needs not only speed but also satisfaction of the sufferers. Tokyo Metropolitan Government prepared the post-disaster recovery and restoration measures in the pre-disaster period, learning lessons from the 1995 Kobe Earthquake.

In 1997, TMG planning Manual for Post-disaster Urban Reconstruction was published, which might be the first manual in the world. This consists of the process management and planning guideline for urban reconstruction. In 1998, TMG Administrative Manual for Post-disaster Life Recovery was published, which was consisted of five chapters; Organization for recovery and restoration, .Principles and concepts of restoration, rebuilding of houses, Recovery of life and services and Recovery of industries and jobs.

In 2001, TMG Grand Design of Urban Reconstruction was published. This shows the goals and views of urban reconstruction and proposals of master plan and projects for Tokyo's urban reconstruction, which have been made according to a result of damage estimation research. In this grand design, seven strategic projects are proposed already before earthquake; 1) renewal of district structure as safer residential districts from the crowded wooden houses districts, 2) improving the crowded wooden houses districts as safer ring zone with green space surrounding central Tokyo, 3) construction of safe ground from lowland under sea level to reclaim it with debris of collapsed buildings, 4)Construction of parks as relies base from disaster in and around densely built-up areas, 5) Renewal of river side zones as water-front space, 6) Expansion of international business center, and 7) renewal of transportation network as motorway system.

The effectiveness of such preparedness of post-disaster recovery and restoration measures is sown in Fig. 6. The direct damage such as collapsed houses and burnt houses can be reduced by pre-disaster measures as the retro-fitting of old houses and fire-proofing of wooden houses. The gap of regional level can be reduced only by the pre-disaster measures. In addition, preparedness of not only emergency response activities but also recovery and restoration measures can reduce the damage directly and indirectly.

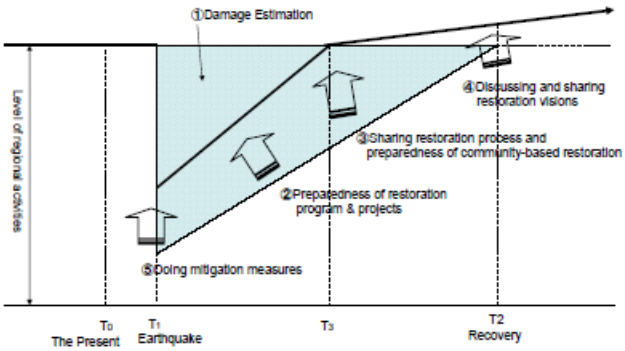

Fig.6 Effectiveness of mitigation through preparedness of post-disaster recovery and restoration measures

In 2003, TMG revised both manuals of urban reconstruction and recovery of life, and published two kinds of new manuals; Earthquake Restoration Manuals of Recovery Process for citizen and for officers. Manual for citizen is an important roll to implement urban reconstruction and other restoration smoothly and satisfyingly. It is to introduce the process of earthquake restoration and the importance of collaboration with residents and local government The process of restoration through collaboration with community and government is shown in Fig.7.

The restoration activities shall start in three days after earthquake, when many residents evacuates in shelter. The rough research of building damage is began within one week and headquarter of earthquake recovery and restoration is established within two weeks. Local government calls to

collaborate with community for urban reconstruction. In the busiest period of disaster response activities, the urban reconstruction projects are begun in collaboration with suffered residents in fig.7.

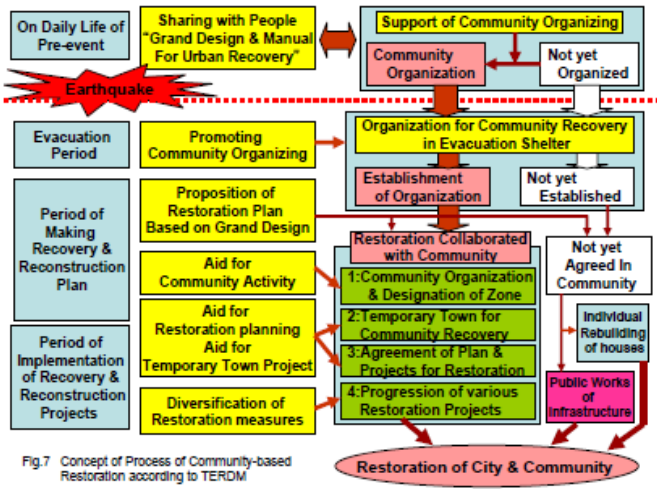

Fig.7 Concept of process of community-based restoration prepared by TMG
(Revised by Nakabayashi after TMG2003)

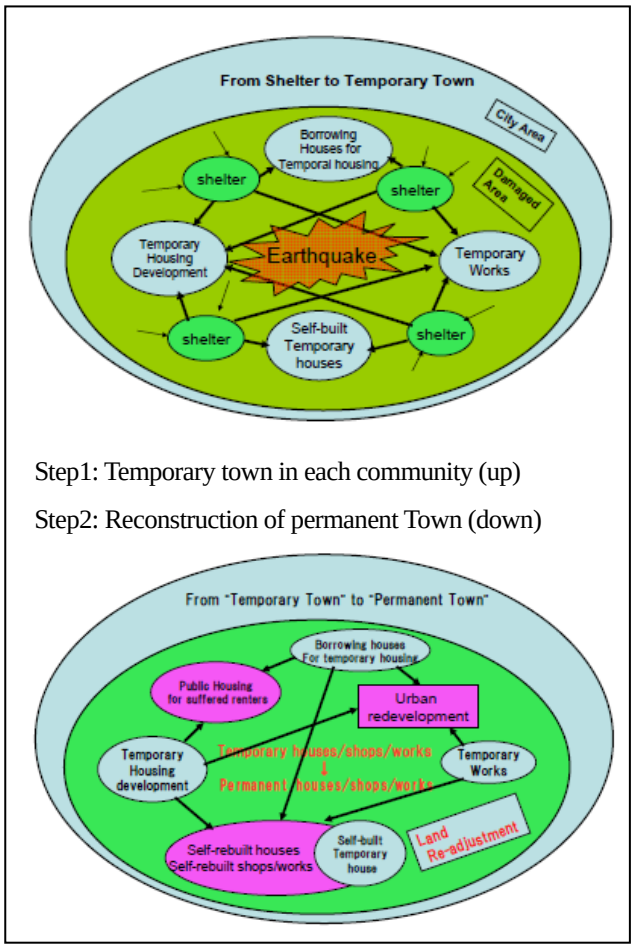

Fig.8 Conceptual process of urban reconstruction from temporary town to permanent town, proposed by TMG

It is a long way to rebuild houses and to restore life for individual in a slightly damaged district. However, it is a longer and more difficult way to reconstruct a severely damaged district in a process of community-based urban renewal project, in collaboration with community and local government. It is necessary to discuss not only among residents but also among community and government for community-based project. But, there are few houses to be continued to live in such damaged community. If many residents seek temporary houses individually, the community meeting for discussion of restoration projects is very difficult to be held.

"Temporary town" is proposed to continue the community activities in a damaged district. If the temporary town is built in each community area, it can make the residents to live in their community and to work on the community-based restoration. And "permanent town" which means reconstructed community are redeveloped from thr "temporary town". (Fig. 8)

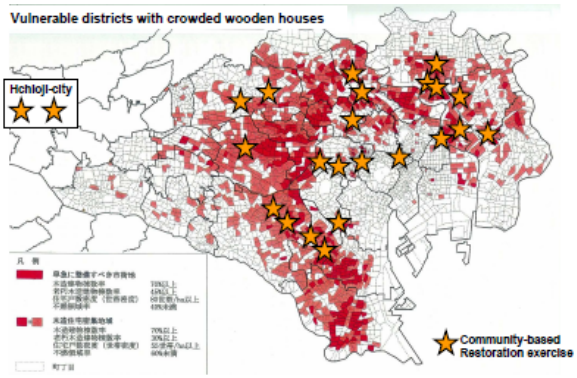

Fig.9 Distribution of community-based restoration exercises and vulnerable districts with crowded wooden houses

Such process of community-based urban reconstruction is different from the process of the 1995 Kobe Earthquake. The author was proposed that it is necessary to exercise such process for officers and for the community and implemented a new style exercise for community-based restoration planning in Nukui town in Nerima ward, western Tokyo in 2003. Since then, this community-based restoration exercise implemented in more than 25 communities.

The residents who participated in this exercise can learn the importance of restoration activities and also the difficulty of restoration. This experience makes them to be encouraged for their community improvement.(Table 3 & 4)

The pre-disaster measures for post-disaster restoration are very important issue not only for Tokyo as a capital city but also for every city in Japan, because Japanese society is becoming the aged and population-decreased society. In the 21st century, restoration issues are important strategic studies for Japan, because many earthquakes will hit the aged and decreased society. The restoration and reconstruction is not only satisfactory for sufferers, but disaster-proofing against next disaster more and more.

Table 3 Resident's mind of participation with community-based restoration projects

Questionnaire	Very much	A little	No decided	No answer
I would like to participate Community-based restoration project as a member od association positively regardless difficulty of community-based recovery and restoration activities, if I can contribute anything for the community/	49%	49%	----	2%
I would like to participate Community-based Restoration Association, which works on community restoration and empowerment project.	55%	36%	6%	3%

Table 4 Resident's evaluation of participation in community-based restoration exercise

	Very much	A little	No decided	Do not so	No answer
Widening neighborhood relationship	45%	43%	9%	2%	2%
I find there are various experts for implementation of disaster restoration, such as lawyer, architect, surveyor and so on.	57%	36%	2%	2%	2%
It is essential to consult with the experts and to get knowledge on implementation of community disaster management and restoration from disaster.	81%	15%	----	----	4%
I can find efforts to be done beforehand by community for preparing disaster such as management of evacuation base by community, and so on.	57%	34%	4%	2%	2%
I can find efforts to be done beforehand by myself for mitigation such as retro-fitting of houses, fixing furniture on wall and so on.	55%	32%	4%	2%	7%

4. CONCLUSIONS

The next Tokyo Earthquake is possible to cause a huge scale of damage, which nobody has experienced yet. Earthquake is a natural phenomenon, but earthquake disaster is a very societal and humanistic phenomenon. Mitigation of earthquake disaster is able to be implemented from not only engineering approach but societal approach. Especially, societal approach is important to develop measures against many million people or houses and measures for urban functional problems.

In this paper, two strategic studies on the walking to home of twenty million persons and the restoration from huge damages are introduced. Both issues are necessary to be approached from societal viewpoint. Additionally, it is important to integrate measures which are organized from various resolutions and which are structured through collaboration works among academic studies, residents and officers. The societal technology have to be developed more and more as well as the engineering technology.

Acknowledgements:

The author acknowledges support from CDMC Special Committee of Tokyo Earthquake and its measures, TMG Committee of damage estimation research and Earthquake disaster recovery and restoration committee. The author can get opportunities to study many things, because the author is a member of both committees. The author also acknowledge the support from the Center for Urban Earthquake Engineering (CUEE) in Tokyo Institute of Technology.

References:

Central Disaster Management Council (2005) "Report on damage estimation of the next Tokyo Earthquake" edited by Special Committee of Tokyo Earthquake and its measures. *http://www.cao.go.jp*

Nakabayashi I. (1985), "Basic Study og urban disaster caused by Earthquake (4); Estimation of persons of long way to home and situations of dispersed families through the analysis of person trip data in Tokyo metropolitan region" *Proceedings of academic meeting "Tokai 1985" of Japan Institute of Architecture, Version of planning, 361-362.*

Nakabayashi I. (2007a) "Preparedness for Recovery and Reconstruction from the next Tokyo Earthquake" Proceedings of 2nd International Conference on Urban Disaster Reduction, Taipei.

Nakabayashi I. (2007b) "Earthquake Vulnerability Assessment and Anti-Earthquake Disaster City Planning in Tokyo." Proceedings of 1st International Symposium of Urban Environmental Sciences, TMU, Tokyo.

Nakabayashi I., Aiba S. and Ichiko T.(2009) "Pre-disaster Restoration Measure of preparedness for Post-disaster Restoration in Topkyo." Journal of Disaster Research Vol.3 No.6.

Tokyo Metropolitan Government (2006) "Report on Damage Estimation of Tokyo caused by the next Tokyo Earthquake", *http;www.bousai.metro.tokyo.jp*

Tokyo Metropolitan Government (2003) "Earthquake Restoration manual; Process Version", *http;www.bousai.metro.tokyo.jp*

Sixth International Conference on Urban Earthquake Engineering
March 3-4, 2009, Tokyo Institute of Technology, Tokyo, Japan

PERFORMANCE-BASED SEISMIC DESIGN OF TALL BUILDINGS IN THE U.S.

Jack P. Moehle[1)]

1) Professor, Pacific Earthquake Engineering Research Center, University of California, Berkeley, USA

Abstract: Building codes in the United States contain prescriptive requirements for seismic design as well as an option for use of alternative provisions. Increasingly these alternative provisions are being applied for the performance-based seismic design of tall buildings. Both practice- and research-oriented aspects of performance-based seismic design of tall buildings are presented.

1. INTRODUCTION

The west coast of the United States experienced a resurgence in the design and construction of tall buildings (defined here as buildings 240 feet (73 meters) or taller) in the past five years. Many of these buildings use high-performance materials and framing systems that are not commonly used for building construction or that fall outside the height limits of current buildings codes. In many cases, prescriptive provisions of governing building codes are found to be overly restrictive, leading to designs that are outside the limits of the code prescriptive provisions. This is allowable through the alternative provisions clause of building codes. For example, the International Building Code [ICC, 2006], which governs construction in much of the U.S. writes "An alternative material, design, or method of construction shall be approved where the building official finds that the proposed design is satisfactory and complies with the intent of the provisions of this code and … is at least the equivalent of that prescribed in this code in quality, strength, effectiveness, fire resistance, durability, and safety."

When the alternative provisions clause is invoked, this normally leads to a performance-based design involving development of a design-specific criteria, site-specific seismic hazard analysis, selection and modification of ground motions, development of a nonlinear computer analysis model of the building, performance verification analyses, development of building-specific details, and peer review by tall buildings design experts. Experience gained in the application of this approach has found its way into written guidelines [e.g., SEAONC, 2007; CTBUH, 2008; LATBSDC, 2008]. These documents generally define what needs to be considered, but leave considerable latitude in their implementation so that the designer is not overly constrained. This paper reviews the currently accepted approaches to performance-based seismic design of tall buildings in the U.S., presents examples, and describes relevant research findings and needs.

2. THE NEW GENERATION OF TALL BUILDINGS

Urban regions along the west coast of the United States recently saw a boom in tall building construction. Buildings as tall as 1200 ft (370 m) are under study. Many of the buildings are residential or mixed-use (including residential) occupancy, though economic changes may lead to alternative functions including office occupancies.

To meet functional and economic requirements, many of the new buildings are using specialized materials and lateral-force-resisting systems that do not meet the prescriptive definitions and requirements of current building codes. Figure 1a and b illustrate the framing system of a 60-story building in San Francisco. The seismic force-resisting system is reinforced concrete core walls with buckling-restrained steel outrigger braces along one axis. The designated gravity framing comprises an unbonded post-tensioned flat-plate system. As the building responds to anticipated earthquake ground shaking, the flat plate and its supporting columns will undergo deformations and develop internal forces that must be considered as part of the design. In addition to the core wall system shown in Figure 1, other framing systems including moment frames, steel-plate walls, and other innovative systems are being considered for various buildings, each with its own special design needs.

3. DESIGN CRITERIA

A design criteria document generally is developed by the designer to clearly and concisely communicate to the design team, the building official, and the peer reviewers the intent and the process of the building structural design. It will include information about the building and its location; the seismic and wind force-resisting systems; sample conceptual drawings; codes and references that the design incorporates in part or full; exceptions to code prescriptive provisions; performance objectives; gravity, seismic, and

wind loading criteria; load combinations; materials; methods of analysis including software and modeling procedures; acceptance criteria; and test data to support use of new components. The document is prepared early for approval by the building official and peer reviewers, and may be modified as the design advances and the building is better understood.

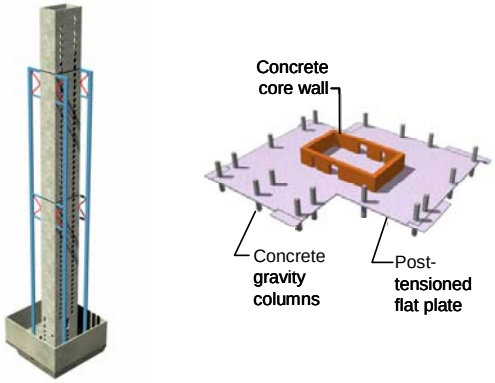

(a) Core wall elevation (b) Floor framing perspective

Figure 1 Example framing system (after Magnusson Klemencic Associates)

The design criteria document must define how the design is intended to meet or exceed the performance expectations inherent in the building code. A common opinion of the general public is that tall building performance should exceed the performance of "ordinary" buildings. This opinion derives from perceptions of high occupancy, emergency response challenges, and the effects on regional image in the event of damage to an iconic building. Another opinion is that mandating special performance objectives for one class of building would be precedent-setting with little technical basis but with important (usually negative) economic consequences. These clearly are public policy issues that should be publicly debated either on a national scale (through the model/national building codes) or at a local scale (through an ordinance in local government). However, given that the primary purpose of building codes is protection of life safety and public welfare, characteristics of tall buildings that present higher risks than normal buildings could be considered for enhanced performance. Examples that fall into this category are cladding and its anchorage, and emergency ingress and egress [Holmes et al., 2008].

Apart from these special characteristics, performance expectations for design of most tall buildings in the U.S. are set equal to those for ordinary buildings. A common interpretation is that the building structural and nonstructural systems and components must be serviceable when subjected to frequent earthquakes (50% probability of exceedance in 30 years, or 50%/30yr) and the building must be stable (that is, not collapse) when subjected to extremely rare shaking (generally taken as 2%/50yr exceedance level, but not more than 1.5 times median deterministic motions). The assumed level of damping will strongly affect the design for the serviceability check; the 50%/30yr shaking level is commonly used with 2-35% of critical damping.

4. SEISMIC HAZARD ANALYSIS AND DESIGN GROUND MOTIONS

Seismic ground shaking generally is determined using site-specific seismic hazard analysis considering the location of the building with respect to causative faults, the regional and local site-specific geologic characteristics, and the selected earthquake hazard levels. The analysis produces a uniform hazard response spectrum defining linear spectral acceleration values for different periods and hazard levels. It also identifies which hypothetical earthquakes dominate the seismic hazard at the site. From this, a set of (almost always seven) ground motion pairs consistent with the site conditions and with the magnitude, distance, and mechanism of the dominant earthquakes is selected for use in nonlinear dynamic analysis of an analytical model of the building. Because magnitude strongly influences frequency content and duration of ground motion, it is desirable to use records from earthquakes within 0.25 magnitude units of the target magnitude [Stewart et al., 2001]. Duration can be especially important for tall buildings because of the time required to build up energy in long-period structures. For sites close to active faults, selected motions should contain an appropriate mix of forward, backward, and neutral directivity consistent with the site [Bray and Rodriguez-Marek, 2004].

The selected ground motions generally are manipulated to better fit the target linear response spectrum using either *scaling* or *spectrum matching*. *Scaling* involves applying a constant factor to individual pairs of horizontal ground motion records to make their response more closely match the design spectrum over a range of periods [ASCE 7-05, 2005]. *Spectrum matching* is a process whereby individual ground motion records are manipulated (usually in the time domain by addition of wave packets) to adjust the linear response spectrum of the motion so it matches the target design response spectrum. Resulting motions should be compared with original motions to ensure the original character of the motions is not modified excessively.

There currently is no consensus on which approach, scaling or spectrum matching, is preferable for nonlinear dynamic analysis, and both procedures are in use. The advantage of scaling is that individual ground motion records retain their original character including peaks and valleys in the response spectrum. However, given the long fundamental periods characteristic of tall buildings (up to 10 sec), it can be difficult to find records with sufficient energy in the long-period range, therefore requiring relatively large scaling factors that may result in unrealistic short-period response. Spectrum matching can alleviate the aforementioned problem with scaling, though there are concerns that these uniformly matched motions will mask the inherent record-to-record variability of building response. On the other hand, given that the number of ground motion pairs is almost universally limited to seven in tall buildings

designs, it is doubtful that any scaling procedure will result in motions that accurately reproduce the true dispersion in building dynamic response.

The uniform hazard spectrum is a composite of the peak response spectral ordinates for many different hypothetical earthquakes that could affect a site; in general, no single earthquake will have a response spectrum matching the uniform hazard spectrum. Recognizing this, Abrahamson [2006] recommends that each of the ground motions used to excite the building model should represent a scenario earthquake, that is, just one of the many earthquakes that contribute to the uniform hazard spectrum. In this case, the selected motion is scaled to the response spectrum of the scenario earthquake, which is less broadband than the uniform hazard spectrum. Baker and Cornell [2006] have recommended that the scenario spectrum should be modified to represent the conditional mean response spectrum, which takes into account the correlation between response spectral amplitudes at different periods. A complication that arises with a tall building is that different engineering demands are controlled by different periods, requiring ground motion sets scaled to several different scenario spectra. There currently is no established way to combine the results from different conditional mean spectra, other than to take the envelope, a result that is likely to be conservative though less so than the uniform hazard spectrum.

Figure 2 presents results of a study of the use of ground motions scaled to different response spectra. DBE refers to the design basis earthquake response spectrum of ICC (2006), which is roughly equivalent to a uniform hazard spectrum, and CMS refers to the conditional mean spectrum conditioned on a single period; three such spectra are shown corresponding to each of the first three translational modes of vibration (in one plane) of a tall core wall building model. The conditional mean spectra match the DBE spectral acceleration at the target period, but generally have lower response ordinates for periods away from the target. Several ground motion records were selected to approximately match the DBE and CMS spectra, and then were used to excite a nonlinear analytical model of the building. Figure 2b shows results of nonlinear dynamic analyses; for shears the results are the mean plus one standard deviation of the peak story shears and for moments the results are the mean of the peak story moments (these statistical measures commonly are used in current design practice). It can be observed that the envelope of the CMS results is nearly as large as the DBE results, and in this example there are locations where the CMS values are higher (attributed to ground motion variations and problem nonlinearities). Generally, little benefit is obtained from the CMS results for response quantities dominated by a single mode, and only marginal benefit is obtained from response quantities with contributions from more than one mode. Given the high expense of developing the spectra, the ground motions, and the building responses, scenario-based ground motions currently are not used for tall building designs.

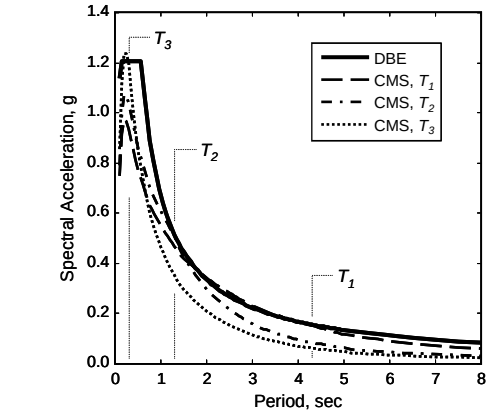

(a) Response spectra

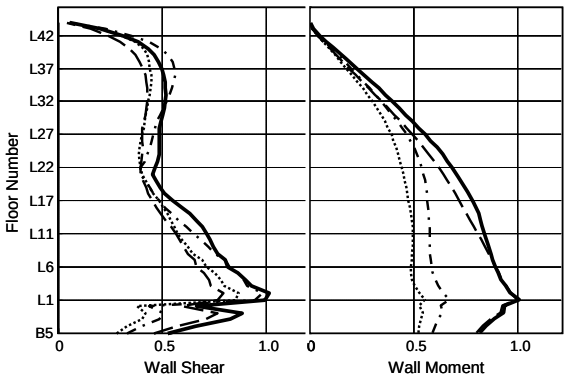

(b) Peak building responses

Figure 2 (a) Design Basis Earthquake and Conditional Mean Spectra and (b) calculated design wall shears and moments (mean plus one standard deviation of peak values for shear and mean of peak values for moment)

5. NONLINEAR DYNAMIC ANALYSIS AND PERFORMANCE VERIFICATION

Performance-based seismic analysis of tall buildings in the U.S. increasingly uses nonlinear analysis of a three-dimensional model of the building. Lateral-force-resisting components of the building are modeled as discrete elements with lumped plasticity or fiber models that represent material nonlinearity and integrate it across the component section and length. Gravity framing elements (those components usually not designated as part of the lateral-force-resisting system) increasingly are being included in the nonlinear models so that effects of building deformations on the gravity framing (imposed deformations and the accumulation of overturning forces over the building height) as well as effects of the gravity framing on the seismic system (for example, increased stiffness and core-wall shears) may be represented directly.

Figure 3a shows statistics of story shear profiles for a tall core-wall building subjected to different levels of earthquake ground motion. (Twenty-seven records from earthquakes having ~M7 at ~10km were scaled to the

first-mode spectral acceleration of the uniform hazard spectrum for 475-year (DBE) and 2475-yr (MCE) mean return periods.) The story shear has considerable dispersion for any level of ground shaking, and the shear increases as the intensity of shaking increases even though total overturning moment is limited by the wall yielding mechanism. Similar patterns can be observed for upper-story wall moments and other design parameters.

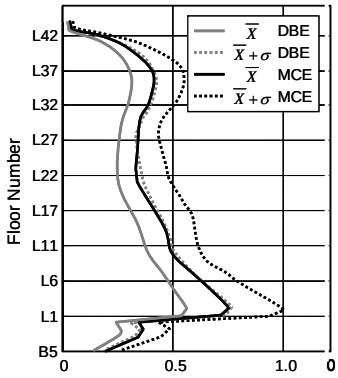

Figure 3 Selected results from nonlinear analysis of a core wall building: Mean and mean plus one standard deviation results of core wall shear for ground motions scaled to Design Basis Earthquake and Maximum Considered Earthquake levels.

Results of nonlinear dynamic analysis are sensitive to modeling assumptions. In reinforced concrete construction, component effective stiffnesses should consider effects of cracking on stiffness and slip of reinforcement from anchorage zones. Usual practice is to base nonlinear component strengths on expected material properties and to include reinforcement strain-hardening effects. By so doing, the computer model response is likely to be closer to best-estimate response and internal actions (e.g., axial forces, shears, and moments) on components expected to remain elastic will be more conservatively estimated. Some results are particularly sensitive to stiffness assumptions, so bounding analyses are not uncommon. Figure 4 illustrates variation in calculated wall shears for different shear stiffness assumptions of walls and podium diaphragms. The effect on shear below the main transfer slab is especially prominent.

The gravity framing system (that part designed mainly to support gravity loads and not seismic forces) typically is included in the analytical models to estimate deformation demands and forces acting on the gravity framing. In U.S. design practice, columns are proportioned for multiple load combinations, including 1.2D + 1.6L and 1.2D + 0.5L + E, where D, L, and E are effects from dead, live, and earthquake, respectively. Given these load combinations and typical values for D, L, and E, the overturning on gravity columns may control their design.

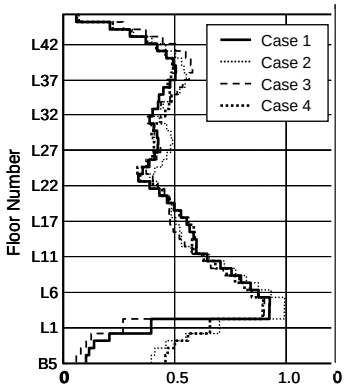

Figure 4 Selected results from nonlinear analysis of a core wall building: Effect of wall and podium diaphragm modeling assumptions on calculated core wall shears.

A nearly universal practice is to use seven ground motion pairs (horizontal components only) to excite a nonlinear model of the building [ASCE 7-05, 2005; LATB, 2008; SEAONC, 2007]. A key question, then, is how to define the design-level response when each of the multiple design ground motions produces its own distinct results. In one study, a core wall building was subjected to 100 different sets of seven pairs of ground motions to identify typical response statistics. On average, the standard deviation of the wall shear demand was approximately 0.3. Thus, the choice of design value (for example, mean, median, or one standard deviation higher) has a significant impact on final design quantities.

Equally important is the selection of the design strength or resistance. Lacking written guidance, designers have proposed design strengths ranging from (a) the nominal strength reduced by a strength reduction factor from the building code to (b) expected strength (based on expected materials properties) with strength reduction factor equal to 1.0. For typical shear wall configurations, and for the code strength reduction factor of 0.75, the difference between these two values is in the range of 1:1.5.

To promote more consistent design approaches, SEAONC [2007] recommends that demands for ductile actions be taken not less than the mean value obtained from the nonlinear response history analysis, whereas demands for low-ductility actions (for example, shear response of walls) should consider the dispersion of the values. The commentary to the SEAONC guidelines notes that in typical cases design actions for low-ductility actions can be defined as the mean plus one standard deviation of the values obtained from the nonlinear response history analysis. SEAONC also recommends that design strengths for low-ductility actions be defined based on the product of the nominal strength (considering specified material properties) and the strength reduction factor from the building code. Simplified analyses of this approach, considering the statistics of seismic demands and resistances, suggest the probability of shear failure is approximately one fifth of the probability of reaching flexural deformation capacities.

Additional development is required to formalize these findings and their adoption in practice.

6. PROPORTIONING AND DETAILING

A significant percentage of recent high-rise building construction in the western U.S. has been for residential and mixed-use occupancies. Thus, much of it has been of reinforced concrete, and the majority of those have used reinforced concrete core walls. Some concrete and steel framing, and some steel walls, also are used.

Under design-level earthquake ground motions, the core wall may undergo inelastic deformations near the base (and elsewhere) in the presence of high shear. Ductile performance requires an effectively continuous tension chord, adequately confined compression zone, and adequate proportions and details for shear resistance. In locations where yielding is anticipated, splices (either mechanical or lapped) must be capable of developing forces approaching the bar strength. Furthermore, longitudinal reinforcement is to be extended a distance $0.8l_w$ past the point where it is no longer required for flexure based on conventional section flexural analysis, where l_w is the (horizontal) wall length.

Walls generally are fully confined at the base and extending into subterranean levels. Confinement above the base may be reduced (perhaps by half) where analysis shows reduced strains, though strains calculated by nonlinear analysis software generally should be viewed skeptically as they are strongly dependent on modeling assumptions (modeling procedures should be validated by the engineer of record against strains measured in laboratory tests). The reduced confinement usually continues up the wall height until calculated demands under maximum expected loadings are well below spalling levels. Transverse reinforcement for wall shear generally is developed to the far face of the confined boundary zone; otherwise, the full length of the wall is not effective in resisting shear. Figure 5 shows an example detail for boundary element confinement and anchorage of shear reinforcement using headed bars. Another accepted detail is to lap the horizontal shear reinforcement with an equal area of hoops or U-bars inserted into the boundary. Hooks on the horizontal reinforcement may not be feasible given the large diameter of the horizontal bars.

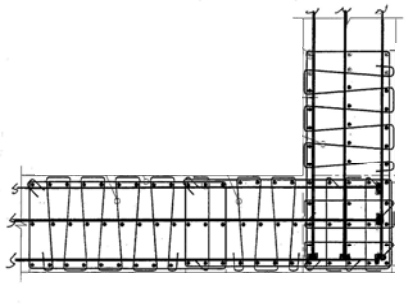

Cross section

Figure 5 Wall cross section details

Coupled core walls require ductile link beams that can undergo large inelastic rotations. In typical cases, the small aspect ratio and high nominal shear stress dictate use of diagonally reinforced coupling beams. To facilitate construction, link beams are now constructed using full cross section confinement rather than individual diagonal confinement (Figure 6).

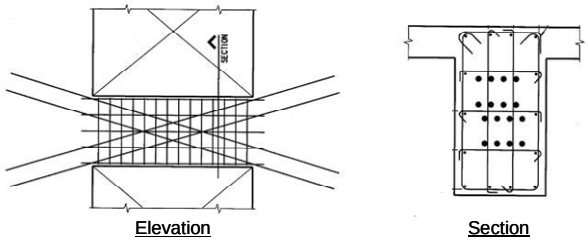

Elevation Section

Figure 6 Typical link beam details

Away from the core walls, gravity loads commonly are supported by post-tensioned floor slabs supported by columns. Slab-column connections are designed considering the effect of lateral drifts on the shear punching tendency of the connection. In most cases, stud rails or other systems are used to reduce the likelihood of punching around the columns. For post-tensioned slabs, which are most common, at least two of the strands in each direction must pass through the column cage to provide post-punching resistance.

7. PEER REVIEW

Few building departments have the expertise to understand and approve the code exceptions and alternative means proposed in a performance-based design. Questions invariably arise regarding use and performance of new materials and systems, selection of appropriate hazard levels and representative ground motions, nonlinear dynamic analysis models and results interpretations, acceptance criteria, and quality assurance in design and construction. Peer review by independent qualified experts helps assure the building official that the proposed materials and system are acceptable. The peer review generally starts early in the process, starting with review of the project design criteria, and follows through to final verification of analysis and design details.

8. CONCLUSIONS

Performance-based earthquake engineering increasingly is being used as an approach to the design of tall buildings in the U.S. Available software, research results, and experience gained through real building applications are providing a basis for effective application of nonlinear analysis procedures. Important considerations include definition of performance objectives, selection of input ground motions, construction of an appropriate nonlinear

analysis model, and judicious interpretation of the results. Implemented properly, nonlinear dynamic analysis specific to the structural system and seismic environment is the best way to identify nonlinear dynamic response characteristics, including yielding mechanisms, associated internal forces, deformation demands, and detailing requirements. Proportions and details superior to those obtained using the prescriptive requirements of the building code can be determined by such analysis, leading to greater confidence in building performance characteristics including serviceability and safety. Although performance-based designs already are under way and are leading to improved designs, several research needs have been identified, the study of which can further improve design practices.

Acknowledgements:

This work had several influences, including the Pacific Earthquake Engineering Research Center (National Science Foundation award EEC-9701568) and several building performance-based engineering review projects in California and Washington. Analytical studies reported here were conducted by T.Y. Yang, post-doctoral researcher at the Pacific Earthquake Engineering Research Center, except the bounding analysis results of Figure 4 were conducted by Professor J.W. Wallace of UCLA. Professor J. Baker of Stanford provided Conditional Mean Spectra and corresponding ground motions presented in Figure 2a. The views expressed are those of the author and not necessarily those of individuals or organizations cited here or in the references.

References:

Abrahamson, N.A. (2006). Seismic hazard: Problems with current practice and future developments. *Proc. of the First European Conference on Earthquake Engineering and Seismology*, Geneva, September 4-7, 2006.

ASCE 7-05 (2005). *Minimum Design Loads for Buildings and Other Structures*, American Society of Civil Engineers.

Baker, J.W. and C. A. Cornell (2006). Spectral shape, epsilon and record selection, *Earthquake Engineering and Structural Dynamics*, 35, 1077-1095.

Bray, J.D., and A. Rodriguez-Marek (2004). Characterization of forward-directivity ground motions in the near-fault region, *Soil Dynamics and Earthquake Engineering*, 24, pp. 815-828.

CTBUH (2008). Recommendations for the Seismic Design of High-Rise Buildings, Council on Tall Buildings and Urban Habitat.

Holmes, W.T., Kircher, C., Petak, W., Youssef, N., Kornfield, L. (2008). Seismic Performance Objectives for Tall Buildings, *PEER Report 2008/01*, Pacific Earthquake Engrg. Research Ctr., Univ. of California, Berkeley.

ICC (2006). *International Building Code*, International Code Council.

LATBSDC (2008). *An Alternative Procedure for Seismic Analysis and Design of Tall Buildings Located in the Los Angeles Region*, Los Angeles Tall Buildings Structural Design Council.

SEAONC (2007). SEAONC *Recommended Administrative Bulletin for San Francisco*, Structural Engineers Association of Northern California, San Francisco.

Stewart, J.P., S.J. Chiou, J.D. Bray, R.W. Graves, P.G. Somerville, N.A. Abrahamson, 2001. Ground motion evaluation procedures for performance-based design, *PEER-2001/09*, UC Berkeley.

Sixth International Conference on Urban Earthquake Engineering
March 3-4, 2009, Tokyo Institute of Technology, Tokyo, Japan

E-DEFENCE PROJECT ON SEISMIC PERFORMANCE OF BRIDGES

Kazuhiko Kawashima[1)], Tomohiro Sasaki[2)], Hiromichi Ukon[3)], and Koichi Kajiwara[4)]

1) Professor, Department of Civil Engineering, Tokyo Institute of Technology, Japan
2) Graduate student, Department of Civil Engineering, Tokyo Institute of Technology, Japan
3) Research fellow, National Research Institute of Earth Science and Disaster Prevention, Japan
4) Senior researcher, ditto
kawashima.k@ae.m.titech.ac.jp, sasaki.t.aa@m.titech.ac.jp, ukon@bosai.go.jp, kaji@bosai.go.jp

Abstract: This paper introduces a large scale shake table experimental program on bridge structures using E-Defense. The program was formulated as one of the US-Japan cooperative research programs based on NEES and E-Defense collaboration. Component model (C1 model) and system model (C2 model) are included in the program. Objectives of C1 model is to clarify the failure mechanism of reinforced concrete bridge piers using as large models as possible to eliminate barriers of scale and loading rate effect. C2 model is to study the complex system behavior of bridges to failure. Background, objectives, proposed models and tests cases are presented with emphasis on C1-1 model.

1. INTRODUCTION

E-Defense was built to advance the scientific knowledge on the earthquake engineering as a consequence of the extensive damage of urban infrastructures in the 1995 Kobe, Japan earthquake. "Why did structures suffer such extensive damage during the Kobe earthquake?," "what were the mechanism of failure?," and "what extent do structures fail under near-field ground motions?" are the basic target and motivations of constricting E-Defense.

A large scale shake table experiment on bridge structures was identified as one of the high priority research areas in the US-Japan cooperative program based on NEES/E-Defense collaboration. A large scale bridge experimental program as well as two other programs (steel buildings and information technology) was initiated in 2005 as one of the US-Japan cooperative research programs.

This paper introduces the E-Defense experiment on the seismic performance of bridge columns.

2. E-DEFENSE PROJECT ON BRIDGE COLUMNS

Since E-Defense was built for clarifying the extensive damage of structures during the 1995 Kobe earthquake, breakthrough experiments which are significantly important as a benchmark test for clarifying the failure mechanism and/or enhancing the seismic performance of structures are expected.

Based on discussions between Japan and US researchers, an experimental program consisting of C1 and C2 experiments was formulated in 2005 (Nakashima et al, 2008). C1 experiment is to clarify the failure mechanism of single reinforced concrete columns with as large section as possible so that restriction of the scale-effect can be eliminate. Because failure of reinforced concrete columns was one of the major mechanisms of the damage during 1998 Loma Prieta, 1994 Northridge and 1995 Kobe earthquakes (Kawashima and Unjoh, 1997), the study on reinforced concrete columns is a high priority research area. On the other hand, C2 experiment is for clarifying the system failure mechanism of a bridge consisting of a deck, columns, abutments, bearings, expansion joints, and unseating prevention devices under an extreme seismic excitation.

Preliminary experiments and analysis as well as design of C1 and C2 models were conducted in 2005 and 2006. Six experiments were originally planned for C1 models in 2007-2008; two columns which were typically built in 1970-1980s and collapsed during 1995 Kobe earthquake. One is a column which fails in flexure (C1-1 model) while the other is a column which fails in shear (C1-2 model). Other four were experiments for verifying the effect of seismic retrofit by steel jacket and carbon fiber jacket (C1-3 and C1-4 models), and experiments for verifying the seismic performance of a column which was built based on the current technology (C1-5 model) and for clarifying redundancy of a recent column under stronger than code specified ground motions (C1-6 model). A series of C2 experiments was originally scheduled in 2009.

However the experiment program was subjected to extensive modification under various constraints. Among six C1 experiments, C1-1, C1-2 and C1-5 experiments were conducted, and C1-6 experiment is expected in 2009. Other experiments including C2 experiment have to be eliminated from the original program.

Because the experimental data on C1-2 and C1-5 models are under analysis, the result on C1-1 model is presented

here.

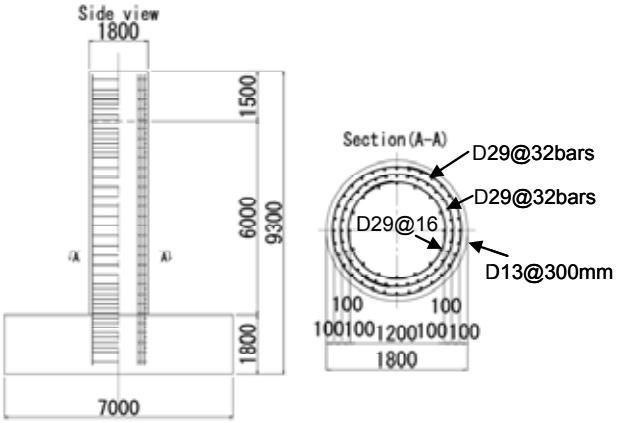

Figure 1 Column built 1960-1970s which fails in flexure (C1-1 column)

Photo 1 C1-1 under Construction

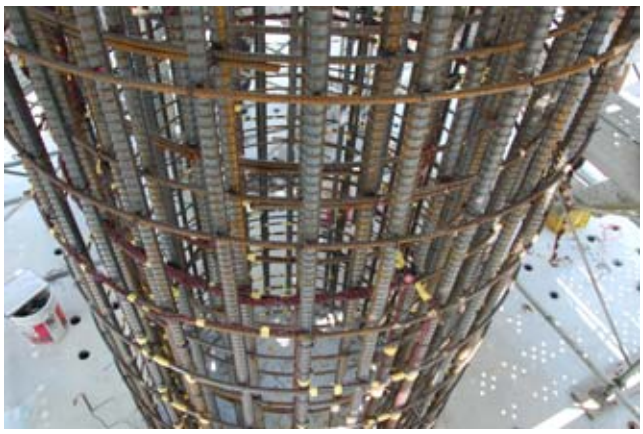

Photo 2 Reinforcements

2. C1-1 MODEL

C1-1 is a 7.5 m tall 1.8 m diameter circular reinforced concrete column as shown in Fig. 1. It was designed based on a combination of the static lateral force method and the working stress analysis specified in the 1964 Design Specifications of Steel Road Bridges, Japan Road Association. Combination of the lateral seismic coefficient of 0.23 and the vertical seismic coefficient of +/-0.11 (upward and downward seismic force) was assumed in design. It was assumed that the column was built on the Type II soil (moderate) site. It was nearly a half scale of prototype columns, therefore it was designed assuming that it was a small prototype column without considering the scaling rule. This is because the scaling rule cannot be explicitly implemented to structures in which plastic deformation is predominant.

The column had reinforcements in three layers, i.e., 32, 32 and 16 longitudinal reinforcements were provided at the outer, middle and inner layers as shown in Photos 1 and 2. Longitudinal and tie reinforcements were deformed 29 mm and 13 mm diameter bars, respectively, with the nominal yield strength of 345MPa. Ties were provided at every 300 mm interval, except the outer ties at the top 1.15 m zone and the bottom 0.95 m zone where they were provided at 150 mm interval. Ties were lap spliced. It was the common practice by the mid 1980s because the importance of the lateral confinement was not considered. The longitudinal reinforcement ratio is 2.02% and the tie volumetric reinforcement ratio ρ_s is 0.32% except the top 1.15m and bottom 0.95 m zones where ρ_s is 0.42%. The design strength of concrete was 27 MPa.

Table 1 shows an evaluation of the seismic performance of C1-1 in the longitudinal direction based on the current design code. The seismic performance of C1-5 column is also presented here for comparison. C1-5 is a 2m diameter circular column with the longitudinal reinforcement ratio of 2.19% and tie volumetric reinforcement ratio of 0.911%. Because the moderate soil condition (Type II) is considered, the design response acceleration S_A is 17.15 m/s^2 for both C1-1 and C1-5. The yield displacements u_y and ultimate displacement u_u are 0.046m and 0.099m in C1-1 and 0.045m and 0.231m in C1-5. The design displacement u_d is evaluated based on u_u and u_y as

$$u_d = u_y + \frac{u_u - u_y}{\alpha u_y} \tag{1}$$

in which α depends on the type of ground motions (near-field or middle-field) and the importance of the bridge. Because α is 1.5 for a combination of the near-field ground motion category and the important bridges category, the design displacement u_d is 0.081m in C1-1 and 0.169m in C1-5.

On the other hand, because the force reduction factor is 1.58 in C1-1 and 2.56 in C1-5, the displacement demand of the column u is 0.328m in C1-1 and 0.168m in C1-5. Consequently, C1-1 is evaluated to be unsafe while C1-5 is

Table 1 Evaluation of C1-1 Column in Comparison with C1-5 Column in the Longitudinal Direction

Demand & Capacity	Properties	C1-1	C1-5
Design Force	Design response spectrum S_A	$1.75 \times 9.8 = 17.15 m/s^2$	
	Force reduction factor	1.58	2.56
	Response acceleration demand	$10.83 m/s^2$	$6.70 m/s^2$
Demand	Displacement demand of the column	0.328m	0.168m
Capacity	Yield displacement capacity u_y	0.046m	0.045m
	Ultimate displacement capacity u_u	0.099m	0.231m
	Design displacement capacity u_d	0.081m	0.169m

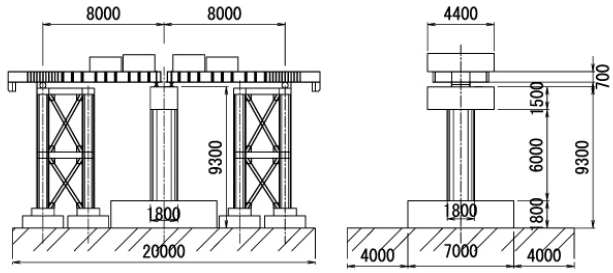

Figure 2 Setup of Model

(a) NNW view

(b) NE view

Photo 3 C1-1 column on E-Defense

safe based on the current seismic design code. From the evaluation of the shear capacity, it is evaluated that both C1-1 and C1-5 models fail in flexure.

3. EXPERIMENTAL SETUP

The C1-1 column was set on E-Defense as shown in Fig. 2 and Photo 3. Two simply supported decks were set on the Column and two steel end supports. The decks are a device to fix four mass blocks on the column and they are not designed to idealize the stiffness and strength of real decks. Each deck was supported by a fixed bearing on the column and a movable bearing (friction bearing) on the end supports as shown in Photos 4 and 5. Two side sliders (friction bearings) were provided at the both sides of the fixed and movable bearings for preventing overturning of the decks around its axis.

A 78 t mass block and a 44.6 mass block per deck are fixed to the decks. The mass blocks are of laminated steel plates. Total mass due to 4 mass blocks, 2 decks, 2 fixed bearings, 2 movable bearings, 8 side sliders and 32 load cells is 302 t. Including masses of the column with a 1.8 m thick footing, 2 steel end supports and table protections, the total mass of the model is slightly over 1,000 t.

A ground acceleration recorded at JR Takatori Station during the 1995 Kobe, Japan earthquake (refer to Fig. 3) was used for the table motion. It is well known that the radiational energy dissipation of a model on a shake table is extremely smaller that the real energy dissipation. Taking account of the soil structure interaction effect, a ground motion with 80% the original intensity of JR Takatori record was used as a command to the table in the experiment. This ground motion is called hereinafter as E-Takatori ground motion.

The model was subjected to a 10%, two 20% and six 30% E-Takatori ground motion excitations to check the overall response and measuring system. No visible cracks occurred during those excitations. Main excitation using the 100% E-Takatori ground motion was conducted twice. Only the response and failure mode for the first 100% E-Takatori excitation are shown in the folowing.

4. SEISMIC PERFORMANCE OF THE C1-1 COLUMN

Fig. 4 shows the response displacements at the top of the

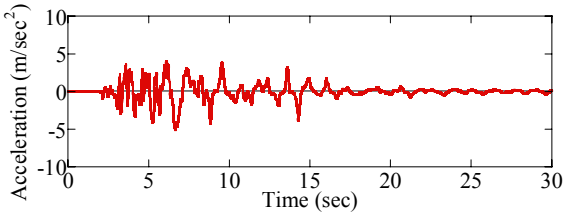

(a) Longitudinal direction

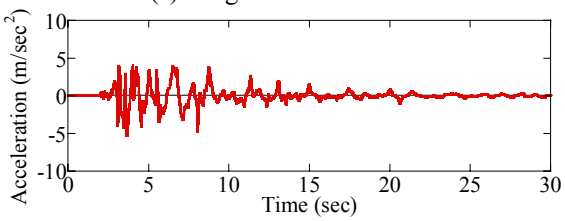

(b) Transverse direction

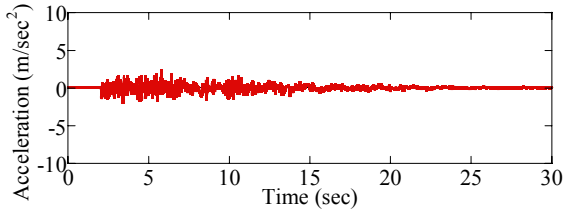

(c) Vertical direction

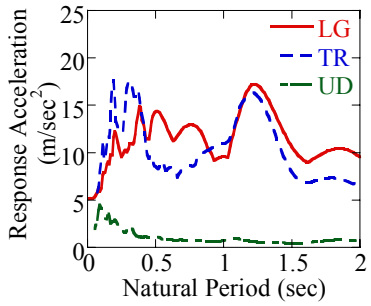

(d) Acceleration response spectra

Figure 3 E-JR Takatori Ground Accelerations

column. The combined displacement of two lateral components had a peak of 0.195 m (2.56 % drift) at 6.9 s. Because the ultimate displacement at the top of the column is 0.091 m, the peak response exceeded the ultimate displacement by a factor of 2.1.

Photo 6 shows progress of failure of the column at the plastic hinge on NE and SW surfaces. It should be noted that N-S and E-W correspond to the longitudinal and transverse directions of the model, respectively. At an instance of 6.9 s, the covering concrete started to spall at SW surface due to compression. At SW, covering concrete spalled between the bottom and 0.6 m from the bottom of the column and several outer longitudinal reinforcements locally buckled between the bottom and 0.2 m from the bottom of the column during the excitation.

Figs. 5 and 6 show strains of the outer longitudinal and tie reinforcements, respectively, at 6.9 s. Strains in the longitudinal reinforcements were over 4000 μ in tension at SE, E, NE, N and NW while they were over 2000 μ in compression at W and SW. Strains in the longitudinal reinforcements are extremely large between 0.25 m below and 1.5 m above the surface of the footing. It is interesting to

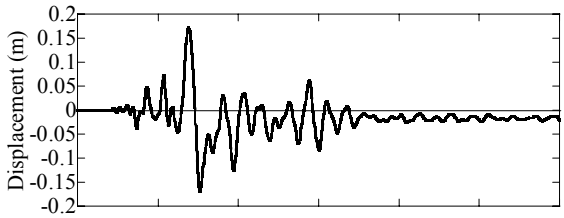

(a) Longitudinal

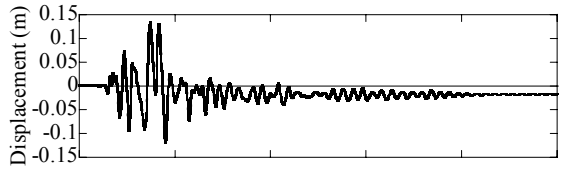

(b) Transverse

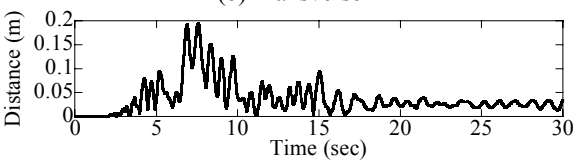

(c) Combined bilateral components

Figure 4 Response Displacement of C1-1 at the Top during the First 100% E-Takatori Ground Acceleration Excitation

(a) 6.9 sec

(b) 8.35 sec

Photo 6 Progress of Failure of C1-1 during the First 100% E-Takatori Ground Acceleration Excitation on SW Surface

note that extensive yielding of longitudinal reinforcements occurs at the zone higher than the anticipated plastic hinge region. Deformation of the longitudinal reinforcements inside the footing contributes to the lateral response of the

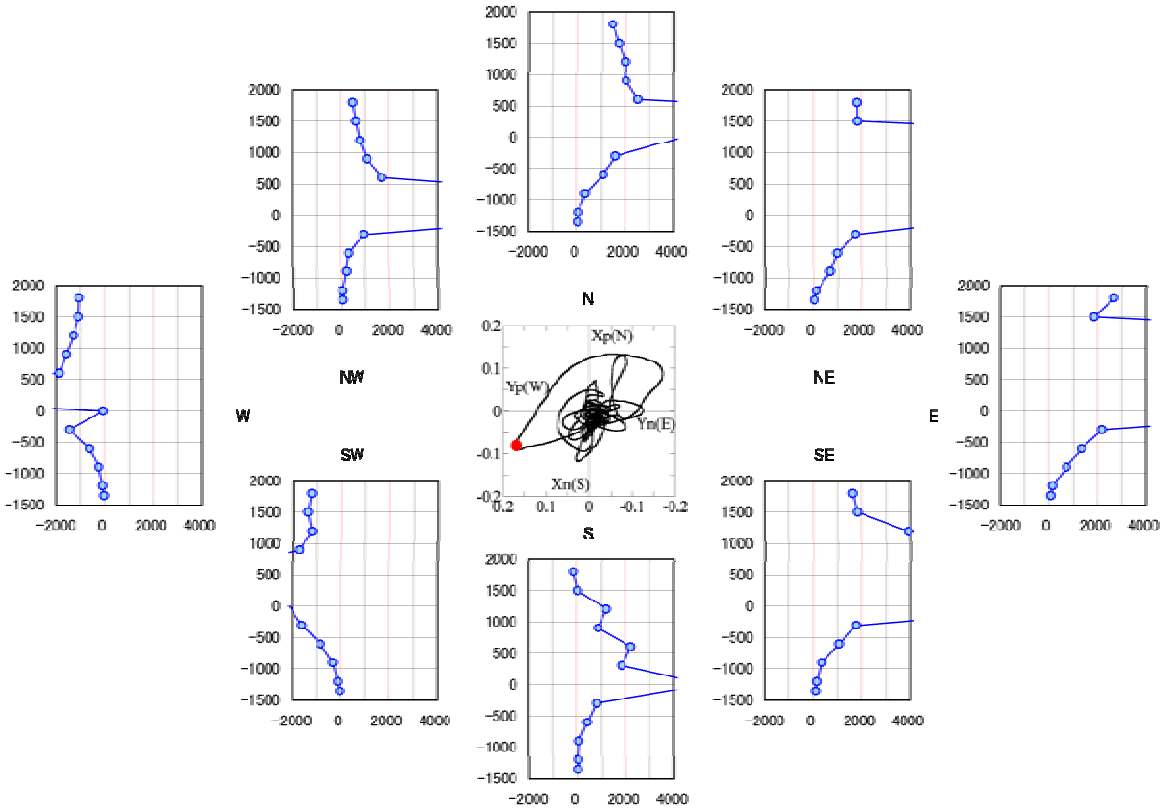

Figure 5 Strains of Outer Longitudinal Bars at 6.9 sec during the First 100% E-Takatori Ground Acceleration Excitation

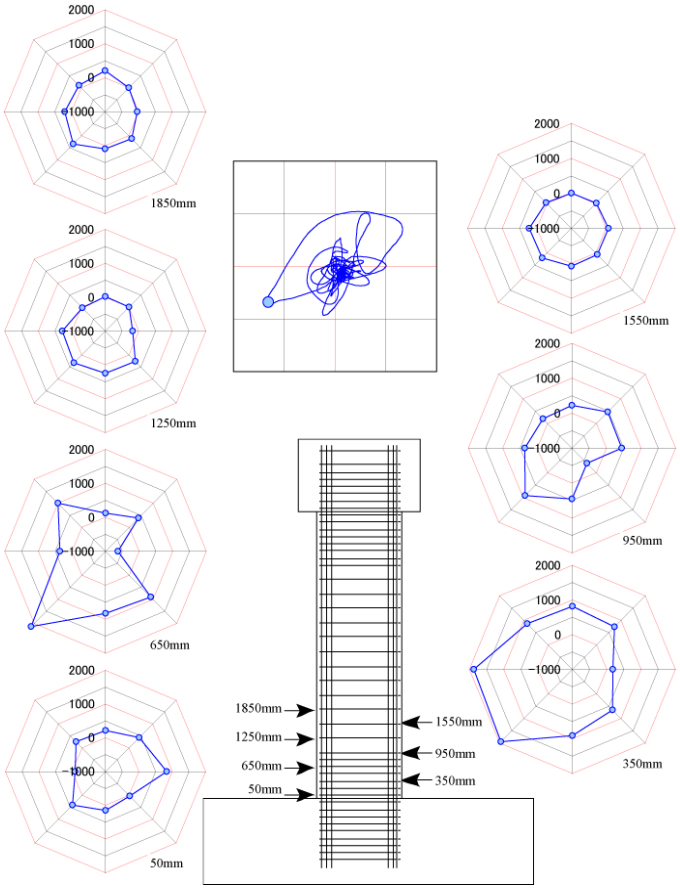

Figure 6 Strains of Ties at 6.9 sec during the First 100% E-Takatori Ground Acceleration Excitation

model.

Although it is not presented here, the lateral confinement among the three layered ties is very complex. The lateral confinement is not uniform around the ties, and it is not the same among the three ties. Mechanism of the lateral confinement by multi-layered ties should be critically investigated.

Strains of the tie reinforcements at an instance of 6.9 s are larger at 0.35 m and 0.65 m above the surface of the footing The maximum strains at the two locations are nearly 2000 μ, slightly larger than the yield strain. It is important to note that strains of tie reinforcements are larger at SW and W where the section is subjected to compression. Obviously this is resulted from the local buckling of longitudinal reinforcements at SW.

5. CONCLUSIONS

C1-1 column which is a typical flexural failure type column in 1970s was excited twice under 3D 100% E-Takatori ground accelerations using E-Defense. It was designed assuming 0.23 lateral seismic coefficient and +/-0.11 vertical seismic coefficient based on the working stress design approach in accordance with the JRA 1964 design codes. Based on the results presented herein, the following conclusions may be deduced:

1) C1-1 column suffered extensive damage under a near field ground motion recorded at JR Takatori Station during the 1995 Kobe earthquake.
2) The lateral confinement of three layered ties is very complex. The lateral confinement is not uniform around the ties, and it is not the same among the three ties. Mechanism of the lateral confinement by multi-layered ties should be critically investigated.
3) Although it was anticipated that yielding of the longitudinal and tie reinforcements was less significant at the zone higher than the plastic hinge, extensive yielding occurred up to 83% and 69% the column diameter in the longitudinal and tie reinforcements, respectively.
4) Deformation of the longitudinal reinforcement inside the footing contributes to the response of the column. Thus its effect has to be included in analysis for evaluating the column drift.
5) Effect of the bilateral excitation should be included in design. The current design still stands on the concept of unilateral excitation.

Acknowledgements:

The E-Defense bridge project was formulated as a US-Japan cooperative research based on NEES and E-Defense collaboration. The C1-1 experiment was conducted based on the extensive support of over 70 members in the Overview Committee (Chair, Iemura, H., Professor Emeritus, Kyoto University), Executing Committee of Large-scale Bridge Experimental Program (Chair, Kawashima, K., Tokyo Institute of Technology), Analytical Correlation WG (Chair, Unjoh, S., Public Works Research Institute), Measurements WG (Chair, Takahashi, Y., Kyoto University), and Dampers and Bearings WG (Chair, Yabe, M., Chodai). Special appreciation is extended to Professor Buckle, I. , University of Nevada, Reno, and Professor Mahin, S., University of California, Berkeley for their kind cooperation for the US-Japan cooperative research..

References:

Kawashima, K. and Unjoh, S. (1997). The damage of highway bridges in the 1995 Hyogo-ken nanbu earthquake and its impact on Japanese seismic design. Journal of Earthquake Engineering, 1(3), 505-542.

Nakashima, M., Kawashima, K., Ukon, H. and Kajiwara, K. (2008). Shake table experimental project on the seismic performance of bridges using E-Defense. 14WCEE, Beijing, China.

Sixth International Conference on Urban Earthquake Engineering
March 3-4, 2009, Tokyo Institute of Technology, Tokyo, Japan

Advancing the State of Earthquake Engineering through Cooperative Research and Large Scale Testing

Steven L. McCabe[1)]

1) Chief Executive Officer, NEES Consortium, Inc. Davis, CA, USA; Professor Emeritus, University of Kansas, Lawrence, KS USA
Steve.McCabe@nees.org

Abstract: The risks faced by societies today from earthquake and other hazards are significant. With increased populations centered in urban areas of high density, the challenges that are present are unique. No longer are studies of limited scope whereby component performance is examined, sufficient. Rather larger and more complex research programs are required to examine these modern issues. With limited resources the solution lies in cooperative research among a team of researchers where technical problems can be studied in depth with a scale sufficient to examine systems of complexity and completeness.

1. INTRODUCTION

The 20th Century was an eventful period of time, not the least because it contained a number of serious earthquakes. A brief list includes the 1906 San Francisco, the 1923 Tokyo and the 1964 Anchorage earthquakes, where damage and loss of life exhibited the need for improved design provisions and a better basic understanding of the mechanics of response to earthquake. These events resulted in an increasing level of effort into understanding the geotechnical, structural and hydrodynamic aspects of response of the built environment to earthquake. Much of this work was based on component tests where small parts of larger ,actual systems were studied. These results formed the basis for an improved understanding and improved design approaches. The focus of this early work was life safety and based on performance over the past 40 years, these efforts have been largely successful.

Starting with the 1989 Loma Prieta earthquake, there has been growing awareness in the US and in Japan of the risk posed by earthquakes to the built environment, especially in urban areas where population density is high. This awareness has transformed into concern over economic losses in addition to life safety. Loma Prieta (1989), Northridge (1994) and Kobe (1995) all exhibited the serious economic impact that a large earthquake can have to a metropolitan area. While the human toll remains the predominant concern, economics and large levels of damage and societal interruption have taken an important role in design decisions

This transformation has occurred in part from the dependence of modern societies on their infrastructure. Urban areas do not generally have the redundancy necessary to permit long interruptions in utility service, highway or bridge availability or other basic services. More rural areas with lower population density may actually cope better in a post-earthquake environment. Thus modern design philosophy is beginning to consider both life safety and economic health as well.

The question is how best to incorporate the concept of economic health to design approaches based on the more basic question of life safety? This step introduces a significant level of sophistication to the process. No longer are approximate force-based methods sufficient. Rather the portfolio of forces, the distribution of forces and moments through the structure for example, as well as the displacement and overturning response become nearly equal considerations. The issue of how does the system respond becomes the question and whether this response acceptable in all of its aspects, not only forces.

This more complete look at response in design has resulted in a move to Performance Based Design concepts and away from more prescriptive methods. The shift in approach requires significantly more information as to *system* behavior under earthquake excitations than required for the earlier force-based methods. By examining system response we can look at more of the entire picture of how an engineering system responds, together with the context of its place in the broader environment. This can result in greatly improved efficiencies in design where members more equally participate in response, or foundation components can be designed with more insight as to demands. But how do we obtain system performance to use in design, especially in a current era of tight budgets and limited support for basic research?

2. Shared Experimental Resources

In this modern era since Loma Prieta, several things have become apparent:

1. Large number or casualties and large economic losses from earthquake are not acceptable
2. Understanding systems behavior is an important element of Performance Based Design
3. Study of systems requires large scale testing laboratories
4. Limited national resources limit the availability of funds to construct these large labs.

What has occurred in both Japan and the US is a response to these new challenges that are quite similar and complementary. With the need for new large scale facilities, both countries have embarked on building laboratories to be used by the research community. In Japan following Kobe, the E-Defense facility was constructed and opened for service. The world's largest and most capable shake table, E-Defense permits study of complete systems under earthquake that have not been possible before. Together with the Dai Dai Toku program, an organized and systematic study of important national technical problems has been undertaken by large teams of investigators. These results are being published and entering design application now. They represent a significant step forward.

The solution in the US came in the late 1990's when Congress funded the George E. Brown, Jr. Network for Earthquake Engineering Simulation (NEES), a 10-year investment aimed at reducing the vulnerability of the United States' infrastructure to the effects of earthquakes. The Network is built around the National Science Foundation's (NSF) $82M funding of 15 geographically-distributed NEES Equipment Sites, together with an integrative IT infrastructure, Fig. 1. The NEES sites include three shake table facilities, two geotechnical centrifuge sites, one tsunami wave basin, one pipeline facility, six large scale testing laboratories and three field sites; all linked with IT systems and managed by the NEES Consortium, Inc.

Through use of the NEES Sites, as well as the table at E-Defense, researchers in the US and Japan seek to reduce the vulnerability of the built infrastructure to the damaging effects of earthquakes through answers to important and complex technical problems whose study is enabled by the Network. A secondary goal is to accelerate the rate at which research discoveries are made and then integrated into methods, technologies and products for engineering practice.

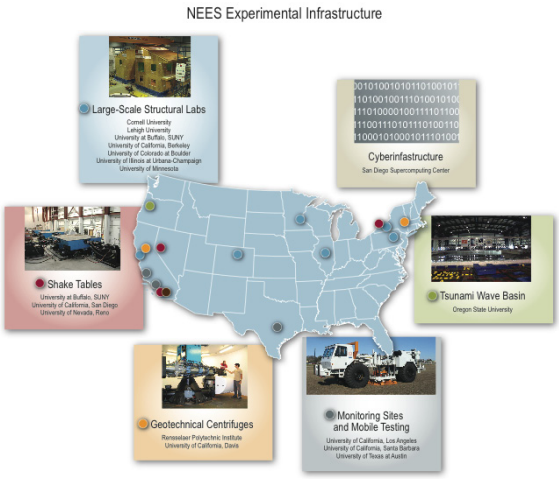

Figure 1 The NEES Equipment Sites

Both NEES and E-Defense represent significant improvements in the state testing abilities world wide. E-Defense and NEES are shared use and permit access by the community to study important large scale problems. As such they used by teams of researchers who work together towards a common goal. This approach represents a shift in methodology where smaller scale studies by one or a few investigators have been replaced in part by these larger projects. This increase in scale requires larger budgets and larger facilities. The outcomes, however, also are larger and likely to have more significant impact on engineering practice and ultimately society.

What has made these two investments by Japan and the US even more important is the cooperation and coordination developed by the two communities. In essence what has developed is a NEES-E-Defense network where researchers have access to a range of facilities from the smaller scale NEES labs all the way to the table in Miki City. Moreover, the research agenda has been cooperative as well with many projects funded by the US NSF being in part driven by issues raised in the Dai Dai Toku. We see an excellent cooperative spirit resulting in even better outcomes and more efficient use of sites in the US and Japan. We truly are witnessing use of shared experimental resources in the largest sense.

Moreover, both the NEES and E-Defense systems are currently undergoing a funding reauthorization for the next period of operation. This demonstrates the linkage between the facilities that has been present since the beginning. In the US this reauthorization also will include selection of a new NEES operations manager. This new entity will replace the NEES Consortium as operator and manager of the Network starting on October 1, 2009. The goals for NEES will be to continue the close cooperation with E-Defense and to continue to work to frame our common research

agendas to the benefit of both research communities, as well as MEXT and NSF as funding agencies.

3. NEES Up Close

As stated earlier, NEES research can be separated from earlier efforts in a number of ways, not the least is the scale of the effort as well as the scale of the specimens. Moreover the scale of the projects permit a more sophisticated integration of effects. For example, many projects include work in a variety of areas including geotechnical and structural work in the same project. These integrated studies allow investigation of not only one aspect of a problem but the coupling effects between different subdisciplines of Civil Engineerings.

At present there are over 100 projects underway in the NEES Network, funded by NSF and other Federal agencies together with projects funded by Caltrans and others. The goal is the study of complex problems that could not be studied previously due to size or testing lab capacities. These 15 sites represent the state-of-the-art in the US and in most cases are not equaled anywhere in the world. The associated NEES research is of a scale that collaborative work is required with project teams formed around expertise, including faculty and practitioners. Integration of the practitioner community has greatly helped focus the research and guide the overall effort with an eye towards implementation. The end result is not only better understanding of basic performance issues but results that can validate new ideas and products as well as lead to new design provisions to improve performance.

Another unique aspect of NEES is the common Data Repository, designed to archive all experimental data generated by projects in the Network. This archive will be in retrievable formats to permit accessing of results over the long term. At present about 20 projects are fully curated with over 1000 registered users of the repository.

Some examples of current projects include:

- Research into the behavior of precast floor diaphragms and the dynamic interactions between floor diaphragms and the primary lateral force-resisting elements. Here the diaphragm flexibility is not negligible. The project is a direct result of performance issues observed following the Northridge earthquake in 1994. The result is a large project partially supported by the Precast/Prestressed Concrete Institute (PCI), the Pankow Foundation and NSF (CMMI-0324522).

  The project has utilized detailed subassembly testing conducted at NEES@Lehigh to determine basic behavior, and together with detailed Finite Element studies, has developed new diaphragm design concepts. A large-scale specimen was tested at NEES@UCSD on their shake table in summer 2008, shown in Fig. 2, to compare with smaller tests and analyses and validate these simulations. The specimen was a half scale, half million kilogram specimen shaken at various levels of ground motion to observe performance of the entire system. Response was observed from progressively larger sharing and illustrated the complexity and uncertainty in designing these systems, which are widely used in the US. Design provisions from this work are under development.

Figure 2 Half Scale Precast Structure Ready for Test on NEES@UCSD Shake Table

- Planar wall research undertaken to determine performance characteristics and design recommendations, Fig. 3. The test specimen is a 1/3-scale model of the bottom three stories of a ten-story building with uniformly distributed longitudinal reinforcement spliced at approximately mid-height of the first story. The University of Illinois NEES@UIUC Load and Boundary Condition Boxes (blue and orange) were used to apply a constant axial load as well as shear and moment at the top of the specimen. Ancillary actuators applied story shears at the top of the first and second stories.

  This innovative testing configuration permits application of realistic forces and moments to the specimen. The results have shown remarkable consistency with observed behavior of these types of walls in actual earthquakes. Design provisions are being developed for review by the American Concrete Institute Building Code Committee for possible inclusion in ACI 318. Research funded by NSF under grant CMMI- 0421577.

Figure 3 Planar Wall Test Specimen Following Testing to a Maximum Drift of 1.5% at NEES@UIUC

- Research to understand sand liquefaction during lateral spreading near pile foundations, see Fig. 4. The project links large scale tests with centrifuge and analysis to determine behavior. The goal is to determine how to design pile foundations against lateral spreading both in simplified terms as well as in terms of providing a basic understanding for appropriate analytical platforms.

  The research uses the University at Buffalo 6m-tall laminar box NEES@UB facility to induce 2D shaking together with the NEES@RPI centrifuge facility, and the large E-Defense shaking table. Project features use of novel advanced sensors to measure soil accelerations, deformations and pressures during shaking; and micromechanical Discrete Element (DEM) numerical experiments and Finite Element (FE) analyses at RPI, UC San Diego and Tulane University; all integrated by an appropriate identification and analysis framework including system identification and visualization capabilities. Research funded by NSF under grant CMMI-0529995.

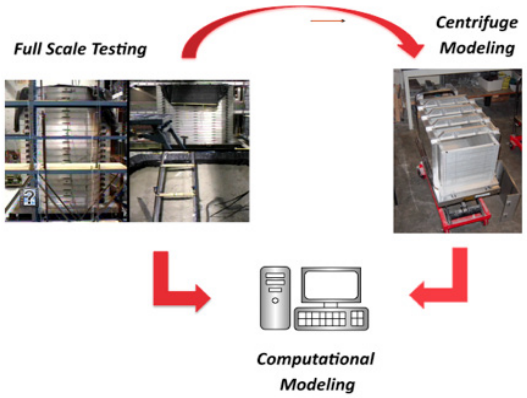

Figure 4 Pile Foundation Liquefaction Study at NEES@RPI

- Research into the performance of wood structures has been of interest in both the US and Japan. The NEESWood project headed by Van De Lindt (CMMI-0529903) is studying the response of midrise wood structures so as to develop performance based design methods for design of these structures. Full scale tests have been completed at NEES@Buffalo, Fig. 5. A companion capstone test will be conducted at E-Defense in 2009.

Figure 5. NEESWood Full Scale Specimen on the NEES University at Buffalo Shake Table Laboratory

By examining the list of NEES projects listed at http://www.nees.org/Research_Activities/ResearchProjects/ the breadth and scope of the projects underway within the Network can be seen.

4. The New Experimental Realties

The introduction of these new testing facilities in the US and Japan have resulted in a large shift in the research enterprise. Project scopes, budgets and specimens all have increased in size. This shift has resulted in larger more significant projects to be addressed. In particular, it can be stated that there are three attributes of this new experimental environment:

1. Projects specimens can be of larger scale.

   This reduces the effects of scale on results and related conclusions. Full scale wood structures have been tested, as has a half scale three story precast concrete building.

2. Project specimens can be more complex.

   Instead of testing components, systems can be tested. These systems can examine more closely the interaction elements to identify how these elements work together to respond to earthquake excitation.

3. Projects specimens and overall projects themselves can be more complete.

   Many projects now include soil-structure-foundation interaction or other formerly isolated effects. Taken together these important aspects of the overall built environment do interact and now can be studied experimentally.

These attributes can be readily seen in the project lists of both E-Defense and NEES. The result of this change will be a greatly improved understanding of system behavior and a reduction in scale effects. Improved design recommendations and professional engineering solutions will be the ultimate effect.

In addition to the changes to the physical testing environment, in the US NEES has shifted the manner in which research is done. The NEES collaborative approach empowers researchers to form problem-focused project teams that serve as 'virtual centers of expertise' constrained neither by geographical location nor by static organizational structures or limited local experimental facilities. Another aspect of NEES is the development of high-impact educational programs to enhance the (1) capabilities of the engineering workforce, (2) community diversity, (3) science and math education, and (4) public understanding of earthquake risks. The NEES collaborative environment itself, including both the shared experimental infrastructure and the integrative cyberinfrastructure, assures open and long-term access to the data resulting from experimental and numerical simulation.

5. Conclusions

As we conclude the first five years of operation of E-Defense and NEES, it can be seen that these two initiatives have been great successes in their own right. When taken together they form an international partnership that is unique and unmatched. Technical developments already are being seen from work performed. The first research projects conducted under NEES are just now finishing. In the next year these results will be published and also seen in design provisions under consideration by ACI, AISC and PCI.

The NEES and E-Defense programs offer tremendous opportunities for developing new understanding of seismic demands and how to mitigate their effects. The cooperation of NEES and E-Defense is an important element of this ongoing progress and should be continued in the next period of operation. Our continued cooperative work on the outstanding issues that we face can greatly benefit both of our counties and our citizens.

Acknowledgements:

The author acknowledges support from the US National Science Foundation for the NEES Consortium, Inc. under grant CMMI-0402490. The support of NSF for NEESinc and for the projects funded under the NEES Research solicitations since 2004 is gratefully acknowledged.

The author also acknowledges the support of the Japan Ministry of Education, Culture, Sport, Science, and Technology (MEXT) for funding research at the E-Defense facility. The cooperation of Dr. Masayoshi Nakashima in furthering the US-Japan cooperation in our joint research efforts is acknowledged and greatly appreciated.

Sixth International Conference on Urban Earthquake Engineering
March 3-4, 2009, Tokyo Institute of Technology, Tokyo, Japan

EARTHQUAKE SURFACE FAULT RUPTURE DESIGN CONSIDERATIONS

Jonathan D. Bray

Professor, Dept. of Civil & Environmental Engineering, University of California, Berkeley, CA, USA
bray@ce.berkeley.edu

Abstract: Buildings, facilities, and lifelines that will be sited across or adjacent to active faults should be designed considering the hazards associated with earthquake surface fault rupture. Observations of surface faulting during earthquakes show how the resulting ground movements affect engineered systems. Lessons learned from these case histories can be extended to provide insight on a particular project through the use of numerical analyses that have been calibrated by field observations and experimental data. Similar to other forms of ground failure, such as mining subsidence, landslides, and lateral spreading, effective design strategies can be employed to address the hazards associated with surface faulting. These design measures include establishing non-arbitrary setbacks based on fault geometry, fault displacement, and site conditions; constructing reinforced earth fills to partially absorb underlying ground movements; using slip layers to decouple ground movements from foundation elements; and designing strong, ductile foundation elements that can resist the resulting earth pressures.

1. INTRODUCTION

Surface fault rupture has severely damaged numerous structures during shallow earthquakes that produce significant ground deformations associated with differential movement along the ruptured fault. The spectacular damage of the Shihkang Dam in Taiwan as a result of nearly 9 m of reverse fault movement through the dam during the 1999 M_w=7.6 Chi-Chi earthquake is just one example. While documentation of these dramatic cases is important, it is noteworthy that many other structures that were never designed for surface faulting did not fail when subjected to significant faulting. Both satisfactory and unsatisfactory performances of engineered systems have been observed during these events.

Avoidance of the trace of an active fault is not always a viable option. There are times when engineered systems either currently overlie active faults or must cross active faults. Sometimes the amount of fault movement is relatively minor so avoidance is not necessary. It is imperative that we develop rational design guidance for those cases when a structure needs to be evaluated and designed to accommodate the hazards associated with surface fault rupture. In this paper, key observations of surface faulting are summarized and earthquake surface fault rupture design considerations are discussed.

2. SURFACE FAULT RUPTURE HAZARDS

2.1 Principal Hazards

The principal hazards of earthquake surface fault rupture are: (a) propagation of the distinct shear rupture plane to the ground surface, (b) differential movement or angular distortion of the ground surface, and (c) extensional or compressive horizontal strains at the ground surface.

The first hazard is obvious and one that should be avoided if possible. However, engineered systems can be designed to deflect or accommodate the extreme differential ground movement that occurs across a displaced fault. If the shear rupture does not reach the ground surface, the ground will still be warped due to the underlying rock fault displacement. In these cases, the engineer should assess the amount of angular ground distortion ($\beta = \delta/L$) and lateral ground strain (ε_L) produced beneath the structure's foundation due to the underlying fault displacement. Similar to other forms of ground movement-induced structural damage (e.g., from mining subsidence or excavations), these engineering parameters can be estimated and the structure can be evaluated with regards to its capacity to accommodate the estimated levels of ground distortion and strain. Son and Cording (2005) provide rational criteria for evaluating damage potential due to the combination of angular distortion and lateral strain (Figure 1).

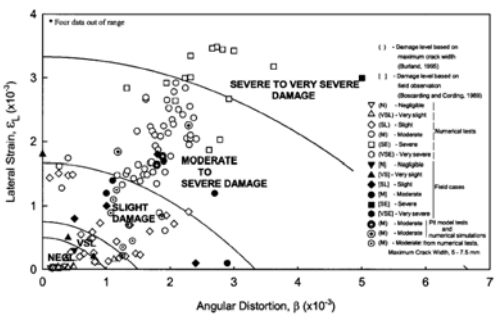

Figure 1 Relationship of Damage to Angular Distortion and Horizontal Extension Strain (Son and Cording 2005)

2.2 Important Factors

The factors that largely control the characteristics of surface faulting in the free-field are (Bray 2001): (a) the type of fault movement (reverse, normal, or strike-slip), (b) the inclination of the fault plane, (c) the amount of displacement on the fault, (d) the depth and geometry of the earth materials overlying the bedrock fault, (d) the nature of the overlying earth materials, and (e) the definition of the fault (i.e., well-established or more recently developed). Engineered systems can alter the ground deformations associated with surface faulting. Detailed descriptions of surface fault rupture are provided in Bray (1990) and Lazarte (1996), and in papers such as Bray et al. (1994a,b) and Bray (2001).

In summary, reverse faults tend to gradually decrease in dip near the ground surface (Bray et al. 1994a). Normal faults tend to refract at the soil-bedrock contact and increase in dip as they approach the ground surface. This refraction and variation of the dip of the normal fault plane may produce gravity grabens. Strike-slip faults tend to follow the almost vertical orientation of the underlying bedrock fault, although the rupture zone may spread or "flower" near the ground surface.

Ductile earth materials may accommodate significant fault movement by warping without actually developing distinct shear surfaces. Ground warping and secondary ground ruptures are most significant over the hanging wall of dip-slip faults (i.e., over the upthrown block for reverse faults and over the downthrown block for normal faults). Once shear failure develops in the overlying warped earth mass, differential movement is localized primarily to thin, distinct failure planes within the earth. However, additional ground deformation will continue to occur adjacent to the fault primarily in the hanging wall of dip-slip faults and in ductile ground adjacent to a strike-slip fault.

Differential movement across an underlying distinct bedrock fault dissipates as the shear rupture plane propagates through previously unfractured overlying soils (e.g., Bonilla 1970, Cole and Lade 1984, Bray et al. 1994a, Lazarte et al. 1994, Lazarte and Bray 1996). A deep, ductile earth mass can “absorb” a relatively minor amount of offset across the underlying bedrock fault. In these cases, a distinct surface rupture does not reach the ground surface; instead, the base movement is “spread out” over a wider zone.

The distance that a distinct bedrock rupture propagates up through overlying earth materials that were previously unfractured is primarily a function of the ductility of the overlying materials and the amount of relative displacement across the bedrock fault. Numerical simulations validated by the results of carefully performed physical model experiments and the trends found in documented field studies indicate that at a specified amount of bedrock fault displacement, the height that the shear rupture will propagate up into the overlying soil can be related to the failure strain of the soil as shown in Figure 2 (Bray et al. 1994b).

Using boundary deformation analyses, the angular distortion and lateral ground strain developed at the ground surface can be estimated. The results of these analyses with the application of engineering judgment may be used to evaluate fault setback criteria when the ground deformation is significant and to evaluate mitigation measures when the level of ground deformation can be made to be tolerable. As the ductility of the soil that overlies the bedrock fault has been found to be an important soil response characteristic, fill-reinforcement materials can be used to optimize the depth of over-excavation and the amount of earth fill required to mitigate the surficial hazards of earthquake fault rupture at a project site (Bray et al. 1993).

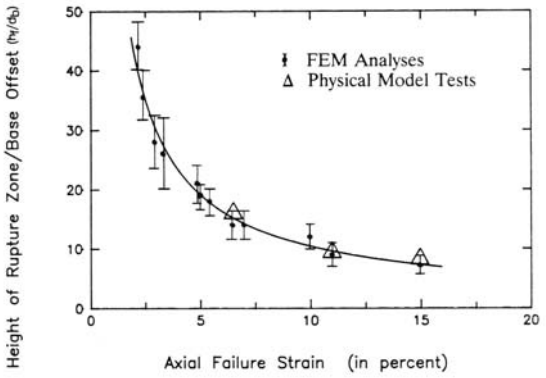

Figure 2 Normalized Height of Shear Rupture Zone in Earth Overlying Base Rock Fault as a Function of its Failure Strain (Bray et al. 1994b)

3. OBSERVATIONS FROM CASE HISTORIES

3.1 General

Specific observations of surface fault rupture serve to illustrate some of the key points that were summarized in the previous section. First, it is insightful to examine field case histories that describe free-field ground deformation resulting from earthquake faulting. Later, the interaction of surface faulting with structures will be examined.

3.2 Free-Field Ground Deformation

Differential ground movement is often concentrated within a relatively narrow zone above the bedrock fault. In many other cases, it is not. Instead, it is spread over a wide zone of distributed shearing.

Careful measurements of ground deformation associated with faulting were made as early as 1906 in the Lawson et al. (1908) report of the 1906 San Francisco earthquake. For example, a detailed survey by H. Schussler of an originally linear fence that was offset by the San Andreas fault rupture provides important insights regarding the characteristics of strike-slip faulting. At this location, Fence “C” exhibited a total lateral offset of 5.2 m over a zone about 370 m wide (Lawson et al. 1908). The survey data were used to construct Figure 3 by Bray and Kelson (2006). The primary fault strand offset Fence “C” approximately 2.2 m, or only about 43% of the total

horizontal movement, within a zone less than 12 m wide. The remaining offset was accommodated as "secondary" faulting or ground warping over a distance of about 100 m on both sides of the primary fault zone. These types of measurements illustrates the characteristics of the free-field ground deformation associated with a significant strike-slip fault movement. They can be used to assess whether engineered systems, such as pipelines, can withstand a fault rupture event.

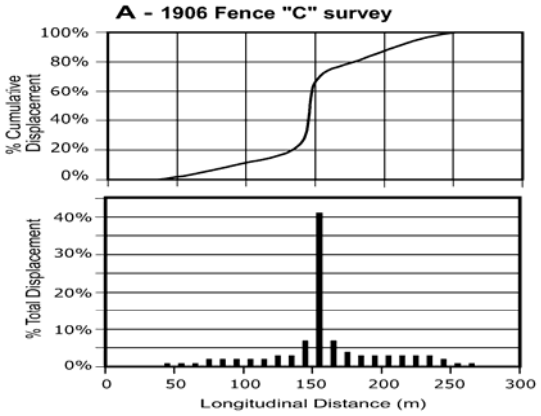

Figure 3 Ground Deformation across the San Andreas fault movement in 1906 as interpreted from the detailed survey of Fence "C" by Schussler in Lawson et al. (1908) (Bray and Kelson 2006)

A more recent example is the surface fault rupture zone produced by the 1992 (M_w = 7.3) Landers, California earthquake. It was often expressed as a broad shear zone, hundreds of meters wide with numerous individual fractures (Lazarte et al. 1994). Although the majority of relative fault displacement often occurred within a zone only 10 m wide or less, significant fractures and ground movements (on the order of a few centimeters, which is sufficient to be of engineering interest for many projects) were observed over a zone 100 m wide or more.

The stress-deformation response of the soil that overlies a ruptured fault was shown to be important. For example, the loose, compressible, wind-blown sand dune shown in Figure 4 spread the distinct bedrock displacement of several meters across a much wider and diffused zone of shearing.

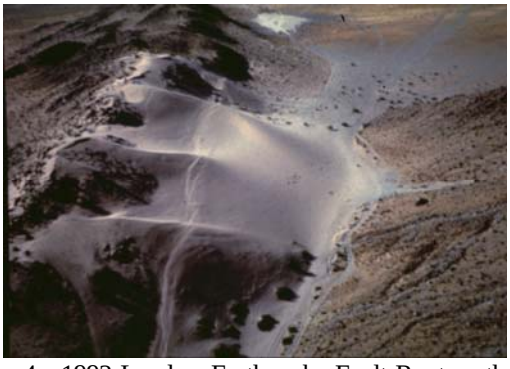

Figure 4 1992 Landers Earthquake Fault Rupture through a Sand Dune (photo by E. Gath).

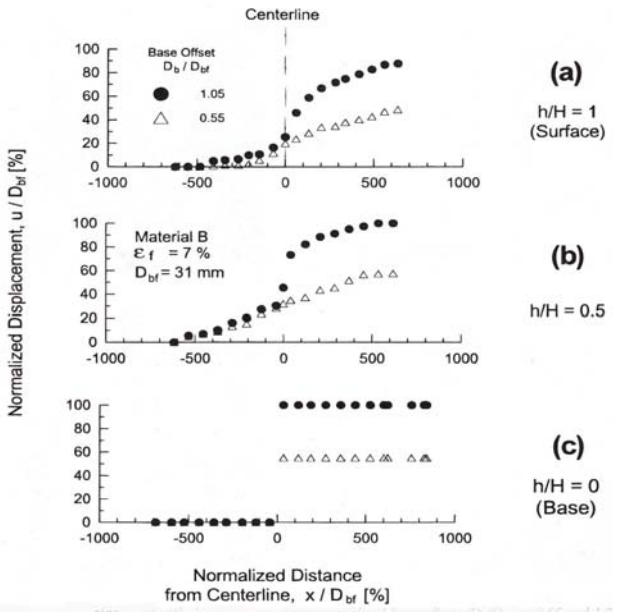

Figure 5 Distribution of Horizontal Displacement with Depth for Increasing Normalized Base Offsets: (a) Surface, (b) Mid-Height, and (c) Base of Model

The development of the shear rupture zone in a ductile, saturated clay deposit overlying a distinct bedrock fault rupture is illustrated in the experiments performed by Lazarte and Bray (1996). In this experiment, a soft mixture of kaolinite and bentonite (3:1) was placed atop a split rigid base, and the right side of the base was displaced horizontally while the left side was kept stationary. Relative displacement was measured at the base of the model and observed at the top of the model. A string-line device at mid-height within the clay allowed the deformation pattern within the clay to be tracked.

As shown in Figure 5, at a base offset of 55% of that required to shear through the height of the clay, the ground deformed in a simple shear mode in the upper half of the clay deposit, even though the distinct shear rupture was imposed at the base of the model. At a larger base offset a distinct shear rupture developed in the middle of the clay. Once this shear developed, the rate of additional warping of the surrounding clay was greatly reduced. A sufficient amount of base deformation was induced so that the distinct shear rupture emerged eventually at the surface of the clay.

The widespread warping of the ground overlying the upthrown block of the Chelungpu reverse fault offset during the 1999 Chi-Chi earthquake is another example of the significant amount of deformation that can occur off the primary trace of a major fault. The warped rice paddies shown in Figure 6 were originally relatively level. Although significant differential movement occurred across the primary trace it can be seen that considerably more vertical ground movement developed in the soil above the hanging wall of this reverse fault. Whereas a setback distance of 15 m might have been adequate on the undeformed ground on the footwall side of this shallow reverse (thrust) fault, it

would not have been adequate on the hanging wall. Thus, setback criteria should be based on geologic principals rather than be based on arbitrary, standardized regulations.

Figure 6 Ground Warping Associated with the 1999 Chi-Chi Earthquake (photo by N. Sitar)

Figure 7 Lack of Secondary Ground Deformation on the Footwall of the Normal Fault Movement near Golcuk during the 1999 Kocaeli Earthquake

The two-story building shown in Figure 7 has no discernable damage (even the glass windows are not broken), although it is situated less than 1 m off the primary trace of the normal fault rupture that occurred in this area during the 1999 (M_w = 7.5) Kocaeli, Turkey earthquake. Again, the ground deformation is not uniformly distributed on each side of a dip-slip fault, so setback criteria should not be the same on each side of a dip-slip fault.

3.2 Effects on Structures

The manner in which surface faulting interacts with structures is illustrated through numerous well-documented case histories. Recent earthquake surface fault rupture events in highly urbanized areas have provided exceptionally insightful observations. For example, at the northern end of the Chelungpu fault in Taiwan, several cases that illustrate the effects of faulting on structures were documented. The four-story reinforced concrete structure shown in Figure 8 was uplifted approximately 4.5 m across its width, which rendered the building unserviceable. However, everyone in the building was able to evacuate. Thus, the life safety objective of most building codes was achieved.

Figure 8 Reinforced Concrete Building Tilted by about 4.5 m of Reverse Fault Displacement without Collapsing

In this case, the reinforced concrete shear walls of the building worked in combination with a reportedly well-reinforced 0.6 m-thick reinforced concrete mat foundation to allow the building to tilt excessively in a nearly rigid body mode. The tilting led to some internal deformation of the building, but the occupants were able to walk down the stairs of the building without incident following the event. At the time that this picture was taken, which is several weeks after the event, the author was still able to walk up the stairs and within the building. Thus, a robust structural system with stiff, high-strength shear walls and a thick reinforced concrete foundation can undergo significant ground deformation associated with surface fault rupture without collapsing.

The two-story building described in Figure 9 by Lettis et al. (2000) is an example of a structure with a robust foundation (i.e., a 30 cm-thick mat overlain with 1 m deep grade beams in a grid layout), which was subjected to significant differential ground displacement, that was largely undamaged. The North Anatolian fault displaced 3 to 3.5 m underneath this structure. It moved the structure some, but there was no observable damage in the building, although its structural system is relatively weak and brittle (i.e., reinforced concrete frame with in-filled walls).

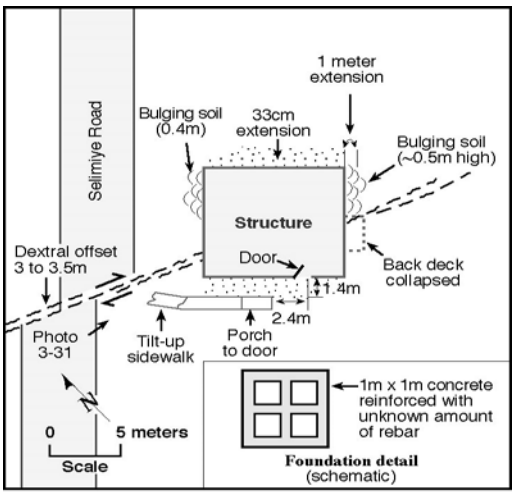

Figure 9 House with Robust Foundation is Not Damaged Significantly as a Result of over 3 m of Right-Lateral Fault Displacement (Lettis et al. 2000)

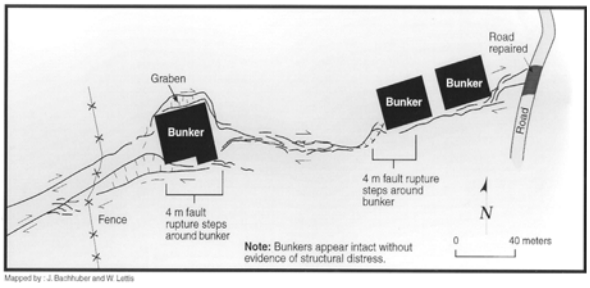

(a)

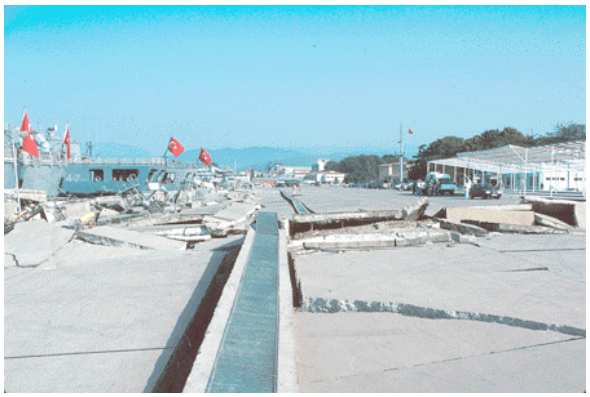

(b)

(c)

Figure 10 Different Responses to Surface Fault Rupture: (a) Heavily Reinforced Concrete Bunkers that Underwent over 4 m of Strike-Slip Offset without Cracking (Lettis et al. 2008); (b) Pile-Supported Wharf Damaged by 2.4 m of Strike-Slip Offset; and (c) Tree Trunk Split and Telephone Pole Undamaged by Surface Faulting (Ulusay et al. 2001)

If significant differential ground movements are produced by surface faulting under a structure, it is preferred that the structure not be "rooted" into the ground. The heavily reinforced concrete bunkers shown in Figure 10a are internally very strong, but they are not fixed into the ground. The shear rupture in this case is more likely to move around the relatively stiff and strong inclusion of these bunkers than to break them. Conversely, the pile-supported wharf structure shown in Figure 10b is fixed into the ground surrounding the primary trace of the fault. As the ground on each side of the trace of the fault displaces relative to each other, the piles go with the ground, and nearly all of the differential ground movement is transferred up into the deck of the wharf. The deck is not sufficiently strong to withstand the large forces induced through the fault movement, so it is heavily damaged as a result of surface fault rupture.

Useful analogies to these different structural responses are the tree and telephone pole responses shown in Figure 10c. The tree in the left photograph is rooted into the ground on each side of the fault. The telephone pole in the right photograph is not rooted into the ground on each side of the fault. Whereas there are numerous observations in the literature of trees that are well rooted on both sides of a displaced fault splitting up their trunk, there are no cases of telephone poles splitting due to surface faulting. The telephone pole, not being anchored into the surrounding ground, may displace as a rigid body, but it does not undergo internal deformation. The tree trunk is split, because its foundation of many strong roots on each side of the fault force all of the differential ground deformation to be concentrated within it.

Therefore, the foundation of a building has a large influence on its structural response to surface faulting. Structures that are tied to the ground (i.e., pile foundations) will undergo the full relative displacement of the ground movements; whereas structures that are allowed to move relative to the ground (i.e., a shallow reinforced concrete mat) will undergo rigid body movement, but the structure will be isolated from much of the damaging effects of the differential ground movements.

A side-by-side comparison of two different structural systems undergoing similar ground deformation resulting from surface fault rupture with different performances is shown in Figure 11. The 8 m-diameter, 0.3 m-thick unreinforced brick forebay was heavily damaged by the distributed ground deformation between the main-trace of the San Andreas fault and an auxiliary fault to the west of it (Lawson et al. 1908). It was deformed into a 9 m by 6.5 m oval. This response can be contrasted to that exhibited by a rectangular-shaped concrete forebay that was constructed of three compartments, each 0.76 m by 0.76 m in plan. The relatively stiff and strong concrete forebay was undamaged, even though it was located about the same distance off of the main-trace and was intersected by the auxiliary fault located to the west of the main-trace.

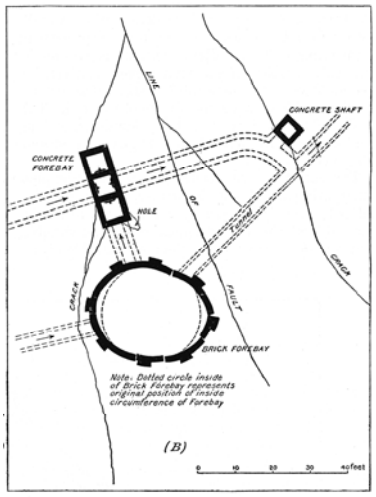

Figure 11 Interaction of Two Structures Situated Astride the San Andreas Fault (Lawson et al. 1908)

Figure 12 Suspension Walkway Bridge Undergoing Relative Movement of its Abutments due to Fault Movement (photo by C. Roblee)

If a long structure or lifeline must traverse a fault that could undergo surface rupture, it may be prudent to design the system to respond flexibly to the differential ground movement. The relative ground displacement that occurs along a line oriented perpendicular to the strike of a strike-slip fault, for example, as shown in Figure 3, must be transferred to a long structure that is aligned along this line if it is eventually locked into the ground at two distant points from the fault trace. In these cases, the structure cannot accommodate the ground deformation through a rigid body mode of deformation and it must be able to deform internally without collapse. The performance of the suspension bridge shown in Figure 12 is an excellent example of a flexible system that can deform internally between its two anchorages without falling. The Trans-Alaskan pipeline was thoughtfully designed when it crossed a major fault (Cluff et al. 2003). The pipeline was moved out of the ground and placed on Teflon-coated supports with sufficient slack to accommodate the anticipated surface fault displacement. It performed exceptional well during the 2002 Denali earthquake. The design was sufficiently flexible to allow the system to withstand the ground movements associated with surface fault rupture without collapsing.

4. DESIGN CONSIDERATIONS

4.1 General

There are four principal means of mitigating the potential hazards associated with earthquake fault rupture: (a) land use planning, (b) engineering geology, (c) geotechnical engineering, and (d) structural engineering. The California Alquist-Priolo Earthquake Fault Studies Act has served as a model for mitigation of this hazard through avoidance. Although it took damage from surface faulting resulting from the 1971 San Fernando earthquake to motivate politicians to enact it, the A-P Act's underpinnings result from the post-1906 San Francisco earthquake mindset (Bray and Kelson 2006). Echoing the sentiments of many scientists and engineers, Humphrey states: *"It is a generally accepted fact that no structure could have withstood the stresses produced by the movement of the earth at the 'fault trace' …"* (Gilbert et al. 1907). The author prefers the more reasonable approach delineated by Derleth: *"If fortunately located … a structure on or near a fault line may not be seriously crippled … Where structures must be built upon treacherous ground or near fault lines, no expense should be spared for good materials, high grade workmanship, and intelligent design."* (Jordan 1907). Through field observations, physical model studies, numerical analyses, and the application of engineering judgment, the mitigation measures summarized in Table 1 are offered as a rational means for achieving "intelligent design."

Table 1 Mitigation Measures for Engineered Systems

LAND USE PLANNING
· Avoid areas with the potential for surface fault rupture
ENGINEERNG GEOLOGY
· Identify and avoid primary faults · Establish non-arbitrary setbacks based on fault and ground conditions · Estimate amount and type of potential fault displacement
GEOTECHNICAL ENGINEERING
· Construct ductile earth fills to spread out fault displacement · Install soil reinforcement · Use slip layers to decouple ground movements from foundation · Keep the base of all foundation elements at the same elevation · Avoid protrusions that would act like cleats to lock the building into the ground · Place compressible materials adjacent to walls and utilities · For dams, use thick, ductile clay cores, thick upstream "crack-stopper" zones, thick downstream filters zones, thick chimney drains, and rockfill zone at the downstream face · Increase freeboard, minimize reservoir height, and enlarge crest width · Site outlet works and spillway off the fault trace
STRUCTURAL ENGINEERING
· Design strong, ductile foundations, such as thickened reinforced mat foundations, waffle slabs, and post-tensioned slabs · Do not use piles or piers that tie structure into the ground · Design structure to be flexible and with isolation joints · Install "catcher bents" or ties for bridge spans that must cross over faults

4.2 Land Use Planning

The intent of the Alquist-Priolo Act of 1972 was to avoid the surface fault rupture hazard by prohibiting the building of structures with human occupancy across the trace of an active fault. To provide some level of conservatism, the Act established the "infamous" 50 ft (15 m) setback criterion. The Act required that an area within this distance of an active fault shall be presumed to be underlain by active branches of that fault unless proven otherwise. Many scientists, engineers, and regulators forget the last part of this sentence (i.e., "unless proven otherwise"). If a comprehensive geologic study demonstrates that the ground adjacent to an active trace does not contain active branches of that fault trace then a structure may be sited directly adjacent to the primary trace. However, most engineers and scientists prefer to setback at least a couple of meters from the trace of a major active fault.

One of the primary deficiencies of the Alquist-Priolo Act is that it treats all active faults the same. Is it reasonable to place the primary trace of the San Andreas fault, which could have meters of movement across it, in the same category as an unnamed minor bending moment fault that may have moved once in the last 11,000 years an amount on the order of a centimeter or two? If land-use regulators allow engineers to mitigate major landslides, mining subsidence, and large liquefaction-induced lateral spreads, why would they not also allow engineering mitigation of the minor ground deformations resulting from movements along a minor fault? Moreover, it is sometimes impossible to avoid all active faults in all cases. It is time to employ a more rational, consistent approach when addressing the earthquake surface fault rupture hazard.

4.3 Engineering Geology

The success of the remaining mitigation approaches depends primarily on a sound interpretation of the geology on regional and project level scales. The importance of a comprehensive geologic study by a well-trained and highly experienced team of engineering geologists cannot be overstated. The results of the geologic study provide the key fault parameters such as fault type, fault geometry, and the amount, sense, and distribution of potential ground movement associated surface fault rupture. Best estimates of each should be provided with upper and lower estimates at about the 84% and 16% levels of probability to capture the inherent uncertainty of this complex phenomenon. Surface faulting, however, is generally no more complex than other earthquake hazards, such as ground shaking, liquefaction, and landsliding. These other hazards are currently characterized through a probabilistic seismic hazard assessment or at least through a pseudo-probabilistic approach that provides some assessment of the variability in the seismic demand parameter. Correspondingly, the surface fault rupture hazard should not be characterized only through a "worst" case deterministic assessment.

As discussed previously, countless observations of surface faulting prove that the ground deformations associated with surface faulting are not equally distributed on each side of the fault. Thus, the engineering geologist should work toward interpreting the geologic information to establish non-arbitrary setbacks based on specific site, fault, and soil characteristics. Although the profession requires continual enhancement of its understanding of the complex fault rupture phenomenon, sound judgment, coupled with reasonable interpretations of surficial geology and crack propagation theory, can be applied to develop earthquake-resistant designs without resorting to arbitrary setback criteria. In most cases, an accurate record of the likely characteristics of a future fault displacement is written into the local geology. Through sound mapping, trenching, and other tools, the engineering geologist can provide a reasonable description of the amount and type of potential fault displacement at the site.

4.4 Geotechnical Engineering

The geotechnical engineer plays an integral role in what should be a multi-disciplinary team of experienced and skilled engineers and scientists that evaluates the surface fault rupture hazard and develops effective design measures.

One of the geotechnical engineer's first approaches is typically to use the inherent capability of soil to "locally absorb" and distribute distinct bedrock fault movements. Previous field, physical model, and numerical studies (e.g. Bray et al. 1994a,b) have found that differential movement across distinct bedrock faults dissipates as the shear rupture plane rises through overlying fills, especially if the fills are reinforced with geosynthetics (Bray et al. 1993). The relative displacement across a distinct bedrock fault is spread across a wider zone in the overlying fill. This spreading of the localized bedrock fault displacement over a wider zone at the ground surface reduces angular distortion and lateral ground strain at the foundation level. Hence, ductile compacted fill or reinforced fill may be used at a site to mitigate the hazards associated with earthquake fault rupture.

There may be times, however, when the geotechnical engineer may consider using a weak soil element, such as a bentonite slurry wall built above a fault trace, to localize most of the differential fault movement across a narrow zone. This would enable the developer to possibly utilize more land by requiring narrower setbacks. The distinct base rock shear dislocation and the associated warping of the adjacent rock will eventually be expressed at the ground surface. The geotechnical engineer can help access the amount and distribution of ground movement and either spread it out over a wider area or localize it to a narrow, more confined zone. This should be part of the design process.

Mat foundations and interconnected spread footings, which should all be at the same elevation, can be constructed atop a double layer of smoothly laid-out polyethylene (plastic) sheets sandwiched between layers of clean coarse sand to fine gravel to "decouple" anticipated ground deformation from the foundation elements. This defensive design measure will minimize the transfer of horizontal strains in the ground below the foundation to the structural foundation elements. Trenches excavated to construct

grade beams and underground utilities can be backfilled with loose soil or styrofoam to reduce lateral earth pressures that can develop on these elements.

Many of these geotechnical design measures have been used successfully in areas subject to ground deformations associated with mining subsidence. There are many good references that describe these approaches (e.g., Kratzch 1983). Potential ground deformation beneath a structure from mining subsidence, excavations, or expansive soils, for example, are routinely accommodated in foundation engineering. Most of these approaches can be employed to address the earthquake surface fault rupture hazard as well.

Geotechnical engineering plays an integral role in developing prudent design measures in earth dams that are built atop or near active faults. Some of these measures are listed in Table 1. The reader is referred to papers such as Sherard et al. (1974) and Bray et al. (1992) for a thorough discussion of these issues.

4.5 Structural Engineering

The constructed facility can be designed by an experienced structural engineer to undergo some limited amount of ground deformation without collapse or significant structural damage. Again, the design of structures subjected to ground deformation resulting from mining subsidence (e.g., Kratzsch 1983) or other forms of ground deformation are generally applicable. Similar to observations of foundation performance undergoing fault rupture, mining subsidence studies indicate that foundation elements should be heavily reinforced to improve ductility. The maximum allowable angular distortion for conventional structures is approximately 1/400, however, specially designed and built structures can tolerate significantly more ground distortion without posing a life safety risk to the building's occupants. The maximum allowable horizontal tensile ground strain below buildings is on the order of 0.3%, but as discussed previously (e.g., Figure 1), it is the combination of angular distortion and lateral strain of the ground, after considering that portion that will be transmitted up into the building's foundation, that is important.

The use of foundation elements that tie the structure into the ground should be avoided. Pile or pier foundations would likely force the superstructure to undergo the full amount of differential ground displacement across the building's footprint. Likewise, a two-level foundation design would likely "lock" the building into the ground. The foundation elements should be designed to minimize the transfer of ground strain into the superstructure.

Post-tensioning the floor slab will improve its ability to bridge over irregular ground deformation of limited extent. However, there is likely no mitigation method (other than avoidance) that is more important than the use of a well-reinforced thickened mat foundation. There are numerous examples of thick reinforced concrete foundations that undergo significant ground deformation without collapse. The use of waffle slabs or an integrated foundation of footings interconnected with substantial grade beams may also provide the foundation stiffness desired to bridge over gaps and span warped ground.

In designing the structure, care should be also given to the selection of its structural system. A redundant, robust structural system can work with the building's foundation elements to reduce internal distortions and enable the structure to respond to ground deformations in primarily a rigid body mode.

In those cases, where the structure and its foundation cannot be designed to withstand the anticipated ground deformation, isolation joints can be employed to control deformation within the structure. Flexible structures are also inherently more stable than stiff long structures that must accommodate differential ground movements across a wide zone. Lastly, if large ground movements are possible, then systems can be installed to keep system components from falling, such as "catcher bents" and "ties."

5. CONCLUSIONS

Earthquake surface fault rupture is an important hazard that must be addressed in areas where major faults may break the ground surface or underlying bedrock faults may produce significant ground warping. Recent major earthquakes have reminded the profession and the public of the potentially devastating effects of surface fault rupture on structures and lifelines. Conversely, the fact that relatively simple structures located across major fault movements were able to survive ground fracturing in terms of life safety suggests that we can design structures to withstand ground deformations associated with surface rupture.

Field observations, experiments, and analysis can be employed to evaluate the hazards associated with surface faulting and to develop effective mitigation measures. Numerous illustrative cases show how differing ground conditions alter the surface expression of faulting and how surface fault rupture affects engineered systems, such as pipelines, earth dams, and buildings. Case histories have shown that the response of engineered systems can be devastating or acceptable, depending on geologic relations and engineering design. Engineering geology in concert with sound engineering practice can be employed to evaluate the hazards associated with surface faulting and to develop reasonable mitigation measures.

These mitigation measures include establishing non-arbitrary setbacks based on fault geometry, fault displacement, and the overlying soil; constructing reinforced earth fills to partially absorb and spread out the underlying ground movements; using slip layers to decouple ground movements from foundation elements; employing foundation systems that do not force the underlying ground movements up into the superstructure; and designing strong, ductile foundation elements that can accommodate some level of deformation without compromising the functionality of the structure.

In addressing the surface fault rupture hazard, the potential pattern of ground deformation should be developed through the use of detailed mapping and trenching at the site.

Measured patterns of surface fault-induced ground deformation from similar types of faulting from past events offer useful insights to complement site-specific studies. Having characterized the likely patterns of expected ground deformation, engineers can site systems across the fault in an optimal manner and design it to accommodate fault-induced ground movements. Building strong, ductile structural foundation elements that can accommodate some level of ground deformation and isolating the superstructure from much of the underlying ground movement are prudent design measures. It is not prudent to tie structures into the ground with foundation elements such as piers and piles.

Acknowledgements:

Partial support for the research efforts presented in this paper was provided over the years by the David and Lucile Packard Foundation and the National Science Foundation. Many students and colleagues have contributed to the author's understanding of earthquake surface fault rupture, and the sharing of their expertise and insights is greatly appreciated. I would also like to thank the Japan Ministry of Education, Culture, Sport, Science, and Technology (MEXT) for establishing the Center for Urban Earthquake Engineering (CUEE) in the Tokyo Institute of Technology, which is providing support for this conference.

References:

Bonilla, M. G. (1970) "Surface Faulting and Related Effects," in Earthquake Engineering, Weigel, R. L., ed., New Jersey, Prentice-Hall, 47-74.

Bray, Jonathan D. (1990) "The Effects of Tectonic Movements on Stresses and Deformations in Earth Embankments," Dissertation, PhD, UC Berkeley, 414.

Bray, J. D., R. B. Seed and H. B. Seed (1992) "On the Response of Earth Dams Subjected to Fault Rupture," *Proceedings of Stability and Performance of Slopes and Embankments - II*, 608-624.

Bray, J. D., A. Ashmawy, G. Mukhopadhyay and E. M. Gath (1993) "Use of Geosynthetics to Mitigate Earthquake Fault Rupture Propagation Through Compacted Fill," *Proceedings of the Geosynthetics '93 Conference*, 1, 379-392.

Bray, J. D., R. B. Seed, L. S. Cluff and H. B. Seed (1994a) "Earthquake Fault Rupture Propagation through Soil," *Journal of Geotechnical Engineering*, ASCE, 120(3), 543-561.

Bray, J. D., R. B. Seed and H. B. Seed (1994b) "Analysis of Earthquake Fault Rupture Propagation through Cohesive Soil," *Journal of Geotechnical Engineering*, ASCE, 120(3), 562-580.

Bray, J. D. (2001) "Developing Mitigation Measures for the Hazards Associated with Earthquake Surface Fault Rupture," in *Seismic Fault-Induced Failures – Possible Remedies for Damage to Urban Facilities*, Japan Soc. Prom. Sci., K. Konagai, Ed., Univ. of Tokyo, Japan, pp. 55-79.

Bray, J. D. and Kelson, K. I.. (2006) "Observations of Surface Fault Rupture from the 1906 Earthquake in the Context of Current Practice," *Earthquake Spectra*, Earthquake Engineering Research Institute, Vol. 22, No. S2, pp. S69-S89.

Cluff, L.S., R.A. Page, D.B. Slemmons, and C.B. Crouse (2003) "Seismic Hazard Exposure for Trans-Alaska Pipeline," Proc. 6th U.S. Conf. on Lifeline Earthquake Engineering, Long Beach, CA, TCLEE, ASCE.

Cole, D. A., Jr. and Lade, P. V. (1984) "Influence Zones in Alluvium Over Dip-Slip Faults," *Journal of Geotechnical Engineering*, ASCE, 110(5), 599-615.

Gilbert, G. K., Humphrey, R. L., Sewell, J. S. and Soule, F. (1907) "The San Francisco Earthquake and Fire of April 18, 1906 and their effects on structures and structural materials," U.S. Geological Survey Bulletin 324, Washington D.C.

Jordan, D.S., Ed. (1907) "The California Earthquake of 1906," A.M. Robertson, San Francisco, CA.

Kelson, K., Bray, J., Cluff, L., Harder, L., Kieffer, S., Page, W., Perkins, W., Rix, G., Roblee, C., Sitar, N., Wells, D., Wright, R., and Yashinsky, M. (2001) "Fault-Related Surface Deformation," Chapter 3 of the Chi-Chi, Taiwan, Earthquake of September 21, 1999 Reconnaissance Report, in *Earthquake Spectra* Journal, Suppl. A to Vol. 17, EERI, 2001, pp. 19-36.

Kratzsch, H. (1983) "Mining Subsidence Engineering, Springer Verlag," Berlin, 543.

Lawson, A.C., et al. (1908) "The California Earthquake of April 18, 1906," *Report of the State Earthquake Investigation Commission*, Carnegie Institution of Washington, Vols. I & II, Washington D.C.

Lazarte, C. A. (1996) "The Response of Earth Structures to Surface Fault Rupture," Ph.D. Thesis, UC Berkeley.

Lazarte, C. A, Bray J. D., Johnson A. M. and R. E. Lemmer (1994) "Surface Breakage of the 1992 Landers Earthquake and Its Effects on Structures," *Bulletin of the Seismological Society of America*, 84(3), 547-561.

Lazarte, C. A. and Bray, J. D. (1996) "A Study of Strike-Slip Faulting Using Small-Scale Models," *Geotechnical Testing Journal*, American Society for Testing and Materials, 19(2), 118-129.

Lettis, W., Bachhuber, J, and Witter, R., with Barka, A., Bray, J., Page, W., and Swan, F., "Surface Fault Rupture," Chapter 2 of the Kocaeli, Turkey Earthquake of August 17, 1999 Reconnaissance Report, in *Earthquake Spectra* Journal, Suppl. A to Vol. 16, EERI, 2000, pp. 11-53.

Sherard, J. L., Cluff, L. S., and Allen, C. R. (1974) "Potentially active faults in dam foundations," *Geotechnique*, **24**, 367-427.

Son, M. and Cording, E. J. (2005). "Estimation of Building Damage Due to Excavation-Induced Ground Movements." *ASCE Journal of Geotechnical and Geoenvironmental Engineering*. 131(2): 162-177.

Ulusay, R., Aydan, O., and Hamada, M. (2001) "The behaviour of structures built on active fault zones: examples from the recent earthquakes of Turkey," in *Seismic Fault-Induced Failures – Possible Remedies for Damage to Urban Facilities*, Japan Soc. Prom. Sci., K. Konagai, Ed., Univ. of Tokyo, Japan, pp. 1-26.

Sixth International Conference on Urban Earthquake Engineering
March 3-4, 2009, Tokyo Institute of Technology, Tokyo, Japan

EARTHQUAKE ENGINEERING AS A COMPONENT OF SUSTAINABLE DEVELOPMENT

Stephen A. Mahin[1)]

1) Byron and Elvira Nishkian Prof. of Structural Engineering, Univ. of California, Berkeley, CA USA
mahin@berkeley.edu

Abstract: The primary goal for seismic-resistant design of ordinary structures is to prevent collapse and loss of life. Thanks to extensive experimental, theoretical and computational research, engineers are able to design wide array of structures capable of withstanding numerous cycles of inelastic deformation during strong earthquakes with minimal probability of collapse. However, this approach, while providing a high degree of life safety, is expected to result in substantial structural and nonstructural damage. The economic and social impacts of this anticipated damage could be far-reaching and profound; and likely contrary to the basic principles of sustainable development increasingly advocated by many owners, architects and policymakers. However, a range of quantitative tools, such as performance-based evaluation, and advanced structural system concepts, can easily extend current earthquake engineering design practices consistent with and supportive of emerging trends related to sustainable design. This paper discusses some of the underlying issues and highlights several approaches to achieve structural systems that are more sustainable.

1. INTRODUCTION

A large ductility capacity is generally required of structures located in regions of high seismicity to ensure economical designs with adequate protection against collapse. For a design level or larger earthquake, this approach results in significant damage to structural and other elements, and permanent offsets -- damage that can impede post-event functionality and require costly, dangerous and disruptive inspections, repairs and, in some cases, demolition. Thus, a challenge increasingly posed to earthquake engineers is to maximize post-event operability and minimize repair costs and other impacts, while protecting public safety.

One approach to this problem is to design stronger and stiffer structures, thereby limiting inelastic action and reducing displacements. This approach increases the quantity of materials required, but may permit use of simpler and cheaper construction details. Since many structures are constructed on poor soil conditions, the need for greater superstructure strength and stiffness can disproportionately increase the complexity and cost of foundations. Stiffening and strengthening a structure would also likely increase accelerations, increasing damage to nonstructural elements, or necessitating more costly nonstructural elements and details.

Another approach is through performance-based design where the various performance objectives are characterized in terms of loss of life, disruption to operation, and direct and indirect losses. Engineering principles and risk management concepts are applied to evaluate how well stated goals are achieved. While this approach provides a powerful quantitative tool for assessing a particular structure, and comparing the likely performance of alternative structures, performance-based engineering as currently used is more of an evaluation technique than a coherent design strategy.

Similar problems are encountered in the planning of critical infrastructure systems and the architectural design of individual structures. The holistic framework articulated in 1987 by the UN's Brundtland Commission is increasingly used to address such issues [Brundtland, 1987]. This framework advocates "meeting the needs of present generations without compromising the ability of future generations to meet their needs." Numerous approaches to sustainable development have evolved from this report, but nearly all emphasize maintaining a balance among resource efficiency, environmental responsibility, well being of occupants, and community sensitivity. To many, sustainable design or so-called green construction focuses on selection of materials and energy efficiency, but as applied in the context of earthquake engineering, includes: durability and longevity; reparability, particularly following an earthquake; more efficient and lower impact construction; efficient use of materials through improved materials, more efficient design methods, and more efficient structural systems and layouts; consideration of material re-use and disassembly for reuse; use of recycled materials; integration of structural forms to help achieve the needs of other disciplines; and reducing the impacts of abnormal events such earthquakes by minimizing the need for repair and disruption of service [Kren, 2006].

Efforts are being carried out by engineers

throughout the world to realize these objectives. For example, precast and prefabricated construction may reduce environmental impacts, reduce disruption caused by shoring and false work, and speed construction. Greater use is being made of fly ash, recycled steel and concrete, and high performance materials. Several investigators have examined replaceable plastic hinges to facilitate post-earthquake repair. Several other approaches to earthquake-resistant design appear ideal when considered from the perspective of sustainable design.

In this paper, three approaches under investigation at UC Berkeley are highlighted that permit durable structures to respond to earthquakes in a controlled nonlinear manner (resulting in cost savings), but that require less or no repair, and suffer only small residual displacements, following an major earthquake. These relate to (1) seismically isolated structures, (2) structures that rock on spread footings or pile foundations, and (3) fixed based structures that self-center as a result of the presence of unbonded longitudinal post-tensioning. Each approach is shown to be effective in reducing design forces compared to designing the structure to remain elastic, and each reduces post-earthquake residual displacements and damages due to drift and acceleration.

2. SEISMIC ISOLATION

Seismic isolation has been widely used to retrofit existing seismically vulnerable structures and to design major new ones. This technology is especially easily to implement for bridges where decks are attached to the supporting columns and abutments via elastomeric or other bearings. To develop improved understanding of the behavior of seismically isolated bridges and gain confidence in design methods, a series of tests and analyses of isolated bridges has been recently completed at Berkeley (e.g., Anderson, 2003). These studies include a variety of different isolator types, bridge dynamic properties, and earthquake characteristics. Three generic types of isolator bearings were considered, including lead rubber bearings, high damping bearings, and friction pendulum bearings. Extensive studies were made to characterize bearings subjected to 3D loading, and to assess the effects of aging. Bridge systems tested include one and two span bridges having substructure periods ranging from nearly zero to more than 2 seconds. More than a dozen bridge configurations were tested to assess the effects of mass eccentricity, stiffness eccentricity, bridge substructure period, bearing type, in-situ variations in bearing properties, yielding of supporting columns, and earthquake excitations. One of the bridge models tested appears in Fig. 1.

Such experimental results were used to develop improved numerical models of the isolation bearings, and to assess the sensitivity of system response to different design parameters, and to uncertainties in these parameters. Various provisions of the AASHTO Guideline Specification [1999] such as those related to treatment of bidirectional excitations were assessed in Anderson and Mahin [2003, 2004]. Overall, good performance was noted for all of the isolated systems studied.

Fig. 1 Shaking Test specimen of simple supported bridge with different substructure stiffness

It has been noted that the design of isolated buildings and bridges can be problematic due to the apparent over-conservativeness of some design provisions, and also because of challenges encountered when designing isolated systems to resist intense near-field ground motions. To resist large near-fault ground shaking, relatively large and strong isolators are often necessitated to control displacements and maintain isolator stability. In these cases, isolators may not act effectively, especially for small events, and require relatively large design forces and trigger excessive accelerations in the superstructure [Morgan and Mahin, 2007]. Thus, efforts are underway to improve isolation for small events, limit displacements for larger events, and reduce floor accelerations.

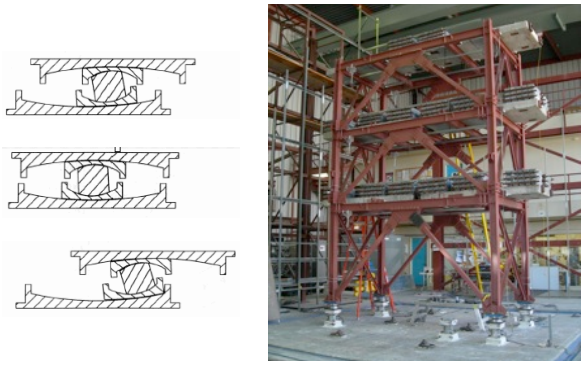

Fig. 2 Triple pendulum slider and test specimen

Several approaches are being pursued at Berkeley, including novel combinations of elastomeric isolators and nonlinear viscous dampers. Another promising approach is the newly developed Triple Pendulum Slider

[Earthquake Protection Systems, 2007]. This device has three independent pendulum mechanisms (Fig. 2). By strategically selecting friction coefficients for each mechanism, hysteretic characteristics can be optimized for occasional, rare and very rare events. Tests (Fig. 2) and analyses demonstrate that the devices can be designed to achieve about the same isolator displacements for a large event, but with smaller drifts and accelerations in the superstructure and with a far greater degree of isolation during smaller events (Fig. 3) [Morgan and Mahin, 2007].

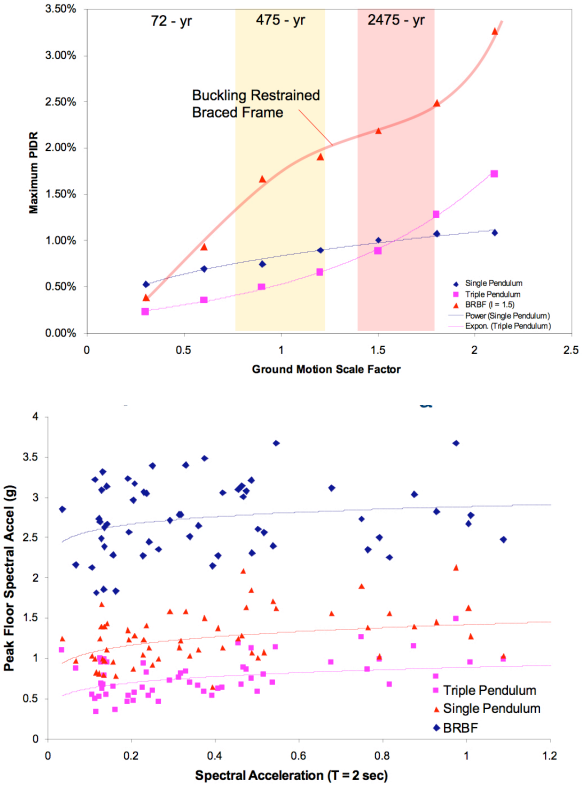

Fig. 3 Interstory drift ratio and floor spectral acceleration for isolated structures with TPS and conventional bearings and buckling restrained braced frames (BRBF) [Morgan *et al*, 2007]

3. ROCKING FOUNDATIONS

Most structures are designed to have a fixed base. For example, conventional bridge structures residing on competent soil are typically designed with rectangular spread footings proportioned to allow for a fixed base response. This generally leads to inelastic behavior at or near the column to footing interface during design level earthquakes. This mode of behavior dissipates input energy, but results in damage to the column and potential permanent lateral displacements. By permitting the bridge piers to rock or uplift on the supporting soil introduces other modes of nonlinearity (rocking) and energy dissipation (soil inelasticity). Explicit consideration of rocking as an acceptable mode of response can reduce required footing sizes. Also, the simultaneous rocking of a properly designed foundation and flexural deformation of the supported column appears to eliminate, or substantially reduce, damage in the column and residual displacements in a bridge with moderate to long fundamental periods following a major earthquake. Of the three approaches discussed in this paper, rocking of bridge foundations relies the most on conventional design and construction methodologies.

Many previous studies have investigated the benefits of allowing a column and footing system to uplift (e.g., [Chopra and Yim, 1985; Housner, 1963]). Analytic studies of bridge column response to one horizontal earthquake component have illustrated the combined effects of rocking and column flexural displacements [Alameddine and Imbsen, 2002; Kawashima and Hosoiri, 2003]). Recent earthquake simulator tests [Sakellaraki et al, 2005] on small-scale steel columns subjected to unidirectional excitation demonstrate the feasibility and benefit of rocking in resisting seismic effects.

Because of the potential economic and performance benefits of using rocking in new construction, and the desirability of developing reliable analysis procedures for evaluating existing bridge structures, a series of experimental and analytical investigations has begun at UC Berkeley and UC Davis with funding from Caltrans. These studies focus on developing guidelines for the design of bridge piers foundations allowed to uplift during severe earthquakes. The work at UC Berkeley focuses on development of design procedures, and validating these via more refined structural analyses and earthquake shaking table tests of moderate-scale models of reinforced concrete bridge columns under multidirectional earthquake excitations. The work at UC Davis focuses on validating this work through a series of geotechnical centrifuge tests. Consideration is limited to good soil conditions where the factor of safety under gravity loads alone exceeds three. Some to the models used in the tests and analyses are shown in Fig. 4.

For the shaking table model, a series of tests examine the effect of one, two and three components of excitation for a simple 1:4.5-scale column on a spread foundation supported on a 50 mm thick neoprene (Duro-60) pad. This pad highly idealizes the soil beneath the footing. The column has a diameter of 410 mm, a longitudinal reinforcement ratio of 1.2%, and spiral reinforcement. Tests have been carried out with columns having a footing width of 3 and 5 times the column width (D_c) and having gravity loads equal to 3% and 10% of $A_g f'_c$. Two near-fault ground motion recordings having several frequency and amplitude scalings were used in the tests. For tests with a $3D_c$ footing width, the column remained elastic, even though comparable fixed based columns would likely suffer substantial damaged. For bridges with moderate to long

fundamental periods, the overall displacement of the mass is similar to or smaller than expected of a fixed base column. For the $5D_c$ wide footing simultaneous yielding of the column and uplift of the footing occurred with similar overall top displacement but reduced plastic hinge rotation demands compared to the fixed base case.

Fig. 4 UC Berkeley shaking table tests and UC Davis centrifuge tests of rocking foundations.

The effect of two- and three-components of excitation was of special interest in these tests. When a footing lifts about a corner under two horizontal components of motion, it may tend to (1) 'roll' towards one edge or the other, resulting in irregular 3D response, or (2) pivot about a vertical axis due to the eccentricity of the reaction point and the center of mass. Where footing rotation was unrestrained about a vertical axis, after about 30 runs there was a permanent rotation about the vertical axis of about 2%. The bridge deck and soil surrounding the footing would restrain this rotation.

Several models were developed for predicting uplift and rocking behavior using the computational framework OpenSees [2003]. The baseline model is a lumped mass fiber column resting on an elastic footing and nonlinear vertical springs. In addition, full 3D finite element models and a generalized bending, rocking and sliding plastic hinge model were also developed [Kutter *et al*, 2006]. Good correlation between computed and test results was achieved for both types of numerical models.

Experimental and analytical investigations indicate that this rocking mechanism provides a viable means of resisting earthquake effects. Except for short period structures, column displacements were similar to or smaller than would be expected for a comparable elastic or yielding pier with a fixed foundation, and the column showed no signs of damage and re-centered following the end of the ground shaking. For cases where column yielding occurs, damage and permanent displacements are greatly reduced. It is recognized that rocking of spread footings may not be possible in many important situations (e.g., poor soil conditions). In such cases, development of special foundation details that permit rocking on pile-supported foundations may be feasible.

4. SELF-CENTERING REINFORCED CONCRETE COLUMN SYSTEMS

Where the base of a bridge column is fixed by large spread footings or piles, a modification of conventional ductile reinforced concrete columns is possible that can greatly improve post-earthquake operability and reduce the extent of necessary repairs. In this case, some of the reinforced concrete column's (RC) longitudinal mild reinforcement is replaced by unbonded post-tensioning strands (typically located in a central conduit). The seismic performance of such partially prestressed, reinforced concrete columns (PRC) was investigated by the Pacific Earthquake Engineering Research Center through quasi-static and dynamic analyses and shaking table tests of single columns and simple bridge systems. The design approach used for these columns [Jeong and Mahin, 2007; Sakai and Mahin, 2004; Sakai et al, 2006] is to reduce the amount of longitudinal reinforcement needed for a conventional ductile design [Caltrans, 1998] by about half, but to add unbonded post-tensioning strands and adjust the amount of transverse confinement such that the envelop of stiffness and strength is similar to that for a conventional ductile column. Under unloading, these columns exhibit a characteristic hourglass or center-oriented hysteretic loop shape.

Six nearly identical columns have been tested to date [Sakai *et al*, 2006]. The self-centering columns are shown in Fig. 5. In Specimens PRC and PRC-2 all of the mild reinforcement is fully bonded to the surrounding concrete. In PRC-U, the mild rebar are debonded locally over a length of $2D_c$ in the plastic hinge region to help reduce steel strain concentrations. In Specimen PRC-U2, the rebars are also debonded, but the level of post-tensioning is increased by about 75% to try to improve re-centering tendencies. Lastly, Specimen PRC-J was constructed with locally unbonded mild reinforcement, the lower baseline prestress force, and a steel jacket (to help confine the plastic hinge region and reduce visible damage in the plastic hinge region following an earthquake). For all of the partially prestressed columns, the post-tensioning was debonded over the full length of the column. All specimens were subjected to two horizontal components of the Los Gatos record from the 1989 Loma Prieta earthquake scaled to

yield, design and maximum excitation levels. This motion typically results in large permanent residual drifts.

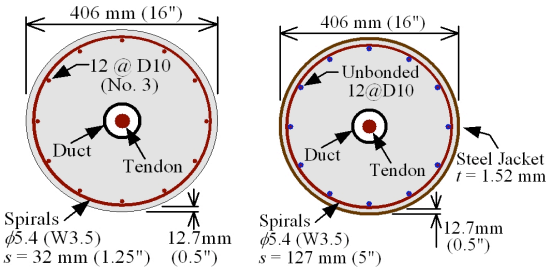

Fig. 5 Cross sections considered for self-centering column investigation

As expected, the conventional column proved to be quite ductile (with ductility demands in excess of 12 during the maximum considered event), but permanent lateral displacements developed during the design and maximum level events, requiring a premature termination of the tests (see Fig. 6(a)) at the end of the maximum level tests where the permanent lateral displacements were more than 10% of the column height. Even at the design level event (displacement ductility of 7.5) the permanent lateral displacement in the ductile column is more than 1%, which would be problematic for continued traffic flow. In contrast, the basic self-centering column at the Design Level excitation had the same or smaller peak displacements, but the permanent offset was very small (Figs. 6(b)).

To improve the self-centering characteristics of the partially prestressed concrete columns, several design modifications were attempted, as mentioned above. As can be seen in Fig. 9(b), these reduced the residual displacements significantly. For the design level events, the residual displacements were essentially insignificant for all of the modified designs. For the maximum considered event (MCE), the displacement ductility demands were quite similar (greater than 10). While unbonding of the mild reinforcement in Specimen PRC-U reduced peak steel strains, it softened the column, some of the longitudinal bars buckled slightly and residual displacements increased somewhat in comparison to Specimen PRC-2 for the MCE. By increasing the level of prestressing in Specimen PRC-U2, the residual displacements under the MCE became smaller than for PRC-2, but the column suffered significant spalling and more buckling of the longitudinal steel. As such, these columns perform better than conventional reinforced concrete columns, but may still require repair following very large shaking.

On the other hand, self-centering column with steel jacketing (Specimen PRC-J), behaved quite well under the MCE, with permanent lateral displacements less than 0.6% of the column height, and no apparent damage (except a small local buckle at the bottom of the steel jacket attributed to contact between the jacket and footing). Thus, this column would appear to minimize the need for post-earthquake repair, and remains plumb enough to avoid reduced traffic flow. Extension of these concepts to the design of concrete cores in building structures is currently under investigation.

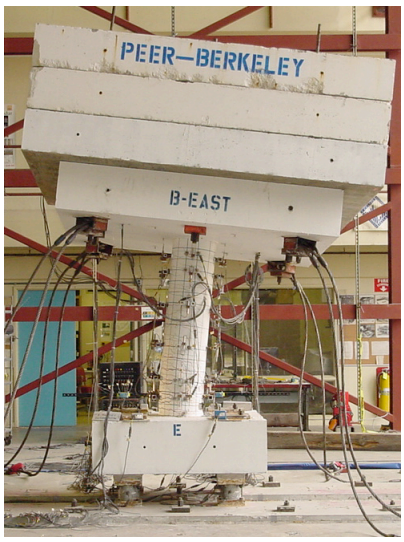

(a) Specimen RC

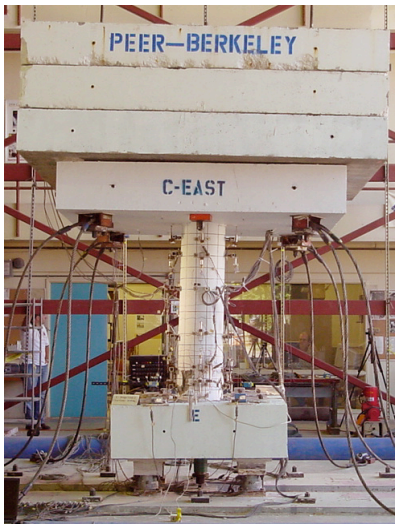

(b) Specimen PRC

Fig. 6 Residual displacements of specimens after maximum level test

A series of numerical simulations was undertaken to evaluate and improve analytical models and assess the cost and performance of self-centering systems [Jeong and Mahin, 2007; Lee and Billington, 2006]. Design guidelines for self-centering columns have been developed [Jeong and Mahin, 2007; Sakai *et al* 2006].

5. CONCLUDING REMARKS

The technology and design approaches described in this paper provide several alternative ways to achieve durable building and transportation structures that

increase post-earthquake serviceability and reduce the need for repair. By permitting structures to undergo significant inelastic deformations during seismic events, yet suffer little damage that would require post-earthquake repairs and impair operability, structural engineers can achieve designs that are durable, dependable, and economical in terms of initial construction cost and the potential losses that might occur in the event of a damaging earthquake. As such, these approaches address the basic principles articulated by sustainable design.

Additional research is needed to refine these concepts, especially with regards to (1) reducing cost and increasing speed of construction, (2) reducing the societal and ecological impacts of construction, (3) and refining concepts such as those presented herein and developing more generally applicable design guidelines. In addition, these design approaches require study to assess reliably the ability of the structure to withstand future seismic events. While typical visible forms of damage may not develop, some forms of damage are hidden (e.g., compaction of soil yielding beneath foundations), dynamic characteristics may have changed, and the remaining ability to dissipate energy may be reduced due to low cycle fatigue. Similarly, the deformed shape of structures designed in using these concepts may differ from conventional fixed base structures, requiring special consideration for the design of architectural, mechanical, electrical and plumbing elements.

6. ACKNOWLEDGEMENTS

Financial support for this research was provided by the California State Department of Transportation, the Earthquake Engineering Research Centers Program of the National Science Foundation, under Award Number EEC-9701568, through the Pacific Earthquake Engineering Research Center (PEER), and a gift from Earthquake Protection Systems. Many students and post-doctoral scholars contributed to this effort, including Eric Anderson, Andy Espinoza, Dr. Hyungil Jeong, Troy Morgan, Andreas Schellenberg and Dr. Junichi Sukai. The observations and conclusions presented are those of the author and do not necessarily represent those of the sponsors.

REFERENCES

AASHTO (1999). "Guide Specifications for Seismic Isolation Design", American Association of State Highway and Transportation Officials, Washington, D.C.

Alameddine, F., and Imbsen, R.A. (2002). "Rocking of Bridge Piers Under Earthquake Loading." *Proceedings,* Third National Seismic Conference on Bridges and Highways.

Anderson, E. (2003). "Performance-Based Design of Seismically Isolated Bridges," *Doctoral Thesis,* University of California, Berkeley, CA, 881 pp.

Anderson, E. and Mahin, S. (2004). "An Evaluation Of Bi-Directional Earthquake Shaking On The Provisions of the AASHTO Guide Specifications For Seismic Isolation Design," *Proceedings,* 13WCEE, Vancouver.

Brundtland, G. (1987). *World Commission on Environment and Development: Our Common Future,* United Nations.

Caltrans (1998). *Seismic Design Criteria,* version 1.1, Calif. Dept. of Transportation, Sacramento, CA.

Chopra, A. K. and Yim, C. (1985). "Simplified Earthquake Analysis of Structures with Foundation Uplift." *Structural Engr.,* ASCE, **111:4**.

Earthquake Protection Systems (2007). *Product Description,* Mare Island, CA.

Housner, G.W. (1963). "The Behavior of Inverted Pendulum Structures During Earthquakes." *Bulletin of the Seismological Society of America,* **52:2**.

Kawashima, K. and Hosoiri, K. (2003). "Rocking Response of Bridge Columns on Direct Foundations," *Proceedings,* Symposium on Concrete Structures in Seismic Regions, Paper No. 118, FIB, Athens.

Kren, A. (2006). *Personal communication*.

Kutter, B., Jeremic, B., Stephen Mahin, S., Ugalde, J., Gajan, S., and Hu, G. (2006). "Seismic Energy Dissipation by Foundation Rocking for Bridge SFS Systems," *Proceedings,* Fifth National Bridge Seismic Conference, San Francisco.

Jeong, H. and Mahin, S. (2007). "Evaluation of Self-Centering Reinforced Concrete Columns by Shaking Table Tests and Numerical Simulations," *PEER Report*, University of California, Berkeley, CA.

Lee, W. and Billington, S. (2006). "Performance based assessment of a self-centering bridge pier system for seismic regions," *Proceedings*, 100th Anniversary Earthquake Conference. EERI, Oakland, CA.

Morgan, T. and Mahin, S. (2007). "Enhancing the performance capabilities of seismically isolated buildings using multi-stage friction pendulum sliding bearings," *Proceedings*, World Forum on Smart Materials and Smart Structures Technology (SMSST '07), Chongqing & Nanjing, China.

OpenSees Development Team (1998-2003). "OpenSees: open system for the earthquake engineering simulations" *http://opensees.berkeley.edu/*.

Sakai, J. and Mahin, S. (2004). "Analytical investigations of new methods for reducing residual displacements of reinforced concrete bridge columns." *PEER-2004/02*, Pacific Earthq. Engrg. Res. Center, Univ. of California, Berkeley, CA.

Sakai, J., Jeong, H. and Mahin, S. (2006). **"**Reinforced Concrete Bridge Columns That Re-Center Following Earthquakes," *Proceedings,* 8NCEE, EERI, San Francisco, CA.

Sakellaraki, D., Watanabe, G. and Kawashima, K. (2005). "Experimental Rocking Response of Direct Foundations of Bridges, *Proceedings,"* 2nd Int. Conf. on Urban Earthquake Engineering, March2005, Tokyo Inst. of Technology, Tokyo.

Sixth International Conference on Urban Earthquake Engineering
March 3-4, 2009, Tokyo Institute of Technology, Tokyo, Japan

CONDITIONS OF FAULT RUPTURE AND SITE LOCATION THAT GENERATE DAMAGING PULSE WAVES

Takao Kagawa[1)]

1) Professor, Tottori University Graduate School of Engineering, Japan
kagawa@cv.totori-u.ac.jp

Abstract: The conditions to generate large pulse like waves that easily lead to beak down engineering structures are discussed. The observed pulses in and around the damaged area due to the recent large earthquakes have predominant period longer than one second, with large peak acceleration and velocity. The pulses are much more dominant in fault normal direction than fault parallel direction. The pulses are considered to be generated due to fault rupture propagation across asperities that radiate strong seismic energy. Ground motion distributions are calculated based on several fault rupture scenario changing locations of site, asperity, and rupture starting point. The conditions that generate particular area affected by the damaging pulses are demonstrated.

1. INTRODUCTION

Recently developed dense observation networks have recorded strong ground motions in earthquake source area. From the records, we can easily find pulse-like ground motions with predominant period longer than one second with large peak ground acceleration and velocity. Such pulses have potential to beak down engineering structures.

The pulses are considered to be result of forward directivity effect due to fault rupture propagation. The record at the Pacoima Dam site due to the 1971 San Fernando earthquake, CA, USA may be an early example of the pulse-like waveform [Heaton, 1982]. It is a problem for seismic design of socially important structures.

We can estimate the particular area where the pulses might affect on, using detailed simulation technique, if we can assume hypothesis fault rupture scenario. Here the conditions that generate large pulses are discussed through several simulations of ground motion distribution.

2. CAUSE OF PULSES

2.1 Forward Directivity

Figure 1 shows an example of strong ground motion records due to the 1992 Landers earthquake, CA, USA [Somerville et al., 1997]. The record at Lucerne site has particular pulse-like wave, meanwhile the waveform at Joshua Tree site has feature of a random wave with long duration and lower amplitude than the former, despite that the latter site is closer in epicentral distance than the former site. The Lucerne site locates in the forward rupture propagating direction and the Joshua Tree site is in backward rupture region.

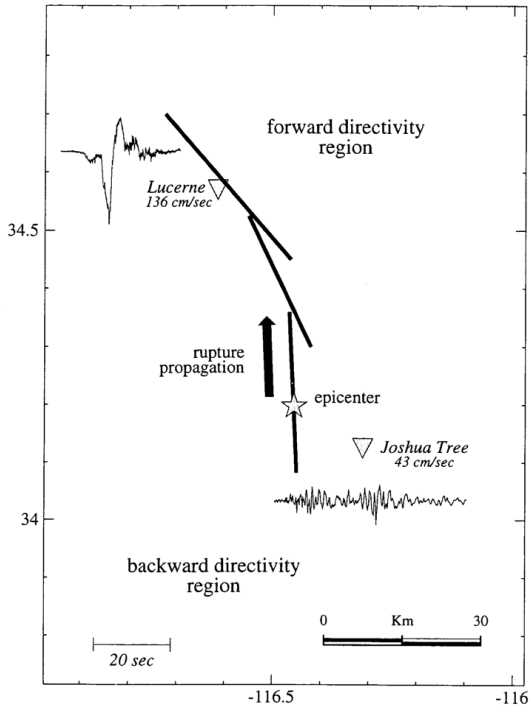

Figure 1 Fault rupture propagation and example of observed records due to the 1992 Landers Earthquake [Somerville et al., 1997]

Figure 2 shows generation of forward directivity pulses. Fault rupture starts from hypocenter of an earthquake rupture, and it propagates over the fault plane with adequate rupture velocity that is usually slightly slower than shear wave velocity. Delay times due to the fault rupture propagation are same at both forward and backward directivity sides. However, it takes shorter time for shear wave propagation according to progress of the fault rupture

to forward directivity side, on the contrary, longer time required to backward directivity side. Accordingly, shear waves generated all over the fault plane arrives almost simultaneously in forward directivity side and it produces pulse like ground motion. Meanwhile, smaller amplitude ground motion with long duration is observed in rupture backward direction.

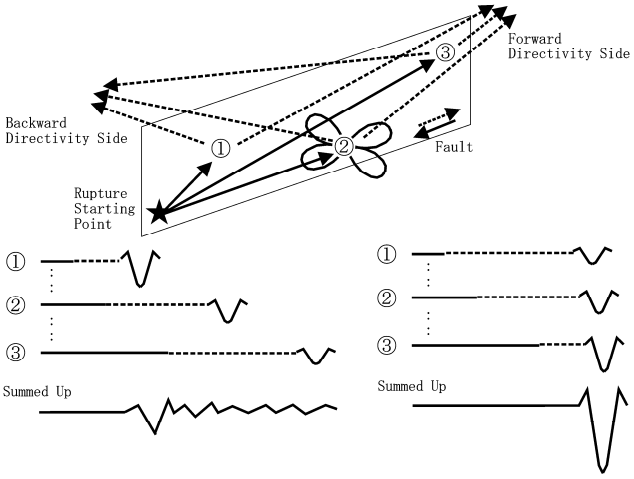

Figure 2 Schematic illustration of directivity effect

Next, we have to discuss an effect of radiation pattern of shear waves. Figure 3 shows 2-D plane view of shear wave amplitude distributed from a strike slip point source with vertical dip angle. Blanc arrows show slip direction. Fine arrows indicate direction of initial ground movement and predominantly vibrating direction. Curving line explains intensity radiated to the direction. The intensity is maximum to the direction of $\theta=-\pi/2, 0, \pi/2, \pi$, and minimum to the direction of $\theta=-3\pi/4, -\pi/4, \pi/4, 3\pi/4$. In case that maximum radiation direction corresponds to forward directivity orientation, a directivity pulse grows toward the extending direction of the fault plane. Note that the directivity pulses are dominant to fault normal component.

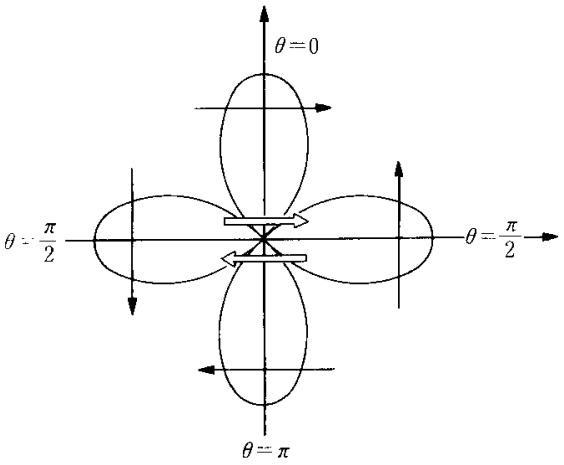

Figure 3 Amplitude distribution of transverse component from a point source [Aki and Richards, 1980]

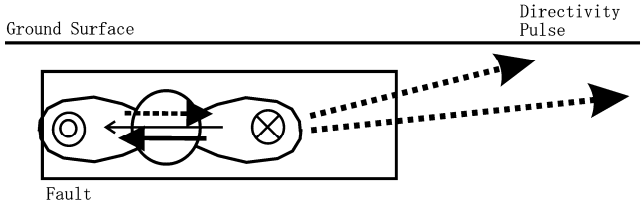

Figure 4 Cross section view of forward directivity effect due to a vertical strike slip fault

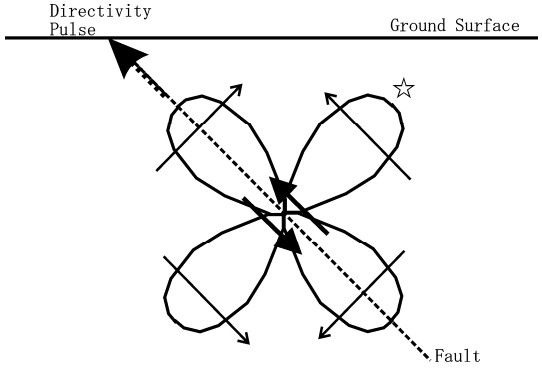

Figure 5 Cross section view of forward directivity effect due to a dip slip fault

Figure 4 shows cross section of vertical strike slip fault, same as Figure 3 but seeing from the direction of $\theta=\pi$. Forward directivity is dominant to the direction in underground, large dash arrows, and its effect propagates away to the extension of fault strike direction. Cross section of a dip slip fault is shown in Figure 5. Dip angle is assumed as $\pi/4$. In the case, forward directivity effect hits the ground surface. This suggests that the ground motion by the dip slip fault is larger than that by strike slip fault.

2.2 Focusing Effect

The 2007 Niigata-ken Chuetsu-oki earthquake attacked the world largest nuclear power plant, Kashiwazaki-Kariwa. The records at the plant and its neighborhoods consist of three pulses. The main fault plane is considered to have south-east dip from minute analysis of aftershock distribution. Using the fault plane, three asperities concerning the three pulses are detected by inversion analyses [Kurahashi et al., 2008, and so on]. The result is shown in Figure 6. The Kashiwazaki-Kariwa nuclear power plant locates on the hanging wall side of the source fault. It is not on the extension of the fault plane where forward directivity effect is dominant. We have to introduce other reason that enhances the pulse-like wave.

Figure 7 shows the schematic illustration of the mechanism. If a site is located on a perpendicular line from a rupture starting point on a fault, seismic waves along the isochrone of rupture front arrives simultaneously to the site, because rupture propagating times and shear wave propagating times are same on the isochrone. If there is an asperity on the isochrone, the summed up waves transform to a large pulse. It is possible on the hanging wall side of

dip slip faults. Amplitude toward the site is also large in the case, see shear wave radiation indicated by star symbol in Figure 5. This mechanism is to be called 'Focusing Effect'. If the rupture of an asperity started from the center of the asperity, the effect might be largest.

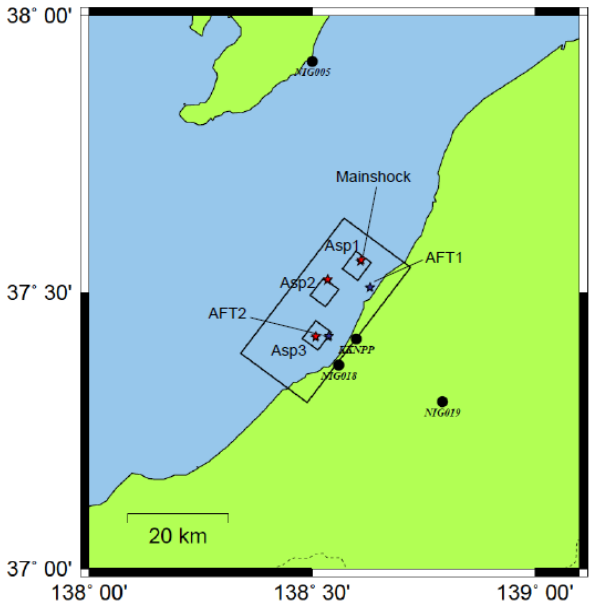

Figure 6 Three asperities of the 2007 Niigata-ken Chuetsu-oki earthquake derived from a fault rupture analysis [Kurahashi et al., 2008]

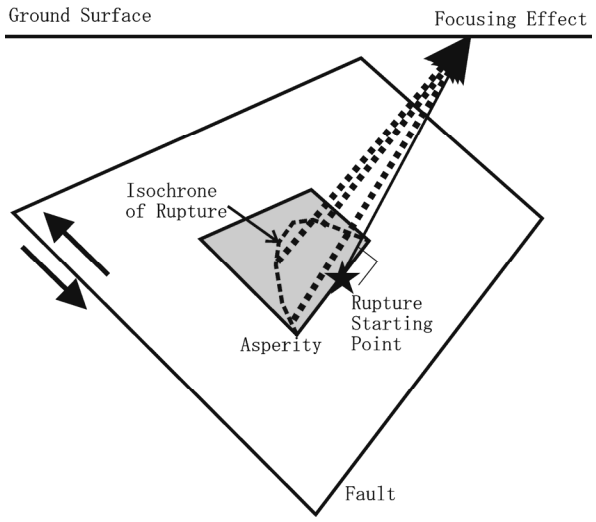

Figure 7 Schematic illustration of focusing effect

2.3 Amplification by Sedimentary Structure

The pulses generated by fault rupture propagate to the target site. The propagation path and site also affect on the pulses. In case there is soft sediment beneath the target site, the pulses are amplified. Non-linear site response might not affect much on the pulses, because their predominant periods are not short enough. For quantitative estimation of the pulse waves, we have to consider the site amplification effect.

3. SIMULATIONS OF SEISMIC INTENSITY DISTRIBUTION

Assuming fault rupture scenario for strong ground motion simulation, we comply with a recipe [Irikura et al., 2004]. The frame work of the recipe are derived from empirical relationships between fault rupture area and rupture parameters; i.e. seismic moment, rupture duration, size of asperity, stress drop, and so on. The relationships are also confirmed by theoretical consideration and dynamic fault rupture simulations. Using the recipe, we can assume general feature of non-uniform fault slip models. Figures 8 and 9 show fault rupture scenarios after the recipe for strike and dip slip faults. Dip angles of strike and dip slip faults are assumed as 90 and 45 degrees respectively. Densely dotted sub-faults indicate asperities and star symbols are rupture starting points. Locations of asperities and rupture starting points are decided arbitrarily. The fault size of all the rupture scenarios is 20km x 20km, resulting seismic moment is 7.6×10^{18}Nm (M_W6.5). Area ratio of asperities against total rupture area is assumed as 0.16 (8km x 8km), and stress drop on asperities are set as 14.4MPa. Top depths of the faults are assumed as 2km. Shear wave and rupture velocities are 3.5km/s and 2.52km/s, respectively. Rupture duration 0.79 second is derived from one-quarter time of rupture propagation across the asperity.

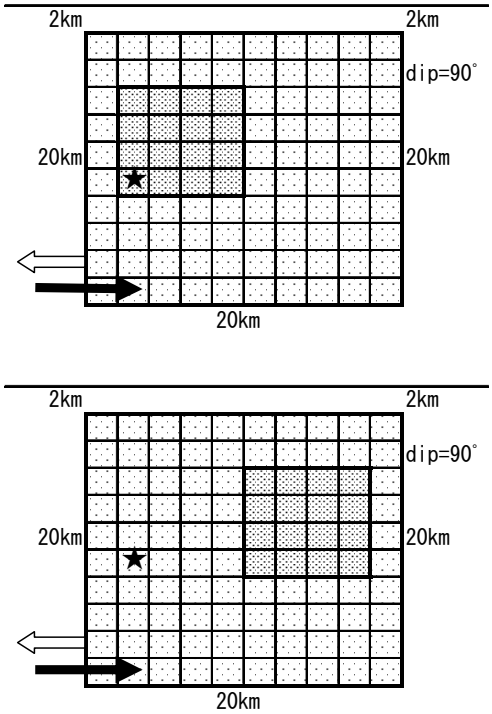

Figure 8 Assumed fault rupture scenario for strike slip earthquakes (Upper: STR1, Lower: STR2)

Ground motions are simulated in area of 50km x 50km with 1km intervals using stochastic Green's function method. The method [Kagawa, 2004] introduces coherent phases in longer period range as to able to generate directivity pulses.

Near and intermediate field terms are also considered after Nozu (2006). JMA, Japan Meteorological Agency, seismic intensities are calculated from simulated three components waveforms.

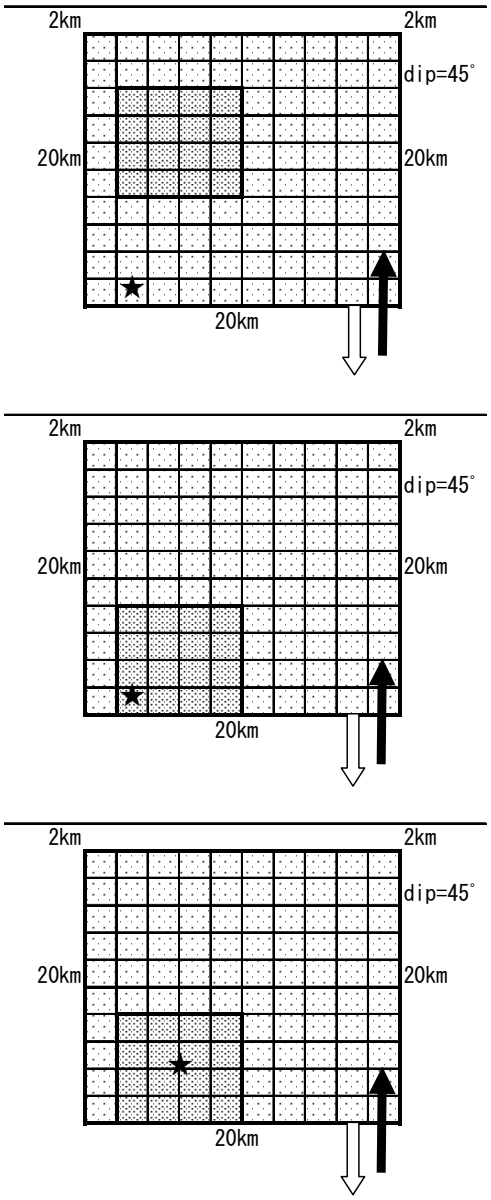

Figure 9 Assumed fault rupture scenario for dip slip earthquakes (Upper: REV1, Middle: REV2, Lower: REV3)

Panels in Figure 10 show seismic intensity distribution of two strike slip scenarios. Thin and thick lines in the panels show surface projections of fault plane and asperity. Small star symbol indicates epicenter. Large seismic intensities are calculated in forward rupture propagating direction of asperity. However the case STR1 has larger seismic intensity spot than the STR2. Dotted circle in STR1 shows the spot. This is caused by a directivity pulse propagate to the surface direction. However, radiation coefficient of shear wave is not large enough to the direction. In the case STR2, directivity pulse from the asperity propagates more horizontally then STR1, and radiation coefficient to the direction is larger than STR1 as shown in Figure 4. This makes large intensity area to prolong far away; dotted circle in STR2.

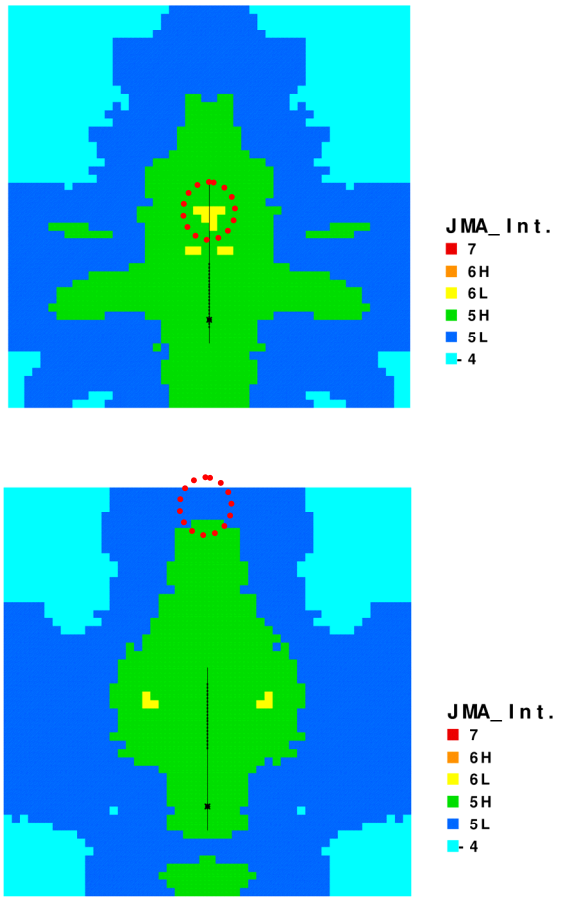

Figure 10 Calculated seismic intensity distribution due to the strike slip earthquakes (Upper: STR1, Lower: STR2)

Seismic intensity distributions of dip slip faults are shown in panels in Figure 11. In the panels, fault perpendicular projections of asperity and rupture starting point are plotted with surface projections of fault plane, asperity, and hypocenter. Case REV1 has high intensity spot attacked by the forward directivity pulse; dotted circle. The calculated seismic intensity in the spot is larger than the case of strike slip; STR1. This is because shear wave radiation is larger than strike slip cases to the forward rupture direction that hit the surface. In another wards, directivity pulse of case STR2 that propagate far away attacks the surface.

Location of rupture starting point at the bottom of asperity in the case REV2 is similar to the case STR1. Relatively large seismic intensity is calculated toward rupture propagating direction across the asperity; doted circle. However, absolute intensity is smaller than the case REV1, because the direction differs from largest shear wave radiating direction and the asperity is farther from the surface than that of REV1.

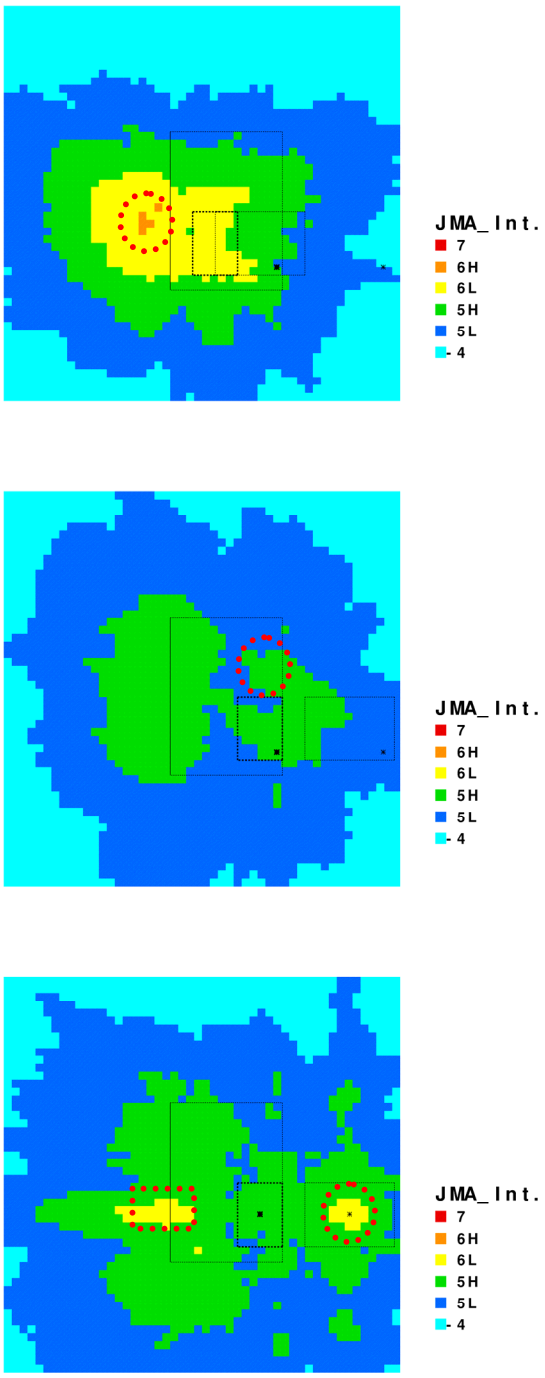

Figure 11 Calculated seismic intensity distribution due to the dip slip earthquakes (Upper: REV1, Middle: REV2, Lower: REV3)

The case REV3 has same asperity location with the case REV2, but the rupture starting point is different. Rupture starts from the center of the asperity. The setting arises the focusing effect around the fault perpendicular projection point of rupture starting point; dotted circle. Seismic intensity of the area is same as the high seismic intensity spot generated by forward directivity effect due to strike slip fault; dotted circle of case STR1 in Figure 10. High seismic intensity spot is also observed in forward directivity region; dotted rectangular. The forward directivity effect toward shallower part of fault in the case REV3 is more notable than the case of REV2. This is because the rupture isochrone to the direction is symmetrical and rupture phases are easy to be coordinated.

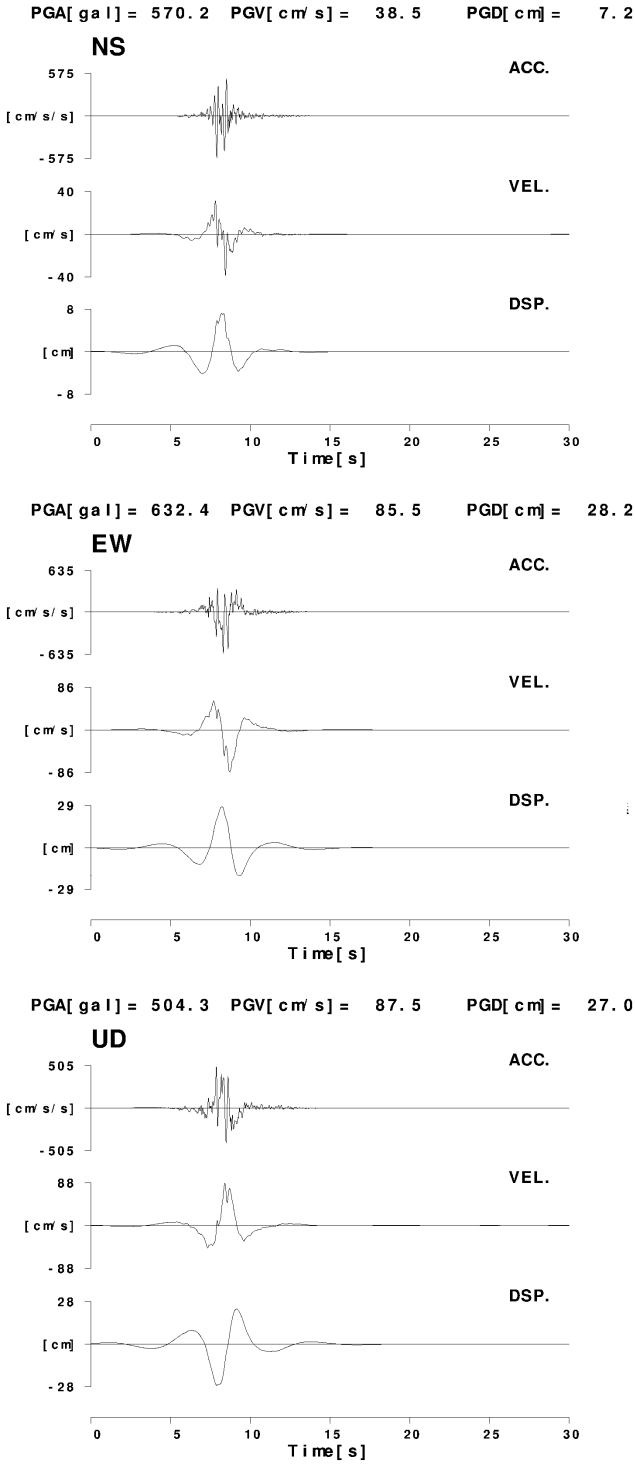

Figure 12 Acceleration, velocity, and displacement waveforms of NS, fault parallel, EW, fault normal, and UD components in the dotted circle region of the case REV1.

Figure 12 shows simulated waveforms in the dotted circle region of the case REV1; upper panel of Figure 11. Fault normal, EW and UD components have larger pulses than that of fault parallel, NS, component in velocity and displacement waveform. This is the forward directivity pulse caused by dip slip fault. The predominant direction of vibration is transverse component of the fault slip direction. We have to note that the forward directivity pulse due to the dip slip fault also affect on the vertical component, meanwhile the pulse by strike slip fault is dominant in the horizontal components.

4. CONDITIONS OF FAULT RUPTURE AND SITE LOCATION TO GENERATE PULSE WAVES

Here we discuss how to generate damaging pulses for the purpose of strong ground motion estimation. We can assume the worst case for the site considering forward directivity effect in Figure 13. In the case, asperity exists between the site and the rupture starting point, and largest radiation takes aim at the site. If the asperities locate the closer to the site, the larger amplitude of pulse wave is generated. Size of asperity controls predominant period of the pulse.

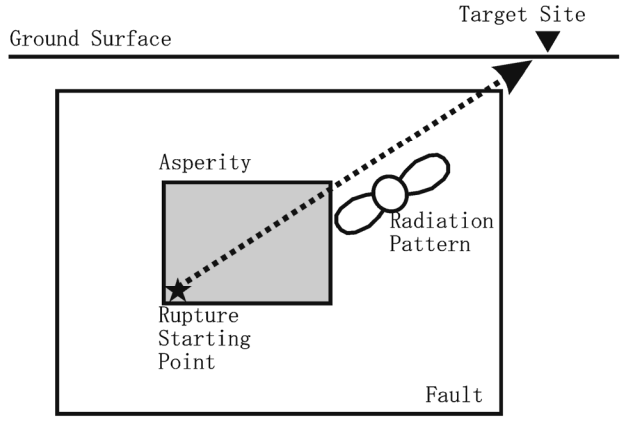

Figure 13 The case that gives large pulse to the target site due to forward directivity effect

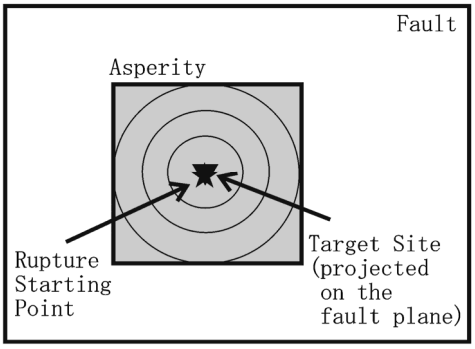

Figure 14 The case that gives large pulse to the target site due to focusing effect The target site is projected on the fault plane.

The worst case considering focusing effect is that rupture starting point locates at the center of an asperity and the point also locates on the perpendicular line of the fault plane from the site. Scale of the asperity also controls predominant period of the pulse, see Figure 14.

5. CONCLUSIONS

We introduced important aspects of the large pulse-like waves as follows.

1) The pulses are generated mainly by the forward directivity effect.
2) Directivity pulses grow up in case that maximum radiation direction corresponds to forward directivity orientation.
3) Directivity pulses are enhanced if asperity exists between target site and rupture starting point.
4) In hanging wall area of dip slip fault, we have to care about focusing effect.
5) The pulses are dominant on fault normal component.
6) The size of asperity controls predominant period of the pulse.
7) The pulses might be amplified by sedimentary structure.

Careful setting of fault rupture scenario is required for estimating strong ground motion in near fault area to express the damaging pulses.

References:

Aki, K. and Richards, P. G. (1980), "Quantitative seismology", Freeman.

Heaton, T. H. (1982), "The 1971 San Fernando earthquake; a double event? ", *Bull. Seism. Soc. Am*., **72**, 2,037-2,062.

Irikura, K. et al. (2004), "Recipe for predicting strong ground motion from future large earthquake", *Proc. 13WCEE*, 1371.

Kagawa, T. (2004), "Developing a Stochastic Green's Function Method having more accuracy in long period range to be used in the Hybrid Method", *Journal of JAEE*, **4**, 21-32. (in Japanese with English Abstract)

Kurahashi, S. et al. (2008), "Source model of the 2007 Niigata-ken Chuetu-oki earthquake using empirical Green's function (SE-dip model) ", *Jpn. Geoscience Union Meeting 2008*, S146-P017. (in Japanese)

Nozu, A. (2006), "A simple scheme to introduce near-field and intermediate-field terms in stochastic Green's functions", *12th JAEE*, 190-193.

Somerville, P. G. et al. (1997), "Modification of empirical strong ground motion attenuation relations to include the amplitude and duration effects of rupture directivity", *Seism. Res. Lett.*, **68**, 199-222.

Sixth International Conference on Urban Earthquake Engineering
March 3-4, 2009, Tokyo Institute of Technology, Tokyo, Japan

SOURCE MODELING OF SUBDUCTION-ZONE EARTHQUAKES FOR LONG-PERIOD GROUND MOTION VALIDATION

Hiroe Miyake[1] and Kazuki Koketsu[2]

1) Assistant Professor, Earthquake Research Institute, University of Tokyo, Japan
2) Professor, Earthquake Research Institute, University of Tokyo, Japan
hiroe@eri.u-tokyo.ac.jp, koketsu@eri.u-tokyo.ac.jp

Abstract: The national seismic hazard map for Japan indicates 30-year probability in the Tokyo metropolitan area to be controlled by megathrust earthquakes along the Sagami and Nankai troughs of the Philippine Sea plate. This indicates that source modeling and realistic ground motion prediction for distant subduction-zone earthquakes are quite important. We have proposed two types of source modeling for four major subduction-zone earthquakes towards long-period ground motion assessment. One type is the previous event source model, and the other type is the characterized source model. The previous event source model with kinematic or pseudo-dynamic approach is useful for ground motion simulation of the future earthquake as well as ground motion validation of the past earthquake. The characterized source model consists of asperities and a background area. The size and slip of the asperities are constrained by the source scaling for subduction-zone earthquakes, where the scaling is based on the compilation of past slip inversion results. This characterized source model is applicable to ground motion prediction for the future earthquake.

1. INTRODUCTION

The national seismic hazard map for Japan indicates 30-year probability in the Tokyo metropolitan area to be controlled by megathrust earthquakes along the Philippine Sea plate, which are four major subduction-zone earthquakes called the Kanto (M_w 7.9), northern Tokyo bay (M_w 7.0 or greater), Tokai (M_w 8.0), and Tonankai (M_w 8.1) earthquakes. We have experienced the 1923 Kanto and 1944 Tonankai earthquakes, however the rest of two are hypothetical earthquakes. For disaster mitigation and hazard assessment in the Tokyo metropolitan area, realistic ground motion prediction based on the physics-based source model and the 3-D velocity structure model are essential.

In 2004, a large offshore earthquake with an M_w of 7.4 occurred off the Kii peninsula, and excited long-period ground motions widely over the Honshu islands of Japan. The event was located at an outer rise of the Philippine Sea plate neighboring the source regions of the 1944 Tonankai and 1946 Nankai earthquakes. Record sections indicate well-developed long-period ground motions as observed within distant basins away from the 1985 Michoacan, Mexico, and 2003 Tokachi-oki, Japan, earthquakes (e.g., Anderson et al., 1986; Koketsu et al., 2005). Miyake and Koketsu (2005) pointed out that the distributions of pseudo-velocity response spectra confirmed this excitation at periods of 5-7 s in the Osaka basin, of 3-5 s in the Nobi basin, and of 7-10 s in the Kanto basin, which corresponds to the seismic characteristics of each basin. The 2004 off the Kii Peninsula earthquake provided a timely warning of damaging long-period ground motions from megathrust events such as the future Nankai, Tonankai, and Tokai earthquakes. Long-period ground motions, which will damage structures with longer natural periods like skyscrapers, long-span bridges, and huge oil tanks in the large sedimentary basins, have been simulated for the megaturust events (e.g., Furumura et al., 2008; Kawabe and Kamae, 2008; Sekiguchi et al., 2008).

We here propose subduction-zone source modeling of the Kanto, northern Tokyo bay, Tokai, and Tonankai earthquakes, and discuss the applicability of the source models for long-period ground motion prediction in the Tokyo metropolitan area.

2. SOURCE MODELING OF SUBDUCTION-ZONE EARTHQUAKES

Recent studies demonstrate that most asperities of subduction-zone earthquakes in Japan rupture repeatedly (e.g., Yamanaka and Kikuchi, 2004; Wu et al., 2008). To quantify the size of asperities, Murotani et al. (2008) performed scaling of characterized source models for subduction-zone earthquakes, and they found ratios of the size and slip between the asperities and rupture area are the same for subduction-zone earthquakes as for crustal earthquakes by Somerville et al. (1999). Considering the above, our strategy of source modeling for subduction-zone earthquakes is as follows: If source models of historical earthquakes exist, we adopt this previous event source model for the ground motion prediction. If not, we construct a characterized source model consisting of asperities and a background area (Miyake et al., 2003), by applying the scaling relations for rupture area and asperity. Fault

parameters are obtained through the recipe for strong ground motion prediction by Irikura and Miyake (2001) and Irikura et al. (2006).

2.1 Kanto Earthquake

Several source models for the 1923 Kanto earthquake have been constructed (e.g., Kanamori, 1971). Most models provide moment magnitude of M_w 8.0. Slip distribution by Wald and Somerville (1995) is inferred from teleseismic and geoedetic data, and that by Kobayashi and Koketsu, (2005) are from strong motion, teleseismic, and geoedetic data. Similar slip distribution among the above analyses suggests that it is stably solved as long as the fault plane and geometry for the source inversions are the same.

(a)

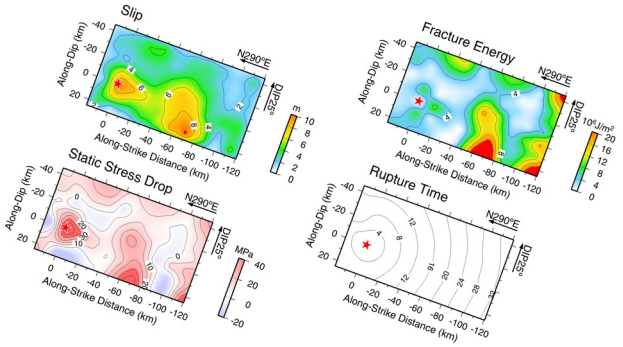

(b)

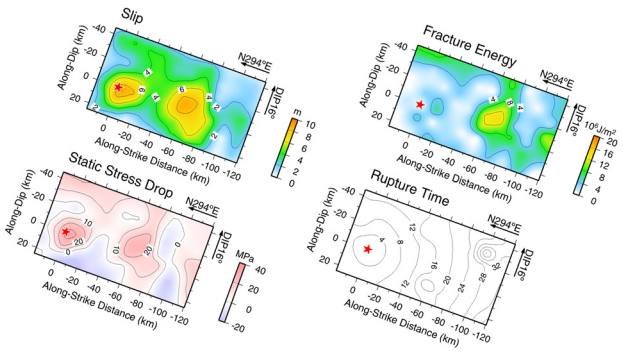

Figure 1. Pseudo-dynamic source modeling for the Kanto earthquake. Distribution of slip, static stress drop, fracture energy, and rupture time are shown for the inverted source models of (a) Kobayashi and Koketsu (2005) with M_w 8.0 and (b) Sato et al. (2005) with M_w 7.9. Stars indicate the epicenters.

Recently Sato et al. (2005) discovered that the top of the Philippine Sea plate is much shallower than the previous estimates. The new estimate is based on the deep seismic reflection profiling performed by the Special Projects for Earthquake Disaster Mitigation in Urban Areas (DaiDaiToku project), and the previous one is from the distribution of seismicity by Ishida (1990). Sato et al. (2005) recalculated the finite-slip inversion for the earthquake with the new plate geometry. The shallower plate geometry changes the location and maximum slip of the asperities for the 1923 Kanto earthquake. The eastern asperity moved about 40 km northward toward Tokyo, and maximum slip was slightly decreased. Figures 1(a) and 1(b) display the slip distributions along the previous and new geometries of the Philippine Sea plate.

The past several years have seen substantial progress in physically based approaches to earthquake source modeling for the prediction of strong ground motion. Using the characteristics of the dynamic faulting based on the frictional law, the pseudo-dynamic source modeling has been proposed by Guatteri et al. (2004). As shown in Figure 1, we applied the pseudo-dynamic source modeling for the inverted slip distribution of Kobayashi and Koketsu (2005) and Sato et al. (2005). Different location of asperities results in the complex pattern of fracture energy and rupture time.

2.2 Northern Tokyo Bay Earthquake

Two characterized source models for the northern Tokyo bay earthquake are set up along the geometry of the Philippine Sea plate by Ishida (1992) and the new geometry by Sato et al. (2005). We use the same outer fault parameters of the Central Disaster Prevention Council with M_w 7.3. Using the locations of two asperities to avoid the slow slip region identified by Hirose et al. (2000) and high reflection coefficients of the seismic profiling carried out by Sato et al. (2005), we have constructed characterized source models consisting of two asperities and a background area. The size and slip of the asperities are constrained by the source scaling of asperities for subduction-zone earthquakes, which was derived by Murotani et al. (2008) based on the compilation of past slip inversion results. The stress drop of rupture area and asperities are 3.0 and 15.8 MPa, respectively. Figure 2 shows an example of the characterized source model for the northern Tokyo bay earthquake. This is a case that a larger asperity is located beneath the center of the Tokyo metropolitan area and a smaller asperity is beneath the Chiba prefecture.

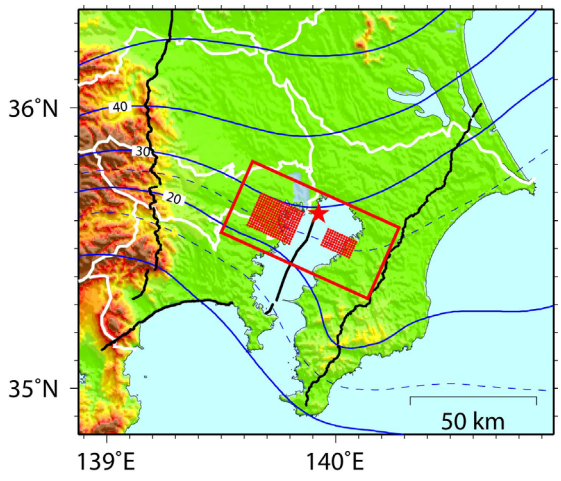

Figure 2. An example of the characterized source models constructed for the northern Tokyo bay earthquake. Star indicates the epicenter. Contours show the top depth of the new geometry of the Philippine Sea plate proposed by Sato et al. (2005).

2.3 Tokai Earthquake

Since the Tokai earthquake is hypothetical, there is no historical source model which can be used for strong ground motion prediction of a future event. However, the segmentation of rupture area and location of asperity have been geophysically investigated. For example, Matsumura (2002) proposed three locked zones figured out from seismicity which could be candidates for future asperities. We constructed a characterized source model that consists of three asperities and a background area, assuming the following geophysical constraints: (1) According to the thermal condition and geometry of the subducting Philippine Sea plate, the rupture along the dip direction extends from 5 to 25 km in depth. (2) Locked zones estimated by the background seismicity are regarded as asperities. (3) The asperities are located not to overlap the regions of slow slip estimated by GPS measurements.

The size and slip of the asperities are constrained by the source scaling for subduction-zone earthquakes by Murotani et al. (2008). The stress drop was adjusted so that asperities for long-period ground motions behave as strong motion generation areas for short-period ground motions. We defined the rupture area of 9,100 km^2 with an average stress drop of 3.0 MPa as outer fault parameters, and the combined asperity area of 1,786 km^2 with a stress drop of 15.8 MPa as inner fault parameters. The moment magnitude M_w of this source model is 8.0. Considering the historical evidence that the source region of the Tokai and Tonankai earthquakes ruptured together, we set the rupture starting point on the neighboring the source region of the Tonankai earthquake.

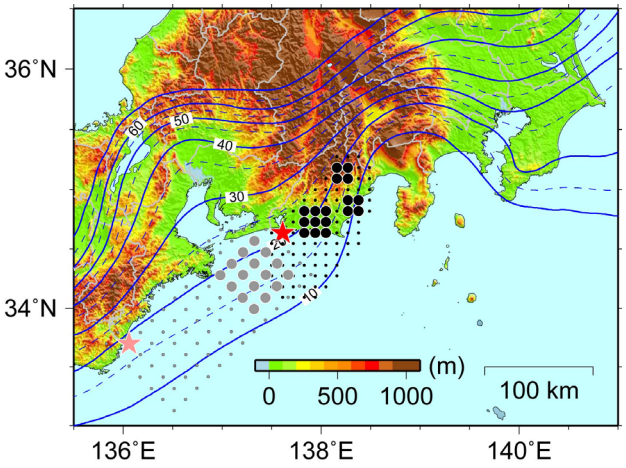

Figure 3. Characterized source models constructed for the Tokai (black tone) and Tonankai (gray tone) earthquakes. Stars indicate epicenters. Contours show the top depth of the Philippine Sea plate.

2.4 Tonankai Earthquake

The source process of the 1944 Tonankai earthquake was inferred from regional and teleseismic data by Ichinose et al. (2003) and regional data by Yamanaka (2004). Both models rupture from southwest to northeast direction with a single asperity, however the asperity location of Ichinose et al. (2003) is deeper, on the other hand, that of Yamanaka (2004) is shallower. We adjusted subfaults of the inverted source models to be on the plate-boundary, and tested the ability of the two source models to reproduce regional records of the 1944 Tonankai earthquake. The heterogeneous slip model of Yamanaka (2004) worked well as the previous event source model to reproduce the regional data.

We then constructed two characterized source models to simulate the Tonankai earthquake, where one has a shallow asperity as shown in Figure 3, and the other has a deep asperity. We modeled the rupture area of 20,475 km^2 with an average stress drop of 1.23 MPa as outer fault parameters, and the asperity area of 3,600 km^2 with a stress drop of 7.0 MPa as inner fault parameters. The moment magnitudes M_w of the characterized source models are 8.1.

3. DISCUSSION AND CONCLUSIONS

We have proposed source modeling for four major subduction-zone earthquakes. To validate the applicability of the source modeling, long-period ground motion simulations were performed by combining the proposed source models and the integrated 3-D velocity structure model in the Tokyo metropolitan area (Tanaka et al., 2005). This geophysical-based 3-D velocity model was constructed by integrating refraction, reflection, borehole, microtremor, and gravity data as well as ground motion spectra.

For the Kanto earthquake, Miyake et al. (2006) performed waveform simulation using the FEM with a voxel mesh in a period range longer than 2 second (Figure 4). They confirmed the simulated ground motions are sensitive to the distribution of asperities in the source model along the shallower plate geometry, where the eastern major asperity is located closer toward downtown Tokyo than in the previous models. The spatial validation of ground motions is important to measure the impact of the shallower plate geometry.

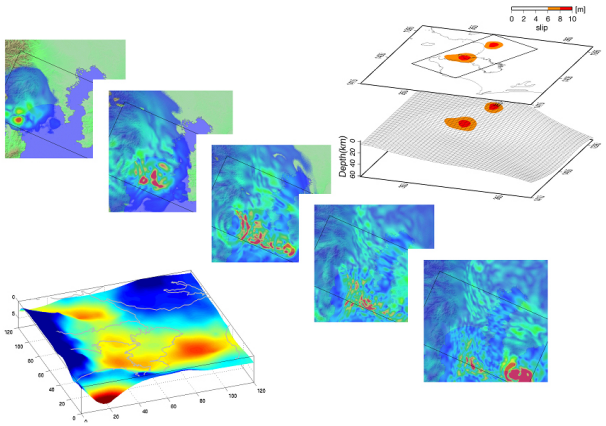

Figure 4. Long-period ground motion validation (center) for the Kanto earthquake based on the previous event source model (upper right; Sato et al., 2005) and the integrated 3-D velocity structure model (lower left; Tanaka et al., 2005).

For the northern Tokyo bay earthquake, ground motion

prediction is performed by the 3-D FDM (< 1.3 Hz). The western basin edge of the Kanto basin complicated the wave propagation, as pointed by Koketsu and Kikuchi (2000). The simulated ground motion was much larger for the source model along the new geometry of the Philippine Sea plate rather than the source model along the previous geometry.

For the Tokai and Tonankai earthquakes, Miyake et al. (2008) performed long-period ground motion prediction using the characterized source models and the integrated 3-D velocity structure model. They confirmed that long-period ground motions at a period of 7-10 s are significantly developed in the Kanto basin, indicating that the impact of damaging long-period ground motion from the future megathrust events against the Tokyo metropolitan area.

In summary, we have confirmed that the previous event source model with kinematic or pseudo-dynamic approach is useful for ground motion simulation of the future earthquake as well as ground motion validation of the past earthquake, and the characterized source model is applicable to ground motion prediction for the future earthquake. In the future direction, it is necessary to expand ground motion simulation into short-period range to compare the detailed seismic intensity distribution. This is a challenging issues to improve realistic source modeling as well as 3-D velocity structure modeling towards broadband ground motion simulation.

Acknowledgements:

This research was supported by the Special Projects for Earthquake Disaster Mitigation in Urban Areas (2002-2006) and in Metropolitan Tokyo Area (2007-2011) from MEXT, Japan.

References:

Anderson, J.G., Bodin, P., Brune, J.N., Prince, J., Singh, S.K., Quaas, R. and Onate, M. (1986). "Strong ground motion from the Michoacan, Mexico earthquake," *Science*, **233**, 1043–1049.

Furumura, T., Hayakawa, T., Nakamura, M., Koketsu, K. and Baba T. (2008). "Development of long-period ground motions from the Nankai Trough, Japan, earthquakes: Observations and computer simulation of the 1944 Tonankai (M_w 8.1) and the 2004 SE Off-Kii Peninsula (M_w 7.4) earthquakes," *Pure Appl. Geophys*., **165**, 585–607.

Guatteri, M., Mai, P.M. and Beroza, G.C. (2004). "A pseudo-dynamic approximation to dynamic rupture models for strong ground motion prediction," *Bull. Seismol. Soc. Am*., **94**, 2051-2063.

Ichinose, G.A., Thio, H.K., Somerville, P.G., Sato, T. and Ishii, T. (2003). "Rupture process of the 1944 Tonankai earthquake (M_s 8.1) from the inversion of teleseismic and regional seismograms," *J. Geophys. Res*., **108**(B10), 2497.

Irikura, K. and Miyake, H. (2001). "Prediction of strong ground motions for scenario earthquakes," *Journal of Geography*, **110**, 849–875 (in Japanese with English abstract).

Irikura, K., Miyake, H., Iwata, T., Kamae, K., Kawabe, H. and Dalguer L.A. (2004). "Recipe for predicting strong ground motion from future large earthquake," *Proc. 13th World Conf. Earthq. Eng*., Paper No.1371.

Ishida, M. (1992). "Geometry and relative motion of the Philippine sea plate and Pacific plate beneath the Kanto-Tokai district, Japan," *J. Geophys. Res*., **97**, 489–513.

Hirose, I., Kawasaki, I., Okada, Y., Sagiya, T. and Tamura, Y. (2000). "A silent earthquake of December 9, 1989, in the Tokyo Bay, as revealed by the continuous observation of crustal movements in the southern Kanto district, central Japan," *Zisin*, **53**, 11–23, 2000 (in Japanese with English abstract).

Kanamori, H. (1971). "Faulting of the great Kanto earthquake of 1923 as revealed by seismological data," *Bull. Earthq. Res. Inst. Univ. Tokyo*, **49**, 13–18.

Kawabe, H. and Kamae, K. (2008). "Prediction of long-period ground motions from huge subduction earthquakes in Osaka, Japan," *J. Seismol*., **12**, 173–184.

Kobayashi, R., and Koketsu, K. (2005). "Source process of the 1923 Kanto earthquake inferred from historical geodetic, teleseismic, and strong motion data," *Earth, Planets and Space*, **57**, 261–270.

Koketsu, K. and Kikuchi, M. (2000). "Propagation of seismic ground motion in the Kanto basin," *Science*, **288**, 1237–1239.

Koketsu, K., Hatayama, K., Furumura, T., Ikegami Y. and Akiyama, S. (2005). "Damaging long-period ground motions from the 2003 M_w 8.3 Tokachi-oki, Japan, earthquake," *Seismol. Res. Lett*., **76**, 67–73.

Matsumura, S. (2002). "Seismicity rate changes in the inferred locked zones of the Tokai region in the latter half of the 1990's," *Zisin*, **54**, 449–463 (in Japanese with English abstract).

Miyake, H. and Koketsu, K. (2005). "Long-period ground motions from a large offshore earthquake: The case of the 2004 off the Kii peninsula earthquake, Japan," *Earth Planets Space*, **57**, 203–207.

Miyake, H., Iwata, T. and Irikura, K. (2003). "Source characterization for broadband ground-motion simulation: Kinematic heterogeneous source model and strong motion generation area," *Bull. Seismol. Soc. Am*., **93**, 2531–2545.

Miyake, H., Koketsu, K., Kobayashi, R., Tanaka, Y., and Ikegami, Y. (2006). "Ground motion validation of the great 1923 Kanto earthquake using source model along the new geometry of the Philippine sea slab and integrated 3D velocity structure model in the Tokyo metropolitan area," *Bull. Earthq. Res. Inst. Univ. Tokyo*, **81**, 267–272.

Miyake, H., Koketsu, K. and Furumura, T. (2008). "Source modeling of subduction-zone earthquakes and long-period ground motion validation in the Tokyo metropolitan area," *Proc. 14th World Conf. Earthq. Eng*, S10–012.

Murotani, S., Miyake, H. and Koketsu K. (2008). "Scaling of characterized slip models for plate-boundary earthquakes," *Earth Planets Space*, **60**, 987–991.

Sato, H., Hirata, N., Koketsu, K., Okaya, D., Abe, S., Kobayashi, R., Matsubara, M., Iwasaki, T., Ito, T., Ikawa, T., Kawanaka, T., Kasahara, K. and Harder, S. (2005). "Earthquake source fault beneath Tokyo," *Science*, **309**, 462–464.

Sekiguchi, H., Yoshimi, M., Horikawa, H., Yoshida, K., Kunimatsu, S. and Satake, K. (2008). "Prediction of ground motion in the Osaka sedimentary basin associated with the hypothetical Nankai earthquake," *J. Seismol*., **12**, 185–195.

Somerville, P., Irikura, K., Graves, R., Sawada, S., Wald, D., Abrahamson, N., Iwasaki, Y., Kagawa, T., Smith, N. and Kowada, A. (1999). "Characterizing crustal earthquake slip models for the prediction of strong ground motion," *Seismol. Res. Lett*., **70**, 59–80.

Tanaka, Y., Koketsu, K., Miyake, H., Furumura, T., Sato, H., Hirata, N., Suzuki, H. and Masuda, T. (2005). "Integrated modeling of 3D velocity structure beneath the Tokyo metropolitan area," *Eos Trans. AGU*, **86**(52), Fall Meet. Suppl., Abstract S21A–0200.

Wald, D.J. and Somerville, P.G. (1995). "Variable-slip rupture model of the great 1923 Kanto, Japan, earthquake: Geodetic and body-waveform analysis," *Bull. Seismol. Soc. Am*., **85**, 159–177.

Wu, C., Koketsu, K. and Miyake, H. (2008). "Source processes of the 1978 and 2005 Miyagi-oki, Japan, earthquakes: Repeated rupture of asperities over successive large earthquakes," *J. Geophys. Res*., **113**, B08316.

Yamanaka, Y. (2004). "Source processes of the 1944 Tonankai and 1945 Mikawa earthquakes," *Chikyu Monthly*, **29**, 739–745 (in Japanese).

Yamanaka, Y. and Kikuchi, M. (2004). "Asperity map along the subduction zone in northeastern Japan inferred from regional seismic data," *J. Geophys. Res*., **109**, B07307.

Sixth International Conference on Urban Earthquake Engineering
March 3-4, 2009, Tokyo Institute of Technology, Tokyo, Japan

ESTIMATION OF STRONG MOTIONS NEAR THE SOURCE REGION FOR THE RECENT EARTTHQUAKES IN JAPAN USING AFTERSHOCK RECORDS

Kentaro Motoki[1], Hiroaki Yamanaka[2] and Kazuoh Seo[3]

1) Assistant Professor, Dept. of Built Environment, Tokyo Institute of Technology, Japan
2) Associate Professor, Dept. of Environmental Science and Technology, Tokyo Institute of Technology, Japan
3) Professor, Dept. of Built Environment, Tokyo Institute of Technology, Japan
kmoto@enveng.titech.ac.jp, yamanaka@depe.titech.ac.jp, seo@enveng.titech.ac.jp

Abstract: It is important to estimate the appropriate seismic motions near the source region, from the engineering view point. We evaluated the earthquake motions during the main shock using aftershock records for Noto Hanto earthquake. The results can be recognized overestimation caused by non-linear effect. We compared the observed strong motions of the main shock to the estimated motions using the aftershock records to investigate the non-linear effect. The non-linear effect can be estimated. We will continue the calculation and the consideration with the subsurface geology about non-linear effect for other earthquakes. But it still remains the problem of difficulty to estimate the strong motion near the source region in the longer period range than 0.5 second using the aftershock records.

1. INTRODUCTION

The disastrous earthquakes have occurred frequently and the lots of buildings and houses have been damaged for recent decades. It is important to estimate the appropriate seismic motions near the source region, from the engineering view point. We conducted aftershock observations on the damage area to investigate the effects of surface geology (e.g. Motoki *et. al*. 2006). The site effect was successfully estimated, but the estimation of the strong motions during the main shock have not been reached yet. We evaluated the earthquake motions during the main shock using aftershock records, in the Monzenmachi town for Noto Hanto earthquake (Motoki *et. al.* 2008). The result was about 50 cm/s on the hill area surface geology is Pliocene, but they were estimated more than 4000 cm/s^2 or 200 cm/s at some points on the soft soil. These can be recognized overestimation. This phenomena is caused by that earthquake motions behave elastically while the amplitude is low. The realistic motions including plastic behavior can not be estimated. It is necessary to estimate this non-linear effect. The appropriate reduction induced by non-linear effect will make a realistic estimation using aftershock records.

In this study, we calculate the strong motions during the main shock using aftershock records and we investigate the non-linaer effect from the difference of the estimated motions from the observed motions. We used the records of the 2005 West off Fukuoka Prefecture earthquake.

2. DATA SET

Figure 1 shows the staion of the earthquake motions and the epicenters the main shock and the aftershocks using as the element earthquake. The records that non-linear effect does not include are preferable in this study. We selected the stations that the amplitude is less than 100 cm/s^2. The stations where the amplitude is less than the records we use could not triggered during the aftershock motions. Besides we picked up the stations which surround the fault area. Despite the accelerations are exceed 100cm/s^2 at 2 stations, NGS021 and NGS022, we use them to decrease the directional bias from the source. The distances of the stations from the epicenters are about 100 km. Table 1 shows the specification of these events. These information was evaluated by F-net and Hi-net. We use 2 events for this study. the event A is the largest aftershock. The event B occured considerably near to the event A. The fault strike, dip and slip angle of the main shock and these aftershocks were estimated similar to each other. We calculate strong motions using these events respectively, and attempt to think about errors in this study.

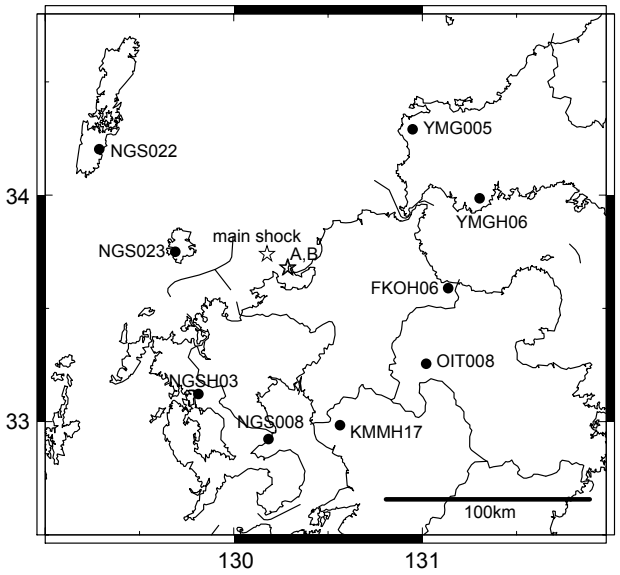

Figure 1 Distribution of Strong Motion Station used for this study and Epicenters of the main shock and aftershocks

Table 1 List of the earthquakes Studied and Source Scaling Parameters

Event	Date	Depth(km)	Mw(M0[Nm])	C	N
A	2005/4/20 6:11	13.5	5.4 (1.31E+17)	1.0	4
B	2005/4/20 9:09	13.3	4.8 (1.50E+16)	1.13	8
main shock	2005/3/20 10:23	9.2	6.6 (7.80E+18)		

3. SOURCE MODEL

The aftershock motions are used as the empirical Green's function and we adopted the filter function which multiplies in synthesization proposed by Irikura *et. al.* (1997). For this technique, the scaling parameters C and N is estimated from the constant levels of accelaration and displacement amplitude spectra of the events with the following the equation

$$N = \left(\frac{U_0}{u_0}\right)^{0.5}\left(\frac{a_0}{A_0}\right)^{0.5} \qquad C = \left(\frac{u_0}{U_0}\right)^{0.5}\left(\frac{A_0}{a_0}\right)^{1.5}$$

Where, U_0 and u_0 show the constant levels of the amplitude of the displacement spectra for the large and small events, respectively. A_0 and a_0 indicate the constant levels of the acceleration spectra. Namely, U_0/u_0 and A_0/a_0 mean the constant level of the spectral ratio in the longer period range and the shorter period range, respectively. Figure 2 shows the source spectral ratio function of the main shock to the event B. For Fourier analysis, we use about 40 second from the S wave arrivals. The thick line indicate the average of the spectra. In the shorter period range, the flat level can be easily detect but in the longer period range, it is difficult to find it. The seismic moment evaluated by F-net is used for the displacement flat level which means flat level in spectral ratio in the longer period range. The evaluated scaling factor is listed on Table 1.

Since the location of the hypocenter is different from each other, the travel time from the hypocenter is also different. Therefore the time shifting is needed to move the hypocenter. The S-wave arrival time of the aftershocks was picked up to evaluate the apparent velocity to calculate time shifting. We evaluate as 3.25 km/s the apparent velocity.

We put the strong motion generation area (SMGA), refering to the source model estimated by the previous researches (e.g. Nozu, 2007). And, unknown parameters representing the location, the trigger point, the size and the rise time were fixed with trial and error. we could obtain the proper parameters with grid search to fit the acceleration envelop and the velocity waveforms filtered 0.2 - 1.0Hz.

Figure 3 shows the comparison of waveforms between synthetic and observed for the main shock. These synthetic waveforms seem to give a good fit to observed in accelerations, velocities and displaecements. Most of accelerations are estimated bigger than observed motions, comparing to the velocity and displacement. This tendency appears strongly at NGS022 and NGS023 where the observed accelerations are higher than 100 cm/s.

Figure 4 shows the comparison of pseudo velocity response spectra at NGSH03 for the horizontal component. Both of the estimated motions is good fitting at the observed motions in the period range longer than 0.3 second, especially the spectra with event B can be said just fitting. In the shorter period range, the response is higher than observed ones. In most of the stations, such tendency were recognized.

4. COMPARISON OF STRONG MOTIONS BETWEEN ESTIMATED MOTION AND OBSERVED MOTIONS

In this section, we notice the stations where the amplitudes of the observed accelerations are high. The sources model derived in the previous section are userd for the estimation of the strong motion at these stations.

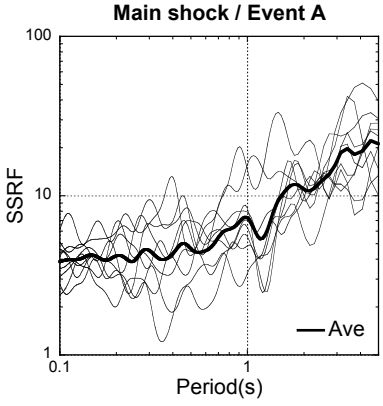

Figure 2 Source Spectral Ratio Function of the main shock to the event A.

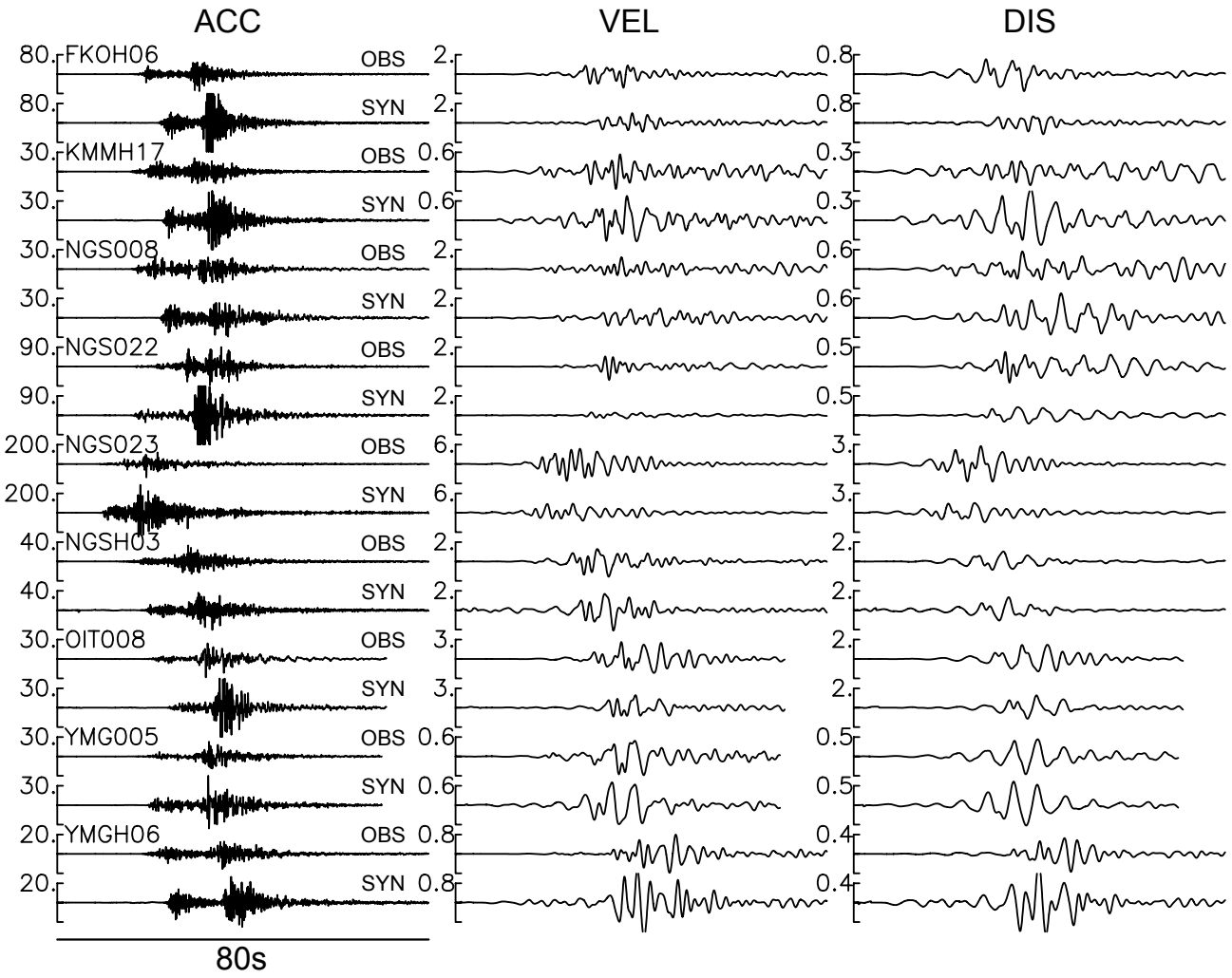

Figure 3 Comparison between waveforms synthesized from event A and observed waveforms of the main shock

Figure 5 shows the comparison of PGA and PGV between estimated motions and observed motions. Estimated PGA and PGV in this figure were geometrical average of calculated value using aftershock motion of Event A and B. We calculated PGA low pass filtered with 5Hz, because high frequency range might be affected by fmax. In the PGA non-filtered, the estimated values are much higher than observed ones. The ratio is higher than those of PGA with filtered and PGV. PGA is dominated by the amplitude of shorter period range, and such range is strongly affected by non-linear effect. Therefore, estimated PGA is considerably higher than observed PGA. But it cannot be recognized the difference by the amplitude in the ratio of estimated PGA to observed PGA, despite non-linear behavior must appear clearly during high amplitude shaking. 2 reasons can be considered for this phenomena. One is that the appearance and the degree of the plastic deformation of the soil depend on the strength of the soil. The subsurface soils are different from each other station. It can be considered that the dispersion is caused by the subsurface structure.

Another one is the error affected by other phenomena. The ratio of the estimated PGV to the observed one can

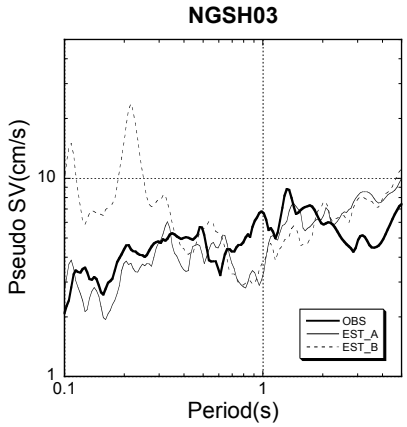

Figure 4 Comparison of Pseudo Velocity Response Spectra between observed motions and synthetic motions at NGSH03

be recognized less than the that of PGA. non-linear effect includes in the PGV ratio, but the dispersion seen in PGA is also recognized. Figure 6 shows the comparison of pseudo velocity response spectra between the estimated motions and the observed motions at FKO006 where PGV ratio is low and FKOH09 where the ratio is high. In this

figure, all estimated response is bigger than observed one in the shorter period range less than 0.4 second. It can be considered it caused by the non-linear effect. in the longer period range, it can be seen the error that cannot be explained with non-linear effect. The station where such error includes can be easily find by the PGV ratio.

Figure 7 shows the PGA rario of the estimated motions to the observed motions. It is difficult to find the directional bias in this figure. The fluctuation of the PGV ratio can be seen near the source area from this figure. This characteristic show that the station near the source is strongly affected by the source characteristics. On the other hand, the empirical Green's function method is composed of the omega square model, and the source model and calculation model are simple. The complexity of the source cannot be expressed properly. For distant station, the source model can be make simple, because the complexity can be regarded as uniformity from adequately far point. Though it is difficult to estimate strong motions near the source region with far site acculately, the decreasing factor by non-linear effect can be calculated. It can be considered that it is necessary to change the calculation model for the purpose.

5. CONCLUSIONS

We compared the observed strong motions of the main shock to the estimated motions using the aftershock records. The non-linear effect can be estimated. We will continue the calculation and the consideration with the subsurface geology about non-linear effect for other earthquakes. But it still remains the problem of difficulty to estimate the strong motion near the source region in the longer period range than 0.5 second using the aftershock records.

Ackknowledgements:

We thank the K-NET, KiK-net, F-net, Hi-net of the National Research Institute of Earth Science and Disaster Prevention for providing the strong motion data and the seismic information.

References:

Irikura, K., Kagawa, T. and Sekiguchi, H. (1997) "Revision of the empirical Green's function method by Irikura (1986)," Program and Abstracts of the Seismological Society of Japan, **2**, B25

Motoki K. Yamanaka, H. and Seo, K. (2008), "An Estimation of Strong Motions in Damaged Areas for the Noto Hanto Earthquake in 2007 Using Ground Motion Data from Aftershock Observations," *Proc. of Fifth Intern. Conf. on Urban Earthq. Eng.*, Tokyo Institute of Technology, 111-114

Motoki K. Yamanaka, H., Seo, K. and Kawase, H. (2006), "An Estimation of Site Amplification by Irregular Subsurface Structure near Kego Fault from Aftershock Records of the 2005 West off Fukuoka Prefecture Earthquake," *J. of Structural and Construction Eng.*, AIJ, 129-136

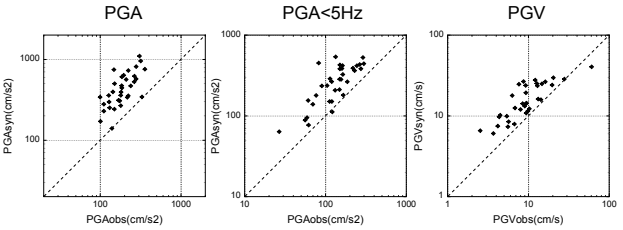

Figure 5 Comparison of PGA(left), PGA low pass filterered with 5Hz(middle) and PGV(right) at stations where PGA is more than 100cm/s^2

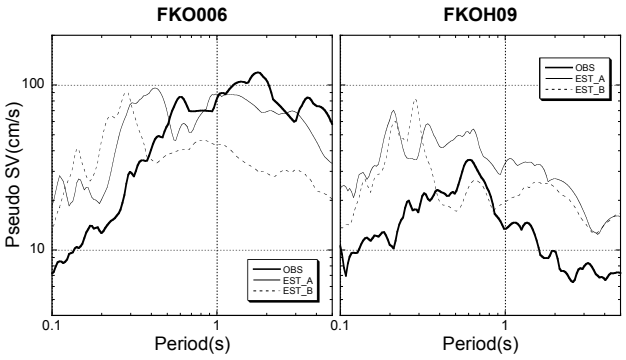

Figure 6 Comparison of Pseudo Velocity Response Spectra between observed motions and synthetic motions at FKO006, where PGV ratio is low and FKOH09, where PGV ratio is high.

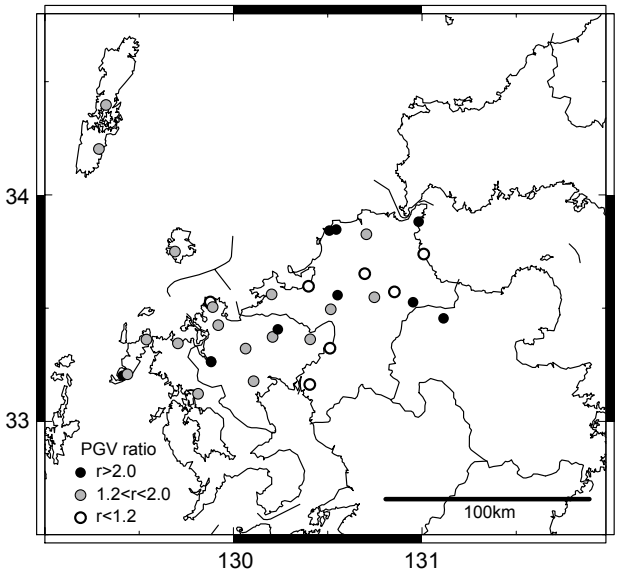

Figure 7 Distribution of PGV ratio of estimated motions to the observed motions

Nozu, A.(2007), "Valuable slip Rupture Model for the 2005 West off Fukuoka Prefecture, Japan, Earthquake," ZISIN *J. of the Seismological Society of Japan*, **59**(3), 253-270

Sixth International Conference on Urban Earthquake Engineering
March 3-4, 2009, Tokyo Institute of Technology, Tokyo, Japan

VARIABILITY IN RESPONSE SPECTRA OF GROUND MOTION FROM MODERATE CRUSTAL EARTHQUAKE USING STOCHASTIC GREEN'S FUNCTION METHOD

Tatsuya Itoi[1)], Saburoh Midorikawa[2)], Junzo Kito[3)]
Hiroyuki Miura[4)], Yasuo Uchiyama[5)], and Shigehiro Sakamoto[6)]

1) Technology Center, Taisei Corporation, Japan
2) Professor, Dept. of Built Environment, Tokyo Institute of Technology, Japan
3) Former Graduate Student, Dept. of Built Environment, Tokyo Institute of Technology (Central Japan International Airport), Japan
4) Assistant Professor, Dept. of Built Environment, Tokyo Institute of Technology, Japan
5) Technology Center, Taisei Corporation, Japan
6) Technology Center, Taisei Corporation, Japan
ititty00@pub.taisei.co.jp, smidorik@enveng.titech.ac.jp, Junzo_Kito@cjiac.co.jp, hmiura@enveng.titech.ac.jp, yasuo.uchiyama@sakura.taisei.co.jp, shigehiro.sakamoto@sakura.taisei.co.jp

Abstract: In this paper, the variability in the acceleration response spectra (h=0.05) of ground motion due to the random source parameters for shallow crustal earthquakes is investigated. Firstly, the slip models of the past crustal earthquakes in Japan are compiled and statistically investigated. Secondly, ground motions are simulated at several receivers for different events using the stochastic Green's function method, where events have different asperity distribution and hypocenter location. Then, the variability of the acceleration response spectra is evaluated. The variability increases as the period of the response spectra increases. Finally, the effects of other source parameters are also evaluated. The variability of the simulation results is comparable to the inter-event error in an attenuation relationship, suggesting that the inter-event error can be explained by the effects of the random source parameters.

1. INTRODUCTION

In probabilistic seismic hazard analysis (PSHA), the ground motion variability is modeled according to the residual errors in an attenuation relation. An attenuation relation is derived from the observed strong ground motions from various events, recorded at stations with different site conditions, which yields larger scattering in the residual errors. Therefore, PSHA is considered to give an unrealistic ground motion level especially on a rock site for large return periods.

For more sophisticated PSHA, factors affecting the variability of ground motions have been examined using observed ground motion records (e.g. Midorikawa & Ohtake 2003, Ikeura & Noda 2005). Numerical simulation of ground motions has also been performed to examine the effects of random source parameters on ground motions (e.g. Strasser & Bommer 2005, Miyakoshi *et al.* 2008), which covers the disadvantage of observed records, especially the insufficiency of the number of near-field records. The random source parameters, however, were not sufficiently consistent with the source models evaluated for the past earthquakes.

In this study, firstly, the slip models of the past crustal earthquakes in Japan are compiled and statistically examined, to construct a random source event model. Then, ground motions are simulated at several receivers for different events using the stochastic Green's function method, where events have different source parameters. Finally, the variability in the acceleration response spectra is evaluated and compared with residual errors in an attenuation relation.

2. STATISTICAL CHARACTERISTICS OF SLIP MODEL FOR CRUSTAL EARTHQUAKE

First, the inversion slip models of the past crustal earthquakes in Japan are compiled for the statistical analysis. Table 1 shows the list of 18 earthquakes examined (12 strike slip faults and 6 reverse faults). Figure 1 shows an example of slip models, where the fault area and the asperity area are trimmed based on the method proposed by Somerville *et al.* (1999).

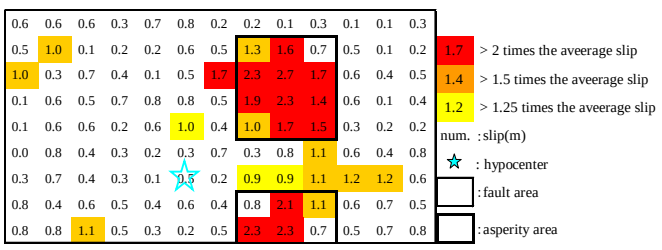

Figure 1 Characterization of Slip Model for 2005 Fukuoka Seiho Oki Earthquake (based on Asano & Iwata, 2006)

Table 1 Earthquake List of Slip Model

no.	yy/mm/dd	name of earthquake	Mw	mecha nism	reference	S_a/S	Vr(km/s)
1	1945/1/13	Mikawa	6.6	RV	Kikuchi et al. (2003)	0.13	2.5
2	1948/6/28	Fukui	6.7	SS	Ichinose et al. (2005)	0.21	2.5
3	1961/8/19	Kita-Mino	6.5	RV	Takeo & Mikami (1990)	0.17	-
4	1969/9/9	Central Gifu	6.4	SS	Takeo & Mikami (1990)	0.27	-
5	1974/5/9	Off Izu-Hanto	6.6	SS	Takeo (1989)	0.20	-
6	1975/4/21	Central Oita	6.4	SS	Takeo & Mikami (1990)	0.22	-
7	1980/6/29	East Off Izu-Hanto	6.6	SS	Takeo (1988)	0.20	-
8	1984/9/14	West Nagano	6.3	SS	Yoshida & Koketsu (1990)	0.19	2.5
9	1995/1/17	Hyogo-ken Nambu	6.9	SS	Koketsu et al. (1998)	0.17	2.5
10	1997/3/26	Northwest Kagoshima	6.1	SS	Miyakoshi et al. (2000)	0.27	-
11	1997/5/13	Northwest Kagoshima	6.0	SS	Horikawa et al. (2001)	0.11	2.3
12	1997/6/25	North Yamaguchi	5.8	SS	Miyakoshi et al. (2000)	0.21	2.5
13	1998/9/3	North Iwate	5.9	RV	Miyakoshi et al. (2000)	0.17	2.5
14	2000/10/6	Tottoriken Seibu	6.8	SS	Iwata & Sekiguchi (2002)	0.19	1.9
15	2003/7/26	North Miyagi	6.1	RV	Hikima & Koketsu (2004)	0.18	3.0
16	2004/10/23	Mid Niigata	6.6	RV	Hikima & Koketsu (2005)	0.19	-
17	2004/10/23	Mid Niigata (after shock)	6.3	RV	Hikima & Koketsu (2005)	0.13	-
18	2005/3/20	West Off Fukuoka	6.6	SS	Asano & Iwata (2006)	0.15	2.1
					mean	0.19	2.43 (2.61)
					standard deviation	0.04	0.28 (0.20)

Parenthesis means the statistics evaluated together with data in Somerville *et al.* (1999)

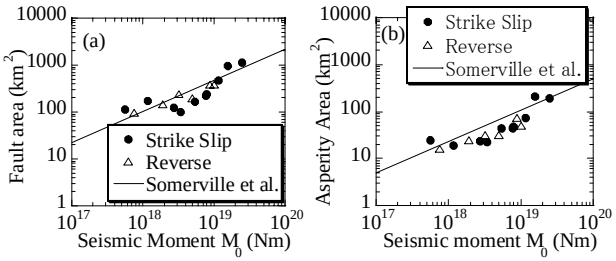

Figure 2 Relation with Seismic Moment: (a) Fault Area, and (b) Asperity Area

Figure 2 shows M_0-S and M_0-S_a relationships, which agree with the relation proposed by Somerville *et al.* (1999). As shown in Table 1, asperity area ratio S_a/S and rupture propagation velocity V_r also agree with Somerville *et al.* (1999) and with the method ("Recipe") by Headquarters for Earthquake Research Promotion in Japan (2008).

Next, the spatial distribution of asperity in a fault plane is examined. As the mechanism of a strike slip fault and a reverse fault is different, it is desirable to examine the characteristics for each fault type separately. However, the number of reverse faults is limited. Hereafter, only the characteristics of strike slip fault are examined. Figure 3 shows the distribution of the asperity area ratio along (a) the strike direction and (b) the dip direction at interval of 0.05 *L* or 0.05 *W*. The dashed line in the figure shows the theoretical distribution if a square asperity is distributed uniformly in a square fault plane. The distribution of asperities along the dip direction disagrees with the theoretical one at close to the fault bottom, though they almost agree with each other in the strike direction.

The hypocenter location is also examined. Figure 4 shows the relative position of hypocenter from the center of the largest asperity, which is normalized by each asperity size. The cross on each hypocenter indicates the mesh size of inversion analysis, and the number in the figure indicates its earthquake name in Table 1. As similar to Mai *et al.* (2005), hypocenters tend to be close to the largest asperity. The hypocenters are located around the lower half of the largest asperity including inside the asperity.

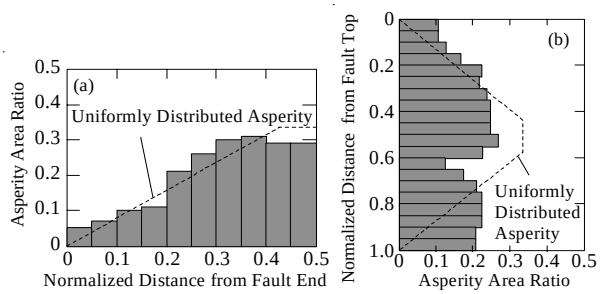

Figure 3 Spatial Distribution of Asperity Area Ratio: (a) Strike Direction, and (b) Dip Direction

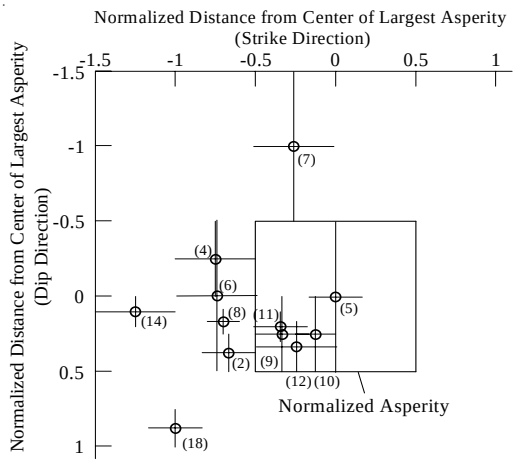

Figure 4 Relative Position of Hypocenter to Largest Asperity

Based on the above-mentioned findings, a random source event model with different asperity distribution and hypocenter location is proposed in the next chapter.

3. RESPONSE SPECTRA FOR DIFFERENT ASPERITY DISTRIBUTION AND HYPOCENTER LOCATION

3.1 Analysis Method and Parameters

A strike slip fault (Mw 6.5) is assumed for ground motion simulation. Table 2 shows the fault parameters arranged by the "Recipe" (HERP 2008). Ground motions are calculated at 12 receivers as shown in Figure 5, where horizontal distances from the fault are from 8 to 50 km.

The asperity distribution and hypocenter location for a random event model are arranged based on the statistics in Chapter 2. 20 asperity distributions are arranged as shown in Figure 6, where the asperity is assumed not to distribute in a border of the upper and lateral edge, where its distance from the fault end is larger than about 0.1*L* or 0.1*W*. As shown in Figure 7, the spatial distribution of modeled asperity is almost consistent with that of the compiled earthquakes. Then, six hypocenters are assumed for each asperity distribution, which distribute uniformly around the lower half of the largest asperity. The total number of events considered is 120.

Ground motions are calculated based on the stochastic Green's function method (Boore 1983, Kamae *et al.* 1991).

Table 2 Fault Parameters

	No. of Asperities	
	1	2
Mw	6.5	
Seismic Moment (N·m)	7.2×10^{18}	
Fault Length (km)	24	
Fault Width (km)	15	
Fault Area (km^2)	360	
Depth of Fault Top (km)	1	
Dip Angle (deg)	90	
Shear Wave Velocity near Fault (km/s)	3.5	
Density near Fault (kg/m^3)	2800	
Rupture Propagation Valocity (km/s)	2.52	
Asperity Area(km^2)	81	83
Asperity Area Ratio	0.23	
Seismic Moment of Asperity (N·m)	3.2×10^{18}	3.3×10^{18}
Stress Drop of Asperity (MPa)	11.4	11.7
Background Area (km^2)	279	277
Seismic Moment of Background (N·m)	4.0×10^{18}	3.9×10^{18}
Stress Drop of Background (MPa)	2.43	1.75

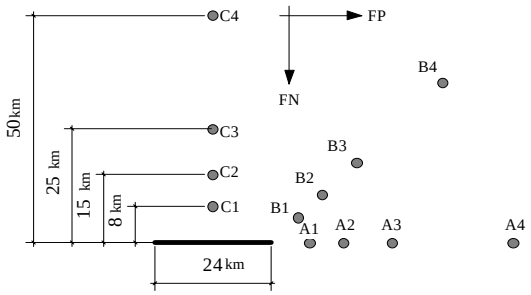

Figure 5 Fault Geometry and Receiver Location

First, ground motions for small earthquakes on each sub-fault are generated. For the radiation pattern, the isotropic value (0.63) is employed for high frequency, while the theoretical value is used for low frequency. Then, small earthquakes are superposed to generate ground motions for a large earthquake according to Irikura *et al.* (1997). 20 ground motions are calculated for each event with different random phases of small earthquakes, where the random phase is arranged to fit the envelope shape dependent on hypocenter distance for short period (Murakami *et al.* 2002) and the theoretical source time function for long period (Kagawa 2004). The total number of ground motions calculated for each receiver is 2400.

3.2 Variability of Simulation Results

3.2.1 Outline of Simulation Results

Figure 8 shows the acceleration time histories and the response spectra at A1, B1, C1 and A4 for an event where asperity distribution is on the second line and the second column in Figure 6 with the lower left hypocenter. As for receivers with the same distance (A1~C1), the response spectrum at C1 is larger than those at other receivers for shorter period (than 1 s), indicating that the difference in the receiver azimuth affects the amplitude of response spectrum for shorter period. For longer period, larger scattering is observed due to the "directivity" effects, or the effects of radiation pattern and rupture propagation.

Figure 9 shows a comparison between histogram of

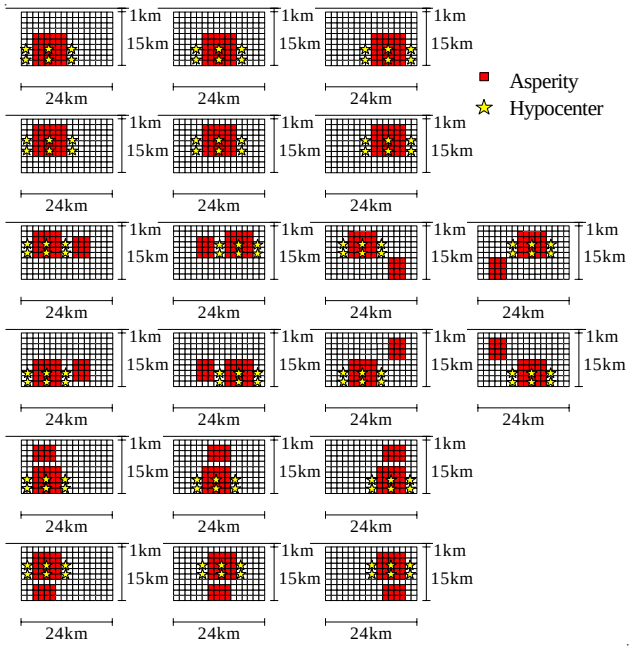

Figure 6 Modeled Asperity Distribution and Hypocenter Location

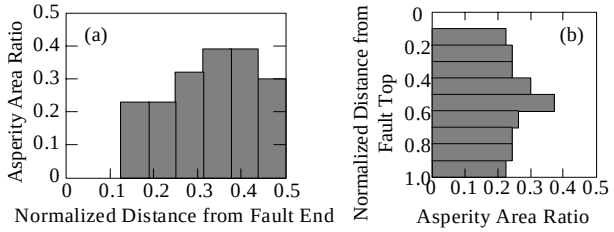

Figure 7 Spatial Distribution of Modeled Asperity Area Ratio: (a) Strike Direction, and (b) Dip Direction

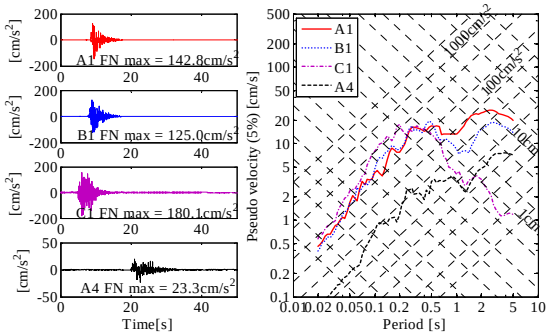

Figure 8 Acceleration Time History and Response Spectra for FN component

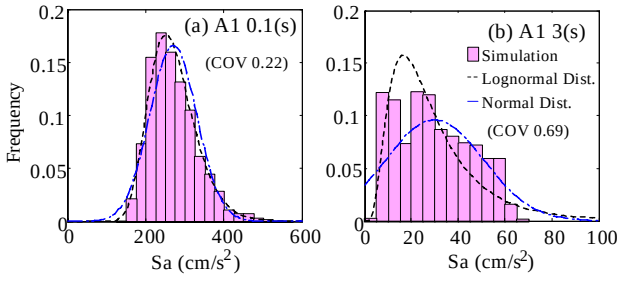

Figure 9 Histogram of All Results for FN comp. at A1: (a) 0.1 s, and (b) 3 s

simulated response spectrum and common probability distribution, the normal and log-normal distribution, with sample mean and standard deviation for period of 0.1 and 3 s. The variability for short period (0.1 s) agrees with the lognormal distribution, while that for long period (3 s) has a complicated shape of distribution and seems to have an upper limit. Though the identification of the upper limit in variability is also a research issue, the variability is measured only by the log standard deviation in this study.

3.2.2 Assumption in Analysis of Variability

The purpose of this study is to compare the variability of simulated ground motions at certain distance with residual errors in an attenuation relation. The variability at receiver is evaluated first, for that purpose. The variability at receiver is influenced by two factors: i) the variability due to asperity distribution and hypocenter location, and ii) the variability due to random phase for small earthquakes. Additionally, the variability at distance is considered to be affected by another factor, the variability due to the azimuth direction of receivers from a fault plane. The variability due to each factor is approximately evaluated as follows.

The variability at the *i*-th receiver $\sigma_{\mathrm{Total}}(i)$ is calculated across all 2400 simulated ground motions at each receiver. Since it is necessary to calculate the variability due to asperity distribution and hypocenter location independent from the effect of random phase (the *k*-th condition), the mean response spectra for random phase (20 ground motions) are calculated firstly for the *j*-th asperity and hypocenter as:

$$\log \bar{S}_a(i,j) = \frac{1}{20}\sum_{k=1}^{20} \log S_a(i,j,k) \qquad (1)$$

Next, the mean response spectra $\bar{S}'_a(i)$ at receiver are calculated for all 2400 ground motions as follows:

$$\log \bar{S}'_a(i) = \frac{1}{120}\cdot\frac{1}{20}\sum_{j=1}^{120}\left(\sum_{k=1}^{20} \log S_a(i,j,k)\right) \qquad (2)$$

Then, the variability due to asperity distribution and hypocenter location $\sigma_{\mathrm{Asp}}(i)$ is calculated as follows:

$$\sigma_{\mathrm{Asp}}(i) = \sqrt{\frac{1}{120}\sum_{j=1}^{120}\left\{\log \bar{S}_a(i,j) - \log \bar{S}'_a(i)\right\}^2} \qquad (3)$$

Then, the variability due to random phase $\sigma_{\mathrm{Phase}}(i)$ is calculated as follows:

$$\sigma_{\mathrm{Phase}}(i) = \sqrt{{\sigma_{\mathrm{Total}}}^2(i) - {\sigma_{\mathrm{Asp}}}^2(i)} \qquad (4)$$

Next, the variability at distance ${}_r\sigma_{\mathrm{Total}}$ is calculated from all simulated ground motions for three receivers with the same distance (2400 x 3 receivers). The variability due to each factor at distance ${}_r\sigma_{\mathrm{Asp}}$, ${}_r\sigma_{\mathrm{Phase}}$ is calculated as average of that at receiver as follows:

$${}_r\sigma^2_{\mathrm{Asp}} = \sum_{i=1}^{3}{\sigma_{\mathrm{Asp}}}^2(i)/3 \quad {}_r\sigma^2_{\mathrm{Phase}} = \sum_{i=1}^{3}{\sigma_{\mathrm{Phase}}}^2(i)/3 \qquad (5)$$

Finally, the variability due to receiver azimuth ${}_r\sigma_{\mathrm{Dir}}$ is evaluated as increase in the variability at distance ${}_r\sigma_{\mathrm{Total}}$ from the variability at receiver as follows:

$${}_r\sigma_{\mathrm{Dir}} = \sqrt{{}_r\sigma_{\mathrm{Total}}{}^2 - {}_r\sigma_{\mathrm{Asp}}{}^2 - {}_r\sigma_{\mathrm{Phase}}{}^2} \qquad (6)$$

Strictly speaking, the variability due to each factor is not independent from each other. They are, however, not able to be completely separated. Therefore, an increase in the variability calculated by Eq. (6) is roughly regarded as an approximation of the variability due to receiver azimuth.

Hereafter, the geometric mean of acceleration response spectra (h=0.05) for two horizontal components is investigated for comparison with an attenuation relation.

3.2.3 Variability at Receiver

Figure 10 shows the variability at receiver for each receiver azimuth. Standard deviation is 0.05 ~ 0.10 for shorter period than 0.5 s. The variability gets larger, as a

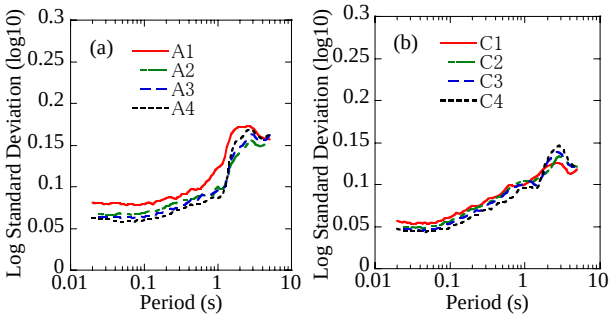

Figure 10 Variability of Response Spectra at Receiver: (a) A Line, (b) C Line

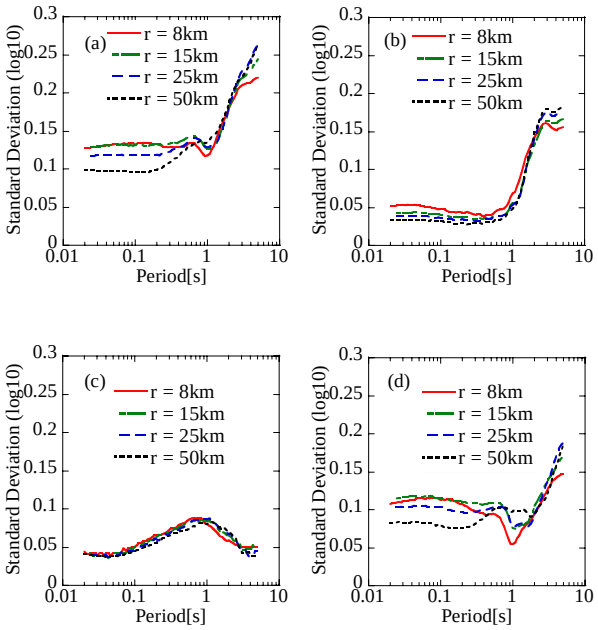

Figure 11 Variability at Distance and Decomposition by Influencing Factor: (a) Total, (b) Asperity Distribution and Hypocenter Location, (c) Random Phase for Small Earthquake, and (d) Receiver Azimuth

receiver is closer to the fault plane. The standard deviation increases for longer period, which is 0.12 ~ 0.17 for longer period than 2 s. The variability for C line is smaller than A line. The large variability at A line is caused because the directivity effects affect the response spectra in case of certain hypocenters, while not in case for other hypocenters. A similar tendency is observed at B line.

3.2.4 Variability at Distance

Figure 11(a) shows the variability at distance. The variability at distance, or the variability across receiver, is larger than the variability at receiver especially for shorter period. The variability tends to increase as a receiver is closer to the fault plane. Standard deviation is about 0.14 for shorter period than 1 s, for the fault distance 8 km and 15 km, while standard deviation is about 0.10 for the fault distance 50 km. This dependence on distance is caused because the short period ground motions are more sensitive to the difference in the distance to asperity, if a receiver is located closer to the fault plane.

Figure 11(b) shows the variability due to asperity distribution and hypocenter location. Similar to Figure 11(a), the variability for shorter period increases, as a receiver is closer to the fault plane.

Figure 11(c) shows the variability due to random phase for small earthquakes, which is stable for different fault distances. Standard deviation is around 0.05 at period shorter than 0.1 s, which has a peak at around 1 s, and decreases as period increases.

Figure 11(d) shows the variability due to receiver azimuth. The variability increases as the period increases. Standard deviation is about 0.1 for shorter period than 0.5 s and for the distance smaller than 25 km. Similar to Figure 11(a) and (b), the variability for shorter period is larger at receivers closer to the fault plane, while the variability for longer period is larger at receivers farther from the fault plane.

These results show that the variability due to asperity and hypocenter is dominant for longer period, while the variability due to receiver azimuth is dominant for wider period, especially for shorter period.

4. COMPARISON WITH RESIDUAL ERRORS IN ATTENUATION RELATION

The variability evaluated for simulated ground motions are compared with the residual errors in an attenuation relation. Asperity area ratio and rupture propagation velocity are considered as other important factors on the ground motion variability by the past researches. The effects of these factors are roughly evaluated as follows. Table 3 shows the asperity area ratio and rupture propagation velocity for the calculation. The stress drop of asperity changes with the asperity area ratio on condition that the total seismic moment is fixed, which means the variability due to asperity area ratio is equivalent of the variability due to the short period level in source spectrum.

Ground motions are calculated for three conditions, i.e. for parameters with mean and with mean plus or minus standard deviation. The asperity distribution and the hypocenter location is fixed same as in the example in Figure 8. The effect due to random phase is removed similarly as discussed in 3.2.2. The variability at receiver due to asperity area ratio or due to rupture propagation velocity is approximately evaluated as follows:

$$\sigma_{S_a}^{\pm}(T) = \left| \log\left\{\bar{S}_a^{\pm}(T)\right\} - \log\left\{\bar{S}_a(T)\right\} \right|$$

$$\sigma_{S_a}(T) = \left(\sigma_{S_a}^{+}(T) + \sigma_{S_a}^{-}(T)\right)/2 \qquad (7)$$

Where, $\bar{S}_a(T)$ and $\bar{S}_a^{\pm}(T)$ are the response spectra for mean source parameter and for source parameter with mean plus/minus standard deviation respectively.

Then, the variability at distance due to each parameter is calculated as an average of the variability at receivers similar to Eq. (5).

Figure 12 shows the variability at distance for each factor at r = 8 km. The total variability is also shown, assuming that each factor is independent from each other. The variability due to asperity area ratio is around 0.04 to 0.08 for all period, which is comparable to or a little larger than the variability due to asperity distribution and hypocenter location for shorter period than 2 s. The variability due to rupture propagation velocity is about 0.04 to 0.10 for longer period than 1 s, while it is quite small for shorter period than 0.2 s, which has less impact except for around 2 s.

Figure 13 compares the evaluated variability with the residual errors in Boore & Atkinson (2008) attenuation relation, which exhibits a moderate variability in Next Generation Attenuation projected by Pacific Earthquake Engineering Research Center (Abrahamson *et al*. 2008). A residual error in an attenuation relation can be separated into inter-event and intra-event errors; the former is roughly due to the effects of source parameters and the latter is due to the effects of local site amplification and propagation path conditions respectively. The variability evaluated in this study is generally an event-to-event variability and the effects of source parameters, thus they are considered a part of the inter-event variability. The variability due to receiver azimuth, however, is a site-to-site variability and considered to be the intra-event variability. Therefore, the variability due to receiver azimuth is compared with the intra-event error, and the variability without the variability due to receiver azimuth is compared with the inter-event error. As

Table 3 Arrangement of Asperity Area Ratio and Rupture Propagation Velocity

	mean	standard deviation
Asperity area ratio S_a/S	0.23	0.04
Rupture propagation velocity V_r	2.52	0.20

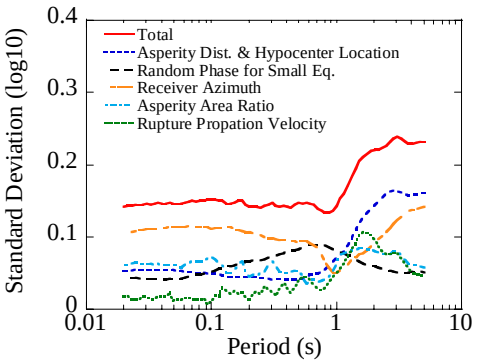

Figure 12 Variability at Distance from Simulation at r = 8 km

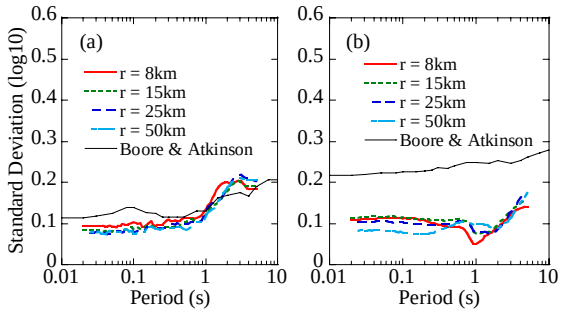

Figure 13 Comparison between Variability at Distance and Residuals Errors in Attenuation Relation: (a) Inter-event Residual, and (b) Intra-event Residual

shown in Figure 13(a), the variability of simulation result is comparable to the inter-event variability in the attenuation relation, while it is much smaller than the intra-event variability in the attenuation relation. This result suggests that the intra-event variability in the attenuation relation is affected by the difference in local site amplification and propagation path condition, which is not considered in this study and should be investigated in a future study.

5. CONCLUSIONS

The slip models of the past crustal earthquakes in Japan are compiled and statistically investigated. Asperity distribution and hypocenter location are mainly examined. Asperity tends to distribute away from the upper and lateral end of a fault plane. Hypocenter is located in and around the lower half of the largest asperity. Ground motions are simulated for a moderate shallow crustal earthquake (Mw6.5) at several receivers for different events using the stochastic Green's function method, where events have different asperity distribution and hypocenter location. The variability of the acceleration response spectra at a certain fault distance is evaluated. The variability increases as the period of the response spectra increases. The effects of other source parameters are also approximately evaluated. Finally, the variability of simulated ground motions is compared with the residual errors in an attenuation relation. The variability of the simulation results is comparable to the inter-event error in an attenuation relationship, suggesting that the inter-event error can be explained by the effects of random source parameters.

Acknowledgements:

This study was partly supported by the Japan Nuclear Energy Safety Organization (JNES).

References:

Abrahamson, N., G. Atkinson, D. Boore, Y. Bozorgnia, K. Campbell, B. Chiou, I. M. Idriss, W. Silva, R. Youngs (2008): Comparisons of the NGA Ground-Motion Relations, Earthquake Spectra, 24(1), pp.45-66.

Asano, K., Iwata, T. (2006): Source process and near-source ground motions of the 2005 West Off Fukuoka Prefecture earthquake, Earth Planets and Space, 58, pp.93-98.

Boore, D.M. (1983): Stochastic Simulation of High-Frequency Ground Motions Based on Seismological Models of Radiated Spectra, Bulletin of Seismological Society of America, 73(6), pp. 1865-1894.

Boore, D.M. and G. M. Atkinson (2008): Ground-Motion Prediction Equations for the Average Horizontal Component of PGA, PGV, and 5%-Damped PSA at Spectral Periods between 0.01 s and 10 s, Earthquake Spectra, 24(1), pp.99-138.

Headquarters for Earthquake Research Promotion (2008): Strong ground motion prediction method ("Recipe") for earthquakes with specified source faults (April 11, 2008) (in Japanese)

Ikeura,T., Noda, S. (2005): Variation of Strong Motion Response Spectra Observed at the Same Site Analysis on Data from Pair Events of the Same Magnitudes and the Same Hypocentral Distance, Journal of JAEE, 5(3), pp. 12-30 (in Japanese with English abstract).

Irikura, K., Kagawa, T., Sekiguchi, H. (1997): Revision of the empirical Green's function method by Irikura (1986), Abstracts the Seismological Society of Japan, B25. (in Japanese)

Kagawa, T. (2004): Developing a Stochastic Green's Function Method having more accuracy in long period range to be used in the Hybrid Method, Journal of JAEE, 4(2), pp. 21-32 (in Japanese with English abstract).

Kamae, K., Irukura, K. Fukuchi, Y. (1991): Prediction of Strong Ground Motion Based on Scaling Law of Earthquake, Journal of Structural and Construction Engineering, AIJ, 430, pp.1-9. (in Japanese with English abstract)

Mai, P. M., Spudich, P., Boatwright, J. (2005): Hypocenter Locations in Finite-Source Rupture Models, Bulletin of the Seismological Society of America, 95(3), pp.965-980.

Midorikawa, S., Ohtake, Y. (2003): Empirical Analysis of Variance of Ground Motion Intensity in Attenuation Relationships, Journal of JAEE, 3(1), pp. 59-70 (in Japanese with English abstract).

Miyakoshi, J., Dan, K., Fukukita, A., Okazaki, A. (2008): Effect of Random Parameters in Semi-Empirical Method on the Results of Ground Motion Predictions, Paper ID: 03-01-0008, The 14th World Conference on Earthquake Engineering.

Murakami, Y., Nobata, A., En, K. (2002): Statistical Envelope Characteristics based on Weak Earthquake Records Observed at Basement in Kinki-District, Annual meeting, Architectural Institute of Japan, B-II, pp.113-114. (in Japanese)

Somerville, P., Irikura, K., Graves, R., Sawada, S., Wald, D., Abrahamson, N., Iwasaki, Y., Kagawa, T., Smith, N., Kowada, A. (1999): Characterizing Crustal Earthquake Slip Models for the Prediction of Strong Ground Motion, Seismological Research Letters, 70(1), pp.59-80.

Strasser, F. O., Bommer, J. J. (2005): Preliminary Simulations with EXWIM: Calibration and Assessment of Ground-Motion Variability in the Near-Source Region, Research report number 05-022-SM, Imperial College London.

Sixth International Conference on Urban Earthquake Engineering
March 3-4, 2009, Tokyo Institute of Technology, Tokyo, Japan

ASYMMETRICAL GROUND MOTION UNDER EXTREME SHAKING DUE TO THE TRAMPOLINE EFFECT

Shin Aoi[1], Takashi Kunugi[1], and Hiroyuki Fujiwara[1]

1) Senior researcher, National Research Institute for Earth Science and Disaster Prevention, Japan
aoi@bosai.go.jp, kunugi@bosai.go.jp, fujiwara@bosai.go.jp

Abstract: Evidence of unusual earthquake ground motion indicating trampoline-like behavior is presented by Aoi et al. (2008b). Records for the 2008 Iwate-Miyagi earthquake in Japan, a reverse-fault crustal earthquake of magnitude Mw 6.9, reveal the largest peak ground acceleration reported to date, exceeding four times gravity. The vertical accelerogram recorded at the free ground surface has distinct asymmetry, with the positive (upward) envelope of the waveform being about 1.6 times larger than the negative (downward) envelope. Records for other strong shaking events display similar asymmetry, implying that this behavior is characteristic of large ground shaking. The asymmetry of the surface record is shown to be explainable by a simple model of a mass bouncing on a trampoline. Simulation of such motion qualitatively reproduces the characteristics of the observed shallow ground motion.

1. INTRODUCTION

Seismograms of ground motion during major earthquakes provide valuable insights into the response of the shallow ground to such events (e.g., the 1994 Northridge, 1995 Kobe, 2001 Kunlun, 2004 Parkfield, and 2007 Off-Chuetsu earthquakes). The deployment of high-density seismograph networks has contributed to recent discoveries concerning ground shaking and complex wave propagation (Frankel, 1999; Koketsu and Kikuchi, 2000; Aoi et al., 2008a), and to the development of ShakeMap, a tool for real-time seismology and earthquake hazard mitigation (Kanamori et al., 1997; Wald et al., 1999).

2. OBSERVED ASYMMETRICITY

2.1 Observed Waveforms

The National Research Institute for Earth Science and Disaster Prevention (NIED) of Japan has deployed and maintained the nationwide seismograph networks of K-NET, KiK-net, Hi-net and F-net (Kinoshita, 1998; Aoi et al., 2000; 2004; Okada et al., 2004) which consists of about 2,000 stations. A station of the KiK-net recently recorded the strongest ground motions observed to date, exceeding four times gravity, during the 2008 Iwate-Miyagi earthquake in Japan. The peak ground acceleration at IWTH25 was 4022 gal, in terms of the vector summation of all three components. The peaks in the north-south, east-west and up-down (vertical) accelerations were 1143, 1435 and 3866 gal, respectively.

This event was a reverse-fault crustal earthquake, extending 30 km in strike and 20 km in the dip direction (Figure 1). The motion was recorded at the IWTH25 (West Ichinoseki) KiK-net station, located on the hanging-wall side of the fault (Oglesby et al., 1998), 3 km southwest of the epicenter. The IWTH25 station is equipped with three-component accelerometers, installed at both the free

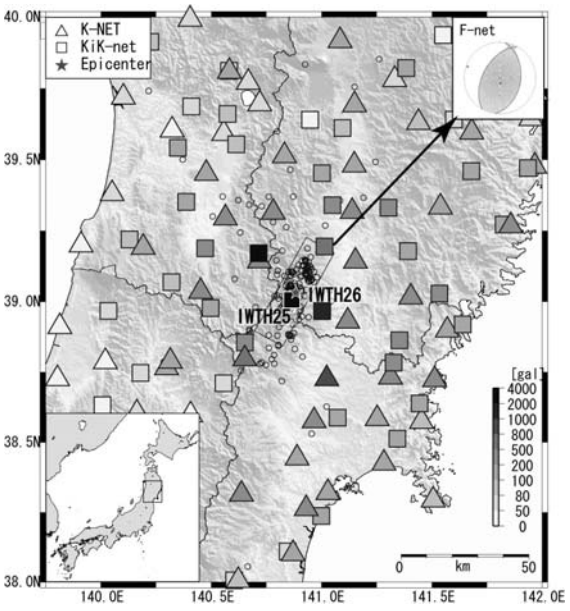

Figure 1. Map of fault region for the 2008 Iwate-Miyagi earthquake in Japan (June 14, 2008, 8:43 JST). Triangles and Squares show the K-NET and KiK-net stations, respectively, colored with the observed PGA (peak ground acceleration). Star and white circles denote epicenter of mainshock and aftershocks. General fault region is outlined in black. Focal sphere shows mechanism estimated from F-net broadband data.

surface and at the bottom of a 260 m borehole. All KiK-net stations have recently been re-equipped by new instruments. The surface sensors have been upgraded from 2000 to 4000 gal in maximum measurable acceleration.

The recorded waveforms are shown in Figure 2A. The recorded peak ground acceleration (PGA) at the surface was extraordinarily high: 4022 gal, in terms of the vector summation of all three components, and 1143, 1435 and 3866 gal in the north-south, east-west and up-down (vertical), respectively. Taking into account the downhole (GL -260 m) record at the same site at a soft rock (S wave velocity = 1810 m/s; Figure 2B) have rather large amplitude of 640 and 1039 gals for the vertical and horizontal directions respectively, one of the essential factor of the large PGA on the surface is due to the large incident acceleration at the subsurface layer.

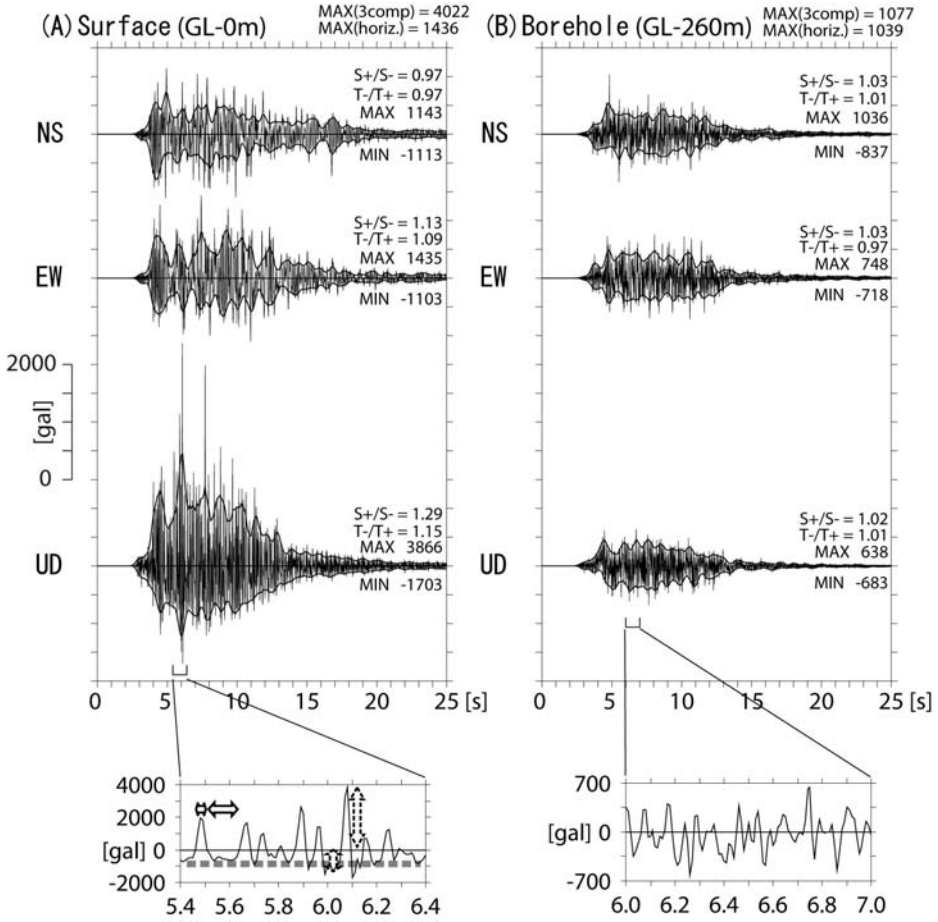

Figure 2. (A) Accelerograms recorded at IWTH25 during the 2008 Iwate-Miyagi earthquake. (Left) Surface record. (Right) Downhole (GL -260 m) record. The origin of the time axes is 8:43:44 JST. Gray areas denote envelopes of upward and downward motion in each accelerogram. Lowest column display the magnifications of vertical component accelerogram of the surface and downhole U-D sensors for 1 s time windows including the maximum shaking for each component shown by brackets under the seismograms.

During a field survey performed by NIED one week after the earthquake, we found no trace, in the neighborhood of the IWTH25 station, of stones displaced and tossed around during the strong shaking. We checked the sensors in person after the Iwate-Miyagi mainshock to ensure that no abnormal circumstances had affected the records. The sensors successfully recorded a large number of aftershocks, including one event with acceleration exceeding gravity.

2.2 Analysis of Asymmetry

The waveform and envelope of the up-down (U-D) component at the surface are strongly asymmetric with respect to the horizontal zero-axis (Figure 2A), whereas the remaining surface and downhole (GL -260 m) components are broadly symmetric. As the downhole envelope and shape of the waveform, and the PGA ratio between the horizontal and vertical components, are not considered unusual, the asymmetric phenomenon occurs near the surface, that is, from GL -260 m to the surface. The vertical ground motion has much larger high frequency content than for the horizontal components and the waveform asymmetry becomes visible above 8 Hz.

Independent estimates of the envelopes for the positive and negative polarity motions were determined by applying a triangular (1 s duration) smoothing filter to the maximum positive and negative amplitudes of the horizontal and vertical components every 0.1 s. (Figure 2). In the time window of roughly 4-14 s corresponding to large amplitude motion, the envelope determined from positive polarity is clearly larger than the envelope for negative polarity by a factor of 1.6 by peak value and 1.29 by area. After the 14 s time point, the amplitudes of both envelopes become very similar.

Only at the surface in the 4-14 s window, the upward pulses have high amplitude and sharp peaks, whereas the downward pulses are smaller in amplitude and have less abrupt peaks. Furthermore, the widths of the upward pulses are generally shorter than the corresponding downward pulses. Typical waveform during asymmetrical behavior is shown in the lowest column of Figure 2A of surface component, whereas the corresponding waveform for GL -260 m is quite ordinary. The pulse widths of the upward and

Table 1. List of stations and events plotted in Figure 3(A).

Event #	station	date and time	magnitude Mw*	epicentral distance [km]	fault type**	PGA:surface [gal]		PGA:downhole [gal]	
						down	up	down	up
1	IWTH25	2008/06/14 08:43	6.9	3.3	RF	−1703	3866	−683	638
2	NIG019	2004/10/23 17:56	6.6	7.0	RF	−545	820		
3	AKTH04	2008/06/14 08:43	6.9	25	RF	−847	1094	−116	138
4	IWTH26	2008/06/14 08:43	6.9	9.4	RF	−707	927	−167	160
5	TTRH02	2000/10/06 13:30	6.6	6.7	SS	−539	775	−267	317
6	MYG011	2003/05/26 18:24	7.0	58	RF	−680	825		
7	NIG021	2004/10/23 18:34	6.3	25	RF	−200	220		
8	IWTH04	2003/05/26 18:24	7.0	48	RF	−480	1280	−114	88
9	IWTH27	2003/05/26 18:24	7.0	27	RF	−637	615	−86	74
10	HKD020	2004/12/14 14:56	5.7	8.6	RF	−368	363		
11	HKD100	2003/09/26 04:50	7.9	84	RF	−316	461		
12	IWTH25	2008/06/14 23:42	4.6	3.3	RF	−378	343	−67	61
13	NIG021	2004/10/23 17:56	6.6	21	RF	−521	564		
14	IWT007	2003/05/26 18:24	7.0	53	RF	−474	592		

* Mw listed this table is estimated by F-net (http://www.hinet.bosai.go.jp/fnet/top.php?LANG=en).
** fault type: RF and SS mean reverse fault earthquake and strike slip earthquake, respectively.

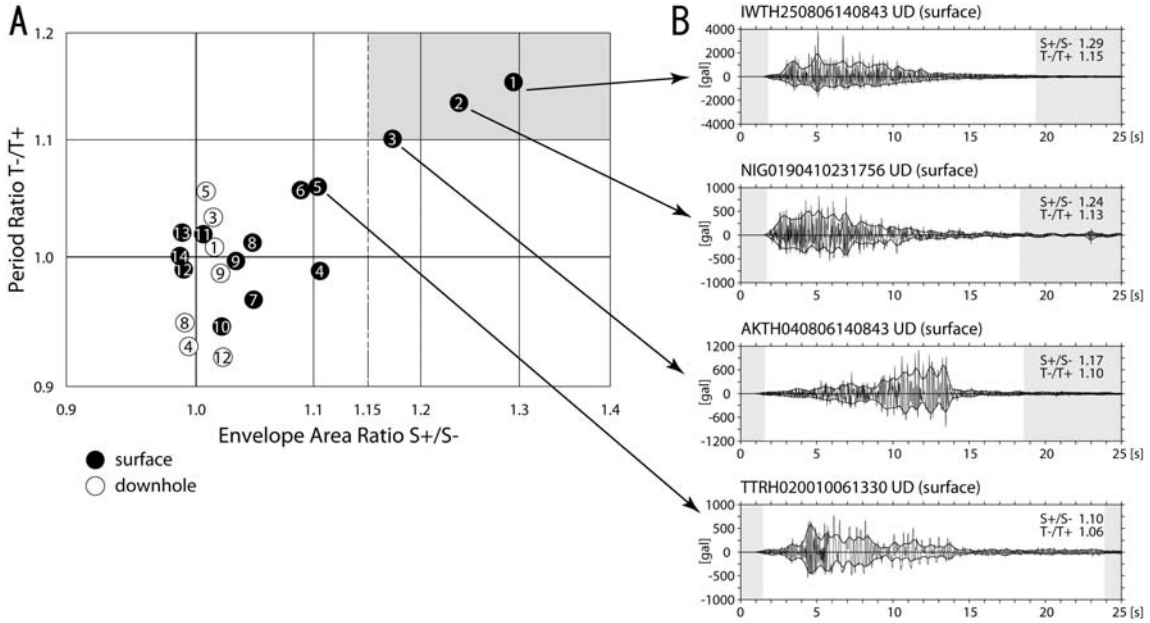

Figure 3. (A) Plot of S+/S- vs. T-/T+ ratio for vertical component of 14 records with PGA exceeding gravity picked from all of the K-NET and KiK-net database. Close and open circles denote surface and downhole values (downhole measurements available only for KiK-net). Gray area denotes region of S+/S- > 1.15 and T-/T+ > 1.10 where the indexes show strong waveform asymmetry. (B) Waveforms displaying strong asymmetry. Indexes shown are calculated for the time windows shown in white in each waveform trace.

downward components were investigated separately by the half-period zero-crossing method, where a positive/negative pulse period is defined as twice the time between two consecutive seismogram zero-crossings corresponding to positive or negative pulses. The periods of upward motion are distinctly shorter than the periods of downward motion in the time window of 4-14 s on the surface. These two patterns of asymmetry are only observed in the 4-14 s time window, with the seismogram being broadly symmetrical at later times.

Two indexes are introduced here as measures of waveform asymmetry; the ratio between the areas of the positive (S+) and negative (S-) envelopes, and the ratio between the average pulse periods of the negative (T-) and positive (T+) motions. These two indexes were calculated for the longest continuous time window over which the envelop amplitudes were greater than 5% of the maximum amplitude. For the surface mainshock recorded at IWTH25, these two indexes are S+/S- = 1.29 and T-/T+ = 1.15.

2.3 Asymmetry Observed in Other Earthquakes

To investigate the presence of such asymmetry in other records we used 14 accelerograms exceeding gravity (vector summation of three component) picked from among approximately 200,000 records in the K-NET and KiK-net database (Table 1). Among these 14 records, two display distinct asymmetry similar to that seen for the present IWTH25 record where we judge the threshold of S+/S- > 1.15 and T-/T+ > 1.10 shown by gray area in Figure 3A. It should be emphasized that the S+/S- and T-/T+ ratios have a lower-bound limit close to unity, particularly for the S+/S- ratio. Moreover both ratios have tendency to increase as ground acceleration rise. At IWTH25, a largest aftershock indicated by event number 12 in the figure had quite symmetrical feature implying the asymmetrical tendency is not the original nature of this station. Event number 5, a strike-slip earthquake, also has a tendency of waveform asymmetry, suggesting that the occurrence of waveform asymmetry is not peculiar to reverse fault for strong shaking events. Yet there are cases in which strong asymmetry was not observed, in spite of strong shaking. Number of cycles or frequency of ground shaking may be one of the key factors for occurrence of waveform asymmetry and, investigating the conditions giving rise to waveform asymmetry is a topic for future research.

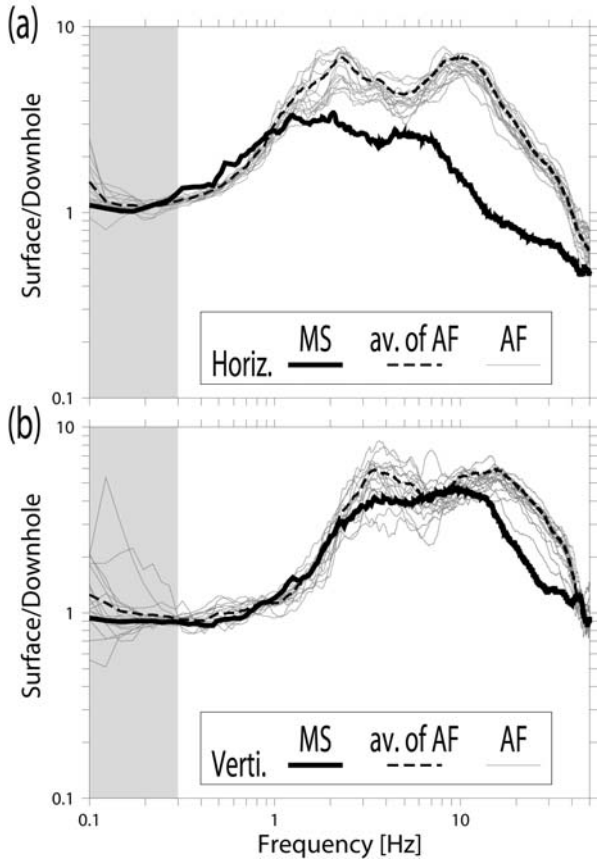

Figure 4. Fourier spectral ratios between surface and downhole records for the vertical (a) and horizontal (b) components. Thick, dotted and thin lines are for ratios of mainshock, average ratios of aftershocks and ratios of each aftershock, respectively. 16 aftershocks whose PGAs are between 10 to 100 gal, are selected.

3. TRAMPOLINE MODEL

Let us consider the mechanism of the waveform asymmetry. Earthquake ground motion is generally well approximated by wave propagation across an elastic medium satisfying a wave equation, implying that it should demonstrate no polarity with respect to amplitudes in positive and negative directions for any symmetric input motion. During strong shaking, it is well known that the non-linear behavior of the ground becomes important (Idriss and Seed, 1968; Field et al., 1997; Bonilla et al., 2002; 2005). Figures 4 show the Fourier spectral ratios between surface and downhole records for aftershocks which approximate the expecting amplification factor between downhole and surface sites under a linear behavior. The ratio for mainshock is smaller than the average of the ratios of aftershocks due to the anticipated non-linearity as is frequently observed during intense shaking, and the degree of the amplification for mainshock is not much larger that is expected. However, this kind of conventional non-linearity does not satisfactorily explain the occurrence of waveform asymmetry.

It is suggested here that when the subsurface is struck by strong shaking, the assumption of elastic deformation of the ground fails. Under the strong downward acceleration, the medium stress condition becomes tensile implying that tensile cracks or apertures may develop within the media and the ground loses its cohesion. By analogy, consider the scenario of an open box filled with cohesionless material like sand. At low shaking acceleration in the vertical direction, the sand behaves like an elastic medium. As the shaking increases in intensity, the sand continues to deform elastically with upward motion under compressional stress, yet begins to separate during downward acceleration. The sand particles lose contact, resulting in a reduction of interactions between grains and the inability of the medium to convey stresses. This situation is essentially a free-fall state. When the acceleration turns upward, the sand grains are highly compressed toward the bottom of the box and undergo rapid upward acceleration. This behavior can also be understood by considering the motion of a person bouncing on a trampoline (Cartoon of Figure 5A). In this case, there are two forces acting on the person; down-going gravity, and the upward force applied when the person hits the trampoline, which is larger than gravity. Two forms of waveform asymmetry are applicable in this case; the asymmetry of amplitude because the downgoing acceleration is limited to -1×g while the upgoing acceleration is much larger, and the asymmetry of period because the time to be pushed up is shorter than the time to be pulled down to the mat by gravity.

This "trampoline" model is illustrated in Figure 5. The motion of a rigid mass bouncing on the trampoline is shown in Figure 5A. The pulse waveform in Figure 5A was obtained using the Gaussian function with the constraint that the pulse shape integrates to zero over each single cycle. Figure 5B denotes the elastic deformation of the mass which is picked out from the later portion of the downhole records which is expected to be elastically behaved. Assuming the

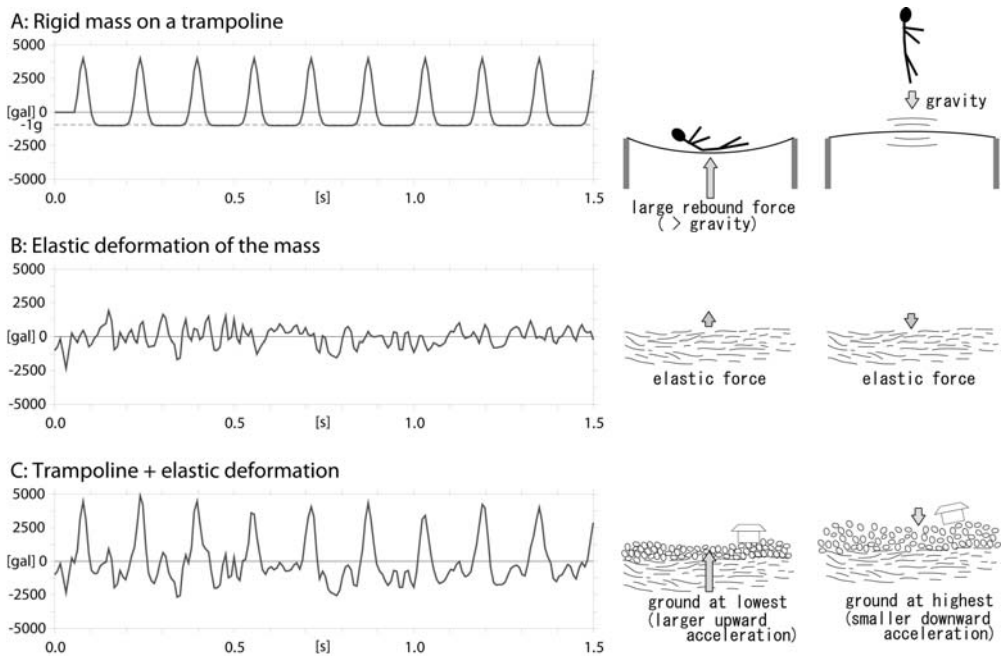

Figure 5. (A) Motion of a rigid mass bouncing on the trampoline. The motion in this case is represented by pulses with constant period and maximum amplitude. (B) Motion due to the elastic deformation of the mass. (C) Simulated ground motion which is the summation of (A) and (B), assuming the asymmetrical ground motion is composed by the trampoline-like motion (A) and the elastic behavior (B).

asymmetrical ground motion is composed by the trampoline-like motion and the elastic behavior, the total motion of (A) and (B) is shown as the simulated ground motion in Figure 5C. This motion is qualitatively similar to the observed vertical waveform shown in the inset of Figure 2A of surface record, satisfactorily explaining the generation of asymmetrical ground motion, and also the existence of a maximum downward acceleration of close to -1×g.

As the ground is not rigid and cannot be entirely approximated as a cohesionless material, and is affected by natural factors such as friction, other interactions, and complexity of the medium, the true behavior is more complex than the trampoline analogy. However, the fundamental ground motion is considered to accord well with a model in which elastic deformation applies at low acceleration, while high acceleration results in tensile behavior and a loss of cohesion. Such asymmetry of motion may be general characteristic of large ground shaking, since the ground surface is free in the normal upward direction and is unable to constrain the medium under strong downward acceleration.

References:

Aoi, S., Obara, K., Hori, S., Kasahara, K., and Okada, Y. (2000). "New Strong-Motion Observation Network: KiK-net," *EOS. Trans. AGU*, **81**(48), Fall Meet. Suppl., Abstract S71A-05.

Aoi, S., Kunugi, T., and Fujiwara, H. (2004). "Strong-Motion Seismograph Network Operated by NIED: K-NET and KiK-net," *J. Japan Assoc. Earthq. Eng*., **4**, 65-74.

Aoi, S., Honda, R., Morikawa, N., Sekiguchi, H., Suzuki, H., Hayakawa, Y., Kunugi, T., and Fujiwara, H. (2008a). "Three-Dimensional Finite Difference Simulation of Long-Period Ground Motions for the 2003 Tokachi-oki, Japan, Earthquake," *J. Geophys. Res.*, **113**, B07302.

Aoi, S., Kunugi, T., and Fujiwara, H. (2008b). "Trampoline Effect in Extreme Ground Motion," *Science*, **322**, 727-730.

Bonilla, L.F., Steidl, J.H., Gariel, J.C., and Archuleta, R.J. (2002). "Borehole Response Studies at the Garner Valley Downhole Array, Southern California," *Bull. Seismol. Soc. Am*., **92**, 3165-3179.

Bonilla, L.F., Archuleta, R.J., and Lavallee, D. (2005). "Hysteretic and Dilatant Behavior of Cohesionless Soils and Their Effects on Nonlinear Site Response: Field Data Observations and Modeling," *Bull. Seismol. Soc. Am*., **95**, 2373-2395.

Field, E.H., Johnson, P.A., Beresnev, I.A., and Zeng, Y. (1997). "Nonlinear Ground-Motion Amplification by Sediments during the 1994 Northridge Earthquake," *Nature*, **390**, 599-602.

Frankel, A.D. (1999). "How Does the Ground Shake?," *Science*, **283**, 2032-2033.

Idriss, I.M. and Seed, H.B. (1968). "An Analysis of Ground Motions during the 1957 San Francisco Earthquake", *Bull. Seismol. Soc. Am.*, **58**, 2013-2032.

Kanamori, H., Hauksson, E., and Heaton, T. (1997). "Real-Time Seismology and Earthquake Hazard Mitigation," Nature, 390, 461-464.

Kinoshita, S. (1998). "Kyoshin net (K-NET)", *Seismol. Res. Lett.*, **69**, 309-332.

Koketsu, K. and Kikuchi, M. (2000). "Propagation of seismic ground motion in the Kanto basin, Japan," *Science*, **288**, 1237-1239.

O'Connell, D.R.H. (2008). "Assessing Ground Shaking," *Science*, **322**, 686-687.

Oglesby, D.D., R. J. Archuleta, R.J., and Nielsen, S.B. (1998), "Earthquakes on Dipping Faults: The Effects of Broken

Symmetry", *Science*, **280**, 1055-1059.

Okada, Y., Kasahara, K., Hori, S., Obara, K., Sekiguchi, S., Fujiwara, H., and Yamamoto, A. (2004). "Recent Progress of Seismic Observation Networks in Japan ---Hi-net, F-net, K-NET and KiK-net ---," *Earth Planets Space*, **56**, xv-xxviii.

Wald, D.J., Quitoriano, V., Heaton, T.H., Kanamori, H., Scrivner, C.W., and Worden, C.B. (1999). "TriNet "ShakeMaps": Rapid Generation of Peak Ground Motion and Intensity Maps for Earthquakes in Southern California," *Earthquake Spectra*, **15**, 537-555.

Sixth International Conference on Urban Earthquake Engineering
March 3-4, 2009, Tokyo Institute of Technology, Tokyo, Japan

A MODEL OF GROUND STRUCTURE ESTIMATED BY MICROTREMOR ARRAY OBSERVATIONS IN HSINCHU, TAIWAN.

H. Morikawa[1], T. Noguchi[2], H.-T. Chen[3], T. Kobayashi[4], and K. Iwahori[5]

1) Associate Professor, Department of Built Environment, Tokyo Institute of Technology, Japan
2) Assistant Professor, Department of Civil Engineering, Tottori University, Japan
3) Professor, Department of Civil Engineering, National Central University, Taiwan
4) Under Graduate Student, Department of Civil Engneering, Tokyo Institute of Technology, Japan
5) Under Graduate Student, Department of Civil Engneering, Tottori University, Japan
morika@enveng.titech.ac.jp, noguchit@cv.tottori-u.ac.jp, chenhtofpadau@seed.net.tw,
kobayashi.t.ba@m.titech.ac.jp, iwahori05007@cv.tottori-u.ac.jp

Abstract: To obtain a detailed model of the three-dimensional ground structure, the microtoremor surveys have been carried out at nine sites around Hsinchu area, Taiwan using large arrays. Using these data of miroseisms, velocity structures to bedrock are estimated and the results at some of the sites are reported preliminarily. The bedrock, whose shear wave velocity is estimated as 3 km/s, is found at about 1-km depth from the surface. A layer with about 2 km/s, furthermore, is also found in only the middle of the target area, where corresponds to a limited area between two faults: Hsinchu and Hsincheng faults. It, however, is difficult to explain the gravity anomaly from the obtained velocity structures: especially, we could not find any deep structures in the area of the lowest gravity anomaly, where is observed in south-eastern area.

1. INTRODUCTION

To estimate the earthquake ground motions, it is very important to know the ground structure, especially, deep and three-dimensional structure, because the ground motions excited by a large earthquake predominate components with long period which relates to the deep structure. For this purpose, we have many kinds of technique for the geological survey, though some of them may be costly. The microtremor and gravity survey are easy to conduct the survey and not so expensive techniques. Thus, for estimating the three-dimensional ground structure over a large area, these techniques are useful and provide good information without much cost. Especially, the microtremor array survey is suitable to estimate the detailed velocity structure at a specific site using the phase velocity.

The geological setting of Taiwan is really complicated because there is the boundary between the Eurasia and Philippine plates and we can find so many active faults in the Taiwan island. This means that the seismic activity is very high in Taiwan. Under this circumstance, we focus the target for our survey on Hsinchu city, Taiwan, where many industrial factories, especially for IT, computer, semiconductor companies are located. We, therefore, may say that Hsinchu area should be key for the Taiwanese economy.

From this, it is very important to know the ground structure and to estimate some strong ground motions in this area. As a first step to estimate earthquake ground motion for earthquake disaster mitigation, we will try to make a detailed model of three-dimensional shape of the surface for the bedrock which is defined, hereafter, as hard rock like granite.

For this purpose, we have carried out the gravity survey and microtremor array observations for the short period range [1, 2, 3]. However, the gravity anomary obtained from the gravity survey depends on the density structure. This means that it is difficult to determine the velocity structure absolutely. We, thus, have to introduce some other information in order to determine the velocity structure with abolute values of depth to the bedrock. The array observations of microseisms, which are microtremors with long period such as 1 to 10 second, are carried out to determine the deep structure. Using these data of miroseisms, velocity structures to bedrock are estimated and the results at some of the sites are reported preliminarily.

2. GEOLOGICAL SETTING AROUND HSINCHU CITY, TAIWAN

Hsinchu city is located at the north-western area of Taiwan as shown in Figure 1. The altitude of north-western part is very low and the south-eastern part is very high such as more than 1000m. The topographical map is shown in Figure 2. In the are of this figure, the higest altitude is

Figure 1 Location of Hsinchu city

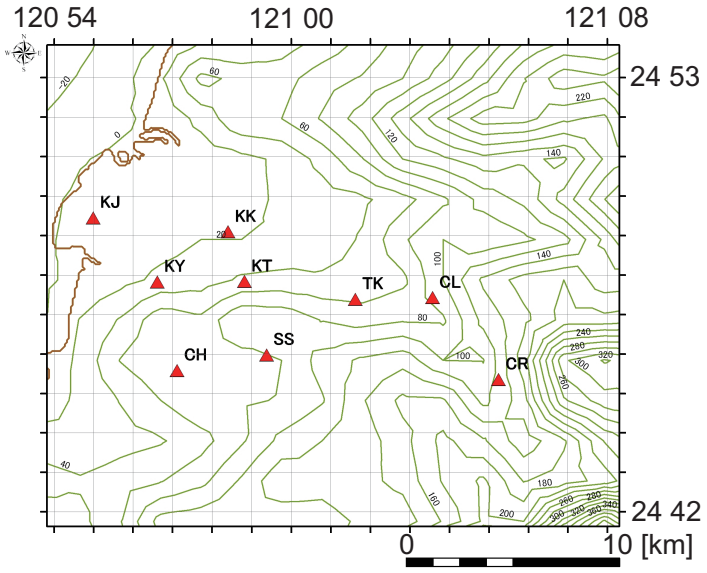

Figure 2 Topographical map around Hsinchu city (contour lines). Horizontal and vertical coordinates show the longitude and latitude, respectively. In this map, triangles stand for the observation sites of microtremor arrayy, and the two-character words for site codes.

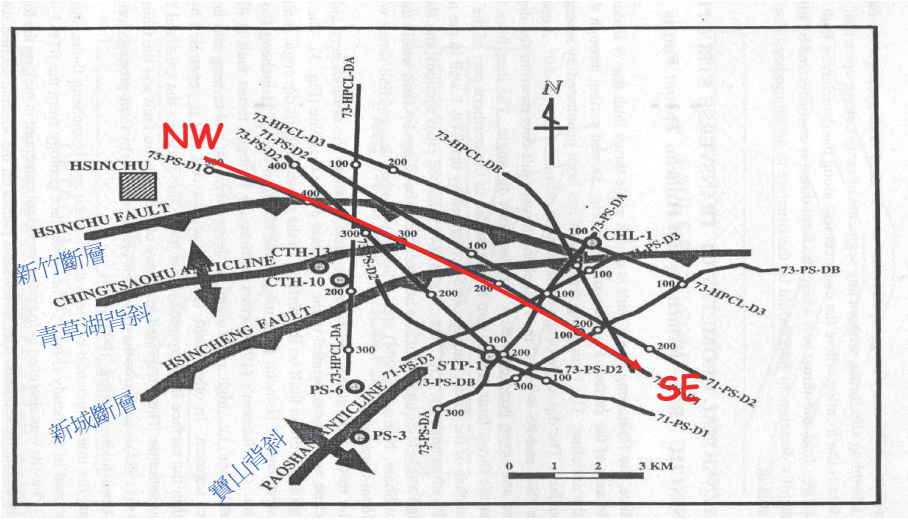

Figure 3 Faults and geological system around Hsinchu city (after Shu-Fan [4])

about 400m. Furthermore, we can find many faults around Hsinchu city as shown in Figure 3. In the southern part of Hsinchu city, anticline and syncline, whose directions are north-eastern to south-western, are found and the fault is recognized between them. The Hsincheng fault is considered as an active fault and it is key issue to consider mitigation of the earthquake disaster. Furthermore, we can see the similar structure in the northern part of Hsinchu city, which includes the anti- and syncline structure with Hsinchu fault.

From some results of gravity survey (for example, after Shu-Fan [4] and Morikawa et al. [1]), the peculiar low anomaly of gravity is found in the southern part of Hsinchu city. They consider existence of the oil around this low anomaly area, and carried out many kinds of survey to know the ground structure including the deep borehole and dense gravity survey. Unfortunately, in this area, there is no oil, but we can see the geological profiles along some lines. Figure 4 is an example of the detailed profiles. Furthermore, using the information of the gravity anomaly, the density structure is proposed as shown in Figure 5. Although these maps might be made by considering the gravity anomaly, the authors have no information about the detailed processes to make the profiles.

3. OBSERVATIONS AND RESULTS OF MICROTREMOR ARRAY OBSERVATIONS

To determine the velocity structure, we carried out array observations of microseisms at 9 sites around Hsinchu city, where are shown in Figure 2, during September 16th to 27th. For this observation, we used moving-coil-type velocity sensors, whose natural period is 2 seconds, and digital recorder with 24-bit resolution $\Delta\Sigma$ A/D converter,

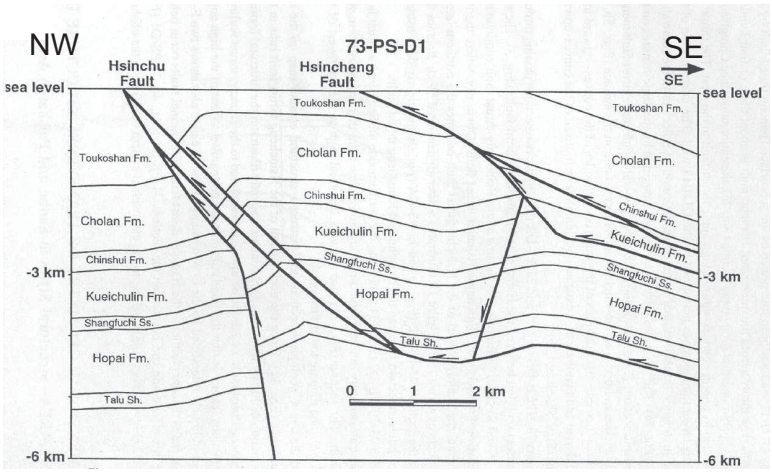

Figure 4 Section profile on the NW-SE line of Figure 3 (after Shu-Fan [4])

年代	地層		地下密度 潘 (1965)	地表密度 謝與胡 (1972)	地表密度 本研究
更新世	台地堆積		——	——	1.85
	紅土台地堆積		——	——	1.90
	大南澗層		——	——	1.95
上新一更新世	甜樂山層	上部	——	1.90-2.00	2.09
		下部		2.10	
上新世	半屯層		2.30	2.20	
	錦水頁岩		2.35	2.30	
中新世	桂竹林層		2.45	2.40	
	南莊層	上福基砂岩	2.54	2.40	——
		河排層		2.40	
	南港層		2.55		
	石底層		2.56		
	大寮層		2.57	——	
	木山層		2.60		

Figure 5 Examples of the available density structure [4]. The right column is obtained by the results of a research in 1975.

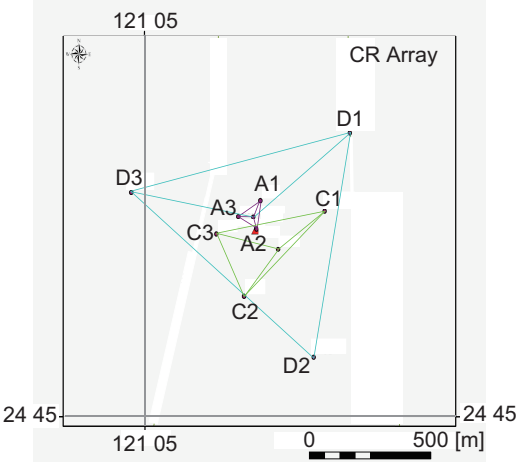

Figure 6 An example of the array collocation of site CR. The array radii are 50, 200, and 490 m.

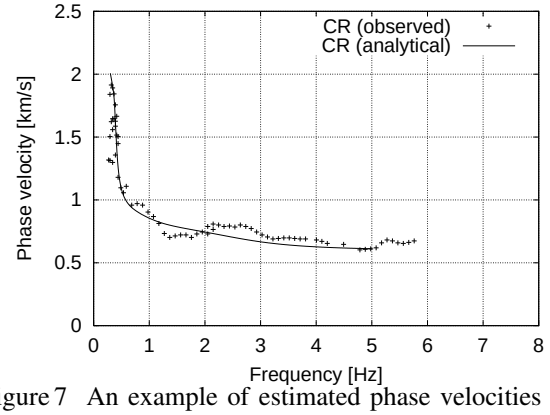

Figure 7 An example of estimated phase velocities (site CR). The plus signs are the observed values and the solid line is analytical dispersion curve obtained from a velocity structure model.

which include an analog gained filter and GPS clock system. The time is synchronized by the GPS clock and data is recorded by sampling rate 800 Hz after passing the low pass filter with cut off frequency of 10 Hz. Before the observations, a step response of the pendulum is recored to perform the correction of istrumental characteristics during the process of analysis.

Radii of the arrays are 60 m to 500 m and the radii depend on the sites. An example of the array collocation is shown in Figure 6. The observation is performed at 4 sites simultaneously. For the analysis, the spatial autocorrelation (SPAC) method [5] is applied and phase velocities are estimated. Figure 7 shows an example of the results.

4. DISCUSSION

To estimate the velocity structure, we search a structure to satisfy the observed phase velocity using a heuistic approach based on forward calculations. As a result, the layers with some different shear wave velocities (hereafter, V_s) are determined: roughly speaking, the values of V_s are 500 m/s, 800 m/s, 1.2 km/s, 2.0 km/s, and 3.0 km/s, which is considered as a bedrock such as granite. The profiles of the velocity structures are shown in Figure 8 for five sites.

The basement can be found at about 1-km depth from the surface. The thickness of the sediments, which correspond to alluvial and/or diluvium with shear wave velocity less than 600 m/s is almost same for the five sites. At the seashore, site KJ, the thickness of the sediments is slightly larger than the other sites and very soft soil with about 250 m/s is determined. This properties may be reasonable from the geological viewpoints. A layer with $V_s \approx 2$ km/s, furthermore, is founed at only the middle of the target area: KY, KT, and TK, where corresponds to a area surrounded by Hsinchu and Hsincheng faults.

The location of sites for the array observations is very close to the NW-SE line of Figure 3. From the Figure 4, the geological structure around the middle of the two faults is very different from the other area. The results obtained from the array observations may reflect the ge-

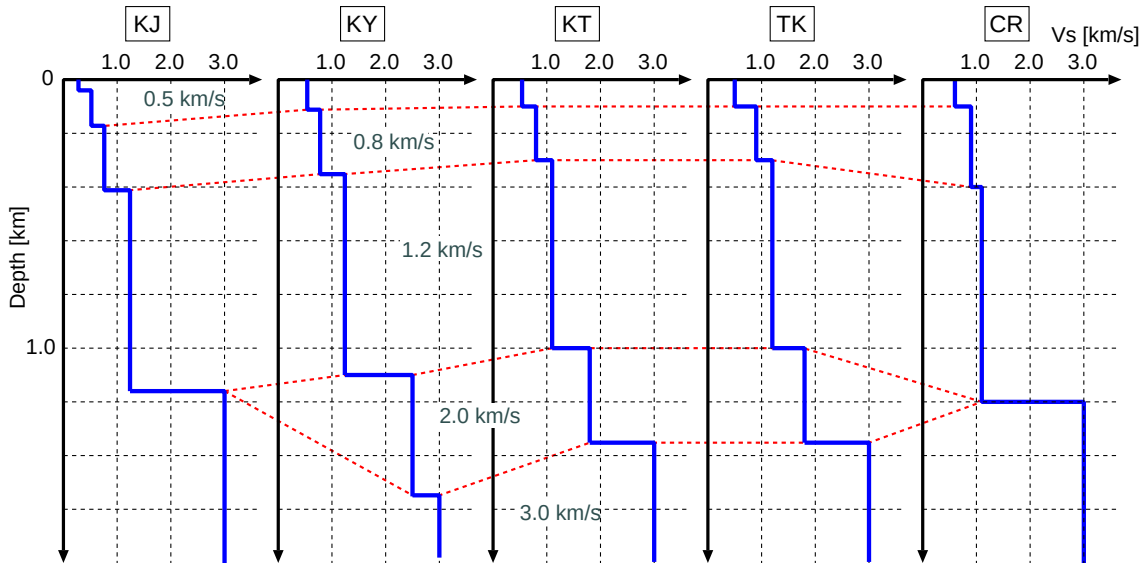

Figure 8 Velocity structures at each site. The dashed lines connet the correspondent layers and the numbers shown between the dashed lines denote the approximate values of shear wave velocity for each layer.

ological properties, though it is very difficult to say the correspondence between the layers proposed geologically (Figure 4) and ones obtained by this analysis (Figure 8).

From the gravity survey, a very low gravity anomaly is observed around the site CR (Morikawa et al. [1, 2, 3]). This suggests that the basement is very deep in this area. However, the depth to the bedrock estimated by the microtremors is not so deep at site CR. This may be caused by the very low density structure around site CR. In the present time, it is difficult to explain this inconsistency between density and velocity structure.

5. CONCLUSIONS

We have carried out the microtremor observation of large arrays at 9 sites around Hsinchu area, Taiwan. Using observed data, we estimated the phase velocities and velocity structures at the sites using the spatial autocorrelation method and a heuistic approach based on forward calculations. The results from this research are listed as follows:

- The depth to the bedrock, whose shear wave velocity is about 3 km/s, is about 1 km.
- In the sediment, 4 or 5 layers are determined: 500 m/s, 800 m/s, 1.2 km/s, and 2.0 km/s. Only at seashore, very soft soil, whose velocity is 250 m/s, is determined.
- The layer with velocity 2.0 km/s is found at only the area surrounded by Hsinchu and Hsincheng faults. This structure seems to relate to the geological setting in this area.
- Although the gravity anomaly is very low in the south-eastern area, the depth to the bedrock, wich is estimated from microtremors, is almost same for the sites. To explain this inconsistency, some more geological infomation is necessary.

Acknowledgments:

Many students of graduate and under graduate school of civil engineering, National Central University, Taiwan are gratefully acknowledged for their kind supports for the microtremor observations in Hsinchu area.

References:

[1] Morikawa, H., Komazawa, M., Chen, H.-T., Shosaka, T., and Takahashi, C., "A model of ground structure and numerical simulation of an earthquake ground motion around Hsinchu city, Taiwan on the baseis of gravity survey," *Proc. 2007 Taiwan-Japan Symposium on the Advancement of Urban Earthquake Hazard Mitigation Technology*, National Central University, Taiwan, September 26–27, 2007.9, pp. 73–80.

[2] Morikawa, H., Chen, H.-T., Takahashi, C., Kawatsure, H., and Komazawa, M., "Detailed study on ground structure around Hsinchu city, Taiwan using gravity and microtremor surveys," *Proc. of fifth International Conference on Urban Earthquake Engineering*, Tokyo, Japan, March 4–5, 2008.3, pp.89–94.

[3] Morikawa, H., Komazawa, M., Chen, H-T., Takahashi, C., Shosaka, T., and Kawatsure, H., "A model of ground structure to estimate earthquake ground motions around Hsinchu city, Taiwan on the basis of gravity and microtremor surveys," *Proc. of 14th World Conference on Earthquake Engineering*, Beijing, Chaina, October 12–17, 2008.10, paper No. 02-0034.

[4] Shu-Fan, Report on the ground structure around Hsinchu district, through the personal communication with Prof. Yen of National Central University, Taiwan.

[5] Matsushima, T. and H. Okada, Determination of Deep Geological Structures under Urban Areas using Long-Period Microtremors, *Butsuri-Tansa*, Vol. 43, pp.21–33, 1990.

Sixth International Conference on Urban Earthquake Engineering
March 3-4, 2009, Tokyo Institute of Technology, Tokyo, Japan

DAMAGE OF THE 2008 WENCHUAN, CHINA EARTHQUAKE OBSERVED IN SATELLITE OPTICAL AND SAR IMAGES

Hiroyuki Miura[1] and Saburoh Midorikawa[2]

1) Assistant Professor, Dept. of Built Environment, Tokyo Institute of Technology, Japan
2) Professor, Dept. of Built Environment, Tokyo Institute of Technology, Japan
hmiura@enveng.titech.ac.jp, smidorik@enveng.titech.ac.jp

Abstract: The characteristics of the satellite optical and SAR (synthetic aperture radar) images observed in a catastrophically damaged area by the 2008 Wenchuan, China earthquake are examined. From the comparison of the pre- and post-event optical images observed in Qushan town, Beichuan county, the completely collapsed buildings and the landslides are clearly identified. The visual damage detection using the optical images shows that totally about 80% of the buildings are classified into severe damage or complete collapse. From the post-event SAR image, large landslides and slope failures are identified.

1. INTRODUCTION

On May 12, 2008, a gigantic inland earthquake (Ms8.0, Mw7.9) attacked the Sichuan province in China, that was named the 2008 Wenchuan, China earthquake. About 87,000 people were killed or missing, 370,000 were injured, and more than four million houses were damaged. Severe building damage is mainly distributed in mountainous areas located above the fault. Landslides and slope failures buried lots of buildings in villages. They also produced isolation of people by road blockages and quake lakes by river blockages. In order to capture the distribution of the damage in a large area, remote sensing data from satellites would be useful.

In remote sensing technology, optical and synthetic aperture radar (SAR) sensors are widely used. Optical images are easily recognizable for human because the images cover visible spectral bands that correspond to visible range of human. It is, however, difficult to observe the earth's surface in cloud-covered areas. On the contrary, SAR systems can image the earth's surface without being influenced by weather condition. This advantage would be powerful to capture affected areas immediately after a disaster.

After the Wenchuan earthquake, many optical and SAR images were acquired in the affected areas. This paper describes the characteristics of the satellite optical and SAR images in a catastrophically damaged area to discuss the performance of the images for damage detection.

2. TARGET AREA AND SATELLITE IMAGES

Figure 1 shows the isoseismal map of the 2008 Wenchuan earthquake (China Earthquake Administration, 2008) with the locations of major cities in Sichuan province, China. The seismic intensity scale in China almost corresponds to the Modified Mercari intensity scale. The seismic intensity XI areas are distributed in Wenchuan county located near the epicenter and in Beichuan county located about 130km northeast from the epicenter.

The target area is Qushan town in Beichuan county that was catastrophically damaged due to the earthquake. Table 1 shows the characteristics of the satellite images used in this study. ALOS (Prism/Avnir2), and FORMOSAT images are optical data with the spatial resolution of 3m, and 2m, respectively. The TerraSAR-X image is SAR data with the

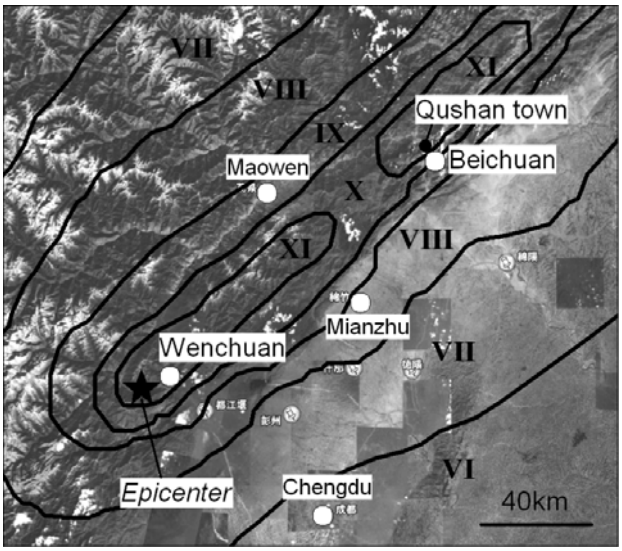

Figure 1 Isoseismal map of the 2008 Wenchuan, China earthquake (China Earthquake Administration, 2008) with locations of major cities

resolution of 3m. The images used in this study are the pre-event ALOS image, post-event FORMOSAT image and post-event TerraSAR-X image.

3. DAMAGE OBSERVED IN SATELLITE IMAGES

Qushan town in Beichuan county located about 130km northeast from the epicenter was struck by the strong ground motion whose seismic intensity is XI. Number of the residents in the town was about 22,000 before the earthquake. About 12,000 people that correspond to 55% of the residents were killed in the earthquake. Because of the heavy damage, the town was abandoned and all the survived residents were evacuated from the town.

Figures 2 (a) and (b) show the satellite images in the built-up area of Qushan town. Large landslides and slope failures are clearly observed from the post-event image as shown by black line areas in Fig. 2(b). Figure 3 shows the aerial photograph captured from the direction shown by arrow in Fig. 2(b) (Munich Re Group, 2008). The solid square in Fig. 2(b) corresponds to the area of the aerial photo. The photo shows that many buildings are completely collapsed. The buildings located in the western part of the area are buried in the soils flowed by the large landslide. The road blockages by the landslides in the eastern part of the area are also identified in the photo.

Table 1 Characteristics of Satellite Images

Town	Qushan, Beichuan county		
Timing	Pre	Post	Post
Date	Mar. 31, 2007	May 14, 2008	May 16, 2008
Sensor	Optical	Optical	SAR
Satellite	ALOS (Prism/Avnir-2)	FORMOSAT	TerraSAR-X
Polarization	—	—	HH
Resolution	3 m	2 m	3 m

Visual detection of building damage is applied using the pre- and post-event optical images. Firstly, locations of buildings are detected from the pre-event image. Even from 3m-resolution satellite image, however, it is difficult to identify the locations of rather small buildings. Minimum building size detected from the image is approximately 10 to 15m.

The damage level of the buildings is classified by comparing the pre- and post-event images. The post-event image and the ground photographs are shown in Figs. 4. In the completely collapsed building, the roof and outline of the /building cannot be identified from the satellite image and many rubbles are observed around the building. In the severely damaged building, although the roof and outline of the building can be identified, the rubbles are observed around the building in the image. In the slightly damaged or undamaged building, the significant change cannot be observed between the pre- and post-event images.

Because it is difficult to classify moderate damage, slight damage and no damage even from a high-resolution satellite image (Miura *et al.*, 2006), the damage levels are finally classified into three categories; complete collapse, severe damage, and slight or no damage. The characteristics of the post-event image for each damage level are summarized in Table 2. The buildings completely buried in soils of a landslide are classified into complete collapse. The buildings whose roof damage is clearly identified are classified into severe damage. Based on the criteria shown in Table 2, the damage detection is applied to building by building.

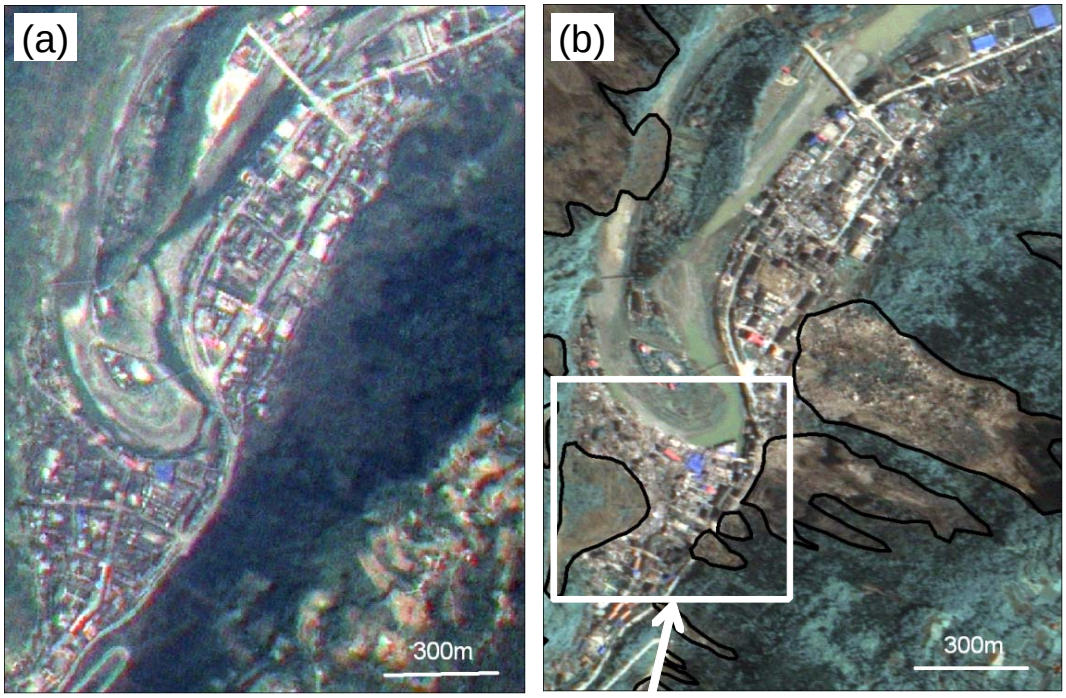

Figures 2 (a) Pre-event ALOS Image, (b) Post-event FORMOSAT Image

Figure 3 Photograph at Southern Part of Qushan Town, Beichuan County (Munich Re Group, 2008)

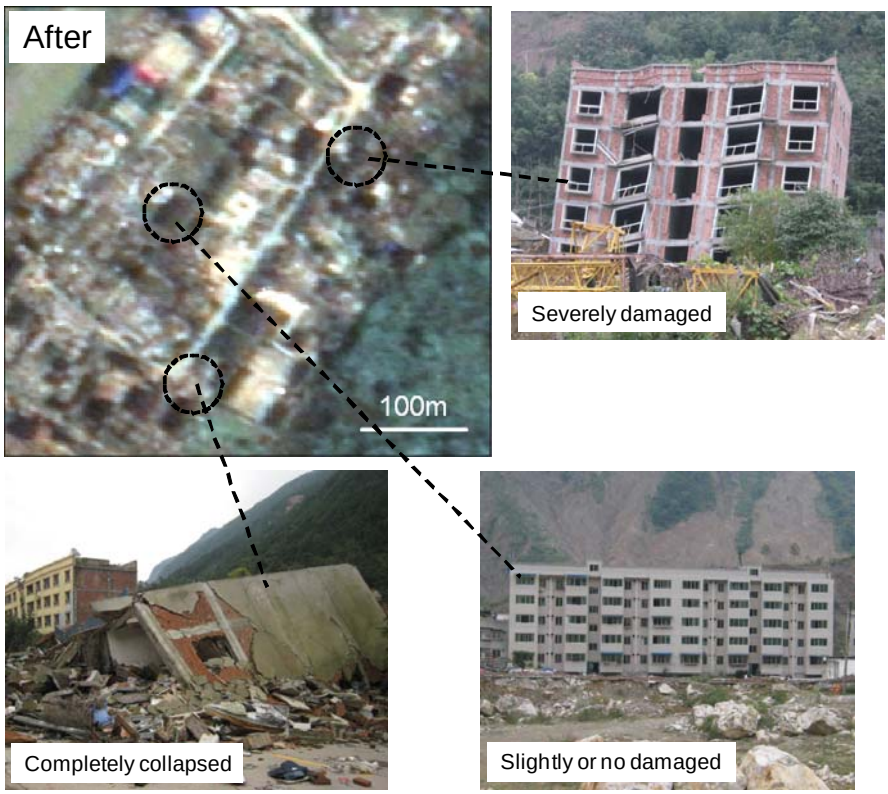

Figures 4 Post-event Satellite Image and Ground Photographs

The result of the visual detection of the building damage is shown in Fig. 5. The number of the damaged buildings and the damage ratio are shown in Table 3. Totally the locations of 457 buildings are detected. The numbers of completely collapsed and severely damaged buildings are 273 and 96 that are about 60% and 20% of the total, respectively. The number of slight or no damaged buildings is 88 that is about 20% of the total. The result shows that approximately 80% of the buildings are classified into severe damage or complete collapse.

Figure 6 shows the TerraSAR-X image observed after the earthquake. The spatial resolution of the image is 3m, much higher resolution than that of the previous SAR image. Compared with the optical images, however, the performance for the visual interpretation of the SAR image is not fine because color information is not obtained and speckle noises are distributed on the image. Outlines of small buildings cannot be identified from the SAR image. Therefore, it is difficult to detect the building damage only from the post-event SAR image. On the other hand, it is much easier to identify the landslides because the scale of most of the failures is larger than several tens of meters. In the large-scale landslides as shown by A and B in Fig. 6, the texture of the digital number seems to be rougher than that in other vegetated area.

Since the observation of the TerraSAR-X has just started since Dec. 2007, the number of the archived data is limited. Unfortunately the TerraSAR-X image was not

Table 2 Criteria for Classification of Building Damage

Damage level	Characteristics of image
Complete collapse	Roof and outline of building are not identified. Many rubbles are observed around building. Building is buried in soils of a landslide.
Severe damage	Rubbles are observed around building although roof and outline of building are identified. Damage on building roof is observed.
Slight or no damage	Significant change on roof and around building is not identified.

Table 3 Numbers of Buildings Classified by Visual Damage Detection

Damage level	Num. of buildings	Percentage (%)
Complete collapse	273	59.7
Severe damage	96	21.0
Slight or no damage	88	19.3
Total	457	100.0

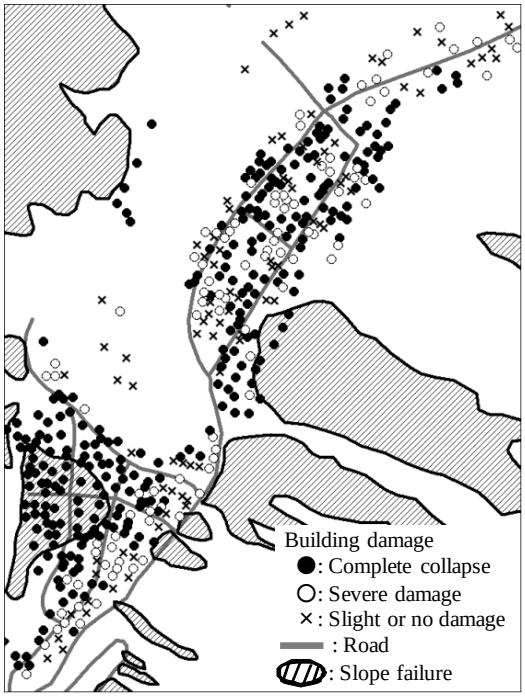

Figure 5 Result of Visual Detection

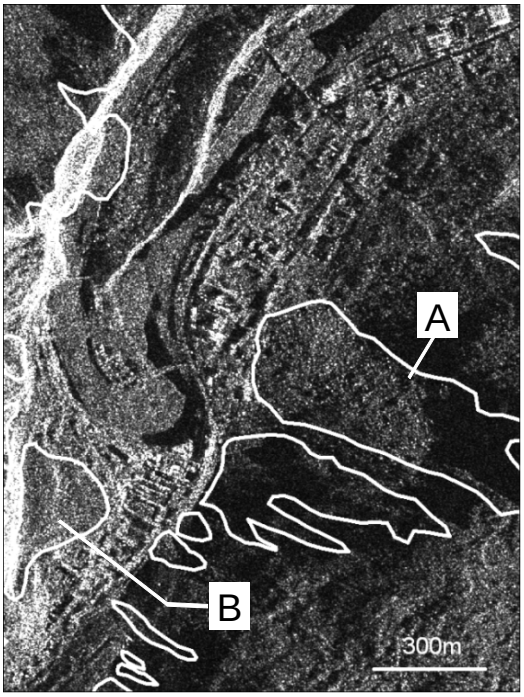

Figure 6 Post-event TerraSAR-X Image

acquired in Beichuan area before the earthquake. When pre- and post-event images are available, SAR images might be powerful tool to detect earthquake-induced damage areas. The data archive should be enriched for the quantitative application of the damage detection.

4. CONCLUDING REMARKS

The characteristics of the satellite optical and SAR images observed in the catastrophically damaged area by the 2008 Wenchuan, China earthquake are examined. From the comparison of the pre- and post-event optical images observed in Qushan town, Beichuan county, the completely collapsed buildings and the landslides are clearly identified. The visual building detection is applied to building by building . The result shows that totally about 80% of the buildings are classified into severe damage or complete collapse. The characteristics of the post-event SAR image are also examined by comparing the optical images. Although it is difficult to detect the damage of individual building, large landslides and slope failures are identified.

Acknowledgements:

The TerraSAR-X image was provided by PASCO Co.. This study is partially supported by the Global COE Program "International Urban Earthquake Engineering Center for Mitigating Seismic Mega Risk".

References:

China Earthquake Administration, (2008), "General Introduction to Engineering Damage during Wenchuan Earthquake", *Journal of Earthquake Engineering and Engineering Vibration*, Vol.28S, 114p.

Miura, H., Wijeyewickrema, A. C. and Inoue, S., (2006), "Evaluation of Tsunami Damage in the Eastern Part of Sri Lanka Due to the 2004 Sumatra Earthquake Using Remote Sensing Technique", *Proceedings of 100th Anniversary 1906 San Francisco Earthquake Conference*, Paper No.8NCEE-856.

Munich Re Group, (2008), "The 2008 Sichuan Earthquake: A Predictable Disaster with Unpredictable Consequences?", Severe Winter and Earthquake -Two Significant Events in China, No. 302-05851.

Sixth International Conference on Urban Earthquake Engineering
March 3-4, 2009, Tokyo Institute of Technology, Tokyo, Japan

A DIGITAL ARCHIVE BASED ON WEB-GIS TECHNOLOGY MONITORING DAMAGE, RECOVERY AND DEVELOPMENT OF A COMMUNITY AFFECTED BY AN EARTHQUAKE

Masasuke Takashima[1] and Hirotaka Ikeda[2]

1) Associate Professor, Department of Disaster and Environmental Research, Fuji Tokoha University, Japan
2) Professor, Department of Disaster and Environmental Research, Fuji Tokoha University, Japan
takashim@fuji-tokoha-u.ac.jp, ikeda_h@fuji-tokoha-u.ac.jp

Abstract: It is important mission for affected local community to accumulate, organize and disseminate disaster experience to their next generation and other communities which have not been struck by disaster yet. The mission can be achieved in decentralized community websites developed by various individuals and organizations which has different social position and viewpoint which is called community archive network in this paper. After Mar. 2007 Noto peninsula earthquake, community archive network has been formed on recovery and revitalization of Anamizu town, one of the most damaged municipality. To add new viewpoint and function on it, we developed web-GIS digital archive which is specialized to shows spatial configuration of the process, its chronological change and to provide practical topics in disaster response operation and community revitalization activity.

1. INTRODUCTION

1.1 Disaster Experience as a Local Community Resource

One big reason of difficulty on disaster management comes from scarcity of disaster experience. When disaster happens, many people in affected community were wondering what and how they should do and seeking the precedents from past disaster. Additionally, once disaster happens, people who had experience of response and recovery in past disasters contacted affected communities and give them advices. Those advices only who has disaster experience can provide were highly appreciated by newly affected communities. In that sense, It can be said disaster experience is a precious resource of local community. It is important mission for affected local community to accumulate, organize and disseminate disaster experience to their next generation and other communities which have not been struck by disaster yet. The internet and web technology would be a powerful tool for the mission among other media. How web technology can be utilized for such mission is a large issue.

1.2 Community Archive Network

Since Mar. 2007 Noto peninsula earthquake, authors could have a opportunity to record recovery process of Anamizu Town through supporting activity on adoption of individual recovery chart system which Takashima et al. (2008a,b) proposed, joining "Recovery Salon"(Yoshida et al. (2008)), interviewing local people such as affected households and local volunteers and other field survey. To archive and disseminate those records, we decided to build up a digital community archive on the web.

Around same time, various individuals and organizations in Anamizu town, not only us, was concerned with damage, recovery and revitalization of their own community and built up website to archive and disseminate what they saw, heard and experienced from their own position. In this paper, we call those websites "community site". Community site treats recovery and revitalization process of Anamizu town community as a major topic from the viewpoint or social position of individuals or organizations who manage the site as. Those community sites on Anamitu town have a variety of viewpoints and styles. We recognized that what we could record is a part of whole process and that they are forming a large archive network on Anamizu town community. We call it "community archive network" in this paper. To develop our community site to add new viewpoint and function on it, the viewpoint and function of community archive network on Anamizu town was analyzed. As a result, we developed web-GIS digital archive which shows spatial configuration of the process, its chronological change and provide practical topics in disaster response and community revitalization as follows.

2. Community Archive Network on Anamizu Town

2.1 Analysis of the Community Archive Network

Table 1 shows a part of community sites which form community archive network on recovery and revitalization process of Anamizu town. To make this list, candidate sites (15,400 sites as of the end of Jan. 2009) were retrieved by Google from the web with retrieval term of "Anamizu", "Earthquake" and "Recovery". Then, sites treat topics on recovery and revitalization of Anamizu town were picked up as community sites from the candidate sites. A site introduced in other community sites was also verified as a candidate. Those sites can be categorized from several

Table 1 community sites on Anamizu town

	Site Title	1)	3)	4)	7)
1	Gambarankaine Noto, Anamizu (Keep chin up, Noto, Anamizu)	Weblog	Anamizu Town Recovery Action Conference	Events, activities, e.t.c. related to recovery and revitalization of Anamizu town.	*
2	Subarashii Noto(Fantastic Noto)	Weblog	Self-owned Buisiness	Foods in season, Fishing, Events around Noto area including recover from the e.q..	*
3	Anamizu Eye's Yomura	Weblog	Individual	Photographs of seasonal scenes and events including the e.q..	
4	Anamizu Hyakkei (Scenes of Anamizu)	Weblog	Individual	Photographs of seasonal scenes and daily life seen in Anamizu including recovery from the e.q..	
5	Café Lawell 6109	Weblog	Anamizu Downtown Revitalization Committee	Events and Activity hosted by Anamizu shopping street including revitalization event after the e.q..	*
6	Anamizu Portal Site	BBS	College	Reports, Ideas, Opinions, News from people concerned with Anamizu town.	*
7	Noto Peninsula Earthquake Information	Ordinary	Anamizu Town	Damage situation after the e.q. and response of local government.	*
8	Bride of Noto Supporter's Blog	Weblog	Anamizu Town	Interchange between filming team of "Bride of Noto"(filmed in Anamizu) and people in Anamizu	
9	Zen-san's Canoe Diary	Weblog	Individual	Zen-san's daily life in Anamizu town and canoeing including recovery from the e.q.	
10	Blue Lightning Diarys	Weblog	Individual	Daily life in Anamizu town and cinema including situation of Anamizu town after the e.q.	

aspects such as 1) form of presentation (Weblog, BBS, ordinary site, e.t.c.), 2) type of media used in the site (text, image, movie, sound, CG, etc.), 3) social position of website owner (individuals, commercial organization, NPO, public sectors, etc.), 4) topic treated in the site, 5) spatial configuration, 6) chronological progress, 7) verifiability.

2.2 Coordination with Other Community Sites

Many sites adopt weblog style. Weblog manages contents chronologically. So, it is easy to find when and what happened if the process of recovery and revitalization is recorded in weblog. But, without intentional viewpoint setting, it is impossible to follow chronological progress even in weblog [appendix 1]. Most sites contain many photograph records not only text. But there are no movie records. Practical topics in disaster response and community revitalization which potential users such as local government staff, local volunteers and community leaders in future disaster would be highly concerned with is not provided in organized manner although various organization and individuals describe the situation after the e.q. from various viewpoints. Webmaster of some sites are anonymous. It is difficult to verify the contents of those sites [appendix 2]. No positioning information is provided with the contents. It is impossible to know where a photograph on a site was taken and how large a damage area a webmaster mentions on a site extended spatially.

To add new viewpoint and function on community archive network, our community site focuses on following four points.

1) to provide contents with positional information on web-GIS to shows spatial configuration of the situation

2) to organize contents chronologically with fixed viewpoint to show progress of the situation clearly.

3) to use movies to show the situation more vividly.

4) to provide practical topics in disaster response and community revitalization including response operation of local government and local volunteers, planning and implementation of shopping street revitalization by community leaders, useful for potential affected community in future disaster.

3. STRUCTURE OF ARCHIVE

3.1 Web Site Development

Our site, "Anamizu Community Archive (ACA)" was developed with HTML, JavaScript and Google Maps API to implement web-GIS and interactive information display on the site. Google Maps API allows web site developer to overlay various vector (point, polyline and polygon) and raster data (Aerial Photo, Satellite Image, e.t.c. [Appendix 3)] (Gibson, R., 2006). URL of the site is "http://ddm. fuji-tokoha-u.ac.jp/anamizu/anamizu.htm". Figure 1 shows overview of the site.

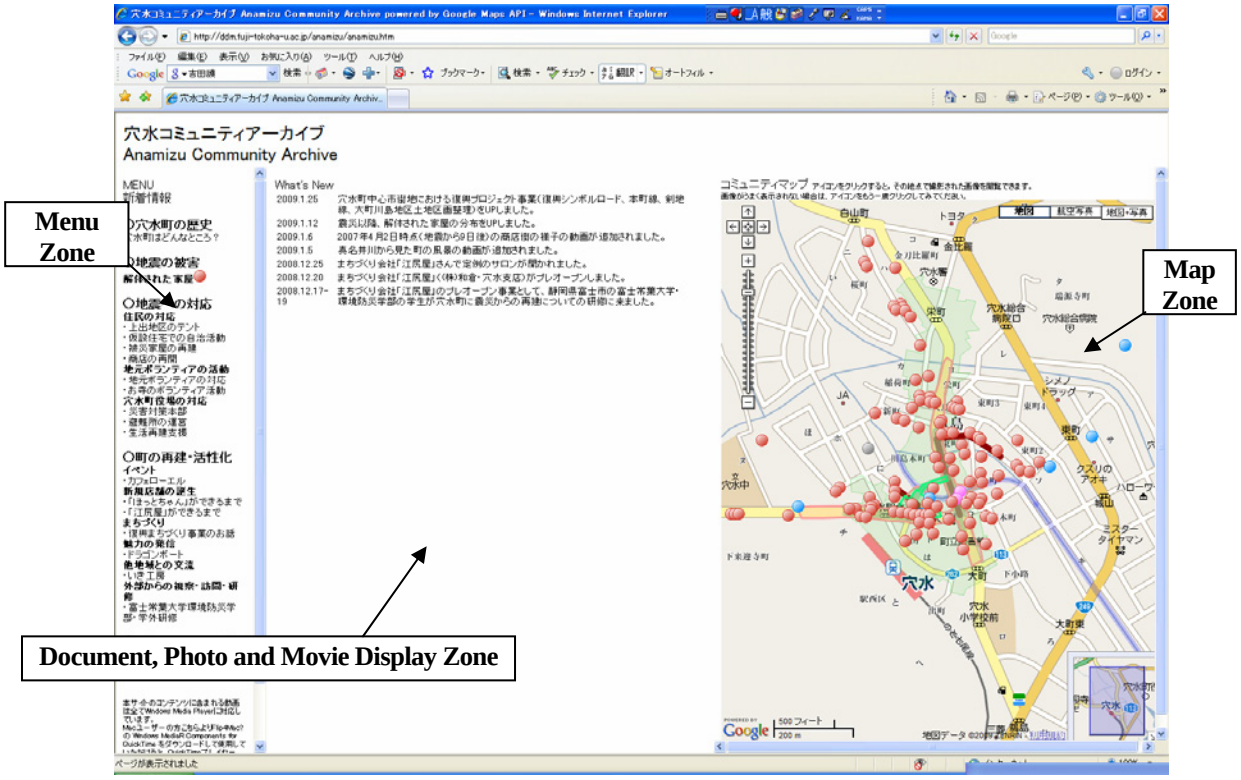

Figure 1 Overview of Anamizu Community Archive

3.2 Data

ACA provides records of the e.q. and recovery from it in following four phases, 1)Anamizu town before the e.q., 2)the e.q. and damages due to it, 3)response to the disaster and 4) recovery and revitalization of the community. On each phase, interview with persons who played an important role in particular operation or event or in community development is provided in text and movies to describe the situation at the time. And also, As of now, following topics are contained on each phase in ACA. Each topic is linked with objects on web-GIS to show where it happened and how it extended.

1)Anamizu town before the e.q.
-Brief introduction of Anamizu town (text, movie)
2)The e.q. and damages due to it
-Housing Damages (photo, point, aerial photo)
3)Response to the disaster
-Demolition of Damaged House (photo, point)
-Activity of community leaders (text, movie, point)
-Life in temporary housings (text, movie, point)
-Activity of local volunteers (text, movie, point)
-Emergency operation center of Anamizu town (text, movie, point)
-Operation of evacuation centers of Anamizu town (text, movie, point)
-Individual household recovery assistance of Anamizu town (text, movie, point)
-Public housing for disaster victims (photo, point)
4) Recovery and revitalization of the community.
-Land readjustment project (text, photo, movie, polygon)
-Road expansion project (text, photo, movie, polyline)
-Streetscape planning (text, photo, movie, polygon)
-Rebuilding damaged housing (text, photo, movie, point)
-Restart of affected self-owned businesses (text, photo, movie, point)
-Newly opened shops after the e.q. (text, photo, movie, point)
-Café Lowell (text, photo, movie, point and polygon)
-Hasebe Festival (text, photo, movie, point and polygon)
-Oyster Festival (text, photo, movie, point and polygon)
-Recommended Canoeing Course and scenes of Anamizu town from the river(text, photo, movie, point and polyline)

Figure 2-5 shows examples of display of several topics.

4. CONCLUSIONS

Anamizu community archive provides web-GIS function which shows spatial configuration of the situation, its chronological change and practical topics in disaster response and community revitalization in community archive network on Anamizu town. Disaster is a huge process including many physical and social phenomena concerned with various individuals, groups and organization. It is practically impossible for one individual, group or organization to provide whole process of a disaster. Only network of community site which are managed by people who are concerned with the disaster from their unique viewpoint or social position can describe the total picture. It is important to form mutually complementary relation between community sites so that community archive network works well. Framework of coordination among community sites must be discussed for further study.

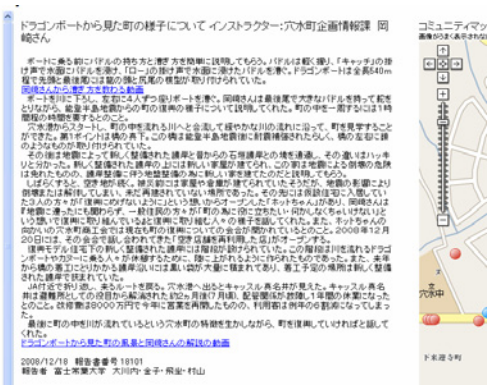

Figure 2 Display of text data (Interview record)

Figure 3 Map view (Distribution of Demolished Housings)

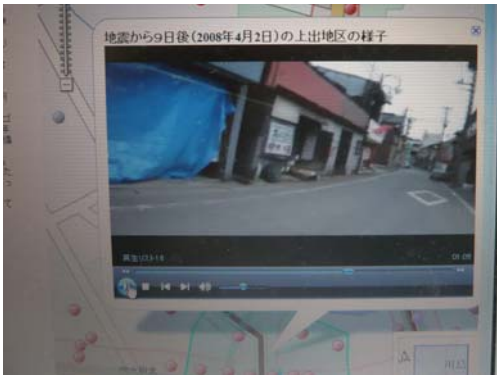

Figure 4 Movie record (Kamide St. 9 days after the e.q.)

Figure 5 Photo record (Newly open shop after the e.q.)

Acknowledgements:

The authors acknowledge support from Japan Ministry of Education, Culture, Sport, Science, and Technology (MEXT) for Support for Improvement of Education and Study Methods in Support Programs for Enhancement of Sophistication and Uniqueness of Faculty Education 2008, "Training and Support Activity at Affected Community as a Disaster Education".

Appendix:

1) For example, when a viewer met up with a photograph of a damaged housing in a weblog and wanted to follow subsequent development of the housing, he cannot follow if webmaster did not follow.
2) Actually, local people can recognize who manage those anonymous sites.
3) As of now, high resolution satellite image is provided on only a part of the world, for example, densely inhabited area. For other part including Anamizu town, only low resolution satellite image is provided.

References:

Takashima, M., Tanaka, S., and Shigekawa, K.,(2008), "Case Studies on the Household Recovery Assistance Operation Based on Customer Relationship Management in Recent Earthquake Disasters in Japan", *Proceedings. of 14th World Conference on Earthquake Engineering*, CD-ROM.

Takashima, M., Tanaka, S., and Shigekawa, K., (2008), "Household Recovery Consulting Using Household Recovery Support Chart in Anamizu Town After the March 2007 Noto Peninsula Earthquake", *Journal of Disaster Research, Vol.3, No.6*(printing)

Yoshida, M., Matsuda, Y. and Tatano, Y. (2008), "Implementation of community development support in recovery Phase", *Proceedings of 27th Conference on Japan Society of Natural Disaster Research.*

"Gambarankaine Noto, Anamizu (Keep your chin up, Noto, Anamizu)", Weblog by Anamizu Town Recovery Action Conference for Recovery from Noto Peninsula Earthquake, http://www.anamizu-fukkou.com/ (in Japanese).

"Subarashii Noto(Fantastic Noto)", Weblog by Kou-zushi, http://kouzushi.org/ (in Japanese)

"Anamizu Eye's Yomura", Weblog by Kitamura, S., http://anamizeyes.exblog.jp/ (in Japanese)

"Anamizu Hyakkei (Scenes of Anamizu)", Weblog, http://blog.livedoor.jp/redstar99/ (in Japanese)

"Café Lawell 6109", Weblog by Anamizu Downtown Revitalization Committee, http://lowell.blog62.fc2.com/ (in Japanese)

"Anamizu Portal Site", Weblog by Ishikawa Polytechnic College, ttp://www2.ishikawa-pc.ac.jp/anapo/index.aspx.

"Noto Peninsula Earthquake Inforamtion", Anamizu Town, http://www.town.anamizu.ishikawa.jp/anamizu/anamizu_gyosei/fukkou/shinsai.jsp

"Bride of Noto Supporters' Blog", Weblog by Planning and Information Division of Anamizu Town, http://notonoyome.exblog.jp/i6

"Blue Lightning Diarys", Weblog, http://blog.livedoor.jp/makochan311/

Gibson, R., Erle, S., Musha, H., Fukuchi, T. and R. Musha, (2006), "Google Maps Hacks", O'Reilly Japan, (in Japanese).

Sixth International Conference on Urban Earthquake Engineering
March 3-4, 2009, Tokyo Institute of Technology, Tokyo, Japan

LANDSLIDES DURING THE 2008 IWATE-MIYAGI-NAIRIKU, JAPAN EARTHQUAKE OBSERVED IN HIGH-RESOLUTION SAR IMAGES

Saburoh Midorikawa[1] and Hiroyuki Miura[2]

1) Professor, Department of Built Environment, Tokyo Institute of Technology, Japan
2) Assistant Professor, Department of Built Environment, Tokyo Institute of Technology, Japan
smidorik@enveng.titech.ac.jp, hmiura@enveng.titech.ac.jp

Abstract: The 2008 Iwate-Miyagi-Nairiku, Japan earthquake (Mw6.9) struck the northern part of Japan. The earthquake produced many landslides which caused isolation of people at small villages in mountain areas. After the earthquake, high resolution SAR images in the damage area were acquired by the TerraSAR-X satellite which was launched in 2007. This paper describes landslides observed in the high-resolution SAR image and the preliminary analysis of the image for landslide detection.

1. INTRODUCTION

On June 14, 2008, a major inland earthquake (M_J7.2, M_W6.9) struck the northern part of Japan. The earthquake was named the 2008 Iwate-Miyagi-Nairiku earthquake by Japan Meteorological Agency. Twenty-three people were killed or missing, about 500 were injured, and more than 2,000 houses were damaged. Although the damage was rather small in comparison with the magnitude of the earthquake, many landslides were observed and caused isolation of people at small villages in mountain areas. After the earthquake, high resolution SAR (synthetic aperture radar) images in the damage area were acquired by the TerraSAR-X satellite which was launched in 2007. This paper describes landslides observed in the high-resolution SAR image and the preliminary analysis of the image for landslide detection.

2. EARTHQUKE AND DAMAGE

The earthquake is a shallow crustal event with a focal depth of 8 km, due to reverse-faulting on a fault striking the north-northeast and dipping down to the west. The fault plane is 20 km in length and 12 km in width, the average slip is 3.5 m, and the dip angle is about 30 degree. The moment magnitude is 6.9. Figure 1 shows the seismic intensity distribution with surface projection of the fault plane. The observed maximum intensity is the JMA intensity 6 upper which corresponds to the M.M. intensity 10. The observed peak horizontal accelerations exceed 1 g at several sites and 0.5 g at about twenty sites.

The damage of houses was observed at Kurihara city and other cities around the epicentral zone as shown in Table 1. In total, about 2,000 houses were damaged. The epicentral zone is on the mountain area where population is small. This is one of the reasons that the building damage was relatively small.

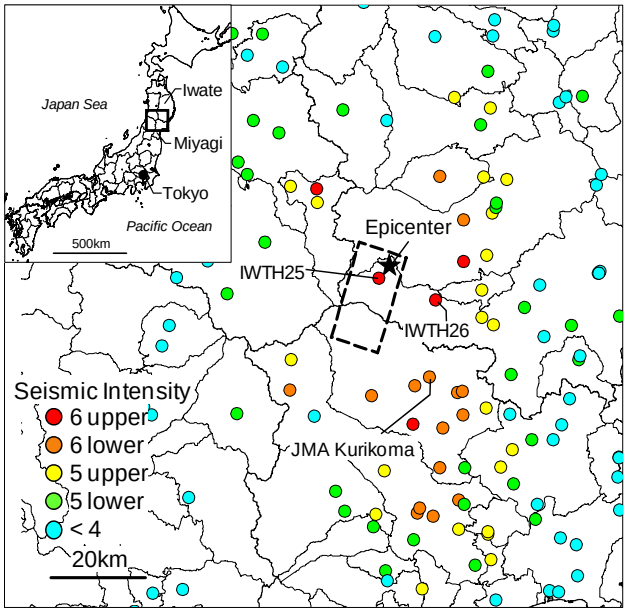

Figure 1 Seismic Intensity Distribution

Table 1 Damage of houses (as of Nov. 17, 2008)

Prefectrure	Municipality	Severely Damaged Houses	Moderately Damage Houses	Partially Damaged Houses
Iwate Pref.	Ohshu City	1	2	419
	Ichinoseki City	1	2	145
	others	0	0	44
Miyagi Pref.	Kurihara City	30	125	1366
	Ohsaki City	1	6	160
	others	0	2	36

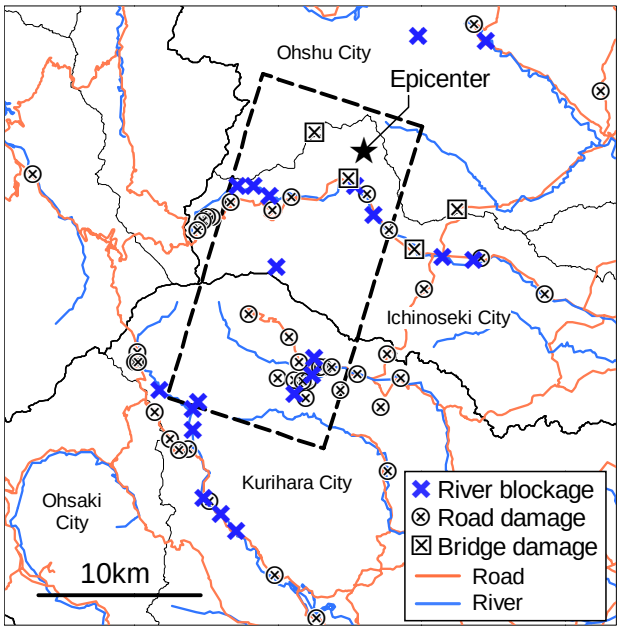

Figure 2 Locations of damage of roads and bridges

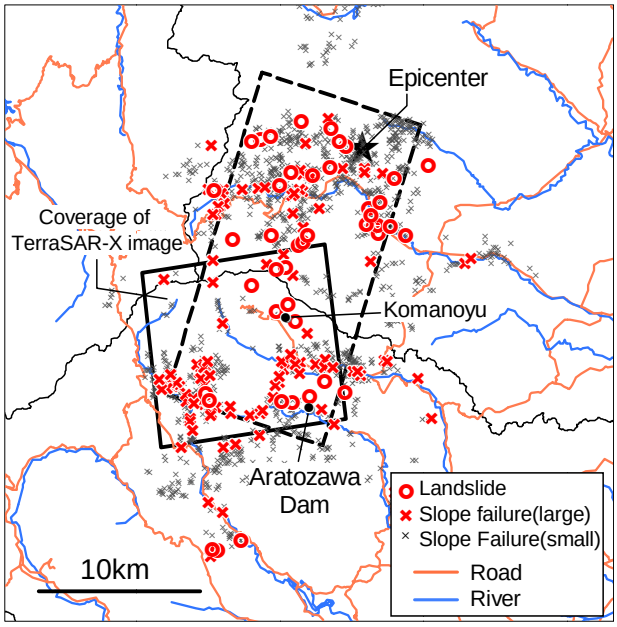

Figure 3 Locations of landslides and slope failures

The damage of roads was extensive. People at mountain villages were isolated by interruption of roads. Figure 2 shows the distribution of damage of roads and bridges reported by Geographic Survey Institute (2008), Miyagi Prefecture (2008) and Iwate Prefecture (2008). The damage is concentrated in and around the epicentral area.

The damage of roads was mainly due to landslides and slope failures. Figure 3 shows locations of landslides and slope failures compiled by Geographic Survey Institute (2008). Extensive damage was observed just above the fault plane. A largest landslide occurred at upper stream of the Aratozawa dam as show in Photo 1. The area of 1.2 km in length and 0.8 km in width slid down about 100 m.

Photo 1 Aratozawa dam and landslide

3. ANALYSYS OF SAR IMAGE

Two days after the earthquake, the high-resolution SAR image was acquired by the TerraSAR-X satellite (PASCO, 2008). The satellite was launched on June, 2007, and started the service on Dec. 2007. The area of the image is about 10 km by 10 km shown by a square in Fig. 3. Table 2 summarizes the characteristics of the image.

The image is shown in Fig. 4. The spatial resolution of the image is 1 m. Figure 5 shows comparison of the aerial photograph and SAR image at the Aratozawa landslide. At the landside area, the texture of the SAR image seems rough. At the west side of the cliff caused by the landslide, the image is dark because of the incident angle of west-southwest.

Table 2 Characteristics of TerraSAR-X image

Radar Frequency	9.65 GHz (X-band)
Wavelength	3.1 cm
Observation Date	16 May, 2008
Time	17:37 (JST)
Polarization	HH
Mode	SpotLight
Spatial Resolution	1m
Orbit Direction	Ascending
Incidence Angle	49.3°

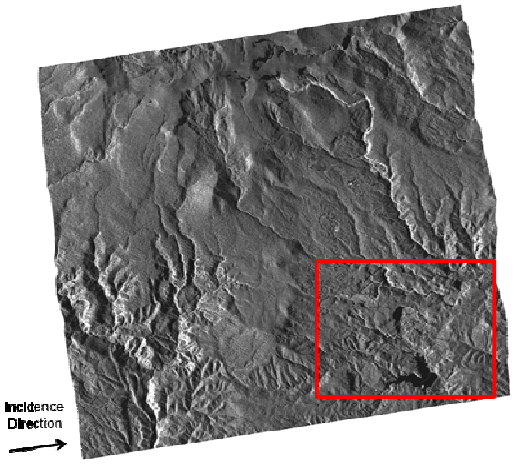

Figure 4 High-resolution SAR image

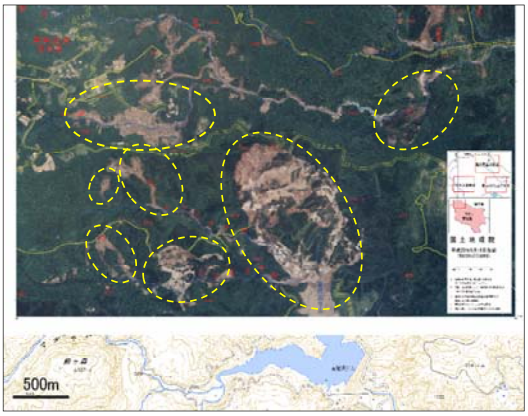

(a) aerial photograph

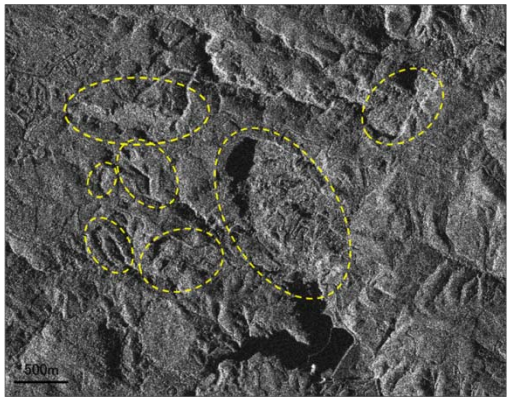

(b) high-resolution SAR image

Figures 5 Images of Aratozawa landslide

The texture analysis of the image is one of the useful approaches for automated detection of a landslide area. Variance, skewness and kurtosis are often used to extract the feature of texture (Shimoda, 1997);

$$M = \text{Mean} = \frac{\sum x_{ij}}{n} \quad (1)$$

$$SD^2 = \text{Variance} = \frac{\sum (x_{ij} - M)^2}{n} \quad (2)$$

$$Vc = \text{Variation Coef.} = \frac{SD}{M} \quad (3)$$

$$Sk = \text{Skewness} = \frac{\sum (x_{ij} - M)^3}{n\, SD^3} \quad (4)$$

$$Kw = \text{Kurtosis} = \frac{\sum (x_{ij} - M)^4}{n\, SD^4} \quad (5)$$

where x_{ij} is pixel value at pixel ij and n is number of pixels in a window. The distributions of the variation coefficient, skewness and kurtosis are computed from the SAR image, as shown in Figs. 6. In the figures, higher and lower values are shown by dark and light colors, respectively, and landslide areas are shown by solid lines. Areas with higher skewness show better correlation with landslide areas, indicating that the skewness is a good classifier for detection of a landslide area.

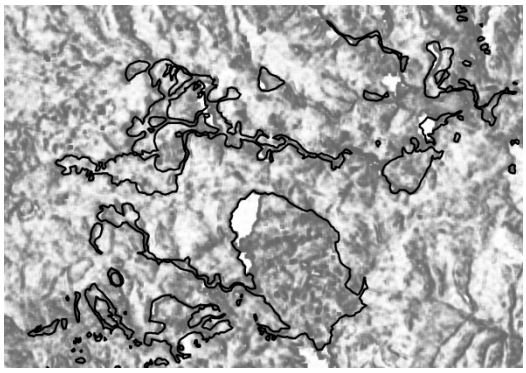

(a) variation coefficient

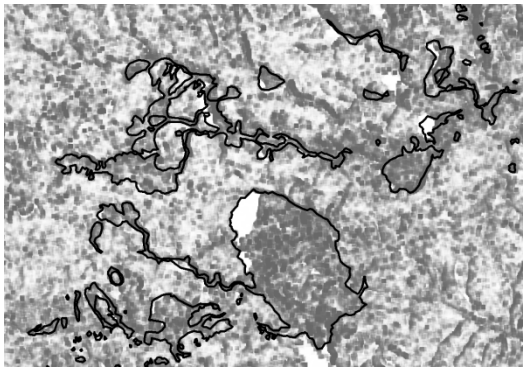

(b) skewness

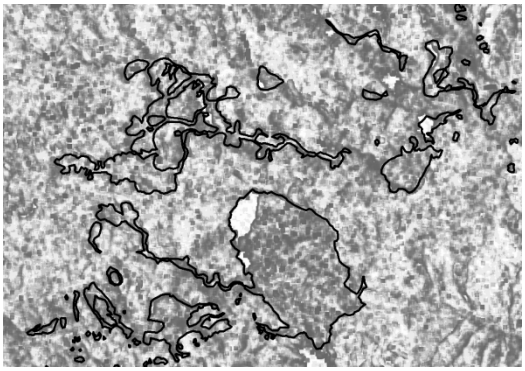

(c) kurtosis

Figures 6 Comparison of distributions of the variation coefficient, skewness and kurtosis

The effect of the window size to the distribution of the skewness is examined. Figures 7 show the comparison of the distributions of the skewness for different window sizes. From the figures, the skewness for a larger window size seems to have better correlation with landslide areas. For a quantitative analysis of the window size effect, the ROC (Receiver Operating Characteristic) analysis is applied.

The ROC analysis is a technique for visualizing, organizing and selecting classifiers based on their performance (Fawcett, 2006). In the analysis, the true positive rate and false negative rate are computed for different threshold levels of the skewness which separate landslide and non-landslide areas. The definitions of the true positive rate and false negative rate are shown in Table 3.

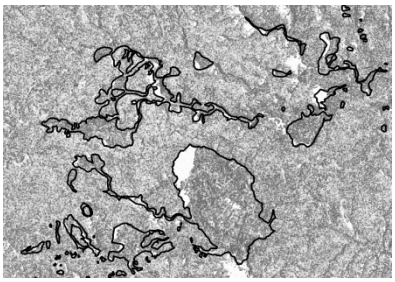

(a) 15 x 15 pixels

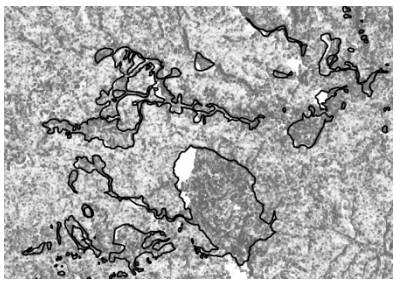

(b) 31 x 31 pixels

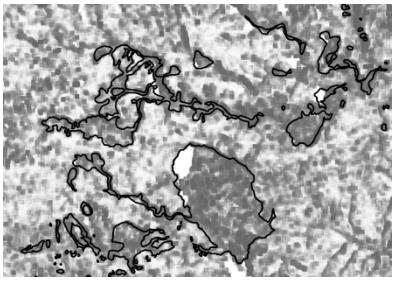

(c) 71 x 71 pixels

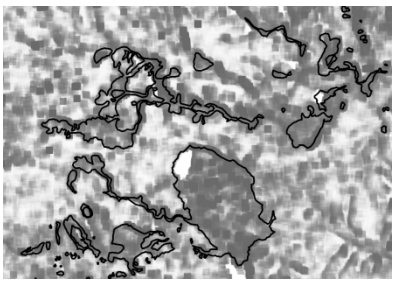

(d) 111 x 111 pixels

Figures 7 Comparison of distributions of skewness for different window sizes

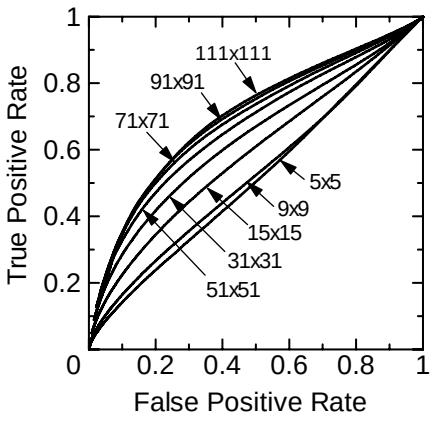

Figure 8 ROC curves

Table 3 Confusion matrix by true-false and positive-negative rates

		Truth	
		True	False
Estimated	Positive	True Positive Rate	False Positive Rate
	Negative	True Negative Rate	False Negative Rate

The ROC graph is a two-dimensional graph in which the true positive rate and false negative rate are plotted on the Y axis and X axis, respectively. The ROC curve is created from the points for different threshold levels, as shown in Fig. 8. In the figure, the upper left point represents perfect classification. The classifier is evaluated to have better performance if the curve is closer to the upper left point of the figure. The curves for larger window size are closer to the upper left point. The difference, however, of the curves is small when the window size is larger than 70 x 70 pixels.

If the window size is large, the spatial resolution of the evaluation becomes worse. Therefore the use of the window size of 71 x 71 pixels will give the best estimate. In this case, the true positive rate and false positive rate are about 0.7 and 0.4, respectively, and the performance of the evaluation is not so high. It seems that many of the misdetections occur at mountain ridges. The further examination considering topography may be useful to improve the performance of detection.

4. CONCLUSIONS

The 2008 Iwate-Miyagi-Nairiku, Japan earthquake produced many landslides. After the earthquake, the 1 m resolution SAR image was acquired in the damage area. At the landside area, the texture of the SAR image seems rough. The skewness of the image shows better correlation with the landslide area, suggesting that the skewness is a good classifier for detection of a landslide area.

Acknowledgment:

The TerraSAR-X image was provided by PASCO Co.. This study is partially supported by the Global COE Program "International Urban Earthquake Engineering Center for Mitigating Seismic Mega Risk" sponsored by Ministry of Education, Culture, Sports, Science and Technology (MEXT), Japan.

References:

Fawcett, T. (2006), "An Introduction of ROC Analysis," *Pattern Recognition Letters*, Vol.27, No.8, pp.861-874.

Geological Survey of Japan (2008), http://unit.aist.go.jp/actfault katsudo/ jishin/iwate_miyagi/index.html

Iwate Prefecture (2008), http://www.pref.iwate.jp/

Miyagi Prefecture (2008), http://www.pref.miyagi.jp/kohou/iwate miyagi-jishin.htm

PASCO Co. (2008), http://www.pasco.co.jp/disaster/detail/080614/ index.html

Shimoda, H. (1997), "*Image Processing Text Book*," Computer Graphic Arts Society (in Japanese)

Sixth International Conference on Urban Earthquake Engineering
March 3-4, 2009, Tokyo Institute of Technology, Tokyo, Japan

MODELING OF INTERDEPENDENCY ASSOCIATED WITH A SYSTEM FAILURE OF CRITICAL INFRASTRUCTURE NETWORKS IN VIEWS OF A SEISMIC DISASTER RISK

Gaku Shoji[1] and Masafumi Tabata[2]

1) Associate Professor, Graduate School of Systems and Information Engineering, University of Tsukuba, Japan
2) College of Engineering Systems, University of Tsukuba
gshoji@kz.tsukuba.ac.jp, live-your-dreams_m@edu.esys.tsukuba.ac.jp

Abstract: In this paper interdependency associated with a system failure of critical infrastructure networks is evaluated in views of a seismic disaster risk. Selecting electric power supply systems, gas supply systems, and water treatments distributed in Tokyo metropolitan area for analysis, these related structures and structural components are modeled as network nodes and links taking into account their functional interdependency. To reveal the trend of network system reliability and analyze its variation, numerical simulation by using network parameters of average degree $\langle k \rangle$, characteristic path length L, clustering coefficient C, relative size of the largest cluster S, average size of the isolated clusters $\langle s \rangle$ and accessibility ratio R_a, is carried out in the case that the nodes exposed to the high seismic hazard are affected.

1. INTRODUCTION

Over the past few decades, a considerable number of studies have been made on evaluation of system reliability associated with mechanical and functional failures of critical infrastructure networks (CINs) due to a seismic hazard (for instance, Ang and Cornell 1974, Taleb-Agha 1977, Shinozuka et al. 2004). However, among them very few attempts have been made at such evaluation considering interdependency associated with a system failure of CINs due to a seismic hazard (for instance, Hoshiya and Ohno 1987, Nojima and Kameda 1995). It is for the reason that dependency of maintaining related structures and structural components of each CIN on the other CINs' functions has been becoming too complicated qualitatively every year to be examined and to be modeled quantitatively. On the other hand, the social concern with catastrophic damage in a Mega city such as Tokyo due to a system failure of CINs in a seismic disaster has been rapidly growing for the last several years.

For the reason above, this paper discuses analytical modeling of interdependency associated with a system failure of CINs in views of a seismic disaster risk. Four critical infrastructures distributed in Tokyo metropolitan area are selected: electric power supply systems, gas supply systems, water supply systems and sewerage systems. These related structures and structural components are modeled as network nodes and links taking into account the functional interdependency, and the behaviour of network parameters is analyzed to reveal the trend of network system reliability and its variation in the case that the nodes exposed to the high seismic hazard are affected.

2. SUBJECT CRITICAL INFRASTRUCTURE NETWORKS AND SEISMIC HAZARD

2.1 Subject Critical Infrastructure Networks

In this study, four critical infrastructure networks (CINs) distributed in Tokyo metropolitan area are dealt with: electric power supply systems (EPSS), gas supply systems (GSS), water supply systems (WSS) and sewerage systems (SS). In numerically modeling these systems, as identical locations and number of related structures and structural components in subject area as those of original prototype systems are approximately detected by referring related references (Central Disaster Prevention Council 2005, Disaster Prevention Conference of Tokyo Metropolitan 2006, Tokyo Electric Power Company, Inc. 2006, Tokyo Gas Company, Ltd. 2008, Bureau of Waterworks Tokyo Metropolitan Government 2006, Bureau of Sewerage Tokyo Metropolitan Government 1998) and by modifying the obtained network models by the results from hearing survey for expertise managing those CINs, since we can not get the numerical information associated with completely exact locations and number of those prototype systems from open resources. Following network models should be recognized to be crude approximations and ones of typical CINs' topologies.

In modeling EPSS, facilities associated with power stations, extra-high voltage substations, primary substations, intermediate substations and distributing substations are modeled as 169 nodes, and transmission lines transferring electric power at 500kV, 275kV, 154kV, 66kV and 22kV and distribution lines distributing electric power to customers at 6.6kV are modeled as 242 links, as shown in Figure 1 (a). In the same way in modeling GSS production facilities and pressure governors are modeled as 193 nodes, and high,

(a) EPSS (b) GSS (c)WSS (d) SS-A (e) SS-B

Figure 1 Network Models

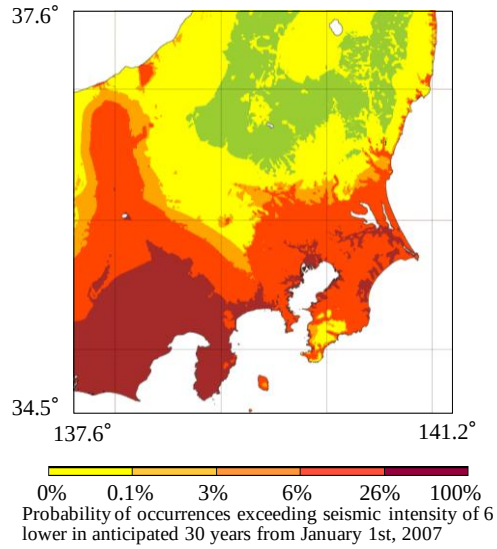

Figure 2 Anticipated Seismic Hazard (J-SHIS 2007)

middle and low pressure pipelines between a pressure governor and the others are modeled as 230 links, as shown in Figure 1 (b). In modeling WSS, facilities associated with water resources (intake weirs), reservoirs, purification plants and water supplying stations are modeled as 159 nodes, and water conveyance channels between these facilities are modeled as 200 links, as shown Figure 1(c). In modeling SS, two systems (SS-A and SS-B) in subject area are selected to be analyzed since the area managed by each sewerage system is clearly separated with the other areas. Pumping stations and water reclamation centers are modeled as 97 nodes in modeling SS-A and 98 nodes in SS-B, and sewers piping wastewater from pumping stations to water reclamation centers are modeled as 100 links in SS-A and 97 links in SS-B, as shown in Figure 1 (d) and (e).

2.2 Anticipated Seismic Hazard

To assume a seismic hazard in the targeted area which EPSS, GS, WS, SS-A and SS-B network models locate in, we use the probability of occurrences exceeding seismic intensity of 6 lower in anticipated 30 years from January 1st , 2007 by courtesy of J-SHIS (2007) (Figure 2). By comparing locations of subject network nodes and links with those of meshes displayed in Figure 2, the number of nodes locating at a mesh corresponding to higher seismic hazards, which probability of occurrences becomes more than 26%,

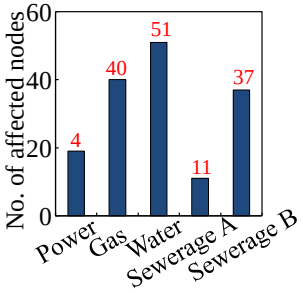

Figure 3 Number of Nodes in a Mesh Matching High Seismic Hazards on Subject Networks

is identified, as shown in Figure 3. In following Section 4, by varying the order of failures of those nodes, the variation of values of network parameters will be simulated.

3. NETWORK PARAMETERS

Six network parameters are used as indices to measure the characteristics of subject networks by referring and modifying the approach by Watts and Strogatz (1998) and Albert et al. (2000): average degree $\langle k \rangle$, characteristic path length L, clustering coefficient C, relative size of the largest cluster S, average size of the isolated clusters $\langle s \rangle$, and accessibility ratio R_a.

Average degree $\langle k \rangle$ is expressed as follows;

$$\langle k \rangle = \frac{1}{n} \sum_{i=1}^{n} k_i \qquad (1)$$

where n is the total number of nodes and k_i is the number of nodes connected to node i. Average degree $\langle k \rangle$ quantifies the average connectivity of each node to the neighboring nodes. Characteristic path length L is expressed as follows;

$$L = \frac{1}{n^p} \sum_{j=1}^{n^p} L_j \qquad (2)$$

where n^p is the number of pairs by any nodes (at most $n^p = n(n-1)/2$), and L_j is the shortest path length

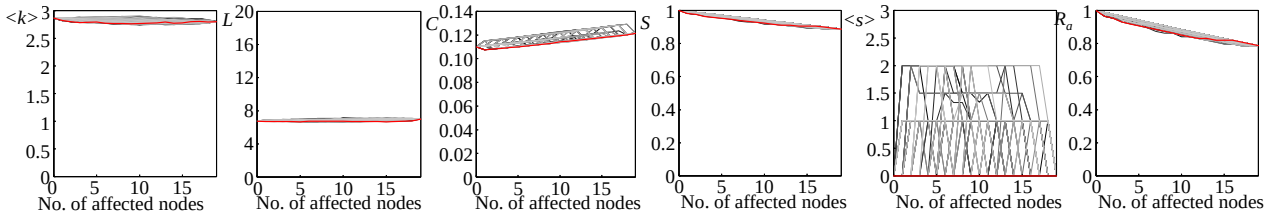

(a) EPSS

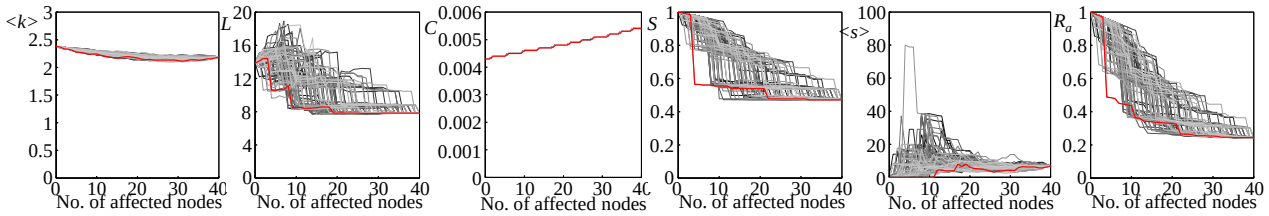

(b) GSS

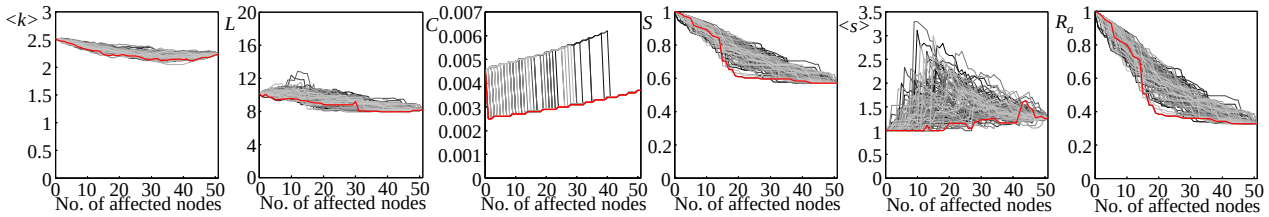

(c) WSS

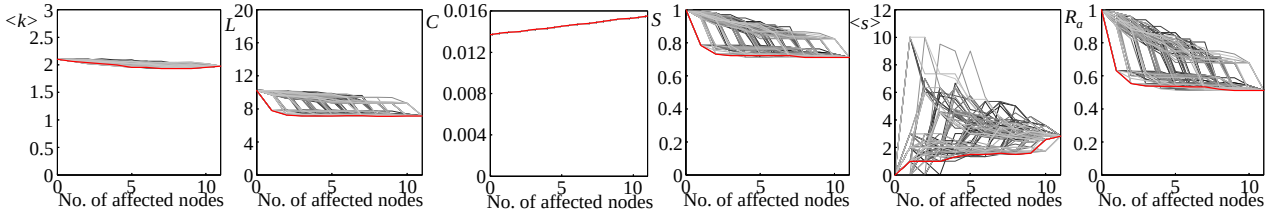

(d) SS-A

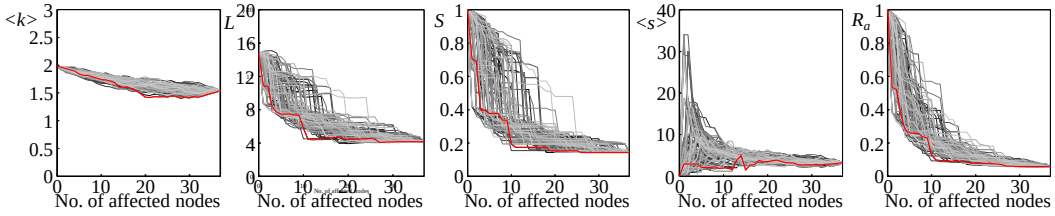

(e) SS-B

Figure 4 Variation of Values of Network Parameters on Independent Network Models

of node pair j. Characteristic path length L quantifies the average minimum number of links between any two nodes. Clustering coefficient C is expressed as follows;

$$C = \frac{1}{n}\sum_{i=1}^{n}\frac{n_i^p}{{}_{k_i}C_2} \tag{3}$$

where ${}_{k_i}C_2$ is the number of pairs by any nodes neighboring on node i (at most ${}_{k_i}C_2 = k_i(k_i-1)/2$) and n_i^p is the number of pairs with actually interconnected links among the pairs selected from the combination of ${}_{k_i}C_2$. Clustering coefficient C quantifies the amount of fragmentation on subject networks, which describes the average connectivity between the neighboring nodes connected to each node. Large clustering coefficient C is associated with high average connectivity and small fragmentation on subject networks, whereas small clustering coefficient C with low average connectivity and large fragmentation. Average degree $\langle k \rangle$, characteristic path length L, and clustering coefficient C are fundamental network parameters that describe the characteristics of subject networks under given network's topology

In addition, to quantify the degree of variation associated with network characteristics as network topology va-

rying from initial one due to random failures of high-seismic-hazard nodes, relative size of the largest cluster S and average size of the isolated clusters $\langle s \rangle$ are computed as follows;

$$S = \frac{Cl^{aft}}{Cl^{ini}} \tag{4}$$

$$\langle s \rangle = \frac{1}{n^c} \sum_{m=1}^{n^c} Cl_m \tag{5}$$

where Cl^{aft} is the number of nodes contained in largest cluster (size of the largest cluster) on subject networks after high-seismic-hazard nodes are assumed to be affected and removed in turn (affected networks) in the following numerical simulation described in Section 4 and Cl^{ini} is the size of the largest cluster on initial networks under the condition before high-seismic-hazard nodes are affected. In Eq.(5), n^c is the number of clusters except the largest cluster, and Cl_m is the number of nodes contained in cluster m except the largest cluster (size of cluster m). Lastly, accessibility ratio R_a is expressed as follows;

$$R_a = \frac{n_{aft}^p}{n_{ini}^p} \tag{6}$$

where n_{aft}^p is the number of pairs by any accessible nodes of affected networks, and n_{ini}^p is that of initial networks. Accessibility ratio R_a quantifies the redundancy of subject networks once some of their nodes are affected due to a seismic hazard.

4. NUMERICAL SIMULATION

4.1 Simulation Scheme

Variation of values of six network parameters as previously described in Section 3 is numerically simulated with increase of the number of affected nodes on subject networks under random removals. The nodes which match the high-seismic-hazard ones of subject networks as previously shown in Fig. 3 (refer Section 2.2) are randomly selected by the sampling based on generated uniform random numbers and above numerical trials are repeated 100 times. In the following figures, vertical axis denotes the variation of values of six network parameters and horizontal axis denotes the number of affected and removed nodes on subject networks. Thus, based on this simulation scheme, we can obtain 100 simulated curves which describe the variation of values of six network parameters.

In evaluating the variation, we focus the curves which indicate smaller values than the other curves (that are called as 'lower-trend curves'), and the curves which indicate larger values than the other curves (that are called as 'higher-trend curves'). Lower-trend curves indicate that connectivity, redundancy, or accessibility on subject networks becomes relatively lower and their fragmentation becomes higher than that of the other curves under random failures of high-seismic-hazard nodes. Meaning of higher-trend curves is contrary to that of lower-trend curves.

Figure 5 Interdependency Network Model

4.2 Case Studies on Subject Independent Networks

Figure 4 show the numerical results associated with six network parameters based on the simulation scheme above: average degree $\langle k \rangle$, characteristic path length L, clustering coefficient C, relative size of the largest cluster S, average size of the isolated clusters $\langle s \rangle$, and accessibility ratio R_a. These cases are ones in no consideration of interdependency between subject network models. The value of clustering coefficient C on SS-B remains zero even under random failures of affected nodes, then there is no figure corresponding to C on SS-B in Fig.4(e).

From Fig.4, focusing on lower-trend curves on characteristic path length L, from the stand of their total tendency SS-B has strongest tendency that network's connectivity falls down under random failures of high-seismic-hazard nodes than the other networks: GSS second, SS-A third, WSS fourth, and EPSS weakest. On the other hand, in the range that the number of affected nodes is small among their whole number, network's connectivity of EPSS, GSS, and WSS increases in spite of increasing affected nodes. The reason of this is that their redundancy becomes relatively higher than that of SS-A and SS-B. With regard of the tendency of the variation of fragmentation, SS-B has also strongest tendency that size of the clusters becomes small (fragmentation becomes high) with increase of affected nodes than the other networks: GSS second, WSS third, SS-A fourth, and EPSS weakest. These implications based on the simulation scheme above are very useful for evaluating the network system reliability under random failures in views of a seismic disaster risk.

4.3 Case Studies Considering Interdependency between Subject Networks

Figure 5 shows the network model with interdepen-

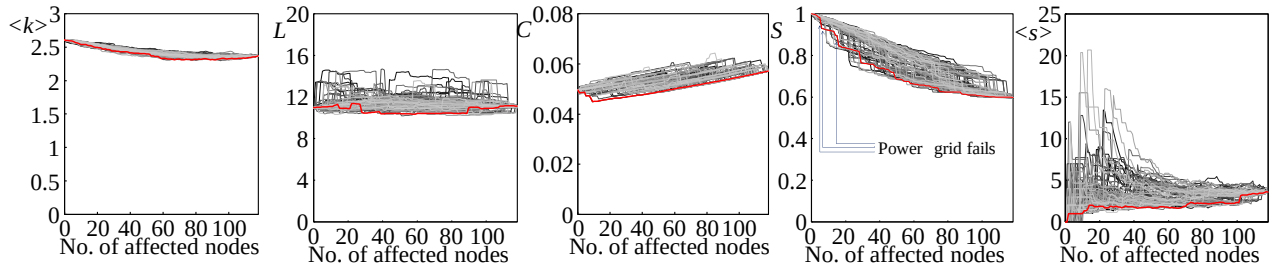

Figure 6 Variation of Values of Network Parameters Considering Interdependency of Subject Networks

dency between subject networks considered. In this model, purification plants and water supplying stations in WSS network model, and pumping stations and water reclamation centers in SS-A and SS-B network models are assumed to be functionally dependent on electric power supply from primary substations, intermediate substations or distributing substations in EPSS network model. These nearest substations from purification plants, water supplying stations, pumping stations and water reclamation centers are detected and functional connectivity between them is introduced by modeling new 44 links. Hence, new network model consisted of 523 nodes and 693 links in consideration of functional interdependency between EPSS, WSS, SS-A and SS-B can be formed as Fig. 5.

Figure 6 show the numerical results associated with the network parameters on interdependency network model under random failures of 118 high-seismic-hazard nodes based on same simulation scheme as in Section 4.2. From the general views of Fig. 6 compared with Fig.4, the results clearly show that the tendency of variation of values of the network parameters varies compared with that of each independent network model. In particular focusing on the lower-trend curves regarding relative size of the largest cluster S among the parameters, in the range that the number of affected nodes is less than 20, failures of power substations cause the immediate drop of these values. We can interpret this trend that connectivity, fragmentation, redundancy and accessibility on interdependency network model are strongly dependent on failures of specific power substations at the first stage of random failures of high-seismic-hazard nodes. It has been recognized qualitatively that electric power supply is the first important requirement for maintaining the functions of the other CINs. In contrast, our results demonstrate quantitatively above issue based on the network analyses on functional interdependency network model by using the network parameters.

5. CONCLUSIONS

This paper discussed analytical modeling of interdependency associated with a system failure of critical infrastructure networks (CINs) in views of a seismic disaster risk. Four critical infrastructures distributed in Tokyo metropolitan area are focused on: electric power supply systems (EPSS), gas supply systems (GSS), water supply systems (WSS) and sewerage systems (SS-A and SS-B). These related structures and structural components are modeled as network nodes and links taking into account the functional interdependency, and six network parameters of average degree $\langle k \rangle$, characteristic path length L, clustering coefficient C, relative size of the largest cluster S, average size of the isolated clusters $\langle s \rangle$, and accessibility ratio R_a, are analyzed to reveal the trend of networks system reliability and its variation in the case that the nodes exposed to the high seismic hazard are failed. The following results are deduced below:

1) From case studies on subject independent networks, SS-B has strongest tendency that network's connectivity falls down and the clusters are fragmented into under random failures of high-seismic-hazard nodes than the other networks: GSS second, WSS third, SS-A fourth, and EPSS weakest. This indicates that connectivity and redundancy of EPSS model become relatively higher than those of the other models: SS-A second, WSS third, GSS fourth, and SS-B weakest.

2) From case studies considering interdependency between subject networks, connectivity, redundancy, fragmentation and accessibility on interdependency network model are strongly dependent on failures of specific power substations at the first stage of random failures of high-seismic-hazard nodes. These results demonstrate quantitatively the related key issue associated with a system failure of CINs due to their functional interdependency.

Acknowledgements:

This research was sponsored by the Ministry of Education, Culture, Sports, Science and Technology (MEXT) under a grant as Special Funds for Disaster Prevention and Reduction associated with the anticipated Tokyo Metropolitan Earthquake (leader, Professor H. Hayashi at DPRI, Kyoto University and F. Yamazaki at Chiba University).

References:

Ang, A. H-S. and Cornell, C. A. (1974), "Reliability Bases of Structural Safety and Design," *Journal of the Structural Division, Proceedings of the American Society of Civil Engineers*, **100**(ST9), 1755-1769.

Taleb-Agha, G. (1977), "Seismic Risk Analysis of Lifeline Networks," *Bulletin of the Seismological Society of America*, **67**(6), 1625-1645.

Shinozuka, M., Chang, S. E. and Dong, X. (2004), "Assessment of Disaster Resilience of Lifeline Systems," *Proceedings of the 3rd Asian-Pacific Symposium on Structural Reliability and its Applications*, 1-17.

Hoshiya, M. and Ohno, H. (1987), "Inter-Chain Effect of Lifelines on their Aseismic Performance," *Journal of Structural Mechanics and Earthquake Engineering*, Japan Society of Civil Engineers, **386**(I-8), 387-396.

Nojima, N. and Kameda, H. (1995), "Seismic Risk Assessment of Urban Lifelines under System Interactions," *Journal of Structural Mechanics and Earthquake Engineering*, Japan Society of Civil Engineers, **507**(I-30), 231-241.

Special Investigation Committee on Disaster Prevention for Tokyo Earthquake, Central Disaster Prevention Council (2005), "Report of Special Investigation Committee," http://www.bousai.go.jp/jishin/chubou/shutochokka/houkoku.pdf.

Disaster Prevention Conference of Tokyo Metropolitan (2006), "Publication of Tokyo Regional Disaster Prevention Measures," http://www.bousai.metro.tokyo.jp/japanese/knowledge/material_h.html.

Tokyo Electric Power Company, Inc. (2006), "Operational Plan for Disaster Prevention," http://www.tepco.co.jp/cc/pressroom/bousai.pdf.

Bureau of Waterworks, Tokyo Metropolitan Government (2006), "Operational Plan for Seismic Disaster Prevention," http://www.waterworks.metro.tokyo.jp/press/h18/press060825.pdf.

Bureau of Sewerage, Tokyo Metropolitan Government (1998), "Operational Plan for Seismic Disaster Prevention (Chapter of Emergency Policy) ."

Bureau of Sewerage, Tokyo Metropolitan Government (1998), "Operational Plan for Seismic Disaster Prevention (Chapter of Prevention Policy)."

Tokyo Gas Company, Ltd. (2008), "Operational Plan for Disaster Prevention," http://www.tokyo-gas.co.jp/safety/bousai.pdf.

Japan Seismic Hazard Information Station (J-SHIS) (2007), "National Seismic Hazard Maps for Japan," http://www.j-shis.bosai.go.jp/

Watts, D. J. and Strogatz, S. H. (1998), "Collective Dynamics of 'Small-World' Networks," *Nature*, **393**, 440-442.

Albert, R., Jeong, H. and Barabási, A-L. (2000), "Error and Attack Tolerance of Complex Networks," *Nature*, **406**, 378-381.

Sixth International Conference on Urban Earthquake Engineering
March 3-4, 2009, Tokyo Institute of Technology, Tokyo, Japan

ECONOMIC IMPACTS OF DISASTERS: A GLOBAL ANALYSIS

Yasuhide Okuyama[1)]

1) Associate Professor, International University of Japan, Japan
okuyama@iuj.ac.jp

Abstract: The economic impacts of major disasters in the world are estimated and analyzed in this paper. The global trends of major disasters between 1960 and 2007 are analyzed based on the available damage data and economic models constructed for this study. In addition, the economic impacts of the 2004 Indian Ocean Earthquake and Tsunami are estimated and investigated in the international context. The results indicate the complex nature of economic impacts of disasters and therefore highlight the importance of appropriately evaluating and accounting for the economic impacts.

1. INTRODUCTION

More than 7,000 major disasters have been recorded since 1970, causing at least $2 trillion in damage, killing at least 2.5 million people, and adversely affecting societies (UN, 2008; p. xiii). And, some 75% of the world's population lives in areas affected at least once by natural disaster between 1980 and 2000 (UNDP, 2004). It is also reported that the frequency and economic impacts of natural disasters has been increasing in the recent years (UN, 2008). These statistics alone can make natural disasters one of the major issues and urgent tasks to tackle in the world. However, little has been known about the economic impacts of natural disasters, due partly to lack of the standardized definition and also to the difficulty for measuring it.

In this present paper, the global trend of economic impacts of major disasters during 1960 and 2007 is estimated and analyzed, and the detailed economic impacts of 2004 Indian Ocean Earthquake and Tsunami are estimated and investigated. In the following section, the concepts and methodologies for economic impact of disasters are discussed in connection with development. Section 3 illustrates and analyzes the global trend of major disasters. Then, the detailed impact estimation for 2004 Tsunami case is presented and analyzed in Section 4. The final section concludes the paper with some remarks based on the findings and for the future agenda.

2. ECONOMIC IMPACTS OF DISASTERS

2.1 Concepts and Methodologies

It is useful to clarify the terminologies regarding economic impacts of disasters: *damages* are by economics definition the damages on stocks, which include physical and human capitals; *losses* are business interruptions, such as production and/or consumption, caused by damages and can be considered as first-order losses; *higher-order effects*, which take into account the system-wide impact based on first-order losses through interindustry relationships; and *total impacts* are the total of flow impacts, adding losses (first-order losses) and higher-order effects. While some researchers critique that the higher-order effects of disaster are "more a possibility than a reality" (Albala-Bertrand, 1993, p. 104), the estimation of higher-order effects has been attempted to "gauge individual and community vulnerability, evaluate the worthiness of mitigation, determine the appropriate level of disaster assistance, improve recovery decisions, and inform insurers of their potential liability" (Rose, 2004, p. 13).

Various economic modeling frameworks have been employed to estimate the higher-order effects of a disaster. Perhaps, the most widely used modeling framework is the IO model (for example, Cochrane, 1974, 1997; Wilson, 1982; Kawashima et al. 1991; Boisvert, 1992; Gordon and Richardson, 1996; Rose et al. 1997; Rose and Benavides, 1998; and Okuyama et al., 1999). The popularity of IO models for disaster related research is based mainly on the ability to reflect the economic interdependencies within a regional economy in detail for deriving higher-order effects, and partly on its simplicity. On the other hand, this simplicity of the IO model creates a set of weaknesses, including its linearity, its rigid structure with respect to input and import substitutions, a lack of explicit resource constraints, and a lack of responses to price changes (Rose, 2004). In order to overcome these weaknesses in the context of disasters, several attempts of refinement and extension of the IO framework have been proposed (the detailed discussions on such extensions can be found in Okuyama, 2007).

Other modeling frameworks have been also employed to estimate higher-order effects of disasters. The social

accounting matrix (SAM) has been utilized to examine the higher-order effects across different socio-economic agents, activities, and factors. Notable studies using SAM include Cole (1995, 1998, and 2004) among others. Like IO models, the SAM approach has rigid coefficients and it tends to provide upper bounds for the estimates. On the other hand, the SAM framework, as well as extended IO models, can derive the distributional impacts of a disaster in order to evaluate equity considerations for public policies against disasters. An alternative modeling framework to the IO and SAM is CGE analysis (for example, Boisvert, 1992; Brookshire and McKee, 1992; Rose and Guha, 2004; and Rose and Liao, 2005). Unlike IO and SAM models, CGE models are non-linear in common practice, can respond to price changes, can incorporate input and import substitutions, and can explicitly handle supply constraints. However, Rose and Liao (2005) claim that most CGE models are intended for long-run equilibrium analysis; hence, in contrast with the rigidity of the IO model, a CGE model generally leads to the underestimation of economic impacts due to its flexible adjustment feature. It is argued, however, that CGE models provide lower impact estimates than IO models, partly because "not all causations in CGE models are unidirectional, i.e., functional relationships often offset each other" (Rose, 2004, p. 27). Another weakness of CGE models is that the assumption of optimizing behavior can be considered questionable under disaster situations, where increased uncertainties arise in the near and distant future. Of course, the more extensive data requirement for CGE modeling presents a major weakness for empirical analysis of disasters.

Econometric models, which are based on time-series data that may not include any major disasters, appear ill-suited for disaster impact analysis. Ellson et al. (1984), however, argue that they examined the damage estimates of major earthquakes in the United States and found that the damages do not appear really outside of the historical variability of the regional economy in response to more traditional shocks and cyclical fluctuations. Furthermore, econometric models are statistically rigorous, can provide stochastic estimates, and have forecasting capabilities. They do require a large data set (time-series as well as cross-section) though, and cannot easily distinguish between direct and higher-order effects (Rose, 2004).

2.2 Economic Impacts and Development

Most empirical studies with cross-country data investigating the relationship between development level and disaster losses conclude that correlation between them is negative, i.e. "the higher the level of development, the smaller both the number of deaths, injured, and deprived, and the relative material losses" (Albala-Bertrand, 1993, p.202). Similar results are found in Anbarci et al., 2005; Kahn, 2005; Toya and Skidmore, 2005, among others. This appears consistent with the disaster theory that as countries develop and grow, they should have sufficient resources, such as financial and/or technological ones, to better manage disaster risk through the implementation of countermeasures and to better manage the adverse impact of disasters. Some policy analysts have suggested that a way to reduce disaster damages and losses for less developed countries should be to develop and grow faster (for example, Okonski, 2004, and Hoke, 2005).

However, with the recent increasing complexity of social and economic structure and interdependency within and across countries, this relationship may not be as straightforward as it seems. According to Lester (2008), direct losses from disaster (as % of GDP) appear to have a negative correlation with GDP per capita; however, as GDP per capita increases, the complexity of economic system also increases and thus the higher-order effects (as % of GDP) has a positive correlation with GDP per capita; as a result, the total impact over GDP per capita has an inverted "U" shape curve. This implies that the most potentially affected economies by disaster will tend to be middle-income-level economies. This observation is shared with Benson and Clay (1998). They claimed that the most vulnerable economies are not the most underdeveloped, since least developed countries tend to have simple economic structures, such as agriculture. While middle-income-level economies with some diversifications seem more secure, because of intertwined economic activities between industries, however, the higher-order-effects can be much greater than in a simple agro-economy, and the total impacts from a disaster can be larger than in a simple economy. This is exactly the point that flow analysis models aim to address—the complexity of economic activities across industries lead to spread higher-order effects to larger extent. At the same time, Kellenberg and Mobarak (2008) claim that this inverted U shape relationship could be attributable to behavioral changes at micro level in response to income increase. They argue that the risk-return trade off will swing in favor of return (consumption) at low levels of income where the marginal utility of consumption is higher, but then will swing to risk mitigation as income increases (the marginal utility of consumption becomes relatively low). Their empirical analysis of 133 countries over 28 years showed the stronger tendency of this inverted U shape non-linearity for floods, landslides, and windstorms than for extreme temperature events or earthquakes. This result implies that "the achievement of the simultaneous goals of natural disaster risk reduction and poverty elimination cannot be assumed to be complementary for all disaster types" (p. 779). In this context, particularly for ex-ante analysis to assess disaster risk, it is advisable to control income level and disaster type in the analysis of disaster impact so that different effects are taken into account.

3. GLOBAL TREND OF DISASTERS

Natural hazards occur around the world with a wide range of intensities. In order to set the cases for global aggregate of impact estimation, economic damage, or loss data of disasters need to be collected. No standardized definitions or frameworks of economic damage and loss are

set so far, except the use of ECLAC methodology (UN ECLAC, 2003) for recent disasters. Thus, it is difficult to collect the consistent measurement of economic damage and loss data for past disasters. However, there are a few sources offer the economic damage or loss data of past disasters: EM-DAT database by Centre for Research on the Epidemiology of Disasters (CRED) of Université Catholique de Louvain, NatCat database by Munich Re, and Sigma data base by Swiss Re. In this present study, economic damage data are gathered from EM-DAT and NatCat databases. The disaster cases are selected from the ones occurred during 1960 and 2007. As mentioned above, there is no standard definition of economic impact; furthermore, economic damage, loss, and impact of disasters are used interchangeably in various documents, including official ones. In fact, EM-DAT uses 'estimated damage' while NatCat's data is labeled as 'overall losses'. Whereas EM-DAT and NatCat databases used different terms for economic data of disasters, they are considered as damages—damages on capital stock.

Then, the disaster cases are combined between two databases, and are screened by intensity in order to reduce the number of cases by eliminating smaller ones. The intensity condition is set as: damages should be greater than or equal to US$ 20 million (current), and either should be greater than 1% of current GDP for high-income countries or 2% of current GDP for low income countries. The number of cases after this screening becomes 184. In order to be used as the input to estimate disaster losses and higher-order effects, these damage (stock) data were converted first to flow measure, i.e. losses, based on the available and estimated capital data and the current GDP data using capital-to-output ratio. The derived losses are further converted to changes in final demand through dividing losses by the inverse of diagonal terms in the direct input coefficient matrix. Then, the total impact of each disaster is estimated by plugging this final demand changes into the respective accounting multiplier matrix, constructed specifically to this study.

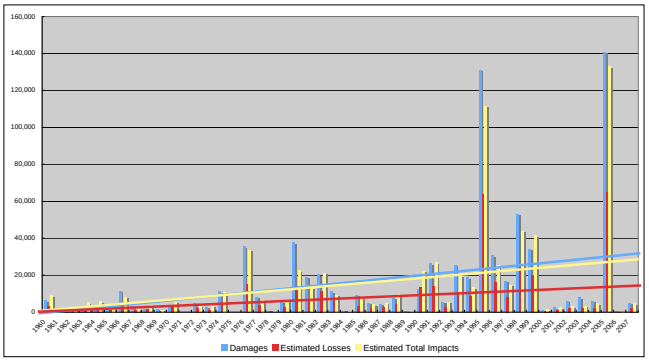

Figure 1 Trends of Economic Impacts of Selected Disasters between 1960 and 2007 (values are in constant 2007 US$)

Figure 1 illustrates the estimated trends of aggregated damages, losses, and total impacts for each year. A gradual increase of all the three economic impacts is observed until year 2000, with an exception of 1995 including the Hanshin-Awaji (Kobe) Earthquake in Japan. Between 2001 and 2004, a lull of economic impacts was observed; and then, year 2005 becomes another exception with the Hurricane Katrina in the U.S. This lull might be caused by the screening of events, excluding smaller cases. For instance, multi-national disasters, such as 2004 Indian Ocean Earthquake and Tsunami, are separated to each affected country and are screened; thus, some affected countries in such events are not included.

The relationships among damages, losses, and total impacts appear different each year. For example, in 1990, the aggregated total impacts are the largest, followed by the aggregated losses and the aggregated damages. In 1999, for instance, the aggregated total impacts are the largest, followed by the aggregated damages and the aggregated losses. On the other hand, in many years, aggregated damages are the largest, followed by the aggregated total impacts and aggregated losses. Since the estimation of losses (and higher-order effects based on losses and SAM) relies a great deal on capital stock data, which are rarely available and thus are estimated based mostly on the available data for recent years, the above observations of relationship among these economic impacts cannot be easily generalized. In addition, the relationship between losses and total impacts needs further attention, because the damages and/or losses to specific industries can cause different higher-order effects: for example, damages and/or losses of manufacturing industry may result in a production bottleneck via forward linkage (supply chain) and backward linkage (demand chain) and can cause effects in a broader range of industries, depending on how the domestic (or international) interindustry relationships are intertwined.

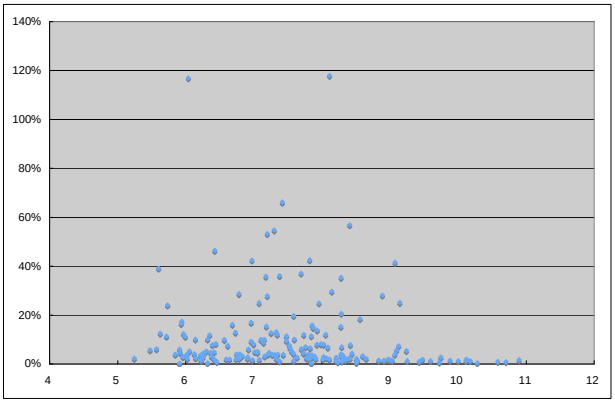

Figure 2 Relationship between GDP per capita and Impact on GDP (X-axis is natural log of GDP per capita)

With a casual visual inspection, the distribution of 184 cases, seen in Figure 2, displays the tendency of inverted 'U' curve relationship between the natural log of GDP per capita and the share of total impacts over GDP (hereafter GDP impact). While both tails, lower and higher GDP per capita countries, indicate relatively low GDP impact, many middle level GDP per capita countries have higher GDP impact values. Two outliers, with extremely large GDP impact rate, are 1963 storm in Haiti and 1988 storm in St. Lucia,

small island nations hit by hurricanes. This observation appears to prove that the theory of inverted 'U' curve relationship can be found with total impact of disasters.

A series of statistical analyses is performed to see whether or not the inverted U curve relationship actually exists. The results show that inverted U curve relationship (non-linear function form) in either all events case or any type of disasters is not statistically significant, contrary to the above visual inspection. On the other hand, a negative linear relationship is found statistically significant with climatological, geophysical, and hydrological events. For the cases with all the 184 events and with meteorological events, neither linear nor non-linear form is statistically significant. The negative linear relationship is, in fact, consistent with the traditional disaster theory, in which as development level, i.e. per capita income, increases, the risk for disaster impacts decreases.

4. DETAILED IMPACT ESTIMATION: 2004 INDIAN OCEAN EAQTHQUAKE AND TSUNAMI

The December 2004 Indian Ocean disaster was caused by an earthquake, and the earthquake generated a tsunami, carrying many million tons of water in a series of very large waves that traversed the Indian Ocean in a matter of hours. These waves hit beaches, flooding low-lying lands coastal areas. The destruction was widespread: the most seriously affected areas were Banda Aceh, Indonesia, as well as in tourism resorts in Thailand, Sri Lanka, and the Maldives. Many small and medium sized rural villages located along the beachside in the five countries were also wiped out (ADPC, 2005).

According to the above preliminary assessment of damages and losses, total of 281,900 persons died as a result of the earthquake and tsunami; 189,500 persons were injured, physically and psychologically, and required immediate or medium term treatment; and, 1.2 million persons became homeless and even a year after the tsunami many were still housed in temporary camps, a sizable fraction of which still requires shelter, food and health services. The total economic effect of this event was estimated as US$ 5.6 billion for damages and 4.3 billion for losses over five countries—Indonesia, India, Sri Lanka, Maldives, and Thailand. In this section, the total impacts of this event are analyzed below for Indonesia and Thailand using 2000 Asian International IO table, published from the Institute of Developing Economies.

Indonesia

The total damage and loss in Indonesia were estimated as US$ 2,664 million and 1,136 million, respectively (ADPC, 2005). The Housing sector had the largest damage with 1,398 million (52% of total damage). The Transport sector had the second largest damage, 409 million. The Productive sector, especially Agriculture and Industry (manufacturing), also had the sizable damage. On the other hand, the losses were concentrated on these Productive sectors, 550 million for Agriculture and 280 million for Industry, and together, they had about 73% of total loss.

The derived impacts are US$ 2,386 million (0.93% of 2004 GDP) for the total impact (output) and 1,219 million for income impact. The most significant output impact falls on Manufacturing with 814 million (with 280 million of output decrease as loss), followed by Agriculture with 672 million. The sectors with large impact tend to be accompanied with large losses, while the other sectors with small or no losses, such as Mining, Utilities, and Construction, have limited higher-order effects. This may lead to the relatively small impact multiplier of 2.10.

Thailand

The total damages and losses in Thailand were estimated to US$ 509 million and 1,690 million, respectively. The damages were concentrated on Tourism with 376 million (74% of the total damage), resulted from the washed out resorts and hotels on the beaches. Other noticeable damages were on Agriculture. The losses were also mostly on Tourism with 1,470 million (87% of the total loss), and Agriculture and Industry had some losses around 100 million each.

The derived impact on output and income are US$ 3,205 million (1.99% of 2004 GDP) and 1,240 million, respectively. The total impacts fall mostly on Services (including tourism industry) with 1,535 million (48% of the total output impact). Meanwhile, Manufacturing has a sizable impact of 872 million (27% of the total output impact), indicating that the Thailand's domestic industries are interwoven and interdependent to some extent so that the higher-order effects spread across the sectors. However, the calculated impact multiplier is 1.90, a relatively low value. This implies that while the tourism industry is one of the major industries in Thailand, the losses are concentrated on one industry (Tourism) and thus the higher-order effects are somehow limited and not widely spread to the entire economy.

International Analysis (including Indonesia and Thailand)

As seen above, the impacts of the event appear not so large within the two countries (0.93% of GDP in Indonesia and 1.99% of GDP in Thailand). With increased economic dependency between countries through international trades, this simultaneous damages and losses in multiple neighboring countries may bring the higher-order effects to other surrounding countries.

Table 1 indicates the impacts for these countries. Except those directly affected countries, Indonesia and Thailand, Japan has the largest total impact in this system, with US$ 428 million. The United States has the second largest total impacts of 306 million. China follows these two countries and has 156 million of the total Impact. Among the sectors, Manufacturing has the most significant impact in total (2,307 million) and for each country in this system. This also an evidence of interdependency of manufacturing firms through international trades.

Comparing to the total impacts in Indonesia and Thailand and to their own GDPs, these higher-order impact can be considered as negligible for each country. At the same time, for the system as a whole, the total impacts (output) become 6,761 million with the impact multiplier of 2.39, and these numbers are noticeably larger than the total of the above two countries. For the multi-country disaster case such as this Indian Ocean Earthquake and Tsunami, this type of international analysis is indispensable to capture the comprehensive picture of the impacts.

Table 1 Total Impacts of 2004 Indian Ocean Earthquake and Tsunami: International Comparison

	Output Impact								Income Impact
Sector in model	Agri-culture	Mining	Manu-facturing	Utilities	Con-struction	Trade and Transport	Services	Total	
Indonesia	672	69	814	30	20	370	412	2,386	1,219
Thailand	228	33	872	132	3	401	1,535	3,205	1,240
Malaysia	2	5	36	1	0	5	9	58	22
Philippines	1	0	7	1	0	2	2	14	5
Singapore	0	0	33	1	0	7	9	50	12
China	19	7	96	6	1	14	14	156	39
Taiwan	2	0	42	1	1	9	15	69	24
Korea	3	0	59	2	0	7	19	90	26
Japan	8	1	230	11	4	64	110	428	154
USA	13	4	120	7	2	47	114	306	143
Total	948	118	2,307	192	30	926	2,239	6,761	2,885

5. CONCLUSIONS

The results for global trend analysis in this paper were derived from the damage data of EM-DAT and NatCat database. These damage data are highly aggregated without having any sector-level information. For an analysis of historical trends and international comparison, the aggregation level in this study is acceptable due to the data availability. On the other hand, further detailed analysis, based disaggregated sectors and/or space, can reveal a more comprehensive figure of disaster impacts, as presented with the 2004 Indian Ocean Earthquake and Tsunami case. While more sophisticated analysis requires further precise numerical input data (West and Lenze, 1994), some standardized framework, such as the ECLAC methodology (UN ECLAC, 2003), can guide how the more detailed disaster data can be gathered in a consistent way. And, if some common economic model of nations, such as SAM with certain level of disaggregation, becomes available, the estimation and examination of disaster impacts will provide not only clearer and more complete but also broader and more robust picture of what have happened in a disaster. In this regard, the role of international organizations is particularly important.

Some researchers claim that the short-term impact of disasters are negligible, since relief, recovery, and reconstruction activities start immediately after the occurrence of hazards, bringing some positive impacts to the economy, and the counteraction measures that a society inherently has against such a calamity would respond to reduce the higher-order effects (Albala-Bertrand, 1993). This may be true, if the negative impacts of losses and higher-order effects and the positive impacts of relief and reconstruction are added up; in empirical disaster studies, the total impacts are indeed sometimes negligible, offsetting negative and positive impacts, or even positive in some cases. However, these results do not lead to the conclusion that disasters have no impact on the economy. A thorough investigation of disaster impacts requires a detailed analysis, which separates negative and positive impacts, and not merely adding them up, in order to assess how negative and positive impacts interact each other and affect various segments of society differently. Negative impacts of higher-order effects surely exist as seen in this paper, and their proper recognition and estimation can enable policy makers to contemplate how ex-ante loss reduction measures can be formed effectively and efficiently.

Acknowledgements:

This research was supported by the Global Facility for Disaster Reduction and Recovery (GFDRR) and the World Bank. The author would like to express deepest gratitude to Apurva Sanghi and Sebnem Sahin for their support, encouragement, and patience. The author would like to also thank Reinhard Mechler for the use of NatCat data and advice.

References:

Albala-Bertrand, J.M. (1993) *The Political Economy of Large Natural Disasters: With Special Reference to Developing Countries*. Oxford, UK: Clarendon Press.

Anbarci, N., Escalerasb, M., and Register, C.A. (2005) Earthquake fatalities: the interaction of nature and political economy, *Journal of Public Economics*, 89, pp. 1907–1933.

Asian Disaster Preparedness Center (ADPC) (2005) *Regional Analysis of Socio-Economic Impacts of the December 2004 Earthquake and Indian Ocean Tsunami*, Bangkok, Thailand.

Benson, C. and Clay, E. (1998) The impact of drought on sub-Saharan African economies, Technical paper 401, Washington DC: World Bank.

Boisvert, R. (1992) Indirect losses from a catastrophic earthquake and local, regional, and national interest, in: *Indirect Economic Consequences of a Catastrophic Earthquake*, pp. 207-265 (Washington, DC: National Earthquake Hazards Reduction Program, Federal Emergency Management Agency).

Brookshire, D. and Mckee, M. (1992) Other indirect costs and losses from earthquakes: issues and estimation, in: *Indirect Economic Consequences of a Catastrophic Earthquake*, pp. 267-325 (Washington, DC: National Earthquake Hazards Reduction Program, Federal Emergency Management Agency).

Cochrane, H.C. (1974) Predicting the economic impacts of earthquakes, in: H.C. Cochrane, J.E. Haas and R.W. Kates (Eds) *Social Science Perspectives on the Coming San Francisco Earthquakes—Economic Impact, Prediction, and Reconstruction*, Natural Hazard Working Paper No.25 (Boulder, CO: University of Colorado, Institute of Behavioral Sciences).

Cochrane, H.C. (1997) Forecasting the economic impact of a Midwest earthquake, in: B.G. Jones (Ed.) *Economic Consequences of Earthquakes: Preparing for the Unexpected*, pp. 223-247 (Buffalo, NY: National Center for Earthquake Engineering Research).

Cole, S. (1995) Lifeline and livelihood: a social accounting matrix approach to calamity preparedness, *Journal of Contingencies and Crisis Management*, 3, pp. 228-40.

Cole, S. (1998) Decision support for calamity preparedness:

socioeconomic and interregional impacts, in: M. Shinozuka, A. Rose and R.T. Eguchi (Eds) *Engineering and Socioeconomic Impacts of Earthquakes*, pp. 125-153 (Buffalo, NY: Multidisciplinary Center for Earthquake Engineering Research).

Cole, S. (2004) Geohazards in social systems: an insurance matrix approach, in: Y. Okuyama and S.E. Chang (Eds) *Modeling Spatial and Economic Impacts of Disasters*, pp. 103-118 (New York: Springer).

Ellson, R.W., Milliman, J.W. and Roberts, R.B. (1984) Measuring the regional economic effects of earthquakes and earthquake predictions, *Journal of Regional Science*, 24, pp. 559-579.

Gordon, P. and Richardson, H.W. (1996) The business interruption effects of the Northridge earthquake (Lusk Center Research Institute, University of Southern California, Los Angeles, CA).

Hoke, Z. (2005) In natural disasters the poor are hardest hit, *Voice of America News*, http://voanews.com/english/archive/2005-01/2005-01-13-voa12.cfm, accessed on 10/16/08.

Kahn, M.E. (2005) The death toll from natural disasters: the role of income, geography, and institutions, *The Review of Economics and Statistics*, 87 (2), pp. 271–284.

Kawashima, K., Sugita, H. and Kanoh, T. (1991) Estimation of earthquake induced economic damage, *Report of Public Works Research Institute*, 186, pp. 1-57. (In Japanese.)

Kellenberg, D.K. and Mobarak, A.M. (2008) Does rising income increase or decrease damage risk from natural disasters? *Journal of Urban Economics*, 63, pp. 788-802.

Lester, R. (2008) Climate change, development and the insurance sector", Policy Research Working Paper, World Bank.

Okonski, K. (2004) Economic growth saves lives, *Wall Street Journal Asia*, December 29, 2004.

Okuyama, Y. (2007) Economic modeling for disaster impact analysis: past, present, and future, *Economic Systems Research*, 19 (2), pp. 115-124.

Okuyama, Y., Hewings, G.J.D. and Sonis, M. (1999) Economic impacts of an unscheduled, disruptive event: a Miyazawa multiplier analysis, in G.J.D. Hewings, M. Sonis, M. Madden and Y. Kimura (Eds) *Understanding and Interpreting Economic Structure*, pp. 113-144 (Berlin: Springer).

Rose, A. (2004) Economic principles, issues, and research priorities in hazard loss estimation, in: Y. Okuyama and S.E. Chang (Eds) *Modeling Spatial and Economic Impacts of Disasters*, pp. 13-36 (New York: Springer).

Rose, A. and Benavides, J. (1998) Regional economic impacts, in: M. Shinozuka, A. Rose and R.T. Eguchi (Eds) *Engineering and Socioeconomic Impacts of Earthquakes*, pp. 95-123 (Buffalo, NY: Multidisciplinary Center for Earthquake Engineering Research).

Rose, A. and Guha, G.S. (2004) Computable general equilibrium modeling of electric utility lifeline losses from earthquakes, in: Y. Okuyama and S.E. Chang (Eds) *Modeling Spatial and Economic Impacts of Disasters*, pp. 119-141 (New York: Springer).

Rose, A. and Liao, S.Y. (2005) Modeling regional economic resilience to disasters: a computable general equilibrium analysis of water service disruptions, *Journal of Regional Science*, 45, pp. 75-112.

Rose, A., Benavides, J., Chang, S.E., Szczesniak, P. and Lim, D. (1997) The regional economic impact of an earthquake: direct and indirect effects of electricity lifeline disruptions, *Journal of Regional Science*, 37, pp. 437-458.

Toya, H. and Skidmore, M. (2005) Economic development and the impacts of natural disasters, Working Paper 05-04, Department of Economics, University of Wisconsin – Whitewater.

United Nations Development Programme. (2004) *Reducing Disaster Risk: A Challenge for Development.* New York, NY: UNDP.

United Nations Economic Commission for Latin America and the Caribbean (UN ECLAC) (2003) *Handbook for Estimating the Socio-Economic and Environmental Effects of Disasters*, Santiago, Chile.

United Nations. (2008) *World Economic and Social Survey 2008: Overcoming Economic Insecurity*. New York, NY: UN.

West, C.T. and Lenze, D.G. (1994) Modeling the regional impact of natural disaster and recovery: a general framework and an application to hurricane Andrew, *International Regional Science Review*, 17, pp. 121-150.

Wilson, R. (1982) Earthquake vulnerability analysis for economic impact assessment (Information Resources Management Office, Federal Emergency Management Agency, Washington, DC).

Sixth International Conference on Urban Earthquake Engineering
March 3-4, 2009, Tokyo Institute of Technology, Tokyo, Japan

PROBABILITIES AND SHAKEMAPS OF THE POTENTIAL EARTHQUAKES IN TAIWAN

K. L. Wen[1], M. W. Huang[2], T. H. Wu[2], C. L. Chang[3], S. Y. Liu[3], M. C. Kuo[3], and Y. W. Chang[4]

1) Professor, Institute of Geophysics, National Central University, Taiwan
Deputy Director, National Center for Research on Earthquake Engineering, Taiwan
Deputy Division Head, National Science & Technology Center for Disaster Reduction, Taiwan
2) Associate Research Fellow, National Science & Technology Center for Disaster Reduction, Taiwan
3) Assistant Research Fellow, National Science & Technology Center for Disaster Reduction, Taiwan
4) Assistant Research Fellow, National Center for Research on Earthquake Engineering, Taiwan
wenkl@earth.ncu.edu.tw, mwhuang@ncdr.nat.gov.tw, wu@ncdr.nat.gov.tw, evachang@ncdr.nat.gov.tw, lsy@ncdr.nat.gov.tw, bettyk@ncdr.nat.gov.tw, ywchang@ncree.org.tw

Abstract: Taiwan is located on the boundary between Eurasia Plate and Philippines Sea Plate and earthquakes occur frequently. Since the seismic hazard is inevitable in Taiwan, it is suggested to reduce the seismic hazard. Promotion of seismic hazard mitigation is time-consuming and needs comprehensive resources. Due to limited resources for hazard mitigation, it is suggested to set priority first for regions with high potential of earthquake disaster. In this study, we separated the earthquake source in Taiwan into regional and fault sources, and calculated the potential earthquake probabilities in next 10 to 50 years respectively. For regional source, we analyzed the 13 regions, which used by Taiwan Power Company for Nuclear Power Plant's seismic safety evaluation. We set up the earthquake probability models, and calculate the probabilities for the potential earthquake of each region. As for fault sources, we refer to the active fault parameters investigated by the Central Geological Survey of Taiwan, MOEA, set up the characteristic earthquake probability model, and calculated the probabilities for potential earthquake of each fault. Finally, we estimated the ground motion potential of peak ground acceleration by attenuation relation of PGA for each fault, and the PGA values are improved in prediction by taking into account the site effect. In this study, we can identify the region with high potential earthquake probabilities, these results can be used for seismic hazard prevention and disaster mitigation in Taiwan.

1. INTRODUCTION

Taiwan island is located on the boundary where the Philippines Sea Plate collides with the Eurasia Plate and earthquakes occur frequently in this area. Many disastrous events brought a lot of loss in human being and property in the past hundred years. The latest event is the Chi-Chi Taiwan earthquake with M_L7.3 in 1999 (Shin and Teng 2001; Teng et al. 2001) associated with Chelungpu fault ruptures. It is important to prompt the hazard estimation. The earthquakes can be classified into two sources. The first one is earthquakes associated with surface fault ruptures (also called characteristic earthquake), and the other one is from blind fault ruptures (regional earthquake). An earthquake catalogue with uniform local magnitude, M_L, for about one hundred years in Taiwan was developed by Shin (1993) and Yeh et al. (1995) by combining the catalogue of the Central Weather Bureau (CWB) and the Institute of Earth Science (IES), Academia Sinica. Since 1995, the National Science Council (NSC) and the Central Geological Survey (CGS) have started projects of the systematic survey on active fault. Their efforts focus toward investigating the fault trace, long- and short-period slip rates, the potential earthquake magnitude, and the return period, etc.

In this study, we estimate the probabilities of earthquake recurrence in next 10 to 50 years, respectively, for large regional earthquakes and characteristic ones, and then predict its peak ground acceleration (PGA). For regional earthquakes, the earthquakes with $M_L \geq 5$ are selected due to completeness of the catalogue and hazard evaluation. For the characteristic earthquake, we firstly focus on the recurrence of the 13 active faults defined by the CGS. Finally, the ground motions induced by earthquakes are predicted by an attenuation equation which takes site effects into account.

2. PROBABILTY OF POTENTIAL EARTHQUAKE

As mentioned above, the earthquake sources can be classified into regional and fault sources. Firstly, we estimate the potential magnitude of earthquake for the 13 regions and for characteristic faults. Secondly, the probabilities of earthquake recurrence in next 10 to 50 years are calculated for earthquake with $M_L \geq 5$, $M_L \geq 6$, $M_L \geq 7$ and the potential magnitudes, respectively. Thirdly, the probabilities of recurrence for characteristic faults are evaluated in next 10 to 50 years.

2.1 Probability for Regional Earthquake

2.1.1 Scaling of magnitude and frequency

The earthquake catalogue released by CWB over the period of from 1900 to April 2008, in which the earthquakes with $M_L \geq 5$ are selected in this study. Based on the criteria of seismic zoning of the Taiwan Power Company for Nuclear Power Plant's seismic safety evaluation, 13 regions are analyzed. In Figure 1, the circle denotes the distribution of earthquakes at a period spanning from 1900 to April 2008, while the solid lines depict the 13 regions with codes as S001, S002, etc. The statistic of seismicity following *G-R* law (Gutenberg and Richter 1944) describes the relationship between magnitude and frequency in form of Eq. (1).

$$\log N(m) = a - bm, \qquad m_o \leq m \leq m_u \qquad (1)$$

In Eq. (1), m represents the magnitude, and $N(m)$ expresses the frequency of earthquake with magnitude larger and equal to m. Meanwhile, the constants of a and b can be calculated from best fit of Eq. (1). Under the consideration of seismology and earthquake engineering, we take m_o as lower limit for hazard estimation, and m_u as upper limit for the potential earthquake in a specific region. As mentioned above, the m_o is set to 5 in following evaluation. Figure 2 is an example and shows seismicity of region S011. As shown in Figure 2(a), the earthquakes with various magnitudes occur with time from 1900 to April 2008, and it is observed that earthquakes with $M_L \geq 6$ occur repeatedly every 10 to 20 years. Figure 2(b) shows an example of magnitude and frequency relationship (solid circles), which follows the *G-R* magnitude and frequency relationship, and the solid line is the best fit in form of Eq. (1), where a=5.07 and b=1.01.

2.1.2 Magnitude of the potential earthquake

From the past earthquake, we can derive the potential magnitude of earthquake. Iida (1976) proposed the relation between magnitude and strain energy in form of Eq. (2).

$$\log(E) = 12.66 + 1.4M_L \qquad (2)$$

In Eq. (2), the E represents the strain energy. The evaluation of the potential magnitude can be done through two lines enveloped the released strain energy cumulated with time. The slopes of the two lines express the energy released constantly in this region and the potential magnitude can be derived from Eq. (2). As shown in Figure 3, we have the energy released in the region S011 over the period from 1900 to April 2008 and the potential magnitude is about 7.1.

2.1.3 Recurrence model and results

In this study, we adopt the recurrence model of lognormal model (Utsu 2002) based on the concept of the Poisson process (Angnos and Kiremidjian 1988). The effect of aftershock is removed from the catalogue through the method proposed by Gardner and Knopoff (1974). Given $f(t)$ as the probability density function (*PDF*), t as the interevent time, the model can be expressed as follows:

$$f(t) = \frac{1}{\sqrt{2\pi}\sigma t} e^{\frac{-(\ln t - \mu)^2}{2\sigma^2}} \qquad (3)$$

where the σ and μ are mean and standard deviation of *PDF*, respectively. The probability density function can be derived from Eq. (1) for the 13 regions and obtained the values of σ (recurrence time) and μ. Then we take the occurrence time of the last event into account. The probabilities of recurrence of earthquake with $M_L \geq 5$, $M_L \geq 6$, $M_L \geq 7$, and potential magnitude are listed in Table 1, Table 2, Table 3, and Table 4, respectively. Asterisk in Table 1, Table 2, Table 3, and Table 4 denotes insufficient data to estimate the probabilities. As shown in Table 1, the probabilities of earthquake with $M_L \geq 5$ in next 10 years are almost 100% for all regions, except for region S001 (86.96%) and S012 (75.15%) due to low seismicity with high standard deviations. The return period for earthquakes with $M_L \geq 6$ are nearly in next 10 to 20 years, but three regions, i.e., S003 (6.53 years), S006 (7.96 years), and S008 (10.50 years), belong to regions with high seismic hazard (Table 2). For earthquakes with $M_L \geq 7$, the most hazardous area is region S003 in the future (Table 3). Two regions, i.e., S003 and S006, belong to high probabilities of recurrence for earthquakes with $M_L \geq 7$ (Table 4). The highest probabilities of recurrence for potential earthquakes with $M_L \geq 7$ locate at region S003 and exceed 10% in next 10, 20, 30, 40, and 50 years.

2.2 Probability for Characteristic Earthquake

Based on the concept of time-predictable model on the characteristic earthquakes, we can estimate the probability of recurrence for each fault. Young and Coppersmith (1985) used slip rate of faults on evaluation of probability for avoiding the underestimating probability of large earthquake. Table 5 shows return period estimated from trenching survey and monitoring of active faults, and averaged return period used in this study. The longest return period is 1500 years for the Hsincheng fault, and the shortest one is 110 years for the Milun fault. Taking occurred time of last event, we can estimate the probabilities of each fault system. Results are listed in Table 6. The larger probabilities of Tachienshan-Chukou fault and Milun fault with potential magnitude 7.3 are 5.43% and 9.39%, respectively, in next 10 years.

3. SHAKE MAP

After estimating the probability of earthquakes recurrence, we can predict the ground motion induced by both of the potential area source earthquakes and the characteristic ones. The main factors that affect the attenuation relationship are the existence of site effects. It is believed that the systematic bias mainly comes from the site effects. Therefore, it is necessary to take account of the site effects in applying the attenuation relationship of PGA, and the results in estimation of seismic hazard will be improved.

Up to date, the sites for stations of the Taiwan Strong-motion Instrumentation Program (TSMIP) deployed by the CWB and Central Mountain Array (CMA) deployed by the IES, Academia Sinica still not been classified explicitly. In this study, we used two steps to predict the best results of PGA shake map.

First step, we got the first PGA of each site by attenuation relationship of PGA (Jean 2001), which used more than 3000 seismic records from 59 earthquake events to study the attenuation relationship of PGA, which follows the model proposed by Campbell (1997). The attenuation equation can be expressed as follow:

$$Y_{att}=0.00369e^{1.75377m}[R+0.12220e^{0.78315m}]^{-2.05644} \quad (4)$$

where Y_{att} is predicted PGA value and R is the closest distance to the source.

Second step, the site correction of each station of the TSMIP and CMA can be simplified by the following law:

$$ln(PGA_{obs})_S = C_0 + C_1 \times ln(Y_{att})_S \quad (5)$$

where $(PGA_{obs})_S$ is the observed PGA value, and $(Y_{att})_S$ is the predicted PGA value obtained from the attenuation relationship law. In Eq. (5), the values of C_0 and C_1 are the site-dependent parameters for corrections on site effects. The selection criteria for earthquakes are M_L>4.0 and focal depth<50 *km*. All seismograms are well recorded by the Taiwan Rapid Earthquake Information Release System (TREIRS) system, TSMIP system and CMA system. The results reasonably agree with the surface geology from published maps.

Figure 4 shows two example of the shake map for two high hazardous faults, i.e., (a) Tachienshan-Chukou Fault with potential magnitude M_L7.3 and recurrence probability 5.43% in next 10 years, and (b) Milun Fault with potential magnitude M_L7.3 and recurrence probability 9.39% in next 10 years.

4. SUMMARY

From Tables 1, 2, 3, and 4, four regions, i.e., S003, S006, S008, and S009 belong to high seismic potential high hazards. On the contrary, the regions, i.e., S001, S004, and S012 are low seismic hazards. Compared with the tectonic of Taiwan area, it shows regions close to collision zone between plates with high seismic hazards, and far away from collision with low ones. The probabilities of Tachienshan-Chukou fault and Milun fault with potential magnitude 7.3 are 5.43% and 9.39%, respectively, in next 10 years. According to shake map of Tachienshan-Chukou fault with M_L7.3, the shake intensity reaches sixth degree for large area with high population and should pay more attention.

Acknowledgements:
The authors acknowledge support from the National Science Council under the Grant No. NSC95-2745-M-008-003 and NSC96-2625-Z-008-012.

References:

Anagnos, T. and Kiureghian, A.S. (1988), "A Review of Earthquake Occurrence Models for Seismic Hazard Analysis," *Probabilistic Engineering Mechanics*, **3**(1), 3-11.

Campbell, K.W. (1997), "Empirical Near-source Attenuation Relationships for Horizontal and Vertical Components of Peak Ground Acceleration, Peak Ground Velocity, and Pseudo-absolute Acceleration Response Spectra," *Seism. Res. Lett.*, **68**(1), 154-179.

Gutenberg, B. and Richter, C.F. (1944), "Frequency of Earthquake in California," *Bull. Seism. Soc. Am.*, **34**, 185-188.

Iida, K. (1976), "Earthquake Energy-magnitude Relation, Strain Rate and Stress Drop in Earthquake, Seismic Efficiency Factor, and Parameters of Faulting," Dept. of Earth Science, Nagoyo University.

Jean, W.Y. and Loh, C.H. (2001), "A Study on the Classification of Site Effects and Its Application to the Seismic Hazard and Microzonation," 10th International Conference on Soil Dynamics and Earthquake Engineering, SDEE'2001, Volume of Extended Abstracts, 82.

Shin, T.C. and Teng, T.L. (2001), "An Overview of the 1999 Chi-Chi, Taiwan, Earthquake," *Bull. Seism. Soc. Am.*, **91**(5), 895-913.

Teng, T.L., Tsai, Y.B., and Lee, W.H.K. (2001), "Preface to the 1999 Chi-Chi, Taiwan, Earthquake Dedicated Issue," *Bull. Seism. Soc. Am.*, **91**(5), 893-894.

Utsu, T. (2002), "Statistical Features of Seismicity," In: Lee, W.H.K., H. Kanamori, P.C. Jennings, and C. Kisslinger, (Eds.), International Handbook of Earthquake & Engineering Seismology, 81A, Academic Press, 719-732.

Youngs, R.R., and Coppersmith, K.J. (1985), "Implications of Fault Slip Rates and Earthquake Recurrence Models to Probabilistic Seismic Hazard Estimates," *Bull. Seism. Soc. Am.*, **75**, 939-964.

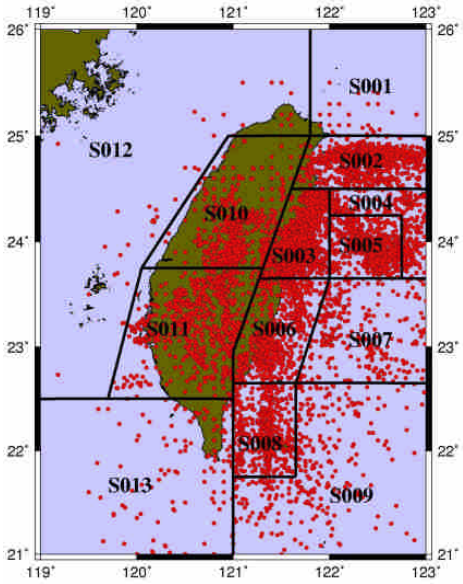

Figure 1 The Distribution of Earthquake with $M_L \geq 5$ at a Period of from 1900 to April 2008.

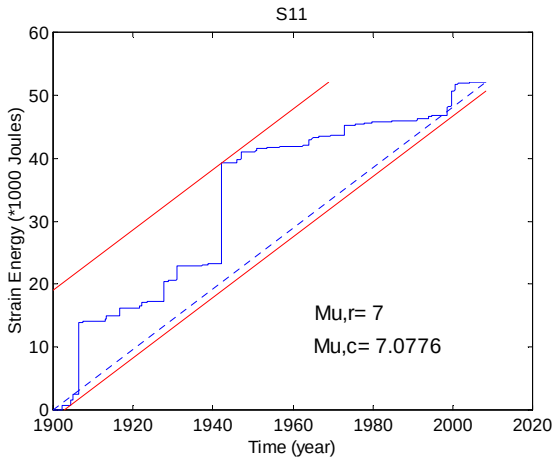

Figure 3 The Released Strain Energy Cumulated Over the Period of From 1900 to April 2008 in the Region S011.

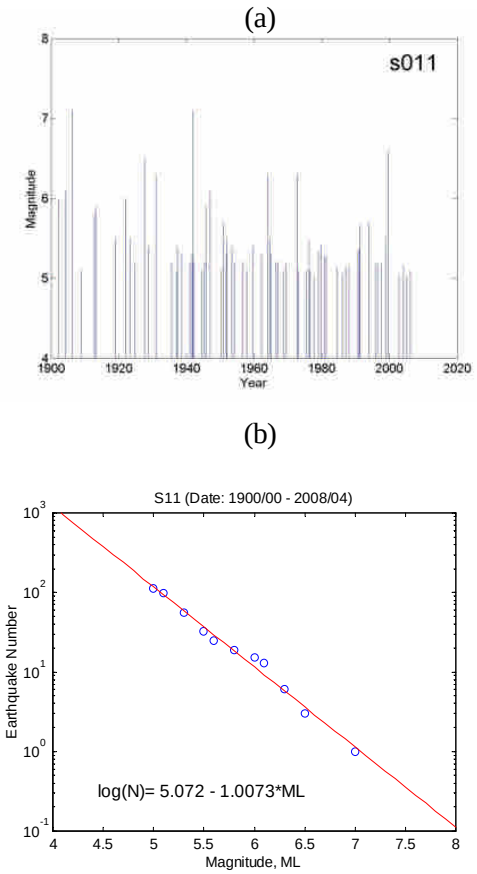

Figure 2 (a) Earthquakes Occur from 1900 to April 2008 in the Region S011. (b) The Solid Circles Show the Magnitude and Frequency Relationship in the Region S011 and the Solid Line is the Best fit.

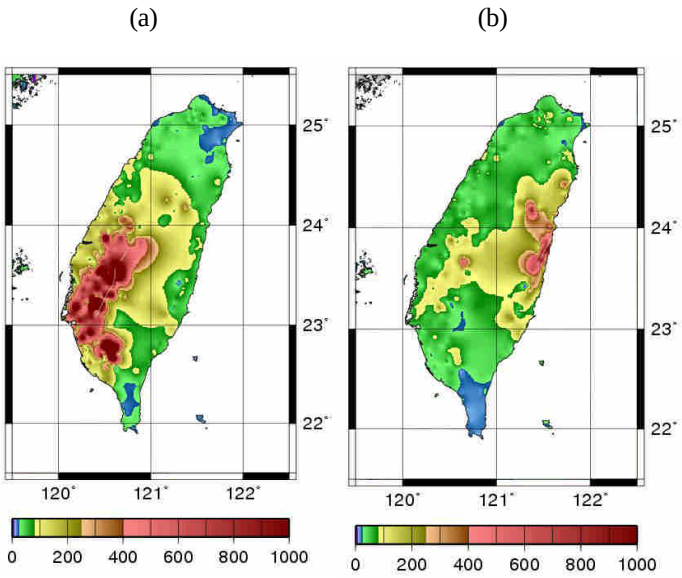

Figure 4 Two Examples of Shake Map for (a) Tachienshan-Chukou Fault (M_L=7.3, 5.43% in Next 10 Years) and (b) Milun Fault (M_L=7.3, 9.39% in Next 10 Years)

Table 1 Probabilities for $M_L \geq 5$ in Next 10, 20 30, 40, and 50 Years

Zone	G-R Law		CV	Last Event	Probability for T_p Years				
					10	20	30	40	50
S001	5.10	5.20	1.02	2003.04	86.96	96.89	98.99	99.60	99.82
S002	1.20	1.38	1.15	2007.01	99.34	99.94	99.99	100.00	100.00
S003	0.60	0.70	1.16	2006.03	99.91	100.00	100.00	100.00	100.00
S004	1.84	2.26	1.23	2004.09	96.36	99.45	99.86	99.95	99.98
S005	0.59	0.74	1.26	2006.06	99.95	100.00	100.00	100.00	100.00
S006	0.75	0.89	1.19	2006.03	99.94	100.00	100.00	100.00	100.00
S007	1.44	1.31	0.91	2006.09	99.47	99.97	100.00	100.00	100.00
S008	1.33	1.35	1.01	2007.07	99.63	99.98	100.00	100.00	100.00
S009	1.35	1.20	0.89	2007.03	99.67	99.98	100.00	100.00	100.00
S010	2.16	2.94	1.36	1999.07	91.87	98.28	99.46	99.79	99.90
S011	0.92	0.92	1.00	2006.02	99.93	100.00	100.00	100.00	100.00
S012	5.07	4.51	0.89	1988.05	75.15	92.05	97.00	98.73	99.41
S013	3.12	2.62	0.84	1993.09	96.50	99.64	99.94	99.98	100.00

Table 2 Probabilities for $M_L \geq 6$ in Next 10, 20 30, 40, and 50 Years

Zone	G-R Law		CV	Last Event	Probability for T_p Years				
					10	20	30	40	50
S001	*	*	*	*	*	*	*	*	*
S002	9.84	11.32	1.15	2002.4	72.67	89.66	95.29	97.58	98.65
S003	4.57	5.30	1.16	2001.5	85.77	96.24	98.67	99.44	99.73
S004	27.43	33.74	1.23	2004.9	45.71	69.11	81.03	87.64	91.57
S005	6.98	8.80	1.26	2006.6	85.81	95.93	98.41	99.26	99.62
S006	6.87	8.18	1.19	2006.3	85.44	95.93	98.46	99.31	99.65
S007	10.72	9.76	0.91	1989.6	61.84	83.20	91.83	95.71	97.60
S008	9.41	9.50	1.01	2002.7	73.88	90.91	96.19	98.19	99.06
S009	10.98	9.77	0.89	2007.1	62.97	87.32	94.94	97.72	98.87
S010	16.31	22.18	1.36	1999.7	59.73	79.91	88.67	93.06	95.49
S011	9.93	9.93	1.00	1999.7	70.76	89.06	95.19	97.64	98.74
S012	*	*	*	*	*	*	*	*	*
S013	19.47	16.35	0.84	1955.3	38.31	60.53	74.03	82.49	87.94

Table 3 Probabilities for $M_L \geq 7$ in Next 10, 20 30, 40, and 50 Years

Zone	G-R Law		CV	Last Event	Probability for T_p Years				
					10	20	30	40	50
S001	*	*	*	*	*	*	*	*	*
S002	115.17	132.44	1.15	1922.7	11.76	21.77	30.41	37.88	44.38
S003	50.21	58.25	1.16	1957.1	22.63	39.04	51.29	60.60	67.79
S004	*	*	*	*	*	*	*	*	*
S005	147.15	185.41	1.26	1910.7	11.13	20.61	28.83	35.97	42.22
S006	117.56	139.90	1.19	1968.2	14.65	26.63	36.58	44.88	51.86
S007	206.39	187.81	0.91	1979.0	5.04	10.73	16.72	22.72	28.55
S008	130.11	131.41	1.01	1996.7	6.09	14.70	23.92	32.76	40.81
S009	170.85	152.05	0.89	1972.1	6.86	14.22	21.62	28.75	35.44
S010	200.17	272.23	1.36	1999.7	5.64	13.02	20.60	27.77	34.32
S011	255.25	255.25	1.00	1942.0	6.38	12.53	18.43	24.01	29.26
S012	*	*	*	*	*	*	*	*	*
S013	573.19	481.48	0.84	1900.4	0.47	1.02	1.66	2.39	3.20

Table 4 Probabilities for $M_{u,r}$ in Next 10, 20 30, 40, and 50 Years

Zone	G-R Law		CV	Last Event	$M_{u,r}$	Probability for T_p Years				
						10	20	30	40	50
S001	172.45	175.90	1.02	1907.5	5.8	10.79	20.16	28.40	35.65	42.04
S002	407.27	468.36	1.15	1922.7	7.3	3.34	6.66	9.96	13.21	16.39
S003	174.97	202.97	1.16	1951.8	7.3	8.53	16.16	23.04	29.25	34.87
S004	639.54	786.64	1.23	2004.9	6.7	0.35	1.66	3.86	6.71	9.95
S005	252.36	317.97	1.26	1910.7	7.1	8.35	15.78	22.46	28.47	33.90
S006	198.38	236.07	1.19	1968.2	7.1	10.51	19.73	27.86	35.02	41.33
S007	206.39	187.81	0.91	1979.0	7.0	5.04	10.73	16.72	22.72	28.55
S008	476.34	481.11	1.01	1936.6	7.2	0.55	1.89	4.02	6.78	9.98
S009	636.91	566.85	0.89	1972.1	7.2	1.26	3.03	5.25	7.85	10.72
S010	1101.29	1497.75	1.36	1999.7	7.3	0.08	0.32	0.74	1.34	2.11
S011	577.13	577.13	1.00	1942.0	7.1	2.77	5.72	8.82	11.99	15.19
S012	142.84	127.13	0.89	1920.9	5.9	8.15	15.70	22.71	29.16	35.07
S013	573.19	481.48	0.84	1900.4	7.0	0.47	1.02	1.66	2.39	3.20

Table 5 Return Period for Characteristic Faults From Trenching Survey and Monitoring of Active Faults

Fault Name	Estimated return period (yr)			Return Period Used in This Study (yr)
	Trenching Survey	Monitoring of Active Fault		
		Long-term	Short-term	
Hsincheng F.	1300~1850	*	167~237	1500
Shihtan F.	*	*	167	300
Shenchoshan F.	*	*	138	
Tuntzuchiao F.	*	*	424	
Chelungpu F. (northern)	341~892	392~980	641~5769	375
Chelungpu F. (middle)	298~731	269~476	374~749	
Chelungpu F. (southern)	408~625	212~532	103~516	
Meishan F.	*	*	409~631	300
Tachienshan F.	*	*	8~390	200
Chukou F.	*	*	*	
Hsinhua F.	*	16~152	20~206	120
Milun F.	*	*	67~178	110
Yuli F.	*	*	625~2187	240
Chishang F.	240	*	*	
Chimei F.	*	*	*	

Table 6 Probabilities for Characteristic Faults in Next 10, 20 30, 40, and 50 Years

Fault Name	Return Period	T_e	Last Event	M_u	Probability in T_p Year(%)				
					10	20	30	40	50
Hsincheng F.	1500	196.0	1811	6.60	0.00	0.01	0.01	0.02	0.02
Shihtan F.	300	72.7	1935/4/21	7.1	0.35	0.94	1.82	3.04	4.61
Shenchoshan F.									
Tuntzuchiao F.									
Chelungpu F.	375	8.3	1999/9/21	7.3	0.00	0.00	0.00	0.00	0.01
Meishan F.	300	101.8	1906/3/17	7.1	1.21	2.77	4.70	6.98	9.57
Tachienshan F.	200	100.0	*	7.3	5.43	11.28	17.36	23.51	29.61
Chukou F.									
Hsinhua F.	120	61.1	1946/12/5	6.1	8.50	18.10	28.03	37.69	46.69
Milun F.	110	56.2	1951/10/22	7.3	9.39	19.99	30.82	41.16	50.60
Yuli F.	140	56.1	1951/11/25	7.3	0.41	1.18	2.44	4.23	6.58
Chishang F.									
Chimei F.									

Sixth International Conference on Urban Earthquake Engineering
March 3-4, 2009, Tokyo Institute of Technology, Tokyo, Japan

ESTIMATION OF SHALLOW SOIL MODELS FOR THE KANTO BASIN, JAPAN, USING SITE AMPLIFICATIONS FROM SPECTRAL INVERSION OF STRONG MOTION DATA

Hiroaki Yamanaka[1], Mitihiro Ohori[2], and Saburo Midorikawa[3]

1) Associate Professor, Dept. of Environmental Science and Technology, Tokyo Institute of Technology, Japan
2) Research Scientist, DONET, Japan Agency for Marine-Earth Science and Technology, Yokohama, Japan
3) Professor, Dept. of Built Environment, Tokyo Institute of Technology, Japan
yamanaka@depe.titech.ac.jp, ohorim@jamstec.go.jp, smidorik@enveng.titech.ac.jp

Abstract: Site amplification factors in a period range of 0.5 to 20 Hz were estimated from a spectral inversion of strong motion data at more than 600 stations in the Kanto basin, Japan. Since the site amplification for sedimentary layers over the basement of Vs of about 2.5 km/s at a reference station were used as the constraint condition in the spectral inversion, the estimated site amplification can be regarded as effects of shallow and deep soils over the basement. We, next, inverted the site amplifications to a 1D S-wave velocity model at each site by fitting the amplification with theoretical one of S-wave using a heuristic inversion method by Yamanaka (2007). Distributions of the S-wave velocities of the shallow and deep soils are obtained from results of the inversion of the site amplifications. We also map averaged S-wave velocity of soils in a depth of 30meters. The amplification is closely related with the averaged S-wave velocity.

1. INTRODUCTION

Estimation of site amplification is one of the important tasks in strong motion prediction. Accurate soil model parameters of shallow and deep soils must be prepared in reliable evaluation of site effects at a site with sediments. In the Kanto basin, 3D models of S-wave velocity structure for deep soils over basement were proposed and validated for performance of simulation of earthquake ground motion (e.g., Yamanaka and Yamada, 2006). Although there are many data for profiles of shallow soils with a depth of about several tens of meters, 3D model of the shallow soils has not been proposed yet in entire of the Kanto basin.

Recently strong motion records of small and moderate events at many stations are available in the Kanto basin from dense strong motion observations operated by several agencies. Site amplifications were estimated from the observations (e.g., Kawase and Matsuo, 2004; Kawakami et al., 2004). The amplification factor estimated contains effects of soils beneath each station, and was used to deduce S-wave velocity model (Kawase and Matsuo, 2004).

In this study, site amplification factors in a period range of 0.5 to 20 Hz were estimated from a spectral inversion of strong motion data at more than 600 stations in the Kanto basin, Japan. We, next, inverted the site amplification to a 1D S-wave velocity model at each site by fitting the amplification with theoretical one of vertically propagating S-wave. 3D distribution of shallow soils is constructed from the results of the inversion at each site.

2. SPECTRAL INVERSION

2.1 Data

To derive the site amplification spectra from strong motion records, we analyzed 23 earthquakes with Mj from 4.1 to 6.1, which occurred beneath the Kanto plain during interplate earthquakes and slab earthquakes concerned with the Philippine plate and the Pacific plate. The source depths of targeted events were in the range of 20 to 101 km with an average depth of 63 km. The F-net focal mechanisms showed that most of events had low-dip reverse faulting components, except that a few cases involved strike faulting components.

We used the strong motion data recordings during the events from the three strong motion networks: the K-NET, the KiK-net and the SK-net. To highlight the S-wave portion rather than other waves and to avoid nonlinearity of surface layers, we selected targeted data and stations in and around the Kanto plain in what follows. (a) The maximum acceleration must be less than 100 cm/s^2. (b) The hypocentral distance must be less than 150 km. (c) After passing (a) and (b), recordings from five events or more must remain for each station. Finally, we selected 115 stations from the K-NET, 42 stations from the KiK-net, and 519 from the SK-net. Most of these stations were located inside the Kanto plain, whereas several stations surrounding the Kanto plain were included from the viewpoints of possible reference sites and azimuthal coverage. The locations of these selected stations are shown in Figure 1 with those of the epicenters of the events.

2.2 Data Processing

To estimate the site effect from spectral inversion method, we took 20 s time window for the S-wave portions from the NS and EW components. The beginning and the end of the window were tapered with 1 s cosine taper. Then, we calculated the Fourier spectral amplitude from a complex signal x(t)+iy(t), where x(t) and y(t) denote two orthogonal horizontal components. The amplitude spectrum was smoothed by a Parzen window with a width having frequency dependence: given by 0.1*f with the minimum of 0.1 Hz and the maximum of 1.0 Hz. Totally, we calculated 1777 spectra for the K-NET, 499 for the KiK-net, and 5442 for the SK-net.

2.3 Spectral Inversion Method

Based on the assumption that the spectral amplitude was expressed by the product of the source, path, and site effects, we separated these effects by solving simultaneous logarithmic equations. We basically used the method proposed by Iwata and Irikura (1986) except a slight modification. The spectral amplitude between 0.8 and 20 Hz was analyzed. First, we carried out the first stage inversion based on the KiK-net borehole recordings and modeled the frequency dependent Qs-value (quality factor of the S-wave) along the propagation path with assumed S-wave velocity of 4km/s. Spectral amplitudes were corrected for the path effect with the anelasticity (Qs-value) and the geometrical spreading that is the same as inverse of hypocentral distance. Next, to eliminate the trade-off between source effects and site effects in spectral inversion, we examined the spectral ratios between the surface and borehole data for 42 KiK-net stations and found that SITH10 was the most preferable stations as reference site in this study. After modifying the initial subsurface structure model based on the PS logging to fit the theoretical spectral ratio with the averaged observed data as shown in Figure 2, we calculated the transfer function of the surface ground motion at SITH10 against the vertical plane S-wave incidence at the bedrock with the S-wave velocity of 2500 m/s. Finally, we conducted the spectral inversion using the above transfer function as additional information and estimated the site amplification spectra for all stations of our interest.

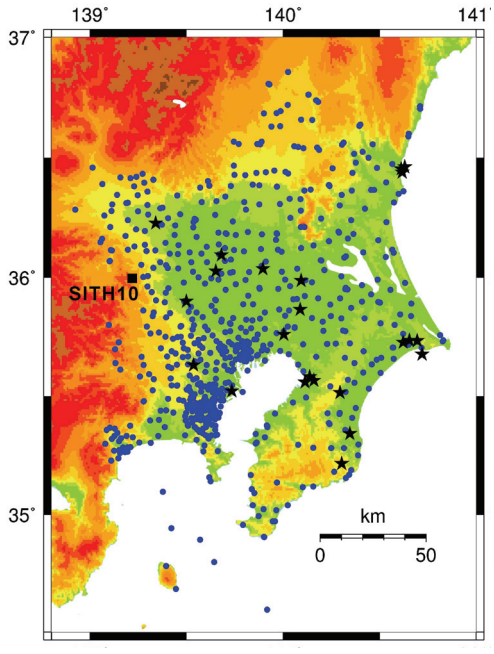

Figure 1 Locations of stations (circles) and epicenters (stars).

2.4 Results

The Qs-value for the propagation path is estimated as shown in Figure 3. Although the spectral inversion method allows estimating Qs-value at each frequency, the estimated Qs are well approximated with a linear relationship of $Q_s(f) = 101 f^{0.667}$ as can be seen in the figure. The Qs-value is coincident with results of previous studies of similar spectral inversion using earthquake records in and around the Kanto basin (e.g., Kinoshita, 1994; Yamanaka et al., 1998). Although the source spectra do not shown here, most of them are similar to spectral shapes for the ω^{-2} model.

The examples of the site amplifications separated by the spectral inversion are shown in Figure 4. These stations are located between the eastern and western edges of the basin.

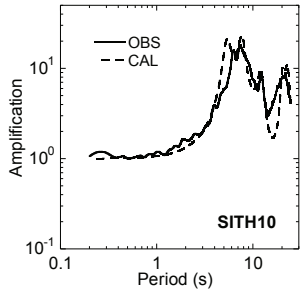

Figure 2 Comparison of observed spectral ratio between records on the surface and at the bottom of borehole with theoretical one at SITH10. This S-wave model is used as defining reference site effects in the spectral inversion.

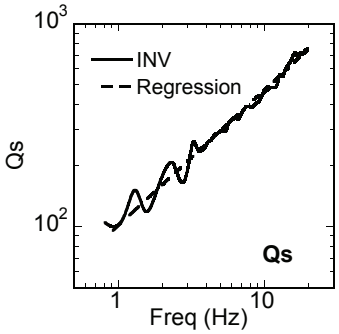

Figure 3 Qs-value for propagation path derived from spectral inversion.

The amplification at TKYH13 in the mountainous area is characterized by a strong peak at a frequency of 10 Hz suggesting effects of superficial low-velocity layers. On the other hand, a large amplification at a frequency of less than 1 Hz can be identified at TKYH11 and CHB_FUN in the central part of the basin with an amplitude decrease at a frequency higher than 10 Hz. It is noted that the site effects at CHBH14 located in the eastern margin of the basin differs from that of TKYH13 with a relative large amplification at a frequency less than 1Hz. This suggests that surface soils models are different from each other in the eastern and western margins of the Kanto basin.

The estimated site amplifications at all the sites are mapped at several frequency bands. Figure 5 shows the distributions of the amplifications at frequencies of 1, 5 and 16 Hz. The amplifications at a frequency of 1Hz are large in most of the sites in the basin, except for those at the marginal part of the basin. This pattern of the amplification map can be still identified in the distribution for 4Hz, although the amplification factors are smaller than that for 1Hz at most of the stations. On the other hand, the amplifications at a frequency of 16 Hz are different from those for 1 and 4 Hz with large amplification factors in the marginal part and amplitude decreases in the central part of the basin. The amplitude decrease at a frequency of 16Hz can be interpreted as the same as explained above.

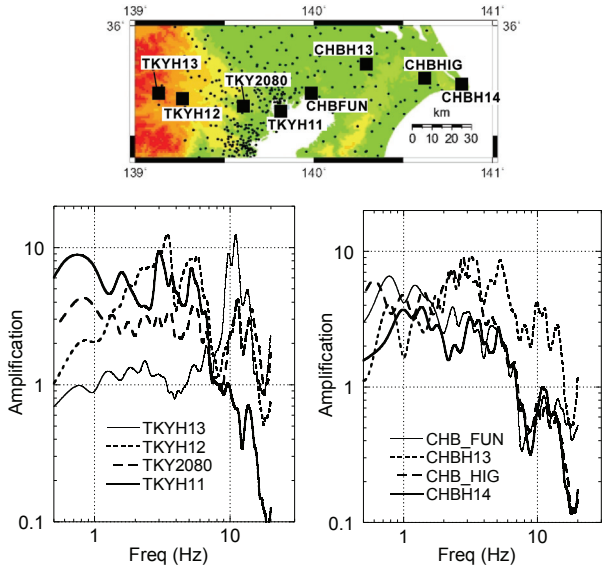

Figure 4 Site amplifications at sites shown by solid squares in the upper figure.

3. ESTIMATION OF SOIL PROFILES

3.1 Inversion method for Vs-profiling

The site amplification at each site was inverted to a 1D soil profile by fitting its with theoretical one of vertical S-waves. Since the separated values correspond to amplifications of S-waves in shallow and deep soils over the basement having an S-wave velocity of 2.5 km/s, we invert the amplification to a soil model over the basement. S-wave velocity and thickness of each layer in the soil model are optimized in the inversion. Anelastic attenuation of soil layers is defined as a function of S-wave velocity (Vs) and frequency (f) using $(Vs/b)f^a$. The coefficients, a and b are constant for all the layers of soil model at each site. These coefficients are also optimized in the inversion of the site amplification. Since S-wave velocity structure of deep soils over the basement is three-dimensionally revealed from microtremor array explorations by Yamanaka and Yamada (2006), we assumed a 4-layer model with constant S-wave velocities of 0.3-0.8, 1.0, 1.5 and 3.0 km/s for the deep soils. For the shallow soils, we assumed 2 layers over the engineering bedrock which is the same as the first layer of the deep soils model. These parameters are optimized so as to fit

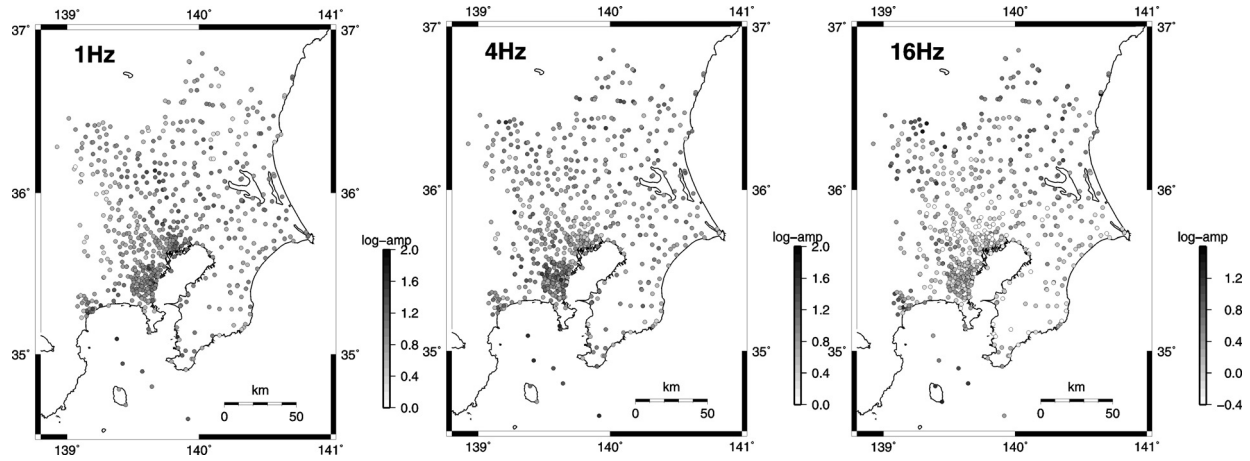

Figure 5 Distributions of site amplifications at frequencies of 1, 4 and 16Hz.

observed amplification with theoretical one using a hybrid heuristic inversion method proposed by Yamanaka (2007). Details of the procedure can be also seen in Takekoshi and Yamanaka (2009). Only search limits of each parameter are given in the method. Density of each layer is also given in advance. The misfit to be minimized in the inversion is defined by summation of root mean square of difference between the observed and theoretical amplifications. It is noted that the search limits of S-wave velocity and thickness for the deep part of the soils are set to be about 10 % of 1D profile from the 3D model by Yamanaka and Yamada (2006). Therefore the deep soils from the inversion are not so different from the existing 3D model.

3.2 Results

Figure 6 shows the example of S-wave velocity profiles of shallow parts of the soil models at TKYH11 and CHBH13. The comparison between the observed and calculated amplifications at the two sites is shown in Figure 7. The shallow S-wave velocity model at TKYH11 is characterized with the very low-velocity surface layer with an S-wave velocity of less than 80m/s. This low-velocity layer is responsible for the amplitude decrease at frequencies higher than 6 Hz as can be seen in Figure 6. However the observed and calculated amplifications are not well fitted with each other. The assumption of the same attenuation model is not adequate for extremely low-velocity layers. On the other hand, the observed amplification at CHBH13 is well reconstructed with the theoretical one at frequency higher than 10Hz. In the figure, the theoretical amplifications for deep soil models are also shown for understanding effects of shallow soils. The shallow soils affect the amplification in entire frequency range at TKYH13, while effects of shallow soils are limited in a frequency higher than 2 Hz at CHBH13.

The distributions of S-wave velocity for the top layer and the depth to the top of the third layer corresponding to the engineering bedrock are depicted in Figure 8. The low S-wave velocity of 70-100 m/s can be seen in many stations near the coast of the Tokyo and Sagami bays. The depth to the engineering bedrock is deep as 40 to 50 meters in the central and western parts of the basin. It becomes shallow in the western and northern margins of the basin.

S-wave velocity profiles at some of the stations of the K-NET are available to the top 20 meters from the surface. We therefore compared averaged S-wave velocity (AVS20) in the top 20 meters between our profiles and those from the K-NET to understand appropriateness of our results. Figure

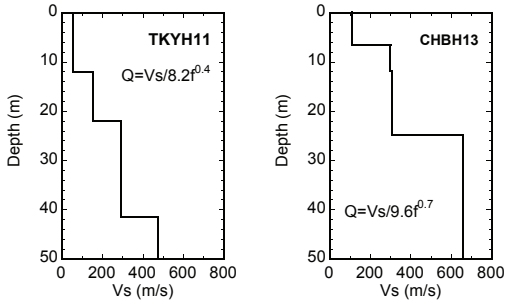

Figure 6 S-wave velocity profiles at TKYH11 and CHBH13 from inversions of site amplifications.

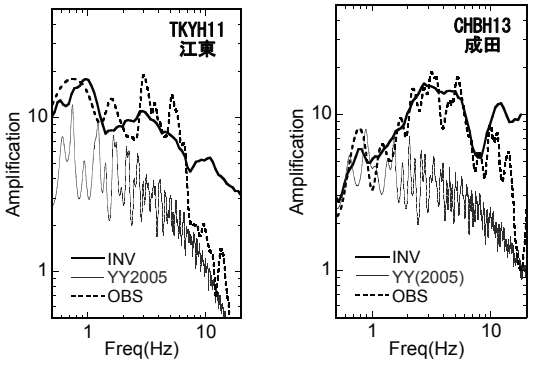

Figure 7 Comparison of observed site amplifications with calculated ones for the inverted S-wave profiles in Figure 6.

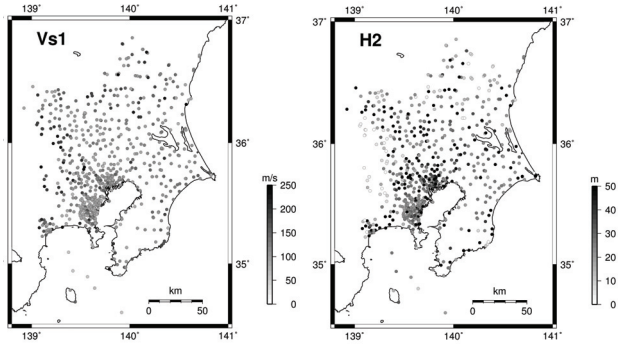

Figure 8 Distributions of S-wave velocity of the top layer of inverted S-wave profiles (left) and depth to top of the third layer corresponding to the engineering bedrock (right).

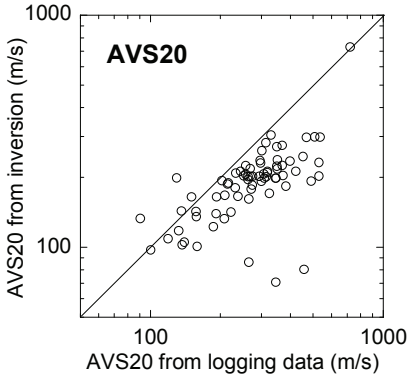

Figure 9 Comparison between averaged S-wave velocity in the top 20 meters of our inverted models and models revealed by logging at the stations of the K-NET.

9 shows the comparison of the averaged S-wave velocities. The averaged S-wave velocities in our models are similar to those of the K-NET up to 400m/s. The AVS30 is usually used in an assessment of ground motion amplification instead of the AVS20. Therefore we calculated AVS30 from the soil profiles. Figure 10 shows the distribution of AVS30. The AVS30s at most of the stations in the basin are from 200 to 300m/s, and some of the stations have low AVS30s of less than 100m/s. Large AVS30s can be identified at the sites in the marginal part of the basin.

3.3 Relationship between amplification and soil models

The amplifications are compared with the AVS30 for the inverted soil models. We calculated the average of the site amplification in a period range from 0.8 to 5Hz, because the amplifications at frequencies more than 6Hz are not well simulated with the inverted soil model as can be seen in Figure 7. The comparison is shown in Figure 11. The amplifications are closely related with the AVS30 at the sites with an AVS more than 150 m/s. It is noted that the amplifications at eh sites with an AVS30 more than 2km/s are from 1 to 2. This agrees with the assumptions where we estimated amplification of shallow and deep soils over the basement having an S-wave velocity of 2.5km/s.

The predominant periods for the shallow soil models are using the equivalent S-wave velocity, *Ve*, that is defined as

$$V_e = \frac{d_1 + d_2}{d_1/Vs_1 + d_2/Vs_2}$$

where $Vs_{1,2}$ and $d_{1,2}$ are the S-wave velocities and thicknesses for the top and second layers. The predominant period is calculated from $4(d_1+d_2)/V_e$. Figure 12 displays the distribution of the predominant periods. Most of the predominant periods are estimated between 0.4 to 0.8 seconds. It becomes more than 1 second at the sites in the coast of the Tokyo and Sagami bays, where the AVS30s are smaller than 150 m/s. The sites in the marginal part of the basin have short predominant periods of less than 0.2 seconds.

4. CONCLUSIONS

The site amplifications of deep and shallow soils were estimated from a spectral inversion of earthquake ground motion data in the Kanto basin together with the Q-value of the propagation path and source spectra for the moderate events. The estimated amplifications were also used to determine shallow soil models. We used a hybrid heuristic inversion technique to find Vs-wave velocity structure and Q-values of soil models over the basement by fitting the amplifications with theoretical ones of vertical S-waves. The inverted soil models were validated by comparing AVS20 from PS-loggings. We discussed the relationship between shallow soils and the amplifications.

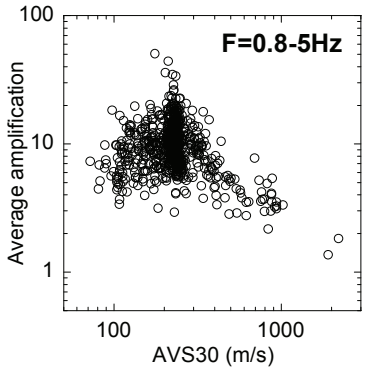

Figure 11 Comparison between AVS30 for the inverted model and average amplification in a period range

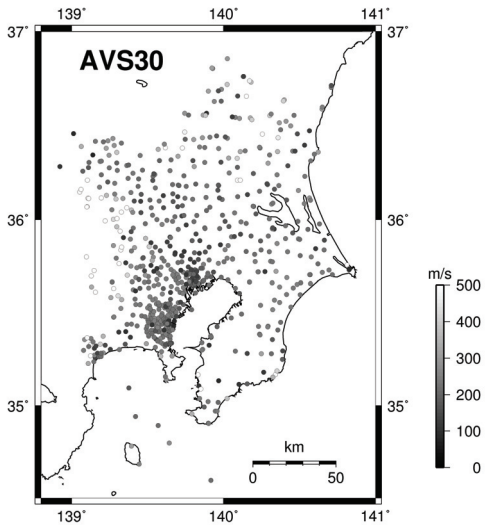

Figure 10 Distributions of averaged S-wave velocity in the top 30 meters of inverted soil models.

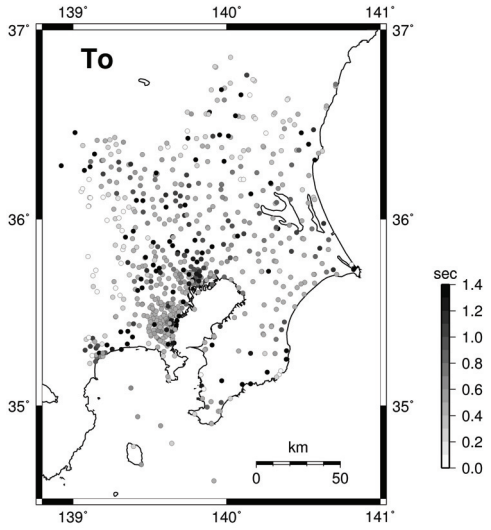

Figure 12 Distributions of predominant periods of shallow soils of S-wave velocity models derived from inversion of site amplifications.

Acknowledgements:

In this study, we used the strong motion data of the K-NET, KiK-net operated by the National Research Institute for Earth Science and Disaster Prevention (NIED) and the SK-net by the Earthquake Research Institute, University of Tokyo. We also used the ground motion data observed by the KKNET Chiba, which was compiled into the SK-net. The focal mechanism information of the F-net by NIED was used. Our sincere gratitude is given to whom it may concern.

References:

F-net (Broadband Seismograph Network) operated by National Research Institute for Earth Science and Disaster Prevention, http://www.fnet.bosai.go.jp/fnet/.

Iwata, T. and Irikura, K. (1986), "Sparation of Source, Propagation and Site Effects from Observed S-waves, " *Journal of Seism. Soc. Japan (Zisin)*, 39, 579-593 (in Japanese).

K-NET (Kyoshin Network) operated by National Research Institute for Earth Science and Disaster Prevention, http://www.kyoshin.bosai.go.jp/kyoshin/.

Kawakami, Y., Koketsu, K. and Hisada, Y. (2004), "Relation between the geographical classifications and the site amplifications estimated from the observed seismic records in Kanto plain," *Summaries of Technical Papers of Annual Meeting Architectural Institute of Japan,* B-2, 687-688 (in Japanese).

Kawase, H., and Matsuo, H. (2004), "Relationship of S-wave velocity structure and site effects separated from the observed strong motion data of K-NET, KiK-net and JMA Network, *Journal of Japan Association Earthq. Eng*., 4, 126-145 (in Japanese).

Kinoshita, S. (1994), "Frequency-dependent attenuation of shear waves in the crust of southern Kanto area, Japan", *Bull. Seism. Soc. Am*., 84, 1387-1396.

KiK-net (Digital Strong-Motion Seismograph Network) operated by National Research Institute for Earth Science and Disaster Prevention, http://www.kik.bosai.go.jp/kik/.

SK-net (Seismic Kanto Network) operated by the Earthquake Research Institute, the University of Tokyo, http://www.sknet.eri.u-tokyo.ac.jp/.

Takekoshi, M. and Yamanaka, H. (2009), "Waveform inversion of shallow seismic refraction data using hybrid heuristic search method," *Geophysical Exploration,* 62, accepted.

Yamanaka, H. and Yamada, N. (2006), "Modeling 3D S-wave velocity structure of Kanto basin for estimation of earthquake ground motion,"*Geophysical Exploration (Butsuri Tansa)*, 59, 549-560 (in Japanese).

Yamanaka, H. (2007), "Inversion of surface-wave phase velocity using hybrid heuristic search method, "*Geophysical Exploration (Butsuri Tansa)*, 60, 265-275 (in Japanese).

Yamanaka, H., Nakamaru, A., Kurita, K., and Seo, K. (1998), "Evaluation of site effects by an inversion of S-wave spectra with a constraint condition considering effects of shallow weathered layers , "*Journal of Seism. Soc. Japan (Zisin),* 51, 193-202 (in Japanese).

Sixth International Conference on Urban Earthquake Engineering
March 3-4, 2009, Tokyo Institute of Technology, Tokyo, Japan

LONG-PERIOD SITE RESPONSE IN THE TOKYO METROPOLITAN AREA

Kenichi Tsuda[1)], Takashi Hayakawa[1)], Kazuki Koketsu[2)], and Hiroe Miyake[3)]

1) Researcher, Center for Atomic Energy Engineering, Institute of Technology, Shimizu Corporation, Tokyo, Japan
2) Professor, Earthquake Research Institute, University of Tokyo, Tokyo, Japan
3) Assistant Professor, Earthquake Research Institute, University of Tokyo, Tokyo, Japan
kenichi.tsuda@shimz.co.jp, takashi.hayakawa@shimz.co.jp, koketsu@eri.u-tokyo.ac.jp, hiroe@eri.u-tokyo.ac.jp

Abstract: We have derived the spatial variation of site response for the greater Tokyo metropolitan area in the long -period range of 2 to 4 s. The site responses have been obtained by the spectral inversion method developed by Tsuda *et al.* (2006). The general features of spatial variation of site response roughly correlate with the surface geology classification by Wakamatsu and Matsuoka (2006). The effect of focal mechanism on site response is included, because the site responses estimated at three KiK-net stations with this effect is closer to the observed one than the site responses estimated without this effects. In particular, site responses near nodes or lobes of the radiation pattern are much affected by this effect. Our results indicate that the geometrical relation of a target site to the seismic source is important for the site response estimation and the inclusion of focal mechanism effect can lead to more realistic ground motion predictions for a specific scenario event.

1. INTRODUCTION

The observed ground motions are constituted by three different factors: seismic source (source effects), wave propagation through heterogeneous earth's interior (path effects), and local geological conditions (site effects). This relationship can be represented by the following equation;

$$O(t) = S(t) * P(t) * G(t) \qquad (1)$$

where * is the convolution operator, O(t) is the observed records, S(t) means the source effects of earthquake ruptures, P(t) means the path effects of wave propagation through the heterogeneous earth's interior, and G(t) means the site response close to the stations. This basic equation has been used to estimate site response based on the observed records.

Among those three effects, site response plays an important role for the ground motion prediction since Reid (1910) pointed out that the level of ground motion correlates with the type of surface geology. Previously, estimation of site response for the period of 0.1-2 s was important, because the number of low-profile buildings with 0.2-0.5 s resonant period was much large compared to large scale structures such as high-rise buildings, oil storage tanks, and base-isolated building *etc.* with usually longer resonant period (1 s or longer). However, increasing number of such large scale structures (e.g., Fukuwa and Tobita, 2008) leads to the recognition of the importance of spatial variation of site response for a long-period range.

In addition to the increasing of such large scale structures, the Tokyo metropolitan area has a very high possibility to have the large earthquakes that can produce very damaging long-period ground motions in near future (The Headquarters for Earthquake Research Promotion, 2007). Such large events can produce the near-source long period ground motions (Koketsu and Miyake, 2008) as well. This means that estimation of site response for longer period in order to predict the long-period ground motions for future earthquakes is an urgent task.

In this study, the site responses for a long-period range (longer than 1 s) have been estimated by using the spectral inversion method (Tsuda *et al.*, 2006). Since this method is reference-independent, site response from the seismological basement to the surface might be estimated. Because some previous studies showed the effects of focal mechanism on the observed ground motions in a long-period range, we have taken into account the effects of focal mechanism into site response estimation. We have used the data recorded at the Tokyo metropolitan area where there are more than 800 strong motion sites. After we obtain site response on all the sites, we have investigated the spatial variation of site response.

2. DATA

We have used the observed data collected by the Seismic Kanto Strong motion-network (SK-net), K-NET and KiK-net. The SK-net began operation after the 1995 Kobe earthquakes for the purpose of seismic hazard mitigation around the Kanto area. This array consists of three-component accelerometers for more than 800 surface

stations and more than 70 borehole stations (Seismic Kanto Research Project, 2001). For this study, we selected 19 events that occurred around the Kanto area. Each event was recorded on almost all of the KiK-net borehole accelerographs as well as most surface stations (Table 1). The epicenters, shown as solid red circles, and the station distribution are shown in Figure 2. The solid blue triangles denote the stations used to determine source and path parameters. The focal depths are greater than 50 km; magnitudes range between 4.5-5.8. Average hypocentral distances to the array vary from 50 to 130 km (Figure 1). In Table 1, we give the source location, focal depth and magnitude determined by the F-net/NIED for each event. We also show the source parameters (seismic moment: *Mo*, and corner frequency: *fc*) in the same table.

Table 1: List of earthquakes used in this study. Mo and fc denote the estimated seismic moments and corner frequencies by Tsuda *et al.* (2008): Mo (NIED) is those determined by F-net/NIED (Fukuyama *et al.*, 1998).

	Event (Date)	Lat.† (N)	Long.† (E)	Depth† (km)	Mw	Moment† [Nm]	Moment§ [Nm]	fc§ [Hz]
1	3/13/03	36.09	139.87	50	4.9	2.34E+16	2.41E+16	1.95
2	4/8/2003	36.07	139.91	44	4.8	2.11E+16	1.58E+16	1.69
3	5/10/2003	35.81	140.11	65	4.7	1.37E+16	2.00E+16	1.41
4	5/12/2003	35.87	140.09	50	5.2	7.07E+16	3.87E+16	1.28
5	5/17/03	35.74	140.7	53	5.3	1.13E+17	1.03E+17	0.71
6	8/18/03	35.8	140.11	71	4.8	1.92E+16	2.55E+16	1.55
7	9/20/03	35.22	140.3	56	5.7	3.53E+17	2.22E+17	0.89
8	10/15/03	35.61	140.05	68	5.1	5.15E+16	5.32E+16	1.60
9	7/10/04	36.08	139.89	50	4.7	1.21E+16	1.34E+16	2.10
10	7/17/04	34.83	140.36	59	5.6	2.39E+17	1.40E+17	1.34
11	8/6/04	35.61	140.06	71	4.7	1.27E+16	1.92E+16	1.98
12	10/6/04	35.99	140.09	65	5.7	4.52E+17	2.80E+17	0.78
13	2/8/05	36.14	140.09	65	4.9	2.20E+16	1.88E+16	2.11
14	2/16/05	36.04	139.9	53	5.4	1.33E+17	7.44E+16	1.52
15	4/10/05	35.73	140.62	50	5.8	4.95E+17	5.52E+17	0.42
16	6/20/05	35.73	140.69	51	5.5	1.94E+17	1.26E+17	0.81
17	7/23/05	35.58	140.14	73	4.7	4.74E+17	4.64E+17	0.84
18	7/28/05	36.13	139.85	51	4.7	1.17E+16	9.58E+15	3.00
19	8/7/05	35.56	140.11	73	4.5	6.88E+15	1.30E+16	2.35

†These parameters were determined by National Institute for Earth Science and Disaster Prevention (NIED), Tsukuba, Japan.

§ Resultant source paramters

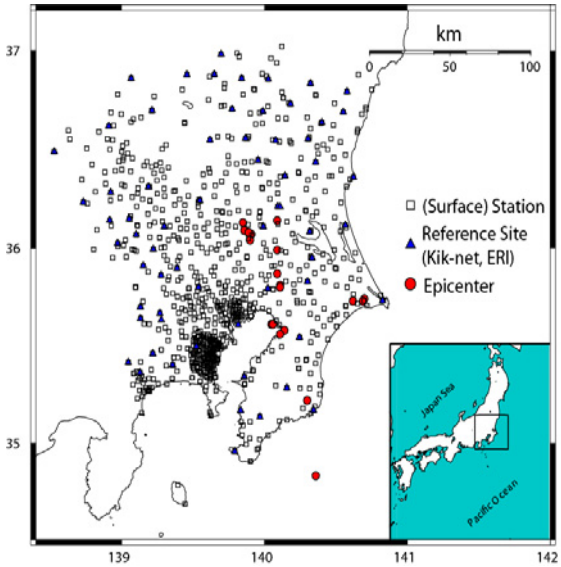

Figure 1: Geography of the Kanto region. Epicenters of the events listed in the Table 1 are plotted in map view by solid circles. Solid triangles colored by blue denote the reference station used to determined source and path parameters by Tsuda *et al.* (2008). Open squares mean the surface stations used in this study.

For our analysis, we used the two horizontal components at each site. A 10 s time window beginning 1.0 sec before the first *S*-wave arrival was picked for all events. We applied a cosine window taper of 0.5 sec to both ends of the record. After the Fourier amplitude spectrum of each component was calculated, we used vector summation of the two horizontal components as the amplitude spectrum. During checking the observed data, we eliminated the data including noise in longer period range.

3. ESTIMATING SITE RESPONSE

3.1 Spectral Inversion Analysis

In order to estimate site response, we have to separate the source and path effects from observed records. We have applied the spectral inversion analysis developed by Tsuda *et al.* (2006) to separate these three factors. Tsuda *et al.* (2008) applied this method to estimate site response in the Tokyo metropolitan area for a period range of 0.1-2 s. Then we have derived the site response for a period range of 2-4 s.

Explaining the detail concept for the spectral inversion analysis is found on many articles (Iwata and Irikura, 1988; Bonilla *et al.*, 1997; Yamanaka *et al.*, 1998; Satoh *et al.*, 2001) and is beyond this study, we show the brief introduction of this method.

The observed ground motion for linear response—can be expressed as a convolution of the source, path, and site (Eq1). In a frequency domain, this equation can be rewritten as a multiplication:

$$|A(f)| = |S(f)|\,|Site(f)|\,R^{-1}\,e^{-\pi f R / Q(f)\beta} \qquad (2)$$

where f is frequency, $|A(f)|$ is the acceleration amplitude spectrum of the recorded ground motion, $|S(f)|$ is the source spectrum, $Q(f)$ is the quality factor, which is assumed to be frequency dependent, $|Site(f)|$ is the site response amplitude, R is the distance from source (Table 1) to site, and β is the average shear wave velocity of the medium (3.7 km/s, Yamanaka *et al.*, 1998). To estimate the site response, it is necessary to isolate these three factors from observed records. In general, isolating each element requires constraints to avoid tradeoffs among these three elements. A standard constraint is to impose a condition on a rock station. Another approach is to define a source spectrum for a specific 'reference' event. Because some shallow borehole records (reference station) may be contaminated the borehole response itself, we used a method to separate the source, path and site effect that is independent of a reference station (Tsuda *et al.*, 2006).

Equation 3 uses Boatwright's (1978) representation of a source spectrum (Brune, 1970), in which the amplitude of the source spectrum has a nonlinear dependence on the corner frequency:

$$|S(f)| = C\, M_o (2\pi f)^2 \cdot f_c^2 / (f^4 + f_c^4)^{0.5} \qquad (3)$$

where

$$C = (G_0 \cdot F^{rad}) / (4\pi\rho V_S^3) \qquad (4)$$

C depends on the radiation parameter of the source: F^{rad} is the effects of this radiation pattern coefficients on site response estimation will be discussed, the material parameters for source area (3000 [kg/m³] for density: ρ and 4.5 [km/sec] for shear wave velocity: V_S) and the free surface effect G_o is included. We assumed that the radiation pattern coefficient F^{rad} is frequency-independent. The seismic moment M_o and corner frequency f_c are determined from the spectrum (Brune, 1970). We show the source parameters estimated by Tsuda *et al.* (2008) in Table 1 and Figure 2. The resultant seismic moments agree with the values determined by F-net/NIED (Figure 2 (a)), and calculated stress drop based on the resultant corner frequency (Figure 2 (b)) follows the previous studies (Brune, 1970). These indicate that their estimates for source parameters are reasonable. We have used these parameters to estimate source spectrum based on Eq (3).

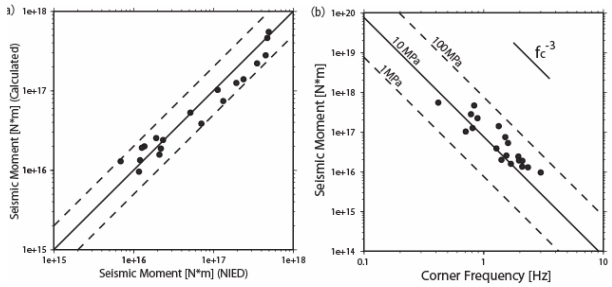

Figure 2: (a) Seismic moments from Tsuda *et al.* (2008) are compared with those from F-net/NIED. Dashed lines show a factor of two. (b) Seismic moment is plotted versus corner frequency for the 19 events. Lines of constant stress drops (Brune) are plotted. Within a factor of two the stress drops are ~10 MPa.

Including the path effect introduces a nonlinear dependence on frequency when the attenuation parameter $Q(f)$ is assumed to have a power law dependence on frequency: $Q(f)=Q_o f^{\prime}$. In this study, we have used the $Q(f) = 107 f^{0.52}$ derived by Tsuda *et al.* (2008). This model agrees with the other models derived for this area.

3.2 Estimating Site Response

Importance of Radiation Pattern: After having the source effects for each events and path effect, we have derived the site response for 2-4 s. Compared to the site response for the short period range, the source effects such as the focal mechanism in a long-period (2-4 s) ground motions for site response are getting pronounced (Kamae *et al.*, 1990). We have calculated the RMS of vector amplitude normalized by the maximum values for *S*-wave for a 2-4 s period range at each site. We show the spatial distribution of RMS peak ground velocity vectors and radiation pattern coefficients as the examples in Figure 3. The radiation pattern coefficient is getting very small when the geometrical relation of the site to the source is located on the nodes (blue-shaded area). On the other hand, the coefficient is very large when its geometrical relation is located on the lobes (red-shaded area). As we show the figures, the difference of two cases (lobes and nodes) can be the factor of 3. This suggests that we need to the effects of focal mechanism on the estimation of site response in a long-period range (2-4 s).

Site Response Estimation with Focal Mechanism: In this study, we have incorporated the effects of focal mechanism into estimating site response. We calculated the radiation coefficients (Aki and Richards, 2002) for each record based on the mechanism determined by F-net/NIED (Fukuyama *et al.*, 1998) and substitute it into Eq 4. After we calculate source spectrum (Eq 3), the site response has been derived by using $Q(f)$. We averaged the site response calculated for each event. We show the contour map of site response for 2-4 s in Figure 4(a). The general feature of spatial variation of site response looks similar to the site response map based on the classification of surface geology (Wakamatsu and Matsuoka, 2006), i.e. the region of very weak soil like swanpy area, shown in the Figure 4(b) has large site response.

In Figure 5, we have compared the predominant periods of our resultant site response and those from H/V ratios of microtremor measurements at K-NET sites (Tanaka *et al.*, 2005). We plotted the predominant periods from only sites with apparent ones, because the apparent predominant periods of H/V ratio clearly agree with the site response estimates from other methods, such as spectral inversion method, spectral amplitude ratio *etc* (Bonilla *et al.*, 1997; Satoh *et al.*, 2001). Thus, we picked these sites based on the criteria that the difference between peak and trough of site response function is more than 50%. As shown in the figure, the predominant periods from our resultant site responses agree with H/V ratios, indicating that our estimates of site response are reasonable.

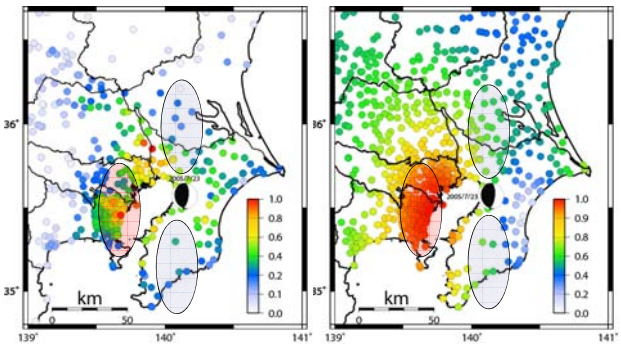

Figure 3: Distribution of normalized RMS observed peak ground velocity vectors for the event 17 (2005/7/23). Each value is the hypocentral distance corrected values at R =100 km (left). Spatial variation of radiation pattern coefficients of the same event for all sites (right).The focal mechanism has been determined by F-net/NIED.

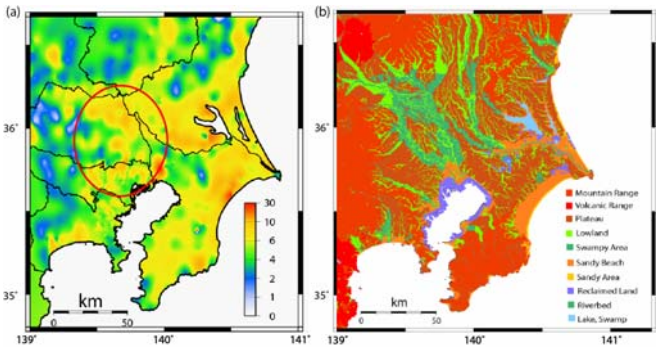

Figure 4: Spatial distribution of site response for a period range of 2-4 s (a). The area with large site response values (around red circle of left figure) correspond to the very weak surface geology, such as swanpy area classified by Wakamatsu and Matsuoka (2006) (b).

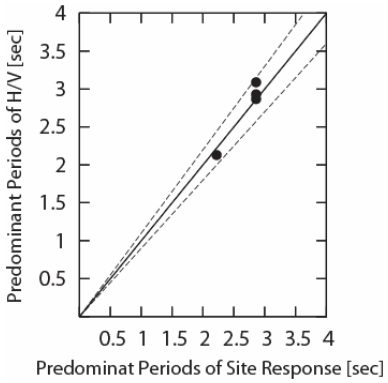

Figure 5: Comparison of predominant period of site response estimates. The solid line denotes the equal values of predominant periods.

4. DISCUSSION

The difference of site response between two cases for different F^{rad} (theoretical radiation and isotropic radiation) is discussed in this chapter. The derived site response in this study includes the effects of focal mechanism. This means that the theoretical radiation of seismic wave is assumed. However, the isotropic radiation (F^{rad} in Eq 4 is set to be 0.63, Boore and Boatwright, 1984) of seismic wave is usually assumed for the estimation of site response in short period range and the necessity of incorporation of the effects of focal mechanism into site response estimation is not clear yet in long period range. We calculated the site response with assuming isotropic radiation and show the spatial variation in Figure 6 (right). As we compare the results of theoretical radiation (Figure 6, left), the general features of spatial variation of site response is very similar. However, if we take the ratio of these two values, the hatched area in Figure 7 has some differences between two site responses. Because this area corresponds to the node of theoretical radiation based on the geometrical relation for many events (Figure 1), site responses tends to be large (radiation pattern coefficients in Eq 4 becomes small) compared to the other area.

In order to examine the effects of radiation pattern on site response as well as to validate our results, we compared our results with observed spectral amplitude ratio (surface / borehole) on some KiK-net sites. We picked three sites inside the Kanto basin (locations are also shown in Figure 7) that their borehole depth is "close" to the seismological basement *i.e.*, the *S*-wave velocity of borehole depth is close to 3.0 [km/sec]. Also their location is close to the area with big difference of site response (radiation pattern coefficients). However, because the definitions of our resultant site response corresponds to the ratio from the seismological basements (not borehole depth) to the surface, correction of the observed spectral ratio: $R_o(f)$ (surface/borehole) is necessary. The correction is based on the ratio of material impedance as follows (Shearer, 1999)

$$R_C(f) = (\rho_1\beta_1 / \rho_2\beta_2)^{0.5} \cdot R_o(f) \qquad (5)$$

where ρ_i, β_i, are the material properties (density and shear wave velocity) of seismological basement (i=1) and borehole depth (i=2).

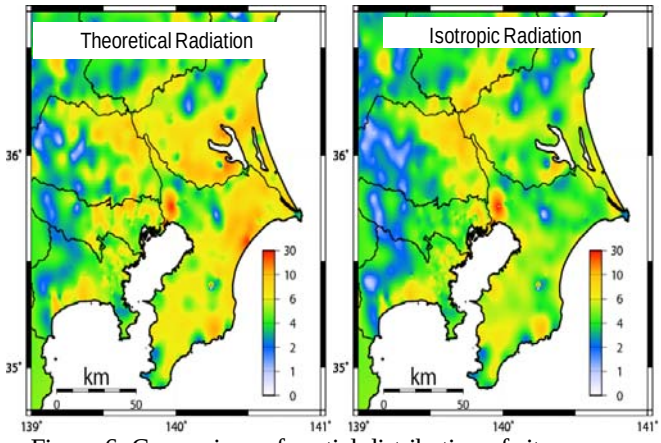

Figure 6: Comparison of spatial distribution of site response between theoretical radiation (left) and isotropic radiation (right) for a period range of 2-4 s.

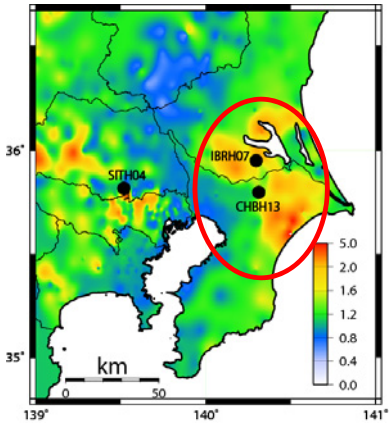

Figure 7: Spatial variation of site response ratio (theoretical radiation / isotropic radiation) for a period range of 2-4 s.

We used the values of material property at the borehole depth given by NIED and the generic values at the seismological basement ($\rho = 2.9$, $\beta = 3.7$ [km/sec]) based on previous studies (e.g. Tsuda et al., 2008; Ludwig *et al.*, 1970) are assumed. In Figure 8, we show the comparison of our site response (red curve for theoretical radiation and green curve for the isotropic radiation) and corrected site response (blue curve). As shown for all sites, the site response based on theoretical radiation (red line) is getting closer to the corrected observed spectral ratio (blue line) for the frequency range of 0.25 Hz (4 sec) - 0.5 Hz (2 sec). This indicates that modeling site response including the effects of radiation pattern might lead to the better estimation of site response at site that their geometrical relation is node (or lobe) of theoretical radiation.

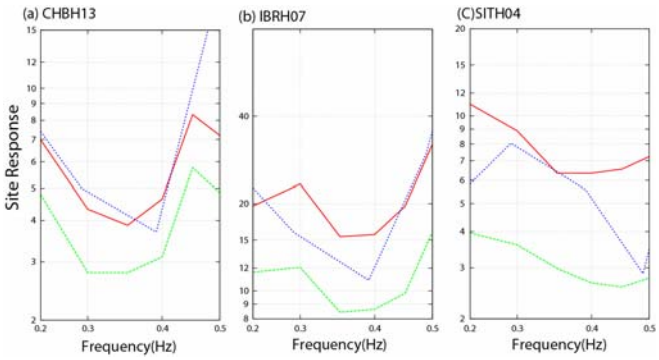

Figure 8: Comparison of site response for theoretical radiation (red), isotropic radiation (green), and corrected observed spectral ratio (blue) at three KiK-net sites.

5. SUMMARY

In this study, we have derived the long-period (2-4 s) site response with the effects of focal mechanism. The agreement of spatial variation of observed values of RMS of vector amplitudes for 2-4 s *S*-wave with of radiation coefficients suggest the necessity of incorporation of focal mechanism into the estimation of site response. The general features of spatial variation of site response agree with the other studies based on the classification of surface geology. Also the predominant periods of our site responses agree well with those from H/V ratios of microtremor, indicating that our estimates of site response are reasonable.

Our resultant site responses with considering the effects of focal mechanism are closer to the observed spectral ratio corrected based on the material impedance ratio. This indicates that modeling site response including the effects of radiation pattern might lead to the better estimation of site response in a long-period range. Incorporating the effect of complex velocity structure beneath the Kanto area on ray paths into estimating site response and our results into developing velocity model might be the next steps. The development of velocity model leads to the better understandings of ground motion complexity and is useful for the ground motion prediction for the future large disastrous events (e.g., Sekiguchi *et al.*, 2008).

Acknowledgements:

We thank to Prof. Saruboh Midorikawa for his invitations. Creating some figures is helped by Mr. N. Matsui from Esco Corporation.

References:

Aki, K. and P. Richards. (2002). Quantitative Seismology, 2nd edition, University Science Books.

Boatwright, J. (1978). Detailed spectral analysis of two small New York State earthquakes, *Bull. Seism. Soc. Am.* **68,** 1117-1131.

Bonilla, L.F., J. H. Steidl, G. T. Lindley, A. G. Tumarkin, and R. J. Archuleta (1997). Site amplification in the San Fernando valley, California: variability of site-effect estimation using the S-wave, coda, and H/V methods, *Bull. Seism. Soc. Am.* **87**, 710-730.

Boore, D. M., and J. Boatwright. (1984). Average body-wave radiation coefficient, *Bull .Seism. Soc. Am.* **74**, 1615-1621.

Borcherdt, R.D. (1970). Effects of local geology on ground motion near San Francisco Bay, *Bull. Seism. Soc. Am.* **60**, 29-61.

Brune, J. N. (1970). Tectonic stress and the spectra of seismic shear waves from earthquakes, *J. Geophys. Res*, **75,** 4997-5009.

Fukuyama, E., M. Ishida, D. S. Dreger, and H. Kawai (1998). Automated seismic moment tensor determination by using on-line broadband seismic waveforms, *Zisin.* **51**, 149-156. (Japanese with English abstract)

Fukuwa, N., and J. Tobita (2008), Key parameters governing the dynamic response of long-period structures, *J. Seismol*., **12**, 295-306.

Iwata, T., and K. Irikura. (1988). Source parameters of the 1983 Japan Sea earthquake sequence, *J. Phys. Earth*. **36**, 155-184.

Kamae, K., K. Irikura, and Y. Fukuchi (1990), Prediction of strong ground motion for M7 earthquake using regional scaling relations of source parameters, *J. Struct. Constr. Eng.* **416,** 57–70 (Japanese with English abstract).

Koketsu, K., and H. Miyake (2008), A seismological overview of long-period ground motion, *J. Seismol.*, **12**, 133-143.

Ludwig, W. J., J.E. Nafe, and C. L. Drake (1970), "Seismic refraction", *The Sea*, **4**, 53-84.

Mai, M. (2007), Ground Motion: Complexity and scaling in the near field of earthquake ruptures

Reid, H. F. (1910). The California earthquake of April 18, 1906, Publication 87, V21, Carnegie Institute of Washington, Washington, D.C.

Seismic Kanto Research Project, Earthquake Research Instiutute, University of Tokyo. (2001), http://www.sknet.eri.u-tokyo.ac.jp/ (in Japanese).

Satoh, T., H. Kawase, and S. Matsushima (2001), Differences between site characteristics obtained from microtremors, S-waves, P-waves, and codas, *Bull. Seism. Soc. Am.* **91,** 313-334.

Sekiguchi, H., H. Horikawa, and M. Yoshimi (2008), Broadband ground motion prediction in Kanto basin due to hypothetical Kanto earthquakes, Programme and Abstracts, The 7th General Assembly of Asian Seismological Commission.

Shearer, P. (1999). "Introduction to Seismology", Cambridge University Press.

Tanaka, Y., K. Koketsu, H. Miyake, T. Furumura, H. Sato, N. Hirata, H. Suzuki, and T. Masuda (2005), Integrated modeling of 3D velocity structure beneath the Tokyo metropolitan area, *EOS Trans*, AGU, 86(52), Fall Meeting Suppl, Abstract S21A-0200.

The Headquarters for Earthquake Research Promotion (2007) Report ' National Seismic Hazard Maps for Japan

Tsuda, K, Y. Hisada, and K. Koketsu (2008). Estimation of site

response for Kanto Plain by use of the data from dense strong motion seismograph array, in preparation to *Bull. Seism. Soc. Am.*

Tsuda, K., Archuleta, R., and Koketsu, K. (2006). Quantifying spatial distribution of site response by use of the Yokohama High-Density Strong Motion Network, *Bull. Seism. Soc. Am.* **96,** 926-942.

Yamanaka, H., A. Nakamaru., K. Kurita., and K. Seo. (1998). Evaluation of site effects by an inversion of S-wave spectra with a constraint condition considering effects of shallow weathered layers, *Zisin* **51,**193-202 (in Japanese with English abstract).

Wakamatsu, K., and M. Matsuoka. (2006). Development of the 7.5-arc-second engineering geomorphologic classification database and its application to seismic microzoning, *Bull. Earthq. Res. Inst.* **81**, 317-324.

Sixth International Conference on Urban Earthquake Engineering
March 3-4, 2009, Tokyo Institute of Technology, Tokyo, Japan

CORRELATION METHODS REVISITED WITH A CONSEQUENCE OF SEISMIC INTERFEROMETRY

Toshiaki Yokoi[1)]

1) Senior Research Scientist, International Institute of Seismology and Earthquake Engineering, Building Research Institute, Japan
tyokoi@kenken.go.jp

Abstract: First, the power partition ratio among the normal modes of Rayleigh waves is formulated based on Seismic Interferometry and applied to derive the formulas of Spatial AutoCorrelation Method (SPAC) and Centerless Circular Array Method (CCA) for multi-modal case in that the eigen functions of the modes play the role of combining their contribution. Second, the numerical validation check using the simulated microtremor records for given horizontally layered structures shows that these formulas can reproduce well the dispersion curves obtained by the conventional way of analysis of SPAC and CCA. Further more, the dual mode inversion based on this formula for CCA shows a good performance in comparison with the given underground velocity structures. Therefore the formulas derived here are supported and also the appropriateness of Seismic Interferometry.

1. INTRODUCTION

In this study the theoretical derivation of the formulas of two notable correlation methods for geophysical exploration, *i. e.*, Spatial AutoCorrelation Method (SPAC, Aki 1957; Okada 2003) that is already used widely and Centerless Circular Array Method (CCA, Cho *et al.* 2006) that is new and powerful as shown below is shown for multi-modal case based on the power partition ratio among the normal modes of Rayleigh waves that is a theoretical consequence of the recently developed research topic so called Seismic Interferometry (*retrieval of elastodynamic Green's function*, Refer Wapenaar *et al.* 2008), and the results of the numerical validation check for these formulas. Further more, the performance of the dual mode inversion based on them is shown.

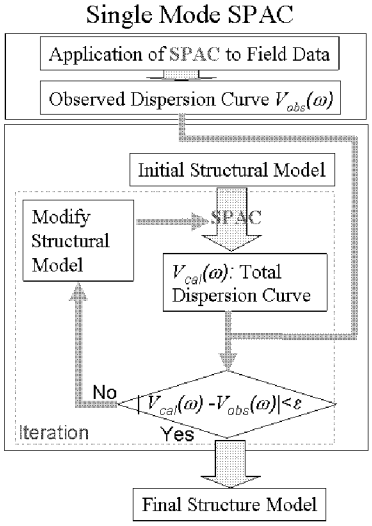

Figure 1 Flow chart of the conventional SPAC method.

1.1 Spatial Auto Correlation Method (SPAC)

After the pioneering work of Aki (1957), the methods based on correlation analysis of microtremor field has been developed for about fifty years and among them SPAC as summarized by Okada (2003). The principle is:

$$\rho(r_{AB},\omega) = \frac{1}{2\pi}\int_0^{2\pi} \frac{\mathrm{Re}\{E[C_{A,B}(\omega)]\}}{E[C_{A,A}(\omega)]} d\theta = J_0(kr_{AB}), \quad (1)$$

where $E[\ ]$ denotes the *ensamble* average over time that is practically calculated by the block averaging over time, $C_{A,B}(\omega)$ the cross-spectra of the records obtained at x_A and x_B. $(E[C_{A,A}(\omega)]E[C_{B,B}(\omega)])^{1/2}$ is often used in place of $E[C_{A,A}(\omega)]$ in order to correct very local amplification. The integrand of Eq.(1) together with its corresponding imaginary part is called *complex coherence function* (CCF, Shiraishi *et al.* 2006). The wavenumber $k(\omega)$ is estimated by fitting $J_0(kr)$ with the observed SPAC coefficient $\rho(r,\omega)$. Then, the frequency dependent phase velocity or so called dispersion curve $c(f)$ can be inverted to the underground shear wave velocity structure by a heuristic search (*e. g.*, Genetic Algorithm, Simulated Annealing and/or Neighborhood Algorithm) as shown in Figure 1. A huge number of successful examples can be found in the journals and the conference proceedings in the related study fields.

Feng *et al.* (2007), *e. g.*, assumed that the observed phase velocity sticks to the mode that has the biggest amplitude response at each frequency, applied it for microtremor array analysis for long period range and obtained acceptable results. The dispersion curve, however, sometimes immigrates from one mode to another gradually in real cases. Therefore the problem of SPAC in multi-modal case is still open for discussion.

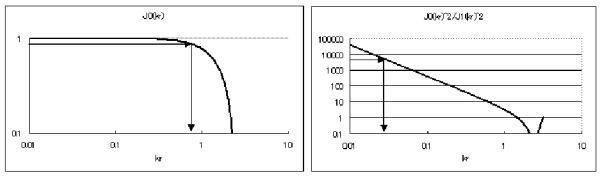

Figure 2 Explanation of CCA's advantage at long wavelength range. *Left*: SPAC coefficient $J_0(kr)$ is almost unity for $kr<0.2$. *Right*: CCA's one $\{J_1(kr)/J_0(kr)\}^2$ gives a high resolution for the estimated kr.

1.2 Centerless Circular Array Method (CCA)

Cho *et al.* (2006) have proposed a series of new techniques based on the generic formulation for circular microtremor array. Among them Centerless Circular Array method (CCA) is focused on here as well as SPAC in relation with another recently developed big research topic Seismic Interferometry**.**

The coefficient for CCA is:

$$s(r,\omega)=\frac{PSD\left\langle\int_{-\pi}^{\pi}Z(t,r,\theta)d\theta\right\rangle}{PSD\left\langle\int_{-\pi}^{\pi}Z(t,r,\theta)\exp^{-i\theta}d\theta\right\rangle}=\frac{J_0(kr)^2}{J_1(kr)^2}, \qquad (2)$$

where $PSD< >$ denotes power spectral density, the numerator and the denominator of the second member the power spectral density of the zero and the first order's coefficients of Fourier expansion over azimuth, respectively, $Z(\ )$ the vertical component of microtremor observed at the radius r, azimuth θ and at the time t, $J_1(\ )$ the first kind Bessel function of the first order,.

CCA is advantageous in comparison with SPAC especially in the long wavelength range, namely for big values of λ/r where λ is wavelength. Cho *et al.* (2006) has reported that the maximum resolvable one reaches up to several tens times of the array radius. Another notable advantage is that only one circular array with small radius can cover a wide frequency range. In contrast SPAC requires combining arrays of various sizes, because only a narrow range of kr is available for a precise estimation of the phase velocity due to low resolution at small kr range (Figure 2) and contamination by incoherent noises at large kr range (Cho *et al.* 2008).

Cho *et al.* (2006) showed also the formulation of CCA coefficient in multi-modal case where the power partition ratios of the modes play the key role. Their estimation, however, is remained unsolved and open for discussion.

1.3 SEISMIC INTERFEROMETRY (SI)

Here, I use the term *Seismic Interferometry* for *the retrieval of elastodynamic Green's function* (EGF) from microtremor, although its coverage seems to be much wider.

A pioneering work had appeared in earlier times (*e. g.*, Claerbout 1968). This topic has been consciously recognized mainly in the 21st century (Refer Wapenaar *et al.* 2008). Wapenaar and Fokkema (2006) show the following with point sources located along the buried surface.

$$2\,\mathrm{Re}\left\{\hat{G}_{p,q}^{v,\tau}(x_A,x_B,\omega)\right\}\hat{S}(\omega) \approx \frac{2}{\rho_d c_P}\left\langle\left\{\hat{v}_p^{obs}(x_A,\omega)\right\}^{*}\cdot\hat{v}_q^{obs}(x_B,\omega)\right\rangle, \qquad (3)$$

where the right member is the cross spectra of the observed particle velocity at x_A and x_B on the free surface, $< >$ denotes a spatial *ensemble* average, * the complex conjugate, $S(\omega)$ the power spectra that is assumed to be the same for all sources, the contents of { } in the left member EGFs in the frequency domain that is the p-th component of velocity observed at x_A due to an unit traction force applied to the q-th direction at x_B, Re{} the real part of the complex quantity, ρ_d and c_P the density and P-wave velocity respectively on and outside of the buried surface that are isotropic and homogeneous. The left member is equal to the sum of the causal and the acausal ones. The assumption used by Wapenaar and Fokkema (2006) at starting their theoretical derivation of SI, however, can not be proved directly. The only approach available may be to compare the consequences of SI with the reality and the existent studies.

Yokoi and Margaryan (2008) reviewed SPAC and showed the way how to get a similar expression from SI, and further the consistency between them using field data.

2. CONSEQUENCE OF SI

EGF in the left member of Eq. (3) is described as follows on the assumption of the dominance of surface waves that seems appropriate approximation because both of x_A and x_B are located on the surface.

$$\hat{G}_{z,z}^{v,\tau}(x_A,x_B,\omega)\approx-\omega\sum_{n=0}^{\infty}\left\{\hat{r}_2(k_n,0)\right\}^2 J_0(k_n r_{A,B}), \qquad (4)$$

where the subscript n shows the mode numbering, and $\hat{r}_i(k_n,z)^2=r_i(k_n,z)^2/4c_n^R(\omega)U_n^R(\omega)I_1^{R(n)}(\omega)$ denotes horizontal (i=1) and vertical (i=2) eigen functions (z=0 means at the free surface) normalized by the product of the phase velocity $c_n^R(\omega)$, the group velocity $U_n^R(\omega)$ and the energy integral $I_1^{R(n)}(\omega)=\frac{1}{2}\int_0^{\infty}\hat{\rho}(z)\left\{r_1(k_n,z)^2+r_2(k_n,z)^2\right\}dz$ for Rayleigh waves, $\hat{\rho}(z)$ the density distribution (Refer Aki and Richard 2002). Eq. (4) can be expressed using the notations given by Harkrider (1964) as follows.

$$w(\omega)=L(\omega)\sum_n\left[w_s(D)/w_0\right]_n A_n J_0(k_n r), \qquad (5)$$

where the content of [ ] is unity for the station at the surface, $L(\omega)$ the source spectra is unity for Green's function, A_n layering effect, *i. e.*, the response of layered media. Tokimatsu *et al.* (1992) called A_n medium response and derived the formula of the phase velocity in multi-modal case assuming the power partition ratio could be denoted A_n^2/c_n.

Following the notation given by Saito and Kabasawa (1993),

$$w(\omega)=-\omega\sum_n\left[\bar{y}_1(k_n,z)/2I_3(k_n)\right]J_0(k_n r) \quad . \qquad (6)$$

where $z=0$ for station at the surface, $\bar{y}_1(k_n,z)$ denotes depth dependency of the vertical displacement normalized by its value at the surface, $I_3(k_n)$ is a energy integral of the eigen function. Eq. (6) shows clearly the correspondence of the variables in Eq. (4) and those of DISPER80 (Saito 1988).

2.1 Power Partition Ratio

The zero-offset version of Eq. (3) combined with Eq. (4) gives the power of vertical component as follows

$$\left\langle \left\{\hat{v}_z^{obs}(x_A,\omega)\right\}^* \cdot \hat{v}_z^{obs}(x_A,\omega)\right\rangle \approx -\hat{\rho} c_P \omega \hat{S}(\omega) \sum_{n=0}^{\infty} \left\{\hat{r}_2(k_i,0)\right\}^2 . \quad (6)$$

Then, the power partition ratio of Cho *et al.* (2006) becomes

$$\alpha_i(\omega) = \left\{r_2(k_i,0)\right\}^2 \Big/ \sum_{n=0}^{\infty} \left\{\hat{r}_2(k_i,0)\right\}^2 , \quad (7)$$

clearly different from $A_n^2 c_n$ of Toskimatsu *et al.* (1992) that is, however, given by the waves propagating to only one direction. Therefore any contradiction is not found.

2.2 SPAC Coefficient for Multi-Modal Case

Yokoi and Margaryan (2008) derived the formula of CCF for dual-mode case based on Eq. (4) and SI as:

$$\begin{aligned} (\gamma_z)_{A,B} &= \beta \cdot J_0(k_0 r_{A,B}) + (1-\beta) \cdot J_0(k_1 r_{A,B}), \\ \beta &= \mathrm{Re}\left\{\hat{r}_2(k_0,0)^2\right\} \Big/ \left[\mathrm{Re}\left\{\hat{r}_2(k_0,0)^2\right\} + \mathrm{Re}\left\{\hat{r}_2(k_1,0)^2\right\}\right], \end{aligned} \quad (8)$$

where $(\gamma_z)_{A,B}$ denotes CCF calculated from the records obtained at stations x_A and x_B. According to Eq. (7), β is the power partition ratio of the fundamental mode. Note that the average over azimuth of Eq. (8) gives SPAC coefficient at the left member and leaves the right member unchanged. Considering on the process of derivation, Eq. (8) can be extended for multi-modal case (Yokoi and Margaryan 2008).

2.3 CCA coefficient for Multi-Modal Case

Substituting (6) into the formula for multi-modal case given by Cho *et al.* (2006), *e. g.*, the formula for dual mode (the fundamental and the first higher ones) is obtained.

$$\begin{aligned} s(r,\omega) &= \frac{G_{z0z0}(r,r;\omega)}{G_{z1z1}(r,r;\omega)} = \frac{\beta_0 J_0^2(k_0 r) + \beta_1 J_0^2(k_1 r)}{\beta_0 J_1^2(k_0 r) + \beta_1 J_1^2(k_1 r)}, \\ \beta_0 &= \mathrm{Re}\left\{\hat{r}_2(k_0,0)^2\right\}, \ \beta_1 = \mathrm{Re}\left\{\hat{r}_2(k_1,0)^2\right\} \end{aligned} \quad (9)$$

3. NUMERICAL VALIDATION CHECK

Validation of the power partition ratio shown in Eq. (7) is checked by applying its consequence Eq. (9) to the synthetic microtremor waveform records in order to eliminate the problems due to different characteristics among channels of observation system.

3.1 Synthetic Microtremor Records and Processing

Two sets of synthetic records provided for *NBT*, *i. e.*, N101 and N104 are used (Cornou *et al.* 2006) that are calculated using the finite difference codes (Moczo and Kristec 2002) for the given horizontally layered media as shown in Figure 3 and Figure 4 (point sources (*gray dots*) and stations (*black dots*) in *top left* panels, array configurations in *bottom left*, the given model of P- (*gray*) and S- (*black*) waves' velocity structure in *top right*, and theoretical dispersion curves of the fundamental (*solid*) and the first higher (*broken*) modes of Rayleigh (*black*) and Love (*gray*) waves in *bottom right*). Their wave fields are neither isotropic nor dominated by the fundamental mode.

First, the SPAC coefficients of various inter-station distances are converted to *kr* and then to *c(f)* using the fifth order polynomial that approximates the inverse function of $J_0(kr)$ in the range of *kr* from zero to the first minimum of $J_0(kr)$. Then, plotted against the frequency, the curves of *c(f)* start growing with unacceptably low value, take a first peak then gradually decrease, take the minimum value etc. then finally increase to unacceptably high value. The frequency range between the first peak and the last minimum is extracted. Second, the frequency range that corresponds to the wave length shorter than $2D$ and longer than $5D$ is eliminated where D denotes the inter-station distance. The former corresponds to the Nyquist wave length (Okada 2006) and the latter the border between acceptable and critical range (Cornou *et al.* 2006). Within the remained frequency range a coincidence or similarity among more than two curves are looked for as well as continuity among them in order to determine the dispersion curve that covers whole target frequency range.

In contrast, CCA does not require the combining dispersion curves, because only one array can cover whole target frequency range. Moreover, the following approximation for long wave length, *i. e.*, small *kr* can be used in this noiseless case.

$$c(\omega) = r\omega \Big/ \sqrt{s(r,\omega) + 2}\,/2 \quad (10)$$

3.2 Performance of CCA in Comparison with SPAC

The provided array configuration for N101 is shown in Figure 3 *left-bottom*. The radii are 6m, 23m and 89m for the inner and middle hexagons and the outer triangle, respectively. The records obtained at these fifteen stations were used all together for SPAC analysis, whereas for CCA

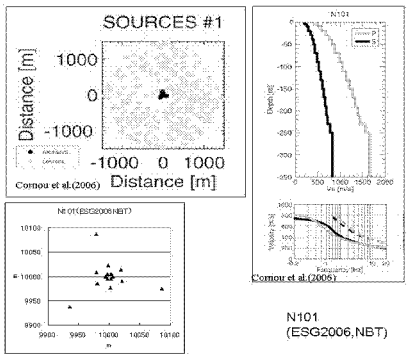

Figure 3 Outline of Simulation of Microtremor for N101. After Cornou *et al.* (2006)

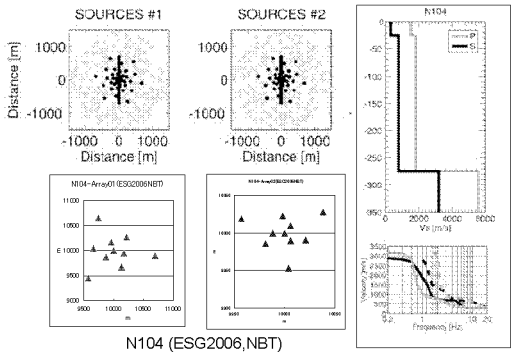

Figure 4 Outline of Simulation of Microtremor for N104. After Cornou *et al.* (2006)

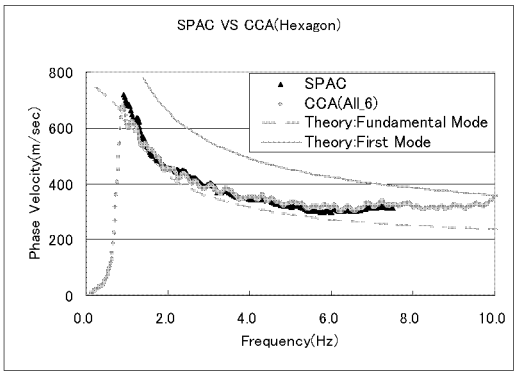

Figure 5 Comparison of dispersion curves: those obtained by SPAC (89m radius with 15 components) and by CCA (6m radius with 6 components).

only the six station of the inner hexagon are used. The duration of the provided records is about eleven minutes and whole dataset were used. The very good mutual coincidence as shown in Figure 5 where *black dots* denote the dispersion curve determined by SPAC, *grey dots* that determined by CCA is an evidence for that CCA can be considered as the more efficient alternative way to obtain the dispersion curve. Note that in this example CCA covers the frequency range from about 0.9Hz to 10Hz and its maximum resolvable wave length is surprisingly about 122 times of the radius 6m.

These dispersion curves, however, lay together between the theoretical fundamental (*gray broken*) and the first higher (*gray solid*) mode curves (Figure 5).

3.3 Validity of Power Partition Ratio

Two examples are shown below for the validity of Eq. (9) and then Eq. (7), *i. e.*, the power partition ratio theoretically forseen by SI.

N101 case: The theoretical amplitude of the fundamental mode is always bigger than that of the first higher mode (Figure 6 *left*). Then, the theoretical dispersion curve calculated using Eq. (9) lays itself between two modes (Figure 6 *center*). I propose to call this theoretical one *false phase velocity*, because this does not correspond to any real elastic wave. Namely, this is a ghost owed by applying the single mode assumption to the multi-modal case. Figure 6 *right* shows the good coincidence of the theoretical *false phase velocity* with the observed one. The fall off at the low frequency is due to the limitation of the ability of CCA using this small size array.

N104 case: The observed dispersion curve is determined by the conventional way of SPAC, because the dataset N104 is composed of the records obtained only by the triangular arrays of which radii are about 12m, 23m, 47m, 180m, 350m and 700m. The theoretical amplitude of the fundamental mode becomes smaller than that of the first higher modes at around from 2 Hz to 4 Hz (Figure 7 *left*). Eq. (9) foresees *the false phase velocity* sticks to the first higher mode's one in this frequency range whereas to the fundamental mode's one at out side of this range (Figure 7 *center*). This complicated behavior of *the false phase velocity*, however, coincides well to the observed one as shown in Figure 7 *right,* where the contribution of each array is drawn independently. A gap appears in the observed ones due to the threshold of the wave length from *2D* to *5D*.

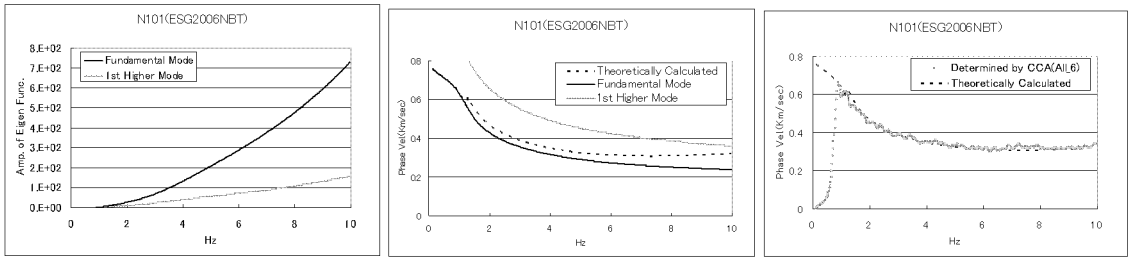

Figure 6 (*Left*) Amplitude of the fundamental (*black*) and the first higher (*gray*) modes, (*Center*) theoretical dispersion curve of the fundamental (*black solid*), the first higher (*gray solid*) modes and that based on Eq. (9) for *r=6m* (*black broken*). (*Right*) Comparison of theoretical dispersion curve based on Eq. (9) (*black broken*) with that determined by hexagonal CCA of *r=6m* (*gray dotted*).

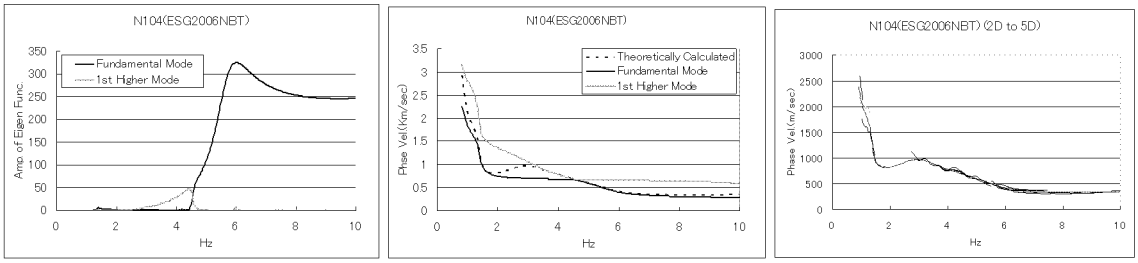

Figure 7 (*Left*) Amplitude of the fundamental (*black*) and the first higher (*gray*) modes, (*Center*) theoretical dispersion curve of the fundamental (*black solid*), the first higher (*gray solid*) modes and that based on Eq. (9) for *r=6m* (*black dotted*), and (*Right*) theoretical dispersion curve based on Eq. (9) (*thick smooth curve*) compared with that determined by SPAC for various inter-station distances (*thin curves*).

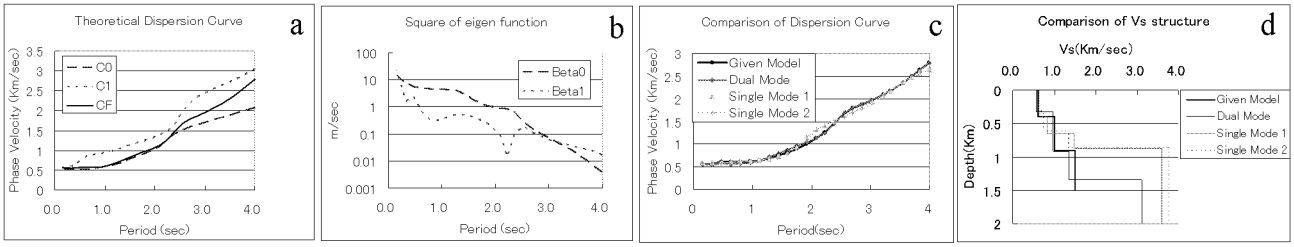

Figure 8 Case-1: a) Phase velocity of the fundamental mode c_0 (*broken*), the first higher mode c_1 (*dotted*) and the false phase velocity c_F (*solid*) calculated based on Eq. (9) for the model structure given in Table 1. b) Power partition ratio β_0 and β_1. c) Comparison of dispersion curves. d) Comparison of Vs structures. *Vs* of the given model grows to 4.8 Km/sec at 1.5 Km depth. For c) and d) Given model is drawn by *thick soli*d curve, the result of dual mode inversion by *thin black solid* one, that of the single mode inversion Single-1 and Single-2 by *thin gray solid* and *thin gray broken* curves, respectively.

4. DUAL MODE INVERSION FOR RAYLEIGH WAVE DISPERSION CURVE

The power partition ratio is a function only of the eigen functions of layered media as shown in Eq. (7), then uniquely defined once under ground velocity structure is given. Therefore, Eq. (8) and/or Eq. (10) can be involved in the iterative process of inversion using a heuristic search.

In the single mode SPAC shown in Figure 1 the theoretical dispersion curve is directly calculated from the modified velocity structure in each iterative step without calculating the theoretical SPAC coefficients. For dual mode SPAC, this must be calculated using Eq. (8) in each step and the dispersion curves for various inter-station distances must be combined in order to eliminate the small *kr* range that does not have sufficient resolution and big *kr* range that is affected much by incoherent noises. In contrast Eq. (9) gives the theoretical CCA coefficient from the given modified velocity structure and the theoretical dispersion curve is calculated using Eq. (10) in a straight forward way.

Here, examples are shown for application of the dual mode inversion for dispersion curve of Rayleigh wave using Eqs. (9) and (10). Heuristic search is conducted by Down Hill Simplex Method combined with Very Fast Simulated Annealing (DHSM-VFSA) using the optimum schedule with the parameters t_0=*1.0, a=0.6, c=1.3* (Yokoi 2005). For each iterative step, the densities ρ are fixed to the initial values, *Vp* calculated from *Vs* using the empirical formula (Kitzunezaki *et al.* 1990): *Vp*=1.11*Vs*+1.29 (Km/sec).

Table 1 Given model and the search range for Case-1 (After Yamanaka 2001). *Vp*, *Vs* in Km/sec, thickness *H* in Km, density ρ in g/cm^3. *: 3.6 for Dual and Single-1, 6.0 for Single-2.

Given Model				Search Range	
Vp	*Vs*	*H*	ρ	*Vs*	*H*
1.956	0.6	0.4	1.8	0.4-0.9	0.2-1.0
2.400	1.0	0.5	2.0	0.7-1.3	0.2-1.0
2.955	1.5	0.6	2.3	1.2-1.8	0.2-1.0
4.842	3.2	∞	2.5	2.6-3.6*	-

Case 1 is conducted for checking the algorithm and the program for the dual mode inversion. The given structure model and the search range of thickness *H* and *Vs* are shown in Table 1 (Yamanaka 2001). β_0 in Eq. (9) is bigger than β_1 in the period range shorter than about 2.5 Hz, whereas for the longer period β_1 becomes bigger (Figure 8 b), and the *false phase velocity* $c_F(\omega)$ curve tends to get closer to the theoretical dispersion curve of the first higher mode (Figure 8 a). It may be difficult to detect the influence of the first higher mode if this curve is shown alone.

DHSM-VFSA is applied to this curve for the dual mode inversion and single mode one. The latter has two trials. One has the upper limit of Vs of the basement 3.6 Km/sec (Single-1) and another 6.0 Km/sec (Single-2), all other parameters are the same for these two trials.

The fitted dispersion curves coincide well to the given model (Figure 8 c) although Single-1 and -2 are a relatively more deviated than the dual mode inversion. The inverted *Vs* structure of the dual mode inversion follows the given model well from the surface to about 1.3 Km depth (Figure 8 d). It seems that the discrepancy at the deeper part is due to the cut off at the period 4.0 sec. In contrast Single-1 and Single-2 start deviating at about 0.5 Km depth, and give a basement depth much less than the given model.

Table 2 Search range of *Vs* (Km/sec) and thickness *H* (Km) for Case-2

Vs	*H*
0.3-0.9	0.01-1.0
0.7-1.3	0.2-1.0
1.2-1.8	0.2-1.0
2.6-3.6	-

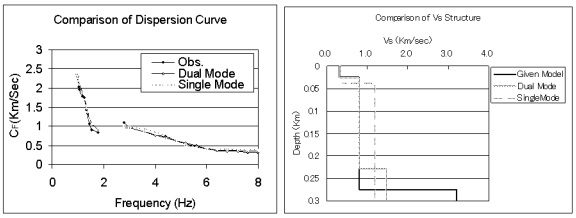

Figure 9 Comparison of Dispersion curves (*left*) and *Vs* structure (*right*) for Case-2.

Case-2 (N104): The observed dispersion curve shown in Figure 7 *right* is inverted using the search range in Table 2. In comparison with Table 1, the lower limits of *Vs* and *H* of the shallowest layer are changed to 0.3 Km/sec and 0.01 Km, respectively, because the observed dispersion curve converges to about 0.3 Km/sec at the high frequency side and the given *H* of the shallowest layer is less than 0.2 Km.

Dual mode inversion can be performed using all the data shown in Figure 9 *left*, whereas single mode inversion can not give a conversion. Then, the used frequency range is narrowed for the single mode inversion to those higher than about 2.8 Hz, namely the high frequency side of the gap in Figure 9 *left*. The deviation of the fitted curves are acceptable, where *black solid*, *gray solid* and *gray broken* curves denote those corresponding to the given model, the dual mode inversion and the single mode one, respectively.

Vs structure given by the dual mode inversion (*gray solid*) follows well the shallowest two layers of the given model (*black solid*), whereas the depth and *Vs* of the basement is not estimated correctly due to the cut off at low frequency side at 0.9 Hz (Figure 9 *right*). In contrast, the result of the single mode inversion (*gray broken*) gives higher *Vs* for the second shallowest layer.

4. CONCLUSION

Two correlation methods of microtremor exploration SPAC and CCA, and also Seismic Interferometry are reviewed, first. The power partition ratio of microtremor composed of the eigen function of layered media is theoretically derived and used to derive the formulas of SPAC and CCA coefficients for multi-modal case.

Second, numerical experiments are conducted using the synthetic microtremor waveform records and show the good performance of CCA in comparison with SPAC, the validity of the derived power partition ratio and these formulas. Namely, CCA can be considered as a more efficient alternative way to determine the dispersion curve and these formulas give the theoretical dispersion curves coincident to the observed ones. Further more, the dual mode inversion using one of these formulas (for CCA) is tested and show a better performance than the conventional single mode inversion.

These results support the appropriateness of the CCA coefficients for multi-model case, the power partition ratio, therefore SPAC coefficients derived here, the algorithm of dual mode inversion proposed here and further more Seismic Interferometry, *i. e.,* the retrieval of the elastodynamic Green's function.

ACKNOWLEDGEMENT

I would like to thank Dr. C. Cornou, Dr. M. Ohrnberger, Prof. D. Boore, Prof. K. Kudo and Prof. P.-Y. Bard who are the organizers of Noise Prediction Test that was held in *Third International Symposium on Effect of Surface Geology on Seismic Motion*, 2006, Grenoble, France, and Prof. M. Saito for the subroutine package of digital filter (Saito 1978) and DISPER80 (Saito 1988) for data processing.

REFERENCES

Aki, K. and Richard, P. G.. (2002), "Quantitative Seismology, 2nd Edition," University Science Books.

Cho, I., Tada, T. and Shinozaki, Y. (2006), "Centerless circular array method: Inferring phase velocities of Rayleigh waves in broad wavelength ranges using microtremor records," *Jour. Geophys. Res.*, **111**, B09315.

Cho, I. Tada, T. and Shinozaki, Y. (2008), "Assessing the Applicability of the Spatial Autocorrelation Method: A Theoretical Approach," *Jour. Geophys. Res.*, **113**, B06307.

Clearbout J. F. (1968), "Synthesis of a layered medium from its acoustic transmission response," *Geophysics*, **33**, 264-269.

Cornou, C., Ohrnberger, M., Boore, D. M., Kudo, K. and Bard, P.-Y. (2006), "Derivation of Structural Models from Ambient Vibration Array Recordings: Result from an Interpretational Blind Test," in *Proc. 3rd Int. Symp. on the Effects of Surface Geology on Seismic Motion,* eds Bard, P.-Y. , Chaljub, E., Cornou, C., Cotton, F. and Gueguen, P., LCPC Editions, Paper Number: NBT.

Feng, S., Sugiyama, T., Horikawa, H. and Yamanaka, H. (2006), "Multi-mode Pahse Velocity Inversion with Reference to Medium Response," , *Proceedings of the 114th SEGJ Conference*,27-30

Harkrider, D. G. (1964), "Surface Waves in Multi-Layered Elastic Media I.," *Bull. Seism. Soc. am.*, **54**(2), 627-679.

Kitsunezaki, C., Goto, N., Kobayashi, Y., Ikawa, T., Horike, M., Saito, T., Kuroda, T., Yamane, K. and Okuzumi, K. (1990), "Estimation of P- and S- Wave Velocities in Deep Soil Deposits for Evaluating Ground Vibrations in Earthquake," *Jour. Japan Soc. Nat. Dis. Sci.*, **9**(3),1-17 (*in Japanese*).

Moczo, P. and Kristek, J. (2002), "Sesame report D02.09", available on *http://SESAME-FP5.obs.ujf-grenoble.fr*

Okada, H. (2003), "Microtremor Survey Method," *Geophysical Monograph, No. 12*, Society of Exploration Geophysicists, Tulsa

Saito, M. (1978), "An Automatic Design Algorithm for Band Selective Recursive Digital Filters," *BUTURI-TANSA*, **31**(4), 112-135 (*in Japanese*).

Saito, M. (1988), "DISPER80: A Subroutine Package for the Calculation of Seismic Normal Mode Solutions," *Seismological Algorithms*, Doorbos, D. J. (Ed.), 293-314, Academic Press.

Saito, M. and Kabasawa, H. (1993), "Computations of Reflectivitiy and Surface Wave Dispersion Curves for Layered Media II. Rayleigh Wave Calculations," BUTSURI-TANSA, **46**(4), 283-298 (*in Japanese*).

Shiraishi, H. and Matsuoka, T. and Asanuma H. (2006), "Direct Estimation of the Rauleigh Wave Phase Velocity in Microtremor," *Geophys. Res. Lett.*, **33**, L18307.

Tokimatsu, K., Tamura, S. and Kojima, K. (1992), "Effects of Multiple Mode on Rayleigh Wave Dispersion Characteristics," *Jour. Geotech. Engn.*, **118**, 1529-1543.

Wapenaar, K. and Fokkema, J. (2006), "Green's Function Representations for Seismic Interferometry," *Geophysics*, **71**, SI33-SI46.

Wapenaar, K., Draganov, D. and Robertsson, J. O. A. (Eds.) (2008) "Seismic Interferometry: History and Present Status," *Geophysics Reprint Series No. 26*, Soc. of Exploration Geophysicists, Tulsa.

Yamanaka, H. (2001), "Application of Simulated Annealing to Inversion of Surface Wave Phase Velocity – Comparison of Performances between SA and GA Inversions -," *BUTURI-TANSA*, **54**(4), 197-206, (*in Japanese)*.

Yokoi, T. (2005), "Combination of Down Hill Simplex Algorithm with Very Fast Simulated Annealing Method", *Prog. and Abst, Seism. Soc. Japan 2005 Fall Meeting*, B049 (*in Japanese*).

Yokoi, T. and Margaryan, S. (2008), "Consistency of the Spatial Autocorrelation Method with Seismic Interferometry and its Consequence," *Geophys. Prospecting*, **56**, 435-451.

Sixth International Conference on Urban Earthquake Engineering
March 3-4, 2009, Tokyo Institute of Technology, Tokyo, Japan

PROPAGATION OF RAYLEIGH WAVES IN AN IRREGULAR GROUND

Shoichi Nakai[1] and Hiroto Nakagawa[2]

1) Professor, Graduate School of Engineering, Chiba University, Japan
2) Graduate Student, Graduate School of Engineering, Chiba University, Japan
nakai@faculty.chiba-u.jp, nakagawa-hiroto@graduate.chiba-u.jp

Abstract: In this paper, wave propagation in an irregular ground due to an incident Rayleigh wave is formulated by combining the thin layered element method and the finite element method. Based on the numerical analysis, the following conclusions are made: 1. The thin layered element method can be used as a very good alternative to the theoretical solution method. 2. When an incident Rayleigh wave propagates toward an irregular ground, different types of Rayleigh wave modes as well as body waves are generated. 3. The contribution of body waves that are generated by irregularity is large only in the frequency range close to the natural frequency of a layered ground.

1. INTRODUCTION

A detailed soil profile is requisite for an accurate estimation of the behavior of a ground during earthquakes. There are a number of methods available that are used for this purpose. Among others, microtremor measurement is one of the most popular ways and has been conducted extensively. It is accepted that the peak frequency of its horizontal-to-vertical spectral ratio (H/V spectrum) obtained from microtremor measurement corresponds to the natural frequency of a surface soil. This correspondence has been explained by the theory of surface wave propagation in a layered medium (Tokimatsu and Arai 1998). Since the closed form solution to this problem is available, this approach is used as a basis for the identification process of a soil profile. However, difficulty arises in the case of an irregular ground where the parallel layer assumption is not established (Horike 1993). The problem of wave propagation in an irregular ground is crucial when the landform is complex as in the case of Japan and has been studied by a number of researchers. However, most of studies were made from the viewpoint of body wave propagation and only a few dealt with surface waves (Drake 1972, Uebayashi 2006).

The objective of this study is to examine Rayleigh wave propagation in an irregular ground based on the combined method of thin layered element and finite element.

2. THIN LAYERED ELEMENT METHOD

2.1 Eigenvalue Problems

A soil which is a horizontally layered linear elastic medium is considered, as shown in Figure 1. Suppose the displacement at an arbitrary point in a layer be expressed as $v(z)\exp(i\omega t - ikx)$. Applying the finite element technique in the z-direction in conjunction with this expression leads to the following eigenvalue problem in terms of the wave number k and the modal displacement amplitude $\{v\}$ (Lysmer 1970, Waas 1972):

$$\left(k^2[A] + ik[B] + [G] - \omega^2[M]\right)\{v\} = \{0\} \qquad (1)$$

in which, $[A]$, $[B]$ and $[G]$ are the stiffness matrices and $[M]$ is the mass matrix. Each of these matrices consists of element matrices with the size of 6 x 6 for the plane strain condition when quadratic elements are utilized.

Eq. (1) is a quadratic eigenvalue problem. A numerical technique can be applied to find eigenvalues and corresponding eigenvectors. Emphasis can be placed on the fact that among these eigenvalues there exist "physical" modes which correspond to actual Rayleigh waves.

2.2 Line Load Excitation and Corresponding Amplitude Function

The load-displacement relationship, i.e. the dynamic

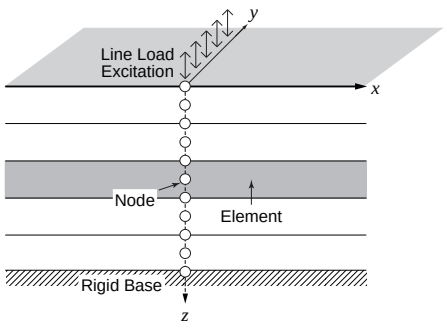

Figure 1 Thin Layered Element Method

stiffness matrix, at a vertical boundary of a semi-infinite layered region is called a transmitting boundary and is given for the region extending toward right and left as:

$$\begin{aligned}[R] &= i[A][V][K][V]^{-1} + [D] \\ [L] &= i[A][\underline{V}][K][\underline{V}]^{-1} + [D]\end{aligned} \tag{2}$$

Where $[V]$ is the matrix which contains mode shapes in its column, $[K]$ is the diagonal matrix which contains wave numbers on its diagonal and $[D]$ is related to $[B]$ through $[B]=[D]^T-[D]$. The analysis of a left layered region is analogous to that of a right layered region. The dynamic stiffness matrix, $[L]$, of a left layered region may be computed from $[R]$ by changing only the sign of all the coefficients that relate horizontal forces to vertical displacements or vertical forces to horizontal displacements.

Since $[R]+[L]$ is the stiffness matrix at the vertical boundary $x=0$, we can calculate the displacement at the vertical boundary, $\{u\}^R$, when an external force acts at $x=0$. The mode participation factor, $\{\alpha\}$, can be obtained as follows:

$$\{\alpha\} = [V]^{-1}\{u\}^R \tag{3}$$

It is worthy of note that the participation factors of the "physical" mode represent their medium responses (Harkrider 1964), or amplitude functions.

2.3 H/V Spectra due to Surface Waves

By consulting the work done by Tokimatsu and Arai(1998), the horizontal-to-vertical displacement ratio at the ground surface, i.e. the H/V spectrum, due to Rayleigh and Love waves can be computed from the modal amplitudes and the participation factors by the following expressions:

$$\begin{aligned}(H/V)_R &= \left(\frac{\sum_s \alpha_s^2 \left(v_{xs}/v_{zs}\right)^2 \left\{1+\gamma^2\left(v_{xs}/v_{zs}\right)^2/2\right\}}{\sum_s \alpha_s^2 \left\{1+\gamma^2\left(v_{xs}/v_{zs}\right)^2/2\right\}} \right)^{1/2} \\ \gamma^2 &= \frac{2\sum_s \alpha_s^2 \left(v_{xs}/v_{zs}\right)^2}{\left(R/L\right)^2 \sum_s \beta_s^2 - \sum_s \alpha_s^2 \left(v_{xs}/v_{zs}\right)^2} \\ (H/V) &= (H/V)_R \sqrt{1+1/\left(R/L\right)^2}\end{aligned} \tag{4}$$

Where, γ is the H/V ratio of excitation forces and R/L is the Rayleigh to Love wave amplitude ratio in horizontal motions.

2.4 Verification of Accuracy

In order to verify the accuracy of the thin layered element method, a two layered soil has been analyzed in terms of phase velocities, modal amplitude distributions, H/V spectra, displacements due to a line load excitation and amplitude functions. Properties of the soil are shown in Figure 7. Results are shown in Figures 2

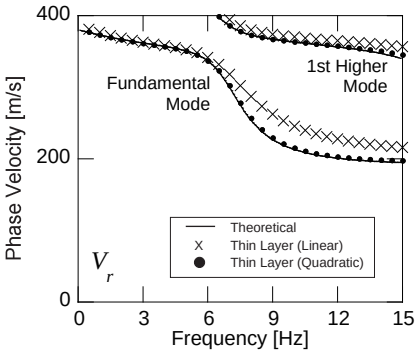

Figure 2 Phase Velocities

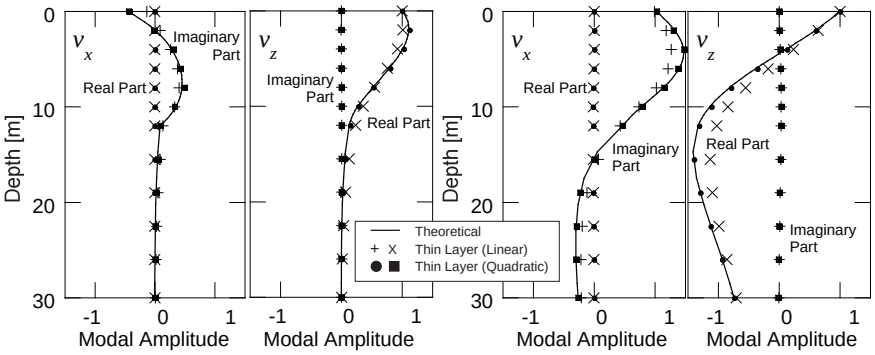

Figure 3 Rayleigh Wave Mode (10Hz, Fundamental and 1st Higher)

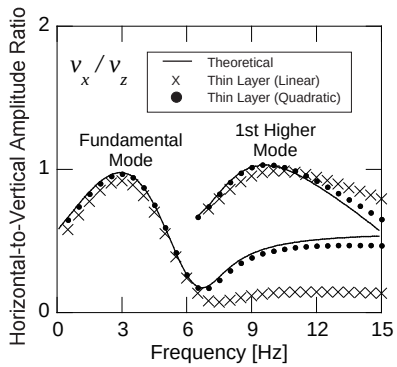

Figure 4 H/V Spectra

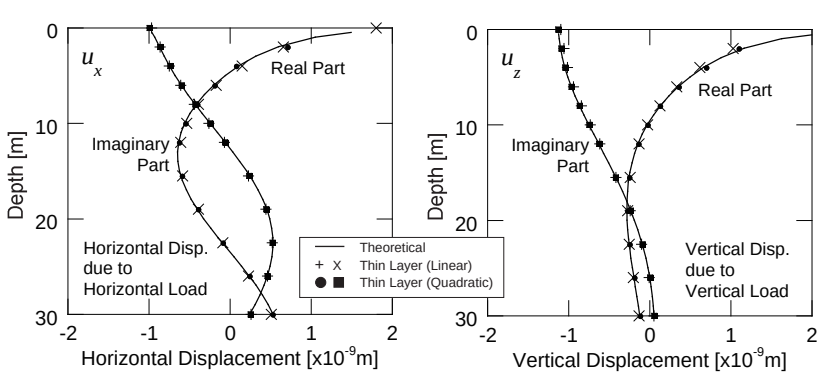

Figure 5 Displacement due to Line Load Excitation (10Hz)

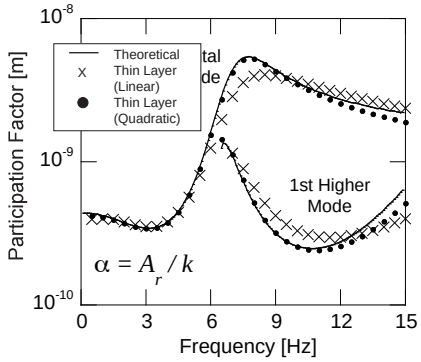

Figure 6 Mode Participation Factors (Amplitude Functions)

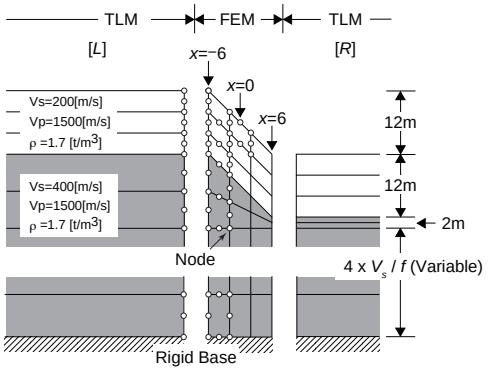

Figure 7 Finite Element Analysis Model

through 6, in the form of a comparison with those obtained by linear elements and theoretical solutions (Saito and Kabasawa 1993, Nakai and Fukuwa 1984). As we can see from these figures, the thin layered element method in conjunction with quadratic elements gives far more accurate results compared to linear elements and can be considered a very good alternative to the theoretical solution method.

3. INCIDENT RAYLEIGH WAVE IN AN IRREGULAR GROUND

A number of studies have been made on the surface wave propagation based on the hypothesis that the soil medium is horizontally layered. The applicability of H/V spectra of microtremors to estimating dynamic properties of the ground is usually discussed in this context. However, we often encounter a situation in which it is difficult to assume horizontal layering. In this study, a two-dimensional finite element approach in conjunction with the thin layered element method described above has been used to investigate Rayleigh wave propagation in an irregular ground. A similar topic was discussed by the previous researchers (Drake 1972, Regan and Harkrider 1989, Uebayashi 2006).

3.1 Method of Analysis

The analysis method is based on the so-called substructure approach in elastodynamics. In this approach, an infinite medium is divided into a near field and a far field. In the analysis of the near field, the impedance matrix of the far field is attached to the near field at its boundary and the driving force due to an incident wave from the far field is applied to the boundary.

Suppose that a soil model is divided into three parts along the vertical boundaries as shown in Figure 7. The driving force due to an incident Rayleigh wave propagating from left can be expressed as:

$$\left\{ f_c^* \right\}_s = [L]\alpha_s \{v\}_s + \{p\}_s \qquad (5)$$

where, $[L]$ is the impedance matrix of a left layered soil, s is the mode number, α is the mode participation factor, $\{v\}$ is the mode shape and $\{p\}$ is the traction corresponding to $\alpha\{v\}$ at the boundary of the left layered soil.

3.2 Analysis Model

In this study, an irregular ground with a slope is considered, as shown in Figure 7. The soil consists of two layers and their boundary is parallel to the ground surface. The underlying layer is assumed as a half-space. The angle of inclination of the slope is 45º and the height is 12m, same as the thickness of the surface layer. As shown in the figure, the surface layer consists of three quadratic elements, while 22 elements are allotted to the underlying layer. The fixed condition is assumed at the bottom boundary but its depth varies with frequency in order for the half space approximation to be made, following the relationship: $H = 4V_s / f$, where V_s is the shear wave velocity of the underlying layer. In order to suppress body wave reflection from the bottom boundary, relatively large damping of 30% to 50% is assumed in the lower part of the model.

3.3 Wave Field due to an Incident Rayleigh Wave

Figure 8 shows the wave field in an irregular ground due to an incident Rayleigh wave either from the left or the right layered soil. The analysis frequency is 10Hz and there exist two sets of Rayleigh wave mode for this frequency, i.e. the fundamental and first higher modes, respectively. Thus, Figure 8 consists of four cases of results. Each case has four diagrams: cross sectional distributions of the amplitude and the phase of horizontal and vertical displacements.

It is clearly seen from the phase diagrams that body waves are generated as reflected waves from the slope (represented by a series of concentric circle patterns). Thus, wave propagation becomes fairly complex due to the existence of irregularity. If we look at the upland and the lowland away from the slope, it is noticed that the phase patterns become vertical as the distance from the slope increases. This explains that the body waves attenuate rapidly compared to the surface waves because of large geometric damping. Finally, if we look at the surface layer situated in the back of the slope with respect to the direction of wave incidence, a pattern of

multiple reflections are seen, especially in the amplitude diagrams. This implies that the fundamental and first higher mode waves interfere with each other.

3.4 Contribution of Rayleigh and Body Waves

In order to examine the contribution of Rayleigh and body waves to the wave field, the nodal displacement, $\{u\}$, along the vertical line at a given horizontal coordinate has been decomposed into the eigenmodes corresponding to a hypothetical parallel layer at its horizontal coordinate. Mode separation can be done by:

$$\{\alpha\} = [V]^{-1}\{u\} \quad (\because \{u\} = [V]\{\alpha\}) \tag{6}$$

Since the mode participation factor $\{\alpha\}$ corresponds to the amplitude of each mode, the contribution of the Rayleigh wave mode of order s is computed by Eq. (7):

$$\eta_s = |\alpha_s| \Big/ \left(\sum_{s=1}^{M} |\alpha_s| + \left| \sum_{s=M+1}^{N} \alpha_s \right| \right) \tag{7}$$

$$\eta_b = 1 - \sum_{s=1}^{M} \eta_s \tag{8}$$

in which, M is the number of physical Rayleigh wave modes and N is the total number of generalized Rayleigh wave modes. Since the rest of (N–M) modes other than M physical Rayleigh wave modes is considered the contribution of body waves, its ratio is computed by Eq. (8).

Figure 9 shows the resulting contribution ratio which corresponds to Figure 8. As can be seen from the figure that the contribution of the body wave accounts for about 20 per cent of the total displacement near the slope and it decreases in accordance with the distance from the slope. In addition, the contribution of the first higher mode increases with the increasing distance from the slope, while that of the fundamental mode decreases inversely. This suggests that the damping of the fundamental mode is larger than that of the higher mode.

4. EFFECT OF IRREGULARITY ON THE CHARACTERISTICS OF MICROTREMORS

4.1 Wave Propagation from Multiple Sources

According to Tokimatsu and Arai (1998), the microtremor wave field can be expressed by the superposition of surface waves generated from an infinite number of point load excitations that surround the observation point. In this study, a two-dimensional analogy is considered by superposing the Rayleigh waves generated from a number of line load excitations that surround the irregular ground. Since the thin layered element method utilizes an analytical expression in the horizontal direction, superposition is fairly easy to perform. In the analysis, it is assumed that a total of 100 line load excitations are distributed on the ground excluding the area that extends over one wave length of each mode from the shoulder and the foot of the slope. Displacements due to the Rayleigh wave modes generated from each excitation are superposed in the form of power representation.

4.2 H/V Spectrum

Figure 10 shows thus obtained H/V spectral ratios. In addition, three color bars on the right hand side represent the H/V spectral ratios of the fundamental mode, the first higher mode and the superposed mode of a two layered soil. From this figure, it is seen that the ratio varies a lot near the frequency of 4Hz, which corresponds to the natural frequency of the surface layer (4.2Hz). This suggests that body waves generated from the slope travels a long way at this frequency (Tokimatsu and Tamura 1995). In the high frequency range over 6Hz, the spectral shape is complex near the slope due to its influence but it seems to converge gradually to the spectral ratio of the superposed mode of the two layer solution. This discussion may suggest a possibility of supporting the claim that the peak of a H/V spectral ratio can be explained by the theory of body wave propagation.

4.3 Contribution of Rayleigh and Body Waves

Separation of Rayleigh and body waves in the hypothetical microtremor wave field of an irregular ground with a slope has been performed based on the concept described in 3.4. The contributions of the Rayleigh wave mode and the body wave can be computed by the following expressions:

$$\zeta_s = \sqrt{\sum_{i=1}^{W} |\alpha_{si}|^2} \Big/ \left(\sum_{s=1}^{M} \sqrt{\sum_{i=1}^{W} |\alpha_{si}|^2} + \sqrt{\sum_{i=1}^{W} \left| \sum_{s=M+1}^{N} \alpha_{si} \right|^2} \right)$$
$$\zeta_b = 1 - \sum_{s=1}^{M} \zeta_s \tag{9}$$

in which, W is the total number of incident waves. In the case of W=1, ζ_s is equal to η_s given by Eq. (7).

Figure 11 shows the resulting contribution ratios. It is seen in this figure that the contribution of the fundamental mode decreases in the vicinity of the natural frequency of the surface layer, 4.2Hz. In contrast, the contribution of the body waves increases in this frequency range to the extent of 30 to 40 percent of the total near the slope. The influence is far-reaching as well. Thus, in the vicinity of the natural frequency of the surface layer, the influence of generated body waves is very large compared to the rest of the frequency range. In fact, in the vicinity of the natural frequency of the second order, 12.5Hz, this tendency is not clear. The fact that the body waves play an important role in the frequency range close to the natural frequency implies that a difficulty may be encountered in identifying the phase velocity in

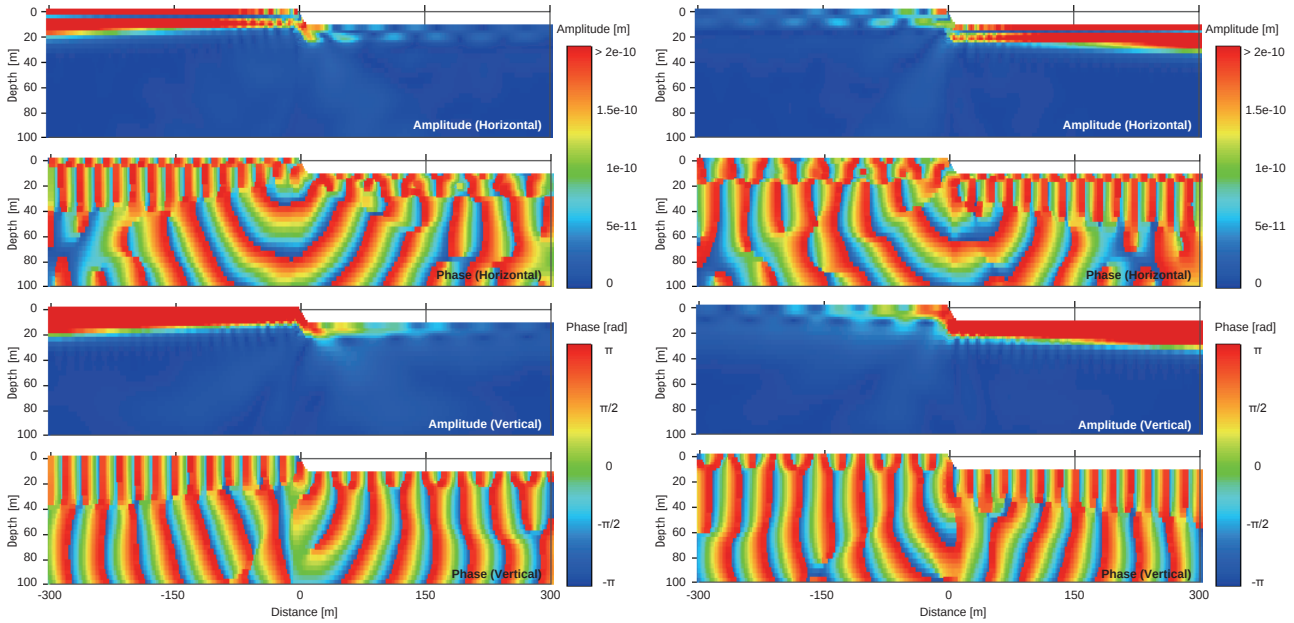

(a) Fundamental Mode Incidence from Left

(b) Fundamental Mode Incidence from Right

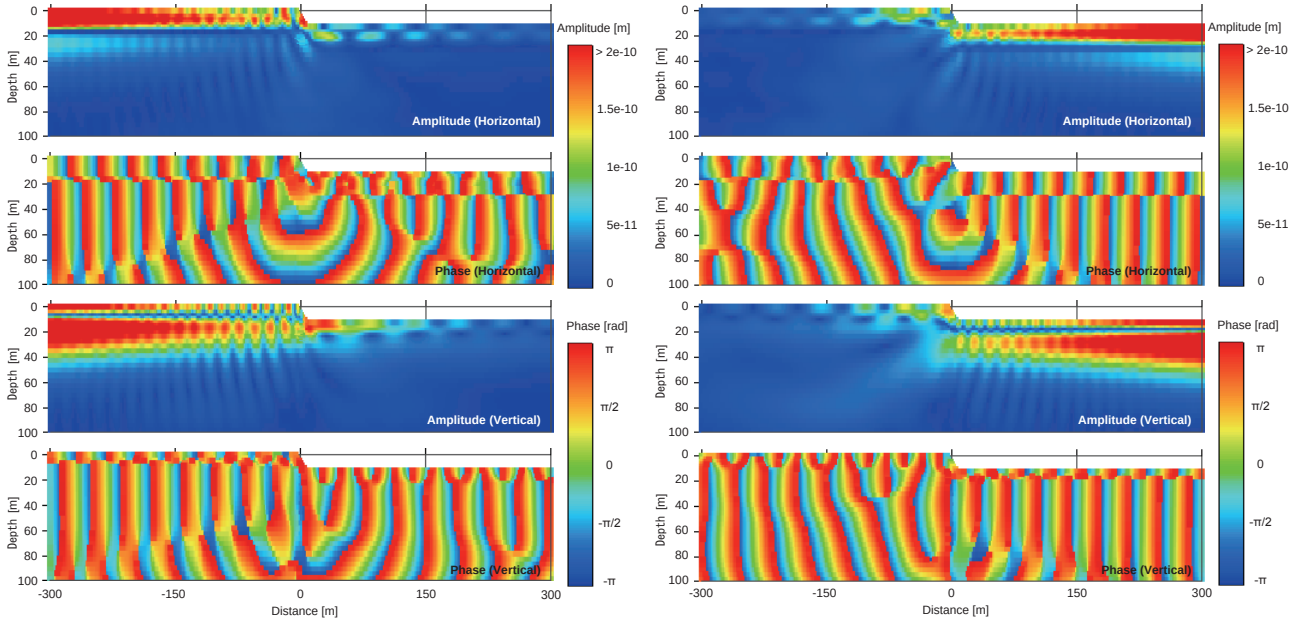

(c) 1st Higher Mode Incidence from Left

(d) 1st Higher Mode Incidence from Right

Figure 8 Wave Field due to Incident Rayleigh Wave (10Hz)

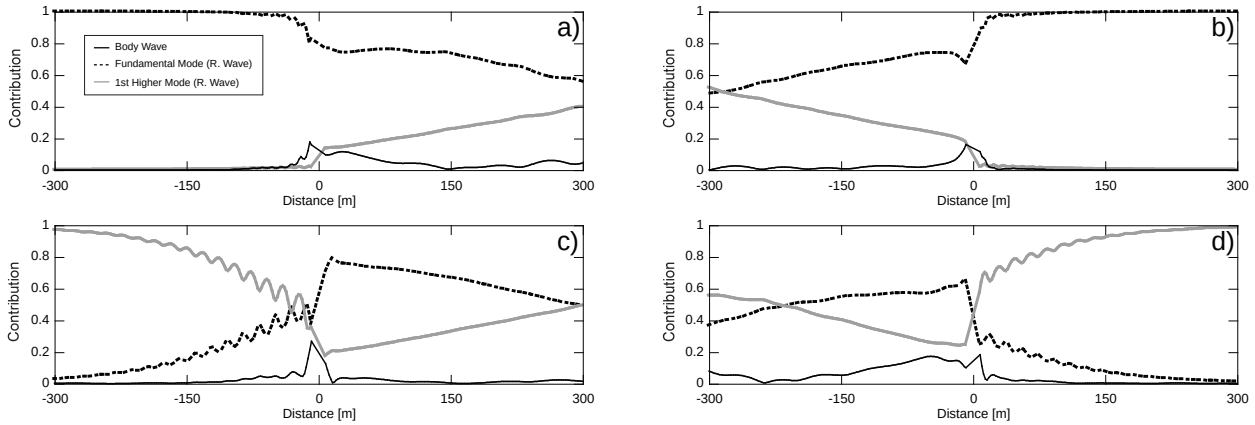

Figure 9 Contribution of Rayleigh and Body Waves (10Hz)

this frequency range from microtremor array observations.

A striped pattern in the vicinity of 6.5Hz found in the contribution diagram of the fundamental mode shown in Figure 11 is due to the influence of the first higher mode which dominates in this frequency range as shown in Figure 6. In fact, the contribution diagram of the first higher mode in Figure 11 reads a fairly high value of 30 percent.

The contribution ratio may change depending on the intensity of the sources, the stiffness of the surface soil, as well as the contrast between the surface layer and the underlying layer. A further investigation is required for the detailed discussion.

5. CONCLUSIONS

From this study, the following conclusions can be made: (1) H/V spectra of a horizontally layered medium as well as the surface wave modes can be obtained based on the thin layered element method. (2) When an incident Rayleigh wave propagates toward an irregular ground, different type of Rayleigh wave modes as well as body waves are generated. (3) In the microtremor wave field due to multiple line load excitations, body waves generated from a slope dominate in the vicinity of the natural frequency of a layered soil.

References:

Drake, L. A. (1972), "Love and Rayleigh Waves in Nonhorizontally Layered Media," Bull. Seism. Soc. Am., **62**(5), 1241-1258.

Harkrider, D. G. (1964), "Surface Waves in Multilayered Elastic Media I. Rayleigh and Love Waves from Buried Sources in a Multilayered Elastic Half-Space," Bull. Seism. Soc. Am., **54**(2), 627-679.

Horike, M. (1993), "Studies on Microtremors," Zishin, **46**(2), 343-350 (in Japanese).

Lysmer, J. (1970), "Lumped Mass Method for Rayleigh Waves, Bull. Seism. Soc. Am., **60**(1), 89-104.

Nakai, S. and Fukuwa, N. (1984), "Dynamic Behavior of an Embedded Structure - Boundary Element Analysis of Approximate Three-Dimensional Soil-Structure Interaction -," Transaction of AIJ (Architectural Institute of Japan), (344), 81-92 (in Japanese).

Regan, J. and Harkrider, D. G. (1989), "Seismic Representation Theorem Coupling : Synthetic SH Mode Sum Seismograms for Non-homogeneous Paths," Geophys. J., **98**, 429-446.

Saito, M. and Kabasawa, H. (1993), "Computations of Reflectivity and Surface Wave Dispersion Curves for Layered Media," Butsuri-Tansa, **46**(4), 283-298 (in Japanese).

Tokimatsu, K. and Tamura, S. (1995), "Contribution of Rayleigh and Body Waves to Displacement Induced by Vertical Point Force on a Layered Elastic Half-space," J. Struct. Constr. Eng., AIJ, (476), 95-101 (in Japanese).

Tokimatsu, K. and Arai, H. (1998), "Effects of Rayleigh to Love Wave Amplitude Ratio on Microtremor Horizontal -to-Vertical Spectral," J. Struct. Constr. Eng., AIJ, (511), 69-75 (in Japanese).

Uebayashi, H. (2006), "Inversion of Microseism Horizontal-to-Vertical Spectral Ratio for Determining the Boundary Shape of a Basin Structure -Verification by numerical experiment-," J. Struct. Constr. Eng., AIJ, (603), 69-76 (in Japanese).

Waas, G. (1972), "Analysis Method for Footing Vibrations through Layered Media," Tech. Report S-71-14, Report 3, Univ. of Calif. Berkeley.

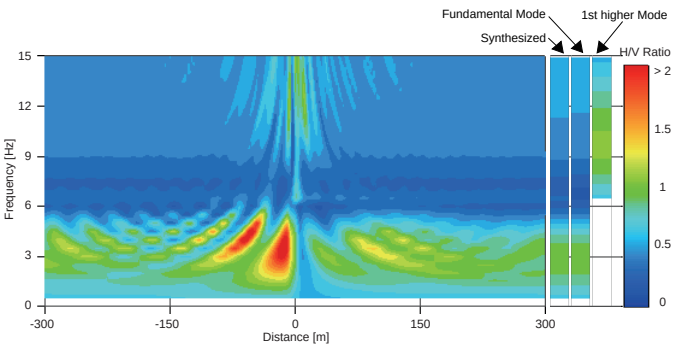

Figure 10 H/V Spectra

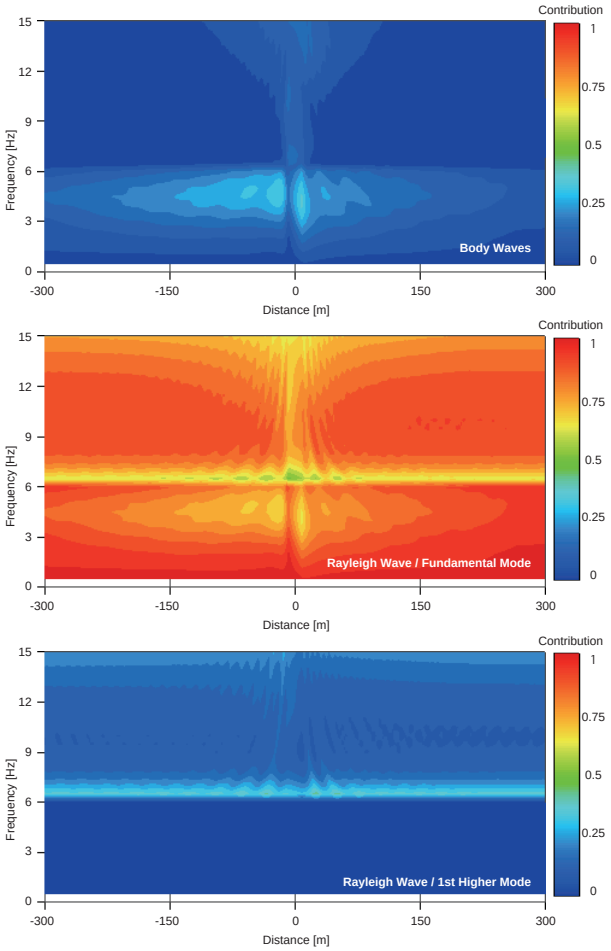

Figure 11 Contribution of Rayleigh and Body Waves

Sixth International Conference on Urban Earthquake Engineering
March 3-4, 2009, Tokyo Institute of Technology, Tokyo, Japan

SEISMIC STRUCTURAL RESPONSE AND STRONG GROUND MOTION SIMULATION BASED ON MULTI-SCALE ANALYSIS

Tsuyoshi Ichimura[1] and Muneo Hori[2]

1) Associate Professor, Department of Civil Engineering, Tokyo Institute of Technology, Japan
2) Professor, Earthquake Research Institute, University of Tokyo, Japan
ichimura@cv.titech.ac.jp,hori@eri.u-tokyo.ac.jp

Abstract: In order to estimate a structure's seismic response considering spatial and temporal variations of earthquake motion, an effective approach is full three-dimensional numerical simulation considering a fault-structure system; fault processes, wave propagation, amplification near the surface and the seismic behavior of the structure. However, it is difficult to realize such an approach because of its huge computational cost. In this paper, we present an efficient approach based upon a multi-scale analytical method for estimation of the strong ground motion and the seismic response of large-scale complex structure considering a fault-structure system in an assumed scenario earthquake. Application examples are also presented to show its potential usefulness and effectiveness.

1. INTRODUCTION

With advancements of construction technology, increasingly large-scale and complex structures are being constructed, which might have a disastrous impact on social activity if their function is lost. Particularly, reasonable accurate estimation of such structures' seismic response is important for mitigation of earthquake disasters.

The seismic behavior of such structures is usually complicated because the structure comprises complex parts. In addition, this seismic behavior might be more complicated because its behavior is affected by spatial and temporal variation of earthquake motion such as phase differences in the horizontal direction and amplification differences near the surface along its depth and so on, because they are larger than conventional structures.

To estimate a structure's seismic response considering spatial and temporal variations of earthquake motion, an effective approach is full three-dimensional (3-D) numerical simulation considering a fault-structure system including fault processes, wave propagation, amplification near the surface and the seismic behavior of the structure. As depicted in Fig. 1, it is difficult to realize such an approach because of its huge computational cost.

On the other hand, studies of earthquake motion prediction are conducted for practical engineering purposes (e.g. 1)). In addition, recent studies of 3-D seismic wave propagation simulation in a large-scale domain and 3-D numerical simulations for dynamic behavior of large-scale structure can handle more realistic models (e.g., 2), 3), 4), 5), 6), 7), 8) for wave propagation simulation, and 9), 10), 11) for structural analysis). A better approach would estimate behavior with equivalent accuracy to enable computation from the fault to the structure directly with integration of these recent advancements in numerical simulation methods.

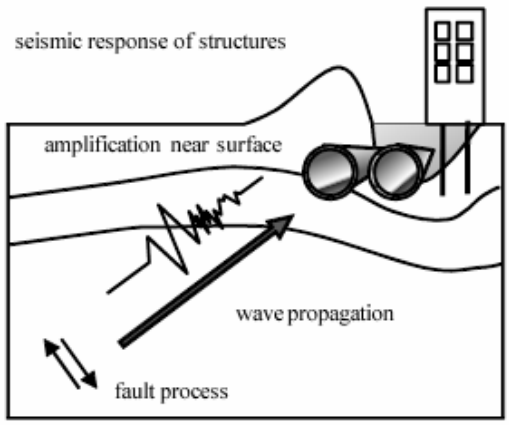

Figure 1 fault-structure system

In this paper, we present an efficient approach, based upon a multi-scale analytical method, to estimate the strong ground motion and the dynamic behavior of structure considering a fault-structure system. Our approach can estimate its behavior with equivalent accuracy to that of direct computation and with much less numerical effort than direct computation, by decomposing the system shown in Fig. 1 to the system portrayed in Fig. 2 with reasonable approximation. Each decomposed problem can be estimated using conventional methods with only implementations of these methods to this framework.

The following is the contents of this paper. First, the proposed method is briefly presented in section 2. In section 3, as an application example, dynamic behavior of large-scale structure is estimated using our approach.

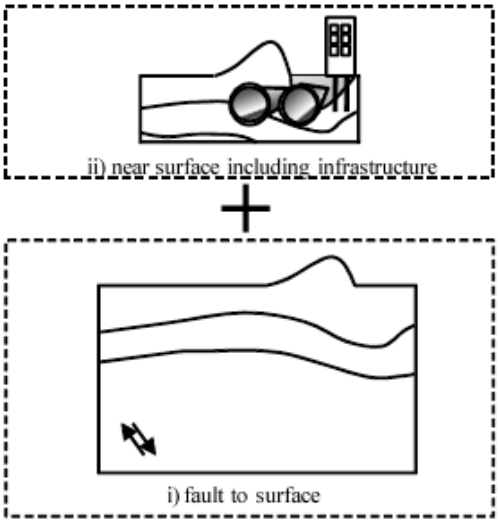

Figure 2 decomposed system

2. Methodology

In this section, to estimate responses of structure with equivalent accuracy to that of direct analysis considering a fault-structure system, we present an efficient analytical method based upon the multi-scale analytical method which we have earlier proposed as an earthquake motion prediction method (see 8), 12)). Furthermore, its validity of application to seismic structural response analysis is numerically verified in 13). This approach can decompose the target problem shown in Fig. 1 to decomposed problems presented in Fig. 2 with reasonable approximation. Here, we summarize the concept and the procedures of multi-scale analytical method using singular perturbation expansion; see 8), 12) for details.

The following wave equation for a displacement function, ui, is the target equation in the target body V,

$$\mathrm{d}_i(c_{ijkl}(\mathbf{x})\mathrm{d}_l u_k(\mathbf{x},t)) - \rho(\mathbf{x})\ddot{u}_j(\mathbf{x},t) = 0,$$

where c_{ijkl}, ρ, d_i and **x** are the elastic tensor, density, spatial derivative ($\partial/\partial x_i$), and position vector. Using singular perturbation expansion as $u_i(\mathbf{x}) \approx u_i^{(0)}(\mathbf{X}) + \varepsilon u_i^{(1)}(\mathbf{X},\mathbf{x}) + \cdots$ this target equation can be approximately decomposed to the following Equations based upon multi-scale analytical method:

$$\mathrm{D}_i(\bar{c}_{ijkl}(\mathbf{X})\mathrm{D}_l u_k^{(0)}(\mathbf{X},t)) + \bar{\rho}(\mathbf{x})\ddot{u}_j^{(0)}(\mathbf{X},t) = 0, \quad \text{1-a)}$$

$$\mathrm{d}_i(c_{ijkl}(\mathbf{x})(\mathrm{d}_k u_l^{(1)}(\mathbf{X},\mathbf{x},t) + \mathrm{D}_k u_k^{(0)}(\mathbf{X},t)) + \rho(\mathbf{x})(\varepsilon\ddot{u}_j^{(1)}(\mathbf{X},\mathbf{x},t) + \ddot{u}_j^{(0)}(\mathbf{X},t)) = 0. \quad \text{1-b)}$$

Here, $\mathbf{X} = \varepsilon\mathbf{x}$ is a slow spatial variable and ε (<<1) is a non-dimensional parameter that represents the relative size of heterogeneities to V. For these analyses, $D_i = \partial/\partial X_i$, and $\bar{\rho}$ is the apparent density that is given as the average of ρ over $\Omega_{\mathbf{X}}$, which is a small domain around **X**, and $\bar{c}_{ijkl}$ is equivalent elastic tensor; see 8), 12) for the detail of definition.

We summarize the procedures of the multi-scale analysis as follows.

i) Compute $\bar{c}_{ijkl}$.
ii) Solve Eq.1-a) for $u_i^{(0)}$ in the whole domain from fault to surface (Fig. 2-i): macro-analysis).
iii) Solve Eq.1-b) for $u_i^{(1)}$ in a small domain near the surface including structure using $u_i^{(0)}$ (Fig. 2-ii): micro-analysis).
iv) Obtain an approximate solution as $u_i^{(0)} + \varepsilon u_i^{(1)}$.

By definition, $u_i^{(0)}$ is regarded as a solution of lower spatial resolution from a low-resolution model, $\bar{c}_{ijkl}$ and $\bar{\rho}$ because it depends slowly on **X**. This $u_i^{(1)}$ gives corrections of higher spatial resolution to the low-resolution solution when the target structure model is refined as c_{ijkl} and ρ. Approximate solutions can be computed with much less numerical effort than directly computing u_i.

It is noteworthy that decomposition of a target system based on multi-scale and sub-structure approaches have been conducted in earthquake simulation; for examples, see 14)-23); see 24), 25) for a brief history. As described previously, the present multi-scale analysis differs slightly from those of previous studies because it is based on singular perturbation expansion; see 26) for a brief history of singular perturbation expansions applied to astronomy and mechanics.

3. Application Example

	V_p (m/s)	V_s (m/s)	ρ (tf/m^3)	h
soil	300	100	1.7	0.06
1st layer	1800	500	2.0	0.03
2st layer	2560	1000	2.2	0.02
3st layer	3200	1700	2.3	0.001
4st layer	5800	3360	2.7	0.001
RC	3373	2127	2.5	0.001

Table 1 material properties

As an application example, seismic response of large-scale complex structure considering fault-structure system is estimated by the proposed method. The target structure is main and side ramp tunnel of the underground highway, which is located in layered media (see Figure 3). Its side ramp tunnel connects the main tunnel in deep underground with the top surface of soft soil layer. Material properties are summarized in Table 1. Point source shown in Figure 3-a) is considered as an assumed scenario earthquake, whose properties are the following: (strike, dip, rake) = (0, π/2, 0), Moment is 5×10^{17} (Nm), which has first ordered slip-velocity function with 0.5 (sec) rise time. Target frequency is set to 2 Hz and frequency components more than 2 Hz is removed from the resulting wave profiles. Target time duration is 65.536 (sec) with time increment 0.004 (sec).

Figure 4 presents the computed wave field around target structure by using proposed multi-scale analysis method. Although the wave field is almost like plane wave, the soft soil layer generates the complicated wave field along its layer. This complicated wave field causes the complicated dynamic response of the underground highway tunnel. As shown here, our proposed method enables us to compute the complicated dynamic behavior of target structure in the assumed scenario earthquake considering fault-structure

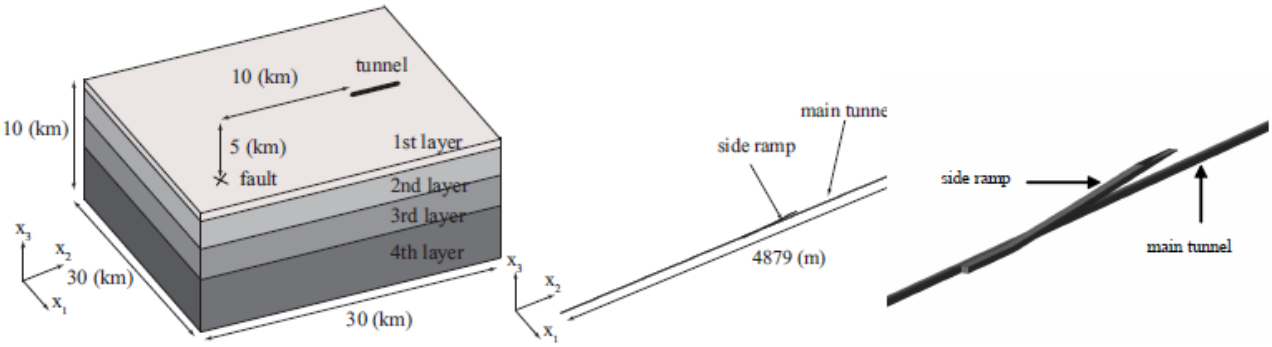

a) whole model b) underground highway model c) close-up view of tunnel

Figure 3 three dimensional numerical simulation model of large-scale underground highway considering fault-structure system

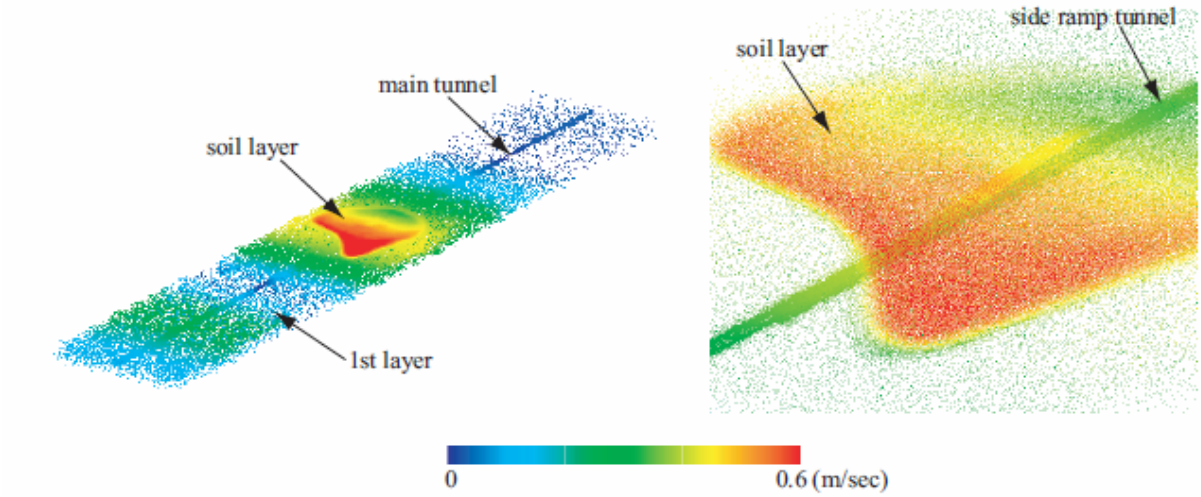

Figure 4 velocity distribution around target structure 6.8 seconds after fault begins to rupture: around target structure (left panel) and close-up view of target structure and soft soil layer (right panel).

system.

4. CONCLUSIONS

This paper presents the method to compute the complicated dynamic response of target structure in the assumed scenario earthquake considering fault-structure system. The application example is also shown to present its usefulness and effectiveness. Although in this application example we use simple crust structure and fault model, actual 3-D crust structure and large-scale fault model can be considered in our method. In the near future, we will compute seismic responses of the important structures with high resolution and high accuracy in mega-earthquake such as near-field earthquake beneath Tokyo area.

References:

1) Irikura K, Miyake H, Iwata T, Kamae K, Kawabe H, Dalguer LA., Recipe for predicting strong ground motion from future large earthquake. *Proc. of the 13th World Conference on Earthquake Engineering* 2004; 1371.

2) Koketsu K, Fujiwara H, Ikegami Y., Finite-element simulation of seismic ground motion with a voxel mesh. *Pure Appl. Geophys.* 2004; 161: 2463-2478.

3) Komatitsch D, Liu Q, Tromp J, Suss P, Stidham C, Shaw JH., Simulations of ground motion in the Los Angeles Basin based upon the spectral element method. *Bulletin of the Seismological Society of America* 2004; 94: 187-206.

4) Bielak J, Ghattas O, Kim EJ., Parallel octree-based finite element method for large-scale earthquake ground motion simulation. *Computer Modeling in Engineering and Sciences* 2005; 10: 99-112.

5) Furumura T., Large-scale parallel simulation of seismic wave propagation and strong ground motions for the past and future earthquakes in Japan. *Journal of the Earth Simulator* 2005; 3: 29-38.

6) Kaeser M, Dumbser M., An arbitrary high-order discontinuous Galerkin method for elastic waves on unstructured meshes - I. The two-dimensional isotropic case with external source terms. *Geophys. J. Int.* 2006; 166: 855-877.

7) Ma S, Liu P., Modeling of the perfectly matched layer absorbing boundaries and intrinsic attenuation in explicit finite-element methods. *Bulletin of the Seismological Society of America* 2006; 96:1779-1794.

8) Ichimura T, Hori M, Kuwamoto H., Earthquake Motion Simulation with Multiscale Finite Element Analysis on Hybrid Grid. *Bulletin of the Seismological Society of America* 2007; 97: 1133-1143.

9) Ogino M, Shioya R, Kawai H, Yoshimura S., Seismic Response Analysis of Nuclear Pressure Vessel Model with ADVENTURE System on the Earth Simulator. *Journal of the Earth Simulator* 2005; 2: 41-54.

10) Elgamal A, Lu J, He L, Law K, Yang Z., Techniques for Simulation of Large-Scale Nonlinear Soil-Structure Systems. *International Workshop on Constitutive Modelling, Development, Implementation, Evaluation, and Application* 2007.
11) Dobashi H, Ochiai E, Ichimura T, Yamaki Y, Hori M, Yamada T, Ohbo N, Moriguchi M., 3D FE Analysis for Seismic Response of Complicated Large-Scale Ramp Tunnel Structure. *ECCOMAS Thematic Conference on Computational Methods in Structural Dynamics and Earthquake Engineering* 2007.
12) Ichimura T, Hori M., Macro-Micro Analysis Method for Wave Propagation in Stochastic Media. *Earthquake Engineering & Structural Dynamics* 2006; 35: 419-432.
13) T. Ichimura, M. Hori, Structural Seismic Response Analysis Based on Multiscale Approach of Computing Fault-Structure System, *Earthquake Engineering & Structural Dynamics*, DOI: 10.1002/eqe.861 (in press).
14) Clough RW, Penzien J., *Dynamics of Structures* 1975, McGraw-Hill, New York, 584.
15) Kausel E, Whitman RV, Morray JP, Elsabee F., The spring method for embedded foundations. *Nucl. Eng. Des.* 1978; 48: 377-392.
16) Bielak J, Christiano P., On the effective seismic input for nonlinear soil-structure interaction systems. *Earthquake Eng. Struct. Dyn.* 1984; 12: 107-119.
17) Mita A, Luco JE., Dynamic response of embedded foundations: a hybrid approach. *Comput. Methods Appl. Mech. Eng.* 1987; 63: 233-259.
18) Regan J, Harkrider DG., Numerical modelling of SH Lg waves in and near continental margins. *Geophys. J. Int.* 1989; 98: 107-130.
19) Bielak J, MacCamy RC, McGhee DS, Barry A., Unified symmetric BEM-FEM for site effects on ground motion-SH waves., *J. Eng. Mech.* 1991; 117: 2265-2285.
20) Aydinoglu MN., Consistent formulation of direct and substructure methods in nonlinear soil-structure interaction. *Soil Dyn. Earthquake Eng.* 1993; 12: 403-410.
21) Fah D, Suhadolc P, Mueller S, Panza GF., A hybrid method for the estimation of ground motion in sedimentary basins: Quantitative modeling for Mexico City. *Bull. Seism. Soc. Am.* 1994; 84: 383-399.
22) Zahradnik J, Moczo P., Hybrid seismic modeling based on discrete-wavenumber and finite-difference methods. *Pure Appl. Geophys.* 1996; 148: 21-38
23) Oprsal I, Zahradnik J. Three-dimensional finite difference method and hybrid modeling of earthquake ground motion. *J. Geophys. Res.* 2002; 107 (B8): 2161.
24) Moczo P, Bystricky E, Kristek J, Carcione JM, Bouchon M., Hybrid modeling of P-SV seismic motion at inhomogeneous viscoelastic topographic structures. *Bull. Seism. Soc. Am.* 1997; 87: 1305-1323.
25) Bielak J, Loukakis K, Hisada Y, Yoshimura C., Domain Reduction Method for Three-Dimensional Earthquake Modeling in Localized Regions, Part I: Theory. *Bulletin of the Seismological Society of America* 2003; 93: 817-824.
26) Smith DR., *Singular Perturbation Theory, An Introduction with Applications*. Cambridge University Press: Cambridge, 1985.

Sixth International Conference on Urban Earthquake Engineering
March 3-4, 2009, Tokyo Institute of Technology, Tokyo, Japan

EXAMINATION OF EFFECTS OF ARRAY LAYOUT ON SOURCE INVERSION BY STRONG-MOTION DATASET OF THE 1979 IMPERIAL VALLEY EARTHQUAKE

Michihiro Ohori[1], Arihide Nobata[2], and Kentaro Motoki[3]

1) Research Scientist, DONET, Japan Agency for Marine-Earth Science and Technology, Yokohama, Japan
2) Research Manager, Technical Research Institute, Obayashi Corporation, Tokyo, Japan
3) Assistant Professor, Dept. Environmental Eng., Tokyo Institute of Technology, Yokohama, Japan
ohorim@jamstec.go.jp, nobata.arihide@obayashi.co.jp, kmoto@enveng.titech.ac.jp

Abstract: In this study, based on the strong-motion data from the 1979 Imperial Valley, California, earthquake (Mw6.5), we studied effects of array layouts on waveform source inversion. After obtaining a reference solution for a slip distribution on the fault plane using all stations involved, we conducted a number of array layouts of strong-motion stations and examined the accuracy of the waveform inversion results from different indexes, such as the discrepancy of a fault-slip distribution against the reference solution, the degree of waveform matching between syntheses and records, the deviation of characterized source parameters from the empirical prediction, and so on.

1. INTRODUCTION

In estimating source rupture process, the importance of seismometer array configurations was pointed out by Miyatake et al. (1986), Iida et al. (1988, 1990), and Iida(1990). Their papers inspired us to confirm effects of array layouts on source study using actual strong-motion data. Miyatake et al. (1986) proposed a method of prediction analysis for the accuracy of source inversion of strong-motion data, and examined the accuracy of a rupture process for the strike-slip fault, using two straight-line arrays: a fault-parallel array consisting of stations aligned along a fault-strike, and a fault-perpendicular one consisting of stations aligned perpendicular to a fault-strike. They concluded that the former layout provides a more reliable solution than the latter one. They also discussed the array installed in the Imperial Valley area. The stations tested was 20 stations in the United States (Case A), 14 El Centro strong-motion-array stations only, these being almost linearly aligned perpendicular to the fault-strike (Case B), and all 26 stations in the United States and Mexico (Case C). They concluded that Case C provided the best solution, Case A the second best, and Case B the third.

Using a method proposed by Miyatake et al. (1986), Iida et al. (1988) determined the optimum array configurations for source inversion; 'Optimum' means that the highest accuracy of source inversion is acquired with the same number of array stations and the same process of fault rupturing. They concluded that the optimum array geometry consists of two different types of stations regardless of the target fault types: stations surrounding the fault area with good azimuthal coverage and stations close to the fault and aligned parallel to the strike. They pointed out that the former stations play an important role in resolving the early stage of the fault rupturing whereas the latter stations significantly resolve the later stage of the fault rupturing. In addition, from comparison with their optimum array geometries, they indicated that the ones proposed on the basis of an empirical judgment at the 1978 International Workshop on Strong-Motion Earthquake Instrument Arrays were not the best ones.

Iida (1990) studied thorough investigation extending the theoretical approach with a half-space Green's function. Comparison between his revised optimum array geometries and their previous ones clarified that different types of waves recorded at each station may weaken the dependency of the array configuration of the effect of the source characteristics. It should be noted that the fault-perpendicular array layout, which was disadvantageous in Miyatake et al. (1986) and Iida et al. (1988), gives almost the same accuracy as the fault-parallel array geometry. He also found some resemblances between his re-evaluated optimum array configuration and the above-mentioned Workshop geometries. Iida et al. (1990), moreover, elaborated the effect of physical waves to the source process derived from the waveform inversion.

With the background mentioned above, it should be noted that Iida and his colleagues' works treated only the far-field S-waves in a full-space (Miyatake et al., 1986; and Iida et al., 1988) or full-wave field in a half-space (Iida et al., 1990; Iida, 1990), thus their work was not based on realistic underground structures. In addition, actual strong-motion data were not used: a moment-release distribution was not estimated. Instead, moment-release variances were evaluated based on a principle of the propagation of errors. We therefore consider that their conclusions should be

confirmed as much as possible by performing waveform inversion for actual strong-motion data recorded on realistic underground structures. This is our main purpose in the present study.

Based on the strong-motion data from the 1979 Imperial Valley, California, earthquake (Mw6.5), we study the effect of array layout on waveform source inversion. After obtaining a reference solution for a slip distribution on the fault plane using all stations involved, we tested a number of array layouts of strong-motion stations and examined the accuracy of the waveform inversion results from different indexes, such as the discrepancy of a fault-slip distribution against the reference solution, the degree of waveform matching between syntheses and records, the deviation of characterized source parameters from the empirical prediction by Somerville et al. (1999), and so on.

2. FAULT RUPTURE PROCESSES OF THE 1979 IMPERIAL VALLEY EARTHQUAKE

To verify effects of strong-motion array layout on source inversion, we require a strong-motion dataset that are recorded at a number of stations in the near field. In addition, to demonstrate our results, it would be effective to select an earthquake in which the rupture process was investigated. Therefore, we decided to target the 1979 Imperial Valley earthquake. It should be noted that our interest is not in the rupture process itself, but in effects of the strong-motion array configuration on waveform inversion. In this section, we review studies of the fault rupture process for the 1979 Imperial Valley earthquake.

Using the strong-motion data to model this event, Olson and Apsel (1982) and Hartzell and Heaton (1983) performed waveform inversion, while Hartzell & Helmberger (1982) and Archuleta (1984) conducted forward modeling. Hartzell & Helmberger (1982) and Hartzell & Heaton (1983) treated only the Imperial Fault, but Olson & Apsel (1982), and Archuleta (1984) modeled the Brawley Fault as well as the Imperial Fault. Archuleta (1984) indicated that contribution of the Brawley-Fault to seismic moments was only 4% of the total seismic moment, and that the Brawley Fault affected only a nearby small area. Results of Olson and Apsel (1982) were in accordance with those of Archuleta (1984). Archuleta (1984) gives an excellent summary of the other three works, so we follow the work of Hartzell & Heaton (1983), in terms of an inversion scheme and a fault discretization.

Hartzell & Heaton (1983) conducted a linear waveform inversion of the near-field strong-motion data, and the teleseismic-body wave data, and both. As for the near-field data of interest to us, they inverted a velocity waveform dataset that was obtained by integration of the accelerograms and of 0.1 to 1.0 Hz bandpass-filtering. Owing to lack of underground structure information to satisfy the observed P-S time interval, they used only two horizontal components. Of more than 30 source models they tested, the best-fit model was obtained for a rupture velocity of 0.85β, where β is the local S-wave velocity. In the model, each subfault was allowed to rupture three times with different slip rates, and the seismic moment M0, and the fault-dip were estimated as 5×10^{18} Nm and $90\pm5^{\circ}$, respectively. The strike slip component was dominant compared with the dip one. From an inspection of the rupture process on the fault plane, they interpreted that the 1979 event as two sequential events: a foreshock of M5 occurring around the hypocenter, followed by a mainshock of M6 about 15 km north-west.

It should be noted that a keen insight of Archuleta (1984) were found in the way he took a careful look at data. He observed the obvious similarities in pulse shapes common to different groups of stations, for example, HVP, E03, and E02 for fault-parallel components, E04, E05, E06, and E07 for fault-perpendicular ones. He felt that if he could reproduce one or two stations of a group, the others might be well predicted. Thus, he successfully conducted the forward modeling from only the data of 10 stations; BCR, EMO, HVP E03, E04, E05, E06, E07, and E11. Figure 1 might be useful for those who are unfamiliar with the array deployment around the Imperial Valley.

3. STRONG-MOTION DATA

3.1 Data Acquisition

In California State, great efforts have been paid to deploy and operate accelerometer networks in near-fault areas, and a great quantity of strong-motion accerograms has been successfully recorded. In the Imperial Valley area, one of the most dense seismometer networks has been installed, and the network recorded near-field ground shaking during the 1979 Imperial Valley earthquake. It is worth noting that this event accelerated studies of source inversion, as was mentioned in the former section. Recently, the Southern California Earthquake Center has released an immense amount of data of the Strong Motion Data Base (SMDB) via Internet. Seismologists and earthquake engineers all over the world can now download data of interest from the SMDB World Wide Web. We downloaded the data recorded at 34 stations during the 1979 Imperial Valley earthquake.

3.2 Processing

In Figure 1, we show the epicenter of the 1979 Imperial Valley earthquake and the strong-motion stations in and around the Imperial Valley area. On the United States side, most of the stations were operated by the United States Geological Survey (USGS), the exceptions being EMO, WSM, and NIL, which were operated by the California Department of Geology and Mines (CDMG). All the stations on the Mexico side were operated by collaboration between the University of California, San Diego (UCSD) and the University of National Mexico (UNAM). In our final inversion, 26 stations are selected. The first and last two seconds of time window were cut off with semi cosine-shaped tapers. We then added zeros after each original record to make a record length of 163.84 s. After the

records were transformed into the frequency domain with a fast Fourier transform (FFT), they were bandpass-filtered between 0.1 and 1.0 Hz, and integrated once. Using an inverse FFT, we finally obtained velocity waveforms with a sampling time of 0.08 s.

3.3 Time Correction

At most stations, trigger times of accelerometers as listed in Table 1 of Archuleta (1982) were available. To estimate timings of records approximately, we preliminarily inverted waveforms of some stations using the trigger times, and synthesized waveforms at other stations using the resulting slip distribution. The underground structure we used was assumed by simplifying a structure in previous studies (Hartzell & Helmberger, 1982; Hartzell & Heaton, 1983). The quality factors for the P- and S-waves were properly considered. To accommodate the time lag between data and synthesis, we calculated the correlation function between syntheses and records at all stations and estimated the timing shift approximately. After correcting the time of all the stations, we performed another preliminary inversion for all the stations used here, to find the exact time shift. In this way, we corrected the time of all stations to extract the first 40 s record as an inversion target.

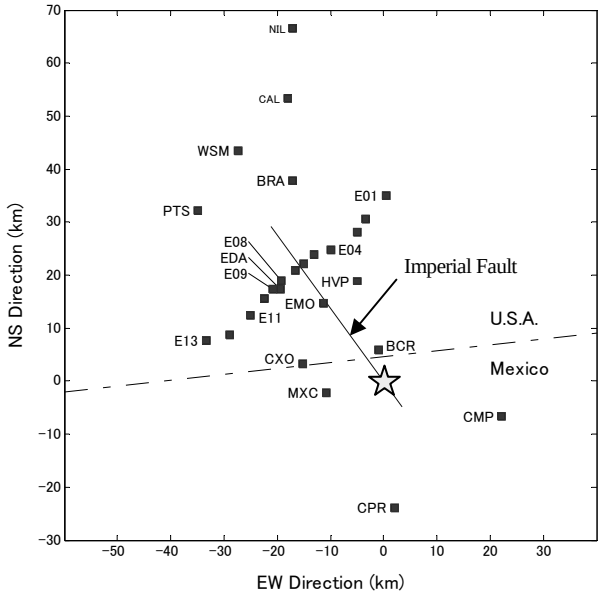

Figure 1: Location map of the epicenter and strong motion observation stations around the Imperial Fault. The epicenter is located at the origin with a star.

4. METHOD

4.1 Basic Equations

We use a linear inversion technique with multiple time-windows (Hartzell & Heaton, 1983). The equations to be solved are obtained by equating the synthesized and observed waveforms,

$$Ax = d \qquad (1)$$

where A denotes the matrix of subfault synthetics, d the observed data vector, and x the solution vector. Using algorithms of Lawson & Hansen (1974), we can solve the equations of Eq. (1) with non-negative constraints, and derive a subfault-slip distribution. Furthermore, to stabilize the solution, we impose a moment minimization constraint on Eq. (1):

$$Ex = 0 \qquad (2)$$

where E denotes the identical matrix. A slip-distribution is obtained by solving Eq. (1) and Eq. (2) simultaneously. Using the slip-distribution, we can calculate synthesized waveforms and compare them with the observed ones.

4.2 Unknown Parameters to be Determined

It was shown that a strike slip was dominant compared with a dip slip in previous studies such as Hartzell & Helmberger (1982) and Hartzell & Heaton (1983). So we will consider only the strike-slip amount of each subfault as unknowns to be determined in our inversion. The number of unknowns to be determined is 168, which is equal to the product of the number of subfaults (56) and the number of rupture times on each subfault (3) in what follows.

4.3 Fault Discretization

Referring to the model by Hartzell and Heaton (1983), the Imperial Fault is modeled as a vertical strike-slip fault with a length of 42 km and a width of 10 km. The rectangular fault is divided into 14 subfaults along the strike direction, and 4 along the plunge direction, so that the total number of subfaults is 56. The length of each subfault is 3 km, and the width of subfault is 2.5 km.

4.4 Source Time Function and Rupture Propagation

We use a triangle-shaped slip-velocity function with a rise time of 0.8 s. To obtain the best fit between the observed and synthesized seismograms, three rupture velocities, 0.9β, 0.85β, and 0.8β are tested, where β indicates the local S-wave velocity. The earthquake hypocenter is located at 10 km in depth, and the rupture propagates from the hypocenter to all directions. Because of the layered media, the rupture front is complicated [e.g., see Figure 6 of Archuleta (1984)]. The arrival time of rupture front at the center of each subfault is calculated by simple ray tracing. To take into account multiple ruptures, we allow each subfault to slip three times: first at the arrival time of the rupture front, then at a later time by half of a rise time, and finally at another later time by a rise time. Therefore, every subfault slips three times with a time interval of 0.4 s.

4.5 Green's Functions

In calculating the Green's functions, we used a computer code of 'grflt6.f' developed by Hisada (1994, 1995) by which seismic responses of a multi-layered medium subjected to a double-couple source are evaluated.

Velocity responses for underground structure due to a unit strike slip were calculated. Synthesized waveforms were filtered with the same bandpass filter as was applied to the observed waveforms.

4.6 Staion Selection

The stations selected by Olson & Apsel (1982) were similar to the stations of layout C of Miyatake et al. (1986). Olson and Apsel (1982) pointed out that waveform fitting of Mexican records was not as good as that of American records, because of complexities observed in Mexican records. Based upon the degree of waveform-matching between the records and the synthetics by a preliminary source inversion, we selected 26 stations employed in this study. In Figure 1, the targeted stations are shown by solid squares.

5. METHOD

5.1 Reference Solution

To find the best fault rupture velocity, we tested three cases: Case 1 (0.9 β), Case 2 (0.85 β), and Case 3 (0.8 β). Although the slip distributions on the fault plane obtained are not shown because of the limited space. Case 1 and Case 2 give similar results, the slip distribution has a single, peak area at much the same location in three cases. The peak location gets separate from the hypocenter as the rupture velocity increases. This is a trade-off between the rupture velocity and the asperity location, as shown in previous studies (e.g., Hartzell and Heaton, 1983). On the other hand, the slip distribution of Case 3 has two slip peaks in an asperity. This characteristic is found in Hartzell and Helmberger (1982) and Hartzell and Heaton (1983) when the rupture velocity is close to 0.8 β. A common feature among these thee cases, is that the large peak area is located at a deeper position in the fault zone. The maximum slip on the fault plane is estimated to be 3.27 m, 3.64 m, and 3.20 m for Cases 1-3, respectively. The calculated seismic moment, M_0 among three cases is almost the same: 4.74×10^{18} Nm for Case 1, 4.60×10^{18} Nm for Case 2, and 4.80×10^{18} Nm for Case 3. Because of limited space, the waveform results are not shown, but good fitting between the synthesized waveforms and observed ones are found for Cases 1 to 3. To measure the degree of the fitting, we adopt a normalized error criterion defined by

$$\varepsilon_T = \sqrt{\sum_{i=1}^{NT}\left|d_i^{est} - d_i^{obs}\right|^2 \Big/ \sum_{i=1}^{NT}\left|d_i^{obs}\right|^2} \qquad (3)$$

where N_T denotes the total number of the time-series record, d_i^{est} the i-th data of the synthesized waveform, and d_i^{obs} the i-th data of the observed waveform.

Comparing the errors of Cases 1 to 3, Case 2 gave a slightly better accuracy than the others. Therefore, we defined the slip distribution obtained of Case 2 as a reference solution. Hereafter, we fix the rupture velocity as 0.85 β.

5.2 Station Layouts

To understand how the station layout influences the inversion result, we constructed several array layouts and examined the inversion results from them, assuming the slip distribution result from Case 2 as the reference solution, As shown in Table 1, 12 cases were tested. Among them, 6 cases are classified into three types of layouts: fault-perpendicular (Cases A1, A2), fault-surrounding (Cases B1, B2), and fault-parallel arrays (Cases C1, C2). Next, to find the effect of combination between two cases from different groups, we examined Cases A1B1, A1C1, and B1C1. Case A1B1 is a mixture of A1 and B1. Cases A1C1 and B1C1 are constructed in the same manner. Remaining three cases were tested for different purpose. Case D1 consists of 10 near-fault stations which Archuleta (1984) used for his forward modeling. Cases D2 and D3 consist of 18 and 21 stations from the United States. The difference between them is whether or not they include the Mexican stations. These kinds of layouts were examined theoretically in Miyatake et al. (1986).

5.3 Indexes for Effects of Station Layouts

To compare the inversion results from different cases and to investigate quantitatively the accuracy of the station layout on the waveform inversion, we evaluated the following different indexes: (a) the degree of waveform matching between syntheses and records, ε_T of Eq.(3), which is calculated from waveforms at 26 stations for any case, (b) the discrepancy of a fault-slip distribution against the reference solution (Case 2), ε_1 , ε_2, defined by Eq. (4) and (5),

$$\varepsilon_1 = \sum_{i=1}^{NF}\left|x_i^{est} - x_i^{ref}\right| \Big/ \sum_{i=1}^{NF}\left|x_i^{ref}\right| \qquad (4)$$

and

$$\varepsilon_2 = \sqrt{\sum_{i=1}^{NF}\left|x_i^{est} - x_i^{ref}\right|^2 \Big/ \sum_{i=1}^{NF}\left|x_i^{ref}\right|^2} \qquad (5)$$

where N_F denotes the total number of subfaults, x_i^{est} the total slip of the i-th subfault for each of the cases we tried, and x_i^{ref} is the total slip for Case 2, and (c) the difference between characterized source parameters and the empirical predictions by Somerville et al. (1999), where the extraction of the rupture area, S_{RA} and the total asperity area, S_{ASP} is conducted and the ratio between the total asperity area and the rupture area, S_{ASP}/S_{RA} is calculated. We compare above indexes from different cases with attention on the dependence on the number of stations N_S and the seismic moment, M_0.

6. RESULTS

Waveforms inversion results from different station layouts are summarized in Table 2. Those for Cases 1 and 3 are listed for reference purposes only. In Figure 2, we show

ε_T, ε_1, and ε_2 as well as N_S in each inversion. From comparison among the results for Cases As, Bs, and Cs, we notice that the accuracy of the fault-parallel type (Cases C1, C2) is better than the fault-perpendicular one (Cases A1, A2) and the fault-surrounding one (Cases B1, B2), nevertheless the number of stations used is the minimum among them. As for M_0, Cases As give the largest values among all cases tested. From comparison with Cases As and Cs, it is confirmed that a fault-parallel array gives us a much better resolution than a fault-perpendicular array. This fact agrees with the results in Miyatake et al. (1986) and Iida et al. (1988) rather than those in Iida (1990).

The examination of the results of Cases A1B1, A1C1, and B1C1 comapered with their elementary layouts, Case A1, B1, and C1 suggests us that a combination of different types of array layouts seems to enhance effectively the accuracy of the source inversion. In particular, Case A1C1 gives the best solution among them.

Focusing on the remaining cases, a considerably good solution given by Case D1 implies the excellent insight in the way Archuleta (1984) selected the stations. We also notice that Cases D1 and A1C1 give similar results each other, where both cases involve the all stations used in Case C1 and greatly enhance the accuracy with addition of other stations. In Cases D2 and D3, inversion results are similar to each other and they have relatively slight discrepancy from reference solutions.

In Figure 3, we plot S_{RA} and S_{ASP} versus M_0 from this study in comparison with the predicted values by the empirical relationship of Sommerville et al. (1999). We examine the effect of the array design from the viewpoint of the deviation of characterized source parameters from the empirical prediction by Somerville et al. (1999) and Irikura et al. (2001). S_{RA} in most cases coincidents with the empirical prediction within a standard deviation (1.6). On the other hand, S_{ASP} in six cases exceeds the empirical prediction beyond a standard deviation (1.34). S_{ASP}/S_{RA} in most cases except Cases A1 and A2 is in a good agreement with empirical expectation (0.22 on average) by a factor of 1.2. In Cases As, two asperities are resolved and S_{ASP}/S_{RA} is increased with 0.1 by contribution from the second largest asperity, whereas in other cases only single asperity is extracted. Also, S_{RA} and S_{ASP} from this study is scattering around the results based on the slip model by Hartzell and Heaton (1983), which is listed in Table 6 of Sommerville et al. (1999). The discrepancy between them is mostly within a factor of 1.2.

7. CONCLUSION

Through the study, using the strong-motion dataset of the 1979 Imperial Valley, California, earthquake, we investigated effects of strong-motion array layouts on waveform source inversion. Some basical findings about the station layout described in Miyatake et al. (1986) and Iida et al. (1988) were confirmed by performing waveform inversion for actual strong-motion data recorded on realistic underground structures, so the importance of the array design on the source study was recognized. Among the findings observed through this study, it should be emphasized that the deployment of the stations along the fault-strike is the most significant to enhance the accuracy of waveform inversion for the strike-slip faulting.

Acknowledgements:

The strong-motion data used in this article were recorded by USGS and CDMG and downloaded through the Internet site of Strong Motion Data Base, Southern California Earthquake Center. My sincere gratitude is given to all people involved in this project. In addition, I would like to express my appreciation to Prof. Yoshiaki Hisada, Kogakuin University, for giving me a chance to use his Green's function for multi-layered media. Our sincere gratitude is given to Dr. Masahiro Iida, Earthquake Research Institute, University of Tokyo, for his critical reading and constructive comments to the manuscript in an early stage.

References:

Articulate, R. J. (1982), "Analysis of near-source static and dynamic measurements from the 1979 Imperial Valley Earthquake", Bull. Seism. Soc. Am., 72, pp. 1927-1956.

Archuleta, R. J. (1984), "A faulting model for the 1979 Imperial Valley Earthquake", J. Geophys. Res., 89, pp. 4459-4588.

Hartzell, S. and D. V. Helmberger (1982), "Strong-motion modeling of the Imperial Valley Earthquake of 1979", Bull. Seism. Soc. Am., 72, pp. 571-596.

Hartzell, S. H. and T. H. Heaton (1983), "Inversion of strong ground motion and teleseismic waveform data for the fault rupture history of the 1979 Imperial Valley", California, Earthquake, Bull. Seism. Soc. Am., 73, pp. 1553-1583.

Hisada, Y. (1994), "An efficient method for computing Green's functions for a layered half-space with sources and receivers at close depths", Bull. Seism. Soc. Am., 84, pp. 1456-1472.

Hisada, Y. (1995), "An efficient method for computing Green's functions for a layered half-space with sources and receivers at close depths (Part 2)", Bull. Seism. Soc. Am., 85, pp. 1080-1093.

Iida, M., Miyatake T., and K. Shimazaki (1988), "Optimum strong-motion array geometry for source inversion", Earthquake Eng. Struct. Dyn., 16, pp. 1213-1225.

Iida, M. (1990), "Optimum strong-motion array geometry for source inversion Ⅱ", Earthquake Eng. Struct. Dyn., 19, pp. 35-44.

Iida, M., Miyatake, T., and K. Shimazaki (1990), "Relationship between strong-motion array parameters and the accuracy of source inversion and physical waves", Bull. Seism. Soc. Am., 80, pp. 1533-1552.

Irikura, K. and H. Miyake (2001), "Prediction of strong motions for scenario earthquakes", Journal of Geography, 110, pp. 849-875. (in Japanese with English abstract)

Lawson, C. L. and D. J. Hanson (1974), "Solving least squares problems", Prentice-Hall Inc., Englewood Cliffs, New Jersey.

Miyatake, T., Iida M., and K. Shimazaki (1986), "The effect of strong-motion array configuration on source inversion", Bull. Seism. Soc. Am., 76, pp. 1173-1185.

Olson, A. H. and R. J. Apsel (1982), "Finite faults and inverse theory with applications to the 1979 Imperial Valley Earthquake", Bull. Seism. Soc. Am., 72, pp. 1969-2001.

Somerville, P., K. Irikura, R. Graves, Robert, S. Sawada, D. Wald, N. Abrahamson, Y. Iwasaki, T. Kagawa, N. Smith, and A. Kowada (1999), "Characterizing crustal earthquake slip models for the prediction of strong ground motion", Seism. Res. Lett., 70, pp.59-80.

Strong Motion Data Base, Southern California Earthquake Center, http://www.crustal.ucsb.edu/scec/smdb/, last accessed on 1 September, 2000.

Table 1: Station selection in each array layout.

Case \ Stn.	1 CMP	2 CPR	3 MXC	4 BCR	5 CXO	6 EMO	7 HVP	8 E01	9 E02	10 E03	11 E04	12 E05	13 E06	14 E07	15 E08	16 EDA	17 E09	18 E10	19 E11	20 E12	21 E13	22 BRA	23 PTS	24 WSM	25 CAL	26 NIL
1, 2, 3	○	○	○	○	○	○	○	○	○	○	○	○	○	○	○	○	○	○	○	○	○	○	○	○	○	○
A1								○		○	○			○			○		○		○					
A2								○	○	○	○	○	○	○	○	○	○	○	○	○	○					
B1	○	○	○		○			○													○	○	○			
B2	○	○	○		○			○													○	○	○	○	○	○
C1				○		○								○												
C2				○		○	○							○												
A1B1	○	○	○		○			○		○	○			○			○		○		○	○	○			
A1C1				○		○		○		○	○			○			○		○		○					
B1C1	○	○	○	○	○	○		○						○							○	○	○			
D1				○		○	○			○	○	○	○	○	○				○							
D2				○	○	○	○	○		○	○	○	○	○	○				○		○	○	○	○	○	○
D3	○	○	○	○	○	○	○	○		○	○	○	○	○	○				○		○	○	○	○	○	○

Table 2: Summary of inversion results for different array layouts.

Case	Layout Type	*Ns*	M_0 ($\times 10^{18}$ Nm)	ε_T	ε_1	ε_2	S_{RA} (km^2)	S_{ASP} (km^2)	S_{ASP}/S_{RA}
1	whole (0.90β)	26	4.74	0.72			293	75	0.26
2	whole (0.85β)		4.60	0.71			360	75	0.21
3	whole (0.80β)		4.80	0.73			270	60	0.22
A1	perpendicular	7	7.00	0.90	1.02	0.99	270	105	0.39
A2	perpendicular	14	6.91	0.86	0.82	0.82	270	120	0.44
B1	surrounding	8	4.16	0.91	0.86	0.69	420	90	0.21
B2	surrounding	11	4.14	0.90	0.84	0.69	420	90	0.21
C1	pallarrell	3	4.27	0.82	0.66	0.67	420	105	0.25
C2	pallarrell	4	4.53	0.80	0.65	0.64	420	105	0.25
A1B1	A1&B1	13	5.51	0.79	0.53	0.46	270	75	0.28
A1C1	A1&C1	9	4.69	0.75	0.25	0.21	360	75	0.21
B1C1	B1&C1	11	3.65	0.82	0.47	0.50	420	75	0.18
D1	Archuleta (1984)	10	5.08	0.73	0.25	0.22	360	75	0.21
D2	with no Mexican sites	18	4.72	0.72	0.19	0.17	360	75	0.21
D3	with Mexican sites	21	4.58	0.72	0.14	0.13	360	75	0.21

[Note] Case 2 is used as a reference solution.

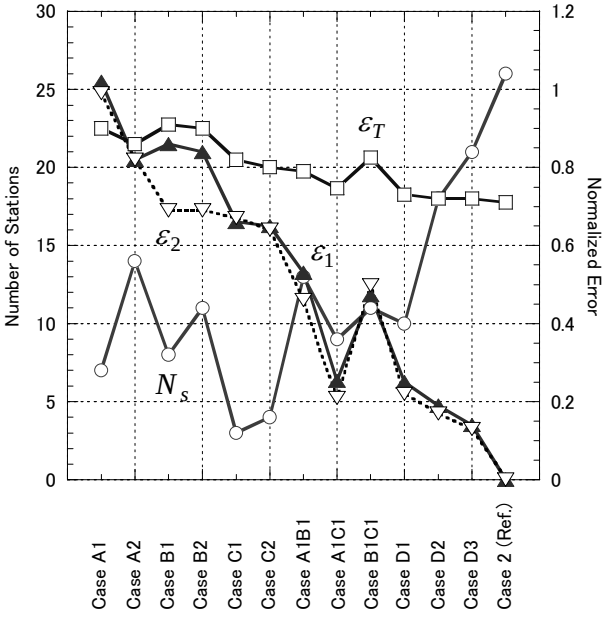

Figure 2: Comparison of ε_T, ε_1, ε_T and N_s in each inversion. Note that ε_T was evaluated by using data and synthesized waveforms for 26 stations.

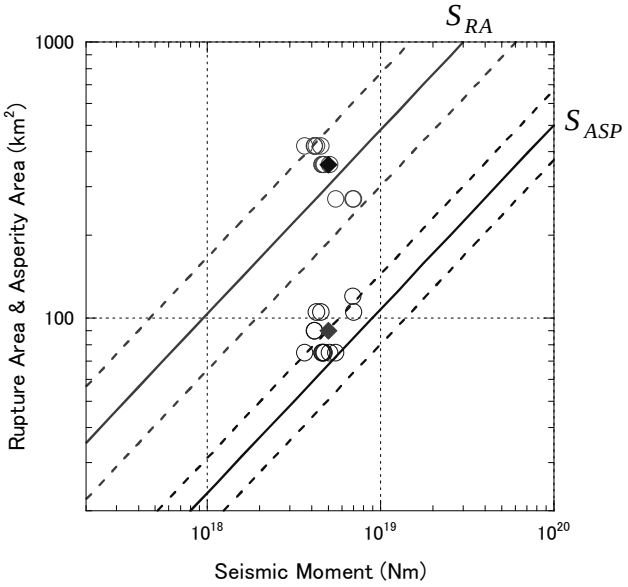

Figure 3: Comparison of S_{RA} and S_{ASP} versus M_0. Results from the present study are denoted by open circles, and empirical prediction by solid lines. Dashed lines indicate the range of a standard deviation. Solid diamonds indicate the result for the same event listed in Table 6 of Sommerville et al. (1999).

Sixth International Conference on Urban Earthquake Engineering
March 3-4, 2009, Tokyo Institute of Technology, Tokyo, Japan

JOINT INVERSION OF S-WAVE, RECEIVER FUNCTION AND PHASE VELOCITY OF RAYLEIGH WAVE TO S-WAVE PROFILE OF DEEP SEDIMENTARY LAYERS

Haruhiko Suzuki[1)] and Hiroaki Yamanaka[2)]

1) OYO Corp., Japan
2) Associate Professor, Department of Civil Engineering, Tokyo Institute of Technology, Japan
suzuki-haruhiko@oyonet.oyo.co.jp, yamanaka@depe.titech.ac.jp

Abstract: We propose an joint inversion method for estimation of a 1D S-wave velocity structure of deep sedimentary layers using S-wave parts of earthquake records, receiver function, and phase velocity of Rayleigh wave for evaluating site amplification. Genetic algorithm is used in inversion to find an optional model that has the minimum misfit between observed and synthetic data. Using joint inversion method we can avoid the trade-off relation between S-wave velocity and thickness of a layer..

1. INTRODUCTION

It is important to evaluate characteristics of source, path and site effects for strong motion prediction. S-wave velocity structure is one of the most important factors. Recently many 3D subsurface structural models were constructed for strong motion estimation (e.g., Horikawa et al., 2003; Yamanaka and Yamada, 2006). These models were constructed using reflection, refraction and microtremor array surveys. Although there are many geophysical data in urban area, there are a few data in small plains.

On the other hands, strong motion seismograph networks (K-NET) have been constructed in Japan after Hyogo-ken Nanbu earthquake in 1995 to cover whole of Japan. If an S-wave velocity structure can be constructed using these strong motion data, we can construct a 3D subsurface structural model in the area there are a few geophysical data.

Several methods are now available to construct the S-wave velocity structure using earthquake records, such as receiver function method (e.g., Kurose and Yamanaka,2006), phase velocity analysis of surface waves (Mikoshiba and Kinoshita,1989; Miura and Midorikawa,2001), group velocity analysis of surface waves (Yamanaka et al,1989) and spectral analysis between horizontal and vertical components of surface waves (Kudo and Sakaue,1984). Although it is important to estimate characteristics of S-wave for the strong motion prediction, the method to evaluate S-wave velocity structural model using S-wave parts of earthquake data. Hikima and Kokestu (2005) recently evaluated an S-wave velocity structural model from comparison of observed S-wave with theoretical one using the reflectivity method. Because non linear least square method is used in inversion process, it takes much amount of calculation at high frequency range. Furthermore we have to decide many parameters of source in their procedure.

In this study, we use the smoothed ramp function for source time function in modeling S-wave part. In inversion process we use a genetic algorithm to find an optimal model. Because of using simple source time function, we use small earthquake. At first, we perform the numerical experiment to applicability of the method. We also conducted numerical experiments of joint inversion of the S-wave, the receiver function and the phase velocity of Rayleigh wave by referring Kurose and Yamanaka (2006) to avoid trade-off problems between shear wave velocity and thickness in s-wave form inversion.

2. WAVEFORM INVERSION FOR S-WAVE PART

2.1 Inversion Method

Concept of estimation of S-wave velocity structure in our method is displayed in Figure 1. Details can be seen in Suzuki and Yamanaka (2008). We calculate velocity wave form at surface using Haskell method (Haskell,1960).

Before inversion, we decide t1, t2 and t3 in Figure 1. T1 is first arrival of S-wave. T2 is the end time of direct S-wave. T3 is the end time of analysis. Misfit e_i between observed and synthetic waves of S-wave from t1 to t3 is defined in the form Eqn1. τ_i is defined to minimize e_i.

$$e_i = \sum_{t=t1}^{t2} \left(\frac{O_i(t)}{A_i^o} - \frac{C_i(t+\tau_i)}{A_i^s} \right)^2 \qquad (1)$$

where, Oi, A_i^o, Ci, A_i^s are observed velocity wave, the maximum amplitude of observed wave, synthetic velocity wave, the maximum amplitude of synthetic wave, respectively. The misfit between observed and synthetic waves from t2 to t3 is defined in the form Eqn2.

$$E_{SH} = \sum_{i=1}^{M} \sum_{t=t2}^{t3} \left(\frac{O_i(t)}{A_i^o} - \frac{C_i(t+\tau_i)}{A_i^s} \right)^2 \quad (2)$$

where, M is number of earthquake data. S-wave velocity structure is optimized to minimize E_{SH}. Minimization of E_{SH} is performed by genetic algorithm (GA). The parameters in the inversion are S-wave velocity and thickness of each layer, a, b, incident angle and rise time (Tr in the followings). S-wave velocity of the basement is fixed. Density of each layer is synthetic from Vs in the Eqn3 (Ludwig et al., 1973).

$$\rho(g/cm^3) = -0.0450Vs^2 + 0.4316Vs + 1.7106 (Vs \le 3.2) \quad (3)$$
$$\rho(g/cm^3) = 0.0448Vs^2 + 0.2481Vs + 1.3760 (Vs > 3.2)$$

2.2 Numerical Experiments

In numerical experiments, we use the model displayed in Figure 2b. A band pass filter from 1sec to 5sec is used for synthetic observed data. The random phase noise with an amplitude of 30% of its Fourier specta is added. Incident angles are 0degree (Event1), 30degree (Event2) and 45degree (Event3). Trs are 1.0s (Event1), 1.25s (Event2) and 1.5s (Event3).

The four-layers model is used in the numerical experiments. Populations, generations, rate of crossover and rate of mutation are 200, 100, 0.7 and 0.01, respectively, according to Yamanaka and Ishida (1996) Search area is displayed in Table 1.

Comparisons between observed and synthetic waveforms are displayed in Figure 2a. Comparisons of parameters between the true and inverted models are displayed in Figure 2b. The synthetic wave is similar well to the observed wave. Parameter distributions of the acceptable models for the inversions in the numerical experiment are displayed in Figure 3. The threshold was set to be equal to the minimum E_{SH}*1.07 and E_{SH} *1.14 in the acceptable model estimation (Kurose and Yamanaka, 2006). Rectangle areas in the figure indicate the search areas of each parameter. The S-wave velocities and thicknesses of the first, second and third layers are displayed in Figure 3a. These parameters agree well with those of the true model. In Figure 3b, there is trade-off between Vs and thickness.

3. JOINT INVERSION

3.1 Method

In order to resolve the trade-off relation between S-wave velocity and thickness, we try to apply joint inversion of S-wave part with receiver function and phase velocity of Rayleigh wave. The synthetic observed data are displayed in Figures 4a, 4b and 4c, respectively. It is noted that the phase velocity data is incomplete with lack of long-period phase velocity, considering difficulties to obtain such a data in actual field observation. The misfits between the observed and synthetic data are defined in the form Eqn3 and Eqn4. The random noises that's Fourier amplitude is 60% of the synthetics are added to the S-wave and receiver function. Furthermore, we added 10 % noises to the phase velocity.

$$E_{RF} = \left(1/N^{RF} \right) \sum_{j=1}^{N_{RF}} \left[\left(R_j^{obs} - R_j^{cal} \right) / R_{\max}^{obs} \right]^2 \quad (4)$$

$$E_{PV} = \left(1/N^{PV} \right) \sum_{j=1}^{N_{PV}} \left[\left(C_j^{obs} - C_j^{cal} \right) / C_j^{obs} \right]^2 \quad (5)$$

where, R_j^{obs}, R_j^{cal}, $R_{\max}^{obs}$ and N^{RF} are the observed, the synthetic, the max value and data numbers of the receiver function, respectively. C_j^{obs}, C_j^{cal} and N^{PV} are the observed, the synthetic and data numbers of the phase velocity, respectively.

The misfit between the observed and synthetic data is defined in the form Eqn6.

$$E = p_{SH} \cdot E_{SH} + p_{RF} \cdot E_{RF} + p_{PV} \cdot E_{PV} \quad (6)$$
$$p_{SH} + p_{RF} + p_{PV} = 1 \quad (7)$$

In the case of the joint inversion using all data, each p is equal to 0.333. In the joint inversion, S-wave velocity of basement is searched. The search area is from 2.6 to 3.4km/s.

2.2 Results

The results of the joint inversion are displayed in Figure 5 showing the models with misfits less than 0.0038. There is the trade-off relation between shear-wave velocity and thickness in only S-wave and receiver function inversion in Figures 5a and 5b. Figure 5c indicates the result of only phase velocity inversion. Because the phase velocity used here is insufficient in the period range, basement depths don't agree with that of the true model. Difference of S-wave velocity models of S-wave and phase velocity inversion is smaller than that of S-wave and receiver function inversion. Figure 6 shows the S-wave velocity structure from joint inversion using all data. Figure 7 shows the averaged standard deviations of S-wave velocity and thickness. The case of joint inversion using all data, standard deviation is smallest. Figure 8 shows the coefficient of regression analysis for calculating the standard deviation from the results in Figure 7 with a liner relationship. The coefficient of the S-wave is smaller than that of the receiver function. Because the phase velocity data is insufficient, the coefficient of the phase velocity is bigger than the others. Even if using the insufficient data like period limited phase velocity in the joint inversion, the accuracy of inversion can be improved.

3. CONCLUSIONS

We proposed an inversion method for estimation of a 1D S-wave velocity structure of deep sedimentary layers using S-wave part of earthquake records for evaluating site amplification. We conducted numerical experiments using synthetic data. Using joint inversion method of the S-wave part with the other data, such as receiver function and phase velocity we can avoid the trade-off relation between S-wave velocity and thickness.

References:

Haskell, N. A. (1960): Crustal reflection of plane SH waves, J. Geophys. Res., 65, 4147-4150.

Hikima, K. and K. Koketsu (2005): Rupture processes of the 2004 Chuetsu (mid-Niigata prefecture) earthquake, Japan: A series of events in a complex fault system, Geophys. Res. Lett., 32, doi:10.1029/2005GL023588.

Horikawa, H., K. Mizuno, T. Ishiyama, K. Satake, H. Sekiguchi, Y. Kase, Y. Sugiyama, H. Yokota, M. Suehiro, T. Yokokura, Y. Iwabuchi, N. Kitada and A. Pitarka1 (2003): A three-dimensional subsurface structure model beneath the Osaka sedimentary basin, southwest Japan, with fault-related structural discontinuities (in Japanese with English abstract), Annual report on active fault and paleoearthquake researches,7, 225-259.

Kudo and Sakaue (1984): Oil-sloshing in the huge tanks at Niigata due to the Nihonkai-Chubu earthquake of 1983(in Japanese with English abstract), Bull. Earthq. Res. Inst. Univ. Tokyo, 59, 361-382

Kurose, T., H. Yamanaka (2006): Joint inversion of receiver function and surface-wave phase velocity of sedimentary layers, Geophysical Exploration (Butsuri-Tansa), 59, 93-101.Mikoshiba and Kinoshita, 1989.

Ludwig, W. J., S. Murauchi, N. Den, P. Buhl, H. Hotta, M. Ewing, M. Asanuma, T. Yoshii and N. Sakajiri (1973): Structure of East China Sea-West Philippine Sea Margin off Southern Kyushu, Japan, J. Geophys. Res., 78, 2526-2536.

Mikoshiba, T and S. Kinoshita (1989): Strong later phases recorded at Fuchu strong-motion array observation during a swarm of 1987 off Fukushima Pref. earthquakes, Report of the National Research Center for Disaster Prevention, 41, 95-104.

Miura, H. and S. Midorikawa (2001): Effects of 3-D Deep Underground Structure on Characteristics of Rather Long-Period Ground Motion – Examination in and around Yokohama City –(in Japanese with English abstract), ,J. Seismol. Soc. Jpn, 54, 381– 395.

Yamanaka, H., K. Seo and T. Samano (1989): Effects of sedimentary layers on surface-wave propagation, Bull. Seism. Soc. Am., 79, 631-64.

Yamanaka and Ishida (1996),: Application of genetic inversion to inversion of surface wave dispersion , Bull. Seism. Soc. Am., 86, 436-444.

Yamanaka, H. and N. Yamada (2006): Modeling 3D S-wave velocity structure of Kanto basin for estimation of earthquake ground motion (in Japanese with English abstract), BUTSURI-TANSA, 59, 549-560.

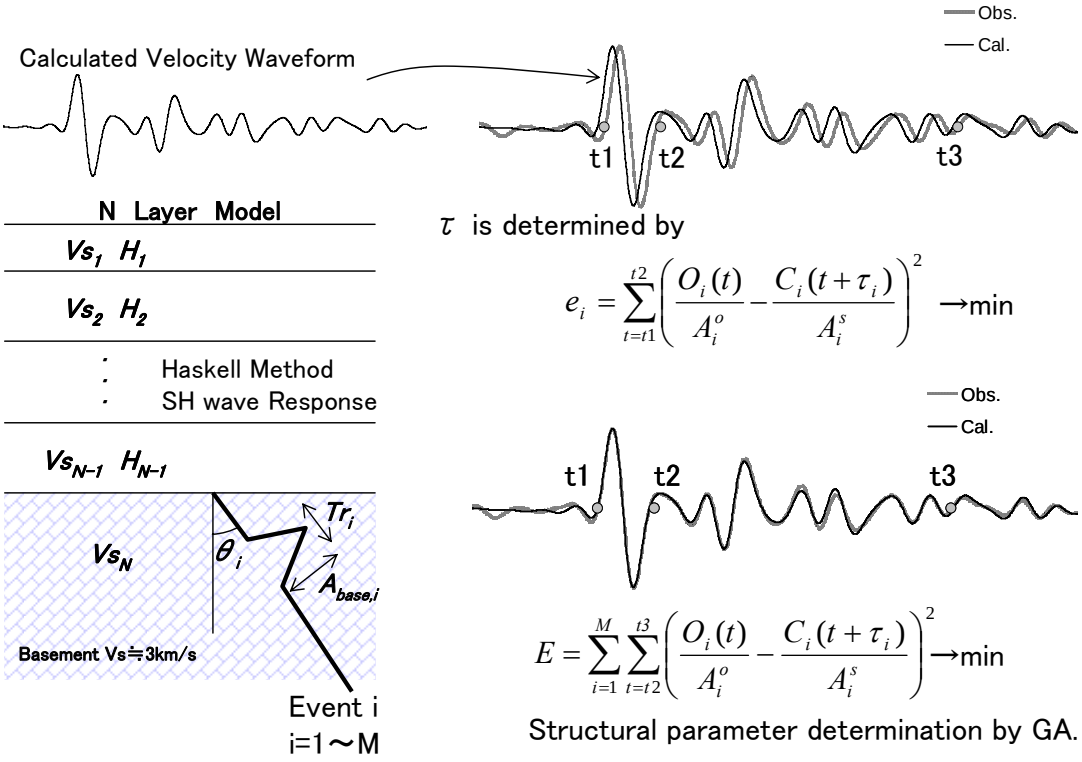

Figure 1 Concept of estimation of S-wave velocity structure using a waveform in inversion.

Table 1 Search limits in inversion. Values in parenthesis indicate true model.

Layer No.	Vs(km/s)	H(km)	Event No.	Tr(s)	Angle(°)	a	b
1lay	0.3-0.7 (0.5)	0.02-0.5 (0.2)	Event1	0.9-1.2 (1.0)	0-50 (0)	1−20 (5)	0.3−2.0 (1.0)
2lay	0.6-1.5 (1.0)	0.05-1.0 (0.8)	Event2	1.1-1.3 (1.25)	0-50 (30)		
3lay	1.4-2.2 (1.8)	0.1-1.5 (0.6)	Event3	1.4-1.6 (1.5)	0-50 (45)		
4lay	3.0 (3.0)	-					

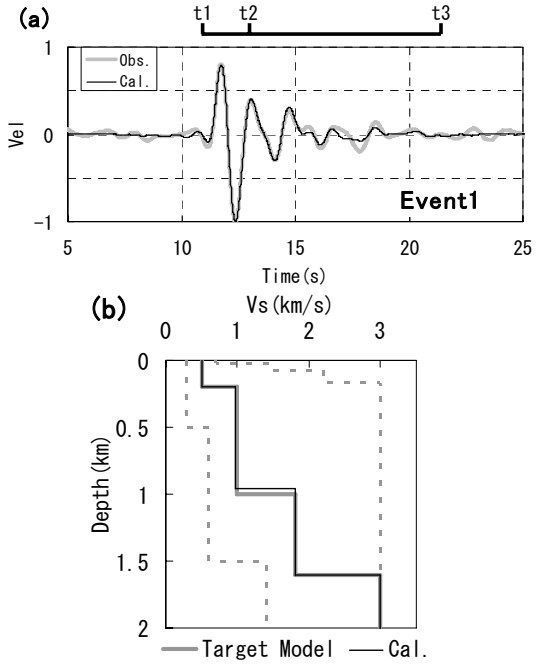

Figure 2 Comparisons between observed and synthetic waveforms for (a)Evnet1-1. Gray thick lines and black thin lines indicate observed and synthetic velocity waveforms, respectively. (b) Comparison between true and inverted models. A gray thick line and black thin line indicate true and inverted velocity structures, respectively. Gray broken lines indicate search areas in the inversion.

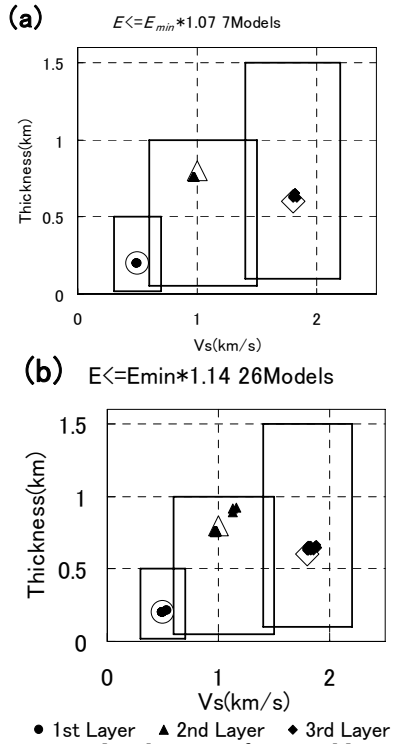

Figure 3 Parameter distributions of acceptable models for the inversions in numerical experiment for Model1. The threshold was set to be equal to the minimum (a) Emin*1.07, (b)Emin*1.14. Solid circles, triangles and lozenges indicate S-wave velocity and thickness of the first, second and third layers, respectively. .

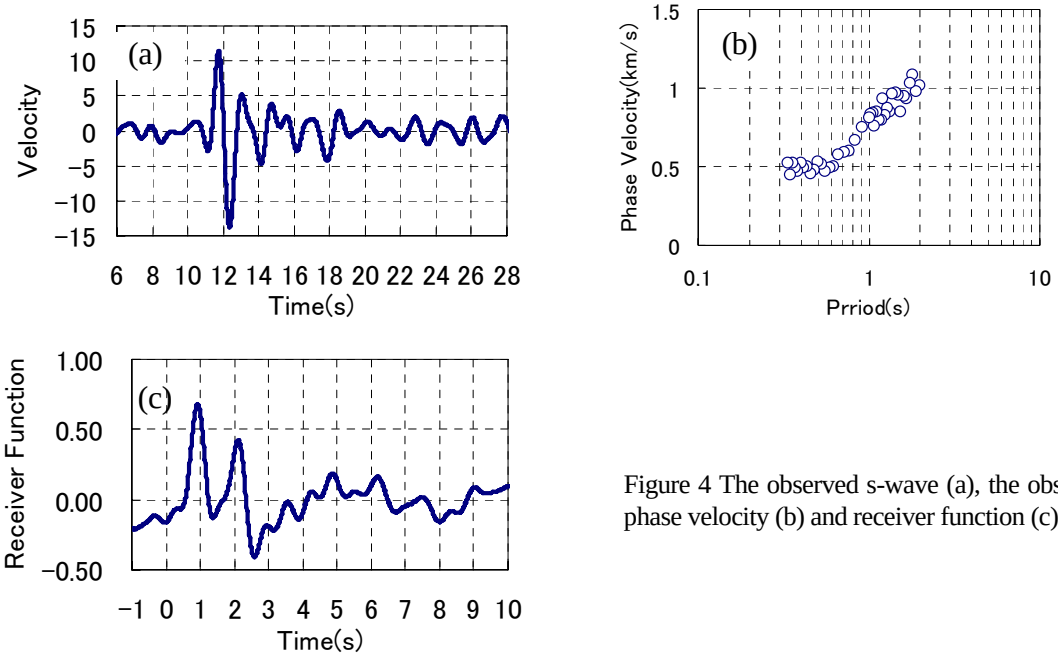

Figure 4 The observed s-wave (a), the observed phase velocity (b) and receiver function (c).

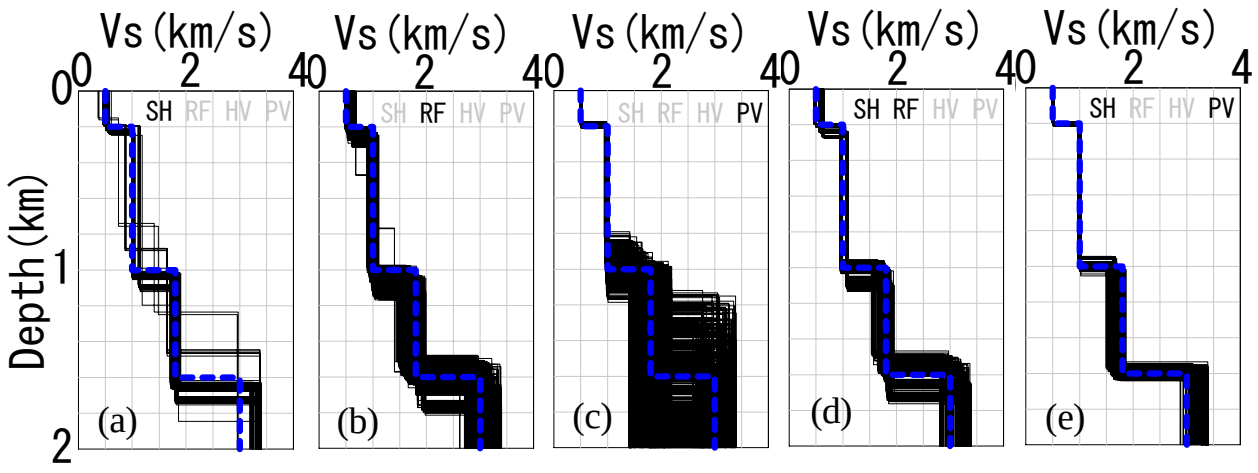

Figure 5 The s-wave velocity structure (a) S-wave (b) receiver function (c) phase velocity (d) s-wave and receiver function (e) s-wave and phase velocity. Blue lines indicate true model.

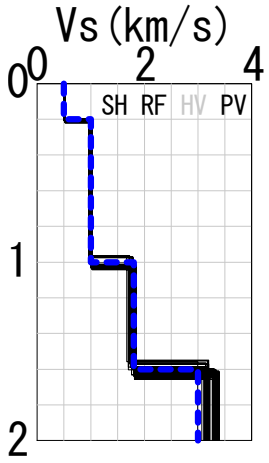

Figure 6 The s-wave velocity structure using all data. A blue lines indicates true model

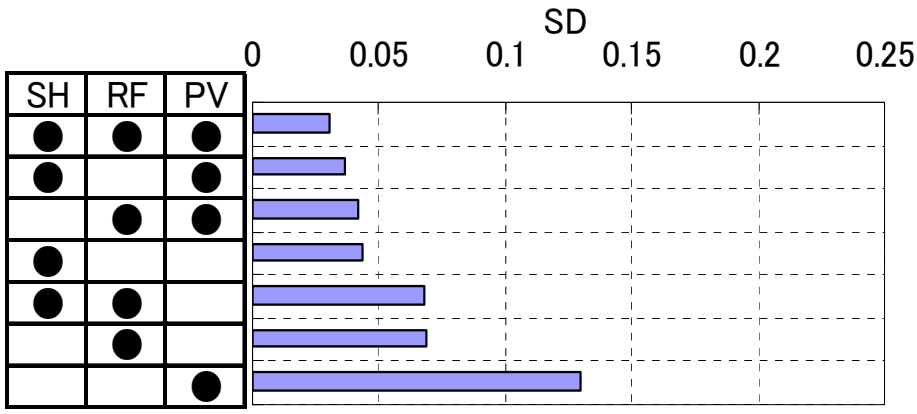

Figure 7 The averaged standard deviation of S-wave velocity and thickness. SH: S-wave data; RF: receiver function data; PV: phase velocity data

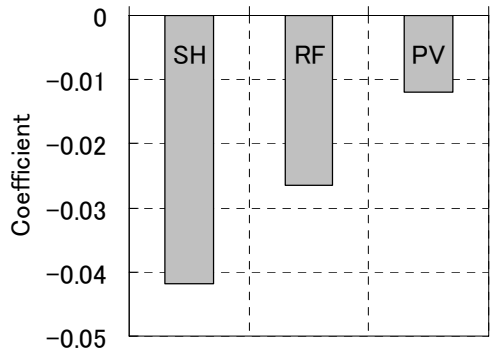

Figure 8 The coefficient of regression analysis

Sixth International Conference on Urban Earthquake Engineering
March 3-4, 2009, Tokyo Institute of Technology, Tokyo, Japan

ESTIMATION OF SPECTRAL AMPLIFICATION OF GROUND USING H/V SPECTRAL RATIO OF MICROTREMORS AND GEOMORPHOLOGICAL LAND CLASSIFICATION

Shigeki Senna[1], Saburoh Midorikawa[2], and Kazue Wakamatsu[3]

1) Researcher, National Research Institute for Earth Science and Disaster Prevention, Japan
2) Professor, Department of Built Environment, Tokyo Institute of Technology, Japan
3) Professor, Department of Civil and Environmental Engineering, Kanto-Gakuin University, Japan
senna@bosai.go.jp, s.midorik@enveng.titech.ac.jp,wakamatsu@kanto-gakuin.ac.jp

Abstract: This study aims to estimate the spectral amplification factor of ground from the H/V spectral ratio of microtremors. The empirical amplification factor is calculated from the ratio of the response spectrum of the record to that on the engineering bedrock obtained from the attenuation relationship, for the K-NET and KiK-net observation sites. The empirical amplification factor is compared with the H/V spectral ratio of microtremors at different geomorphologic conditions. The relationships for estimation of the spectral amplification factor from the H/V spectral ratio are proposed for three geomorphologic groups. For the 2007 Niigata-ken-chuetsu-oki earthquake, the proposed method is applied. The estimated spectra show good agreements with the observed ones, and the effectiveness of the method is confirmed.

1. INTRODUCTION

In order to estimate the distribution of earthquake damage, it is necessary to properly evaluate the distribution of earthquake motion, and hence it is important to evaluate the characteristics of ground at different sites. However, there are practical problems when systematically evaluating amplification characteristics of ground over wide areas, such as data sparseness and excessive labor required. For this reason, an existing practice is to estimate the amplification characteristics of ground from its relationship with geomorphological conditions and other elements that can be obtained from simpler information.

In this study, the spectral amplification factor is obtained as the ratio of the response spectrum from measurement records to that derived from the attenuation relationship on the engineering bedrock. The relationship between this quantity and the H/V spectral ratio of microtremors is considered for each geomorphological class, with the objective of deriving a relationship for obtaining the spectral amplification factor from the H/V spectral ratio of microtremors.

2. DATA

2.1 Source of strongmotion data

In this study, the spectral amplification factor is obtained as the ratio of the response spectrum on the land surface according to observation records to that on the engineering bedrock calculated using the attenuation relationship. The attenuation relationship of the response spectrum is based on Kanno et al. (2006), which is a recent research work. The observation records on the land surface used were obtained from May 1996 to December 2006 (in K-NET and KiK-net). Upon selecting the records, the following conditions were chosen so as to match those used by Kanno et al. (2006) when deriving the attenuation relationship, attempting to avoid the occurrence of nonlinear effects due to strong earthquake motion, thus achieving better correspondence with microtremor data: (1) Mw = 5.5 or more, (2) maximum acceleration of up to 100 gal, (3) distance from epicenter of less than 200 km, (4) at least 5 earthquake data per observation site.

2.2 Source of microtremor data

Microtremor records from K-NET observation sites lasting approximately 1 to 2 hours, spanning the period from July 2005 to November 2006 were obtained. As to KiK-net observation sites, the observation covered all 680 sites for at least 15 to 20 minutes during the period from July 2006 to August 2007. The measurements were made using a high-performance acceleration sensor (manufactured by Japan Aviation Electronics Industry, model JA-40GA04). For further details, refer to Senna et al. (2006) . Moreover, microtremor data were collected at 59 sites in order to complement the data in geomorphological classes for which K-NET and KiK-net observation sites do not exist or exist in insufficient numbers. Figure 1 shows the distribution of the observation data used; it can be seen that the observation sites are spread throughout Japan.

Table 1 Number of data observation sites for each geomorphological class

GEOM ID	Name of geomorphological class	Number of observation sites contained in earthquake data that can be evaluated through the attenuation relationship (K-net, KiK-net)	Number of observation sites using microtremors (This study)
1p	Mountain(Pre-Tertiary)	17	52
1t	Mountain (Tertiary)	5	26
2	Mountain footslope	13	37
3	Hill	10	53
4	Volcano	4	12
5	Volcanic footslope	19	39
6	Volcanic hill	3	10
7	Rocky strath terrace	3	10
8	Gravelly terrace	81	161
9	Terrace convered with volcanic ash soil	31	53
10	Valley bottom lowland	87	215
11	alluvial fan	35	77
12	Natural levee	8	14
13	Back marsh	20	50
14	Abandonced river channels	0	33
15	Delta and coastal lowland	31	56
16	Marine sand and gravel bars	21	54
17	Sand dune	7	10
18	Reclaimed land	5	20
19	Filled land	5	55
Total		405	1037

3. METHOD FOR CALCULATING THE H/V SPECTRAL RATIO OF MICROTREMORS AND SPECTRAL AMPLIFICATION FACTOR, AND COMPARISON OF RESULTS

3.1 Method for calculating microtremor data

The microtremor data were processed by selecting from observation records 10 segments with 81.92-second duration showing relatively good amplitude stability. For each segment, the Fourier spectrum and the H/V spectral ratio were obtained. The results were then averaged. The problems above are not significant when method binomial filter (Marchand and Marmet (1983)) is used, which is why this method was chosen to determine the H/V spectral ratio (number of items: 500).

3.2 Method for calculating the spectral amplification ratio

The spectral amplification ratio is calculated as follows. In the present research, the spectral amplification is defined as in equation (1), which is the ratio of the spectrum obtained from actually observed earthquake records to that on the engineering bedrock estimated using the attenuation relationship of the response spectrum, where the results of both records are expressed in logarithmic scale. The spectrum on the engineering bedrock is based on the formula used by Kanno et al. (2006)[1].

$$\log_{10} G_j(T) = \frac{\sum_{i=1}^{n} \left\{ \log_{10} O_{ij}(T) - \log_{10} P_{ij}(T) \right\}}{n} \quad (1)$$

where, $G_j(T)$ is the spectral amplification factor at observation site j, $O_{ij}(T)$ is the observed value at observation site j during earthquake i, $P_{ij}(T)$ is the estimated value on the engineering bedrock at observation site j for earthquake i, and n is the number of records from observation site j.

3.3 Comparison of the spectral amplification factor and the H/V spectral ratio

Figure 1 shows a comparison between the spectral amplification factor and the H/V spectral ratio for microtremors related to all 19 geomorphological classes of Table 1 except 'old river courses' (ID = 14), where the results for 30 sites are shown. A trend that can be inferred from this figure is that for 'mountainous areas' corresponding to detailed geomorphological class IDs 1p and 1t to 7, the H/V spectral ratio of microtremors is larger than the spectral amplification factor. In addition, in most cases the spectrum either has a flat shape or contains peaks with a short periodicity. For geomorphological class IDs from 8 to 11 corresponding to 'highlands', in most cases the H/V spectral ratio of microtremors approximately matches the spectral amplification factor. For geomorphological class IDs from 12 to 19 corresponding to 'lowlands', the compared values are approximately the same near the predominant period. However, in other periods the spectral amplification factor is larger. In many cases, the H/V spectral ratio shows a trough resulting in large differences especially at periods smaller than the predominant period. Thus, the relationship between the spectral amplification factor of microtremors and the H/V spectral ratio shows peculiarities depending on the geomorphological class. By considering and compensating such peculiarities one can expect to estimate the spectral amplification factor from the H/V spectral ratio of microtremors with relatively high accuracy.

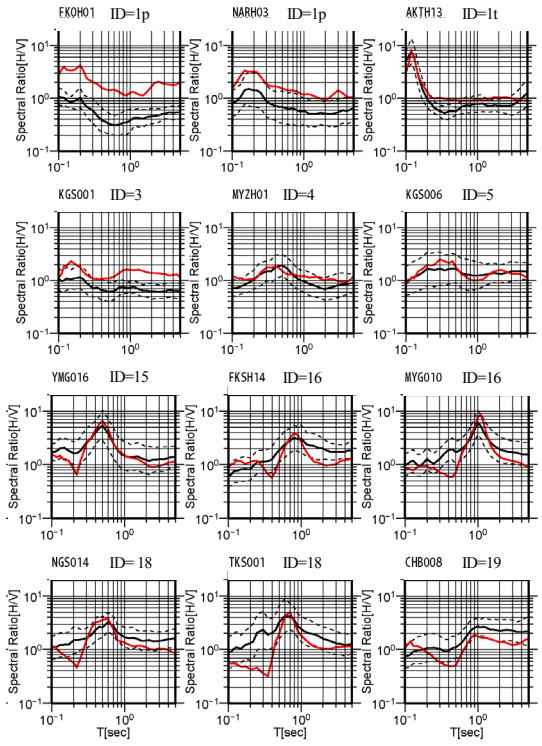

Figure 1 Comparison between spectral amplification factor and H/V spectral ratio of microtremors
Note: The captions on the graphs indicate observation site codes within K-NET and KiK-net (top) and the geomorphological ID

4. CONPENSATION COEFFICIENT OF THE H/V SPECTRAL RATIO OF MICROTREMORS FOR ESTIMATING THE SPECTRAL AMPLIFICATION FACTOR

Based on the results of the previous section, an analysis is carried out on the ratio of the H/V spectral ratio of microtremors to the spectral amplification factor for each geomorphological class, in order to estimate the spectral amplification factor from the H/V spectral ratio of microtremors. First, a global difference can be observed in both values, and the corresponding bias is eliminated. Then, trend differences between the region around the predominant period and other periods are corrected. Using equation (2), the average value a_j of the ratio of the spectral amplification factor $G_j(T)$ at observation point j to the H/V spectral ratio $HV_j(T)$ of microtremors is calculated for period values T_l from 0.1 to 2 seconds. The granularity q for period values is set to 25 points from 0.1 to 2.0 seconds similarly to Kanno et al. (2006).

$$a_j = \frac{\sum_{l=1}^{q} \frac{HV_j(T_l)}{G_j(T_l)}}{q} \qquad (2)$$

Moreover, observation values related to observation sites a_j belonging to the same geomorphological class k are averaged and defined as the average compensation factor α_k for geomorphological class k. Figure 2 shows the value of α_k for each geomorphological class, as well as its distribution.

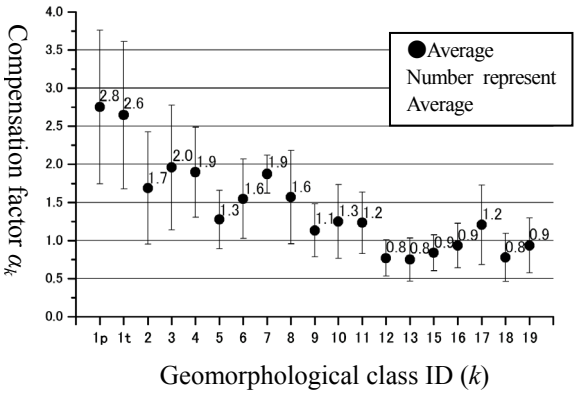

Figure 2 Relation between compensation factor α_k and geomorphological class k (there are no data available for geomorphological class ID = 14 (‘old river courses’))

To compensate for that effect as well, the spectral amplification factor at the observation site is compensated by α_k before calculating the ratio b_j (T/T_0) with respect to the H/V spectral ratio. Since the predominant period differs depending on the site, the value T/T_0 corresponding to period T normalized by the maximum period of microtremors T_0 is adopted as a parameter. The peak period T_0 corresponds to the maximum peak in the range of 1.0 to 2.0 seconds. Based on the shapes of peaks and troughs of the normalized H/V spectral ratio for different gemorphological classes, they are roughly classified into three groups: group A (geomorphological group for ‘mountainous areas’), group B (geomorphological group for ‘highlands’), and group C (geomorphological group for ‘lowlands’).
Considering the changes according to geomorphological groups and peak values of the H/V spectral ratio of microtremors, a model of the compensation factor is created in order to estimate the spectral amplification factor from the H/V spectral ratio of microtremors. The results of Figure 3 are modeled using a COS-type function. β_m is the compensation factor for observation sites belonging to geomorphological group m. The model was created so as to assume the value 1 for inputs up to 0.1, taking the minimum value for 0.4 and the maximum value for 1.0, then becoming 1 again for 2.0 and above. Therefore, the outputs for T/T_0 = 0.1, 0.4, 1.0 and 1.5 as well as the shape of the model were adjusted in order to approximate the one in Figure 3. Below are the basic functions (3-1 to 3-5) used in the model,
and the shapes generated by the compensating equations (Figure 4).

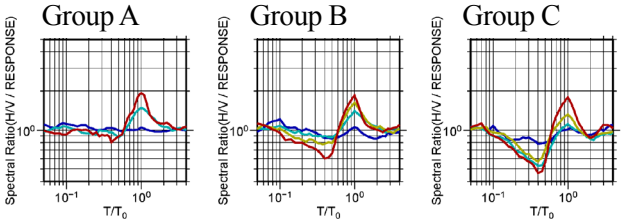

Figure 3 Average ratio of the H/V spectral ratio of microtremors to the spectral amplification factor corrected by α_k for each geomorphological group plotted on the T/T_0 axis (T normalized by the period T_0 corresponding to the peak of the H/V spectral ratio of microtremors)

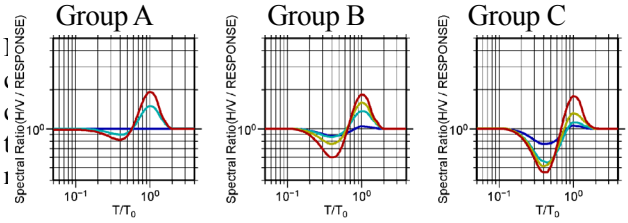

Figure 4 Shape of the compensation factor β_m for each group(modeling of Figure 7)

$$\beta_m(T/T_0) = c + d \cdot \cos(1.67\pi \cdot (T/T_0) + 0.95) \quad (0.1 \le T/T_0 < 0.4) \qquad (3-1)$$
$$\beta_m(T/T_0) = a + b \cdot \cos(3.33\pi \cdot (T/T_0) - 1.00) \quad (0.4 \le T/T_0 < 1.0) \qquad (3-2)$$
$$\beta_m(T/T_0) = e + f \cdot \cos(2\pi \cdot (T/T_0) + 6.0) \quad (1.0 \le T/T_0 < 1.5) \qquad (3-3)$$
$$\beta_m(T/T_0) = g + h \cdot \cos(\pi \cdot (T/T_0) + \pi) \quad (1.5 \le T/T_0 < 2.0) \qquad (3-4)$$
$$\beta_m(T/T_0) = 1.0 \quad (2.0 \le T/T_0) \qquad (3-5)$$

according to Matsuoka et al. (2005), and the compensating factor α_k used is 0.9, which is the one obtained as the global average for 'lowlands'. The results of the considerations in this section about compensation factors (α_k and β_k) are shown in Table 3.Using the results of the previous section, the response spectrum on the land surface is estimated according to Equation (4).

$$SA_s(T) = \frac{HV_j(T)}{\alpha_k \cdot \beta'_m(T)} \cdot SA_b(T) \qquad (4)$$

First, the H/V spectral ratio at the observation site HV_j(T) is compensated by dividing it by the compensation factor α_k related to each geomorphological class and by the compensation factor β_m (β'_m (T)) related to the geomorphological group. The response spectrum SA_S(T) on the land surface is obtained by multiplying the above result by the expected acceleration response spectrum SA_b(T) on the engineering bedrock. β'_m (T) corresponds to the value of (β_m (T/T_0)) when the period T_0 at the peak of the H/V spectral ratio is changed to T. As to the range where Equation (4) can be applied, little can be said because β'_m (T) has been modeled for T/T_0 ranging from 0.1 to 2.0, but it can be assumed that a reasonable range is up to 2 seconds due to the small influence of surface waves. Moreover, most H/V spectral ratios of microtremors used in the present research contain one large peak. Complex shapes having two large peaks or the like may need further consideration.

5. EXAMPLE APPLICATION TO THE 2007 NIIGATA-KEN-CHUETSU-OKI EARTHQUAKE

The response spectrum on the land surface for the Niigata-ken-chuetsu-oki earthquake which occurred on July 16, 2007 was calculated according to Equation (4) and the list of amplification factors. The calculated results were compared to the response spectra from observation records and the ones calculated based on the amplification factors on the engineering bedrock according to Kanno et al. (2006). Subject observation sites are located within 200 km from the epicenter and the obtained records are up to 100 gal, in accordance with the conditions of section 2.1. The total number of sites is 159. Figure 5 illustrates the expected positions of fault planes of the earthquake and the 159 observation sites of K-NET and KiK-net that fulfill the earthquake selection conditions of section 2.1.

Figure 6 shows examples of results. The red lines in the figure indicate acceleration response spectra of observed records. The blue lines are the results of the present research, and the black lines are the results obtained by Kanno et al. (2006). The results by Kanno et al. (2006) consist of smooth spectra in which the peaks of

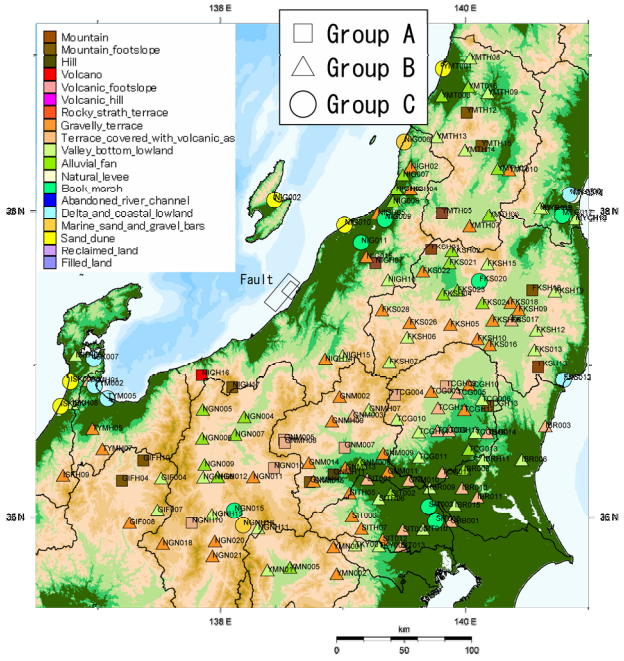

Figure 5 Distribution of fault planes and target observation sites (159) of the Niigata-ken-chuetsu-oki earthquake used in the calculations. The symbols in the figure indicate geomorphological groups A, B, and C, and the colors indicate geomorphological classes.

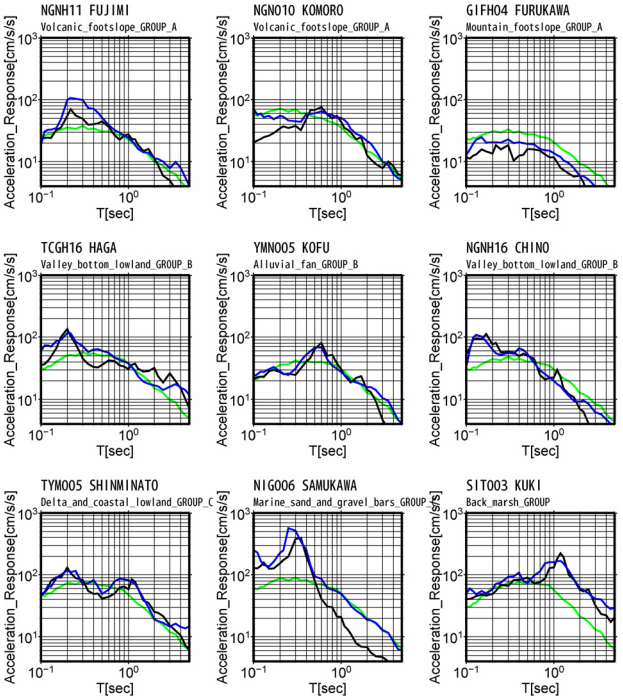

Figure 6 Comparison between predicted and measured acceleration response spectra (5% attenuation)(black line: observation results of the Niigata-ken-chuetsu-oki earthquake, blue line: results estimated by this study, green line: results estimated from AVS30 by Kanno et al. (2006))

the observation records do not appear. On the other hand, it can be seen that the results of the present research reflect the predominant peak related to the ground from the H/V spectral ratio of microtremors and contain the peaks existing in the observation records. Therefore, in many sites they show better correspondence with observation records.

In Figure 7, ●marks show the logarithmic standard deviation of the ratio of observed spectra to the spectra estimated in the present research, and ○ marks show the logarithmic standard deviation of the ratio of the observed spectra to the spectra estimated according to Kanno et al. (2006). The results of the present research have a smaller deviation with respect to observed data for periods of 0.15 seconds or more compared to the results by Kanno et al. (2006), indicating that a better accuracy has been achieved. It is worth noting that the logarithmic standard deviation of the results obtained in the present research ranges from 0.22 to 0.31, and these values cannot be considered small. However, the logarithmic standard deviation of the attenuation relationship on the engineering bedrock which was used in order to obtain the response spectrum is around 0.4 (Kanno et al. (2006)). Thus, a certain amount of error is already present upon evaluating the response spectrum on the engineering bedrock, which in turn prevents the final error from becoming smaller.

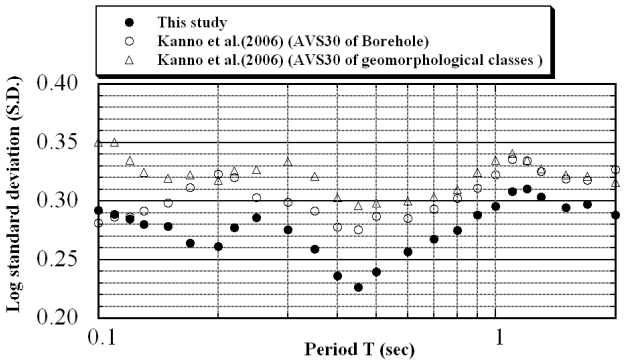

Figure 7 Standard deviation of the ratio of the logarithm of the observed to the estimated spectra of the Niigata-ken-chuetsu-oki earthquake (values estimated by the present research are represented by ● and those estimated according to Kanno et al. (2006) are represented by ○)

However, the logarithmic standard deviation of the attenuation relationship on the engineering bedrock which was used in order to obtain the response spectrum is around 0.4 (Kanno et al. (2006)). Thus, a certain amount of error is already present upon evaluating the response spectrum on the engineering bedrock, which in turn prevents the final error from becoming smaller.

6. CONCLUSIONS

With the objective of estimating the spectral amplification factor from the H/V spectral ratio of microtremors, the spectral amplification factor was obtained from the ratio of the response spectrum extracted from observation records to the response spectrum on the engineering bedrock derived from the attenuation relationship of the response spectrum according to Kanno et al. (2006). The relationship between this quantity and the H/V spectral ratio of microtremors was investigated. Using the results above, a relational formula was derived in order to estimate the spectral amplification factor from the H/V spectral ratio of microtremors for each geomorphological class. Using this relation, and taking into consideration the 2007 Niigata-ken-chuetsu-oki earthquake, the spectral amplification factor for each site was obtained from microtremor measurements and the geomorphological class. The response spectrum for each site was estimated by multiplying the obtained value by the response spectrum on the engineering bedrock estimated from the attenuation relationship. The estimated response spectrum fits well the observation records in many sites, reflecting the predominant period of the ground related to the H/V spectral ratio of microtremors and the spectral peaks seen in the observation records. Therefore, the effectiveness of the present method for estimating the response spectrum on the land surface was confirmed.

Acknowledgements:

In the present research, we made use of earthquake records, ground data and microtremor databases from the National Research Institute for Earth Science and Disaster Prevention, K-NET and KiK-net. We also received advice on the attenuation relationship of the response spectrum from Dr. Nobuyuki Morikawa of the Disaster Prevention Center of the National Research Institute for Earth Science and Disaster Prevention(NIED).

References:

Boore, D.M., W.B. Joyner and T.E. Fumal : Equations for Estimating Horizontal Response Spectra and Peak Ground Acceleration from Western North American Earthquakes : A Summary of Recent Work, Seism. Res. Lett., Vol.68, 1997, pp.154-179.

Kanno,T,A.Narita,N.Morikawa,H.Fujiwara,and Y.Fukushima: A New Attenuation Relation for Strong Ground Motion in Japan Based on Recorded Data, Bull. Seism. Soc. Am., Vol.96, 2006, pp.879-897.

Rodriguez, V. and S. Midorikawa : Comparison of Spectral Ratio Techniques for Estimation of Site Effects Using Earthquake Motions Recorded at Surface and in Boreholes, and Microtremor Data, Earthquake Engineering & Structural Dynamics, Vol.32, No.11, 2003, pp.1691-1714.

P.Marchand and L.Marmet : Binomial smoothing filter : A way to avoid some pitfalls of least-squares polynomial smoothing. Rev.Sci.Instrum, 1983, pp.1034-1041.

Sixth International Conference on Urban Earthquake Engineering
March 3-4, 2009, Tokyo Institute of Technology, Tokyo, Japan

SPATIAL SPECTRAL CHARACTERISTICS OF HIGH RESOLUTION SATELLITE IMAGE AT EACH GEOMORPHOLOGY FOR DETAILED GEOMORPHOLOGIC CLASSIFICATION MAPPING

Kazunori Ishii[1], Saburoh Midorikawa[2] and Hiroyuki Miura[3]

1) Graduate Student, Department of Built Environment, Tokyo Institute of Technology, Japan
2) Professor, Department of Built Environment, Tokyo Institute of Technology, Japan
3) Assistant Professor, Department of Built Environment, Tokyo Institute of Technology, Japan
kazishii@enveng.titech.ac.jp, smidorik@enveng.titech.ac.jp, hmiura@enveng.titech.ac.jp

Abstract: As a preliminary study for detailed mapping of geomorphologic classification, the spatial spectral characteristics of high-resolution satellite image at different geomorphology units are examined. The spectral decays of the power spectrum are computed from the digital number of the QuickBird image whose resolution is 0.7m by using 2D-FFT. The result shows that the spectral decay is different for each geomorphology and would be useful for detailed geomorphologic classification.

1. INTRODUCTION

In order to obtain a ground shake map due to a scenario earthquake, the distribution of site amplification factors is indispensable. The geomorphologic classification map whose mesh size is 1km has been used to compute the distribution of site amplification factors for the national seismic hazard map for Japan. The Central Disaster Prevention Council of Japan is encouraging detailed ground shake mapping with mesh size of 50m as an incentive to citizens' disaster mitigation actions such as seismic retrofit of their own houses.

The detailed mapping requires a high-resolution digital map of soil information such as geomorphologic classification. It is, however, a time and labor consuming task to create such a digital map from the existing analog maps. For detailed geomorphologic classification mapping, the correlation between geomorphology and land use pattern was examined [Ishii et al., 2007]. Since the land use pattern is closely related with land cover estimated from satellite image, primary detailed mapping was conducted by using the simple classification rules based on the characteristics of the satellite image and digital elevation model [Ishii et al., 2007].

In the previous study, however, only the characteristics of the digital number for each pixel of the image were used. In order to quantitatively evaluate the land use pattern in an urban area from the image, the size and density of buildings should be discussed. The spatial spectral characteristic of the image would be one of the powerful information to evaluate the land use pattern. In this study, the spatial spectral characteristics of high resolution satellite image at each geomorphology are examined to improve the estimation accuracy of the geomorphologic classification in the previous study.

2. CHARACTERISTIC OF TARGET AREA

2.1 Target area and data

The target area of this study is Tsurumi ward, Yokohama, Japan. Figure 1(a) shows the 250m-mesh geomorphologic classification map constructed by Wakamatsu et al. (2006). In the area, various geomorphologic units are distributed such as the terrace covered with volcanic ash soil (LT), the valley bottom lowland (VL), the natural levee (NL), the back marsh (BM), the abandoned river channel (FR), the delta and coastal lowland (D), the marine sand and gravel bars (SB), the filled land (LF) and the river bed. In order to examine the detailed geomorphology, the 50m mesh geomorphologic classification map is constructed from the old topographical map. Figure 1(b) shows the constructed 50m-mesh map.

Figure 1(c) shows the QuickBird image used in this study. The image was observed in May, 2007. The spatial resolution of the image is 0.7m. The image consists of 4 bands. The bands 1, 2 and 3 indicate blue, green and red bands, respectively. The band 4 indicates near infrared band.

Figure 1(d) shows the DEM in the target area constructed from airborne laser scanner data. The spatial resolution of the DEM is 1m. Figure 1(e) shows the land use map constructed by Geographical Survey Institute (2007). The spatial resolution of the data is 10m. Totally

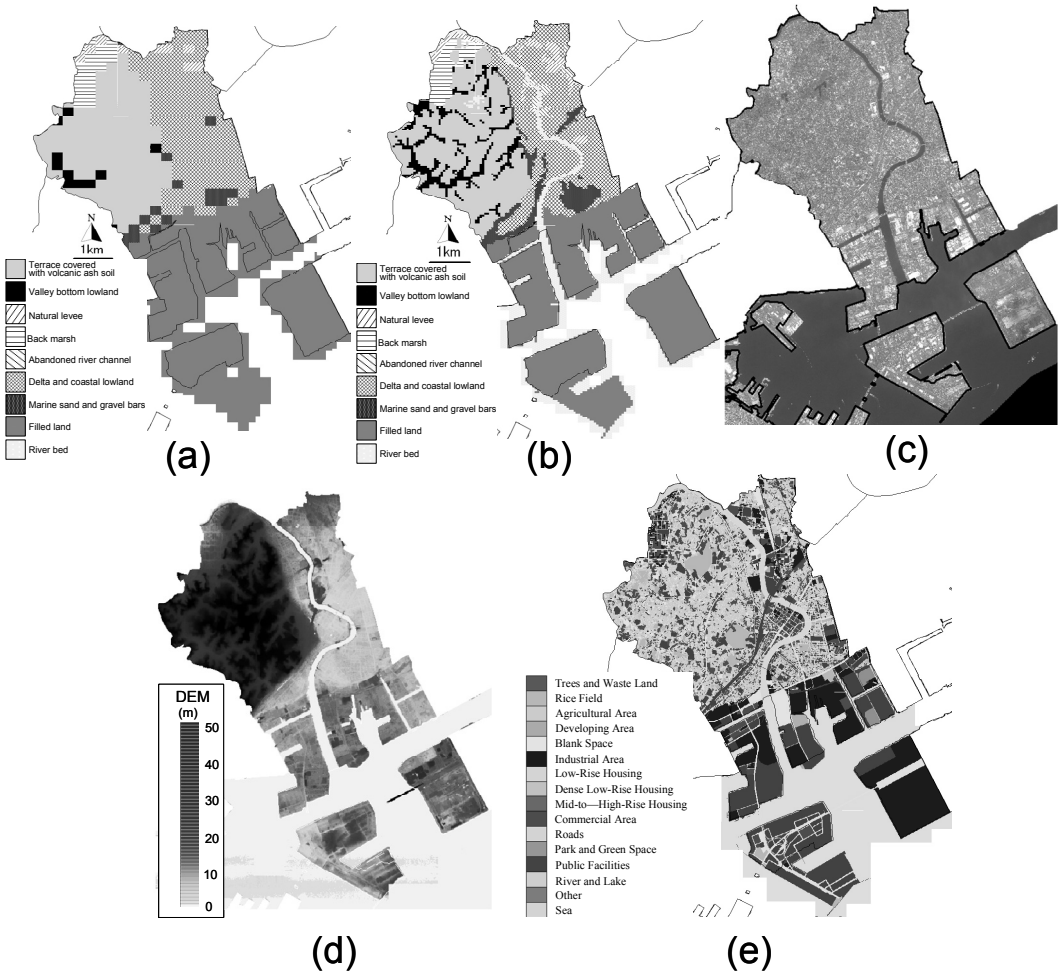

Figures 1 (a) 250m-mesh geomorphologic classification map, (b) Manually constructed 50m-mesh geomorphologic classification map, (c) Quick bird image, (d) DEM, (e) Land use map

13 land use units are distributed in the area.

2.2 Relationship between geomorphology and land use

In order to examine the relationship between the geomorphology and the land use, the number of meshes at each land use unit is aggregated for each geomorphologic unit. Figure 2 shows the area proportions of the land uses for each geomorphologic unit. The vegetated area corresponds to trees/wasteland, parks/green space or agricultural area.

In the terrace area such as LT and VL, the residential areas such as the low-rise housing and the mid-to-high-rise housing accounts for about 40% and the vegetated area accounts for 15 to 20%. The vegetated areas are mainly distributed in the boundary between the terrace and the lowland. Since the terrain of the boundary is steep slope and it is difficult to develop built-up area to the slope, the vegetations such as trees are remained in the boundary.

In the lowland area such as NL, FR and D, the area proportion of the vegetated areas is less than 5% because the built-up area is mainly developed in the lowlands. In NL, the area proportion of the low-rise housing is about 40%. It suggests that the low-rise buildings are densely distributed in the area. In BM and FR, the area proportions of the commercial and the public facilities areas is 30 to 50%. Because BM and FR had been easily inundated by floods, the residential areas have not been significantly developed in these geomorphologies.

D is covered with multiple land use units not only the low-rise housing but also the commercial and the industrial areas. In SB, the area proportions of the low-rise housing and the roads are 40% and 25%, respectively. Since LT is newly developed area, the area proportions of the industrial and the public facilities areas are about 80%.

The results indicate that the characteristics of the land use pattern are different at different site geomorphology. It suggests that there would be some correlation between the geomorphology and satellite images because the land use pattern would be closely related with satellite images. In the next chapter, the relationship between the high-resolution satellite image and the land use is examined.

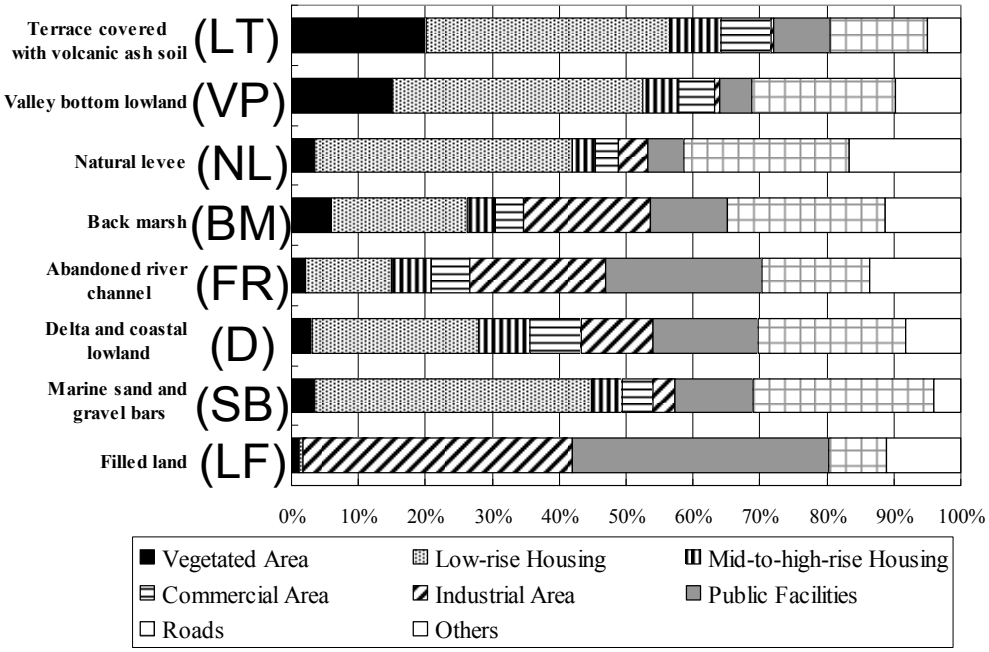

Figure 2 Area Proportions of Land Use for Each Geomorphology

3. SPATIAL SPECTRAL ANALYSIS

3.1 Analysis of 2D-FFT

In this study, the land use pattern is examined from the high-resolution satellite image. By analyzing the image in frequency domain, size and density of features such as buildings can be quantitatively evaluated. In this study, the two-dimensional Fourier transformation known as 2D-FFT (e.g., Kitagaki et al., 2003) is used to evaluate the spatial spectral characteristics of the image.

Figures 3 show the schematic diagram of 2D-FFT. Figure 3(a) and (b) show an example of the satellite image and the distribution of the digital number, respectively. In the 2D-FFT, the Fourier transformation is applied to the signal wave of the digital number for *x*-direction and *y*-direction. The equation of 2D-FFT is described as following equation (1);

$$F(u,v) = \int\int f(x,y) \cdot e^{-i2\pi(ux+vy)} dxdy \qquad (1)$$

Here, *f(x, y)* shows a value of digital number in the position (*x, y*) on an image. *F* (*u, v*) shows a result of the 2D-FFT where *u* and *v* are wave numbers along the *x* and *y* component, respectively.

Figure 3(c) shows the spatial spectrum of the image computed by Eq. (1). Horizontal and vertical axes indicate wave number for *u*-component and *v*-component, respectively. The brightness of the figure indicates the power spectrum of the image. The center origin of the figure represents the power spectrum for the lowest frequency.

In order to evaluate the spatial characteristics by an index, the relationship between the frequency of the image and the power spectrum are examined. The values of the power spectrum located in the same distance from the origin point are summed as shown in Fig. 3(d). Figure 3(e) shows the relationship between the wave length and the summed power spectrum. The vertical axis indicates the normalized power spectrum. The points shown in by arrows in Fig. 3(d) correspond to the points in Fig. 3(e). Because the minimum size of a building is almost 8m, the target wave length is from 80 to 8 m in this study.

3.2 Spectral decay

The suitable window size for the 2D-FFT analysis is examined. The candidate sizes of the window, 64 by 64, 128 by 128 and 256 by 256(pixels) are used because the target window size of the geomorphologic classification map is 50 by 50 m. In the result, the window size of 256 by 256 pixels (180m) seems more adequately to evaluate the land use pattern. Therefore, in this study, the image of 256 by 256 is used.

Figures 4(a) shows examples of images for low-rise housing area and industrial area. Figure 4(b) shows the comparison of the curves for the low-rise housing area with the industrial area. The spectral decays are computed from the curves by the least square method. In the low-rise housing area, small buildings are densely distributed.

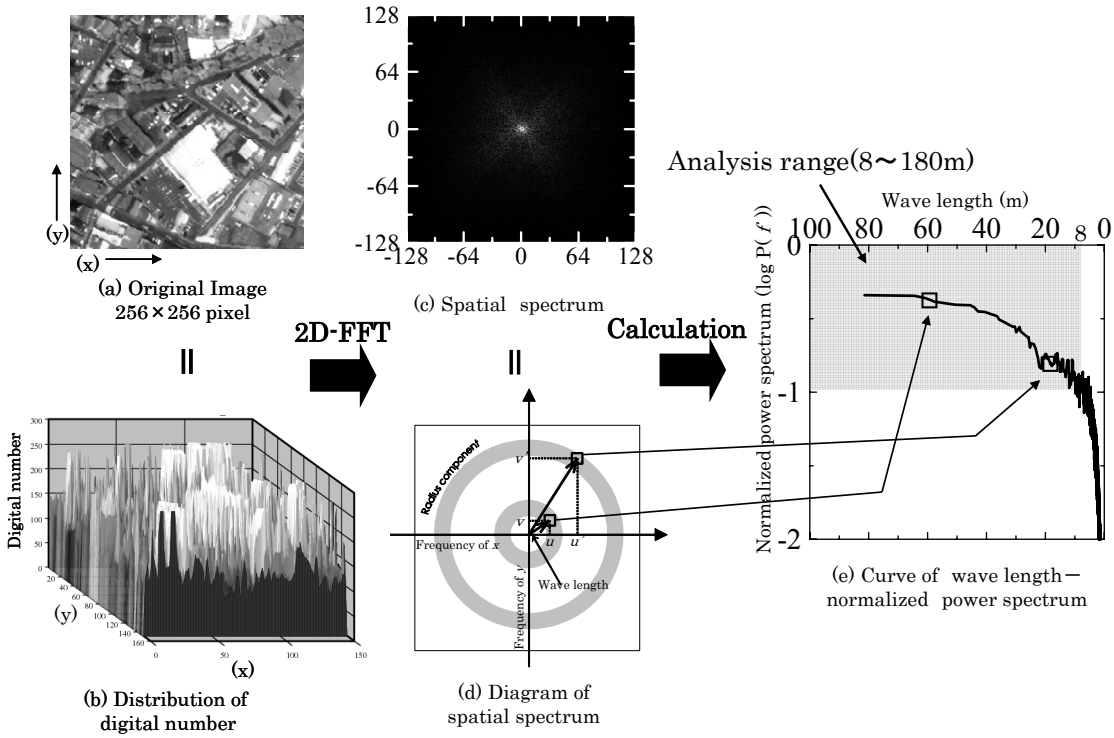

Figures 3 Schematic diagram of 2D-FFT

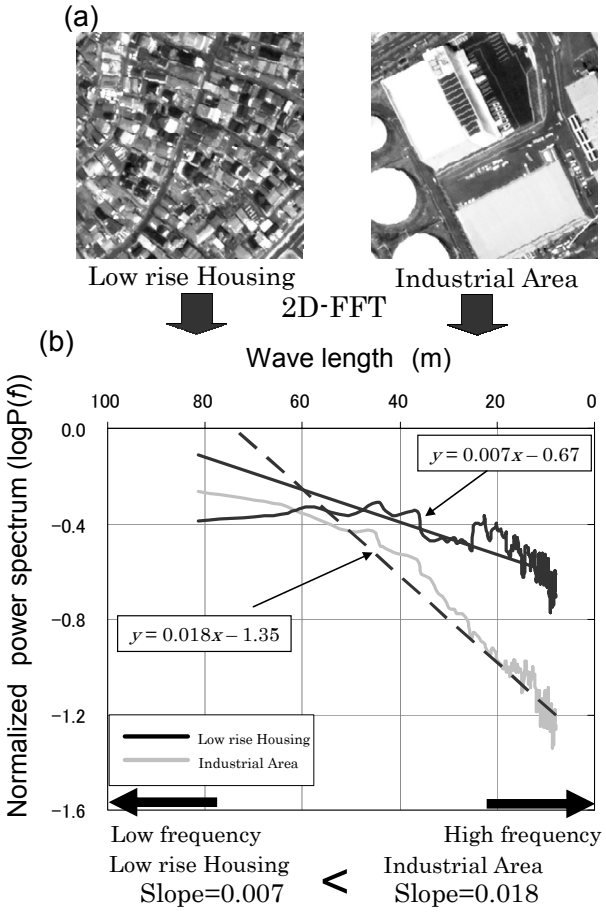

Figures 4 Schematic Diagram of evaluation of images by using 2DFFT

Because the distribution of the digital number for the dense small buildings is complicated, the higher frequency component would be predominant. On the other hand, the industrial area is covered with a large building. Because the digital numbers are almost constant in a large building, the lower frequency component would be predominant. The spectral decay of the industrial area is larger than that of the low-rise housing area because the lower frequency component is dominant in the industrial area. Then, the spectral decay computed by the 2D-FFT would be useful to evaluate the spatial spectral characteristics of the image.

4. RESULTS AND DISCUSSIONS

Figures 5 (a) and (b) show the distribution of the spectral decay computed from the band 1 and 4, respectively. Solid lines in the figures indicate the boundaries of the 50m-mesh geomorphologic classification map (see Fig. 1 (b)). Darker mesh indicates large spectral decay. In the previous study [Ishii et al., 2007], the geomorphologic classification was relatively inaccurate at the areas of (i) to (iv) shown by circles in Figs. 5. Therefore, this study focuses on the areas of (i) to (iv).

Figures 6 (a) and (b) show the relationship between the spectral decay and geomorphology. The vertical axis is the spectral decay. The horizontal axis is geomorphology. The diamonds and error bars are the averages and the standard deviations of the spectral decay for each geomorphology. The geomorphology units are

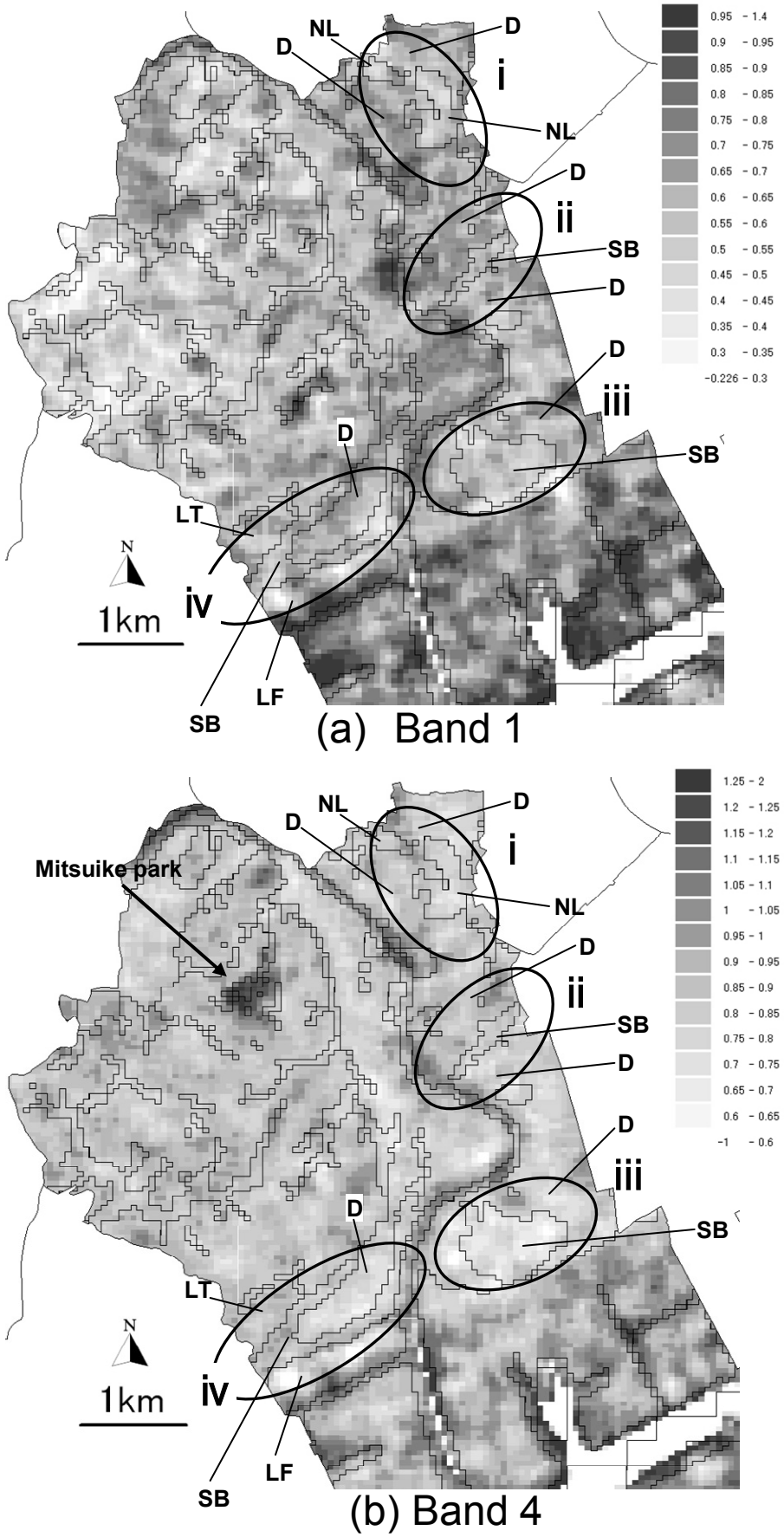

Figures 5 Distribution of spectral decay at Tsurumi ward
a: Spectral decay of band1, b: Spectral decay of band4

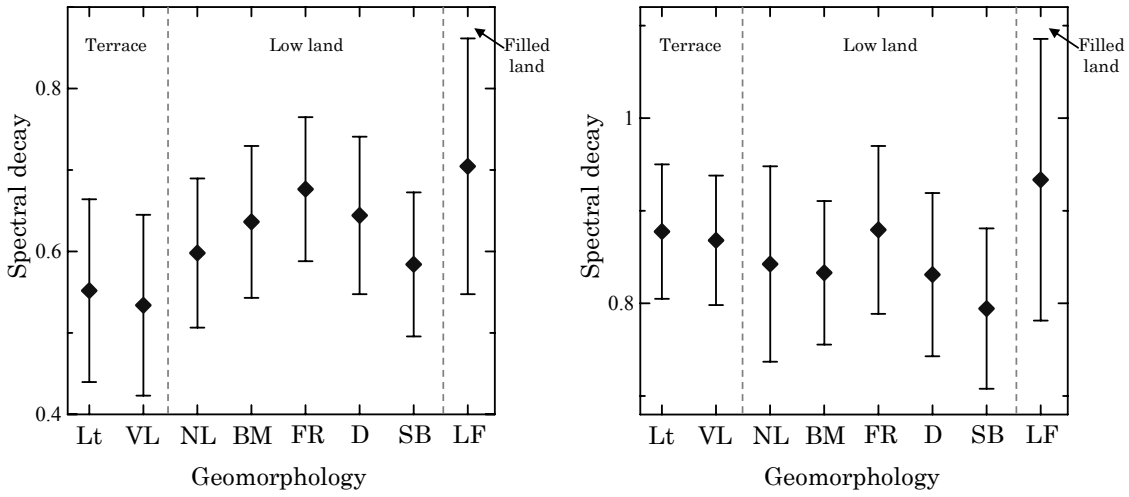

Lt:Terrace covered with volcanic ash soil, VL:Valley bottom lowland,
NL:Natural levee, BM:Back marsh, FR:Abandoned river channel,
D:Delta and coastal lowland, SB:Marine sand and gravel bars, LF:Filled land

Figure 6 Relationship between geomorphology and spectral decay

broadly classified into three categories such as terrace, low land and filled land.

The spectral decay of the band 1 is higher at LF than at other areas. A lot of lower frequency components are included in the geomorphology, suggesting that large buildings are distributed in this area. In fact, large-scale buildings such as industrial plant and public facilities are mainly distributed in LF as shown in Fig. 2.

In the area (i) in Fig. 5(a), NL is surrounded by D. In the areas (ii) and (iii), SB is surrounded by D. The spectral decay of NL and SB is smaller than that of D. As shown in Fig. 2, low-rise housing area is dominant in NL and SB while low-rise housing and public facilities are distributed in D. The difference of the spectral decay would reflect the difference of the land use patterns in each geomorphology.

On the contrary, in the area (iv), the difference of the spectral decay in each geomorphology such as SB, D, and LT is not clearly observed. Because the distribution of SB is complicated in the area, several land use patterns would be also complexly distributed.

For the band 4 shows in Fig. 5(b), the difference of the spectral decay between the geomorphologies in the areas of (i) to (iv) is not clear. Because the band 4 strongly reflects vegetation activity, the difference in the highly developed low land area would be small. As shown by arrow in Fig. 5(b), the spectral decay in densely vegetated area such as a large park (Mitsuike park) is higher than that in other area. On the other hand, the spectral decay of the band 4 in low-rise housing area such as the area (iii) is low because the density of the vegetation is small.

These results show that the spectral decay is strongly correlated with the land use patterns and is different in each geomorphology. By using the spectral decay computed the satellite image, the accuracy of the detailed geomorphologic classification mapping would be improved especially in the low land area.

5. CONCLUSIONS

As a preliminary study for detailed mapping of geomorphologic classification, the spatial spectral characteristics of the high-resolution satellite image at different geomorphology units are examined. The spectral decays of the power spectrum are computed from the digital number of the QuickBird image whose resolution is 0.7m by using 2D-FFT. The result shows that the spectral decay is different for each geomorphology and would be useful for detailed geomorphologic classification.

Acknowledgements:

This study was done as a part of "Development of Integrated Geo physical and Geological Information Database" supported by Special Coordination Funds Promoting Science and Technology of the Japanese Ministry of Education, Culture, Sports, Science and Technology.

References:

Geographical Survey Institute (2007), "Digital Map 5000 (Land Use) Metropolitan Area 2000" (in Japanese)

Ishii, K. Midorikawa, S. Miura, H. (2007), "Detailed Mapping of Engineering Geomorphologic Classification Using Digital Elevation Model and Satellite Image," *Journal of Social Safety Science*, No.9, pp. 121-129(in Japanese with English Abstract).

Kitagaki, R. Kanematsu, M. Noguchi, T. (2003), "Evaluation of Features of Color Distribution Related to Visual Impression of Architectural Cladding Surfaces by using 2DFFT," *6th Asian Design International Conference,* pp.24-27.

Wakamatsu, K., Matsuoka, M., and Hasegawa, K. (2006). GIS-Based Nationwide Hazard Zoning Using the Japan Engineering Geomorphologic classification map, *Proceedings of the 8th U.S National Conference on Earthquake Engineering*, Paper No. 849.

Sixth International Conference on Urban Earthquake Engineering
March 3-4, 2009, Tokyo Institute of Technology, Tokyo, Japan

REVIEW OF HISTORICAL EARTHQUAKES AND ITS DAMAGE ON RELIGIOUS ARCHITECTURE IN REPUBLIC OF TURKEY

Masahi Morita[1] and Saburoh Midorikawa[2]

1) Post-Doctoral Research Fellow, Center for Urban Earthquake Engineering, Tokyo Institute of Technology, Japan
2) Professor, Dept. of Built Environment, Tokyo Institute of Technology, Japan
mmorita@enveng.titech.ac.jp, smidorik@enveng.titech.ac.jp

Abstract: Destructive earthquakes have successively occurred in Republic of Turkey while the great number of cultural heritages remains there. To protect those heritages representing the regional culture and identity is as significant as to protect human lives and their properties from earthquakes. From this viewpoint, this paper reviews the earthquake activity and damages of religious buildings in Turkey. Since more than 150 earthquakes occurred in Turkey over the past century, its damage has became among the most enormous in the world. In this situation, the inventory survey on mosques and minarets in Kocaeli earthquake (1999) clearly shows the seismic vulnerability of minarets and masonry mosques in contrast to new RC mosques. Hereafter, we continue to collect this kind of detailed report more and to grasp the actual condition of earthquake damage in such historical buildings.

1. INTRODUCTION

Republic of Turkey has suffered from serious damage of many earthquakes from a long time ago because of the North Anatolian Fault (NAF), the East Anatolian Fault (EAF), both of which are one of the greatest active faults in the world, and the Western Turkey Graben Complex in the Aegean region. Recently, large earthquakes have struck in those areas in succession, like at Dinar (1 October 1995, Mw=6.4), Kocaeli (17 August 1999, Mw=7.6), Düzce (12 November 1999, Mw=7.2) and Bingöl (01 May 2003, Mw=6.4).

Turkey is, at the same time, also known as an intersecting place between eastern and western civilizations, hence diverse civilizations have been developed there due to the repetition of migration and settlement by a large number of ethnic groups. A lot of historical monuments as the evidences that such civilizations have left behind, for example, Hellenistic temples, Roman antiquities, Hittite remains, Early Christian churches and monasteries, Islamic religious buildings and so on, are existing at present. Historical monuments showing the past wisdom of mankind and historic cityscape created by those monuments are very precious cultural heritages for not only us but also the next generation.

Since Turkey is one of the world's most seismologically active counties as mentioned above, a lot of valuable cultural heritages are not divorced from seismic hazard. It goes without saying that a first priority on urban disaster protection and reduction against destructive earthquakes is to protect human lives and their properties. It is, however, also significant to protect those heritages which show a cultural identity in each region from earthquakes. That is, there is a need to construct an earthquake disaster protection and reduction system including conservation of cultural heritages and historic cityscape. For it, it is necessary to grasp the history of culture and disaster-affected status in this area. Considering damages, disaster protection and rehabilitation processes of cities having historical monuments enables to learn what has been lost and how this present situation has been produced. In addition, making use of findings obtained from such historical facts and lessons is contributory to establish a better disaster protection and reduction system with recognizing characteristics of the regional history and tradition.

This paper, as a starting point of a study from this viewpoint, reviews the earthquake activity and damages of religious buildings in Turkey with focusing on studies already done and reports on damage investigation in recent destructive earthquake.

2. EARTHQUAKE ACTIVITY AND DAMAGE IN TURKEY

2.1 Earthquake Damage in Turkey and Other Countries

Table 1 and Figure 1 show the number of earthquakes and fatalities and the total estimated damage (US$ million) in each country. Data were acquired from the “Significant Earthquake Database” in NOAA's National Geophysical Data Center (NGDC) for the time interval 1900 to 2008. Earthquakes contained in this database are that fit at least one of the following criteria: Moderate damage (approximately $1 million or more), 10 or more deaths,

Magnitude 7.5 or greater, Modified Mercalli Intensity X or greater, or the earthquake generated a tsunami. However estimated damages were converted into the price in 2008 with the "CPI Inflation Calculator" service provided by U.S. Bureau of Labor Statistics.

As shown Fig. 1, 10 countries including Turkey had more than 100 earthquakes meeting the criteria mentioned above. In Turkey, the number of earthquakes after 1900 was 154 that ranks 6th in the world. The total number of fatalities is about 98,000 that ranks 7th and the total estimated damage is more than US$25 billion that ranks 6th. Though the number of earthquakes and fatalities in Iran and Indonesia are more than ones in Turkey, the total estimated damage in those countries is below one in Turkey. Meanwhile, in the United States whose earthquake occurrence is almost equivalent to one of Turkey, the number of fatalities is remarkably few as 1,155 despite approximately US$80 billion of the total estimated damage. Only three countries, Japan, China and Italy, exceed Turkey in all 3 categories. Thus, Turkey ranks in high places in every category worldwide. Therefore, earthquakes cause much alarm for her.

Table 1 Number of Earthquakes, Fatalities and Estimated Damage

Country	EQ num.	Fatality	US$ mil.
China	286	646,538	150,537
Indonesia	224	196,119	4,610
Japan	206	123,940	203,431
Iran	181	176,312	16,449
United States	159	1,155	79,662
Turkey	154	97,546	25,098
Russia	116	2,063	17,261
Italy	115	120,603	65,735
Chile	102	32,111	9,103
Philippines	101	4,265	1,223
Peru	99	70,239	3,490
Greece	95	1,509	8,807
Mexico	92	12,015	8,486
India	68	63,768	5,620
Taiwan (China)	63	10,774	17,852

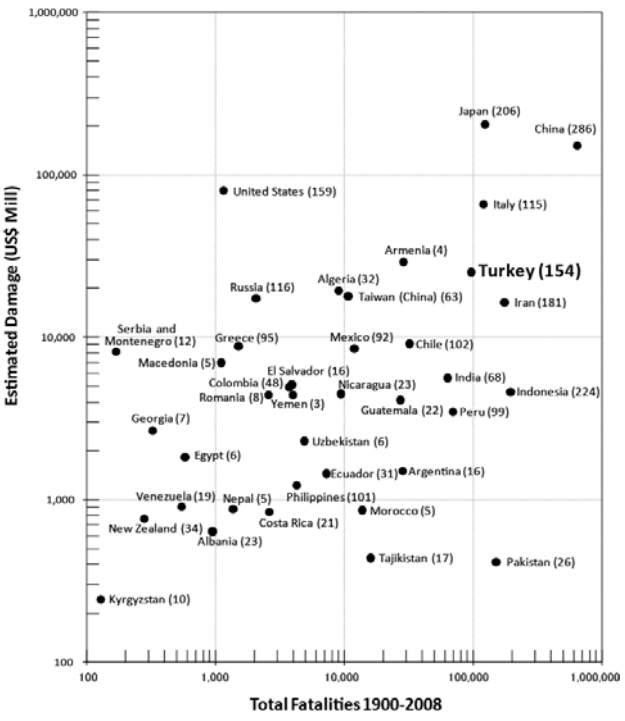

Figure 1 Fatalities and Estimated Damage in Earthquakes by Country

2.2 Historical Earthquakes in Turkey

For forecasting future earthquake occurrence and assessing seismic hazard, one of the effective approaches is to examine earthquakes already occurred in detail. A historical earthquake catalogue underlies this approach. Although there are several catalogues as to historical earthquakes in Turkey and neighboring countries, the newest catalogue compiling previous catalogues cyclopaedically was published last year (Tan et al. 2008). It contains 2284 earthquake records between 2100 B.C. and 1963 A.D. Based on this catalogue and by reference to the databases of ISC, USGS and Boğaziçi University Kandilli Observatory and Earthquake Research Institute (KOERI) for earthquakes after 1964, Figure 2 shows the distribution of the earthquakes with magnitudes greater than 5.5.

It is evident from Figure 2, 3 that many earthquakes occurred along the NAF and around the Sea of Marmara. As Dewey (1976) and Toksöz et al. (1979) indicated, the NAF

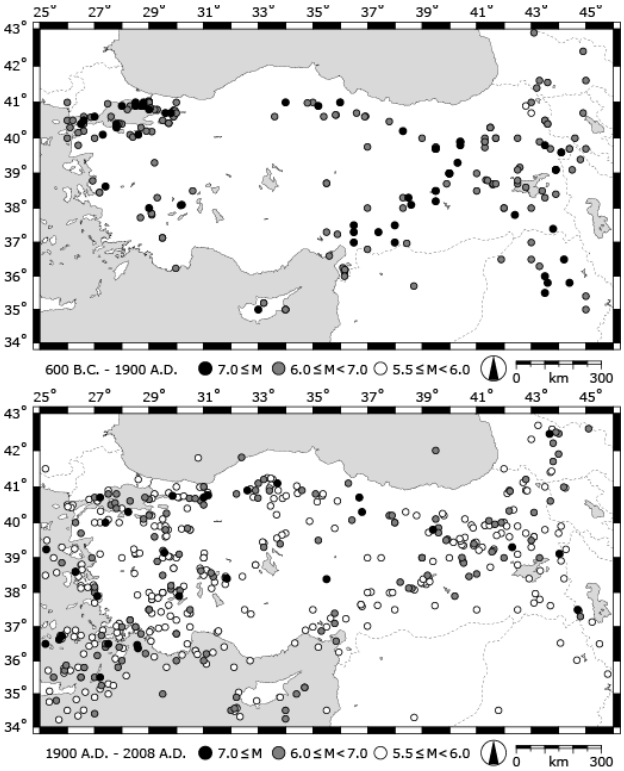

Figure 2 Seismicity Map of Turkey

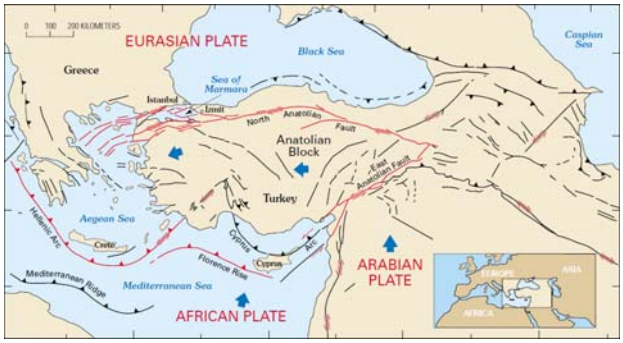

Figure 3 Tectonic Map of Turkey (after USGS 2000)

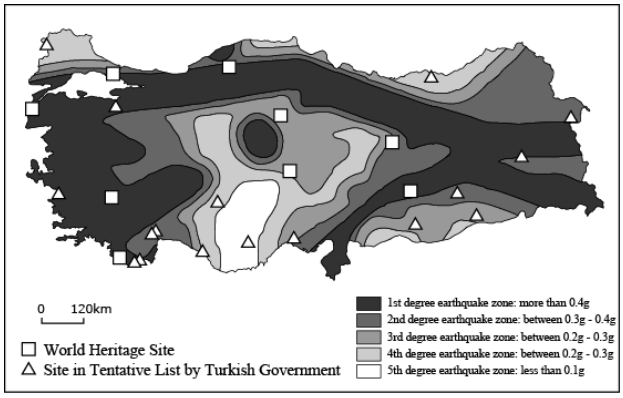

Figure 4 Location of Cultural Heritage Sites on Modified Earthquake Zoning Map of Turkey (Modified from Earthquake Research Department, Ministry of Public Works and Settlement, Turkey)

shows characteristic seismic activity that is the sequence of earthquakes with magnitude 6.8 and greater from the Erzincan earthquake (1939) to the Kocaeli and Düzce earthquakes (1999). Moreover, the epicenters of these earthquakes migrated from west to east over time. Focusing on this feature, many researchers have attempted to forecast future earthquake occurrence around NAF and Istanbul (e.g., Stein et al. 1997 and Yılmaz et al. 2004). According to the recent study (Parsons et al. 2000) with considering the influence of earthquakes in 1999, the probability of strong shaking (MMI >= VIII) around Istanbul and the sea of Marmara is estimated 62±15% within 30 years and 32±12% within 10 years from May 2000. On the other hand, it is also noteworthy that the earthquake (Mw=6.7) recurred at Erzincan in 1992 when about 50 years had passed since the previous earthquake.

In the southwestern part of Turkey, especially Aegean region, earthquakes with magnitude 7.0 and greater have occurred though not to the frequency of the NAF. A lot of earthquakes with magnitude 6.0 and greater also have been observed. Since Hellenistic civilization flourished around this region in ancient times, a large number of Greek Architecture now exist. Then, the population in this region is increasing with rapid development as a sightseeing area and summer resort for not only Turkish but also foreigners. Moreover, earthquakes with magnitude 6.0 and greater also continue intermittently to be recorded along the EAF from 600 B.C. Thus, these regions also require an adequate preparation for earthquake like Istanbul and areas around the NAF.

2.3 Location of Historical Sites

There are 9 World Heritage sites and 18 sites registered in the Tentative List for World Heritage by the Turkish government. Figure 4 shows the locations of those sites on the Seismic Zone map. 7 of 9 World Heritage sites are located within the zone 1 and 2. Including sites in the Tentative List, total 16 sites (about 59 %) are located within the zone 1 and 2. A great number of monuments other than cultural heritages shown here is dotted within the zone 1. For example, Erzurum, the largest city in eastern Turkey, has more than 50 buildings and traditional houses in the Seljuk and Ottoman period just inside the city. That is, it can be said that most cultural heritages are always exposed to great risk for collapsing by earthquakes.

3. REVIEW OF REPORTS ON DAMAGE INVESTIGATION ABOUT RELIGIOUS BUILDING IN RECENT DESTRUCTIVE EARTHQUAKES

Most of historical monuments in Turkey are religious buildings as same as in many countries. Above all, mosques are the most significant facilities since mosques even if they are old have been daily used until now and have been also newly constructed. In order to protect such buildings from earthquakes, a detailed damage investigation is important. However, what kind of survey was conducted and what was reported in fact? Here, we overview the contents of the reports by the Japanese investigation team as an example since we could not collect the investigation reports published within Turkey in this time.

The Japanese investigation team conducted inventory surveys and reported on total 59 mosques in Gölcük and Düzce in 1999 earthquakes (AIJ et al. 2001). According to this report, 48 of 59 mosques suffered moderate or less damage (Grade 1 & 2, Table 2). Most of these mosques are new RC construction after 1950's. Only 3 mosques totally collapsed. One of them is the oldest mosque (1912) among mosques surveyed and is solely of stone masonry. Its size, frame system and plan for further consideration are not reported while this mosque would have been a good example to think earthquake protection for older masonry mosques remaining in other cities. Contrary to mosques, 22 minarets were severely damaged (Grade 4 & 5). All of these damaged minarets are of RC or masonry. None of timber minarets were damaged. The same situation of damage was reported from the inventory survey on minarets in Adapazarı (Sudo et al. 1999). These show that a RC or masonry minaret is badly vulnerable to an earthquake. Since a minaret breaks at a base in many cases, it wreaks further damage to surrounding buildings. In fact, one mosque, the

Table 2 Damage of Mosques and Minaret in Kocaeli Earthquake (Modified from AIJ et al. 2001)

Gölcük		Mosque					
		1	2	3	4	5	T
Minaret	none	5	1		1		
	1	2	1				3
	2	1					1
	3	2	1			1	4
	4						0
	5	4	2	2			8
	Total	14	5	2	1	1	

Düzce		Mosque						
		1	2	3	4	5	D	T
Minaret	none		2					2
	1	10	1	1				12
	2	3	3					6
	3			2				2
	4		1					1
	5	2	6			1		9
	Demolish	1		1	1		1	4
	Total	16	13	4	1	1	1	

Bold number: Damage level accorgind to the EMS-98

none: Mosque without minaret

Demolish: Collapsed by the 17 August Earthquake, then demolished

dome of which was collapsed by the broken minaret, was recorded in the report mentioned above.

On the other hand, as for the Erzincan earthquake, the survey on the damage of mosques was conducted as a part of the inventory survey on buildings and then only 3 damaged mosques were reported with brief description (AIJ 1993). Conversely, it indicates that few mosques were damaged at that time. Since Erzincan experienced the catastrophic damage by the previous earthquake in 1939, the city itself was reconstructed. At the same time, the mosques founded in 14th and 16th century were totally collapsed. Therefore, RC mosques were rebuilt so that most of them seemed to avoid heavy damage. However, no damage buildings were also reported as to other common buildings. In the Bingöl earthquake (2003), it is unclear how many mosques were damaged as whole while some cases such as a collapse of minaret were individually reported (JSCE 2004). Furthermore, both reports don't contain the information such as size and plan of mosques. It is hard to think that the number of mosques is about that reported in Erzincan and Bingöl. Mosques also vary in size and form. A whole number of mosques, which is even an approximate number, and the damaged mosques' size should be shown as being done concerning to common buildings. It would enable advanced discussion as the reported mosque was whether a peculiar case or not.

4. CONCLUDING REMARKS

Over the past century, more than 150 earthquakes occurred in Turkey. Its damage is among the most enormous in the world. In this situation, detailed reports on earthquake damage will provide useful information for the different activities related to the safety of the historical monuments. In general, a damage investigation survey on common buildings is relatively done in detail. Compared with it, the information amount concerning to religious architecture is little in the reports of Erzincan earthquake and Bingöl earthquake. The report in the 1999 Kocaeli earthquake, on the other hand, clearly shows the seismic vulnerability of minarets and masonry mosques in contrast to new RC mosques. From now on, we try to accurately grasp the actual condition of earthquake damage in such historical buildings by collecting and weighing this kind of detailed report, especially ones published within Turkey.

Acknowledgements:

This study is supported by the Global COE Program "International Urban Earthquake Engineering Center for Mitigating Seismic Mega Risk" in Tokyo Institute of Technology supported by Japan Ministry of Education, Culture, Sport, Science, and Technology (MEXT).

References:

Architectural Institute of Japan (AIJ) (1993), "Report on the Damage Investigation of the 1992 Turkey Earthquake," Tokyo: AIJ

Architectural Institute of Japan (AIJ), Japan Society of Civil Engineers (JSCE), Japanese Geotechnical Society (JGS) (2001), "Report on the Damage Investigation of the 1999 Kocaeli Earthquake in Turkey," Tokyo: AIJ

Dewey, J. W. (1976), "Seismicity of Northern Anatolia," *Bulletin of the Seismological Society of America*, **66**, 843-868.

Japan Society of Civil Engineers (JSCE) (2004), "The Bingöl Earthquake of May 1, 2003" http://www.jsce.or.jp/report/19/report/report200307.pdf

Parsons, T., Toda, S., Stein, R. S., Barka, A. and Dieterich, J. H. (2000), "Heightened Odds of Large Earthquakes near Istanbul: An Interaction-Based Probability Calculation," *Science*, **Vol.288**, 661-665

Stein, R. S., Barka, A. and Dieterich, J. H. (1997), "Progressive Failure of the North Anatolian Fault Since 1939 by Earthquake Stress Triggering," *Geophysical Journal International*, **Vol.128**, 594-604.

Sudo, K., et al. (1999), "Preliminary Report on the 17 August 1999 Kocaeli Earthquake, Turkey," *Journal of Natural Disaster Science*, **Vol.21 No.2**, 65-85.

Tan, O., Tapırdamaz, M. C. and Yörük, A. (2008), "The Earthquake Catalogues for Turkey," *Turkish Journal of Earth Sciences*, **Vol.17**, 405-418. (First published online 28 December 2007)

Toksöz, M. N., Shakal, A. F. and Michael, A. J. (1979), "Space-time Migration of Earthquakes along the North Anatolian Fault Zone and Seismic Gaps," *Pure and Applied Geophysics*, **117**, 1258-1270.

U.S. Geological Survey (2000), "Implications for Earthquake Risk Reduction in the United States from the Kocaeli, Turkey, Earthquake of August 17, 1999," *U.S. Geological Survey Circular*, **1193**

Yılmaz, V., Erişoğlu, M. and Çelik, H. E. (2004), "Probabilistic Prediction of the Next Earthquake in the NAFZ (North Anatolian Fault Zone), Turkey," *Dogus University Journal*, **5(2)**, 243-250

Sixth International Conference on Urban Earthquake Engineering
March 3-4, 2009, Tokyo Institute of Technology, Tokyo, Japan

DEVELOPMENT OF BRAND-NEW PORTABLE EARTHQUAKE SIMULATOR USING HOLONOMIC OMNI-DIRECTIONAL PLATFORM

R.Yamaguchi[1)], M.Wang[2)], M.Matsudaira[3)], Y.Hirayama[4)], S.Midorikawa[5)], and S.Hirose[6)]

1) Ph.D candidate, Department of Mechanical and Aerospace Engineering, Tokyo Institute of Technology, Japan
2) Undergraduate Student, Department of Mechanical and Aerospace Engineering, Tokyo Institute of Technology, Japan
3) Technical Manager, Division of Mechatronics, Hakusan Corporation, Japan
4) Research Director, Division of Communication System, Hakusan Corporation, Japan
5) Professor, Department of Built Environment, Tokyo Institute of Technology, Japan
6) Professor, Department of Mechanical and Aerospace Engineering, Tokyo Institute of Technology, Japan
yamaguchi.r.ac@m.titech.ac.jp, ou.t.ab@m.titech.ac.jp, matsu@hakusan.co.jp,
hirayama@hakusan.co.jp, smidorik@enveng.titech.ac.jp, hirose@mes.titech.ac.jp

Abstract: We developed a portable earthquake simulator which can reproduce a waveform of a two-dimensional earthquake vibration using a holonomic omni-directional platform. By adopting a compact platform with large payload capacity, the simulator can be applied to applications for which vibration is felt by actually getting on top of the simulator in various places or for applications in vibration tests for larger structures.

1. INTRODUCTION

Devices to simulate and reproduce vibration of ground and floor surfaces of structures (hereinafter referred to as the "earthquake simulator") have been conventionally developed. Most of these devices adopt a platform driven by actuators attached to the ground or simple wheeled vehicle to make one directional vibration [1]. These are used in various applications such as enhancing awareness of disaster preparedness through experience of earthquake disaster simulations, and earthquake resistance tests and usability assessments for large and small facilities and structures.

However, to give real sensation to the mounted person, a large platform and its actuation mechanism with significant output power are required.

There is constant demand for compact and portable devices which can reproduce earthquake vibrations in unspecified places.

Accordingly, we developed a mobile and portable earthquake simulator by using a holonomic omni-directional platform with high payload.

2. CHARACTRISTICS OF EARTHQUARK AND OBJECTIVE OF THE DEVICE

The earthquake simulator addressed in this research has been developed with the objective of reproducing vibrations of ground or floor surfaces of structures by self-motion to the same scale and with satisfactory accuracy according to measured or forecasted data.

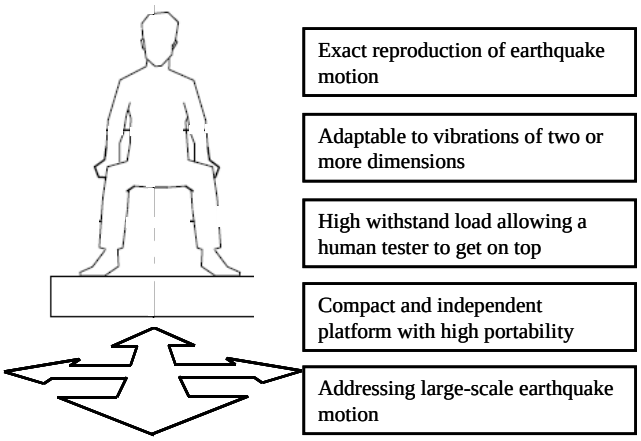

Figure 1 Concept of Vuton simulator

It has been designed to carry a person or a relatively large payload, as the objects to be placed on top, and it is put in motion through his/her own operation or the operation by a nearby operator (Figure 1).

The earthquake motion to be reproduced will be of a scale which allows a human to experience. It is our intention to contribute to disaster prevention efforts by allowing this device to respond to major earthquakes with an intensity of 6 or lower.

With regard to the earthquake motion which causes a great amount of damage, rough standards for the relationship between the characteristics of earthquake motion and the damage caused by the same are proposed, for example, on the National Research Institute for Earth Science and Disaster Prevention (NIED) website [2]. According to the results, the areas recording a maximum

acceleration of 8 m/sec^2 or more and a maximum velocity of 1 m/sec or more in earthquake motion can be defined as heavy damage areas.

In the meantime, it has been recently pointed out that the response of tower buildings in central areas of Tokyo, Nagoya and Osaka reaches a maximum acceleration of 2 to 7 m/sec^2 for a long period of approximately 2 to 5 sec, bringing the possibility of severe damage to those tower buildings when the Tokai, Tonankai and Nankai earthquakes occur [3]. Since the displacement of such vibrations extend to the order of meters, conventional devices with short motion range prove difficult in reproducing such vibrations for such areas.

Aside from the reproduction of earthquake motion actually observed, it is also assumed that this device enables simple and safe experiences of earthquake vibrations in the fields of education and public information as well as use as relates to the effects of comparative evaluation of seismic isolated structures. The reproduction of large displacements, such as the reproduction of vibrations of affected oil tanks during the Tokachi-oki Earthquake in 2003, should be brought into view.

Figure 2 presents a triaxial graph to show the relationships among acceleration, velocity, displacement and period. With period (sec) on the horizontal axis and velocity (m/sec) on the vertical axis, the upward-sloping line represents acceleration (m/s^2) and the downward-sloping line represents displacement (m). All of these are plotted on the logarithmic scale. In addition, positions corresponding to each of seismic intensity scale 1 to 7 are plotted (line I1 to I7) based on the relationships among the period, acceleration and seismic intensity (theoretical value) shown on the Japan Meteorological Agency [4] website. The bold line represents the measurable range of the accelerometer used in the strong-motion seismograph network of NIED. Although the movement range of the simulator as a target does not cover the heavy damage area or overall long-period vibration, the simulator enables reproduction of an intensity 6 upper for a period of one second and expression of displacements without limit.

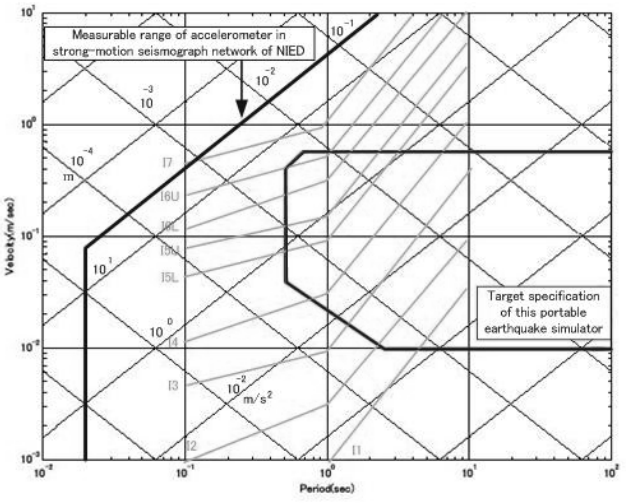

Figure 2 Triaxial graph shown in the target specification of simulator. The approximate relationships of seismic intensities of Japan Meteorological Agency (I1 to I7) are also shown .

Generally, basic mechanical performance can be discussed in terms of movement velocity, acceleration and response performance in addition to allowable load, in designing mobile machines. Therefore, we intend to set appropriate maximum velocity, maximum acceleration and reproduction frequency in consideration of earthquake areas plotted in Figure 2.

3. CHARACTRISTICS OF VUTON CRAWLER USED IN THIS DEVICE

Fig. 3 shows an overview of the Vuton crawler [6] [7], the basic element of holonomic omni-directional platform which is proposed as the earthquake simulator in this document.

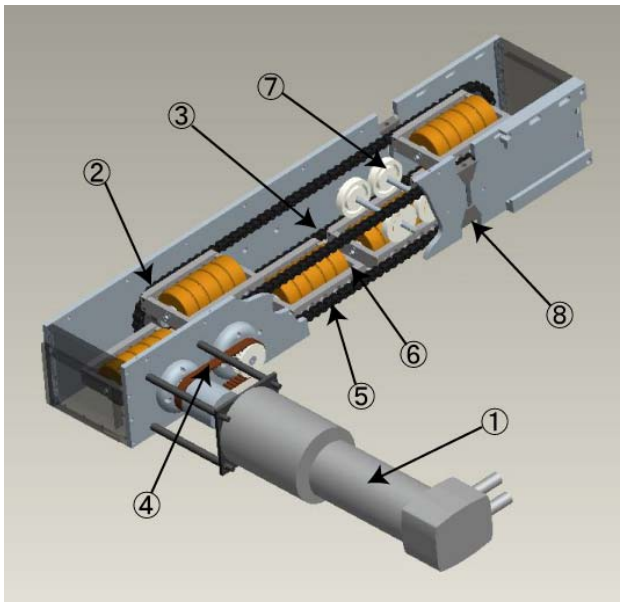

Figure 3 The Vuton crawler

The Vuton crawler is a platform to be driven by synchronization of chains (3) (5) in two rows with the geared motor (1), sprockets (2) and the belt (4). Multiple square frames (6) storing rubber wheels are connected to a pair of chains at its diagonal points with pins. When the chains rotate, rubber wheels contact the ground and produce thrusting motion to the direction of the chain. On the other hand, each rubber wheels can freely rotate around the axes and allow free locomotion to the perpendicular direction of the chain. As the squire frames (6) are supported by multiple guide rollers (7), the payload is effective supported. Wage (8) adjust the length of the chains,

By the above, the Vuton crawler functions as a driving

thruster in one direction and as a free rotating supporting base in its perpendicular direction. When three or more units of the Vuton crawler are located on the bottom of the device at different angles, thrust can be produced in any direction by performing proper coordination control.

Until now, several types of platforms such as the omni wheel [5] were proposed. Compared with these former omni-wheels as shown for example in Fig.4, the Vuton crawler has several advantages as shown below.

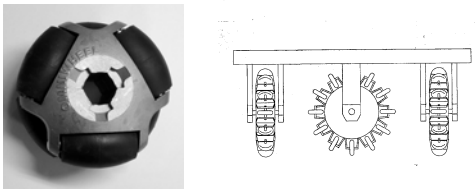

Figure 4 Example of omni-directional platform

1. A high payload is achieved. It is because multiple roller units always simultaneously contact the ground, and the roller units are always oriented horizontally with the effect of special chain driving mechanism and the roller shapes long cylindrical configuration, and thus the weight of the platform is evenly supported by the side of multiple cylinder-shaped rollers and making the rollers' ground contact areas large. Furthermore, the compactness of this device becomes a great advantage as an earthquake simulator which supports and drives a heavy object.
2. Contact pressure with a floor surface can be reduced with same reason of 1). This enables the device to have larger gripping force on the floor and it is advantageous to produce high lateral acceleration. It is also advantageous to reduce the damage of the floor surface on which the device is driven.
3. High transportability due to its low profile.

4. DESIGN OF JISHIN-THE-VUTON

We designed the earthquake simulator using Vuton crawler on which a person can mount on top of it and experiences earthquake vibrations. We named it as "Jishin-The-Vuton". Expected performance of the "Jishin-The-Vuton" is shown on the triaxial graph in Figure 2. Jishin-The-Vuton reproduces earthquake vibrations on a two-dimensional surface by controlling/driving internally mounting 4 sets of Vuton crawlers simultaneously (Figure 5). Jishin-The-Vuton can reproduce the planar X and Y directional translation motions and rotational motion around the vertical axis. However, to match the usual motion of the earthquakes, only X and Y directional translation motions are used. In this case, opposing Vuton crawlers are always generating motion with same velocity.

A design was conducted under conditions that the weight of a person getting on top of Jishin-The-Vuton is 80 (kg) and the power of the motor mounted on each crawler module is 400 (W). Other design values are as shown in Table 1.

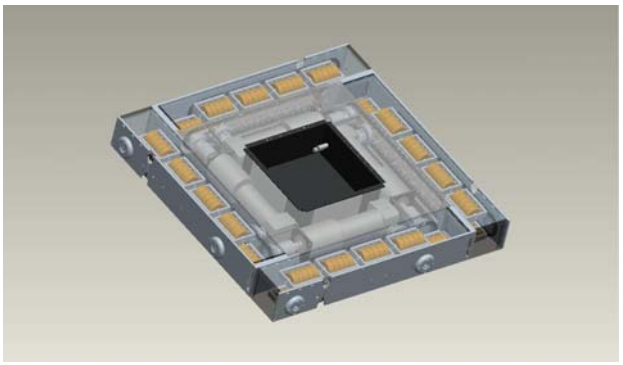

Figure 5 Crawler arrangement

Table 1 Design values of Jishin-The-Vuton

Items	Design value /Specification value	Remarks
Device dimensions	744 x 744 x 115 [mm]	Design values
Device weight	65 [kg]	Design values
Maximum motor torque	747[mNm]	Maxon EC60
Gear reduction ratio	13.7	Maxon GP31
Maximum motor speed	7000[RPM]	Maxon EC60
Sprocket diameter	30[mm]	Design values
Maximum running speed	1.23[m/sec]	According to the maximum motor rated speed
Maximum running acceleration	5.2[m/sec^2]	Theoretical value according to the maximum thrust of two crawlers

4.1 Setting of acceleration and velocity performance

Vuton crawler of the Jishin-The-Vuton drives a pair of chains by DC motor with reducer. The reduction ratio of the reducer should be judged by the trade-off between the realizable maximum velocity and the maximum acceleration.

In this design, the reduction ratio takes on a little larger value to allow the torque required for acceleration of the device itself and the load to be properly produced. Although the maximum velocity has to be lower, it was done as a result of considering that the magnitude of loss torque is evaluated.

Although the velocity is limited, the producible velocity still covers a substantial portion of the velocity area of the earthquake vibration which is regarded as causing heavy damage as shown in Figure 2.

4.2 Setting of frequency performance

The Jishin-The-Vuton adopts a system of realizing velocity or acceleration data of seismic waveforms given in advance by servo control, so the frequency range of realizable seismic waveforms virtually has no limitation on the long-period side. The long-period frequency generally tends to have large amplitude. However, since Jishin-The-Vuton is of a portable type, stroke has no

limitation and it is sufficiently possible to reproduce the long-period earthquake motion and vibration of high-rise buildings due to this.

On the other hand, the short-period side has limitations for backlash and rigidity of the crawler platform, the time constant of the motor itself, and performance of the drive amplifier, as is the case with other vibration exciters of other systems.

The Jishin-The-Vuton was designed with around 5 (Hz) as an immediate target to set. It is assumed that the grip performance reduction of the crawler on the floor surface and the expansion/contraction of the chain motor-driven platform of the crawler would be direct factors in reducing short-period reproduction performance. These influences become evaluation items after the manufacture of this device. However, it is assumed that electrical equipment such as the servo amplifier and motor can properly support this specification value.

4. DEVELOPMENT OF JISHIN-THE-VUTON

In consideration of the results of the design study described in the preceding section, an actual "Jishin-The-Vuton" is prototyped. Jishin-The-Vuton has nearly the same shape and is approximately 1.3 times as large as previous equipment as shown in Figure 6.

From the standpoint of performance, it can be driven in both the X-axis and Y-axis directions with one earthquake motion tester (assumed weight: 80 kg) placed on top.

The lead acid battery stored in the device is used as a driving power source. Two systems (one is a system in which an external AC power source is converted from AC to DC and incorporated and the other is a system to drive with an internal battery) are realizable depending on the operation mode. When either system is adopted, it is assumed that a commercial power source of AC 100V, which is generally available, is used as the power required for driving or charging.

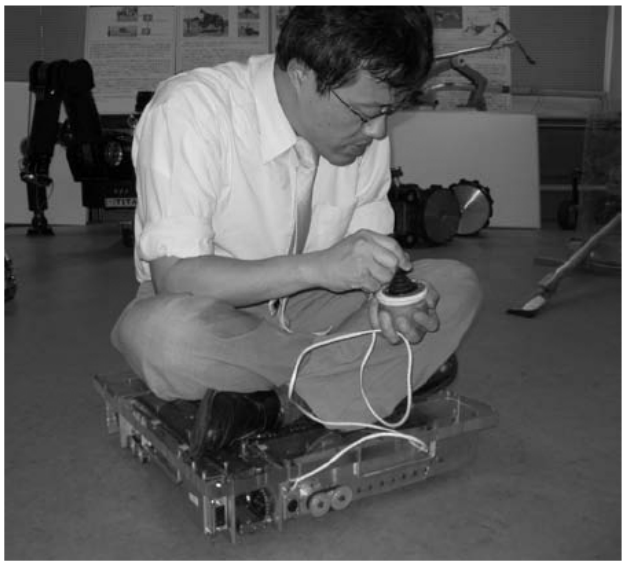

Figure 6 Vuton crawler test equipment

As a control device, a Windows PC is used. Seismic waves can be reproduced by transmitting motion data from a PC via serial communication (CAN bus) in real-time with a dedicated servo amplifier used for motor control.

Seismic wave data has the specification to read text files in CSV format which is made compatible with the commercial seismometer (SU-102; Hakusan Corporation). As a result, the seismic wave data measured in buildings, etc., can be reproduced as it is.

6. FUTURE DEVELOPMENT

A prototype device of Jishin-The-Vuton will be evaluated using the actual machine and the following items will be evaluated so that they are reflected in the next prototyping and product.

1. Grip performance limitation of the crawler on the floor surface, especially limit performance evaluation in high acceleration and short-period areas. Clarification of unconfirmed technical problems such as vibration.
2. Validation of device design. Study on better balance between velocity and acceleration, and sensory evaluation on reproduction performance of seismic waves by an actual occupant.
3. Validity of system design. Evaluation of user-friendliness of operation system and study on functions such as the settings required in the control system. Validation of the format of seismic wave data.

The specification and performance of this prototype were conducted with the absolute intention of experiencing seismic waves by one occupant. However, the platform of Jishin-The-Vuton can be applied to testing equipment which readily conducts vibration tests for large-load structures or compact equipment by contrast. Feasibility for commercialization will be sought including the above.

Furthermore, we intend to address the pattern of conducting earthquake reproduction tests with unlimited displacement for large structures by driving multiple units of Jishin-The-Vuton in synchronization, as a future challenge.

Figure 7 shows an image of 4 units of Jishin-The-Vuton which are used concurrently. At this time, the same seismic data will be reproduced if the movement of each device is translation only. However, if each device rotates around the vertical axis, arithmetic processing such as coordinate transformation will be individually required and the technology of synchronized operation involving communication between Jishin-The-Vuton units may also be required.

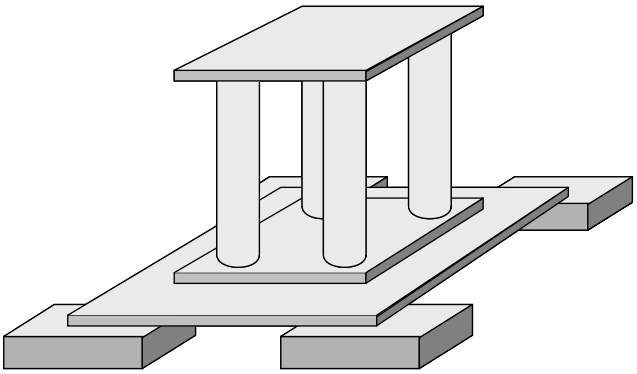

Figure 7 Concept of multiple collaboration of Jishin-The-Vutons

References:

[1] Website of Oyo Seismic Instrumentation Corp: "Jisoh- Bururu"
http://www.oyosi.co.jp/jisobururu.pdf

[2] Website of National Research Institute for Earth, Science and Disaster Prevention
Relationships among maximum acceleration, maximum velocity and seismic intensity
http://www.k-net.bosai.go.jp/k-net/topics/chuetsuoki20070716/pgav5v20070716.html

[3] Structural response and performance for long period seismic ground motions, Architectural Institute of Japan, 2007

[4] Website of the Japan Meteorological Agency: Relationships among period, acceleration and intensity (theoretical value)
http://www.seisvol.kishou.go.jp/eq/kyoshin/kaisetsu/comp.htm

[5] Website of Kornylak Corporation: "Omniwheel"
http://www.omniwheel.com/omniwheel/omniwheel.htm

[6] S.Hirose and S.Amano(1993), "The VUTON: High Payload, High Efficiency Holonomic Omni-Directional Vehicle," Proc. of the 6th Symp. On Robotics Research, pp.253-260, 1993.

[7] R.Damoto and S.Hirose(2002),"Development of Holonomic Omnidirectional Vehicle "Vuton-II" with Omni-Discs", Journal of Robotics and Mechatronics Vol.14, No.2, 186-192, 2002

Sixth International Conference on Urban Earthquake Engineering
March 3-4, 2009, Tokyo Institute of Technology, Tokyo, Japan

Review and Analysis of Seismic Damages of RC Frame Structures in Wenchuan Earthquake

Yingmin Li[1)], Jun Han[2)], Liping Liu[3)], Nina Zheng[2)], Liping Wang[2)], Jianwei Liu[2)], Qixiang Tian[4)], Yun Tang[4)]

1) Professor, College of Civil Engineering, Chongqing University, Chongqing, China
2) PhD candidate, College of Civil Engineering, Chongqing University, Chongqing, China
3) Associate Professor, College of Civil Engineering, Chongqing University, Chongqing, China
4) Postgradute, College of Civil Engineering, Chongqing University, Chongqing, China
liyingmin@cqu.edu.cn, hanjun009@126.com, liuliping@cqu.edu.cn

Abstract: Frame structures in the Wenchuan earthquake generally reach the goal of the current seismic code. Meanwhile, some typical damages to be conscientiously introspected also occur, which mainly conclude (1) the "strong column-weak beam" failure mechanism is rarely realized, (2) serious cracks and damages occur to the infill wall and the enclosure structure, (3) unreasonable plan configuration of infill wall leads to the torsional failure, (4) unreasonable elevational configuration of infill wall makes the ground floor as the weak story, (5) discontinuous arrangement of the infill wall along the story height leads to the damage of short columns, (6) stairs without seismic design are severely destroyed, and (7) severe damage occurs to the frame structure in the slope land. Based on the seismic damage phenomena mentioned above, this paper uses the elastic and plastic analysis to investigate the failure mechanism and the way to avoid them. At last, some design recommendations are provided, and the trend for further revision of the seismic code is suggested.

1 CHARACTERISTIC OF DAMAGE

5.12 Wenchuan earthquake is called "blood of the shaking table test" for the price of heavy casualties and huge financial losses. It caused severe damage and destruction to large number of buildings. It can be said that during this earthquake event buildings in different intensity areas with different completion ages and types have been subjected to a dynamic test. We must collect the earthquake disaster data and continue further research in time, from which we could learn some valuable experience and lessons, as what we did in the Tangshan earthquake. Wenchuan earthquake will be remembered as another milestone in the history of earthquake disaster prevention technology development of China. As the classic type of structure used in disaster area, frame structures generally showed better seismic performance in this earthquake and essentially reached seismic fortification goal (China Ministry of Construction 2001). Meanwhile, there are some typical damages need to be seriously investigated, which mainly includes:

(1) Frame structures meet the object of the seismic design code on a whole. Some structures are somewhat severely damaged but not collapsed in rare earthquake intensity areas, some are slight to moderate damaged or basically intact medium earthquake intensity areas and some are completely intact in small earthquake intensity areas (Fig.1).

Fig.1 Basically intact RC structures in Wenchuan earthquake

(2) The "strong column-weak beam" failure mechanism advocated in codes is rarely realized. Frame structures commonly appear column hinge and little beam hinge as shown in Fig. 2. Such damage pattern has shocked many researchers and engineers and motivated everyone to determine the reason that the beam-column hinge mechanism advocated by the code is not formed. Inspection of the effectiveness of the measures for strong column-weak beam specified in the current code and

Fig.2 Column plastic hinge mechanism of RC frame structure in Sichuan Wen chuan earthquake

research for the necessity and methods are problems that

need to be solved urgently.

(3) As the main partitions of frame structures, masonry infill walls have been seriously damaged in the Wenchuan earthquake, as shown in Fig. 3. There are following type of damages: 1) the infill wall serving as the first line of defense in the earthquake is suffered severe cracking and damage. Also, in the small and medium earthquake intensity areas, the damage of infill walls has caused serious damage and economic losses. This has become an important feature of the earthquake damage, how to control the damage level (maintenance degree) of infill wall under different seismic level has become an important topic; 2) Infill walls along the height with discontinuous layout may cause abrupt change in stiffness which may in turn form the weak layers at the bottom. As shown in Fig. 3(b), in the ground floor of the frame structure where no infill wall is

(a) (b)

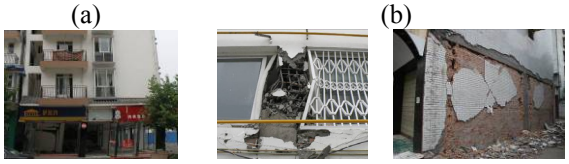

（c） (d) (e)

Fig.3 Damages resulted from the infill wall in Wenchuan Earthquake

configured, serious plastic hinge damage, which leads to the formation of layer lateral displacement mechanism, occurs at both ends of the columns with the story drift angle up to 1 / 12 as much. But the floors above the ground floor is intact; 3) Asymmetric layout of infill wall leads to a whole torsional damage. As shown in Fig. 3(c), on the street side the frame structure occupied as shops, few infill walls are configured while on the other side the back walls are fully covered. In this earthquake, severe eccentric and torsional damage occurred to the structure; 4) Short-column damage occurred to the frame columns restricted by the infill walls below windows (Fig. 3 (d)); 5) The oblique bracing effect of infill walls caused the additional shear at the column ends, aggravated the damage of columns (Fig. 3(e)).

(4)The stair was damaged severely, as shown in Fig. 4, which mainly consists of the rupture of the stair slabs, torsional failure of stair beams and damage of supporting columns due to short column effect. This is a typical damage of concern, mainly because of the lack of overall seismic design of stairs.

(a) (b) (c)

Fig.4 Damage of the stairs of the frame in the Earthquake

(5) Frame structures in slope land areas were damaged severely, as shown in Fig. 5, which mainly include the damage of shorter columns and pile columns (Fig. 5(a, b)) and the damage of the stilt floor (Fig. 5(c)).

（a） （b） （c）

Fig.5 Damage of frame structures in slope land areas during the Wenchuan earthquake

2. SEISMIC DAMAGE ANALYSIS

2.1 Strong column-weak beam failure mechanism analysis

To simulate the bending performance of columns with variable axial force and the descent segment of the structural response in an efficient way, the fiber model based on the flexibility method (Han et al. 2008) is used on Opensees (Silvia et al. 2006) platform, and the effects of slabs (including the slab bars), over-strength, and the redistribution of internal forces are taken into account in the analysis models. According to the code, several 6-storey regular frame structures in the different intensity regions are designed for nonlinear dynamic analysis and pushover analysis, to study the failure mechanism of the structures, and then they are compared with the damage phenomenon to verify the effectiveness of strong column-weak beam measures in seismic code. Finally, the minimum requirement which can achieve the failure mechanism of the main beam hinge that seismic code advocates is trial calculated and explored.

2.1.1 Example Design

According to the current seismic code six 3 × 2 span-6-storey frame structures for 6 to 9 degree region were designed under small earthquake according to the Class □ site, first zone (characteristic period as 0.35s). 3 spans in X direction (width = 6m), 2 spans in Y direction(width = 5m), The height is 3.9m for the ground floor, and 3.3m for others. The axial compression ratio of the bottom column and the story drift angle are controlled to meet the minimum requirement of seismic design code. The bars in the bottom of the beam were adjusted based on T-shaped section, and the bars in the top of the beam were adjusted based on double reinforcement section.

2.1.2 Nonlinear dynamic analysis results

For frame structures in all the intensity area mentioned above, four seismic waves are selected for dynamic time-history analysis, including three actual ground motion records selected using the dual-band method(Yang et al., 2000), and an artificial wave simulated using the ARMA model compatible with

response spectrum specified in code.

Fig. 6 gives the distribution of plastic hinge and rotation angles of the frame structures in all the intensity zone at the moment that some drift angle reaches its maximum with the artificial wave (statistically significant) input at rare earthquake level. As can be seen, in 6 degree region individual plastic hinge appears at the ends of frame beam, no column hinge appears; in 7 degree region, more column hinges and less beam hinges

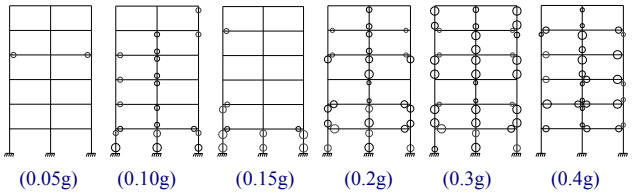

Fig.6 Plastic hinge distribution of frame for different seismic fortification intensity at the time reaching max. story drift angle

appear, and a clear lateral displacement mechanism is presented in ground floor; compared to 7 degree region, the hinge area of the frame in 8 degree region is more fully and more beam hinges appear. Column hinges are still predominant, and there are some clear lateral displacement mechanisms in the 2nd floor in 8 degree 0.2g area and in th 2nd ,4th and 6th floors in 8 degree 0.3g region; in 9 degree region, beam hinges are predominant in the frame structure (Tg =0.4s), which dissipate the majority of the seismic energy.

Figure 7 gives the average and the maximum of the story drift angle for all floors under the rare earthquake

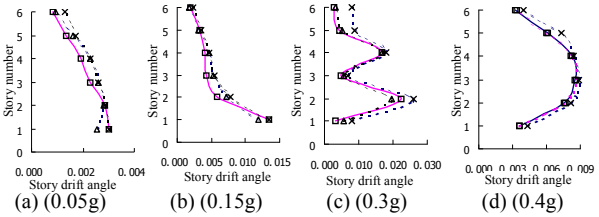

Fig.7 Average story drift angle curve of frame for different seismic fortification intensity by rare earthquake action max in the all time at the time of max story drift angle at the time of max top floor displacement

level at two moments that the vertex displacement and the drift angle of a certain floor reach their maxima. As is shown, except for 8 degree 0.3g, the largest story drift angle in other intensity zones did not exceed 0.02 as is regulated by the code. However, in 7 degree region the drift angle in the ground floor is considerably large, and the weak story appears there; the drift angle in 2nd and 4th floors in 8 degree region increase sharply which leads to the occurrence of weak stories. Note that this pattern of story drift angle is different from the story drift angle caused by Wenchuan earthquake in 7 degree region, earthquake force that the structure in Wenchuan earthquake suffered is larger than the one that the code forecast.

Fig. 8 gives frame column having the largest layer drift angle moment-curvature hysteretic curve under rare earthquake in all the intensity area (7 degree (0.15g), 8 degree (0.3g) as the examples). As can be seen from the chart, frame columns in 6 degree region are basically in the pre-yielding state; in 9 degree region the frame columns obviously entered the yielding state, curvature ductility demand is about 4.5, the bearing capacity does not decrease significantly after yielding, the overall ductility is good; in 7- and 8-degree regions frame columns under a major earthquake pulse are apparently pulsed into yielding, the bearing capacity declines significantly after yielding. And weak stories are easy to appear, overall ductility is poor. Therefore, frame columns in 7 and 8 degree regions are easy to result in ductile failure under strong earthquake.

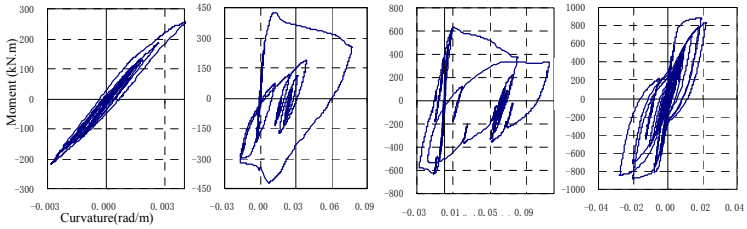

Fig.8 Moment-Curvature curve of frame column with max. story drift angle for different seismic fortification intensity by rare earthquake action

Therefore, the earthquake force in 6 degree region is weak and the earthquake force has no controlling effect, the seismic behavior of the frame structures will satisfactory. In 9 degree region, with the capability measures the seismic grade 1 frame structures will also

Table1 Measures of avoiding column hinge mechanism

Measures	Limit value (7degree)	Limit value (8degree)
Increasing coefficient of strong column-weak beam (α)	α =2.0	α =1.8
Decreasing the axial compression ratio (β)	α =0.65 β =1.6	α =0.65 β =1.4
Increasing the designed seismic force (F)	0.6F	0.5F

behave well in rare earthquake. But in 7 and 8 degree regions, because of the request of axial compression ratio and strong column-weak beam coefficient are relaxed, the lateral displacement mechanism, usually appearing as column hinges, are easy to occur. And the structural ductility is weak, which is easily failed in rare earthquake, which is consistent with the phenomenon in the 7 degree regions in Wenchuan Earthquake.

Using the measures in Table 1 to improve the seismic performance in predictive rare earthquake may avoid column hinges: 1) to assure none or few column hinges occur at the same axial compression ratio, the strong column-weak beam coefficient must be highly

increased;

2) more strict axial compression ratio and strong column-weak beam coefficient are to be specified;

3) the small earthquake design seismic force for the frame structures in 7 and 8 degree regions should be increased, which means the decrement of reduction factor of seismic force, some plans such as "mid earthquake force-mid ductility" in low danger earthquake region of the IBC2006 code can be adopted.

2.2. The effect the infill wall on seismic behavior of Frame Structures

Based on the elastic analysis, static nonlinear analysis (ATC1996, Chopra 1999) and nonlinear dynamic analysis are applied to the frame structures which are designed according to the current Chinese seismic codes, the effects of infill walls on the internal force, stiffness and deformation of the frame structures are studied, especially in the strong earthquake.

Fig. 9 gives analysis of models M1-M3, which are designed under Fortification Intensity of 7 degree, site class of II, third frame Anti-Seismic Grade,

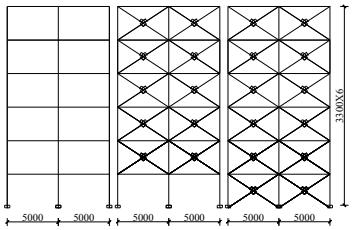

（a）M1 （b）M2 （c）M3

Fig.9 Analysis models M1-M3

Table 2 The types of infill wall

model	M2-or M3-		
	1	2	3
Type of the infill wall	100mm hollow brick (MU2.5+M 2.5)	100claybrick （MU5+M5） 200hollowbrick （MU2.5+M2.5 ）	200clay brickwall （MU10+M2.5） 200 hollow brick （MU5+M5）

first classification of designed earthquake. M1 is designed with no infill walls. M2 is designed with infill walls except the ground floor. M3 is full of infill walls.

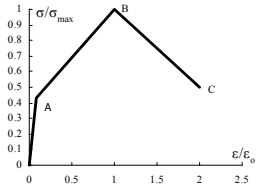

Fig.10 σ - ε curve of the infill wall

Table 2 gives the types of infill wall of different materials. The software SAP2000 Version 11 is used for analysis. Equivalent compression strut model is used to simulate the infill wall. Fig. 10 gives the nonlinear hysteretic curve of equivalent compression strut. The stiffness of First Polygonal Line (O-A) is adopted in the elastic analysis.

2.2.1 Effect on the natural period

The infill wall will greatly affect the global stiffness of the frame and shorten the natural period. To consider the effect of infill walls, a stiffness reduction factor（0.6-0.7）is suggested in the current seismic design code of China. However, such a roughly estimated factor cannot reflected the whole situation. By changing lateral stiffness ratio between the infill wall and the frame structure (calculated according to the initial elastic stiffness), the n_k- Ψ_T curve is shown in Fig. 11. It is obvious that when n_k >2 , Ψ_T <0.60, when n_k is between 4 and 9(T. Paulay et al., 1992), Ψ_T is between 0.4 and 0.5, which is obviously smaller than that in the code.

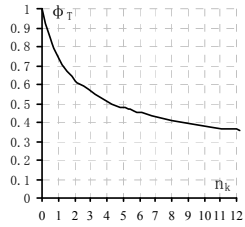

Fig.11 the effect to T caused by change of K on every floor

2.2.2 Effect on the internal force of the frame

In the figure 12, the axial and shear force of all models at performance point under frequent earthquake are shown (the corresponding results for moment which

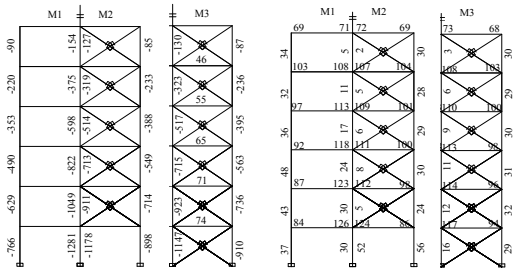

（a）axial force （b） shear force

Fig.12 Internal force analysis of model1-3(α max=0.08)

are the same as shear force are not provided here). It is obvious that if infill walls are taken into account, below conclusions can be drawn: bending effect of the structure will be more evident; overturning moment are partially caused by the tensile and compressive force of columns. When the frame structure is full of infill walls, a considerable earthquake force will be imposed on infill walls, thus the internal force of frame part will be decreased. In this case, the seismic capacity of structure will benefit from the infill walls. But for the frame structure with infill walls in higher floors except for the ground floor, the effect of infill walls is negative.

2.2.3 Effect on the deformation

Fig. 13 gives the story drift angle of all the models at the different seismic performance points. As is seen, mode M3 keeps the story drift at lowest level. The story

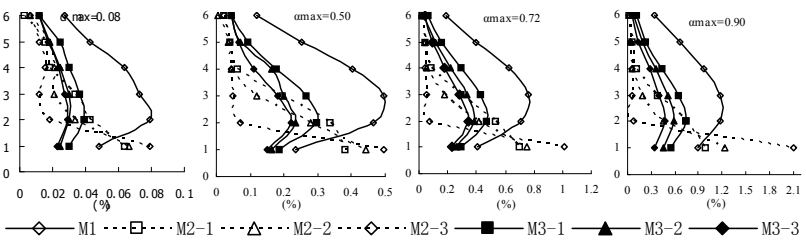

Fig.13 Story drift angle of model M1-M3 (α max=0.08,0.5,0.72,0.90)

drift in the ground floor of M2 dramatically increases when α max>0.72. Therfore, the seismic capacity of model M2 is poorer than M1.

2.2.4 Effect on the distribution of the plastic hinges

Figs. 14-16 show the distribution of plastic hinges at different earthquake levels and performance points. It shows:

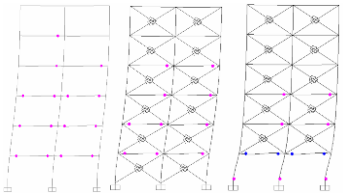

Fig.14 Plastic hinges (α max=0.50)

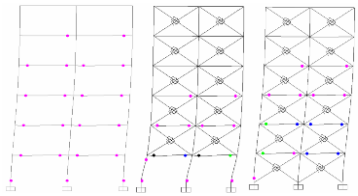

Fig.15 Plastic hinges (α max=0.72)

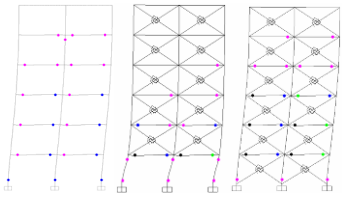

Fig.16 Plastic hinges (α max=0.90)

1) M1 only appears beam hinges in 7 degree rare earthquake. At the bottom ends of columns in the ground floor, plastic hinges will appear in larger earthquake and beam hinges will be fully developed.

2) Because in M2 the ground floor is the weak story, the plastic hinges will appear at the bottom ends of columns in 7 degree rare earthquake, the thicker infill wall is, the more plastic hinges appear there; in models M2-2 and M2-3, plastic hinges appear at both ends of the columns in the ground floor in super rare earthquake, then the lateral displacement mechanism is formed with plastic hinges inadequacy developed, which is worse to seismic capability; the distribution of plastic hinges in M2-1 is similar with M1;

3) Compared to M1, the beam hinges in M3 is less and inadequacy developed; in super rare earthquake plastic hinges will appear at the bottom ends of columns in the ground floor; generally the existence of infill wall will decrease the damage to beams and columns, which is beneficial for anti-seismic.

2.2.5 Restrict effect of the infill wall

The restrict effect of the infill wall can be divided into two types: 1) The support effect is located on some extent range of the joint connecting with the column or beam(Fig.17) when the infill wall is set in a even way on storey height, which will bring about additional shear force. As shown in Fig. 1(e), damage will occur if this effect is neglected in design. 2) The damage due short column effect (Fig. 1(d)) will occur when the calculating height of the column reduces as a result of digging a hole in the infill wall. The way to handle the first restrict effect is to neglect the shear bearing capacity of the infill wall, and the columns are designated to bear the shear when the natural period has been discounted. We can treat it as a equivalent by redistributing its shear according to D-value method, however, the actual circumstances is that the more the stiffness is, the larger the seismic force will be .The conclusion we can make from Table 3 is that it is easy to draw an analogy between D-value method and period discount method when calculating shear force; The shear force redistributed by the diagonal brace effect can meet the calculation by the other two method while there is a big gap of shear force in the side column. Therefore, the period discount method will make the shear in the end of column insufficient and the shear failure will occur while the top of the wall and the end of beam are not compacted or masonry on the top of the wall crushed earlier.

Table3 Comparison of additional shear force for models M3-1, M3-2 and M3-3

Model	Shear force in the side column (kN)			Shear force in the central column (kN)		
	diagonal bracing method	D-value method	period discount method	diagonal bracing method	D-value method	period discount method
M3-1	43.6	36.2	35.3	49.2	47.4	47.2
M3-2	58.2	46.7	42.5	64.6	61.3	56.9
M3-3	74.4	59.0	63.0	83.8	76.9	71.1

To inspect the second restrict effect, i.e., the effect of short column, we set the infill wall at the 2/3 of height of per storey, at the same time, we change the stiffness of the wall and adopt the pushover analysis. The result of calculation indicates that before the bending hinge appears, the shear failure will occur in a obvious way in the side and central columns (Fig.18).

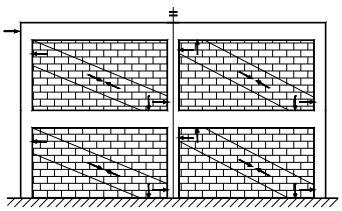
Fig.17 the diagonal strut effect Of the infill wall

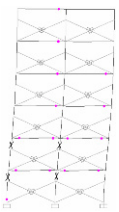
Fig.18 Plastic hinges （α max=0.72）

2.3 Seismic damage analysis of slope frame structures

Using pushover method to analyze the designed example, this section analyzes the short column damage, and columns mixed in piles damage of slope land frame.

Fig. 19 gives the basic information of the examples：the span in both X and Y direction is 6m., 2 spans in X direction, 4 spans in Y direction. Storey height is 3m. Fortification intensity is 7 degree (0.1g), site classification is Ⅱ. The bottom columns

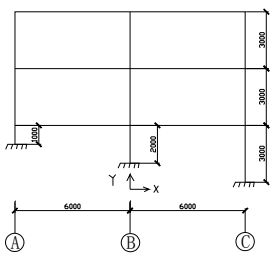

Fig.19 the model for slope frame

heights of the slope frame structures are 1m, 2m and 3m.

2.3.1 Short column effect

By comparing the shear force and the shear capacity when the bottom column plastic hinge appears as shown in Fig. 20(a), whether the bending failure is prior to the shear failure is studied. The results can be summarized as follows: 1) If the stirrups in column A are

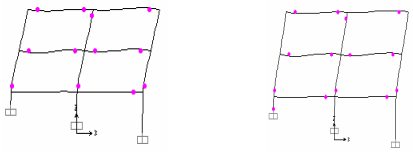

(a) .the slope land frame (b) .the slope land frame with the pile column

Fig.20 the distribution of the plastic hinge

full-length closely spaced, and the section is smaller than 550mm × 550mm, the shear failure is prior to the bending failure according to pushover analysis; 2) The stirrups are not closely spaced or lower than the design demands, the column is more easy to shear failure.

2.3.2 Columns mixed in piles

It is common that the bottom columns are replaced by the pile foundation in practice, 3-floor slope frame is taken as an example. The bottom column section is 550mm×550mm. Under the rare earthquake of 7 degree there is no plastic hinge, no bending failure and no shear failure, as shown in Fig. 20(b). However, if the model is modified by changing the column section to pile section (800mm) with the minimum reinforcement ratio in the longitudinal direction as 0.2% and spiral stirrups as Φ8 at 200mm, and changing the columns in the bottom story to 1 pile and 2 columns, 2 piles and 1 column, or piles only, it is very easy to find plastic hinges and bending failure in piles according to the pushover analysis, though the pile section is larger. So, it is unreasonable that the bottom column is replaced by the pile without bending design (without the consideration of horizontal load).

2.3.3 Design Measures

To improve the performance of short columns in slope frame structures, three ways are advised: changing the area of the column sections, changing the height and stirrup densification spacing of short columns.

2.4 Seismic damage analysis of stairs

The design-examples respectively provide static analysis and elastoplastic time-history analysis under earthquake action for the stairs using the software SAP2000.The static analysis is aimed for analyzing distribution of axis force, shear force and moment of the stairs under seismic action, while the elastoplastic time-history analysis studies the damage condition of stair components based on the plastic hinges under different setting of bracing columns, stair beams and stair slabs.

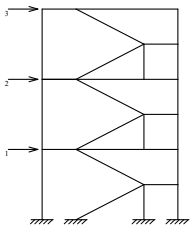

Fig. 21 The analysis Model for stairs

2.4.1 Static analysis

Simplified model is used in this analysis, and a framework near stair well is adopted in the model. The stair slab is taken as inclined beam, the vertical load is not considered, and axis and shear deformation are ignored. The model is shown in Fig. 21. The corresponding axis force, shearing force and moment are respectively shown in Fig. 22.Inclined slabs suffer a

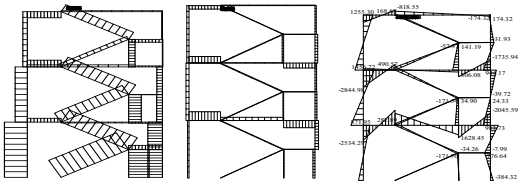

(a) axial force(b) shear force (c) moment

Fig.22 Internal force of stairs under horizontal loads

considerable axial force while shearing force and moment are relatively small, and shear force of frame beams connecting the stair slabs are larger. Therefore, it is reasonable that the stair slab is simplified as the inclined strut with hinged joints at both ends.

2.4.2. Elastoplastic time-history analysis

This calculating model stimulates middle cored teaching building (Fig. 23) .Time-history analysis is taken by setting up different plastic hinges distrib-ution to support columns for staircase ladder beams, ladder beams, ladders plates. Approximately, beam elements are used for simulate the staircase inclined plates.

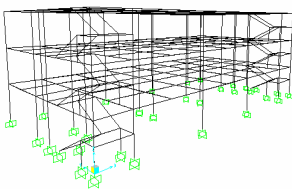

Fig.23 Finite element model

The distribution of plastic hinges under rare earthquake of 7 degree is shown in Fig. 24. In Fig. 24(a), torsional hinges appear in the ladder beams and axial force hinges appear in the inclined plates. In Fig. 24(b), shear force hinges appear in the ladder beams and moment hinges appear in the inclined plates. And in Fig. 24(c), shear force hinges appear in the ladder beams and axial force hinges appear in the inclined plates.

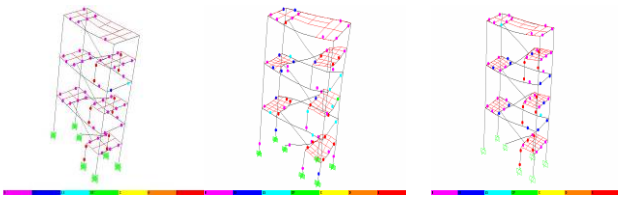

(a) α max=0.50 (b) α max=0.90 (c) α max=0.90

Fig.24 Distribution of the plastic hinges

As can be seen, for inclined plates plastic hinges are not severe under moment action and no hinges due to axis force appear. So it can be seen that inclined plate go into plastic state first under moment action and then

damage under axis force. Plastic hinges will occur to the ladder beams under shear or torsion force, and will be more severe under simultaneous shear-torsion action. Staircase columns are more likely to damage in the earthquake action.

3.Conclusion and Suggestion

3.1 Strong column-weak beam failure mechanism

(1) The beam hinge mechanism or beam-column hinge mechanism under rare earthquake cannot be realized in frame structures designed in accordance with the existing code, except the class 1 frame structures in 9 degree regions. Few hinges occur to the frame structures in 6 degree region; more column hinges occur to the class 3 frame structures in 7 degree regions and the class 2 frame structures in 8 degree regions to form a layer lateral displacement mechanism, thus their seismic performance is poor; in the frame structures in 9 degree regions beam-column hinge mechanism appears, and the ductility and energy performance is good;

(2) The calculation results are basically similar with the phenomena occurred in Wenchuan earthquake. In the frame strctures in 6 degree fortified district, which experienced rare earthquakes in Wenchuan earthquake (such as Mian yang), basically no hinge appears; in the frame structures in 7 degree fortified district, which suffered the predicted strong earthquake or larger (such as Du jiang yan, Bei chuan and Ying xiu), few beam hinges appear, but much more column hinges appear, especially at both ends of columns in the ground floor;

(3) With the same force-reduction coefficient, structures of different intensity take different seismic measures, which will lead to different seismic performance and seismic reliability under rare earthquake, i.e., the "R-μ" relation implied in the seismic code of China is unreasonably inconsistent;

(4) Keep the design axial compression ratio of frame columns at low level is necessary in any intensity region.

3.2 . The effect on seismic behavior of Frame Structure due to the infill wall

(1) The contribution of non-flexibility infill wall to the stiffness cannot be neglected. It is not adequate to reduce the natural period, using a reduction factor ranging from 0.6 to 0.7, according to the current code. In fact, we can adopt different reduction factors base on different amount of infill walls.

(2) The non-flexibility infill walls can not only strengthen the stiffness of structures but also strengthen the restrict conditions. The main effects include: 1) it will reduce the period of the structures and change the stiffness distribution in structures; 2) The non-uniform infill walls may change the failure mode as well as the position of weak story, which will make the desired failure mode difficult to occur. 3) It will change the restrict conditions and the non-linear performance of lateral force-resisting members in elevation direction. A typical damage is discontinuous arrangement of the infill wall along the story height leads to the damage of short columns.

(3) When we design the frame structure, it is critical to make the calculation model conform to the actual situation as far as possible. So we make the suggestion as below: 1) It is a feasible idea to make the infill wall as the first defense line, nevertheless, we should take the control of extent on damage along with extent on repairable in to account. 2) In the processes of dynamic analysis, regularity classification and stiffness control, the contribution of infill walls to the stiffness of structures should be considered adequately. 3) Soft connection can be used if the contribution of infill walls is neglected. 4) To remove or set infill wall arbitrarily in large-scale should be avoided.

3.3 slope land frame structure

It is unreasonable to design the slope frame structures as the common ones. We should avoid designing short column in the bottom story. We can do partial excavation in slope field to increase the height of the column or change it into regular structure; also we can improve the performance of short column through increasing the section of the columns in the ground floor, increasing the height of the shorter columns and deducing stirrups spacing; and we should avoid to replacing the column in the ground with piles, or the piles should be designed as columns.

3.4 stair

If the beams, slabs and columns of stairs are designed without seismic calculation, they are prone to be damaged. So the seismic design of stairs should be specified in the code, and the methods and measures for stairs seismic design are in urgent need.

References:

China Ministry of Construction. GB50011-2001(2001), “Code for seismic design of buildings,” Beijing: China Architecture and Building Press.

Silvia.Mazzoni, F.McKenna, M.H.Scott and G.L.Fenves. (2006), “Opensees Users Manual,” PEER, University of California at Berkeley.

Yang Pu, Li Yingmin, Wang Yayong, et al. (2000), “ A study on improvement of Push-over analysis,” *Journal of Building Structures*, 21(1): 44-50.

Han Jun, Zhang Yi, Zheng Nina, et al. (2008), “Analysis on nonlinear seismic response of multi-story torsion-irregular structures,” *The 14th World Conference on Earthquake Engineering*, October 12-17. Paper No. 03-01-0046

T. Paulay, M. J. N. Priestley. (1992), “Seismic design of reinforced concrete and masonry buildings,” John Wiley & Sons, Inc.

ATC. (1996), “Seismic evaluation and retrofit of concrete buildings, ATC40,” Redwood city, Applied Technology Council.

A.K. Chopra, R.K.Goel. (1999), “Capacity-demand-diagram methods for estimating seismic deformation of inelastic structures:SDF systems,” University of California,Berkeley. California, US.PEER.

Sixth International Conference on Urban Earthquake Engineering
March 3-4, 2009, Tokyo Institute of Technology, Tokyo, Japan

SEISMIC RETROFIT OF RC MEMBERS USING FRP WITH VERY LOW YOUNG'S MODULUS AND HIGH DEFORMATION CAPABILITY

Susumu KONO[1], Masato DOI[2], Jungyoon Lee[3], Hitoshi TANAKA[4]

1) Associate Professor, Dept. of Architecture and Architectural Engineering, Kyoto University, Japan
2) Graduate Student, Dept. of Architectural Engineering , Kyoto University
3) Associate Professor, Department of Architectural Engineering, Sungkyun Kwan University, Korea
4) Professor, Disaster Prevention research Institute, Kyoto University
kono@archi.kyoto-u.ac.jp, jylee@skku.ac.kr, tanaka@sds.dpri.kyoto-u.ac.jp

Abstract: This paper proposes a use of fiber reinforced polymers (FRP) with very low Young's modulus and high deformation capability to solve various issues of ordinary FRP's. "Super Reinforced with Flexibility (SRF)" is a polyester fiber reinforced polymer which has 1/40 of Young's modulus, 1/35 of tensile strength, 10 times larger fracture strain, and 2/3 of price compared to carbon fiber reinforced polymer (CFRP). SRF has potential to substitute CFRP for its high seismic performance and ease of construction. In an experimental program, two identical structural wall specimens with eccentric openings and five cantilever column specimens were constructed with and without SRF strengthening to study effects of SRF on the shear and confining mechanisms. Strengthened specimens showed larger shear strengths and ductility. Test results were studied to consider the resisting mechanism of concrete structures strengthened with SRF.

This paper was presented at the 14th World Conference on Earthquake Engineering, Beijing, China, 2008.

1. INTRODUCTION

There are many seismic retrofit schemes for structural walls and columns which are main seismic as well as vertical load resisting components. It is traditional to construct additional concrete and/or steel structural walls or braced steel frames and anchor them to existing RC walls or frames. This type of strengthening method has a long history and is considered as one of the most common methods. However, it necessitates heavy construction effort. Since fiber reinforced polymers (FRP) began to play an important role in the civil engineering in 1990's, carbon fiber reinforced polymer (CFRP) has been used on columns first and then on structural walls to increase the shear strength and confinement. CFRP retrofit procedures are much easier compared to steel jacketing and steel bracing, but the surface needs to be smoothened and a part of the concrete needs to be taken to avoid sharp corners. The epoxy resin used with CFRP is sometimes too stimulus for construction workers and residents of buildings. Although it has superior seismic performance and ease of construction, CFRP has not been necessarily considered as the best retrofit materials.

FRP with low Young's modulus (SoftFRP) was developed in late 1990's and early 2000's. They were manufactured from relatively economical materials like polyacetar [1] or polyester [2] to substitute expensive CFRP in the beginning. FRP with high Young's modulus like CFRP may fracture when it experiences large tensile strain at cracks. However, it was found that a large deformation capability of SoftFRP was more effective to strengthen concrete structures since it is highly resistant to the local concentration of tensile strain at cracks.

Super Reinforcement with Flexibility (SRF) was developed as a construction material in 1999 and considered as one of SoftFRP's. Its typical mechanical properties are compared with those of CFRP and a mild steel plate in Table 1. Young's modulus is 1/40 of that of CFRP or ordinary steel. The tensile strength is 1/35 of CFRP and the strain at the tensile strength is ten times larger. The properties on the tensile strength and strain are similar to those of an ordinary mild steel plate. It should be noted that SRF costs 2/3 of CFRP and much easier to purchase locally. The research on SRF was first published regarding retrofit of reinforced concrete columns in 2000 [2]. Since then, retrofit on RC columns has been studied extensively [3]. Studies on the use of SRF to retrofit structural walls have just begun recently [4][5][6].

This study explains the experimental works on structural walls and columns strengthened with SRF. The effect of SRF on the enhancement of shear strengths and confinement are explained. The resisting mechanism of members strengthened with SRF is discussed to understand the behavior of SoftSRF.

Table 1 Typical mechanical properties of SRF, CFRP and steel plate

Material	Young's modulus (GPa)	Yield strenth (MPa)	Tensile strength (MPa)	Strain at tensile strength (%)
SRF (SRF465)	6.3	63	580	17
CFRP	235	* -	3400	1.5
Steel plate (SS400)	220	325	400	20

* CFRP is basically linear elastic and does not yield.

2. EXPERIMENT ON STRUCTURAL WALLS

2.1 Experimental setup

Two identical structural wall specimens were constructed with eccentric openings as shown in Figure 1. One specimen without any strengthening is designated as L1 and the other specimen strengthened with SRF sheet is designated as L4. A single layer of SRF sheet was applied on the south face of the wall and anchored to the north face as shown in Figure 2. The beams of the second and third floor (B2 and B3) next to the openings were also strengthened with a single layer of SRF. The specimens were designed as a lower portion of a six-story structural wall. Materials used commonly for both specimens are listed in Table 2 and mechanical properties of materials are listed in Table 3. Polyurethane adhesive was used for placing SFR on the concrete surface.

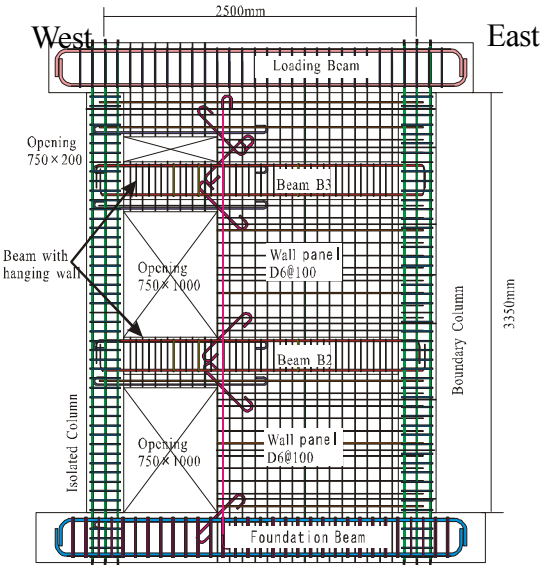

(a) Configuration and reinforcement arrangement (L1, L4)

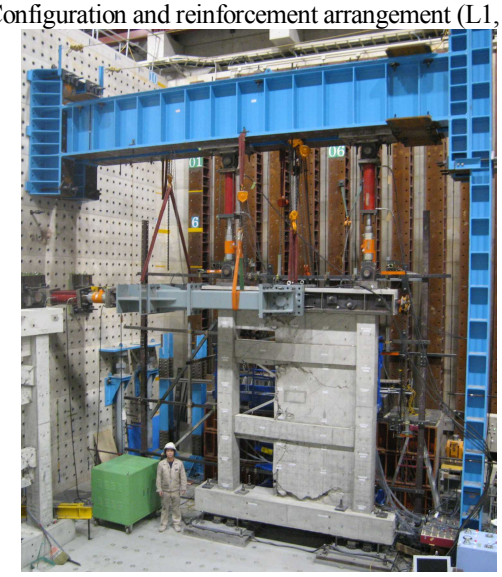

(b) Loading system

Figure 1 Specimen and loading system (Unit: mm)

The lateral load was applied to the loading beam as shown in Figure 1(b) and the drift at the midspan of loading beam was controlled. The loading protocol was two cycles each at drift angles of 0.05%, 0.1%, 0.25%, 0.5%, 0.75%, 1.0%. The vertical load was applied to the top of each column based on Eqs. (1) and (2) so that the contraflexure point was 2500 mm above the foundation beam. The detail of the experiment may be referred to the companion paper [7].

$$N_e = +0.42Q + 244kN \quad (1)$$

$$N_w = -0.42Q + 244kN \quad (2)$$

where Q is the lateral load.

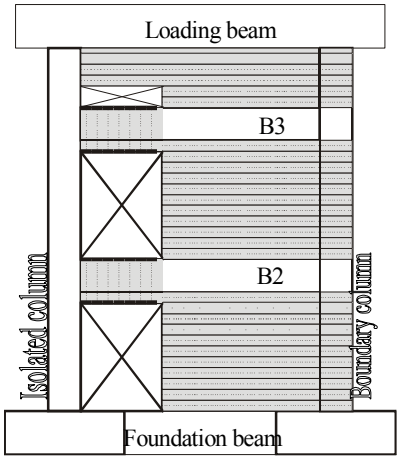

(a) South face

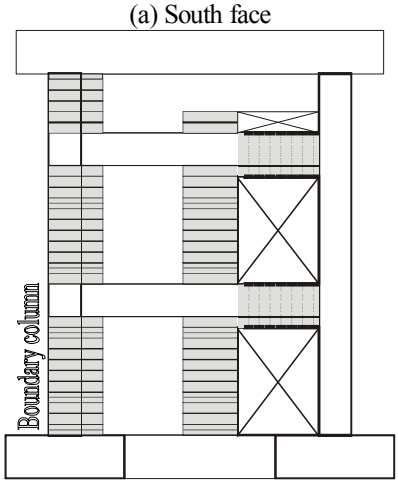

(b) North face

Figure 2 SRF configuration placed on L4

Table 2 Section size and reinforcing bars in common

Member	Section size	Longitudinal bar		Shear reinforcement	
		Type	Steel ratio	Type	Steel ratio
Boundary column	300×300mm	8-D19	2.55%	2-ϕ 10@75	0.63%
Beam	200×300mm	2-D13	0.47%	2-ϕ 6@100	0.32%
Wall	t=80mm	D6@100(Staggered) 0.4% in both vertical and horizontal shear reinforcement			

2.2 Experimental results

Crack distributions are shown in Figure 3 and damage after loading test is shown in Figure 4. The first shear crack of L1 was found at the first floor wall panel at drift angle (R) of +0.04%, and the number of cracks kept increasing till R=0.5%. Then the vertical reinforcement buckled at the wall base of the first floor at the region enclosed by a circle. The concrete started to spall locally from this drift angle. Then the shear sliding failure along the foundation beam took place along the wall base at R=+1.5% and the lateral load dropped suddenly. L4 strengthened with SRF sheet had the initial shear cracks at R=+0.05% and the number of cracks increased until R=0.5%. At the part of B2 enclosed with a circle in Figure 3(b), the flexural crack opened by large amount and the maximum load was reached at R=0.68% in the positive direction. Peak load in negative direction was reached when the shear failure occurred at the third floor wall panel since the force path, shown in dotted arrow in Figure 3(b), was not secured due to a opening. In positive direction, the force path was secured and the wall resisted the external force until R=1.25%. Degradation of load carrying capacity in positive direction started at R=1.25% at which the sliding shear failure occurred just below the loading beam.

Table 3 Mechanical Properties of Reinforcement

(a) Reinforcing bars for L1

Type	Yield strength (MPa)	Maximum strength (MPa)	Young's modulus (GPa)
D6	425	538	204
D10	366	509	180
D13	369	522	189
D16	400	569	194
D19	384	616	183
ϕ 10	985	1143	197
Separator	1260	1461	759

(b) Reinforcing bars for L4

Type	Yield strength (MPa)	Maximum strength (MPa)	Young's modulus (GPa)
D6	425	538	204
D10	352	496	186
D13	362	529	188
D19	411	605	189
D25	387	541	194
φ10	1033	1221	204

(c) Concrete

Specimen	Compressive strength (MPa)	Tensile strength (MPa)	Young's modulus (GPa)
L1	28.9	-	26.0
L4	26.8	2.3	20.4

(d) SRF Sheet

Width (mm)	Thickness (mm)	Young's modulus (MPa)	Tensile strength (MPa)	Strain at failure (%)
100	2.5	5800	400	10

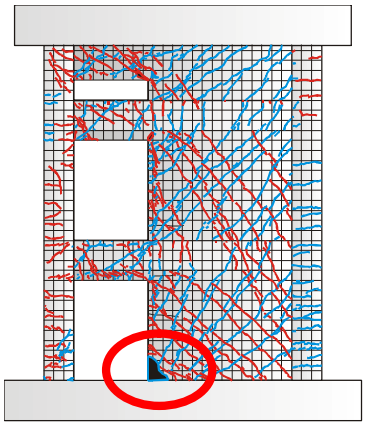

(a) L1

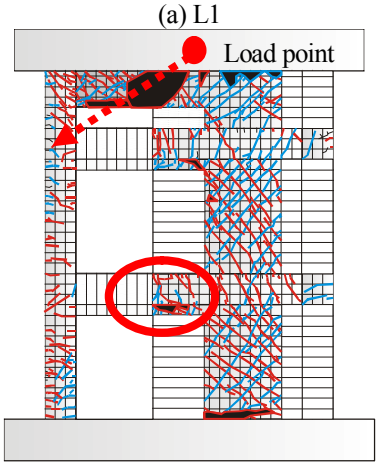

(b) L4

Figure 3 Crack distribution at R=0.75%

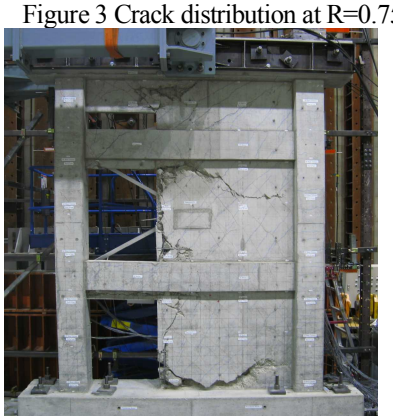

(a) L1

(b) L4

Figure 4 Photographic view after the loading test

Lateral load – drift angle relations are shown in Figure 5 and the initial stiffness and shear strengths are summarized in Table 4. Test results of N1, which had no openings nor strengthening, is also listed in the table as a reference. It is clear that SRF did not affect the initial stiffness but affected the shear strengths. Since the degradation of the shear strength from the positive peak to R=+1.3% was gentler than that of L1, it may be said that the confinement of SRF increased the ductility of the structural wall.

When the shear strength of L4 was computed, the effect of SRF was taken into account by adding the equivalent amount of shear reinforcement steel to the equation. The equivalent amount of steel was determined so that the steel at yielding carries the same magnitude of force which a given amount of SRF carries at the stain of 0.57%. The computed and experimental shear strengths in Table 4 agree well in the positive direction and the employed equation is considered reasonable.

3. EXPERIMENT ON COLUMNS

3.1 Experimental setup

An experiment was also conducted using five RC column specimens. Their configurations and test variables were the existence of steel hoop and amount of SRF as shown in Figure 6 and Table 5. Concrete had compressive strength of 27.4 MPa and Young's modulus of 19.6 GPa. Mechanical properties of steel and SRF are listed in Table 6. Axial force was kept constant at 30% of the axial compressive strength of the column and the lateral load was cyclically applied twice each at the pre-selected drift angles. The loading protocol for C30N0 and C30N4 differed from that of other three specimens as can be seen in Figure 7. The detail of the loading system may be referred to the companion paper [9].

3.2 Experimental results

Lateral load – drift angle relations are shown in Figure 7 and the peak values in positive and negative directions are listed in Table 5. The computed shear capacities were smaller than the flexural capacity for three specimens but all five specimens seemed to have reached the flexural capacities. This is because a large amount of the shear force was resisted by the horizontal component of the inclined axial force trajectory from loading point to the neutral axis at the column base since the column was stocky. Hence Figure 7 shows the confining effect of SRF on the plastic hinge region.

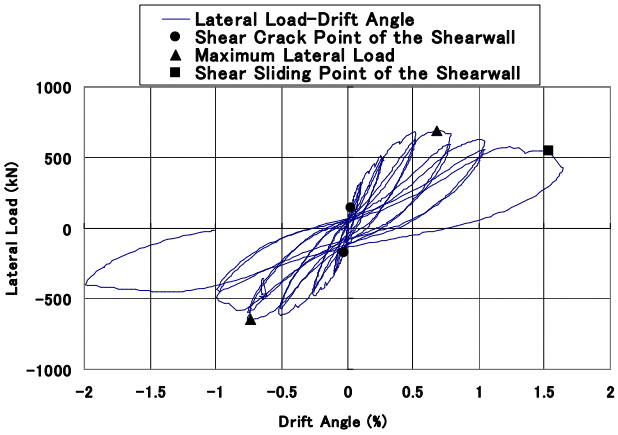

(a) L1

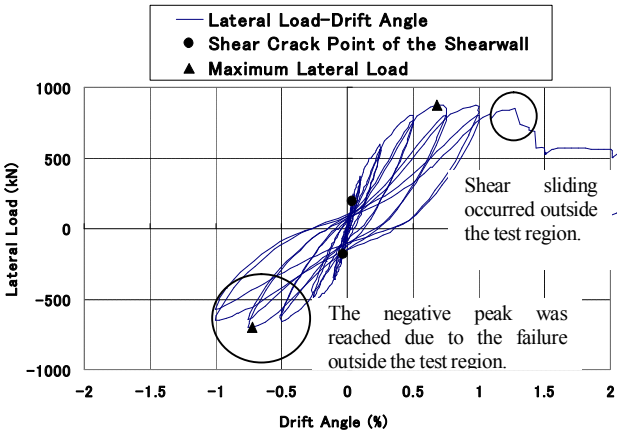

(b) L4

Figure 5 Lateral load – drift angle relations

Table 4 Summary of loading test results

Specimen	Positive direction				Negative direction			
	Maximum load Qe, (kN)	**Computed strength Qc, (kN)	Drift angle (%)	Initial stiffness (10^5kN/rad)	Maximum load Qe, (kN)	Computed strength Qc, (kN)	Drift angle (%)	Initial stiffness (10^5kN/rad)
*N1	1179	1120	0.48	16.0	-1039	1120	-0.42	13.4
L1	686	633	0.68	5.9	-649	633	-0.74	6.7
L4	873	904	0.68	5.7	***(-705)	904	-0.73	5.6

* N1 is a specimen without any openings. ** Qc was computed from Ref. [8] considering the reduction factor due to openings. *** The value is not considered as the real maximum since the wall panel at the third floor, which is outside the test region, failed.

Table 5 Summary of test variables and test results

Specimen	Shear reinforcement		Computed strength		Experimental strength	
	Mild steel hoop	SRF	Shear Qvu (kN)	Flexure Qmu (kN)	Positve +Qe (kN)	Negative -Qe (kN)
C30N0	None	None	80*[1]	125	129	-
C30N4	D6@60 (p_w=0.0042)	None	137*[1]		119	-
C30F2R	None	One-layer zebra stripe (p_{wef}=0.0025)	94*[2]		124	-136
C30F2C	None	Three layers of one side stripe (p_{wef}=0.0025)	94*[2]		132	-132
C30F4	None	One layer spiral stripe (p_{wef}=0.0050)	145*[2]		133	-133

*1 Based on the AIJ standard [10]. *2 Based on SRF specifications [11] *3 p_{wef} is the equivalent reinforcement ratio

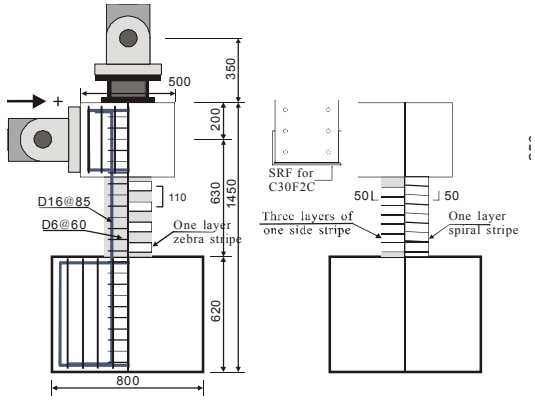

(a) C30N4 (b) C30F2R (c) C30F2C (d) C30F4

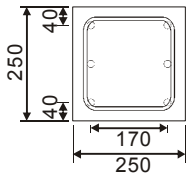

(e) Section of C30N4

(Other specimens had no steel shear reinforcement.)

Figure 6 Specimen configurations (Unit: mm)

Table 6 Mechanical properties

(a) Steel reinforcing bar

Bar type	Yield strength (MPa)	Tensile strength (MPa)	Young's modulus (GPa)
D6	425	538	204
D16	320	478	182

(b) SRF

Sheet type	Width thickness (mm)	Effective Young's modulus (MPa)	Fracture strength (MPa)	Strain at Fracture (%)
SRF450	50×4	5800	400	10

C30F2C had three layers of SFR only on one side of the section and SRF was extended to the adjacent two sides for anchorage. Its lateral load – drift angle relation was similar to that of C30F2R until the concrete started to fail in shear at R=2%. C30F2R showed the steady and slow degradation of lateral load carrying capacity until the end of the loading test. C30F4 had double amount of SRF compared to C30F2C and C30F2R and hence the degradation of load carrying capacity was much slower than that of C30F2R. C30F4 carried larger lateral load than the other four specimens for a given drift angle as can be seen from the envelope curves in Figure 7. It can be seen that SRF effectively confined the core concrete at the plastic hinge region to greatly enhance the ductility.

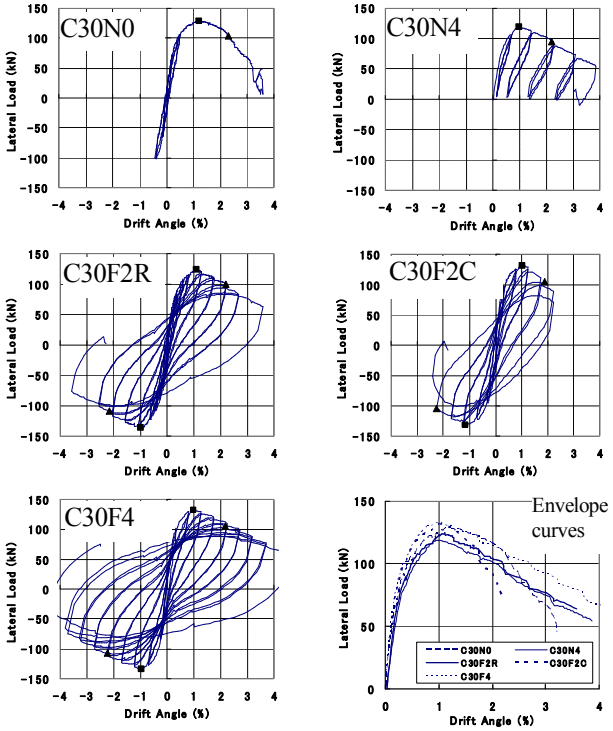

Figure 7 Lateral load – drift angle relations and their envelop curves

4. DISCUSSIONS

Shear strength of the structural wall (L4) in the positive direction was enhanced by 27%. This can be explained that SRF worked as additional horizontal reinforcement. However, it is interesting to consider reasons behind it. Both SRF and polyurethane adhesive have low stiffness but high deformation capability. With SRF attached on concrete surface, cracks did not concentrate locally but rather distributed evenly over wall panels, and consequently

the number of cracks increased for a given drift. Since the number of cracks increased, the width of cracks decreased. The cracks with smaller width made the aggregate interlock more effective resulting in the enhancement of shear capacity. SRF also alleviated deterioration of the load carrying capacity by preventing the spalling of concrete. Even after the concrete of the compression strut failed in compression, crushed concrete stayed in the original position since SFR held it. This kept the shear resisting mechanism continue to work even if concrete crushed in the compression strut. Consequently, the degradation after the peak became gentler.

Confining effects of SRF was also confirmed from the experiment on column specimens. In addition to the increase of moment capacity, the ductility after the capacity was greatly enhanced. This confining mechanism is very similar to other FRP materials. Even if concrete failed in compression, concrete was confined within the enclosed SRF and did not come out from the SRF enclosure. Hence the sudden drop of load was avoided.

In addition to the force resisting mechanisms stated above, SRF has a function to relieve stress concentration due to its large deformation capability. The corners of the RC members do not have to be round like they should be when using CFRP, which is sensitive to sharp corners. FRP can be also applied to large bridge columns, brick-walls and lumber structures as well for its design flexibility, ease of handling at construction and low price.

5. CONCLUSIONS

Fiber reinforced polymers with low Young's modulus was used to retrofit RC structural walls and RC columns in experiments. Their large deformation capability greatly improved seismic performance of structural walls and columns compared to the carbon fiber reinforced polymers and also relieved stress concentration. It is very easy to handle fiber reinforced polymers with low Young's modulus as a construction material. The fiber reinforced polymers with low Young's modulus will greatly improve the current construction practice.

ACKNOWLEDGEMENTS

A part of this research was financially supported by Miracle Three Corporation and Grant-in-aid, Ministry of Education, Culture, Sports, Science and Technology (PI: H. Tanaka). SRF and adhesive materials used in the experiment were donated by Structural Quality Assurance, Inc. and precious advice and technical support was given by Dr. Shunichi Igarashi. The authors acknowledge M. Warashina and K. Mori, graduate students at Kyoto University, for their contribution to the experimental works and data processing.

REFERENCES

[1] Iihoshi, C., Fukuyama, H. and Tanaka, H., "Strengthening effects of RC members with polyacetal fiber sheets," International Symposium on Earthquake Engineering Commemorating Tenth Anniversary of the 1995 Kobe, Kobe/Awaji, Japan, January 2005, on CD-ROM.

[2] Igarashi, S., "Soft Retrofitting for old buildings", Proceedings of the third Japan-Turkey workshop on earthquake engineering, February 22, 2000, Istanbul.

[3] For example, Kabeyasawa, T., Tasai, A. and Igarashi, S., "A new Method of Strengthening Reinforced Concrete Columns against Axial Load Collapse during Major Earthquake", EASEC-8, Singapore, 2001.

[4] Sanada, Y., Murase, M., Kabeyasawa, K., Thuat, D. V. and Igarashi, S., "Experimental study on strengthening of reinforced concrete shear wall using polyester sheet," Transactions of AIJ annual meeting, AIJ, 2005, C2, pp. 609 – 612.

[5] Kabeyasawa, T., Kabeyasawa, T., Kabeyasawa, T., Kim, Y. and Tojo, Y., "Experimental study on shape and reinforcing of RC walls, Part 1 and 2" Transactions of AIJ annual meeting, AIJ, 2007, C2, pp. 461 – 464.

[6] Warashina, M., Mori, K., Doi, M., Sakashita, M., Kono, S., Tanaka H. and Watanabe, F., "Shear Behavior of Multi-Story Shearwalls with Eccentric Openings" Transactions of AIJ annual meeting, AIJ, 2008, C2.

[7] Warashina, M., Kono, S., Sakashita, M. and Tanaka, H., "Shear behavior of multi-story RC structural walls with eccentric openings," 14th World Conference on Earthquake Engineering, Beijing, 2008.

[8] Architectural Institute of Japan (1999), "Design Guidelines for Earthquake Resistant Reinforced Concrete Buildings Based on Inelastic Displacement Concept", AIJ. (In Japanese)

[9] Lee, J. Y., Kono, S., Watanabe, F. and Cheong, Y. G. "Softening behavior of RC columns under cyclic loading," 14th World Conference on Earthquake Engineering, Beijing, 2008.

[10] Architectural Institute of Japan (2005), Design Standard for Steel Structures -Based on Allowable Stress Concept-, AIJ. (In Japanese)

[11] Structural Quality Assurance, Inc., "Specifications for Design and Construction of Retrofitting Existing Building Structures Using SRF," Assessment Version from The Japan Building Disaster Prevention Association, The second edition, pp. 5.18-5.24, 2007.

Sixth International Conference on Urban Earthquake Engineering
March 3-4, 2009, Tokyo Institute of Technology, Tokyo, Japan

FORMULATION OF BI-AXIAL NON-LINEAR RESTORING FORCE CHARACTERISTICS WITH SLIPPING BEHAVIOR BY USING THE THEORY OF PLASTICITY

Koshiro Nishimura[1] and Katsuki Takiguchi[2]

1) Assistant Professor, Dept. of Architectural and Building Engineering, Tokyo Institute of Technology, Japan
2) Professor, Dept. of Mechanical and Environmental Informatics, Tokyo Institute of Technology, Japan
nishimura.k.ac@m.titech.ac.jp, ktakiguc@tm.mei.titech.ac.jp

Abstract: In this study, bi-axial non-linear restoring force characteristics with slipping behaviors were formulated by using the theory of plasticity. A slipping type of bi-axial restoring force model was proposed in the previous paper by the authors. The proposed model, which a tensor was used to express slipping behaviors, was an extended model of a bi-axial elastic perfectly plastic type model that was based on an analogy to the theory of plasticity. A parallel system of slipping type and elastic-perfectly plastic type of bi-axial restoring force model was used in the formulation. Numerical results with the parallel system and static loading test results of R/C shear wall specimens were compared to verify the restoring force model.

1. INTRODUCTION

It is necessary to model restoring force characteristics of building structures properly when dynamic behaviors of the structures subjected to earthquake excitation are analyzed. R/C members have tendency to show slipping behaviors, which deformation increase and decrease with little varying lateral force in the quite low load condition, in case of one-directional cyclic load combined bending and shear. R/C beams with insufficient bond of longitudinal bars and R/C walls shows slipping behaviors. In the previous study, three-directional loading tests of R/C members without bond were carried out to understand slipping behaviors (Nishimura et al. 2006). R/C members without bond of longitudinal bar shows slipping behaviors in their one-directional force-deformation relationships. Then bi-axial non-linear restoring force model of slipping type was proposed (Nishimura et al. 2006). The proposed model, which a tensor was used to express slipping behaviors, was an extended model of an elastic-perfectly plastic type bi-axial model that was based on an analogy to the theory of plasticity. It was confirmed that the proposed model could roughly describe the test results in the previous study.

The slipping type model has no energy dissipation in hysteresis loop under cyclic loading of constant amplitude. Therefore, in this paper, a parallel system of slipping type and elastic perfectly plastic type of bi-axial restoring force model was used to describe the energy dissipation under cyclic loading. Then numerical results of the parallel system were compared with static loading test results of R/C shear wall specimens to verify the restoring force model. The R/C shear wall specimens, which were single-bay and single story wall, were subjected to two-directional cyclic lateral loading under a constant axial load.

2. RESTORING FORCE MODEL

2.1 Parallel System of Bi-axial Restoring Force Model

As shown in Figure 1, a parallel system of slipping type and elastic perfectly plastic type of bi-axial restoring force model was used in this paper. The both types of model were based on the theory of plasticity, and had two components of force and displacement, which were (P_X, P_Y) and (δ_X, δ_Y). Figure 2 shows uni-axial restoring force characteristics of these models.

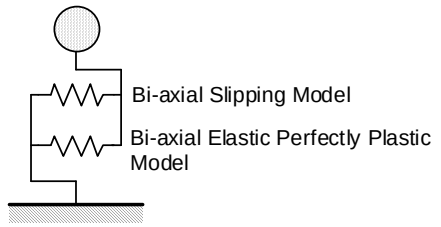

Figure 1 Parallel System

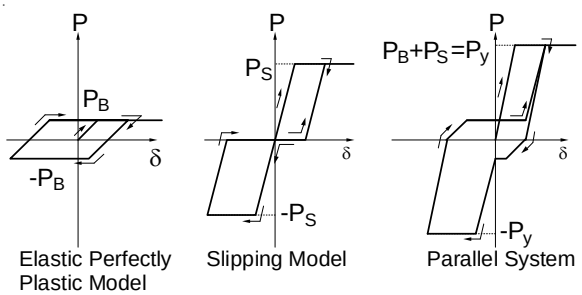

Figure 2 Uni-Axial Restoring Force Characteristics

2.2 Outline of Slipping Type Restoring Force Model

The slipping type of bi-axial restoring force model was proposed by the authors (Nishimura et al. 2006). The slipping type model, which a tensor was used to express slipping behaviors, was an extended model of an elastic-perfectly plastic type bi-axial model that was based on an analogy to the theory of plasticity. A concept of the model can be drawn as Figure 3 that a roller, which consist with a mass and an elastic member, moves in slipping area surrounded with rigid wall.

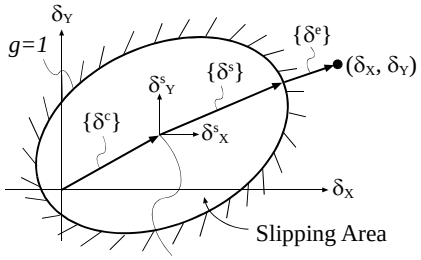

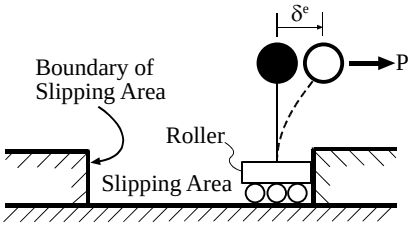

Figure 3 Slipping Model

As shown in Figure 3, total displacement vector $\{\delta\}$ is assumed as follows.

$$\{\delta\} = \{\delta^e\} + \{\delta^s\} + \{\delta^c\} \tag{1}$$

$\{\delta^e\}$, $\{\delta^s\}$, and $\{\delta^c\}$ are vectors of elastic displacement, slipping displacement, and center of slipping area, respectively. $\{\delta^s\}$ and increment of $\{\delta^c\}$ are assumed as follows.

$$\{\delta^s\} = [D] \cdot \{n\} \tag{2}$$

$$[dD] = \frac{k_s}{\left\|\{d\delta^p\}\right\|} \cdot \begin{bmatrix} d\delta_X^{p\,2} + k_o \cdot d\delta_Y^{p\,2} & (1-k_o) \cdot d\delta_X^p \cdot d\delta_Y^p \\ (1-k_o) \cdot d\delta_X^p \cdot d\delta_Y^p & k_o \cdot d\delta_X^{p\,2} + d\delta_Y^{p\,2} \end{bmatrix} \tag{3}$$

$$\{d\delta^c\} = (1-k_s) \cdot \{d\delta^p\} \tag{4}$$

$[D]$ is tensor for expressing the slipping area and $[dD]$ is increment of $[D]$. $\{n\}$ is a unit vector and $\{d\delta^p\}$ is increment of plastic displacement vector in elastic-plastic state of the model. As shown in Figure 4 and Figure 5, a coefficient k_s is degree of slipping behaviors, and a coefficient k_o is expanding ratio of slipping area in orthogonal direction in elastic-plastic state. Figure 6 shows expanding stage of slipping area, which is expressed by an equation $g(\delta^s)=1$

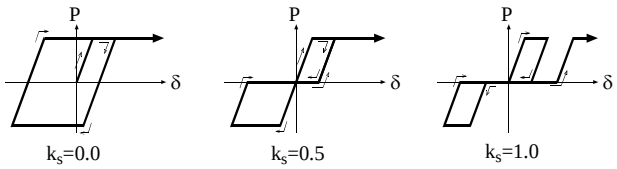

Figure 4 Coefficient k_s in Eq. (3)

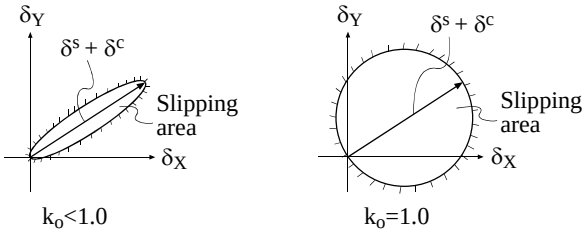

Figure 5 Coefficient k_o in Eq. (3)

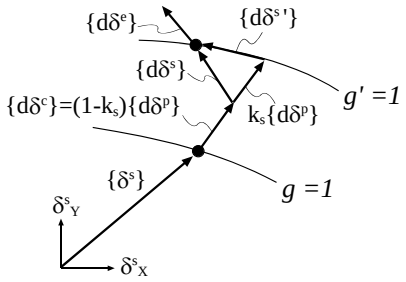

Figure 6 Expansion Stage of Slipping Area

As shown in upper figure in Figure 3, direction of force vector $\{P\}$ must be in the same direction as normal direction of slipping area, and $\{P\}$ is also given by elastic rigidity $[K^e]$. Therefore, the force vector can be given as follows, where $\{\nabla g\}$ is gradient of the function $g(\delta^s)$.

$$\{P\} = \kappa \cdot \{\nabla g\} \ , \ (\kappa \geq 0) \tag{5}$$

$$\{P\} = [K^e] \cdot \{\delta^e\} \tag{6}$$

The function $g(\delta^s)$ is given by Eq. (2) and an equation $\{n\}^T \{n\}=1$ because $\{n\}$ is a unit vector.

$$g = \frac{\{\delta^s\}^T \cdot [T] \cdot \{\delta^s\}}{2} \ , \text{ where } [T] = 2 \cdot [D]^{-1} \cdot [D]^{-1} \tag{7}$$

Figure 7 shows a yield surface that is assumed as an equation $f(P)=1$. In this paper, the yield surface was assumed as ellipse. The function $f(P)$ is given as follows, where components of a matrix $[U]$ are constants when its characteristics are assumed as perfectly plastic.

$$f = \{P\}^T \cdot [U] \cdot \{P\} \tag{8}$$

The flow rule of the theory of plasticity can be written as follows. $\{\nabla f\}$ is gradient of $f(P)$.

$$\{d\delta^p\} = d\lambda \cdot \{\nabla f\} \tag{9}$$

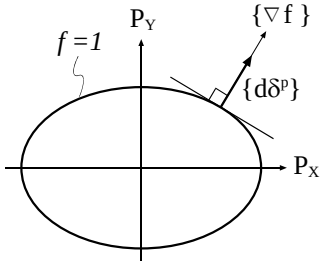

Figure 7 Yield Surface

2.3 Incremental Force and Displacement Relationships

2.3.1 Elastic State

In elastic state, relationship between incremental force and displacement is written as follows because total of incremental displacement is equal to incremental elastic displacement.

$$\{dP\} = [K^e] \cdot \{d\delta\} \tag{10}$$

2.3.2 Slipping State

In slipping state, incremental force-displacement relationship is written as follows, where $[K^s]$ is a zero matrix, because total of incremental displacement is equal to incremental slipping displacement and there is no elastic displacement.

$$\{dP\} = [K^s] \cdot \{d\delta\} \tag{11}$$

2.3.3 Elastic-Slipping State

In elastic-slipping state, total of incremental displacement is equal to the sum of $\{d\delta^e\}$ and $\{d\delta^s\}$, where $\{d\delta^e\}$ and $\{d\delta^s\}$ are increment of $\{\delta^e\}$ and $\{\delta^s\}$, respectively. $\{P\}$ and increment of $\{P\}$, $\{dP\}$, are given as follows by Eq. (5) and (7).

$$\{P\} = \kappa \cdot [T] \cdot \{\delta^s\} \tag{12}$$

$$\{dP\} = d\kappa \cdot [T] \cdot \{\delta^s\} + \kappa \cdot [T] \cdot \{d\delta^s\} \tag{13}$$

The following equation is given by dg=0.

$$\{\nabla g\}^T \cdot \{d\delta^s\} = 0 \tag{14}$$

Relationship of $\{dP\}$ and $\{d\delta\}$ is given as follows by Eq. (6), (13), and (14).

$$\{dP\} = [K^{es}] \cdot \{d\delta\} \tag{15}$$

where

$$[K^{es}] = [K^e] \cdot [A]^{-1} \cdot \frac{\{\nabla g\} \cdot \{\nabla g\}^T}{\{\nabla g\}^T \cdot [A]^{-1} \cdot \{\nabla g\}} \cdot [A]^{-1} \cdot [K^e] + \kappa \cdot [T] \cdot [A]^{-1} \cdot [K^e]$$

and

$$[A] = [K^e] + \kappa \cdot [T]$$

2.3.4 Elastic-Slipping-Plastic State

In elastic-slipping-plastic state, total of incremental displacement is equal to the sum of $\{d\delta^e\}$, $\{d\delta^s\}$, and $\{d\delta^c\}$. The following equations are given by replacing $\{d\delta^s\}$ in Eq. (13) and (14) with ($\{d\delta^s\}$-$k_s\{d\delta^p\}$).

$$\{dP\} = d\kappa \cdot [T] \cdot \{\delta^s\} + \kappa \cdot [T] \cdot \left(\{d\delta^s\} - k_s \cdot \{d\delta^p\} \right) \tag{16}$$

$$\{\nabla g\}^T \cdot \left(\{d\delta^s\} - k_s \cdot \{d\delta^p\} \right) = 0 \tag{17}$$

The following equation is given by df=0.

$$\{\nabla f\}^T \cdot \{dP\} = 0 \tag{18}$$

Incremental force and displacement relationship is given as follows by Eq. (4), (6), (8), (9), (16), (17), and (18).

$$\{dP\} = [K^{esp}] \cdot \{d\delta\} \tag{19}$$

where $[K^{esp}] = [K^{es}] - \dfrac{[K^{es}] \cdot \{\nabla f\} \cdot \{\nabla f\}^T \cdot [K^{es}]}{\{\nabla f\}^T \cdot [K^{es}] \cdot \{\nabla f\}}$

2.4 Elastic Perfectly Plastic Type Restoring Force Model

The elastic perfectly plastic type model in parallel system was used to describe an area of hysteresis loop under cyclic loading. When coefficient k_s in Eq. (3) is equal to zero, the slipping model perfectly agrees with the elastic perfectly plastic type model, as shown in Figure 4.

3. VERIFICATION OF MODEL

3.1 Static Loading Test of Shear Wall Specimens

In this paper, numerical results of the parallel system were compared with static loading test results of R/C shear wall specimens (Nishimura et al. 2008) to verify the restoring force model. Three-directional static loading tests of three identical specimens were mentioned here. Figure 8 and Table 1 show detail and material properties of specimens. The specimens had a wall plane and two columns. The column had four longitudinal bars of D6, and D4 were used for shear reinforcements and wall plane reinforcements. Figure 9 shows loading setup of the specimen. X, Y, and Z

axes were wall plane direction, orthogonal direction against wall plane, and vertical direction, respectively.

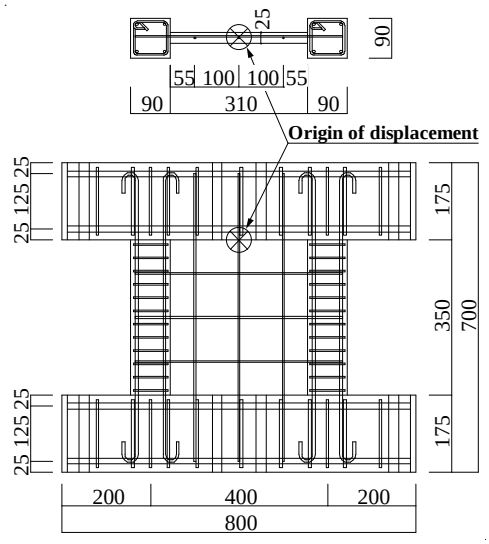

Figure 8 Detail of Specimen

Table 1 Material Properties of Specimen

Name of Specimens	Concrete		Deformed Bar		
	F_C [N/mm^2]	E_C [kN/mm^2]	Name	σ_y [N/mm^2]	E_S [kN/mm^2]
SW-R-U	22.9	20.5	D4	366	185
			D6	348	187
SW-R-B	22.9	20.5	D4	366	185
			D6	348	187
SW-B-1	37.7	26.7	D4	379	190
			D6	383	197

F_C: Compressive strength, σ_y: Yield strength
E_C: 1/3 secant modulus of elasticity, E_S: Young's modulus

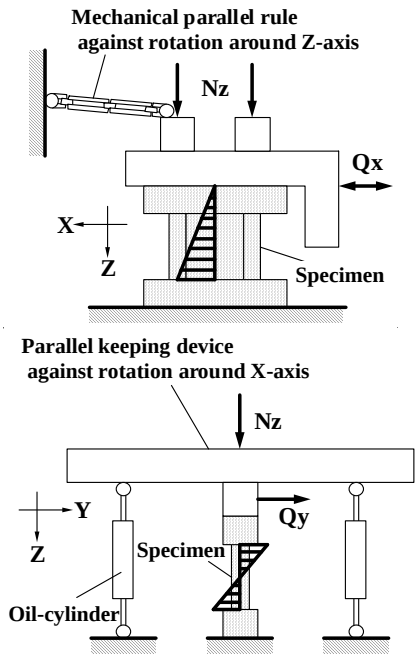

Figure 9 Loading Setup

The specimen SW-R-U was applied cyclic loading in X-direction under 0.07 of constant axial load ratio, and test result of this specimen was used to decide stiffness of the restoring force model. SW-R-B was applied cyclic loading in X-direction under constant Y-directional load and 0.07 of constant axial load ratio, and SW-B-1 was applied cyclic loading in Y-direction under constant X-directional load and 0.1 of constant axial load ratio. Test results of these two specimens were compared with numerical results.

3.2 Modeling of Restoring Force Characteristics

Figure 10 shows simplified restoring force characteristics in X and Y directions. A light broken curve on Q_X-R_X plane was the test result of SW-R-U. R_X and R_Y were deformation angles of the specimens. The simplified lines were bi-linear, and had parallelogram hysteresis loop and didn't have degradation of unloading rigidity. Yield point stiffness in X-direction was decided based on the test result of SW-R-U, and the stiffness in Y-direction was calculated by method written in AIJ standard (Architectural Institute of Japan, 1999). Yield strengths in X and Y directions were calculated on the condition that concrete and deformed bars were assumed as rigid perfectly plastic material, which strength were F_C and σ_y in Table 1, and bending strengths of sections of each material were added as added strength became maximum.

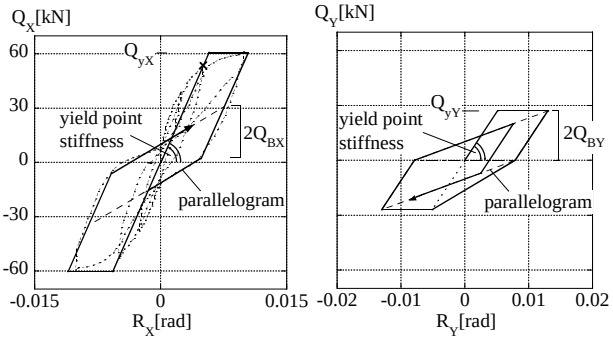

Figure 10 Restoring Force Characteristics of Shear Wall in X and Y directions

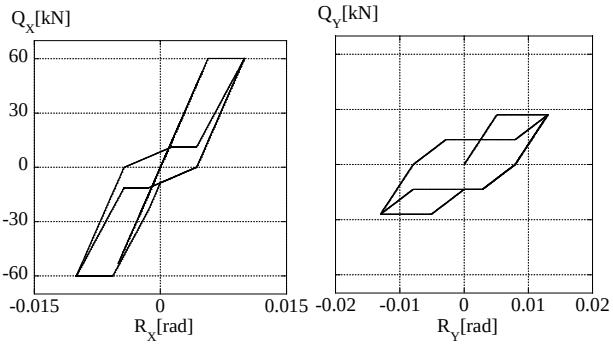

Figure 11 Relationships of Force and Deformation of Parallel System in X and Y directions

Next, the simplified restoring force characteristics shown in Figure 10 were divided into slipping type and elastic perfectly plastic type models. As shown in Figure 10, the yield strength of elastic perfectly plastic type model was

decided as twice of that was equal to height of parallelogram, which were $2Q_{BX}$ and $2Q_{BY}$. The parallelogram in X-direction was decided by using the test result of SW-R-U, and that in Y-direction was assumed as $2Q_{BY}$ was equal to Q_{yY}. The stiffness of two types of model were decided as both model yielded at the same time. Figure 11 shows force-deformation relationships of parallel system model in X and Y direction, respectively.

3.3 Comparison Between Test and Numerical Results

Figure 12 and 13 show comparison between test and numerical results of SW-R-B and SW-B-1, respectively. Solid line and broken line were numerical and test results, respectively. In numerical analysis of SW-R-B, (R_X, R_Y) were input data in the range from (a) to (b), and (R_X, Q_Y) were inputted in the range from (b) to (c). The result of SW-B-1 was also calculated in the same way as SW-R-B.

As shown in Figure 12, calculation of Q_X-R_X relationship showed good agreement with the test result, and Y-directional deformation, which direction was the same as direction keeping force constant, could be roughly estimated. In case of SW-B-1, area of hysteresis loop of calculation was larger than that of test result. It can be considered that is because this model wasn't considered rigidity degradation on unloading. The numerical result in R_X-R_Y relationship showed good agreement with the test results.

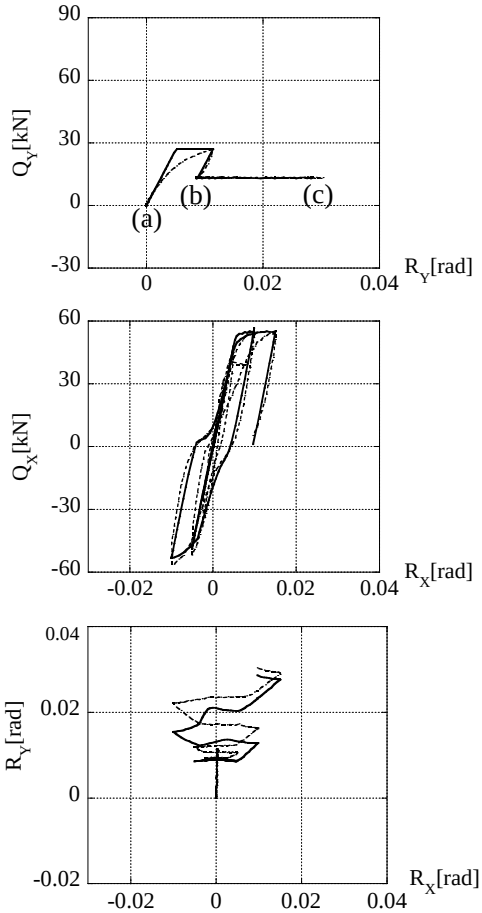

Figure 12 Comparison between Test and Numerical Result of Specimen SW-R-B

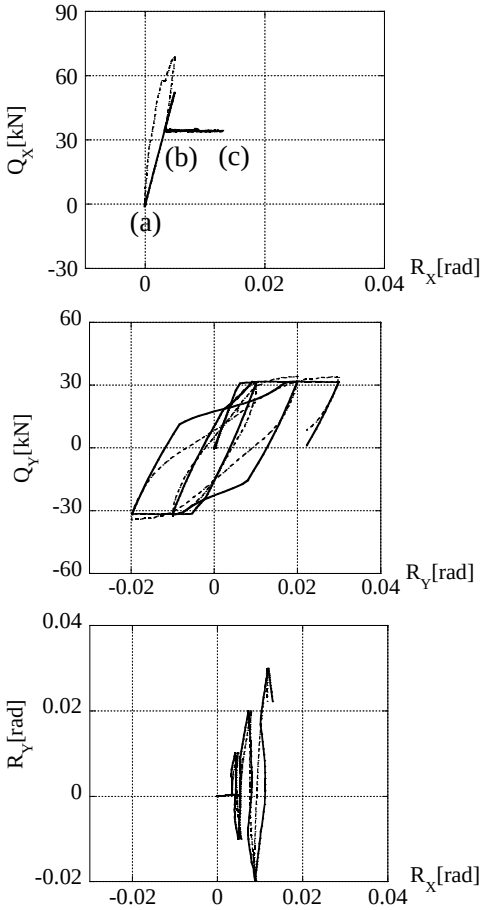

Figure 13 Comparison between Test and Numerical Result of Specimen SW-B-1

4. CONCLUSIONS

Bi-axial nonlinear restoring force characteristics of reinforced concrete shear wall specimens were modeled by using parallel system of slipping type and elastic perfectly plastic type models those were based on the theory of plasticity. It was confirmed that the model could roughly estimate the test results of specimens subjected to two-directional cyclic loading under constant axial load.

References:

Architectural Institute of Japan. (1999), "AIJ Standard for Structural Calculation of Reinforced Concrete Structures, -Based on Allowable Stress Concept-, revised 1999", Architectural Institute of Japan, (in Japanese).

Nishimura, K., Takiguchi, T., and Kojima, K. (2008), "Experimental Study on Behavior of Reinforced Concrete Shear Walls Subjected to Three-directional Loading", *Proceedings of Eleventh East Asia-Pacific Conference on Structural Engineering & Construction (EASEC-11)*, Taipei, Taiwan, Paper No. B07-07.

Nishimura, K., Nguyen, H. H., and Takiguchi, T. (2006), "Study on Formulation of Slipping Type Multi- Axial Restoring Force Characteristics of R/C Members", *Journal of Structural and Construction Engineering*, Architectural Institute of Japan, No.609, pp145-154, (in Japanese).

Sixth International Conference on Urban Earthquake Engineering
March 3-4, 2009, Tokyo Institute of Technology, Tokyo, Japan

EFFECT OF AXIAL LOAD ON THE SHEAR-TRANSFER MECHANISM DURING SHEAR DAMAGE PROGRESS IN R/C COLUMNS

Yasuji Shinohara [1] and Shizuo Hayashi[2]

1) Associate Professor, Structural Engineering Research Center, Tokyo Institute of Technology, Japan
2) Professor, Secure Materials Center, Tokyo Institute of Technology, Japan
yshinoha@serc.titech.ac.jp, hayashi.s.ac@m.titech.ac.jp

Abstract: Recent approaches to the design of reinforced concrete (RC) members have paid attention not only to shear failure as a primary cause of collapse, but also to shear damage from the viewpoint of serviceability and durability. Tests were performed on RC columns having axial load ratios of 0 to 0.3, and shear reinforcement ratios of 0.29% and 0.63% in order to study the influence of axial load and shear reinforcement upon the shear-transfer mechanism while shear damage was in progress. Resistance against shear damage increases with an increase in shear reinforcement, but the shear-transfer ability, due to the concrete contribution, decreases with an increase in shear reinforcement and axial load. A method for evaluating shear damage has been proposed based on the shear-transfer mechanism of concrete and reinforcement.

1. INTRODUCTION

As earthquake-resistant design of reinforced concrete (RC) buildings is making the transition to performance-evaluation design from technical-specification design (AIJ 2004), it is necessary not only to gather information on maximum shear carrying capacity relevant to safe performance, but also to evaluate subsequent operating performance and durable performance for continuous use, based on the damage to a building after an earthquake. In RC buildings, crack width is treated as a measure of damage evaluation in many cases, and plays an important role in the verification of damage limits. However, the shear-crack width in RC buildings that may occur in future earthquakes is not clearly estimated in current practical-use design due to the complicated stress-transfer mechanism of shear behavior.

Nakamura et al. (2005) clarified shear-crack behavior from the generation of a shear crack through to shear failure, and proposed a method of evaluating shear damage by making shear-crack width into an index. Their damage-evaluation method consists of the three processes shown in Fig. 1. They are: 1) the relation between the width of a shear crack at peak load (w_p) and that at unloading (w_r) (Kawai, S. *et al*. 2003), (2) the relation between the width of a shear crack at peak load and the strain of shear reinforcement (Handa, N. *et al*. 2004), and (3) the relation between the strain of shear reinforcement and shear force. According to the above-mentioned process, the maximum shear force experienced, V_1, can be estimated from the strain of shear reinforcement at peak load through crack width, w_{p1}, at the peak, calculated from the residual-crack width, w_{r1}, at unloading. The reverse process can be used to estimate residual-crack width, w_{r2}, to the assumed shear force, V_2. The shear force carried by a RC member is divided into three categories by referring to the Shear-friction Model (Moehle, J.P. et al. 2002) by means of a free body, which is used to evaluate the ultimate shear strength. They are the contributions from shear reinforcement, V_H, aggregate interlocking, V_i, and the arch mechanism of concrete, V_a. The arch mechanism of the concrete carries the total shear force before shear cracking, and it is assumed that the concrete contribution decreases linearly with an increase in the strain of shear reinforcement (crack width) after cracking. Moreover, when the compressive stress that acts on the diagonal compressive strut of the truss mechanism reaches the effective compressive strength of the concrete, it is supposed that the arch mechanism will disappear based on the truss arch theory. The strain of shear reinforcement, ε_{au}, in which the arch mechanism disappears, is computed, and a damage evaluation is performed.

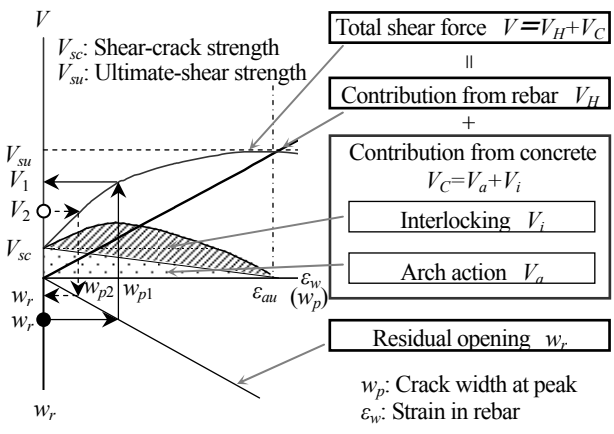

Figure 1 Concept of evaluation method for shear damage

However, the above-mentioned damage-evaluation method is proposed for a specimen without axial load. It has been pointed out in past research that axial load has an important effect on shear-crack behavior and damage evaluation. Therefore, in order to establish a more practical damage-evaluation method, it is necessary to store and compile data on a specimen that has axial load, and to verify the damage-evaluation method.

The main objectives of the present study are (1) to clarify the effect of axial load and shear reinforcement on shear-crack behaviors in RC columns based on the flexure-shear tests, (2) to propose a damage-evaluation method that takes axial load into consideration, and (3) to investigate the transition of the shear-transfer mechanism during the progress of shear damage in RC columns.

2. OVERVIEW OF EXPERIMENTS

2.1 Details of Test Specimens

The specimen used in the current study was designed so that it could be compared with previous specimens (Shinohara, Y. *et al*. 2007). The specimen configuration and the rebar arrangement are shown in Fig. 2. The common factors are the concrete strength (Fc45), the cross-sectional dimension (340 mm x 340 mm), the shear-span ratio (1.3) and the main reinforcement (8-D22). The variation factors are the shear reinforcement ratio of two levels (0.29%, 0.63%) and the axial load ratio of three levels (0, 0.15, and 0.30). Specimen details are shown in Table 1. The specimen designation is expressed by the concrete strength, the axial load ratio (%), and the shear reinforcement ratio (% × 100). All RC column specimens were designed to reach shear failure before the longitudinal reinforcement yield. For this reason, a high-strength screw reinforcement was used for the main reinforcement, and the end was welded to an anchor plate. Moreover, a high-strength welded square-shaped steel shear reinforcement was used, and additional rebar (D13) was positioned at intervals as shear reinforcement to prevent the columns from splitting due to bond failure. As the previous-specimen was designed to be compared with a specimen that introduced lateral prestress, the thickness of its covering concrete was reduced, as shown in Fig. 2. This difference is taken into consideration with regard to the handling of the number of shear reinforcements on the crack surface in the shear force contribution. The mix proportion of the concrete was the same as the previous-specimen.

Table 1 List of test specimens

Test Designation	σ_B N/mm^2	E_c N/mm^2	σ_y N/mm^2	p_w (%)	$_w\sigma_y$ N/mm^2	σ_0/σ_B
RC45-0-29	47.8	3.45×10^4	1190	0.29	1280	0
RC45-15-29*	44.2	3.34×10^4	1190	0.29	1470	0.15
RC45-30-29*	50.8	3.51×10^4	1200	0.29	1460	0.30
RC45-0-63	47.1	3.38×10^4	1190	0.63	1450	0
RC45-15-63	48.9	3.74×10^4	1190	0.63	1450	0.15
RC45-30-63	49.0	3.47×10^4	1190	0.63	1450	0.30
RC90-15-63*	91.9	4.21×10^4	1190	0.63	1410	0.15

*=previous specimens, σ_B=compressive strength of concrete, E_c=elastic modulus of concrete, σ_y=yield stress of longitudinal reinforcement, p_w=ratio of shear reinforcement, $_w\sigma_y$= yield stress of shear reinforcement, σ_0=axial stress of column

2.2 Loading and Measuring Method

A loading device is shown in Fig. 3. After introducing a predetermined axial load into the specimen using a 2000 kN oil jack, constant axial load was maintained with the controller until test termination. Cyclic horizontal loading was applied by displacement control so that antisymmetric flexural would occur in the specimen. The horizontal force was decreased when the rotation angle of the column amounted to ±1/400, ±1/200, ±1/100, ±1/67, ±1/50, and ±1/33, until peak load was reached. The relative displacement (horizontal and vertical) between the stubs was measured using a displacement-measuring jig attached to the up-and-down stub. Strain on the main reinforcement was measured at the ends of the test section to check the flexural yielding of the main reinforcement. In order to examine the correspondence to shear-crack behavior, the strain on the shear reinforcement was measured by attaching two (three) strain gauges on the front-face side and one gauge on the back side for all the reinforcements (Fig. 2).

All the shear-crack width generated above the shear reinforcement was measured at peak and unloading in each cycle using a digital microscope with a resolution of 0.01 mm. Furthermore, the sliding displacement of the crack

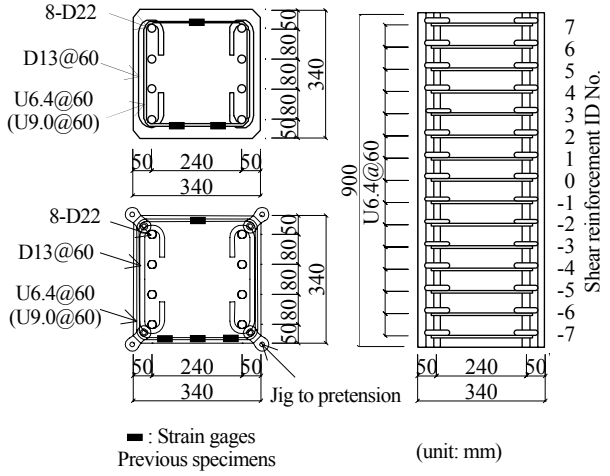

Figure 2 Details of test specimen

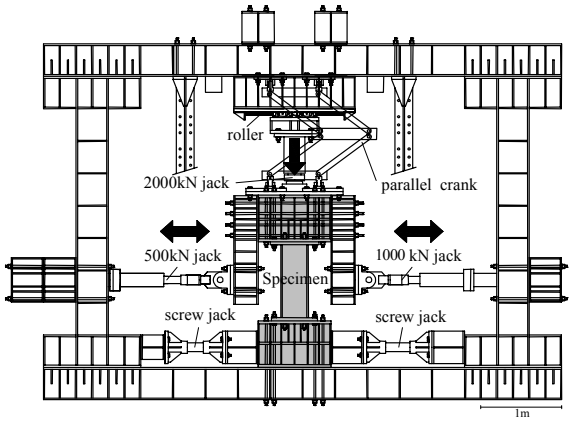

Figure 3 Loading apparatus

direction was measured between the reinforcements in which shear reinforcement has little effect on the sliding.

3. EXPERIMENTAL RESULT S

3.1 Shear Force and Rotation Angle Curves

Figure 4 shows the shear force Q-rotation angle R curves obtained from the experiments, and compares them to the analytical results. Table 2 shows the shear-crack strength and ultimate shear strength obtained from the experiment, the FEM analysis, and the calculation according to design guidelines (AIJ 1997). As for crack behavior, a flexural crack appeared in the flexural tensile region by 0.25% of the rotation angle, and it extended in a diagonal direction, and grew into a flexure-shear crack. Then, a shear crack occurred midway up the column before and behind the rotation angle of 0.5%. At maximum capacity, a tiny perpendicular crack appeared in the compression zone (the front face and side face) of the ends of the specimen, and eventually it reached compression-shear failure, accompanied by the partial exfoliation of the compressive cover concrete. The shear strength did not increase greatly despite the amount of reinforcement having been increased more than twofold, from 0.29% to 0.63%, because the carrying capacity was determined by the compression failure

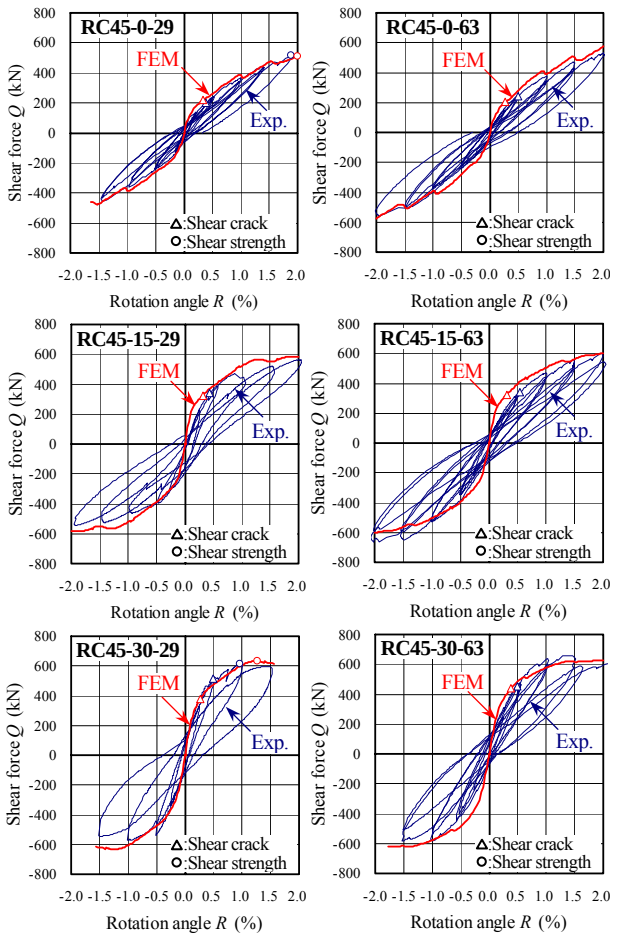

Figure 4 Comparison between analytical and experimental Q-R curve

Table 2 Shear-crack strength and ultimate shear strength

Test Designation	${}_{exp}Q_{sc}$ (kN)	${}_{exp}Q_{su}$ (kN)	${}_{FEM}Q_{sc}$ (kN)	${}_{FEM}Q_{su}$ (kN)	${}_{cal}Q_{sc}$ (kN)	${}_{cal}Q_{su}$ (kN)
RC45-0-29	203	515	222	512	176	520
RC45-15-29	343	595	324	585	339	617
RC45-30-29	515	617	380	634	496	648
RC45-0-63	243	662	202	578	175	617
RC45-15-63	338	603	325	603	363	628
RC45-30-63	453	660	440	625	483	629

${}_{exp}Q_{sc}$ =shear crack strength by experiment, ${}_{exp}Q_{su}$ =ultimate shear strength by experiment, ${}_{FEM}Q_{sc}$ =shear crack strength by FEM, ${}_{FEM}Q_{su}$ =ultimate shear strength by FEM, ${}_{cal}Q_{sc}$ =shear crack strength by AIJ 1997, ${}_{cal}Q_{su}$ =ultimate shear strength by AIJ 1997

of the concrete. With an increase in axial load, shear-crack strength and stiffness increased, but the shortening in the axial direction resulting from the sliding displacement of the crack surface became remarkable after the shear cracking.

3.2 Shear Crack Behavior

The crack pattern at the maximum shear load of each specimen is shown in Fig. 5. When computing the contribution ratio of the shear force in Section 4, the assumed final failure surface is also shown by the broken line in this figure. Generally, the crack angle also changes with shear loading. In particular, in the RC45-15-63 specimen, a flexure-shear crack that appeared around 0.5% of the rotation angle in the reinforcement location of the top +3 to +6 and lower -3 to -6 develops to the top +2 to +6 and lower -1 to -6 by 1% of the rotation angle, and the up-and-down flexure shear crack connects by 1.8% of the

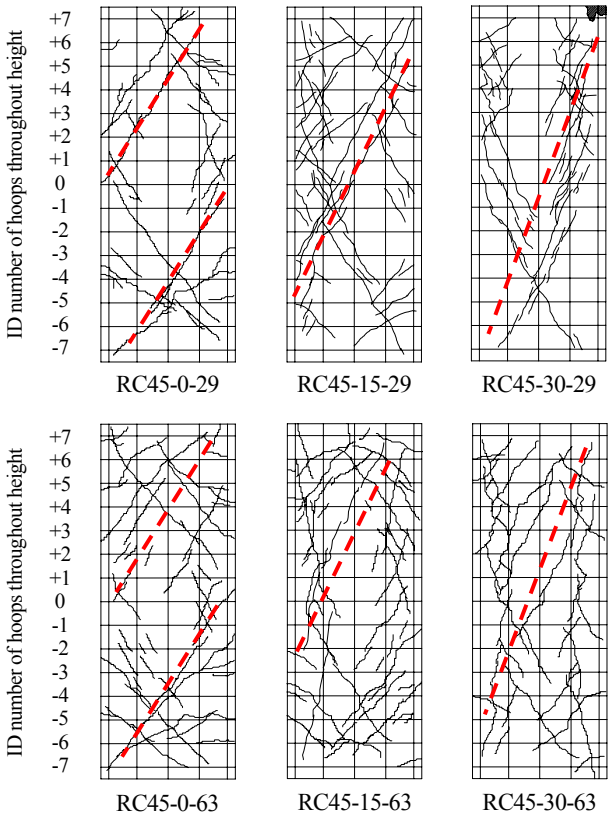

Figure 5 Crack patterns at maximum shear loads

rotation angle, and finally it changes to a one-shear crack. In this paper, therefore, the final-failure surface assumed in the free body model is determined, judging from the reinforcement location where the crack appeared notably at the maximum strength, and from the strain of the shear reinforcement increased. With an increase in axial load, the slope of the final-failure surface becomes steeper and approaches the member axis.

Figure 6 compares and shows the crack width (Δ: triangular symbols) computed from the strain of the shear reinforcement, and the total crack width (□: square symbols) measured by microscope on the corresponding shear reinforcement for each shear-reinforcement height. The rotation angle at the time of comparison is the rotation angle in which there are no loose areas in the cover concrete, and a clear crack width has been measured. In the axial load ratio of 0.30 series, the rotation angle is 1/100, and the rotation angle is 1/67 for the 0 and 0.15 series. Crack width measured by microscope is the surface value, and generally becomes wider compared with the crack width of the shear-reinforcement location evaluated by the strain of the reinforcement. However, as the tensile strain of the concrete is disregarded, and fine cracks may be overlooked, on the whole, both crack widths exhibit the same behavior. Therefore, it seems appropriate to use the strain of shear reinforcement as a measure of evaluation of shear damage related to shear-crack width. Crack width (◊: diamond symbols) as evaluated from the elongation of lateral reinforcement by FEM analysis is also shown in the figure. As compared with the same rotation angle, Fig. 6 also shows that doubling the amount of shear reinforcement reduces crack width by half.

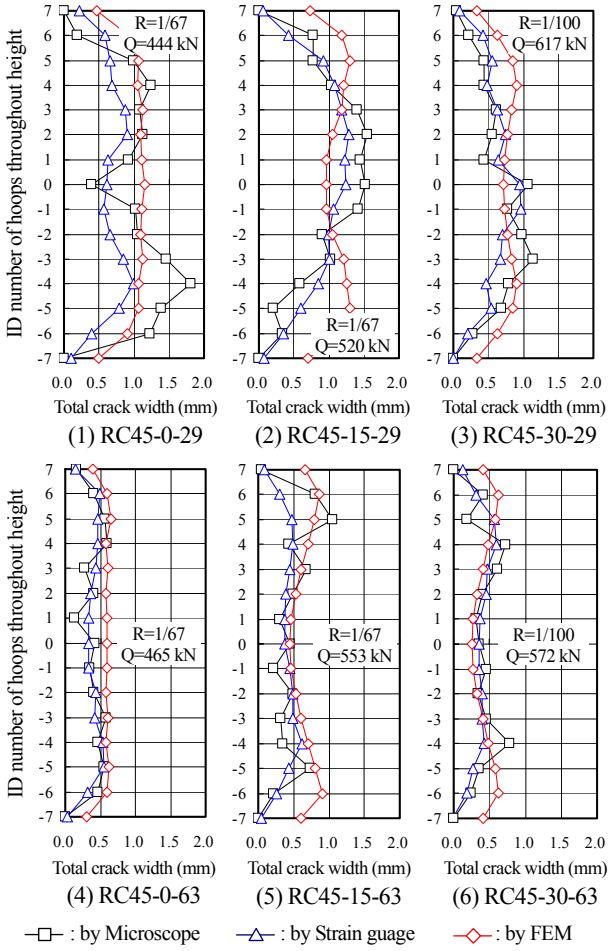

Figure 6 Total crack width obtained from microscope, strain of shear reinforcement and FEM analysis

4. SHEAR DAMAGE AND CONTRIBUTION RATIO OF SHEAR FORCE

4.1 Shear Force Transfer Model

From the viewpoint of shear-damage evaluation, the contribution ratio of shear force is examined by considering shear reinforcement strain as having a close relation to shear-crack width, as shown in Fig. 6. It is assumed that the shear force of the column is transmitted by three shear-transfer mechanisms: (1) shear reinforcement, V_H, (2) the arch mechanism of concrete, V_a, and (3) aggregate interlocking, V_i. The dowel action of the main reinforcement is disregarded because of its limited effect. If the failure surface is set up in the shear-transfer model of Fig. 7, the contribution from shear reinforcement is computable by measuring its strain. The angles, θ, of the failure surface set up in this paper are assumed to be 57 degrees, 64 degrees, and 69 degrees to the axial load ratios of 0, 0.15, and 0.3, respectively, judging from the final crack pattern of the experiment (see Fig. 5). The contribution, V_H, from shear reinforcement is the total tensile force of the number of shear reinforcements that cross the crack surface, and the tensile force is computed by multiplying average strain, ε_{AVE}, of the reinforcement by Young's modulus, E_s, and sectional area, na_w, of the shear reinforcement.

$$V_H = \varepsilon_{AVE} \cdot E_s \cdot n \cdot a_w = \varepsilon_{AVE} \cdot E_s \cdot j_t \cdot \tan\theta \cdot b \cdot p_w \qquad (1)$$

The distance, j_t, between the main reinforcements is 300 mm in the previous RC45-15-29, RC45-30-29, and RC90-15-63 specimen (see Fig. 2).

Nakamura et al. (2005) assumed that the contribution of shear force, V_a, from the arch mechanism of concrete disappears, when the concrete compressive stress, ${}_c\sigma_t$, produced by the truss mechanism reaches the effective compressive strength of the concrete, $\nu\sigma_B$, based on the Ultimate Strength Concept. Therefore, from ${}_c\sigma_t=\nu\sigma_B$, the strain of the shear reinforcement, ε_{au}, in which the arch mechanism disappears is defined by the following equation:

$$\varepsilon_{au} = \frac{\nu\sigma_B}{p_w \cdot E_s (1+\cot^2\phi)} \qquad (\varepsilon_{au} \le \varepsilon_y) \qquad (2)$$

where cot φ is set to two, within the limits that the arch mechanism produces. However, as the effect of axial load is not taken into consideration by this equation, ε_{au} will be overestimated to the member bearing the axial load. Then, in order to reflect the influence of axial load, the strain obtained by converting the axial stress into the direction of the concrete compressive strut of the truss mechanism and

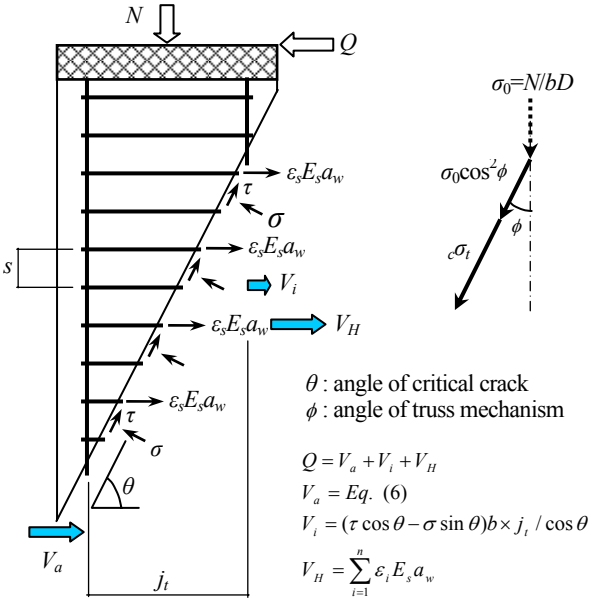

Figure 7 Free body diagram for end support region of columns and shear force contributions

deducting from the effective compressive strength of the concrete is defined as the shear-reinforcement strain in which the arch mechanism disappears. However, this paper also does not question the difference in the angle of the compressive strut in the arch mechanism and the truss mechanism.

$$\varepsilon_{au} = \frac{\nu\sigma_B - \sigma_0\cos^2\phi}{p_w \cdot E_s(1+\cot^2\phi)} \qquad (\varepsilon_{au} \le \varepsilon_y) \tag{3}$$

$$\nu = 0.7 - \sigma_B/200 \quad \text{for} \quad \text{Fc45}$$

$$\nu = 0.25 + 11/\sigma_B \quad \text{for} \quad \text{Fc90}$$

The initial value of the contribution of shear force, V_a, from the arch mechanism of concrete is defined by Eq. (4) for shear-crack strength, V_{sc}, in Design Guidelines (AIJ 1997), supposing that the concrete carries the total shear force before the shear crack is generated. After shear cracking, Eq. (5) is obtained by assuming that V_a decreases linearly with the increase in the strain of shear reinforcement, and that it becomes zero by the strain, ε_{au}, in which the arch mechanism disappears.

$$V_{sc} = \sqrt{\sigma_T^2 + \sigma_T \cdot \sigma_0} \cdot b \cdot D/1.5 \qquad (\sigma_T = 0.33\sqrt{\sigma_B}) \tag{4}$$

$$V_a = V_{sc}\left(1 - \frac{p_w \cdot E_s \cdot (1+\cot^2\phi)}{\nu\sigma_B - \sigma_0\cos^2\phi} \cdot \varepsilon_{AVE}\right) \tag{5}$$

If the shear slide increases in a crack, the surfaces facing each other across the crack will contact and stresses, τ and σ, will be transmitted in parallel and in the normal direction to the crack surfaces (Fig. 7). The contribution of shear force, V_i, from this aggregate interlock is obtained as Eq. (8) from the simple solution (6) and (7) of the stress-transfer constitutive equations that are controlled by the ratio of the shear slide to the crack width, which is proposed by Li and Maekawa (Li et al. 1989). It is not realistic to evaluate the aggregate interlocking effect on all individual cracks using Li and Maekawa's model. Therefore, the average aggregate interlocking effect is evaluated using the shear-crack width obtained from the strain of the shear reinforcement to the final failure surface, and the shear slide by Eq. (9). Eq. (9) is determined to become a bigger sliding value than the shear slide, $\delta = 0.71w^{1.65}$, without the axial load (Nakamura et al. 2005).

$$\tau = m\frac{\psi^2}{1+\psi^2} \tag{6}$$

$$\sigma = m \cdot \left(\frac{\pi}{2} - \cot^{-1}\psi - \frac{\psi}{1+\psi^2}\right) \tag{7}$$

$$m = 3.83\sigma_B^{1/3}, \quad \psi = \delta/w$$

$$V_i = (\tau\cos\theta - \sigma\sin\theta)b \cdot j_t/\cos\theta \tag{8}$$

$$\delta = 1.0w^{1.65} \tag{9}$$

4.2 Strain of Shear Reinforcement and Contribution of Shear Force

Figure 8 shows each contribution ratio of shear force computed based on the average strain of the shear reinforcement of the failure surface, as described in the previous section. The total shear force by the experiment, Q, the contribution of the shear reinforcement, Q_H, and the contribution of the concrete, $Q_c = Q - Q_H$ are shown using a line having a marker. The total shear force, $V_{c+H} = V_c + V_H$, the contribution ratio of the shear reinforcement, V_H, and the contribution ratio of the concrete, $V_c = V_a + V_i$, are calculated by the method given in the previous section and shown in a solid line. Furthermore, the broken line shows shear force, V_{a+H}, which ignores the shear force from aggregate interlocking, and the shear force, V_a, from the arch mechanism of concrete. It is assumed that the aggregate interlocking effect will disappear if compressive stress reaches effective compressive strength.

Eq. (1) which evaluates the contribution of shear force from shear reinforcement is finally in agreement with the experiment because it is dependent upon the reinforcement number that exists in the final-crack surface. However, in a specimen with a low axial load, as the flexure-shear crack proceeds at the upper and lower ends of the specimen first, and then the crack-progress behavior changes to the final-crack surface, the number of shear reinforcements reckoned to contribute to shear force will differ with crack progress, and the shear stiffness will also change. As a strong correlation exists between the strain of the shear reinforcement and the width of the shear crack, the slopes of the curves in Fig. 8 express the resistance to the widening of a crack (it is called "crack stiffness" below) after shear crack. Although the crack stiffness increases with the increase in the amount of shear reinforcement, it tends to decrease with an increase in the axial load. Especially the V_{a+H} curve of the RC45-30-63 specimen (see Fig. 8 (6)) that has a high axial load and a large amount of shear reinforcement shows a negative slope, and the curve by the experiment also shows the same slope (see the ellipse parts by the dotted line). This is because the strain of shear reinforcement in which the arch mechanism disappears is very small and the shear force from shear reinforcement does not reach shear-crack strength. On

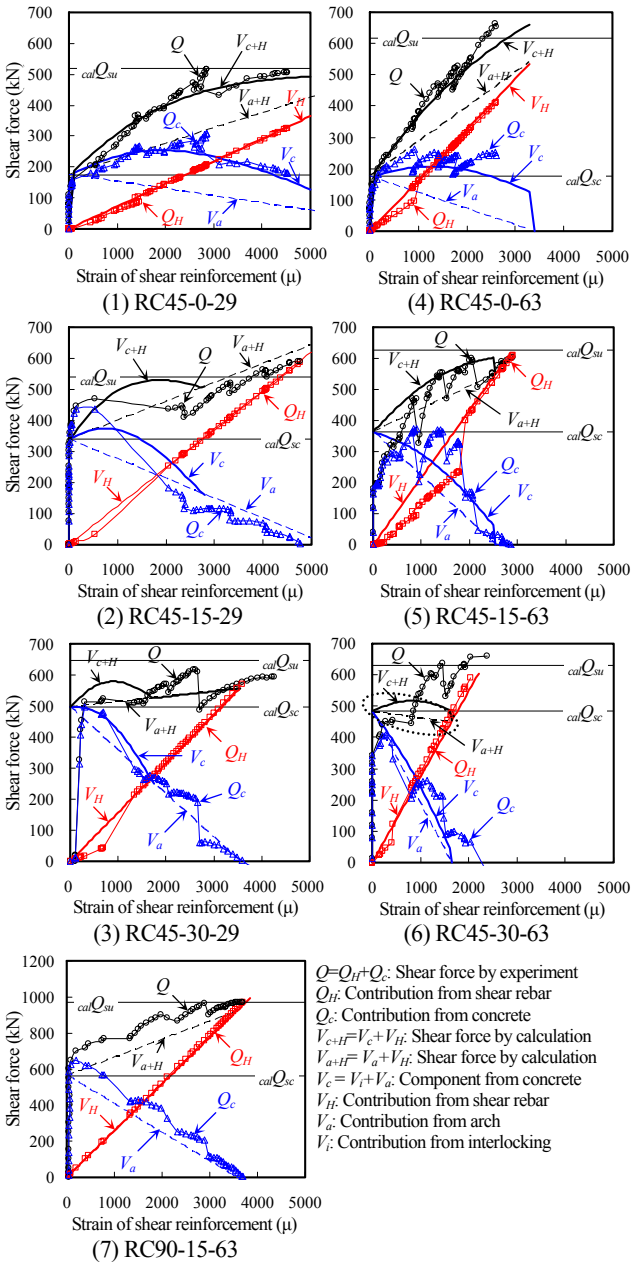

Figure 8 Relation between average strain of shear reinforcement and shear force component by proposed method

generating the shear crack, the shear reinforcement cannot carry the shear force carried by the concrete before cracking, so the reinforcement strain (crack width) increases rapidly.

The shear-reinforcement strain, ε_{au}, is shown in Table 3 to give a comparison of the three results from Eq. (5), the experiment, and the FEM analysis. It can be seen that Eq. (5), which incorporates the effect of axial load, can mostly estimate the shear-reinforcement strain, ε_{au}, in which the arch mechanism disappears. With an increase in axial load and shear reinforcement, as the compressive stress of the concrete strut increases, ε_{au} decreases, and the arch mechanism disappears at an early stage. Thus, the amount of shear reinforcement has both an action that improves crack stiffness after cracking, and an action that extinguishes the arch mechanism in the early stage.

Table 3 Average strain of shear reinforcement, ε_{au}, (μ)

Test Designation	RC45-0-29	RC45-15-29	RC45-30-29	RC45-0-63	RC45-15-63	RC45-30-63	RC90-15-63
Experiment	—	4810	3630	—	2860	2270	3690
Eq.(5)	7600	5340	3540	3390	2540	1630	3550
FEM	—	4520	3960	—	2850	2120	—

5. CONCLUSIONS

1) If the amount of shear reinforcement is doubled, the crack width is controlled by about half, and the crack tends to be distributed.
2) If the amount of shear reinforcement increases, resistance to the widening of the crack (crack stiffness) will also increase, but if the axial load increases, crack stiffness will decrease. This is because shear reinforcement functions also to control the shear-sliding displacement due to the axial load.
3) As a close relation exists between the strain of the shear reinforcement and the width of the shear crack, the strain of shear reinforcement can be used as a measure to evaluate quantitatively shear damage based on shear-crack width.
4) With the increase in axial load, as compressive stress by axial load is added to the compressive stress of concrete by the truss mechanism, the compressive stress in the concrete reaches effective compressive strength at an early stage, and the arch mechanism of the concrete disappears.
5) The amount of shear reinforcement has both the function of improving crack stiffness after cracking, and removing the arch mechanism at an early stage.

References:

Architectural Institute of Japan (2004), 'Guidelines for Performance Evaluation of Earthquake Resistant Reinforced Concrete Buildings', AIJ.

Nakamura, Y. *et al*. (2005), 'Shear Crack Behavior and Evaluating Methods of Shear Crack Width of RC Columns to Damage Process', *Proceedings of the Japan Concrete Institute*, Vol.27, No.2, pp.211-216.

Kawai, S. *et al*. (2003), 'The Influence of Axial Load and Section Shape of RC Column to Damage Process', *Proceedings of the Japan Concrete Institute*, Vol.25, No.2, pp.265-270.

Handa, N. *et al*. (2004), 'Damage Process Estimation of RC Column using Shear Crack Behavior', *Proceedings of the Japan Concrete Institute*, Vol.26, No.2, pp.217-222.

Moehle, J.P., Elwood, K.J. and Sezen, H. (2002), 'Gravity Load Collapse of Building Frames during Earthquakes', ACI SP-197, Behavior and Design of Concrete Structures for Seismic Performance, ACI, pp215-238.

Shinohara, Y. *et al*. 2007, 'Effect of Active Confinement on Shear Behavior for High-Strength Concrete Columns Prestressed Laterally', *J. Struct. Const. Eng.*, AIJ, [613], pp.113-120.

Architectural Institute of Japan (1997), 'Design Guidelines for Earthquake Resistant Reinforced Concrete Buildings Based on Inelastic Displacement Concept', AIJ.

Li, B. Maekawa, K. and Okamura, H. : Contact Density Model for Stress Transfer across Cracks in Concrete, *J. of the faculty of eng., The university of Tokyo,* Vol. XXXX, No.1, pp.9-52, 1989

Sixth International Conference on Urban Earthquake Engineering
March 3-4, 2009, Tokyo Institute of Technology, Tokyo, Japan

YIELD SURFACE AND BEHAVIOR OF 3D ASYMMETRICAL RC FRAMES WITH SHEAR WALLS

Hisato Hotta[1)], Kenichi Fuchizawa[2)]

1) Assoc.Prof.,Graduate School of Science and Engineering, Tokyo Institute of Technology, Dr.Eng.
2) Graduate Student, Graduate School of Science and Engineering, Tokyo Institute of Technology
hotta@arch.titech.ac.jp, fuchizawa.k.aa @m.titech.ac.jp

Abstract: As for reinforced concrete multi-story buildings in which open frames and wall frames are paralleled alternately and with asymmetric plans, this paper indicates that there is a case transverse displacement is accumulated during the vibration in wall direction through several numerical analyses. It is concluded that the reason of that phenomenon is because the yield surface is not symmetric and transverse component of the plastic displacement is always positive or negative regardless of the direction of the displacement of the wall.

1. INTRODUCTION

In the case of 3D reinforced concrete structures in which open frames and wall frames are paralleled alternately as shown in Fig.1 subject to horizontal external load in the wall direction (X direction), transverse beams by which the open frames and the wall are connected are forcibly deformed due to the difference of vertical elongation of the columns between in the open frames and in the wall ones. When such structures have an asymmetrical plan as shown in Fig.2 and the external force is loaded in X direction, the direction of the story drift is different from X direction, because the shear force and the bending moment of the transverse beams at both sides of the wall frame are different. As for asymmetrical structure, it is very often that the direction of the deformation is not equal to the direction of the force. In this case inverse force causes inverse deflection in general, however, in the case above mentioned, deformation in Y direction is always positive whether the external force in X direction is positive or negative, therefore, there is some possibility the transverse inelastic deformation accumulates during the vibration in one direction in those structures. The objective of this study is to show that such phenomenon exists actually through static and dynamic analyses in numerical space.

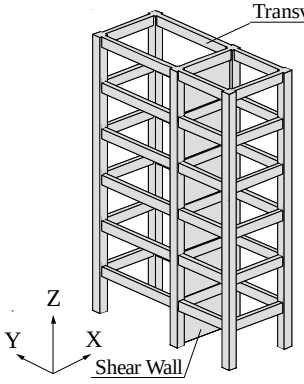

Figure1 Analytical Object

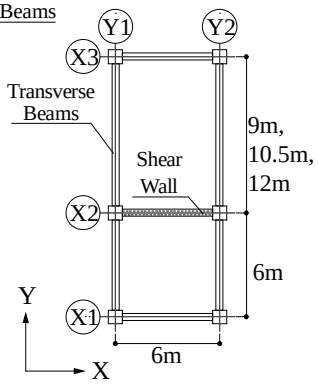

Figure2 Planning

2. DIMENSION AND DETAIL OF ANALYTICAL OBJECT

An analytical object is 2-span-1-bay-6-story reinforced concrete structure that has already shown in Figs1 and 2 in the previous paragraph. Typical span length was set to 6 meters and only the span length between X1 and X2 was varied from 6, 9, 10.5 and 12 meters as shown in Fig.2. The dimension and the amount of the longitudinal rebars for the beams, columns and the wall are indicated in Table 1. The specifications of the beams indicate in Table 1 is for the one with the length of 6 meters and when the length is varied, the

Table1 Specification of Analytical Object

story	Column		Beam			Shear Wall		Weight (kN)	Floor height (cm)
	B×D (cm)	rebars	B×D (cm)	top rebars	bottom rebars	thickness (cm)	reinforcing ratio (%)		
6	70×70	24-D25	35×70	4-D25	4-D25	20	0.48	1950	400
5	75×75		40×80					2080	
4	75×75		45×85					2120	
3	80×80	32-D25	45×90				0.60	2200	
2	80×80		50×95					2270	
1	85×85		50×95					2480	

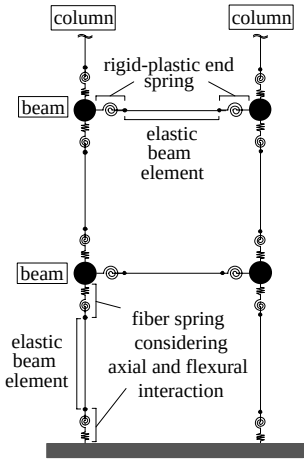

Figure 3 Frame Model

depth is also varied in proportion to the length, however, the amount of the longitudinal reinforcement is fixed, therefore, for example the beam with the length of 12 meters has the ultimate end moment 2 times as large and the same ultimate shear strength as the typical one has. The weight and the height of each story are also indicated in Table 1. The story height was 4 meters for every story. All the columns were assumed to share 1/6 of the story weight in this analysis

3. NUMERICAL MODELING OF ANALYTICAL OBJECT

As shown in Fig.3, members were modeled to several series springs. The beams were modeled to an elastic beam element of which stiffness EI and EA with rigid-plastic springs at both the ends. Hysteretic rules for the end spring was assumed degrading stiffness tri-linear model. The columns were also modeled to an elastic beam element with rigid-plastic springs at both the ends. In order to take account of an interaction between an axial and a flexural behavior, fiber springs as the end springs were applied for the columns. The walls were modeled to an elasto-plastic beam element in in-plane direction and assumed to have no stiffness in transverse direction.

Boundary condition between the structure and the ground was assumed rigid. All slabs were assumed rigid in plane.

4. ANALYTICAL RESULTS

4.1 Pushover analysis

Two directional pushover analyses were carried out. The angle between X axis and the direction of external force loaded at the 6th floor (θ) was changed from –90 degree to 90 degree with interval of 5 degree. The vertical distribution of the external force was the sum of the elastic response of the all modes by SRSS method.

Figure 4 shows the base shear versus drift angle at the 1st story relationship of each frame in the case the length of transverse beam is 9 meters and the direction of the external force is 0 degree. Because the analytical object has asymmetrical plan, the base shear of the open frames X1 and X3 are not coincident. The orbit of the displacement of the 1st and the 6th floors are drawn on X-Y plane in Figs. 5 and 6. As shown in the figures, the direction of the displacement is almost 0 degree initially and the component in Y direction gradually developed after cracking of the transverse beams (marked by ○ in the figures) and yielding of the ones (marked by ●.) The direction of the displacement is fixed after yielding of the transverse beams. The wall is yielded due to bending at the bottom at the mark □ in Fig.5.

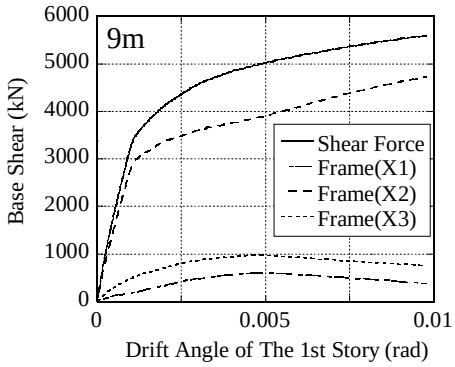

Figure 4 Base Shear – Story Drift Angle Relationship

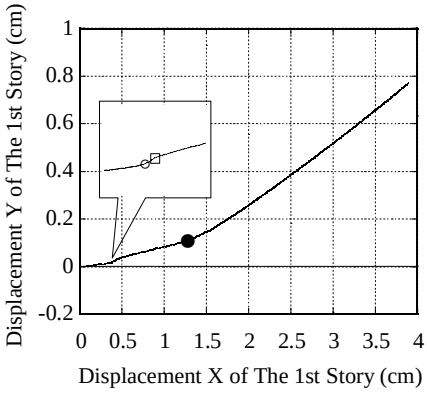

Figure 5 Y-X Directional Displacement Relationship of The 1st Story

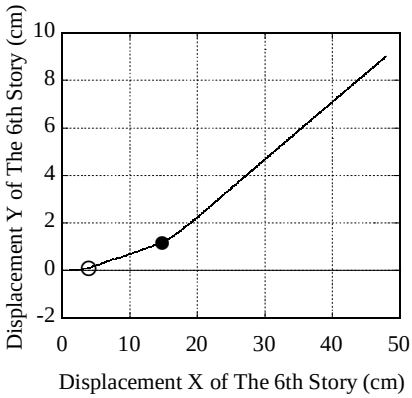

Figure 6 Y-X Directional Displacement Relationship of The 6th story

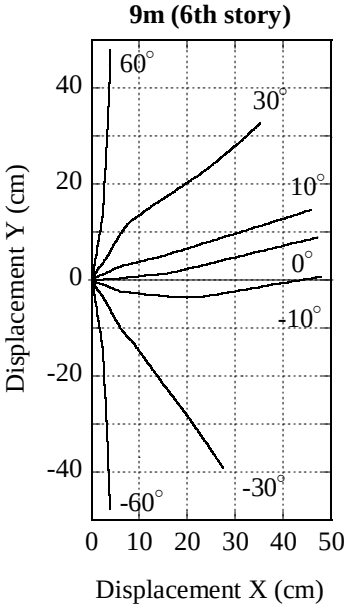

Figure 7 Y-X Displacement Relationship at Each Load Direction

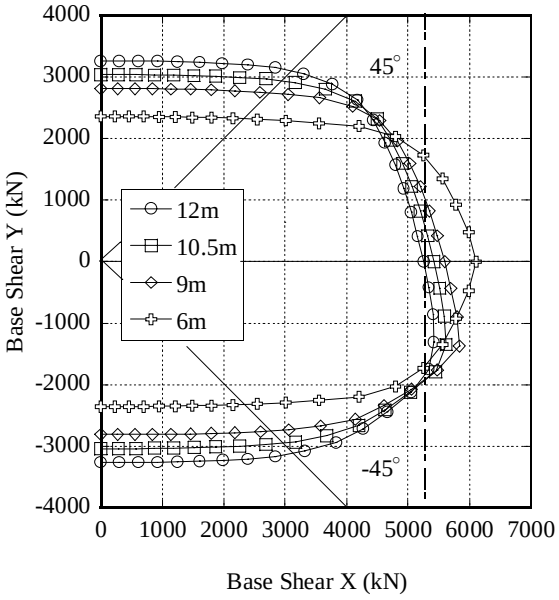

Figure 8 Yield Surfaces of The Analytical object with different Length of Transverse Beams

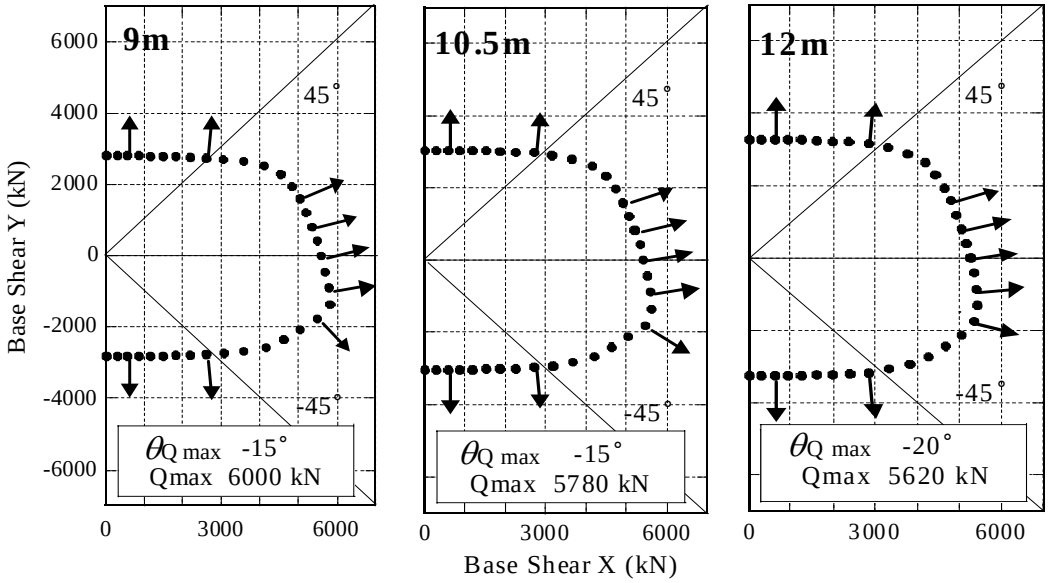

Qmax is Maximum strength and θQmax is then Direction of external

Figure 9 Relationship of Yield Surfaces and Plastic Deformation Direction

The orbits of the displacement of the 6th floor in the several cases the direction of the external are varied are drawn in Fig.7. Y component of plastic displacement is always positive in the case θ is ranged at least from –10 to 10 degree as shown in Fig.7. Also as shown in Fig.7, both directions of the displacement in the cases θ = 30 degree and θ = –30 degree are considerably different.

4.2 Yield surface

Yield surfaces are indicated in Fig.8 for all variations of the length of transverse beams. The base shear at the mean story drift angle of 0.02 rad is regarded as ultimate strength and plotted on X-Y plane because the structures reach to almost collapse mechanism at that drift angle. Chained line in Fig.8 stands for the ultimate base shear in X direction in the case the effect of the transverse beams is neglected. The yield surface is symmetric about both X and Y axes for the structure having the symmetrical plan, however, it is not symmetric about Y axis for asymmetric structure. The effect of the transverse beams becomes small according as the length of one side transverse beam changes from 6 meters to 12meters as shown in Fig.8.

The yield surfaces are drawn with the direction of plastic deformation in Fig.9 for each analytical object with different length of transverse beams. It can be recognized that the direction of the plastic deformation is perpendicular to the yield surface.

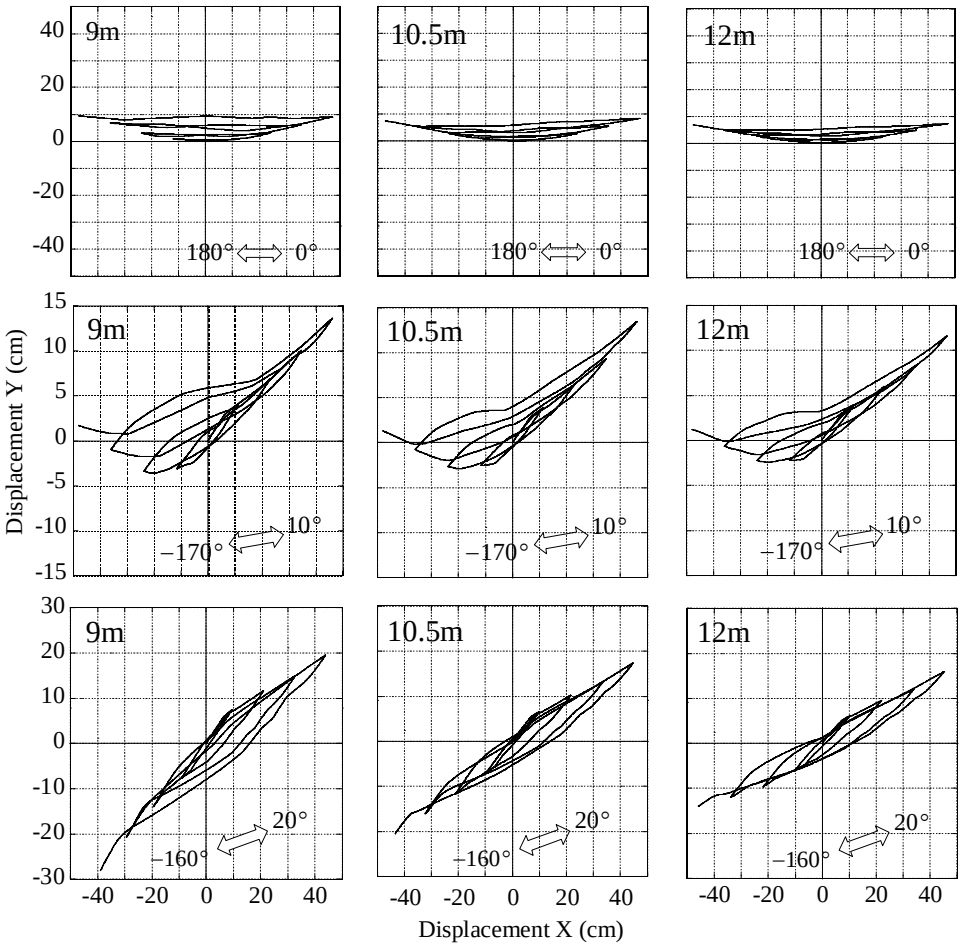

Figure 10 Y-X Displacement Relationship by Cycle Loading Analysis

4.3 Cyclic behavior

Figure 10 shows the orbit of the displacement of the 6th floor obtained by cyclic analyses. In the case $\theta = 0$ degree, the displacement in Y direction was gradually accumulated according to the number of the cycle. In the case $\theta = 10$ degree, the displacement in Y direction was negative during loading in opposite direction before yielding, however, it was reversed after yielding.

4.4 Dynamic analysis

Dynamic analyses were also carried out for the analytical object. The inputted ground motions were sine wave with constant amplitude of 400 gal and the direction of them was 0 degree in q. The integration interval was set to 0.002 second and Newmark-β method ($\beta = 1/6$) was used for the numerical integration of the equation of motion. Dumping factor of 5% was assumed for all modes determined by initial stiffness.

Figures 11-15 show the results in the case the period of the sine wave is 1.2 second. In addition, the length of transverse beam at one side is 9 meters. The natural period of the analytical object is 0.52 second in X direction and 1.02 second in Y direction. Figure 11 shows the time history of the displacement of the 6th floor in X direction. Figure 12 shows the one in Y direction. Figures 13 and 14 show the end moment versus the end rotation angle relationships for the transverse beams Y11 and Y21 located at the 1st floor. Figure 15 shows the end moment of the base columns 13' s bottom. After the negative peak at almost 2 seconds (marked by ● in the figures,) the transverse beam Y11 is yielded and the displacement in Y direction is gradually accumulated. In accordance with increasing the displacement in Y direction, the rotation angle at the end of the beams and the end moment in Y direction of the column 13 are also increased.

Figures 16-19 show the results in the case the period of the sine wave is 0.8 second and the natural period of the analytical object is 0.38 second in X direction and 0.73 second in Y direction. The length of the transverse beam is also 9 meters. Why the natural period is different from the former example is that the mass of the floor is reduced to 1/2 in this example. Similar to the former example, the displacement in Y direction is also accumulated in this example. Moreover in this case, the displacement in Y direction eventually becomes larger than the one in X direction.

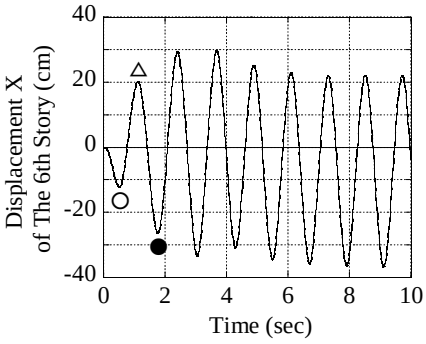

Figure 11 Time History of X Directional Displacement of The 6th Story

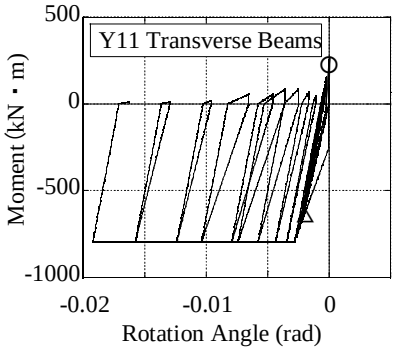

Figure 13 Moment-Rotation Angle Relationship of The Y11 Transverse Beams

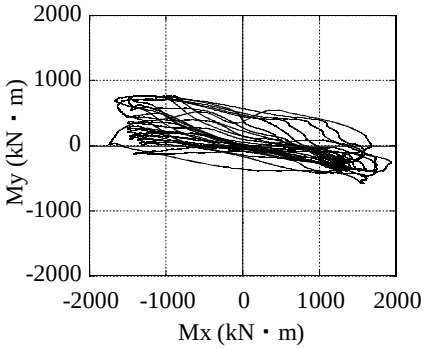

Figure 15 X-Y Directional Moment Relationship of The Column 13

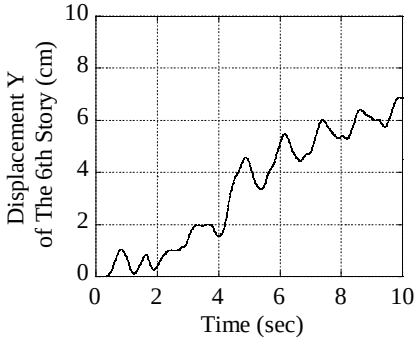

Figure 12 Time History of Y Directional Displacement of The 6th Story

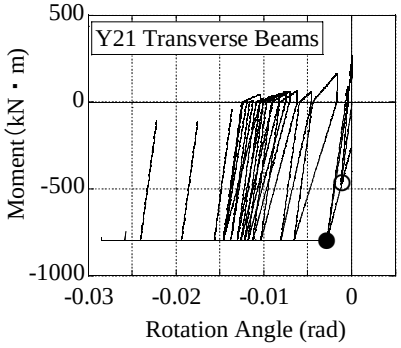

Figure 14 Moment-Rotation angle Relationship of The Y21 Transverse Beams

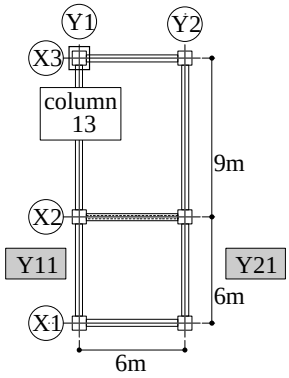

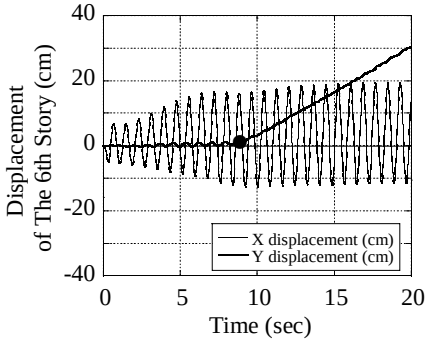

Figure 16 Time History of X-Y Directional Displacement of The 6th Story

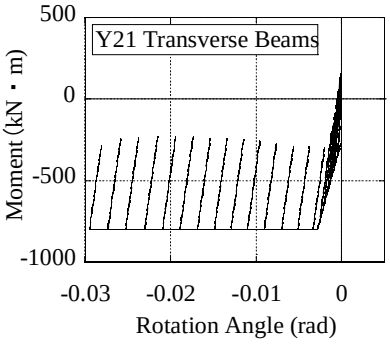

Figure 18 Moment-Rotation Angle Relationship of The Y21 Transverse Beams

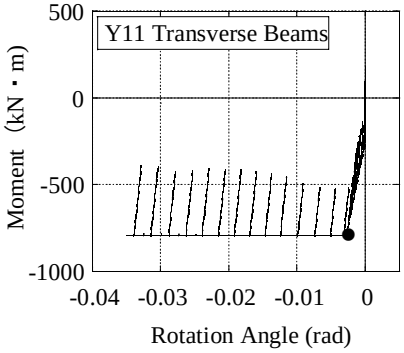

Figure 17 Moment-Rotation Angle Relationship of The Y11 Transverse Beams

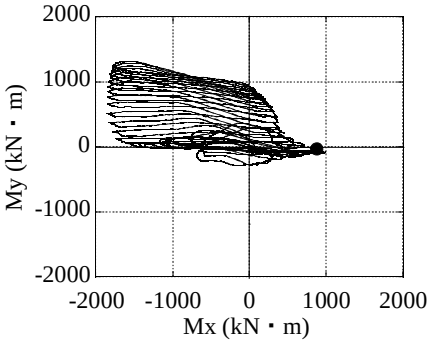

Figure 19 X-Y Directional Moment Relationship of The Column 13

5. CONCLUSIVE REMARKS

As for reinforced concrete multi-story buildings in which open frames and wall frames are paralleled alternately and with asymmetric plans, there is a case transverse displacement is accumulated during the vibration in wall direction through several numerical analyses. The reason of that phenomenon is because the yield surface is not symmetric and transverse component of the plastic displacement is always positive or negative regardless of the direction of the displacement of the wall.

References:

Aono M. and Ichinose T. (2007) "Yield surface and seismic response of RC frames with eccentricity", Journal of Structural Engineering Vol. 53B 1-8 (in Japanese).

"Guideline for evaluating performance of reinforced concrete structures" Gihoudo Shuppan 2000 (in Japanese)

Hotta H. and Nagao M. (2003) "Inelastic torsional response analyses for 3D RC frame composed of bare RC frames and independent shear walls" Proc. of the 9th East Asia-Pacific Conference on Structural Engineering and Construction SME-120

Sixth International Conference on Urban Earthquake Engineering
March 3-4, 2009, Tokyo Institute of Technology, Tokyo, Japan

REINFORCED CONCRETE BEAM-COLUMN JOINTS: AN OVERLOOKED FAILURE MECHANISM

Hitoshi Shiohara

Associate Professor, Department of Architectural Engineering, The University of Tokyo, Japan
shiohara@arch.t.u-tokyo.ac.jp

Abstract: This paper proposes a series of simple mathematical expressions useful in predicting the ultimate behavior of two-dimensional reinforced concrete beam-column joints. The expressions are based on a model that reflects observations of the crack pattern at failure, and its compatible kinematic field, overlooked in prior research. The kinematic model, called a Nine Parameters (DOF) model is combined with non-linear constitutive relations for concrete and steel to bear simple algebraic expressions for the ultimate moment capacity and moment at balanced failure of interior beam-column joints. Simple equations for the upper bound value of the amount of reinforcement precluding the joint failure before yielding of longitudinal reinforcement are also presented. This paper treats a special case of a symmetric interior beam-column joint subjected to four symmetric couples of forces transmitted among the four connected members, without joint shear reinforcement or mid-layer longitudinal reinforcement in the column. In addition, the amount of longitudinal reinforcements in the beams and columns are identical. The algebraic expressions for the moment at balanced failure of a beam-column joint is developed and the factors affecting the upper bound reinforcement are identified.

1. INTRODUCTION

The analytical tool for seismic design of reinforced concrete moment resisting frame usually assumes that the beam-column joint does not fail and that integrity of the adjacent members is maintained. But in reality, some beam-column joints with particular combinations of design parameters such as dimensions, reinforcement ratios and combination of member end forces may exhibit a concentration of damage at the beam-column joint. This causes difficult repair work post earthquake, and may prevent flexural hinge from reaching its expected moment capacity, thus limiting energy dissipation by stable hysteretic cycles. As a result, the seismic performance is jeopardized.

Hence, the seismic design of beam-column joints should ensure that: (1) damage is not concentrated in the beam-column joint, and (2) the moment capacity and stiffness of the members framing into the joint follow the flexural theory.

To date, there have been no practical design models based on mechanism that are capable of predicting and controlling the seismic performance of beam-column joints based on the geometry, reinforcing details, and mechanical properties of the materials. The development of theoretical modeling of beam-column joint have lagged far behind other aspects of reinforced concrete structures, despite the crucial roles these joints play in overall seismic performance.

The well-known but empirical idea of failure of beam-column joints subjected to lateral load, is that shear failure develops due to excessive shear forces in the column induced by the bending moment at the ends of beams. The majority of past research developing mathematical models have been based on this idea. Paulay et al. (1978) have proposed a design concept to preclude shear failure of RC beam-column joints. They define joint shear at the flexural capacity at beam ends. Then a truss mechanism in beam-column joint resisting the joint shear is derived. The truss mechanism is used to design sufficient shear capacity to make the beam-column joint elastic and decrease the nonlinear deformation in the joint. However a typical calculation using this model shows that a quite a large percentage of joint horizontal hoop reinforcement is required and this is not practical.

Ichinose (1988) and Fujii (1989) have independently proposed a similar combined mechanism of truss and struts resisting the joint shear in which the contribution of each element is determined considering the equilibrium of the joint shear force as well as axial forces and moments. The assumptions in these models are not simple and the validity and scope are not clear. The calculation procedure is also too complicated for practical design.

Cheung et al. (1991) have proposed a practical design method as a revision to the original truss mechanism by Paulay. By adding the contribution by a variable strut to shear resistance, reflecting bond deterioration of the longitudinal bars passing through the joint, the

required joint shear reinforcement can be reduced. Although the model is clear, it still requires a large percentage of joint reinforcement and is adopted only in New Zealand.

Hwang (1999), Ingham et al. (2001) and other researchers have tried to apply Strut and Tie Model (STM) to the beam-column joint for predicting strength of the joint for design. However each model is applicable to one particular configuration and reinforcing detail and as a result this approach is not widespread.

Prior research dealing with modeling of RC beam-column joints commonly uses models that consider equilibrium and the failure condition of the elements using a shear transfer mechanism that assumes the longitudinal reinforcing bars are infinitely strong in tension. Hence, the joint shear failure is defined due to one of the following conditions: (1) the concrete reaches its compressive strength, (2) bond failure occurs between the longitudinal bars and the concrete, or (3) the joint reinforcement yields. The objective in modeling of the joint strength is to use it in a capacity design that requires the joint shear strength to exceed the induced joint shear at the flexural capacity of the beam or column. The rationality of such models depends on the validity of the hypothesis that the joint shear failure is the result of overloading the joint shear force resistant mechanism.

The starting point of this research is distinctly different from past research. It is based on the fact that during a joint shear failure observed in the author's tests the joint maintains its ability to resist joint shear while the deformation of the beam-column joint increases as longitudinal reinforcing bars passing through the joint yield (Shiohara 2001).

The objective of this paper is to identify the kinematics and failure pattern common to reinforced concrete beam-column joint that have been overlooked by the past research due to the emphasis of empirical equations on joint shear failure. A new mathematical model and algebraic expressions are proposed which are compatible with the kinematics and considers the mechanical properties of beam-column joint. A series mathematical expressions is shown for ultimate moment, moment at balanced failure and critical reinforcing ratio for beam-column joints based on the kinematics and the failure mechanism. This paper treats a special case of a symmetric interior beam-column joint subjected to symetric couples of forces without joint shear reinforcement or mid-layer longitudinal reinforcement in the column. In addition, the amount of longitudinal reinforcements in the beams and columns are identical.

2. OBSERVED FAILURE OF A BEAM-COLUMN JOINT

To establish a rational model for design considering the ultimate limit state, the failure mechanism must be based on realistic behavior. Very few past experimental research papers on beam-column joints have shown more than an idealization of a crack pattern and joint shear deformation. **Photo 1** shows a crack image of a vertically cut surface through an interior beam-column joint subjected to quasi-static reverse cyclic displacements. This is specimen C1 tested by the author (Kusuhara and Shiohara 2007).

2.1 Crack Image of Beam-Column Joint Observed in Test

This specimen was designed to develop a weak beam-strong column mechanism. Clear beam yielding was observed, and the observed moment in the beam reached its theoretical flexural capacity. The story shear-story drift relation showed stable but typical slip behavior, and there was no degradation of story shear beyond a story drift of 4% due to cyclic loading. However, the analysis of observed deformation revealed that the component of joint deformation was unexpectedly large.

This suggests that the joint shear increased until the end of the test because the story shear never degraded. The joint deformation increased with keeping the capability to resist to the joint shear. To ascertain the kinematics in the beam-column joint, specimen C1 was unloaded without reloading to diminishing the residual displace-

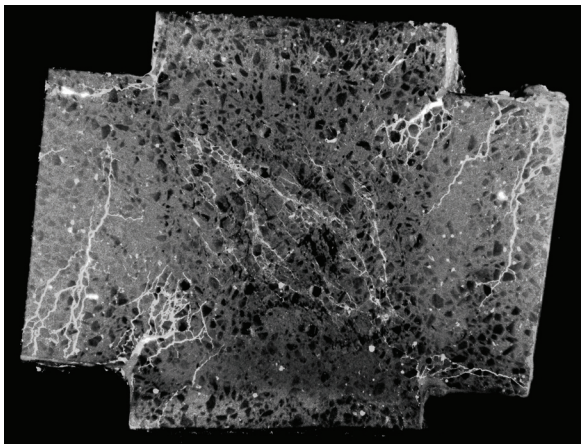

Photo 1 Crack image on the vertical surface cut out after test courtesy of Fumio Kusuhara

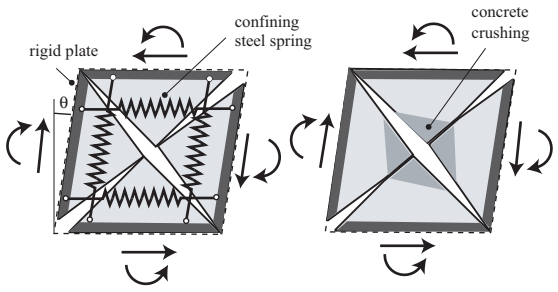

Figure 1 Moment resisting mechanism of beam-column joint

ment, and the cracks were injected with epoxy resin tagged with a fluorescent pigment. After the epoxy hardened, the specimen was cut out. The cracks became visible due to the fluorescent in the resin, allowing details of the crack width and the distribution to be more easily identified as shown in **Photo 1**.

The photo reveals several previously unidentified mechanisms within a beam-column joint that (1) there were several clear flexural cracks at the beam ends; (2) there were a significant number of diagonal cracks in the joint; (3) cracks opened at the beam end at the column face extending diagonally from the upper right corner and lower left corner to the inside of the joint. The crack width was significant and the "trunk" of the crack diverged to many hair line cracks. (4) Many fine diagonal cracks passed through the upper left and lower right portion of the center of the joint. However all these cracks did not penetrate from corner to corner, but the tip of diagonal cracks was arrested. This suggests the widely-opened crack closed due to a large compressive stress perpendicular to the crack direction under load reversal. (6) The concrete damage is obvious at the center of the beam-column joint, while the surrounding regions within the beam or column seems to exhibit little cracking. This may be attributed to the confining effect by the end sections of the beam and column. The distribution of cracks and resulting damage pattern may be explained by considering the beam-column joint divided into four rigid triangular parts rotating relative to each other. As shown in **Fig. 1**, movement, damage and cracks concentrated along the diagonal lines of the beam-column joint are evident.

This paper proposes a model to more accurately represent the behavior of a beam-column joint; This failure mechanism has been overlooked by previous researchers. Most researches, including that reported in text books has explained joint shear failure in terms similar to the shear failure of 1-D flexural element. As shown in **Fig. 1**, there is no diagonal crack completely through the joint (a feature of diagonal tension failure); there is no diagonal sliding of a compressive strut due to concrete crushing, (a feature of compressive shear failure); and there is no vertical or horizontal sliding. Therefore, it is concluded that the failure mechanism of a beam-column joint is fundamentally different than the shear failure of columns or beams.

2.2 Inadequacy of Uniform Shear Strain Assumption

In contrast to the observed beam-column joint behavior previously stateed, most models for beam-column joints usually assume that a uniform shear strain exists in the joints, as depicted in **Fig. 2**. This model has only one parameter representing the deformation of the joint. Hence, this model could be called a one-parameter model. However, the one-parameter model (OPM) does not have sufficient parameters to represent the deformation so that a joint could satisfy the continuity of displacements and stress at each end of the member connected to the joint. The model can only satisfy equilibrium and compatibility for arbitrarily selected components. Therefore, the OPM can not be a reasonable basis of force-deformation relations based on the stress-strain relationship of the material. In addition, the model can not be verified experimentally.

3. FAILURE MECHANISM OVERLOOKED

The OPM for a beam-column joint is too simplistic, does not include enough parameters to represent the actual joint deformations, and can not satisfy the compatibility as well as the equilibrium at the ends of the members connected to a joint. Hence, more parameters are required to mathematically represent a joint.

4.1 Nine Parameters Model for Beam-Column Joint

Judging from the cracks in the beam-column joint shown in **Photo 1**, the region inside of the column face adjacent to the beam end as well as the region inside of the beam face adjacent to the column end have exhibit little damage. This is due to the confining effect of the member ends and generally applicable to a wide variety of beam-column joints. Therefore, the general state of deformation of a beam-column joint is assumed to be represented by the lateral displacement and rotation of the

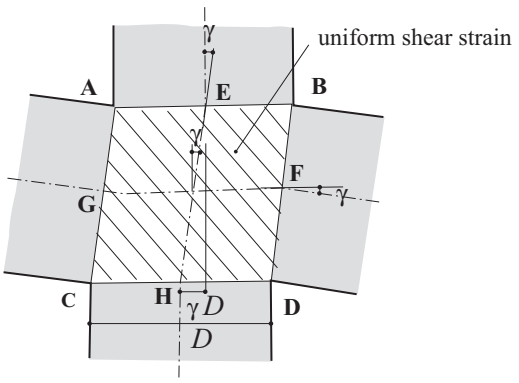

Figure 2 One parameter model (OPM) for a beam-column joint

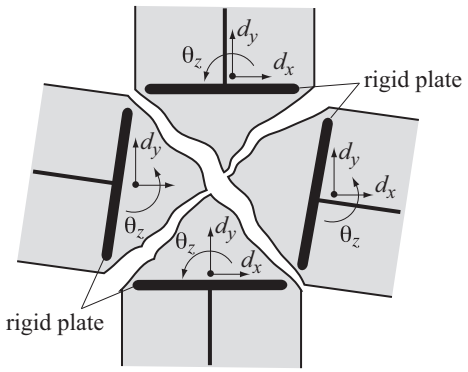

Figure 3 Nine Parameter Model (NPM) for a beam-column joint

four rigid plates as shown in **Fig. 3**. The deformation of this model is represented by the displacement of three plates relative to the other plates. The independent number of degrees of freedom is $12 \times 4 - 3 = 9$ for each joint. Therefore, this model is called the Nine-Parameter Model (NPM) hereafter in this paper. The state of the deformation of this model is represented by the displacement of three plates relative to the other panel.

In structural analysis of plane frames, each node has three degree of freedom representing the two translations and one rotation. For the compatibility of between the joint and member ends the same assumption is convenient.

3.2 Constitutive Equations of Nine Parameter Model (NPM)

Constitutive equations or stiffness equations for a beam-column joint can be established as the relationship of twelve components of displacements and twelve components of force. The constitutive equations of the joint may be derived based on finite element modeling techniques, while the assumptions of the Nine Parameter Model (NPM) can be summarized as follows: (1) From the displacement of the four rigid plates estimate the magnitude and direction of the two principal strains; (2) replace the reinforcing steel and concrete with a non-linear uniaxial spring based on the direction of principal strain; (3) assume nonlinear constitutive rule for the steel and concrete and a bond spring, if necessary; (4) use the equilibrium of forces applied to the plate and the internal forces; and (5) sum all the internal forces applied to a rigid plate to obtain the three components of nodal force acting on the rigid plate.

By following this procedure, the stiffness relationship between the twelve components of force and displacement at the four nodes is established. Because the NPM has built-in degrees of freedoms to satisfy the compatibility and the equilibrium to the members, it can reflect all the interaction of member force and behavior of a beam-column joint. The One-Parameter Model is clearly deficient due to an insufficient number of degrees of freedom. Thus, the extension of the OPM to frame analysis requires arbitrary assumptions, which introduces errors in the model. For example, it neglect the interaction of joint behavior with axial force as well as shear force at the member ends. So the extension of OPM for frame analysis needs arbitrary assumptions, which significantly constrains the scope of the model.

3.3 Macro Element Model based on Nine Parameter Model

The basic constitutive equation of the Nine-Parameter Model could be solved by different analytical techniques. Numerical modeling is one option. Tajiri and the author have implemented the Nine Parameter Model using uniaxial springs similar to a fiber model for flexural analysis (Tajiri and Shiohara 2006). They assumed the direction of principal stress in concrete is in the direction of the diagonal from the corner to the corner. Concrete, steel and a bond link were modeled with a non-linear cyclic hysteresis spring. They used this model for statically non-linear cyclic frame analysis.

The author has also used the Nine-Parameter Model for analysis of an interior beam-column joint assuming that the critical section is the diagonal line (Shiohara 2004). By solving the nonlinear simultaneous equations for the nine equilibrium conditions, they obtained the ultimate moment capacity. Shin and Shiohara have applied the same idea to determine the ultimate moment capacity of corner joints (Shiohara and Shin 2006). These model are used to evaluate the moment capacity of a joint subjected to arbitrary combination of member forces including axial forces, shear and moments, (combined forces on beam-column joint); however the behavior of such parts are not well known experimentally. By these NPM implementations, it is straightforward to account for; (a) movement of the contra flexure point, and (b) configuration of the joint, (interior, exterior, corner, etc.). However, solving the nonlinear equations with nine variables requires non-linear numerical solving tools and is not appropriate for the routine design.

3.4 Simplification of Nine Parameter Model by Condensation of Degree of Freedom

An alternative implementation of an NPM solution is herein proposed. Simplified algebraic expressions are derived by assuming symmetry and reducing the number of parameters. Algebraic expressions are helpful to reveal the generic properties of an RC beam-column joint.

In an interior beam-column joint, the moment, shear and axial force are usually almost symmetric. Thus it is

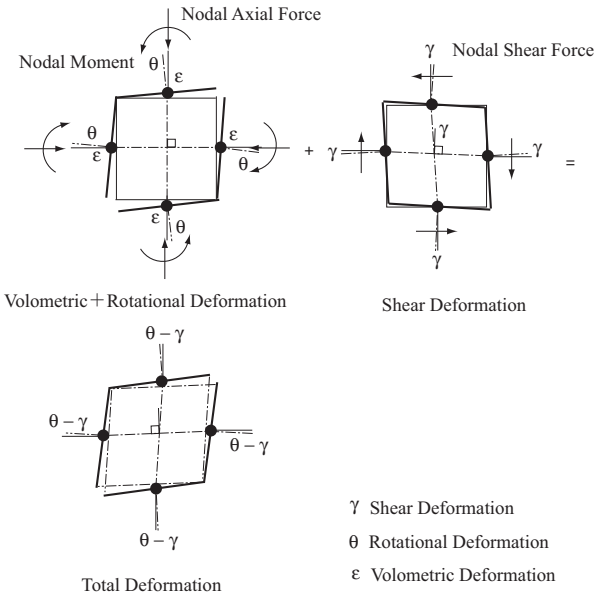

Figure 4 Three independent deformation mode of beam-column joint by reducing the number of degree of freedom considering the symmetry

assumed that the magnitude of axial forces, shear forces and moment transferred from the member to the joint are in symmetry with respect to two lines of 45 degrees from the member axis. With this assumption, the number of independent components of force decreases from nine to three: axial force, shear and moment. As shown in **Fig. 4**, the corresponding deformation mode include volumetric strain, ε ; shear strain, γ ; and rotational deformation, θ.

The volumetric strain, ε, is defined as the translational movement of the rigid plate in the direction of the member axis. It has no contribution to story drift. The shear strain, γ, is defined as the translational movement of the rigid plate in the transverse direction of the member axis. The rotational deformation, θ, is defined as the rotation of the rigid plate. The contribution of the shear strain γ and the rotational deformation θ to the story drift is $\theta - \gamma$.

The set of beam-column joint deformations defined here is more complete than OPM, which considers only shear strain in the joint. In the NPM modeling, each component of force and deformation is measurable by instrumentation in test. This makes it possible to evaluate the validity of the model by comparing test and model prediction. Whereas, instrumentation of the joint shear and joint shear strain addressed in OPM is challenging and often prohibitive. Therefore evaluation of the validity of the OPM is limited.

4. ULTIMATE MOMENT CAPACITY OF PLANE SYMMETRIC INTERIOR BEAM-COLUMN JOINT

In the previous section, a general solution using the NPM is described. This section introduces, the constitutive equations of the Nine Parameter Model for a symmetric beam-column joint with three independent and shows algebraic solutions. Several useful expressions for a RC beam-column joint in ultimate strength design of a RC Frame are introduced.

In defining a generic beam-column joint, the following is assumed: (1) the widths of beam and column are equal, and the shape is symmetric in the vertical and horizontal directions; (2) The beam-column joint is subjected to four identical couples of forces and no shear or axial force is transmitted. As no shear acts at the member ends to the beam-column joint, only the axial displacement and rotational displacement are considered among the deformation components shown in **Fig. 4**.

4.1 Strain and Stress Fields before Concrete Cracking in Beam-Column Joint

Figure 5 portrays the distribution of bi-axial elastic strain and elastic stress within the joint caused by symmetric movement of the surrounding rigid plates with a rotational angle θ, before cracking in concrete. As no axial forces are assumed, the center of the rotation coincides with the axis of the member. Due to symmetry, the direction of principal strain is identical to the direction of the diagonal line. The value of strain is estimated as the change in distance in the diagonal direction divided by the distance of the rigid plates. **Figure 5** also shows the strain diagram along the diagonal. Within the rectangular zone **GEFH**, the principal strain is in tensile in the direction **CB** and in compression in the direction **AD**. Within the triangular zone **AGE** and **HDF**, a state of bi-axial compression exists, and **CHG** and **BEF**, bi-axial tension exits. The values of principal strain and stress are maximum at points on the diagonals. As the strain at points C and B are infinitely large stress concentration, concrete cracking is expected to initiate shortly after loading. The first cracks are expected to form in the upper right and lower left corners and extend inward to the center. The next zone at which the tensile strain causes cracking is along the diagonal. In the rectangular zone of **GEFH**, cracking is expected to initiate at the center and proceed outward along **AD**. Hence, the crack formed as shown in **Photo. 1**.

4.2 Strain and Stress Fields after Cracking in Beam-Column Joint

Consider the strain and stress fields in a beam-column joint after the cracking. Due to cracking of the concrete, the tensile force in the concrete is relieved while the crack width increases. In addition, the tensile force in the reinforcing bars crossing the crack increases as stresses

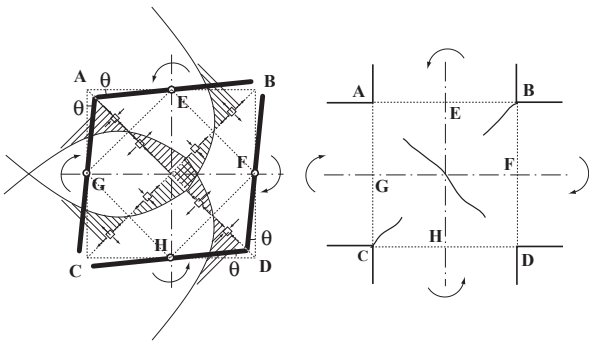

Figure 5 Stress and strain before cracking

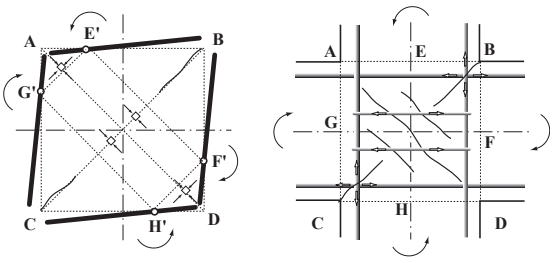

Figure 6 Formational of diagonal compressive strut and increase in tensile force in transverse reinforcement in a beam-column joint after cracking

redistribute. As shown in **Fig. 6**, the longitudinal reinforcement adjacent to point **C** and **B** carries tensile forces. Near the center of the beam-column joint, tensile forces arise in the joint reinforcement. As the cracked concrete does not transfer tension, the bi-axial stress state shifted to a uniaxial compressive stress state along the direction of **AD** after cracking. The triangular zones of **CGH** and **EFB** changes to no stress zones.

As the deformation increases, the tensile strain in reinforcing bars crossing the cracks increases, and the stress in the reinforcing bars passing through the joint increases. Due to equilibrium of the axial force, the longitudinal strain is usually larger than the concrete compressive strain, the volumetric strain of the beam-column joint increases and the center of rotation of the rigid plate shifts to one corner. Thus, the volumetric strain increases, the tensile strain in the joint reinforcement increases, and a uniaxial concrete compression zone of **G'H'F'E'** and a bi-axial compression zone **AGE** and **HDF** develop.

4.3 Ultimate State of Beam-Column Joint

The nodal moment in a beam-column joint which is reached at the ultimate state is defined herein as the *ultimate moment capacity of a beam-column joint*. The algebraic expression is derived as follows.

If the rotation of the rigid plates increases further, the tensile strain in longitudinal reinforcement increases at the location where it crosses the opening cracks. The resisting moment reaches its maximum when the rebar yields in tension, while width of the diagonal crack continues to increase. As a result, the deformation of the beam-column joint increases. This concentrates the compressive force in the diagonal compression strut and causes the strut become to narrower. Ultimately, the compressive strain in the concrete along the center line of the diagonal strut reaches a critical value at which the strut crushes and decrease of volumetric strain of the beam-column joint begins. The location of the crushing is usually at the center of the beam-column joint because of confinement around the boundary by the ends of framing member into the joint. The crack pattern observed in the test shown in **Photo 1** correlates well with the description of ultimate. So the algebraic equations for (1) ultimate moment capacity and (2) the condition of balanced failure are investigated next based on the ultimate state, equilibrium and failure criteria for concrete and steel.

4.4 Ultimate Moment Capacity of Beam-Column Joint

The geometry of the beam-column joint is square, and the depth of the columns and the beams are denoted by D. The width of the column and the beam is b. The longitudinal reinforcing bars passing through the beam-column joint in the vertical and horizontal directions are placed in symmetric positions at the top and bottom of the section. The distance between the extreme layers of reinforcements is defined as gD, where g is the *distance ratio of longitudinal reinforcements*. For example, the value of g is zero if the longitudinal bar are only at the center of gravity of the section. The value of g is less than 1.0 and typical value is around 0.7. For simplicity, it is assumed there is no transverse reinforcement in the beam-column joint and the beam-column joint is subjected to four symmetric moments M_j. In addition, there is no thrust force or shear force transmitted through the beam-column joint. The longitudinal reinforcement is assumed to have elasto-plastic stress-strain behavior, with yield point of f_y and resists only axial force. The compressive strength of concrete is f_c', and cracked concrete transmits no tension.

Figure 7 shows the notations representing the internal forces and the location of the forces. T_1 and T_2 represent the resultant forces in longitudinal bars on the diagonal lines. C_1 and C_2 represent the resultant forces in the concrete in the vertical and horizontal directions. Due to symmetry, the magnitude of forces in the vertical and horizontal directions is identical on the diagonal lines. The direction of the compressive principal stress is always parallel to the diagonal line.

Based on the compressive strain in the concrete estimated in **Fig. 6**, the compressive stress contributing to the resultant force C_1 in the direction of **AD** is distributed perpendicular to the diagonal line **AD**. In contrast, the compressive strain related to the resultant force C_2 is distributed from the corner to the inside perpendicular to the diagonal line **AD**. Thus the location of the resultant forces C_1 and C_2 is determined reflecting the magnitude of the

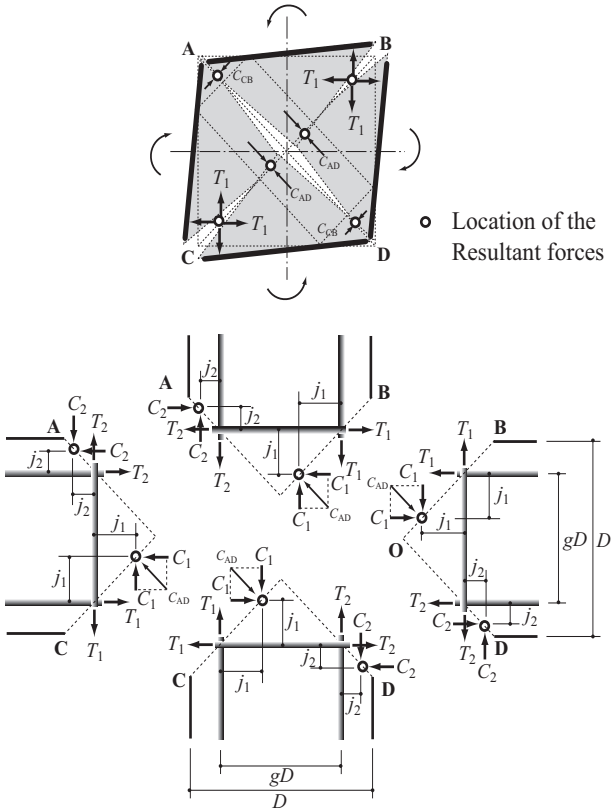

Figure 7 Notations for internal resultant forces acting across the diagonal lines

forces. The distribution of the compressive stress is assumed to be well modelled by the stress block used in flexural theory of reinforced concrete, because the distribution of the compressive strain is approximately linear in compressive zone as shown in **Fig. 5**. The ratio of the concrete compressive stress in the stress block to the compressive strength f_c' is denoted as β_3. By using β_3, the location of the resultant C_1 is at a distance $C_1/(2b\beta_3 f_c')$ from the center of the joint for both the vertical and horizontal direction. Similarly, the location of the resultant C_2 is a distance $C_2/(2b\beta_3 f_c')$ from the corner of the joint for both the vertical and horizontal directions.

The horizontal and vertical distances between the resultant forces T_1 and C_1 is denoted by j_1, while the horizontal and vertical distances between the resultant forces T_2 and C_2 is denoted by j_2.

To apply the principle of virtual displacement, a beam-column joint is separated into four free bodies by diagonal lines **AD** and **BC** as shown in **Fig. 8**. The virtual displacement is applied such that each segment rotates $\delta\theta$ around the location of the resultant C_1 and C_2. The virtual work by the external force M_j is $2M_j\delta\theta$ while the virtual work by the reinforcing bars passing across the diagonal cracks is $4(j_1T_1 + j_2T_2)\delta\theta$. The concrete resultants C_1 and C_2 do not contribute to the virtual work because virtual displacement is rotation around the location and transverse displacement to the direction of concrete resultant forces.

Using the principle of virtual displacements, the equation of equilibrium is obtained as follows,

$$M_j = 2(j_1T_1 + j_2T_2) \tag{1}$$

The distances of the resultant forces j_1 and j_2 can be estimated, considering the $T_1 = C_1$ and $T_2 = C_2$ as follows,

$$j_1 = \frac{1}{2}D\left(g - \frac{T_1}{bD\beta_3 f_c'}\right) \tag{2}$$

$$j_2 = \frac{1}{2}D\left((1-g) - \frac{T_2}{bD\beta_3 f_c'}\right) \tag{3}$$

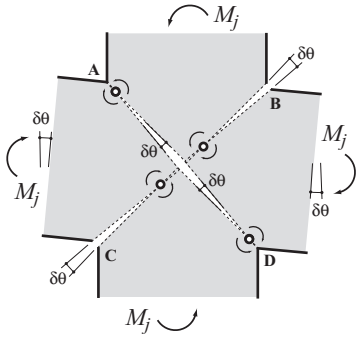

Figure 8 Virtual displacement

By denoting *stress gradient coefficient* α as the ratio of the tensile force T_1 in the reinforcing bars passing through the joint on the diagonal line on the tensile side to the tensile force T_2 on the compressive side, T_1 can be replaced by T and T_2 by αT. Substituting **Eqs. 2** and **3** to **Eq. 1** yields the following equation for the moment M_j,

$$M_j = DT\left\{\alpha + g(1-\alpha) - \frac{(1+\alpha^2)T}{bD\beta_3 f_c'}\right\} \tag{4}$$

The stress gradient coefficient α is a variable that reflects the location of the longitudinal reinforcement in the section. If the *longitudinal reinforcement distance ratio g* is close to unity, the tensile stress at the closing crack T_2 is relatively small while T_1 is relatively large. The value of α is small in this case, and sometimes can reach zero. However, $T_1 - T_2$ represent the stress gradient due to bond resistance. Thus sufficient bond stiffness and strength are necessary along the longitudinal bar. If *g is* 1/2, the value of T_1 becomes a tensile force due to the diagonal crack opening from the corner, while the value of T_2 also becomes tension due to the diagonal crack at the center. This corresponds to α is closing to unity. As the bond stress becomes smaller, the bond stiffness and strength along the longitudinal reinforcement are not required. If *g is* zero, the value for T_1 and T_2 is the same because the reinforcement is at the same location, and the value of α is unity. If the longitudinal bars passing through the joint are debonded, there is no bond resistance and thus the value of α is unity, despite of a non-zero value of *g*. Clearly, the value of the stress gradient coefficient α is valuable depending upon the value of *g*. In general, the ultimate moment of joint M_j is dependent on the value of α and *g*.

For the case of a joint subjected to four identical couples of forces M_j, the tensile yield of the horizontal and vertical longitudinal bars in the beam-column joint commence simultaneously. This assumes the sectional area and the yield point of longitudinal bars for beams and columns are identical. In this case, the moment resistance reaches a plateau and does not increase with joint deformation if the value of α keeps constant. Anyway, the further elongation of longitudinal reinforcements passing through the joint increase the rotation of the rigid plate. Therefore, with the crushing of the concrete due to excessive concentration of compressive strain along the diagonal of **AD** or the corner points; **A** and **D**, the ultimate moment capacity will be reached. The ultimate moment capacity of beam-column joint M_{ju} is derived by substituting T_y for T in **Eq. 4**:

$$M_{ju} = DT_y\left\{\alpha + g(1-\alpha) - \frac{(1+\alpha^2)T_y}{bD\beta_3 f_c'}\right\} \tag{5}$$

where T_y :resultant force of the longitudinal bars at tensile yielding, $(= \Sigma a_t f_y)$; Σa_t : total sectional area of tensile longitudinal reinforcement; f_y : yield strength of tensile longitudinal reinforcement. As seen in **Eq. 5**, M_{ju}

is a quadratic equation of the stress gradient coefficient α, the value of M_{ju} is maximized when the value of α is $(1/2)(1-g)((bD\beta_3 f_c')/T_y)$. The value of $(bD\beta_3 f_c')/T_y$ and g of a typical reinforced concrete joint is around 0.1 and 0.7 respectively. Hence the value of M_{ju} is estimated to be maximized at the value α around 1.5. So in this case, the M_{ju} gently increases as the value of α increases from 0.0 to 1.0. Hence, it is concluded that the moment capacity for such typical beam-column joint gently increase as the stress gradient coefficient α increase. As can been seen, the moment capacity of beam-column joint is reflecting the stress condition of compressive reinforcement.

For simplicity, reinforced concrete beam-column joint in moment resisting frames may categorized into one of two typical types. A Type I joint shown in **Fig. 9** is a beam-column joint designed with two layers of longitudinal reinforcement in the beam and column sections for tension and the other for compression. The joint has sufficient bond capability along the longitudinal reinforcement and a stress gradient coefficient α of approximately zero. A Type II joint has longitudinal reinforcements located near the mid depth of the beam and column section and a stress gradient coefficient α of approximately 1.0. Beam column joints with debonded bars in the joint are included in Type II joint.

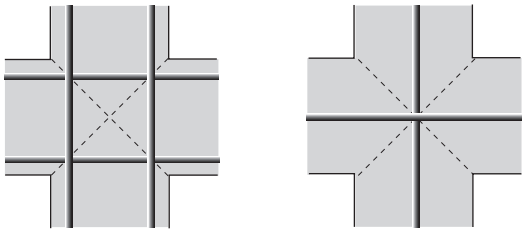

$g \cong 1 \quad \alpha = 0$ $\qquad$ $g \cong 0 \quad \alpha = 1$

(a) Type I joint $\qquad$ (b) Type II Joint

Figure 9 Classification of typical RC beam-column joints

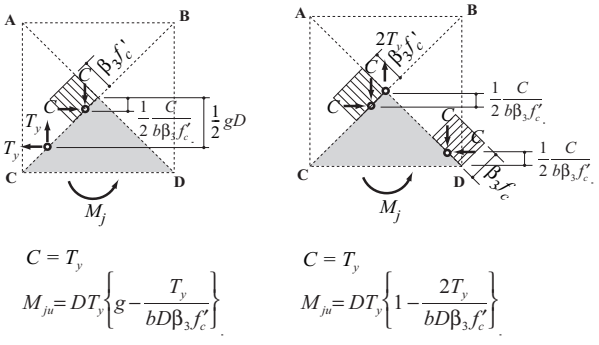

(a) Type I Joint $\qquad$ (b) Type II Joint

Figure 10 Internal stress at ultimate moment capacity of beam-column joint

For these two types of beam-column joints, the ultimate moment capacity M_{ju} from **Eq. 5** is simplified to **Eq. 6** and **Eq. 7** by substituting the approximations of α = 0 for Type I joints and α = 1 for Type II joints respectively.

$$M_{ju} = DT_y\left\{g - \frac{T_y}{bD\beta_3 f_c'}\right\} \text{ Type I joint} \qquad (6)$$

$$M_{ju} = DT_y\left\{1 - \frac{2T_y}{bD\beta_3 f_c'}\right\} \text{ Type II joint} \qquad (7)$$

The internal stress at the ultimate moment capacity is shown in **Fig. 10**. The moment capacity of a Type I beam-column joint using **Eq. 6** is compared with a moment capacity of beam section in **Fig. 11**. For the Type I joints and beams, a typical distance ratio of longitudinal reinforcement g of 0.7 is assumed together with a factor β_3 of 0.85 for concrete stress block. It is observed that the moment capacity of a beam-column joint is always smaller than that of the beam section. Therefor, it is predicted that a beam-column joint failure would occur even if the longitudinal bars reach tensile yield and the moment capacity of the joint is smaller than that predicted by flexural capacity of beam section. As mentioned previously, this applies for cases in which the column and beam sections are identical and the amount of vertical and horizontal reinforcement are the same.

4.5 Balanced Failure of Beam-Column Joint

If excessive amount of longitudinal reinforcing bars are provided for the concrete section, crushing of concrete precede the tensile yield of reinforcement in beam-column joint. This type of special failure of beam-column joint is defined as balanced failure of beam-column joint after the balanced failure of flexural theory. The moment at balanced failure of beam-column joint is denoted by M_{jb} hereafter. In general, the condition of balanced failure is expressed that the tensile strain in tensile reinforcement

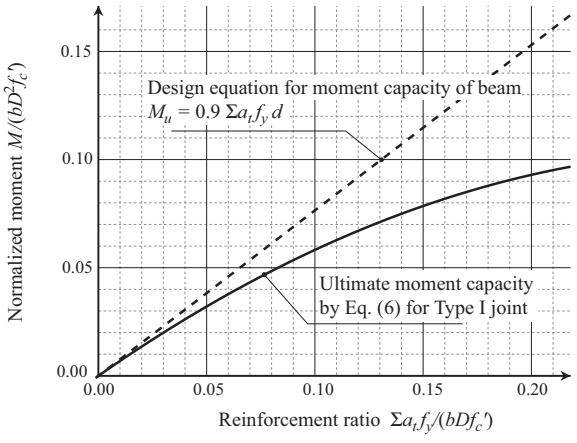

Figure 11 Comparison of moment capacity of beam and beam-column joint

no longer increases even if the rotational deformation increase. By applying this condition, the balanced failure of beam-column joint is obtained as shown in **Fig. 12**.

In the type I joint, the diagonal compressive strut is dominant and the width of the strut increase as more longitudinal reinforcing bars are provided. If the line of neutral axis **G'H'** and **E'F'** go beyond the crossing point of the vertical and horizontal longitudinal reinforcement, the rotational deformation of rigid plates decreases of tensile strain. Hence this is the condition of the balanced failure for type I joint and the height of the concrete stress block at the balanced failure is obtained as $(1/2)gD\beta_1$, where β_1 is the factor representing the ratio of the height of the stress block to the distance of neutral axis to most compressive end of the section as used in the flexural theory of reinforced concrete section. As the resultant of tensile reinforcement T is equal to the compressive resultant of the concrete, the following equations are obtained for Type I joint,

$$T = \frac{1}{2}gbD\beta_1\beta_3 f_c' \quad \text{Type I joint} \tag{8}$$

Therefore M_{jb}, the moment at balanced failure of a Type I joint is derived by substituting **Eq. 8** to **Eq.5** and given as follows,

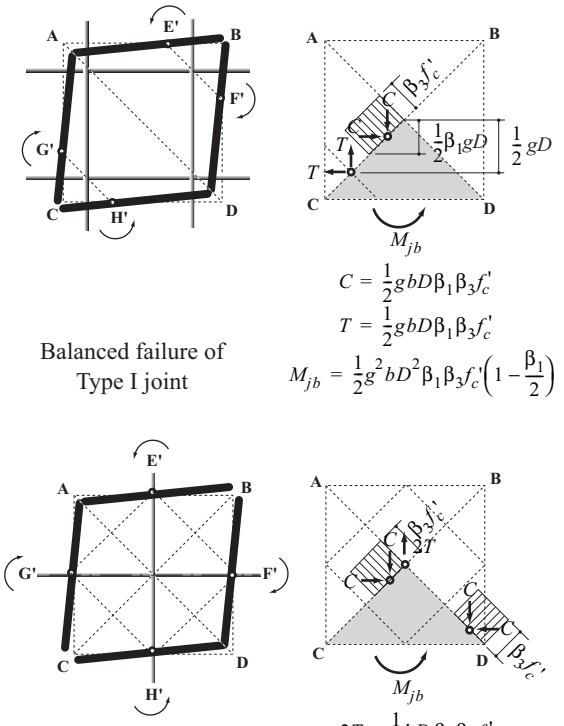

Figure 12 Moment at balanced failure of beam-column joint for Type I joint and Type II joint

$$M_{jb} = \frac{1}{2}g^2 bD^2\beta_1\beta_3 f_c'\left(1-\frac{\beta_1}{2}\right) \quad \text{Type I joint} \tag{9}$$

On the contrary for the Type II joint, compressive resultant at the diagonal strut at center and at the two corners near **A** and **D** need to be identical. Hence the volumetric strain of the joint changed from expansion to contraction when the height of neutral axis is $D/2$ and the height of the stress block of concrete is $(1/4)D\beta_1$.

$$T = \frac{1}{4}bD\beta_1\beta_3 f_c' \quad \text{Type II joint} \tag{10}$$

Therefore M_{jb}, the moment at balanced failure of a Type II joint is derived by substituting **Eq. 10** to **Eq. 6**. and given as follows,

$$M_{jb} = \frac{1}{4}bD^2\beta_1\beta_3 f_c'\left(1-\frac{\beta_1}{2}\right) \quad \text{Type II joint} \tag{11}$$

It is predicted from the discussion above that if amount of longitudinal reinforcement passing through the joint is larger than the value give by **Eq. 8** or **Eq. 10**, the concrete crushing precedes the yielding and maximum attained moment is given by **Eq. 9** and **Eq. 11**. The values given by **Eq. 8** and **Eq. 10** are upper bound amount of reinforcement necessary to preclude the balanced failure of beam-column joint.

The factors affecting the value of M_{jb} for Type I joint include the dimension factor of bD^2, concrete compressive strength f_c', factors defining the shape of concrete stress block $\beta_1\beta_3(1-\beta_1/2)$ and g. The moment at balanced failure M_{jb} for Type II joint is not influenced by the distance ration of longitudinal reinforcement g.

5. CONCLUSIONS

The conclusions of this paper are summarized as follows:

1. The kinematics of the failure of a reinforced concrete beam-column joint is appropriately modeled as the domain surrounded by four rigid plates, because the beam-column joint is confined by the ends of the beams and columns framing into the joint.
2. If the four rigid plates for an interior beam-column joint rotate symmetrically due to lateral loading, the direction and the distribution of principal stress and strain is reasonably estimated. This explains in rational way the observed location and the direction of concrete cracks.
3. If the rotation of the four rigid plates increases, the concrete cracks cause redistribution of stress, resulting in loosing the tensile resistance to the transverse direction of crack. This explains how the diagonal compression strut develops and grows in a reinforced concrete beam-column joint in a rational way.
4. Based on the foregoing mechanism, the ultimate moment capacity of a beam-column joint is defined as

the moment at which the concrete crushes in the extreme compressive fiber, after the longitudinal reinforcing bar yields.

5. Considering equilibrium and the yield condition of steel and concrete, algebraic expressions for the ultimate moment capacity of beam-column joint is brought.
6. Balanced failure of a beam-column joint is defined as a crushing of concrete and yielding of the longitudinal reinforcement simultaneously. The amount of reinforcement at balanced failure is defined as an upper bound value.
7. The algebraic expressions for the moment at balanced failure of a beam-column joint is developed and the factors affecting the upper bound reinforcement are identified. It is shown that the longitudinal reinforcement ratio should be less than the upper bound to preclude joint failure due to concrete crushing only.

This paper treats a special case of a symmetric interior beam-column joint subjected to couples of forces without joint shear reinforcement or mid-layer longitudinal reinforcement in the column. In addition the amount of longitudinal reinforcement in the beam and column are identical. This simplification allows a focus on the introduction of a novel concept of moment capacity of beam-column joint, balanced failure of beam-column joint and upper bound amount of longitudinal reinforcement with emphasis on the derivative of appropriate mathematical expressions. However, the extension of these mathematical expressions for more realistic general cases are feasible for composing validation to test data. Such cases include beam-column joints (1) subjected to combination of axial force, shear and moment, (2) designed according to the weak-beam strong-column concept, and (3) with joint shear reinforcement etc.. These topics will be addressed in future publication.

ACKNOWLEDGEMENT

The author acknowledges Dr. Eric E. Matsumoto, associate professor of structural engineering, Department of Civil and Environmental Engineering, California State University, Sacramento, for his valuable advises and suggestion for the development of ideas and for the publication of this paper.

REFERENCES

Paulay, T., R. Park and M. J. N. Priestley (1978), "Reinforced Concrete Beam-Column Joints Under Seismic Actions," *ACI Journal*, **75**(11), 585-593.

Ichinose, T. (1988), "Required Joint Shear Reinforcement for RC Interior Beam-Column Joint of Good Bond Condition," *Structural Journal of AIJ*, **383**, 88-96. (in Japanese)

Fujii, S., S. Morita (1989), "Shear Resisting Mechanism of RC Exterior Beam-Column Joint," *Structural Journal of AIJ*, **398**, 61-71. (in Japanese)

Cheung P. C., T. Paulay and R. Park, (1991), "Some Possible Revisions to the Seismic Provisions of the New Zealand Concrete Design code for Moment Resisting Frames," Proc. Pacific Conference on Earthquake Engineering, Nov. 1991, 79-90.

Hwang, S. and H. Lee (1999), "Analytical Model for Predicting Shear Strengths of Exterior Reinforced Concrete Beam-Column Joints for Seismic Resistance," *ACI Structural Journal*, **96**(5), 846-857.

To, N.H.T., J.M. Ingham and S. Sritharan (2001), "Monotonic Non-linear Analysis of Reinforced Concrete Knee Joints using Strut-and-tie Computer Models," *Bulletin of the New Zealand Society for Earthquake Engineering*, **34**(3), 169-185.

Shiohara, H. (2001), "New Model for Shear Failure of RC Interior Beam-Column Connections," *Journal of Structural Engineering*, *ASCE*, **127**(2), 152-160.

Kusuhara F., and H. Shiohara (2007), "Damage and Restoring Force Characteristics of RC Beam-Column Joint subjected to Multi-Axial and Combined Loading. Proc. of Annual Convention, Japan Concrete Institute, **29**(4), 235-239. (in Japanese)

Tajiri, S., H. Shiohara and F. Kusuhara (2006), "A New Macro Element of Reinforced Concrete Beam-Column Joint for Elasto-Plastic Plane Frame Analysis," Proc. of 8th National Conference on Earthquake Engineering, San Francisco, April 2006, Paper No. 674/CD-ROM.

Shiohara, H. (2004), "Quadruple Flexural Resistance in R/C Beam-column Joints," Proc. of the 13WCEE, Vancouver, B.C., Canada, August 1-6, 2004.

Shiohara, H. and Yong Woo Shin (2006), "Analysis of Reinforced Concrete Knee joint based on Quadruple Flexural Resistance," Proc. of 8th National Conference on Earthquake Engineering, San Francisco, April 2006, Paper No. 1173/CD-ROM.

Sixth International Conference on Urban Earthquake Engineering
March 3-4, 2009, Tokyo Institute of Technology, Tokyo, Japan

Experimental Study on Mechanical Behavior of Cruciform Frame with Floor Slab Constructed using PC-Mild-Press Joint Method

Hiroyasu Sakata[1)], Hajime Sakagami[2)], Akira Wada[3)] , and Yasuhiro Matsuzaki[4)]

1) Associate Professor, Structural Engineering Research Center, Tokyo Institute of Technology, Japan
2) Graduate Student, Department of Built and Environment, Tokyo Institute of Technology, Japan
3) Professor, Structural Engineering Research Center, Tokyo Institute of Technology, Japan
4) Professor, Department of Architecture, Tokyo University of Science, Japan
hsakata@serc.titech.ac.jp, sakagami.h.aa@m.titech.ac.jp, wada@serc.titech.ac.jp, uhh01853@nifty.com

Abstract: The PC-Mild-Press joint method is one of method which can control damage of structures with concrete. Authors have already carried out study and have clarified its mechanical behavior and damage. However, the effects of the floor slab on the structural behavior of the frame with have not been clarified. In this study, experiments were conducted on a cruciform frame with a floor slab constructed by the PC-Mild-Press Joint method to determine its mechanical behavior and damage. The study focused on the effects of damage control when a prestress force was introduced into the floor slab using unbonded prestressing bars for the main floor slab reinforcement. The evaluation of damage in the floor slab derived from the crack width and the section analysis of interface's M – θ are proposed.

1. Introduction

The prestressing binding jointing method (hereinafter PC-Mild-Press Joint Method) is used to joint high-quality high-strength (F_c=50N/mm^2 and above) precast prestressed concrete members using a tensioning force of about 50% of the standardized yield strength (hereinafter P_y) of the prestressing steel. Damage is controlled by inducing elastic rotation due to separation of bound surfaces (hereinafter interface) under a large earthquake. Previous studies[1-3)] have shown that a frame constructed using this method have origin-oriented-type hysteretic characteristics where residual deformation is small even under large frame deformations. Previous studies have also clarified the effects of damage control where damage was concentrated at the interface. However, the effects of the floor slab on the frame have not been clarified. Those effects cannot be ignored from the viewpoint of damage control, which is the focus of this study. In this study, experiments were carried out a cruciform frame with a floor slab constructed by the PC-Mild-Press Joint Method to determine its mechanical behavior and damage. The study focused on the effects of damage control when a prestress force was introduced into the floor slab using unbonded prestressing bars for the main floor slab reinforcement.

2. Test outline

2.1 Specimen

The parameters and material properties of the specimens are shown in Table-1, and the configuration and beam section of the specimens are shown in Figure-1. They were prepared for this study by attaching an orthogonal beam, a short beam and a floor slab to the cruciform specimen employed for reference 1). They were built to scale of about 1/3. Reinforcement and concrete were placed in the floor slab, after the individual members were binding-jointed and column prestress was introduced. A total of three

Table.1. Parameters of Specimen and Material Properties

Member	Specimen	concrete		Main Reinforcing Bar								Shear Reinforcement		Joint
				PC Strand and PC bar							Deformed Bar			
		Compressive strength	Young's Modulus	Number(Material)	Yield Strength	Young's Modulus	Prestress Force		σ_P※1/η_P※2	σ_N※3/η_N※4	Number(Material)	Number (Material)	p_w	Number (Material)
		$_c\sigma_B$	$E_c(\times10^4)$		σ_y	$E_s(\times10^5)$	1piece	sum						
		N/mm^2	N/mm^2		N/mm^2	N/mm^2	kN/piece	kN	N/mm^2/—	N/mm^2/—			%	
Column	No.1	61.8	3.64	8-φ13(SBPR 930/1080)	1057	1.93	49	392	3.83/0.062	7.28/0.118	20-D16(SD295A)	D10@85 (SD345)	1.05	SD345 (2-D10)
Beam	No.2 No.3	62.6 63.3	3.58 3.67	3/3(SWPR 7B)	1580	2.13	78	468	4.84/0.078	—	—	D10@80 (SD295A)	0.78	
Slab	No.1	40.5	3.25	—	—	—	—	—	—	—	16-D6(SD295A)	—	—	
	No.2	40.8	3.15	6-φ9.2(SBPR 1080/1230)	1199	1.94	14.7	88.2	0.84/0.021	—	8-D6(SD295A)	—	—	
	No.3	43.2	3.07	12-φ9.2(SBPR 1080/1230)	1199	1.94	14.7	176	1.69/0.039	—	—	—	—	

※1, σ_P(=N_P/b/D) ; N_P: Prestress Force ,b: Column Width , Beam Width or Slab thickness ,D: Column Depth , Beam Depth or Slab Width,※2, η_P(= σ_P/$_c\sigma_B$),※3, σ_N(=N_N/b/D) ; N_N: Axial Force=745kN, Column Width , Beam Width or Slab thickness ,D: Column Depth , Beam Depth or Slab Width,※4, η_N(= σ_N/$_c\sigma_B$)

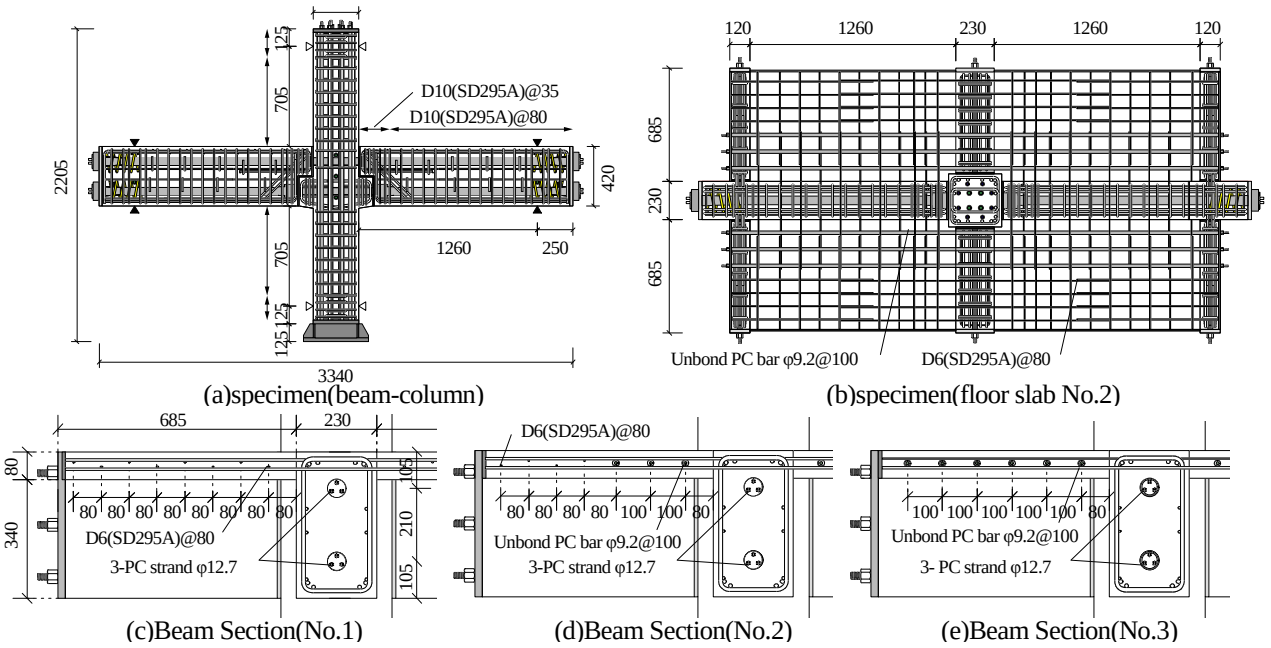

(a)specimen(beam-column) (b)specimen(floor slab No.2)

(c)Beam Section(No.1) (d)Beam Section(No.2) (e)Beam Section(No.3)

Fig.1. Specimens and Beam Sections

specimens were prepared, while the type of main reinforcement of the floor slab was set as a parameter. Specimen No.1 employed deformed bars D6(SD295A) as the main reinforcement. Specimen Nos. 2 and 3 employed unbonded prestressing bars ϕ9.2 (Type C, No.1) as the main reinforcement and prestress force was introduced to them. The unbonded prestressing bars employed in Specimen No. 2 were arranged for the range of 0.1*l* (*l*: beam's internal span = 2520mm) from both sides and deformed bars were employed for the other range in the same manner as No. 1. Specimen No. 3 employed unbonded prestressing bars for all the main reinforcement.

2.2 Tensioning method

A beam prestress force of about 78 kN (= 0.5 P_y) per unit strand was introduced using the 7-strand Type B, ϕ12.7. A column prestress force of about 48 kN (= 0.4 P_y) per unit bar was introduced using the prestressing bar Type B, No. 1, ϕ13. Prestressing bars Type B, No. 1 ϕ19 were arranged in the orthogonal beam and short beam so that their prestresses were equalized with that applied to the beam. The tensioning force per unbonded prestressing bar of Specimen Nos. 2 and 3 was set at about 14.7 kN/bar (= 0.17 P_y) to make the prestress force acting to the floor slab of Specimen No.3 the same as the tensile force causing yield of all the deformed bars of Specimen No.1.

2.3 Loading method

The loading apparatus and loading cycle are shown in Figure-2. Alternate monotonically increasing load was applied to the specimens using a jack provided at each end of the beam. The load settings were set to simulate the horizontal force acting during an earthquake. The capital support and column-base support needed to have a pin mechanism at mid-story height and a pin roller mechanism, respectively. Thus, the supports were sandwiched with steel and fixed in the loading frame using prestressing bars with a spherical washer. Then, the column reaction was

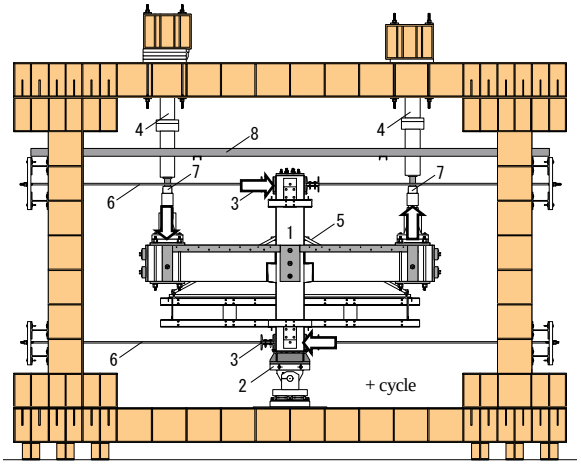

1:Specimen, 2:Pin-roller, 3:Column pin, 4:490kN oil jack, 5:Holder for displacement measurement, 6:PC bar, 7:Load cell, 8:Steel member for lateral deformation control

(a)Loading Apparatus

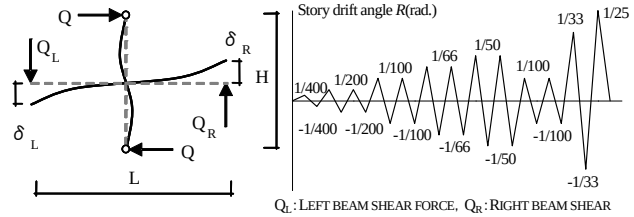

Q_L: Left beam shear force, Q_R: Right beam shear force, L: Span (2840mm), H: Height (=1830mm), Δ_L: Vertical displacement at left beam loading point, Δ_R: Vertical displacement at right beam loading point

(b)Deformation of Specimen (c)Loading Cycle

Fig.2. Loading Apparatus and Loading Cycle

obtained by binding them. A column axial force of 745 kN was also introduced using the unbonded prestressing bars inside the column.

3. Test results and investigations

3.1 Failure characteristics

The ultimate state of the binding surface of the column and beam (hereinafter beam interface) and floor slab is shown in Figure-3. Separation occurred in all the specimens at the beam interface during a cycle of the story drift angle

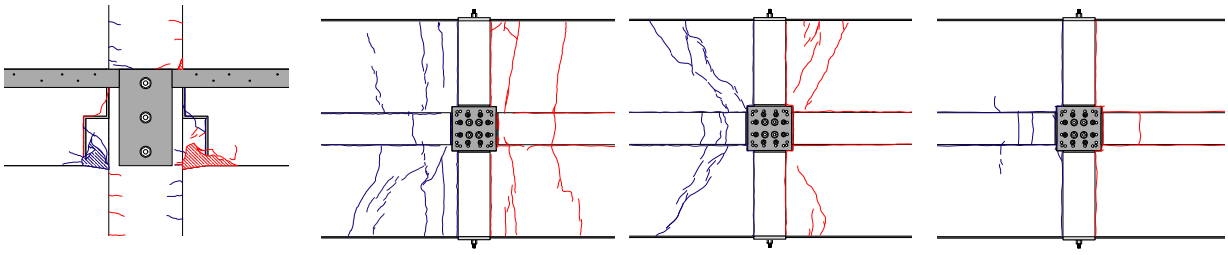

(a)Beam-Column Joint (No.1) (b) Floor Slab(No.1) (c) Floor Slab(No.2) (d) Floor Slab(No.3)

Fig.3. Failure Aspect(R=1/25rad.)

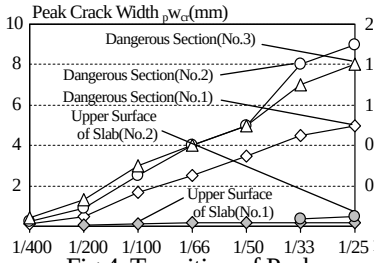

Fig.4. Transition of Peak Crack Width

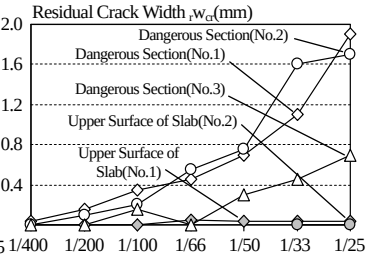

Fig.5. Transition of Residual Crack Width

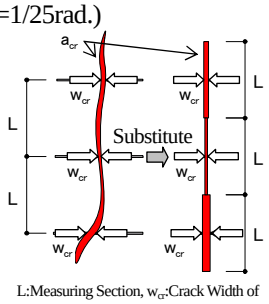

【Attitude of Cracking Area】

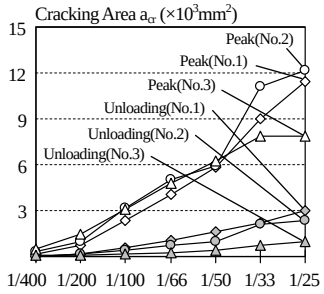

(a)Total Area

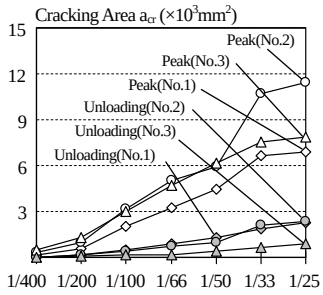

(b)Dangerous Section

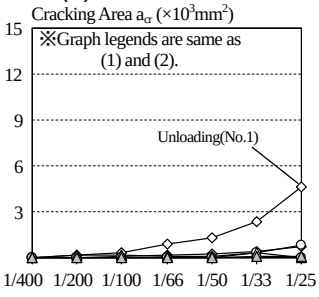

(c)Upper Surface of Slab

Fig.6. Transition of Cracking Area

(hereinafter R) 1/400 rad. Separations of the beam upper end occurred almost simultaneously at the beam interface and the contact surface between the orthogonal beam and the floor slab (hereinafter floor critical section). A crack appeared on the floor slab surface at R = 1/200 rad cycle in Specimen No. 1. It became parallel with the orthogonal beam within 0.5D (D: beam height) of the column face. Thereafter, as the deformation increased, the crack zone extended toward the beam loading point, and to the outside of the floor slab parallel with the orthogonal beam. In Specimen No. 2, a crack appeared within 0.5D of the column face at R = 1/100 rad cycle. However, unlike Specimen No. 1, a crack started at the outside of the floor slab and extended to inside as the deformation increased. It also extended toward the column diagonally to the orthogonal beam. This would be because the cracking load increased due to the prestress force, as the crack approached the column. In Specimen No. 3, only microcracks less than 0.04mm appeared at R = 1/25 rad cycle. Bending cracks appeared in the column at R = 1/200 rad in all the specimens. Thereafter, the crack zone extended toward the column reaction point as the deformation increased. Crack width was very small: less than 0.1mm during unloading. The beam interface was crushed at the beam's lower end and at the column corbel at R = 1/66 rad cycle in Specimen No. 1 and at R = 1/100 rad cycle in Specimen Nos. 2 and 3. Almost all the cover concrete of the corbel had segregated before loading finished.

3.2 Characteristics of floor slab cracking

The changing crack width at the cycle peak and the residual crack width of the floor slab are shown in Figures-4 and 5. Measurement was focused on the cracks crossing the main reinforcement of the floor slab. Crack width at the main reinforcement location was measured using a crack scale (minimum 0.05mm).

The majority of the floor slab deformation was concentrated at the floor's critical section in all the specimens. The crack width was very large relative to that on the floor slab surface. In particular, the crack width at the floor's critical section at the cycle peak in Specimen Nos. 2 and 3 where unbonded prestressing bars were used was about twice that of Specimen No.1. However, residual cracking on the floor's critical section of Specimen No. 3 showed about half the crack width of Nos. 1 and 2. This would be because the deformed bars of Specimen No. 2 caused larger residual crack. Unbonded prestressing bars were used in No.2 in the same manner as No. 3.

Next, crack area was investigated as an index of the extent of floor slab damage. Changing residual areas with changing cycle peaks are shown in Figure-6. Crack area was calculated from an equivalent rectangle with measured crack width at the measurement point and length between main reinforcement of the floor slab (= measurement interval). Figure-6 shows the total crack area on the surface (= floor critical section + floor slab surface), floor critical section and slab surface.

The residual crack area tended to decrease in the specimens with larger prestress force owing to the unbonded prestressing bars. However, crack area on the critical section of Specimen No. 2 rapidly increased after R = 1/33 rad, resulting in a similar residual crack area to that of No. 1. Crack area on the floor slab surface also increased after R = 1/66 rad in Specimen No. 1, which used all deformed bars. It was found from the above that the prestress force introduced by the unbonded prestressing bars could gather the deformation into the floor critical section, restrain crack

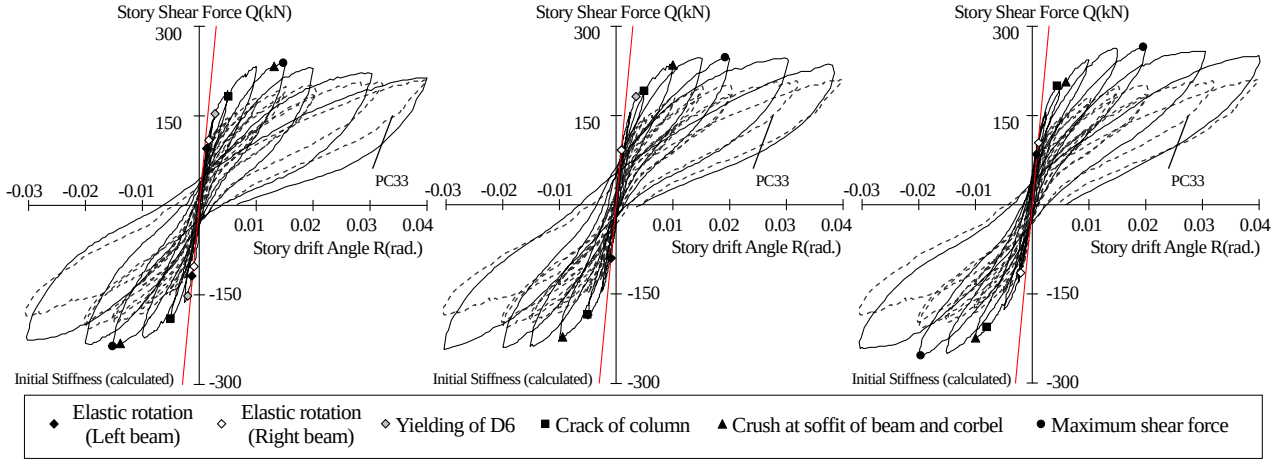

(1)No.1 (2)No.2 (3)No.3

Fig.7. Story Shear Force Q(kN)－Story Drift Angle R(rad.) Relationship (1st Cycle)

expansion into the floor slab surface and control the residual crack width.

3.3 Story shear force – story drift angle

Story shear force versus story drift angle relation (hereinafter Q-R relation) for changing residual deformation angle and changing equivalent viscous damping factor are shown in Figures-7, 8 and 9, respectively. The initial rigidity shown in Figure-7 was calculated by taking into account the rigid zone of the column-beam interface. For the rigid zone, the RC standard[4] figure was taken for the column, and the range up to the column face position was taken for the beam. PC33 was a cruciform[1] specimen without a floor slab. As for the subject specimens, it had three prestressing steel strands each for the upper and lower mat and had a beam in which the same prestress force was introduced. It is noted that the design standard strength of the concrete was 90 N/mm^2.

After the beam interface was separated, the rigidity of all the specimens gradually decreased. Changes in the separation load due to the changing variable of the specimen, i.e. the bar arrangement of the floor slab and the introduced prestress, could not be visually confirmed. Thereafter, the deformed bars of the main reinforcement of Specimen Nos. 1 and 2 reached yield strain by R = 1/200 rad. Then, bending crack appeared at the column in all of the specimens and rigidity greatly decreased. Thereafter, crushing started at the beam's lower end and at the column corbel. Story shear force very slowly increased and reached a maximum. After the maximum strength was reached, it did not greatly decrease. The prestressing steel strands of the beam, the prestressing bars of the column and the unbonded prestressing bars of the main reinforcement of the floor slab did not reach yield. Also, all the specimens showed origin-oriented hysteresis. Up to R = 1/50 rad, the specimens with a larger ratio of deformed bars in the main reinforcement of the floor slab showed larger residual deformation, as shown in Figure-8. In particular, after R = 1/100 rad, Specimen No. 1 showed about twice the residual deformation as the other specimens. It showed near spindle-shaped hysteretic characteristics. It was also found that residual deformation could be controlled to the same

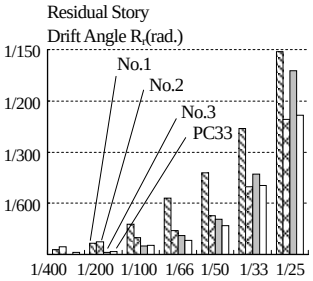

Fig.8. Transition of Residual Story Drift Angle

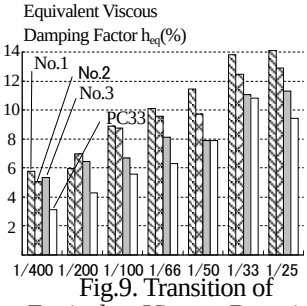

Fig.9. Transition of Equivalent Viscous Damping

level as PC33 without a floor slab by introducing a prestress force into the floor slab. Specimens with smaller residual deformation tended to have smaller equivalent viscous damping factor, as shown in Figure-9.

3.4 Strain characteristics

Strain distribution in the main reinforcement of the floor slab in the critical section of Specimen Nos. 1 and 3 are shown in Figure-10. All reinforcement in the section reached yield strain by R = 1/200 rad in Specimen No. 1, in which deformed bars were used. Larger strains were observed in the reinforcement located closer to the beam. Change in strain with changing bar arrangement was not observed in Specimen No. 3, in which unbonded prestressing bars were used, and the strain in the section was uniformed. Also, yield strain was not reached even in the final cycle.

Strain distributions in the direction of the main floor slab reinforcement of Specimen Nos. 1 and 3 are shown in Figure-11. Specimen No. 1 showed a triangular distribution of which the apex was the strain in the floor's critical section. Bond length was generally constant at about 145mm until the strain in the floor critical section reached yield strain. Thereafter, as the deformation increased, the zone where strain yield was reached expanded toward the beam loading point. Specimen No. 3 strained uniformly over all the unbonded prestressing bars. Also, it was found that the effects of local bending of the prestressing bars in the floor critical section were small.

3.5 Jointing moment – rotational angle

The left jointing moment versus rotational angle relation (hereinafter M – θ relation) is shown in Figure-13. The rotational angle was obtained from the displacement relative

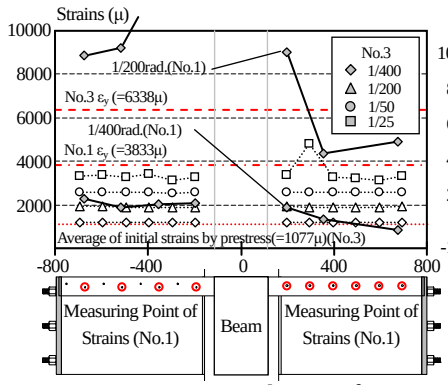

Fig.10. Strain Distribution of Main Reinforcing Bar of Slab of No.1 and No.3 (Dangerous section of slab)

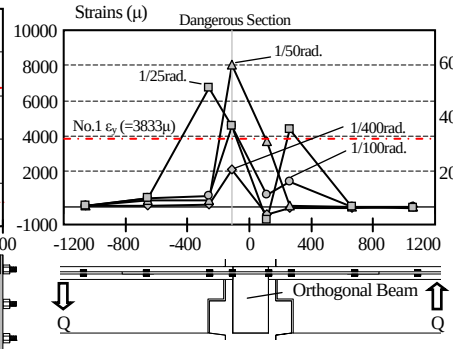

Fig.11. Strain Distribution of Main Reinforcing Bar of Slab of No.1 (Direction of Reinforcing bar)

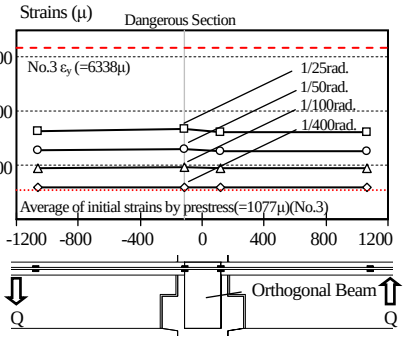

Fig.12. Strain Distribution of Main Reinforcing Bar of Slab of No.3 (Direction of Reinforcing bar)

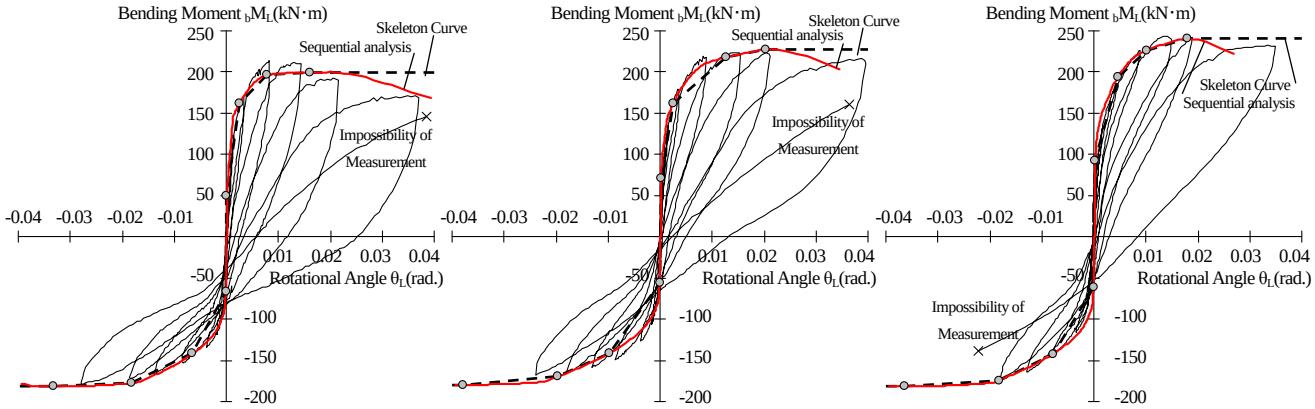

(a) No.1 (b) No.2 (c) No.3

Fig.13. Bending Moment M(k·Nm)- Rotational Angle θ(rad.) Relationship (Left Beam)

to the column face measured with a displacement meter placed in the beam's upper and lower ends. The figure shows the points up to the limit where measurement became impossible with the displacement meter due to crushing at the beam's lower end. Results of the section analysis described in Section 3.6 are also shown in Figure-13. Rigidity gradually decreased in all the specimens after the beam interface underwent separation. The maximum strength for the tensile upper end case resulted in 1.17 (No. 1), 1.29 (No. 2) and 1.35 (No. 3) times that for the compressed upper end case. As the ratio of unbonded prestressing bars in the floor slab increased, the increasing factor increased. This was considered to be because the unbonded prestressing bars at maximum strength had incremental strain from the initial introduced strain caused by parting from the floor's critical section. The incremental strain of the prestressing bars of Specimen Nos. 2 and 3 at maximum strength was 1098 μ and 1144 μ, respectively. The tensile force in the main reinforcement of the floor slab calculated from the above was 176 kN (No. 1), 275 kN (No. 2) and 343 kN (No. 3). It was found that specimens with larger ratios of unbonded prestressing bars had higher contributions to the bending strength of the floor slab. It is noted that increase in tensile force due to strain hardening of the deformed bars was not taken into account. For the case of a compressed upper end, the restoring force showed hysteretic characteristics of the origin-oriented type in all specimens. For the tensile upper end, a restoring force showing origin-oriented type characteristics was found in specimens with larger ratios of unbonded prestressing bars.

3.6 Evaluation of story shear force – story drift angle

The Q – R relation of the cruciform frame was calculated from the envelope curve of the M –θ relation obtained from section analysis taking into account the floor slab. The calculated relation was compared with the experimental one. The analysis employed the method proposed in the previous study[5], taking into account the parting of the prestressing steel strands. The envelope curve showed a total of four kinked points. The first was where the main reinforcement of the floor slab started parting from the interface. The second and third were where the minimum and maximum rotational angles occurred, i.e, where compression rim strain became the strain at the compressive strength from the cylinder test, where main reinforcement of the floor slab reached yield strain and where the prestressing steel strands reached their elastic limit strain. The elastic limit strain was defined as the strain at the limit of the range where stress was proportional to strain, according to Young's modulus. It was set to 80% of 0.2 %-offset-based calculated strain.

The model employed for the section analysis is shown in Figure-14. The concrete was studied by dividing it into cover part and core part, as shown in Figure-14(a). For the stress – strain relation, Provics' equation[6] and Nozaki/Son's equation[7] were employed for the cover part and core part, respectively. The steel was regarded as bilinear. For the participation width of the floor slab, the total width of the floor slab and the RC standard[4] equation were employed for the tensile and compressed upper ends, respectively. Bending moment was obtained as shown in Figure-14(a).

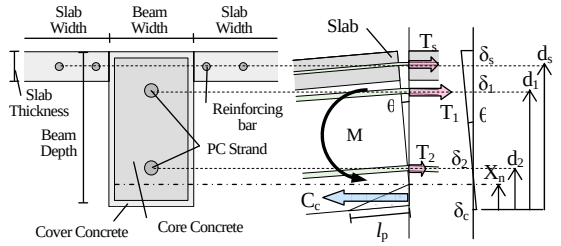

(a)Model of Section (b) Model of Deformation

Fig.14. Model for Sectional Analysis

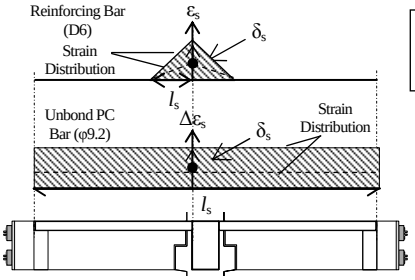

$$\varepsilon_s, \Delta\varepsilon_s = \delta_s / l_s \quad (1)$$

δ_s:Bond Slip Displacement, ε_s,$\Delta\varepsilon_s$:Strain(D6),Incremental Strain(Unbond PC Bar)
l_s: Bond Length (=145mm: D6, =2550mm:Unbond PC Bar)

Fig.15 Model of Strain Distribution of Main Reinforcing Bar

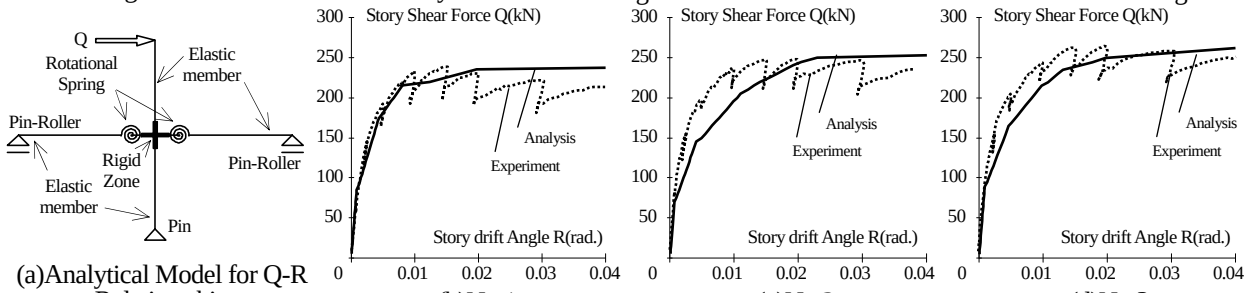

(a)Analytical Model for Q-R Relation ship (b)No.1 (c)No.2 (d)No.3

Fig.16. Story Shear Force Q(kN)－Story Drift Angle R(rad.) Relationship (Analysis)

It was assumed that the deformed plane could remain plane. Steel parting δ_i and concrete shrinkage δ_c were estimated by assuming rotation center position X_n against arbitrary rotational angle θ. Then, the rotation center position X_n that satisfied the force balance was obtained from convergence calculations where corresponding incremental strain $\Delta\varepsilon_i$ and strain ε_c were incorporated. Then, the bending moment was obtained. To calculate the strain against the elongation of the main floor slab reinforcement, the strain distribution of the main floor slab reinforcement was modeled. The strain distributions of the deformed bars and unbonded prestressing bars as main reinforcement of the floor slab (Figures-11 and 12) were used for modeling, as shown in Figure-15. Strain ε_s (deformed bar) and incremental strain $\Delta\varepsilon_s$ (unbonded prestressing bar) were obtained corresponding to the elongation δ_s. For the deformed bars, a triangular distribution was assumed, where the apex was the strain of the critical section until yield strain was reached and the bond length was constant. For the unbonded prestressing bars, constant strain over all the prestressing bar was assumed. The results of the section analysis taking into account the effects of the floor slab using the above method are shown in Figure-13. It was found that the calculated results closely followed the experimental results. The cruciform frame model and the results of the analysis of the Q – R relation are shown in Figure-16. The envelope curve obtained from the section analysis shown in Figures-13(a) through (c) was employed as the rotational spring of the beam interface in the analysis model shown in Figure-16(a). The rigid zone was determined to refer to the RC standard[4] and ranged up to the column face for the column and beam, respectively. It was found that the calculated Q – R relation using the above model was capable of representing the experimental results.

4. Summary

1) Characteristics of a restoring force of the origin-oriented type were observed even in the cruciform frame with floor slab. In particular, the following was noted for the specimens where prestress was introduced using unbonded prestressing bars. Those specimens even with the floor slab were capable of controlling residual deformation in almost the same manner as those without a floor slab.
2) Based on the evaluation of damage to the floor slab derived from the crack width, the following was noted. Specimens where prestress was introduced into the floor slab using unbonded prestressing bars restrained the crack extension to the floor slab surface and were superior in damage control.
3) Conducted section analysis incorporating the parting of the floor slab and steel member was capable of evaluating the M – θ relations at the interface and Q – R relations of frame.

References:

Hiroyasu Sakata et al. (2004) "Experimental Study on Mechanical Behavior OF Damage Controlled Precast-Prestressed Concrete Structure with P/C Mild-Press-Joint," *Journal of Structural and Construction Engineering Transactions of AIJ*,**576**,125-136.

Toshifumi Nakai et al. (2006) "Structural performance of -shaped frame with P/C Mild-Press-Joint," *Journal of the Japan Concrete Institution*,**28-2**,535-540.

Toshiaki Seto et al. (2007) "Study on Mechanical of Behavior of Beam-Column-Foundation in Frame with P/C Mild–Press –Joint,"*Journal of the Japan Concrete Institution* ,**29-2**,475-480.

AIJ (1999) "AIJ Standard for Structural Calculation of Reinforced Concrete Structure"

Hajime Sakagami et al. (2008) "Study on Hysteretic Loop of Frame with P/C Mild–Press–Joint ," *Journal of the Japan Concrete Institution*,**30-2**,529-534.

Sandor Popovics (1973): "A Numerical Aproach to the Complete Stress-Strain Curve of Concrete," *Cement and Concrete*, **3**, 583-599,

Kenji Sakino et al. (1994) "Stress-Strain Curve of Concrete Confined by Rectilinear Hoop" *Journal of Structural and Construction Engineering Transactions of AIJ*,**461**,95-104.

Sixth International Conference on Urban Earthquake Engineering
March 3-4, 2009, Tokyo Institute of Technology, Tokyo, Japan

DAMAGE-FREE REINFORCED CONCRETE BUILDINGS WITH GOOD REPAIRABILITY

Kazushi Shimazaki

Professor, Dept. of Architecture and Building Engineering, Kanagawa University, JAPAN
Email: shimazaki@kanagawa-u.ac.jp

Abstract: Recently, owners of buildings wish to continue using their buildings with low repair cost even after a severe earthquake. To achieve this, it is necessary to reduce the damage or to ensure good repairability of members. A building system consisted with "coupled shear core walls with damper" and flat plate slabs is one of the buildings having an ability of such demand. In this structural system, a large part of the horizontal force is resisted by the core wall, and most of the energy of the earthquake is absorbed in parts such as the boundary beam damper connected to the core walls. Repairability of these members is one of the most important factors in order to reuse the building. This paper examines the behavior of these members with de-bonded diagonal reinforcements to reduce the damage and so ensure good repairability.

1. INTRODUCTION

The goal of earthquake resistant design in any country is to protect life in very severe earthquakes by providing buildings with the strength and durability required to resist collapse. After a severe earthquake such as the Great Hanshin Earthquake, however, the demands of building owners changed: they want to be able to use the buildings again, at a low repair cost. In response, damage control design has recently become popular. This requires good repairability even for RC members to improve the performance of the member. On the other hand, the performance requirements of buildings during planning are diverse, such as improved habitability and large open spaces for flexibility. The structural system combined with RC core walls connected by damper beams and flat plate slabs as shown in Figure 1 is one structural type which meets these performance requirements.

In this structural system, a large part of the horizontal force is resisted by the core wall, and most of the energy of the earthquake is absorbed in parts such as the boundary beam damper connected to the core walls. To satisfy the ductility demand of the beams, diagonal reinforcements have been used [1]. Many experimental studies were carried out on using diagonal reinforced beams as members of a tube structure [e.g. 2, 3]. Although these beams showed very ductile behavior, the number of concrete cracks was quite large and damage to the beams prevented repair work. In those beams, the diagonal reinforcements yielded on the tension side only because concrete struts work with them on the compression side. This increases the number of concrete cracks, and increases the beam length. Repair work is thus laborious.

On the other hand, as a large part of the horizontal force is to be resisted in the core walls, severe shear force and bending moment act at the bottom of the walls. Diagonal cracks caused by this shear force reduce the shear stiffness of the core wall substantially. As shear stiffness cannot be restored by repair works, it is desirable to minimize such diagonal cracks. The horizontal cracks caused by bending moment will be closed by the action of the dead load after an earthquake; this damage, unless severe, is acceptable.

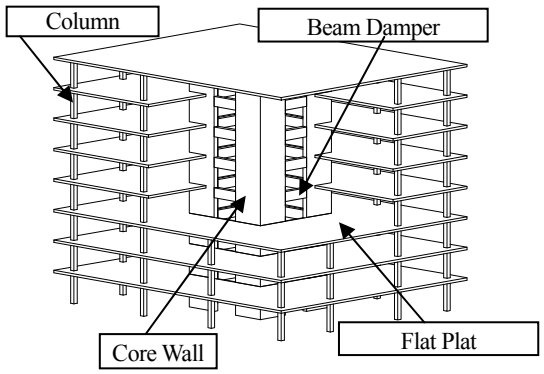

Figure 1 Prototype Building

To improve the performance of the earthquake resistant wall, a 45-degree arrangement of bars, the combination of precast and pre-stressed, and removal of the bond of the main reinforcement of the wall and so on have been proposed[Sittipunt et al. 2000, Yahya et al. 2002, FIB 2003]. The objectives of these proposals were to ensure good ductile capacity, not to reduce the damage.

In order to reduce the damage of the structural system shown in figure 1, this study tested the damage reduction type boundary beams and earthquake resistant walls having de-bonded diagonal reinforcing bars which are expected to act as a brace.

2. De-Bonded Diagonally Reinforced Beam

2.1 Test specimens

The dimensions of the specimens are shown in Figure 2. All beams had eight diagonal reinforcement bars with four longitudinal reinforcement bars and web reinforcements. The section is 200 mm thick, 400 mm high and 1000 mm long. The overall length of the specimen is 2800 mm with end stubs of 400 mm thick, 1400 mm high and 900 mm long at both ends. These dimensions are one-third scale of the prototype structure shown in Figure 1. The specimens are divided into two series, one nominal and the other progressive.

The first of the series is summarized in Table 1. The primary experimental parameter is the bond of diagonal reinforcements, the second is the amount of web reinforcement, and the third is the strength ratio of rebar and concrete. Specimens #N-1 and #N-2 are common diagonal reinforcement beams, and specimens #N-3 to #N-8 are beams with de-bonded diagonal reinforcements. The amount of web reinforcement provided for #N-1 and #N-3 is consistent with the current AIJ standard [4, experimental equation]. For #N-2 and #N-4, the amount is calculated according to the AIJ design guidelines [5, truss model equation] with R = 1/50 inelastic rotational ability. For #N-5, 6, 7 and 8, the amount at both end parts is doubled. The concrete compressive strength and the yield stress of the reinforcements are summarized in Table 1.

The other series (I series) is summarized in Table 2. These are improved ones having small notches near the beam end to reduce concrete cracks and thus improve repairability. Specimen #I-1 has 4-D16 parallel reinforcements anchored into the stub and the others have 2-D10 parallel reinforcements without anchoring into the stub. The notches are at the beam-end for specimen #I-1, and at 150 mm inside from the beam-end for specimens #I-2 through 6. All diagonal reinforcements are de-bonded. The amount of web reinforcement of #I-1 is the same as in #N-1 and 3, and the others are the same as in #N-5 to 8. The concrete compressive strength and the yield stress of the reinforcements are summarized in Table 2. Specimens #I-1, 2, 4, and 5 have axial reinforcements to deduce axial elongation. #I-1 and 2 are with bond and #I-4 and 5 are without. To create de-bonded reinforcement bars, wax and de-bond material (butylene rubber) were used for the deformed bars.

Loading cycles were applied to increase drift angle R with 3 repeated cycles. Only at the level of R = 1/100 was the loading cycle conducted with 6 repeated cycles. These were determined by dynamic response analysis for the prototype building shown in Figure 1 during a severe earthquake to satisfy the energy dissipation ability. Specimens #6 and #8 were repaired after at the level of the R = 1/100 cycle for #6, and 1/67 for #8. Then they were reloaded from the level of R = 1/200.

2.2 Experimental Results

During the response in the R = 1/700 cycle, bending cracks were observed for all specimens at beam-ends. In the

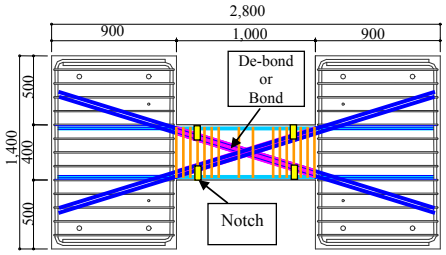

Figure 2: Dimensions of Test Specimens

Table 1 : List of the first series' specimens

Specimen		No.N-1	No. N-2	No. N-3	No. N-4	No. N-5	No. N-6	No. N-7	No. N-8
Section									
b×D(mm)		200×400							
Concrete (N/mm²)		54	51	54	51	51	64	48	32
Parallel bars	Bars	2-D16							
	σ_y(N/mm²)	476	459	476	459		432	456	
X Shape bars	Bars	4-D16 Bond		4-D16 De-bond			4-ϕ 16 De-bond	4-ϕ 19 De-bond	4-ϕ 16 De-bond
	σ_y(N/mm²)	476	459	476	459		386	380	383
Web bars	Bars	2-D6 @150	2-D6 @100	2-D6 @150	2-D6 @100	2-D6 @100/@50			
	σ_y(N/mm²)	331	337	331	337		308	349	
	p_w (%)	0.21	0.32	0.21	0.32	0.32/0.64			
Tested year		2000	2001	2000	2001		2002	2003	

Table 2 : List of the I series' specimens

Specimen		No.I-1	No. I-2	No. I-3	No. I-4	No. I-5	No. I-6
Section							
b×D(mm)		200×400					
Concrete(N/mm²)		54	64	64	49	33	33
Parallel bars	Bars	2-D16	2-D10				
	σ_y(N/mm²)	476	370		380		
Axial bars	Bars	4-D16 Bond	2-D16 Bond	-	2-ϕ 19 De-bond		-
	σ_y(N/mm²)	476	849		380		
X Shape	Bars	4-D16 Bond	4-ϕ 19 De-bond				
	σ_y(N/mm²)	476	386		380		
Web	Bars	2-D6 @150	2-D6 @100/@50				
	σ_y(N/mm²)	331	308		349		
	p_w (%)	0.21	0.32/0.64				
Tested year		2000	2002		2003		

R = 1/400 cycle, bending-shear cracks were observed for the nominal series specimens. Diagonal shear cracks occurred at the center in the R = 1/100 cycle except in specimens # N-3 and 6. For the specimens with de-bonded diagonal reinforcements (#N-3-8), cracks concentrated on both edge parts and the number of cracks was small. For the I-series specimens, a very small number of cracks concentrated on both edge parts with no shear crack at the center until large deformation occurred, except in #I-1. Crack patterns in the R = 1/100 are shown in Figure 3.

The load-deflection behavior of the specimens are shown in Figure 4. Significant differences were not observed between the hysteretic response of the specimens until the R = 1/40 cycle for N-series specimens. During the response in the R = 1/40 cycle, strength degradation was observed due to shear yield for specimen #N-1, of diagonal reinforcements buckling at the center in negative loading for specimen #N-2, of bond failure for specimen #N-3, and of diagonal shear slip at the end for specimen #N-4. No degradation was observed for specimens #N-5, 6, 7, and 8.

For I-series specimens, the load-deflection curves are fat, and energy dissipation ability is larger than in the N-series specimens, except in #I-1. Specimens #I-2, 4, and 5

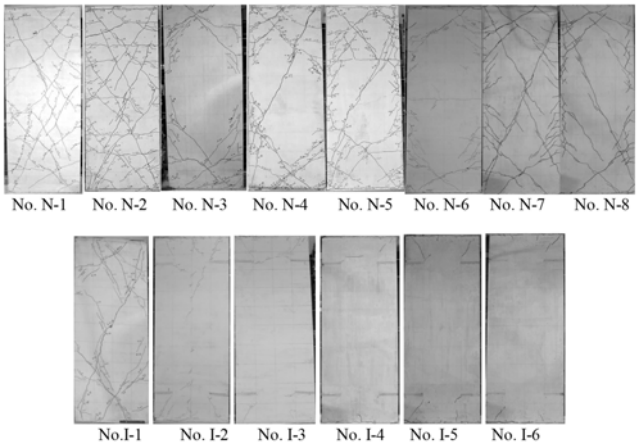

Figure 3 : Crack Patterns (R=1/100)

have pinching phenomenon at the occurrence of large deformation after R = 1/67. This seems to be caused by the axial bars that work as bending bars. In the relation of #I-2 at the second R = 1/40 cycle, the load dropped because one of the X bars fractured at the welded part. These bars of specimens #I-2 and 3 were quench-hardened for strengthening, and weldability was not good.

Figure 5 shows the change of deformation components of bending deformation and shear deformation. The shear deformation part increases with increasing total deformation caused by shear cracks. Specimen #N-1 had large shear cracks in the center part, so the shear deformation part becomes much larger than that of the other specimens with slight cracking in the center. As specimen #N-6 had no shear cracks during the R = 1/100 cycles, shear deformation is the smallest of the N-series specimens. Specimens of I-series had no shear cracks even at the occurrence of large deformation, except #I-1, so that shear deformation is minimal.

Figure 6 shows the equivalent damping factor of each specimen calculated from the first half cycle of the applied load – total deflection relationship shown in Figure 4. Significant differences were not observed in the equivalent damping factor between all N-series specimens. This means that the energy dissipation ability is the same, despite the clear difference of crack patterns shown in Figure 3 caused by the presence or absence of bond of the diagonal reinforcements. For I-series specimens, the equivalent damping factor becomes large compared with the N-series' value after the R = 1/100 cycle. For the #I-2 specimen, the value was reduced because bond cracks of the axial reinforcements developed and stiffness degrading near zero load occurred as shown in Figure 4.

2.3 Macro model and damage evaluation

To evaluate the load resisting system and the condition of whether or not shear cracks developed at the central part, the load-carrying model was investigated as shown in Figure 7. A beam is divided into two systems, one diagonal steel bar truss system with concrete strut and the other a parallel-reinforced beam. As the tension force and the compression force should be equal for both the diagonal

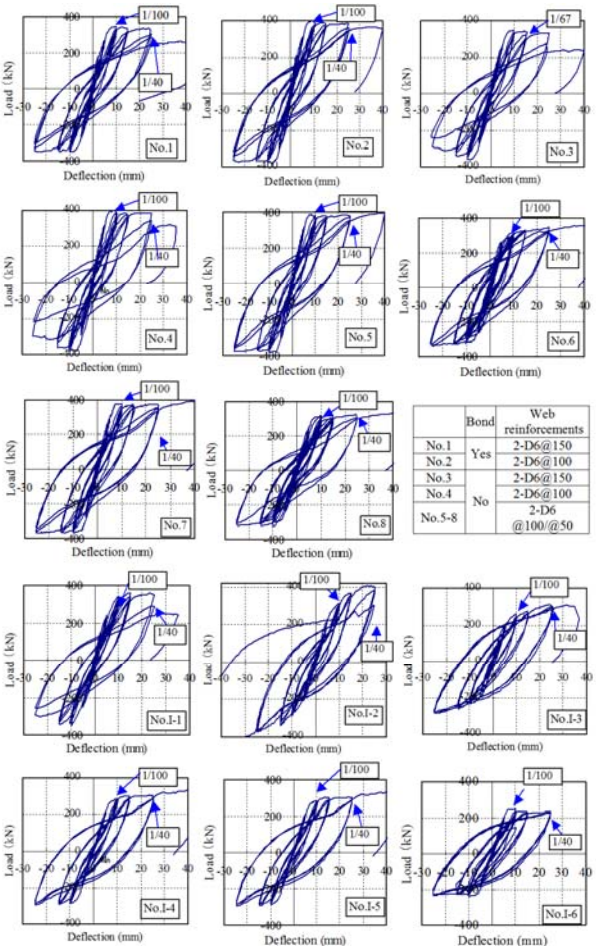

Figure 4 : Load-Deflection Curves

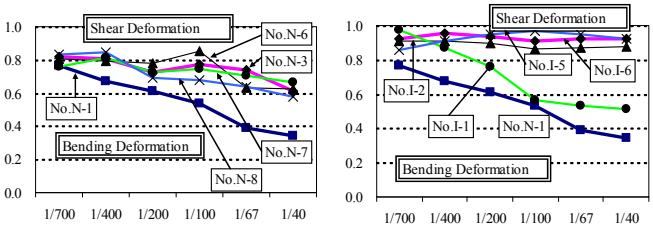

Figure 5: Changing of deformation component

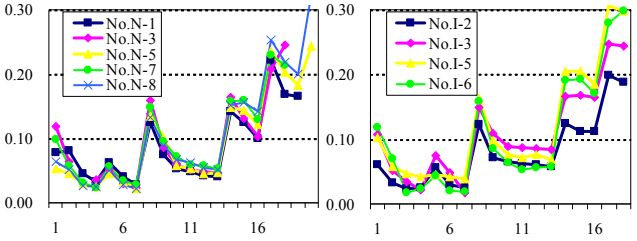

Figure 6: Fluctuations in equivalent damping factor

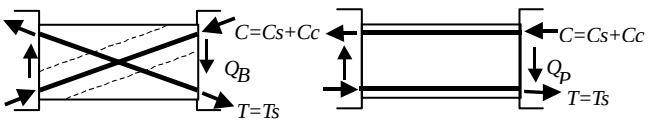

(a)X Brace System (b)Parallel Beam System

Figure 7 : Macro model

truss system and the parallel beam system, the compression force of concrete struts can be evaluated from the difference of force of the diagonal steel bar estimated from strain gage data. The ratio of *Cs*/*Ts* is shown in Figure 8(a)(b) for specimens #N-5, 6, 7 and 8 at the R = 1/400 and 1/200 cycles. These values are almost constant despite the difference of concrete strength or yield strength of the steel bars. It is about 0.15 for the X brace system and 0.35 for the parallel beam system.

For the parallel reinforcement beam, the compression stress of concrete was calculated by elastic beam theory using steel bar force (*Ts*) estimated from strain data. The area of compression was assumed from extreme compression fiber to neutral axis calculated from strain data of steel bars. According to the elastic beam theory, there is no compression stress of concrete in the middle part of the beam. Figure 8(c) shows the depth of compression area for specimens #N-5, 6, 7 and 8 at the R = 1/400 and 1/200 cycles. In this figure, the calculated values using the elastic beam theory for the parallel beam section are also plotted. These values are also almost constant, and are about 0.2 times the total depth. This compression area is used for the brace system to obtain the compression stress of concrete struts. Shear force for concrete was calculated by subtracting the vertical force of the diagonal steel bar (*Ts*+*Cs* in Figure 7(a)) from the total shear force. Maximum shear stress of concrete is calculated as 1.5 times the mean shear stress for the all-rectangular section.

Using horizontal component of compression stress, tension stress by Poisson's effect (ν= 1/6), and shear stress, the principal tension stress is calculated by Mohr's circle. Figure 9 shows the calculated results at the calculated maximum load as the ratio to the square root of concrete strength in Figure 9(a), and to the concrete strength in Figure 9(b). Shear stress is also plotted in the same figure. The principal stress and the shear stress are almost the same. The specimens having large tension stress had the diagonal shear crack at an early load cycle. It seems that this model shows good agreement for examining the load-carrying system. I-series specimens have no compression concrete strut because of the notch. Therefore, as steel bars carry almost all of the shear force, the tension stress of concrete becomes nearly zero. The test results showed no diagonal shear crack.

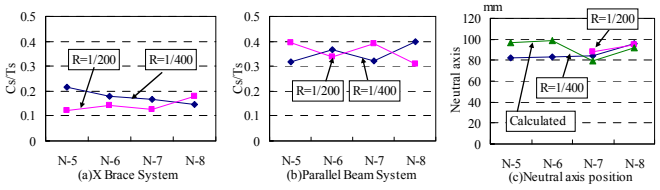

Figure 8 : Ratio of compression force to tension force

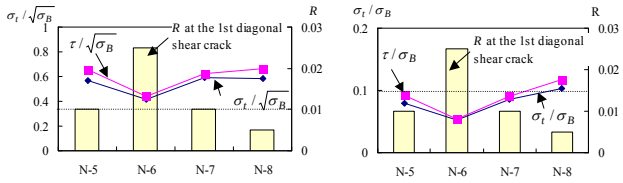

(a) Ratio to squirt of concrete strength (b) Ratio to concrete strength

Figure 9 : Ratio of tension stress

3. Shear Walls with De-bonded Diagonal Reinforcements

3.1 Test specimens

Six wall specimens of 1800 mm height, 900 mm width and 120 mm thickness were tested. They were part of the lower 2.5 stories of the prototype building shown in Figure 1. Following a preliminary analysis, the top of the specimen is at the height of the point of contraflexure of the first story core wall. The section arrangements of bars are shown in Table 3 and Figure 10.

WP1 is a common parallel reinforced wall. WX1 has de-bonded diagonal reinforcements arranged instead of the edge vertical reinforcing bars of 6-D13 of WP1, and additional 6-D6 were arranged at that place for confining bars. WSX1 was divided at each story assuming a precast panel, and WSX2 has crack generation plates of 0.6-mm thickness which divide the panel horizontally into three parts. Each gap between the panels was filled with grout mortar. The edge vertical reinforcement of both WSX1 and WSX2 was de-bonded and fixed at the panel boundary by fixing plates of 40x40x6 mm and nuts. The other reinforcements in the panel were the closed type and were anchored in it. WTX1 is a T-shape specimen with an orthogonal wall for concentration of the L type flange wall. WTX2 has D16 reinforcing bars instead of D6 at the other end of the flange wall (hereafter called "free end"). The bar is cut off at 160 mm in the lower stub, and de-bonded in the stub. This is expected to increase the compressive strength at the free end and not increase the tensile strength. The former prevents concrete crushing caused by the large tensile strength of the orthogonal wall, and the latter prevents an increase in the number of cracks.

Table 3: Test specimens

Specimen		WP1	WX1	WSX1	WSX2	WTX1	WTX2
b×D(mm)	Main Panel	120×900					
	Orthogonal					350×120	
σ_B(N/mm^2)		44		43		43	
Vertical bars	End	6-D13 (σy=371N/mm^2)	6-D6 (σy=368N/mm^2)	12-D13 (σy=390N/mm^2)		14-D13 (σy=368N/mm^2)	
	Center	14-D13 (σy=371N/mm^2)		14-D13 (σy=368N/mm^2)		6-D6 (σy=374N/mm^2)	4-D6、2-D16
	Orthogonal					8-D16 (σy=388N/mm^2) 、6-D6	
Diagonal bars			12-D13 (σy=371N/mm^2)	12-D13 (σy=376N/mm^2)		12-D13 (σy=376N/mm^2)	
Horizontal bars		2-D10@70 (σy=387N/mm^2)		2-D10@70 (σy=353N/mm^2)		2-D10@70 (σy=353N/mm^2)	
Confining bars	Upper	2-D6@70 (σy=368N/mm^2)		2-D6@70 (σy=374N/mm^2)		2-D6@70(σy=374N/mm2)	
	Lower					2-D6@35 (σy=374N/mm2)	

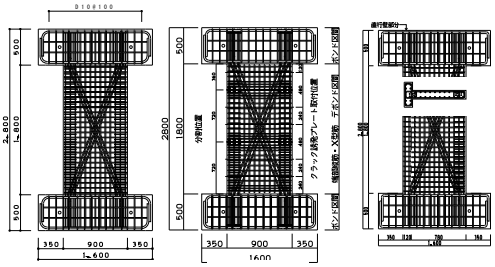

Figure 10: Section arrangements of bar

Cyclic horizontal force is applied at the top of the wall under constant axial compression load of 392 kN for the plane type walls, and 490 kN for the T shape walls (σ_0= 3.6N/mm^2). The loading cycle is one cycle at R = 1/700, three at R = 1/400 and 1/200, six at R = 1/100, three at R = 1/67, and finally one way loading to R = 1/33.

3. 2 Experimental results

Crack patterns at R= 1/200 and 1/100 of each test specimen are shown in Figure 11. Bending cracks occurred in the cycle at R = 1/700 for all test specimens. Bending shear cracks occurred at R = 1/400 for WP1, WTX1 and WTX2, and at R = 1/200 for WX1.

At R = 1/200, the diagonal bending shear crack was conspicuous for WP1, whereas for WX1, the horizontal crack region was wide and there were few diagonal shear cracks. For WTX1 and WTX2, when the orthogonal wall side became compressed, horizontal cracks were observed in the tension side but when the orthogonal wall side became tension, only diagonal cracks were observed. Also, few diagonal cracks were observed in WSX1 and WSX2.

At R = 1/100, signs of concrete crushing in the bottom part were observed for WP1, WX1, WSX1 and WSX2. The maximum crack width except at the bottom boundary was 0.2 mm for WP1, and 0.05 mm for WX1. For WTX1, the edge D6 reinforcing bars buckled and fractured during repeating loading. The concrete crushed region expanded to the central part with increasing damage to the edge. For WTX2, concrete crushing stayed in the concrete surface. For WSX1 and WSX2, the diagonal cracks decreased substantially compared with WX1. The remaining crack width at the bottom boundary of the wall panel was about 0.4 mm for both WSX1 and WSX2.

At R = 1/67, for WTX1, the concrete crushing progressed in both end parts, and for WTX2, it progressed into the center part. At R = 1/33, the concrete crushed part progressed in both end parts for WP1, WX1, WSX1 and WSX2, however the axial load was maintained until the last cycle. Hence, the deformation capacity is sufficient.

The relationships of horizontal force and top displacement of the specimens are shown in Figure 12. For all specimens except the T-shape model, the maximum load was maintained until at R = 1/67, after which the strength declined gradually. For WX1, the vertical reinforcement of D6 in the edge part buckled at R = 1/40 and the strength declined. For WTX1, after the strength declined at R = 1/100, concrete was crushed in the compression side, and D6 reinforcements broke. Then, the cycle was reduced once at R = 1/67, and additional one-way loading for the orthogonal wall compression side was performed until R = 1/40. For WTX2, the control displacement of the first cycle at R = 1/67 exceeded the target value caused by range-over of the control displacement gauge and the data could not be obtained. The gray line in the figure is the value estimated from the test minute. At R = 1/100 cycle, even concrete was crushed in the unconfined region, the strength kept the maximum value, and the strength declined at R = 1/67 caused by buckling of D13 rebars. In the figure, the solid

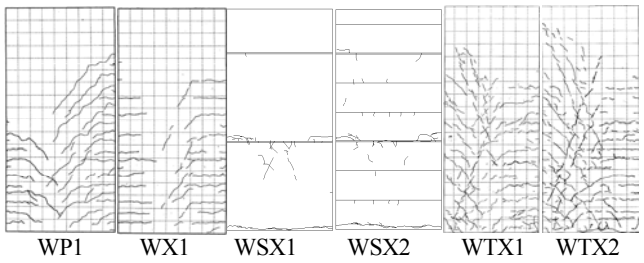

(a) R = 1/200

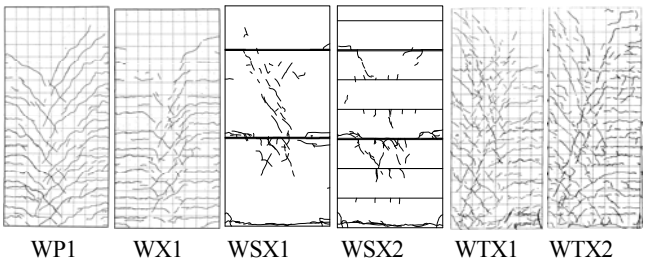

(a) R = 1/100

Figure 11: Crack pattern

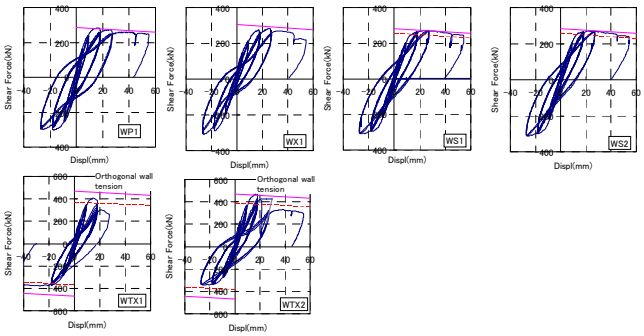

Figure 12 : Relationships of horizontal force and top

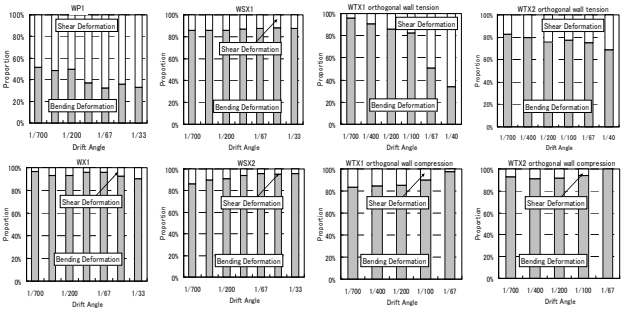

Figure 13 : Bending and shear deformation

and dashed lines are calculated values.

The calculated value, which is the sum of the shear force at the full plastic moment of parallel reinforcements and the yield strength of the horizontal components of the diagonal reinforcements, is shown by the solid line in Figure 12. The line was modified with deflection by considering the P-Delta effect of the vertical load and the horizontal component of inclined vertical load. WP1 withstood the shear force at the full plastic moment until large deformation. The strength of WX1, WSX1 and WSX2 at large deformation was less than the calculated value. For WTX1 and WTX2, the test values were small compared with the calculated ones on the positive side where the orthogonal wall becomes a tension side. In the negative side where the

orthogonal wall becomes a compression side, the tested values were quite low.

The dashed line is the calculated load-deflection relations considering the strain distribution. The compression stress of X bars is assumed to be 1/4 of the yield stress for WSX1 and 1/2 for WSX2. The test results were higher than the calculated values until large deformation. For WTX1 and WTX2, because the de-bonded X bars do not work fully, the calculation values ignored the X bars. They showed good agreement with the test results.

Bending deformation was calculated by integrating the curve obtained from the piecewise axial displacement difference of both wall edges. Shear deformation was calculated by subtracting the bending deformation from the total horizontal deformation. Figure 13 shows the deformation components of bending and shear deformation at the peak point of each loading cycle. The shear deformation component accounts for over 50% of the total deformation for WP1 of the common parallel reinforcing type wall. For WX1 having the de-bonded X type reinforcing bars, the bending deformation component accounts for over 80% and increases with deformation except at the final stage. This corresponds to the phenomenon that the shear crack of WX1 decreases and that the bending crack stretches to the center part. For WSX1 in which the panel wall was divided in each story, the bending deformation component accounts for over 85%, and 90% for WSX2 in which panels divided the horizontal direction into three parts. For WTX1 with the orthogonal wall, the deformation component ratio is almost the same as the value of WX1 when the orthogonal wall is the compression side, in contrast with the tension side, and the shear deformation component becomes larger because of the large shear force caused by large bending strength. At large deformation, the compression concrete of the wall edge was crushed and slipped at the base boundary, and so the shear deformation component increased. In WTX2 which has heavy confining reinforcements in the compression area, the shear deformation component does not increase as much as WTX1, even in the case of large deformation.

Figure 14 shows the equivalent damping factor of each specimen. Over R = 1/100, as the X bars do not yield in the compression side, the load-deflection curve shows an inverted S shape, and the equivalent damping factor of WX1 is less than that of WP1. The values of WSX1 and WSX2 are approximately equal to WX1. The damage was substantially reduced compared with WX1 but having equal energy absorbing capacity. For WTX1 and WTX2, when the orthogonal wall is in the compression side, the value is slightly larger than the value of WX1. When the orthogonal wall is in the tension side, however, the value of WTX2 with heavy confining reinforcements in the compression area is smaller than that of WTX1 because of small damage.

4. CONCLUSIONS

This paper examined the RC members with diagonal reinforcements to reduce damage during a severe earthquake for good repairability. The main findings are as follows:

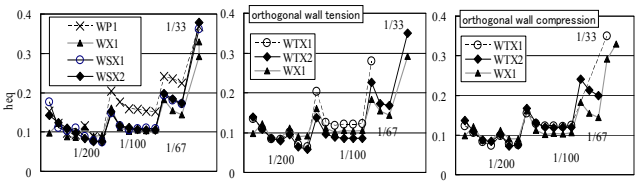

Figure 14 : Equivalent damping factor

1. The results of this experimental investigation demonstrated that de-bonded diagonal reinforcements are an effective means to reduce the number of cracks.
2. For the beams, the macro model showed good agreement with the tested results.
3. For shear walls, by forming a panel wall at each story and de-bonding the main vertical reinforcements in the panel, the bending deformation component increases with concentration in the panel boundary. As a result, shear cracks and bending cracks in the panel center do not occur, and so the wall has good repairability.
4. The horizontal strength of the wall can be calculated as the summation with shear strength of the parallel arrangement wall and the horizontal component of X bar brace yield strength with whole area of tension brace and a half area of compression brace in safe side until large deformation. The stress of concrete on the compression side becomes large because the compression X bars do not result in yielding. An adequate amount of confining reinforcement is necessary to secure deformability in the case of large deformation.

Acknowledgements:

This study was funded by Frontier Research Program of MEXT and Grants-in-Aid for Scientific Research of JSPS. The opinions and findings do not necessarily represent those of the sponsor.

References:

1. Park, R. and T. Paulay, Reinforced Concrete Structures, A WILEY-INTERSCIENCE PUBLICATION, 1975
2. Eto, H., K. Yoshioka, et al., Aseismic design of 41 story reinforced concrete tube structure –Part 4 Ultimate shear strength of short beams-, Summaries of technical papers of annual meeting, C, Architectural Institute of Japan, 1989, pp.773-774 (In Japanese)
3. Shimazaki, K. and Y. Hayakawa, Experimental study for ductility of short beams, Proceedings of the Japan Concrete Institute, 1990, pp.179-184 (In Japanese)
4. AIJ, AIJ Standard for structural Calculation of Reinforced concrete Structures –Based on Allowable Stress Concept–, Architectural Institute of Japan, 1999.
5. AIJ, Design Guidelines for Earthquake Resistant Reinforced Concrete Buildings Based on Inelastic Displacement Concept, Architectural Institute of Japan, 1999.
6. Sittipunt, C. and wood, S. L. (2000). Development of reinforcement details to improve the cyclic response of slender structural walls, 12th World Conference on Earthquake Engineering, Paper 1770.
7. Yahya, C., Kurama, Y., Sause, R., Pessiki, S., and Lu, L.W. (2002). Seismic Response Evaluation of Unbonded Post-Tensioned Precast Walls, ACI Structural Journal, Vol. 99, No. 5, pp. 641-651
8. FIB (2003). Seismic design of precast concrete buildings, state of art report, fib bulletin, No.27

Sixth International Conference on Urban Earthquake Engineering
March 3-4, 2009, Tokyo Institute of Technology, Tokyo, Japan

P-DELTA EFFECTS IN EARTHQUAKE EXCITED STRUCTURES

Christoph Adam[1)]

1) Professor, Faculty of Civil Engineering, University of Innsbruck, Austria
christoph.adam@uibk.ac.at

Abstract: The paper summarizes ongoing research efforts to quantify the destabilizing effect of gravity loads (P-delta effect) on highly inelastic non-deteriorating structures subjected to strong motion seismic excitation. The median excitation intensity at structural collapse is of particular interest and is referred to as collapse capacity of the structure. Characteristic structural parameters of inelastic single-degree-of-freedom systems for collapse induced by gravity loads are identified. The representation of the collapse capacity as a function of the corresponding elastic structural period leads to collapse spectra, which are based on a set of 40 recorded ordinary ground motions. The application of these collapse spectra for the prediction of the collapse capacity of regular multi-degree-of- freedom frame structures is discussed.

1. INTRODUCTION

Gravity loads reduce the lateral stiffness of structures. This destabilizing effect is referred to as P-delta effect. For realistic buildings this reduction of stiffness is in general insignificant as long as the structure is deformed in its elastic range. However, modern earthquake resistant design allows inelastic deformations in specified parts of the structure, and in combination with the P-delta effect the post-tangential stiffness may become negative, if the building is very flexible. For such conditions the displacements tend to be amplified in a single direction, and during the impact of strong motion earthquakes the risk of structural failure is increased potentially.

In this paper a methodology is presented, which allows a fast quantification of the P-delta effect in seismic excited highly inelastic structures. Emphasis is given to the structural collapse capacity.

2. SINGLE-DEGREE-OF-FREEDOM SYSTEMS

2.1 The P-delta Effect in Inelastic Single-Degree-of-Freedom Systems

The effect of gravity loads in single-degree-of-freedom (SDOF) oscillators with inelastic spring characteristics is evaluated considering an inverted mathematical pendulum of length h as shown in Figure 1. The rigid rod of the pendulum is supported by an elastic-plastic rotational base spring with initial stiffness k_r. A rotational viscous damper with parameter r_r, which is connected in parallel with the spring, models structural viscous damping. For the aim of this study geometric linear vibrations ($|\varphi| \ll 1$) are investigated, which are characterized by the horizontal displacement x of the lumped mass m. The given ground acceleration $\ddot{x}_g$ represents the seismic excitation.

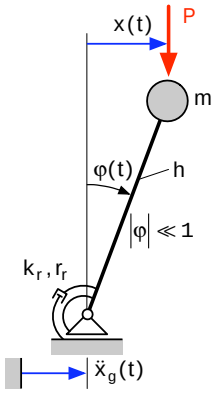

Figure 1 Considered SDOF oscillator

The non-dimensional equation of motion of this system can be derived as follows (Adam, 2008),

$$\frac{1}{\omega^2}\ddot{\mu} + 2\zeta\frac{1}{\omega}\dot{\mu} + \left(\bar{f}_S - \theta\mu\right) = -\frac{\ddot{x}_g}{g\,\gamma} \qquad (1)$$

In this equation μ represents the horizontal displacement related to the yield displacement x_y, $\bar{f}_S$ is the spring force normalized by means of the yield strength f_y of the corresponding translational spring, and γ denotes the yield strength coefficient,

$$\mu = \frac{x}{x_y} \;,\; \bar{f}_S = \frac{f_S}{f_y} \;,\; \gamma = \frac{f_y}{mg} \qquad (2)$$

g is the acceleration of gravity. Parameters ω and ζ denote the natural circular frequency and the viscous damping coefficient of the linear system, respectively,

$$\omega = \sqrt{\frac{k}{m}} \;,\; k = \frac{k_r}{h^2} \;,\; \zeta = \frac{r}{2\omega m} \qquad (3)$$

The so-called stability coefficient θ characterizes the stability of the corresponding elastic system with infinite yield strength. It is a function of the gravity load *P*, stiffness, and geometry,

$$\theta = \frac{P}{k\,h} \tag{4}$$

If $\theta < 1$ the equilibrium of the elastic structure is stable, otherwise it is unstable. $\theta = 1$ is the limit of stability.

From the structure of Eq. (1) it can be concluded that the gravity load leads to a "shear deformation" of the normalized hysteretic force-displacement relationship by the amount of the stability coefficient θ. Figure 2 illustrates this behavior for a single load cycle of a bilinear hysteretic loop. In a realistic building usually the stability coefficient is smaller than 10% ($\theta < 0.1$), and thus, the reduction of the lateral stiffness is of minor significance. However, if the stability coefficient is larger than the hardening ratio α, $\theta > \alpha$, the slope of the post-yield tangent stiffness becomes negative, compare with Figure 2. In such a condition the ratcheting effect occurs when subjected to severe seismic excitation and the structure may approach a state of dynamic instability at a rapid rate (Bernal, 1998). It is noted that the ratcheting effect refers to the fact that the displacement is amplified in a single direction.

It is emphasized that a negative post-yielding stiffness is a precondition for dynamic instability, i.e. $\alpha - \theta < 0$ (or $\theta - \alpha > 0$, alternatively).

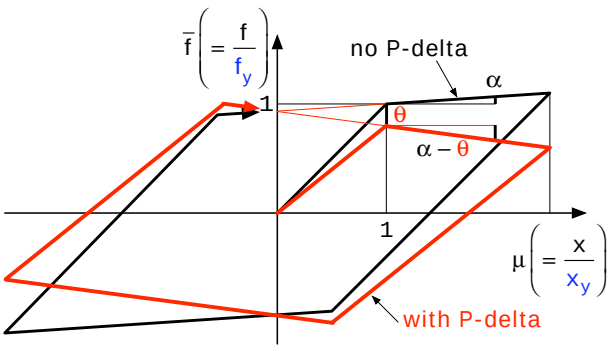

Figure 2 Normalized bilinear cyclic structural behavior without (black lines) and with gravity load (red lines)

The effect of gravity loads on inelastic SDOF oscillators subjected to the normalized earthquake excitation $\ddot{x}_g / (g\gamma)$ is characterized by means of the following parameters (Adam and Spiess, 2007):

- The elastic structural period $T = 2\pi / \omega$,
- the slope of the post-tangential stiffness expressed by the difference $\theta - \alpha$, and
- the viscous damping coefficient ζ (which is of minor significance).

2.2 Collapse Spectra and Design Collapse Spectra

The P-delta effect in SDOF systems of type described above is investigated utilizing real seismic induced ground motions. The considered earthquake data are taken from the bin LMSR-N, which contains 40 ground motions recorded in Californian earthquakes of moment magnitude between 6.5 and 7 and closest distance to the fault rupture between 13 km and 40 km. These ground motions were recorded on NEHRP site class D and selected from the PEER (Pacific Earthquake Engineering Research) Center Ground Motion Database (Medina and Krawinkler, 2003). This set of ordinary records has strong motion duration characteristics, which are not sensitive to magnitude and distance. A statistical evaluation of this bin of records and its detailed description are provided in Medina and Krawinkler (2003).

For a given SDOF system with assigned initial period T, slope $\theta - \alpha$, viscous damping coefficient ζ, and a given ground motion record several time history analyses are performed. In each subsequent run the normalized intensity $\ddot{x}_g / (g\gamma)$ is increased incrementally according to the IDA procedure (Vamvatsikos and Cornell, 2002). The procedure is stopped at the certain level of intensity, where the displacement μ grows to infinity. The corresponding normalized peak ground acceleration (PGA)

$$\frac{\max\left|\ddot{x}_g\right|}{g\gamma} \tag{5}$$

is referred to as collapse capacity of the considered structure for this specific ground motion record. IDAs are performed for the entire set of ground motion records, and the statistical evaluation of the outcomes, i.e. the median value, is considered as the representative collapse capacity CC for this set of records as a function of T, $\theta - \alpha$, ζ. Subsequently, the structural parameters are varied and the procedure is repeated.

Plotting the median collapse capacity CC against the elastic period T for fixed values of $\theta - \alpha$ and $\zeta = 0$ leads to collapse spectra. In Figure 3 a series of derived collapse spectra are presented, each corresponding to a specific value of the slope $\theta - \alpha$. All results are based on a bilinear hysteretic loop and a viscous damping coefficient of $\zeta = 0.05$.

Smoothing of collapse spectra results in design collapse spectra. Figure 4 shows the design collapse spectra, which are derived from the collapse spectra of Figure 3.

It is intended to provide engineers involved in earthquake resistant structural design with design collapse spectra. The practical application is simple, since the initial period and the slope of the considered SDOF structure must be estimated only. Subsequently, the appropriate related collapse capacity CC is to be multiplied by the actual value of $g\gamma$, compare with Eq. (1),

$$CC_{SDOF}\left(= \max\left|\ddot{x}_g\right|\right) = CC\, g\gamma \tag{6}$$

and a reasonable approximation of the median collapse intensity of the actual SDOF system CC_{SDOF} is obtained.

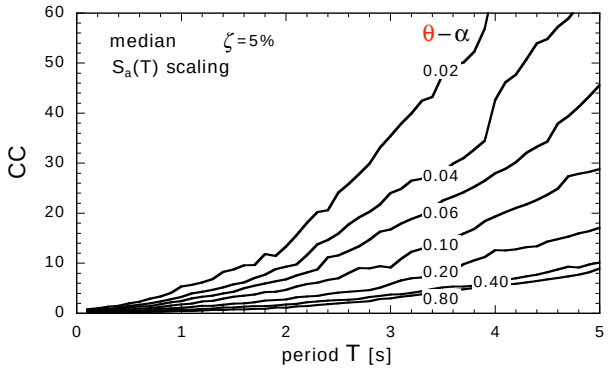

Figure 3 Collapse spectra for bilinear material behavior

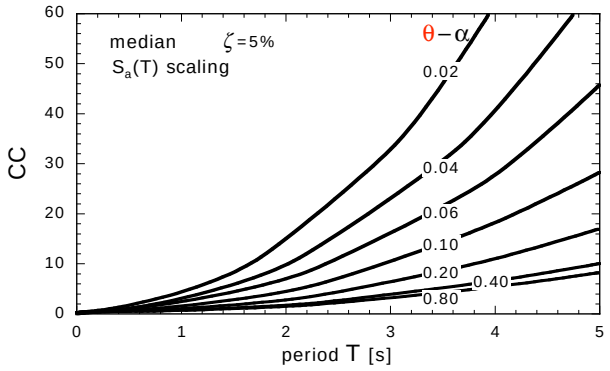

Figure 4 Design collapse spectra for bilinear material behavior

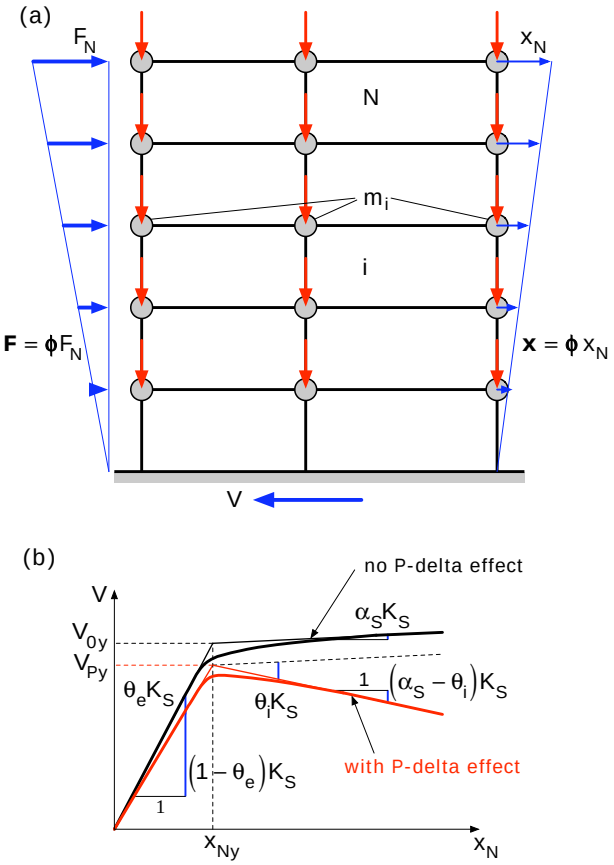

Figure 5 (a) Planar MDOF frame structure, load pattern of the pushover analysis, and shape of deflection.
(b) Corresponding global pushover curves without and with P-delta effect.

3. MULTI-DEGREE-OF-FREEDOM SYSTEMS

3.1 The P-delta Effect in Inelastic Multi-Degree-of-Freedom Systems

Earthquake excited multi-degree-of-freedom (MDOF) structures with non-deteriorating hysteretic material behavior, which are vulnerable to the P-delta effect, are considered. As an example in Figure 5(a) a planar frame structure is shown. It is desirable to apply the presented design collapse spectra also for the prediction of the collapse capacity of MDOF structures.

In a first step it must be determined, if the structure is vulnerable to gravity loads. For this purpose a pushover analysis is conducted, and the base shear V is plotted against the roof deformation x_N. If the post-tangent stiffness of the resulting global pushover curve is negative, the global capacity must be assessed.

3.2 Equivalent Single-Degree-of-Freedom System

The proposed procedure is based on the assumption that the dynamic properties of the actual structure are reflected with sufficient accuracy by an equivalent single-degree-of-freedom (ESDOF) system (Adam et al., 2004). The parameters of the ESDOF system are defined utilizing a time-independent shape vector $\boldsymbol{\phi}$, which describes the lateral deformation of the MDOF building regardless of its magnitude, and on results of two pushover analyses applied to the original structure, one ignoring and the other accounting for the gravity loads, respectively. Details of the ESDOF system can be found in Fajfar (2002) and Adam et al. (2004). The horizontal displacement D of the ESDOF system is related to the roof displacement x_N,

$$D = \frac{m^*}{L^*} x_N \quad , \quad L^* = \boldsymbol{\phi}^T \mathbf{M} \mathbf{e} \quad , \quad m^* = \boldsymbol{\phi}^T \mathbf{M} \boldsymbol{\phi} \qquad (7)$$

and the backbone curve of the ESDOF spring force f_S^* is derived from the base shear V of the global pushover curve (without P-delta effect) according to

$$f_S^* = \frac{m^*}{L^*} V \qquad (8)$$

$\mathbf{M}$ denotes the mass matrix of the original frame structure, and $\mathbf{e}$ is the influence vector, which represents the displacements of the stories resulting from a static unit base motion in direction of the ground motion $\ddot{x}_g$. For the considered ESDOF model it is assumed that the deformation pattern $\mathbf{x}$ and the load pattern $\mathbf{F}$ of the pushover analysis are affine as shown in Figure 5(a), Fajfar (2002).

In contrast to a real SDOF system no unique stability coefficient does exist for an ESDOF oscillator. As shown in Figure 5(b) the stability coefficient is different in the elastic

and inelastic range of deformation, since the backbone curve of the ESDOF system is derived from the global pushover curve of the corresponding building. A bilinear approximation of the backbone curve leads to an elastic stability coefficient θ_e and to an inelastic stability coefficient θ_i. Analyses have shown that θ_i is always larger than the elastic one θ_e, $\theta_i > (>)\theta_e$ (Krawinkler and Medina, 2003). Hence, loading of the ESDOF system by means of an equivalent gravity load, which is derived from the elastic stability coefficient θ_e, leads to a "shear deformation" of the hysteretic loop of the ESDOF system, where the post-tangent stiffness is overestimated. Consequently, the hazard of collapse would be underestimated. In Ibarra (2003) it is proposed to employ an auxiliary backbone curve, which features a uniform "auxiliary" stability coefficient θ_a. The parameters of the auxiliary backbone curve can be found in Ibarra (2003) and Adam and Spiess (2007).

Subsequently, an appropriate hysteretic loop is assigned to the auxiliary backbone curve, which is sheared by θ_a when the ESDOF system is loaded by the equivalent gravity force P^*, compare with Eq. (4),

$$P^* = \theta_a k_a^* h \tag{9}$$

Eventually, the equation of motion of the ESDOF system may be expressed in full analogy to a real SDOF system, compare with Eq. (1),

$$\frac{1}{\omega_a^{*2}}\ddot{\mu}^* + 2\zeta\frac{1}{\omega_a^*}\dot{\mu}^* + \left(\bar{f}_S^* - \theta_a\mu^*\right) = -\frac{\ddot{x}_g}{g\,\gamma^*} \tag{10}$$

The parameters of this equation are defined in Adam (2008).

The equivalent base shear coefficient γ^* of the ESDOF system is linked to the base shear coefficient $\bar{\gamma}$ of the MDOF system according to

$$\gamma^* = \frac{\bar{\gamma}}{\lambda_{MDOF}} \quad , \quad \bar{\gamma} = \frac{V_y}{Mg} \quad , \quad \lambda_{MDOF} = \frac{L^{*2}}{m^* M} \tag{11}$$

V_y is the base shear at yield, and M the (dynamic effective) total mass of the MDOF structure.

3.3 Application of Collapse Spectra to Multi-Degree-of-Freedom Systems

Design collapse spectra according to Figure 4 are applied for the assessment of the global seismic stability of the considered MDOF frame structures utilizing the period of the ESDOF system, $T^* = 2\pi / \omega_a^*$, and the difference of the auxiliary stability coefficient and hardening coefficient $\theta_a - \alpha_S$. Since the difference between the period of the ESDOF system and the fundamental period of the MDOF system is small the latter may be employed (Adam, 2008). A prediction of the related collapse capacity CC of the ESDOF system is obtained. The actual collapse capacity of the ESDOF system, i.e. the median intensity of earthquake excitation at collapse, is subsequently determined from (Adam, 2008),

$$CC_{ESDOF} = CC\, g\gamma^* = CC\, g\bar{\gamma} / \lambda_{MDOF} \tag{12}$$

This result approximates the collapse capacity of the actual MDOF structure,

$$CC_{MDOF} \approx CC_{ESDOF} \tag{13}$$

4. CONCLUSIONS

In this paper collapse spectra are presented, which allow a quantification of the P-delta effect on non-deteriorating inelastic SDOF oscillators with bilinear hysteretic loop. In particular, the median PGA, which leads to P-delta induced collapse, is identified as function of the initial structural period, the normalized slope of the post-tangent stiffness, and the viscous damping coefficient.

The application of these collapse spectra for prediction of the global collapse capacity of inelastic regular MDOF frame structure is described. The procedure is based on pushover analyses on the original structure and equivalent SDOF systems.

Acknowledgements:

The author gratefully acknowledges a travel grant from the Tokyo Institute of Technology.

References:

Adam, C. (2008) "Global collapse capacity of earthquake excited multi-degree-of-freedom frame structures vulnerable to P-delta effects", *Proceedings of the Taiwan - Austria Joint Workshop on Computational Mechanics of Materials and Structures*, November 15-17, 2008, National Taiwan University, Taipei, Taiwan (Yang, Y.B., ed.), pp. 10 - 13.

Adam, C., Ibarra, L.F. and Krawinkler, H. (2004), "Evaluation of P-Delta effects in non-deteriorating MDOF structures from equivalent SDOF systems," *Proceedings of the 13th World Conference on Earthquake Engineering*, August 1-6, 2004, Vancouver B.C., Canada. DVD-ROM paper, 15 pp., Canadian Association for Earthquake Engineering 2004.

Adam, C. and Spiess, J.-P. (2007), "Simplified evaluation of the global capacity of stability sensitive frame structures subjected to earthquake excitation" (in German), *Proceedings of the D-A-CH Meeting 2007 of the Austrian Association of Earthquake Engineering and Structural Dynamics*, September 27 - 28, 2007, Vienna, CD-ROM paper, paper no. 30, 10 pp.

Bernal, D. (1998), "Instability of buildings during seismic response," *Engineering Structures*, **20**, 496-502.

Ibarra, L.F. (2003), "Global collapse of frame structures under seismic excitations", PhD Thesis, Stanford University.

Fajfar, P. (2002), "Structural analysis in earthquake engineering - a breakthrough of simplified non-linear methods". *Proceedings of the 12th European Conference on Earthquake Engineering*, CD-ROM paper, paper ref. 843, 20 pp., Elsevier.

Medina, R.A. and Krawinkler, H. (2003), "Seismic demands for nondeteriorating frame structures and their dependence on ground motions." Report no. 144. The John A. Blume Earthquake Engineering Center, Stanford University.

Vamvatsikos, D. and Cornell, C.A. (2002), "Incremental dynamic analysis," *Earthquake Engineering and Structural Dynamics*, **31**, 491-514.

Sixth International Conference on Urban Earthquake Engineering
March 3-4, 2009, Tokyo Institute of Technology, Tokyo, Japan

NONLINEAR ANALYSIS OF BUILDINGS WITH ELEVATED LOWER LEVELS IMPACTED BY TSUNAMI WATER-BORNE MASSIVE OBJECTS AND POTENTIAL FOR PROGRESSIVE COLLAPSE

Kavinda M. Madurapperuma[1] and Anil C. Wijeyewickrema[2]

1) Graduate Student, Department of Civil Engineering, Tokyo Institute of Technology, Japan
2) Associate Professor, Department of Civil Engineering, Tokyo Institute of Technology, Japan
ma.k.aa@m.titech.ac.jp, wijeyewickrema.a.aa@m.titech.ac.jp

Abstract: Tsunami resistant buildings where the lower levels are elevated by means of RC columns to allow the free flow of tsunami waves, have been recently constructed in certain countries. However these columns are very vulnerable to impact due to water-borne massive objects. Tsunami field survey observations show that building destruction is often exacerbated by the impact of tsunami water-borne massive objects such as automobiles, barges, boats, empty storage tanks and shipping containers. In this paper, impact of tsunami water-borne massive objects on a RC building is carried out by using a fiber-based discretization model in OpenSEES. The *contact stiffness approach* which is based on a single-degree-of-freedom (SDOF) model is used to obtain impact force-time history. In addition, the potential for progressive collapse of the building due to loss of one or more first-story columns is investigated. Numerical results show that frame system suffers extensive damage due to impact of water-borne massive objects. It is found that the loss of a single column due to impact does not indicate potential for progressive collapse but the subsequent loss of an adjacent column (due to a similar impact) leads to progressive collapse of the building.

1. INTRODUCTION

The Indian Ocean tsunami that occurred on December 26, 2004 has resulted in massive destruction to coastal communities with more than 275,000 fatalities, and severe damage to buildings, bridges and other infrastructure (Inoue et al. 2007). Many RC buildings collapsed or were severely damaged due to the impact of massive objects such as automobiles, barges, boats, empty storage tanks and shipping containers (Ghobarah et al. 2006). However, post-tsunami reconnaissance surveys have reported that buildings that had only columns in the first-story (i.e., no infill walls) performed well during the Indian Ocean tsunami (Dias et al. 2006). Based on tsunami field observations and research studies, new tsunami resistant buildings have been constructed, where the lower levels are elevated by means of RC columns to allow the free flow of tsunami waves. An example of a recently constructed RC frame building is shown in Fig. 1. However, columns of the first-story are very vulnerable to impact due to tsunami water-borne massive objects. Failure of one or more columns may overstress critical members of the building leading to progressive collapse.

In this paper, the impact of tsunami water-borne massive objects on a RC building that is designed according to the new design concept, that the first-story is open space with only columns (i.e., no infill walls) allowing free flow of tsunami waves, is considered. Previously the authors (Madurapperuma and Wijeyewickrema 2008) used the *impulse-momentum approach* and assumed a triangular shape for the impact force-time history. In this study, the *contact stiffness approach* which is based on a single-degree-of-freedom (SDOF) model is used to obtain the impact force-time history. Essential factors such as object mass, contact stiffness and impact speed are incorporated. In addition, the potential for progressive collapse of the building due to loss of one or more first-story columns is investigated.

Fig. 1. A tsunami resistant building with elevated lower level in Sri Lanka.

2. DESCRIPTION AND STRUCTURAL DESIGN OF THE BUILDING

The building considered is a three-story RC school building, located in a tsunami inundation zone that can also

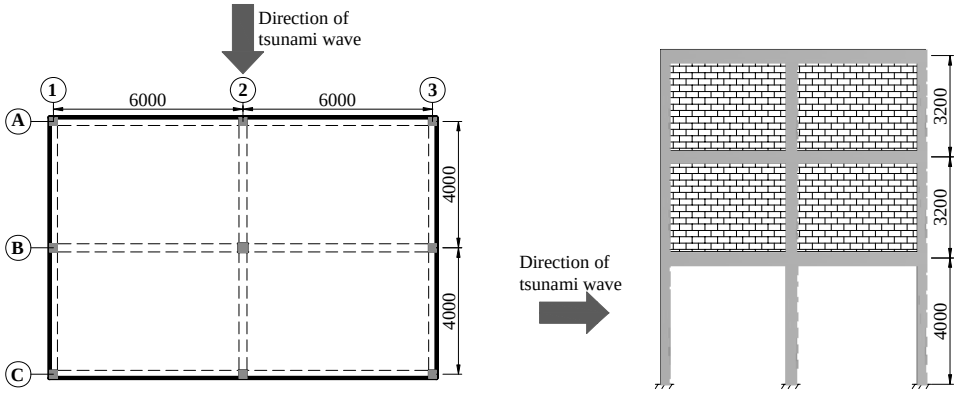

(a) Plan (b) Elevation

Fig. 2. Building configuration used in the study (all dimensions in mm).

Table 1. Section and reinforcement details of beams and columns.

Reinforcement	4 m beams (400×250 mm^2)			6 m beams (500×250 mm^2)			All columns (300×300 mm^2)
	Support		Middle	Support		Middle	
	Top	Bottom		Top	Bottom		
Longitudinal[a]	2-No. 5	2-No. 5	2-No. 5	3-No. 5	3-No. 5	3-No. 5	8-No. 5
Transverse[b] (shear)	No. 3 stirrups, at 175 mm over 1318 mm each end			No. 3 stirrups, at 175 mm over 2675 mm each end			No. 3 ties, at 200 mm

[a] Number of bars-diameter; No. 5: 16 mm.
[b] No. 3: 10 mm.

be used for tsunami evacuation purposes. The plan and elevation of the building are shown in Fig. 2. The first-story is an open space with only columns allowing the free flow of tsunami waves. The building was designed according to the strength design method specified in ACI 318-02 (ACI 2002) using SAP2000 (2004). The building is assumed to be located in a non-seismic region, hence seismic loads are not considered in the design. The dead loads consisted of loads from member self-weight and uniformly distributed 4.6 kN/m and 12.88 kN/m loads due to masonry walls along the perimeter beams of 6 m and 4 m, respectively. In addition, uniformly distributed load of 8.68 kN/m was applied over the interior 4 m beams for partitions. Design live loads were determined using the code provisions of IBC 2003. The design live loads consisted of uniformly distributed loads of 0.96 kPa on roof slab and 1.91 kPa on floor slabs. The slab thickness was taken as 150 mm for the roof and the floors. The concrete cover was 35.5 mm for all beams and columns. Normal weight concrete with a specified compressive strength of 27.6 MPa and reinforcing steel with yield strength of 414 MPa were used. The design details of beams and columns are summarized in Table 1.

3. EVALUATION OF TSUNAMI FORCES

In the present study, the dominant forces are hydrodynamic force and impact force due to water-borne massive objects. The hydrodynamic force F_H exerted on first-story columns can be evaluated from

$$F_H = \frac{1}{2}\rho C_D B(hu^2)_{\max}, \tag{1}$$

where ρ is the fluid mass density including sediment (1200 kg/m^3), C_D is the drag coefficient (2.0 for square columns), B is the breadth of the column in the plane normal to the direction of flow, h is the flow depth, and u is the tsunami flow velocity at the location of the column (pg. 72, FEMA (2008)). The tsunami flow velocity u is calculated from the two equations,

$$\eta = \frac{1}{36\tau^2}(2\sqrt{2}\tau - \tau^2 - 2\zeta)^2, \tag{2}$$

$$\upsilon = \frac{1}{3\tau}(\tau - \sqrt{2}\tau^2 + \sqrt{2}\zeta), \tag{3}$$

where $\eta = h/R$, $\upsilon = u/\sqrt{2gR}$, $\tau = t\tan\theta\sqrt{g/R}$, $\zeta = z/R$; in which g is the gravitational acceleration, R is the runup, t is the time ($t = 0$ at the shoreline), θ is the beach slope and z is the ground elevation at the location of the column measured from the shoreline (pg. 132, FEMA (2008)). Eqns. (2) and (3) can be used to determine υ for a given η and ζ. The term $(hu^2)_{\max}$ in Eq. (1) can be estimated using flow velocities for different water depths.

The *contact stiffness approach* which is based on a SDOF model is used to estimate impact force-time history. It is assumed that the impact occurs over a short duration such that damping can be neglected (pg. 215, Stronge 2000).

The equation of motion for such a model is

$$m_{obj}\ddot{x} + k_{eff}x = 0, \quad (4)$$

where m_{obj} is the mass of the object, x is the summation of compression of the contact region in the direction of motion and k_{eff} is the effective contact stiffness i.e., $1/k_{eff} = 1/k_{obj} + 1/k_l$; in which k_{obj} is the frontal stiffness of the object and k_l is the local stiffness of the column. By considering the $p-\Delta$ curve obtained by loading the structure quasi-statically at the impacted point, the stiffness k_l can be obtained. Applying initial conditions $x = 0$ and $\dot{x} = v_{i,obj}$ at $t = 0$, where $v_{i,obj}$ is the velocity of the object before impact, and using the equation $F = k_{eff}x$, the time varying object velocity v_{obj} and impact force F can be expressed as

$$F = v_{i,obj}\sqrt{k_{eff}m_{obj}}\,\sin\left(t\sqrt{k_{eff}/m_{obj}}\right), \quad (5)$$

$$v_{obj} = v_{i,obj}\cos\left(t\sqrt{k_{eff}/m_{obj}}\right). \quad (6)$$

It is assumed that the velocity of the object before impact $v_{i,obj}$ is the same as tsunami flow velocity u, and that the object comes to rest without rebounding from the column.

4. FINITE ELEMENT MODELS

The frame system is analyzed using a fiber-based discretization model in OpenSEES (2009). The 2-D model is used to simulate impact response of the frame system and the 3-D model is used to investigate the potential for progressive collapse of the building. The water-borne object is assumed to impact on column A2 (Fig. 2(a)) hence the frame along grid line 2 is modeled for 2-D analysis. The stiffness of floor slabs to beam response is considered in 3-D analysis where beams are modeled as T or L sections following the ACI 318-05 (ACI 2005) design specifications. The effective flange widths are taken as one-quarter and one-twelfth of span lengths of beams for T-beams and L-beams, respectively. The both frame systems are modeled using *nonlinearBeamColumn* element which is a distributed plasticity type force-based element with fiber sections accounting for the spread of plasticity both over the cross-section and along the member length. Material properties for concrete and reinforcing bars are defined through conventional stress-strain models available in OpenSEES. The concrete material response is simulated using the *Concrete02* material model. The model proposed by Mander et al. (1988) is used to estimate the core concrete strength accounting for the amount of confinement provided by transverse reinforcement. The material model *Steel02* is used to simulate the steel material response. The material properties for nonlinear material modeling of concrete and reinforcing bars are given else where (pg. 4-5, Madurapperuma (2007)). The gravity loads on the frame systems are determined using roof and floor tributary areas corresponding to dead load plus 25% of the design live load.

5. NUMERICAL ANALYSIS

For the dynamic analysis, the modified Newton-Raphson iterative scheme, the Newmark method for time integration with $\beta = 0.25$, $\gamma = 0.5$ and time step $dt = 0.00005$ s are used. The Rayleigh damping parameters are calculated assuming a 5% mass-proportional damping ratio.

5.1 Impact Analysis

It is assumed that the building is located 2.0 m above the shoreline and the land is inundated by a tsunami runup of 12.0 m (i.e., $z = 2.0$ m and $R = 12.0$ m). The tsunami water-borne objects are automobiles (Table 2) and impact the column A2 (Fig. 2(a)) at 2.0 m above the ground level. By considering $p-\Delta$ curve in Fig. 3, $k_l = 24{,}000$ kN/m was obtained. Then the effective contact stiffness k_{eff} was obtained using the frontal stiffness values given in Table 2. The time histories of the impact force and the automobile velocity are obtained using Eqns. (5) and (6), respectively and shown in Fig. 4. The hydrodynamic force is first applied as a uniform load (i.e., 22.75 kN/m for a height of 0.54 m) with gravity loads and a static analysis is carried out. Then the impact force-time history as shown in Fig. 4(a) is applied as a point load at 2.0 m above the ground level and a nonlinear dynamic analysis is carried out.

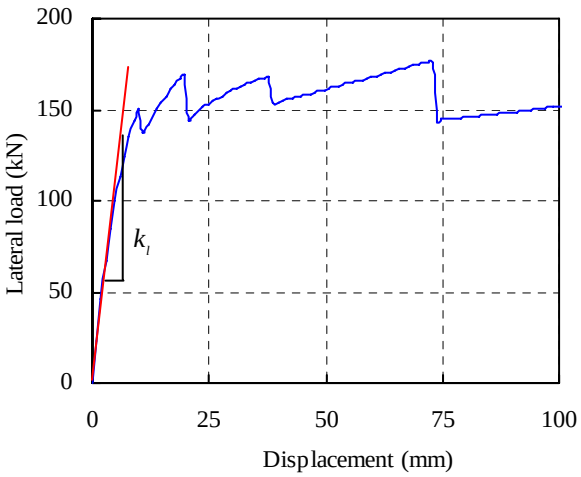

Fig. 3. Response of column A2 when the frame system is quasi-statically loaded at 2.0 m above the ground level.

The displacement and moment-curvature responses of the column A2 at 2.0 m above the ground level are shown in Fig. 5. In Fig. 5(a) the column displacement at 2.0 m above ground level attains a peak value of approximately 32 mm after 0.0548 s and then decreases to a constant value of 19 mm due to impact of the 1909 kg van. This peak displacement is more than 4 times the peak displacement due to impact of the 1138 kg car at the same level. It is

Table 2. Kinetic energies for different types of water-borne objects.

Water-borne object	Dimensions (m)	Mass (kg)	Frontal stiffness (kN/m)	Draft (m)	Velocity (m/s)	Kinetic energy (kJ)
Car	3.5×1.25[a]	1138[b]	1000[b]	0.42	8.86	44.7
Medium size van	4.5×1.5[a]	1909[b]	2000[b]	0.53	8.27	65.3

[a] length × width, [b] Wagstrom et al. 2004.

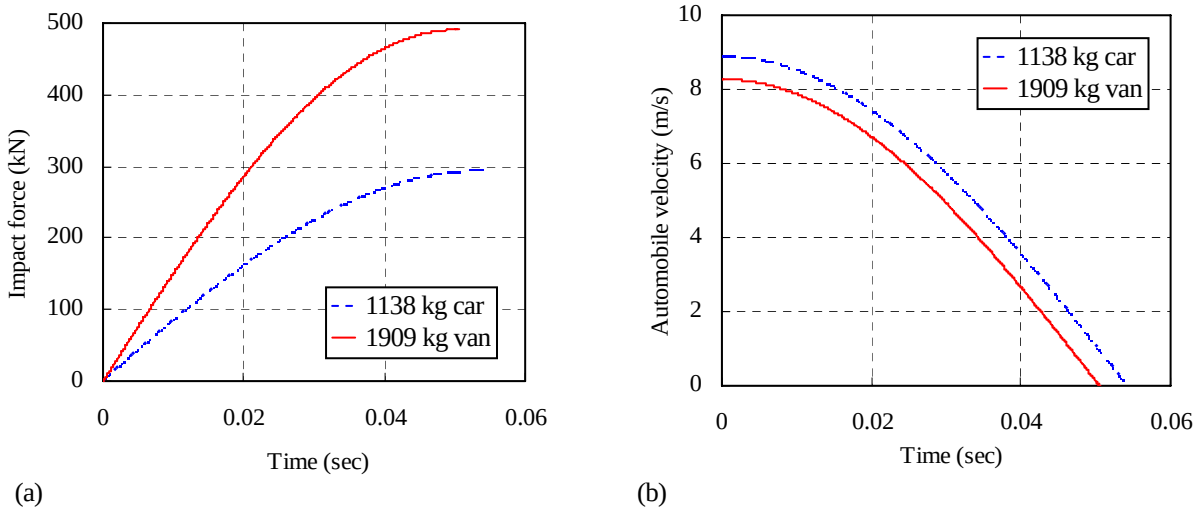

(a) (b)

Fig. 4. Time histories of (a) impact force, and (b) automobile velocity.

expected that the cracking and spalling of concrete followed by the yielding and buckling of steel reinforcements cause the constant displacement which is not equal to that before impact (i.e., displacement due to hydrodynamic force and gravity loads). In Fig. 5(b), when the 1909 kg van impacts the column, the moment drops after spalling of the cover concrete and a plastic hinge forms with extensive inelastic behavior due to buckling of reinforcements at the impacted section. However, when the 1138 kg car impacts the column, the inelastic behavior in the moment-curvature response is very small compared to that of the 1909 kg van.

The base shear and moment-curvature responses of the column A2 at the support section are shown in Fig. 6. In Fig. 6(a) base shear increases with increase in impact force up to 111 kN after 0.0364 s and then a sudden drop of shear force can be seen for impact of the 1909 kg van. Shear failure can be expected at the support because the spacing of the transverse (shear) reinforcement in the column (see Table 1) is relatively wide. However, shear failure cannot be seen for the impact of 1138 kg car and the base shear of the column A2 after the impact is equal to that before impact (i.e., base shear due to hydrodynamic force and gravity loads). Examining moment-curvature response in Fig. 6(b)

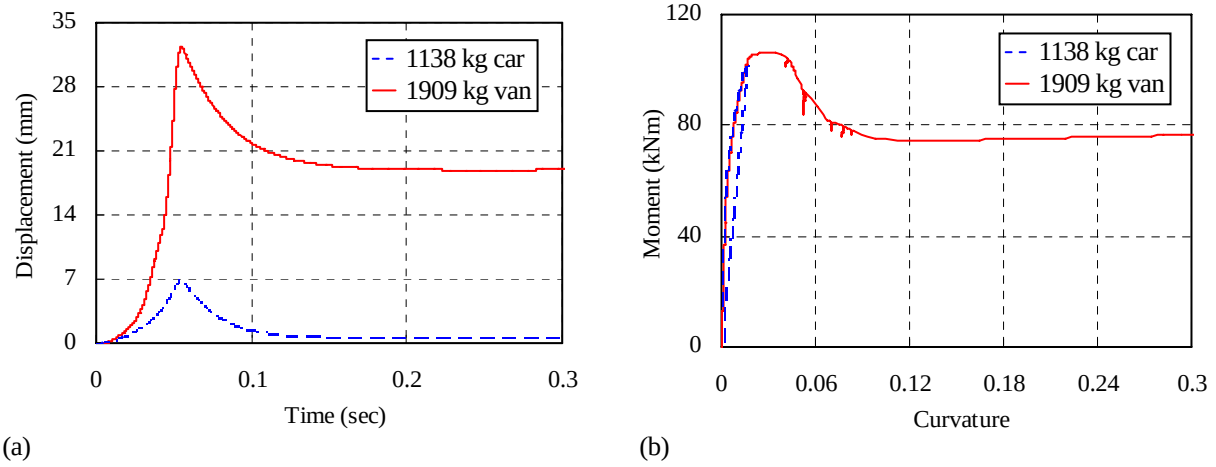

(a) (b)

Fig. 5. Response of the column A2 at 2.0 m above the ground level: (a) horizontal displacement, and (b) moment-curvature.

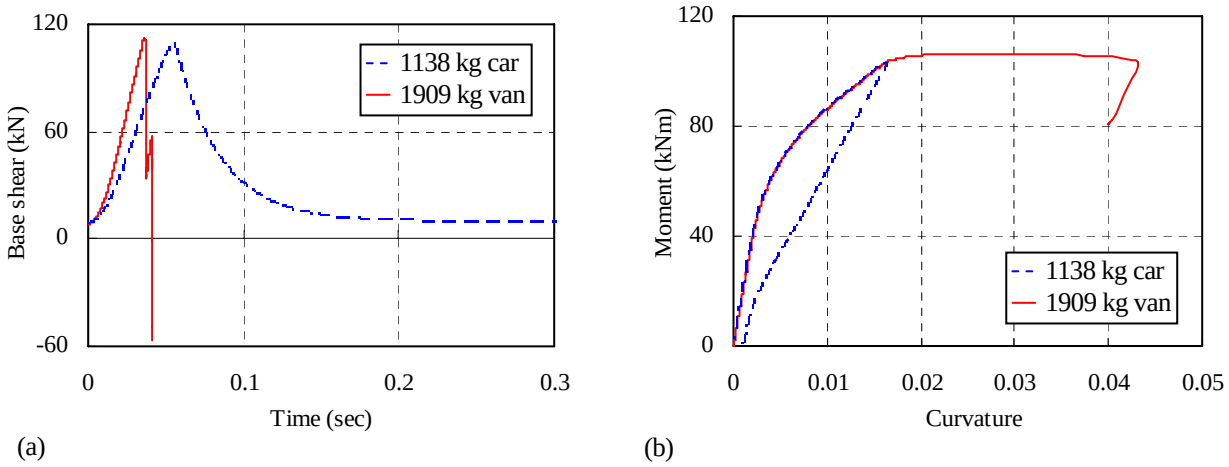

Fig. 6. Response of column A2 at the support section: (a) base shear, and (b) moment-curvature.

shows that the support moment exceeds its yield capacity and a plastic hinge forms with extensive inelastic behavior due to impact of the 1909 kg van. Again the plastic deformation at the support is relatively small due to impact of the 1138 kg car. Therefore, it is seen that the column A2 suffers extensive damage due to impact of the 1909 kg van.

5.2 Progressive Collapse Analysis

The potential for progressive collapse of the building due to loss of columns A2 and A1 (Fig. 2(a)) is investigated using the 3-D model. The gravity loads are applied and the end forces of columns A2 and A1 are determined. First, the potential for progressive collapse of the building due to loss of column A2 is investigated. The column A2 is removed from the model and the column end forces obtain from the previous analysis are applied externally at the top node of the column A2 to establish the equilibrium. The results of such analysis are identical to those of initial analysis where the column was not removed. Then equal and opposite column end forces are applied to the top node of column A2 to simulate the loss of column A2 and dynamic analysis is carried out. The node corresponding to the top of column A2 attains a peak vertical displacement of 17.2 mm and finally decreases to a constant value of 17 mm as seen in Fig. 7. Examining the axial force histories (but not shown here)

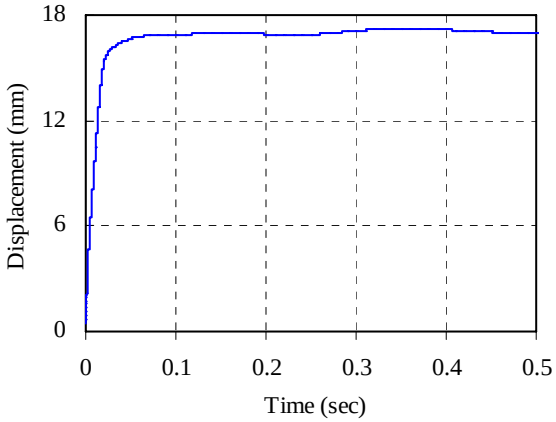

Fig. 7. Vertical displacement response at the top node of column A2.

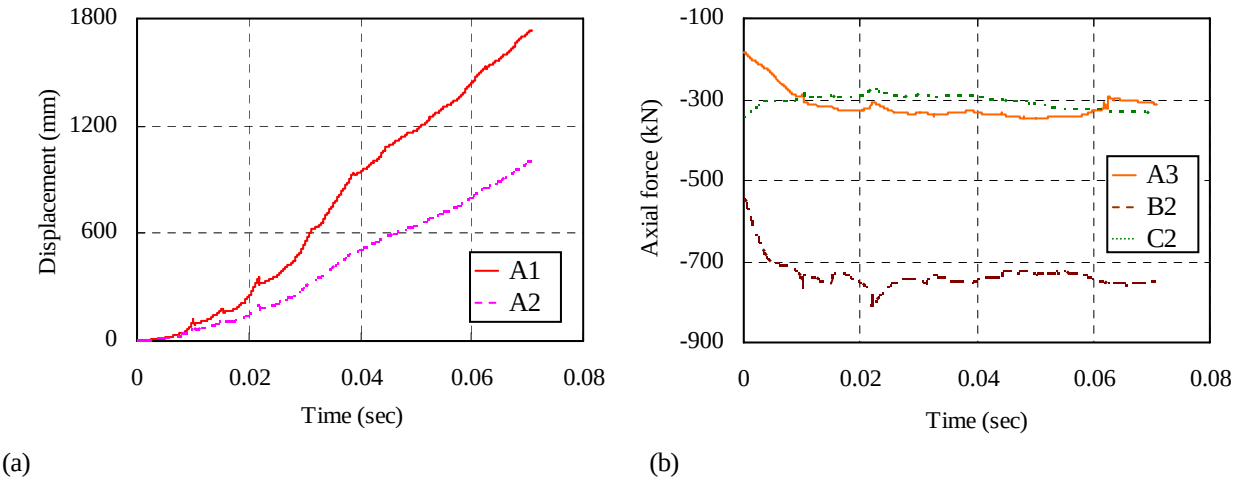

Fig. 8. Response of the frame system due to loss of columns A2 and A1: (a) vertical displacement at the top node of column A1 and A2, and (b) column axial forces.

shows that axial forces are generally not affected resulting stable behavior of the building. Since the loss of a single column did not indicate a potential for progressive collapse, the frame system was investigated to simultaneous loss of columns A2 and A1. The response of the frame system due to loss of columns A2 and A1 is shown in Fig. 8. In Fig. 8(a) the vertical displacements of top nodes of the columns A2 and A1 increased rapidly up to a maximum of 1005 mm and 1737 mm, respectively and then system instability was seen due to nonconvergence of the equilibrium equation at the last load step after 0.0707 s. In Fig. 8(b) the axial force in column B2 increases from 545 kN to a maximum of 810kN while the axial force in column C2 decreases from 348 kN minimum of 274 kN due to an overturning moment acting on the frame system. Therefore, it is seen that the frame system cannot maintain the static force equilibrium due to loss of columns A2 and A1 resulting potential for progressive collapse of the building.

6. CONCLUDING REMARKS

The impact of tsunami water-borne automobiles on a RC building is considered using a fiber-based discretization model in OpenSEES. The *contact stiffness approach* which is based on a single-degree-of-freedom (SDOF) model is used to obtain the impact force-time history. Numerical results show that the frame system is safe when impacted by water-borne automobiles with a mass less than or equal to 1138 kg. But the frame system suffers extensive damage when impacted by the 1909 kg automobile. In the progressive collapse analysis, it is found that loss of a single column does not severely affect the stability of the building but the subsequent loss of an adjacent column (due to a similar impact) leads to potential for progressive collapse of the building. It is noted that the findings of this analysis may not be the same for a different building configuration. The incorporation of walls which was not considered in this study is expected to influence the collapse response of the building.

Therefore, it can be concluded that impact may cause devastating damage to critical structural members of the building according to the mass and type of the water-borne object. Failure of a column due to a very large impact load cannot be avoided and it would be costly to design a building for such impact loads. However, there are certain mitigation measures that could be explored to protect critical buildings that can be used for tsunami evacuation purposes. One of the impact mitigation strategies for buildings with open first-story is the inclusion of redundancies in the open first-story to avoid collapse of the building due to failure of one or two columns. Another impact mitigation strategy is the construction of impact resisting barriers which absorb and dissipate most of the impact energy to protect critical buildings.

Acknowledgements:

The first author gratefully acknowledges a Monbukagakusho scholarship from the Japanese government. The authors are very grateful to Prof. Kohji Tokimatsu, GCOE Program Leader of Center for Urban Earthquake Engineering (CUEE), Tokyo Institute of Technology, for his advice and support. Financial support from CUEE is gratefully acknowledged.

References:

American Concrete Institute (ACI) (2002), "Building Code Requirements for Structural Concrete," ACI 318-02, Farmington Hills, Mich.

American Concrete Institute (ACI) (2005), "Building Code Requirements for Structural Concrete and Commentary," ACI 318-05, Farmington Hills, Mich.

Dias, P., Dissanayake, R. and Chandratilake, R. (2006), "Lessons Learned from Tsunami Damage in Sri Lanka," *Proceedings of Institution of Civil Engineers (ICE)*, **159**(2), 74-81.

Federal Emergency Management Agency (FEMA) (2008), "Guidelines for design of structures for vertical evacuation from tsunamis," Publication number FEMA P646, Washington, D.C.

Ghobarah, A., Saatcioglu, M. and Nistor, I. (2006), "The Impact of the 26 December 2004 Earthquake and Tsunami on Structures and Infrastructure," *Engineering Structures*, **28**, 312-326.

Inoue S., Wijeyewickrema, A. C., Matsumoto, H., Miura, H., Gunaratna, P., Madurapperuma, K. M., and Sekiguchi, T. (2007), "Field Survey of Tsunami effects in Sri Lanka due to the Sumatra-Andaman Earthquake of December 26, 2004," *Pure and Applied Geophysics*, **164**(2-3), 395-411.

International Building Code (IBC) (2003), International Code Council, Inc., Country Club Hills, Illinois.

Madurapperuma, K. M. (2007), "Impact Response of Buildings due to Tsunami Water-Borne Massive Objects," M.Eng. Thesis, Dept. of Civil Engineering, Tokyo Institute of Technology, Tokyo, Japan.

Madurapperuma, K. M. and Wijeyewickrema, A. C. (2008), "Damage to Reinforced Concrete Buildings with Elevated Lower Levels Impacted by Tsunami Water-Borne Massive Objects," *Proceedings of Fifth International Conference on Urban Earthquake Engineering*, Tokyo, Japan, 447-452.

Mander, J. B., Priestly, M. J. N. and Park, R. (1988), "Theoretical Stress-Strain Model for Confined Concrete," *Journal of Structural Engineering*, ASCE, **114**(8), 1804-1826.

OpenSEES (2009), "Open system for earthquake engineering simulation," <http://opensees.berkeley.edu> (Jan. 17, 2009).

SAP2000 (2004), "Integrated Finite Element Analysis and Design of Structures," Computers and Structures, Inc., Berkeley, Calif.

Stronge, W. J. (2000), "Impact Mechanics," Cambridge University Press, Cambridge.

Wagstrom, L., Thomson, R. and Pipkorn, B. (2004), "Structural Adaptivity for Acceleration Level Reduction in Passenger Car Frontal Collisions. *International Journal of Crashworthiness*, **9**(2), 121–127.

Sixth International Conference on Urban Earthquake Engineering
March 3-4, 2009, Tokyo Institute of Technology, Tokyo, Japan

PIEZORESISTIVE FRCS WITH HIGH TOUGHNESS AND DYNAMIC SENSING ABILITIES FOR EARTHQUAKE RESISTANT STRUCTURES

N. Banthia

Professor, Distinguished University Scholar & Canada Research Chair in Infrastructure Rehabilitation
Department of Civil Engineering, The University of British Columbia, 2024-6250 Applied Science Lane
Vancouver, BC, Canada V6T 1Z4

banthia@civil.ubc.ca

Abstract: The usefulness of fiber reinforced concrete (FRC) in various civil engineering applications is indisputable. Fiber reinforced concrete has so far been successfully used in slabs on grade, shotcrete, architectural panels, precast products, offshore structures, structures in seismic regions, thin and thick repairs, crash barriers, footings and hydraulic structures. This paper discusses the performance of FRC under quasi-static and dynamic loading conditions. The paper further illustrates that FRCs carrying carbon fibers and carbon nano-tubes possess sensing abilities that can help us develop smart and intelligent infrastructure with elegantly integrated sensing and health monitoring abilities.

1. INTRODUCTION

Concrete in most instances is loaded at the strain rates approximated in our standardized tests. However, there are dynamic events in which the strain rates may significantly exceed those obtained in standardized tests (1) such as in fast moving traffic ($\dot{\varepsilon}=10^{-6}$–$10^{-4}s^{-1}$), gas explosions ($\dot{\varepsilon}=5x10^{-5}-5x10^{-4}\,s^{-1}$), earthquakes ($\dot{\varepsilon}=5x10^{-3}$–$5x10^{-1}\,s^{-1}$), pile driving ($\dot{\varepsilon}=10^{-2}$–$10^{0}\,s^{-1}$) and aircraft landing ($\dot{\varepsilon}=5x10^{-2}$–$2x10^{0}s^{-1}$). Inappropriately, though, the properties of materials used in the design of these structures are derived from standardized tests that are run at low quasi-static strain-rates (generally around $10^{-6}s^{-1}$). Concrete is highly strain-rate sensitive in compression (2), tension (3) and flexure (4).

A large amount of energy is often imparted to the structure during a dynamic event. If the structure is not capable of absorbing the incoming energy, a failure during the event itself may ensue. Concrete, unfortunately, is a very brittle material with a poor energy absorption capacity. Research in the last thirty years has indicated that the ideal way to enhance the post-fracture stress transfer capability in concrete is by reinforcing it with fibers (Figure 1). Fibers bridge matrix cracks and undergo pull-out processes resulting in a significant enhancement in the fracture toughness of the material.

2. PERFORMANCE OF FRC

2.1 Critical Fiber Volume, Strain Hardening and Multiple Cracking

It emerges therefore that fiber-reinforced cementitious composites can be classified into two broad categories: normal performance (or conventional) fiber-reinforced cementitious composites and high-performance fiber-reinforced cementitious composites (HPFRCC). In normal performance FRCs with low to medium volume fraction of fibers, fibers do not enhance the tensile/flexural strength of the composite and benefits of fiber reinforcement are limited to either a reduction in the plastic shrinkage crack control (5) or to enhancement of energy absorption ('toughness') in the post-cracking regime only (6). For high performance fiber reinforced composites, on the other hand, with high fiber dosages, benefits of fiber reinforcement are noted in an increased tensile strength, strain-hardening response before localization and enhanced 'toughness' beyond crack localization. Fiber volume fraction at which fibers can be expected to produce an increase in the tensile/flexural strength is given by (7).

$$V_f \geq (V_{f\,critical}) = \frac{1}{1+\frac{\tau_{fu}}{\sigma_{mu}}\frac{l_f}{d_f}(\lambda_1\lambda_2\lambda_3-\alpha_1\alpha_2)} \qquad (1)$$

where, τ_{fu} is the average interfacial bond strength at the interface, σ_{mu} is the tensile strength of the matrix, l_f is the fiber length and d_f is the fiber diameter. λ_1, λ_2, λ_3 are efficiency factors related to length, orientation and grouping, respectively, and α_1 and α_2 are constants pertaining to uncracked state of the composite. For a given FRC, Equation 1 guarantees that if the critical

volume fraction is exceeded, composite will depict strain hardening and show multiple cracking. Some such curves for carbon fiber reinforced concrete in tension are given in Figure 2. Note the presence of strain hardening in the composite beyond 2% by volume.

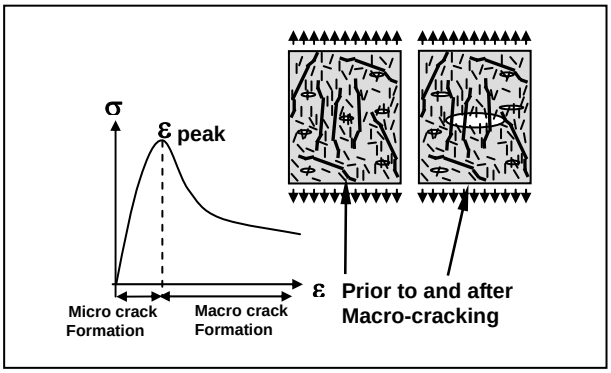

Figure 1 Principles of Fiber Reinforcement. Micro-fibers delay crack localization and then enhance the pull-out resistance of macro-fibers in the softening zone.

In FRCs with volume fractions higher than the critical, after the bend-over point, BOP, (Figure 2), multiple cracking is expected to occur and the composite is expected to crack in segments of lengths between x and $2x$ (where x is the transfer) length given by:

$$x = 2\left(\frac{V_m}{V_f}\right)\left(\frac{\sigma_{mu}}{\tau_{fu}}\right)\left(\frac{d_f}{4}\right) \tag{2}$$

In the softening regime, where the load starts to drop, the response of the composite is completely dependent upon the bond-slip behaviour of the fibers under an applied pull-out load. The response in the softening regime can therefore be assembled by first expressing the bond-slip behavior of a given fiber and then integrating the contribution of all fibers across a crack. In the case of pure tension, the stress vs crack separation, $\sigma_{tension}(w)$, curve can be expressed as [7]:

$$\sigma_{tension}(w) = \frac{V_f}{\pi d_f{}^2/4}\int_{\alpha=0}^{\pi}\int_{z=0}^{(L_f/2)\cos\alpha} f(\alpha,w)\,p(\alpha)p(z)\,dz\,d\alpha \tag{3}$$

where, $f(\alpha, w)$ is the bond-slip response of a single fiber at a crack opening (w) and inclination angle α, $p(\alpha)$ and $p(z)$ are probability density functions of the orientation of fiber w.r.t. the tensile loading direction and centroidal distance of the fiber from the crack plane, respectively.

2.2 Fracture Representation

Equation (3) is a rather simplistic approach to FRC. It assumes that the composite goes from an uncracked

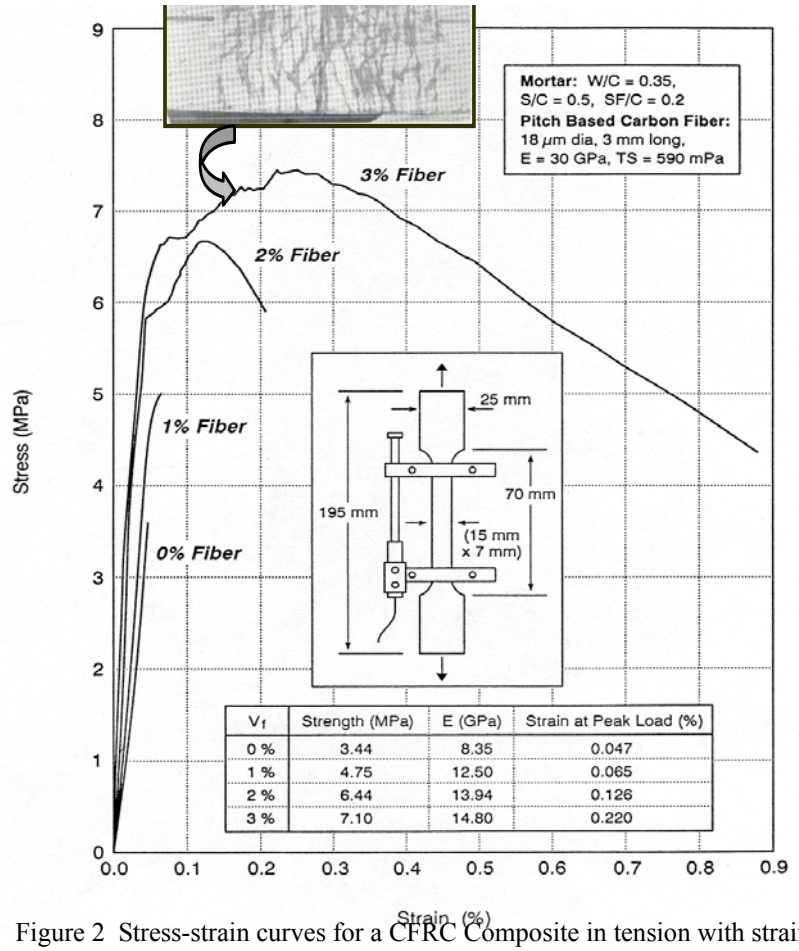

V_f	Strength (MPa)	E (GPa)	Strain at Peak Load (%)
0 %	3.44	8.35	0.047
1 %	4.75	12.50	0.065
2 %	6.44	13.94	0.126
3 %	7.10	14.80	0.220

Figure 2 Stress-strain curves for a CFRC Composite in tension with strain-hardening and multiple cracking at high fiber volume fractions

state to a cracked state (albeit showing multiple cracking at $V_f > V_{fcritical}$). In reality, concrete is a micro-fracturing, strain-softening material, and in the case of fiber reinforced concrete, in addition to crack closing pressure due to aggregate interlocking, fiber bridging occurs behind the tip of a propagating crack where fibers undergo bond-slip processes and provide additional closing pressures. The fracture processes in fiber reinforced cement composites are therefore complex and advanced models are needed to simulate these processes. Attempts have been made to model fracture in FRC using the cohesive crack model [8] as well as the J-integral [9]. However, strictly speaking, these are only crack initiation criteria and fail to define conditions for continued crack growth. To define both crack initiation and growth, there is now general agreement that a continuous curve of fracture conditions at the crack tip is needed as done in an R-curve [10]. An R-curve (Figure 3) is a significantly more suitable representation of fracture in FRCs, as one can monitor variations in the stress intensity as the crack grows and derive a multi-parameter fracture criterion. Some R-Curves are shown in Figure 4 [10].

Figure 2 Stress-Strain Curves for a A CFRC Composite in Tension with Strain-Hardening and Multiple Cracking at High Fiber Volume Fractions

2.3 Performance Under Dynamic Loading

In spite of continued efforts in this area, our understanding of the engineering properties of concrete and fiber reinforced concrete under dynamic loading (such as those occurring during impact, blast and earthquake loading) remains severely limited. In the case of fiber reinforced concrete, while an improvement in impact properties is widely reported, the exact magnitude of these improvements is uncertain. On a worrisome note, steel fibers are reported (11) to fracture across cracks at high rates of loading and thus produce a brittle response at very high strain-rates. Shear properties of FRC under impact have not been studied at all. In Figure 5, the static load-displacement plots in flexure for HPFRCC are compared with those for normal FRC (12). Notice a significantly better response in HPFRCC. The impact response of HPFRCC is compared with that of normal FRC in Figure 6 in terms of total energy absorbed (typically area under the load-deflection curve shown in Figure 5, but under dynamic conditions). Notice the very high impact resistance of HPFRCC over conventional FRC. Notice also the gradual decrease in the energy absorption capacity of SFRC with an increase in the dynamic stress-rate, and the corresponding increase in the energy absorption capacity of PFRC in the same impact range. A general notion of the stress rate sensitivity may be obtained from the formulation proposed by Nadeau *et al* (13). This is shown in Figure 7 where flexural strength of HPFRCC is compared with plain and normal strength FRC as a function of stress-rate. Note that HPFRCC is less sensitive to stress-rate than traditional normal strength FRC, and that a steep rise in the stress-rate sensitivity (*knee* in the curve, point D) in the case of HPFRCC occurs at a higher value of applied stress-rate than normal strength FRC.

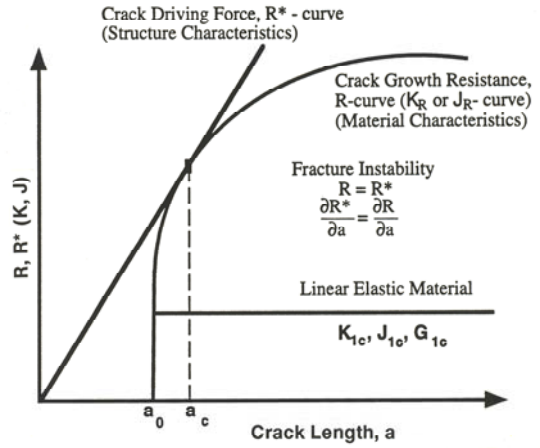

Figure 3 R-Curve representation of fracture in FRC

2.4 Piezo-Resistivity and Sensing Abilities

Structural health monitoring (SHM) using reliable fiber optic sensors (FOSs) strategically integrated into structural systems is part of an effective approach towards infrastructure management. Unfortunately, FOSs are prohibitively expensive.

Fortunately, fiber reinforcement of cementitious materials with conducting media such as carbon fibers and carbon nano-tubes can produce Piezoresistive materials that are highly conductive and can sense changes with strain, temperature and the chemical environment through impedance changes. These Piezoresistive Fiber Reinforced Cementitious Composites (PFRCC) can therefore be either embedded in concrete or applied in a Near Surface

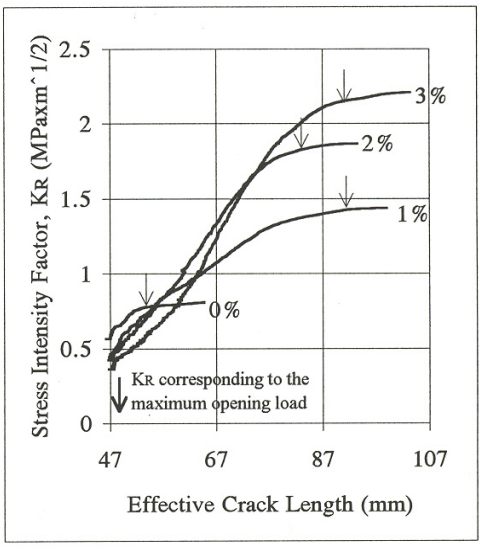

Figure 4 R-Curves generated from a crack growth test

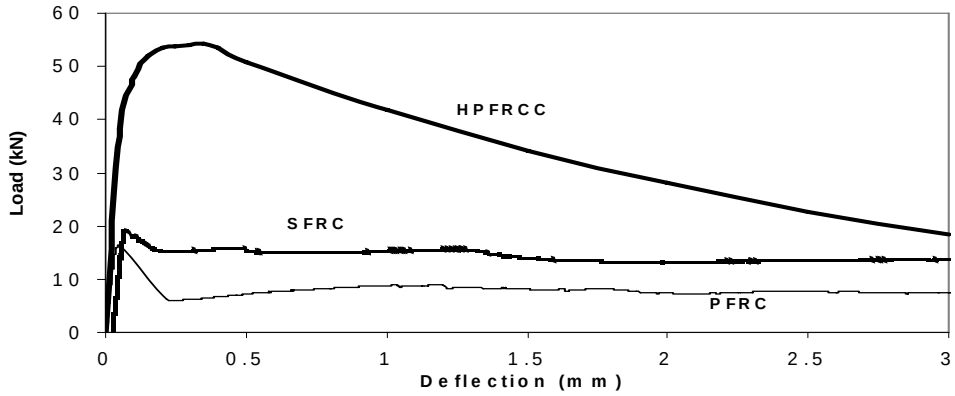

Figure 5 Quasi-static flexural response of normal steel FRC (SFRC), Normal polypropylene FRC (PFRC) and HPFRCC (with steel fiber)

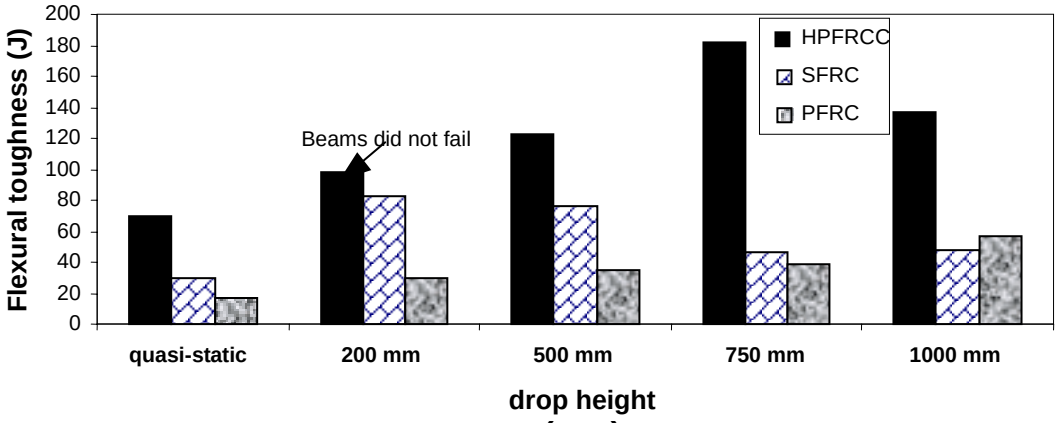

Figure 6 Impact toughness of normal FRC (SFRC and PFRC) and HPFRCC

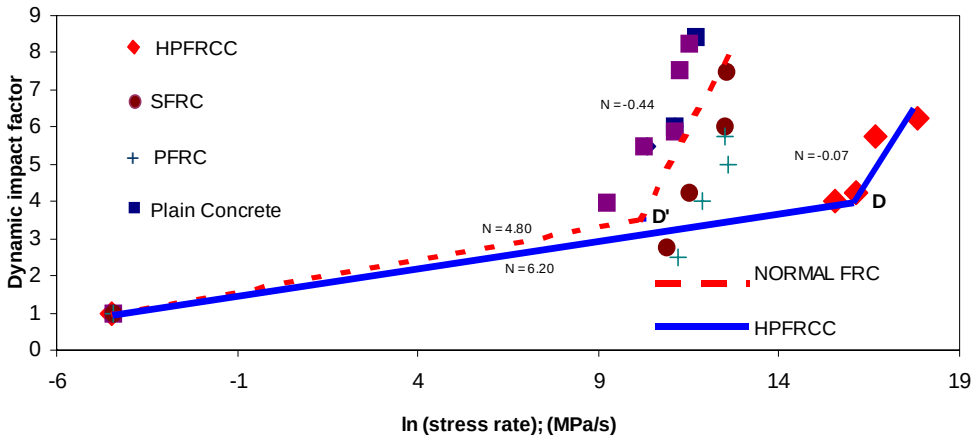

Figure 7 Rate Effects in Normal FRC and HPFRCC

Mounted (NSM) form to detect structural condition. Some results from such sensors are given in Figure 8 (14-16). Notice in the stress vs. resistivity plot that at the creation of a macro-crack (Point A) the sensor resistivity increases suddenly (Point B), implying that such sensors can be effective 'crack-detectors'.

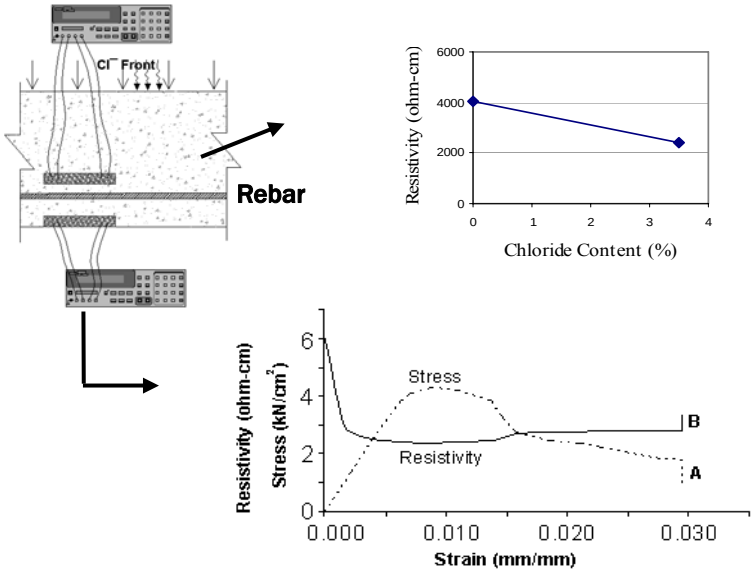

Figure 8 Piezo-resistive FRC (PFRC) sensors capable of detecting chloride content and strains (14).

Unfortunately, signals from the PFRCC remain unreliable due to three reasons: first, polarization (16) occurs (due to the generation of gases) degrading the quality of the signal; second, Joule's effect occurs where current generates heat; and finally, dimensional changes due to shrinkage further diminish the reliability of the signal. It is often proposed to resolve these by: employing a high frequency alternating current, using high pressure steam curing (autoclaving) to maximize dimensional stability and by introducing dummy sensors for elimination/referencing purposes.

3. CONCLUDING REMARKS

The use of fiber reinforced concrete for both new construction and repair appears highly promising. Fibers control shrinkage cracking, abate micro-cracks from coalescing and enhance ductility, toughness, impact resistance and fatigue endurance. With their high resistance to crack nucleation and growth, fibers reduce the permeability of concrete and prevent the ingress of deleterious agents thereby delaying both material degradation and steel corrosion. Some fibre reinforced cementitious composites when reinforced with conducting media such as carbon fibers and carbon nano-tubes can act as smart materials and piezo-resistive sensors, enabling effective structural health monitoring.

References:

1. Comite Euro-International du Beton (CEB) (1988), Bulletin 187, 3.6.
2. Grote, D.L. et al. (2001), *Int. J. Impact Engineering*, **25**, 869-910.
3. Zielinski, A.J. and Reinhardt, H.W. (1982), *Cem. & Conc. Res.* **12**, 309-319.
4. Banthia, N., Mindess, S. Bentur, A. and Pigeon, M. (1989) *Expt. Mech.,* **29**(2), 63-69.
5. Banthia, N. and Gupta, R. (2006), Influence of Polypropylene Fiber Geometry on Plastic Shrinkage Cracking, *Concrete, Cement and Concrete Research*, **36**(7), 1263-1267.
6. Banthia, N. and Dubey, A. (2000), Measurement of Flexural Toughness of Fiber Reinforced Concrete using a Novel Technique, Part 2: Performance of Various Composites, *ACI Materials Journal*, **97**(1), 3-11.
7. Banthia, N. (2005), FRC for Bridge Decks, Proc. Int. Workshop on Innovative Bridge Deck Technologies, ISIS Canada, Winnipeg, 195-214.
8. Hillerborg, A. (1980), *Cement and Concrete Composites*, **2**, 177-84.
9. Mindess, S. et al, (1977), *Cement and Concrete Research*, **7,** 731-742.
10. Banthia, N. and Genois, I. (2000), "Controlled Crack Growth Tests for Optimization of Micro-Fiber Reinforced Cement Composites", ACI, Special Publication: Application and Testing of Fracture Mechanics Concepts (Ed. C. Vipulanandan), SP-201, 55-74.
11. Banthia, N. et al. (1987), *Materials and Structures.* (RILEM), **20**, 293-302.
12. Bindiganavile, V. and Banthia, N. (2002), *ACI Materials Journal*, **99**(6), 543-548.
13. Nadeau, J.S., Bennet, R. and Fuller, E.R. (Jr). (1982), *J. of Mater. Sci*. **17**, 2831-2840.
14. Chacko, R. (2005), MASc Thesis, Dept of Civil Engineering, The University of British Columbia, 110 pp.
15. Chacko, R. M., Banthia, N., and Mufti, A. A., (2007), *Can. J. of Civil Engineering*, **34**(3), 284-290.
16. Banthia, N., Djeridane, S. and Pigeon, M. (1992), *Cement and Concrete Research*, **22**(5), 804-814.

Sixth International Conference on Urban Earthquake Engineering
March 3-4, 2009, Tokyo Institute of Technology, Tokyo, Japan

FINITE ELEMENT ANALYSES OF CONCENTRICALLY LOADED ANCHORAGE ZONES WITH PRESENCE OF SUPPORT REACTIONS

Songwut Hengprathanee[1] and Carin L. Roberts-Wollmann[2]

1) Assistant Professor, Dept. of Civil Engineering, Kasetsart University, Thailand
2) Associate Professor, Dept. of Civil and Environmental Engineering, Virginia Tech, USA
fengsoh@ku.ac.th, wollmann@vt.edu

Abstract: Linear Elastic finite element analyses are used for the parametric study of rectangular anchorage zones with the presence of a support reaction. The finite element program called DIANA was selected for the study. In this paper, the investigation of two load configurations consisting of concentric and inclined concentric loads is presented. The influence of several parameters, including anchorage ratio, inclination angle of prestressing load, magnitude of the reaction force, the location of the reaction force, and bearing plate ratio, is studied. Improved equations, which are modified from the equations presented in the AASHTO Standard Specifications (2002) based on the result from the study of concentrically loaded anchorage zones, are proposed.

1. INTRODUCTION

After Burdet's recommendations of anchorage zone design (1990), based on the study of rectangular sections of several configurations, were adopted into the AASHTO Standard Specifications (1994), they were acknowledged as conservative methods to design bursting reinforcement and were assumed to provide sufficient guidance for general anchorage zone design. However, in addition to the cases of inclined and eccentric load configurations, which are often found in the end regions of post-tensioned concrete girders, support reactions are also often found in this critical part of the structure. The support reaction was proven to have a significant effect on the bursting force according to the experimental study of Wollmann (1992). Unfortunately, only a few load configurations were investigated, and detailed recommendations for anchorage zones with support reactions have not yet been clearly addressed in any available code provisions. The study of anchorage zones of rectangular post-tensioned girders with the presence of a support reaction is the major focus of this research.

2. OBJECTIVES

This paper focuses on the following objectives.

1. The investigation of the behavior of anchorage zones with a support reaction under two load configurations including concentric and inclined concentric.
2. The investigation of the effect of various parameters related to the anchorage zone with a support reaction. Parameters of the study comprise typical anchorage ratios (a/h where a is the width of anchorage device and h is the lateral dimension of girder cross section), angle of inclination of prestressing load (α), magnitude of support reaction (R), location of support reaction (l), and support bearing plate ratio (b/h where b is the width of bearing plate).
3. The evaluation of the applicability of the method of determining the bursting force and the location of the force in the anchorage zone presented in the AASHTO Standard Specifications (2002), to the design of an anchorage zone with support reaction.

3. SCOPE OF WORK

This study focuses on the behavior of the bursting region in anchorage zones with a support reaction in order to examine the expressions used to determine the bursting force in the general anchorage zone and the location of the force presented in the AASHTO Specifications. The equations are improved by including several parameters related to the design of the anchorage zone which the equations presented in the code exclude.

4. BACKGROUND

According to the AASHTO Standard Specifications (2002), anchorage zone at the end of a member is considered to have a length of one and one half of the depth of the section. The body of the anchorage zone can be divided into two regions: local zone and general zone (see Figure 1).

The local zone is the region covering and ahead of the anchorage device. The local zone transfers the prestressing

force into the general zone. The primary design concern in the local zone is the very high bearing stress under the anchorage device. The main component of the local zone, besides the anchorage device and surrounding concrete, is spiral or tie confining reinforcement. A special anchorage device needs to pass an acceptance test, which is presented in the AASHTO Standard Specifications.

The general zone is the region of concrete outside the vicinity of the local zone into which the high concentrated prestressing forces from the anchorage device spread throughout the region and become linearly distributed across the entire cross section at some location ahead of the anchorage device. This behavior of stress distribution can be described by using Saint Venant's principle. The AASHTO Specifications define the dimensions of the general zone to be the same as that stated for the overall anchorage zone. The design methods for the general zone may be selected from one of these three methods: equilibrium-based plasticity models (generally referred to Strut-and-Tie Models); elastic stress analysis based on elastic material properties, equilibrium equations, and strain compatibility (generally referred to finite element method); other approximate methods such as approximate stress analyses and design presented in the specifications based on a study by Burdet.

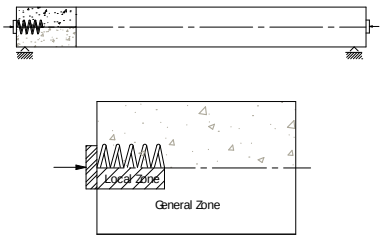

Figure 1 Anchorage Zone in PC Girder

According to the AASHTO Standard Specifications, the equations below can be used to calculate the bursting force and the location of the force, which can be used to locate the centroid of bursting steel, respectively:

$$T_{burst} = 0.25\Sigma P_u(1-\frac{a}{h}) + 0.5\left|\Sigma(P_u \sin\alpha)\right| \qquad (1)$$

$$d_{burst} = 0.5(h-2e) + 5e\sin\alpha \qquad (2)$$

where T_{burst} is the bursting force in the anchorage zone acting ahead of the anchorage device and transverse axis (N), P_u is the factored tendon force (N), d_{burst} is the distance from the anchorage device to the centroid of the bursting force (mm), a is the lateral dimension of the anchorage device or group of devices in the direction considered (mm), e is the eccentricity of the anchorage device or group of devices, with respect to the centroid of the cross section, always taken as positive (mm), h is the lateral dimension of the cross section in the direction considered (mm), and $\propto$ is the angle of inclination of a tendon force, with respect to the centerline of the member, positive for concentric tendons or if the anchor force points toward the centroid of the section, negative if the anchor force points away from the centroid of the section. Some limitations of the application of these equations are described in the specifications. Figure 2 shows the typical model of anchorage zone in this study.

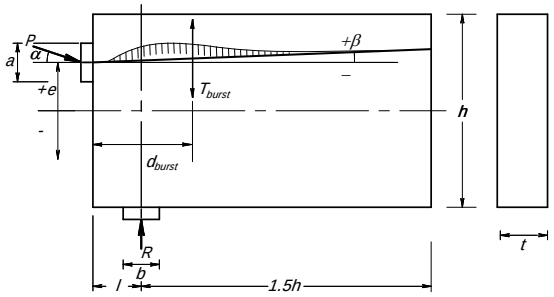

Figure 2 Typical Model of Anchorage Zone with a Support Reaction

5. PARAMETERS

5.1 Anchorage Ratio (*a/h*)

The anchorage ratio has a major influence on the magnitude of the bursting force according to equation (1). The most frequently discussed load configuration in anchorage zone studies is a concentric load (load applies directly at the centroid of girder cross section). The first term on the right side of equation (1) accounts for the effect of the anchorage ratio. However, it is known that the first term of equation (1) results in unconservative predictions for anchorage ratios of less than 0.15 (Burdet, 1990). The anchorage ratios used for the present study were chosen to be 0.10, 0.20, 0.35, and 0.50. An additional ratio of 0.00 was inserted into the study to complete the characteristic plot of magnitude of bursting force versus anchorage ratio.

5.2 Inclination Angle of Prestressing Force (α)

In reality, there is rarely a case in which a prestressing force is applied horizontally for post-tensioned structures. The second term of equation (1) accounts for the inclination effect. The term can be explained as 50 percent of the total shear force resulting from the vertical component of the inclined load. Generally, the angle of inclination is smaller than 10 degrees. This study investigated the effect of inclination of prestressing load with two selected angles consisting of 6 degrees and 9 degrees, which should cover all possible angles that can be found in typical prestressed concrete girders.

5.3 Magnitude of Reaction Force (*R*)

The reaction force can be estimated as a proportion of the force. Based on engineering experience, the magnitude of the support reaction on one side of a girder can rise above 10 percent of the prestressing force. Therefore, the parameter of the magnitude of the reaction force consists of four numbers: 0.00 (no reaction applied), 0.05, 0.10, and

0.15 times prestressing force

5.4 Location of Support Reaction (*l*)

The parameter of the location of the support reaction consists of three values relative to the width of the beam section (*h*): 0.125*h*, 0.25*h*, and 0.5*h*. The first value represents the case of a support reaction placed relatively close to the anchorage surface. The largest value illustrates the effect of a support reaction located at a distance equal to half of the section width (the location of d_{burst} if the inclination angle and eccentricity are invalid according to equation (2) presented in the specifications).

5.5 Bearing Plate Ratio (*b/h*)

Besides the magnitude of support reaction, the bearing plate width of the support reaction was suspected to have a significant effect on the behavior of the anchorage zone as well. The parameter of the bearing support ratio was divided into three cases comprising the ratios of 0.0 (simple concentrated load), 0.125, and 0.250. The values of the bearing support ratio were set to monitor the behavior of stresses from immediately above the bearing region to the extreme top fiber of the beam.

5.6 Eccentricity (*e*)

Since this paper presents only the behavior of concentrically loaded anchorage zones, the parameter of eccentricity is set as zero.

5.7 Summary

All parameters are summarized in Table 1.

Table 1 Summary of Parameters

a/h	*Angle*	*R/P*	*l/h*	*b/h*	*e/h*
0.00	0	0.00	0.125	0.000	0.00
0.10	6	0.05	0.250	0.125	
0.20	9	0.10	0.500	0.250	
0.35		0.15			
0.50					

6. RESULTS

6.1 Bursting Force

Figures 3 and 4 show examples of the relations between bursting forces and locations of the support reactions for concentric and 9 degree inclined concentric load configurations for all values of *a/h* and *R/P* while *b/h* is set as zero. When the reaction force is applied close to the anchorage surface, the bursting force from each value of *R/P* is obviously different for each *a/h* ratio. When the force is further away, approaching the position of *l/h* equal to 0.50, the bursting force from each plot converges to the lowest value. This can be concluded that the largest bursting force with respect to the location of the reaction force can be determined from the load configuration with the closest location of the support reaction to anchorage surface. The furthest position of support reaction establishes otherwise. Therefore, the equation for determining the bursting force is developed from the results with the *l/h* ratio equal to 0.125.

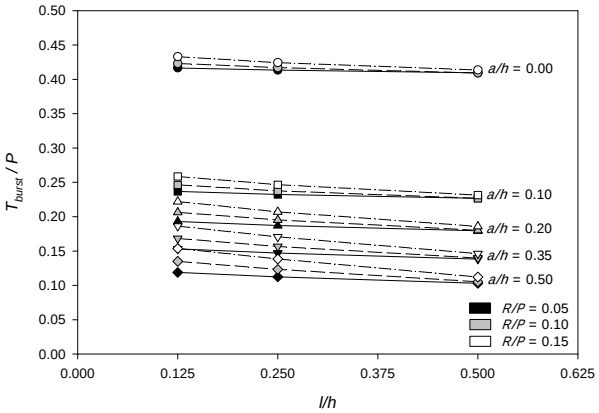

Figure 3 Bursting Force vs. Location of Support Reaction for Concentric Load (0 Degree Inclination), *b/h* = 0.0

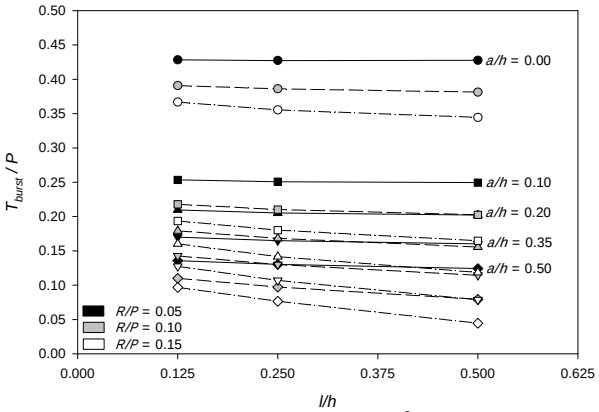

Figure 4 Bursting Force vs. Location of Support Reaction for 9 Degree Inclined Concentric Load, *b/h* = 0.0

Figure 5 shows an example of the relation of the bursting force and the bearing plate ratio for 9 degree inclined concentric load. All plots are essentially horizontal lines, which can be concluded that the bearing plate width (*b/h*) has no effect on the bursting force.

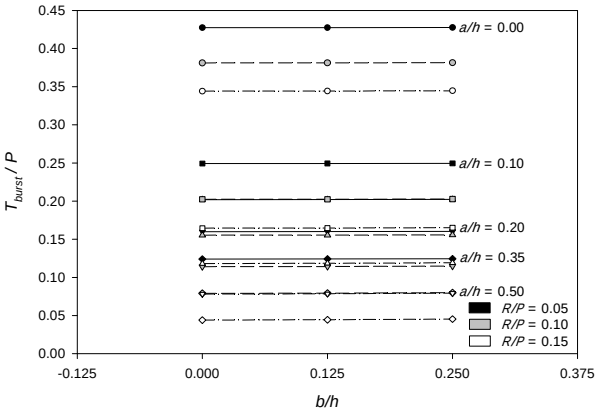

Figure 5 Bursting Force vs. Bearing Plate Ratio for 9 Degree Inclined Concentric Load, *l/h* = 0.50

The effect of inclination can be generally described as 50 percent of the vertical component of the inclined prestressing load. Figure 6 shows the relation between the bursting force and the inclination angle for a concentrically loaded anchorage zone. The plots from the finite element results for each anchorage ratio are almost parallel to one another. The comparison of the plot of the anchorage ratio of 0.20 with the plot using equation (1) is given. The plot from the equation is a straight line with a steeper slope compared to those from the finite element method. As the angle increases, the difference between the bursting force from the finite element method and the equation becomes larger. A closer prediction of the bursting force due to the inclination angle can be formulated by decreasing the value of the coefficient 0.50 in the second term of equation (1) to the value of 0.40.

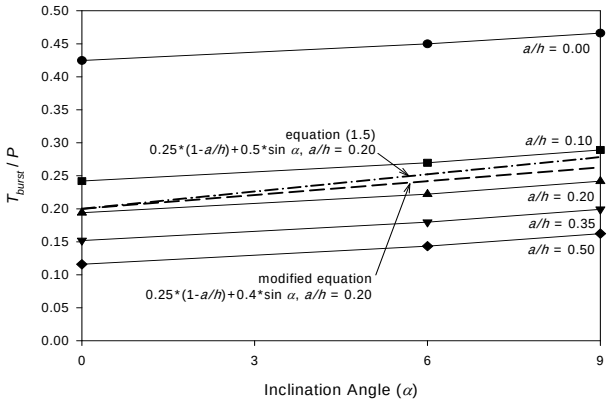

Figure 6 Bursting Force vs. Inclination Angle for Concentric Load, $b/h = 0.0$

Figure 7 shows an example of the relation between the bursting force and the reaction force. The plots do not vary linearly as the magnitude of the reaction force increases. The slopes vary as the value of *R/P* increases. A unique characteristic detected from all plots is that they vary in a concave upward manner. Therefore, a conservative equation for determining a bursting force can be found by using a line drawn from one end of the plot to the other end (see Figure 7).

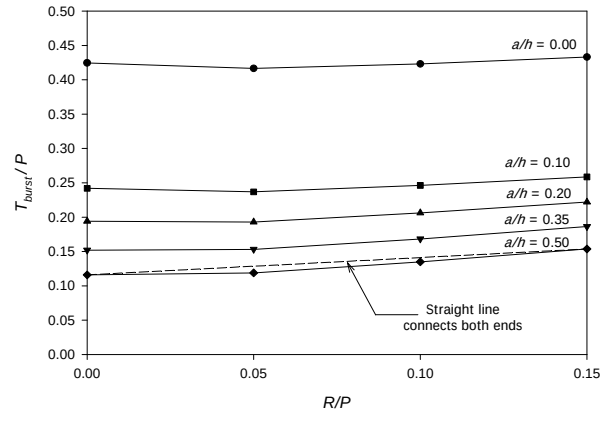

Figure 7 Bursting Force vs. Reaction Ratio for Concentric Load, $l/h = 0.125$, $b/h = 0.0$

To achieve the most conservative equation to determine the bursting force for all concentric load configurations, the equation must be developed from the line which contains the largest increasing slope from all the results of concentric and incline concentric load configurations. The effect of the magnitude of the reaction force in inclined concentrically loaded anchorage zones with 6 degree and 9 degree angles are presented in Figures 8 and 9, respectively. The shape of each plot is still concave upward. Figure 9 indicates that with an inclination angle of 9 degrees the plots slope downward with the smallest bursting force at the *R/P* ratio of 0.15.

To arrive at a conservative method to calculate the bursting force, the method illustrated earlier for the formulation of the bursting force in the concentric load configuration is applied to establish the term representing the influence of the reaction force due to the inclination of the prestressing force. A straight line was drawn to connect the bursting force of the *R/P* ratio of 0.00 and 0.15 in order to find the maximum slope for all load configurations. A summary of all slope values is listed in Table 2 with bold character for the maximum slope value for each inclination angle of concentric load configurations.

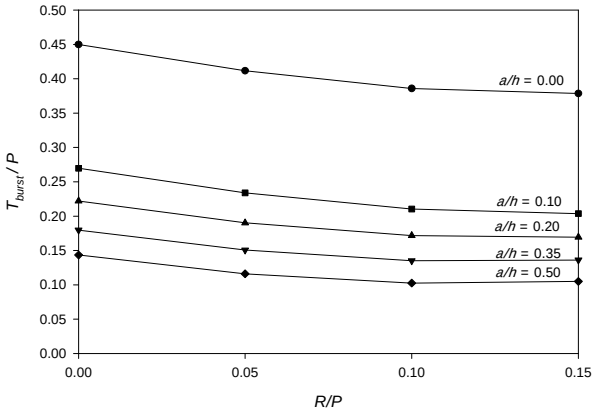

Figure 8 Bursting Force vs. Reaction Ratio for 6 Degree Inclined Concentric Load, $l/h = 0.125$, $b/h = 0.0$

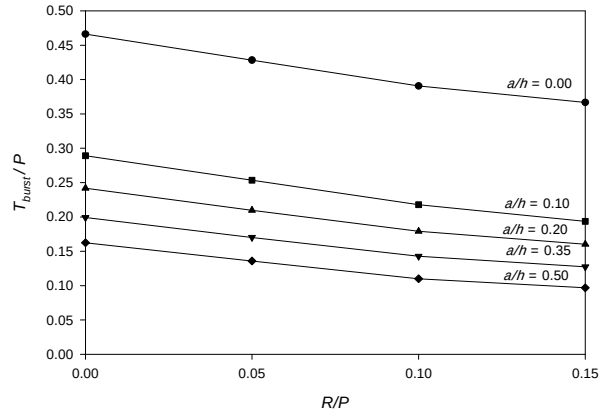

Figure 9 Bursting Force vs. Reaction Ratio for 9 Degree Inclined Concentric Load, $l/h = 0.125$, $b/h = 0.0$

Because of the relation with the inclination angle, the

maximum slopes in all the load configurations including concentric with zero, 6, and 9 degrees are plotted relative to the inclination angles as shown in Figure 10. The plot of inclination angle and maximum increasing slope resulting from all concentric load studies decreases as the inclination angle increases. This relationship can be approximated using a linear equation which is also presented in the figure.

Table 2 Slopes of All Straight Lines for T_{burst} of All Concentric Load Configurations

		l/h		
	a/h	*0.125*	*0.25*	*0.5*
Concentric Load	0.00	0.0555	-0.0022	-0.0735
	0.10	0.1105	0.0311	-0.0705
	0.20	0.1860	0.0857	-0.0553
	0.35	0.2288	0.1239	-0.0395
	0.50	**0.2514**	0.1492	-0.0255
6 Deg. Inclined Concentric Load	0.00	-0.4746	-0.5593	-0.6587
	0.10	-0.4403	-0.5409	-0.6696
	0.20	-0.3514	-0.4811	-0.6570
	0.35	-0.2910	-0.4300	-0.6392
	0.50	**-0.2567**	-0.3925	-0.6222
9 Deg. Inclined Concentric Load	0.00	-0.6626	-0.7382	-0.8112
	0.10	-0.6373	-0.7270	-0.8289
	0.20	-0.5433	-0.6681	-0.8212
	0.35	-0.4784	-0.6142	-0.8032
	0.50	**-0.4373**	-0.5724	-0.7857

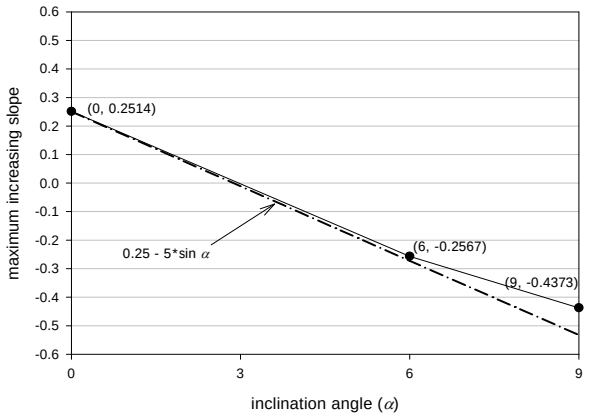

Figure 10 Equation for Bursting Force Prediction

By adding this approximate equation to the modified equation stated earlier, the new expression to determine the bursting force for all concentrically loaded anchorage zones can be written as shown below:

$$T_{burst} = 0.25P(1-\frac{a}{h}) + 0.4P\sin\alpha + R(0.25-5\sin\alpha) \quad (3)$$

6.2 Location of Bursting Force

Figure 11 shows the comparison of the plots of d_{burst} from three different methods consisting of finite element method, the first term of equation (2), and a modification of the term. By including the term of anchorage ratio (as the second term of the modified equation shown in Figure 11), a better agreement is produced in which the new plot more closely parallels the plot from the finite element method. A physical explanation of the modified term is that the distance of the bursting force extends from the anchorage surface for a distance of half of its section width plus a quarter of the anchorage plate width. This modified equation needs to be further developed to include the effect of the support reaction.

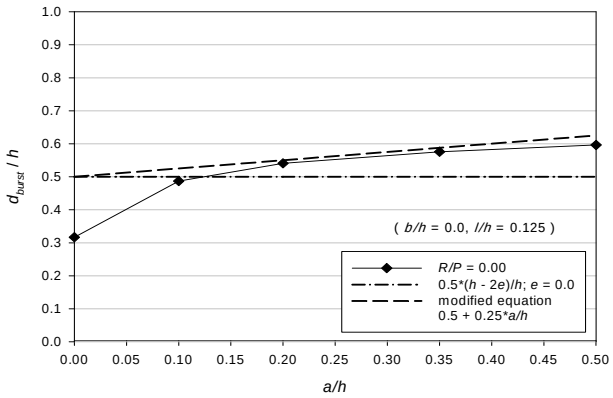

Figure 11 Comparison of d_{burst} with Modified Equation

The bearing plate ratio (*b/h*) has the same effect on the location of the bursting force as on the magnitude of the bursting force. The distance d_{burst} does not vary with the change of the bearing support width. Therefore, based on the study of concentrically loaded anchors, the parameter *b/h* is not considered in the formulation of bursting force location as well.

Figure 12 shows the relation between d_{burst} and three inclination angles: zero, 6, and 9 degrees with no support reaction. All plots for each anchorage ratio are essentially parallel lines. A single slope can be used in a linear equation to establish the behavior of d_{burst} with respect to the inclination angle. Therefore, a modified equation can be formulated by adding a term representing the effect of the inclination angle. As shown in the figure, a result from using the modified equation is compared for the case of *a/h* equals to 0.20. In the equation, the value 0.25 was selected as a multiplier for the angle term, similar to that used in the bursting force formulation.

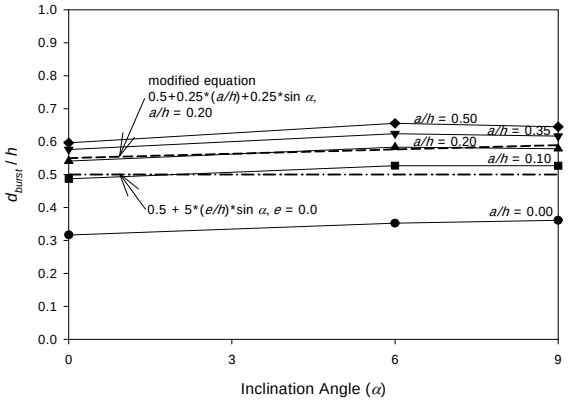

Figure 12 Comparison of d_{burst} with Modified Equation

The magnitude of the reaction force (*R/P*) is significant for the location of the bursting force as can be seen in Figure 13, a method similar to that used for the bursting force formulation (previous section) was used for finding an equation for estimating the bursting force location. A straight line connecting the ends of each plot (an example is shown in Figure 13) is used for determining the slope. Instead of using the largest increasing slope, the expression for determining the location of bursting force is formulated using the average of slopes from all straight lines for each inclination angle.

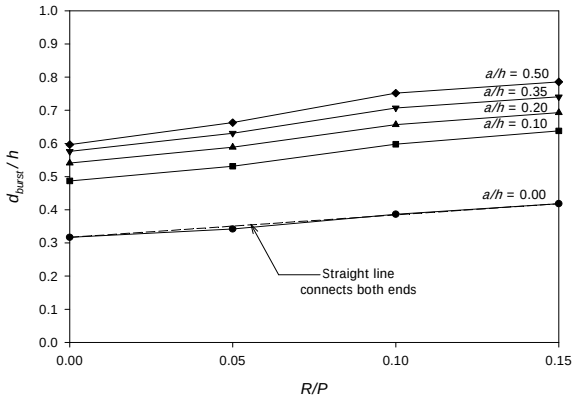

Figure 13 Bursting Force Location vs. Inclination Angle with No Support Reaction

Slopes of each straight line from all concentric load configurations are listed in Table 3 along with the resulting of average slope. After determining the average values of each inclination angle, a term representing the effect of the *R/P* ratio on an inclined load configuration can be estimated. Figure 14 shows the estimation plot. A linear equation can be applied to approximate the plot of the average slopes. Equation (a) in the figure is developed from the numbers given in Table 3. Equation (b) in the figure is a simplified version of equation (a), which provides an acceptable estimation.

Table 3 Slopes of All Straight Lines for d_{burst} of All Concentric Load Configurations

		l/h			
	a/h	*0.125*	*0.25*	*0.5*	*Average*
Concentric Load	0.00	0.6767	0.7138	0.7337	
	0.10	1.0058	1.1738	1.3631	
	0.20	1.0151	1.2915	1.6913	1.3430
	0.35	1.0987	1.4759	2.1348	
	0.50	1.2620	1.7501	2.7582	
6 Deg. Inclined Concentric Load	0.00	0.0121	-0.1043	-0.4366	
	0.10	0.3376	0.2629	-0.1999	
	0.20	0.3151	0.3515	-0.0208	0.1926
	0.35	0.3023	0.4322	0.1905	
	0.50	0.3333	0.5539	0.5585	
9 Deg. Inclined Concentric Load	0.00	-0.1382	-0.2674	-0.6142	
	0.10	0.2231	0.1088	-0.4281	
	0.20	0.2063	0.2080	-0.2776	-0.0076
	0.35	0.1859	0.2750	-0.1516	
	0.50	0.1814	0.3533	0.0217	

Since all parametric studies for zero, 6, and 9 degree inclined concentrically loaded anchorage zones with support reactions have been conducted, the final equation for determining the location of bursting force can be established as shown below:

$$d_{burst} = 0.5h + 0.25a + 0.25h\sin\alpha + \frac{R}{P}h(1.5 - 10\sin\alpha) \quad (4)$$

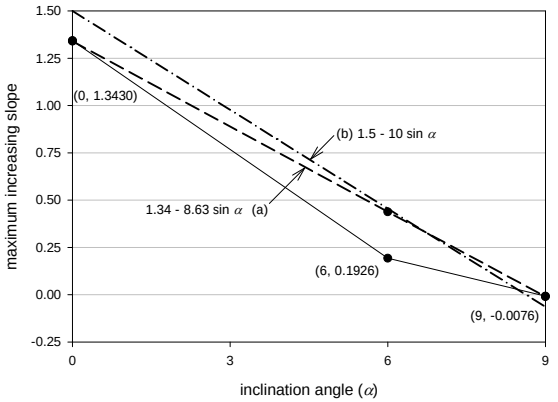

Figure 14 Equation for the Prediction of the Location of Bursting Force

7. CONCLUSION

The study of the behavior of concentrically loaded anchorage zones with support reactions results in the modification of the equations to determine bursting force and its location presented in the AASHTO Standard Specifications (equation (1) and (2)). Two improved equations (equation (3) and (4)) are used for calculating the bursting force and its location, respectively. After comparing the results using these new equations with those from the specifications, the new equations provide more conservative value for T_{burst} and closer value for d_{burst} to the results from finite element analyses (Hengprathanee, 2004). However, the equations are effective only in the case where the value of *a/h* larger than 0.15 and they are not yet applicable for eccentrically loaded anchorage zones with the presence of support reactions.

References:

American Association of State Highway Transportation Officials (AASHTO). (1994) *Standard Specifications for Highway Bridges*, 1st Ed.

American Association of State Highway Transportation Officials (AASHTO). (2002) *Standard Specifications for Highway Bridges*, 1st Ed.

Burdet, O.A. (1990). *Analysis and Design of Post-Tensioned Anchorage Zones Concrete Bridges*, Ph.D. Dissertation, University of Texas at Austin.

Hengprathanee, S. (2004). *Linear and Nonlinear Finite Element Analyses of Anchorage Zones in Post-Tensioned Concrete Structures*, Ph.D. Dissertation, Virginia Polytechnic Institute and State University at Blacksburg.

Wollmann, G.P. (1992). *Anchorage Zones in Post-Tensioned Concrete Structures*, Ph.D. Dissertation, University of Texas at Austin.

Sixth International Conference on Urban Earthquake Engineering
March 3-4, 2009, Tokyo Institute of Technology, Tokyo, Japan

MECHANICAL PROPERTIES IMPROVEMENT OF REINFORCED CONCRETE BEAMS SUBJECTED TO HIGH-SPEED LOADING

Mitsuyasu Iwanami[1)], Taku Matsubayashi[1)], Hiroshi Yokota[2)], Takeshi Yamada[3)], and Naoto Takehana[3)]

1) Structural Mechanics and Materials Division, Port and Airport Research Institute, Japan
2) LCM Research Center for Coastal Infrastructures, Port and Airport Research Institute, Japan
3) Kobe Steel, Ltd, Japan
iwanami@pari.go.jp, matsubayashi@pari.go.jp, hiroy@pari.go.jp
yamada.takeshi@kobelco.com, takehana.naoto@kobelco.com

Abstract: In this paper the applicability of PVA short fibre was experimentally investigated to improve mechanical properties of reinforced concrete members subjected to high-speed loading such as impact loading observed in port structures. In the experiment, mechanical behaviour of reinforced concrete beams with PVA short fibre under repeated high-speed loads was examined by conducting falling-weight loading tests. In the tests, PVA short fibre content and loading speed were changed to investigate their influences on the mechanical properties of the beams. As the results, it was found that the number of repetition of high-speed loading until ultimate failure was greatly affected by the loading speed, and the degree of the effect was considerably changed between 2.0m/s and 2.5m/s in the loading speed. Also, it was made clear that the number of repetition of high-speed loading was increased in case of concrete beams reinforced with PVA short fibre. It was because that degradation of flexural rigidity of the beam due to repeated high-speed loads was mitigated by the existence of PVA short fibre. Accordingly, it was concluded that mechanical properties of reinforced concrete beams subjected to high-speed loading can be improved by mixing PVA short fibre into concrete.

1. INTRODUCTION

In case of port concrete structures such as caisson-type breakwaters, huge impulsive wave forces are acting repeatedly, resulting in ultimate failure of reinforced concrete (RC) members. When wave-energy dissipating concrete blocks are installed in front of the caissons, the blocks might be moved during storms, causing impact forces due to collision of the block to the caisson wall. In the present design of such port concrete structures (Port and Harbor Association of Japan 2007), it is one of the problems that scatters of impulsive wave forces and dynamic behaviour of concrete structures are not taken into account. Also, in case of concrete structures subjected to seismic actions, structural members may be damaged by cyclic high-speed loads due to inertia forces during earthquake motions. However, it has not made clear how RC members are degraded under repeated high-speed loads, causing reduction in residual performance of concrete structures.

In addition, it is necessary to examine countermeasures to improve mechanical properties of RC members against repeated high-speed loads. In the previous study (Ito et al. 2004a), it is revealed that shear capacity of RC members can be improved in static conditions by mixing PVA (Polyvinyl alcohol) short fibre into concrete. Based on this, it is expected that dynamic mechanical properties of RC members will be improved by PVA short fibre. Therefore, in this study, to investigate the applicability of PVA short fibre to improve mechanical properties of concrete structures under repeated high-speed loads such as concrete caissons of breakwater and structures subjected to seismic forces, dynamic behaviour and failure process of RC beams reinforced with PVA short fibre were examined by conducting falling-weight loading tests. In the tests, PVA short fibre content and loading speed were changed to investigate their influences on the mechanical properties of the beams.

2. EXPERIMENT

2.1 PVA Short Fibre

PVA short fibre was used to improve physical properties of concrete. In general, steel short fibre may be promising to improve concrete properties (Hannant 1978). In case of use in marine environments, steel short fibre will cause the problems relating to corrosion of steel so that the applicability of synthetic short fibre was examined in this study. One of the synthetic short fibre, PVA short fibre, was used to make fibre reinforced concrete in this study because of high tensile strength and high resistance against corrosion compared with other types of synthetic short fibre. Also, it is expected that PVA short fibre can adhere chemically to cement matrix, causing excellent bond strength between the

Table 1 Fundamental Properties of PVA Short Fibre

Diameter (mm)	Length (mm)	Linear density (g/m)	Density (g/cm^3)	Tensile strength (N/mm^2)	Young's modulus (kN/mm^2)
0.66	30	0.0444	1.3	880	29.4

Table 2 Mixture Proportion of Concrete

Concrete type	Fibre content (vol. %)	G_{max} (mm)	Slump (cm)	W/C (%)	s/a (%)	Air (%)	Unit weight (kg/m^3)			
							W	C	S	G
N	0	20	18	55.0	46.0	4.5	178	325	807	991
F	1.5		-							

Table 3 Concrete Properties and Calculated Mechanical Properties of RC Beams

Concrete type	Concrete properties		Mechanical properties of RC beams	
	Compressive strength (N/mm^2)	Young's modulus (kN/mm^2)	Flexural capacity (kN)	Shear capacity (kN)
N	33.0	26.6	58.0	161.4
F	30.8	26.0	57.6	159.1

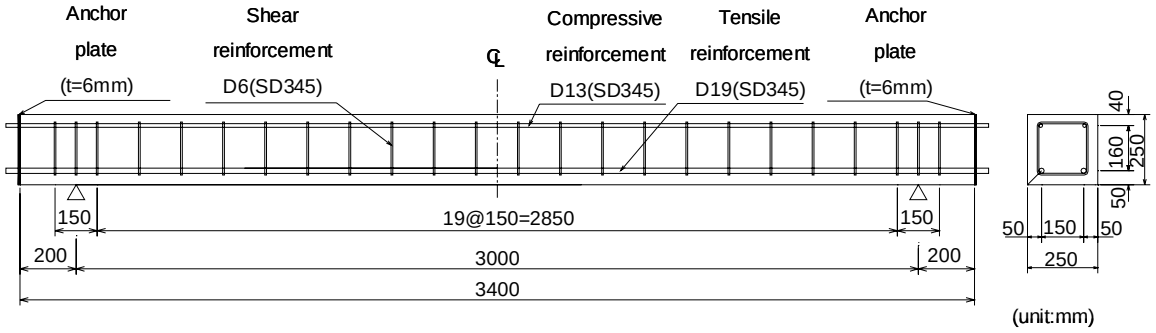

Figure 1 Shape and Dimensions of Test Beams

fibre and the matrix.

Due to its lower density, PVA short fibre can mitigate the problem of segregation during casting of concrete, which has often been observed when the concrete was reinforced by steel short fibre. Based on these facts, it is expected that dynamic mechanical properties of concrete members will be improved by PVA short fibre as well as static ones. The fundamental properties of PVA short fibre used in this experiment are summarised in Table 1.

2.2 Concrete Properties

Fibre reinforced concrete was produced by adding PVA short fibre into normal concrete. Therefore, the bulk properties of fibre reinforced concrete were the same as that of normal concrete. Table 2 presents the mixture proportions of each concrete. The fibre reinforced concrete contained PVA short fibre in volume ratio of 1.5%. This volume ratio was thought to be the maximum value considering constructivity of fibre reinforced concrete (Ito, et al. 2004b).

Table 3 presents concrete properties obtained from compressive tests on cylinder specimens at the time of falling-weight loading tests, mentioned later.

2.3 Test Beams

In this experiment, two kinds of RC beams were prepared: normal concrete beams (N-series) and fibre reinforced concrete beams (F-series). Beams of both series were 250mm in width, 250mm in height, and 3300mm in length, as shown in Figure 1. They were provided with two deformed steel bars in upper and lower sides, respectively.

Table 4 Test Case

Concrete type	Designation	Loading method	Loading speed (m/s)
N	N-S	Static	-
	N-V2	Falling-weight	2.0
	N-V2.5		2.5
	N-V3		3.0
	N-V4		4.0
F	F-S	Static	-
	F-V2	Falling-weight	2.0
	F-V2.5		2.5
	F-V3		3.0
	F-V4		4.0

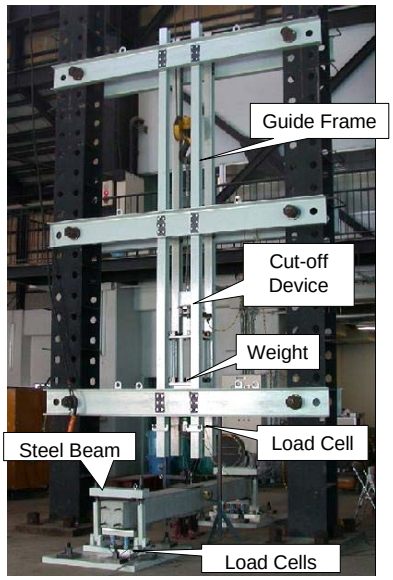

Figure 2 Falling-Weight Loading Test Machine

Shear reinforcements were arranged with the intervals of 150mm in order to make the beam fail in bending. Table 3 presents calculated mechanical properties of RC beams in static conditions. The calculation was carried out according to Japanese design standard (Japan Society of Civil Engineers 2008). The mechanical properties of RC beams in terms of flexural capacity and shear capacity were almost the same between N-series and F-series beams because there was little difference in physical properties between normal concrete and fibre reinforced concrete.

2.4 Falling-Weight Loading Test

Table 4 summarises the test cases of this experiment. The loading tests were conducted by static loading and repeated high-speed loading with the constant speed of loading. The loading speed was set at 2.0m/s, 2.5m/s, 3.0m/s and 4.0m/s. For repeated high-speed loading, an falling-weight loading test machine was used, as shown in Figure 2. A steel weight is lifted to the predetermined height by a small crane, and the weight free-falls along a guide frame by releasing a hook. The weight is dropped onto the top surface of a test beam at the midspan. The mass of the weight is 400kg, and the contact face of the weight has a spherical shape with a diameter of 565mm. To prevent the test beam from bouncing out of the test machine, the test beam is fixed with the steel beams at the supporting points. To reduce scatters of dynamic response, caused by damage of concrete at the top surface of the beam, a rubber sheet of 10mm in thickness is placed at the contact position of the beam.

The ultimate state of the beam was defined as the cumulative residual midspan displacement reached 2.0% of the span length, that is 60mm. This definition was determined based on the previous research (Japan Society of Civil Engineers 2004). The high-speed loads by falling-weight were applied repeatedly until the ultimate state.

The dynamic force developed by the contact between the weight and the beam was measured using a load cell installed in the weight. The reaction forces at supporting points were measured using load cells installed in the supporting devices. The midspan displacement of the beam was measured using a laser-type displacement sensor. Also, concrete cracks in the beam were observed periodically.

3. RESULTS AND DISCUSSION

3.1 Result of Static Loading Test

Figure 3 shows the relationships between static loads and midspan displacements obtained from the static loading tests on N-S and F-S beams. Comparing these two curves, even though the type of concrete was different, the flexural rigidity and yield load were almost the same. The maximum load of F-S beam was larger than that of N-S beam, but the difference was very small. It was confirmed that the mixing of PVA short fibre hardly affected the mechanical properties and failure process of RC beams which failed in bending.

From Figure 3, it was found that tensile steel bars yielded when the midspan displacement reached about 12mm, regardless of the type of concrete. Also, crushing of top concrete occurred in both beams when the midspan displacement reached about 30mm.

3.2 Relationship between Loading Speed and Midspan Displacement

Figure 4 shows the relationships between loading speed and midspan displacement at the first high-speed loading. The maximum midspan displacements of N-series beams were 13.3mm, 18.4mm, 25.0mm and 38.2mm for the loading speeds of 2.0m/s, 2.5m/s, 3.0m/s and 4.0m/s, respectively. Similarly, the maximum midspan

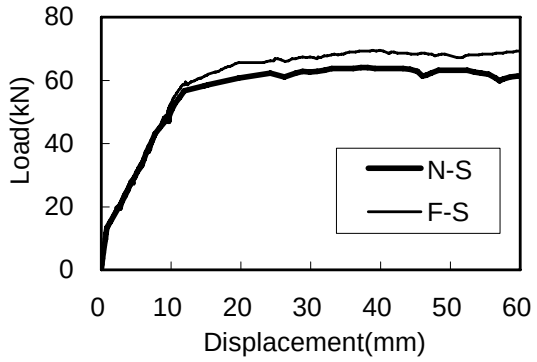

Figure 3 Result of Static Loading Test

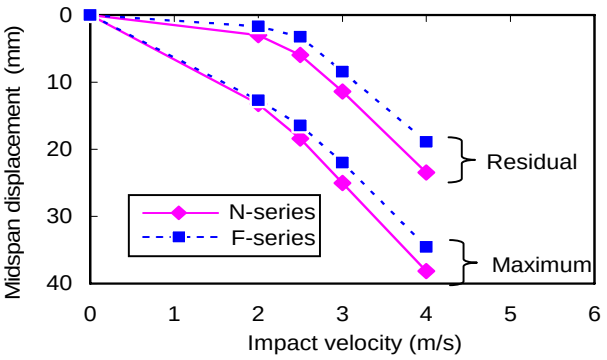

Figure 4 Loading Speed vs Midspan Displacement

displacements of F-series beams were 12.7mm, 16.4mm, 22.0mm and 34.6mm. It was found that the maximum displacements of F-series beams became smaller than N-series ones, indicating improved flexural rigidity of the beams.

Here, it is supposed that the dependence of strain rate on physical properties of concrete and steel bars was ignored and that dynamic behaviour of RC beams during high-speed loading was identical to that of static loading. Comparing Figure 4 with Figure 3, it could be regarded that the high-speed load with the loading speed of 2.0m/s was equivalent to static load not to make tensile steel bars yield. Similarly, the high-speed loads with the loading speeds of 2.5m/s and 3.0m/s were equivalent to static load to make tensile steel bars yield but not to cause crushing of top concrete, and the high-speed load with the loading speed of 4.0m/s was equivalent to static load to cause both yielding of tensile steel bars and crushing of top concrete.

3.3 Number of Repetition of High-Speed Loading until Ultimate State

Table 5 summarises the result of repeated high-speed loading tests in term of the number of repetition of loading speed until the ultimate state. Because high-speed loads were applied to the beams repeatedly, even comparatively small loads could make the beam fail at last. For example, in case of the loading speed of 2.0m/s, the beam reached the ultimate state after 590 times of loading for N-V2 and 105 times of loading for F-V2. In addition, the beams reached the ultimate state after less number of repetition when the loading speeds were larger. The difference in the number of repetition of high-speed loading until the ultimate state was remarkable in the range of 2.0m/s and 2.5m/s in loading speed.

Table 5 Number of Repetition of High-Speed Loading until Ultimate State

	Loading speed (m/s)			
	2.0	2.5	3.0	4.0
Designation	N-V2	N-V2.5	N-V3	N-V4
Number of repetition	105	15	5	3
Designation	F-V2	F-V2.5	F-V3	F-V4
Number of repetition	590	25	9	3

Comparing F-series beams with N-series beams, the number of repetition for F-series beam was 5.6 times more than N-series one in case of 2.0m/s in loading speed. Similarly, the number of repetition for F-series one was 1.7 times more in case of 2.5m/s, and 1.8 times more in case of 3.0m/s, respectively. However, in case of 4.0m/s, the beams of both series failed after the third loading, showing no improvement of the mechanical properties. Therefore, it was found that mechanical properties of RC beams subjected to high-speed loading could be improved by mixing PVA short fibre into concrete, in particular the effect of PVA short fibre became significant when the loading speed was relatively small.

3.4 Change in Midspan Displacement during Repeated High-Speed Loading Test

Figure 5 shows the cumulative residual and maximum midspan displacements of the beam with increase in number of repetition of high-speed loading. In case of 2.0m/s in the loading speed, midspan displacement of the beam progressed remarkably at the stage of small number of repetition. Then, after a slow progress, midspan displacement again increased acceleratedly, approaching the ultimate state. The whole tendency of this relationship drew an S-shape curve. On the other hand, in cases of 2.5m/s, 3.0m/s and 4.0m/s, the progress of midspan displacement was almost linear with increase in number of repetition, which was greatly different from the case of 2.0m/s. The reason for this difference was considered why the high-speed load with the impact velocity of 2.0m/s was equivalent to static load not to make tensile steel bars yield, as explained in **3.1**. Therefore, the failure process was

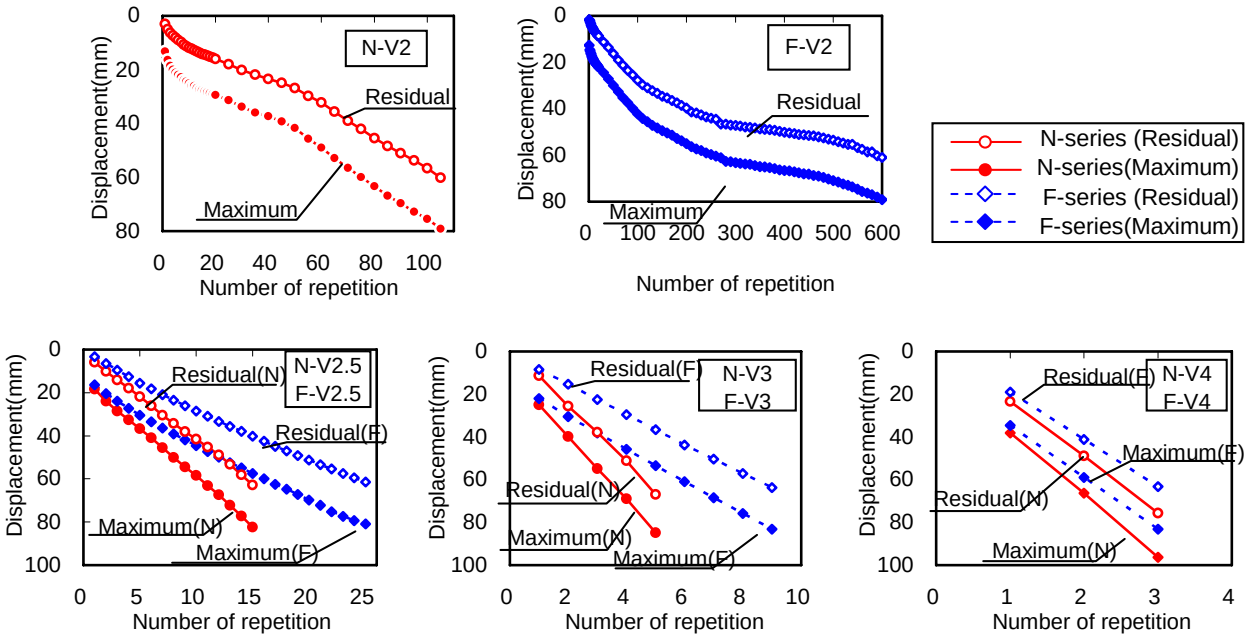

Figure 5 Change in Midspan Displacement with Number of Repetition

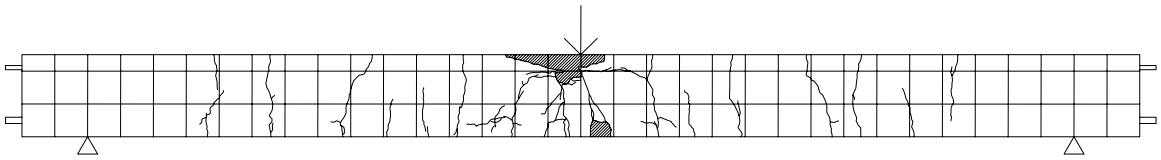

(a) N-V2 Beam (Number of Repetition=105, Cumulative Residual Midspan Displacement=60.2mm)

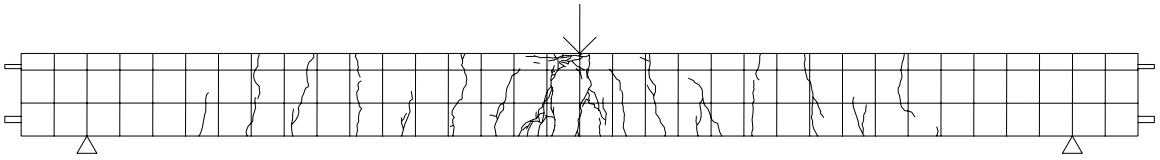

(b) F-V2 Beam (Number of Repetition=100, Cumulative Residual Midspan Displacement=27.8mm)

Figure 6 Crack Pattern of Test Beams subjected to Repeated High-Speed Loading

similar to that of RC beams typically failed in fatigue. In case of the loading speed of more than 2.5m/s, the high-speed load was regarded as static load which could make tensile steel bars yield, causing linear relationship between number of repetition and midspan displacement, as shown in the lower graphs of Figure 5. It was because the number of repetition of high-speed loading until the ultimate state changed drastically in the range between 2.0m/s and 2.5m/s in loading speed.

In addition, as shown in Figure 5, in case of N-V2 beam, the progress of cumulative residual displacement was accelerated after the number of repetition exceeded 50 (maximum displacement = 42mm; residual displacement = 27mm). This number of repetition coincided with the stage when crushing area of top concrete was spread greatly, according to the result of visual observation. On the other hand, in case of F-V2 beam, the cumulative residual displacement increased acceleratedly after the number of repetition exceeded 470 (maximum displacement = 69mm; residual displacement = 52mm). In this case, crushing of top concrete and spalling of concrete cover was not remarkable. As a whole, the increment of cumulative residual displacement for one loading was relatively small. For these facts, it was considered that PVA short fibre transferred

tensile stress in cracked concrete together with reinforcing bars and prevented concrete cover from spalling off, improving mechanical properties of the beam subjected to high-speed loading.

Figure 6 shows crack patterns of N-V2 and F-V2 beams after approximately 100 times of loading. N-V2 beam reached the ultimate state already, showing crushing of top concrete and spalling of concrete cover. However, crushing of top concrete of F-V2 beam was very limited so that spalling of concrete cover was not observed. Therefore, it was confirmed that PVA short fibre mitigated damage of RC beams subjected to repeated high-speed loading, resulting in improvement of mechanical properties of the beam under repeated high-speed loads.

4. CONCLUSIONS

The conclusions of this study are as follows:

(1) The number of repetition of high-speed loading until the ultimate state increased in case of RC beams with PVA short fibre, compared with normal reinforced concrete beams. It was because degradation of flexural rigidity of the beam was mitigated due to improved properties of concrete by PVA short fibre.

(2) Mechanical properties of RC members subjected to high-speed loading such as concrete caissons of breakwater will be improved by mixing PVA short fibre into concrete, especially in cases that the loading speed is relatively low.

References:

Hannant, D. J. (1978), "*Fibre Cements and Fibre Concrete*," John Wiley & Sons.

Ito, H., Iwanami, M. and Yokota, H. (2004a), "Experimental Study on Shear Capacity Evaluation of RC Beams with PVA Short Fiber," *Journal of Materials, Concrete Structures and Pavements*, No.774/V-65, pp.123-138.

Ito, H., Iwanami, M. and Yokota, H. (2004b), "Experimental Investigation on Constructivity of Fibre Reinforced Concrete," *Technical Note of Port and Airport Research Institute*, No.1087.

Japan Society of Civil Engineers (2004), "*Practical Methods for Impact Test and Analysis*," Structural Engineering Series 6.

Japan Society of Civil Engineers (2008), "*Standard Specifications for Concrete Structures - Structural Design*."

Port and Harbor Association of Japan (2007), "*Technical Standards and Commentaries for Port and Harbour Facilities in Japan*."

Sixth International Conference on Urban Earthquake Engineering
March 3-4, 2009, Tokyo Institute of Technology, Tokyo, Japan

DEFORMATION CAPACITY OF CORRODED RC COLUMN UNDER SEISMIC LOAD

Michiaki Oyado[1], Toshiyuki Kanakubo[2] and Akira Yasojima[3]

1) Senior Researcher, Structures Technology Division, Railway Technical Research Institute, Japan
2) Associate Professor, Institute of Engineering Mechanics, University of Tsukuba, Japan
3) Assistant Professor, Graduate School of Engineering, Hiroshima University, Japan
oyado@rtri.or.jp, kanakubo@kz.tsukuba.ac.jp, yasojima@hiroshima-u.ac.jp

Abstract: This paper describes the discussion about the fundamental properties of the deformation capacity of the deteriorated reinforced concrete columns due to the corrosion in order to verify the safety performance of existing reinforced concrete structures against the seismic load. In this discussion, the experimental results are taken into consideration where eleven cantilever column specimens with the modeled corrosion were subjected to the cyclic loading test. From the load- displacement relationships, it has been confirmed that the corrosion at the loading sides causes reduction of the deformation capacity at the former loading stages, on the other hand, the corrosion at the transverse sides causes that reduction at the latter loading stages. The main reason of that result can be assumed that the buckling of the corroded main bars causes the reduction of the deformation capacity earlier, but the corrosion of hoops at the transverse sides causes only the reduction of the lateral reinforcing strength.

1. INTRODUCTION

To maintain reinforced concrete (RC) structures safe against the seismic load, it is important to evaluate the strength and deformation capacity of the structural members. A number of evaluation methods have been proposed so far for calculating structural performance of newly constructed RC members until now. On the other hand, the evaluation method of the safety performance for the existing deteriorated RC structure is not clarified, particularly when it is damaged by the corrosion. The strength or the deformation capacity of the slender RC beams or columns may well decrease due to the corrosion of main bars and hoops.

In order to present the evaluating method of the deformation capacity for the corroded RC member, authors have carried out the experimental study (2007) about the deformation capacity of the corroded RC column, in which 11 cantilever formed RC column specimens were subjected to the horizontal cyclic loading. This paper describes the discussion about the effect due to the difference of the location of the corrosion.

2. TEST PROGRAM

2.1 Details of test specimen

In this study, eleven deteriorated cantilever column specimens were subjected to the cyclic loading. Table 1 gives the relevant properties of the specimens and Figure 1 shows the details of the specimen. All of the specimens are designed in accordance with the Japanese design standard for railway structures (2007) and the previous experiments by Takiguchi et al. (1999) which deal with no corroded RC column. They were 1650 mm long (from the top horizontal loading axis to the bottom fixed end) and had the same overall dimensions of a 450x450mm square cross section. The specimens were tested for three relevant properties; corrosion parts, corrosion levels and modeling methods of the corrosion. They were provided by the normal concrete whose compressive strength is about 30.5 N/mm^2 and the reinforcing bars whose tensile yielding strength is about 383/366(main bar/hoop) N/mm^2.

Table 1 Relevant properties of specimens

<table>
<tr><th rowspan="3">No.</th><th colspan="4">Reinforcing bar</th><th rowspan="3">Hoop bar
D:deformed bar
ϕ: small size round bar (mm)</th></tr>
<tr><th colspan="2">Main bar</th><th colspan="2">Hoop bar</th></tr>
<tr><th>Corrosion Side</th><th>Corrosion Method</th><th>Corrosion Side</th><th>Corrosion Method</th></tr>
<tr><td>1</td><td colspan="4">No corrosion (control)</td><td rowspan="5">D10 @47.5</td></tr>
<tr><td>2</td><td>Transv.</td><td rowspan="2">Electric</td><td>Transv.</td><td rowspan="2">Electric</td></tr>
<tr><td>3</td><td rowspan="3">Loading side</td><td rowspan="2">Loading side</td></tr>
<tr><td>4</td><td rowspan="2">Scraped</td><td>Scraped</td></tr>
<tr><td>5</td><td colspan="2">No corrosion</td></tr>
<tr><td>6</td><td colspan="2" rowspan="4">No corrosion</td><td colspan="2">All sides</td><td>ϕ9 @69</td></tr>
<tr><td>7</td><td rowspan="2">Transv.</td><td rowspan="2">Scraped</td><td rowspan="2">D10 @47.5</td></tr>
<tr><td>8</td><td>Loading</td></tr>
<tr><td>9</td><td colspan="2">All sides</td><td>ϕ6 @47.5</td></tr>
<tr><td>10</td><td>Loading side</td><td>Scraped*</td><td colspan="2">No corrosion</td><td>D10 @47.5</td></tr>
<tr><td>11</td><td colspan="2">Scraped*</td><td colspan="2">All sides*</td><td>ϕ9 @69</td></tr>
</table>

* Corrosion Position (Height from bottom fixed end of the column, top surface of the stub) is 400±100(mm) , others 225±100(mm)

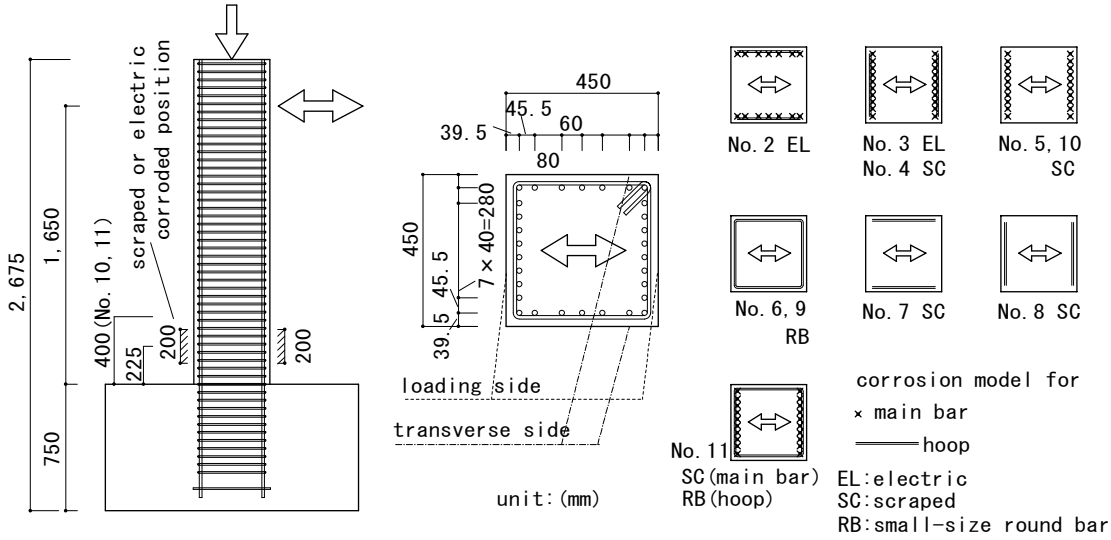

Figure 1 Details of specimen

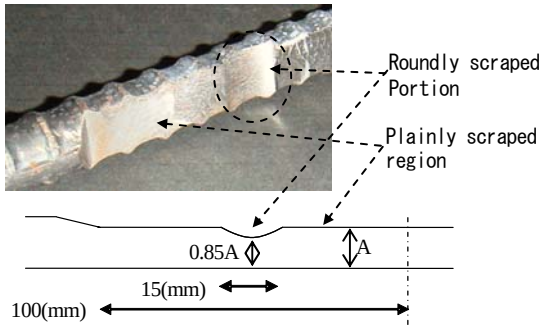

A : averaged cross sectional area as 15% reduced from original nominal area

Figure 2 Scraped bar

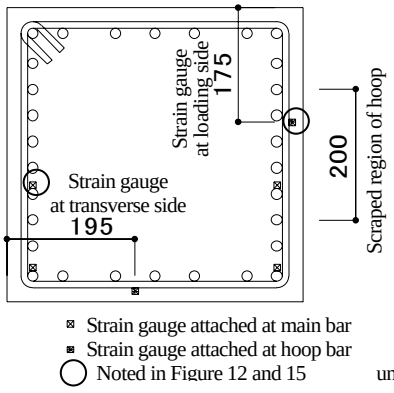

Figure 3 Position of strain gauge

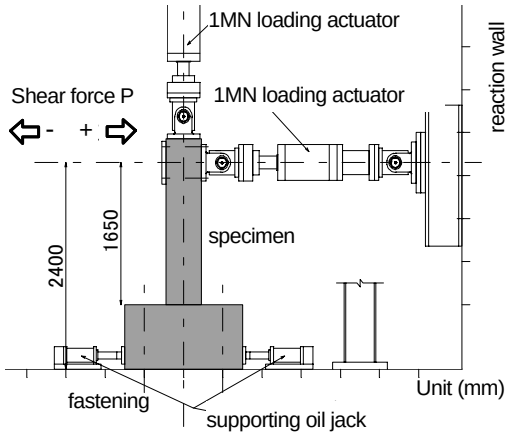

Figure 4 Test setup

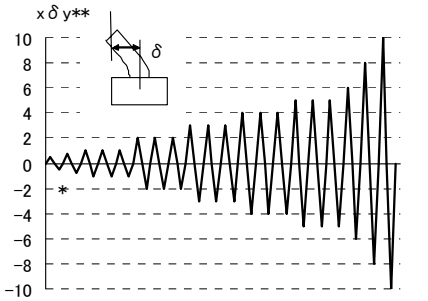

* loaded for only 1 cycle at Py/2 and 3Py/4
(Py is the calculated strength of the column yielding)
** δ y is the displacement at which the main bar of the test specimen No.1 yields

Figure 5 Loading program

2.2 Method of corrosion modeling

To simulate the corrosion of the reinforcing bars, two column specimens No.2 and No.3 were subjected to the electric accelerated corrosion process referring to the previous experiments by authors (Oyado et al. 2003). After a minimum period of 28 days after casting, an external water tank was attached to two sides of the specimens. Electrical direct current from the electric (galvanostatic) power supply was adopted between the reinforcing bars and the cupper electrode plates in the external water tank.

On the other hand, other six specimens No.4, 5, 7, 8, 10 and 11 were provided with the pre-scraped and whittled deformed bars and two column specimens No.6 and No.9 were provided with the small size round-bars to simulate mechanical properties of the corroded reinforcing bars, so

that those scraped reinforcing bars or small size round- bars could avoid unexpected corrosion uncertainness and the tensile strain values of those bars could be measured. The outward appearance of the scraped main bar and its scraping method are shown in Figure 2, showing that the scraped region was formed by the plainly scraped region and the roundly scraped portion. The scraped bars were modeled to have the same distribution of cross sectional area as the substantially corroded bars measured by the 3D scanner, referring to the previous experiments by authors (Oyado et al. 2006). The ratio of averaged / maximum cross sectional reduction is planned to be about 15% / 30% respectively. Figure 3 shows the position of the strain gauges attached to the reinforcing bar.

2.3 Loading test

Figure 4 shows the test setup for the column specimens, and Figure 1 also shows the loading point and directions in the cyclic loading test.

Each RC column specimen was subjected to the horizontal cyclic loading statically with the vertical constant axial loading. Figure 5 shows the shear force loading program. Each column specimen was loaded under the gradually- increasing cyclic loading.

3. TEST RESULT AND CONSIDERATION

3.1 Effect due to difference of corroded sides

The P-δ (shear loading versus displacement) relationship of the specimens No.2 and No.3 are shown in Figure 6,

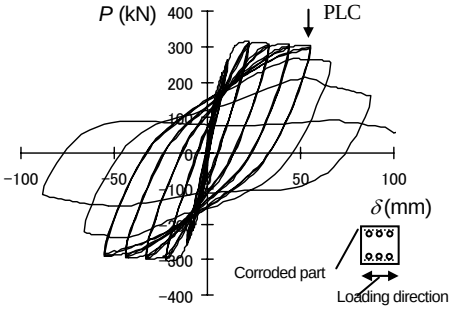

(a) Specimen No.2

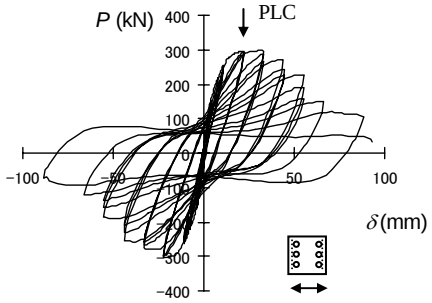

(b) Specimen No.3

Figure 6 P-δ relationship

and the envelope curves of these P-δ relationships are compared in Figure 7. In the following figures of the P-δ relationships, the point of peakload- carriable loading cycle (PLC) is noted as shown in Figure 6 for example. The point PLC is defined as the maximum loading cycle by which the strength reduction doesn't appear in spite of the 3 times repeated loading within the same maximum displacement. According to Figure 7, it is obvious that the corrosion of reinforcing bars decreases the deformation capacity of the RC column. From the standpoint of Figure 6, it is observed that the test specimen No.2 could sustain shear loading till the PLC of $5\delta_y$ (δ=55mm). On the other hand, it is observed that the test specimen No.3 could sustain shear force till the PLC of $2\delta_y$ (δ=22mm), showing that the shear loading P was being reduced after the loading step of $3\delta_y$ ($\delta \geq$33mm) according to 3 times repeated loading. In these ways, it is clarified that the corrosion at the loading sides is more effective to reduce its deformation capacity of the column than that at the transverse sides.

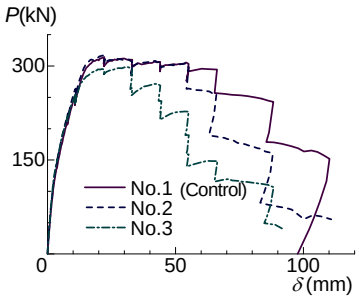

Figure 7 Envelope curves of P-δ relationships
(Effect due to difference of corroded sides)

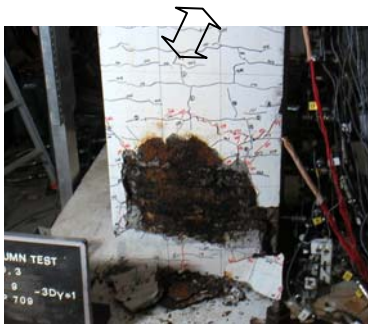

(a) Specimen No.3 (electric corroded)

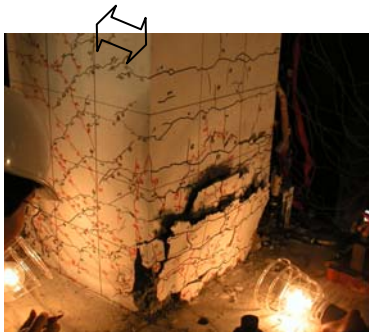

(b) Specimen No.4 (scraped)

Figure 8 Conditions of Spalling

3.2 Comparison in method of corrosion modeling

Figure 8 shows the condition at the beginning of the spalling of the column side surface of the specimen No.3 to No.4, in which scraped or electric corroded bar was arranged at the loading side. Early spalling before the loading step at the displacement $4\delta_y$ was visible in the test specimen No.3 and No.4. The cover concrete at the corrosion area was fallen all in one together in the test specimen No.3 and No.4, whereas in the no corroded control specimen No.1, the cover concrete near the fixed end was fallen portion by portion gradually. The failure condition of the specimen No.4 provided with the scraped bars is similar to that of the electric corroded specimen No.3. Figure 9 shows the envelope curve of the P-δ relationship of the specimen No.4 compared with the specimen of electric corroded No.3 and control No.1. It is judged that providing scraped bars can be a good modeling method of the substantial corrosion.

3.3 Comparison in location of corrosion of hoop

The P-δ relationship of the specimens No.7 and No.8 are shown in Figure 10 respectively. The point PLC of the specimen No.7 and No.8 is the same $5\delta_y$ (55mm). The envelope curves of these P-δ relationships are compared in Figure 11. The envelope curve of the specimen No.8 is almost equal to that of the control specimen No.1, in spite of having the scraped hoops at its loading sides as the corrosion model. On the other hand, according to the P-δ curve of the specimen No.7 whose hoop bars were scraped at its transverse sides, it can be observed that the shear strength P after the PLC of $5\delta_y$ (55mm) is smaller than that of the

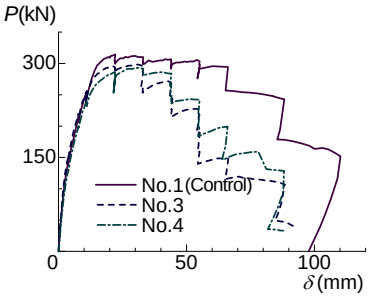

Figure 9 Envelope curves of P-δ relationships
(method of corrosion modeling)

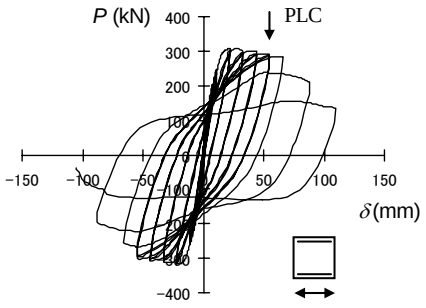

(a) Specimen No.7

Figure 10 P-δ relationship

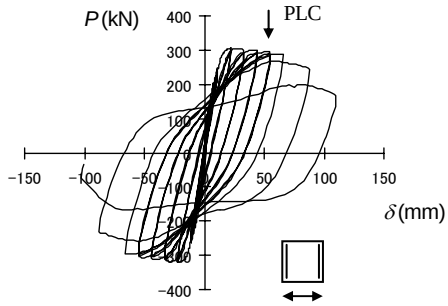

(b) Specimen No.8

Figure 10 P-δ relationship

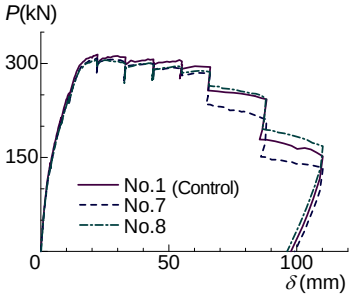

Figure 11 Envelope curves of P-δ relationships
(Comparison of location of hoop corrosion)

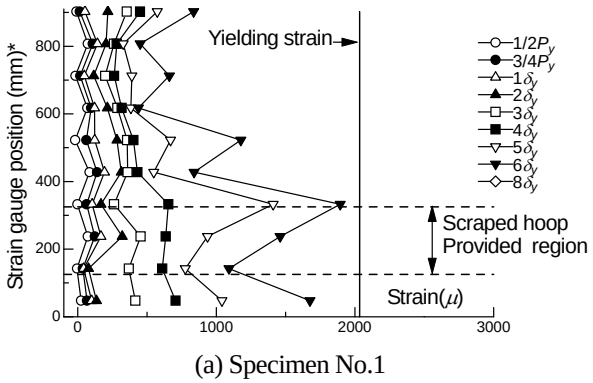

(a) Specimen No.1

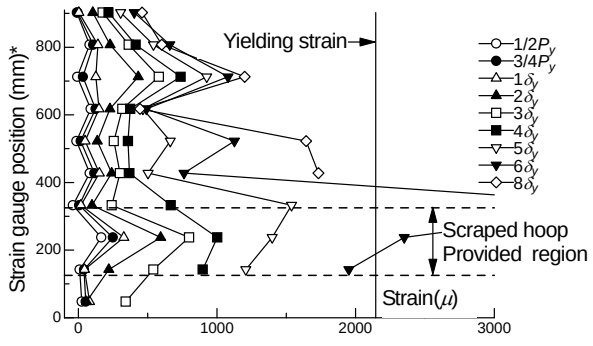

(b) Specimen No.8

* height from bottom fixed end (top of stub)

Figure 12 Strain distribution of hoop at loading side

other specimen No.1 and No.8, despite that the PLC of the specimen No.7($5\delta_y$) is as much as that of the specimen No.8. Therefore it can be pointed out that the hoop corrosion at the transverse side brings no effect to the former loading stage before the PLC point, but makes the shear strength reduction at the latter loading stage after the PLC point.

The strain distribution of the hoop reinforcing bar at the loading side was shown in Figure 12. The strain distribution of the specimen No.8 doesn't have any significant difference from the control specimen No.1. In spite of having thinner hoops than the original ones, there isn't any apparent evidence of being much elongated in the specimen No.8. One of the main reason is that the hoop at the loading sides doesn't contribute to resist against the buckling of the main bar.

Therefore it can be judged that the corrosion of hoops at the loading sides brings almost no effect to the deformation capacity of the RC column, but that at the transverse sides can make its loading capacity decrease at the latter loading stage after the PLC point.

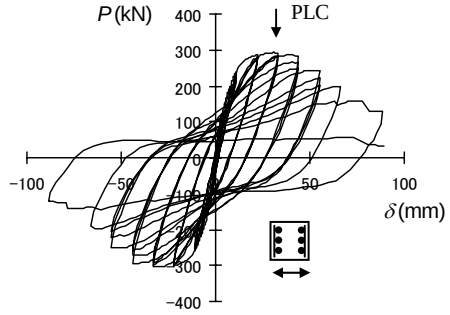

(a) Specimen No.4

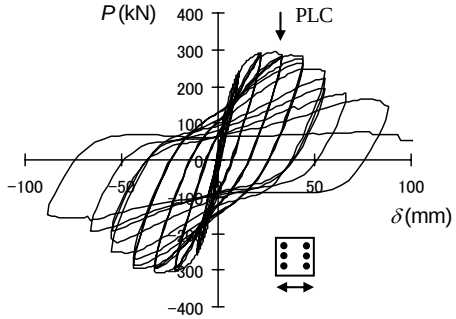

(b) Specimen No.5

Figure 13 P-δ relationship

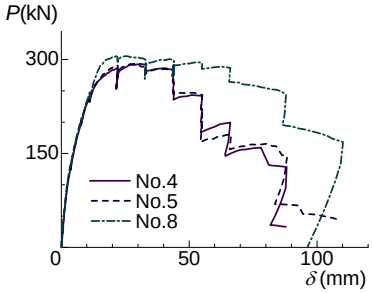

Figure 14 Envelope curves of P-δ relationships
(Comparison of with/without main bar corrosion)

3.4 Effect of main bar corrosion

The P-δ relationship of the specimens No.4 and No.5 are shown in Figure 13, and the envelope curves of these P-δ relationships including that of specimen No.8 are compared in Figure 14. The P-δ curve of the specimen No.5 is almost equal to that of the specimen No.4, in spite of not having the scraped hoops at its loading sides as the corrosion model. As mentioned in previous section, the P-δ curve of the specimen No.8 in which scraped hoop bars are arranged at the loading side is almost equal to the control specimen No.1. Therefore the envelope curve of the specimen No.8 can be assumed as to be equal to that of the control specimen No.1. Comparing the envelope curve of the specimen No.4 and No.5 to that of the specimen No.8, it is clear that the deformation capacity of the RC column with the corrosion at the loading side should be reduced from that of the original no- corroded one, no matter if the hoop corrosion at the loading side exists or not. Therefore it can be pointed out that the corrosion at the loading side decreases the deformation capacity of the RC column, and that phenomena is caused not by the corrosion of hoop bar but by that of main bar.

The strain distributions of the main bars of the test specimens No.5 is shown in Figure 15 in accordance with that of the control specimen No.1. According to these figures (a),(b), the length of the tensile yielded region in the test specimen No.5 is shorten within the scraped region.

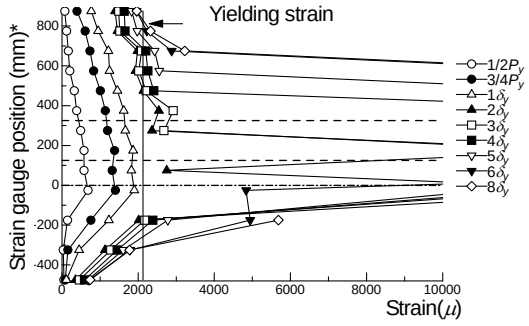

(a) Specimen No.1 (tensile)

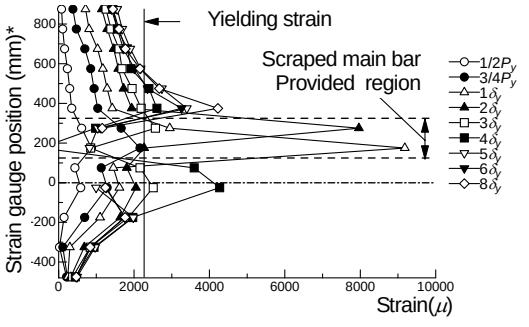

(b) Specimen No.5 (tensile)

* height from bottom fixed end (top of stub)

Figure 15 Strain distribution of main bar

On the other hand, according to that figure of (c)(d), the length of the compressive yielded region in the test specimen No.5 is widen to the scraped region of the main bar. It can be assumed that the damaged area of the main bar due to loading is concentrated into the scraped (corrosion modeled) region, so that the buckling of the corroded main bar can be easily caused due to the elongation of the buckling length.

Therefore, the fact can be derived that the effect of corrosion at the loading sides is conduced not by the corrosion of hoop but by the corrosion of main bar, because the latter causes the buckling of the main bar easily due to the elongation of the buckling length.

4. CONCLUSION

In order to verify the safety performance of existing RC structures against the seismic load, the fundamental properties of the deformation capacity of the deteriorated reinforced concrete columns due to the corrosion was discussed based on the previous experimental result by authors. According to this discussion, it is obvious that the corrosion of reinforcing bars decreases the deformation capacity of the RC column. It is also clarified that providing scraped bars can be a good modeling method of the substantial corrosion. From the standpoint of the effect due to the difference of the location of the corrosion, the followings are obtained as the fundamental knowledges to evaluate the deformation capacity;

i. The corrosion at the loading sides is more effective to reduce the deformation capacity of the column than that at the transverse sides.

ii. The corrosion of hoop at the loading sides brings almost no effect to the deformation capacity of the RC column, but that at the transverse sides can make its loading capacity decrease at the loading stage after the PLC point.

iii. The corrosion at the loading side decreases the deformation capacity of the RC column, and that phenomena is caused not by the corrosion of hoop bar but by that of main bar.

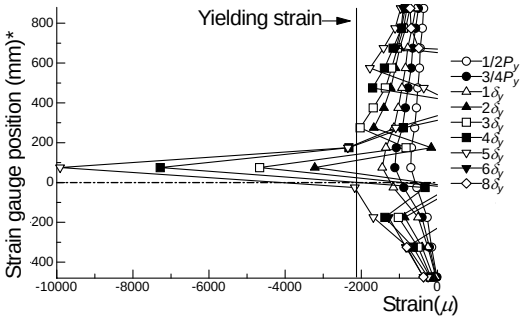

(c) Specimen No.1 (compressive)

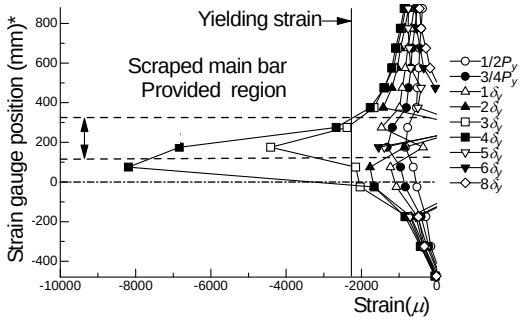

(d) Specimen No.5 (compressive)

* height from bottom fixed end (top of stub)

Figure 15 Strain distribution of main bar

Acknowledgements:

This work is financially supported in part by the Japanese Ministry of Land, Infrastructure and Transport.

References:

Oyado, M., Saito, Y., Yasojima, A., Kanakubo, T., Yamamoto, Y., " Structural Performance of Corroded RC Column under Seismic Load," *1st International Workshop on Performance, Protection and Strengthening of Structures under Extreme Loading*, JPN12, 2007.

Outline of Design Standards for Railway Structures and Commentary (Seismic Design), Railway Technical Research Institute JAPAN, 2007

Takiguchi, M., Watanabe, T., Sato, T. and Tanaka, H., "Evaluation of Ductility for Reinforced Concrete Members," *Quarterly Report of RTRI*, Vol.40, No.3, 1999, pp.165-170.

Oyado, M., Hasegawa, M. and Sato, T., "Characteristics of Fatigue and Evaluation of RC Beam Damaged by Accelerated Corrosion," *Quarterly Report of RTRI*, Vol.44, No.2, 2003, pp.72-77.

Oyado, M., Kanakubo, T., Yamamoto, Y. and Sato, T., "Influence of Corrosion of Reinforcing Bars on Bending Performance of Reinforced Concrete Members," *Journal of Materials, Concrete Structures and Pavements, JSCE*, Vol.62 (2006), No.3, 2006, pp.542-554. (in Japanese)

Sixth International Conference on Urban Earthquake Engineering
March 3-4, 2009, Tokyo Institute of Technology, Tokyo, Japan

Residual Load Carrying Capacity of RC Beams with Spatially Variability of Corrosion

T. Miki[1] and J. Niwa[2]

1) Associate Professor, Department of Civil Engineering, Kobe University, Japan
2) Professor, Department of Civil Engineering, Tokyo Institute of Technology, Japan
mikitomo@port.kobe-u.ac.jp, jniwa@cv.titech.ac.jp

Abstract: This paper presents an evaluation of the residual structural performance of RC members damaged due to steel corrosion. A lattice model is focused on and developed to evaluate the shear resisting mechanism of corroded RC beams. An interface element is modeled for the bond behavior between corroded steel and concrete and is incorporated into the lattice model. The target is set on landing piers that were removed at 2004 because of deteriorations in service for about 40 years. The lattice model is extended to a three dimension to consider corrosion conditions of steels which varied spatially in the analysis. The analysis shows that the 3D lattice model can reasonably evaluate the yielding and maximum loads of RC structural members with corrosion-damaged steels.

1. INTRODUCTION

An appropriate method for the maintenance of existing RC structures has been required to keep the structures being the initial required performance. Deteriorations such as steel corrosion due to the permeation of chloride ions should be considered as one of the durability problem regarding RC structures. When steel corrosion in RC structures progresses, cracks, induced by the expansion pressure of corrosion products, occur in the cover concrete. The previous study (Kato et al. 2004) has shown that flexural capacities of RC beams decreased due to the deterioration of bond properties between a reinforcing bar and concrete. The decrease in the flexural capacity is much larger than that in the capacity which is estimated from the cross-sectional loss of a reinforcing bar.

For the deteriorated RC structures, it is required to evaluate the residual performance of the structures in the maintenance system, and the analytical tool to evaluate the performance is keenly needed. The aim of this study is to establish the method to evaluate the residual performance of RC structures using given information on the deterioration such as steel corrosion.

In the lattice model (Niwa et al. 1995, Miki and Niwa 2004), a RC member is discretized into truss elements. This is objective and simple modeling which can be used to explain the shear resisting mechanism of RC structural members. Suzuki et al. (2006) have considered the cross-sectional loss of reinforcing bars due to steel corrosion, and introduced interface elements modeled by using shear springs and vertical springs in the lattice model. The interface elements were able to express the deterioration of bond properties due to corrosion. Their research clarified that the updated lattice model was able to evaluate the structural performance of RC beams with corrosion-damaged steels. These analytical investigations were performed using the 2D lattice model in their study. In addition, the targets of the analysis were RC beams with corrosion-damaged steels by means of electric acceleration method. Concerning this reproduction method, Morinaga (1996) has pointed out that the electric corrosion condition was distributed more uniformly than that in the actual RC structures. When the steel corrosion spatially distributed among the actual structures, it is difficult to evaluate the response of such structures appropriately by using 2D analysis. This study aims to evaluate the residual performance of RC structural members using the 3D lattice model. In the model, the corrosion condition spatially distributed in the actual structures is considered.

2. ANALYTICAL MODEL

2.1 Outlines of Lattice Model

The lattice model consists of concrete members and reinforcement members, as shown in Figure 1. In a RC beam, the concrete is modeled into flexural compression members, flexural tension members, diagonal compression members, diagonal tension members, horizontal members and an arch member. The longitudinal and transverse reinforcing bars are modeled into horizontal and vertical members, respectively. The diagonal members are arranged at regular intervals with inclined angles of 45 and 135 degrees with respect to the longitudinal axis of a beam. The arch member connecting the nodes at the opposite diagonal corners between the loading point and a support in the beam is arranged according to the direction of the internal flow of compressive stresses.

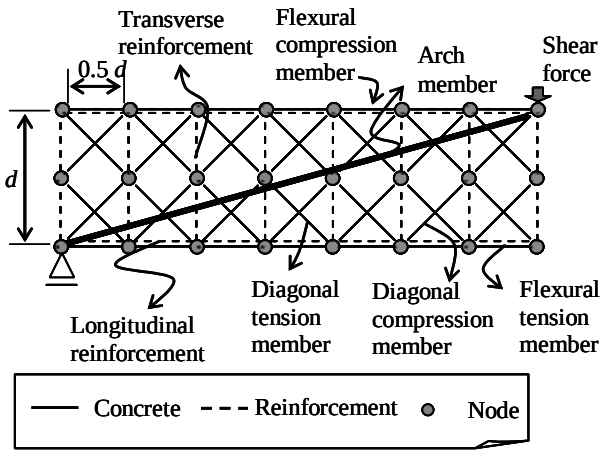

Figure 1 Schematic diagram of lattice model in side view

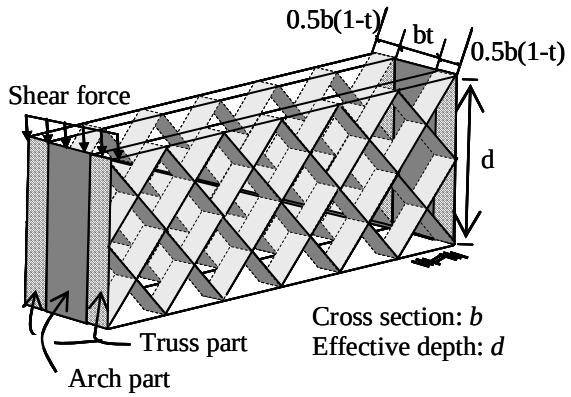

Figure 2 Cross-section of RC beam modeled by lattice model

Figure 2 illustrates a schematic diagram of cross-section of a RC beam modeled by the lattice model. The concrete is divided into truss and arch parts. When the value of t is defined as a ratio of the width of an arch part to the width of cross-section, the widths of an arch part and a truss part are given as bt and $b(1-t)$, respectively, where t ranges from 0 to 1. The value of t is determined based on the theorem of the minimization of the total potential energy for the lattice model with the initial elastic stiffness. The total potential energy is obtained from the difference between the summation of the strain energy in each element and the external work. The pre-analysis using the lattice model is carried out to determine the value of t according to the minimum total potential energy.

2.2 Material Constitutive Model

a) Concrete model

For a cracked concrete, the compressive softening behavior of concrete proposed by Vecchio and Collins (1986) is considered. The ability of cracked concrete to resist the compressive stress decreases as increase in the transverse tensile strain. For the flexural compression members, the stress-strain relationship proposed by Maekawa and Fukuura (1999) is used. As for the flexural tension members, which are provided around reinforcing bars, the tension-stiffening model (Okamura and Maekawa 1991) is applied in order to consider the bond effect between the concrete and reinforcing bars. On the other hand, when interface elements that will be mentioned later on are installed in the model, the 1/4 tension softening model (Uchida and Rokugo 1991) is applied as brittle behavior of plan concrete.

For the diagonal tension members, the 1/4 tension softening model (Uchida and Rokugo 1991) is applied. The stress-strain relationships proposed by Naganuma and Ohkubo (2000) are used, for the cyclic behavior of concrete under both compression and tension.

b) Reinforcing bar model

The envelope curve for the stress-strain relationship in tension of reinforcing bars is modeled as the average behavior in concrete by Maekawa and Fukuura (1999). As for the stress-strain relationship in compression, bi-linear model in which the tangential stiffness after yielding is set as 0.01 E_s, where E_s denotes the Young's modulus of a reinforcing bar, is used.

2.3 Interface Elements Between Reinforcing Bar and Concrete

Figure 3 shows the outlines of the interface elements. The nodes are arranged such that the nodes of steel are located between the adjacent nodes of concrete. The

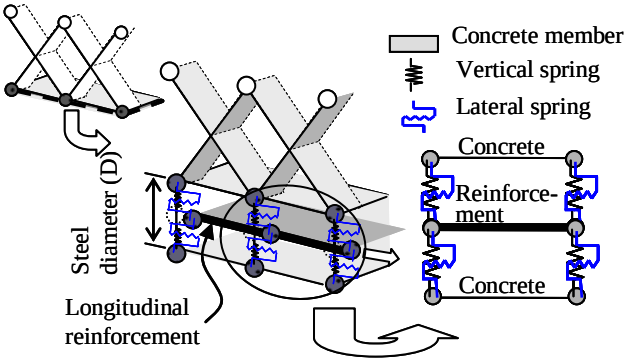

Figure 3 Outlines of interface elements

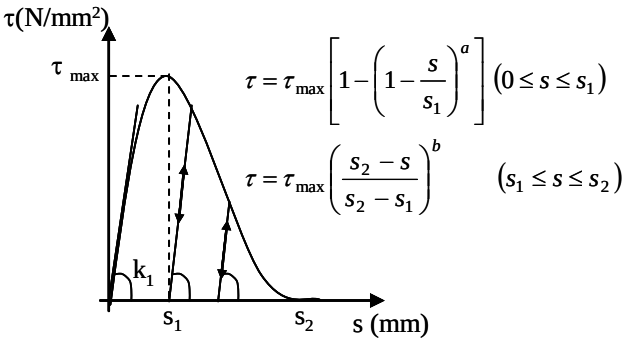

Figure 4 Bond property in the shear spring

thickness of the interface element is assumed to be as same as the diameter of a reinforcing bar (D). These nodes are connected with vertical springs transmitting the vertical stress and lateral springs transmitting the shear stress. The vertical spring is modeled as a linear elastic spring in which the tangential stiffness is as same as the Young's modulus of concrete, E_c. As for the lateral spring, it is assumed that the bond stress is uniformly distributed on the surface of the longitudinal reinforcing bar and the bond force on the surface is calculated by the bond stress being multiplied by the steel surface. In this study, τ (bond stress)-s (slip between steel and concrete) relationship as shown in Figure 4 is applied to the lateral spring. The parameters of this model are the maximum bond stress τ_{max}, the slip displacement at τ_{max}, s_1, the slip displacement at $\tau = 0$, s_2 and the exponential coefficients, a and b. Here, the exponents of a and b in the equations are determined based on the extensive parametric analysis. These are assumed to be constants; $a = 1$ and $b = 4$ in this study.

Based on Kato's study (2003), which is related with the ratio of the cross-sectional loss of a reinforcing bar to the degree of bond deterioration between a reinforcing bar and concrete, s_1 and s_2 are set as values of 0.1 mm and 0.2 mm, respectively. Figure 5 shows results in axial test and the analysis using appropriate parameters for the bond-slip behavior of the lateral spring. From the parametric analysis, it can be assumed that τ_{max} is determined by Eq. (1) using a ratio of cross-sectional loss of a reinforcing bar, x (%).

$$\tau_{max} = -0.16x + 4.0 \qquad (1)$$

3. RESIDUAL PERFORMANCE OF RC MEMBERS WITH CORROSION-DAMAGED STEELS

3.1 Target for 2D Analysis

The target is the shear loading tests conducted by Matsuo et al. (2004) on RC beams with the reinforcement artificially corroded by the electrolytic method. Since ion migration accelerated in a sodium chloride solution as shown in Figure 6, the corrosion of reinforcement occurred in this region. The specimens were RC beams with or without transverse reinforcement. The rectangular cross section had the width of 200 mm, the depth of 400 mm and the effective depth of 350 mm as shown in Figure 6. The corrosion target region which is soaked in the sodium

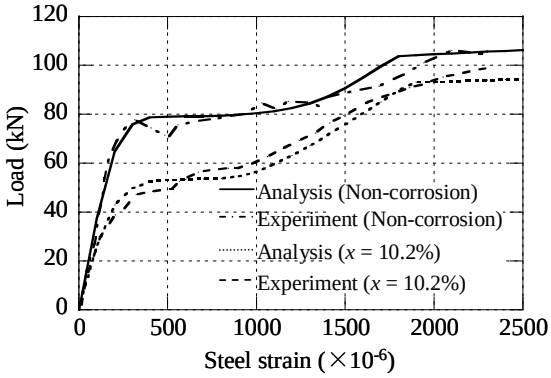

Figure 5 Load-steel strain relationship of RC members in the axial tension test and the analysis

chloride solution corresponds to the span between the supports (2400 mm). The material properties of concrete and reinforcement are listed in Table 1. The experimental cases are listed in Table 2.

The 2D lattice model is illustrated in Figure 7. The value of t, the number of nodes and elements are also shown in this figure. Cross-sectional loss of longitudinal and transverse reinforcements and the bond deterioration between longitudinal bar and concrete are considered in the

Table 1 Material Properties

Concrete	
Compressive strength (N/mm^2)	47.8
Young's modulus (kN/mm^2)	36.4
Longitudinal reinforcements (D19)	
Yielding strength (N/mm^2)	429
Young's modulus (kN/mm^2)	191
Transverse reinforcements (D6)	
Yielding strength (N/mm^2)	279
Young's modulus (kN/mm^2)	191

Table 2 Experimental and Analytical Parameters

ID	Cross-sectional loss of steel (%)		τ_{max} (N/mm^2)
	Long.	Trans.	
A-0h	0	0	4.0
A-36h	1.3	21.3	3.8
A-72h	2.8	38.0	3.55
A-144h	10.6	52.9	2.3

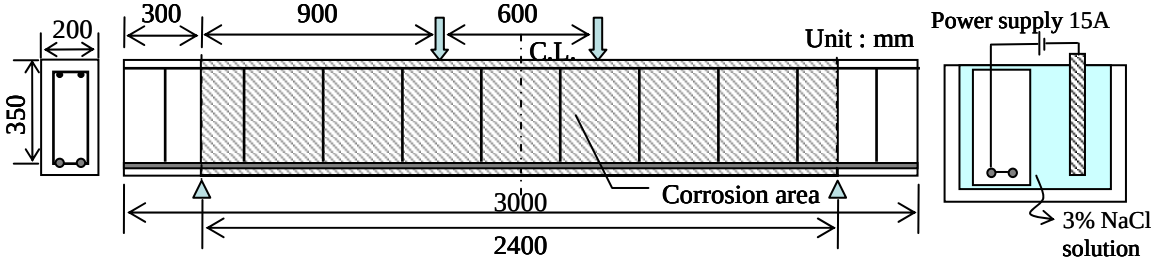

Figure 6 Specimen Details and Test Setup

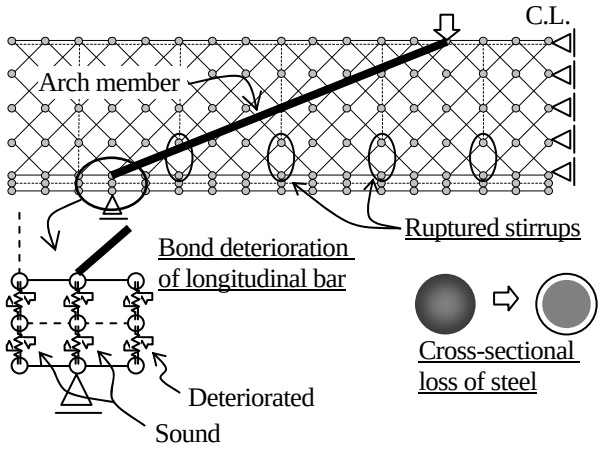

Figure 7 Modeling of damaged RC beams

lattice model in order to represent damaged RC beams as shown in Figure 7. In addition, the ruptured transverse reinforcement due to corrosion at lower corners was predicted not to be able to work at the anchorage in the concrete web. For taking into account the insufficient anchorage of transverse reinforcement, no transverse element is provided in the area near the longitudinal reinforcement as shown in Figure 7. In contrast, the anchorage of longitudinal reinforcement is strong enough in the shear loading test, since the anchorage zone at both ends of the beam is set to be outside of the corrosion area.

3.2 Load-Displacement Relationships

Figure 8 shows the load-displacement relationships obtained from the experiment and lattice model analysis. In the analysis, it is assumed that the rapid compression softening behavior of the arch member leads to the brittle shear failure of RC beams. Therefore, if the compression softening of the arch member occurs before the yield of the longitudinal reinforcement, the diagonal tension failure will be predicted. The point of arch softening (C) and yielding of longitudinal bar (Y) obtained from the analysis are indicated in this figure. In addition, the failure modes of experiment and analysis are shown in this figure. The analysis shows a good agreement with the experiments. The beams A-0h and A-36h show brittle shear failures both in the experiment and analysis. In the experiment, the beam A-72h shows shear-compression failure while in the analysis shear failure was predicted.

Interestingly the analysis shows that the shear carrying capacity of the beams is improved with the increase in cross-sectional loss of the reinforcement. To understand why the shear carrying capacity of damaged RC beams is improved as corrosion of the reinforcement proceeds further, we evaluate the resisting mechanism of the beams in terms of the behavior of each member of the lattice model. Figure 9 shows the contribution of arch member to the shear force, V_{arch} in the beams of A series. The comparison with the results indicates that the analysis predicts the increase in the V_{arch} as the steel corrosion proceeds. In the analysis, especially in the beam A-144h, the bond between concrete and longitudinal reinforcement significantly degraded within the shear span of the beam. The arch member of concrete in the lattice model represents tied arch action in the shear carrying mechanism of the RC beam. Consequently, the increase in the shear carrying capacity can be explained by the premature formation of the tide arch mechanism in the RC beam. It should be noted that for all specimens in this study, the longitudinal reinforcement has been anchored properly. In addition, it was observed in the experiment that the crack along the longitudinal reinforcement resulted in the bond deterioration by the expansion pressure due to the steel corrosion.

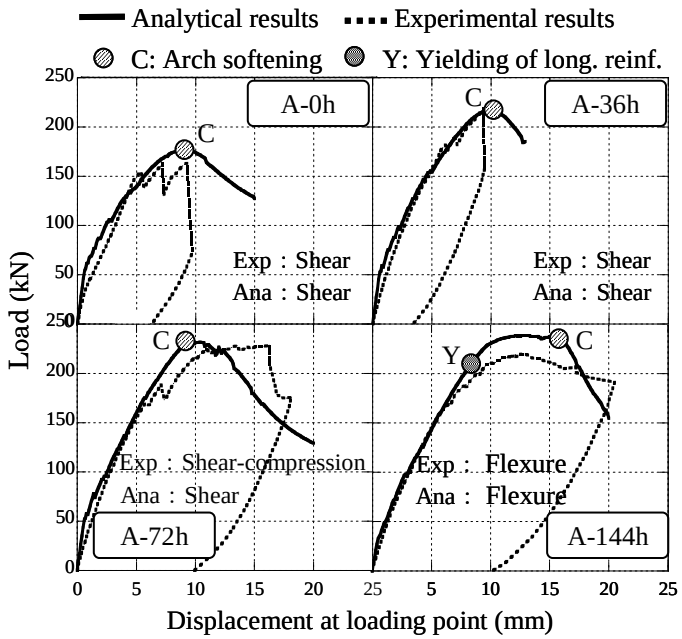

Figure 8 Load-displacement relationships

3.3 Target for 3D Analysis

In this study, the experimental tests conducted by Kato et al. (2006) are used as a target of the analysis. The specimens were six rectangular RC beams taken out from two slabs of the pier which had been in

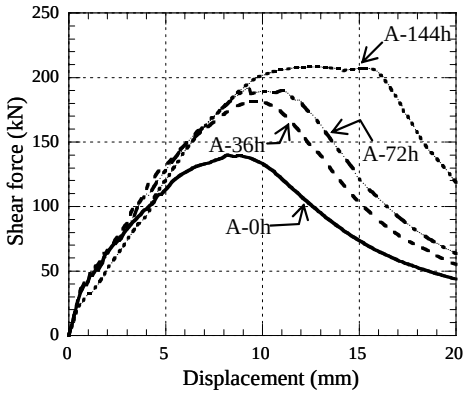

Figure 9 Contribution of arch member to the shear force

Table 3 Dimension of specimens

Name	Series 1			Series 2		
	1-1	1-2	1-3	2-1	2-2	2-3
Width b(mm)[*1]	699	535	798	732	569	812
Depth h(mm)[*1]	300	300	300	310	310	310
N_u [*2,*3]	3	4	3	3	3	3
N_l [*2,*4]	5	4	6	5	5	6

*1 : mean, *2 : round bar of 13mm diameter
*3 : number of upper reinforcing bars
*4 : number of lower reinforcing bars

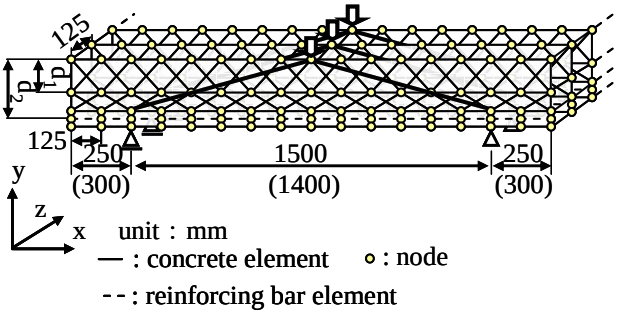

Figure 10 Configuration of 3D lattice model

service for about 40 years. The pier was removed in 2004 because of serious deterioration such as cracks and spalling of cover concrete. Table 3 shows the dimension of the specimens.

The material tests of reinforcing bars and core concrete which were taken from the beams after bending tests were conducted. The average yield strength and the average Young's modulus of reinforcing bars among the beams were 358 N/mm^2 and 218 kN/mm^2, respectively. The average compression strength and the average Young's modulus of concrete were 38.6 N/mm^2 and 29.1 kN/mm^2, respectively.

Figure 10 shows the configuration of the 3D lattice model for these specimens. In this model, the 2D lattice models are arranged at the location of reinforcing bar in the z direction, and each 2D model is connected by the truss members in the x-z and y-z planes. To reflect effective depth of upper and lower reinforcing bars, the nodes of the reinforcing bar elements are arranged at the location of reinforcing bars (d_1 and d_2) in the y direction. In the Series 1, d_1 and d_2 are 140 and 250 mm, respectively, and in the Series 2, d_1 and d_2 are 150 and 260 mm, respectively.

The ratio of cross-sectional loss of reinforcing bar is defined as a ratio of the weight-loss of corroded reinforcing bar from its initial weight to that of original reinforcing bar. Lower reinforcing bars were taken from RC beams within the bending span after bending tests, and all reinforcing bars were divided into 14 samples with the length of 100 mm. The ratios of cross-sectional loss were measured for each sample, and the distributions of the ratios of cross-sectional loss of lower reinforcing bars were calculated as shown in Figure 11. The figure clearly shows that the corrosion conditions of each reinforcing bar varied spatially. In these specimens, the ratios of cross-sectional loss tend to be highest in the center part of the bending span. In the specimen 2-3, although one reinforcing bar shows the maximum loss ratio 51 %, the other shows no corrosion in the center part of the bending span. Remarkable variation of the maximum loss of reinforcing bars can be confirmed for all beams taken from one slab. It seems likely that the causes of these variations of corrosion condition are initial defects such as unfilled concrete in the concrete cover.

The cross-sectional loss of the reinforcing bar elements and τ_{max} of the shear spring elements are determined by using Eq. (1) substituted the ratio of cross-sectional loss measured within the bending span. These values express the influence of deterioration of bond properties in the analysis. Because the ratio of cross-sectional loss of reinforcing bars except between the supports are not measured, these ratios in the region from the support to the beam end are assumed to the constant values that are measured at the support.

3.4 Results of the 3D Lattice Model Analysis

Figure 12 shows the load-displacement relationship obtained from the analysis and the experiments. As can be seen in the figure, the initial stiffness of RC beams obtained from the experiment, which indicates the stiffness before load-induced cracking of the beam, shows good agreement with that predicted in the analysis. However, the predictions of the cracking load are remarkably higher than those of the experiment in all beams. The stiffness after cracking obtained from the analysis is also different from those of the experimental results. As for the deformation capacity, even though the analysis predicted slightly smaller than the experiments, the analysis for all beams captured the

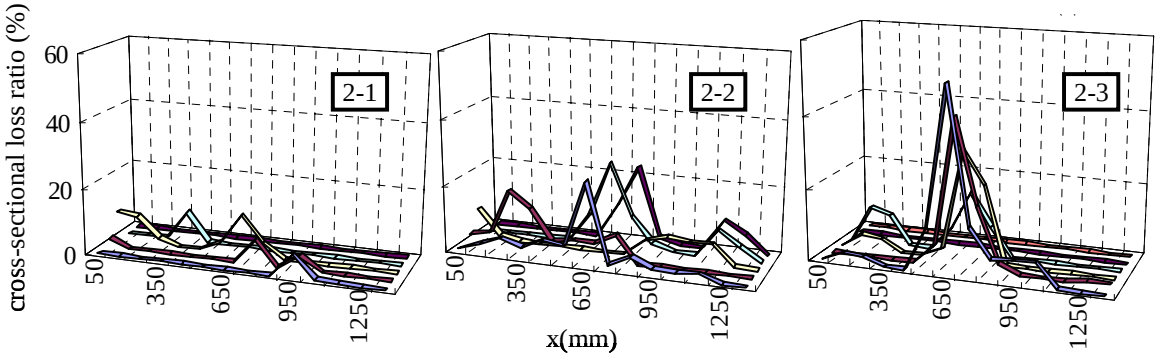

Figure 11 Cross-sectional loss distribution of lower reinforcing bars

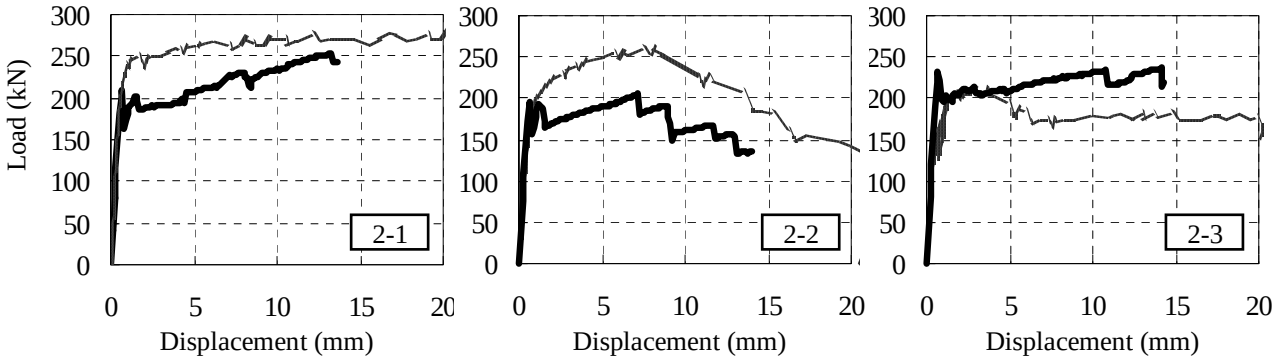

Figure 12 Load-displacement relationships computed by 3D lattice model

experimental behavior approximately.

The cracking loads obtained from the analysis are higher than those of the experiments in all beams. The cause of overestimations is no consideration in the analysis for the reduction of concrete cross-sectional due to the initial defects such as unfilled concrete in the concrete cover and the corrosion cracking.

The discussion on Eq. (1) which expresses the maximum bond stress between a reinforcing bar and concrete is also required. This relationship is based on the experiment in which the maximum ratio of cross-sectional loss of a reinforcing bar measured is about 10 %. However, all specimens selected as the targets in this study show more than 10 % of the maximum ratios of cross-sectional loss of reinforcing bars, and the largest ratio is 51 %. To evaluate the residual performance of the structures with further accuracy, it is required to confirm the applicability of Eq. (1) to use in the analysis of actual RC structures having severely corroded reinforcing bars.

4. CONCLUSIONS

In this study, the RC structural members deteriorated in actual condition are selected as targets of the analysis. The residual performance of RC structural members is evaluated by using the 3D lattice model. In the model, the interface elements considering the bond deterioration between concrete and reinforcing bars are introduced.

The conclusions obtained from this research are shown as follows:

1) In the case of the RC structural members with actual corrosion conditions in a reinforcing bar, it is difficult to evaluate the behavior of these members by 2D analysis. This is because the corrosion conditions of a reinforcing bar indicates the spatial dispersion in structural members and the corrosion condition cannot be averaged into the two-dimension properly.
2) The 3D lattice model analysis can appropriately evaluate the residual structural performance of RC structural members with corrosion-damaged steels, especially for the yielding and maximum loads.

References:

Kato, E., Iwanami, M., Yokota, H., Ito, H. and Sato, F. (2003), Bond Behavior between Corroded Rebar and Concrete, *Technical Note of the Port and Airport Research Institute*, **1044**.

Kato, E., Iwanami, M., Yamaji, T. and Yokota, H. (2006), Structural Performance and Deterioration due to Chloride Attack of Reinforced Concrete Deck of Existing Piers, *Technical Note of the Port and Airport Research Institute*, **1140**.

Maekawa, K. and Fukuura, N. (1999), Re-formulation of Spatially Averaged RC Constitutive Model with Quasi-orthogonal Bi-directional Cracking, *Journal of Materials, Concrete Structures and Pavements*, **634**(45), 157-176.

Miki, T. and Niwa, J. (2004), Nonlinear Analysis of RC Structural Members Using 3D Lattice Model, *Journal of Advanced Concrete Technology*, **2**(3), 343-358.

Morinaga, S. (1996), Remaining Life of Reinforced Concrete Structures after Corrosion Cracking, *Durability of Building Materials and Components*, 127-137.

Naganuma, K. and Ohkubo, M. (2000), An Analytical Model for Reinforced Concrete Panels under Cyclic Stresses, *Journal of Structural and Construction Engineering*, **536**, 135-142.

Niwa, J., Choi, I.C. and Tanabe, T. (1995), Analytical Study for Shear Resisting Mechanism Using Lattice Model, *Concrete Library International*, **26**, 95-109.

Okamura, H. and Maekawa, K. (1991), Nonlinear Analysis and Constitutive Models of Reinforced Concrete, Gihodo-Shuppan.

Suzuki, N., Miki, T. and Niwa, J. (2006), Lattice Model Analysis for Evaluation of Shear Loading Capacity of Damaged RC Beams, *Proceedings of the Japan Concrete Institute*, **28**(2), 235-240.

Uchida, Y. and Rokugo, K. (1991), Determination of Tension Softening Diagrams of Concrete by Means of Bending Tests, *Journal of Materials, Concrete Structures and Pavements*, **426**(14), 203-212.

Vecchio, F. J. and Collins, M. P. (1986), The Modified Compression Field Theory for Reinforced Concrete Elements Subjected to Shear, *ACI Journal*, **83**(2), 219-231.

Sixth International Conference on Urban Earthquake Engineering
March 3-4, 2009, Tokyo Institute of Technology, Tokyo, Japan

SHEAR FAILURE MECHANISM OF RC DEEP BEAMS IN FRAME STRUCTURES SUBJECTED TO THE SEISMIC LOADING

Ken Watanabe[1], Toshiya Tadokoro[2], Yukihiro Tanimura[3], and Junichiro Niwa[4]

1) Assistant Professor, Department of Civil Engineering, Tokyo Institute of Technology, Japan
2) Assistant Senior, Concrete Structures, Railway Technical Research Institute, Japan
3) Laboratory Head, Concrete Structures, Railway Technical Research Institute, Japan
4) Professor, Department of Civil Engineering, Tokyo Institute of Technology, Japan
ken@cv.titech.ac.jp, tadokoro@rtri.or.jp, tanimura@rtri.or.jp, jniwa@cv.titech.ac.jp

Abstract: Reinforced concrete (RC) deep beams are used as a structural member having a shear span to effective depth ratio of not exceeding 1.0 as well as for the application to frame structures, caisson foundations, and corbels. There is, however, a peculiar problem in the analysis of RC deep beams; the variety of supporting condition for RC deep beams induces various failure modes. The goal of this research is to identify the shear failure mechanism as well as the shear loading capacity of RC deep beams. To tackle with this objective, the research has focused on internal strain distributions of the RC deep beams under external loading. Based on experimental results, this paper concluded the failure mode and the loading capacity of RC deep beams associated with supports condition and the specimen design.

1. INTRODUCTION

Reinforced concrete (RC) deep beams are widely used as a structural member having shear span to effective depth ratio of not exceeding 1.0 as well as for application to frame structures, caisson foundations, corbels. Civil engineers in Japan have considered the shear carrying capacity of RC deep beams loaded under the simple-supported condition, and the shear compression failure with principle compressive stress flows from the load point to supports after the occurrence of diagonal cracks (Niwa 1984). There is, however, a peculiar problem in the analysis of RC deep beams; the variety of supporting method for RC deep beams subjected to the seismic force induces various moment diagrams. For example, the moment diagram in RC deep beams used for caisson foundations shows the symmetry with respect to the middle of the span under vertical loading. On the other hands, the moment diagram in RC deep beams used for frame structures shows the anti-symmetry moment diagrams under horizontal loading. Because the failure mechanism is corresponding to the moment diagram, the shear carrying capacity of RC deep beams is strongly depending on types of civil engineering structures. A few studies have explained and predicted the failure mode of RC deep beams, which was influenced by the support condition (MacGregor and Wight 2004). The difference in failure modes between predicted and experimental results has caused a large safety factor in the design of shear carrying capacity and deformation capacity of RC structures.

The goal of this research is to identify the shear failure mechanism of RC deep beams in frame structures subjected to the seismic loading. This paper discussed the effect of supports condition on the shear failure mechanism as well as the shear carrying capacity of RC deep beams. Based on experimental and finite element method (FEM) results, this paper concluded the failure mode and the shear carrying capacity of RC deep beams associated with the supporting condition and the transverse reinforcement ratio, r_w.

2. EXPERIMENT AND ANALYSIS PROGRAMS

2.1 Test under Symmetry Moment Diagram

(1) Specimen Fabrication

Figure 1 illustrates the scheme of tested RC deep beam with name of DB408S. (Tanimura et al. 2004) The loading span ($2a$) was 800 mm, and the effective depth (d) was 400 mm; the shear span to the effective depth ratio (a/d) was equal to 1. The beam width was 300 mm. Specimens were longitudinally reinforced by four deformed PC tendons of 29 mm in diameter (D29: the yield strength f_{sy} = 458 N/mm^2 and the Young's modules E_{sc}=1.60×10^5 N/mm^2); the longitudinal reinforcement ratio was 2.14 %. Table 1 summarized specifications of specimens: DB400S and DB408S. Stirrups with deformed steels of 13 mm in diameter (D13) were arranged in DB408S with the interval of 100 mm. D13 had f_{sy} of 368 N/mm^2 and E_{sc} of 1.46×10^5 N/mm^2. The transverse reinforcement ratio (p_w) of DB408S was 0.84 %.

(2) Loading Test

A three points bending test of the specimen was conducted. The specimen was placed over the roller supports

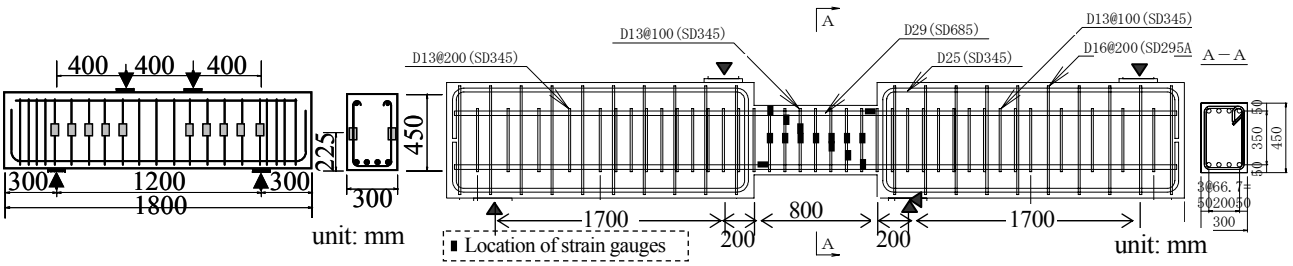

Figure 1 Specimen detail (DB408S)

Figure 2 Specimen detail (DB408A)

Table 1 Properties of specimens and experimental results

Specimen	Loading condition	Stirrup ratio, r_w, (%)	Compressive strength, f_c', (N/mm^2)	Shear carrying capacity, (kN)	
				V_{sb} *1	V_{ab} *2
DB400S	Symmetry	0.0	29.0	632	-
DB408S		0.84	29.3	804	
DB400A	Anti-symmetry	0.0	28.6	-	381
DB408A		0.84	28.9		621

*1: Shear carrying capacity under simple-supported condition,
*2: Shear carrying capacity under anti-symmetry condition.

of the loading plate with 100 mm width and the friction reducing pads inserted. The friction reducing pads consisted of two Teflon sheets with sandwiched grease. A concentrated load was applied at the mid-span, and a steel plate with 100 mm width was set at the loading point.

2.2 Test under Anti-Symmetry Moment Diagram

(1) Specimen Fabrication

Figure 2 illustrates the scheme of tested RC deep beam named DB408A. The test span with length of 2a=800 mm was sandwiched by two stabs with the length of b at both sides. The effective depth (d) of 400 mm, and the beam width of 300 mm. Table 1 summarized specifications of specimens: DB400A and DB408A. The value of a/d was 1.0, and p_w was 0.0 or 0.84 %. The average compressive strength of cylindrical specimens (f_c') was 28.6 N/mm^2 at the loading test. Specimens were longitudinally reinforced by four deformed PC tendons of 29 mm in diameter (D29: f_{sy}= 721 N/mm^2 and E_{sc}=1.94×10^5 N/mm^2); the longitudinal reinforcement ratio was 2.14 %. Stirrups with D13 were arranged in DB408 with the interval of 100 mm. D13 had f_{sy} of 369 N/mm^2 and E_{sc} of 1.91×10^5 N/mm^2. The specimen detail at the test span of DB400A or DB408A is the identical with DB400S or DB408S.

Three-axis strain gauges were installed inside the specimens to calculate the direction and the magnitude of principle strain. The gauges were attached on the surface of the acrylic rod with an interval of 100 mm, and embedded at the center of the cross-section to measure the strain of concrete.

(2) Loading Test

Four-point bending test was conducted to apply the anti-symmetry moment diagram to the test span. Steel plates with 250 mm width were placed at the loading point and supports. A set of deflection gauges was installed to measure the relative displacement between both stabs of the beam. The applied load was measured by using load-cells at loading points and supports. Strain gauges were pasted on the surface of longitudinal reinforcements and stirrups at its middle height and the diagonal line as shown in Figure 2.

(3) FEM Analysis

The nonlinear FEM using DIANA has been conducted to analyze the mechanical behavior of whole specimen: DB400A and DB408A. Four-node quadrilateral isoperimetric plane stress elements in a two dimensional configuration were adopted for a concrete. The reinforcement elements were modeled for internal bonded reinforcing bars to have the perfect bond with concrete. Parabolic model and the tension softening model proposed by Hordijk (1991) were utilized as the concrete constitutive model for compression and tension. The compressive fracture energy was 50 N/mm, and the tensile fracture energy was 0.15 N/mm. Two stabs at both ends of the test span were assumed to be a perfect elastic body having the elastic modulus of E_c.

3. EXPERIMENTAL RESULTS AND DISCUSSIONS

3.1 Shear Force-Displacement Relationship

Figure 3 shows the effect of r_w and on shear force–displacement curves of RC deep beams under the symmetry and the anti-symmetry moment diagrams. Both figures indicate that the inclination of these ascending curves seemed to be similar under the identical loading condition, even the value of r_w was different. On the other hands, the shear carrying capacity, the shape of descending branch, and cracks distributions were different depending on the value of r_w and loading conditions. Figure 3(b) also compares the curves of the experimental and FEM results. Even there were some gaps; the curve obtained by FEM was able to demonstrate the shear force at the generation of diagonal cracks, the inclination of the experimental curves, and the shear carrying capacity.

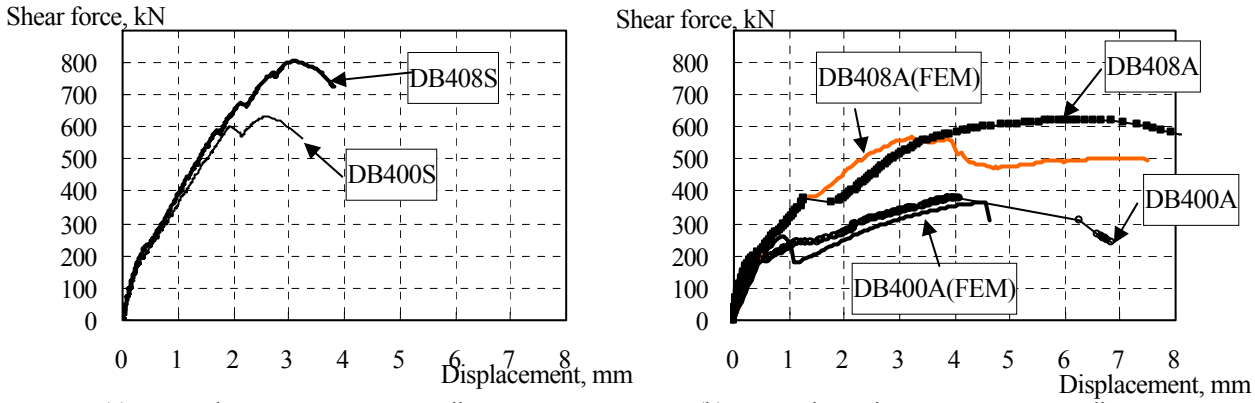

(a) Test under symmetry moment diagram (b) Test under anti-symmetry moment diagram

Figure 3 Shear force-displacement relationships.

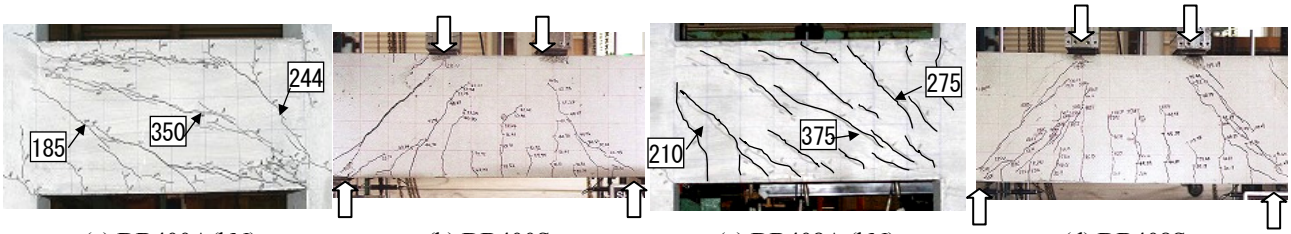

(a) DB400A(kN) (b) DB400S (c) DB408A (kN) (d) DB408S

Figure 4 Difference of the failure mode in RC deep beams.

3.2 Crack Distributions and Failure Modes

Figure 4 summarize the cracked specimen when the shear force (V) reached its maximum (the peak). The cracks distributions were different by p_w and support condition.

(1) Simple-Supported Condition (Figure 4(b) (d)**)**

When RC deep beams were subjected to loading under simple-supported condition (DB400S and DB408S), flexural cracks were first observed at the bottom zone of the mid-span. Then, inclined shear cracks suddenly developed along the direction between the loading point and the support at the shear cracking load. While further load was applied, the shear cracks in both shear spans and many flexural cracks developed with the increase in the deflection. The concrete near the loading point began to fail where non-linear behavior was significant near the peak. Finally, the one side of the compressive arch failed with compression when the load reached its maximum. Strain of stirrups arranged in DB408S did not reach the yield strain.

(2) Anti-symmetry Condition (Figure 4(a) (c))

Figure 4 (a) (c) shows the cracked specimen of DB400A and DB408A. The number in the figure indicated the shear force when the crack was observed. Shear-flexural cracks at both ends of a span the first and the second cracks were observed. Then, DB408A contained many cracks developed along the longitudinal reinforcements with the increase in the displacement. A diagonal shear crack suddenly developed at the middle of the beam span when the shear force reached the shear cracking force, and propagated throughout the beam span. The shear force applied to DB400A reached its maximum at the generation of the

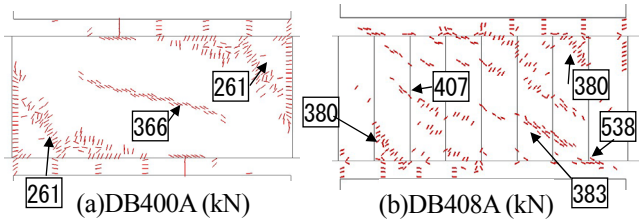

(a)DB400A (kN) (b)DB408A (kN)

Figure 5 Difference of the crack distributions by p_w (FEM).

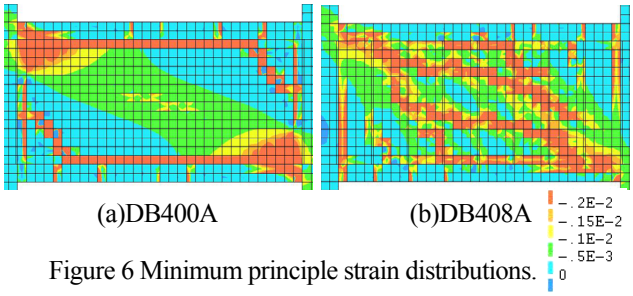

(a)DB400A (b)DB408A

Figure 6 Minimum principle strain distributions.

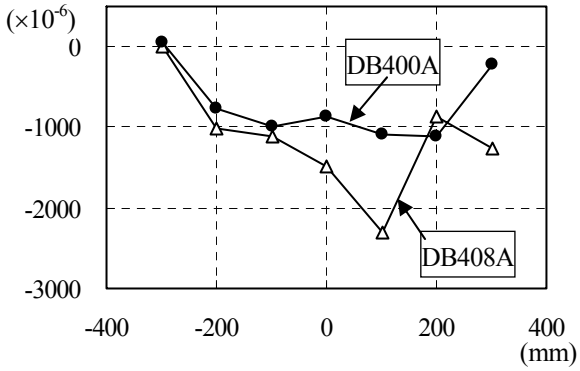

Figure 7 Minimum principle strain distributions.

diagonal shear crack. On the other hands, DB408A carried higher loading after the generation of the diagonal crack. Some stirrups arranged in DB408A were yielded, and the number of cracks along longitudinal reinforcements increased with the increase in the shear force.

Figure 5 shows the crack distributions at the peak obtained through the FEM. The figure contains the shear force at the generation of shear-flexural cracks and a diagonal shear crack. These values of the shear force were corresponding to the experimental data in Figure 4 (a) (c).

(3) Anti-symmetry Condition

Figures 4 (a)(b) and (c)(d) compared the cracks distribution that was depending on the support condition. The RC deep beam loaded with the simple-supported condition (DB400S, DB408S) was failed at the compressive struts formed diagonally between the loading plates and supports. The diagonal cracks usually occur in both shear spans. On the other hands, the specimens: DB400S and DB408S, were failed with the different way as stated in **3.2(2)**. The shape of diagonal crack connecting both ends of a span, and a large number of cracks along longitudinal reinforcements were observed. The difference of crack distributions according to support conditions leaded to be the difference in the shear carrying capacity.

3.3 Principle Strain Distributions

Figure 6 is the contour of the minimum principle strain at the peak in FEM. Strain concentration area were diagonally generated in the whole tested span. Figure 7 plots the experimental results of minimum principle strain measured by using the acrylic rod method along the longitudinal direction. The experimental results were measured at the middle height of the specimen. The effect of stirrups on the minimum principle strain of concrete was obtained by comparing the results of DB400A and DB408A. The minimum principle strain of concrete was decreased with the arrangement of stirrups. The contribution of the compressive strut on carrying the shear force under loading was increased with the increase in p_w. To measure the internal strain distribution by using the acrylic rod method will support for evaluating the shear carrying mechanism of RC deep beams, which were changed by supports condition.

3.4 Effect of Supports on the Shear Carrying Capacity

Figure 8 illustrates the effect of the support condition on the shear strength of RC deep beams: (a) shows the comparison of the shear carrying capacity under the anti-symmetry condition (V_{ab}) with that of under the simple-supported condition (V_{sb}), both values were normalized by $f_c'^{2/3}$ to reduce the effect of variation of the compressive strength. The values of V_{ab}/V_{sb} were less than 1.0: V_{ab}/V_{sb}=0.61 at p_w= 0.0 % and V_{ab}/V_{sb}=0.78 at p_w= 0.84 %. This means that the shear carrying capacity of RC deep beams was strongly depending on the support condition.

In addition, the value of V_{ab}/V_{sb} increased with the increase in p_w. The shear carried by stirrups (V_s) was calculated by subtracting V_{ab} of DB400 from that of DB408. Figure 8(b) plots the values of V_s according to the support

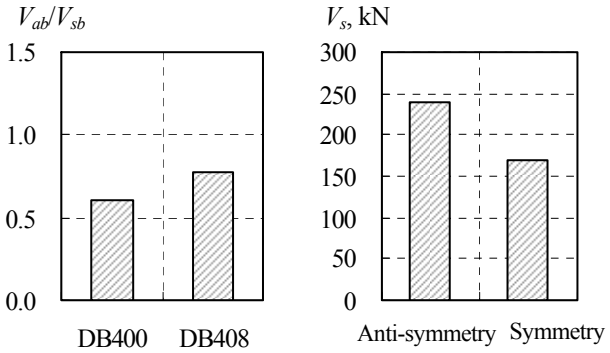

(a) Comparison of shear carrying capacities.

(b) Contribution of stirrups, V_s.

Figure 8 Effect of support condition on shear strength of RC deep beams.

condition. The value of V_s was increased with the increase in a/d and p_w. There is a gap in V_s of RC deep beams subjected to two different supported conditions: V_s of RC deep beams subjected to the anti-symmetry moment diagram was larger than that of RC deep beams subjected to the symmetry moment diagram. According to discussion in 3.2, RC beep beams under simple-support condition (DB400S, DB408S) was failed in the shear compression: the compressive failure of concrete seemed to be related to the peak load, V_{sb}. On the other hands, DB400A and DB408A had a remarkable diagonal crack observed at the mid-span of the beam: the shear carrying capacity under the anti-symmetry condition (V_{ab}) seemed to be related to the shear tension failure. The gap of the shear carrying capacity (V_{ab} and V_{sb}) and the shear carried by stirrup (V_s) between two support conditions would be related to the difference of failure criteria in both RC deep beams.

4. CONCLUSIONS

The difference of support conditions leaded to be the difference in crack distributions as well as the shear carrying capacity. The values of V_{ab}/V_{sb} were less than 1.0. This means that the shear carrying capacity of RC beep beams under the anti-symmetry condition was smaller than that of RC beep beams under the simple-support condition. The contribution of stirrups on shear carrying capacity of RC deep beams obtained in these specimens was larger than that of RC deep beams subjected to the simple-supported condition.

References:

MacGregor, J. G. and Wight, J. K. (2004), "Reinforced Concrete Mechanics and Design," Prentice Hall.

Niwa, J. (1984), "Equation for Shear Strength of Reinforced Concrete Deep Beams Based on FEM Analysis," Concrete Library of JSCE, 4, 283-295.

Tanimura, Y., Sato, T., Watanabe, T. and Matsuoka, S. (2004), "Shear Strength of Deep Beams with Stirrups," Journal of Materials, Concrete Structures and Pavements, JSCE, 760, 29-44. (in Japanese)

Sixth International Conference on Urban Earthquake Engineering
March 3-4, 2009, Tokyo Institute of Technology, Tokyo, Japan

FRAME ANALYSIS OF PASSIVELY CONTROLLED WOODEN FRAME USING HYSTERESIS MODEL BASED ON EXPERIMENT OF JOINT

Kazuhiro Matsuda[1], Hiroyasu Sakata[2], Kazuhiko Kasai[3] and Yoji Ooki[4]

1) JSPS Research Fellow, Japam (Graduate Student, Department of Built Environment, Tokyo Institute of Technology, Japan)
2) Associate Professor, Structural Engineering Research Center, Tokyo Institute of Technology, Japan
3) Professor, Structural Engineering Research Center, Tokyo Institute of Technology, Japan
4) Research Associate, Structural Engineering Research Center, Tokyo Institute of Technology, Japan
matsuda@serc.titech.ac.jp, hsakata@serc.titech.ac.jp, kasai@serc.titech.ac.jp, ooki@serc.titech.ac.jp

Abstract: The wooden wall with shear link passive control mechanism involving with K-brace has been developed by authors, and the effectiveness of the K-brace was confirmed by some dynamic loading tests. This paper proposes an accurate, framed analytical model for the wooden energy dissipation wall with damper. The analytical model was constructed by using spring elements whose properties derived from the experimental results of the joint tests. The comparison between the analytical results and the experimental results by dynamic loading tests showed good agreement. The detailed response of the wooden wall with passive control mechanism could be obtained from the analysis.

1. INTRODUCTION

In the Hanshin-Awaji (Kobe) Earthquake that occurred in 1995, the number of collapses or seriously damaged of wooden houses were approximately 250,000. It is said that approximately 10 million wooden houses are insufficient for earthquake resistant in Japan, and those houses need to be reinforced immediately. Moreover, to design new wooden houses to be resistant to earthquakes, it is important to investigate rational methods applying the passive control to wooden houses.

In order to mitigate the damage of wooden houses and seismic response, K-brace passive control wall was developed (Kasai and Sakata et al. 2005, Figure 1) and a lot of experimental studies using the wall were carried out, such as dynamic cyclic loading tests of the passive control walls (Matsuda et al. 2008), shaking table tests of 1-story or 2-story wooden frames (Sakata et al. 2007 and Matsuda et al. 2007), and so on. However, analytical studies need to be carried out to develop more effective passive control wall and to propose the design method.

Therefore the objective of this study is to propose accurate, framed analytical model for the K-brace passive control wall. To make the model, modeling the joint between column and horizontal member is important. In this study, the analytical model was constructed by using spring elements whose properties derived from the experimental results of the joint tests. Also the accuracy of the framed analytical model is confirmed by the comparison between the analytical results and the experimental results of dynamic loading tests.

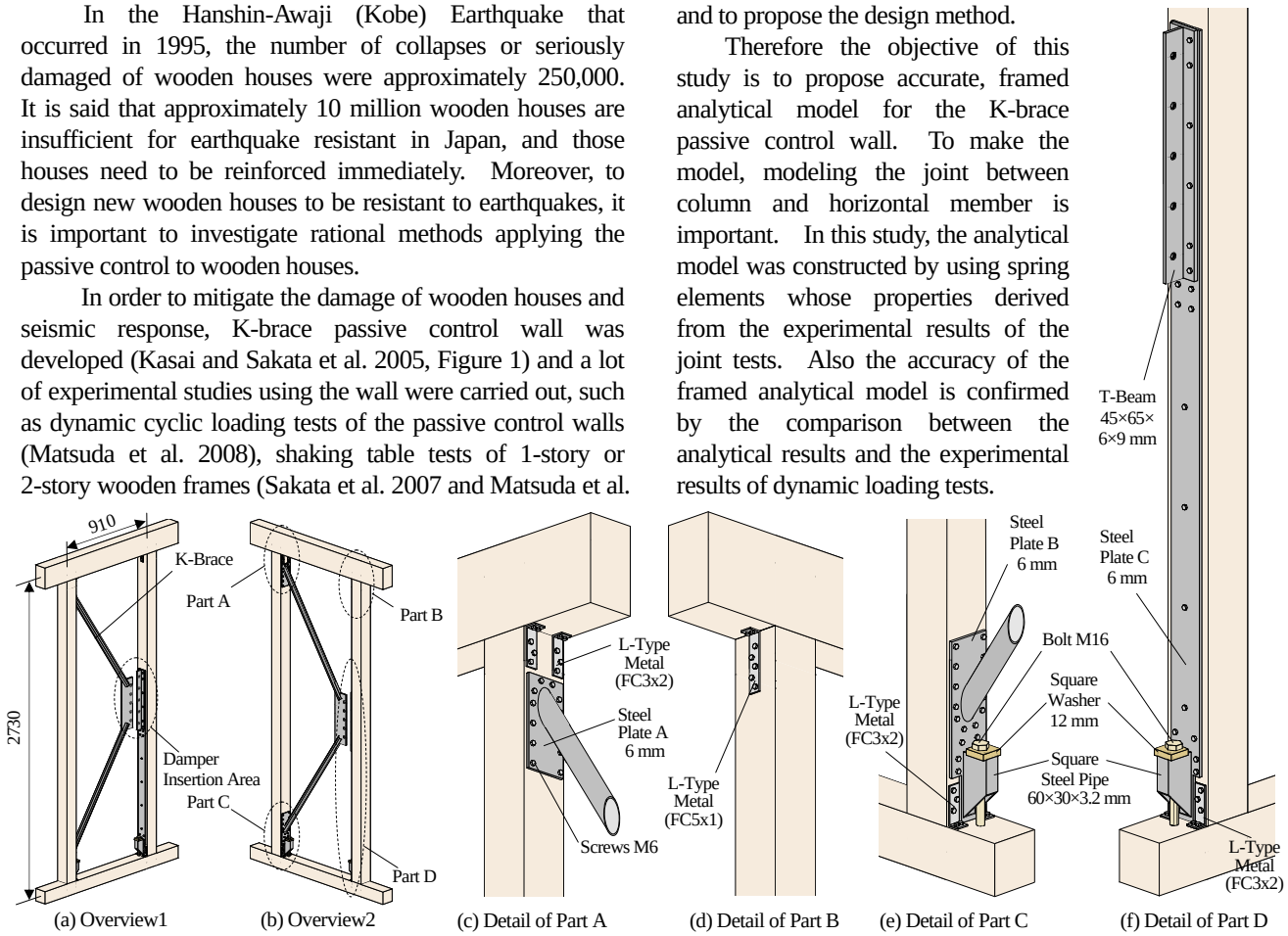

Figure 1 Detail of K-Brace Passive Control Wall

2. OUTLINE OF PASSIVE CONTROL WALL

The feature of K-brace passive control wall is shown below (Figure 1). When the wall deforms by horizontal force, there is vertical deformation between the brace and the steel plate and the damper is inserted in the place. The wall is classified in to a series of so-called shear link type. In order to reduce the effect of the column's bending, the edge of the brace is fixed near the joint of the column and horizontal member. There are many advantages because the contents of the wall are able to fit in inside of frames. For example it is possible to fix without an attachment of other walls. K-brace is screwed on wooden frames by a lot of screws because of high factor of safety.

A stub tenon, L-type metal and bolt (hold-down metal) are allocated in the joint of the column and horizontal member. The L-type metal includes "FC5" and "FC3" which indicate the number of screws on the column. "x1" and "x2" indicate the number of the metals. The square steel pipe is fillet-welded to steel plate B and C (Figure 1(e), (f)). Energy absorption capacity is increased as much as possible by allocating the bolt closer to the column, and integrating the steel plate C into the hold-down metal.

3. TESTS OF JOINT

3.1 Specimens

The specimens are basically picked out from the joints of the K-brace passive control wall, in addition HD (general hold-down metal: Figure 2), they are listed in Table 1. FC5x2 is compared with FC5x1 and FC3x2, HD is compared with 1K-D and 1K-V. All specimens have also stub tenon (30mm×85mm×52mm).

3.2 Setup and Measurement Method

As shown Figure 3, the horizontal member is fixed on the steel beam by two anchor bolts, and the column is pin-connected with the actuator. In the case of 1K-D and 1K-V, the locations of the anchor bolts are considered for the wall tests.

The relative displacement between the column and the horizontal member (u), and the slippage of the column and metal (u_{slip}) are measured. In the case of having a bolt, the axial force of the bolt (N_B) is measured, and initial axial force is 10 ± 0.5kN. In the case of 1K-D and 1K-V, the lift of horizontal member (u_{lift}) is measured.

3.3 Load Scheme

The number of each specimen consists of one monotonic loading test and three cyclic loading tests. All tests are static loading. The scheme of cyclic loading depends on u_y which is calculated from the monotonic loading test. The amplitudes of each step are 1/10, 1/4, 1/2, 1, 2, 4, 6, 8, 12 of u_y in sequence and 3 times each step. As for 1K-D, 1K-V, the tests are recessed when the axial force of the bolt reaches 55kN.

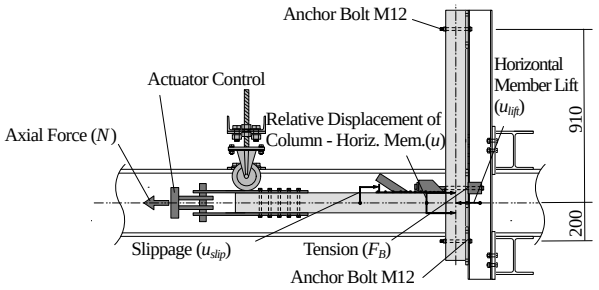

(a) 1K-D

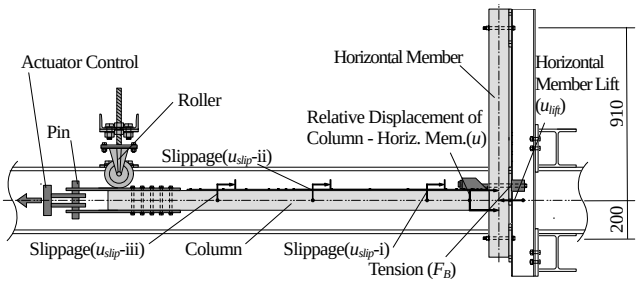

(b) 1K-V

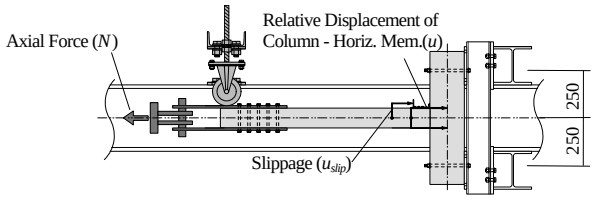

(c) FC3x2, FC5x1, FC5x2

Figure 3 Setup and Measurement Method

Table 1 Specimens

Name	1K-D	1K-V	FC5x1	FC3x2	FC5x2	HD
Specimen	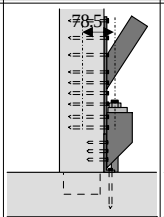	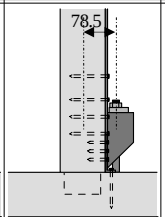	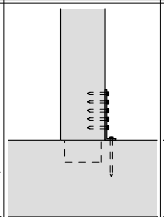	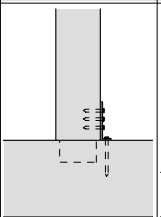	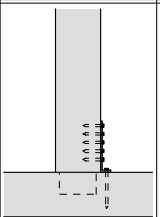	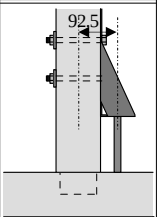
Horiz. Mem.	105×105×1310	105×105×1310	180×105×700	180×105×700	105×105×700	105×105×700
Column	105×105×1100	105×105×2000	105×105×1100	105×105×1100	105×105×1100	105×105×1100
L-Type Metal	3×2	3×2	5×1	3×2	5×2	-
Bolt	M16	M16	-	-	-	M16

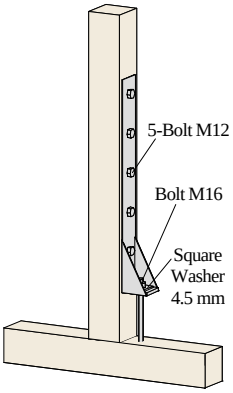

Figure 2 HD

3.4 Tests Results

Figure 4 illustrates relationships of axial force and displacement, Figure 5 illustrates comparison of average envelope curve. Plus direction means tension and minus direction means compression. In order to design the effective passive control wall, it is important to control the behavior of the joint. Therefore 1K-D and 1K-V are more appropriate for passive control wall than HD, because their stiffness against axial force is higher than HD.

4. FRAME MODEL OF PASSIVE CONTROL WALL

4.1 Outline of Frame Model

Figure 6 illustrates outline of frame model. Basically linear beam elements which have same condition to the test, are arranged in the center of the members. Each beam elements are connected by the joint elements which consist of three springs: axial spring, shear spring and rotation spring (Figure 7). However the area between the edge of the beam and the surface of the column assume rigid and the steel pipe brace set for truss elements.

Viscoelastic element which is proposed by Kasai et al. (2001, 2002), is arranged at between the intersection of the brace and the steel plate. There are two types of joint element: FC3x2, FC5x1 (Figure 1). Detail of setting the each spring is described from 4.3.1 to 4.3.3. The two nodes which are framed in by break line at Figure 6, are set so that

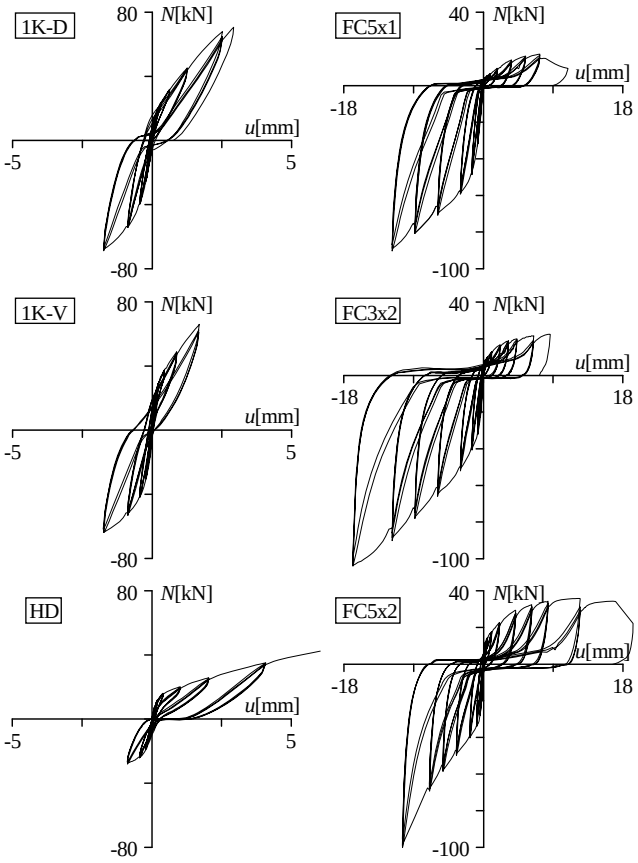

Figure 4 Relationships of Axial Force and Displacement

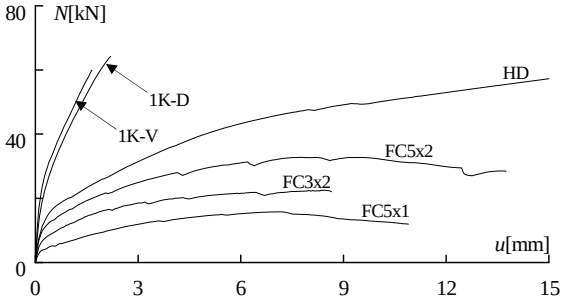

Figure 5 Comparison of Average Envelope Curve (Relationships of Axial Force and displacement)

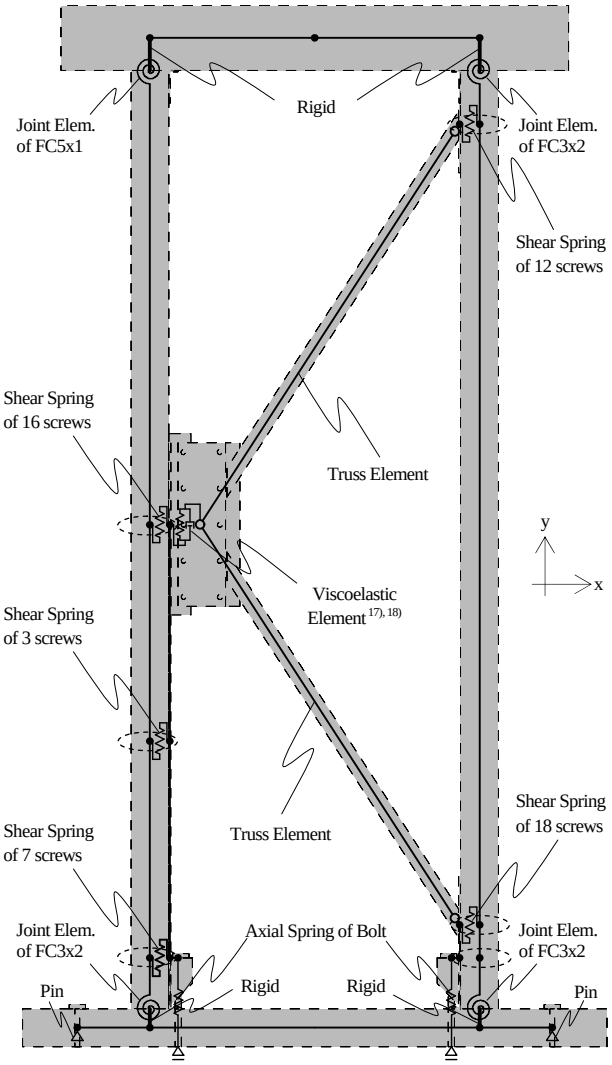

Figure 6 Outline of Frame Model

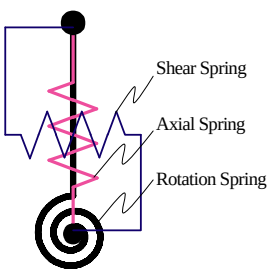

Figure 7 Joint Element

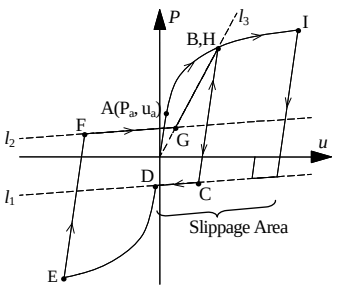

Figure 8 Hysteresis Rule

the two nodes behave together about horizontal displacement and rotation, due to assume only shear slippage between the column and steel plate. The shear springs between the nodes are set depending on shear performance of per screw which is set from the test of joint, because the steel plate is screwed on column by a number of screws (4.3.4). The axial springs of bolt are set from the test of joint (4.3.5).

4.2 Hysteretic Rules of Springs

Figure 8 illustrates hysteresis rule. After arriving at the elastic limit (Figure 8 A), force increases gradually, and the envelope curve is calculated by Equation (1).

$$\Delta P_x = \frac{\left(k_i - k_p\right)\Delta u_x}{\left(1.0 + \left(k_i \Delta u_x / M_0\right)^n\right)^{1/n}} + k_p \Delta u_x \qquad (1)$$

Where ΔP_x and $\Delta \upsilon_x$ are increment from P_a and u_a. k_i and k_p are initial and second stiffness. n and M_0 are coefficient to decide the shape of the curve.

This hysteretic rule is applied to the four springs: axial, rotation and shear springs of the joint, and shear spring of the screw. In slippage area, force is set 0 to make the models into simple.

4.3 Envelope Curves of Springs

[Axial springs of the joint]

Figure 9 and Figure 10 illustrate the established curve of axial spring of the joints. The established curve is fitted to the average of four envelope curves which are obtained by chapter 3. In the case of negative direction, the specimen whose maximum displacement is the smallest of all curve, is regarded when the average curve is obtained.

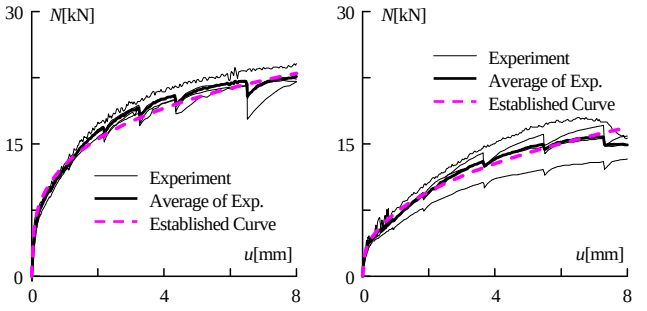

(a) FC3x2 (b) FC5x1

Figure 9 Established Curves of Axial Spring of Joints (Pos. Direc.)

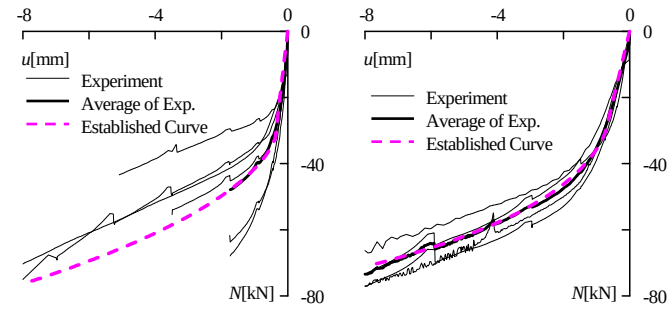

(a) D = 105mm (b) D = 180mm

Figure 10 Established Curves of Axial Spring of Joints (Neg. Direc.)

[Rotation springs of the joint]

As for FC5x2, the envelope curves of rotation spring are obtained by using a past data (Kasai et al. 2004). The established curves of FC3x2 and FC5x1 are fitted to 0.75 times and 0.5 times of FC5x2. Because FC3x2 and FC5x1 have 0.75 and 0.5 times smaller stiffness than FC5x2 in Chapter 3. Figure 11 illustrates the established curve of rotation spring of the joints.

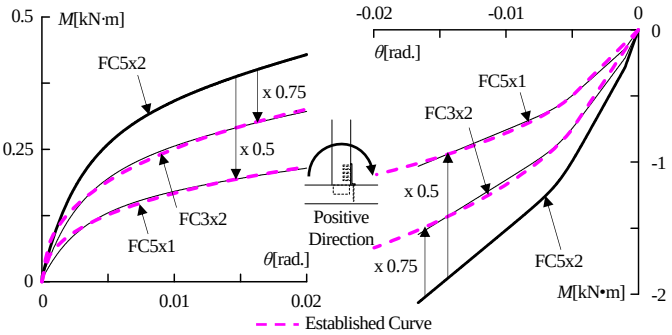

(a) Positive Direction (b) Negative Direction

Figure 11 Established Curves of Rotation Spring of Joints

[Shear springs of the joint]

As for FC5x2 and stub tenon, the envelope curves of shear spring are obtained by using a past data (Kasai et al. 2004). The established curves of FC5x1 are fitted to the average curve of FC5x2 and stub tenon. The established curves of FC3x2 are fitted to the curve of FC5x2. Because the screws which are arranged at the edge part, hardly have effect against shear force of the joint. Figure 12 illustrates the established curve of shear spring of the joints.

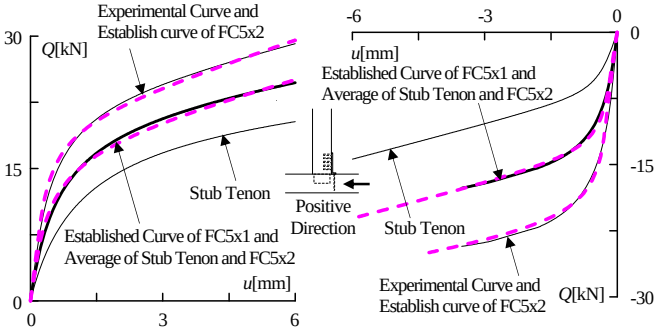

(a) Positive Direction (b) Negative Direction

Figure 12 Established Curves of Shear Spring of Joints

[Shear springs per screw]

It is assumed that behavior per screw is same, although the number of screw varies according to each joint. Figure 13 illustrates the established curve of a screw. The shear force per screw is calculated by dividing axial force of the bolt by 18. The slippage is obtained by u_{slip} (Figure 3). The established curve is fitted to the average of four envelope curves which are obtained by chapter 3 (1K-D).

[Axial springs of bolt]

Figure 14 illustrates the established curve of axial spring of the bolt. The relationships (Figure 14(a)) are obtained by the tests of chapter 3 (1K-D and 1K-V). u_B is calculated by Equation (2), regarding the lift of the horizontal member and the slippage of the metal.

$$u_B = u + u_{lift} - u_{slip} \qquad (2)$$

In the case of experimental curves, the curves start from N_B = 10kN because of the initial tension 10kN of the bolt. However it is assumed that the influence of the initial tension is small, and the initial tension is left out of consideration. Therefore u_B is moved by 0.8mm regarding the displacement of initial tension 10kN. The established curve is fitted to the enveloped curve which was moved by 0.8mm like Figure 14 (b). Figure 15 illustrates hysteresis rule of bolt.

5. FRAME ANALISIS RESULTS

As for hysteresis of 1P and 3P passive control wall, Figure 16 and 17 illustrate comparison of experimental results (Matsuda et al. 2008) and analytical results. Where P means 910mm length and 3P framed model has two K-brace passive control walls at both ends symmetrically. Each left graphs indicate relationships between story shear force and story drift (System). And each right graphs indicate relationships between damper force and damper displacement. Analytical results are obtained by liberating enforced deformation to the center of the beam and the enforced deformation is same to test (Matsuda et al. 2008). In both 1P and 3P, analytical results correspond to experimental results with high accuracy.

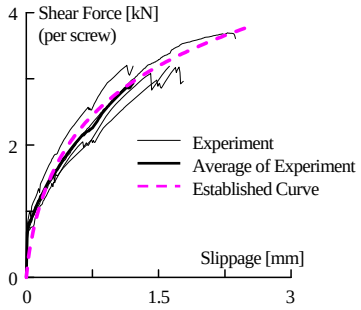

Figure 13 Established Curve of Screw

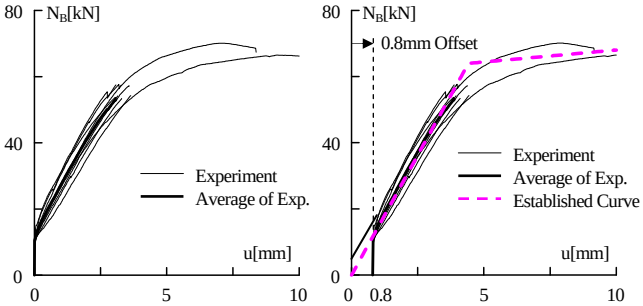

Figure 14 Established Curves of Axial Spring of Bolt

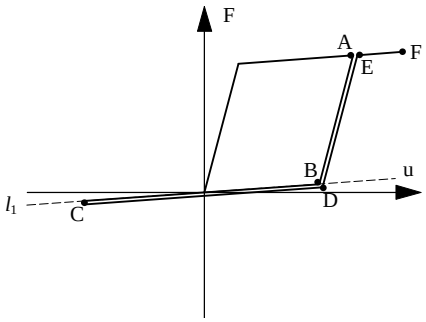

Figure 15 Hysteresis Rule of Bolt

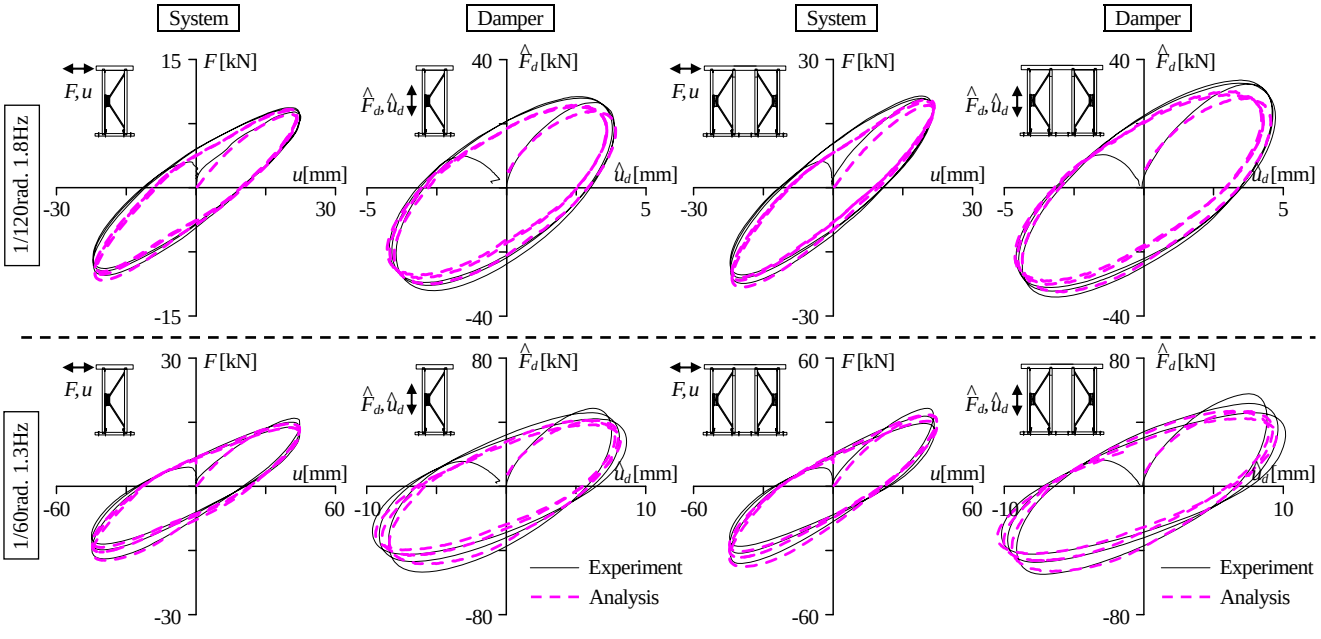

Figure 16 Comparison of 1P Passive Control Wall

Figure 17 Comparison of 3P Passive Control Wall

In the case of 3P passive control wall having viscoelastic damper, the shear force per wall increase because the beam rotation is restrained (Matsuda et al. 2008). Figure 18 illustrates ratio between 1P and 3P, and figure 19 illustrates variation of beam rotation. By these two figures, experimental results are duplicated by analysis including the deformation mode and the effect of continuous beam.

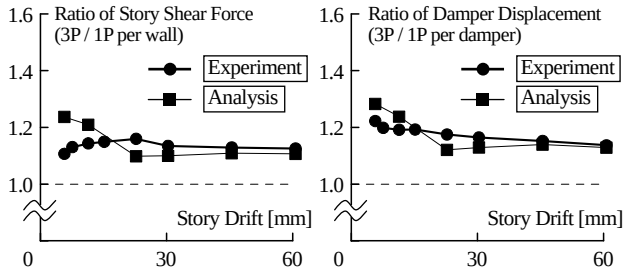

(a) Story Shear Force (Per Passive Control Wall)

(b) Damper Displacement

Figure 18 Ratio Between 1P and 3P

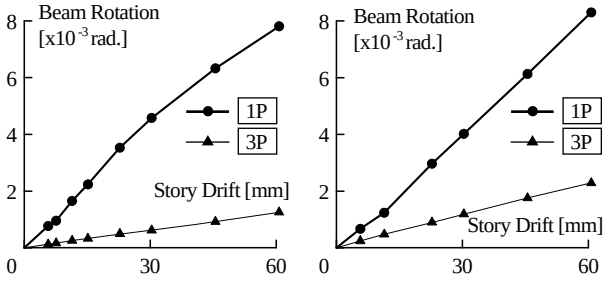

(a) Experiment [9]

(b) Analysis

Figure 19 Variation of Beam Rotation

6. CONCLUSIONS

Tests of joint, whose specimens consist of the joint of K-brace passive control wall, are carried out and the mechanical behavior is figured out. The framed analytical method of the K-brace passive control wall is proposed using the test results. Moreover, the analytical results and the experimental results by dynamic loading tests (Matsuda et al. 2008) are compared. Major finding are

- 1K-D and 1K-V (joints of K-brace passive control wall) are more appropriate for passive control wall than HD (general hold-down metal), because their stiffness against axial force is higher than HD.
- The analytical results which are obtained from frame model analysis, correspond to experimental results by dynamic loading tests with high accuracy. The frame model focuses on the joints, and the joints consist of three springs: axial spring, shear spring and rotation spring. The hysteresis rule of the springs is considered for slippage.
- The analytical method is able to duplicate experimental results including the deformation mode and the effect of continuous beam.

By using this framed analytical model, whole behavior of the frame is able to be estimated without whole frame test if there are relationships between force and displacement as for only the joint. Because the framed analytical model reflects the detail elements which the frame consists of, such as metals, screws, bolts and so on. Therefore this analytical method is effective for improving the wall and developing new walls.

Moreover, this frame model is useful against larger frame than 3P, because it is possible to expand the frame model from 1P to 3P with high accuracy. However in the case of 2-story frame analysis, it is necessary to study more because this study is confined about 1-story frame.

References:

Kasai, K., Sakata, H., Wada, A. and Miyashita, T. (2005): "Dynamic behavior of a wood frame with shear link passive control mechanism involving k-brace", Journal of Structural and Construction Engineering, No.598, 2005.12, pp.51-60 (In Japanese)

Matsuda, K., Sakata, H., Kasai, K. and Ooki, Y. (2008): "Experimental study on dynamic response of wooden frames with passive control", Journal of Structural Engineering, Vol.54B, 2008.3, pp.149-156 (In Japanese)

Sakata, H., Kasai, K., Wada, A., Midorikawa, M., Ooki, Y., Nakagawa, T. and Matsuda, K. (2007): "Shaking table tests of wood frames with velocity-dependent dampers", Journal of Structural and Construction Engineering, No.615, 2007.5, pp.161-168 (In Japanese)

Matsuda, K. and Kasai, K. and Sakata, H. and Ooki, Y. and Wada, A. (2007): "Shaking table tests of two-story frames with passive control system", Proceedings of 4th International Conference on Urban Earthquake Engineering, Center on Urban Earthquake Engineering, 2007.3, pp.369-374, Yokohama, JAPAN

Kasai, K., Teramoto, M., Okuma, K and Tokoro, K. (2001): "Constitutive rule for viscoelastic materials considering temperature frequency, and strain sensitivities, part 1 Linear model with temperature and frequency sensitivities", Journal of Structural and Construction Engineering, No.543, 2001.5, pp.77-86 (In Japanese)

Kasai, K. and Tokoro, K. (2002): "Constitutive rule for viscoelastic materials considering temperature frequency, and strain sensitivities, part 2 Nonlinear model based on temperature-rise, strain and strain-rate", Journal of Structural and Construction Engineering, No.561, 2002.11, pp.55-63 (In Japanese)

Kasai, K., Wada, A., Sakata, H., Ooki, Y. and Miyashita, T. (2004): "Passive control for mitigating seismic damage to wood houses, part 1 Behavior and design of joints, dampers, and system", Passive control symposium 2004, 2004.11, pp.169-184 (In Japanese)

Sixth International Conference on Urban Earthquake Engineering
March 3-4, 2009, Tokyo Institute of Technology, Tokyo, Japan

PRACTICAL MODELING OF REINFORCED-CONCRETE BEAM-COLUMN JOINTS

Anna Birely[1)], Laura Lowes[2)], and Dawn Lehman[3)]

1)Graduate Student Researcher, Dept. of Civil & Environmental Engineering, University of Washington, Seattle, WA, USA
2) Associate Professor, Dept. of Civil & Environmental Engineering, University of Washington, Seattle, WA, USA
3) Assistant Professor, Dept. of Civil & Environmental Engineering, University of Washington, Seattle, WA, USA
birely@u.washington.edu, lowes@u.washington.edu, delehman@u.washington.edu

Abstract: Behavior of beam-column joints can significantly impact seismic performance of reinforced concrete moment-frame structures. Models capable of predicting joint performance are needed in the design and evaluation of such structures. One method of modeling joints, proposed in the ASCE/SEI Standard 41-06, is to use rigid offsets at the ends of beam and column elements. The adequacy of this model is evaluated and modifications are proposed. To account for post-yield behavior and loss of lateral load carrying capacity, a simple nonlinear model, easily implemented in commercial software such as SAP 2000, is proposed. Lumped-plasticity beam elements are modified to account for joint nonlinearity, and rotational limits are introduced to capture strength loss. The resulting model successfully indicates brittle and ductile joint performance. All models are evaluated using a dataset comprising of 45 joint sub-assemblage tests.

1. INTRODUCTION

Beam-column joints in reinforced concrete moment frames can contribute significantly to frame flexibility and strength loss during an earthquake. Thus, practical models are required to enable engineers to simulate joint response and the consequent impact on overall frame response.

A wide range of models for RC beam-column joints are found in the literature. One of the simplest, found in the ASCE/SEI Standard 41-06 (2006), includes rigid offsets at the ends of beam and column elements that are varied in length to alter flexibility of the joint region. Other recent models include those presented by Anderson (2003) in which empirically calibrated nonlinear rotational springs connect beam and column centerline elements. Nonlinear models in which finite-volume joint macro-elements have been proposed (Shin and Lafave 2004, Mitra and Lowes 2007, Lowes et al., 2003) to account for flexibility due to slip of beam longitudinal reinforcement and shear action within the joint core. However, few of these models meet requirements for widespread use in practice: 1) compatibility with commonly employed commercial software packages, 2) support for rapid model building, 3) computational efficiency and robustness, and 4) acceptable accuracy over a range of design configurations.

In this study, two practical methods for modeling joint response are presented: a modification to the ASCE/SEI Standard 41-06 acceptable for elastic analysis and a nonlinear model in which beam plastic hinges are modified to account for joint flexibility. Models are validated using an extensive, wide-ranging experimental data set.

2. Experimental Data

For evaluation of existing models and calibration of proposed models, a data set of planar interior beam-column joint sub-assemblages was developed from that presented by Mitra and Lowes (2007). The data set consists only of subassemblages without i) slabs or transverse beams, ii) failure modes of beam shear, column flexure or column splice failure, and iii) smooth reinforcing bars. All specimens were subject to reversed cyclic lateral loading. Specifically, the specimens include in the data set are DWX1, DWX2, DWX3 (Durrani & Wight, 1985); OKAJ1, OKAJ2, OKAJ3, OKAJ4, OKAJ5 (Otani, Kobayashi, & Aoyama, 1984); MJ1, MJ2, MJ3, MJ5, MJ6, MJ12, MJ13 (Meinheit & Jirsa, 1984); PEER14, PEER22, PEER0850, PEER0995, PEER4150 (Alire, 2002 and Walker, 2001); PR1, PR2, PR3, PR4 (Park & Ruitong, 1988); NKOKJ1, NKOKJ3, NKOKJ4, NKOKJ5, NKOKJ6 (Noguchi & Kashawazaki, 1992); OSJ1, OSJ2, OSJ4, OSJ5, OSJ6, OSJ7, OSJ8, OSJ10, OSJ11 (Oka & Shiohara, 1992); KOAC1, KOAC3 (Kitayama, Otani, & Aoyama); PM1 (Park & Milburn, 1983); HC, A1 (Endoh, Kamura, Otani, & Aoyama, 1991); B11, B12 (Beckingsale, 1980).

For the current study, test specimens were evaluated to determine if the joint designs met the criteria specified for categorizing joint design and thus expected seismic performance in the ASCE/SEI Standard 41-06 and the ACI Building Code (2008). ACI compliance was determined on the basis of joints meeting the requirements for 1) concrete compressive strength and reinforcement yield strength, 2) the ratio of the sum of the column flexural strengths to the sum of the beam flexural strengths 3) presence of lap splices or termination of beam reinforcement in the joint 4) ratio of

column height to beam longitudinal reinforcement diameter 5) amount and spacing of joint transverse reinforcement and 6) maximum nominal shear strength of joint. Eleven joints were found to be ACI Compliant and 34 were ACI Non-Compliant, having failed to meet at least one of the above requirements.

3. Rigid Offset Models

Rigid offset models are easily incorporated in commercial structural analysis software and provide engineers a tool for accounting for joint flexibility within a linear elastic model of a structure. Centerline elements are assigned flexural, shear and torsional stiffness to accurately represent beams and columns. To account for the joint volume at the beam column connection, rigid offsets are introduced at the end of the elements, essentially defining the joint region as rigid. By adjusting the offset length, the joint can be made more or less flexible. FEMA 356 (2000) recommends offset lengths such that the full joint region is modeled as rigid (Figure 1a). The ASCE/SEI Standard 41-06 recommends lengths of the beam and column rigid offsets based on the relative flexural strength of these elements. For significantly strong columns relative to beam strength, rigid offsets are only used in the column, as shown in Figure 1b. If beams are significantly stronger than the columns, offsets are used in the beams, as shown in Figure 1c. When beam and column strength are relatively the same, beams and columns have rigid offsets equal to half the length defining the volume of the joint, as shown in Figure 1d.

To improve accuracy of the rigid offset method for accounting for joints, this study proposed a model in which offsets were included in both the beams and columns, with the lengths defined as a percentage, β, of the joint dimensions (see Figure 1e). This value was determined for the full data set as well as for subsets of the data based upon compliance with the ACI Code. Two approaches were used. The first found β_{opt} by minimizing the error measure:

$$\sum \varepsilon^2 = \sum_{i=1}^{N} \left(\frac{\Delta^{exp\ i} - \Delta^{sim\ i}}{\Delta^{exp\ i}} \right)^2 \qquad (1)$$

where Δ^{exp} and Δ^{sim} are the measured and simulated displacements of the specimen at the computed yield strength of the beam. Next, the offset length minimizing the normalized displacement error at first yield for each joint was found and averaged, excluding those joints with a physically unrealistic optimal length, to produce β_{avg}. Results are shown in Table 1.

Table 1 also presents an evaluation of the ability of the existing (FEMA 356 and ASCE 41) and proposed (β_{opt} and β_{avg}) models to predict the story drift under an applied column shear corresponding to theoretical first yield of the beams. Review of the error measures indicates that the FEMA 356 recommendations simulate a joint response

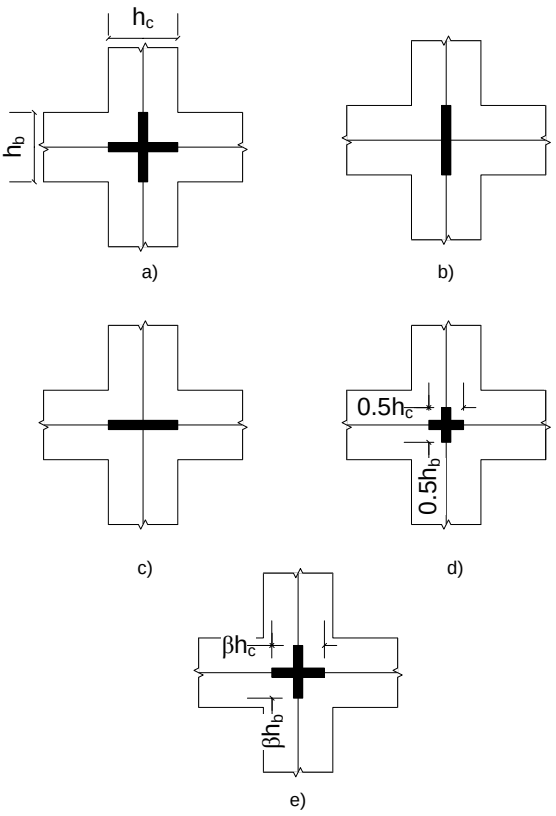

Figure 1 Offset configuration recommendations of FEMA 356 (a), ASCE 41 (b-d), and proposed offset length (e)

significantly stiffer than the real systems. The ASCE 41 model is more flexible than the real system. The proposed models offer an improvement, although minimal, in the error prediction at first yield.

4. Nonlinear Model

Rigid offset models fail to capture changes in joint stiffness associated with beam yielding and strength loss due to joint damage. To facilitate nonlinear modeling of joint response using commercial software, a nonlinear joint model is proposed that can be implemented by modifying the moment-rotation history for a plastic-hinge in the lumped-plasticity elements typically used in nonlinear frame analysis.

4.1 Model Definition

Models proposed by previous researchers (Anderson, 2003) using nonlinear moment-rotation springs to represent joint flexibility place the spring at the beam-column intersection. In this study, this concept is modified by moving the joint moment-rotation representation of the joint to plastic hinges located in the beams and defining the joint region as rigid using rigid offsets.

To define a joint using a moment-rotation relationship, geometry is used to relate the joint shear stress (τ) and shear strain (γ) to moments and rotations, respectively. The moment-rotation stiffness, k, of the joint spring can be

Table 1 Evaluation of Existing and Proposed Rigid Offset Models

Data Set	Effective Stiffness Model	Rigid Offset Model	β	$\Sigma\varepsilon^2$		ε_{avg}	
				$\beta \neq 0$	All β	$\beta \neq 0$	All β
All	FEMA 356	FEMA 356	-	7.46	15.97	0.53	0.59
	ASCE 41	ASCE 41	-	0.56	3.19	0.04	0.17
		β_{opt}	**0.44**	0.54	2.97	0.02	0.15
		β_{avg}	**0.38**	0.56	2.80	-0.01	0.13
ACI Compliant	FEMA 356	FEMA 356	-	1.26	3.90	0.5	0.59
	ASCE 41	ASCE 41	-	0.13	0.76	-0.04	0.15
		β_{opt}	**0.62**	0.11	0.89	0.02	0.2
		β_{avg}	**0.56**	0.11	0.81	-0.01	0.18
ACI Non-Compliant	FEMA 356	FEMA 356	-	6.20	12.07	0.54	0.59
	ASCE 41	ASCE 41	-	0.43	2.42	0.06	0.18
		β_{opt}	**0.39**	0.39	2.13	0.01	0.14
		β_{avg}	**0.34**	0.40	2.04	-0.01	0.12

written as:

$$k = \frac{M}{\theta} = \frac{\chi_\tau \tau}{\chi_{gamma}\gamma} \tag{2}$$

where geometry determines the modifiers:

$$\chi_\tau = \frac{A_j L_c}{\frac{L_c}{jd}\left(1-\frac{h_c}{L_b}\right)-1} \tag{3}$$

$$\chi_\gamma = \left(1-\frac{h_c}{L_b}-\frac{h_b}{L_c}\right) \tag{4}$$

and h_b, L_b, h_c, and L_c are the height and length of the beams and columns, A_j is the cross-sectional area of the joint, and jd is the lever arm of the beam moment. Introducing the concrete shear modulus

$$G = \frac{\tau}{\gamma} \tag{5}$$

The joint stiffness in the proposed model is defined as

$$k_i = \alpha_i \frac{\chi_\tau}{\chi_\gamma} G \tag{6}$$

for each segment, i, of spring. A bilinear spring is considered, thus requiring calibration of stiffnes parameters α_1 and α_2.

Beam moment-cruvature analyses (performed in Opend Sees (McKenna, et. al., 2007)) are used to define moment-rotation springs by assuming an assumed plastic hinge length of one-half the beam depth. The beam and joint springs are placed in series, producing a modified plastic hinge model for the beams that accounts for joint flexibility. Rotational limits are placed on the beam and joint springs to account for loss of lateral load carrying capacity.

4.2 Model Calibration

4.2.1 Initial Stiffness

The initial joint stiffness was calibrated by optimizing the secant stiffness of the plastic hinge at the column shear corresponding to initial yielding of the beams, where the joint initial stiffness is defined as

$$k_1 = \alpha_1 \frac{\chi_\nu}{\chi_\gamma} G \tag{7}$$

and the calibrated stiffness parameter is:

$$\alpha_1 = 0.0415 \tag{8}$$

4.2.2 Post-Yield Stiffness

The post-yield stiffness of the joint spring, defined as

$$k_2 = \alpha_2 \frac{\chi_\nu}{\chi_\gamma} G \tag{9}$$

was established (using data for joints in which both beams yielded) to accurately simulate post-yield response and to enable calibration of rotation limits for the joint shear spring and beam spring. The resulting stiffness parameter is:

$$\alpha_2 = 0.0111 \tag{10}$$

Table 2 Error Evaluation of Modified Plastic Hinge Model

Data Sub-sets	Error[1]	1st Yield	2nd Yield	Peak		10% Loss	
		Disp	Disp	Disp	Load	Disp	Load
All[2]	Average	5.59	13.89	-27.01	5.89	27.05	6.98
	Stand. Dev.	22.75	24.74	77.08	9.55	36.07	11.64
Ductile	Average	7.09	17.46	-60.88	7.48	8.74	1.34
	Stand. Dev.	25.06	24.76	91.17	7.59	37.15	9.64
Limited Ductility	Average	-4.45	-1.18	-3.29	13.32	46.73	11.09
	Stand. Dev.	22.54	22.29	59.31	9.15	48.95	12.96
Brittle	Average	-	-	1.40	1.24	-	-
	Stand. Dev.	-	-	49.11	9.67	-	-

[1]All errors are given as percents

[2]For 1st and 2nd yield, excludes joints not reaching yield load

4.2.1 Rotational Limits

When calibrating rotational limits, a methods for classifying and predicting the failure mode of the joints was desired, as joints failing in a brittle manner were expected to require different limits than those failing in a ductile manner. Classification of the joints was done using the experimental displacement ductility, μ_Δ, at which a 10% loss in the maximum strength occurred. Displacement ductility was defined such that the unity value occurred at the column shear associated with theoretical beam yielding. Joints were identified as "Brittle" if they did not reach this column shear. For those joints reaching or exceeding this load, those with a displacement ductility of at least 4.0 were identified as "Ductile". All other joints were identified as "Limited Ductility". Eighteen joints were identified as "Brittle", twenty as "Ductile", and seven as "Limited Ductility".

The rotational limit for beam response was calibrated by minimizing the average drift error at strength loss of ductile joints, with θ_{bm}^{fail} defined as a function of the beam curvature and plastic hinge length.

$$\theta_{bm}^{fail} = l_p \phi_{bm}^{fail} \tag{11}$$

where l_p is the plastic hinge length and

$$\phi_{bm}^{fail} = 0.0056 \tag{12}$$

Joint rotational limits, calibrated by minimizing the average drift error of brittle joints at strength loss, are defined as a function of joint shear strains and system geometry.

$$\theta_{joint}^{fail} = \chi_\gamma \gamma_{joint}^{fail} \tag{13}$$

$$\gamma_{joint}^{fail} = 0.0071 \tag{14}$$

4.3 Model Validation

To evaluate the proposed nonlinear model, pushover analyses were performed on models of the joint sub-assemblages. The analytical load-drift envelopes were compared with the experimental envelopes using the error measure in (15) at key points in the load-drift histories: 1st yield, 2nd yield, peak strength and 10% loss of lateral load carrying capacity. The average and standard deviations are provided for the load and drift at these points in Table 2. At the column shear corresponding to first yield, the displacement is predicted very well, indicating the ability of the proposed model to adequately capture the initial stiffness of the assemblages. The behavior following this point is also well predicted. Brittle joints have a low error for displacement and load at the peak. Although there is significant scatter in this error for the displacement, the peak load has a low standard deviation, indicating the accuracy of the model in predicting the strength capacity of the brittle joints. For ductile and limited ductility joints, the error in the displacement prediction of the peak load provides limited information on model accuracy, as the moment capacity of the beam, determined through moment-curvature analysis, controls this aspect of the model.

$$\varepsilon_\Delta = \frac{\Delta_{experimental} - \Delta_{analytical}}{\Delta_{experimental}} \tag{15}$$

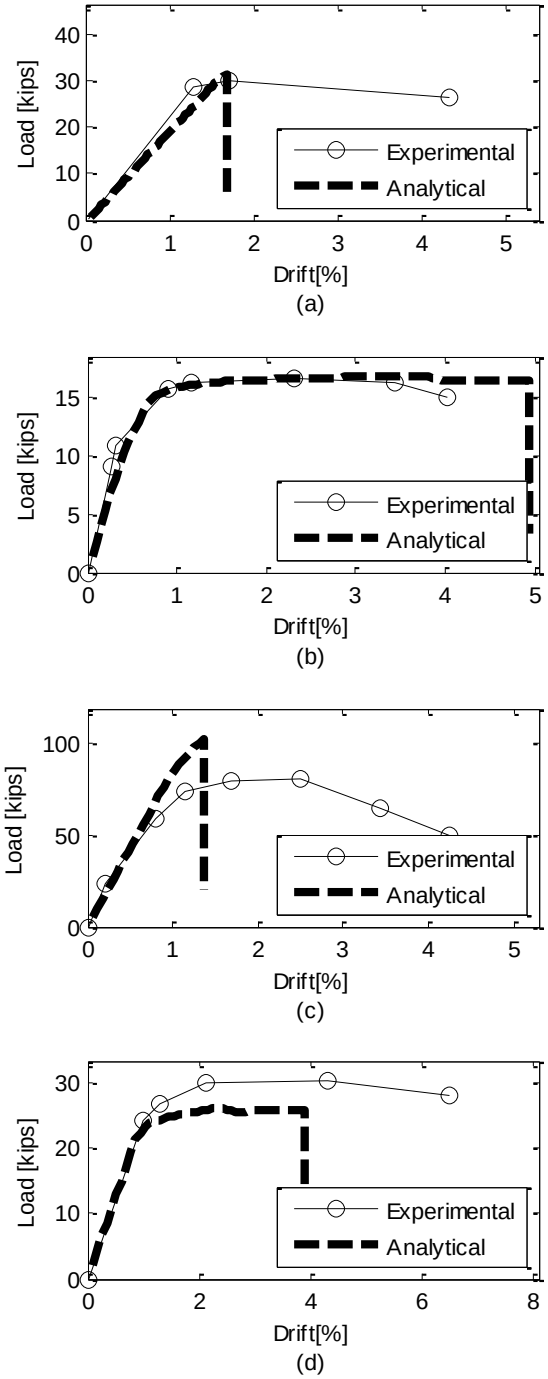

Figure 2 Envelopes for (a) best brittle prediction, MJ3, (b) best ductile prediction, PR3, (c) worst brittle prediction, PEER22, AND (d) worst ductile prediction, HC

For all "Ductile" joints, strength loss was simulated to occur when the beam rotation limit was reached; For all "Brittle" joints, strength loss was simulated to occur when the joint spring rotation limit was reached. Thus, the model accurately predicts the failure mechanism for these joints. Of the seven "Limited Ductility" joints, six exhibited strength loss when the joint rotation limit was reached, and thus exhibited brittle failure in the simulation. Only specimen PEER14 reached the beam rotational limit prior to reaching the joint rotation limit, and thus exhibited ductile response in the simulation.

Figures 2a and 2b show the best simulation of experimental response for brittle and ductile joints respectively. The worst simulations of brittle and ductile joint behavior are shown in Figures 2c and 2d, respectively.

3. CONCLUSIONS

Using a data set of 45 planar interior reinforced-concrete beam-column joint sub-assemblages, the rigid offset modeling recommendations provided by ASCE/SEI Standard 41-06 were evaluated and found to provide for a more accurate simulation of joint behavior at first beam yield than the recommendations put forth by the FEMA 356 Pre-Standard. Modifications were proposed to these recommended offset lengths and were found to provide a slight improvement in prediction of yield displacement.

The data set joint was then used to calibrate a proposed nonlinear model to account for joint nonlinearity and loss of lateral strength carrying capacity. Lumped-plasticity beam elements were modified by introducing a bilinear rotational spring element. Rotational limits on the joint spring and the traditional beam moment-curvature plastic hinge account for strength loss and allow the model to accurately represent brittle and ductile modes of strength loss.

Acknowledgements:
Support of this work was provided primarily by the Earthquake Engineering Resarch Centers Program of the National Science Foundation, under award number EEC-9701568 through the Pacific Earthquake Engineering Research Center (PEER). Any opinions, findings, and conclusions or recommendations expressed in this material are those of the authors and do not necessarily reflect those of the National Science Foundation.

References:

ACI Committee 318 (2008), "Building code requirements for structural concrete (ACI 318-08) and Commentary(ACI 318R-08)", American Concrete Institute, Farmington Hills, Michigan

ACI-ASCE Joint Committee 352 (2005), "Recommendations for design of beam-column connections in monolithic reinforced concrete structures", American Concrete Institute, Farmington Hills, Michigan

Alire, D. (2002), "Seismic evaluation of existing unconfined reinforced concrete beam-column joint", M.S.C.E, Department of Civil Engineering, University of Washington.

Anderson, M. (2003), Analytical modeling of existing reinforced concrete beam-column joints, M.S.C.E, Department of Civil Engineering, University of Washington.

ASCE (2000), Pre-standard and Commentary for the Seismic Rehabilitation of Buildings (FEMA-356), American Society of Civil Engineers prepared for the Federal Emergency Management Agency, Reston, Virginia.

ASCE (2007), Seismic Rehabilitation of Existing Buildings (ASCE/SEI 41-06). American Society of Civil Engineers.

Berry, M., and Eberhard, M. (2003), Performance Models for Flexural Damage in Reinforced Concrete Columns. Pacific Earthquake Engineering Research Center, Berkeley, California.

Durrani, A.J., and Wight, J.K. (1982), Experimental and analytical study of beam to column connections subjected to reverse cyclic

loading. Technical Report, Department of Civil Engineering, University of Michigan.
Endoh, Y., Kamura, T., Otani, S., and Aoyama, H. (1991), "Behavior of RC beam-column connections using light-weight concrete. Transactions of Japan Concrete Institute Vol. 13, pp. 319-326.
Higashi, Y., and Ohwada, Y. (1969), "Failing behaviors of reinforced concrete beam-column connections subjected to lateral loads," Memoris of Faculty of Technology Tokyo Metropolitan University, Tokyo, Japan, Vol. 19, pp. 91-100.
Kitayama, K., Otani, S., and Aoyama, H. (1987), "Earthquake resistant design criteria for reinforced concrete interior beam-column joints," In Pacific Conference on Earthquake Engineering, Wairakei, New Zealand, pp. 315-326.
Kunnath, S.K. (1998), "Macromodel-Based Nonlinear Analysis of Reinforced Concrete Structures," Structural Engineering Worldwide, Elsevier Science, Ltd., Oxford, England, paper no. T101-5.
Lowes, L.N. and Altoontash, A. (2003), Modeling the response of reinforced concrete beam-column joints, Journal of Structural Engineering, ASCE Vol. 129, No. 12, pp. 1686-1697.
Lowes, L.N., Mitra, N., and Altoontash, A. (2004), A beam-column joint model for simulating the earthquake response of reinforced response of reinforced concrete frames, Pacific Earthquake Engineering Research Center, Berkeley, California.
MacGregor, J., and Wight, J., K., 1997, Reinforced concrete: mechanics and design, 3rd Edition, Prentice Hall, Upper Saddle River, New Jersey.
Mazzoni, S., McKenna, F., and Fenves, G. (2007), OpenSees Examples Manual Version 1.7.3, http://opensees.berkeley.edu/OpenSees/manuals/usermanual/index.html
Mazzoni, S., McKenna, F., and Fenves, G. (2007), OpenSees User Manual for OpenSees Version 1.7.3, http://opensees.berkeley.edu/OpenSees/manuals/usermanual/index.html
McKenna, F., Fenves, G.L., et al (2007), Open Systems for Earthquake Engineering Version 1.7.3, http://opensees.berkeley.edu
Meinheit, D.F., and Jirsa, J.O. (1977), The shear strength of reinforced concrete beam-column joints, Technical Report, University of Texas at Austin.
Mitra, N. (2007), An analytical study of reinforced concrete beam-column joint behavior under seismic loading, Dissertation, Department of Civil Engineering, University of Washington.
Mitra, N., and Lowes, L.N. (2007), "Evaluation, calibration, and verification of a reinforced concrete beam-column joint," Journal of Structural Engineering, Vol. 133, No. 1, pp. 105.
Noguchi, N., and Kashiwazaki, T. (1992), "Experimental studies on shear performances of RC interior column-beam joints," In Tenth World Conference on Earthquake Engineering, Madrid, Spain, pp. 3163-3168.
Oka, H., and Shiohara, H. (1992), "Tests on high-strength concrete interior beam-column joints sub-assemblages," In Tenth World Conference on Earthquake Engineering, Madrid, Spain, pp. 3211-3217.
Otani, S., Kobayashi, Y., and Aoyama, H. (1984), "Reinforced concrete interior beam-column joints under simulated earthquake loading," In US-New Zealand-Japan seminar on design of reinforced concrete beam-column joints, Monterey, California.
Park, R., and Ruitong, D. (1998), "A comparison of the behavior of reinfroced concrete beam column joints designed for ductility and limited ductility," Bulletin of the New-Zealand national society for Earthquake Engineering, Vol. 21, No. 4, pp. 255-278.
Walker, S. (2001), Seismic performance of existing reinforced concrete beam-column joints, M.S.C.E, Department of Civil Engineering, University of Washington.

Sixth International Conference on Urban Earthquake Engineering
March 3-4, 2009, Tokyo Institute of Technology, Tokyo, Japan

BRIDGE ABUTMENT LATERAL EARTH PRESSURE EXPERIMENTS

Patrick Wilson[1] and Ahmed Elgamal[2]

1) Graduate Student Researcher, Dept. of Structural Engineering, University of California San Diego, La Jolla, California, USA
2) Professor, Dept. of Structural Engineering, University of California San Diego, La Jolla, California, USA
prwilson@ucsd.edu, elgamal@ucsd.edu

Abstract: During strong earthquake excitation, a bridge deck may impact the abutments and mobilize resistance due to passive earth pressure. Including this abutment contribution in seismic bridge design will reduce the demand on the bridge piers and foundation. In consideration of such bridge abutment force-displacement resistance, static and shake table full scale abutment passive earth pressure tests are presented and discussed. Static pushover test results and numerical simulations are used to calibrate hyperbolic force-displacement backbone curves to represent the abutments in bridge analyses and simulations. Parameters for implementation of these curves are presented to account for a range of practical design assumptions. A cyclic loading abutment spring model is described in order to employ the calibrated hyperbolic backbone curves in dynamic numerical bridge simulations. Shake table excitation test results suggest that inertial forces in the backfill also affect the available passive resistance. On this basis, backfill resistance variation is presented for a 1 g lateral acceleration pulse.

1. INTRODUCTION

A series of collaborative tests and simulations has been underway to investigate the seismic response of reinforced concrete bridges, including soil-structure interaction. For that purpose, facilities of the George E. Brown, Jr. Network for Earthquake Engineering Simulation (NEES, http://nees.org) have been employed to perform shake table experiments. One-quarter scale bridge models are being tested at the University of Nevada at Reno (Saiidi 2004). In addition, investigation of the abutment contribution to the dynamic bridge response was conducted at the University of California in San Diego as discussed in this article.

In seismic design (AASHTO 2007, Caltrans 2004), an abutment system relies on the soil backfill to provide resistance to longitudinal bridge deck displacement. During strong shaking, if the deck impacts the abutment, a sacrificial portion (the backwall) can break off into the backfill. Resistance to further displacement of the deck and backwall is then provided by passive earth pressure within the densely compacted soil (Shamsabadi et al. 2007). This abutment resistance can decrease the demand placed on other seismic components such as the bridge columns and foundation (AASHTO 2007). As a result, an accurate representation of the abutment backfill resistance may lead to a more economic seismic bridge design.

To aid in this regard, experiments performed on an abutment backwall, full scale in height, are described in this paper. Experimental results and numerical simulations are employed to provide abutment spring models for a range of possible design considerations and assumptions. These models can be used to represent the abutment contribution to the longitudinal seismic bridge response in pushover type analyses or dynamic bridge simulations. Related recent research includes Cole and Rollins (2006), Shamsabadi et al. (2007) and Stewart et al. (2007).

2. FULL SCALE TESTS

In this study, static pushover experiments were performed initially to record the abutment-backfill longitudinal force-displacement capacity. Next, dynamic shake-table excitation experiments were conducted to investigate the influence of ground shaking on the mobilized passive earth resistance, and to provide a basis for calibration of the dynamic computational models. The experiments were performed inside a large steel soil container on an outdoor shaking table (Figure 1) at the Englekirk Structural Engineering Center (ESEC) in San Diego, California.

Figure 1: Soil container on shake table

2.1 Test Setup

Primary components of the experimental configuration (Wilson 2009) included a large laminar soil container (Figure 1), a model of a section along the width of an abutment (Figure 2), a loading mechanism (Figure 3) and a compacted sand backfill (Figure 4). A restraining system

(not shown) was applied to the laminar box to create a rigid container configuration for the abutment tests. The inside dimensions of the soil container were about 2.9, 6.7 and 2.5 meters in width, length and height, respectively. The model abutment consisted of a separate fixed seat box resting beneath a suspended backwall (Figure 2), which supported 1.7 meters of backfill. Hydraulic jacks reacted through load cells onto concrete-filled steel posts (Figure 3) to push the wall into the backfill while measuring the applied load.

Figure 2: Abutment backwall section suspended above seat box

Figure 3: Loading mechanism behind backwall

Well-graded sand with about 7 percent fines (cohesion of about 14 kN/m^2 was observed in direct shear tests, Wilson 2009) was compacted (Figure 4) for each test in compliance with Caltrans (1999) standard specifications for structural backfill. The unit weight of the dense sand backfill was approximately 20.6 kN per cubic meter. Dimensions of the backfill were about 2.9, 5.6 and 2.1 meters in width, length and height.

Figure 4: Backfilling and compaction inside soil container

As mentioned above, the testing program consisted of both static push-over and dynamic excitation tests. First, the hydraulic jacks (Figure 3) were used to push the backwall into the backfill during two different static pushover tests. In the testing configuration, the wall was free to move upwards. The force-displacement relationship was recorded up to and beyond the peak measured resistance. In additional experiments, dynamic excitations were imparted on the system by the shaking table while the hydraulic jacks (Figure 3) were locked in a fixed position. Changes in measured force and pressure were recorded throughout the shake-table excitations (Wilson 2009).

2.2 Static Pushover Tests

Applied force and horizontal displacement were recorded as the abutment backwall was pushed into the backfill in two separate tests. Results from the two static pushover tests were combined to create an average force-displacement relationship (per meter of width) for the abutment (Figure 5).

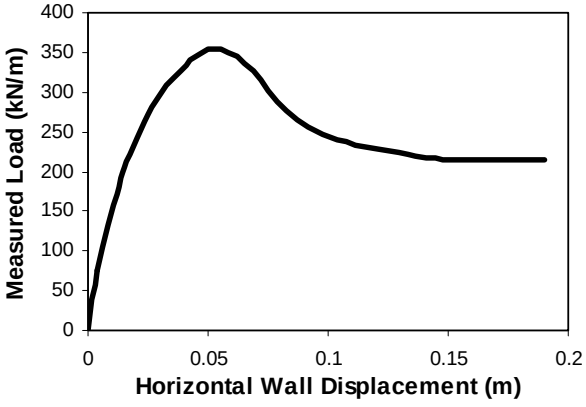

Figure 5: Average backbone load-displacement curve

In these tests, the measured load increased until it reached a peak and then decreased to a steady-state level (Figure 5). The wall was observed to move slightly upward as it was being displaced horizontally, resulting in low mobilization of friction between the wall and the backfill. This low mobilization of wall-soil friction

resulted in measurement of a lower-bound conservative force-displacement curve as discussed further in a later section.

While the recorded behavior was similar for the two tests, the peak measured load was about 15% lower in the second test compared to the first. This difference may be attributed to a more dried out backfill condition during the first test resulting from a longer time between model construction and testing (17 more days). The residual steady-state resistance was essentially the same for both tests. Measured peak loads were close to currently accepted peak passive earth pressure predictions (Wilson 2009).

The force-displacement relationship of Figure 5 (average of 2 tests) provides a representation of the abutment backfill resisting behavior. As mentioned earlier this curve was obtained for the 1.7 meter high test backfill (typical height of 5.5 feet according to Shamsabadi et al. 2007). In these tests, the plane-strain backfill soil friction angle was estimated at about 48 degrees (i.e., triaxial friction angle of about 40 degrees, Terzaghi et al. 1996). The mobilized wall-soil friction angle was on the order of 3 degrees (Wilson 2009).

2.3 Dynamic Excitation Tests

In the shake table experiments, earthquake-like motions were imparted in 1-D with the direction of shaking normal to the backwall face. These tests were conducted with the backwall approximately in its original (zero displacement or near at-rest) position and also with the wall displaced into the backfill (with a significant portion of passive earth resistance already mobilized). A modified acceleration time history (Figure 6) from the 1994 Northridge earthquake (Century City Station record) as well as a sine wave motion (not shown) were scaled to different peak ground accelerations (up to 1.2 g) and used as the input excitations.

The results shown in Figure 7 are from a shake table excitation test that was performed after the backwall was pushed to mobilize a portion of passive resistance in the backfill (about 260 kN per meter of width, Figure 7). Figure 7 shows the total force measured by the load cells (Figure 3) throughout the input motion of Figure 6. These experimental results clearly illustrate how the inertial forces imposed on the backfill and backwall during shaking cause the level of mobilized resistance to increase and decrease.

From Figures 6 and 7, peak acceleration of about 0.7 g during the earthquake record excitation resulted in an instant (just before 15 seconds, Figure 7) when the measured force was reduced by more than 50 kN/m from the initial static value of 260 kN/m. Additionally, at the end of shaking the static force was about 30 kN/m lower than the initial value (Figure 7). For subsequent tests with larger input accelerations, significantly greater reductions in the mobilized passive resistance were also observed (Wilson 2009). However, for tests with smaller input accelerations (up to about 0.5 g), only minor changes in the initial passive force were observed (Wilson 2009).

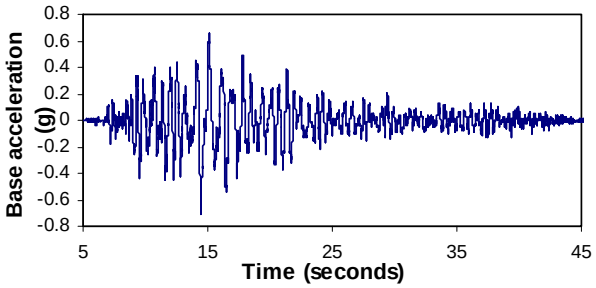

Figure 6: Recorded base acceleration during an earthquake input (Northridge 1994) test

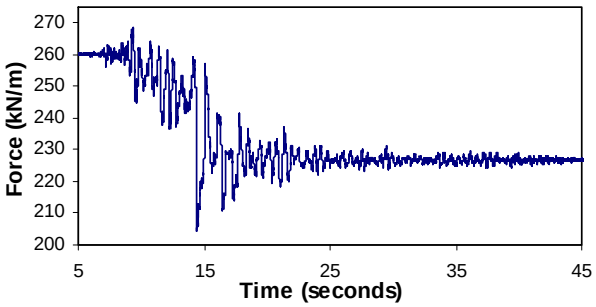

Figure 7: Load cell force-time history during the earthquake input test

The above inertial effects may suggest that the actual abutment passive resistance lies within a range of the static backbone curve (Figure 8). The upper and lower bound curves of Figure 8 were developed by imposing the measured changes in mobilized pressure for 1 g of input acceleration over the average backbone curve (for a near at-rest initial static resistance scenario). Such a variation in the available resistance may have a substantial impact on the dynamic bridge response.

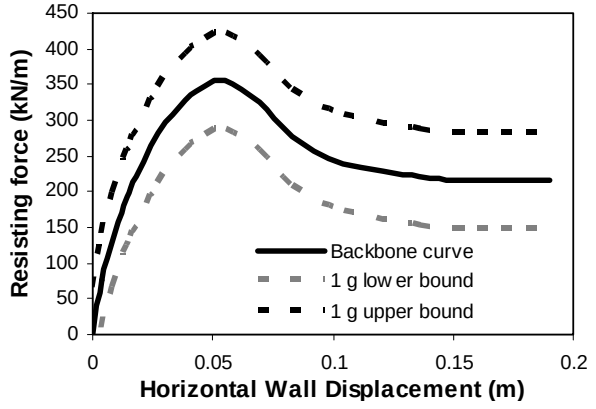

Figure 8: Envelope of possible abutment passive resistance range at a 1 g pulse of base acceleration

In order to investigate further, results from several conducted dynamic excitation experiments with input accelerations of up to 1.2 g are currently being analyzed using nonlinear finite element (FE) models. These models can later be implemented to represent the abutments with

soil backfills in full bridge simulations. However, until that analysis is completed, and consistent with current design practice (Caltrans 2004, AASHTO 2007, Shamsabadi et al. 2007), the abutment models presented in the sections below are based only on the static backfill force-displacement capacity.

3. HYPERBOLIC ABUTMENT STIFFNESS BACKBONE CURVES

Recent work by Shamsabadi et al. (2007) proposed a hyperbolic relationship for representing the nonlinear abutment stiffness in monotonic pushover analyses by:

$$F = \frac{F_{ult}(2Ky_{\max} - F_{ult})y}{F_{ult}y_{\max} + 2(Ky_{\max} - F_{ult})y} \qquad (1)$$

where F is the resisting force, y is the horizontal displacement, F_{ult} is the peak resisting force, K is the secant stiffness at $F_{ult}/2$ and y_{max} is the maximum horizontal displacement. Duncan and Mokwa (2001) also defined the following equivalent relationship:

$$F = \frac{y}{\frac{1}{K_{\max}} + R_f \frac{y}{F_{ult}}} \qquad (2)$$

where K_{max} is the initial tangent stiffness and R_f is the failure ratio (refer to Duncan and Mokwa 2001 for a description of the failure ratio).

The above hyperbolic curves have been shown to work well for representing measured force-displacement results from large scale passive earth pressure experiments up to the peak measured resistance (Duncan and Mokwa 2001, Cole and Rollins 2006, Shamsabadi et al. 2007). In this section, calibrated parameters which can be used with the hyperbolic formulae of Equations 1 and 2 are presented (Table 1). These parameters were determined based on the static pushover experimental results as well as from calibrated FE simulations as described below.

Table 1: Calibrated hyperbolic model parameters

Model	K (kN/m/m)	F_{ult} (kN/m)	y_{max} (m)	K_{max} (kN/m/m)	R_f
1	14500	355	0.055	21500	0.7
2	18000	215	0.2	32000	0.95
3	12500	485	0.07	22000	0.95
4	13000	550	0.075	18500	0.7
5	15000	330	0.2	30000	0.95

The model parameters of Table 1 were calibrated for the 1.7 meter tall wall, per meter of abutment width, for the five scenarios described below. To scale for width, K or K_{max} and F_{ult} should be multiplied by the abutment width in meters. These models assume that no resistance occurs until the expansion gap has closed completely (space between bridge and wall). Each model is limited to a displacement range of y_{max} beyond the expansion gap length. Resistance further than this level is apt to decrease for situations of a dense sand backfill such as the one employed herein (large strain shear strength reduction, Terzaghi et al. 1996).

Models 1 and 2 are based on the experimental results with the above mentioned soil shear strength properties (Figure 5). As mentioned previously, the testing configuration allowed the backwall to move upwards as it was pushed into the backfill. These models may be used as lower-bound conservative estimates for the abutment stiffness, when restriction of vertical wall movement is not guaranteed, or when the wall-soil friction between the abutment backwall and backfill is unknown.

The first model represents the average force-displacement relationship measured in the two static pushover tests up to the peak resistance. By limiting the displacement range, this model is able to benefit from the pre-softening backfill peak strength. This benefit of added capacity may be applicable, for instance, to laterally stiff bridges which do not exceed 8 cm of longitudinal bridge deck displacement in the design earthquake of interest.

The second model considers the possibility of abutment displacements that reach beyond the level of the peak resistance range measured in the experiments. This model conservatively relies only on the residual steady-state resistance measured in the experiments.

Models 3, 4 and 5 are based on FE simulation (Plaxis 2D plane-strain model) results. This FE model was carefully developed and calibrated first based on the experimental results (Wilson 2009). During the calibration phase, the FE model backwall (rigid plate elements with the actual wall mass) was permitted to move vertically, as in the physical tests. To consider the possible scenario of a wall restricted from moving upwards (e.g., integral abutment case or due to large friction between the bridge deck and backwall), the FE model was then adapted by restricting the vertical backwall movement and adding an assigned interface friction between the model wall and backfill. Hyperbolic model parameters (Table 1) were then calibrated to match the FE simulation results.

Model 3 assumes that the wall-soil interface friction is 30% of the soil friction angle. Similar to the first model, by limiting the displacement range, the third model is able to benefit from the peak backfill strength.

The fourth scenario assumes greater wall-soil friction (50% of the soil friction angle) than the third with all other factors being the same. This added friction results in greater backfill resistance compared to model 3. In the FE simulations, larger values of wall-soil friction were not found to result in a further substantial increase in resistance.

Similar to the second, the fifth model considers the possibility of displacements that reach beyond the level of the peak resistance range measured in the numerical simulations. This model was calibrated by employing the backfill residual plane-strain friction angle of 40 degrees in

the FE model (i.e., triaxial friction angle of about 34 degrees according to Terzaghi et al. 1996). In this case, wall-soil friction was assumed equal to 30% of the soil friction angle. Larger wall-soil friction angles did not result in a substantial increase in resistance in the FE simulation.

4. ABUTMENT CYCLIC LOADING SPRING MODELS

To apply the hyperbolic abutment stiffness backbone curves to dynamic bridge simulations, a cyclic loading model is described in this section (Figure 9). Within the overall collaborative framework of the project (Saiidi 2004), this cyclic model has recently been implemented and is available for use in the FE platform OpenSees (Mazzoni et al. 2006). For that purpose, a "HyperbolicGapMaterial" was developed and added to OpenSees by Matthew Dryden of the University of California at Berkeley, as a part of his PhD study under the supervision of Professor Gregory Fenves.

The cyclic model follows the hyperbolic backbone curve for virgin loading but adds an unloading and reloading stiffness K_{ur} for subsequent cycles (Figure 9). This model assumes that if the bridge deck pushes the abutment backwall into the backfill and then retreats, the backwall essentially remains at its furthest penetration (the small soil cohesion helps the deformed backfill to retain its shape). On subsequent loading cycles (Figure 9), it is assumed that the abutment loses its resisting capacity up to the point of prior unloading. A value of K_{ur} = 21500 kN/m (per meter of width) was estimated based on the initial stiffness and instances of unloading and reloading in the static pushover experiments (Wilson 2009). For the implemented model, $K_{ur} = K_{max}$ (Table 1) may also be adopted as the unloading and reloading stiffness.

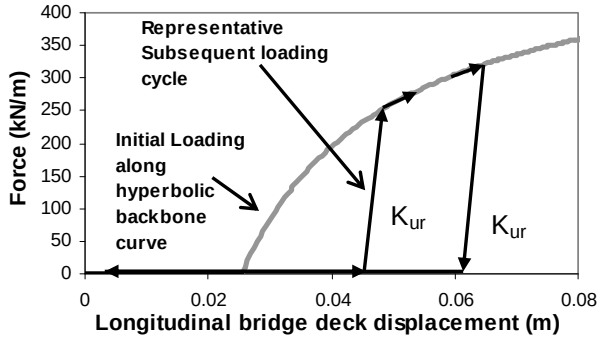

Figure 9: Abutment cyclic loading model description

5. CONCLUSIONS

Recent full scale experiments to consider the bridge abutment longitudinal force-displacement resisting capacity have been described in this article. Static pushover test results provided a basis for developing hyperbolic model parameters to represent the abutment in monotonic pushover analyses. A cyclic loading model was described to employ the hyperbolic force-displacement relationships in dynamic computational analyses. Dynamic excitation test results suggest that earthquake induced inertial forces on the backfill may affect the available abutment force-displacement resistance. However, this effect may be negligible at shaking levels of up to 0.5 g. Finite element simulations are currently being employed to further investigate this issue.

Acknowledgements

Support for this research was provided by the National Science Foundation (NSF) NEESR grant number 0420347 under the overall direction of Professor M. Saiid Saiidi of the University of Nevada at Reno (UNR). Discussions with Dr. Anoosh Shamsabadi of Caltrans have provided valuable insights. The authors acknowledge Matthew Dryden and Professor Gregory Fenves (grant Co-PI) of the University of California at Berkeley for their implementation of the described cyclic loading model in OpenSees.

References

AASHTO (2007). Proposed Guide Specifications for LRFD Seismic Bridge Design. American Association of State Highway and Transportation Officials, Washington D.C.

Caltrans (1999). "Standard specifications." California Dept. of Transportation, Sacramento, CA.

Caltrans (2004). "Seismic design criteria, version 1.3." California Dept. of Transportation, Sacramento, CA.

Cole, R., and Rollins, K. (2006). "Passive earth pressure mobilization during cyclic loading." Journal of Geotechnical and Geoenvironmental Engineering, 132(9), 1154-1164.

Duncan, M., and Mokwa, R. (2001). "Passive earth pressures: theories and tests." Journal of Geotechnical and Geoenvironmental Engineering, 127(3), 248-257.

Mazzoni, S., McKenna, F., and Fenves, G. (2006). Open System for Earthquake Engineering Simulation User Manual. Pacific Earthquake Engineering Research Center, University of California, Berkeley, CA, USA.

Saiidi, M. S. (2004). "Seismic Performance of Bridge Systems with Conventional and Innovative Design." <http://nees.unr.edu/4-spanbridges/index.html> (Nov. 10, 2007).

Shamsabadi, A., Rollins, K., and Kapuskar, M. (2007). "Nonlinear soil-abutment-bridge structure interaction for seismic performance-based design." J. of Geotechnical and Geoenvironmental Eng., 133(6), 707-720.

Stewart, J. P., Taciroglu, E., Wallace, J, W., Ahlberg, E. R., Lemnitzer, A., Rha, C., Tehrani , P. K., Keowan, S., Nigbor, R. L., and Salamanca, A. (2007). Full scale cyclic testing of foundation support systems for highway bridges. Part II: Abutment backwalls, UCLA – SGEL, Report 2007/02, Department of Civil Engineering, University of California, Los Angeles, Los Angeles, CA.

Terzaghi, K., Peck, R., and Mesri, G. (1996). Soil mechanics in engineering practice, 3rd edition, John Wiley and Sons, Inc. New York, NY.

Wilson, P. (2009). "Large-scale measurement and simulation of lateral earth pressure for bridge abutment and retaining wall seismic design." Ph.D. thesis, Dept. of Structural Eng., University of California, San Diego, CA (in progress).

Sixth International Conference on Urban Earthquake Engineering
March 3-4, 2009, Tokyo Institute of Technology, Tokyo, Japan

COMPARISON OF DYNAMIC STRUT-AND-TIE AND FIBER BEAM-COLUMN MODELS FOR THE UCSD SEVEN-STORY FULL-SCALE BUILDING SLICE TEST

André R. Barbosa[1)], Marios Panagiotou[2)], Joel P. Conte[3)], and José I. Restrepo[3)]

1) Graduate Student, Dept. of Structural Engineering, University of California, San Diego, USA
2) Assistant Professor, Dept. of Civil and Environmental Engineering, University of California, Berkeley, USA
3) Professor, Dept. of Structural Engineering, University of California, San Diego, USA
abarbosa@ucsd.edu, panagiotou@ce.berkeley.edu, jpconte@ucsd.edu, jrestrepo@ucsd.edu

Abstract: A full-scale seven-story reinforced concrete wall building slice was tested at the Large High Performance Outdoor Shake Table of the George E. Brown Jr. Network for Earthquake Engineering Simulation (NEES) equipment site at the University of California at San Diego (UCSD). The reinforced concrete wall building slice was subjected to four different and consecutive earthquake records of increasing levels of peak ground acceleration. The test structure consisted of a web wall that provided the primary lateral force resistance to the building, a flange wall, gravity columns, a segmental precast post-tensioned column, and flat slabs at every floor level that were supported by the web wall and the gravity columns. During the experiment, the level of damage of the building increased with the increasing intensity of the shake table motions. Most of the damage was located in the web wall. In this paper, two different two-dimensional computational models for numerical simulation of the nonlinear response of the test structure are presented. In the first model, a recent dynamic nonlinear strut-and-tie approach is used to model the web wall, while, in the second, the web wall is modeled using force-based nonlinear fiber beam-column elements. In both computational models, particular attention was given to the three-dimensional coupling between the walls, the slab and the gravity columns, which had a significant influence on the building's dynamic response. Comparisons of the predicted response with the measured test results show that, in general, the adopted strategies produced good estimates of the measured response for the quantities of interest (displacements, accelerations, forces, strains), and the nonlinear strut-and-tie approach is a promising alternative for modeling structural walls.

1. INTRODUCTION

A full-scale seven-story reinforced concrete wall building structure was tested on the NEES-UCSD shake table in the period October 2005-January 2006. The shake table tests were designed so as to damage the building progressively through four historical seismic motions reproduced on the shake table. The test structure was designed with a displacement-based, capacity approach for a site in Los Angeles. A primary objective of the shake table test was to demonstrate that the building slice behaved satisfactorily with the use of about half of the reinforcing longitudinal steel that would be typically necessary by current codes in similar walls (e.g., UBC-97, 1997), and to verify that undesirable shear failures were precluded through capacity design, a practice not prescribed in the latest codes for structural wall buildings, even for high seismic risk areas (ACI 381-08). A secondary objective was to study the ability of different analytical models to predict the experimental response (NEES/UCSD, 2006).

The modeling and analysis of reinforced concrete wall buildings under severe earthquake excitations has been a challenging problem for the engineering community. Extensive experimental research has been carried out to study the behavior of reinforced concrete walls and frame wall systems, and several nonlinear formulations for modeling of concrete walls have been developed. Even though refined modeling approaches for nonlinear dynamic analysis of reinforced concrete walls can be adopted, they typically involve significant pre- and post-processing efforts and very time consuming computations. Therefore, there is a need for use of relatively simple models that provide accurate estimates of the nonlinear dynamic response quantities with reduced computer run times (Wallace, 2007).

In the past two decades, the research community has arrived at a general consensus that, for reinforced concrete flexural walls, the modeling approaches that strike a good balance between accuracy of the estimated nonlinear response and computational efficiency include the use of fiber beam-column elements (Spacone et al., 1996) or the use of Multiple-Vertical-Line-Elements (MVLEs) (Vulcano et al., 1987). More recently, models have been also been proposed to incorporate the interaction between flexural/axial behavior and shear behavior (Wallace, 2007). Panagiotou and Restrepo (2006) proposed another approach that involves the use of two-dimensional nonlinear strut-and-ties and accounts directly for shear-flexure interaction in a reinforced concrete wall.

This paper presents a pair of advanced two-dimensional computational models for numerical simulation of the

nonlinear dynamic response of the full-scale seven-story reinforced concrete wall building slice that was tested on the NEES-UCSD shake table. In the first model, the dynamic nonlinear strut-and-tie approach is used to model the web wall, while, in the second, the web wall is modeled using force-based nonlinear fiber beam-column elements. Realistic nonlinear inelastic constitutive models are used for the structural concrete and reinforcing steel. In order to capture the main effects of the three-dimensional response on the two-dimensional models, particular attention was given to the three-dimensional interaction between the walls, the slab and the gravity system, which had a significant influence on the building's dynamic response. Both models are subjected to the same sequence of seismic base excitation that was measured in the test. Representative responses of the models to the sequence of the shake table inputs are presented and compared to the experimental response.

2. TEST DESCRIPTION

The test structure is a slice of a full-scale reinforced concrete structural wall building and consists of a main wall (web wall), a back wall perpendicular to the main wall (flange wall), concrete slabs at each floor level, an auxiliary post-tensioned column to provide torsional stability, and four gravity columns to transfer the weight of the slabs to the shake table. Figure 1a displays a picture of the test structure mounted on the shake table, while an elevation view and general dimensions of the structure above the foundation is shown in Figure 1b. Figure 2 displays a plan view of the structure with wall and slab dimensions at different levels. The total height of the specimen above the foundation is 19.2m and the height from the top face of the shake table platen is 19.92m. More details about the test structure can be found in Panagiotou et al. (2007).

The experimental program investigated the response of the cantilever web wall to different levels of base excitation. The input acceleration records were applied parallel to the web wall (E-W direction). A sequence of dynamic tests (Conte et al. 2007) was applied to the test structure including ambient vibration, free vibration, and forced vibration tests (white noise and seismic base excitations). In total 68 tests were performed. The ambient vibration, free vibration, and white noise vibration tests were designed for system and damage identification, while the seismic base excitations were designed so as to progressively damage the structure. The seismic base excitations correspond to four historical seismic records (see Panagiotou et al. (2007) for complete description) which are designated EQ1, EQ2, EQ3, and EQ4 in order of increasing intensity.

3. NONLINEAR MODELING AND ANALYSIS PARAMETERS

This section describes two computational models used for numerical simulation of the dynamic nonlinear behavior of the full-scale seven-story reinforced concrete wall building structure that was tested on the NEES-UCSD shake table. The first model is analyzed using the nonlinear dynamic analysis program for earthquake engineering *RUAUMOKO-2D* (Carr, 1998), while the software *OpenSees* (Mazzoni et al, 2006), a finite element analysis platform for earthquake engineering simulation, is used for analysis of the second model.

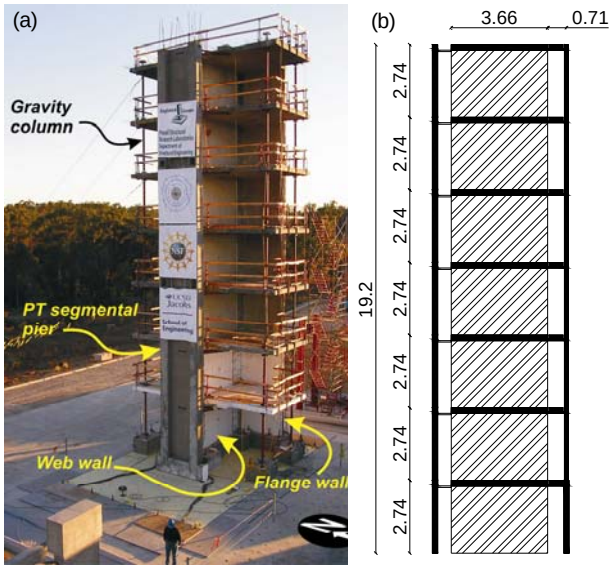

Figure 1. R/C shear wall building slice: (a) Picture of the test structure, and (b) Elevation dimensions (unit: m)

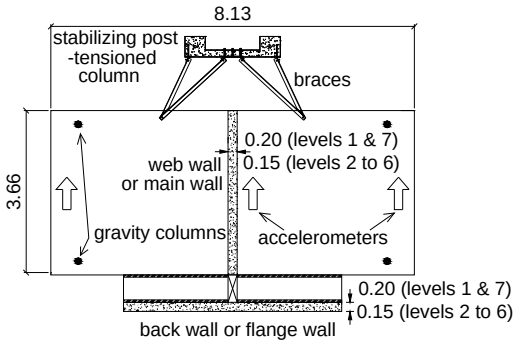

Figure 2. Plan view of the test structure (unit: m)

To the extent possible, when two different software packages are used, the models are almost identical. The main difference between them is the approach used for modeling the web wall. In the first, a dynamic nonlinear strut-and-tie approach is used, while, in the second, the web wall is modeled using force-based nonlinear fiber beam-column elements.

In the development of both finite element models, special considerations was given to the three-dimensional framing effects. Panagiotou et al. (2007) demonstrated that the kinematic interaction between the primary lateral resisting element (web wall) and the secondary structural components (flange wall, slab, slotted-slab, and gravity columns) played a very important role in the experimental response of the building slice structure. The

three-dimensional framing of the slab into the wall had a significant effect on the magnitude of bending moments and shear forces that developed in the web wall. Since the framing action has the effect of increasing the system forces in the web wall (Bertero et al. 1985), it may also be termed as kinematic overstrength. Another source of kinematic overstrength was provided by the slotted slab connection between web wall and flange wall.

Figure 3 shows the main characteristics of the finite element models, where the framing actions are modeled through a number of nonlinear springs. Details for each of the models are described in the following sections.

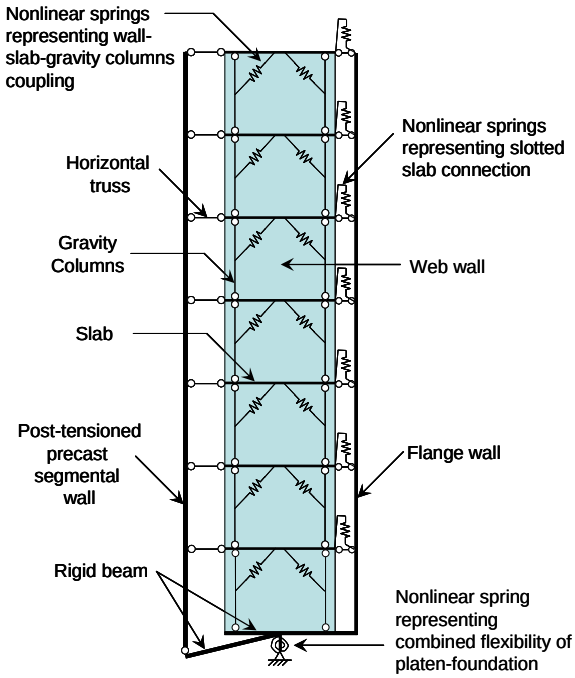

Figure 3. Overview of the main characteristics present in both 2-D mathematical models of the building slice.

3.1 Dynamic nonlinear strut-and-tie model

The computational model of the building-slice test structure described in this subsection makes use of the nonlinear strut-and-tie approach. The model was first presented by Panagiotou and Restrepo (2006). For completeness of this paper, the main characteristics of the model are summarized herein. The mass was lumped at the mid-length of the web wall, at mid-height of the slab at every floor. The web wall was modeled using a dynamic nonlinear strut-and-tie approach. For the post tensioned precast segmental pier and the flange wall, beam-column elements with concentrated plastic hinges at both ends were used with bilinear origin oriented hysteresis moment-rotation characteristics. To model the effects of coupling between the slab-wall-gravity columns, properly calibrated multiple nonlinear shear springs of different inelastic characteristics were used in order to reproduce the measured axial force in the gravity columns. The steel braces that connected the post-tensioned column to the slab were modeled as elastic truss elements. Elastic truss elements were also used to model the gravity columns. The slotted slab connection between the web and flange walls was modeled as a combination of three parts: first, truss elements representing the nonlinear hysteretic behavior of the concrete and reinforcing steel present in the slot; second, bilinear vertical shear springs representing the moment capacity of the slots; and third, bilinear vertical shear springs with initial gap to account for effects of dowel action of the reinforcing steel present in the slot. A nonlinear bilinear rotational spring was located at the base of the wall in order to model the observed flexibility of the foundation-platen.

The dynamic nonlinear strut-and-tie model used to model the web wall was first introduced by Panagiotou and Restrepo (2006). For the purpose of explaining the approach, Figure 4 shows a structural wall segment (panel) that could correspond to a story of Figure 3, say the second story, for example. For this wall panel (Figure 4), the nonlinear strut-and-tie model consists of four parts: (1) horizontal frame elements representing the effective width of the slabs at the floor levels; (2) truss elements in the vertical direction representing concrete and reinforcing steel; (3) truss elements in the horizontal direction corresponding to horizontal reinforcing steel; (4) variable angle truss elements representing the diagonal concrete struts with an effective area that is the product of the effective width of each strut by the width of the wall, where the effective width of the struts is computed as the length of the wall diagonal divided by the number of diagonals in each direction.

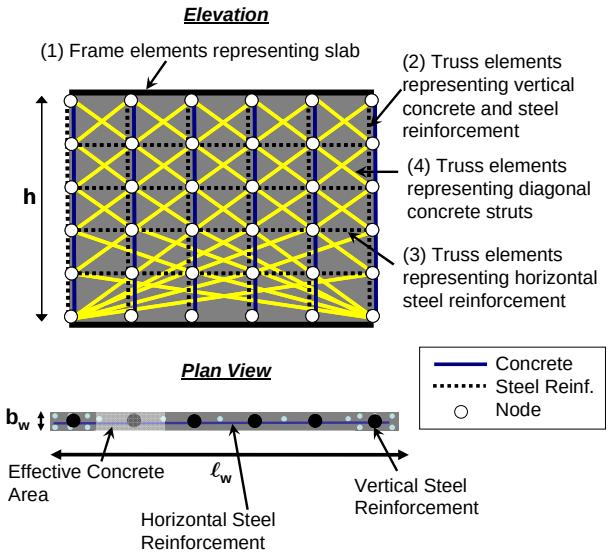

Figure 4. Strut-and-tie model for a structural wall panel.

In the nonlinear strut-and-tie model, perfect bond is assumed between the concrete and reinforcing steel. Phenomena such as tension stiffening, tension softening, bond-slip, or bar buckling, for example, may be incorporated into the definition of the nonlinear behavior of the truss elements.

Two different levels of discretization were used along the height of the web wall (see Figure 5(a)). In the first two stories, a more refined strut-and-tie mesh was constructed.

This level of detailing allowed for better estimation of the nonlinear response of the plastic hinge region that developed in the first two floors. For levels three through seven, the wall was expected to behave in an elastic manner and thus less refined meshes were defined. It is worth noting that, the model implemented in *RUAUMOKO* accounts for reduction of compressive stresses of diagonally cracked concrete with increase of transverse tensile strain.

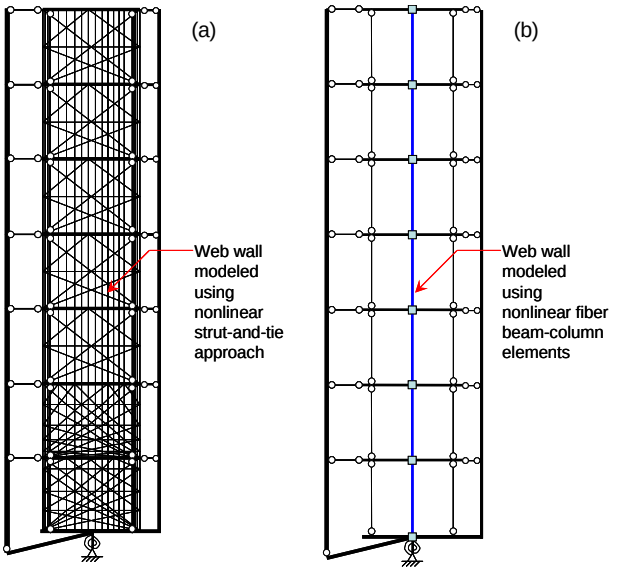

Figure 5. Elevation showing discretization of the web wall in the finite element model using: (a) nonlinear strut-and-tie approach; (b) nonlinear fiber beam-column elements

The total number of nodes of the model was 434 and the total number of elements 1494. Refer to Panagiotou and Restrepo (2006) for a complete and more detailed description of the model, including the hysteretic modeling of the various components.

3.2 Fiber beam-column model

The computational model of the test structure that involves the use of nonlinear fiber beam-column elements was developed in *OpenSees* (Mazzoni et al., 2006). The web wall is modeled with one nonlinear fiber beam-column element per story (see Figure 5 (b)). Each element is divided into five fiber sections, which are located at the Gauss-Lobatto integrations points. The fiber sections are defined from the wall cross-sectional geometry, and longitudinal reinforcing steel. Each section is subdivided into 80 concrete layers and steel fibers are located according to the drawing specifications. The concrete uniaxial model used was the Popovics/Mander model (Concrete04 in *OpenSees*). Exponential tension stiffening effects are also considered in the concrete model. For the reinforcing steel, the stress-strain behavior is described by the uniaxial nonlinear Menegotto-Pinto model. The material parameters for the uniaxial stress-strain constitutive laws are calibrated based on material testing results (Panagiotou et al. 2007). For the fiber sections of the element located at the first level, two different confined concrete zones and one unconfined concrete zone were defined. For all other levels, the concrete was modeled as unconfined. The flange wall was also modeled using nonlinear fiber section beam-column elements. The post-tensioned column was modeled using nonlinear beam-column elements, in which the section has a bilinear hysteretic moment-curvature relation and linear elastic axial and shear behaviors. The effect of coupling between the slab-wall-gravity columns was modeled using the same approach described for the nonlinear strut-and-tie finite element model.

The total number of nodes of the model was 74, while the total number of elements was 124 elements.

3.3 Analysis parameters

The parameters described in this section were used in the analysis of both computational models shown in Figure 5. The simulation to all recorded shake table motions was performed with a single continuous sequence of concatenated 30 sec acceleration records from EQ1 through EQ4. Rayleigh damping based on the initial stiffness was used. Parameters for the Rayleigh model were 0.5% damping ratio for the first mode and 2.0% for the second mode. The Newmark constant average acceleration method was used to integrate the equations of motion. The time step of the input motions was equal to 0.02 sec and the integration time step was 0.005 sec. A nonlinear geometry formulation of the elements (corotational formulation of large displacement theory) was used in the analysis.

Note that the damping ratios used for these nonlinear analyses are significantly lower than the traditional values used in the design of reinforced concrete structures (typically 5% or higher). However, it should be emphasized that, first of all, the tested structure corresponds to a “bare” structure, and additionally, the traditional values used in design correspond to “equivalent” viscous damping ratios and should not be used for a nonlinear finite element model of a structure that explicitly accounts for material inelastic behavior (hysteretic energy dissipation).

4. ANALYSIS RESULTS AND COMPARISONS

In this section, results from the nonlinear time history analysis of both computational models are compared to the experimental results. Figure 6 shows the measured versus computed time histories of the roof relative horizontal displacement, while Figure 7 compares the time history of the system total base shear response for EQ4. In these figures, grey solid lines correspond to the experimental values, black solid lines to the computed results from the nonlinear strut-and-tie model (“S&T”) and the red dotted lines to the computed results from the model using nonlinear fiber beam-column elements (“NL Fiber Ele”). In general, for both displacement and system forces, excellent agreement is achieved in terms of amplitude and frequency content under the multiple cycles of the response. Difference between measured and the computed response is observed after the peak displacement response for EQ4. This

discrepancy is due to the effect of the lap splice failure (Panagiotou et al. 2007), which was not represented in both computational models.

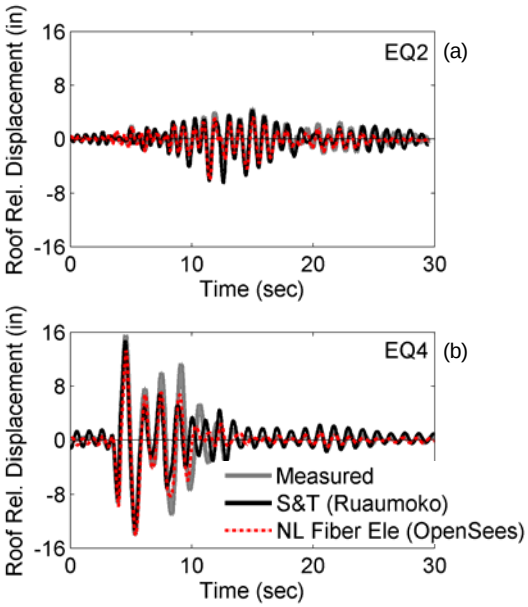

Figure 6. Time histories of measured and computed roof relative horizontal displacement for: (a) EQ2, and (b) EQ4

Figure 8 shows the envelopes of key response quantities of interest for EQ1, EQ2 and EQ4. Results for EQ3 are not shown so that the figures are more legible, since results for EQ2 and EQ3 almost overlap. The response quantities shown are total horizontal acceleration, relative horizontal displacement, system shear forces and system bending moments along the height of the web wall. Note that both measured and computed shear forces at a given level correspond to the sum of inertial forces above that level, while system bending moments are computed as the sum of the products of the inertia forces and the associated vertical distance measured above that level. In Figure 8, the correlation between measured and simulated response is again very good. In EQ1, the nonlinear fiber beam-column model overestimates the shear force at the base more than the strut-and-tie model. The difference between the simulated and the measured data may be due to small differences in the models used for concrete in tension, as the tension stiffening plays an important role for the initial low amplitude cyclic response.

Figure 9 shows the measured and computed strains in the reinforcing steel for EQ3 at a fiber 7.5 in from the western face of the wall, which corresponds to the location of the LVDT used to measure concrete strains. The computed values for the strut-and-tie model (black lines) show very good agreement with the measured strains. The results of the nonlinear beam column model (red dotted line) show a big discrepancy with respect to the measured strains. This was expected due to localization of the plastic curvatures, typical of nonlinear beam-column elements. Therefore, the computed curvature response needed regularization.

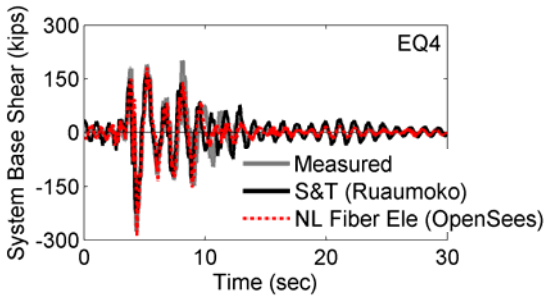

Figure 7. Time history of measured and computed system total base shear for EQ4.

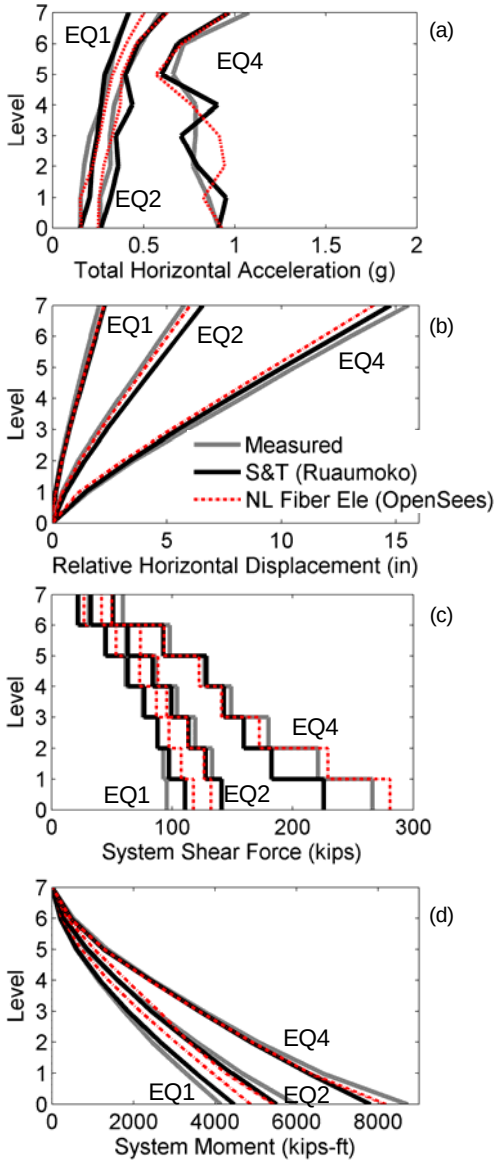

Figure 8. EQ1, EQ2 and EQ4 - Envelopes of measured and computed: (a) total horizontal accelerations, (b) relative horizontal displacement, (c) system shear forces, and (d) system bending moment.

Following the work of Coleman and Spacone (2001), the computed curvatures are regularized using Eq. (1):

$$\phi^{REG} = \phi_y + \frac{w_{IP} L^2 \left(1 - w_{IP}\right)}{L_P \left(L - L_P\right)} \phi_p^{MODEL} \qquad (1)$$

where ϕ^{REG} is the regularized curvature, $\phi_y = 2\varepsilon_y / l_w$ is the yielding curvature (with ε_y the yielding strain of steel), l_w is the wall length, w_{IP} is the weight of the integration point, L is the length of the element, L_P is the plastic hinge length (taken as $L_P = 0.5 l_w$) , and ϕ_p^{MODEL} is the model output curvature.

After transforming the regularized curvatures to regularized strains, these are plotted in Figure 9 (green line). It is apparent that the computed strain response, after being regularized, is in good agreement with the measured response. Note that the residual plastic strains are also computed with reasonable accuracy.

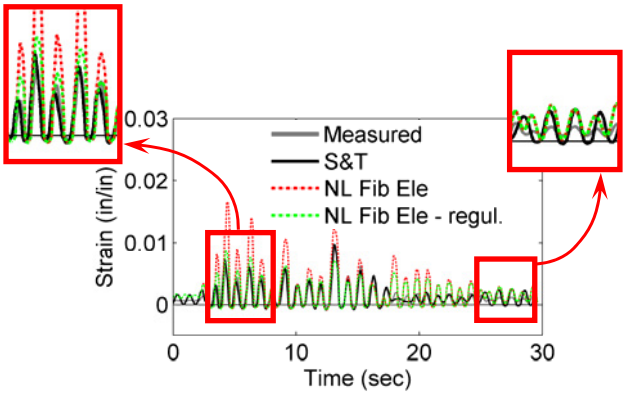

Figure 9. Strain time history at the Western side of the web wall for EQ3

5. CONCLUSIONS

A full-scale seven-story reinforced concrete wall building slice was tested on the NEES-UCSD shake table. This paper describes two computational models that were used to simulate the flexure dominated nonlinear behavior of the test structure subjected to four consecutive table motions taken as earthquake records of increasing peak ground acceleration. In the first model, a novel dynamic nonlinear strut-and-tie approach was used to model the web wall, while, in the second, the web wall was modeled using force-based nonlinear fiber beam-column elements. In both models, particular attention was given to the three-dimensional coupling between the walls, the slab and the gravity system, which had a significant influence on the building's dynamic response. Comparisons of the predicted and measured responses show that: (1) in general, the adopted modeling strategies produced good estimates of the measured response for the quantities of interest, (2) best correlations between computed and measured responses were obtained for low values of damping ratios, (3) regularized strains from force-based beam-column elements proved to be good estimates for measured strains, and (4) the nonlinear strut-and-tie model proved to be an attractive alternative for modeling structural walls.

Acknowledgements:

Partial supports of this research by the Englekirk Center Industry Advisory Board and by Lawrence Livermore National Laboratory with Dr. David McCallen as Program Leader are gratefully acknowledged. The first author would also like to acknowledge the Center for Urban Earthquake Engineering of the Tokyo Institute of Technology and the Pacific Earthquake Engineering Research Center for the invitation and support to attend this conference. Partial support provided by the Department of Civil Engineering of the Universidade Nova de Lisboa and the Portuguese Science Foundation (BD/17266/2004) is also acknowledged. Any opinions, findings, and conclusions or recommendations expressed in this material are those of the authors and do not necessarily reflect those of the sponsors.

References:

ACI Committee 318: ACI 318-08 (2008), "Building Code Requirements for Structural Concrete and Commentary", *American Concrete Institute*, Farmington Hills, MI, 456 pp

Bertero, V. V., Atkan, A. E., Charney, F., and Sause, R. (1985), "Earthquake Simulator Tests and Associated Experiments, Analytical and Correlation Studies of One-Fifth Scale Model," in *Earthquake Effects on Reinforced Concrete Structures, U.S.-Japan Research, ACI Publication SP-84*, American Concrete Institute, Detroit, 375-424.

Carr, A.J,: Ruaumoko (1998), "Ruaumoko – A Program for Inelastic Time-History Analysis". Department of Civil Engineering, University of Canterbury, New Zealand.

Coleman, J, and Spacone, E. (2001) "Localization Issues in Nonlinear Force-Based Frame Elements." *ASCE Journal of Structural Engineering*, Volume **127**(11), 1257-1265

Conte, J.P., Moaveni, B., He, X., and Barbosa, A.R. (2007) "System and damage identification of a seven-story reinforced concrete building structure tested on the UCSD-NEES shake table" Keynote paper in *Proceedings of EVACES07, Experimental Vibration Analysis for Civil Engineering Structures*, Portugal

Mazzoni, S., Scott, M.H., McKenna, F., Fenves, G.L., et al. (2006). "Open System for Earthquake Engineering Simulation - User Manual (Version 1.7.3)". *Pacific Earthquake Engineering Research Center*, University of California, Berkeley

NEES/UCSD, (2006), *Seminar on Analytical Modeling of Reinforced Concrete Walls for Earthquake Resistance*, La Jolla, California.

Panagiotou, M., and Restrepo, J. I., 2006, "Model Calibration For The UCSD 7-Story Building Slice." *NEES/UCSD Seminar on Analytical Modeling of Reinforced Concrete Walls for Earthquake Resistance*, La Jolla, California.

Panagiotou, M., Restrepo, J. I. and Conte, J.P., (2007), "Shake table test of a 7-story full scale reinforced concrete structural wall building slice – Phase I: Rectangular wall", *Report No UCSD/SSRP–07/07*, University of California San Diego

Spacone, E., Filippou, F.C., and Taucer, F.F. (1996) "Fiber Beam-Column Model for Nonlinear Analysis of R/C Frames. I: Formulation." *Earthquake Engineering and Structural Dynamics*, **25**(7), 711-725

Uniform Building Code: UBC-97 (1997), International Conference of Building Officials, Whittier, California, 1997.

Vulcano, A., and Bertero, V. V. (1987), "Analytical Models for Predicting the Lateral Response of RC Shear Walls: Evaluation of Their Reliability," *EERC Report No. UCB/EERC-87/19*, Earthquake Engineering Research Center, University of California, Berkeley, Calif., 1987, 99 pp

Wallace, J.W., (2007), "Modelling issues for tall reinforced concrete core wall buildings," *The Structural Design of Tall and Special Buildings* **16**(5), 615-632

Sixth International Conference on Urban Earthquake Engineering
March 3-4, 2009, Tokyo Institute of Technology, Tokyo, Japan

EVALUATION OF COMPRESSIVE FRACTURE BEHAVIOR OF HIGH-STRENGTH CONCRETE UNDER CYCLIC LOADING BY DIGITAL IMAGE CORRELATION METHOD

Yasutaka Noma[1], Ken Watanabe[2], and Junichiro Niwa[3]

1) Graduate Student, Department of Civil Engineering, Tokyo Institute of Technology, Japan
2) Assistant Professor, Department of Civil Engineering, Tokyo Institute of Technology, Japan
3) Professor, Department of Civil Engineering, Tokyo Institute of Technology, Japan
ynoma@cv.titech.ac.jp, ken@cv.titech.ac.jpl, jniwa@cv.titech.ac.jp

Abstract: This research is aimed at evaluating the compressive fracture behavior of high-strength concretes under cyclic loadings by means of the digital image correlation method. In the present research, the lateral strain, depicting the vertical cracks formed under the uniaxial compressive load, was employed to find the damage extent of high-strength concretes. The applicability of the digital image correlation method was investigated to estimate the fracture behavior of high-strength concrete under uniaxial cyclic loadings. As a result, the failure process, derived from the initiation and the propagation of cracks, was visualized and distinguished as strain concentration regions obtained from the changes in calculated values of the lateral strain during loading and reloading stages.

1. INTRODUCTION

Under seismic loads, the collapse of concrete structures is caused by the initiation and the propagation of cracks. Structures showing signs of damage should be verified whether the structural performance required in design can be satisfied, depending on the extent of damage. Hence, it is important to evaluate damage extents of concrete structural elements under dynamic loadings.

Various image measurement methods were developed and employed to measure deformations of concrete elements and structures in order to clarify the fracture phenomena (Matsuo et al. 2004, Machida 1978). The advantage of the image measurement methods is the ability to measure two-dimensional deformations of structural elements without making contact with the target unlike in the case of methods based on strain and displacement gages. One such procedure is the digital image correlation method, developed and studied by Chu T. C. et al. (1985). The digital image correlation method has been already applied to the area of structural concrete (Choi et al. 1999, Sagawa et al. 2007), with good results. Cracks which are directly related to the failure of concretes can be easily observed by the digital image correlation method. This information of failure growths is useful to obtain the fracture phenomena of concrete.

In this research, uniaxial cyclic compressive tests were carried out to evaluate the compressive fracture behavior of high-strength concretes in terms of damage extent under cyclic loadings as dynamic simulation tests. The digital image correlation method was applied to analyze the variation of the lateral strains at the surface of concrete specimens. Damage growths of high-strength concrete, such as crack initiation and propagation, changes in the values of the lateral strain were evaluated by using the digital image correlation method during loading and reloading stages.

2. EXPERIMENTAL PROCEDURE

2.1 Material, Mix Proportion, Concrete Strength

Table 1 shows the type and the physical properties of cement, fine aggregate, coarse aggregate and admixture. The mix proportions used in the experiments and the compressive strengths measured according to JIS A 1108 are presented in Table 2. Water to cement ratio (30%) is constant for all mix proportions.

For the experimental program, two series of specimens with different mix proportions for the mortar part were used. One is the series that mix proportions in the mortar part are constant depending on the quantity of coarse aggregate. For the second series, the amount of fine aggregates of mix proportions in the mortar part decreases as the increase of the quantity of coarse aggregate. Mix proportions, in the mortar part, were evaluated by the mass ratio of water, fine aggregate and cement (W : S : C). For the first series, W : S : C is constant and the unit weight of water and cement decreases as the increase of the quantity of coarse aggregate. W : S : C was 1:5.51:3.33. For the second series, the water to cement ratio is constant as the increase of the quantity of coarse aggregate. However, the amount of fine aggregate decreases with the increase in the quantity of coarse aggregate. W : S : C is varied from 1:3.74:3.33 to 1:1.09:3.33. Each series included a variation of the quantity

Table 1 Employed Material

Materials		Physical Properties
Cement	High Early Strength Cement	Density 3.14 g/cm^3, Specific surface are 4620 cm^2/g
Fine Aggregate	Obitsu Land Sand	Density in SSD 2.65 g/cm^3, Absorption 1.55 %
Coarse Aggregate	Oume Crushed Stone	Density in SSD 2.63 g/cm^3, Absorption 0.67 %, G_{max} 20 mm
Admixture	Super Plastisizer	Polycarboxylate type, Density 1.05 g/cm^3

Table 2 Mix Proportion and Compressive Strength

Series	Mark	G_{max} (mm)	W : S : C	The Quantity of Coarse Aggregate (ℓ/m^3)	W/C (%)	s/a (%)	Unit Weight (kg/m^3)				Compressive Strength (N/mm^2)
							Water	Cement	Fine Aggregate	Coarse Aggregate	
Ⅰ	450-5.51	20	1 : 5.51 : 3.33	450	30	36.8	126	419	693	1184	80.5
	550-5.51			550		27.7	102	339	560	1447	82.5
Ⅱ	450-3.74		1 : 3.74 : 3.33	450		32	150	500	561	1184	73.7
	550-1.09		1 : 1.09 : 3.33	550		16.9	150	500	296	1447	72.7

of coarse aggregate of 450, and 550 ℓ/m^3. The target values of slump and air content were 20.0±3.0 cm and 2.0±2.0%, respectively. Compressive strengths for series Ⅰ tends to be higher than that for series Ⅱ.

2.2 Details of Specimens

Uniaxial cyclic compressive tests were conducted on rectangular specimens with the size of 150×150×(50±3) mm as shown in Figure 1. Usually, the surface of concretes is uniform gray because of a thin layer of mortar covering it. Therefore, the distribution of luminance values at the surface of concretes becomes constant. The digital image correlation method used in this research can trace the change of pixels color and compute the displacement of the surface of the concrete specimen by utilizing the random distribution of the luminance values. Hence, it is required to devise a procedure to arrange the random distribution of luminance values at the surface of measuring objects for the digital image correlation method. Such a procedure was proposed and used by Sagawa et al. (2007). Concrete specimens with sizes of 150 × 150 × (50 ± 3) mm were obtained from cutting rectangular specimens with the size of 150×150×200 mm, using concrete cutter. The cutting procedure was performed after the predefined curing period passed. After cutting, coarse aggregate and mortar parts were exposed at the surface of the concrete specimens and the luminance values could be randomly distributed (Figure 1).

2.3 Details of Tests

In order to be able to observe the compressive fracture behavior under cyclic loading by the digital image correlation method, uniaxial cyclic compressive tests were carried out on rectangular specimens like the above. The cyclic process is shown in Figure 2. The loading was repeated twice. The compressive fracture behavior for the loading and the reloading state will be discussed in the subsequent chapter.

Pictures including specimens were taken by using the

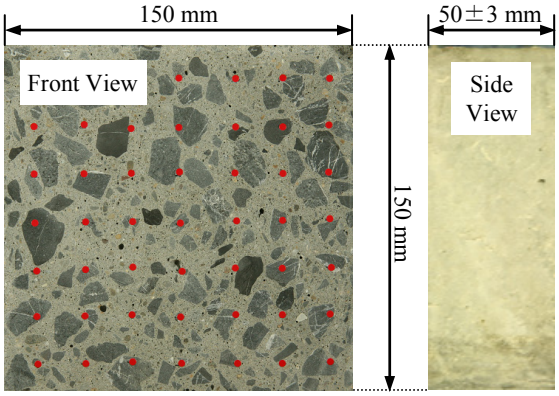

Figure 1 The Outline of Specimens

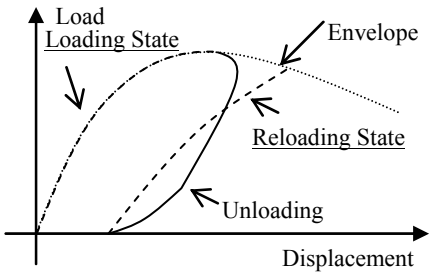

Figure 2 Cyclic Processes

high-resolution digital camera during loading and reloading states. In order to ensure the high quality of the pictures taken during the test, the digital camera was fixed on a tripod.

To exclude influences of natural daylight and generic illumination in testing, the testing machine was covered by a black-out curtain, and light-emitting diode illumination which can be used under direct-current voltage was used. The calibration of the high-resolution digital camera was conducted in order to remove influences of strains of camera lenses, internal and external parameters that might influence the quality of the pictures taken during testings. Several pictures were taken by keeping the load constant for each stage during tests.

The friction at the boundary between the specimen and the loading plates was reduced by inserting the friction reducing pads. The image analysis conducted in this research can not measure the displacement in the depth direction. Hence, loading tests were conducted without the removal of influences of boundary restraints. This restraint condition is constant in all cases.

3. PROCEDURE OF THE IMAGE ANALYSIS

3.1 The Degital Image Correlation Method

The digital image correlation method is the method which can trace and compute displacements of designated arbitrary pixels by conducting matching of luminance values of the measuring object on the pictures taken before and after deformation. The area-based displacement distribution on the entire visual field can be obtained by repeatedly conducting this process.

In particular, the distribution of luminance values at the subset on the image before deformation is used. The subset is an arbitrary area on the image. In this analysis, the similarity function which can evaluate the coincidence between the distribution of luminance values within the subset before and after deformation is used. The coordinate after deformation can be obtained by searching the coordinate which show the most correlated similarity.

3.2 Details of Analyses

The target of the analysis was the area with the dimension of about 120×120 mm at the surface of the rectangular concrete specimens, as shown in Figure 3. About 8000-10000 pixels were selected with an interval 25 ×25 pixels within this area.

Searching processes of pixels after deformation can be divided into pixel units and in sub-pixel units, which is less than the integer number units of pixels. The sum of squared difference was used for the search method in pixel units. The search in sub-pixel units was conducted according to the method proposed by Shimizu et al. (2004). It is reported that this method can predict the coordinate after deformation with a high accuracy and search the two-dimensional coordinate at the same time. The similarity function was calculated by using the distribution of luminance values of the analyzing object before and after the deformation with the size of subset of 61×61 pixels. The coordinate in sub-pixel units after the deformation was computed by conducting the above process within 61×61 pixels area with a central focus on the pixel before the deformation on the image obtained after the deformation.

Influences caused by the distortion of image were removed by using the aberration correction to obtain the coordinates (Steger et al. 2008). The compressive fracture behavior was evaluated by running the analysis when the applied load was 60, 80, 90, 95% of the first and second peak loads both during the loading and reloading stages, respectively. The maximum value of the average lateral strain and the two-dimensional distribution of the lateral

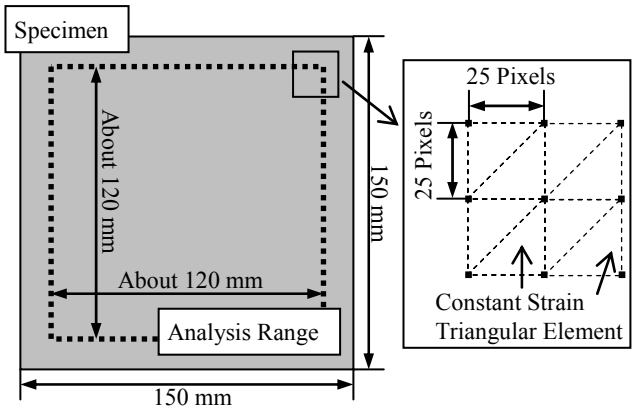

Figure 3 The Outline of Analyses

strain was calculated. The average lateral strain was computed by using the coordinates of the points located on the right and left edges of the area under consideration. The maximum average lateral strain was calculated from these results. The displacement and the lateral strain in each element were interpolated by means of shape functions for a constant strain triangular element.

In fact, it is considered that fracture mechanisms in concrete should be three-dimensionally discussed (Izumi et al. 1980). However, it is impossible to obtain three-dimensional information in this research. The two-dimensionally idealized fracture mechanisms at the surface of concretes were evaluated in this research.

4. RESULTS OF IMAGE ANALYSIS

Figures 4 and 5 show the strain distributions obtained by the digital image correlation method from the images taken during the loading and reloading stages in the uniaxial cyclic compressive loading test. The maximum average lateral strain is shown in Tables 3 and 4.

Vertical cracks can be visualized as local strain concentrations by using the digital image correlation method. The strain concentration regions can be confirmed as a result of the damage growths in all specimens. It is possible to evaluate the fracture behavior of concrete specimens by observing these damage conditions.

Vertical cracks can be confirmed in the region enclosed by a rectangle, Figure 4 (1)[(a)], at 60% of the first peak load during the loading stage, for all cases. On the strain distributions of 450-5.51 and 550-5.51 specimens, for which the compressive strengths are higher than those of the series Ⅱ, inclined cracks, diagonally connected, were formed in the region enclosed by a circle, Figures 4 (1) [(b)(c)(d)] and (2)[(c)(d)]. In some compressive tests of concrete, inclined cracks were generated and propagated. It is reported that these phenomena are influences of the boundary restraints of specimens (Van Mier et al. 1997). Furthermore, it is reported that the compressive strengths of concrete specimens increase due to the effect of the boundary restraints (Van Mier et al. 1997).

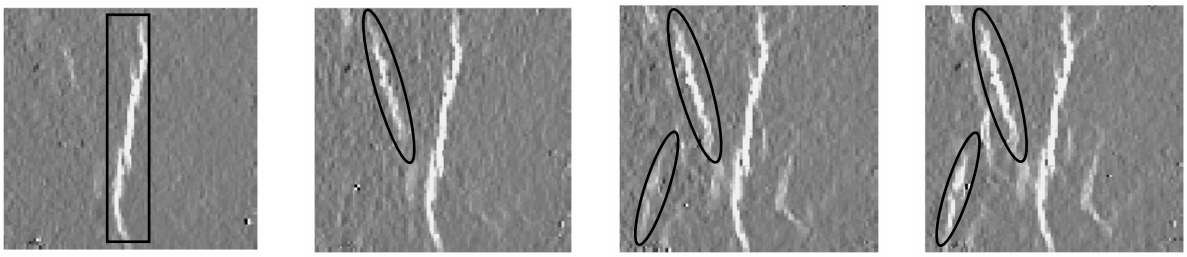

(a) 60% (b) 80% (c) 90% (d) 95%

(1) 450-5.51 (Series-Ⅰ)

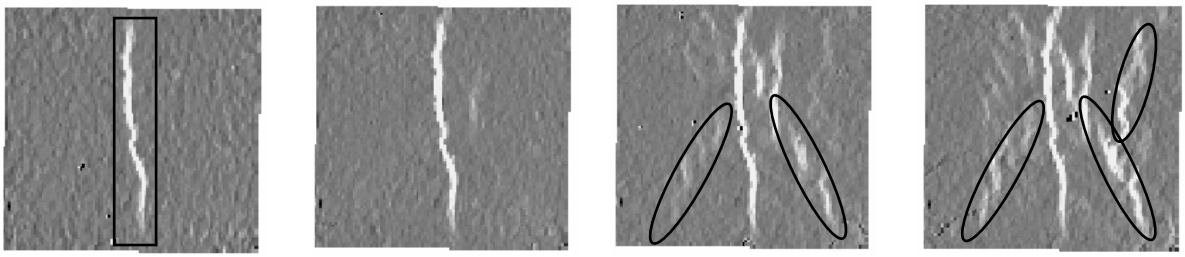

(a) 60% (b) 80% (c) 90% (d) 95%

(2) 550-5.51 (Series-Ⅰ)

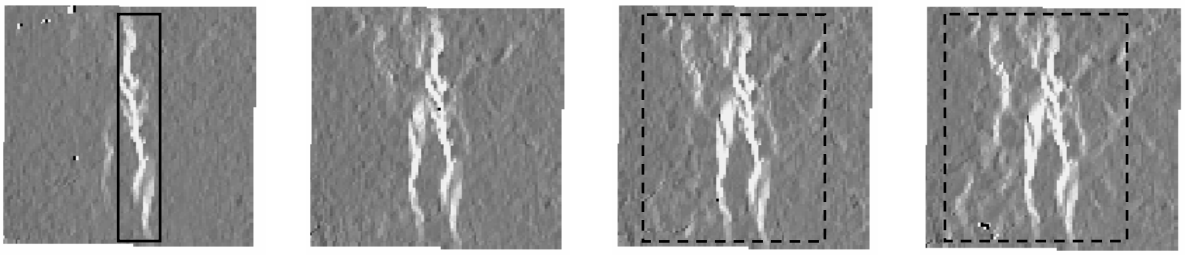

(a) 60% (b) 80% (c) 90% (d) 95%

(3) 450-3.74 (Series-Ⅱ)

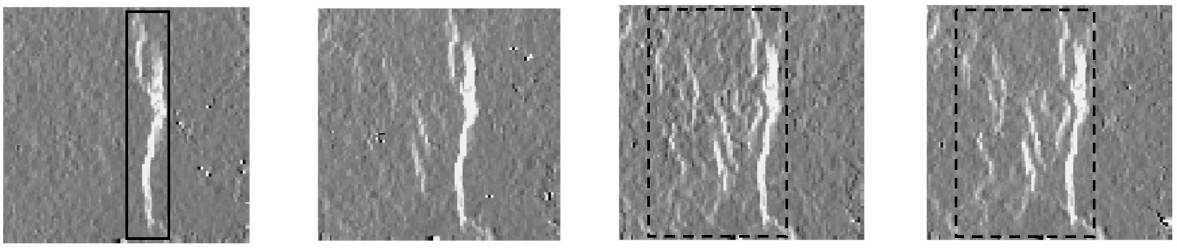

(a) 60% (b) 80% (c) 90% (d) 95%

(4) 550-1.09 (Series-Ⅱ)

The crack width of splitting cracks formed at the central part, increased with the progression of loadings. Only the crack width at the central part increases if boundary restraint effect works. Accordingly, it is considered that inclined cracks are generated.

In the series Ⅰ, compressive strengths increase comparing to those of series Ⅱ with formations of inclined cracks. These phenomena have been considered to depend on the restraint conditions such as the material of loading plates and the slenderness of the specimens (Van Mier et al. 1997). However, boundary restraint effects, such as the formation of inclined cracks, are different depending on series in spite of the same restraint conditions. It is considered that the restraint effect is varied depending on the internal factors such as W : S : C. The restraint mechanism derived from the boundary restraint inside the specimens is

-10000×10^{-6} 0 10000×10^{-6}

Figure 4 Lateral Strain Distributions (Loading State)

Table 3 The Maximum Average Lateral Strain (Loading State)

	450-5.51	550-5.51	450-3.74	550-1.09
60%	1098×10^{-6}	713×10^{-6}	794×10^{-6}	1051×10^{-6}
80%	1608×10^{-6}	1047×10^{-6}	1567×10^{-6}	1446×10^{-6}
90%	1884×10^{-6}	1630×10^{-6}	1931×10^{-6}	1695×10^{-6}
95%	2142×10^{-6}	2067×10^{-6}	2261×10^{-6}	1881×10^{-6}

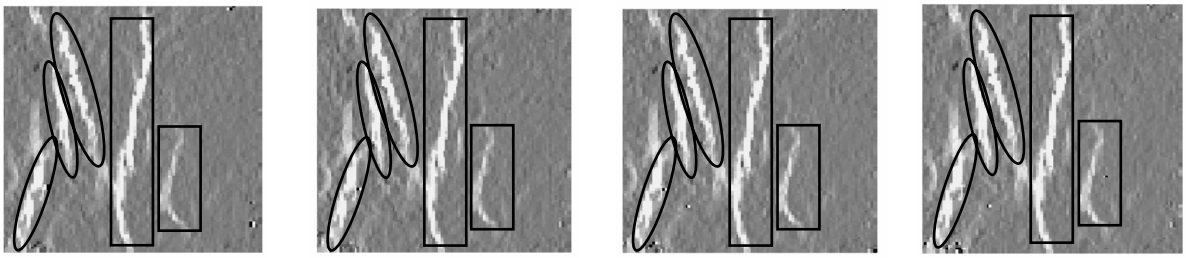

(a) 60% (b) 80% (c) 90% (d) 95%

(1) 450-5.51 (Series-Ⅰ)

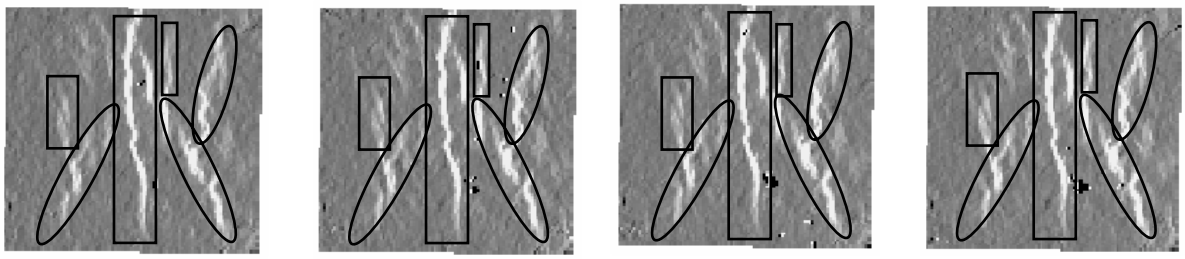

(a) 60% (b) 80% (c) 90% (d) 95%

(2) 550-5.51 (Series-Ⅰ)

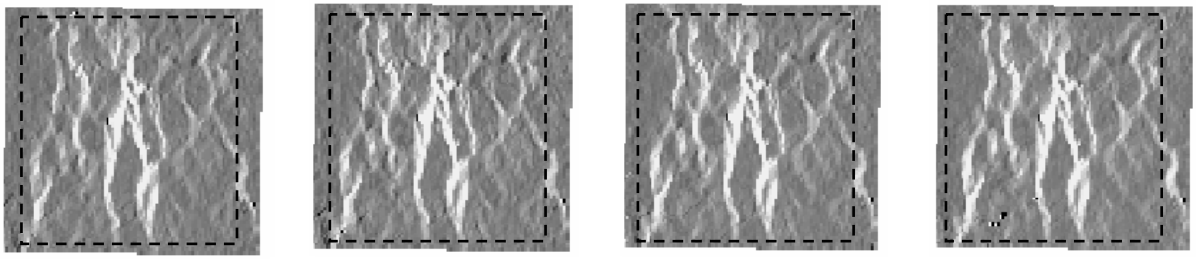

(a) 60% (b) 80% (c) 90% (d) 95%

(3) 450-3.74 (Series-Ⅱ)

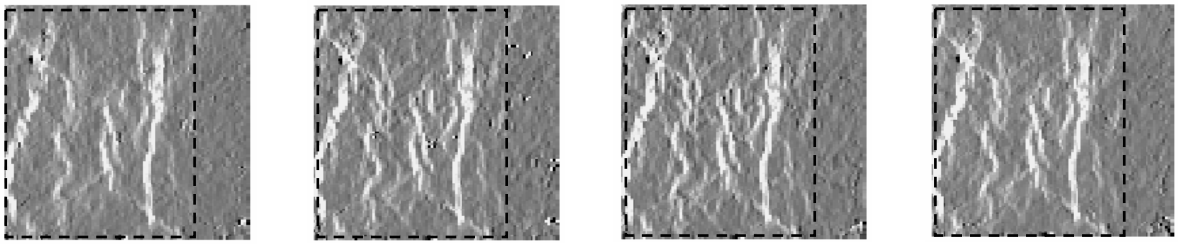

(a) 60% (b) 80% (c) 90% (d) 95%

(4) 550-1.09 (Series-Ⅱ)

significant in series Ⅰ.

Many vertical cracks could be confirmed, in the region enclosed by a rectangle written in a wavy line from 90% of the first peak load during loading stage, from the strain distributions of 450-3.74 and 550-1.09. On the other hand, inclined cracks could not be confirmed from the strain distributions of 450-3.74 and 550-1.09. It can be considered that compressive strengths of 450-3.74 and 550-1.09 are lower than those of 450-5.51 and 550-5.51 because of the formation of many vertical cracks.

The maximum average lateral strain increases with the progression of loading in all specimens. This increase of the maximum average lateral strain is mainly derived from crack initiations and propagations.

Vertical cracks and inclined cracks could be confirmed, in the region enclosed by a rectangle and a circle written in a

-10000×10^{-6} 0 10000×10^{-6}

Figure 5 Lateral Strain Distributions (Reloading State)

Table 4 The Maximum Average Lateral Strain (Reloading State)

	450-5.51	550-5.51	450-3.74	550-1.09
60%	2318×10^{-6}	1853×10^{-6}	2447×10^{-6}	2248×10^{-6}
80%	2428×10^{-6}	2060×10^{-6}	2722×10^{-6}	2461×10^{-6}
90%	2626×10^{-6}	2165×10^{-6}	2885×10^{-6}	2567×10^{-6}
95%	2750×10^{-6}	2340×10^{-6}	3087×10^{-6}	2735×10^{-6}

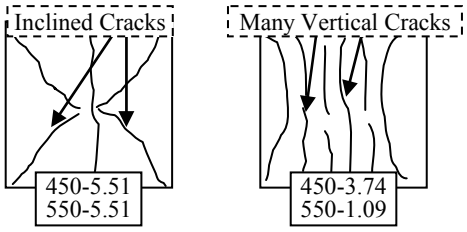

Figure 6 Crack Patterns of Specimens

solid line, at 60% of the second peak load, from the strain distributions of 450-5.51 and 550-5.51 during reloading stage. At the same time, vertical cracks were able to be observed, in the region enclosed by a rectangle written in a wavy line, at 60% of the second peak load, from the strain distributions of 450-3.74 and 550-1.09 during the reloading stage. In all cases, any initiation and propagation of cracks were not generated from 60% to 95% of the second peak load during the reloading state.

However, the maximum average lateral strain increases with the progression of loading in all specimens, as shown in Table 4. It is considered that this increase of the maximum average lateral strain is derived from the increase of the crack widths of formed cracks without the initiation of new cracks or the propagation of the existing cracks.

Figure 6 shows the crack pattern diagrams observed during the experiments. Inclined cracks were confirmed on specimens 450-5.51 and 550-5.51 whose compressive strengths were higher than those of 450-3.74 and 550-1.09. Many vertical cracks were confirmed from specimens 450-3.74 and 550-1.09.

Figure 7 shows the fracture behavior considered in loading and reloading states. Crack initiations and propagations were observed from strain distributions obtained from the digital image correlation method during the loading state in all cases. However, crack initiation and propagation behaviors were not observed during the reloading state in all cases. It is considered that the crack widths increased during the reloading state due to the increase of the maximum average strain.

5. CONCLUSIONS

Uniaxial compressive fracture behaviors of high-strength concretes under cyclic loadings were investigated by using the digital image correlation method. The followings summarize the obtained results.

1. Compressive strengths of concretes in the series for which W : S : C is constant and cracks are inclined were higher than the specimens for which W : S : C is not constant and fracture growth accompanied by many vertical cracks.
2. The phenomenon that inclined cracks generated from the boundary restraint effect is observed from specimens with identical W : S : C indicated that the influences of restraints are dependent not only on the material of the loading plates and the aspect ration of the specimens but also on other parameters that characterize the internal behavior of concrete.
3. The results of the digital image correlation method indicate that cracks are initiated and propagated during the loading state and crack widths increase during the reloading state.
4. It is considered that the digital image correlation method is applicable to evaluate the extent of damage of concrete under cyclic loadings.

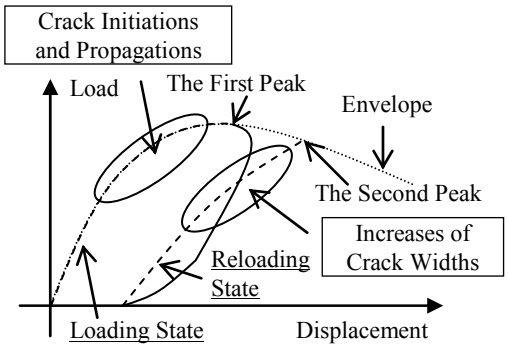

Figure 7 Fracture Behaviors for Each State

Acknowledgements:

The authors acknowledge support from the Japan Society for the Promotion of science. This study is also partially supported by Grants-in-Aid for Scientific Research, by the Ministry of Education, Science and Culture (A No.19206050).

References:

Matsuo, T., Sakai, M., Matsumura, T. and Kanazu, T. (2004), "An Experimental Study on Shear Resisting Mechanism of RC Beams with Corroded Reinforcement," *Concrete Research and Technology*, Japan Concrete Institute, **15**(2), 69-77.

Machida, A. (1978), "Fundamental Studies on Splitting Tensile Strength Tests of Concrete," *Proceedings of Japan Society of Civil Engineers*, Japan Society of Civil Engineers, **279**, 99-112.

Chu, T. C., Ranson, W. F., Sutton, M. A. and Peters, W. H. (1985), "Application of Digital-Image-Correlation Techniques to Experimental Mechanics," *Experimental Mechanics*, Society for Experimental Mechanics, **25**(3), 323-244.

Choi, S. and Shah, S. P. (1999), "Propagation of Microcracks in Concrete Studied with Subregion Scanning Computer Vision," *American Concrete Institute Materials Journal*, American Concrete Institute, **96**(2), 255-261.

Sagawa, Y., Onoue, K., Uchino, M. and Matsushita, H. (2007), "Applocation of Digital Image Correlation Method tp Strain Mesurement of Mortar Specimen under Uniaxial Compression," *Journal of the Japan Society for Experimental Mechanics*, The Japan Society for Experimental Mechanics, **7**(2), 20-26.

Shimizu, M. and Okutomi, M. (2004), "Two-Dimensional Simultaneous Sub-Pixel Estimation for Area-Based Matching," *The Institute of Electronics, Information and Communication Engineers Transactions on Information and Systems*, The Institute of Electronics, Information and Communication Engineers, **J87-D-2**(2), 554-564.

Steger, C., Ulrich, M. and Wiedemann, C. (2008), "Machine Vision Algorithms and Applications," Tokyo Shoseki Insatsu Kabusikigaisha.

Izumi, M., Mihashi, H. and Sasaki, T. (2004), "A Study of the Concrete Fracture Mechanism under Uniaxial Compressive Load," *Transactions of Architectural Institute of Japan*, Architectural Institute of Japan, **289**, 11-25.

Van Mier, J. G. M. et al. (1997), "Strain-Softening of Concrete in Uniaxial Compression," *Materials and Structures*, International Union of Laboratories and Experts in Construction Materials, Systems and Structures, **30**, 195-209.

Sixth International Conference on Urban Earthquake Engineering
March 3-4, 2009, Tokyo Institute of Technology, Tokyo, Japan

PARAMETRIC STUDY FOR SHEAR CARRYING CAPACITY OF SEGMENTAL CONCRETE BEAMS WITH EXTERNAL TENDONS

Dinh Hung Nguyen[1], Ken Watanabe[2], and Junichiro Niwa[3]

1) PhD. Candidate, Graduate School of Civil Engineering, Tokyo Institute of Technology, Japan
2) Assistant Professor, Department of Civil Engineering, Tokyo Institute of Technology, Japan
3) Professor, Department of Civil Engineering, Tokyo Institute of Technology, Japan
nguyen@cv.titech.ac.jp, ken@cv.titech.ac.jp, jniwa@cv.titech.ac.jp

Abstract: This paper presents a parametric study for segmental concrete beams with external tendons. The effect of the joint position and the prestress level are observed as important parameters in the shear mechanism transferred across a segmental joint by using nonlinear FEM. A simplified truss model has been modified based on the nonlinear FEM results to predict the shear carrying capacity and the critical diagonal compression member of segmental concrete beams with external tendons. The predicted results show a good agreement with the experimental results.

1. INTRODUCTION

External prestressing was developed in the early period of prestressed concrete bridges. The application of external prestressing with the precast segmental construction has both time saving in construction and substantial cost due to the reduction of dead load from the concrete section for the substructure. For this reason, the application of external prestressing has become more popular and widely used for bridge structures in recent years.

However, the segmental structure can become weak during the strong excitations due to an earthquake, especially in the high seismic zone with a high shear force. When an earthquake occurs, a segmental joint will be opened due to lack of longitudinal reinforcements. The area at a segmental joint to transfer shear force is reduced. It leads the collapse of segmental beams. Therefore, it is necessary to confirm that the shear failure does not take place in the precast segmental concrete structure.

Calculating for the shear carrying capacity of slender segmental concrete beams with external tendons has previously been based on empirical equations of monolithic beams. Recently, a simplified truss model for estimating the shear carrying capacity of segmental concrete beams with external tendons was proposed by Sivaleepunth et al. (2008). This simplified truss model was extended from the monolithic concrete beams with external tendons (Sivaleepunth et al. 2007) that was proposed and conducted a parametric study using nonlinear finite element method (FEM). Their model yields a greater accuracy if the critical segmental joint still remains in contact. In case the joint opening the shear force transferred cross a segmental joint has not a comprehensive explanation in this model. This model was also proposed without taking into account the influence of joint position in the shear span (Nguyen et al. 2007) because of the segmental joint closest to the loading point was the critical joint. Moreover, the shear mechanism of the slender segmental concrete beams was different from that of monolithic beams with external tendons as explained by Nguyen et al. 2008. On the other hand, the investigation of the effect of concrete stress at the bottom extreme fiber by nonlinear FEM analysis for the model propose by Sivaleepunth et al. (2008) was not good agreement with the experiment results by Nguyen et al. 2008.

In addition, MacGregor et al. (1989) have explained the local behavior of the segments near an opening joint. After a segmental joint opens a compressive strut is formed from the loading point to the lower corner of the segment. Another inclined strut runs across the segmental joint from the loading point to other segment. This shear behavior mechanism of segmental concrete beams with external tendons explained by Nguyen et al. (2008) was different from that of monolithic beam.

In this study, a simplified truss model has been modified to calculate the shear carrying capacity of slender segmental concrete beams with external tendons. In order to obtain the objective, the nonlinear FEM was used to clarify the shear force transferred across a segmental joint. The concentrated stress flow crossed to a segmental joint from the nonlinear FEM results is used to modify the simplified truss model. The shear carrying capacity calculated from the modified model is compared with the nonlinear FEM and experimental results to confirm the applicability of the model.

2. PARAMETRIC STUDY USING FEM

2.1 FEM analysis

Nonlinear FEM analysis using DIANA system had been carried out to examine the shear failure mechanism of

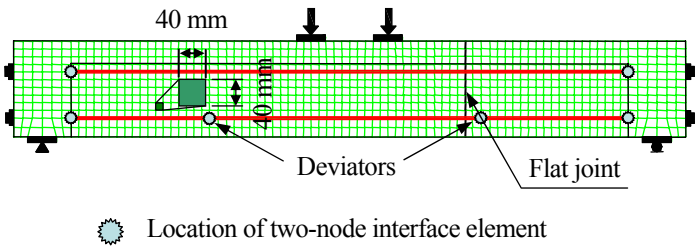

Figure 1 Mesh of finite element

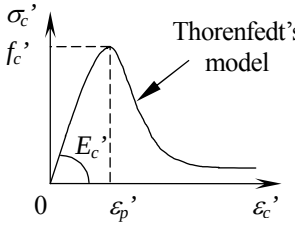

Figure 2 Compression model for concrete

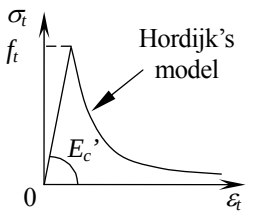

Figure 3 Tensile model for concrete

segmental concrete beams under the effect of significant parameters, which is discussed later. The concrete beams were modeled with a two-dimensional element, namely a four-node quadrilateral isoparametric plane stress element as shown in Figure 1. Thorenfeldt et al. (1987) and Hordijk's model (1991) were applied as the constitutive models of concrete in compression and tension as shown in Figures 2 and 3, respectively. The properties of concrete such as compressive and tensile strengths, elastic young modulus were archived from experimental results.

Longitudinal reinforcements were modeled by the embedded reinforcement element in DIANA system. External tendons were modeled by a two-node truss element. The stress–strain relationship for external tendons and reinforcing bars were appropriately represented by a bilinear elasto-plastic constitutive model. The properties of external tendons and reinforcement bars were obtained from experimental results.

To represent the interfacial behavior between external tendons and deviators or a concrete beam, the two-node interface element in DIANA system was applied. The coefficient stiffness of this interface element was adopted from Sivaleepunth et al. (2008) to model that the friction between the tendons and the deviators or concrete at ending parts of the beams was neglected.

Figure 1 also showed that the flat joint model had been applied to reproduce the real geometry joint by using the two-line interface element in DIANA system. Since the cracking observed in experiments (Nguyen et al. 2007, 2008) corresponded with the development of one single crack from a segmental joint that accumulated all the deformations, the discrete crack model was selected for the interface elements at segmental joints in this study.

2.2 Parametric study

In order to understand shear force transferred across a segmental joint, a number of important parameters were surveyed in the nonlinear FEM analysis. The prestressing force in terms of concrete stress at the bottom fibers, the compressive strength of concrete, f'_c, the ratio of shear span to effective depth, a/d, the effective depth, d were considered in this study. A distance from segmental joint to the loading joint, a_j, was investigated in terms of a_j/d. All the parameters were tabulated in Table 1.

The external tendons were applied in both tensile zone (lower tendons) and compressive zone (upper tendons). It was ensured that whole segmental joint was suffered from compression and the beam failure was occurred in concrete

Table 1 Summary of parameters

Parameters	Range	No. of case
a/d	3 to 4.5	4
a_j/d	0.5 to 2.5	5
σ_l (N/mm^2)	3 to 20	3
f'_c (N/mm^2)	30 to 65	3
d (mm)	400 to 600	3

before the yielding of external tendons. Because of segmental concrete beams, concrete stress in the extreme fiber of beams was not resisted tension. Therefore, the concrete stress in the top extreme fiber of beams was 0 N/mm^2. The initial prestressing force, f_{pe}, was introduced for the upper and lower tendons so that concrete stresses in the bottom extreme fiber of about 19 N/mm^2, 15 N/mm^2 and 10 N/mm^2.

Concrete strength, f'_c, and ratio of shear span to effective depth, a/d, have been significant parameters for shear problem. Concrete strength varied from 30 N/mm^2 to 65 N/mm^2, ratio of shear span to effective depth was changed in range from 3 to 4.5. While the effective depth of beams ranged from 400 mm to 600 mm.

Joint position has been also affected on a joint opening that influenced on the shear transfer mechanism across a segmental joint. Ratio of the distance from segmental joint to loading point to effective depth of segmental beams, a_j/d, was changed from 0.5 to the 2.0.

3. SIMPLIFIED STRUSS MODEL

3.1 Evaluate the inclination angle of concentrated stress flow and divide the model

Based on nonlinear FEM results, the stress flow transferred across a segmental joint was investigated to modify the simplified truss model for segmental concrete beams with external tendons. These nonlinear FEM analysis results were compared to the experimental results in order to confirm the applicability of the former. A contour figure of the principal compressive stress, σ_2, at 90% of analytical resistance of shear carrying capacity was utilized to predict the inclination angle of the concentrated stress flow across the segmental joint.

In order to predict shear failure, concentrated stress flow from the loading point was investigated. Figure 4 marks the location of the maximum absolution value of σ_2 at each Gauss's point in the location of the concentrated stress

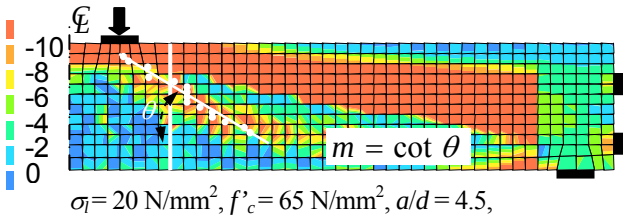

σ_l= 20 N/mm^2, f'_c= 65 N/mm^2, a/d = 4.5,
a_j/d = 0.5, d = 400 mm

$$\frac{1}{nS_xS_y}\sum_{i=1}^{n}\left(x_i-\bar{x}\right)\left(y_i-\bar{y}\right)\geq 0.95$$

$\bar{x}$, $\bar{y}$: Mean of x and y

n : Number of data considered

S_x, S_y : Standard deviation of x and y

Figure 4 Evaluation of inclination of concentrated stress flow in term m value

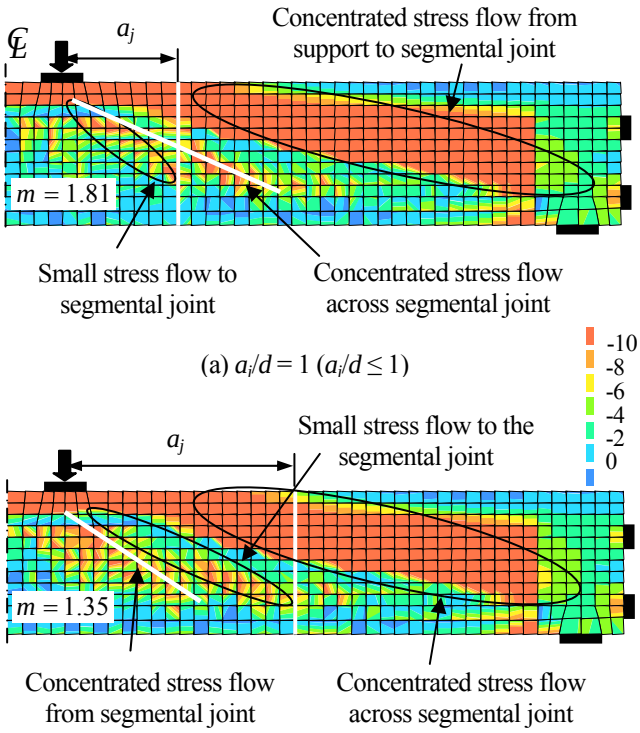

σ_l= 20 N/mm^2, f'_c= 65 N/mm^2, a/d = 4.5, d = 400 mm

Figure 5 Contour figure of principal stress σ_2 varying of joint position (a_j/d).

flow from the loading point. This was based on a set of X-Y coordinates and the correlation coefficient calculated from the equation shown in Figure 4. The marked Gauss's points with high values of correlation coefficient (≥0.95) were utilized to determine the inclination angle of concentrated stress flow. The concentrated stress flow from the loading point was evaluated in terms of m, where $m = \cot\theta$ and θ is an angle of the concentrated stress flow inclining from longitudinal axis.

The local behavior of a segmental joint near an opening

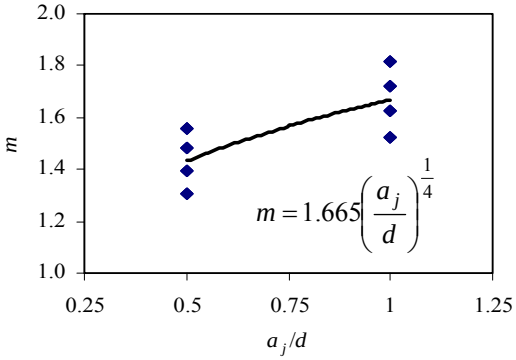

(a) $a_j/d \leq 1$

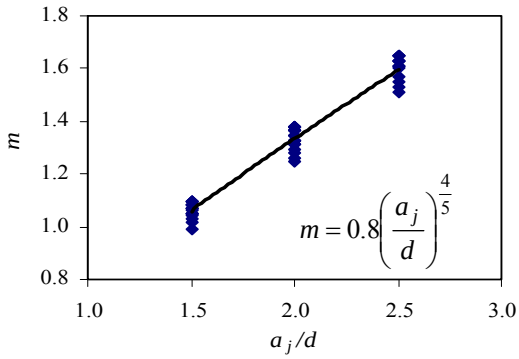

(b) a_j/d > 1

Figure 6 Relationship of m and a_j/d.

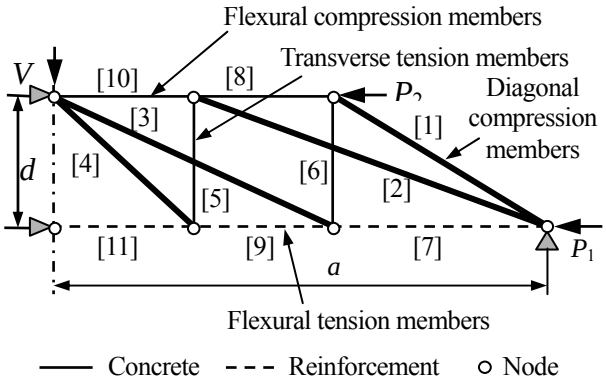

Figure 7 Schematic diagram of simplified truss model (a half of beam).

joint explained by MacGregor et al. (1989) presents a agreement with the experimental and nonlinear FEM results. Figure 5 shows the contour figure of segmental beams with the effect of the joint position. It was found that correlation position of the concentrated stress flow with a joint position was affected by the joint position. For the beam with $a_j/d \leq$ 1.0, a separately concentrated stress flow crossed the segmental joint from the loading point, while other stress flow started from support to segmental joint as shown in Figure 5(a). However, for the beam with a_j/d > 1.0 as shown in Figure 5(b), a concentrated stress flow crossed the segmental joint was from the support. This stress flow did not converge to the loading point, while a separately concentrated stress flow from the loading point did not cross the segmental joint. A slightly compressive strut from the

loading point to the lower corner of the segment was observed. Figure 6 shows the summary of the relationships between the *m* values from nonlinear FEM analysis results and joint position. That means joint position strongly influenced on the inclination of concentrated stress flow.

Figure 7 shows the schematic diagram of the simplified truss model (a half beam) which was adopted in this study based on the comprehensive explanation for the shear failure mechanism of segmental concrete beams with external tendons. In this simplified truss model, one compression member was adopted from the bottom of the web at the edge of the critical segmental joint. As discussed about the correlation position of the concentrated stress flow compared with the joint position, the shear failure mechanism can be divided into two types of failure pattern as shown in Figure 8. Model 1 was for the segmental concrete beam with $a_j/d \leq 1.0$, a concentrated stress flow was across the segmental joint from the loading point as presented in Figure 8(a). Model 2 was for the segmental concrete beam with $a_j/d > 1.0$, a concentrated stress flow was across the segmental joint from the support as presented in Figure 8(b).

In Model 1, the distance *md* was adopted as the horizontal distance from the loading point to the ended node of member [3]. The compression member [4] was adopted from the bottom of the web at edge of the segmental joint. In Model 2, the distance *md* was adopted as the horizontal distance from the loading point to the ended node of member [4], while the compression member [3] was adopted from the bottom of the web at edge of the segmental joint.

These *m* values were affected on not only joint position, a_j/d, but also other parameters. In the case of segmental concrete beams, concrete stress in the extreme fiber of beams is not resisted tension. Therefore, only concrete stress at the bottom extreme fiber, σ_l, was consider in an *m* value. The location of the deviators had less effect on *m* value as mentioned by Sivaleepunth et al. (2008) and the experimental results (Nguyen et al. 2007). Moreover, relationships between *m* value and other parameters such as a/d, f'_c and *d* were also investigated. It was found that *m* values are influenced by the a/d, a_j/d and σ_l. Formulae of *m* value for Model 1 and Model 2 can be written as follow Eq. (1) and Eq. (2), respectively.

$$m = 1.584\left(\frac{a_j}{d}\right)^{\frac{1}{4}}\left(\frac{a}{d}\right)^{\frac{3}{8}}(\sigma_l)^{-\frac{1}{7}} \quad (1)$$

$$m = 0.505\left(\frac{a_j}{d}\right)^{\frac{4}{5}}\left(\frac{a}{d}\right)^{\frac{1}{10}}(\sigma_l)^{\frac{1}{10}} \quad (2)$$

3.2 Cross section of members

Names of member were presented in Figure 7. The cross sectional area of the transverse tension member [5] was assumed to be the distance from the critical joint position to the loading point multiplied by the web thickness, while the cross sectional area of member [6] was assumed to be the distance from the critical segmental joint to the support multiplied by the web thickness. The cross sectional area of members [5] and [6] take into account the area of the transverse reinforcement in its length multiplied by the ratio

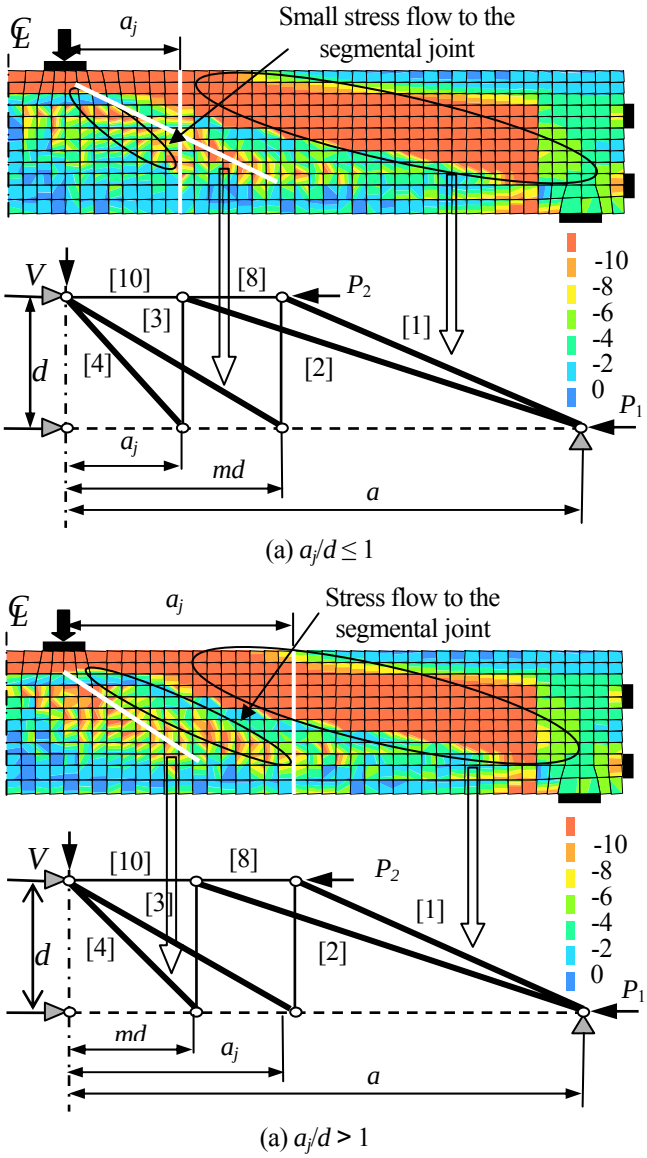

Figure 8 Division of modified models

of elastic stiffness of reinforcement to elastic stiffness of concrete, E_s/E_c. The cross sectional area of the flexural compression struts was set at $t_f b_f$, where t_f and b_f were the thickness and the width of flange. The cross sectional area of external tendons was employed as the cross sectional area of the flexural tension member.

The thickness of the compression struts of the simplified truss model was also formulated based on the nonlinear FEM results. The compressive stresses in the vertical direction at each Gauss's points, σ_{yi}, at 90% of the shear carrying capacity were considered. The distribution of the ratio of σ_{yi} and the maximum value $\sigma_{yi\text{-}max}$, ($\Delta_i = \sigma_{yi}/\sigma_{yi\text{-}max}$) in horizontal direction of beams was used to calculate. The horizontal width, t_i, of the distribution where Δ_i was equal to 0.1 was measured to determine the thickness of compression struts. In the modified model, the members [1] - [2] and members [3] - [4] were considered to be affected by the support and loading plates. Three levels of Gauss's points in the web below the flange were considered to evaluate the effect of the loading plate. The average value

of the horizontal width at the vicinity of the loading plate was t_l. While three levels of Gauss's points in the web above the level of external tendons were considered to evaluate the effect of the support plate. The average value of the horizontal width at the vicinity area of support plate was t_s. The cross sectional area of each strut can be assumed as the value of t_l or t_s multiplied with web thickness, b_w, and its inclination angle compared to the longitudinal direction.

The effect of the width of loading, w_l, and support, w_s, plates, the effective depth, d, and the ratio of flange width to web width, b_f/b_w, stirrups, and the longitudinal reinforcement on the thickness of compression member were explained by Sivaleepunth et al. (2008). Because of the discontinuity of the longitudinal reinforcement at a segmental joint, the effect of longitudinal reinforcement was insignificant. In this study, the effects of the a/d and a_j/d were considered. The values of t_l and t_s can be estimated for Model 1 as shown in Eps. (3) and (4). Meanwhile, the values of t_l and t_s can be estimated for Model 2 as shown in Eps. (5) and (6).

$$t_s = 2\left(w_s + 0.1d\right)\left(\frac{b_f}{b_w}\right)^{\frac{1}{5}}\left(1+\left(\frac{A_{sv}}{b_w s}\right)^{\frac{1}{4}}\right)\left(0.193\left(\frac{a}{d}\right)^{\frac{3}{2}}\left(\frac{a_j}{d}\right)^{\frac{1}{5}}\right) \quad (3)$$

$$t_l = \left(w_l + 0.1d\right)\left(\frac{b_f}{b_w}\right)^{\frac{1}{5}}\left(1+\left(\frac{A_{sv}}{b_w s}\right)^{\frac{1}{4}}\right)\left(0.193\left(\frac{a}{d}\right)^{\frac{3}{2}}\left(\frac{a_j}{d}\right)^{\frac{1}{5}}\right) \quad (4)$$

$$t_s = 2\left(w_s + 0.1d\right)\left(\frac{b_f}{b_w}\right)^{\frac{1}{5}}\left(1+\left(\frac{A_{sv}}{b_w s}\right)^{\frac{1}{4}}\right)\left(0.122\left(\frac{a}{d}\right)^{\frac{3}{2}}\left(\frac{a_j}{d}\right)^{\frac{2}{3}}\right) \quad (5)$$

$$t_l = \left(w_l + 0.1d\right)\left(\frac{b_f}{b_w}\right)^{\frac{1}{5}}\left(1+\left(\frac{A_{sv}}{b_w s}\right)^{\frac{1}{4}}\right)\left(0.122\left(\frac{a}{d}\right)^{\frac{3}{2}}\left(\frac{a_j}{d}\right)^{\frac{2}{3}}\right) \quad (6)$$

3.3 Evaluate of shear carrying capacity

In order to calculate the shear carrying capacity of segmental concrete beams with external tendons, equivalent elastic analysis was utilized. The member force, F_i, of each member was calculated based on the Castigliano's second theorem, the theorem of minimum strain energy. Secant modulus, E_{cu}, was utilized for calculating the compression struts, while initial elastic modulus was applied for flexural compression members. The resistance of each member, R_i, was calculated by multiplying f'_c by concrete softening parameter and the correlatively cross sectional area, A_i. The shear carrying capacity and the critical member were estimated when the maximum value of ratio of F_i to R_i was equal to 1 [max $(F_i/R_i) = 1$, i = 1÷4].

4. ACCURACY OF PROPOSED METHOD

In order to verify the validity of the modified simplified truss model, the calculated results from the modified simplified truss model were compared with the collected experimental results. A total of 12 segmental concrete beams with external tendons using epoxy to connect the segments were utilized for comparision. Seven of the segmental beams were presented by Hosoda et al. (2002) and Sivaleepunth et al. (2008). The other segmental beams were conducted by Nguyen et al. (2007, 2008). In the data collected there appear several factors such as a/d, a_j/d, d, f'_c and σ_l and are tabulated in Table 2.

The modified models were applied to determine the shear carrying capacity of beams and the critical compression member. The shear carrying capacity calculated from the simplified truss model was compared with that from the experimental results as presented in Table 2. Meanwhile the critical compression member was used to compare with the crack pattern of the beam at the ultimate stage as shown in Figure 9. In Figure 9, the bold dashed line represents the critical compression strut of each beam.

In addition, the predicted results of shear carrying capacity from the modified model from this study are compared with those from simplified truss model by Sivaleepunth et al. (2008). Figure 10 presents the validity of each model. The validity of the prediction equations was also examined by using results from the statistical analyses in terms of mean values, standard deviations, and correlation coefficients as given in Table 2. Based on the predicted results for the shear carrying capacity, it was found that the modified simplified truss models offer better accuracy in prediction of shear carrying capacity for segmental concrete beams with external tendons

5. CONCLUSIONS

This paper has presented a comprehensive parametric evaluation by the application of nonlinear FEM analysis to the shear failure mechanism of segmental concrete beams with external tendons. Some important parameters such as shear span to effective depth ratio, position of segmental joint, prestress level, compressive strength of concrete and effective depth were carried out in this study. The shear mechanism of a segmental joint with a joint opening by the compression stress flow was well explained in this study. It was found that joint position and prestress level strongly affect the tendency of change of inclination angle of the concentrated stress flow. In slender segmental concrete beams with external tendons, the segmental joint nearest the loading point dominated the response of the segmental concrete beams. The nonlinear FEM analysis results was showed that when $a_j/d \leq 1.0$, a compression stress flow from the loading point crossed the critical segmental joint. While $a_j/d > 1.0$, a concentrated stress flow from a support crossed the critical segmental joint. From these tendencies, two formulae for calculating the inclination angle of concentrated stress flow were proposed in terms of m value.

The simplified truss model was modified based on the parametric study of m values. The thickness of diagonal compression members is also formulated based on the nonlinear FEM analysis results with taking into account the influence of support and loading plates, effective depth, shear span to effective depth ratio, position of segmental

Table 2 Summary of experimental data used to compare with the calculated results

References	Beams	a/d	a_j/d	d (mm)	f'_c (N/mm^2)	σ_l (N/mm^2)	P_{EXP} (kN)	P_{cal}(kN)	P_{EXP}/P_{cal}	Failure member
Present	SJ25	3.5	2.50	400	65.7	19.5	480.3	490.3	0.98	4
	SJ15		1.50		68.9	19.2	406.8	471.2	0.86	2
	SJ10-19		1.00		65.7	20.0	453.9	414.0	1.10	2
	SJ-05		0.50		64.6	19.9	423.0	424.2	1.00	1
	SJ10-10		1.00		65.7	10.7	394.6	426.5	0.93	3
Sivaleepunth et al. (2008)	S40		0.50		35.6	11.3	251.4	253.6	0.99	3
	S80				32.1	11.0	230.9	233.4	0.99	3
	H40				67.6	18.5	439.4	434.5	1.01	1
	H80				65.8	19.6	439.7	427.2	1.03	1
Hosoda et al. (2002)	Seg-1	3.6	0.40	500	52.9	10.8	324.0	310.0	1.05	3
	Seg-2				54	10.8	448.0	376.0	1.19	3
	Seg-3				58.8	10.8	355.0	329.5	1.08	3

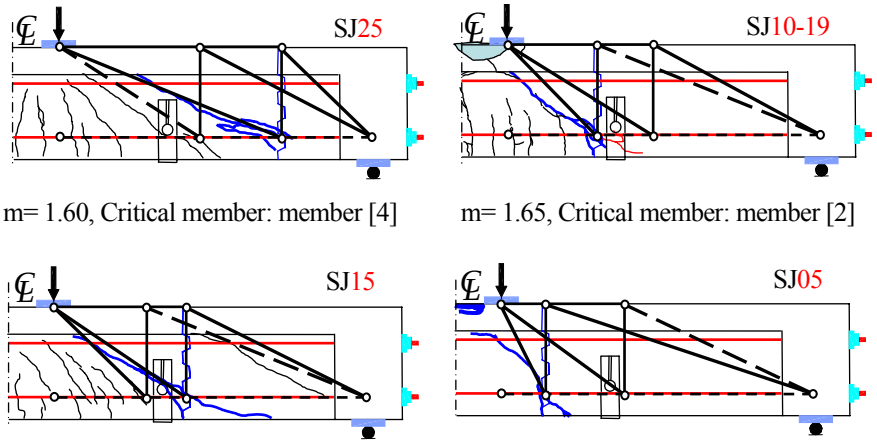

Figure 9 Critical member and crack pattern

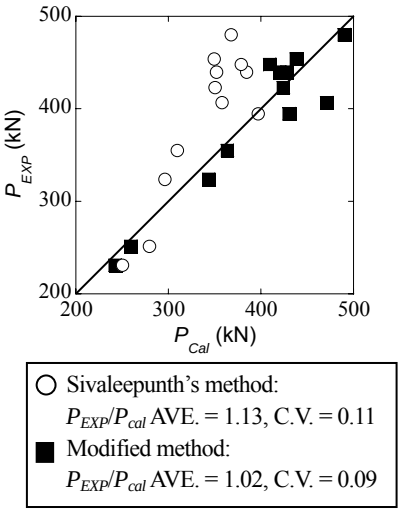

Figure 10 Validation of equation

joint, prestress level and compressive strength of concrete. An equivalent elastic analysis was applied to the simplified truss models to predict for the shear carrying capacity of segmental concrete beams with external tendons. The shear carrying capacity assessed from modified simplified truss models provided better accuracy in comparison with the measured values and the existing prediction model for segmental concrete beams with external tendons.

References:

Japan Society of Civil Engineers (JSCE) (2002), "Standard Specification for Concrete Structures," Structure Performance Verification.

Sivaleepunth, C., Niwa, J., Bui, K. D., Tamura, S. and Hamada, Y. (2007), "Simplified Truss Model for Externally Prestrtessed Concrete Beams," *Journal of Materials, Concrete and Pavements*, JSCE, **63**(4), 562-574.

Sivaleepunth, C., Niwa, J., Nguyen, D. H., Hasegawa, T. and Hamada, Y. (2008), "Shear Carrying Capacity of Segmental Prestrtessed Concrete Beams," *Journal of Materials, Concrete and Pavements*, JSCE, **Publishing**.

MacGregor, R. J. G. Kreger, M. E. and Breen, J. E (1989), "Evaluation of Strength and Ductile of Precast Segmental Box Girder Construction with External Tendons," *Research Report*, No. 365-3F.

Thorenfeldt, E., Tomaszewicz, A. and Jensen, J. J. (1987), "Mechanical Properties of High-Strength Concrete and Application in Design," *Symposium Procceding*, Utilization of High-Strength Concrete, Norway.

Hordijk, D. A. (1991), "Local Approach to Fatigue of Concrete," *PhD thesis*, Delft University of Technology

Nguyen, D. H., Niwa, J., Sivaleepunth, C. and Hasegawa, T. (2008), "Influence of Joint Position on Shear Behavior of Segmental Concrete Beams with External Tendons," *Proceeding of JCI*, **30**(3), 565-570.

Nguyen, D. H., Watanabe, K., Niwa, J., and Hasegawa, T. (2009), "Influence of Prestress Level on Shear Behavior of Segmental Concrete Beams with External Tendons," *Proceeding of JCI*, **Under review**.

Sixth International Conference on Urban Earthquake Engineering
March 3-4, 2009, Tokyo Institute of Technology, Tokyo, Japan

MID-COLUMN POUNDING WITH HEAVY ADJACENT BUILDING CONSIDERING SOIL-FOUNDATION INTERACTION

Kabir Shakya[1], Anil C. Wijeyewickrema[2], and Tatsuo Ohmachi[3]

1) Graduate Student, Department of Civil Engineering, Tokyo Institute of Technology, Japan
2) Associate Professor, Department of Civil Engineering, Tokyo Institute of Technology, Japan
3) Professor, Department of Built Environment, Tokyo Institute of Technology, Tokyo, Japan
shakya.k.aa@m.titech.ac.jp, wijeyewickrema.a.aa@m.titech.ac.jp, ohmachi@enveng.titech.ac.jp

Abstract: An analysis of seismic pounding with a heavy adjacent reinforced concrete building with non-equal story heights, including soil-foundation interaction is presented in this paper. Soil-foundation interaction is considered by using the discrete model and pounding between buildings is incorporated through impact elements which consist of a gap element and a Kelvin-Voigt element. The response of buildings are presented in terms of impact forces, base shear, interstory displacements and normalized story shear to evaluate the performance when buildings are subjected to two near field and two far field earthquakes. The buildings under consideration experience larger maximum impact forces and maximum interstory displacements due to the near field earthquakes for both fixed foundation and foundation with soil flexibility cases. The largest maximum interstory displacements occurred when there is no pounding. In general, the buildings with fixed foundations experience higher base shear and maximum normalized story shear.

1. INTRODUCTION

During earthquakes, insufficiently separated adjacent buildings having different dynamic characteristics may vibrate out of phase and collide causing non-structural and structural damage to the buildings. In the past, because of rapid urbanization and the associated increase in real-estate values, especially in urban areas, many buildings were constructed even up to their property lines with insufficient or no gap between adjacent buildings. The location and magnitude of impact force depend on characteristics of input ground motion, geometric configurations and dynamic characteristics of buildings, soil parameters and gap between the adjacent buildings. In order to eliminate seismic pounding, building codes such as IBC (2003) have provided a clause to make a provision of sufficient separation between adjacent buildings. However, there is no such clause in IBC (2006). Due to constraints in availability of land and in order to fulfill functional requirements, adjacent buildings may be constructed with different floor heights which may give rise to eccentric and mid-column pounding.

Investigating the damage during past earthquakes, five major types of pounding, viz., mid-column pounding, heavier adjacent building pounding, taller adjacent building pounding, eccentric building pounding and end building pounding have been reported by Jeng and Tzeng (2000). In order to simulate earthquake induced pounding between adjacent structures, Anagnostopoulos (1988) used the spring-damper element in which the damping constant is represented in terms of coefficient of restitution. To perform more accurate simulation of structural pounding during earthquakes, Jankowski (2005) incorporated a non-linear viscoelastic element. The analytical results were then compared with the results of experiments performed by van Mier et al. (1991) to find the characteristics of concrete-to-concrete impact and steel-to-steel impact. The effects of soil flexibility on seismic pounding for adjacent multi-story buildings of differing total heights was highlighted by Rahman et al. (2001) by using the discrete model proposed by Mullikan and Karabalis (1998). In the present paper too, the discrete model is used to incorporate soil-foundation interaction. Figure 1 shows the discrete model composed of foundation mass, dampers and springs. Shakya et al. (2008) investigated the effects of underlying soil on mid-column pounding of reinforced concrete buildings in a row.

In most of the cases, the effects of underlying soil are ignored when performing seismic pounding analyses. However, consideration of underlying soil adds extra degrees of freedom at the foundation level and also allows energy dissipation. Hence, it is necessary to consider

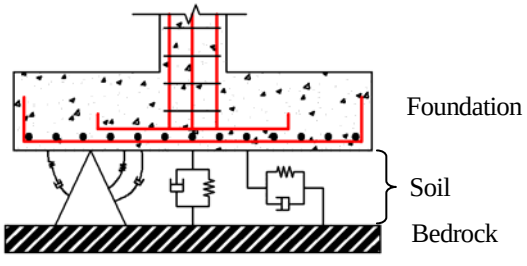

Fig. 1. Discrete model for soil-foundation interaction.

effects of underlying soil on the seismic pounding analysis of buildings. In the present paper, analytical results of mid-column pounding with heavy adjacent building upon considering soil-foundation interaction, are presented in terms of impact forces, base shear, interstory displacements and normalized story shear.

2. POUNDING FORCE AND IMPACT ELEMENT

Elastic or viscoelastic impact elements are often used to model pounding between adjacent structures. The Kelvin-Voigt element (linear spring-damper element) is mostly used to model impact between two colliding structures. The viscous component of the Kelvin-Voigt element is activated with the same damping coefficient during the whole time of contact. The force in Kelvin-Voigt element $F(t)$ during impact is given by

$$F(t) = k_L \delta(t) + c_L \dot{\delta}(t), \qquad (1)$$

where, $\delta(t)$ is the relative displacement of colliding structural elements, $\dot{\delta}(t)$ is the relative velocity between colliding elements, k_L is the stiffness and c_L is the damping coefficient and is given by

$$c_L = -2 \ln e_r \sqrt{\frac{k_L m_1 m_2}{\left[\pi^2 + (\ln e_r)^2\right](m_1 + m_2)}}, \qquad (2)$$

where, e_r is the coefficient of restitution, m_1 and m_2 are masses of structural members. The impact elements are inserted between buildings as shown in Fig. 2(a) to simulate contact of buildings and pounding force. The link element shown in Fig. 2(c) is created by combining the gap element shown in Fig. 2(b) with Kelvin-Voigt model. The force-deformation relationship of gap element is given by

$$f_G = \begin{cases} k_G[(u_i - u_j) - gap] & \text{if } u_i - u_j > gap, \\ 0 & \text{if } u_i - u_j < gap, \end{cases} \qquad (3)$$

where, f_G is the force, k_G is the spring constant, u_i and u_j are the nodal displacements of nodes i and j and gap is the initial gap opening. The stiffness of gap element k_G is considered as $100k_L$, to avoid error in convergence and to ensure that it works nearly rigidly when the gap is closed. The force transmits from one structure to another only when contact occurs. For concrete-to-concrete impact, $k_L = 93,500$ kN/m and $e_r = 0.65$ showed good correlation between the numerical simulation results of Jankowski (2005) and experimental results provided by van Mier et al. (1991). Anagnostopoulos (1988), Azevedo and Bento (1996), Mouzakis and Papadrakakis (2004) and Jankowski (2006) have also used $e_r = 0.65$ for concrete to concrete impact. In the present study also $k_L = 93,500$ kN/m and $e_r = 0.65$ are used.

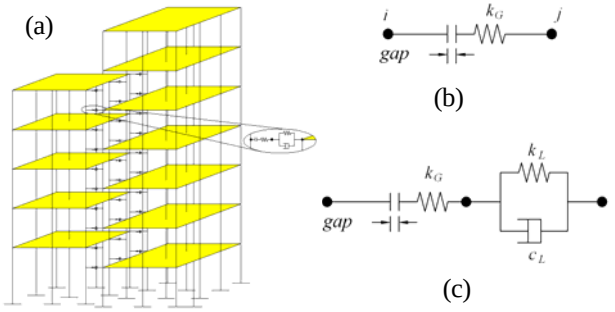

Fig. 2. (a) Buildings connected with impact elements; (b) gap element; and (c) impact element composed of gap element and Kelvin-Voigt element.

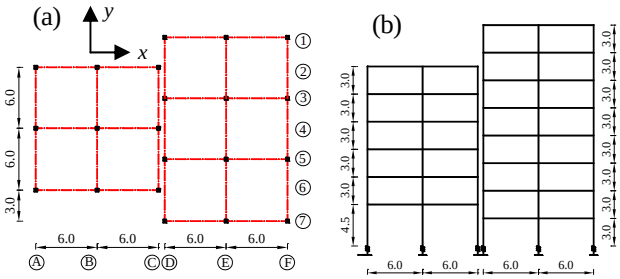

Fig. 3. The 6-story and 8-story buildings: (a) plan; and (b) elevation.

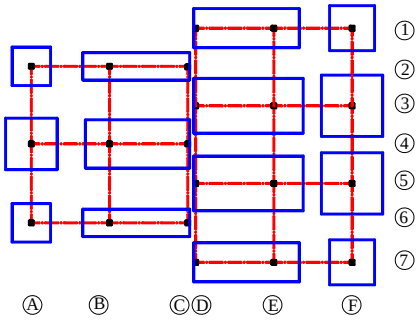

Fig. 4. Foundation arrangement plan.

3. DESCRIPTION OF BUILDINGS AND DESIGN

The plan and elevation of the 6-story and 8-story buildings as shown in Fig. 3, are considered for the analysis,. The story height of the first floor of the 6-story building is 4.5 m while all other story heights of 6-story and 8-story buildings are 3.0 m, which gives rise to mid-column pounding. The software SAP2000 is used to analyze the buildings considering 5% damping ratio. Concrete with compressive strength $f_c' = 27$ N/mm^2, unit weight $\gamma_c = 24$ kN/mm^3, modulus of elasticity $E_c = 24,281$ N/mm^2, and Poisson's ratio $\nu_c = 0.2$ and reinforcing steel with yield strength $f_y = 414$ N/mm^2 are used for analysis and design. The buildings are assumed to be located at site class D (stiff soil), seismic use group II and seismic design category A. Live load of 2 kN/m^2, roof load of 1 kN/m^2,

Table 1. Footing details.

Grid	A	B	C	D	E	F
1/7				8.15 × 3.00 × 0.50		3.50 × 3.50 × 0.45
2/6	3.00 × 3.00 × 0.40	8.20 × 2.10 × 0.40				
3/5				8.75 × 4.20 × 0.60		4.75 × 4.75 × 0.60
4	4.00 × 4.00 × 0.50	8.20 × 3.70 × 0.60				

(All dimensions are in m)

partition wall load of 1 kN/m^2 and earthquake loads are calculated according to IBC 2003. The structural components including foundations of the buildings are designed to fulfill the code requirements of ACI 318-02. The buildings are provided with 180 mm thick floor slabs which are considered as rigid floor diaphragms and 300 mm × 500 mm beams. Assuming allowable bearing capacity of 150 kN/m^2 for silty gravel soil, square and rectangular footings are designed. The dimensions of footings are given in Table 1 and the arrangement of footings is shown in Fig. 4.

4. NUMERICAL ANALYSIS AND RESULTS

The mass, damper and spring coefficients of each footing are calculated from Eqs. (2.42a)-(2.44) and Tables 2-4 of Wolf (1988) (pg. 32-36), using the designed footing size (Table 1) with 1.5 m embedment and soil properties: density $\rho_s = 16.5$ kN/m^3, Poisson's ratio $\nu = 1/3$ and shear modulus $G = 55.30$ N/mm^2. The gap between the buildings are assumed to be 50 mm. Two far field earthquakes, 1940 El Centro (Imperial Valley irrigation station, N-S component, PGA = 0.298g, M_w = 7.0) and 1968 Hachinohe (Hachinohe city station, N-S component, PGA = 0.229g, M_w = 7.9) and two near field earthquakes, 1994 Northridge (Sylmar county hospital parking lot station, N-S component, PGA = 0.843g, M_w = 6.7) and 1995 Kobe (0 KJMA station, N-S component, PGA = 0.821g, M_w = 6.9) are used as earthquake inputs along *x*-direction. Time history analysis is conducted using Newmark method with $\beta = 0.25$, $\gamma = 0.5$ and time step $\Delta t = 0.002$ sec.

Table 2 shows the fundamental time periods and frequencies of the buildings. An increase in fundamental time period of the buildings is observed when underlying soil is considered. From the Fourier spectrum of input

Table 2. Dynamic properties of buildings.

Foundation Type	Fundamental Period (sec)		Natural Frequency (Hz)	
	6-Story	8-Story	6-Story	8-Story
Fixed	0.9693	1.0855	1.0317	0.9212
With soil Flexibility	0.9893	1.1117	1.0108	0.8995

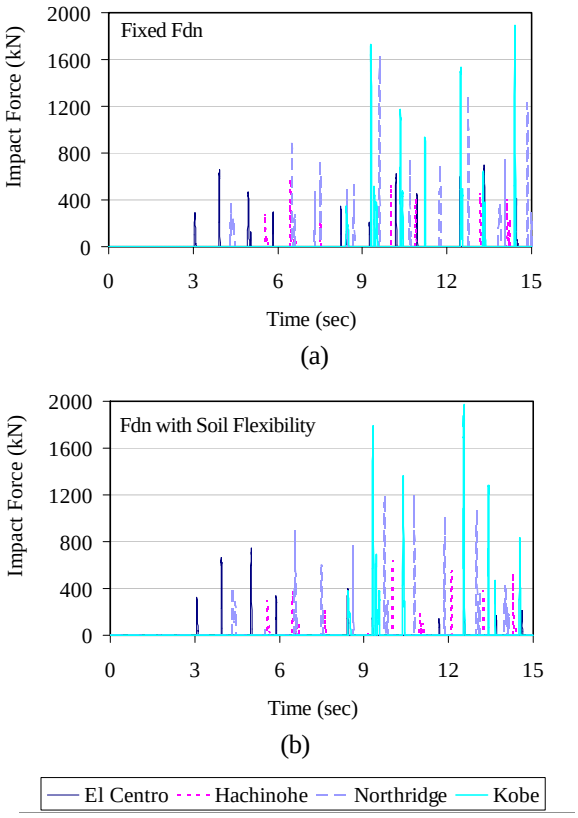

Fig. 5. Impact force time history at roof level of 6-story building column C4.

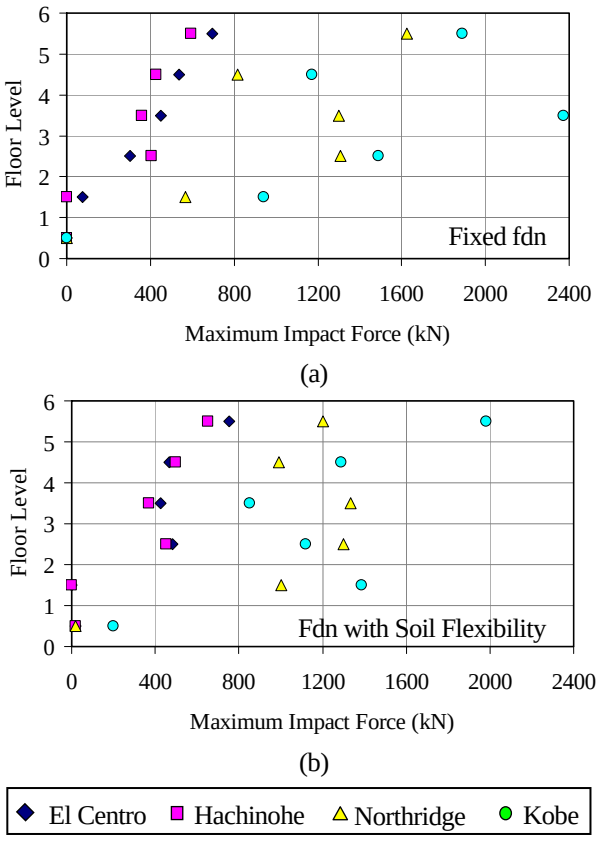

Fig. 6. Maximum impact force at 6-Story building column C4.

ground motions, the dominant frequencies of El Centro, Hachinohe, Northridge and Kobe earthquakes are found to be 2.151 Hz, 0.361 Hz, 0.633 Hz and 1.417 Hz, respectively. The dominant frequency of Northridge earthquake is close to the fundamental frequency of 8-story building considering foundations with soil flexibility (i.e., foundation represented by the discrete model) and that of Kobe earthquake is close to the fundamental frequency of 6-story building with fixed foundations.

The impact force time history at roof level of 6-story building, column C4, is shown in Fig. 5 where it can be seen that the collision between buildings occurs at different times with different magnitudes. Only for Northridge earthquake the magnitude of maximum impact force is reduced when foundation with soil flexibility is considered. Kobe earthquake has the dominant effect for both fixed foundation case and foundation with soil flexibility case. Higher magnitude of impact forces are observed in the case of near field earthquakes. On comparing the maximum impact forces at each floor level of 6-story building, column C4 (Fig. 6), it is clearly seen that the largest maximum impact forces

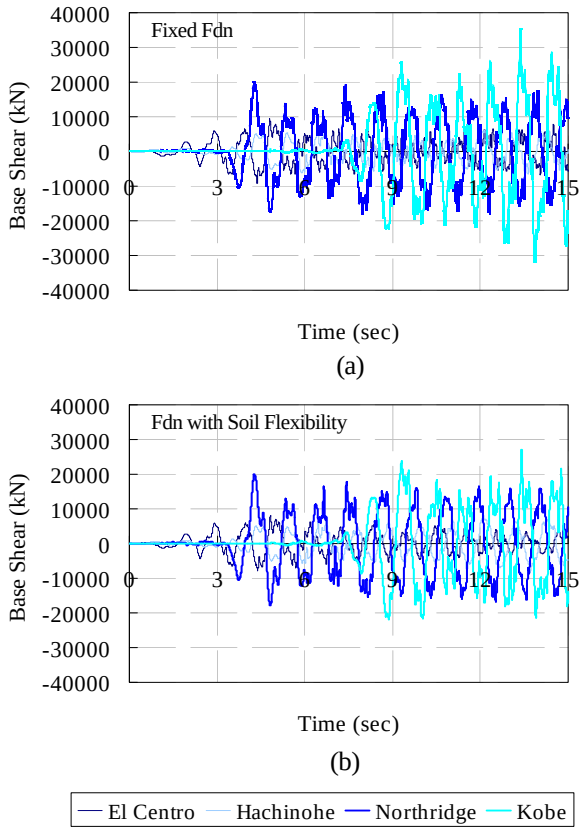

Fig. 7. Base shear time history.

Table 3. Ratio of max. base shear to weight of buildings.

	Fixed Foundation	Foundation with Soil Flexibility
El Centro	0.293	0.246
Hachinohe	0.218	0.246
Northridge	0.612	0.615
Kobe	1.091	0.830

have been reduced for near-field earthquakes when foundations with soil flexibility is considered.

Figure 7 shows the base shear time history of the buildings with fixed foundations and foundations with soil flexibility when pounding occurs between the buildings. The total weight of the buildings is 32,577 kN. The ratio of the maximum base shear to the weight of the buildings due the considered earthquakes are tabulated in Table 3, where it can be seen that for the buildings with foundations with soil flexibility, the ratios have been reduced in the case of El Centro and Kobe earthquakes, however, slight increase is observed in the case of Hachinohe and Northridge earthquakes.

Maximum interstory displacement of the buildings at columns C4 and D5 for fixed foundation no pounding, fixed foundation with pounding and foundation with soil flexibility with pounding, cases are shown in Fig. 8. Reduction in interstory displacement is observed while pounding between adjacent buildings occur. The largest maximum interstory displacements in all the buildings are observed when there is no pounding (Figs. 8 (a)-(b)). For El Centro and Kobe earthquakes maximum interstory displacements are reduced upon considering foundations with soil flexibility, however, slight increase in maximum interstory displacements are observed for Hachinohe and Northridge earthquakes (Figs. 8(c)-(f)). Except for 8-story building with fixed foundation no pounding case (Fig. 8(a)), Kobe earthquake resulted in the maximum interstory displacement. In this regard, it is clearly seen that near field earthquakes yield significant effect on interstory displacements for the given buildings.

Maximum normalized story shear defined as the ratio of maximum story shear resulting from pounding to maximum story shear for fixed foundation without pounding, is used as another parameter to express the response of the buildings. Figure 9 shows the maximum normalized story shear of 6-story and 8-story buildings with fixed foundations and foundations with soil flexibility. Maximum normalized story shear in all the floor levels of buildings considering foundations with soil flexibility is less than that of buildings with fixed foundations only in the cases of 8-story building due to El Centro earthquake (Fig. 9(a)) and 6-story buildings due to El Centro and Kobe earthquakes (Figs. 9(b), (h)). When the buildings are subjected to Hachinohe earthquake, in both 6-story and 8-story buildings, larger maximum normalized story shear is observed in the buildings with foundations with soil flexibility (Figs. 9(c), (d)). The largest maximum normalized story shear for the buildings with foundation with soil flexibility is found to be 2.496 due to Hachinohe earthquake (Fig. 9(d)) while that for the buildings with fixed foundation 3.469 due to Kobe earthquake (Fig. 9(h)).

5. CONCLUSIONS

The importance of considering underlying soil on the study of seismic pounding is presented in this paper. The

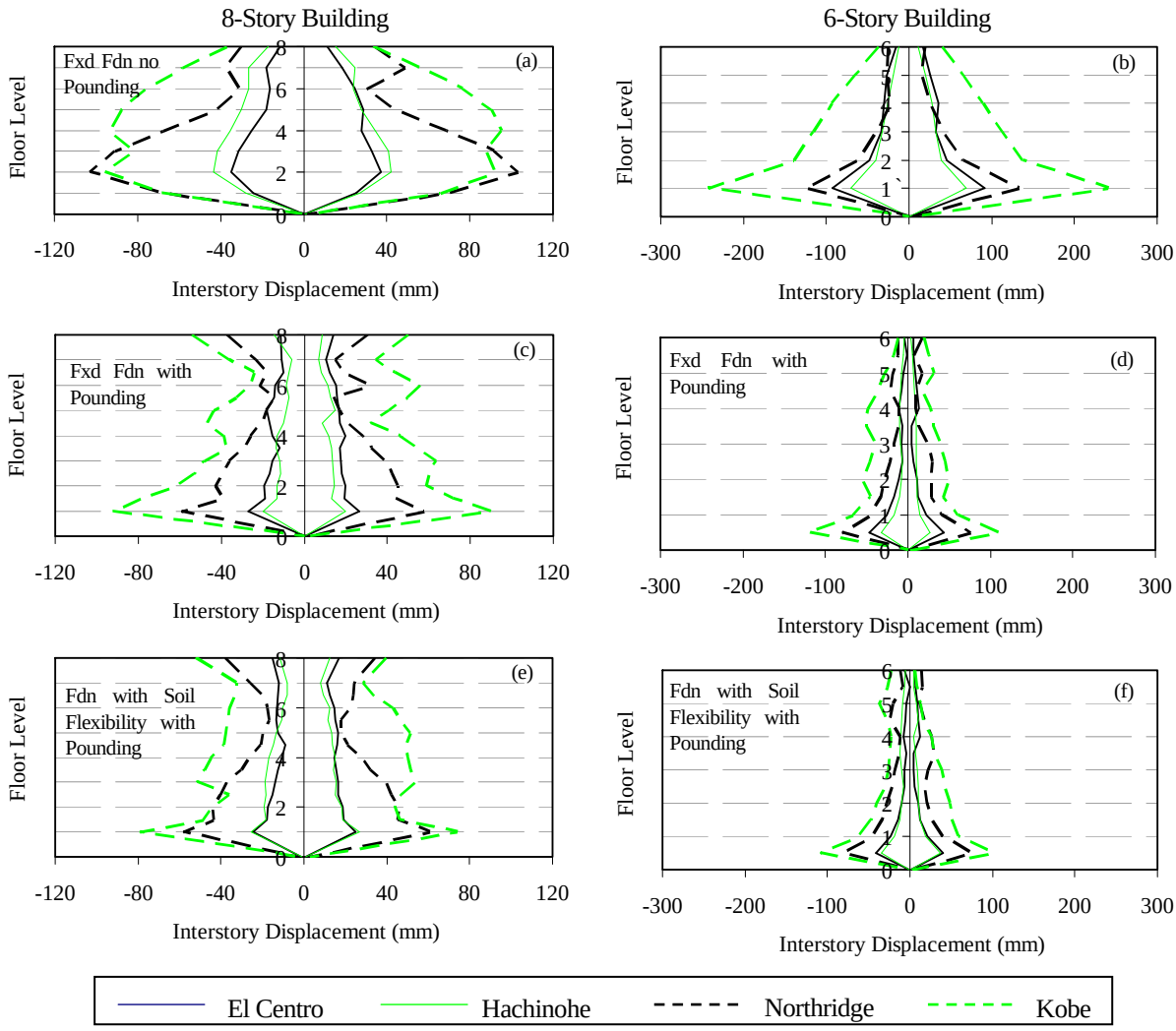

Fig. 8. Maximum interstory displacement of columns C4 and D5.

6-story and 8-story buildings having different story heights at the first floor are subjected to two near field and two far field earthquakes which caused mid column pounding in the buildings. The building responses are expressed in terms of impact forces, base shear, interstory displacements and normalized story shear. The maximum interstory displacements are observed when there is no pounding. In most cases, the results show the reduction in maximum impact forces, base shear, maximum interstory displacements and maximum normalized story shear when soil effects are taken into account. The results indicate that Kobe earthquake is dominant for both fixed foundations and foundations with soil flexibility cases in the considered buildings. In most cases, response of the buildings under consideration are more significant due to near field earthquakes and adopting soil-foundation interaction for pounding analysis is beneficial.

Acknowledgements:

The first author gratefully acknowledges a Monbukagakhusho scholarship from the Japanese government. The authors are very grateful to Prof. Kohji Tokimatsu, GCOE Program Leader of Center for Urban Earthquake Engineering (CUEE), Tokyo Institute of Technology, for his advice and support. Financial support from the CUEE through the project "Development of Practical Urban Earthquake Engineering Research for Mitigation of the Metropolitan Great Earthquake Disaster", is gratefully acknowledged.

References:

American Concrete Institute (ACI) (2002), "Building Code Requirements for Structural Concrete" ACI 318-02, Farmington Hills, Michigan.

Anagnostopoulos, S. A. (1988), "Pounding of Buildings in Series During Earthquakes", *Earthquake Engineering and Structural Dynamics*, **16**, 443-456.

Azevedo, J. and Bento, R. (1996), "Equivalent Viscous Damping for Modeling Inelastic Impacts in Earthquake Pounding Problems", *Eleventh World Conference on Earthquake Engineering*, Acapulco, Mexico, Paper No. 1063.

International Building Code (IBC) (2003), International Code Council Inc., Country Club Hills, Illinois.

International Building Code (IBC) (2006), International Code Council Inc., Country Club Hills, Illinois.

Jankowski, R. (2005), "Non-linear Viscoelastic Modelling of Earthquake-Induced Structural Pounding", *Earthquake Engineering and Structural Dynamics*, **34**, 595-611.

Jankowski, R. (2006), "Pounding Force Response Spectrum Under Earthquake Excitation", *Engineering Structures*, **28**, 1149-1161.

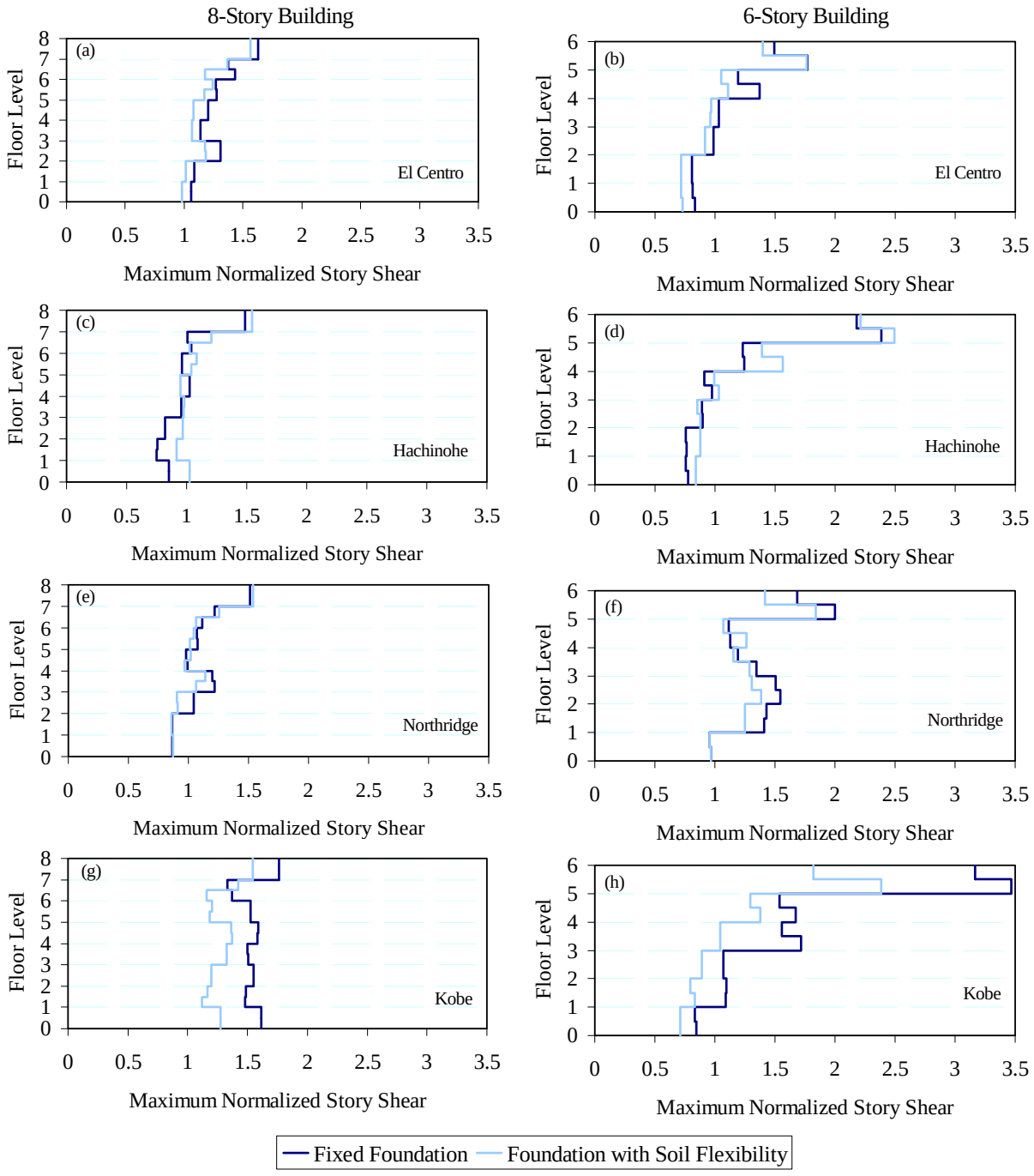

Fig. 9. Maximum normalized story shear: (a), (b) El Centro; (c), (d) Hachinohe; (e), (f) Northridge; and (g), (h) Kobe earthquakes.

Jeng, V. and Tzeng, W. L. (2000), "Assessment of Seismic Pounding Hazard for Taipei City", *Engineering Structures*, **22**, 459-471.

Mouzakis, H. P. and Papadrakakis M. (2004), "Three Dimensional Nonlinear Building Pounding with Friction During Earthquakes", *Journal of Earthquake Engineering*, **8**, 107-132.

Mullikan, J. S. and Karabalis, D. L. (1998), "Discrete Model for Dynamic Through-the-Soil Coupling of 3-D Foundations and Structures", *Earthquake Engineering and Structural Dynamics*, **27**, 687-710.

Rahman, A. M., Carr A. J. and Moss P. J. (2001), "Seismic Pounding of a Case of Adjacent Multiple-Storey Building of Differing Total Heights Considering Soil Flexibility Effects", *Bulletin of The New Zealand Society for Earthquake Engineering*, **34**(1), 40-59.

Shakya, K., Wijeyewickrema, A. C., and Ohmachi, T. (2008), "Mid-column seismic pounding of reinforced concrete buildings in a row considering effects of soil", *Proceedings of the Fourteenth World Conference on Earthquake Engineering*, Beijing, China, Paper No. 05-01-0056.

van Mier, J. G. M., Preuijssers, A. F., Reinhardt, H. W., and Monnier, T. (1991), "Load-Time Response of Colliding Concrete Bodies", *Journal of Structural Engineering*, **117**, 354-374.

Wolf, J. P. (1988), "Soil-Structure-Interaction Analysis in Time Domain", Prentice Hall Inc.

Sixth International Conference on Urban Earthquake Engineering
March 3-4, 2009, Tokyo Institute of Technology, Tokyo, Japan

COMMUNICATION TO OVERCOME BARRIERS TO MITIGATION

Guna Selvaduray[1)], and James Lee[2)]

1) Associate Dean for Research and Professor, College of Engineering, San Jose State University, California, U.S.A.
2) Associate Professor, Dept. of Sociology, San Jose State University, California, U.S.A.
guna.selvaduray@sjsu.edu, james.lee@sjsu.edu

Abstract: Earthquake mitigation has not been implemented to the extent that would be desirable, as a result injuries and damages that occur as a result of an earthquake are higher than need be. The faculty and staff of San Jose State University were surveyed to identify the barriers to mitigation, so that effective communications means can be developed. The sample was fully aware that the region they live in is prone to earthquakes. However, mitigation implementation was significant only for those measures that are required by codes or regulations. The main reasons cited for not implementing mitigation were all subjective, such as "inconvenient". The incentives that could potentially improve mitigation implementation were found to be mainly financial in nature, including provision of free labor and free items. Close personal relationships with individuals who incurred injuries or damage, or to a person who has mitigated, was also found to be a motivator for mitigation implementation. In order for communications aimed at reducing earthquake-caused injuries and damages to be effective, the psychological framework of the recipient needs to be taken into account. In other words, a bottoms-up approach, rather than a top-down approach, is necessary.

1. INTRODUCTION

There are several aspects to disaster communications. These can be divided into two major categories: (1) communications needs and means after a disaster occurs, and (2) communications needs and means prior to the occurrence of a disaster. Each of these categories can be further subdivided into different components. One major aspect of post-disaster communications deals with communications among emergency response personnel, at all levels, with the aim of improving coordination among the various agencies so that the extent of the disaster can be not only contained, but also held to the minimum possible extent. Another aspect of post-disaster communications is focused on keeping the general public appropriately informed of developments, including information on how and where to seek disaster assistance and how the public can obtain information on the fate and whereabouts of their loved ones.

In the case of pre-disaster communications, the bulk of the effort is usually focused on "preparedness" for the disaster, i.e., what the public sector and residents should have, and do, so that when a disaster occurs the response will be carried out in a timely and efficient manner, and in that process, minimize the consequences of the disaster. One aspect of pre-disaster communications that has not received as much attention as all other aspects is the manner in which information regarding mitigation has been communicated to the general public so that the magnitude of the disaster can be minimized by minimizing the vulnerability of the community.

The different aspects of disaster communications outlined above all require different approaches in order for them to be effective. In particular, when the public sector is attempting to reach out to the residents in the community, the means of communication employed needs to be such that it is "acceptable" by the target audience and resonates with them.

2. RESEARCH BACKGROUND, OBJECTIVES AND METHODOLOGY

The research on which this paper is based was undertaken on the premise that pre-disaster communication aimed at improving the levels of implementation of mitigation among residents has not been very effective thus far, as a result of which the implementation of mitigation is not as wide-spread as would be desired. The communications on mitigation methods has tended to be "top-down", with the public sector, academicians and consultants telling the residents what they should do. Relatively little research has been done thus far on attempting to understand the barriers, from a resident's perspective, that impede implementation of mitigation. It is expected that by understanding the barriers to mitigation, communications means that assist residents at overcoming the barriers can be developed.

The population in the U.S.A. in general, and California in particular, is extremely diverse. Not only is there diversity in terms of educational and income levels, but there

is also significant diversity in terms of ethnic origins and the age at which residents immigrate to California. One of the objectives of this research was to determine if factors such as national origin, the number of years a particular individual has lived in California, the age at which a particular individual immigrates to California, an individual's disposable income, among others, affect the extent to which that particular individual takes mitigation measures.

This research was also focused on homeowners, and in particular nonstructural hazard mitigation within homes. This focus was developed for a number of reasons. In general, homeowners who are primarily middle class, receive relatively little disaster assistance. Since their incomes are sufficiently high to disqualify them from most aid programs, they have to bear the financial burden of repairing damage to their homes and possession. Further, nonstructural hazard mitigation is relatively inexpensive, as compared to structural mitigation, and is also amenable to being undertaken by the homeowner.

A survey that could be administered electronically was developed. The target population group selected for this initial survey was the faculty and staff of San Jose State University (SJSU). The survey was hosted by the university's Survey Policy Research Institute. An email was sent to all employees of SJSU, requesting them to take the survey. The survey was designed specifically to elicit information on why homeowners are not taking steps to mitigate potential earthquake hazards. The examples of mitigation measures that were included in the survey were the following:

- Have you had an engineer evaluate your home for resistance to earthquake damage?
- Have you secured your home to its foundation?
- Have you strapped down your water heater?
- Have you fitted gas and other appliances with flexible connections?
- Have you bolted large furniture items into place (e.g., bookshelves/entertainment centers)?
- Have you placed safety straps on large appliances (e.g., televisions or refrigerators)?
- Have you placed safety latches on cabinets?
- Have you secured heavy wall hangings, art/paintings, or mirrors?
- Have you secured decorative glassware or other table top items (e.g., with putty)?
- Have you braced, reinforced, replaced, or removed your masonry chimney?
- Have you braced masonry and concrete walls?
- Have you placed plastic film over window glass?

Afterward, respondents were asked if they had taken those measures or not. If they had not, they were asked the reason(s) why they had not,

Another set of questions attempted to find out if respondents would be more likely to take mitigation actions if they had themselves experienced earthquake-caused injuries or damage, or if someone they knew had had that experience. The questions addressing this aspect of the survey were:

- Have you, or anyone you know, ever been injured in an earthquake?
- If you or someone you know were injured in an earthquake, how likely would you be to take steps to prevent future earthquake injuries in your home?
- What relationship to you was the person(s) who was injured in an earthquake? (check all that apply)
- Did this event lead you to take steps to prevent future earthquake injuries in your home?
- Have you, or anyone you know, experienced an earthquake that caused damage to their home or items within their home?
- If you or someone you know had home damage in an earthquake, how likely would you be to take steps to prevent future earthquake damage in your home?
- What relationship to you was the person(s) who experienced home damage in an earthquake? (check all that apply)
- Did this event lead you to take steps to prevent future earthquake damage to your home?
- Do you have friends, family, or neighbors who have taken steps to prevent earthquake damage or injuries in their homes?
- If your friends, family, or neighbors were to take steps to prevent earthquake damage or injuries in their homes, how likely would you be to take similar action in your home?
- What is your relationship to those who took steps to prevent damage or injury from an earthquake? (check all that apply)
- Did the actions of your friends, family, or neighbors to prevent earthquake damage or injuries lead you to take earthquake damage or injury prevention measures in your home?

A third set of questions attempted to find out what incentives could be provided in order to encourage or motivate respondents to take mitigation actions. The incentives were:

- Discount on homeowner's insurance
- Tax incentive(s)
- Discount on mortgatge
- Free items needed for mitigation actions
- Free advice
- Free service or labor
- More information on regulations and codes.

In addition to direct causes for lack of mitigation actions, the survey also attempted to examine the potential effect of various demographic factors such as education level, income level, and length of residence in California, among others, on mitigation actions. A total of 320 employees took the survey. Out of this sample population, 221 were homeowners.

3. SURVEY RESULTS

Approximately two thirds of the respondents owned their homes. Regardless of whether they were home-owners or renters, two thirds also live in single family homes.

3.1 Awareness of Likelihood of Earthquake Occurrence

All respondents were aware that earthquakes occur in San Jose. The vast majority (71 %) felt that the likelihood of an earthquake occurring in San Jose within the next year was only "somewhat likely"; 12 % responded "very likely" and 17 % responded "not likely". When the time frame was increased to 10 years, 65 % felt that it was very likely that an earthquake would occur. The majority thought that it was "somewhat likely" that an earthquake will cause injuries (51 %) and damage to property (63 %). The perception here is that property damage is more likely than injuries.

3.2 Mitigation Information and Actions

Approximately half of the respondents stated that they had researched information on earthquake damage prevention. The reasons cited for not having done any research on earthquake damage prevention, in declining order were: (a) requires too much time, (b) inconvenient, (c) not enough information, and (d) too expensive. Close to 11 % of the respondents thought that this research was not necessary and another 8.5 % thought that it was either ineffective or not useful.

23 % reported that their homes had been evaluated, for seismic resistance, by an engineer. The primary reason for not having the home evaluated by an engineer was that it was too expensive (35 %). Other reasons cited include: not enough information (18 %), unnecessary (14 %), and inconvenient (12 %).

Approximately 50 % of the respondents had either not anchored their homes to the foundation or did not know if it had been. Of those who had not anchored their homes to the foundation, 40 % had not done so because it was too expensive, 18 % stated that they did not have enough information, 10 % stated that it required too much time, and another 10 % thought that it was ineffective. Another 8 % of the respondents stated that it was inconvenient.

With regards to water heaters, the vast majority reported that their water heaters had been strapped. This is very likely the outcome of the Uniform Plumbing Code which has required, since 1991, that water heaters be strapped to the wall. Only 7 % reported that their water heaters had not been strapped to the wall.

The response with regard to fitting major gas appliances with flexible piping connections was similar to that regarding water heaters. Only 6 % reported that their appliances had not been fitted with flexible piping connections.

When it came to bolting large furniture items in place, 63 % reported that they had not done this. The main reasons for not doing so included inconvenient (25 %), requires too much time (17 %), not enough information (8 %), and too expensive (6 %). However, 16 % thought that this was not necessary, with another 5 % who thought that it was not effective.

Only 11 % had restrained their large appliances such as refrigerators and TV sets, with 85 % reporting that they had not done it. The reasons for not placing safety straps on the large appliances are: inconvenient (23 %), not enough information (21 %), and requires too much time (10 %). 21 % thought that it was not necessary, 9 % thought that it was not useful or effective, and 4 % thought it was too expensive.

Only 15 % had installed safety latches on their kitchen cabinets while 80 % had not. The primary reasons cited for not doing so were: inconvenient (30 %), insufficient information (14 %), requires too much time (13 %). 18 % thought that it was not necessary and another 11 % thought that it was not effective.

3.3 Effect of Personal Relationships on Mitigation

Only a small fraction (7 %) stated that they personally knew someone who had been injured in an earthquake – in most cases a friend. However, 95 % of those who responded to this question stated that they would be either somewhat likely, or very likely, to take steps to prevent future injuries from earthquakes. 68 % stated that they did take steps to prevent future injuries; however, 32 % stated that this knowledge did not result in their taking any action to prevent future injuries.

A much larger proportion (70 %) responded that they personally knew someone who had incurred earthquake-caused damage to their homes, primarily a friend or themselves. 97 % of the respondents stated that they would be either somewhat likely, or very likely, to take steps to prevent future earthquake-caused damage, and 58 % stated that they had actually done so. The other 42 % stated that the personal experience or knowledge did not lead them to take preventive actions.

3.4 Incentives for Mitigation Actions

As perhaps could be expected, the majority responded that they would be very likely to take mitigation actions if incentives were provided.

Approximately 96 % responded that if free service or labor were provided, then they would be either *very likely* or *somewhat likely* to take mitigation actions, with 70 % *stating very likely*.

The provision of free items for mitigation also drew very favorable responses, with a total of approximately 95 % responding *very likely* or *somewhat likely*; 63 % stated that they would be *very likely* to take mitigation actions if free items were provided.

A close third in popularity among the incentives was "tax incentives". Approximately 60 % stated that they would be *very likely*, and another 36 % stated that they would be *somewhat likely*, to take mitigation actions.

The combined response of *very likely* and *somewhat likely* for insurance discounts was also very high, with a total

of 93 %.

The respondents also stated that free advice would motivate them to mitigate, but only 48 % stated that they would be *very likely* to do so. Similarly, more information on regulations and codes, while being a motivator, was not as strong as those described above, with only 36 % responding as being *very likely* to take mitigation actions.

3.5 Effect of Demographics on Mitigation

The analysis on the effect(s) of demographics on mitigation actions is on-going at the current time and the results are forthcoming.

4. DISCUSSION OF RESULTS

4.1 Sample

The population that was surveyed in this research constitute a public university's faculty and staff. The demographic information collected indicates that the sample is probably not as representative of the general population as could be desired, especially if one considers the population of the City of San Jose and Santa Clara County. For example, 71 % of the respondents were white, the median age was between 51 and 55, 85 % have a college degree or more, and the median household income was between $110,000 and $129,999. The City of San Jose has fewer whites, a younger population, less education, and lower median household income.

Nevertheless, if this study is treated as a pilot, the results of which can be built upon, it does yield valuable information that can be used in developing effective means of communicating the necessity to take mitigation actions when one lives in earthquake country.

4.2 Implications of Results for Communications

The entire sample is aware that earthquakes occur in the San Jose area; the differences arise only in terms of the time-frame within which people think the earthquake will occur. As such, the efforts thus far to make residents aware that they live in earthquake country can be considered as having been successful. The respondents also think that property damage is more likely than injuries.

However, when it comes to mitigation, the "success rate" is not as impressive. The highest level of mitigation was found for strapping of water heaters, which is required by the Uniform Plumbing Code. All licensed plumbers, when they install a new water heater, are required to strap it to the wall. The approach of making a mitigation action a legal requirement, with the professional responsible for implementation, has been successful. This is very similar to the effort that has been taken to improve the seismic resistance of structures, since the early 20th Century. The building codes are reviewed every three years and updated as necessary, especially after damaging earthquakes. The individuals responsible for implementing the building codes and standards are the professionals, i.e., the building design professionals such as engineers and architects, building and other contractors who do the actual construction, and the building inspectors of the local jurisdictions.

The success rate with mitigation actions that are voluntary, with the responsibility resting on the homeowner, is not equally impressive.

The primary reasons cited for not taking mitigation actions were really quite subjective, namely, factors such as requires too much time, inconvenient, not enough information, and too expensive. The respondents also identified incentives that they felt they would respond to, namely, free service or labor, free items, tax incentives, and insurance discounts.

If the two - reasons for not mitigating and incentives for mitigating - are viewed jointly, it appears that the primary impediment to taking damage prevention actions is financial. However, this could be the result of only financial questions being posed in the incentives set. A revised set of possible incentives, based on the results of this pilot survey, needs to be developed.

However, based on the results from the current survey the respondents seem to indicate that the household mitigation options are not worth doing because of convenience issues; but, they are willing to either do them if someone else will pay for it or have them done. So, it is not that the respondents think of mitigation options as being too expensive. Rather, it appears that they think of it as not being as valuable as it would cost to do it.

It was also found that personal relationships can play a role in an individual's decision/motivation to take mitigation actions.

The development of damage reduction communications with the residents of earthquake prone areas need to take the items described above into consideration, in order to make the efforts of the public sector more worthwhile and effective.

5. CONCLUSIONS

While people are aware that they live in an earthquake prone region, this knowledge alone is apparently insufficient for them to be motivated to proactively take mitigation actions that would reduce injuries and property damage. The "barriers" to taking earthquake damage reduction steps, by the homeowner, appears to be a matter of that individual prioritizing how he/she will use his/her time and resources. The major incentive that people identified as being a motivator to take actions were all directly or indirectly related to finances and financial incentives. Injuries or damage incurred by others with close personal relationships also appear to have an important effect, though not as strong as the financial incentive. Legislation and/or codes requiring mitigation implementation, however, appears to be very successful.

There is a need for the development of communications techniques that take into account the findings of this research thus far. Greater emphasis should be placed on the financial aspects of mitigation. Another

area that can also be emphasized further are injuries and damage that could be incurred.

6. ACKNOWLEDGEMENTS

The authors gratefully acknowledge Kim Shunk, Director, Office of Emergency Services, City of San Jose, for funding this study. Dr. Melinda Jackson, Professor, Political Science Department, and Director, Survey Policy Research Institute, San Jose State University, kindly arranged for email distribution of the survey and for electronic compilation of the results. Ms. Crystal Paul, Graduate Student, Sociology Department, San Jose State University, was instrumental in the data analysis.

Sixth International Conference on Urban Earthquake Engineering
March 3-4, 2009, Tokyo Institute of Technology, Tokyo, Japan

QUICK DAMAGE DETECTION OF URBAN AREAS USING DIGITAL AIRBORNE IMAGES

Fumio Yamazaki[1], Daisuke Suzuki[2], and Yoshihisa Maruyama[3]

1) Professor, Graduate School of Engineering, Chiba University, Japan.
2) Graduate Student, Graduate School of Engineering, Chiba University, Japan.
3) Assistant Professor, Graduate School of Engineering, Chiba University, Japan.

yamazaki@tu.chiba-u.ac.jp, daisuke.s.9-18@graduate.chiba-u.jp, ymaruyam@tu.chiba-u.ac.jp

Abstract: Remote sensing technology is effective to grasp the damage distributions from various natural disasters, such as earthquakes, tsunamis and volcanic eruptions. After the 2007 Off-Mid-Niigata, Japan earthquake, aerial images were taken in the stricken area by several air survey companies in Japan. Airborne remote sensing is more suitable to collect detailed damage distribution because it provides higher resolution images than satellite remote sensing does. The post-event image taken by a digital aerial camera (DMC) is employed in this study to detect building damages. Since visual damage inspection takes time to perform for the whole areas that are subjected to severe ground motion, an object-based technique is proposed to extract debris from buildings. The proposed method is expected to contribute for the damage assessment at an early stage after the occurrence of an earthquake.

1. INTRODUCTION

Aerial photography has been used widely for aerial surveying and photogrammetry. Because of its very high spatial resolution, aerial photographs were employed to detect damages due to earthquakes (e.g., Ogawa and Yamazaki, 2000). Digital aerial cameras, recently developed and introduced for aerial photography, have much higher radiometric resolution than traditional film (analog) aerial cameras do. Thus, even though the spatial resolution is almost the same level, e.g. 0.1 m, a digital aerial camera can capture much clearer images of the earth surface than an analog camera does.

Another important feature of digital aerial cameras is that they have a near infrared (NIR) band as well as RGB visible bands. Using the NIR band, detection of vegetation becomes quite easy. Through the pan-sharpening procedure, very-high resolution pseudo-color images can be obtained by combining these 4 multi-spectral bands and the panchromatic band. Note that the spatial resolution of high-resolution satellites currently available is 0.6 m (QuickBird) at the maximum, and thus the digital aerial images can be used for extraction of detailed damages of buildings and infrastructures (Mitomi et al., 2002; Maruyama et al., 2006).

This paper highlights the capability of digital aerial images in detecting various damages due to earthquakes. In the recent earthquakes in Japan, such as the 2004 Mid-Niigata, the 2007 Noto Peninsula, and the 2007 Off-Mid-Niigata earthquakes, the affected areas were captured by digital aerial cameras as well as by film aerial cameras and high-resolution satellites. Especially for the 2007 Off-Mid-Niigata earthquake, digital aerial cameras captured the affected area both before and after the event. Pixel-based and object-based image processing techniques are applied to those digital images, and their accuracy to extract building damage is discussed.

2. DIGITAL AERIAL IMAGES OF KASHIWAZAKI CITY

The central part of Niigata Prefecture, Japan was hit by a strong M_{JMA}=6.8 earthquake on July 16, 2007. A total 1,330 houses were collapsed or severely damaged and 15 people were killed in Niigata Prefecture. Kashiwazaki City was most severely affected in the prefecture with 1,120 collapsed or severely damaged houses and 14 deaths. A fire broke out in Kashiwazaki-Kariwa nuclear power plant from a transformer. Due to the strong shaking exceeding the safety shutdown level, the operation of the power plant has been suspended since then.

Figure 1 shows the study area of this study (Higashi-honmachi), a central part of Kashiwazaki City. Aerial surveys of the city were conducted by three different organizations; Kashiwazaki City Government on 27 April, 2007 (before the earthquake), Asia Air Survey Co., Ltd. and Geographical Survey Institute (GSI), Japan on 19 July, 2007 (two days after the earthquake). The pre-event images of the city government were taken by UltraCam-D digital camera (Leberl and Gruber, 2005) while the post-event images of Asia Air Survey were obtained by DMC digital camera (Hinz, 1999). UltraCam and DMC are the most selling large-format aerial digital cameras in the world. The post-event images by GSI were taken by RC30 analog (film) camera.

Figure 1. Digital aerial image with 12.2 cm resolution for a part of Kashiwazaki City, which was taken two days after the 2007 Mid-Off-Niigata earthquake by Asia Air Survey Co., Ltd.

One of the most advantageous features of aerial digital cameras is that they have a near infrared (NIR) band as well as RGB visible bands. Vegetation is often the cause of changes between two images taken in different seasons. However, using NIR and red (R) bands of digital cameras, vegetation is easily extracted in terms of the normalized vegetation index (NDVI), calculated by

$$NDVI = (NIR - R) / (NIR + R) \quad (1)$$

where R and NIR are the reflectance of the red and near-infrared bands, respectively. NDVI is a simple and reliable index to identify the existence of vegetation, and therefore widely applied to assess the characteristics of the earth surface in the field of satellite remote sensing.

Another important feature of digital aerial images is its high radiometric resolution. Since digital images contain much less noise than scanned-analog photos do, much clear edges can be extracted. Edge extraction is one of the important tools to extract building damage (Mitomi et al., 2002), to estimate the overturning ratio of tombstones due to earthquakes (Nitto and Yamazaki, 2006), and to extract vehicles from aerial images (Liu et al., 2007).

3. PIXEL-BASED SUPERVISED CLASSIFICATION

First, a conventional pixel-based classification was carried out for the post-earthquake digital image (Figure 1) based on the maximum likelihood method, the most common supervised classification method. In the classification, 8 bit values of RGB and NIR bands were used and twelve classes were selected as training data: black roof, white roof, gray roof, red roof, blue roof, road, ground, paved ground, shadow, tree, grass, and debris.

The result of the classification is shown in Figure 2. Vegetation (tree and grass) were correctly classified because the NIR band was used. However, salt-and-pepper noises are seen (Matsumoto et al., 2006) in all the parts of the image. Such noises were generated because the digital aerial image has very-high spatial-resolution which captures fine details, especially in pixel-based classification. Thus, many small

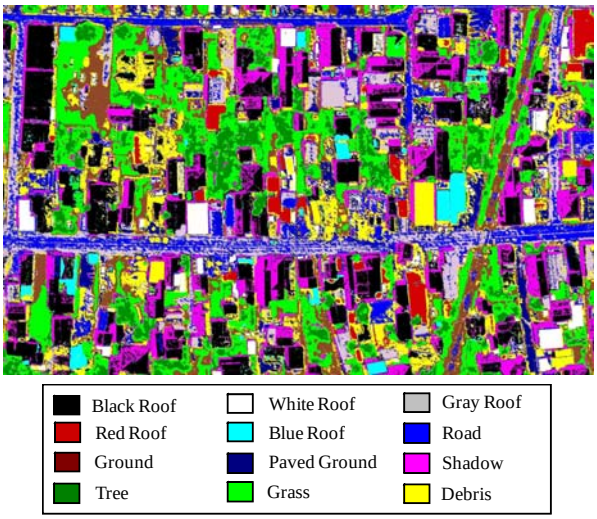

Figure 2. The result of pixel-based supervised classification for the post-event image.

Figure 3. The result of visual extraction of debris.

misclassifications are seen, especially for black-roofs by capturing individual roof-tiles. Another cause of misclassifications is the effect of sunlight. Since sunlight comes from the right side of the image, the brightness of right- and left-side roofs is different.

Figure 3 shows the result of visual extraction of debris for the post-event image. Comparing the debris areas in Figure 2 (yellow) and Figure 3 (red), those by the pixel-based classification look to overestimate the actual debris areas. Debris does not have unique spectral characteristics because it consists of the mixture of woods, mud and roof-tiles. Therefore, a lot of misclassifications as debris were seen in the ground and non-damaged roofs with the color of no training data. Mitomi et al. (2002) introduced a sort of spatial filtering to reduce the salt-and-pepper noise classified as debris. In such approaches, the size of spatial window should be assigned properly, depending on the size of target objects.

4. OBJECT-BASED SEGMENTATION AND SUPERVISED CLASSIFICATION

4.1 Object-based Approach and Segmentation

To solve the salt-and-pepper problem in high-resolution images, object-based classification has recently been introduced. Yamazaki and Kouchi (2006) compared the result from pixel-based classification and that from object-based one for debris detection using QuickBird images in the 2003 Boumerdes, Algeria earthquake. In the study, however, only the post-event image was used and thus, pre-event information, e.g. the location of buildings, was not used effectively. Usefulness of object-based classification is further investigated by Matsumoto et al. (2006) in building damage detection from QuickBird images obtained before and after the 2006 Central Java earthquake. Building areas were extracted for both the pre-event and post-event images by pixel-based and object-based classifications, and their areas were compared. The results showed that the object-based method is suitable to reduce the noise to extract debris from other objects.

In the present study, the digital aerial images with much finer spatial-resolution were employed in performing object-based classification using e-Cognition software (Baatz et al., 2004). Image segmentation was carried out as the first step to make "objects" using the post-event 4 band image. In e-Cognition, the segmentation process is determined by 5 parameters: *Layer Weight*, *Compact Weight*, *Smooth Weight*, *Shape Factor*, and *Scale Parameter*. The most important parameter is *Scale Parameter*, which determines the object size. *Shape Factor* is to determine the importance level of spectral heterogeneity or shape heterogeneity in segmentation. When *Shape Factor* moves toward 0, the spectral heterogeneity is more concerned. On the contrary, if it moves toward 0.9, the shape heterogeneity is more concerned. The spectral heterogeneity is decided by *Layer Weight*, which gives the weight for each spectral band. The shape heterogeneity is decided by *Compact Weight* and *Smooth Weight*; the summation of these values should be 1.0. When *Compact Weight* is larger than *Smooth Weight*, the segmented image objects become a more round shape. On the contrary, when *Smooth Weight* is larger than *Compact Weight*, they become to have smoother borderlines.

Starting from pixels, segmentation runs the merger between two objects and is terminated when an assigned condition is reached. This condition is defined based on the fusion value *f*, which measures the changes when merging. If *f* equals to or becomes bigger than the squared scale parameter, the condition is reached. Although it is difficult to decide the appropriate values of the parameters suitable to all land cover classes, the user can decide the suitable values to a few focused classes, e.g. building, road, and car.

The appropriate parameters for the size of a car was used in this study because the aerial images have very high spatial-resolution and we want to extract debris larger than say, 3-5 m. Considering its resolution (12.2 cm) and the target size of objects (car), *Scale Parameter* was determined as 40 for the post-event image. Figure 4 shows the result of segmentation for the study area and the parameters used. From the figure, objects like cars, roofs, and debris are seen to be segmented properly as one or a few adjacent objects.

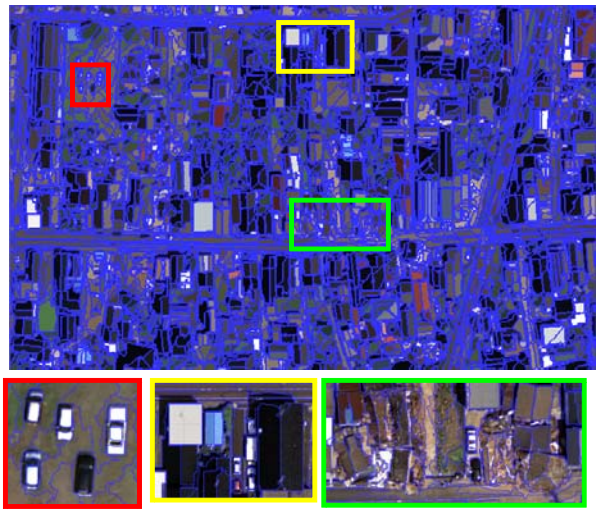

Segmentation parameters
Scale Parameter = 40, *Layer Weight* = 1.0
Shape Factor = 0.5, *Compact Weight* = 0,
Smooth Weight = 1.0

Figure 4. The result of image segmentation for the post-event 4 band image.

4.2 Object-based Supervised Classification

After segmentation, the training areas for all the classes used in the pixel-based classification were assigned as those for the object-based supervised classification. The objects' mean values and standard deviations of 4 spectral bands were used as the indices of classification. In e-Cognition, not only these layer values of image objects but also various feature values of image objects, such as shape, can be considered.

The characteristic object features for debris are with a complex shape and a smaller area than others. In order to extract debris accurately, the object features, that are *Border Length* and *Shape Index*, were employed in the classification.

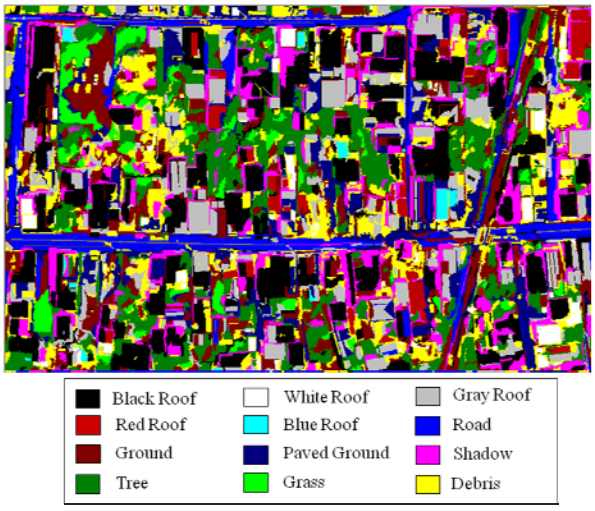

Figure 5. The result of object-based supervised classification for the post-event 4 band image.

The border length is the length of borderline of an image object and the shape index means the degree of complexity of an image object; if an image object has a complex shape, the shape index is given as a high value. The nearest neighbor method was used in a classification step.

The result of the object-based classification for the post-event images is shown in Figure 5. Comparing with the pixel-based classification result (Figure 2), the object-based method looks to classify the images into proper object groups. Salt-and-paper noise is no more seen in case of the object-based classification. Comparing the object-based classification result with the visual inspection result (Figure 3), however, it looks not so satisfactory. The classification result includes a lot of commission errors; some objects like cars, intact roofs, bare grounds, are classified as debris. Since debris contains various materials and possesses various shapes, some objects without proper training areas may be misclassified as debris.

Another drawback of classification methods, both pixel-based and object-based, is necessity to assign many classes and their training data. Actually, if the extraction of debris is the main objective, the classification results for other classes are not so important. If we must extract earthquake damages from many aerial images, the selection of proper classes and training data is time consuming. Thus we will focus only on debris and introduce a level-slice method after the object-based segmentation process.

5. OBJECT-BASED LEVEL-SLICE METHOD FOR DEBRIS EXTRACTION

In order to perform quick damage extraction from digital aerial images, a multi-level slice method is introduced after the object-based segmentation process. Since we focus on the extraction of debris from collapsed houses, color information is not so important. The color of debris is dependent on its material, e.g. roof-tiles, woods, soil, and there is no unique color. Thus a panchromatic image or an intensity (brightness) image is employed instead of RGB color layers. In this study, the intensity (I) is obtained by

$$I = 0.3R + 0.59G + 0.11B \qquad (2)$$

To exclude vegetation, the normalized vegetation index (NDVI) is considered to be another layer value to be used for segmentation and level-slice. For these two layers, segmentation was performed using the same parameter values as Figure 4.

After segmentation, the characteristics of debris objects were investigated in terms of their object features. In this study, the two layer values, *I* and *NDVI*, and five features related to the object shape, *Area*, *Length*, *Width*, *Border Length*, *Average Length of Edges*. To determine the conditions of these object feature values, debris from collapsed houses and roofs of non-damaged houses were used as training areas as shown in Figure 6.

Figure 7 shows the mean and standard deviation of the intensity value for the objects shown in Figure 6. It is observed that the standard deviation for the debris objects is

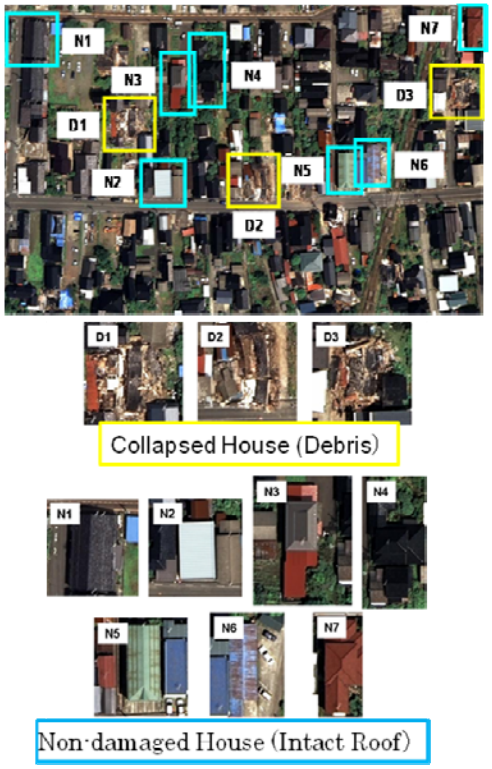

Figure 6. Training areas to determine the condition of object features for debris.

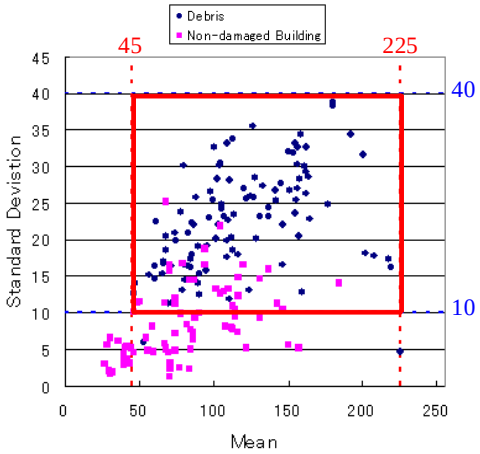

Figure 7. The mean and standard deviation of the intensity of the objects shown in Figure 6. The bounds were used to extract debris objects.

generally bigger than that for the intact roofs. The objects with the mean NDVI value larger than 0.17 were excluded as vegetation in this case. Figure 8 plots the relationship between *Area/Border Length* and *Average Length of Edges* for the training areas. The both values represent irregularity of objects and their conditions to select debris objects are shown in the figure. Figure 9 shows the relationship between *Width* and *Length* for the training areas. To exclude large intact roofs, upper limits were assigned for *Width* and *Length*. Long thin objects, like road lines and shadows, were removed by assigning the threshold of *Length*/*Width*.

The objects satisfying all these conditions were assumed to be considered as debris as shown in Figure 10. Comparing this figure with the visual inspection result, the extracted objects are much more than actual debris. Especially, there are still many small objects which were misclassified as debris. To reduce these commission errors, the pre-event digital image taken by UltraCam-D was employed. The similar debris extraction procedure was applied to this image and the result was shown in Figure 11. Since the debris' threshold values determined for the post-event image were used, many "debris" areas were extracted, as obvious commission errors. The common "debris pixels" in Figures 10 and 11 were removed from Figure 10 to reduce commission errors.

Since there still remain many commission errors, the objects smaller than a minimum area (A_{min}) were further excluded from debris. Figure 12 shows the accuracy of debris extraction with respect to A_{min}. The overall accuracy is considered as the average of producer accuracy and user accuracy. To increase A_{min} value, the user accuracy increases because commission errors (area A in Figure 12) are removed, and the producer accuracy decreases due to reduction of the correctly extracted area (B in Figure 12). The average of the two accuracies gets its maximum value when A_{min} reaches about 58 m^2. But this maximum value does not show a clear peak, a slight change in the extraction procedure may give other A_{min} value.

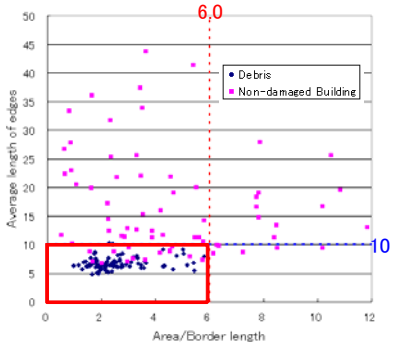

Figure 8. The relationship between *Area/Border Length* and *Average Length of Edges* for the training areas. The bounds were used to extract debris objects.

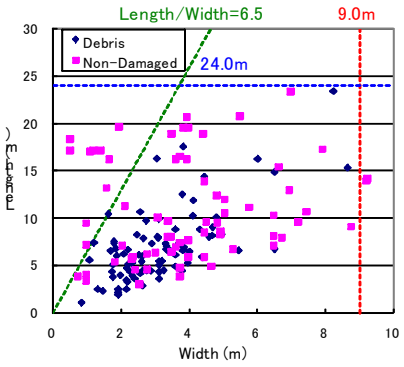

Figure 9. The relationship between *Width* and *Length* for the training areas. The bounds were used to extract debris objects.

Figure 10. The result of extracted debris by the object-based level-slice method. Many small commission errors are seen.

Figure 11. The result obtained by applying the debris extraction procedure to the pre-event digital image.

Figure 13 shows the filtered debris areas at this A_{min} value and the debris areas are in good agreement with the visual inspection result. But this area-filter value is considered to be too large since it is almost the same level as the footprint of an ordinary house in Japan, and hence this kind of area-based accuracy evaluation may have some limitation.

Evaluation of accuracy is further carried out in an object-based manner; if an extracted object has a 50% overlap with an actual debris area, it is counted as correct. Figure 13 shows the accuracy of debris extraction by this object-based counting with respect to A_{min}. The maximum accuracy is obtained when A_{min} reaches about 58 m^2, the

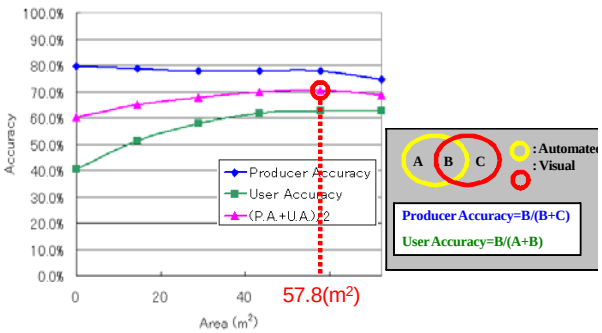

Figure 12. Area-based accuracy of extracted debris by the object-based level-slice method.

Figure 12. The result of extracted debris after subtraction of the pre-event debris areas and applying the minimum area filter (A_{min}=58m^2).

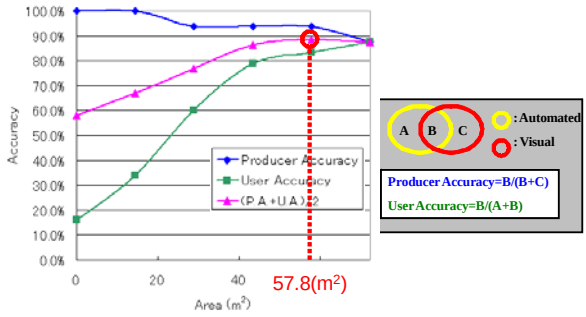

Figure 13. Object-based accuracy of extracted debris by the object-based level-slice method.

same as the area-based accuracy evaluation. However, the peak was much clearer than the previous evaluation. If we try to estimate the number of collapsed houses from aerial images, counting the number of extracted objects by this scheme may give acceptable accuracy. However, the determination of object feature values still need to be tested for many other examples.

6. CONCLUSIONS

Automated building damage extraction was conducted using a digital aerial image captured after the 16 July 2007 Mid-Off-Niigata earthquake. First, a pixel-based maximum likelihood classification was performed. As the result, salt-and-pepper noises and misclassifications were seen. An object-based supervised classification was then performed assigning 12 classes as training data. Although the object-based classification method gives an acceptable level of accuracy, assigning proper classes and training data is time consuming for a large area. Thus a level-slice method was introduced after object-based segmentation. Selecting the intensity and NDVI as layer values and employing several feature values of debris objects, the object-based level-slice method was carried out. The similar debris extraction was also carried out for the pre-event image to remove commission errors in the level-slice debris extraction. Since many small misclassifications were still observed, a minimum area-filter was further applied to remove them. The extracted debris areas show a reasonable level of accuracy, especially in the object-based producer and user accuracy. To enhance the accuracy further, the method should be tested for larger areas and more examples.

Acknowledgements:

The aerial digital image used in this study was provided from Asia Air Survey Co., Ltd and Kashiwazaki City Government.

References:

Baatz, M., Benz, U., et al. (2004). Definiens Imaging, e-Cognition user guide 4, 76-78.

Hinz, A. (1999). The Z/I digital aerial camera system, *Proceedings of the 47th Photogrammetric Week 1999*, Wichmann Verlag, Heidelberg, 109-115.

Leberl, F. and Gruber, M. (2005). ULTRACAM-D: Understanding some Noteworthy Capabilities, *Photogrammetric Week 05*, Dieter Fritsch, Ed. Wichmann Verlag, Heidelberg 57-68.

Liu, W., Yamazaki, F., Vu, T.T., and Maruyama, Y. (2007). Speed Detection of Vehicles from Aerial Photographs, *Proc. 27th Asian Conference on Remote Sensing*, CD-ROM, 6p.

Maruyama, Y., Yamazaki, F., Yogai, H., and Tsuchiya, Y. (2006). Interpretation of Expressway Damages in the 2004 Mid Niigata Earthquake Based on Aerial Photographs, *Proceedings of the First European Conference on Earthquake Engineering and Seismology*, Geneva, Switzerland, CD-ROM, Paper No. 738, 8p.

Matsumoto, K., Vu, T.T., and Yamazaki, F. (2006). Extraction of Damaged Buildings Using High Resolution Satellite Images in the 2006 Central Java Earthquake, *Proc. 27th Asian Conference on Remote Sensing*, CD-ROM, 6p.

Mitomi, H., Matsuoka, M., and Yamazaki, F. (2002). Application of Automated Damage Detection of Buildings due to Earthquakes by Panchromatic Television Images, *The 7th U.S. National Conference on Earthquake Engineering*, CD-ROM, 10p.

Nitto, T. and Yamazaki, F. (2006). Estimation of Overturning Ratio of Tombstones by Image Analysis of Aerial Photographs, *Proc. 27th Asian Conference on Remote Sensing*, CD-ROM, 6p.

Ogawa, N. and Yamazaki, F. (2000). Photo-Interpretation of Building Damage due to Earthquakes using Aerial Photographs, *Proc. 12th World Conference on Earthquake Engineering*, CD-ROM, 8p.

Yamazaki, F., and Kouchi, K. (2006). Automated Damage Detection of Buildings from High-Resolution Satellite Images, *Proceedings of the First European Conference on Earthquake Engineering and Seismology*, Geneva, Switzerland, CD-ROM, Paper No. 714, 7p.

Sixth International Conference on Urban Earthquake Engineering
March 3-4, 2009, Tokyo Institute of Technology, Tokyo, Japan

STUDY ON AN INFORMATION MANAGEMENT SYSTEM OF PUBLIC OFFICE TO SUPPORT EMERGENCY RESPONSE ACTIVITIES - CASE STUDY OF NAGOYA PORT -

Kenichi Ishibashi[1)]

1) Associate Professor, Faculty of Environment and Information management, Nagoya Sangyo University, Japan
kishibas@nagoa-su.ac.jp

Abstract: This document describes the information collecting system under the emergency condition and manage it. This proposal is focusing the management cost and keep good working under the emergency condition. A by-product of the system, user of the system are hard to make a mistake.

1. INTRODUCTION

From late of 20's century, we had some serious disaster, Hanshin-Awaji Earthquake in Japan, Big Tsunami in Indian Ocean and more. Its make a heavy loss of lives. In case of Japan, central government founded Central Disaster Prevention Council (CDPR) by the law. CDPR is working to prevent and mitigate the natural hazards. And CDPR is focusing to business continuity of public and private sector such as to create the BCP (Business Continuity Plan)/BCM (Business Continuity Management). Assuming that natural hazard is happened and makes damage in particular area. If it has a restoration power (e.g. socio-economical aspects) from the disaster, it's damage is relative low. Because public/private sector has a BCP/BCM, they know the way to recover from the disaster and can manage limited resources (human/physical resource). Public sector and private sector is setting same aim, saving a life under the emergency activity, however their aims are different under the recovery process.

2. AIMS AND OBJECTS

2.1 Aims

In this paper, it focused on the public sector's activity under the emergency situation when disaster happened. This paper aims to clear the conditions collecting the information about damages by disaster and related information.

Generally, natural hazards (Earthquake, Tsunami and more) has uncertainty. In other words, no one knows exact time these hazards happened. Science has been progressing, unfortunately we can not predict the occurrence time, place and its scale accurately. So it needs that to make the strategy to prevent natural hazards and mitigate the damage by it. If the society has equipped these strategies, this society will recover from the damage.

In this paper, it discusses the way of collecting and using the information by the public sector. Nagoya Port Office set the test case

Focusing an Emergency Activities, its aims to save suffers and enable to prevent the second disaster. Most important things are to get the accurate information about damages and adequate correspondences. Nowadays, some systems to support the emergency activities. Considering the error (system based error and human based error), dual use (Emergency use and Daily use) is suitable. That is, the frequency of using the system is very high under the dual use case. Then stuff who use the system are familiar with the system and system based error is easy to find out. Finally, average cost of the system is getting low.

2.2 Objectives

According to cost of the system, it is to be desired that installation and maintenance cost is getting low. However, it is not able to cut down on expense of the system. Because proposed system is needed the high reliability, the cost is very expensive at the result. Considering the cost benefit, cost is not changed depending on the system requirements. Then solution is frequency of using the system is getting higher.

In this paper, it shows that requirement for integrated information system to collect and deliver the information in public sector.

3. SYSMTEM REQUIRMENT FOR EMERGENCY RESPONSE ACTIVITY

3.1 System Requirements

Focusing the information collect process, that's not to say that all information collect process are automated. For example, it is able to get the transfer pathway data by the people using the GPS sensor and make the alert for a landslip automatically.

Most of the information collect process is human

activity based. In other words, observer is going to the damaged area, they observe the damage and evaluate. Therefore, evaluation result has an ambiguity. To prevent the vagueness, a third person is able to assess the damage. To give an actual example, to take the photo for damaged area with a measure.

It is desired that information collecting and reporting process are real-time processing. That is, conditions of the damaged area are changed time by time. Two of them are quite different, human and physical resources for emergency response are wasted.

According to former researches, members of the disaster countermeasures office are showing a tendency to keep on working in a few days. After emergency activities are converged, they fall ill. To prevent it, transferring their duties, it needs to easy to transfer. However, transferring process is different from normal transferring process. Most important point are quickness and accuracy.

3.2 Framework

As noted that requirements of the system are easy operation and easy to understand the damages. According to these conditions, GIS (Geographical Information System) is suitable.

3.3 Management of the system

ccording to the brochure of Port and Airport Department, the Chubu Regional Bureau (CRB-MLIT) shows tha

To focus the management of the system, there is some possibility of doing that it is not working perfectly. Because, most of them (system) are specialized for emergency use only. Moreover, users of this system are not familiar with it, there is some possibility to make a mistake. To prevent, this system is usually used for lesson for emergency activity or inspect the berth. After all, users are get skilled and difficult to make a mistake. Furthermore average cost of the system is getting lower. Consequently, the system is able to use daily and emergency case.

4. CASE STUDY OF NAGOYA PORT

4.1 About Nagoya port

According to the brochure of Port and Airport Department, the Chubu Regional Bureau (CRB-MLIT) shows that Nagoya Port is important role, that is the hub function of the industrial sector in Chubu region. Figure 1 shows that current status of international logistics in Chubu Area. It is clear that Nagoya Port is dominating other ports. More specific, imported items are industrial raw materials (e.g. LNG and crude oil) and exported items are machinery products, such as automobiles and industrial machinery.

Otherwise, Chubu region is designated as an affected area for “Tokai Earthquake”, “Tonankai Earthquake” and “Nankai Earthquake”. CDPR is setting an Expert Study Panel for predict the effect by these earthquake. Figure 2 shows that expected Tsunami heights and arrival times at coastal areas of Chubu region. It is clear that outside of Ise

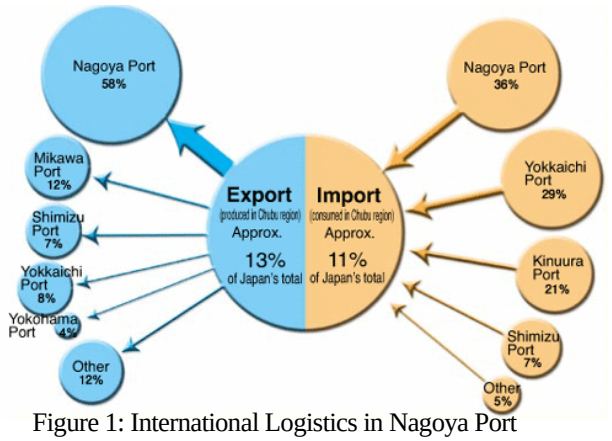

Figure 1: International Logistics in Nagoya Port

Bay, huge Tsunami is arriving up to 30 minutes after the earthquake. Otherwise inner area of Ise Bay, medium level (up to 3 m) is arriving more than 30 minutes after the earthquake.

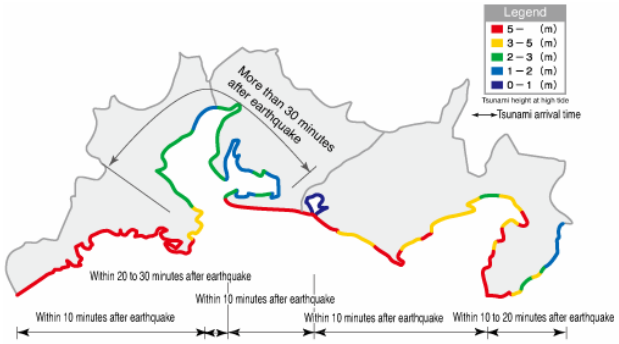

Figure 2: Tsunami Alert Area Map

50 years ago, Ise Bay was attacked by Big-scaled Typhoon, “Isewan Typhoon”. It made a high tide water, enormous people were suffered. Since 2008, the Chubu Regional Bureau (MLIT) has setting an Expert Study Group about high tide water and flood which is tackling to predict the damage by it.

CRB-MLIT is stated that “In the hinterland of Ise Bay, is an area of enormous manufacturing industry concentration and lively economic activity, with Nagoya as its core”. Nagoya Port is located the front line to face a natural hazards such as high tide water, Tsunami. Nagoya Port Office (NPO) has prevent and mitigation programs for each natural hazards, which aims to shorten the recovery time.

4.2 Emergency Program in Nagoya Port Office

NPO is assigned a role in an emergency action program which to assess the berth by their officer under the emergency case (such as Earthquake, Tsunami, High Tide Water). Moreover, if their own berth was safe, they have to support other local area office which damaged heavily.

However, no one has exact information that who came to the office within one hour after disaster happened. Because, disaster has much uncertainty (time, location and scale). And nobody knows exactly time to assess the damages of the berth. It is clear that key player of emergency action program is NPO’s officer.

In this case study, it focuses the officer's activity. An emergency action program is decomposed three parts, first one is checking officers' safety, second one is gathering condition for every officer, last one is to assess damages for each berth.

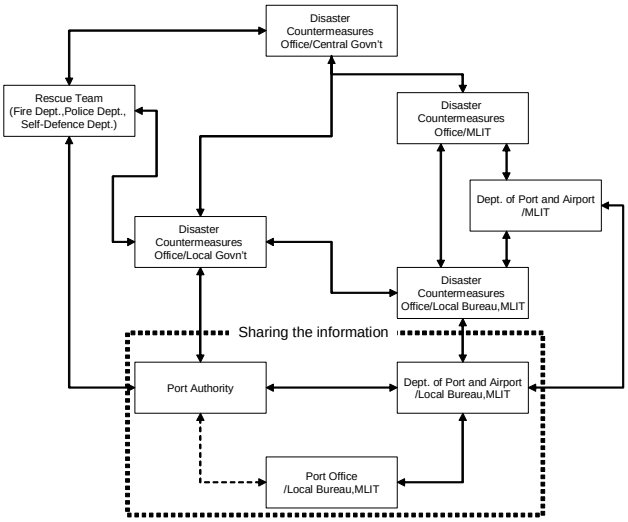

Figure 3: Relations for every public sector

4.3 Experimental System in Nagoya Port

NPO has equipped "Saigai-Infoweb" system which enables to collect the damages at the berth using the mobile phone (Show Figure 4). To specify the system, officers of the NPO are going to every damaged area, then they are taking a photo by their own/public mobile phone which include GeoCode (latitude and longitude). And they send the data (photo with GeoCode) via email by the mobile phone. NPO is collecting above data, they can check the damage easily.

Figure 4:Screen-shot (saigai-infoweb)

However, NPO has only Saigai-Infoweb, which does not cover all emergency activities. Then they can not handle with all data seamlessly. At the result, they can not supply effective information to emergency activities. We are discussing about the integrated system based on the LBS (Location Based Service) to support the emergency activities (Figure 5).

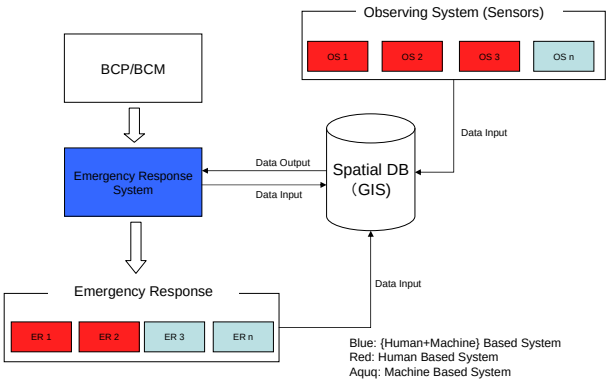

Figure 5: Integrated System Concept

Figure 5 is the overall concept for new integrated system. It mentioned below, NPO is working for assessing their own berth, emergency response and supporting other damaged local office/port. Again it note that these activity is depended on their officers. In other words, NPO is eager to get the information, number of officers within one hour after disaster happened.

Hereafter, introducing collaboration work with NPO, WAVE (Waterfront Vitalization and Environment Research Center) and author.

Figure xxx is concept based system. NPO has the BCP (Business Continuity Plan) for "Tokai Earthquake". We are just making the "Emergency Response System" which based on the BCP of the NPO. This system is issuing some emergency activities, which include assessing the berth, restoration work and supporting the other damaged local office to officers.

As it note that if Disaster Countermeasures Office does not have accurate information about officers' condition, it does not take an effective action. In the right side of Figure xxx, we set the observing system using some sensors. In Figure xxx, "OS 1, OS 2, …, OS n" means that observation system one to n. OS 1 is the "Confirmation of the safety for officers". It enables to confirm the officers' safety and grasp the number of officers to involve the emergency activity. These observing system is get data (e.g. damaged road, berth and more) every moment, then spatial DB is collecting these data. Finally, Disaster Countermeasures Office is easy to make a decision.

From 2008, we are tackling to make the system focused on the Emergency Response System.

5. CONCLUSION

In this paper, it explored the logic integrated Emergency Response System And to inform the Nagoya Port Office experimental study.

Acknowledgements:

The author expresses an acknowledgement deeply to support and discussion with Nagoya Port Office (Mr. Ito, Mr, Miyahara, , Mr. Okazaki: Deputy Director, Mr. Kasugai: Director) and Port and Airport Department (Mr. Takei: Senior Planning Officer for Port

and Airport, Mr. Horita: Senior Planning Officer for Port and Airport and Mr. Tanabe: Director), the Chubu Regional Bureau, Ministry of Land, Infrastructure, Transport and Tourism, Japan.

Sixth International Conference on Urban Earthquake Engineering
March 3-4, 2009, Tokyo Institute of Technology, Tokyo, Japan

CYBER CITY IMPLEMENTATION AND APPLICATIONS TO HAZARD MITIGATION

Fuan Tsai*[1)], Tea-Ann Teo[2)], Liang-Chien Chen[3)], Wenko Hsu[4)], and Dung-Mou Hung

1) Associate Professor, Center for Space and Remote Sensing Research & Dept. Civil Engineering, National Central University, Taiwan
2) Post-Doc. Research Fellow, Center for Space and Remote Sensing Research, National Central University, Taiwan
3) Professor, Center for Space and Remote Sensing Research & Dept. Civil Engineering, National Central University, Taiwan
4) Research Fellow, Research Center for Hazard Mitigation and Prevention, National Central University, Taiwan

ftsai@csrsr.ncu.edu.tw, ann@csrsr.ncu.edu.tw, lcchen@csrsr.ncu.edu.tw, wenko@ncu.edu.tw

Abstract: This paper presents a systematic approach for implementing 3D digital city for hazard mitigation. Prismatic and polyhedral building models with complicated roof types are constructed from topographic maps, aerial photographs and airborne LIDAR data independently or with data fusion. Photo-realistic façade textures are generated from close-range digital images and video sequences. In addition, Level of Detail (LOD) techniques are developed to processing high resolution terrain meshes and building models for high performance visualization and real-time analysis. The developed 3D digital city systems are employed in sophisticated applications including urban earthquake modeling and flooding potential analysis. It is demonstrated that 3D digital city can not only provide critical parameters to the modeling analysis, but also can be used as an intuitive platform for decision support.

1. INTRODUCTION

Three-dimensional (3D) digital city (cyber city) is an emerging and fast-growing topic in the research and applications of spatial information science. A cyber city is a virtual replica of a real city in a computer-generated environment. It not only resembles the layouts and geometry of various city objects, but also should contain the activities and functionalities of a real city. As the technologies in remote sensing advance, new types of data from assorted sensors and with different characteristics have become available for the reconstruction of important objects in a city. Similarly, the new technology developments in geoinformatics have enabled cyber city systems with advanced designs and implements as well as more powerful processing and analysis capabilities for sophisticated applications. For example, it might be difficult to obtain adequate information to accurately predict potentials of building damages in a earthquake assessment analysis from conventional 2D GIS systems. On the other hand, a 3D digital city can provide the modeling systems more complete parameters to perform real 3D assessments. In addition, the modeling results can be integrated into the 3D digital city for realistic presentation and intuitive decision-support operations.

This paper presents a systematic approach to construct photo-realistic 3D digital city systems from assorted remote sensing and other spatial datasets, including topographic maps, aerial photographs, airborne Light Detection and Ranging (LIDAR) data, and close-ranged digital photographs and video sequences. High performance visualization algorithms are also presented for real-time, interactive exploration and applications of the constructed 3D digital city. Example applications to earthquake and flooding potential assessments are also discussed to demonstrate the usability of the developed system

2. 3D DIGITAL CITY

A cyber city constitutes various objects. Among them, terrain, buildings and roads are probably the most important. Remote sensing data from different sources can be used to construct them. However, different datasets have different characteristics. For example, optical imagery provides good spectral information of ground targets but with little geometric properties. On the other hand, LIDAR point clouds are accurate in range measurement but they are discrete and without topological relationship. Consequently effective strategies and algorithms must be employed to fully utilize the advantages of different data.

2.1 Building Modeling

As buildings are the most ubiquitous objects in a city, building model is also one of the most important components in a digital city. In this study, prismatic and polyhedral building models with flat and complicated roof structures are reconstructed from topographic maps, aerial photographs and LIDAR datasets. These data can be used independently or by data fusion. Figure 1

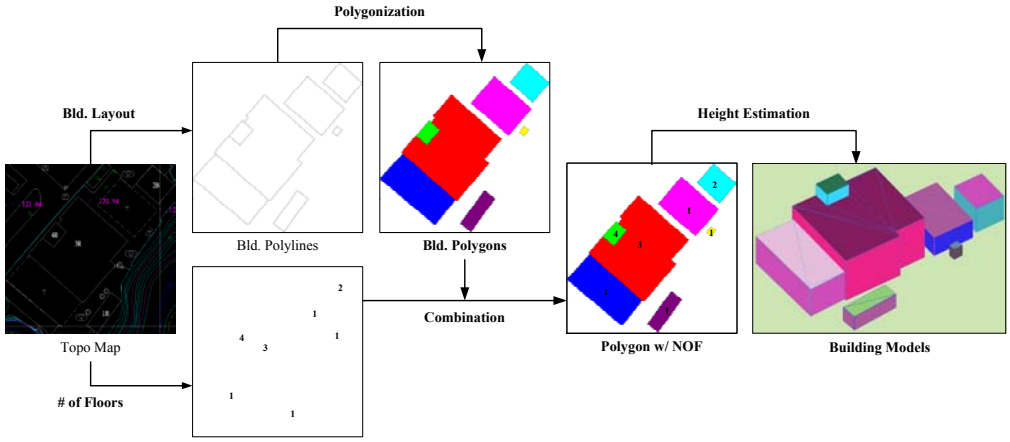

Figure 1: Building modeling from topographic maps

demonstrate a procedure for quickly constructing block-based building models from topographic maps that provide 2D building layouts but only annotate the number of floors for each building. As a result, the building heights need to be estimated and all roofs are assumed flat.

On the other hand, stereo aerial photographs and LIDAR datasets provide better information about building heights and roof structures. However, the former usually requires intensive human operations to identify feature points and lines, and the later are discrete point clouds without topological relationship. Therefore, algorithms were developed to extract 3D line segments from both datasets and shape them to form building models. For example, a modeling procedure based on extracted 3D line segments (Rau & Chen, 2003) is used to construct building models as displayed in Figure 2.

To fully utilize the advantages of different datasets, algorithms were also developed to generate building models from fusion of multiple datasets. For example, a Split-Shape-Merge method (Teo et al., 2007) was used to model complicated buildings from topographic maps and LIDAR point clouds as displayed in Figure 3. The method combines accurate building layouts extracted from topo maps and height information from LIDAR point clouds to construct building models.

2.2 Façade Texture Mapping

The methods described above can only produce geometric outlines of building models. For photo-realistic digital city modeling, model facets must attach realistic façade textures to provide realistic look and feel and, more importantly, accurate texture attributes. Conventionally, this task is labor-intensive and time-consuming. A polygon-based texturing mapping system was developed to facilitate this process (Tsai and Lin, 2007). This research further developed an interest-point matching algorithm to automate the generation of façade textures from close-range images and video sequences. A self-mending procedure was also developed to correct most of occlusions of the texture images.

On individual texture images, corner points are extracted using Harris Corner Detector as listed in Eq. (1):

$$R = \det M - (traceM)^2$$

$$M = \begin{bmatrix} \frac{(\partial I)^2}{\partial^2 x} \otimes w_{u,v} & \left(\frac{\partial I}{\partial x}\right)\left(\frac{\partial I}{\partial y}\right) \otimes w_{u,v} \\ \left(\frac{\partial I}{\partial x}\right)\left(\frac{\partial I}{\partial y}\right) \otimes w_{u,v} & \frac{(\partial I)^2}{\partial^2 y} \otimes w_{u,v} \end{bmatrix} \quad (1)$$

$$w_{u,v} = e^{-(u^2+v^2)/2\sigma^2}$$

Overlapped texture images are mosaicked automatically according to the "relative image displacement" and normalized cross-correlation (NCC) restrains as listed in Eq. (2).:

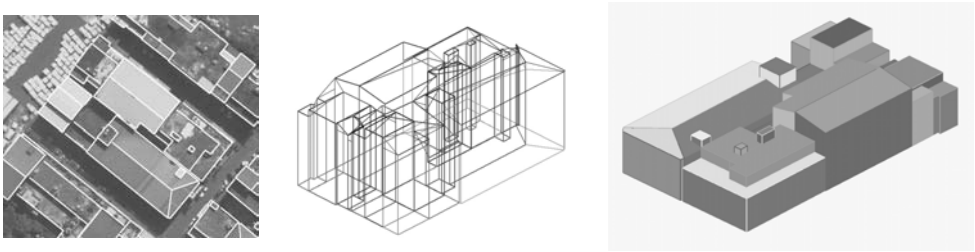

Figure 2: Building modeling from aerial photographs.

$$NCC = \frac{\sum\left[G_t(u,v)-\bar{t}\right]\cdot\left[G_s(u,v)-\bar{s}\right]}{\left\{\sum\left[G_t(u,v)-\bar{t}\right]^2\sum\left[G_s(u,v)-\bar{s}\right]^2\right\}^{0.5}} \quad (2)$$

Figure 4 shows an example of the feature point matching result. As displayed in the figure, most of the feature points are matched correctly. Therefore, using the matched feature points as tie points to merge overlapped images will generate complete texture mosaics continuous in geometry.

applications is the system performance. A 3D digital city often consists of high resolution terrain meshes, images and hundreds to thousands of objects. The vast amount of data is a great challenge for visualization and analysis tasks. To this regard, view-dependent Level of Detail (LOD) process is an effective solution to interactive rendering and visual-enabled operations. For terrain meshes, this research utilizes a quad-tree based terrain LOD processing mechanism (Tsai and Chiu, 2008) to create multiple LOD terrain tiles adaptive to different

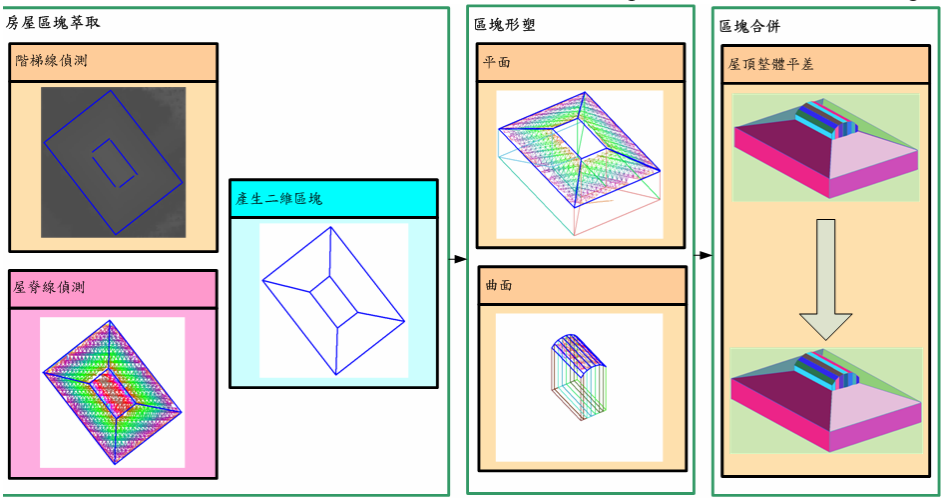

Figure 3: Building modeling from fusion of LIDAR and topographic maps.

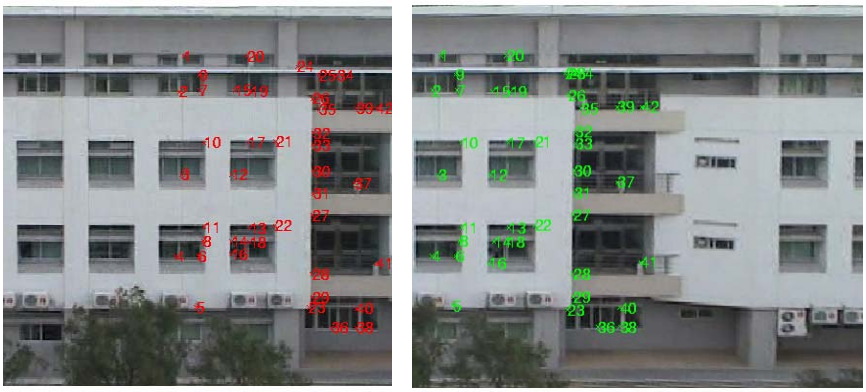

Figure 4: Automatic matching of feature points.

Façade texture images acquired with close-range digital cameras or video camcorders often consists of occlusions caused by trees, cars and other foreign objects. These occlusions should be identified and mended to generate complete and accurate texture attributes of buildings in a 3D digital city. Figure 5 shows a systematic procedure for self-mending the occlusions. The idea is that most building façades have symmetric appearances, so by identifying the axis of symmetry, most of the occlusions can be corrected by mirroring. As a result, photo-realistic 3D digital city systems as displayed in Figure 6 can be constructed with algorithms described above.

2.3 Performance Consideration

A practical factor for real-time cyber city

viewing conditions. The key issue is to identify appropriate thresholds for quad-tree processing of terrain meshes based on the ground sampling distance (GSD) based on viewing parameters. Figure 7 demonstrates an example of the generated LOD mesh datasets for a terrain tile. Detail discussions about terrain LOD processing can be found in the mentioned reference and are not repeated here. Based on a previous test (not shown in this paper), using this LOD processing, large-scale terrain meshes can be rendered efficiently in interactive fly-through applications and with at least 25 frames per second performance, which is adequate for real-time applications.

Building model is another target that requires LOD processing in the visualization of 3D digital city systems. A divide-and-conquer strategy has been developed to

Figure 5: Automatic identification of mirroring axis and region for self-mending occlusions. From upper left to lower right: (a) original; (b) region growing; (c) area histogram filtering; (d) homogeneity test; (e) location filtering; (f) identified mirroring axis and region.

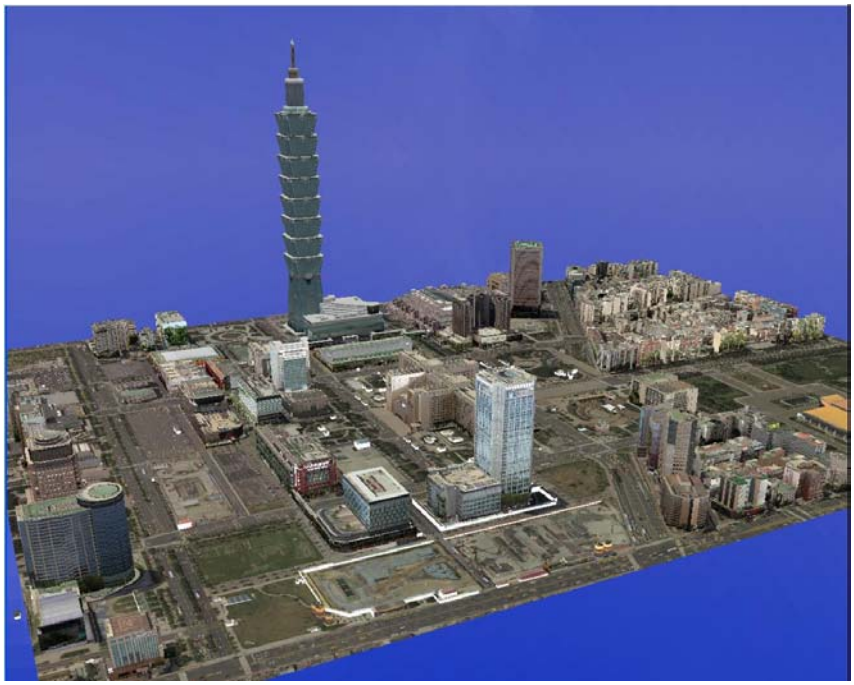

Figure 6: 3D digital city with photo-realistic façade texture mapping.

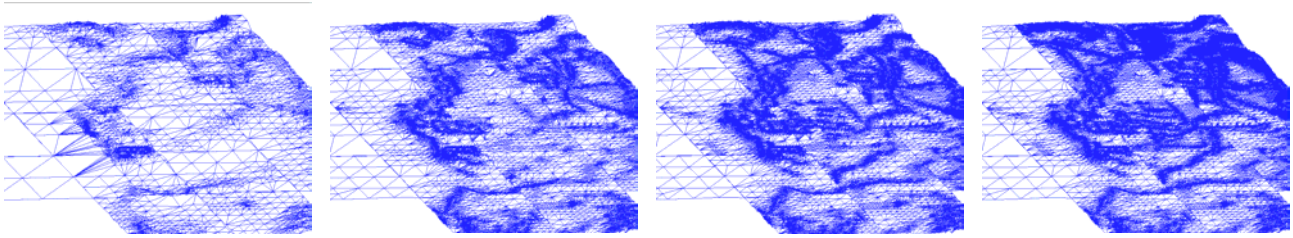

Figure 7: LOD of terrain meshes (from course to fine).

deal with this issue. The algorithm is based on the simplification on 2D orthographic projects of 3D building models as described in Lin et al., 2008. The idea and an example are illustrated in Figure 8. First, orthographic projections are generated from complicated 3D building models. Secondly, simplifications are performed on the 2D projections. Then a generalized 3D building model is generated by reconstituting from the simplified 2D projections. The process can be repeated until the generalization is satisfied.

Combining the terrain and building LOD processes with image pyramid schemes for terrain and façade

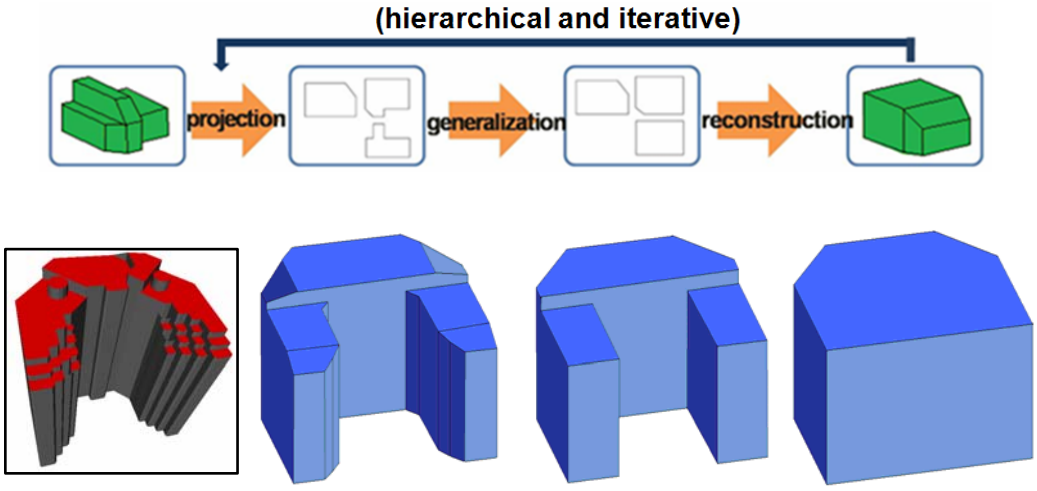

Figure 8: LOD generation of 3D building models.

texture images, the developed 3D digital system will have a high performance suitable for real-time, interactive exploration, analysis and applications. For Internet-based applications, the system performance can be further improved with data streaming and adaptive transmission.

3. APPLICATIONS TO HAZARD MITIGATION

The developed 3D digital systems were applied to hazard modeling and mitigation studies. Figure 9 displays the modeling results of flood perils in Hsin-Chu County of Taiwan under a 200-year frequency precipitation condition. The modeling was done using a flood potential modeling algorithm (Chang et al., 2008) with parameter inputs derived from the 3D digital city system. The same cyber city system is also used as a platform for hazard evaluation, management and other decision support tasks. As demonstrated in the figure, 3D digital city provides a more realistic and intuitive platform for interactive analysis.

Similar 3D digital city systems are also applied to urban earthquake modeling analysis. Figure 10 shows building damage potentials of an earthquake modeling for a business and residential district in Taipei. In this figure, buildings with more than 50% probability of moderate damage during the simulated earthquake are displayed in solid textures and those with less than 50% probability are in transparent façade textures. Similar queries for different levels of damages can also be made interactively in the same cyber city system and with real-time response. This way, it provides a convenient exploratory platform for identifying damage potentials and subsequent decision support for strategic mitigation operations.

The earthquake modeling and assessment was carried out with a well developed earthquake modeling system that is specifically designed for seismologic studies in Taiwan (Chiang and Hsu, 2004). In this analysis, the 3D digital city system not only acts as a graphical presentation and query platform, but more importantly, it also provides critical parameters (for example, building heights, estimations of volumes/weights etc.) to the modeling system, which are usually difficult to obtain from traditional two-dimensional models.

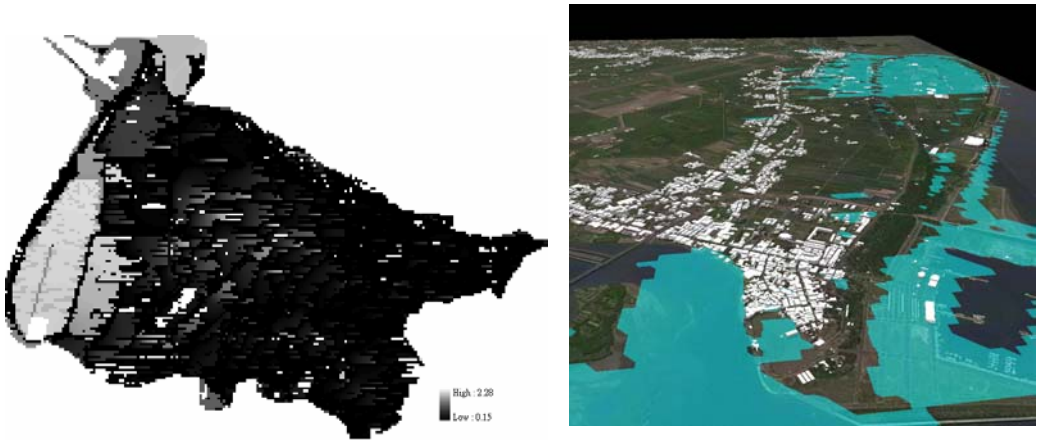

Figure 9: Modeling of flood perils for 200-year precipitation (left: 2D; right: 3D).

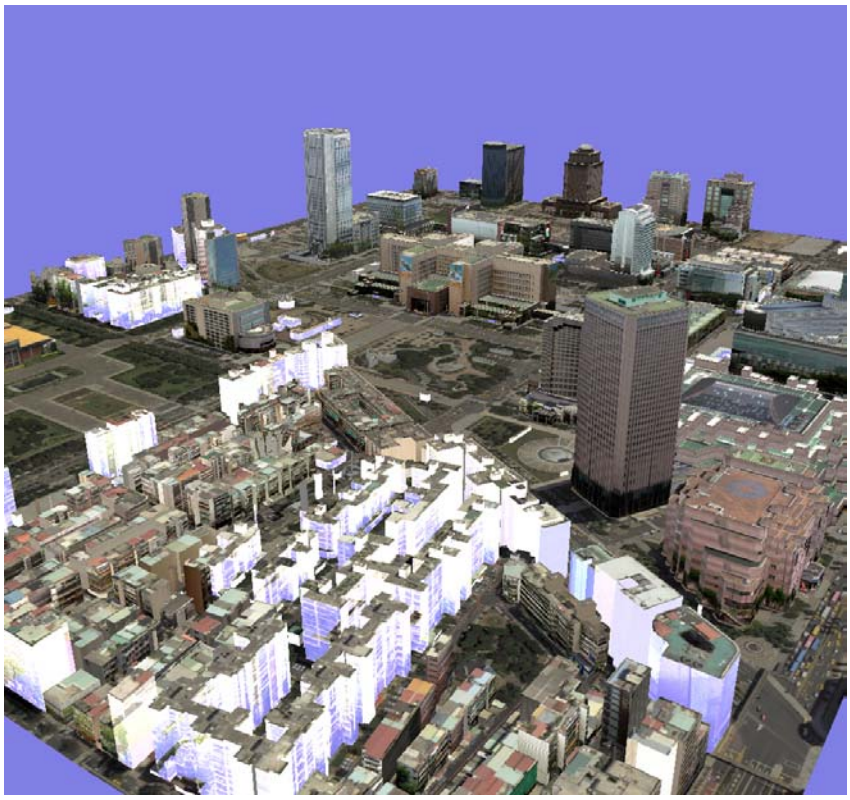

Figure 10: Building damage potentials of urban earthquake modeling. Solid textured buildings are the ones with 50%+ probability of moderate damage after a simulated earthquake.

4. CONCLUSION

This study developed a systematic approach to construct a photo-realistic 3D digital city for hazard mitigation. The digital city consists of accurate 3D building models constructed from topographic maps, aerial photos and LIDAR surveys. Realistic façade texture mosaics were generated from close-range digital images and videos based on feature points. Occlusions were corrected with developed self-mending algorithms to provide complete and accurate texture attributes. LOD algorithms for terrain meshes and building models were also implemented to improve system performance. Interactive real-time 3D visualizations of modeled flood perils and urban earthquake modeling were presented to demonstrate the capability of the system in hazard mitigation. The 3D digital city can be used as an intuitive platform for decision support. More importantly, it can also provide sophisticated applications critical parameters, which are difficult to obtain from conventional 2D models.

Acknowledgements:

This study was supported, in part, by the National Science Council and Ministry of Interior of Taiwan under project Nos. NSC-96-2221-E-008-068 and H-950925. The authors would like to thank the Research Center of Hazard Mitigation and Prevention for providing earthquake and flooding peril modeling supports.

References:

Change, CC, W Hsu and MD Su (2008), "Modeling Flood Perils and Flood Insurance Program in Taiwan", *Proceedings of 2008 American Agricultural Economics Association Annual Meeting*, July 27-29, 2008, Orlando Florida, CD-ROM.

Chiang, W. and W. Hsu (2004), "Taiwan Earthquake Model Upgrade 2004", *Proceedings of Innovative Solutions for Global Risk Management*, 27 May, 2004.

Lin, WR, F. Tsai and JJ Chen (2008), "Level of Detail Generation of 3D Building Models", *Proceedings of 29th Asian Conference on Remote Sensing*, Nov. 10-14, 2008, Colombo, Sri Lanka, CD-ROM.

Rau, J-Y and Chen, L-C (2003), "Robust Reconstruction of Building Models from Three-Dimensional Line Segments", *Photogrammetric Engineering and Remote Sensing*, **66**(2), 181-188.

Teo, TA, LC Chen, JY Rau and SJ Chen (2007), "Building Reconstruction Using a Split-Shape-Merge Method", *Asian J. Geoinformatics*, **7**(3), 31-44.

Tsai, F and HC Chiu (2008), "Adaptive Level of Detail for Terrain Rendering in Cyber City Applications", *International Archive of Photogrammetric Engineering, Remote Sensing and Spatial Information Sciences*, **XXXVII**(B4), 579-584.

Tsai, F and HC Lin (2007), "Polygon-based Texture Mapping for Cyber City 3D Building Models", *International J. Geographical Information Science*, **21**(9), 965-981.

Sixth International Conference on Urban Earthquake Engineering
March 3-4, 2009, Tokyo Institute of Technology, Tokyo, Japan

EARTHQUAKE EVACUATION FROM PEAK-HOUR UNDERGROUND RAILS

Junichi Obata[1] and Yasunori Muromachi[2]

1) Undergraduate, Department of Civil Engineering, Tokyo Institute of Technology, Japan
2) Associate Professor, Department of Built Environment, Tokyo Institute of Technology, Japan
obata@cv.titech.ac.jp, ymuro@enveng.titech.ac.jp,

Abstract: In this study, we studied how the passengers of the underground rail were affected by a large earthquake attack during peak-hours. We indicated preliminary results of our questionnaire survey by which each respondent was requested to answer behavioral alternatives in case of a large earthquake, and found that the knowledge of the passengers on the invulnerable underground rails might affect the behaviors they would choose in response to earthquake.

1. INTRODUCTION

According to the Damage Estimates of an Earthquake with an Epicenter in the Tokyo Metropolitan Area issued by Tokyo Metropolitan Government (2000), the scale of damage in relation to rails is estimated relatively smaller than that in relation to houses and buildings partly because civil engineering structure such as rail has mostly been reinforced against large earthquakes. However, the scale of damage will be dependent not only on the structural design of the railroad but on the behaviors of the passengers. Even when the damage of the railroad structure is very small, a large earthquake might induce passengers into risky behaviors, and cause unexpectedly large scale of damages. Especially during peak-hours, many passengers are riding on the fully-packed underground rails where the psychological situation of the passenger is difficult to predict, and the way of evacuation is unclear and limited in case of a large earthquake attack. In addition, frequent service during peak-hour might make the railroad companies to leave many trains stacked long after a large earthquake happens.

In this study, we discuss how the passengers of the underground rail are affected by a large earthquake attack during peak-hours. In the second section, we briefly review some preceding studies and discuss possible scenarios for earthquake evacuation from peak-hour underground rails. In the third section, we indicate preliminary results of our questionnaire survey by which each respondent is requested to answer behavioral alternatives when a large earthquake attacks peak-hour underground rails. While we understand that it is extremely difficult to ask respondents how they behave under a specific situation such as earthquake, we believe that the questionnaire survey is helpful in finding possible scenarios and considering which scenario might be more likely than others for the specific situation. In the last section, we make some concluding remarks by summarizing our findings.

2. PRECEDING STUDIES AND OPERATION OF PEAK-HOUR UNDERGROUND RAILS

According to Editorial Committee for the Report on the Hanshin-Awaji Earthquake Disaster (1998) and Yamato, T. et al. (1996), Great Hanshin-Awaji Earthquake collapsed the Daikai Station located underground along the Kobe Rapid Transit. While the Earthquake happened before peak-hours, the scale of damage might have been larger if it happened during peak-hours not because of vulnerability in structural design but because of fully-packed underground trains. In Tokyo Metropolitan Area, there are many underground rails operating during peak-hours whose service frequency is 20 to 30 trains per hour and volume of passengers is about 10 to 80 thousand per hour per direction. If a large earthquake occurs during peak-hours, it is likely that the companies operating underground rails need to stop all the trains and inspect all the sections of the track, which might take considerable time and make some passengers stay inside the trains until the companies confirm the safety of the track.

The psychological situations of the passengers might be very different from the usual one especially when they are constrained to the underground trains after a large earthquake. Furuta (2003) summarized possible ways of understanding human behavior in case of emergency and considered human psychology in the three states of individual, group and social levels. Gotoh et al. (2006) studied the causes and tendencies for raising a panic in the underground streets by conducting a questionnaire survey. However, the number of past studies whose focus is given to the peak-hour underground rails is limited. Because some of

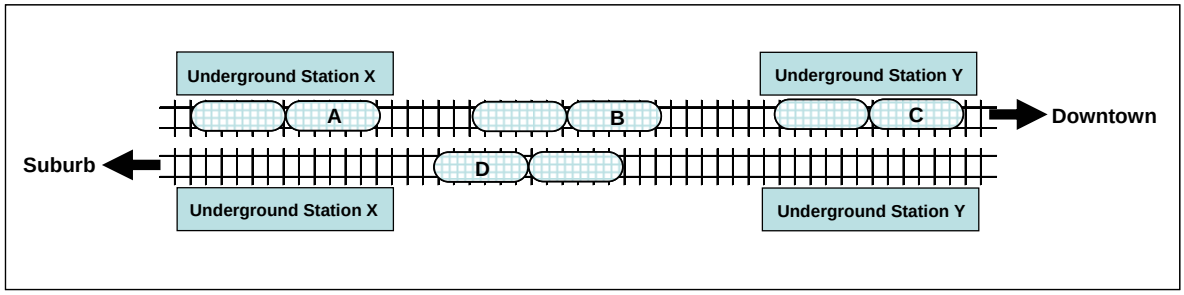

Figure 1 Diagram of Morning Peak-hour Underground Trains

the large metropolitan areas such as Tokyo are heavily dependent on the dense underground rails, the vulnerability against disaster when they are used at full capacity needs more discussion.

As a study area, we selected one section of an underground rail which connects downtown and suburban areas of Tokyo Metropolitan Area. The section contains six underground stations and carries about 80 thousand passengers per peak-hour. Figure 1 shows the diagram of a part of the section we selected. The diagram indicates that Case A and Case C trains are stopping at underground station X an Y, while Case B train is running between the two stations, because during morning peak-hours service frequency is quite high for downtown bound. On the other hand, Case D train is running between the underground stations Y and X, while there are no trains stopping at the two stations because the service is less frequent for suburban bound during morning peak-hours.

In case a large earthquake happens, the passengers on the Case A and Case C trains are able to evacuate from underground space through underground stations X and Y, while the passengers on the Case B train might be made to stay inside the train until the railroad company confirms the safety of the track between the Case B train and underground station Y, and the Case C train departs from the station Y. The passengers on the Case D train might also need to wait for the railroad Company's safety inspection, but they can approach the underground station X immediately after the safety of the track between the Case D train and the station X is assured. It is likely that, if a large earthquake occurs during peak-hours, the passengers on the Case B train bounded for downtown need to stay in the most congested train for a long time, and that how long they must wait for evacuation from the peak-hour underground rail is not uncertain. If it takes an unexpectedly long time, the psychological situation of the passenger may well become different from the usual situation.

For studying the Cases assumed in Figure 1, we conducted a survey of the planned and actual train schedule during peak-hours from 0800 to 1000 for the study section of the underground rail. The summary of the results is indicated in Table 1. The first two rows show the shares of the time for the trains stopping at the stations ('On Station') and that for the trains running between the stations ('Between Stations'). We assumed that each train stopped at each station for 30 seconds. The third row shows the share of the time between 0800 and 1000 when the train of Case B indicated in Figure 1 is found according to the planned train schedule and observed from our survey of actual train operation on the survey days (20/25 November 2008).

Table 1 Operation of Peak-hour Underground Trains

Downtown Bound	On Station*	Between Stations*	Case B Trains
According to Train Schedule	15.6%	84.4%	25.8%
20 Nov 2008	28.6%	71.5%	58.6%
25 Nov 2008	29.2%	70.8%	64.8%
Suburb Bound	**On Station***	**Between Stations***	**Case B Trains**
According to Train Schedule	18.2%	81.8%	3.1%
20 Nov 2008	31.6%	68.4%	25.8%
25 Nov 2008	31.0%	69.1%	28.1%

*) excluding express services

Table 1 demonstrates that, when a large earthquake happens during morning peak-hours, the passengers on our study section are more likely to be located between stations than on stations. For the planned train schedule, the share of the case between stations is about 80 percent for both downtown and suburb bound trains, however, for our survey days, the share is reduced to be about 70 percent mainly because of chronically delayed trains during morning peak-hours.

While the share of the time when the train of Case B is found to be less than 30 percent for downtown bound according to the planned train schedule, the share is observed to be about 60 percent according to our survey. In other words, if a large earthquake occurs during morning peak-hours, the probability of being passengers who are left for a long time inside the congested train is more than 50 percent for downtown bound trains. This is because of highly frequent services as well as chronically delayed trains during morning peak-hours. It is also noted that even for suburb bound trains, the share is observed to be about 25 percent on our survey days.

According to our survey of the planned schedule and

actual train operation during peak-hours for the study section, the share of the time when the train of Case B is observed is about 60 percent for downtown bound and about 25 percent for suburb bound trains. In case a large earthquake happens, the passengers on the Case B train might be made to stay inside the train until the railroad company confirms the safety of the track in principle. However, some passengers might not follow the railroad company's directions if it takes a long time and the psychological situations of the passenger become different from the usual situation. We discuss the issues in the next section.

3. PASSENGER'S BEHAVIOR IN RESPONSE TO A LARGE EARTHQUAKE

In order to study the passenger's behavior in response to a large earthquake, we conducted a questionnaire survey by which we asked the passengers on the study section of the underground rail about the perception of safety for underground rails in terms of earthquake and likely behaviors after a large earthquake happens, as well as demographic characteristics. We assumed two types of the passengers who get on/off the station within the study section, and who only pass through the section. We also prepared two types of the questionnaires with/without the information that 'structures of underground rails have mostly been so reinforced against large earthquakes that it is unlikely that an earthquake with an epicenter in the Tokyo Metropolitan Area whose magnitude is 7.3 will cause damages on transport.' In this paper, we only indicate preliminary results of our questionnaire survey and the dataset is limited to the passengers with the information.

The survey was conducted from December 2008 to January 2009. We distributed about 1,100 questionnaires among the passengers of two kinds out of which about 460 questionnaires were returned by post mail. The number of the returned questionnaires with the information was 245 as of the end of January, which constitutes a dataset for the study in this paper. The outline of the questionnaire survey is indicated in Table 2.

In the questionnaire, we asked respondents whether they knew the information. According to the results, only about 15 percent of the respondents answered 'yes.' First, we assume the passengers on Case A train in Figure 1 where the train is stopping at the station when a large earthquake happens. According to the result, more than 60 percent of the respondents with the knowledge ('Know') on the invulnerable underground station against earthquake and more than 20 percent of the respondents without the knowledge ('Do Not Know') expressed their anxiety for safety in case of earthquake, as indicated in Figure 2. As of the types of anxieties, irrespective of the knowledge, most of the respondents were anxious about the items of 'Locked in Underground,' 'Blackout,' and 'Panic,' out of which 'Panic' and 'Blackout' were more concerned by the respondents with the knowledge, while 'Locked in Underground' by the respondents without it, partly because the respondents with

Table 2 Outline of the Questionnaire Survey

	Passengers Passing through the Study Section	Passengers Getting on/off the Stations within the Section
Questionnaires Distributed	613	461
Questionnaires Returned	280	183
Questionnaires with Information Returned	143	102
Respondents Who Knew the Information	24	13

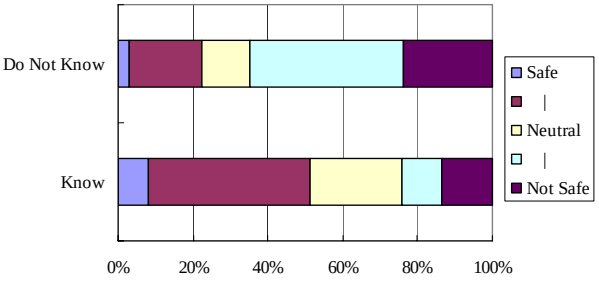

Figure 2 Perception of Safety by Respondent's Knowledge

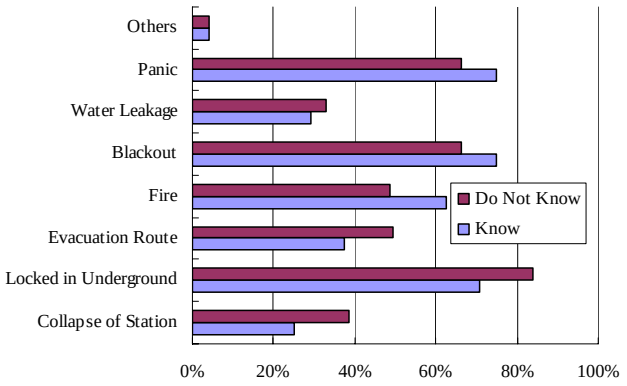

Figure 3 Types of Anxieties by Respondent's Knowledge

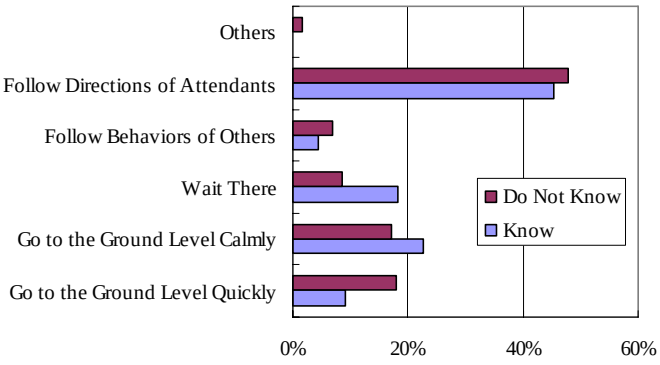

Figure 4 Types of Behaviors by Respondent's Knowledge

the knowledge were more confident in the structural design of underground station against earthquake, as demonstrated in Figure 3.

We also asked respondents how they would behave at the station in response to a large earthquake. The result is indicated in Figure 4. While most of the respondents chose 'follow directions of attendants,' the respondents with the knowledge chose 'wait there' more and 'go to the ground level quickly' less than the respondents without it. In addition, we prepared the question that 'how much percentage of the people around you going to the ground level will make you follow their behaviors?' (Yamagishi (1990)) and the result is shown in Figure 5. The equilibrium is found in the range between 90 and 100 percent, which means most of the respondents will choose to go to the ground level by following other people's behaviors. However, the tendency for the respondents with the knowledge is less so than the respondents without it, because they understand underground stations are relatively safe.

Second, we assume the passengers on Case B train in Figure 1 where the train is left between the stations if a large earthquake happens. We asked the respondents 'how many minutes can you stay inside the congested train?' and the result is indicated in Figure 6. The difference is not clear in terms of the respondent's knowledge, however, some respondents with the knowledge intend to stay even inside the congested train for more than one hour. We also asked the question that 'how much percentage of the people around you going outside of the train will make you follow their behaviors?' and the result is indicated in Figure 7. The equilibrium is found in the range between 70 and 100 percent, which means most of the respondents will choose to go outside of the train by following other people's behaviors. The respondents with the knowledge are slightly more inclined toward going outside of the train, partly because they are confident in safety of underground rails.

4. CONCLUDING REMARKS

In this study, we studied how the passengers of the underground rail were affected by a large earthquake attack during peak-hours. We discussed possible scenarios for earthquake evacuation from peak-hour underground rails. Also, we indicated preliminary results of our questionnaire survey by which each respondent was requested to answer behavioral alternatives in case of a large earthquake, and found that the knowledge of the passengers on the invulnerable underground rails might affect the behaviors they would choose in response to earthquake.

References:

Editorial Committee for the Report on the Hanshin-Awaji Earthquake Disaster (1998), "Report on the Hanshin-Awaji Earthquake Disaster 10: Damage and Restoration of Transportation and Agricultural Facilities," Japan Society of Civil Engineers.

Yamato, T., *et al*. (1996), "Damage to Daikai Subway Station of Kobe Rapid Transit System and Estimation of Its Reason during the 1995 Hyogoken-Nanbu Earthquake," *Journal of Structural and Earthquake Engineering*, Japan Society of Civil Engineers, **537/I-35**, 303-320.

Furuta, T. (2003), "Safety and Crisis Management (2) Human Behavior in Case of Emergency," *Regional Development Studies*, Toyo University, **6**, 239-254.

Gotoh, K., *et al*. (2006), "Survey for Consciousness and Action during Underground Street Disaster by the Questionnaire Method," *Proceedings of the Symposium on Underground Space*, Japan Society of Civil Engineers, **11**, 151-156.

Yamagishi, T. (1990), "Social Dilemma," Saiensusha.

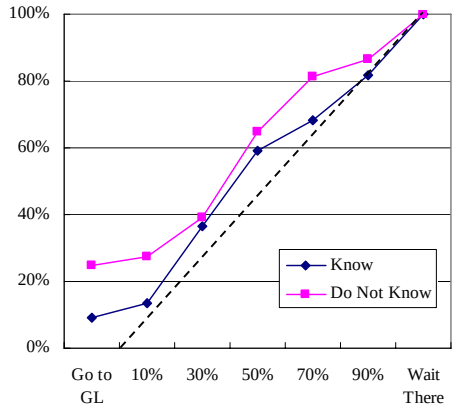

Figure 5 How Much Percentage of the People around You Going to the Ground Level will Make You Follow Their Behaviors?

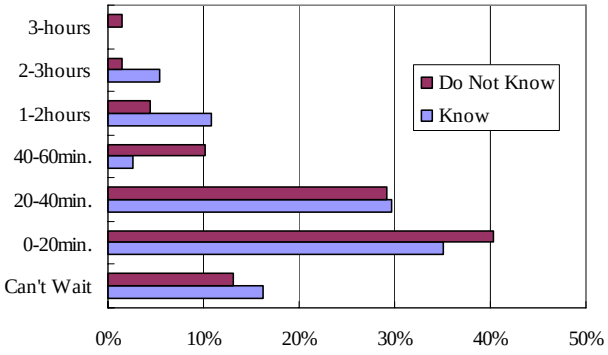

Figure 6 Waiting Time by Respondent's Knowledge

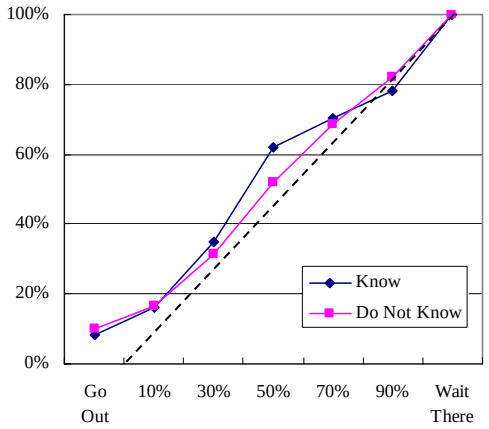

Figure 7 How Much Percentage of the People around You Going Outside of the Train will Make You Follow Their Behaviors?

Sixth International Conference on Urban Earthquake Engineering
March 3-4, 2009, Tokyo Institute of Technology, Tokyo, Japan

TOWARDS A COMPUTATIONAL MODEL FOR CONSTRUCTIVE DECISION MAKING

Haruyuki Fujii

Associate Professor, Department of Architecture, Tokyo Institute of Technology, Japan
hfujii@arch.titech.ac.jp

Abstract: This article introduces a constructive methodology of designing, describes the similarities between the constructive methodology and decision-making under changing situation, and proposes the requisites for such decision-making.

1. INTRODUCTION

The purpose of decision-making is to determine what should be done in order to make good progress towards a preferred situation. We could say that decision-making is one of important actions in design if we regard the notion of design as referring, in a broader sense, to a constructive methodology, which is explained later.

Decisions under rapidly changing situations, such as situations in rebuilding process after an earthquake, have to be made on the basis of incomplete or uncertain information. The situations often require prompt actions to change them into preferred ones or to avoid making them worse. The decisions on what to do in those situations cannot afford to be made after deliberation on the basis of complete and certain information even though it is ideal to make decision after deliberation. However, it doesn't mean to accept acting always act without much deliberation. Even if decisions are made on the basis of incomplete or uncertain information, it is desirable that the decisions are made so as to increase the possibility of changing the situations into preferred ones (Simon 1996).

This article introduces a role of decision-making in design as a constructive methodology and describes the nature of such decision-making that is made under changing situation. The discussion on the nature of design is given elsewhere (Fujii 2009). The content of this article is a revision of the discussion with respect to decision-making under changing situations.

DESIGN AND DECISION-MAKING

The notion of design refers to an activity of forming a new schema coupling things and their assigned significances as well as of embodying the schema in a certain artifact, concurrently (Fujii 2009, Nakashima 2009). A certain thing is produced in an environment as the result of an activity of design and a certain phenomenon is promoted as the consequence of the interaction between the product and other things in the environment. We call a thing produced with the purpose of promoting something as an artifact. An artifact is generated by making or performing a thing as well as by giving significance to the thing. An existing thing could be a new artifact if certain significance is given to the thing. A schema describes the constitution of an artifact, the mechanism how the artifact brings about certain situations, and the course of events to embody the artifact.

Decisions are made to determine the goal of design, the features of a scheme to realize the goal, the features of an artifact to be embodied. The goal of design is described as the features of phenomena promoted as the consequences of generating an artifact. The decisions are made on the basis of the decision-maker's beliefs about the nature of law related to the things in question and about the existing situations. The immediate products of design are a new schema and an artifact as an instance of the schema. The indirect products of design are the expected phenomena as instances of the given significance and the unpredicted phenomena as secondary effects. The secondary effects could be either favorable or unfavorable. It is desirable that decisions are made in the conviction that the expected phenomena will emerge with minimal unfavorable effects. If the effects are favorable then they may be expected explicitly in the succeeding decision-making. If they are unfavorable the schema and the artifact are modified so as to avoid such phenomena.

Design is the combination of generation and analysis. The two parts are performed sequentially or synchronized with each other. In generation, a scheme of the artifact that is expected to have the potentiality to change the current situation into preferred one is formed. Generation produces a course of actions to embody the artifact, too. In analysis, it is predicted what if the artifact is embodied and located in a particular environment to let the artifact interact with the environment. The beliefs about the nature of law and information retrieved from the existing situations are used as

grounds for the prediction. If it is convinced that the artifact has the expected potentiality on the basis of the consequence of prediction then a course of action to change the current situation into preferred one is determined. If not, the schema of the artifact and some beliefs are modified on the basis of the difference between the preferred situation and the predicted situation.

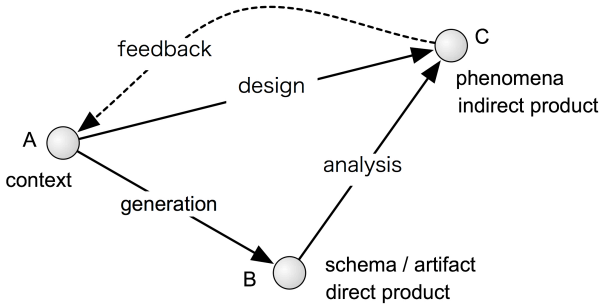

Figure 1 An Image of design

Design is constructive. The crucial nature of design is that a new schema has to be formed on the basis of the current beliefs and hypotheses about the nature of law and the existing situations. The beliefs and hypotheses about the new schema are constructed before the new schema is determined. In its nature, decisions in design have to be made on the basis of incomplete beliefs and the hypotheses with which the beliefs are complemented. The beliefs and hypotheses will probably be modified when the interactions between an artifact with the schema and its environment are analyzed. If the schema is not consistent with the modified beliefs, the schema loses some of the grounds. It is hard to consider all of important aspects prior to generation. Some aspects that have not been considered are found to be important through the interaction. Therefore, the concurrent cycle of generation and analysis is repeated. This means that design is constructive and has dialectic nature and that decisions are made as drawing the trajectory towards the goal and adjusting it to the encountered situations.

3. FEATURES

We assume that a thing is differentiated from the other things by its features. The features of a thing define the characteristics of the thing. A process of design is formulated as a process in which the features are being made explicit. Decision-making is formulated as the event to determine the features among the alternatives.

The features are classified as proximal features or distal features depending on the level of the granularity, scale, and abstraction adopted for the observation of the thing that has the features. The classification is relative since the level for the observation changes. A proximal feature is the feature that articulates a distal feature. A distal feature is the feature that emerges as an appearance of the unified totality of proximal features. The proximal features are recognized as the constituents of the distal feature, but the distal feature cannot be explained completely in terms of the proximal features. For example, the comfortableness of an architectural space could be a distal feature whose proximal features are the thermal comfort of the space, the safety from fire, earthquakes, and intruders, the usability, the beauty, and so on. The thermal comfort of a space could also be a distal feature whose proximal features are the temperature, the humidity, the wind velocity, the metabolic ratio of the occupant, and so on.

The features are also classified as accessible features, controllable features, inaccessible features, or emergent features depending on the level of accessibility to the features. We assume that a feature can be directly determined or controlled in design if it is perceived as a proximal feature. A feature can be determined directly in the sense that it can be specified whether a schema, an artifact, or a phenomenon in question has the feature or not. We call such a feature as an accessible feature, or A-feature in short. A feature can be controlled in the sense that it is possible to specify the feature indirectly but conclusively by determining other features. We call such a feature as a deducible feature, or D-feature. It is presupposed that an A-feature and a D-feature have a causal relation that an A-feature is the cause of a D-feature. For example, the material, the shape, and the dimension of a wall of a building are A-features since they can be directly determined. The heat conductance and the heat capacity of the wall are D-features since they are conclusively specified if the material, the shape, and the dimension of the wall are determined. An inaccessible feature, or I-feature in short, is a feature that cannot be determined, controlled, or affected. An emergent feature, or E-feature in short, is the feature that emerges as an appearance of the unified totality of A-features, D-features, and I-features. Those features can give influence on the E-feature. The thermal comfort of a space can be affected by controlling the temperature by determining the structure of the walls of the space. An E-feature, here, is a distal feature whose proximal features are the A-features, D-features, and I-features. As it is relative to observation whether a feature is proximal or distal, a feature seen as an E-feature in an observation can be seen as an A-feature, D-feature, or I-feature in another observation.

Two types of classifications construct a hierarchical structure of the duality of proximal features, i.e., A-features and D-features, and distal features, i.e., E-features.

It is often the case that the significance of a thing being designed is described in terms of E-features promoted by the thing. In design, A-features are determined directly and D-features are controlled under the constraints described by I-features in the expectation that the E-features emerge upon the interaction among the features. An artifact is specified in terms of A and D-features. The significance of the artifact is described in term of E-features. The schema embodied by the artifact is described as the relation among A, D, I, and E-features. Design explores the specific features towards the preferred situation as well as the relation among the features. A process of generation in design is formulated as a process where relations among features are assumed and A-features

are determined with respect to the relations. Decisions on the acceptance of the assumptions and the adoption of the features are made. A process of analysis is formulated as a process where D-features are deduced from the A-features and it is predicted, on the basis of the assumptions, whether the expected E-features emerge upon the interaction among the A-features, the D-features, and the I-features or not. Decisions on whether design has been completed, should be continued, or has to be stopped are made. The assumptions about the relations are modified to fill the gap between the prediction and the expectation in the succeeding generation process. The decisions on the direction of the modification are made.

4. THE NATURE OF LAW FOR DESIGN

A process of forming a schema and embodying it as an artifact is not an arbitrarily or randomly performed activity. All of A-features are not determined arbitrarily or randomly. Some A-features are determined on certain grounds. The relations among the features derived from the nature of law are consciously applied to form a schema with the conjecture that an artifact with the schema facilitates the expected features. It is essential for the success of schema forming to refer the nature of law that governs the features. It is preferable but not necessary to know what exactly the content of the nature of law is (Taketani 1963). It is important to do something with he consciousness of existence of the nature of law. The nature of law could be subjective, or private, in the sense that it represents personal understandings of the world formed through the experience. It is not necessary that the nature of law is objective or public in the sense that it is verified in a so-called scientific manner, either. Even though it is subjective or private, it plays an important role to define the direction of design. To form a schema is to construct the hypothetical relations among the features. The hypothetical relations should be consistent with the relations among the features that are governed by the nature of law. We assume that the objective type of the nature of law navigates the designer towards a rational direction and that the subjective type of the nature of law navigates the designer towards a creative direction.

The nature of law is expressed in some ways. (A) Some laws are expressed in the form of an equilibrium governing A-features, D-features, and I-features. The features must be in the same proximal level. A distal feature is not expressed in the equilibrium since a distal feature is defined as the feature that cannot be described by its proximal features completely. Formal and scientific knowledge is expressed in this form. Heat balance and dynamic system are expressed as equilibriums. (B) Some laws are expressed as qualitative or quantitative causalities between two things. A thing is expressed as the cause of the other thing, or a thing is expressed as the effect of the other thing. Procedural knowledge, which couples means and ends and is applied to plan a course of actions in generation, is expressed in this form. The relations between the emergent behavior of a system and the behavior of the constituents of the system are also expressed in this form. At least one of the two things can be an action. When an action is the cause of the other thing, the thing is the result or consequence of the action. When an action is the effect of the other thing, the thing facilitates the action. Proximal features as well as distal features can characterize the things involved in this form of expression. Therefore, vertical causality (Nakashima, Suwa, and Fujii 2007), which bridges different conceptual levels, is expressed in this form. The notion of vertical causality refers to the causality among the features in the different conceptual level. The relations among the proximal features controlled directly and the distal features brought about as the consequence of the control are expressed. (C) The rest of the nature of law is tacit and not expressed explicitly in the forms described above. It could be expressed implicitly in a narrative form. Intuitive beliefs about the nature of law, which determine which features should be focused in design, cannot be expressed in the form of either equilibrium or causality. The focused features are important to determine the direction of generation and analysis.

5. POLYSEMIC DUALITIES

The discussion above suggests that there are polysemic dualities in design. Design aims at producing an artifact as well as promoting a certain phenomena as the significance of the artifact. The significance is evaluated from a practical point of view concerning whether existing situations can be changed into preferred ones as well as from a theoretical point of view concerning how the relations between the artifact and the phenomena are understood on the basis of the nature of law. Design applies the nature of law for generation and analysis as well as constructs the nature of law in generation and analysis. The schema associating an artifact with the significance is formed with respect to the nature of law as well as the nature of law is modified constructively to understand the unexpected consequences of forming the schema. The proximal features as well as the distal features describe the things involved in design. It depends on the conceptual level of observation if a feature is proximal or distal. The dualities of proximal features and the distal features organize the hierarchical structure corresponding to the levels of observation. Design produces an individual schema as well as a general schema.

A schema defines the composition of an artifact, from which artifacts in the same class are embodied, and formulates the mechanism underlies emergence of the expected situations upon the interaction between the artifact and the environment. A schema is individual in the sense that it is formed so as to fulfill particular expectations in a certain context. A schema is general in the sense that it is possible to apply the schema to different contexts so as to produce similar individuals that fit the contexts. The individuality and the generality are mutually necessary even though they vary in accordance with interests in design on which the emphasis falls. A general schema is an abstraction of the interested

features from an individual schema. The significant features of interest are selected for the abstraction. The general schema should be transmitted to instantiate other individual schemata. Adding some features to the general schema in accordance with the context where the individual is being formed forms an individual schema.

6. CYCLE OF DECISION-MAKING

We model a process of design in terms of the forms of inferences, i.e., deduction, induction, and abduction. Peirce (1887) modeled a process of scientific inquiry as cycles of abduction, deduction, and induction. We will see that the model of a design process is similar to that of scientific inquiry if we focus on the forms of inferences employed in scientific inquiry and design. Decisions in design are based on the consequences of these inferences. This implies that decision-making in changing situation is similar to decision-making in scientific inquiry.

(Step-0) Every design is motivated by the consciousness of one's will to produce an artifact so as to promote preferred situation. An exploration into the schema that realizes the will begins. For example, if the urban infra- and supra-structures are destroyed by a disaster and our preferable everyday life is obstructed by the tragedy then we will intend to restore the everyday life by rebuilding the urban infra- and supra-structures. (Step-1) The designer imagines, on the basis of the past and present experiences, how the situations will change if a certain schema is embodied. The designer invents some hypotheses that shall fulfills the will, and selects the one that seems promising. Decision which hypothesis should be the most promising and be adopted is made. A schema that is consistent with the hypothesis is formed. There is no logical way to invent or select the most plausible hypothesis and to design the consistent artifact. Even if we investigate the existing situations and correct a plenty of information on the current situation, we have to make decision with some intuition. (Step-2) The designer predicts the conditional experiential consequences that would be logically or probably derived in accordance with certain inference rules if the selected hypothesis were true and the schema were embodied. Decision whether the schema should be embodied is made. If the decision is made, a course of actions to embody the schema is planned. Then, decision how the schema should be embodied is made. (Step-3) The designer actually embodies the schema and verifies how far the predicted consequences are consistent with the experiential observations as estimating the proportion of truth of the hypothesis. Decisions whether the schema and the hypothesis are sensibly correct, or require some inessential modification to fulfills the intention, or must be rejected are made. If the second decision is made, then the direction of the modification is determined. (Step-R) Step-1, 2, and 3 are repeated until the designer forms the schema that enables the preferred situation.

Either abduction or induction doesn't have logical inference rules that guarantee the truth of the consequences in spite that deduction does. Therefore, the success of design as well as scientific inquiry depends not only on the procedural schema like the rules of deductive reasoning but also on the heuristic capacities to be employed to select the most plausible hypothesis, to classify the empirical observations, and to imagine a course of action towards the goal.

In the case of emergency, some decision-making should be done timely even though the decision has to be made under incomplete and uncertain information. It is, of course, wise to wait for the result of analysis of the situation on the basis of enough information only when it is clear that the result waited is essential for adequate decision-making and is clear what to do depending on the result. The worst thing is to just wait for the situation where information for decision-making is complete and certain without any plan to do with the information waited. Commitment to selected hypothesis and the flexible attitude that is not afraid of the replacement of the hypotheses are the keys to decision-making under rapidly changing situation.

7. CONCLUSIONS

A role of decision-making in design as a constructive methodology is introduced, and the nature of such decision-making that is made under changing situation is described.

ACKNOWLEDGMENT

Discussions given in this article are mostly the result of an on-going and long discussion with Hideyuki Nakashima (Future University – Hakodate) and Masaki Suwa (Keio University), and partially inspired by discussions with Yoshitsugu Aoki (Tokyo Institute of Technology).

REFERENCES:

Fujii, H. (2009), "Nature of Design – From an Architectural Point of View", *Special Issue of Japan Society for the Science of Design*, in press.

Nakashima, H. (2009), "Design of Constructive Design Process", *Special Issue of Japan Society for the Science of Design*, in press.

Nakashima, H., Suwa, M., and Fujii, H. (2007), "Vertical Causality (in Japanese)", *Proc. 24th Annual Meeting of Japanese Cognitive Science Society*,42-47.

Peirce, C. S. (1887), "Science and Immortality.", *Charles Peirce, Selected Writings*, 345-379, Dover.

Simon, H. A. (1996), *The Science of the Artificial*, Third edition. The MIT Press.

Taketani, M. (1963, 1969), *Science and Technology* (in Japanese), Keiso-Shobo.

Sixth International Conference on Urban Earthquake Engineering
March 3-4, 2009, Tokyo Institute of Technology, Tokyo, Japan

A REVIEW OF RECOVERY PROCESS OF CHI-CHI EARTHQUAKE SINCE 1999

Liang Chun Chen[1)]

1) Professor, National Taiwan University, Graduate Institute of Building and Planning, Taiwan
lcchen@ntu.edu.tw

Abstract: The Chi-Chi earthquake, occurred in 21, September, 1999 with magnitude 7.3 and epicenter on Central Taiwan, has already passed about 10 years. This earthquake had caused over 103,000 buildings collapsed or partial collapsed, more than 2,505 people death or missing. In addition, many public facilities, including schools, universities, city government halls, bridges, roads, were damaged. The lifelines, such as electric power system, gas pipe-line, or tap-water system, were also destroyed. Furthermore, local industries and economic activities on the disaster areas being closely linked with people life were seriously ruined. The huge earthquake losses with costing more than 11 billions have gradually recovered during passing 10 years. Looking back for the recovery processes, it is worthy to figure out the reconstruction process in detail and find out the facilitating or impairing factors of earthquake recovery. According to this research analysis and the recovery experiences of 7 years after the earthquake, the physical recovery, such as public constructions, would be more easily done than unphysical recovery, such as livelihood, industry or mental health recovery. Besides, comparing to the given process and flow path for recovery, regulated by the government, the actual implementations of recovery processes are quite different. Both the direct influencing factors induced by earthquake disasters and external influencing factors caused by non-earthquake disasters may have unexpected impacts to earthquake recovery. The results of this research will be referred to recovery for future large-scale earthquakes.

1. INTRODUCTION

The Chi-Chi Earthquake, occurred at 1:47 local time, in 21, September, 1999 with magnitude 7.3 and epicenter on Central Taiwan, because of fault dislocation, was the largest scale earthquake from 1935 until now. The Chi-Chi Earthquake has drawn a lot of attention. Not only has this earthquake caused thousands of people deaths or missing and huge property losses on the disaster areas, but also it was the first large-scale earthquake after Taiwan modernization. Therefore, the large-scale disaster management processes, including emergency response, relieving the victims, recovery or reconstruction, were dealt on very limited recognition or preparedness. In other words, the recovery process of the Chi-Chi Earthquake is progressed on condition of error tries. On this year, 2009, to be the tenth year of the Chi-Chi Earthquake, looking back for the recovery 10 years, it is worthy to review and reorganize the recovery process or reconstruction experiences so that the research results could be useful to manage large-scale earthquake disaster for the future, or even could facilitate recovery process smoothly or mitigate earthquake disaster.

Based on above-mentioned the research motives, the articles and documents related to the Chi-Chi earthquake will be gathered, reviewed and analyzed. First, the recovery processes about 7 years[1] after the earthquake will be reorganized so as to figure out the priority for dealing with various affairs of earthquake recovery by time series. Secondly, the influencing factors of the achieved percentage of recovery scheduled progress for various recovery affairs will be analyzed. Finally, by analyzing the influencing factors, the primary suggestions and reviews will be proposed for disaster mitigation and earthquake recovery so that the research results could be referred for researchers for their studying related to the large-scale earthquake.

The main contents of this paper are included: 1) The disaster general description for the Chi-Chi Earthquake; 2) The initial stage for recovery process; 3) The process for recovery; 4) Analysis of the main influencing factors for recovery process; 5) The primary conclusion and suggestions.

2. THE DISASTER GENERAL DESCRIPTION FOR THE CHI-CHI EARTHQUAKE

2.1 Disaster Descriptions of the Chi-Chi earthquake

The dislocation of the "*Chelunpu* Fault" with north to south direction and the epicenter on the central Taiwan caused the Chi-Chi earthquake. The devastation of the Chi-Chi earthquake is huge, including 2,455 deaths and 50 missing. In addition, 755 people had hurt seriously and over ten thousand people had light injuries. The property damages were also significant. There were 38,935 units of

[1] "921 Earthquake (Chi-Chi earthquake) Post-disaster Recovery Commission, the Executive Yuan" was established after the Chi-Chi earthquake and was closed on February, 4. 2005. It took about 6 years and 4 mouths. All unfinished recovery works were returned to related central government to implement continuously. Therefore, 7 years was used to be a time period for analysis.

houses collapsed and 45,320 units of houses partial collapsed[2]. Besides, many public infrastructures, such as school buildings, government offices, bridges, roads, lifelines, and large-scale farming or manufacturing equipments, are damages seriously by the earthquake. According to the government statistics, the direct losses are as huge as 115 hundred million US dollars.

2.2 Characters of damage

There were several characters for this disaster and victims areas as the followings:

1. *Victim areas were across several administrative districts*: With magnitude 7.3 of the Chi-Chi earthquake, but the focus of the earthquake was only 8 km depths. Besides, the length of the thrust dislocation of the *Chelunpu* Fault of the earthquake were across 96 Km[3] from north to south. Therefore, the fault which expressed significant energy caused strong shakes and devastation. The length of the disaster areas form the north to the south was about 105 Km and from east to west was about 80 Km. The disaster areas includes 31 cities, towns or counties totally, if Taipei city, Taipei county, Chia-Yi city and Chia-Yi county far away from the disaster areas were also counted, which had damaged by this earthquake with deaths and buildings collapsed.

2. *Serious landscape changes and geological destructions*: Because of fault dislocation significance (e.g. the northern end of the fault changed it location vertically about 11 M) and the eastern side of the upper part of the fault was mountain and village areas so that the geological structures were fragile. Therefore, the movements of the fault thrust significantly had caused many damages, such as about 180 collapses or landslides, about 130 places for stones or earth piles. In particular, the broken area of earth's surface of *Jiou-Fen-Er-Shan* was about 200 hectares. The landslide area of *Tsau-Ling* had produced earthworks with the volumes about one hundred million and twenty million M3.

3. *Public facilities and infrastructures are damaged seriously*: Most parts of the disaster impacted areas were on the farming areas or villages with less urbanization and lower density of population. The public facilities and infrastructures located on the farming area or village were aged styles. Besides, most of roads and bridges were located across mountain areas with steep landform or across over the north-to-south fault. Therefore, there were many school buildings, accounted totally 1,546, which were damaged at different levels. The 293 school buildings must be removed for reconstruction. The 250 public facilities, such as administrative buildings, public activity centers, fire fighting and police offices, are whole collapsed. At least 600 public facilities were partial damaged dangerously.

4. *Earthquake timing reduced the death or injury numbers*: As the above-mentioned, thousands of school buildings and public facilities were damaged seriously or totally collapsed. However, the earthquake timing on daybreak may reduce the death or injury numbers in the public facilities, because there was almost no one inside the buildings.

5. *Both the lower-floor old style of houses and the higher assembled style of buildings were destroyed together simultaneously*: Because of most of the disaster areas on farming or village, many lower-floor old styles of houses (e.g. house made of soil and earth bricks) were on this kind of areas. Meanwhile, many higher assembled styles of buildings are constructed on the disaster area with high density of population, such as on the township areas. Therefore, both the lower-floor styles of houses and the higher assemble styles of building were destroyed together simultaneously on the same disaster areas during this earthquake so as to increase the difficulty and complication for recovery.

6. *The agriculture and tourism with the most negative impacts on the farming or village areas of disaster:* As the above-mentioned, most of the disaster areas were on farming or village areas so that the local agriculture were damaged seriously. Besides, before this terrible earthquake, the disaster areas had existed many beautiful see-sights and natural landscapes. Multi-culture characters, such as aboriginal, Fukien, Ha-KKa, Taiwanese or Mainlander cultures, also give a good opportunity for developing tourism industry.

7. *Given land system impeded the recovery process*: Most of the disaster areas were on remote mountain areas. According to Taiwanese given land system, most of the remote areas belong to government or reserved for aboriginal. Therefore, the disaster victims without land ownership, even though they had lived or farmed there for several generations, could not have the land owner right. Therefore, the given land system increased the difficulties and complications for recovery.

3. THE INITIAL STAGE FOR RECOVERY PROCESS

3.1 Launching for earthquake recovery

After the Chi-Chi earthquake, Taiwanese government took part in the disaster rescue, response and recovery affairs. For instance, in 40 minutes, "the Central Response Center for Large-scale Earthquake" is established. The Center announced 9 emergency orders and 15 important measures for disaster rescue were decided. In addition, before the daybreak, the deputy-minister of the Interior Department had arrived at the disaster area (e.g. Nan-tou county) for establishing "the Progressing Command Center of Central Disaster Reduction". At the stage of emergency response, in about one mouth, not only stepping into many affairs, including rescue, handling corpses, transporting necessary materials, staying victims or repairing electric systems, but also the center launched to prepare the recovery processes.

The recovery processes were complex and long-term

[2] The data is gathered form The Architecture and Building Research Institute, the Ministry of Interior. If it is counted by the unit of household, the totally collapsed households were 50,652 and partial collapsed household were 53,615.

[3] The main thrust fault is 85 Km from north to south, extending 11 Km from east to north, totally 96 Km (data resource: Central weather Bureau).

works, and the major processes at the government side as the followings:

1. *Establishing the necessary organizations or task-forces;*
2. *Announcing the necessary regulation;*:
3. *Getting financial resources*;
4. *Others:* there were several measures for livelihood, mental health and settlement of victims.

It is worthy to mention that "921(the Chi-Chi earthquake) Post-disaster Guiding Principles for the Disaster Recovery Affairs", announced on November, 9, by the Executive Yuan and illustrated with the **Figure 1**. The principles were the key for supporting influentially to recovery affairs.

Comparing to the government side, on the non-government side, in about one month, the NGOs participated in preparing the recovery affair for a long-term supporting, except for devoting to emergency rescues, including:

1. *Establishing the necessary organizations and taking into recovery planning:* There were several examples worthy to mention. For instances, "921(the Chi-Chi earthquake) relief and recovery Commission of Christianity" was organized by Presbyterian Church in Taiwan. "921 Earthquake (the Chi-Chi earthquake) Assistant Recovery Division of Buddhism" was organized by Luminary Buddhist Group. Also, "Association of National Civil Post-disaster Recovery, Coordination and Supervision" was established by multi-NOGs. "921 Large-scale Earthquake (the Chi-Chi earthquake) Recovery and Relief Special Project of Tzu-Chi Foundation" was drafted by the Charity Foundation of Tzu-Chi.
2. *Supporting to building temporary staying houses:* For instance, the Tzu-Chi Foundation was signed with Nan-Tou County government for constructing simply equipped houses to settle down the victims.
3. *Responsibility for rebuilding damaged school buildings:* On, October, 19, there were 8 NGOs, volunteer organizations or enterprises, such as Tzu-Chi Foundation, Fu-bon Cultural & Educational Foundation and International Lion Clubs, announced their responsibility for rebuilding damaged school buildings with a ritual, namely "Signing Ritual for Responsibility and Donation".
4. *Mental health recovery:* Many religious groups and volunteer organizations began to accompany with the victim and take part in their mental health recovery after the earthquake psychological trauma almost at the first time. It took time and also need a lot of human resources for this kind of social works.

4. THE RECOVERY PROCESSES

There were many factors to influence the recovery process for a large-scale earthquake of recovery, including timing, magnitude, impacted victims, recovery priority and complex etc. The whole recovery process was difficult to describe clearly, since the Chi-Chi earthquake has been to almost ten years. Therefore, in this paper, I will try to use the content framework of "921 (the Chi-Chi earthquake) Post-disaster Guiding Principles for the Disaster Recovery Affairs" for analysis, including: 1). Lifelines, such as electric system, water providing system etc.; 2). Transportation systems, such as roads, bridges and railways etc.; 3). Water conservancy engineering, such preventing flood engineering and irrigation canals etc.; 4). Geological engineering recovery, such as landslide, mudflows recovery etc.; 5.) Public facilities, such as administrative office, civil activity etc.; 6.) Campus recovery, such as universities building, primary school buildings etc.; 7.) Culture heritages and historical architectures; 8.) Housing; 9.) Livelihood; 10.) Industry; and 11.) Community. Totally, 11 item contents for analyzing recovery processes by categorized important contents, including the implemented period of the specific recovery projects (such as Dong-Shi Bridge had been constructed and finished, Shi-Gang Dam has been repaired and Don-Shi community had been completed) and the project outcomes, illustrated with the **Figure 2** so as to identify the recovery processes as the followings:

4.1 In the initial one or two months after the earthquake

The main works were still focus on the emergency rehabilitations for safe assurance and livelihood function, including restoring water or electric systems, recovering transportation, constructing the temporary bridge, dealing with the barrier lack and dike, building temporary settlement house, rebuilding classrooms, caring livelihood and mental health.

4.2 In the half a year after earthquake

The emergency rehabilitations had almost finished at the initial stage, but the lifelines with serious damages, landslide recoveries, bridge and dike constructions were still implemented continuously. Besides, the public facilities, such as school buildings, administrative offices and assembled houses, were still halted. The victims' livelihood was supported by the project of "Working substitutes for money relief only". Some labor welfares, such as relax restrictions for labor insurance payments and subsidizing the labor healthy insurance were provided. The industrial revitalizations were processing to recovery agriculture facilities, local business equipments, and dairy market revitalizations. It is worthy to mention that the devoted civil foundations to help to rebuild communities, cooperating with the related government departments. The devoted civil foundations also announced their responsibility and denotation for reconstructed school buildings so as to regain students back to attend schools for studying. Besides, the government regulated several acts and regulations, including launching the "921 earthquake (the Chi-Chi earthquake) post-disaster recovery commissions" on February, 2, 2002, announcing the "Simplified Application of Building Licenses for disaster areas of 921earthquake (the Chi-Chi earthquake). In addition, several important policies are launched, including "Industrial revitalization Plan of Five Years" approved by Council for Economic Planning and Development (CEOD) on January,

20, and "Livelihood Revitalization Plan" approved by CEOD, on February, 10. These acts, regulations and plans were useful to assure the recovery policy strategies and renew the given regulations. Meanwhile, the basic land measuring tasks, such as land re-measures and cadastres renewal were processed in this stage.

4.3 In one year after earthquake

As the above-mentioned, in the half of a year, the basic physical infrastructures and unphysical recoveries were implemented continuously. At this stage, at about ten months after the earthquake, the recovery of public facilities, such as school buildings, administrative offices and civil activity centers, began constructions. In addition, the community recoveries based on the method of "resident's participation" increased to about 60 communities, in two months and one year. However, most of the housings were rebuilt, extending to one or two years after this earthquake, which had impacted directly to victims' life.

4.4. In 7 years after the earthquake

Except for limited rebuilding cases, most of infrastructures, such lifelines, roads, bridges, were reconstructed completely. Most of the campuses were rebuilt accomplishedly in the period of three years and half one year. In addition, most of the public facilities, culture heritages and historical architectures took more time, about 4 years, to be rebuilt or repaired. During the recovery period, many typhoons and downpours attacked the disaster area so as to cause many natural hazards, such as landslides, collapses, floods. The natural hazards had negatively impacted to recover the geological reconstruction, water conservancy reconstruction, some bridges and roads, so that the kinds of reconstructions had extended to 6 or 7 years to be done, and some of them are still not completed. Besides, livelihood, industrial and housing recovery took the longest time, because these related to complex social issues. It is worthy to mention that the major direction of industrial recovery had changed after 3 or 4 years of the earthquake. Comparing to the initial stage, the industrial recovery had changed from traditional agricultural development to a new style of industrial development. The new style of industries included eco-tourism, local culture, wine-making technique, and leisure for increasing work opportunities of local residents. Finally, considerable quantities of housing reconstructions were still delayed so that a part of victims lived still in temporary houses constructed at the initial stage. Only limited individual households had reconstructed completed, after applying construction licenses. The reconstructions of assembled buildings and larger-scale communities began at the end of the three years after the earthquake.

In sum, the recovery of the Chi-Chi earthquake in one year was focus on the reconstruction of lifelines, roads and bridges. Some acts, regulations and recovery plans were drafted and recovery mechanisms were designed at the initial stage. Then, the seriously damaged campuses began to reconstruct and most of the public facilities had been done in 3 or 4 years. However, the flood control works, geological engineering and irrigation works, housing reconstructions, livelihood and industrial recoveries were difficulty in recovery completely, until the final stage, because of diversity and complex factors.

5. ALYSIS OF THE MAIN INFLUENCING FACTORS

In this paper, I try to figure out why the recovery processes and time periods are diversity and what are the main influencing factors caused the different results, even though all of the recovery works began at the same time, according to my analysis as the followings:

5.1The complications and difficulties with difference in degrees

The recovery affairs related with many dimensions, including the physical reconstructions (e.g. pubic infrastructure constructions or geological works) or the unphysical social recoveries (e.g. livelihood and industrial recovery). Besides, both of the physical and unphysical recoveries may have mixed together so as to increase the complications of recovery. For instances, hundreds of household reconstructed and moved together into the assembled houses, which holding the same land right. Therefore, the recovery of complications and difficulties with difference in degrees would influence directly or indirectly the recovery implementations.

5.2The necessary recovery regulations for large-scale earthquake were still not completed

Whiling the large-scale earthquake, many physical and unphysical (social) conditions may change dramatically. Furthermore, the emergency response and rehabilitation were usually urgent. Therefore, it is difficult to follow the regular procedures or normal methods to deal with the recovery affairs. The laws, regulations or administrative procedures related to recovery fitted in with the ordinary time, which operated at the emergency time after a large-scale disaster, becoming rigid and inconvenient obviously. For instances, the laws or regulations related to the review institutions of urban planning and urban renew, the community renew of assembled houses with common land right of victims, the applying procedures of bank loans, or even general administrative applications would become hardly to be operated.

5.3The affordable necessary human and finical resources for recovery were still lack

All of the human and finical resources of Taiwanese government for recovery are based on related laws or regulations. However, during the disaster recovery processes in emergency time period, it is difficult to use ordinary budget quota or human resources to deal with the recovery affairs. In particular, in the disaster areas, the administrators themselves are the victims so as to reduce their recovery abilities, both in qualities and quantities. In Taiwan case, in the Chi-Chi area, it has been lasted several

generations with no attacked by the large-scale earthquake so that the given budget quota and human resources were lack for many recovery affairs.

5.4 Basic information gathers and administrative methods were not accurate

To assure the correct in basic information, such as census register data, land transcript, cadastres, etc., is important for implementing the widespread and complex recovery affairs. For instance, if a disaster reconstruction in a large land with multi-land rights of victims, with most of the buildings totally collapsed, should be implemented, then the above-mentioned basic information is needed to plan, design or rebuild for recovery. However, in the Chi-Chi earthquake case, the disaster area was located on the old style village or street, the necessary basic information is lack on records and files so as to influence the emergency recovery affairs.

5.5The radical changes caused by the large-scale earthquake were difficult to control

Because of the large-scale of the Chi-Chi earthquake with magnitude 7.3 and the total length of the thrust fault is about one hundred meters, the large-scale earthquake caused movements, both vertically and horizontally, and dramatic changes of the earth surfaces so that many safe threaten issues, fragile and long-term factors were induced.

5.6 Unexpected events

Excepting for above-mentioned influencing factors caused by the large-scale earthquake, during the very long time recovery processes, there were still many unexpected events to influence the recovery affairs. These events included natural or artificial, physical or unphysical (social) dimensions. For instance, several strong typhoons and downpours had attacked the disaster areas. Besides, the Taiwanese Present Champion and the party-rotation on 2000 could be also treated to be an important influencing factor for recovery. For local agriculture on the disaster areas, Taiwan jointed the WTO (World Trade Organizations) had key impacts of recoveries and agricultural revitalization.

6. CONCLUSIONS AND SUGGESTIONS

6.1Conclusion

In this paper, by through gathering and arranged the documents related to the Chi-Chi earthquake for passing 7 years. Then the recovery affairs and processes are categorized and compared so as to analyze the influencing factors of the scheduled progresses and time period. The results are explained as the following:

1. *Three types of recovery affairs*: As the above-mentioned, the recovery processes of the Chi-Chi earthquake included 11 the major items of contents. These 11 items of contents had different from time periods and completed priorities. Basically, the recovery contents can be induced into three types: 1). Type of physical environment or space: the recovery works related to physical environment or space, such as lifelines, traffic transportation, water conservancy, geo-constructions; 2). Type of social recovery: The recovery works were focus on social dimensions or individual recoveries, such as livelihood, industrial and community recovery; 3) Type of mix with physical environment and social dimensions, such as the campus and public facilities recoveries. According to my analysis, the first recovery type is easy to be implemented and quick to get reconstruction result. The third type is more difficult than the first type to be launched immediately. However, if the implementing mechanism of the third type is adjusted, it could be finished in the limited time period. Even though the second type is highly related to individual victims or local communities with request for beginning at the initial stage, the second type of recovery works are impeded by influencing factors. Therefore, the second type is the most difficult in implementation and extends to a long time period, because it is easy to be influenced by external factors. In sum, the differences of the three types are formed basically the recovery processes.

2. *Analysis of the influencing factors of recovery*: The long term recovery processes were impacted always by the external influencing factors. Meanwhile, all recovery works were still in progresses. The influencing factors included basically two categories: one is about natural or physical factors; the other side is about human or social factors. The former physical factors can be separated into two subtypes: one is direct influencing factors caused by this earthquake; the other is another influencing factors caused by natural hazards, not directly caused by this earthquake. For instance, the strong earthquake caused to the landforms change, rock crack or landslide, which could be treated as the former subtype of influencing factors. Another natural hazard, such as typhoon or downpour or another earthquake, caused to more serious conditions of disaster, could be treated as the latter subtype of influencing factors. The latter type of social influencing factors can also be separated into two subtypes: one is direct influencing factors related to recovery, which is controllable or expected, form the point of disaster management view; the other is unexpected influencing factors, which is uncontrollable. For instance, drafting regulations related recovery and arranging basic information of victims could be treated as the former of social direct influencing factors includes. For instance, the Present Champion following the party rotation during the recovery processes of the Chi-Chi earthquake and Taiwan joined to the WTO, could be treated as the unexpected influencing factors. The former subtype of social direct influencing factors will have strong affections to the recovery affairs, or even impeded the related recovery works. The latter subtype of social indirect influencing factors will increase complications for recovery or delay the recovery processes.

3. *Interaction of three types of recovery affairs and two influencing factors:* As the 6.1 above-mentioned, the first type of recovery affairs is easy to be affected by the natural or physical influencing factors. On the other hand, the type of social recovery is easy to be affected by the social

influencing factors, not only to impede to launch the recovery works, but also to increase the complications and difficulties of recovery works. However, no matter the physical influencing factors or the social influencing, the more influencing factors are involved in the recovery processes, the more difficulties the recovery works are implemented. That may explain why the recovery processes have differences in scheduled progresses and time period, during the passing 7 years after the Chi-Chi earthquake.

6.2 Temporary Suggestions

According to the analysis of the recovery works, processes and influencing factors of the Chi-Chi earthquake, two temporary suggestions are proposed here for referring to future researches and practical implementations:

1. *Enhancing abilities of earthquake mitigation and emergency response*: According to present technologies, it is impossible to eliminate the earthquake itself in scale or to predict it accurately. However, it is possible to mitigate the disaster situations in advance by necessary methods. Therefore, how to enhance the abilities of earthquake and increasing the efficiency of emergency response are key issues to reduce greatly the recovery workloads and enhance the recovery efficiency.
2. *Reducing the influencing factors of recovery*: It is difficult to change the needs of recovery works after earthquake. However, the influencing factors of recovery, which may affect the recovery progresses, can be changed or even reduced. According to the above-mentioned analysis, it is impossible to eliminate completely the natural or physical influencing factors. However, it may have the way to reduce negative impactions. Specifically, no matter the first influencing factor caused by earthquake itself or another influencing factors caused by natural hazards will affect the recovery works. In other words, how to mitigate various secondary disasters and quick response during the recovery processes are important issues, which can reduce the recovery obstructions. Analyzing the social influencing factors, excepting for the unexpected influencing factors which can not be dealt by disaster management, most of the social influencing factors can be handled in advance. Some lessons can learn from the case of the Chi-Chi earthquake. For instance, revising recovery acts or regulations and recreating recovery mechanism in advance for enhancing the recovery abilities, cultivating human resources for recovery response and implementation, adjusting the budget procedure, assuring budget quota for recovery, operating recovery organization flexibly, or investigating basic recovery information for disaster management. All these recovery works should be implemented before earthquake disasters in advance.

In brief, the recovery works of large-scale earthquake can be implemented smoothly, only if the recovery works are ready before disaster attacks, not waiting until to be attacked by disaster. In addition, depending on various disaster experiences, each recovery works needs to be adjusted and enhanced. In other words, the preparedness of the four phases (e.g. mitigation, preparedness, response and recovery) of disaster management is not only for response, but also to take into account the recovery need so as to arrange necessary recovery works in advance.

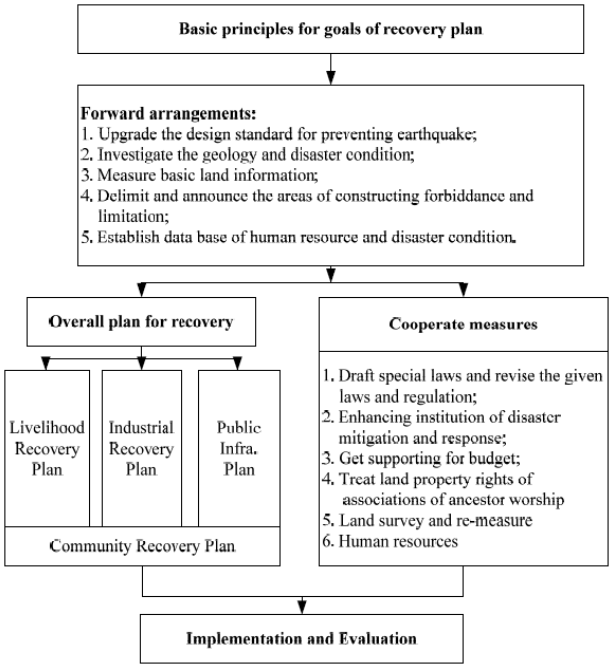

Figure 1: Chi-Chi earthquake Post-disaster Guiding Principles for the Disaster Recovery Affairs

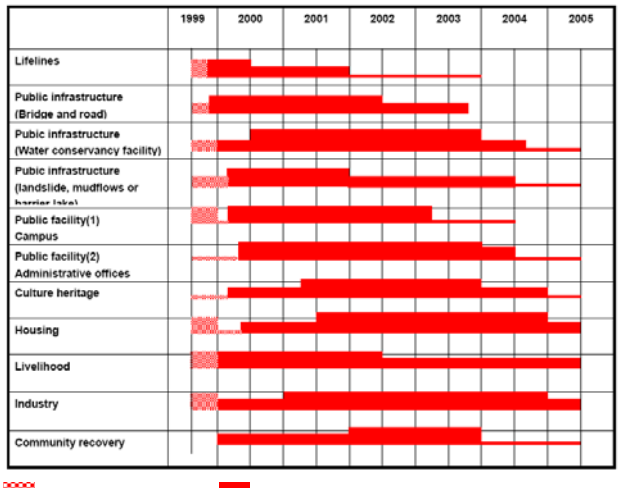

Ps. The width of line is illustrated with the quantity of recovery works

Figure 2: Recovery processes classified by work contents of the Chi-Chi Earthquake

Sixth International Conference on Urban Earthquake Engineering
March 3-4, 2009, Tokyo Institute of Technology, Tokyo, Japan

A STUDY ON ADMINISTRATIVE SUPPORT IN REVIVAL PROCESS FROM THE NIIGATA CHUETSU EARTHQUAKE IN 2004

Masahiro SAWADA[1)]

1) Associate Professor, Ph.D., Nagaoka Intitute of Design, Japan
sawada@nagaoka-id.ac.jp

Abstract: In the Niigata-Chuetsu 2004, Villages in mountainous regions proved to be particularly vulnerable as they were isolated when rivers and roads were blocked, forcing many residents to temporally evacuate their home and take refuge in evacuation shelters. Recovery was expected to be a prolonged process as many homes and facilities were seriously damaged. The earthquake also accelerated depopulation and the overall aging of the population , issues that had been present from well before the earthquake, ant the prospect of entire communities vanishing has become even more real in people's mind.

The objective of this paper is to examine the current situation and explore modes of support that would be crucial for enabling sustainable recovery efforts in affected villages.

1. Introduction

The Niigata Chuetsu Earthquake (hereafter referred to as the "Chuetsu Earthquake") caused extensive damage to roads and rivers, primarily because the region is one of the most landslide-prone in Japan and also because it had been hit by heavy rainfall from typhoon 23 for several days immediately before the earthquake. Municipalities in intermediate mountainous regions proved to be particularly vulnerable as they were isolated when rivers and roads were blocked, forcing many residents to temporarily evacuate their familiar surroundings and take refuge in evacuation centers. Recovery was expected to be a prolonged process as many homes and facilities were seriously damaged. The earthquake also accelerated depopulation and the overall aging of the population, issues that had been present from well before the earthquake, and the prospect of entire communities vanishing has become even more real in people's minds.

Today, four years after the earthquake, most roads have been repaired and preventive work has been performed at locations that were affected by landslides. Agricultural land, such as paddies and fields on which residents depended for their livelihood, has also been restored. However, actions that are considered essential for sustaining these villages have only now started to take shape if at all. The Chuetsu Earthquake contrasted with the Great Hanshin Awaji Earthquake of 1995 in that it was an intermediate mountainous region disaster. As such, while recovery efforts were related closely to disaster recovery efforts for intermediate mountainous areas in general, it is important to study the conditions of this particular disaster to gain insight since 70% of the land in Japan is found on similar terrain. The objective of this paper is to examine the current situation and explore modes of support that would be crucial for enabling self-sustainable recovery efforts in affected villages.

2. Consequences of evacuating all residents of Yamakoshi

Of the many municipalities in intermediate mountainous areas that were affected by this earthquake, Yamakoshi probably received the most attention due to the extent of its devastation. All roads that connected the district to cities and towns such as Nagaoka and Ojiya were severed in multiple locations, virtually isolating the entire the district. This situation led to the decision two days after the earthquake by then mayor to evacuate all residents to Nagaoka city. The evacuation order was issued to all villages of the district. With no time to clean up their homes, residents carried whatever they could and evacuated to evacuation centers, primarily schools, in Nagaoka (the two municipalities of Yamakoshi and Nagaoka were to consolidate the following April). After this initial phase, residents moved to temporary housing facilities built in the Nagaoka New Town district on the west side of Nagaoka, more than an hour's drive from their homes. Plans were made to group evacuees by home village and measures were taken to make life as easy as possible for what was expected to be a prolonged period of evacuation. For example, while these temporary houses were originally cleared only for residential use, officials authorized evacuees to open retail shops. Evacuees were also loaned agricultural land adjacent to the Yokodai complex, the largest of the temporary housing complexes (evacuees from areas other than Tanesuhara and Mushigame villages were housed here).

The extent of damage in the Yamakoshi district varied from village to village. Buildings in Tanesuhara, the largest village in Yamakoshi, and Mushigame, the closest village to Nagaoka, sustained relatively little damage and evacuees could have returned home once the roads and essential utilities were restored. However, under the slogan "We're

going back to Yamakoshi," officials maintained the evacuation order on the entire district regardless of the extent of damage to individual villages. This demonstrated the residents' commitment to tackle the issue and shoulder the load of recovery as a community, regardless of the varying degrees of damage to their respective villages. This decision drew attention from people around the country and helped bring in a broad range of relief supplies to the evacuees. On the other hand, while residents of Ojiya city and Kawaguchi town, whose buildings sustained damage similar in extent to those in some villages of Yamakoshi, were issued only an evacuation warning and were able to perform limited repair work on their homes, residents of Yamakoshi had to spend their time in evacuation. This was a major factor in delaying the commencement of recovery efforts at Yamakoshi. In fact, hardly any new recovery action had been initiated when the evacuation order was lifted on July 22, 2005. Finally, in July 2007, residents agreed to form a resident-initiated organization for recovery.

3. Support for returning and support for leaving

In addition to the issue of depopulation and the resulting aging of the population, communities in intermediate mountainous regions affected by the Chuetsu Earthquake must tackle a range of other issues to sustain themselves, including declining agricultural output and heavy snowfall. Because part-time farmers commute to work in nearby Nagaoka or Ojiya, concerns were raised immediately after the earthquake that these people may decide to relocate to these cities. On the other hand, many of the very elderly wished to live self-sufficiently in areas that they were familiar with, relying on their pension and the produce they grow in their fields. These widely differing needs posed a major challenge in developing a roadmap for recovery. Other municipalities affected by the disaster faced similar challenges, as was evident in their lists of victim relief measures.

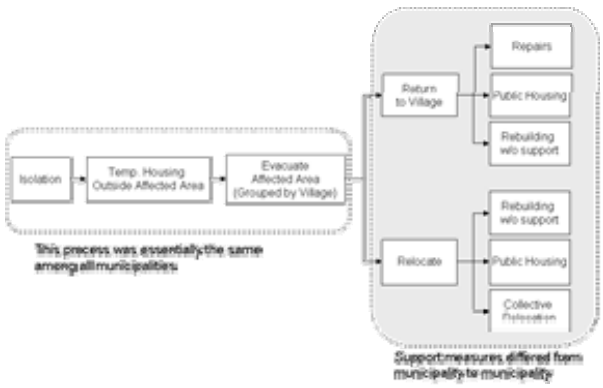

Fig. 1 Flow Chart of Village Rebuilding Efforts

As shown in Figure 1, residents living in isolated villages were evacuated to temporary housing built outside of their own villages, and various measures were taken to rebuild and restore normal living conditions during the two-year period that was determined to be the timeframe for evacuation in temporary housing. While virtually all municipalities implemented similar measures during the process of building temporary housing outside of affected districts, measures implemented after this stage varied widely. In the case of Yamakoshi (currently Yamakoshi district, Nagaoka city), six out of fourteen villages sustained devastating damage. In an effort to support households in these villages who elected to return and live in the district, the municipality created village recovery plans for each village and has actively supported the residents' efforts. In these cases, officials employed the "Small-scale Residential District Improvement Project" scheme in order that residents would be eligible for support for rebuilding their local areas. Officials applied this scheme, which was originally created to improve environments in densely built residential neighborhoods, to intermediate mountain areas to support rebuilding by households who elected to return to the mountains. Meanwhile, the Yamakoshi district extends almost no support to people who have decided to leave the district since the earthquake.

4. Damage in the Higashiyama area of Ojiya city and housing reconstruction

The Higashiyama area of Ojiya city consists of about 10 villages concentrated along route 291, which runs from Ojiya city to Yamakoshi village. As stated previously, because of the severed roads, an evacuation order was in effect for more than one year, forcing people to live in temporary housing in Ojiya city. As a result, farming of carp and raising bulls for bull-fighting, which are the characteristic products of this area, was either temporarily stopped or moved to another area.

In terms of housing reconstruction, all the damaged areas immediately after the earthquake were offered an emergency repair system, a livelihood reconstruction support scheme, and a housing reconstruction scheme among others. However, after the evacuation order was issued, construction companies and the like were prevented from entering the area, and thus were not able to be sufficiently active. As a result, the buildings within the area were considered to be “totally destroyed”. In order to supplement the loss of opportunity to make use of the emergency repair system, relief money was distributed and a livelihood reconstruction support system was created by the prefecture.

Table 1 Number of households in each village

Villaget name	No. households		
	Before the earthquake	After the earthquake	Percentage of pre-earthquake
Junidaira	11	0	0.0%
Shiodani	49	19	38.8%
Nigoro	39	11	28.2%
Utogi	33	15	45.5%
Iwamagi	31	19	61.3%
Tsumurisawa	13	5	38.5%
Asahi	40	27	67.5%
Terasawa	23	21	91.3%
Nakayama	16	16	100%
Koguriyama	33	20	60.6%
TOTAL	277	153	55.2%

This housing reconstruction support system for residents of the intermediate and mountainous disaster areas, including the Higashiyama area of Ojiya city, utilized the "Disaster Prevention Mass Movement Promotion Project" which has been used for other natural disasters, and adopted a policy of mass movement to a comparatively convenient part of Ojiya city and support for housing reconstruction. In accordance with this intention, it was decided to move all the residents of Junidaira village, which is located in the most secluded part of the Higashiyama area and which was near to a natural dam caused by the earthquake, and thus the village ceased to exist. Apart from this, about half of the residents of Shiodani village, which comprised 49 households before the earthquake, agreed to move and reconstructed their lives away from the village. In this case, as a procedure for carrying out the mass movement for the purposes of disaster prevention, it was necessary that the land around the households that wished to move was declared a disaster-prone area, and after the declaration, even if there were residences remaining, there were limitations on their use. Therefore, apart from Junidaira village where all households decided to move, the land use around the houses of households that decided to move away from Shiodani became restricted and the area fell into decay, and no measures could restore the situation. For those households that wished to remain there, the situation was a huge contrast to that in Yamakoshi village, where support was provided by reconstructing the former housing areas and building public housing.

In the Higashiyama area, the trend toward depopulation before the earthquake was accelerated after it hit. Apart from Nakayama village where all households remained and Terasawa village where 80% of households remained, the number of households was greatly reduced, and in virtually all villages there was even concern that they would become marginal villages (Table 1). Additionally, looking at the population structure of the Higashiyama area in 5-year intervals, the traditional pattern of many elderly residents populating intermediate or mountainous areas has been strengthened.

5. Initiatives to establish a recovery design for the Higashiyama area

5-1. Creation of the "Higashiyama Recovery Map"

In Shiodani area, the residents alongside external aid workers were the first to start specific activities aimed at the restoration of the village. However, in Higashiyama area as a whole more than a year passed after the earthquake before activities got into full swing. In the past during the Boshin war, this area was an important base when government forces were attacking Nagaoka, and many historical remains exist, including Enoki Toge. These episodes came to light during interviews while various information was being gathered concerning Higashiyama area with the objective that it would be useful for the future restoration. Efforts toward the preparation of a Higashiyama restoration map started about 18 months after the earthquake. Repeated workshops were held in each village, uncovering the thoughts and feelings of the residents toward the area and its the resources. As this process was repeated on countless occasions, Higashiyama area became united; the feeling of realizing the sustainable restoration of the villages became stronger, although in a different form to that of Yamakoshi village where various aid had already been provided.

As the mood among the area residents arose, aid was provided from the Niigata Prefecture Chuetsu Earthquake Restoration Fund, which had been established by the Government with the objective of providing compensation for community restoration tasks and aid on soft aspects. For example, initially this was almost entirely spent on hard aspects, but by this time concerns had turned toward the individual victims and the restoration of the villages and as such, efforts turned towards the development of support items. At the same time as the workshops were being held to create the restoration map, dialog was established between members of the Higashiyama Area Restoration Committee, which became the mouthpiece for the area, and the administrators of the restoration funds. In this dialog, aid was developed to support the creation of the restoration map, and aid was investigated for the establishment of a restoration plan aimed at sustainable restoration. It was with such a mood that the Area Restoration Committee turned toward establishing the restoration plan for Higashiyama area as a whole.

5-2. Activities of the recovery design establishment project

From April 1, 2007, the Niigata Prefecture Chuetsu Earthquake Restoration Fund established an aid item for "work in support of establishing the restoration design". This was for supporting external specialists and experimental events for establishing a restoration plan utilizing the area's characteristics in order to work toward the independent restoration of the damaged areas. It provided an upper limit of 7 million yen to be used between fiscal years 2007 and 2011, to provide 100% support for costs. In the Higashiyama area, the restoration fund administrators judged that the time was ripe as the restoration map had already been established, so the policy for the aid was determined soon after this aid item was made available. Hence, the policy for specific work was examined, mainly by the Higashiyama Area Restoration Committee. The workshops that had already been held in all the areas were held again, with the main objective of providing a vision of the work plan for achieving the independent restoration. In addition, as a result of discussions between the chairman and members of the restoration committee, who feared that the sustainability of the villages with only half of their households remaining would be lost, work was carried out to try to reflect, to some degree, "future integration of the community" into the restoration plan.

The opinions of each of the villages and those of the restoration committee were summarized, and in July 2007 the recovery process plan was produced as the Higashiyama Recovery Plan with the slogan "Comfortable living Higashiyama".

5-3. Activities of the recovery design establishment project

The recovery plan consisted of the following two basic policies, and five measures.

■ **Basic Policy 1** "To create new vigor with 1+2+2.5"

Aiming to build the community with not only the residents, but with "2.5 people with heart" that are strongly associated with the community through the earthquake

■ **Basic Policy 2** "To achieve comfortable living by having the appropriate facilities in the appropriate place"

To reduce the burden of maintenance while developing new services, by reviewing existing resources

□ **5 Measures**

1. To recognize the "connection" brought about by the earthquake
2. To review and revitalize the culture and traditions (of oneself, of the community)
3. To carry out rich exchange activities using the attractive items arising from item 1.
4. To identify people who want to contribute to the sustainability (2.5 people with heart) and to provide them with their field of activities
5. To achieve a sustainable area with "1＋2＋2.5"

In Higashiyama area, half the households chose to move from the area to reconstruct their lives after the earthquake. Compared with the case if the earthquake had not happened, this was almost the same rate of depopulation as would occur over the period of one generation. Therefore, the task of sustaining the village suddenly became an urgent issue to be tackled, and most residents had difficulty understanding that achieving sustainability was their problem. However, as typified by the example of Shiodani area referred to earlier, a continuous engagement with external aid workers who were present was started. In such circumstances, the organization of the villages became reorganized to a certain extent over a period of time; they received the necessary support from the external aid workers, and they resolved to create a comfortable living environment for the residents of later generations.

In fact, in order to gain the understanding of each individual resident for this abstract plan, and to raise the awareness of the need for integration of the community, after the plan was established the main members of the Area Restoration Committee and external aid workers involved in establishing the plan held discussion meetings in each village to discuss the plan. A time schedule for implementing the plan was also established. Specific measures were put in place for the residents to create by themselves an environment in which the villages could be sustained independently once Government support through the restoration fund would end, 10 years after the earthquake.

6 Ensuring sustainability by integration of the village

6-1. Establishment of a village investigation committee and its discussions

With the number of households in each village reduced, not only did it become difficult to find people to take the roles of area head (or mayor within a town) and various types of staff as had been previously appointed in the villages, but it also became difficult for each village to independently cover the meeting costs and personnel costs associated with such overseeing activities. A "village investigation committee" was established based on the restoration plan, in which several members from each village, members of the Higashiyama Area Restoration Committee, and government workers participated. This committee is continuing its discussions at present to determine specific forms of integration, while clarifying the population statistics of the future and the financial circumstances of each village. In fact there is still resistance towards integration of the villages, and sufficient agreement has not been reached. However, as there is a strong feeling that this problem should not be passed onto the next generation, the debate is intensifying.

6-2. Future activities toward ensuring sustainability

Among many residents in their 50s and older that carry out various roles within the present villages, there is not much of a sense of crisis that it may become difficult to sustain the villages in the future, and it cannot be denied that the discussions have gone around in circles on some points. However, in parallel with the discussions occurring in the investigation committee, new initiatives have started across the entire area, mainly among the young women, such as planning and holding Bon Odori (traditional summer dance) festivals and the like. Above all, these activities arise out of the residents' own activities, and if these initiatives continue, their results will provide many important hints for the future sustainability of other mountainous areas nationwide.

7. Conclusion

In closing, it is often said that natural disasters have a way of making a region's existing issues apparent and accelerating them. The crucial element in transforming disasters into an opportunity for positive change, incorporating different modes of awareness and utilizing ties with neighboring regions, are people. Therefore, our most important challenge would be to identify ways to establish a context where people can exercise their initiative; generous support may not be the only or best way for enabling such actions. The situation must become an opportunity for developing self-sustainability and this is a theme that we must carefully continue to explore into the future.

References

1) The Editing Committee, "History of the Niigata-Chuetsu Earthquake Revival Record", Gyosei Publication, 2006
2) Higashiyama Promotion Committee, "The Map of Revitalization Process, Ojiya-Higashiyama", 2006

Sixth International Conference on Urban Earthquake Engineering
March 3-4, 2009, Tokyo Institute of Technology, Tokyo, Japan

DYNAMIC RELATION BETWEEN DEMAND AND SUPPLY OF TEMPORARY HOUSING FOLLOWING URBAN DISASTERS

Keiichi Sato[1], Itsuki Nakabayashi[2], and Saburoh Midorikawa[3]

1) Research Associate, Institute of Social Science, The University of Tokyo, Japan
2) Professor, Graduate School of Urban Science, Tokyo Metropolitan University, Japan
3) Professor, Center for Urban Earthquake Engineering, Tokyo Institute of Technology, Japan
keiichi-s@iss.u-tokyo.ac.jp, nakabasi@comp.metro-u.ac.jp, smidorik@enveng.titech.ac.jp

Abstract: An occurrence of future great earthquake in the Tokyo metropolitan area is concerned. Recently, the Japanese Cabinet Office had much discussion about damage assessment, disaster prevention strategy, and evacuation countermeasures for the earthquake but less so about a temporary housing problem after an evacuation. For considering the temporary housing problem, we constructed the database of temporary housing, household's behavior model, and the micro simulation which illustrates temporary housing situation. Although the amount of demand and the amount of supply are not clear, the simulation using one assessment has been performed. This paper examines dynamic relations of the demand of temporary housing, and the supply.

1. Introduction

The Japanese Cabinet Office had much discussion about damage assessment (2004), disaster prevention strategy (2005), and evacuation countermeasures (2006-08) for the anticipated Tokyo Metropolitan Earthquake. After a huge amount of evacuation, a scale of temporary housing problem will appear. However, so far the deliberation of the temporary housing problem following the Tokyo Metropolitan Earthquake has been superficial.

In the Tokyo Metropolitan Earthquake, the number of about 0.3 million to 0.9million complete-collapse buildings is predicted by Japanese Cabinet Office in 2004. Considering the number of buildings and the number of households, about 0.5 to 1.5 million households will lose their houses. In Japan, the prefabricated houses (prefabs) play the central role in the temporary housing countermeasures; however, the number of prefabs will be insufficient when the Tokyo Metropolitan earthquake occurs. On the other hand, approximately one million vacant rental housings are existed in the Tokyo metropolitan area. These vacant housings can be utilized for victims' temporary living spaces (Sato et al. 2007a). However, the argument of supply amount is not enough to solve the problem because of the complexity of the temporary housing problem. There are many types of temporary housing (prefab, rental housing, relative's home and etc), and each household have each choices.

For considering the problem mentioned above, we constructed the database of temporary housing (Sato et al. 2007a), household's behavior model (Sato et al. 2007b), and the micro simulation which illustrates temporary housing situation (Sato et al. 2008). Although the amount of demand and the amount of supply are not clear, the simulation using one assessment has been performed. This paper examines dynamic relations of the demand of temporary housing, and the supply.

Specifically, changes of the simulation results are checked from fluctuating settings of the demand and the prefabs supply. Since the purpose of this paper is checking the relation between demand and supply, a policy condition is fixed at the current system (Disaster Relief Law and Natural Disaster Victims Relief Law).

In this study, the following research step is conducted to figure out the dynamic relations between demand and supply.

1. *Setting of the micro-data of temporary housing (prefabs, rental housings, and households who require temporary housings).*
2. *Run the micro-simulation of several cases (9 cases)*
3. *Grasp the dynamic relations between demand and supply from the several simulation results.*

2. SETTING OF THE MICRO DATA

The Tokyo metropolitan area has 5 prefectural governments with about 300 city governments. Because size of administrative segmentation is not appropriate for the simulation, we divided the area into original 24 sections as showing in the Figure1. Data settings and the simulation are conducted by the original 24 areas.

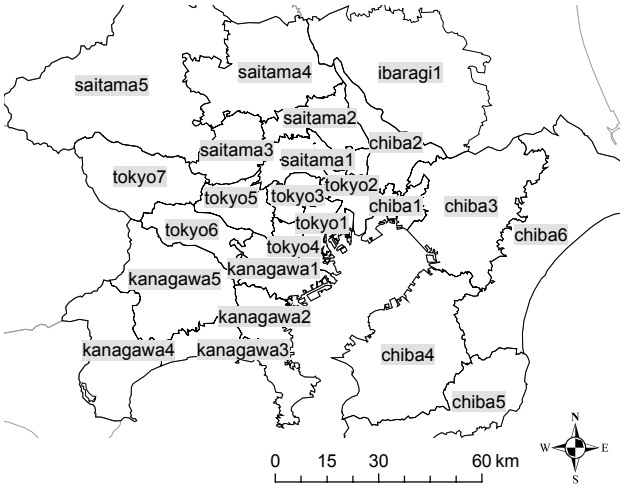

Figure 1 Area Setting of the Simulation

2.1 Micro Data of the Prefabs

The supply amounts of the prefabs are placed from the temporary housing site lists of prefectural governments. Since the data of private land are imperfect, the data of only public land is used. This data can be used as micro data.

In this paper, three patterns of 0.1million, 0.2million, and 0.3million were prepared as the number of prefab supplies. The numbers of prefab supplies in each area are generated from the number of households who require temporary housing using the Cabinet office's report (2004) and the number of prefabs which can be constructed in public space. Micro data which use in the simulation picked up at random from the temporary housing site lists of prefectural governments.

Table 1 Settings of Prefab supply

area	prefabs which can be constructed in public space	case 0.1million prefabs	case 0.2million prefabs	case 0.3million prefabs
tokyo1	13,133	5,867	11,734	13,133
tokyo2	14,775	6,601	13,201	14,775
tokyo3	33,412	14,928	29,853	33,412
tokyo4	11,211	5,008	10,017	11,211
tokyo5	16,462	7,354	14,709	16,462
tokyo6	8,865	3,960	7,921	8,865
tokyo7	2,060	0	0	2,060
kanagawa1	19,552	8,735	17,469	19,552
kanagawa2	25,512	11,397	22,795	25,512
kanagawa3	35,517	15,867	31,734	35,517
kanagawa4	5,990	0	0	0
kanagawa5	55,145	0	0	48,394
saitama1	5,259	2,349	4,699	5,259
saitama2	4,479	2,001	4,002	4,479
saitama3	4,117	0	0	4,117
saitama4	13,600	0	0	13,600
saitama5	14,056	0	0	0
chiba1	21,816	9,746	19,492	21,816
chiba2	2,391	1,068	2,136	2,391
chiba3	11,458	5,119	10,238	11,458
chiba4	7,987	0	0	7,987
chiba5	2,248	0	0	0
chiba6	9,196	0	0	0
ibaragi1	–	0	0	0
total	338,241	100,000	200,000	300,000

2.2 Micro Data of Rental Housing

Although damage appears in about 140,000 of about 1,050,000 vacant rental housings located in the tokyo metropolitan area in case of the anticipated earthquake, about 910,000 vacant rental housing make practical use possible (Sato et al. 2007a). Sato et al. (2008) generated micro data of rental housing which can be used after the Tokyo Metropolitan Earthquake, using aggregated data (national statistical data about housing and land, earthquake damage assessment, and the information about rental housing on the internet). In this paper, the generated micro data is used directly.

Table 2 Setting of Rental housing

area	All Vacancy on Rental Housing	Vacancy on Rental Housing which can be used following the Tokyo Metropolitan Earthquake
tokyo1	96,010	74,583
tokyo2	81,410	45,703
tokyo3	110,860	88,623
tokyo4	51,850	33,972
tokyo5	70,790	64,724
tokyo6	35,250	33,775
tokyo7	8,830	8,751
kanagawa1	86,040	78,420
kanagawa2	53,150	49,154
kanagawa3	45,140	39,806
kanagawa4	11,160	11,050
kanagawa5	52,000	49,868
saitama1	63,910	59,392
saitama2	30,420	28,616
saitama3	28,990	28,106
saitama4	27,700	26,719
saitama5	13,090	13,090
chiba1	43,910	35,435
chiba2	25,900	23,710
chiba3	53,040	49,650
chiba4	23,250	22,827
chiba5	2,930	2,861
chiba6	7,790	7,641
ibaragi1	31,230	30,881
total	1,054,650	907,355

2.3 Micro Data of households who require housing

The Japanese Cabinet Office's expert panel published the trial assessment in 2007. According to the report, approximately 1.6 million household will have their houses damaged because of the Tokyo Metropolitan Earthquake, but 0.3 million households will be able to repair their damaged house. Thus, 1.3 million households which deducted 0.3 million from 1.6 million are regarded as the number of households who require temporary housing at the maximum of the anticipated earthquake.

In this paper, three patterns of 1.3 million, 1.0 million, and 0.7 million are discussed as the numbers of households who demand temporary housing. The Micro data of the demand is generated from Sato et al. (2008).

Table 3 Settings of household who require temporary housing

area	Households who require temorary housing using Cabinet Offeice's Report(2004)	case 1.3million	case 1million	case 0.7million
tokyo1	230,597	228,487	175,760	123,032
tokyo2	332,943	329,898	253,766	177,636
tokyo3	190,408	188,666	145,128	101,590
tokyo4	139,750	138,472	106,517	74,562
tokyo5	25,149	24,919	19,169	13,418
tokyo6	4,994	4,948	3,806	2,664
tokyo7	0	0	0	0
kanagawa1	67,534	66,916	51,474	36,032
kanagawa2	42,007	41,623	32,017	22,412
kanagawa3	33,976	33,665	25,896	18,127
kanagawa4	0	0	0	0
kanagawa5	0	0	0	0
saitama1	70,778	70,131	53,947	37,763
saitama2	10,066	9,974	7,673	5,371
saitama3	0	0	0	0
saitama4	0	0	0	0
saitama5	0	0	0	0
chiba1	99,193	98,286	75,605	52,923
chiba2	31,440	31,153	23,964	16,775
chiba3	33,165	32,862	25,278	17,695
chiba4	0	0	0	0
chiba5	0	0	0	0
chiba6	0	0	0	0
ibaragi1	0	0	0	0
total	1,312,000	1,300,000	1,000,000	700,000

3. MICRO-SIMULATION

3.1 Outlines of the Micro Simulation Model

The simulation flow is summarized below.

1. Fix the individual data of households who lose their houses. Gather housing data about the prefabs and rental housing.
2. Extract the household who looks for a temporary housing at random.
3. Extract a rental housing based on victim's preference from the rental hosing data. Extract the prefabs from the supply role. In a severe situation, there is a possibility that rental housing and the prefab does not exist.
4. Calculate choice probability based on generated choice problem and constructed discrete choice model and then assign of choice result using a random number.
5. Delete selected supply data.
6. Extract the next household who looks for a temporary housing at random and compute 3 to 5 again. Repeat the same calculation to all households.

One calculation is completed the flow above. Since the result of choices is assigned by the random numbers, calculation has to perform repeatedly about several times. By totaling a repetition calculation result, we can grasp what we can expect to happen in the temporary housing situation.

This simulation was programmed by the C language. One simulation takes about 30 minutes using general workstation under the following setting; 0.1 million prefabs, 0.9 million rental housings, and 1.0 million households who require temporary housing.

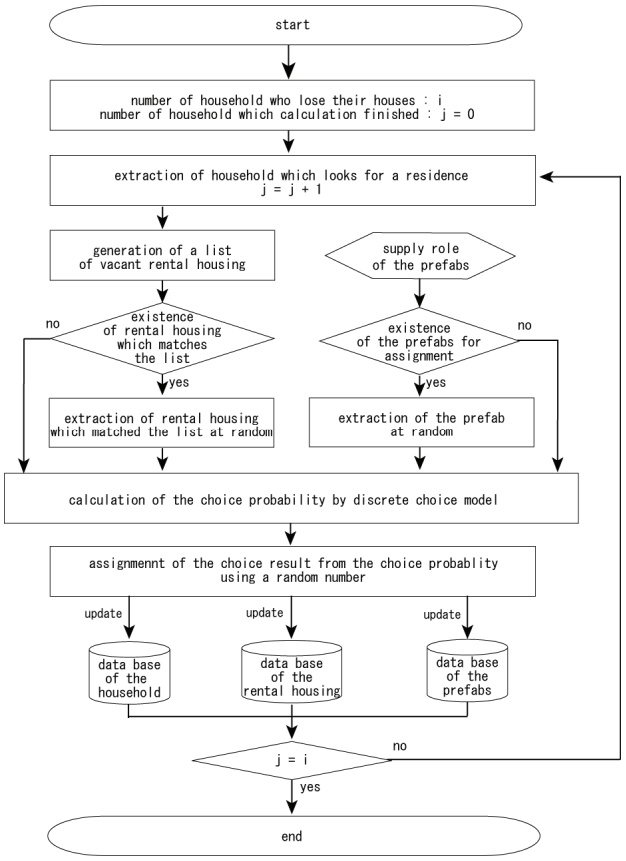

Figure 2 Flow Chart of the Micro Simulation

3.2 Case Set

Table 4 shows the result of the case set of the simulation as mentioned above. The case sets have nine patterns by combination of three sets of the demand and three sets of the supply. Codes of each case are described in the Table 4.

Table 4 Case set of the micro simulation

		supply amount of prefabs		
		0.1million	0.2million	0.3million
number of household who require temoary housing	1.3million	case130-10	case130-20	case130-30
	1.0million	case100-10	case100-20	case100-30
	0.7million	case70-10	case70-20	case70-30

3.3 Effect of Fluctuations of the Supply

First, we checked an effect of fluctuations of the prefabs number. In this section, the number of the demand set only 1.3 million, and the number of the prefabs set from 0.1 million to 0.3 million. The average values of 10 times simulation are summarized in Figure 3.

Even when the number of prefabs was increased, there was no large change to the number of households who remain living in shelters. This suggests that, if many prefabs are constructed, even those households who can live somewhere else in fact may also move in those prefabs. In

order to solve the problem, it is important to acknowledge that it is inadequate to simply supply many prefabs, and to employ a distribution method of prefabs that can be suggested from the results of this research.

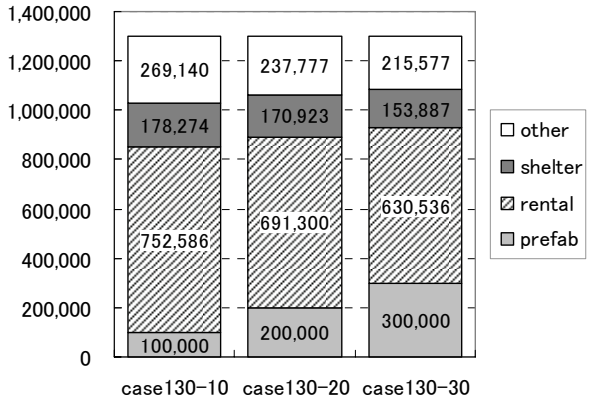

Figure 3 Effect of fluctuations of the prefabs number

3.4 Effect of Fluctuations of the Demand

Next, we checked an effect of fluctuations of the household number. In this section, the number of the prefabs set only 0.1 million, and the number of the households who require temporary housing set from 1.3 million to 0.7 million. The average values of 10 times simulation are summarized in Figure 4.

When housing damage occurs lower than an assessment, households who remain shelter can also be reduced. Although 0.9 million rental housing existed, all these housing are not used in three cases. It is difficult to move into the rental housing which has preferable conditions. Considering the condition of temporary housing, just reducing the housing damage will be inadequate, and importance of the countermeasures to the problem of lengthening shelter can be pointed out.

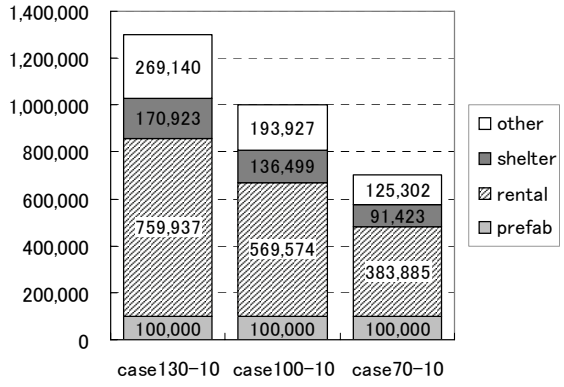

Figure 4 Effect of fluctuations of the demand

3.5 Dynamic Relations between the Demand and the Supply

At last, we checked total relations between the demand and the supply. The micro simulations of 9 cases mentioned at Table 4 were calculated in each 10 times, and the average value of the households who remain shelter was described in Table 5.

The number of households who remain shelter is mitigated by increasing supplies of prefabs from 0.10 to 0.3 million. The rate of mitigation changes with numbers of the households who require temporary housing. In the case of 1.3 million households, the rate is 86%. In the case of 0.7 million households, the rate become 47%. It can say that if mitigation of housing damage is progressed, it increases the effect of the prefabs to solve the problem of lengthening shelters.

Table 5 Number of the Households who Remain Shelters in the 9 Cases

		supply amount of prefabs			reduction rate from 0.1 million of the supply to 0.3 million
		0.1million	0.2million	0.3million	
number of households who require temorary housing	1.3 million	178,274	170,923	153,887	86.3%
	1.0 million	136,499	119,200	90,163	66.1%
	0.7million	91,984	64,808	43,407	47.2%

4. CONCLUSION

This paper examined the dynamic relation between demand and supply of temporary housing in association to the anticipated Tokyo Metropolitan Earthquake by using the micro simulation. The relation has the following three characters. 1) Even if the number of prefabs is increased, the large change to the number of households who remain shelter is not seen. In order to solve the problem, a distribution method of prefabs will become important. 2) When the housing damage occurs lower than the assessment, households who remain shelter can be reduced. 3) The result from checking dynamic relation between the demand and the supply suggests that if mitigation of housing damage is progressed, it increases the effect of the prefabs to solve the problem of lengthening shelters.

Acknowledgements:

The authors acknowledge support from Japan Ministry of Education, Culture, Sport, Science, and Technology (MEXT) for the Center for Urban Earthquake Engineering (CUEE) in Tokyo Institute of Technology.

References:

Sato, K. and Midorikawa, S. (2007a), "Distribution characteristic of Vacancy on Rental Housing which can be used following the Tokyo Metropolitan Earthquake," *Journal of Social Safety Science*, **9**, 47-53.(Japanese)

Sato, K., Nakabayashi, I. and Midorikawa, S. (2007b), "Discrete Choice Analysis of Temporary Hougsing Choice After Urban Earthquake Disaster," *Proc.Fourth International Conference on Urban Earthquake Engineeringe*, 561-568.

Sato, K., Nakabayashi, I. and Midorikawa, S. (2008), "A Micro Simulation for Temporary Housing Countermeasures using Earthquake Damage Assessment," *Journal of the City Planning Institute of Japan* , **43(3)**, 715-720.(Japanese)

Sixth International Conference on Urban Earthquake Engineering
March 3-4, 2009, Tokyo Institute of Technology, Tokyo, Japan

DISCUSSION PROCESS AMONG AFFECTED PEOPLES TO REACH A CONSENSUS ON A RECONSTRUCTION PROGRAM AFTER A DISASTER: A CASE STUDY OF THE HANSHIN-AWAJI EARTHQUAKE

Hideki Kaji [1] and Mari Yahagi[2]

1) Professor, Center for Urban Earthquake Engineering (CUEE), Tokyo Institute of Technology, Japan
2) Graduate of the Master Program of Media and Governance, Keio University
hkaji@plum.ocn.ne.jp, yahagimari@hotmail.com

Abstract: The early reconstruction of damaged houses caused by a disaster is the most anxious matter for the affected peoples. Individual piecemeal reconstructions efforts, however, in some cases, are not allowed by the local development authorities, when they have an idea of taking the opportunity for rebuilding a disaster-resilient district on urban renewal basis. Thus serious argument between the affected peoples and the local development authorities may begin. This paper tries to analyze the consensus process between such two parties. The urban renewal project of Rokkoumichi-Minami district in Kobe city (noted as Rokkoh-south district hereafter) after the Hanshin-Awaji Earthquake has been selected as a case study. The paper aims to clarify the consensus process over different conflicts on the Disaster Prevention Park Plan proposed by the local government, through a contents analysis of the minutes of Citizens Committee on the Rokkoh-South Urban Renewal Project.

1. INTRODUCTION

About one month after the Hanshin Awaji Earthquake, the Kobe city government announced the urban redevelopment plans on the six districts where the damage were most severely caused. And next month, 24 areas, including them, were additionally designated as the intensive reconstruction promotion areas, where urban rehabilitation, redevelopment, or land readjustment projects were supposed to be urgently implemented (Figure 1, URL).

Rokkoh-south district, taken as a case study district in this paper, was the one among the six redevelopment districts. In this district with population of 1400 persons, 65% of houses (180units) were totally or half collapsed because most of them were vulnerable old wooden houses.

The urban redevelopment plan proposed by the local government was designed by arranging three high-rise residential buildings, a shopping mall and public facilities around a large disaster prevention park with one ha in the central part. It was also proposed that the project would fully be implemented under the local government initiative.

One of the reason why the local government had decided to reconstruct the district in such large scale development, was of cause due to severity of damage, but its real intention was laid in the fact that the district had been nominated as an eastern sub-center even before the Earthquake, and thus it was good timing for the government to make it reality. Though one ha of the park was too large, it was vital for the local government to receive the subsidy from the central government.

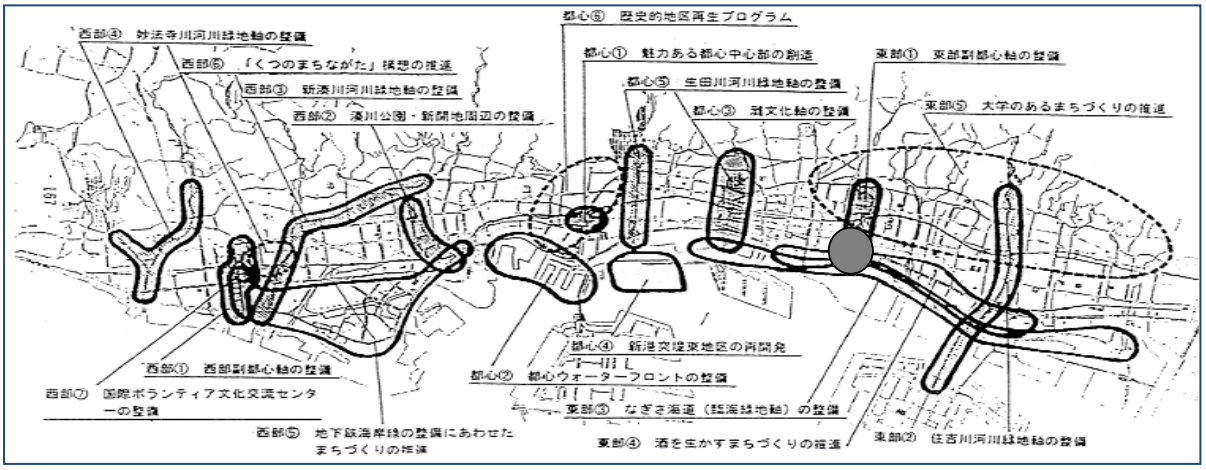

Figure 1 Intensive Reconstruction Promotion Areas

2. BEGININNG OF THE ARGUMENT

2.1 Counter plan

This sudden notice of the proposal was brought to the affected peoples of the district when they least expected it. In fact, more than 60% of residents were out of the area when the plan was announced. Naturally they all expressed against the plan, complaining that the procedure was too much one-sided and the plan did not reflect any people's will at all.

Thus, some voluntary peoples of the district organized "Citizen's Group for Discussing about Reconstruction of Rokkoh-south Area (noted as the Group hereafter).

The Group, then drew up a counter reconstruction plan, which included variety of citizen's idea, for appealing their ambition, and at the same time it submitted, some 460 comments and opinions about the governmental plan, requesting for reconsideration (See figure2 and 3).

The Kobe city government however neglected the counter plan and rejected these comments and opinions under the reasons that they were those from the minor group, and authorized the plan as an official one.

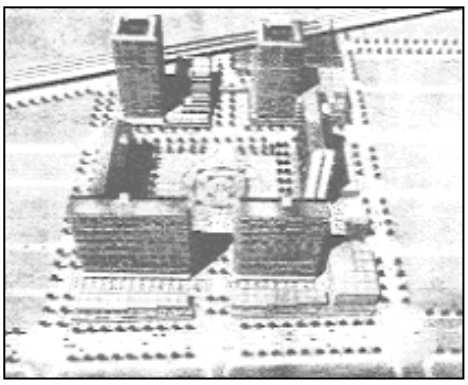

Figure 2 Government Plan

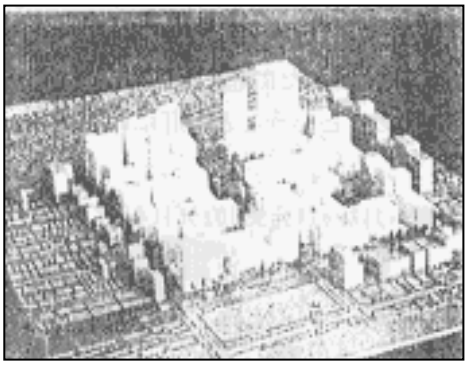

Figure 3 Citizen's Plan

2.2 Citizen's Machizukuri Committee

Even after the authorization, people's campaign against the plan was not ceased, and became rather radical. Consequently, the government could not help changing its mind. Thus it proposed to the peoples that they should organize the official "Citizen's Machizukuri (=city planning) Committee of Rokkoh-south District (noted as the Committee hereafter)", which was regularized by the Kobe municipal ordinance, and promised that the government was ready to revise the authorized plan based on the opinions raised by the Committee.

It was a very exceptional formality to the Urban Planning Law in Japan that once an authorized city plan might later be revised by people's opinion. This case has been called as "Two Step Authorization Formality of City Planning".

At beginning, the peoples refused to organize the Committee, because they distrusted the government and were afraid of being wheedled. Finally, however, they found that the Committee must be an only channel to appeal their opinions, and accepted the governmental proposal.

Thus, four committees on the residential bloc bases, and one joint committee consisted of the representatives of the four committees were organized.

3. AIM AND METHODOLOGY OF THE PAPER

.

After nine month's discussions in the Committees, the affected peoples and the local government had reached to a consensus of opinion, and the redevelopment project started the construction work in July 1997. In March 2004, nine years after the earthquake, the construction of 14 buildings were completed, and in September 2005, the project was perfectly ended by the accomplishment of the central park.

Thus, this paper aims at examining how and when the peoples and the local government have reached to a consensus, in particular, of the large-scale park with one ha, by reviewing the discussion minutes of the Committee during the period from June 2005 to March 2006.

The procedure and methodology of the contents analysis of the minutes' statements are as follows:

a. Coding individual statements in the minutes,
b. Classification of the statement contents by PM analysis,
c. Attitude appraisal of the statements by PAC analysis,
d. Classification of the statements based on arguments for or against the project
e. Scoring the individual statements, and
f. Calculating average consensus score of each meeting.

This contents analysis of the statements was applied only to the statements from the people's side, taking account of the government statements as a exogenous input.

4. PM-PAC METHOD

4.1 PM analysis

Looking at the individual statements in the discussion minutes, it may be found that they imply two different discussion points. They are;

- Statement which is more or less related to the redevelopment plan itself, and
- Statement which is rather related to a meeting or discussion procedure.

Misumi, Japanese psychologist, has advocated this classification to analyze a concept of leadership in a group dynamics (Misumi, 1994), and he named as P-function (the former) and M-function (the latter), respectively. The P-function stands for performance function and helps to lead

a conclusion, which a meeting seeks as a goal. While, M-function stands for maintenance function and helps to keep fairness and order in a meeting.

Though Misumi's theory was applied to analyze a function of leadership in a group dynamics, the paper expands the idea analogically to the individual statements in the meeting, assuming that they also play these functions through discussions. Since there is, of course, those statements which are not related to both function, all statements will be then classified into three groups; P, M, and neutral (=0).

4.2 PAC analysis

It is also observed in communication through a discussion that some statements are very rational and impressive and thus have powerful leading function of P or M to the members, while some are very emotional and selfish and thus do not give any influence on a discussions, or give rather negative effect. Such attitude of the speaker may also important in the discussion process, in particular, when the meeting seeks a consensus of opinion as a goal.

In a communication theory, Sugita has pointed out that a communication pattern can be characterized by three personalities with members based on their self (Referred by Nishikawa, 2002). They are Parent, Adult, and Child. The Parent-attitude has a critical orientation, the Adult-attitude has a rational orientation, and the Child-attitude has a free and wild orientation.

Though Sugita's definition of these three personalities takes account the change of the self depending on interrelation of members, the authors have simplified it as fixed attitude (noted as PAC analysis) and applied them to appraise an influence of statements on discussion. That is;

-The statement with Adult-attitude has powerful leading function of P or M.

-The statement with Parent or Child-attitude has weak or rather negative function of P or M.

4.2 Combination and scoring

Above all, the individual statements recorded in the discussion minutes of the meetings of the Rokkoh-south Machizukuri Committee can be characterized by the PM-function and the two attitude of Adult or Parent/Child –attitude. It is therefore summarized as shown in the Table 1, where NP or NM implies that P-function or M-function is weak and rather negative.

Table 1 Combination of PM and PAC

↓Attitude Function→	P	Neutral	M
Adult	P	0	M
Neutral	0	0	0
Parent/Child	NP	0	NM

A statement has sometimes P and M-function at the same time, and thus P/NP-function and M/NM-function should be combined to illustrate a statement by these abbreviations, where the figure 0 means that the statement does not imply that function (see Table 2)

Table 2 Types of a statement

	M	0	NM
P	P-M	P	P-NM
0	M	0	NM
NP	NP-M	NP	NP-NM

Since this classification of the statements shows how far a statement gives an influence on discussion to reach a consensus or how far it contributes to maintain the discussion order. In order to illustrate it numerically, the authors have judged the extent by arbitrarily giving a score to each cell (Table 3).

Table 3 Scoring

	M	0	NM
P	5	4	3
0	4	0	2
NP	3	2	1

5. ARGUMENT FOR OR AGINST THE PROJECT

The individual statements imply implicitly or explicitly that the speaker's arguments are for or against the governmental plan. The main point of the arguments was as a matter of course laid on the size of the disaster prevention park in this case.

Although there were various nuances of meaning in the respective arguments, the statements can principally be classified into three types: agree, disagree, and neutral to the proposal. By putting three scores of +2, -2, and 0 to these types respectively and then by combining the above mentioned PM-PAC scores, the following matrix will be obtained. This matrix can be applied to evaluate a statement in terms of how far and to which direction it contributes for leading the discussion.

Table 3 Extent of contribution for leading consensus

Direction→		Agree	Neutral	Disagree
↓ PM-PAC score		+2	0	-2
PM	5	+10	0	-10
P	4	+8	0	-8
M	4	+8	0	-8
P-NM	3	+6	0	-6
NP-M	3	+6	0	-6
NP	2	+4	0	-4
NM	2	+4	0	-4
NP-NM	1	+2	0	-2

6. SCORING STATEMENTS

6.1 Score of individual statement

The individual statement in a meeting, thus, can be illustrated in a numerical manner, in terms of the extent of contribution for leading a discussion to a consensus. The consensus is not always positive or for the plan, but sometimes negative or against it. The distribution of the

scores of all individual statements in nine meetings from 5th to 14th is illustrated in figure 4. As seen in the figure, almost all members were against the 1 ha park at the 5th meeting, though the extent was not so intensive. In other words, there was a negative consensus among the members at that time.

At the 6th meeting, two persons changed to the positive side, while other two persons drastically opposed. AT the 8th meeting, a consensus among the members was totally disappeared. The 9th meeting was very critical. The opinions for the 1 ha park might dominated those against it. At the 10th and 12th meeting, some opinions against the 1 ha park were raised but minor, and the final outcome was already certain.

7. AVERAGE SCORE AND EXOGENIOUS FACTOR

This process can become clearer when the average of the statements score is calculated by meeting. The figure 5 shows it together with some exogenous inputs made by the city government and the consultant which was assigned to support the citizen's group.

It seemed that the people could not help reaching a consensus when they found that the government might not change its intention at the 9th meeting, but finally accepted when the government made a concession to slightly reduce the area of the park.

8. CONCLUSIONS

It is quite doubtful that the citizens really have agreed to the 1ha park through the discussions with the local government.. As Ms. Ito pointed out, they might partially understand the importance of 1 ha park, but more substantial reason was that they were eager to settle down as earlier as possible (Ito, 2003). In this sense, time must be one of the most important factors which lead a discussion to a consensus, as seen in this case.

Finally, the paper may be appreciated in a sense that it has developed a method to visualize the discussion process to reaching a consensus in numerical manner. The authors do expect another application case of the method.

References:

-http://web.kyoto-inet.or.jp/org/gakugei/mokuroku/tosi/fukkou/kinmoku/kin12gif/n.gif

-Misumi N, (1994) "Behavior Science for leadership", Asakurashoboh,

-Nishikawa K.,(2002),"Communication Process", NIheisha

-Ito A.(2003), "A Machizukuri Project for Reconstruction by Urban Redevelopment - A case of Rokkohmichieki- south district", Symposium hosted by the Hyogo Geography Association

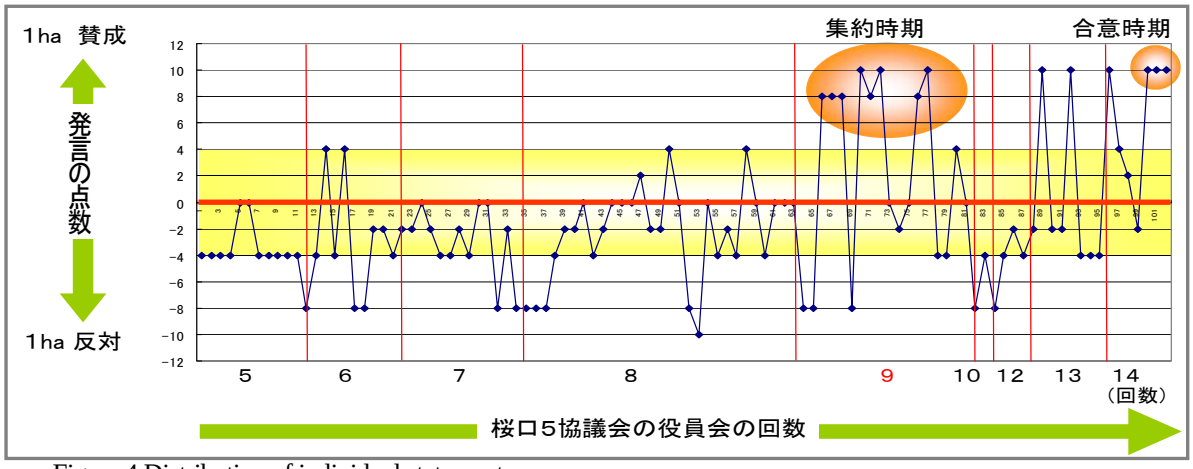

Figure 4 Distribution of individual statement score

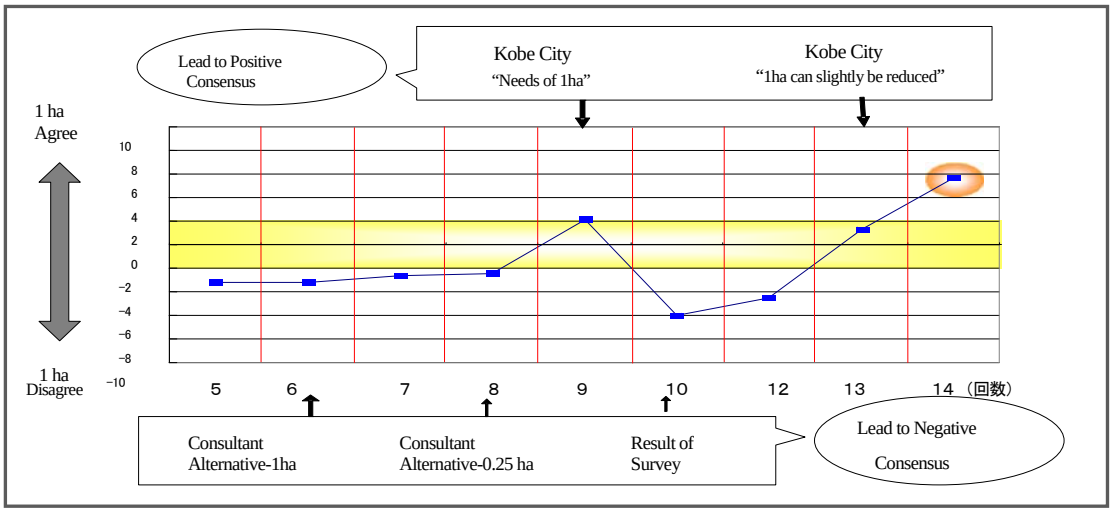

Figure 5 Average score of statements

Sixth International Conference on Urban Earthquake Engineering
March 3-4, 2009, Tokyo Institute of Technology, Tokyo, Japan

A STUDY ON URBAN DISASTER MITIGATION BY A BUILDING-REPLACEMENT CONTROL METHOD WHICH ASSUMED THE GAIN-MAXIMIZING BEHAVIOR MODEL

Yusuke Meshitsuka[1)]

1) Assistant Professor, Department of Architecture and Building Engineering, Tokyo Institute of Technology, Japan
meshi@arch.titech.ac.jp

Abstract: In this study, a theoretical model of fireproof improvement is constructed and some basic comparative relations are confirmed. And as a result of interpretations of this model about the effect of specification of a floor-area ratio, a usability of floor-area ratio system for control of fireproof improvement became theoretically clear.

1. INTRODUCTION

It is said that there is high possibility of suffering the large-scale damage after a huge earthquake and the damage caused by a fire is especially serious.

Fireproof improvement of city area is not progressing easily though it is highly required (figure 1 and figure 2). One of the reasons is considered to be that fireproof improvement is progressed only by building-replacement of private ownership buildings. It is also considered to be the reason that many flammable wooden buildings have been rebuilt to wooden buildings again.

However, it seems to be a bigger problem that an effective control method of building-replacement from wooden building to fireproof building (such as reinforced concrete buildings, steel-reinforced concrete buildings, etc.) is not found out.

From above mentioned recognition, in this study, the profit model of the individuals who make decision of rebuilding is constructed. And some fundamental knowledge is shown from a basic comparative analysis.

Figure 1 Scenery of a old residential area in Tokyo

Figure 2 An aerial photograph of a old residential area in Tokyo (Google Earth)

2. PERSONAL PROFIT-DAMAGE MODEL

2.1 General model

When people build a building in Japanese city, the use of a building is limited under the principle of use zoning. Moreover, the building structure type is also limited by fire protection zone system. Therefore, profit and loss which are obtained from a building are dependent on such conditions. However, in this section, general model without specifying a use type and structure type is constructed.

Now, p represents disaster probability which is a probability of suffering the damage from a disaster during a year. L represents the amount of loss when the building is suffered from a disaster. M represents the amount of profit per year which is obtained when the building is not suffered from a disaster.

Then, the expected value of profit and loss during the first year can be represented as follows.

$$E_1 = (1 - p)M - pL \quad \text{----- (1)}$$

The current value of above profit and loss can be represented by the following equation. Where r represents annual rate of price.

$$Q_1 = \frac{E_1}{1+r} = \frac{(1-p)}{1+r}M - \frac{p}{1+r}L$$

----- (2)

The expected value of profit and loss which is obtained during 2nd year is represented as follows. Note that this profit and loss are acquired only when the building has not suffered with a disaster during first year.

$$E_2 = (1-p)^2 M - (1-p)pL$$

----- (3)

The current value of above profit and loss can be represented as follows.

$$Q_2 = \frac{E_2}{(1+r)^2} = \frac{(1-p)^2}{(1+r)^2}M - \frac{(1-p)p}{(1+r)^2}L$$

----- (4)

Then the current value of profit and loss during i-th year can be represented by the following equation.

$$Q_i = \frac{(1-p)^i}{(1+r)^i}M - \frac{(1-p)^{i-1}p}{(1+r)^i}L$$

----- (5)

The current value of total profit and loss can be calculated by following equation, where T represents the period when the building was used.

$$Q = \sum_{i=1}^{T} Q_i = \sum_{i=1}^{T}\left\{\frac{(1-p)^i}{(1+r)^i}M - \frac{(1-p)^{i-1}p}{(1+r)^i}L\right\}$$

----- (6)

Above variables Q can be represented as follows.

$$Q = \left(M - \frac{p}{1-p}L\right)\frac{1-p}{1+r}\cdot\frac{1-\left(\frac{1-p}{1+r}\right)^T}{1-\left(\frac{1-p}{1+r}\right)}$$

$$! = \left(M - \frac{p}{1-p}L\right)\frac{1-p}{r+p}\left\{1-\left(\frac{1-p}{1+r}\right)^T\right\}$$

----- (7)

Furthermore, since the disaster probability (p) and the annual rate of price (r) are small enough compared with 1, the following approximation is available.

$$\left(\frac{1-p}{1+r}\right)^T \cong \frac{1-pT}{1+rT}, 1-\left(\frac{1-p}{1+r}\right)^T \cong \frac{rT+pT}{1+rT}$$

----- (8)

Under above approximation, the current value of total profit and loss Q is represented as follows.

$$Q = \left(M - \frac{p}{1-p}L\right)\frac{1-p}{r+p}\cdot\frac{rT+pT}{1+rT}$$

$$= \{(1-p)M - pL\}\frac{T}{1+rT}$$

----- (9)

Then the current value of total gain which is earned in building-replacement is represented by following equation where C represents initial construction cost.

$$R = Q - C = \{(1-p)M - pL\}\frac{T}{1+rT} - C$$

----- (10)

The building owner should make a decision as the above-mentioned total gain R becomes its maximum.

2.2 Basic comparative analysis

In order to make clear following analysis, two quantities are defined which are called whole-period-profit and whole-period-loss.

$$M_T = \frac{T}{1+rT}M, \qquad L_T = \frac{T}{1+rT}L$$

----- (11)

Then the current value of total earning which is earned in building-replacement is represented as follows.

$$R = (1-p)M_T - pL_T - C$$

----- (12)

Now the values of these variables differ between wooden building and fireproof building. We distinguish between these two types of building with superscript notation such as $p^{(w)}$ and $p^{(p)}$ in order to identify the difference clearly. The variables of fireproof building are represented by the sum of the variables of a wooden building and the difference as follows.

$$p^{(w)} = p, \qquad p^{(p)} = p - \Delta p$$

----- (13.1)

$$M_T^{(w)} = M_T, \qquad M_T^{(p)} = M_T + \Delta M$$

----- (13.2)

$$L_T^{(w)} = L_T, \qquad L_T^{(p)} = L_T + \Delta L$$

----- (13.3)

$$C^{(w)} = C, \qquad C^{(p)} = C + \Delta C$$

----- (13.4)

The quantities of differences $\Delta p, \Delta M, \Delta L, \Delta C$ have positive value under the following assumptions.

Assumptions

1. The probability of suffering the damage from a disaster of fireproof building is lower than it of wooden building.

2. The profit of fireproof building is higher than it of wooden building. (At a same location, the upper limit of floor area of fireproof building is larger than it of wooden building, because fireproof building can go vertical.)

3. The loss of fireproof building is smaller than it of wooden building. (Because of compartmentation, the fire of a fireproof building is extinguished within certain scale at high probability.)

4. The construction cost of fireproof building is more than it of wooden building.

Therefore, when wooden building is chosen, the current value of total profit which is earned in building-replacement is represented as the following equation.

$$R^{(w)} = (1-p)M_T - pL_T - C$$

----- (14)

And when fireproof building is chosen, it is represented as the following formula.

$$R^{(p)} = (1-p+\Delta p)(M_T + \Delta M_T) - (p-\Delta p)(L_T - \Delta L_T) - (C + \Delta C)$$

----- (15)

Therefore, the difference of current value of total profit between fireproof building and wooden building is represented as follows.

$$\Delta R = R^{(p)} - R^{(w)} = (1-p)\Delta M_T + \Delta p M_T + \Delta p \Delta M_T + \Delta p L_T + p\Delta L_T - \Delta p \Delta L_T - \Delta C$$

----- (16)

Here, in the right-hand side of an above equation, $\Delta p \Delta M_T$ and $\Delta p \Delta L_T$ are regarded as negligible small. Then ΔR is represented as follows.

$$\Delta R = (1-p)\Delta M_T + \Delta p M_T + \Delta p L_T + p\Delta L_T - \Delta C$$

----- (17)

When above variable has minus value, the building owner is expected to choose fireproof building. When it has plus value, the building owner is expected to choose wooden building.

Then the following equations can be calculated from equation (17) .

$$\frac{\partial \Delta R}{\partial p} = -\Delta M_T + \Delta L_T, \qquad \frac{\partial \Delta R}{\partial \Delta p} = M_T + L_T$$

----- (18.1)

$$\frac{\partial \Delta R}{\partial M_T} = \Delta p, \qquad \frac{\partial \Delta R}{\partial \Delta M_T} = 1 - p$$

----- (18.2)

$$\frac{\partial \Delta R}{\partial L_T} = \Delta p, \qquad \frac{\partial \Delta R}{\partial \Delta L_T} = p$$

----- (18.3)

$$\frac{\partial \Delta R}{\partial C} = 0, \qquad \frac{\partial \Delta R}{\partial \Delta C} = -1$$

----- (18.4)

The following relations are obtained from equation (18) and above mentioned assumptions.

$$\frac{\partial \Delta R}{\partial \Delta p} > 0, \qquad \frac{\partial \Delta R}{\partial M_T} > 0, \qquad \frac{\partial \Delta R}{\partial \Delta M_T} > 0,$$

$$\frac{\partial \Delta R}{\partial L_T} > 0, \qquad \frac{\partial \Delta R}{\partial \Delta L_T} > 0, \qquad \frac{\partial \Delta R}{\partial \Delta C} < 0$$

$$\frac{\partial \Delta R}{\partial C} = 0$$

As a result, we can naturally confirm following facts under the above-mentioned assumptions.

1. The increase of the difference of disaster probability Δp which results from the improvement of fireproof performance of fireproof building promotes fire-proof improvement.

2. The increase of whole-period-profit M_T promotes fire-proof improvement.

3. The increase of the difference of total profit in the whole period $\Delta \mathbf{M_T}$ promotes fire-proof improvement.

4. The increase of whole period loss L_T promotes

fire-proof improvement.

5. The increase of the difference of total loss in the whole period ΔL_T which results from the improvement of fire prevention performance of fireproof building promotes fire-proof improvement.

6. The increase of the difference of initial construction cost ΔC obstructs fire-proof improvement.

7. The move of initial construction cost C in itself does not influence fireproof improvement.

2.3 The effect of specification of a floor-area ratio

From the result of 2.2, our model seems to be not far from reality. Then, we try some interpretations from this formulization.

In an actual city in Japan, there are many systems such as use zoning system, floor-area ratio regulation system, fire protection zone system, etc.

Fireproof improvement is directly controlled in fire protection zone because the building is limited to fireproof building when people build a building in this zone. However, there are not much clear examinations about the remote effect on fireproof improvement which is exerted from use zoning system and floor-area ratio regulation system.

In what follows, the effect of fireproof improvement by floor-area ratio regulation system is mainly studied. We discuss two zones as typical types as follows.

1) Low floor-area ratio zone
2) High floor-area ratio zone.

At first, we discuss the case in low floor-area ratio zone. In this zone, the building becomes same size whether fireproof building or wooden building. Hence, the building is considered to earn same quantities of profit whether fireproof building or wooden building. So the difference between the two appears in loss and initial construction cost.

Hereafter, some of signs are omitted on the basis of wooden building in the low floor-area ratio zone. Total profit of wooden building and fireproof building in low floor-area ratio zone are represented as follows.

$$R_L^{(w)} = (1-p)M - pL - C \qquad \text{----- (19.1)}$$

$$R_L^{(p)} = (1-p)M - p(L-\Delta L) - (C+\Delta C) \qquad \text{----- (19.2)}$$

The difference between above two is represented as follows.

$$\Delta R_L = R_L^{(p)} - R_L^{(w)} = p\Delta L - \Delta C \qquad \text{----- (20)}$$

Next, we discuss the case in high floor-area ratio zone. When a wooden building is chosen in this zone, the building size is same as the case in a low floor-area ratio zone because multistoried building cannot be built technically by wooden building.

On the other hand, when fireproof building such as reinforced concrete building is chosen, the building size can become larger by the verticalization and the profit can become bigger. An initial construction cost can become bigger too.

Generally, the more the building goes vertical, the more profits increase, so the profits increment by a verticalization ΔM_H is much larger than construction cost increment ΔC_H.

Total profits in high floor-area ratio zone are represented as follows.

$$R_H^{(w)} = (1-p)M - pL - C \qquad \text{----- (21.1)}$$

$$R_H^{(p)} = (1-p)(M+\Delta M_H) - p(L-\Delta L) - (C+\Delta C_H) \qquad \text{----- (21.2)}$$

Then

$$\Delta M_H - \Delta C_H \gg 0 \qquad \text{----- (22)}$$

$$\Delta R_H = (1-p)\Delta M_H + p\Delta L - \Delta C_H \gg 0 \qquad \text{----- (23)}$$

Eqn (22) is considered to implicate following equation when probability p is small enough.

$$(1-p)\Delta M_H - \Delta C_H > -\Delta C \qquad \text{----- (24)}$$

When above inequality is formed,

$$\Delta R_H - \Delta R_L = (1-p)\Delta M_H - \Delta C_H + \Delta C > 0. \qquad \text{----- (25)}$$

In short, the conditions of fireproof improvement in the high floor-area ratio are easily satisfied than in the low floor-area ratio. Hence, it turned out that there is some possibility to control fireproof improvement indirectly.

4. CONCLUSIONS

Our proposed model seems to be not far from reality since some basic comparative relations were confirmed. As a result of interpretations about the effect of specification of a floor-area ratio, it became clear theoretically that a floor-area ratio system can be used for control of fireproof improvement.

Sixth International Conference on Urban Earthquake Engineering
March 3-4, 2009, Tokyo Institute of Technology, Tokyo, Japan

RELIEF, RECONSTRUCTION AND REHABILIATION FROM THE SICHUAN EARTHQUAKE, CHINA

Wanglin Yan[1], Yoshiyuki Inaba[2] and Akihiro Oba[3]

1)Professor, Faculty of Environmental and Information Studies, Keio University, Japan
2)Doctoral Student, Graduate School of Media and Governance, Keio University, Japan
3)Master Student, Graduate School of Media and Governance, Keio University, Japan
yan@sfc.keio.ac.jp, yi@sfc.keio.ac.jp, perry@sfc.keio.ac.jp

Abstract: The May 12, 2008 Wenchuan earthquake had attacked the land of abundance, Sichuan, caused massive damage. It killed tens of thousands of people and severely damaged the province's industry and infrastructure. After the earthquake, the whole China as well as people all over the world have joined hands in the most difficult and vital moments to fight against the catastrophe. This paper reports the outline of the earthquake and the efforts of relief, reconstruction and rehabilitation by the Chinese central and local governments as well as people.

1. INTRODUCTION

Sichuan Province is located on the upper reaches of the Yangtze River in China's western heartland. Home to more than 87.7 million people, Sichuan is the third most populous province in China, and its plentiful natural resources are spread over 485,000 square kilometers of diverse landscape. As the largest commodity and raw materials market in western China, Sichuan province alone accounts for approximately a quarter of western China's grain production, gross industrial output, and retail sales of consumer goods. Sichuan was the first among the western provinces and autonomous regions to exceed the RMB 1 trillion in GDP, contributing 4 percent to China's national GDP in 2007, and is expected to maintain an annual growth of 12 percent in the next 10 years. Sichuan's favorable investment environment is complemented by pleasant living conditions, and is consistently chosen as one of China's most livable provinces.

Chengdu, the capital city of Sichuan province has been implementing the government-designated Urban-Rural Integration and Co-development Program since 2003. In the city's more developed rural areas, the government has implemented three major reforms: concentrating scattered industries and small businesses into developed zones; encouraging the rural population to move to urban areas; and reprioritizing land to be used for larger-scale projects. In rural areas that are not yet ready for urban-rural integration, the government has taken measures to industrialize traditional agricultural practices, construct rural infrastructure, and reduce rural poverty (McKinsey & Co., 2008).

Such a *land of abundance* on the way toward modernization was unfortunately attacked by the Wenchuan Earthquake on May 12, 2008, caused massive damage. It killed tens of thousands of people and severely damaged the province's industry and infrastructure. This was, undoubtedly, the single most destructive natural disaster that China has seen in recent decades. After the earthquake, the whole China as well as people all over the world have joined hands in the most difficult and vital moments to fight against the severe catastrophe. This paper reports the outline of the massive earthquake and the efforts of relief, reconstruction and rehabilitation by the Chinese central and local governments as well as people.

2. DAMAGES OF THE EARTHAQUAKE

Sichuan Earthquake was the most destructive one with the widest affecting scope and most serious disaster-induced losses ever since the founding of the People's republic of China in 1949. **Magnitude and intensity:** The earthquake measured 8.0 degrees in magnitude and 11.0

degrees in seismic intensity on the Richter scale (Fig.1). After the major quake on May 12, the area suffered nearly 14,000 aftershocks throughout the following month. The earthquake also caused a large number of secondary disasters such as landslides, mud-rock flow, barrier lakes, etc.

Casualties: As of August 7, 2008, the disaster had killed 69,222 people, wounded 374,638, and left 18,176 missing. Government authorities and volunteers were able to rescue 83,988 survivors from the ruins. In total, 29.8 million people are estimated to have been affected by the disaster.

Geographic impact: The earthquake severely damaged an area of over 250,000 square kilometers. In particular, six municipalities or prefectures were extremely hard-hit: Chengdu, Deyang, Mianyang, Ya'an, Guangyuan and the Aba Autonomous Prefecture (Fig.2).

Economic impact: Direct economic losses are estimated at RMB 1.1 trillion, and a total of 21,167 companies were affected. Collapsed and damaged residences numbered 4.4 million, of which 3.5 million were rural houses and 0.98 million were urban residences. Public service facilities, factories, and cultural heritage sites suffered varying degrees of destruction. 139 counties in Sichuan were affected by the earthquake. To better assess the overall damage, affected counties were classified into three categories depending on the severity of the destruction: "extremely hard-hit", "hard-hit", and "affected."

Extremely hard-hit areas: comprise 10 counties, namely Wenchuan, Beichuan, Mianzhu, Shifang, Qingchuan, Mao, An, Dujiangyan, Pinwu and Pengzhou counties. The State Council has designated an one-on-one scheme that all ten of these counties will receive post-quake reconstruction assistance for the next three years from 10 more-developed provinces and municipalities in eastern and southern China (NDRC, 2008).

Fig.1 the Yingxiu Town, the epicenter

Hard-hit areas: comprise 29 counties in total, including Li, Jiangyou, Heishui, Chongzhou, Jiange, Songpan, Xiaojin and Hanyuan counties. These eight counties are also receiving reconstruction assistance from eight more developed provinces and municipalities. Among the remaining 21 hard-hit areas, 13 of them will receive reconstruction assistance from 13 non-affected or lightly-affected areas in Sichuan

Affected areas: include 100 additional counties that suffered losses during the earthquake. Even though the damage sustained in these areas may be less extreme compared to the counties mentioned above, the extent of the destruction in these areas exceeds what is commonly estimated.

Earthquake Induced Landslides: Satellite image

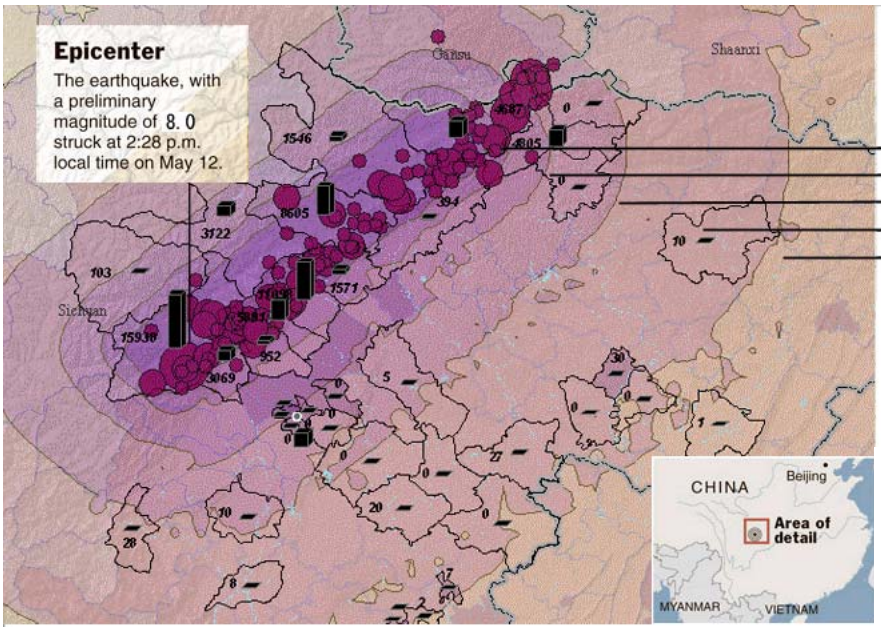

Population in affected zones

LEVEL OF PERCEIVED SHAKING	POTENTIAL STRUCTURAL DAMAGE	ESTIMATED POPULATION
Extreme	Very heavy	606,000
Violent	Heavy/very heavy	668,000
Severe	Moderate/heavy	3,962,000
Very strong	Moderate/heavy	12,351,000
Strong	Light/moderate	15,409,000

Edited by the author.
Map source: Harvard University CGA, http://cegrp.cga.harvard.edu/people
Damage zones and population estimated by the US Geological Survey. Newyork Times, May 12, 2008.

Fig.2 the geographic coverage and estimated damages of the Sichuan Earthquake

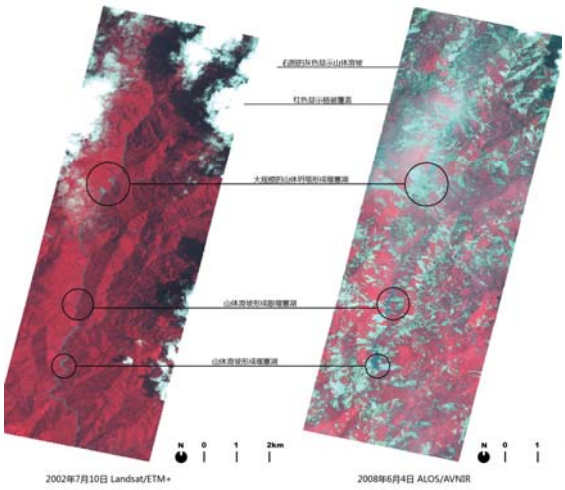

Fig.3 Landslide triggered by the quake

showing hundreds of landslides that were triggered by the event. These slides wiped out thousands of homes, killed thousands of people and blocked rivers with at least 30 unstable dams. The false-color ALOS/AVNIR images (right) in Fig.3 show the landslides in the northeast part of Dujianyan City, in which red indicates vegetation; blue-gray indicates bare ground, buildings, and paved areas; and deep blue indicates water.

3. RELIEF ACTIONS BY GOVERNMENTS

China had achieved a great progress in quake relief and minimized losses from the disaster as Xinhua, the Chinese news agency reported on Sep 16, 2008 (Wen, 2008). According to Premier Wen, rescuers dug out 84,000 survivors from the ruins, moved more than 1.486 million people to safer places and gave medical treatment to 2.96 million injured people. Another 96,000 were sent to hospitals, of whom more than 92,000 were treated and discharged. The government has provided financial aid to 10.584 million people who had financial problems due to the quake, including 286,000 orphans, elderly and handicapped people living alone. It had resettled 15.1 million people whose houses were damaged or whose neighborhoods became dangerous due to the earthquake. In the first three months after the quake, the government distributed 500 grams of grain and 10 yuan (about 1.47 U.S. dollars) for every quake survivor every day in financial difficulty. In the next three months, the government had continued financial aid to these people, including 200 yuan per person and 600 yuan for those living alone every month. The government had also paid 5,000 yuan to the families of the deceased. The government has tried various means to provide temporary housing for survivors, ensure local schools reopen on time and safeguard stability in the quake areas. Meanwhile, most of the infrastructure in the area has been repaired and restored to normal operation, including all major railways, 90 percent of the power transmission lines, all public telecommunications services, the majority of local radio and TV networks, local water conservation facilities, and 97 percent of water plants and water-supply pipelines, which had ensured the supply of drinking water. Strenuous efforts were made to prevent or minimize geological disasters caused by the quake, such as the successful treatment of "quake lakes".

The central government had set up a quake rehabilitation fund and had allocated 70 billion yuan for its use in 2008. The State Council (cabinet) had also issued a series of financial policies for rehabilitation.

4. RECONSTRUCTION PLANS

4.1 Reconstruction plans at central and provincial level

From the later period of rescue activities after the earthquake, the governments have moved quickly to reconstruction and rehabilitation. The Sichuan provincial government has laid out the overall reconstruction objectives as follows:

Complete restoration in three years: Rebuild urban and rural residences, reconstruct all basic public services and infrastructure, restore living conditions for the majority of the population, help socioeconomic development reach or exceed pre-quake levels, and lay a solid foundation for sustainable development.

Revitalize development in five years: Develop a distinctive geographical blueprint for industrial regions, optimize industry structure, establish well-planned towns and villages, install infrastructure to support basic living needs, foster economic advancement and promote higher living standards.

Build a moderately prosperous society in ten years: Speed up the development of areas affected by the disaster in order to take them to a level of moderate prosperity along with the rest of the province.

This has been built upon the basic reconstruction principles as laid out in the *State Overall Planning for Post-Wenchuan Earthquake Restoration and Reconstruction* (NDRC，2008)*:*

- Bear in mind the concept of people first, and give top priority to people's well-being
- Respect nature by arranging a scientific planning
- Make comprehensive considerations and arrangements to ensure coordinated development

- Make mechanism innovations and conduct collaborative construction
- Place safety first and ensure quality
- Strictly practice frugality and protect farmland
- Inherit and carry forward culture, and protect ecology
- Adapt to the local conditions and implement the overall planning in different phases

The government had announced a plan on rehabilitation of 18 badly-hit counties and towns in Sichuan and quake areas in Gansu and Shaanxi provinces, with assistance of 19 provinces and municipalities.

4.2 Reconstruction plan at local level

Under the advice of central and provincial governments, local governments of counties and towns have moved to the post-quake reconstruction quickly, too. Dujiangyan City, a world natural and cultural heritage city with the world famous Dujianyan irrigation system and the Daoist origin of Qingchengshan was a representative.

On May 29, just three weeks after the quake, the Dujiangyan city government and the Bureau of Urban Planning and Management of Chengdu have jointly called for the post-earthquake reconstruction conceptual plan to the international community. 47 planning and design institutes or laboratories of universities of the world have responded to and 10 joint teams were formed to make proposals. We the University of Tokyo, Keio University and Southwest Jiaotong University have established the only Japanese-Chinese joint team and attended the activities. With a short field trip and instructions by the local government held on June 8-9, we worked at the project within one month. A presentation conference was held at Dujianyan City on July 12 and 13 with the attendance of local officials, urban planning and design experts and distinguished scholars. Although time was very limited, all the teams have worked hard and devoted. The proposed conceptual plans cover from urban forms, transportations, green spaces, industry, housing reconstruction and disaster preventions etc.

The conceptual plan by our Japanese-Chinese team was based on the concept of *New Origin of the Abundant Land*, an ecological and sustainable world heritage city in the Western Sichuan Basin. We have reviewed the current master plan with population prediction, allocated residents and immigrants in built-up districts and a new town area. The urban and rural form was designed with the vision of compacted city, conserving the abundance of biodiversity in mountain area and the historical irrigation systems in plain area, saving the productive paddy land and controlling the urban sprawl. A concept called *Water-town Community* wad applied for the rehabilitation of the downtown area (Fig.4). With this concept, the downtown area was divided into 28 water-town communities by the division of fan-frame-styled canal system and ring road network systems. The green spaces, housing and urban facilities were allocated along the canal network. The scrub of damaged building and the temporary and permanent houses would be constructed within community, which is mostly expected for by sufferers.

The conceptual plans from 10 teams were full of new concepts, new operations and additional opinions for governments. They were integrated by the Institute of Urban Planning and Design, Tongji University and authorized at the end of September.

5. Implementation and rehabilitation

In accordance with the objectives of “completing major works of restoration and reconstruction within about 3 years” issued in General Plan for Restoration and Reconstruction Work after Wenchuan Massive Earthquake by State Council (NDRC, 2008), currently Sichuan government and people are speeding up to compile the plans focusing on “5 major reconstructions” (Wei, 2008):

Firstly, housing reconstruction. Up to November 12, the number of rural housing under reconstruction in Sichuan province amounts to 685,000 households, taking up 52.6% of the total; the number of rural housing already completed reaches 195,000 households, taking up 15.5% of the total; those with repair and reinforcement work being completed amounts to 1.94 million households, taking up 87.8% of the total; the number of permanent houses under construction in townships totals 39,000 sets (households) with 92,000 sets (households) already being reinforced.

Secondly, facility reconstruction. The governments have actively pushed forward schools, hospitals and other public utilities reconstruction as well as infrastructure reconstruction such as highway and irrigation projects, of which 4,580 reconstruction projects are already in process. Among all the projects, 1,363 schools have been reconstructed or currently under reconstruction, taking up 40.8% of the total number to be reconstructed; another 340 medical and health care institutions are under construction; construction of 14 traffic projects including Guang-Shan Expressway and National Highway 317 have also been activated.

Thirdly, industrial reconstruction. Of the total 4,812 above-scale industrial enterprises that are earthquake-affected, currently 96.4% have

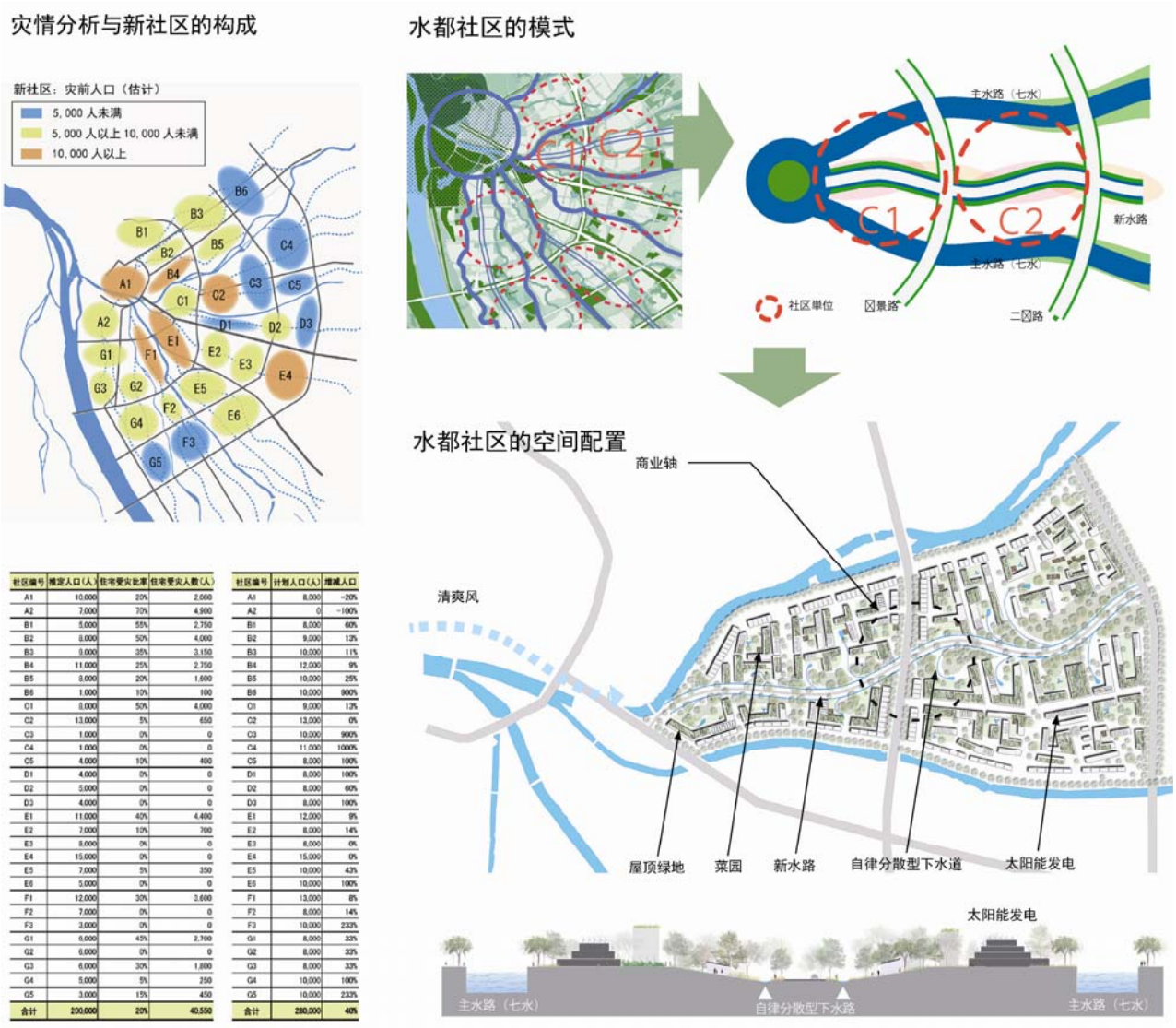

Fig. 4 the Conceptual reconstruction plan made by Sino-Japanese team

basically resumed production; over 94% of commercial circulation businesses and service networks have resumed operation; the efforts of reviving tourism industry has produced initial results.

Fourthly, urban and township reconstruction. The compiling work of urban and rural planning is supposed to be completed by the end of this year. A group of urban public utility projects have already been activated ahead of schedule. Site selection for 25 townships to be relocated has already begun. As for the 3 counties of Beichuan, Wenchuan and Qingchuan as well as the 2 townships of Yingxiu and Hanwang that have drawn everybody's attention, China Academy of Urban Planning and Design has arrived in a timely manner to start compiling after the site selection for Beichuan County was replied to. The initial stage of planning for Wenchuan and Qingchuan counties as well as the 2 townships of Yingxiu and Hanwang has already been completed with good results.

Efforts are under way to organize experts and specialists to conduct evaluation of forest, land and plantation losses in Minjiang River and Jialing River areas so that the compiling work of the ecological rehabilitation planning in these river areas, the restoration and reconstruction planning for the natural habitat of giant pandas and the construction of giant panda corridors can be completed at the soonest time possible with effective execution being carried out. In addition, the reconstruction of people's spiritual home also stays at the focus of attention. Governments have actively implemented psychological rehabilitation projects and carried out over 200,000 person-times of mental health service in the quake-stricken areas. Special lectures on mental intervention have been arranged and more than 600 leaders in the quake-stricken areas have received the training and mental intervention. The project of Safeguarding Qiang Nationality Cultures is in nice and orderly

Fig.5 the plan of XiangE Town (left) and the rebuilding site of XiangE Primary School aided by Shanghai within the One-on-One Support Scheme

progress and the preservation and construction work of earthquake ruins are in full swing.

Up to the end of October, RMB34.49billion of post-disaster restoration and reconstruction funds from central financing has been channeled to Sichuan province; State Development Bank of China and other 4 major state-owned banks have granted a total loan of RMB64.73billion as relief and reconstruction funds; provinces (cities and districts) of pairing-assistance as well as Hong Kong and Macau have reached 1,152 project agreements with Sichuan province with the total funds for reconstruction assistance amounting to almost RMB27billion. Currently, 341 aid projects have been activated with 171 projects already under way.

The Central Government will deploy RMB70 billion from the central budget to set up a Post-quake Restoration Reconstruction Fund. Similar capital injection will be made in the next two years. At the local level, in accordance with the "Post-Wenchuan Earthquake Restoration and Reconstruction One-on-One Support Scheme" (the One-on-One Support Scheme) promulgated by the State Council on 11 June 2008, 18 provinces and municipalities directly under the central government in central and eastern China are designated to support the 18 hard-hit counties/municipalities in Sichuan. Support for reconstruction of the counties/municipalities/ districts not included in the One-on-One Support Scheme will be undertaken by the local governments of the concerned provinces. Under the One-on-One Support Scheme, every year, each province and municipality should offer aid in kind worth at least 1% of its local government revenue for the past year.

6. REMARKS

The central government has recently unveiled 10 policies and measures to expand domestic demand and fuel economic growth, of which the most important ones focus on accelerating post-disaster restoration and reconstruction as well as implementing livelihood projects. Sichuan Provincial Government has decided to center on the rebuilding of beautiful homes after the disaster to expedite the construction of a highland of economic development in western China and try to accomplish a total investment of over RMB3000billion by 2010, of which about RMB790billion will be in place in 2008 and about RMB1200billion in 2009. The journey of the post-disaster restoration and reconstruction is still long under the global economic crisis but the chances are over there.

REFERENCE

McKinsey & Co., 2008, relief, reconstruction and renewal: Report Report on International investment and assistance Needs in Sichuan's Post-quake Restoration and Reconstruction.

NDRC (National Development and Reform Committtee, China), 2008, The State Overall Planning for Post-Wenchuan Earthquake Restoration and Reconstruction (Public Opinion Soliciting Draft), 2008.8.11.

WenJiabao, 2008, Wen speaks on relief, rehabilitation in quake-hit areas. Sep 16, 2008. http://www.gov.cn/english/2008-09/16/content_1097017.htm. [last accessed: Feb 1, 2009].

Wei Hong, 2008, press release by Wei Hong, Vice-governor of Sichuan Province, http://www.china.org.cn/government/scio-press-conferences/2008-11/21/content_16806022.htm. [last accessed: Feb 1, 2009].

Sixth International Conference on Urban Earthquake Engineering
March 3-4, 2009, Tokyo Institute of Technology, Tokyo, Japan

ANALYSIS OF THE VALUE OF INFORMATION IN THE DESIGN OF RESILIENT WATER DISTRIBUTION NETWORKS

Maud Comboul[1], and Roger Ghanem[2]

1) PhD candidate, Dept. of Civil and Environmental Engineering, University of Southern California, USA
2) Professor, Dept. of Civil and Environmental Engineering, University of Southern California, USA
comboul@usc.edu, ghanem@usc.edu

Abstract: The monitoring of water distribution networks by means of sensor placements is intended to act as an early warning system. It is designed to minimize the impact on the network of the potential infiltration of hazardous contaminants. Yet the absence of information about possible contamination events including the knowledge of the injection sources, contaminant types or mass and time of pollution as well as the variability of water network input parameters, such as the nodal demands and the pipe roughness coefficients raise several issues on the design approach to pursue. Through the use of submodular cost functions, which allows us to solve the optimization problem with the improved Greedy algorithm formulated by Leskovec et al. (2007), we were able to introduce stochastic water demands in our simulation. We also framed the problem considering imperfect sensor sensibility while maintaining submodularity. The results showed the high sensitivity of the obtained placements upon the uncertainty quantification of the input parameters as well as the definition of the sensor capabilities.

1. INTRODUCTION

Unobserved contamination will rapidly spread through a water distribution network, thereby potentially harming consumers. Hence networks should be monitored at some locations to prevent the infiltration of a pollutant from spreading undetected. The optimal sensor placement in a water distribution network aspires to minimize the impact of such pollution via the early detection of the contaminant. This NP-hard optimization problem has been the subject of various investigations; see Ostfeld and Salomons (2004), Berry et al. (2005), Carr et al. (2006), Watson et al. (2006), Propato (2006), Shastri and Diwekar (2006) and Leskovec et al. (2007). The primary difficulty comes from the absence of information about the potential contamination events. Because it is impossible to predict before the event occurrence where and when it will happen in the system, the majority of the solution approaches perform the optimization over a very large set of predefined contamination scenarios. Consequently, these optimization methods processed on large networks (with thousands of nodes) require substantial computations. Solution techniques vary from genetic algorithms (Ostfeld and Salomons (2004)) to heuristic approaches (Berry et al. (2005)). The high computational cost as well as the large number of contamination events has led Watson et al. (2006) to focus exclusively on the worst case scenarios. The choice over the possible damage mesures also generated much discussion (Watson et al. (2004), Krause et al. (2008)); several components can quantify the impact of a pollution on a water distribution network, including the detection time, the affected population and the amount of contaminated water. While most of the analyses consider sensors with perfect responsiveness to contamination, Berry et al. (2006) formulated the problem considering imperfect sensors. Another important issue relates to the variability of the flow: small perturbations in the nodal demand values can extensively modify the flow pattern causing different spread of the same contamination scenario. Thus Shastri and Diwekar (2006) have followed a stochastic approach assuming some network input parameters, such as the nodal demands, random rather than deterministic. Several sources of uncertainty in water distribution networks introduce a number of challenges to solve the optimal sensor placement problem, computational viability being one of them. Krause et al. (2008) formulated the problem using cost functions having submodular properties; thus the authors were able to develop a faster Greedy algorithm to find a near optimal solution. This formulation allowed us to perform a thorough study, introducing stochastic parameters in the hydraulic simulations as well as the assumption that sensors can fail to respond to a contamination. The different outcomes obtained using diverse analysis assumptions showed that the resulting sensor placements are highly sensitive to those hypothesis.

2. MATHEMATICAL REPRESENTATION

A water distribution network is embodied in a graph $G(V, E)$ where the nodes $V = v_1, v_2, ..., v_n$ represent the junctions, the sources and the reservoirs while the edges $E = e_1, e_2, ..., e_m$ correspond to the linking pipes. The way the water flows through the network is controlled at all times by the nodal demands, which evolve according to the time of the day, causing the flow to change speed and direction. Consequently, the sensor placement problem requires the ability to perform hydraulic simulations to evaluate the flow pattern at any time, as well as water quality simulations to track how the different contamination scenarios spread through the system. EPANET object library in C++ served as the simulation tool. Several properties of the network were controlled during the simulations; for example, the nodal base demands and the time patterns associated with the nodes were perturbed for the stochastic analysis and the contamination source, mass and time were changed for each scenario. We define the set of all "possible" contamination scenario I, where each scenario $i \in I$ consists of a source, a contaminant type and mass as well as a time and probability of occurrence $P(i)$. During a water quality simulation, contaminant particles are tracked passing through the network allowing for the construction of time series describing the evolution of the contaminant in terms of its concentration at every node: $\forall v \in V$ and $\forall i \in I$, we denote the time series $c_i(v,t), \quad t \in [0,T]$, where T is the total simulation time. For each node, we are mostly interested in the time of the first non-zero concentration, which would also be the time of detection if a sensor was located at that node. In other words, we define $T_i(v)$ to be the time for scenario i to reach node v. Therefore $T_i(v) = t$ such that $c_i(v,t) > 0$ for the first time. Let S be the set of all possible sensor locations. Since the sensors are placed at the nodes, $S \subseteq V$ in our formulation. A $k-$sensor placement A, where $k \leq |S|$ is a subset of S. For a given scenario i, the detection time for a sensor placement A is defined by $T_i(A) = \min_{s \in A} T_i(s)$. In addition, the impact associated with a particular sensor placemant A for a given scenario i is denoted by $\pi_i(T_i(A))$. The impact function π depends on what is to be minimized; in the past, measures of damage have included detection time, consumed or delivered contaminated water and affected population. Usually, it is computed as a sum of the chosen units over the contaminated nodes between the contamination time and the detection time.

3. OPTIMIZATION PROBLEM

3.1 Stochastic system

Given a fixed number k of sensors, the question remains where would they provide the best protection against a potential contamination? Knowing that the set of all possible contamination scenarios is very large (not only could it happen at any node but more importantly at any time, at any concentration level and of any kind), this question raises the issues of defining a representative set of scenarios as well as quantifying damages in a water distribution network after such an event. Abstractly, let $\pi_i(t)$ be the measure of damage if scenario i is detected at time t (if the intrusion is not detected, then $t = \infty$). π is nondecreasing, i.e. $\pi_i(t) \leq \pi_i(t'), \quad \forall t < t'$. One key assumption that allows π to be essentially a function of time, is the idea of global alarm; as soon as a contamination is detected, a global alarm is raised, which prevents further consumption of polluted water. Due to some interesting properties useful to our solution method, we consider the maximization of the damage reduction function instead of the minimization of the impact function itself. For all of scenario i, the damage reduction function generated by a subset of sensor placement A is expressed as follow:

$$R_i(A) = \pi_i(\infty) - \pi_i\left(T_i(A)\right) \tag{1}$$

Let us denote by $R(A)$, the total impact reduction for a sensor placement A, then:

$$R(A) = \sum_{i \in I} P(i) R_i(A) \tag{2}$$

Where $P(i)$ is the probability of occurence for scenario i. As mentioned in the introduction, the flow in water distribution networks can be rather sensitive to fluctuations in the nodal demands. Slight perturbations in the demands can cause the watercourse to change direction in several pipes. Because the way pollution spreads through a network directly follows the flow pattern, the same scenario can draw very different impacts for distinct demand patterns. Thus the efficacy of a particular sensor placement against a specific scenario may be diminished with an altered flow pattern. To account for variability within networks, we performed Monte Carlo simulations with random demands. Every demand pattern sample consists of a perturbed nodal base demand as well as a perturbed nodal time pattern. We used the truncated Gaussian distribution $\tilde{d_v} \sim N(d_v, \epsilon)$, in which the negative values are removed, as well as the Uniform distribution $\tilde{d_v} \sim U(d_v(1-\delta), d_v(1+\delta))$ with different noise levels to generate the samples (d_v and $\tilde{d_v}$ are respectively the original demand value at node v and the new perturbed demand value used in the MC simulations). For each demand realization, we perform a hydraulic simulation and for each contamination scenario we perform a water quality simulation. Finally, we may now formulate our k-sensor placement optimization problem as the set $A \subseteq S$ that maximizes the expected damage reduction over all demand patterns and all scenarios. For instance, we have n samples and for each one, we can compute the total impact reduction for a placement A denoted by $R^{(n)}(A)$. The new optimization formulation is the following:

$$\begin{aligned} \max_{A \subseteq S} \quad & \sum_{j=1}^{n} R^{(n)}(A) = \max_{A \subseteq S} \quad E[R(A)] \\ & |A| = k \end{aligned} \tag{3}$$

This formulation is equivalent to finding A that minimizes the expected damage: $\pi(A) = \sum_{i \in I} \pi_i\left(T_i(A)\right)$.

However the damage reduction function presents some advantages over the damage function itself because it was shown in Krause et al. (2008) to be submodular.

3.2 Imperfect sensor sensibility

To this point, the analysis supposes perfect sensor sensibility, in other words the sensors are theoretically capable of detecting any kind of contaminant at any concentration level. However, the possible failure of a sensor or a group of sensors to detect a contamination is likely to happen if the concentration levels are too low and depending on the chemical type. By imposing a weight factor denoted by $p_i(A)$ for a sensor placement A, which increases with the pollution level at the detection time, the optimization will now favor placements with some elements located closer to the source of higher impact scenarios. Accordingly, we modified the impact reduction function from **??** the following way:

$$\begin{aligned} \max_{A \subseteq S} \quad & R(A) = \max_{A \subseteq S} \sum_{i \in I} P(i) p_i(A) R_i(A) \\ & |A| = k \end{aligned} \tag{4}$$

4. SOLUTION METHOD: THE GREEDY ALGORITHM

Exhaustive searches to find the optimal $k-$sensor placement over all possible placement combinations in water networks is NP-hard and would quickly become computationaly inviable as the number of nodes increases. For that reason, alternative algorithms must be used in order to reduce the computational cost, even if it results in suboptimal solutions. The optimization formulations all possess an interesting common property: the damage reduction function presents some advantages over the impact function because it was shown in Krause et al. (2008) to be submodular. Thus, we know that for all subsets $A \subseteq B \subseteq S$ and element $s \in S$, the properties of the damage reduction function are the following:

1. $R(\varnothing) = 0$
2. $0 \leqslant R(A) \leqslant R(B)$
3. $R(A \cup \{s\}) - R(A) \geqslant R(B \cup \{s\}) - R(B)$

The properties on the reduction function of being non-decreasing and submodular allow the use of the Greedy algorithm to find a near-optimal solution to our optimization problem. The idea behind the Greedy algorithm is simple. It sequentially adds the best sensor location to an existing placement A, starting with the empty set. However it was proved in Nemhauser et al. (1978) that the greedy algorithm produces near-optimal solutions when the objective function is non-decreasing and submodular. Furthermore, they were able to quantify near-optimality and showed that the set A_G resulting from this method was such that $R(A_G) \geqslant (1 - \frac{1}{e})R(A^*)$, where $A*$ is the optimal k-sensor placement. Let T_{qual} be the computation cost to run a water quality simulation using EPANET object library, the total computational cost is now reduced from $O\left(\binom{|S|}{k} + |I|T_{qual}\right)$ to $O\left(k|S| + |I|T_{qual}\right)$

Algorithm 1 Greedy(S,A,s)

$A \leftarrow \emptyset$
for j from 1 to k **do**
  $s^* = argmax_{s \in S} R(A \cup \{s\}) - R(A)$
  $A \leftarrow A \cup \{s^*\}$
end for

Using the submodular property furthermore, Krause et al. (2008) were able to reduce the amount of necessary evaluations of the reduction cost $R(A)$. Let $\delta_A(s) = R(A \cup \{s\}) - R(A), \quad \forall s \in S \setminus A$, notice that $\delta_A(s) \geqslant \delta_{A \cup \{s\}}(s'), \quad \forall s' \in S \setminus A \cup \{s\}$ by definition of submodularity. Therefore by sorting the possible sensor placements s in decreasing order of their associated $\delta_A(s)$, as the set A gets bigger, we do not need to reevaluate $\delta_A(s)$ for all s. It is likely that the sensor placement that is at the top of the queue will remain at the top after reevaluation and if not, only a few need to be reevaluated. The new algorithm is given in Algorithm 2.

Algorithm 2 Improved Greedy(S,A,s)

$A \leftarrow \emptyset$
for all $s \in S$ **do**
  insert $\delta(s) \leftarrow R(\{s\})$ into Q {Q is a queue sorted in decreasing order}
end for
$A \leftarrow s^*$ such that $\delta(s^*) = Q_{top}$
remove element at the top of Q
for j from 1 to k **do**
  repeat
    $\delta_{new}(s) \leftarrow R(A \cup \{s\}) - R(A)$ for s such that $\delta(s) = Q_{top}$
    remove element at the top of Q
    insert $\delta_{new}(s)$ into Q
  until $\delta_{new} = Q_{top}$
  $A \leftarrow A \cup \{s^*\}$ such that $\delta(s^*) = Q_{top}$
  remove element at the top of Q
end for

5. RESULTS AND DISCUSSION

In order to test how the variability in the demand patterns influenced the optimal placement, we completed a series of water simulations with different assumptions on the nodal demands. First, we assumed the demands were known exactly at all time. Then, we introduced randomness by generating the nodal demands and the associated time patterns following different probability distributions. We performed Monte Carlo simulations with either uniformly ($\sim U(d_v(1-\delta), d_v(1+\delta))$) or normally

($\sim N(d_v, \delta d_v)$) distributed nodal demand values, alternatively taking δ magnitudes of 0.1, 0.25 and 0.5. For each assumption on the demands, we run a water quality simulation for every potential contamination scenario. During the quality simulation, we measured the impacts $\pi_i(v)$ that a particular scenario has on the network if a sensor was placed at node v for all possible nodes $v \in V$. In the random demand cases, we computed $E[\pi_i(v)]$, the average impacts over all Monte Carlo simulations. In each context previously described, two sets of optimal sensor placements were found using the Greedy algorithm; one solution for the perfect sensor assumption and one for the imperfect sensor assumption. Finally, we measured how the different solutions performed in particular contexts of analysis by computing the impact or the impact reduction produced by a group of sensors.

The EPANET object library developed by the Environmental Protection Agency was used in C++ to perform all the hydraulic and water quality simulations needed for our problem. In addition, in all of the following results, the quantity to minimize was the affected population, which we assumed directly proportional to the nodal demand values. To simplify the notations, we will use "deterministic placement" (green arcs in figure 2) for the solution set obtained from the deterministic demands and the perfect sensors sensibility assumptions. "Stochastic placement" (red arcs in figure 2) will stand for the solution set obtained from the random demands and perfect sensor assumptions. Finally, "imperfect sensor placement" (blue arcs in figure 2) will denote the solution set obtained from the random demands and imperfect sensor assumptions. For each demand probability distribution, we performed 1000, 2500 and 5000 Monte Carlo simulations. Since the results obtained with 2500 and 5000 simulations consistently agreed with each other, we concluded that convergence was reached for 2500 Monte Carlo runs.

Figure 1 displays the impact function with respect to the number of sensors. All impact functions are monotonically decreasing with the increasing number of sensors. In the top figure, the analysis context assumes random demands and perfect sensor sensibility. It exemplifies that the impact generated with the deterministic placement is suboptimal compared to the stochastic placement. In the bottom figure, the analysis assumptions are random demands and imperfect sensor sensibility. The deterministic and the stochastic placements perform poorly in this context compared to the optimal imperfect sensor placement. In the imperfect sensor context, the impact functions have a much slower decrease rates than in the perfect sensor context, which implies that more sensors are needed to effectively protect the network in the imperfect sensor case. The bar plots 3 and especially 4, which show the impacts associated with particular scenarios, again demonstrate how the performance of a sensor placement set highly depends on the context in which it was generated. Notice how poorly the deterministic placement performs when the sensors have indeed an imperfect responsiveness to contamination. While perfect sensor placements were sensitive to the different kinds of uncertainty in the nodal demand values, the optimal imperfect sensor placement was robust to all probability ditributions and noise levels in the demands.

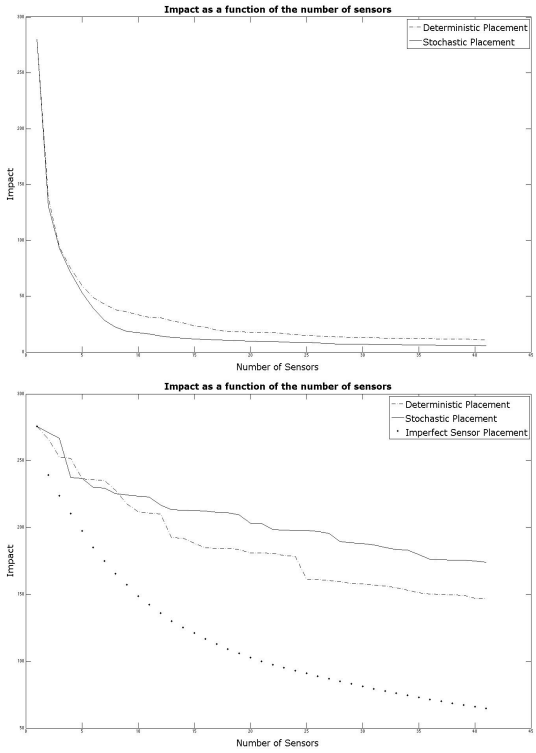

Figure 1: Impact reduction function with respect to the number of sensors. Top figure: perfect sensors and stochastic demands assumptions. Bottom figure: imperfect sensors and stochastic demand assumptions.

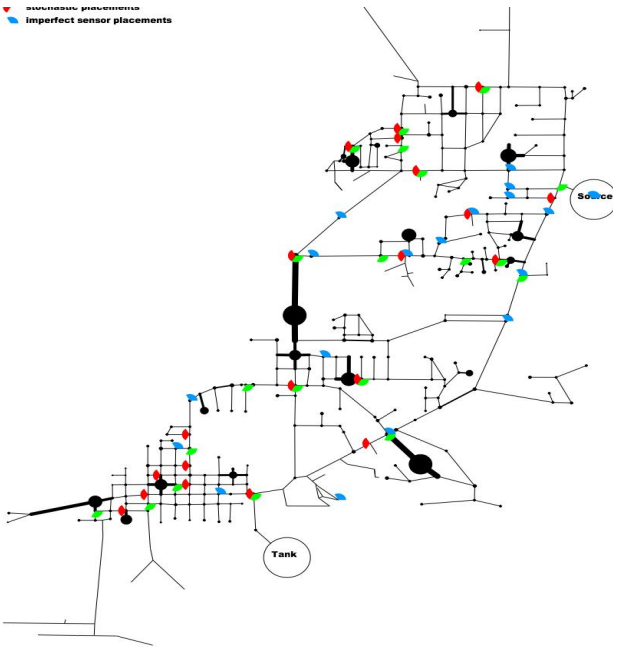

Figure 2: Sensor Placement Problem: 20 resulting sensor placements for the three different analysis approaches

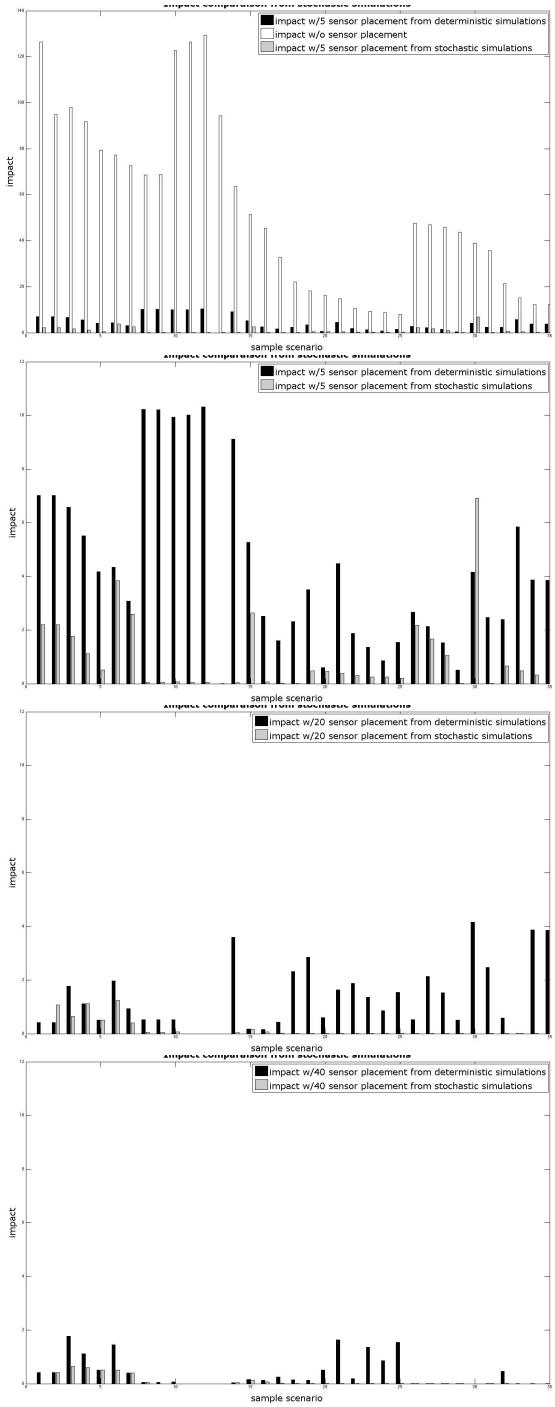

Figure 3: Perfect sensors: impact computed from the stochastic demand simulations as a function of sample scenarios. The impacts produced with the stochastic placement quickly decrease as the number of sensors increases. However, the deterministic placement generates a slower decrease

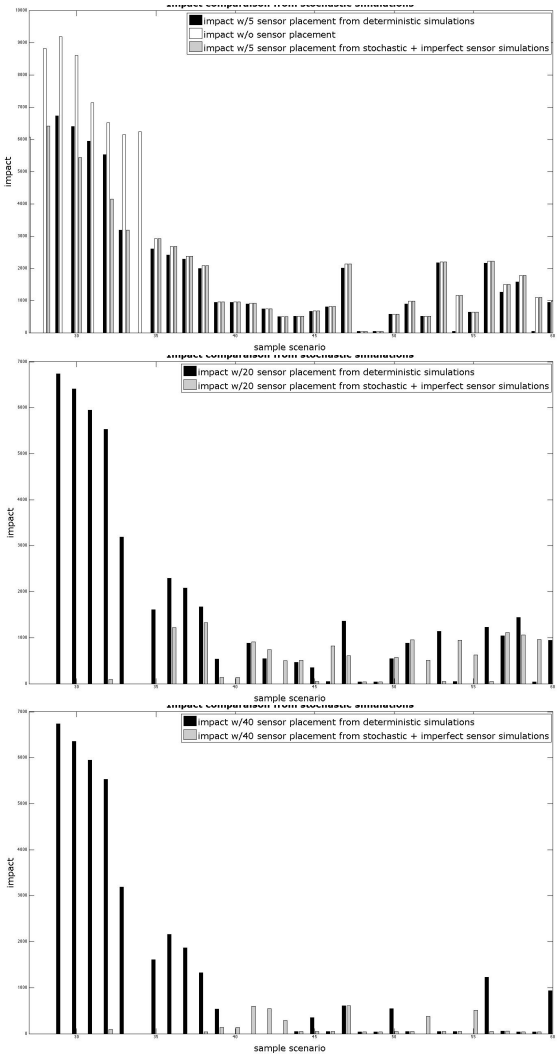

Figure 4: Imperfect sensors: impact computed from the stochastic demand simulations as a function of sample scenarios. In this case, 5 sensors are simply insufficient to reduce the impacts. While increasing the number of sensors greatly reduces the impacts produced with the imperfect sensor placement, the impacts only reduce slightly with the deterministic sensor placement.

6. CONCLUSION AND FURTHER WORK

The EPANET object library allowed us to build an efficient Monte Carlo simulation tool for the study of water network responses to uncertainty in the demand parameters and contamination scenarios. In addition, based on assumptions on the demand probability distributions and the sensor capabilities, we can compute the optimal sensor placement using the fast Greedy algorithm. We can draw several conclusions from our simulation results. First, the obtained sensor locations significantly depend on the initial hypothesis regarding the uncertainty in the water demands as well as the sensor sensibility (figure 2). Secondly, placements that are optimal in a particular context can perform poorly under distinct analysis assumptions (figures 3, 4 and 1). Finally,

the optimal imperfect sensor placement was more robust to fluctuations in the demand values than the perfect sensor placement. However, the number of sensors required to effectively protect the water network significantly increases in the imperfect sensibility case (figure 1).

Because the robustness of the resulting placements to uncertainty in the input parameters is an issue, the optimization formulation could be improved by adding a constraint on the variance of the impact reduction function. In addition, although we have assumed random nodal demands, we should also introduce randomness into the pipe roughness coefficients since these parameters greatly influence the flow patterns as well. To conclude, raising a global alarm as soon as a sensor detects pollution comes at a considerable fixed cost of shutting down the whole system. However, an alternative would be to allow for the containment of the threat by shutting off only the contaminated parts of the network. Hence, a cost associated with the control of the spread could be included in the optimization problem.

References

Berry, J., L. Fleischer, W. Hart, C. Phillips, and J. Watson (2005). Sensor placement in municipal water networks. *Water Resources Planning and Management 131*(3), 237–243.

Berry, J., W. Hart, V. Leung, C. Phillips, and J. Watson (2006). On the placement of imperfect sensors in municipal water networks. In *In Proceedings of the 8th Symposium on water distribution systems*.

Berry, J., W. Hart, J. Uber, and J. Watson (2006). Sensor placement in municipal water networks with temporal integer programming models. *Water Resources Planning and Management: special issue on drinking water distribution systems security*.

Carr, R., H. Greenberg, W. Hart, G. Konjevod, E. Lauer, H. Lin, T. Morrison, and C. Phillips (2006). Robust optimization of contaminant sensor placement for community water systems. *Mathematical Porgramming: Series A and B 107*(1), 337–356.

Krause, A., J. Leskovec, C. Guestrin, J. VanBriesen, and C. Faloutsos (2008). Efficient sensor placement optimization for securing large water distribution networks.

Leskovec, J., A. Krause, C. Guestrin, C. Faloutsos, J. VanBriesen, and N. Glance (2007). Cost-effective outbreak detection in networks. In *In 13th ACM SIGKDD International Conference on Knowledge Discovery and Data Mining*.

Nemhauser, G., L. Wolsey, and M. Fisher (1978). An analysis of the approximations for maximizing submodular set functions. *Mathematical Porgramming 14*.

Ostfeld, A. and E. Salomons (2004). Optimal layout of early warning detection stations for water distribution systems security. *Journal of Water Resources Planning and Management - ASCE 130*(5), 377–385.

Propato, M. (2006). Contamination warning in water networks: general mixed-integer linear models for sensor location design. *Water Resources Planning and Management 132*(4), 225.

Rossman, L. (1999). The epanet programmer's toolkit for analysis of water distribution systems. In *Annual Water Resources Planning and Management Conference*. Environmental Protection Agency.

Shastri, Y. and U. Diwekar (2006). Sensor placement in water networks: a stochastic programming approach. *Water Resources Planning and Management 132*(3), 192–203.

Watson, J., H. Greenberg, and W. Hart (2004). A multiple-objective analysis of sensor placement optimization in water networks. In *Critical Transitions In Water And Environmental Resources Management*.

Watson, J., W. Hart, and R. Murray (2006). Formulation and optimization of robust sensor placement problems for contaminant warning systems. In *Water Distribution Systems Analysis Symposium*.

Sixth International Conference on Urban Earthquake Engineering
March 3-4, 2009, Tokyo Institute of Technology, Tokyo, Japan

A BUSINESS CONTINUITY PLANNING OF TOKYO-TECH SUZUKAKEDAI

Masaki Fujioka [1], Hideki Kaji [2], Tatsuo Ohmachi [3], Saburo Midorikawa [3] and Yoko Iwaguchi [4]

1) Researcher, Center for Urban Earthquake Engineering, Tokyo Institute of Technology, Japan
2) Professor, Center for Urban Earthquake Engineering, Tokyo Institute of Technology, Japan
3) Professor, Dept. of Built Environment, Tokyo Institute of Technology, Japan
4) The Tokio Marine and Nichido Risk Consulting Co., Ltd.
fujioka.m.aa@m.titech.ac.jp, kaji@cuee.titech.ac.jp, ohmachi@enveng.titech.ac.jp, smidorik@enveng.titech.ac.jp
yooko.iwaguchi@tokiorisk.co.jp

Abstract: This paper describes a practical framework of a Business Continuity Plan (BCP) on university activities taking the Suzukake-dai campus of Tokyo Institute of Technology, Japan as a case study. This paper examines the properties of the BCP in general and the necessity for a university to devise the BCP for an unexpected catastrophic event. Finally, this paper presents a case study of the BCP targeted on a research building including 6 laboratories.

1. INTRODUCTION

1.1 What is BCP

The BCP (Business Continuity Plan) is a management strategy plan for organizations to recover and restart their core business after facing disasters. The BCP theory also enables the sustainability of the existing PDCA (plan-do-check-act) cycle. Gradually, the BCP takes important role on the field of corporate risk management. Besides, many companies believe the BCP as a plan of CSRs (Corporate Social Responsibilities).

Thus, the BCP deals the following four requirements;

1. Considerations of every incident that gives severe damage to businesses,
2. Acceptable interruption period taking account of overall business management,
3. Acceptable degree of loss for resuming the business within the above period,
4. Priority investments to fundamental function to be made before the events, and
5. Emergency response guideline for resumption.

1.2 BCP in University Management

There are several different approaches on the BCP between a profit based organization and an education oriented university. There are two major functions for university's operation – management operation and education operation. With regard to the completeness of

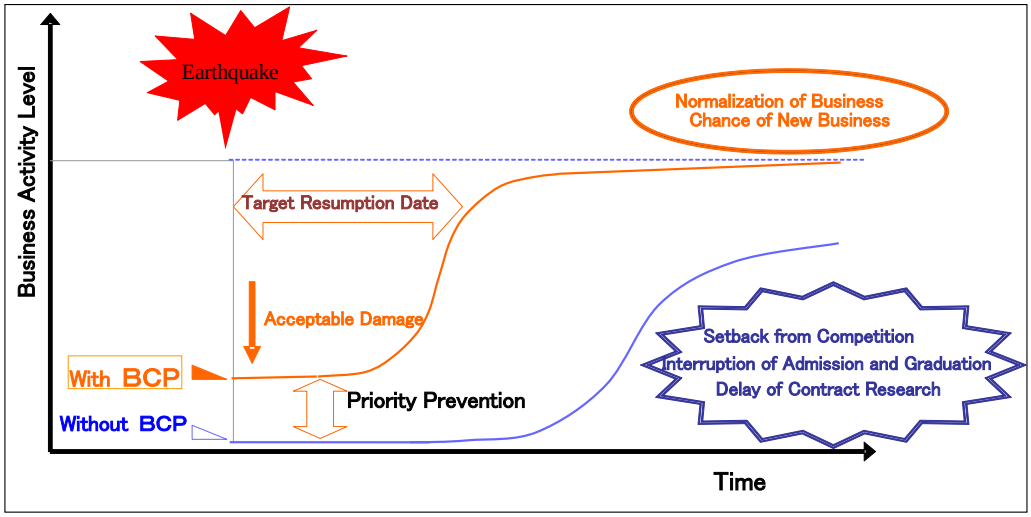

Figure1 Concept of BCP

BCP's execution, a university ought to take the different policies into account. Theoretically, making corporations' BCP follows the Top-Down rule, same with the structure of corporations' decision making. However, the management operation of a university faces diverse horizons of management, such as laboratory based, building based, department based, and university based.

Besides, when a university encounters disaster which causes closing educational operations, postponing examinations, and delaying students' entrance or graduation, the problems are different from corporations' bankruptcy.

A technology-oriented university, like Tokyo-Tech University, suffers the competition issues as well. A leading research center has a lot of jointed projects with other research organizations or companies. A several day delay will lead their results simply as a second brew of tea. In order to minimize loss, the BCP of university or each laboratory not only plans for emergency response but also redact damage plans for business continues and quick recovery.

Thus, even though university faces a huge damage from a big disaster, launching the BCP to reduce damage to the least enables university minimize the bad effectives for management, recover educational programs also research and investigation activities as soon as possible.

Table 1 shows the summary of differences between the conventional disaster mitigation plan and the BCP for university.

Table 1 Difference between Traditional DMP and BCP for University

	Conventional DM plan	BCP for University
Main Purposes	Reducing human injury and death Property loss mitigation Prevent consequential damages	Continuity of fundamental business Early resumption Rearrange education schedule Rearrange research schedule Maintaining social creditability Concerning social responsibility
Area concerned	Overall preparedness Appropriate emergency responses	Allocating of adequate human resources Alternative arrangements
Constraint	None	Human capacity Fundamental equipment Resource materials Market information Lifeline (water and energy)

2. Pilot study of BCP OF TOKYO-TECH SUZUKAKEDAI

In the Suzukake-dai campus, about 500 employees are working. Out of them, 400 persons are researchers such as professor, associate professor, lecturer, and research associate, and others are engineers and administrators. In fact, however, some more part time stuff joins.

Most of researchers perform their research works under the above mentioned departments integrating with educational activities. Apart from theses educational organizations, however, six research organizations are in operation at the campus. They are;

- Chemical Resources Laboratory,
- Precision and Intelligence Laboratory,
- Materials and Structures Laboratory,
- Imaging Science and Engineering Laboratory,
- Frontier Research Center, and
- Center for Biological Resources and Informatics.

2.1 Basic Survey of Current Activities and Damage Estimate

In this survey we focus on one research building called F-Center in convenience. Currently, the six laboratories are performing their research works in the F-Center. The first step of the program is thus to clarify the current activities and working environment of these respective laboratories, and to estimate their loss and damage caused by two emergency events.

The following contents are to be investigated through a questionnaire survey and direct interview survey to research stuff.

A. What kind of research works or experiments are in operation?

B.What kinds of equipment are used under what conditions?

Table 2 usage conditions regarding specific types of equipment

Equipment	Conditions
Gas Chromatography Mitigation	Experimental use (Long term)
Many kinds of Measuring system	Experimental use
Vacuum pump	Experimental use (Long term)
Electrical heating furnace	Experimental use (Long term)
Deep freezer	Always use
……..	……..

Table 2 shows the answer example from interview survey. Many specific types of equipment for experimental purpose are expensive and hard to be replaced. Also, some experiments have to be kept running in order to keep some particular materials warm or cool.

C. What kinds of dangerous materials are used and how are they kept usually?

Table 3 The dangerous materials and its preservations

Dangerous materials	Conditions
Poisonous gas	Preserved in the compressed gas cylinder
Combustible gas	Preserved in the compressed gas cylinder
Chemicals(poison)	Preserved in the Special cabinet

Table 3 shows the answer example about dangerous material and its preservations. Generally, dangerous materials ought to be preserved in the safe ways. However, facing disasters several problems might happen as following descriptions.

- The cabinets for chemicals storage collapse.
- Chemicals spill.
- Some chemicals have not yet been located in the proper places.
- All kinds of air storage cylinders ought to be fastened in the proper ways. But a strong earthquake may loose binders from cylinders, which could cause the gas leak problem.
- The disposal of exhausted cylinders also obstacles human's escaping route.

D. How much energy is normally in use?

Each laboratory has different needs in energy consumption. In ordinary use, all 6 laboratories need 105.4kW for operation. During high-peak energy consumption times, they need totally 182kW to keep all systems running.

2.2 Process analysis

In this study, we surveyed the bad effects of each laboratory after disaster. The questionnaires are about business interruption and the least people and resources to continuing their works.

Our research objection is to make sure project priority for the laboratories' survival. Moreover, we would like to have further discussion on what kind of disaster mitigation should be prepared.

We established the scoring system. The indicators are introduced as following.

WSE: Work stop effective Level

Level1: No effection
Level2: Small effection
Level3: Middle effection
Level4: Big effection
Level5: Huge effection

ATIME: arrival time to the Lab.

Distance : hours
4Km : one hour
4-12km : 3-6 hours
12-20km : 6-12 hours

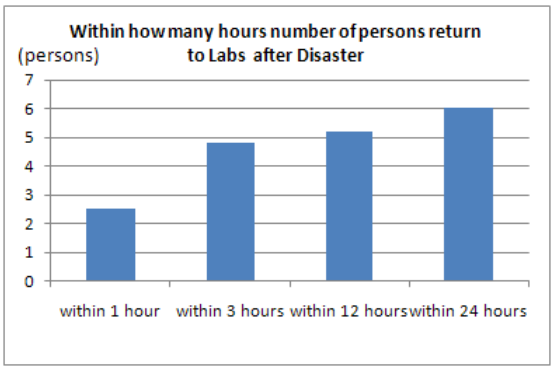

Figure2 Within how many hours number of persons return to the lab

RRP: Resource recovery possibility

Possible : 1
difficult : 2
impossible : 3

RRT: Resource recovery time

one month :1
3 month :2
5 month :3
6 month :4
one year :5

ESP: Effectiveness of stop project

$ESP = WSE * ATIME$

DRR: Difficulty of Recover Rate

$DRR = RRP * RRT$

Figure 3 shows the plot graph about the difficulty of restart and bad effects from business interruption by all projects of each laboratory.

Some projects, like L3-A, face difficulty in restart and get bad effects from their work interruption. One the other hand, some projects don't get severe effects by damage.

It is hard to make comparison between each laboratory. However, the comparison of projects priority inside laboratory is possible.

Our analysis actually conducts lab managers to

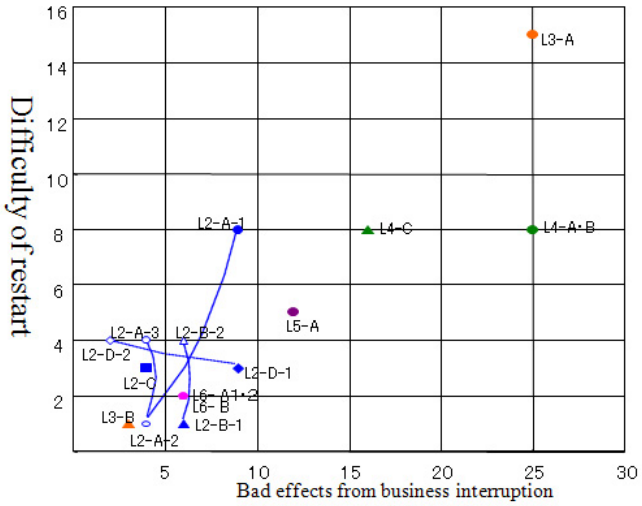

Figure 3 difficulties of restart and bad effects from business interruption by all projects of each laboratory.

consider the perspective of risk management of their usual research activities. Given this experience, lab managers start to exploit alternative resources and calculate the cost to preserve those un-alternative materials.

3. Prepare for BCP of F-center in suzukake-dai chanpus.

In order to enable the BCP, a long term analysis and again and again revise are necessary. At the first step of the BCP, we set some targets for the F-center as below.

1. Never cause any human injury or death
2. Protect important materials on academic purpose
3. Protect every lab's main equipments
4. Every lab reports confirmation about safety of students, researchers, and professors to the chief of F-center within 24 hours.
5. All research activities will be recovered within one week

Next, to realize these targets, there is something we can do as below;

1. Make manual of the BCP for each Lab and Administrator
2. Set up warning systems such as Urgent Earthquake Detection and Alarm System
3. Prepare table type seismic isolator for protect un-alternative resource.
4. Prepare reporting system for the use of confirmation from safe persons.
5. Stable electricity supply after disaster such as UPS or private power generator.

4. Conclusion: for support BCP for Lab.

In this survey, we focus on Business Continuity Plan (BCP) on university activities taking the F-center of Suzukake-dai campus as a case study. From our survey some problems of University were found, such as disaster prevention has not been well prepared, it takes long time to return labs for inspection, and some project faces difficulty of recover after disaster. Also we found some administration operating problem, such as cooperative structure of emergency response. People in lab have received the evacuation manual from university administration. However, when disaster occurs, there is almost no way for technicians return to lab to check the lab situation.

Those problems happened not only in the F-center but also everywhere in the university only if there is a technology oriented department. In the future, we will continue survey and report our next process.

Acknowledgements:

The authors wish to express their gratitude for the support from Tokio Marine & Nichido Risk Consulting Co., Ltd. Japan. Without their support, the project would not become possible.

References:

Taiwan-Japan Joint Symposium on the Advancement of Earthquake Hazard Mitigation Technology, (2008)"A PRACTICAL FRAMEWORK OF THE BCP ON TOKYO-TECH SUZUKAKE-DAI CAMPUS"

Ministry of Cabinet Affairs, (2005) "The First Edition of Guideline of BCP – Towards Damage Mitigation and Capacity Building of Enterprises in Japan"

Japan Chamber of Commerce and Industry, (2007), "Step-up Guidance of BCP for Small and Medium Sized Enterprises"

Poster Sessions, Institute of Social Safety Science, (2008), "Study on the present condition of the earthquake disaster prevention for universities and introduction process of Business Continuity Plan"

Sixth International Conference on Urban Earthquake Engineering
March 3-4, 2009, Tokyo Institute of Technology, Tokyo, Japan

QUESTIONNAIRE SURVEY ON RISK RECOGNITION AND PREPAREDNESS OF CITIZENS

Jun Mihira[1)] , Hideki Kaji[2)] and Saburoh Midorikawa[3)]

1) Graduate Student, Department of Built Environment, Tokyo Institute of Technology, Japan
2) Professor, Center for Urban Earthquake Engineering, Tokyo Institute of Technology, Japan
3) Professor, Department of Built Environment, Tokyo Institute of Technology, Japan
mihira.j.aa@m.titech.ac.jp, hkaji@plum.ocn.ne.jp, smidorik@enveng.titech.ac.jp

Abstract: After the Great Hanshin-Awaji Earthquake in 1995, the importance of self-help and mutual assistance has been more recognized. However, there is a gap between earthquake recognition and preparedness by citizens. To examine the gap, a questionnaire survey is conducted to citizens who participated in the disaster training at Fujisawa city, Kanagawa. The results of the study showed that the higher the life risk recognition of the individual and the regional society is, the more the implementation rate of disaster measures doesn't necessarily rise.

1. INTRODUCTION

The Great Hanshin-Awaji Earthquake in 1995 produced a huge urban disaster. The Police White Paper (1995) shows that 80% of the dead people in the disaster were killed in broken houses. It tells us the necessity of disaster measures by individuals such as earthquake resistant of houses and securing furniture. About 80% of the 35,000 survivors were rescued by family members and neighbors. This suggests the importance of mutual cooperation. Ministry of Internal Affairs and Communications (2002) shows that about 60% of the general public feels the necessity of taking disaster measures. However, it is doubtful that they take disaster measures practically. Therefore, disaster measures by individuals are important.

Although a lot of people are aware of the importance, there are still issues left unsolved. There are some reasons causing a big gap between recognition of importance and practices. Sakano and Ohishi (2008) analyzed that only risk recognition about vulnerability of houses did not bring to take the antiseismic reinforcement.

This study aims to examine the relationship between risk recognition and preparedness based on the questionnaire survey.

2. OUTLINE OF QUESTIONNAIRE SURVEY

The questionnaire survey was conducted to citizens who participate the disaster training in Shonan-Oba district, Fujisawa city, Kanagawa on November 24, 2008. Table 1 shows the face sheet. The participants are considered to be interested in disaster mitigation. The number of the participants is 3% of the residents in the area.

The questionnaires were distributed to 133 persons, and returned from 110 persons. Table 2 is a list of the questions on the questionnaire. Two types of questions were used. Five questions of Section1 were asked about earthquake risk recognition. Twenty-six questions of Section2 were asked whether disaster measures were prepared.

Table 1 Face sheet of the questionnaire

Sex	Number (person)	Relative frequency (%)
Man	50	45%
Woman	60	55%
Age Division	**Number (person)**	**Relative frequency (%)**
Under Age 20	1	1%
Age 20～29	2	2%
Age 30～39	10	9%
Age 40～49	14	13%
Age 50～59	22	20%
Age 60～69	40	37%
Age 70～79	17	16%
Over Age 80	3	3%

Table 2 Two types of question on the questionnaire

Section1	What kind of image do you have for an earthquake? (Answer is choice from 4 levels about intention)
Q1-1	While it is alive, I think I will not encounter an earthquake.
Q1-2	Even if a large earthquake will occur, I will be safe.
Q1-3	If the earthquake will occur, I think that I will fall into the situation with the crisis of the life.
Q1-4	Even if a large earthquake will occur, many of buildings of the Shonan-Oba district will be safe.
Q1-5	If an earthquake will occur, I think many dead and injured people bring in this area.
Section2	What kind of disaster measures have you performed? (Answer is choice from Y/N)
Q2-1	I decide a place where it meets again with a family.
Q2-2	Evacuation procedure has been discussed in the family.
Q2-3	When I sleep, I have put footwear on bedside every night.
Q2-4	When I sleep, I have put wears on bedside every night.
Q2-5	I participated in this training last year.
Q2-6	I participated in the other training this year.
Q2-7	After saving water in a bath, I have gone to bed every night.
Q2-8	I put down the address in a notebook.
Q2-9	I participated in a course of first aid.
Q2-10	I have become a leader for disaster prevention.
Q2-11	I got the qualification of the Bosai-Shi.
Q2-12	I have put securing furniture on chests of the bedroom.
Q2-13	I have put securing furniture on the cupboards.
Q2-14	I have put Opening-and-closing prevention equipment on the cupboard.
Q2-15	I have put securing furniture on the refrigerator.
Q2-16	I have put securing furniture on the bookshelves.
Q2-17	I have a first-aid kit.
Q2-18	I have taken seismic capacity evaluation or antiseismic reinforcement.
Q2-19	I have joined earthquake insurance.
Q2-20	When I go out, I have a whistle for rescue every time.
Q2-21	When I go out, I have a mask every time.
Q2-22	When I go out, I have a radio every time.
Q2-23	I have kept emergency supplies in a rucksack.
Q2-24	I have always kept water (12 liter)
Q2-25	I prepared for emergency rations.
Q2-26	I prepared for restroom goods on using emergency.

3. RESULTS OF QUESTIONNAIRE SURVEY

3.1 Risk Recognition to Individual and to Local Community

Figure 1 shows the distribution of replies concerning the possibility of encountering to a large earthquake. About 45% of respondents feel high possibility of encountering a large earthquake.

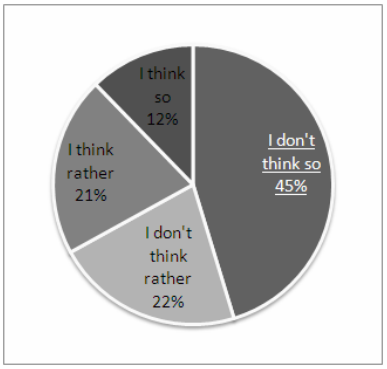

Figure 1 Answer Ratio of *While it is alive, I think I will not encounter an earthquake.*

Figure 2 shows the distribution of replies concerning the possibility of damage. About 40% of respondents feel high possibility of receiving casualty to themselves.

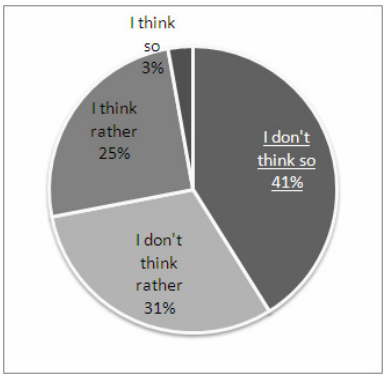

Figure 2 Answer Ratio of *Even if a large earthquake will occur, I will be safe*

Figure 3 is the degree of average recognition classified by age. The average was calculated so that the highest risk is 4 points and the lowest risk is 1 point. The bars of dark color are the degree of average recognition about encountering a large earthquake. The generation of 30's feels the possibility most strongly to encounter a large earthquake, and there is tendency that the more the age goes up, the more the degree is lower.

The reason may be that senior citizens do not encounter a large earthquake because of shortness of life expectancy. The bars of light color are the degree of average recognition about taking casualties. All of generations feel the possibility very strongly to take damages by a large earthquake. Even the younger generation and middle age that have physical strength feel to take casualties.

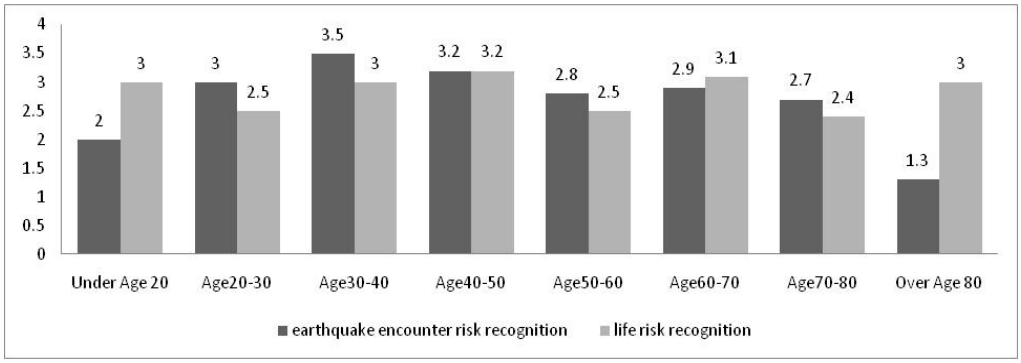

Figure 3 Average value according to age of earthquake risk cognition

The risk in the district was also asked about the risk in the district. Figure 4 shows the distribution of replies concerning the injured person occurrence risk in the region. About 35% of respondent feels as a risk which is high possibility of received damages.

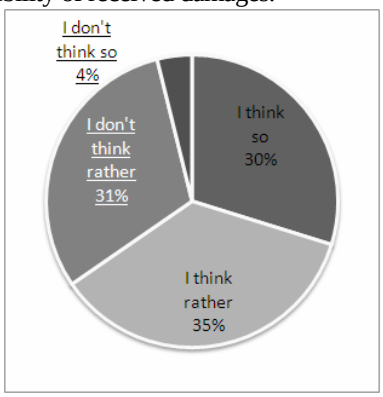

Figure 4 Answer ratio of *Even if a large earthquake will occur, many of citizens in the Shonan-Oba district will be injured.*

3.2 Comparison of Two Types of Life Risk

Table 3 shows the distribution of the recognitions classified by generation. In this result, half of the participant (57 people) evaluates highly both individual and regional society shown by the cells of dark color. And, about 45 % of the participation evaluates that the risk value to individual risk and regional society risk is equal.

Table 3 Correlation of life risk recognition for individual and local community

		Life Risk for Regional Society			
		Low	Rather Low	Rather High	High
Life Risk For Individual	High	2	4	16	**16**
	Rather High	0	5	**16**	9
	Rather Low	2	**21**	5	2
	Low	**0**	1	0	2

3.3 Relationship between Life Risk Recognition and Disaster Measures

In this section, it is examined that there is the difference of implementation rate between person recognizing high life risk and the other. The following hypotheses are built up; the higher the life risk recognition is, the more the implementation rate of disaster measures rises.

In order to examine this hypothesis, Table 4 shows the implementation rate for person recognizing high life risk and for the other people.

From this table, it's clear that for the person recognizing life risk implementation rates higher than for the other person in three question items, “2-7: After saving water in a bath, I have gone to bed every night.”, ”2-8: I put down the address in a notebook.”, ”2-17: I have a first-aid kit.”. But, the result is opposite with 5 items, ”2-13: I have put securing furniture on the cupboards.”, ”2-16: I have put securing furniture on the bookshelves.”, “2-23: I have kept emergency supplies in a rucksack.”, “2-24: I have always kept water (12 liter)”,” 2-25: I prepared for emergency rations.”. In addition, the implementation rates of disaster measures for lives saving and for keeping a standard of living are not very high.

As a result, the higher the life risk recognition of the individual and the regional society is, the more the implementation rate of disaster measures doesn't necessarily rise. Therefore, existence of other factors can be considered.

3.4 Correlation of Different Disaster Measures

Table 5 shows the correlation of a pair of the implementation of disaster measures in 26 question items. If there is positive correlation, the ratio of a person taking both measures is high. If there are negative or no correlation, the ratio of a person taking only one measure is high.

The items are classified into several groups with the same objective; 1) family discussion (2-1,2-2), 2) preparation when going to bed (2-3, 2-4), 3) participating disaster training (2-5, 2-6), 4) furniture-secure measures (2-12, 2-13, 2-14, 2-15, 2-16), and 5) preparation when

Table 4 Relationship of the life risk awareness and disaster measures

	2-1	2-2	2-3	2-4	2-5	2-6	2-7	2-8	2-9	2-10	2-11	2-12	2-13
person with high risk recognition (n=57)	23	15	16	24	14	37	44	30	3	26	0	19	16
Relative frequency (%)	40.4%	26.3%	28.1%	42.1%	24.6%	64.9%	77.2%	52.6%	5.3%	45.6%	0.0%	33.3%	28.1%
other person (n=53)	28	19	14	21	15	33	35	22	4	29	0	24	27
Relative frequency(%)	52.8%	35.8%	26.4%	39.6%	28.3%	62.3%	66.0%	41.5%	7.5%	54.7%	0.0%	45.3%	50.9%

	2-14	2-15	2-16	2-17	2-18	2-19	2-20	2-21	2-22	2-23	2-24	2-25	2-26
person with high risk recognition (n=57)	8	7	9	49	1	26	4	5	6	23	27	25	7
Relative frequency(%)	14.0%	12.3%	15.8%	86.0%	1.8%	45.6%	7.0%	8.8%	10.5%	40.4%	47.4%	43.9%	12.3%
other person (n=53)	10	11	19	39	7	30	3	5	6	34	33	38	8
Relative frequency(%)	18.9%	20.8%	35.8%	73.6%	13.2%	56.6%	5.7%	9.4%	11.3%	64.2%	62.3%	71.7%	15.1%

Table 5 Correlation of disaster measures

	2-1	2-2	2-3	2-4	2-5	2-6	2-7	2-8	2-9	2-10	2-11	2-12	2-13	2-14	2-15	2-16	2-17	2-18	2-19	2-20	2-21	2-22	2-23	2-24	2-25	2-26
2-1	1.00																									
2-2	0.32	1.00																								
2-3	−0.01	0.34	1.00																							
2-4	−0.06	0.22	0.41	1.00																						
2-5	−0.19	0.03	0.10	0.10	1.00																					
2-6	0.15	−0.09	−0.20	−0.25	−0.12	1.00																				
2-7	0.00	0.13	0.15	0.10	0.02	−0.08	1.00																			
2-8	0.10	0.09	0.36	0.06	−0.03	−0.09	0.15	1.00																		
2-9	0.29	−0.08	−0.23	−0.10	0.08	0.21	−0.09	−0.01	1.00																	
2-10	−0.07	−0.15	0.06	−0.03	0.30	−0.12	−0.01	0.23	0.01	1.00																
2-11	0.14	−0.32	−0.09	−0.22	−0.11	0.21	−0.10	−0.18	0.39	−0.02	1.00															
2-12	0.20	0.02	0.00	0.32	−0.03	0.00	0.09	−0.10	0.18	−0.09	0.12	1.00														
2-13	0.06	0.02	−0.18	0.00	−0.30	0.10	−0.26	−0.19	0.07	−0.21	0.06	0.11	1.00													
2-14	0.06	−0.23	0.01	−0.01	−0.24	0.28	−0.29	−0.04	0.13	0.05	0.42	0.00	0.46	1.00												
2-15	0.22	0.02	0.01	0.14	−0.16	0.23	−0.22	−0.05	0.14	−0.11	0.02	0.33	**0.64**	0.50	1.00											
2-16	0.10	−0.09	−0.01	0.03	−0.16	−0.09	−0.18	−0.08	0.12	0.08	0.42	0.20	0.44	**0.59**	0.31	1.00										
2-17	0.22	0.01	0.03	−0.07	−0.37	0.25	−0.13	0.02	0.29	0.03	0.27	0.05	0.48	**0.58**	**0.55**	**0.57**	1.00									
2-18	0.16	−0.12	0.02	−0.04	−0.26	0.15	−0.25	0.12	0.24	0.09	0.26	0.03	0.34	0.49	**0.53**	0.48	**0.82**	1.00								
2-19	−0.01	−0.10	−0.18	−0.18	−0.07	0.05	−0.14	−0.17	0.24	−0.03	0.26	0.02	0.48	0.40	0.43	0.48	**0.62**	0.47	1.00							
2-20	0.12	0.03	0.13	0.03	−0.18	−0.03	−0.13	0.22	0.34	0.13	0.23	0.12	0.31	0.38	0.41	0.46	**0.70**	**0.83**	**0.51**	1.00						
2-21	0.39	0.27	0.17	−0.03	−0.23	0.27	0.02	0.13	0.33	0.05	0.25	0.06	0.21	0.37	0.40	0.35	**0.66**	**0.57**	0.32	**0.56**	1.00					
2-22	0.26	0.24	0.04	−0.06	−0.24	0.21	0.05	0.00	0.31	0.01	0.24	0.03	0.19	0.34	0.38	0.33	**0.64**	**0.55**	0.35	**0.53**	**0.74**	1.00				
2-23	0.37	0.26	0.17	0.18	−0.32	0.07	−0.05	0.06	0.15	0.14	0.11	0.17	0.33	0.25	0.40	0.46	**0.63**	**0.58**	0.27	**0.54**	**0.56**	**0.58**	1.00			
2-24	0.06	0.13	0.10	0.26	−0.17	0.10	−0.12	−0.06	0.24	−0.09	0.12	0.10	0.43	0.23	0.38	0.43	**0.51**	0.41	0.38	0.46	0.47	0.42	**0.53**	1.00		
2-25	0.32	0.29	0.20	0.14	−0.21	0.16	0.19	0.05	0.14	0.02	0.12	0.14	0.40	0.18	0.45	0.38	**0.59**	0.41	0.42	0.39	**0.62**	0.50	**0.72**	0.49	1.00	
2-26	0.30	0.29	0.10	0.21	−0.07	0.16	−0.13	−0.05	0.29	−0.11	0.24	0.16	0.37	0.41	0.54	0.47	**0.55**	0.41	0.43	0.41	**0.60**	**0.57**	**0.60**	**0.64**	**0.59**	1.00

going out (2-20, 2-21, 2-22). Positive correlations are observed at the following pairs;

- ” I have put securing furniture on the cupboards. (2-13)” and “I have put securing furniture on the refrigerator (2-15)”,
- “I have put Opening-and-closing prevention equipment on the cupboard. (2-14)” and “I have put securing furniture on the bookshelves.(2-16)”
- All the questions of preparation when going out.

Negative correlations are observed at the following pairs;

- Family discussion (2-1, 2-2)
- Preparation when going to bed (2-3, 2-4)
- Participating disaster training (2-5, 2-6)

These measures are often taken only one measure. The reason may be that citizens would not like to spend much time for similar measures.

The correlation between of securing furniture plans in kitchen (2-13, 2-14, 2-15) and of securing furniture plan in bedroom (2-12) is negative. The reason may be that citizens pay attention mainly to bedroom furniture, not to kitchen furniture.

The correlation between of preparation of restroom goods (2-26) and of the other preparations of keeping a standard of living (2-23, 2-24, 2-25) is positive. The reason may be that citizens who prepare restroom goods spend money and time for the other preparations of keeping a standard of living. But, it is not for lives saving.

4. CONCLUDING REMARKS

In this paper, the questionnaire survey was made to the participant in the emergency training about risk recognition and disaster measures.

The group of citizen which participates in the disaster training has the high risk recognition to the earthquake. The higher the life risk recognition of the individual and the regional society is, the more the implementation rate of disaster measures doesn't necessarily rise.

Acknowledgements:
The authors acknowledge support from the Global COE program sponsored by Japan Ministry of Education, Culture, Sport, Science, and Technology (MEXT).

References:

Ministry of Internal Affairs and Communications. 2008. Ministry of Internal Affairs and Communications research

National Police Agency. 1995. Police White Paper

Sakano, T. and Ohishi, R.. 2008. Path analysis of risk-avoidance behavior. Tokyo: Self-efficacy and risk Japan Associate for Planning Administration (Session 31)

Sixth International Conference on Urban Earthquake Engineering
March 3-4, 2009, Tokyo Institute of Technology, Tokyo, Japan

REVISION OF SEISMIC DESIGN CODES CORRESPONDING TO BUILDING DAMAGES IN THE 512 WENCHUAN EARTHQUAKE

Wang Yayong[1)]

1) Professor, Institute of Earthquake Engineering, China Academy of Building Research, Beijing , China
yayongwang@sina.com.cn

Abstract: Lots of damages and collapses of buildings were caused in The 512 Great Wenchuan Earthquake. Based on the field survey and studies on damages of different types of buildings, an urgent revision for seismic design codes of buildings has been carried out in time. The revision mainly related to "Standard for classification of seismic protection of building constructions GB50223-2008" and "Code for Seismic Design of Buildings GB50011-2001" is summarized. The definition of seismic fortification class for buildings has been renewed, the seismic class for buildings of school, hospital and those holding large population has been enhanced in the seismic category, the evacuation shelter and information center have been put on higher seismic class in the GB50223-2008 Code. Main issues in the revision of GB50011-2001 are including: (a) The adjustment on the zoning intensity for provinces of Sichuan, Shanxi and Gansu. (b) The basic conception design for retaining wall and foundation of buildings in the mountainous area. (c) The regularity of building configuration.(d)The integration of masonry structure and pre-cast RC floor. (e) The requirements of calculation and detailing for the stair shaft.(f) The limit of using single-bay RC frame structure. Some significant damages in epicenter areas are given herein as the reference in discussion on the consequence collapse, the importance of the multiple defense system and the integration of RC and masonry structures.

1. INTRODUCTION

Lots of damages and collapses of buildings were caused in The 512 Great Wenchuan Earthquake. Based on the field survey and studies on damages of different types of buildings, an urgent revision for seismic design codes of buildings has been carried out within two and half months. The revision of "Standard for classification of seismic protection of building constructions GB50223-2008" and "Code for Seismic Design of Buildings GB50011-2001" is summarized herein in this paper.

It has been observed that most of buildings which were designed and constructed after 1990's while the seismic codes of GBJ11-89 and GB50011-2001 were executed nationwide were performing very well and achieving three seismic fortification objectives in terms of "operational, life-savety and collapse prevetion" for "minor, moderate and major" earthquaqke levels respectively. But, problems still remain in quality control of seismic design and construction. There is a room to improve for the design codes. For example, the lack of multi-defense line or redundancy, large spacious and irregular configulation, "strong beam and weak column" mechanism, improper partition, stair shaft of masonry buildings as well as the poor joints of precast RC floor slabs, etc., caused severe structural damage and collapse in the main shock.

Lesions learnt from the investigation of both damaged and survived buildings in the event shall be put into the code revision.

2. REVISION OF STANDARD GB50223-2008

2.1 Basic Requirement of Seismic Fortification

The 2008 Standard requires that all engineering constructions in earthquake regions, including new, rebuilding and retrofitting ones, shall be definitely classified as a seismic category according to the operation function and occupancy of the building. The seismic category of a building shall not be below one regulated by the Standard, but could be higher if the owner wants and discusses with the designer[1].

2.2 Seismic Classification of Buildings

Four seismic categories are regulated in 2008 Standard as follows:

A: Special Class
B: Important Class
C: General Class
D: Less Important Class

The seismic classification of buildings is based on the earthquake-induced impact on human being and society, and the urgent rescue as well. For example, the seismic category of kindergarten and school buildings is enhanced from Class C to Class B. The tall building with an occupancy over 8000 is also put on Class B. For large scale hospitals of Grade A and B, the seismic class is taken A or B. Particularly, the clinic equipped with surgery and first aid facilities in the rural area is also enhanced to Class B. The seismic category

of those buildings which can be employed as the evacuation shelter, such as the sports hall and conference center has to be Class B or A. The large scale public facilities, such as the culture and entertainment house, the commercial building of multi-story holding big population, and infrastructures of power, water and gas supply are enhanced to Class A or B.

3. REVISION OF THE CODE GB50011-2001 (2008 VERSION)

3.1 New Zoning Map of Earthquake Parameters for Sichuan, Gansu and Shanxi Provinces

After the 512 Wenchuan Earthquake, the earthquake parameters of *PGA* and T_g for 31 cities in Sichuan, Gansu and Shanxi Provinces in the previous Zoning Map have been changed. The seismic intensity of these cities and surroundings is enhanced [2] in accordance with the field survey on damages every kinds of building and geological failures. In Chinese scale, seismic intensity 7, 8 and 9 is corresponding respectively to acceleration 0.1, 0.2 and 0.4g.

3.2 Seismological hazard and Seismic Design of Buildings in Mountainous Regions

The Code 50011-2001(2008 Version) regulates that buildings of Class A, B are forbidden and C not allowed to set up at dangerous sites where seismological hazard such as the landslide, rockslide, earth sunken, ground rupture and debris flow, etc. may be caused by earthquakes. Figure 1 shows Maoba High School building buried by rock slide in Beichuan County of the epicenter region, figure 2 shows an apartment building partly buried by land slide in Wenchuan County, and figure 3 gives an image of an apartment building mostly buried by the debris flow on Sept.24, over seven months late after 512 main shock. The debris flow covered the main streets in Beichuan County, the destroyed city, with mud of thickness from 6 to 40 meters in deep.

Figure 1 The Maoba High School buried by rock slide in Qushan Town, Beichuan County

3.3 Basic Requirements for Seismic Design

3.3.1 Irregularity of Configuration

The Code 50011-2001(2008 Version) stresses the seismic conception design that some measures have to be taken for irregular structures, special studies and enforced measures have to be carried out for buildings with very irregular configuration. Lots of damages were caused due to the irregular configuration of buildings in the earthquake. Figure 4 shows severe failure at RC columns of a building with irregular plan and spacious bottom story. Figure 5 shows the collapse of the second story due to the badly damage in longitudinal brick wall which seats on RC beams of the first floor. Such kind of structures are known having a poor capacity of earthquake resistance[3].

3. 3. 2 Principle of "Strong Column -Weak Beam"

The design strategy of "strong column-weak beam" issued in the Code GB50011-2001(2008 Version) can be expressed by:

$$\sum M_{cy}^{a} > \sum M_{by}^{a} \qquad (1)$$

Where M_{by}^{a} and M_{cy}^{a} are the actual moment resistance of the beam and column, respectively, at the joint.

Figure 2 An apartment building partly buried by land slide in Wenchuan County

Figure 3 A 4-story apartment building mostly buried by debris flow late Sept.2008 in Beichuan County

Figure 4 Damaged bottom RC frame structure (7/9)
Note: (7/9) = (zoning intensity/estimated intensity)

Figure 5 Damaged upper walls of masonry building with bottom RC frame structure (7/9)

Their accurate estimation are rather difficult because of factors related to the complexity of the earthquake action of the three components and the contribution of the in-situ RC floor slabs, so that a factor of $\eta_c \geq 1$ is usually introduced to increase the design moment resistance of columns. Therefore,

$$\sum M_c = \eta_c \sum M_b \qquad (2)$$

To consider the contribution of the floor slabs to the frame beam and other possible influence the factor η_c is generally assumed to be 1.5～2.0, as column is under a very complicated dual loading condition due to the couple of horizontal strong motions. In general, the section design of RC columns can be easily satisfied with the least amount of steel bars, particularly for low rise buildings as in the earthquake affected areas of this event. It can be obviously known that the practical design often results in a mechanism

Figure 6 Plastic hinges of a frame structure (7/11)

Figure 7 Large deflection of cast-in-situ RC beams and slabs of floors (7/11)

of "strong beam-weak column" as often observed in the damage of RC frame structures, and it reveals that the beam resistance or the assumed value of the factor η_c was significantly underestimated, if the Eq. (2) had been applied in the design. Figure 6 shows the plastic hinges of the frame columns of the west wind of the school. Figure 6 shows a plastic hinge at the top of a column of a residential building with 5-story upper masonry structures and a ground story of RC frame structure.

3. 3. 3 Cast-in-Situ RC Slabs of Floor and Roof

The Code GB50011-2001(2008 Version) encourages the usages of cast-in-situ RC slabs of floor and roof for school and hospital building of masonry structures which usually consist of spacious rooms. Figures 7 gives an example of a damaged masonry school building with cast-in-situ RC slabs of floor and roof which was severely damaged but remain hanging and stable.

3. 3. 4 Integration of Confined Masonry Structures and Pre-cast RC slabs of floor and roof

The Code GB50011-2001 (2008 Version) requires that measures be taken to ensure the integration and reliability of joints among pre-cast RC slabs and connection with beam and column. The confined masonry structures are widely used for residence, school and hospital buildings in China. The Code regulates a very strict clauses for the layout and detailing of ring-beam and tie-column for such kind of structures. Unfortunately, lots of pre-cast RC hollow core slabs broke or fell down from floor and roof killing people in the 512 earthquake. Figure 8 shows a partly collapsed school building of masonry structure because of lack of tie-columns arranged. Figure 9 shows the falling pre-cast RC hollow core slabs from a collapsed three story school building of brick structure. It is obvious that no joints among the slabs exist. Figure 10 gives an opposite example. A three story school building of brick structure was seriously injured, even though the bearing walls were partly collapsed, but the pre-cast RC hollow core slabs of floor keep connection owing to the good detailing of joints.

Figure 8 Partly collapsed school building (7/9)

Figure 9 Fallen RC beam and pre-cast floor slabs (7/9)

3. 3. 5 Multiple Seismic Defense Lines of Structures

The Code GB50011-2001 (2008 Version) mentions that seismic design has to ensure a structure system multiple defense lines to avoid structure collapse by the action on the major earthquake level. Some structural members, such as the braces, shear wall for RC frame structure and the coupling beams for RC shear wall structure, may play the role of first seismic defense line which could be damaged firstly to prevent RC columns from injures, and then to prevent the structure from collapse. The RC ring-beam and tie-column can be seen as the second defense line of the confined masonry structure besides of their restraint for brittle bricks and ductility for masonry walls. Figure 11 shows a hospital building of RC single-bay frame structure and a dormitory building of confined brick structure side by side located at a same site. The hospital was badly damaged, leaned and has to be demolished and rebuilt, but the dormitory building survives and remains without any cracks on the brick walls.

3. 3. 6 Details of Seismic Partition

The Code GB50011-2001(2008 version) requires in

Figure 10 Remaining pre-cast RC floor (7/9)

Figure 11 Two buildings side by side at the same site in Pingwu County (7/9)

certain cases that the seismic partition be set for buildings. The arrangement and the size of seismic partition shall be determined in dependence on the seismic intensity, type of structure, structural materials, height of buildings. The upper buildings should be separated completely along the partition to avoid knocking. Figure 12 shows the knocking of two multi-story masonry buildings. Figure 13 shows a sequence collapse caused by collision of two buildings separated by the narrow partition in Beichuan County of the epicenter area. It is not always necessary to have a partition unless the configuration of building is very irregular in plan or elevation. The size of partition should be wide enough.

3. 3. 7 Stair Shaft in Masonry Buildings

The stair shaft is the entrance and exit of buildings, and provides people the way to evacuate from incidents. The failure or collapse of stair shafts may kill or injure escapers, or stack the exit way. The stair shaft in masonry structure may easily be damaged due to their relatively large mass, higher walls, steps between floor and stair platform, and rigidity of step beams etc. The Code GB50011-2001 (2008 Version) regulates that tie-columns be provided at corners of stair shaft and lift tube and at the joints of transverse and longitudinal walls on the step level. A valid connection has to be detailed between beams for steps and platform and so on. The tie-column should be extended up to the top and be connected with the ring-beams of the stair shaft which protrudes beyond the roof. Figure 14 shows a collapsed stair shaft of a 3-story school building due to the wall breaking. Figure 10 shows a RC stair shaft remained with masonry structures besides collapsed. Again, we can see the damaged step beam and the broken stair segment in Figure 15.

4. CONCLUTIONS

Many experts and engineers home and abroad have been several times in the disaster region taking field survey after the 512 Wenchuan Earthquake. The study on damages

Figure 12 Knocking along the partition (7/8)

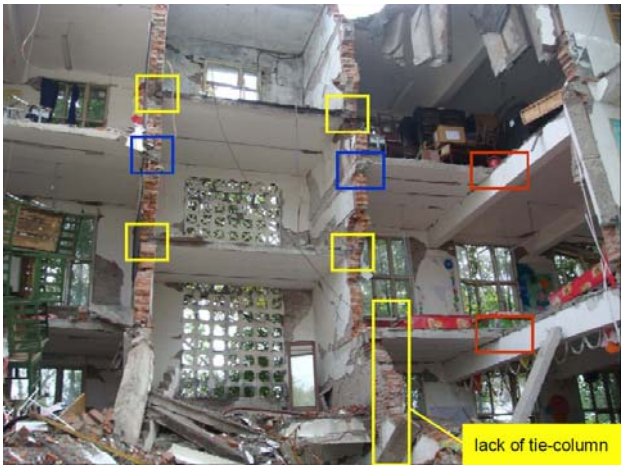

Figure 14 A collapsed stair shaft due to wall broken (7/9)

Figure 13 Sequence collapse caused by collision between office and apartment buildings in Beichuan County (7/11)

Figure 15 Damaged stair shaft of a residence building of masonry structure in Mianzhu City (7/8~9)

of different kinds of buildings constructed in different periods tells the truth that most of buildings which were seismically designed and constructed since 1990's have performed well and are able to achieve the three seismic performance goals, i.e., "operational for minor earthquake, life safety for moderate earthquake, and collapse prevention for major earthquake". Many buildings suffered moderate to severe damage but survived from collapse even the estimated seismic intensity is 3 or 4 degrees higher than zoning intensity (the corresponding peak acceleration is about 10 times larger). The survey and study also show that the basic requirement for seismic design, i.e. the seismic conceptual design, has special significance and is somehow more important than computation to ensure the seismic capacity of structures.

The urgent revision of the Standard GB50223-2008 and Code GB50011(2008 Version) has completed within a period of less three months. Generally speaking, the seismic capacity of different types of structures has been enhanced to a certain degree. Special attention for school, hospital, farmer's houses and those holding massive population has been put into code regulations. To be an engineer, handle of conceptual design is particularly required other than only using the software. The idea of "strong column-weak beam" is the desired requirement for RC structures to realize the goal of "collapse prevention for major earthquake". Unfortunately, a contrast and harmful case of "strong beam-weak column" damage happened in some affected areas because of lack of a deep understanding of the conceptual design. The seismic design should avoid from irregular planning and asymmetric loading system. A well designed seismic structure should employ the integration and large number of internal and external redundancies to prevent collapse partly or as whole due to the failure of individual members. The confined masonry structure with tie-column and ring-beam was created and widely applied in China since the 1976 Tangshan Earthquake. It is noticed that confined masonry structures could in some cases perform better than RC frame structures in seismic area. Attention should be paid to the seismic design for stair shaft of masonry buildings, particularly for schools, hospitals, residential and office buildings. Some injuries and deaths were caused by the collapse and stack of stair shaft that occurred prior to the collapse of the main building.

It is no doubt that there is still a room to improve for the Code 50011-2001. A further updation from all aspects is now carried out and shall be completed by the end of 2009.

References:

The Ministry of Construction of China (2008), "Code for Seismic Design of Buildings GB 50011-2001(2008 Version), China Architecture & Building Press, Beijing.

The Ministry of Construction of China (2008), "Standard for Classification of Seismic Protection of Building Constructions", China Architecture & Building Press, Beijing.

Wang Yayong, "Lessons learned from the 5.12 Wenchuan Earthquake: evaluation of earthquake performance objectives and the importance of seismic conceptual design principles", *Earthquake Engineering and Engineering Vibration*, Vol.7, No.3, September, 2008.

Sixth International Conference on Urban Earthquake Engineering
March 3-4, 2009, Tokyo Institute of Technology, Tokyo, Japan

QUALITY ASSURANCE FOR SEISMIC SAFETY IN CALIFORNIA'S SCHOOLS

James P. Hackett

Supervising Structural Engineer, Division of the State Architect, Sacramento Regional Office, California
Jim.Hackett@dgs.ca.gov

Abstract: Failures of structures from numerous earthquakes around the world have been traced to poor construction practices and significant design deficiencies. For structures located in areas of seismic risk, quality assurance of design and construction is essential. The Division of the State Architect (DSA) in the State of California has operated one of the world's most successful quality assurance programs since 1933. This paper presents the processes of the DSA program and discusses challenges to effective operation of statewide and local quality assurance agencies.

1. INTRODUCTION

In March of 1933, a 6.3 earthquake rocked the community of Long Beach in southern California, causing extensive damage throughout the region. 120 people were killed, 70 public schools suffered severe damage, and over 300 schools suffered moderate to minor damage. Recognizing that public schools and hospitals must provide safe-haven facilities for the public during and after a natural disaster, the California legislature passed a law, henceforth known as the Field Act, revolutionizing quality assurance for public schools throughout the state. The law established a performance objective not only for the protection of life, but also for the protection of property to safeguard the public's infrastructure investment. To ensure quality, four tenets were granted equal importance. California licensed architects or structural engineers were required to be responsible for of the design and observation of construction. The law further established a state-run department, the Division of the State Architect (DSA), to provide rigorous plan review of designs, and to ensure continuous observation of construction by independent inspectors and materials testing by independent laboratories. Today, DSA employs nearly 90 California licensed structural engineers in four regional offices, two satellite offices, and a Headquarters office that provides administrative and support services. The program's success has been substantiated by the excellent performance of public schools in numerous earthquakes. Since 1933, not a single person has lost their life or been seriously injured during a seismic event at a public school.

Figure 1 Hamilton Junior High School after Long Beach Earthquake, 1933

The Field Act has undergone numerous improvements since its inception. The law has been expanded to include the California Community Colleges and state essential service facilities. Initially established to provide seismic and fire safety, the Act now also covers accessibility for the disabled and energy compliance reviews. Following its success, a similar law was adopted for hospitals and health care facilities which is enforced by the Office of Statewide Health Planning and Development (OSHPD). Provisions of the Field Act are regulated in the Title 24, California Code of Regulations.

The Field Act has also influenced quality assurance requirements in the current International Building Code (IBC) to assist local building departments. The Commentary for the 1997 National Earthquake Hazards Reduction Program (NEHRP), "NEHRP Recommended Provisions for Seismic Regulations for New Buildings and Other Structures", introduced similar requirements for a quality assurance plan crediting the tenets of the Field Act.

This paper will present DSA's quality assurance program for seismic safety. Additionally, it will discuss critical challenges to effective operation of statewide and local quality assurance agencies.

2. PLAN REVIEW

All public school building plans are required to be prepared by qualified California licensed architects or structural engineers. Such a requirement is not applicable to local building departments unless specifically adopted by their local government.

The Field Act mandates a rigorous plan review of project designs. Rigorous plan review requires experienced and trained structural engineers, architects and fire safety officers. All reviewers are required to be licensed or show extensive experience in their discipline. Length of time to perform plan reviews range from one day for simple projects to several months for large, complex projects. Review of projects exceeding $100 million may nearly a year to complete.

The plan review process begins by triaging the submitted plans, specifications, calculations and supporting documents for completeness and correctness of structural design assumptions for type of construction. When deficiencies are identified, the clients are notified that start of review will be postponed until all deficiencies are resolved. Incomplete submittals interrupt and delay staff review, and this triage eliminates wasteful effort. Complete submittals are assigned to first available staff.

The structural plan review engineers conduct a thorough review of structural elements and non-structural components within the architectural, structural, mechanical, plumbing and electrical plans. Coordination between disciplines is performed. Geological hazards reports are assessed for site specific ground motions, and other hazards including liquefaction and flooding. Geotechnical reports are reviewed for foundation design and earthwork requirements. The gravity, foundations and lateral load resisting systems, including connection details, are evaluated for applicable code provisions. Calculations are extensively reviewed for appropriate design criteria assumptions and methods of analysis. When necessary, reviewers perform confirming calculations to substantiate design elements. Connection details are also evaluated for constructability, such as inadequate access to achieve field welds or to place reinforcing steel in congested concrete joints. Attachments of architectural finish materials are assessed to prevent falling hazards. Project specifications are coordinated with the plans and current material standards. The construction observation and material testing plan is prepared on a "Testing and Inspection" form (see Table 1) by the project architect or structural engineer and approved by the plan reviewer.

Table 1 Testing and Inspections Form (DSA-103): This form is interactive with users selecting applicable tests from pull-down menus for materials utilized on a project. The type of test and who performs each test is identified.

REQUIRED?	TEST OR SECIAL INSPECTION	TYPE**	PERFORMED BY**	CODE REFERENCE
+	**SOILS**			
+	**CONCRETE**	(based on 2007 CBC, Table 1704A.4)		
+	**MASONRY**	(based on 2007 CBC, Table 1704A.5.3)		
-	**STEEL**	(based on 2007 CBC, Table 1704A.3)		
-	**17. Structural Steel**			
	Material Verification:			
X	**a.** Verify that all materials are appropriately marked and that: • Mill certificates indicate material properties that comply with requirements, • Material sizes, types and grades comply with requirements.	Periodic	*	* By special inspector when directly to project site withou
X	**b.** Test unidentified materials	Test	Lab	**2212A.1.** ASTM A370-06.
X	**c.** Examine seam welds of structural tubes and pipes	Periodic	Special[4]	* See DSA IR 17-3.
	Inspection:			
X	**d.** Verify member locations, bracing and all details constructed in the field.	Continuous	Project	
X	**e.** Verify stiffener locations, connection tab locations and all construction details fabricated in the shop.	Periodic	Special	
+	**18. High Strength Bolts:**			
+	**19. Welding:**			DSA IR 17-3. AWS D1.1-06.
+	**20. Steel Joists and Trusses:**			
+	**21. Spray Applied Fire-Proofing:**			
+	**22. Shop Fabrication:**			
+	**23. Other Steel:**			
+	**WOOD**			
+	**OTHER**			

Comments are made directly onto the plan check sets, and the sets are returned to the project design professional to reply. A key paradigm for plan reviewers is that all comments must be related to compliance with the building code requirements. Personal preferences of staff relating to member and connection design or to presentation of plans are restricted. Prior to return, the plan check sets are "final" reviewed by the supervisor to ensure consistency in nature of comments and that a complete review was performed.

The project design professionals respond to the comments and schedule a "backcheck" appointment to resolve the items directly with the plan reviewer. Working collaboratively on a face-to-face basis has proven to be the most effective and efficient means to resolve issues. During the backcheck, the material testing and inspection program for the construction of the project is approved. Once all items are resolved, the plans and specifications are stamped and initialed by the enforcement agency, and an Approval of Plans Letter is issued. The Approval of Plans Letter equates to a building permit typically issued by most other building departments.

DSA is constantly striving to improve the plan review process. In an effort to become a collaborative partner in the project design, preliminary design meetings with design professionals and owners have been encouraged. Preliminary meetings are recommended at the beginning of design development, the start of construction documents and prior to project submittal. These collaborative meetings have assisted clients in achieving code compliance for all disciplines early in the design process, and have been highly successful in reducing delays and additional project cost.

Figure 2 Polytechnic High School: Fallen Brick Debris over Exit Corridor after Long Beach Earthquake, 1933. Safe passage for exiting buildings must be provided during building design.

3. CONSTRUCTION OBSERVATION

The goal of the construction observation program is to verify completed construction in accordance with the approved plans, specifications and quality assurance plan. To verify compliance, observation is required to be performed by each of the delegated project design professionals, the project inspector and any required special inspectors. Upon completion of construction, each individual files a Final Verified Report stating, under penalty of perjury, that the construction is in compliance with the approved plans. To avoid conflict of interest, project and special inspectors must be hired by the owner, and may not be in the employ of the contractor. DSA District Structural Engineers oversee this process.

3.1 Project Inspector

The project inspector is mandated to provide continuous inspection of all construction. The project inspector is certified by DSA for the classification level associated with the type of construction. A Class 1 certification applies to complex steel, concrete or masonry structures; a Class 2 applies to complex wood structures; while a Class 3 applies to modernizations or light construction. Certification is available for installation and plant fabrication inspection of modular buildings. To become certified for a given class, inspectors are required to pass a written examination, and must attend DSA training courses to maintain certification. To work on a specific project, project inspectors must be approved by the project design professionals, the owner and DSA. Projects of substantial size and complexity may require multiple project inspectors working together.

The project inspector's duties include: inspection of all plans and specifications identifying any deficiencies requiring correction; filing semi-monthly progress reports to the owner, project design professionals and DSA; monitoring and scheduling the required material tests and special inspections. The project inspector is required to track deficiencies until satisfactorily resolved.

3.2 Special Inspectors

Special inspectors possess knowledge and experience pertaining to specific construction materials and/or processes typically associated with material testing laboratories. Special inspections include, but are not limited to, welding, high-strength bolt installation, masonry, post-tensioned concrete and shotcrete construction. Like project inspectors, special inspectors are approved by the project design professionals and DSA, and employed by the owner. Special inspectors submit progress reports, coordinate with the project inspector and track deficiencies through to resolution.

3.3 Project Design Professionals

All project design professionals responsible for a design must observe construction in accordance with the quality assurance plan. Site visits typically occur at construction milestones. The design professional(s) evaluate all progress reports, resolve discrepancies and ensure that associated testing is conducted. Design professionals are also required to keep records of all inspection and material test reports.

4. MATERIAL TESTING

All construction materials are identified and material properties verified with the specifications. Only DSA

qualified material testing laboratories may perform the required tests. Testing laboratories are evaluated and certified by DSA through their Laboratory Evaluation Assurance (LEA) program. To become LEA certified, lab equipment and processes are screened to meet American Society of Testing Materials (ASTM) Standards. Labs must be managed by a California licensed engineer appropriate for their expertise. Staff credentials and training are validated to perform the test procedures and operate equipment.

Lab managers file and retain reports of all fabrication and material tests, and file the Final Verified Report upon completion of their work. Laboratories are responsible to ensure that all fabrication in out-of-state plants is adequately inspected and materials properly identified.

5. DSA DISTRICT STRUCTURAL ENGINEER

To ensure that construction observation and material testing is properly conducted, DSA employs District Structural Engineers (DSE) to oversee the work of the project inspector, special inspectors and contractor. DSE's visit project sites at appropriate milestones of construction to inspect construction, evaluate the project inspector's performance, review inspection and test records, and ensure all deficiencies are being resolved. Site visits provide training opportunities for the project inspectors. When significant deficiencies in construction occur that pose a risk to life safety, the DSE can implement a Stop Work directive until corrective measures are approved. Upon completion of construction and resolution of deficiencies, the DSE authorizes project certification.

Prior to start of construction, the DSE approves the project inspector to work on a project. If the project inspector's performance is determined to be inadequate and accepting of poor construction, the DSE can initiate removal from the project, not approve the inspector for future work, and initiate removal of their certification.

6. PROJECT CERTIFICATION

Once construction is complete, the project design professionals, inspectors and contractors issue signed final verified reports. Upon receipt of all documents and closing fees, DSA issues a Certificate of Compliance. DSA does not issue a certificate of occupancy, nor is occupancy denied if a project is closed without certification. However, failure to achieve certification has significant ramifications. Local school officials may be personally liable for issues that occur due to non-compliance over the life of the facility. Furthermore, DSA does not approve future work to uncertified construction, thereby restricting growth or modernization of the facility.

7. SUPPORT SERVICES

To operate a successful quality assurance program, staff and management need support for various services.

Statewide teams consisting of DSA supervisors and senior staff members interpret code provisions, define administrative policies and procedures, and render decisions on client appeals. Decisions are published and disseminated for staff and public use.

The project inspector and LEA certification programs are administered by engineers and technical staff at the Headquarters office.

Comprehensive technical and procedural training for DSA staff, project inspectors and plan review consultants is required through the DSA Academy. Attendance by project design professionals is encouraged to enhance plan submittal quality. Courses have been developed to teach plan review processes and interpretations for structural, fire safety and access compliance. Multiple courses for Project Inspectors provide guidance in all disciplines of construction. All training courses are continuously updated to remain consistent with the current building code and technological advances. Educational seminars and participation in professional organizations are supported.

DSA is one of only four agencies in the state authorized to amend the California Building Code to ensure life safety and protection of property. DSA code development personnel collaborate with the International Code Council (ICC), the American Society of Civil Engineers (ASCE), and the Structural Engineers Association of California (SEAOC) code development committees and industry representatives throughout the code adoption process. DSA collaborates with the State Fire Marshal for fire safety amendments, and employs staff to write accessibility code for the California Code or Regulations.

8. CHALLENGES AND ADVANTAGES TO STATEWIDE AND LOCAL QUALITY ASSURANCE PROGRAMS

Significant challenges confront operating a successful quality assurance program. Both local and statewide programs are subject to public and political criticisms and incur pressures to change. Advantages exist to both state and locally run building departments. However, publications by the State of California Seismic Safety Commission support the comprehensive quality assurance

program operated by the DSA. The following paragraphs discuss the most significant challenges.

First, the greatest challenge to any quality assurance agency is providing consistent and timely plan review. To owners, time is money. Lengthy plan reviews delay start of construction. Inconsistent comments between plan reviewers can add unexpected design requirements. Appeals further delay plan approval. All result in increased construction costs. Complaints come from owners, contractors, design professionals and sometimes political officials. The Field Act has been challenged on numerous occasions by legislators and contractors as being too costly and cumbersome. The reality is that quality takes time. Furthermore, studies by DSA and the Seismic Safety Commission have identified that the impact of DSA's program increases the cost of construction by less than 4 percent.

DSA has adopted a collaborative philosophy to address timeliness and consistency. The processes for staff training, code interpretation and preliminary meetings described in this paper are in direct response to these criticisms to improve service. To handle peaks in workload, project submittals are shared between regional offices, and some projects are contracted out to qualified private structural engineering firms.

Contrarily, each local building department is independent. California has over 9200 public schools scattered over 58 counties and 480 cities. Many cities and counties enact local ordinances adding provisions beyond model building codes. Experience and licensing of local building department staff varies dramatically between jurisdictions. The balance of timeliness and quality is dependent upon the mission and policies adopted by the jurisdiction operating within their political and economic boundaries. School districts often extend across multiple jurisdictions and require adherence to multiple sets of rules.

Secondly, assurance agencies are subject to influences of public and government entities and the economy. DSA operates under the laws passed by the state legislature and operational policies established by the Governor. The state's economy impacts school funding programs and construction workload. DSA is constantly adapting to the directions of changing leadership while maintaining continuity of service and the principles of their mission. A current example includes DSA transitioning to a paperless work environment, which has had a significant impact on staff training and equipment investment.

Local building departments are influenced by their local politics, governments and economies. The mission and level of rigor a building department can provide is dependant upon what the community can afford. Since development fees are utilized for funding general services, developers can have great influence on local government decisions affecting construction and building department response timelines. Additionally, other local departments, such as fire and public works departments, often attempt to use public school construction to improve facilities, roads or utilities. When successful, these tactics cause school districts and state taxpayers to bear the costs of community enhancements.

Thirdly, costs for operating a quality assurance program must be affordable and appropriate to the mission. Fees supporting DSA are strictly for the department's operating expenses and do not fund other state services. DSA's fees are competitively low compared to those of most cities and counties.

Finally, as knowledge is learned from earthquakes, and building codes become outdated, societies and building departments are faced with evaluating older facilities for adequate seismic safety. DSA has implemented a program for assessment of existing public school buildings and has developed regulations for rehabilitation of deficient structures. The program applies to strengthening existing certified school buildings and to the conversion of commercial buildings into public school use. The provisions also include design criteria for voluntary seismic retrofit of existing buildings at their owner's discretion.

9. CONCLUSION

In numerous earthquakes around the world, failure of many structures has been traceable to poor design and construction practices. Quality design, comprehensive plan review, construction observation and material testing comprise the required quality assurance necessary to reduce the possibility of catastrophic failures. Designers and contractors cannot always be counted upon to place quality over deadlines, funding or profit concerns. Nations, states and municipalities are faced with the difficult challenges of balancing what level of program to provide within their political and business environments, and what they can afford to provide within their economic realities.

California has developed a system which has proven effective during earthquakes since 1933, but it, too, is not immune from the constant pressures to tighten timelines and reduce expenses. What has been proven is that quality assurance saves lives, and therefore should never be compromised.

Acknowledgements:

The author acknowledges the Center for Urban Earthquake Engineering (CUEE), Tokyo Institute of Technology for the opportunity to promote quality assurance during design and construction and to present the program enforced by the Division of the State Architect for public schools in the State of California.

References:

"NEHRP Recommended Provisions for Seismic Regulations for new Buildings and Other Structures," (1997), National Earthquake Hazards Reduction Program, 33-36

"The Field Act and Public School Construction: A 2007 Perspective," (2007), Alfred E. Alquist California Seismic Safety Commission

"Seismic Safety in California's Schools: Findings and Recommendations on Seismic Safety Policies and Requirements for Public, Private and Charter Schools," (2004), State of California Seismic Safety Commission

Sixth International Conference on Urban Earthquake Engineering
March 3-4, 2009, Tokyo Institute of Technology, Tokyo, Japan

Seismic Mass Damper Application in Los Angeles World Airports

H. Kit Miyamoto[1], Amir S.J. Gilani[2], Jaime Garza[3], and Stephen A. Mahin[4]

1) President and CEO, Miyamoto International Earthquake and Structural Engineers, United States
2) Structural specialist, Miyamoto International Earthquake and Structural Engineers, United States
3) Project Manager, Miyamoto International Earthquake and Structural Engineers, United States
4) Professor, Structural Engineering, University of California, Berkeley, United States
kit@miyamotointernational.com, agilani@miyamotointernational.com, jgarza@miyamotointernational.commahin@ce.berkeley.edu

Abstract: In the past, tuned mass dampers (TMDs) have been used in new high-rise structures in North America, Japan, and elsewhere. Most applications have been for wind loading or vibration mitigation. However, recently, TMDs have been considered and use for seismic retrofit of buildings. For stiff walled (such as concrete towers), the use of other energy dissipation devices is impractical. For these cases, TMDs can be used to obtain a significant reduction in the seismic demand by selecting appropriate mass, stiffness, and damping properties. Such approach was chosen for voluntary upgrade of the 44-m tall landmark Theme Building in the Los Angeles International Airport (LAX). Seismic deficiencies, and non-ductile limit states were identified and mitigated by a combination of TMD to reduce demand, and rehabilitation measures to increase strength. The retrofitted structure met its performance goal.

1. INTRODUCTION

The iconic Theme Building at the Los Angeles International airport is a well known structure. A comprehensive investigation was undertaken to assess the performance of its components to dynamic loading. The concrete core, supporting exterior walls, floor slabs, steel supporting arches, and wind stability cables were investigated and retrofitted as necessary. The evaluation and the ensuing voluntary seismic upgrade of the main part of the structure are presented in this paper.

2. DESCRIPTION OF THE BUILDING

The LAX Theme Building is a landmark structure at the Los Angeles International Airport. The building was constructed in 1959. It is comprised of a concrete core and a system of steel arches. Figure 1 presents a recent photograph of the structure. The overall height of the structure is 44 m extending from ground, at elevation 27.5 m, to the apex of the arches at elevation 71.5 m.

Figure 1. Photograph of the building

2.1 Concrete Core

The concrete core is approximately 33 m tall and extends from base to the roof. Access to the building is provided at the first floor and at the plaza level at 38 m. The first floor and plaza slabs are independently supported by a system of exterior concrete walls. At elevation 51 m, there is the restaurant and entertainment area. The observation level is located at elevation 55 m. The concrete core is connected to the four arches at the observation level.

The concrete core consists of a 5.2-m radius annular wall and a system of internal walls. The core thickness is 300 mm above the first floor. The core is supported by a mat foundation and a system of 128 steel H piles. Structural drawings specify 28-MPa normal weight concrete (NWC) up to elevation of 43 m and 21-MPa lightweight concrete (LWC) above. Longitudinal reinforcement consists of two curtains varying from #36M bars at the to #16M bars at the top. Typical splice length is 25 times bar diameter. Figure 2 presents typical cross section of the concrete core.

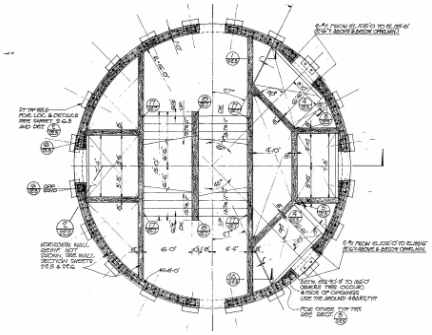

Figure 2. Cross Section of Concrete Core

2.2 Steel Arches

The four steel arches, are 52 m wide, and 41.5 m tall, and are parabolic in shape. To prevent flutter during windstorms, 16 cables are used to connect the upper arches to the concrete core. These cable or rods are used to provide stability for wind loading and bracing for seismic loading.

3. CONDITION ASSESSMENT

3.1 Geotechnical Investigation

Using the available site condition, past seismic events, and active faults that could produce large motions at the site, site-specific response spectra were prepared (Van Beveren & Butelo 2007, and JP Singh 2007). The (Design Earthquake or 475-year event) DE spectrum is anchored at 0.4g and has a peak spectral acceleration of 0.92g. The spectral peaks are similar to the values computed using the ASCE 7 (ASCE 2005) procedure based on the mapped acceleration of the USGS web site (USGS 2007). The fault-normal (FN) and fault-parallel (FP) components have similar spectral amplitudes up to periods of 2-2.5 sec.

Three pairs of spectrum-compatible motions were developed for each level. Recorded earthquake acceleration traces were synthesized such that their response spectra closely matched the target spectra.

Figure 3a present a synthesized acceleration record. The computed response spectrum (average of FN and FP components) and the target spectrum are shown in Figure 3b. The records have acceleration spectra that closely match the target values.

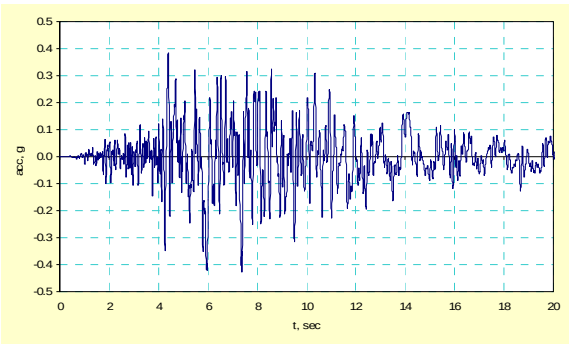

a. Acceleration history

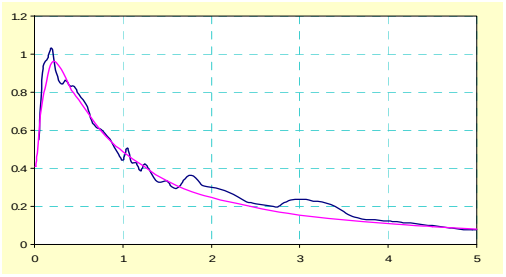

b. Response spectrum

Figure 3. Spectrum-Matched DE Record

3.2 Material Testing

Comprehensive material tests of the structural components were conducted (Twining Laboratories 2007). The testing comprised sampling concrete cores, reinforcement coupons, reinforcement splices, and tests of both fillet and full penetration welds at the upper arches.

ASCE 41 (ASCE 2008) requirements for comprehensive testing were followed. A minimum of three samples for each test component were sampled. Since the concrete strength and unit weight varied along the height and for different walls, 37 concrete cores were extracted and tested.

Table 1 summarizes the test data. Note that the annular wall has compressive strengths of 35 and 32 MPa, for locations were 28 and 21 MPa nominal values were, respectively, specified.

Table 1. Compressive strength of concrete walls, MPa

	NWC	LWC
All wall, nominal	28	21
Annular wall, test	35	32
Exterior walls, test	32	29

The measured splice lengths equaled to or exceeded the nominal values and reinforcement coupons had an average yield and tensile strengths of 350 and 520 MPa, respectively. These values are consistent with the expected strength values as recommended by ASCE 412 for Grade 40 (280 MPa) reinforcement.

3.3 Dynamic field tests

Field tests were conducted by the University of California at Los Angles (Nigbor and Wallace 2007) to determine the dynamic properties of the structure. This data was then used to verify the accuracy of the mathematical model of the building and to design the building retrofit. Field tests consisted of ambient vibration surveys and forced vibration tests. For the latter tests, a concrete pad was cast and anchored at the observation level; see Figure 4. The structure was subjected to low amplitude sinusoidal loading and the acceleration data was collected using accelerometers. Instrumentations were strategically placed, so as to compute the transfer function and mode shape with respect to the roof of the concrete core.

Figure 4. Shakers used for the dynamic field tests

The data was collected in the time domain. It was transferred to the frequency domain and the building frequencies and mode shapes were computed. Figure 5 shows the acceleration power spectral density function obtained from the tests.

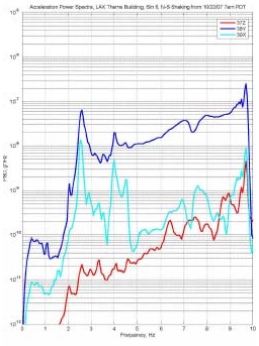

Figure 5. Acceleration power spectra from tests

The peaks in the plot correspond to the building frequencies. The prominent mode is identified at a frequency of approximately 2.5 Hz (0.4 sec). The core fundamental modes in the x and y directions had similar frequencies and mode shapes. The principal modal frequencies are presented in Table 2 Note that the core frequency has a damping ratio of 5-percent of critical.

Table 2. Forced vibration dynamic data

Mode	T, sec	Location	Direction	ξ, %
1	0.54	Upper arch	Y	
2	0.53		X	
3	0.45		Z	
4	0.39	Concrete core	x	5
5	0.38		y	5
9	0.25	Observation & legs	Torsion	
10	0.21			
11	0.18	observation	Z	
12	0.15		Rocking	

4. STRUCTURAL EVALUATION

4.1 Evaluation Criteria

ASCE 41 guidelines were used to assess the seismic performance of the building and to evaluate the effectiveness of the proposed retrofit. The nonlinear dynamic procedure (NDP) was used. Three-dimensional mathematical models of the structure were prepared and were subjected to site-specific motions. The flexural and shear demand were extracted from analysis and compared with computed capacity of the complex cross section at critical elevations.

4.2 Required Performance Objectives

The performance objective for this structure is collapse prevention (CP) for the design earthquake (DE). This is the event with a recurrence interval of 475 years (10% probability of exceedence in 50 years). The excepted level of damage corresponds to major flexural and shear cracks, failure around openings, and large permanent drifts.

4.3 Non-ductile Limit States

To ensure acceptable performance, all brittle modes of failure were checked and mitigated. Typical of this vintage concrete building, this structure has poor reinforcement detailing that does not meet the current requirements to ensure ductile behavior. The following two non-ductile damage states were investigated.

The existing reinforcement has insufficient splice length. All splices have a nominal splice length of 25 times the bar diameter. The splice lengths were inadequate. ACI 318 (ACI 2008a) requires much larger splices for bigger bars embedded in light weight concrete. This mode of failure was eliminated by retrofitting the splice locations or by using reduced yield strength for the reinforcement.

ACI 371 (ACI 2008b) was used to compute the shear capacity of the concrete core. The concrete core has limited shear capacity because of two factors. The openings in the core wall disturb the shear flow path and hence significantly reduce the available shear capacity. Since most openings were oriented parallel to one of the core's principal directions, the shear capacity in that direction was significantly less than the flow in the orthogonal directions. Furthermore, when LWC was used for all the walls, ACI 318 specifies a reduction of 0.75 for shear capacity calculations with LWC. In addition, the shear capacity of transverse reinforcement had insufficient splice length and low volumetric ratio. This mode of failure was accounted for by either increasing the shear capacity at critical elevations or by reducing the seismic demand.

5. MATHEMATICAL MODELS

5.1 Overview

Computer program SAP (CSI 2008) was used to prepare mathematical models of the structure. All pertinent mass and stiffness components were incorporated in the models. Two models were used in analyses; see Figure 6. Model 1 was a three-dimensional model with frame elements used to assess the response of the existing and retrofitted structures and design the TMD. Shell elements were used for Model 2. This model was used for verification studies.

5.2 Calibration of Analysis Models

Model 1 was fixed at base and Icr/Ig was selected as 0.8. Pertinent data from modal analysis are tabulated in Table 3. Comparison of entries in Table 2 and Table 3 show that the analytical model closely predicts the fundamental modes of the core and the upper arches in the principal directions.

Table 3. Analytical modal properties

Mode	T, sec	Loc	Direction
1-2	0.63	Observation	Rocking
5	0.56	Upper arch	Y
6	0.54		X
7	0.43		Torsion
24	0.40	Concrete core	x
25	0.39		y

Since models 1 and 2 had the same seismic mass (22 Mg) and fundamental concrete core frequency (2.5 Hz); they can be considered to be dynamically equivalent. The computed core mode shape from Model 2 and the measured mode shape from field tests is presented in Figure 7. Note that the analytical model closely tracks the field measured fundamental mode shape.

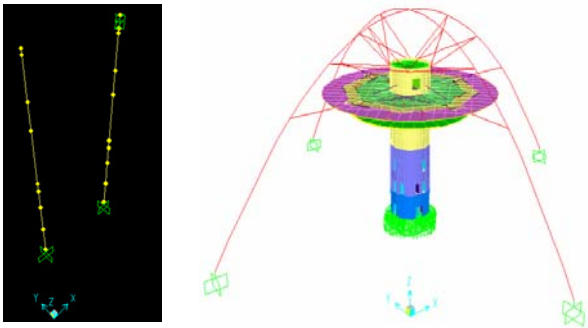

a. Model 1 b. Model 2

Figure 6. Mathematical Models of building

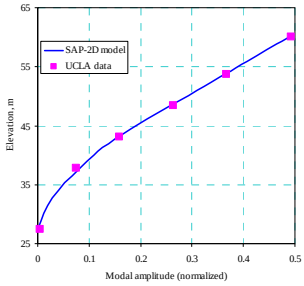

Figure 7. Analytical and experimental mode Shapes

6. FLEXURAL CAPACITY CALCULATIONS

Program xSection (Mahan 2007) was used to compute the flexural capacity of the concrete core at various elevations. The cross section was modeled using fiber elements; see Figure 8a. The strain corresponding to the compressive strength was set at 0.002. The reduced yield strength, as a function of provided splice length and ACI required development length, was computed per ASCE 41 and is shown in Eq 1. Typical moment-curvature results are presented in Figure 8b.

$$f_s = \frac{l_{splice}}{l_d} f_y \qquad (1)$$

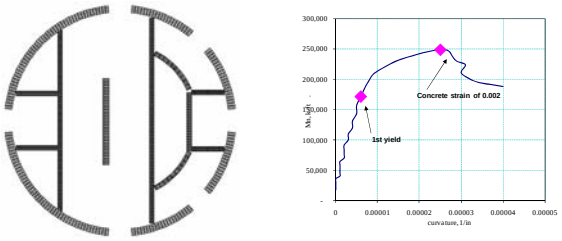

a. Fiber model b. yield stress of reinforcement

Figure 8. Flexural capacity calculations

7. PERFROMANCE OF THE EXISTING BUILING

Figure 9 presents the shear and bending moment distribution along the height of the concrete core. The shear and flexural demands were computed from response history analyses, selecting the maximum values from the three records. The shear and flexural demands exceeded capacity along most of the height of the core.

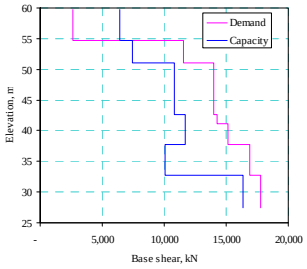

a. Shear

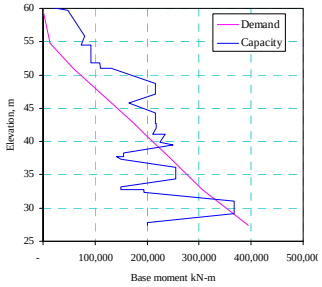

b. Flexure

Figure 9. Existing structure, demand and capacity plots

8. SEISMIC RETROFIT

A comprehensive seismic retrofit was investigated to both increase capacity and to reduce demand. A tuned mass damper (TMD) was selected to reduce seismic demand. This choice was based on structural, aesthetics, and financial considerations. For this type of stiff and tall structure, The conventional retrofits, such as shotcreting the core or adding external pos-tensioning tendons, would have altered the

buildings appearance and hence were not viable.

The addition of TMD will alter the fundamental mode of the concrete core by introducing two modes. In one, the TMD is in-phase with the concrete core, whereas, in another mode, the TMD motion is out-of-phase with the concrete core. Ass result, most of seismic motion is taken up by the TMD and reducing drifts and seismic demand of the concrete core. A high-damped TMD with a mass ratio (defined as mass of TMD to the concrete core) of 25% was selected. The TMD properties were computed based on the procedure developed by Sadek et al (1997) and Villaverde (2002); see Equation 2.

$$f = \frac{1}{1+\mu}(1-\xi)\sqrt{\frac{\mu}{1+\mu}} \quad (2)$$

$$\varsigma = \frac{\xi}{1+\mu} + \sqrt{\frac{\mu}{1+\mu}}$$

In this equation, μ is the ratio of TMD to first mode mass, f is the ratio of TMD to first mode frequencies, ξ, in the damping of the concrete core, and ς is the damping of the TMD. The TMD properties were further optimized by conducting sensitivity analyses with different TMD frequency and damping rations and evaluating response (displacement, acceleration, base shear, overturning moment) reductions.

The reinforcement splices at the three lowest elevations were retrofitted by providing additional confinement. ACI 318 development length depends on the confinement. Such confinement can be provided by drilling holes, pre-compression the cross section using headed reinforcement, and then grouting the holes (Patterson and Mitchell, 2003). By providing full confinement, the lap splices in these locations met the ACI requirements and as such, the reinforcement is expected to reach its full capacity.

At the first floor and at the restaurant, there were large openings in the concrete core, which resulted in significant reduction of shear capacity along one of the core's principal direction. We proposed adding fiber reinforced polymer (FRP) sheets to provide an additional shear capacity of approximately 1800 kN. This would increase confidence in meeting performance level and safety factor.

9. RESPONSE OF RETROFITTED STRUCTURE

Figure 10 presents the shear and bending moment distribution along the height of the concrete core for the retrofitted structure. The shear and flexural demands are less than respective capacities at all elevations. As such, the structure now meets its performance goal. Both demand reduction and capacity increase were required to reach this objectives; neither one alone was sufficient.

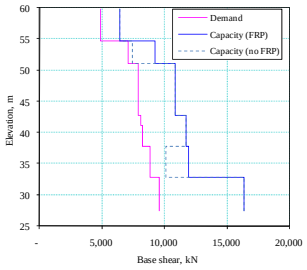

a. Shear

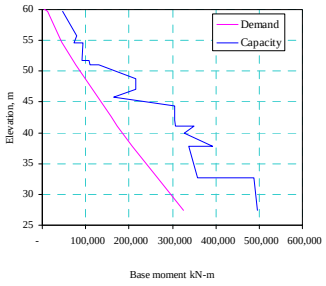

b. Flexure

Figure 10. Retrofitted structure, demand and capacity plots

Figure 11 presents a comparison of roof responses for the existing and retrofitted structures. Drift and force demands were reduced by approximately 30 to 40%.

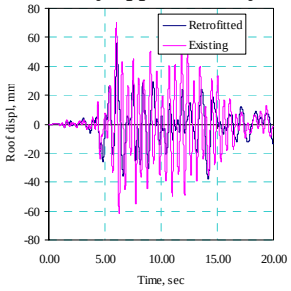

Figure 11. Responses of existing and retrofitted structures

The TMD was placed at the roof of the concrete core. Steel plates were used to provide the TMD mass. Its stiffness and damping was supplied by a system of eight lead rubber bearings and eight fluid viscous dampers respectively (Figure 12). Sufficient gap was provided at the roof to accommodate the motion of the TMD relative to the roof.

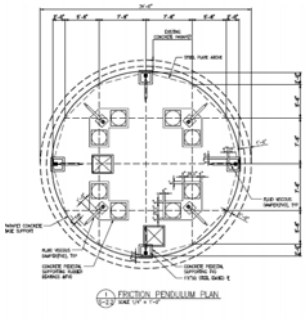

Figure 12. TMD and its components

10. MODEL VERIFICATIONS

Since TMD is tuned to the dynamic response of structure, several sets of analyses were conducted to assess the effect of pertinent parameters on the response of the retrofitted structure.

Table 4 compares the analysis results from Models 1 and 2. The simpler Model 1 was used for design and evaluation, while the detailed Model 2 was used for verification. Good correlation is seen in results.

Table 4. Response of retrofitted models at the roof

	Model 1		Model 2	
	u, mm	a, g	u, mm	a, g
DE-1	56	0.67	56	0.62
DE-2	53	0.54	53	0.60
DE-3	53	0.49	46	0.52
DE-4	48	0.60	48	0.54
DE-5	46	0.41	38	0.52
DE-6	43	0.65	41	0.65

11. CONFIDENCE LEVEL CALCULATIONS

FEMA 351 (FEMA 2000) methodology was used to develop confidence levels for not exceeding the non-ductile limit states. The results are presented in Table 5. The voluntary retrofit has significantly reduced the probability of either shear of bar pullout failures.

Table 5. Limit state probabilities

Limit state	Elevation	Probability (not exceeding)
shear	FRP added	80%
shear	No FRP	45%
bar pullout	Un-retrofitted splice	75%

12. CONSTRUCTION SCHEDULE

The retrofit construction has begun (see Figure 13) and the prototype tests of the TMD components are currently underway. It is anticipated that the construction will be completed in 2009.

Figure 13. Construction photograph

13. CONCLUSIONS

Seismic evaluation of the LAX Theme Building showed that the structure had deficiencies consistent with its construction vintage and would suffer severe damage or collapse in the event of major earthquake. Seismic retrofit was comprised of adding strength and reducing demand.

- TMD with an equivalent mass of 25% was place at the roof and resulted in reduction of over 30% in seismic demand
- Rehabilitation of reinforcement splices, significantly increased flexural capacity of the concrete core.
- We have proposed adding FRP at two critical locations along the core axis with the lowest shear capacity to provide additional safety. Although mot part of the current scope, the client is investigating implementing this item.
- The retrofitted structure met its performance goal and there was moderate to high confidence of satisfactory performance in a major earthquake.

Acknowledgements:
The significant contributions of Messrs. Glenn Ito, Scott Markle, David McCombs, and Jeff Moore, all of LAWA EPMD[1] to this project is kindly acknowledged. Also, the significant contributions of Messrs. Virgil Aoanan C., of VCA Engineers, and Millard A. Lee, of Gin Wong Associates are hereby acknowledged.

References:

Van Beveren and Butelo (2008), Ground Motion Study, Exiting Theme Building Restaurant for the Los Angeles World Airports,
JP Singh (2008), Personal Communications
Twining Laboratories (2007), LAX Theme Building Job No. 070487.1
Nigbor R and Wallace, J (2007), Measurement of Dynamic Properties of the LAX Theme Building, NEES at UCLA
USGS (2007) – USGS Web Site
FEMA (2000), FEMA 351: Recommended Seismic Evaluation and Upgrade Criteria for Existing Welded Steel Moment-Frame Buildings, Federal Emergency Management Agency, Washington DC.
Patterson and Mitchell (2003) Seismic Retrofit of Shear Walls with Headed Bars and Carbon Fiber Wrap, Journal of Structural Engineering, American Society of Civil Engineers, Reston, VA
ACI (2008a) ACI 318-08: Building Code Requirements for Structural Concrete and Commentary, American Concrete Institute, Farmington Hills, MI.
ACI (2008b) ACI 371.R-08 Guide for the Analysis, Design, and Construction of Elevated Concrete and Composite Steel-Concrete Water Storage Tanks American Concrete Institute, Farmington Hills, MI.
ASCE/SEI (2005) ASCE 7" Minimum Design Loads for Buildings and Other Structures, American Society of Civil Engineers, Reston, VA
ASCE/SEI (2006) ASCE 41: Seismic Rehabilitation of Existing Buildings, American Society of Civil Engineers, Reston, VA
Mahan (2007), xSection, Cross section analysis program
Sadek, F., Mohraz, B, Taylor, A., and Chung, R., A (1997) method of estimating the parameters of tuned mass dampers for seismic applications, Structural engineering and structural dynamics.
Villaverde (2002), Aseismic roof isolation system: feasibility study with 13-story building, Journal of Structural Engineering. American Society of Civil Engineers, Reston, VA

[1] Los Angeles World Airports, Engineering and Project Management Division

Sixth International Conference on Urban Earthquake Engineering
March 3-4, 2009, Tokyo Institute of Technology, Tokyo, Japan

SITE-SPECIFIC GROUND MOTIONS FOR EARTHQUAKE DESIGN OF BUILDING STRUCTURES: PRESENT STATE AND FUTURE TREND

Kenichi Kato[1)]

1) General Manager, Kobori Research Complex, Kajima Corporation, Japan
katokenichi@kajima.com

Abstract: The seismic provisions of the Building Standard Law of Japan were revised in 2000 towards a performance-based design code. This is a drastic revision since the input ground motions are defined on the outcropped engineering bedrock in terms of acceleration response spectra. In addition, the revised seismic design code for structures higher than 60 m accepts to use site-specific design ground motions due to scenario earthquakes. This paper shows an example of scenario earthquake from an active fault. To consider their influence on the design of high-rise buildings, results of earthquake response analyses are also presented. Finally, as for the future trend of seismic design, I shall propose the basic concept of ground motion by combining both scenario and non-scenario earthquakes. This paper is rearranged from Kato (2005).

1. INTRODUCTION

In 2000, the seismic provisions of the Building Standard Law of Japan were revised towards a performance-based design code. As shown in Figure 1, the seismic forces of the previous design code were defined in terms of story shear forces as a function of building's period under the categorized soil condition (for example, Midorikawa *et al*., 2004). On the contrary, the revised seismic design code defines the input ground motions on the outcropped engineering bedrock in terms of acceleration response spectra. This is a drastic revision since the input ground motions can directly relate and compared to the observed strong motion records. In addition, the revised seismic design code for structures higher than 60 m accepts to use site-specific design ground motions due to scenario earthquakes. This article shows an example of site-specific design ground motions from scenario earthquakes. Earthquake response analyses of high-rise buildings due to the ground motions are also presented. Occasionally earthquakes are caused by blind faults that cannot be identified in advance. I shall call this type of earthquake "non-scenario earthquake" and show the level of response spectra determined from observed strong motion records in near-source region. Finally, as for the future trend of seismic design, the basic concept of ground motion is proposed by combining both scenario and non-scenario earthquakes, and discusses their availabilities and remaining problems in applying to the performance-based seismic design. This paper is rearranged from Kato (2005).

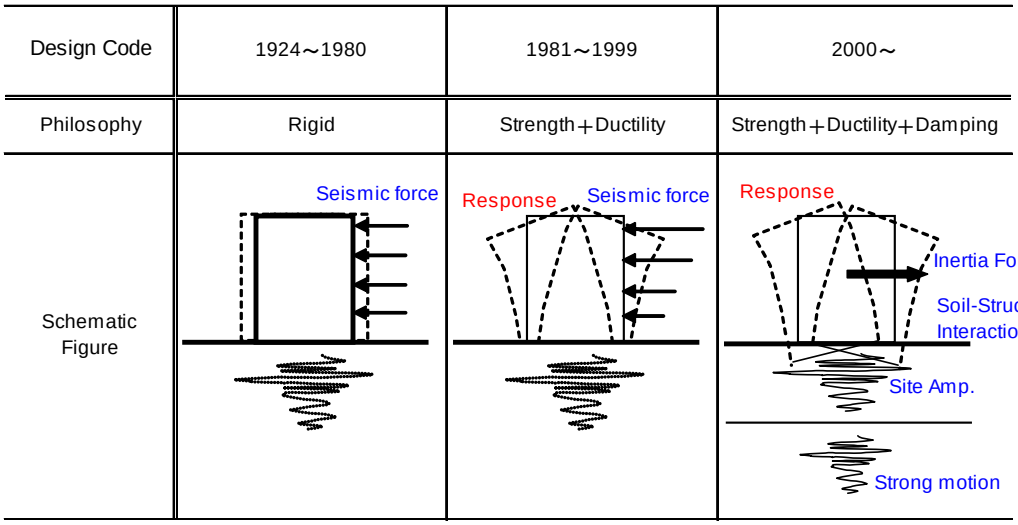

Figure 1 Basic concept of seismic design in each era (Kato, 2005)

2. SCENARIO EARTHQUAKE BY ACTIVE FAULT AND THEIR INFLUENCE ON SEISMIC DESIGN OF HIGH-RISE BUILDING

Near-fault strong motions from the asperity model are synthesized by stochastic Green's function method (Kamae *et al*., 1991). This study was carried out by Yamazoe *et al*. (2004). Figure 2(a) shows the fault model assumed in this study. Fault parameters are estimated on the basis of recipe for predicting strong ground motion from future large earthquake (Irikura *et al.*, 2004). The fault length and width is 20 km and 13 km respectively, and the seismic moment estimated from the fault area by the recipe is $3.98*10^{18}$ Nm corresponding to Mw 6.3. Single asperity is assumed with stress drop of 9.9 MPa. Hypothetical construction site is located 10 km from the surface projection of the fault. The location is corresponding to the direction of forward directivity from the fault plane.

Site-specific design ground motion on the outcropped engineering bedrock with shear wave velocity of 500 m/s is estimated from the stochastic Green's function method, and then site amplification is considered by 1-D stratified medium to obtain surface ground motion. Figure 2(b) shows site-specific design motion on the surface together with ground motions from the seismic provisions of the Building Standard Law of Japan (hereafter I shall call them Standard Law waves). In comparison, El Centro NS component is also shown after normalized to 50 cm/s on the outcropped engineering bedrock. This wave is conventionally used as one of the input ground motions in seismic design.

Figure 2(c) shows their acceleration response spectra with damping factor of 0.05. In the period range shorter than 1.5 s, the site-specific design motion shows smaller amplitude than other waves. On the contrary, the site-specific design motion shows the largest amplitude in the period range from 1.5 to 3 s. This period range corresponds to the predominant period of the asperity with size of 7.6 km square.

Non-linear response analyses of hypothetical 19-storied steel structure are performed. This structure was designed before 2000 year, and the Standard Law waves were not used in the seismic design. Figure 2(d) shows the plan of structure. Grid spacing between columns is 7.5 m. Figure 2(e) shows analytical model of the structure. Columns and girders are modeled as beam elements. Predominant period of this structure is about 2.0 s.

Figure 2(f) shows distribution of structural responses in height such as story shear force, story drift, and maximum ductility ratio of girders due to three input ground motions. In general, allowable limit of the story drift is 0.01 (rad), and allowable limit of the maximum ductility ratio is 2.0 in practical seismic design. The structural responses due to the normalized El Centro NS wave show smaller amplitude than the allowable limit. It indicates that there is no problem as far as the conventional input motion is used. On the other hand, the structural responses due to the Standard Law wave exceed the allowable limit at stories from 3 to 7. The structural responses due to the site-specific design motion show the largest amplitudes in comparison with other input waves, and exceed the allowable limit at many stories. The large amplitude is cause by the resonance, because the predominant period of the structure, 2 s, is very close to the predominant period of input waves that may be originated from the size of asperity. If the site-specific design motion is used as one of input waves, the size or strength of building component such as columns and girders must be modified. Thus, the site-specific design motion plays important roll in performance-based seismic design.

If the predicted ground motions are used as the site-specific ground motions, what kind of design process should we take? I would like to propose four alternative action plans.

(Plan 1) The site-specific ground motions are re-examined. In practical design, asperity is usually set close to the construction site as shown in Figure 2(a), and it may overestimate the predicted ground motions.

(Plan 2) Structural design is re-examined and the size or strength of building component is modified.

(Plan 3) Seismic hazard analysis is performed. If the return period of scenario earthquake is much longer than durable years of the designed structure, results of structural response analysis due to the site-specific ground motions may be treated as reference case.

(Plan 4) Structural control devices are added to reduce the structural responses. For example, base isolation systems, active or semi-active oil damper, and passive damper are available for practical use at this moment.

3. NON-SCENARIO EARTHQUAKES AND ITS IMPORTANCE ON SEISMIC DESIGN

In general, earthquakes occurred in the upper crust are classified into two fault types; the active fault and the blind fault. It is possible to estimate the size and the location of earthquakes due to active faults, since active faults can be identified by the detailed geological surveys such as the lineament analysis from aerial photographs, field investigation, and so on. Based on the estimated fault parameters, earthquake ground motions can be evaluated by empirical, semi-empirical, and theoretical methods as shown in Section 2 in this article. On the other hand, it is impossible to evaluate earthquake ground motions from blind faults based on the same methodology, because the size and the location of blind fault cannot be identified even if the detailed geological surveys aforementioned are conducted. From the viewpoint of seismic design, it is crucial to investigate the level of earthquake ground motions due to blind faults.

Kato *et al*. (2004) selected 41 earthquakes that occurred in the upper crust in Japan and California, shown in Figure 3

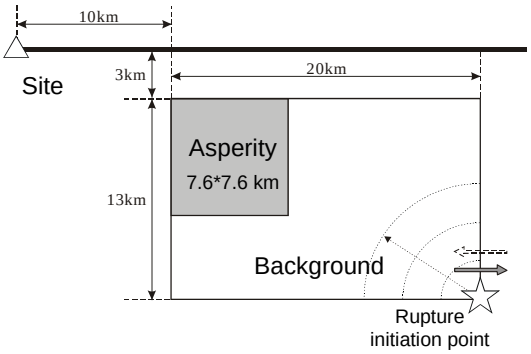

(a) Fault model and location of site

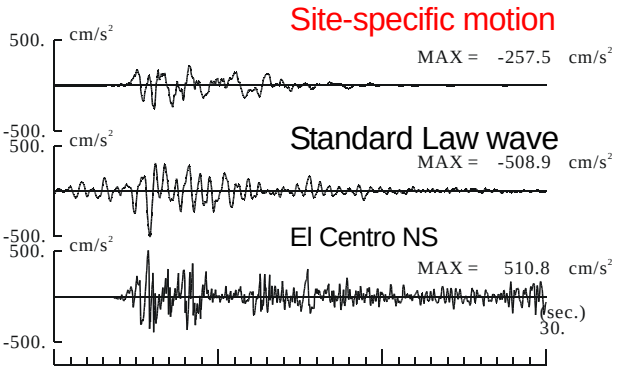

(b) Ground motions on the surface

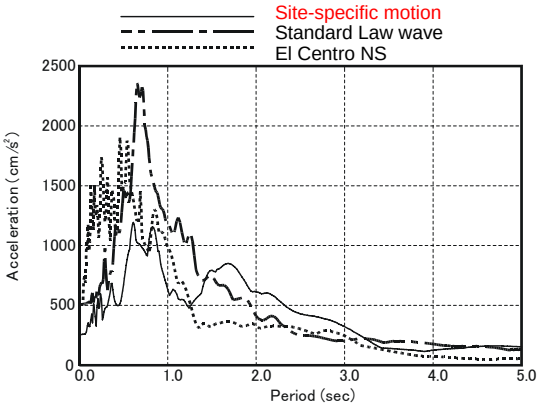

(c) Acceleration response spectra on the surface

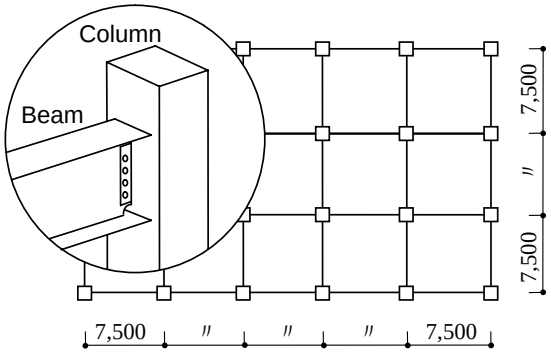

(d) Plan of analyzed steel structure

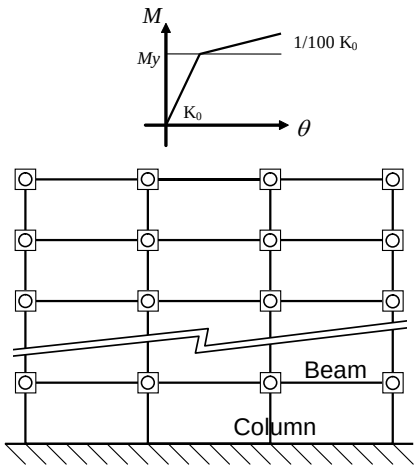

(e) Section of analyzed steel structure

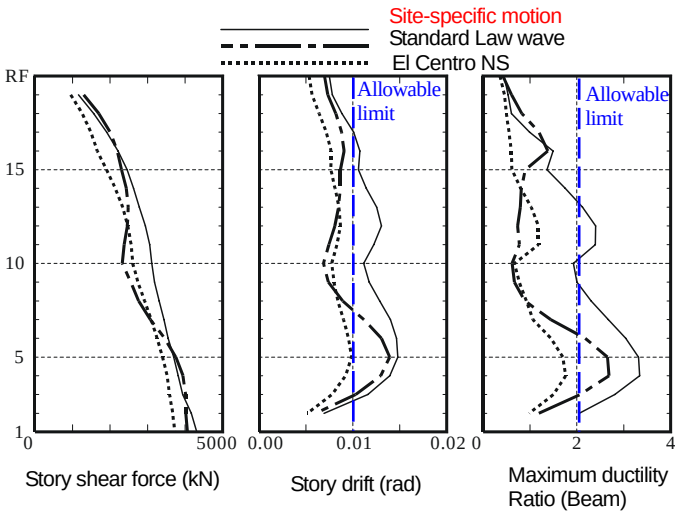

(f) Comparison of structural responses due to 3 input waves

Figure 2 An example of site-specific ground motions from active fault and their influence on the response of 19-storied steel high-rise building (Yamazoe *et al.*, 2004; added and modified)

(a) and (b), and classified them into the active and the blind fault types. These earthquakes were occurred after the initiation of strong motion observations. On the basis of near-source strong motion records observed on rock sites, level of response spectra by blind faults is examined. Figure 4 shows pseudo-velocity response spectra from all 41 events. The spectrum of Building Standard Law is also shown in Figure 4 by dashed line. A large number of observed spectra exceed Standard Law Spectra.

By the detailed geological surveys, the following 4 earthquakes in Japan are picked out as the blind fault type events; the 1984 Nagano-ken-seibu (M_j6.8), the 1997 Yamaguchi-ken-hokubu (M_j6.6), the 1997 March Kagoshima-ken-seibu (M_j6.6), and the 1997 May Kagoshima-ken-seibu earthquake (M_j6.4). M_j is a magnitude determined by Japan Meteorological Agency. Unfortunately near-source strong motion records could not be obtained from the former two events. We add the following 7 earthquakes in our analysis; the 1966 Parkfield (Moment magnitude M_w6.2), the 1978 Santa Barbara (M_w5.8), the 1979 Coyote Lake (M_w5.8), the 1984 Morgan Hill (M_w6.2), the 1987 Whittier Narrows (M_w6.0), the 1991 Sierra Madre (M_w5.6) in California, and the 1998 Iwate-ken-hokubu event (M_j6.2) in Japan. According to the scaling relation of fault parameters, the earthquakes with M_w smaller than 6.2 (M_j smaller than 6.5) are scarcely show the surface fault and difficult to identify the size and the location in advance. Although the above 7 events do not belong to the blind fault type from its strict definition, we incorporate near-source strong motion records from these events into the dataset in order to supplement the shortage of available data.

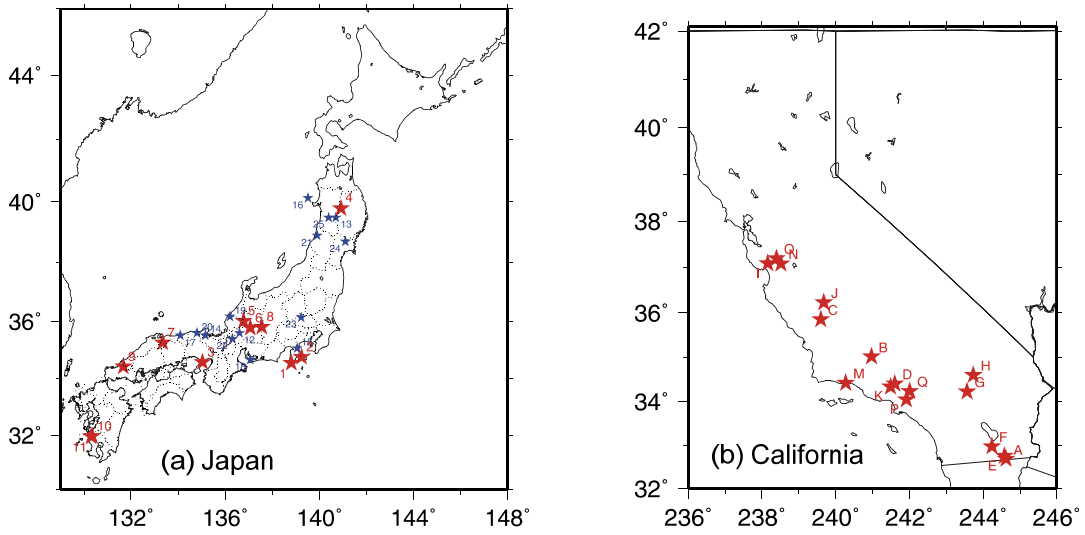

Figure 3 Earthquakes occurred in the upper crust after the initiation of strong motion observations (Kato *et al.*, 2004)

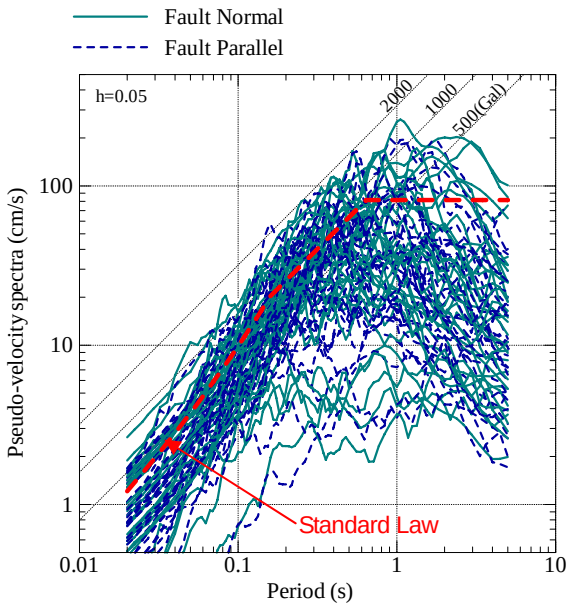

Figure 4 Velocity response spectra for all events shown in Figure 3 (Kato *et al.*, 2004, added and modified)

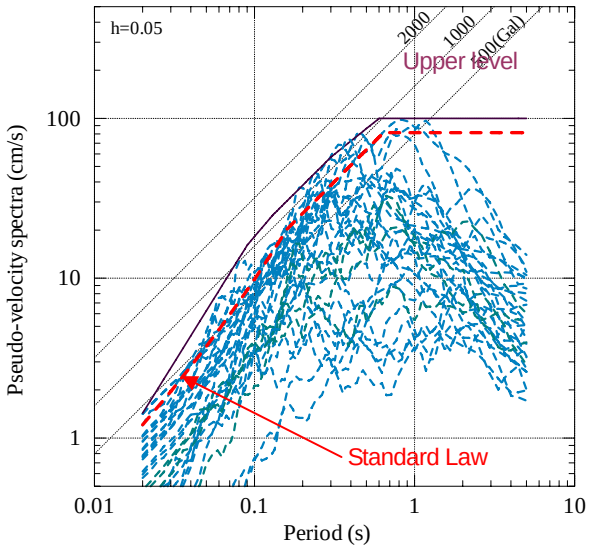

Figure 5 Velocity response spectra for blind faults (Kato *et al.*, 2004, added and modified)

In total, 30 strong motion records of horizontal component observed at 12 stations on rock sites from 9 earthquakes are used to determine the level of response spectra. The minimum distance from the station to the earthquake fault ranges from 3 to 17 km. Figure 5 shows response spectra from blind faults. The level that can envelop the observed response spectra is as follows: the peak ground acceleration is 450 cm/s/s, the flat level of the acceleration response spectra is 1200 cm/s/s, and the flat level of the velocity response spectra is 100 cm/s on rock sites with shear wave velocity V_s of about 700 m/s. The 1984 Nagano-ken-seibu earthquake (M_j6.8) is the largest event by the blind fault in the dataset, but there is no observed record in near-source region. Two observation stations exist at the distance of 24 to 38 km from the earthquake fault, and strong motion records are available.

Kato *et al.* (2004) estimate the level of response spectra in near-source region from the records by correcting the distance effects based on empirical attenuation curve. It is confirmed that the estimated response spectra of the 1984 event are equal to or slightly lower than the upper level shown in Figure 5.

It is important to incorporate the spectral level by blind fault into practical design as a minimum requirement covering whole Japan. The Standard Law spectrum is also shown in Figure 5 by dashed line. This spectrum is defined on the outcropped rock with V_s of about 400 m/s and faster. Observed spectra were recorded on rock sites with V_s of about 700 m/s which are different from the V_s of the Standard Law spectrum. Although it is difficult to directly compare the level of both spectra, most of observed spectra show smaller amplitude than the Standard Law spectrum.

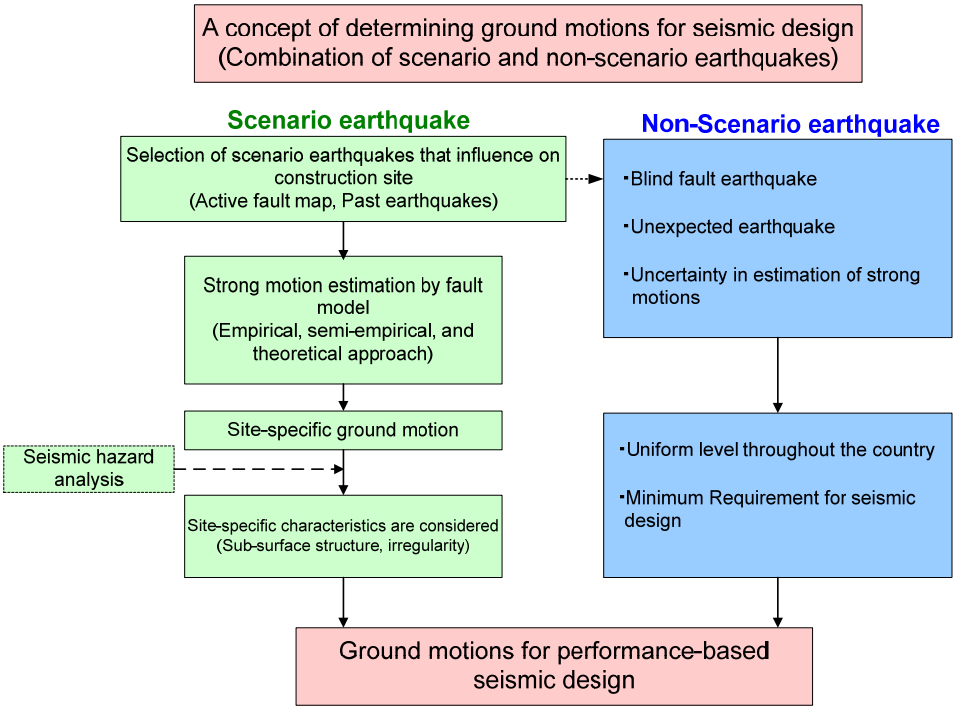

Figure 6 A concept of determining ground motions for seismic design (Kato, 2005)

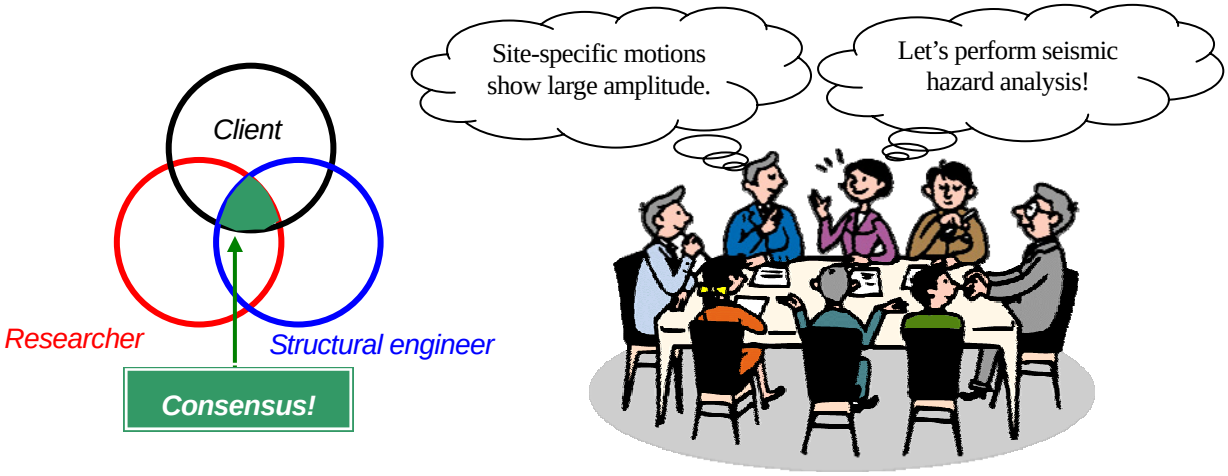

Figure 7 Consensus between researchers, structural engineers, and clients (Kato, 2005)

4. DISCUSSION AND CONCLUSION: FUTURE TREND OF GROUND MOTIONS FOR SEISMIC DESIGN

Figure 6 shows a concept of determining ground motions for seismic design from my point of view. Ground motions are considered via two processes. Left route in Figure 6 corresponds to the scenario earthquake. As I mentioned in Section 2 of this article, site-specific ground motions are evaluated by fault model using empirical, semi-empirical, and theoretical methods. The target events are active fault, plate boundary event, and so on, and they are different in region-to-region considering the seismic activity surrounding the construction site. Strong motion seismology has drastically developed in this decade, and the accuracy of estimating site-specific ground motions is expected to increase.

Right route in Figure 6 corresponds to non-scenario earthquake. Since it is impossible to evaluate earthquake ground motions from blind faults based on the fault model, the level of non-scenario earthquake is determined by observed spectra shown in Figure 5, for example. In addition, non-scenario earthquake has another meaning. No one can deny that an earthquake that is not considered in the assumed scenario will occur in the future. It is evident that the results of strong motion prediction have variation, and there is a possibility to underestimate the actual strong motions. I think non-scenario earthquake has to cover this kind of uncertainties, and is applied as a minimum requirement to whole Japan.

Finally, by combining scenario and non-scenario earthquakes, the ground motion at a construction site is determined. There are many remaining problems when applying the concept in Figure 6 to practical design. For example, site-specific ground motions occasionally show extreme large amplitude in particular at forward direction in near source area. Another problem is the level of non-scenario earthquake. As shown in Figure 7, discussions among researchers, structural engineers, and clients are necessary to solve the problem, and the consensus is the crucial point in performance-based seismic design of structures.

References:

Irikura, K., H. Miyake, T. Iwata, K. Kamae, H. Kawabe, and L. A. Dalguer (2004), Recipe For Predicting Strong Ground Motion From Future Large Earthquake, Proc. 13th World Conf. Earthq. Eng., Vancouver, B.C., Canada, 1371.

Kamae, K., K. Irikura, and Y. Fukuchi (1991), Prediction of strong ground motion based on scaling law of earthquake by stochastic synthesis method, Journal of Struct. Constr. Engng, AIJ, 430, 1-9 (in Japanese with English abstract).

Kato, K., K. Miyakoshi, M. Takemura, D. Inoue, K. Ueta, K. Dan (2004), Earthquake ground motions by blind faults in the upper crust - Categorization of earthquakes based on geological survey and examination of the upper level from strong motion records -, Journal of Japan Association for Earthquake Engineering, Vol.4, No.4 (in Japanese with English abstract).

Kato, K. (2005), Site specific ground motions for performance-based seismic design, International Symposium on Earthquake Engineering Commemorating Tenth Anniversary of the 1995 Kobe Earthquake (ISEE Kobe 2005), A257-A266.

Midorikawa, M., I. Okawa, M. Iiba, and M. Teshigawara (2004), Performance-based seismic design provisions newly introduced to the building standard law of Japan, Journal of Japan Association for Earthquake Engineering, Vol.4, No.3, 162-173.

Yamazoe, M., K. Kato, A., Yamada, M. Takemura (2004), Influence of the difference of source models on earthquake response of high-rise building, Summaries of Technical Papers of Annual Meeting Architectural Institute of Japan, 571-572 (in Japanese).

Sixth International Conference on Urban Earthquake Engineering
March 3-4, 2009, Tokyo Institute of Technology, Tokyo, Japan

COLLABORATIVE RESEARCH ON DEVELOPMENT OF INNOVATIVE STEEL BRACED FRAME SYSTEMS WITH CONTROLLED ROCKING AND REPLACEABLE FUSES

Gregory G. Deierlein[1], Xiang Ma[2], Mathew Eatherton [3], Helmut Krawinkler[1], Sarah Billington[3], and Jerome Hajjar[4]

1) Professor, J.A. Blume Earthquake Engineering Center, Stanford University, USA
2) Graduate Research Assistant, J.A. Blume Earthquake Engineering Center, Stanford University, USA
3) Graduate Research Assistant, Newmark Civil Engineering Laboratory, University of Illinois, USA
4) Professor, Newmark Civil Engineering Laboratory, University of Illinois, USA
ggd@stanford.edu, maxiang@stanford.edu, meather2@uiuc.edu, jfhajjar@illinois.edu

Abstract: This paper describes the development of an innovative new lateral force resisting system that provides improved seismic performance by reducing earthquake-induced damage and facilitating quick repairs after large earthquakes. The design concept is based on a steel braced-frame system that employs controlled rocking, active self-centering (through post-tensioning), and replaceable energy dissipating fuses. Testing and analyses of large-scale fuse and frame subassemblies have demonstrated the viability of the system and provided data to confirm the reliable behavior of the system components. Planning is underway to conduct a large-scale shake table test at the E-Defense facility to fully validate the dynamic system behavior.

1. INTRODUCTION

Traditionally, earthquake design requirements for buildings to resist earthquakes have focused primarily on life-safety (collapse prevention) and have not explicitly addressed damage control that is necessary to limit the risk of significant economic losses and building downtime during a major earthquake. As stated in the Uniform Building Code, "The purpose of the earthquake provisions herein is primarily to safeguard against major structural failures and loss of life, not to limit damage or maintain function (ICBO 1997)". Whereas most engineers are aware of this, typical owners and the general public are not aware of the level of damage that is likely to occur.

The objective of this project is to develop a new type of lateral force resisting system that provides significantly improved performance (reduction in damage, repair costs, and downtime) of buildings subjected to earthquakes. The specific design concepts to achieve the improved performance involve the development of a steel braced-frame system that employs controlled rocking action, active self-centering, and replaceable energy dissipating fuses to both minimize earthquake-induced damage and facilitate quick and economical post-earthquake repairs. When properly designed, the self-centering capabilities of the system will ensure that the system is structurally safe for continued occupancy after a large earthquake.

2. Controlled Rocking System

In concept, there are multiple ways to implement controlled rocking systems using alternative configurations and materials. Shown in Figure 1 are two alternative frame

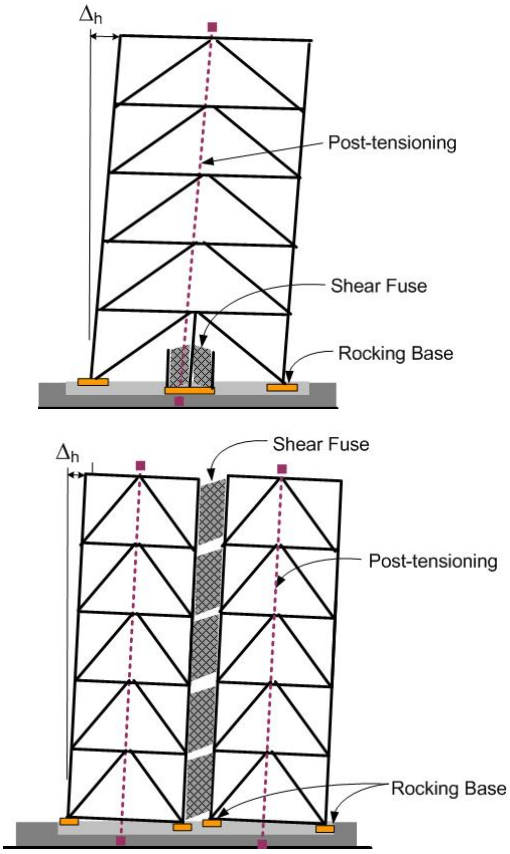

Figure 1 – Schematic of rocking braced frame system (a) single frame configuration, (b) dual frame configuration

configurations that we are investigating. In both configurations, the key components of the system are (a) steel-braced frames, (b) vertical post-tensioning (PT) strands, and (c) replaceable fuses. The braced frames and post-tensioning are designed to remain elastic, while the frame rocks on its base and dissipates energy in the replaceable fuse. In the single frame configuration the energy dissipating fuses are located in the center of the frame, coincident with the post-tensioning. In the dual frame configuration, the shear fuses are located between the two frames. The single frame has the advantage of simplicity, since fewer components are required. The dual frame has the advantage that the configuration amplifies the deformations in the shear fuses, thereby providing greater mobilization of the fuses at low drifts.

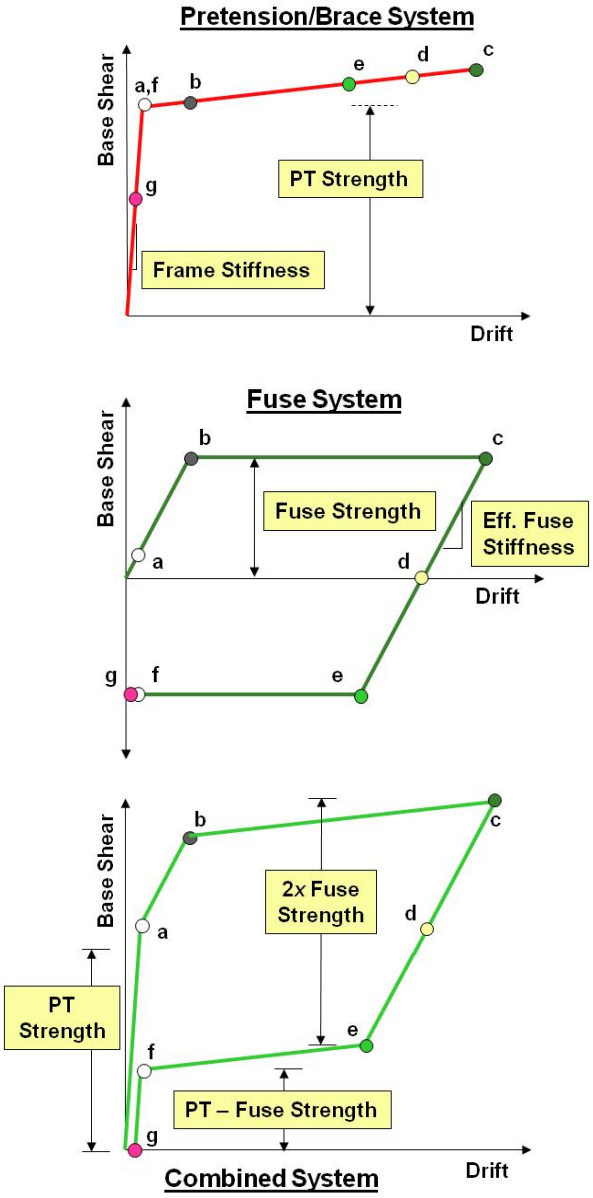

Figure 2 – Force versus deformation characteristics of rocking frame with elastic PT and elastic-plastic fuses

As shown in Figure 2, the overall load-deflection behavior of the combined rocking frame system is based on superposition of strength and restoring actions of the rocking frame with post-tensioning (PT) tendons and the fuse system. The post-tensioned frame exhibits nonlinear elastic response, where the uplift strength and restoring force is controlled by the stresses in the PT plus any gravity loads acting on the frame. The PT strength (at uplift) is proportional to the initial force in the PT strands and the effective over-turning bay dimension of the rocking frame. The fuse system provides energy dissipation through elastic-plastic hysteretic response, although the shape of the hysteresis loop will depend on the specific characteristics of the fuse. The lateral strength provided by the fuse system depends on the fuse strength and the frame geometry. Combined, the two mechanisms result in the "flag shaped" hysteresis loop, where the self-centering ability depends on the difference between the restoring PT force and the fuse strength.

3.0 Energy Dissipating Fuses

The fuse components should be designed with sufficient ductility and toughness that they can dissipate energy throughout the cyclic loading expected during large earthquakes. Moreover, the fuses should be detailed to permit easy replacement in the event they become damaged during a large earthquake. Finally, to help ensure self-centering of the frame after large earthquakes, it is desirable (though not essential) that the fuses exhibit some limited degradation under large deformations.

After considering several alternatives, the authors developed a fuse that consists of a steel plate with "butterfly" shaped links. An example of a fuse that was tested at Stanford University as part of this research is shown in Figure 3. This fuse was fabricated, using standard water-jet cutting, from a thin (6 mm thick) steel plate. For the initial loading region, up to about 7% shear distortion in this example, the fuse links resisted shear force through flexural action with fat hysteresis loops. Beyond deformations of about 7% shear distortion, the links began to buckle in a torsional-flexural mode. At this stage, the flexural resistance of the links decreases and the links begin to resist forces through tension field action. Upon load reversal, the hysteresis loops become pinched as the links buckle in compression and then pick up force again as they stretch in tension. While the pinching decreases the amount of energy dissipated at each cycle, the drop in resistance at large deformations tends to improve the self-centering characteristics of the rocking frame. The degradation in fuse strength also helps to protect the other portions of the rocking frame that are designed to remain elastic under large earthquakes. In this sense, the fuse become sacrificial elements, designed for replacement following a large earthquake.

4.0 Dual Frame Subassembly Tests

With the goal to investigate the rocking frame behavior

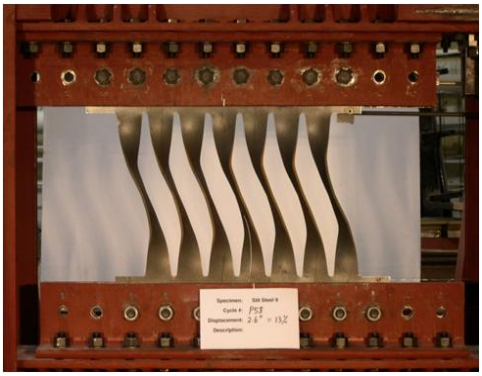

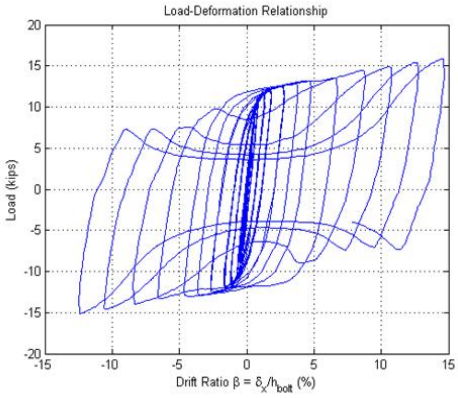

Figure 3 – Energy dissipating shear fuse test fuse

and associated design details, we have recently completed tests of a large (1/2 scale) three-story rocking frame specimen at the University of Illinois NEES facility (Eatherton 2009). Shown in Figure 4 is a photograph of the rocking frame specimen. This specimen is based on the dual frame configuration, as shown previously in Figure 1. In total, seven tests were conducted on the frame to examine alternative fuse designs, varying post-tensioning force, and alternative loading histories.

The test specimen was designed based on a prototype three story office building designed for a typical high seismic site in Los Angeles, California. Based on the design spectrum (characterized by a short period spectral acceleration of S_{DS}=1g and one-second period of S_{1S}=0.6g) and using a seismic response modification factor of R=8 (typical in the U.S. for ductile force resisting systems), the minimum required design base shear coefficient (V/W) for the frame is 0.125. This base shear was used to establish the minimum required strength of the rocking frame, corresponding to the point "b" in the response plot for the combined system in Figure 2. This strength is equal to the overturning resistance provided by the initial PT force (typically on the order of 30% to 50% of the nominal tensile strength of the PT tendons) combined with the nominal yield strength of the shear fuse. The required base shear, calculated using R=8, is about 25% less than would be required for a conventional braced frame.

Shown in Figures 4b and 4c are summary data from one

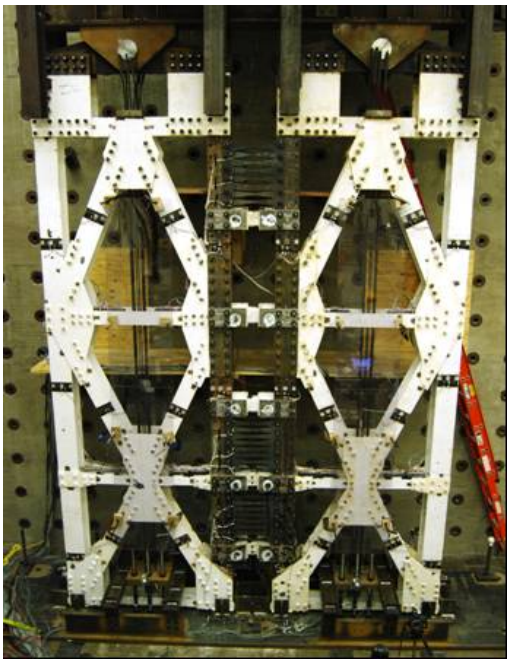

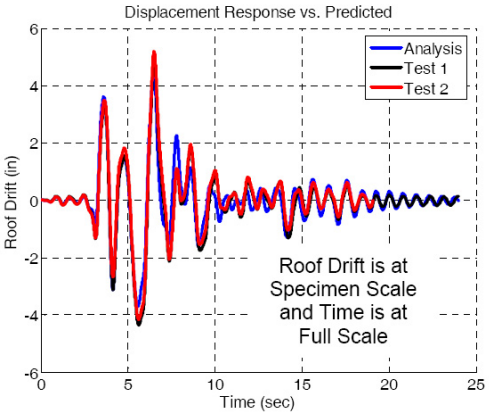

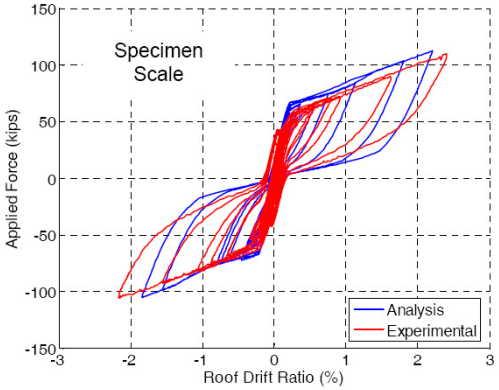

Figure 4 – Dual frame rocking frame test (a) photograph, (b) time-history response, and (c) load-deformation response.

of the rocking frame tests that was loaded pseudo-dynamically under the JMA Kobe record. Included in the figure are pre-tests analyses along with the measured

response. The results shown are for loading of 1.1 times the recorded JMA Kobe ground motion, which has spectral intensities about 2.4 times larger than the Design Basis Earthquake and 1.6 times larger than the Maximum Considered Earthquake. It is quite remarkable that even at this high intensity, the maximum drift ratio was limited to about 0.023 and the frame experience no residual drift. Moreover, there was very limited damage to the fuse and little loss in PT force. Owing to the limited damage under the extreme ground motion and to further demonstrate the reliability of the response, the frame was subsequently subjected to (and survived without significant damage) a second loading with the 1.1 JMA Kobe record.

The agreement between the analysis and measured data in Figures 4b and 4c demonstrate that the response can be accurately predicted with nonlinear analysis models. As the primary yielding element is the shear fuse, accurate modeling can be achieved provided that the shear fuse model is calibrated to the shear fuse response (Figure 3). The slightly pinched hysteretic response in Figure 4c reflects the slight degradation of the fuse at large deformations.

5.0 Single Frame Shaking Table Test

To further examine the performance of the controlled rocking frame system, a large (2/3) scale three-story frame will be tested at the E-Defense facility in August 2009. In addition to demonstrating the reliability of the system and its components, this test will be an important proof-of-concept of the design criteria, constructability, and performance of the system. We are jointly planning this test with collaborators from the Tokyo Institute of Tech. (T. Takeuchi and K. Kasai), Hokkaido University (M. Midorikawa), and E-Defense (M. Nakashima and T. Hikino).

As shown in Figure 5, the shaking table specimen is based on a single rocking frame configuration, where the post-tensioning and fuse are located along the centerline of the frame. The frame is designed for a similar prototype building and design criteria as described previously for the dual-frame configuration tests. Preliminary analyses indicate that the rocking frame will experience maximum story drift ratios of about 0.015 under the JMA Kobe ground motion that is scaled to the MCE level intensity. As observed in the subassembly frame tests, we expect minimal damage to the frame at this intensity.

Four tests of the rocking frame are planned to investigate alternative fuse designs, including a buckling restrained brace damper. The frame tests will utilize a re-usable testbed assembly (shown in white in Figure 5) that provides the inertial mass and bracing for out-of-plane stability (Takeuchi et al., 2008). This re-useable testbed offers significant savings in the required time, budget and complexity of the rocking frame tests.

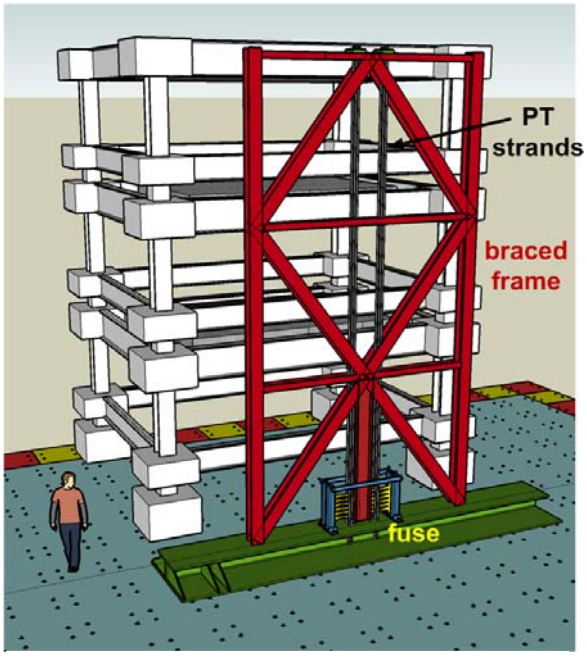

Figure 5 – Schematic of single frame shaking table test planned for E-Defense.

5. CONCLUSIONS

As outlined in this paper, previous and ongoing research has demonstrated the viability of a new structural system that employs controlled rocking to provide enhanced performance under earthquakes. In particular, the proposed system can be designed to essentially eliminate residual displacements, thereby minimizing damage and downtime of the facility. Use of industry standard components, combined with reduced base shear strength for the braced frame, make this equally attractive to conventional braced frame systems, both in terms of first-cost and performance. Durability and robustness, combined with replaceable fuse elements, provide further advantages from a life cycle perspective. While this study has focused on the concepts of controlled rocking and replaceable fuses for steel braced frame systems, similar concepts can be applied to reinforced concrete systems.

Acknowledgements:
This research is supported by the National Science Foundation (Grant No. CMMI-0530756), the American Institute of Steel Construction, Stanford University, and the University of Illinois. The authors acknowledge contributions of our industry partners from the US (David Mar and Gregory Luth) and our Japanese collaborators: T. Takeuchi, M. Midorikawa, T. Hikino, K. Kasai, M. Nakashima, their colleagues and students.

References:

International Conference of Building Officials (1997), *Uniform Building Code*, ICBO, Whittier, CA.

Eatherton, M.R. (2009), "Controlled Rocking of Steel-Framed Building With Replaceable Energy Dissipating Fuses," *PhD. Dissertation Proposal, Univ. of Illinois.*

Takeuchi, T., et al. (2008), "Shaking Table Test Using Multipurpose Test Bed," *Proceedings of 14WCEE*, Beijing, S17-01-002.

Sixth International Conference on Urban Earthquake Engineering
March 3-4, 2009, Tokyo Institute of Technology, Tokyo, Japan

STUDY ON ENERGY-BASED SEISMIC DESIGN METHOD AND THE APPLICATION FOR STEEL BRACED FRAME STRUCTURES

Lieping Ye[1], Guangyu Cheng[2], and Zhe Qu[3]

1) Professor, Department of Civil Engineering, Tsinghua University, China
2) PhD Candidate, Department of Civil Engineering, Tsinghua University, China
3) PhD Candidate, Department of Civil Engineering, Tsinghua University, China
ylp@tsinghua.edu.cn, chengguangyu@mails.thu.edu.cn, qz@mails.thu.edu.cn

Abstract: An energy-based seismic design framework for building structures is proposed with comprehensive understanding of the relationship between energy-based and performance-based seismic design methods. Some fundamental aspects are especially concerned, including spectral input energy E_I, cumulated hysteresis energy ratio E_H/E_I of both SDOF and MDOF systems, system capacity design philosophy of controlling the distribution of hysteresis energy E_H in MDOF systems, methods of determining E_H distribution in building structures as well as the limitations of this method. The proposed framework of seismic design is applied to braced-steel frames to show its effectiveness. The scope of future researches for energy-based seismic design is also outlined, including ground motion intensity indices, distribution of hysteresis energy in MDOF systems, energy-based and displacement-based design methods for individual structural components and energy-based seismic design of irregular structures.

1. INTRODUCTION

Since the first proposal by G. Housner (1956), great progress has been made by researchers in the fundamental aspects of the energy-based seismic design method. One of the major differences between the energy-based seismic design method with other methods, such as the conventional force-based methods and the displacement based method recently, is that a preferable energy-dissipating mechanism is required in the design with the hope that the structure subjected to severe earthquakes will follow the presumed energy-dissipating mechanism and the total energy dissipation capacity of the structure must be greater than the input energy of expected earthquake ground motions. In this way, Engineers are required to fully understand the energy-dissipating behavior of the structure and to control the distribution of structural damages and energy dissipating mechanisms.

Energy dissipation patterns in building structures can be either concentrated or distributed. For seismically isolated buildings, the energy dissipation is concentrated at the isolation layer. Besides, the isolated structure behaves more like a SDOF system, which makes the analysis of such systems much easier. Thus, the energy-based seismic design method was firstly applied to isolated structures (AIJ 2001). On the other hand, energy-based seismic design method was not so far well-developed for structures with distributed energy dissipating mechanisms, such as passive controlled structures with continuously distributed dampers. One of the major difficulties is to estimate the energy distribution among the structural system under severe earthquake, in which case some components of the system were already considerably damaged. This can be very difficult if the damage mode of the system is too arbitrary.

In order to overcome this difficulty, "system capacity design methodology" was proposed by the first author (Ye *et al.* 2002). The main idea is to control the structural damage mode by keeping a main sub-system nearly within its elastic region even when the system is subjected to very severe earthquake. Once the structural system damage mode being controlled, the distribution of energy dissipation will be easier to be estimated. Based on this approach, an energy-based seismic design framework is proposed in this paper.

2. FRAMEWORK OF ENERGY-BASED SEISMIC DESIGN

It is not intended to take the place of the traditional force-based or the recently emerging displacement-based design method by the energy-based design method. Rather, the energy-based seismic design is a supplement to those current design methods, which is expected to make the performance-based seismic design more comprehensive. Strength is a fundamental issue to ensure the structure safety under design earthquake as IO in Figure 1 while for severer earthquakes like LS in Figure 1, displacement limitations proved very helpful to reduce casualty and economic losses. Such displacement limitations are usually dependent on the building occupancies, which are not directly related with the structural seismic capacity or dynamic characteristics. The structural seismic behavior is actually a process of the structure to dissipate the input energy of the ground motion. This is the fundamental concept of the energy-based seismic

design. To ensure the structural safety under very rare earthquakes, the LS state in Figure 1 should be kept far enough away from the collapse point (CP in Figure 1), although the determination of such collapse point is still very difficult. Disastrous earthquakes in the last two decades such as Northridge earthquake in 1994, Kobe earthquake in 1995, Chichi earthquake in 1999 and Wenchuan earthquake in 2008 caused astonishing casualty and economic losses. It is of essential importance to study the collapse behavior of building structures under very rare mage earthquakes. Although it is already out of the scope of this paper, some researches have shown that well-designed energy-dissipating mechanisms are helpful to reduce the collapse probability of building structures under very rare mage earthquakes. As mentioned before, engineers to conduct energy-based seismic design are required to comprehensively understand the energy dissipating mechanism of the structure subjected to severe earthquakes. As a result, the aim of energy-based seismic design is to improve the structure design against severe earthquake (as around LS in Figure 1) by applying more reasonable energy-dissipating mechanisms. Furthermore, energy-based seismic design is not only suitable for seismic-resistant structures, but also for seismic passive control and seismic isolation structures.

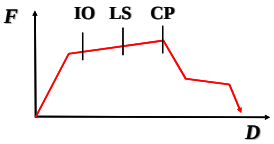

Fig.1 Seismic performance objects of building structures

A design framework as shown in Figure 2 is proposed to achieve the above aim, where the route through ①-③-④-⑤-⑨ is the current displacement-based design and ①-②-⑥-⑦-⑧-⑨ is energy-based design. The energy-based design emphasizes the design of the energy-dissipation mechanism, which is very important for the structure to meet the structural performance objects. The design procedure should be able to ensure that the structure follows the presumed energy-dissipating mechanism under severe earthquakes.

Besides the strength and deformability demands, the following aspects need to be further considered in the energy-based design: (1) Demand of total input energy EI; (2) Hysteresis energy ratio EH/EI (and damping energy ratio ED/EI for structures with viscous dampers); (3) Distribution of hysteresis energy in the structure; (4) Evaluation of component damage.

3. DEMAND OF TOTAL INPUT ENERGY E_I

A lot of researches have been devoted in determining the demand of total input energy E_I. Acceptable design energy spectra (E_I spectra) are already obtained despite of some detailed problems which need further studies. In early researches, E_I spectra were established for elastic SDOF systems. Later, E_I spectra for inelastic SDOF

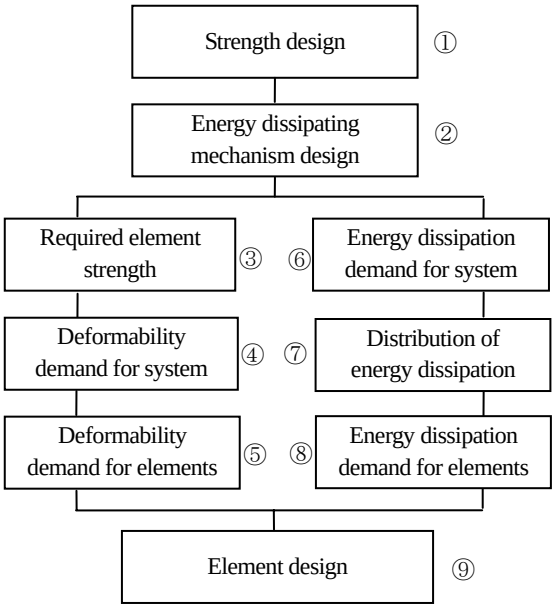

Figure 2 Framework of energy-based seismic design

systems were also established. The E_I spectra used in this study is as below.

3.1 Energy spectra for elastic SDOF systems

The normalized energy spectra for elastic SDOF systems with damping ratio ξ=0.02 are obtained for different site types as shown in Figure 3a, which consists of three branches as below:

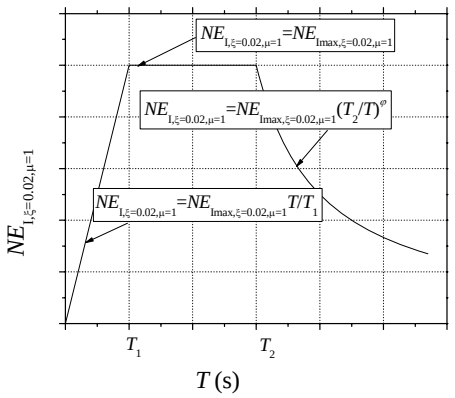

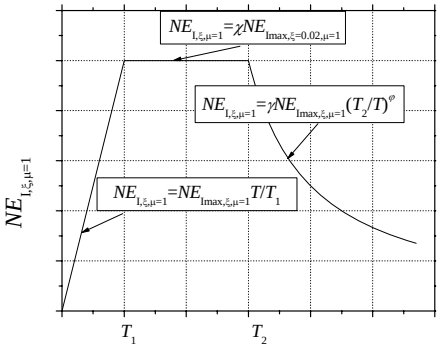

Figure 3 Energy spectra of elastic SDOF systems: (a) Normalized energy spectrum at ξ=0.02 and

(b) Normalized energy spectra at various damping ratios

I: For short period $T<T_1$, a linearly ascending branch, reaching its peak N_{EImax}, ξ=0.02, μ=1 at $T=T_1$;

II: For moderate period $T_1 \leqslant T<T_2$, a plateau equal to N_{EImax}, ξ=0.02, μ=1;

III: For long period $T \geqslant T_2$, a descending branch with parameters φ given in Table 1.

Table 1 Parameters of elastic energy spectra

Site Type	S1	S2	S3	S4
T_1(s)	0.2	0.3	0.4	0.5
T_2(s)	1	1.8	2	2.5
φ	2.2	2.8	2.8	2.8
$NE_{Imax,\xi=0.02,\mu=1}$	1.0	1.2	1.2	1.3

The characteristic periods T_1 and T_2 are determined following the proposal by Decanini *et al.* (2001) as shown in Table 1. The normalized peak values N_{EImax}, ξ=0.02, μ=1 for different site types are also listed in Table 1, which are obtained as the mean plus one standard deviation of the ground motion spectral energy in the period region of $T_1 \leqslant T<T_2$. Based on the analysis by the authors, the energy spectra peak values E_{Imax}, ξ=0.02, μ=1 was suggested as,

$$E_{Imax,\xi=0.02,\mu=1}=NE_{Imax,\xi=0.02,\mu=1}(9.11I^{1.91}) \quad (1a)$$

$$I = \dot{x}_{gmax} t_D^{0.15} \quad (1b)$$

where I is earthquake intensity index; $\dot{x}_{gmax}$ is peak ground velocity and $t_D^{0.15}$ is strong ground motion duration.

Table 2 Damping modification factor

Damping ratio	0.05	0.1	0.2	0.3
χ (Mean)	0.743	0.569	0.426	0.359
χ（Mean+StdDev）	0.819	0.669	0.526	0.452

Considering the influence of system damping ratios on the elastic energy spectra, a set of two damping modification factors χ and γ are proposed to transform the energy spectra at a standard damping ratio of 0.02 to various damping ratios, as shown in Figure 3b. Factor χ, as given in Table 2, is used to modify the normalized peak value. Factor γ, given by Equation 2, is used to modify the descending branch of the spectrum.

$$\gamma = \frac{(4.5\xi - 0.0663)T + 1}{(4.5\xi - 0.0663)T_2 + 1} \qquad T \geq T_2 \quad (2)$$

The design elastic energy spectrum corresponding to different site types and ground motion intensities can then be obtained by multiplying the normalized energy spectrum by the peak values given by Equation 1, as shown in Figure 4.

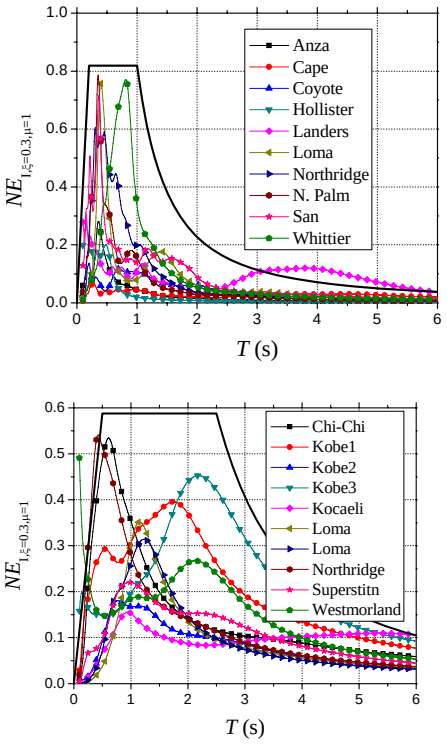

Figure 4 Proposed elastic energy spectra: (a) S1, ξ=0.1 and (b) S4, ξ=0.3

3.2 Energy spectra for inelastic SDOF systems

Inelastic energy spectra are much more sophisticated than elastic ones. The following factors may have considerable influence on them.

(1) Hysteresis model: It was commonly believed that the influence of hysteresis models on energy spectra is insignificant and that it is conservative to use the bilinear model to generate design spectra. However, the author discovers that such a consensus is only applicable in the moderate and long period region. In short period region, the energy spectra of systems with degrading stiffness are generally larger than those with the ideal bilinear model. This effect should be taken into account if short-period structures are to be studied. In this study, only moderate and long period structures are covered. So the energy spectra yielded with bilinear models can be still regarded as conservative.

(2) Post-yielding stiffness: Most researchers didn't give enough attention to the influence of the post yielding stiffness. It is generally believed that energy spectra with post-yielding stiffness ratio η=0 or 0.05 is conservative. In some cases, however, the input energy for hardening systems can be larger than for perfect plastic-elastic systems. In studying the energy spectra of SDOF systems in this paper, bilinear model with η=0.05 is used herein to simulate the hardening behavior. Hardening systems with η>0.05 will be discussed for MDOF systems.

(3) Damping ratio and ductility factor: Damping and inelastic hysteresis are the two aspects of energy dissipation. They both have significant influence over the energy spectra.

Peak spectral input energy decreases with the increasing of the damping ratio and ductility factor. Based on

the analysis by the authors, the average ratio of peak spectral input energy of inelastic systems with various damping ratios $E_{\mathrm{Imax},\xi,\mu}$ to that of elastic systems with ξ=0.02 $E_{\mathrm{Imax},\xi=0.02,\mu=1}$ is suggested as Equation 3.

$$\zeta = \frac{E_{\mathrm{Imax},\xi,\mu}}{E_{\mathrm{Imax},\xi=0.02,\mu=1}} = \left(0.6845 - \frac{0.6393}{\mu} - 0.0882\ln\xi - \frac{0.1517}{\mu}\ln\xi\right)\mu^{-0.57} \quad (3)$$

Considering the standard deviation of ζ is 0.05, the normalized peak spectral input energy for inelastic SDOF system $NE_{\mathrm{Imax},\xi,\mu}$ can be determined by Equation 4.

$$NE_{\mathrm{Imax},\xi,\mu} = (\zeta + 0.05)NE_{\mathrm{Imax},\xi=0.02,\mu=1} \quad (4)$$

The energy spectrum slightly decreases in short period region (T<0.5s) and dramatically increases in moderate and long period regions (T>0.5s) with the increase of the damping ratio when ductility is constant, as shown in Figure 5. On the other hand, the energy spectrum significantly increases in short period region (T<0.5s) and decreases in moderate and long period regions (T>0.5s) with the increase of the ductility factor when the damping ratio is constant, as shown in Figure 6.

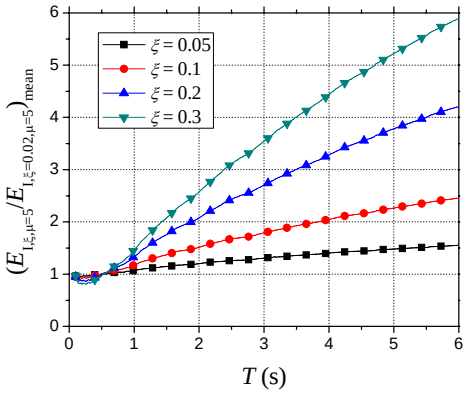

Figure 5 Influence of damping ratio ξ (μ = 5)

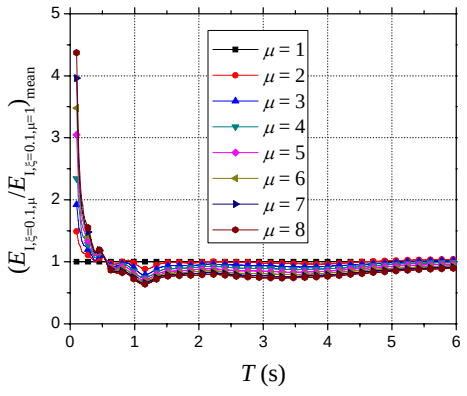

Figure 6 Influence of ductility factor μ (ξ=0.1)

The following modification is applied to the energy spectra in period region $T>T_2$ according to the analysis results in Figure 5 and 6.

$$\frac{E_{\mathrm{I},\xi,\mu}}{E_{\mathrm{I},\xi=0.02,\mu=1}} = (4.5\xi - 0.0663)(13-\mu)\frac{T}{12} + 1.0 \quad (5)$$

where $T \geq T_2$, $\mu \leq 5$

Energy spectrum significantly increases with the increase of ductility factor in short period region. This is mainly due to the increase of the equivalent period of the system. Equation 6 is recommended to calculate the equivalent period.

$$T_{1,\mu} = \frac{T_1}{1 + 0.121(\mu-1)^{0.939}} \quad (6)$$

Figure 7 compares the energy spectra given by time history analysis and the proposed equations for various combinations of damping ratios and ductility factors. It is shown that the proposed energy spectra are accurate enough and conservative.

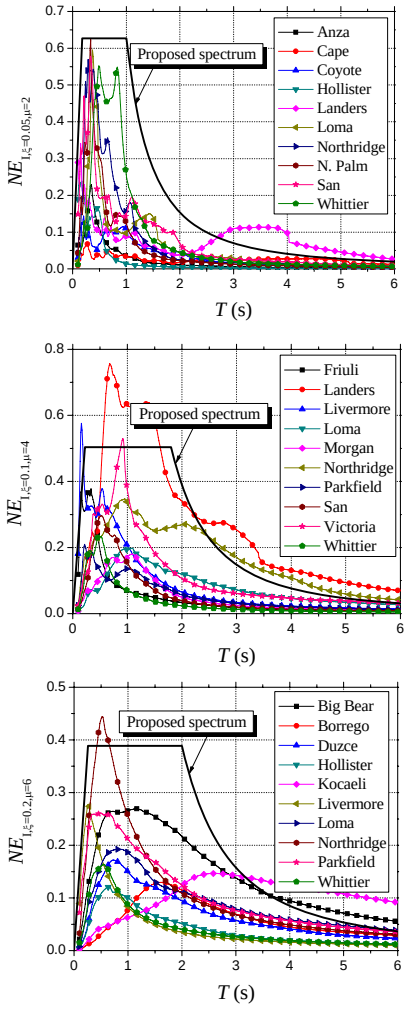

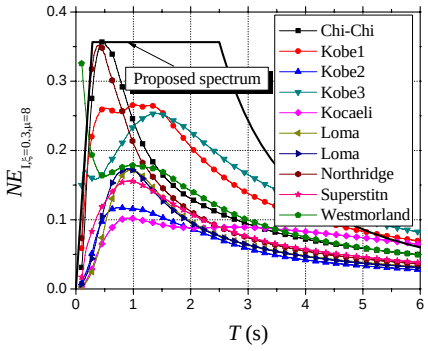

Fig. 7 Proposed inelastic energy spectra: (a)S1 ($\xi = 0.05$, $\mu = 2$), (b) S2 ($\xi = 0.1$, $\mu = 4$), (c) S3 ($\xi = 0.2$, $\mu = 6$) and (d) S4 ($\xi = 0.3$, $\mu = 8$)

3.3 Energy spectra for MDOF systems

Besides the factors influencing the SDOF systems, the earthquake input energy to inelastic MDOF systems are also influenced by the system parameters and ground motion characteristics. It will be extremely complicated to consider all these influencing factors. Bearing in mind that the input energy E_I is a global parameter, the scattering of the influence of different factors on the relationship between the input energy of SDOF and MDOF systems is relatively insignificant if the global system parameters of the SDOF and MDOF are identical. For this reason, the input energy to inelastic SDOF systems $E_{I,SDOF}$ is generally taken as an approximation of that to inelastic MDOF systems $E_{I,MDOF}$. It has been proved accurate enough for engineering practice to use the input energy of SDOF system $E_{I,SDOF}$ as an approximation of that of the MDOF system with the same fundamental period T_0 (Housner *et al.* 1956, Kato *et al.* 1982 and Akiyama *et al.* 1985), i.e.

$$E_{I,MDOF} = E_{I,SDOF}(\xi_1, \mu, T_0) \qquad (7)$$

4. DEMAND FOR HYSTERESIS ENERGY RATIO E_H/E_I

4.1 Demand for hysteresis energy ratio in SDOF systems

Factors influencing the hysteresis energy ratio E_H/E_I of SDOF systems include the damping ratio, the ductility factor and the initial period. For brevity, the influence of these factors on the hysteresis energy ratio E_H/E_I is firstly studied for inelastic SDOF system with bilinear hysteresis and post-yielding stiffness ratio η=0.05. Figure 8 presents some results of E_H/E_I, and following observations are made:

(1) E_H/E_I decreases for larger periods. For given damping ratio and ductility factor, E_H/E_I is approximately linearly descending along the whole range of period.

(2) E_H/E_I decreases for larger damping ratios when constant ductility system is studied.

(3) For given damping ratio, the influence of ductility factors is insignificant in the whole period region when the ductility factor $\mu \geqslant 3$. E_H/E_I increases with the increase of ductility factor. This increase is relatively large in short period region and negligible in long period region.

(4) The standard deviation of E_H/E_I is relatively small. The influences of site soil conditions and ground motion characteristics on E_H/E_I is negligible.

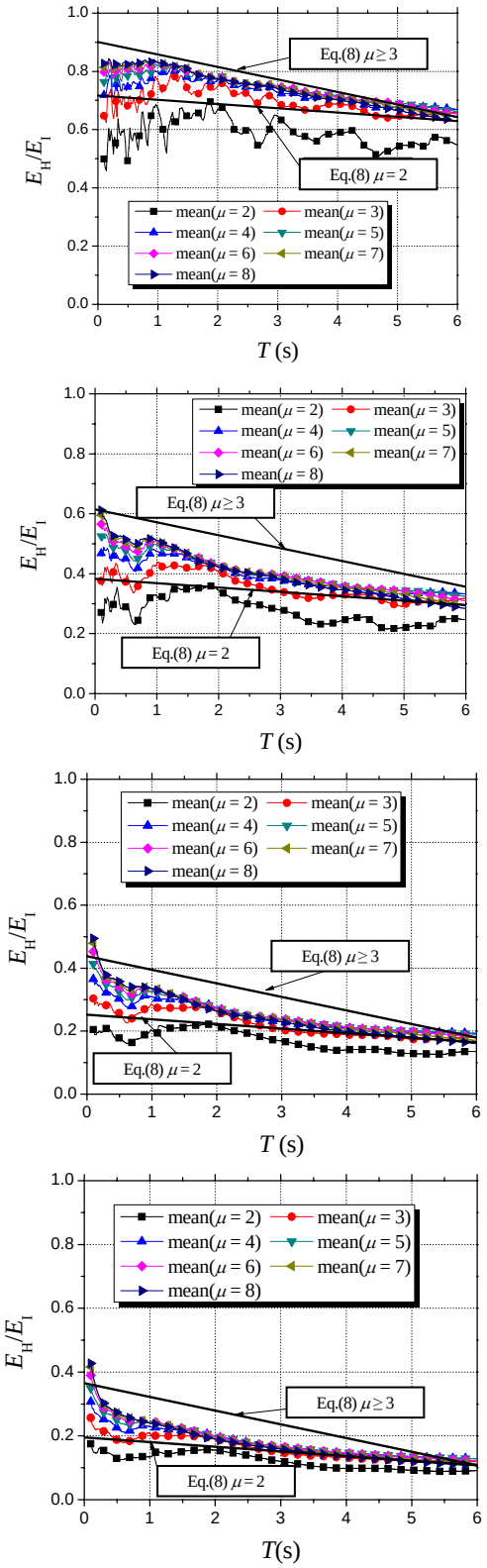

Fig. 8 E_H/E_I for 4 ground motions at various damping ratios: (a) $\xi = 0.02$, (b) $\xi = 0.1$, (c) $\xi = 0.2$ and (d) $\xi = 0.3$

The calculation of E_H/E_I ratio is recommended as Equation 8, which is based on the mean plus one standard deviation value of E_H/E_I ratios from extensive calculations. Values given by Equation 8 are compared with time history analysis results in Figure 8.

$$\frac{E_H}{E_I}=\begin{cases}1 & (\mu=1)\\ -0.0146T+b_1 & (\xi\neq 0,1<\mu\le 2)\\ \left[-0.0146-0.0284(\mu-2)\right]T+b & (2<\mu<3)\\ -0.043T+b_2 & (\mu\ge 3)\end{cases} \quad (8a)$$

where

$$\begin{aligned} b_1 &= -43.6\xi^3+29.87\xi^2-7.22\xi+0.85\\ b &= b_1+(b_2-b_1)(\mu-2)\\ b_2 &= -17.48\xi^3+15.69\xi^2-5.25\xi+1\end{aligned} \quad (8b)$$

4.2 Demand for hysteresis energy ratio in MDOF systems

Based on extensive analysis results, E_H/E_I ratio of MDOF systems can be obtained by modifying those of corresponding SDOF systems in moderate and long period regions. The following equations are suggested.

$$\frac{E_H}{E_I}=\begin{cases}b_1 & (\xi\neq 0,1<\mu\le 2)\\ b & (2<\mu<3)\\ b_2 & (\mu\ge 3)\end{cases} \quad (9)$$

where the values of b_1, b and b_2 are the same as given in Equation 8(b).

5. SYSTEM CAPACITY DESIGN AND ENERGY DISTRIBUTION

5.1 System capacity design

The distribution of hysteresis energy E_H in a structural system is essential to perform the energy-based seismic design. E_H distributions can be very different when the structure is subjected to different earthquake ground motions if its deformation pattern or damage mode is not well-controlled. This has been a major difficulty for a long time to perform energy-based seismic design. As a result, the energy-based method has been applied mainly for SDOF systems. Researches on E_H distribution are quite very limited. Fajfar (1996) proposed a method of determining E_H distribution for reinforced concrete frames and shear wall-frame structures based on pushover analysis. This method was further developed by Chou through modal pushover analysis (MPA) and was applied to steel frames. These methods can still be categorized into some displacement-based design framework and are not fully compatible with the basic principle of the energy-based design, although they found some rational bases for determining of E_H distribution. The energy-based design requires the structure's energy-dissipation capacity to be greater than its energy-dissipation demand. The energy dissipation mechanism should be considered as the first step and be taken as a premise in the following design procedure. It was shown by the author (Ye *et al.* 2002) that structures without carefully chosen energy dissipation mechanisms may suffer from story-mechanisms and the location of damage concentration will be quite arbitrary due to the randomness of earthquake ground motions, even if its mass, stiffness and strength are uniformly distributed along the height. In order to effectively control the energy dissipation mechanism and maximize the system capacity of energy dissipation, "system capacity design" was proposed by the first author (Ye 2004). In system capacity design, the structural system is further divided into two or more sub-systems, one of which is taken as the major sub-system and is responsible for controlling the global structural behavior under severe earthquakes. The major sub-system is designed not to be damaged and most of the energy dissipation occurs in the secondary sub-systems. E_H distribution of thus-designed structural system will be controlled by the major sub-system. The whole structure will behave as a hardening system. Further researches by the authors show that the scattering of the inelastic seismic responses is significantly smaller for hardening systems, which makes the seismic simulation more reliable (Ye *et al.* 2008). As mentioned previously, the design of energy dissipation mechanism is the major difference between the energy-based method and other methods. It is also the basis of energy-based design.

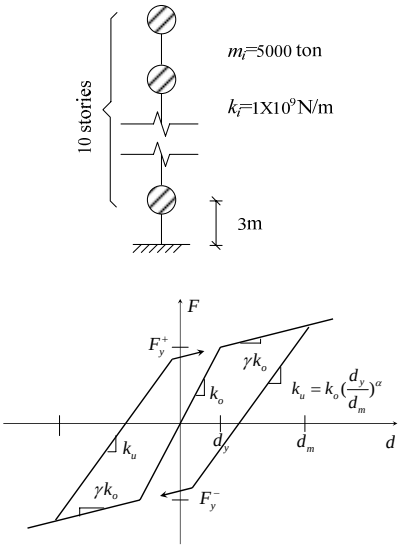

Figure 9 MDOF shear-story model:
(a) Model and (b) Story shear-deformation model

E_H distributions in hardening structure systems are demonstrated by the lumped mass MDOF systems with 5, 10, 20 and 30 degrees of freedom, as shown in Figure 9, are analyzed. Bilinear hysteresis model is adopted. The post-yielding stiffness ratios γ are taken to be 0.05, 0.1, 0.2, 0.3, 0.5 and 0.75, the damping ratios ξ to be 0.02, 0.1, 0.2 and 0.3, the strength reduction factor R to be 1, 2, 4, 6 and 8. Ductility factors μ and cumulated hysteresis energy E_H of individual stories under the El Centro NS ground motion are shown in Figure 10. When the post-yielding stiffness ratio is small (γ<0.5), μ and E_H are badly distributed and tend to concentrate at certain stories.

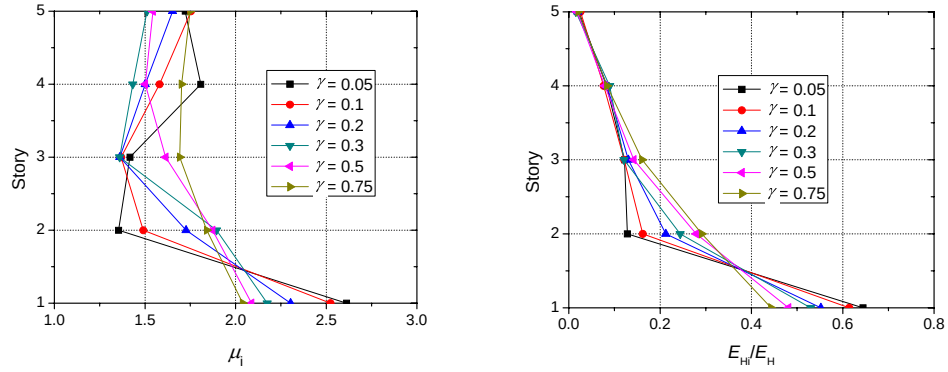

(a) 5DOF system with ξ=0.02, R=2

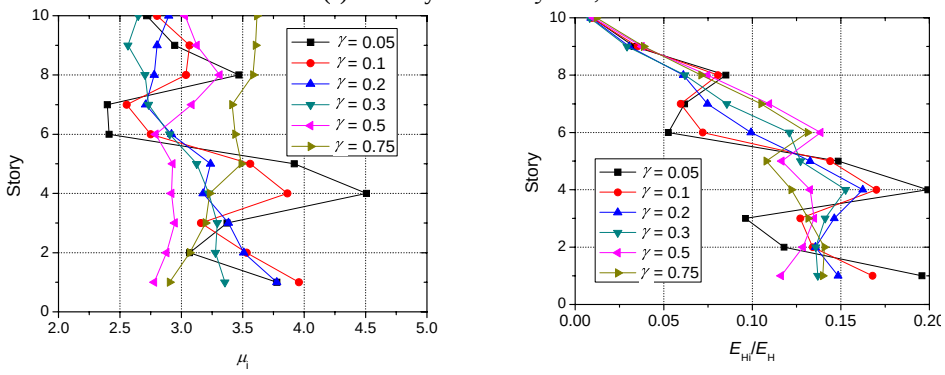

(b) 10DOF system with ξ=0.1, R=4

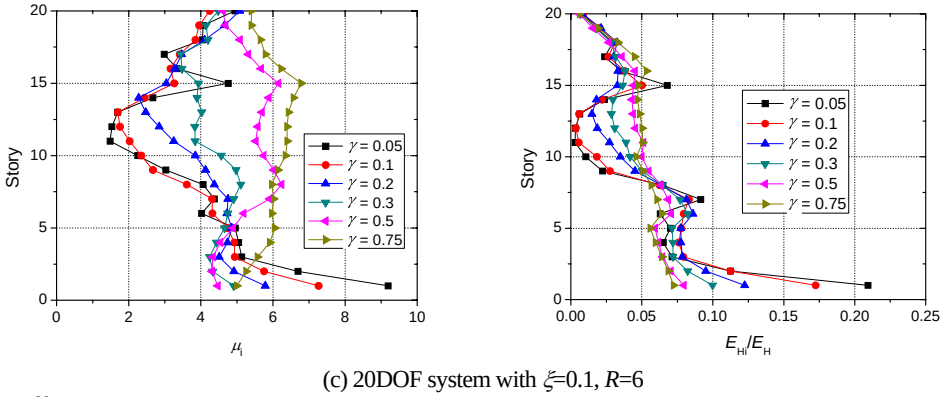

(c) 20DOF system with ξ=0.1, R=6

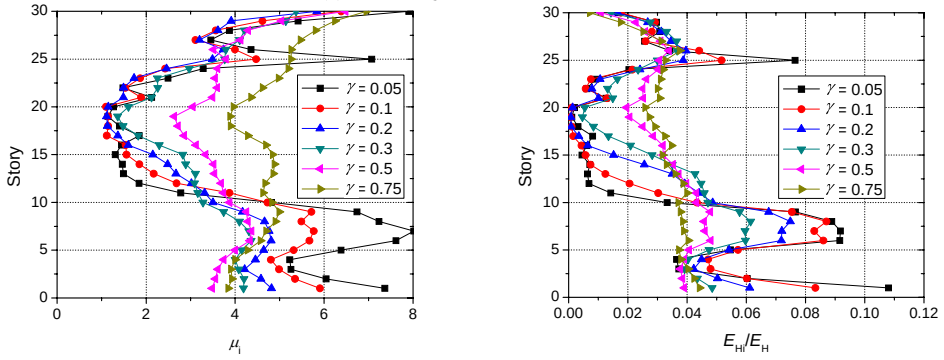

(d) 30DOF system with ξ=0.02, R=8

Figure 10 Distribution of cumulated hysteresis energy

The concentration becomes even severer for systems with more degrees of freedom. When $\gamma \geq 0.5$, μ and E_H distribution becomes uniform and $\mu \approx R$. Larger post-yielding stiffness ratios lead to much smaller inter-story drifts and more uniformly distributed inelastic deformation and damage more uniform.

Based on the analysis of lumped mass MDOF, Nakashima *et al.* (1996) concluded for frames with displacement-related dampers that the deformation concentration can be avoided if no column yields at both of its ends and the post-yielding stiffness ratio $\gamma \geq 0.75$. The work by Connor and Wada *et al.* (1997) shows that this can

be done for frame models if $\gamma \geq 0.33$.

The basic concept of system capacity design is to obtain hardening behavior in the system level. Various measures should be taken to provide a global major sub-system in the structural system. This major sub-system should have very high strength and enough deformability and the damaging sequence in the whole structural system should be well-organized.

5.2 Method for calculating E_H distribution

Three methods of determining E_H distribution have been so far proposed: (1) Uniform distribution (Akiyama 1985); (2) Linear distribution along height (Shen *et al.* 1999 and Akbas *et al.* 2001); (3) Pushover analysis-based method (Chou *et al.* 2003). Uniform distribution has proved inaccurate. The following discussion shows that the linear distribution and the pushover-based distribution can be achieved under certain conditions.

(1) Linear distribution

Akbas *et al.* (2001) concluded that E_H distribution is almost linear for regular steel frames with damping ratio of 0.02. According to the present research, however, E_H distribution can approximately be taken as linear only when the damping ratio $\xi > 0.1$. As a result, the assumption of linear E_H distribution is applicable for structures with additional damping devices. The following linear equations are suggested to calculate E_H distribution:

$$\frac{E_{Hi}}{E_H} = \begin{cases} \dfrac{2(N+1-i)}{N(N+1)} & N < 5 \\ \dfrac{2(N-i)}{N(N-1)} & N \geq 5 \end{cases} \qquad (10)$$

where N is the total number of story and i is the story number. The equation is compared with E_H distribution given by time history analysis in Figure 11. For structures with large damping ratios, Equation 10 agrees well with time history analysis results.

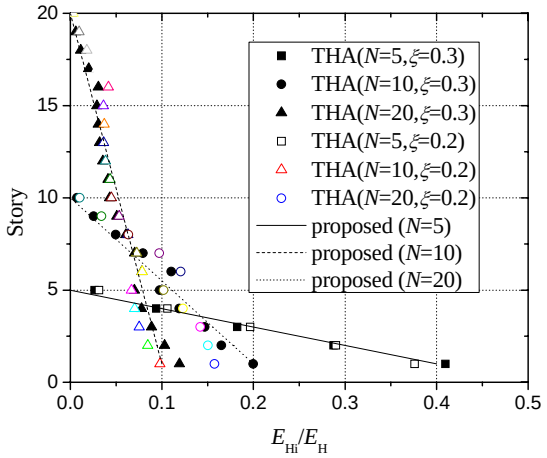

Fig. 11 Proposed linear distribution equation (Eq. 10) of E_H

(2) Pushover analysis-based method

E_H distribution is highly affected by the structure's characteristics when the damping ratio $\xi \leq 0.1$. Pushover analysis is used to determine E_H distribution by Chou *et al.* (2003)[0]. Pushover analysis is capable of estimating the structural peak responses while E_H is cumulated through the whole dynamic process of the structural response to earthquake excitations. As a result, the relationship between E_H and the structural peak response need to be first established. A linear correlation between them can be found when the post-yielding stiffness ratio $\eta \geq 0.5$. Figure 12 compares the plastic deformation energy E_{pi} and cumulated hysteresis energy in individual stories. The plastic deformation energy E_{pi} is defined in Equation 11, which is taken herein as a typical peak response.

$$E_{pi} = (1-\eta_i)(\mu_i - 1) F_{yi} d_{yi} \qquad (11)$$

Good correlations are observed for systems with various numbers of DOF and damping ratios. Equation 12 is suggested to determine E_H distribution from peak story drifts.

$$\frac{E_{Hi}}{\sum_{i=1}^{N} E_{Hi}} = \frac{E_{pi}}{\sum_{i=1}^{N} E_{pi}} \qquad (12)$$

Modal pushover analysis should be used to determine the plastic deformation energy E_{pi} in Equation 11 for high-rise buildings and other structural systems where higher modes contribute a lot.

6 ENERGY-BASED SEISMIC DESIGN OF BRACED STEEL FRAMES

Two parameters are introduced to better describe the concept of system capacity design: capacity coefficient and capacity ratio. The capacity coefficient of an individual component or a sub-system is the ratio of its actual strength capacity to required strength capacity. The capacity ratio is taken as the ratio of the capacity coefficients of different components or sub-systems. By adjusting the capacity ratios of different sub-systems, secondary sub-systems are expected to be damaged and dissipate energy while the major sub-system keeps elastic and controls the global response of the whole system when the system is subjected to a certain level of earthquake. The capacity ratios can be adjusted in the following two ways:

(1) Increase the capacity coefficient of the major sub-system, especially the elastic deformation capacity of the major sub-system in order to increase the post-yielding stiffness of the whole system. High strength and high performance materials are preferable for the major sub-system.

.

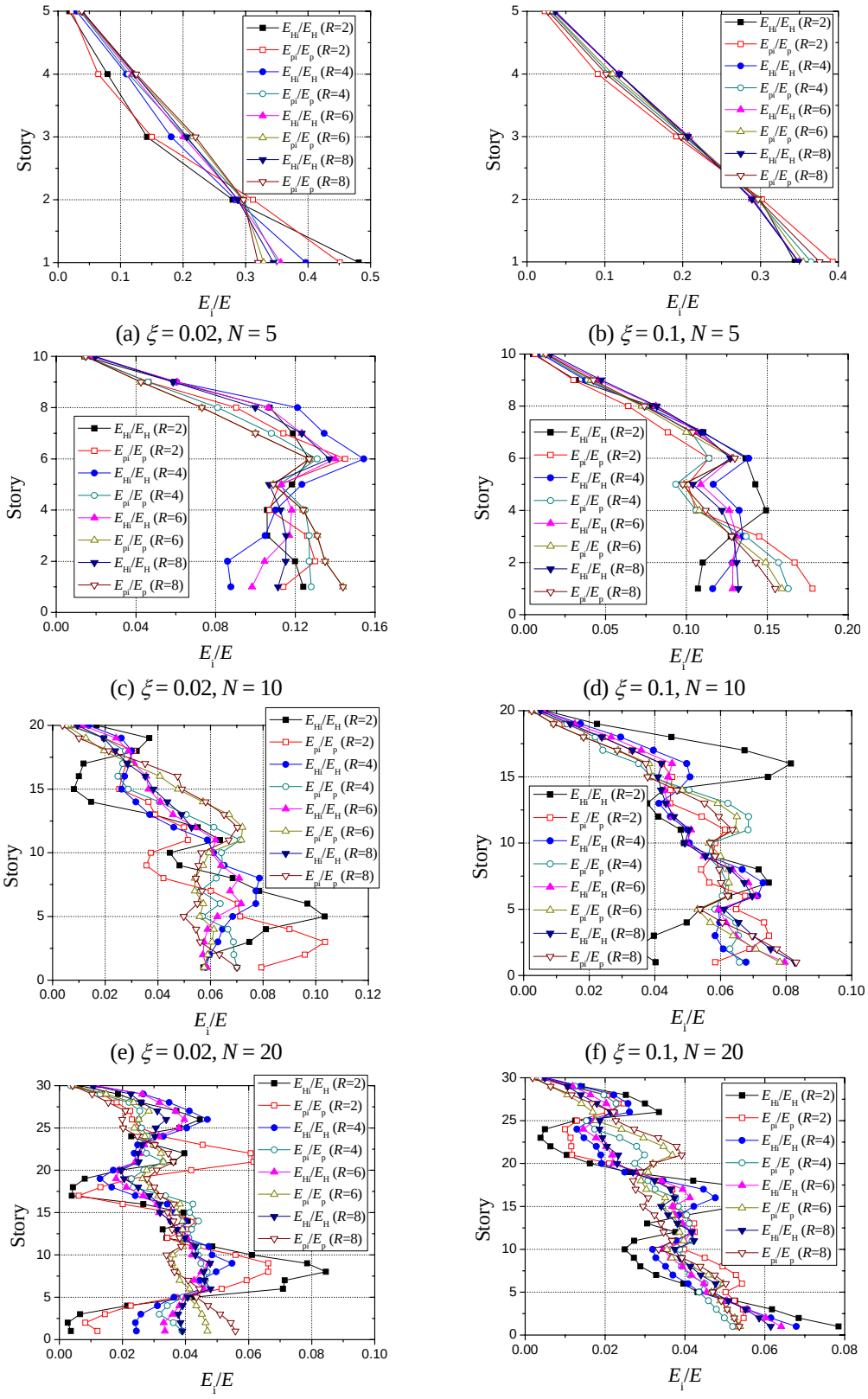

(a) $\xi = 0.02$, $N = 5$ (b) $\xi = 0.1$, $N = 5$

(c) $\xi = 0.02$, $N = 10$ (d) $\xi = 0.1$, $N = 10$

(e) $\xi = 0.02$, $N = 20$ (f) $\xi = 0.1$, $N = 20$

(g) $\xi = 0.02$, $N = 30$ (h) $\xi = 0.1$, $N = 30$

Figure 12 Energy distribution ($\eta = 0.5$)

(2) Distinguish the major sub-system from secondary ones by changing the structural layout. A way of doing this is to make components in the major sub-system insensitive to lateral deformations while those in secondary sub-systems are sensitive

The above energy-based seismic design method is applied

to a steel braced frame as shown in Figure 13. As the vertical load is mainly carried by the frame columns and beams, their performance determines the safety of the whole structural system. As a result, the frame becomes the major sub-system in this system and columns are even more important. Steel braces mainly resist the lateral forces. Their yielding will not affect the vertical capacity of columns. At the same time, braces are more sensitive to lateral deformations than columns. So braces belong to the secondary sub-system.

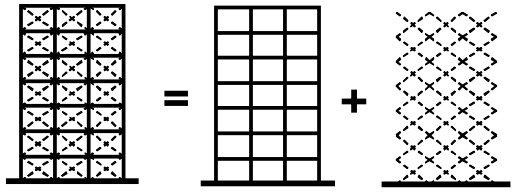

(a)Whole system (b) Major system (c) Secondary system

Figure 13 Braced steel frame and its system hierarchy

The performance objects for the major and the secondary sub-systems are prescribed as below according to the 3-level fortification criterion in Chinese seismic design code:

(1) When subjected to minor earthquakes, both the major and secondary sub-system keep elastic.

(2) When subjected to moderate or design earthquakes, the secondary sub-system (braces) may be damaged and the major sub-system keeps elastic. Rehabilitation is only required checking for the secondary sub-system after the earthquake.

(3) When subjected to major earthquakes, the secondary sub-system (braced) can be heavily damaged but not exceed its deformation capacity. Some frame beams in the major sub-system may be moderately damaged and the columns keep elastic.

High strength steel is used for frame columns in order to achieve the desirable energy dissipation mechanism and the above performance objects and to ensure that the post-yielding stiffness ratio of the whole system $\eta \geq 0.5$. Mild steel with large elongation ratio and low yield strength is used for braces. Material properties are listed in Table 3.

Table 3 Material properties

Comp.	Steel Grade	Steel Type (mm)	f_y(MPa)	f_u(MPa)	Elongation (%)
Column	HT590	19~100	440~540	590~740	≥20
Beam	Q235B	10~40	205~235	375	≥20
Brace	LY100	6~12	90~130	200~300	≥50

The structure is located in VIII seismic fortification area with site condition of Grade II. Peak ground accelerations associated with minor, moderate and major earthquake levels are taken to be 70gal, 200gal and 400gal, respectively. The story height is 5m for the first story and 4m for other stories. The total height of the building is 61m. Every story carries the same dead load of 6kN/m^2 and live load of 2kN/m^2. The structural layout is shown in Figure 14.

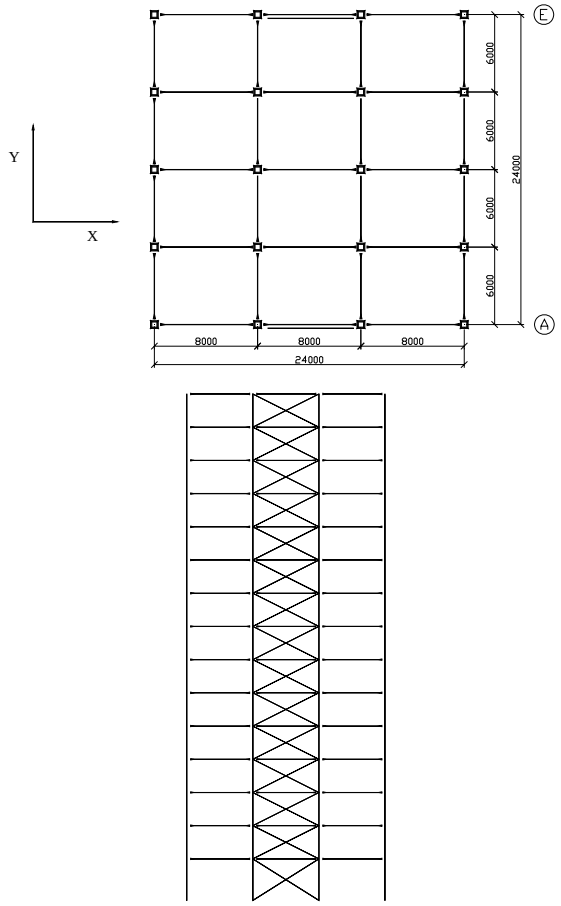

Fig. 14 Structural layout: (a) Plan and (b) Elevation A-E

The cross section geometries of all the components are listed in Table 4. The lateral stiffness of the secondary sub-system is designed to be about 2 times that of the major sub-system. The fundamental period of the structure is 1.62s.

Table 4 Component section dimensions

Story	Column(mm)	Beam(mm)	Brace(mm^2)
1~5	□500×500×20×20	I 500×300×12×20	24464
6~10	□400×400×20×20	I 500×300×12×20	18400
11~15	□350×350×20×20	I 500×300×12×20	13216

By evaluating the E_H distribution and energy dissipation demands for individual components in accordance with the proposed energy-based design method, the braced steel frame proves capable of meeting the energy dissipation demand under major earthquakes. Story responses given by the proposed method and by the time history analysis of 10 ground motion records are compared in Figure 15. The total cumulated hysteresis energy and its distribution given by the proposed method is conservative for engineering purpose compared with the time history analysis results.

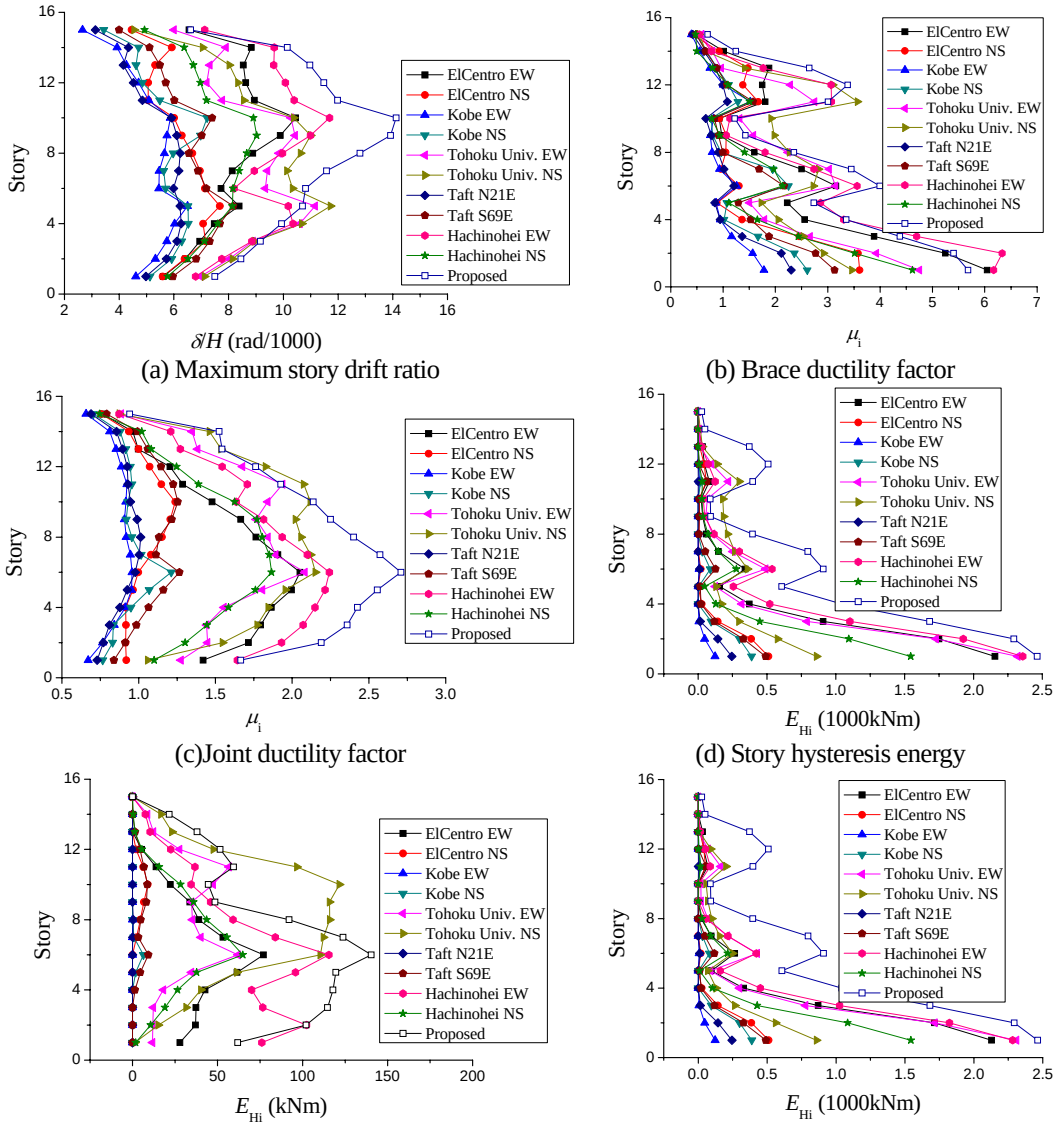

(a) Maximum story drift ratio (b) Brace ductility factor

(c)Joint ductility factor (d) Story hysteresis energy

(e) Joint hysteresis energy (f) Brace hysteresis energy

Figure 15 Comparison between nonlinear time-history analysis and the proposed method

7. CONCLUSIONS

The energy-based seismic design is reviewed and developed in the following aspects: (1) By considering the influences of ground motion characteristics and structural properties on E_I spectra of SDOF systems, elastic E_I spectra for various damping ratios and inelastic E_I spectra for various damping ratios and ductility factors are established. Spectra of hysteresis energy ratio E_H/E_I considering the influences of both ductility factors and damping ratios are also established.

(2) Influences of structural properties on the input energy and its distribution are examined based on inelastic MDOF shear systems. Relationships between energy input and its distribution of inelastic MDOF systems and inelastic SDOF systems are established.

(3) The influence of the post-yielding stiffness ratio on E_H distribution is examined in accordance with the system capacity design concept and the requirement for system hardening. Methods of determining the E_H distribution are proposed and their limitations are summarized.

(4) Energy-based seismic design method for steel braced frames is proposed in accordance with the system capacity design concept. Its validity is demonstrated through a case study.

Energy-based seismic design is an important part in the performance-based seismic design framework. It can be used to comprehensively assess the structural performance and hence ensure the structural safety under severe earthquakes together with structure control concepts and displacement-based methods. More studies are still needed in the following aspects:

(1) Peak ground accelerations have proved not adequate as an earthquake intensity index to represent the structural seismic capacity. More advanced earthquake intensity indices, which can represent the complete characteristics of earthquake ground motions, are required as

a basis to improve energy spectra.

(2) More widely applicable and simpler methods of determining the hysteresis energy distribution in MDOF systems are still needed.

(3) Energy-based seismic design is a supplement to displacement-based methods. Besides the strength and the deformation, the cumulated hysteresis energy is also a design index for individual components. The establishment of methods of evaluating and designing the energy capacity of various structural components requires comprehensive experimental and theoretical studies.

(4) The current study mainly focuses on regular structures. In theory, energy-based seismic design method is also applicable in irregular structures. More researches are needed in this field.

Acknowledgement:

The present research is sponsored by the Ph.D Foundation of Education Ministry of China (No. 200800030001) and the key project of National Natural Science Foundation of China (No. 90815025).

References

AIJ, Recommendation for the design of base isolated buildings, 2001

Akbas B, Shen J, Hao H. Energy approach in performance-based seismic design of steel moment resisting frames for basic safety objective. Structural Design of Tall Buildings, 2001, 10(3):193-217.

Akiyama H. Earthquake resistant limit state design for buildings. Tokyo: University of Tokyo Press, 1985.

Bertero V V, Uang C M. Issues and future directions in the use of an energy approach for seismic-resistant design of structures. In: P. Fajfar and H. Krawinkler, eds. Nonlinear Seismic Analysis and Design of Reinforced Concrete Buildings. Elsevier Applied Science, 1992

Chou C C, Uang C M. A procedure for evaluating seismic energy demand of framed structures. Earthquake Engineering & Structural Dynamics, 2003, 32(2):229-244.

Connor, J. J., Wada A, Iwata M, et al. Damage-controlled structures 1. Preliminary design methodology for seismically active regions. Journal of Structural Engineering, ASCE, 1997, 123(4):423-431.

Decanini L D, Mollaioli F. An energy-based methodology for the assessment of seismic demand. Soil Dynamics and Earthquake Engineering, 2001, 21(2):113-137.

Fajfar P. Equivalent ductility factors, taking into account low-cycle fatigue. Earthquake Engineering & Structural Dynamics, 1992, 21(9):837-848.

Fajfar P, Vidic T. Consistent inelastic design spectra: strength and displacement. Earthquake Engineering & Structural Dynamics, 1994, 23(5):507-521.

Fajfar P, Vidic T, Fischinger M. Seismic demand in medium- and long-period structures. Earthquake Engineering & Structural Dynamics, 1989, 18(4):1133-1144.

Housner G. Limit design of structures to resist earthquakes. Proceedings of the 1st World Conference on Earthquake Engineering. Oakland, California: 1956: 1-12.

Kato B, Akiyama H. Seismic design of steel buildings. Journal of Structural Division, ASCE, 1982, 108(8):1709-1721.

Nakashima M, Saburi K, Tsuji B. Energy input and dissipation behavior of structures with hysteretic dampers. Earthquake Engineering & Structural Dynamics, 1996, 25(5):483-496.

Nurtug A, Sucuoglu H. Prediction of seismic energy-dissipation in SDOF systems. Earthquake Engineering & Structural Dynamics, 1995, 24(9):1215-1223.

Riddell R, Garcia J E. Hysteretic energy spectrum and damage control. Earthquake Engineering & Structural Dynamics, 2001, 30(12):1791-1816.

Shen J, Akbas B. Seismic energy demand in steel moment frames. Journal of Earthquake Engineering, 1999, 3(4):519-559.

Sucuoglu H, Nurtug A. Earthquake ground motion characteristics and seismic energy-dissipation. Earthquake Engineering & Structural Dynamics, 1995, 24(9):1195-1213.

Teran-Gilmore A, Avila E, Rangel G. On the use of plastic energy to establish strength requirements in ductile structures. Engineering Structures, 2003, 25(7):965-980.

Uang C M, Bertero V V. Use of energy as a design criterion in earthquake resistant design. Berkeley, California: Earthquake Engineering Research Center, 1988.

Vidic T, Fajfar P. Behavior Factors Taking into Account Cumulative Damage. In: Proceedings of Tenth European Conference on Earthquake Engineering. Vienna: 1994: 959-964.

Ye, L.P., System capacity design and performance/displacement based seismic design, Building Structures, 34(6), 2004:10-14

Ye, L.P., Jing, J., On seismic design methods of building structures, Proc. 6th National Conference of Earthquake Engineering, Nov. 2002, Nanjing:419-429

Ye, L.P., Lu, X.Z., Ma, Q.L., *et al*., Study on the influence of post-yielding stiffness to the seismic response of building structures, Proc. 14WCEE, No. 05-01-0030, Beijing China, 2008, CD-ROM

Sixth International Conference on Urban Earthquake Engineering
March 3-4, 2009, Tokyo Institute of Technology, Tokyo, Japan

FULL-SCALE EXPERIMENTS AND ANALYSES OF 5-STORY STEEL FRAME WITH DIFFERENT DAMPERS

Kazuhiko Kasai[1)], Yoji Ooki[2)], Hiroshi Ito[3)], Shojiro Motoyui[4)], Tsuyoshi Hikino[5)], and Koichi Kajiwara[5)]

1) Professor, Structural Engineering Research Center, Tokyo Institute of Technology, Japan
2) Assistant Professor, Structural Engineering Research Center, Tokyo Institute of Technology, Japan
3) Postdoctoral Researcher, Structural Engineering Research Center, Tokyo Institute of Technology, Japan
4) Associate Professor, Department of Built Environment, Tokyo Institute of Technology, Japan
5) Researcher, National Research Institute for Earth Science and Disaster Prevention, Japan
kasai@serc.titech.ac.jp, ooki@serc.titech.ac.jp, ihiroshi@enveng.titech.ac.jp, motoyui@enveng.titech.ac.jp, hikino@bosai.go.jp, kaji@bosai.go.jp

Abstract: Realistic three-dimensional shaking table tests will be conducted in March 2009 for full-scale 5-story building specimens with dampers. The building will be tested repeatedly, inserting and replacing each of 4 damper types, i.e., steel damper, oil damper, viscous damper, and viscoelastic damper. For each damper type, 3 different capacities ranging approximately from 400 kN to 1,800 kN were tested, and correlated with analyses. According to analysis results, the deformation of the building will be kept small even against the strong 1995 Kobe earthquake record. The blind analysis contest will be held for pre-test prediction of the experimental results.

1. INTRODUCTION

The Japanese social desire for adopting passive control schemes has increased considerably after the 1995 Kobe earthquake. The schemes are now typically used for major buildings, and are modified and used even for many small residential buildings, in order to better protect the building and its contents. However, because the history of passive control is short, the technology has never been attested under the major and catastrophic earthquakes, while it is increasingly used in Japan. Therefore, it is extremely important to validate reliability of this technology by realistic simulations, before such earthquakes occur.

Pursuant to this, a full-scale building with dampers will be examined in February 2009 using the E-Defense, the world's largest three-dimensional shaking table. The experiment is a part of the 5-year E-Defense steel building project addressing moment-resisting frames, innovative methods for new/existing buildings, protective systems, and nonstructural elements (Kasai et al., 2007). The present paper reports a part of the preliminary study such as full-scale tests and analyses of individual dampers, and three-dimensional analyses of the 5-story building. It also briefly explains the blind analysis contest to be held regarding performance of this building,

2. FULL-SCALE 5-STORY BUILDING SPECIMEN

2.1 Value-Added Building Specimen

As shown in Fig. 1, the building is 5-story with two bays in each direction. Due to the reduction in budget, the building is made smaller than originally planned and described elsewhere (Kasai et al. 2007, 2008). In spite, the test is still by far the largest and the most realistic, among those conducted for passively-controlled buildings. The plan dimension is 10m × 12m, and total height from the upper surface of a stiff foundation beam is 15.8 m. Seismically active weight of the superstructure is 4,730 kN, including all structural and non-structural components as well as a portion of live load.

The frame members of the superstructure consist of wide-flange beam sections of 400 mm deep, and square box column sections of 350 mm × 350 mm. The expected steel yield strength for the beam and column are 358 MPa and 325 MPa, respectively. All the beam and column connections will be a fully-restrained type. The steel deck with concrete on top will be considered and fully composite beams will be created. Note that the beam flange is haunched to increase yield rotation and to delay onset of yielding (Kasai et al. 2007). Some stories of the building will be provided with glass curtain wall, pre-cast light-weight curtain wall, partitions with doors, several types of ceilings with sprinkler systems, and mechanical equipment. The study on the behavior of non-structural components is a part of the major US-Japan collaborative research program. The building will have 12 dampers (Fig. 1) of the same type with three to four different sizes. Four major damper types are considered: they are steel, oil, viscous, and viscoelastic dampers (Section 3).

The specimen is designed to be the "value-added" building whose structural and non-structural components are protected from a major seismic attack. The story drift angle is required not to exceed 0.005 (=1/200) rad. under the so-called level 2 (design basis) earthquake, which is much more stringent than 0.01 (=1/100) rad. usually considered for a conventional building. At the drift angles limited to 0.01

rad., the frame would be almost elastic with no damage. These points will be confirmed in Sec. 2.2 and Sec. 4, by a series of analyses.

2.2 Static and Eigenvalue Analyses

Using the seismically active story weight (Table 1a), the so-called Ai-distributions (BCJ 1991) and the lateral design load distributions (Table 1b) are obtained. The latter is used for static push-over analyses of a three-dimensional building model that includes beam-column elements with

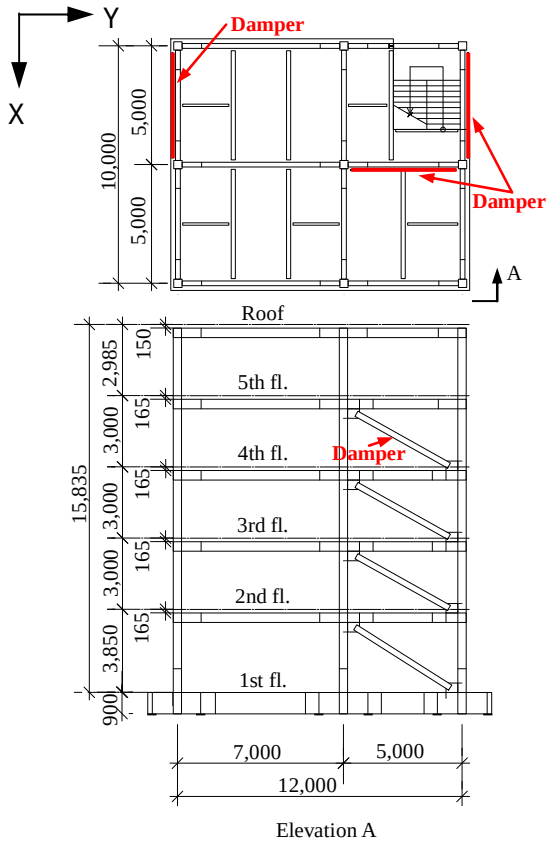

Figure 1 Full-Scale 5-story Building with Dampers (E-Defense Tests)

axial force and bi-axial moment interaction. Table 1c indicates the story stiffness and fundamental vibration periods in x- and y-directions (Fig. 1), which are obtained from the model without and with elastic steel dampers, respectively. In contrast to the steel damper, other three types of dampers are velocity-dependant, and they are therefore examined via dynamic analysis (see Section 4). Fig, 2 shows the results from the static push-over analyses applying the lateral load in either x- or y-direction, and Fig. 3 shows those applying the lateral load in both x- and y-directions simultaneously. From now on the cases will be named as "x-loading case", "y-loading case", and "simultaneous loading case". The solid and dashed lines indicate the results without dampers and with dampers, respectively.

Without Dampers: The story stiffness and vibration period of the frame in x-direction are about 12% larger and 6% smaller than those in y-direction, as indicated by

Table 1 5-Story Specimen: (a) Story Weight, (b) Lateral Force, and (c) Story Stiffness (kN/cm) and Vibration Period

(a)

Story Level	Weight (kN)
5	1455
4	799
3	817
2	822
1	841
Total	4734

(b)

Story Level	Lateral Force	Shear Force
5	0.52	0.52
4	0.17	0.69
3	0.14	0.83
2	0.10	0.93
1	0.07	1.00

(c)

Story Level	Frame		Frame with Steel Damper	
	X	Y	X	Y
5	776	703	945	848
4	805	712	1472	1264
3	929	820	1839	1606
2	1004	878	2256	1992
1	1055	943	2254	2309
Natural Period	0.74 s	0.79 s	0.53 s	0.56 s

Table1c. The vibration periods in x- and y-directions are 0.047 and 0.050 times the building height of 15.8 m, much longer than that (0.03 times) given by the code and considered typically for taller steel moment resisting frames in Japan. In either x- or y-loading case (Fig. 2), the frame shows no plastic hinge until the story drift angle exceeds 0.01 rad. In simultaneous loading case (Fig. 3), the plastic hinge forms at the column base when story drift angle reaches 0.008 rad. However, the hinge does not form in either the beam or column, until the drift angle exceeds 0.01 rad. Note also that the beam haunch detail explained earlier has increased the elastic limit story drift by about 20% , although not shown.

With Steel Dampers: By adding the dampers, the story stiffness and vibration period of the building shifts to 2 and 0.7 times, respectively, as indicated by Table 1c. The steel dampers are designed to yield at the story drift angle o f about 0.002 rad., and energy dissipation occurs well before reaching the target story drift angle of 0.005 rad. (design basis earthquake) and 0.01 rad. (catastrophic earthquake) mentioned in Sec. 2.1. In either x- or y-loading case, the frame shows the first plastic hinge at the column base due to increased column axial force caused by the dampers, but this occurs only after the story drift angle reaches 0.01 rad. In simultaneous loading case (Fig. 3), the plastic hinge forms at the column base when story drift angle reaches 0.0065 rad., earlier than the case without damper. However, it is found that the hinge does not form in either the beam or column, until the story drift angle exceeds 0.01 rad. The possibility of weak story mechanism is also checked for larger drift angles: the increased axial load in the column increases number of column plastic hinges, but has not caused such story mechanism. See for instance Fig. 4, for the story drift angle of 1/75 (0.0133) rad.

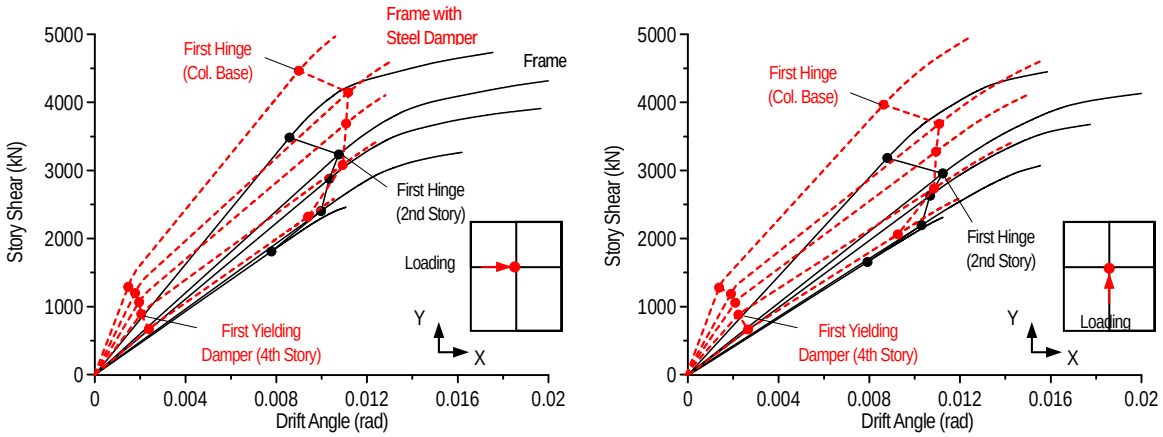

Figure 2 X-Loading Case and Y-Loading Case (Solid Line: Frame, Broken Line: Frame with Steel Damper)

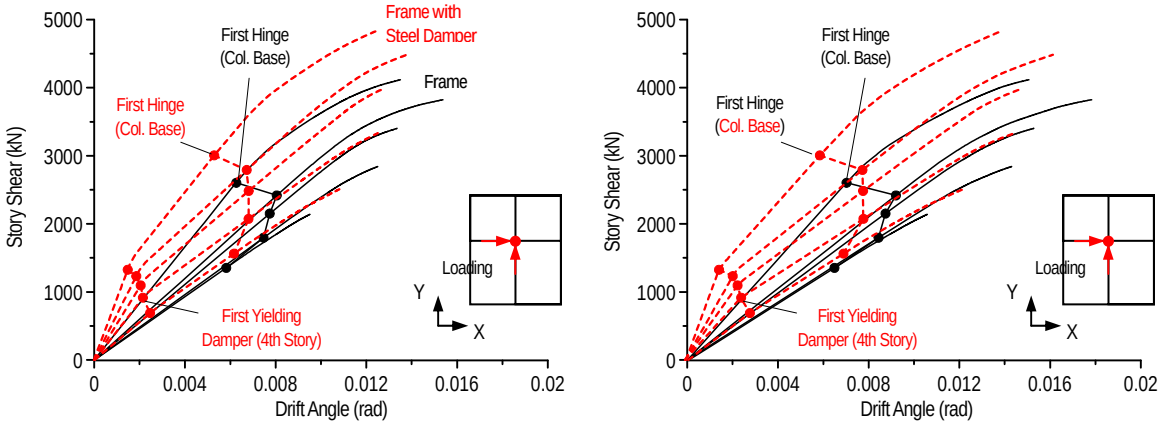

Figure 3 Simultaneous Loading Case: Reponses in X-Direction and Y-Direction, Respectively

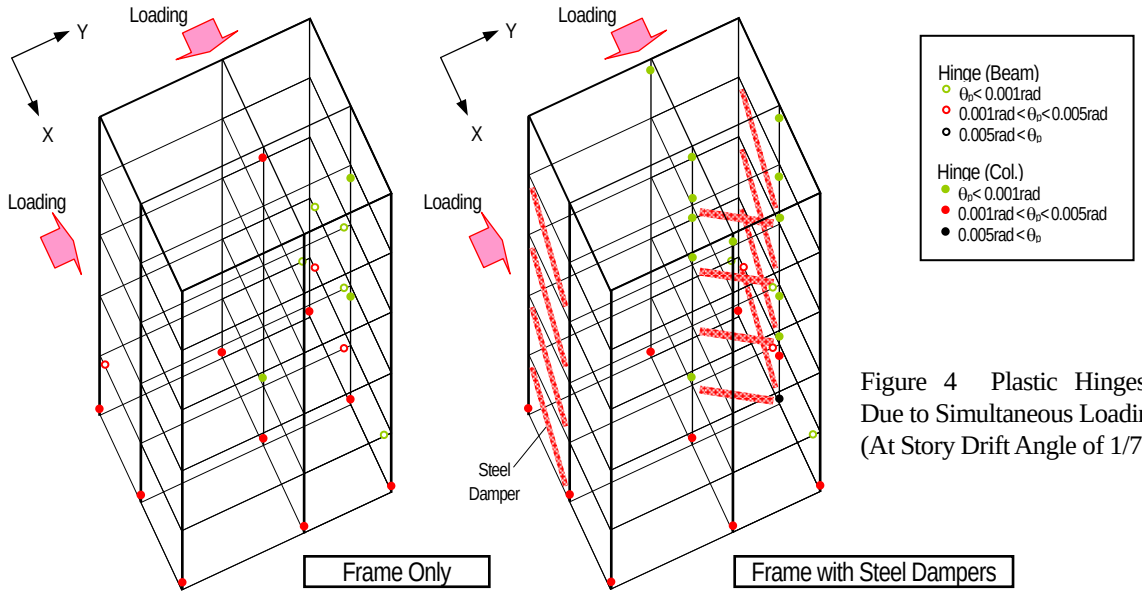

Figure 4 Plastic Hinges Produced Due to Simultaneous Loading (At Story Drift Angle of 1/75 rad.)

3. FULL-SCALE DAMPER TESTS AND ANALYTICAL SIMULATIONS

3.1 Four Types of Dampers

In order to assure performance of the damper to be used in the building as well as to validate analytical model, four types of full-scale dampers (Fig. 5) were dynamically tested at Tokyo Institute of Technology (Kasai et al. 2008). Brief descriptions for each type follow: Steel damper utilizes yielding of steel material for energy dissipation. It shows a round curve bounded by bi-linear lines, and can be analytically modeled by using readily available constitutive rules for steel materials. Oil damper utilizes flow resistance of the oil with low viscosity. The damper typically has a

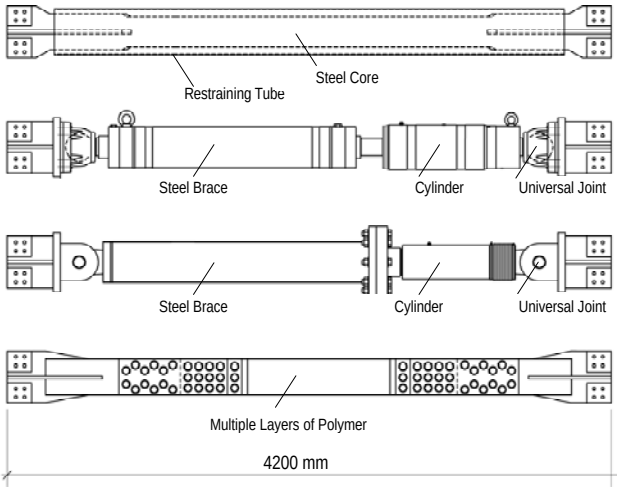

Figure 5 Steel, Oil, Viscous, and Viscoelastic Dampers Tested (From Top to Bottom Three Sizes per Type)

relief mechanism to switch viscous coefficient to a small value when subjected to a large velocity, making the hysteresis to switch from an elliptical shape to a rectangle shape. Viscous damper utilizes flow resistance of the polymer liquid. Its force is proportional to the fractional power of velocity, leading to the hysteresis loop of combined ellipse and rectangle. Viscoelastic damper utilizes molecular motion of a polymer for energy dissipation. Hysteresis loop is an inclined ellipse, and the inclination angle and the fatness of the loop depend on the excitation frequency and the temperature.

3.2 Tests and Analytical Simulations

Dampers of three different sizes per each type were tested, where Fig. 5 shows the largest specimen of each type. As shown in Fig. 6, deformations of various components of the damper-brace assembly are measured, for precise modeling. First, sinusoidal deformation tests are performed, by combining four different peak displacements (0.5, 12, 24, 36 mm) and four frequencies (0.2, 0.5, 1, 2 Hz), except for the loading of combination of 36 mm and 2 Hz that exceeds the performance limit of most dampers. Second, random deformation tests are performed, by using the 1st story drift history obtained from each analysis of 5, 12, and 24-story building models subjected to JMA Kobe NS record and Taft EW record, respectively. Various additional tests are performed on a damper-by-damper basis. For instance, prior to the dynamic tests, steel dampers are statically tested,

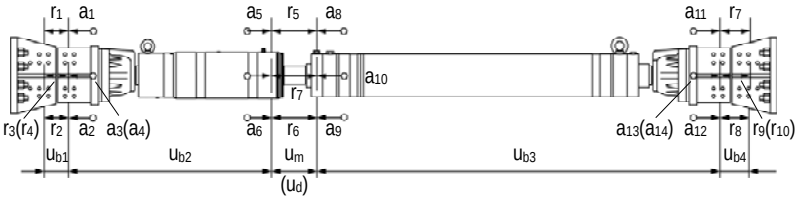

$u_{b1} = (r_1+r_2+r_3+r_4)/4$

$u_{b2} = (a_1+a_2+a_3+a_4)/4+(a_5+a_6+a_7)/3$

$u_{b3} = (a_8+a_9+a_{10})/3+(a_{11}+a_{12}+a_{13}+a_{14})/4$

$u_{b4} = (r_7+r_8+r_9+r_{10})/4$

$u_m\,(u_d) = (r_5+r_6+r_7)/3$

Figure 6 Example for Deformation Measurement (Oil Damper Case)

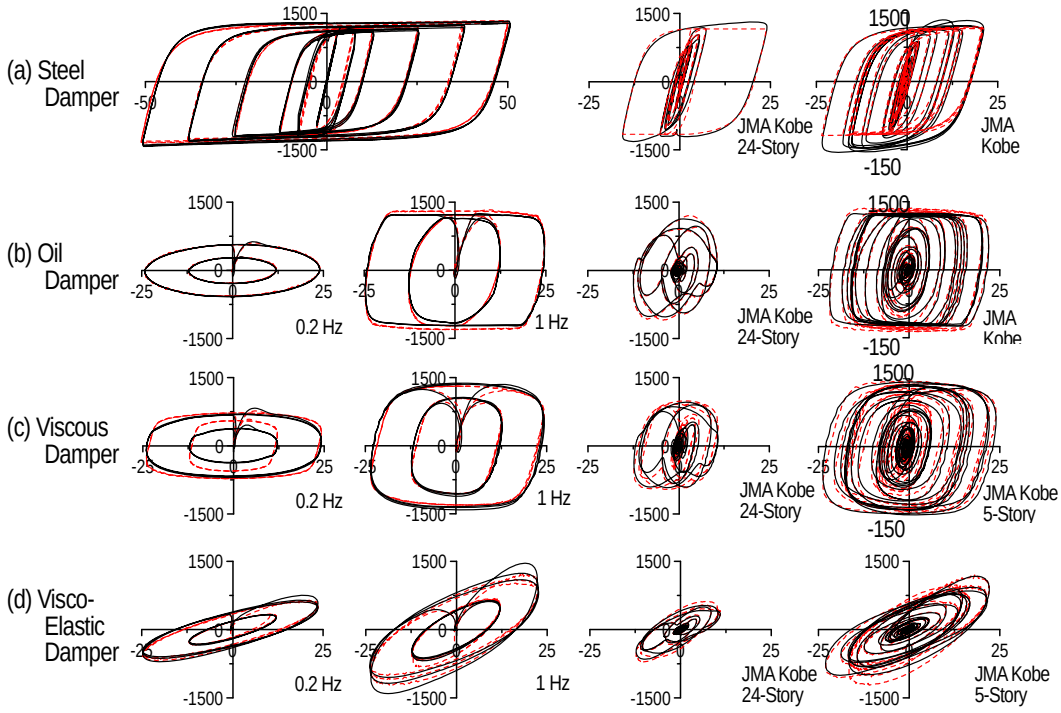

Figure 7 Results of Full-Scale Damper Tests (Solid Lines) and Analytical Simulations (Broken Lines)

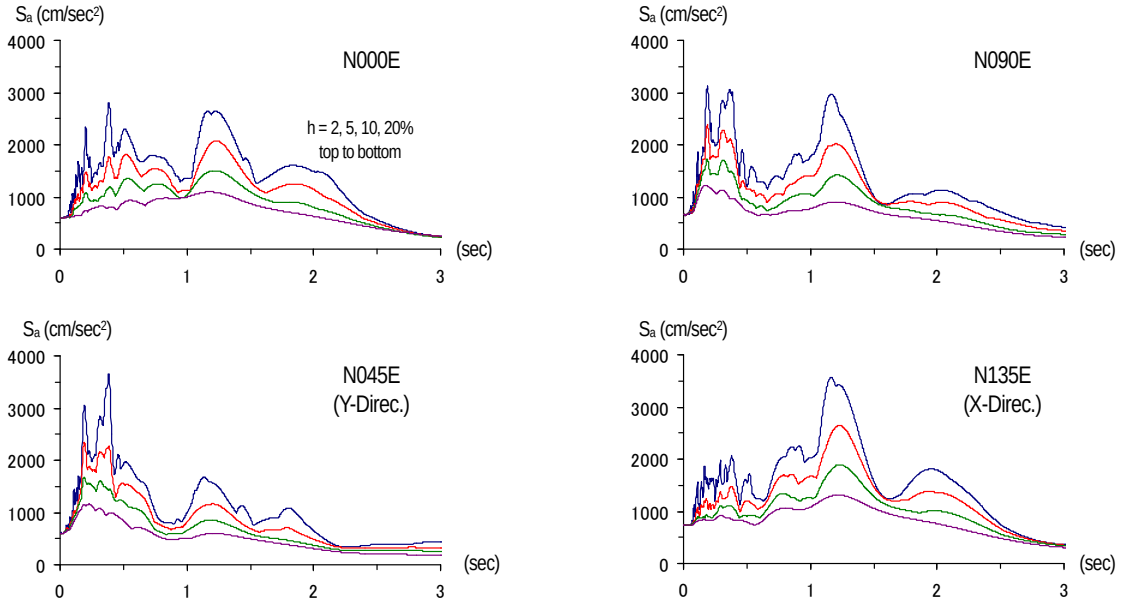

by applying cyclic deformations of gradually increased peak magnitude. Fig. 7 shows the hysteretic curves obtained from tests and analytical simulations (Kasai et al. 2004a, b, and c, Yamazaki et al. 2006), in which the analytical models appear to be reasonably accurate. For steel damper, the model is accurate for the static loading case (Fig. 7a left), but must be improved for the dynamic case (Fig. 7a right). Also, although not shown, the responses of oil damper and viscous damper at small deformations deviate from prediction, which must be considered when designing against wind and traffic vibration. The viscous damper has been typically modeled as a series combination of an elastic spring and a nonlinear dashpot whose force is proportional to fractional power of velocity. The stiffness of the elastic spring is found to be limited, thus, current practice of assuming it infinity for the viscous damper is not always appropriate. Analytical model for the viscoelastic damper appears to be accurate from extremely small to large deformations (Figure 6d). Unlike other dampers, increase of force at the first half cycle is remarkable.

4. DYNAMIC ANALYSES OF 5-STORY BUILDING

Fig. 8a shows acceleration spectra Sa of the JR Takatori Station records during the 1995 Kobe Earthquake. The peak ground velocities from both N000E and N090E records are equally 125 cm/s, the largest among the records during the 1995 event, and they are 2.5 times the velocityconsidered for the design basis (Level-2) earthquake. The records were used for the steel building seismic collapse test in 2007 (Yamada et al. 2008, Suita et al. 2008), and would also be used for the present test. In order to achieve almost equal story drifts in both x- and y-directions, the N000E record may be applied in the direction 45° counter-clockwise from y-axis defined earlier in Figs. 1 to 4. Corresponding Sa in x- and y-directions are shown in Fig. 8b. For the expected effective period of 0.6 to 0.7 sec., the average S_a is 1,500 cm/s^2 or more, when damping ratio is 0.02.

Figs. 9a and 9b show trajectories of the building roof in xy-plane and maximum absolute story drift angle, respectively. The building without dampers has displaced primarily in x-direction, and the largest story drift angle is 0.03 rad., which can cause significant damage in both structural and non-structural elements. In contrast, the story drift angle of the buildings with any damper type is limited to 0.01 rad. protecting structural and most non-structural components. Furthermore, the story shear forces and accelerations are controlled to about 0.7 times, although not shown. Fig. 10 shows damper force vs. axial deformation (relative displacement between the diametrically opposite intersecting points of beam and column centerlines). Due to the energy dissipated and stiffness added by the dampers, (Fig. 10), the excellent performance is obtained, which hopefully will be validated by the full-scale experiments in March 2009. In addition to the above, design basis and smaller earthquakes will also be used in order to observe the value-added performance at various levels.

5. SUMMARIES AND CONCLUSIONS

Realistic three-dimensional shaking table tests will be conducted in March 2009 for full-scale 5-story building specimens with or without dampers. Note that a blind analysis contest, like the one in 2007 for steel building collapse (Ohsaki et al. 2008a, b, and c), will be held as the world-wide competition for analytical prediction prior to the test (see http://www.blind-analysis.jp /index_e.html).

Acknowledgements:
This study is a part of "NEES/E-Defense collaborative research program on steel structures," and was pursued by the Damper and Isolation WG. The Japan team leader for the overall program and the leader for the WG is Kazuhiko Kasai, Tokyo Institute of Technology. The WG members not listed as the authors also contributed to the present effort, and their contributions are greatly appreciated. The authors also acknowledge the financial support provided by the National Research Institute for Earth Science and Disaster Prevention (NIED).

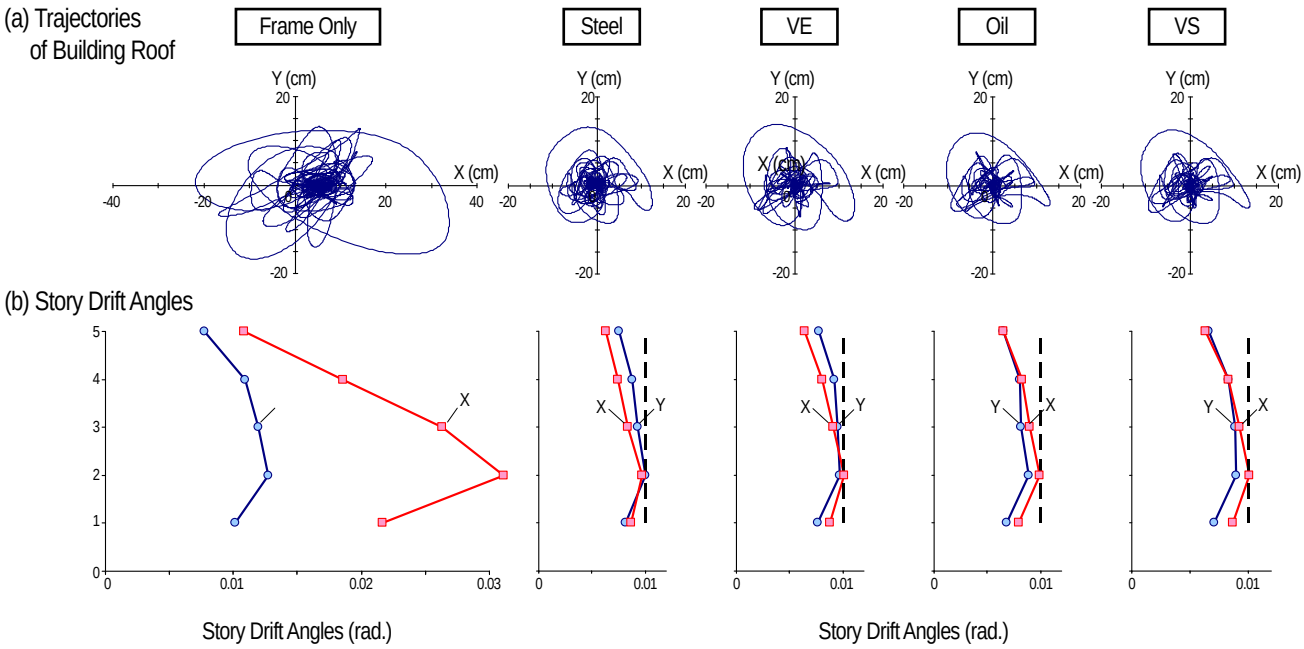

Figure 9 Frame without Dampers vs. Frame with Dampers: (a) Trajectories of Building Roof on XY-Plane, and (b) Absolute Peak Drift Angles

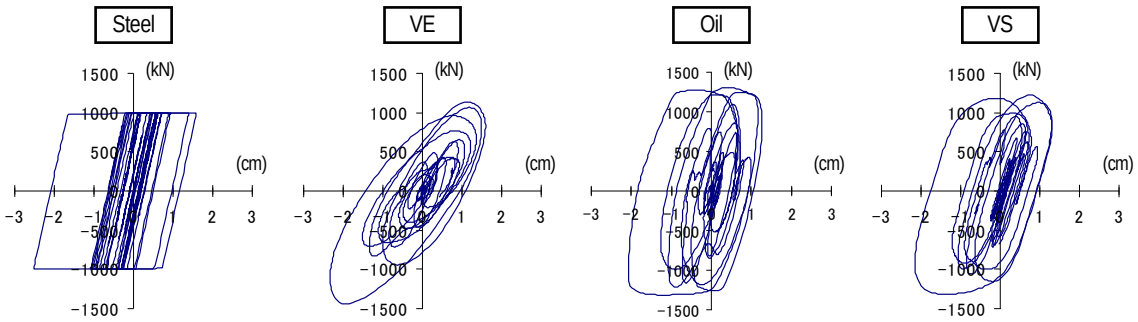

Figure 10 Damper Force vs. Axial Deformation of Added Component (Deformation of Damper, Brace, and Gusset Connections Combined in Series)

References:

BCJ (1991) " Guidelines to Structural Calculation under the Building Standard Law", Building Center of Japan (BCJ).

Kasai, K., Oohara, K., and Sekiguchi, Y. (2004a). "JSSI Manual for Building Passive Control Technology: Part-11 Time-History Analysis Model for Viscous Dampers", 13WCEE, Vancouver, No. 1427

Kasai, K., Takahashi, O. and Sekiguchi, Y. (2004b). "JSSI Manual for Building Passive Control Technology: Part-10 Time-History Analysis Model for Nonlinear Oil Dampers", 13WCEE, Vancouver, No. 1283

Kasai, K., Ooki, Y., Tokoro, K., Amemiya, K. et al. (2004c) "JSSI Manual for Building Passive Control Technology: Part-9 Time-History Analysis Model for Viscoelastic Dampers, 13WCEE, Vancouver, No. 1507

Yamazaki, H., Kasai K., Ono Y., Kaneko H., and Sadasue K. (2006). "Curved Hysteresis Model of Structural Steel under Cyclic Loading, Part 3 Modification of Analysis Model", Proceedings, Annual Meeting, Architectural Institute of Japan (AIJ), C-1, September, 935-936

Kasai, K., Ooki, Y., Motoyui S., Takeuchi T., and Sato, E. (2007). "E-Defense Tests on Full-Scale Steel Buildings: Part 1 – Experiments Using Dampers and Isolators", ASCE Str. Congress, Long Beach, CA.

Yamada, S., Suita, K., Tada, M., Kasai, K., Matsuoka Y., and Shimada Y. (2008). "Collapse Experiment of 4-Story Steel Moment Frame: Part 1 Outline of Test Results", 14WCEE , Beijing, Oct. 12-17

Suita, K., Yamada S., Tada, M., Kasai, K., Matsuoka Y., and Shimada Y. (2008). "Collapse Experiment of 4-Story Steel Moment Frame: Part 2 Detail of Collapse Behavior", 14WCEE , Beijing, Oct. 12-17

Kasai, K., Ooki, Y., Motoyui S., Takeuchi T., Kajiwara, K., and Sato, E. (2008). "Results of Recent E-Defense Tests on Full-Scale Steel Buildings: Part 3 – Experiments on Dampers and Frame Subassemblies", ASCE Structures Congress, Vancouver, B.C., April 24-26.Ohsaki M., Kasai, K., Hikino, T., and Matsuoka, Y. (2008a). "Overview of 2007 E-Defense Blind Analysis Contest Results", 14WCEE , Beijing.

Ohsaki M., Kasai, K., Yamamoto, M., Kiriyama, S. (2008b). "2-D Analysis Methods for 2007 Blind Analysis Contest", 14WCEE , Beijing.

Ohsaki M., Kasai, K., Thiagarajan, G., Yang, Y., and Komiya, Y. (2008c). "3-D Analysis Methods for 2007 Blind Analysis Contest", 14WCEE.

Sixth International Conference on Urban Earthquake Engineering
March 3-4, 2009, Tokyo Institute of Technology, Tokyo, Japan

POSSIBILITY OF STRUCUTURAL DESIGN USING ISOLATION SYSTEM

Yoshiharu Kanebako[1)], Yosuke Matsubara[2)], Sadamitsu Nezu[3)], Yoji Ishibashi[3)], Ryotaro Sakata[2)], and Yoshinori Suzuki[2)]

1) Professor, Center for Urban Earthquake Engineering, Tokyo Institute of Technology, Japan
2) Structural Engineer, Kanebako Structural Engineers, Tokyo, Japan
3) Structural Engineer, Mitsubishi Jisho Sekkei, Tokyo, Japan
kanebako@kanebako-se.co.jp, matubara@kanebako-se.co.jp, sadamitsu.nezu@mj-sekkei.com
yoji.ishibashi@mj-sekkei.com, sakata@kanebako-se.co.jp, suzuki@kanebako-se.co.jp

Abstract: In this paper three projects that we designed in late years are introduced, and possibility of structural design with the seismic isolation system is discussed. In the first project, the site is very narrow, so we considered how to secure usable building area regardless the loss of the seismic isolation clearance space. In the second project, the seismic isolation system should be employed to a complicated building including a large space. The third project was the museum, in which we applied the room seismic isolation system to an exhibition room and a storage room. In those projects, laminated rubber isolators, steel dampers, lead dampers, elastic slide bearings, oil dampers, and friction pendulum bearings were used corresponding to each situation.

1. INTRODUCTION

Techniques of seismic isolation system widely have prevailed and been used extensively from small residences to large buildings and high rise buildings. The main purpose to employ the seismic isolation system is to enhance safety of the building against earthquakes. However, there are creative design buildings that exploit characteristics of this system recently. By combining various seismic isolation devices newly developed effectively, the seismic isolation structure suitable for the building can be planned.

In this paper three projects that we designed in late years are introduced, and possibility of the structural design with the seismic isolation system is discussed. Each of the three projects has particular conditions for use of the seismic isolation system. We exercised our ingenuity so as to respond to the conditions and achieved the seismic isolation structures. In the first project, the site is very narrow, so we considered how to secure usable building area regardless the loss of the seismic isolation clearance space. In the second project, the seismic isolation system should be employed to a complicated building including a large space. The third project was the museum, in which we applied the room seismic isolation system to an exhibition room and a storage room. Base isolation was unable to use because the building was planned to be constructed on the remain.

It is important to choose the optimal seismic isolation devices according to the conditions of each building. In those projects, laminated rubber isolators, steel dampers, lead dampers, elastic slide bearings, oil dampers, and friction pendulum bearings were used.

2. SEISMIC ISOLATION OF THE BUILDING ON A NARROW SITE

2.1 Outline of the Building

This project is an eight-storied building in a commercial avenue includes a bank office in the first and the second floors, rental housings in the third to sixth floors, and the owner's house in the seventh and eighth floors. Since the client strongly requested to enhance earthquake-proof safety and assure asset value, the seismic isolation system was adopted. The site has an odd-shaped, which is 8.7m × 12.7m rectangle missing one corner space of 1.2m × 1.5m.

Considering dimensions of the seismic isolation clearance and retaining walls, the usable space where a building can be constructed on is decreased by 65%. This is quite small to the site with 80% of building coverage. Because of such a factor, adopting the seismic isolation

Figure 1 Outer View

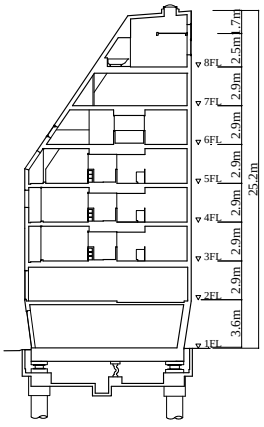

Figure 2 Section

Table 1 Outline of the Building

Name of building	LAPIS
Architect	Iida Archiship Studio
Structural Design	Kanebako Structural Engineers
Location	Minato-ku, Tokyo
Stories	8 above the ground
Total floor area	517 ㎡
Structure	RC structure

system to the buildings on a narrow site is mostly rejected.

In order to get rid of the influence by decrease in dimensions of the building space because of the isolation clearance, we designed the outer shape of the first and the second floors to be concaved inward and tried to ensure as much volume as possible on the upper portion of the building. Overall, the middle portion of the building looks voluminous as the building is sloped from the fifth floor and above due to the setback regulation from road width. Figure 2 is section of the building.

The building with this height is used beam-to-column rigid frames when a normal earthquake proof structure with RC or SRC structures is planned. The size of columns influences the planning. By providing sufficient walls on the upper structure, thickness of the columns and walls was made to be equal. We reduced the building frame dimensions of columns and walls as much as possible in order to utilize the advantages of the seismic isolation system. The basic wall thickness of the upper structure is 250 mm and columns are embedded in them, giving an impression as a boxed wall structure. Windows are allocated on the walls irregularly. This design was difficult with the normal earthquake proof structure and was leaded by the advantage of the seismic isolation structure.

2.2 Design of the Isolation Structure

The building is 13.6m high on the front side facing the road, and the maximum height on the rear side is 25.2m. As the plane shape of the building on the first floor is small, the aspect ratio is from 3.2 to 4.2, which is comparatively large. Thus, we needed to design not to cause tensile force of the isolators. The laminated rubber isolators were set on each of four corners, and a 1 m-thick mat slab was constructed under the first floor to lower the center of gravity height, to be counter weights, and to prevent tensile force. U-shaped steel dampers and lead dampers were used. The outer structure of the lower portion of the seismic layer was moved inward to minimize the thickness of the structural walls and the retaining walls for excavation. The height of retaining walls on the periphery was 1.8m.

Seismic design load is investigated with equivalent linear analysis method, which is notified by the minister of Land, Infrastructure and Transport (No.2009, 2000). Also, we investigated it with the time history response analysis method for verification. The adopted earthquake waves were the artificial waves with a uniform random number phase, Kobe phase, and Hachinohe phase. Figure 6 shows story shear coefficient (C_i) of each floor inspected with equivalent

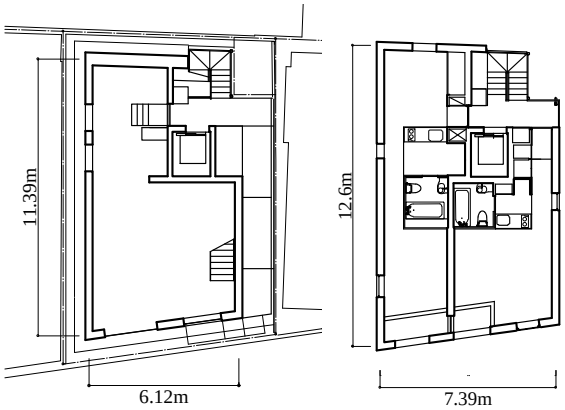

Figure 3 1st Floor Plan

Figure 4 3rd Floor Plan

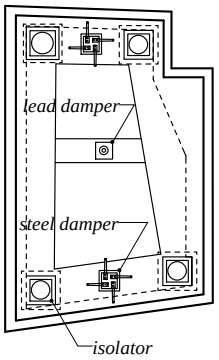

Figure 5 Arrangement of the Isolation Devices

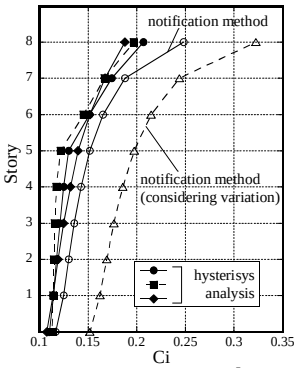

Figure 6 Story Shear coefficient (X-direction)

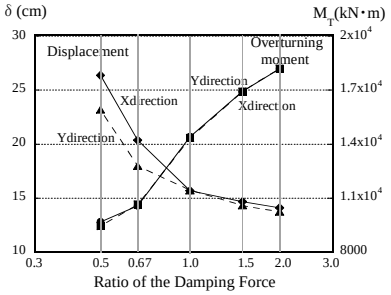

Figure 7 Response of Displacement and Overturning Moment

linear analysis method and time history response analysis. The results of equivalent linear analysis method are larger than time history response analysis. Figure 7 is the response of isolation story displacement (δ) and overturning moment (M_T) by time hysteresis analysis when the damper yield shear force is verified larger or smaller from the design adopted value. In order to minimize the seismic isolation clearance, it is effective to increase the force of the dampers and reduce the response displacement. However, enhancing the force of dampers increase the response acceleration of the upper structure and tensile force is likely to be caused in the isolators. Thus, we needed to select an appropriate damper which reduced the horizontal displacement and did not cause tensile force in the isolators.

The value of horizontal displacement of the isolation story the equivalent linear analysis method was 280mm considered variations. It is larger than the value by hysteresis analysis. The actual clearance was determined to be 300mm.

3. SEISMIC ISOLATION OF A COMPLICATED BUILDING INCLUDING A LARGE SPACE

3.1 Outline of the Building

The second project is a complex building constructed for 150th anniversary of Keio university. This building consists of various facilities such as graduate school facilities, a swimming pool, a lecture hall with seating capacity of 500, recreation center dormitories, multipurpose halls, open sports facilities, and another supporting facilities. The planar shape of the first floor is a rectangle with 130m of the long direction and 60m of the short direction. The appearance of sloped setback from the side of the field is a remarkable characteristic of the building. There is a high-ceiling passage which goes through the building in the longitudinal direction in the middle of the building. This passage divides the stepped lower part from the higher part. There is the 50 m-long swimming pool on the first basement story. It is a large space with an atrium through the seismic isolation stories and the first floor. The deck terrace and a part of the building (setback part) above the pool are supported with the truss structure which span is about 30m.

In order to clarify behavior of the complicated upper structure caused by earthquakes and achieve high earthquake-proof safety as an anniversary complex, the client and the design team judged to use the seismic isolation system. Because the building has two underground stories with deep foundation bed level and includes a parking lot in the underground, a base isolated structure seemed not to be appropriate. Therefore, only the aboveground stories were planned to be isolated. Initially, we considered integrating the truss structure over the poor and the other lower structure and providing a seismic isolation story under the second floor. However, the high-ceiling space from the first to the fourth floors is important in terms of design; the seismic isolation story was arranged under the first floor (Figure 11).

The frame of the pool upper structure is a modified truss structure which transmits a force in one direction, covering the space of 31m × 63m. The truss is double-layered at the inside of the building, but single-layered in outside of the building. One truss member is divided two members in planarly at the outside of the building. This configuration was derived from the purposes to ensure sight lines from spectators' seats and optimize the shape of the stage in the center of the outer stadium (Figure 12, 13).

Table 2 Outline of the Building

Name of building	Keio Hiyoshi Campus Collaboration Complex
Architect	Environmental Design Institute Mitsubishi Jisho Sekkei
Structural Design	Mitsubishi Jisho Sekkei Kanebako Structural Engineers
Location	Yokohama-city, Kanagawa
Stories	7 above the ground, 2 underground
Total floor area	38,207 ㎡
Structure	SRC structure, Steel structure

Figure 8 Outer View

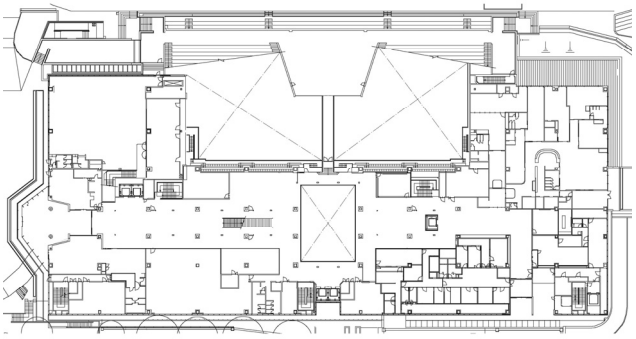

Figure 9 1st Floor Plan

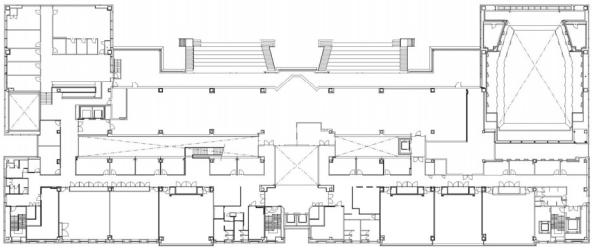

Figure 10 4th Floor Plan

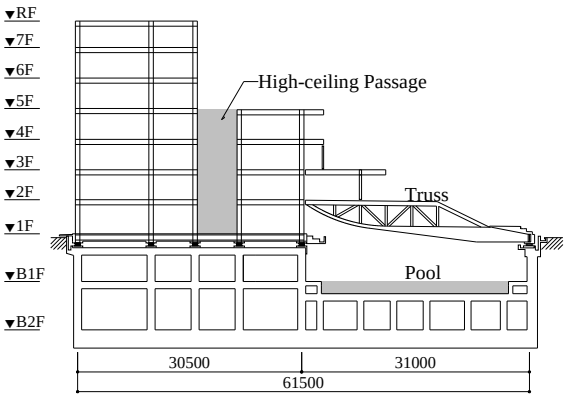

Figure 11 Structural Section

Figure 12 View of the Pool

3.2 Design of the Isolation Structure

The main base-isolated bearing was a laminated natural rubber bearing. Some elastic slide bearings were also used. Oil dampers were used as a damping element. A semi-active seismic isolation system, which switches the damping coefficient of the oil dampers according to the earthquake level, was employed for the purpose of enhancing habitability and earthquake resistance when a medium or small earthquake occurs. It switches the damping coefficient twice for each earthquake. This system sets a lower primary damping coefficient of the oil dampers in the stage of relatively small earthquake motion to reduce the response acceleration. When the ground acceleration goes beyond a certain level, a higher primary damping coefficient is set (Figure 15). This system was suggested and designed by Kazuo Yoshida (the deceased), the former vice-president and Hidekazu Nishimura, professor of Keio University.

Since the steel truss structure over the pool connects the first and the second floors, it makes an effect like a wall brace does when an earthquake occurs and it generates a large stress owing to deformation of the first story. In order to solve this problem, an expansion joint was put between the truss structure and the main frame of the first floor flooring level (Figure 16). To make the truss move integrally with the flooring of the second floor, the elastic slide bearing with a lower friction coefficient (0.01) was used for the supporting point of the first floor level on the edge of the truss (on the outer edge of the building).

3.3 Earthquake Response Analysis

The upper structure of the building is divided into two sections by the high-ceiling passage running through in the longitudinal direction in the middle. These two sections are connected only by the passage slab. Considering these conditions, not only a one-story one-mass model but also a multiple rigid floor model was examined with response analysis method. The design of the joints was based on the result of static analysis and dynamic analysis on the multiple rigid floor models.

The used earthquake waves were three observed waves (EL Centro NS, Taft EW, and Hachinohe NS) and three artificial waves by the notified method (uniform random number phase, Hachinohe phase, and Kobe phase). The response analysis results about story shear coefficient (C_i) and floor acceleration are showed figure 17 and 18. The response acceleration on the highest floor was found to be about 140gal for a rare earthquake motion and about 300gal for a quite rare earthquake motion in both directions, indicating realization of high seismic isolation effect although the steel framed structure, which has relatively small rigidity, was used for the upper structure. We examined the deformation of the seismic isolation story under the condition that a low primary damping coefficient of the variable damping damper was fixed and variations in properties of the seismic isolation materials were considered. The maximum value of the deformation was about 360mm. Thus, the clearance was decided to be 500mm with margin.

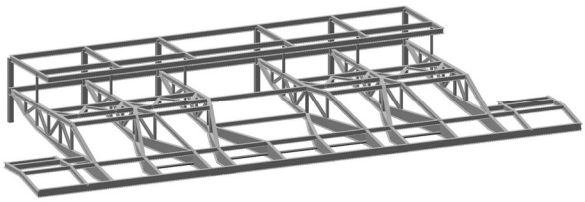

Figure 13 Figure of the Truss Structure

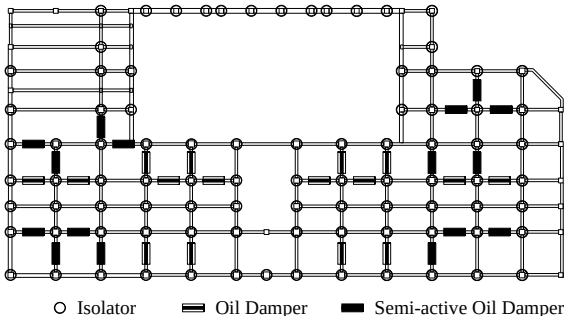

Figure 14 Arrangement of Isolation Devices

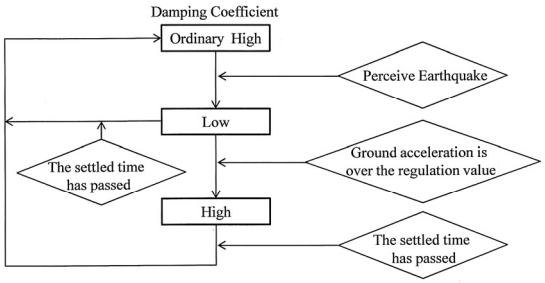

Figure 15 System of changing the damper coefficient

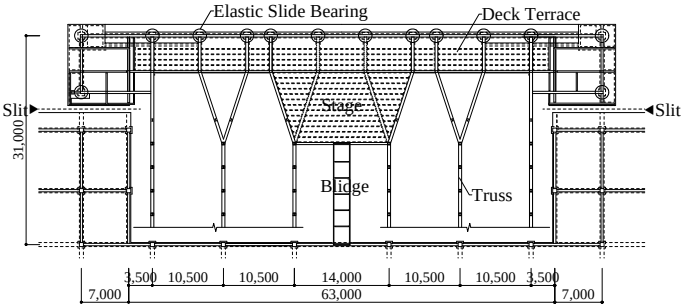

Figure 16 Structural Plan of the Truss

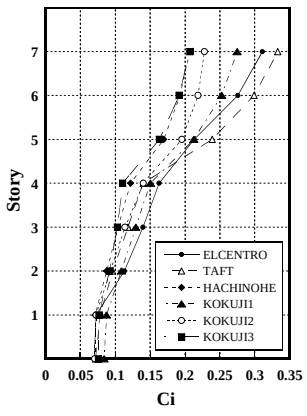

Figure 17 Response of Story Shear Coefficient

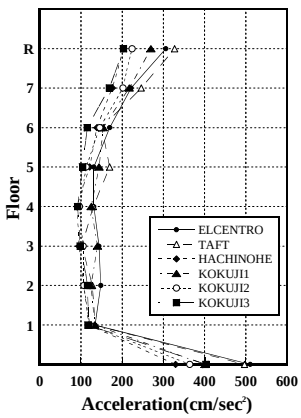

Figure18 Response of Acceleration

4. ROOM ISOLASION PROJECT OF A MUSEUM

4.1 Outline of the Building

The third project is an exhibition facility for a temple with a long history where national treasure-class articles are planned to be exhibited and stored. Constructing the entire building with the seismic isolation system was thought to be the best. However, there are some remains of the Nara period on the site and depth of excavation is limited to 1.5 m from the ground surface for preservation, and applying the base isolated structure for the entire building was impossible. At first, an idea that making the exhibition cases with the seismic isolation system was also discussed, later we thought to construct the entire exhibition room with the seismic isolation structure (Figure 19, 20).

The seismic isolation for the floor has been used for exhibition rooms and computer rooms. This project is characterized by the following two conditions. The first is necessity of the large live load, and the second is a demand for air tightness of the room to prevent the historical articles. On the floor surface, an RC construction floor was placed on the steel beams, and steel frame was set on it in order to support the entire room including walls and ceiling with the seismic isolation (Figure 21, 22).

As the weight to support is light in case of the floor or room isolation, it is difficult to making the natural period of the structure longer by using the laminated rubber isolators in principle. Sliding bearings and rolling bearings are useful to expand the natural period. In this project, the triple friction pendulum bearings were used (Figure 23). These bearings obtains restoring force is generated from the bearing curvature and hysteresis damping from friction force, so the natural period and the damping coefficient are determined regardless of the supported weight. Therefore, this is the most suitable bearing for the seismic isolation for the exhibition room flooring which goes through large variation of the live load. Another feature of this product is that a structural engineer can freely set the performance of the seismic isolation bearing since the curvature and friction coefficient of the bearing are adjustable.

The configuration of the isolation structure is illustrated in figure 24. A steel beam was arranged in a pitch of 2.5 m in one direction. The secondary beams are placed cross direction. 12 seta of the FPB placed at the both side. Viscous dampers were set for each of the X and Y direction so that the force from the damper would act upon the gravity center of the floor. The FPS used in this building does not cause

Table 3 Outline of the Building

Name of building	Todaiji Culture Center
Architect	Archivison
Structural Design	Kanebako Structural Engineers
Adviser of Isolation	Akira Wada
Location	Nara-city, Nara
Stories	3 above the ground, 1 underground
Total floor area	4,773 ㎡
Structure	RC structure, Steel structure

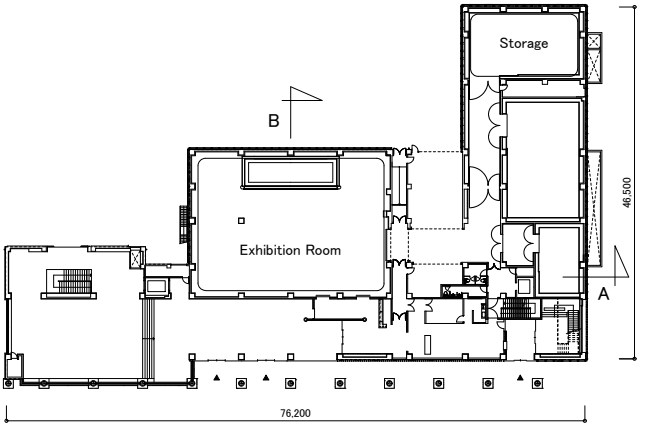

Figure 19 1st Floor Plan

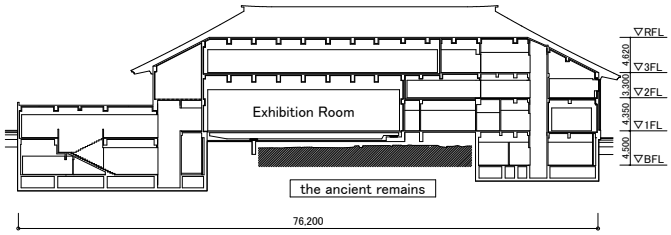

Figure 20 Section (A)

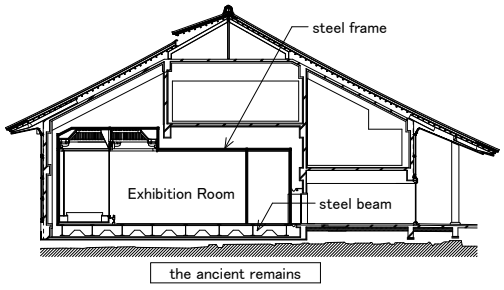

Figure 21 Section (B) : the Isolation Room

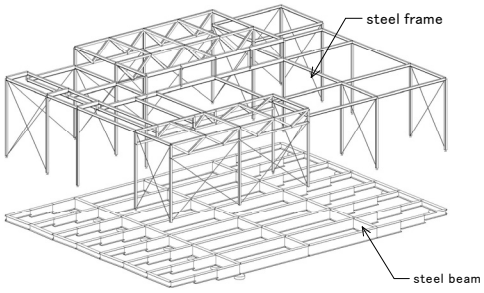

Figure 22 Flame Structure of the exhibition room

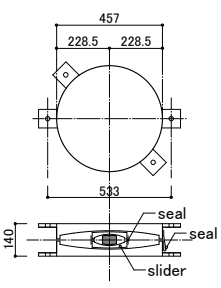

Figure 23 Friction Pendulum Bearing

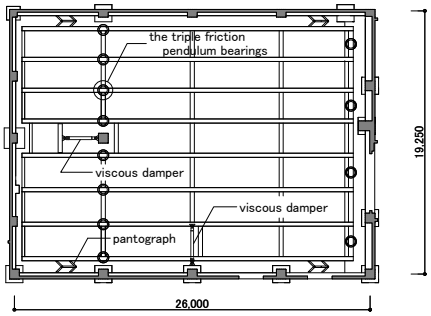

Figure 24 Arrangement of the Isolation Devices and Steel Beams

distortion even though the building weight is unevenly distributed, but the parallel moving apparatuses in the shape of pantograph were set on four points in order to prevent the distortion of the floor surface in consideration of use of the dampers and accidents.

4.2 Design of the Isolation Structure

As the purpose of employing the seismic isolation system was to protect the stored articles, how to evaluate the possible earthquake motion and set criteria of the response acceleration was an important issue to discuss. From the investigation on the historic earthquake motion around the site, the earthquake due to movement of the trough in the Pacific sea, and influence of marginal active fault, we decided to take account of (1) the earthquake motion caused by Nankai earthquake and (2) the earthquake motion caused by the Nara Basin Eastern Edge Fault as possible earthquake motions at the site. The expert committee about To-nankai and Nankai earthquake of the Central Disaster Prevention Council presents probable seismic intensity in each area of western Japan for (1). According to this, the intensity around Nara city is five upper. The earthquake of (2) was examined using "The Earthquake Motion Wave Caused by The Nara Basin Eastern Edge Fault" provided by the Cabinet Office Central Disaster Prevention Council.

The criteria of the response acceleration were determined based on the method of the reference 2). This paper suggests a method to estimate furniture fall rate based on the investigation on the fallen furniture after the actual earthquakes. Due to the relationship between the size of the furniture and flooring natural frequency, the possibility of fall depends on either acceleration or velocity. When the seismic isolation flooring is used like this case, it mostly depends on the acceleration. Assumed that the ratio of the width to the height of the sculptures is 1: 5 and the standard deviation is 0.2, the possibility of falling down is 0.004 for 120gal and 0.005 for 140 gal. The target acceleration was determined to the value below 140gal and the target response displacement was less than 300mm.

A one-mass system model was used for the time history response analysis. The examined earthquake waves were four observed waves (El Centro NS, Taft EW, Hachinohe NS, and JMA Kobe), one artificial wave (uniform random number phase) and the site wave (Nara Basin Eastern Edge Fault). The waves of El Centro, Taft, and Hachinohe are normalized 60 cm/s. Figure 25 is the acceleration response spectrum of these earthquake waves on 30 % damping. The influence of the site wave is remarkable in the range of natural period from 2 to 3 seconds. Figure 26 is the force-displacement relationship of the bearing. The result of the response analysis is summarized Table 4. The response of the earthquake caused by the Nara Fault is the largest and shows 140gal of the response acceleration and 300mm of displacement. Regarding other earthquake motions, the response acceleration is about 110gal or less, and the horizontal displacement is 150mm or less. Thus, the seismic isolation structure is judged to accomplish the purpose of protecting the exhibited articles.

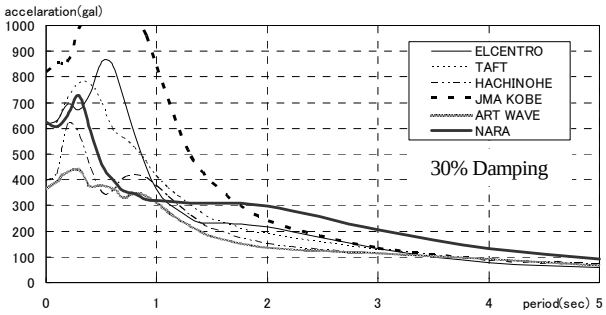

Figure 25 Response Acceleration Spectrum

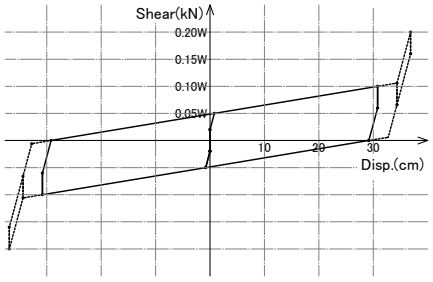

Figure 26 Force-Displacement Relationship of the Triple Friction Pendulum Bearing

Table 4 Maximum Response Value

wave	maximum acceleration (gal)	maximum verocity (kine)	maximum displacement
ELCENTRO	108	52	11.7
TAFT	108	66	14.8
HACHINOHE	105	50	10.9
JMA Kobe	111	81	13.0
ART WAVE	106	28	12.8
NARA	139	70	29.2

5. CONCLUSION

These three projects introduced in this paper were used significantly special seismic isolation structures and required us to jump over different hurdles for each case. The clients' understanding of seismic safety and eagerness for the seismic isolation system largely contributed to realize these buildings. The possibility of isolation structure will spread by using various devices properly taking advantage of the feature.

Acknowledgements:

We would like to express our gratitude to the people involved from Iida Archiship Studio, Environmental Design Institute, Mitsubishi Jisho Sekkei, and Archivison. We also appreciate the guidance offered by Professor Akira Wada and Professor Saburo Midorikawa respectively for the seismic isolation system and probable earthquake motion in designing the museum project.

References:

1) The Central Disaster Prevention Council: Assesmennt of damage by To-nankai and Nankai earthquake, 2003
2) Mika Kaneko: Method to Estimate Overturning Ratios of Furniture During Earthquakes, J. Struct. Constr. Eng. A.I.J, No.551

Sixth International Conference on Urban Earthquake Engineering
March 3-4, 2009, Tokyo Institute of Technology, Tokyo, Japan

PERFORMANCE OF SEISIMIC ISOLATED STRUCTURES FOR LONG-PERIOD GROUND MOTIONS

Mineo Takayama[1)]

1) Professor, Dept. of Architecture, Fukuoka University, Japan
mineot@fukuoka-u.ac.jp

Abstract: In Japan, the Tokai earthquake and the Tonankai earthquake are expected to occur in the near future. It is expected that the vibration continues for a long time in seismic isolated buildings due to a long-period ground motion. In this research, the dynamic experiments of rubber bearings and sliding bearings carried out to verify the energy absorption capacity. The influence that the change in the hysteretic characteristics gave to the maximum response in seismic isolated building was verified by the response analysis. As the results, it was shown that it was important to evaluate the change in the hysteretic characteristics of isolation devices appropriately.

1. INTRODUCTION

Since the 1995 Hyogo-ken Nanbu Earthquake, seismic isolated buildings have dramatically increased. The seismic isolation system has become frequently applied to apartment buildings other than disaster-prevention facilities such as hospitals, so the period of seismic isolated building has become long.

Meanwhile, when the 2003 Tokachi-oki Earthquake occurred, a petroleum tank in Tomakomai was damaged by sloshing of liquid by a long-period ground motion. The duration time of this type ground motion is long and its dominant periods are also long. When the 2004 Niigata Chuetsu Earthquake and the 2007 Niigata Chuetsu-oki Earthquake occurred, large ground motions were observed at the neighborhood of epicenter. The energy spectrum of these ground motions are shown in Fig.1. The input energy level exceeded the Japanese design level.

In this study, firstly, we carried out the dynamic experiments, presuming the long-duration ground motion. The rubber bearings and the sliding bearing were used in this experiment. It showed how the hysteresis characteristics of isolation bearings are changed by being deformed repeatedly for 200 cycles or more. Based upon the experimental results, the maximum response of seismic isolated building was validated by time history analysis.

2. RESPONSE PREDICTION

It can be presumed that seismic isolation layer of seismic isolated building can absorb all earthquake input energy. The characteristics of seismic isolation layer are presumed to be able to be modeled in the bilinear type as shown in Fig.2. Equation (1) was obtained as energy equilibrium equation in seismic isolation layer.

$$W_e + W_p = E \tag{1}$$

W_e of Equation(1) is the elastic vibration energy, and it is obtained in Equation (2) as the energy absorbed by the linear spring (Isolator) K_d shown in Fig.2(b). δ_{max} is the maximum displacement of seismic isolation layer.

$$W_e = \frac{1}{2} K_d \delta_{max}^2 \tag{2}$$

W_p is the elasto-plastic strain energy, which is equivalent to the absorbed energy by the entire elasto-plastic spring (damper) as shown in Fig.2(c). If the yield load and accumulated plastic deformation of damper are Q_d and δ_p, respectively, Equation (3) is obtained.

$$W_p = Q_d \delta_p \tag{3}$$

The energy input E of the earthquake is converted to the equivalent velocity V_E by Equation (4).

$$E = \frac{MV_E^2}{2} \tag{4}$$

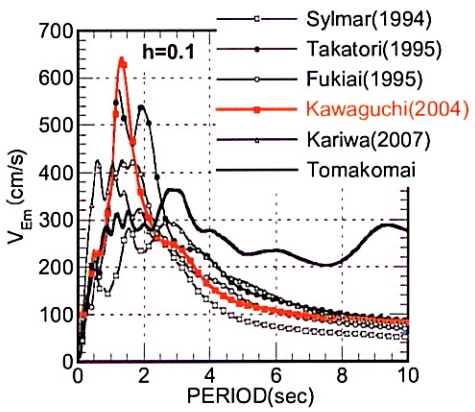

Fig.1 Energy Spectrum

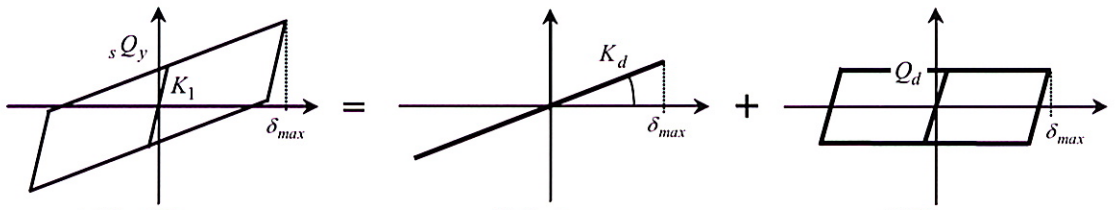

(a) Total System (b) Isolator (c) Damper

Fig.2 Restoring Force Characteristics of Isolation System

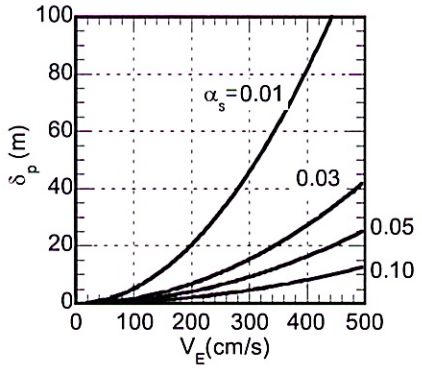

Fig.3 Relationship between Energy Input and Cumulative Plastic Deformation

Substitute Equations (2)-(4) to Equation (1) and sort out it with Equations (5) and (6), then Equation (7) is obtained.

$$T_d = 2\pi\sqrt{\frac{M}{K_d}} \tag{5}$$

$$\alpha_s = \frac{Q_d}{Mg} \tag{6}$$

where, M: the total mass of building

g : the acceleration of gravity

$$\frac{4\pi^2}{T_d^2}\delta_{max}^2 + 2g\alpha_s\delta_p = V_E^2 \tag{7}$$

All earthquake input energy is absorbed by damper ultimately. Therefore $W_p = E$, and the accumulated plastic deformation of damper δ_p is obtained in the simple form like Equation (8).

$$\delta_p = \frac{V_E^2}{2g\alpha_s} \tag{8}$$

The relationship between the accumulated plastic deformation of damper δ_p and V_E is shown in Fig.3. It shows that when α_s is small, the accumulated plastic deformation necessary to absorb earthquake energy becomes very large.

3. EXPERIMENTS OF ISOLATORS

3.1 Rubber Bearings

In order for the energy absorption capacities of lead rubber bearing (LRB) and high damping rubber bearing (HDR) to be confirmed, the dynamic experiment with 200 cycles was conducted. The compressive shear tests were carried out in each test specimen. The compressive stress (surface pressure) was kept at 8N/mm^2 constantly during the test, and the experiment was repeatedly performed at 200% shear strain for 200 cycles. The accumulated deformation was approximately 70m. The input waveform was a sine curve and the frequency was 0.33 Hz. The heat distribution within the rubber bearing was measured with a thermo couple at the experiment. In order for the heat conduction through the experiment equipment to be prevented, a heat insulation board (10mm thickness) was placed between the test specimen and experimental equipment.

Fig. 4 shows the section plan and Table 1 shows the specification of the specimen. The material of rubber of LRB is natural rubber and that of HDR is high-damping rubber. The diameter of test specimen is 225mm and the total rubber thickness is 44mm. The diameter of the lead plug is equivalent to 1/5 the external diameter of the rubber bearing.

Table 1 Specification of Rubber Bearings

Specimen	LRB	HDR
Rubber Material	Natural Rubber (G=0.39N/mm^2)	High Damping Rubber (G=0.62N/mm^2)
Diameter	φ225mm	
Lead Plug	φ45mm	—
Rubber Sheet	2.0mm × 22 layers=44.0mm	
Steel Plate	1.2mm × 21 layers	
Shape Factor	S_1=28.1, S_2=5.11	

Note: S_1: Primary Shape Factor, S_2: Secondary Shape Factor

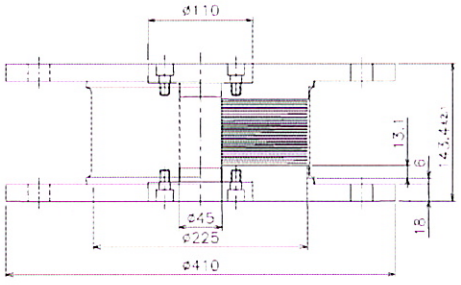

Fig.4 Section Plan of LRB Specimen

Fig.5 and Fig.6 shows the relationship between horizontal displacement and horizontal load obtained by the experiment. The hysteresis characteristics are the largest at

the first cycle, and the hysteresis loop (yield load) becomes reduced with increasing the repeated cycles. As stated above, the characteristics of rubber bearing change by being repeatedly deformed, but, when it was deformed again after it was left for more than one day, the characteristics of rubber bearing showed the same ones as before. It is considered that the characteristics of rubber bearing return to original ones.

The horizontal stiffness of HDR decreased with the repetition of the test and the hysteresis loop area also reduced in size. The equivalent stiffness, *Keq*, decreased with the increased repetition of the test, and the equivalent viscous damping constant, *Heq*, changed only in the range from 0.17 to 0.15.

Fig.7 and Fig.8 show the changes of K_d and Q_d caused by the increase of hysteresis absorption energy W_p. From these figures, the ratio of change of K_d for LRB was -5.4% at the third cycle of 200 cycles and that of Q_d was -41.7%. From these results of LRB, it revealed that although the change of K_d (horizontal stiffness after yield) on the hysteresis curve was small, the yield load largely decreased. It decreased approximately to -30% at around the first 10 cycles, in particular, so we should pay special attention to this point in establishing a restoring force model for response analysis.

Comparing to LRB, K_d and Q_d of HDR are mildly decreasing.

Fig.9 shows the relationship between the temperature measured at the center part of the specimens and the absorbed energy. The temperature measured at the upper part of lead plug reached 100℃ at the maxim and it rapidly decreased after the completion of vibration input. The melting point of lead is approximately 320℃, so the temperature of the lead plug might not have reached the melting point. The temperature of HDR reaches about 90℃ at maximum, but stays below the melting point of rubber.

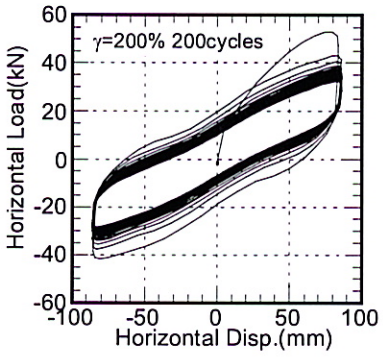

Fig.5 Hysteresis Loop of LRB

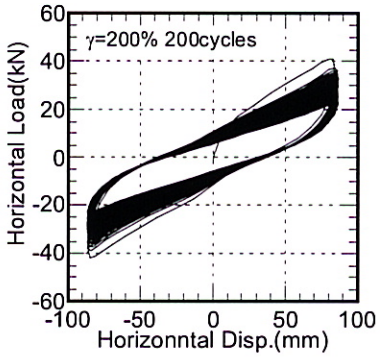

Fig.6 Hysteresis Loop of HDR

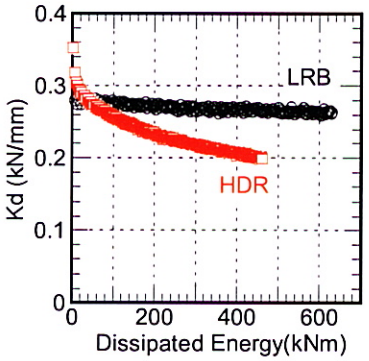

Fig.7 Variation of K_d

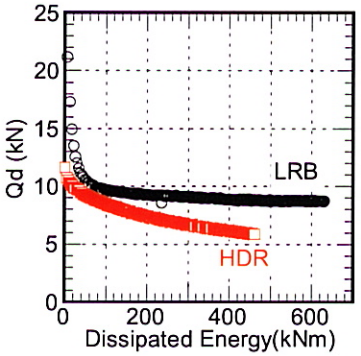

Fig.8 Variation of Q_d

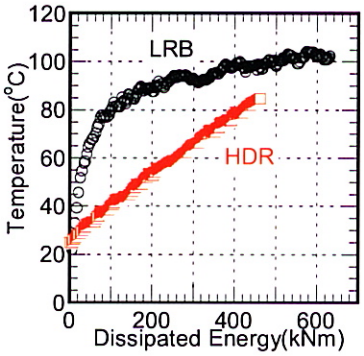

Fig.9 Variation of Temperature

3.2 Sliding Bearing

In order to confirm the energy absorption capacity of a sliding bearing, the dynamic cyclic tests with 540 cycles was carried out. The cyclic deformation was 140mm and the frequency was 0.4Hz (maximum velocity was 35cm/s). The cumulative sliding displacement reaches to around 300m. The compressive stress was defined by the surface area of PTFE, which corresponds to the nominal stress provided by manufacturer. The compressive stress for tests was 10MPa.

Characteristics of test specimens are shown in Table 2. The nominal friction coefficient of the test specimen is 0.13. This sliding bearing is one of conventional material which has been widely used as bridge bearings, and, also has been applied to base isolation devices.

Fig.10 shows the restoring force characteristics of the sliding bearing of 540 cycles. Obviously, it was observed that the friction force decreases as number of cycles increases. Fig.11 shows relationship of the change of friction coefficient and the absorbed energy, and also shows the change of the temperature at the back side of the center part

of stainless plate. At the 540th cycle, the coefficient decreased as almost 40% of the initial value. The temperature rapidly increased up to 250 degree, then finally reached to 300 degree in Celsius. The temperature at the back of PTFE reached only to 150 degree, because of the heat-insulation characteristic of PTFE material. On the other hand, after loading completion, the temperature went down faster in stainless plate than in PTFE.

Table 2 Specification of Sliding Bearing

Bearing	Bearing Dia.	225mm
	Shear Modulus	1.2MPa
	Rubber Layers	2.8mm×10lys.
	PTFE Dia.	160mm
	Nominal Comp. Stress	10MPa
Stainless Plate	Plan Dim.	300mm×500mm
	Material	SUS304 (JIS G 4303)

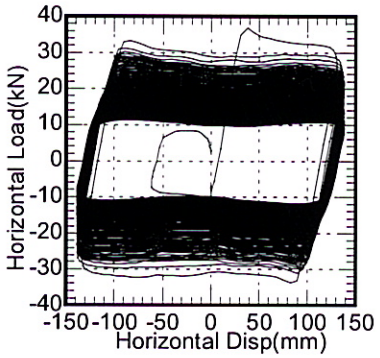

Fig.10 Hysteresis Loop of Sliding Bearing

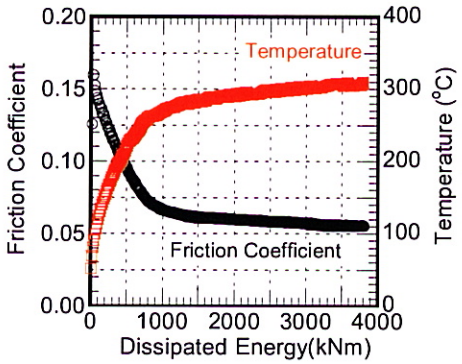

Fig.11 Variation of Friction Coefficient and Temperature

4. TIME HISTORY RESPONSE ANALYSIS

It was revealed by the dynamic experiments of rubber bearing that the energy absorption capacity is decreasing. In order for these changes of characteristics affecting earthquake response to be confirmed, time history response analysis was performed. The analytical model was a one-degree-of-freedom model consisting of seismic isolation layer only. The seismic isolation layer has the bi-linear characteristic as shown in Fig. 2(a).

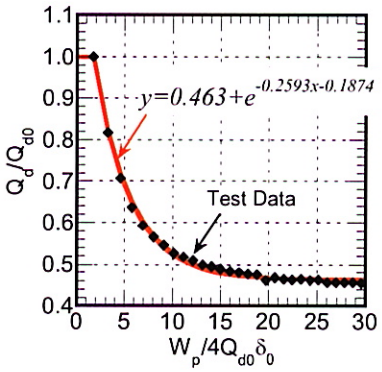

(a) Q_d for LRB Model

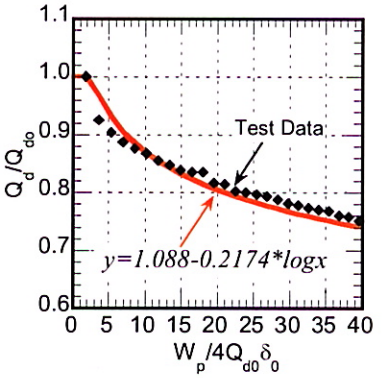

(b) Q_d for HDR Model

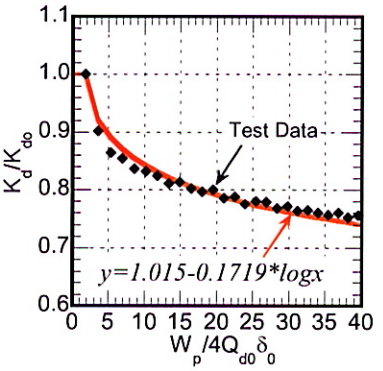

(c) K_d for HDR Model

Fig.12 Dependency of Hysteresis Loop

In modeling of restoring force characteristics of LRB, the horizontal stiffness K_d was fixed, and the yield load Q_d was changed. The relationship between yield load and hysteretic absorption energy W_p is shown in Fig.12(a). The hysteretic absorption energy is standardized by being divided by $4Q_{d0}\delta_0$. Q_{d0} is the initial yield load and δ_0 is assumed as D/S_2. In other words, δ_0 show the deformation equivalent to the thickness of total rubber layers, and it is equivalent to the hysteresis loop area for one cycle of damper shown in Fig.2(c).

In modeling of HDR hysteresis loop, both the horizontal stiffness and yield load were changed as shown in Fig.12(b)(c). A model like these is called a dependency

model. For the purpose of comparison, an analysis was performed by the model maintaining primary characteristics, which is called a constant model.

Table 3 Conditions of rubber bearing to be used in the analytical model

Compressive Stress σ (N/mm^2)	6	8	10	15
Diameter D (m)	1.0			
Mass M (ton)	480.8	641.1	801.4	1202.1
Stiffness K_d (kN/m)	1570.7			
Period T_d (sec)	3.48	4.01	4.49	5.50
Q_{d0} (kN) for LRB	251			
$\alpha_s = Q_{d0}/Mg$	0.053	0.040	0.032	0.021
Q_{d0} (kN) for HDR	208			
$\alpha_s = Q_{d0}/Mg$	0.044	0.033	0.027	0.018

For the preparation of an analytical model, the rubber bearing with the diameter of 1m was presumed, and the situation where the rubber bearing is supporting a given load was modeled. Table 3 shows K_d and Q_d of rubber bearings used for the analysis. The secondary shape factor S_2 is presumed as 5 (δ_0 =0.2m). The compressive stress (surface pressure) σ of the rubber bearing was changed in the range of 6N/mm^2 to 15N/mm^2. The period T_d and yield shear coefficient α_s calculated in Equations (5) and (6) are also shown in Table 3.

For response analysis, an artificial earthquake wave and the waveform observed at the Japan Meteorological Agency (JMA) in Kawaguchi-machi at the time of the 2004 Niigata-ken Chuetshu Earthquake were used. The artificial earthquake wave was prepared with the phase information of waveform observed at Tomakomai when the 2003 Tokachi-Oki Earthquake occurred. Fig.13 shows the time historical waveforms. It revealed that although the acceleration of artificial earthquake wave is not large, it continues for a long period of time.

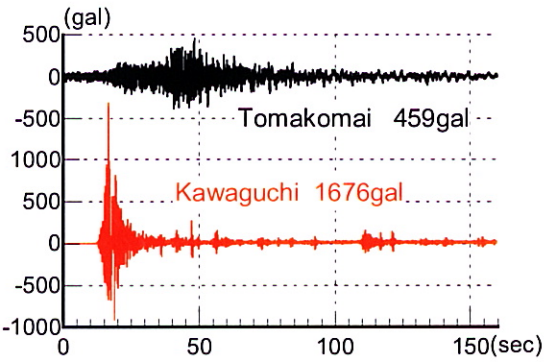

Fig.13 Input Earthquake Wave for Dynamic Analysis

Table 4 shows the maximum displacement of seismic isolation layers obtained from the response analysis. According to the analysis results, where the dependence of characteristics of both LRB and HDR were taken into consideration, the ratio of the results of Tomakomai wave analyzed by the dependency model and the constant model became 1.1-1.3 times. The reason why the ratio of response of HDR is smaller than that of LRB is that the characteristic change of HDR is more moderate than that of LRB, as clearly shown in Fig. 12. Meanwhile, there was no change in the maximum response displacement in the case of Kawaguchi wave.

As shown in Fig. 14 and 15, in the case of Tomakomai wave, many repeated deformations are generated, but in the case of Kawaguchi wave, the repetitions are very few. The cumulative plastic deformation of Tomakomai wave is in the range of 10m to 28m, but Kawaguchi wave is less than 6m. The hysteretic absorption energy W_p of Kawaguchi wave is only 4-6 times of $4Q_{d0}\delta_0$. Meanwhile, that of Tomakomai wave is 10-25 times.

5. CONCLUSIONS

It revealed that both the lead rubber bearing and the high damping rubber bearing produce heat by repeated cyclic loading, and that the change of stiffness after yield is small, but the yield load decreases early in LRB and that the equivalent viscous damping constant does not change so much, even though the equivalent stiffness decreases in HDR.

Test specimens themselves were not crippled by the heat generation and continued to have enough energy absorption capacity. It revealed that, because the mechanisms of heat generation of LRB and HDR are different, the manners of the temperature increase are also different, and that the changing trends of hysteresis loops of LRB and HDR caused by repetition are also different.

The friction coefficient of sliding bearing decrease as the temperature at sliding surface increase. When the surface temperature cooled downed to the room temperature, the friction characteristics was recovered. When using sliding bearing as a friction damping element, decrease of friction coefficient according to the sliding displacement should be properly considered in the design.

In order to correctly evaluate the earthquake response of seismic isolated buildings, it is indispensable to make models of hysteresis characteristics of seismic isolation devices correctly. From the analytical results of changing the restoring force model based on experiment, when the response causes many repetition as in the case of long-period ground motion, it is very important to appropriately make the model of restoring force characteristics according to presumed response deformation and the number of repetition (accumulated deformation).

Acknowledgements:

The author acknowledge that these experiments were carried out by Bridgestone Co.. The author would also like to acknowledge these individuals for their assistance of experiments and

suggestions: Ryuichi Kousaka of Azusa Sekkei Co. Ltd., Takashi Kikuchi of Bridgestone Co., Hironori Hamazaki of Bridgestone Co., Nobuo Murota of Bridgestone Co..

References:

Kousaka R., Hamazaki H., Mutota N. and Takayama M. (2008), "Experimental Study on Durability of Sliding Bearings under Long Duration Dynamic Loading," Proceedings of 14WCEE, Beijing, China

Takayama M., Kousaka and Kikuchi T. (2008), "Durability of Rubber Isolators by Long-Duration Ground Motion due to Large Earthquakes" Proceedings of 14WCEE, Beijing, China

Table 4 The maximum displacement obtained from analysis (m)

(a) Analysis Results of LRB

Input Motion	TOMAKOMAI			KAWAGUCHI		
Hysteresis Model	Dependency Model (A)	Constant Model (B)	Ratio (A/B)	Dependency Model (A)	Constant Model (B)	Ratio (A/B)
σ=6 N/mm^2	0.224 (10.2)	0.171	1.31	0.769 (5.9)	0.769	1.00
σ=8 N/mm^2	0.308 (15.8)	0.271	1.14	0.716 (4.5)	0.713	1.00
σ=10 N/mm^2	0.386 (21.0)	0.305	1.27	0.650 (4.1)	0.646	1.01
σ=15 N/mm^2	0.630 (27.9)	0.503	1.25	0.647 (3.7)	0.647	1.00

(b) Analysis Results of HDR

Input Motion	TOMAKOMAI			KAWAGUCHI		
Hysteresis Model	Dependency Model (A)	Constant Model (B)	Ratio (A/B)	Dependency Model (A)	Constant Model (B)	Ratio (A/B)
σ=6 N/mm^2	0.291 (9.6)	0.252	1.15	0.800 (5.0)	0.798	1.00
σ=8 N/mm^2	0.337 (13.1)	0.320	1.05	0.754 (4.1)	0.751	1.00
σ=10 N/mm^2	0.388 (16.8)	0.339	1.14	0.687 (3.8)	0.686	1.00
σ=15 N/mm^2	0.633 (23.8)	0.567	1.12	0.628 (3.4)	0.628	1.00

Note: The value in parenthesis shows the cumulative plastic deformation δ_p.

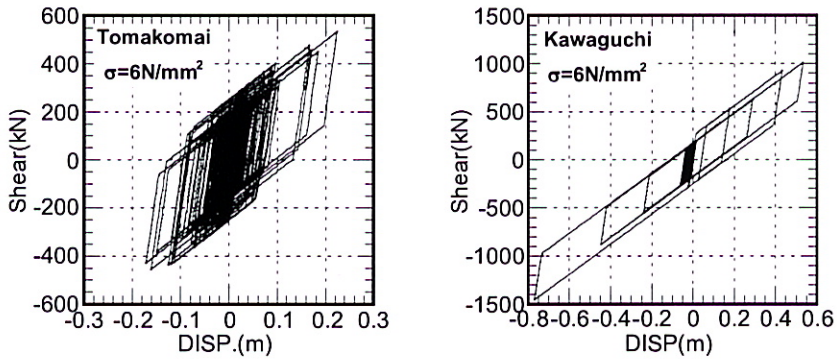

Fig.14 Analysis Results for LRB Model (Compressive Stress σ=6N/mm^2)

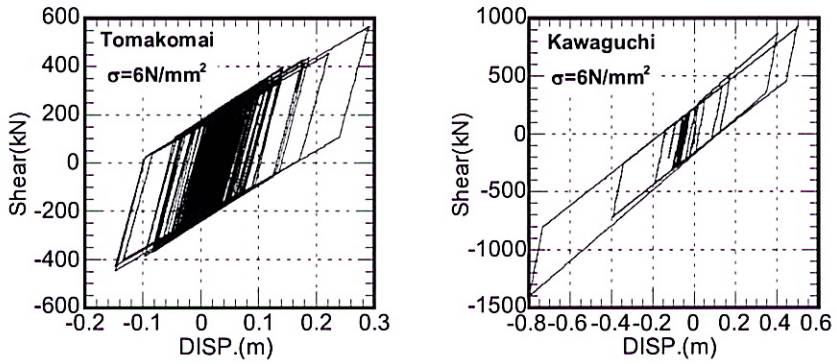

Fig.15 Analysis Results for HDR Model (Compressive Stress σ=6N/mm^2)

Sixth International Conference on Urban Earthquake Engineering
March 3-4, 2009, Tokyo Institute of Technology, Tokyo, Japan

A STRUCTURAL DESIGN METHOD OF BUILDING MASS DAMPER SYSTEM BASED ON MODE CONTROL CONCEPT WITH DYNAMIC MASS

Takeshi Furuhashi[1)], Shinji Ishimaru[2)] and Ippei Hata[3)]

1) Associate Professor, College of Science and Technology, Nihon University, Tokyo, Japan
2) Professor, College of Science and Technology, Nihon University, Tokyo, Japan
3) Assistant Engineer, College of Science and Technology, Nihon University, Tokyo, Japan
furuhashi@arch.cst.nihon-u.ac.jp, ishimaru@arch.cst.nihon-u.ac.jp, i_hata@edu.cst.nihon-u.ac.jp

Abstract: This paper presents a new response control system named as "Building Mass Damper System (BMDS)", which is composed on a basis of "Mode Control Concept" by making use of "Dynamic Masses". BMDS means a Tuned Mass Damper System designed by making use of masses of about from 1/4 to 1/2 stories from the top of the building. The behavior of these masses is controlled by the adjusted dynamic masses in order to maintain a single degree of freedom system. Dynamic mass damper is the name of the device which generates inertia forces to be proportional to the acceleration difference between the installed points. The paper shows BMDS has a higher performance to be able to absorb vibration energies of buildings, which may be applied not only to newly constructed buildings but also to seismic retrofitting of existing buildings.

1. INTRODUCTION

In general, seismic designs of buildings are performed by adjusting the stiffness and the strength and, in recent years, by artificially giving the damping. The response control by making use of these devices means to design the stiffness factor and the damping factor in an equation of motion.

On the other hand, there are studies to control responses by making supplementary masses behave according to the displacement difference between the installed points[1], 2], 3]].

The authors have proposed response control design methods of structures against earthquakes utilizing dynamic mass dampers [4], 5], 6], 7], 8]]. The word of "dynamic mass damper" is named for the device that generates the force to be proportional to the acceleration difference between the installed points.

A high performance "dynamic mass" damper can be realized by using the displacement amplification mechanism such as a rotation mechanism etc, which the magnitude of mass in a vibration phenomena becomes much greater than its actual mass.

Accordingly, the following two quite new response control methods can be proposed. One of them is the mode control design. By adjusting the value of the dynamic mass of the each story, the participation factors of higher modes can be adjusted to be 0. As a result of the mode control, the following characteristics are derived. First, the responses of higher modes disappear. Second, response accelerations decrease. Third, response shear coefficients of all stories are the same. This method is also called "a full mode control", because dynamic masses are installed to all stories except the top story and all higher modes are controlled. A large amount of dynamic masses, however, is required to achieve a full mode control.

The other method is a Building Mass Damper System (BMDS), which is a tuned mass damper designed by making use of masses of about from 1/4 to 1/2 stories from the top of the building.

By the way, when the mass of a tuned mass system is relatively small in comparison with the structure, the system is not adequate to control responses of structures against severe earthquakes. Thereby, the masses of the upper stories may be used as the weight.

One of such ideas is a system installed a seismic isolation layer in the middle story of building. However, it is hard to be widely applied to buildings in the viewpoints of architectural planning and the magnitude of the story drift at the seismic isolation layer against the strong winds such as typhoon.

In order to conquer the weak points, the BMDS is can be proposed by making use of the above mentioned "mode control concept" with dynamic masses.

Because the masses of about from 1/4 to 1/2 stories from the top of the building can be controlled to produce the behavior of a single degree of freedom system. Thereby, the masses of the upper stories work as the large weight of a tuned mass damper. Consequently, the system requires neither seismic layer in the middle of the building, nor dynamic masses installed to all stories except the top story. The system with large weight is adequate to control responses of structures against severe earthquakes[10], 11], 12]].

Thereby, the system may be called "a partial mode control" structure.

2. DYNAMIC MSSS (INERTIA CONNECTION ELEMENT BETWEEN MASS POINTS)

Figure 1 shows the concept of a dynamic mass which is composed of the rotation body with the combined inner wheel and the outer wheel. And the mass m is concentrated at the outer wheel.

Now, we define the amplification ratio β which is the ratio of the radius of the outer wheel to the inner wheel. When the inner wheel is pushed in the direction of the tangent with the acceleration α, the inertia force of the mass m of the outer wheel is $m\beta\alpha$. And the reaction force to push the inner wheel becomes $\beta^2 m\alpha$.

As a result, the mass m of the outer wheel can display the magnitude of $\beta^2 m$ at the position of the inner wheel.

If β is large enough, this mechanism has a property of mass amplification device, named as a dynamic mass that generates the force to be proportional to the acceleration difference between the installed points.

Now, we express the magnitude of dynamic mass as m' ($=\beta^2 m$) in distinction from the real mass m of the structure.

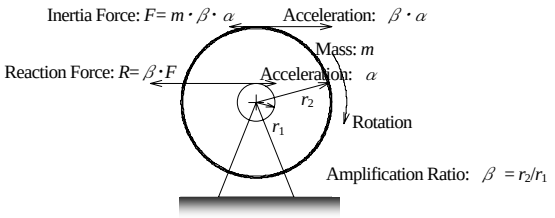

Figure 1 Rotation Body

A practical device of a dynamic mass is composed by a little improvement for a viscous damping device called "Rotary Damping Tube (RDT)" which can convert an axial movement into the gyration of the inner cylinder with a ball screw, and generates the resistance force due to the viscous body filled between the rotating inner cylinder and the fixed cover cylinder.

The displacement of the direction of the tangent of the inner cylinder is amplified to about 5 to 40 time of the axial displacement. The effect of the inertia mass of the rotating inner cylinder is amplified to the square of the displacement amplification ratio. It becomes 1,000 times or more the mass of the inner cylinder[13].

Thus, if the mass at the rotating inner cylinder is designed with a little larger magnitude, the device can be applied for the practical use as a dynamic mass.

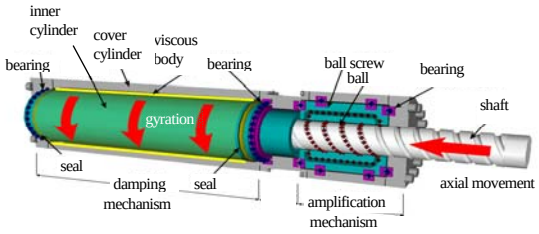

Figure 2 Rotary Damping Tube (RDT)

3. MODE CONTROL DESIGN WITH DYNAMIC MASSES

First, let's review response control design methods using dynamic masses briefly.

The equation of motion for a single degree of freedom system with a dynamic mass m' is given by Eq.1 below, in which the value of η becomes less than or equal to 1.

$$(m+m')\ddot{x}+c\dot{x}+kx=-(m+m')\eta\ddot{y} \tag{1}$$

in which, $\eta=\dfrac{m}{m+m'}$

The equation of motion for a multi degree of freedom system with dynamic masses is given by Eq.2. Each element of $\{\eta\}$ is less than or equal to 1, which indicates the decrease effect of the input.

$$[\hat{M}]\{\ddot{\hat{x}}\}+[\hat{C}]\{\dot{\hat{x}}\}+[\hat{K}]\{\hat{x}\}=-[\hat{M}]\{\eta\}\ddot{y} \tag{2}$$

in which,

$[\hat{M}]=[\hat{M}_0]+[\hat{M}']$

$[\hat{M}_0]$ is ordinary mass matrix,

$[\hat{M}']$ is dynamic mass matrix,

$\{\eta\}=[\hat{M}]^{-1}[\hat{M}_0]\{1\}$

That is, the response control methods using dynamic masses induce the system to be able to decrease the effect of ground motion input etc., which can not be obtained by only controlling the stiffness and the damping.

Thus, we can gain quite new two types of response control method.

One is that the natural period of a structure can be elongated without changing its mode shapes by adding the dynamic masses proportional to the stiffness of each story of the vibration system[5].

The other is the mode control design. By adjusting the value of the dynamic masses of each story, the participation factors of higher modes can be adjusted to be 0.

Next, consider an n-degree of freedom system with dynamic masses, the participation factors of from the 2nd to the n-th mode can be adjusted to be 0 by adding the dynamic masses. The combination of the dynamic masses can be evaluated easily by the following procedure [5].

$$
\left.
\begin{aligned}
&{}_1\omega^2 = \frac{1}{\sum_{i=1}^{n}\left(\frac{1}{k_i}\sum_{j=i}^{n} m_j\right)} \\
&\eta_0 = 0 \\
&\eta_i = \eta_{i-1} + \frac{{}_1\omega^2}{k_i}\sum_{j=i}^{n} m_j \qquad (1 \le i \le n) \\
&\{{}_{n+1}u\}^T = \{\{1-\eta\}^T \;\; 1\} \\
&D_i = \frac{{}_{n+1}u_i}{{}_{n+1}u_{i-1}} \qquad (1 \le i \le n) \\
&m'_n = 0 \\
&m'_i = \frac{m_i + m'_{i+1}(1-D_{i+1})}{\frac{1}{D_i}-1} \qquad (1 \le i \le n-1)
\end{aligned}
\right\} \qquad (3)
$$

Table 1 Evaluation of Dynamic Mass

${}_1\omega$	5.6381	${}_1T$=	1.1144
${}_1\omega^2$	31.788		

i	m_i (ton)	k_i (kN/m)	Σm_i (ton)	$\Sigma(1/k_i \Sigma m_i)$	${}_1u_i = \eta_i$	${}_{n+1}u_i$ =1- η_i	D_i	m'_i (ton)
8	750.0	820,000	750.0	0.00091	1.0000	0.0000	0.0000	0
7	760.0	830,000	1,510.0	0.00273	0.9709	0.0291	0.3346	382.09
6	770.0	840,000	2,280.0	0.00545	0.9131	0.0869	0.5018	1,031.66
5	780.0	870,000	3,060.0	0.00897	0.8268	0.1732	0.6077	2,004.36
4	790.0	890,000	3,850.0	0.01329	0.7150	0.2850	0.6745	3,267.00
3	800.0	900,000	4,650.0	0.01846	0.5775	0.4225	0.7201	4,793.33
2	850.0	910,000	5,500.0	0.02450	0.4133	0.5867	0.7533	6,693.43
1	900.0	920,000	6,400.0	0.03146	0.2211	0.7789	0.7789	8,985.31
0	–	–	–	–	0.0000	1.0000	–	–

Table 2 Eigenvalue Analysis of Controlled System

	1st	2nd	3rd	4th	5th	6th	7th	8th	9th
T	1.114	0.621	0.539	0.459	0.381	0.302	0.220	0.135	0
ω	5.638	10.12	11.66	13.70	16.51	20.83	28.53	46.61	∞
β	1.000	0.000	0.000	0.000	0.000	0.000	0.000	0.000	1.000
u_8	1.000	-0.663	-0.663	-0.669	-0.693	-0.733	-0.816	1.000	0.000
u_7	0.971	-0.601	-0.580	-0.554	-0.521	-0.442	-0.208	-0.987	0.029
u_6	0.913	-0.477	-0.416	-0.325	-0.177	0.137	1.000	0.000	0.087
u_5	0.827	-0.293	-0.172	0.015	0.336	1.000	0.000	0.000	0.173
u_4	0.715	-0.054	0.145	0.457	1.000	0.000	0.000	0.000	0.285
u_3	0.578	0.239	0.535	1.000	0.000	0.000	0.000	0.000	0.423
u_2	0.413	0.590	1.000	0.000	0.000	0.000	0.000	0.000	0.587
u_1	0.221	1.000	0.000	0.000	0.000	0.000	0.000	0.000	0.779
u_0	0.000	0.000	0.000	0.000	0.000	0.000	0.000	0.000	1.000

Table 1 shows the process and the combination of the dynamic masses that adjust the participation factors of all higher modes of the example system to be 0.

Table 2 shows the result of eigenvalue analysis of the system with dynamic masses. The participation factors β from the 2nd to the 8th mode of the controlled system are 0. It must be emphasized that the 9th mode (the (n+1)th mode) of rigid body (i.e., $\omega = \infty$) appears, and it has the physical meaning of transmit of the acceleration related to the ground motion.

This method is also called "a full mode control", because dynamic masses are installed to all stories except the top story and all higher modes are controlled to 0.

Note that a large amount of dynamic masses is required to achieve a full mode control.

4. FIXED POINT'S THEORY OF TUNED MASS SYSTEM

A tuned mass system is often used by making use of supplementary masses. The optimum tuned mass system can be derived by applying the so called the fixed point's theory. There are some expressions of the fixed point's theory depending on the target of control and the assumed input[9].

One of them is given by Eq.4 for reference.

$$
\left.
\begin{aligned}
&\text{Optimum frequency ratio:} \quad \lambda_{OPT} = \frac{\omega_U}{\omega_L} = \sqrt{\frac{2-\mu}{2}} \\
&\text{Optimum damping ratio:} \quad h_{OPT} = \frac{c_2}{2\sqrt{m_2 \cdot k_2}} = \sqrt{\frac{3}{8}\cdot\mu} \\
&\text{in which,} \\
&\text{Upper structure:} \quad \omega_U{}^2 = \frac{k_2}{m_2}, \quad \frac{c_2}{m_2} = 2h_U\omega_U \\
&\text{Lower structure:} \quad \omega_L{}^2 = \frac{k_1}{m_2+m_1}, \quad c_1 = 0 \\
&\text{Frequency and damping ratio:} \quad \mu = \frac{m_2}{m_2+m_1}, \quad \lambda = \frac{\omega_U}{\omega_L} \\
&\text{Frequency of input ground motion:} \quad \omega
\end{aligned}
\right\} \qquad (4)
$$

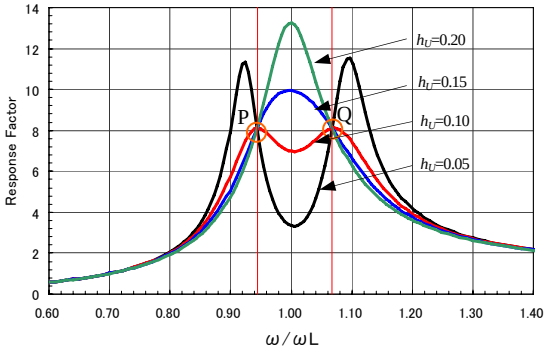

Figure 3 Resonance Curves of Lower Structure

($h_U = 0.05, 0.10, 0.15, 0.20$)

$\mu = \frac{m_2}{m_2+m_1} = 0.03$, $\lambda_{OPT} = 0.99$, $h_{OPT} = 0.105$

Response factor is the ratio of relative response displacement to the input amplitude. The target of control is the response factor of the lower structure. The assumed input is a ground motion. Points P and Q are fixed points.

5. BUILDIN MASS DAMPER SYSTEM BASED ON MODE CONTROL CONCEPT WITH DYNAMIC MASS

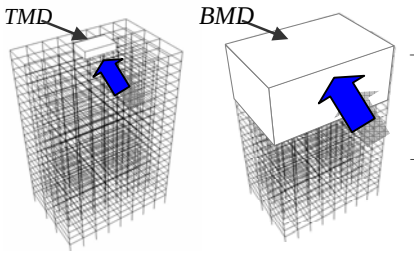

Figure 4 TMD and BMD

Our proposed Building Mass Damper System (BMDS) is designed by the mode control concept on a basis of dynamic masses.

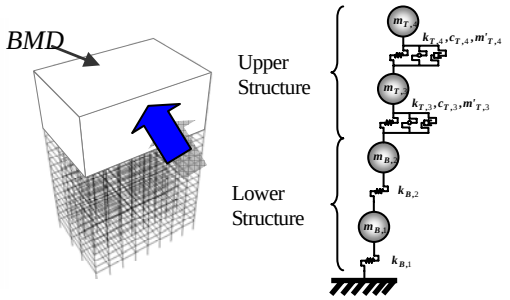

Figure 5 BMD based on mode control with dynamic mass (Hereafter, a dynamic mass is shown by─○─ .)

The procedure to design the BMDS is as follows.

First, define the upper structure. It may be 1/4 to 1/2 from the top of the building depending on the design target and the architectural planning. The rest is treated as the lower structure.

Next, apply the mode-control for the upper structure with dynamic masses by the procedure described in Section 2. As a result, the higher modes responses of the upper structure disappear. Next, the natural period and the equivalent mass of the 1st mode are calculated.

Then, analyze the eigenvalues for the lower structure to gain the natural period and the equivalent mass of the 1st mode of the lower structure.

Thus the optimum frequency ratio and damping ratio are derived by referring to the fixed point's theory of a tuned mass system.

By the way, the adjustment for the optimum frequency ratio is carried out by the following procedure. As mentioned in Section 3, the natural period of the upper structure can be elongated without changing its mode shapes.

That is, keeping the mode control situation, the natural period can be easily changed by adding dynamic masses proportional to the stiffness of each story of the upper structure. Needless to say, oil dampers are installed to each story of the upper structures to achieve the optimum damping ratio.

However, the fixed point's theory can not be simply applied to the BMDS. Because, as a result of the mode control of the upper structure, the (n+1)th mode of rigid body (i.e., $\omega = \infty$) remains as mentioned in Section 3. That is, still the (n+1)th mode has a modal equivalent mass.

Accordingly, this mass must be added to the top of the lower structure in analyzing the eigenvalues for the lower structure. This means that the natural period and the equivalent mass of the 1st mode of the lower structure change. In addition, the optimum frequency ratio and damping ratio also change. Consequently, dynamic masses installed to the upper structure change. The (n+1)th modal mass changes again.

Hence, the iteration analyses become necessary to get the optimum tuned situation of the BMDS, even referring to the fixed point's theory.

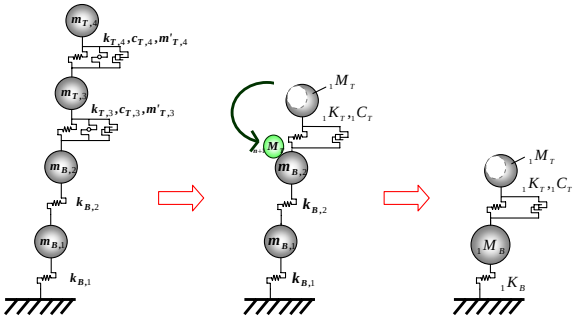

Figure 6 Concept of BMDS based on mode control with dynamic mass

6. SHAKING TABLE TEST

The shaking table test was carried out to verify the efficiency of BMDS. The model is 7 storied. Each floor is supported by linear bearings to allow the horizontal displacement. Restoring force characteristics are provided with rubber bearings. The upper 3 stories are utilized as BMD, where dynamic masses made with ball screws, and oil dampers are installed. The mass amplification factor β^2 of each dynamic mass at the upper stories is about 120.

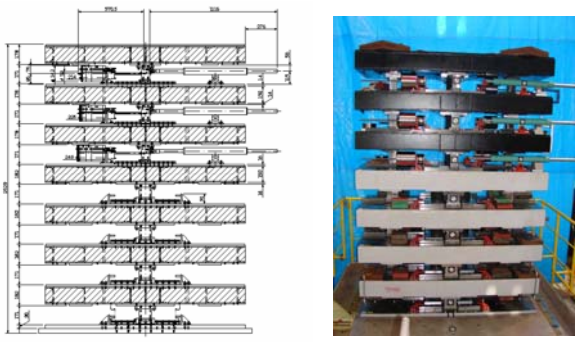

Figure 7 Vibration Model

Table 3 is the outline of the uncontrolled model. Table 4 is its natural periods and damping factors. Table 5 and 6 are the parameters for the BMDS model.

Table 3 Outline of Uncontrolled Model

story	*m* [ton]	*c* [kN·s/m]	*k* [kN/m]
7	0.713	0.88	50.0
6	0.713	0.88	50.0
5	0.713	0.88	50.0
4	0.750	1.58	100.0
3	0.750	1.58	100.0
2	0.750	1.58	100.0
1	0.750	1.58	100.0

Table 4 Natural periods and Damping factors of Uncontrolled Model

mode	period [sec]	damping factor
1st	2.63	0.067
2nd	1.03	0.067

Table 5 Outline of BMDS Model

story	*m* [ton]	*DM* [ton]	*c* [kN·s/m]	*k* [kN/m]
7	0.713	3.400	6.63	50.0
6	0.713	3.757	6.63	50.0
5	0.713	4.351	6.63	50.0
4	0.750	0.000	1.58	100.0
3	0.750	0.000	1.58	100.0
2	0.750	0.000	1.58	100.0
1	0.750	0.000	1.58	100.0

Table 6 Natural periods and Damping factors of BMDS Model

mode	period [sec]	damping factor
1st	2.81	0.120
2nd	1.65	0.135

Figure 8 shows the comparison of the experimental story displacement response factors between the controlled system and the uncontrolled system

In these figures, lines are the calculated values and markers are the results of experiments. Blue color and red color show values of the controlled system and of the uncontrolled system, respectively.

Response factors are significantly decreased of not only the lower structure but also the upper structure (= BMD part). The results show that the experimental values agree with calculated values very well.

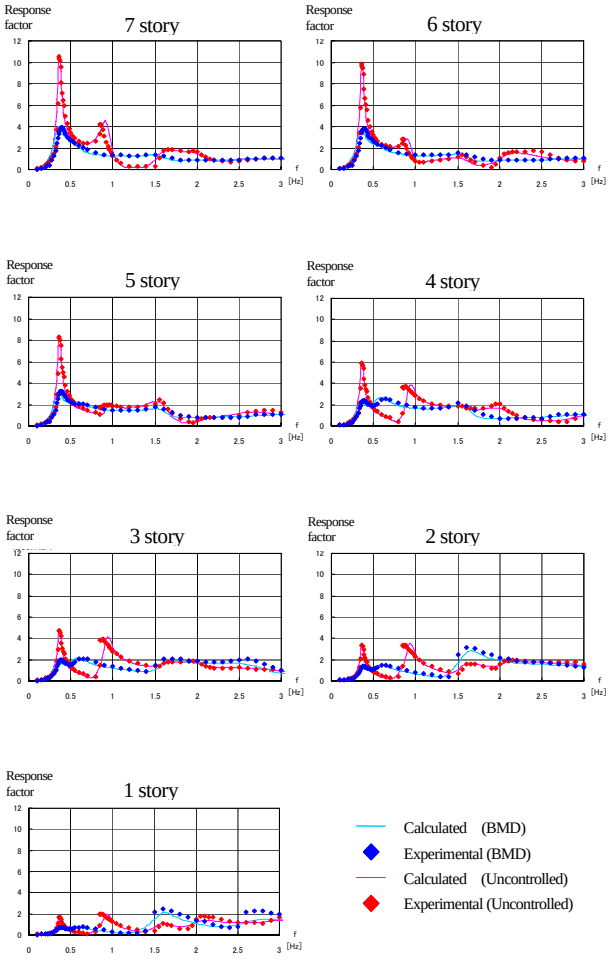

Figure 8 Displacement Response Factors

Next step, response characteristics for earthquake motion waves are investigated. Input waves are these three waves, an artificial wave, TC-IKEDA (recorded during the Tokachi-oki earthquake of 2003) and JMA-KOBE (recorded during the Hyougoken-Nanbu earthquake of 1995).

Figure 9 shows pseudo velocity spectra of elastic systems with viscous damping ratio $h = 0.05$ and $h = 0.4$ for the input waves. The spectrum of the artificial wave has the dominant power range from the 1st mode to the 5th mode. That of TC-IKEDA has the dominant period for the 1st mode. JMA-KOBE has the dominant periods for the 2nd mode and the 3rd mode.

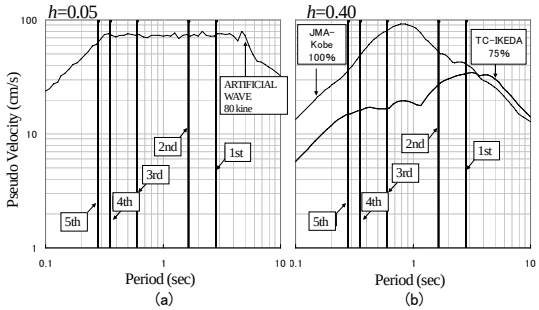

Figure 9 Pseudo Velocity Spectra of Input Waves

Figure 10 is the results of the maximum response accelerations. Figure 11 is the results of the maximum response displacements.

The results show that the seismic performance of BMDS is very high, even if the characteristics of the earthquake motions are quite different.

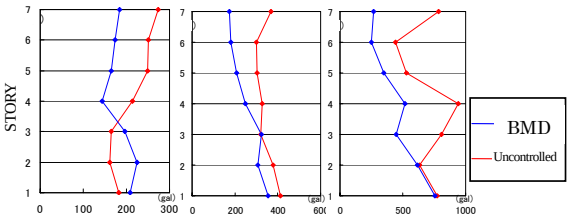

Figure 10 Maximum Response Accelerations

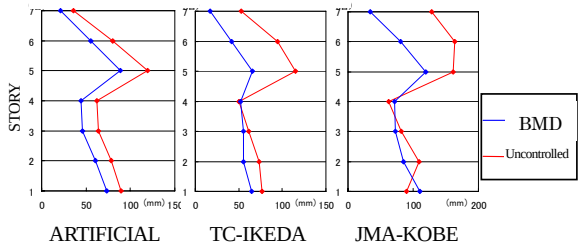

Figure 11 Maximum Response Displacements

7. CONCLUSIONS

This paper proposed the response control methods by making use of dynamic masses.

One of them is to adjust elongation of natural periods with keeping its mode shapes. Another is the full mode control method to eliminate responses of all higher modes. Dynamic masses are installed to all stories except the top story and a large amount of dynamic masses is required to achieve a full mode control.

In addition to this, Building Mass Damper System (BMDS) for high-rise buildings is proposed. This system is based on the mode control concept with dynamic masses. This system requires neither seismic layer in the middle of the building, nor dynamic masses installed to all stories except the top story. It is adequate to control responses of structures against severe earthquakes.

Dynamic masses are installed to a certain part of a building and the part of the building is mode-controlled to control responses of the whole structure. It is also called "a partial mode control" method. It may be applied not only to newly constructed buildings but also to seismic retrofitting of existing buildings.

A model vibration experiment was carried out. The efficiency of BMDS is verified.

References:

1] Kawamata, S., et al. (1986), "Control of Structural Vibration by Inertia Pump Damper Part(1), Part(2)", Summaries of Technical Papers of Annual Meeting, Architectural Institute of Japan, August 1986, 771-774

2] Ishimaru, S. (1994), "Outline of Response Control of Structures against Earthquakes, Design Mechanism and Control Dynamics of Building Structure", Architectural Institute of Japan, November 1994, 199-202

3] Okumura, A. (2000), "Vibration Interception Connection Mechanism", Waseda Univ. Science & Technology Seeds, NO. TLO 2000-002, March 2000

4] Furuhashi, T. and Ishimaru, S. (2004), "Mode isolation by inertial mass, Study on response control by inertial mass no.1", Journal of Structural and Construction Engineering, Architectural Institute of Japan, February 2004, 55-62

5] Furuhashi, T. and Ishimaru, S. (2006), "Response control of multi-degree system by inertial mass, Study on response control by inertial mass no.2", Journal of Structural and Construction Engineering, Architectural Institute of Japan, March 2006, 83-90

6] Saiki, K., Mitsusaka, Y., Furuhashi, T. and Ishimaru, S. (2004), "Study on Characteristic of SDOF system response with Inter-story Inertial Mass Part 1, Part 2 and Part 3", Summaries of Technical Papers of Annual Meeting, Architectural Institute of Japan, August 2004, B-2, 241-246

7] Takeshi Furuhashi and Shinji Ishimaru (2008), "MODE CONTROL SEISMIC DESIGN WITH DYNAMIC MASS", 11-0028, The 14th World Conference on Earthquake Engineering, October 12-17, 2008, Beijing, China

8] Takeshi Furuhashi and Shinji Ishimaru (2008),"MODE CONTROL SEISMIC DESIGN WITH DYNAMIC MASS", Tokyo Tech CUEE, 5th International Conference on Urban Earthquake Engineering, March 4-5, 2008, Tokyo, Japan

9] Seto, K. and Maruyama, K. (2002), "Vibration Engineering", Morikita Publishing

10]ISHIMARU Shinji, FURUHASHI Takeshi, HATA Ippei, MIYAJIMA Youhei, MAKI Ryouta, KOYAMA Sho (2008), "A Basic Study on BMD system with Dynamic Mass (Part 1 A Structural Design Method of BMD with DM Effect)", Summaries of Technical Papers of Annual Meeting, Architectural Institute of Japan, September 2008, B-2, 631-632

11]ISHIMARU Shinji, FURUHASHI Takeshi, HATA Ippei, MIYAJIMA Youhei, MAKI Ryouta, KOYAMA Sho (2008), "A Basic Study on BMD system with Dynamic Mass (Part 2 A Model Experiment and Verification of the Theory)", Summaries of Technical Papers of Annual Meeting, Architectural Institute of Japan, September 2008, B-2, 633-634

12]ISHIMARU Shinji, MIYAJIMA Youhei, USHIZAKA Shinya (2007), "A Structural Design Method of Building Mass Damper Based on Mode Control Concept", Summaries of Technical Papers of Annual Meeting, Architectural Institute of Japan, August 2007, B-2, 709-710

13]Nakaminami, S., et al. (2005), "Development of Viscous Damping Device with Inertia Mass Element", REPORTS OF TECHNICAL RESERCH INSTITUTE OF SUMITOMO MITSUI CONSTRUCTION CO., LTD. No.3, September 2005

Sixth International Conference on Urban Earthquake Engineering
March 3-4, 2009, Tokyo Institute of Technology, Tokyo, Japan

INFLUENCE OF RIGIDITY OF COLUMN BASE ON SEISMIC PERFORMANCE OF STEEL MOMENT FRAME RETROFITTED WITH HYSTERETIC DAMPER

Hayato Asada[1)], Shoichi Kishiki[2)], and Satoshi Yamada[3)]

1) Graduate Student, Structural Engineering Research Center, Tokyo Institute of Technology, Japan
2) Assistant Professor, Structural Engineering Research Center, Tokyo Institute of Technology, Japan
3) Associate Professor, Structural Engineering Research Center, Tokyo Institute of Technology, Japan
asadai@serc.titech.ac.jp, kishiki@serc.titech.ac.jp, naniwa@serc.titech.ac.jp

Abstract: This research aims to develop the seismic performance of steel moment frame retrofitted with hysteretic dampers such as buckling restrained braces, In this paper, effects of rigidity of column bases on seismic behavior of steel frame retrofitted with BRBs was discussed . In order to discuss the effect of rigidity of column base on damage concentration and maximum story drift which are important indicators to examine the retrofitting effects, the nonlinear response analysis is carried out. In this analysis, column bases are modeled using elastic rotational springs connected to columns and simple elastic springs connected to braces in serial. The analytical results show that the rigidity of column bases had effect on damage concentration to the original frames.

1. INTRODUCTION

After 1994 Northledge and 1995 Kobe earthquake, it has been widely-recognized as an important issue to improve poor seismic performances of existing buildings. For this reason, many retrofitting techniques has been studied and developed. Recently, several rehabilitations with hysteric damper such as buckling restrained braces (BRBs) have been reported (Tena-Colunga, 1997, Hasegawa, 2006, Di Sarno, 2006). Some of them include several techniques to connect these braces to original beam-to-column connection (Ichikawa 2006). However, little attention have been given to the effective techniques for attaching braces to column bases in the past. There are several reasons for this. One of them is that actual seismic performance of column base with braces, such as resisting mechanism against seismic load has not been clarified. Many old middle-rise buildings which need seismic rehabilitation have exposed type column bases. Most of their column bases don't have sufficient stiffness and strength. Therefore, to achieve requested structural improvement with additional components such as BRBs, retrofitting technique including repair of original column base may be required. On the other hand, for steel moment frame with BRBs, effects of rigidity of column bases on global performance have not been clarified. So, in this study, in order to investigate the effects of rigidity of column base on seismic performance of steel moment frames retrofitted with BRBs, a series non-linear response analysis of middle-rise steel moment frames retrofitted with BRBs was carried out prior to evaluation of performance of column bases with braces such as strength and restoring force characteristics subjected to earthquake load and developing retrofitting techniques.

2. ANALYTICAL MODEL

2.1 Original building

The original steel building is ordinary 8-story moment resisting frame (weak beam type frame). All bay width is 6 m. Total height of the structure from ground level is 32 m, with story height of 4m. The weight of each story is 1000 kN. Frame members consist of wide flange beam sections (SN400B) and cold-formed square box column sections (BCR295). Yield strength of steel material for beam, column and panel equal to 1.1 times of each nominal yield strengths. Material properties of members are summarized in table 1. The original steel structure was designed using plastic design method. For plastic design procedure, following constraints and assumptions were considered.

1. At the point to form the overall failure mechanism, base shear coefficient equals to 0.25.
2. The earthquake load distribution specified by Optimum Yield-Shear Coefficient Distribution (Akiyama, 1985) is used.
3. The strong column-weak beam philosophy is employed. Specifically, at each story, the sum of design column strength is 1.5 times of the sum of the strength of the beams which is not considered contributions of floor slab at this point.
4. Column and beam section is same in every 3 story from the ground level.
5. Columns and beams have good plastic deformation capacity. The width to thickness ratios of columns and beams correspond to minimum value of FA-rank according to Japanese design provision. (AIJ, 1998 etc) Specifically, b_c/t=30, $b/2t_{bf}$=9 and d/t_{bw}=60 where b_c: column width; t: column thickness; b: beam width, t_{bf}; beam frange thickness;

t_{bw}; beam web thickness; d: D_b(beam height)-2t_{bw}.
6. Positive contributions of floor slab were considered as analytical modeling assumptions. Specifically, strength of beams is 1.2 times of those of steel beam. Their stiffness applied the average value of composite beam calculated based on AIJ standard and steel beam.

2.2 Braces for Seismic Retrofitting

The damper braces are installed in center bay of each story as shown in figure 1. These hysteric dampers are buckling restrained braces. Dampers for seismic retrofitting were designed for the force calculated based on the ratio of damper's shear strength to maximum resistance of each story β_i. the ratio β_i. can be defined by equation(1).

$$\beta_i = \frac{{}_D Q_i}{{}_D Q_i + {}_M Q_i} \qquad (1)$$

Where ${}_M Q_i$: lateral strength of original frame at i-story obtained from plastic design method ; ${}_D Q_i$: Shear (lateral) strength of dampers in i-story.

In this study, β_i was set to 0.3. The lateral strength of original frame is calculated based on the plastic design method described in the previous section. Brace sizes are set to the required cross sectional area A_d (based on a nominal yield stress of LYP 225, 225 N/mm^2 for yielding core.).

The brace stiffness is calculated assuming a yielding length of a half of the brace length. Based on static loading tests of frame with BRBs (Kishiki, 2007) cross-sectional area of the non-yielding zone was three times of the yielding zone. As well as original members, brace size is same in every 3 story from the ground level. The link members connected braces to original frame were modeled as elastic truss elements.

Table 1 Material properties of member

Part	σ_y [N/mm^2]	τ_y [N/mm^2]	E [N/mm^2]	G [N/mm^2]
Column	325	-	205×10^3	79×10^3
Beam	259	-		
Panel	325	188		
Damper	225	-		

Table 2 Dimension of members

Story	Column and Panel	Beam	Damper A_d [mm^2]
7,8	□-354x354x11.8	H-481x213x7.60x11.8	974
4~6	□-442x442x15.6	H-597x264x9.50x14.7	1,866
1~3	□-502x502x16.7	H-662x293x10.5x16.3	2,674

Their equivalent stiffness is six times of yielding core based on stiffness of non yielding zone. Braces were modeled as ideal members capable of resisting axial force only. Dimension of members is summarized in Table 3
papers that is already copyrighted elsewhere.

2.3 Column Base

In this study, main parameter is the rigidity of column base. The column bases were modeled using simple elastic springs connected to braces in serial and elastic rotational spring as show in figure 2. The rigidity of column base was defined by the ratio of axial stiffness of elastic spring connected to braces K_J to axial stiffness of yielding core of BRB K_D and the ratio of the rotational stiffness of column base K_{CB} to the flexural stiffness of column K_c, thus

$$\gamma_1 = K_J / K_D$$
$$\gamma_2 = K_{CB} / K_C \qquad \text{Eqs. (2)}$$

. γ_1 and γ_2 is called in this study, the axial stiffness ratio and the flexural stiffness ratio respectively. The flexural stiffness of column was calculated assuming the point of contrary flexure is the middle point of 1st story height. In analytical study, frame with exposed-type column and sufficient stiffer brace connection is defined as benchmark model.

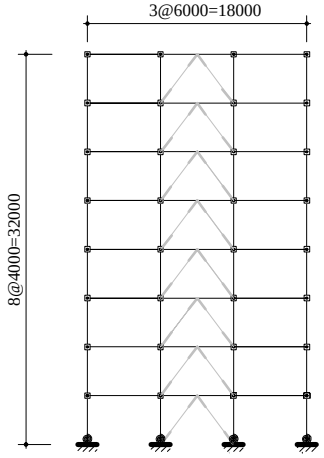

Figure 1 Dimension of Frame and layout of braces

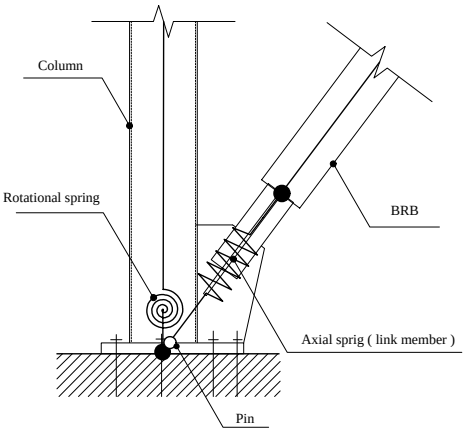

Figure 2 Analytical modeling of column base with brace

From the nominal structural performance of the commercial exposed type column bases (without braces) and previous experimental results, the ratio of axial stiffness γ_1 of 6.0 and also γ_2 of 1.0 was applied to benchmark model.
In order to discuss the effects of rigidity of column bases on seismic performance of steel moment frames retrofitted with BRBs, 7 models with different rigidity of column base was selected. Analytical models were named as follows;

CBX1_X2

where X1: The axial stiffness ratio γ_1 ; X2: The flexural stiffness ratio γ_2 The analytical models are summarized in Table 4. In analysis model, CB6.0_rigid and CB6.0_pin correspond to frame with rigid type column base and frame with pin type column base respectively. The decreases of γ_1 are indirectly-expressed as the degradations of axial and shear stiffness of column base including brace connection.

3. ANALYTICAL METHOD

The analyses were carried out using non-linear dynamic analysis program based on general hinge method (Ogawa et al, 1994). The bi-linear axial-flexural hinges were used to represent concentrated nonlinearity of beams and columns. The nonlinearity of panels also was modeled using bi-linear hysteresis model. The secondary modulus of them was set to 1% of elastic stiffness. Rayleigh damping is adopted, where the damping ratios are 2% for the first and second modes.
Newmark-βmethod (β=1/4) is used for the time integration scheme. The time increment for numerical iteration is 0.001sec.
The models were analyzed using two ground acceleration records namely, the 1940 Imperial valley earthquake (N-S component recorded at El Centro) and the 1968 Tokachi-oki earthquake (E-W component recorded at Hachinohe) two records were adjusted to target energy input level by multiplying amplification factor by acceleration records. Two energy input level was defined for this study level 2 and level 3. L.2 was defined as damage limit input level based on damage controlled design philosophy, at which original members of benchmark structure such as beam, column and panel can remain almost elastic (allowing the maximum ratio of cumulative plastic deformation η for original member of below 0.5) L.3 was defined as 1.5 times of L.2.

4. ANALYTICAL RESULTS

The relations of the fundamental natural periods and the rigidity of column base are plotted in figure 3. These plots indicate that the rigidity of column base have little effect on the fundamental natural periods of frames. Comparison of total energy input of models with various rigidity of column base to benchmark model CB6.0_1.0 is shown in Table 4.
Total energy input is not affected by the rigidity of column base except CB0.5_1.0 inputted Hachinohe EW.
The energy dissipated by member can be expressed by cumulative plastic deformation ratio. This ratio is defined as follows;

Table 3 List of Analytical model

Analytical model	The axial stiffness ratio γ_1	The flexural stiffness ratio γ_2
CB0.5_1.0	0.5	1.0
CB2.0_1.0	2.0	
Benchmark model → CB6.0_1.0	6.0	
CB6.0_0.5		0.5
CB6.0_2.0		2.0
CB6.0_pin		0.0
CB6.0_rigid		∞

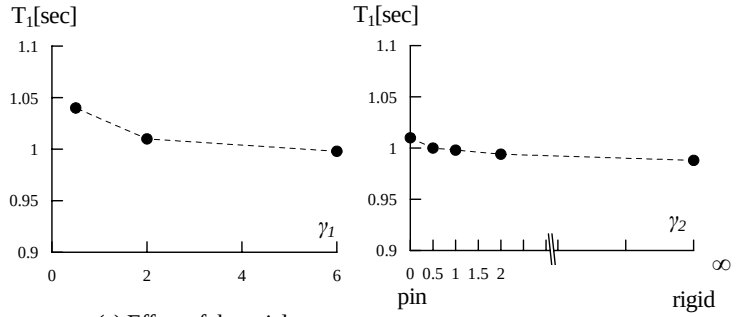

(a) Effect of the axial stiffness ratio γ_1

(b) Effect of the flexural stiffness ratio γ_2

Figure 3 Effect of the rigidity of the column base on 1st mode periods

Table 4 Comparison of total energy input to the benchmark model

Analytical model	El Centro NS_L.2	Hachinohe EW_L.2
CB2.0_1.0	1.00	1.03
CB0.5_1.0	0.99	1.15
CB6.0_0.5	1.00	1.00
CB6.0_2.0	0.99	1.00
CB6.0_rigid	0.98	1.00
CB6.0_pin	0.99	1.00

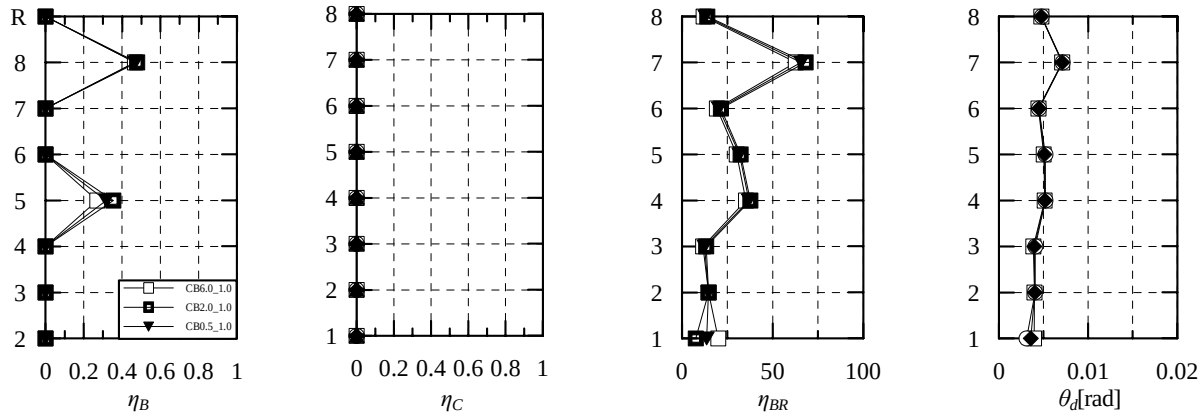

(a) Effect of the axial stiffness ratio γ_1 (El Centro NS component, L.2)

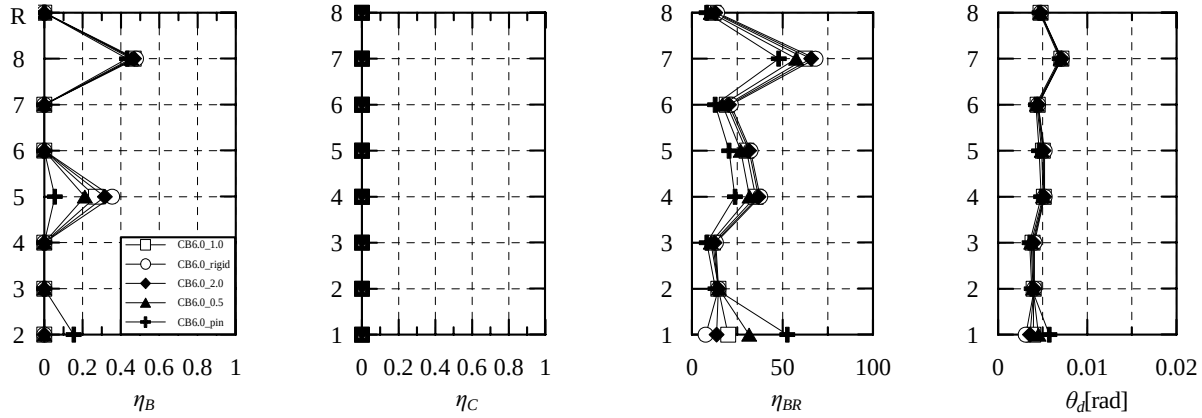

(b) Effect of the flexural stiffness ratio γ_2 (El Centro NS component, L.2)

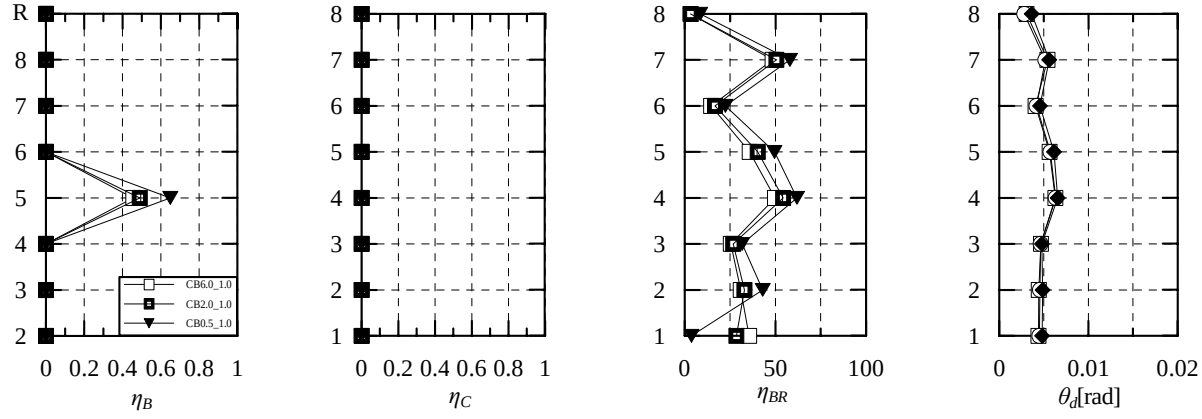

(c) Effect of the axial stiffness ratio γ_2 (Hachinohe EW component, L.2)

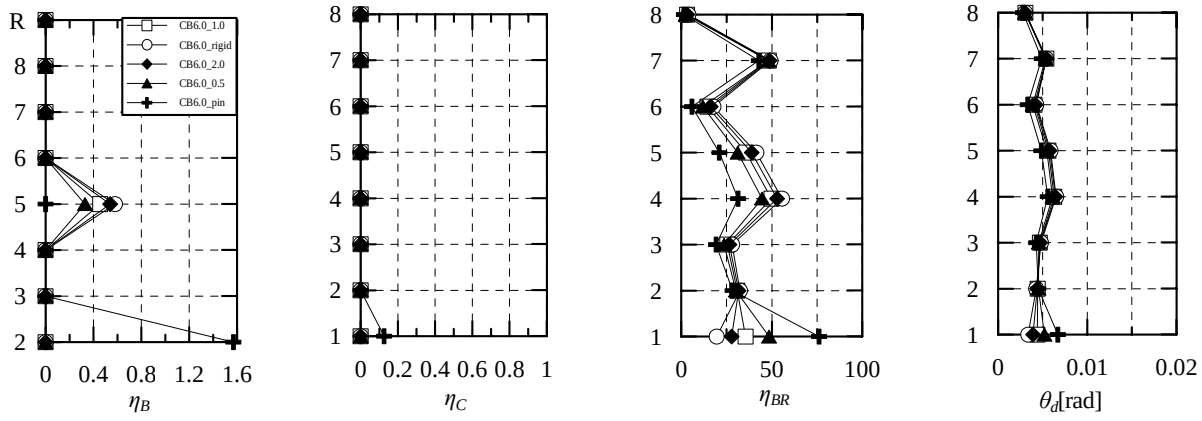

(d) Effect of the flexural stiffness ratio γ_2 (Hachinohe EW component, L.2)

Figure 4 Examples of damage distribution and maximum story drift at each story

$$\eta = \frac{\sum W_p}{Q_y \delta_y} \qquad \text{Eq.(3)}$$

where ΣW_p: cumulated plastic strain energy of member; Q_y: yield strength of member; δ_y: yield deformation of member.

η represents the damage level of members. In order to discuss the effect of rigidity of column base on damage distribution and maximum story drift angle which are important indicators to examine the retrofitting effects, example of damage distributions of each members and the maximum story drifts angle of each story for 7 analytical models with various γ_1 and γ_2 are shown in figure 4.

For beams and columns, the ratios of η_B, η_C were the each maximum ratio of cumulated plastic deformation of one member end existing in each story. The ratio η_{BR} was adopted the mean of the ratios of two dampers installed in each story. In addition, panels were not damaged in any analytical cases. From the analytical results, configurations of damage distribution were affected by the rigidity of column bases. But, the rigidity of column bases had relatively small effect on global deformations. The decrease of the ratio γ_2 contributes to the reduction of damage concentration. However, in case of model with pinned base connection CB6.0_pin, damage concentration is occurred at the original members in the first story. On the other hand, with the decrease of the ratio γ_1, the energy dissipated by the dampers in the first story obviously decreases. But, in comparison with the effects of γ_2, decrease of γ_1 didn't have much effects on damage concentration in that dampers in upper story dissipates energy equally with maintenance of heightwise configuration of energy dissipation. These tendencies became pronounced in the analytical case inputted Hachinohe EW, because the Input energy of lower story is much larger due to relations between frequency characteristics of input wave and those of frames.

To examine the damage transition to the original frame, the indicator ${}_{MF}W_p/{}_{total}W_p$ where ${}_{MF}W_p$: energy dissipated by original frames; ${}_{total}W_p$: total energy dissipated by frame, based on the amount of energy dissipated by frame was adopted. Figure 5 shows the relations of ${}_{MF}W_p/{}_{total}W_p$ and the rigidity of column bases. As the input level was higher, the effect of γ_1 on the damage transition to the original frame was larger in that energy dissipated by the beam for whole story equally increased. That is the decrease of γ_1 has little effects on the damage concentration. On the other hand, the decrease of γ_2 contributes to the reduction of damage to the original frames. However, this contribution is little. In case of pinned type column base, damage of original frames was much larger so that damage concentration was occurred at 1st story.

Figure 6 shows the relations of maximum story drift angle for each case ${}_{max}\theta_d$ and the rigidity of column bases. As previously indicated, because of the damage decentration even though the reduction of energy dissipated by the dampers in the 1st story was occurred due to the decrease of γ_1, there is little change in the maximum story drifts for each analytical case. The tendency of the maximum story drift depending on the γ_1 was similar to those of ${}_{MF}W_p/{}_{total}W_p$.

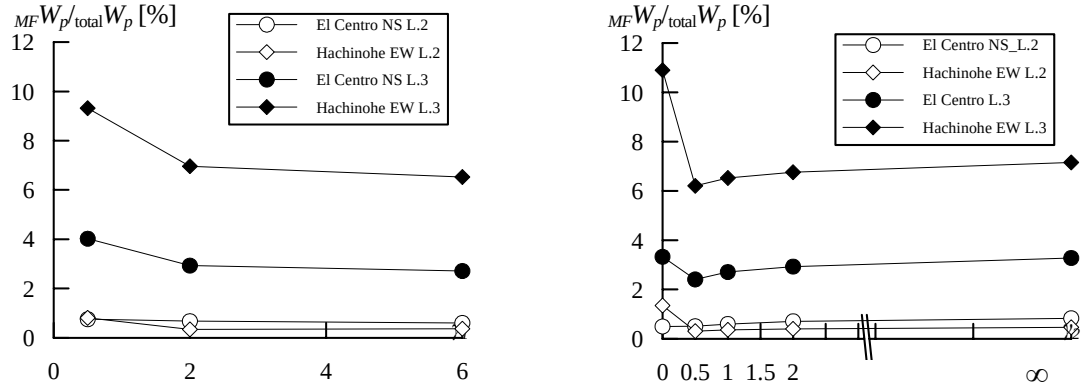

Figure 5 Relations of ${}_{MF}W_p/{}_{total}W_p$ and the rigidity of column bases

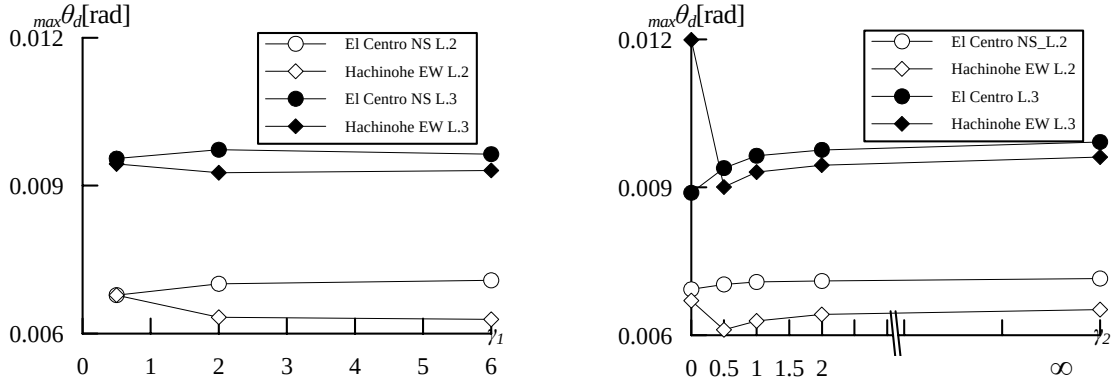

Figure 6 Relations of maximum story drift and the rigidity of column bases

5. CONCLUSIONS

The present analytical work investigated the effect of rigidity of column base on the seismic performance of Moment resisting frames retrofitted with BRBs. The findings are as follows;

- The decrease of the flexural stiffness of column base contributes to the reduction of damage to the original frames. However, this contribution is little. In case of pinned type column base, damage of original frames was much larger so that damage concentration was occurred at 1st story.
- The decrease of the stiffness of axial spring connected to brace in serial have little effects on the damage concentration.

References:

Tena-Coulunga, A. and Vergara, A. (1997). "Comparative Study on the seismic retrofit of a mid-rise building: Steel Bracing vs. Energy dissipation", *Earthquake Engineering and Structural Dynamics*, 26(6), 637-655

Hasegawa, T. (2006). "Study on Seismic Retrofit of Existing Buildings Using Hysteretic Dampers", *Proceedings of annual meeting of Architectural Institute of Japan*, C-2: 685-686 (in Japanese).

Di Sarno, L. (2006). "Bracing Systems for Seismic Retrofitting of Steel Frames", *Proceedings of the 5th International Conference on Behavior of Steel structures in Seismic Areas* (STESSA 2006), Yokohama, Japan, 821-826.

Ichikawa, Y., Okayasu, T., Nakamura, H., Yamada, S., Wada, A., (2005). "Experimental study on Joint of Seismic Retrofitting Brace for Steel Structure Using Shear-key Plate Adhered to Concrete Slab", *Journal of Structural and Construction Engineering*, AIJ, No.596, 133-140.

Akiyama, H. (1985). "Earthquake-Resistant Limit-State Design for Buildings", University of Tokyo Press.

AIJ, (1998). Recommendation for Limit State Design of Steel Structures. (in Japanese)

Ogawa, K., and Tada, M.,(1994). "Combined non-Linear Analysis for Plane Frame", *Proc. of 17th Symposium on Computer Technology on Information Systems and Applications*, 79-84, Architectural Institute of Japan.(in Japanese)

Kishiki, S., Yamada, S., Wada, A., (2007). "Experimental Evaluation of Structural Behavior of Gusset-plate Connection: Global Enhancement of Seismic Performances of Passive-Controlled Structures Part 1", *Journal of Structural and Construction Engineering*, AIJ No.620, 133-140. (in Japanese)

Sixth International Conference on Urban Earthquake Engineering
March 3-4, 2009, Tokyo Institute of Technology, Tokyo, Japan

PEAK RESPONSE EVALUATION METHOD FOR SLIP-HYSTERETIC STRUCTURE CONTROLLED BY VISCO-ELASTIC DAMPER

Kazuhiko Kasai[1], Wuchuan Pu[2], and Kousaku Nishihara[3]

1) Professor, Structural Engineering Research Center, Tokyo Institute of Technology, Japan
2) Postdoctoral Researcher, Center for Urban Earthquake Engineering, Tokyo Institute of Technology, Japan
3) Structural Engineer, Oobayashi Corporation, Japan
kasai@serc.titech.ac.jp, pu.w.aa@m.titech.ac.jp, nishihara.kosaku@obayashi.co.jp

Abstract: This paper proposed a peak seismic response evaluation method for structures with slip hysteresis added with visco-elastic damper, based on the spectrum modification and reduction techniques. With the randomness of earthquake response considered, the equivalent period and equivalent damping of system are derived. The accuracy investigation over a wide range of system parameters and input earthquakes shows good agreement between the proposed method and the nonlinear time history analysis.

1. INTRODUCTION

Vibration control technology has been increasingly used in recent years in various building structures to reduce the structural vibrations produced by earthquake or wind. For timber house structures, study on the new structural formation and damping devices are being advanced significantly (Kasai et al. 2005; Sakata el al. 2005). In particular, the small-sized visco-elastic dampers for timber house are becoming more and more popular due to their economy and constructional efficiency. To achieve an efficient vibration control design, it is important to understand the seismic behavior of damping devices as well as that of main structure, and then to provide a design with good balance between the stiffness and strength of structural components. Particularly, in most timber structures, slip of the hysteresis loops is commonly observed due to localized deformation in connections, which will reduce the energy dissipation capacity of structures significantly. Such characteristics need to be taken into account during structural aseismic analysis and design.

Equivalent linearization is one of the major approaches to estimate the peak seismic response of structures, and significant advances have been made regarding its theory and application in the past decades. However, the research attention devoted to the equivalent linearization method for slip-hysteretic structures has been relatively small. Iwan and Gates (1979) carried on the accuracy investigation of averaged stiffness and energy method on one type of the stiffness degrading system which is different from that considered in this study, and only small damping was investigated. Obviously, a general equivalent linearization method for structures with slip hysteresis is needed.

This study aims to propose a peak seismic response evaluation method for slip-hysteretic SDOF structure passively controlled by visco-elastic damper. Within the hysteresis models previously proposed for timber shearwalls, the combination model of bilinear model and slip model has relatively simple mechanism, and is capable of reproducing exactly the dynamic behavior of shearwall (Araki et al. 2004; Isoda and Kawai 2007). In the present study, this hysteresis model is adopted, and the peak seismic response evaluation method is developed based on this model.

2. EQUIVALENT PERIOD AND DAMPING

2.1 Hysterestic Characteristics

The SDOF system considered is represented by a Kelvin model consisting of a spring element denoting the stiffness of system in parallel with a dashpot element denoting the viscosity (Figure 1(a)). The vibration period T_0 and frequency ω_0 for elastic system is expressed by $T_0 = 2\pi\sqrt{M/K} = 2\pi/\omega_0$ with M being the mass and K being the initial stiffness. In this paper, the small damping ratio of slip element is called as initial damping ratio, while the damping ratio of the system with viscous element included is called as elastic damping ratio h_0.

Figures 1(b), 1(c), and 1(d) show the typical hysteresis loops of slip element, viscous element, and system, respectively. The ω denotes the frequency of external excitation, and it is different from the natural vibration frequency of system. Let the post-yield stiffness ratio, yield deformation, and yield force of slip element be denoted by p, u_y, and F_y. The skeleton curve of slip element is bilinear, the force corresponding to the deformation at which the elastic hysteresis and the slip hysteresis curves intersect is defined to be qF_y, with $q(\leq 1)$ referred to as slip strength ratio. The q describes the degree of slip occurring in hysteresis of structure, and q=1 gives bilinear hysteresis. The viscous element is velocity-dependent, the force is proportional to

the damper velocity, and its hysteresis curve is represented by an ellipse. Combining the hysteresis of the slip element and the viscous element produces the hysteresis curve of system (Figure 1(d)).

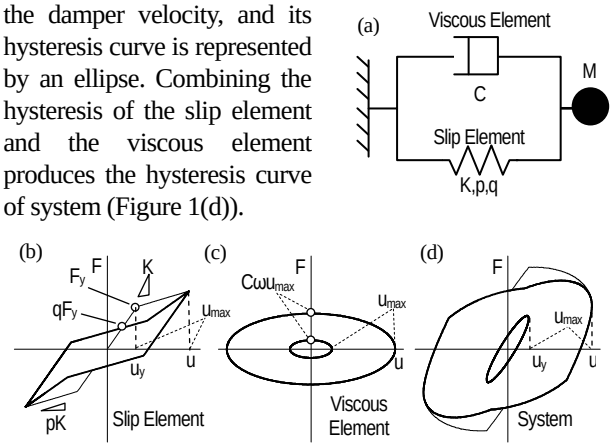

Figure 1 Hysteresis loop of system

2.2 Equivalent Period

The equivalent stiffness is defined as the secant stiffness at the maximum displacement, which can be obtained from Fig. 1(b) as

$$K_{eq} = \frac{F_m}{u_m} = K(1 + p\mu - p)/\mu \tag{1}$$

where u_m = maximum deformation experienced in the past, F_m = restoring force at u_m, and ductility ratio $\mu = u_m/u_y$. With use of the equivalent stiffness defined in Eq.(1), the equivalent frequency and equivalent period of system with amplitude denoted by ductility ratio μ are obtained as

$$\omega_{eq}(\mu) = \omega_0\sqrt{\frac{1 + p\mu - p}{\mu}}\ , \quad T_{eq}(\mu) = T_0\sqrt{\frac{\mu}{1 + p\mu - p}} \tag{2a, b}$$

where ω_0 = elastic vibration frequency, T_0 = elastic period.

Figure 2 shows the curve of equivalent period against ductility ratio. It is observed that the equivalent period increases monotonically with the amplitude of the response, and the smaller the post-yield stiffness ratio, the larger the increase in equivalent period.

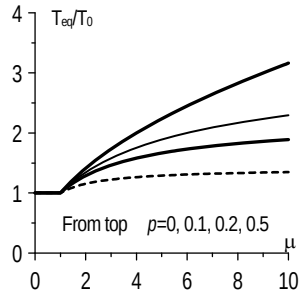

Figure 2 T_{eq}/T_0 versus μ

2.3 Energy Dissipation Accompanied with Peak Deformation Expansion

As mentioned above, the skeleton curve of slip element is bilinear, while its typical hysteresis exhibits slip phenomenon. When peak deformation is expanded, the first hysteresis loop to reach the new maximum deformation and the later hysteresis loops with the same deformation have different shape and subsequently different energy dissipation. We call the former one the peak deformation expansion loop, and the later the stationary loop.

The equivalent damping will be developed based on the typical slip hysteresis, namely the stationary hysteresis. However, before the equivalent damping is obtained, the energy dissipation accompanied with the peak deformation expansion, namely the difference between the peak deformation expansion loop and the stationary loop, needs to be examined. Figure 3 shows the stationary hysteresis loop after the initial loading (Fig. 3(a)), and the stationary hysteresis loop after the amplitude expansion (Fig. 3(b)). Let the energy dissipated by amplitude expansion loop denoted by $E'_p + E_p$, and the energy dissipated by stationary hysteresis loop denoted by E_p, then E'_p is the energy dissipation resulted from the amplitude expansion. E'_p can be obtained geometrically from Fig. 3 as

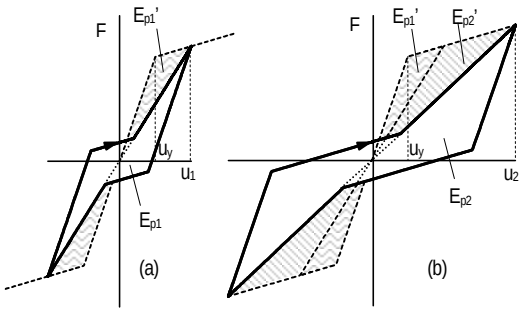

Figure 3 Energy dissipation due to amplitude expansion

$$E'_p = Ku_y^{\,2}(\mu - 1)(1 - p)(1 - q^2) \tag{3}$$

Assume that j cycles of the stationary hysteresis loop are repeated, the accumulated energy is given as $E'_p + jE_p$, and the following equation is obtained.

$$E'_p/(E'_p + jE_p) = 1/[1 + j(1+q)/(1-q)] \tag{4}$$

From Eq. (4), we know that the ratio of the energy dissipation resulted from amplitude expansion to the accumulated energy depends on only q and j, and the ratio decreases as q or j increases.

To understand the energy dissipation of structure in random earthquake response, the nonlinear time history analysis is carried out. The system shown in Fig. 1 is used, and the system parameters are assigned to be elastic period T_0 = 0.4s, 2s, elastic damping ratio h_0 = 0.02, 0.1, 0.3, post-yield stiffness ratio p = 0, 0.5 (excluding $p = q = 0.5$). Three ground motions, BCJ-L2, Hachinohe NS, and JMA Kobe, are applied to each system. The yield displacement of each system is assumed to be the elastic displacement of system subjected to original earthquake wave, and the scale of input motions is then increased gradually so that 3 ductility ratios μ = 2, 4, 10 are obtained. A total of 162 cases of time history analysis are carried out.

From the earthquake response analysis, the $\Sigma E'_p/\Sigma E_p$ is obtained in each case, Fig. 4 shows the $\Sigma E'_p/\Sigma E_p$ averaged over 3 elastic damping ratios per period. The ratio of $\Sigma E'_p/\Sigma E_p$ shows a maximum of about 40% in the case of pulse-like JMA Kobe earthquake, and a maximum of about 15% in the case of BCJ-L2 wave, whose long duration leads to a large number of hysteresis loops of system. Figure

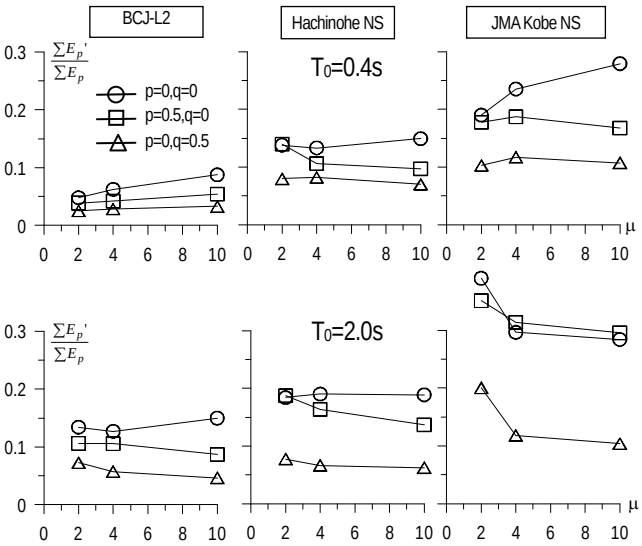

Figure 4 $\sum E'_p / \sum E_p$

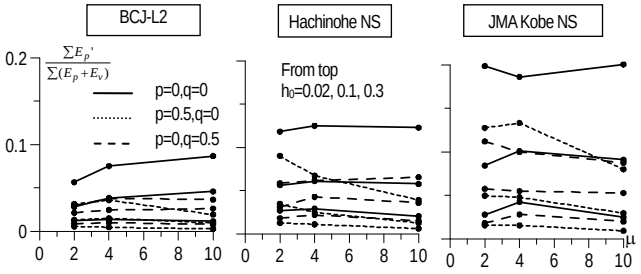

Figure 5 $\sum E'_p / \sum (E_p+E_v)$

5 shows the ratio of $\sum E'_p$ to the total energy dissipated by system. Because the energy dissipated by viscous element is included, this ratio is much small.

Based on the above discussion, except for the case of the combination of h_0=0.02 and the JMA Kobe earthquake, the investigation shows that $\sum E'_p / \sum E_p$ is generally smaller than 0.1. It is considered that the energy dissipation accompanied with the peak deformation expansion has very limited effect; therefore, it will be neglected in the following discussion.

2.4 Equivalent Damping Ratio

The writers (Kasai and Kawanabe 2005; Kasai et al. 2003) have proposed an equivalent damping ratio evaluation method for bilinear system. The equivalent damping for slip system will be developed based on that approach.

During harmonic oscillation of amplitude μ, let $E_p(\mu)$ denote the energy dissipated in damping in each cycle, $E_v(\mu,\omega)$ the energy dissipated in slip hysteresis in each cycle, and $E_s(\mu)$ the potential energy possessed by system at the maximum displacement. They are equal to the area enclosed by force-deformation curves, and given as

$$E_p(\mu) = Ku_y^2(\mu-1)(1-p)(1+q)^2$$
$$E_v(\mu,\omega) = \pi C\omega(\mu u_y)^2 \qquad \text{(5a-c)}$$
$$E_s(\mu) = Ku_y^2\mu(1+p\mu-p)/2$$

Then the equivalent damping ratio of the system is obtained as

$$h'_{eq}(\mu,\omega) = \frac{E_p(\mu)+E_v(\mu,\omega)}{4\pi E_s(\mu)}\cdot\frac{\omega_{eq}(\mu)}{\omega} = h_p(\mu,\omega)+h_v(\mu)$$

$$h_p(\mu,\omega) = \frac{\omega_0}{\omega}\frac{2(\mu-1)(1-p)(1+q)^2}{\pi\mu^{1.5}\sqrt{1+p\mu-p}} \qquad \text{(6a-c)}$$

$$h_v(\mu) = h_0\sqrt{\frac{\mu}{1+p\mu-p}}$$

The ratio of $\omega_{eq}(\mu)/\omega$ in Eq. (6a) serves to revise the equivalent damping in case that the frequency of external excitation is unequal to the equivalent vibration frequency of system. Through such modification, the dependence of E_p on μ is converted into the dependence of h_p on μ and ω; the dependence of E_v on μ and ω is converted into the dependence of h_v on μ.

Substituting the equivalent frequency (Eq.2(a)) into Eq.(6) yields the equivalent damping of system in resonance.

$$h_{eq}(\mu,\omega_{eq}) = \frac{(\mu-1)(1-p)(1+q)^2}{2\pi\mu(1+p\mu-p)} + h_0\sqrt{\frac{\mu}{1+p\mu-p}} \qquad (7)$$

When subjected to random earthquake excitations, the structure may experience a large number of hysteresis loops, and the amplitude of each hysteresis loop vary greatly between 0 and maximum. In view of this randomness, Newmark and Rosenbluth (1971) proposed the averaged damping method, which gives the equivalent damping averaged over the amplitude of 0 to maximum.

$$h_{eq} = \frac{1}{\mu}\int_0^{\mu} h'_{eq}(\mu',\omega_{eq})d\mu' \qquad (8)$$

For slip element in random response, however, both the amplitude expansion hysteresis and the amplitude reduction hysteresis happen. At an amplitude smaller than the maximum deformation experienced, the equivalent damping ratio of the stationary loop and that of the loop after the maximum deformation will be different, because the energy dissipated is unequal. When applying the averaged damping method into the slip system, the effect of the amplitude reduction hysteresis needs further examination.

Figure 6 shows the two types of the amplitude reduction hysteresis. Let μ_a denote the maximum ductility

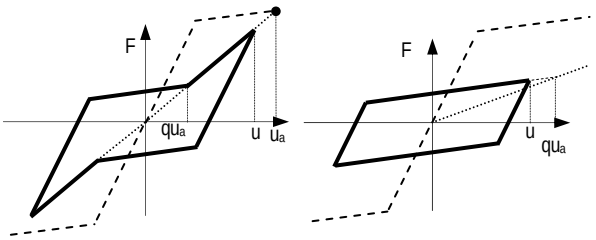

(a) Amplitude reduction hyestersis I $q\mu_{pm} < \mu < \mu_{pm}$ (b) Amplitude reduction hyestersis II $\mu < q\mu_{pm}$

Figure 6 Two types of amplitude reduction hysteresis

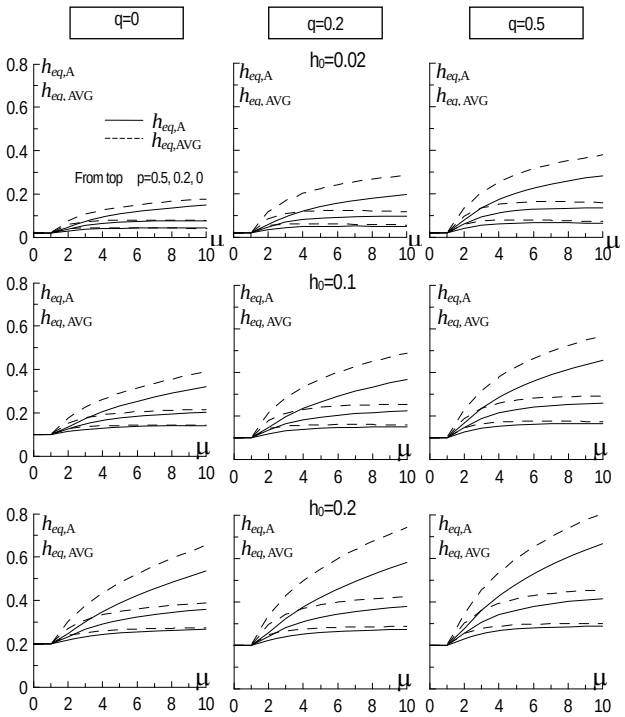

Figure 7 Equivalent damping

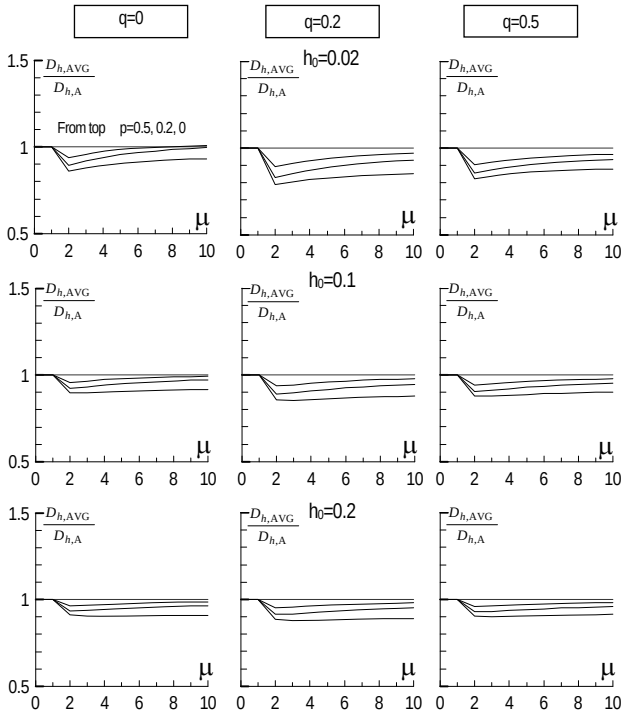

Figure 8 Ratio between damping effect factors

ratio experienced in the past by system. In the similar way, the equivalent damping ratios for the two types of amplitude-reduction cycles are obtained as

$$h_{eq}(\mu,\omega_{eq})=\frac{(\mu_a-1)(1-p)(\mu+q\mu_a)^2}{2\pi\mu^2\mu_a(1+p\mu_a-p)}+h_0\sqrt{\frac{\mu_a}{1+p\mu_a-p}} \quad (q\mu_a\le\mu<\mu_a)$$

$$h_{eq}(\mu,\omega_{eq})=\frac{2q(\mu-q)(1-p)}{\pi\mu(q+p\mu-pq)}+h_0\sqrt{\frac{\mu}{q+p\mu-pq}} \quad (\mu<q\mu_a) \qquad (9a, b)$$

Assume that case 1: the amplitude of hysteresis loops increase from 0 to the maximum continuously, and case 2: the amplitude of hysteresis loops decrease from the maximum to 0 continuously. The equivalent damping of these two cases, $h_{eq,A}$, $h_{eq,B}$ can be obtained by substituting Eq. (7) and Eq. (9), respectively, into Eq. (8).

Let h_0=0.02, 0.1, 0.2, q=0, 0.2, 0.5, p=0, 0.2, 0.5, the equivalent damping $h_{eq,A}$, the mean equivalent damping between case 1 and case 2 ($h_{eq,A}$+$h_{eq,B}$)/2 are shown in Fig. 7 against the ductility ratio. It is observed that the equivalent damping becomes larger with the amplitude reduction hysteresis being considered.

To examine how the amplitude reduction hysteresis affects the response prediction, the damping effect factor which will be described in detail later is investigated. In response prediction, only damping effect factor is affected by the variation in equivalent damping. The damping effect factors $D_{h,A}$ and $D_{h,AVG}$ obtained from $h_{eq,A}$ and ($h_{eq,A}$+$h_{eq,B}$)/2, respectively, are compared.

$$D_{h,\mathrm{AVG}}/D_{h,\mathrm{A}}=\sqrt{(1+25h_{eq,\mathrm{A}})/(1+25h_{eq,\mathrm{AVG}})} \qquad (10)$$

Figure 8 shows the ratio $D_{h,AVG}/D_{h,A}$. It is seen that the difference between $D_{h,A}$ and $D_{h,AVG}$ is generally less than 10% of $D_{h,A}$ for most cases. It is a negligible quantity.

Based on the above discussion, it is reasonable to consider only the stationary hysteresis to evaluate the equivalent damping. Therefore, by substituting Eq.(7) into Eq.(8), the equivalent damping ratio for slip system is obtained as

$$h_{eq}=\frac{(1+q)^2}{2\pi p\mu}\ln\left(\frac{f(\mu)}{\mu^p}\right)+\frac{h_0}{\mu}\left\{\frac{\sqrt{\mu\cdot f(\mu)}+p-1}{p}+\ln\left(\frac{\sqrt{p\mu}+\sqrt{f(\mu)}}{\sqrt{p}+1}\right)^{\frac{p-1}{p\sqrt{p}}}\right\}$$

$$f(\mu)=1+p\mu-p \qquad (11a, b)$$

3. PEAK RESPONSE EVALUATION METHOD BASED ON SPECTRUM SPECIFICATION AND REDUCTION

3.1 Peak Response Evaluation Method

The ductility ratio of system with elastic damping ratio h_0 varies between 1 and maximum ductility ratio μ, and subsequently, the equivalent period of system varies randomly between elastic period T_0 and the equivalent period at the maximum ductility ratio, T_{eq}. When calculating the velocity response of system, it is more reasonable to use the equivalent response spectrum given by Eq. (12) than to use directly the response spectrum value at the equivalent period obtained from the maximum ductility ratio.

$$\bar{S}_{pv}(T_{eq},h_0)=\frac{1}{T_{eq}-T_0}\int_{T_0}^{T_{eq}}S_{pv}(T,h_0)dT \qquad (12)$$

The above equation gives the average of response spectrum over the range of (T_0, T_{eq}).

Furthermore, the reduction of elastic response spectrum resulted from the increasing of damping ratio from h_0 to h_{eq} will be accounted for by using the damping effect factor proposed by Kasai et al. (2003), as shown in Eq. (13).

Table 1 Input earthquake waves

No.	Earthquake: Record Name	PGA (cm^2/s)	Duration Time (s)	Evaluated Duration
1	Artificial Earthquake: BCJ-L2	355.66	120.0	65.28
2	Imperial Valley 1940: El centro NS	341.70	53.74	24.40
3	Tokachi-oki 1968: Hachinohe NS	270.09	71.99	41.28
4	Hyogoken Nanbu 1995: JMA Kobe NS	820.56	30.06	8.10
5	Hyogoken Nanbu 1995: JR Takatori EW	656.98	40.95	9.93
6	Kushiro Oki 1993: JMA Kushiro N063E	692.81	157.4	18.89
7	Northridge 1994: Sylmar NS	826.76	59.98	5.32
8	Iran 1978: Tabas N344E	919.02	49.98	18.06
9	Kern Country 1952: Taft EW	175.90	54.38	28.84
10	Miyagi Oki 1978: Tohoku Univ. NS	257.98	40.98	19.50

$$D_h = \sqrt{(1+\alpha h_0)/(1+\alpha h_{eq})} \tag{13}$$

Based on the investigation by Kasai et al. (2003), the coefficient α of 25 is appropriate if the real earthquake records are used, and in case of artificial earthquakes, the other values (such as 75 for BCJ-L2) should be used.

With use of D_h, the velocity response can be obtained easily, and displacement response can be obtained based on the relationship between pseudo-velocity and displacement.

$$u_{\max} = \frac{T_{eq}}{2\pi}\bar{S}_{pv}(T_{eq}, h_{eq}) = \frac{T_{eq}}{2\pi} D_h \bar{S}_{pv}(T_{eq}, h_0) \tag{14}$$

The computation process for peak displacement is the same as described in Kasai et al. (2003). In addition, if the initial damping ratio 0.02 instead of elastic damping ratio is used, the only thing needed is to change h_0 in Eqs. (13) and (14) to 0.02.

When maximum displacement occurs, the velocity of system is zero, and accordingly, the velocity-dependent damping force is zero. Therefore, the force of system at maximum displacement equals to the restoring force of slip element. It is given by

$$F' = F_y \mu \ (\mu \le 1), \quad F' = F_y(1 + p\mu - p) \quad (\mu > 1) \tag{15}$$

The maximum force is the same as that of bilinear system (Kasai and Kawanabe 2005), and is given by

$$F_{\max} = F_y \mu \sqrt{1 + (\varsigma C \omega_{eq}/K)^2} \qquad (\mu \le \mu_A)$$
$$F_{\max} = F_y \left[\mu \sqrt{p^2 + (\varsigma C \omega_{eq}/K)^2} + 1 - p \right] \quad (\mu \ge \mu_A) \tag{16a-c}$$
$$\mu_A = \left[\sqrt{1 + (\varsigma C \omega_{eq}/K)^2} + \sqrt{p^2 + (\varsigma C \omega_{eq}/K)^2} \right] / (1+p)$$

For long period・high damping system, notable discrepancy may arise between the velocity spectrum S_v and pseudo-velocity spectrum S_{pv}. The longer the period of system, and the higher the damping ratio, the difference between S_v and S_{pv} is larger. The ς in Eq. (16) is the coefficient intended to reduce such difference. The ς is given as the function of h_0 and T_{eq} (Kasai et al. 2009) by Eq. (17).

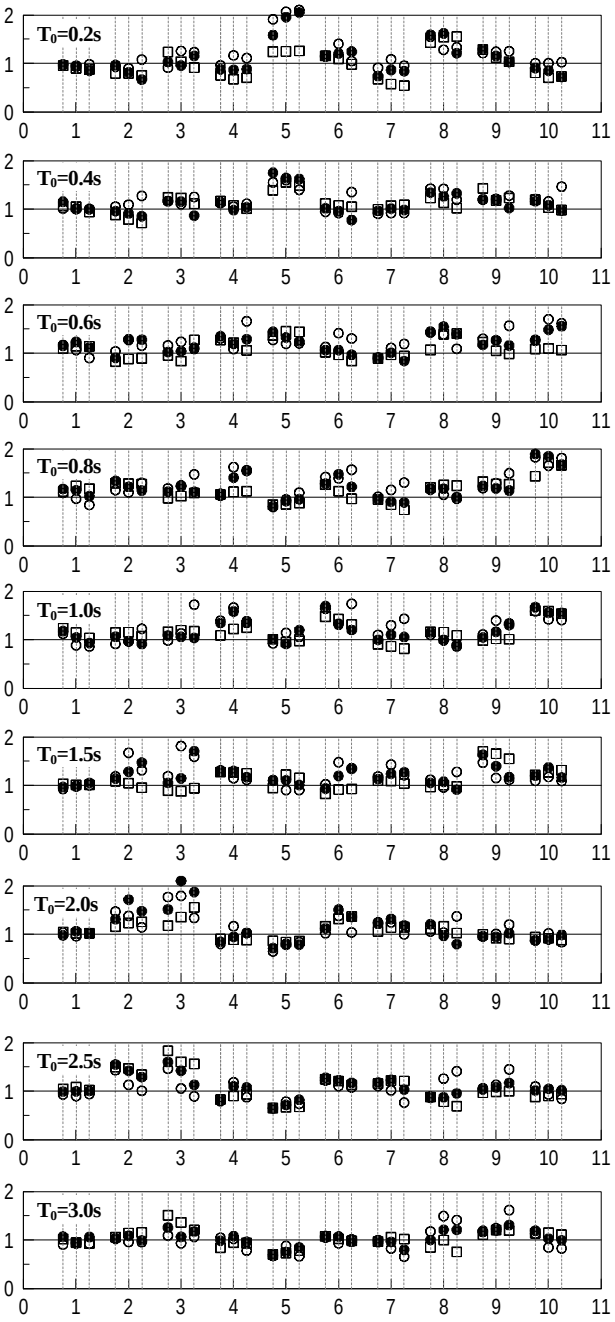

Figure 9 Accuracy of displacement prediction (Horizontal axis: Earthquake number; Vertical axis: ratio of prediction to time history analysis. ○ p=0; ● p=0.2; □ p=0.5)

$$\varsigma = (0.6h_0 + 0.1)(T_{eq} - 0.8) + 1 \tag{17}$$

3.2 Accuracy Examination

The accuracy of the proposed evaluation method is examined through comparison with the nonlinear time history analysis. Let elastic period T_0 = 0.2~3.0s (5 types from 0.2s to 1.0s with interval of 0.2s, 4 types from 1.5s to 3.0s with interval of 0.5s), elastic damping ratio h_0 = 0.02, 0.1, 0.2, 0.3, post-yield stiffness ratio p = 0, 0.2, 0.5, slip strength ratio q = 0, 0.2, 0.5, 1, a total of 1296 (= 9×4×3×4) systems are considered. Each system is subjected to 10 ground motions as shown in Table 1 (one artificial

Table 2 Accuracy of the displacement prediction

Period T_0	Mean (Standard deviation)	
0.2s	1.09(0.32)	1.13 (0.25)
0.4s	1.13(0.20)	
0.6s	1.18(0.20)	
0.8s	1.20(0.25)	1.13 (0.24)
1.0s	1.19(0.23)	
1.5s	1.17(0.21)	
2.0s	1.11(0.26)	
2.5s	1.06(0.24)	
3.0s	1.03(0.18)	

earthquake wave and 9 real earthquake waves); the yield displacement is assumed to be the elastic response of system subjected to original earthquake wave, and the scale of input motions is then adjusted so that 3 different ductility ratios μ = 2, 4, 10 are obtained. A total of 12960 cases of time history analysis are performed.

The peak response evaluation based on the proposed method is carried out by using the given system parameters and the ductility ratio obtained from time history analysis, where the response spectra with 2% damping ratio are used.

For each of the cases mentioned above, the ratio of prediction result to time history analysis result is obtained, and they are averaged over 4 elastic damping ratios, 4 slip strength ratios per combination of period, earthquake, post-yield stiffness ratio, and ductility ratio. The average values are shown in Fig. 9. Next, such values are further averaged over 10 earthquakes per period and per period region (short period region (0.2s~0.6s) and middle・long period region (0.8s~3.0s) are considered), and the results are shown in Table 2. Generally, the proposed method produces good accuracy without notable dependence on the input earthquakes or system properties.

Figure 10 shows the accuracy of the maximum force prediction of the proposed method per elastic damping ratio h_0. The present method produces good agreement between the prediction and the time history analysis. Although a small increase in the standard deviation is observed as the damping ratio increases, the proposed method predicts the maximum force very accurately thanks to the revision on the pseudo-velocity spectra.

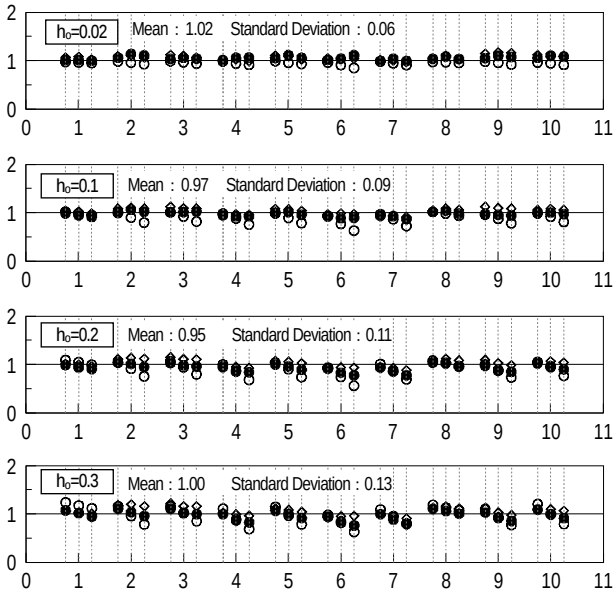

Figure 10 Accuracy of force prediction (Horizontal axis: Earthquake number; Vertical axis: ratio of prediction to time history analysis. ○ p=0; ● p=0.2; □ p=0.5)

4. CONCLUSION

This paper proposed a peak seismic response evaluation method for structures with slip hysteresis added with viscous element based on the spectrum modification and reduction techniques. With the randomness of earthquake response considered, the equivalent period and equivalent damping are derived. The accuracy of the propose method was examined by comparing the prediction results with the nonlinear time history analysis results over a wide range of system parameters, and it is found that both the displacement and force prediction produce good agreement with the time history analysis results.

REFERENCE

Kasai K., Sakata H., and Wada A. et al., "Dynamic Behavior of a Wood Frame with Shear Link Passive Control Mechanism Involving K-Brace," *Journal of Structure and Construction Engineering*, No.598, 51-59, 2005.12

Sakata H., Kasai K., and Wada A. et al., "Experimental Strudy on Dynamic Behavior of Wood Frame with Shera Link Passive Control Mechanism Involving Plywood Panel," *Journal of Structure and Construction Engineering*, No.594, 65-73, 2005.8

Iwan W.D. and Gates N.C., "Estimating Earthquake Response of Simple Hysteretic Structures," *Journal of the Engineering Mechanics Division*. June 1979

Araki Y., Koshihara M., Ohashi Y. et al., "A Study on Hysteresis Model for Earthquake Response Analysis of Timber Structures," *Journal of Structure and Construction Engineering*, No.579, 79-85, 2004.5

Isoda H. and Kawai N., "Hysteresis Model of Walls on Japansese Conventional Construction: Study on seismic behavior of wooden construction," *Journal of Structure and Construction Engineering*, No.616, 157-163, 2007.6

Kasai K., Kawanabe Y., "Equivalent Linearization to Predict Dynamic Properties and Seismic Peak Responses of a Structural System with High Viscous Damping and Hysteretic Damping," *Journal of Structure and Construction Engineering*, No. 591, pp.43~51, 2005.5

Ito H. and Kasai K., "Equivalent Method for Cumulative Plastic Deformation of Damper Based on Maximum Deformation of Elasto-Plastically Damped Structure", *Journal of Structure and Construction Engineering*, No. 607, pp.53-61, 2006.9

Newmark, N.M. and Rosenblueth, E. "Fundamentals of Earthquake Engineering." Prentice-Hall Inc., 1971

Kasai K., Ito H., and Watanabe A., "Peak Response Prediction Rule for a SDOF Elasto-Plastic System Based on Equivalent Linearization Technique," *Journal of Structure and Construction Engineering*, No.571, pp.53~62, 2003.9

Kasai K., Yamashita T., and Yamazaki Y. et al., "Spectrum-Based Response Prediction of Asymmetric Structure with Supplemental Viscous Damping," *Journal of Structure and Construction Engineering*, 2009.2

Sixth International Conference on Urban Earthquake Engineering
March 3-4, 2009, Tokyo Institute of Technology, Tokyo, Japan

SEISMIC RESPONSE MODELS FOR SACRAMENTO-SAN JOAQUIN DELTA LEVEES

Ross W. Boulanger[1)] and Tadahiro Kishida[2)]

1) Professor, Dept. of Civil and Environmental Engineering, University of California, Davis, USA
2) Staff engineer, URS Corporation, Oakland, California, USA
rwboulanger@ucdavis.edu, tadahiro_kishida@URSCorp.com

Abstract: Seismic response and performance of the levee system is an important concern for the long-term management of the Sacramento-San Joaquin Delta. An overview is provided of research on developing regression models for the dynamic properties of the organic soils and peats that underlay large portions of the levee system and on seismic response models for predicting dynamic response and Newmark-type slope displacements. Sources of uncertainty and their propagation in hazard evaluations are discussed.

1. INTRODUCTION

The Sacramento-San Joaquin Delta in California is a complicated network of channels and reclaimed islands, which collects water from about 45% of California's surface area and directs it to San Francisco Bay. There are about 1700 km of levees and over 60 islands with ground surface levels up to 8 m (25 feet) below adjacent water ways (California 1995). Delta waterways are a critical link in California's water delivery system, conveying water from northern California to aqueducts and canals at the southern end of the Delta, which then convey it further south to cities and farmers.

The Delta is facing a number of complex problems with competing needs for the environment, water supply, and economy (Lund et al. 2007). Risks associated with floods and earthquakes continue to increase because of increasing urbanization, ongoing subsidence of the islands, the potential for rising water levels, and stress on the ecosystem. Earthquake-induced levee failures and the resulting rapid inundation of the inner islands have the potential to significantly reduce the freshwater supply for California, in addition to damaging the natural habitat, crops and civil infrastructure.

Levees in the Delta are commonly non-engineered, having been constructed over the past hundred years by a variety of methods and organizations. A typical levee cross-section is shown in Fig. 1. The levees often contain loose to medium-dense sands and silts that are susceptible to liquefaction, and are commonly underlain by deposits of organic soil or peat. About 74 levee failures leading to island inundations have occurred since 1950, with about 6 of these failures occurring under non-storm water levels and the remainder occurring when the adjacent water levels were elevated (e.g., storm events). There are no reported failures due to earthquakes, but the progressive increase in levee heights as islands subsided over the past several decades means that levees with current heights have never experienced significant shaking.

This paper describes research on developing regression models for evaluating nonlinear seismic wave amplification and performance for levees in the Sacramento-San Joaquin Delta where the subsurface soils include thick deposits of soft clay and silt, organic soil, and peat. A program of laboratory testing was performed to characterize the dynamic properties of organic soils, and a regression model for their properties was developed (Kishida et al. 2009a, 2009b). One-dimensional and two-dimensional equivalent-linear site response analyses were performed using a broad range of input motions, soil profiles, and realizations of dynamic soil properties. The resulting site amplification factors were checked for dependence on various characteristics of the input motions and dynamic soil profiles, and the sources of uncertainty in the site amplification factor were evaluated (Kishida 2008). The propagation of uncertainties through to the computed hazards or risks are illustrated and discussed.

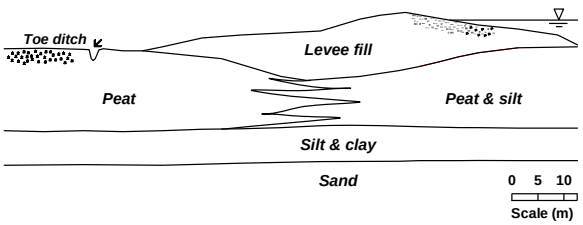

Figure 1 A levee cross-section from Sherman Island

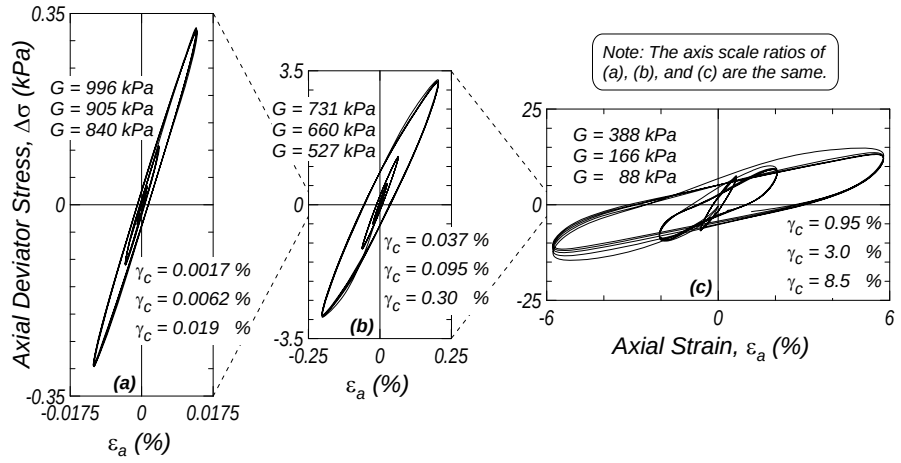

Figure 2 Stress-strain curves for an organic soil: Secant shear modulus (G) is listed for the 1st cycle of loading at γ_c of (a) 0.0017%, 0.0062%, 0.019%, (b) 0.037%, 0.095%, 0.30%, (c) 0.95%, 3.0%, and 8.5% [Wehling et al. 2003]

2. DYNAMIC PROPERTIES OF ORGANIC SOILS

Dynamic properties of organic soils in the Delta were studied through a program of sampling and testing from different locations, the compilation of a database of dynamic properties, and the development of a regression model for dynamic properties (see Kishida et al. 2009a, 2009b). Data from outside the Delta were obtained from Seed and Idriss (1970), Stokoe et al. (1996), and Kramer (2000). Soils included in the database ranged from highly fibrous peat to amorphous organic clays with organic contents (OC) ranging from 14 to 81%, water contents ranging from 88 to 495%, total densities (ρ) ranging from 1.06 to 1.45 Mg/m3, and effective consolidation stresses (σ'_{vc}) ranging from 11 to 135 kPa. Laboratory tests included cyclic triaxial tests at UC Davis and resonant column / torsional shear tests at UT Austin. Stress-strain behavior obtained in a cyclic triaxial test is shown in Fig. 2, illustrating the reduction in secant shear modulus (G) and increase in hysteretic damping ratio (ξ) with increasing shear strain amplitude (γ_c).

In the regression models, the values of G and ξ were modeled as nonlinearly dependent on γ_c, consolidation stress (σ'_{vc}), and organic content (OC). Details of the regression model and its parameters are given in Kishida et al. (2009b). Fig. 3 shows G/G_{max} and ξ curves obtained from the regression models for σ'_{vc} = 15, 45, and 135 kPa and OC of 15 and 60%. G/G_{max} tends to locate higher with increasing OC, while ξ locates lower with increasing OC. G/G_{max} also tends to locate higher with increase of consolidation stress for low organic content (OC) soil, and does not vary with different consolidation stress for highly organic soil. ξ decreases with increase of consolidation stress for low organic soil, and does not vary with different consolidation stress for highly organic soil.

Fig. 4 shows the residuals between the predicted and measured values of ln(G) plotted against the predictor variables, loading frequency (f) and number of cycles (N). The residuals are uniformly distributed, indicating that the model is unbiased and has a standard deviation of about 0.33 in ln(G). Thus, the mean plus one standard deviation estimate of G is 1.39 times the mean estimate of G, while the mean minus one standard deviation estimate is 0.72 times the mean estimate.

A database of in situ shear wave velocities (V_s) was used to adjust the regression model for in situ conditions; i.e., to account for factors such as sampling disturbance, load path, loading frequency, and state of stress. The adjustment to G was assumed to not affect the ratio of G/G_{max}. Variances and correlations in the regression models were developed.

3. SEISMIC RESPONSE

Seismic wave amplification at soft soil sites depends on the input motions, the soil profile, and the nonlinearity of the subsurface soils. Intensity measures of input motions such as peak ground acceleration (PGA) or spectral acceleration (Sa) can be used as an estimator of nonlinearity in the site amplification. Idriss (1991) presented the nonlinear seismic wave amplification at soft soil sites against the PGA on rock based on earthquake observations. Fiegel (1995) and Arulnathan (2001) performed dynamic centrifuge model tests of soft and organic soil profiles, and showed that equivalent-linear site response analyses were reasonably capable of approximating the nonlinear seismic wave amplification. Baturay and Stewart (2003) showed that 1D equivalent-linear site response analyses provided improved accuracy, relative to empirical models, in predicting spectral accelerations (at periods less than about 1 s) at soft soil sites where strong ground motion records had been obtained. Stewart and Kwok (2008) demonstrated that nonlinear analyses may provide improved estimates of ground motion relative to equivalent-linear analyses when ground strains approach about 1%.

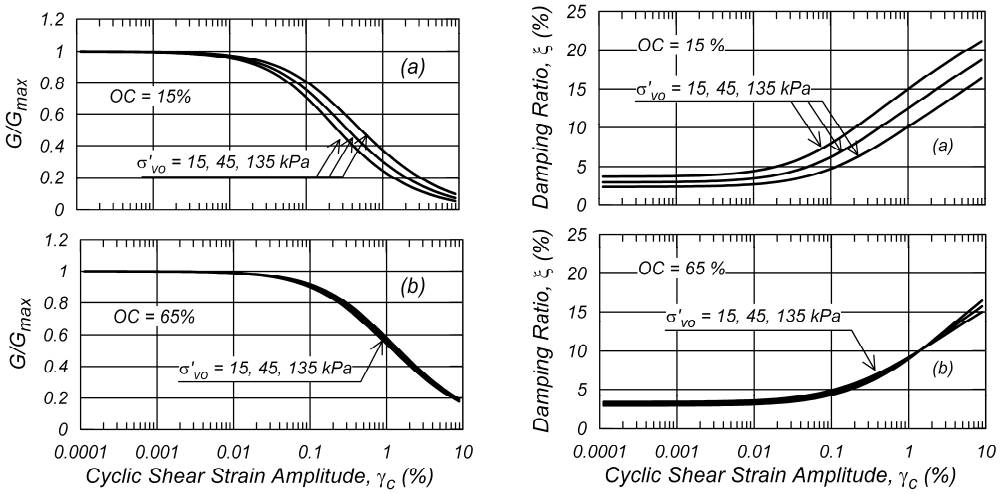

Figure 3 Regression model results for organic soils with organic contents of 15 and 65% at different confining stresses.

The NGA ground motion database organized by Pacific Earthquake Engineering Research Center (http://peer.berkeley.edu/nga/) was used in selecting the input motions for site response analysis. Ground acceleration records from sites classified as NEHRP (1994) site D (180 m/s < V_{s30} < 360 m/s) were used as input motions. The full set of site D recordings were used for one-dimensional site response calculations for select soil profiles, after which a subset of 264 recordings were selected for one- and two-dimensional analyses of additional soil profiles. This subset of records had peak horizontal accelerations (PGA) ranging from 0.004 g to 1.78 g, and were recorded at distances of 1.1 km to 296 km during earthquakes with moment magnitudes (Mw) of 4.3 to 7.9. No scaling or modification of input motions was performed.

Eighteen soil profiles were selected from 13 different levees in the delta for use in one-dimensional analyses. All the profiles were obtained from crests of levees (e.g., Fig. 1). All profiles have a stiff sand deposit below approximately 20 to 30 m depth that has V_s values corresponding to NEHRP site D. Peat and organic soil layers ranged from 0 m to 13.5 m thick at the various soil profiles.

For predominantly sand or clay layers, dynamic properties were estimated as follows. Small strain stiffness (G_{max}) was obtained from density (ρ) and shear wave velocity (V_s) with $G_{max} = \rho V_s^2$ when V_s and ρ were available. When V_s was not available, regression equations were used to estimate G_{max}. Normalized modulus reduction (G/G_{max}) and damping ratio (ξ) curves were based on EPRI (1993) for sands and on Vucetic and Dobry (1991) for clays.

Uncertainty in dynamic soil properties was modeled in Monte Carlo simulations using different soil profile realizations. In general, five different realizations were used for each soil profile. For select cases, up to twenty realizations were used. The covariance matrix of dynamic soil properties was obtained by combining a covariance matrix based on the covariance between residuals of dynamic soil properties as measured in the laboratory, and a

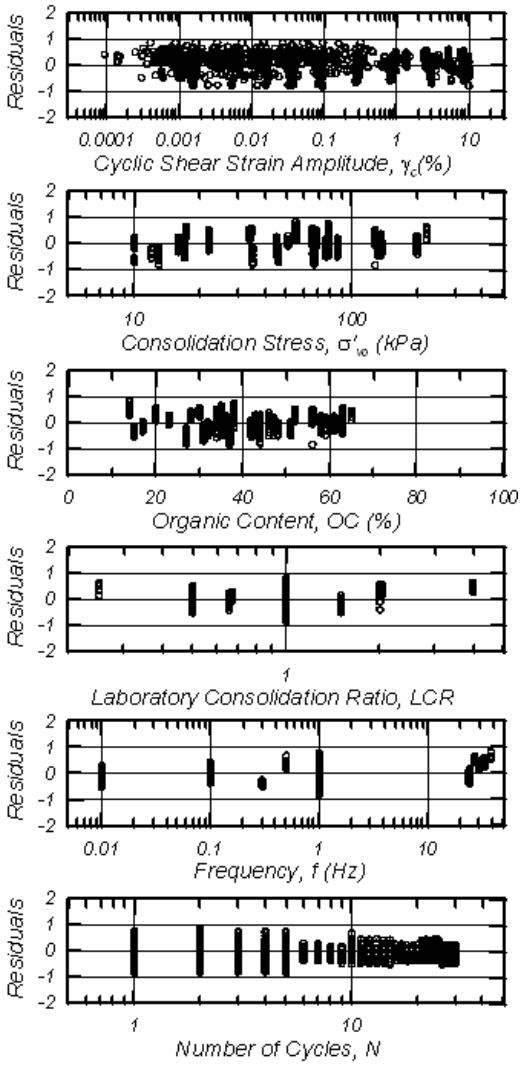

Figure 4 Residuals between predicted and measured values of ln(G) for organic soil

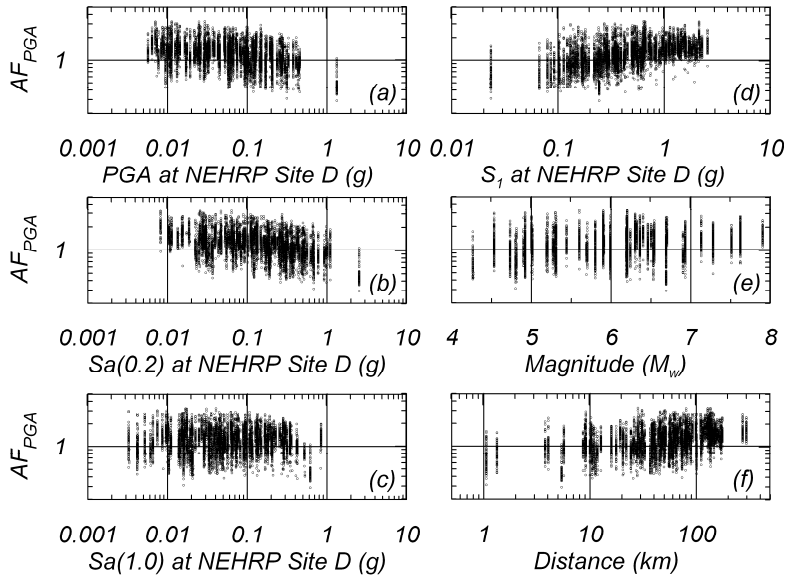

Figure 5 Site amplification factor versus possible predictor variables

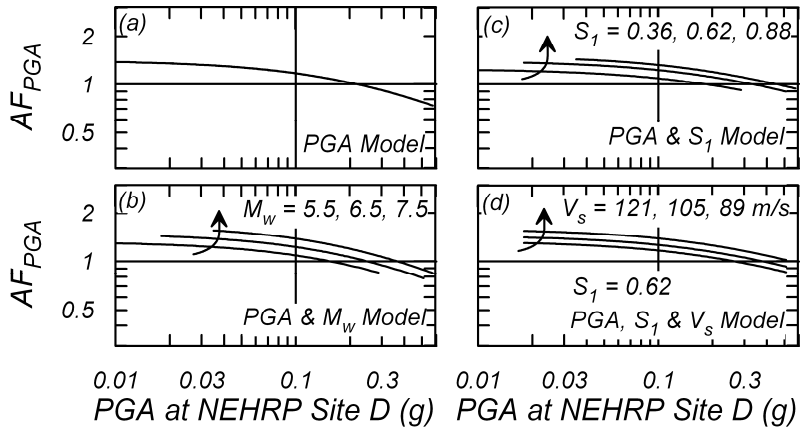

Figure 6 Four different site amplification models for PGA

covariance matrix for spatial correlation of soil properties. Spatial correlation was applied within the same geological layer and assumed to have a 2.0-m scale of fluctuation with exponential decay.

Computed one-dimensional site amplification factors of PGA from NEHRP site D outcrop to levee crest at Delta are plotted against possible predictor variables in Fig. 5. Five different models were developed for the site amplification factor (AF): AF as a constant; AF as a function of PGA; AF as a function of PGA and M_w; and AF as a function of PGA and the ratio S_1 = Sa(1.0)/Sa(0.2) for the outcrop motion; and AF as a function of PGA, S_1 and V_s in the upper 10 m . For example, the AF model for PGA based on the outcrop PGA and S_1 is as follows.

$$ln(AF_{PGA}) = -0.105 - 0.397 ln(PGA + 0.245) + 0.186 ln(S_1) + \tau_{profile} + \tau_{property} + \varepsilon_{motion} \quad (1)$$

These models produced standard deviations in $\ln(AF_{PGA})$ of 0.39, 0.37, 0.35, 0.34, and 0.32, respectively, indicating that the additional predictor variables did produce improved accuracy in predicting AF_{PGA}. Four of these models are compared in Fig. 6 for predicting AF_{PGA}.

Sources of uncertainty in the AF were evaluated by considering the random effects assigned to the soil profiles and properties, respectively. This evaluation showed that approximately 25-40% of the variance in AF_{PGA} was due to uncertainties in the input ground motions, about 50-65% was due to uncertainties in the soil profiles and about 10% was due to uncertainties in the dynamic property relationships.

Two-dimensional equivalent-linear dynamic finite element analyses were performed for a set of levee cross-sections to evaluate the differences between one- and two-dimensional responses. These analyses also used Monte Carlo simulations with a range of input ground motions and soil property realizations. The two-dimensional analyses indicated an increase in peak horizontal

acceleration at the crest of about 19% on average. Amplification factor relationships for levee crests were developed by combining the results of the one- and two-dimensional analyses.

The impact of different site effects models on seismic hazard is illustrated by an example analysis for one levee location in the western Delta. Fig. 7 shows a comparison of the resulting PGA hazard curves for the NEHRP site D outcrop and for the levee crest based on four site amplification models. For a mean annual frequency of exceedance of 0.0021 (i.e., 10% in 50 year motion), the expected PGA values are 0.43 g at a site D outcrop and 0.86, 0.65, 0.58, and 0.52 g at the levee crest for the four site amplification models, respectively. The differences between the levee crest results for the different site amplification models become smaller for more frequent events and larger for less frequent events. Expected PGA values at the levee crest progressively decrease between each of these four site amplification models because the models progressively become both more sufficient and efficient (e.g., as represented in their lower standard deviations). Use of a constant AF_{PGA} increasingly over-estimates the seismic hazard as the frequency of the event decreases, because nonlinear site response is important at these higher shaking intensity levels. The nonlinear AF_{PGA} model based on $PGA_{site\ D}$ alone produced the highest hazards of the three nonlinear models because it had the largest variance of the three models and was insufficient in its representation of the nonlinear site effects. The vector model based on $PGA_{site\ D}$ and S_1 produced smaller hazard results than the vector model based on $PGA_{site\ D}$ and M_w, with the differences being largely due to the former model being slightly more efficient (e.g., lower standard deviation) than the latter model.

These site effects models are expected to reasonable at low to moderate shaking levels (e.g., PGA less than about 0.3 g) that produce ground strains less than about 1% (Stewart and Kwok 2008) and are only for levee responses in the absence of liquefaction or slope instability; these hazard results can be used to assess the potential for triggering of liquefaction or for use in uncoupled methods of estimating slope deformations, while recognizing that the actual crest motions under very strong shaking would be significantly reduced by the occurrence of slope yielding or liquefaction. These site effects models are expected to be used in combination with nonlinear analyses for the evaluation of levee performances at higher shaking levels or with the effects of liquefaction (e.g., URS 2008).

Regression models were also developed for Newmark sliding block displacements that were computed for the input NEHRP (1994) site D ground motions and the computed seismic coefficient time series from the dynamic analyses. Four models were developed by adapting the functional form by Saygili and Rathje (2008); these models computed displacements as functions of k_y and PGA (or k_y and $k_{h,max}$ for the seismic coefficient data set), as a function of k_y, PGA, and M_w, as a function of k_y, PGA, and S_1, and as a function of k_y, PGA, S_1, and S_2 = Sa(0.2)Sa(5.0)/Sa(1.0)PGA. The PGA-S_1-S_2 regression model is compared to three other

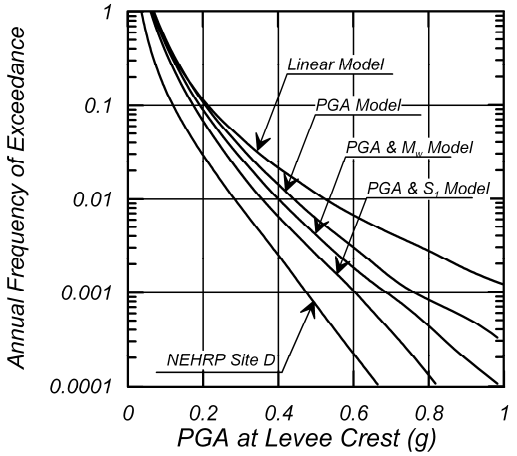

Figure 7 Residuals between predicted and measured values of ln(G) for organic soil

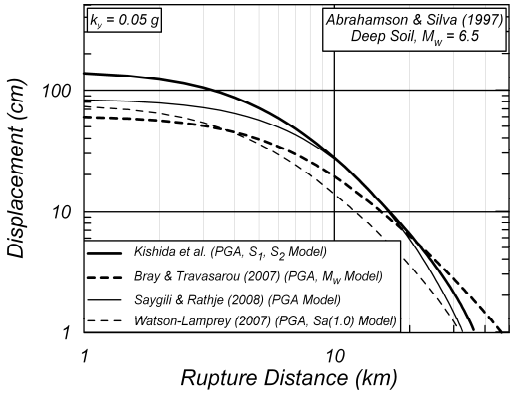

Figure 8 Expected values of Newmark sliding block displacements by four different models

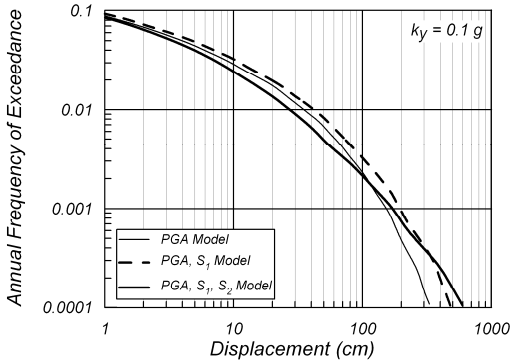

Figure 9 Effect of site response model on Newmark sliding block displacement hazards

models by Bray and Travasarou (2007), Watson-Lamprey (2007), and Saygili and Rathje (2008) in Fig. 8 showing the attenuation of expected Newmark sliding block displacements with distance from the rupture surface for strike-slip event with M_w=6.5 and with k_y=0.05g. The differences between the displacements predicted by these four models are attributed to the differences in their predictor variables and the sufficiency of those predictor variables to describe ground motion characteristics important to

Newmark sliding block displacements. The four models are, however, reasonably consistent for many practical purposes.

The influence of different Newmark sliding block regression models on displacement hazard is illustrated by the example results shown in Fig. 9. This figure shows displacement hazard curves computed using the PGA, PGA-S_1, and PGA-S_1-S_2 models. The PGA-S_1 model resulted in the highest displacements, while the PGA-S_1-S_2 model, which is the most sophisticated to implement, resulted in the smallest displacements at mean annual frequencies of exceedance greater than 0.002. The PGA model resulted in intermediate values of displacement at mean annual frequencies of exceedance greater than 0.002. The differences in displacement hazard can be attributed to: (1) differences in the mean predictions of sliding block displacement for the different combinations of earthquake magnitudes and distances that contribute to the seismic hazard at this location, and (2) differences in the standard deviations for each sliding block regression model. The displacement hazard curves computed using these three models are not, however, significantly different for practical purposes. Additional examples demonstrated that accounting for the uncertainties in the sliding block model and yield coefficient (k_y) are significantly more important for probabilistic evaluations of potential slope displacements.

3. CONCLUSIONS

This paper provided an overview of research directed toward characterizing nonlinear seismic wave amplification effects for levees in the Delta. This research has included sampling and testing of organic soils, the development of regression models for the dynamic properties of organic soils, one- and two-dimensional dynamic response analyses, and an analysis of how uncertainties propagate through the computed seismic hazards. Understanding the propagation of uncertainties in the hazard and risk analyses provided valuable guidance on the effective direction of further engineering studies.

The regional evaluation of seismic levee performance warrants the judicious use of both equivalent-linear and nonlinear analysis methods to assess the potential for liquefaction triggering and slope deformations across a broad range of conditions. The simplified models presented herein are based on equivalent-linear analyses, and are expected to be reasonably accurate up to moderate shaking levels. Nonlinear analyses should be used to evaluate levee responses at stronger shaking levels and for the direct evaluation of levee deformations (e.g., URS 2008). The collection of strong ground motion recordings on Delta levees remains an important goal for the verification of these different dynamic analysis methods.

Acknowledgements:

This research was supported by the California Department of Water Resources (CDWR), State of California. The views and conclusions contained in this paper are those of the authors and should not be interpreted as necessarily representing the official policies, either expressed or implied, of the State of California. The authors appreciate the contributions of Mike Driller, Timothy Wehling, and Norm Abrahamson throughout the various studies that are summarized in this paper.

References:

Arulnathan, R., Boulanger, R. W., and Idriss, I. M. (2001). "Site response of organic soils." Proc., 4th Intl Conf on Recent Advances in Geotechnical Earthquake Engineering and Soil Dynamics, S. Prakash, ed., U of Missouri-Rolla, Paper 1.07.

Baturay, M. B., and Stewart, J. P. (2003). Uncertainty and bias in ground-motion estimates from ground response analyses. Bulletin of Seismological Society of America, 93, 2025-2042.

Bray, J. D., and Travasarou, T. (2007). Simplified procedure for estimating earthquake-induced deviatoric slope displacements, J. Geotech. and Geoenvir. Engrg., ASCE, 133(4), 381-392.

California (1995). Sacramento–San Joaquin Delta Atlas, Department of Water Resources, Sacramento, California.

Electric Power Research Institute (1993). Guidelines for site specific ground motions, Rept. TR-102293, 1-5, Pala Alto, California.

Fiegel, G. L. (1995). "Centrifugal and analytical modeling of soft soil sites subjected to seismic shaking." Doctoral thesis, Dept of Civil and Envir. Engrg., University of California, Davis, CA.

Idriss, I. M. (1991). Earthquake ground motions at soft soil sites, Proceedings: 2nd Intl Conf on Recent Advances in Geotechnical Earthquake Engineering and Soil Dynamics, 2265-2272.

Kishida, T., (2008). Seismic site effects for the Sacramento-San Joaquin Delta, Doctoral thesis, Dept of Civil and Environmental Engineering, University of California, Davis, CA.

Kishida, T., Wehling, T. M., Boulanger, R. W., Driller, M. W., and Stokoe, K. H., II (2009a). "Dynamic properties of highly organic soils from Montezuma Slough and Clifton Court." J. of Geotech. and Geoenvironmental Engineering, ASCE, 135(4), in press.

Kishida, T., Boulanger, R. W., Abrahamson, N. A., Wehling, T. M., and Driller, M. W. (2009b). "Regression models for dynamic properties of highly organic soils." Journal of Geotechnical and Geoenvironmental Engineering, ASCE, 135(4), in press.

Kramer, S. L. (2000). Dynamic response of Mercer Slough Peat, J. of Geotech. and Geoenv. Engineering, ASCE, 126(6): 504-510.

Lund, J., Hanak, E., Fleenor, W., Howitt, R., Mount, J., and Moyle, P. (2007). Envisioning Futures for the Sacramento-San Joaquin Delta. Public Policy Institute of California, San Francisco, CA.

Saygili, G., and Rathje, E. M. (2008). Empirical predictive models earthquake-induced sliding displacements of slopes, J. of Geotech. and Geoenvir. Engineering, ASCE, 134(6), 790-803.

Seed, H. B., and Idriss, I. M. (1970). Analyses of ground motions at Union Bay, Seattle during earthquakes and distant nuclear blasts, Bulletin Seismological Society of America, 60(1): 125-136.

Stewart, J. P., and Kwok, Annie O. L. (2008). "Nonlinear seismic ground response analysis: Code usage protocols and verification against vertical array data." GEESD IV, Geotech. Special Pub No. 181, Zeng, Manzari, and Hiltunen, editors, ASCE.

Stokoe, II, K. H., Bay, J. A., Rosenbald, B. L., Hwang, S. K., and Twede, M. R. (1996). In situ seismic and dynamic laboratory measurements of geotechnical materials at Queensboro Bridge and Roosevelt Island, Geotechnical Engineering Report GR94-5, Civil Engineering Dept., Univ. of Texas at Austin, June.

URS (2008). Delta Risk Management Strategy Phase 1, Risk Analysis Report (Draft 4), by URS Corp/Jack R. Benjamin & Associates, Inc., for CA Dept of Water Resources, July.

Vucetic, M., and Dobry, R. (1991). Effect of soil plasticity on cyclic response. J. Geotechnical Engineering, ASCE, 117(1): 89-107.

Watson-Lamprey, J. A. (2007). Selection and scaling of ground motion time series, Ph.D. thesis, Univ. of California, Berkeley.

Wehling, T. M., Boulanger, R. W., Arulnathan, R., Harder, L. F., and Driller, M. W. (2003). Nonlinear dynamic properties of a fibrous organic soil. J. of Geotech. Geoenvir. Engrg., (129(10), 929-939.

Sixth International Conference on Urban Earthquake Engineering
March 3-4, 2009, Tokyo Institute of Technology, Tokyo, Japan

CURING PRESSURE DEPENDENCY OF COMPRESSIVE STRENGTH OF CEMENT-TREATED SAND

Akihiro Takahashi[1)], Shunsuke Tanimoto[2)], and Hideki Sugita[2)]

1) Associate Professor, Dept. of Civil and Environmental Engineering, Tokyo Institute of Technology, Japan
(Formerly, Public Works Research Institute, Japan)
2) Public Works Research Institute, Japan
takihiro@cv.titech.ac.jp, s-tanomo@pwri.go.jp, sugita@pwri.go.jp

Abstract: In practice, strength assessment of the cement-treated soil is made by unconfined compression tests on samples cured without any confining pressure. However, the cement-treated soils are usually cured under a certain confining pressure, resulting in the better interlocking and bonding of soil particles as compared to that under the very low confining pressure for the sandy ground. To examine strength change of the cement-treated sand with curing pressure, a series of undrained triaxial compression tests were performed. Test results reveal that the compressive strength for the samples cured under the very low confining pressure does not change with the confining pressure, while it increases with the confining pressure for the samples cured in the pressurised triaxial cell. The sample having the same density as the sample cured in the pressurised triaxial cell but cured under the very low confining pressure has more or less the same compressive strength as the sample cured in the pressurised triaxial cell. This suggests the possibility of improvement of the strength assessment of the cement-treated soil using samples cured without confining pressure.

1. INTRODUCTION

Large settlement of levees in the past earthquakes was primarily induced by liquefaction of foundation soils (TCCRFE, 1996). The liquefied soil beneath a levee laterally spreads away from the levee, resulting in the large settlement of the levee. Such deformation mode of the levee is also observed in physical model tests (e.g., Koga & Matsuo 1990, Okamura & Matsuo 2002). To mitigate the levee settlement induced by the lateral spreading of the liquefied foundation soils, remedial measures are often made to the foundation near toes of a levee and many types of remedial measures have been proposed. Among others solidification of the liquefiable foundation near the toes is widely used in practice.

To create such solidified blocks in the liquefiable ground, the deep mixing method (e.g., Terashi 2003) is often adopted. For mix design of cement-treated ground, the unconfined compression tests are performed to determine amount of cement to achieve strength specified in design. In preparation of samples for the unconfined compression test, thoroughly mixed cement and soil are cast in moulds and then are cured under the very low confining pressure. However, as the length of a vertical soil cement column created with the deep mixing method is relatively long (more than the depth of the liquefiable layers bottom,) the in-situ treated soil is always cured under a certain amount of overburden pressure. Probably this results in the better interlocking and bonding of soil particles for the in-situ treated soils, i.e., the larger strength as compared to the samples cured under the very low confining pressure. In other words, there is a possibility that the strength obtained by the unconfined compression test for the mix design is too conservative, due to leaving the confining pressure during curing out of consideration.

In this study, to examine strength change of the cement-treated sand with curing pressure, a series of undrained triaxial compression tests as well as unconfined compression tests were performed.

2. SOIL TESTED AND TEST PROCEDURES

The sand used was Edosaki sand (ρ_s=2.68Mg/m^3, D_{50}=0.26mm, F_C=8.1%, U_C=3.2, w_{opt}=15%). The sample preparation procedures for the cases without confining pressure during curing are as follows: Firstly the sand thoroughly mixed with the Portland cement with a near-optimum water content was compacted in layers (JGS 0812: 2000) to a dry density of 1.41Mg/m^3 (bulk density: 1.57Mg/m^3), corresponding to a relative compaction of 85%. The specimen is a cylindrical shape whose diameter is 50mm and height is 100mm. The maximum density (the reference density for the relative compaction) and the optimum water content were determined according to the standard test method for soil compaction using a rammer (JIS A 1210: 1999, Method A-b, which is equivalent to ASTM D698-07e1,

Table 1: Test conditions and undrained shear strength obtained.

Series	Cement content	Dry density before shearing (Mg/m^3)	Confining pressure during curing	Confining pressure before shearing	$q_u / 2$ *1	s_u *2
N	0%	1.42	–	50	–	24.3
		1.43		100		39.8
		1.44		200		70.7
A	5%	1.42	~ 0	50	290	222
		1.41	~ 0	100		239
		1.42	~ 0	200		252
B		1.44	50	50	367	265
		1.45	100	100	381	319
		1.48	200	200	399	372
C		1.44	~ 0	50	311 *3	323
		1.45	~ 0	100	321 *3	315
		1.48	~ 0	200	348 *3	348

Unit for pressures and strengths: kPa
*1: Obtained by unconfined compression test
*2: Obtained by undrained triaxial compression test
*3: Estimated from empirical correlation between dry density and q_u in this study.

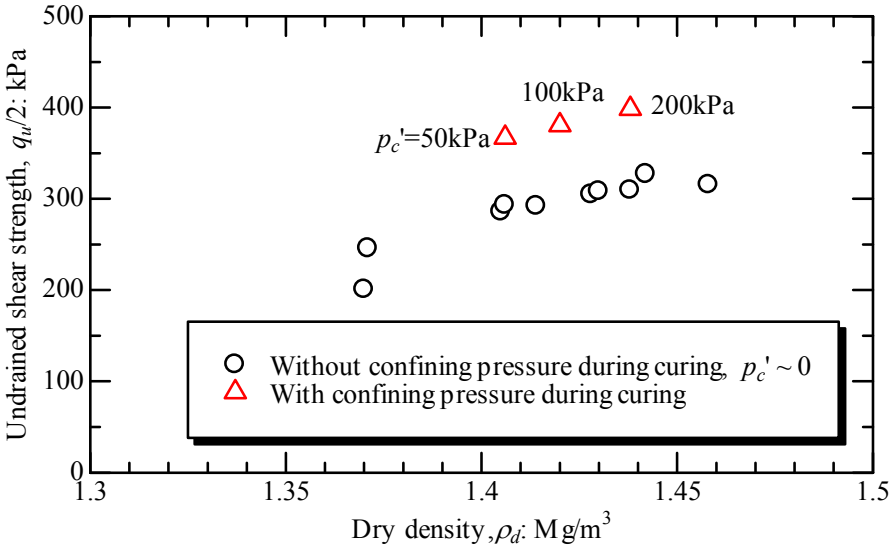

Figure 1: Variations of undrained shear strength obtained by unconfined compression test with dry density before shearing.

Method A.) And then the specimen in a mould was wrapped with plastic film and moist cotton waste and was cured for a week at a temperature of 21°C before shearing.

For purpose of comparison, three types of samples were prepared, namely, samples cured (A) under the very low confining pressure (mentioned above), (B) under a prescribed pressure and sheared at the same confining pressure, and (C) under the very low confining pressure but the density of samples was the same as that cured with the confining pressure. In Series B, the specimen was set in a triaxial cell and was cured at a prescribed confining pressure (isotropically consolidated) for a week at a temperature of 25°C before shearing. In Series C, the initial density of the specimen was adjusted to that of the Series B before shearing. In addition to these, tests without cement were also conducted (Series N.) Test conditions and undrained shear strength obtained are summarised in Table 1.

3. TEST RESULTS AND DISCUSSION

Variations of the undrained shear strength obtained by the unconfined compression test with the dry density before shearing are shown in Fig. 1. The undrained shear strength increases with the dry density and the plots for the cases with confining pressure during curing are

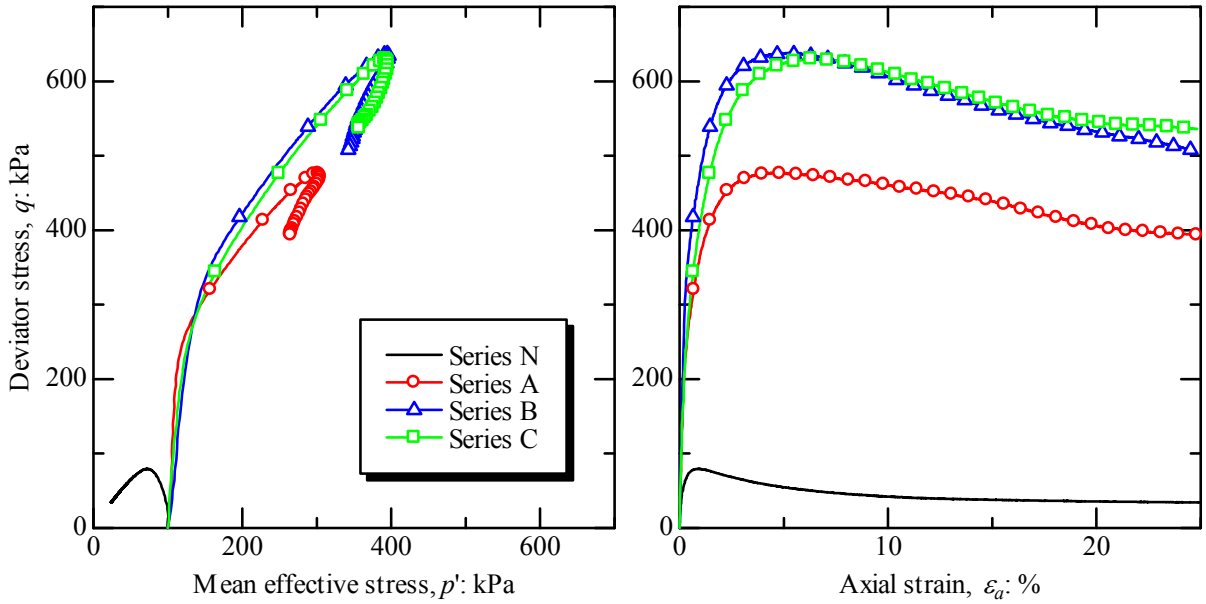

Figure 2: Stress paths (Left) and stress-strain relations (Right) for p_0'=100kPa.

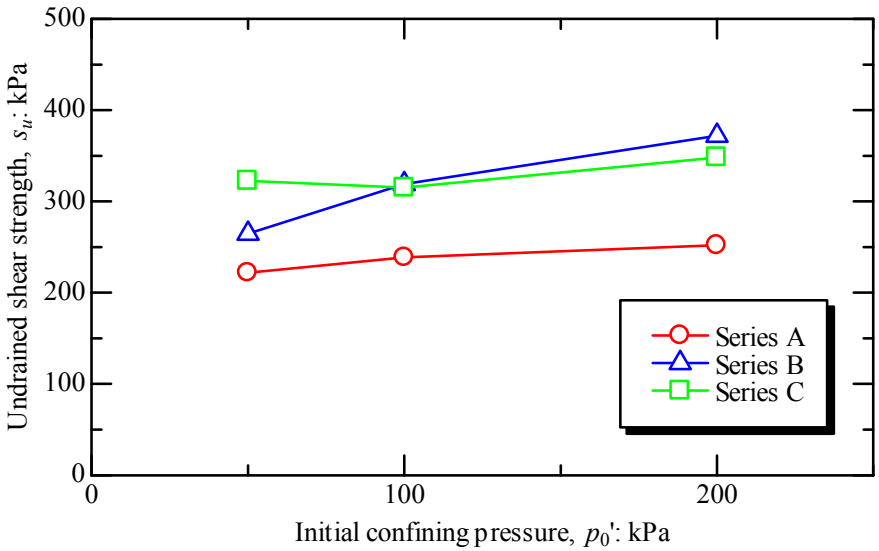

Figure 3: Variations of undrained shear strength obtained by undrained triaxial compression test with initial confining pressure.

well above those almost without curing pressure. These indicate that there is a possibility that the undrained strength obtained for the mix design, i.e., the strength obtained by the unconfined compression tests on samples cured under very low confining pressure, is too conservative.

Figure 2 plots stress paths and stress-strain relations obtained by the undrained triaxial compression test with p_0'=100kPa for all the series. For the case without cement treatment (Series N), the soil was contractive and the marked softening was observed after reaching peak in the stress—strain relation. On the other hand the samples with cement (Series A, B & C) were dilative and the moderate softening occurred after reaching the peak.

The undrained strength changes with the confining pressure for Series A, B & C are plotted in Fig. 3. The plots reveal that the compressive strength for the samples cured under the very low confining pressure (Series A) does not change with the confining pressure, while it increases with the confining pressure for the samples cured in the pressurised triaxial cell (Series B). The sample having the same density as the sample cured in the pressurised triaxial cell but cured under the very low confining pressure (Series C) has more or less the same compressive strength as the sample cured in the pressurised triaxial cell (Series B) except the case with p_0'=50kPa. This suggests the possibility of improvement of the strength assessment of the

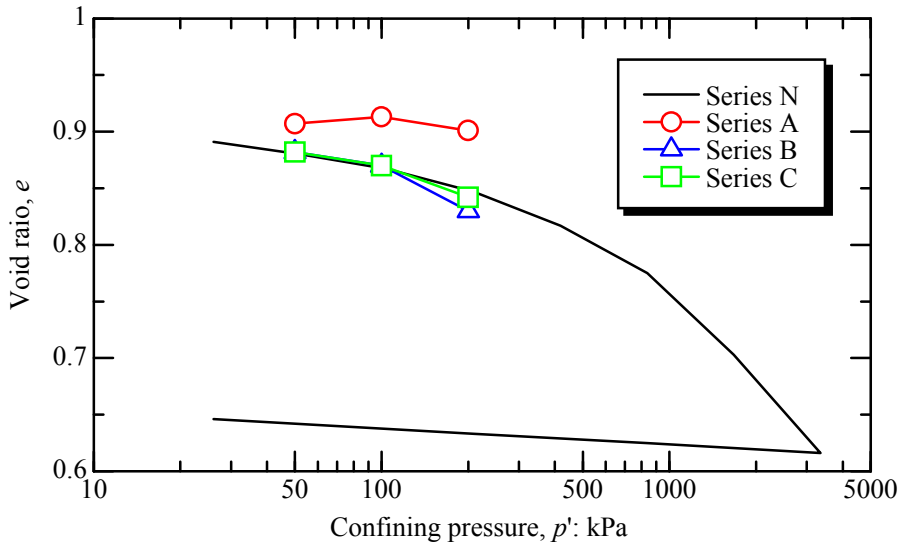

Figure 4: State points just before shearing in e–log(p') space, together with compression and swelling curve for sand without cement treatment

cement-treated soil using samples cured without confining pressure, provided the density of the treated soil after curing is known.

Figure 4 plots the state points just before shearing in e–log(p') space, together with the compression and swelling curve for sand without cement treatment. The compression and swelling curve for sand without cement treatment was obtained by the one-dimensional compression and swelling test, i.e., the oedometer test, and the plot was made by assuming that the earth pressure coefficient is 0.5, i.e., $p'=(1+2\times0.5)\sigma_v'/3$ where σ_v'=vertical stress. As expected, the state points just before shearing for the samples cured under the very low confining pressure (Series A) are well above the compression curve for sand without cement treatment. On the other hand, the state points just before shearing for the samples cured in the pressurised triaxial cell (Series B) and for the samples cured in the pressurised triaxial cell but cured under the very low confining pressure (Series C) are on the curve for sand without cement treatment. The latter fact suggests that the density of the in-situ treated sand, i.e., the density of the treated soil after curing, can be estimated using the compression curve for sand without treatment.

4. SUMMARY

To examine strength change of the cement-treated sand with curing pressure, a series of undrained triaxial compression tests were performed. Test results suggest the possibility of improvement of the strength assessment of the cement-treated soil using samples cured without confining pressure provided the density of the treated soil after curing is known. The density of the treated soil after curing can be estimated using the compression curve for sand without treatment.

References:

Koga, Y. & Matsuo, O., "Shaking table tests of embankments on liquefiable sandy ground", *Soils and Foundations*, Vol.30, No.4, 162-174, 1990.

Okamura, M. & Matsuo, O., "Effects of remedial measures for mitigating embankment settlement due to foundation liquefaction", *Int'l J. Physical Modelling in Geotechnics*, Vol.2, No.2, 1-12, 2002.

Technical Committee on Countermeasures for River Facilities against Earthquake, Interim Report (in Japanese), 1996.

Terashi, M., "The State of Practice in Deep Mixing Methods", *Grouting and Ground Treatment, Johnsen, Bruce & Byle (eds.)*, *ASCE Geotechnical Special Publication*, No.120, 25-49, 2003.

Sixth International Conference on Urban Earthquake Engineering
March 3-4, 2009, Tokyo Institute of Technology, Tokyo, Japan

RELATION OF VOLUME STRAIN INCREMENT AND PORE WATER PRESSURE GENERATION UNDER CONSTANT LOAD AND CONSTANT VOLUME CYCLIC SIMPLE SHEARING

Chung-Jung Lee[1], Chin-Hong Lin[2], Yu-Chen Wei[2], Wen-Yi Hung[3]

1) Professor, Department of Civil Engineering, ,National Central University, Taiwan
2) Graduate student, Dept. of Civil Engineering, National Central University, Taiwan
3) Postdoctoral Fellow, Department of Civil Engineering, National Central University, Taiwan
cjleeciv@cc.ncu.edu.tw , u0116000@cc.ncu.edu.tw, hungwy@ncu.edu.tw

Abstract: The relations of stress and dilatancy rate for the sand under simple shear loading were first proposed. Adopting the concept that the volume change due to cyclic shearing in the constant load tests were compensated by the volume change due to vertical stress change in the constant load tests were compensated by the volume change due to vertical stress change in the constant volume tests. Then an incremental pore water pressure generation model was developed.

1. INTRODUCTION

Cyclic simple shear tests can more closely simulate field conditions, such as rotations of principal stress directions, and may be used to study the deformation of sand during earthquakes. Cyclic simple shear causes a tendency of volumetric contraction or dilatancy of sandy soil, whether it is loose or dense. For saturated sandy soil in the drained condition the volumetric strain will occur. In the undrained condition, on the other hand, the tendency of volume change will transfer the normal load from the soil skeleton to the water, causing a rise or a drop in pore water pressure and a reduction or increase in the effective stress, depending on contraction or dilatancy tendency. The generation of pore water pressure in sandy soils under cyclic shearing, such as earthquakes or any other source of vibrations induced loadings, has been studied (Martin et al. 1975; Byrne and McIntyre 1994; Seed et al. 1975; Polito et al. 2008). The model developed by Seed et al. (1975) relates the pore water pressure generated to the cycle ratio, which is the ratio of the number of applied cycle of loading to the number of the cycles required to cause liquefaction. Polito et al. proposed the pore water pressure generation model, which relates the pore water pressure generation to the energy dissipated within the soil. Byrne and McIntyre (1994) applied the volumetric constraint that arose from the presence of the pore fluid to model the saturated undrained response to cyclic loading.

It is not easy to conduct the truly undrained shearing in the simple shear apparatus, therefore, a undrained shear test was generally conducted by performing the drained tests at constant volume. The changes in the measured vertical stress during constant volume simple shear tests should be correspond to the changes of pore water pressure measured in an undrained test. In order to be similarity between the undrained and the constant volume tests the apparatus has to impose a uniform deformation with no volume change. In the study the relationship between the stress-dilatancy relation in the drained test and the corresponding pore water changes in the undrained test is compared and an incremental pore water pressure generation model is established for the cyclic simple shearing.

2. EQUIPMENTS AND TESTING POCEDURES

2.1 Simple Shear Apparatus

The apparatus used in the study is shown in Figure 1. The shear box is the Kjellman type. A cylindrical specimen (100 mm in diameter and 30 mm in height) was enclosed in a rubber membrane supported by the stacked thin alumina rings coated with Teflon to minimize the friction between. Because the stacked rings prohibited lateral deformation, the specimen was first subject to K_o consolidation and then sheared at the condition of without lateral deformations as well. A vertical air actuator is used to apply vertical stress, while the cyclic horizontal shear stress can be applied with either a DC motor or an air actuator controlled with a computer. The vertical and horizontal loads were measured with two load cells and the vertical settlement and the horizontal displacement were measured with LVDTs, respectively. Both constant load and constant volume simple shear tests can be conducted with a load control mode or a displacement control mode.

2.2 Test Sand characteristics and Test Procedures

Ottawa sand and Fulung sand were used in the tests. The specimens having various relative densities were prepared with a multiple sieve pluviation method. The characteristics of Ottawa sand and Fulung sand are summarized in Table 1. The prepared specimen was

consolidated with various vertical stresses and then cyclically sheared to failure in the constant load or in the constant volume conditions. In the constant load tests the vertical settlement, horizontal displacement, and horizontal load were continuously measured, while in the constant volume tests the vertical load, horizontal displacement, horizontal load and vertical displacement were measured as well.

Figure 1 Simple shear Apparatus

Table 2 Physical properties of the crushed quartz sand

	G_s	D_{50}, in mm	C_u	[1] e_{max}	[1] ε_{min}
Ottawa sand	2.63	0.22	1.31	0.778	0.487
Fulung sand	2.67	0.19	1.22	1.01	0.671

[1] The maximum and minimum densities of the sand were measured in the dry state, according to the method (JSF T 161-1990) specified by the Japanese Geotechnical Society.

3. DERIVATION OF FORMULAE

3.1 Stress Dilatancy Relation in Constant Load Tests

The deformation behavior of sand during cyclic shear loading was studied based on a particulate approach considering slip and non-slip contacts between the grains on a microscopic shear plane (Ueng and Lee 1990). In the cyclic simple shear condition the relation of the shear stress ratio, τ / σ_y, and the average dilatancy rate ($d\varepsilon_v^p / |d\gamma^p|$), which is related to the distribution of contact angles between grains, on the macroscopic plane is expressed as :

For the positive and negative shear stress

$$\frac{\tau}{\sigma_y} = \tan\phi_u + \sec^2\phi_u \times \alpha(\theta) \times \frac{d\varepsilon_v^p}{|d\gamma^p|} \qquad (1\text{-a})$$

$$\frac{\tau}{\sigma_y} = -\tan\phi_u - \sec^2\phi_u \times \alpha(\theta) \times \frac{d\varepsilon_v^p}{|d\gamma^p|} \qquad (1\text{-b})$$

where τ = the shear stress along the shear plane and σ_y = the normal stress on the horizontal plane; ϕ_u =basic friction angle; $\alpha(\theta)$ =a positive value related to the number of slip and non-slip contacts; $d\varepsilon_v^p$ and $d\gamma^p$ are the plastic normal strain increment and plastic shear strain increment, respectively. The elastic strain increments are neglected in the study. Here τ was considered to be positive if clockwise, and $|d\gamma^p|$ was always positive regardless of the shearing direction, therefore, a positive dilatancy rate, ($d\varepsilon_v^p / |d\gamma^p|$) indicates dilatant behavior, whereas a negative dilatancy rate indicates contractive behavior during shearing. Figure 2-a demonstrates the relation of shear stress and shear strain. Eqs. 1-a and 1-b can be plotted in Figure 2-b, which show that upon reversal of the shear stress or strain the specimen becomes highly contractive.

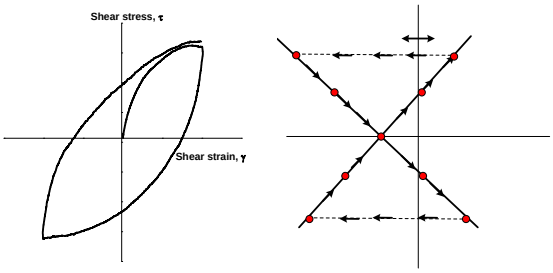

(a) (b)

Figure 2 (a) Shear stress vs. shear strain;
(b) Shear-volume coupling relations (Ueng and Lee 1990).

3.2 Change rate of vertical Stress in Constant Volume Simple Shear Tests

Consider a sample subjected to shearing in the constant load simple shear condition. Let dV_1^p = the increment (or decrement) of plastic volume change (dilation or contraction) due to slips at grain contacts during shearing. It has been shown that dV_1^p is a function of magnitude of shear stress, relative density, and the number of shearing cycles. Now assume the same shear stress applied on the identical sample but in the constant volume simple shear condition. The slips at grain contacts resulting in the increment (decrement) of plastic volume change, dV_1^p must occur as well and the increment of or decrement of vertical stress, $d\sigma_y$ was found. The increment (or decrement) of vertical stress would cause the volume change in sand structure. The vertical stress increment was considered to be positive and the vertical stress decrement to be negative. Because no vertical stress is carried by the water because of no water in the sample, the compatibility condition of no volume change during constant volume shearing gives the following equation.

$$dV_1^p = V_o \times \frac{d\sigma_y}{D_1} \qquad (2\text{-a})$$

$$d\varepsilon_{v1}^p = \frac{dV_1^p}{V_o} = \frac{d\sigma_y}{D_1} \qquad (2\text{-b})$$

in which V_o =total sample volume; D_1 = tangent constrained modulus when the current vertical stress larger than the initial consolidation stress or unloading tangent constrained modulus when the current vertical stress smaller than the initial consolidation stress. Substituting Eq.2-b into

Eqs.1-a and 1-b, the relation of the shear stress ratio and the change rate of vertical stress is given as:

$$\frac{\tau}{\sigma_y} = \pm tan\phi_u \pm \frac{sec^2\phi_u \times \alpha(\theta)}{D_1} \times \frac{d\sigma_y}{|d\gamma^p|} \quad (3)$$

in which $\frac{d\sigma_y}{|dr^p|}$ =change rate of vertical stress.

If the same stress was applied on the identical but saturated sample and in the undrained simple shear condition, the same plastic volumetric increment, dV_1^p, occurs. The water is assumed to be incompressible. Thus, the increment (or decrement) of pore water pressure, *du*, results in the volume change, dV_2.

$$dV_2 = V_o \times \frac{(-du)}{D_2} \quad (4\text{-a})$$

$$d\varepsilon_{v2} = \frac{dV_2}{V_o} = \frac{-du}{D_2} \quad (4\text{-b})$$

D_2 has the identical value as D_1 if neglecting the sample anisotropy. Under the condition of zero volume change:

$$d\varepsilon_{v1}^p = d\varepsilon_{v2} \quad (5)$$

Thus the relation of the increment of pore water pressure in the undrained simple shearing and the increment of the vertical stress in the constant volume shearing is:

$$du = -d\sigma_y \quad (6)$$

Hence the vertical stress decrement in the constant volume simple shear condition can be regarded as the pore water pressure increment and the vertical stress increment is regards as the pore water pressure decrement in the undrained simple shear condition. Substituting Eq. 6 into Eq. 3, incremental pore water pressure generation model is written as:

$$\frac{\tau}{\sigma_y} = \pm tan\phi_u \mp \frac{sec^2\phi_u \times \alpha(\theta)}{D_1} \times \frac{du}{|d\gamma^p|} \quad (7)$$

3.3 Errors of Insufficient Frame Stiffness

Similar to the membrane penetration and the compliance of pore water pressure measuring system to affect the pore water pressure measurement in a triaxial undrained test, the insufficient frame stiffness of the vertical load ram and its joint connection may cause the inevitable vertical deformation and results in the apparent volume change, dV_3, which can be measured with two LVDTs mounted at the vertical load ram throughout the constant volume simple shear test. During constant volume shearing, a positive dV_1^p (dilation) increases the vertical load on the load ram and produces negative value of dV_3, therefore, the less vertical load change (the less negative excess pore water pressure) would be measured. In contrast, a negative dV_1 (contraction) decreases the vertical load and produces positive value of dV_3 and results in the less vertical load change (less positive excess pore water pressure) being registered. Consequently Eqs.(2-a) and (2-b) can be rewritten as:

$$dV_1^p + dV_3 = V_o \times \frac{d\sigma_y}{D_1} \quad (7\text{-a})$$

$$d\varepsilon_{v1}^p = \frac{dV_1^p}{V_o} = \frac{d\sigma_y}{D_1} - \frac{dV_3}{V_o} \quad (7\text{-b})$$

Substituting Eq.7-b into Eqs.1-a and 1-b, the modified relation of the shear stress ratio and the change rate of vertical stress is derived as:

$$\frac{\tau}{\sigma_y} = \pm tan\phi_u \pm \frac{sec^2\phi_u \times \alpha(\theta)}{D_1} \times \left(\frac{d\sigma_y}{|d\gamma_p|} - \frac{dV_3/V_o \times D_1}{|d\gamma_p|}\right) \quad (8)$$

These errors can be eliminated as small as possible by increasing the stiffness of the loading frame as stiff as possible.

4. TEST RESULTS AND DISCUSSION

4.1 Stress Dilatancy Relation for Constant Load Tests

The stress dilatancy relation can be obtained from the constant load cyclic simple shear tests. Figures 3 and 4 show the relations of stress and dilatancy for Ottawa sand and Fulung sand with different relative densities at different vertical stresses under cyclic simple shear test. These stress dilatancy relations can be written as:
For Fulung sand

$$\frac{\tau}{\sigma_y} = \pm 0.45 \pm 1.815 \frac{d\varepsilon_v^p}{|d\gamma^p|} \quad (9)$$

For Ottawa sand

$$\frac{\tau}{\sigma_y} = \pm 0.42 \pm 1.68 \frac{d\varepsilon_v^p}{|d\gamma^p|} \quad (10)$$

Here τ was considered to be positive if clockwise. $|d\gamma^p|$ was always positive regardless of the shearing direction, therefore, a positive dilatancy rate, ($d\varepsilon_v^p / |d\gamma^p|$) indicates dilatant behavior, whereas a negative dilatancy rate indicates contractive behavior despite of scattering data observed at the beginning of the stress reversal due to difficulty in measuring the extremely small deformation responding to a rather larger stress change.

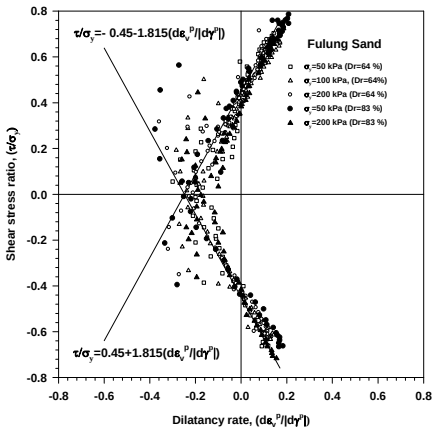

Figure 3 Relations of stress dilatancy for Fulung sand

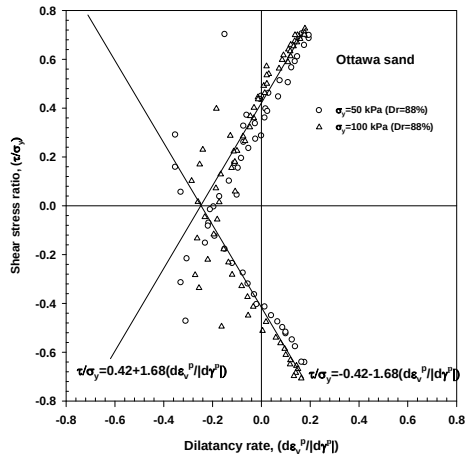

Figure 4 Relations of stress dilatancy for Ottawa sand

The stress dilatancy relation is true for all densities and all the vertical consolidation stress for a given sand. The equations (Eqs. 9 and 10) can quite correctly capture the shear volume coupling effects under strain controlled conditions.

4.2 Relation between Shear Stress Ratio and Change Rate of Vertical Stress for Constant Volume Tests

The stress – dilatancy relation measured from the test results of the constant load tests as shown in Figs. 3 and 4 can give the relation of shear stress ratio and change rate of vertical stress for constant volume tests per Eq. 3 as follows:
For Fulung sand

$$\frac{\tau}{\sigma_y} = \pm 0.45 \pm \frac{1.815}{D_1}\frac{d\sigma_y}{|d\gamma|} \tag{11}$$

For Ottawa sand

$$\frac{\tau}{\sigma_y} = \pm 0.42 \pm \frac{1.68}{D_1}\frac{d\sigma_y}{|d\gamma|} \tag{12}$$

The unloading tangent constrained modulus D_1, which is calculated from the 1-D consolidation test, varies with the type of sand, relative density of specimen, and the magnitude of consolidation pressure. Assume that unloading and reloading follow the same path, they show elastic behavior. The slope of unloading-reloading path (swelling index) is denoted as C_s. D_1 can be computed with Eq. 13:

$$D_1 = \frac{d\sigma_y}{d\varepsilon_v} = \frac{\sigma_y}{C_s} \tag{13}$$

Then the relation between shear stress ratio and change rate of vertical stress in the constant volume tests is written as:
For Fulung sand

$$\frac{\tau}{\sigma_y} = \pm 0.45 \pm \frac{1.815 \times C_s}{\sigma_y}\frac{d\sigma_y}{|d\gamma|} \tag{14-a}$$

For Ottawa sand

$$\frac{\tau}{\sigma_y} = \pm 0.42 \pm \frac{1.68 \times C_s}{\sigma_y}\frac{d\sigma_y}{|d\gamma|} \tag{14-b}$$

Fig. 5 shows the good comparison of the measured and the predicted change rate of vertical stress vs. the shear stress ratio for the Fulung sand under cyclic shear loading. Substituting Eq. 6 into Eq. 14-a and 14-b, therefore the incremental pore water pressure generation model can be give as follows for the Fulung sand and the Ottawa sand:

$$du = \left[\left(\frac{\tau}{\sigma_y} \mp 0.45\right) \times \frac{\sigma_y}{1.815 \times C_s}\right] \times |d\gamma^p| \tag{15-a}$$

$$du = \left[\left(\frac{\tau}{\sigma_y} \mp 0.42\right) \times \frac{\sigma_y}{1.68 \times C_s}\right] \times |d\gamma^p| \tag{16-b}$$

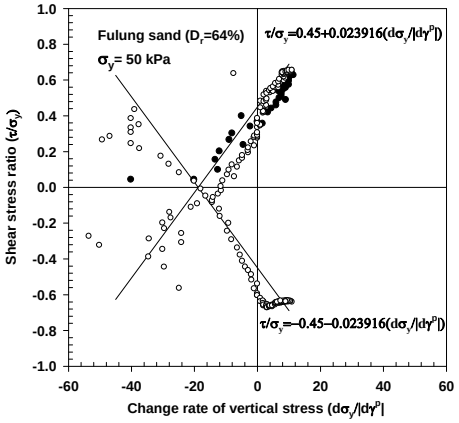

Figure 5 Relations of τ/σ_y and $(d\sigma_y/d|\gamma^p|)$ for Fulung sand

5. CONCLUSIONS

The relations of stress and dilatancy rate for the sand under simple shear loading were first proposed. Adopting the concept that the volume change due to cyclic shearing in the constant load tests were compensated by the volume change due to vertical stress change in the constant volume tests. Then an incremental pore water pressure generation model was developed.

References:

Martin, G.R., Finn, W.D., and Seed, H.B. (1975), "Fundamentals of liquefaction under cyclic loading,"*Journal of Geotechnical Engineering*, American Society of Civil Engineers, **101**(5), 423-438.

Byrne, P.M. and McIntyre, J. (1994), "Deformations in granular soils due to cyclic loading," *Proceedings of Settlement'94: Vertical and Horizontal Deformations of Foundations and Embankments*, **Vol.2**, 1864-1896.

Seed, H.B., Martin, P.P., and Lysmer, J. (1975), "The generation and dissipation of pore water pressure during soil liquefaction," *No. EERC-75-26*, University of califirnia, Berkerley, California.

Politi, C.P., Green, R.A., Lee, J. (2008), "Pore pressure generation models for sands and silty soils subjected cyclic loading," *Journal of Geotechnical and Geoenviromental Engineering*, American Society of Civil Engineers, **134**(10), 1490-1500.

Ueng, T.S., and Lee, C.J. (1990), "The deformation behavior of sand under shear - A particulate approach," *Journal of Geotechnical Engineering*, **116**(11), pp.1625-1640.

Sixth International Conference on Urban Earthquake Engineering
March 3-4, 2009, Tokyo Institute of Technology, Tokyo, Japan

EFFECTS OF MOISTURE CONTENT OF SOIL ON NATURAL SLOPE FAILURE DURING THE 2004 NIIGATA-KEN CHUETSU EARTHQUAKE

Hirofumi Toyota[1] and Susumu Takada[2]

1) Associate Professor, Department of Civil and Environmental Engineering, Nagaoka University of Technology, Japan
2) Graduate Student, Energy and Environment Science Course, Nagaoka University of Technology, Japan
toyota@vos.nagaokaut.ac.jp, stakada@m3.gyao.ne.jp

Abstract: Numerous landslides occurred in hilly and mountainous areas during the 2004 Niigata-ken Chuetsu Earthquake. Social problems developed when many towns became isolated because landslides cut off traffic and public service lifelines. The hilly areas are composed mainly alternate layer of soft sandstone and mudstone deposited in quaternary or tertiary period. This geomorphology formed by folding presents a prominent landslide area in this region. This area has been utilized as rice terraces or carp breeding ponds because of plenty of water in the ground all the time. In addition, there was rainfall of more than 100 mm caused by Typhoon No. 23 two days before the earthquake in Chuetsu area. Block samples were extracted from the failure sites. The samples obtained were mainly low-cemented sandy soils. Triaxial tests of the samples under saturated and unsaturated conditions were conducted to examine the soils' strength properties and estimate slope stability.

1. INTRODUCTION

The Niigata-ken Chuetsu Earthquake whose main tremor was magnitude of 6.8 occurred in a mid part of Niigata-ken (Chuetsu area) at 17:56 on 23 October 2004 and seriously damaged infrastructures of hilly and mountain area which are Kawaguchi town, Ojiya city, Nagaoka city, etc. (Fig. 1). This earthquake is an epicentral earthquake of thrust fault with hypocentre of about 10 km depth and characterised that frequent strong aftershocks led to increasing damage.

Chuetsu area has been compressed in northwest-southeast directions due to the crustal movement and constituted folded mountains formed by quite young tertiary deposits. The region exhibits catchment area dotted with many rice terraces and carp breeding ponds. In addition, rainfall of more than 100 mm was recorded from typhoon No. 23, which passed through the Chuetsu area two days before the earthquake. Daily rainfall of 21 October 2004 at Nagaoka city, based on data from the Japan Meteorological Agency, reached 115 mm. Under those circumstances, numerous landslides occurred in Yamakoshi of Nagaoka city (formerly Yamakoshi village). Social problems developed when many towns became isolated because landslides cut off traffic and public service lifelines. Soil from landslides closed river channels and formed natural dams along the Imo River, which flows north to south in Yamakoshi. The natural dams submerged some towns and emergency measures were promptly undertaken to prevent debris flows caused by natural dam breaks.

In the paper, observed ground water level was shown and effects of moisture content of soil on natural slope failure were examined by conducting the monotonic and cyclic triaxial tests using the saturated and unsaturated samples.

2. CHARACTERISTICS OF SLOPE FAILURE

More than 3000 landslides occurred during the earthquake, especially along the Imo River in Yamakoshi area. According to a geological map (Takeuchi and Kato, 1994), alternation of mudstone and sandstone (sandstone dominate) of the Quaternary deposit forms this place.

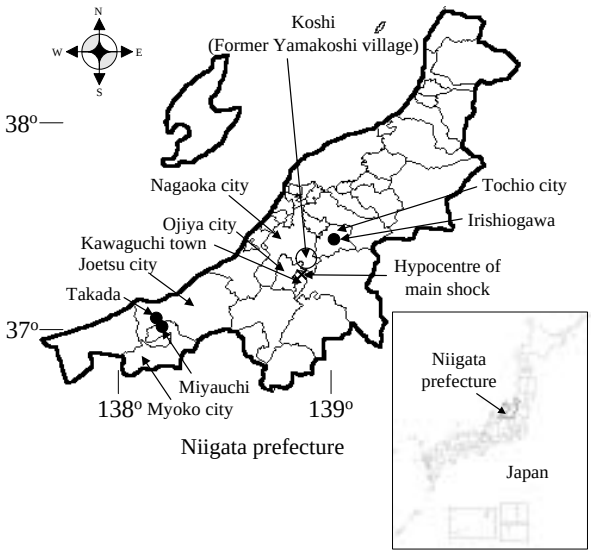

Figure 1 Map of Niigata prefecture

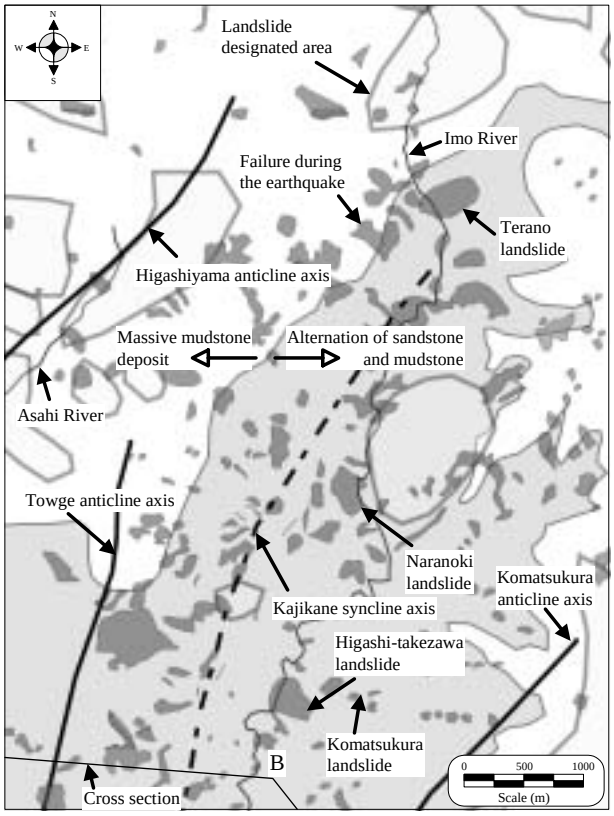

Figure 2 Landslide distribution and geological map of Yamakoshi area

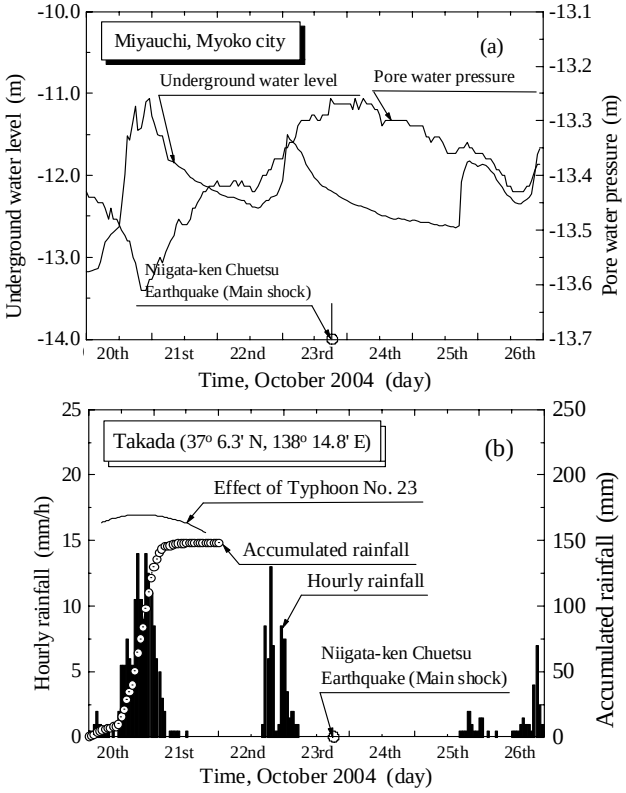

Figure 3 Records of water pressure and hourly rainfall during the earthquake at Miyauchi of Myoko city

Figure 2 was prepared by overlaying the landslide locations during the earthquake (Geographical Survey Institute, 2004) on a simplified geological map provided by Takeuchi et al. (2004). Landslide designated areas obtained from a conservation map of Niigata prefecture (1982) are also indicated in the figure. The west side of the map, which is classified in the Asahi River basin (Fig. 2), is geologically an Araya deposit that is massive dark grey mudstone. Shifting toward the east side of the map, which is classified in the Imo River basin (Fig. 2), the deposit changes to alternation of sandstone and mudstone named Kawaguchi and Wanatsu deposits. Alternation of sandstone and mudstone is distributed mainly along the Imo River, except in its upper course. Numerous landslides occurred during the earthquake in areas with alternated layers of sandstone and mudstone compared with massive mudstone deposits. This finding engenders the conclusion that sandy natural slopes are more fragile than clayey natural slopes during earthquakes. On the other hand, landslide-designated areas are distributed mainly in the massive mudstone deposits. Moreover, the notable geological features of this region are syncline and anticline structures. They form a complex topography in which synclinal axes and anticlinal axes are arranged with a short interval (Fig. 2). For that reason a peculiarly cuesta topography appears in this region. Fragile and weak slopes are therefore easily formed.

According to those findings, several reasons of frequent landslides were reported in Toyota et al. (2006): 1. The unstable slops were created because the river had scoured the toe of the slope, 2. A complex topography in which synclinal axes and anticlinal axes are arranged with a short interval was formed and it is easily weathered, 3. Sandstone and sandy mudstone, which are soft and fragile, are distributed widely around this area.

3. MEASUREMENT OF WATER PRESSURE IN PREVIOUS LANDSLIDE AREAS

Water level and pore water pressure have been measured by our laboratory since 1995 in old landslide areas, which are Miyauchi of Myoko city and Irishiogawa of former Tochio city. Topographical maps and ground profiles of the measuring points are reported in Toyota et al. 2006. Figures 3 and 4 respectively show the records of water pressure and hourly rainfall at Miyauchi and Irishiogawa. The values of water pressure have been acquired using a data logger on the hour. This means that the water pressures were measured after 4 minutes from the main shock because the earthquake occurred at 17:56. The rainfall data of the nearest areas from our measuring points were selected from among data provided by the Japan Meteorological Agency. The measuring points of Miyauchi and Irishiogawa are about 6 km and 4 km apart from the rainfall-recorded points, respectively. Rainfall occurred by typhoon No. 23 of 20 Oct. 2004. The accumulated rainfall reached 100 mm in those

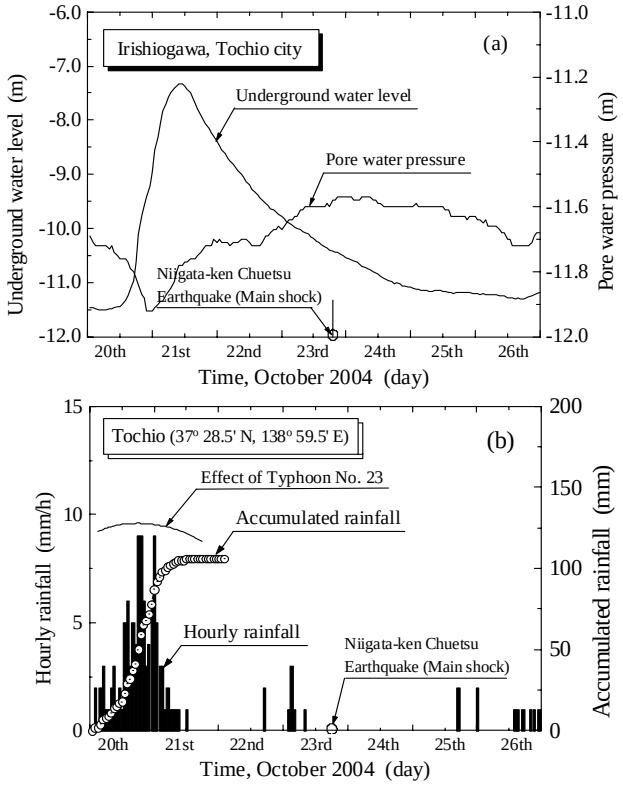

Figure 4 Records of water pressure and hourly rainfall during the earthquake at Irishiogawa of former Tochio

areas (Figs. 3(b) and 4(b)). The groundwater level rose quickly with the rainfall: about 2 m in Miyauchi and 4 m in Irishiogawa. The difference in the rise of groundwater between Miyauchi and Irishiogawa is considered to result from their geological and topographical features. These areas are inferred to be catchment areas because elevated underground water levels descend gradually over a few days. The rise in groundwater table induced by the typhoon had dropped by about 1 m in Miyauchi and 3 m in Irishiogawa by the time of the Niigata-ken Chuetsu Earthquake. Similar behaviour was observed concerning the pore water pressure at both areas: the pore water pressure dropped on 20 Oct. 2004 with low atmospheric pressure; it then increased gradually. Although the pore water pressure reached a peak at the time of Niigata-ken Chuetsu Earthquake, the pore water pressure increase of about 20 cm in the water head is too small to affect slope failure. The pore water pressure sensors might not be installed near the slip surface where pore water pressure will change most during a certain event. It seems that there was considerable rainfall on the night before the earthquake at Miyauchi (Fig. 3(b)).

4. SOILS PROPERTIES OBTAINED FROM SLOPE FAILURE SITES

4.1 Grain Size Distributions of Soils

Figures 5 shows grain size distribution of the soil

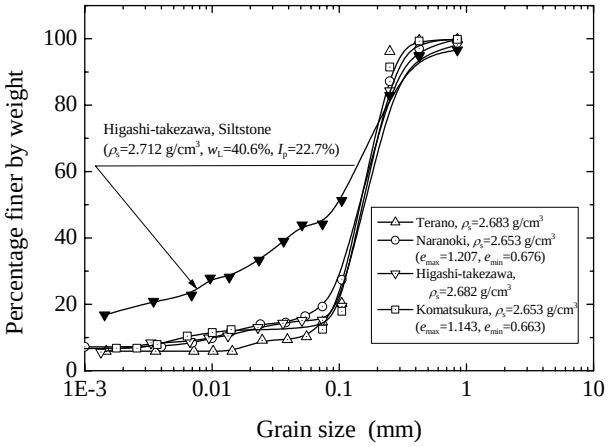

Figure 5 Grin size distributions obtained from failure sites

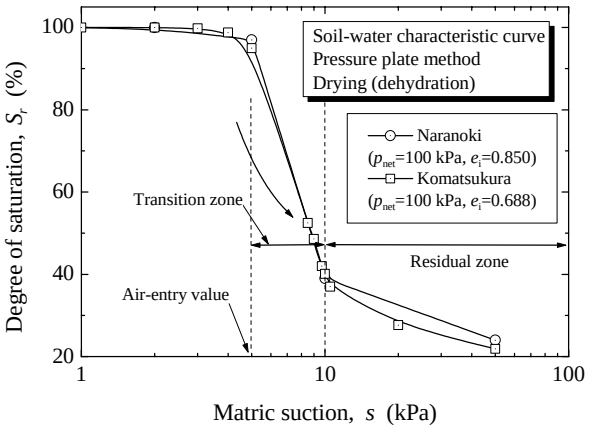

Figure 6 Soil water characteristic curves obtained from failure sites

samples taken from slope failure sites (Fig. 2). All samples from the main scarps of slope failure sites are sand including less than 10% fines. This means that sandy natural slopes are more fragile than clayey natural slopes during earthquakes. The exposed mudstone at Higashi-takezawa is composed mainly of silt; that is, siltstone. These results agree with information from the geological map, which shows alternation of sandstone and mudstone strata. The maximum and minimum void ratios based on Japanese industrial standards (JIS A 1224) are respectively 1.207 and 0.676 in Naranoki sand and 1.143 and 0.663 in Komatsukura sand.

4.2 Sample Preparation

Block samples were obtained from a sandy layer of the failure site in Naranoki and trimmed to make specimens for triaxial tests in the laboratory. The soil is very soft and can be easily broken and shaped by hand. Reconstituted specimens were made using the wet tamping method (Ishihara, 1993). Soil of 5% water content was strewn in the mould that is the same size with the specimen. Then, tamping was applied to the soil with flat bottom of 2cm

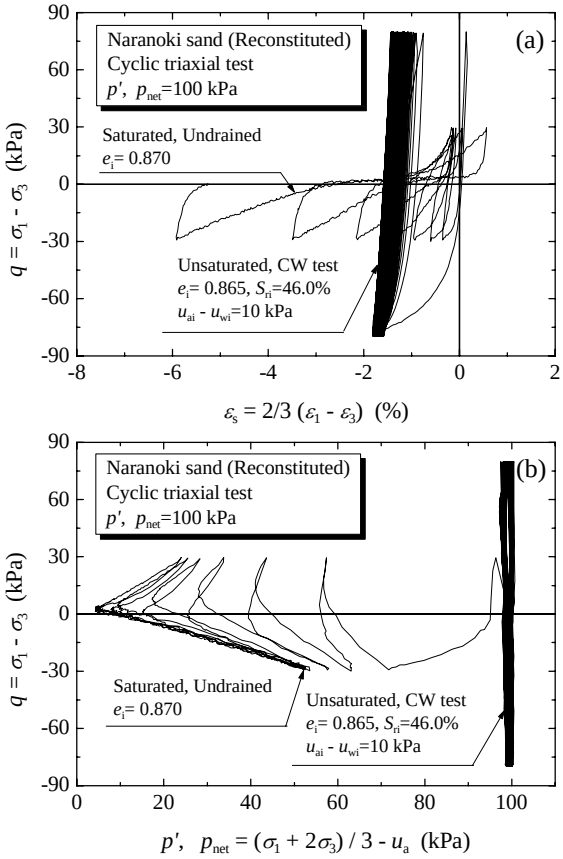

Figure 7 Comparison of cyclic shear behaviour between saturated and unsaturated specimens: (a) stress-strain, (b) stress path failure sites

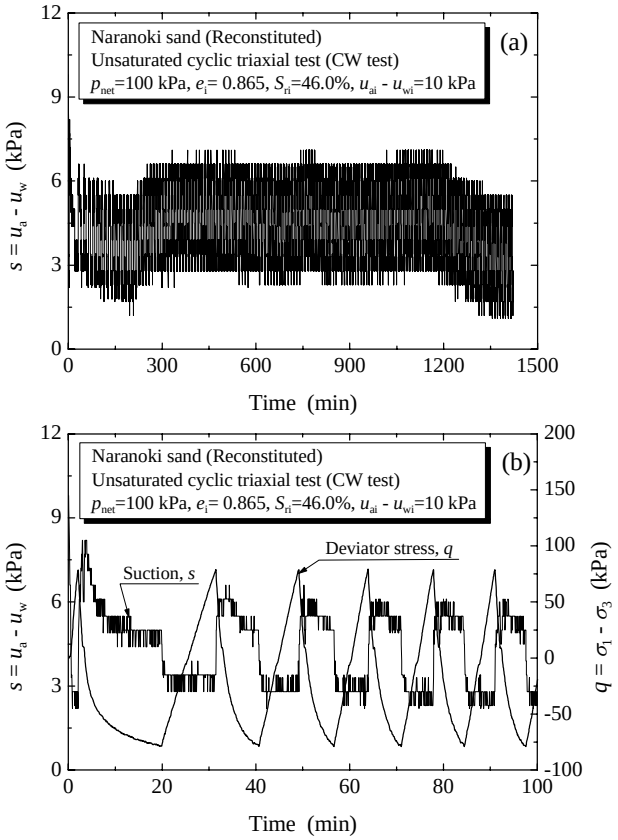

Figure 8 Variation of suction during cyclic loading in CW condition of unsaturated specimen

diameter tamper. Tamping energy was controlled to make a given density of specimen. Amount of soil strewn in one time was calculated in advance so as to make about 2cm layer. These procedures were repeated five times. Using that method, reconstituted specimens having the same void ratio with undisturbed specimen were made. Specimens were d=50 mm in diameter and h=100 mm in height in triaxial tests. The specimens were saturated using the vacuum saturation procedure.

The drying portion of the soil-water characteristic curve obtained from the pressure plate method using a ceramic filter is shown in Fig. 6. The experiment was carried out under net mean principal stress, p_{net}=100 kPa, using triaxial apparatus. This result suggests that the air entry value of the soil is approximately 5-10 kPa. The degree of saturation dramatically decreases at the air entry value because of the sandy soil specimen. Therefore, when the soil is under stable conditions, the soil is in either fully saturated or in a low degree of saturation.

The results of monotonic loading tests using triaxial and box shear apparatuses have been reported in Toyota et al. 2006. Cyclic undrained triaxial tests of constant deviator stress amplitude were also performed with constant axial strain rate of 0.1 %/min.

4.3 Cyclic Shear Behaviour on Unsaturated Soil

It is well known that liquefaction resistance fairly increase with small decrease of saturation degree from a saturated state (Yoshimi et al., 1989). The cases where lateral flow of unsaturated ground had occurred during earthquakes were reported, and then many researchers have studied liquefaction and flow characteristics under unsaturated state (e.g. Kazama et al., 2006 and Nakazawa et al., 2007). Here, unsaturated specimens of Naranoki sand were prepared by applying 10 kPa suction to saturated specimens. According to Fig. 6, the degree of saturation became relatively low in this situation.

It is very difficult to keep undrained condition where both pore-air and pore-water are not allowed to drain because air can pass through a rubber membrane. Therefore, pore-air drained and pore-water undrained conditions, which is referred to as a constant water content (CW) test, were adopted for the study. Cyclic shear tests were carried out under constant total mean principal stress, p, in the unsaturated specimens to simulate the closer behaviour to real seismic loading, while under constant cell pressure in the saturated specimens. The cyclic loading speed is set as 0.1%/min considering the insensitive response of water pressure because of low permeability of a ceramic filter.

The representative result of stress-strain relationship and stress path are respectively shown in Fig. 7 (a) and 7(b)

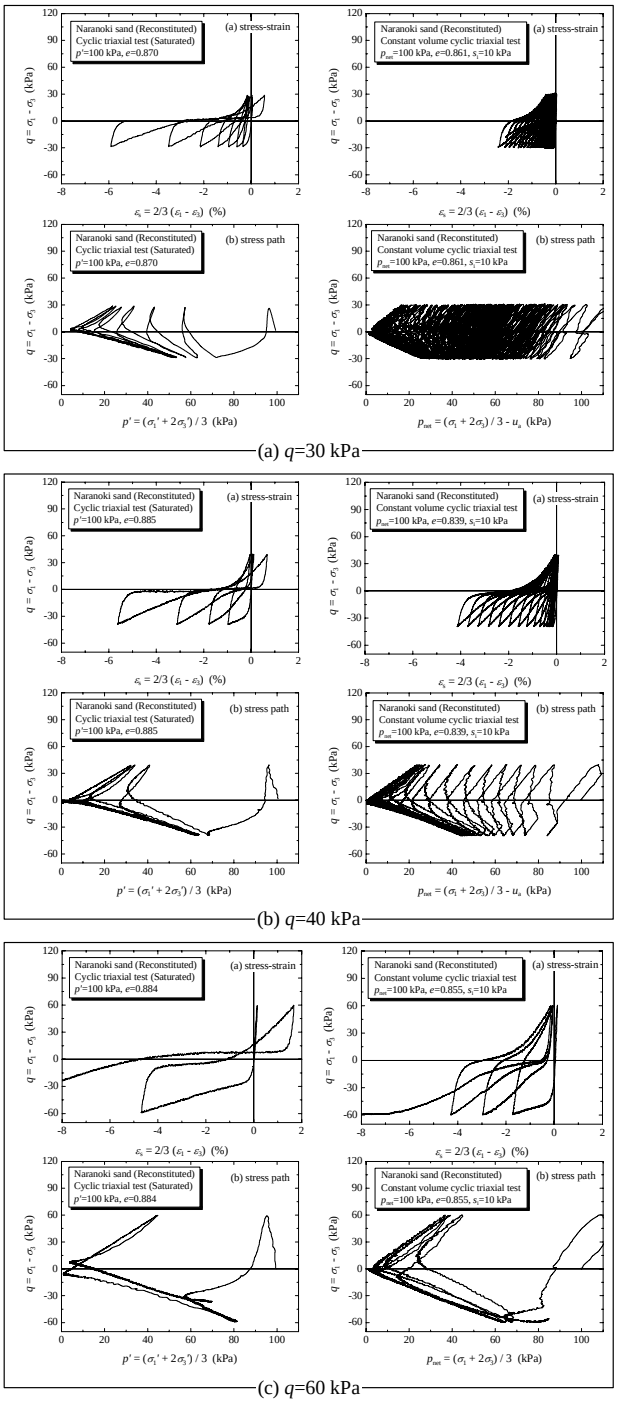

(a) q=30 kPa

(b) q=40 kPa

(c) q=60 kPa

Figure 9 Cyclic shear behaviour on undrained saturated and constant volume unsaturated specimens: (a) cyclic deviator stress, q=30 kPa, (b) q=40 kPa, (c) q=60 kPa

to compare between saturated (cyclic deviator stress, q=30 kPa) and unsaturated specimen (cyclic deviator stress, q=80 kPa). In the case of saturated specimen, well-known cyclic behaviour is presented where deformation develops more in extension direction because of weak direction. In the case of unsaturated specimen, at first, the specimen considerably deforms to extension direction, and then the residual deformation to extension direction tends to converge with the number of cycles. Stress path keeps the p_{net} constant because of air-drined condition under constant p. It can be understand that in unsaturated soil, whose degree of saturation is low, the stiffness against a cyclic loading is increased with the cyclic loading and the softening behaviour like liquefaction of saturated soils never occurs.

Although the u_a is constant in unsaturated condition, the u_w varies during shearing because of water-undrained condition. Figure 8 shows the change of suction during cyclic loading in CW condition of unsaturated specimen. Suction decreases from 10 kPa to 2 kPa in the initial compression loading and varies between 7 kPa and 3 kPa. From Fig. 8(b), suction dramatically increases just after the q become the maximum value and sharply decreases around the minimum (negative) value of the q.

After applying cyclic loading, shear strengths of the specimens under monotonic loading were demonstrated in Toyota 2006. According to the results, there is little effect of cyclic loading on static shear strength of the unsaturated soil. The reason may be considered that the effects of densification and decrease of suction due to cyclic loading on static shear strength are cancelled each other.

Next, in order to purely investigate the effect of moisture content, cyclic shear tests of unsaturated specimens (s=10 kPa) were conducted under constant volume condition where the cell pressure was controlled to maintain a constant volume. Although it is difficult to image that the unsaturated ground keeps its volume constant during earthquakes, this testing condition contributes to estimate the cyclic strength of soils having aging or cementation. Since enough undisturbed samples could not be obtained, the cohesion of undisturbed sample is represented by the apparent cohesion of unsaturated soil. Toyota et al. (2006) demonstrated that the both cohesions that are less than 10 kPa are similar.

Figure 9 shows the comparison between undrained saturated and constant volume unsaturated specimens on cyclic shear behaviour at different cyclic deviator stress. Similar behaviour with undrained saturated soil is presented in constant volume condition of unsaturated soil. The deformation develops to extension direction in every case. More number of cycles is needed to reach liquefaction in unsaturated soil than that in saturated soil. This is considered as the effect of apparent cohesion in unsaturated soil on liquefaction strength.

Figure 10 shows the relationships between cyclic stress ratio and number of cycles to certain double amplitude of axial strain. Although the apparent cohesion is less than 10 kPa as static strength, the number of cycles remarkably increases as shown in the figure. From the results it is inferred that soils having aging or cementation have enough liquefaction resistance. Relatively high liquefaction strength is expected in soils having aging and low moisture content. However, increase of moisture content induces the decrease of cyclic shear strength. Therefore, detailed investigation is necessary to discuss the slope stability during earthquakes because especially pore water pressure increases and shear strength decreases in the case of high moisture content.

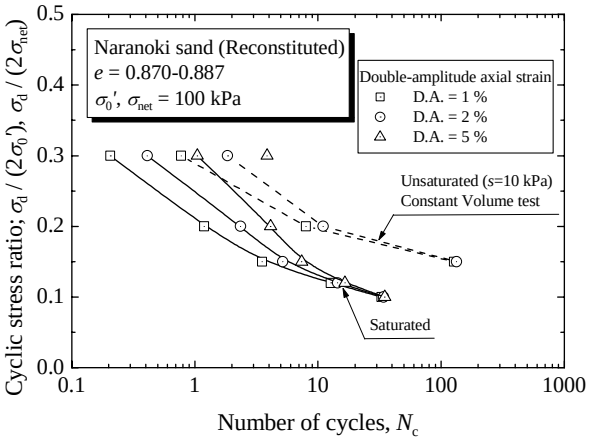

Figure 10 Increase of liquefaction strength due to apparent cohesion

5. CONCLUSIONS

A detailed investigation and laboratory testing were carried out on slope failures during the Chuetsu Earthquakes. Main findings from the study are summarised as:

1. The greater part of slope failures during the earthquake occurred at alternating sandstone and mudstone strata, but landslides, which moved gradually during snow melting season, have usually occurred at massive mudstone of quaternary and tertiary deposits.
2. The groundwater table was raised about 2 m in Miyauchi and 4 m in Irishiogawa, which are old landslide area, by typhoon No. 23. But the rise in groundwater table had dropped about 1 m in Miyauchi and 3m in Irishiogawa by the time of the Niigata-ken Chuetsu Earthquake.
3. The sandstones of Yamakoshi area are fragile on earthquakes because the cementation and ageing effects are small. However, the liquefaction resistance considerably increases due to addition of small cohesion and the decrease of moisture content.

Acknowledgements:

Soil testing was conducted with the assistance of students from the Geotechnical Engineering Laboratory, the Department of Civil and Environmental Engineering, Nagaoka University of Technology. The authors express sincere appreciation for their contributions to this study.

References:

Geographical Survey Institute (2004), "Disaster Map of Niigata-ken Chuetsu Earthquake," (http://zgate.gsi.go.jp/niigatajishin/index.htm).

Ishihara, K. (1993), "Liquefaction and flow failure during earthquakes," *Géotechnique*, **43**(3), pp. 349-415.

Kazama, M., Takamura, H., Unno, N., Sento, N. and Uzuoka, R. (2006), "Liquefaction Mechanism of Unsaturated Volcanic Sandy Soils," *Journals of the Japan Society of Civil Engineers*, Division C, **62**(2), 546-561. (in Japanese)

Nakazawa, H., Ishihara, K., Tsukamoto, Y. and Kamata, T. (2007), "Characteristics of Undrained Shear Behaviour of Sandy Soil Under Partially Saturated Conditions," *Journals of the Japan Society of Civil Engineers*, Division C, **63**(2), 334-343. (in Japanese)

Niigata prefecture (1982), "Conservation Map" (in Japanese).

Takeuchi, K. and Kato, S. (1994), "1:50,000 Geological Map of the Takada-Tobu region," Geological Survey of Japan.

Takeuchi, K., Yanagisawa, Y., Miyazaki, J. and Ozaki, M. (2004), "1:50,000 Digital Geological Map of the Uonuma region, Niigata Prefecture (Ver.1)," *GSJ Open-file Report*, no. 412 (http://www.gsj.jp/GDB/openfile/files/no0412/index.html).

Toyota, H. (2006), "Estimation of Natural Slope Failures Induced by the 2004 Niigata-ken Chuetsu Earthquake," *Proceedings of the Second Japan - Taiwan Joint Workshop on Geotechnical Hazards from Large Earthquakes and Heavy Rainfall*, Niigata, 49-55.

Toyota, H., Wang, J., Nakamura, K. and Sakai, N. (2006), "Evaluation of Natural Slope Failures Induced by the 2004 Niigata-ken Chuetsu Earthquake," *Soils and Foundations*, **46**(6), 727-738.

Yoshimi, Y., Tanaka, K. and Tokimatsu, K. (1989), "Liquefaction Resistance of a Partially Saturated Sand," *Soils and Foundations*, **29**(3), 157-162.

Sixth International Conference on Urban Earthquake Engineering
March 3-4, 2009, Tokyo Institute of Technology, Tokyo, Japan

DYNAMIC SOIL PROPERTIES BACK-CALCULATED FROM STRONG MOTIONS RECORDED AT TWO DOWNHOLE ARRAYS DURING THE 2007 NIIGATA-KEN CHUETSU-OKI EARTHQUAKES

Kohji Tokimatsu[1], Yoshiaki Ibaraki[2], and Hiroshi Arai[3]

1) Professor, Center for Urban Earthquake Engineering, Tokyo Institute of Technology, Japan
2) Undergraduate Student, Department of Architecture and Building Engineering, Tokyo Institute of Technology, Japan
3) Senior Research Engineer, Building Research Institute, Japan
kohji@o.cc.titech.ac.jp, ibaraki.y.aa@m.titech.ac.jp , arai@genken.go.jp

Abstract: Dynamic properties of soil deposits at two sites (one near Unit 5 and the other near the Service Hall) at the Kashiwazaki-Kariwa nuclear power plant were back calculated using strong motion recordings obtained during the 2007 Niigata-ken Chuetsu-oki earthquakes. The method used to figure this inversion was genetic algorithm, coupled with a one-dimensional equivalent linear response analysis, in which damping ratios will vary with the Fourier shear strain amplitude in the frequency domain. Our back-analysis has demonstrated that the surface layer at the Service Hall consisting of Holocene and Pleistocene dune sands showed strong nonlinear behavior during the main shock, with the underlying Pliocene Nishiyama Formation remaining elastic. The Pleistocene Yasuda Formation occurring near the ground surface at Unit 5, as well as the underlying Nishiyama and Shiiya Formations, also remained nearly elastic, but exhibited higher damping ratios. It is believed that the different dynamic soil behavior between the two sites may have led to the strikingly different site amplification between the two sites during the main shock.

1. INTRODUCTION

The Niigata-ken Chuetsu-oki earthquake (M_j=6.8) that occurred on July 16, 2007, with an epicenter off the Niigata Prefecture, affected not only the coastal areas of the southwestern Niigata prefecture but also the Kashiwazaki-Kariwa nuclear power plant of Tokyo Electric Power Company (TEPCO). The operation of the plant has been halted for more than one and a half years, presumably due to very strong ground shaking at the site and the resulting settlements of backfills around critical buildings.

A total of 97 accelerometers were installed at the site (TEPCO 2007a). These include free-field downhole arrays near the Units 1, 5, and 6 reactor buildings as well as near the Service Hall. Strong motion time histories during the main shock were successfully digitized and stored for 33 locations including the downhole array at the Service Hall. Unfortunately, however, the digital recordings obtained at the other 63 locations including the other downhole arrays close to the reactor buildings were overwritten with aftershock data and lost. Only exceptions are their peak acceleration values and pen-writing time history recordings including NS components at Unit 5 (TEPCO 2007a, 2007b; Tanaka et al. 2008). Recently, those hardcopy recordings have been successfully digitized (Tanaka et al. 2008).

The downhole array recordings near the Service Hall as well as near Unit 5 seem to be particularly important not only to determine the input rock outcrop motions for analytically reviewing dynamic behavior of the critical buildings but also to estimate nonlinear dynamic soil properties at the site that are definitely required for such analysis. The objective of this paper is to estimate dynamic soil properties based on an inverse analysis of the downhole array recordings using genetic algorithms combined with a one-dimensional equivalent linear response analysis.

2. SITE CONDITIONS AND OBSERVED RECORDS

The Kashiwazaki-Kariwa nuclear power plant is located along the coast on the north of Kashiwazaki city and about 16 km southeast of the epicenter. Figure 1 shows a map of

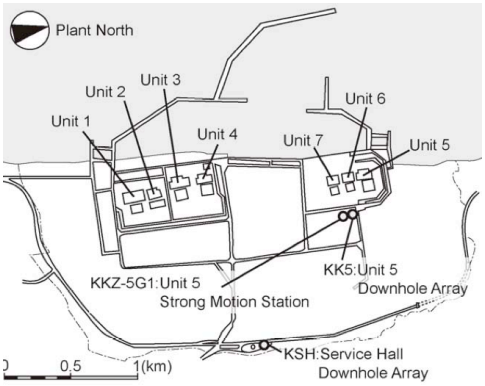

Figure 1 Map Showing Locations of Downhole Array

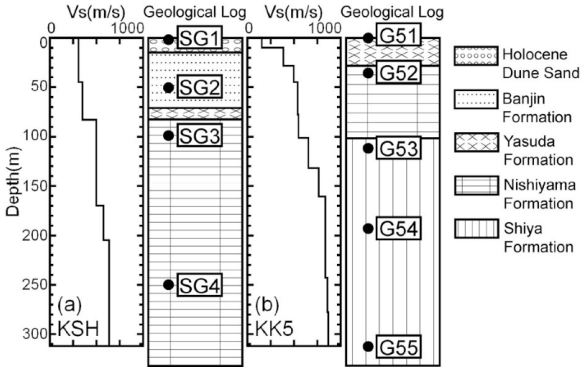

Figure 2 Goelogical and Geophysical Logs at Two Sites

the site together with the locations of the Unit 5 and Service Hall downhole arrays.

Figure 2 shows the geological and geophysical logs along with the locations of the downhole accelerometers. The elevation of the Service Hall on a sand dune is 67.5 m, which is 55.2 m higher than that of Unit 5 (12.3 m). The sand dune at the Service Hall that was formed in the Holocene and Pleistocene eras deeply overlies the Pleistocene Yasuda Formation and the Pliocene Nishiyama Formation. The Pleistocene Yasuda Formation, in contrast, outcrops at Unit 5, overlying the Pliocene Nishiyama and Shiiya Formations. The shear wave velocities, V_{so} of the Holocene sand dune (New sand dune), the Pleistocene sand dune (Banjin Formation), and the Yasuda, Nishiyama, and Shiiya Formations vary from 300- 850 m/s.

The Service Hall downhole array includes three-component accelerometers installed at four different depths (SG1-SG4), while the Unit 5 array at five different depths (G51-G55) with an additional one on the ground at the observation house nearby (5G1), as shown in Figure 2. The NS and EW directions of the accelerometers were set to the two principal axes of the plant buildings and thus were rotated clockwise 18.9 degrees from the true ones.

The downhole array recordings for the main shock as well as two aftershocks that occurred at 15:37 hrs and 17:42 hrs on the same day, herein called aftershocks L and S, are used for this study (TEPCO 2007a-2007c). Since the acceleration time history at G51 during the main shock is unavailable, it was replaced with the nearby recording at 5G1. Figure 3 shows the NS acceleration time histories observed with the Service Hall and Unit 5 arrays during the main shock and Table 1 summarizes peak NS accelerations observed with the arrays during the three events. Note that

Table 1 Peak NS Accelerations in Two Arrays during Three Earthquakes

Sensor ID	Peak acceleration (m/s^2)			Sensor ID	Peak acceleration (m/s^2)		
	S	L	Main		S	L	Main
SG1	0.35	1.6	3.5	G51/ 5G1	0.39	2.2	9.6
SG2	0.15	1.3	3.4	G52	0.31	1.4	4.2
SG3	0.17	1.4	4.0	G53	0.22	1.1	3.9
SG4	0.18	1.4	4.3	G54	0.16	1.3	4.2
				G55	0.16	1.2	4.1

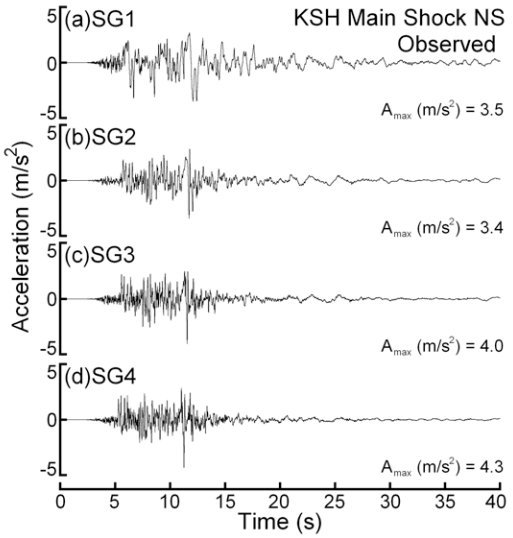

Figure 3(a) NS Acceleration Time Histories Recorded with Service Hall Array (KSH)

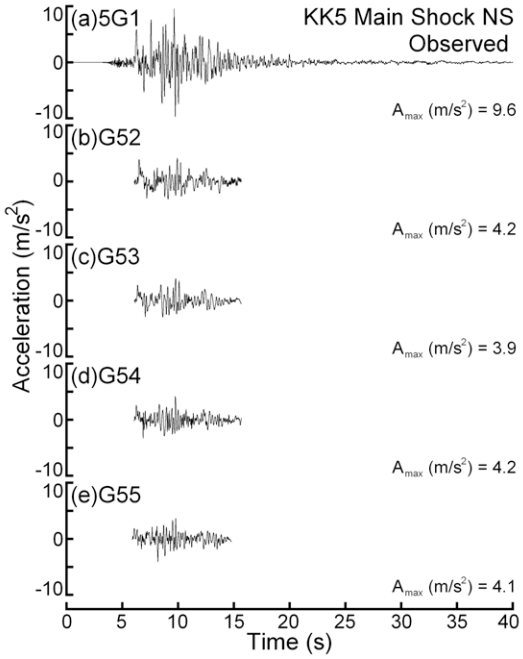

Figure 3(b) NS Acceleration Time Histories Recorded with Unit 5 Array (KK5)

the pen-writing records were digitized only for duration of about 10 s.

The acceleration response at the Service Hall array during the main shock was de-amplified toward the ground surface, with a peak value decreasing from 4.3 m/s^2 at a depth of 250 m to 3.5 m/s^2 near the ground surface, losing their short period component. This contrasts well with the remaining data sets including the main shock response at Unit 5, where the peak acceleration tends to increase toward the ground surface, without losing short period motions. This suggests that the difference in dynamic soil properties between the two sites may have led to the different site response observed during the earthquakes.

3. INVERSION USING GENETIC ALGORITHMS

Dynamic soil properties were back-calculated for the deposits of the two sites at the Kashiwazaki-Kariwa nuclear power plant based on the strong motion downhole array recordings during the 2007 Niigata-ken Chuetsu-oki earthquakes. The goal of this inversion is to find a soil layer model that minimizes the misfit between observed and computed Fourier amplitudes and phase angles between any of the two depths in an array defined as:

$$F = \sum_{i=1}^{K-1}\sum_{j=i+1}^{K}\int_{f_1}^{f_2} w^2\left\{\log_{10}(A_{o_{ij}}(f)) - \log_{10}(A_{c_{ij}}(f))\right\}^2 df + \alpha\sum_{i=1}^{K-1}\sum_{j=i+1}^{K}\int_{f_1}^{f_2} w^2\left\{P_{o_{ij}}(f) - P_{c_{ij}}(f)\right\}^2 df \quad (1)$$

in which A_o, A_c, P_o and P_c are the observed and computed Fourier amplitude ratios and phase angles between the i-th and j-th accelerometers in the array, K is the number of accelerometers at different depths, f_1 and f_2 are the minimum and maximum frequencies to be considered, w is a weighting factor defined as 1/f, and α is a constant.

It is assumed that A_c in the above equation be determined with a one-dimensional equivalent-linear response analysis of a deposit subjected to a vertically incident SH waves. The damping ratios of the deposit are assumed to be dependent on the Fourier amplitude of shear strain in the frequency domain (e.g., Sugito et al, 1993), which is an extended version of SHAKE (Schnabel et al, 1972) to improve its over-damping nature in the short period range during strong shaking. It is also assumed that the target soil deposit consists of N sub-layers including the bottom half space, each characterized by the mass density, thickness, equivalent shear wave velocity, and the damping ratio in the frequency domain defined as:

$$h(f)=h_{min}+(h_{max}-h_{min})(\gamma_{eff}(f)/\gamma_{ref})/(1+\gamma_{eff}(f)/\gamma_{ref}) \quad (2)$$

$$\gamma_{eff}(f) = 0.8\gamma_{max}\cdot\Gamma(f)/\Gamma_{max} \quad (3)$$

in which h_{min} and h_{max} are the minimum and maximum damping ratios; γ_{ref}, γ_{max}, $\gamma_{eff}(f)$, $\Gamma(f)$ and Γ_{max} are the reference shear strain, maximum shear strain in the time domain, effective shear strain for a given frequency *f*, Fourier amplitude of shear strain at a given *f*, and the maximum Fourier amplitude of shear strain in the frequency domain, respectively. Thus, once knowing all the soil properties in the deposit, A_c and P_c in Eq. (1) can be determined, by an iterative process until h(*f*) becomes compatible with Fourier amplitude of shear strain.

Adopted in the optimization using Eq. (1) is genetic algorithm (GA; Goldberg, 1989, Kobayashi et al., 1999). Four parameters including the equivalent shear wave velocity, minimum and maximum damping ratios and reference shear strain of each sub-layer are then sought with other parameters such as the thickness and mass density being predetermined, together with N=15 or 14, I=4 or 5, T=81.92 s, f_{max}=25 or 5 Hz, f_{min}=0.2 Hz, and a=0.10.

In the GA space, an 8-bit Gray coded integer is used for each of the unknown parameters. This leads to a 4x8x(N-1)-bit integer (chromosome) for an individual soil layer model consisting of N sub-layers with four unknown parameters each. An initial population of 200 soil layer models is generated randomly, covering the range of possible solutions, and the succeeding generation of the same population is reproduced until the 500th generation. The parameter search ranges are 0-5% for h_{min}, 15-40% for h_{max}, 10^{-4}-10^{-2} for γ_{ref} and (0.05-0.5)V_{so}-(0.7-1.2)V_{so} for V_s.

A roulette wheel-selection is used to choose and mate a pair or the new generation based on the fitness of each individual soil layer model defined by 1/F, with a crossover rate of 0.7 and a mutation rate of 0.02. The soil layer model having the best fitness in the final generation is assumed to be the solution for one trial. A total of ten trials were made for each set of the array data observed during the main shock and the two aftershocks L and S.

4. DYNAMIC SOIL PROPERTIES FROM INVERSION

Figures 4 and 5 compare the Fourier amplitude ratios computed for the back-calculated soil layer models having the best fitness with those of the observed records for the aftershock L and the main shock. A good agreement exists between the observed and computed amplitude ratios, indicating that the back-calculated soil profiles are reasonably reliable.

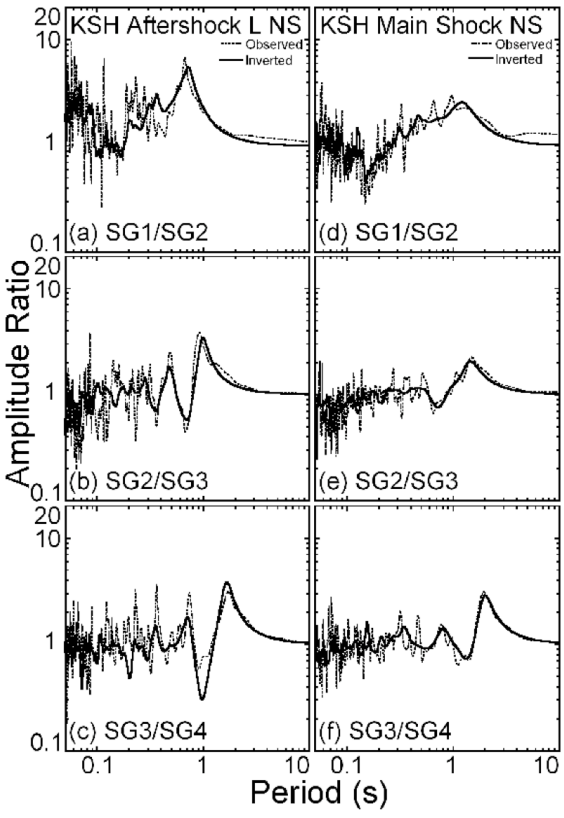

Figure 4 Observed and Computed Amplitude Ratios during Aftershock L and Main Shock at Service Hall Array

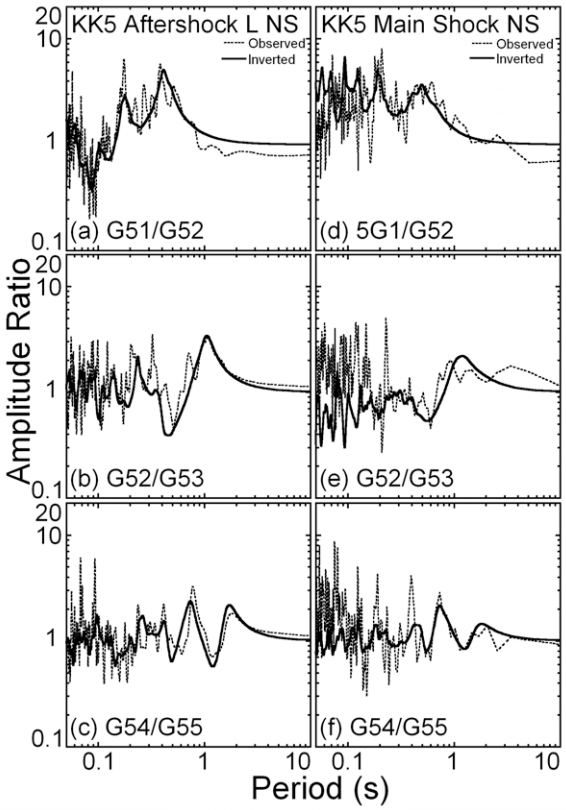

Figure 5 Observed and Computed Amplitude Ratios during Aftershock L and Main Shock at Unit 5 Array

Figure 6 shows the distribution of back-calculated equivalent shear wave velocity with depth for the three events compared with an available V_s profile determined by PS logging. The estimated shear wave velocities at depths smaller than about 70 m at the Service Hall are significantly smaller in the main shock than in either of the two aftershocks. In contrast, those at deeper depths at the Service Hall as well as most of the layers at Unit 5 during the three events are almost identical. The back-calculated shear wave velocities are generally consistent with the

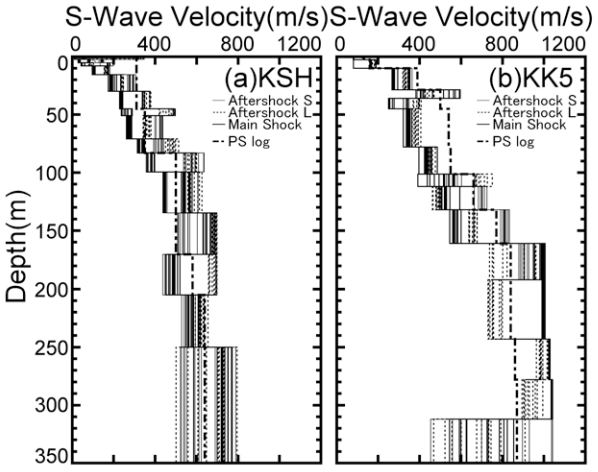

Figure 6 Observed and Back-calculated Shear Wave Velocity Profiles at Two Sites

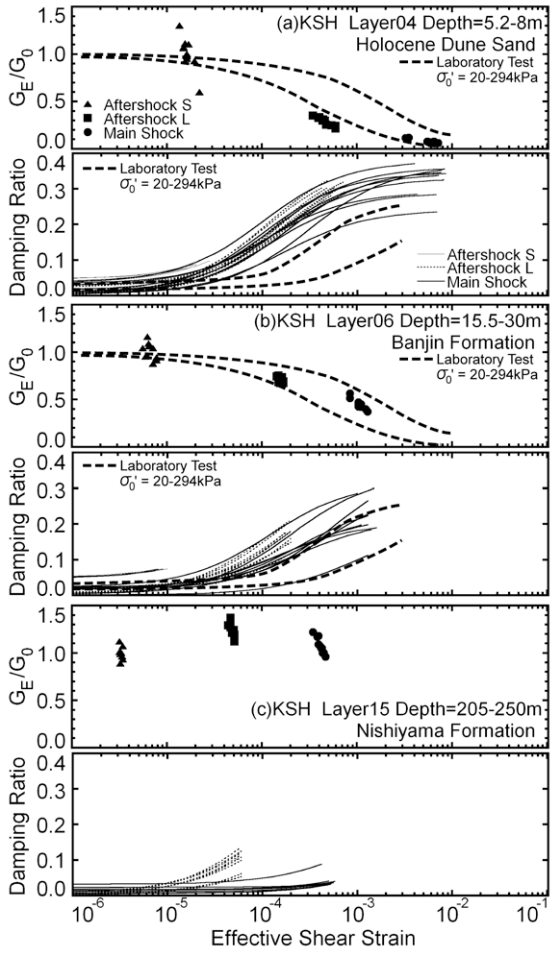

Figure 7 Back-calculated Dynamic Soil Properties at Service Hall Compared with Laboratory Test Results

available shear wave velocity profile, except for the shallow depths where even the back-calculated V_s for the aftershock S are significantly smaller than the available V_s values. This poses a question about the accuracy of the available V_s profile at the shallow depths.

Figures 7 and 8 show the back-calculated strain-dependent shear modulus and damping ratios of the two sites during the three earthquakes. The shear modulus has been normalized with respect to the elastic shear modulus estimated using $G_o = \rho V_s^2$ in which V_s is the average of the back-calculated values for the aftershock S. The shear modulus ratios of the sand dune deposits at the Service Hall as well as the Yasuda Formation at Unit 5 decrease to 0.05-0.5 and their damping ratios increase to about 20-35% with shear strains up to 2×10^{-3} - 3×10^{-2} during the main shock. Also shown in the figures are the laboratory test data for sand tested under confining pressures (Kokusho, 1980) similar to those of the dune sands. The back-calculated shear modulus ratios are consistent with those of the previous study but the back-calculated damping ratios are slightly higher than those of the previous study. The back-calculated shear modulus ratios of the Pliocene Nishiyama and Shiiya Formations are about 1.0 and do not

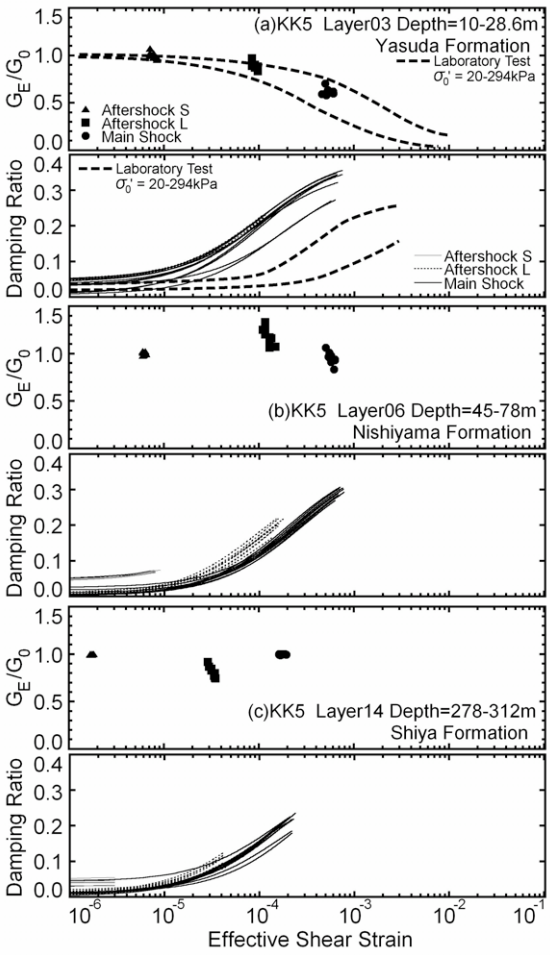

Figure 8 Back-calculated Dynamic Soil Properties at Unit 5 Compared with Laboratory Test Results

show any significant nonlinear behavior irrespective of the level of ground shaking but the back-calculated damping ratios of those formations at Unit 5 vary depending on shear strain and are significantly higher than expected. It is believed that the different dynamic soil behavior between the two sites may have led to the strikingly different site amplification between the two sites during the main shock.

5. CONCLUSIONS

Dynamic soil properties are back-calculated using the strong motion downhole array recordings at the Kashiwazaki-Kariwa nuclear power plant during the 2007 Niigata-ken Chuetsu-oki earthquakes. The back-analysis has shown the following conclusions:

(1) The surface layer at the Service Hall consisting of Holocene and Pleistocene dune sands showed strong nonlinear behavior during the main shock, with the underlying Pliocene Nishiyama Formation remaining elastic.

(2) The Pliocene Yasuda Formation that occurs near the ground surface at the Unit 5 as well as the underlying Nishiyama and Shiiya Formations also remained almost elastic, but had higher damping ratios.

(3) The different dynamic soil behavior between the two sites could have led to completely different site amplification between the two arrays during the main shock.

ACKNOWLEDGEMENTS

The strong motion array records and geological and geophysical logs at the Service Hall of the Kashiwazaki-Kariwa nuclear power plant, used in this study, were provided by Tokyo Electric Power Company (TEPCO 2007a and 2007b).

REFERENCES

Goldberg, D. E. 1989. Genetic Algorithms in Search, Optimization and Machine Learning, *Addison-Wesley Publishing Company, Inc.*, 412pp., 1989.

Kobayashi, K., Kyuke, H., Uetake, T., Mashimo, M., and Kobayashi, H. 1999. Estimation of Q value for soil layers by simultaneous inversion of transfer functions at many sites Part 3, Summaries of Technical Papers of Annual meeting, Architectural institute of Japan, B-2, 255-256 (in Japanese).

Kokusho, T. 1980. cyclic triaxial test of dynamic soil properties for wide strain range, Soils and Foundations, Vol. 20, No. 2, 45-60.

Schnabel, P. B., Lysmer, J. and Seed, H. B. 1972. SHAKE-A Computer Program for Earthquake Response Analysis of Horizontally Layered Sites, EERC Report, No.72-12.

Sugito, M., Goda, H., Masuda, T. and Etsunada, K. 1993. Equi-linearlized method with frequency-dependent shear modulus and damping, *Proceedings of the 28th Japan National Conference on Soil Mechanics and Foundation Engineering*, 1129-1132 (in Japanese).

Tanaka S., Mashimo, M., Yuzawa, Y., Nakajima, Y., Takahashi, H., and Kudo, K. 2008. Strong motion during the 2007 Niigata-Chuetsu-oki earthquake at down-hole sites in the Kashiwazaki-Kariwa nuclear power station-Digitizing the pen-writing monitoring-record and estimation of strong motions at depths-, Journal of JAEE, Vol. 8, No. 3, pp. 63-78.

TEPCO. 2007a. Report on analysis of observed records at Kashiwazaki-Kariwa Nuclear Power Plant during the Niigata-Chuetsu-Oki earthquake 2007.

TEPCO. 2007b. Acceleration time histories at Kashiwazaki-Kariwa nuclear power plant during the 2007 Niigata-ken Chuetsu-oki earthquakes, Main shock at 10:13 a.m. on July 16, 2007, CD-ROM.

TEPCO. 2007c. Acceleration time histories at Kashiwazaki-Kariwa nuclear power plant during the 2007 Niigata-ken Chuetsu-oki earthquakes, 6 aftershocks, CD-ROM.

Sixth International Conference on Urban Earthquake Engineering
March 3-4, 2009, Tokyo Institute of Technology, Tokyo, Japan

MITIGATION OF GEOTECHNICAL SEISMIC DAMAGE IN SUBURBAN RESIDENTIAL AREA

Suguru Yamada[1], Ikuo Towhata[2] and Ryouhei Tanaka[3]

1) Assistant Professor, Department of Civil Engineering, University of Tokyo, Japan
2) Professor, Department of Civil Engineering, University of Tokyo, Japan
3) Graduate Student, Department of Civil Engineering, University of Tokyo, Japan
suguru@geot.t.u-tokyo.ac.jp, towhata@geot.t.u-tokyo.ac.jp, rtanaka@geot.t.u-tokyo.ac.jp

Abstract: Geotechnical damages of the residential developments caused by earthquakes lead to house collapses which have serious influence on the civic life for several years. A large number of seismic damages of residential lands were reported at the recent large earthquake events, and most of them were caused in the residential developments. It has been pointed out that a lot of damage to residential developments is due to the use of fill which did not have the organic material removed from surface of base slope. This paper describes results obtained from shaking table tests that aimed to examine the seismic behaviour of a fill placed on a remaining slope surface soil, and to develop appropriate seismic reinforcements for residential fills. As a result, it was found that an ambitious reinforcement, which should is placed in a base slope, is needed to stabilize the fill having a residual surface soil, because the backfill soil may otherwise slide down as a block along the slope.

1. INTRODUCTION

Many residential developments have been constructed in suburban hilly areas by filling soil upon natural slopes. These residential developments suffered from significant damages frequently during past earthquakes. Hence, development of mitigation of seismic damages is important. However, since a residential land is a personal property, the expenses for the seismic reinforcements must be borne by the landlord. Currently, the costs of existing reinforcements for the fill are extremely high for the personal expense. Thus, the number of personal residential development which has been reinforced against earthquakes is extremely small in comparison with that of the public earth structures. Therefore, it is necessary to develop earthquake-resistance techniques with lower cost that should be inexpensive enough for personal expense.

On the other hand, fills situated upon natural slope with an organic soil layer on its surface often collapse when subjected to strong seismic shaking. According to the current design code of the residential development, an existing surface soil must be removed before filling soil because of its low shear strength. However, there are a large number of small fills situated on slopes with residual surface soil constructed several decades ago as a residence. In order to develop an effective, economical aseismic technique for small residential developments, it is necessary to understand the seismic behaviour of fills situated upon residual surface soil. In the present study, a series of shaking table tests were carried out on model grounds of small residential fills. The effectiveness of the seismic reinforcements of a fill on the slope was examined.

2. EXPERIMENTAL METHOD

2.1 Model Ground

Figure 1 shows the configuration and material of the model ground used in the present study. A model slope and a model retaining wall of "L" shape were placed in an acrylic box which was firmly fastened to the shaking table. The size of acrylic box was 60 cm in height, 255 cm in length and 40 cm in depth. The base slope was made of a blockboard with the depth of 30 cm and 10 degrees in angle. The model retaining wall was also made of blockboard with height of 21.5 cm, 38 cm in depth and 7 cm in foot length. The gap between the acrylic box and model retaining wall was filled by a sponge to prevent backfill soil from leaking. Toyoura sand (e_{max}=0.98, e_{min}=0.61, Gs=2.64) in dry condition was employed for making both the base ground and the fill. The base ground was made by the tamping method with 70% relative density. The fill was made with the relative density of 50% by air pluviation. The model slip plane was made by cutting a plastic sheet into chips and laying them on the model slope to reproduce a weak residual surface soil.

Two kinds of seismic reinforcements, which were ground anchorage and nailing, were studied in the experiments. Schematic diagrams of the model anchorage and the model nailing are shown in Fig.2 and Fig.3, respectively. A kite string of 16cm in length was used as a model anchor. The string was connected to the model retaining wall and embedded in the base slope to reproduce a state where a retaining wall and a base slope were connected with each other. For the model nailing, the silicon resin was glued on the kite string, which was 23 cm in length, in order to increase the skin friction overall the string.

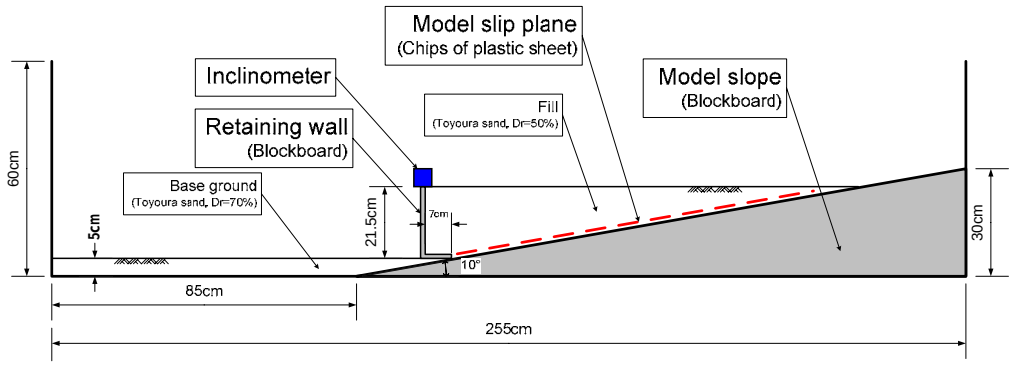

Figure 1: Model ground

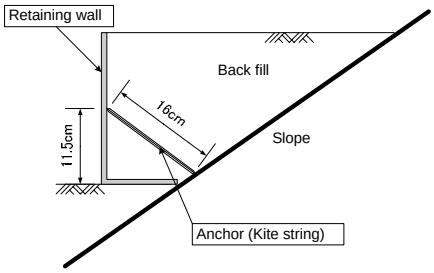

Figure 2: Model anchor

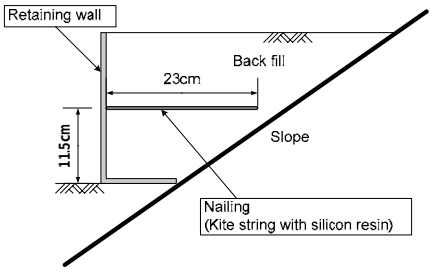

Figure 3: Model nailing

Table 1: Experimental conditions

No	Reinforcement	Model slip plane
1	Unreinforced	Absent
2	Unreinforced	Used
3	Nailing (2)	Absent
4	Nailing (8)	Absent
5	Nailing (8)	Used
6	Anchor (8)	Absent
7	Anchor (2)	Used

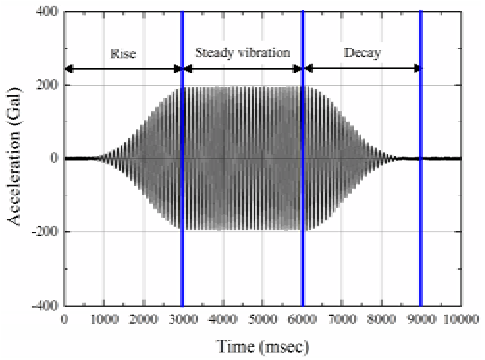

Figure 4: Time history of input acceleration

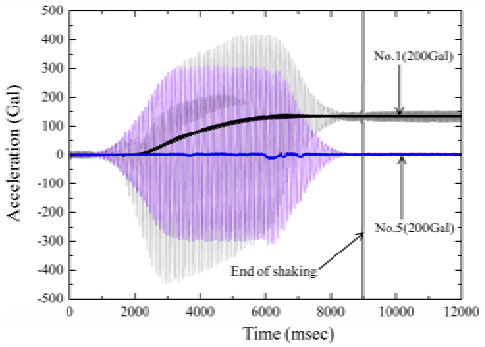

Figure 5: Response acceleration at top of retaining wall

2.2 Test Conditions and Procedures

Seven shaking table tests were performed with different experimental conditions as shown in Table 1; i.e., the reinforcement type, the extent of reinforcement and the slope surface condition with or without a plastic sheet. The number in the parenthesis in Table 1 designates the number of reinforcement in the corresponding experiment.

In all experiment cases, the model grounds were shaken by acceleration of 100, 200, 300, 400 and 500 Gal for 9 seconds. Fig. 4 illustrates an example of the input acceleration which was recorded by an accelerometer installed on the shaking table. The input acceleration was increased to the target acceleration in 3 seconds after the beginning of shaking, and was kept constant for the next 3 seconds, followed by decay in the last 3 seconds. The horizontal displacement, D_H, of the model retaining and the settlement of the fill were recorded at the end of each shaking. D_H was defined as the horizontal displacement at the top edge of the model retaining wall, which was obtained by reading the value of the scale of a ruler. The tilting angle of the model retaining wall, θ, was obtained by reading the static (gravity) offset of an accelerometer record at the top. Fig. 5 shows examples of the response acceleration at the top of the model retaining wall. The solid curves in the figure indicate the average trends. The constant acceleration occurred immediately after the end of shaking. This constant acceleration was employed for the calculation of the wall tilting angle, θ.

D_H was divided into two components which were due to sliding and tilting of the model wall. The tilting component of the horizontal displacement of the model retaining wall, D_{HI}, was obtained from simple calculation using θ and the length of the model wall; 21.5 $cm \sin\theta$. Then,

the sliding component of the horizontal displacement of the model retaining wall, D_{HS}, was obtained by subtracting D_{HI} from D_H. The magnitude of subsidence of the fill was measured by using a ruler at 0, 10, 20, 30, 40, 50, 60 and 70cm from the model retaining wall. It should be noted that these recorded values were cumulative values, because a stronger acceleration was applied after shaking with weaker intensity.

3. EXPERIMENTAL RESULTS

Figure 6 shows the relationships between the horizontal displacements of the model retaining wall, D_H, and the input acceleration for all experiments. The value of D_H is the sum of D_{HS} and D_{HI}, as described in the previous chapter. The solid symbols in Fig. 6 show the results when the model slip plane was installed at the base.

Results of experiments on an unreinforced retaining wall (No.1 and No.2) demonstrate that large horizontal deformation occurred under more than 200 Gal of acceleration, regardless of the use of the model slip plane. However, No.1 and No.2 show different D_H at all the accelerations, because D_H of No.1 at 100 and 200 Gal was small due to tilting of the model retaining wall in the early stage of shaking. Since the increment of D_H under greater acceleration is similar in both No.1 and No.2, it is reasonable to state that there is no effect of the model slip plane on the horizontal displacement of the unreinforced retaining wall.

In the experiments with anchors (No.6 and No.7), very small horizontal deformation was observed up to 400 Gal of acceleration with or without the model slip plane. Some increase of horizontal displacements was observed at 400 and 500 Gal of acceleration in No.7, because the kite string of anchorage was disconnected from the base (visual inspection the 500 Gal test). It was thus confirmed that the use of anchorage is very effective in seismic reinforcement of a fill that rests on a slope with residual surface soil.

As for nailing, different D_H values were observed (No.3, No.4 and No.5). Test No.4 shows minor D_H in all the acceleration range while that of No.2 shows considerable D_H at 300 Gal or more. This suggests that nail reinforcement is as effective as anchorage when the number of nailing is sufficient. In other words, it is possible to adjust the extent of seismic reinforcement in accordance with the safety requirement of the landlord. Moreover, considerable D_H occurred in No.5 test in spite of eight nails. Thus, nailing is not effective when a fill is underlain by a weak slip plane.

In order to study the seismic behaviour of fills with different types of reinforcement, the horizontal deformation of the model retaining wall was examined by dividing it into the sliding component, D_{HS}, and the tilting component, D_{HI}. The variation of D_{HS} and D_{HI} along with the acceleration are shown in Figs. 7 and 8, respectively. It can be stated that approximately equal D_{HS} occurred when unreinforced retaining wall was used (No.1 and No.2). However, No.2 shows smaller D_{HI} than No.1, which was caused by tilting of a model retaining wall in the early stage of shaking as mentioned above. In No.6 and No.7 where anchors were applied, extremely small D_{HS} and D_{HI} were observed over

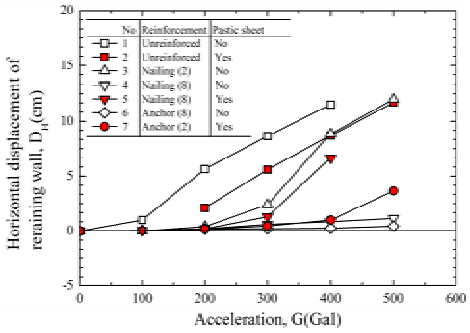

Figure 6: Relationships between horizontal displacement atop the retaining wall and intensity of base shaking.

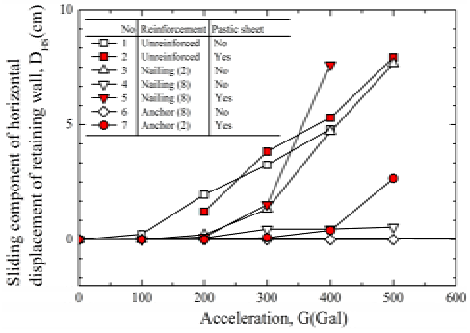

Figure 7: Sliding component of horizontal displacement atop the retaining wall changing with intensity of base shaking.

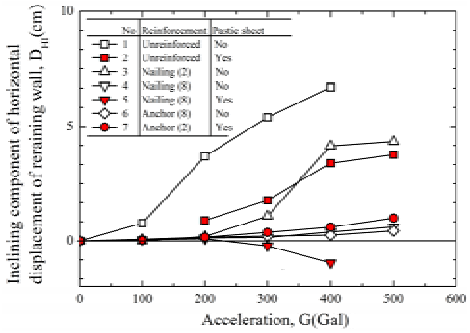

Figure 8: Inclining component of horizontal displacement atop the retaining wall changing with intensity of base shaking.

the entire acceleration range except for No.7 with 500 Gal excitation.

D_{HS} and D_{HI} similar to that of No.6 and No.7 were observed in No.4 with 8 nails and without a model slip plane. This result shows that seismic reinforcing effect comparable to anchorage is achieved when many nailing rods are installed. On the other hand, No.5 shows much larger D_{HS} than No.4 and negative D_{HI}. It is believed that this is because the backfill soil moved down as a single block along the base model slip plane.

Figure 9 shows the distribution of backfill subidence caused by 300 Gal and 400 Gal excitation. The magnitude of subsidence was measured on the surface of the fill at every 10 cm from the model retaining wall. In general, subsidence is more significant when horizontal displacement of the model retaining wall is greater. For example, the magnitude

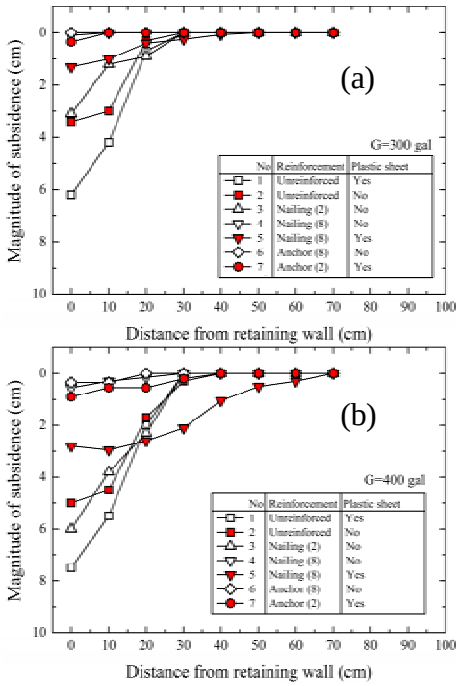

Figure 9: Distributions of magnitudes of the subsidence of fill against distance from retaining wall; (a) 300 Gal and (b) 400 Gal

of subsidence is greatest in the experiment performed without reinforcement (No.1), and is least when anchors were installed (No.6); see Fig.10. In addition, it can be seen that subsidence occurred within 30 cm from the model retaining wall except for No.5.

In the case of No.5, eight nails and a model slip plane were installed. It is observed that when the magnitude of subsidence of the fill decreased, the range of subsidence increased. Fig.11 (a) and (b) demonstrate deformation of model grounds after 400-Gal shaking in No.2 and No.5. The range to which subsidence extended and the location of a shear failure plane are therein illustrated. It was observed in No.5 that shear failure appeared at a far place from the model retaining wall and the backfill soil moved down as a soil mass. In the case of No.2, on the contrary, the slip failure plane appeared at 20cm from the model retaining wall.

4. CONCLUSIONS

A series of shaking table tests were conducted on model grounds in which retaining wall supported a backfill resting on a slope. The following conclusions were drawn on the basis of the experimental investigation.

1. The anchorage reinforcement is effective against the earthquake, regardless of the existence of a residual surface soil on the base slope.
2. The backfill soil moves down along the base slope when there is a residual surface soil on the base slope. In this case, it is difficult to inhibit the horizontal displacement of the retaining wall and the subsidence of the fill without connecting the retaining wall to the base slope by anchors or using a large number of nailing rods.
3. The reinforcement by means of many nailing rods decreases the magnitude of subsidence of the fill. However, the range of subsidence extends to farther places.
4. Consequently the deformation of the fill can be controlled by applying an appropriate number of nailing rods. Hence, it may be possible to develop the seismic reinforcement for a personal residential development that can control the deformation of the fill, i.e. the displacement of the retaining wall or subsidence of the fill in accordance with the safety requirement of a landlord.

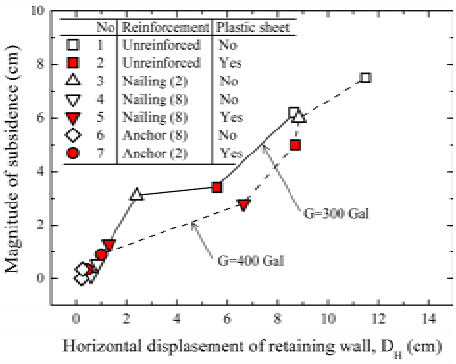

Figure 10: Relations between magnitudes of subsidence at 0 cm from retaining wall and horizontal displacement of retaining wall.

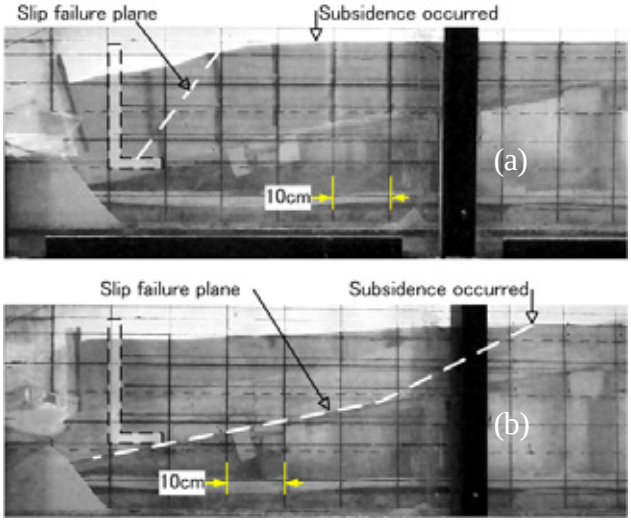

Figure 11: Slip failure plane after shaking with 400gal; (a) No.2 and (b) No.5

References:

Asada, A. (1982), "A method for estimating and increasing the stability of artificial housing ground during earthquake," *Soils and Foundations*, Vol.22, No.4, 192-202. (in Japanese)

Asada, A. (2005), "Assessment of seismic risk in residential areas under future Miyagi-ken-Oki earthquake and its mitigation, Draft report.

JGS (2007), "Guideline for Aseismic Investigation and Mitigation for Residential Developments," Research committee on aseismic investigation and mitigation for residential developments, Jpn. Geotech. Soc. (in Japanese)

Sixth International Conference on Urban Earthquake Engineering
March 3-4, 2009, Tokyo Institute of Technology, Tokyo, Japan

UNCERTAINTY PROPAGATION IN GEOTECHNICAL EARTHQUAKE ENGINEERING

Robb Eric S. Moss[1)]

1) Asst. Prof. of Geotechnical, Earthquake, and Risk Engineering, Cal Poly San Luis Obispo, CA
rmoss@calpoly.edu

Abstract: This paper describes recent advances in evaluating, quantifying, and propagating various forms of uncertainty in geotechnical earthquake engineering problems. Important developments in the fields of liquefaction engineering, dynamic slope stability, engineering seismology, and lifeline engineering are discussed. The benefits gained through proper treatment of uncertainty include; a well defined measure of the most likely engineering results, a well defined estimate of extreme results, a probability of likelihood ascribed to different realizations, and a mathematical format that lends to performance-based engineering assessment. This paper is by no means comprehensive but highlights some recent studies that contribute to improved probabilistic methodology in the realm of geotechnical earthquake engineering.

1. INTRODUCTION

Uncertainty in its various forms is an unavoidable component of engineering analysis. Geotechnical earthquake engineering is ripe with uncertainty primarily because of the inherent variability of geotechnical materials and the stochastic nature of earthquake ground motions. Capturing and translating uncertainty through any engineering analysis is necessary for resolving the mean or median response with any confidence, and for estimating the dispersion of possible results. Geotechnical earthquake engineering is a pseudo-empirical discipline where theory dictates the trends of the analytical models but data drives the shape, coefficients, and values of the numerical results. A model used in geotechnical earthquake engineering is only as good as its accuracy with respect to the empirical data.

Uncertainty can be conceptually lumped into two groups; the inherent variability of the underlying phenomena, and uncertainty as a function of modeling, measuring, and other engineering machinations that are not part of the phenomena. These are termed aleatory and epistemic uncertainty respectively. These two groups of uncertainty can have a strong influence on the outcome of some engineering analysis and are often not easily separable. Recent advances in probabilistic methods have lead to improved uncertainty analysis in geotechnical earthquake engineering and related fields. This paper describes a select (and by no means comprehensive) group of studies which the author feels demonstrates improvements in how uncertainty is quantified and propagated through the analysis thereby providing a broader understanding of the problem at hand and the desired outcome. The select group of studies is biased towards the author's work but also draws on work from others that strive for the same goal of propagating uncertainty for improved understanding and accuracy.

2. METHODS OF UNCERTAINTY PROPAGATION

The basis for error propagation is founded in the fundamentals of statistics and probability. Statistics is the means of quantifying past occurrences and probability the means of predicting future occurrences. In civil engineering early applications of statistics and probability were well described by Benjamin and Cornell (1970) and Ang and Tang (1975). Quantifying uncertainty can be accomplished through various statistical means if sufficient data exists, or by ascribing a probability distribution based on theory, assumptions, and/or expert solicitation. Quantifying engineering uncertainty using all forms of available information subscribes to the Bayesian philosophy of probability and uncertainty.

Propagating uncertainty involves "pushing" the uncertainty through the model, equation, or analysis to arrive at final results representative of the formulation and the contributing uncertainty. This can be accomplished with exact methods if certain conditions are met (e.g. sum of normally distributed random variables), approximate methods that can often give reasonable results (i.e. first order second moment approximation), and simulation methods (e.g. Monte Carlo simulation). Reliability analysis is a special case of error propagation where the mathematical formulation is defined by a relationship between load and resistance with the goal of characterizing failure. The relative contribution of epistemic and aleatory uncertainty in uncertainty propagation can be complex and there is little agreement as to how best separate the two (Helton 2004). But the methods of propagating uncertainty are well established and can be readily applied to most geotechnical earthquake engineering problems. The following are selected studies that demonstrate useful applications of uncertainty propagation.

2. LIQUEFACTION ENGINEERING

Liquefaction engineering starts with the assessment of the likelihood of liquefaction triggering for a particular soil deposit. Field data drives liquefaction analysis because lab data in most cases fails to capture critical *in situ* soil conditions. There exists uncertainty in the input variables on both the load and the resistance side of the phenomenon. Recent work by Cetin et al. (2004) and Moss et al. (2006) focused effort on quantifying the uncertainty in the earthquake loading, in the form of the cyclic stress ratio (CSR), and the dynamic soil resistance, in the form of corrected resistance values from the SPT and CPT. The results show (Figure 1) the probabilistic relationship between load and resistance that provides a means of making a performance-based engineering decision of the likelihood of liquefaction triggering for a particular soil deposit. This probabilistic relationship is a byproduct of quantifying the uncertainty of each input variable and then propagating that uncertainty through the mathematical interaction of the variables in a reliability format.

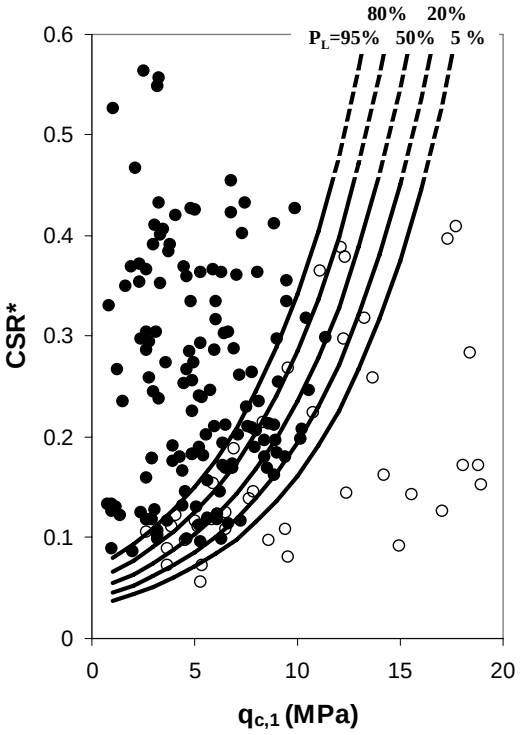

Figure 1 Liquefaction triggering curves for the CPT (from Moss et al. 2006). The x-axis is a normalized cone tip resistance and the y-axis a normalized earthquake load. Probability of liquefaction curves from 5% to 95% are shown.

Cetin et al. (2004) and Moss et al. (2006) capture and propagate the uncertainty from the back-analysis of a liquefaction case history database using FORM (first order reliability method), SORM (second order reliability method), and MC (Monte Carlo) simulations. Work by Fang et al. (2006) focuses on including the uncertainty in the forward-analysis of liquefaction triggering using FORM. The work by Fang et al. assesses the uncertainty from the site specific aspects of loading and resistance, providing a probabilistic forward-analysis that combines with the uncertainty from the back-analyzed case histories to give a comprehensive probabilistic approach.

The probability of liquefaction at a site is conditional on the probability of a particular level of ground shaking being exceeded. Kramer and Mayfield (2007) present a study that integrates the probability of ground shaking with the probability of liquefaction which results in an annualized return period of liquefaction. The return period of liquefaction provides a more consistent measure of liquefaction potential when comparing sites from different seismo-tectonic regions. This work lends to more uniform liquefaction hazard maps on a regional and national scale.

One issue that is often overlooked is the uncertainty that creeps into an analysis when converting between *in situ* index tests (e.g. CPT to SPT). Moss and Hollenback (2009) discuss this issue with respect to post-liquefaction effective stress normalized undrained strength (s_u/σ_{vo}'), commonly called liquefied residual strength or mobilized shear strength ratio. When converting from one index test to another, the measurement uncertainty from the index test combine with the statistical uncertainty between the correlated index tests to produce a compounded uncertainty. This can result in ambiguous and inaccurate estimates of the median converted value as well as large dispersion. Even in the simple process of converting from one index test value to another, the propagation of uncertainty should be performed to evaluate the impact of this uncertainty on the final results.

3. DYNAMIC SLOPE STABILITY

Dynamic slope stability is a concern for natural and man-made slopes. The work by Bray and Travasarou (2007) provides an improved simplified slope displacement model that captures the uncertainty associated with the seismic loading and the dynamic slope resistance. The bulk of the uncertainty in dynamic slope stability is due to the inherent variability of the input ground motion. Bray and Travasarou (2007) statistically account for this variability by evaluating almost 700 ground motions and corresponding displacements using a nonlinear fully coupled stick-slip sliding block model. The resulting slope displacement model can be used in a fully probabilistic manner for predicting the distribution of anticipated slope displacements in a hazard analysis.

A novel aspects of this research is the use of mixed random variables (discrete and continuous) to separate slopes that exhibit small displacements that would be of no engineering concern from slopes that exhibit displacements that warrant engineering attention. Figure 2 shows the distribution of the mixed random variable used to model this dual-mode displacement response. A mixed random variable is useful for removing the bias of slopes that indicate negligible engineering displacements.

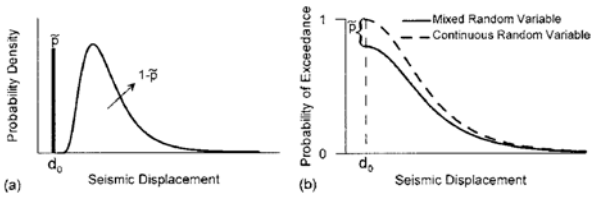

Figure 2 Mixed random variable used for seismic slope displacement analysis; (a) probability density function and (b) probability of exceedance for mixed and continuous random variable (from Bray and Travasarou, 2007).

4. ENGINEERING SEISMOLOGY

Geotechnical earthquake engineering projects rely on engineering seismology models to define the loading for design. Many sources of uncertainty contribute to the overall uncertainty for a particular measure of seismic loading. Probabilistic seismic hazard analysis (PSHA) provides a means of combining the most readily quantifiable sources of uncertainty into a comprehensive probabilistic measure of seismic loading at a particular site. The dispersion of PSHA results however can be ill defined and there is much debate as to the scale and magnitude of the true dispersion. This is particularly important for long return period projects such as nuclear power plants where the project life is often in the 10,000 year range and uncertainty drives the upper bound values (Bommer et al. 2004). Several recent studies have delved into the source and impact of uncertainty in seismic loading and are discussed here.

Moss (2009) and Moss and Der Kiureghian (2006) evaluate the influence of parameter uncertainty on the variance of ground motion prediction equations. The focus of this work is primarily evaluating the influence of measurement uncertainty of V_{S30} (thirty meter shear wave velocity) on the resulting overall uncertainty of a ground motion prediction equation (defined by the standard deviation in natural log units). The measurement uncertainty in V_{S30} is quantified using existing blind and comparative studies in Moss (2008). This uncertainty is then propagated through the ground motion prediction equations using Bayesian regression as well as the approximate methods of Monte Carlo simulation and FOSM (first order second moment). Figure 3 shows a 10% reduction that can be achieved by evaluating the influence of V_{S30} measurement uncertainty on the overall uncertainty in a ground motion prediction equation.

Wang and Takada (2007) present an excellent paper using Bayesian updating to, in most cases, reduce the uncertainty of a site specific ground motion prediction by using new data near the site. This paper presents the mathematical methodology, closed-form solution using conjugate priors, and data-based example showing the utility. By updating a regional ground motion prediction equation using recent site specific recordings the authors achieved an appreciable reduction in the standard deviation thereby affording a better defined median ground motion for design purposes.

Atkinson (2006) presented an interesting study delving into the impact of site effects and travel path on the overall uncertainty of ground motion prediction equations. The argument made is that regression of a large database of ground motions from diverse regions that are questionably grouped together results in an artificially large dispersion. To control for site and travel path effects Atkinson looked at the dispersion of a single site that experienced multiple earthquakes. The results, based on the limited data set for this site, indicate that site effects alone contribute 10% of the uncertainty as measured by the standard deviation, and that travel path and site effects together can contribute 40% to the uncertainty. Controlling for site and travel path effects is not necessarily feasible in a predictive analysis but this study raises questions about a weak correlation between V_{S30} and the complexity of site effects, and binning strong motion data from diverse regions to define the dispersion. A large database of diverse motions will provide a stable median value and well defined trends, but dispersion may be more accurately estimated on a site specific basis if there exist enough recordings at the site, or on a region specific basis where the data is carefully binned to reflect the travel path and site effects consistent with the site of interest.

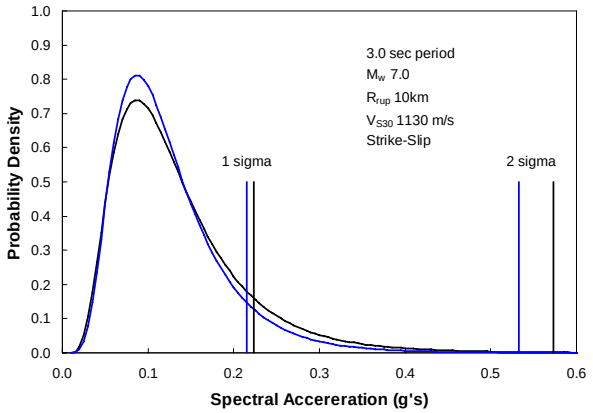

Figure 3 The influence of V_{S30} measurement uncertainty on ground motion prediction equation is most pronounced at the longer periods. Here the Chiou and Youngs (2008) ground motion prediction equation is used as the basis to demonstrate a 10% reduction in one standard deviation for the 3.0 second period spectral ordinate when V_{S30} uncertainty is properly accounted for within the regression procedure (from Moss 2009).

5. LEVEE/LIFELINE ENGINEERING

Engineering of lifelines presents interesting problems that are unique to spatially distributed man-made structures. With respect to geotechnical engineering there has been progress following the large consequences of the levee failures in New Orleans from Hurricane Katrina. Levee risk has been an ongoing concern in the Netherlands since catastrophic failures there in the 1950's. Probabilistic

methods are the obvious choice for assessing the failure potential of levees and levee systems however implementing uncertainty propagation for levee analysis and design has proven difficult. Static stability methods pertain to geotechnical earthquake engineering because static analysis is the starting point for dynamic analysis of levee systems in seismic parts of the world like Japan, China, and the western US.

The US Army Corp of Engineers commissioned as study for revising the methodology of levee analysis using risk and reliability concepts. Wolff (1994) developed approximate methods for levee analysis that are compatible with existing Corp deterministic methods, however these methods have not been adopted to date. Corp guidelines for seismic dam analysis (HQUSACE 1997) are more advanced than that for seismic levee analysis and provide a template for engineering issues that relate to both types of structures.

The current forefront of probabilistic levee analysis is driven by the levee systems in the California Bay Delta. In the Delta there are over 1000 km of waterways hemmed by poorly engineered and poorly maintenanced levees that protect land largely below sea level. To compound the problem there is a high likelihood of seismic activity in the vicinity that can load these levees dynamically. At risk are major transportation corridors, power transmission lines, high dollar agricultural fields, residential housing areas, metropolitan areas, and a water transmission system that delivers fresh water to over 20 million users in Central and Southern California. The author's research is focused on improving methods for quantifying risk and propagating uncertainty for the Delta levee system (Moss and Eller 2007). In this ongoing research, that is as yet unpublished, a number of novel concepts have been implemented in the realm of levee risk analysis. Some of these are listed below.

Spatial variability of soil properties is a reality for long linear engineered structures such as levees. To properly account for the influence of spatial variability on stability analysis a general relative variogram, GRV (Issaks and Srivastava 1989), is calculated for each levee reach using evenly spaced *in situ* data. The GRV determines the length of a levee reach by defining the distance needed to achieve a minimum statistical correlation, thereby ensuring the maximum statistical independence between levee reaches. The GRV is also compatible with, and includes in this study, point estimates of measurement uncertainty represented by the squared coefficient of variation (Figure 4).

The GRV of the foundation soils for a reach are constrained by the geomorphology and depositional environment of the soil, and the GRV of the levees are constrained by the composition material, construction methods, and level of maintenance. Spatial variability in other studies, if is accounted for at all, is treated as a fixed pseudo-probabilistic value with an ambiguous mathematical basis. It has been found that probability of failure calculations are highly sensitive to the reach length and a robustly defined reach length will provide a quantitative basis for eliminating this sensitivity.

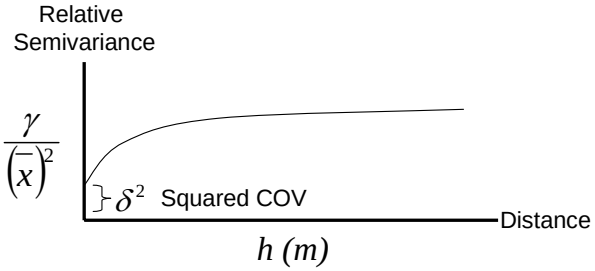

Figure 4 Conceptual diagram of exponential curve of a general relative variogram, GRV. The x-axis is the lag or distance. The y-axis is the semivariance divided by the squared mean of the spatial sample. The nugget or intercept value is the squared coefficient of variation, a point estimate of measurement uncertainty. The reach length where statistical correlation is minimized is at the sill or exponential plateau. Semivariance is calculated from SPT, CPT, and V_S measurements.

In following the lead of the Dutch (van Manen and Brinkhuis 2005) the calculation of risk, usually the product of the probability of failure and the consequences of failure in that order, is performed in reverse order setting the consequences first and then working through the failures modes that could result in the consequences. This is a subtle change but provides a consequences driven analysis that identifies all the possible failure modes that could result in a particular consequence. This results in a much more efficient means of computing the risk and focuses effort on the highest consequence scenarios.

The failure of a levee, regardless of the particular failure mode, is controlled by the weakest levee section along the length of the levee and the lowest resistance values within that levee section. In system reliability terms this is a series system with failure occurring within the weakest component. In observing past levee failures (e.g. 17th Street Canal failure as discussed in Seed et al., 2008) it has been found that the weakest levee section is often controlled by extreme low values in resistance, yet static and dynamic levee stability analyses are often performed using mean or median values of resistance. It is more appropriate to apply extreme value statistics to the resistance to better define the most probable location of the failure and the dispersion of the low values. A Type III smallest or Weibull distribution is used in this research to better define the lowest values in a particular weak levee section. The continuity or spatial extent of these extreme low values will be mapped by extrapolating the median trends of the levee or foundation GRV to the extreme values. As in the case of the variograms, the *in situ* data is used to define the statistics of the extreme values both in their point distributions and spatial continuity.

Time is a factor not just for the load variables (i.e. seasonal water loads or stochastic seismic loads) but also for resistance variables. Soil strength changes occur due to various geotechnical processes, and overall levee degradation occurs due to biological or maintenance factors.

The distributions of the resistance variables will be subjected to time alterations based on degradation/aggradation models of the altering effects. The probability of failure is calculated per levee reach throughout the Delta at a fixed point in time, then recalculated for each time increment progressively to capture the time rate effects of the altered resistance distributions.

This research on the risk analysis of the Bay Delta uses FORM (first order reliability method) and MC (Monte Carlo) simulations in a structural reliability formulation to calculate the component failure probabilities for each levee reach. The reverse risk modeling is performed using an event tree format with the consequences driving the analysis. A very important component of this work is the final calibration using existing failure case history data that provides a rough estimate of the time rate of failure and the general spatial distribution of failures. This bounds and provides a check on the reasonableness of the results. Calibration is performed ostensibly on the static (non-seismic) failure modes. Being that the static and dynamic resistance values are integrally linked, this then provides some means of bounding the dynamic failure modes.

6. CONCLUSIONS

A review of some recent research pertaining to liquefaction engineering, dynamic slope stability, engineering seismology, and levee/lifeline engineering has been presented in this paper. The thread that ties all this research together is the common goal of propagating uncertainty through the respective problems to determine how this uncertainty influences the results. Probabilistic methods for propagating uncertainty are coming of age and geotechnical earthquake engineering is the ideal field for these methods due of the large amount of uncertainty that exists in both the loading and resistance aspects of these problems. This review has been biased towards the author's work but effort was made to include important progress made by other researchers with similar interests. By quantifying and propagating uncertainty, as demonstrated in these types of earthquake engineering problems, more reliable engineering analysis and design can be accomplished.

References:

Ang, A. H.-S., and Tang, W. H. (1975). Probability Concepts in Engineering Planning and Design, Vol. 1., John Wiley and Sons, Inc.

Atkinson, G. M. (2006). "Single-Station Sigma." Bulletin of Seismological Society of America, 96(2), 446-455.

Benjamin, J., and Cornell, C. A. (1970). Probability, Statistics, and Decision for Civil Engineers, McGraw-Hill, New York.

Bommer, J. J., Abrahamson, N. A., Strasser, F. O., Pecker, A., Bard, P.-Y., Bungum, H., Cotton, F., Faeh, D., Sabetta, F., Scherbaum, F., and Struder, J. (2004). "The challenge of defining the upper limits on earthquake ground motions." Seismological Research Letters, 70(1), 82-95.

Bray, J. D., and Travasarou, T. (2007). "Simplified Procedure for Estimating Earthquake-Induced Deviatoric Slope Displacements." Journal of Geotechnical and Geoenvironmental Engineering, 133(4), 381-392.

Cetin, K. O., Seed, R. B., Der Kiureghian, A., Tokimatsu, K., Harder, L. F., Kayen, R. E., and Moss, R. E. S. (2004). "SPT-Based Probabilistic and Deterministic Assessment of Seismic Soil Liquefaction Potential." Journal of Geotechnical and Geoenvironmental Engineering, 130(12).

Chiou, B., and Youngs, R. R. (2008). "An NGA Model for the Average Horizontal Component of Peak Ground Motion and Response Spectra." Earthquake Spectra, 24(1), 173-215.

Fang, S. Y., Juang, C. H., and Tang, W. H. (2006). "A Probabilistic Model for Liquefaction Triggering Analysis using SPT." GeoShanghai 2006 ASCE.

Helton, J. C. (2004). "Alternative representations of epistemic uncertainty." Reliability Engineering & System Safety, 85, 1-10.

HQUSACE. (1997). "Dam Saftey Assurance Program." Engineer Regulation 1110-2-1155, Washington, D.C.

Issaks, E. H., and Srivastava, R. M. (1989). An Introduction to Applied Geostatistics, Oxford University Press.

Kramer, S. L., and Mayfield, R. T. (2007). "Return Period of Soil Liquefaction." Journal of Geotechnical and Geoenvironmental Engineering, 133(7), 802-813.

Moss, R. E. S. (2008). "Quantifying Measurement Uncertainty Associated with Thirty Meter Shear Wave Velocity (VS30)." Bulletin of Seismological Society of America, 98(3), 1399-1411.

Moss, R. E. S. (2009). "Reduced Uncertainty of Ground Motion Prediction Equations through Bayesian Variance Analysis." Pacific Earthquake Engineering Research Center, PEER, Report (in press)

Moss, R. E. S., and Der Kiureghian, A. (2006). "Incorporating Parameter Uncertainty into Attenuation Relationships." 8th U.S. National Conference on Earthquake EngineeringSan Francisco.

Moss, R. E. S., and Eller, J. M. (2007). "Estimating the Probability of Failure and Associated Risk of the California Bay Delta Levee System." GeoDenver, ASCE conf. proc..

Moss, R. E. S., and Hollenback, J. C. (2009). "Discussion of "Analyzing Liquefaction-Induced Lateral Spreads using Strength Ratios" by Scott M. Olsen and Cora I. Johnson. August 1, 2008 Vol. 134, No. 8, pp. 1035-1049." Journal of Geotechnical and Geoenvironmental Engineering, in press.

Moss, R. E. S., Seed, R. B., Kayen, R. E., Stewart, J. P., Der Kiureghian, A., and Cetin, K. O. (2006). "Probabilistic Seismic Soil Liquefaction Triggering Using the CPT." Journal of Geotechnical and Geoenvironmental Engineering, 132(8).

Seed, R. B., Bea, R. G., Athanasopoulos, A. G., Boutwell, G. P., Bray, J. D., Cheung, C., Cobos-Roa, D., Harder, L. F., Moss, R. E. S., Pestana, J. M., Riemer, M. F., Rogers, J. D., Storesund, R., Vera-Grunauer, X., and Wartman, J. (2008). "New Orleans and Hurricane Katrina. III: The 17th Street Drainage Canal." Journal of Geotechnical and Geoenvironmental Engineering, 134(5), 750-761.

van Manen, S. E., and Brinkhuis, M. (2005). "Quantitative flood risk assessment for Polders." Reliability Engineering & System Safety, 90, 229-237.

Wang, M., and Takada, T. (2007). "Bayesian updating for site-specific attenuation relation with limited number of data." ICASP10 Tokyo.

Wolff, T. F. (1994). "Evaluating the Reliability of Existing Levees." Report to U.S. Army Engineer Waterways Experiement Station, Geotechnical Laboratory, Vicksburg, MS

Sixth International Conference on Urban Earthquake Engineering
March 3-4, 2009, Tokyo Institute of Technology, Tokyo, Japan

3-D time-domain fast multipole BEM based on the convolution quadrature method for seismic analysis

Sohichi Hirose[1)] and Takahiro Saitoh[2)]

1) Professor, Department of mechanical and environmental informatics, Tokyo Institute of Technology, Japan
2) Assistant Professor, Department of nuclear power and energy safety engineering, University of Fukui, Japan
shirose@cv.titech.ac.jp, tsaito@taku.anc-d.fukui-u.ac.jp

Abstract: This paper presents a new time-domain fast multipole boundary element method (BEM) based on the convolution quadrature method (CQM) for 3-D seismic analysis. In this formulation, the convolution integrals of the time-domain boundary integral equation is numerically approximated by CQM. Moreover, the fast multipole method (FMM) is adapted to improve the computational efficiency for large size problems. First, the time-domain BEM formulation based on CQM is described for 3-D wave propagation. Next, a brief description on how to apply FMM to the time-domain BEM based on CQM is presented for 3-D scalar and elastic wave propagation. As numerical examples, 3-D scalar wave scattering by rigid spheres are solved to validate the proposed method.

1. INTRODUCTION

Seismic motions produced at an earthquake fault propagate in ground as elastic waves and sometimes cause tremendous destruction of buildings and infrastructures. Therefore, the understanding of elastic waves can help not only predict ground motions by earthquake but also reduce seismic damages.

Normally, a seismic problem can be solved by modeling the ground as an infinite or half-space. Since the boundary element method (BEM) is a suitable numerical approach for wave analysis in an infinite or half space domain, BEM has been used for many years for seismic analysis (Abe et al. 1993, Kataoka 1996). In general, transient problems can usually be solved for unknown time-dependent quantities by a direct time-domain BEM with a time stepping scheme. However, the use of direct time-domain BEM sometimes causes the instability of time stepping solutions. Moreover, the time-domain BEM needs much computational time and memory for large size problems.

To overcome these difficulties, a new time-domain boundary element method is developed for seismic analyses. In the formulation of the new time-domain BEM, the convolution quadrature method (CQM), first proposed by Lubich (1988) is applied to achieve the stability behavior in a time stepping scheme. The convolution integrals of the time-domain boundary integral equations are numerically approximated by the quadrature formulas, whose weights are computed using the Laplace transform of the fundamental solution and a linear multistep method. In addition, the fast multipole method (FMM) developed by Greengard and Rokhlin (1987) is utilized to improve the computational efficiency of the time-domain BEM.

As a first step for the development of a seismic wave simulator, in this paper, the new time-domain BEM formulation is presented with the focus on 3-D scalar wave propagation, which gives basic concept to understand the 3-D elastic wave propagation. As numerical examples, 3-D scattering problems by spherical scatterers subjected to a incident plane wave are implemented by the new time-domain BEM.

2. TIME-DOMAIN BEM BASED ON CQM FOR 3-D WAVE PROPAGATION

We consider a 3-D scalar wave scattering problem in an exterior domain D as shown in Figure 1. When the incident wave u^{in} hits the boundary surface S^c of the scatterer $\bar{D}$ and the ground surface S^f, scattered and reflected waves are generated by the interaction with the scatterer and the ground surface, respectively. Assuming the zero initial conditions, i.e., $u(\boldsymbol{x}, t = 0) = 0$ and $\partial u(\boldsymbol{x}, t = 0)/\partial t = 0$, the displacement field u satisfies the governing equation and boundary conditions as follows:

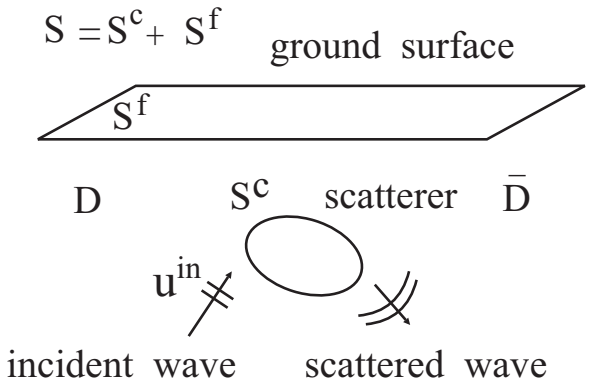

Figure 1 A 3-D analysis model.

$$\nabla^2 u(\boldsymbol{x},t) = \frac{1}{c^2}\frac{\partial^2 u(\boldsymbol{x},t)}{\partial t^2} \quad \text{in } D, \tag{1}$$

$$u(\boldsymbol{x},t) = \breve{u}(\boldsymbol{x},t) \quad \text{on } S_1,$$

$$q(\boldsymbol{x},t) = \frac{\partial u(\boldsymbol{x},t)}{\partial n} = \breve{q}(\boldsymbol{x},t) \quad \text{on } S_2, S_2 = S \backslash S_1 \tag{2}$$

where c is the wave velocity and $\partial/\partial n$ shows the differentiation for the outer normal direction on the surface S. In addition, $\breve{u}(\boldsymbol{x},t)$ and $\breve{q}(\boldsymbol{x},t)$ are given boundary conditions.

The time-domain boundary integral equation for 3-D wave propagation for $\boldsymbol{x} \in S$ can be expressed by

$$\frac{1}{2}u(\boldsymbol{x},t) = u^{\text{in}}(\boldsymbol{x},t) + \int_S G(\boldsymbol{x},\boldsymbol{y},t) * q(\boldsymbol{y},t) dS_y - \int_S H(\boldsymbol{x},\boldsymbol{y},t) * u(\boldsymbol{y},t) dS_y \tag{3}$$

where $G(\boldsymbol{x},\boldsymbol{y},t)$ and $H(\boldsymbol{x},\boldsymbol{y},t)$ denote the time-domain fundamental solution and its double layer kernel (Kobayashi 2000) in 3-D wave propagation, respectively. In addition, $(*)$ is the symbol of time convolution. To evaluate the convolution integrals of Equation 3, we use the convolution quadrature method (CQM) developed by Lubich. According to CQM, Equation 3 is arranged into the following equation for $n_{\text{-th}}$ step, e.g.,

$$\frac{1}{2}u(\boldsymbol{x},n\Delta t) = u^{\text{in}}(\boldsymbol{x},n\Delta t) + \sum_{\alpha=1}^{M}\sum_{k=1}^{n}\Big[A^{n-k}(\boldsymbol{x},\boldsymbol{y}^\alpha)q(\boldsymbol{y}^\alpha,k\Delta t) - B^{n-k}(\boldsymbol{x},\boldsymbol{y}^\alpha)u(\boldsymbol{y}^\alpha,k\Delta t)\Big] \tag{4}$$

where Δt denotes the time increment and M is the number of elements. Moreover, A^m and B^m are influence functions, which are defined as follows:

$$A^m(\boldsymbol{x},\boldsymbol{y}) = \frac{\mathcal{R}^{-m}}{L}\sum_{l=0}^{L-1}\int_S \tilde{G}(\boldsymbol{x},\boldsymbol{y},s_l)e^{\frac{-2\pi i m l}{L}}dS_y \tag{5}$$

$$B^m(\boldsymbol{x},\boldsymbol{y}) = \frac{\mathcal{R}^{-m}}{L}\sum_{l=0}^{L-1}\int_S \tilde{H}(\boldsymbol{x},\boldsymbol{y},s_l)e^{\frac{-2\pi i m l}{L}}dS_y \tag{6}$$

where i is the imaginary unit. In Equations 5 and 6, $\mathcal{R}$ and L are the parameters of CQM (Lubich 1988) . Moreover, $\tilde{G}(\boldsymbol{x},\boldsymbol{y},s)$ and $\tilde{H}(\boldsymbol{x},\boldsymbol{y},s)$ are the Laplace domain fundamental solutions, which are defined with the Laplace parameter s as follows:

$$\tilde{G}(\boldsymbol{x},\boldsymbol{y},s) = \frac{1}{4\pi r_{\boldsymbol{xy}}}e^{-s r_{\boldsymbol{xy}}} \tag{7}$$

$$\tilde{H}(\boldsymbol{x},\boldsymbol{y},s) = \frac{1}{4\pi}e^{-s r_{\boldsymbol{xy}}}\left(-\frac{s}{r_{\boldsymbol{xy}}} - \frac{1}{r_{\boldsymbol{xy}}^2}\right)\frac{\partial r_{\boldsymbol{xy}}}{\partial n_y} \tag{8}$$

where $r_{\boldsymbol{xy}}$ is given by $r_{\boldsymbol{xy}} = |\boldsymbol{x} - \boldsymbol{y}|$. Note that s is defined by $s = s/c$ due to the simple expression in Equations 7 and 8. The calculations of Equations 5 and 6 are identical to the discrete Fourier transform. Therefore, Equations 5 and 6 can be evaluated rapidly by means of the fast Fourier transform (FFT) algorithm. Arranging Equation 4 according to the boundary conditions, we obtain

$$\begin{aligned}&\frac{1}{2}u(\boldsymbol{x},n\Delta t) + \sum_{\alpha=1}^{M}[B^0(\boldsymbol{x},\boldsymbol{y}^\alpha)u(\boldsymbol{y}^\alpha,n\Delta t)\\ &-A^0(\boldsymbol{x},\boldsymbol{y}^\alpha)q(\boldsymbol{y}^\alpha,n\Delta t)] = u^{\text{in}}(\boldsymbol{x},n\Delta t)\\ &+\sum_{\alpha=1}^{M}\sum_{k=1}^{n-1}[A^{n-k}(\boldsymbol{x},\boldsymbol{y}^\alpha)q(\boldsymbol{y}^\alpha,k\Delta t)\\ &-B^{n-k}(\boldsymbol{x},\boldsymbol{y}^\alpha)u(\boldsymbol{y}^\alpha,k\Delta t)].\end{aligned} \tag{9}$$

For the $n_{\text{-th}}$ time step, all the quantities on the right-hand side of Equation 9 are known. Therefore, the unknown values $u(\boldsymbol{y}^\alpha,n\Delta t)$ or $q(\boldsymbol{y}^\alpha,n\Delta t)$ in the $n_{\text{-th}}$ time step can be obtained by solving Equation 9. Unfortunately, we cannot solve large scale problems with a large number of boundary elements M because the computational time and required memory are proportional to the number of elements in Equation 9. Therefore, the time-domain BEM based on CQM is accelerated by the fast multipole method (FMM) (Greengard and Rokhlin 1987) in this research.

3. TIME-DOMAIN FAST MULTIPOLE BEM BASED ON CQM

3.1 3-D scalar wave propagation

The FMM, developed by Greengard and Rokhlin (198-7), is a technique for reducing computational time and memory requirements for a large-scale problem. Since the FMM and its application to the BEM have been described in detail in other published papers (Nishimura 2002, Saitoh et al. 2009), we will summarize only the essential formulas here.

We first consider a point $\boldsymbol{y_0}$ near the source point $\boldsymbol{y}$ on the surface S as shown in Figure 2. In this section, we define the vector $\boldsymbol{x}-\boldsymbol{y}$ as $\boldsymbol{r_{xy}}$ and its unit vector as $\hat{\boldsymbol{r}}_{\boldsymbol{xy}}$. The FMM for 3-D wave propagation is based on the following series expansion (Abramowitz 1965, Epton and Dembart 1995) :

$$\frac{e^{-sr_{\boldsymbol{xy}}}}{r_{\boldsymbol{xy}}} = \frac{2s}{\pi}\sum_{n=0}^{\infty}\sum_{m=-n}^{n}(2n+1)\mathcal{K}_n^m(sr_{\boldsymbol{xy_0}})\bar{\mathcal{I}}_n^m(sr_{\boldsymbol{y_0y}}) \tag{10}$$

where the bar $\bar{\cdot}$ indicates the complex conjugate. The functions $\mathcal{I}_n^m(sr_{\boldsymbol{y_0y}})$ and $\mathcal{K}_n^m(sr_{\boldsymbol{xy_0}})$ have the following relations;

$$\mathcal{I}_n^m(sr_{\boldsymbol{y_0y}}) = I_n(sr_{\boldsymbol{y_0y}})Y_n^m(\hat{\boldsymbol{r}}_{\boldsymbol{y_0y}}) \tag{11}$$
$$\bar{\mathcal{I}}_n^m(sr_{\boldsymbol{y_0y}}) = I_n(sr_{\boldsymbol{y_0y}})\bar{Y}_n^m(\hat{\boldsymbol{r}}_{\boldsymbol{y_0y}}) \tag{12}$$
$$\mathcal{K}_n^m(sr_{\boldsymbol{xy_0}}) = K_n(sr_{\boldsymbol{xy_0}})Y_n^m(\hat{\boldsymbol{r}}_{\boldsymbol{xy_0}}) \tag{13}$$
$$\bar{\mathcal{K}}_n^m(sr_{\boldsymbol{xy_0}}) = K_n(sr_{\boldsymbol{xy_0}})\bar{Y}_n^m(\hat{\boldsymbol{r}}_{\boldsymbol{xy_0}}) \tag{14}$$

where I_n^m and K_n^m are the modified spherical Bessel functions of the first and second kind, respectively. Moreover, Y_n^m is the spherical harmonics defined by

$$Y_n^m(\hat{\boldsymbol{r}}_{\boldsymbol{y_0y}}) = \sqrt{\frac{(n-m)!}{(n+m)!}}P_n^m(\cos\theta)e^{im\phi} \tag{15}$$

where θ and ϕ are azimuthal and zenith angles in the spherical coordinate system, respectively, and P_n^m is the associated Legendre function. Using Equation 10, we have the multipole expansion for 3-D scalar wave propagation as follows:

$$\int_S \frac{e^{-sr_{\boldsymbol{xy}}}}{r_{\boldsymbol{xy}}}q(\boldsymbol{y},k\Delta t)dS_y = \frac{2s}{\pi}\sum_{n=0}^{\infty}\sum_{m=-n}^{n}(2n+1) \times \mathcal{K}_n^m(sr_{\boldsymbol{xy_0}})M_{n,m}^G(\boldsymbol{y}_0) \tag{16}$$

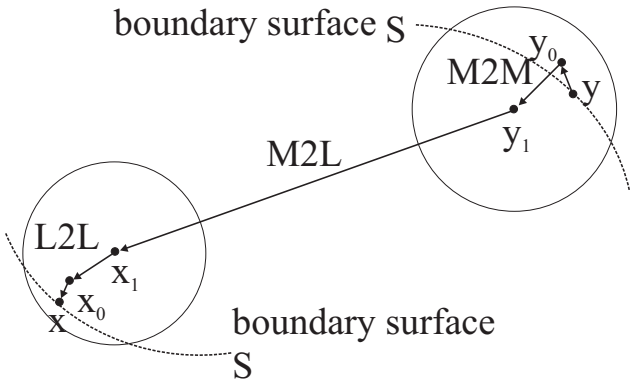

Figure 2 M2M, M2L and L2L.

where $M_{n,m}^G(\boldsymbol{y_0})$ is called the multipole moment on the multipole point $\boldsymbol{y_0}$, which is defined as follows:

$$M_{n,m}^G(\boldsymbol{y_0}) = \int_S \bar{\mathcal{I}}_n^m(sr_{\boldsymbol{y_0y}})q(\boldsymbol{y},k\Delta t)dS_y. \tag{17}$$

Similarly, the multipole moment $M_{n,m}^H(\boldsymbol{y_0})$ for the double layer kernel of the fundamental solution can be obtained by using Equations 8 and 10. Note that all multipole moments for all source points $\boldsymbol{y}$ can be evaluated independently from the field point $\boldsymbol{x}$. Corresponding to the multipole expansion defined in Equation 16, the local expansion is calculated as follows:

$$\int_S \frac{e^{-sr_{\boldsymbol{xy}}}}{r_{\boldsymbol{xy}}}q(\boldsymbol{y},k\Delta t)dS_y = \frac{2s}{\pi}\sum_{n=0}^{\infty}\sum_{m=-n}^{n}(2n+1) \times \bar{\mathcal{I}}_n^m(sr_{\boldsymbol{xx_0}})L_{n,m}(\boldsymbol{x_0}) \tag{18}$$

where $L_{n,m}(\boldsymbol{x_0})$ is the local expansion coefficient on the point $\boldsymbol{x_0}$ near the field point $\boldsymbol{x}$ as shown in Figure 2. After the multipole moments are obtained once for each source point $\boldsymbol{y}$, we can quickly evaluate the matrix vector products of Equation 4 using the fast multipole algorithm with an oct-tree structure which is prepared in advance to implement M2M, M2L and L2L translations recursively.

Now, the functions $\bar{\mathcal{I}}_n^m$ and $\mathcal{K}_n^m$ have the following expansions:

$$\bar{\mathcal{I}}_n^m(sr_{\boldsymbol{yy_1}}) = \sum_{n'=0}^{\infty}\sum_{m'=-n'}^{n'}\sum_{l=|n-n'|}^{n+n'}(-1)^{m'} \times\alpha(n,n',l)\mathcal{W}_{0,0,0}^{n,n',l}\mathcal{W}_{m,m',-m-m'}^{n,n',l}e^{\frac{\pi}{2}\mathrm{i}(l+n'-n)} \times\bar{\mathcal{I}}_{n'}^{-m'}(sr_{\boldsymbol{yy_0}})\mathcal{I}_l^{-m-m'}(sr_{\boldsymbol{y_0y_1}}) \tag{19}$$

$$\mathcal{K}_n^m(sr_{\boldsymbol{x_0y_0}}) = \sum_{n'=0}^{\infty}\sum_{m'=-n'}^{n'}\sum_{l=|n-n'|}^{n+n'}(-1)^{m+n'} \times\alpha(n,n',l)\mathcal{W}_{0,0,0}^{n,n',l}\mathcal{W}_{m,m',-m-m'}^{n,n',l}e^{\frac{\pi}{2}\mathrm{i}(n+n'-l)} \times\mathcal{I}_{n'}^{-m'}(sr_{\boldsymbol{x_0x}})\mathcal{K}_l^{m+m'}(sr_{\boldsymbol{x_0y_0}}) \quad (20)$$

where $\alpha(n,n',l)$ is defined by $\alpha(n,n',l) = (2n'+1)(2l+1)\mathrm{i}^{-n+n'+l}$ and $\mathcal{W}_{n_1,n_2,n_3}^{j_1,j_2,j_3}$ denotes the Wigner 3j symbol (Messiah 1967) . Substituting Equation 19 into Equation 17, we obtain M2M to translate the multipole expansion on the point $\boldsymbol{y_0}$ into that on a different point $\boldsymbol{y_1}$ as follows:

$$M_{n,m}(\boldsymbol{y_1}) = \sum_{n'=0}^{\infty}\sum_{m'=-n'}^{n'}\sum_{l=|n-n'|}^{n+n'}(-1)^{m'} \times\alpha(n,n',l)\mathcal{W}_{0,0,0}^{n,n',l}\mathcal{W}_{m,m',-m-m'}^{n,n',l}e^{\frac{\pi}{2}\mathrm{i}(l+n'-n)} \times\mathcal{I}_l^{-m-m'}(sr_{\boldsymbol{y_0y_1}})M_{n',-m'}(\boldsymbol{y_0}). \quad (21)$$

M2L is used to express the local expansion coefficient $L_{n,m}(\boldsymbol{x_1})$ on the local point $\boldsymbol{x_1}$ by the coefficient of the multipole expansion $M_{n,m}(\boldsymbol{y_1})$ on the point $\boldsymbol{y_1}$. Substituting Equation 20 into Equation 16, we obtain M2L as follows:

$$L_{n,m}(\boldsymbol{x_1}) = \sum_{n'=0}^{\infty}\sum_{m'=-n'}^{n'}\sum_{l=|n-n'|}^{n+n'}(-1)^{m+m'+2n} \times\beta(n,n',l)\mathcal{W}_{0,0,0}^{n',n,l}\mathcal{W}_{m',m,-m-m'}^{n',n,l}e^{\frac{\pi}{2}\mathrm{i}(n+n'-l)} \times\mathcal{K}_l^{m+m'}\left(sr_{\boldsymbol{x_1y_1}}\right)M_{n',m'}(\boldsymbol{y_1}) \quad (22)$$

where $\beta(n,n',l)$ is defined by $\beta(n,n',l) = (2n'+1)(2l+1)\mathrm{i}^{n-n'+l}$. Using Equations 18 and 19, the center of the local expansion is shifted from $\boldsymbol{x_1}$ to $\boldsymbol{x_0}$ by L2L as follows:

$$L_{n,m}(\boldsymbol{x_0}) = \sum_{n'=0}^{\infty}\sum_{m'=-n'}^{n'}\sum_{l=|n-n'|}^{n+n'}(-1)^{-m} \times\beta(n,n',l)\mathcal{W}_{0,0,0}^{n',n,l}\mathcal{W}_{m',-m,-m'+m}^{n',n,l}e^{\frac{\pi}{2}\mathrm{i}(l+n-n')} \times\mathcal{I}_l^{m-m'}\left(sr_{\boldsymbol{x_0x_1}}\right)L_{n',m'}(\boldsymbol{x_1}). \quad (23)$$

Note that we have to truncate the infinite series of such Equations 10, 19 and 20 taking p terms in the practical calculations of FMM.

3.2 3-D elastic wave propagation

In this section, the brief description of the time-domain fast multipole BEM based on CQM is presented for 3-D elastic wave propagation. The Laplace domain fundamental solution $\tilde{U}_{ik}(\boldsymbol{x},\boldsymbol{y},s)$ for 3-D elastodynamics is expressed as follows:

$$\tilde{U}_{ik}(\boldsymbol{x},\boldsymbol{y},s) = \frac{1}{4\pi\mu s_T^2}\left\{e_{rji}e_{rlk}\frac{\partial^2}{\partial x_j\partial y_l}\frac{e^{-s_Tr_{\boldsymbol{xy}}}}{r_{\boldsymbol{xy}}} + \frac{\partial^2}{\partial x_i\partial y_k}\frac{e^{-s_Lr_{\boldsymbol{xy}}}}{r_{\boldsymbol{xy}}}\right\} \quad (24)$$

where μ is shear modulus, e_{ijk} is the permutation symbol, and s_β is given by $s_\beta = s/c_\beta(\beta = L \text{ or } T)$. Substituting Equation 10 into Equation 24, and considering the influence functions for 3-D elastodynamics, we have the multipole expansion as follows:

$$\begin{aligned}&\int_S \tilde{U}_{ik}(\boldsymbol{x},\boldsymbol{y},s)t_k(\boldsymbol{y},k\Delta t)dS_y \\ &= \sum_{n=0}^{\infty}\sum_{m=-n}^{n}A_ne_{rji}\frac{\partial}{\partial x_j}[\mathcal{K}_n^m(s_Tr_{\boldsymbol{xy_0}})]M_{r,n,m}^{U_T}(\boldsymbol{y_0}) \\ &+ \sum_{n=0}^{\infty}\sum_{m=-n}^{n}B_n\frac{\partial}{\partial x_i}[\mathcal{K}_n^m(s_Lr_{\boldsymbol{xy_0}})]M_{n,m}^{U_L}(\boldsymbol{y_0}) \quad (25)\end{aligned}$$

where $A_n = -(2n+1)/(2\pi^2\mu s_T)$ and $B_n = -s_L(2n+1)/(2\pi^2\mu s_T^2)$. Furthermore, u_k and t_k show the displacement and traction components, respectively. The coefficients $M_{n,m}^{U_L}(\boldsymbol{y_0})$ and $M_{r,n,m}^{U_T}(\boldsymbol{y_0})$ are the multipole moments on the multipole point $\boldsymbol{y_0}$ for 3-D elastodynamics, which are defined as follows:

$$M_{n,m}^{U_L}(\boldsymbol{y_0}) = \int_S\frac{\partial}{\partial y_l}[\bar{\mathcal{I}}_n^m(s_Lr_{\boldsymbol{yy_0}})]t_l(\boldsymbol{y},k\Delta t)dS_y \quad (26)$$

$$M_{r,n,m}^{U_T}(\boldsymbol{y_0}) = \int_S e_{rlq}\frac{\partial}{\partial y_l}[\bar{\mathcal{I}}_n^m(s_Tr_{\boldsymbol{yy_0}})]t_q(\boldsymbol{y},k\Delta t)dS_y \quad (27)$$

Thus, we have two types of multipole moments with respect to longitudinal and transverse waves for 3-D elastodynamics. Note that M2M, M2L and L2L translations for 3-D elastodynamics are the same as for 3-D scalar wave propagation.

4. NUMERICAL EXAMPLES

The proposed method is now applied to analyze the scalar wave scattering by rigid spheres. For all numerical calculations, boundary conditions are supposed to be $q = \partial u/\partial n = 0$ on the surfaces of rigid spheres. The boundary surfaces of each rigid sphere are divided into 384 elements, which are discritized with the constant approximation. In the calculations of Equations 5 and 6, the parameters L and $\mathcal{R}$ are taken as $L = 128$ and $\mathcal{R} \simeq 0.9475$, respectively.

4.1 Scalar wave scattering by a rigid sphere

We firstly consider the scalar wave scattering by a rigid sphere with the radius a as shown in Figure 3. In this analysis, the time increment is $c\Delta t/a = 0.05$ and the total time

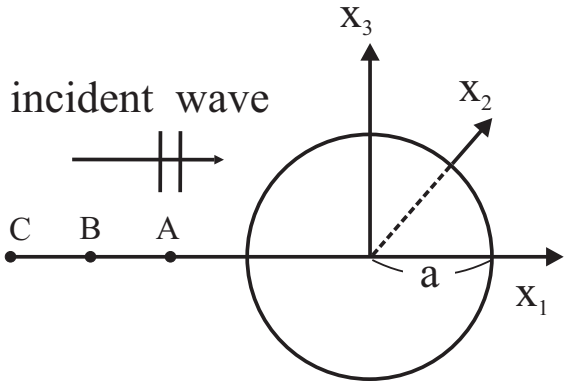

Figure 3 Scalar wave scattering by a rigid sphere.

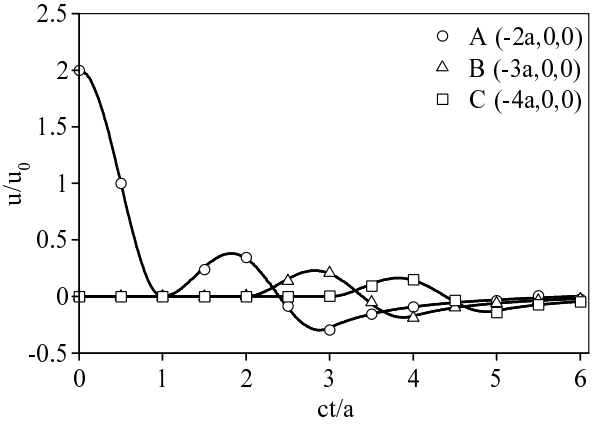

Figure 4 Total displacements u/u_0 as a function of time at A, B and C in Figure 3.

steps $N = 128$. The displacement of the incident wave is given by

$$u^{\text{in}}(\boldsymbol{x}, t) = u_0\left(1 - \cos\pi\left[\frac{ct}{a} - \frac{x_1 + a}{a}\right]\right), \quad \begin{cases} [\alpha] = \alpha & \text{for} \quad 0 \le \alpha \le 2 \\ [\alpha] = 0 & \text{otherwise} \end{cases} \tag{28}$$

where u_0 is the displacement amplitude. This problem has been analytically solved in the frequency domain (Schmerr, L. W. 1988). The transient solution can be obtained by superposing the results in the frequency domain by means of the fast Fourier transform (FFT). Figure 4 shows the total displacements as a function of time at point A$(-2a, 0, 0)$, B$(-3a, 0, 0)$ and C$(-4a, 0, 0)$ in Figure 3. In Figure 4, the solid lines show the numerical results by the time-domain BEM based on CQM. Numerical results are in good agreement with the analytical numerical results obtained by FFT.

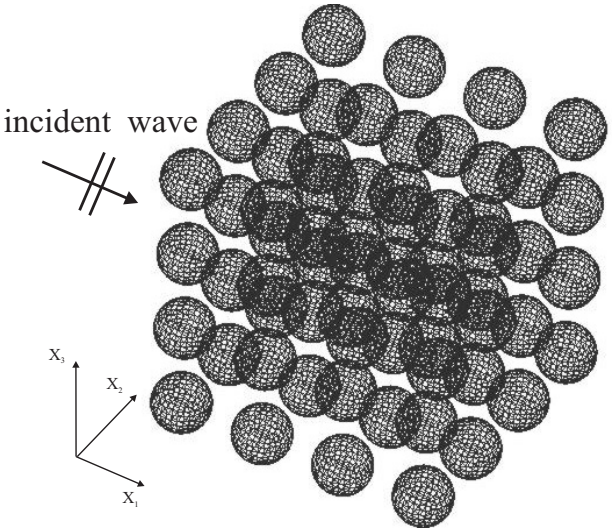

Figure 5 Scalar wave scattering by 64 rigid spheres.

4.2 Scalar wave scattering by 64 cavities

Next, we consider the scalar wave scattering by 64 rigid spheres with the diameter a and the rigid spacing $2a$ between two adjacent rigid spheres along each axis as shown in Figure 5. The time increment is $c\Delta t/a = 0.05$ and the total time steps $N = 128$. The incident wave defined in Equation 28 is also used for this analysis. Figure 6 and Figure 7 show the total displacements u/u_0 on $x_3/a = 0.0$ plane and $x_1/a = 0.0$ plane, respectively. In each figure, (a) and (b) indicate the total displacements at $ct/a = 3.2$ and $ct/a = 6.35$, respectively. We can confirm the multiple scattering by the interaction between 64 rigid spheres and the incident wave. In this calculations, the desktop computer with 2GB memory and Intel(R) Xeon(R) CPU 5310 1.6GHz is used. Note that this problem could not be solved by the conventional time-domain BEM because of the restriction of the required memory.

5. CONCLUSIONS

In this paper, the new time-domain fast multipole BEM based on CQM was developed for 3-D scalar wave propagation. In addition, the formulation for 3-D elastodynamics was also shown. As numerical examples, scalar wave scattering by rigid spheres were demonstrated to validate the proposed method. The new time-domain fast multipole BEM based on CQM is very effective for large scale problems. However, our proposed method has been improved. Further refinement of the formulations and our Fortran code are desirable for seismic analyses and engineering applications.

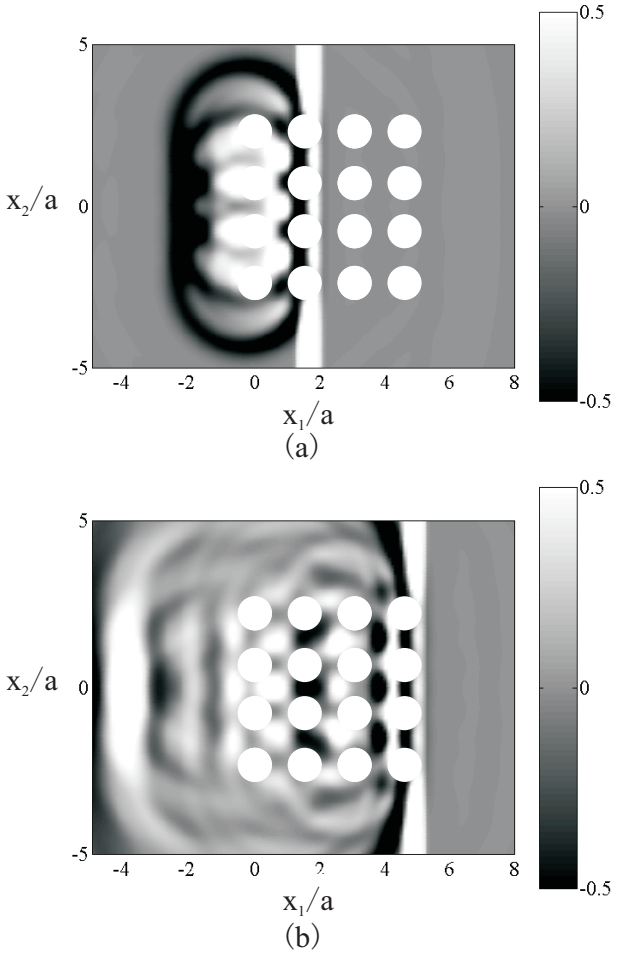

Figure 6 Total displacements u/u_0 on $x_3/a = 0.0$ plane. (a): $ct/a = 3.2$. (b): $ct/a = 6.35$.

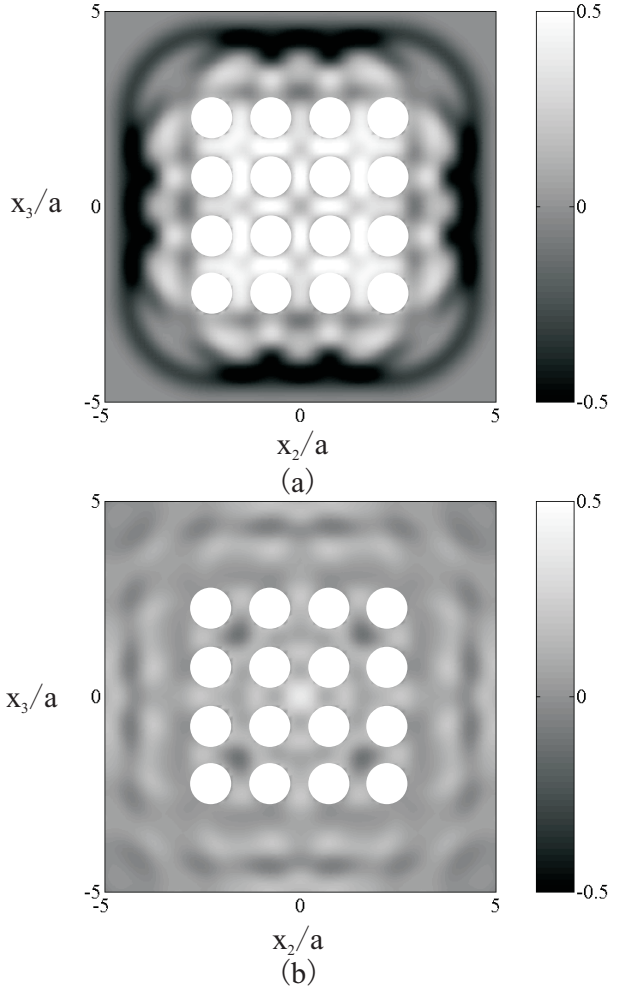

Figure 7 Total displacements u/u_0 on $x_1/a = 0.0$ plane. (a): $ct/a = 3.2$. (b): $ct/a = 6.35$.

References:

Abe, K., Yoshida, Y. and Nakamura, T. (1993), "Near field seismic analysis by three-dimensional time domain boundary element method, *Journals of the Japan Society of Civil Engineers*, No.471/I-24, 125-133 (in Japanese).

Kataoka, S. (1996), "Simulation of the 1995 Hyogo-ken Nanbu Earthquake by a 3-D BEM", *Technical Report, Department of Civil Engineering, Tokyo Institute of Technology*, No.54, 11-20 (in Japanese).

Lubich, C. (1988)," Convolution quadrature and discretized operational calculus I", *Numer. Math.*,**52**, 413-425.

Lubich, C. (1988)," Convolution quadrature and discretized operational calculus Ⅱ ", *Numer. Math.*,**52**, 129-145.

Greengard, L. and Rokhlin, V. (1987)," A fast algorithm for particle simulations", *Journal of Computational Physics*, **73**, 325-348.

Kobayashi, S. et al. (2000), "Wave analysis and boundary element methods", Kyoto University Press (in Japanese).

Nishimura, N. (2002), " Fast multipole accelerated boundary integral equation methods", *Applied Mechanics Review*, 55-4, 299-324.

Saitoh, T., Hirose, S. and Fukui, T. (2009), "Convolution quadrature boundary element method and acceleration by fast multipole method in 2-D viscoelastic wave propagation, *Theoretical and applied mechanics Japan* (in press).

Abramowitz, M. (1965), "Handbook of Mathematical Functions", Dover.

Epton, M. A. and Dembart, B. (1995), "Multipole translation theory for the three-dimensional Laplace and Helmholtz equations", *SIAM J. Sci. comput.* **16**, 865-897.

Messiah, A. (1967), "Quantum Mechanics", John Wiley & Sons (North Holland), New York.

Schmerr, L. W. (1988), "Fundamentals of ultrasonic nondestructive evaluation", Plenum Press, New York.

Sixth International Conference on Urban Earthquake Engineering
March 3-4, 2009, Tokyo Institute of Technology, Tokyo, Japan

Comparison of Surface Motions of a Partially Improved Ground Using 1D, 2D and 3D Ground Models

Huei-Tsyr Chen[1], and Yu-Cheng Wang[2]

1) Professor, Department of Civil Engineering, National Central University, Taiwan
2) Former Graduate Student, Department of Civil Engineering, National Central University, Taiwan
chenht@cc.ncu.edu.tw

Abstract: Using the 10 spectrum-compatible artificial earthquake motions as the input motions, in this paper the 1D, the 2D and the 3D nonlinear finite element models are used to compute the surface ground motions of a ground with an improved zone. The differences among the ground motions generated using the three ground models are then explored through the comparison of their response spectra. It is found that the seed number affects the characteristics of the artificial earthquakes significantly. For a soil stratum with an improved zone of finite dimension, the 2D analysis gives the largest surface ground motion, while the 1D analysis gives the smallest surface ground motion. From the preliminary analyses a 1D analysis can be justified only when the width of one side is about 15 times that of the other side.

1. INTRODUCTION

It is well known now that the ground motion at a site is affected by source mechanism, path and local site conditions through the past observations and theoretical investigations. It has been found in many instances that even for locations at several tens of meters apart the characteristics of ground motions may differ significantly. Such differences can lead to different degrees of damage within the affected area, which can be seen in many publications (Ohbo et al., 1994; Campillo et al., 1988; Akamatsu et al., 1996).

In general the irregular ground can be classified into three categories: irregular topography, irregular soil stratum and irregular bedrock. Many studies have been conducted to explain the effect of each category on the earthquake ground motions. Moczo et al. (1994) studied the effect of lateral inhomogeneity of soil stratum on the earthquake ground motions and found that the significant differences can be observed for soil stratum with lateral inhomogeneity. Chen and Ho (2000) investigated the seismic response of a basin with symmetric shape for different angles of side rock and found that the horizontal ground acceleration near the region of side rock decreases with increasing angle of side rock. Tu (2008) adopted a 2D finite element model to investigate the effect of seismic bedrock configuration on the surface ground motions of soft ground; for a seismic bedrock of triangular shape, it is found that for regions near the ends of model the characteristics of ground motions are significantly affected by the configuration of the seismic bedrock and the earthquakes and to predict better ground motion the configuration of seismic bedrock must be determined as exactly as possible.

For certain occasions, a structure may be built on top of a soft ground. One way to ensure adequate bearing capacity of soil is to improve the site by using ground improvement technique. For such a soil stratum with a zone of improvement it is essentially a three-dimensional problem. Thus, using the 10 spectrum-compatible artificial earthquake motions as the input motions, in this paper the 1D, the 2D and the 3D nonlinear finite element models are used to compute the surface ground motions of an improved zone. The differences among the ground motions generated using these three ground models are then explored through the comparison of their response spectra.

2. METHOD OF ANALYSIS

The methodology adopted in this study consists of two stages: (1) the artificial earthquake motion compatible with the Level 2 design spectrum specified at the engineering bedrock as given in the performance-based seismic design code for buildings in Japan is generated, and (2) the artificial earthquake motion generated in step (1) is then used as the input motion for the surface ground motion calculation using the selected finite element model. The Level 2 design spectrum (unit: cm/sec^2) is defined as follows where T is the period.

$$0.64 \le T < 5.0 \quad S_0 = 512/T \tag{1a}$$

$$0.16 \le T < 0.64 \quad S_0 = 800 \tag{1b}$$

$$T < 0.16 \quad S_0 = 320 + 3000T \tag{1c}$$

2.1 Generation of Artificial Earthquake

Many methods have been proposed for generating artificial earthquakes. In this study the one adopted is to express the acceleration in terms of complex exponentials as

$$a(t) = f(t)\sum_{k=0}^{n} A_k \exp i(\omega_k t + \phi_k) \qquad (2)$$

where a(t) is the acceleration, A_k the kth Fourier amplitude, ϕ_k the kth Fourier phase angle, ω_k the selected frequency and f(t) the envelope function which approximately envelopes the time history of the entire earthquake record and represents the nonstationary property of earthquake motion. However, observing the close correlation between the shape of distribution of difference of Fourier phase angles for any two consecutive frequencies and the wave shape of an earthquake motion, Ohsaki (1979) proposed the so-called "phase difference method" in which the independent random numbers are assigned for the desired numbers of phase difference. Assuming ϕ_1=0, the kth Fourier phase angle is then computed using

$$\phi_{k+1} = \phi_k + \Delta\phi_k \qquad k=0,1,.2,\ldots..n\text{-}1 \qquad (3)$$

Shown in Fig. 1 is the shape of distribution of difference of Fourier phase angles adopted in this study; in the figure, T_R is the rise time to reach the full amplitude, T_L is the time to decrease the amplitude, T_D is the duration of the motion and NDIF is the number of the intervals used to obtain the corresponding accumulated function. This approach do not need f(t) as shown in equation (2) and is shown to have the uniform convergence. In this study, a program NCUARTEQ (Wang 2000) based on the "phase difference method" was used for generating the spectrum-compatible earthquake motions. The ω_k was chosen arbitrarily to cover the entire frequency range of the design spectrum. During the iterative process, the quantities ω_k, and ϕ_k remained unchanged, while only the A_k was adjusted so that the response spectrum of the generated artificial earthquake motion can envelope the design spectrum. It is also noted that we adopted the criterion listed in Standard Review Plan (NRC 1989) where the calculated response spectrum of the artificial earthquake is considered to envelope the design spectrum when no more than five points and no more than 10% of the value below the design spectrum.

2.2 Analysis of Seismic Ground Motion

In this study the seismic ground response was computed using the program NCULIQUID3 (Chen 2002) which is a three-dimensional nonlinear effective stress finite element program in U-W form based on Biot's equations. The constitutive relation for soil is the cap model (Sandler et al. 1976) and the pore pressure model developed according to the cap model is the one proposed by Pacheco (1989). In addition, the viscous boundary accounting for two-phase nature of soil is used to model the lateral infinite extent of soil stratum (Akiyoshi et al. 1994).

$$\begin{bmatrix} M_{uu} & M_{uw} \\ M_{wu} & M_{ww} \end{bmatrix} \begin{Bmatrix} \ddot{U} \\ \ddot{W} \end{Bmatrix} + \begin{bmatrix} C_{uu} & 0 \\ 0 & C_{ww} \end{bmatrix} \begin{Bmatrix} \dot{U} \\ \dot{W} \end{Bmatrix} + \begin{bmatrix} K_{uu} & K_{uw} \\ K_{wu} & K_{ww} \end{bmatrix} \begin{Bmatrix} U \\ W \end{Bmatrix}$$
$$= -\begin{bmatrix} M_{uu} & 0 \\ 0 & 0 \end{bmatrix} \{J\} \ddot{U}_g \qquad (4)$$

where U_i is the displacement of soil particle and W_i the displacement of water relative to soil particle. The submatrix C_{uu} is a Rayleigh damping matrix to account for the damping mechanism other than the nonlinearity of soil. The vector $\{J\}$ is made up of 1 and 0 to account for the desired direction of input motion. $\ddot{U}_g$ is the input motion specified at the bedrock of soil stratum. A note is to be made that no effect of underground water is considered in this study.

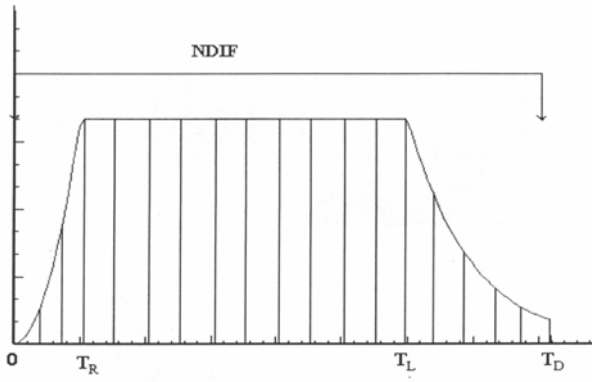

Figure 1 Distribution of Phase Difference

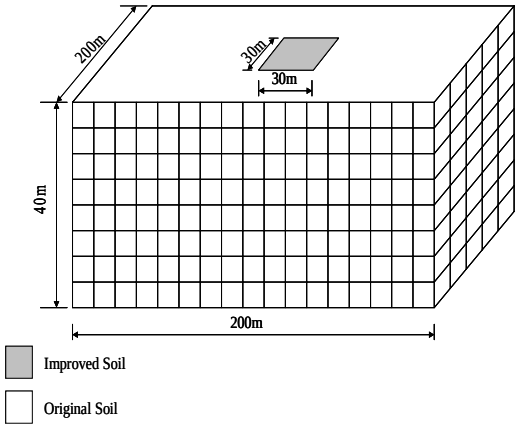

Figure 2 3D Finite Element Ground Model

Shown in Fig. 2 is the hypothetical three-dimensional ground model employed in this study. The shaded region is the improved zone and the improvement is made such that its shear wave velocity changes from 170m/sec to 300m/sec. The depth of soil stratum is 40m and the width of

improvement region is 30m x 30m x 20m. Through the convergence test runs, it was found that when the boundary of domain of analysis was set up at a location of 100m from the center of the model (indicated as 40x40x8 in the figure), the response spectrum of the surface ground motion converges and this was the size of the finite element model used in this study. Although three components of motions on the ground surface can be obtained from the finite element model, in order to compare with the 1D and the 2D results, only the horizontal motion which is parallel to the input motion at the bedrock was considered. The ground motions at the center of improved-zone surface were then analyzed. Table 1 describes the parametric values of the ground model.

Table 1 Parametric Values for Soil Stratum

Parameters	Original soil	Improved soil
Shear-wave velocity (m/sec)	170	300
Poisson ratio	0.44	0.46
Mass density (t/m^3)	1.9	2.1
Cohesion (kN/m^2)	12	100.5
Friction angle (degree)	10	26.7
Cap model parameter R	4.0	1.6
Cap model parameter W	0.18	0.18
Cap model parameter D (1/kN)	$5x10^{-6}$	$5x10^{-6}$

3. RESULTS AND DISCUSSIONS

3.1 Artificial Earthquakes

It is known that there are infinite numbers of artificial earthquakes which can be generated to envelope the same design spectrum. Chen and Ou (2004) used the following numbers as the seed numbers for the random number generator subroutine: 10579, 123, 130579, 2223, 2459, 290197, 5791, 6079, 7983 and 8953 to generate the distribution of phase differences associated with T_R=5.0 seconds, T_L=15.0 seconds, T_D=20.48 seconds and NDIF=100. Table 2 shows the time to reach the maximum acceleration of each artificial earthquake which varies significantly with the seed number, indicating that the seed number plays an important role in generating the spectrum-compatible artificial earthquakes. These 10 artificial earthquakes were adopted in this study to investigate the effects of these earthquakes on the seismic responses of a ground with an improved zone.

3.2 Response Spectra from 1D, 2D and 3D Analyses

In the seismic ground motion analysis a 1D analysis is frequently performed because of its easy implementation. However, for the case where a portion of ground is improved, it becomes essentially a three-dimensional problem. In such a situation both the 1D and the 2D conditions are violated and whether the 1D and the 2D analyses are still applicable needs further investigation.

Table 2 Time to Reach Peak Acceleration of Artificial Earthquakes

Seed	Peak Value (gal)	Time (sec)
123	381.19	9.05
2223	-345.84	11.45
2459	391.29	9.66
5791	-357.89	12.35
6079	-369.72	4.89
7983	338.99	11.7
8953	-371.79	14.12
10579	-339.97	13.8
130579	-387.32	10.12
290197	-364.75	10.01

Shown in Figs. 3 and 4 are the response spectra computed from the surface motions at the center of the surface of improved soil zone as described in the section 2.2. These ground motions are obtained using the 1D, the 2D and the 3D analyses. It can be seen that the response spectra for the surface ground motions are influenced by the seed numbers. For the case using the seed number 123, the peak value is at period of 1 second, while for the case using the seed number 130579 its peak value is at period about 0.4 seconds; in addition, the significant difference can also be observed for the peak values.

On the other hand, the response spectra of the 1D analysis are very different from those of the 2D and the 3D analyses with the spectral values of the 2D analysis being the largest and those of the 1D analysis being the smallest over the periods below about 3 seconds. The reason for such a difference is that in the 1D analysis the improved zone is assumed to extend laterally to infinity and during the strong earthquake most of the wave energy is trapped at the bottom soft soil region and dissipated by the nonlinear soil behavior; for the 2D analysis the improved zone is surrounded by the soft soil region and "floats" on top of the soil stratum during the strong earthquake, resulting in larger ground motions, while in the 3D analysis the propagation of wave in the third direction dissipates a little more energy than the 2D analysis, leading to smaller responses. Despite this, for the periods above 1.8 seconds, there is almost no difference between the 2D and the 3D analyses.

Table 3 shows the periods associated with the peak spectral accelerations for the surface motions of improved soil zone computed using 10 artificial earthquakes. Except for the case with seed number 130579, the 2D and the 3D analyses give almost the same period associated with each seed number, while the periods from the 1D analysis are significantly lower than those of the 2D and the 3D analyses.

Shown in Figure 5 are the peak spectral accelerations of

the surface motions computed using 10 artificial earthquakes. For each seed number used for generating the artificial earthquake, the 2D analysis renders the highest peak spectral acceleration, followed by the 3D analysis, while the 1D analysis gives the smallest peak spectral acceleration. A note should be made that 1D analysis gives the values less than one half of those obtained using the 3D analysis, while the 2D analysis gives conservative results.

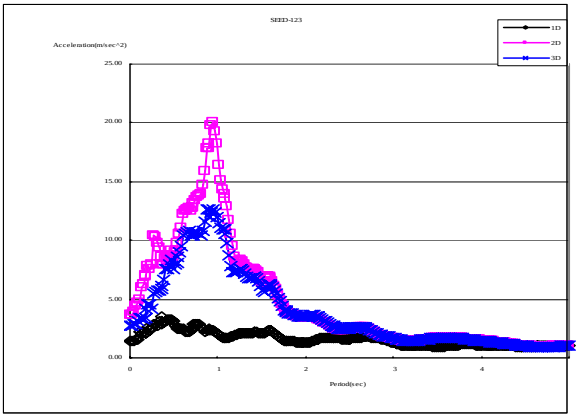

Figure 3 Response Spectra of Surface Ground Motions of Improved zonefrom 1D, 2D and 3D Analyses with Seed Number 123

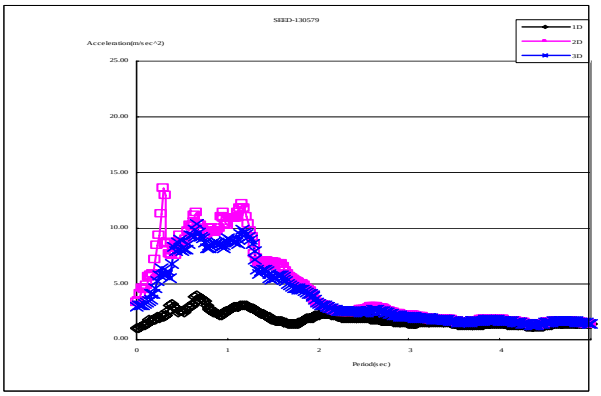

Figure 4 Response Spectra of Surface Ground Motions of Improved zone from 1D, 2D and 3D Analyses with Seed Number 130579

From the above discussions, it can be concluded that for the case of a soil stratum with an improved zone and the surface ground motion is desired over that zone, it will be inappropriate to perform the 1D ground motion analysis.

In order to further explore the suitability of adopting 1D analysis, three cases were studied. Case A has the improved zone of 30m x 30m x 20m with depth of soil stratum of 40m. Case B has the improved zone of 30m x 30m x 10m with depth of soil stratum of 40m. Case C has the improved zone of 30m x 30m x 10m with depth of soil stratum of 20m. During the 2D analysis, the widths of one side of the improved zone considered were 60m, 100m, 200m, 400m, and 600m, respectively. The 1D and the 2D analyses were performed using the artificial earthquake generated using seed number 2223. The response spectra of the surface motions of improved zone for these three cases are shown in Figs. 6-8. It can be seen that for Case B and Case C there are significant differences as width increases from 100m to 200m, while for Case A this occurs as width increases from 200m to 400m. On the other hand, for Case B and Case C, as the width increases to 400m, the spectral curves obtained from both 1D and 2D analyses almost coincide, while some differences can still be observed for Case A. Although more analyses involving different situations need being studied, from this preliminary study, it seems that for an improved zone in an otherwise homogeneous soil stratum, if one side has width of approximately 15 times that of the other side, 1D analysis can then be used.

Table 3 Periods Associated with the Peak Spectral Accelerations for the Surface Motions of Improved Zone

Seed	Period (sec)		
	3D	2D	1D
123	0.97	0.97	0.37
2223	0.93	0.93	0.55
2459	0.93	0.93	0.31
5791	1.03	1.03	0.33
6079	1.07	1.07	1.01
7983	1.11	1.01	0.35
8953	0.87	0.87	0.43
10579	0.85	0.85	0.29
130579	0.69	0.31	0.69
290197	0.83	0.93	0.33

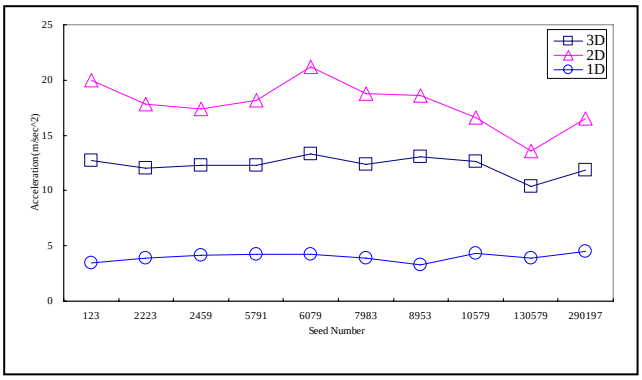

Figure 5 Peak Spectral Accelerations of the Surface Motions of Improved zone Computed Using 10 Artificial Earthquakes.

4. CONCLUSIONS

Using 10 spectrum-compatible artificial earthquake motions as the input motions, in this paper the 1D, the 2D and te 3D nonlinear finite element models are used to compute the surface ground motions of a ground with an improved zone. The differences among the ground motions generated using these three ground models are then explored through the comparison of their response spectra. It is found that the seed number affects the characteristics of the artificial earthquakes significantly. For a soil stratum with an improved zone of finite dimension, the 2D analysis gives the largest surface ground motion, while the 1D analysis gives the smallest surface ground motion. From the preliminary analyses a 1D analysis can be justified only when the width of one side is about 15 times that of the other side.

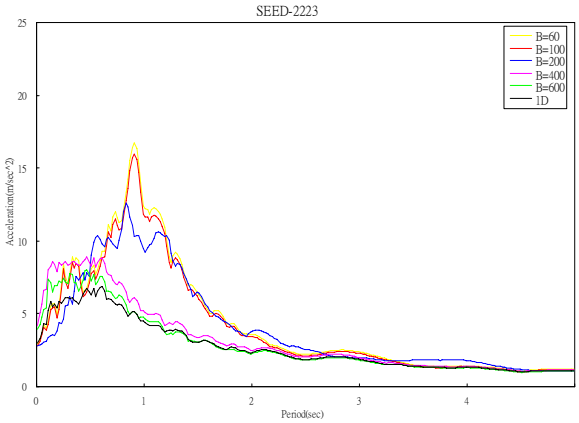

Figure 6 Response Spectra for Various Widths of Improved Zone of Case A

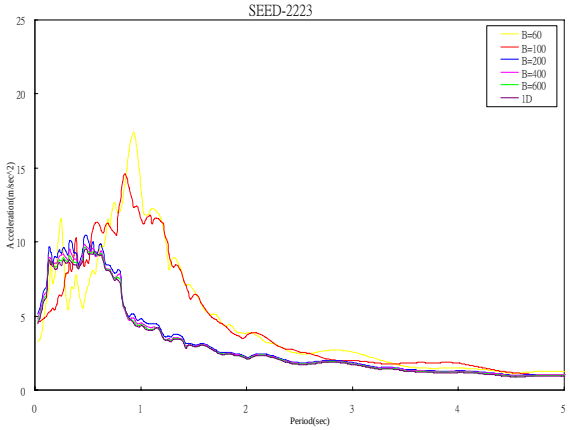

Figure 7 Response Spectra for Various Widths of Improved Zone of Case B

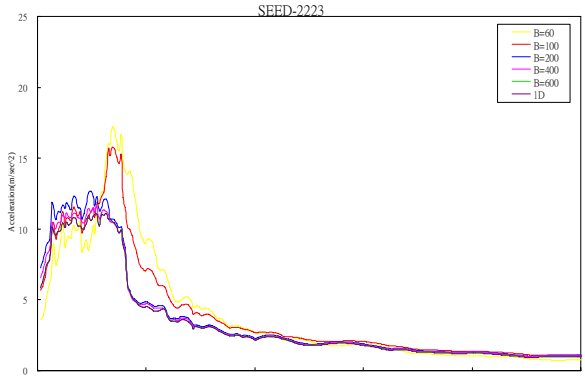

Figure 8 Response Spectra for Various Widths of Improved Zone of Case C

References:

Ohbo, N., Iwadate, T., Yagishita, F., Shibata, M. (1994), "Case Studies of Lateral Geological Inhomogeneity and Wooden Houses Damage during Past Earthquake in Japan," Proceedings of 10th European Conference on Earthquake Engineering, Vol.1, pp.399-404.

Campillo, M., Gariel, J.C., Aki, K. and Sanchez-Sesma, F. (1988), "Destructive Ground Motion in Mexico City: Source, Path and Site Effects during Great 1985 Michoacan Earthquake," Bulletin of Seismological Society of America, Vol.78, pp.451-477.

Akamatsu, J., Saito, H., Jido, M., Morikawa, H., Nishimura, K. and Komazawa, M. (1996), "Effects of Irregular Bedrock Configuration in a Sedimentary Basin on Ground Vibration Characteristics- Possible Cause of Damage Distribution of 1995 Hansin-Awaji Great Earthquake Disaster," Proceedings of 11th World Conference on Earthquake Engineering, Paper No. 1655.

Moczo, P., Labak, P. and Rovelli, A. (1994), "Effects of the Lateral Heterogeneity beneath Roman Colosseum on Seismic Ground Motion," Proceedings of 10th European Conference on Earthquake Engineering, Vol.1, pp.377-383.

Chen, H.T. and Ho, J.C. (2000), "Effects of Ground Water on Seismic Responses of Basin," 12th World Conference on Earthquake Engineering, Paper No.770.

Ohsaki, Y. (1979), "On the Phase Difference of Phase Content in Earthquake Ground Motions." *Earthquake Engineering and Structural Dynamics*, 7, 427-439.

Wang, J.M. (2000), "The effect of Phase Angle of Spectrum-Compatible Artificial Earthquake on the Floor Response Spectra." *Master Thesis*, Department of Civil Engineering, National Central University, Chungli, Taiwan (in Chinese).

Standard Review Plan (1989), US Nuclear Regulatory Commission, Rev.2.

Chen, W.H. (2000), "Effectiveness of Diaphragm Wall in Reducing the Potential of Soil Liquefaction Induced by Earthquakes," *Master Thesis*, Department of Civil Engineering, National Central University, Chungli, Taiwan (in Chinese).

Sandler, I.S., Dimaggio, F.L., Baladi, G.Y. (1976), "Generalized

Cap Model for Geological Materials," *Journal of Geotechnical Engineering Division*, ASCE 1976. **102**(7), 683-699.

Pacheco, M.P. (1989), "Pore Pressure Predictions in Finite Element Analysis," *International Journal for Numerical and Analytical Methods in Geomechanics*, 13, 477-491.

Akiyoshi, T., Fuchida, K., Fang, H.L. (1994), "Absorbing Boundary Conditions for Dynamic Analysis of Fluid-Saturated Porous Media," *Soil Dynamics and Earthquake Engineering*, 13,387-397.

Chen, H.T. and Ou, G.Y. (2004), "Seismic Responses of Structures Subjected to Artificial Ground Motions Generated Using 1D and 2D Ground Model," *Proceedings of 13th World Conference on Earthquake Engineering*, Paper No. 1765.

Tu, C.S. (2008), "Effects of Irregular Seismic Bedrock Configuration on Surface Ground Motions ," *Master Thesis, Department of Civil Engineering, National Central University, Taiwan (in Chinese).*

Sixth International Conference on Urban Earthquake Engineering
March 3-4, 2009, Tokyo Institute of Technology, Tokyo, Japan

SOIL-WATER-AIR COUPLED ANALYSIS OF SEEPAGE AND SEISMIC BEHAVIOR OF RESIDENTIAL FILL

Ryosuke Uzuoka[1], Tomohiro Mori[2], Takashi Chiba[2], Kenji Kamiya[2] and Motoki Kazama[3]

1) Associate Professor, Dept. of Civil and Environmental Engineering, Tohoku University, Japan
2) Graduate Student, Dept. of Civil and Environmental Engineering, Tohoku University, Japan
3) Professor, Dept. of Civil and Environmental Engineering, Tohoku University, Japan
uzuoka@civil.tohoku.ac.jp, mori@soil1.civil.tohoku.ac.jp, chiba@soil1.civil.tohoku.ac.jp, kamiya@soil1.civil.tohoku.ac.jp, kazama_motok@.civil.tohoku.ac.jp

Abstract: A dynamic three-phase coupled analysis is newly proposed. The equations governing the dynamic deformation of unsaturated soil are derived here based on porous media theory and constitutive models. The weak forms of the momentum balance equations of the overall three-phase material and the continuity equations (mass and momentum balance equations) of the pore fluids (water and air) at the current configuration are implemented in a finite element model. The discretized equations are solved by fully implicit method and the skeleton stress is also implicitly integrated. Seepage and seismic behaviors of an actual fill slope during 2008 Iwate-Miyagi Nairiku earthquake are discussed.

1. INTRODUCTION

Fill slopes located on an old valley have been dam-aged because the ground water table was high after rainfall. Moreover the capillary zone in an artificial ground with a volcanic soil with high water retention is usually thick; therefore it possibly liquefies during earthquake (Uzuoka et al. 2005).

Cyclic triaxial tests with unsaturated soil have been performed by many researchers (e.g. Yoshimi et al. 1989, Selim & Burak 2006). Recently liquefaction mechanism of unsaturated soil has been discussed (e.g. Okamura & Soga 2006, Unno et al. 2008) and it is suggested that the behaviors of pore air and suction play an important role during liquefaction of unsaturated soil.

Liquefaction analyses of saturated ground based on Biot's porous media theory have been studied since 1970s. Liquefaction analyses of unsaturated ground have been performed using porous media theory (e.g. Meroi & Schrefler 1995). Most liquefaction analyses, however, assumed that pore air pressure was zero and the behavior of pore air was not directly treated. Therefore, liquefaction analysis without considering suction cannot precisely predict the seismic behavior of unsaturated fill slope.

In this study, a dynamic three-phase coupled analysis is newly proposed. The equations governing the dynamic and finite deformation of unsaturated soil are derived here based on porous media theory. The soil water characteristic curve (SWCC) modeling is one of the most important issues to reproduce the change in suction and water saturation during cyclic loading. A simplified SWCC model with logistic function is proposed to reproduce the wetting process during cyclic loading.

Numerical simulations of seismic behavior of an actual fill slope are performed with the proposed numerical method. The material parameters of the constitutive models are determined through the calibration of the laboratory tests. Seepage and seismic behaviors of an actual fill slope during 2008 Iwate-Miyagi Nairiku earthquake are discussed.

2. NUMERICAL METHOD

2.1 Balance and Constitutive Equations

Firstly the basic equations are derived based on porous media theory (e.g. de Boer 2000, Schrefler 2002). The partial densities of soil skeleton, pore water and air are defined as follows,

$$\begin{aligned} \rho^s &= n^s \rho^{sR} = (1-n)\rho^{sR} \\ \rho^w &= n^w \rho^{wR} = n s^w \rho^{wR} \\ \rho^a &= n^a \rho^{aR} = n s^a \rho^{aR} = n(1-s^w)\rho^{aR} \end{aligned} \tag{1}$$

where ρ^s, ρ^w and ρ^a are the partial densities of soil skeleton, pore water and air respectively. ρ^{sR}, ρ^{wR} and ρ^{aR} are the real densities of each phase, n^s, n^w and n^a are the volume fractions of each phase. n is the porosity, s^w is the degree of water saturation and s^a is the degree of air saturation.

Mass balance equation for α phase (α = s, w, a) is

$$\frac{D^\alpha \rho^\alpha}{Dt} + \rho^\alpha \operatorname{div} \mathbf{v}^\alpha = 0 \tag{2}$$

where $D^\alpha \square / Dt$ is the material time derivative with respect to

α phase, $\boldsymbol{v}^\alpha$ is the velocity vector of α phase. The mass exchange among three phases is ignored here. The linear momentum balance equation of α phase is

$$\rho^\alpha \frac{D^\alpha \mathbf{v}^\alpha}{Dt} = \rho^\alpha \mathbf{a}^\alpha = \operatorname{div} \boldsymbol{\sigma}^\alpha + \rho^\alpha \mathbf{b} + \hat{\mathbf{p}}^\alpha \tag{3}$$

where $\boldsymbol{a}^\alpha$ is the acceleration vector of α phase, $\boldsymbol{\sigma}^\alpha$ is the Cauchy stress tensor of α phase, $\boldsymbol{b}$ is the body force vector, $\hat{\mathbf{p}}^\alpha$ is the interaction vector of α phase against other phases.

Constitutive equations are the followings. The partial Cauchy stress of each phase is assumed as

$$\begin{aligned} \boldsymbol{\sigma}^s &= \boldsymbol{\sigma}' - (1-n)(s^w p^w + s^a p^a)\mathbf{I} \\ \boldsymbol{\sigma}^w &= -n s^w p^w \mathbf{I}, \quad \boldsymbol{\sigma}^a = -n s^a p^a \mathbf{I} \end{aligned} \tag{4}$$

where $\boldsymbol{\sigma}'$ is the skeleton stress tensor (e.g. Gallipoli et al. 2003), p^w is the pore water pressure and p^a is the pore air pressure. These pressures are defined as positive in compression. The interaction vector for each phase is assumed as

$$\begin{aligned} \hat{\mathbf{p}}^s &= -\hat{\mathbf{p}}^w - \hat{\mathbf{p}}^a \\ \hat{\mathbf{p}}^w &= p^w \operatorname{grad} n^w - \frac{n^w \rho^{wR} g}{k^{ws}} n^w \mathbf{v}^{ws} \\ \hat{\mathbf{p}}^a &= p^a \operatorname{grad} n^a - \frac{n^a \rho^{aR} g}{k^{as}} n^a \mathbf{v}^{as} \end{aligned} \tag{5}$$

where g is the gravity acceleration, k^{ws} and k^{as} is the permeability coefficient of water and air respectively. The compressibility of pore water under an isothermal condition is assumed as

$$\frac{D^s \rho^{wR}}{Dt} = \frac{\rho^{wR}}{K^w} \frac{D^s p^w}{Dt} \tag{6}$$

where K^w is the bulk modulus of pore water. The compressibility of pore air under an isothermal condition assumed as

$$\frac{D^s \rho^{aR}}{Dt} = \frac{1}{\Theta \bar{R}} \frac{D^s p^a}{Dt} \tag{7}$$

where Θ is the absolute temperature, $\bar{R}$ is the specific gas constant of air. The constitutive relation between water saturation and suction is assumed as

$$\frac{D^s s^w}{Dt} = c \frac{D^s p^c}{Dt} = c \frac{D^s (p^a - p^w)}{Dt} \tag{8}$$

where c is the specific water capacity. The specific water capacity is calculated from the soil water characteristic curve (SWCC). The SWCC is assumed as

$$\begin{aligned} s^w &= (s_s^w - s_r^w) s_e^w + s_r^w \\ s_e^w &= \left\{1 + \exp(a_{lg} p^c + b_{lg})\right\}^{-c_{lg}}, \quad p^c = p^a - p^w \end{aligned} \tag{9}$$

where s^w_s is the saturated (maximum) degree of saturation, s^w_r is the residual (minimum) degree of saturation and s^w_e is the effective water saturation. The relationship between s^w_e and suction p^c is assumed as a logistic function with the material parameters a_{lg}, b_{lg} and c_{lg}. The logistic SWCC is continuous function at $p^c = 0$; therefore the convergence in the iterative numerical scheme can be achieved. The SWCC during undrained cyclic shear has a similar shape as "wetting" curve (Unno et al. 2008). The above SWCC is modified to fit "wetting" curve during undrained cyclic shear as shown in later. The permeability coefficient of water and air are assumed to be dependent on the effective water saturation as

$$k^{ws} = k_s^w (s_e^w)^{\xi_k}, \quad k^{as} = k_s^a (1 - s_e^w)^{\eta_k} \tag{10}$$

where k^w_s is the saturated (maximum) coefficient of water permeability, k^a_s is the dry (maximum) coefficient of air permeability, ξ_k and η_k are the material parameters.

Combining these equations, we derive the governing equations which include the momentum balance equations of the overall three-phase material and the mass and momentum balance equations (continuity equations) of the pore water and air with the following assumptions. 1) The soil particle is incompressible, 2) the mass exchange among phases is neglected, 3) The material time derivative of relative velocities and advection terms of pore fluids to the soil skeleton are neglected, 4) an isothermal condition are assumed. The momentum balance equations of the overall three-phase material is derived as

$$\rho \mathbf{a}^s = \operatorname{div}\left\{\boldsymbol{\sigma}' - (s^w p^w + s^a p^a)\mathbf{I}\right\} + \rho \mathbf{b} \tag{11}$$

where ρ is the overall density of three-phase material. The mass and momentum balance equations of the pore water and air are derived as

$$\begin{aligned} &\left(\frac{n s^w \rho^{wR}}{K^w} - n\rho^{wR} c\right)\frac{D^s p^w}{Dt} + n\rho^{wR} c \frac{D^s p^a}{Dt} \\ &+ s^w \rho^{wR} \operatorname{div} \mathbf{v}^s \\ &+ \operatorname{div}\left\{\frac{k^{ws}}{g}\left(-\operatorname{grad} p^w + \rho^{wR}\mathbf{b} - \rho^{wR}\mathbf{a}^s\right)\right\} = 0 \end{aligned} \tag{12}$$

$$\begin{aligned} &\left(\frac{n s^a}{\Theta \bar{R}} - n\rho^{aR} c\right)\frac{D^s p^a}{Dt} + n\rho^{aR} c \frac{D^s p^w}{Dt} \\ &+ s^a \rho^{aR} \operatorname{div} \mathbf{v}^s \\ &+ \operatorname{div}\left\{\frac{k^{as}}{g}\left(-\operatorname{grad} p^a + \rho^{aR}\mathbf{b} - \rho^{aR}\mathbf{a}^s\right)\right\} = 0 \end{aligned} \tag{13}$$

This simplified formulation is called u-p^w-p^a formulation. Although the governing equations are derived in the regime of finite strain, we assume infinitesimal strain in the following study for simplicity.

2.2 Constitutive Equation for Skeleton Stress

A simplified elasto-plastic constitutive equation for skeleton stress is used here. Assuming that plastic deformation occurs only when the deviatoric stress ratio changes, the yield function is assumed as

$$f = \left\|\boldsymbol{\eta} - \boldsymbol{\alpha}\right\| - k = \left\|\mathbf{s}/p' - \boldsymbol{\alpha}\right\| - k = 0 \tag{14}$$

where p' is the mean skeleton stress, $\boldsymbol{s}$ is the deviatoric stress tensor, k is the material parameter which defines the elastic

region. $\boldsymbol{\alpha}$ is the kinematic hardening parameter (back stress) and its nonlinear evolution rule (Armstrong & Frederick 1966) is assumed as

$$\begin{aligned} \dot{\boldsymbol{\alpha}} &= a\left(b\dot{\mathbf{e}}^{p} - \boldsymbol{\alpha}\dot{\varepsilon}_{s}^{p}\right) \\ \dot{\varepsilon}_{s}^{p} &= \left\|\dot{\mathbf{e}}^{p}\right\| \end{aligned} \tag{15}$$

where a, b are the material parameters, $\dot{\mathbf{e}}^{p}$ is the plastic deviatoric strain rate tensor. With non-associated flow rule, the plastic potential function is assumed as

$$g = \left\|\boldsymbol{\eta} - \boldsymbol{\alpha}\right\| + M_{m}\ln\left(p'/p'_{a}\right) = 0 \tag{16}$$

where M_{m} is the material parameter which defines the critical state ratio, p'_{a} is p' when $\left\|\boldsymbol{\eta} - \boldsymbol{\alpha}\right\| = 0$. Finally the elastic module are assumed as

$$K^{e} = -K^{*}p' \quad G^{e} = -G^{*}p' \tag{17}$$

where K^{e} is the elastic bulk modulus, G^{e} is the elastic shear modulus, K^{*} and G^{*} are the dimensionless elastic module respectively.

2.3 Finite Element Formulation and Time Integration

Weak forms of the equations (11) - (13) are implemented in a finite element formulation. Newmark implicit scheme is used for time integration. The primary variables are the second-order material time derivative of displacement of soil skeleton $\mathbf{a}^{s}$, pore water pressure $\ddot{p}^{w}$ and pore air pressure $\ddot{p}^{a}$. The weak forms are linearized and solved by Newton-Raphson method iteratively at each time step. The linearized forms of the weak forms are derived as

$$\begin{aligned} &D\delta w^{s}[\Delta\mathbf{a}^{s}] + D\delta w^{s}[\Delta\ddot{p}^{w}] + D\delta w^{s}[\Delta\ddot{p}^{a}] = -\delta w^{s}_{(k)} \\ &D\delta w^{w}[\Delta\mathbf{a}^{s}] + D\delta w^{w}[\Delta\ddot{p}^{w}] + D\delta w^{w}[\Delta\ddot{p}^{a}] = -\delta w^{w}_{(k)} \\ &D\delta w^{a}[\Delta\mathbf{a}^{s}] + D\delta w^{a}[\Delta\ddot{p}^{w}] + D\delta w^{a}[\Delta\ddot{p}^{a}] = -\delta w^{a}_{(k)} \end{aligned} \tag{18}$$

where $D\delta w^{s}[\Delta\mathbf{a}^{s}]$ is directional derivative of δw^{s} with respect to $\Delta\mathbf{a}^{s}$, the $\delta w^{s}_{(k)}$ is the residual at the iteration step of (k). The iteration is continued until the norm of the residual vectors becomes less than the convergence tolerance of 1.0×10^{-7}. In the finite element formulation, Galerkin method and isoparametric 8-node elements are used. The soil skeleton displacement and the fluid pressures are approximated at 8 nodes and 4 nodes respectively to avoid a volumetric locking.

2.4 Implicit Stress Integration

Implicit stress integration and consistent tangent modulus at infinitesimal strain (e.g. Simo & Taylor 1985) are used to achieve the convergence of global iteration of (18). The return mapping algorithm in stress space is used as

$$\begin{aligned} \mathbf{r}_{1} &= \boldsymbol{\sigma}' - \boldsymbol{\sigma}'^{(\mathrm{tr})} + \Delta\gamma\mathbf{c}^{e}\frac{\partial g}{\partial\boldsymbol{\sigma}'} \\ \mathbf{r}_{2} &= \boldsymbol{\alpha} - \boldsymbol{\alpha}_{n} + \Delta\boldsymbol{\alpha} \\ r_{3} &= f \end{aligned} \tag{19}$$

where $\boldsymbol{\sigma}'^{(\mathrm{tr})}$ is the trial skeleton stress for a given strain increment at the global iteration step, $\Delta\gamma$ is the plastic multiplier, $\boldsymbol{c}^{\mathrm{e}}$ is the elastic tensor, $\boldsymbol{\alpha}_{\mathrm{n}}$ is $\boldsymbol{\alpha}$ at the previous time step, $\Delta\boldsymbol{\alpha}$ is the increment of $\boldsymbol{\alpha}$. Until the norm of left-handed residual vector $\boldsymbol{r}$ of (19) becomes less than the convergence tolerance of 1.0×10^{-10}, the nonlinear equations of (19) are solved iteratively by Newton-Rapshon method with respect to $\boldsymbol{\sigma}'$, $\boldsymbol{\alpha}$ and $\Delta\gamma$. The skeleton stress and back stress for a given strain increment at the global iteration step are obtained by local iteration of (19) at each stress integration point. The consistent tangent modulus is obtained as

$$\mathbf{c}^{ep} = \frac{\partial\boldsymbol{\sigma}'}{\partial\boldsymbol{\varepsilon}^{e(tr)}} = \frac{\partial\boldsymbol{\sigma}'}{\partial\boldsymbol{\varepsilon}} \tag{20}$$

where $\boldsymbol{c}^{\mathrm{ep}}$ is the elasto-plastic tensor, $\boldsymbol{\varepsilon}^{\mathrm{e(tr)}}$ is the trial elastic strain (given strain). The differentiation of (20) is carried out at each converged stress derived from the local iteration of (19).

3. NUMERICAL DATA FOR SIMULATION

Numerical predictions of seismic behavior of an actual fill slope are performed with the proposed numerical method. The fill slope is located at a residential area in Sendai city, Japan. The seismic motions on the fill and moisture content in the fill have been measured by the authors since 2006 (Mori et al. 2008).

3.1 Material Parameters

The fill material is silty sand. The physical and mechanical properties are investigated with in-situ and laboratory tests. The material parameters of the constitutive models for skeleton stress and SWCC are determined through the calibration of the undrained cyclic triaxial tests with unsaturated soil. The de-tailed description of the testing method is referred to Unno et al. (2008).

The specimen was made of silty sand obtained from the in-situ fill. The initial dry density of the specimen was about 1.2 g/cm3 which roughly agreed with the dry density of the in-situ fill. The effective degree of water saturation was from about 23 % to 60 % by controlling air pressure during the isotropic consolidation process. The pore water pressure was almost zero after the consolidation and the pore air pressure increased with the decrease in water saturation. The net stress was about 45 kPa for all specimens and the mean skeleton stress varied with the initial suction dependent on initial water saturation.

The cyclic shear was applied to the specimen under undrained air and water conditions. The input axial strain was the sinusoidal wave with multi step amplitudes whose single amplitudes were 0.2, 0.4, 0.8, 1.2, 1.6, and 2.0 with every ten cycles. The frequency of the sinusoidal wave was 0.005 Hz. This loading rate is slow enough to achieve an equilibrium condition between air and water pressure.

Figure 1 (a) shows SWCC during the undrained cyclic triaxial tests. The measured SWCC are not on the main drying and wetting curves obtained from water retention tests; therefore the scanning curves should be used to reproduce the SWCC during undrained cyclic shear. The

logistic SWCC function of (9) is modified to reproduce the scanning curves with simple scaling method in Figure 1 (b).

$$s_e^w = \frac{1-s_{e0}^w}{1-s_{e1}^w}\left[1+\exp(a_{lg}\,p_a^c + b_{lg})\right]^{-c_{lg}} + \left(1-\frac{1-s_{e0}^w}{1-s_{e1}^w}\right) \quad (21)$$

$$p_a^c = \frac{p_1^c}{p_0^c}\left\{\frac{p_0^c}{p_0^c - p_2^c}(p^c - p_0^c) + p_0^c\right\}$$

where $p^c{}_0$ and $s^w{}_{e0}$ are the initial suction and effec-tive water saturation respectively, $p^c{}_1$ (= $p^c{}_0$) and $s^w{}_{e1}$ are the suction and effective water saturation on main wetting curve respectively and $p^c{}_2$ is the suction on the scanning curve at $s^w{}_e$ = 1. The modified logistic SWCC roughly reproduce the measured SWCC during undrained shear in Figure 1 (a). Further investigation on SWCC during undrained shear is necessary for more precise reproduction.

In the triaxial test simulations, the finite element formulation presented in the previous section is not used. Assuming that the variables in the specimen are homogeneous, only the local equilibrium is considered. Table 1 shows the calibrated material parameters of the constitutive model. Figure 2 shows the time histories of pore water pressure, pore air pressure, suction, mean skeleton stress (positive in compression) and void ratio from tests and simulations in the case with the initial effective water saturation of 46 %. In the test results (denoted "Test" in the figures), the pore water and air pressure increase, while the suction and mean skeleton stress decrease during cyclic undrained shear. In this case, the suction and the mean skeleton stress do not attain zero, which means that the specimen do not liquefy completely. In the simulated results (denoted "Model" in the figures), the model well reproduces the overall tendency of the test results. Therefore, the simplified constitutive equation of soil skeleton is applicable to predict pore water and air responses of unsaturated soil in the framework of three-phase porous media theory. The modifications of the constitutive equations are necessary for more precise reproduction.

3.2 Finite Element Model and Boundary Conditions

Figure 3 shows the cross section of the in-situ fill slope. Figure 3 (b) shows the close view of the slope where three seismometers are installed. Assuming plane strain condition, the cross section is used for finite element modeling. The fill is elasto-plastic material and the air, clay and base rock are linear elastic material with Lame coefficients λ and μ. Kelvin type viscosity is assumed in all materials and its viscous coefficient is proportional to the elastic modulus with a multiplier coefficient α. Table 1 and 2 show the material parameters for all layers. Smooth infiltration of rain to the fill is simulated with "aerial elements" which have a special SWCC and large permeability of water in vertical direction (Uzuoka et al. 2008). Use of the aerial elements makes no numerical treatment (e.g. switching between natural and basic boundary) on the surface.

The soil displacement at the bottom boundary is fixed in all directions and the lateral boundaries are vertical rollers. The bottom and lateral boundaries are impermeable and a

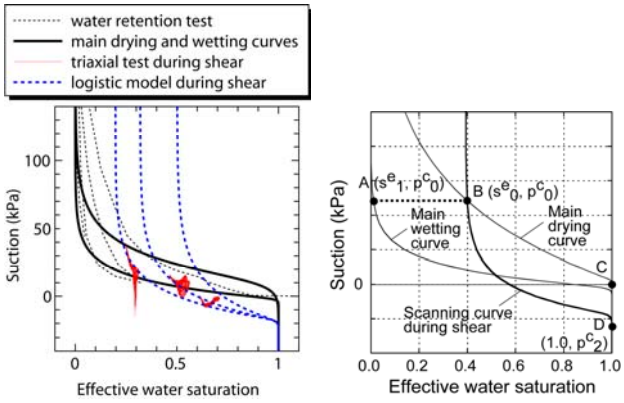

(a) Test and model (b) Scaling method

Figure 1 Soil water characteristic curves (SWCC)

Table 1 Material parameters of silty sand from the fill

Elasto-plastic model parameters	
Dimensionless shear modulus, G^*	1011
Dimensionless bulk modulus, K^*	758
Nonlinear hardening parameter, a	5879
Nonlinear hardening parameter, b	-1.47
Critical state stress ratio, M_m	1.47
Yield function parameter, k	0.0085
SWCC parameters	
Maximum degree of saturation, $s^w{}_s$	0.99
Minimum degree of saturation, $s^w{}_r$	0.35
Main drying curve, a_{lg}, b_{lg}, c_{lg}	1.5, 3.0, 0.05
Main wetting curve, a_{lg}, b_{lg}, c_{lg}	0.25, -2.5, 0.2
Scaling parameter, $p^c{}_2$ (kPa)	-15
Physical parameters of water and air	
Bulk modulus of water, K^w (kPa)	2.0×10^6
Real density of air, ρ^{aR} (t/m^3)	1.23×10^{-3}
Gas parameter, $1/(\bar{R}\Theta)$ (s^2/m^2)	1.25×10^{-5}

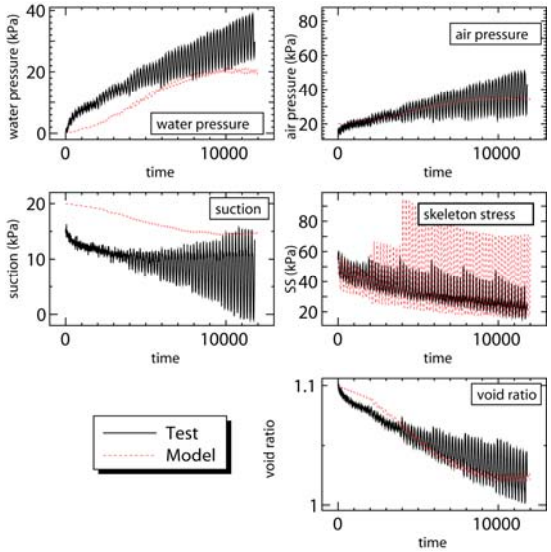

Figure 2 Test and simulation with initial effective water saturation of 46 %

part of the surface on the clay layer is permeable with zero water pressure.

Figure 4 shows the time history of input acceleration. This acceleration history is a deconvolved wave from observed wave at S4 during 2008 Iwate-Miyagi Nairiku earthquake with elastic wave propagation theory. The coefficients in Newmark implicit time integration are 0.5 and 0.25. The time increment is 0.002 seconds.

4. NUMERICAL RESULTS OF SEEPAGE AND SEISMIC ANALYSES

Simulations of the seismic responses of the unsaturated fill slope during 2008 Iwate-Miyagi Nairiku earthquake are performed.

4.1 Initial Conditions with Seepage Analyses

The moisture condition in the fill is strongly dependent on weather conditions before the earthquake. Before the 2008 Iwate-Miyagi Nairiku earthquake there were no heavy rain; therefore low ground water table is assumed in this study. Rainfall is applied on the top boundary in the seepage analyses without inertia terms in (11) - (13). Because of difficulties to reproduce the actual rainfall history since distant past, the precipitation is assumed as 175 mm/year. This amount of infiltration roughly corresponds to the amount of measured flux at the toe of the fill when it has not rained for about a week before the measurement. Figure 5 shows the distributions of water saturation after the precipitation after the steady state is achieved. The ground water table roughly agrees with the measured one without heavy precipitation before the measurement.

4.2 Seismic Response of the Fill

Following the seepage analyses, the seismic response analyses are performed with the input acceleration in Figure 4. Figure 6 shows the time histories of observed and computed acceleration at top of the fill (S2) and slope of the fill (S3). At the top of the fill (S2), the simulation well reproduces the observed acceleration before about 5 seconds. After about 5 seconds, computed acceleration is larger than the observed one until about 10 seconds. Meanwhile the simulation underestimates the observed one after about 10 seconds. It is possible that these errors are mainly due to the underestimation of undrained cyclic strength of in-situ soil. Similar underestimation of the observed acceleration is shown at slope of the fill (S3). Figure 7 shows the Fourier spectrums of observed and computed acceleration at S2 and S3. The simulations well reproduce the predominant frequencies while the simulations underestimate the amplitudes at high frequency range.

Figure 8 shows the distributions of skeleton stress reduction ratio after 15 seconds in both cases. The skeleton stress reduction ratio is defined as $1 - p'/p'_0$ where p'_0 is the initial value of p'. The skeleton stress reduction ratio in the saturated fill below the ground water table reaches almost one at some elements; liquefaction occurs in some saturated area although no liquefaction evidence was observed at the site. It is possible that the underestimation of undrained cyclic strength of in-situ soil causes this error.

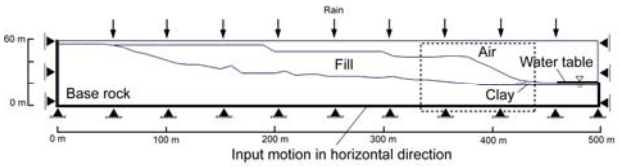

(a) Whole model

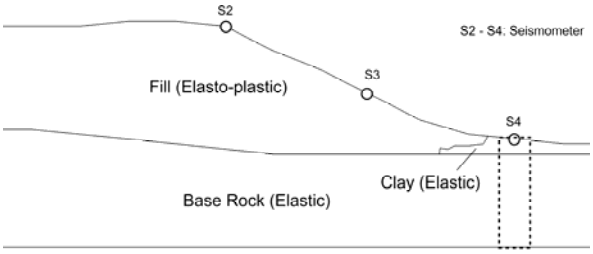

(b) Close view at the slope

Figure 3 Cross section of the fill

Table 2 Material parameters for seismic analysis

	Rock	Fill	Clay	Air
n	0.27	0.57	0.64	1.0
ρ^{sR} (t/m^3)	2.72	2.59	2.72	0.0
ρ^{wR} (t/m^3)	1.0			
k^w_s (m/s)	-	1.0×10^{-7}	1.0×10^{-7}	10.0
k^a_s (m/s)	-	1.0×10^{-8}	1.0×10^{-8}	10.0
ξ_k / η_k	-	3.0/0.333	3.0/0.333	0.1/10.0
λ (kPa)	4500000	-	186116	0.01
μ (kPa)	4500000	-	46529	0.001
α	0.0032	0.0013	0.0013	-

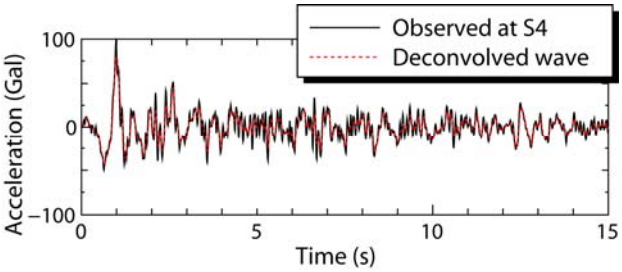

Figure 4 Time history of input acceleration (deconvolved wave at the base)

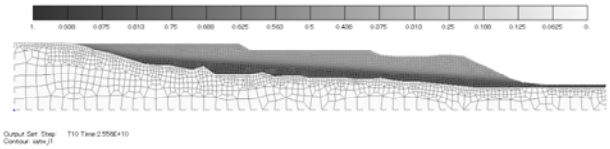

Figure 5 Distribution of degree of water saturation before the earthquake

5. CONCLUSIONS

A dynamic three-phase coupled analysis is newly proposed. The equations governing the dynamic deformation of unsaturated soil are derived here based on porous media theory and constitutive models. The finite element formulation is solved by fully implicit method and the skeleton stress is also implicitly integrated. Seepage and seismic behaviors of an actual fill slope during 2008 Iwate-Miyagi Nairiku earthquake are simulated. The simulation well reproduced the observed acceleration until about 5 seconds. It is possible that the errors are mainly due to the underestimation of undrained cyclic strength of in-situ soil.

References:

Armstrong, P.J. & Frederick, C.O. (1966), "A mathematical representation of the multiaxial Bauschinger effect," C.E.G.B. Report RD/B/N731, Berkeley Nuclear Laboratories, Berkeley, UK.

de Boer, R. (2000), "Contemporary progress in porous media theory," *Applied Mechanics Reviews*, **53**(12), 323-369.

Gallipoli, D., Gens, A., Sharma, R. and Vaunat, J. (2003), "An elasto-plastic model for unsaturated soil incorporating the effects of suction and degree of saturation on mechanical behaviour," *Geotechnique*, **53**(1), 123-135.

Meroi, E.A. and Schrefler, B.A. (1995), "Large strain static and dynamic semisaturated soil behavior," *Int. J. for Numerical and Analytical Methods in Geomechanics*, **19**(8), 1-106.

Mori, T., Kazama, M., Uzuoka, R. and Sento, N. (2008), "Fill slopes: Stability assessment based on monitoring during both heavy rainfall and earthquake motion," *Proc. of Landslides and Engineered Slopes*, 1241-1246.

Okamura, M. and Soga, Y. (2006), "Effects of pore fluid compressibility on liquefaction resistance of partially saturated sand," *Soils and Foundations*, **46**(5), 93-104.

Schrefler, B.A. (2002), "Mechanics and thermodynamics of saturated/unsaturated porous materials and quantitative solutions," *Applied Mechanics Reviews*, **55**(4), 351-388.

Selim, A. and A. Burak, G. (2006), "Cyclic stress-strain behavior of partially saturated soils," *Proc. 3rd Int. Conf. on Unsaturated Soils*, 497-507.

Simo, J.C. and Taylor, R.L. (1985), "Consistent tangent operators for rate-independent elastoplasticity," *Computer Methods in Applied Mechanics and Engineering*, 48, 101-118.

Unno, T., Kazama, M., Uzuoka, R. and Sento, N. (2008), "Liquefaction of unsaturated sand considering the pore air pres-sure and volume compressibility of the soil particle skeleton," *Soils and Foundations*, **48**(1), 87-99.

Uzuoka, R., Sento, N., Kazama, M. and Unno, T. (2005), "Landslides during the earthquake on May 26 and July 26, 2003 in Miyagi, Japan," *Soils and Foundations*, **45**(4), 149-163.

Uzuoka, R., Kurihara, T., Kazama, M. and Sento, N. (2008), "Finite element analysis of coupled system of unsaturated soil and water using aerial elements," *Proc. the Conference on Computational Engineering and Science* 13, 219-222. (in Japanese)

Yoshimi, Y., Tanaka, K. and Tokimatsu, K. (1989), "Liquefaction resistance of a partially saturated sand," *Soils and Foundations*, **29**(3), 157-162.

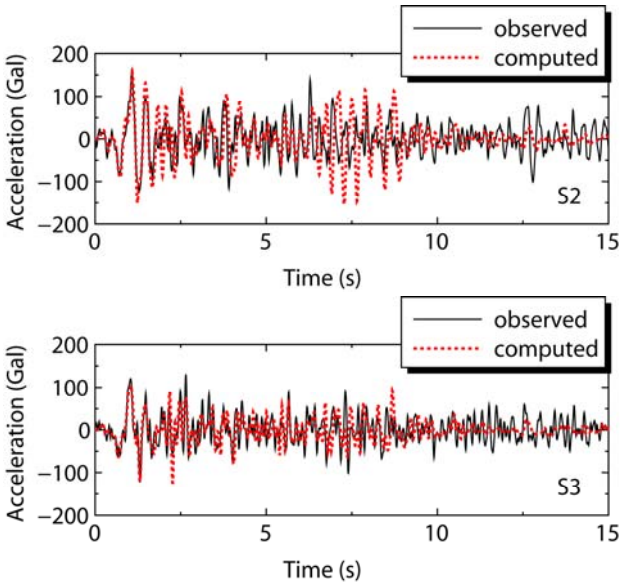

Figure 6 Time histories of observed and computed acceleration at top of the fill (S2) and slope of the fill (S3)

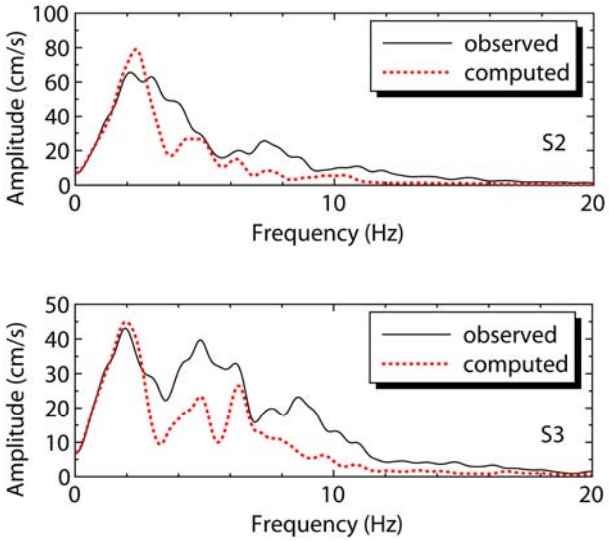

Figure 7 Fourier spectrums of observed and computed acceleration at top of the fill (S2) and slope of the fill (S3)

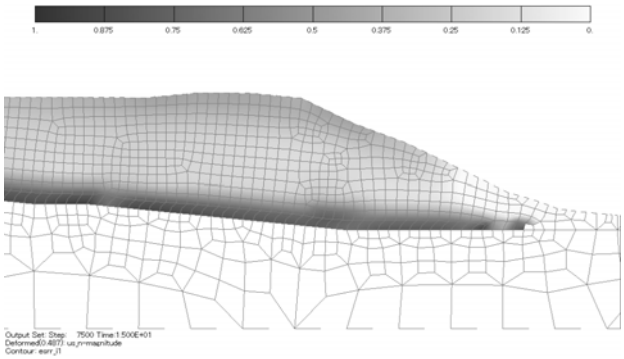

Figure 8 Distribution of skeleton stress reduction ratio after the earthquake (displacement/model = 30)

Sixth International Conference on Urban Earthquake Engineering
March 3-4, 2009, Tokyo Institute of Technology, Tokyo, Japan

EFFECTS OF EXISTING PILES ON LATERAL RESISTANCE OF NEW PILES BASED ON CENTRIFUGE TESTS

Shuji Tamura[1], Keisuke Adachi[2], Sakamoto Tadashi[3], Yasuhito Higuchi[2] and Yasuhiro Hayashi[4]

1) Associate Professor, DPRI, Kyoto University, Japan
2) Graduate Student, Kyoto University, Japan
3) Researcher, Shimizu Corporation, Japan
4) Professor, Kyoto University, Japan
tamura@sds.dpri.kyoto-u.ac.jp

Abstract: To investigate effects of existing piles on the lateral response of a new pile when piles of an old building are left derelict, cyclic lateral-loading centrifuge tests were performed on a new pile located at the center of 2 × 2 existing piles. Results suggest the following conclusions. (1) The amplitude of the earth pressure of the existing piles is small when the new pile's lateral displacement is small. Consequently, the existing piles have no marked effects on the new pile's lateral resistance. (2) The amplitude of the earth pressure increases not only at the right side but also at the left side of the existing pile when the new pile moves to the left side and its lateral displacement becomes larger. Therefore, the horizontal subgrade reaction of existing piles is small and the existing piles slightly increase the new pile's lateral resistance.

1. INTRODUCTION

Many urban areas are located on soft ground such as reclaimed land in Japan. Recently, urban renewal has proceeded and the number of cases that replacement of old buildings supported by pile foundations has increased. The piles are extracted or reused as piles of new buildings or are often left derelict when the buildings are rebuilt. In cases where the piles of old buildings are reused, several studies have been made of the connection of pile heads (e.g., Sei et al. (2001), Horii et al. (2007)). Reportedly, a flexible connection at the pile head is suitable for the reuse of piles. In cases where piles of old buildings are left derelict, the existing piles can affect the lateral response of the new piles of buildings. Miyata and Suzuki (2004) reported, based on a study using the 3D finite difference method, that effects of existing piles on the lateral resistance of the new pile are slight. However, that numerical analysis was performed using a small pile displacement (2 cm); no experimental studies have ever been reported. Therefore, knowledge of effects of existing piles on a new pile's lateral response remains limited.

Based on results of cyclic lateral-loading centrifuge tests performed on a new pile located at the center of 2 × 2 existing piles, this study will specifically examine the effects of existing piles on the new pile's lateral response when piles of an old building are left derelict.

2. CENTRIFUGE TESTS PERFORMED

2.1 Test cases

Centrifuge tests were performed at 40 × *g* centrifugal acceleration using a geotechnical centrifuge at the Disaster Prevention Research Institute, Kyoto University. Figure 1 portrays the centrifuge test cases. In Case 1, a single pile, representing a pile of a new building, was embedded in dry sand. In Case 2, in addition to a single pile, a 2 × 2 pile group, representing piles of an old building, were also embedded in dry sand. The single pile and the 2 × 2 pile groups are defined respectively as new

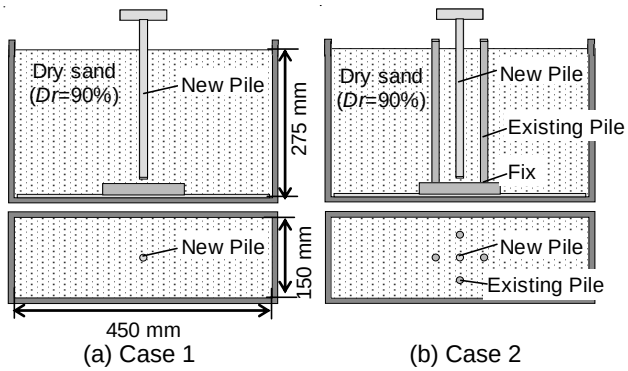

Figure 1 Test cases

Table 1 Conditions of new and existing piles in prototype and model scale

		unit	Prototype	Model
Existing piles (2×2)	Diameter	m	0.48	0.012
	EI	kN m²	0.824×10^{5}	0.322×10^{-1}
New pile (single)	Diameter	m	0.48	0.012
	EI	kN m²	4.198×10^{5}	1.640×10^{-1}

piles and existing piles. The pile models were prepared in a rigid aluminum alloy box that was 450 mm long, 150 mm wide, and 300 mm high. The soil model used for the dry sand deposit was Toyoura sand (D_{50}=0.21 mm) with *Dr*=90%. The sand layer was prepared by pluviating dry sand.

2.2 Test models

The existing piles were modeled with a 12-mm-diameter, 268-mm-long, and 0.7-mm-thick round brass pipe. The bending stiffness *EI* of existing piles was 0.322×10^{-1} kN·m^2. The pile heads were free; their tips were linked rigidly to the rigid box, as presented in Fig. 2. The new pile was modeled with a 12-mm-diameter, 296-mm-long, and 2.0-mm-thick round stainless steel pipe. The bending stiffness of the new pile was 1.64×10^{-1} kN·m^2. The pile head was rigidly linked with the footing; its tip was free. The center-to-center distance of the existing piles was 60 mm (5*D*), in which *D* is the pile diameter. The new pile was located at the centrally, equidistant from each of the 2 × 2 existing piles. The surfaces of new and existing piles are smoother than that of the prototype pile. For that reason, Toyoura sand was pasted on the surfaces of piles. Conditions of the piles in the prototype and model scale are presented in Table 1.

Figure 2 shows strain gauge pairs attached to the exterior faces of the new pile and Pile D of the existing piles. Pairs of strain gauges were placed at 28 mm intervals. Earth pressure transducers were also attached to the new pile and Pile D at depths of 60 mm and 120 mm at the piles' left and right sides. The base line of the earth pressure amplitude was set to zero before loading tests. The location of sensors for the new pile in Case 1 was the same as that in Case 2.

Lateral displacement cycles were applied to the footing of the new pile with aboveground height of 56 mm through an electric actuator. The footing was fixed rigidly with the load frame. The lateral load was transmitted from the loading frame to the pile along a horizontal guide frame with a sway motion. The displacements were monitored using a displacement transducer. The corresponding load was calculated by differentiation of the strain at the pile head above the ground. The loading tests were performed without exceeding the new pile's elastic limit.

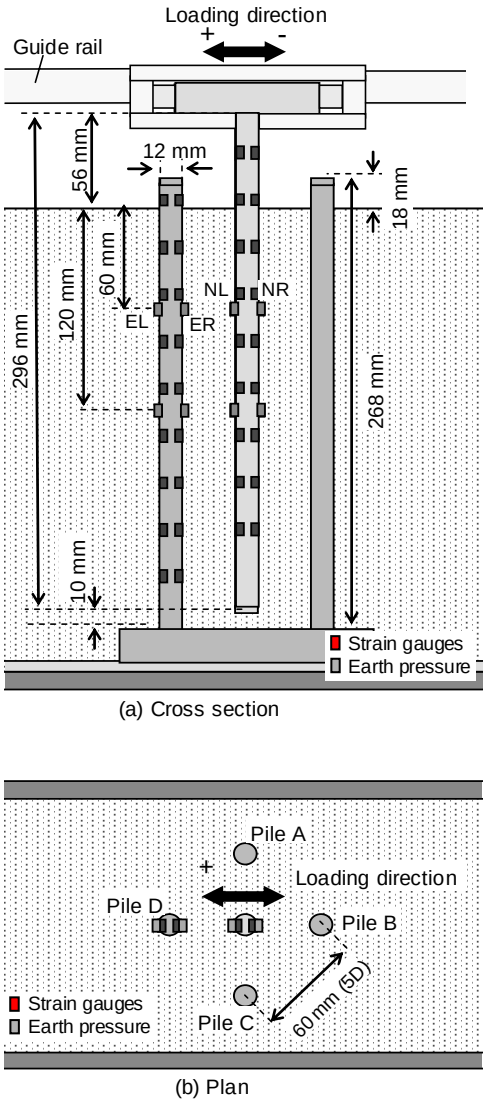

Figure 2 New and existing piles (Case 2)

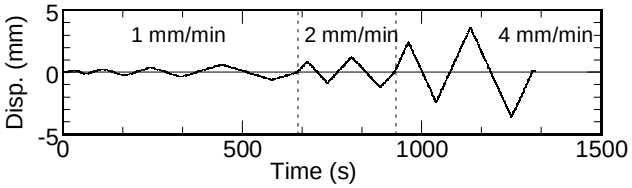

Figure 3 Lateral displacement of new pile in model scale (Case 1)

The load tests were performed using a controlled-displacement approach with amplitudes ranging from 0.12 mm in the first cycle to 3.6 mm in the last cycle. Figure 3 presents time histories of the displacement of the pile head with aboveground height of 56 mm in Case 1. The velocity of lateral loading is changed with the pile head displacement as 1 mm/min (*y/D*=0.01–0.05), 2 mm/min (*y/D*=0.07–0.1) and 4 mm/min (*y/D*=0.2–0.3), in which *y* is the amplitude of pile head displacement peaks. The loading velocity is low. Therefore, "dynamic effects"

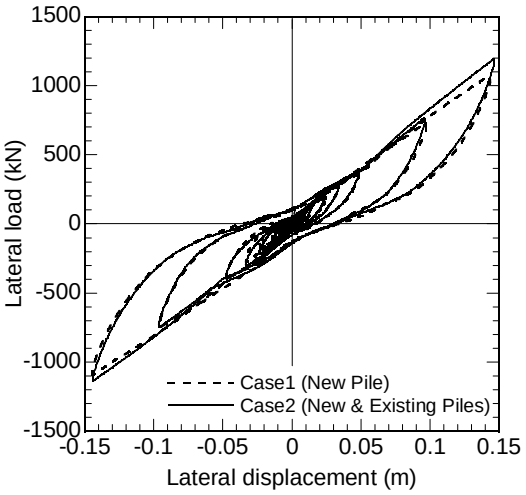

Figure 4 Relation between lateral displacement and lateral load of new pile

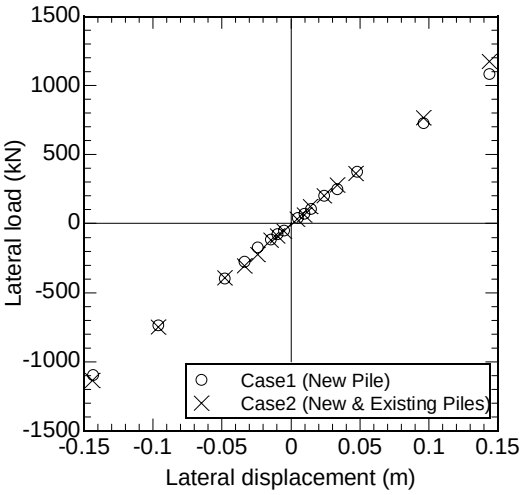

Figure 5 Relation between lateral displacement and lateral load peak of new pile

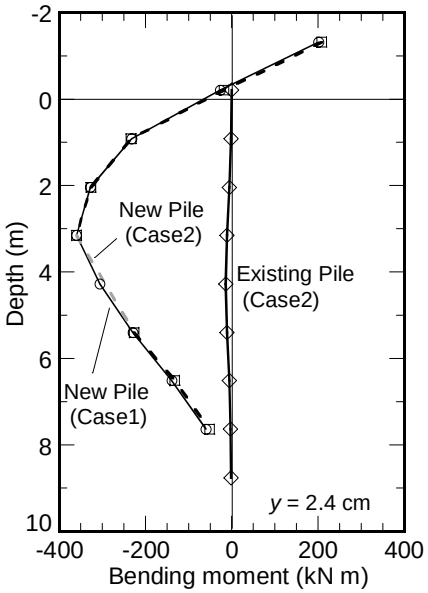

Figure 6 Vertical distribution of bending moment at y=2.4 cm

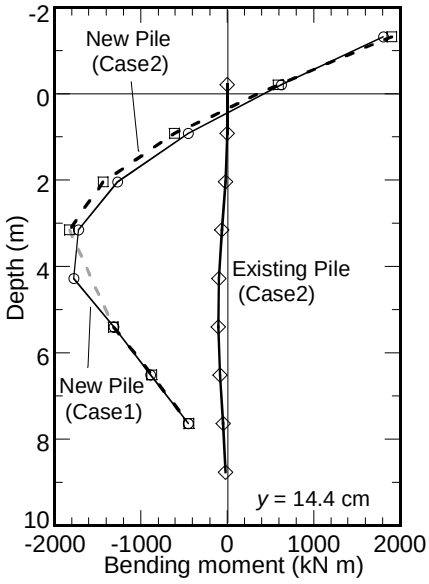

Figure 7 Vertical distribution of bending moment at y=14.4 cm

are negligible. All data presented in the following sections are of prototype scale.

3. TEST RESULTS

3.1 Lateral displacement and lateral load

Figure 4 shows the relation between the lateral displacement and the new pile's lateral load in Cases 1 and 2 to elucidate effects of the existing piles on the lateral load. The hysteretic responses in Cases 1 and 2 are almost identical. Figure 5 presents a comparison of the lateral displacement and the peak value of the lateral load. The lateral load tends to increase linearly with the relative displacement in both cases. The lateral load peaks in Cases 1 and 2 are almost identical for lateral displacement of less than 2 cm. The lateral load in Case 2 is slightly larger than that in Case 1 for larger lateral displacement, which indicates that the lateral resistance of a new pile located in a place surrounded by existing piles shows a tendency of a slight increase.

3.2 Bending moments of new and existing piles

The vertical distributions of the bending moments of new piles in Cases 1 and 2; the existing piles in Case 2 at y=2.4 cm (y/D=0.05) and 14.4 cm (y/D=0.3) are portrayed in Figs. 6 and 7. The strain data of the new pile at G.L.-4.1 m in Case 2 were not recorded. The vertical distribution of the bending moment of the new pile in Case 2 is identical to that in Case 1 at y=2.4 cm. The bending moment amplitude of the existing pile is extremely small, indicating that the bending moments of

existing piles are affected slightly by the new pile's lateral loading.

The maximum amplitude of the bending moment of the new pile in Case 2 is slightly larger than that in Case 1 at y=14.4 cm. The bending moment occurred at the middle part of the existing pile, indicating that the respective bending moments of existing piles are affected by the new pile's lateral loading. The bending moment at the existing pile tip is extremely small, suggesting that the fixed boundary condition did not affect the existing piles' lateral response.

4. KINEMATIC INTERACTION BETWEEN NEW AND EXISTING PILES

The horizontal subgrade reaction of piles corresponds to the difference between the left-side and right-side earth pressures. Figure 8 depicts the time histories of lateral displacement and earth pressure at the left and right sides of the new pile in Case 1. The amplitude of the left-side earth pressure (NL) increases, but the amplitude of the right-side earth pressure (NR) is extremely small when the new pile moves to the left side, which indicates that a horizontal subgrade reaction acts on the new pile in a direction from left to right and its amplitude is almost identical to that of the left-side earth pressure.

To investigate the kinematic interaction between new and existing piles, the time histories of the new pile's lateral displacement, and earth pressure at the left and right sides of the new pile and existing pile (Pile D) in Case 2 are shown in Fig. 9. The tendency of the earth pressure of the new pile resembles that presented in Case 1. The amplitude of the left-side earth pressure (NL) increases, but the amplitude of the right-side earth pressure (NR) is extremely small when the new pile moves to the left side. In contrast, the tendency of the earth pressure of the existing pile differs greatly from that of the new pile. The amplitude of the earth pressure increases not only at the right side (ER) but also at the left side (EL) of Pile D when the new pile moves to the left side and its lateral displacement becomes larger. The left-side earth pressure is about half of the amplitude of the right-side earth pressure.

5. DISCUSSION

The small earth pressure of the existing pile (ER), as portrayed in Fig. 9(c), indicates that the existing pile receives a small force from the loading of the new pile when the new pile's lateral displacement is small. Therefore, the existing piles have no marked effects on the new pile's lateral resistance. The increase of the right -side earth pressure of the existing pile (ER) indicates

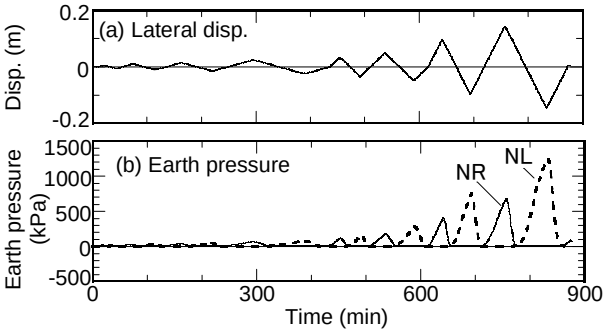

Figure 8 Lateral displacement and earth pressure of new pile at G.L.-2.4 m

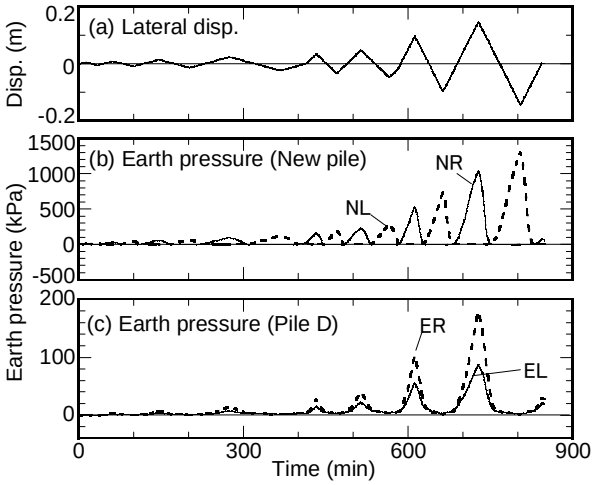

Figure 9 Lateral displacement, earth pressure of new pile and earth pressure of existing pile (Pile D) at G.L.-2.4 m

that the existing piles receive the force from the loading of the new pile through the soil between the new and existing piles when the new pile's lateral displacement increases. The increase of the left side earth pressure of the existing pile (EL) indicates that the force from the new pile transmits to the outside soil of the existing pile. Therefore, the horizontal subgrade reaction of the existing piles is small: the existing piles do not substantially affect the new pile's lateral resistance.

6. CONCLUSIONS

Cyclic lateral-loading centrifuge tests were performed on the new pile located at the center of the 2 × 2 existing piles. The following conclusions are drawn:

1) The amplitude of the earth pressure of the existing pile is small when the new pile's lateral displacement is small. Therefore, the existing piles have no marked effects on the new pile's lateral resistance.
2) The amplitude of the earth pressure increases not only

at the right side but also at the left side of the existing pile when the new pile moves to the left side and its lateral displacement increases. Therefore, the horizontal subgrade reaction of the existing piles is small and the existing piles slightly increase the new pile's lateral resistance.

Acknowledgments:

The authors are grateful for financial support from the Ministry of Land, Infrastructure, Transport and Tourism, Japan.

References:

Sei, H., Chatani, F. and Fujii, A. (2001), "Enhancing seismic performance of pile foundation by using existing piles and non-rigid connection method of pile head", *Summaries of Technical Papers of Annual Meeting Architectural Institute of Japan*, B-1, Structures I, pp. 429–430. (in Japanese)

Horii, Y., Nagao, T., Kawata M., Ishizawa S. and Ono, S. (2007), "Reuse of existing piles using flexible connection at pile head", *Journal of Architecture and Building Science*, AIJ, Vol. 13, No. 25, pp. 81–84. (in Japanese)

Miyata, A. and Suzuki, M. (2004), "Influence of old piles left underground on new pile resistance", *Annual Report of Kajima Technical Research Institute*, Kajima Corporation, No. 52, pp. 29–34. (in Japanese)

Sixth International Conference on Urban Earthquake Engineering
March 3-4, 2009, Tokyo Institute of Technology, Tokyo, Japan

STABILITY OF OIL TANK SUPPORTED BY PILED-RAFT FOUNDATION ON LIQUEFIABLE SAND

Jiro Takemura[1)], Shinichiro Imamura[2)], and Takashi Yagi[3)]

1) Associate Professor, Department of Civil and Environmental Engineering, Tokyo Institute of Technology, Japan
2) Senior Researcher, Nishimatsu Technical Research Center, Nishimatsu Construction Co. Ltd, Kanagawa, Japan
3) Head of Civil Engineering Inspection Section, Hazardous Materials Safety Techniques Association, Tokyo, Japan
jtakemur@cv.titech.ac.jp, sinichiro_imamura@nhsimatsu.co.jp

Abstract: In this study, dynamic centrifuge model tests were performed to investigate the mechanical behavior of oil tank supported by piled-raft foundation on liquefiable sand. In the centrifuge tests, two types of foundation were modeled, one is slab foundation and the other piled-raft foundation. The piles used for the latter foundation is relatively short and embedded in the loose sand, and the vertical load supported by the raft, (RLP: Raft Load Proportion) was about 50% before shaking. Various types of sensor were instrumented in the models, such as accelerometers, pore water pressure transducers, displacement transducers, and strain gages of the piles. Beneath the foundation, excess pore water pressures generated by the shaking are higher for the raft foundation than the slab foundation especially at the deep depth near the pile tips. The higher excess pore water pressure causes the decrease of pile bearing load, resulting in the increase of RLP. Although the settlement of the piled raft foundation was larger than that of the slab foundation due to the increase of raft load, the uneven settlement was smaller for the piled raft foundation than the slab foundation.

1. INTRODUCTION

Majority of existing oil storage tanks in Japan were constructed before early 1970's when the soil liquefaction was first considered in the design of tank foundation. Since the 1995 Hyogoken Nanbu earthquake, originally the 1964 Niigata earthquake and the 1978 Miyagiken-oki earthquake (Ishihara at al., 1980), it has become an urgent matter for geotechnical engineers to assess the seismic stability of existing oil storage tanks and implement proper countermeasures against soil liquefaction. In the assessment of the oil tank with slab foundation, liquefaction potential, P_L, is adopted and a layer with F_L less than a unity can be allowable if the P_L in the ground less than 5.0. However, for the pile foundation, the liquefaction is not allowed and some countermeasures should be applied when it is expected.

Piled raft foundation is considered as a rational foundation system for the subsoil with medium strength, because the slab (raft) and piles can share the design load. However, the soil-structure interaction of this type of foundation is very completed with variation of the load proportion of raft and piles. To study the mechanical behavior of the piled raft foundation, centrifuge model tests have been conducted by various researchers both on static and dynamic conditions (e.g., Horikoshi et al. (2003a, 2003b). However, dynamic behavior of the piled raft foundation on liquefiable sand has not been well studied.

In this study, dynamic centrifuge model tests were performed to investigate the mechanical behavior of oil tank supported by piled-raft foundation on liquefiable sand. In the centrifuge tests, two types of foundation were modeled, one is slab foundation and the other piled-raft foundation. The piles used for the latter foundation is relatively short and embedded in the loose sand, and the vertical load supported by the raft, (RLP: Raft Load Proportion) was about 50% before shaking. The effects of soil liquefaction on the load proportion of raft and piles, and resulting foundation behavior are discussed in this paper.

2. CENTRIFUGE TESTS

2.1 Soil used and Model Foundation

In centrifuge modeling, a viscous liquid is often used as the pore-fluid to overcome the mismatch in the similitude concerning seepage and dynamic events. In this study, however, fine silica sand No.8 having relatively low permeability was used with water as the pore-fluid. Properties of the silica are shown in Table 1. In 50g, the permeability of sand in prototype scale is 50 times that in 1g as shown in the table. Liquefaction curve obtained from cyclic triaxial tests on the silica sand No.8 with Dr=50% is shown in Figure 1

Two types of foundation, 1) slab foundation and 2) piled raft foundation were used in the centrifuge tests. Test set up for the dynamic centrifuge model of piled raft foundation is shown in Figure 2. A large laminar box, with the inner dimensions of 300mm in height, 400mm in width and 650mm in length (Imamura et al., 2002) was used. Circular tank with 140mm in diameter was rested on the raft

Table 1 Properties of silica sand No. 8

Specific gravity: G_s	2.65
Mean particle size: D_{50} (mm)	0.100
Particle size: D_{10} (mm)	0.041
Coefficient of uniformity: U_c	2.93
Max. void ratio: e_{max}	1.333
Min. void ratio: e_{min}	0.703
Permeability coefficient.: k (m/sec) (k in prototype scale under 50g)	2.0×10^{-5} (1.0×10^{-3})

Table 2 Specifications of model pile

Material	Stainless steel
Diameter or width (D)	8 mm
Thickness (t)	0.5 mm
Flexural rigidity (EI) (EI in prototype scale under 50g)	16 Nm^2 (86MN/m^3)

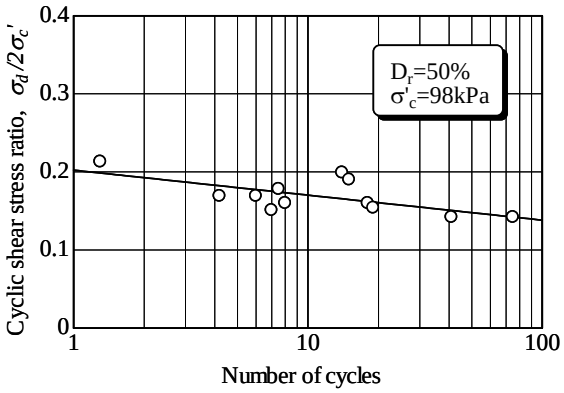

Figure 1 Relationship between cyclic stress ration and number of cycles: Silica sand No.8

or slab with 160mm in diameter and 15mm in thickness. The raft/slab model is made of 10mm thick aluminum plate and 5mm acrylic plate as shown in Figure 3. Height of center of gravity of the tank model was 66mm from the base of the raft/slab. Total mass of tank and raft parts was 4.02kg, which gives 100kPa of average load intensity at the raft base. A stainless steel tube with the specification given in Table 2 was used as the model piles with embedment length of 150mm. Seven piles were fixed to the raft. Strain gages were attached outer surface of the piles for measuring the bending moment and axial forces at the location shown in Figure 2. The silica sand No. 8 was glued on the raft base and the pile surface to make rough condition.

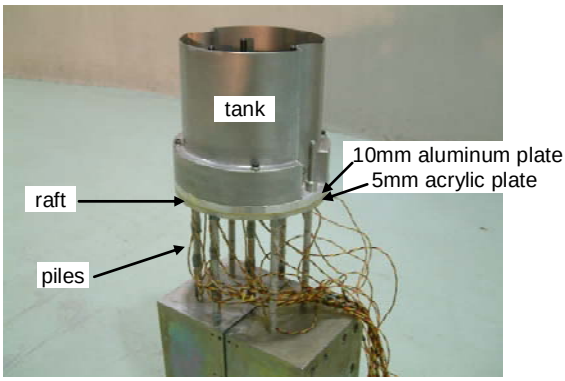

Figure 3 Piled raft foundation model and model tank

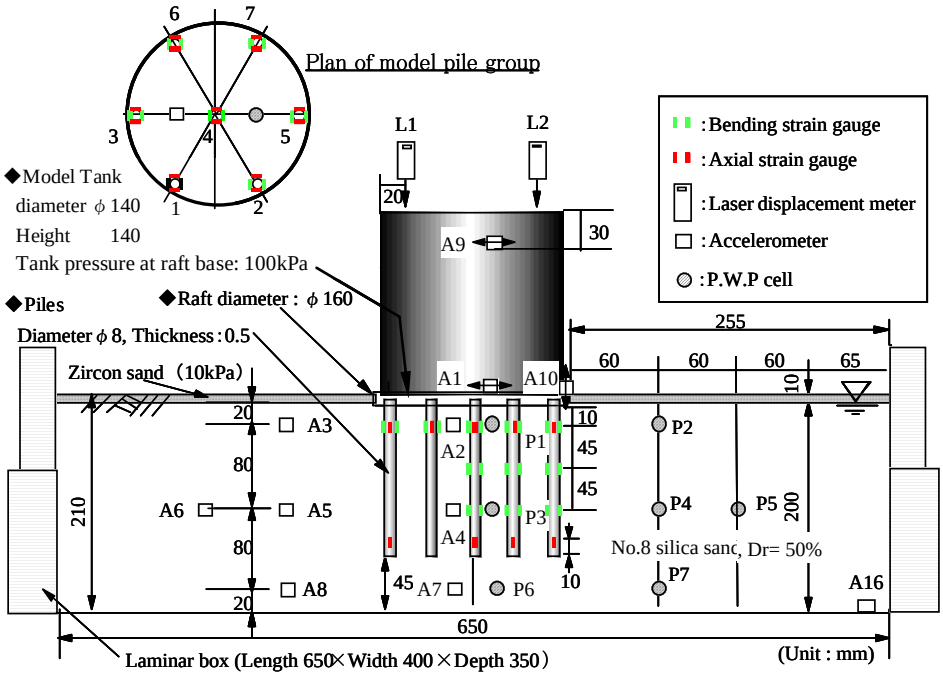

Figure 2 Test setup and location of sensors for piled raft model.

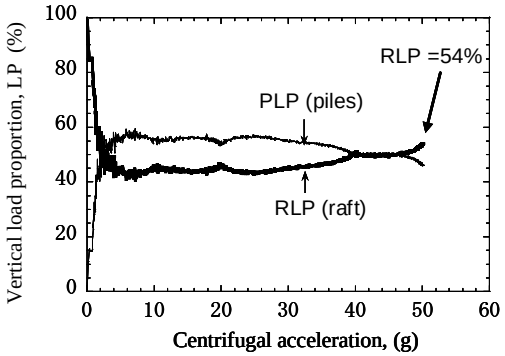

Figure 4 Variation of vertical load proportions of piles and raft due to centrifugation.

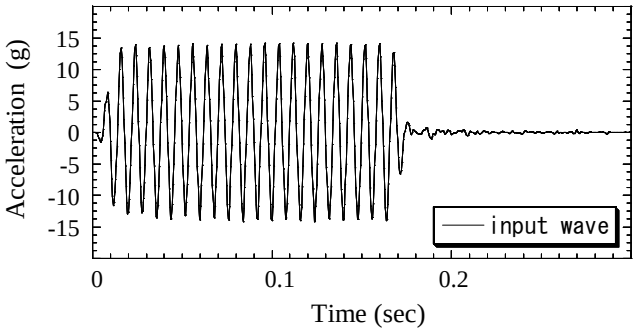

Figure 5 Horizontal input acceleration (A16)

2.2 Model preparation and test procedures

In the model preparation, the piles were temporarily fixed at predetermined positions using guide rods and then 200mm thick dry silica sand layer with Dr=50% was made by air pluviation in the box. Having flattened the surface by applying vacuum, the model raft was carefully placed on the surface and the model piles were fixed to the raft. 10mm thick Zircon sand was laid on the surface of the silica sand to give the surcharge pressure of 10kPa in 50g. During the sand preparation, various sensors were placed at the location shown in Figure 2. The foundation was vertically loaded on the lab floor to diminish the gap at the foundation base, which might cause the uneven settlement and load distribution of the base. After the loading, the model was aerated with carbon dioxide gas from the bottom of the box, and then saturated with the deaired water.

Setting the displacement sensors in the model, the box was mounted to the centrifuge and preloading was applied to the model by the centrifugation to 50g in order to measure the load proportion of the raft and piles. The preloadings in 1g and 50 g were also conducted for the slab foundation model to apply the same loading history as the piled raft foundation model.

Confirming the raft load proportion (RLP) close to the target value (50%) in the preloading to 50 g, the centrifugal acceleration was again increased to 50g. The variation of RLP in the second centrifugation is shown in Figure 4. The RLP was 54 % before the shaking test. In 50g centrifugal acceleration, the corresponding prototype was a 7m diameter oil tank supported by 8m raft (slab) on 10m depth sand deposit. All tests were carried out by the dynamic geotechnical centrifuge (effective radius: 3.80m, maximum payload: 19.2MN-m/sec^2) of Nishimatsu Construction Co., Ltd (Imamura et al., 1998). Input wave for the tests is shown in Figure 5. A sinusoidal wave with acceleration amplitude of 13g, frequency of 100Hz (20cycles) was applied to the model for duration of 0.2sec. This input motion is the horizontal acceleration of 260gal, frequency of 2Hz and duration of 10 sec in prototype scale. Locations of various probes installed in the model are shown in Figure 2 On the measurements, particular attentions were paid to the load proportion of raft and piles, the settlements of the tank, dynamic responses of the oil tank and excess pore water pressures underneath the foundation. In the discussions of the following chapter, test results are all given in prototype scales.

3. TEST RESULTS AND DISCUSSIONS

3.1 Variation vertical load proportion

Figures 6 show the variation of axial forces of piles at central and outermost points in the loading direction. In the figure, the axial forces measured at pile head and tip are drawn. Decreases of the axial force at the head and tips were greater for the outer pile than the central one. Attenuation of amplitude of the axial force at the tip was more than that at the head and the force difference between the head and tip, that is, shaft friction, was kept almost constant during the shaking. These facts imply that the decrease of tip resistance was more significant at the deeper depth near the pile tip than the shallow depth beneath the daft.

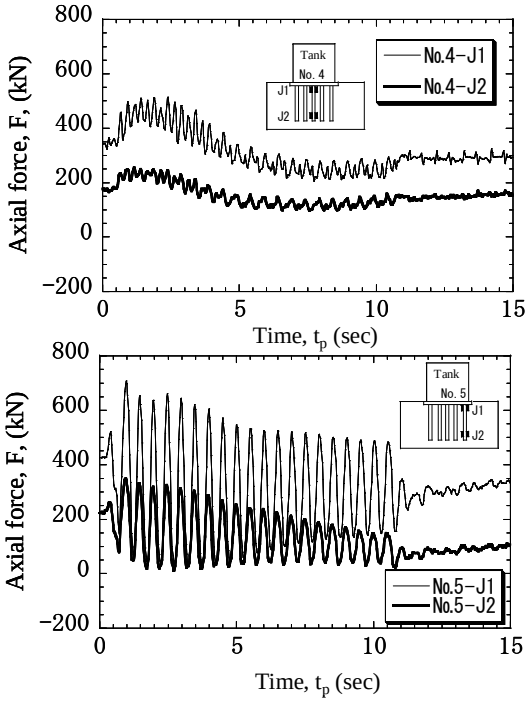

Figure 6 Variation of axial forces of pile during shaking

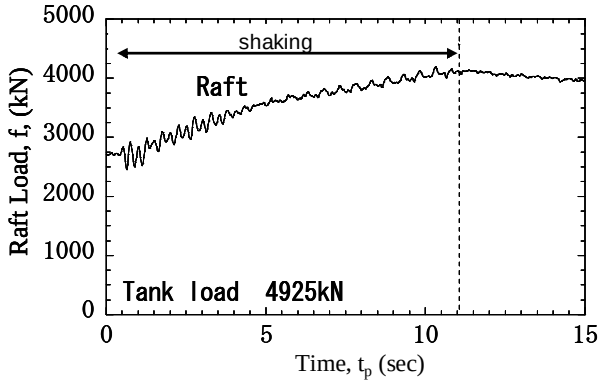

Figure 7 Variation of raft load during shaking

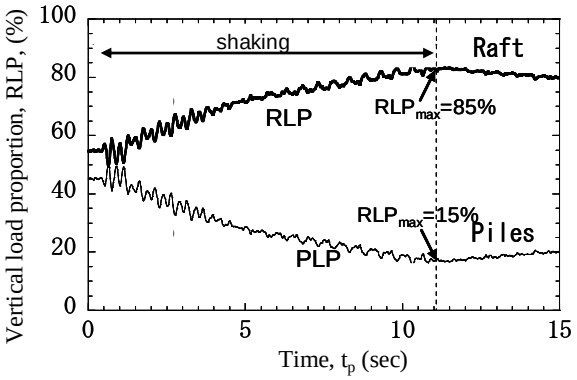

Figure 8 Variation of vertical load proportions during shaking

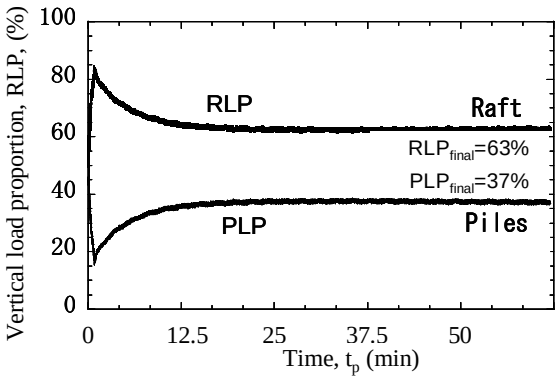

Figure 9 Variation of vertical load proportion after shaking with $t_p(=N^2t_m)$

The load carried by the raft increased during shaking due to the decrease of pile baring load as shown in Figure 7. As a result, the raft load proportion, RLP, increased from the initial value of 54% to the maximum vale of 85% at the end of shaking as shown in Figure 8. This increase of RLP corresponds to the raft base pressure increase of 31kPa. After the shaking, the pile bearing load was regained and the RLP gradually decreased to the final value of 63% (Figure 9).

3.2 Pore pressure behavior

Observed excess pore water pressures (Δu) normalized by the effective vertical stress, σ'_{v0}, during shaking are

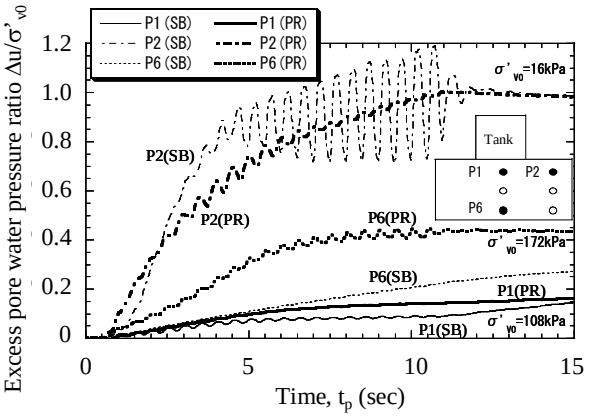

Figure 10 Variation of normalized excess pore pressure in the model ground during shaking with $t_p(=Nt_m)$

compared between the model with slab foundation and the model with piled raft foundation in Figure 10. At the free field (P2), the Δu reached to σ'_{v0}, implying the clear liquefaction. It is interesting to see that large amplitude of Δu was observed at the later part of shaking in the slab foundation model, but this is not the case for the piled raft foundation. It may be considered that the cyclic mobility and additional cyclic load from the tank were more eminent in the former foundation than the latter.

At the portion beneath the raft or slab, the Δus were much smaller than the σ'_{v0}, showing the effect of stain confinement by the foundation. The difference of Δu between the two foundations is more significant at the portion beneath the foundation than the free field. The increase of raft load during the shaking could be considered as a reason of the difference. However, from the fact that difference of Δu at the shallow point (P1) and the deep point (P6) were about 6 kPa and 40kPa in the later stage of shaking respectively, the large difference at deeper portion can be attributed to the difference in degree of liquefaction.

3.3 Settlement behavior

Observed averaged settlements of the two foundations during the shaking are compared in Figure 11. The settlement of the slab foundation seems to increase almost linearly with shaking time but the settlement rate gradually decreases with the time. On the other hand, the settlement rate of the pile raft foundation shows the increase at the time of about 6sec when the Δu at P6 reached the large value. Figure 12 shows the averaged settlement of two foundations after the shaking. The long term settlement can be observed in the piled raft foundation, which could be attributed to the variation of RPL after the shaking (see Figure 9). Dud to the increase of settlement rate during the shaking and the long term settlement after the shaking, averaged settlement caused by the shaking was larger for the pile raft foundation than the slab foundation as shown in Figure 13. However, differential settlement of the tank was smaller for the raft foundation than the slab foundation (Figure 14). This confirms the advantage of the piled raft foundation for

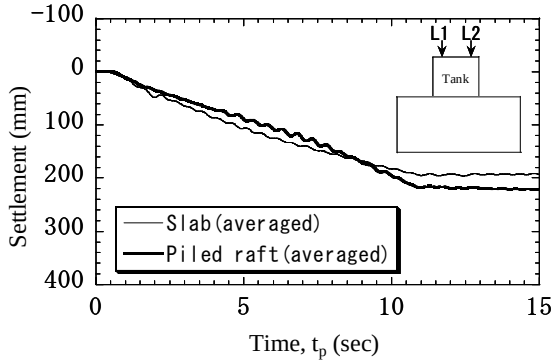

Figure 11 Settlement of tank during shaking with $t_p(=Nt_m)$

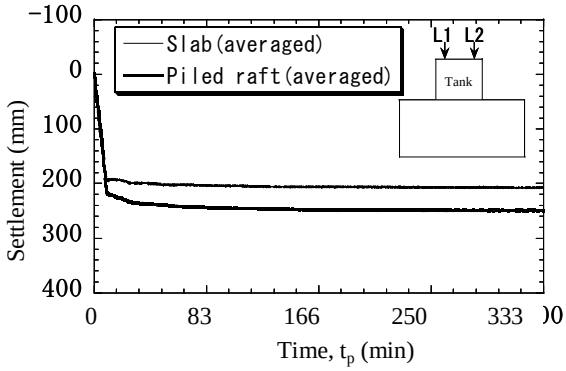

Figure 12 Settlement of tank after shaking with $t_p(=Nt_m)$

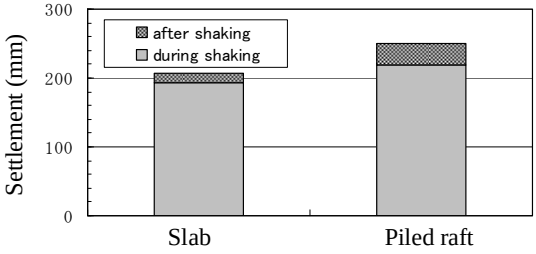

Figure 13 Average settlement of foundation due to shaking.

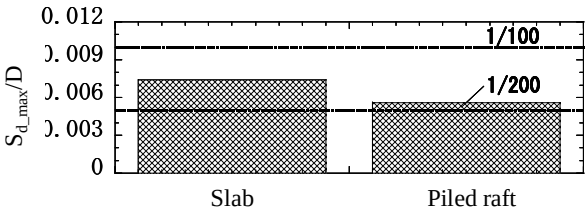

Figure 14 Normalized differential settlement of foundation due to shaking.

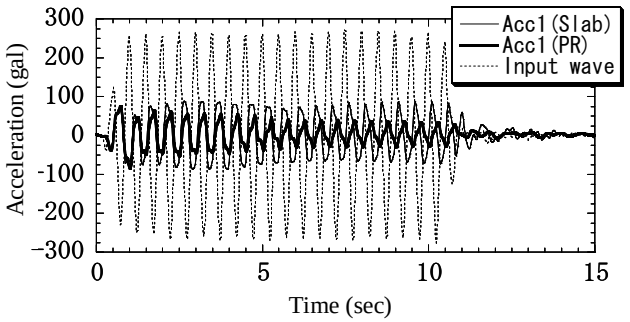

Figure 15 Acceleration response of foundation in the horizontal direction.

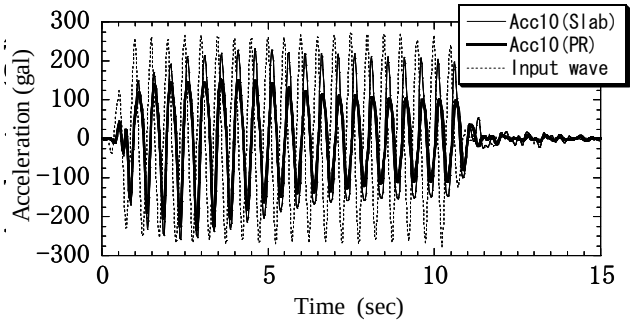

Figure 16 Acceleration response of foundation in the vertical direction.

reducing the inclination of the tank even against the settlement caused by the liquefaction of subsoil.

3.4 Acceleration responses of the foundation

Horizontal accelerations observed at the raft/slab base (Acc1) and vertical accelerations observed at the outermost point of the raft/slab (Acc10) are shown together with the input horizontal base motion in Figures 15 and 16 respectively. The horizontal accelerations of the foundations are much smaller than the input acceleration, showing the attenuation of motion due to the deterioration of the sand stiffness by liquefaction. The amplitude of the horizontal acceleration of the piled raft foundation shows further attenuation at the time of about 6sec, which is similar to the behavior of foundation settlements discussed in Figure 11. From the relatively large amplitude of vertical acceleration, rocking motion of the tank can be observed. The degree of the rocking motion seems larger for the slab foundation than the piled raft foundation. This observation agrees with the pore water pressure response of P2 (Figure 10) and the lager differential settlement of the slab foundation (Figure 14).

3. CONCLUSIONS

The following conclusions were derived from the centrifuge model tests of the slab and piled raft foundations.

(1) The load carried by the raft or the raft load proportion, RPL, of the pile raft foundation increases during shaking due to the decrease of pile baring load. The decrease of tip resistance is more significant than the shaft resistance. After shaking, the pile bearing load was regained and the RLP gradually decreased to the final value, which is larger than that before shaking.
(2) The difference of excess pore water pressure between the models with the two types of foundation is more significant at the portion beneath the foundation than the free field, especially for deep depth near the pile tip.
(3) Settlement behavior of the pile raft foundation is affected by the liquefaction at the deep depth near the pile tip. Due to the larger excess pore water pressure at the pile and the change of RLP, the averaged settlements during and after shaking were larger for the pile raft foundation that the slab foundation. However, the piled raft foundation has an advantage of reducing the inclination of the tank.

References:

Horikoshi, K., Matsumoto, T., Hashizume, Y., Watanabe, T. and Fukuyama, H. (2003a) "Performance of piled raft foundations subjected to static horizontal loads" Int. Jour. of Physical Modelling in Geotechnics, 3(2), 37-50.

Horikoshi, K., Matsumoto, T., Hashizume, Y. and Watanabe, T. (2003b) "Performance of piled raft foundations subjected to dynamic loading" Int. Jour. of Physical Modelling in Geotechnics, 3 (2), 51-62.

Imamura, S., Hagiwara, T. and Nomoto, T. (1998), "Nishimatsu dynamic geotechnical centrifuge", Proc. of Centrifuge 98, Vol.1, 25-30.

Imamura, S. & Fujii, N. (2002), Observed dynamic characteristics of liquefying sand in a centrifuge, Proc. of Physical Modeling in Geotechnics, 195-200.

Ishihara, S., Kawase, Y. and Nakajima, M. (1980), "Liquefaction characteristics of sand deposits at an oil tank site during the 1978 Miyagiken-oki Earthquake, Soils and founda-tions, 20 (2), 97-111.

Sixth International Conference on Urban Earthquake Engineering
March 3-4, 2009, Tokyo Institute of Technology, Tokyo, Japan

STUDIES ON VARIOUS PILE GROUP MODELS USING EFFECTIVE STRESS ANALYSIS

Kiyoshi Fukutake[1)]

1) Senior Researcher Institute of Technology, Shimizu corporation, Japan
kiyoshi.fukutake@shimz.co.jp

Abstract: Various detailed analyses have been done by FEM about dynamic analysis of pile foundations. But most of them were conducted under two-dimensional condition, and the detailed analyses for examining the behavior under three-dimensional conditions ware few. Especially, it is hard to find the research that treats liquefiable ground. In this paper, behaviors of pile group foundations under two- and three-dimensional condition are discussed using effective stress analysis. In addition, simplified modeling method of pile group foundations is proposed, and the applicability is evaluated.

1. INTRODUCTION

The ground/foundation/structure system to be analyzed was of a three-dimensional structure composed of piles and walls with varying physical properties and geometric shapes. Three-dimensional models have conventionally been approximated by two-dimensional models frequently in the case where three-dimensional analysis was difficult. Then, piles were modeled as a sheet pile extending infinitely along the direction of length. Horizontal ground motions have N-S and E-W components and need to be evaluated using multi-directional input ground motions. Two-dimensional models, however, can evaluate only unidirectional component. The results of cyclic element tests (simple shear tests) show that multi-directional shear causes higher dilatancy than unidirectional shear and the resistance to liquefaction is reduced (Ishihara et al 1980, Fukutake et al. 1989). The deviation from actual phenomena can be eliminated by three-dimensional analysis. Thus, two-dimensional analysis has some limitations. Three-dimensional effective stress analysis, however, requires great efforts and is not generally used in design.

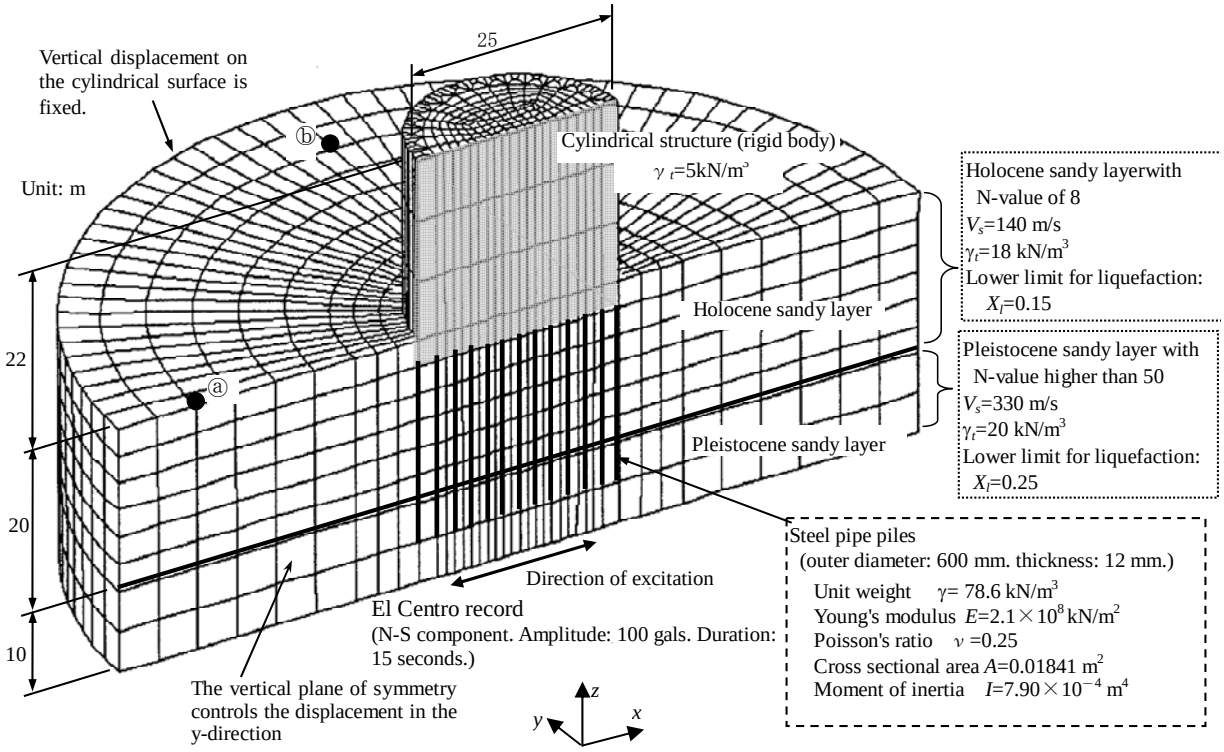

Figure 1 FEM model of cylindrical structure/ground system supported on a pile foundation (half model)

The FEM program code for three-dimensional effective stress analysis called "*HiPER*" (Fukutake 1997) to assess the dynamic response of structures on liquefiable ground was developed. In this method a simplified constitutive model is used to represent the nonlinear behavior of soil involving liquefaction called "bowl model" (Fukutake, 1989 and 1997). The applicability of the method has been examined by comparing computed results with observed data (Fukutake et al., 1992, Ohtsuki et al., 1994, Fukutake, 2008).

In this paper, behaviors of pile group foundations under two- and three-dimensional condition are discussed using effective stress analysis. In addition, simplified modeling method of pile group foundations is proposed, and the applicability is evaluated.

2. Analysis of pile foundations - two- or three-dimensional analysis

2.1 Interactions among the ground, pile foundation and structure

This section focuses on the structures supported on pile foundations in soft sandy ground, and presents the forces acting on the cross-section of each pile and the percentage of load carried by each pile, and the behavior of the ground around the foundation that were obtained from three-dimensional analysis (Fukutake et al. 1996a). A comparison was also made with the results of two-dimensional analysis, and the limitations in the application of two-dimensional analysis are described. Loads were applied only in one direction. Figure 1 shows an FEM (finite-element method) model of the ground/structure system used for analysis. The model represents half of the symmetrical system. The cylindrical structure is supported on the Pleistocene sandy layer using piles. The locations of the piles are shown in Figure 2.

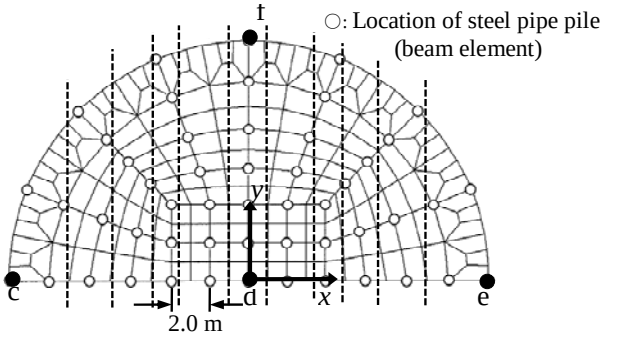

Figure 2 Finite elements representing the structure and piles

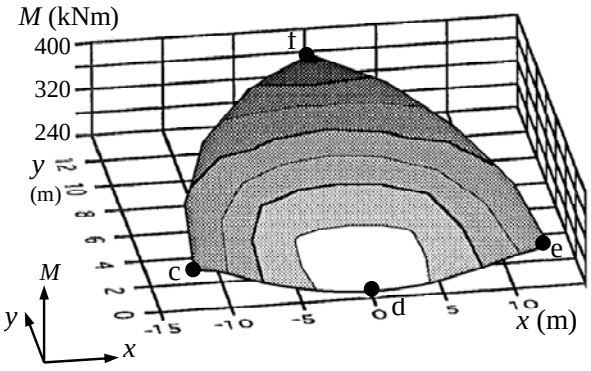

Figure 3 Maximum bending moment at each pile head

The maximum bending moment at each pile head is shown in Figure 3. The height (vertical axis) indicates the maximum bending moment. Symbols *c* through *f* correspond to the locations of piles shown in Figure 2. The

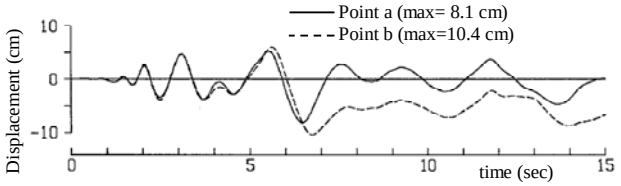

Figure 4 Displacement of ground surface (*x*-direction)

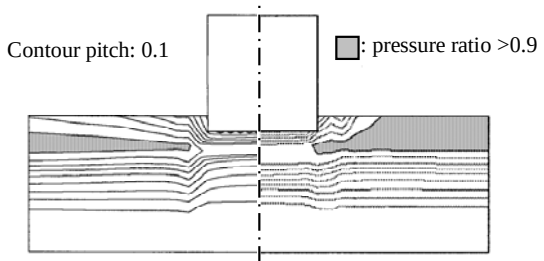

(a) Two-dimensional analysis ℄ (b) Three-dimensional analysis

Figure 5 Maximum contour of excess pore water pressure ratio

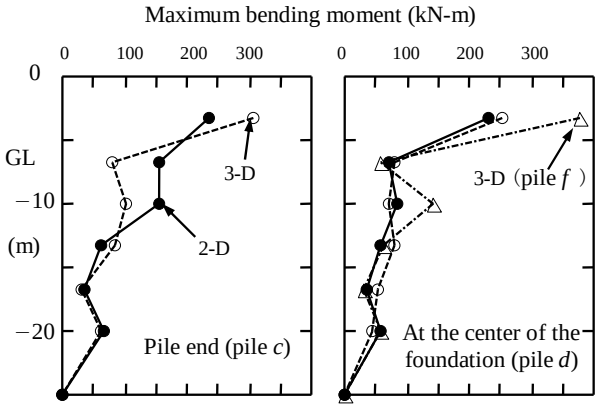

(a) Maximum bending moment of pile at different depths

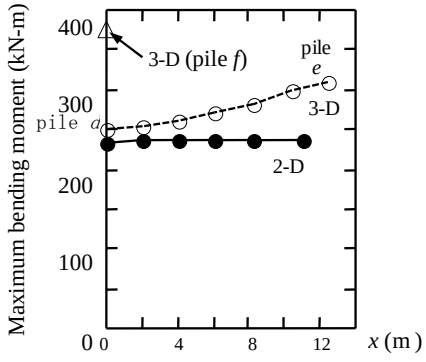

(b) Maximum bending moment at pile head

Figure 6 Comparison of pile stresses for pile group foundations in two- and three-dimensional analyses

distribution of maximum bending moments is shaped like a bowl. The maximum bending moment is lowest at pile *d* at the center of the foundation. The highest maximum bending moment occurred at pile *f* on the edge of the foundation. If the maximum bending moment at pile *d* is supposed to be 1.0 (lowest), the moment at piles *c* and *d* will be 1.22 and 1.53 (highest), respectively. Loads are applied simultaneously in two directions, x and y, during an actual earthquake. Then, the forces acting on the cross section are expected to be nearly the same at piles along the circumference connecting piles *c*, *f* and *e* . Thus, the piles near the edge of the foundation carry higher percentage of load than those near at the center. Figure 4 shows time histories of surface displacements at nodes *a* and *b* shown in Figure 1. Both nodes are at a radius of 40 m from the center of the structure. The amplitude was higher at node *b* than at *a*. The oscillation was greater on the far side than on the near side. Permanent deformation also occurred at *b*. Deformation was controlled at *a* owing to the pile foundation, and the amplitude was also lower than at *b*. Such information on deformation cannot be obtained by two-dimensional analysis.

In order to identify the applicability of two-dimensional analysis, the same structure was also analyzed using a two-dimensional model62). A circular pile foundation/ground system was represented by a model for analyzing a two-dimensional plane strain problem. (i) For representing the cylindrical structure with a diameter of 25 m by a rectangular model for performing a two-dimensional analysis of plane stress, a length of a side *D'* was set to be 22.16 m so that the contact area could be the same in the two- and three-dimensional models. (ii) The piles of the circular foundation were divided by dotted lines into several groups (Figure 2) and each group was modeled using a beam element by summing the forces acting on the cross section of the pile and the moment of inertia for each pile. (iii) The length of the ground was adjusted so as to express the effects of three-dimensional analysis somewhat accurately, and the stiffness of soil between piles was adjusted so that the percentages of load carried by the piles might be the same as in the three-dimensional model63).

Figure 5 shows the contours of the maximum excess pore pressure ratios obtained as a result of the two- and three-dimensional analyses. The results are nearly the same. The area of liquefied soil is slightly wider near the ground surface in the three-dimensional analysis. In three-dimensional analysis, the ground had an oscillation component in the direction of depth (y direction) although loading was applied unidirectionally. In two-dimensional analysis on the other hand, no y-direction component existed. As a result, the shear strain of the soil was higher in three-dimensional analysis. Figure 6 shows the pile stresses of pile group foundations in two- and three-dimensional analyses. There are differences near the head of pile *c*, indicating the effect of the two-dimensional model. The results of two- and three-dimensional analyses are in good

Table 1 Analytocal cases of pile fouindation (4 cases)

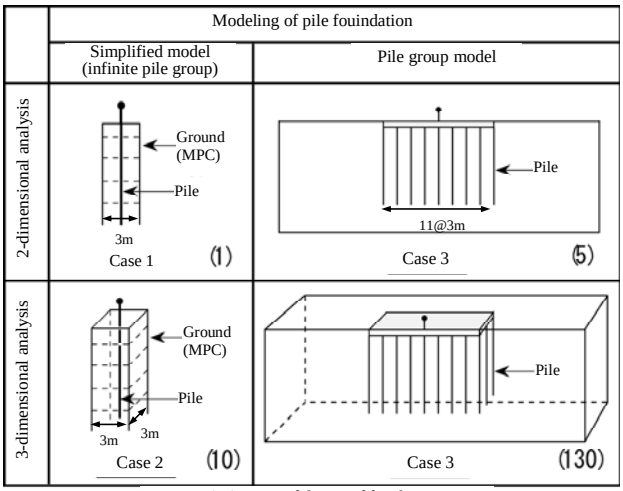

( ): Ratio of degree of freedom

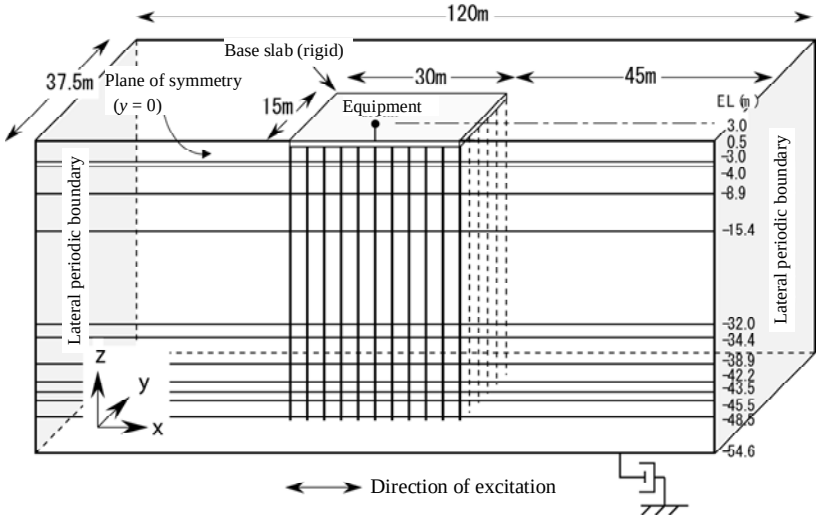

Input ground motion: Shin-Kobe record during the Kobe Earthquake 1995

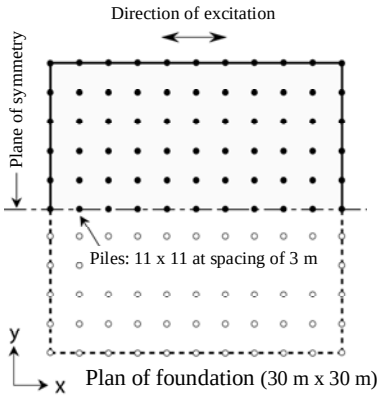

PHC piles (class B. Diameter: 600 mm)

- Holocene ground: Mainly composed of sandy silt. V_s=130～250 m/s
- Bearing ground: Gravel. V_s=360 m/s

Figure 7 GIS three-dimensional pile group foundation model (half model)

agreement with each other at pile *d* at the center of the foundation. The Figure also shows using a triangle the forces acting on the cross section of pile *f* obtained by three-dimensional analysis. The forces are greater than the result by two-dimensional analysis. Evaluating the forces acting on the cross section of pile *f* is difficult by two-dimensional analysis. The result by two-dimensional analysis is on the dangerous side. Figure (b) shows maximum bending moments at pile heads. The results of three-dimensional analysis are the values on the plane of symmetry (along the line connecting *d* and *e* in Figure 2). The results of three-dimensional analysis are higher at the pile end but there is not such a tendency for the results of two-dimensional analysis. As shown above, evaluating the forces acting on pile cross section is difficult in two-dimensional analysis in the case where piles are arranged in a circle in a circular foundation.

2.2 Development of various pile group models

Pile group foundations with numerous piles exhibit complicated behavior. For example, the percentages of load carried by pile groups vary according to the effect of pile groups or the locations of piles. It is therefore ideal to thoroughly examine the behavior of pile group foundations by three-dimensional analysis using a model of the entire foundation. FEM analysis of a three-dimensional model of a structure/pile group/ground system, however, requires high calculation capacity and central processing units. Then, a two-dimensional pile group model is frequently used that focuses on a vertical section. In the case where numerous piles are used, large-scale analysis is required, and piles are modeled as if they formed a wall in two-dimensional analysis. Piles are generally modeled as beam elements but beam elements are linear and have no volume. If piles are arranged densely, the volumes of the piles are not ignorable. Presented below are two examples of the results of effective stress analysis considering the above problems.

(1) Two- and three-dimensional models of pile group foundations and simple modeling methods

In order to reduce the burden on three-dimensional analysis using a pile group model, an analysis method using a simpler model of a pile group is presented (Fujikawa et al., 1997). The applicability of the analysis using the simpler model was verified by comparing the results with the results of three-dimensional analysis using a model of the entire pile group. Analyzed were the piles supporting gas insulated switchgear. Figure 7 shows a three-dimensional model. In the analysis, excess pore pressure occurred but did not induce liquefaction. The simple model is an infinite pile group model of a pile and the surrounding area supported by the pile using MPC condition (Side nodes are tied to each other shown in Figure 10). Analysis cases are shown in Table 1. In the two-dimensional pile group model (case 3), the physical properties of eleven piles along the direction of length were integrated. The values eleven times the moment of inertia *I* and cross sectional area *A* for a single pile were given to a beam element.

The maximum bending moment M_{max} of each pile is shown in Figure 8 for comparison. There is a soil boundary at the depth shown in Figure 8 and M_{max} is highest at the depth. M_{max} is higher near the edge than at the center of the foundation. A comparison of M_{max} along the direction of length using a three-dimensional model shows that M_{max} is higher in row F on the outer edge than in row A in the plane of symmetry by approximately 25%. In the two-dimensional model, piles were modeled like walls and were vulnerable to the effect of soil reaction, resulting in high M_{max}. The Figure also shows the values obtained using simple models. Ordinary values were produced either in two- or three-dimensional analysis. Figure 9 shows the distribution of M_{max} at the pile head in a three-dimensional model. M_{max} is highest at pile F1 in the corner. The Figure indicates three-dimensional distribution of percentages of load carried by the piles.

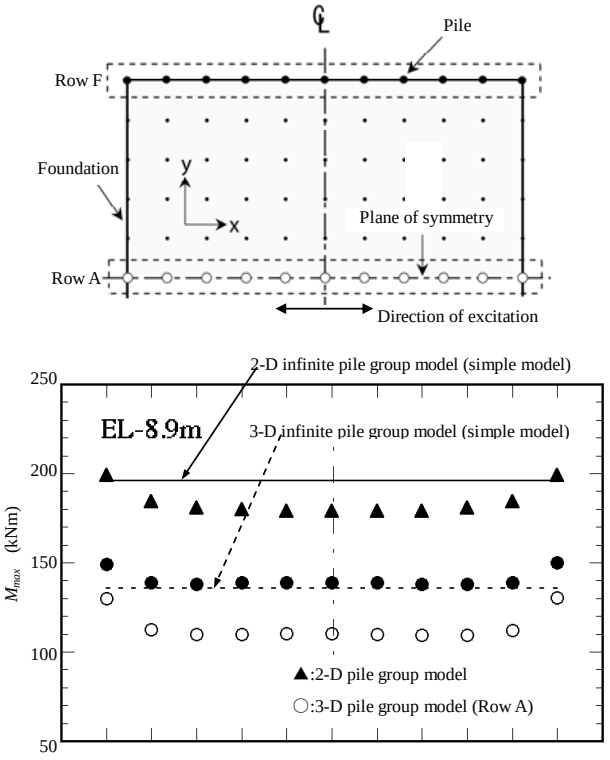

Figure 8 Maximum bending moment of each pile at soil boundary

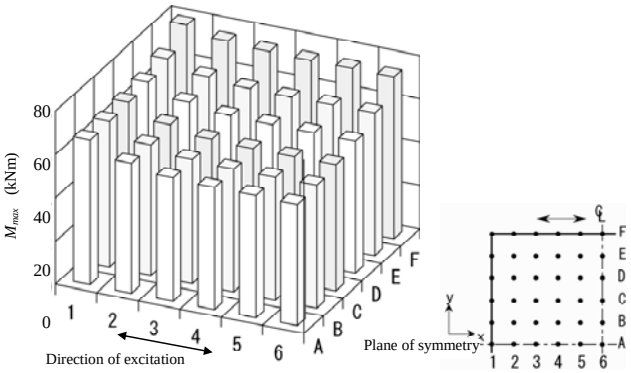

Figure 9 Maximum bending moment at pile head (three-dimensional model)

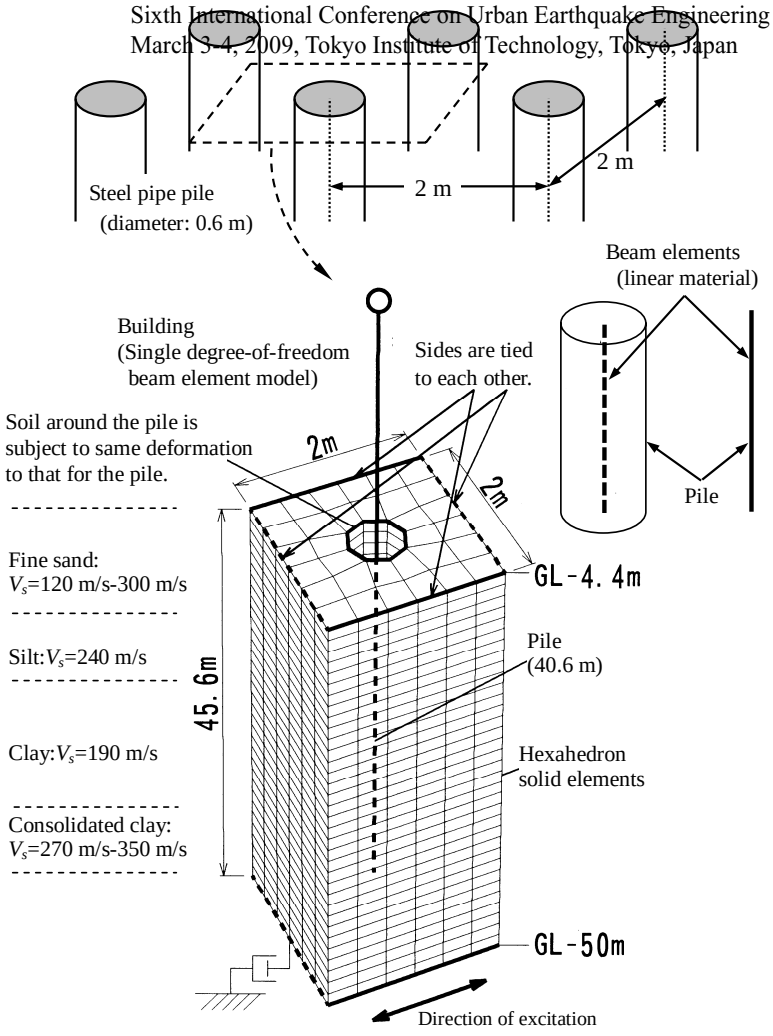

Figure 10 Consideration of the volume of pile in an infinite pile group model (in the case of three-dimensional analysis)

Table 2 Pile group model composed of an infinite number of piles using a repetitive boundary a single beam element (plan view)

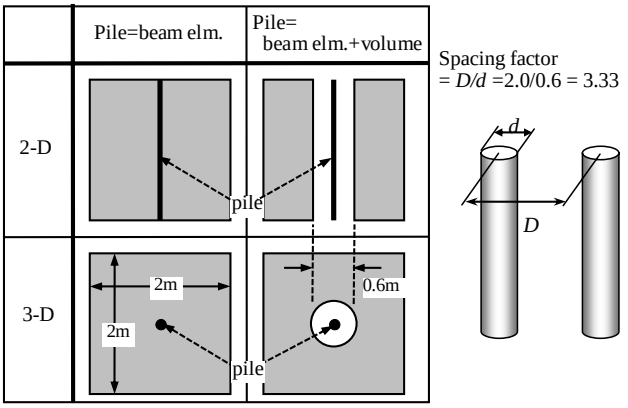

The results obtained using a simple model were nearly in agreement with the results of analysis using a pile group model. When applying the simple model to an infinite pile group, the following points should be kept in mind. In pile group foundations, the percentage of load carried by the pile varies according to the location of the pile, and the stress is higher in piles on the edge than in those at the center of the foundation. The simple model cannot represent the effect. The simple model is unsuitable for the models in which the rocking of the foundation is predominant. In the case where the ground in the vicinity of the pile exhibits three-dimensional behavior getting around the foundation, the behavior of the ground causes the piles on the edge of the foundation to be subjected to high stress concentrations, which cannot be examined using the simple model. The limitations in the application of the simple model should therefore be considered.

(2) Effect of the volume of pile

Analysis was made of a thermal power plant built in the liquefaction-prone soils and supported on a pile group foundation composed of thousands of pilesnote. A simple analysis model was adopted as shown in Figure 10 (Fukutake et al. 1996b). The piles were installed indefinitely at spacings of 2 m in the model. If the number of piles increases and the spacing of piles D is reduced as compared with the pile diameter ϕ, the volumes of piles cannot be ignored. A model was also used for analysis in which the volume of the pile was removed. In the model, space of octagonal cross section circumscribing a 0.6-m-diameter 40.6-m-deep cylinder was created in a soil mass 2 m long, 2 m wide and 45.6 m deep to represent the volume removed by the pile. The pile was modeled using beam elements, and the node inside the cylinder of octagonal cross section is connected to a node in the beam element at the same depth under the same displacement condition. The analysis cases are shown in Table 2

Figure 11 shows the time histories of excess pore pressures in a fine sand layer (As1 layer) at a depth of 8 m below ground level. The pore pressure increased slightly faster in the case where the volume of the pile was taken into consideration. Little difference was found between two- and three-dimensional analyses. Few variations were found according to the location at the same depth. (The soil around a pile behaved nearly like the soil between piles.) This is because the soil was deformed like the piles as the piles were installed densely at spacings of 2 m. Figure 12 shows the maximum bending moments at different depths for comparison. The maximum bending moment was highest at the pile head and second highest at a depth of 21 m below ground level in all of the cases. At a depth of 21 m below ground level, there exists a boundary between the As2 (liquefied) layer and Ac1 (non-liquefied) layer. The maximum bending moment near the pile head is slightly higher in the case where the volume of the pile was considered. No significant difference was, however, generally found in all of the four cases. This is true either for two- or three-dimensional analysis.

If focus is placed on the stress of the pile in the pile group model, the volume of the pile has a small effect and a

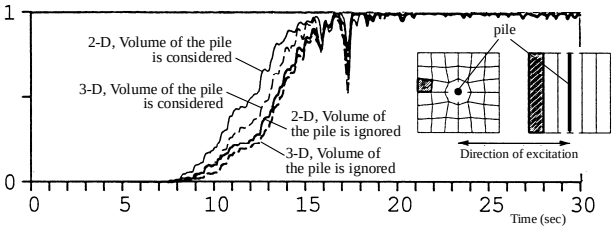

Figure 11 Time histories of excess pore pressures in fine sand layer (As1 layer) at a depth of 8 m below ground level

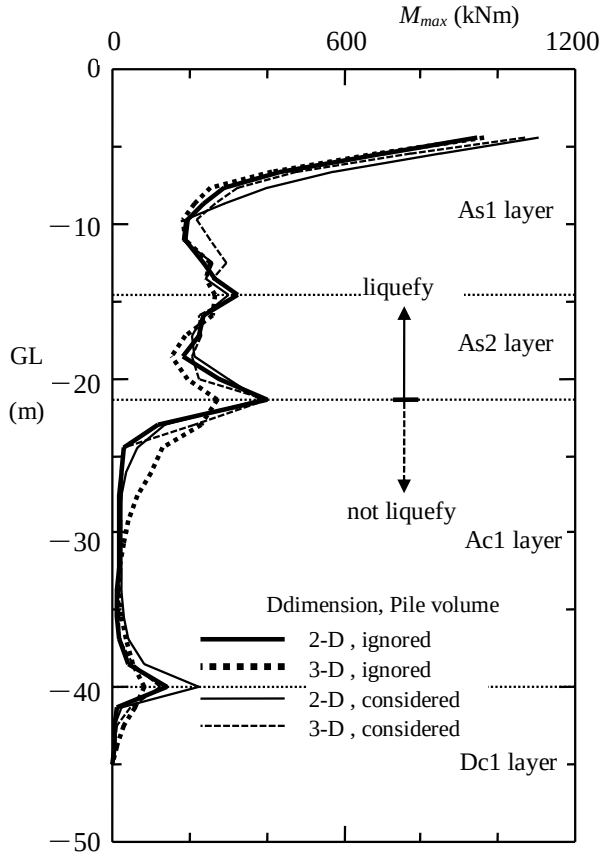

Figure 12 Maximum bending moment of the pile (infinite pile group model)

model considering no pile volume is sufficient from an engineering viewpoint. There is little difference in result between two- and three-dimensional analyses. Two-dimensional analysis is applicable if piles are installed at a small spacing.

3. CONCLUSIONS

In this paper, behaviors of pile group foundations under two- and three-dimensional condition are discussed using effective stress analysis. In addition, simplified modeling method of pile group foundations is proposed, and the applicability is evaluated. In the three-dimensional model, the soils are likely to go around or through the pile. Larger soil deformation (strain) is likely to occur than in the two-dimensional model and liquefaction is also likely to occur. The bending moment of the pile is complicated because of the three-dimensional dynamic interaction. In three-dimensional analysis for example, the difference in percentage of load carried by the pile group can be represented. The percentage is high at the piles along the circumference of the foundation. In two-dimensional analysis, there are cases where the difference in percentage of load carried by the pile cannot be represented explicitly.

Three-dimensional analysis enables the modeling that reflects the actual phenomena. The behavior of a structure and the ground in the vicinity during an earthquake including the dynamic interaction of the structure and the ground can be examined highly reliably. Three-dimensional effective stress analysis enables detailed evaluation of liquefaction control works. More economical and safer designs of foundations than in the past are possible.

Developing well balanced and functional models is important. Complicated models are not always effective. Models vary depending on what knowledge is required to what extent in analysis.

References:

Fujikawa, S., Ueda, M., et al.. (1997), "A study on simplified method for pile group modeling in nonlinear dynamic analysis," *JSCE Journal of Earthquake Engineering*, **24**, 629-632.

Fukutake, K. and Matsuoka, H. (1989), "A unified law for dilatancy under multi-directional simple shearing," *Proceedings of Japan Society of Civil Engineers*, **412/III**, 143-151

Fukutake, K., Ohtsuki, A. and Fujikawa. S. (1992), "Three-dimensional liquefaction analysis for simulating response of ground due to Superstition Hills earthquake 1987," *Proc. Annual convention of JSSMFE*, 1103-1106

Fukutake, K., Ohtsuki, A. and Yoshimi, Y. (1996a), "Analytical evaluation of reducing stress in piles with soil cement improvement," *11th World Conference on Earthquake Engineering*, Acapulco

Fukutake, K., Ohta, Y., et al. (1996b), "A Study on Modeling of Structure- Pile- Ground System for Effective-Stress-Analysis Part 5, comparison between 3D and 2D analysis, and effect of pile volume," *Annual Meeting Architectural Institute of Japan*, Structures II, 465-466.

Fukutake, K. (1997), "Studies on three-dimensional liquefaction analyses of soil-structure system considering multi-directional shearing of soil," doctoral thesis of Nagoya Institute of Technology.

Fukutake, K., Sato, M., Tabata, K. and Taji, Y. (2008) "E-Defense shaking table tests on soil-pile-foundation interaction in liquefiable deposit Part 3:Prediction analyses using R-O model & Bowl model," *Annual Meeting Architectural Institute of Japan*, Structures I, 709-710.

Ishihara, K. and Yamazaki., F. (1980), "Cyclic simple shear tests on saturated sand in multi-directional loading," *Soils and Foundations*, **20**, No. 1 45-59.

Ohtsuki, A., Fukutake, K., Fujikawa, S. and Sato, M. (1994), "Three dimensional effective analysis for evaluating response of group pile foundation under liquefaction," *Proceedings of Japan Society of Civil Engineers*, **495/I**, 101-110.

Sixth International Conference on Urban Earthquake Engineering
March 3-4, 2009, Tokyo Institute of Technology, Tokyo, Japan

BENDING, BEARING AND BUCKLING: EFFECTS OF AXIAL LOAD ON PILE RESPONSE IN LIQUEFIABLE SOILS

Jonathan Knappett[1], and Gopal Madabhushi[2]

1) Lecturer, Division of Civil Engineering, University of Dundee, UK
2) Reader, Dept. of Engineering, University of Cambridge, UK
j.a.knappett@dundee.ac.uk, mspg1@eng.cam.ac.uk

Abstract: The design of piled foundations to resist the effects of earthquake-induced liquefaction commonly focuses on lateral bending moments induced in the piles. Axial load in the piles is rarely considered, despite these loads often being substantial at the time of earthquake (including superstructural loads and any axial dynamic loads). Recent research has identified two key axial pile failure mechanisms in liquefying soil, namely instability (buckling) and bearing capacity failure. The former occurs due to the loss of lateral soil restraint to the pile which essentially behaves as an unsupported column. The latter is a result of a reduction in pile tip bearing capacity due to excess pore pressure rise within the bearing layer. This paper will describe these two competing modes of failure based on observations from dynamic centrifuge testing. An analytical solution to determine the elastic critical (buckling) load for floating piles will be presented, along with an analytical relationship describing the loss in pile bearing capacity. Both of these solutions allow for determination of the limiting load for a downwards-propagating liquefaction front. Finally, these relationships will be used to investigate the vulnerability of steel and reinforced-concrete piles of varying dimensions founded in saturated sandy soils during earthquake induced liquefaction.

1. INTRODUCTION

Foundation designers are familiar with the need to design piled foundations to resist the lateral loads imposed on them due to earthquake shaking. These include inertial forces transmitted to the piles due to vibration of the supported superstructure, and kinematic loads which arise due to relative displacement between the pile and the surrounding soil. Traditional design methods have focused on determining the peak shear forces and bending moments induced within the piles such that the pile section may be detailed to provide sufficient shear and moment capacity. For piles in level liquefiable soils, both sophisticated numerical methods in the time domain and simpler pseudo-static methods have been presented (e.g. Liyanapathirana and Poulos, 2005) and validated against centrifuge models and case histories.

In concentrating on the damaging effects of lateral forces on piled foundations, it is easy to forget that the main purpose of a pile is to carry axial load due to the weight of the supported structure. Such loads lead to second-order effects when determining the bending response of a pile due to the axial load inducing P-Δ moments within the pile section when the pile is deflected laterally. In liquefiable soils, the degradation of soil stiffness around the pile leads to a dramatic reduction in the overall stiffness of the soil-pile system such that these second order effects can be significant, particularly for piles with low bending stiffness. Indeed, the loss in soil stiffness can be enough that the pile suffers unstable collapse (buckles). This has recently been demonstrated by centrifuge testing conducted at the University of Cambridge by Bhattacharya (2003) and Knappett and Madabhushi (2009).

For unstable collapse to occur the axial load carried by the pile must be reacted at some point towards the tip of the pile (shaft load is typically small by comparison to end-bearing in cohesionless soil). This condition will clearly be met for piles which are socketed into bedrock at the tip, as this will provide a resilient foundation throughout an earthquake, even if the soil above it liquefies. For the more common case of floating piles bearing in sand layers, the situation is not so clear. Knappett and Madabhuhsi (2008a) have further demonstrated that as excess pore pressure builds up around a pile due to liquefaction of the surrounding soil, the shaft and base capacities reduce, leading to settlement which may be sufficiently large to cause damage to the supported structure. Furthermore, as the excess pore pressure at pile tip level exceeds approximately half of the initial vertical effective stress, bearing capacity failure can occur for common values of the initial (static) factor of safety of the piles (FoS).

Floating pile groups may therefore suffer from instability or bearing failure depending on the pile and soil properties. If the lateral stiffness of the foundation is low compared to the bearing capacity, instability may be more likely to occur, while bearing failure may dominate for

shorter, stiffer piles founded in more competent layers. This paper aims to address this issue by developing analytical solutions which can model both the reduction in lateral stability/buckling as soil progressively liquefies, and the simultaneous reduction in vertical bearing capacity to determine which is the critical mode of failure for a range of pile configurations, and the amount of liquefaction (or, alternatively, the excess pore pressure profile) at which this occurs.

2. OBSERVATIONS OF UNSTABLE COLLAPSE FROM CENTRIFUGE TESTS

Bhattacharya et al. (2003) and Knappett (2006) undertook a number of centrifuge tests to investigate unstable collapse (buckling) as a potential mechanism of failure in liquefiable soils. This mode of failure is based on the premise that when the soil surrounding the pile is fully liquefied, the soil will have negligible lateral stiffness such that the pile behaves as an unsupported column carrying (significant) axial load. An axially-loaded column will become unstable (buckle) when the axial load exceeds a critical value, P_{cr}. This load can be found using Euler's well-known equation

$$P_{cr} = \frac{\pi^2 EI}{(\beta L_p)^2} \quad (1)$$

where EI is the bending stiffness of the column (or pile), L_p is the pile length and β is a fixity factor which accounts for the fixity at the top and tip of the pile.

Between them, Bhattacharya et al. (2003) and Knappett (2006) compiled a database of 18 piled foundations, including 10 single piles (Bhattacharya) and 8 2 × 2 pile groups (Knappett), surrounded by loose liquefiable saturated sand (relative density of 35 – 50%). In all tests the piles were fully fixed against displacement and rotation at the tips, both to avoid bearing failure so that instability could be studied in isolation and to represent rock-socketed piles. Various different fixities at the head were considered to represent a range of different values of β. Harmonic ground shaking was applied to each model, inducing liquefaction over the full depth of the soil. The model piles were fabricated from 6000 series aluminum and designed to have outside diameters (D_0) and bending stiffnesses representative of 0.5m diameter steel tubular piles at prototype scale.

The collated data from these tests is shown in Figure 1. In this figure, loading is expressed in terms of the axial stress within the pile. This is plotted against slenderness ratio defined as

$$slenderness \quad s = \beta L_p \sqrt{\frac{A}{I}} \quad (2)$$

where A is the cross-sectional area of the pile and I the second moment of area. High values of slenderness ratio represent long flexible pile behaviour while low slenderness ratios represent short 'stocky' piles. In addition to the centrifuge data, a curve representing Eq. 1 has also been plotted, though it should be noted that at low slenderness ratios (< 50 in this case), the load required to cause axial yielding is lower than the critical (buckling) load and the pile will 'squash' instead of buckle. With the exception of one test, all of the datapoints represent piles at slenderness ratios high enough that unstable collapse is the critical mode of failure.

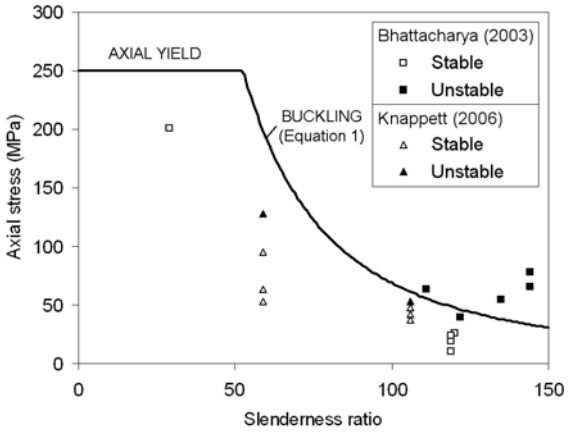

Figure 1 Evidence for unstable collapse at full liquefaction as a failure mode based on centrifuge test results.

Figure 1 clearly shows that if piles carry sufficient load to exceed the critical load in the liquefied soil, the piles will become unstable. This paper will develop an analytical solution which extends this work to consider floating piles (i.e. with different pile tip fixity conditions) and soil layers which are only partially liquefied.

Continuing the analogy of a pile in liquefied soil behaving as an unsupported column, axial load will also serve to amplify any lateral deflections in piles, such as those induced by seismic shaking or due to lateral spreading of the surrounding liquefied ground. Eq. 3 may be used to estimate this amplification, where P is the axial load carried and Δ the lateral deflection. Knappett and Madabhuushi (2009) have demonstrated that this approach is generally conservative (i.e. overpredicting amplification) due to the non-zero strength of liquefied soil.

$$amplification = \frac{\Delta(P)}{\Delta(P=0)} = \frac{1}{1-P/P_{cr}} \quad (3)$$

3. OBSERVATIONS OF BEARING FAILURE FROM CENTRIFUGE TESTS

Knappett and Madabhushi (2008a) undertook further centrifuge testing on 2 × 2 model pile groups passing through loose liquefiable sand and bearing in a layer of dense sand. These tests were instrumented to measure the average pile group vertical displacement (i. e. that at the centre of the pile cap) as liquefaction progressed. The

models were representative of end-bearing piles tested at varying initial static safety factors (FoS) and pile lengths passing through soil layers of varying thickness, the details of which are summarized in Table 1. In the table, H_1 represents the thickness of the upper (loose) layer. All piles were embedded by $10D_0$ in the underlying dense sand layer ($D_r \approx$ 85-90%).

Figure 2 shows the vertical displacement (w) of some of the pile groups, normalized by pile diameter, and plotted against normalized base load and the excess pore pressure ratio at pile tip level ($r_{u,base}$). The excess pore pressure ratio (r_u) is defined as

$$r_u = \frac{\Delta u}{\sigma'_{v0}} \tag{4}$$

where Δu is the excess pore pressure developed at a given depth due to the earthquake and σ'_{v0} is the initial vertical effective stress at that depth. A value of $r_u = 0$ therefore represents the 'no liquefaction' case and $r_u = 1$, the 'full liquefaction' case. The base capacity was determined by the method presented in Knappett and Madabhushi (2008b), in which by considering the popular solution for pile tip bearing capacity presented by Vesic (1972) it was shown that the ultimate base load in liquefying soil during an earthquake ($Q_{bE,ult}$) can be related to the static ultimate base load ($Q_{b0,ult}$) by

$$\frac{Q_{bE,ult}}{Q_{b0,ult}} = \left(1 - r_{u,base}\right)^{\frac{3-\sin\phi}{3(1+\sin\phi)}} \tag{5}$$

where ϕ is the friction angle of the soil and $r_{u,base}$ is the value of r_u at the tip of the pile.

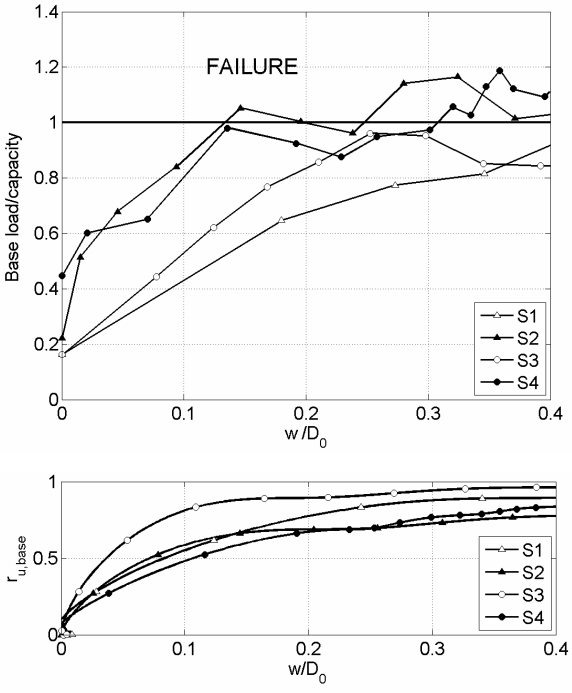

Figure 2 Evidence for liquefaction-induced bearing failure as a failure mode based on centrifuge test results.

Table 1 Centrifuge model configurations for bearing failure tests shown in Figure 2.

Group ID	L_p (m)	H_1 (m)	FoS
S1	15.2	10.4	5.9
S2	15.2	10.4	4.5
S3	15.2	10.4	5.9
S4	15.2	10.4	2.2

As the total axial load carried by the piles (due to the weight of the superstructure) does not change during the earthquake, it is clear from Figure 2 that increasing excess pore pressures lead to a reduction in pile capacity at the tip and consequent large vertical displacements. These can exceed 1 pile diameter at high $r_{u,base}$, though only values of $w < 0.4D_0$ have been plotted in Figure 2 for clarity. If the bearing capacity of the pile reduces below the critical load, then it is clear that the pile will settle rather than buckle.

4. ANALYTICAL MODELS FOR FLOATING PILES IN LIQUEFIABLE SOILS

4.1 Analytical model of pile instability

The previous sections have demonstrated that there is physical evidence for both instability and bearing failure as possible pile failure modes when axial loads are considered. In this and the following sections analytical solutions will be developed to model the changes in both the critical buckling load (P_{cr}) and the bearing capacity (P_{bc}) as liquefaction progresses. Floating (rather than rock-socketed) piles embedded within a single homogeneous layer of soil are considered for simplicity and to highlight some of the important parameters affecting the competition between these two modes more clearly.

It is well known that soil deposits do not instantaneously liquefy over their full depth when subject to seismic shaking. Florin and Ivanov (1961) demonstrated that liquefaction begins at the top of a liquefiable deposit and progresses downwards as shaking continues. This is because the soil near the surface (and therefore at lower σ'_{v0}) requires less excess pore pressure to be generated to reach $r_u = 1$ than layers at depth. This leads to the concept of a liquefaction front which moves downwards in the soil as liquefaction progresses, with the soil above this front being fully-liquefied ($r_u = 1$).

Figure 3 details schematically the vertical effective stress conditions within the soil around a floating pile group as the liquefaction front progresses to a depth z_L. Florin and Ivanov (1961) have shown that the actual distribution of excess pore pressure with depth within a uniform soil deposit is represented by a continuous curve. For the purpose of the analyses presented herein, a simple bi-linear approximation to the excess pore pressure distribution can be made in which soil shallower than z_L is at full liquefaction ($r_u = 1$ or $\sigma'_v = 0$), with the excess pore pressure being constant with depth below z_L. This is shown in Figure

3. The resulting distribution of vertical effective stress has a value of zero down to z_L and increases linearly below this depth. This is identical to the stress conditions around idealised partially embedded piles with a free-standing length of z_L, as demonstrated in Figure 3.

The instability of partially embedded piles has been studied by many authors including Reddy and Valsangkar (1970) and Gabr et al. (1997). Each of these solutions utilises the Rayleigh-Ritz method to determine the elastic critical (buckling) load. This method considers the stored energy in the soil-pile system due to elastic flexure of the pile and elastic deformation of the soil (U) and the potential energy of the external axial pile load (V) for a given lateral displacement, y(x). Determination of the critical loads is accomplished by applying the principle of minimum potential energy which may be expressed mathematically as

$$\frac{\partial(U+V)}{\partial c_n} = 0 \tag{6}$$

where c_n represents the magnitude of the Fourier components used to describe the deflected shape of the pile y(x) (see later). The expressions for U and V as a function of the lateral pile deflection are presented as Eqs. 7 and 8.

$$U = \frac{EI}{2}\int_0^{L_p}\left(\frac{d^2y}{dx^2}\right)^2 dx + \frac{D_0}{2}\int_0^{L_p-z_L} p(x)y\,dx \tag{7}$$

$$V = -\frac{1}{2}\int_0^{L_p} P(x)\left(\frac{dy}{dx}\right)^2 dx \tag{8}$$

where $x = L_p - z$, i.e. a coordinate measured upwards from the tip of the pile, $p(x) = k \cdot y(x)$ and is the lateral soil-pile reaction, and P(x) the axial load in the pile at a given height above the pile tip. Of the solutions described previously, that of Gabr et al. (1997) is the most versatile as it is able to account for different distributions of horizontal subgrade reaction, k (i. e. k = constant or $k = \eta_h z$, where η_h is the modulus of subgrade reaction) and axial pile load distribution, P(x) (split between base and shaft resistance).

In order to use Eqs. 6 – 8, an expression for the lateral deflected shape of the pile must be assumed which is consistent with the boundary conditions on displacement and rotation at the top and tip of the piles. This represents the mode shape for unstable collapse and Eq. 6 is used to find a compatible critical load in this mode. In this paper, floating piles in homogeneous soil are considered, for which y(x) is given by Eq. 9 after Gabr et al. (1997):

$$y(x) = c_0 + \sum_{n=1}^{N} c_n \sin\frac{2n-1}{2L_p}\pi x\,. \tag{9}$$

Eq. 9 represents y(x) in terms of N+1 Fourier components, each of magnitude c_n. Increasing the magnitude of N allows more complex (and more discontinuous) mode shapes to be modeled. In the work described herein, N = 50 has been assumed.

Substituting Eqs. 7, 8 and 9 into Eq. 6 yields a set of N+1 homogeneous linear equations in terms of the unknown coefficients c_n (n = 0 to N) which may be written as

$$[A]\underline{c}_n = 0\,. \tag{10}$$

The system of equations described by Eq. 10 has a non-trivial solution for $\underline{c}_n$ only if the determinant of [A] is zero. This is a statement of the generalised eigenvalue problem which can be solved by standard methods. The lowest eigenvalue (λ_1) for this system of equations is related to the fixity factor (β) introduced in Eq. 1 by

$$\lambda_1 = \frac{1}{\beta^2}\,. \tag{11}$$

Hence, the critical load may be found using Eq. 1.

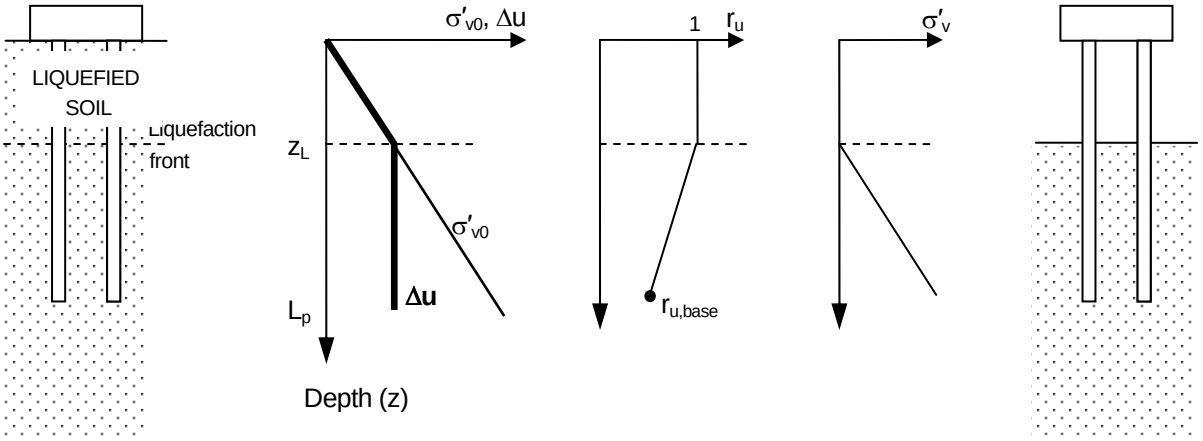

Figure 3 Distribution of vertical effective stress around a pile group in partially-liquefied soil and equivalence to the case of partially-embedded piles.

4.2 Analytical model of bearing capacity

Base capacity in liquefying soil is related to the static base capacity according to Eq. 5. In an homogeneous soil (Figure 3), it has already been shown that the pile is analogous to a partially-embedded pile with free-standing length z_L. The shaft capacity ($Q_{sE,ult}$) is therefore assumed to reduce proportionally from the static value ($Q_{s0,ult}$) according to the length of the pile below z_L, as represented by

$$\frac{Q_{sE,ult}}{Q_{s0,ult}} = 1 - \left(\frac{z_L}{L_p}\right)^2 . \qquad (12)$$

Referring to Figure 3, $r_{u,base}$ may be correlated to z_L such that Eqs. 5 and 12 may be expressed in terms of the same variable (i. e. $r_{u,base}$). For the bi-linear model, the excess pore pressure at depth z_L is given by $\Delta u(z_L) = \gamma' z_L$. As this is constant below z_L, and the initial vertical effective stress at depth L_p is $\sigma'_{v0}(L_p) = \gamma' L_p$, the excess pore pressure ratio at depth L_p (i.e. $r_{u,base}$) is given by

$$r_{u,base} = \frac{\Delta u(L_p)}{\sigma'_{v0}(L_p)} = \frac{z_L}{L_p} . \qquad (13)$$

The parameter $r_{u,base}$ therefore represents the normalized liquefaction front depth and Eq. 12 may be expressed in terms of $r_{u,base}$ by substitution of Eq. 13. The total pile capacity, $P_{bc} = Q_{bL,ult} + Q_{sL,ult}$, in the liquefying soil may therefore be determined in terms of a single value of $r_{u,base}$.

5. COMPETITION BETWEEN MECHANISMS

The methods detailed in the previous sections can be used to determine the variation in both P_{cr} and P_{bc} with $r_{u,base}$ for a given pile and soil configuration (L_p, EI, D_0, ϕ, $Q_{b0,ult}$, $Q_{s0,ult}$). These loads may then be compared with the actual pile load for a given initial FoS to determine the failure mode which is expected.

This process has been repeated for a range of pile properties representative of both steel tubular and solid circular reinforced-concrete (RC) piles with diameters from 0.3 – 0.75 m. Pile lengths from 5 – 30 m have been considered for each class of pile and FoS = 2 was selected as representative of piles designed based on conventional static conditions alone.

In determining representative bending stiffnesses for piles of different diameter the following expression has been used for steel tubular piles

$$EI = E_s \frac{\pi}{4}\left[\left(\frac{D_0}{2}\right)^4 - \left(\frac{D_0}{2} - t\right)^4\right] \qquad (14)$$

where E_s is the Young's modulus of the steel and t is the wall thickness (t = 16 mm assumed herein). For the RC piles, determination of EI is more complicated due to the composite construction. The concrete can only carry compressive stresses, such that only part of the area will contribute to the stiffness, while all of the reinforcing steel may contribute. By using standard transformed area theory, which may be found in any standard textbook on reinforced concrete (e. g. Kong and Evans, 1987), it is possible to derive a formula for the overall bending stiffness of the section

$$EI = E_c\left\{\frac{49D_0^4}{2000} + \frac{\alpha A_s}{4}\left[2\left(\frac{D_0}{2} - c\right)^2 - \frac{\alpha A_s}{\pi}\right]\right\} \qquad (15)$$

where E_c is the Young's modulus of the concrete (here taken as E_c = 30 GPa), A_s is the total area of steel distributed around the circumference of the pile, c is the cover depth to the reinforcing steel and α is the modular ratio (= E_s/E_c).

For the soil properties, a linearly increasing variation of subgrade reaction with depth has been assumed, with η_h = 6.6 MNm^{-3} representing loose saturated soil (relative density $D_r \approx 30\%$) based on API recommendations (API, 1993). The soil is further assumed to have a friction angle of 32° and no cohesion. Due to the hypothetical nature of the soil profile considered, initial static shaft and base capacities have been computed using common analytical methods. Shaft capacity was found using

$$Q_{s0,ult} = \pi D_0 L_p \bar{\sigma}_{v0} K \tan\delta \qquad (16)$$

where K was taken to be K_0 (= 1-sinϕ) which represents an upper bound on the earth pressure coefficient for bored piles, and a lower bound on that for displacement piles after Kulhawy (1984). Base capacity was determined after Berezantzev et al. (1961), as modified by Cheng (2004). The resulting diagrams detailing expected failure modes for the piles under consideration are presented in Figure 4. The dashed line in this figure at L_p = 5m represents the minimum length of pile considered in this study considering common lengths of field piles.

Figure 4 clearly shows the combinations of pile length and amount of liquefaction propagation resulting in bearing or buckling failure, and a safe zone (i.e. conditions below ultimate) within which serviceability conditions will dominate (i.e. lateral displacement due to bending, amplified by axial instability effects, and pile settlement). From this, a number of practical conclusions can be drawn relating to the design of piles in liquefiable soils:

1. For a given pile size/material, shorter piles will be less flexible such that bearing failure will dominate over buckling.
2. As the piles become longer, instability takes over as the dominant failure mechanism.
3. As the pile is made stiffer (i.e. using a steel tubular pile instead of RC, or diameter increased), longer pile lengths can be used before instability becomes problematic.
4. Partial liquefaction around the pile tip, although not causing ultimate failure, may still have effects on the lateral and vertical displacements of the foundation.(i.e. within the 'safe' region)

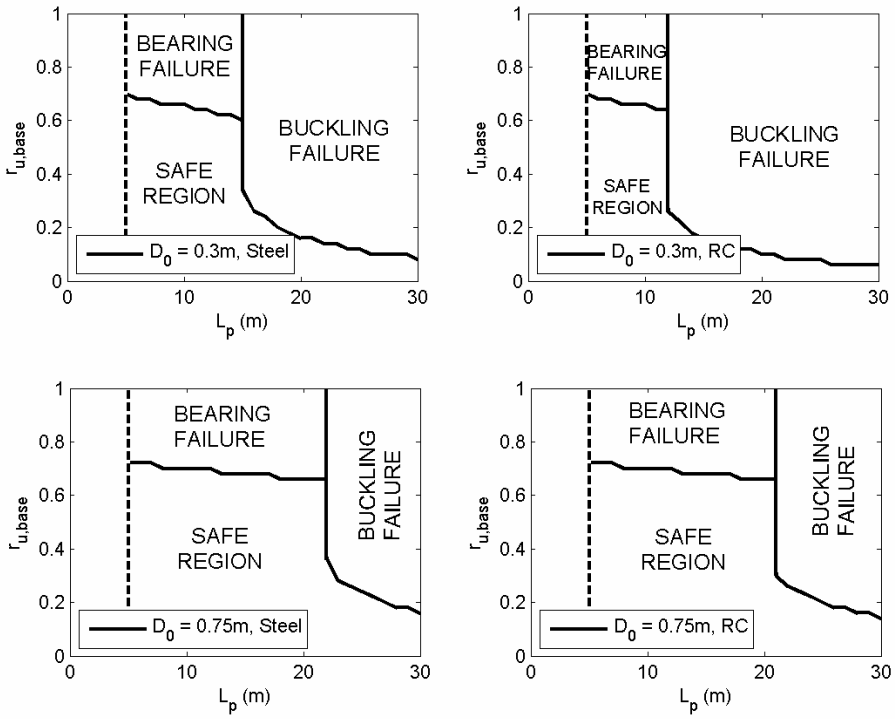

Figure 4 Charts showing combinations of amount of liquefaction ($r_{u,base}$) and pile length (L_p) leading to bearing and buckling axial pile failures (FoS = 2).

6. CONCLUSIONS

This paper has presented physical evidence from centrifuge testing that identifies instability (buckling) and bearing failure as possible modes of axial pile failure in liquefiable soil. Analytical solutions have been developed which allow both buckling load and bearing capacity to be determined for floating piles in soil which may only be fully liquefied over part of the length of the pile. This has been used to identify critical parameters governing the effects of axial load on pile response in liquefiable soil.

Acknowledgements:

The authors acknowledge financial support from the Engineering and Physical Sciences Research Council, UK (EPSRC) for providing financial support for the first author.

References:

API (1993). "Recommended practice for planning, design and constructing fixed offshore platforms." *API RP2A, Working Stress Design, 20th Ed*, American Petroleum Institute.

Berezantzev, V. G., Khristoforov, V. S. and Golubkov, V. N. (1961). "Load bearing capacity and deformation of piled foundations." *Proc. 5th Int. Conf. on Soil Mechanics and Foundation Engineering*, Paris, **2**, 11-15.

Bhattacharya, S., Madabhushi, S. P. G. and Bolton, M. D. (2003). "An alternative mechanism of pile failure in liquefiable deposits during earthquakes." *Géotechnique*, **54**(3), 203-213.

Cheng, Y. M. (2004). "N_q factor for pile foundations by Berezantzev." *Géotechnique*, **54**(2), 149-150.

Florin, V. A. and Ivanov, P. L. (1961). "Liquefaction of saturated sandy soils." *Proc. 5th Int. Conf. on Soil Mechanics and Foundation Engineering*, Paris, **1**, 107-111.

Gabr, M. A., Wang, J. J., and Zhao, M. (1997). "Buckling of piles with general power distribution of lateral subgrade reaction." *Journal of Geotechnical and Geoenvironmental Engineering*, American Society of Civil Engineers, **123**(2), 123-130.

Knappett, J. A. (2006). "Piled foundations in liquefiable soils: accounting for axial loads." *PhD Thesis*, University of Cambridge, UK.

Knappett, J. A. and Madabhushi, S. P. G.. (2008a). "Liquefaction-induced settlement of pile groups in liquefiable and laterally-spreading soils." *Journal of Geotechnical and Geoenvironmental Engineering*, American Society of Civil Engineers, 134(11), 1609-1618

Knappett, J. A. and Madabhushi, S. P. G. (2008b). "Designing against pile tip bearing capacity failure in liquefiable soils." Proc. 2nd BGA International Conference on Foundations, Dundee, **2**, 1237-1246.

Knappett, J. A. and Madabhushi, S. P. G.. (2009). "Influence of axial load on lateral pile response in liquefiable soils, Part I: Physical Modelling." *Géotechnique* (Accepted for publication).

Kong, F. K. and Evans, R. H. (1987). "Reinforced and prestressed concrete." *E&FN Spon*, London, 3rd Ed.

Kulhawy, F. H., (1984). "Limiting tip and side resistance, fact of fallacy." *ASCE Symposium on Analysis and Design of Pile Foundations*, San Francisco, 80-98.

Liyanapathirana, D. S. and Poulos, H. G. (2005). "Seismic lateral response of piles in liquefying soil." *Journal of Geotechnical and Geoenvironmental Engineering*, American Society of Civil Engineers, **131**(12), 1466-1479.

Reddy, A. S. and Valsangkar, A. J. (1970). "Buckling of fully and partially embedded piles." *Journal of the Soil Mechanics and Foundations Division*, American Society of Civil Engineers, **96**(SM6), 1951-1965.

Vesic, A. S. (1972). "Expansion of cavities in infinite soil mass." *Journal of the Soil Mechanics and Foundations Division*, American Society of Civil Engineers, **98**(SM3), 265-289.

Sixth International Conference on Urban Earthquake Engineering
March 3-4, 2009, Tokyo Institute of Technology, Tokyo, Japan

AN APPROACH TO STUDY DYNAMIC STABILITY OF PILE-SUPPORTED STRUCTURES IN LIQUEFIABLE SOILS

S.Bhattacharya[1], N.A.Alexander[2] S.Adhikari[3]

1) Lecturer in Dynamics, Earthquake Engineering Research Centre, University of Bristol (U.K)
2) Senior Lecturer in Structural Engineering, Earthquake Engineering Research Centre, University of Bristol (U.K)
3) Professor, Department of Aerospace Engineering, Swansea University (U.K)
S.Bhattacharya@bristol.ac.uk, Nick.Alexander@bristol.ac.uk, S.Adhikari@swansea.ac.uk

Abstract: Collapse and/or severe damage of pile-supported structures are still observed after strong earthquakes despite the fact that a large factor of safety against axial capacity and bending due to lateral loads is employed in their design. A recent investigation has conclusively shown that a pile may become laterally unsupported in the liquefiable zone during strong shaking and due to the axial load acting on it. This led to another failure mechanism: Buckling instability. Also, during seismic liquefaction, the axial load on the pile in the liquefied zone increases due to the loss of shaft resistance. Due to this extra axial load, the stiffness of the pile-soil system reduces and so does the first natural vibration frequencies. This paper aims to show that at the point of instability the fundamental vibration mode and buckling mode shapes are identical. A method is shown to analyse dynamic stability of piles in liquefiable soils.

1. INTRODUCTION

Collapse and/or severe damage of pile-supported structures are still observed after strong earthquakes despite the fact that a large factor of safety against axial capacity and bending due to lateral loads is employed in their design. All current design codes employ a large margin of safety against the hinge formation (using partial factors on load and material stress), yet occurrences of pile failure due to liquefaction are abundant. Bhattacharya (2003) has shown that in some cases, the overall factor against plastic hinging at collapse has been of the order of 4 to 8. This is strong evidence that there are perhaps other mechanisms governing these failures, which the code does not consider. A critical review of the current theories of pile failure can be found in Bhattacharya and Madabhushi (2008).

In Japan, following some earthquakes, piles were excavated or extracted from the subsoil, borehole cameras were used to take photographs, and pile integrity tests were carried out. These studies hinted the location of the cracks and damage patterns for the piles. The main observations in terms of hinge formation or cracks in the pile are:

1. Cracks were observed near the bottom and top boundaries between liquefied and non-liquefied layers. Often cracks were observed at the pile head.
2. Plastic hinges also formed not only at the boundaries of the liquefiable and non-liquefiable layers but also at various depths.
3. Horizontal displacements of the piles were measured in some cases of pile failure. In some cases, the displacement of the piles was found to agree with the horizontal displacement of the ground.
4. There are few cases where plastic hinges formed at the middle of the liquefied layer. It has been reported, Yoshida et al (2005) that this damage was observed when the structure was very close to the quay wall which moved towards the sea significantly.

The above observation indicates that the stresses in the pile during the earthquakes exceeded the yield stress of the material of the pile. As a result, design of pile foundation in seismically liquefiable areas still remains a constant source of attention to the earthquake geotechnical engineering community.

2. THEORIES OF PILE FAILURE

2.1 Bending mechanism due to kinematic loads on the pile and inertia of the superstructure

The current understanding of pile failure as hypothesised by some codes of practice is as follows: In an earthquake if loose sands are saturated, they lose strength as excess pore water pressure is generated and the soil tends to liquefy. This means that if the soil is on a slope it will flow down-slope which is often termed as lateral spreading. Lateral spreading is a term used to represent the permanent lateral ground displacement after an earthquake. Up to now it has been assumed that the failure of these buildings were caused by the lateral pressure of the flow of the liquefied sand and any non-liquefied stabilised crust resting on the top of the liquefied soil. This mechanism is therefore based on flexure of the pile causing a bending failure. This mechanism forms the basis for the design guidelines developed by JRA (1996, 2002). Many researchers recently suggested that in the presence of non-liquefied crust, the lateral loading created by liquefied ground can be ignored as

the lateral passive earth pressures created in the non-liquefied crust dominate the lateral loading generated on the pile foundation.

The movement of the superstructure i.e. inertia force can also induce bending moments in the pile. However, Ishihara (1997) notes that during an earthquake soil liquefaction starts at approximately the instant of peak acceleration. He argues that since the seismic motion has already crossed its peak, subsequent shaking will be less intense, so that the lateral force applied by the superstructure will not be significant. Therefore, the effects of inertia of the superstructure on the pile stresses are considered separately and are not combined with the lateral spreading effects.

2.2 Buckling mechanism arising due to unsupported length of the pile in liquefiable zone

A recent investigation by Bhattacharya et al (2004), Bhattacharya et al (2005) conclusively showed that a pile becomes laterally unsupported in the liquefiable zone during strong shaking which led to another failure mechanism. The soil around the pile liquefies and it loses much of its stiffness and strength, so the piles now act as unsupported long slender columns, and simply buckles under the action of the vertical superstructure (building) loads. The stress in the pile section will initially be within the elastic range, and the buckling length will be the entire length in the liquefied soil. Lateral loading, due to slope movement, inertia or out-of-line straightness, will increase lateral deflections, which in turn can cause plastic hinge to form, reducing the buckling load, and promoting more rapid collapse. Therefore, this hypothesis is based on a buckling mechanism. This has later been verified by other researchers; see for example Lin et al (2005), Kimura and Tokimatsu (2007), Shanker et al (2007).

Though buckling mechanism can classify pile failures (good performance or otherwise), the location of hinge formation/ cracks in the piles cannot be explained by buckling instability theory. Criticisms of buckling mechanism can be found in Yoshida et al (2005). This led to the search of any other mechanism of failure.

3.0 DYNAMIC STABILITY OF PILED FOUNDATIONS (UNIFIED BUCKLING MECHANISM AND RESONANCE)

Structurally, buckling of a slender column can be viewed as a complete loss of lateral stiffness to resist deformation. It is commonly known as an instability phenomenon. During liquefaction, if a pile buckles - it can be concluded that the lateral stiffness of the pile is lost. From a dynamics point of view as the applied axial load approaches the buckling load it can also be observed that the fundamental natural frequency of the system drops to zero, Thompson and Hunt (1984). Essentially, at the point where the natural frequency drops to zero, the inertial actions on the system no longer contribute. Thus, the system's dynamical equations of motion degenerate into a statics stability problem.

During seismic liquefaction, the axial load on the pile in the liquefied zone increases due to the loss of shaft resistance. Due to this extra axial load, the stiffness of the pile-soil system reduces and so does the vibration frequencies. At the point of instability the fundamental vibration mode and buckling mode shapes are identical. Thus, as the soil transforms from solid to a fluid-like material i.e. from partial-liquefaction stage to full-liquefaction stage, the modal frequencies and shapes of the pile change.

Considering the first natural frequency of the pile-soil-superstructure system, it is suggested that the "other mechanism" may probably be the two effects arising from the removal of the lateral support the soil offers to the pile while in liquefied state. They are

(a) Increase in axial load in the pile in the potentially unsupported zone due to loss of shaft resistance;

(b) Dynamics of pile-supported structure due to frequency dependent force arising from the shaking of the bedrock and the surrounding soil than can cause dynamic amplification of pile head displacements leading to resonance type failure.

Essentially, under service conditions (no earthquake and no-liquefaction) the first natural frequency of a structure or the fundamental time period can be estimated without considering the effect of the piles. Typically, a building will have a fundamental time period of about 0.1 times the number of storey. For a 5 storey building, the time period is 0.5sec an the first natural frequency is therefore 2Hz. However when the soil starts to liquefy, the piles become an integral part of the structure and take part in the vibration. As a result, the time period alters significantly and cannot be ignored in analysis/design. In most cases, the frequency will decrease. This paper is therefore aimed at explicitly quantifying the first natural frequency due to the effects of (1) Axial force, (2) Dynamic excitation and (3) Reduction of the lateral support due to liquefaction. An attempt has been made to develop a simplified procedure.

3.1 Winkler models for liquefied soil

BNWF [Beam on Non-Linear Winkler Foundation] or "p-y" method is commonly used in practice for analyzing piles. In "p-y" method, the soil is modelled as non-linear springs where 'p' refers to the lateral soil pressure per unit length of pile and the 'y' refers to the lateral deflection. Figure 1 shows a particular p-y model for non-liquefied soil and its corresponding liquefied condition based on an empirical method. The reduction of strength is carried out using p-multiplier and typical values of this multiplier can be found in AIJ (2001), RTRI (1999), Liu and Dobry (1995). It may be noted that the initial stiffness (i.e. the initial slope of p-y curve) degrades when the soil transforms from being solid to fluid. A detailed discussion on the shape of p-y curves for liquefied soil can be found in Dash et al (2008).

However, analysis of the full-scale tests such as Rollins et al (2005), centrifuge tests such as Bhattacharya et al (2005), laboratory tests on liquefied soil by Yasuda et al (1998), 1-g pipe pulling tests, Takahashi et al (2002) suggests that the shape of the "p-y" curve for liquefied soil should look like a S-curve. Figure 2(a) shows the change of "p-y" curves when the soil is transformed from being solid to fluid-like medium. Figure 2(b) shows the shape following Dash et al (2008).

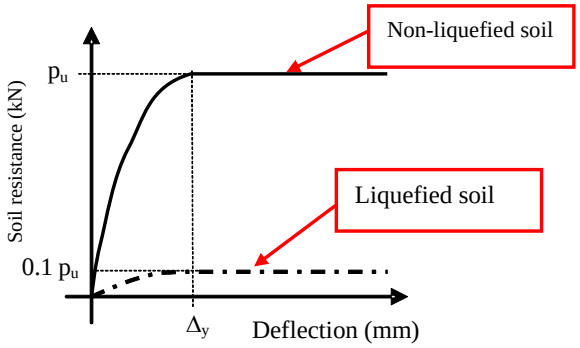

Figure 1: p-y curve for non-liquefied soil and liquefied soil using p-multiplier

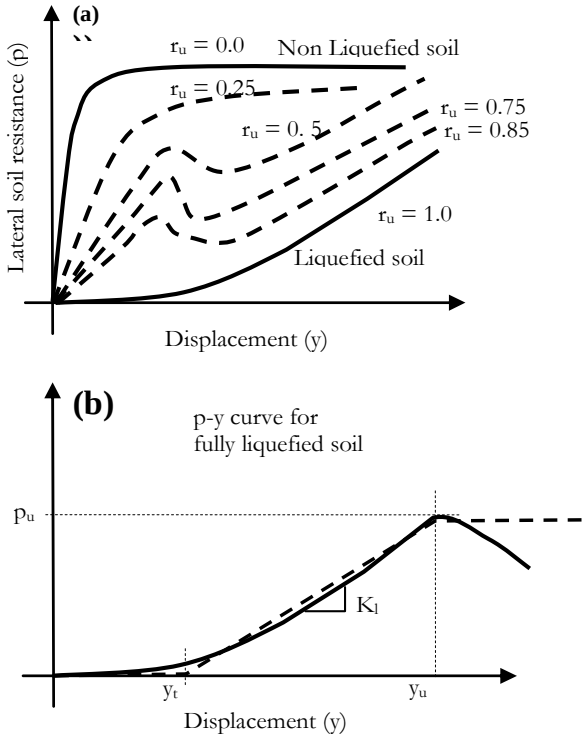

Figure 2: (a): p-y curve for saturated sandy soil during the process of liquefaction; (b) Simplified p-y curve for liquefied soil, Dash et al (2008).

3.1 Vibration of piles in liquefied soil

A pile passes through different stages of loading during an earthquake due to the transformation of the supporting soil from being a solid to a fluid. In one stage, when the soil has not fully liquefied, the transverse bending is expected to govern the internal stresses within the pile. As the liquefaction progresses, the coupled buckling (due to the unsupported length of the pile) and frequency-dependent resonance force would govern the internal stresses in the pile. The key physical aspect that the authors aim to emphasize is that the motion of the pile (and consequently the internal stresses leading to the failure) is a coupled phenomenon. This coupling is, in general, nonlinear and it is not straightforward to exactly distinguish the contributions of the different mechanisms towards an observed failure. It is however certainly possible that one mechanism may dominate over the others at a certain point of time during the period of earthquake motion and till the dissipation of excess pore water pressure.

A coupled dynamical analysis combining (a) transverse bending, (b) dynamic buckling and (c) resonance motion can be carried out for a comprehensive understanding of the failure mechanism of piles during an earthquake. The purpose of this paper is therefore to understand the vibrational characteristics of the piled foundation at full liquefaction. This has design implications as it is necessary to predict the lateral and vertical dynamic loads in the pile at full liquefaction.

4. METHODOLOGY OF ANALYSIS FOR DYNAMIC STABILITY – ENERGY METHOD

In this section of the paper, a generalized method is adopted to analyse the dynamic stability of piled foundation in liquefiable soils.

4.1 Potential Energy

The potential Energy U of this system is composed of three terms (i) the flexural strain energy of the pile group, (ii) the loss of stiffness energy due to compressive loading of the pile group and (iii) the spring stiffness energy of the soil (c.f. Winkler) springs. The soil spring stiffnesses vary linear with depth; where k_w is the soil spring stiffness at the toe of the pile, i.e. $z = L$.

$$U = \tfrac{1}{2} E I \int_0^L y''^2 dz - \tfrac{1}{2} N \int_0^L y'^2 dz + \tfrac{1}{2} k_w \int_0^L \tfrac{z}{L} y^2 dz \quad (1)$$

By employing a Rayleigh-Ritz spatial-temporal solution composed of a sum of a vector of orthogonal functions $\boldsymbol{\phi}$, equation (2), the potential energy can be re-expressed in quadratic form as (3) and (4). The non-dimensional stiffness matrices are (i) $\mathbf{K}_p$ for the pile flexural stiffness, (ii) $\mathbf{K}_s$ for the soil springs and (iii) $\mathbf{K}_b$ for the loss of stiffness due to the axial load N. $\mathrm{x} \in \mathbb{R}^n$ is vector generalised coordinates. Two non-dimensional system parameters are

introduced axial load factor ν and soil to pile stiffness ratio factor η ,see (5).

$$y = L\mathbf{x}(t)^T \boldsymbol{\phi}(\xi), \qquad z = \xi L \tag{2}$$

$$U = \tfrac{1}{2}\tfrac{EI}{L}\mathbf{x}^T\left(\mathbf{K}_p + \eta\mathbf{K}_s - \nu\mathbf{K}_b\right)\mathbf{x} \tag{3}$$

$$\mathbf{K}_p = \int_0^1 \boldsymbol{\phi}''\boldsymbol{\phi}''^T d\xi, \quad \mathbf{K}_s = \int_0^1 \xi\boldsymbol{\phi}\boldsymbol{\phi}^T d\xi, \quad \mathbf{K}_b = \int_0^1 \boldsymbol{\phi}'\boldsymbol{\phi}'^T d\xi \tag{4}$$

$$\nu = \frac{NL^2}{EI}, \qquad \eta = \frac{k_w L^4}{EI} \tag{5}$$

Any orthogonal series that satisfies the boundary conditions can be employed; but the challenge is to find this special orthogonal series. First, let us consider employing an $n+q$ term Legendre polynomial series, where P_i is the i^{th} order Legendre polynomial. The pile displacement y can be defined (7) in term of vector of shape functions $\boldsymbol{\phi}_1$ and $\boldsymbol{\phi}_2$ can be defined as (6). Essentially the q generalised coordinates $\mathbf{x}_q$ will be constrained by the natural boundary condition leaving n unconstrained generalised coordinates $\mathbf{x}$.

$$\boldsymbol{\phi}_1^T = \left[P_0, P_1, \cdots P_{q-1}\right], \ \boldsymbol{\phi}_2^T = \left[P_q, P_{q+1}, \cdots P_{q+n-1}\right] \tag{6}$$

$$y = L\left(\boldsymbol{\phi}_1^T\mathbf{x}_q + \boldsymbol{\phi}_2^T\mathbf{x}\right) = L\mathbf{x}^T\boldsymbol{\phi} \tag{7}$$

The corresponding boundary condition of a pile [i.e. fixed-free (cantilever pile) etc] can be imposed.

4.1 Linear Buckling Analysis

By applying Euler-Lagrange equations to (3) we obtain an eigenvalue problem given by equation 8. From the smallest eigenvalue ν_1, the first mode and critical buckling load N_1 can be obtained, see equation 9.

$$\left(\mathbf{K}_p + \eta\mathbf{K}_s\right)\mathbf{x} = \nu\mathbf{K}_b\mathbf{x} \tag{8}$$

$$N_1 = \nu_1\frac{EI}{L^2} \tag{9}$$

By employing the corresponding boundary conditions of the pile, appropriate orthogonal series can be obtained. This is then employed with computational algebra package to obtain matrices $\mathbf{K}_p$, $\mathbf{K}_s$ and $\mathbf{K}_b$.

4.2 Kinetic Energy

The kinetic energy of this system can be stated as equation 10; where m_b is the mass of the building, m_s is half the mass per unit depth of the soil stack, and m_p is the mass per unit length of the pile.

$$T = \tfrac{1}{2}m_b\dot{y}(0)^2 + \tfrac{1}{2}\left(m_p + m_s\right)\int_0^L \dot{y}^2 dz \tag{10}$$

This can be expressed in the quadratic form (11) where $\mathbf{M}$ is the system non-dimensional mass matrix which is expressed in terms of pile and soil to building mass ratio α.

$$T = \tfrac{1}{2}m_b L^2\dot{\boldsymbol{x}}^T\mathrm{M}\dot{\boldsymbol{x}} \tag{11}$$

$$\mathbf{M} = \boldsymbol{\phi}(0)\boldsymbol{\phi}(0)^T + \alpha\int_0^1 \boldsymbol{\phi}\boldsymbol{\phi}^T d\xi \tag{12}$$

$$\alpha = \frac{\left(m_p + m_s\right)L}{m_b} \tag{13}$$

4.3 Equation of free vibration

The dimensionless Euler-Lagrange equations of free vibrations are given by (15); where time is scaled by the introduction of τ , see (14).

$$\tau = st, \ s^2 = \frac{EI}{m_b L^3} \tag{14}$$

$$\mathbf{M}\ddot{\mathbf{x}} + \left(\mathbf{K}_p + \eta\mathbf{K}_s - \nu\mathbf{K}_b\right)\mathbf{x} = \mathbf{0} \tag{15}$$

$$\left(\mathbf{K}_p + \eta\mathbf{K}_s - \nu\mathbf{K}_b\right)\mathbf{x} = \lambda\mathbf{M}\mathbf{x} \tag{16}$$

The fundamental natural frequency, of the pile/soil/structure system, ω_1 is obtained by solving the generalised eigenvalue problem (16) and determining its smallest eigenvalue λ_1.

5. AN EXAMPLE CASE STUDY

In this section an example problem shown in Figure 3 is taken. The pile is assumed to be fixed at some depth below the liquefied layer. In other words, the pile extends quite a considerable depth in non-liquefiable hard layer below the liquefiable layer. The pile head is free to translate but fixed against rotation. The boundary condition is shown by equation 17.

$$y(1) = y'(1) = y'(0) = 0 \tag{17}$$

The buckling load is calculated by solving the generalised eigenvalue problem (Equation 8) for various η, the smallest eigenvalue ν_1 is found and Figure 4 can be displayed. It may be noted that the graph tends to the Eulerian beam results as $\eta \to 0$.

Figure 5 displays a contour plot of λ_1 vs. the soil/pile stiffness ratio η and axial load factor ν. This is obtained for a fixed value of mass ratio α.

$$\omega_1^2 = s^2 \lambda_1 \tag{18}$$

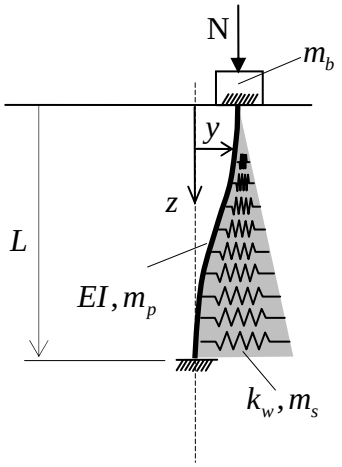

Figure 3: Example problem considered in this paper

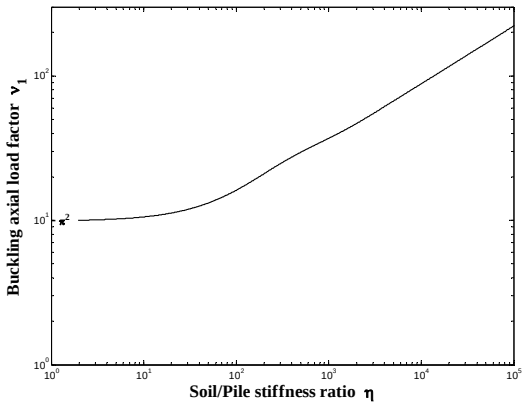

Figure 4: Buckling Load eigenvalue, ν_1 equation (8 & 9), for the boundary condition shown in Figure 3.

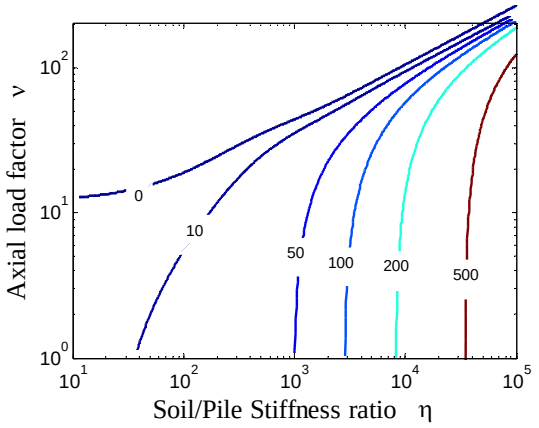

Figure 5: Natural Frequency eigenvalues, λ_1 equation (16 & 18), for the boundary condition shown in Figure 3

5. DISCUSSION

The following points may be observed:

1. As the soil/pile stiffness increases, the buckling load of the system increases. As a result, buckling of piles are never considered a problem unless the soil is extreme soft clay or liquefied soil.
2. As soil liquefies, the soil/pile stiffness decreases and the buckling load decreases (see Figure 4).
3. For low soil/ pile stiffness, the buckling load can be estimated by considering the pile as an unsupported column (see Figure 4).
4. For a particular axial load ratio of the pile, as the soil/ pile stiffness decreases, the first natural frequency of the system also decreases.
5. Zero contours in frequency plot (see Figure 5) is identical to the buckling load factors obtained in Figure 4

6. CONCLUSIONS

Dynamic stability of a pile-supported structure has been considered. During seismic liquefaction, two effects arises due to the removal of the lateral support the soil offers to the pile. They are

(a) Increase in axial load in the pile in the potentially unsupported zone due to loss of shaft resistance;

(b) Dynamics of pile-supported structure due to frequency dependent force arising from the shaking of the bedrock and the surrounding soil than can cause dynamic amplification of pile head displacements leading to resonance type failure.

Under service conditions (no earthquake and no-liquefaction) the first natural frequency of a structure or the fundamental time period can be estimated without considering the effect of the piles. However when the soil starts to liquefy, the piles become an integral part of the

structure and take part in the vibration. As a result, the time period alters significantly and cannot be ignored in analysis/design. In most cases, the frequency will decrease.

This paper shows a simple method to analyse the combined problem of stability and dynamics. This paper explicitly quantified the first natural frequency due to the effects of (1) Axial force, (2) Dynamic excitation and (3) Reduction of the lateral support due to liquefaction for one boundary condition of a pile.

Acknowledgements:

The first author acknowledges the support from Japan Ministry of Education, Culture, Sport, Science, and Technology (MEXT) for establishing the Center for attending the 6th Urban Earthquake Engineering (CUEE) in Tokyo Institute of Technology.

References:

AIJ (1988, 2001): Architectural Institute of Japan, Recommendations for design of building foundations, (in Japanese)

Bhattacharya, S and Madabhushi, S.P.G (2008): "A critical review of methods of pile design in seismically liquefiable soils", Bulletin of Earthquake Engineering, Volume 6, No 3, pp 407-447.

Bhattacharya, S., Bolton, M.D. and Madabhushi, S.P.G. (2005): "A reconsideration of the safety of the piled bridge foundations in liquefiable soils", Soils and Foundations, Volume 45, August 2005 issue, No 4, pp 13-26.

Bhattacharya, S., Madabhushi, S.P.G., and Bolton, M.D. (2004): "An alternative mechanism of pile failure in liquefiable deposits during earthquakes", Geotechnique 54, April issue, No.3, pp 203-213.

Bhattacharya, S (2003): Pile Instability during earthquake liquefaction, PhD thesis, University of Cambridge (U.K).

Dash, S.R., Bhattacharya, S., Blakeborough, A. and Hyodo, M (2008): "P-Y curve to model lateral response of pile foundations in liquefied soils", Paper number 04-01-0089, Proceedings of the 14th World Conference on Earthquake Engineering, Oct 12-17, 2008, Beijing.

Ishihara, K (1997): Terzaghi oration: "Geotechnical aspects of the 1995 Kobe earthquake", Proceedings of ICSMFE, Hamburg, pp 2047-2073.

JRA (2002, 1996): Japanese Road Association, Specification for Highway Bridges, Part V, Seismic Design.

Kimura, Y. and Tokimatsu, K. (2007): "Buckling stress of slender pile with lateral displacement at the pile head in liquefied soils", Journal of Structural and Construction Engineering, AIJ (Architectural Institute of Japan) No 617, pp 169-175, July 2007.

Lin et al (2005): "Damage of piles caused by lateral spreading – Back study of three cases", ASCE Geotechnical Special Publication No 145 on Seismic Performance and Simulation of Pile Foundations in Liquefied and Laterally Spreading Ground, (Boulanger and Tokimatsu eds),

Liu, L and Dobry, R (1995): "Effect of liquefaction on lateral response of piles by centrifuge model tests", NCEER report to FHWA. NCEER Bulletin, January 1995, Vol 9, No. 1.

Rollins, K.M., Gerber, T.M., Dusty, L.J. and Ashford, S.A. (2005): "Lateral resistance of a full-scale pile group in liquefied sand", Journal of Goetechnical and Geo-environmental Engineering (ASCE), Vol 131, No 1, January 2005

RTRI: Rail Technical Research Institute code – 1999 edition

Shanker, K., Basudhar, P.K. and Patra, N.R. (2007): "Buckling of piles under liquefied soil condition", Geotechnical and Geological Engineering (Springer), Volume 25, pp 303-313.

Takahashi, A., Kuwano, J., Arai, Y., and Yano, A. (2002): "Lateral resistance of buried cylinder in liquefied sand" Proceedings of the international conference on physical modelling in geotechnics, ICPMG-02, St Johns, Newfoundland, Canada, July 2002.

Thomson, J.M.T and Hunt, G.W (1984): "Elastic Instability phenomenon", Wiley, Chichester.

Yasuda, S., Terauchi, T., Morimoto, H., Erken, A. and Yoshida, N (1998): "Post liquefaction behaviour of several sands" 11th European Conference on Earthquake Engineering, Balkema, Rotterdam, ISBN 90 5410 982 3

Yoshida, N, Towahata, I., Yasuda, S. and Kanatani, M. (2005): Discussion to the paper by Bhattacharya et al. (2004) on "An alternative mechanism of pile failure in liquefiable deposits during earthquakes", Geotechnique, 55, No 3, pp 259-263.

Sixth International Conference on Urban Earthquake Engineering
March 3-4, 2009, Tokyo Institute of Technology, Tokyo, Japan

ESTIMATION OF KINEMATIC FORCE ACTING ON PILES IN LATERALLY SPREADING GROUND

Hiroko Suzuki[1] and Kohji Tokimatsu[2]

1) Assistant Professor, Department of Architecture and Building Engineering, Tokyo Institute of Technology, Japan
2) Professor, Department of Architecture and Building Engineering, Tokyo Institute of Technology, Japan
hsuzuki@arch.titech.ac.jp, kohji@o.cc.titech.ac.jp

Abstract: Kinematic force arising from ground displacement during laterally spreading ground is estimated through large shaking table tests conducted on soil-pile models. The models had two single piles with different stiffness that penetrated an inclined sand deposit with a slope angle of 2 degrees. The displacements and bending strains of both stiff and flexible piles increase when the ground moves downstream in the initial stage of shaking. Those of the stiff pile, however, tend to decrease in the later stage of shaking, while those of the flexible pile do not show such a trend. The difference in displacement bending strain and displacement between the two piles is due to the different pile stiffness between the two. Namely, the stiff pile can resist ground movement, while the flexible pile can follow ground movement. The pseudo static analysis is conducted in order to simulate the test results. The computed results including pile stresses are in good agreement with the observed ones.

1. INTRODUCTION

The Hyogoken-Nambu earthquake (M=7.2) that occurred on January 17, 1995, caused many geotechnical problems particularly in the reclaimed land area along the coastline of Kobe city. A large number of buildings supported on piles in liquefied and laterally spreading areas settled and/or tilted without significant damage to their superstructures (BTL Committee 1998). Subsequent studies have shown that kinematic force on piles that was induced by large cyclic and/or permanent ground displacement was the major cause of the distress.

To clarify the abovementioned kinematic forces arising from ground displacement during liquefaction and lateral spreading, 1-g and centrifuge shaking table tests have been conducted (e.g., Wilson et al. 2000, Abdoun et al. 2003, Boulanger et al. 2003 and Tokimatsu and Suzuki 2004). Despite many studies, there still exits a controversial argument on how liquefied and laterally spreading soil behave like and whether the p-y behavior, defined as the relation of subgrade reaction with relative displacement between soil and pile, be modeled as a viscous fluid (e.g., Towhata et al. 1999) or solid material (Railway Technical Research Institute 1997 and Architectural Institute of Japan 2001).

The objective of this study is to investigate the kinematic force acting on piles subjected to lateral spreading and its effects on pile behavior. Two large shaking table tests were conducted for this purpose in which two single piles having different stiffness set in an inclined sand deposit with or without a non-liquefied crust layer.

2. LARGE SHAKING TABLE TESTS

To investigate kinematic force arising from ground displacement on pile behavior during liquefaction-induced lateral spreading, shaking table tests were conducted using the large shaking table facility at the National Research Institute for Earth Science and Disaster Prevention, in Tsukuba in 2004. Figure 1 shows soil-pile systems prepared in a laminar shear box, 5.5m in height, 12.0m in width and 3.5m in length, that was set on the shaking table with a slope angle of 2 degrees. The sand deposit constructed in the laminar shear box also had an inclined surface with a slope angle of 2 degrees, in which two single piles 6m in length were set apart.

The two single piles had the same diameter but different wall thickness and different stiffness. One located downstream was a steel pipe with a diameter of 318.5mm and a wall thickness of 6mm. The other located upstream was a stainless steel pipe with a diameter of 318.5mm and a wall thickness of 3mm. The downstream pile is hereby called the stiff pile (PS-1 and PS-2 in Figure 1) and the upstream pile the flexible pile (PF-1 and PF-2 in Figure 1). Both piles had a free rotational condition at their heads and a fixed boundary with the laminar shear box base at their tips.

The inclined sand deposit prepared in the inclined laminar box had a thickness of 5.0 m. As shown in Figure 1, the water table was at 1.0 m below the lowest ground surface for Test 1 or at the same level as the highest ground surface for Test 2. To prepare the sand deposit for Test 1, after fixing the piles in the inclined base layer of cemented mortar, the laminar shear box was filled with water to a certain level (4.0 m high from the base) and wet

Kasumigaura Sand was pluviated into the water. Dry sand was, then, air-pluviated to form the top non-liquefiable layer above the water table. To prepare the sand deposit for Test 2, the water was poured above the top non-liquefied layer after the shaking event of Test 1. For both the test, a sinusoidal wave with a frequency of 2Hz was used as an input base motion, with a maximum acceleration of 2.0 m/s^2. Before each shaking event, a geophysical test and cone penetration test were conducted to characterize soil profile.

The test models were densely instrumented with accelerometers, displacement transducers, strain gauges, pore water pressure transducers and earth pressure transducers. In particular, to investigate factors influencing subgrade reaction of piles during lateral spreading, pore pressure transducers were installed on both downstream and upstream sides of the two piles.

3. KINEMATIC EFFECTS ON PILES WITH DIFFERENT STIFFNESS

Photo 1 shows the laminar shear box before and after Test 2. The permanent deformation of the laminar box after the test, induced by lateral ground spreading, was more than 1 m at the top (Photo 1(b)).

Figure 2 shows time histories of major values for Tests 1 and 2, i.e, displacements of the ground surface (laminar box edge at the same height) and the pile heads, bending strains at the pile tips (0.5m above the laminar box base), pore water pressures and accelerations of the shaking table. The value of the flexible pile displacement exceeded a measurable range after 13 s, as shown in Figure 2(j).

The pore water pressure reaches the initial effective stresses, causing soil liquefaction within 5 s after the start of shaking (Figure 2(f)(m)). The ground displacement increases downstream (on the negative side) with cyclic fluctuation, increasing pile displacement and bending strain in the initial stage of shaking (Figure 2(a)-(e)(h)-(l)). In both tests, the displacement and bending strains of the stiff pile, however, decrease in the later stage of shaking (Figure 2(b)(d)(i)(k)), while those of the flexible pile do not show such a trend (Figure 2(c)(e)(j)(l)). The bending strain of the stiff pile is slightly larger in Test 1 than in Test2 (Figure 2(d)(k)), indicating that the presence of the non-liquefied crust layer might have affected an increase in bending strains. The bending strain of the flexible pile, in contrast, is significantly larger in Test 2 than in Test 1 (Figure 2(e)(l)). Probably, the flexible pile had yielded in Test 1 and

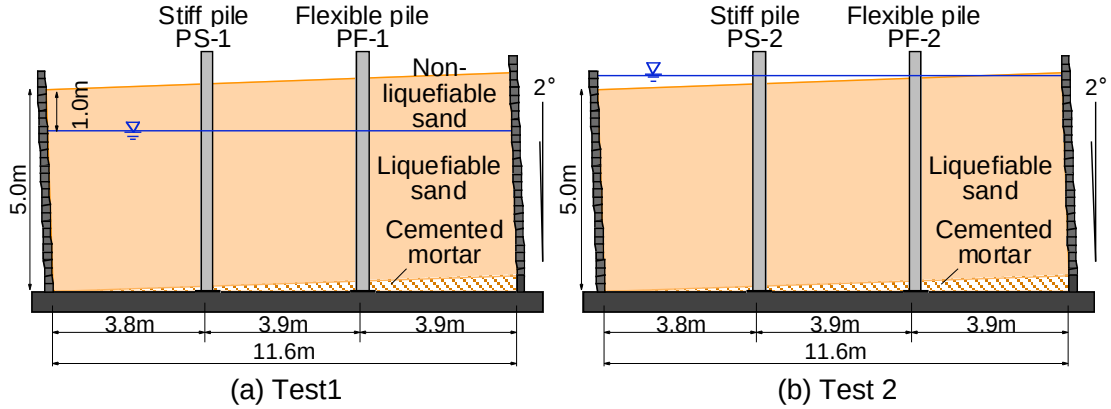

Figure 1 Soil-pile test models

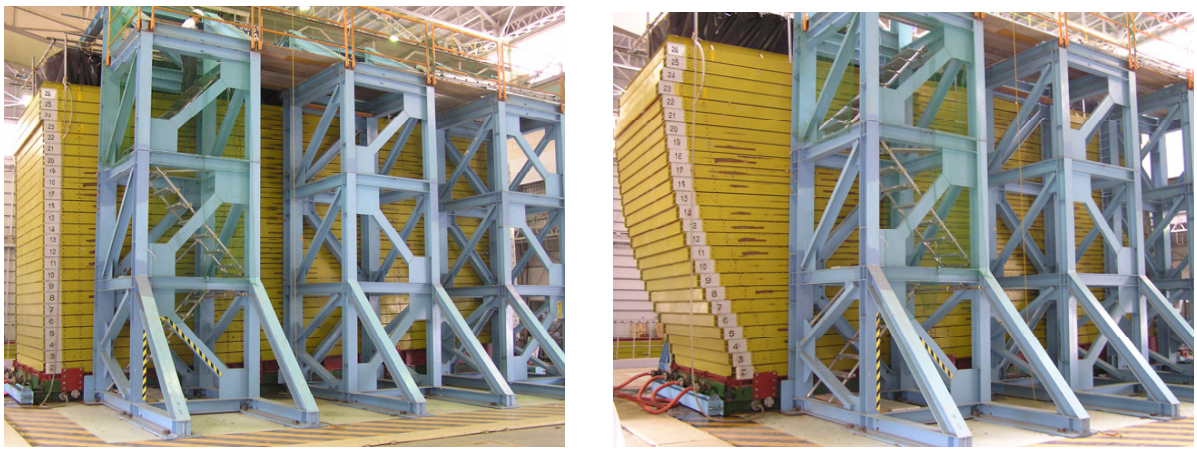

(a) Before shaking (b) After shaking

Photo 1 Deformation of laminar box in Test 2

deformed more in Test 2.

Figure 3 compares distributions of bending strains of the stiff and flexible piles in two instances, i.e. 5.6 s and 20 s, for Tests 1 (Figure 3(a)(b)) and 2 (Figure 3(c)(d)). The bending strains of the stiff pile in both tests are much larger at 5.6s than at 20.0s (Figure 3(a)(c)), while those of the flexible pile are almost the same between the two instances (Figure 3(b)(d)). This confirms that the effects of kinematic forces depend on pile stiffness, resulting in the difference in pile behavior during laterally spreading. In addition, the difference in bending strains between 5.6 s and 20 s for the stiff pile is more significant in Test 2 than in Test 1 (Figure 3(a)(c)). This finding suggests that the presence of non-liquefied top layer affects changes of bending strains with time.

To investigate the difference in behavior between the stiff and flexible piles, the p-y relation, i.e. the relation of subgrade reaction with relative displacement between a pile and ground, is computed from the observed bending strain on the assumption that pile stiffness is unchanged with depth throughout shaking. Figure 4 shows the relation of relative displacement with subgrade reaction and the pore water pressures observed on both downstream and upstream sides of the stiff and flexible piles in Test 1. When the piles and the ground move downstream, the pore water pressure on the downstream side of the piles decreases significantly with that on the upstream side almost constants (Figure 4(b)(c)(e)(f)). At this stage, the subgrade reaction becomes large (Figure 4(a)(d)). When the piles and ground move upstream, the pore water pressures on both sides of the piles increase or maintain almost constant (Figure 4(b)(c)(e)(f)). At this stage, the subgrade reaction decreases (Figure 4(a)(d)). This indicates that the subgrade reaction in laterally spreading ground is induced by the pore water pressure changes in soil around a pile (Tokimatsu and Suzuki 2004).

A comparison of the trends between the stiff and flexible piles shown in Figure 4(a)(b)(d)(e) suggests that a decrease in pore water pressure on downstream side as well as an increase in subgrade reaction, induced by the cyclic relative displacement, are more significant in the stiff pile than in the flexible pile. This is probably due to the difference in relative displacement between the two piles. Namely, the stiff pile, that can resist the ground movement, suffers larger displacement relative to the ground, while the flexible pile, that can follow the ground movement, yield smaller relative displacement.

The subgrade reaction and pore water pressure changes are small with time, as shown in Figure 4(a)(b)(d)(e), with increasing permanent relative displacement. It is interesting to note that the value of subgrade reaction of the stiff pile is bounced to almost zero

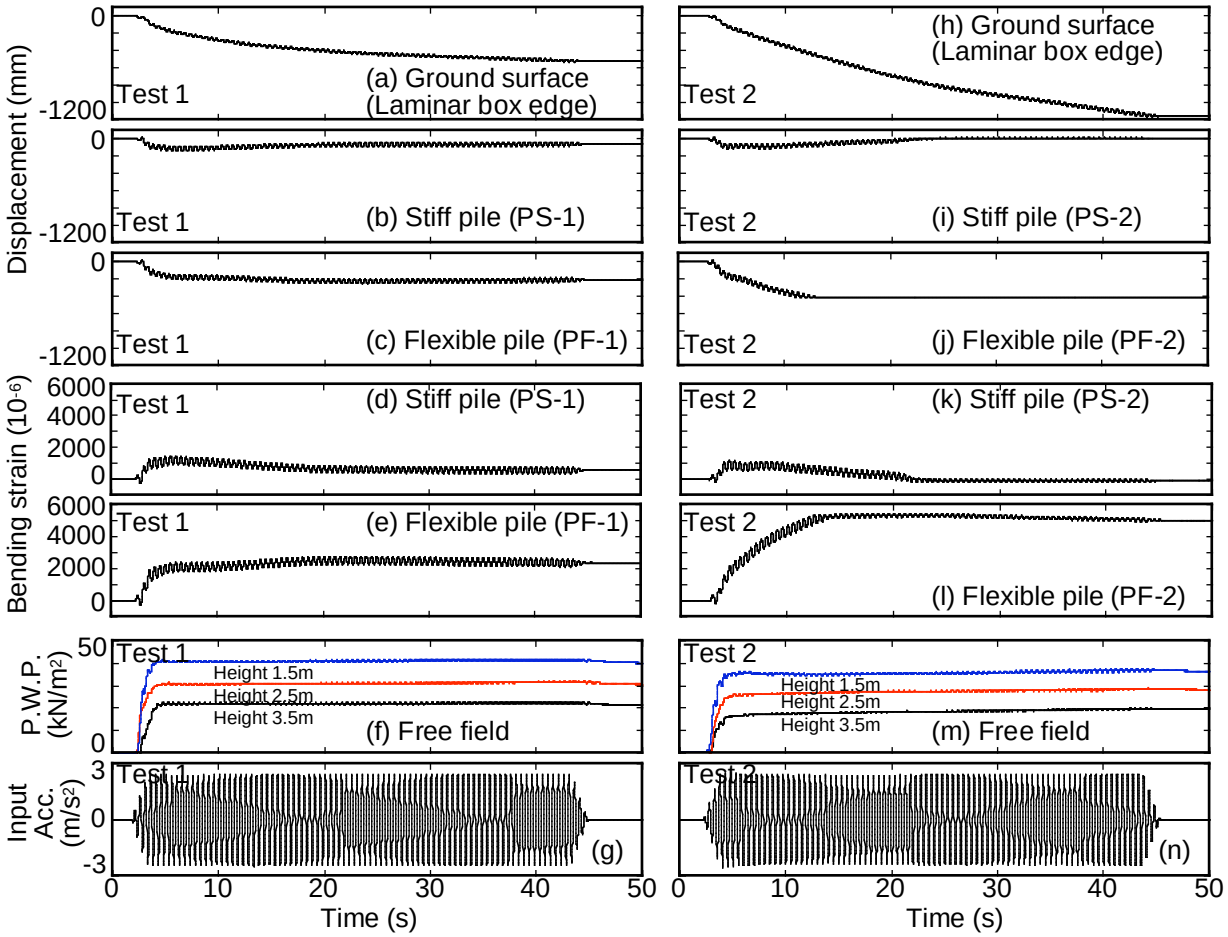

Figure 2 Time histories of major values in Tests 1 and 2

at every cycle, while that of the flexible pile is not (Figure 4(a)(d)). This relates to the difference in bending strains between the stiff and flexible piles, in which the bending strain of the stiff pile decreases in the later stage of shaking, while that of the flexible pile does not.

4. ESTIMATION OF PILE STRESSES BASED ON PSEUDO-STATIC ANALYSIS

To estimate kinematic effects in laterally spreading ground, pseudo static analysis is conducted on soil-pile models. Simplified pseudo static methods using the p-y spring are based on the following equations (Architectural Institute of Japan 1988, 2001 and Railway Technical Research Institute 1997):

$$EI\frac{d^4y}{dx^4} = -p \tag{1}$$

$$p = k_h B\left(y - y_g\right) \tag{2}$$

in which E and I are the Young's modulus and the moment of inertia of a pile, y and y_g are the horizontal displacement of a pile and ground, x is the depth, p is the subgrade reaction, k_h is a coefficient of horizontal subgrade reaction, and B is a pile diameter. The coefficient of subgrade reaction k_h is given by the following equation (Tokimatsu et al. 2002):

$$k_h = k_{h1}\frac{2}{1+\left|y_r/y_1\right|}\beta \tag{3}$$

in which k_{h1} is the reference value of k_h, defined as a function of N-value. y_1 is the reference value of y_r and β is a scaling parameter for a reduction in coefficient of subgrade reaction.

To estimate pile stresses of the stiff and flexible piles in the laterally spreading soil, it is assumed that the ground displacement is equal to the observed one, the value of which is 200 mm at 5.5 s and 400 mm at 20 s. k_{h1} is given by the N-value computed from the CPT resistances measured prior to each shaking table tests and y_1 is one percent of a pile diameter. β is assumed to change from 0.1 in 5.5 s to 0.02 in 20 s, to take into account the degradation of soil stiffness during lateral spreading.

Figures 5 and 6 compare the estimated and observed bending strains of the stiff and flexible piles for the two instances, i.e. 5.5 s and 20 s, in Tests 1 and 2. The estimated bending strain of the flexible pile is almost the same between the two instances (Figures 5 and 6(b)(d)). In contrast, the estimated bending strain of the stiff pile is

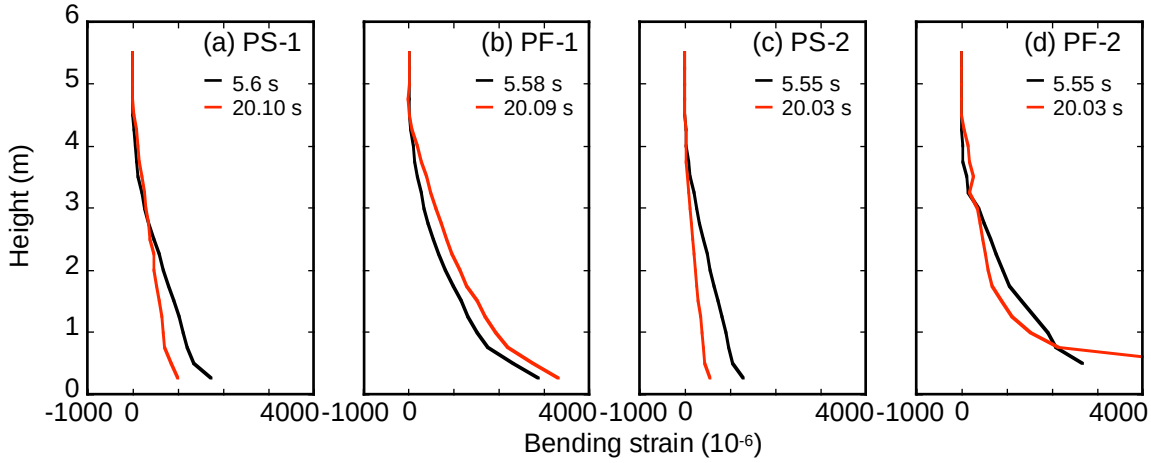

Figure 3 Distributions of bending strains in Tests1 and 2

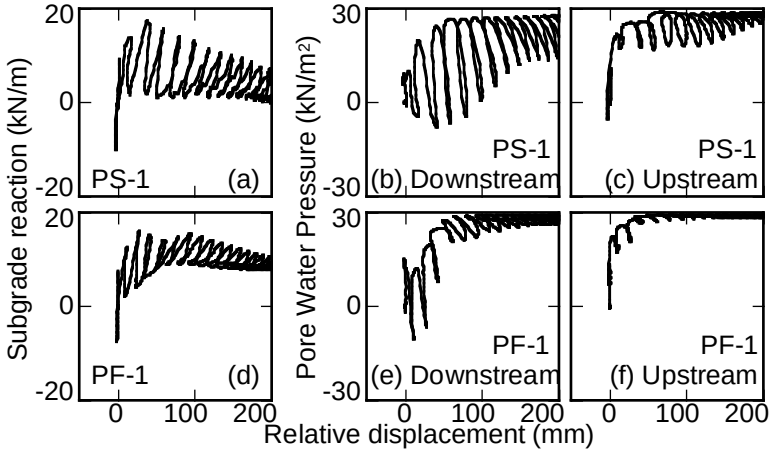

Figure 4 Relation of relative displacement with subgrade reaction and pore water pressures in Test 1

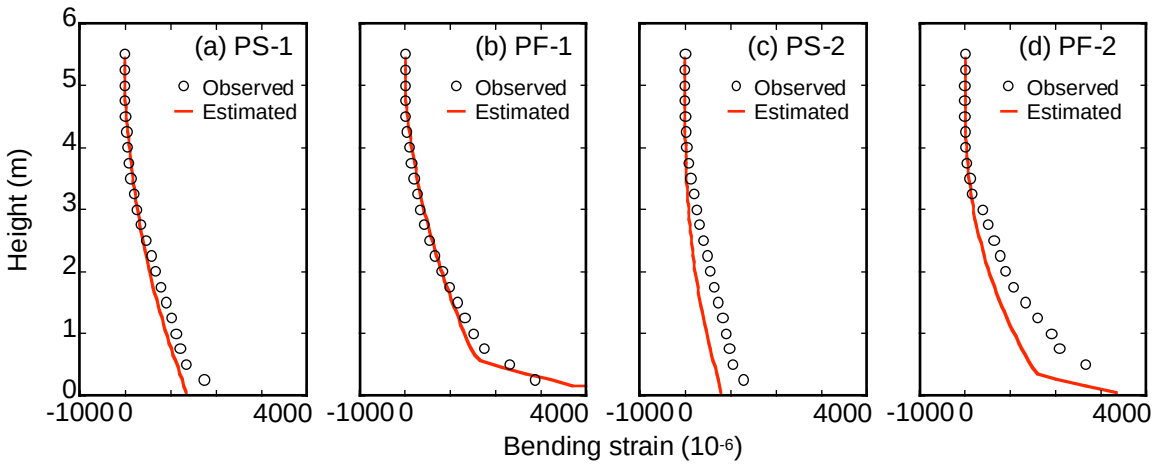

Figure 5 Distributions estimated and observed bending strains for 5.5 s

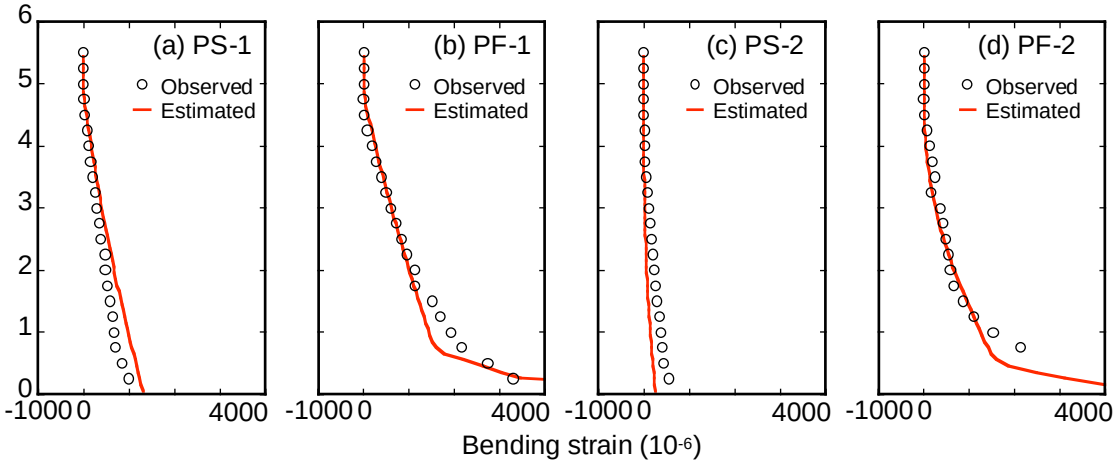

Figure 6 Distributions estimated and observed bending strains for 20 s

smaller at 20 s than at 5.5 s, despite of the larger ground displacement in 20 s (Figures 5 and 6(a)(c)). The decease in bending strain of the stiff pile is probably related to the degradation of soil stiffness induced by the large relative displacement. Namely, the subgrade reaction of the stiff pile reaches the ultimate value due to large relative displacement before the large strain enough to cause pile yielding develops. In contrast, the flexible pile yields before the subgrade reaction reaches the ultimate value. In addition, the estimated bending strain of the stiff pile is larger in Test 1 than in Test 2, while that of the flexible pile is almost the same between the two. This suggests that the effects of non-liquefied crust layer are more significant on the stiff pile than on the flexible pile. Abovementioned trends in estimated bending strains are in good agreement with the observed ones.

4. CONCLUSIONS

The effects of kinematic force on piles having different stiffness in laterally spreading ground were estimated based on large shaking table tests and pseudo static analysis. The results have shown the following:

The displacements and bending strains of both stiff and flexible piles increase when the ground moves downstream in the initial stage of shaking. Those of the stiff pile, however, tend to decrease in the later stage of shaking in the later stage of shaking, while those of the flexible pile do not show such a trend. This is probably because the stiff pile can resist ground movement, resulting in the large relative displacement, which induces the ultimate subgrade reaction before the yielding of pile. In contrast, the flexible pile can follow the ground movement and yields before the subgrade reaction reaches the ultimate value.

The effect of kinematic force arising from the non-liquefied crust layer is more insignificant on the flexible pile than on the stiff pile. This is because the kinematic force arising from liquefied layer could cause the yielding of the flexible pile.

Acknowledgements:

The study described herein was made possible through a US-Japan collaboration research among National Institute for Earth Science and Disaster Prevention, Rensselaer Polytechnic Institute, University of California, San Diego, Tokyo Institute of Technology

and Tokyo Soil Research Co. The authors express their sincere thanks to the above organizations.

References:

Abdoun, T., Dobry, R., O'Rourke, T. D. and Goh, S. H. (2003), "Pile response to lateral spreads: centrifuge modeling", *Journal of Geotechnical and Geoenvironmental Engineering*, ASCE, **129** (10), 869-878.

Architectural Institute of Japan (1988, 2001), "Recommendations for design of building foundations" (in Japanese).

Boulanger, R. W., Kutter, B. L., Brandenberg, S. J., Singh, P. and Chang, D. (2003), "Pile foundations in liquefied and laterally spreading ground during earthquakes: Centrifuge experiments & analyses", Center for Geotechnical modeling, Department, of Civil Engineering, UC, Davis, Report No. UCD/CGM-03/01.

BTL Committee (1998), Research Report on liquefaction and lateral spreading in the Hyogoken-Nambu earthquake (in Japanese).

Railway Technical Research Institute (1997), "Foundation design codes for railway structures" (in Japanese).

Tokimatsu, K., Suzuki, H. and Saeki, E. (2002), "Modeling of horizontal subgrade reaction of pile during liquefaction based on large shaking table", *Journal of Structural and Construction Engineering*, AIJ, **559**, 135-141 (in Japanese).

Tokimatsu, K., Suzuki, H. and Sato, M. (2005), "Effects of dynamic soil-pile-structure interaction on pile stresses, *Journal of Structural and Construction Engineering"*, AIJ, **587**, 125-132 (in Japanese).

Towhata, I., Vargas-Monge, W., Orense, R. P. and Yao, M. (1999), "Shaking table tests on subgrade reaction of pipe embedded in sandy liquefied subsoil", *Journal of Soil Dynamics and Earthquake Engineering*, **18** (5), 347-361.

Wilson, D. W., Boulanger, R. W. and Kutter, B. L. (2000), "Observed seismic lateral resistance of liquefying sand", *Journal of Geotechnical and Geoenvironmental Engineering*, ASCE, **126** (10), 898-906.

Sixth International Conference on Urban Earthquake Engineering
March 3-4, 2009, Tokyo Institute of Technology, Tokyo, Japan

SHAKING TABLE TESTS ON SOIL-PILE-STRUCTURE MODELS WITH SEMI-RIGID PILE HEAD CONNECTIONS

Sadayuki Ishizaki[1)], Masato Majima[2)], Toshiaki Nagao[3)], Hideki Funahara[1)], Kazuki Aoshima[1)]

1) Research Engineer, Technology Center, Taisei Corp., Japan
2) President, Soil Design Inc., Japan
3) Senior Research Engineer, Technology Center, Taisei Corp., Japan
sada.ishizaki@sakura.taisei.co.jp, masato.majima@soil-design.co.jp, toshiaki.nagao@sakura.taisei.co.jp, hideki.funahara@sakura.taisei.co.jp, kazuki.aoshima@sakura.taisei.co.jp

Abstract: Shaking table tests are conducted on soil-pile-structure models to investigate the seismic behaviour of buildings with semi-rigid pile head connections. The dynamic test results show that (1) The semi-rigid pile head connection is effective to reduce bending moment of piles and footing beams; (2) In case of semi-rigid pile head connections, the shear force of pile head at the end of building tend to increase, when axial force increase; and (3) The maximum acceleration of superstructure with semi-rigid pile head connections is slightly smaller than that of rigid one in this study.

1. INTRODUCTION

In the conventional design of pile heads, anchoring the main reinforcement of pile head to the pile cap has prevailed. Pile heads are connected nearly rigidly. Under the condition, extremely large inertia forces acting from the building during an earthquake are likely to greatly increase the bending moment at the pile head and cause damage exclusively to pile heads. In the Hyogoken-nambu Earthquake of 1995, the failure of pile heads partly ascribable to the nearly rigid connection caused differential settlement or inclination of numerous structures. In the wake of the event, various semi-rigid pile head connection methods were developed that permit the rotation of pile heads as more effective pile design methods. Their effectiveness for reducing damage to piles has been verified by structural tests (Hara et al. 2002, Ohtsuki et al. 2001, Hiraide et al. 2004). The existing researches have, however, made studies focusing only on the static structural properties of pile head connections. Few examples are available of verifying in tests the effectiveness of semi-rigid pile head connection methods for reducing damage using the whole building while considering the dynamic soil-pile-structure interaction. In this study, shaking table tests were conducted using soil-pile-structure models to examine the effectiveness of semi-rigid pile head connection methods for reducing seismic damage to piles and footing beams, and the effects on the response of the building.

2. TEST OUTLINE

2.1 Models

2.1.1 Building, Piles and Soil Assumed

The building, piles and soil assumed in the tests are listed in Table 1. The model similarity law was defined based on the work by Iai (1989) as shown in Table2. The scale was 1/15 for length and time. No similarity law was applied in the height of the building.

2.1.2 Types of Models

The types of models are shown in Table 3. Used as the test parameters were the type of pile head connection (rigid

Photograph 1 Model of Soil-pile-structure system (S-S Model)

or semi-rigid connection) and the aspect ratio (height) of the building for the semi-rigid connection models. The aspect ratio of the building was selected as a parameter because the semi-rigid pile head connection was designed to have varying rotation characteristics according to the axial force and because it was necessary to identify the effects of varying axial forces on the behavior of the semi-rigid pile head connection.

2.1.3 Soil Models

A general view of the model is given in Photograph 1 and the model is outlined in Figure 1. The laminar shear box was composed of 13 layers of 10-cm-high aluminum plates. The box measured 2.7 m in the direction of shaking, 1.2 m transverse to the direction of shaking and had a depth of 1.5 m. The soil model was created using silica sand No. 5. The target relative density was set at 90% to minimize the variations of soil properties due to soil compaction at each round of shaking. The soil was compacted using a vibrator while controlling the weight and height of the sand spread in the box. Soil was created for a rigid pile head connection model, a semi-rigid connection model and another semi-rigid connection model with a higher building aspect ratio. The relative densities were 94%, 92% and 91%, respectively. Little change was found in relative density before and after shaking.

2.1.4 Pile-foundation-structure Models

Aluminum pipes with an outer diameter of 70 mm and a thickness of 1.5 mm were used as piles. In order to identify the difference in stress between end and midpoint piles, two spans constituted the foundation in the direction of shaking and a single span in the direction perpendicular to the direction of shaking. Pile ends were connected using pins.

Table 1 Building, Piles and Soil Assumed in This Study

Building	Eleven-storied Reinforced Concrete Rigid-frame Structure with a Period of 0.8 Second
Piles	Cast-in-place Reinforced Concrete Pile with an Axial Diameter of 1200 mm
Soil	Surface Soil Depth: 25 m. γ = 16 kN/m^3. N-value: 10. Vs = Approximately 150 m/sec

Table 2 Model Similarity Law

Physical Quantities	Model/Actual Ratio. λ = 15
Length	$1/\lambda$
Density	1
Strain	$1/\lambda$
Acceleration	1
Displacement	$1/\lambda^2$
Angel of Rotation	$1/\lambda$
Time	$1/\lambda$
Force	$1/\lambda^3$
Moment	$1/\lambda^4$
Shear Modulus	1

Table 3 Types of Models

Symbol of Model	Type of Pile Head Connection	Superstructure	
		Aspect Ratio	Peak Period in the Transfer Function
R-S	Rigid Connection	Lower	0.069
S-S	Semi-rigid Connection		0.076
SH-S		Higher	0.065

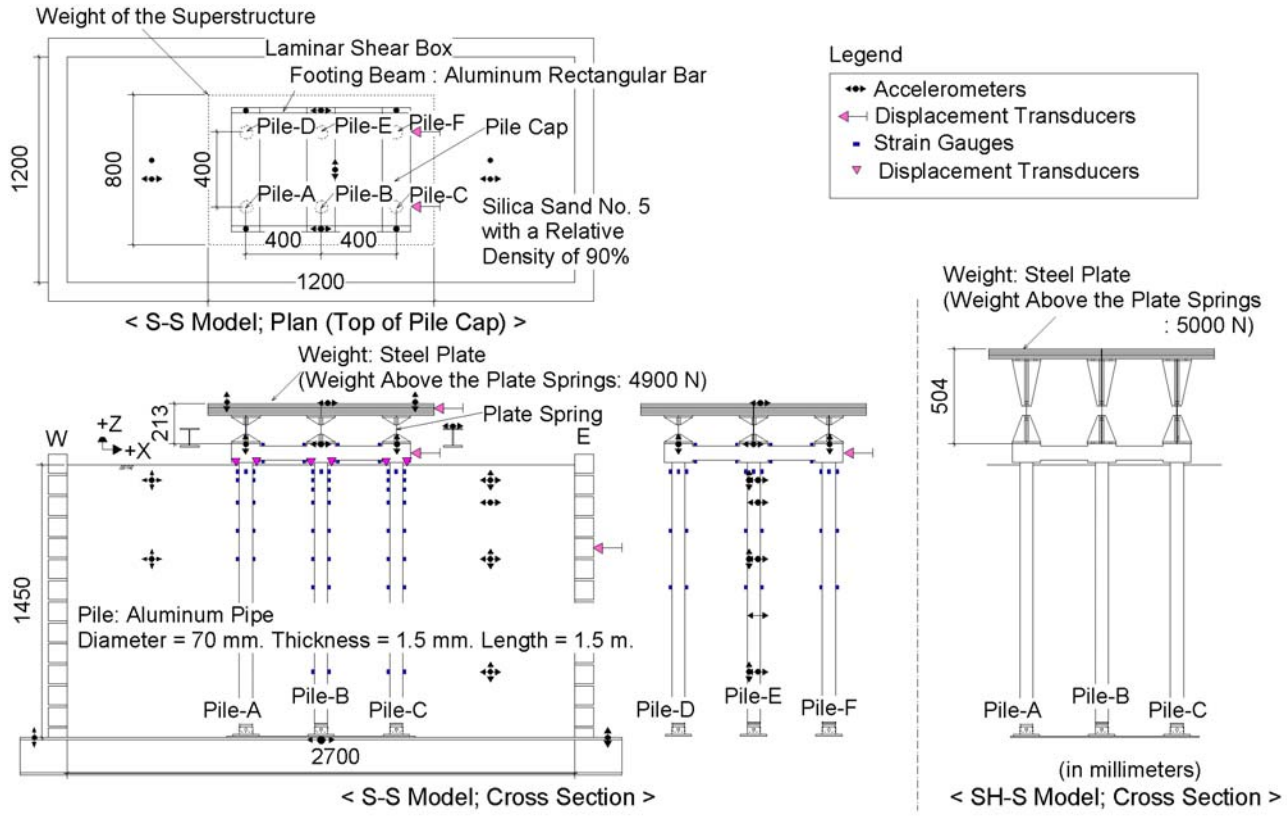

Figure 1 Outlines of Models and Measurement Items

Pile heads were connected either rigidly or semi-rigidly according to the type of connection. Two piles aligned in the direction perpendicular to the direction of shaking were connected together using a pile cap. Three rows of pile caps were connected to one another via the footing beams.

The building model was composed of a weight (steel plates), plate springs and angle bars for fixing the weight and springs and connecting them to the pile cap. In the building model with the lower aspect ratio, the distance between the top of the pile cap and the top of the weight was set at 213 mm. In the model with the higher aspect ratio, the distance was set at 504 mm. The thickness and width of plate springs were adjusted so as to obtain the designated period. The total of weights of the angle bars and weight above the plate springs was 4900 N in the building model with the lower aspect ratio or 5000 N in the building model with the higher aspect ratio. Nearly the same total weight was adopted.

White noise excitations were conducted after the development of the soil-pile-structure models. The peak ratios of Fourier spectrum of the acceleration of the pile cap to that of the acceleration of the top of the building during white noise excitation are shown in Figure 3.

2.1.5 Pile Head Connection Models

The cross section of the pile head connection is shown in Figure 2. For rigid connection, the pile head was filled with gypsum, sandwiched between divided sections of a pile cap and fastened using bolts.

For semi-rigid connection, a pile cap was simply placed on the pile head as in the actual structure (Hara et al. 2002). The pile head was designed to have varying rigidity according to the axial force in the pile head bonding plane. Pile heads were unlikely to contact the pile cap when the frame of the building was assembled in the test. Bolts were therefore installed to connect the pile heads to the pile cap before conducting the test to apply an axial force of approximately 300 N to 500 N.

The rotation characteristics at the pile head connection were identified in preliminary static tests. A cantilever beam composed of a pile cap and a pile was used as a model. Piles were subjected to loading and unloading in a direction perpendicular to the axis and the bending moment and the angle of rotation at pile head were measured. Several initial axial forces were applied to the semi-rigid connection Model.

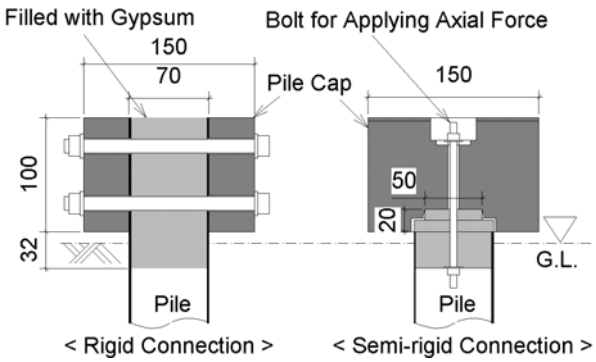

Figure 2 Cross Section of Pile Head Connection in the Direction of Excitation

A comparison was made in relationship between the bending moment and the angle of rotation at the pile head between the rigid connection and semi-rigid connection models (Figure 3). In the semi-rigid connection models, the initial rigidity was small, and the angle of rotation increased drastically as the bending moment increased. The relationship between the bending moment and the angle of rotation was represented by nearly the same curve either in loading or unloading. Thus, the models exhibited nonlinear elastic behavior. The bending moment was found to correspond to the initial axial force.

2.2 Measurement Parameters

Measurement parameters are shown in Figure 1. Measured were the horizontal and vertical accelerations of shaking table, soil and structure; lateral displacements of pile cap, building and laminar box; strains of piles and footing beams; angles of rotation of pile heads; and strain of bolt for applying axial forces to the semi-rigid connection models. Static measurements were taken for the pile head and the bolt for applying axial forces before excitation to grasp the initial axial force.

2.3 Method of Processing Measured Data

A schematic drawing in Figure 4 shows the distribution of bending moments in the piles and footing beams when inertia force acted on the building. The locations where the bending moments in pile heads and footing beams were measured are shown in the figure. The shear force of the pile and soil reaction were obtained by differentiating bending moment in the vertical direction once and twice, respectively.

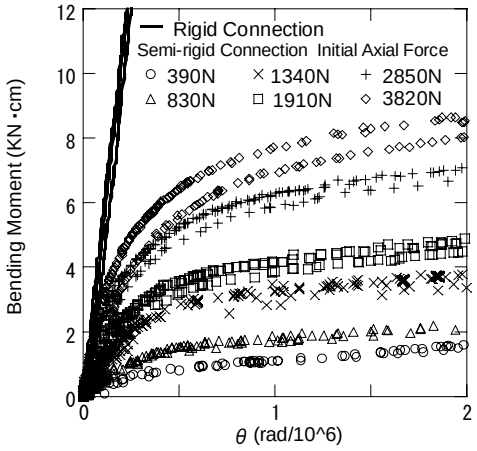

Figure 3 Results of Preliminary Test at Pile Head Connection

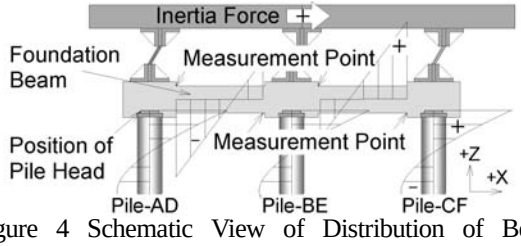

Figure 4 Schematic View of Distribution of Bending Moment

The axial force that was induced by the weight of the building and the axial force that was applied using a bolt acted on the plane of pile head bonding in the semi-rigid connection models. For the axial force at the pile head in this study, the axial force obtained from the strain of the pile and the load applied by the bolt for applying axial forces were used. The pile head axial force varied slightly from pile to pile. The rigidity against pile head rotation was also considered to vary according to the axial force. In the subsequent discussions, therefore, the bending moments in the pile and footing beams were evaluated using a mean value for two piles perpendicular to the direction of excitation. For example, a mean value was obtained between Piles-A and -D, and represented as Pile-AD.

The soil displacement was obtained by integrating the acceleration record twice.

2.4 Cases of Excitation

Cases of excitation are listed in Table 4. The N-S component of the Hachinohe record was used as an input motion for excitation. The amplitude was adjusted to obtain a maximum horizontal velocity of 50 cm/sec for Level 2 ground motion and a maximum horizontal velocity of 25 cm/sec for Level 1 ground motion as under actual conditions. Level 2 ground motions of Hachinohe record are shown in Figure 5.

3. Test Results and Discussions

3.1 Discussions on the Results of Application of Level 2 Ground Motion of Hachinohe Record

The results of excitation using Level 2 ground motion of the Hachinohe record (with a peak horizontal velocity of 50 cm/sec) were compared in SH-S, S-S and R-S. The distributions of axial forces right before excitation are shown in Table 5 for the semi-rigid pile head connection models. The axial force was carried predominantly by Pile-BE in S-S and by Pile-AD in SH-S.

Table 4 Cases of Excitation

Input Level		Input Wave
Peak Acceleration: 30 gal		White Noise
Level 1	Equivalent to Peak Horizontal Velocity of 25 cm/sec	Hachinohe Record
Level 2	Equivalent to Peak Horizontal Velocity of 50 cm/sec	

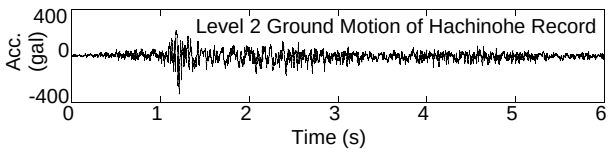

Figure 5 Input Ground Motion

Table 5 Axial Force Before Excitation

Symbol of Model	Pile-AD	Pile-BE	Pile-CF
SH-S	1700N	1100N	1400N
S-S	1200N	2000N	900N

3.1.1 Major Time Histories

The time histories in the period between the first and second seconds are shown in Figure 6. The acceleration of the building was slightly lower in SH-S and S-S than in R-S (Figure 6 (a)). The varying pile head axial force in SH-S was approximately 1.5 times that in S-S and R-S. The effect of a larger aspect ratio of the building was therefore found (Figure 6 (i)). The pile head bending moment tended to be lower in semi-rigid connection models (SH-S and S-S) than in R-S (Figures 6 (d) through (f)).

3.1.2 Relationship between Pile Head Bending Moment and Angle of Rotation, and Relationship between Pile Head Axial Force and Angle of Rotation

The relationship between pile head bending moment and angle of rotation, and that between pile head axial force and angle of rotation are shown in Figure 7 for respective models. Judging from the relationship between pile head bending moment and angel of rotation for the semi-rigid pile

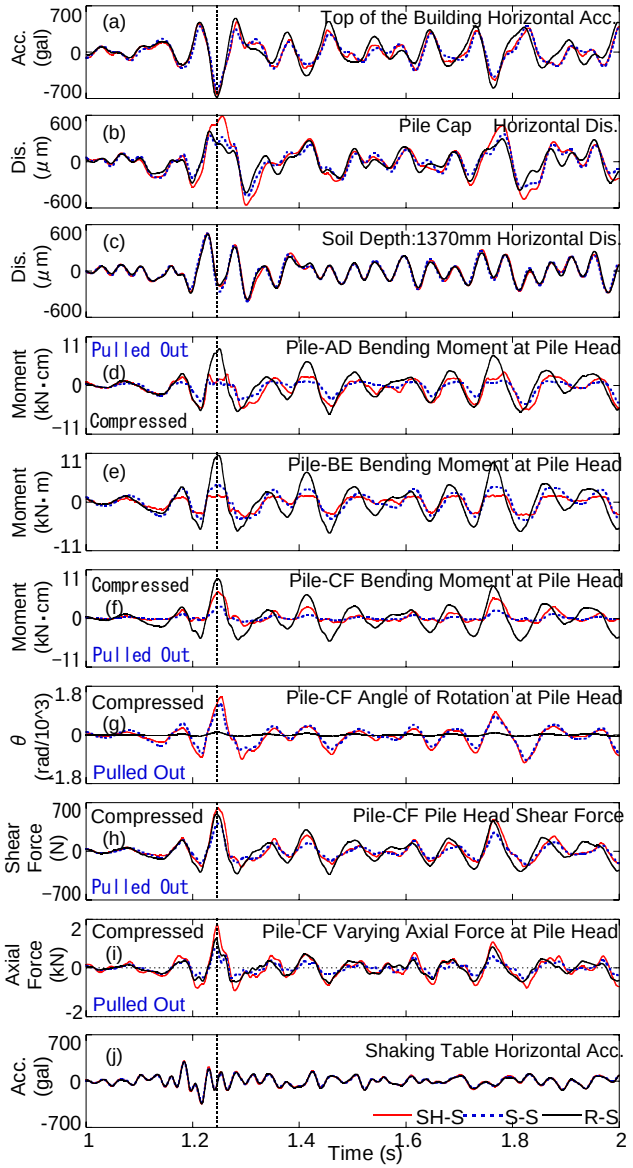

Figure 6 Major Time Histories

head connection models, the semi-rigid pile head connection models had lower initial rigidity than the rigid pile head connection model as shown in preliminary tests and exhibited non-linear elastic behavior. In the midpoint piles (Pile-BE) of the semi-rigid connection models, the axial force varied little. The bending moment dropped more steadily than in R-S (Figures 7 (b) and (e)). In the end piles of each model (Piles-AD and CF), the moment peaked out at different values in the piles subjected to compression and in the piles subjected to pullout force. The moment in the piles subjected to compression to which larger axial force acted was higher than the moment in the piles subjected to pullout force. In the end piles of SH-S, an incremental axial force approximately 1.3 times the initial axial force at the maximum occurred because the aspect ratio of the building was set higher (Figures 7 (d) and (f)). Then, a higher moment occurred in the piles according to the axial force when subjected to compression than in S-S (Figures 7 (a) and (c)).

3.1.3 Distribution of Bending Moments in Piles and Footing beams

Figure 8 shows distributions of bending moments in the piles and footing beams nearly at T = 1.24 seconds when the maximum inertia force acted from the building. The bending moment in the piles in the semi-rigid pile head connection models (SH-S and S-S) was lower at the pile head and higher in the soil than in the rigid pile head connection model (R-S). In the midpoint piles with little variation in axial force in the semi-rigid connection models, the pile head bending moment was lower than in the rigid connection model. Moreover, the maximum bending moment that occurred in the soil was 40 to 50% of the maximum pile head bending moment that occurred in R-S.

For the end piles (Piles-AD and CF) of the semi-rigid connection models, bending moments were distributed differently in the piles subjected to compression due to overturning moment (Pile-CF) and in the piles subjected to pullout force due to overturning moment (Pile-AD) (Figures 8 (b) and (d)). In the piles subjected to compression, the moment in the semi-rigid connection models was close to that in the rigid connection model at pile head, and was higher than in the rigid connection model in the soil. In the piles subjected to pullout force, on the other hand, the moment was considerably lower at pile head. The distribution of moments was similar to that for pinned pile head. The phenomenon was more outstanding in SH-S with the higher aspect ratio than in S-S. When a large varying axial force acted, the maximum bending moments in the semi-rigid connection models at all depths decreased to 50 to 70% of that at pile head in R-S.

The bending moment that occurred in the footing beams of S-S, like the bending moment at the pile head to which the footing beams were connected, decreased to 40 to 70% of that in R-S. The bending moment that occurred in the footing beam of SH-S were higher than that in the S-S because the bending moment increased at the column base as a higher aspect ratio was specified for the building.

3.1.4 Distributions of Shear Forces Occurring in Piles

The distributions of shear force in the pile at T = 1.24 seconds are shown in Figure 9. The shear force occurring in the pile in the semi-rigid connection models was larger in the soil than in the rigid connection model. The maximum shear force occurred at pile heads. The shear force at pile heads in S-S was smaller than in R-S because the response of the building was slightly reduced as the pile heads were semi-rigidly connected. In SH-S, the pile head shear force in the midpoint piles (Pile-BE) and in the piles subjected to pullout force (Pile-AD) was slightly smaller than in the rigid connection model. But in the piles subjected to compression (Pile-CF), the pile head shear force was 1.3 times that in R-S.

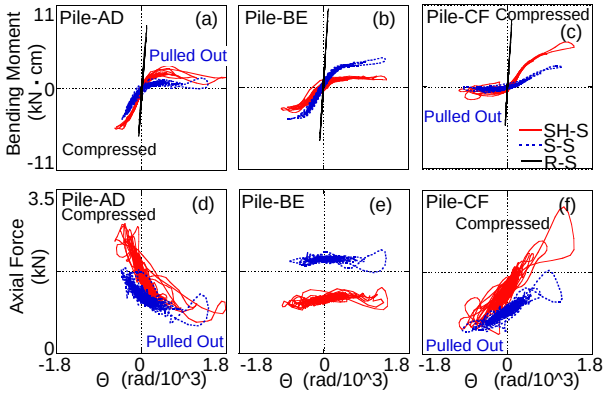

Figure 7 Pile Head Bending Moment and Angle of Rotation, and Pile Head Axial Force and Angle of Rotation

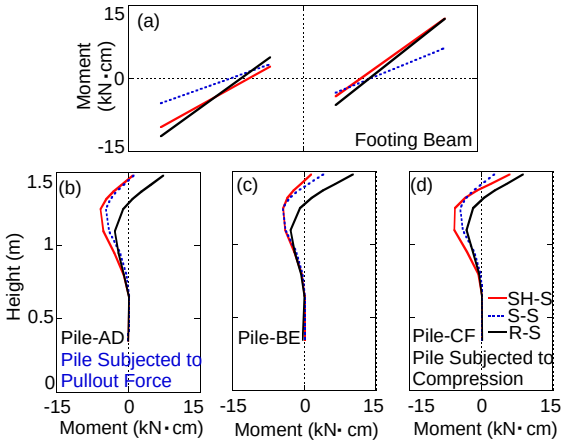

Figure 8 Distributions of Bending Moments of Pile and Footing (Nearly at T = 1.24 Seconds)

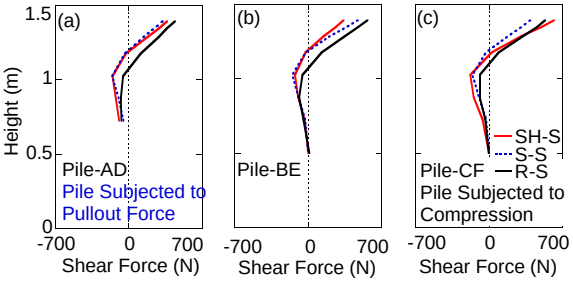

Figure 9 Distributions of Pile Shear Forces (Nearly at T = 1.24 Seconds)

3.1.5 Distributions of Soil Reactions Occurring in Piles

The distributions of soil reactions at T = 1.24 seconds for respective models are shown in Figure 10. In R-S, the soil reaction in the front piles (Pile-CF subjected to compression) was nearly the same as in the midpoint piles (Pile-BE). The soil reactions in both front and midpoint piles were larger than the soil reaction in the rear piles (Pile-AD subjected to pullout force) (Figure 10 (c)) for two reasons. First, the heads of the midpoint piles were restrained by the footing beams from both sides and the pile heads were more firmly fixed. Second, the soil reaction acting on the rear piles was reduced due to the interaction with the front piles. In S-S, large soil reaction occurred in the midpoint piles subjected to large initial axial force. The soil reaction in the front piles was smaller than in the midpoint piles. In SH-S with considerable variations of axial force, extremely large soil reaction occurred in the front piles (piles subjected to compression) and the soil reaction was smaller in the midpoint piles and rear piles. Then, it was concluded that the pile head shear force in the piles subjected to compression was larger in SH-S than in R-S because the piles subjected to compression were fixed more firmly owing to axial force variation and because the soil reaction acting on the rear piles was reduced because of the positioning of piles.

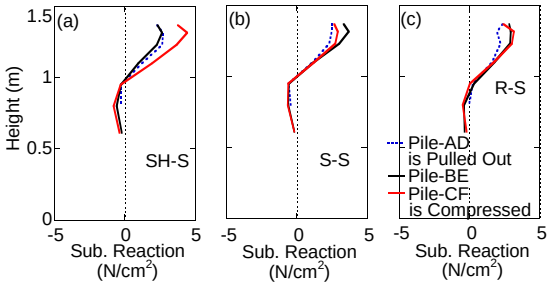

Figure 10 Distributions of Soil Reactions Occurring in Pile (Nearly at T = 1.24 Seconds)

4. CONCLUSIONS

Shaking table tests were conducted using models that represented the soil, pile foundation and building to identify the seismic behavior of a building that adopted the semi-rigid pile head connection method. The test results were compared among a rigid pile head connection model, a semi-rigid connection model and another semi-rigid connection model with a higher aspect ratio of the building. The conclusions obtained are described below.

1) The bending moments in the piles and footing beams of the semi-rigid pile head connection models were lower than in the rigid connection model. The semi-rigid connection was found effective for steadily reducing the bending moment in midpoint piles in particular with little variation of axial force. In the case where Level 2 ground motion was applied for excitation, the bending moment was reduced to approximately 40% of that in the rigid connection model. In the end piles with great variation of axial force, the bending moment was also reduced to approximately 70% on the average.

2) It was confirmed that the pile head shear force in the semi-rigid pile head connection models concentrated in the end piles subjected to compression (front piles) because of the variation of axial force and the positioning of piles. The pile head shear force in the semi-rigid connection models was 1.3 times that in the rigid connection model at the maximum. It was also confirmed that the pile head shear force in the midpoint piles tended to decrease where great input motion was applied because of the reduction of the response of the building or the concentration of shear force in the piles subjected to compression.

3) It was verified in the test that the acceleration response of the building was slightly smaller in the semi-rigid connection models than in the rigid connection model when Level 2 ground motion was used for excitation. This is ascribable to the relationship between the frequency characteristics of input motion and the period of the system composed of the soil, pile foundation and building. It was also found that the displacement of the foundation was slightly greater in the semi-rigid connection models than in the rigid connection model.

This study was conducted as part of the special project for earthquake disaster mitigation in urban areas (theme II significant improvement of seismic performance of structures) launched by the Ministry of Education, Culture, Sports, Science and Technology.

References:

Hara, T. Yasuda, S. Kawabata, I. Komuro, T. Korenaga, T. Tatsuno, S. (2002), "Development of Pile Head-Foundation Joint without Anchorage of Pile Rebar," Summaries of Technical Papers of Annual Meeting, AIJ, C-2, 187-190.

Ohtsuki, A. Tazoh, T. Aoki, T. Mano, H. Isoda, K. Iwamoto, T. Arakawa, N. Ishihara, T. Ohkawa, M. (2001), "A Pile-head Device with Spherical Contact-surface for Decreasing the Bending Moment," Summaries of Technical Papers of Annual Meeting, AIJ, B-2, 451-454.

Hiraide, T. Sugimura, Y. Ohsugi, F. (2004), " Experimental Study on Mechanical Properties of Pile Headjoint for Prestressed High Strength Concrete Piles Using Unbonded Stud Bars," Journal of Structural and Construction Engineering, AIJ, 581, 71-78.

Iai, S. (1989), "Similitude For Shaking Table Tests on Soil-Structure-Fluid Model in 1g Gravitational Field," Soils and Foundations, 29(1), 105-118.

Sixth International Conference on Urban Earthquake Engineering
March 3-4, 2009, Tokyo Institute of Technology, Tokyo, Japan

PSEUDO-STATIC SEISMIC RESPONSE OF URBAN MOUNTAIN TUNNEL IN SAND

Shuhei Shibayama[1], Jun Izawa[2], Akihiro Takahashi[3], Jiro Takemura[3] and Osamu Kusakabe[3]

1) Doctoral student, Department of Civil Engineering, Tokyo Institute of Technology, Japan
2) Assistant Professor, Department of Civil Engineering, Tokyo Institute of Technology, Japan
3) Associate Professor, Department of Civil Engineering, Tokyo Institute of Technology, Japan
4) Professor, Department of Civil Engineering, Tokyo Institute of Technology, Japan
sh4880@cv.titech.ac.jp, jizawa@cv.titech.ac.jp, takihiro@cv.titech.ac.jp, jtakemur@cv.titech.ac.jp, kusakabe@cv.titech.ac.jp

Abstract: It is widely accepted that underground structures have high seismic stability because of confining effects from the surrounding ground. However, tunnel structures have experienced serious damages. Although the need for seismic performance of tunnels is emphasized in specifications for tunnels, it is required to understand detailed mechanisms on the interaction between the structure and soil. There are many uncertain factors which affect soil-structure interaction, e.g., the arch action of ground, deformation of ground together with tunnel and lining structures. Arch action of the ground is expected to occur due to tunnel and ground deformation during the construction process of the mountain tunnel, and it might be changed by the earthquake-induced ground deformation. In order to investigate the pseudo-static seismic response of the urban mountain tunnel in sandy ground and effect of tunnel lining end fixity, centrifuge model tests were carried out in this study. In conclusion, following results were obtained. Firstly, the formation of arch action is affected by tunnel rigidity. Secondly, the arch action is rapidly deteriorated in case which has highly structural rigidity. Thirdly, after arch action is deteriorated, the significant earth pressures are developed when rigidity is highly.

1. INTRODUCTION

Recently, the number of construction of urban tunnels has been increasing because of intensive use of urban areas. In order to reduce construction cost of the urban tunnels, mountain tunnels have extended its application to urban area in sandy ground at relatively shallow depth.

Underground structures were considered having high seismic stability because of a confining effect from the tunnel surroundings (Kawashima 1994). However, tunnel structures have experienced serious damages in Hyogoken-Nanbu Earthquake (Asakura et al. 1996), and consequently the design codes for tunnels were revised (JSCE 1996 and JSCE 2001). The revised specification recommends taking into account the soil-structure interactions by proper methods, such as the seismic displacement method. This method is a kind of pseudo-static approach in which seismically induced ground motion is applied to the tunnel through soil springs. This soil-structure interaction is affected by many factors, e.g., stress conditions of soil, deformation of ground together with tunnel structure, surface condition of tunnel and lining structures, thus, there are many uncertainties in the application of the seismic displacement method. Although the need for seismic performance of urban tunnels is emphasized in JSCE standard specifications for tunnels, it is required to understand detailed mechanisms on the soil-structure interaction under various conditions.

Arch action of the ground above a mountain tunnel is expected to occur due to tunnel and ground deformation during tunnel construction, i.e. stress releasing of the ground is generated, and the earth pressure acting on the tunnel lining is much smaller than that by shield tunneling method. According to previous studies (Kusakabe et al. 2008), the experimental results showed that the earth pressure changes due to deterioration of the arch action which is caused by ground deformation, however its effect on different types of tunnel structures have not been investigated. In this study, active type shear tests in a centrifuge were carried out to understand the pseudo-static seismic response of the urban mountain tunnel in sandy ground, especially the effect of tunnel lining end fixity on earth pressure change due to earthquake-induced ground deformation.

2. CENTRIFUGE MODEL TESTS

2.1 Introduction

Seismic stability of a tunnel is usually evaluated by the seismic displacement method. The method evaluates stress exerted on tunnel by applying the lateral displacements of ground to the tunnel in a pseudo-static approach, because the effect of inertia force acting to the underground structure can be neglected as compared with super structures. Figure 1 shows an active type shear box used in this study. The seismic displacement method was experimentally

reproduced by using this shear box. Validity of the experimental method for a rectangular tunnel and its countermeasures in sand has been confirmed by the previous study (Izawa et al. 2006). In this study, seismic behavior of tunnels was investigated by the experimental simulation of the seismic displacement method using the active type shear box in a centrifuge.

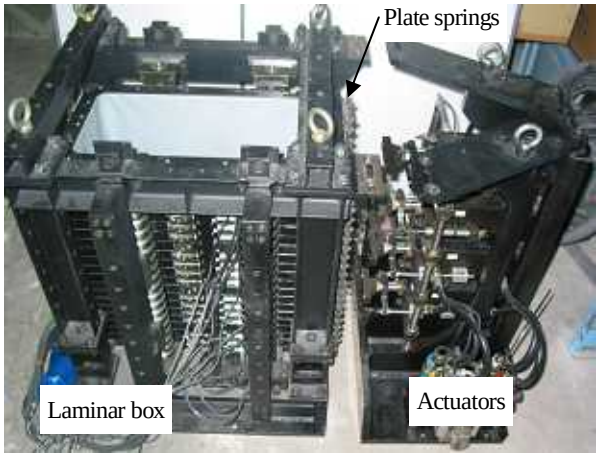

Figure 1 Active type shear box

Table 1 Specifications of shear box

Maximum centrifugal acceleration		100G
Actuator	Number	4
	Stroke	±20mm
	Force capacity (20.5Mpa oil pressure)	25.8kN (outward) 18.0kN (inward)
	Peak velocity	133mm/sec
Laminar box	Dimensions (inner)	W452mm B202mm H524mm
	Number of laminae	20+fixed one

2.2 Test and model description

The active type shear box comprises two parts; a laminar box and actuators. The laminar box consists of 20 stacked 24mm laminae with a roller bearing support and one fixed lamina at the base of the box. The shear deformation of the box was imposed by four hydraulic actuators connected to the four laminae at specific elevations. Lateral displacements of the other laminae were created by transmitting forces from the actuators to them through four linked sets of 0.6mm plate springs. A rectangular shape rubber sleeve was placed on the inner wall of the box to prevent the soil particles from getting into the gaps of the laminae. Thin stainless vertical sheets and a horizontal sheet of 0.2mm thickness with rough surface were fixed to both the inner end walls and the base of the box, respectively. These sheets are used for mobilizing the shear stresses on the inner boundary when the box is sheared. The specifications of the shear box are shown in Table 1.

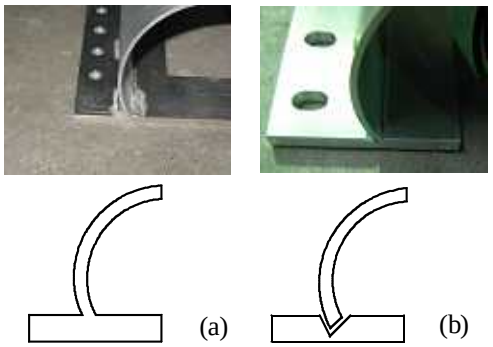

Figure 2 Arrangement of lining end condition : (a) Fixed model, and (b) Free model

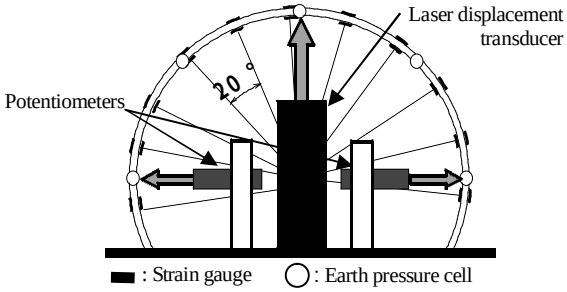

Figure 3 Positions of sensors

Assuming horseshoe-shaped mountain tunnel in sandy ground, a semi-circular aluminium model tunnel was used, in which only tunnel lining and invert were modeled. The model lining has a diameter of 100mm, a height of 75mm and a thickness of 2mm with smooth surface, which approximately corresponds to a 5m diameter tunnel with a RC lining of 300mm thickness in the prototype scale. In order to investigate the effect of tunnel lining end condition to the pseudo-seismic behavior of the tunnel, two types of the semi-circular model tunnels were used in this study. Figure 2 shows the detailed arrangements of the two types of lining end conditions. One of the models (termed as fixed model hereafter) had the lining of which both ends of the model were rigidly fixed to a 5mm thick steel invert as shown Figure 2 (a). The other model (termed as free model hereafter) had the end condition that the both ends of the tunnel lining have a sharp V shape of 90 degrees, which were placed in a 90 degree V shape notch of a 5mm thick steel invert fixed on the base, allowing rotation at the end of the lining as shown in Figure 2 (b).

In total, 22 strain gages were attached on both outer and inner sides of the two models in pairs to obtain bending moment distributions of the tunnel lining and 5 earth pressure cells of 6.2mm diameter and 0.75mm thick were embedded to measure the earth pressure distributions acting on the outer surface of the linings at the tunnel crown, spring lines and the midpoints between the crown and the spring lines. In addition, to measure vertical and horizontal convergences, a laser displacement transducer and two potentiometers were placed inside the tunnels model. Figure

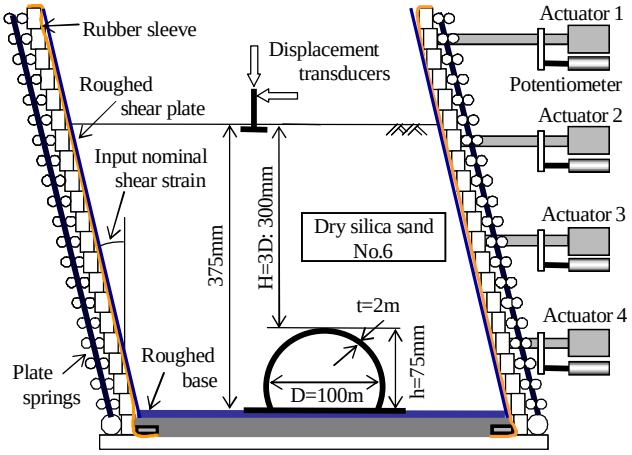

Figure 4 Model setup

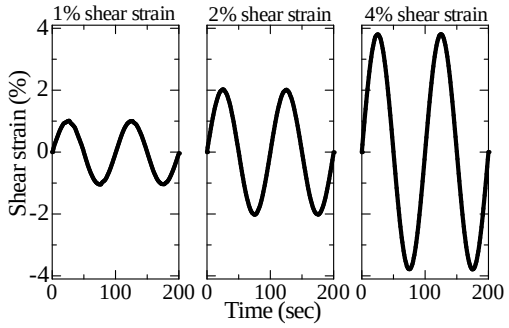

Figure 5 input shear strain history

3 illustrates the positions of these sensors attached to the tunnel model lining.

Figure 4 illustrates the schematic diagram of a model setup for the test, which was used in all test cases in this study. Dry silica sand No.6 (G_s=2.64, D_{50}=0.51mm, Uc=1.74, e_{max}=0.922, e_{min}=0.565) was used for the model ground. After the model tunnel was placed on the base of the laminar box, the model ground was constructed by air pluviation method to achieve a relative density of 80% (γ_d=15.8kN/m^3, ϕ=41deg.). The height of the model ground was selected to be 375mm, creating the tunnel cover, H of 300mm which corresponds to a tunnel cover-diameter ratio, H/D of 3. The vertical and horizontal displacements were measured at the ground surface by a potentiometer and a laser displacement transducer respectively.

The horizontal displacements were linearly imposed by the actuators with depth in a centrifugal acceleration of 50G, i.e. the displacements were proportional to the height from the base, so that the shear strains at any point in the vertical direction were the same. The input nominal shear strain history is shown in Figure 5. The two cycles sinusoidal nominal shear strains with frequency of 0.01 Hz (which corresponds to 0.0002Hz in prototype scale), of which amplitudes were 1%, 2% and 4% respectively, were imposed to the model ground continuously in the centrifugal acceleration of 50G.

2.3 Results and discussion

Figure 6 shows the time history of the normalized radial earth pressures at tunnel crown by a whole overburden pressure, $\gamma_d H$, during the pseudo-static shear test, for both cases of the fixed and free model. In the figure, broken and solid lines indicate the normalized earth pressure at tunnel crown of the fixed and free model, respectively. The dashed sinusoidal waves indicate input shear strains during the test, showed before in Figure 5. From Figure 6, it is observed that the initial earth pressures of the both cases before the first shearing (shear strain amplitude of 1%) were smaller than the overburden pressure (which were about 53% for fixed model and 26% for free model of the overburden pressure), probably due to the formation of arch action during the period of increasing centrifugal acceleration up to 50G.

Terzaghi (1948) proposed the concept of the loosening earth pressure acting on the crown as illustrated in Figure 7, in which the arch action of the ground was considered. The loosening earth pressure is calculated by Eq. (1),

$$\sigma_l = \frac{B\left(\gamma - c/B\right)}{K\tan\phi}\left(1 - e^{-K\tan\phi\, H/B}\right) \qquad (1)$$

$$, B = \frac{D}{2}\cot\left(\frac{\pi/4 + \phi/2}{2}\right)$$

where σ_l= loosening earth pressure, γ= unit weight of soil, c= cohesion of soil, K= coefficient of lateral earth pressure, ϕ= angle of shearing resistance of ground, C= tunnel-cover depth and D= diameter of the tunnel as shown in Figure 6. According to Terzaghi's study, K-value may be selected to be unity. By substituting H=15m (=0.300m*50G), D=5m (=0.100m*50G), K=1, c=0, γ=γ_d=15.8kN/m^3 and ϕ=41deg. into equation (1), the calculated and normalized value of the loosening earth pressure was plotted in Figure 6 (indicated by lower chained line). The initial earth pressure at the crown of the free model is almost equal to the Terzaghi's loosening earth pressure, while the earth pressure at the crown of the fixed model is about twice larger than that of free model.

Figure 8 shows relationships between the earth pressure at crown and vertical convergence δ_v of the crown divided by the tunnel diameter D at the time when the initial state and after the each two cycles of shearing events (which corresponding to the initial states and elapsed time in the each shearing event of 200 seconds in the Figure5). The term 'after' means that the shear box is back to the initial position with no shear strain was applied to the models. In the figure, the normalized overburden pressure and loosening earth pressures were also plotted. Two solid lines in the lower left indicate the changes of earth pressure during the increasing centrifugal acceleration up to 50G for the both cases, in which gradients of these lines indicate the structural rigidity of the tunnel models in vertical direction. Because of high structural rigidity of the tunnel model, at the initial state, the

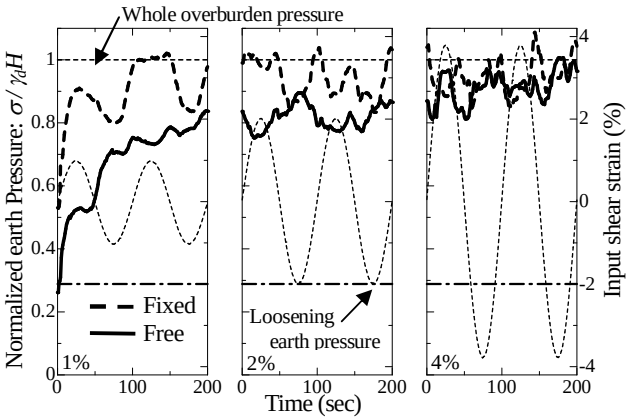

Figure 6 Time history of normalized earth pressure acting on tunnel crown

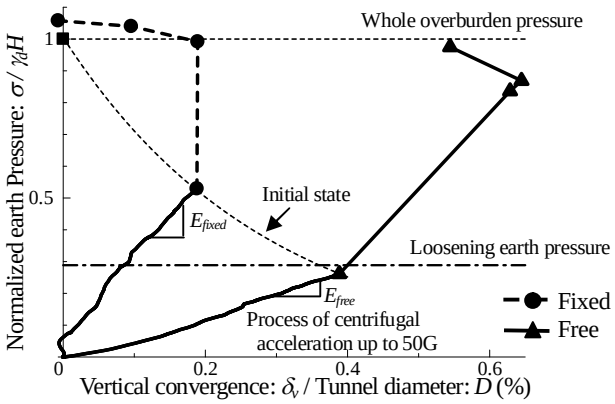

Figure 8 Relationship between normalized earth pressure and vertical convergence at tunnel crown

fixed model was not deformed enough with respect to the state that has been assumed by Terzaghi. The vertical convergence δ_v of the fixed model (0.19mm) is about half the value of the free model (0.39mm). Note that these displacements are in model scale.

Then, as shown in Figures 6 and 8, after shearing, the earth pressures at the crown of the both models increase and approach the overburden pressure. The earth pressure at crown of the fixed model almost reached the overburden pressure after first one cycle of shear history of 1%, while for the free model the earth pressure gradually increased and reached the overburden pressure in 4% shearing event. The results suggest that deterioration of the arch action of the ground above tunnel crown occurs by the shearing, and in the case of tunnel with high rigidity (fixed model), the arch action of the ground is rapidly deteriorated as compared with the case of low rigidity tunnel (free model).

Figures 9 and 10 present distributions of the measured earth pressures of both the fixed and free models measured before and after two cycles of 1% and 4% shearing, respectively. The term 'before' in these figures corresponds to the test elapsed time of 0 second in the each shearing event in Figure 5 (before 1% shearing event corresponds to the initial state with no shearing histories).

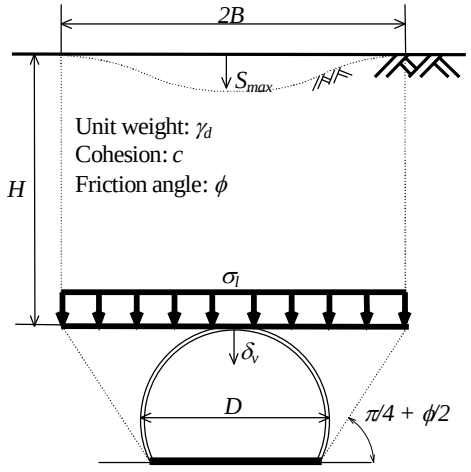

Figure 7 Loosening earth pressure

Radial earth pressures acting on tunnel lining without the influence of the ground deformation are plotted as a chained line in Figures 9 and 10, which are calculated according to the following Eq. (2) by assuming the coefficient of earth pressure at rest, K_0 =0.5.

$$\sigma_r = \left(\frac{1+K_0}{2} - \frac{1-K_o}{2} \right) \sigma_v \cos 2\theta \qquad (2)$$

where σ_r= earth pressure in the radial direction, σ_v= vertical earth pressure ($\sigma_v=\gamma_d z$), γ_d= unit weight of the ground, z= depth, K_o= coefficient of earth pressure at rest and θ= angle from the horizontal axis in the anti-clockwise direction. The loosening earth pressure was also plotted in the Figures 9 and 10.

From Figure 9 at the initial state (before 1% shearing), in the case of the free model, the earth pressures at both tunnel shoulders are slightly smaller than the calculated radial earth pressures at rest, while that of the fixed model are almost equal to the calculated these. As compared with the case of the fixed model, the arch action due to the tunnel deformation of the case of the free model might affect the wider area above the tunnel.

In Figure 9, the earth pressures increased after first shearing event (1% shearing) and the earth pressure distributions changed in the both cases of the fixed and free model, while in Figure 10 the earth pressure distributions before and after 4% shearing event for the both cases showed no appreciable change before and after event. This experimental fact suggests that the arch action is deteriorated by shearing and the earth pressure distribution after several shearing events reach the certain distribution in which the earth pressures at the tunnel shoulders are significant. Especially for the case of the fixed model**,** the considerable earth pressures at tunnel shoulders are much larger than those for the case of free model.

Figure 11 shows the distributions of the bending

moments measured when the maximum positive shear strain was first applied in the 1% and 4% shearing event, respectively, corresponding to the elapse time of 25seconds in Figure 5. In Figure 11, solid line with square points and dashed line with circle points indicate distribution of bending moment for the fixed and free models, respectively.

The previous experiments (Yamada et al., 2002 and Izawa, et al. 2006) indicated that the shear deformation of the ground generates the maximum bending moment in the tunnel at the shoulder around 45^{o} measured from the tunnel crown. The present data shown in Figure 11 also support the previous experimental observation.

As shown in Figure 11, the bending moment distributions when the maximum shear strain was first applied in the 1% and 4% shearing event for the both cases of the fixed and free model are almost the same. However, in Figure 11, the values of the bending moment at the right end of the tunnel lining are quite different between the free and fixed models. The results indicated that the difference of the tunnel lining end conditions only affect to the bending moments near the ends of the tunnel lining. It is noticed that the bending moment at the both side ends for the free model

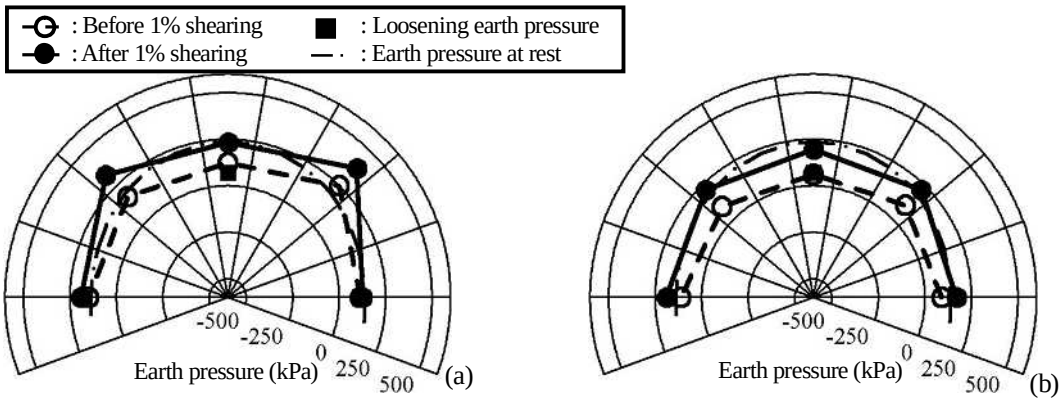

Figure 9 Distributions of earth pressures before and after two cycles of 1% shearing:
(a) Fixed model, and (b) Free model

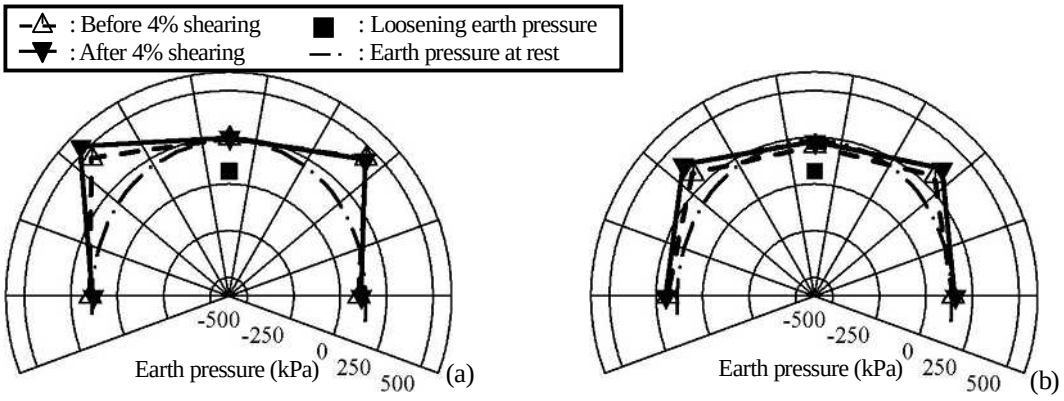

Figure 10 Distributions of earth pressures before and after two cycles of 4% shearing:
(a) Fixed model, and (b) Free model

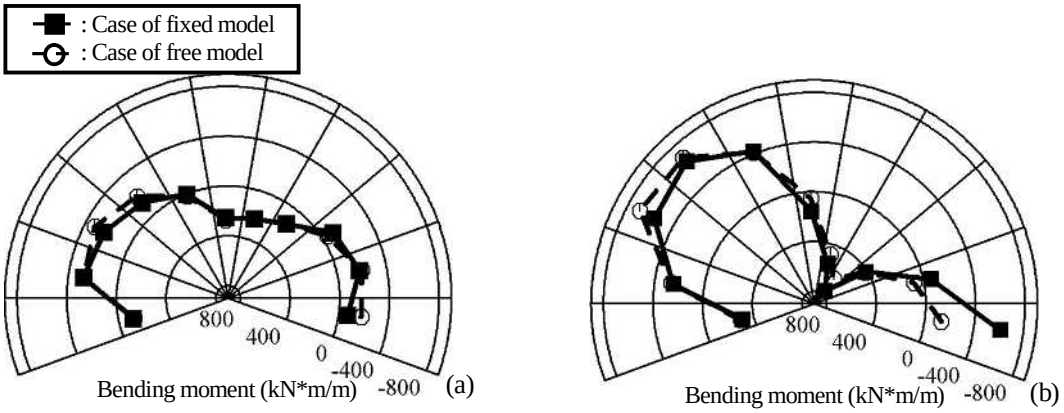

Figure 11 Distributions of bending moments measured when maximum positive shear strain was first applied:
(a) In 1% shearing cycles, and (b) In 4% shearing cycles

exhibit some value, suggesting that the end conditions of the free model might not be an ideal hinge condition in this test.

3. CONCLUSIONS

This paper presented some results of the active type shear box tests in a centrifuge by modeling the two types of semi-circular aluminum tunnels in sand to understand the pseudo-static seismic response of the urban mountain tunnel in sandy ground, especially the effect of the tunnel lining end fixity on the earth pressure change due to the earthquake-induced ground deformation. According to the results, the following findings were obtained.

1. The initial earth pressures acting on the tunnel crown before the first shearing are smaller than the calculated whole overburden pressure due to the formation of arch action. The formation of arch action is strongly affected by deformation of the ground and structural rigidity of the tunnel.

2. The deterioration of the arch action of the ground above tunnel crown occurs by shearing, and in the case of tunnel with high rigidity, the arch action of the ground is rapidly deteriorated as compared with the case of low rigidity tunnel.

3. After arch action is deteriorated, the earth pressure distribution reaches to the certain distribution which the earth pressures at both shoulders are significant. Especially in the case of tunnel with high rigidity**,** the considerable earth pressures are much larger than that for the case of low rigidity tunnel.

Acknowledgements:

This research was partially supported by Grant-in-Aid for Scientific Research (A), 2005-2007, No. 17206050, "Seismic stability of the large cross-section urban tunnel with located in relatively shallow depth". The authors gratefully acknowledge the funding for this research from the 21st Century Centre of Excellence (COE) program entitled "Evolution of Urban Earthquake Engineering".

References:

Kawashima, K. (1994), "Seismic Design of Underground Structures," Kajima Publishing Co. Ltd., (In Japanese)

Asakura, T. and Sato, Y. (1996), "Damage to Mountain Tunnels in Hazard Area," *Soils and Foundations Special Issue on Geotechnical Aspects of the January 17 1995 Hyogoken-Nanbu Earthquake*, 301-310.

Japan Society of Civil Engineers (1996), "Standard Specifications for cut and cover tunnels," (in Japanese)

Japan Society of Civil Engineers (2001), "Japanese Standard for Shield Tunneling -1996- The Third Edition,"

Kusakabe, O., Takemura, J., Takahashi, A., Izawa, J. and Shibayama, S. (2008), "Physical Modeling of Seismic Responses of Underground Structures," *Proc. 12th Int'l Conf. of Int'l Association for Computer Methods and Advances in Geomechanics*, 1459-1474.

Izawa, J., Kusakabe,O., Nagatani, H., Yamada, T. and Ohbo, N. (2006), "Centrifuge Modeling on Seismic Behavior of Rectangular Tunnels," *Physical Modeling in Geotechnics 6th ICPMG*, 1163-1169.

Terzaghi, K. (1948), "Theoretical Soil Mechanics," John Wiley and Sons, 66-76.

Yamada, T., Nagatani, H., Igarashi, H. and Takahashi, A. (2002), "Centrifuge Model Tests on Circular and Rectangular Tunnels Subjected to Large Earthquake-induced Deformation," *Proc. of the 3rd Int'l Symp. on Geotechnical Aspects of Underground Construction in Soft Ground*, 673-678.

Sixth International Conference on Urban Earthquake Engineering
March 3-4, 2009, Tokyo Institute of Technology, Tokyo, Japan

CENTRIFUGE MODEL TEST OF PILED RAFT FOUNDATION SUBJECTED TO HORIZONTAL LOAD

Kouhei Sawada[1)], Jiro Takemura[2)], and Sakae Seki[3)]

1) Graduate student, Department of Civil and Environmental Engineering, Tokyo Institute of Technology, Japan
2) Associate Professor, Department of Civil and Environmental Engineering, Tokyo Institute of Technology, Japan
3) Technician, Department of Civil and Environmental Engineering, Tokyo Institute of Technology, Japan
sawada.k.ab@m.titech.ac.jp, jtakemur@cv.titech.ac.jp, seki@cv.titech.ac.jp

Abstract: Piled raft foundation has been recognized as an economical foundation system with the combined effects of raft and piles. However, the proportion of vertical load carried by the raft and piles, and these effect on the behavior of foundations subjected to horizontal load have not been well understood. In order to discuss the effect of the proportion of vertical load carried by the raft and piles, and the moment loads on the behavior of horizontally loaded piled raft foundations, vertical and horizontal loading tests were carried out on piled raft models and their components (pile group and raft models) in dry Toyoura sand by using a geotechnical centrifuge.

1. INTRODUCTION

Piled raft foundation has been recognized as an economical and rational foundation system, because piled raft foundations can support the weight of superstructures by the raft and piles. However, the behavior of the piled raft foundation is complex especially when horizontally loaded, because the contact condition between the raft base and the ground varies during the loading, resulting in complicated soil structure interaction.

Design concepts of piled raft foundations are to take advantage of the bearing capacity of the raft and to reduce the settlement of foundations to acceptable level by piles. Piles in the piled raft foundations play roles in reducing the settlement and transferring a part of the load to the deep ground. Although considerable researches on the piled raft foundations subjected to the vertical load have been carried out, it seems that a number of researches on the behavior of horizontally loaded piled raft foundations are limited. However, it is very important to clarify the behavior of piled raft foundations in highly seismic areas such as Japan.

Physical modeling studies on the behavior of piled raft model subjected to static or dynamic horizontal loads are reported. In the static and dynamic 1g model tests conducted by Matsumoto et al. (2004a, 2004b), the influences of moment loads and pile head connection conditions on the behavior of piled raft were discussed. In the static and dynamic centrifuge model tests conducted by Horikoshi et al. (2003a, 2003b), the proportion of the horizontal load carried by raft and pile were investigated for the different pile head connection conditions. However, in above researches, the influences of moment load relative to horizontal load applied to the foundations and the proportion of the vertical load carried by the raft (raft load proportion, RLP, Figure 1) were not taken as a parameter. It is important to consider the influence of moment load especially on the foundation of tall superstructure, such as, bridge pier, high rise building, and tower.

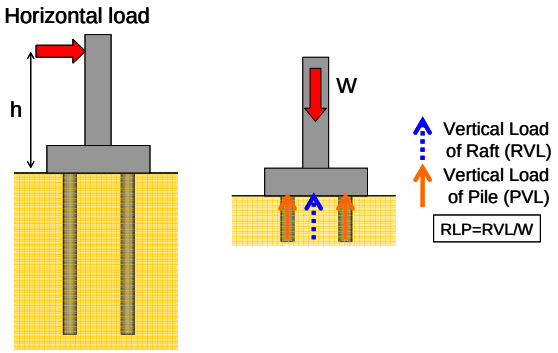

Figure 1 Definition of horizontal loading height h and RLP

In this research, centrifuge model tests were conducted to investigate the influence of the moment load and RLP for three types of foundation models, raft, pile group and piled raft.

2. MODEL DESIGNS AND TEST PROCEDURE

2.1 Model piled raft and superstructure

The static vertical and horizontal loading tests were conducted on the piled raft, the pile group and the raft alone in this study. Figure 2 shows the raft and pile models used in this study. Stainless steel raft with 80mm*80mm*20mm is divided into three parts and the model piles are clutched between the parts. Sandpaper was glued on the raft base to

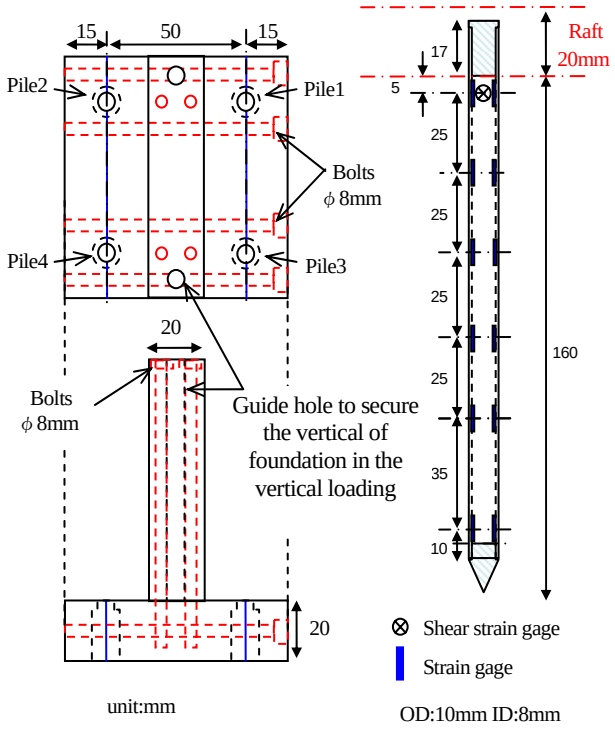

Figure 2 Model raft and pile

make rough base condition. On top of the raft, stainless steel thick plate with 80mm height and 20mm thickness is fixed as the superstructure, to which horizontal load is applied at different height. Total mass of the raft and plate is 2kg, which is equivalent to 980 N of vertical dead load under 50g centrifugal acceleration.

The model pile is stainless steel made with 10mm outer diameter and 0.5mm thickness. Strain gages are attached inside the piles to measure bending moment and axial force. A set of strain gages is also attached at the outer surface of pile head to measure the shear force. Table 1 shows the properties of the model pile. Four piles were rigidly fixed to the raft in the square arrangement of 50mm spacing (S). This model was used for both the tests of piled raft and pile group. In the pile group model, 5mm gape between the raft base and the ground surface was provided to avoid the interaction between them.

2.2 Model preparation

Soil used for the tests is dry Toyoura sand with the physical properties given in Table 2. The model container is made of aluminum with inner dimension of 800mm in length, 250mm in breadth and 400mm in depth. Figure 3 shows the test setup, which was prepared as follows.

1) The model ground was made by air pluviation with a depth of 230mm and target relative density of 50%.

2) In 1g the piles were penetrated into the ground by deadweight with a guide to secure the verticality of the piles.

3) Centrifugal acceleration was increased up to 50g and the piles were further penetrated by deadweight.

4) Centrifugal acceleration was down to 10g to penetrate piles by the two way actuator until the raft base contacted to the ground for the piled raft model or reached 5mm above

Table 1 Properties of model pile

Properties	Model	Prototype
Material	Stainless steel	Concrete
Diameter	10mm	500mm
Thickness	0.5mm	Solid
Embedment depth	160mm (piled raft) 155mm (pile)	8mm 7.75m
Longitudinal rigidity EA	2.98×10^{-3}GN	7.46GN
Bending rigidity EI	3.37×10^{-8}GNm^2	0.211GNm^2

Table 2 Physical properties of Toyoura sand

Specific gravity (G_s)	2.65
Mean particle diameter (D_{50})	0.162
Maximum void ratio (e_{max})	0.973
Minimum void ratio (e_{min})	0.609

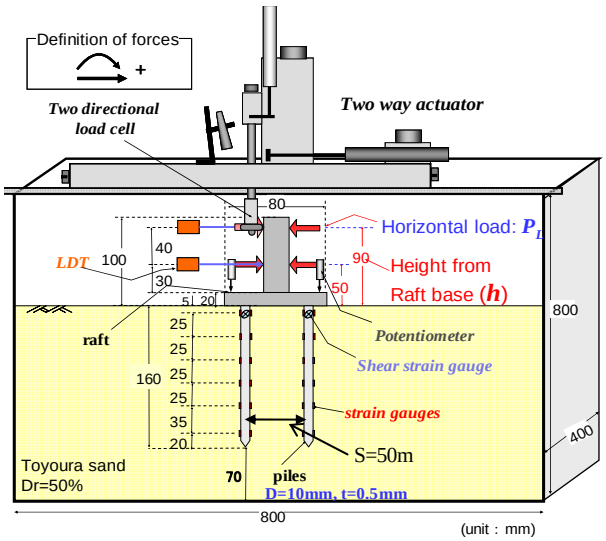

Figure 3 Model set-up and location of sensors

the ground for the pile group model.

5) Centrifugal acceleration was down to 1g, for removing the guide and setting all instrumentations.

Displacement of the model foundation was measured by potentiometers and lazar displacement transducers. Shear force, bending moment and axial force of the pile are measured by strain gage. Applied vertical and horizontal load were measured by two directional load cell attached to the actuator. The locations of the instrumentations are shown in Figure 3.

2.2 Procedures of loading tests

Having completed the model setup, the centrifugal acceleration was increased to 50g for both vertical and horizontal loading tests. Horizontal load was applied by the two way actuator from left side and then right side at two different heights from the raft base, h=50mm and 90mm, as shown in Figure 3. Rightwards horizontal load, displacement and clockwise moment are taken positive in this study. This loading cycle was repeated until the displacement measured at h=50mm was prescribed value shown in Table 3. Vertical and Horizontal loading were conducted by displacement control, with loading rate of 0.0162 mm/s and 0.155 mm/s

Table 3 Test cases

Model case	Details of Test	Applied horizontal displacement	Relative Density
R1	Raft (Vertical Loading)		50.3%
R2	Raft (Horizontal Loading, h/S=1)	±1mm (50mm), +5mm (250mm)	50.3%
R3	Raft (Horizontal Loading, h/S=1.8)	±1mm (50mm) (h/S=1), +5mm (250mm) (h/S=1.8)	46.0%
P1	Pile (Vertical and Horizontal Loading)	±1mm (50mm), ±2mm (100mm)	49.6%
PR1	Piled raft (Vertical and Horizontal Loading, h/S=1, 1.8)	±1mm (50m) (RLP24%), ±2mm (100mm) (RLP10%)	53.0%
PR2	Piled raft (Vertical and Horizontal Loading, h/S=1)	+2mm (100mm) (RLP35%)	53.0%

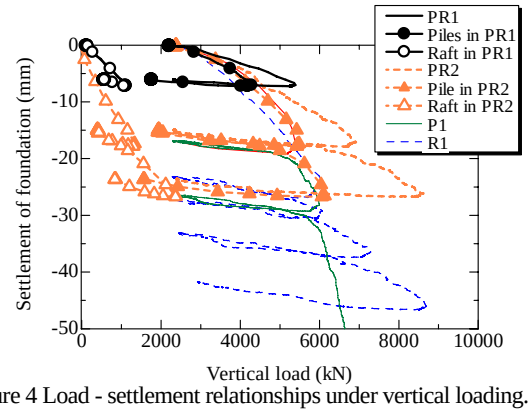

Figure 4 Load - settlement relationships under vertical loading.

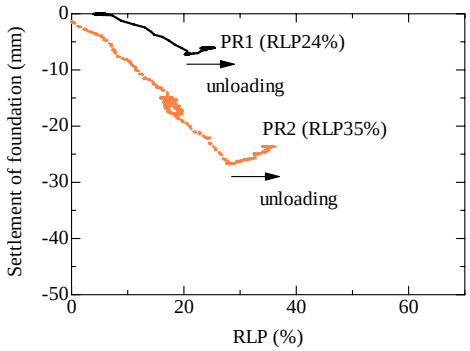

Figure 5 Variation of RLP-with settlement of raft

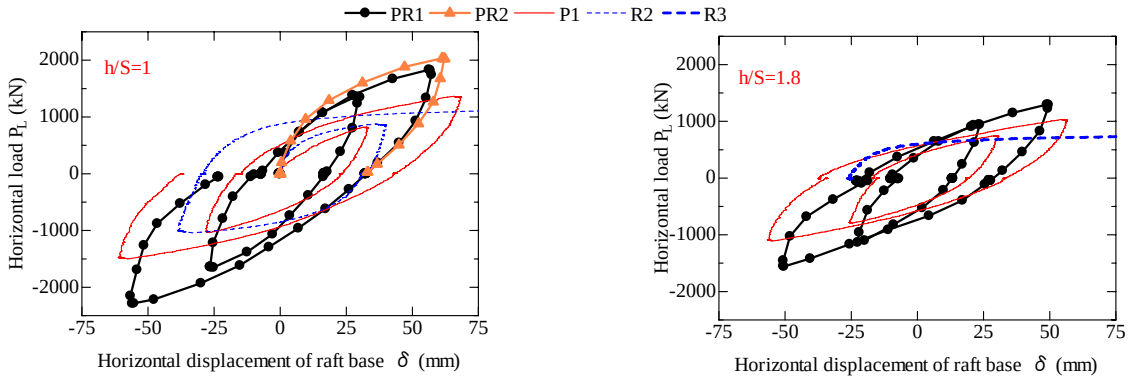

Figure 6 Relationships between horizontal load and horizontal displacement of raft base.

respectively. By the instrumentations shown in Figure 3, measured are the horizontal displacements of the raft base, δ, the rotation of the foundation, θ, and the shear force, the bending moment and the axial force of the piles. The moment load, M_L, applied to the foundation is estimated by multiplying horizontal load, P_L, by the height h. Vertical load applied to the raft is estimated by subtracting total axial force at the pile heads from the total vertical load, and horizontal load applied to the raft is estimated by subtracting total shear forces at the pile heads from the applied horizontal load.

In the following section, tests results are given in prototype scale.

3. RESULTS AND DISCUSSION

3.1 Vertical loading tests

Vertical load–settlement curves measured in vertical loading tests were shown in Figure 4. The loads carried by the piles and the raft in the piled raft are also given in the figure. The vertical load includes deadweight of the raft and the superstructure. The bearing capacity of piled raft is larger than those of pile group and raft. The bearing capacity of raft component in the piled raft increases with increase of the settlement of foundation. The bearing load of the pile components of piled raft is similar to that of pile group. Under the condition of this study, the bearing load of pile components is larger than that of the raft component of the piled raft in the initial stage and RLP increases with settlement as shown in Figure 5. RLP also increase the in unloading stage, implying negative friction mobilized in the piles. RLP can be controlled by this pre-vertical loading process before the horizontal loading.

3.2 Horizontal loading tests of piled raft and components

Figure 6 shows δ - P_L relationships of three foundation models for the normalized loading height h/S=1.0 and 1.8 respectively. In all the foundations, the increase of the

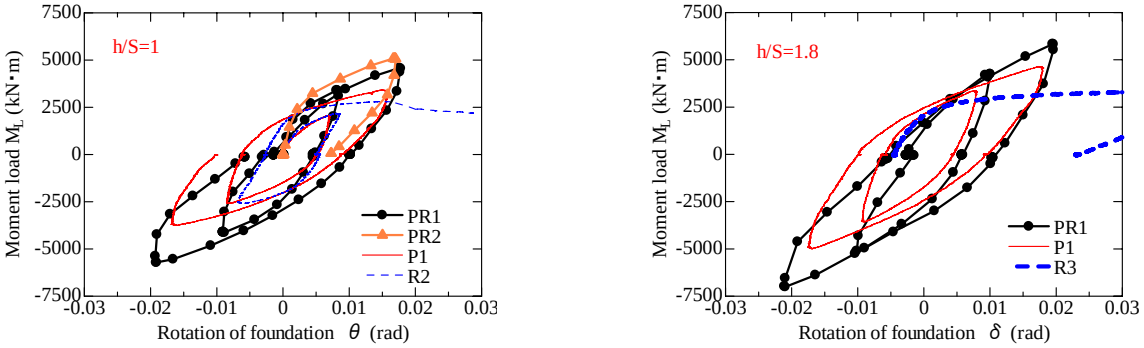

Figure 7 Relationships between moment load and rotation of foundation.

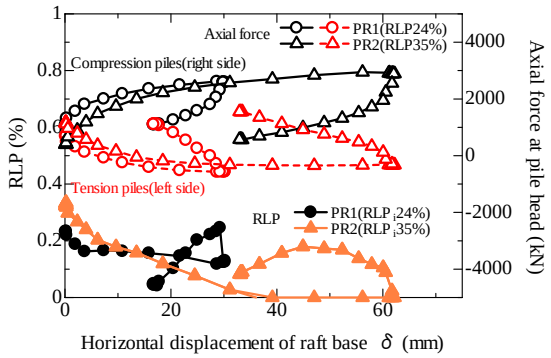

Figure 8 Variation of RLP and axial loads

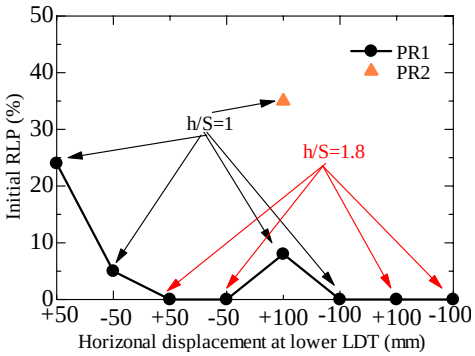

Figure 9 Initial RLP in each loading cycle

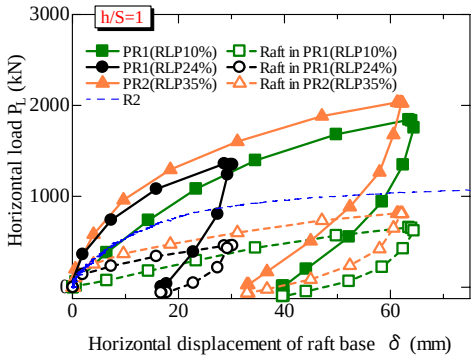

Figure 10(a) Horizontal load carried by piled raft foundation and raft:h/S=1

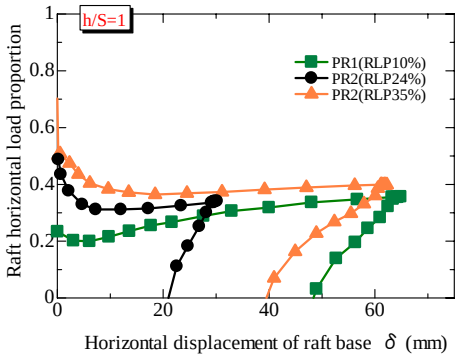

Figure 10(b) Variation of proportion of horizontal load carried by raft:h/S=1

horizontal displacement due to the increase of the horizontal load are larger in the cases of h/S=1.8 than those of h/S=1.0. The horizontal bearing load of the piled raft is the largest. Although the horizontal displacement can be restrained in the raft foundation in the range of small load, it increases rapidly with the increase of the horizontal load implying clear failure of the foundation. On the other hand, the horizontal resistance of the pile group foundation is smaller than that of the raft foundation in the small δ range, but it increases with the displacement showing the larger resistance in the large δ than the raft foundation. Figure 7 shows θ - M_L relationships for h/S=1.0 and 1.8. The moment resistance of PR2 with large RLP (35%) is larger than that of PR1. The raft foundation has larger moment resistance in the beginning than the pile group foundation, but the moment resistance of the pile group foundation increases with the moment load, which is similar to the δ - P_L relationships seen in Figure 6.

The variation of RLP and axial loads of tension (left side) piles and compression (right side) piles are shown in Figure 8. The RLP varied during the loading and reached to different value before loading, by which the initial RLP in each loading cycle were different and decreased as the loading increased as shown in Figure 9.

Figures 10(a) and 11(a) show δ - P_L relationships of the piled raft foundations with different initial RLP for h/S=1.0 and 1.8 respectively. The load carried by the raft and the raft foundation are also shown in the figures. The variation of the raft horizontal load proportion with δ for h/S=1.0 and 1.8 are shown in Figures 10(b) and 11(b) respectively. The horizontal displacement, δ, in the figure, is the increment from the onset of each loading. The horizontal resistance of the piled raft foundation with larger initial RLP is larger than that with smaller initial RLP. This can be attributed to the larger horizontal load carried by the raft for the former than the latter. The difference of the piled raft foundation with different initial RLP is more distinct at small δ. In the cases with h/S=1.0 the horizontal resistances of the piled raft foundations are lager than that of raft, while for the cases with h/S=1.8 the resistances of piled raft foundations are

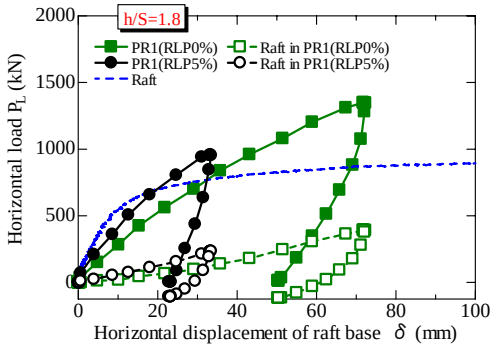

Figure 11(a) Horizontal load carried by piled raft foundation and raft:h/S=1.8

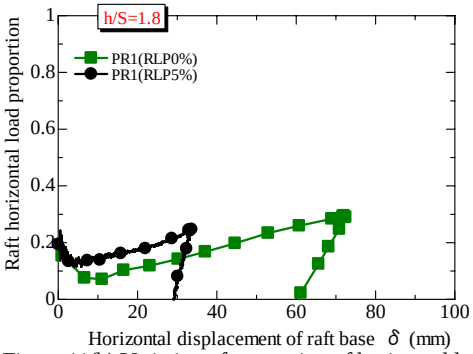

Figure 11(b) Variation of proportion of horizontal load carried by raft:h/S=1.8

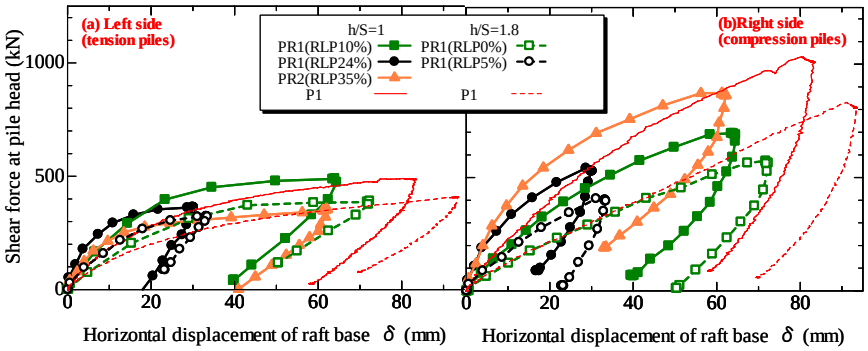

Figure 12 mobilization of horizontal resistance of piles

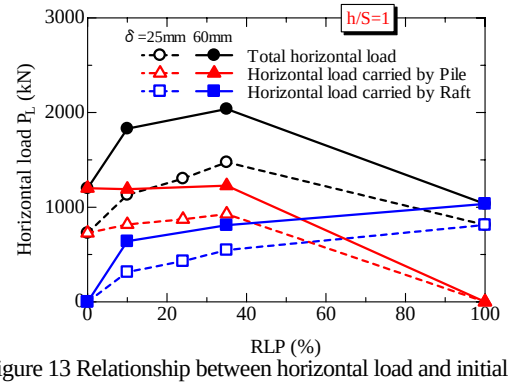

Figure 13 Relationship between horizontal load and initial RLP

smaller than that of the raft foundation at small δ. This can be explained by the small initial RLP in the cases of h/S=1.8. However, even in the cases with small initial RLP, it can be seen that the increase of the horizontal resistance of raft part in the piled raft foundation is larger than that of the raft foundation at large δ, giving the increase of the raft horizontal load proportion as shown in Figures 10(b) and 11(b).

Figures 12 shows the relationship between δ and shear force measured at the pile heads in tension (left side) piles and compression (right side) piles. The shear forces in the case of h/S=1 are larger than those in the case of h/S=1.8 for both tension and compression piles. The shear force of the tension piles is smaller than the compression piles especially at large δ. The shear forces of the piled raft foundation are greater than that of pile group foundations. The effect of RLP is clearly seen in the compression piles, the larger RLP is, the larger shear force.

Figure 13 shows the relationships between the RLP and horizontal load at δ = 25mm and 60mm for the cases of h/S=1.0. RLP= 0% and 100% represent the pile group foundation and the raft foundation respectively. The increase of the horizontal load by the increase of δ is the largest in the piled raft foundation. The total horizontal load and the load carried by the raft component increase with RLP in the range adopted in this research. Although the horizontal load carried by the pile components slightly increases with RLP, that is almost equal to that of the pile group foundation. The total horizontal load and the load carried by the raft component similarly increase with RLP, confirming that RLP affects on the raft components strongly.

Figure 14 shows θ - M_L relationships of three types of foundation for the cases of h/S=1.0. The rotation, θ, in the figure is the increment from the onset of the horizontal load. Similar behavior is observed in θ - M_L relationship as seen Figures 10(a) and 12. Figure 15 shows relationships between the RLP and moment resistance at θ=0.008 and 0.015 (rad). Moment resistance increases with the increase of RLP in the piled raft foundations. The increase of moment resistance caused by the increase of θ is larger, in the order of piled raft, pile group, raft.

Figure 16 shows bending moment profiles of left pile and right pile at P_L=±540(N) for the cases of h/S=1.0. Bending moments of the piled raft foundation are smaller than those of pile group foundation. The bending moments of the piled raft foundations are smaller for the case with larger RLP. The reason for this behavior is considered that a part of the horizontal load and the moment load are carried by the raft component in the piled raft foundation.

Figure 17 shows observed settlements of the foundation due to cyclic loading. It can be confirmed that the settlement

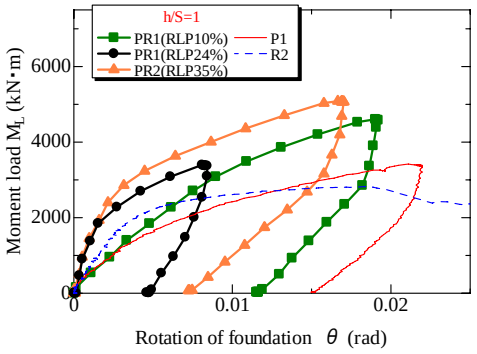

Figure 14 Moment load – raft rotation curves

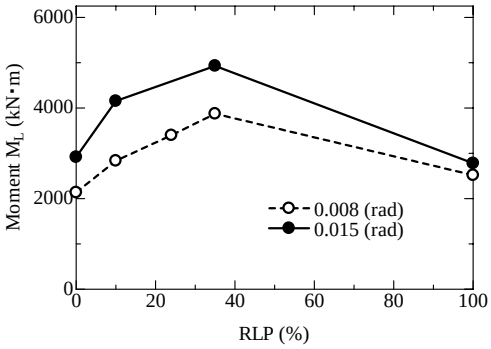

Figure 15 Relationship between moment load and initial RLP

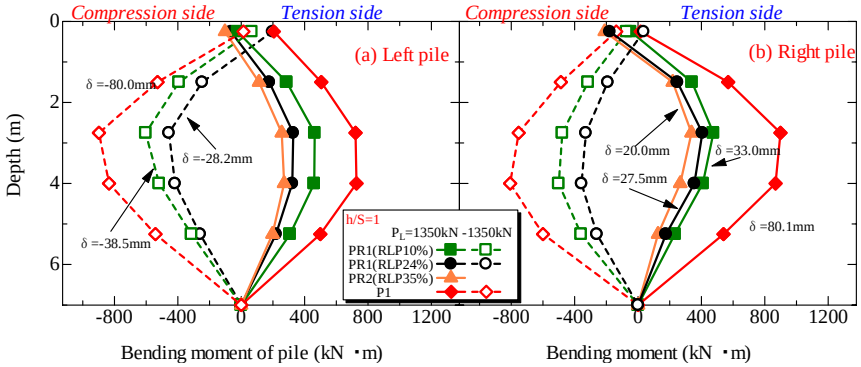

Figure 16 Bending moment of piles during horizontal loading.

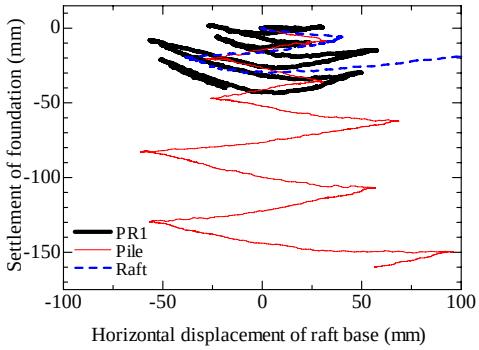

Figure 17 Observed settlements of the foundation caused by cyclic loading

of piled raft foundation is much smaller than those of the pile group foundation and the raft foundation.

3. CONCLUSIONS

Vertical and horizontal loading tests were conducted on piled raft, pile group and raft foundation models by using a geotechnical centrifuge. The following conclusions were derived from this study.

1) The proportions of vertical load carried by the raft and piles vary during horizontal loading cycles. This variation affects the horizontal and moment resistance of the piled raft foundation.
2) Piled raft foundations have high horizontal resistance and moment resistance because the horizontal and moment load resistances of the raft part are effectively mobilized by preventing the rotation of the foundation with piles. The larger RLP is up to 35%, the smaller displacement and rotation.
3) Horizontal load carried by the raft and the piles (shear forces at pile head) increase with RLP. The increase of the raft component is much larger than that of pile components.
4) Piled raft foundation can reduce the settlement of foundation and the bending moment of piles caused by cyclic loads.

References:

Horikoshi, K., Matsumoto, T., Hashizume, Y., Watanabe, T. and Fukuyama, H. (2003a) "Performance of piled raft foundations subjected to static horizontal loads" Int. Jour. of Physical Modelling in Geotechnics, Vol. 3, No. 2, pp. 37-50.

Horikoshi, K., Matsumoto, T., Hashizume, Y. and Watanabe, T. (2003b) "Performance of piled raft foundations subfected to dynamic loading" Int. Jour. of Physical Modelling in Geotechnics, Vol. 3, No.2, pp. 51-62.

Matsumoto, T., Fukumura, K., Kitiyodom, P., Horikoshi, K., Oki, A. (2004a) "Experimental and analytical study on behaviour of model piled rafts in sand subjected to horizontal and moment loading" Int. Jour. of Physical Modelling in Geotechnics, Vol. 4, No. 3, pp.1-19.

Matsumoto, T., Fukumura, K., Horikoshi, K., Oki, A. (2004a) "Shaking table tests on model piled rafts in sand considering influence of superstructures" Int. Jour. of Physical Modelling in Geotechnics, Vol. 4, No. 3, pp.21-38

Sixth International Conference on Urban Earthquake Engineering
March 3-4, 2009, Tokyo Institute of Technology, Tokyo, Japan

TRAIN-INDUCED WAVE PROPAGATION IN GROUND USING FINITE/INFINITE ELEMENT MODELING IN ABAQUS

Ramin Motamed[1)], Kazuya Itoh[2)], Sohichi Hirose[3)], Akihiro Takahashi[4)], and Osamu Kusakabe[5)]

1) JSPS Postdoctoral Fellow, Dept. of Civil Engineering, Tokyo Institute of Technology, Japan
2) Researcher, Construction Safety Research Group, National Institute of Occupational Safety and Health, Japan
3) Professor, Dept. of Mechanical and Environmental Informatics, Tokyo Institute of Technology, Japan
4) Associate Professor, Dept. of Civil Engineering, Tokyo Institute of Technology, Japan
5) Professor, Dept. of Civil Engineering, Tokyo Institute of Technology, Japan
motamed@cv.titech.ac.jp, k-ito@s.jniosh.go.jp, shirose@cv.titech.ac.jp, takihiro@cv.titech.ac.jp, kusakabe@cv.titech.ac.jp

Abstract: This paper aims to investigate the application of numerical modeling in train-induced ground vibration problems and appropriate mitigation measures. A finite/infinite element model was developed in ABAQUS to study (1) propagation characteristics of the train-induced ground vibrations, (2) effectiveness of different vibration countermeasures in reducing the ground vibrations induced by the trains. In this regard, first the numerical results were validated using geotechnical centrifuge tests conducted at Tokyo Institute of Technology and theoretical solutions. Second, a parametric study on both geometrical and material properties of the wave barriers was conducted to investigate the effectiveness of these mitigation measures to reduce the ground vibration. Three different vibration countermeasures considered in this study include installation of concrete wall, improved soil, and EPS. Conclusions are made regarding the selection of appropriate parameters for the three abovementioned barriers in reducing the train-induced ground vibrations.

1. INTRODUCTION

The ground vibrations induced by trains can propagate through the surrounding soils to adjacent buildings, causing annoyance to residents or resulting in malfunction of sensitive instruments located inside. Therefore, how to mitigate the train-induced vibrations transmitted to the ground that support the vibration sources has become an important issue in densely populated metropolitan areas and for structures housing vibration-sensitive equipment (Yang and Hung 1997). Zerwer et al. (2002) employed ABAQUS in finite element modeling of Rayleigh waves and notified the importance of proper mesh dimensions and damping characteristics in the finite element simulation. They presented equations to calculate the linear Rayleigh damping coefficients (average) with minimum variance within the frequency bandwidth of interest. Hall (2003) also applied the ABAQUS in the numerical modeling of train-induced ground vibration studies and reported an acceptable agreement between the numerical simulation and the field measurements. Yang et al. (2003) conducted a parametric study on train-induced wave propagation in soils using finite/infinite element modeling and concluded the mechanism of wave propagation in layered grounds for practical applications. Yang and Hung (1997) also implemented the same finite/infinite scheme to study the effect of wave barriers for the reduction of train-induced ground vibrations. They performed a parametric study on geometrical and material properties of the wave barriers and recommended the optimal values for isolating the train-induced ground vibrations. Moreover, a detailed literature review on the vibration screening methods can be found in Ahmad and Al-Hussaini (1991). However, few works have been carried out to further investigate the effect of wave barrier characteristics, both geometrical and material, to reduce the train-induced ground vibrations using ABAQUS in connection with geotechnical centrifuge tests.

In this respect, this research aims to investigate the train-induced ground vibrations and appropriate countermeasures using numerical approach by the dynamic three-dimensional finite element program ABAQUS. This software was employed using the supercomputer facilities of Tokyo Institute of Technology called TSUBAME. Considering the high frequency nature of train-induced vibrations, ABAQUS/Explicit was employed in this study and the main part of the model was developed in ABAQUS/CAE as a visualization tool. In addition, the infinite element was utilized to reproduce the infinite boundaries and prevent the wave reflections.

First, the propagation of waves in the ground was investigated by applying an impact-type loading. Then, the attenuation of maximum acceleration on the surface ground was obtained and the results were compared to the data from geotechnical centrifuge tests conducted at Tokyo Institute of Technology (Itoh 2003) and the theoretical solutions (Bornitz 1931). These comparisons confirmed the reliability

of the numerical modeling in this study.

Second, the effect of barriers in reduction of ground vibration was investigated by modeling a wave barrier at the transmission path. Three different types of barriers were evaluated in this study considering their stiffness: concrete wall, improved soil, and EPS. A benchmark model was also analyzed without any mitigation measure, and then the models with countermeasures were compared to evaluate their effectiveness.

2. FINITE/INFINITE ELEMENT MODELING IN ABAQUS

2.1 Characteristics of Wave Propagation in Ground

As the first step in this study, it was attempted to establish the reliability of ABAQUS in the numerical modeling of wave propagation problems. The axisymmetric model was applied to simulate the ground for a more realistic modeling. The finite element part of the model was built using ABAQUS/CAE as a visualization tool. Figure 1 displays the finite/infinite element parts of the model ground. The dimensions of the model were selected based on the geotechnical centrifuge tests; hence the results could be quantitatively compared. In other words, the centrifuge test results (Itoh 2003) were used to validate the present numerical model and confirm the reliability of the ABAQUS in the train-induced ground vibration studies.

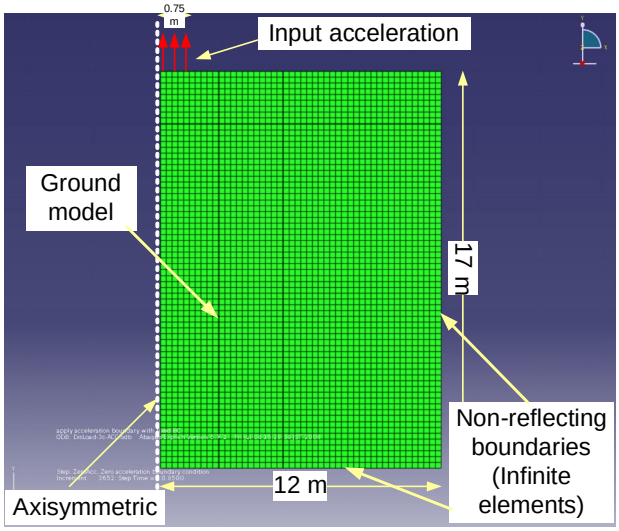

Figure 1 Finite/infinite element model of ground

According to the ABAQUS manual (ABAQUS, Inc. 2007), the Explicit scheme was adopted in this study for analysis, because it is suitable for high-speed dynamic events such as stress wave propagation in medium. ABAQUS/explicit uses a central difference rule to integrate the equations of motion explicitly through time, using the kinematic conditions at one increment to calculate the kinematic conditions at the next increment. The term "explicit" refers to the fact that the state at the end of the increment is based solely on the displacements, velocities, and accelerations at the beginning of the increment. This method integrates constant accelerations exactly. For the method to produce accurate results, the time increments must be quite small so that the accelerations are nearly constant during an increment (ABAQUS, Inc. 2007). The automatic time incrementation option was activated in all analyses to prevent any numerical instability.

The axisymmetric model, shown in Fig. 1, measured 12×17 m^2 and consisted of 3380 elements and 3498 nodes. The element size in the model was 0.25 m considering the material with the lowest shear wave velocity. The elements comprised of 4-node, linear, axisymmetric, solid, and reduced-integration elements (CAX4R). The ground was a homogenous isotropic elastic medium without any damping at this step. Material properties of the ground were identical as in centrifuge tests and are tabulated in Table 1 (Itoh 2003).

Then, an impulse type input motion was applied at the center of the model ground (Fig. 1) and the propagation of this wave throughout the ground was studied. Figure 2 shows the time histories of acceleration on the ground surface at different distances from the source.

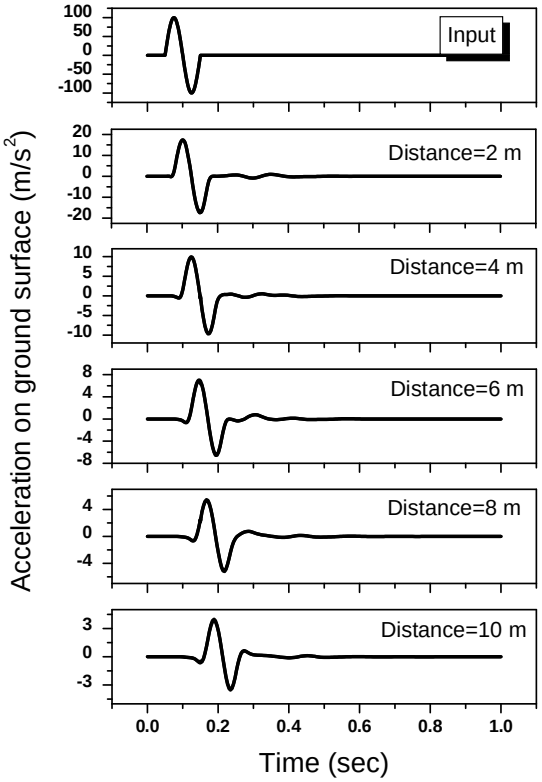

Figure 2 Time histories of acceleration on ground surface at different distances from source

The graphic interface of ABAQUS was used as a postprocessor to visualize the propagation of waves in the ground, and an example of this visualization is depicted in Figure 3. This figure displays the wave fronts at the time of 0.1 sec. Then, two different wave types were recognized (1) P-wave: compression wave with higher velocity and smaller amplitude, (2) S-wave: shear wave with lower velocity and

larger amplitude. Hence, the first disturbance in the propagated wave time history, e.g. Figs. 2 and 3 here, is attributed to the arrival of P wave and the second corresponds to the S wave. This recognition was conducted considering the time history records (Fig. 2) and visualized format (Fig. 3) and then it was possible to calculate the propagation velocity of abovementioned waves in both theoretical and visualized forms.

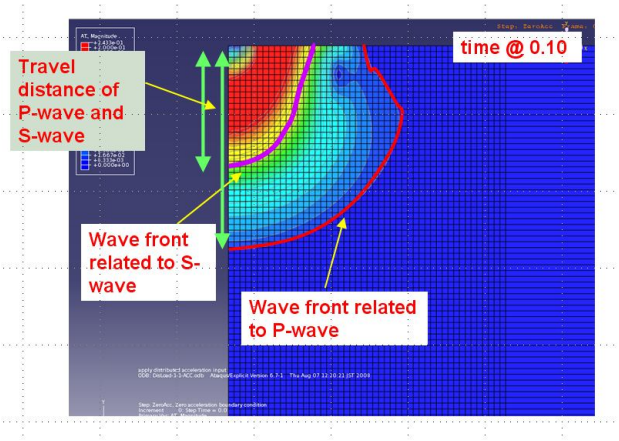

Figure 3 Visualization of wave front propagation in ground using ABAQUS/CAE

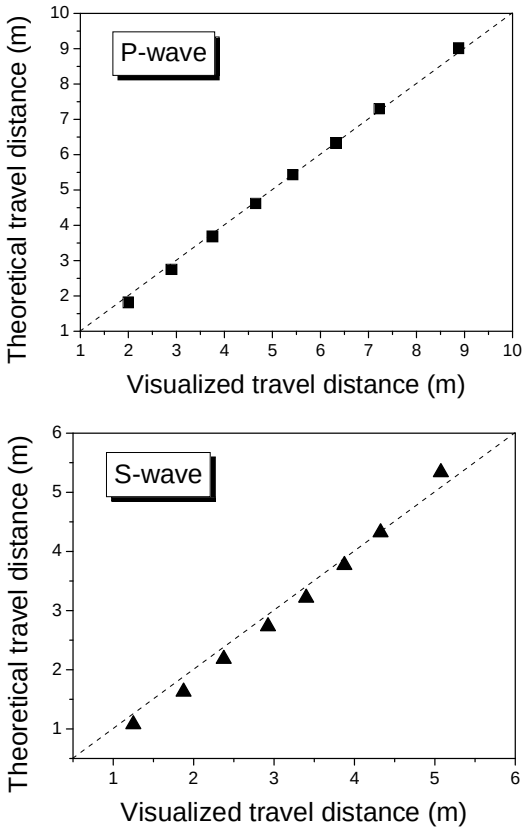

Figure 4 Theoretical and visualized travel distances of wave fronts

Therefore, a comparison between the two travel distances was made and the results are given in Figure 4. As is shown, there is a strong agreement between these two approaches, confirming the results of ABAQUS.

Table 1 Material properties of ground (Itoh 2003)

Material	Shear modulus (kN/m^2)	Poisson's ratio	Dry unit weight (kN/m^3)
Soil (Dr=80%)	17.9×10^3	0.23	15.435

2.2 Finite Element Analyses of Train-Induced Ground Vibrations

After confirming the reliability of ABAQUS in the wave propagation phenomenon, the finite element model was modified to investigate the train-induced ground vibrations. In this study, geotechnical centrifuge tests were employed to validate the finite element results, and this part explains the procedure we followed. Further information about the centrifuge tests can be found in Itoh (2003).

One important modification to the numerical model was to consider the material damping. This option was applied to the model in ABAQUS using Rayleigh damping coefficients. The Rayleigh damping parameters provide a linear material attenuation (Eq. 1).

$$D = \frac{\eta_1}{2\omega} + \frac{\eta_2 \omega}{2} \quad (1)$$

where D is damping ratio, η1 is mass damping parameter, η2 is stiffness damping parameter, and ω is circular frequency. In the Rayleigh damping approach, two mass and stiffness constants are defined to produce an average damping ratio within a bounded frequency range while having a minimum variance. This method and the related equations are elaborated in detail in Zerwer et al. (2002). Table 2 provides the damping coefficients for the ground, producing a 5% damping in the specified frequency bandwidth.

Another important issue was to consider the increase in the shear modulus of soil with the increase in the depth or overburden pressure. Therefore, the ground was divided into four layers (Fig. 5) and each layer was assigned a specified shear modulus to reproduce the real condition of the field.

Table 2 Rayleigh damping coefficients

Rayleigh damping coefficients		Average damping ratio	Minimum variance for damping	Frequency bandwidth (Hz)
Mass constant	Stiffness constant			
3.4163	0.001124	5%	0.1	1.5 ~ 40

Since the boundary condition in the centrifuge tests was almost fixed (a rigid box with sponges attached), the boundaries in the finite element model (Fig. 1) were changed into a fixed conditions, providing a similar circumstances to

the centrifuge tests. Therefore, reflected waves existed in both approach records.

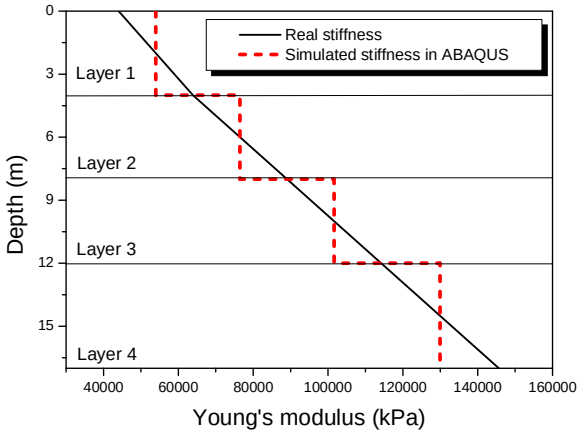

Figure 5 Variation of Young's modulus with depth (Jung 1998)

The input motion in the finite element model was identical as the centrifuge test, being similar to an impulse type input motion (Fig. 6). The frequency of this input motion was 10Hz which is located in the frequency range of train-induced ground vibrations (Yoshioka 2000 and Itoh et al. 2005).

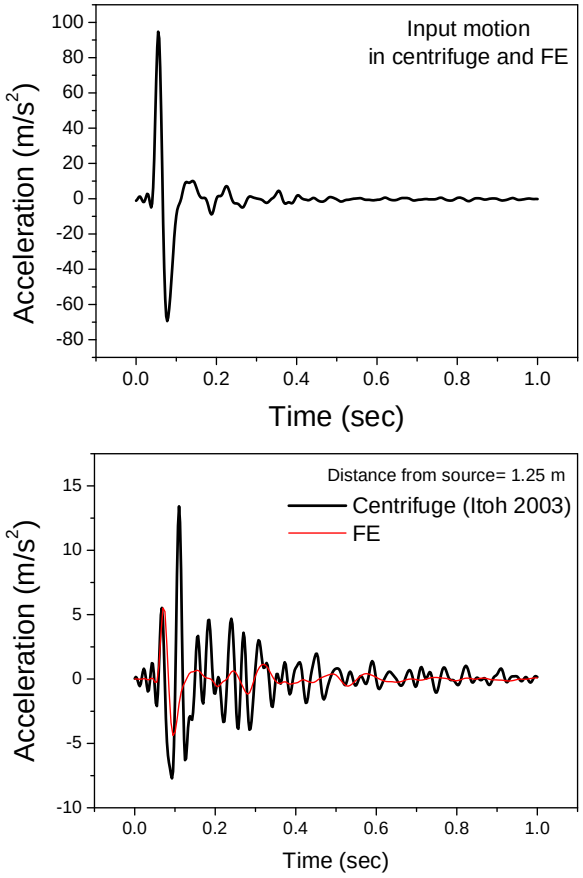

Figure 6 Time histories of input and recorded accelerations in numerical modeling and centrifuge experiment

Figure 6 shows an example for the comparison between the finite element model and the centrifuge test. As can be seen, the records on the ground surface at the distance of 1.25 m from the source displays a reasonable agreement specially for the case of first arrival wave which is believed to be free from any reflected wave.

In the next step, the peak values of the first arrival waves were selected to draw the attenuation curves for the surface ground waves. Figure 7 illustrates the comparison between the finite element model and the centrifuge tests, and the results display a reasonable agreement. Moreover, this figure includes the attenuation curve from a theoretical approach. Bornitz (1931) suggested theoretical attenuation curves for both body and surface waves which included geometrical and material damping. It should be noted here that the curved assigned to Bornitz (1931) in Fig. 7 indicated the attenuation for the surface waves and demonstrates an acceptable agreement with the finite element and centrifuge results.

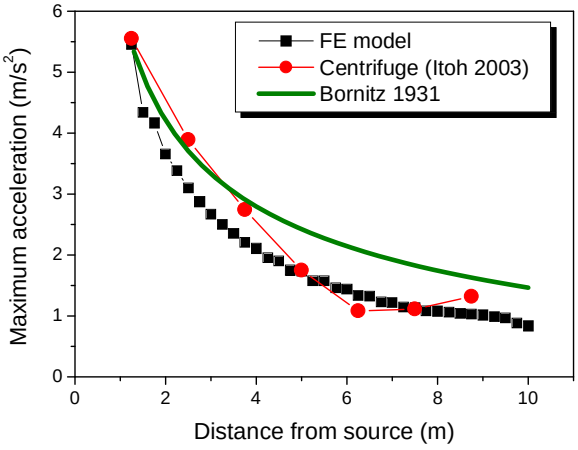

Figure 7 Comparison between attenuation curves for waves on ground surface derived from numerical modeling, centrifuge tests and theoretical method

2.3 Finite/Infinite Element Modeling of Mitigation Measures to Reduce Ground Vibration

After confirming the validation of finite element analysis in this study, it was attempted to evaluate the effect of wave barriers as a mitigation measure to reduce the ground vibrations.

In the centrifuge tests, an impact type point loading was applied through a ball-dropping system which details can be found in Itoh (2003) and Itoh et al. (2002). Wave barrier was installed at a distance from the source, which was 2.25 m, to reduce the ground vibrations. A schematic illustration of the wave barrier system is depicted in Fig. 8.

In this section, the screening effect of wave barriers in numerical modeling is thoroughly investigated and the results are compared with the centrifuge tests. Moreover, the effects of barrier parameters, both geometrical and material, are evaluated by performing a parametric study.

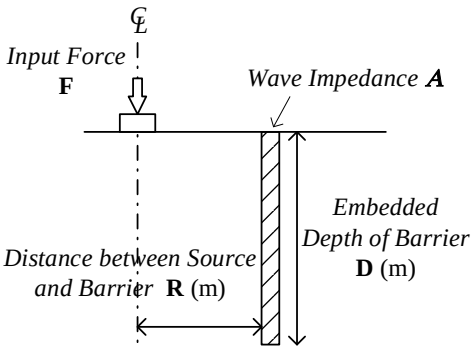

Figure 8 Schematic illustration for wave barriers in geotechnical centrifuge tests (Itoh et al. 2002)

The finite element model was improved in this part by inclusion of infinite elements to model the infinite boundary and minimize the wave reflections. Lysmer and Kuhlemeyer (1969) introduced the viscous boundaries (dashpot) for the analysis of dynamic problems involving infinite continues systems; hence an infinite half space could be successfully modeled as a finite element model. ABAQUS implements the principle of this theory for defining a non-reflecting boundary condition using infinite elements.

Three types of wave barriers were employed in the centrifuge tests including Aluminium, Acryl and Expanded Poly-Styrol (EPS) which stand for concrete wall, improved soil, and EPS itself in the prototype scale, respectively. Please refer to Table 3 for their properties. All these barriers were considered at the distance of 2.25 m from the source of vibration, because of the limitations in the centrifuge testing which imposed this restriction, and this study also followed the same configuration for the uniformity.

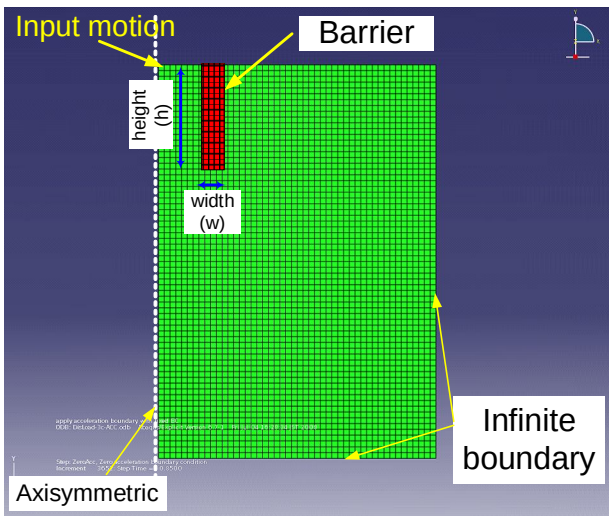

Figure 9 Model of wave barrier in finite element program – width=w and height=h

Figure 10 displays the time histories of the vertical accelerations on the ground surface of a model with the Aluminium barrier which had the configuration of width= 0.5 m and height= 10 m. As can be seen, the amplitude of the acceleration decreased as the distance from the source increased.

Table 3 Material properties of wave barriers (Itoh 2003)

Material	Shear modulus (MN/m^2)	Poisson's ratio	Dry unit weight (kN/m^3)	Damping ration (%)
Aluminium	25.6×10^3	0.34	26.5	1
Acryl	12.1×10^2	0.35	11.8	1
EPS	11.1×10^{-1}	0.10	0.12	5

Furthermore, a benchmark model was run without any mitigation measure, providing an appropriate reference for the comparison. Figure 11 shows the attenuation curves of the maximum vertical acceleration on the ground surface for different barriers in addition to the benchmark model. As can be seen, all the barriers decreased the ground vibration in comparison with the benchmark model except the EPS barrier at the area between source and the barrier and on the barrier itself. Figure 11 indicates that EPS barrier magnifies the ground vibration at the area near to the barrier, while beyond the barrier it performs likewise other barriers and reduced the ground vibration. It should be mentioned here that the some amplifications of the ground vibration near the EPS barrier has been observed during a series of field tests which further information can be found in Itoh (2003).

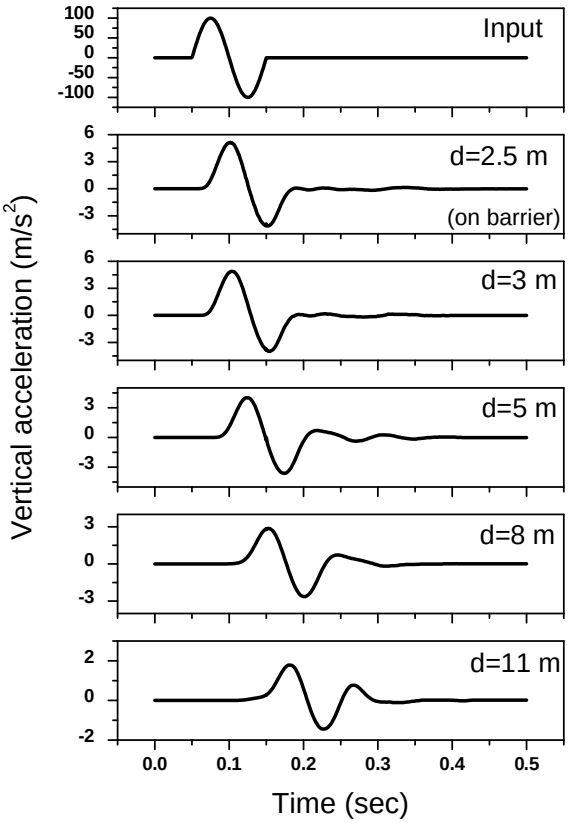

Figure 10 Time histories of vertical acceleration on ground surface at different distances (d) from the source – model with Aluminium barrier (w=0.5 m and h=10 m)

Furthermore, Fig. 11 provides the evidence that in deep barriers, i.e. 10 m here, stiff materials would more significantly reduce the ground vibration compared to the soft materials.

In order to investigate the effect of barrier depth, several models were run with different penetration depths (h=2.5, 5.0, 10, 15 m), and Fig. 12 displays two examples of the results for the case of Aluminium and EPS barriers. These two materials represent the stiff and soft barriers, respectively.

The results in Fig. 12 imply that increasing the depth could effectively enhance the performance of a stiff barrier, i.e. Aluminium here, while this parameter showed a little effect on the soft barrier, i.e. EPS. Hence, deeper depth in the stiff barriers would mean a better performance in the ground vibration reduction.

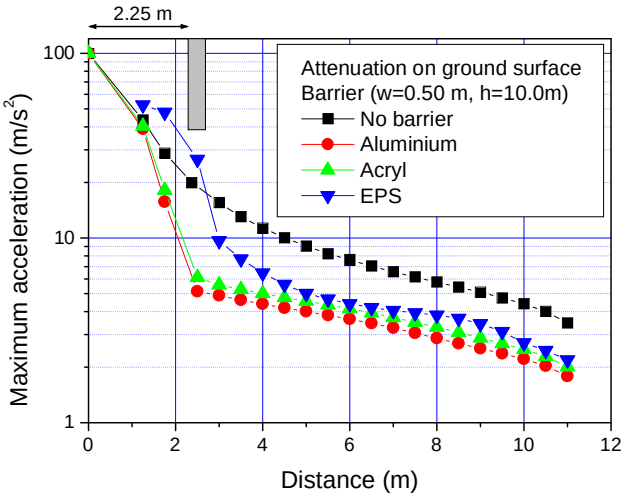

Figure 11 Attenuation curves of vertical acceleration on ground surface for different barriers (w=0.5 m. h=10 m)

In addition, a comparison was made between the numerical modeling results and the mitigation experiments in the geotechnical centrifuge tests and an example is presented in Fig. 13 for the case of the Aluminium barrier.

A parameter called Reduction Factor (R.F.) was introduced in this study to provide a quantitative comparison between the ABAQUS and the centrifuge tests, since amplitude of the input motion in the centrifuge tests was not constant. This parameter represents the efficiency of a barrier in the ground vibration reduction as follows:

$$R.F. = \frac{(A_w - A_m)}{A_w} \times 100 \qquad (2)$$

where R.F. is reduction factor (%), A_w is maximum ground acceleration without any mitigation measure, and A_m is maximum ground acceleration with a vibration countermeasure. The positive R.F. represents effective vibration mitigation, while a negative value stands for vibration amplification.

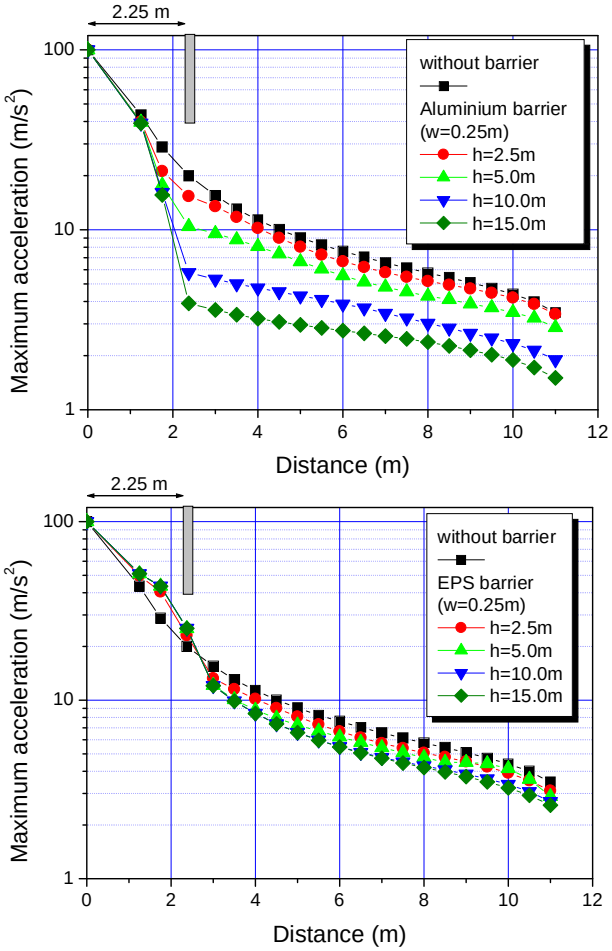

Figure 12 Attenuation curves of vertical acceleration on ground surface for Aluminium and EPS barriers for different depths (width=0.25 m)

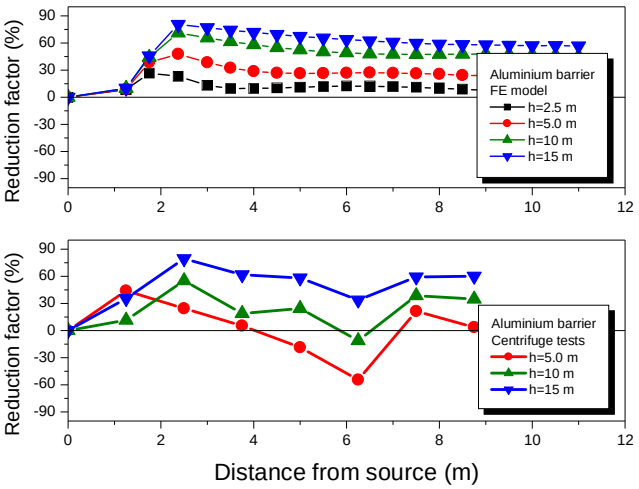

Figure 13 Comparison between numerical results from ABAQUS and geotechnical centrifuge tests (Itoh 2003) for case of Aluminium barrier (width=0.25 m)

The comparison in Fig. 13 demonstrates an acceptable agreement between these two approaches. In other words,

Fig. 13 again confirms the validity and reliability of the finite/infinite element modeling in ABAQUS for the studies related to the train-induced ground vibration and the mitigation measures. Moreover, it is to be noted here that some negative R.F. values near the boundary in the centrifuge test would be accounted for the wave reflection phenomenon as a result of the rigid side of experimental container.

3. CONCLUSIONS

In this study, finite/infinite element modeling of the train-induced ground vibration was conducted using ABAQUS and the following conclusions are drawn:

(1) Reliability and validity of the present finite/infinite element model in ABAQUS was confirmed using the geotechnical centrifuge tests.
(2) Wave barriers as the mitigation measures were employed and their efficiency in the ground vibration reduction was investigated in detail.
(3) It was shown that increasing the depth is an effective tool in enhancing the performance of stiff barriers, while this solution would result in insignificant outcome for the case of soft barriers.
(4) Stiffer materials provide a more effective vibration countermeasure than soft ones for the deep barriers.
(5) Reasonable agreement was established between the mitigation experiments in centrifuge and the results from ABAQUS which enables us to consider ABAQUS as a reliable measure for this type of studies.

Acknowledgements:

The first author acknowledges the support from the Japan Society for the Promotion of Sciences (JSPS) to conduct this research through a postdoctoral fellowship. This support is very much appreciated.

References:

Itoh, K. (2003), "Physical Modelling of Wave Propagation From Ground Vibration and Vibration Countermeasures," PhD Dissertation, Tokyo Institute of Technology.

Itoh, K., Koda, M., Lee, K.I., Murata, O., and Kusakabe, O. (2002), "Centrifugal Simulation of wave Propagation Using a Multiple Ball Dropping System," *International Journal of Physical Modelling in Geotechnics*, **No. 2**, 33-51.

ABAQUS, Inc. (2007), "ABAQUS version 6.7 user's manual".

Lysmer, J., and Kuhlemeyer, R.L. (1969), "Finite Dynamic Model for Infinite Media," *Journal of the Engineering Mechanics Division of the ASCE*, American Society of Civil Engineers, 95(EM4), 859–877.

Zerwer, A., Cascante, G., and Hutchinson, J. (2002), "Parameter Estimation in Finite Element Simulations fo Rayleigh Waves," *Journal of Geotechnical and Geoenvironmental Engineering*, American Society of Civil Engineers, **128** (3), 250-261.

Hall, L. (2003), "Simulations and Analyses of Train-Induced ground Vibrations in Finite Element Models," *Soil Dynamics and Earthquake Engineering* **23**, 403-413.

Yang, Y.B., Hung, H.H., and Chang, D.W. (2003), "Train-Induced Wave Propagation in Layered Soils Using Finite/Infinite Element Simulation," *Soil Dynamics and Earthquake Engineering* **23**, 263-278.

Yang, Y.B. and Hung, H.H. (1997), "A Parametric Study of Wave Barriers for Reduction of Train-Induced Vibrations," *International Journal for Numerical Methods in Engineering* **40**, 3729-3747.

Ahmad, S. and Al-Hussaini, T.M. (1991), "Simplified Design for Vibration Screening by Open and In-Filled Trenches," *Journal of Geotechnical Engineering*, American Society of Civil Engineers, **117** (1), 67-88.

Bornitz, G. (1931), "Uber die Ausbreitung der von Grozklolbenmaschinen erzeugten Bodenschwingungen in die Tiefe," Springer-Verlag, Berlin.

Yoshioka, O. (2000), "Basic Characteristics of Shinkansen-Induced Ground Vibration and its Reduction Measures," *Proceedings of International Workshop WAVE 2000*, Balkema, Bochurn, 219-240.

Itoh, K., Zeng, X., Koda, M., Murata, O., and Kusakabe, O. (2005), "Centrifuge Simulation of wave Propagation due to Vertical Vibration on Shallow Foundations and Vibration Attenuation Countermeasures," *Journal of Vibration and Control*, **No. 11**, 781-800.

Sixth International Conference on Urban Earthquake Engineering
March 3-4, 2009, Tokyo Institute of Technology, Tokyo, Japan

CYCLIC VOLUME CHANGE OF UNSATURATED SOILS WITH VARYING FINES CONTENTS

Eric Yee[1], Pendo M. Duku[2], and Jonathan P. Stewart[3]

1) *Graduate Student, Department of Civil and Environmental Engineering, University of California, Los Angeles, USA*
2) *Staff Engineer II, Fugro West Consultants, Ventura, California, USA*
3) *Professor and Vice Chair, Department of Civil and Environmental Engineering, University of California, Los Angeles, USA*
mailericyee@ucla.edu, pduku@fugro.com, jstewart@seas.ucla.edu

Abstract: Cyclic simple shear laboratory testing has been performed to evaluate the effects of relative density, fines content, saturation, and overburden pressure on seismic compression behavior of sands having fines with low plasticity. It was observed that vertical strains increased as relative density, and overburden pressure decreased, and as fines content increased. It was also observed that vertical strains generally decreased at intermediate levels of saturation. These results can be used to develop a preliminary empirical volumetric strain material model linking shear strain demand to volumetric strain.

1. INTRODUCTION

During strong earthquake shaking, unsaturated soils have a tendency to accumulate contractive volumetric strains. This process is termed seismic compression and has been identified to cause significant levels of damage in past seismic events (Pyke et al. 1975, Stewart et al. 2001, Stewart et al. 2002, Tokimatsu 2008). As a result, settlement from seismic compression is becoming an integral component of modern geotechnical seismic design practice (e.g., CGS, 2005).

The state-of-practice for estimating settlements from seismic compression is the simplified procedure by Tokimatsu and Seed (1987). A critical component of this procedure relates shear strain demand and number of strain cycles to volumetric strain, also known as a volumetric strain material model (VSMM). However, the Tokimatsu and Seed VSMM was based on laboratory test data by Silver and Seed (1971) for only one clean sand material. Recently, Duku et al. (2008) updated the VSMM for clean sands based on laboratory test data of 16 materials. Like the earlier Tokimatsu and Seed (1987) approach, this VSMM accounts for the decrease of seismic compression with increasing relative density. However, the Duku et al. (2008) approach also captures the decrease of volumetric strain with increasing overburden pressure. Nonetheless, both of these VSMMs remain limited in that they are only applicable to clean sands.

Laboratory test data to help develop VSMMs for soils with fines have been presented by Pyke et al. (1975), Whang et al. (2004), and Whang et al. (2005). Pyke et al. (1975) performed a limited number of cyclic simple shear tests on well-graded clayey sand. The researchers tested samples at two densities, γ_d = 1.78 and 1.94 g/cm^3, with an average water content of 10%. Whang et al. (2004) performed cyclic simple shear testing on four soils with high fines contents, FC = 40–54% and plasticity indices, PI = 2–15. Their findings showed that compacted plastic soils have lower seismic compression when compacted at high saturation (wet of line of optimums) than when compacted at lower saturations. Soils with low plasticity fines (PI~2) did not show a significant effect of saturation. Their tests also showed lower levels of seismic compression for these clayey sands than for clean sands. Whang et al. (2005) investigated the effects of density, saturation, and fines content on the seismic compression behavior of several synthetic non-plastic silty sands (fines were rock-flour). They found intermediate levels of saturation, S~30%, produced vertical strains that were less than samples with S>60% and that increasing fines content increased vertical strains under constant relative compaction. The effect of fines content on seismic compression for sands containing finite but low plasticity fines has not yet been systematically investigated and is the subject of the present (ongoing) research.

To help tackle these issues, this paper presents data to evaluate seismic compression behavior of sand with varying fines content of low plasticity. In particular, this investigation extends on the research done by Duku et al. (2008) and systematically concentrates on the effects of relative density, fines contents, saturation, and overburden pressure on seismic compression.

2. LABORATORY TESTING

The soil materials tested were reconstituted mixtures of sand and fine-grained materials. These materials were derived from bulk samples of natural soils retrieved from three locations in southern California (an unknown location

in southern California, downtown Los Angeles, and Santa Clarita Valley). To reflect the origin of these soils, they are referred to as GPI, Wilshire, and Newhall#2. In each case, the fine and coarse fractions were separated by sieving the natural materials through the number 200 sieve and the clean sand was obtained by washing the coarse fraction. The original GPI, Wilshire, and Newhall#2 soils had FC ~ 35, 22, and 14% respectively.

Mixtures of clean sand and varying levels of corresponding fines were used for cyclic simple shear testing and their soil properties are listed in Table 1. This testing was performed using the UCLA Digitally Controlled Simple Shear device (Duku et al. 2007), with sample preparation and testing protocols described by Duku et al. (2008).

Table 1 Soil Properties for Materials Tested.

Material	FC (%)	C_U	C_C	LL	PI
Natural GPI	35	–	–	21	0.7
GPI mixtures	0	3.2	1.1	–	–
	10	–	–	18	NP
	20	–	–	19	NP
	35	–	–	21	0.3
	50	–	–	–	–
	100	–	–	28	14
Natural Wilshire	22	–	–	19	3
Wilshire mixtures	0	3.8	1.1	–	–
	10	–	–	16	NP
	35	–	–	20	7
	50	–	–	25	9
	100	–	–	41	16
Natural Newhall#2	14	–	–	19	NP
Newhall#2 mixtures	0	3.6	0.9	–	–
	10	–	–	–	–
	50	–	–	–	–

3. TEST RESULTS

3.1 Form and Parameterization of Results

The laboratory test results for each specific material are summarized with the following VSMM:

$$(\varepsilon_v)_{N=15} = a(\gamma_c - \gamma_{tv})^b \quad (1)$$

$$C_N = R\ln(N) + c \quad (2)$$

where:

γ_c = uniform cyclic shear strain amplitude

γ_{tv} = volumetric threshold shear strain (0.01-0.03%)

$(\varepsilon_v)_{N=15}$ = volumetric strain with 15 cycles of loading

N = number of strain cycles

$C_N = (\varepsilon_v)_N / (\varepsilon_v)_{N=15}$

$a, b, R, and\ c$ = coefficients from regression analysis

In this paper, we do not consider the parameterization of R.

3.2 Effect of Relative Density and Fines Content

The effect of relative density was investigated by preparing dry samples for each sand-fines combination listed in Table 1. These test results were nonlinearly regressed according to Eq. (1) with sample results shown in Figure 1.

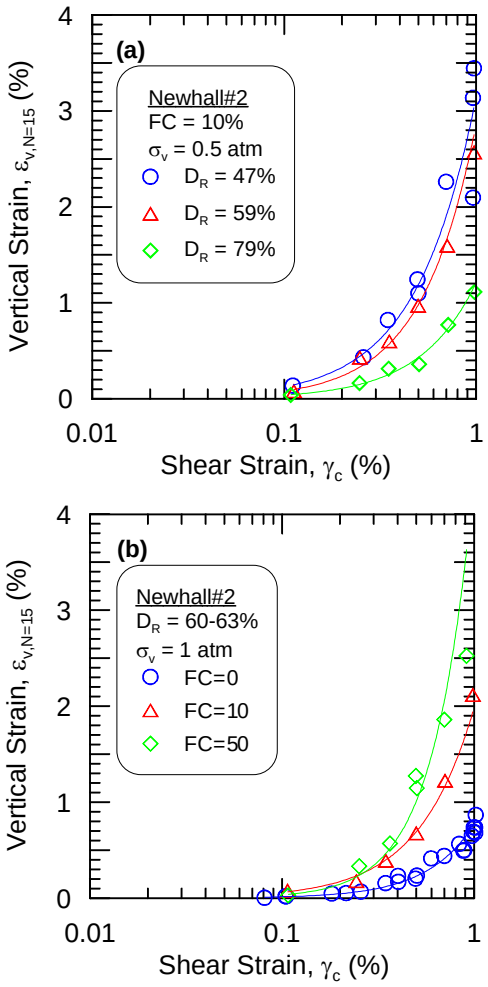

Figure 1 (a) Effect of D_R on vertical strains from seismic compression of Newhall#2 soil with FC=10% at σ_v=0.5atm and (b) effect of fines content for D_R=60-63% and σ_v=1atm.

The observed behavior of increasing vertical strain as relative density decreases is consistent with past observations in clean sands (Silver and Seed 1971, Youd 1972, Duku et al. 2008).

The observed behavior of increasing vertical strain as fines content increases is in agreement with the findings of Whang et al. (2005) on sands with non-plastic fines. A closer look into parameter *a* of Eq. (1) reveals a positive correlation with fines content as shown in Figure 2a. Interestingly, a plot of parameter *b* with fines content in Figure 2b shows that *b*

does not vary significantly with fines content. Duku et al. (2008) similarly found that *b* did not vary significantly across multiple compositional and environmental factors.

The observed effect of increasing vertical strain as fines content increases can be explained by the concept of the limiting fines content, FC_L. The FC_L is defined as the maximum amount of fines that can be contained in the void space between sand particles while maintaining a contiguous sand skeleton. Thevanayagam (1998) postulated that a soil mixture is a delicate matrix comprised of two submatrices, a coarser-grain matrix and finer-grain matrix. For FC < FC_L, the finer-grain matrix does not participate in the transfer of contact frictional forces, or their contribution is secondary. Thevanayagam (1998) also defines intergranular void ratio, e_s, as the void ratio of the coarse fraction only and interfine void ratio, e_f, as the void ratio of the fines fraction only.

Using the concept of FC_L, it can be seen in Figure 3 that for FC < FC_L, e_s increases as FC increases and e_f decreases as FC increases. At FC < FC_L, the soil will exhibit an increase in seismic compression susceptibility because e_s controls the soil behavior for this range of FC. For FC > FC_L, a decreasing e_f would suggest a reduction in vertical strain, however the opposite occurs. This is attributed to the highly compressible nature of the fine-grained matrix. Therefore, for an increasing FC > FC_L, the effect of decreasing e_f is counterbalanced by the increasing volume of highly compressible fines and giving rise to the observed increase in vertical strains.

These trends are generally in agreement with the results of undrained testing of saturated silty sands by Polito and Martin (2001). They found that the liquefaction resistance for a fixed relative density is lower for high FC (> FC_L) than for low FC (< FC_L). This is consistent with the increased compressibility observed in the present study. However, this trend may not hold for materials of higher plasticity.

3.3 Effect of Saturation

The effects of saturation were investigated for GPI and Wilshire materials. Sample effects are shown in Figure 4 at D_R=60% for a Wilshire FC=20% mixture. The test results show similar results for low and high levels of saturation. However, for intermediate saturation levels, the volumetric strains are lower. These observations are consistent with previous investigations by Whang et al. (2004).

To help explain the saturation effects, parameter *a* was normalized against *a* at S=0% and matric suction tests were performed on partially saturated soil mixtures using the filter paper method (ASTM D5298-03). Figure 5 is a plot of the normalized *a* values and the results of the matric suction tests.

Figure 5a shows a decrease in *a* for S~30–50%, indicating less vertical strain at those saturation levels while Figure 5b shows an increase in matric suction at those same saturation levels. The matric suction increases the effective stress in the sample, which in turn increases soil moduli. The increase in soil moduli would reduce the susceptibility to volume change upon cyclic loading.

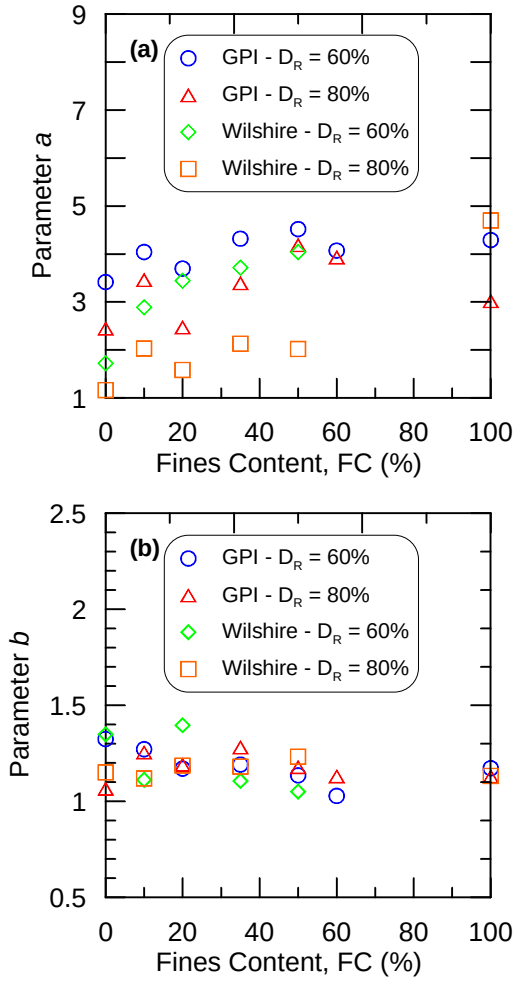

Figure 2 (a) Trend in parameter *a* with respect to FC for a fixed D_R and (b) plot of the corresponding parameter *b*'s.

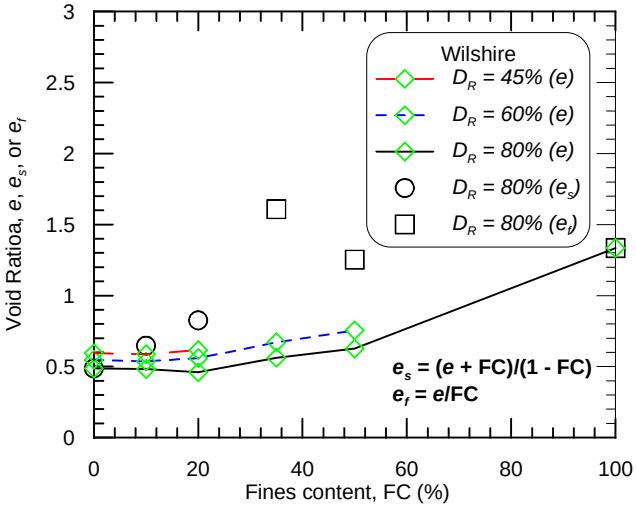

Figure 3 Global (*e*), intergranular (e_c), and interfine (e_f) void ratio versus fines content for Wilshire mixtures. Plot shows FC_L~20%.

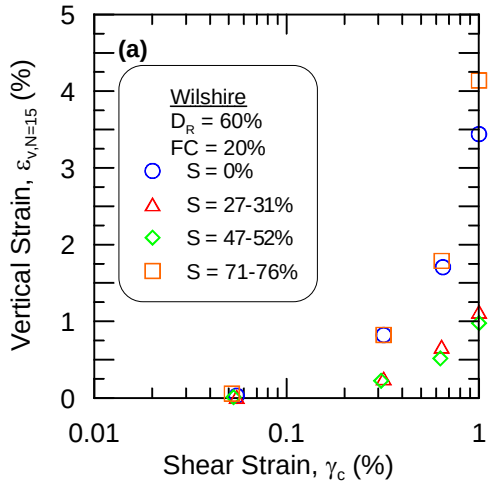

Figure 4 Effect of saturation on vertical strains from seismic compression of Wilshire mixture with FC=20%.

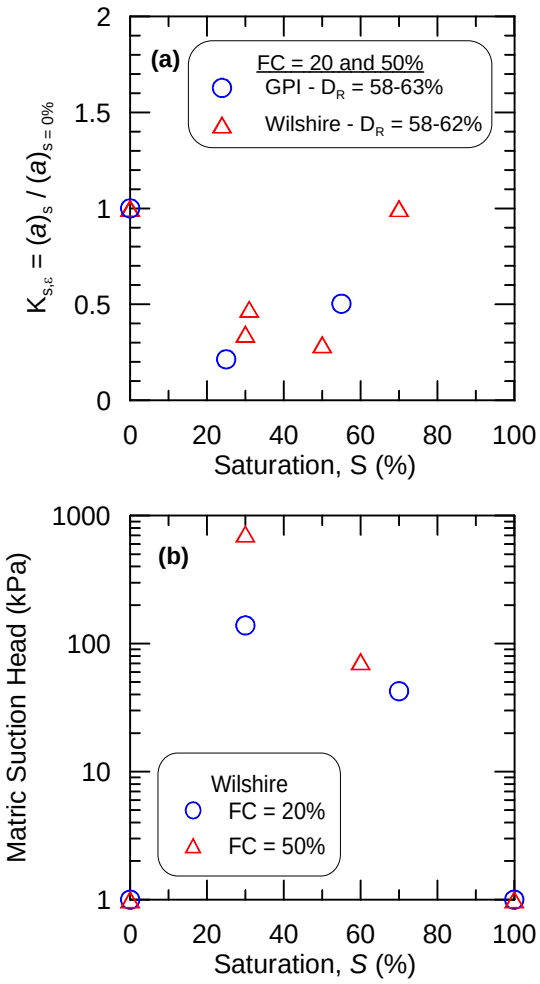

Figure 5 (a) Effect of saturation on normalized parameter *a*, and (b) matric suction test results for Wilshire mixtures.

3.4 Effect of Overburden

The effect of overburden pressure was investigated by preparing dry normally consolidated specimens of Newhall#2 mixtures under vertical stresses of σ_v=0.5, 1, 2, and 4 atm prior to cyclic loading. Example results are given in Figure 7(a), showing $(\varepsilon_v)_{N=15}$ decreasing as overburden pressure increases. Sample normalized results are shown in Figure 7(b) with the recommended correlation for clean sands by Duku et al. (2008) for reference.

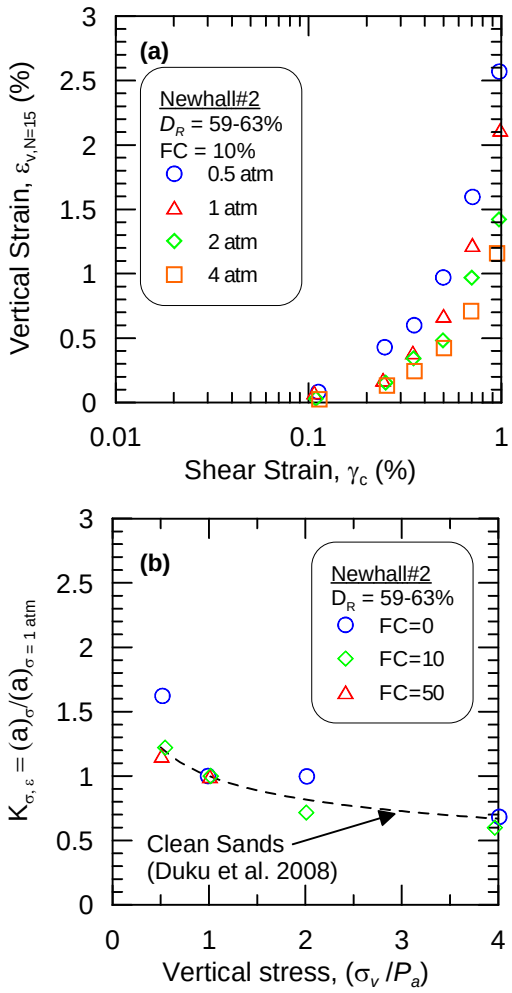

Figure 7 (a) Effect of overburden pressure on vertical strains from seismic compression of Newhall#2 soil with FC=10% at D_R=59-63% and (b) normalized parameter *a* using the data from (a).

The dependence of seismic compression on overburden pressure is clearly identifiable from the test results. The overall trend is in agreement with the findings by Duku et al. (2008), which is different from previous findings by Silver and Seed (1971) and Youd (1972), who found no dependence of seismic compression on overburden pressure in clean sands.

This trend of lowered vertical strains for higher overburden pressures is consistent with the findings on saturation, where high matric suction (higher interparticle stresses) resulted in lower vertical strains when compared to the vertical strains from samples with low matric suction. The higher overburden pressures would increase confining stresses and soil moduli thereby reducing volume change susceptibility.

4. CONCLUSIONS

Three reconstituted mixtures of sand and fine-grained materials underwent cyclic simple shear testing to investigate the effects of relative density, fines content, saturation, and overburden on seismic compression behavior. Test results indicated increasing seismic compression susceptibility for:

1. decreasing relative density,
2. increasing fines content,
3. intermediate saturation levels, and
4. decreasing overburden pressures.

These results represent a progress report on work in progress. We are not yet prepared to propose a VSMM for fine grained compacted soils due to the limited size of the database.

Acknowledgements:

Support for this work was provided by the U.S. Geological Survey (USGS), Department of the Interior, under USGS award No. 05HQGR0050. This support is gratefully acknowledged. The views and conclusions contained in this document are those of the authors and should not be interpreted as necessarily representing the official policies, either expressed or implied, of the U.S. Government.

References:

ASTM D5298-03 "Standard test method for measurement of soil potential (suction) using filter paper," *Annual Book of ASTM Standards, Section 4: Construction, Vol. 04.08, Soil and Rock*, American Society for Testing and Materials, Philadelphia.

California Geological Survey (CGS). (2005), "Engineering geology and seismology for public schools and hospitals in California," *Report to Accompany California Geological Survey Note 48 Checklist*, Sacramento, California, R.H. Sydnor, ed.

Duku, P.M., Stewart, J.P., Whang, D.H., and Venugopal, R. (2007), "Digitally controlled simple shear apparatus for dynamic soil testing," *Geotechnical Testing Journal*, American Society for Testing and Materials, **30**(5), 368-377.

Duku, P.M., Stewart, J.P., Whang, D.H., and Yee, E. (2008), "Volumetric strains of clean sands subject to cyclic loads," *Journal of Geotechnical and Geoenvironmental Engineering*, American Society of Civil Engineers, **134**(8), 1073-1085.

Polito, C.P. and Martin, J.R. II (2001), "Effects of nonplastic fines on the liquefaction resistance of sands," *Journal of Geotechnical and Geoenvironmental Engineering*, American Society of Civil Engineers, **127**(5), 408-415.

Pyke, R., Seed, H.B., and Chan, C.K. (1975), "Settlement of sands under multidirectional shaking," *Journal of Geotechnical Engineering*, American Society of Civil Engineers, **101**(4), 379-398.

Silver, M.L., and Seed, H.B. (1971), "Volume changes in sands during cyclic loading," *Journal of Soil Mechanics and Foundations Division*, American Society of Civil Engineers, **97**(9), 1171-1182.

Stewart J.P., Bray, J.D., McMahon, D.J., Smith, P.M., and Kropp, A.L. (2001), "Seismic performance of hillside fills," *Journal of Geotechnical and Geoenvironmental Engineering*, American Society of Civil Engineers, **127**(11), 905-919.

Stewart J.P., Smith P.M., Whang D.H., and Bray J.D. (2004), "Seismic compression of two compacted earth fills shaken by the 1994 Northridge earthquake," *Journal of Geotechnical and Geoenvironmental Engineering*, American Society of Civil Engineers, **130**(5), 461-476.

Thevanayagam, S. (1998), "Effect of fines and confining stress on undrained shear strength of silty sands," *Journal of Geotechnical and Geoenvironmental Engineering*, American Society of Civil Engineers, **124**(6), 479-491.

Tokimatsu, K. (2008), "Geotechnical problems in the 2007 niigata-ken chuetsu-oki earthquake," *Proceedings of the conference of Geotechnical Earthquake Engineering and Soil Dynamics IV*, Sacramento, California, May 18-22, 2008, 1-30.

Tokimatsu, K., and Seed, H.B. (1987), "Evaluation of settlements in sand due to earthquake shaking," *Journal of Geotechnical Engineering*, American Society of Civil Engineers, **113**(8), 861-878.

Whang, D.H., Stewart, J.P., and Bray, J.D. (2004), "Effect of compaction conditions on the seismic compression of compacted fill soils," *Geotechnical Testing Journal*, American Society for Testing and Materials, **27** (4), 371-379.

Whang, D.H., Moyneur, M.S., Duku, P., and Stewart, J.P. (2005), "Seismic compression behavior of nonplastic silty sands," *Proceedings of the International Symposium on Advanced Experimental Unsaturated Soil Mechanics*, A. Tarantino, E. Romero, and Y.J. Cui (eds.), Trento, Italy, June 27-29, A.A. Balkema Publishers, pp 257-263.

Youd, T.L. (1972), "Compaction of sands by repeated shear straining," *Journal of Soil Mechanics and Foundations Division*, American Society of Civil Engineers, **98**(7), 709-725.

Sixth International Conference on Urban Earthquake Engineering
March 3-4, 2009, Tokyo Institute of Technology, Tokyo, Japan

DUCTILE REINFORCED CONCRETE BEAM-COLUMN JOINTS WITH ALTERNATIVE DETAILING

Barbara Chang[1)], Tara Hutchinson[2)], and Robert Englekirk[3)]

1) Graduate Student, Structural Engineering Department, University of California, San Diego, United States
2) Associate Professor, Structural Engineering Department, University of California, San Diego, United States
3) Adjunct Professor, Structural Engineering Department, University of California, San Diego, United States
Corresponding Author: tara@ucsd.edu

Abstract: Based on current special moment frame design requirements, conventional reinforced concrete beam-column joints in frame-braced buildings designed to resist seismic loads suffer severe damage when plastic hinging is taken to design limits. Furthermore, construction of these conventional beam-column joints is costly and labor intensive. Alternative systems, which reliably localize and minimize the spread of damage, are desirable. Such systems must consider minimizing cost, easing constructability, and increasing performance reliability. In a unique industry-academia collaborative testing program alternative detailing was evaluated. Specifically, four full-scale interior beam-column specimens were tested under reversed cyclic quasi-static loading, with details incorporating: (i) high strength concrete, (ii) embedded ductile rods, (iii) post-tensioning, (iv) precast construction and/or (v) high strength reinforcing steel. Experimental data describing the response of these systems is necessary to support design procedures for the proposed alternative systems as presented by Englekirk and Wang (2008) in a companion report. Observations from the experiments indicate that all specimens exhibit stable hysteretic behavior with no strength degradation up to drifts of 5.5%. At design plastic rotations expected of conventional beam-column joints, specimens exhibited no joint spalling with only minor damage along beam members. It is most impressive that with minimal damage and no strength degradation, these specimens were able to demonstrate well developed damage mechanisms that performed markedly better than conventionally designed subassemblies. Results from these experiments will support future widespread use of alternative systems and the *out-of-the-box* design approaches needed in the engineering community to improve the performance, reliability, and constructability while decreasing cost of critical lateral load resisting elements in seismically active areas. In this paper, the second specimen of the test series, which was constructed of precast beams, high-strength reinforced concrete, and post-tensioning will be discussed.

1. INTRODUCTION

1.1 Background

In the United States, newly constructed reinforced concrete frame structures in regions of high seismicity are designed according to the codified standards of the International Building Code (IBC 2003) and the American Concrete Institute (ACI 318, 2005). These standard design codes attempt to assure structural systems attain acceptable thresholds of life safety during moderate or severe seismic events. Both intermediate moment frames and special moment resisting frames must be designed in accordance with Chapter 21 of ACI 318 ("Special Provisions for Seismic Design").

The critical beam-column joint region of these systems, for monotonically constructed braced frames, follow design guidelines of ACI 352. Provisions for reinforcement within these subsystems, as currently outlined in ACI, result in significant congestion of the reinforcing steel, particularly through the critical joint. Rebar congestion slows construction, increases labor cost, and increases difficulty in placing concrete, especially through the joint region. Moreover, there is the question of reinforcement overlap or bends to provide adequate development length within the joint. This further leads to unavoidable reinforcement congestion. There are other pragmatic points of concern, for example, when higher strength concrete columns are desired (e.g. in taller building construction), resulting in the columns cast separately from the beams. Clearly precast systems would lead to better quality control under these conditions than monolithically constructed systems.

Despite the excessive reinforcement within the joint, modern designed cast-in-place (CIP) reinforced concrete frame bracing systems are expected to exhibit damage at drift ratios of approximately 2%. Concrete spalling within the joint region and along the beam will accordingly result in joint strength degradation. Although the spalling and crushing of the concrete may be critical for dissipation of seismically induced energy, it is distinctly unsightly and may be alarming for the general public.

A number of innovative systems have been explored to relieve the aforementioned issues. For example, use of high strength concrete, high strength steel, precast members, post-tensioning of members, and/or ductile connectors have

been explored [e.g. Stone et al., 1995; Warcholik and Priestley, 1997, 1998a,b; Day, 1999; Kim, 2000; Ertas et al., 2006]. Early work at the National Institute of Standards, for example, paved the way for the concept of Hybrid precast assembled frames, which capitalize on the concept of post-tensioning to provide re-centering capabilities to the frame (Stone et al., 1995).

In earlier work by Stone et al. (1995), hybrid moment-resisting precast beam-column concrete connections were tested. The study concludes that precast systems were able to achieve certain seismic advantages over conventionally reinforced specimens. The hybrid system is self-centering and has essentially no residual drift. Large drift capacity of 6% with 55% of the beam strength retained was observed. Negligible damage occurred in the specimen at up to 6% drift, while low strains in the transverse steel (below $0.15f_y$) and no shear distress were detected.

Ertas et al. (2006) cited the advantages of precast reinforced concrete for construction of ductile moment-resisting frames. In using precast members in construction, high-quality structural elements, construction efficiency, time saving, and lower overall costs may all be realized. The authors conclude that these types of connections performed well, although assembly of cast-in-place connections may need extra formwork on-site, which contributes somewhat to time and cost. In addition, high quality-control procedures may be necessary to ensure good seismic performance of welded connections.

Subsequent tests at the University of Washington on 2/3 scale hybrid frame beam-column specimens further substantiated the benefits of such systems, while incorporating precast members and mild reinforcing steel (Day, 1999; Kim, 2000). The restoring capability of post-tensioning in these experiments reduced residual displacements, and the use of precast elements minimized the amount of severe damage under large displacements and localized it at the beam-column interface. Yielding of the mild steel reinforcement (for beam continuity) provided the necessary energy dissipation.

Tests summarized in the various reports by Warcholik and Priestley (1997, 1998a,b) investigated the comparative performance of high strength and normal strength reinforced concrete beam-column joints. Specimen reinforcement was Grade 60 mild steel, and one sample used Dywidag ductile rods (DDR) for load transfer through the joint. Although the use of high strength concrete improved the performance of the beam-column joint, the amount of measurable improvement was less than expected. Joint distress (cracking and spalling) was observed at $\mu_\Delta = 1.5$, and extreme joint distress was observed at higher values of displacement ductility. The specimen with DDRs in the joint achieved a large amount of ductility and its beams remained elastic for most of the test. The authors conclude that joint shear reinforcement should be increased to satisfy shear demand.

Another approach to address rebar congestion and shear demand is the use of high-strength steel in design of reinforced concrete elements. High strength steel are now available at over 100 ksi (690 MPa) yield strength with greater strain capacity than standard Grade 60 steel. Use of high strength steel reduces the amount of transverse reinforcement in structural members by as much as 40%, compared to Grade 60 steel. A reduction in the amount of rebar used translates to less rebar congestion, which may decrease construction cost. Other side benefits may include improved constructability (better fit between vertical and horizontal structural elements), less construction labor, and less demand on hoisting equipment at the construction site (Post, 2007).

The improved performance of beam-column subassemblies through the use of ductile connections, hybrid systems, or other methods may contribute to increased building safety, while additionally reducing construction time and cost. Thus, further study of alternative design methods to conventional reinforced-concrete design needs to be explored for seismically active regions.

1.2 Test Program Scope

In this paper, we summarize the second specimen from a unique industry-academe collaborative testing program in which innovatively designed beam-column subassemblies are experimentally evaluated. Four full-scale interior beam-column specimens were tested under reversed cyclic quasi-static loading, with details incorporating: (i) high strength concrete, (ii) embedded ductile rods, (iii) post-tensioning, (iv) precast construction, and (v) high performance reinforcing steel. Specimen #1 and #4 used high strength concrete in the column, welded wire mesh Baugrids for transverse reinforcement in the joint region, and Dywidag ductile rods. Specimen #2 (the specimen presented) was constructed from high strength concrete in the column, precast beams, post-tensioning, and Dywidag ductile rods and connectors. Specimen #3 investigated high strength MMFX reinforcing steel with normal strength concrete. Performance of the subassemblies is evaluated in terms of global shear versus drift, energy dissipation, and damping; local moment-curvature, shear stress-strain in the joint region, reinforcing steel and ductile embed strains. In addition, physical observations of damage are carefully monitored using digital images and videos.

2. SPECIMEN DETAILS

2.1 Construction

Specimen #2 consisted of a 30 x 36 inch (0.76 m x 0.91 m) high-strength concrete column [target 10 ksi (69.0 MPa); actual Day Of Test 10.3 ksi (71.0 MPa)] of total length 14.5 feet (4.42 m) cast horizontally and erected vertically. Extending 12.0 feet (3.66 m) in either direction, precast 19x30 inch (North) (0.48 m x 0.76 m) and 19x36 inch (South) (0.48 m x 0.91 m) normal strength reinforced concrete beams were attached via a Dywidag ductile connector (DDC) assembly. (See Figure 1.) The beams had a target compressive strength of 5 ksi (34.5 MPa) and DOT of 7.3 ksi (50.3 MPa). Normal strength slabs [DOT 3.3ksi (22.8 MPa)] were cast when the beams were in place, forming a

T-cross section. Following slab construction, 11-0.6" diameter (1.5 cm diameter) post-tensioned strands were installed (un-grouted) to an initial stress of 190 ksi (1310 MPa) with a total PT force of 450 kips (2.0 MN). The column was reinforced with Grade 60 #7 bars and #11 bars, and Grade 60 #5 bars transverse reinforcement in the beam column joint area. Joint load transfer was provided by eight DDR rod connectors (four per beam face) embedded in the column, with three paired sets connected through a coupler block to Threadbar embedded in the beam and one paired set (upper north beam) that connected directly to the Threadbar without the coupler block. The latter set connected directly to the Threadbar was absent the DDC as it was embedded in the deeper (19x36 inch) beam at the precast plant. Material tests on the DDR's indicate ε_y = 4000 με and σ_y of near 60 ksi (414 MPa). Materials used for construction of all specimens were characterized from test done in the UCSD Powell Laboratories.

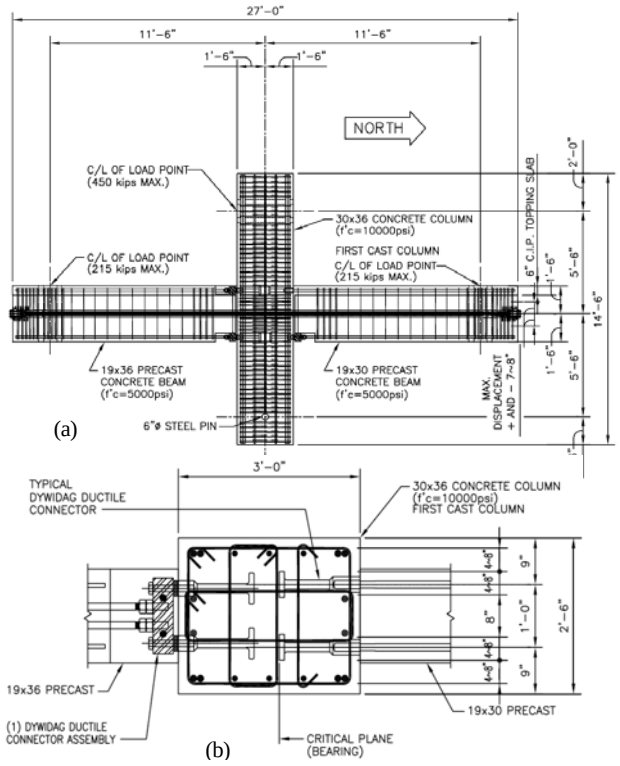

Figure 1 Construction drawings of (a) elevation view and (b) plan view of beam-column joint.

2.2 Test Protocol and Assembly

The specimen consisted of a full-scale interior beam-column configuration tested in a simply-supported frame configuration, whereby the column supports were allowed to rotate but not translate. Loading of the specimen was controlled through beam end displacements in a reversed, cyclic push-pull method applied through two 220 kip (980 kN) vertically placed MTS actuators. A constant axial compression of 150 kips (670 kN) is applied to the column during reversed cyclic loading through a stiff cross-beam and tie-rod assembly. A single 500 kip (2.2 MN) actuator is used to maintain zero displacement at the top of the column. The bottom of the column is restrained from translation through a steel pin. A schematic of the configuration is shown in Figure 2. Positive convention of the subassembly is taken as upwards motion of the North actuator and simultaneous downwards motion of the South actuator. In subsequent discussions, a push cycle refers to this positive notation, while a pull cycle refers to the opposite direction, i.e. with the north actuator moving downward and the south actuator moving upwards. Lateral bracing was provided for to restrict potential out-of-plane movement of the beams. (See Figure 3.)

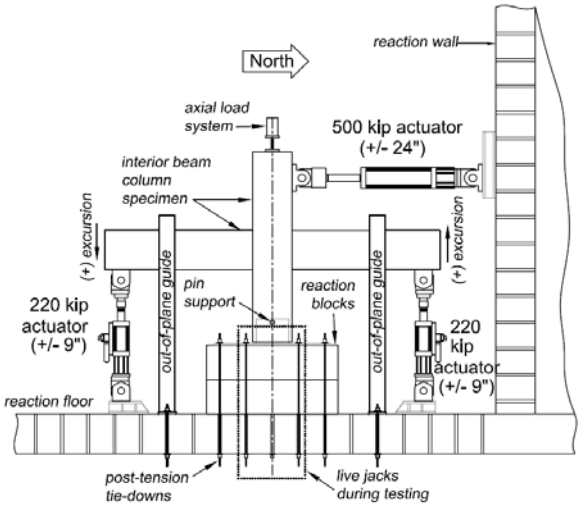

Figure 2 Schematic of test setup.

Figure 3 Specimen #2's test assembly prior to testing.

2.3 Instrumentation

Specimen was monitored using normal and high elongation (15-20%) strain gages, linear potentiometers, inclinometers, and load cells. Fifty-six strain gages and twenty-eight linear potentiometers were used. Nearly 100 channels of data were used for the test. Strain gages were placed within the joint region, along the beam near to the column face, and along the column. Linear potentiometers were placed externally on the specimen to record movement of the beam-column joint region and to monitor boundary

conditions of the specimen. Inclinometers were placed to monitor column rotation in the plane of loading and in the transverse plane of loading. The vertical beam end actuator ΔP cells and displacement transducers were calibrated by MTS prior to testing, and other instruments are calibrated on a regular basis internally by Powell Laboratory staff.

2.4 Test Execution

Specimens were tested under quasi-static reversed cyclic displacement-controlled loading applied in opposing directions at the beam ends. Axial loading was first applied to the specimens and monitored throughout testing. Beam end deformations were subsequently applied as a multiple of the theoretical yield displacement of the first specimen Δ_y = 1.06" (2.7 cm) to a target displacement ductility. Three cycles were applied for each target displacement ductility less than $2\Delta_y$; two cycles were applied for target displacement ductility including and between $2\Delta_y$ and $4\Delta_y$; and one cycle was applied for $6\Delta_y$ and $8\Delta_y$.

The protocol defined deviates slightly from the traditional constant cycle (typically 3) per amplitude protocol typically adopted. In this case, the selected cycle count N is decreased with increasing displacement demand to reflect the fact that during building simulations and from measurements taken during real earthquakes, N has been shown to decrease with increasing period (Krawinkler, 1996). Moreover, real earthquakes have many more lower amplitude (pre-yield) excursions than post-yield, which implies that more cycles in the pre-yield (stiffer) and less in the post-yield regions of the imposed loading history are warranted.

3. RESULTS

3.1 Global Response

Global hysteretic response of the specimen is shown in Figure 4a, which presents the beam shear *V* as averaged by the two vertical actuators versus the beam end average drift ratio γ. Stable hysteretic response is observed, with peak strengths of 760 kN and 623 kN (170 and 141 kips) measured in the push and pull directions, respectively. Asymmetric response of the specimen is attributed to the difference in detailing of the compressive block regions (slab overhangs). The push direction reflects the monolithically cast slab (North beam) placed in compression, whereas the pull direction places the South beam in compression, where a blocked-out region was constructed to allow access to the DDC. Little strength degradation was observed for this specimen.

Comparison of the specimen response with cast-in-place specimen tests performed at UC Berkeley are presented in Figure 4b. Popov et al. (1972) demonstrates the compatible performance of our precast specimen #2 with a conventionally designed specimen. The Popov et al. (1972) specimen is a cantilever beam (lever arm length of 2m) with a cross-section of 0.28 m x 0.74m (15" x 29") and reinforcement using #9 rebar. The strength of this section has a nominal moment of 946 kN-m (8370 kip-in) and supports a nominal load of 476 kN (107 kips). These similar characteristics of the Popov et al. specimen make it a reasonable choice for comparison to specimen #2. In the comparison to these cast-in-place beams, specimen #2 is able to achieve a higher beam end drift ratio (γ = 7%) and, during the last cycles, does not suffer from acute degradation of strength. The Popov et al. specimen is able to reach an drift ratio of γ = 5%, but degrades sharply afterwards (Figure 4b).

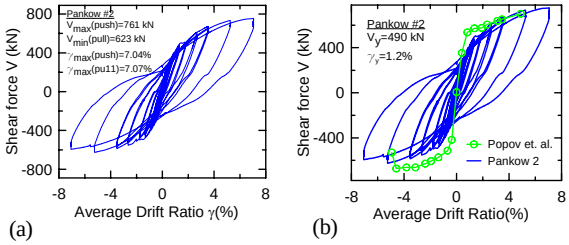

Figure 4 (a) Global shear force versus drift ratio response and (b) Comparison of specimen response to conventionally designed beam (Popov, et al., 1972).

Energy dissipated is calculated as the area under the global shear force versus drift ratio hysteresis response, on a per cycle basis. The resulting hysteretic energy dissipated (Figure 5a) indicates increasing energy dissipated with increasing drift ratio. Each complete cycle of the loading protocol has been considered, and therefore multiple values are observed at a given drift ratio γ.

One may normalized the energy dissipated by the amount determined at the previous cycle at the end of testing and represent these data as a percent (Figure 5b). For example, Figure 5b shows that at a drift ratio of approximately 4.6%, only half the amount of energy is dissipated as compared to the last cycle at drift ratio 7%. A polynomial fit to this data indicates the following regression:

$$E_{norm}(\gamma) = -1.52 + 4.32\,\gamma + 1.49\,\gamma^2 \qquad (1)$$

where γ is in %.

It is also useful to calculate the equivalent viscous damping ζ (Chopra, 2001) as a function of the drift ratio. The resulting viscous damping values as a function of drift ratio are shown in Figure 5c. Increasing drift ratio γ is matched with increasing equivalent viscous damping ζ. A good amount of damping is realized in the specimen with a maximum of ζ = 22% at a drift ratio of γ= 7%. Linear regression through these data indicates the following relation:

$$\zeta(\gamma) = 2.70\,\gamma + 5.46 \qquad (2)$$

where ζ is equivalent viscous damping (in %) and γ is the average drift ratio (in %).

3.2 Local Response

Curvature of the specimen is calculated on both the

North and South beams using the external linear potentiometers placed near the joint at approximately 0.28D [where D = 36 inches (0.91 m), the depth of the beam]. Curvature is calculated by taking the difference between vertical sets of linear potentiometers and dividing by the gage length between them. Moments are subsequently calculated at the location of the corresponding gage length. Figure 6 presents the moment versus curvature response near to the joint, x = 0.28D from the face of the column. Moment versus curvature plots for specimen #2 do not represent the entire testing sequence because the instruments recording the curvature data were damaged during testing. Due to this instrument failure, recording of South beam moment versus curvature data was stopped during the last cycle μ_Δ= 8 of the testing protocol, and North beam moment versus curvature data was stopped before the μ_Δ = 6 target cycle. Therefore, the data presented is not complete.

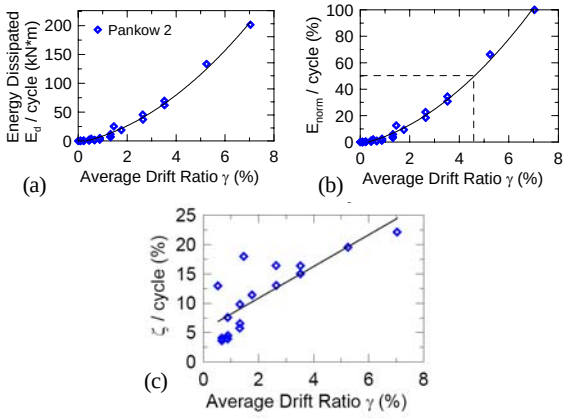

Figure 5 (a) Energy dissipated per cycle, (b) Normalized energy dissipated per cycle, and (c) Equivalent viscous damping per cycle.

The theoretical value of EI can be calculated using the compressive strength from concrete cylinder tests and the effective moment of inertia. Experimental results for EI (from the slope of the moment-curvature plots in Figure 6) give an average EI that is approximately 17% greater than the theoretically calculated EI, estimated with (Nilson et al. 2004):

$$I_{eff} = \left(\frac{Mcr}{Ma}\right)^3 I_{ut} + \left[1 - \left(\frac{Mcr}{Ma}\right)^3\right] I_{cr} \qquad (3)$$

where I_{eff} is the effective moment of inertia, M_{cr} is the cracking moment of the section, M_a is the maximum moment, I_{ut} is the uncracked transformed section moment of inertia, and I_{cr} is the cracked section moment of inertia.

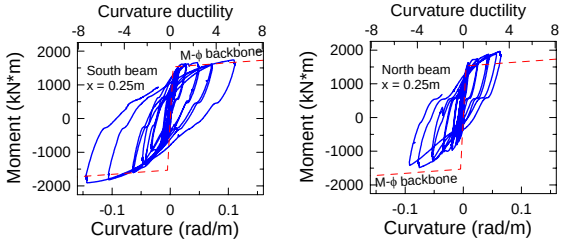

Figure 6 Moment-curvature response of specimen

Joint distortion is measured with linear potentiometers placed in plane with the surface of the column face. Linear potentiometers were secured to the surface of the joint to form a rectangle. One linear potentiometer was placed at the top of the rectangle, one at the bottom, one across the diagonal, and one on each opposing side. Overall joint strain is in units of radians (Figure 7a). The maximum value of the joint stress is 42% of the joint shear stress capacity (10.5 MPa) per the method in ACI 352 (2002). (See Figure 7b.)

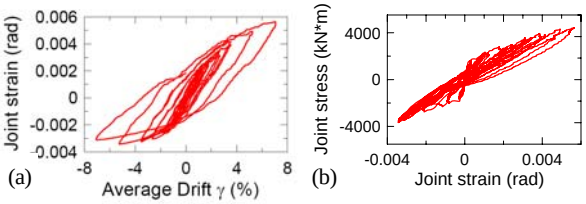

Figure 7 (a) Joint strain versus average drift ratio and (b) Joint stress versus joint strain.

3.3 Physical Observations

Onset of damage to specimen #2 was facilitated via minimal flexural cracks developing symmetrically within the beams near the column face. (Development of shear cracks within the joint region were observed at γ = 1.33%, with continued extension of flexural cracks within the beams. Load transfer at the Dywidag ductile connector block resulted in development of vertical cracks on the North beam at γ= 1.77%. Throughout testing, the slab-column interface was monitored and the two details compared. Notable cracking pattern variations were observed for post-yield, and differences associated with cover concrete spalling were apparent. Flexural cracks did not continue to propagate along the beam; however, shear cracking associated strut mechanism development continued within the joint region. Local detailing variations resulted in significant damage to the slab-beam section, where slab wings were cast separately. At completion of γ = 5.25%, incipient buckling of lower Dywidag bars (Threadbars) was apparent as a region of cover concrete spalled at the lower North beam. Nonetheless, the joint region was fully intact.

Final failure was attributed to compression buckling and subsequent fracture of a beam transverse bar in the North beam upon the final push cycle to 7% drift. Upon unloading of the specimen, two Dywidag ductile bars (Threadbars) that previously buckled, fractured under tension loading (Figure 8). Despite the fractured transverse and longitudinal steels in the North beam, the specimen observed highly stable performance with minimal damage up to this point as demonstrated in Figure 9 and 10.

4. CONCLUSIONS

Select results from a testing program undertaken to evaluate promising alternative beam-column subassembly details are presented. The specimen of interest (denoted as

Specimen #2), a precast, post-tensioned, full-scale model of an interior joint within a building, performed extremely well, sustaining large drift demands with little to no strength degradation and presenting well defined load transfer mechanisms. An attained average drift ratio γ of 7% was achieved. Maximum beam end vertical shear force attained by the specimen before failure was 760 kN.

(a) (b)

Figure 8 (a) Photographs of progression of local failure at bottom of North beam (a) drift ratio γ = -7% (compression buckling of longitudinal bars and fracture of transverse bar) and (b) end of test (subsequent fracture of Dywidag ductile bars [Threadbars]

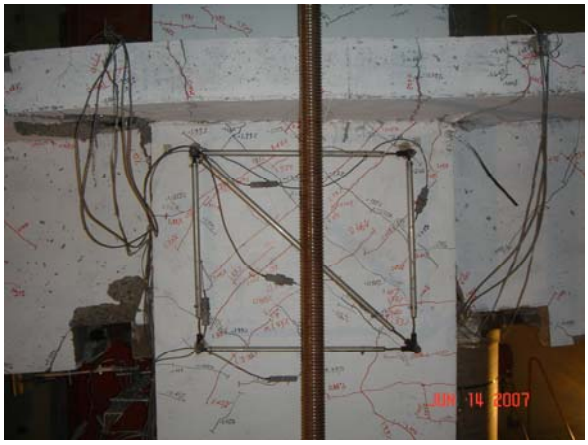

Figure 9 Joint region at final cycle to drift ratio γ = 7%

Figure 10 Overall specimen at final cycle to drift ratio γ = 7%

Comparison of hysteretic energy dissipation from all specimens showed increasing energy dissipation with increasing drift ratio. Specimen #2, assembled using the DDR technology, provided greater energy dissipation capacity and observed broad hysteresis loops. This specimen (and others) exhibited overall superior hysteretic damping. Even at low drift ratios of 0.5%, equivalent viscous damping ζ ranged from 3% to 12%. At higher drift ratios of 5.5% to 7.0%, equivalent viscous damping ζ values varied from 20% to 23%.

In terms of local response, the moment versus curvature behavior indicated the ratios of experimental to theoretical *EI* were well correlated. Using an effective moment of inertia I_{eff} to calculate theoretical *EI*, the experimental *EI* of specimen #2 was within 20% of the theoretical *EI*.

At the life-safety plastic rotation limit of FEMA 356 (2000) [0.02 rad], the specimens observed far less than life safety-levels of damage. Similarly, the specimen was stable at the FEMA 356 collapse prevention plastic rotation limit of 0.03 radians. Joint shear stress was derived from the moment generated by the global shear force. The maximum joint shear stress in the specimens ranged from 42% of the shear stress capacity per the method in ACI 352 (2002), indicating a margin of safety of 2.4. This factor of safety is substantiated by physical observations during testing. At no point in the loading did the beam-column joint itself actually fail.

Varied beam details of the specimen described herein resulted in variation in the damage to beams. The South slab sustained heavy damage near a prescribed cut-out used for connection of the DDRs, while and the North slab, which did not have a cut-out portion, was not significantly damaged. Furthermore, shear stress transfer at the cold joint developed a splitting of the connection between the t-flanges and beam and correspondingly larger stress localization within the 'beam' portion of the South beam – thereby resulting in more damage to this beam. Buckling of the South top and North bottom Threadbars were observed, which precipitated fracture of the North bottom Threadbars.

Physical damage to the specimen was characterized by well developed and distributed flexural cracks along the beams, which extended to shear cracks upon impending final failure of the specimens. The critical joint region remained intact, with well developed diagonal strut mechanisms. Very little loss of cover concrete was observed in the joint region during testing.

These experiments support the design recommendations presented by Englekirk and Wang (2008) in a companion report. Alternative systems are successful in circumventing the development of a plastic hinge in the beams and minimizing damage at design levels. Additionally, the Dywidag ductile rods are able to undergo large deformations beyond yield. Ductile beam-column subassemblies are necessary for ductile braced frame structures – and innovative design is needed to minimize damage at these critical regions. Details investigated herein provide steps in this direction.

Acknowledgements:

This work was supported by funding from the Charles Pankow Foundation. Additional financial support (material and labor) was provided by Dywidag Systems International USA, Inc (DSI), Morley Contractors, MMFX Tech Corp, Baumann Eng, and Clark Pacific. Guidance for this program was provided by the Englekirk Center Industry Advisory Board. The aforementioned support is greatly appreciated.

The authors would like to acknowledge the efforts of the technical staff at the UC San Diego Charles Lee Powell Laboratory, in particular Dr Christopher Latham, Mr Andrew Gunthardt, and Mr Robert Parks. We also thank Professor Frieder Seible, Dean of the Jacobs School of Engineering for his enthusiasm and support of this research program. Opinions, findings, and conclusions are those of the authors, and do not necessarily reflect those of any of the sponsoring partners.

References:

ACI 318 (2005). Building Code Requirements for Structural Concrete (ACI 318-05) and Commentary (ACI 318R-05). American Concrete Institute.

ACI 352 (2002). Recommendations for Design of Beam-Column Connections in Monolithically Reinforced Concrete. ACI-ASCE Joint Committee 352, American Concrete Institute.

Chang, B., Hutchinson, T., and Englekirk R. (2008) "Experimental Seismic Performance Evaluation of Innovative Beam-Column Subassemblies." University of California, San Diego, Department of Structural Engineering, Report No. SSRP 08/01, 2008.

Chopra, A. (2001). Dynamics of Structures. Prentice Hall.

Day, S. (1999). "Cyclic load testing of precast hybrid frame moment-resisting connections." University of Washington, Master of Science in Civil and Environmental Engineering, December 1999.

Englekirk, R. (2003). Seismic Design of Reinforced and Precast Concrete Buildings. John Wiley and Sons, Inc.

Englekirk, R. and Wang, J. (2008). "Structural systems research project: Design procedures for innovative beam column subassemblies to be used in regions of moderate and high seismicity." University of California, San Diego, Department of Structural Engineering, Report No. SSRP-08/06, 2008.

FEMA 356 (2000). Prestandard and Commentary for the Seismic Rehabilitation of Buildings. American Society of Engineers, Virginia.

IBC (2003). International Building Code. International Code Council.

Kim, J. (2000). "Final report on testing of hybrid frame corner beam-column sub-assembly with continuous post-tensioning steel." University of Washington, Structural Research Laboratory, April 2000.

Krawinkler, H. (1996). "Cyclic loading histories for seismic experimentation on structural components." Earthquake Spectra, 12(1).

Nilson, A., Darwin, D., and Dolan, C. (2004). Design of Concrete Structures. McGraw-Hill.

Pauley, T. and Priestley, M. (1992). Seismic Design of Reinforced Concrete and Masonry Structures. John Wiley and Sons, Inc.

Popov, E., Bertero, V., and Krawinkler, H. (1972). "Cyclic behavior of three r.c.flexural members with high shear." University of California, Berkeley, Report No. EERC 72-5, EERC, October 1972.

Post, N. M. (2007). "High-strength rebar called revolutionary." Engineering News Record, August 27/September 3.

Stone, W., Cheok, G., and Stanton, J. (1995). "Performance of hybrid moment-resisting precast beam-column concrete connections subjected to cyclic loading." ACI Structural Journal, 91(2), 229-249.

Warcholik, G. and Priestley, M. (1997). "Structural systems research project: High strength concrete joints tests." University of California, San Diego, Report No. TR-97/10, July 1997.

Warcholik, G. and Priestley, M. (1998a). "Structural systems research project: High strength concrete joints tests." University of California, San Diego, Report No. TR-98/12, July 1998.

Warcholik, G. and Priestley, M. (1998b). "Structural systems research project: High strength concrete joints tests." University of California, San Diego, Report No. TR-98/01, July 1998.

Sixth International Conference on Urban Earthquake Engineering
March 3-4, 2009, Tokyo Institute of Technology, Tokyo, Japan

COMBINED GROUND MOTION SPATIAL VARIATION AND LOCAL SITE AMPLIFICATION EFFECT ON BRIDGE STRUCTURE RESPONSES

Hong Hao[1], Kaiming Bi[2] and Nawawi Chouw[3]

1) Professor, School of Civil and Resource Engineering, the University of Western Australia, Australia
2) PhD student, School of Civil and Resource Engineering, the University of Western Australia, Australia
3) Associate professor, Dept. of Civil and Environment Engineering, University of Auckland, New Zealand

hao@civil.uwa.edu.au, bkm@civil.uwa.edu.au, n.chouw@auckland.ac.nz

Abstract: Intensive research results on seismic ground motion spatial variation modeling and its effect on structural responses have been reported in the literature. Most of the previous works assume the site is flat and homogeneous. A few studies considered the local site effect on ground motion amplifications, but only implicitly. In this paper, local site amplification effect is modeled explicitly based on the one-dimensional wave propagation theory, which is combined with the ground motion wave passage and incoherent effect to model ground motion spatial variations. The spatial ground motion model is used to simulate spatial ground motion time histories compatible with the target loss of coherency model and power spectral density model at individual locations in an engineering site. The spatial ground motion is then used as input in spectral analysis and nonlinear time history analysis of responses of a segmental bridge crossing a canyon site. Ground motion spatial variation and local site amplification effect on bridge responses are discussed in the paper.

1. INTRODUCTION

Because of wave propagation in heterogeneous site, earthquake ground motions at multiple supports of large dimensional structures inevitably vary. Such variations could have significant influences on structural responses. Intensive research works have been conducted in the last three decades to study earthquake ground motion spatial variation and its effect on structural responses. A few ground motion spatial variation models have been developed and reported in the literature. These include theoretical models based on wave propagation in a random medium (Sobczky 1991) and empirical models (Bolt, et al. 1982, Harichandran and Vanmark 1986, Loh an Yeah 1988, Hao, et al. 1989, Abrahamson, et al. 1991). All these models are based on the assumption that the site under consideration is flat and homogeneous. Therefore the ground motion power spectral densities at various locations can be considered as the same. The spatial ground motion variations are associated with only the loss of coherency and phase shifts owing to wave propagation. Many studies of ground motion spatial variation effects on structural responses are based on these spatial ground motion models. These studies include stochastic response analysis of a simply supported beam (Harichandran and Wang 1988), a continuous beam (Harichandran and Wang 1990, Zerva 1990), an arch with multiple horizontal input (Hao 1993), an arch with multiple simultaneous horizontal and vertical excitations (Hao 1994), a symmetric (Hao and Duan 1996) and an asymmetric building structure (Hao and Duan 1995), an isolated highway bridge (Ates, et al. 2005), and a cable-stayed bridge (Dumanoglu and Soyluk 2003). Most of these studies assumed linear elastic responses. Many researchers have also performed time history analysis of structural responses to spatially varying ground motions. In these studies, both linear elastic, nonlinear inelastic responses, pounding responses, soil-structure interaction effects were considered. The spatial ground motion time histories were obtained either by considering the wave passage effect only (Jankowski, et al. 2000), or stochastically simulated to be compatible to a selected empirical coherency loss function (Hao 1989, Monti, et al. 1996, Sextos, et al. 2003b, Chouw and Hao 2005).

However, the assumption of uniform intensity for spatial ground motions will lead to inaccurate ground motion prediction when a site has varying soil and geometrical conditions such as a canyon site as shown in Figure 1. At a canyon site, the spatial ground motions at the base rock may still be assumed to have the same intensity, but on ground surface at points 1, 2 and 3 will have very different amplitude and frequency contents owing to wave propagation through different wave paths that cause different site amplifications. Uniform ground motion power spectral density assumption in such a situation may lead to erroneous estimation of structural responses.

To overcome this problem, Der Kiureghian, et al. (1997) proposed a transfer function to model the site effect on seismic wave propagation. In the model, the ground motion power spectral density function is represented by a Tajimi-Kanai power spectral density function but with site-dependent parameters. Typical site-dependent parameters, i.e., the central frequency and damping ratio for

three generic site conditions, namely, firm, medium firm and soft site are defined. Some researchers used this spatial ground motion model in studying the structural responses (Zembaty and Rotenburg, 2002, Soyluk and Dumanoglu 2003, Sextos, et al. 2003a). The advantage of the model (Der Kiureghian, et al. 1997) is that it is straightforward to use. The drawback of the model is that it can only approximately represent the local site effects on ground motions. For example, it is well known that seismic wave will be amplified and filtered when propagating through a multi-layer site. The amplifications occur at various vibration modes of the site therefore the energy of surface ground motions concentrates at a few frequencies corresponding to these modes. The power spectral density function of the surface ground motion may have multiple peaks. This cannot be modelled in the Tajimi-Kanai power spectral density function. In a recent study (Hao and Chouw 2006), derivation of earthquake ground motion spatial variation on a site with uneven surface and different geological properties was presented. In the latter study, the spatial base rock motion was modelled by a Tajimi-Kanai power spectral density function (Tajimi 1960) together with an empirical coherency loss function (Hao, et al. 1989). Power spectral density functions of the surface ground motions were derived based on the one dimensional wave propagation theory. Compared to the model by Der Kiureghian, et al. (1997), the latter study explicitly models the wave amplification in terms of site conditions such as the soil depth and properties. Therefore the latter model gives more realistic prediction of local site effects on seismic ground motions.

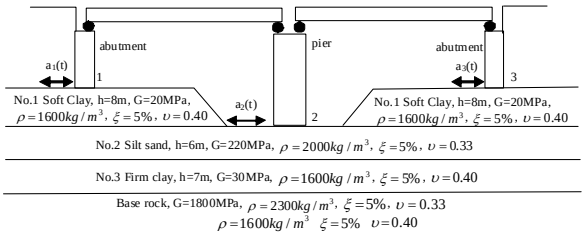

Figure 1. A bridge model crossing a canyon site

In the present study, the derivations are made first to extend the work by Hao and Chouw (2006) to include multi-layers at a site to study the site amplification effect on spatial ground motions. The derived model is then used to simulate spatially varying ground motion time histories on surface of a canyon site as shown in Figure 1. Examples of stochastic and nonlinear time history analysis of bridge responses to spatial ground motions are performed. In stochastic response analysis, only linear elastic responses are considered. In nonlinear time history analysis, inelastic bridge properties and pounding between adjacent bridge decks and between deck and abutment are considered. Numerical results are presented. Discussions of the combined ground motion spatial variation and site amplification effects on bridge responses are made. The numerical results demonstrate the significant effect of the ground motion spatial variation and site amplification effects on bridge responses.

2. SPATIAL GROUND MOTION MODEL AND SIMULATION

From the work by Wolf (1985), for harmonic excitation with frequency ω, the dynamic equilibrium equations can be written as

$$\nabla^2 e = -\frac{\omega^2}{c_p^2} e \quad \text{or} \quad \nabla^2 \{\Omega\} = -\frac{\omega^2}{c_s^2} \{\Omega\} \tag{1}$$

where $\nabla^2 e$ and $\nabla^2 \{\Omega\}$ is the Laplace operator of the volumetric strain amplitude e and rotational-strain-vector $\{\Omega\}$. c_P and c_S are the P- and S-wave velocity, respectively. The out-of-plane displacements with the amplitude v is caused by the incident SH wave, while the in-plane displacement with the amplitude u and w depend on the combined P and SV waves. The amplitude v is independent of u and w, hence, the two-dimensional dynamic stiffness matrix of each soil layer for the out-of-plane and in-plane motion, $[S_{SH}^L]$ and $[S_{P-SV}^L]$, can be formulated independently by analysing the relations of shear stresses and the displacements at the boundary of each soil layer. Assembling the matrices of each soil layer and the base rock, the dynamic stiffness of the total system can be formulated and denoted by $[S_{SH}]$ and $[S_{P-SV}]$, respectively. The dynamic equilibrium equation of the site in the frequency domain is thus

$$[S_{SH}]\{u_{SH}\} = \{P_{SH}\}, \quad [S_{P-SV}]\{u_{P-SV}\} = \{P_{P-SV}\} \tag{2}$$

where $\{u_{SH}\}$ and $\{P_{SH}\}$ are out-of-plane displacements and load vector corresponding to the incident SH wave, $\{u_{P-SV}\}$ and $\{P_{P-SV}\}$ are in-plane displacements and load vector of the combined P and SV waves. The stiffness matrices $[S_{SH}]$ and $[S_{P-SV}]$ depend on soil properties, incident wave types, incident angle and circular frequency ω. The dynamic load $\{P_{SH}\}$ and $\{P_{P-SV}\}$ depend on the base rock properties, incident wave type, incident wave frequency and amplitude. By solving Equation (2) in the frequency domain, the relationship between the base rock motion and that at each soil layer can be formed, and the transfer function between surface and base rock motion, $H(i\omega)$, for each wave path is determined. More detailed information can be found in Wolf (1985).

In this study the ground motion at the base rock is modeled by a filtered Tajimi-Kanai power spectral density function as (Ruiz and Penzien 1969)

$$S_g(\omega) = |H_P(\omega)| S_0(\omega) = \frac{\omega^4}{(\omega_f^2 - \omega^2)^2 + (2\omega_f \omega \xi_f)^2} \frac{1 + 4\xi_g^2 \omega_g^2 \omega^2}{(\omega_g^2 - \omega^2)^2 + 4\xi_g^2 \omega_g^2 \omega^2} \Gamma \tag{3}$$

in which $|H_P(\omega)|^2$ is a high pass filter, $S_0(\omega)$ is the

Tajimi-Kanai power spectral density function. In this study the central frequency and damping ratio of the Tajimi-Kanai power spectral density function are taken as $\omega_g = 10\pi rad/s$ and $\xi_g = 0.6$ those of the high pass filter are $\omega_f = 0.5\pi$, $\xi_f = 0.6$; and the scale factor $\Gamma = 0.0034 m^2/s^3$. These parameters correspond to a ground motion time history with duration $T = 20s$ and peak ground acceleration (PGA) $0.2g$ (Hao 1998).

The cross power spectral density function between ground motions at two points *i'* and *j'* at base rock can be expressed as

$$S_{i'j'}(i\omega) = S_g(\omega)\gamma_{i'j'}(i\omega) \tag{4}$$

in which $\gamma_{i'j'}(i\omega)$ is a coherency function between motions at the two points, and is defined as (Sobczyk 1991)

$$\gamma_{i'j'}(i\omega) = \left|\gamma_{i'j'}(i\omega)\right| \exp(-i\omega d_{i'j'}\cos\alpha / v_{app}) = \exp(-\beta\omega d_{i'j'}^2 / v_{app}) \cdot \exp(-i\omega d_{i'j'}\cos\alpha / v_{app}) \tag{5}$$

where $d_{i'j'}$ is the distance between the two points, α is the incident angle of the ground motion into the site, β is a parameter controls the level of cross correlation of ground motions, and v_{app} is the apparent velocity. The auto and cross power spectral density function of motion on ground surface can be expressed as

$$S_j(\omega) = \left|H_j(i\omega)\right|^2 S_g(\omega)$$
$$S_{ij}(i\omega) = H_i(i\omega)H_j^*(i\omega)S_{i'j'}(i\omega) \tag{6}$$

where H_i and H_j are respectively the transfer functions for seismic wave propagating from *i'* and *j'* at the base rock to *i* and *j* on ground surface. These spectral density functions can be directly used in stochastic response analysis of structural responses to multiple ground excitations, and they can also be used to simulate spatially varying ground motion time histories (Hao, et al. 1989).

To illustrate the ground motion simulation, assume a seismic wave propagating into the site shown in Figure 1 with an incident angle of 60º, and β=0.0005 for highly correlated ground motions, d_{12}= d_{23}=100 m, and the apparent velocity is calculated to be v_{app} =1768 m/s based on the site conditions and the incident angle, the sampling frequency is taken as 100 Hz, PGA=0.2g, and the ground motion duration is assumed to be 20 sec. The simulated base rock and surface motion time histories are shown in Figure 2 and Figure 3, respectively. The comparison of the corresponding power spectral density function and the coherency loss of the simulated motion with the target model functions are also shown in the respective figure. As shown the simulated motions match well the ground motion model at the base rock and on ground surface. It should be noted that an envelope function (Jennings, et al. 1968) with t_0=2s and t_n=10s are applied to modulate the simulated stationary time histories. More detailed information on ground motion simulation can be found in (Hao, et al. 1989).

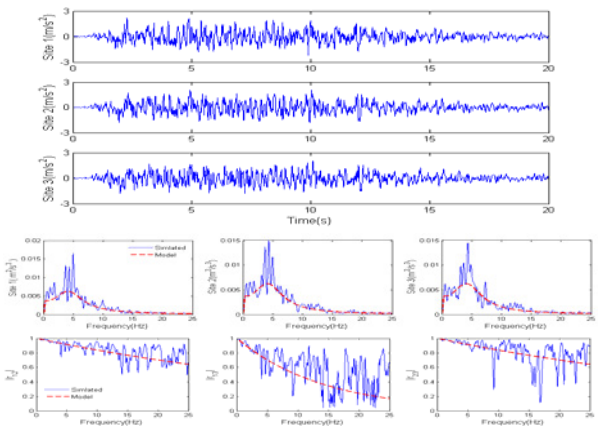

Figure 2 Simulate ground motion histories at the base rock and their power spectral density and coherency loss function

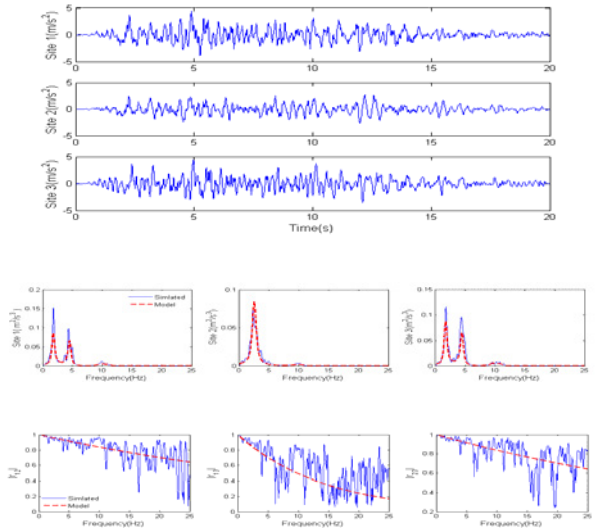

Figure 3 Simulate surface ground motion histories and their power spectral density and coherency loss function

3. STOCASTIC RESPONSE ANALYSIS

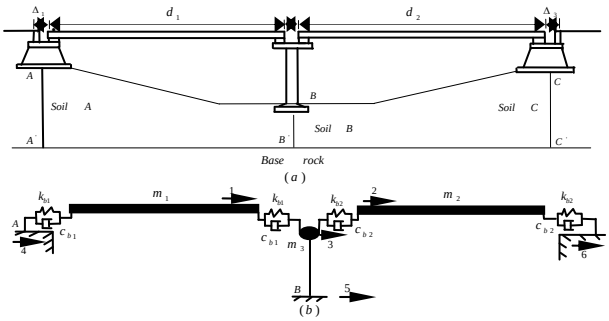

Figure 4 A bridge model

Consider a bridge structure shown in Figure 4, it is simplified as two rigid decks supported on spring-dashpot representing the bearings, which are supported on bridge pipers and abutments. The dynamic equilibrium equation of the system shown in Fig.1 can be written as

$$\begin{bmatrix} M_{ss} & 0 \\ 0 & 0 \end{bmatrix}\begin{Bmatrix} \ddot{y} \\ \ddot{v}_g \end{Bmatrix}+\begin{bmatrix} C_{ss} & 0 \\ 0 & 0 \end{bmatrix}\begin{Bmatrix} \dot{y} \\ \dot{v}_g \end{Bmatrix} +\begin{bmatrix} K_{ss} & K_{sb} \\ K_{sb}^T & K_{bb} \end{bmatrix}\begin{Bmatrix} y \\ v_g \end{Bmatrix}=\begin{Bmatrix} 0 \\ 0 \end{Bmatrix} \tag{7}$$

where $[M_{ss}]$ is the lumped mass matrix, $[C_{ss}]$ is the viscous damping matrix and $[K_{ss}]$ is the stiffness matrix corresponding to the structure degrees of freedom. $[K_{sb}]$ is the coupling stiffness matrix between the structure degrees of freedom and the support degrees of freedom, $[K_{bb}]$ is that corresponding to the support movements, $[y]$ is the total displacements of the structure and $[v_g]$ is the ground displacements at the bridge supports. The modal vibration equation can be derived as

$$\ddot{q}_k + 2\xi_k\omega_k\dot{q}_k + \omega_k^2 q_k = -\frac{\varphi_k^T[K_{sb}]}{\varphi_k^T[M_{ss}]\varphi_k}[v_g] \tag{8}$$

where φ_k is the kth vibration mode shape of the structure, q_k is the kth modal response, ω_k and ξ_k are the corresponding circular frequency and viscous damping ratio, respectively. The kth modal response in the frequency domain is

$$\bar{q}_k(i\omega) = H_k(i\omega)\sum_{m=1}^{r}\psi_{mk}\bar{v}_{gm}(i\omega) \tag{9}$$

in which r is the total number of supports, and

$$H_k(i\omega) = \frac{1}{\omega_k^2 - \omega^2 + 2i\xi_k\omega\omega_k} \tag{10}$$

is the kth mode frequency response function; and

$$\psi_{mk} = -\frac{\varphi_k^T[K_{sb}^m]}{\varphi_k^T[M_{ss}]\varphi_k} \tag{11}$$

is the quasi-static participation coefficient for the kth mode corresponding to a movement at support m, $[K_{sb}^m]$ is a vector in coupled stiffness matrix $[K_{sb}]$ corresponding to support m. The structure response of the jth degree of freedom is

$$y^j(t) = \sum_{k=1}^{l}\varphi_k^j q_k(t) \tag{12}$$

where l is the number of modes considered in the calculation, and φ_k^j is the kth mode shape value corresponding to the jth degree of freedom. The relative displacement between the two bridge decks is

$$\Delta_2(t) = y^1(t) - y^2(t) = \sum_{k=1}^{l}\varphi_k^1 q_k(t) - \sum_{k=1}^{l}\varphi_k^2 q_k(t) \tag{13}$$

The power spectral density function of Δ_2 can be derived as:

$$S_{\Delta_2}(\omega) = \frac{1}{\omega^4}\sum_{i=1}^{r}\sum_{j=1}^{r}[\sum_{k=1}^{l}(\varphi_k^1 - \varphi_k^2)H_k(i\omega)\psi_{mk} \sum_{s=1}^{l}(\varphi_s^1 - \varphi_s^2)H_s^*(i\omega)\psi_{ns}]S_{ij}(i\omega) \tag{14}$$

Similarly, the relative displacement between abutment and deck is

$$\Delta_1(i\omega) = y^1(t) - v_{g1}(t)$$
$$\Delta_3(i\omega) = y^2(t) - v_{g3}(t) \tag{15}$$

The power spectral density functions of Δ_1 and Δ_3 are

$$S_{\Delta_1}(\omega) = \frac{1}{\omega^4}\sum_{i=1}^{r}\sum_{j=1}^{r}\left[\sum_{k=1}^{l}\varphi_k^1 H_k(i\omega)\psi_{ik}\sum_{s=1}^{l}\varphi_s^1 H_s^*(i\omega)\psi_{js}\right] S_{ij}(i\omega) - \frac{2}{\omega^4}\mathrm{Re}\left[\sum_{i=1}^{r}\sum_{k=1}^{l}\varphi_k^1 H_k(i\omega)\psi_{ik}S_{1i}(i\omega)\right] \tag{16}$$

$$S_{\Delta_3}(\omega) = \frac{1}{\omega^4}\sum_{i=1}^{r}\sum_{j=1}^{r}\left[\sum_{k=1}^{l}\varphi_k^2 H_k(i\omega)\psi_{ik}\sum_{s=1}^{l}\varphi_s^2 H_s^*(i\omega)\psi_{js}\right] S_{ij}(i\omega) - \frac{2}{\omega^4}\mathrm{Re}\left[\sum_{i=1}^{r}\sum_{k=1}^{l}\varphi_k^2 H_k(i\omega)\psi_{ik}S_{3i}(i\omega)\right] \tag{17}$$

where 'Re' denotes the real part of a complex quantity. The mean peak responses can be obtained by using the method discussed in (Der Kiureghian 1980)

Consider the bridge model shown in Figure 4, let the span length be 100m, the two deck mass are $m_1 = m_2 = 1.2\times10^6 kg$. The lumped mass on top of the pier is $m_3 = 2\times10^5 kg$. The bearing stiffness of the left span is assumed to be $k_{b1} = 6\times10^6 kN/m$, which corresponds to the uncoupled frequency of left span $f_1 = 0.5Hz$. The bearing stiffness of the right span varies in the numerical calculations to obtain different frequency ratios f_2/f_1. The uncoupled vibration frequency of the two spans are defined as $f_1 = \sqrt{2k_{b1}/m_1}/2\pi$, and $f_2 = \sqrt{2k_{b2}/m_2}/2\pi$. The effective isolation of the bridge decks requires relatively flexible bearings and stiff pier. The stiffness of the pier used in the study is $k_p = 10^8 kN/m$. The viscous damping ratios for all the bearings and the pier are assumed to be 5%.

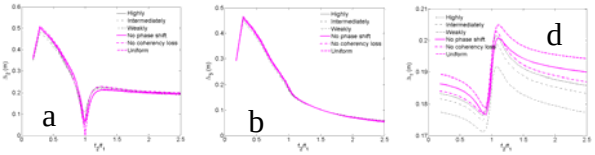

Figure 5. Effect of ground motion spatial variation on the required separation distance (a) Δ_2, (b) Δ_3, (c) Δ_1

To investigate the influence of spatially varying ground motions on the required separation distance, highly, intermediately and weakly correlated ground motions are considered. For comparison, spatial ground motions with intermediate coherency loss without considering phase shift, spatial ground motions without considering coherency loss, and uniform ground motion are also considered. To preclude the effect of site amplification, it is assumed that the bridge located on the base rock, i.e. $h_A = h_B = h_C = 0m$. The mean minimum required separation distance to avoid seismic pounding between two adjacent bridge decks (Δ_2), between the abutment and bridge deck (Δ_3 and Δ_1) are

shown in Figure 5.

As shown in Figure 5(a), with an assumption of uniform excitation, the relative displacement between the two adjacent bridge decks (Δ_2) is small when the fundamental frequencies of the adjacent structures are similar, and is zero when $f_2 = f_1$. The ground motion spatial variation effect is most significant when f_2 / f_1 is close to unity, weakly correlated ground motions cause larger relative displacement than highly correlated ground motions. The ground motion spatial variation effect is, however, not so pronounced if the vibration frequencies of the two spans differ significantly. In these situations the out-of-phase vibration of the two spans owing to their different vibration frequencies contribute most to the relative displacement of adjacent bridge decks. When $f_2 / f_1 > 1.5$, the results are almost a constant with the increase of the frequency ratio. This is because when the structure is relatively stiff as compared to the ground excitation frequency, the dynamic response of the right span is small. The displacement response of the right span is caused primarily because of the quasi-static response associated with the non-uniform ground displacement at the multiple bridge supports, and the quasi-static response is independent of the structure vibration frequency, and is a constant once the ground displacement is defined. As shown in Figure 5(a), there is one obvious peak occurring at $f_2 / f_1 = 0.3$. This corresponds to the predominate frequency of the base rock ground displacement. These observations imply that the maximum relative displacement occurs when the vibration frequency of the uncoupled system coincides with the central frequency of the ground displacement.

Very few researchers studied the required separation distance between bridge deck and abutment to avoid pounding although pounding damages between bridge deck and abutment have been observed in many previous earthquakes. In this study, the relative displacement between decks and abutments are calculated. The abutment is assumed to be rigid and has the same displacement of the respective ground displacement. For the separation distance of Δ_3 as shown in Figure 5(b), one obvious peak occurs when the coupled system resonates with the base rock ground displacement. The effect of ground motion spatial variation is not prominent. Uniform ground motion assumption gives a good estimation of the relative displacement. This observation indicates that the ground motion spatial variation effect is not significant in this considered bridge example. As can be seen from Figure 5(c), although the stiffness of the left span remains unchanged, the relative displacement between the left abutment and the deck (Δ_1) is not a constant with the change of f_2 because of the coupling through the centre pier. The coupling effect is significant when f_2 / f_1 is close to unity and is not so pronounced when the vibration frequencies of the two spans differ prominently. It is interesting to find that the spatially varying ground motions have positive effects on Δ_1, i.e. weakly correlated ground motions result in a smaller required separation distance and the largest required separation distance corresponds to the uniform ground excitation case. The largest relative displacement between the left deck and abutment occurs when the two spans have similar vibration frequencies.

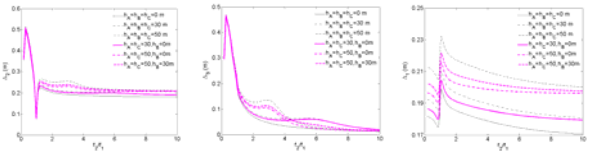

Figure 6. Effect of soil depth on the required separation distance (a) Δ_2, (b) Δ_3, (c) Δ_1

Local soil site conditions have a great influence on the structure responses because of the site filtering and amplification effect on the ground motions. Figure 6 shows the required separation distance of Δ_2, Δ_3, and Δ_1 corresponding to different soil depth. Soil properties assumed are: density 1500kg/m^3, shear wave velocity 300m/s and damping ratio 0.05.

As shown, when one or all the bridge supports are located on the soil site, additional peaks can be observed. One example is as shown in Figure 6(a) and (b), when $h_A = h_C = 50m$ (h_B varies from 0 to 50 m), another obvious peak occurs at $f_2 / f_1 = 3$. This is because when $f_2 / f_1 = 3$, f_2=1.5Hz, the corresponding bearing stiffness of the right span is $k_{b2} = 5.4 \times 10^7 kN/m$. It is found that at this stiffness the 2nd modal vibration frequency of the coupled system is 1.4Hz, which coincides with the predominant vibration frequency of the ground motion on the 50m soil site, indicating resonance occurs at this frequency ratio. Similar conclusions can also be drawn when the soil depth is 30m with the site vibration frequency 2.4Hz. These observations indicate that larger separation distance is required when the structure resonates with local site. The local soil site conditions have a more significant effect on Δ_3 than Δ_2, especially when $f_2 / f_1 > 1.2$. This is because Δ_3 depends on the absolute response of the structure, while Δ_2 depends on the relative response of the adjacent structures. The softer site results in larger absolute structure response (Δ_3), which only slightly increases the relative displacement (Δ_2). As for Δ_1, fluctuations can be seen when f_1 and f_2 are close to each other because of the coupling effect as discussed above.

4. NONLINEAR DYNAMIC RESPONSE ANALYSIS

Spectral analysis is difficult to be applied for nonlinear structural responses analysis. To model nonlinear and pounding responses, time history analysis is a better choice. In this study, nonlinear time history analysis is carried out by using the computer program DRAIN-2DX (Powell 1993). The bridge model considered is the one shown in Figure 1 and the input time histories are those shown in Section 2. Pounding between adjacent decks and between deck and abutments are modeled by a gap element with bilinear stiffness and dashpot. Both pier and deck are modeled by beam-column element with their respective yield surfaces.

The pounding force between adjacent decks, and between deck and abutments, shear force and bending moment of the pier are calculated. Figure 7 shows some typical results. Owing to page limitation, other numerical results are not presented in the paper. It is found that ground motion spatial variation, local site effect, and bearing stiffness are the most critical parameters that affect the bridge responses.

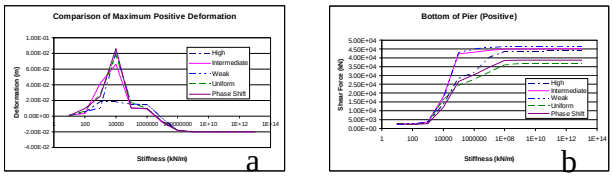

Figure 7 Responses corresponding to different spatial ground motions and bearing stiffness, a) pounding force between decks, b) shear force in the pier

5. CONCLUSIONS

This paper presents a model of ground motion spatial variations on a nonuniform site with different soil properties and soil depths, and examples of spatial ground motion time history simulations, stochastic response and nonlinear time history analysis of bridge structure responses to spatial ground motions. Numerical results demonstrated the importance of both ground motion spatial variation and local site amplification effect on structural responses.

References:

Abrahamson NA, Schneider JF and Stepp JC (1991), "Empirical spatial coherency functions for application to soil-structure interaction analyses," *Earthquake Spectra*, **7**, 1-27.

Ates S, Dumanoglu AA and Bayraktar A (2005), "Stochastic response of seismically isolated highway bridges with friction pendulum systems to spatially varying earthquake ground motions." *Engineering Structures*, **27**(13): 1843-58.

Bolt BA, Loh CH, Penzien J, Tsai YB, Yeah YT. (1982), Preliminary report on the SMART-1 strong motion array in Taiwan." *Report No. UCB/EERC-82-13, University of California at Berkeley*.

Chouw N, Hao H. (2005), "Study of SSI and non-uniform ground motion effects on pounding between bridge girders." *Soil Dynamics and Earthquake Engineering*, **25**(10), 717-28.

Der Kiureghian A. (1980), "Structural response to stationary excitation." *J. of Engineering Mechanics*, **106**(6), 1195-1213.

Der Kiureghian A, Keshishian P, Hakobian A. (1997), "Multiple support response spectrum analysis of bridges including the site-response effect and MSRS code." *Report No. UCB/EERC-97/02, University of California at Berkeley.*

Dumanoglu AA, Soyluk K. (2002), "Response of cable-stayed bridge to spatially varying seismic excitation." *5th Int Conf on Structure Dynamics.* Munich, Germany. Vol.2, 1059-64.

Dumanoglu AA, Soyluk K. (2003), "A stochastic analysis of long span structures subjected to spatially varying ground motions including the site-response effect." *Engineering Structures*, **25**(10), 1301-10.

Hao H. (1989), "Effects of spatial variation of ground motions on large multiply-supported structures." *Report No. UCB/EERC-89-06, University of California at Berkeley.*

Hao H. (1993), "Arch responses to correlated multiple excitations." *Earthquake Eng. and Structural Dynamics*, **22**(55), 389-404.

Hao H. (1994), "Ground-motion spatial variation effects on circular arch responses." *Journal of Engineering Mechanics*, ASCE, **120**(11), 2326-41.

Hao H. (1998), "A parametric study of the required seating length for bridge decks during earthquake." *Earthquake Engineering and Structure Dynamics*, **27**(1), 91-103.

Hao H, Chouw N. (2006), "Modeling of earthquake ground motion spatial variation on uneven sites with varying soil conditions." *The 9th International Symposium on Structural Engineering for Young Experts*, Fuzhou - Xiamen, China, 79-85.

Hao H, Oliveira CS, Penzien J. (1989), "Multiple-station ground motion processing and simulation based on SMART-1 array data." *Nuclear Engineering and Design*, **111**(3), 293-310.

Hao H, Duan XN. (1996), "Multiple excitation effects on response of symmetric buildings." *Engineering Structures*, **18**(9),732-40.

Hao H, Duan XN. (1995), "Seismic Response of Asymmetric Structures to Multiple Ground Motions." *Journal of Structure Engineering*, ASCE, **121**(11), 1557-64.

Harichandran RS, Vanmarcke EH. (1986), "Stochastic variation of earthquake ground motion in space and time." *Journal of Engineering Mechanics*, ASCE, **112**(2), 154-74.

Harichandran RS, Wang W. (1988), "Response of simple beam to spatiality varying earthquake excitation." *Journal of Engineering Mechanics*, ASCE, **114**, 1526 - 1541.

Harichandran RS, Wang W. (1990), "Response of indeterminate two–span beam to spatially varying seismic excitation." *Earthquake Eng. and Structural Dynamics*, **19**(2):173-87.

Jankowski R, Wilde, Y Fujino Y. (2000), "Reduction of pounding effects in elevated bridges during earthquakes." *Earthquake Engineering and Structural Dynamics*, **29**(2), 195-212.

Jennings PC, Housner GW, Tsai NC. (1968), "Simulated earthauqke motions." *Report of Earthquake Eng. Research Lab, EERL-02, California Institute of Technology.*

Loh CH, Yeah YT. (1988), "Spatial variation and stochastic modelling of seismic differential ground movement." *Earthquake Eng and Structural Dynamics*, **16**(4), 583-96.

Monti G, Nuti C, Pinto E. (1996), "Nonlinear response of bridges to spatially varying ground motion." *Journal of Structure Engineering*, ASCE, **122**, 1147-59.

Powell GH (1993), "Drain-2DX element description and user guide – version 1.10," *Report No. UCB/SEMM-93/18, University of California Berkeley*.

Ruiz P, Penzien J. (1969), "Probabilistic study of the behaviour of structures during earthquakes." *Report No. UCB/EERC-69-03, University of California at Berkeley.*

Sextos AG, Pitilakis KD and Kappos AJ. (2003a), "Inelastic dynamic analysis of RC bridges accounting for spatial variability of ground motion, site effects and soil-structure interaction phenomena. Part 1: Methodology and analytical tools." *Earthquake Engineering and Structural Dynamics*, **32**(4), 607-27.

Sextos AG, Pitilakis KD and Kappos AJ. (2003b), "Inelastic dynamic analysis of RC bridges accounting for spatial variability of ground motion, site effects and soil-structure interaction phenomena. Part 2: Parametric study." *Earthquake Engineering and Structural Dynamics*, **32**(4), 629-52.

Sobczky K. (1991), "Stochastic wave propagation." *Kluwer Academic Publishers*, the Netherlands.

Tajimi H. (1960), "A statistical method of determining the maximum response of a building structure during a earthquake." *Proceedings of 2nd World Conference on Earthquake Engineering*, Tokyo, 781-96.

Wolf JP. (1985), "Dynamic soil-structure interaction." *Prentice Hall*, Englewood Cliffs, NJ

Zembaty Z, Rutenburg A. (2002), "Spatial response spectra and site amplification effect." *Engineering Structures*, **24**(11), 1485-96.

Zerva A. (1990), "Response of multi-span beams to spatially incoherent seismic ground motion." *Earthquake Engineering and Structural Dynamics*, **19**, 819-32.

Sixth International Conference on Urban Earthquake Engineering
March 3-4, 2009, Tokyo Institute of Technology, Tokyo, Japan

SHAKE TABLE TESTS FOR DEVELOPMENT OF RAPID REPAIR METHOD FOR DAMAGED REINFORCED CONCRETE BRIDGE COLUMNS

Junichi Sakai[1] and Shigeki Unjoh[2]

1) Senior Researcher, Center for Advanced Engineering Structural Assessment and Research, Public Works Research Institute, Tsukuba. Japan
2) Chief Researcher, Center for Advanced Engineering Structural Assessment and Research, Public Works Research Institute, Tsukuba. Japan
sakai55@pwri.go.jp, unjoh@pwri.go.jp

Abstract: To ensure the structural safety against aftershocks and serviceability of bridges after an extreme earthquake, two rapid repair methods for a reinforced concrete bridge column are proposed. One method is based on carbon fiber sheet jacketing using quick-drying materials, and the other uses mechanical anchors for fiber band jacketing. Reinforced concrete bridge columns that suffered flexural damage at the bottom of the columns during strong ground shaking were repaired by the proposed methods and a series of shake table tests was conducted to evaluate the effectiveness of the methods. The repair works were completed within 8 hours and 5 hours for the methods of quick-drying materials and mechanical anchors, respectively. The tests revealed that both the proposed methods restore the seismic performance of reinforced concrete columns. Stable response and hysteresis of the repaired columns were observed during the shake table tests although the initial stiffness decreased by 50% due to seismic damage.

1. INTRODUCTION

When an extreme earthquake occurs, roads and bridges are fundamental infrastructure to evacuate the affected people and to transport the emergency equipment and materials. For these emergency activities, it is essential to evaluate the structural safety and serviceability of such structures immediately after the event, and to conduct repair works as soon as possible if the structural damage affects the performance of the structures.

After the 2004 Niigata-ken Chuetsu, Japan, earthquake, several bridges were closed for about one week due to damage of reinforced concrete bridge columns as shown in Figure 1 since it took about one week to recover the function of the damaged columns (National Institute for Land and Infrastructure Management and Public Works Research Institute, 2006). Additionally, repeatedly occurrences of relatively large aftershocks (Sakai and Mahin, 2004) affected the structural safety of the damaged columns and interrupted the repair works.

Therefore, there is a strong need to develop a method for immediate earthquake damage detection and a method for rapid seismic repair of structural damage. The authors have been conducting research projects for developing these methods, and have proposed a system utilizing an intelligent sensor unit (Sakai, Kobayashi and Unjoh, 2007) for the former part of the project.

Figure 1 Seismic Damage and Its Repair by Carbon Fiber Sheet Jacketing:
(a) Damage, (b) Repaired with Mortal, and (c) Completed with Carbon Fiber Sheet Jacketing
(National Institute for Land and Infrastructure Management and Public Works Research Institute, 2006)

Table 1 Specimens

	Specimen A	Specimen B	Specimen C
Setup	Single Column Style	With Girders	With Girders
Cross Section	ϕ600 mm	ϕ600 mm	ϕ600 mm
Effective Height in LG (in TR)	3 m (3 m)	2.5 m (3.65 m)	2.675 m (3.811 m)
Inertia Mass in LG (in TR)	27 ton (27 ton)	37.8 ton (26.6 ton)	36.4 ton (25.5 ton)
Axial Stress at Bottom	0.99 N/mm^2	1.04 N/mm^2	1.01 N/mm^2
Longitudinal Reinforcement Ratio (Size: Number)	1.01% (D10 : 40)	2.02% (D10 : 80)	2.42% (D10 : 96)
Transverse Reinforcement Ratio (Size: Pitch)	0.33% (D6:75 mm)	0.21% (D3:50 mm)	0.49% (D6:100 mm)
Flexural Strength in LG	95 kN	184 kN	215 kN
Initial Period in LG (in TR)	0.28 sec (0.27 sec)	0.25 sec (0.38 sec)	0.28 sec (0.39 sec)
Scaling Factor	4	3	4
Directions of Input Signals	3 Dimention	3 Dimention	1 Horizontal
Amplitude of Input Signals for 1st Series	10%, 20%, 30%, 50%, 60%	10%, 80%	10%, 50%, 80%, 120%
Amplitude of Input Signals for 2nd Series	10%, 50%, 60%	10%, 55%, 80%	10%, 80%, 120%

Table 2 Material Properties

Concrete	A	B	C
Elastic Modulus (kN/mm^2)	28.5	28.8	26.7
Compressive Strength (N/mm^2)	23.0	27.9	31.9

Longitudinal Reinforcement	A	B	C
Elastic Modulus (kN/mm^2)	182.8	178.3	186.5
Yield Strength (N/mm^2)	391.5	351.4	394.0

Transverse Reinforcement	A	B	C
Elastic Modulus (kN/mm^2)	182.9	212.9	185.2
Yield Strength (N/mm^2)	380.4	280.4	327.0

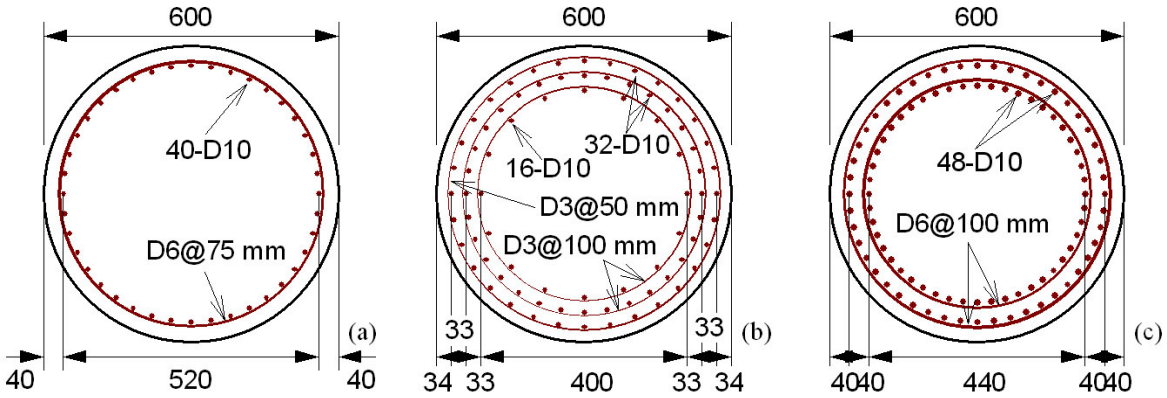

Figure 2 Cross Sections of Specimens: (a) Specimen A, (b) Specimen B, and (c) Specimen C

This paper introduces the experimental study on the latter part of the project. About the development of the rapid seismic repair methods, Yarandi and Saatciglu (2008) proposed a repair method by transverse prestressing.

This paper proposes two rapid seismic repair methods for a reinforced concrete bridge column, and the effectiveness of the proposed methods were investigated through a series of shaking table tests.

2. TEST SETUP AND SPECIMENS

Tables 1 and 2 summarizes the details of specimens, and material properties, and Figures 2 and 3 show the cross section of the specimens and the test setup. Three reinforced concrete bridge columns with circular section were tested. These specimens are the small-scaled models of bridge columns designed in accordance with the 1970's design codes. All the columns were designed to be failed in flexure at the bottom of the column. In the test program, seismic damage was induced through the first series of shake table

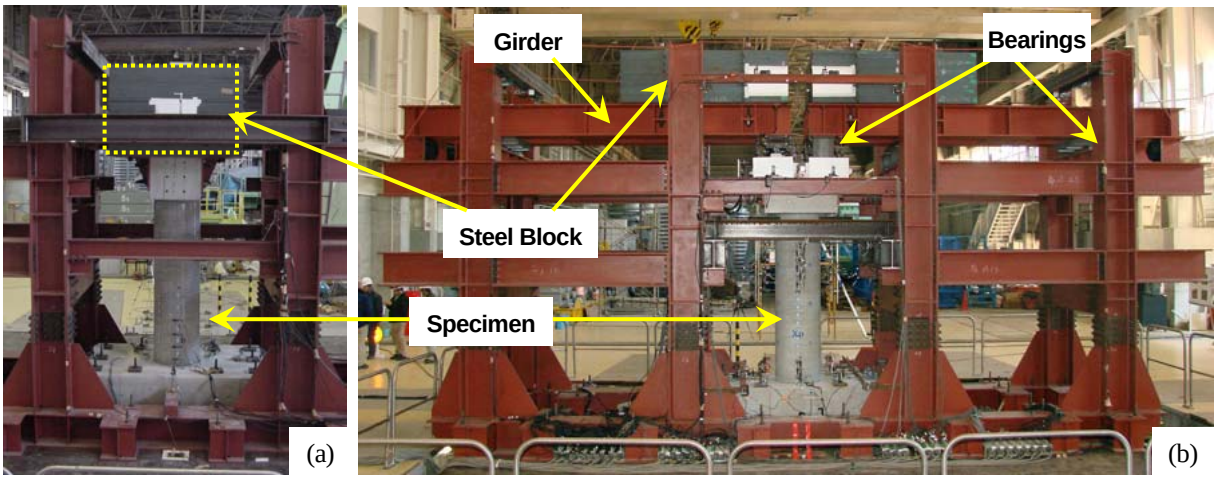

Figure 3 Test Setup: (a) Single-Column Style, and (b) Setup with Girders

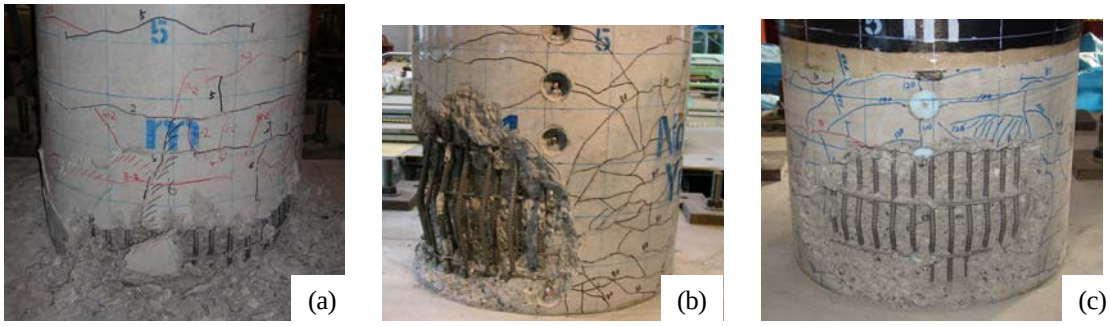

Figure 4 Flexural Damage before Repair: (a) Specimen A, (b) Specimen B, and (c) Specimen C

tests, the seismic damage were repaired by proposed methods describes in Chapter 3, and then the second series of shake table tests was conducted to investigate the effectiveness of the proposed repair methods.

Because each specimen has each objective for the first series of the tests, the test setup, inertia mass, and specimen details were different as shown in Table 1. Specimen A was tested to evaluate the effect of aftershocks. Specimen B was tested to investigate the failure mechanisms of reinforced concrete bridge columns that were severely damaged during the 1995 Kobe earthquake (Sakai, Unjoh and Ukon, 2008). Specimen C was tested to evaluate the failure mechanism of columns that fails in flexure at early termination of longitudinal reinforcement and the effect of strengthening of the damaged portion.

For input ground motions, ground accelerations measured at JR Takatori station during the 1995 Kobe earthquake (Nakamura, 1995) were used. Specimens A and B were tested under three dimensional ground motions, and Specimen C was tested under one horizontal ground motion. The amplitudes of the last test of the first series, which are called the main shock hereinafter, were 60%, 80%, and 120% of the original record for Specimens A, B and C, respectively. The time of the input signals was scaled using a time scale factor considering the similitude requirements.

All the specimens have similar damage at the bottom of the column, such as spalling of cover concrete and rebar buckling even though the test conditions were different each other. No fracture of rebar was observed. After repaired the seismic damage by the proposed methods, the second series of the tests was conducted. The second series of the tests had three phases: the first phase was the elastic level test, the second and third phases were the nonlinear level tests to investigate the seismic performance of the repaired columns for strong aftershocks. The amplitude of the elastic test was 10% of the original records, and that of the nonlinear test is about 70% (65%~80%) and 100% of the main shock.

White noise was inputted to the shake table prior to each test to investigate the dynamic properties and change of natural period of the specimens.

3. RAPID REPAIR METHODS

3.1 Requirements of Rapid Repair Method

Requirements of rapid repair method are determined in this project as follows:

1. To restore the seismic performance to ensure temporal structural safety against aftershocks.
2. To complete the repair works within a day.
3. To conduct the repair works easily without using heavy duty machines.
4. Repair materials have ability for long-term storage.

The first one is required from the seismic performance point of view. The second to forth ones are required to restore the seismic performance of the damaged structure as soon as possible.

According to these requirements, this research proposes

Figure 5 Repair by CFS Jacketing with Quick-Drying Materials:
(a) Repaired by MMA Mortar, (b) CFS Jacketing with MMA impregnation resin, and (c) Completion of Repair

Figure 6 Repair by Fiber Band Jacketing with Mechanical Anchors:
(a) Repaired by Mortar, (b) Tightening Bands with Mechanical Anchor, and (c) Completion of Repair

Table 3 Requirements and Performance of Proposed Methods

Requirement	Qucik-Drying Materials	Mechanical Anchor
1. Seismic Performance	◎	○
2. Rapidity of Repair Work	○	◎
3. Easy Handling of Repair Work	○	○
4. Ability of Long-Term Storage	×	○

Table 4 Properties of Repair Materials

Mortar	A	B	C
Elastic Modulus (kN/mm^2)	19.5	8.6	25.1
Compressive Strength (N/mm^2)	63.3	28.4	56.1

Fiber Sheet/Band	A	B	C
Elastic Modulus (kN/mm^2)	236.0	244.0	4.1
Tensile Strength (N/mm^2)	4140	4250	332.0
Elongation (%)	1.75	1.74	20~30

two methods: one is based on carbon fiber sheet (CFS) jacketing with using quick-drying materials, the other uses mechanical anchors for fiber band jacketing. Table 3 summarizes the features of the proposed methods.

3.2 Carbon Fiber Sheet Jacketing with Quick-Drying Materials

Repair works of carbon fiber sheet (CFS) jacketing generally needs several days for its completion because drying process of materials, which are mortar, primer and impregnation resin, needs more than 10 hours each. To satisfy Requirement 2, this research proposes use of quick-drying materials for mortar, primer, and impregnation resin, and Methyl Methacrylate (MMA) resin is selected for this purpose. This method was applied to Specimens A and B, and the number of layers of jacketing was changed.

Repair works as shown in Figure 5 were conducted in the next day of the first series of tests and finished in about 8 hours. Buckled longitudinal bars were used as-is and transverse bars were removed. Injection of resin into cracks was not conducted. The damaged portion was repaired with the MMA mortar, and then sheets were bonded to the mortar with the MMA impregnation resin. The sheet with 0.111 mm thickness was used, and one layer and two layers were used for Specimens A and B. The volumetric ratios of CFS for Specimens A and B are 0.074% and 0.148%, respectively. Table 4 summarizes the properties of materials that used for repair.

Although this method is expected to have good performance for Requirements 1, 2 and 3, this may not be able to satisfy Requirement 4 because resin materials are generally effective within about 6 months, and thus, these are not suitable for long-term storage.

3.3 Fiber Band Jacketing with Mechanical Anchors

To accelerate the repair works and to improve the ability for long-term storage, one that does not use resin materials is proposed. The method uses mechanically-anchored fiber bands, and has advantages for Requirements 2 and 4 in particular. This method is applied to Specimen C. Metal buckles and polyester fiber bands that are generally used for packing are selected for this method.

Repair works as shown in Figure 6 were conducted in the next day of the first series of tests and finished in about 5

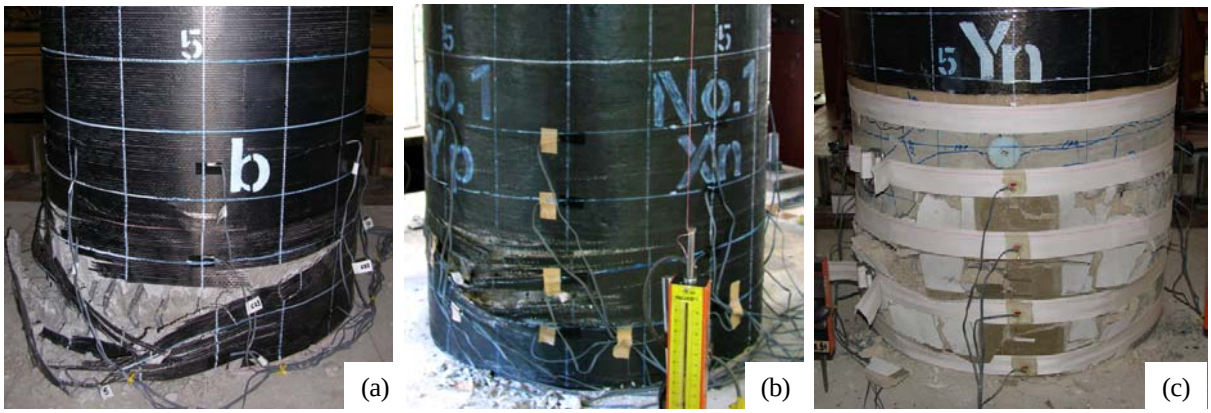

Figure 7 Final Failure Mode: (a) Specimen A, (b) Specimen B, and (c) Specimen C

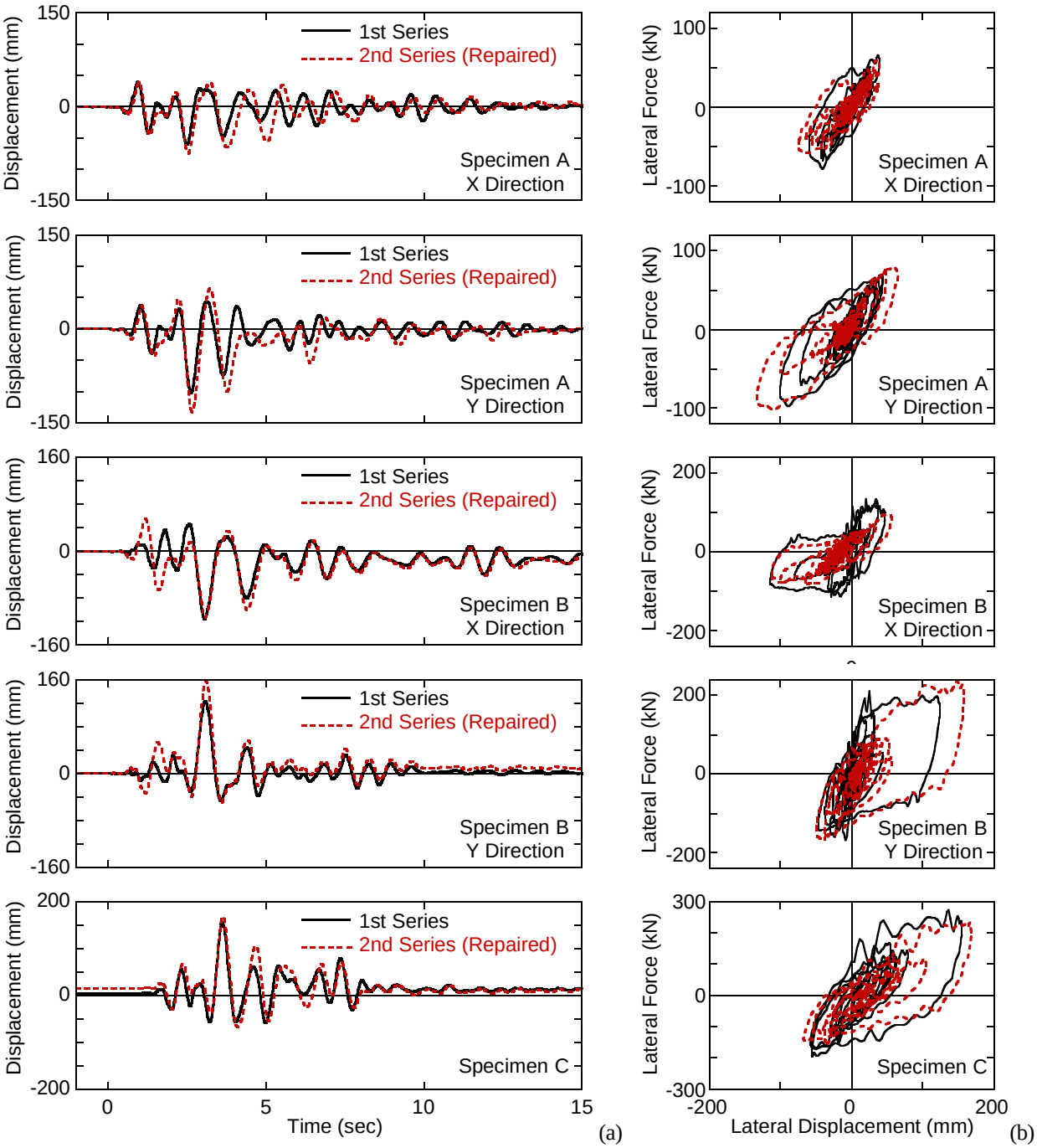

Figure 8 Response of Specimens: (a) Response Displacement, and (b) Force versus Displacement Hysteresis

hours. In this method, not only buckled longitudinal reinforcement but also transverse reinforcement were used as-is. Resin injection into cracks was not conducted. The damaged portion was repaired with ultra rapid-hardening shrinkage compensating mortar, and then polyester fiber bands were placed with mechanical anchors. The band with 45 mm-width and 1.2 mm thickness was placed in 100 mm-pitch with the prestressing force of 1.2 kN. The transverse reinforcement is about equivalent to 0.5 layers of CFS jacketing. Table 4 also shows the properties of the ultra rapid-hardening shrinkage compensating mortar, and polyester fiber bands.

4. EFFECT OF PROPOSED REPAIR METHODS

Figure 7 shows the final failure modes of the specimens, and Figure 8 compares the response lateral displacement, and the lateral force versus lateral displacement hystereses during the test under the main shock between the first and second series.

During the test under about 70% intensity of the main shock, minor fracture of the carbon fiber sheets was observed for both the Specimens A and B. During the final test under 100% intensity of the main shock, the sheet was fractured as shown in Figure 7 and MMA mortar was crushed and spalled. On the other hand, although cracks of mortar were observed during the second phase test, no fracture of the fiber bands was observed. The largest tensile strain of the band was 0.9% during the test. During the final test, although damage of the mortar progressed and the tensile strain of the band increased up to 1.4%, spalling of the mortar was minor because the bands did not fracture due to the elongation capacity of the bands.

The initial stiffness of the specimen decreased by about 50% after repaired comparing with the virgin status of the specimens. Even though the flexural strength capacity at around yield displacement decreased due to the deterioration of the stiffness, the capacity was almost similar when the lateral displacement reached the maximum response as shown in Figure 8. Maximum response of the specimen during the final test increased by 9 to 28% for the repaired columns, but no deterioration of the flexural capacity was observed. Stable response and hysteresis of the repaired columns indicated that the seismic performance of the specimens was restored by the proposed methods.

5. CONCLUSIONS

This paper proposes two rapid seismic repair methods for a reinforced concrete bridge column and the effectiveness of the proposed methods were investigated through a series of shaking table tests. Below are the conclusions determined from the study:

- Requirements of the rapid repair method were clarified. Not only restoring the seismic performance but also the rapidity of the work and ability for long-term storage of materials are important.
- Two rapid seismic repair methods are proposed. The one uses quick- drying materials for carbon fiber sheet jacketing, and the other uses mechanical anchors for fiber band jacketing. The repair works were completed within 8 and 5 hours for the first and second methods, respectively.
- Minor fracture of the carbon fiber sheets of Specimens A and B, which were repaired by CFS jacketing with quick-drying materials, was observed during the test under 70% intensity of the main shock, and then, the sheet was fractured and crushing and spalling of the mortar was observed during the test under 100% intensity of the main shock.
- No fracture of bands of Specimen C, which was repaired by fiber band jacketing with mechanical anchors, occurred even during the test under 100% intensity of the main shock. Spalling of mortar was minor.
- Both the methods restore the seismic performance of reinforced concrete columns. Stable response and hysteresis of the repaired columns were observed during the shake table tests although the initial stiffness decreased by 50% due to seismic damage.

References:

Nakamura, Y. (1995), "Waveform and Its Analysis of The 1995 Hyogo-Ken Nanbu Earthquake," *JR Earthquake Information* 23c, Railway Technical Research Institute, Japan.

National Institute for Land and Infrastructure Management, and Public Works Research Institute (2006), "Report on Damage to Infrastructures by The 2004 Mid-Niigata Prefecture Earthquake," *Research Report of National Institute for Land and Infrastructure Management*, No. 27, and *Research Report of Public Works Research Institute*, No. 203, Japan.

Sakai, J., Kobayashi, H., and Unojh, S. (2007), "Real-time Earthquake Damage Detection System for Bridge Structures," *Proceedings of 23rd US-Japan Bridge Engineering Workshop*, 131-142, Tsukuba, Japan.

Sakai, J. and Mahin S. A. (2005), "Nonlinear Response Spectra for Strong Ground Motion Records from The 2004 Niigata-Ken Chuetsu Earthquakes," *Journal of Japan Association for Earthquake Engineering*, **5**(1), 17-27.

Sakai, J., Unojh, S., and Ukon, D. (2008), "Earthquake Simulation Tests of Bridge Column Models Damaged During 1995 Kobe Earthquake," *Proceedings of 14th World Conference of Earthquake Engineering*, CD-ROM S17-02-001, Beijing, China.

Yarandi, M. and Saatcioglu, M. (2008), "Rapid Seismic Repair of Shear Damaged Concrete Bridge Columns by Transverse Prestressing," *Proceedings of 14th World Conference of Earthquake Engineering*, CD-ROM 12-01-0256, Beijing, China.

Sixth International Conference on Urban Earthquake Engineering
March 3-4, 2009, Tokyo Institute of Technology, Tokyo, Japan

SEISMIC PERFORMANCE VERIFICATION OF THE AKASHI-KAIKYO BRIDGE AGAINST LARGE-SCALE EARTHQUAKES

Kazuo Endo[1], Motoi Okuda[2] and Susumu Fukunaga[3]

1)-3) Engineer, Long-span Bridge Engineering Center, Honshu-Shikoku Bridge Expressway Co., Ltd., Japan
kazuo-endo@jb-honshi.co.jp, motoi-okuda@jb-honshi.co.jp, susumu-fukunaga@jb-honshi.co.jp

Abstract: Presented in this paper is the seismic performance verification of the Akashi-Kaikyo Bridge, the world's longest suspension bridge, against large-scale earthquakes. In the verification, an analytical model incorporated nonlinear behaviors, such as plastic deformation of steel members, bearing failure and collision between a girder and an anchorage, was used for dynamic analyses. Furthermore some limited damages, which had less effect on seismic performance, were permitted. As a result, it was found that the target seismic performance criteria were possibly ensured by taking some minor countermeasures.

1. INTRODUCTION

The Akashi-Kaikyo Bridge, connecting Honshu and Awaji Island, is the world's longest suspension bridge with a center span of 1,991m, as shown in Figure 1. The bridge was designed based on specific design codes developed for this bridge and opened in 1998. In the original seismic design, although site-specific design seismic force was determined in consideration of the information regarding earthquake histories, earthquakes occurring in plate-boundaries and geotechnical conditions around the bridge site, an inland near-field earthquake, such as the Hyogo-ken Nanbu Earthquake in 1995, was not considered in the design seismic force. The bridge is located in seismic-prone area, where plate boundaries and several inland active faults exist nearby. According to the latest findings, there is concern that a large-scale earthquake exceeding the original design seismic force would occur and seismic risk for the bridge would increase. On the other hand, the bridge is designated as a lifeline corridor for emergency transportations or restoration works immediately after a large-scale earthquake since there is no alternative route between Honshu and Awaji Island except for the bridge.

Above mentioned background motivated us to commence seismic performance upgrading for the bridge. In this paper, the seismic performance verification of the Akashi-Kaikyo Bridge against large-scale earthquakes is presented. After performing the verification, it was found that the target seismic performance criteria were possibly ensured by taking some minor countermeasures.

2. SEISMIC PERFORMANCE VERIFICATION

2.1 Seismic Performance Verification Flow

A flowchart of the seismic performance verification is illustrated in Figure 2. In the verification, after defining seismic performance criteria and site-specific large-scale

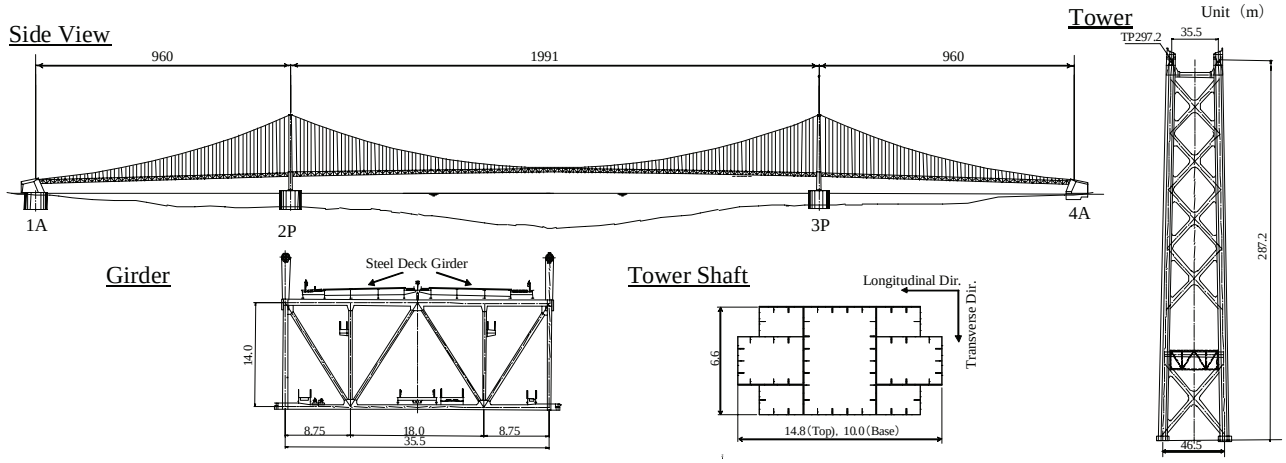

Figure 1 General View of Akashi-Kaikyo Bridge

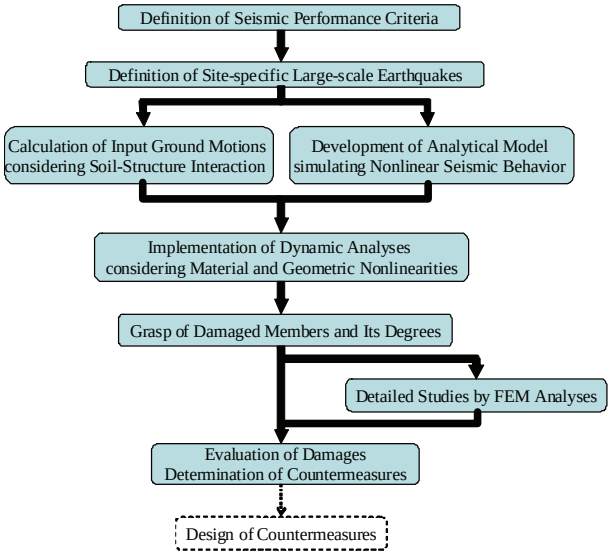

Figure 2 Flowchart of Seismic Performance Verification

earthquakes, several analyses which could simulate the nonlinear seismic behavior accurately were performed in order to assess the performance reasonably.

2.2 Seismic Performance Criteria

Since the bridge must undertake a role as an emergency transportation route in case of a large-scale earthquake, it is required not only to remain stable, but also to provide most operations and functions following an earthquake. Therefore, target seismic performance criteria were specified in terms of two aspects, seismic safety and serviceability, as follows;

Seismic Safety

- ✓ To prevent the bridge collapse and ensure the life safety

Seismic Serviceability after Events

- ✓ To be repairable for damaged structural members
- ✓ To ensure the serviceability for emergency traffic immediately after events by emergency inspections or temporary repair works
- ✓ To ensure the serviceability for normal traffic in a short period after events.

2.3 Large-scale Earthquake

Owing to comprehensive fault surveys and various researches mainly performed after the Hyogo-ken Nanbu Earthquake in 1995 by government agencies, earthquake source information around the bridge site has become apparent. Besides, an estimation method of strong ground motions with fault models has been developed and practically used in some areas. Accordingly, seismic ground motions of site-specific large-scale earthquakes were calculated with fault models based on the information.

Seismic ground motions used for the seismic performance verification were defined as indicated in Figure 3. These are rock outcropping motions on the bedrock where S-wave velocity (Vs) is 2 km/s. Two types of scenario earthquakes were considered; one is the Tounankai-Nankai Earthquake which is an interplate earthquake, the other is an

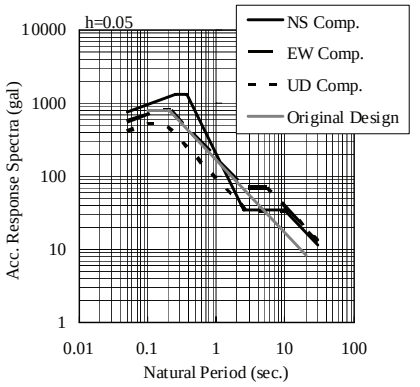

(a) Tounankai-Nankai EQ.

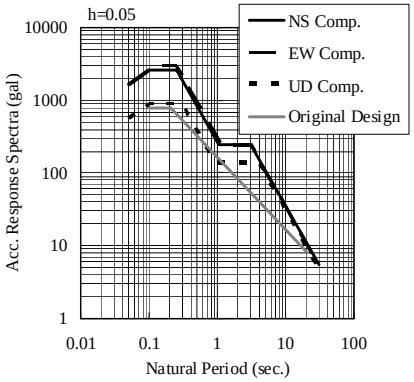

(b) Rokko-Awaji Fault EQ.

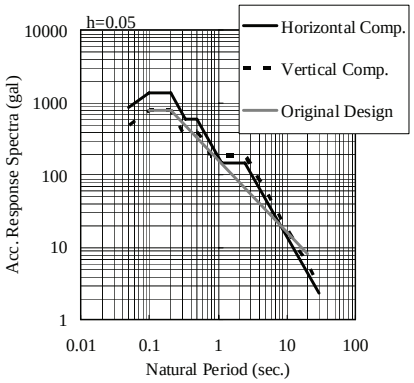

(c) Unknown Inland Active Fault EQ.

Figure 3 Site-specific Large-scale Earthquake

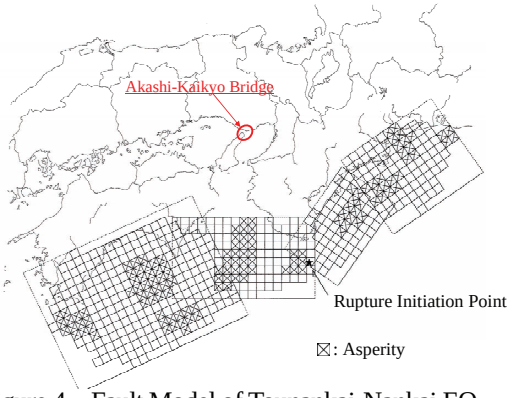

Figure 4 Fault Model of Tounankai-Nankai EQ.

earthquake coming from the Rokko-Awaji Fault which is an inland near-field earthquake. A fault model for the Tounankai-Nankai Earthquake is shown in Figure 4. In addition to the two types of scenario earthquakes, a seismic

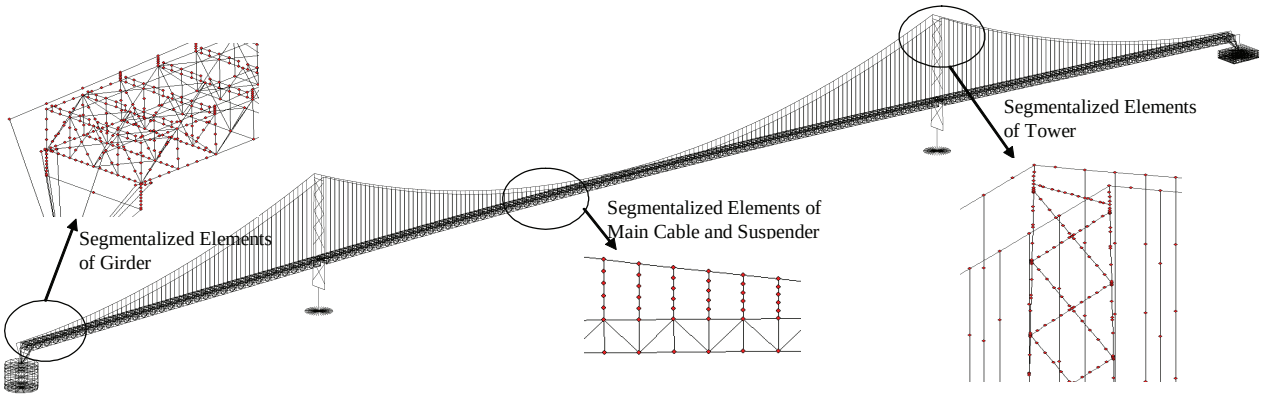

Figure 5 3D Full Bridge Model

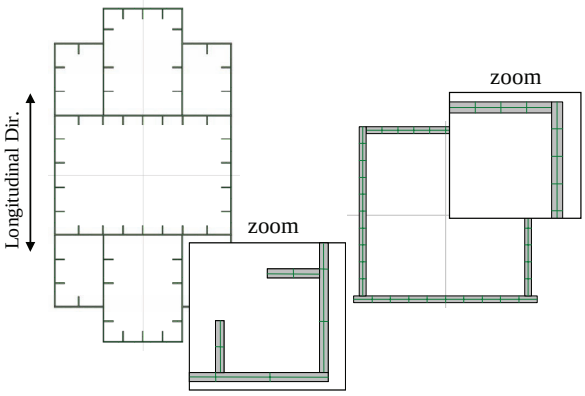

(a) Tower Shaft (b) Lower Chord of Girder

Figure 6 Analytical Model of Tower and Girder

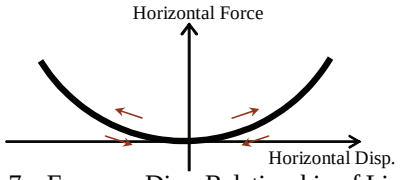

Figure 7 Force vs. Disp. Relationship of Link

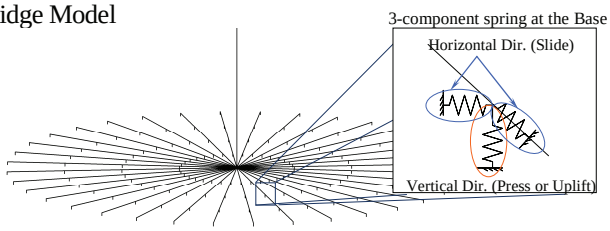

(a) Tower Foundation

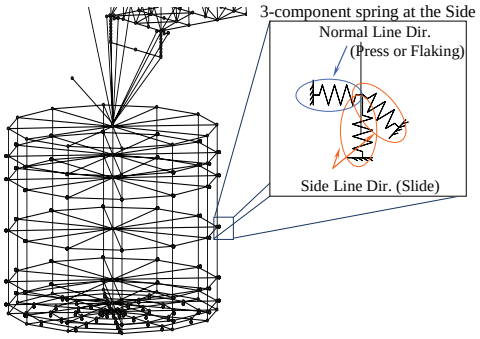

(b) Anchorage Foundation

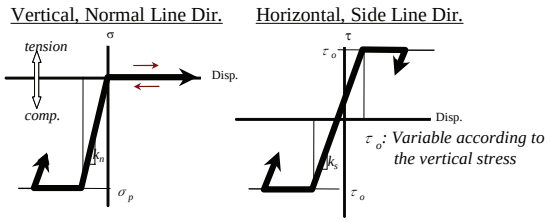

(c) Constitutive Law

Figure 8 Analytical Model of Foundation

ground motion coming from an earthquake with a magnitude of M_J6.8 occurring just beneath the site was considered. This means the consideration for the possibility that an unknown inland active fault might exist near the site. All the seismic ground motions were estimated by a hybrid method (green's function method + 3D finite difference method).

2.4 Analytical Model

A 3D full bridge model used for dynamic analyses is illustrated in Figure 5. Several idealizations, which were able to simulate nonlinear seismic behaviors accurately, were incorporated in the analytical model. Each structural element was idealized as follows;

(1) Tower, Girder

Since the elements were subjected to bidirectional bending moments and axial force fluctuations, those were idealized by fiber elements, which were able to take into account those influences on material nonlinearity. Segmentalized cross sections by fiber elements are shown in Figure 6. The constitutive law was assumed to be elastic-linear kinematic strain hardening model with 0.01E (E: Young's modulus) as the second gradient.

(2) Main Cable, Suspender, Center Stay

The members were idealized by linear beam elements of which flexural stiffness was almost zero. Cable behaviors, such as sagging due to the tension force losing, were simulated by the fine segmentation of cable members (see Figure 5) as well as the implementation of geometric nonlinear analyses. Stay ropes, which restrain excessive relative displacement between the girder and the main cable, are installed only in the center span.

(3) End Link, Tower Link

The members were idealized by linear truss elements. Link behaviors, as indicated in Figure 7, were simulated by

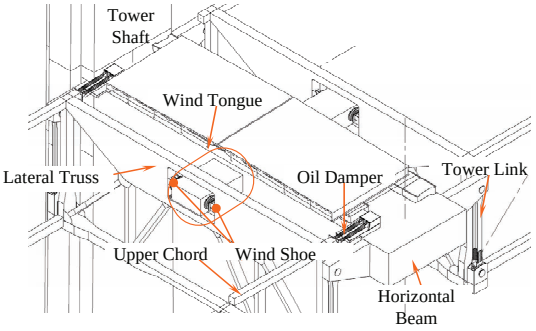

(a) Overview at XPT between Girder and Tower

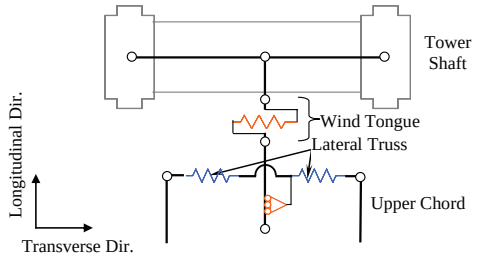

(b) Installation of Spring Element

Figure 9 Analytical Model of Wind Shoe and Tongue

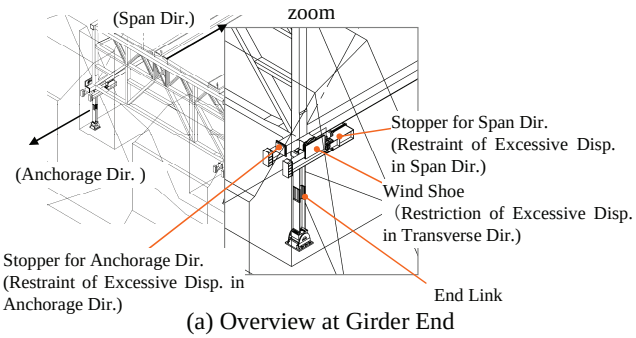

(a) Overview at Girder End

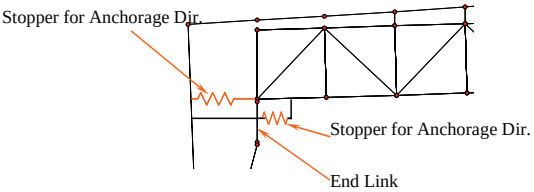

(b) Installation of Spring Element

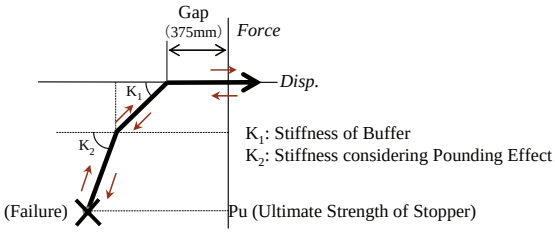

(c) Force vs. Disp. Relationship

Figure 10 Analytical Model of Pounding Effect

the implementation of geometric nonlinear analyses.

(4) Foundation

Nonlinear spring elements were installed at interfaces between the soil and the foundation in order to simulate its uplift and slip behaviors. The analytical model is schematized in Figure 8.

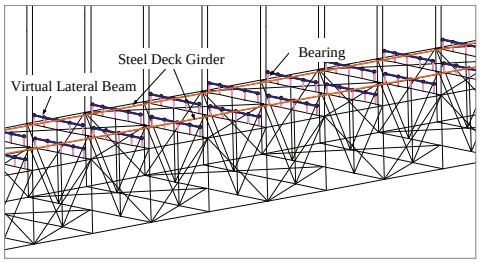

(a) Idealization of Steel Deck Girder

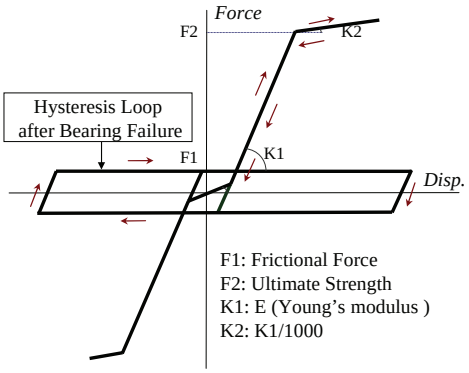

(b) Force vs. Disp. Relationship of Bearing

Figure 11 Analytical Model of Bearing Failure Effect

Table 1 Analytical Conditions

Analytical Method		Time history response analyses with material and geometric nonlinearities
Numerical Integration Method		Newmark's β method (β=0.25)
Damping Type		Member based stiffness-proportional damping
Time Interval		0.0025 sec.
Damping Ratios of Members	Tower, Girder	0.01
	Cable	0.01
	Tower Foundation	0.10
	Anchorage Foundation	(Impedances calculated by soil-structure interaction analyses)
Input Motion		Effective seismic motion
Loading Direction		3 directions (Longitudinal, Transverse and Vertical)

(5) Wind Shoes and Wind Tongues

The girder is restrained in transverse direction by wind shoes attached to lateral trusses and wind tongues attached to horizontal beams at the tower position. This restraint was idealized by linear spring elements as schematized in Figure 9.

(6) Pounding between Girder and Anchorage

Nonlinear spring elements were installed at interfaces between the girder and the anchorage in order to consider the pounding effect between those members. A stopper for anchorage direction of the girder collides against the anchorage due to the excessive displacement in the anchorage direction, while the girder collides against a stopper for span direction due to the excessive displacement in the span direction. The analytical model is schematized in Figure 10.

(7) Failure of Steel Deck Girder Bearing

Nonlinear spring elements were installed at the steel

Table 2 Analytical Results and Damage Evaluation

Structural Element			Results	Damage Evaluation
Tower	shaft	middle	strain ratio (maximum response/buckling strength) = 0.98	-
		base	strain ratio (maximum response/buckling strength) = 1.03	acceptable
	diagonal		strain ratio (maximum response/buckling strength) = 0.76	-
	horizontal	upper	strain ratio (maximum response/buckling strength) = 0.59	-
		lower	strain ratio (maximum response/buckling strength) = 1.42	acceptable
	anchor bolt		strain ratio (maximum response/yield strength) = 0.59	-
	base concrete		strain ratio (maximum response/strength) = 0.98	-
Main Cable	cable		tensile force ratio (maximum response/ultimate strength) = 0.45	-
	slide at saddle		minimum safety factor = 2.7	-
Suspender	rope		tensile force ratio (maximum response/ultimate strength) = 0.25	-
	slip of cable band		minimum safety factor = 1.7	-
Center Stay	rope		tensile force ratio (maximum response/ultimate strength) = 0.86	-
	slip of cable band		minimum safety factor = 1.1	-
Girder	upper and lower chord		strain ratio (maximum response/buckling strength) = 0.81	-
	diagonal		strain ratio (maximum response/buckling strength) = 0.52	-
	lateral		strain ratio (maximum response/buckling strength) = 0.82	-
	pounding at anchorage		pounding	acceptable
	pounding at tower		no pounding	-
	stopper		axial force ratio (maximum response/yield strength) = 1.29	acceptable
Steel Deck	bearing		failure at some bearings	acceptable
Link	tower link		axial force ratio (maximum response/yield strength) = 0.28	-
			displacement ratio (maximum response/allowable value) = 0.30	-
	end link		axial force ratio (maximum response/buckling strength) = 0.47	-
			displacement ratio (maximum response/allowable value) = 0.19	-
Wind Shoe (Tongue)			horizontal force ratio (maximum response/yield strength) = 0.81	-
Expansion Joint			failure at some joints	not acceptable (taking countermeasure)
Oil Damper			failure at all dampers	acceptable
Foundation	stability		minimum safety factor = 1.1	-

deck plate bearings in order to simulate its failure. Steel deck plates were idealized by linear beam elements. The analytical model is schematized in Figure 11.

(8) Oil Dampers

Effects of oil dampers between the girder and the tower, which were installed to improve aerodynamic stability of the tower in the original design, were incorporated in the full bridge analytical model using mass, spring and dashpot elements (see Figure 9 (a)).

2.5 Analytical Condition

Nonlinear dynamic analyses with considering both material and geometric nonlinearities were performed to simulate the seismic behaviors. As input motions into the analytical model, effective seismic motions considering soil-structure (kinematic) interaction were applied in three directions simultaneously. Analytical conditions are tabulated in Table 1.

2.6 Analytical Result and Damage Evaluation

Results of the seismic analyses and damage evaluations are tabulated in Table 2. In the table, a hatching section indicates that some damage or nonlinear behavior was developed. Responses by the Rokko-Awaji Fault Earthquake were dominant for the results among the three earthquakes. As a result, responses of the tower exceeded its buckling strength at the base of tower shafts and the lower horizontal beam, whereas responses of other main structural elements, such as the main cable, suspenders and the girder were within elastic range. In addition, some damages at sub structural elements, such as stoppers at the girder ends, bearings of the steel deck, expansion joints, and oil dampers, were generated.

For the damage evaluation of the tower, detailed studies were performed by FEM analyses, which were pushover analyses using shell elements. Figure 12 shows the results of the lower horizontal beam. These indicate that the structure has redundancy beyond the maximum moment of dynamic analyses and the degree of local buckling is small enough to repair it. Besides, there is concern that strengthening of the horizontal beam might lead to the damage of the tower shaft, which is not desirable for the seismic performance of the entire bridge system. Therefore, the damage was assessed to be acceptable. In addition, the damages of other sub structural elements, such as stoppers at the girder ends, bearings of the steel deck and oil dampers, were also assessed to be acceptable since the damages of those elements do not have much influence on operations and functions of the bridge and are repairable under traffic condition. On the other hand, the damage of expansion joints was assessed to be not acceptable. Since expansion joints of the bridge are huge ones as shown in Figure 13, those

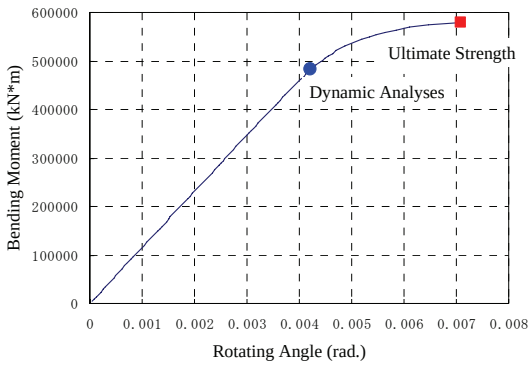

(a) Moment vs. Angle Relationship

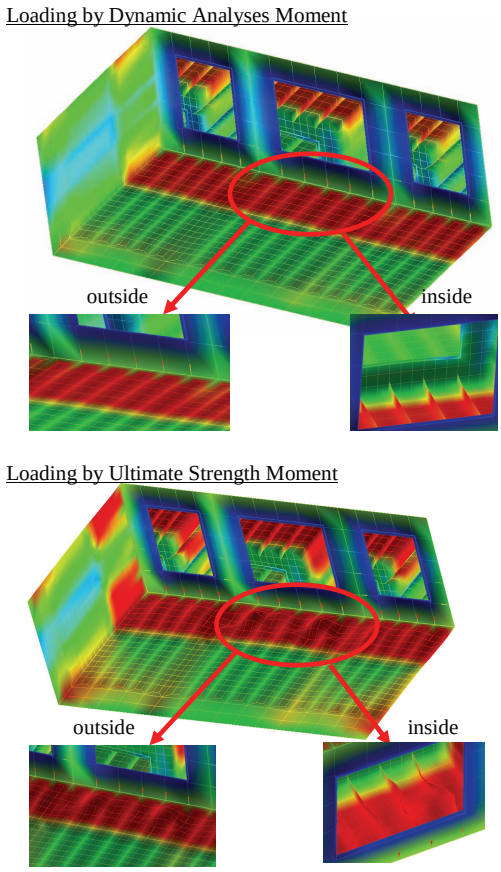

(b) Deformation Diagram (Scale Factor: 10)

Figure 12 FEM Analyses of Tower Horizontal Beam

failures might result in large holes, approximately 2.5-meter-long in the longitudinal direction, on the road surface. Accordingly, there is a fatal possibility that a vehicle might fall from a 60-meter-height during an earthquake. A provisional countermeasure for the expansion joints is shown in Figure 14. PC cables aim to lead failure to a universal joint when the joints spread beyond its allowable range, while brackets aim to support the expansion joints vertically after the universal joints fail.

3. CONCLUSIONS

This paper presented the seismic performance

Figure 13 Expansion Joint

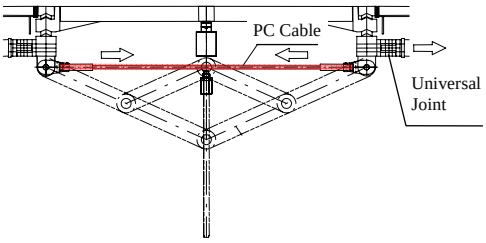

(a) Installation of PC Cable

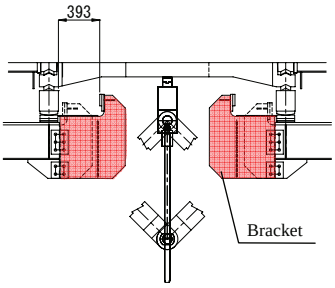

(a) Installation of Bracket

Figure 14 Provisional Countermeasure

verification of the Akashi-Kaikyo Bridge against large-scale earthquakes. Seismic ground motions of site-specific large-scale earthquakes for the verification, which are larger than the original design one by and large, were estimated by a hybrid method using fault models based on the recent information from government agencies. After performing nonlinear dynamic analyses with a 3D full bridge model and FEM analyses with shell models, it was found that most of the structural elements were sound and the target seismic performance criteria were possibly ensured by taking some minor countermeasures even though the seismic force got larger. The primary reason of this result seems that effects of earthquake were not dominant load combination for most of the structural elements in the original design and there were some margins against an earthquake. In order to provide safe transportation of the Akashi-Kaikyo Bridge during a large-scale earthquake, the countermeasures are scheduled to be conducted in a few years.

Acknowledgements:

The authors wish to acknowledge useful supports from the Honshi Seismic Reinforcement Study Committee participants (chairman: Dr. Iemura, the professor emeritus of the Kyoto University)

Sixth International Conference on Urban Earthquake Engineering
March 3-4, 2009, Tokyo Institute of Technology, Tokyo, Japan

VERIFICATION TESTS OF THE DYNAMIC BEHAVIOR OF THE FRICTION-BASED ROTATIONAL DAMPER USING SHAKING TABLE

Akihiro Toyooka[1], Takehiko Himeno[2], Yasuhisa Hishijima[3], Hirokazu Iemura[4] and Imad H. Mualla[5]

1 Assistant Senior Researcher, Railway Technical Research Institute, Japan
2 Professional Eng., Kawaguchi Metal Industry, Japan
3 Head of Tech. Dept., Kawaguchi Metal Industry, Japan
4 Professor Emeritus, Kyoto University, Japan
5 Chief Technical Officer of DAMPTECH, DTU, Denmark
Email:akitoyo@rtri.or.jp, himeno@kawakinkk.co.jp, hishijima@kawakinkk.co.jp, iemura@catfish.kuciv.kyoto-u.ac.jp, ihm@damptech.com

Abstract: A friction damper is regarded as one of the most effective structural control devices in view of regulating the inertia force induced from the upper structures and effective energy dissipation. Despite a large number of friction dampers or bearings have been used for civil and architectural structures, those devices generally require large deformation and stable vertical load induced on the device in order to attain a desirable control performance.

In order to overcome such difficulties, a new friction-based damper was developed. The new damper has several steel arms that are linked each other by a bolt in order for them to rotate freely, and carefully manufactured disk friction materials are embedded in that link. By connecting these arms to the upper and lower structures, horizontal deformation of the structure is converted into the rotational motion of the link and disk.

In this research, dynamic performance of the proposed damper was studied through a large-scale shaking table tests on which the girder and bearings were mounted. It was confirmed through periodical loading tests that the damper generated the stable friction force regardless of the loading frequency. It was also found that the damper successfully introduced the supplemental damping to the structure under earthquake motions.

1. INTRODUCTION

Due to its proven efficiency, the concept of seismic protection based on supplemental damping is gaining momentum within the engineering community worldwide. Friction dampers are often employed in passive response control systems because of their high-energy dissipation potential at relatively low cost and they are easy to install and maintain. Most of the bridges around the world are having dampers. Dampers, they become a very essential and important part of the bridges in order to protect the bridges from heavy dynamic vibration caused by seismic, wind and traffic vibration, and also as bridge retainers.

There exists a variety of devices capable of absorbing seismic energy. The research reported herein is focused in particular on the performance of a new Friction Damper Device (FDD) developed by Mualla (Mualla, 2000) for frame structures. The complete damping system includes FDDs supported by secondary structure. A comprehensive testing of different models and sizes were carried out at the Technical University of Denmark (DTU). A special high tech friction material was heavily evaluated and tested. This friction material performed very well in all aspects and seems very promising one.

However, further research was needed to verify the performance of the damping system in bridges and elevated highways in full-scale application under seismic ground shaking. This paper presents results of a co-operative international research program with Kawaguchi Metal Industry, Kyoto University and DAMPTECH for experimental investigation of the FDD using for bridges. In this research, the prototype damper designed for civil engineering structures was developed and tested using the large-scale shaking table facility. The girder consisting of the counterweight, bearings and prototypes of the proposed damper were mounted on the shake table and excited by sinusoidal waves as well as strong earthquakes. Through the series of tests, the dynamic relation between friction force and displacement, its dependency on loading frequency and the amount of the supplemental damping introduced to the structure are briefly discussed in this research. More detail information is found in the previous paper (see Toyooka, 2008).

2. BASIC CONCEPT OF THE NEW DAMPER

The schematic of the proposed damper is shown in Figures 1. The damper has several steel arms one ends of which are linked each other by a bolt in order for them to rotate freely, and carefully manufactured disk friction materials are embedded in that link. By connecting both ends of these arms to the upper and lower structures, horizontal deformation of the girder is converted into the rotational motion of the link and disk. This rotational

vibration is then dissipated by a friction between layered disks and steel arms. Consequently, horizontal force of the damper (F in Figure 2 (b)) balances with the friction moment M, depending on the moment arm length L.

One of the key features of the proposed damper is its easiness of installation and maintenance. It requires significantly less space for installation compared to the traditional friction dampers in order to attain the large friction energy dissipation. In addition, the axial force that significantly affects the performance of the friction type device is easily controlled by a torque of the fastening bolt, independent from the vertical load of the upper structure. That is to say, the damper can be installed in a short time without a need to high tech equipments or highly trained qualified staff. From the viewpoint of the long-term durability, the damper has a very stable performance over many cycles because of the special friction material. The damper shows a reliable performance over multiple earthquakes. Also, the damper is easily maintained if necessary and if required, can be easily replaced after severe earthquakes.

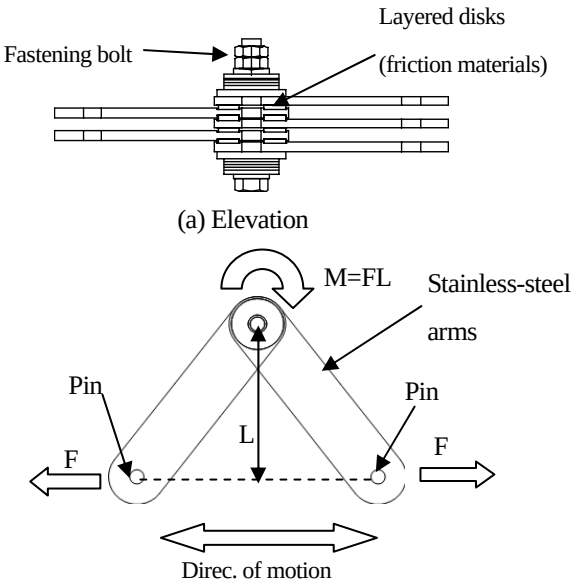

Figure 1 Basic principle of the proposed damper

3. SHAKING TABLE TEST

3.1 Test setup

The prototype of the proposed damper was designed on the basis of the concepts mentioned above, and its dynamic behavior was assessed by using the large-scale shaking table facility in Disaster Prevention Research Institute of Kyoto University. The shake table has a capability to drive the table (5.0 m×3.0 m) up to 1.0 G in acceleration and 150 kine in velocity with maximum specimen weight of 150 kN. The maximum strokes are 300 mm in longitudinal, 250 mm in transverse, and 200 mm in up-down directions.

As shown in Photo 1, large-scale model of an isolated girder was assembled on the shake table. The model of the girder was a steel-made slab (W4150 mm×D2650 mm×H400 mm), the weight of which was approximately 100 kN. For supporting the girder, two different setups were prepared as shown in Figure 2. The girder was supported by four natural rubber bearings (Setup 1), or two natural rubber bearings plus four slide bearings (Setup 2). The setup 1 was prepared for both sinusoidal and earthquake excitation tests, and setup 2 for sinusoidal loading tests. The specifications of the rubber bearing for setups 1 and 2 are shown in Table 1. For slide bearings in setup 2, 290-mm-square stainless-steel plates and polyamide portion were combined, the friction coefficient of which was approximately 0.05. The natural periods of these systems were 0.42 sec and 0.60 sec, respectively. As seen in Figure 2, four damper specimens were then prepared and placed at the every edges of the girder.

Table 1 Specifications of the rubber bearings

Shear modulus	0.8 N/mm^2
Rubber thickness per layer	10 mm
Number of layers	7
Equivalent stiffness (strain=136%)	0.553 kN/mm
Equivalent damping ratio (strain=136%)	7.97 %

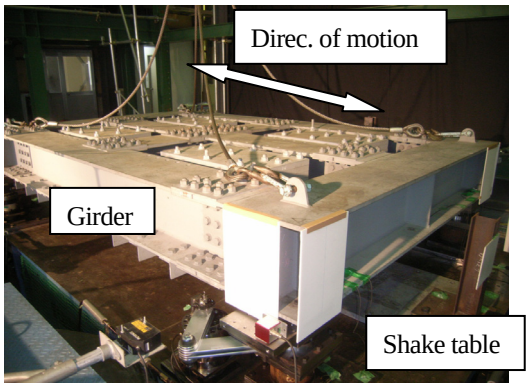

Photo 1. Test setup (Damper specimen and sensors)

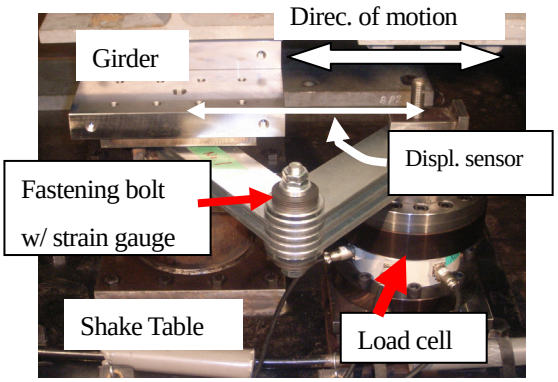

Photo 2. Close view of the damper

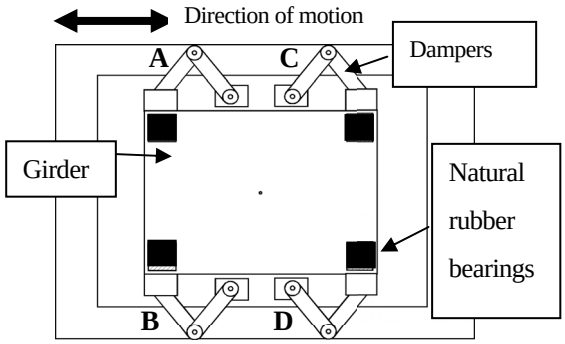

(a) Test setup 1 (Natural period = 0.42 sec)

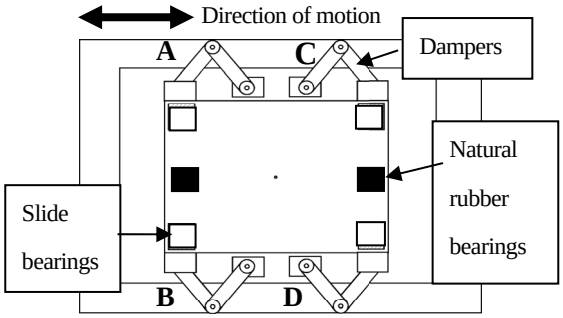

(b) Test setup 2 (Natural period = 0.60 sec)

Figure 2 Schematics of the test setups

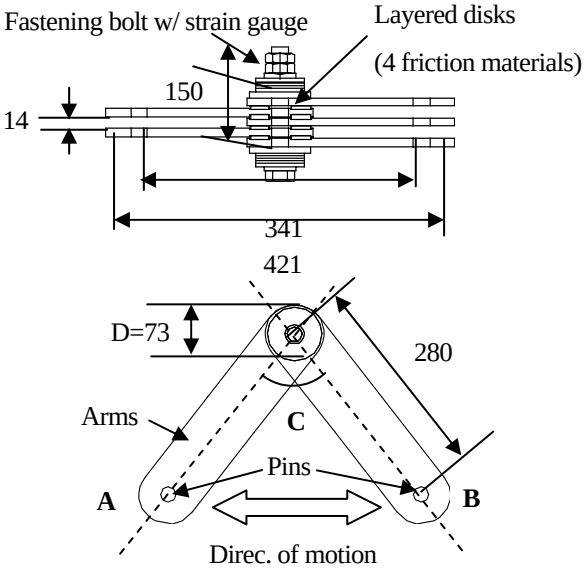

Figure 3 Specification of the damper specimen (unit: mm)

3.2 Data acquisition

Several accelerometers and laser displacement transducers were embedded on the girder and the shake table in order to comprehend the motion of the girder. For the damper specimens, three different types of sensors were installed: wire displacement sensor, load transducer and bolt gauge. The wire displacement sensors were used to measure the relative displacement between two links attached to the girder and the shake table. The load transducers were attached to the all dampers to directly measure the damper's horizontal forces, regardless of the characteristics of the behavior of the total test setup.

The bolt gauge, embedding a strain gauge in the fastening bolt, was prepared to comprehend the initial torque as well as the fluctuation of the axial force during the test.

3.3 Specification of the damper specimen

As shown in Figure 2, total four dampers were prepared and installed to the test system. Figure 3 shows the specification of the damper specimen for the test. Both ends of the arm, A and B in the figure, were attached to the girder model and the load transducer mounted on the shake table using pins (see Photo 2). Prior to the every loading test, the fastening bolt in Figure 3 was fastened so that the initial axial force was approximately 15 kN. In addition, initial angle of the damper, C in the figure, was also measured to estimate the changes of the rotation angle by means of the arm length and relative displacement between A and B in the figure.

3.4 Input motions

The shaking table was driven in longitudinal direction by both sinusoidal and earthquake motions. The number of sinusoidal motions with various amplitude and frequency were prepared to clarify the dependencies of the damper's dynamic behavior on stroke and stroke velocity.

As for earthquake excitations, two different types of the acceleration waveforms based on strong motion records were used. The recorded earthquake at Onnetto bridge during the 1994 Hokkaido-Toho-Oki earthquake (Onneto Br. wave) was selected for assuming inter-plate earthquake, a duration time of which is relatively long. On the contrary, the North-South component of the JR Takatori station record during the 1995 Hyogoken-Nanbu earthquake (JR Takatori wave) was also chosen as very-rare inland intense earthquake. Thise waveforms are shown in Figure 4. The time steps of these waves were scaled by means of a law of similarity so that the apparent natural periods of the test setup 1 were approximately 0.85 sec and 1.06 sec, respectively. This conversion intended to excite the damper with a large displacement, namely, no corresponding real structures were assumed in the series of tests.

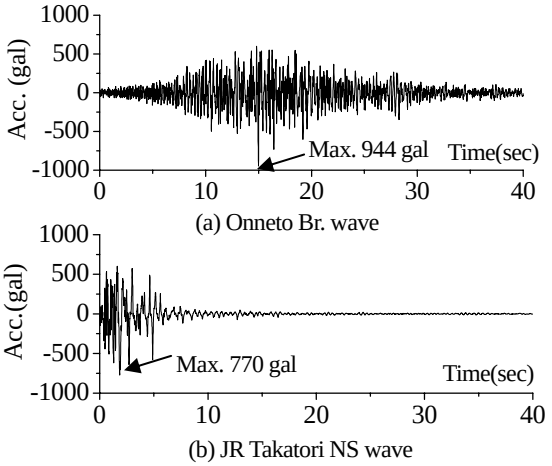

Figure 4 Input earthquake motions

4.TEST RESULTS AND DISCUSSIONS

4.1 Sinusoidal loading tests

Figure 5 shows the representative relations between total damper forces and displacements under sinusoidal motions; 1) Test setup 1 was subjected to the frequency of 1.7 Hz and maximum acceleration of 300 gal (Figure 5(a)) and 2) Test setup 2 excited by a motion of 2.8Hz, 300 gal (Figure 5(b)). The horizontal forces in the figure were obtained by the sum of four dampers. Since the frequencies of input motions were adjacent to the natural frequencies of test systems in both cases, dampers were supposed to the various levels of excitations as the displacement was gradually approaching to the steady-state response. As seen in the figure, dampers generated stable friction forces under periodical motion, regardless of the displacement levels. It consequently follows that the proposed damper holds the same advantage as ordinal friction devices over other types of devices that regulates the interactive force between upper and lower structures up to its friction level. It should be noted that the proposed device attained such a performance without requiring large amount of sliding area.

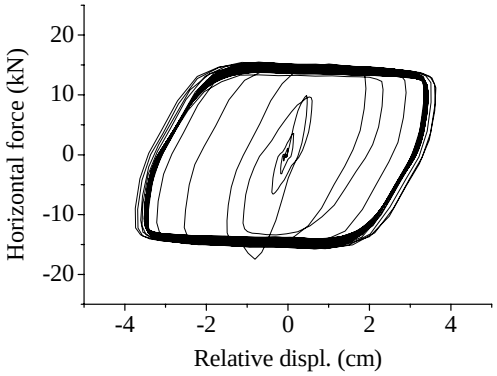

(a) Sin 2.8 Hz, 300gal (Test setup 1)

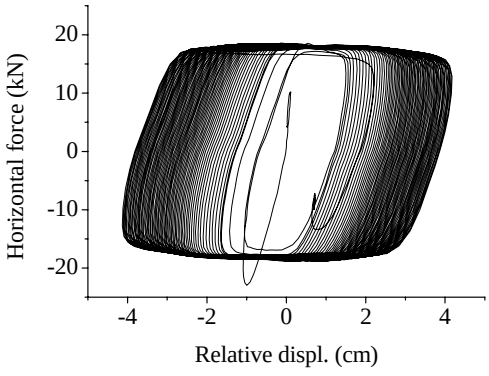

(b) Sin 1.7 Hz, 300 gal (Test setup 2)

Figure 5 Damper forces v.s. relative displacements relations

One of the significant and interesting features of the damper is its dependency on loading frequency. Several cyclic excitation tests were carried out in order to examine the fluctuation of the moment under various loading speeds. Table 2 shows the list of frequency and maximum acceleration for the test setups 1 and 2. The loading frequencies were selected in order to attain a certain amount of damper stroke and to cover dominant natural periods of the common civil engineering structures. In each test case, a mode of the absolute momentum force over time history is selected as representative value of the damper's total hysteresis. The obtained momentum force was then divided by the initial axial force of the fastening bolt to eliminate the dependency of the stress induced on the friction material. Figure 6 illustrates the relation between the normalized moments and corresponding loading frequencies, correlation coefficient of which was -0.28. It can be observed that the momentum force was not significantly affected by the loading frequency. In other words, the proposed damper has a capability to attain stable energy dissipation under wide-range of loading frequencies.

Table 2 Test cases for sinusoidal loadings

Test setup 1		Test setup 2	
Freq.(Hz)	Acc (gal)	Freq.(Hz)	Acc (gal)
2.0	400, 450	1.0	300
2.4	300	1.5	300
2.5	300	2.3	250
2.8	300	2.5	250
2.9	300	2.6	250
3.0	300	2.7	250
3.3	300	3.0	250
3.5	300		

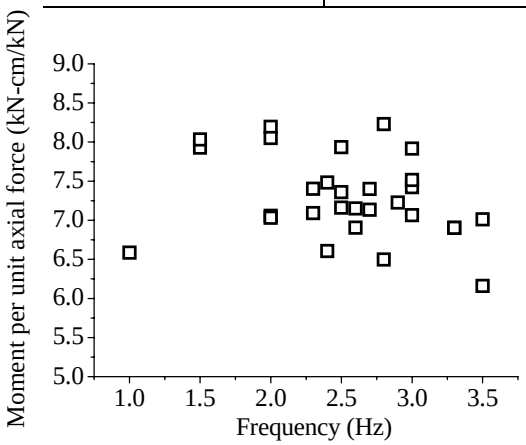

Figure 6 Excitation frequency versus moment per unit axial bolt force

4.2 Earthquake loading tests

On the basis of the sinusoidal loading tests, earthquake excitation tests were conducted using the test setup 1 to verify the damper's capability of energy dissipation under non-periodical excitation.

Figure 7 shows hysteretic loops of four dampers' total horizontal forces and relative displacements under Onneto Br. and JR Takatori motions. It is observed from the figure that the damper behaved as an elasto-plastic material, the horizontal forces of which were saturated in the range of approximately 20 to 25 kN.

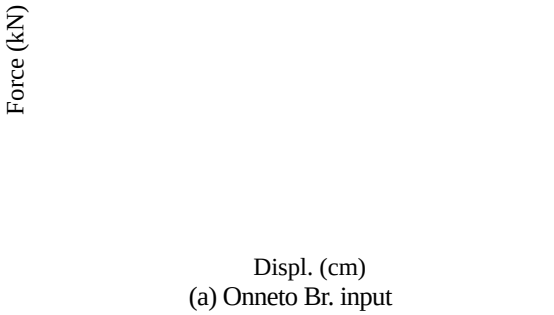

(a) Onneto Br. input

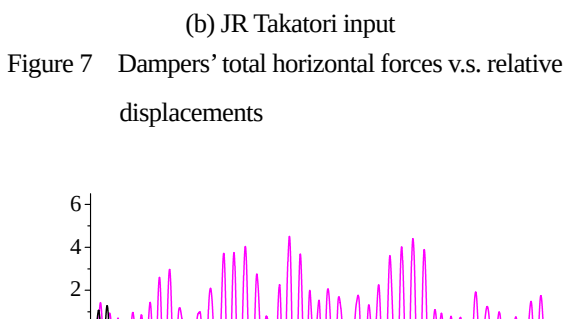

(b) JR Takatori input

Figure 7 Dampers' total horizontal forces v.s. relative displacements

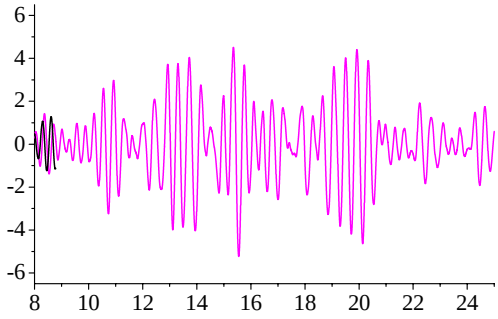

(a) Onneto Br. input

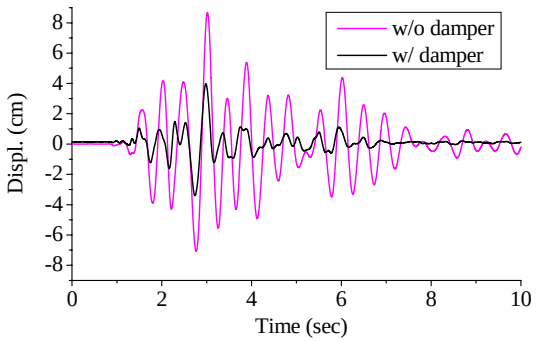

(b) JR Takatori input

Figure 8 Relative displacements (shake table –girder) with and without dampers

As for the vibration reduction performance, Figure 8 illustrates the time histories of the girder's relative displacements from the shake table under earthquake motions as a comparison with and without dampers. The responses without dampers were calculated by numerical simulations incorporating the specifications of the girder and bearings. It is found from these time histories that the maximum responses of the displacement were reduced from 5.23 cm to 4.04 cm (reduced by 22.8 %) in case of Onne Br. motion, and 8.68 cm to 3.98 cm (reduced by 54.2 %) in JR Takatori input. This difference in response reduction effect partly arises from the amount of the damping induced to the test system, depending on the frequency characters of the input motion.

In order to assess the energy dissipation performance of the damper quantitatively, the amount of the supplemental damping induced by the damper was estimated by a following procedures. Figure 9 shows inertia force versus displacement relations of both earthquake motions. The hysteretic loops of dampers are also depicted in the same figures. It is clearly observed from the figure that the damper's forces in both cases were restrained at its friction force, whereas the total inertias increased in accordance with the displacement. The residual force, arises from the structural elements such as rubber supports and other damping elements included in the test system, was obtained by subtracting the damper's force from the inertia.

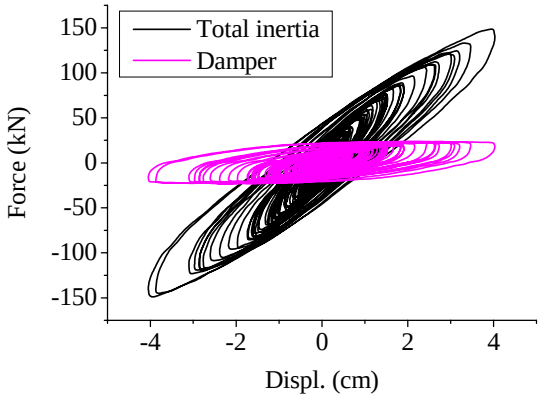

(a) Onneto Br. input

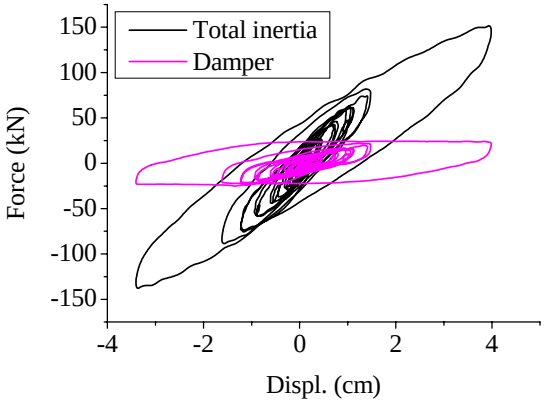

(b) JR Takatori input

Figure 9 Inertial and damping forces vs displacements

Suppose the hysteretic behaviors with regard to the inertial as well as the residual forces are expressed by a linear combination of displacement and velocity, say,

$$I(t) = kx + cv, \quad F_s(t) = k_s x + c_s v \tag{1}$$

Where, I and F_s are forces due to inertia and structural elements, k, c are equivalent stiffness and damping coefficients of the total test system, k_s, c_s are those for the residual force, and x, v are experimentally obtained displacement and velocity. These stiffness and viscous coefficient were identified by employing a nonlinear least square method, minimizing the following evaluation functions.

$$E_e = \int_0^T \left| \left(I_e(t) - I(t) \right) x(t) \right|^2 dt \tag{2}$$

$$E_s - \int_0^T \left| \left(F_{se}(t) - F_s(t) \right) x(t) \right|^2 dt \tag{3}$$

In these functions, I_e and F_{se} express experimentally obtained inertial and residual forces, and T is a duration of motion. This procedure determines the model parameters so as for the energy dissipation time history of the model to trace that of experiment as closely as possible. Given these parameters, equivalent damping ratios for the total system (h_t), residual force (h_s) and damper (h_d) were calculated as follows.

$$h_t = \frac{c}{2\sqrt{mk}}, \quad h_s = \frac{c_s}{2\sqrt{mk}}, \quad h_d = h_t - h_s \tag{4}$$

Where, m is a mass of the girder. Figure 10 shows the contribution of the structural damping (h_s) and damper (h_d) to the total damping ratio with regard to both input motions. It is found that the supplemental dampings due to the damper increased the system's total damping almost twice as the original one. It is concluded from series of tests that the proposed damper has a capability to dissipate seismic energy effectively without transmitting excessive inertia force to the main structure even under strong motions.

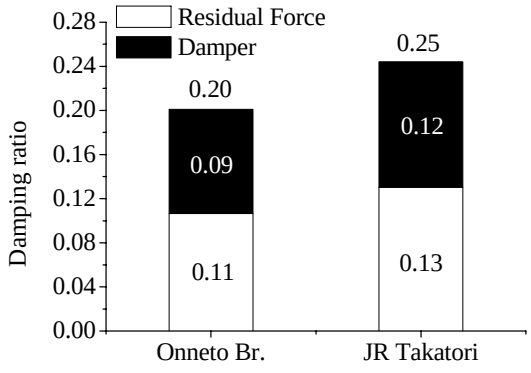

Figure 10 Estimated damping ratios due to residual force and dampers

5. CONCLUSION

In this research, the new friction damper applicable for civil engineering structures was newly developed. The damper holds several features advantageous over traditional structural control devices, such as tiny space for installation and easiness of performance adjustment. The prototype of the damper was assembled, and its dynamic behavior was investigated through large-scale shaking table tests. It was clearly confirmed from periodical loading tests that the device generated the stable energy dissipation and friction force regardless of the input frequency or amplitude. It was also found that the damper successfully introduced the supplemental damping to the structure under both long-term and intense earthquakes, the amount of which was approximately 10%.

ACKNOWLEDGEMENT

The dedication of Mr. Ichikawa (Engineering staff of Kyoto University), DAMPTECH Co., Kawaguchi Metal Industries Co., Ltd., Mr. Yokita (alumnus of Kyoto Univ., now Kyushu Electric Power Company), Mr. Takahashi (graduate student of Kyoto Univ.), Nomura Jyuuki Ltd., staff and students of Kyoto University for carrying out the shaking table tests is fully appreciated.

REFERENCES

Mualla, I.H. (2000a). Experimental Evaluation of a New Friction Damper Device, 12th World Conference on Earthquake Engineering, Auckland, New Zealand.

Mualla, I.H. (2000b). Parameters Influencing the Behavior of a New Friction Damper Device. SPIE's 7th International Symposium on Smart Structures & Materials, SS2000, CA, USA, 2000.

Toyooka, A., Himeno, T., Hishijima, Y., Iemura, H., and Mualla, I.H. (2008), "Verification tests of the dynamic behavior of the novel friction-based rotational damper using shaking table," Proc. of the 14th World Conference on Earthquake Engineering, Beijing, China.

Mualla, I.H., and B. Belev. (2001) Performance of Steel F rames with a New Friction Damper Device Under Earthquake Excitation. J. of Engineering Structures, Elsevier (in press).

Aiken, I.D. & Kelly, J.M. (1990). Earthquake simulator testing and analytical studies of two energy-absorbing systems for multistory structures. Report No. UCB/EERC-90-03, University of California, Berkeley.

Kelly, J.M. (1999). The role of damping in seismic isolation. Earthquake Engng. Struct. Dyn 28:3-20.

I. H. Mualla, L.O. Nielsen, B. Belev, W. I. Liao, C. H. Loh, A. Agrawal. (2002). Performance of Friction-Damped frame Structure: Shaking Table Testing and Numerical Simulations, 7th U.S. National Conference on Earthquake Engineering, Boston, USA.

Nielsen LO, Mualla IH, Iwai Y. (2004). Seismic Isolation with a new Friction-Viscoelastic Damping System, 13th World Conference on Earthquake Engineering, Vancouver, Canada.

Sixth International Conference on Urban Earthquake Engineering
March 3-4, 2009, Tokyo Institute of Technology, Tokyo, Japan

SEISMIC RETROFIT DESIGN OF TEMPOZAN CABLE-STAYED BRIDGE

Hiroshi Kobayashi[1)], Nobuhiro Mashima[2)], Hiroyuki Nagareta[3)], and Tsutomu Nishioka[4)]

1) Survey and Design Group, Osaka Business and Maintenance Dept., Hanshin Expressway Co. Ltd, Japan
2) Survey and Design Group, Osaka Business and Maintenance Dept., Hanshin Expressway Co. Ltd, Japan
3) Specific Planning Group, Planning Dept., Hanshin Expressway Co. Ltd, Japan
4) Design Management and Engineering Research Group, Engineering Dept., Hanshin Expressway Co. Ltd, Japan
hiroshi-kobayashi@hanshin-exp.co.jp, nobuhiko-mashima@hanshin-exp.co.jp, hiroyuki-nagareta@hanshin-exp.co.jp, tsutomu-nishioka@hanshin-exp.co.jp

Abstract: This paper describes the seismic retrofit for Tempozan Bridge on Hanshin Expressway. Tempozan Bridge is continuous three-span of 640m (120+350+170m) cable-stayed bridge. For evaluating the seismic performance of this bridge, huge possible earthquakes at the bridge site are considered as input motions of 3-D dynamic analysis. As the result of the analysis, the scenario of seismic damage and policy of retrofits are determined. It is evaluated that adopting the shear panel dampers at diagonal braces of the towers, is particularly effective for absorbing the seismic energy. The seismic performance of shear panel damper is verified experimentally.

1. INTRODUCTION

After 1995 Kobe Earthquake, seismic retrofits for existing bridges have been implemented steadily in Japan. Hanshin expressway had already completed seismic countermeasures such as reinforcing the piers and adopting the bridge restrainer systems for most of general elevated bridges. However, in case of long-span bridges or special type bridges, the seismic countermeasures are making little headway because these bridges require advanced analysis techniques and it is not rational to apply the same methods for general bridges. When these bridges were damaged heavily, the influence such as cost and time for recovery could be greater than those of general bridges. Therefore, early seismic retrofits for long-span bridges or special-type bridges are recommended.

As a case example for seismic damage of cable-stayed bridge, Higashi Kobe Bridge (Bridge length; 885m, center span length; 485m) on Hanshin expressway at 1995 Kobe Earthquake is known. This bridge has a long natural period of 4.4 second for longitudinal direction, it caused little damage in longitudinal direction, but in transverse direction, wind shoes which support the transverse force were destroyed and secondary eye-bar pendulum supports which resist constant uplift force were broken. As the result, side span of the bridge was lifted up and the difference in level of 1m occurred in the road surface. In the case of the other cable-stayed bridges on Hanshin expressway, the seismic damage from 1995 Kobe Earthquake was minor. However, there is a risk which suffers from a huge possible earthquake in the future, it is necessary to evaluate the seismic performance of present structural condition and to determine the optimal retrofitting. In this paper, the study for seismic retrofit on Tempozan Bridge is described. Tempozan Bridge is continuous three-span of 640m (120+350+170m) cable-stayed bridge as shown in Figure 1 and Figure 2.

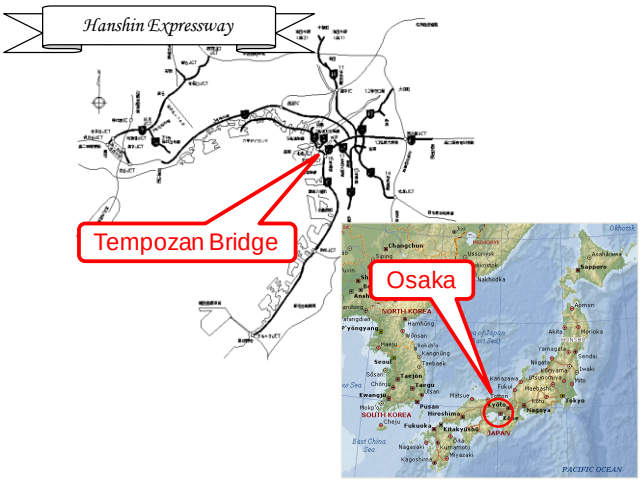

Figure 1 Location of Tempozan Bridge

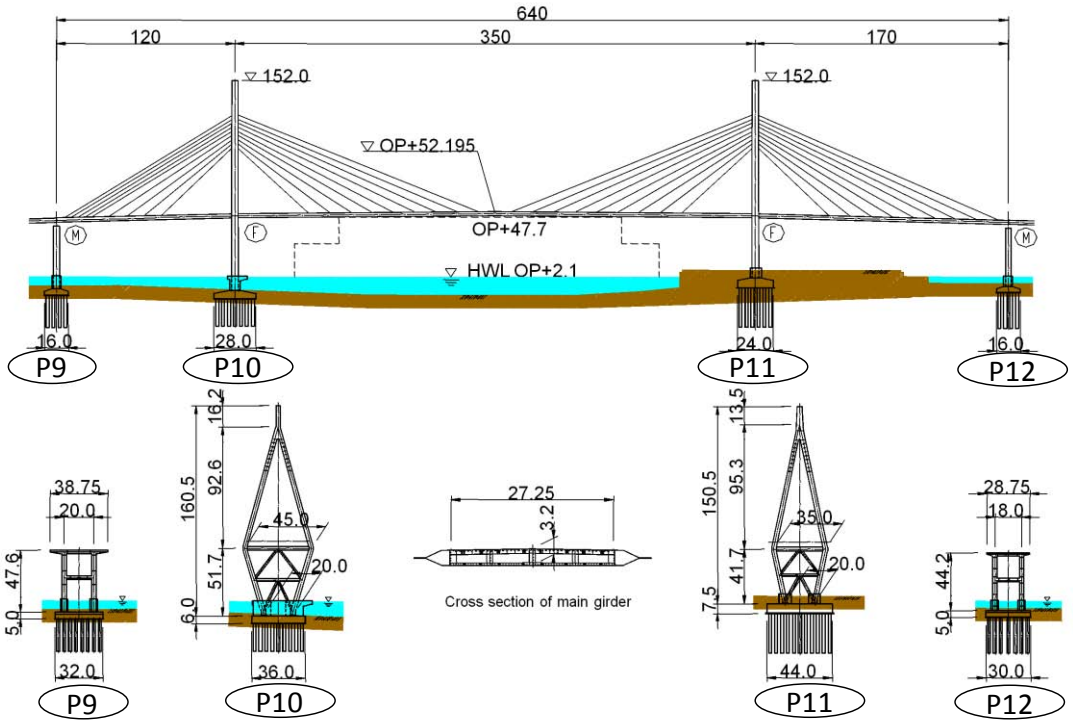

Figure 2 General view of Tempozan Bridge

2. OUTLINE OF TEMPOZAN CABLE-STAYED BRIDGE

Tempozan Bridge has continuous steel box-girder which is supported by stay cables from two steel towers, and two steel rigid-frame piers at both ends. For constant uplift force caused by imbalanced side span distribution, pendulum supports are adopted at both ends.

Because the main girder is 50 meters above water level, this bridge is longitudinally fixed at two flexible towers P10 and P11 in consideration of seismic design. It results in longer natural period of more than 3 seconds in the longitudinal whole structure oscillation mode and this long period alleviates the seismic inertia force on the superstructure.

For the transverse seismic force, horizontal beam and diagonal bracing are installed at lower section from the main girder in the towers and at both ends on the rigid-frame piers, the wind shoes are installed to prevent too much displacement.

3. EVALUATION OF SEISMIC PERFORMANCE

3.1 Input earthquake motion

As for input earthquake motion, natural period characteristic of Osaka Bay area is considered. For this study, the scenario earthquake at the bridge site, which was made by hybrid method on the basis of three-dimensional subsurface structure of Osaka basin, is used. To put it concretely, at first basic design, spectral envelope (hereinafter referred to as spectral envelope) is made from six varieties of acceleration response spectrums which are selected from preliminary examination; next adjusted input wave for final study is adopted. The comparison of the spectral envelope and the acceleration response spectrums of Japanese specifications for highway bridges are shown in Figure 3.

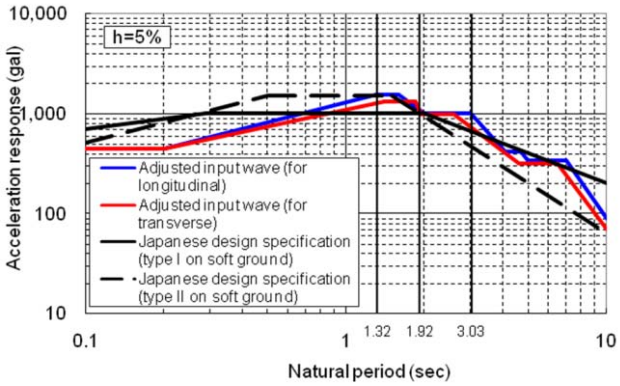

Figure 3 Comparison of spectral envelope and acceleration response spectrums of Japanese specifications for highway bridges

3.2 Dynamic analysis model

Cable stayed bridge is very flexible structure, especially in Tempozan Bridge, large horizontal displacement is caused at the earthquake. Therefore, the following influences to the sectional force on the member with geometric nonlinearity

were studied by limited displacement analysis.

1. The horizontal force on pendulum support caused by the relative displacement on the end of girder.
2. The additional bending moment at the member on the tower caused by longitudinal earthquake input.
3. The additional bending moment at the member on the tower caused by transverse earthquake input.

As the results of the analyses, it became clear that the influences with geometric nonlinearity were sufficiently small except to the horizontal force on pendulum support. The pendulum support was modeled as illustrated in Figure 4. Whole bridge model for dynamic analysis is shown in Figures and each member models which were considered as non-linear elements are shown in Table 1. The results of eigenvalue analysis are shown in Table 2.

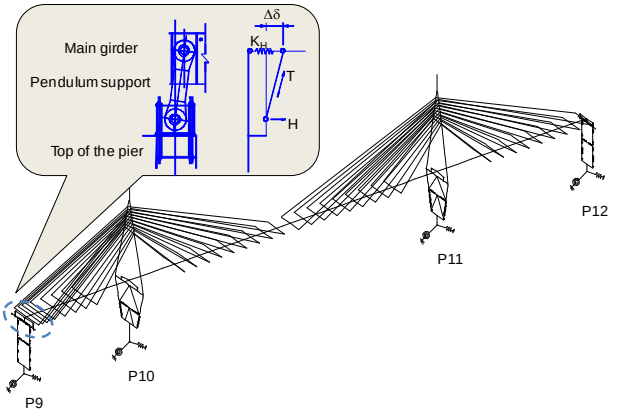

Figure 4 Dynamic analysis model for whole bridge and the pendulum supports

Table 1 Non-linear member models

Bending members	Axial members (Diagonal bracings of the towers)
M-ϕ curve (Bilinear model)	N-ε curve (Elastic-perfectly plastic solid model)
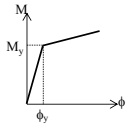	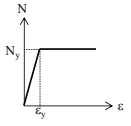
Shear members (Horizontal beams of the piers)	Pendulum supports
S-γ curve (Bilinear model)	H-Δδ curve (Nonlinear spring)
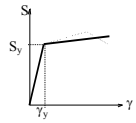	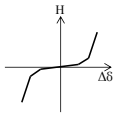

Table 2 The result of eigenvalue analysis

Dominant Vibration Mode	Longitudinal	Transverse	
		Main span	Side span
Natural Period [sec]	3.33	2.13	1.40
Effective Mass Ratio M_X	21%	10%	22%

3.3 Result of analysis and policy of retrofit

Non-linear time history response analysis for dynamic analysis model shown in Figure 4 was conducted making use of the input earthquake motion which described above.

a) Responses of longitudinal direction

The analytical result for longitudinal response is shown in Figure 5. This bridge is fixed at two towers and so seismic inertia forces are transmitted to the tower members through the supports at the towers. Therefore, the horizontal reaction forces of the supports at the towers and response curvatures at the base of towers enlarge, so each response value exceeded the yield value largely. At the same time, relative displacement responses between main girder and the top of the end piers are as large as approximately two times allowable displacement of the pendulum supports.

b) Responses of transverse direction

The analytical result for transverse response is shown in Figure 6. The horizontal reaction forces exceeded the allowable horizontal reaction forces at three supports of four. The response sectional forces exceeded the yield resistances on the diagonal braces, horizontal beams and column members at the towers. The response strains at the diagonal braces exceeded the yield point partly. The end piers are rigid double-deck frame pier which have large aspect ratio, large shearing force acting on the horizontal beams and the response shearing force at the central part of the beams exceeded the yield point. The responses of curvature at the basis and the corner zones of the end piers exceeded the yield point at most parts.

c) The Scenario of seismic damage and policy of retrofits

Fatal damage situations that would happen in Tempozan Bridge by huge earthquake are evaluated as follows:

i) The horizontal reaction force for transverse direction or excessive horizontal displacement for longitudinal direction cause damage of the wind shoe which is linked to damage of the pendulum supports. When the pendulum supports are destroyed, excessive displacement and stress as shown in Figure 7 would act, and there could be a possibility of the collapse of the bridge.

ii) When the pivot supports which fix this bridge is destroyed, the main girder would move and hit to the tower as shown in Figure 8. Then there is possibility of the damage or collapse of the tower, which would directly lead to collapse the bridge.

iii) Although it would not directly lead to collapse of the bridge, there is a possibility that buckling or damage of the member which caused from excessive stress, would lead to unacceptable residual deformation.

Among these damage situations, i) and ii) are really fatal damage situation and these must be evaded. However,

in the case of iii), the required performances (e.g. allowable deformation of the member) need to be determined concretely with consideration for level of damage, effects on other member, repair difficulty level, and so on. The policies of retrofits for Tempozan Bridge based on the scenario of seismic damage are summarized as Table 3.

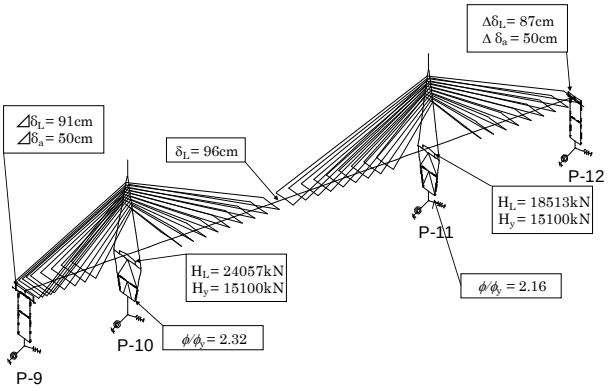

Figure 5 The analytical results for longitudinal response

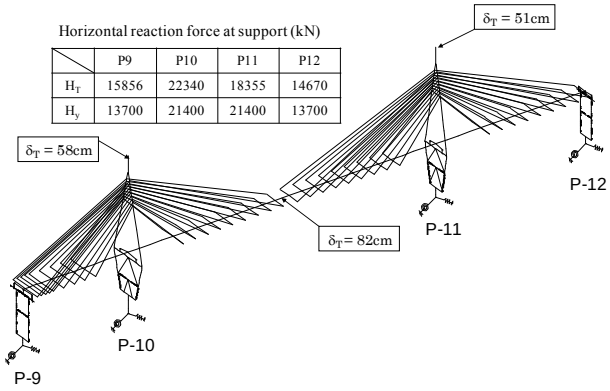

Figure 6 The analytical results for transverse response

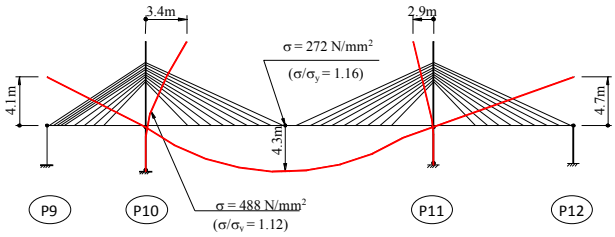

Figure 7 Response displacement and stress after destroying the pendulum support

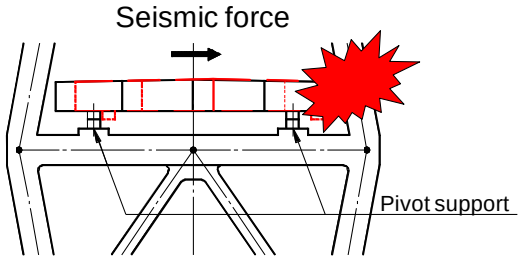

Figure 8 Collision between tower and main girder after destroying the pivot support

Table 3 The policy of retrofits for Tempozan Bridge

Members			Input direction	Policy for retrofit
Supports	Pendulum support		Longitudinal	Adopting a device which limits relative displacement between main girder and end pier less than 50 cm
	Wind support		Transverse	Strengthen the supports or adopting displacement limit devices
	Pivot support		Longitudinal	
			Transverse	
Towers	Column member		Longitudinal	Guarantee required ductility by obtaining enough energy absorption
	at near the base		Transverse	
	Diagonal brace		Transverse	
	Horizontal beam		Transverse	Guarantee required ductility by reinforcing for local buckling
End piers	Horizontal beam		Transverse	Strengthen for shear buckling and guarantee shear ductility
	Column member	Corner zone	Transverse	Guarantee required ductility by reinforcing for local buckling
		Near the base	Transverse	
Main	Center of main span		Transverse	Prevention of buckling of outer web
Whole bridge			Longitudinal	Decrease of seismic response by installation of seismic isolation device or damping device and guarantee required ductility of each
			Transverse	

4. CONTENTS OF RETROFITTING

Based on the policies summarized as Table 3, seismic retrofitting for Tempozan Bridge will be executed. The methods and the effect of each object members are described as follows.

4.1 Towers

a) Methods of retrofitting

At lower part of the towers, concrete will be filled as shown in Figure 9 for the purpose of guaranteeing the ductility for longitudinal and transverse direction. Additionally, shear panel damper that use low yield point steel panels will be installed at diagonal braces of the towers

which resist a horizontal force during earthquake as shown in Figure 9 for the purpose of decreasing the acting horizontal force less than shear yield point and absorbing the seismic energy.

b) Verification of effect

The shear panel damper was modeled as shown in Figure 10. H_y in Figure 10 is determined as 90% as horizontal component of buckling capacity at the diagonal braces. Initial size of shear panel damper was decided that permissible strain of the shear panels are 3%.

Comparison of seismic response displacements at focused points between before and after installation of shear panel damper are shown in Figure 11. Response displacement in transverse direction at the top of P10 was increased slightly caused by plastic deformation of the shear panel damper. However, the other responses including horizontal reaction force of the supports were decreased by adoption of the shear panel dampers. Maximum responses on the tower members were all fitted into elastic range as shown in Figure 12 except the shear panel dampers.

Focused on seismic responses on shear panel dampers, it is confirmed that maximum response of shear strain did not reach to their allowable value of 3% but the number of times which exceed elastic range was quite a lot. Therefore, decrease of allowable shear strain on the shear panel damper that caused by repeated plastic deformation was concerned, cumulative plastic shear strain which is calculated as shown in Figure 13 was determined as performance indicator and verification test was executed.

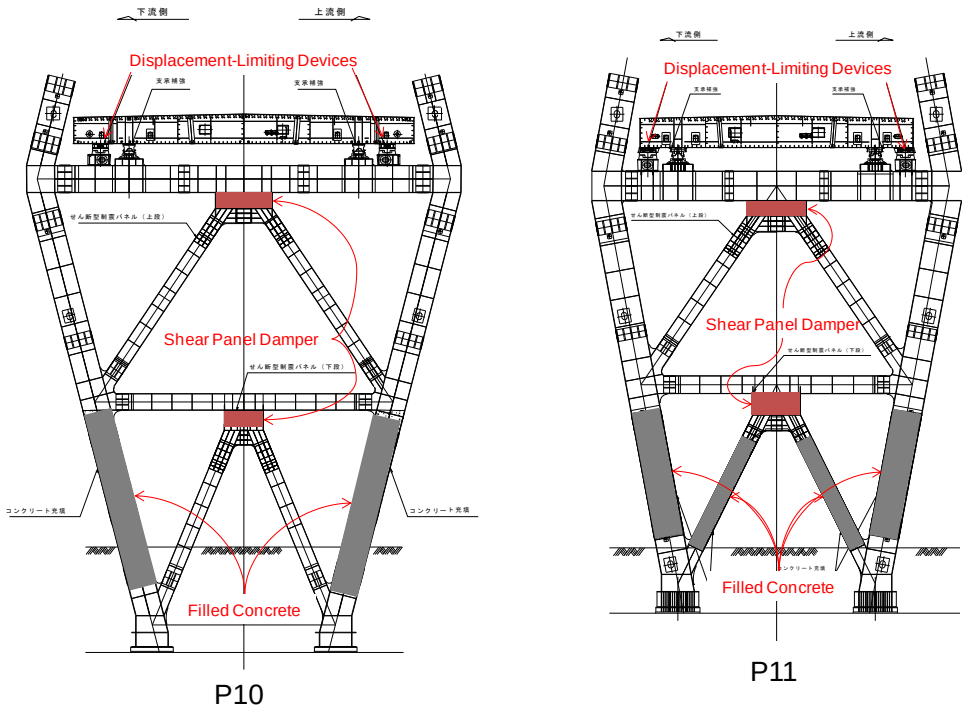

Figure 9 The retrofit method for the towers

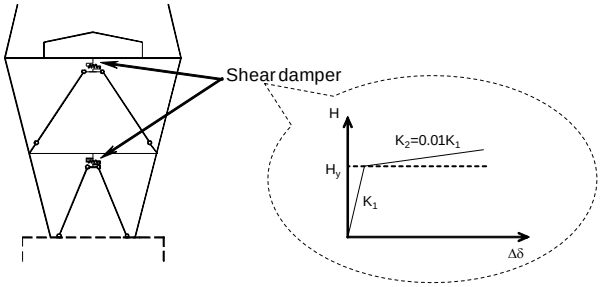

Figure 10 The relationship between horizontal force and displacement of shear panel damper model

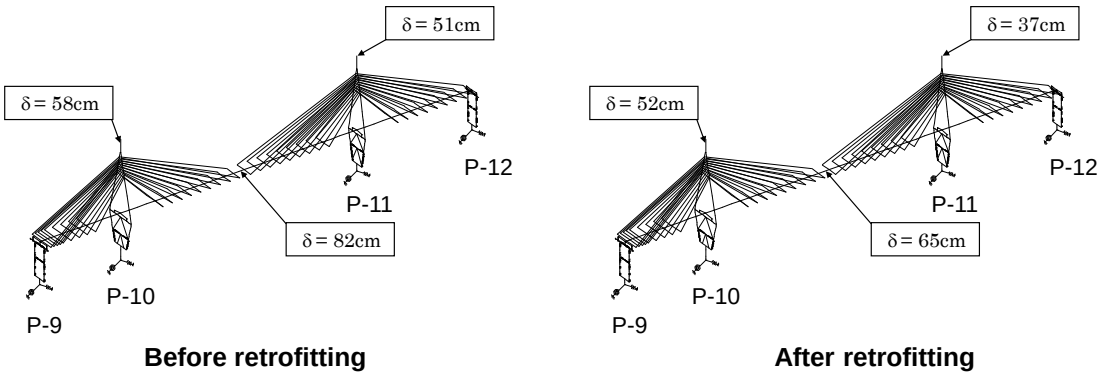

Figure 11 The effect of the shear panel dampers in seismic response

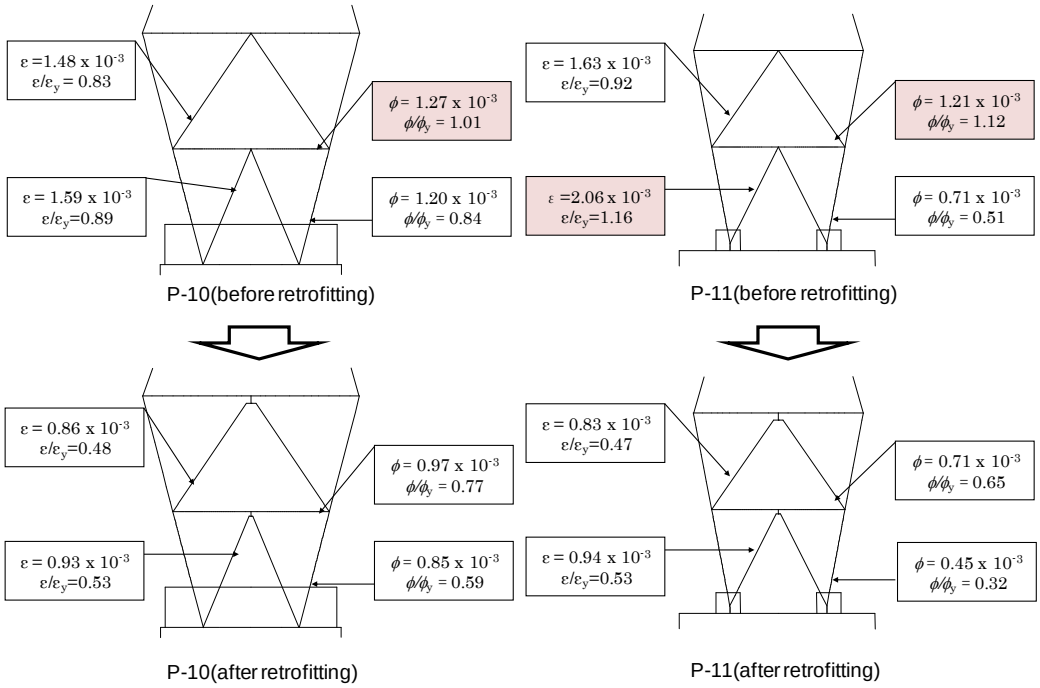

Figure 12 Maximum responses on the tower members

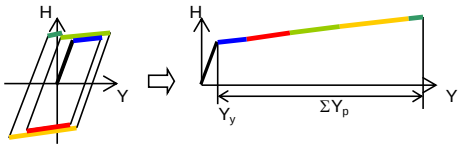

Figure 13 Calculation of cumulative plastic shear strain

4.2 End piers

To achieve the performance described in Table 3, required ductility for transverse direction at end piers must be guaranteed. Concrete filling in near the base of the column members and adopting horizontal stiffeners in horizontal beams will be implemented for increasing their ductility.

4.3 Bearing supports

To achieve the performance described in Table 3, the pivot supports (fixed support) on the towers will be strengthened in longitudinal direction, and displacement-limiting devices and high-damping rubber bearings will be installed on the end piers for limiting the relative displacement between main girder and end pier. In transverse direction, displacement-limiting devices will be installed for preventing the destruction of wind shoes on the end piers. In vertical direction, uplift-preventive cable will be installed between main girder and the end piers as a fail-safe device on the assumption that the pendulum support would be destroyed.

5. VERIFICATION TEST FOR SHEAR PANEL DAMPER

5.1 Experiment objective

Verification test for shear panel damper which are

installed in gusset plate at diagonal brace of the towers was conducted in order to confirm or verify following items:

a) Hysteresis curve (H-γ relationship)

In order to verify the validity of hysteresis model for shear panel damper in dynamic analysis (shown in Figure 10), the relationship between horizontal load and shear strain would be confirmed by cyclic loading test.

b) Deformation performance (Low-cycle fatigue)

Allowable shear strain γ_a for deformation performance check and allowable cumulative plastic shear strain $\Sigma\gamma_p$ (shown in Figure 13) would be configured from the result of these tests.

c) Influence of axial force that acts on the shear panel damper

Influence of axial force to the performance of the shear panel damper would be confirmed because they are installed in gusset plate at diagonal brace of the towers where vertical axial force acts due to dead load.

5.2 Specimen and setup

The specimen and the setup of these tests are shown in Figure 14 and Figure 15. Three same type specimens which were designed as allowable shear strain of 6% were made and they were named C1, C2, and C3. Each specimen was loaded horizontally under axial force of 0kN, 240kN (for dead load situation) and 360kN (for live load situation). Horizontal loading was conducted with displacement (strain) control and increased step by step of 1% strain in both directions.

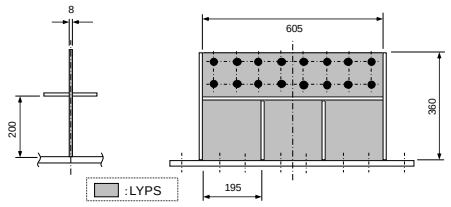

Figure 14 The specimen of the verification test

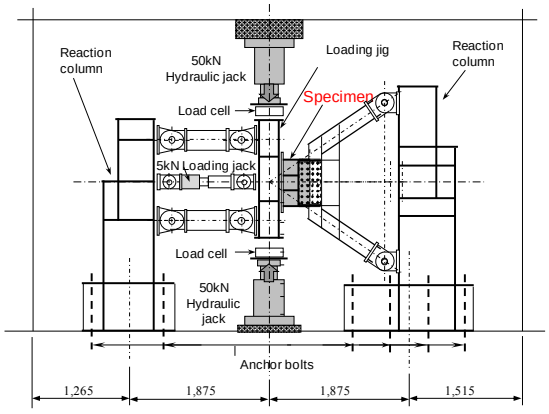

Figure 15 The setup of the verification test

5.3 Results of the test

All tests were stopped because large gap between specimen and supporting jig occurred. Every specimen were loaded cyclically in both direction to 9% of shear strain, but C1 specimen under no axial force continued to be loaded monotonically until 18% of shear strain. Decreases of load were not observed clearly in all specimens during the tests.

a) Horizontal load-shear strain relationship

Relationships between horizontal load and shear strain (H-γ relationship) of each specimen are shown in Figure 16. The bi-linear relationship shown in Figure 10 and tri-linear relationships which consider the effect of the members to restrain the shear panel are also shown in the figures. According to the graph, H-γ relationship of shear panel damper has the following characters:

i) Yield load Hy is increased during the cyclic load in the plastic region.
ii) Stiffness (shown as slope of H-γ curve) in plastic region is decreased as frequency of repetition loading increases.
iii) H- γ relationship is affected by the stiffness of not only the shear panel but the members that restrain the panel.
iv) The difference of the hysteresis with the axial force is seldom seen.

b) Cumulative plastic shear strain and deformation performance

As the results of dynamic analysis, cumulative plastic shear strains of four shear panel dampers which would be adopted in Tempozan Bridge are 0.211 to 0.377. It shows that the shear panel dampers of this bridge will suffer about 0.4 of cumulative plastic shear strain during a huge earthquake, therein stable performance will be required. The cumulative plastic shear strains of the test specimen are estimated from H-γ relationship shown in Figure 16 and they are 1.745 in C1 and 2.064 in both C2 and C3. It is confirmed that the shear panel dampers are able to expect sufficient performance during a huge earthquake from the fact that the decrease of loading capacity is not observed during the test.

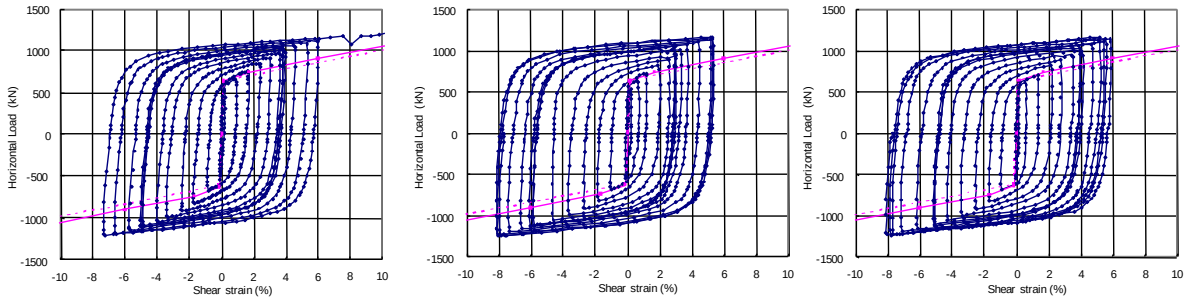

Figure 16 H-γ relationship of each specimen

6. CONCLUSIONS

This paper describes the study on seismic retrofit of Tempozan Bridge in Hanshin Expressway and verification test for shear panel damper. Contents are collected below:

- The input earthquake motions for this study were developed from the scenario earthquakes which would be estimated to occur at the bridge site.
- The influences with geometric nonlinearity of the bridge were studied before conducting 3-D dynamic analysis. As the result of the study, they are sufficiently-small except to the horizontal force on pendulum support.
- As the results of the dynamic analysis, the following scenario is assumed; when the pivot supports which fix this bridge is destroyed, the main girder moves and hits to the tower. Then there is possibility of the damage or collapse of the tower, which would directly lead to collapse of the bridge.
- Although it would not directly lead to collapse of the bridge, there is a possibility that buckling or damage of the member which caused from excessive stress, would lead to unacceptable residual deformation.
- Responding to the assumed scenario, concrete will be filled at lower part of the towers for increasing the ductility, and shear panel damper will be set at diagonal braces of the towers for the purpose of absorbing the seismic energy.
- Verification tests for shear panel damper were carried out. As the result, their seismic performances were verified and the difference of the hysteresis with the axial force was seldom seen.

References:

Ishibashi T, Hamada N, Kanaji H, Noguchi J and Kobayashi Y.(2005), "Seismic Evaluation on existing 3-span continuous steel cable-stayed bridge which is 640m long," *Proceedings of the 8th Symposium on earthquake-resistant design of bridges based on the post-earthquake retained bearing strength method*, Japanese Society of Civil Engineers, (In Japanese)

Nagareta H, Hamada N, Kobayashi H and Nishioka T.(2008), "Verification Test for Shear Panel Damper Using Low-Yield Point Steel," *Proceedings of the 11th Symposium on earthquake-resistant design of bridges based on the post-earthquake retained bearing strength method*, Japanese Society of Civil Engineers, (In Japanese)

Sixth International Conference on Urban Earthquake Engineering
March 3-4, 2009, Tokyo Institute of Technology, Tokyo, Japan

DYNAMIC ANALYSIS OF BRIDGES IN THE ULTIMATE STATE UNDER EARTHQUAKES

Tzu-Ying Lee[1], Po-Hung Chen[2], and Ren-Zuo Wang[3]

1) Assistant Professor, Department of Civil Engineering, National Central University, Taiwan
2) Former Graduate Student, Department of Civil Engineering, National Central University, Taiwan
3) Associate Researcher, National Center for Research on Earthquake Engineering, Taiwan
tylee@ncu.edu.tw, c0937823804@gmail.com, rzwang@ncree.org.tw

Abstract: This study is aimed to analyze the ultimate situation of isolated bridges with unseating prevention devices under extreme earthquakes. Since the Vector Form Intrinsic Finite Element (VFIFE) has the superior in managing the engineering problems with material nonlinearity, discontinuity, large deformation, large displacement and arbitrary rigid body motions of deformable bodies, it is selected to be the analysis method in this study. The analysis methods for sliding of structures and fracture of elements are herein developed to predict the failure process of the bridges. Through numerical simulation of an isolated bridge with a five-span simply-supported deck and unseating prevention devices, the ultimate state is demonstrated. The results confirm that the VFIFE is a powerful computation method to simulate the failure device of the isolators, columns and unseating prevention devices and to predict the collapse situation of bridges.

1. INTRODUCTION

In the past extreme earthquakes, such as Kobe earthquake and Chi-Chi earthquake, a number of bridges suffered damage with unseating of the superstructures. Isolated bridges have been extensively used to mitigate the induced seismic forces by a shift of natural period. However, the trade-off is that the deck displacement becomes excessively large when subjected to a ground motion with large intensity or unexpected characteristics. Such a large displacement may increase the hazard of the unseating of decks. Therefore, unseating prevention devices are important for isolated bridges in particular (Kawashima and shoji 2000). Lately, modern bridge seismic design has been developed toward the seismic performance design on whole bridges as well as their elements. Understanding of the performance of the components of isolated bridges, such as bearings, unseating prevention devices, columns, under extreme condition shall be favorable to determine the goal of performance. In this paper, a new nonlinear structural dynamic analysis method is studied to simulate the dynamic behavior of the isolated bridges with unseating prevention devices under extreme earthquakes.

The Vector Form Intrinsic Finite Element (VFIFE), a new computational method developed by Ting et al. (2004), is adopted in this study because the VFIFE has the superior in managing the engineering problems with material nonlinearity, discontinuity, large deformation, large displacement and arbitrary rigid body motions of deformable bodies. To simulate the extreme situation of bridges, the analysis methods for sliding of structures and fracture of elements are developed in this study. Numerical simulation of a practical isolated bridge with unseating prevention devices is conducted to predict the failure process. The results present the design concept of the fracture sequence of the structural components. Due to the insufficient strength of the unseating prevention devices, the unseating of decks occurs under an ultimate condition.

2. VECTOR FORM INTRINSIC FINITE ELEMENT

The Vector Form Intrinsic Finite Element has been developed based on theory of physics mainly to simulate failure response of a structural system due to applied loads. The first step in VFIFE analysis is to construct a discrete model for a continuous structure. It is noted that the continuous element mass must be lumped into the adjoining nodes. The equations of motion are established at each node for all degrees of freedoms by using Newton's Second Law of Motion. Assume that a structural system consists of a finite number of particles with mass, which are connected by deformable elements without mass. A particle designated as α has a mass value $\mathbf{M}^{\alpha}$ and a displacement $\mathbf{d}^{\alpha}(t)$ at time t. The equation of motion for particle α is

$$\mathbf{M}^{\alpha}\ddot{\mathbf{d}}^{\alpha}(t) = \mathbf{P}^{\alpha}(t) - \mathbf{f}^{\alpha}(t) \tag{1}$$

where $\mathbf{P}^{\alpha}$ is the applied force or equivalent force acting on the particle; $\mathbf{f}^{\alpha}$ is the total resistance force exerted by the elements surrounding the particle, or the internal force. Each element without mass is in static equilibrium.

Since the failure progress of structures involves changes in material properties and structural configuration, discrete time domain analysis is adopted to solve the equations of

motion, Eq. (1). In calculating the internal forces, a set of deformation coordinates is defined for each element and for each time increment. Compared to the traditional finite elements, the feature of VFIFE is the calculation of rigid body motion and deformation of elements through the deformation coordinates in each time increment. By doing so, VFIFE can deal with large displacement, deformation and rigid body motion simultaneously without numerical instability.

For multi-degree-of-freedom systems, it is not necessary to assemble the global property matrices of structures in VFIFE analysis, i.e. matrix algebraic operation is waived. In stead, only scalar calculation is needed for each particle.

The central difference method, an explicit time integration method, was adopted to solve the equations of motion Eq. (1) by Ting et al. (2004). The acceleration $\ddot{\mathbf{d}}_i^{\alpha}$ can be approximated as

$$\ddot{\mathbf{d}}_i^{\alpha} = \frac{\mathbf{d}_{i+1}^{\alpha} - 2\mathbf{d}_i^{\alpha} + \mathbf{d}_{i-1}^{\alpha}}{(\Delta t)^2} \tag{2}$$

where Δt is the incremental time.

Substitution of Eq. (2) into Eq. (1) gives

$$\hat{\mathbf{K}}^{\alpha}\mathbf{d}_{i+1}^{\alpha} = \hat{\mathbf{P}}_i^{\alpha} \tag{3}$$

where

$$\hat{\mathbf{K}}^{\alpha} = \frac{1}{(\Delta t)^2}\mathbf{M}^{\alpha} \tag{4}$$

$$\hat{\mathbf{P}}_i^{\alpha} = \mathbf{P}_i^{\alpha} - \mathbf{f}_i^{\alpha} + \frac{2\mathbf{M}^{\alpha}}{(\Delta t)^2}\mathbf{d}_i^{\alpha} - \frac{\mathbf{M}^{\alpha}}{(\Delta t)^2}\mathbf{d}_{i-1}^{\alpha} \tag{5}$$

3. SIMULATION OF ULTIMATE STATE

Bridges may undergo nonlinear behavior even structural failure when subjected to extreme earthquakes. In the past large earthquakes, a number of bridges suffered deck unseating, which is high nonlinearity along with rigid body motion, such as in the 1995 Kobe, Japan earthquake, and the 1999 Chi-Chi, Taiwan earthquake. To simulate the failure progress of bridges, the failure mechanism of major components of bridges should be taken into account.

Isolated bridges with unseating prevention devices are investigated in this study. The studied failure components are isolators, unseating prevention devices and plastic hinges of columns. Firstly, high-damping-rubber isolators idealized as a bilinear model are used in the target bridge. Assume that the isolators fracture as the deformation reaches rupture deformation. Once the isolator breaks, there is no restoring shear force between the superstructure and column other than the friction force at the interfaces. When the relative displacement between superstructure and column exceeds the unseating length, the superstructure will lose the supporting force provided by the column and fall down from the column due to the gravity force.

The failure of isolators represents a typical failure mechanism completing material linear and nonlinear hysteretic behavior, fracture, and sliding of structures. The writers (Lee et al. 2008) have developed the nonlinear elements in VFIFE in the previous study. This paper herein presents the analytical methods for sliding structures and fracture of elements in VFIFE.

3.1 Sliding of Structures

After the isolator ruptures, the interface between the superstructure and the column turns to a sliding surface if the relative displacement between the superstructure and the column is still within the unseating length. The motion on the sliding surface can be separated into stick and slip phases. When the friction force is smaller than the maximum static friction force, there is no relative motion in the interface, i.e. in stick phase. Once the friction force overcomes the maximum static friction force, relative movement starts in the interface and the friction force converts to dynamic friction force, i.e. in slip phase. In this study, assume that the maximum static friction force is equal to the dynamic friction force, and the dynamic friction coefficient remains constant during sliding.

In the calculation process of VFIFE, the material properties and structural configuration are assumed to be unchangeable in each time increment. Therefore, the interface should be in either stick phase or slip phase during the incremental time. Before solving the response at next time step $i+1$, the condition at the interface must be determined. In this study shear-balance procedure, which was proposed by Wang et al. (2001) for analyzing sliding structures by state-space approach, is used to judge which phase the interface is in.

The first step is to calculate the friction force in the interface on assumption of stick phase. It is noted that the relative displacement is null in stick phase. The interface is in stick phase if the calculated friction force is less than the dynamic friction force while it is in slip phase if the calculated friction force is equal or larger than the dynamic friction force.

Figure 1 illustrates the motion of the superstructure with mass $\mathbf{M}^p$ and the column with $\mathbf{M}^b$ at time step i and $i+1$. The equations of motion for the two masses in the central difference equations are

$$\hat{\mathbf{K}}^p\mathbf{d}_{i+1}^p = \hat{\mathbf{P}}_i^p - \mathbf{f}_{Fi} \tag{6}$$

$$\hat{\mathbf{K}}^b\mathbf{d}_{i+1}^b = \hat{\mathbf{P}}_i^b + \mathbf{f}_{Fi} \tag{7}$$

where $\mathbf{f}_{Fi}$ is designated the friction force in the interface. If the interface is in stick phase, the relative displacement $\mathbf{u}_i = \mathbf{d}_i^p - \mathbf{d}_i^b$ between the superstructure and the column at time step i is the same as the relative displacement $\mathbf{u}_{i+1} = \mathbf{d}_{i+1}^p - \mathbf{d}_{i+1}^b$ at time step $i+1$.

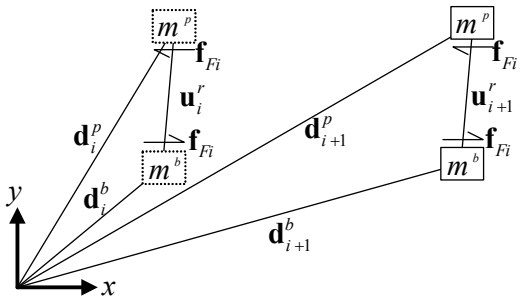

Fig.1 The motion of the superstructure and the column

$$\mathbf{d}_{i+1}^p - \mathbf{d}_{i+1}^b = \mathbf{d}_i^p - \mathbf{d}_i^b \tag{8}$$

Rearranging and substituting Eqs. (6) and (7) into Eq. (8), the calculated friction force $\tilde{\mathbf{f}}_{Fi}$ is obtained as

$$\tilde{\mathbf{f}}_{Fi} = \frac{\hat{\mathbf{K}}^b \hat{\mathbf{P}}_i^p - \hat{\mathbf{K}}^p \hat{\mathbf{P}}_i^b - \hat{\mathbf{K}}^p \hat{\mathbf{K}}^b \left(\mathbf{u}_i^p - \mathbf{u}_i^b\right)}{\hat{\mathbf{K}}^p + \hat{\mathbf{K}}^b} \tag{9}$$

If the calculated friction force $\tilde{\mathbf{f}}_{Fi}$ is less than the dynamic friction force, the assumption of stick phase is true and the calculated friction force can be used in the next time increment, i.e. $\mathbf{f}_{Fi} = \tilde{\mathbf{f}}_{Fi}$. Otherwise, the interface is in slip phase. The friction force $\mathbf{f}_{Fi}$ must be substituted by dynamic friction force μN, i.e. $\mathbf{f}_{Fi} = \mu N$. The above can be summarized as

$$\begin{cases} \mathbf{f}_{Fi} = \mu N & \text{if } \tilde{\mathbf{f}}_{Fi} \geq \mu N, \text{ slip phase} \\ \mathbf{f}_{Fi} = \tilde{\mathbf{f}}_{Fi} & \text{if } \tilde{\mathbf{f}}_{Fi} < \mu N, \text{ stick phase} \end{cases} \tag{10}$$

where μ is dynamic friction coefficient; N is the normal force in the interface.

3.2 Fracture of Elements

The first design principle of isolated bridges is the appropriate utilization of isolators and dampers to shift the main periods of vibration and increase the energy-dissipation capacity of the structures (Priestley et al. 1996). High damping rubber bearings and lead-rubber bearings, which have both the functions, are commonly utilized. Both bearings can be idealized by a bilinear model. In addition, it has been shown in the past study that the columns of isolated bridges may exhibit nonlinear behavior under extreme earthquakes (Lee and Kawashima 2007). The bilinear model can also be used to idealize reinforced concrete columns and steel columns. It must be carefully managed in constructing the bilinear element of VFIFE is the loading, unloading and reloading paths. The unseating prevention devices are designed to provide the final protective function against unseating. The unseating prevention devices are generally with non-working length before they are triggered to function. Therefore they are idealized as elements with a hook or/and a gap.

All properties and configuration of elements are assumed to be unchangeable in each time interval $t_i \leq t \leq t_{i+1}$ in VFIFE. The internal forces are calculated based on the element properties and configuration at the initial time t_i. The deformation coordinates of elements are redefined at the beginning of each time step. Therefore, once an element undergoes nonlinear or discontinuous behavior, all changes are reflected at the beginning of next time step.

In this study, the aforementioned elements are considered failure components. Assume that an element fracture as its deformation reaches rupture deformation. Whether the element failures or not is checked at the beginning of each time step. Once the element meets the fracture condition, the element and its restoring forces are released from the system.

4. NUMERICAL SIMULATION

A isolated bridge having a five-span simply-supported deck with a total length of 5@40 m = 200 m and a width of 12 m, which is supported by four reinforced concrete columns with a height of 12 m in each and two abutments, is analyzed to predict failure condition under extreme earthquakes as shown in Figure 2. The target bridge is designed based on the Japan highway bridge design codes. The columns and isolators are idealized as a perfect elastoplastic model with a fracture ductility of 11.5 and as a bilinear elastoplastic model with a fracture shear strain of 4, respectively. After isolators rupture, the dynamic friction coefficient at the interface is assumed to be 0.15.

Steel tendons are installed at each expansion joint as the unseating prevention devices. The tendons are simulated by a tension element with a yielding force of 839 kN, an ultimate force of 932 kN and a hook of 60 cm. The pounding effect of two adjacent decks is also considered by using an element with a gap of 96 cm. The damping ratios of the system are assumed 5% for the first and second modes. In simulation, the isolated bridge is subjected to near-field ground motions recorded at JR Takatori station, magnified by 150% , in the 1995 Kobe, Japan earthquake.

Figure 3 shows the failure process of the target bridge, where the first characters B, C, D, R of the notions denote the isolator, column, deck and tendon, respectively. It is observed that both isolators, B9 and B10, of the rightmost side span fail first because of pounding effect of the deck and the abutment at 4.76 sec. Losing the restoring forces from the isolators, the deck D5 pulls the tendons at the abutment so as to cause fracture of the tendons at 4.84 sec. Then the innermost column C3 exceeds the fracture ductility at 4.94 sec. The isolators B4, B5, B8 fail sequentially. It is noted that decks D3, D4, D5 and column C3 form a massive sliding structure, which leads a large rigid body motion. At 6.6 sec. the deck D3 loses support from the column C2 and the unseating prevention device R3 is triggered to drag the deck D3. However, the strength of the tendons R3 is not enough to resist the inertial force and gravity force so that it breaks at 7.12 sec. In the following, the deck D3 falls and causes the fracture of tendons R5 and the unseating of the deck 4.

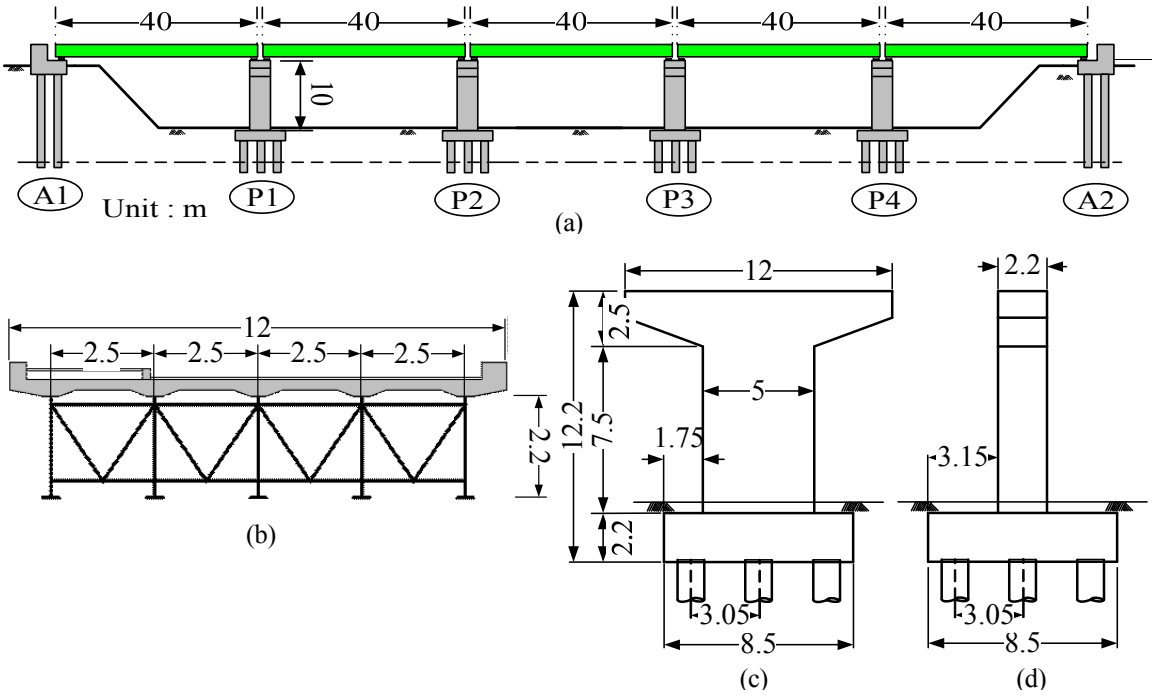

Fig.2 A five-span simply-supported bridge: (a) elevation (b) lateral view of superstructure (c) lateral view of column and (d) side view of column

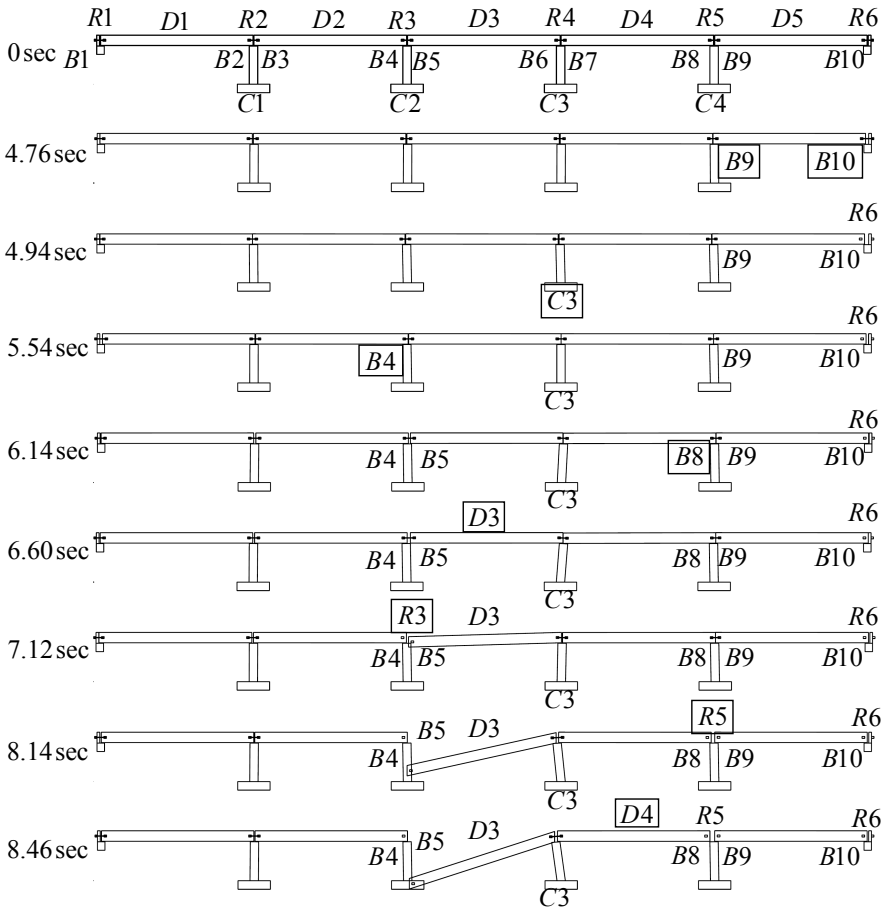

Fig.3 The failure sequence of the target bridge under 150% JR Takatori ground motion

From the numerical simulation of the isolated bridge with unseating prevention devices, the design concept of failure sequence of the structural components is demonstrated. In general, the isolators fail first followed by the columns. The last is the unseating prevention devices. It is noted that the unseating prevention devices designed based on the code still suffer failure so that it causes unseating during the extreme earthquake.

5. CONCLUSIONS

Since the VFIFE has the advantages in managing the engineering problems with material nonlinearity, discontinuity, large deformation, large displacement, arbitrary rigid body motions of deformable bodies and even fracture and collapse, it is adopted in this study to analyze the isolated bridges with unseating prevention devices under an extreme earthquake. In this study, the analysis method for the ultimate conditions, sliding of structures and fracture of elements are developed. An isolated bridge with a five-span simply supported deck, designed based on the Japan highway bridge design codes, is analyzed. The numerical simulation successfully predicts the failure process of the bridges under an extreme earthquake. The results also demonstrate the design concept of the failure sequence of the structural components. The unseating prevention devices are triggered and provide resistant force against unseating. However, the strength of the unseating prevention devices is not enough finally as to result in the falling of deck. The results confirm that the VFIFE is a powerful computation method to simulate the failure device of the isolators, columns and unseating prevention devices and to predict the collapse situation of bridges.

References:

Kawashima, K. and Shoji, G. (2000), "Effect of Restraints to Mitigate Pounding Between Adjacent Decks Subjected to a Strong Ground Motion," *12th World Conference on Earthquake Engineering*, Paper No. 1435 (CD-ROM), Auckland, New Zealand.

Lee T.-Y. and Kawashima K. (2007), "Semiactive Control of Nonlinear Isolated Bridges with Time Delay," *Journal of Structural Engineering*, ASCE, **133**(2), 235-241

Lee, T.-Y., Chen, P.-H. and Wang, R.-Z. (2008), "Nonlinear Dynamic Analysis of Isolated Bridges with Unseating Prevention Devices," The Fifth International Conference on Urban Earthquake Engineering, Center for Urban Earthquake Engineering (CUEE), Tokyo Institute of Technology, Tokyo, Japan, March 4-5, 2008.

Priestley, M. J. N., Seible, F. and Calvi, G. M. (1996), "Seismic Design and Retrofit of Bridges," John Wiley & Sons, New York, USA.

Ting, E. C., Shih, C. and Wang, Y. K. (2004), "Fundamentals of a Vector Form Intrinsic Finite Element: Part I. Basic Procedure and a Plane Frame Element," *Journal of Mechanics*, **20**(2), 113-122.

Wang Y.-P., Liao, W.-H. and Lee, C.-L. (2001), "A state-space approach for dynamic analysis of sliding structures," *Engineering Structures*, **23**, 790-801

Sixth International Conference on Urban Earthquake Engineering
March 3-4, 2009, Tokyo Institute of Technology, Tokyo, Japan

RESPONSE OF MULTI-SPAN BRIDGES SUBJECTED TO SEISMIC EXCITATION

Adam Crewe[1)], and James Norman[2)]

1) Senior Lecturer, Earthquake Engineering Research Centre, University of Bristol, UK
2) Senior Engineer, Ramboll Whitbybird, Bristol Office, UK
A.J.Crewe@bristol.ac.uk, James.Norman@rambollwhitbybird.com

Abstract: Multiple support excitation (MSE) during earthquakes is a significant hazard for structures with large distances between ground support points. Typically this applies to long-span bridges, with Eurocode 8 recommending that bridges longer than 600m are assessed under the effects of MSE. Much research has been carried out on modelling long span bridges with MSE both numerically and analytically, however very few experimental programmes have successful investigated the effect of MSE on bridges. In addition, previous analytical work has suggested that for shorter multi-span bridges (less than 200m) MSE can also have an effect on the overall bridge response which is at odds with the recommendations in Eurocode 8. This paper summarises the results of a series of tests at Bristol University looking at the effect of MSE on bridges. To generate the different input motions at each of the bridge piers a set of five parallel single axis shaking tables have been used to shake a variety of different bridge configurations. These tests have confirmed that, even for short multi-span bridges, MSE can have a significant effect on the bridge response and that the response of some piers may be underestimated if only synchronous ground motion is assumed.

1. INTRODUCTION

When an earthquake occurs the ground moves and when this movement occurs at the interface between a structure and the ground the structure is excited by the ground motion. In design of building structures the ground movements are usually considered to be the same at all points, however for large structures such as dams, bridges, pipe lines and oil rigs, the ground movement will be different along the length of the structure. This difference is caused by the finite wave speed of the ground motion which leads to differences in arrival times at the points of interface. Differences can also be caused by refraction and reflection of the seismic waves, differences in ground conditions and the differing interactions of each foundation with the ground, which all lead to a loss of coherence of the input motions. All of these effects result in multiple support excitation (MSE).

Theoretical and numerical analysis of MSE has consisted of the use of various numerical approaches, in particular the pseudo-static approach (Altinisik & Severn. 1981), and computer-based approaches using various 2D and 3D finite element analysis programmes (Sextos et al. 2003) to analyse structures and investigate their dynamic behaviour. Investigation into MSE for bridges has also been done numerically using mathematical stochastic analysis methods. These methods have included observations of the wave passage, incoherence and local site effects on long-span cable-stayed bridges and investigations have concluded that the wave passage effect was the most significant effect, especially in soft soils (Zhang & Lu. 2004).

Although there is a significant body of analytical work on the effects of MSE on bridges there has been little experimental work to validate the analytical models. Previous work by Norman et al. (2004) showed that even a simple two DOF model can be significantly affected when subjected to MSE. This paper summarises effect of MSE on more complex physical models (including a 1:50 scale model of multi-span viaduct bridge). The results from both the experimental and numerical models (finite element models) are compared, and the effect of MSE on the response of multi-span bridges is considered.

2. PHSICAL TESTS ON BRIGDES WITH MSE

2.1 MSE Test Bed

At Bristol University an MSE test bed has been specifically designed to test the effect of MSE on long span bridges. It comprises of 5 single axis shaking tables which are independently controlled by 5 actuators (figure 1).

Figure 1. The multiple support excitation test bed.

Full details of the construction of the test bed can be found in previous work by the authors (Norman and Crewe 2008).

2.2 Bridge models tested with MSE

This test bed has been used to test a variety of different bridge arrangements under different types of MSE excitation. Initially a four span viaduct bridge was considered. The prototype bridge was 200m long with three piers at equal spacing. The prototype dimensions were based on previous numerical MSE models which used a similar arrangement and showed that MSE can have a significant effect on the response of this size structure (Lupoi et al. 2005). This prototype bridge has also been used in other experimental work on bridges with synchronous inputs (Zapico et al. 2003 and Pinto et al. 1996). The length is such that Eurocode 8, part 2, 2005 recommends considering MSE if the soil type is non-uniform but does not recommend considering MSE when the soil type is uniform. This viaduct bridge also had adjustable pier lengths to allow simulation of differing valley topographies. Two typical arrangements, a uniform valley with 3 long piers i.e. LLL, and double valley with a shorter central pier i.e. LSL, that have been investigated are shown in figure 2.

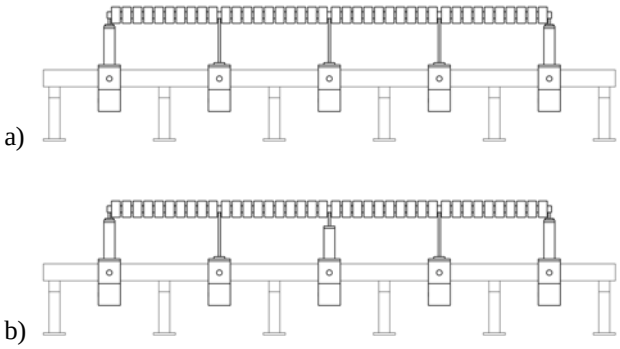

Figure 2. Schematics of the MSE experimental test bed
(a) with the LLL viaduct bridge attached
(b) with the LSL viaduct bridge attached.

The LLL viaduct bridge can be seen attached to the MSE test bed in figure 3.

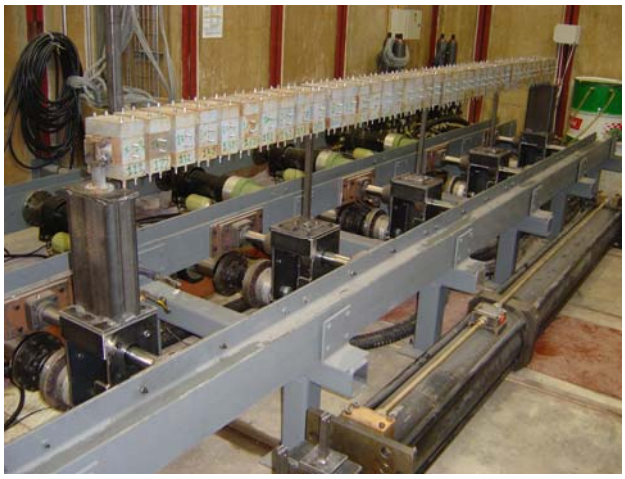

Figure 3. The LLL viaduct bridge on the test bed.

In addition to many tests on this type of viaduct bridge, the effect of MSE on long span cable stay bridges has also been tested using this test bed (Dick et al. 2006). One of these cable stay bridge tests can be seen in figure 4.

Figure 4. A cable stay bridge model on the test bed.

3. MSE EXCITATION

3.1 Eurocode compatible time histories

Initial tests used EC8 response spectra compatible displacement time histories which were generated using the method given in Clough and Penzien (1993). An earthquake duration of 40 seconds real time was chosen as suitable because it significantly longer than the Eurocode's (EC8-1) lower limit of 10s. Type 1 response spectra for a firm soil type A and a soft soil type D were used and are subsequently referred to as 1A and 1D respectively. The displacements were calculated from the acceleration time histories using a numerical form of integration and high pass filters to prevent drift of the input motion, which could lead to damage to the experimental models. The input time histories, in terms of acceleration and displacement, and the design response spectra and actual response spectra are given in figures 5 and 6 for the firm, 1A, and soft, 1D, soil types respectively.

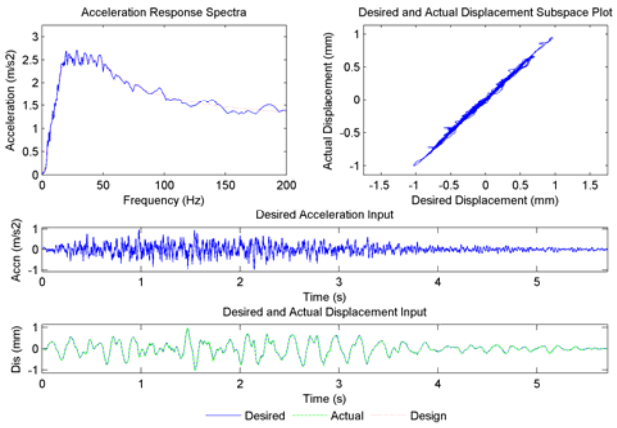

Figure 5. Inputs for response spectra type 1, firm soil type A.

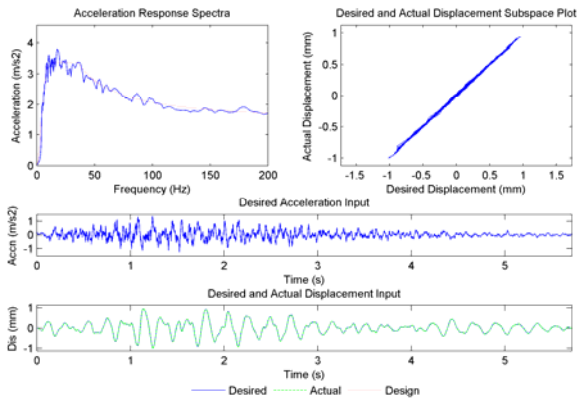

Figure 6. Inputs for response spectra type 1, soft soil type D.

For each artificial earthquake used at least two simulations were run, one using synchronous inputs and the other using time delays calculated from the surface ground velocity given by Eurocode 8. Typically a surface velocity of 1000m/s was used for firm ground and 180m/s for soft ground, which produced time delays of 7ms and 39ms respectively between each pier position at model scale.

3.2 SMART1 array time histories

In addition to the tests using Eurocode compatible time histories, the LLL viaduct bridge has been tested using real earthquake data recorded from the SMART1 array. More details on these tests can be found in Alexander et al. (2006) and Crewe & Norman (2006).

4. TYPICAL RESULTS

4.1 Finite Element Modelling

A finite element model of the multi-span viaduct bridge was created using the DIANA FE package. The displacement inputs were those measured from the physical model to allow direct comparison with the experimental data. The FE bridge model can be seen in figure 7. The end conditions of the bridge model are all fully fixed, except for the two abutment ends where the ends are pinned in plan.

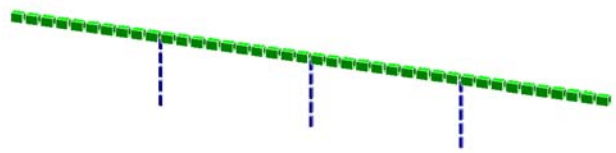

Figure 7. Finite element model of prototype bridge

Finite element model updating was used to tune the response of the finite element model to the experimental model by adjusting the added mass on the deck to match the first modal response. The tuned numerical model had a similar first (5.38Hz) and third mode (16.5Hz), but the second mode frequency was slightly low (9.14Hz as compared to 10.15Hz). The damping value of the first mode of the experimental model was calculated to be in the order of 0.5%. A damping coefficient of 300kg/s was used in the finite element model and damping was modelled using a series of dashpots between nodes.

4.2 Experimental test results for LLL bridge

Figure 8 shows a typical set of responses of the LLL bridge at the top of the three piers for a Type 1A time history with a 7ms delay between each pier. The plots show both the numerical and experimental results. The time histories show a good level of correlation between the numerical and experimental results. The peak responses are approximately the same, see table 1, and the majority of the signal is in phase. The time histories for pier 2, the central pier, show the highest level of correlation. This is due to the fact that the second mode of vibration does not contribute to displacements at this point and, as the numerical model was better tuned to the first and third modes, any error in the second mode response is not seen in the data. Piers 1 and 3 do not show such a strong correlation again because of the way the model was tuned, this time the second mode response contributes more significantly to the time histories at these pier.s

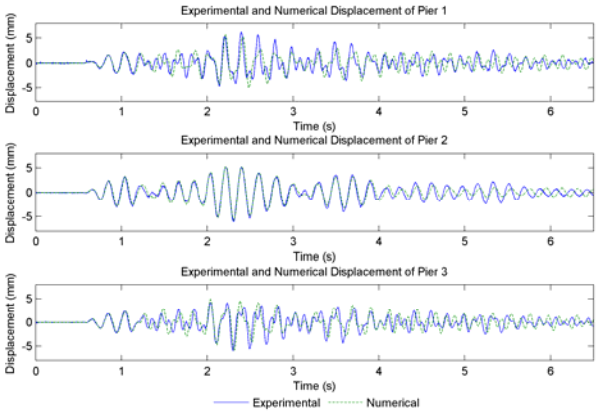

Figure 8. LLL viaduct bridge: displacement at the top of the three piers when subjected to 1A time history, with a 7ms time delay between each support, (top to bottom piers 1-3 respectively).

In figure 8 we can also see that whilst there is strong agreement in amplitude during the majority of the shake, as the displacements of the input excitation diminish and return to zero, the amplitudes and phase for the numerical model and the experimental results start to drift. This was predominantly due to the fact that the damping in the finite element model was created using linear dashpot dampers and was considered to be uniform across the model, however in the experimental model the damping is much more complex and non-linear and therefore as the input motion reduces back to zero and the damping becomes more prevalent in the response of the structure variations between the numerical and experimental results occur.

Table 1. For LLL viaduct bridge, peak displacement at the top of each pier for each input case and both model types.

Soil Type	Input Type	Model	Pier 1	Pier 2	Pier 3
			Peak Disp. (mm)		
Firm 1A	Synchronous	Experimental	**5.000**	6.088	**4.385**
		Numerical	4.217	6.184	4.310
	Asynchronous	Experimental	**6.284**	6.067	**5.945**
		Numerical	5.639	5.813	5.878
Soft 1D	Synchronous	Experimental	4.639	6.201	4.443
		Numerical	4.575	6.293	4.577
	Asynchronous	Experimental	1.837	1.770	2.075
		Numerical	1.849	2.485	2.128

For the firm soil type with a high ground surface velocity and therefore a short time delay, it can be seen from figure 8 and table 1 that the overall response and peak responses of piers 1 and 3 in the bridge are greater for the asynchronous case (by up to 35%) than for the synchronous case. This is because the first mode of the bridge (5Hz) occurs before the peak plateau of the type 1A design response spectra whereas the spectra has significantly more energy to impart at 10Hz (the second bridge mode) if this second mode is excited. However, when the input is synchronous the second mode cannot be excited as the model is symmetrical and the second mode is asymmetrical. When an asynchronous input occurs the second mode can be excited, which in this case has lead to a greater overall response.

Figures 9 and 10 show partial snapshots of the deck's displaced shape in plan, taken from the numerical model. In figure 9 (synchronous excitation) the response of the bridge is completely symmetrical, whereas in figure 10 (asynchronous excitation) we can see that a large part of the response is not symmetrical. This supports the argument that synchronous excitations cannot excite asymmetrical modes but when asynchronous excitations occur, both symmetrical and asymmetrical modes are excited and the combination of these modes can lead to an increase in response.

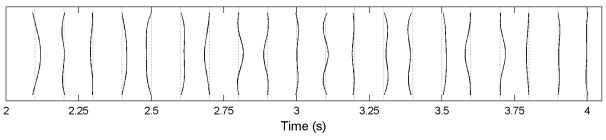

Figure 9. The displaced shape of the LLL viaduct bridge deck calculated using FE analysis at discrete time intervals of 0.1s for the 1A time history, synchronous input.

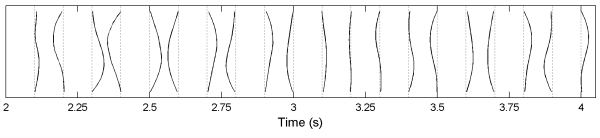

Figure 10. The displaced shape of the LLL viaduct bridge deck calculated using FE analysis at discrete time intervals of 0.1s for the 1A time history, with 7ms delay between supports.

4.3 Experimental test results for LSL bridge

The LSL viaduct bridge represents a bridge spanning over a double valley. In this configuration the bridge is again symmetrical and the first mode is a symmetrical mode, however the second modal frequency is much closer to the first mode compared to the LLL case. The same artificially generated time histories were used as in the LLL case although in this case the time delay between the piers was varied from 0ms (synchronous) to 10ms (a significant level of MSE). Each test was repeated twice and both sets of results were included in the analysis. The FE model again had the same inputs as the recorded experimental inputs and the FE analysis was run with both sets of data.

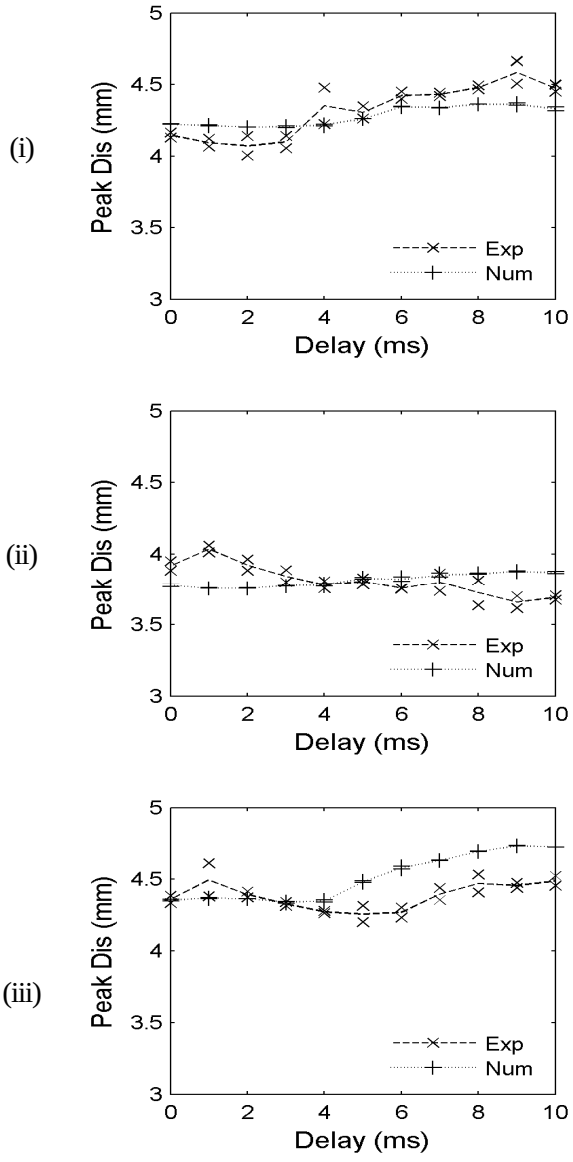

Figure 11. Peak response for piers 1-3, (i-iii) respectively of the LSL viaduct bridge comparing the experimental and numerical model excited by 1A time history with varying delay.

Figure 11 shows the peak responses for all 22 tests performed using response spectra type 1A inputs. The

peak responses from the experimental results varied when repeated, whilst for the numerical model the two values fall much more closely together. As the inputs into the numerical model were those measured during each experiment we can see that the experimental model was much more sensitive to very slight changes in the input motion and that other factors such as non-linear damping must be altering the response of the experimental model. However the difference recorded for the numerical model is much smaller and we can be certain that the only change in this case was the input motion.

Generally the response plots (figure 11) show a good correlation in peak response between the experimental and numerical models. For piers 1 and 3 the experimental and numerical peak displacements increase as the delay increases. For the middle pier (pier 2) the numerical values show a slight increase with increased delay while the experimental values increase initially but then reduce.

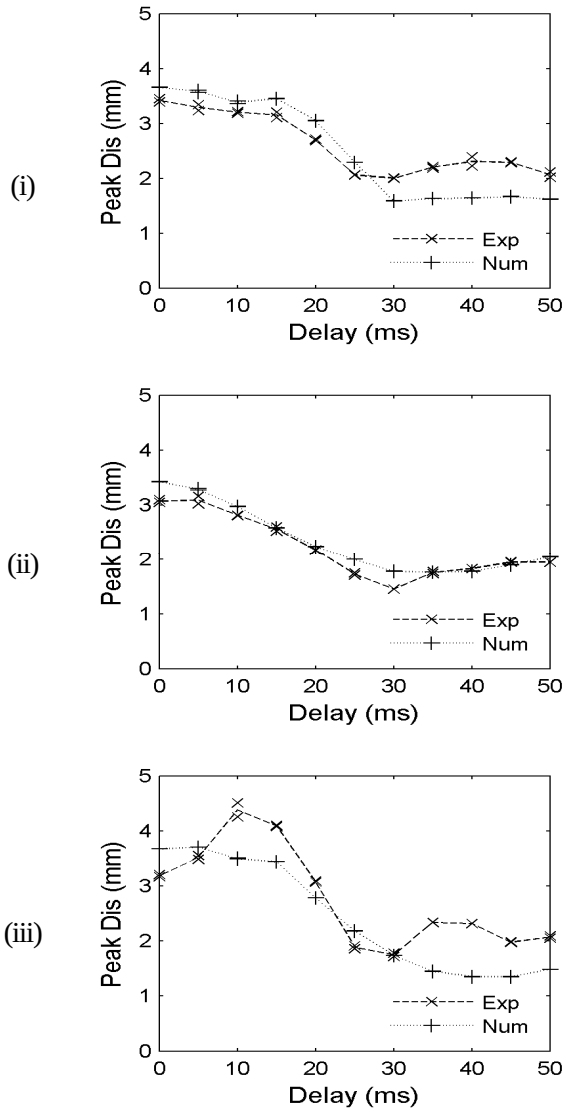

Figure 12. Peak response for piers 1-3, (i-iii) respectively of the LSL viaduct bridge comparing the experimental and numerical model excited by 1D time history with varying delay.

It is interesting to compare the results in figure 11 with those in figure 12 which shows similar data but this time with type 1D input motion. For response spectra type 1D a greater range of time delays was used as the surface wave velocity can be significantly less than for ground type 1A. Once again 22 tests were run, two using each input set with varying delays. In this case, except for pier 3, the peak response reduces as the time delay increase. For pier 3 an increase is observed in the experimental model peaking at 10ms; however this is not reflected in the numerical model. In general the numerical model and experimental model show a strong level of agreement and follow the same trends, except where noted at pier 3.

Looking at the results from both bridge arrangements it can be seen that whilst the response spectra 1A time history produced larger results for both bridge arrangements, the response spectra type 1D time history did not. This sensitivity of the bridge response to the particular time history combined with the fact that MSE can have a significant impact on bridge makes applying Eurocode 8 very difficult. In particular, for bridges that might response baldly to MSE, which this research has shown may be significantly shorter than 600m, Eurocode 8, part 2, 2005 recommends the use of time history analysis, where the time histories are generated using loss of coherence models as given in Appendix D of Eurocode 8.

Eurocode 8 Appendix D recommends using the incoherence model suggested by Der Kiureghian (1996) which has five unknowns in it including wave velocity and distance between supports. It also recommends that enough time histories should be analysed so that they yield stable estimates of the mean of the maximum response of interest. It does not state if this is to be carried out whilst varying each of the variables to assess variations in wave velocity and position of the epicentre of the earthquake. However, if this is assumed then a large number of analysis will need to be carried out which will be very time consuming for a large FEA model.

This has therefore led to the development of a simplified procedure for ascertaining the effect of MSE on multi-span bridges. Initially a simplified model is created which accounts for both the stiffness of the piers and of the bridge deck (Alexander et al., 2006) and has the minimum necessary number of modes. For a typical viaduct bridge the first three modes of the structure account for practically all the participating mass (Lupoi et al., 2005) and therefore a three DOF beam model would be a suitable model. Then a large series of time histories, calculated in accordance with the Eurocode 8, part 1, 2004 and Eurocode 8, part 2, 2005, is run through this simplified model. The response of the bridge should be considered taking into account all variables affecting the loss of coherence, and the time histories ranked so as to represent the maximum to minimum response of the structure. A selection from the ranked time histories should then be selected which produce stable estimates of the mean of the maximum responses of interest. Finally, the full FEA model should be analysed using the suite of time histories selected using the simplified model to determine

the actual range of bridge responses that might be expected. This methodology is much more likely to identify the full effect of MSE on a bridge compared to simply running the full FEA model on a small randomly selected set of all the possible time histories.

5. CONCLUSIONS

The experimental tests at Bristol showed a high level of agreement with the relatively simple FE models. These tests have shown that whilst the 1A time history produced larger results for both bridge arrangements, the 1D time history did not. At present these and other tests do not suggest that the difference in response, when considering asynchronous inputs, is specifically related to the different response spectra but rather that the behaviour of the bridge is related to the specific form of the time history. We can nevertheless conclude that asynchronous inputs, even with small time delays sometimes produce increases in response, but that they can also significantly damp out the response of a bridge and which behaviour occurs is very dependent on the original time history.

A methodology for quickly determining which of the many possible MSE input motions to a bridge is likely to cause the most extreme response has been proposed. This uses a simplified bridge model to quickly develop a good understanding of the response of the bridge to a suite of time histories. The worst of these time histories are then used as input to the full FE bridge model for the design.

Acknowledgements:

The authors wish to thank Engineering and Physical Sciences Research Council (EPSRC) for funding this research under grant GR/R99539/01.

References:

Eurocode 8 Part 2: Bridges, EN1998-2.

Alexander N.A., Norman J., Virden D., Crewe A. & Wagg D. (2006), "Effects of orientation to the epicentre on the response of long span bridges subject to multiple support excitation using SMART-1 array data and corroborative experimental results", Proc. 8th Nat. Conf. on Earthquake Eng., San Francisco, USA.

Altinisik D. and Severn R.T. (1981), "Multiple-support and asynchronous base excitation of structures", Proceedings of the Institution of Civil Engineers. 71, 407-426.

Clough, R.W. and Penzien, J., (1993), "Dynamics of structures", Second Edition, McGraw-Hill, USA.

Crewe A.J. & Norman J.A.P (2006), "Experimental modelling of multiple support excitation of long span bridges". 4th International Conference on Earthquake Engineering, Taipei, Taiwan, October 12-13, Paper No. 127

Der Kiureghian A. (1996), "A Coherency Model for Spatially Varying Ground Motions", Earthquake Engineering and Structural Dynamics, Vol. 25, PP 99-111.

Dick C., Metters E., Norman J.A.P and Crewe A.J. (2006). "Response of cable stay bridges subjected to multiple support excitation". 1st European Conf. on Earthquake Engineering & Seismology, Geneva, Switzerland, 3-8 September, Paper Number 222.

Lupoi A., Franchin P., Pinto P.E. & Monti G. (2005), "Seismic design of bridges accounting for spatial variability of ground motion", Earthquake Eng. and Struct. Dynamics, Vol. 34, PP 327-348, 2005.

Norman J.A.P. and Crewe A.J. (2008), "Development and control of a novel test rig for performing multiple support testing of structures" 14th World Conference on Earthquake Engineering, October 12-17, Beijing, China.

Norman J.A.P., Virden D.W., Crewe A.J., Wagg D.J. & Severn R.T. (2004), "Understanding the dynamics of multi-degree-of freedom structures subject to multiple support earthquake excitation", Proc 13th World Conf on Earthquake Eng., Vancouver, Canada, Paper 3324.

Pinto A.V. (1996), "Pseudodynamic and shaking tables on RC bridges, European consortium of earthquake shaking tables (ECOEST)", Prenomative Research in Support of Eurocode 8, Report No. 5.

Sextos A.G., Pitilakis K.D. & Kappos A.J. (2003), "Inelastic dynamic analysis of RC bridges accounting for spatial variability of ground motion, site effects and soil-structure interaction phenomena, Part 1: Methodology and Analytical tools". Earthquake Eng. and Struct. Dynamics, 32(4), 607-627.

Zapico J.L., Gonzalez M.P., Friswell M.I., Taylor C.A. & Crewe A.J. (2003), "Finite element model updating of a small scale bridge", Journal of Sound and Vibration, 268(5), 993-1012.

Zhang C. & Lu L. (2004), "Seismic response analysis of long-span cable-stayed bridge under multi-support random excitations", Journal of Southeast University (Natural Science Edition), 34, 249-252.

Sixth International Conference on Urban Earthquake Engineering
March 3-4, 2009, Tokyo Institute of Technology, Tokyo, Japan

DUCTILITY EVALUATION OF SRC PIERS CONSIDERING RESTORABILITY AND ULTIMATE STATE

Hideki Naito[1], Mitsuyoshi Akiyama[2] and Motoyuki Suzuki[3]

1) Research Professor, Dept. of Civil and Environmental Engineering, Tohoku University, Japan
2) Associate Professor, Dept. of Civil and Environmental Engineering, Tohoku University, Japan
3) Professor, Dept. of Civil and Environmental Engineering, Tohoku University, Japan
naito@civil.tohoku.ac.jp, akiyama@civil.tohoku.ac.jp, suzuki@civil.tohoku.ac.jp

Abstract: This paper presents an experimental and analytical investigation of the ductility evaluation and a damage prediction method for SRC piers. With regard to the cyclic loading tests of SRC columns, the restorable limit state and the ultimate limit state are defined as the spalling of the cover concrete and the local buckling of the H-shaped steel, respectively. To evaluate the displacement at the restorable limit state, the plastic curvature distribution at the spalling of the concrete cover was modeled to the rectangle distribution, and its curvature was calculated by buckling analysis of the longitudinal bars. The displacement at the ultimate limit state was calculated by integrating the curvature distribution based on the local buckling analysis of the H-shaped steel. Using experimental tests including those of other authors, it was confirmed that the proposed method can appropriately evaluate the displacement at the restorable limit state.

1. INTRODUCTION

Severe earthquakes occur frequently in Japan. Hence, important structures such as expressways and railways and so on should be designed for safety against large seismic ground motions. Concrete-encased steel structures, some -times known as steel-reinforced concrete (SRC), have high strength and ductility because concrete and H-shaped steel are integrated. Recently, in Japan, many SRC piers have been constructed because of their high ductility and strength (seismic performance).

However, the load capacity, large deformation property and damage process of the SRC piers have not been sufficiently clarified, and studies on the seismic performance of SRC piers are few in number. Therefore, the seismic design of SRC piers has referred to that for RC piers. In such a design, the high strength and ductility of SRC piers is ignored. If the damage to SRC piers as a result of large earthquakes, for example, the cracking and spalling of cover concrete and local buckling of longitudinal bars and H-shaped steel, can be predicted appropriately, seismic design of SRC piers considering the restorative efforts required after large earthquakes can be useful. It is necessary to define the limit states of SRC columns corresponding to damage levels and to propose a ductility evaluation and damage prediction method.

In this paper, to propose a seismic design method for SRC piers based on the definition of limit states for damage levels, reversal cyclic loading tests of SRC columns were examined. Moreover, theoretical values using the proposed method were compared with experimental results including those of other authors.

2. CYCLIC LOADING TESTS OF SRC COLUMNS

2.1 Outline of Experimental Tests

Reversal cyclic loading tests of RC and SRC columns were examined. The details of these specimens are shown in Table 1 and Figure 1. The shear spans are 1500 mm in all of

Table 1 Specimen details

Specimen number	Shear span (mm)	Sectional size (mm)	H-shaped steel		Longitudinal bars			Ties			Concrete strength (N/mm^2)
			Size (mm) $H_s \times B_s \times t_w \times t_f$	Yield strength (N/mm^2)	Diam-eter (mm)	Num-ber	Yield strength (N/mm^2)	Diam-eter (mm)	Spac-ing (mm)	Yield strength (N/mm^2)	
No.0	1500	650×650	(RC column)	---	19	18	424	13	100	435	20.7
No.1S	1500	500×500	300×200×10×15	376	16	10	442	10	100	457	25.3
No.3S			300×250×10×15	293	13	8	409	10	100	390	25.2
No.4S			300×250×10×15	293	13	8	409	6	300	317	28.6

the RC and SRC columns. Each SRC column and RC column has almost the same load capacity under the flexural and shear loading. While the size in the RC section was 650 mm × 650 mm, the size in the SRC sections could be reduced to 500 mm × 500 mm.

In these experimental tests, a horizontal cyclic load was added to the top of the SRC columns without axial loading. The material strength is shown in Table 1.

2.2 Load-Displacement Relation and Damage Process

As a comparison of RC and SRC columns, the load -displacement relations of specimens No.0 and No.1S are shown in Figure 2. In the experiment on specimen No.0 (RC), the longitudinal bars reached the yield strain at 6.4 mm horizontal displacement, at which point the bending cracks became large and small shear cracks appeared. At 36.2 mm horizontal displacement, the buckling of longitudinal bars caused spalling of the cover concrete; the load-displacement relation shown in Figure 2 clearly reflects the decreased load. After the spalling of the cover concrete, the RC columns collapsed because the shear cracks became large.

On the other hand, in specimen No.1S (SRC), the yield displacement is 6.4 mm. At 72.9 mm ($9\delta_y$) horizontal displacement, even though spalling of cover concrete and buckling of longitudinal bars have occurred, the load capacity does not decrease as in No.0 (RC). In these specimens, the longitudinal bars fracture after buckling. At 143 mm ($15\delta_y$) horizontal displacement, the core concrete outside the H-shaped steel spalls, and local buckling of the H-shaped steel appears. No.1S appears to have sustained strength and a large energy absorption capacity under cyclic loading at 200 mm horizontal displacement because the H-shaped steel is confined in concrete and cracking in the steel flange does not occur.

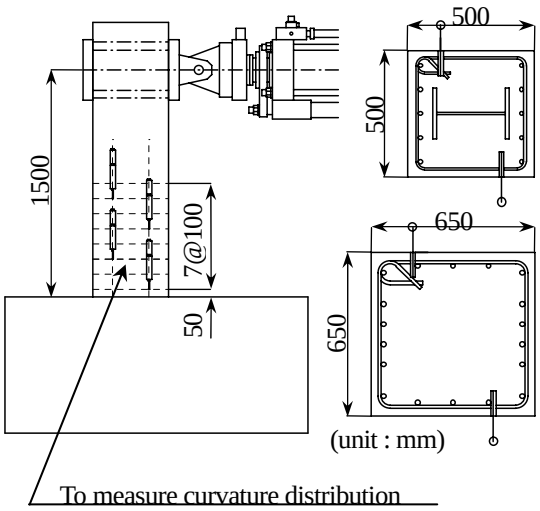

Figure 1 Loading arrangements

In No.3S with a relatively large amount of steel, both spalling of the cover concrete and buckling of longitudinal bars were induced at 45.3 mm ($9\delta_y$) horizontal displacement. After the buckling of longitudinal bars, the load capacity and the energy absorption capacity showed little change because of the large steel content. However, at 123 mm ($24\delta_y$) horizontal displacement, the steel flange buckled in places,

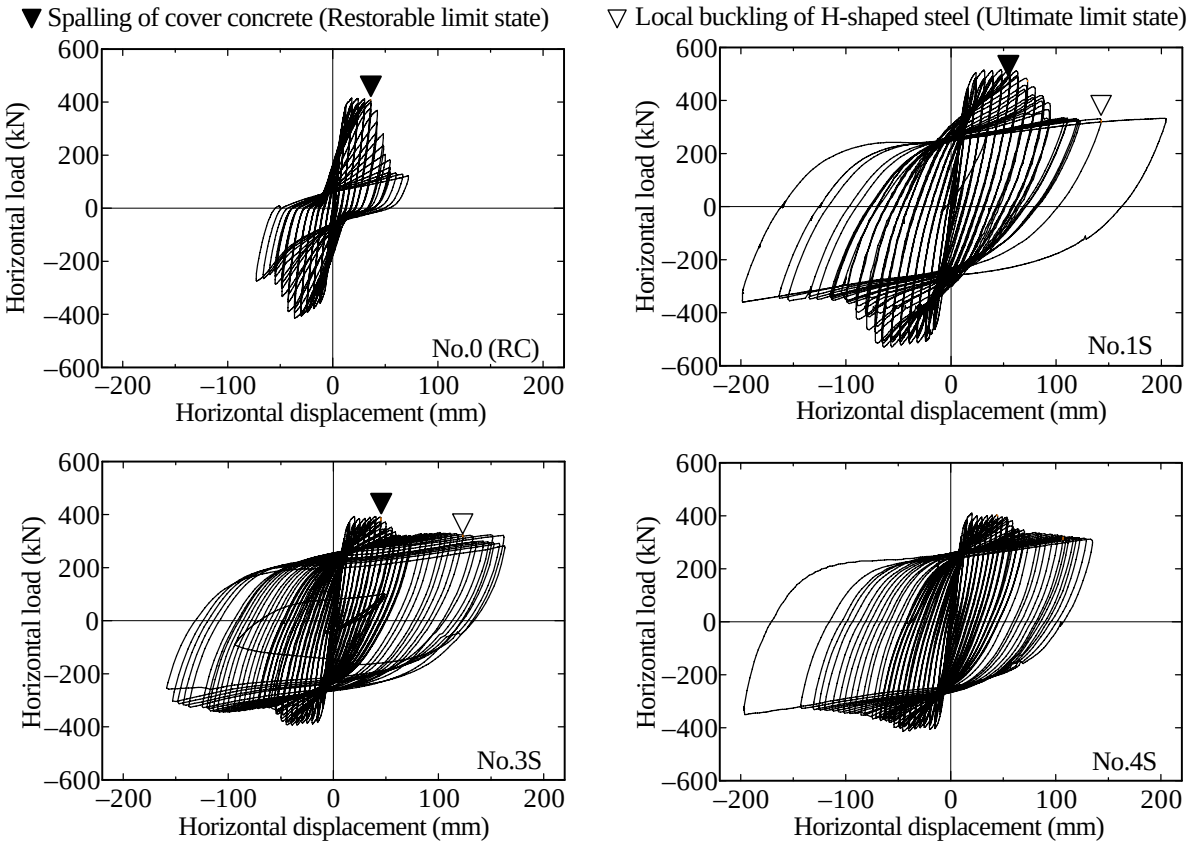

Figure 2 Load-displacement relations

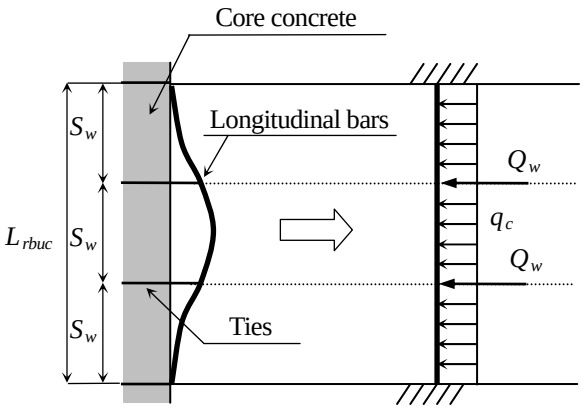

Figure 3 Buckling model of longitudinal bars

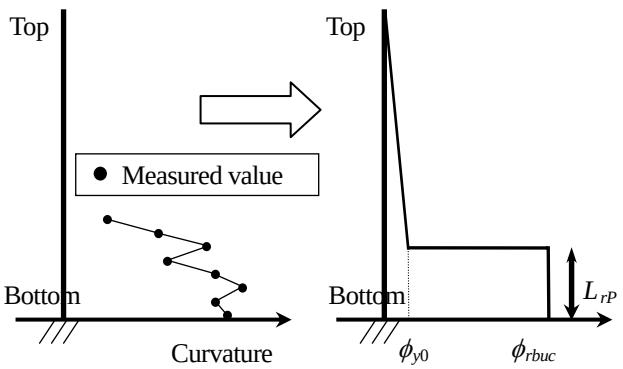

Figure 4 Curvature distribution at the restorable state

with the brittle collapse caused by cracking in the steel flange.

With regard to the amount of ties, No.3S (standard tie content) and No.4S (reduced tie content) were compared. Both these SRC specimens have a large steel content. Despite the different of tie content, the load-displacement relation and the damage process of No.3S and No.4S were almost same. As No.4S showed no cracking in the H-shaped steel, it demonstrated sustained strength and large energy absorption at 200 mm horizontal displacement.

2.3 Restorable and Ultimate Limit State

With regard to experimental tests, for the both RC and SRC columns, enormous damage (e.g., the buckling and fracture of longitudinal bars) is caused after the spalling of the cover concrete. Therefore, the spalling of cover concrete is the common restorable limit state for RC and SRC columns. If the dynamic responses of the SRC members remain within this restorable limit state, the structure can be repaired in the short term by crack injection repair, etc.

On the other hand, SRC columns with a large steel content have high ductility and large energy absorption after the spalling of the cover concrete. In these experimental tests, No.3S underwent brittle collapse due to cracking in the steel flange after local buckling. Referring to other experimental reports, SRC columns are collapsed by cracking in the steel flange or flange-web weld after the local buckling of the H-shaped steel. However, the damage mechanism of SRC columns before the cracking in the H-shaped steel is not clear, and there are few experimental data. The ultimate limit state has to be defined as the local buckling of the H-shaped steel.

3. DUCTILITY EVALUATION OF THE RESTORABEL LIMIT STATE

3.1 Damage Prediction of the Buckling of Longitudinal Bars

Referring to our previous studies, a damage prediction method of the spalling of cover concrete based on the buckling model was proposed. Then, the restorable displacement could be calculated using the buckling model shown in Figure 3.

The equivalent curvature ϕ_{rbuc} of the restorable limit is written as

$$\phi_{rbuc} = -\frac{1}{\alpha_{rb} d_r} \ln\left[\left(\frac{\sigma_{ry}}{E_r} - b_b \Delta\varepsilon_B\right)\left(\frac{2 S_w N_{rbuc}}{\pi D_r}\right)^2 - \gamma\right] + \frac{\Delta\varepsilon_B}{d_r} \quad (1)$$

$$\Delta\varepsilon_B = \left[\frac{2(D_r/S_w)}{3 N_{rbuc} a_x}\left\{g(N_{rbuc})\frac{\sigma_{rm}}{\sigma_{ry}} - 1\right\}\right]^2 \quad (2)$$

$$g(N_{rbuc}) = 1 + \frac{a_x \pi N_{rbuc}}{16(D_r/S_w)N_{ru}}\left\{q_c N_{rbuc} S_w + Q_w f(N_{rbuc})\right\} \quad (3)$$

$$f(N_{rbuc}) = \begin{cases} ({N_{rbuc}}^2 - 1)/N_{rbuc} & (N_{rbuc} \text{ is odd}) \\ ({N_{rbuc}}^2 + 2)/N_{rbuc} & (N_{rbuc} \text{ is even}) \end{cases} \quad (4)$$

$$q_c = k_{qc} \beta_{qc} d_1 D_r {\sigma_c}^{2/3} \quad (5)$$

$$\beta_{qc} = \begin{cases} 1 - 0.75\varepsilon_{\max}/\varepsilon_c & (\varepsilon_{\max} \le \varepsilon_c) \\ 0.25 & (\varepsilon_{\max} \ge \varepsilon_c) \end{cases} \quad (6)$$

where α_{rb}=180, γ=0.045, a_x=0.65, b_b=1/100, k_{qc}=0.03, d_r= the distance from the compression bars to the tensile bars in the cross section, N_{rbuc}=the numbers of tie's space in the buckling length L_{rbuc} (for instance, N_{rbuc}=3 in Figure 3), σ_{ry}= the yield stress of longitudinal bars, E_r=the Young's modulus of the bars, S_w=the spacing of the ties, D_r=the diameter of the bars, σ_{rm}=the tensile strength of the bars, $N_{ru}=A_r\sigma_{rm}$, and A_r=the area of the cross section of the bars. The preservation of the ties is given as $Q_w=a_{we}\sigma_{wy}/N_{rein}$, N_{rein}=the number of the bars on a side of the cross section preserved by the ties, σ_{wy}=the yield strength of the ties, and a_{we}=the effective cross-sectional area of ties given for each tie as $a_{we}=a_w$ (outer tie) and $a_{we}=2.2a_w$ (inner tie) where aw the area of the cross section of a tie itself. σ_c=the compression strength of the cover concrete, and d_1=the distance from the center of the cross section of the bar to the edge of the cover concrete. To take the damage by the compression loading into account, the compression strain and the decreased tensile strength are linked by β_{qe}, where ε_c the compression strain at the maximum strength of the cover concrete, and $\varepsilon_{\max}$ the compression strain of the bar. Here, the numbers of tie's space N_{rbuc} is given as minimum value.

In Figure 4, the plastic curvature distribution is modeled to the rectangle distribution with the equivalent curvature ϕ_{rbuc} and the plastic hinge length L_{rP}. Here, the plastic hinge length L_{rP} is written as

$$\delta_{rbuc} = \delta_{y0} + (\phi_{rbuc} - \phi_{y0})(h - L_{rP}/2)h \quad (7)$$

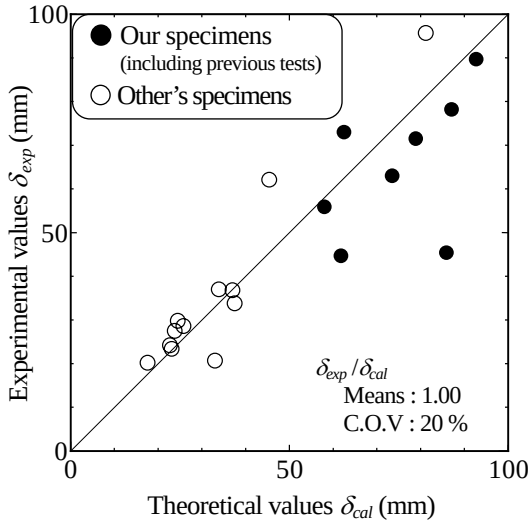

Figure 5 Evaluating the restorable displacement

$$L_{rP} = L_{p0}\left\{\left(1+0.04\,t_{ek}\right)M_m/M_{y0} - 0.25\right\} + 12\left(D_r - 12\right) \quad (8)$$

$$L_{P0} = 0.5d + 0.05h \quad (9)$$

where h=the shear span, and d=the effective height of the cross section, t_{ek}=the sectional ratio of the H-shaped steel and longitudinal bars, M_m=the flexural strength (bending moment), and M_{y0}=yield moment.

3.2 Comparison with the Experimental Results

The proposed method was applied and a comparison made between the theoretical values and the 20 experimental values. In the theoretical and experimental values, the effect of the pulling out of the longitudinal bars from the footing is taken into account. From the comparison shown in Figure 5, it is observed that the results from experimental trials are appropriately evaluated by the proposed method.

4. DUCTILITY EVALUATION OF THE ULTIMATE LIMIT STATE

4.1 Damage Prediction of the Local Buckling of H-shaped Steel

The ultimate strain (buckling strain) of the steel flange has been formulated considering the concrete fixing. In Figure 6, the steel flange is fixed around 3 sides and another side is free. In this study, the deflection of the steel flange w was assumed as

$$w = \delta \sin^2 \frac{\pi x}{L_{sbuc}}\left(1 - \cos\frac{\pi y}{2b}\right) \quad (10)$$

where L_{sbuc}=the local buckling length of the steel flange, b =the width of the steel flange, x and y are the axes of the coordinates shown in Figure 6. Referring to our previous study, the potential energy within the steel flange is written as

$$\Delta U = \frac{1}{2}D_p \int_0^{L_{sbuc}}\int_0^b \left\{\kappa_1\left(\frac{\partial^2 w}{\partial x^2}\right)^2 + 2\kappa_2\left(\frac{\partial^2 w}{\partial x^2}\right)\left(\frac{\partial^2 w}{\partial y^2}\right) + \kappa_3\left(\frac{\partial^2 w}{\partial y^2}\right)^2 + 4\kappa_4\left(\frac{\partial^2 w}{\partial x \partial y}\right)^2\right\} dxdy \quad (11)$$

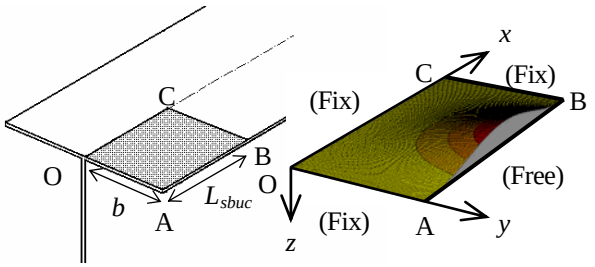

Figure 6 Buckling model of steel flange

$$D_p = \frac{E_s\, t_f^{\,3}}{12} \quad (12)$$

$$\kappa_1 = \frac{1+3\left(E_{2nd}/E_{sct}\right)}{2-4\nu+3\left(E_s/E_{sct}\right)-\left(1-2\nu\right)^2\left(E_{2nd}/E_s\right)} \quad (13)$$

$$\kappa_2 = \frac{2-2\left(1-2\nu\right)\left(E_{2nd}/E_s\right)}{2-4\nu+3\left(E_s/E_{sct}\right)-\left(1-2\nu\right)^2\left(E_{2nd}/E_s\right)} \quad (14)$$

$$\kappa_3 = \frac{4}{2-4\nu+3\left(E_s/E_{sct}\right)-\left(1-2\nu\right)^2\left(E_{2nd}/E_s\right)} \quad (15)$$

$$\kappa_4 = \frac{1}{-1+2\nu+3\left(E_s/E_{sct}\right)} \quad (16)$$

$$E_{sct} = \frac{\sigma_{sy} + E_{2nd}\left(\varepsilon_{sbuc} - \varepsilon_{sy}\right)}{\varepsilon_{sbuc}} \quad (17)$$

where ΔU=the potential energy within the steel flange, E_s=the Young's modulus of the steel, ν=the Poisson ratio, t_f =the thickness of the steel flange, σ_{sy}=the yield stress of the steel, ε_{sy}=the yield strain of the steel, E_{2nd}=the stiffening coefficient after the yield of the steel, and σ_{sbuc}=the ultimate strain for the local buckling of the steel flange.

The energy ΔT caused by axial stress is written as

$$\Delta T = \frac{t_f}{2}\int_0^{L_{sbuc}}\int_0^b \sigma_{sbuc}\frac{\partial^2 w}{\partial x^2}dxdy \quad (18)$$

The buckling strength σ_{sbuc} is given from the equilibrium equation as $\Delta U = \Delta T$.

$$\sigma_{sbuc} = \frac{D_p \pi^2}{b^2 t_f}\left\{\left(3-\frac{8}{\pi}\right)\left(\frac{b}{L_{sbuc}}\right)^2\kappa_1 + \frac{3}{256}\left(\frac{L_{sbuc}}{b}\right)^2\kappa_3 + \left(\frac{1}{8}-\frac{1}{2\pi}\right)\kappa_2 + \frac{1}{4}\kappa_4\right\}\Big/\left(\frac{3}{4}-\frac{2}{\pi}\right) \quad (19)$$

$$\sigma_{sy} + E_{2nd}\left(\varepsilon_{sbuc} - \varepsilon_{sy}\right) = \sigma_{sbuc} \quad (20)$$

The ultimate strain ε_{sbuc} and the buckling strength σ_{sbuc} are given as minimum values.

The plastic curvature distribution of the H-shaped steel column for the ultimate limit state (local buckling of the H-shaped steel) is shown in Figure 7. Moreover, the ultimate displacement of the SRC column is calculated by integrating the plastic curvature. The ultimate displacement δ_{sbuc} is written as

$$\delta_{sbuc} = \left\{\phi_{bot}\, L_{sP1}\left(3h - L_{sP1}\right) + \phi_a L_{sP}\left(3h - L_{sP1} - L_{sP}\right) + \phi_{sy}\left(h - L_{sP1}\right)\left(2h - L_{sP1} - L_{sP}\right)\right\}/6 \quad (21)$$

where these symbols are shown in Figure 7.

4.2 Comparison with the Experimental Results

In our experimental tests, local buckling of the H-shaped steel was caused in No.1S, No.3S and No.4S. In

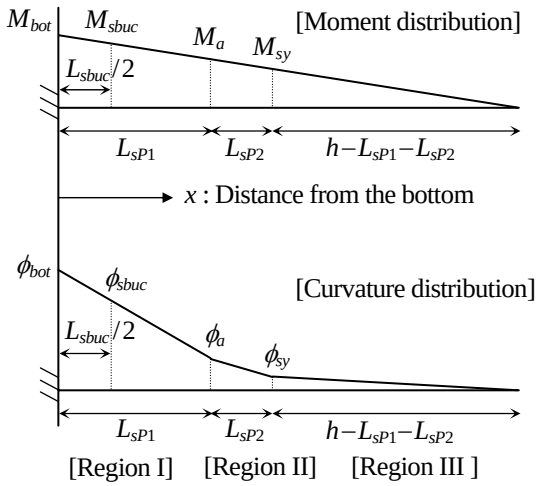

Region Ⅰ : Plastic region of compressive and tensile flanges
Region Ⅱ : Plastic region of only compressive flange
Region Ⅲ : Elastic region of compressive and tensile flanges

M_{sy} : Yield moment
M_a : Moment at $x=L_{sP1}$
M_{sbuc} : Moment at $x=L_{sbuc}/2$
M_{bot} : Moment at the bottom
ϕ_{sy} : Yield curvature
ϕ_a : Curvature at $x=L_{sP1}$
ϕ_{sbuc} : Curvature at $x=L_{sbuc}/2$
ϕ_{bot} : Curevature at the bottom
h : Shear span , L_{sbuc} : Buckling length
L_{sP1} : Length of the region I
L_{sP2} : Length of the region II

Figure 7 Curvature distribution at the ultimate limit state

Table 2 Evaluation of the ultimate displacement

		Ultimate displacement δ_{sbuc} (mm)	Buckling length L_{sbuc} (mm)	Plastic region L_{sP} (mm)
No.1S	Proposed method	89	192	321
	Experimental result	143	200	250
No.3S	Proposed method	98	125	345
	Experimental result	123	100	350
No.4S	Proposed method	74	237	308
	Experimental result	106	200	350
No.2 (Azuma et al.)	Proposed method	121	66	1165
	Experimental result	150	–––	–––

addition, referring to experimental trials in other author's study, local buckling of H-shaped steel was also caused and underwent brittle collapse due to cracking in the steel flange after local buckling. A comparison between the proposed method and these 4 experimental results is shown in Table 2. The theoretical results of the ultimate displacement are smaller than the experimental results. But the local buckling length L_{sbuc} and plastic length L_{sP} ($=L_{sP1}+L_{sP2}$) are almost the same as that in the experimental results.

5. CONCLUSION

This paper presents an experimental and analytical investigation of the seismic performance of SRC piers. As the result of the reversed cyclic loading tests of SRC columns, two limit states considering the damage level of SRC columns were shown. The restorable limit state and the ultimate state were defined as the spalling of the cover concrete and the local buckling of the H-shaped steel, respectively.

Moreover, ductility evaluation and a damage prediction method for the two limit states are proposed. Comparing the theoretical values and the experimental trials, it has been confirmed that the proposed method can appro -priately evaluate displacement at the restorable limit state (the spalling of the cover concrete) and the ultimate limit state (the local buckling of the H-shaped steel) of SRC columns.

References:

Mitsuyoshi AKIYAMA, Hideki NAITO and Motoyuki SUZUKI (2003), "Calculation Method of Ultimate Curvature of RC and SRC Section Based on Analytical Model for Axial Reinforcement Buckling and Its Application to Ductility Evaluation of These Columns," *Journal of Materials, Concrete Structures and Pavements*, Japan Society of Civil Engineers, No.725/V-58, 113-129.

Hideki NAITO, Mitsuyoshi AKIYAMA, Masato TAKADA, Shinsuke SHIMIZU, Kee-Nam HONG and Motoyuki SUZUKI (2005), "Modeling of Plastic Curvature Distribution of SRC Columns Subjected to Reversal Cyclic Loading and Its Application to Ductility Evaluation of Columns Predicting Buckling of Longitudinal Bars," *Journal of Structural Engineering*, Japan Society of Civil Engineers, Vol.51A, 1415-1424.

Hideki NAITO, Nobutaka SHIRAHAMA, Mitsuyoshi AKIYAMA, Masato TAKADA and Motoyuki SUZUKI (2006), "Ductility Evaluation of SRC Columns Predicting the Local Buckling of the H-Shaped Steel," *Journal of Materials, Concrete Structures and Pavements*, Japan Society of Civil Engineers, 62(4), 698-712.

Sixth International Conference on Urban Earthquake Engineering
March 3-4, 2009, Tokyo Institute of Technology, Tokyo, Japan

TRANSPORTATION NETWORK PROTECTION UNDER SEISMIC HAZARDS

Changzheng Liu[1] and Yueyue Fan[2]

1) PhD Candidate, Dept. of Civil and Environmental Engineering, University of California, Davis, USA
2) Assistant Professor, Dept. of Civil and Environmental Engineering, University of California, Davis, USA
czliu@ucdavis.edu, yyfan@ucdavis.edu

Abstract: This paper focuses on the problem of allocating limited retrofit resources over multiple highway bridges to improve the resilience and robustness of the entire transportation system against seismic hazard. We model it as a two-stage stochastic programming problem that minimizes an expected system cost including repair cost and system operation cost. Using a real-world case study, we demonstrate potential benefits brought by rigorous system optimization approaches in seismic hazard mitigation planning.

1. INTRODUCTION

The subject of disaster prediction, mitigation, and response has been a recurring theme in human history and is receiving increasing attention from many science and engineering disciplines, as shown in the work by Housner et al. (1994), Okuyama et al. (2004), Yashinsky (1998), Werner et al. (1999), and Shinozuka et al. (2000). While technologies continue to play an important role in disaster mitigation, effective management of mitigation resources is equally important in order to make the best use of available mitigation technologies. The focus of this paper is on seismic retrofit of highway networks.

Despite of the unpredictable nature of disasters in terms of location, time, and magnitude, seismic retrofit appears to be one of the effective mitigation methods for highway bridges. For example, in the 1994 Northridge earthquake, the highway bridges that had been retrofitted survived the earthquake even though some were within 100 meters of collapsed structures. On the other hand, retrofitting highway bridges can be costly in terms of monetary and manpower resources. This naturally raises a research question: how should limited resources be allocated to candidate facilities for retrofit so that the total loss of the entire transportation system caused by future earthquakes is minimized?

Two main challenges need to be addressed in order to answer the above question. First of all, individual bridges should be considered as a whole system instead of being treated separately. Federal highway administration (FHWA) seismic retrofit manual (Werner et al. 1999) states that retrofit decisions are made according to seismic hazard and the importance of individual components. However, individual components in a transportation system are actually not independent of each other. Highway system components (e.g. bridges and road) are spatially connected as a network. Any change in individual components may lead to a change in global behavior of a network. The behavior of network users and resultant traffic flow should also be studied in order to fully estimate network performance under a post-disaster environment. As pointed by Werner et al. (1999), such system issues are not currently considered in seismic retrofit practice due primarily to the lack of adequate system-based evaluation and decision tools.

Another challenge in retrofit decision making is to cope with uncertainty that is caused by random disaster events and seismic performance of highway bridges. Integrated efforts are needed from both earthquake engineers and transportation system analysts.

In this paper we will show how probabilistic risk assessment of individual highway bridges can be integrated with network theory and stochastic optimization techniques to produce effective retrofit decisions from a system viewpoint.

The organization of this paper is as follows. Section 2 will detail methodologies including network vulnerability analysis and stochastic programming model. A case study based on Alameda County highway network is given in section 3. Using this case study, we will demonstrate potential real-world applications of the presented methods. Advantages, limitations, and possible future extensions of this research are discussed in Section 4.

2. METHDOLOGIES

2.1 Network Vulnerability Analysis

In order to better protect transportation networks, it is important to first understand network behavior under disasters. In the literature, it is called network vulnerability analysis (see e.g. the work by Albert et al 2000), which examines the changes of network performance with the

gradual removal of network nodes and links by simulating attacks and random failure. In this subsection, we will present some preliminary results on a real world example, Alameda County Highway Network in California.

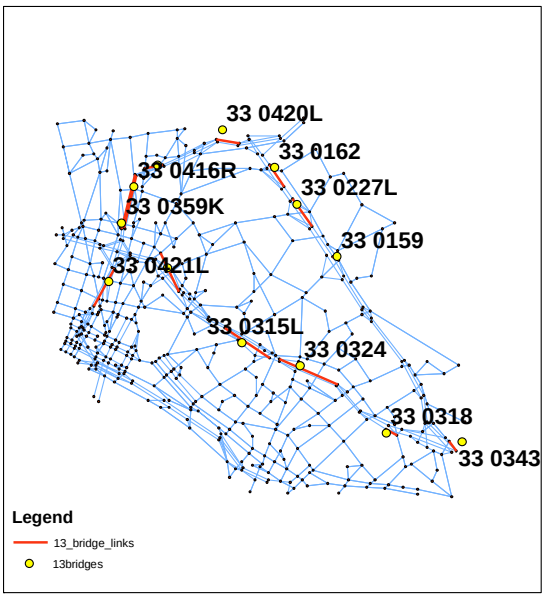

Figure 1 Alameda County Road Network with 504 nodes and 1424 links

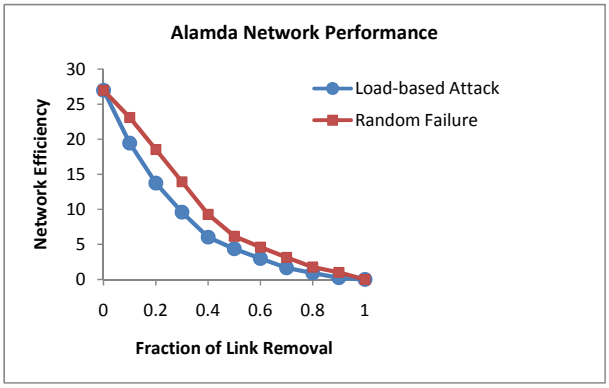

Figure 2 Changes in Global Efficiency of Alameda Network as a Function of Link removal

Figure 2 depicts the change of Alameda network performance as a function of link removal. Here network efficiency or global efficiency is defined by the following equation.

$$E(G) := \frac{\sum_{i \neq j} \frac{1}{t_{ij}}}{N(N-1)} \quad (1)$$

Where G refers to a network with N nodes, and t_{ij} is the shortest cost from node i to j.

Network efficiency is an indicator of network connectivity and its value decreases when a network is damaged and loses partial connectivity.

Load is used to measure the importance of one link and hence load-based attack refers to removing links according to the ranking of link load. The load of a link is defined as the number of shortest paths that pass through the link.

Figure 2 shows load-based attack degrades the network more than random failure especially during the initial stage of link removal. We also observe that removing 20% links by attack will largely degrade network performance (network efficiency decreases by one half), which may imply the necessity of protecting critical network links.

2.2 Stochastic Programming Model

2.2.1 Model Notations and Assumptions

We formally define Network Retrofit Problem as: which bridges should be retrofitted for given budget constraints and hazard estimates in order to reduce the potential system damage quantified by the total structural and travel delay loss? In the framework of two-stage stochastic programming, the first stage of the retrofit problem is to make retrofit decisions before an earthquake happens, while the second stage is to evaluate the total loss due to a realized earthquake including repair cost and increased travel delay in the network. The second stage cost (recourse cost) is a random variable dependent on the first-stage retrofit decision and the particular realization of bridge damages. Our objective is to minimize the expected earthquake loss through pre-disaster retrofit subject to the limited budget. In the rest of this subsection, we will introduce notations and assumptions used in the model.

Notations related to network topology**:**

Let us denote a transportation network as $G(N, A)$, where N is the set of nodes with size n and A is the set of network links with size m. Denote $\bar{A}$ ($\bar{A} \subset A$) as the set of links that are subject to earthquake hazards and thus the candidates for retrofit. The size of $\bar{A}$ is $\bar{m}$. The binary decision variable u_a is 1 if link a is to be retrofitted and 0 otherwise. Variable u_a is a first-stage decision variable. For each commodity[1] $k \in \{1...K\}$, $x^k \in R_+^m$ is the link flow vector, and $q^k \in R^n$ is the vector of demands and supplies of commodity k at each node. Denote f_a as the total flow on link a, i.e., $f_a = \sum_{k=1}^{K} x_a^k, \forall a \in A$.

Notations related to uncertain risk events:

Let $\boldsymbol{\xi}$ represent random events of pre-retrofit link damage states, and ξ be one realization of $\boldsymbol{\xi}$; Let $\boldsymbol{\Xi}$ be the post-retrofit link damage state which depends on u and

[1] In transportation network literature, the flow between each origin-destination pair is often considered as one commodity. Different commodities represent travel between different origin-destination pairs.

ξ, and $\Xi(\xi,u)$ be one realization of random event $\boldsymbol{\Xi}$. Only binary damage state is considered, with 1 indicating damage and 0 otherwise. For example, if there are three bridges in question, a possible value that ξ may take is [0 1 0]. The relationship between ξ, u, and $\Xi(\xi,u)$ for link a is described as

$$\Xi(\xi,u)_a = \begin{cases} \xi_a(\xi_a - u_a), & \forall a \in \bar{A} \\ 0, & \forall a \in A \setminus \bar{A} \end{cases} \quad (2)$$

For a scenario, if the pre-retrofit damage state of link a is 1 ($\xi_a = 1$), but the link is retrofitted (u_a=1), the value of $\Xi(\xi,u)_a$ is 0, indicating that the link will be intact under this scenario. On the other hand, if the link is not retrofitted but its pre-retrofit damage state is 1, the value of $\Xi(\xi,u)_a$ would be 1, indicating that the link will be damaged. If the pre-retrofit damage state of link a is 0 ($\xi_a = 0$), then the link is always in good condition no matter whether it is retrofitted or not.

Traffic flow assumption:

In transportation network literature, traffic is often assumed to be in equilibrium condition, where no traveler can gain more by simply changing her own routing decisions, as shown in the work by Wardrop (1952). This assumption works well in a normal situation in which travelers can learn about and adapt to day-to-day traffic condition. However, how to model travelers routing behavior in a sudden changing environment (such as following a catastrophic disaster) is still arguable. In this paper, we assume that traffic flow can be controlled to achieve system optimal condition. The total costs estimated under this assumption may be considered as a lower bound of the costs in reality.

2.2.2 Model Formulation

The network retrofit problem is formulated as follows:

Network Retrofit Problem (*NRP*)

$$\min_{u} \quad 0 + \underset{\xi \in \Xi_d}{E} \{Q(u,\boldsymbol{\xi})\} \quad (3)$$

$$s.t. \quad < c_1, u > \leq B \quad (4)$$

$$u \in \{0,1\}^{\bar{m}}, \quad (5)$$

where

$$Q(u,\xi) := \min_{x^k} \quad < c_2, \Xi(\xi,u) > + \gamma < f, t(f) > \quad (6)$$

$$s.t. \quad Wx^k = q^k, \quad \forall k = 1...K \quad (7)$$

$$x^k \leq (e - \Xi(\xi,u))M, \forall k = 1...K \quad (8),$$

$$f = \sum_{k=1}^{K} x^k, x^k \in R_+^m \quad (9)$$

where c_1 is the retrofit cost vector, B is the total budget for retrofitting, and c_2 is the repair cost vector. Vector e has all entries 1, i.e., $e_a = 1, \forall a \in A$. The link travel time t depends on the link flow f. Their relationship is usually described by a non-decreasing function such as the Bureau of Public Roads (BPR) function. The notation W represents the node-link adjacency matrix, and M is an arbitrarily large positive number.

Condition (4) represents the budget constraint. Condition (5) simply restricts u to be binary. Expression (6) states the second-stage cost including the repair cost term $< c_2, \Xi(\xi,u) >$ and the weighted flow cost $\gamma < f, t(f) >$, where γ is the weight coefficient converting time to monetary value. This cost becomes known once the earthquake hazard has been realized, thus is the recourse cost quantifying the effectiveness of the first-stage decision. Condition (7) is flow conservation constraint for second stage problem. Condition (8) restricts the link flow to zero if the link is damaged by the earthquake. Finally expression (3) describes our objective as to minimize the expected second stage cost. Note that the first stage retrofit cost is incorporated in the budget constraint, instead of contributing to the total system cost. System modelers may consider adding retrofit cost directly to the objective function. This modeling choice would not change the structure of the model.

Under the assumption of finite discrete distributions of the uncertain parameters, the stochastic programming model can be equivalently formulated as a deterministic equivalent program (DEP), which is a mixed-integer nonlinear program. In order to overcome the numerical complication caused by integer first-stage decision variables in network retrofit problems, we have developed an efficient solution algorithm (Liu et al., 2007) by utilizing decomposition (Benders, 1962), linearization, and successive approximation techniques (Van Slyke et al. 1969).

3. CASE STUDY

We use the Alameda network to demonstrate the potential real-world applications of the methods discussed in this paper. This network has 510 nodes, 1424 links, and 2401 origin-destination flows.

Seismic Risk Assessment of Highway Bridges in the Study Area: Seismic damage to a highway bridge is usually classified into five categories, ranging from no damage to complete collapse. Advanced structural analysis can lead to probabilistic assessment of structural damage for a given earthquake, in terms of a set of discrete probabilities associated with each of the five damage categories. Seismologists, on the other hand, have predictions to the probabilities of various earthquake occurrences. The two sets of probabilistic estimations from earthquake-structural engineers and seismologists can be combined to prepare the damage prediction. Detailed description of assessing damage states of bridges in the study area, considering their spatial and structural correlation, can be found in the work by Lee et al. (2006).

Thirteen highway bridges in the study area are found vulnerable while being evaluated under 31 potential

earthquake events that are likely to affect Alameda County. Most of these earthquake events are not severe enough to cause functional damage to the bridges. After aggregating all no-damage scenarios, we have totally six damage scenarios to consider. The probabilities of these damage scenarios are computed based on the Poisson arrival rates of the 31 earthquake events and a 10-year planning horizon. Table 1 provides information of the damage scenarios and the retrofit and replacement costs of each candidate bridge.

Other parameters: Parameter γ converts two-hour peak time delay to yearly (assuming reconstruction of a bridge takes one year) dollar value. It is set as (1/60)*8*365*20=973.3, where (1/60) is to convert minutes to hours, 365 is to convert daily to yearly value, 20 is the average value of time for travelers in the study area, and 8 is the two-peak-hour conversion factor to daily impact estimated for the San Francisco Bay Area [2]. Link performance function follows the standard BPR function in the form of

$$t_a^0[1+\alpha(\frac{x_a}{c'_a})^\beta] \quad (10)$$

where t_a^0 and x_a are free flow travel time and flow for link a respectively, α and β are parameters, and c'_a is the "practical capacity" of link a .The values of these parameters are set to be $\alpha = 0.15$; $\beta = 4$; $c' = c$.

In this case study, there are 13 integer variables and 418,656 (1424 links x 49 origins x 6 scenarios = 418,656) continuous variables. Retrofit budget considered ranges from 0.5 to 8 million dollars, resulting in 15 to 2048 possible retrofit solutions. Benders decomposition based solution algorithm (Benders, 1962) is implemented to find optimal solutions. The optimal retrofit strategies under different budget constraints are reported in Table 2.

We observe that an optimal solution resulting from low budget may not necessarily be a subset of an optimal solution from high budget, which indicates that retrofit decisions based on simple engineering ranking approaches may be questionable. Let us consider 4 M$ budget as an example. A commonly used engineering approach is to rank the candidate bridges for retrofit based on the traffic volume they carry and their seismic risk estimates. Assuming equal importance of the two factors, the ranks of the thirteen bridges are computed and reported in Table 1. Bridge 33C0315L is ranked highly by the engineering method because of its large traffic volume and the relatively high seismic risk it is subject to. However, this bridge is not chosen for retrofit by the stochastic programming model, demonstrating that a high-volume link may not be as critical as it seems depending on the redundancy of the network and consequently the flexibility it has to redistribute flow.

We also observe positive impact that a retrofit program may bring to the society. Apparently, there is a tradeoff between the planning investment and the recourse cost. As plotted in Figure 3, the expected second stage recourse cost EQ (including repairing cost and travel delay cost) decreases as more retrofit funding is invested. As more retrofit fund becomes available, the total system cost (first-stage retrofit cost plus the expected second-stage cost) also decreases until a certain point (5M$ in this case) is reached. For example, as the retrofit budget increases from 0.5M$ to 4M$, the total system cost decreases from 12.9M$ to 11.7M$. The gained benefit is about 10%.

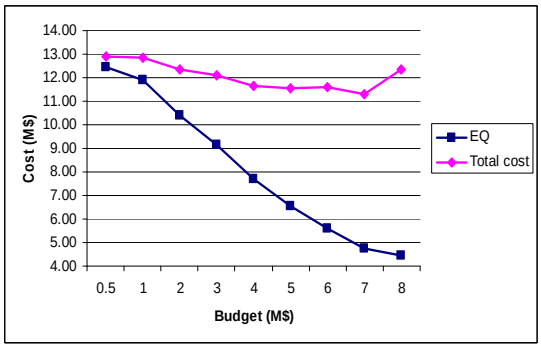

Figure 2 Retrofit budgets vs. system costs

3.1 Stochastic vs. Deterministic Approaches

Wait-and-see approach (Birge, 1997) is a commonly used deterministic approach which seeks an optimal solution for each scenario, as if we could wait and see the realization of random events and then make decisions accordingly. Since wait-and-see approach provides a set of scenario-dependent solutions, simple heuristic rules are often used to aggregate these solutions to a single one that can be implemented.

In Table 3, we give wait-and-see policies for all the scenarios. Retrofit budget is 4M$ in this experiment. The "scenario cost with perfect information" reports the recourse cost of each scenario when the corresponding wait-and-see policy is followed. This is the least possible cost for each scenario. The "expected cost over all scenarios" evaluates the performance of the wait-and-see policies in an expected sense. As expected, the stochastic programming solution provides the least expected cost compared with wait-and-see policies. The difference ranges from 210K to 10.56M dollars.

Wait-and-see solution (Birge, 1997) is defined as $WS = E_\xi[Q(u(\xi),\xi)]$, where $u(\xi)$ is the wait-and-see policy for scenario ξ . In this case study, the WS value is 5.03M$. Expected recourse cost from stochastic programming solution is 7.69M$. Therefore, the expected value of perfect information (EVPI) is 7.69 - 5.03 = 2.66M$. The EVPI of stochastic programming solution suggests that effort in improving estimates of uncertain parameters is worthwhile, even though stochastic programming model may be less sensitive to imperfect information than its deterministic correspondents.

3.2 Value of Stochastic Programming Solutions

[2] This conversion factor is estimated based on peak duration and daily vehicle hours in year 2006 provided by Metropolitan Transportation Commission (unpublished).

One may have noticed that different modeling approaches may lead to quite different policies. Stochastic programming approach explicitly considers the entire range of uncertain scenarios thus hedging better against uncertainty. However, it also increases computational complexity dramatically. Sometimes, as system analysts, we may need to justify whether the extra effort on modeling and solving stochastic programming is worthwhile. The concept of Value of Stochastic programming Solution (VSS) (Birge, 1997) can be used to answer this question quantitatively.

Let us denote u^* as the optimal solution suggested by a commonly used engineering approach. If the solution u^* is implemented, the expected earthquake loss across all possible damage scenarios is $EEV := E_{\xi}(Q(u^*, \xi))$. Similarly, let us denote the expected loss calculated in the stochastic programming model as $SP := \min E_{\xi} Q(u, \boldsymbol{\xi})$. Then the VSS is defined as $VSS = EEV - SP^u$. In general, a bigger VSS indicates higher benefit of using stochastic programming approach.

Since damage scenarios are represented by binary numbers, simply taking expectation of random parameters is not reasonable. If we consider the most likely scenario (scenario 2 in this case), the retrofit solution under 4M$ budget constraint is to retrofit bridges 33C0359K, 33C0421L, 33C0289S, 33C0315L, 33C0159, 33C0318, and 33C0324. In this case, VSS = 8.79-7.69=1.1 million dollars. The relative gain is 12.6%. The relatively large value of stochastic programming solution justifies the use of more sophisticated modeling techniques and the extra computational efforts.

3.3 Evaluating the Reliability and Robustness of Stochastic Programming Solution

The cumulative probabilities of not exceeding a certain cost threshold are plotted in Figure 3 for the stochastic programming, most likely, engineering ranking, and wait-and-see policies. Stochastic programming solution is more reliable than its deterministic correspondents in this case study. For example, at 80% reliability level, SP solution can guarantee a cost threshold of 10M$, but the most-likely-scenario solution can only guarantee a threshold of 17M$. If the goal is not to exceed 18M$ total cost, the SP solution has 98% of chance of achieving such a goal; while the wait-and-see policy (from scenarios 1 and 3) only has less than 90% of chance of achieving such a goal.

Planning decisions are usually made before the actual realization of random variables occurs. However, the public usually judges a decision in the aftermath of an incident when all the uncertain information is already revealed. If one knows perfectly which scenario will actually happen, one could make the optimal retrofit plan to achieve the minimum cost accordingly. This is the wait-and-see solution. The gap between the actual cost and the best possible cost is called "regret," which is often used to measure the robustness of a solution. Mathematically, regret is defined as $Q(u,\xi) - Q(u(\xi),\xi)$, where $u(\xi)$ is the wait-and-see policy for scenario ξ, and u is the policy being evaluated. As shown in Table 3, the relative regrets (regret divided by wait-and-see solution) in all possible scenarios are small.

Results in this case study show that the stochastic programming solution performs well in terms of expectation, reliability, and robustness. However, we need to emphasize that this observation is case specific. Given different distributions of uncertain parameters or different problem settings, tradeoffs among different risk measures may appear.

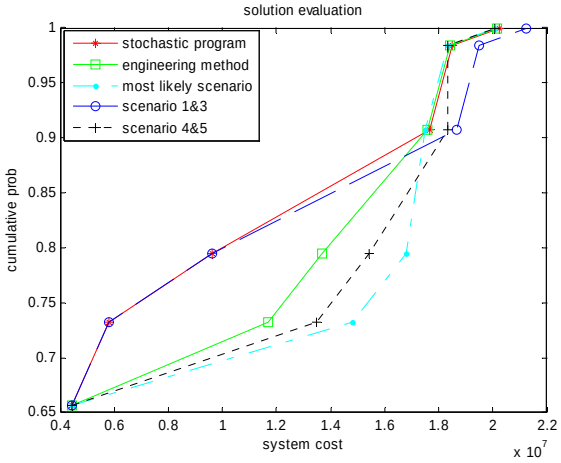

Figure 3 Reliability Evaluations of Different Retrofit Solutions

4. Discussion

Using a real-world case study, we have shown how stochastic programming method can be used to support retrofit planning decisions. By incorporating advanced stochastic system modeling techniques, we are able to achieve a solution that is cost effective and reliable. Nevertheless, we are still at an early stage of this research where the focus is mainly on theory and model development. Several issues arising from retrofit practice are not yet considered. For example, from construction view point, bridges are often grouped during a retrofit project and thus the retrofit decisions would be made over clusters instead of individual bridges. If the clusters are predefined, then the proposed formulation is still suitable. However, if clustering decision needs to be made simultaneously with the retrofit decision, this requirement would impose one more layer of complexity to the model. Other practical issues include considerations of the convenience and safety of detour during construction.

Another extension is to study network performance under a post-disaster environment. This includes further study to network vulnerability analysis emphasizing topology, and the behavior of network users.

Acknowledgements:
The authors acknowledge support from Pacific Earthquake Engineering Research Center (PEER).

References:

Housner, G. W., and C. C. Thiel. ed. (1994) "Continuing Challenge: The Northridge Earthquake of January 17, 1994", Report to the Director, California Department of Transportation, by the Seismic Advisory Board. Sacramento, CA: Caltrans.

Okuyama, Y. and S.E. Chang. Co-Editors. (2004). Modeling Spatial Economic Impacts of Disasters, Springer-Verlag.

Yashinsky, M. (1998). "Performance of Bridge Seismic Retrofits during Northridge Earthquake", Journal of Bridge Engineering, Vol.3, No.1, 1998, pp. 1-14.

Werner, S.D., C.E. Taylor, J.E. Moore, and J.S. Walton (1999). Seismic Retrofitting Manuals for Highway Systems, Volume I, Seismic Risk Analysis of Highway Systems, and Technical Report for Volume I, Multidisciplinary Center for Earthquake Engineering Research, Buffalo, New York.

Shinozuka, M., I. Juran, and T. O'rouke. Co-Editors. (2000). Proceedings of Workshop on Mitigation of Earthquake Disasters by Advanced Technology (MEDAT-1), MCEER Technical Report.

Albert, R., H. Jeong, and A.L. Barabasi (2000). "Error and attack tolerance of complex networks", Nature. 406,378-382.

Wardrop, J. (1952) "Some theoretical aspects of road traffic research", Proceeding of the Institute of Civil Engineers, 2(1):325-378.

Liu, C.Z. and Fan, Y.Y. (2007), "A Two-Stage Stochastic Programming Model for Transportation Network Retrofit", Transportation Research Board 86th Annual Meeting Proceedings. D.C.

Benders JF (1962). "Partitioning procedures for solving mixed variables programming problems", Numerische Mathematik Vol. 4, 1962, pp. 238-52.

Van Slyke, R.M., and R.J.B. Wets (1969). "L-shaped programs with applications to optimal control and stochastic linear programming", SIAM journal of applied mathematics Vol. 17, 1969, pp. 638-663.

Lee, R. and Kiremidjian A.S. (2006). "Probabilistic Seismic Hazard Assessment for Spatially Distributed Systems", Proceedings of Fifth National Seismic Conference on Bridges & Highways.

Birge, J. R., and F. V. Louveaux (1997). Introduction to stochastic programming. New York, NY: Springer.

Table 1: Model input data: damage scenarios and cost data

National Bridge Index (NBI)	Replacement Cost	Retrofit Cost	Scenarios						Engineering Ranking
			1	2	3	4	5	6	
33C0343	$833,833	$208,458	0	0	0	1	1	0	8
33C0318	$1,144,154	$286,038	0	1	0	1	1	0	4
33C0159	$1,024,100	$256,025	0	1	0	1	1	0	7
33C0324	$1,806,588	$451,647	0	1	1	1	1	0	2
33C0227L	$706,420	$176,605	0	1	0	1	1	0	5
33C0162	$1,980,990	$495,247	0	1	1	1	1	0	7
33C0315L	$3,878,490	$969,622	0	1	0	1	1	0	1
33C0420L	$1,737,450	$434,362	0	0	0	0	1	0	9
33C0289S	$489,940	$122,485	0	1	0	1	1	0	2
33C0414L	$1,361,008	$340,252	1	1	1	1	1	0	6
33C0416R	$9,007,614	$2,251,903	1	1	1	1	1	0	2
33C0359K	$1,746,030	$436,507	0	1	0	1	1	0	6
33C0421L	$5,871,690	$1,467,922	1	1	1	1	1	0	3
Probability of Each Damage Scenario (%)			7.6	11.3	6.2	7.7	1.6	66	

Table 2: Optimal retrofit strategies and expected system costs EQ

Budget (M$)	Retrofit Strategies	EQ (M$)
0.5	33C0414L 33C0289S	12.44
1	33C0414L 33C0289S 33C0162	11.91
2	33C0414L 33C0421L 33C0227L	10.38
3	33C0414L 33C0416R 33C0289S 33C0159	9.13
4	33C0416R 33C0421L 33C0159	7.69
5	33C0414L 33C0359K 33C0416R 33C0421L 33C0162	6.54
6	33C0414L 33C0359K 33C0416R 33C0421L 33C0289S 33C0227L 33C0162 33C0159 33C0324	5.59
7	33C0414L 33C0416R 33C0421L 33C0289S 33C0315L 33C0227L 33C0162 33C0318 33C0324	4.76
8	ALL	4.45

Table 3: Performance of wait-and-see and the stochastic programming solutions

	Wait-and-See Policy	**Scenario Cost with Perfect Information (million $)**	**Expected Cost over All Scenarios (million $)**	**Scenario Cost of SP Solution**	**Relative Regret of SP Solution**
Scenario 1	33C0416R 33C0421L	5.81	7.90	5.81	0
Scenario 2	33C0359K 33C0421L 33C0289S 33C0315L 33C0159 33C0318 33C0324	17.51	8.79	17.65	0.8%
Scenario 3	33C0416R 33C0421L	9.61	7.90	9.61	0
Scenario 4	33C0414L 33C0359K 33C0421L 33C0289S 33C0315L 33C0343 33C0324	18.32	8.70	18.48	0.9%
Scenario 5	33C0414L 33C0359K 33C0421L 33C0289S 33C0315L 33C0343 33C0324	20.06	18.25	20.22	0.8%
Scenario 6	None	4.45	13.02	4.45	0
Stochastic Program (SP) Solution	33C0416R 33C0421L 33C0159		7.69		

Sixth International Conference on Urban Earthquake Engineering
March 3-4, 2009, Tokyo Institute of Technology, Tokyo, Japan

CRACK PROPAGATION IN UNDER-MATCHED JOINTS UNDER SEISMIC LOADING

Atsushi Tanabe[1)]

1) Assistant Professor, Department of Civil Engineering, Tokyo Institute of Technology, Japan
tanabe@cv.titech.ac.jp, -

Abstract: There is a possibility of under-matched welded joint in case of high strength steel and old structures. In case of beam-to-column connection, there is high possibility of under matching and weld defects and it means high risk of fatigue cracking during earthquakes. When seismic force applied to under-matched joint, deposit metal yields first and it cause strain concentration and plastic constraint in the deposit metal. Previous study about butt welded joints showed that the strain concentration at a weld defect reduces crack initiation life significantly short, and the crack propagation life is become shorter but constraint effects decrease shortage of propagation life. However, the fatigue performances of cruciform joints are not clear yet. This study is aiming to clarify the fatigue performance of cruciform joint under seismic loading by using FEM analysis. As a result, the reduction of fatigue performance by under-matching is not severe.

1. INTRODUCTION

All of codes and specification request that the yield strength of the deposit metals should be higher than the yielding strength of base metals. However, this requirement cannot always be satisfied because of following reasons. (1) Softer welding materials are used intentionally in order to improve weldability, because stronger welding materials usually have bad weldability. (2) Actual yield strength of base metal can be significantly higher than the value in the provision for yield strength. In addition, old structures have more possibility of under matching because of low welding technology.

Moreover, old structure may have weld defect, too (Miki 2007). In fact, fatigue problems were found at the beam-to-column connection of steel bridge frame piers (Morikawa 2002). The interaction between the defect and under-matching may cause fatigue problem under earthquakes.

When seismic force is applied to under-match welded joints, weld metal yields first and constrained by non-yielded base metal. Stress triaxiality, is introduced by such constraint (Henry and Luxmoore 1997, Hancock et al. 1993). Because of stress triaxiality in deposit metal, under-matched welded joints had almost same tensile strength as usual welded joints, but it had a tendency of low elongation (Satoh and Toyoda 1971). This triaxiality may also affect to fatigue behavior. In case of under-matched welded joints with defect or incomplete penetration, high strain concentration occurs at the defects. This high strain concentration may reduce fatigue strength. Tanabe and Long (2007) showed that in case of butt welded joint, defect containing under-matched welded joints had extremely short initiation life due to strain concentration caused by interaction of defects and under-matching. Tanabe and Padungsriborworn (2008) showed that the propagation life of under-matched butt welded joints was between the propagation life of base metal and of weld metal due to stress triaxiality caused by plastic constraint by non-yielded base metal. However, the behavior of under matched cruciform joint which is used in the beam-to-column connections was not clear.

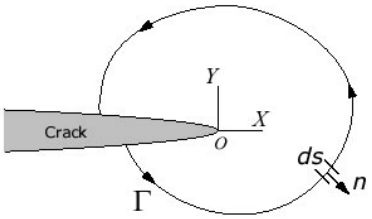

Figure 1 Definition of J-integral

Crack propagation under plastic strain can be evaluated by fracture mechanics parameter, J-integral and J-integral range. J-integral is defined as contour integral (see Eq. (1) and Figure 1), and it has path-independency (Rice 1978).

$$J = \int_{\Gamma} \left(W dy - \sum_i T_i \frac{\partial u_i}{\partial x} d\Gamma \right) \quad (1)$$

Where, T_i ($=\sigma_{ij} n_j$) is surface force along the contour Γ, $\partial u_i / \partial x$ is gradient of stress in x direction (parallel to crack surface and perpendicular to crack front), W is strain energy density, defined as Eq. (2), for non-linear elastic material.

$$W = \sum_{i,j} \int_0^{\varepsilon_{ij}} \sigma_{ij} d\varepsilon_{ij} \quad (2)$$

Crack propagation life N_p can be calculated by Eq. (3) (Dowling and Begley 1976, Dowling 1977).

$$N_p = \int_{a_0}^{a_f} \frac{1}{\frac{da}{dN}} da \quad (3)$$

Where, a_0: initial crack size, a_f: final crack size, *da/dN*: crack propagation rate. The *da/dN* has relationship with ΔJ. , *da/dN* was obtained by Eq. (4)

$$\frac{da}{dN} = C(\Delta J)^m \quad (4)$$

Where, C and m is material constant, in case of steel, $C = 3.32 \times 10^{-4}$, m=1.375.

ΔJ of plastic deformed material can not be calculated from the time history of J, because J-integral is defined for non-linear elastic material. Thus, ΔJ is calculated by summation of elastic part and plastic part as shown in Eq. (5) (Dowling and Begley 1976, Dowling 1977).

$$\Delta J = \Delta J^{(e)} + \Delta J^{(p)} = \frac{K_I}{E'} + \frac{Area}{Bb} \quad (5)$$

Where K_I: stress intensity factor (mode I), *E'*: equivalent elastic constant, *E* for plain stress condition and $E/(1-\nu^2)$ for plain strain condition, *Area*: the area in load-crack opening curve considering crack closure (see Figure 2), *B*: width and *b*: ligament size. In this calculation, the equivalent load range ΔP_e, which considering crack closure, was used for calculation of stress intensity factor K_I. Based on this equation, Hoshide et al. (1982) showed that J-integral range can be calculated more accurately by using load-crack opening displacement relationship instead of load-displacement relationship, and that using loading part of the relationship is better for the estimation.

This study is aiming to clarify the fatigue performance of cruciform joint under seismic loading. Non-linear Finite Element method was used to obtain strain concentration, J-integral and J-integral range, and the fatigue performance was evaluated.

2. EVALUATION OF CRACK INITIATION LIFE

Crack initiation life was discussed by local strain, because crack initiation lives were strongly related with local strain at crack initiation point (Tanabe and Long 2007). Therefore, the effects of under-matching on the crack initiation life were considered by the relative change of local strain concentration at a weld root and weld toe by nonlinear FEM analysis.

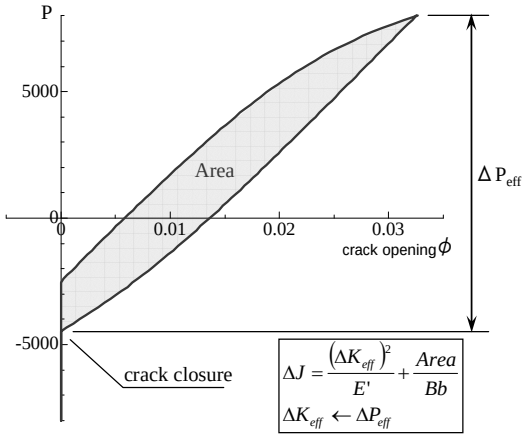

Figure 2 Area for Determination of plastic ΔJ

2.1 FEM Analysis

Strain at the weld root and weld toe was analyzed by using ABAQUS. Figure 3 shows the FEM model of cruciform joint and boundary conditions. Considering symmetrical condition, a quarter parts was modeled by using second order plane strain elements. Minimum mesh size is about 0.2mm. Tip of weld root and weld toe are modeled as r=1 mm in order to eliminate singularity. The radius r is decided by referring effective notch stress which defined by IIW fatigue design recommendation. Nominal stress was applied at the end of beam flange.

Two matching conditions were considered: even matching (EM), which consists of BM only, and under matching (UM) which consists of BM and WM10. Figure 4 shows the true stress-logarithm strain relationships of BM and WM10. Bi-linear kinematic hardening is used. Yield strength of base metal was 500MPa. 10% under-match weld metal's yield strength was 450MPa. Hardening coefficient H is same for all material: 2000MPa (=E/100).

2.2 Analysis Result

Figure 3 shows the relationship between applied nominal stress and local strain at the root and toe. In case of this type joints, weld toe and root yield almost same far field stress of 120MPa. After local yielding, local strain at the weld toe increases faster than at weld root. This difference may caused by stress triaxiality. High stress triaxiality reduces the growth of plastic strain. Because of such stress triaxiality, even under matched joint, strain growth was slow. By increasing far field stress, strain at the weld root increased rapidly and it exceed the local strain at the weld toe. This fact may indicate that weld toe is severe under live load but weld root is severe under seismic load. By considering matching condition, under-matched case had higher local strain.

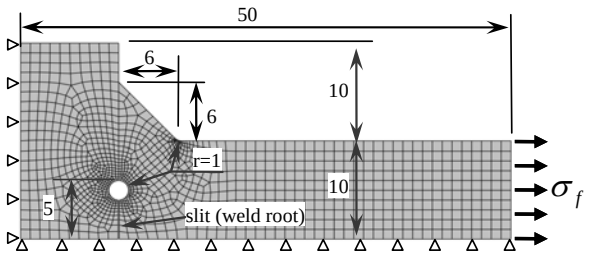

Figure 3 FEM model

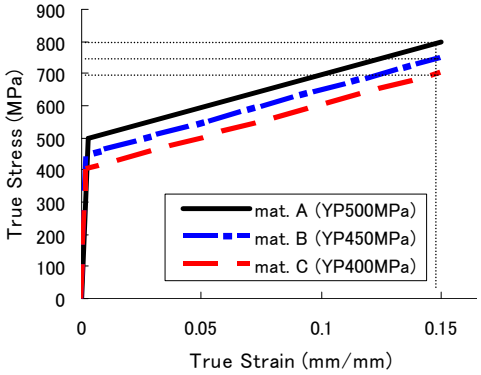

Figure 4 Stress-Strain relationships

3. EVALUATION OF EFFECTS ON ΔJ

In this chapter, propagation life was discussed with fracture mechanics parameters J-integral J and J-Integral Range Delta-J and brittle fracture toughness. At first, fracture strength (Tanabe and Padungsriborworn 2008) was considered to grasp final crack size and then propagation rate was considered by Delta-J.

3.1 Fracture Strength

Final crack size a_f can be determined from brittle fracture strength and maximum stress. Where, the brittle fracture strength is the far field stress when brittle fracture occurred. In this study, Crack Tip Opening Displacement (CTOD) δ_c=0.1mm was used as criterion of fracture toughness (Miki et al. 1999, Miki et al. 2000, Tanabe and Padungsriborworn 2008). The fracture toughness δ_c was converted to J_c by using Eq. (6) (ASTM 2006).

$$\delta = \frac{J}{m\sigma_Y} \tag{6}$$

$$\sigma_Y = \frac{\sigma_{YS} + \sigma_{TS}}{2} \tag{7}$$

$$m = A_0 - A_1\left(\frac{\sigma_{YS}}{\sigma_{TS}}\right) + A_2\left(\frac{\sigma_{YS}}{\sigma_{TS}}\right)^2 - A_3\left(\frac{\sigma_{YS}}{\sigma_{TS}}\right)^3 \tag{8}$$

$$\begin{Bmatrix} A_0 \\ A_1 \\ A_2 \\ A_3 \end{Bmatrix} = \begin{Bmatrix} 3.62 \\ 4.21 \\ 4.33 \\ 2.00 \end{Bmatrix}, \ when \ \left(\frac{\sigma_{YS}}{\sigma_{TS}}\right) \geq 0.5 \tag{9}$$

Where, σ_{YS}: Yield Stress, σ_{TS}: Tensile Strength.

Fracture strength can be obtained from J_c and far field stress-J relationship. The relationship between far field stress and J-integral was calculated by FEM analyses.

3.2 Parameters

Considered parameters are combination of material and nominal stress range.

3.3 FEM Model

Figure 5 shows FEM model. Boundary conditions and loading condition are also shown in Figure xx. Analysis code was ABAQUS, 2nd order plain strain 2D solid element was used. By considering symmetric condition, quarter model was used. Degenerate elements were used to around crack tip in order to consider singularity. Loads were applied as nominal stress in the beam flange. Five times cyclic load were applied the end of beam flange as a pressure.

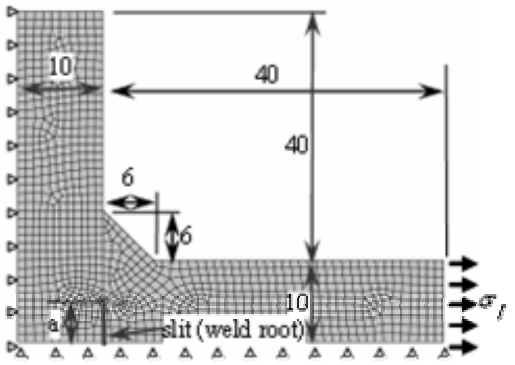

(a) Root crack model

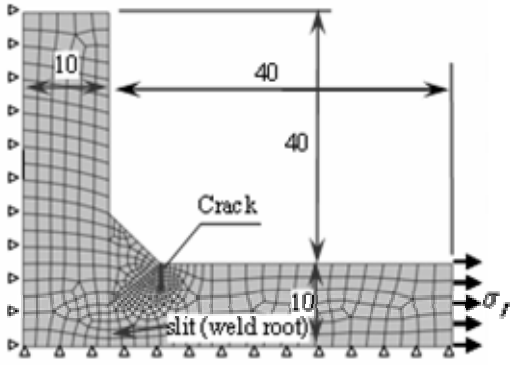

(b) Toe crack model

Figure 5 FEM model for J-integral analysis

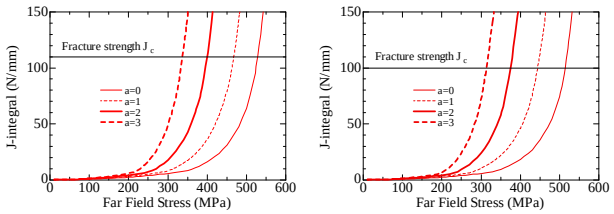

Even matching Under matching

(a) Root crack

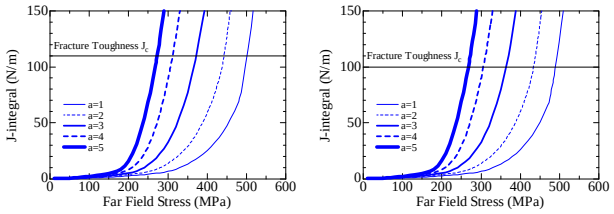

Even matching Under matching

(b) Toe crack

Figure 6 Change of J-integral and Fracture Toughness

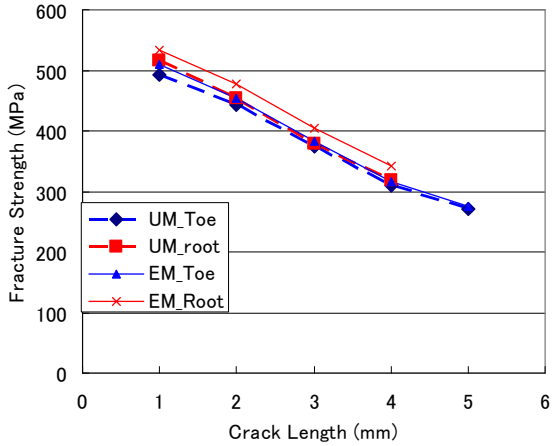

Figure 7 Fracture strength

3.4 FEM Results

Figure 6 shows the change of J-Integral by nominal stress. From this results and fracture strength of material, fracture strengths were calculated. The calculated fracture strengths were shown in Figure 7. From this result, Fracture toughness is strongly related with crack size and root crack had comparably higher fracture toughness. Under matched joints had smaller fracture strength than even matched joints. However the difference is not large and it just reduce fracture strength. Therefore, we may say that fracture strength was reduced by the change of material but there is small effect by the constraints due to under matching.

From this figure, final crack size can be calculated by maximum far field stress. If maximum stress is 400 MPa, final crack size will be about 2.5 mm.

Figuere 8 shows load-crack opening displacement relationship of root crack when far field stress range is 800 MPa (+/- 400MPa). From this result, J-integral ranges were calculated as Figure 9. From this figure, under-matched joint had few percent higher J-integral ranges. This fact indicates that crack propagation life become short in case of under-matched joint, but such effect is not so severe.

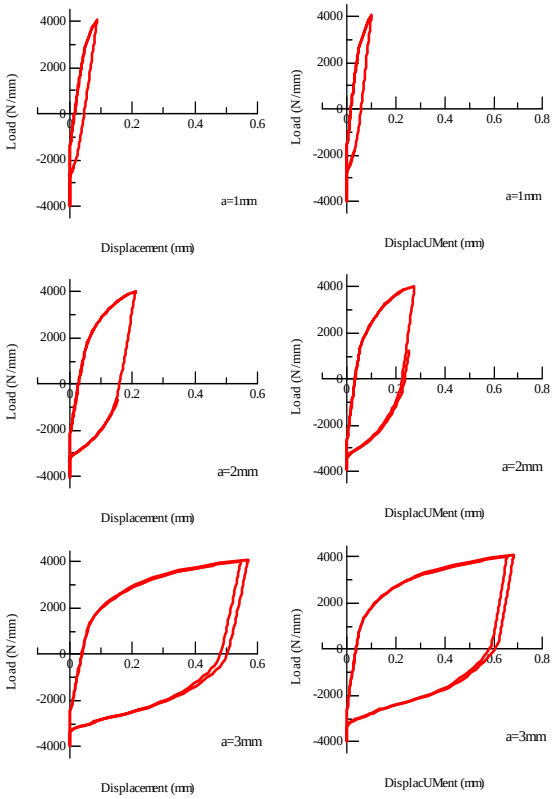

Even match Under match

Figure 8 Load-Crack opening relationship ($\Delta\sigma$ =800MPa)

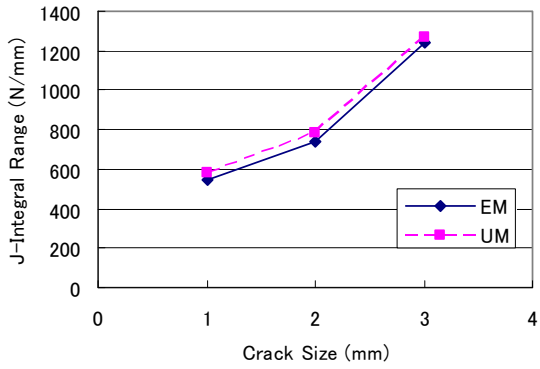

Figure 9 Comparison of J-integral range

4. CONCLUSIONS

In this study, fatigue performances of partial penetrated cruciform joints were discussed by using FEM analysis. The following results were obtained.

1. Under seismic loading, local strain at weld root is higher than at weld toe. Thus, there is high possibility of root cracking.

2. Under matching had comparably small effect on the J-intagral and J-integral range for cruciform joints than the effect for butt welded joint.
3. Under matched joint had little percent higher J-integral range than even matched joints. Thus, it may have shorter propagation life, but the reduction of life was not severe.

References:

ABAQUS, Inc. (2004) ABAQUS Analysis User's Manual, Ver.6.5

ASTM (2006), "Standard Test Method for Measurement of Fracture Toughness", ASTM Designation: E1820-06, 2006

Dowling, N. E. and Begley, J. A. (1976), "Fatigue Crack Growth During Gross Plasticity and the J-Integral", *Mechanics of Crack Growth, ASTM STP 590*, 82-103

Dowling, N. E. (1977), "Crack Growth During Low-Cycle Fatigue of Smooth Axial Specimens", *Cyclic Stress-Strain and Plastic Deformation Aspects of Fatigue Crack Growth, ASTM STP 637*, 97-121

Hancock, J. W., Reiter, W. G. and Parks, D. M. (1993), "Constraint and toughness parameterized by T. Constraint Effects in Fracture", *ASTM STP1171*, ASTM, 21–40

Henry, B. S. and Luxmoore, A. R. (1997), "The stress triaxiality constraint and the Q-value as a ductile fracture parameter", *Engineering Fracture Mechanics*, **57**(4), 375–390

Hoshide, T., Tanaka, K. and Nakata M. (1982) Experimental Investigation on Fatigue Crack Growth Law under Elastic, Elastic-Plastic and General Yield Conditions, *Journal of the Society of Materials Science*, Japan, 566-572

Miki, C., Kyuba, H. and Okinaka, K. (1999) A Study on the material of the brittle fractured bridge pier. *Proceedings of JSCE*, (612), 45-53

Miki, C., Sasaki, E., Kyuba, H. and Takenoi, I (2000) Deterioration of Fracture Toughness of Steel by Effect of Tensile and Compressive Prestrain, *Proceedings of JSCE*, (640), 165-175

Miki, C., Fahimuddin, F. and Anami, K. (2001), "Fatigue Performance of Butt-Welded Joints Containing Various Embedded Defects", *Structural Engineering / Earthquake Engineering of JSCE*, **18**(1), 13s-28s

Rice, J.R. (1968), "A Path Independent Integral and the Approximate Analysis of Strain Concentration by Notches and Cracks", *Journal of Applied Mechanics*, ASTM, **35**(2), 379–386

Satoh, K. and Toyoda, M. (1971), "Effect of Mechanical Heterogeneity on the Static Tensile Strength of Welded Joints", *Journal of the Japan Welding Society*, **40**(9), 885-900

Tanabe, A. and Long, X. (2007), "Fatigue Behavior of Defect-containing Under-matched Welded Joints Under Plastic Strain", *Proc. of Fourth International Conference on Urban Earthquake Engineering*, 261-268

Sixth International Conference on Urban Earthquake Engineering
March 3-4, 2009, Tokyo Institute of Technology, Tokyo, Japan

EFFECT OF STRONG VERTICAL COMPONENT OF NEARFIELD GROUND MOTION ON THE SEISMIC PERFORMANCE OF AN RC BRIDGE

Hiroshi Matsuzaki[1] and Kazuhiko Kawashima[2]

1) Assistant Professor, Department of Civil Engineering, Tokyo Institute of Technology, Japan
2) Professor, Department of Civil Engineering, Tokyo Institute of Technology, Japan
matsuzaki.h.aa@m.titech.ac.jp, kawashima.k.ae@m.titech.ac.jp

Abstract: Nearfield ground motions recorded in recent years have revealed that the intensity of vertical component can be larger than that of the lateral component. In this study, the effect of strong vertical ground motion on the response of a standard girder bridge supported by RC columns was investigated based on the fiber element analysis. Axial force at the bottom of the column varies extensively due to the vertical vibration mode of the bridge excited by the strong vertical ground motion. However, the effect of this large axial force variation on the response of the bridge is very limited.

1. INTRODUCTION

In the seismic design of bridges, the effect of vertical component of ground motions on the response of structures is not considered. This is because the intensity of vertical component is much smaller than that of lateral component in general, and that the fundamental vibration modes of bridges are in the lateral direction. On the other hand, nearfield ground motions recorded in recent years have revealed that the intensity of vertical component can be larger than that of the lateral component. KiK-net Ichinoseki-nishi record in 2008 Iwate-Miyagi Nairiku earthquake is a typical example, and the PGA of the vertical component reached about 4g. This nearfield record shows that strong vertical ground motion can be generated, contrary to the previous strong ground motions, if the hypocenter depth is shallow and the observation point is very close to the source.

The axial force changes significantly with strong vertical ground motions such that design spectra have been proposed (for example, Papazoglou and Elnashai 1996, Elnashai and Papazoglou 1997). However, in these studies the vertical components are slightly larger than the lateral components. Furthermore, studies on the effect of vertical strong ground motions on the response of bridges are insufficient. In this study, the effect of strong vertical ground motion on the response of a standard girder bridge supported by RC columns is investigated.

2. INPUT GROUND MOTIONS

One of the input strong ground motions is the KiK-net Ichinoseki-nishi record in 2008 Iwate-Miyagi Nairiku earthquake as shown in Figure 1. PGA of NS and EW components are 11.4 m/sec^2 and 14.3 m/sec^2, respectively, and that of UD component reaches 38.7 m/sec^2. Response acceleration spectra (h=5%) is shown in Figure 2, and it is recognized that components corresponding to the periods around 0.1-0.3 sec are predominant, and the response acceleration of UD component at 0.1 sec reaches 92.4 m/sec^2.

As shown in Figure 2, response acceleration of UD component exceeds that of the lateral component in the range of 0.3 sec or less of the natural period, thus processed UD component by 3 Hz low-pass filter is also considered as follows

$$\begin{cases} w(f) = 1, & f \le 3\text{Hz} \\ w(f) = 0, & f > 3\text{Hz} \end{cases} \tag{1}$$

As described in more detail below, amplitudes in frequencies corresponding to the vertical vibration modes of the bridge analyzed in this study are absolutely zero by the 3Hz low-pass filter. UD component of KiK-net Ichinoseki-nishi record after low-pass filter process and its response acceleration spectrum are shown in Figure 3 and Figure 4, respectively. As shown in Figure 4, by cutting frequencies higher than 3 Hz, response accelerations in corresponding frequency range decrease.

JR Takatori Station record in Figure 5 is also used for comparison as one of conventional strong ground motions that the vertical component is not the governing component. As shown in Figure 6, for the JR Takatori Station record, the response acceleration of the UD component is smaller than that of the lateral component. This is in contrast to the KiK-net Ichinoseki-nishi record.

3. TARGET BRIDGE AND ANALYTICAL MODEL

As shown in Figure 7, a five-span continuous I-girder

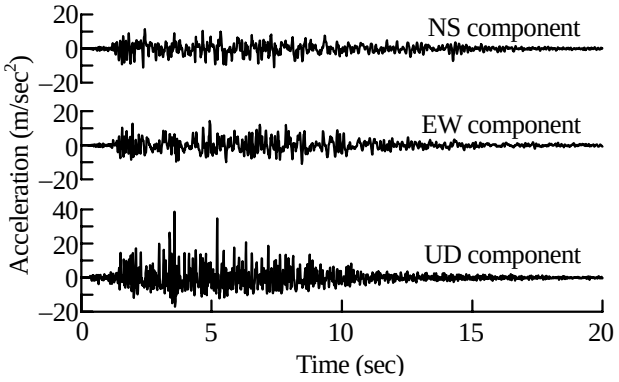

Figure 1 KiK-net Ichinoseki-nishi Record (2008 Iwate-Miyagi Nairiku Earthquake)

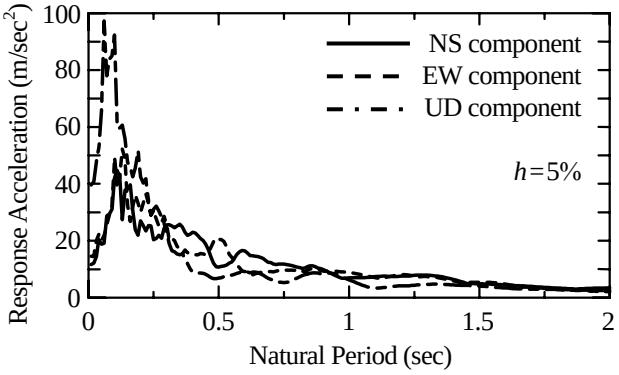

Figure 2 Response Acceleration Spectra (KiK-net Ichinoseki-nishi Record)

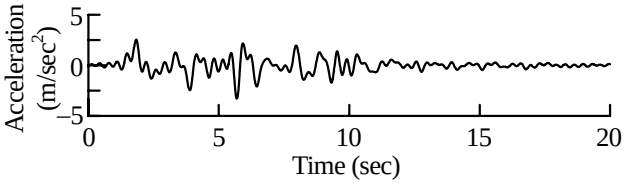

Figure 3 3Hz Low-pass Filtered UD Component (KiK-net ichinoseki-nishi Record)

bridge supported by cantilevered RC columns and pile foundations were analyzed in this study. In the analysis, plastic hinge zones at the bottom of the columns were idealized by fiber elements, elastomeric bearings and soil springs were idealized by linear springs, and the others by 3D linear beam elements. The stress vs. strain relation of the confined concrete was assumed based on Hoshikuma et al (Hoshikuma et al., 1997). Unloading and reloading hystereses were idealized based on a model by Sakai and Kawashima (Sakai and Kawashima, 2006). Furthermore, the Menegotto-Pinto model (Menegotto and Pinto, 1973) was used to idealize the stress vs. strain hystereses of the longitudinal bars.

The natural periods of the bridge are 1.17 sec in the longitudinal direction, and 1.00 sec in the transverse direction, respectively, in case the plastic hinge zone is elastic. Figure 8 shows the first mode (0.86 Hz) shape corresponding to the natural period of the longitudinal direction and the ninth mode (4.33 Hz) shape where vertical

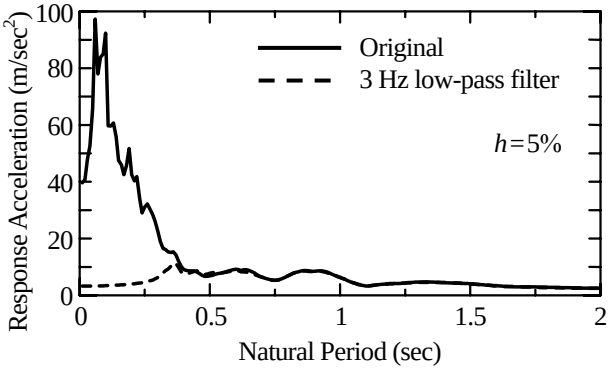

Figure 4 Effect of 3 Hz Low-pass Filter on the Response Acceleration Spectrum

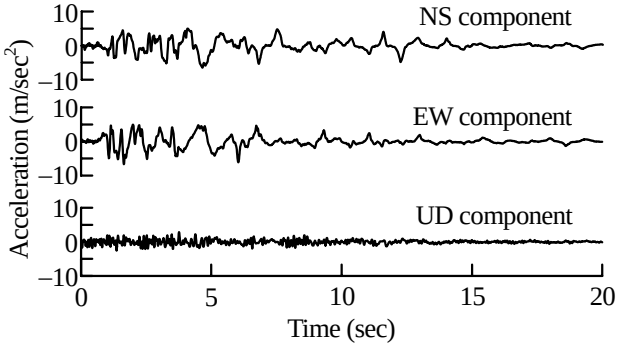

Figure 5 JR Takatori Station Record (1995 Hyogo-ken Nanbu Earthquake)

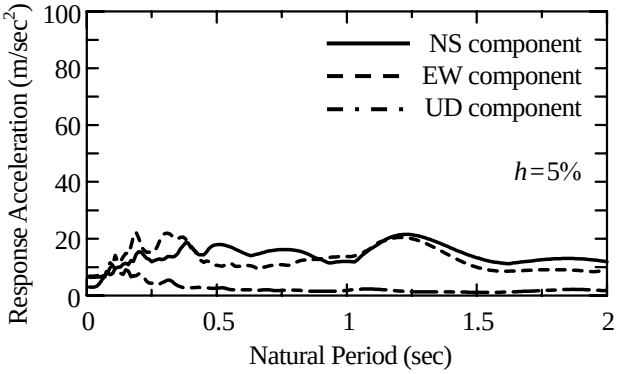

Figure 6 Response Acceleration Spectra (JR Takatori Station Record)

vibration of girders governs. As described before, in this study, 3 Hz low-pass filter processed vertical ground motion was also considered, and high frequency components corresponding to the vertical vibration modes of the bridge were absolutely removed.

In the dynamic response analysis, Rayleigh damping was used. Element damping constants were set to 2 % for bridge elements and 20 % for soil spring elements. The first mode and the sixth mode were used to set parameters in the Rayleigh damping.

The time history analysis was conducted using Newmark β method (β=1/4). The time step interval of integration is 0.001 sec.

EW, NS, and UD components of KiK-net

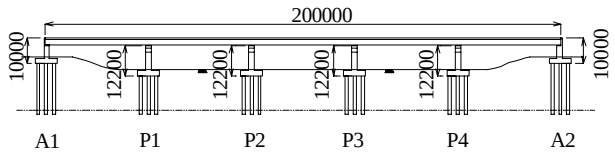

(a) A Five-Span Bridge

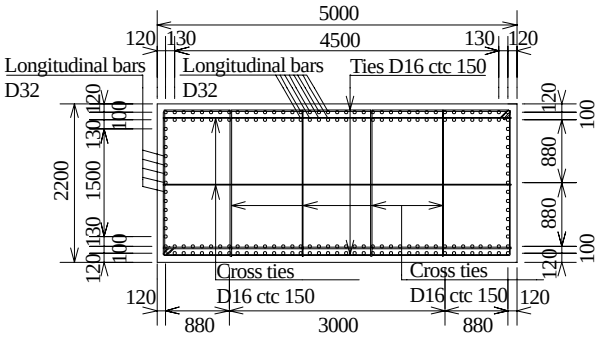

(b) Column Section

Figure 7 Target Bridge

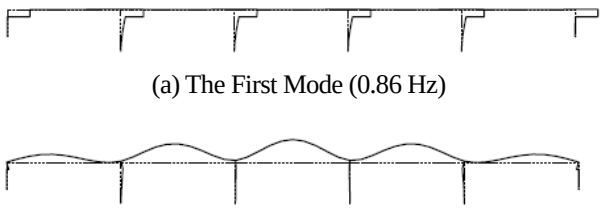

(a) The First Mode (0.86 Hz)

(b) The Ninth Mode (4.33 Hz)

Figure 8 Natural Mode Shapes of the Bridge

Ichinoseki-nishi record and JR Takatori Station record were imposed to the analytical model in the longitudinal, transverse as well as vertical directions simultaneously.

4. THE EFFECT OF VERTICAL GROUND MOTION ON THE RESPONSE OF AN RC BRIDGE

Figure 9 and Figure 10 show the displacement of the deck at P1 column in case KiK-net Ichinoseki-nishi record and JR Takatori Station record is imposed, respectively. There is almost no difference between the displacement by the original KiK-net Ichinoseki-nishi ground motion and by the ground motion which includes 3 Hz low-pass filter processed vertical ground motion. Comparing the displacement in the transverse direction, it is recognized that there is short-period variation for the KiK-net Ichinoseki-nishi ground motion (Figure 9(b)) compared to that of JR Takatori Station record (Figure 10(b)). This short-period variation remains even if 3 Hz low-pass filter processed ground motion is imposed. Hence, this short-period variation is generated by the lateral ground motion which also has predominant frequencies in the

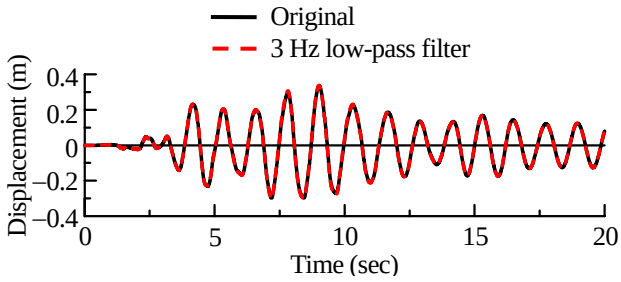

(a) Longitudinal Direction

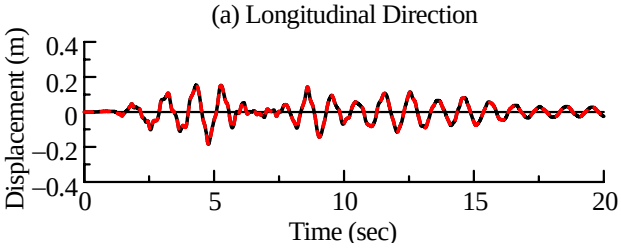

(b) Transverse Direction

Figure 9 Deck Displacement at P1 Column (KiK-net Ichinoseki-nishi Record)

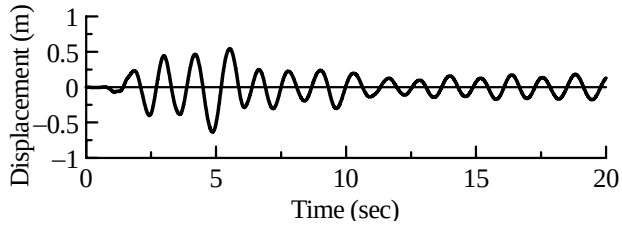

(a) Longitudinal Direction

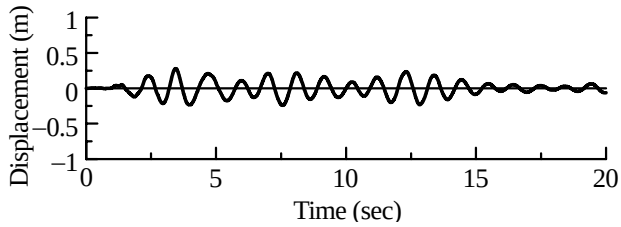

(b) Transverse Direction

Figure 10 Deck Displacement at P1 Column (JR Takatori Station Record)

shorter period as shown in Figure 2.

Figure 11 and Figure 12 show the moment vs. curvature hystereses at the plastic hinge zone of P1 column in case KiK-net Ichinoseki-nishi record and JR Takatori Station record is imposed, respectively. In case the original KiK-net Ichinoseki-nishi ground motion is imposed, the hystereses curve is not smooth. On the other hand, in case low-pass filter processed Ichinoseki–nishi or JR Takatori Station record is imposed, the hystereses curve is smooth. This varying moment vs. curvature hystereses, in case the original KiK-net Ichinoseki-nishi record is imposed, is due to the varying axial force acting at the bottom of the column as shown in Figure 13. The maximum tension force corresponds to the compressive force equal to the dead load. This extensive axial force variation is excited by the vertical ground motion which has predominant frequencies corresponding to the vertical vibration modes of the bridge. As shown in Figure 14, in case JR Takatori Station record is

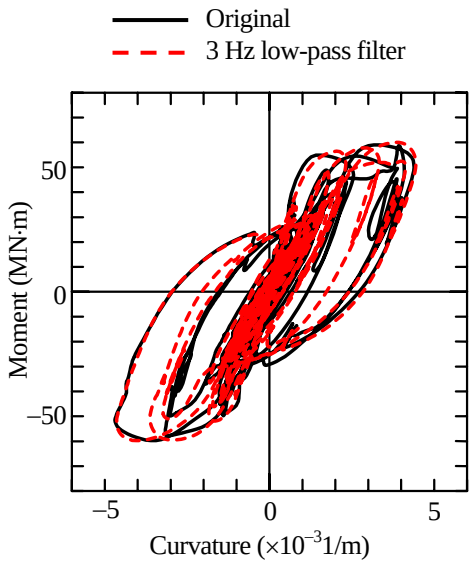

Figure 11 Moment vs. Curvature Hystereses in the Longitudinal Direction at the Plastic Hinge Zone of P1 Column (KiK-net Ichinoseki-nishi Record)

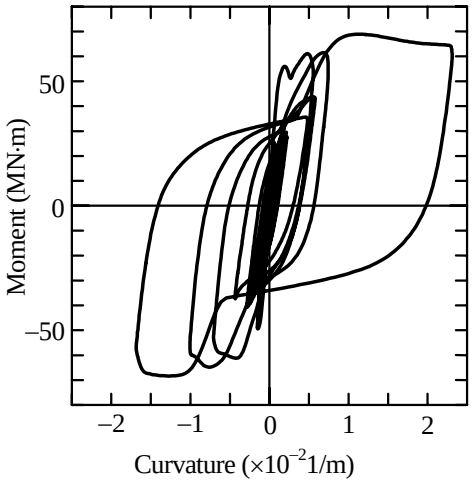

Figure 12 Moment vs. Curvature Hystereses in the Longitudinal Direction at the Plastic Hinge Zone of P1 Column (JR Takatori Station Record)

imposed, tension force slightly acted on the column. However, this long period variation is due to the lateral displacements of the columns supporting the continuous girder, not due to the vertical ground motion.

The effect of the axial load varying from 1 N/mm^2 tension load to 2.7 N/mm^2 compression load on the seismic performance of RC columns was investigated based on the reversed cyclic loading tests and fiber element analysis (Sakai and Kawashima, 2002). From the experimental results, it was found that restoring hystereses under varying axial load which includes tension load corresponding to 1 N/mm^2 was also stable and there was no typical deterioration of lateral force capacity. Furthermore, fiber element analysis also had good correlation with the

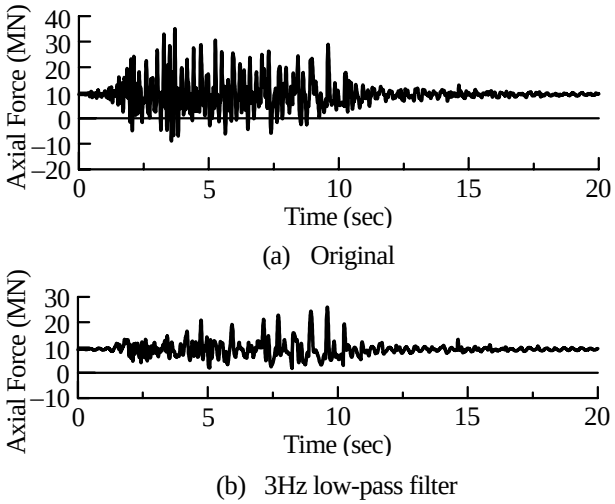

Figure 13 Axial Force at the Bottom of P1 Column (KiK-net Ichinoseki-nishi Record)

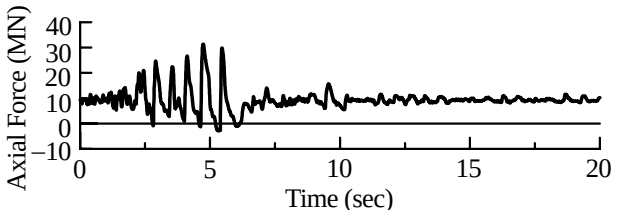

Figure 14 Axial Force at the Bottom of P1 Column (JR Takatori Station Record)

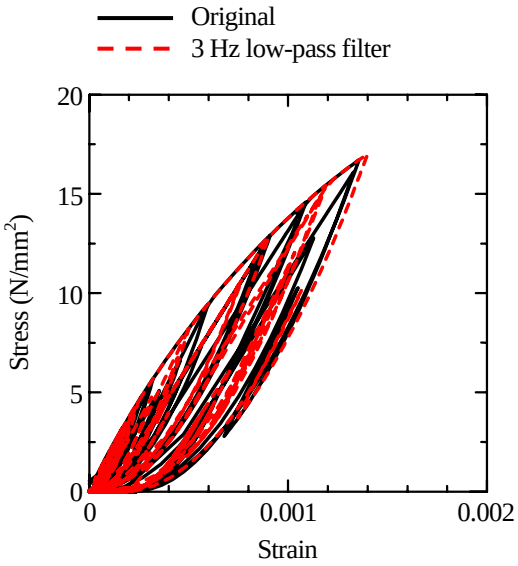

Figure 15 Stress vs. Strain Hystereses of Core Concrete (KiK-net Ichinoseki-nishi Record)

experimental data under tension load as well as under compression load.

Stress vs. strain hystereses of the core concrete and that of the outermost longitudinal bars in the plastic hinge zone of P1 column are shown in Figure 15 and Figure 16, respectively. Neutral axis at the bottom of the column varies

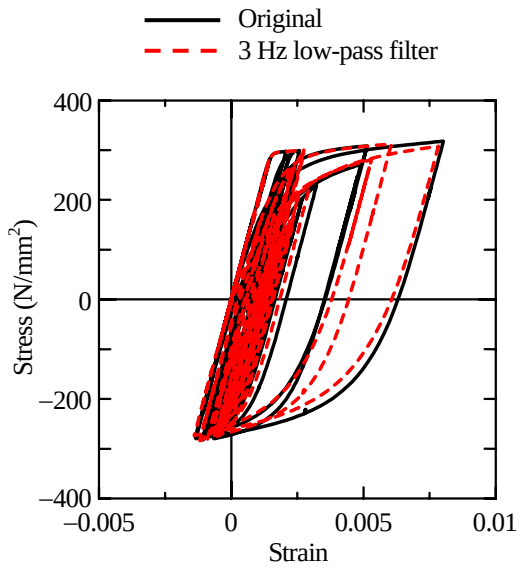

Figure 16 Stress vs. Strain Hystereses of Longitudinal Bars (KiK-net Ichinoseki-nishi Record)

due to the variation of the axial force influenced mainly by the vertical ground motion. Hence, the maximum strains of core concrete and longitudinal bars are slightly changed by 3 Hz low-pass filter process.

The effect of the vertical ground motion on the response of a bridge has been discussed in this paper. From the analysis, the variation of the axial force is excited due to the vertical ground motion which has predominant frequencies in the short period. It has been also shown that the variation of the axial force has little effect on the response of the bridge. In this study, only KiK-net Ichinoseki-nishi record was used as a ground motion which has a strong vertical component, and only a standard type of girder bridge supported by RC columns was analyzed. Thus, it is necessary to study the effect of vertical ground motions on the response of bridges not only for girder bridges but also for arch bridges and cable-stayed bridges which have coupled vibration modes in the vertical and horizontal direction.

5. CONCLUSIONS

The effect of strong vertical ground motion on the response of a standard girder bridge was investigated using the KiK-net Ichinoseki-nishi record observed in 2008 Iwate-Miyagi Nairiku earthquake. From the analysis presented herein, the following conclusions may be deduced:

1) When strong vertical ground motion is imposed, the vertical vibration of the girder is excited and axial force varies extensively such that tension force can act at the bottom of the column. Large variation of the axial force may change the bending capacity of the column such that its effect on the response of the bridge should be carefully investigated. From the analysis presented, there is a limited effect of the axial force variation due to the vertical ground motion on the displacement of the girder, moment vs. curvature hystereses and stress vs. strain hystereses of core concrete and longitudinal bars.
2) The research on the seismic performance of RC column under tension loading has been insufficient. As discussed in this study, tension force can act on the column if the seismic source is close to the structure site. Hence, more studies on this area are needed.
3) In this study, only a standard girder bridge is analyzed. Arch bridges and cable-stayed bridges, which have coupled vibration modes in the vertical and horizontal direction, should also be analyzed.

References:

Elnashai, A. S. and Papazoglou, J. (1997), "Procedure and spectra for analysis of RC Structures subjected to strong vertical earthquake loads," *Journal of Earthquake Engineering*, ASCE, **1**(1), 121-155.

Hoshikuma, J., Kawashima, K. and Taylor, A.W. (1997), "Stress-Strain Model for Confined Reinforced Concrete in Bridge Piers," *Journal of Structural Engineering*, ASCE, **123**(5), 624-633.

Papazoglou, A. J. and Elnashai, A. S. (1996), "Analytical and field evidence of the damaging effect of vertical earthquake ground motion," *Earthquake Engineering and Structural Dynamics*, **25**(10), 1109-1137.

Sakai, J. and Kawashima, K. (2002), "Effect of varying axial loads including a constant tension on seismic performance of reinforced concrete bridge piers," *Journal of Structural Engineering*, JSCE, **48A**, 735-746.

Sakai, J. and Kawashima, K. (2003), "Modification of the Giuffre, Menegotto and Pinto model for unloading and reloading paths with small strain variations," *Journal of Structural Mechanics and Earthquake Engineering*, JSCE, **738**, 159-169.

Sakai, J. and Kawashima, K. (2006), "Unloading and Reloading Stress-Strain Model for Confined Concrete," *Journal of Structural Engineering*, ASCE, **132**(1), 112-122.

Sixth International Conference on Urban Earthquake Engineering
March 3-4, 2009, Tokyo Institute of Technology, Tokyo, Japan

MITIGATION STRATEGIES FOR REGIONAL LOSS ASSESSMENT

Joshua S. Steelman[1] and Jerome F. Hajjar[2]

1) Graduate Research Assistant, Dept. of Civil and Environmental Engrg., University of Illinois at Urbana-Champaign, Urbana, IL, USA
2) Professor, Dept. of Civil and Environmental Engrg., University of Illinois at Urbana-Champaign, Urbana, IL, USA
jsteelm2@illinois.edu, jfhajjar@illinois.edu

Abstract: In recent years, there has been a surge of interest in analyzing seismic impacts on a regional basis. The regional approach is especially apropos in regions of low-to-moderate seismicity, where the risk to individual structures is not sufficient to justify extensive analyses and proactive mitigation in the minds of many stakeholders. However, the aggregate effects across a study region for low-probability, high-consequence events justify investigations and planning at the regional level. The shift toward studying regional effects has also been propelled by the development and integration of tools to address the various aspects of seismic risk and loss within GIS environments. One example of these activities is the Consequence-Based Risk Management approach adopted by the Mid-America Earthquake Center, including the development of refinements for various stages of seismic risk assessment and integration within the open source, GIS-based environment of MAEViz. This paper will address approaches and concerns available to equip and assist decision-makers when assessing loss across large regions by illustrating applications to a regional test bed investigated using MAEViz.

1. INTRODUCTION

In regions of low-to-moderate seismicity, many stakeholders do not find the risk to exposed assets to be sufficient to justify extensive analyses and proactive mitigation efforts. However, in such areas, the potential exists for infrequent but large magnitude events, capable of simultaneously causing extensive damage to buildings, transportation networks, and utilities. Even in regions of high seismicity, the regional response to an unusually strong event has only recently become the focus of large scale investigations.

A number of regional studies have been conducted and reported in published literature for various locations worldwide. In the United States, studies have been documented for six individual cities in the New Madrid Seismic Zone (NMSZ) of Mid-America (CUSEC, 1985). A study was also performed in greater detail specifically for Memphis, TN (Abrams and Shinozuka, 1997). FEMA has developed a loss assessment tool, HAZUS (FEMA, 2006), which has been updated and expanded through multiple releases since 1997. HAZUS has been employed for several documented studies, including commercial studies, such as Charleston, SC (URS, 2001), Northridge, CA (Reis et al., 2001), a repetition of the NMSZ six-city study by CUSEC (2003), Seattle, WA (Ballantyne et al., 2005), and an eight state study of the New Madrid Seismic Zone (Elnashai et al., 2008).

Numerous other commercial studies have been conducted worldwide, some of which have been performed by professional risk assessment firms using proprietary software. Among studies within academic research, notable published studies for losses on a regional scale include papers focusing heavily on western Turkey, as well as other Mediterranean areas such as Italy (e.g., Bal et al., 2008; Erdik et al., 2008; Teramo et al., 2008; Spence et al., 2008). Much of this work serves to form background and establish general guidelines of good practice when performing regional loss assessment. Strategies for decision-making and prioritizing mitigation efforts are not yet uniformly well established. This paper outlines a comprehensive procedure for regional loss assessment and decision support based on integration of several new algorithms within the open source, GIS-based environment of MAEViz (MAEViz, 2008), using Shelby County, TN (including Memphis, TN) in the USA as a case study.

2. INITIAL RISK ASSESSMENT

2.1 General Approach

The core components of the regional seismic risk assessment in this work include: inventory collection, hazard definition, vulnerability assessment, and estimation of social and economic consequences. Each step as established within this work will be described in greater detail in the following sections.

2.2 Inventory Collection

Inventory information for Shelby County, TN was collected for buildings and bridges in the study region from several sources. Building-by-building data was acquired specifically for this study by extrapolating from tax record data through a neural network model, calibrated by surveys of sample buildings in the study region (French and

Muthukumar, 2006). Demographic information was extracted on a census track-basis, and disaggregated as required for algorithms that mesh with demographic data. Example statistics for buildings within the study region are shown in Tables 1 and 2 (French and Muthukumar, 2006). The Tables show concentrations of exposure (replacement value) for combinations of general structure types and general occupancies. C, M, S, and W represent concrete, masonry, steel, and wood, respectively. Likewise, RES, COM, and IND indicate residential, commercial, and industrial occupancies. Agricultural, religious, government, and educational buildings are not shown; even excluding single-family structures, those occupancies only account for about 0.4% of the study region exposure according to the dataset. Bridge data for the study region was obtained from the National Bridge Inventory (FHWA, 2007).

Table 1 Example Exposure Data for Study Region, Including Single-Family Residences

		GENERAL OCCUPANCY			
		RES	COM	IND	Grand Total
GENERAL STRUCTUR TYPE	C	0.8%	6.7%	2.8%	10.4%
	M	2.4%	3.9%	0.5%	6.8%
	S	1.0%	6.5%	1.0%	8.5%
	W	73.8%	0.5%	0.0%	74.3%
	Total	78.0%	17.6%	4.3%	100.0%

Table 2 Example Exposure Data for Study Region, Excluding Single-Family Residences

		GENERAL OCCUPANCY			
		RES	COM	IND	Grand Total
GENERAL STRUCTUR TYPE	C	2.7%	23.0%	9.6%	35.4%
	M	8.1%	13.4%	1.8%	23.4%
	S	3.4%	22.2%	3.3%	29.1%
	W	10.3%	1.8%	0.0%	12.2%
	Total	24.5%	60.4%	14.7%	100.0%

2.3 Hazard Definition

The study region under consideration is subject to a potentially large seismic hazard with a long recurrence interval. To appreciate the consequences of such hazards, a probabilistic hazard approach is not likely to provide a fair representation. The probabilistic hazard will provide a long-term view of seismic hazard, taken over a time interval that may span hundreds or thousands of years, but the approach effectively smoothes the spike of activity that potentially characterizes this region.

To capture the true nature of a low-probability, high-consequence event, a seismic source was selected consistent with the historical seismology of the region. The magnitudes of the 1811-1812 earthquakes are generally estimated to be ranging from moment magnitude 7.0 to 8.1 (Petersen et al., 2008). For this study, a moment magnitude of 7.9 was selected and located at Blytheville, AR, based on guidance provided by geotechnical experts within the Mid-America Earthquake Center. Appropriate formulae were then employed to predict the effects of the seismic source throughout the study region. Attenuation equations developed by Fernandez and Rix (2006) were selected to account for the particular seismological characteristics of this region.

When smoothed spectra based on the USGS attenuation functions and soil adjustment coefficients recommended by the U.S. National Earthquake Hazard Reduction Program (NEHRP) are compared with spectra associated with the two representative soil profiles ("Uplands" and "Lowlands") in the study region considered by Fernandez and Rix (2006), the most significant difference between the two sets of curves is that the NEHRP coefficients generally assume that soil deposits will amplify ground accelerations, whereas the Fernandez and Rix equations implicitly account for nonlinearity in deep soil deposits, such as the 1000 m thick layer underlying Memphis, TN, thus leading to lower acceleration and higher displacement response of surface soils.

2.4 Vulnerability Assessment

There are a number of ways that vulnerability may be assessed for buildings in a study region. The methodologies employed in the various studies mentioned previously vary widely in their vulnerability assessment. HAZUS uses an overdamped capacity spectrum method (CSM) approach (FEMA, 2006), in which a linear elastic acceleration-displacement spectrum is adjusted to account for hysteretic response of a structure by adding "effective hysteretic damping" to elastic damping. Plotting the adjusted hazard spectrum superimposed with a capacity curve and finding the point of intersection, termed the performance point, is expected to yield a reliable prediction of building displacement response when subjected to an earthquake. The methodology has remained unchanged in every release of HAZUS, however, Fajfar (1999) cites discussions in which key assumptions of the overdamped CSM are called into question, most notably including the lack of a "physical principle that justifies the existence of a stable relationship between the hysteretic energy dissipation of the maximum excursion and equivalent viscous damping."

The risk assessment for the study region in this work was based on nonlinear time history analyses of various structure types. Several structure types were studied by constructing detailed models to capture the numerous complicated aspects inherent in nonlinear seismic response. Fragility functions have been developed for light wood frame construction, both 1- and 2-story structures, and considering both slab-on-grade construction and frames constructed with crawl spaces (Ellingwood, 2006; Ellingwood et al., 2008). Fragility functions have also been developed to represent 2-story and 4-story partially restrained steel moment frames, 3-story fully restrained steel moment frames, and 6-story X-braced steel frames (Ellingwood, 2006). Extensive studies of concrete frames have also been conducted (Bai and Hueste, 2006; Erberik and Elnashai, 2006; Hueste and Bai, 2003; Ramamoorthy et al., 2006).

If a structure type occurred in the inventory for which a

fragility set was not available (e.g., reinforced masonry), then a fragility set obtained from the parameterized fragility method (Jeong and Elnashai, 2007) was substituted, which incorporated the expected characteristics for the local ground motion in the study region (Fernandez, 2007). The parameterized fragility method was expanded to consider degradation models, as well as provide nonstructural fragilities in addition to structural fragilities, as described in Steelman and Hajjar (2008). In addition to the adjustments made in that paper, several parameters were adjusted prior to invoking the parameterized fragility engine for this study. Elastic damping ratios were generally reduced to reflect common estimates found in the literature. Also, uncertainty parameters were calculated as a combination of modeling and capacity uncertainty terms obtained from the HAZUS Technical Manual (FEMA, 2006), and demand uncertainties arising from variability in response to ground motion records. Finally, appropriate bridge fragilities were also implemented to represent bridge construction typical of the Central and Eastern US (Choi et al., 2004; DesRoches et al., 2003; DesRoches et al., 2006). The required hazard input for each fragility set was determined by the researcher who originally performed each study. All fragilities took the form of a lognormal distribution.

2.5 Social and Economic Loss Estimation

This final component of loss assessment includes consideration of a range of individual metrics related to social and economic loss (Bai et al., 2007; Green and Feser, 2007; Peacock, 2007; Padgett and DesRoches, 2007). Examples include repair and replacement costs of buildings and bridges, injuries requiring hospitalization, fatalities, business losses due to disruption of normal operations, and population dislocation. In each case, probabilities of discrete damage states from the vulnerability assessment are combined with coefficients and demographic data as appropriate to provide estimates of losses. Sample aggregated results for the case study scenario are given in Table 3.

Table 3 Initial Risk Assessment Summary

Buildings Repair / Replacement	$4.80 x10^9
Bridges Repair / Replacement	$10.6 x10^6
Hospitalizations	984
Fatalities	188
Business Interruption	$964 x10^6
Business Inventory Damage	$83.8 x10^6
Displaced Households	14,900
Displaced Persons	37,900
% Requiring Short Term Shelter	27.1
Loss of Property Tax Revenue	$42.4 x10^6

Bridge functionality was also investigated, yielding the results shown in Figure 1. The figure shows that the transportation system is severely impacted by the earthquake, with only 2% of bridges fully operational immediately after the earthquake. Current predictions estimate, however, that many of the bridges that are damaged can be repaired within several days if adequate materials and personnel are available. Similarly to the results shown in Table 3, functionality estimates for the bridges are based on direct correlation from damage output of the vulnerability assessment.

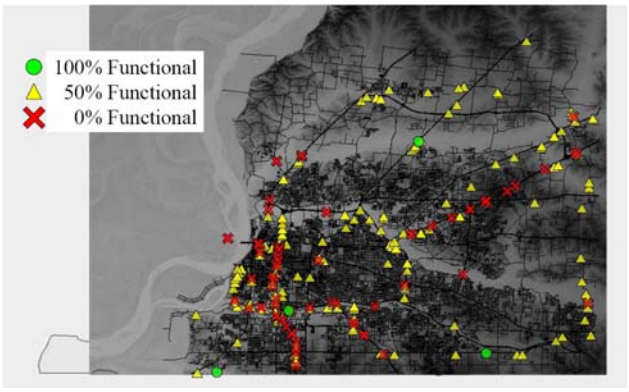

Figure 1 Bridge Functionality Immediately Following Earthquake (28% Non-Functional, 70% @ 50% Functional)

3. MITIGATION PLANNING

3.1 Planning Based on Direct Effects

For the case study region, two methods of mitigation planning and prioritization (i.e., decision support) were employed: Comparative Equivalent Cost Analysis (ECA) and Multi-Attribute Utility Analysis (MAUA). Applications of each framework were carried out as described in Park (2004). The ECA is a relatively simple technique, where the primary calibration involves assigning dollar values to certain key commodities that do not inherently have a dollar value associated with them, such as a human casualty. For this study, estimates were developed based on forensic economic literature (Dillingham, 1985; Hahn, 1996; Karels, 2003; Miller, 1990; Viscusi, 1993), so that a death was estimated to be worth approximately $8.5 million, and an injury was estimated to be worth $1 million.

Additional required data to perform the ECA include vulnerability data for retrofit options and some method of estimating costs to install retrofits. The approach used for these scenarios was to develop additional fragility sets using the parameterized fragility method, as described previously, including implementing parameters (e.g., strength ratio, period) tabulated for higher (i.e., improved) "code levels" in the HAZUS documentation. Costs were estimated for these retrofits based on FEMA 156/157 (FEMA, 1994; FEMA, 1995) as described in Steelman and Hajjar (2008). The optimum retrofit assignments were calculated for each building in the study region, based on maximizing the cost-benefit ratio and ensuring that only ratios greater than one were acceptable.

The cost to install all optimum retrofits is $602 million. However, when reviewing the results at the building level, a subset of buildings is found to provide exceptionally high benefit in return for the required investment. A group of eight hospitals provide benefit-cost ratios in excess of 40. The selected hospital locations are indicated in Figure 2 as

white circles overlaying a map of hospitalizations by tract. The total cost to retrofit this subset is estimated at $10.5 million, but the total projected benefit is $555.6 million. This subset of buildings also happens to share the same structure type: steel frame. Although not explicitly considered algorithmically, the selected subset may potentially permit the use of similar retrofit designs and details for multiple buildings.

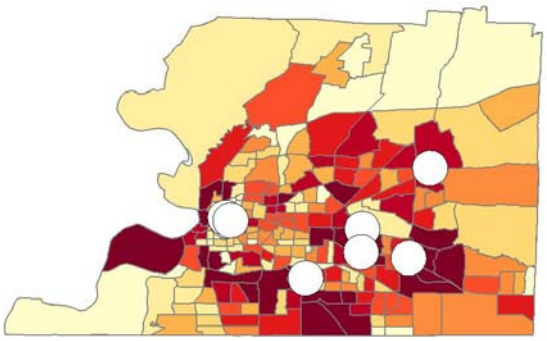

Figure 2 Selected Retrofits according to ECA

The MAUA , in turn, seeks to quantify performance parameters of the region in a relative "utility" sense. In this context, utility may be viewed as an indicator of satisfaction. The maximum value is 1, and this is assumed to be the value for the study region prior to the earthquake. As repair costs increase and casualties mount, the utility drops. The utility function can be any non-increasing function desired by a decision-maker. For this case study, two functions were implemented to reflect two risk attitudes: a cubic function to represent a risk-averse attitude, and an exponential to represent a risk-seeking attitude. Both curves satisfy the requirements of bounding utility by 0 (0.001 for Risk-Seeking) and 1. The Risk-Averse attitude is characterized by a desire to avoid high-risk, defined as scenarios for which utility is near zero. Thus, the maximum gradient of utility perceived by a Risk-Averse decision-maker occurs as the estimated losses near low utility values. The Risk-Seeker, in turn, would perceive little difference between alternatives or low utility values. Utility functions for each attitude are shown in Figure 3.

The limit parameters for the analyses were determined by scaling and calibrating from published losses for the 1994 Northridge earthquake. Limits of 621 persons killed, 3249 persons injured, and a total economic loss of $4.8 billion were used to establish thresholds of zero utility. Optimum retrofits were established for these cases by computing a change in utility for the region resulting from installation of a retrofit, and then normalizing that change in utility for the study region by the cost of the retrofit. The decision-making influences were also varied as part of the study by considering four cases. To calculate utility for a region, the individual utility values are weighted and summed, so the relative influences of various concerns can be incorporated by scaling weighting factors. The four cases considered, with values established in this work, were: (1) 0.25 weight for economic loss, injuries, fatalities, and loss of essential facility functionality, (2) 0.85 weight on economic loss, (3) 0.45 weight on each of injuries and fatalities, and (4) 0.85 weight on essential facility functionality. Figures 4 and 5 show optimum retrofits based on utility gradient for cases 2 and 3, respectively.

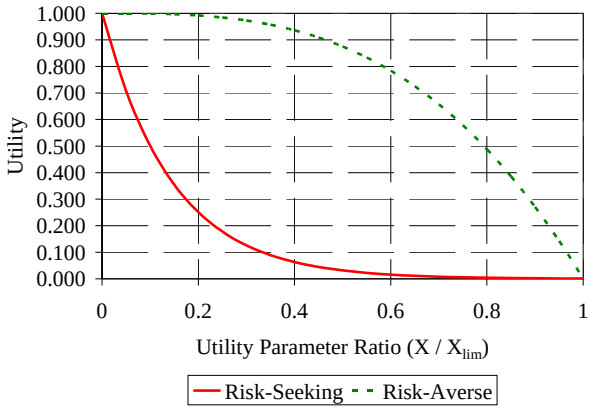

Figure 3 Utility Functions for MAUA

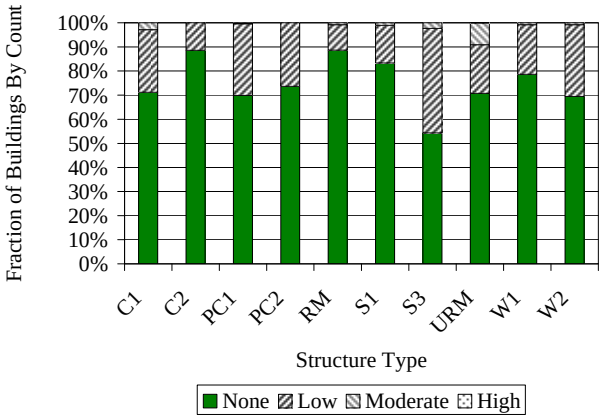

Figure 4 Optimum Retrofit Code Level for MAUA Case 2

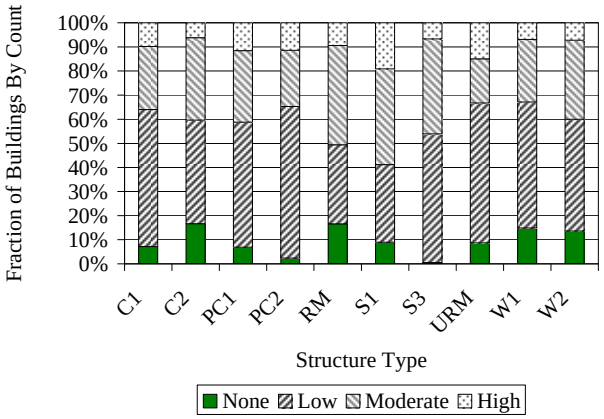

Figure 5 Optimum Retrofit Code Level for MAUA Case 3

The results in Figure 4, in particular, are fairly similar to the ECA result. As shown in Figures 4 and 5, the weight attributed to the value of life by a decision-maker has a pronounced effect on the result of the analysis. The calculations that lead up to the risk assessment, combined with the calculations for the various retrofit options for each structure are computationally intensive, but the final output, in this case, provides direct guidance for the most attractive retrofit options for each structure in the region.

3.2 Planning Based on Multi-Level Interactions

Planning based on multi-level interactions is suited to the current GIS platforms commonly employed for regional seismic risk assessments. One example would be to include consideration of bridge and hospital functionality in casualty estimation. The visual representation of such concerns becomes highly complex and difficult to discern, as in Figure 6, however, the current state-of-the-art is poised to leverage the advantage of GIS to enable these considerations to be considered within the decision framework.

For example, in Figure 6, a primary area of concern would be the northeast region. There is only one hospital nearby, and that hospital is projected to sustain heavier damage than most other hospitals in the region. Decreased functionality of that hospital, combined with extensive damage to the bridges along the primary route providing access to the hospital, leads to a compelling argument to focus mitigation efforts in that geographic region.

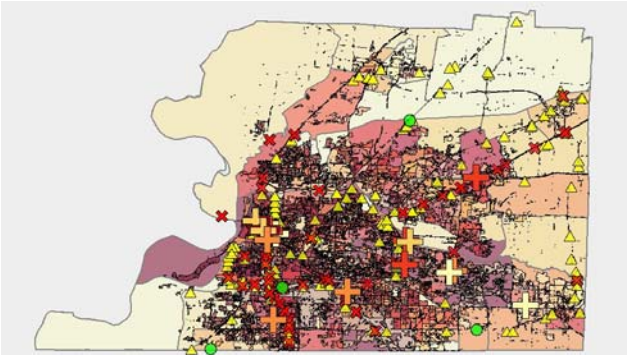

Figure 6 Multi-Level Representation of Injury Risk Factors

4. CONCLUSIONS

Two algorithms suited to evaluating competing retrofit options based on direct effects were presented. The primary consideration for both algorithms is to select suitable decision weights. This presents decision-makers with a conundrum when requiring the assignment of definitive values and influence to considerations of human life, pain, and suffering. However, reasonable values can be estimated from forensic literature and incorporated into regional seismic risk assessments to arrive at justifiable retrofit strategies. Furthermore, the utilization of point-wise inventory allows the prioritization, building-by-building, as a part of the retrofit plan.

Acknowledgements:

This research was supported by the Mid-America Earthquake Center, headquartered at the University of Illinois at Urbana-Champaign, under NSF Grant No. EEC-97010785, and by the University of Illinois at Urbana-Champaign. The authors would like to thank the researchers throughout the MAE Center who have provided guidance and information for this research. Any opinions, findings, and conclusions or recommendations expressed in this material are those of the authors and do not necessarily reflect the views of the National Science Foundation or other sponsors.

References:

Abrams, D. P. and Shinozuka, M. (eds.) (1997). "Loss Assessment of Memphis Buildings," Technical Report No. NCEER-97-0018, National Center for Earthquake Engineering Research, State University of New York at Buffalo, Buffalo, New York.

Bai, J.-W. and Hueste, M. D. (2006) "Seismic Fragility Analysis for a Retrofitted Five-Story Reinforced Concrete Building," Draft Internal Report, Mid-America Earthquake Center Report, University of Illinois at Urbana-Champaign, Urbana, Illinois.

Bai, J. W., Hueste, M., and Gardoni, P. (2007). "Probabilistic Assessment of Structural Damage due to Earthquakes for Buildings in Mid-America," *Journal of Structural Engineering*, ASCE, submitted for publication.

Bal, I.E., Crowley, H., and Pinho, R. (2008) "Development of a Displacement-Based Earthquake Loss Assessment Method for Turkish Buildings," Proceedings of the 14th World Conference on Earthquake Engineering, Beijing, China, October 12-17, 2008, International Association of Earthquake Engineering, Beijing, China.

Ballantyne, D., Bartoletti, S., Chang, S., Graff, B., MacRae, G., Meszaros, J., Pearce, I., Pierepiekarz, M., Preuss, J., Stewart, M., Swanson, D., and Weaver, C. (2005). Scenario for a Magnitude 6.7 Earthquake on the Seattle Fault, Earthquake Engineering Research Institute, Oakland, California.

Central United States Earthquake Consortium (CUSEC) (1985). "An Assessment of Damage and Casualties for Six Cities in the Central United States Resulting from Earthquakes in the New Madrid Seismic Zone," Internal Report, Central United States Earthquake Consortium, Memphis, Tennessee.

Central United States Earthquake Consortium (CUSEC) (2003). "Comparison Study of the 1985 CUSEC Six Cities Study Using HAZUS," Internal Report, Central United States Earthquake Consortium, Memphis, Tennessee.

Choi, E., DesRoches, R., and Nielson, B. (2004). "Seismic Fragility of Typical Bridges in Moderate Seismic Zones," *Engineering Structures*, **26**(2), 187-199.

Crowley, H., Pinho, R., and Bommer, J. (2004). "A Probabilistic Displacement-based Vulnerability Assessment Procedure for Earthquake Loss Estimation," *Bulletin of Earthquake Engineering*, **2**, 173-219.

DesRoches, R., Leon, R. T., and Dyke, S. (2003). "Response Modification of Bridges," Internal Report, CD Release 03-08, Mid-America Earthquake Center, Urbana, Illinois.

DesRoches, R., Padgett, J. E., Elnashai, A. S., Kin, Y. S., and Reed, D. (2006) "MAE Center Transportation Test Bed," Proceedings of the 8th U.S. National Conference on Earthquake Engineering, San Francisco, California, April 18-22, 2006, Earthquake Engineering Research Institute, Oakland, California.

Dillingham, A. E. (1985). "The Influence of Risk Variable Definition on Value-of-Life Estimates," *Economic Inquiry*, **23**(2), 277-294.

Elnashai, A. S., Cleveland, L. J., Jefferson, T., and Harrald, J. (2008). "Impact of Earthquakes on the Central USA," Mid-America Earthquake Center, University of Illinois at Urbana-Champaign,

Urbana, Illinois.
Ellingwood, B.R., Rosowsky, D.V., and Pang, W.C. (2008). "Performance of Light-Frame Wood Residential Construction Subjected to Earthquakes in Regions of Moderate Seismicity," *Journal of Structural Engineering*, **134**(8), 1353-1363.
Erberik, M. A., and Elnashai, A. S. (2006). "Loss Estimation Analysis of Flat-Slab Structures," *Natural Hazards Review*, **7**(1), 26-37.
Erdik, M., Cagnan, Z., Zulfikar, C., Sesetyan, K., Demircioglu, M.B., Durukal, E., and Kariptas, C. (2008) "Development of Rapid Earthquake Loss Assessment Methodologies for Euro-Med Region," Proceedings of the 14th World Conference on Earthquake Engineering, Beijing, China, October 12-17, 2008, International Association of Earthquake Engineering, Beijing, China.
Fajfar, P. (1999). "Capacity Spectrum Method Based on Inelastic Demand Spectra," *Earthquake Engineering and Structural Dynamics*, **28**, 979-993.
Federal Emergency Management Agency (FEMA) (1994). "FEMA-156, Typical Costs for Seismic Rehabilitation of Existing Buildings, Second Edition. Volume 1 – Summary," Federal Emergency Management Agency, Washington, D.C.
Federal Emergency Management Agency (FEMA) (1995). "FEMA-157, Typical Costs for Seismic Rehabilitation of Existing Buildings, Second Edition. Volume 2 – Supporting Documentation," Federal Emergency Management Agency, Washington, D.C.
Federal Emergency Management Agency (FEMA) (2006). "HAZUS-MH MR2 Users and Technical Manual," Federal Emergency Management Agency, Washington, D.C.
Fernandez, J. A. (2007). "Numerical Simulation of Earthquake Ground Motions in the Upper Mississippi Embayment," Ph.D. Dissertation, School of Civil and Environmental Engineering, Georgia Institute of Technology, Atlanta, Georgia. <http://geosystems.ce.gatech.edu/soil_dynamics/research/groundmotionsembay/>
Fernandez, J.A. and Rix, G.J. (2006). "Soil Attenuation Relationships and Seismic Hazard Analyses in the Upper Mississippi Embayment". Proceedings of the 8th U.S. National Conference on Earthquake Engineering, San Francisco, California, April 18-22, 2006, Earthquake Engineering Research Institute, Oakland, California.
French, S. P., and Muthukumar, S. (2006). "Memphis Building Stock Inventory Shapefiles and Databases, Version 4," Center for Geographic Information Systems, Georgia Institute of Technology, Atlanta, Georgia, personal communication.
Green, T., and Feser, E. (2007) "Business Interruption and Inventory Loss Modeling by a Modified HAZUS Approach," Department of Urban and Regional Planning, University of Illinois at Urbana-Champaign, Urbana, Illinois, personal communication.
Hahn, R. W. (1996). *Risks, Costs, and Lives Saved: Getting Better Results from Regulation*, American Enterprise Institute, Washington, D.C.
Hueste, M. D., and Bai, J.-W. (2003). "Predicting the Seismic Performance of a RC Building in the Central U.S.," Proceedings of the Fifth US-Japan Workshop on Performance-Based Earthquake Engineering Methodology for Reinforced Concrete Building Structures, Moehle, J. P. and Kabeyasawa, T. (eds.), September 9-11, 2003, Hakone, Japan, Earthquake Research Institute, University of Tokyo, Tokyo, Japan.
Jeong, S. H., and Elnashai, A. S. (2007). "Probabilistic Fragility Analysis Parameterized by Fundamental Response Quantities," *Engineering Structures*, **29**, 1238-1251.
Karels, T. R. (2003). "Economic Considerations --- AFCI Replacements," Memorandum, United States Consumer Product Safety Commission, Washington, D.C.
MAEviz (2008). "MAEviz Software," Mid-America Earthquake Center, University of Illinois at Urbana-Champaign, Urbana, Illinois, http://mae.ce.uiuc.edu/software_and_tools/maeviz.html , February 12.
Miller, T. R. (1990). "The Plausible Range for the Value of Life – Red Herrings Among the Mackerel," *Journal of Forensic Economics*, **3**(3), 17-29.
Padgett, J. E., and DesRoches, R. (2007). "Bridge Functionality Relationships for Improved Seismic Risk Assessment of Transportation Networks," *Earthquake Spectra*, **23**(1), 115-130
Park, J. (2004). "Development and Application of Probabilistic Decision Support Framework for Seismic Rehabilitation of Structural Systems," Ph.D. Thesis, School of Civil and Environmental Engineering, Georgia Institute of Technology, Atlanta, Georgia.
Peacock, W. (2007) "Displaced Household and Short Term Shelter Requirements by a Modified HAZUS Approach," Hazard Reduction and Recovery Center, Texas A&M University, College Station, Texas, personal communication.
Petersen, M.D., Frankel, A.D., Harmsen, S.C., Mueller, C.S., Haller, K.M., Wheeler, R.L., Wesson, R.L., Zeng, Y., Boyd, O.S., Perkins, D. M., Luco, N., Field, E.H., Wills, C.J., and Rukstales, K.S. (2008). "Documentation for the 2008 Update of the United States National Seismic Hazard Maps," Open-File Report 2008–1128, United States Geological Survey, Reston, Virginia.
Pinho, R., Crowley, H., and Bommer, J. (2008) "Open-Source Software and Treatment of Epistemic Uncertainties in Earthquake Loss Modelling," Proceedings of the 14th World Conference on Earthquake Engineering, Beijing, China, October 12-17, 2008, International Association of Earthquake Engineering, Beijing, China.
Ramamoorthy, S.K., Gardoni, P., and Bracci, J.M. (2006) "Seismic Fragility and Confidence Bounds for Gravity Load Designed Reinforced Concrete Frame of Varying Height," *Journal of Structural Engineering*, **134**(4), 639-650.
Reis, E., Comartin, C., King, S., and Chang, S. (2001). "HAZUS99-SR1 Validation Study," Federal Emergency Management Agency, Washington, D.C.
Spence, R., So, E., Cultrera, G., Ansal, A., Pitilakis, K., Costa, A.C., Tonuk, G., Argyroudis, S., Kakderi, K., and Sousa, M.L. (2008) "Earthquake Loss Estimation and Mitigation in Europe: A Review and Comparison of Alternative Approaches," Proceedings of the 14th World Conference on Earthquake Engineering, Beijing, China, October 12-17, 2008, International Association of Earthquake Engineering, Beijing, China.
Steelman, J., and Hajjar, J. (2008). "Systemic Validation of Consequence-Based Risk Management for Seismic Regional Losses," Mid-America Earthquake Center, University of Illinois at Urbana-Champaign, Urbana, Illinois.
Teramo, M., Crowley, H., Lopez, M., Pinho, R., Cultrera, G., Cirella, A., Cocco, M., Mai, M., and Teramo, A. (2008) "A Damage Scenario for the City of Messina, Italy, Using Displacement-Based Loss Assessment," Proceedings of the 14th World Conference on Earthquake Engineering, Beijing, China, October 12-17, 2008, International Association of Earthquake Engineering, Beijing, China.
URS Corporation (2001). "Comprehensive Seismic Risk and Vulnerability Study for the State of South Carolina," Internal Report, South Carolina Emergency Preparedness Division, West Columbia, South Carolina.
Viscusi, W. K. (1993). "The Value of Risks to Life and Health, Journal of Economic Literature," *Journal of Economic Literature*, **31**(4), 1912-1946.

Sixth International Conference on Urban Earthquake Engineering
March 3-4, 2009, Tokyo Institute of Technology, Tokyo, Japan

SEISMIC PERFORMANCE OF STEEL KNEE BRACED FRAME STRUCTURES

H.-L. Hsu[1], J.-L. Juang[2] and C.-H. Chou[3]

1) Professor, Dept. of Civil Engineering, National Central University, Taiwan
2) Post-doctoral research fellow, Research Center for Hazard Mitigation and Prevention, National Central University, Taiwan
3) Graduate student, Dept. of Civil Engineering, National Central University, Taiwan
t3200178@ncu.edu.tw, jjl1@ncu.edu.tw

Abstract: This study focused on the experimental evaluation of the seismic performance of steel knee braced frame structures with energy dissipation mechanism. A series of cyclic loading tests were conducted on the steel special moment resisting frame and the proposed knee braced frames. Test results validated that the demand in the beam-column connection design was alleviated by the proposed design method. Test results also showed that the strength and stiffness of the proposed design were effectively enhanced. Comparisons in energy dissipation between the steel special moment resisting frame and the knee braced moment resisting frames further justified the applicability of the proposed method.

1. INTRODUCTION

Steel structures possess high strength and significant ductility, thus are effective structural forms for earthquake-resistant designs [Tsai and Popov 1990, Kim et al. 2002, Uang and Fan 2001]. However, the load carrying efficiency of such designs, such as special moment resisting frame (SMRF), is sometimes limited when story drift is a concern, as shown in Figure 1(a). Application of brace elements to the SMRF to enhance the structural stiffness and to reduce the frame deformation is usually adopted as a solution in such design [Martinelli et al. 1996, Remennikov and Walpole 1997]. Although significant improvement in structural stiffness is achieved in the braced frames, as shown in Figure 1(b), a major reduction in the structural ductility is inevitable. In order to improve the seismic performance of the steel frame structure, a modified form that adopts knee brace elements in the corner regions of the beams and columns, namely knee-braced moment resisting frame (KBRF), is proposed in this study.

In general, the application of knee braces to the steel frame is capable of reducing the lateral displacement of the structure. Furthermore, the plastic hinge in the SMRF frame could be shifted from the critical beam-column connection region to the location where knee brace and beam joined [Hsu and Jean 2003]. This characteristic not only prevents the brittle fracture and reduces the demand in the beam-column connection designs, but also provides a possible energy dissipation mechanism in the shifted plastic hinge zone. In this regard, an energy dissipating mechanism that consists of reduced section plates is proposed to further improve the seismic performance of the KBRF structures.

This study focused on the experimental evaluation of the seismic performance of steel knee braced moment resisting frame with energy dissipation mechanism. A series of cyclic loading tests were conducted on the SMRF and KBRF structures with difference arrangements of energy dissipation devices. Relationships between the energy dissipation devices and the structural performance were quantitatively investigated so that design references could be established.

2. EXPERIMENTAL PROGRAM

2.1 Specimens

Seven steel frames, including two SMRF and 5 KBRF, were fabricated for testing. One of the two special moment resisting frames was designed to be semi-rigidly connected, and the other was rigidly connected in the beam-column connections, respectively. This selection was made to establish the comparison data between the SMRF and KBRF, and to investigate the effectiveness of the proposed energy dissipation devices. The 5 knee-braced frames were composed of identical beam and column sections, however, energy dissipation devices with different sectional details. The beams were cut at the locations where energy dissipation devices were placed. Semi-rigid connections were used in the KBRF structures, as less beam-column demand was expected. Test results from the KBRF tests were compared with those from the SMRF frames, and were used to validate the above-mentioned assumptions.

The beam and column sections used in all tests were

ASTM A-36 H175x175x7.5x11, and H244x175x7x11, respectively. The knee brace section used in the KBRF tests was composed of a pair of ASTM A-36 L100x100x13 angles. Five types of energy dissipation plates with different sectional geometries were fabricated from ASTM A-36 thin plates. The steel special moment resisting frames were labeled SF series, and the steel knee braced moment resisting frames were denoted KF series, respectively. The specimen details are described in Table 1 and shown in Figure 2.

2.2 Test set-up

Performance of each frame structure was evaluated by the cyclic loading test. A servo-controlled actuator, driven under a series of increasing displacement commands, was clamped to the test specimen at the beam level. The column bottoms of the test frame were hinged to a stiffened floor beam that was fastened on the strong floor. Structural responses of each test frame were measured using installed stain gages, displacement transducers, and tiltmeters, respectively. Lateral support system was provided in the center portion of the test frame so that out-of-plane instability could be prevented. The test set-up is shown in Figure 3.

3. EXPERIMENTAL OBSERVATIONS

For rigid SMRF structure subjected to cyclic load, yielding was first observed at the beam flanges near the beam-column connection regions. Although significant structural ductility was achieved during the test, brittle fracture of the welds due to heavy stress concentration was also observed at large deformation. Similarly, for semi-rigid SMRF subjected to lateral load, the top and bottom angles that connected the beam and columns deformed due to excessive stress. These phenomena led to significant reduction in strength and energy dissipation, and validated the importance of alleviating the demand of of beam-column connection designs.

For KBRF subjected to cyclic load, load-deformation relationship similar to those of SMRF at elastic stage was observed, except that the former exhibited higher strength and stiffness. Yielding of the energy dissipating plates located at the beam-brace connection regions was observed when the drifts were increased. At these stages, elongation and shortening of plates that subjected to tensile and compressive stresses alternated when the cyclic load was applied. This phenomenon led to stable energy cumulation through plastic plate deformation. This energy dissipation mechanism was sustained when the plates remained functional.

4. COMPARISONS AND INTERPRETATIONS

4.1 Strength and stiffness

Figure 4 shows the load-deformation relationships of the tested frame structures. It can be found from the figure that both semi-rigid and rigid SMRF exhibited significant deformation capabilities, however, the strength of the former was less than the latter. This characteristic justified the importance of beam-column connection rigidity to the structural performance of steel special moment resisting frames. Although the performance of the rigid SMRF structure was proven by the previous comparison, the fractures of the welds in the connection region, as mentioned in previous section, also indicated that a remedy to reduce the high cost in the beam-column connection fabrication was essential.

This concern can be resolved by the structural responses of the proposed KBRF with energy dissipation devices. As shown in the comparison of Figure 5, the strength and stiffness of the KBRF structures were approximately 2.98 and 4.47 times of those of the rigid SMRF with the same column and beam sections, even though the former was only designed with semi-rigid connections. The comparisons validated the feasibility of the proposed design in simultaneously reducing the cost and enhancing the performance.

4.2 Energy dissipation capacity

Energy dissipations were evaluated by the cumulative areas of the hysteretic loops of the test structures. Figure 6 compares the energy dissipation between the SMRF and KBRF with various energy dissipation devices. It can be found from Figure 6(a) that higher energy dissipation capacity was achieved when KBRF frame was equipped with thicker energy dissipation plates, even though the plates possessed the same cross-sectional area.

It can be further observed from the comparisons as shown in Figure 6(b) that the energy dissipation of the KBRF was approximately 101.65% higher than that of the semi-rigid SMRF, when the structure reached 5% drift. This phenomenon justified the effectiveness of the proposed design in the energy dissipation enhancement of the steel framed structures. Figure 6(b) also compares the energy dissipation between the proposed KBRF and the rigid SMRF. It can be found from the comparison that the energy dissipation capacity of a semi-rigidly connected KBRF structure was also high than that of a rigidly connected SMRF structure. This phenomenon, combined with the higher strength and stiffness efficiency of KBRF, validated the applicability of the proposed method to the seismic design of steel framed structures.

5. CONCLUSIONS

This paper presented the test information of steel special moment resisting frames and knee-braced moment resisting frame with energy dissipation plates. Relationships

between structural performance and the proposed design details were evaluated. Test results validated that the demand in the beam-column connection design was alleviated by the proposed design. Test results also showed that the strength and stiffness of the proposed design were effectively enhanced. Comparisons in energy dissipation between the steel special moment resisting frame and the knee braced moment resisting frame with energy dissipation plates justified the applicability of the proposed method.

Acknowledgements:

The test specimens were supported by the National Center for Research on Earthquake Engineering (NCREE), Taiwan, which is gratefully acknowledged. The authors also wish to extend their appreciation to Professor K. C. Tsai and the staff of NCREE for their advice and assistance.

References:

Tsai, K.C. and Popov, E.P. (1990).“Seismic panel zone on elastic story drift in steel moment resistance frames.” *Journal of Structural Engineering*, American Society of Civil Engineers,**116**(12), 3285-3301.

Kim, T.; Whittaker, A. S.; Gilani, A. S. J.; Bertero, V. V.; Takhirov, S. M. (2002), “Cover-plate and flange-plate steel moment-resisting connections”, *Journal of Structural Engineering*, American Society of Civil Engineers, **128(**4), 474-482.

Uang, C. M.; Fan, C. C. (2001), “Cyclic stability criteria for steel moment connections with reduced beam section”, *Journal of Structural Engineering*, American Society of Civil Engineers, **127**(9), 1021-1027.

Martinelli L., Mulas M.G., and Perotti F. (1996). “The seismic response of concentrically braced moment resisting steel frames.” *Earthquake Engineering & Structural Dynamics*, **25**(11), 1275-1299.

Remennikov A.M. and Walpole W.R. (1997). “Analytical prediction of seismic behavior for concentrically braced steel systems.” *Earthquake Engineering & Structural Dynamics*, **26**(8), 859-874.

Hsu H. L. and Jean S. Y.(2003) “Improving seismic design efficiency of petrochemical facilities”, *Practice Periodical on Structural Design and Construction*, American Society of Civil Engineers, **8**(2), 107-117.

Table 1 Specimen Labels

Specimen	Beam-column connection	Knee brace	Energy dissipation devices			
			b_e (mm)	t_e (mm)	L_e (mm)	Cross area (mm^2)
MF-S	Semi-rigid	N.A.	N.A.	N.A.	N.A.	N.A.
MF-R	Rigid	N.A.	N.A.	N.A.	N.A.	N.A.
KF120x12	Semi-rigid	L100x100x13	120	12	150	1440
KF140x12	Semi-rigid	L100x100x13	140	12	150	1680
KF160x12	Semi-rigid	L100x100x13	160	12	150	1920
KF120x16	Semi-rigid	L100x100x13	120	16	150	1920
KF140x14	Semi-rigid	L100x100x13	140	14	150	1960

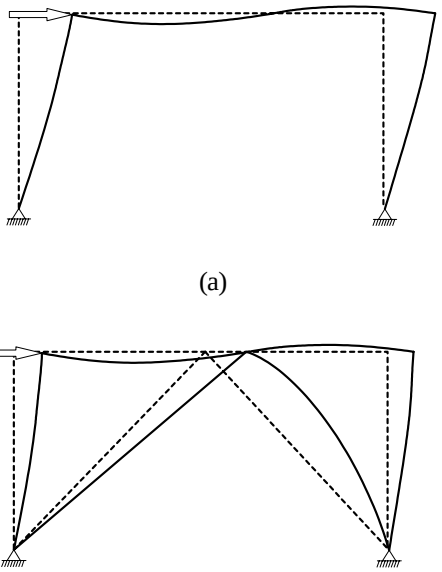

(a)

(b)

Figure 1 Description of Frame Structures Subjected to Lateral Load: (a) Steel Special Moment Resisting Frame; (b) Braced Frame

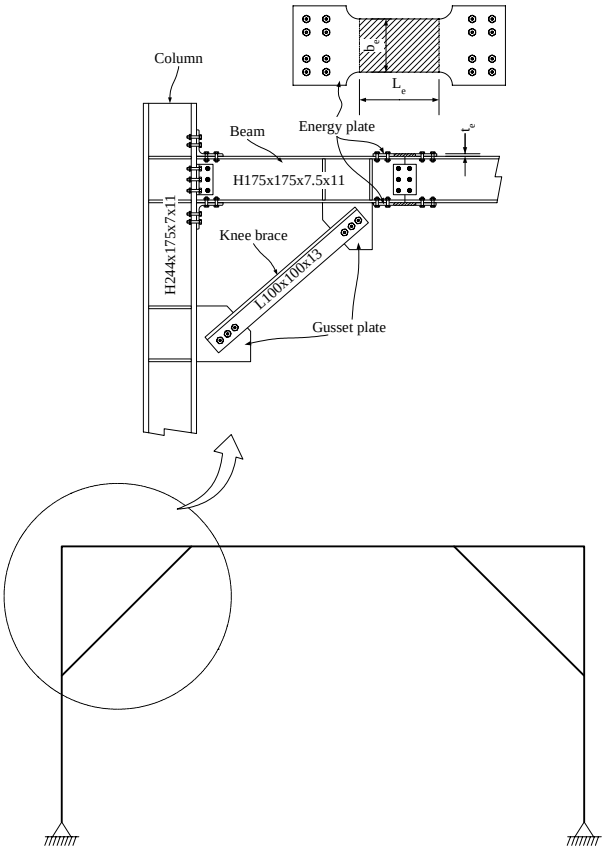

Figure 2 Specimen Details

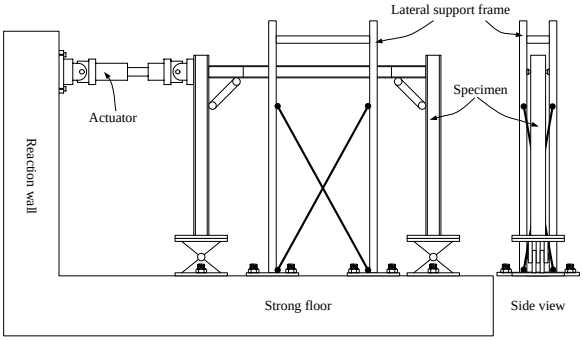

Figure 3 Test Set-up

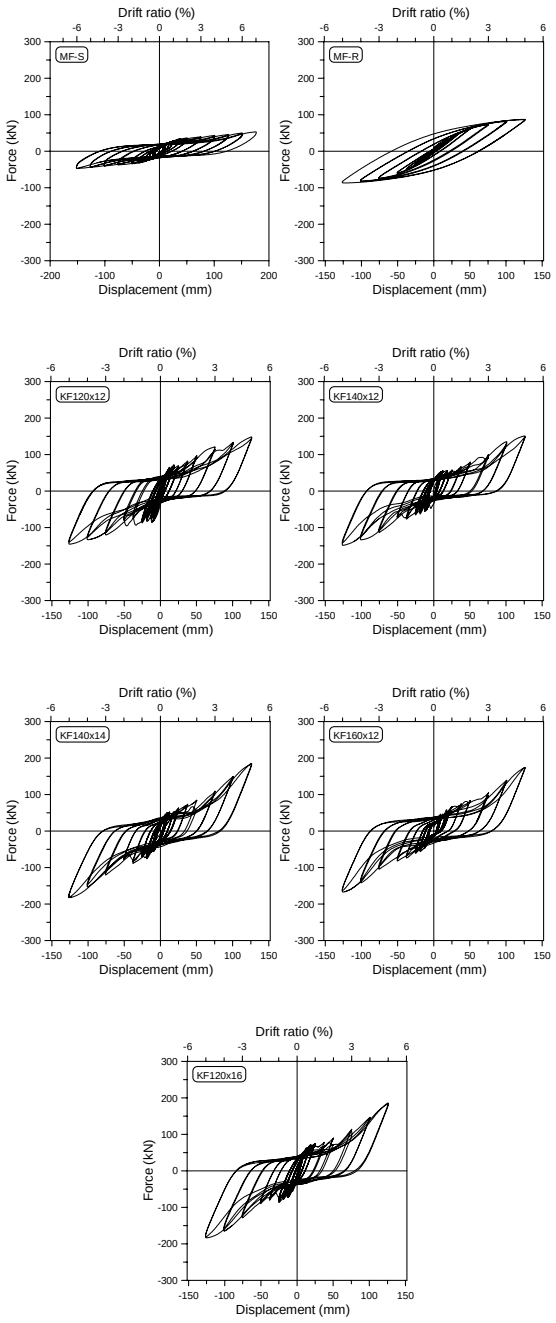

Figure 4 Load-deformation Relationships of the Tested Frame Structures

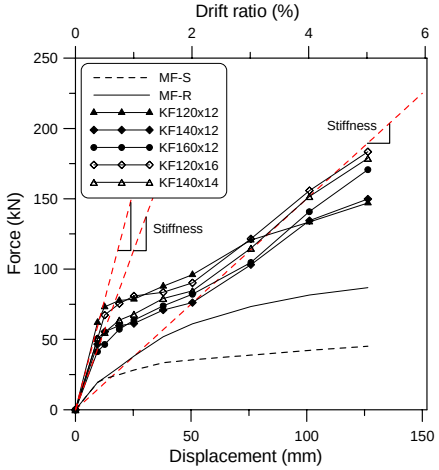

Figure 5 Comparisons of Strength and Stiffness of the Tested Frame Structures

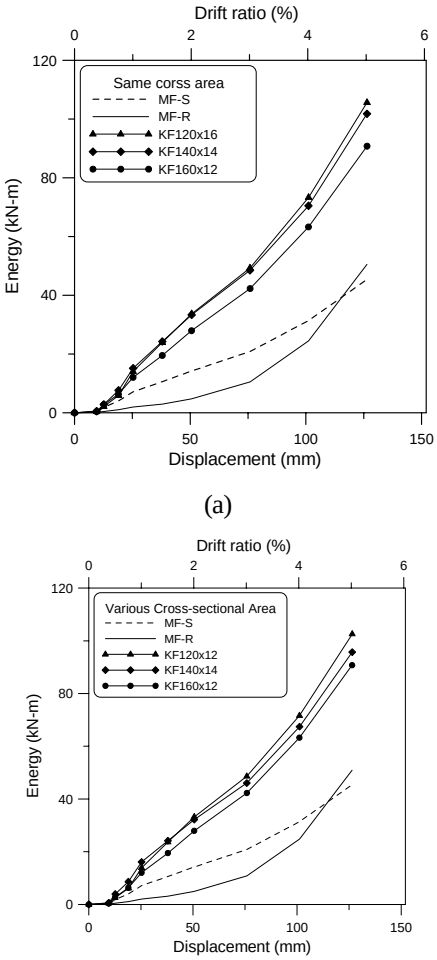

Figure 6 Comparisons of Energy Dissipation for the Tested Frame Structures: (a) Energy Dissipating Plates with Same Cross-sectional Area; (b) Energy Dissipating Plates with Various Cross-sectional Area.

Sixth International Conference on Urban Earthquake Engineering
March 3-4, 2009, Tokyo Institute of Technology, Tokyo, Japan

SHAKING TABLE TEST OF STEEL FRAME FOCUSING ON THE STRENGTH AND STIFFNESS ECCENTRICITY OF HYSTERESIS DAMPERS

Satoshi Yamada[1)]

1) Associate Professor, Structural Engineering Research Center, Tokyo Institute of Technology, Japan
naniwa@serc.titech.ac.jp

Abstract: Recently, buildings with hysteresis dampers as earthquake resistant member are increasing. The damper is used for not only new construction but also seismic repair. In case of seismic repair, strength eccentricity or stiffness eccentricity may occur in damper system by the constraint of floor planning. It becomes an important problem to evaluate the effect of the eccentricity in damper system on earthquake performance of building structures. In this study, in order to clarify this problem experimentally, a series of full-scale shaking table test of single story steel frame is carried out. Main parameter in this experiment is strength eccentricity and stiffness eccentricity in damper system.

1. INTRODUCTION

In Northridge Earthquake (1.17.1994, U.S.A) and Hyogoken- Nanbu Earthquake (1.17.1995, JAPAN), many moment resistant steel frames were suffered. Typical damage was fracture at the beam-to-column connections. By investigations of damage in those earthquakes, it was clarified that earthquake resistant performance of conventional weak beam type moment frame is not sufficient. Therefore, passive control structures became popular.

A lot of research works on passive control design are already done. (WADA et. al 1991) Many of them are researches of dampers or researches of 2-D frame with dampers. Research on the eccentricity of strength and rigidity caused by balance of the arrangement of dampers is rare. (Lin et.al. 2003) For example, in case of seismic repair, strength eccentricity or stiffness eccentricity may occur in damper system by the constraint of floor planning. It becomes an important problem to evaluate the effect of the eccentricity in damper system on earthquake performance of building structures.

In this study, in order to evaluate effect of strength and stiffness eccentricity of dampers experimentally, a series of full-scale shaking table test of single story steel frame was carried out. In the experiment, eccentricity of strength and stiffness were changed by adjusting the performance of dampers set in the both side of frame.

2. SPECIMEN

Specimen, shown in Figure 1, is 1story 1bay by 1bay steel frame with brace type dampers. This frame consists of rigid floor and elastic columns. Counter weight is fixed to the rigid floor. Columns are circular hollow section steel tubes with enough strength. Dampers are installed in both side of plane. Span length of the frame is 4m in each direction and story height is 2.5 m. Total weight of the specimen is 330kN. Natural period of frame without damper is 0.67 sec.

In this experiment, influence of the strength and stiffness eccentricity in damper system on earthquake performance of building structures is focused. Parameters of the specimen are strength and stiffness of dampers. Damper used in this experiment is slit-plate damper installed in the brace as shown in Figure 2. Of course out of plane stiffness was insufficient, guide system was installed around the slit-plate as shown in Figure 3. The clearance of about 2mm was installed between the steel angle and wide flange member. Teflon sheet was set in the clearance in order to prevent generating friction.

Changing thickness of plate, width of strut and material of plate, four types of slit plates of a, b, c, and d were prepared. Shapes, strength and stiffness of slit plates are shown in Table 1. In the table, yield strength and yield deformation of slit-plate ($P_{ys,cal}$, $\Delta_{ys,cal}$) are calculated by Eqs. (1) and (2). (Amadeo et.al. 1998)

$$P_{ys,cal} = n_s \cdot \frac{\sigma_{ys} \cdot B^2 \cdot t}{2 \cdot H'} \quad (1)$$

$$D_{ys,cal} = \frac{3 \cdot \sigma_{ys} \cdot H_T \cdot B_s}{4 \cdot E \cdot H'} \cdot \left[\left(\frac{H'}{B_s} \right)^2 + 2.6 \right] \quad (2)$$

Where ns is number of strut, σ_{ys} is yield

strength of plate, B is width of strut, t is thickness of strut, E is Young's modulus, $H'=H+(2r^2/H_T)$, H is the length of parallel part of strut and $H_T=H+2r$ is total length of strut.

$P_{yd,cal}$ is yield strength of brace type damper. $K_{d,cal}$ is axial stiffness of brace type damper calculated by $P_{ys,cal}$, $\Delta_{ys,cal}$, axial stiffness of wide flange section brace member and axial stiffness of connection.

In this experiment, damper A, which installed slit-plate a, is the standard. Damper B has equivalent stiffness and half strength of damper A. Damper C has equivalent strength and half stiffness of damper A. Damper D has half stiffness and half strength of damper A. Combining these 4 types of dampers, total 6 specimen such as AA, AB, AC, AD, BC, and DD were set.

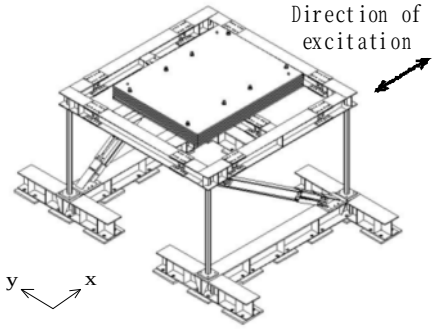

Figure 1 Specimen

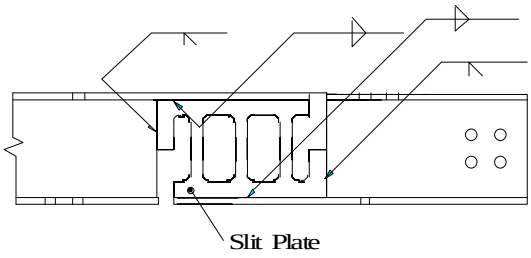

Figure 2 Slit plate installed in brace

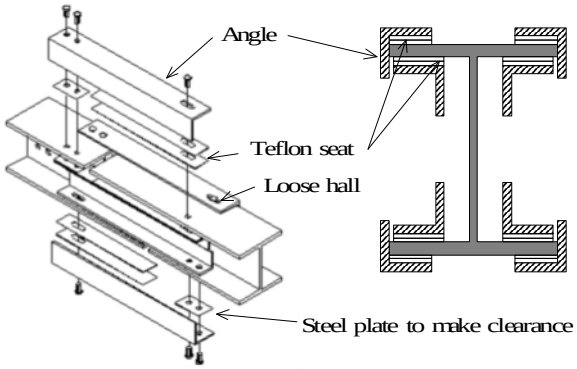

Figure 3 Guide System

Table 2 Specification of slit plate and damper brace

Slit Plate		sys* (MPa)	ns	Bs (mm)	t (mm)	H (mm)	r (mm)	$\Delta_{ys,cal}$ (mm)	Ks,cal (kN/mm)	Pys,cal (kN)
a	SM490A	444	3	22	12	100	10	1.01	37.8	38.1
b	SS400	283	3	18	9	70	10	0.43	39.6	17.1
c	SM490A	374	3	21	16	130	10	1.36	22.1	30.1
d	SS400	283	3	20	9	100	10	0.69	21.7	15.0

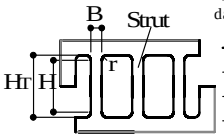

damper	Slit Plate	Pyd,cal (kN)	Kd,cal (kN/mm)	Qyd,cal (kN)	hKd,cal (kN/mm)
A	a	38.1	33.5	32.8	24.8
B	b	17.1	34.9	14.7	25.8
C	c	30.1	20.9	25.9	15.5
D	d	15.0	20.2	12.9	14.9

3. EXCITATION

In this experiment, the large-scale shaking table NIED (National Research Institute for Earth Science and Disaster Prevention) was used. When damper was changed, free vibration test was carried out to examine the fundamental natural period and damping foator. Then, several seismic excitations with different input level were applied to the specimen. In the seismic excitation, NS component of 1995 JMA-Kobe Record and EW component of 1968 Hachinohe record are used as input wave. List of the main excitation is shown in Table 2. The excitation level is expressed as the peak velocity.

Table 2 List of excitation

Excitation	Input Wave	Peak Velocity
Free vibration	pulse	(m/s)
Level 1-1	JMA-Kobe NS	0.1
Level 1-2	Hachinohe EW	0.125*
Level 2-1	JMA-Kobe NS	0.2
Level 2-2	Hachinohe EW	0.25**

* in case of AA 0.15

** in case of AA 0.3

4. MEASUREMENT

Main measurement items in this experiment are (1) acceleration of shaking table, (2) displacement, acceleration and rotation of mass, (3) axial deformation and applied axial force of slit plate, and (4) applied shear force to columns. Acceleration of each point was measured by accelerometers as shown in Figure 4 (1). Displacement, rotation and deformation were measured by displacement transducers as shown in Figure 4. Applied force was measured by strain gauges glued in elastic portion as shown in Figure 4.

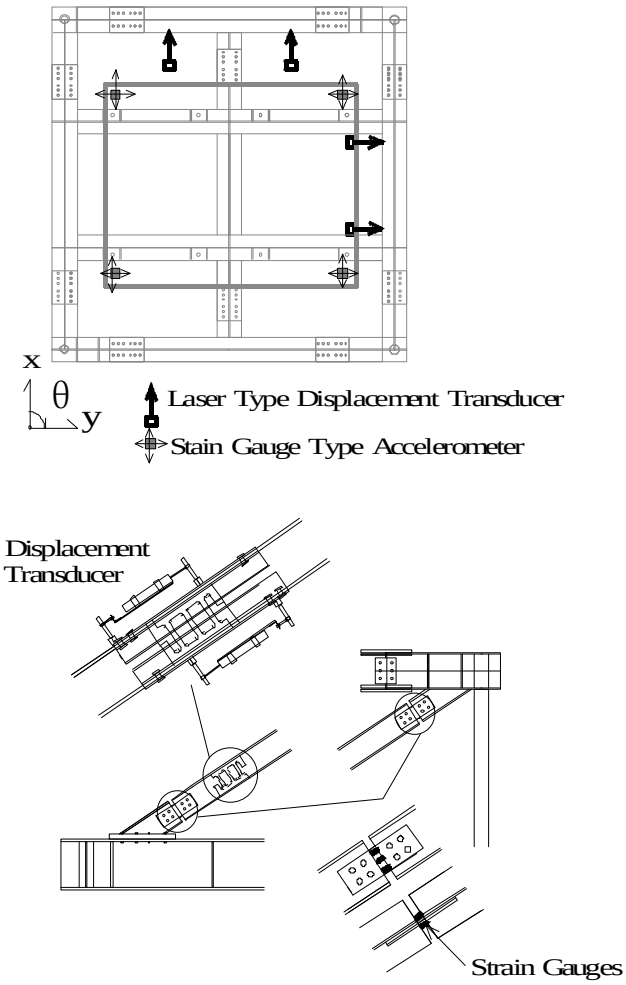

Figure 4 Measurement system

5. EXPERIMENTAL RESULT

Experimental results are summarized in Table 3. In the table, T and h are the fundamental natural period and damping factor corresponding to the fundamental natural period obtained by free vibration test. $\delta_{\max}$ is the maximum drift of each plane. K_b is the elastic axial stiffness of brace type damper evaluated by experimental results of level-2 excitation. K_s is also the elastic stiffness of slit plate evaluated by experimental results. P_{ys} * and K_2 / K_s are the yield strength and second modulus ratio of slit plate in each excitation. $W_{p,b}$ is the dissipated energy by brace type damper. Behavior of the specimen in excitation is shown in Figure 6 represented by hysteresis of slit-plate.

High damping of 6% to 9% are generated by friction between angle and wide flange section brace. In this experiment, damping force is measured as a part of axis resistance of damper. Because damping force and restoring force can not be separated, damping force is evaluated as a part of restoring force. Therefore, the dissipated energy by damper $W_{p,b}$ includes dissipated energy by damping.

Initial yield strength of slit plate P_{ys} * corresponds to calculated value $P_{ys,cal}$. On the other hand, elastic stiffness K_s is much less than calculated value $K_{s,cal}$. It is thought to be caused by insufficiency of restraint by guide system. As a result, eccentricity factor R_e, defined in Japanese Building Design Law, became 0.08 for specimen AB, 0.09 for specimen AC, 0.17 for specimen AD and 0.16 for specimen BC respectively. Those values cover realistic range of $0.15 \leq R_e$. Therefore, reduced stiffness of slit plate is not a problem.

Specimen AB of $R_e = 0.08$ show in plane behavior in the elastic range. After yield of weaker damper B, grown eccentricity of stiffness generates rotation of specimen and deformation of damper B progresses. Specimen n AC of $R_e = 0.09$ show similar behavior with specimen AB. But, rotation of specimen caused by yield of weaker damper is not so significant. It is because eccentricity of strength of specimen AC is less than that of specimen AB. Specimen AD of $R_e = 0.17$ show rotational behavior in elastic range. It is after yield of weaker damper D that the rotational behavior became significant. Specimen BC of $R_e = 0.16$ show similar behavior with specimen AC.

In this experiment, effect of eccentricity of stiffness is not so significant. But effect of eccentricity of strength is significant in plastic range.

Table 3 Experimental Results

Specimen	plane	Brace Damper	T(sec) h(%)	Kb (kN/mm)	Ks (kN/mm)
A A	plane 1	A	0.26	12.2	15.5
	plane 2	A	6.5	13.3	15.2
A B	plane 1	A	0.24	12.5	15.2
	plane 2	B	9.6	13.3	15.5
A C	plane 1	A	0.20	13.5	14.5
	plane 2	C	8.2	10.8	13.1
A D	plane 1	A	0.27	12.6	15.7
	plane 2	D	6.6	10.1	10.2
B C	plane 1	B	0.26	15.7	20.7
	plane 2	C	7.3	10.4	11.6
D D	plane 1	D	0.39	7.7	10.0
	plane 2	D	9.1	10.0	10.5

Specimen	Level 1-1 Kobe NS				
	dmax+ (mm)	dmax- (mm)	Pys* (kN)	K2/Ks	Wp,b (kN・mm)
A A	3.61	-2.85	–	–	191
	3.35	-2.60	–	–	159
A B	2.65	-2.31	–	–	91
	3.00	-2.05	18.6	0.18	212
A C	3.00	-2.30	–	–	137
	3.71	-2.61	–	–	182
A D	2.74	-2.54	–	–	143
	5.01	-5.46	18.4	0.10	501
B C	3.25	-1.90	18.1	0.15	223
	3.25	-2.76	–	–	145
D D	5.86	-4.40	16.5	0.16	467
	4.15	-4.65	16.1	0.11	401

Specimen	Level 1-2 Hachinohe EW				
	dmax+ (mm)	dmax- (mm)	Pys* (kN)	K2/Ks	Wp,b (kN・mm)
A A	4.86	-3.15	–	–	414
	3.80	-3.00	–	–	331
A B	2.55	-2.21	–	–	163
	2.90	-1.95	18.4	0.23	200
A C	2.75	-2.10	–	–	138
	3.31	-2.25	–	–	184
A D	3.39	-2.20	–	–	163
	6.52	-3.41	16.9	0.14	501
B C	3.66	-1.85	19.1	0.11	203
	2.85	-2.66	–	–	203
D D	7.01	-3.61	17.2	0.13	486
	5.65	-3.05	15.4	0.10	442

Specimen	Level 2-1 Kobe NS				
	dmax+ (mm)	dmax- (mm)	Pys* (kN)	K2/Ks	Wp,b (kN・mm)
A A	8.57	-5.90	38.0	0.24	1213
	6.65	-6.96	37.5	0.26	1104
A B	5.80	-5.13	38.7	0.21	577
	8.32	-10.07	26.1	0.05	2108
A C	5.89	-5.85	37.2	0.25	832
	10.28	-7.31	33.0	0.10	1461
A D	6.13	-5.29	–	–	666
	12.38	-14.64	23.8	0.07	3181
B C	7.96	-9.97	26.1	0.01	2012
	7.41	-5.78	32.6	0.14	902
D D	14.38	-14.41	22.4	0.06	2951
	10.79	-13.05	22.5	0.04	2557

Specimen	Level 2-2 Hachinohe EW				
	dmax+ (mm)	dmax- (mm)	Pys* (kN)	K2/Ks	Wp,b (kN・mm)
A A	14.93	-6.70	41.4	0.16	2368
	11.09	-7.10	40.4	0.19	2141
A B	7.26	-4.10	–	–	881
	15.28	-7.16	28.2	0.05	2108
A C	7.83	-4.95	39.2	0.25	1039
	13.74	-6.41	36.8	0.10	1751
A D	8.20	-4.32	–	–	880
	17.74	-11.93	23.7	0.08	3209
B C	15.52	-7.31	27.0	0.04	2191
	9.87	-5.14	31.9	0.09	1298
D D	16.93	-13.41	22.3	0.04	2634
	13.14	-12.05	22.7	0.06	2276

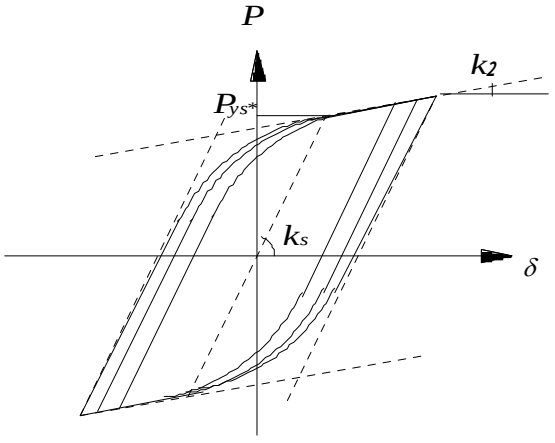

Figure 5 P_{ys} * and K_2 / K_s

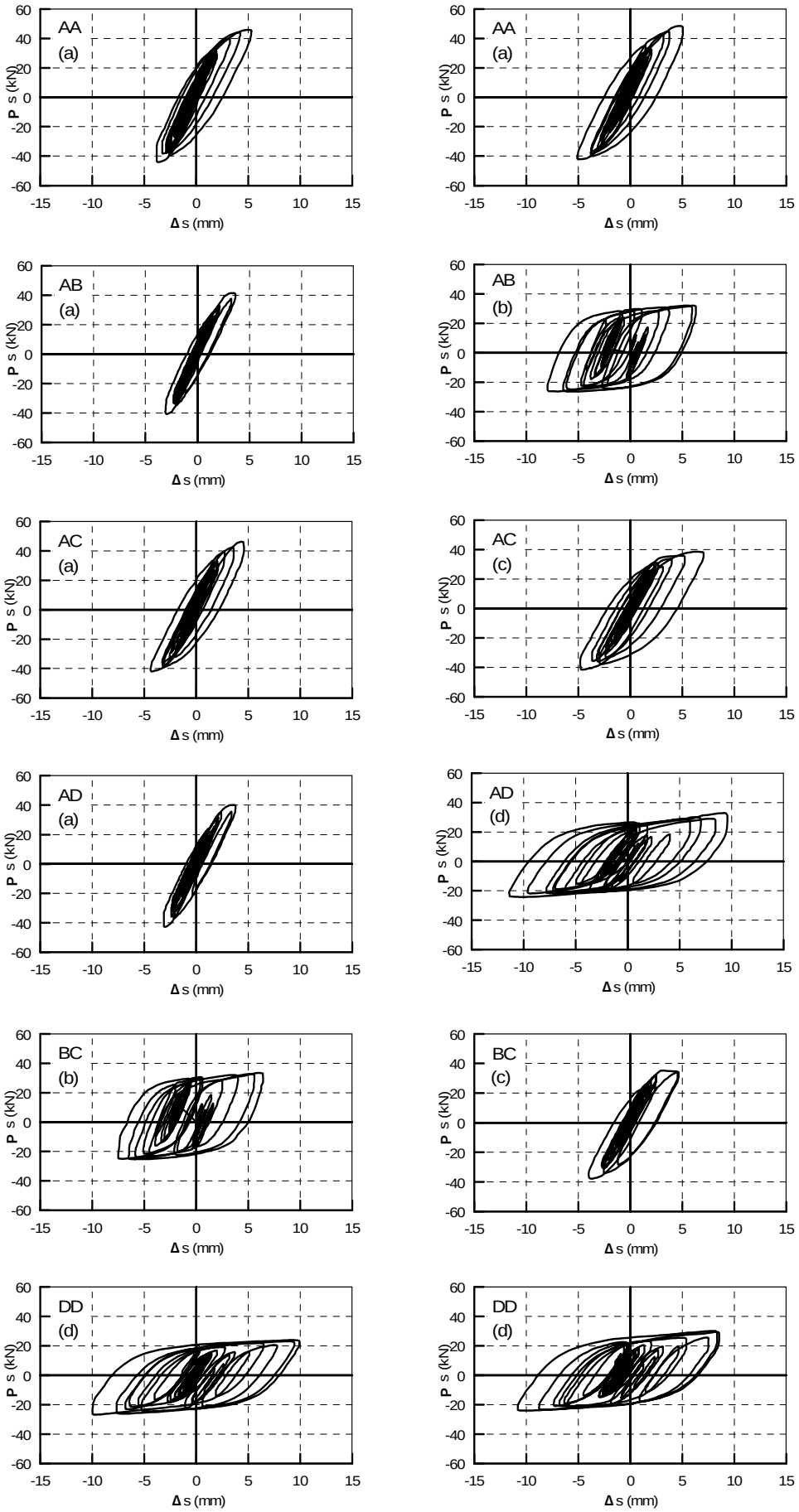

Figure 6 Hysteresis of slit-plate in Level 2-1 excitation

6. CONCLUSION

In this study, in order to evaluate effect of strength and stiffness eccentricity of dampers experimentally, a series of full-scale shaking table test of single story steel frame was carried out. In the experiment, eccentricity of strength and stiffness were changed by adjusting the performance of dampers set in the both side of frame. From experimental results, following conclusions are obtained.

1. Effect of eccentricity of stiffness of hysteresis dampers is not so significant.
2. Effect of eccentricity of strength of hysteresis dampers is significant in plastic range.

References:

Amadeo BENAVENT CLIMENT, Sang-Hoon OH and Hiroshi AKIYAMA (1998); Ultimate energy absorption capacity of slit-type steel plates subjected to shear deformations, J. Struct. Constr. Eng., A.I.J., No.503, pp.139-147

Wen-Hsiung Lin and Anil K. Chopra (2003); Asymmetric one story elastic systems with non-linear viscous and viocselastic dampers: Simplified analysis and supplemental damping system design, Earthquake Engineering and Structural Dynamics, vol.32, pp.579-596

Akira WADA(1991) Damage Tolerant Structure, Proceedings of Fifth U.S. Japan Workshop on The Improvement of Structural Design and Construction Practices, Applied Technology Council, 27-39.

Sixth International Conference on Urban Earthquake Engineering
March 3-4, 2009, Tokyo Institute of Technology, Tokyo, Japan

ELASTO-PLASTIC BEHAVIOR FOR TWO STORY BRACED FRAMES WITH LEANING COLUMNS

Yoshihiro Kimura[1)], and Yui Mihata[2)]

1) Associate Professor, Dept. of Structural Engineering, Nagasaki University, Japan
2) Graduated Student, Graduated School of Science and Technology, Nagasaki University, Japan
ykimura@nagasaki-u.ac.jp, d708115b@cc.nagasaki-u.ac.jp

Abstract: In general, steel concentrically braced frames are designed to resist lateral force by means of truss action. Design considerations for columns in these frames are therefore governed by the column axial force and column moment demands are generally ignored. However, if the columns cannot carry moment, then dynamic inelastic time-history analyses show that a soft-story mechanism is likely to occur causing large concentrated deformations in only one story. Such large concentrations of damage are not generally seen in real frames since columns are generally continuous and they possess some flexural stiffness and strength. This paper develops relationships for column property and drift concentration within a frame based on pushover and dynamic analyses. It is shown that continuous seismic and gravity columns in a structure significantly decrease the possibility of large drift concentrations.

1. INTRODUCTION

Concentrically braced frames (CBFs) are not generally considered to perform as well in earthquakes as some other types of structure. Two reasons for the lower performance expected for CBFs are the possibility of a pinched hysteresis loop, and the possibility of a soft-story mechanism. A pinched hysteresis loop due to braces which buckle is often considered less desirable than a full hysteresis loop. The restraint buckling members can prevent the braces from buckling allowing a full hysteresis loop (Fujimoto et al., 1988). Large concentrations of deformation may also occur in braced frames, especially if the column flexural stiffness is low. This behavior may be understood for the 2 story braced frame shown in Figure 1 (Kimura and MacRae, 2002) (MacRae, Kimura and Roeder, 2004). If the member sizes at both levels are identical, and the frame members are unable to carry moment, elastic deformation will occur upon initial loading, but because the story shears in the bottom story are greatest, it will yield first. Once yielding occurs in the bottom story, all inelastic deformation will occur there.

This paper describes the effect of continuous columns on the seismic response of two story frames with concentric buckling restrained braces. The main seismic resistant element is the braced frame. After the braces yield, the column prevents large soft drift concentrations. Equations for estimating the column moment demand and drift concentration factor are developed. Recommendations for column stiffness and strength, to keep the frame elastic for a specified drift concentration, are then proposed. Finally, dynamic analyses are performed and the column moment demand and equations for the drift concentration factor are developed.

2. STATIC BEHAVIOR FOR TWO STORY BRACED FRAME WITH LEANING COLUMNS

2.1 Development of Equations for Story Drift and Column Moment of Two Story Braced Frames

Continuous columns over the height of the frame, whether they are gravity or seismic columns, resist the tendency for concentration of deformation in one story. The amount of drift concentration will depend on the column flexural stiffness.

The two story braced frame with an elastic column at pinned base will deform as shown in Figure 1. The lateral force distribution is given from A_i distribution, in Japanese seismic design code (Building Center of Japan 2001), and then the lateral force at Level 2 is about 1.8 times as that at Level 1. After yielding of the braces with strain hardening, most of additional shear forces are carried out by the columns at pinned bases and the other are carried out by the yielded braces. The story shear forces, V_{si}, at Levels i, are shown in Eq. (1). The shear force at level 2 is equal to about 0.644 of that at Level 1 (φ =0.644), and it can be calculated from the lateral forces, F_1 and F_2, where the magnitude of F_2 is assumed to be about 1.8 times that of F_1.

$$V_{s1} = V_{f1} + V_c \,,\quad V_{s2} = \varphi V_{s1} \,,\quad V_{s2} = V_{f2} - V_c \tag{1}$$

$$V_c = 3K_1 \alpha \delta_{c-1} \tag{2}$$

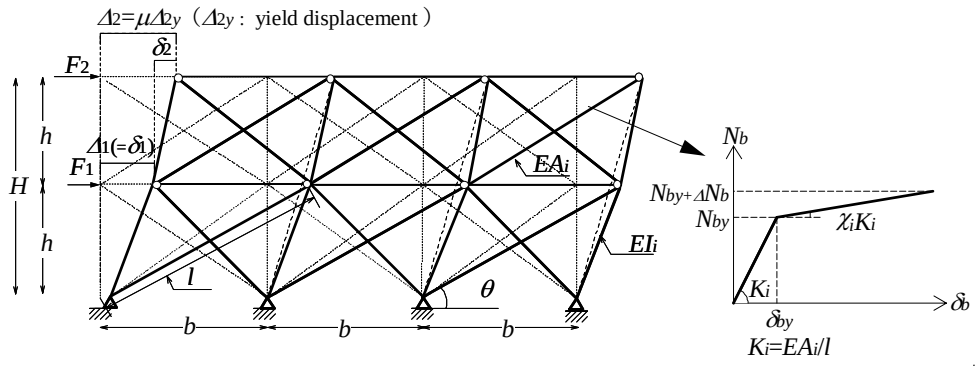

Figure 1 Model of Two Story Braced Frame:
(a) Loading and deformation conditions, (b) Relationship between axial force and axial displacement

$$\alpha = \sum_{i=1}^{m} EI_i / h^3 \Big/ \sum_{i=1}^{n} EA_i \cos^2\theta / l \tag{3}$$

where V_{fi} show the shear forces for braces, V_c shows the column shear forces, and α is the ratio of the column flexural stiffness to brace axial stiffness. The drift concentration factor, γ is developed being classified into three stages such as following.

i) frame displacements before yielding of brace on 1st story

Before brace yielding, the displacements, $\delta_{1\text{-}1}$ and $\Delta_{2\text{-}1}$ on each story are:

$$\delta_{1-1} = \frac{l^3}{EAb^2} V_{f1-1}, \quad \Delta_{2-1} = \delta_{1-1} + \delta_{2-1} = \frac{l^3}{EAb^2}(V_{f1-1} + V_{f2-1}) \tag{4}$$

where l, b, h and H are shown in Figure 1. When braces yield, the total displacement at each level δ_1 and Δ_2 is developed from frame shear forces at yield, V_{f1y} and Eqs. (2) ~ (4).

$$\delta_{1-1} = \frac{l^3}{EAb^2} V_{f1y}, \quad \Delta_{2-1} = \delta_{1-1} + \frac{l^3}{EAb^2}\frac{2\varphi + 3\alpha(\varphi+1)}{2+3\alpha(\varphi+1)} V_{f1y} \tag{5}$$

The column and the brace shear forces on first story, $V_{c\text{-}1}$ and $V_{f2\text{-}1}$ are obtained using yield shear force, V_{f1y} as shown in Eq. (6).

$$V_{c-1} = \frac{3\alpha(1-\varphi)}{2\beta + 3\alpha(\varphi+1)} V_{f1y}, \quad V_{f2-1} = \frac{2\varphi + 3\alpha(\varphi+1)}{2+3\alpha(\varphi+1)} V_{f1y} \tag{6}$$

ii) incremental displacements after yielding of braces on first story to both story braces yielding

After first story braces yielding, the shear forces are represented as incremental form in the following.

$$\Delta V_{s1-2} = \Delta V_{f1-2} + \Delta V_{c-2}, \quad \Delta V_{s2-2} = \varphi \Delta V_{s1-2}, \quad \Delta V_{s2-2} = \Delta V_{f2-2} + \Delta V_{c-2} \tag{7}$$

$$\Delta V_{c-2} = 3K_1 \alpha \delta_{c-2} \tag{8}$$

$\delta_{1\text{-}2}$ and $\Delta_{2\text{-}2}$ are obtained using the increment of brace shear forces on each story, $\Delta V_{f1\text{-}2}$, $\Delta V_{f2\text{-}2}$ of Eqs. (7) and (8) as shown in Eq. (9).

$$\delta_{1-2} = \frac{l^3}{\chi_1 EAb^2}\Delta V_{f1-2}, \Delta_{2-2} = \delta_{1-2} + \delta_{2-2} = \frac{l^3}{EAb^2}\left(\frac{\Delta V_{f1-2}}{\chi_1} + \Delta V_{f2-2}\right) \tag{9}$$

where χ_i is the ratio of second order stiffness to elastic stiffness. $\Delta V_{f1\text{-}2}$, $\Delta V_{f2\text{-}2}$ are obtained from Eqs. (7), (8) and (9) using yield shear force, V_{f1y}.

$$\Delta V_{f1-2} = \frac{\chi_1(\mu-1)\{2+3\alpha(\varphi+1)\}}{2\{1+\varphi\chi_1+3\alpha(\varphi+1)\}}\left\{\frac{2\varphi+3\alpha(\varphi+1)}{2+3\alpha(\varphi+1)}+1\right\}V_{f1y} \tag{10}$$

$$\Delta V_{f2-2} = \frac{(\mu-1)\{2\varphi\chi_1+3\alpha(\varphi+1)\}}{2\{1+\varphi\chi_1+3\alpha(\varphi+1)\}}\left\{\frac{2\varphi+3\alpha(\varphi+1)}{2+3\alpha(\varphi+1)}+1\right\}V_{f1y} \tag{11}$$

The increment of lateral displacement on each story, $\delta_{1\text{-}2}$, and $\Delta_{2\text{-}2}$ are obtained from Eqs. (9) ~ (11) using V_{f1y}.

$$\Delta\delta_{1-2} = \frac{(\mu-1)\{2+3\alpha(\varphi+1)\}}{2\{1+\varphi\chi_1+3\alpha(\varphi+1)\}}\left\{\frac{2\varphi+3\alpha(\varphi+1)}{2+3\alpha(\varphi+1)}+1\right\}\frac{l^3}{EAb^2}V_{f1y} \tag{12}$$

$$\Delta\Delta_{2-2} = (\mu-1)\Delta_{2y} = (\mu-1)\left\{\frac{2\varphi+3\alpha(\varphi+1)}{2+3\alpha(\varphi+1)}+1\right\}\frac{l^3}{EAb^2}V_{f1y} \tag{13}$$

And the increment of column shear force on each story, $\Delta V_{1\text{-}2}$ is given using V_{f1y} as shown in Eq. (14).

$$\Delta V_{c-2} = \frac{3\alpha(\mu-1)(1-\varphi\chi_1)}{2\{1+\varphi\chi_1+3\alpha(\varphi+1)\}}\{\frac{2\varphi+3\alpha(\varphi+1)}{2+3\alpha(\varphi+1)}+1\}V_{f1y} \quad (14)$$

iii) incremental displacements after both story braces yielding

After both stories braces yielding, the shear forces are represented as incremental form in the following such as case ii).

$$\Delta V_{s1-3} = \Delta V_{f1-3} + \Delta V_{c-3}, \quad \Delta V_{s2-3} = \varphi\Delta V_{s1-3}, \quad \Delta V_{s2-3} = \Delta V_{f2-3} - \Delta V_{c-3} \quad (15)$$

$$\Delta V_{c-3} = 3K_1\alpha\delta_{c-3} \quad (16)$$

When both story braces yield, the relationship between shear force and yield shear force on second story, $V_{f2\text{-}1}$, $\Delta V_{f2\text{-}2}$ and V_{f2y} are given in the following.

$$V_{f2y} - V_{f2-1} = \Delta V_{f2-2} \quad (17)$$

The ductility, μ_s at both stories yielding is obtained from Eqs. (7), (8), (11) and (17).

$$\mu_s = 1 + \frac{2\{1+\varphi\chi_1+3\alpha(\varphi+1)\}(1-\varphi)}{\{2\varphi\chi_1+3\alpha(\varphi+1)\}\{\varphi+1+3\alpha(\varphi+1)\}} \quad (18)$$

In $\mu_s < \mu$, the incremental lateral displacement on each story, $\delta_{1\text{-}3}$, $\Delta_{2\text{-}3}$ are given using the incremental shear forces on each story, $\Delta V_{f1\text{-}3}$, $\Delta V_{f2\text{-}3}$.

$$\delta_{1-3} = \frac{l^3}{\chi_1 EAb^2}\Delta V_{f1-3}, \Delta_{2-3} = \delta_{1-3} + \delta_{2-3} = \frac{l^3}{EAb^2}(\frac{\Delta V_{f1-3}}{\chi_1} + \frac{\Delta V_{f2-3}}{\chi_2}) \quad (19)$$

$\Delta V_{f1\text{-}3}$, $\Delta V_{f2\text{-}3}$ are obtained from Eqs. (15), (16) and (19) using yield shear force, V_{f1y} in the following.

$$\Delta V_{f1-3} = \frac{(\mu-\mu_s)\chi_1\{2\chi_2+3\alpha(\varphi+1)\}}{2\{\chi_2+\varphi\chi_1+3\alpha(\varphi+1)\}}\{\frac{2\varphi+3\alpha(\varphi+1)}{2+3\alpha(\varphi+1)}+1\}V_{f1y} \quad (20)$$

$$\Delta V_{f2-3} = \frac{\chi_2(\mu-\mu_s)\{2\varphi\chi_1+3\alpha(\varphi+1)\}}{2\{\chi_2+\varphi\chi_1+3(\varphi+1)\}}\{\frac{2\varphi+3\alpha(\varphi+1)}{2\beta+3\alpha(\varphi+1)}+1\}V_{f1y} \quad (21)$$

The increment of lateral displacement on each story, $\delta_{1\text{-}3}$, and $\Delta_{2\text{-}3}$ are obtained from Eqs. (19) ~ (21) using V_{f1y}.

$$\delta_{1-3} = \frac{(\mu-\mu_s)\{2\chi_2+3\alpha(\varphi+1)\}}{2\{\chi_2+\varphi\chi_1+3\alpha(\varphi+1)\}}\{\frac{2\varphi+3\alpha(\varphi+1)}{2+3\alpha(\varphi+1)}+1\}\frac{l^3}{EAb^2}V_{f1y} \quad (22)$$

$$\Delta_{2-3} = (\mu-\mu_s)\Delta_{2y} = (\mu-\mu_s)\{\frac{2\varphi+3\alpha(\varphi+1)}{2+3\alpha(\varphi+1)}+1\}\frac{l^3}{EAb^2}V_{f1y} \quad (23)$$

And the increment of column shear force on each story, $\Delta V_{c\text{-}3}$ is given using V_{f1y} as shown in Eq. (24).

$$\Delta V_{c-3} = \frac{3\alpha(\mu-1)(\chi_2-\varphi\chi_1)}{2\{\chi_2+\varphi\chi_1+3\alpha(\varphi+1)\}}\{\frac{2\varphi+3\alpha(\varphi+1)}{2+3\alpha(\varphi+1)}+1\}V_{f1y} \quad (24)$$

iv) development of drift concentration factor and column moment

The total lateral displacement on each story is given as shown in Eq. (25).

$$\delta_1 = \sum_{i=1}^{N}\delta_{1-i}, \Delta_2 = \sum_{i=1}^{N}\Delta_{2-i} \quad (25)$$

where N shows the stage of frame deformation such as i) ~ iii). The drift concentration factor, γ is given from Eq. (26).

$$\gamma = \frac{MAX\left([\Delta_2-\delta_1],\delta_1\right)/h}{\Delta_2/H} \quad (26)$$

The column moment at each stage is obtained from the Eqs. (6), (14) and (24) for shear forces.

$$M_c = \sum_{i=1}^{N}V_{c-i}h \quad (27)$$

2.2 Drift Concentration for Two Story Brace Frames

Figure 2 (a) and (b) compare actual and theoretical relationships for drift concentration factor, γ for specified second order stiffness, χ_i. *Analysis A* shows γ from Eq. (26). These curves shown depend on which equation governs. *Analysis B* shows γ from a frame analysis using the computer program DRAIN-2DX (Prakash et al. 1993). Here, the beam and column members were made rigid axially, and the frame members were pinned at their ends. *Analyses A* and *B* are consistent. In Figure 2 (a) and (b), the kink in the curve shows where braces behavior changes from first story only to both stories yields. Its value is different among 4 kinds of curves. The value of μ at the kink does not depend on the magnitude of χ_i and 4 kinds of curves almost same for 0.1 of α in Figure 2 (b), even though they are different for 0.01 of α in Figure 2 (a).

In Figure 2 (a) and (b), the soft story mechanism occurs when only first story braces yield. The drift on second story increases after second story braces yield, and then the drift concentration factor, γ suddenly reduces.

Figure 3 compares actual and theoretical relationships for drift concentration factor, γ for specified second order stiffness, χ_i with frame ductility of 4. As would be expected, γ tends to unity as the column flexural stiffness increases. It may be seen from Figure 3 that the column is effective in

reducing story drift concentration when the column stiffness ratio, α, is greater than about 0.1. As the magnitude of second order stiffness, χ_i is greater, γ tends to reduce in α of less than 0.1.

2.3 Column Moment for Two Story Brace Frames

Figure 4 (a) and (b) compare actual and theoretical relationships for column maximum moment demand for specified ductility levels from Eq. (27). In Figure 4 (a) and (b), the kink in the curve shows where braces behavior changes from first story only to both stories yields. The value of column maximum moment does not depend on the second order stiffness value of braces, when only first story braces yields. As the second order stiffness, χ_i is greater, the magnitude of ductility demand at second braces yielding is small and the slope after the kink becomes high. The magnitude of the moment at both story braces yielding is different in Figure 4 (a), but it is almost same in Figure 4 (b).

Figure 5 compares actual and theoretical relationships for column maximum moment for specified second order stiffness with frame ductility of 4. For columns with high stiffness and braces with low second order stiffness, the column maximum moment occurs at second story yielding. For more flexible columns subject to lower ductility demands, the top story remains elastic at the target ductility. For values of α greater than about 0.1, the column moment is almost same even though the second order stiffness is different. In values of α less than about 0.1, the column moment for small second order stiffness is higher than that for the large stiffness, and in values of α greater than about 0.1, the column moment for small second order stiffness is lower than that for the large stiffness. Columns should be designed for this maximum moment according to Eq. (27).

3. DYNAMIC BEHAVIOR FOR TWO STORY BRACED FRAMES WITH LEANING COLUMNS

In the previous section, the equations for the static drift concentration factor were developed for various brace second order stiffnesses and column flexural stiffnesses assuming the lateral force distribution from A_i distribution in Japanese seismic design code. And two story braced frame with a 3600 mm interstory height, h, and a bay width, B of 9000mm is to designed such as Figure 1. During an earthquake the inertial forces are constantly changing, so that γ may be different from that described above. These frames with χ_i=0.001, 0.01, 0.05 and 0.1 were selected and the

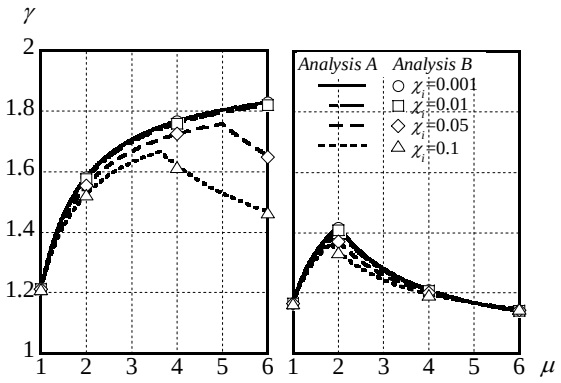

Figure 2 Relationship between Drift Concentration Factor and Frame Ductility: (a) α=0.01, (b) α=0.1

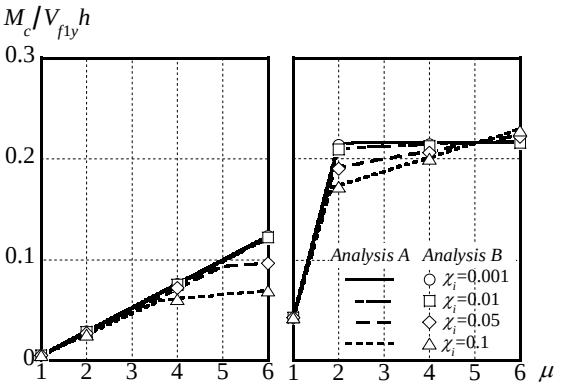

Figure 4 Relationship between Column Moment and Frame Ductility: (a) α=0.01, (b) α=0.1

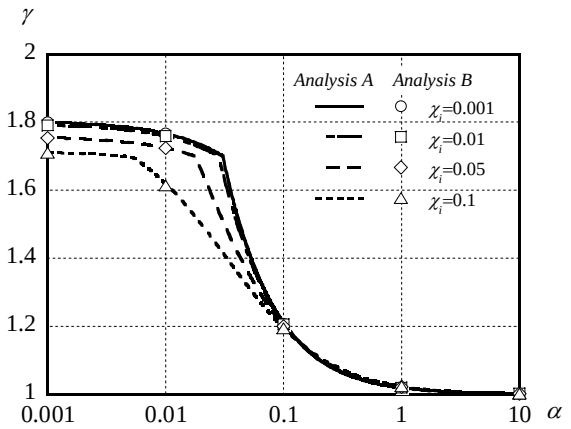

Figure 3 Relationship between Drift Concentration Factor and Column Flexural Stiffness: μ=4

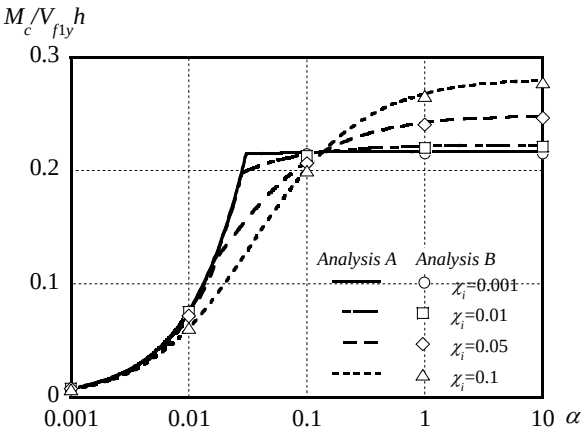

Figure 5 Relationship between Column Moment and Column Flexural Stiffness: μ=4

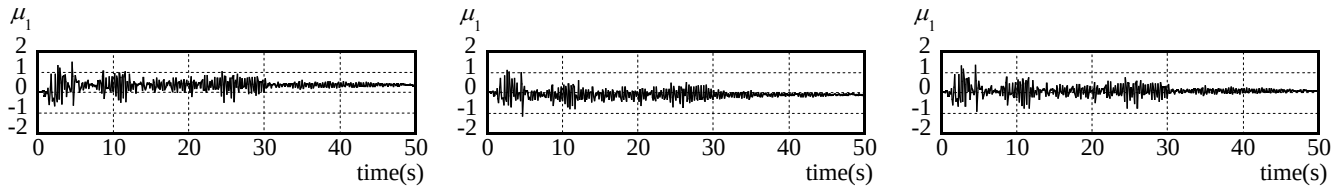

Figure 6 Time History of First Story Ductility, μ_1: (a) α=0.01, χ_i=0.001, (b) α=1, χ_i=0.001 (c) α=0.01, χ_i=0.1

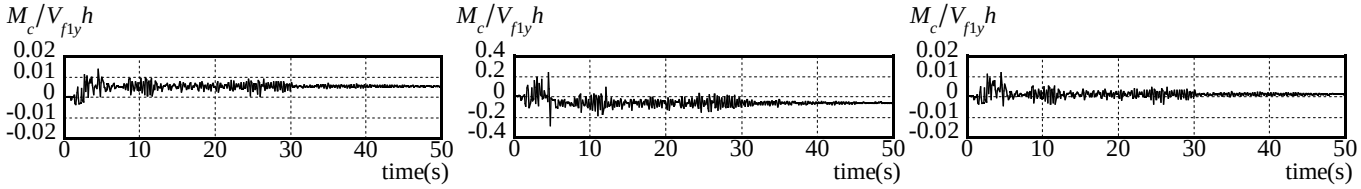

Figure 7 Time History of First Story Column Moment: (a) α=0.01, χ_i=0.001, (b) α=1, χ_i=0.001 (c) α=0.01, χ_i=0.1

earthquake records were used with El Centro NS/EW Hachinohe NS/EW Kobe NS/EW Taft NS/EW and Tohoku NS/EW whose maximum value of velocity was 50 *kine* and 75 *kine*, in order to investigate the effect of the column stiffness under large lateral deformation of the braced frames after braces yielding.

Damping was applied as 2% of critical in the first and second mode using a Rayleigh damping model. The kinematic hardening law is applied to hysteresis loop of braces. Newmark's constant average acceleration integration method was used in the inelastic dynamic time history analysis. The first mode response period for the two story frame was about 0.332s.

Figure 6 (a) ~ (c) show the time history of the ductility on first story whose maximum story ductility occurs. For α=0.01 and χ_i=0.001, the value of maximum ductility demand arrive at 1.5 and the residual deformation occurs. The value of maximum ductility demand for α=1 and χ_i=0.001, is more restraint than that for α=0.01 and χ_i=0.001 because of high column stiffness. The maximum ductility demand for α=0.01 and χ_i=0.1 is more restrained than that for α=0.01 and χ_i=0.1, so that the second order stiffness of the braces is useful for the restraint of soft story mechanism.

Figure 7 (a) ~ (c) show the time history of column moment on first story whose column maximum moment occurs. The column maximum moment for α=1 and χ_i=0.001 is larger in 3 kinds of frames. It is shown that its magnitude depends on just column stiffness.

Figure 8 compares the static and dynamic drift concentration factor, γ and γ_d. The dynamic drift concentration factor, γ_d was computed from the peak story drift and the peak roof drift even though these may occur at different times. It may be seen that the γ_d is similar to the γ, so the γ_d can also be estimated using Eq. (26).

Figure 9 compares the static and dynamic column moment, M_c and M_{cd} whose value is defined as that when the maximum drift occurs. It may be seen that the M_{cd} is similar

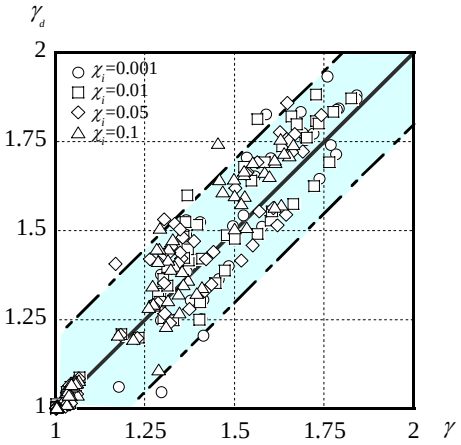

Figure 8 Comparison between Dynamic Drift Concentration Factor and Static Drift Concentration Factor

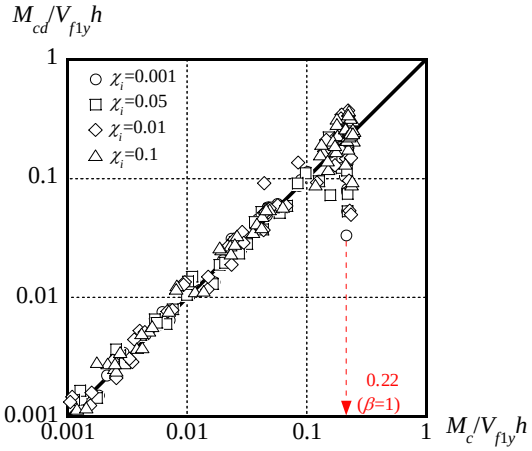

Figure 9 Comparison between Dynamic Column Moment and Static Column Moment

to the M_c, so the M_{cd} can also be estimated using Eq. (27) except 0.22 of $M_c/V_{f1y}h$. The reason why the dynamic and static drift concentration factor, γ_d and γ are different there is the following. In dynamic analysis, the column moment increases due to inertia force. On the other hand, in static analyses, the moment becomes almost constant even though the column stiffness ratio, α changes such as Figure 5.

4. CONCLUSIONS

Closed-form equations were derived to estimate the drifts for different applied forces based on equilibrium, compatibility and constitutive relations. Pushover and dynamic analyses were then performed to investigate the soft story mechanism of the two story braced frames with elastic columns. It was shown that:

1) The deformation of two story braced frames consists of three stages which are i) elastic frame response before yield, ii) only one story yielding, and iii) both stories yielding. The drift concentration factor and the column moment for the three stages above can be found from Eqs. (26) and (27).
2) The magnitude of the drift concentration factor or the column moment is influenced by the column stiffness ratio and braced second order stiffness.
3) The peak drift concentration factor during shaking and dynamic column moment can be estimated as the static drift concentration factor and static column moment.

Acknowledgements:

The authors acknowledge support from Japan Ministry of Education, Culture, Sport, Science, and Technology (MEXT), Grant-in Aid for Scientific Research (C) 19560574.

References:

Fujimoto M., Wada A., et al. (1988), "A Study on Unbonded Braces with Stiffened Concrete Steel Tube," *Journal of Structural Mechanics and Earthquake Engineering*, vol.34B, pp249-258.

Kimura Y. and MacRae G. (2002), "The Effect of the Column Flexural Stiffness on Story Drift Concentration Mechanism of 2 Story Braced Frames," *Journal of Structural Construction Engineering*, AIJ, 560, 189-195.

MacRae G. A., Kimura Y., and Roeder C. W. (2004), "Effect of Column Stiffness on Braced Frame Seismic Behavior," *Journal of Structural Engineering*, American Society of Civil Engineers, **130**(2), 381-391.

Prakash V., Powell G. H. and Campbell S. (1993), "DRAIN-2DX Base Program Description and User Guide Version 1.10," Department of Civil Engineering, University of California, Berkeley, Report No. UCB/SEMM-93/17&18.

Tremblay, R. (2003), Achieving a Stable Inelastic Seismic Stability of Concentrically Braced Steel Frames, Engineering Jour. AISC, Vol.40, No.2, pp.111～129

Building Center of Japan (2001), " The Building Standard Law of Japan "

Sixth International Conference on Urban Earthquake Engineering
March 3-4, 2009, Tokyo Institute of Technology, Tokyo, Japan

HYSTERETIC BEHAVIOUR OF THIN WEB PLATE UNDER CYCLIC BENDING-SHEAR LOADING

Kikuo Ikarashi[1)]

1) Associate Professor, Department of Architecture and Building Engineering, Tokyo Institute of Technology, Japan
ikarashi.k.aa@m.titech.ac.jp

Abstract: In this paper, hysteresis characteristics of thin web plates are investigated. The parameters of investigation are depth-thickness ratio and aspect ratio of web. The influence of flanges is also taken into consideration. First, the anti-symmetric bending shear cyclic loading experiments are carried out by H-section specimens, whose web aspect ratio is 1 and 2. Their depth-thickness ratios are based on the elastic buckling critical depth-thickness ratio; the smaller one, the almost equal one and the larger one. And each hysteresis characteristics are confirmed from the obtained load-deformation curve. Next, the same load-deformation curve as experiments is obtained by the FEM numerical analysis in various assumptions of depth-thickness ratio and material, and the hysteresis characteristics are confirmed. At this time, the part when the shelf appears in load-deformation curve is paid attention.

1. INTRODUCTION

The large deformation behavior of thin web plates with larger depth-thickness ratio than their elastic criticality is extremely steady under applied loading into one direction. For instance, it can be anticipated that thin web plates maintain constant strength after yield. However, it is hard to declare that their hysteresis characteristics under cyclic loading have been understood at length. Therefore, it is necessary to clarify the hysteresis characteristics to use thin web plates at large deformation within the buckling behavior.

Tere are many study of thin shear panel behavior. And it is acknowledged that thin panels exhibited stable S-shaped hysteresis loops with the amount of energy absorbed per cycle increasing with the maximum amplitude of the displacement. For instance, it is shown by Roberts and Ghomi (1991). What seems to be lacking, however, is hysterisis loop shape. Especially, little is known about the strength of the shape like a shelf in the load-displacement curve. In this study, the cyclic loading experiments are carried out by thin web plates, and the basic hysteresis characteristics are investigated. Moreover, the factors that cause the hysteresis characteristics to show the shape like a shelf in the load-deformation angle curve are investigated by the FEM numerical analysis.

2. THE CYCLIC BEHAVIOR OF THIN WEB

2.1 Outline of experiments

Figure 1 shows the loading model. In this experiment, the anti-symmetric bending shear stress is applied on the H-shaped specimen with two beams for adding force at both ends. Handle the shearing deformation angle γ within 1/100, 1/50, and 1/25 circularly until the circumscription of the device. Table 1 shows the list of specimens. Aspect ratio of the specimens is 1 or 2, and each of the section shape No.1, No.3, and No.5 corresponds to No.6, No.7, and No.8. The web slenderness is over the value given by equation (1), except for No.1 and No.6.

$$\left(\frac{b}{t}\right)_0 = \sqrt{\frac{k\pi^2}{12\left(1-\nu^2\right)}\frac{E}{\tau_y}} \tag{1}$$

$$\tau_y = \frac{\sigma_y}{\sqrt{3}} \tag{2}$$

Here, E:Young's modulus, k :Plate buckling coefficient, ν :Poisson's ratio, τ_p:Shear yield stress, σ_y:Yield stress. Bounding condition of web plate is assumed fixed and under the pure shear, so k=14.58 that is shown by Galambos (1998).

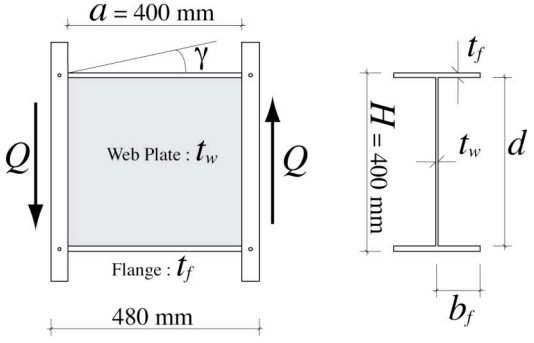

Figure 1 Specimen

Table 1 List of specimens

Specimen	Section	a (mm)	d/t_w	A_f/A_w	${}_wQ_p$ (kN)	Q_{cr} (kN)	Q_{max} (kN)
No.1	H- 400 x 150 x 6 x 9	400	63.1	0.57	393	1590	1365
No.2	H- 400 x 50 x 3 x 9	400	122	0.38	196	209	205
No.3	H- 400 x 80 x 3 x 9	400	123	0.59	198	208	205
No.4	H- 400 x 200 x 3 x12	400	123	2.00	199	210	207
No.5	H- 400 x 50 x 2.2 x 9	400	172	0.52	134	78.4	97.7
No.6	H- 400 x 150 x 6 x 9	800	63.2	0.57	398	1100	840
No.7	H- 400 x 80 x 3 x 9	800	123	0.60	200	148	167
No.8	H- 400 x 50 x 2.2 x 9	800	172	0.53	125	54.7	80.6

Table 2 Mechanical properties

Test-piece	t (mm) thickness	σ_y (N/mm^2) yield stress	σ_u (N/mm^2) tensile strength	E (N/mm^2) Young's modulus	*Elong.* (%) elongation
ss400	2.2 (web)	274	438	208000	31.7
	3.0 (web)	292	438	204000	29.9
	6.0 (web)	296	432	210000	25.8
	9.0 (flange)	295	459	209000	28.3
	12 (flange)	266	443	206000	30.8

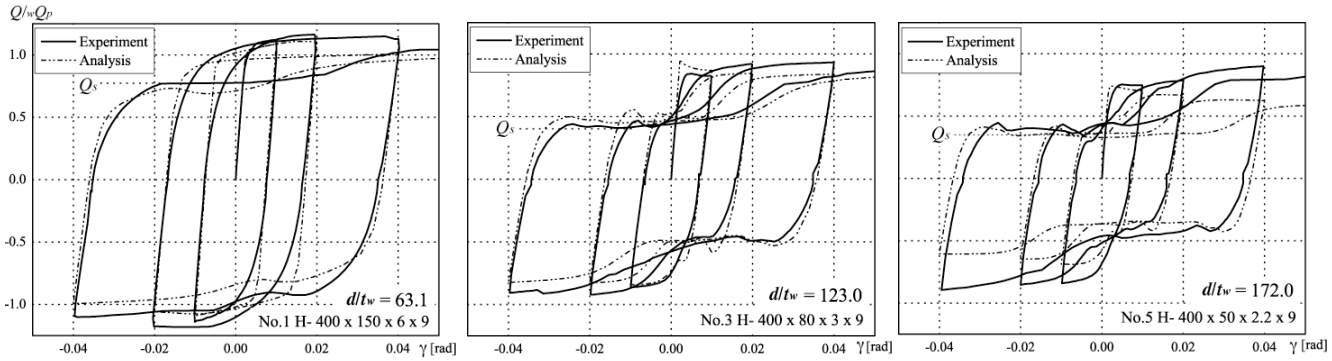

Figure 2 Load-deformation relationships (aspect ratio is 1)

Table 2 shows the mechanical properties of the steel material. The steel material is used SS400 here. SS400 is a Japanese standard structural steel material. Tensile strength of this material is nominally 400N/mm^2.

2.2 Influence of depth-thickness ratio of web whose aspect ratio is 1

Figure 2 indicates the load-deformation curves of No.1, No.3, and No.5. These are different in depth-thickness ratio of web panel, but almost equal in sectional area ratio of web to flange. The load-deformation curve obtained from the FEM numerical analysis is also in the figure, and the perpendicular axis means the dimensionless value divided by ${}_wQ_p$ (shearing yield strength of thin web plate). From figure of No.1, the hysteresis characteristics show a spindle shape up to γ =0.02 in the specimen No.1 which has smaller depth-thickness ratio than its elastic criticality obtained by equation (1).

However, form the other figure of the relationship between load and deformation, and it can be discovered a shelf is shaped into along with the deformation enlarging. On the other hand, the buckling occurs early on specimens No.3 with almost equal depth-thickness ratio to its elastic criticality and No.5 which has larger depth-thickness ratio than its elastic criticality, and the rigidity dwindle down to 0 under a certain load when the oscillation increases. Then, the deformation goes on with constant strength until the tension field is formed, and the strength rises to the experienced deformation peak of the previous loop almost in a line after tension field is formed.

After buckling, this strength Q_s when the shelf arises in the load-deformation curve keeps almost constantly without changing by the hysteresis cycle. Therefore, it is proved that Q_s is influenced by neither loading hysteresis nor the differences of positive and negative, and depends on its initial section shape. Moreover, it can be thought that the reduction is not vast and the deformation advances with the strength constant though the strength diminishes in some measure when the shelf happens in the load-deformation curve. Therefore, it can be considered that the strength Q_s when the shelf appears is an important element to comprehend the hysteresis characteristics of thin web plates under cyclic shear loading.

2.3 Influence of shape of flange

By the way, in the past research by Ikarashi, Suzuki and Shimizu (2004), it has been demonstrated that the rigidity of flange has effects on Q_s. In this study, it is thought that the influence of the strength, not only borne by web but also by flange is included. Figure 3 shows the relationship between load and deformation divided by the difference of flange shape. From the graph, it is aware that the strength Q_s when the shelf appears becomes larger and larger with sectional area of flanges increasing.

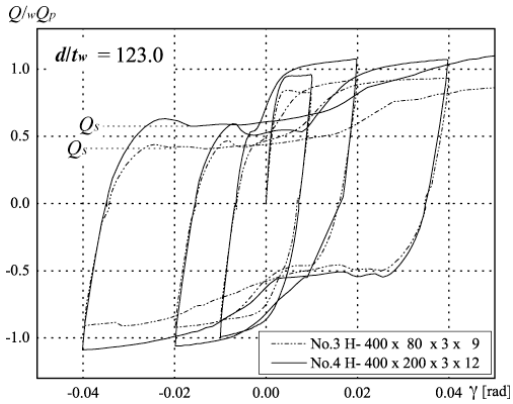

Figure 3 Influence of flange on Q_s

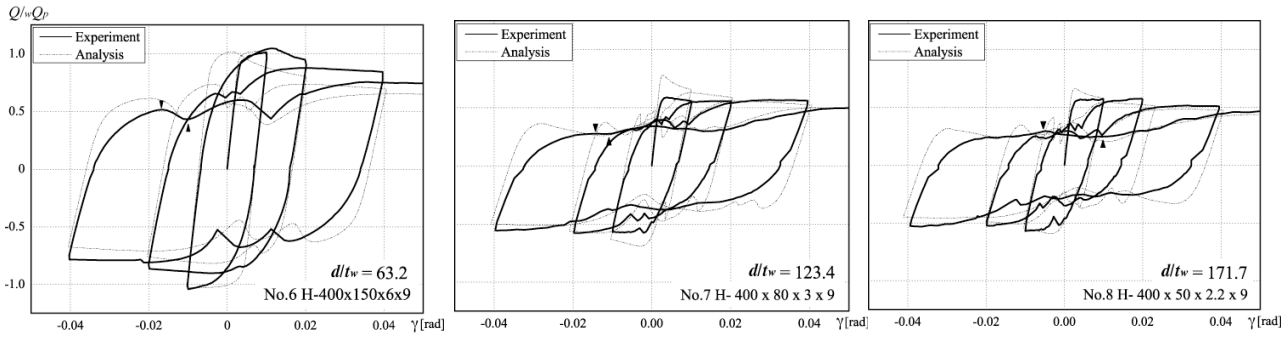

Figure 4 Load-deformation relationships (aspect ratio is 2)

2.4 Influence of aspect ratio of web

Figure 4 shows the load-deformation curve of the experiment results of aspect ratio 2. Figure 5 shows the skeleton curves of No.1 and No.6 which have the same sectional shape. The skeleton curve is different, though the sectional shapes are equal. As for the strength after the maximum strength, the specimen whose aspect ratio is 2 is smaller than the one whose aspect ratio is 1. For No.7 and No.8, a similar tendency can be confirmed by No.3 and No.5, though they are not published in figure. Moreover, it can be seen from Figure 4 that the hysteresis characteristics of No.6 with smaller depth-thickness ratio than its elastic criticality shows a spindle shape as well as No.1 in Figure 2 until the deformation advances to some degree.

However, it begins causing the strength to decrease in large deformation. At this time, two minimum values in the loop might be found in the case of aspect ratio 2, though the deformation advances with constant strength Q_s in each case of aspect ratio 1. About No.7 and No.8 whose depth-thickness ratio of web is comparatively large, the strength Q_s unremarkably decreases in the range of the shelf along with the deformation advancing. Afterwards, the constant strength is kept as well as aspect ratio 1, and the shelf hysteresis characteristics come to be indicated.

3. CONSIDERATION ABOUT THE STRENGTH IN THE SHELF RANGE

3.1 Influence of depth-thickness ratio of web whose aspect ratio is 1

Figure 6 indicates the collapse mechanism of flange. In

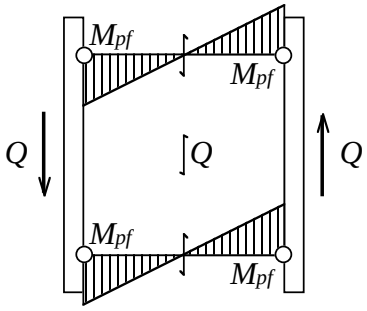

Figure 6 Collapse mechanism of flange

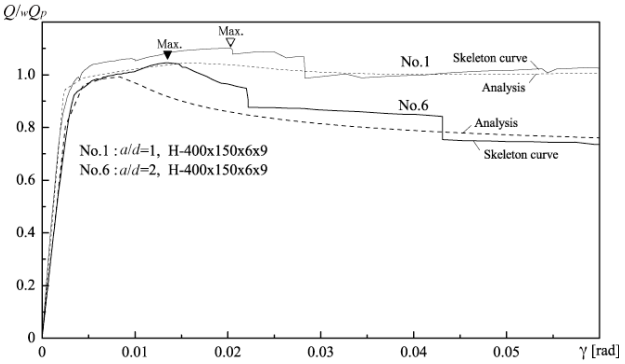

Figure 5 Skeleton curve (No.1 and No.6)

order to consider the strength of flanges, it thinks about Q_f (the strength of flanges) which is calculated from full plasticity moment M_{pf} at both ends of the flange, and the one that Q_f was subtracted from Q_s is defined as ${}_wQ_s$ (the strength of only web panel) in this study. M_{pf}, Q_s, Q_f are indicated by follow equation. Here, bf: flange width, t_f: flange thickness, a: plate length, σ_y: yield stress of flange.

$$M_{pf} = \frac{b_f t_f^{\,2}}{4}\sigma_y \tag{3}$$

$$Q_f = \frac{2M_{pf}}{a}\cdot 2 \tag{4}$$

$${}_wQ_s = Q_s - Q_f \tag{5}$$

It is thought that the hysteresis characteristics of thin web plates with larger depth-thickness ratio than their elastic criticality under cyclic shearing loads can be modeled by Q_s and the maximum strength Q_{max}. In this study, the minimum value of the strength when the shelf appears is defined as Q_s, and the influence that depth-thickness ratio of web has on Q_s is considered. Figure 7 is the graph where ${}_wQ_s$ of each depth-thickness ratio obtained from the numerical analysis by FEM are plotted with experimental value when thickness of web is varied and depth of web is appointed 400mm. For comparing, the curves are obtained from formulas of shearing yield strength (6), elastic buckling strength on surrounding fixed condition (7), the maximum strength evaluation (9) in the graph. The maximum strength is obtained by diagonal tension field strength. Here, A_w : Web cross area, b :web depth, a :web length.

$$ {}_wQ_p = \tau_y \cdot A_w \tag{6}$$

$$ Q_{cr} = \tau_{cr} \cdot A_w \tag{7}$$

$$ \tau_{cr} = \frac{kE\pi^2}{12\left(1-\nu^2\right)}\left(\frac{t_w}{b}\right)^2 \tag{8}$$

$$ Q_{\max} = Q_{cr} + Q_T \tag{9}$$

$$ Q_T = \frac{\sigma_T A_w}{2\sqrt{1+\left(\frac{a}{b}\right)^2}} \tag{10}$$

$$ \frac{\sigma_T}{\sigma_y} = 1 - \sqrt{\frac{\tau_{cr}}{\tau_y}} \tag{11}$$

And λ is given by

$$ \lambda = \left(\frac{b}{t_w}\right) \Big/ \left(\frac{b}{t_w}\right)_0 \tag{12}$$

in which $(b/t_w)_0$ is given by equation (1).

Corresponding to Figure 2 and Figure 7, the influence that the depth-thickness ratio of web has on ${}_wQ_s$ can be separated into three ranges according to the depth-thickness ratio of web. In this analysis, when the depth-thickness ratio of web is smaller than its elastic criticality (less than d/t_w=100), the hysteresis characteristics also show a spindle type at first, then turn a shape like shelf with the deformation increasing after buckling. It was confirmed that the value of ${}_wQ_s$ at that time diminished every time gradual increase loading was repeated. It can be con-firmed the behavior is especially easy to trace during d/t_w =100～200 (mainly handled in this experiment) that the depth-thickness ratio of web is almost equal to its elastic criticality and it is able to verify that the ${}_wQ_s$ can be evaluated by the maximum strength $Q_{max}/2$. In the range where depth-thickness ratio is over d/t_w =200, the ${}_wQ_s$ will continue to decrease further, and the value of ${}_wQ_s$ can be perceived from elastic buckling strength curves. Moreover, in the past research (T. V. Galambos, 1998) though it is made out the maximum strength of thin square web can be evaluated by Q_{max} in the range where depth-thickness ratio is larger than its elastic criticality, it cannot be understood in the range where smaller. In this study, in the range where depth-thickness ratio is smaller than its elastic criticality, the shelf appears in the load that is lower than Q_{max} /2 and the value becomes smaller every time gradual increase loading is repeated. Therefore, ${}_wQ_s$ cannot be evaluated by only the maximum strength Q_{max}, the influence from the other factors should be considered.

3.2 Influence of material characteristics

Figure 8 is the graph where ${}_wQ_s$ is plotted from the relationship of the load-deformation, and the relationship obtained from the analysis that assumes different materials about the model whose aspect ratio is 1. For the material data, the relationship between stress and strain is shown in this figure. σ_y=2.8 Ⅱ is the model of the stress-strain relationship obtained from tensile test for SS400 steel

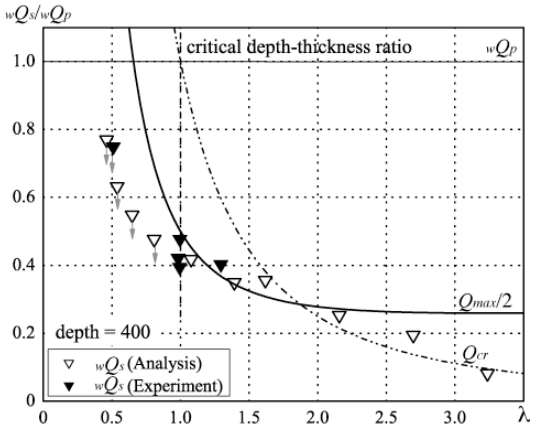

Figure 7 Influence of web depth-thickness ratio on ${}_wQ_s$ (aspect ratio is 1)

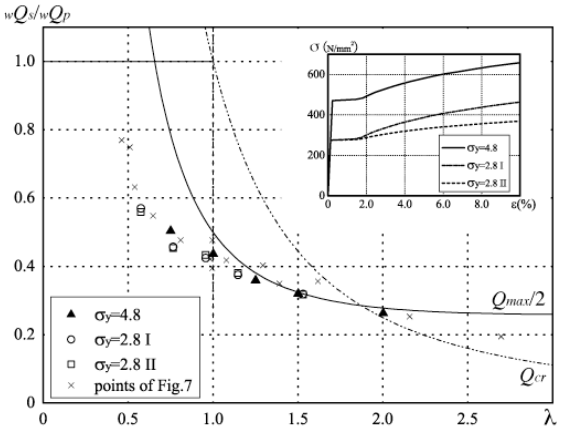

Figure 8 Influence of material characteristics on ${}_wQ_s$ (aspect ratio is 1)

material. Additionally, the models which are different in the point of yield stress (σ_y =4.8) and strain hardening region (σ_y =2.8 Ⅱ) are also used here. The distribution of the plot corresponds to the tendency of Figure 7. Therefore, it is speculated that the strength when the shelf appears does not depend on the yield stress and the strain hardening characteristics of material greatly.

3.3 Influence of depth-thickness ratio of web whose aspect ratio is 2 on ${}_wQ_s$

Figure 9 is the graph by plotting the first maximum value, the first minimum value, and the middle value in the final loop in order to try the evaluation as same as Figure 7. The influence of the strength borne by flange is subtracted from the strength obtained just like Figure 6, and the strength only of web panel is shown. Moreover, the horizontal axis in the figure is shown by using the depth-thickness ratio divided by the elastic critical depth-thickness ratio and buckling strength Q_{cr} / ${}_wQ_s$ which is independent on aspect ratio and yield stress.

As a result, it can be confirmed that the distribution of the middle value shows a similar tendency to whose aspect ratio is 1. It can be confirmed that the value of ${}_wQ_s$ whose aspect ratio is 2 is smaller than that of $Q_{max}/2$, though it is be able to understand the value of ${}_wQ_s$ by $Q_{max}/2$ and Q_{cr} of the

thin web plates which have larger depth-thickness ratio than their elastic criticality when the aspect ratio is 1. The plot of the middle value is almost included between $Q_{max}/2$ and $Q_{max}/3$ if using $Q_{max}/3$ here.

4. CONCLUSIONS

The cyclic loading experiments are carried out by thin web plates whose aspect ratio is 1 or 2, and their hysteresis characteristics are confirmed. As it turns out that the strength Q_s when the shelf is shaped into until tension field is formed after shear buckling and the maximum strength Q_{max} of web can be used to predict the cyclic behavior of thin web plates with larger depth-thickness ratio than their elastic criticality. Moreover, it can be comprehended the strength ${}_wQ_s$ (only of web panel) that Q_f was subtracted from Q_s can be understood by Q_{max} and elastic buckling strength Q_{cr}.

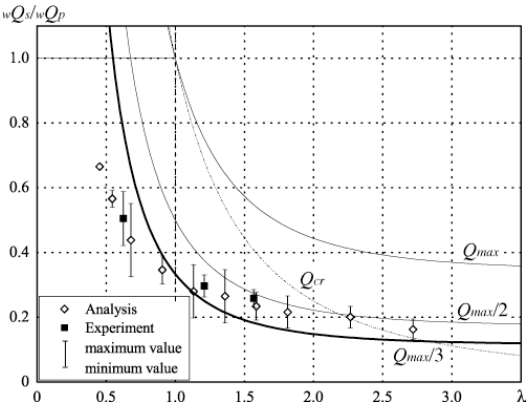

Figure 9 Influence of web depth-thickness ratio on ${}_wQ_s$ (aspect ratio is 2)

Acknowledgements:

This work was supported by KAKENHI (18560543)

References:

K. Ikarashi, T. Suzuki & M. Shimizu (2004), A study on behavior after shear buckling of thin square web, Summaries of Technical Papers of Annual Meeting; Architectural Institute of Japan, C-1, pp793-796 (in Japanese)

T. M. Roberts & S. S. Ghomi (1991), Hysteretic Characteristic of Unstiffend Plate Shear Panels, Thin-Walled Structures, 12, 145-162

T. V. Galambos (1998), Stability Design Criteria for Metal Structures, Fifth Edition

Sixth International Conference on Urban Earthquake Engineering
March 3-4, 2009, Tokyo Institute of Technology, Tokyo, Japan

INNOVATIONS IN STEEL PLATE SHEAR WALL DESIGN

Michel Bruneau[1], Ronny Purba[2], Bing Qu[3], Gordy Warn[4], and K.C. Tsai[5]

1) Professor, Dept. of Civil, Structural and Environmental Engineering, University at Buffalo, Buffalo, NY 14260, USA
2) Graduate Research Assistant, Dept. of Civil, Structural and Environmental Engineering, University at Buffalo, Buffalo, NY 14260, USA
3) Assistant Professor, Department of Civil Engineering, CalPoly,, San-Luis Obispo, CA, USA
4) Assistant Professor, Dept. of Civil Engineering, PennState, PA, USA
5) Director, National Center for Research in Earthquake Engineering, Taipei, Taiwan
bruneau@buffalo.edu, purba@buffalo.edu bqu@calpoly.edu gwarn@engr.psu.edu kctsai@ncree.gov.tw

Abstract: Steel Plate Shear Walls (SPSWs) are rapidly becoming an appealing alternative lateral force resisting system for building structures in high seismic areas. This paper presents results of some recent research to expand the range of applicability of SPSWs. Emphasis is on improving the understanding of seismic and blast performance of SPSWs (in a multi-hazard perspective). Preliminary results of an investigation into the behavior of SPSWs with infill panels designed to resist various percentage of the specified lateral load are also presented.

1. INTRODUCTION

A steel plate shear wall (SPSW) consists of infill steel panels surrounded by boundary beams and columns. Per North American practice, these panels are allowed to buckle in shear and subsequently form diagonal tension fields. The selection of SPSW as the primary lateral force resisting system in buildings has become more popular in recent years, and SPSW have been used increasingly as practicing engineers discover the benefits of this option (Sabelli and Bruneau 2007). This paper provides an overview of selected innovations in SPSW design, namely:

- Information on special perforated SPSW;
- Results on full scale testing of a two-story SPSW to investigate behavior intermediate beams as well as the replaceability of buckled steel plates and performance of the so repaired SPSW following an earthquake;
- Preliminary experimental results on the blast resistance of SPSW.

2. SPECIAL PERFORATED SPSW

A recent experimental investigation of single-story, single-bay SPSW frames was conducted to investigate the behavior of specially detailed ductile perforated SPSWs designed to accommodate utility passage and having anchor beams with Reduced Beam Sections (RBS) connections (see Vian and Bruneau 2004;2009). Two specimens were designed to accommodate utility passage, one having multiple holes specially laid-out in the steel panel, (P) and the other with quarter-circle corner cutouts (CR). An additional specimen was designed with a solid infill panel (S2) as a reference specimen. The specimen P also has reduced panel strength and stiffness compared to the corresponding SPSW having a solid panel. The results of the experimental program showed all specimens resisted a history of increasing cyclic displacement up to a minimum drift of 3% and that the perforated panel reduced the elastic stiffness and overall strength of the specimen by 22% and 15%, respectively, as compared with the solid panel specimen. Figure 1 shows the deformed shape of specimen P at a lateral displacement corresponding to 3% interstory drift, and contours representing the magnitude of the von Mises stress.

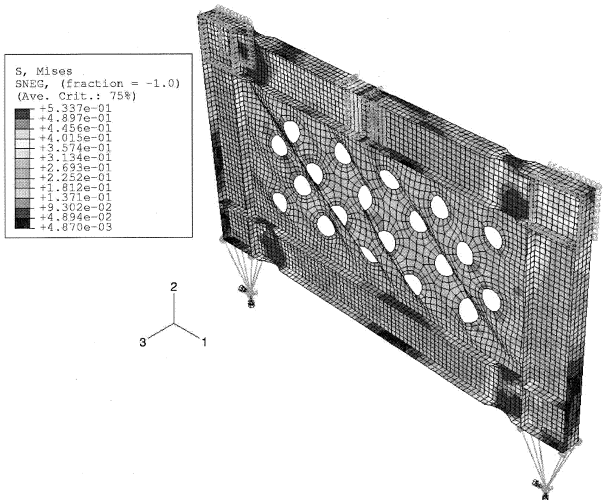

Figure 1. Deformed Shape of FE Models: of Specimen P (from Vian and Bruneau 2004;2009)

The yield strength of a solid panel (Thorburn and Kulak, 1983), V_{yp}, is calculated as

$$V_{yp} = 0.5F_{yp} \cdot t \cdot W_{panel} \cdot \sin 2\alpha \qquad (1)$$

where F_{yp} is the panel yield strength, t is the panel thickness, W_{panel} is the panel width and α is the inclination of the tension field force with respect to the vertical.

Finite element analyses of full SPSW were performed to investigate the relationship between perforation diameter and infill panel strain, to verify the accuracy of the individual strip model results and to investigate the influence of the boundary element stiffness/rigidity on the stress and strain distribution in the panel (Purba and Bruneau 2007).

Figure 2 illustrates typical maximum in-plane principal strain contours for the panel (Figure 2a) and strip (Figure 2b) FE models. Figure 3 presents total uniform strip elongation ($\varepsilon_{un}=\delta/L$) versus perforation ratio (D/S_{diag}) for maximum principal strain (ε_{max}) values of 1, 5, 10, 15 and 20% from analyses performed using the Strip and Panel models. For a given D/S_{diag} and ε_{max} the total uniform strip elongation from the Strip and Panel models agree well.

For example, for a D/S_{diag}=0.35 and ε_{max}=15% a total uniform strip elongation of, approximately, 1.8 is observed in the Strip and Panel models. Although some differences are observed at the 20% monitoring strain, however, in all cases a less than 15% difference is observed and considered acceptable.

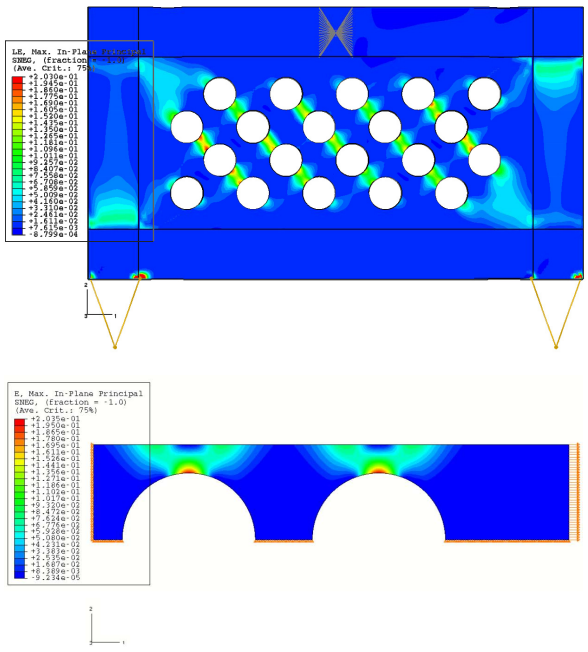

Figure 2. Maximum In-Plane Principal Strain from FE Models: (a) Panel (b) Strip

Results of analyses performed with the full SPSW model were used to formulate a design equation to assess strength of the SPSW panels having multiple perforations. For comparison purposes, a SPSW having a solid infill panel was also analyzed. For both the solid and perforated SPSW models, the infill panel strength was determined by subtracting the strength of the boundary frame determined from an additional analysis of the boundary frame alone. Figure 4 presents infill plate strength ratios ($V_{yp.perf}/V_{yp}$) versus perforation ratios (D/S_{diag}) for frame drifts (γ) of 1, 2, 3, 4 and 5%. Based on the results presented in Figure 4, the following equation is proposed:

$$\frac{V_{yp.perf}}{V_{yp}} = \left[1 - \alpha \frac{D}{S_{diag}}\right] \qquad (2)$$

where α is equal to 0.7 based on the results of the linear regression analysis.

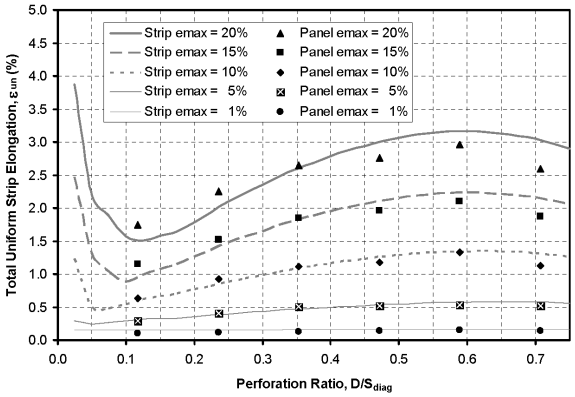

Figure 3. Uniform Distributed Strip Axial Strain $_{un}$ versus Perforation Ratio D/S_{diag}

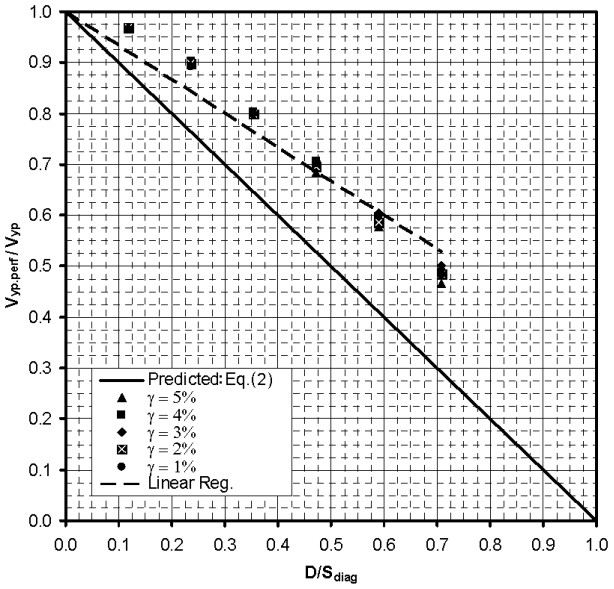

Figure 4. Infill Plate Strength Ratios ($V_{yp,perf}/V_{yp}$) versus Perforation Ratio (D/S_{diag})

3. TESTING OF FULL-SCALE TWO-STORY SPSW

Monotonic, cyclic and shaking table tests on SPSW in North America have shown that SPSW can exhibit high initial stiffness, behave in a ductile manner and dissipate significant amounts of hysteretic energy (Timler and Kulak, 1983; Tromposch and Kulak, 1987; Cassese et al., 1993; Elgaaly et al., 1993; Driver et al., 1998; Rezai, 1999; Lubell et al., 2000; Berman and Bruneau, 2005; Vian and Bruneau, 2005). To investigate the replaceability of infill panels following an earthquake, and the seismic behavior of intermediate beams in SPSW, a full scale two-story SPSW specimen was fabricated and tested. The specimen with equal height and width panels at each story was 8000 mm high and 4000 mm wide between boundary frame member centerlines. The infill panels and boundary frame members were sized based on the recommendations provided by Berman and Bruneau (2003). Beams and columns were of A572 Gr.50 steel members. Infill panels were specified to be SS400 steel which is similar to ASTM A36 steel in this case. The RBS connection design procedure (FEMA350, 2000) was used to detail the beam-to-column connections at top, intermediate and bottom level respectively.

In a first phase the specimen was tested under three pseudo-dynamic loads using the Chi-Chi earthquake record (TCU082EW) scaled up to levels of excitations representative of seismic hazards having 2%, 10% and 50% probabilities of exceedance in 50 years, subjecting the wall to earthquakes of progressively decreasing intensity. Despite the numerous ancillary calculations that checked the adequacy of the specimen, the intermediate concrete slab and the south column base suffered premature failures during the first earthquake record. The tests resumed after the specimen was strengthened at these locations. It then behaved satisfactory upon retest. No fracture was found in the boundary frame and it was deemed to be in satisfactory condition allowing for the replacement of infill panels for the subsequent phase of testing.

The buckled infill panels flame-cut and replaced by new panels welded on the other side of the fish plates used along the boundary frame members to connect the infill panels. The repaired specimen was tested under pseudo-dynamic load corresponding to the Chi-Chi earthquake record (TCU082EW) scaled up to the seismic hazard of 2% probability of occurrence in 50 years.

Observation of the obtained hysteretic curves shows that the first story dissipated more hysteretic energy than the second story. Both the first and second story exhibited stable displacement-force behavior, with some pinching of the hysteretic loops as the magnitude of drifts increased, particularly after the development of a small fracture along the bottom of the shear tab at the north end of the intermediate beam at drifts of 2.6% and 2.3% at the first and second story respectively. After the pseudo-dynamic test, the boundary frame was in good condition except for the aforementioned damage in the shear tab of the intermediate beam. There were notable plastic deformations at the column bases and RBS connections at all levels. All welds within the SPSW specimen were intact after the test.

The next stage of testing involved cyclic test on the SPSW specimen in order to investigate the ultimate behavior of intermediate beam and the cyclic behavior and ultimate capacity of SPSW system after sever earthquakes. The damaged shear tab was replaced by a new one prior to conducting the cyclic test. A displacement-controlled scheme was selected for the cyclic test.

The specimen and hysteretic curves after the cyclic test, along with the results of pseudo-dynamic tests, are shown in Figure 5 It is observed the initial stiffness of the SPSW specimen in the cyclic test was smaller than that in pseudo-dynamic test. Because the previous pseudo-dynamic test stretched the infill panels up to specimen drifts of 2.6% and 2.3% at the first and second story respectively, the hysteretic loops exhibited pinching up to those drifts. Hysteretic loops were then full until drifts of 2.8% and 2.6% at the first and second story respectively in Cycle 7, when complete fracture occurred along the shear tab at the north end of the intermediate beam. A similar fracture developed along the shear tab at the south end of the intermediate beam when the specimen was pulled towards to the reaction wall in this cycle.

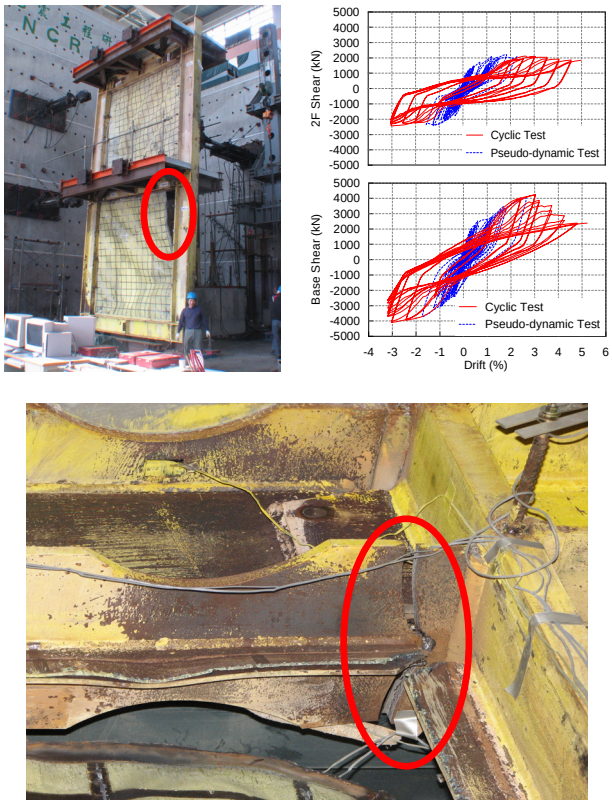

Figure 5. Specimen and hysteretic curves

Rupture of the shear tabs triggered fracture of the bottom flange at the north end of the intermediate beam. At drifts of 3.3% and 3.1% at the first and second story respectively in Cycle 9, the bottom flange at the north end of the intermediate beam fractured as shown in Figure 5. However, no fractures developed in the reduced beam flange regions

of the intermediate beam. The welds connecting the infill panels to the fish plates around the north end of the intermediate beam also fractured over a substantial length to a more severe extent after the specimen experienced drifts of 5.2% and 5.0% at the first and second story respectively. These events significantly changed the load path within the system. However, the SPSW specimen was still able to exhibit stable displacement-force behavior. The cyclic test ended at drifts of 5.2% and 5.0% at the first and second story respectively, when a sudden failure occurred in the load transfer mechanism, i.e. when a fatal longitudinal crack developed along the top concrete slab of the specimen. More information about the testing results of Phase I and II is presented elsewhere (Lin et al 2007 and Qu et al 2007).

This data was then used to investigate the load distribution in the horizontal boundary elements of SPSW (Qu and Bruneau 2008; Qu et al. 2008). New models resulting from this study have made it possible to explain the observed failures and formulate design recommendations to prevent their recurrence in future design.

4. BLAST RESISTANCE OF SPSW

Some engineers have advocated the use of SPSW in buildings and other structures to resist out-of-plane blast loading. Although nonlinear finite element analyses suggest that SPSWs might be capable of resisting substantial out-of-plane impulsive loads and sustaining large inelastic deformation, there has been no experimental validation of the analytical results. To gain an improved understanding of the behavior of SPSWs subjected to out-of-plane blast loading an experimental investigation was conducted. For this study, 0.4 scale models were fabricated based on a representative prototype SPSW designed to resist seismic loading following the AISC Seismic Provisions (2005). Each SPSW consisted of two Vertical Boundary Elements (W310x79), two Horizontal Boundary Elements (S200x34) with RBS and a 1.9 mm thick infill plate measuring 1372 mm by 1270 mm connected to the boundary frame through fishplates (L76x51x4.8). The VBE elements were specified ASTM A992 Grade 50 whereas the HBEs and fishplates were ASTM A572 Grade 50. Due to thickness constraints of the infill plate a hot-rolled commercial sheet stock (ASTM A1011) was specified with a measured yield strength of 330 MPa and an elongation at break of 32%. The VBEs of each SPSW were cast directly into a foundation beam and supported at the center line of the top HBE by a steel reaction frame. The boundary frame dimensions were 1830 mm and 1575 mm from center-to-center of the VBEs and HBEs, respectively.

Table 1 presents summary information for the primary plate tests consisting of two explosive detonations. Test number 1 (SPSW 1) is representative of a hand placed explosive with a charge weight of W (equivalent weight of TNT) at a standoff distance of X at the center of the infill plate and a height of 0.9 m (mid-height of the infill plate). Test number 2 (SPSW 2) is representative of a vehicle bomb with a charge weight of 3W at a standoff distance of 2.4X at the center of the infill plate and a height of 0.9 m.

Table 1. Summary information for blast testing

Test No.	Specimen	Charge Weight w	Standoff Distance x	Charge Height z
				(m)
1	SPSW 1	W	X	0.9
2	SPSW 2	3W	2.4X	0.9

Figure 6 presents a photograph of the backside of SPSW 1 following test number 1. The maximum residual out-of-plane deformation at the center of the plate was 133 mm. The residual plastic elongation at the center of the plate in the horizontal and vertical directions was calculated to be 1.85% and 1.25%, respectively. Although not illustrated here, substantial inelastic deformations were observed in the fishplate and HBE elements. For SPSW 2 (Figure 7), failure occurred at the weld connecting the infill plate to the fishplate around three quarters of the perimeter of the plate. The measured length of the plate in the horizontal direction was approximately equal to the original length suggesting the welds failed prior to yielding of the plate. Although no inelastic deformation was observed in the plate, substantial inelastic deformations were observed in the fishplate and HBE elements, especially the bottom HBE. In both tests, partial length fractures were observed in the full penetration groove welds connecting the HBE flanges to the VBEs.

Figure 6. Backside of SPSW 1 After Test 1

Figure 7. SPSW 2 After Test 2

5. CONCLUSION

This paper provided an overview of recent development on SPSW. It was shown that: (i) regular layout of perforations can be used to reduce the strength of SPSW infills; (ii) it is possible to replace buckled steel plates without major impact on seismic performance, thus allowing repair of SPSWs following an earthquakes, and; (ii) SPSW can be design to have some level of blast resistance.

Acknowledgements:

This work was supported in part by the Earthquake Engineering Research Centers Program of the National Science Foundation under Award Number ECC-9701471 to the Multidisciplinary Center for Earthquake Engineering Research. However, any opinions, findings, conclusions, and recommendations presented in this paper are those of the authors and do not necessarily reflect the views of the sponsors.

References:

AISC (2005), Seismic Provisions for Structural Steel Buildings, American Institute of Steel Construction, Chicago, IL.

Berman, J. W., and Bruneau, M. (2003), "Plastic Analysis and Design of Steel Plate Shear Walls," Journal of Structural Engineering, ASCE, Vol. 129, No. 11, pp. 1448-1456.

Berman, J.W., and Bruneau, M. (2005), "Experimental Investigation of Light-Gauge Steel Plate Shear Walls", Journal of Structural Engineering, ASCE, Vol.131, No.2, pp 259-267.

Caccese, V., Elgaaly, M., and Chen, R., (1993), "Experimental Study of Thin Steel-Plate Shear Walls Under Cyclic Load", Journal of Structural Engineering, ASCE, Vol. 119, No. 2, Feb. 1993, pp. 573-587.

Driver, R.G., Kulak, G.L., Kennedy, D.J.L., and Elwi, A.E. (1998), "Cyclic Test of Four-Story Steel Plate Shear Wall", Journal of Structural Engineering, ASCE, Vol. 124, No. 2, Feb. 1998, pp 112-130.

Elgaaly, M., Caccese, V., and Du, C. (1993), "Postbuckling Behavior of Steel-Plate Shear Walls Under Cyclic Loads", Journal of Structural Engineering, ASCE, Vol. 119, No. 2, Feb. 1993, pp. 588-605.

Federal Emergency Management Agency (FEMA). (2000). "Recommended Seismic Design Criteria for New Steel Moment-Frame Buildings." FEMA 350. Prepared by the SAC Joint Venture for FEMA, Washington, D.C.

Lin, C.H., Tsai, K.C., Lin, Y.C., Wang, K.J., Qu, B., and Bruneau, M. (2007), "Full Scale Steel Plate Shear Wall: NCREE/MCEER Phase I Tests." Proceeding of the 9th Canadian Conference on Earthquake Engineering, Ottawa, Canada.

Lubell, A.S., Prion, H.G.L., Ventura, C.E., and Rezai, M. (2000), "Unstiffened Steel Plate Shear Wall Performance Under Cyclic Loading", Journal of Structural Engineering, ASCE, Vol. 126, No.4, pp. 453-460.

Qu. B, Bruneau, M. Lin, C.H., Tsai, K.C. and Lin, Y.C. (2007),"Full Scale Steel Plate Shear Wall: MCEER/NCREE Phase II Tests." Proceeding of the 9th Canadian Conference on Earthquake Engineering, Ottawa, Canada.

Qu, B, Bruneau, M., (2008). "Seismic Behavior and Design of Boundary Frame Members in Steel Plate Shear Walls", Technical Report MCEER-08-0012, Multidisciplinary Center for Earthquake Engineering Research, State University of New York at Buffalo, Buffalo, NY, 2008.

Qu, B, Bruneau, M., Lin., C.H., Tsai, K.C., (2008). "Testing of Full Scale Two-story Steel Plate Shear Walls with RBS Connections and Composite Floors", Technical Report MCEER-08-0010, Multidisciplinary Center for Earthquake Engineering Research, State University of New York at Buffalo, Buffalo, NY, 2008

Purba, R., and Bruneau, M. (2007). "Design Recommendations for Perforated Steel Plate Shear Walls" Tech. Rep. MCEER-07-0011, Multidisciplinary Center for Earthquake Engineering Research, State University of New York at Buffalo, Buffalo, N.Y.

Rezai, M. (1999), "Seismic Behavior of Steel Plate Shear Walls by Shake Table Testing", Ph.D. Dissertation, University of British Columbia, Vancouver, British Columbia, Canada.

Sabelli, R. and Bruneau, M. (2007). "Steel Plate Shear Walls." Steel Design Guide, American Institute of Steel Construction, Inc., Chicago, Ill.

Timler, P.A. and Kulak, G.L. (1983), "Experimental Study of Steel Plate Shear Walls", Structural Engineering Report No. 114, Department of Civil Engineering, University of Alberta, Edmonton, Alberta, Canada.

Thorburn, L. Jane, Kulak, G. L., and Montgomery, C. J. (1983). "Analysis of Steel Plate Shear Walls," Structural Engineering Report No. 107, Department of Civil Engineering, The University of Alberta, Edmonton, Alberta, May 1983.

Tromposch, E.W., and Kulak, G.L. (1987), "Cyclic and Static Behaviour of Thin Panel Steel Plate Shear Walls", Structural Engineering Report No. 145, Department of Civil Engineering, University of Alberta, Edmonton, Alberta, Canada.

Vian, D., Bruneau, M., 2004. "MCEER's Experimental Research on Steel Plate Walls," Structural Engineers Association of California 2004 Convention, Monterey, California, pp. 211-215.

Vian D.and Bruneau M.(2005). "Steel Plate Shear Walls for Seismic Design and Retrofit of Building Structure", Technical Report MCEER-05-0010, Multidisciplinary Center for Earthquake Engineering Research, Buffalo, N.Y.

Vian, D., Bruneau, M., Tsai, K.C., and Lin, Y.-C. (2009). "Special Perforated Steel Plate Shear Walls with Reduced Beam Section Anchor Beams I: Experimental Investigation," ASCE Journal of Structural Engineering, Vol.135, No.3 (in press).

Sixth International Conference on Urban Earthquake Engineering
March 3-4, 2009, Tokyo Institute of Technology, Tokyo, Japan

A TRIAL OF SEISMIC FRAGILITY EVALUATION OF LARGE LATTICE DOME SUPPORTED BY BUCKLING RESTRAINED BRACES

Shiro Kato[1] and Shoji Nakazawa[2]

1) Professor, Dept. of Architecture and Civil Engineering, Toyohashi University of Technology, Japan
2) Associate Professor, Dept. of Architecture, Gifu National College of Technology, Japan
kato@tutrp.tut.ac.jp nakazawa@st.tutrp.tut.ac.jp

Abstract: A trial to evaluate seismic fragility of a large dome supported by buckling restrained braces is performed and discussed in comparison with a dome supported by ordinary tension active braces. In order to evaluate the fragility depending on an adopted bracing system, the damages burdened to the dome structure due to earthquakes are calculated and interpreted as total fragility in terms of assumed seismic intensity varying from minor to major earthquakes. The procedure for calculating the total fragility, almost similar to functional loss, utilizes a simple event tree modeling, where the total fragility is counted considering the damages to structural members, non-structural walls and ceilings. Based on a simple calculation, an example is illustrated to see how the buckling restrained braces are effective or not effective as an anti-seismic reinforcement.

1. FUNCTION IN AND AFTER EARTHQUAKE

Dome structures and other similar facilities including sport halls for community schools have been effectively served as refuges for certain duration in case of large earthquakes. The importance of this kind of facility as refuges has been proven in Kobe Earthquake in 1995 and other earthquakes in Japan. Such an effective case was also found in the southern part of United States where Houston Steel Dome was used after a severe damage due to the Hurricane Katrina in 2005.

Anti-earthquake braces have been applied and intrinsically indispensable to keep safety for not only structures but also, more important, lives of many people gathering within a building. Recently buckling restrained brace of anti-earthquake has been recognized more effective than ordinary tension-active braces, and they are being adopted in several cases. One typical example, Shimokita Dome [1] shown in Figure 1, is recently constructed. In Japan, sport halls are strongly expected to serve as refuges in case of severe disasters, structural design of lattice domes tends to adopt buckling restrained braces to reduce damages for sure safety.

At present several important investigations [2, 3, 4] have been perfomed with respect to seismic risk of structures in general, however, data has not been well accumurated to evaluate the seismic risk based on probability concept [5]. Accordingly, the present study limits the content to a calculating procedure of fragility with emphasis on the seismic performance of this kind of domes supported by buckling restrained braces, and discusses, using calculated fragility in case of a simple example, on how the structures can function against strong earthquakes.

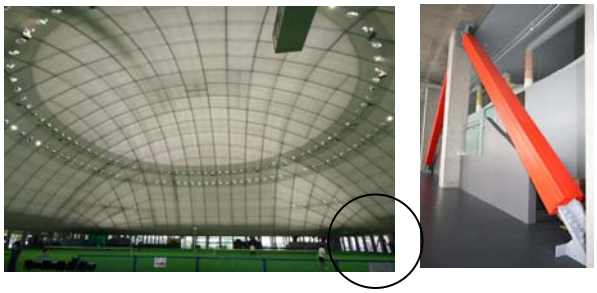

Figure 1 Example of buckling restrained braces adopted as anti-earthquake component supporting a large lattice dome

2. GEOMETRY OF STRUCTURE

2.1 Decomposition into Dome and Substructure

First, a dome with a diameter of 100 meters is assumed for analysis as one of the typical examples for sport halls of medium size. The structure is shown in Figure 2, where the total building is divided here into two parts: the dome and the substructure supporting the dome. The substructure is composed of diagonal braces and vertical columns, both covered with wall finishing as non-structural material. The dome may be of double layer or single layer, and in this study it is assumed a single layer steel lattice roof, where a ceiling of large area is finished inside the roof.

Although bracing elements in real buildings are not so dense as shown in Figure 2, such a arrangement is assumed for analytical simplicity. Accordingly, the sectional area of each dense bracing element is assumed relatively small as given in Table 1 compared with real braces.

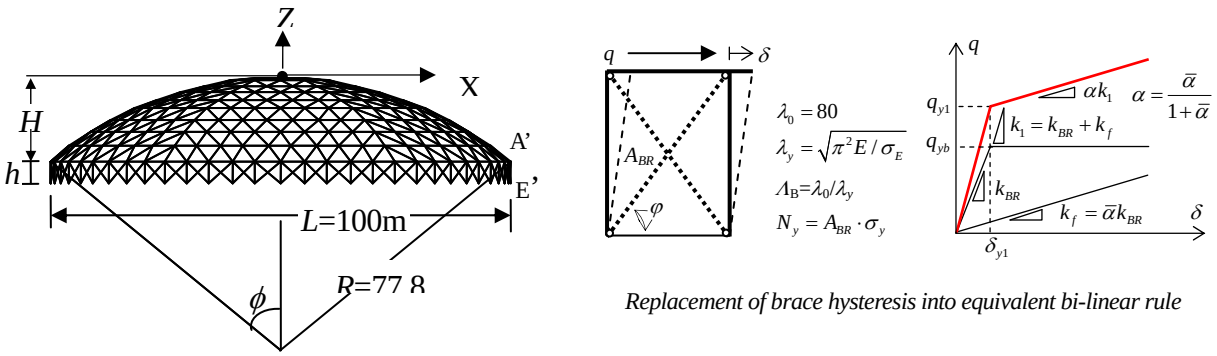

Replacement of brace hysteresis into equivalent bi-linear rule

Figure 2 Steel single layer lattice dome with a large area of ceiling, being supported by earthquake resistant braces.

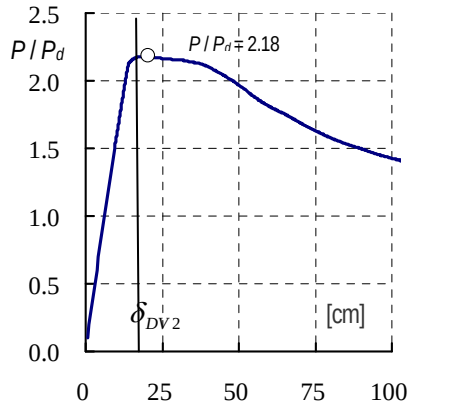

Vertical displacement at Node a

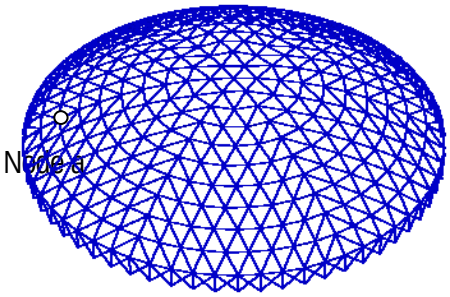

Figure 3 Static behavior of dome

2.2 Structural Members and Ceiling for Roof

For the single layer lattice dome composed of tubular steel members, the design load is assumed as given in Table 2. A limitation is added that the members within the dome roof have a same diameter of 512mm and the tension ring has a diameter twice the roof members. The members are proportioned for the thickness of tubular members in a way that the dome has a bearing capability to resist the two times dead load, $p_{d0} = 1470 N/m^2$ per unit area, and also that it resists the additional static earthquake load , P_{E0}, with 0.6 as the base shear coefficient defined at the dome base. The earthquake load P_{E0} is prepared using a linear earthquake response of dome under El Centro NS with a peak acceleration of A_{max}=320cm/s^2. The total weight of the dome is assumed as W_t=17400kN including tension ring, and the weight of the wall is included as a part of substructure. The elastic modulus E and yield strength σ_y are assumed as $205\times10^3 N/mm^2$ and $235 N/mm^2$, respectively. The detail of members and other structural characteristics are abbreviated due to limited space.

2.3 Buckling Restrained Brace and Tension-active Brace

Two types of brace elements are assumed for comparison to investigate the effectiveness to reduce the damage to the total structure. One is a buckling restrained brace with bi-linear hysteresis, and the other is a slip type brace. The data is given in Table 1. A_{BR} is the area of each brace element, K_{BR} is the shear rigidity of one set of braces as given in the right part of Figure 2, and κ represents the elastic shear rigidity of other structural element except for the brace element, being assumed 0.2 as the ratio to the brace rigidity. Δ_{y1} is the story drift for initial yield. The axial rigidity of columns is assumed very large, and the vertical displacements at column heads are fixed zero in the analysis. The combination of brace with the dome is expressed, for examples, as (α_{y0}=0.3, slip type) or (α_{y0}=0.3, bi-linear). For example, Dome (α_{y0}=0.3, slip type) means a dome supported by slip type braces with 0.3 as yield base shear coefficient.

2.4 Bearing Capacity of Dome under Dead Load

The bearing capacity is illustrated in Figure 3, where the load-displacement relationship is given at Node a. The result is based on an elasto-plastic buckling analysis of the Dome (α_{y0}=0.3, bi-linear) using a geometrically and materially nonlinear analysis [6]. From Figure 3, it is verified that the dome satisfies the design requirement for dead load that the dome should endure the load twice the dead load. Other cases with a different value of α_{y0} are almost same and abbreviated in this paper.

3. EARTHQUAKE MOTIONS FOR ANALYSIS

To investigate the fragility of a real dome requires a set of earthquake motions that are selected by reflecting the site seismic activity. However, the dome studied in this paper is non-real. Accordingly, artificial earthquake motions are prepared based on the design spectrum for Soil Characteristics II of Japan Building Code [7], defined for the serviceability limit level with $\lambda_E = 1.0$ for a design damping

Table.1 Brace elements

	design base shear coefficient for braces α_{y0}	yield stress σ_y	$A_{BR}(cm^2)$	$K_{BR}(kN/cm)$	$\kappa = K_F / K_{BR}$	story drift at first yield Δ_{y1} (cm)
Buckling restrained braces (bi-linear type)	0.2	$235N/mm^2$	2.811	117.8	0.2	0.834
	0.3		4.216	176.7		0.834
	0.4		5.622	235.6		0.834
slip type braces	0.3		4.216×2	176.7		0.834

Table.2 Design load for ultimate limit

	design load as dead load	design load as earthquake	characteristics
Dome	two times the dead load	dead load plus earthquake load with 0.6 as a base shear coefficient defined at dome base	Total weight for structures Wt=17400kN, h=500cm, $\cos\phi$=0.766, ℓ_b = 543cm

Table.3a Assumption of damage intensity to structural members and ceilings on roof: $\delta_{DV1} = 12cm$ $\delta_{DV2} = 18cm$ $A_{DH1} = 800cm/s^2$ $A_{DH2} = A_{DV2} = 1600cm/s^2$

Damage intensity	Maximum response limit over which damage follows due to the response
A No damage	The maximum vertical displacement δ_{DV}; $\delta_{DV} \le \delta_{DV1}$, and maximum vertical acceleration response A_{DV}; $A_{DV} \le A_{DV1}$, and maximum horizontal acceleration response A_{DH}; $A_{DH} \le A_{DH1}$.
B Moderate	Not A and Not C
C Severe damage	The maximum vertical displacement δ_{DV}; $\delta_{DV} \ge \delta_{DV2}$, and maximum vertical acceleration response A_{DV}; $A_{DV} \ge A_{DV2}$, or maximum horizontal acceleration response A_{DH}; $A_{DH} \ge A_{DH2}$.

Table.3b Assumption of damage intensity to wall composed of braces and finishing: $\delta_{SH1} = 2.5cm, \delta_{SH2} = 5cm$

Damage intensity	Maximum response limit over which damage follows due to the response
A No damage	The horizontal displacement at top of wall δ_{SH}; $\delta_{SH} \le \delta_{SH1}$:
B Moderate	Not A and Not C
C Severe damage	The horizontal displacement at top of wall δ_{SH}; $\delta_{SH} \ge \delta_{SH2}$:

factor of h_0=5%. The code defines ultimate limit level corresponding to 5 for λ_E. For investigation of the fragility of dome, twelve artificial ground earthquake motions are simulated using phases drown from twelve recorded earthquake accelerations. They are El-Centro NS, Taft EW and other recorded accelerations that are often applied in anti-earthquake design. Roughly the average peak acceleration for $\lambda_E = 1$ corresponds to 115cm/s^2. In the response analysis performed later, the simulated acceleration motions are applied to domes by changing the peak value of simulated acceleration.

4. FRAGILITY OF STRUCTURE

4.1 Rule for Damage Identification

The damage is evaluated roughly for the structural members and the roof as well as the wall of substructure. Since the precise judgment of damage is fairly difficult at present, the definition is just an assumption. The damage of structural members depends on magnitudes of stress and strain exerted in them, and the damage of the finishing of walls and ceiling depends on how they are fixed with the structural members. And in some cases, the damage of non-structural elements especially on roof depends on the acceleration response at their attached positions.

For approximate fragility analysis, two parts are classified globally. One is the roof including structural members and ceilings on the dome. The other one is the wall composed of braces and wall finishing. The criteria for the global damage to the structural members and ceilings on roof are assumed as given in Table 3.a. The damage of roof is assumed to be represented by the responses at Node a, shown in Figure 3. As the critical terms to judge the damage,

the maximum vertical displacement at Node a, δ_{DV}, is first adopted, since the displacement at this point will be estimated dominant under earthquake motions. And also, maximum vertical acceleration response A_{DV} and maximum horizontal acceleration response A_{DH} are adopted for judging the damage to ceilings on the roof. Based on an assumption without precise reasoning since such reasoning will be the research problem in the next step, critical values of $\delta_{DV1}=12cm$, $\delta_{DV2}=18cm$, $A_{DH1}=A_{DH1}=800cm/s^2$, and $A_{DH2}=A_{DV2}=1600cm/s^2$ are assigned as given in Table 3.a. The vertical displacement of $\delta_{DV2}=18cm$ at Node a in Figure 3 seems to correspond to the ratio of 18cm/ℓ_b, almost 1/100 as the relative vertical drift.

The criteria for the global damage of wall, braces and finishing within wall, are assumed as given in Table 3.b. The damage is assumed to be represented by the maximum sway drift, δ_{SH} , at the wall top. Since the height of wall is relatively low, the damage due to accelerations is assumed negligible, and the damage to wall finishing is judged here based on the maximum sway. Also based on an assumption, often adopted in Japan without precise reasoning, critical values of $\delta_{SH1}=2.5$cm and $\delta_{SH2}=5.0$cm are assigned as given in Table 3.b just as assumption. The value of $\delta_{SH2}=5.0$cm corresponds to one hundredth the wall height, $h/100$.

Table.4a Rule of Fragility: Evaluation Type Ev1

Walls and braces / Dome and ceilings		Damage intensity		
		A	B	C
Damage intensity	A	0	0.50	1.00
	B	0.50	0.50	1.00
	C	1.00	1.00	1.00

Table.4b Rule of Fragility: Evaluation Type Ev1

Walls and braces / Dome and ceilings		Damage intensity		
		A	B	C
Damage intensity	A	0	0.50	1.00
	B	0.50	0.75	0.50
	C	1.00	1.00	1.00

4.2 Rules for Fragility of the Total Building

An assumption is made here that the total fragility, defined here as the ratio of accumulated damage to the complete damage, is counted by the combination between the damages to roof and wall. The event tree is shown as a rule assumed in Table 4. Two cases are applied for comparison to see how the results will be different based on the two rules. The difference of rule is only the combination of intensity B of wall and braces and intensity B of dome and ceilings.

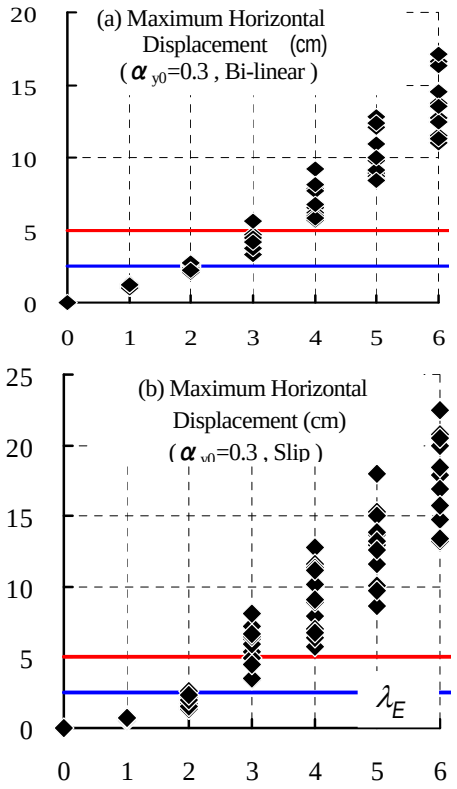

Figure 4 Comparison of Displacements of Substructure

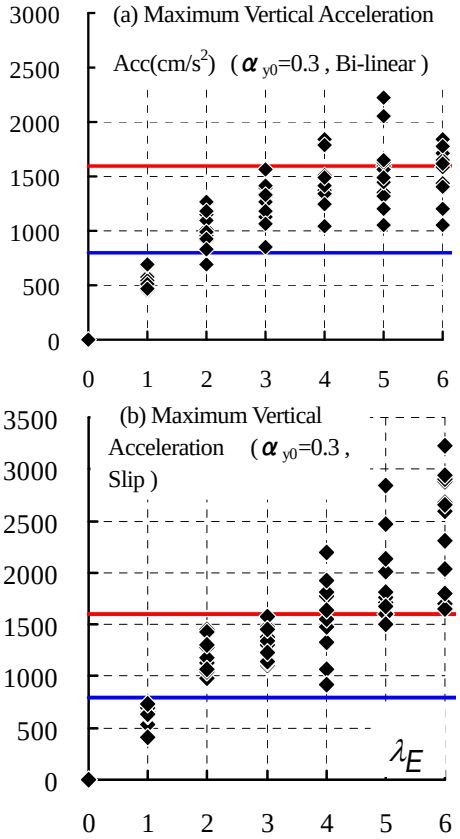

Figure 5 Comparison of Acceleration of Roof

5. EXAMPLES OF EVALUATED FRAGILITY

5.1 Comparison of Responses of Buckling Restrained Brace with Slip Type Brace

Comparison of responses of dome is shown in Figures 4 and 5 only for dome responses and for yield base shear coefficient $\alpha_{y0} = 0.3$.

Although enough data are not shown in figures for the horizontal displacement and accelerations at the top of column, a tendency is found that the horizontal displacement, shown in Figure 4, grows lager than $h/100$ in both cases of slip type and bi-linear type when the earthquake intensity crosses over 3. Additional observation is found to show that the horizontal displacement is a little lager in case of slip type than bi-linear type.

Also, a large difference is found in the responses of horizontal acceleration at the top of columns, although data not shown in figures here. Within the range less than $\lambda_E = 2$, not so much difference is found, however, the response grows rapidly larger in case of slip type brace once the earthquake intensity exceeds $\lambda_E = 3$.

As for the vertical displacement at Node a, no difference is found between two brace types, except for the earthquake intensity beyond $\lambda_E = 5$. When, in case of slip type brace, the earthquake intensity exceeds the level of $\lambda_E = 5$, the structural members experience the critical point marked with a circle in Figure 3 and the dome tends to be displaced largely. In case of bi-linear type brace, the vertical displacement is not so increased proportionally to the input earthquake intensity. This will be the effects of energy absorbing capacity of the buckling restrained brace. In this case, the dome of slip type brace will experience a large damage if the input earthquake grows beyond ultimate limit level of $\lambda_E = 5$.

Figure 5 shows a similar tendency found in the response of vertical acceleration, where vertical acceleration responses grow largely in case of slip type brace over the range beyond $\lambda_E = 4$. If an assumption is made that ceilings on the roof is very sensitive to fall down, the dome of slip type brace will experience a larger damage than that of bi-linear type brace.

From these results, one may expect that both domes with different braces will experience some damage once the intensity exceeds $\lambda_E = 2$, and that the damage will be amplified much larger over the range of $\lambda_E = 3$, and that finally the dome will be almost damaged when the earthquake intensity exceeds the value of $\lambda_E = 4$. The damage is reflected on the fragility of structures shown in Figures 6 to 10.

5.2 Comparison of Damage Depending on Brace Types

Examples of damage distribution are given in Figures 6 and 7, where the damage is counted as the accumulated number experiencing the damages classified in Table 3. For one dome, twelve earthquake motions are applied in same earthquake intensity. Accordingly, the total number is 12 in every case in Figures 6 and 7. Comparison between Figures 6 and 7 suggests that damage in case of buckling restrained brace will be smaller than in case of slip type brace. This tendency becomes clearer once the earthquake intensity increases. This tendency would be increased if the effect of the acceleration response at the column top would have been reflected to damage evaluation of substructure, since the acceleration response, not illustrated here, at the column top is much larger in case of slip type brace than bi-near hysteresis for buckling restrained brace.

6. FRAGILITY EVALUATED BASED ON THE PROPOSED RULE

Figures 8 to 10 show the fragility evaluated based on the rule defined in Table 4. For one earthquake intensity, one obtains twelve results for fragility based on the rule in Table 4: some have a value of 0.0, some have 0.5, and some have 1.0 among the twelve fragility results. Using the twelve results an average fragility is calculated as a mean value and it is plotted as a mean value in Figures 8 to 10. However the standard deviation in terms of intensity λ_E is abbreviated in the figures. If the fragility is zero in Figures 8 to 10 for a certain earthquake intensity, it means that the structure will survive earthquake without any damage, and on the other hand, if the fragility is 1.0 for a certain earthquake intensity, it means that the structure will reach a complete damage and be of no use after earthquake. If the fragility is 0.5 for an intensity, it means that probability for surviving will be half after earthquake.

Comparison of Figures 8 and 9 shows that the fragility changes dependent on the rule, EV1 or EV2 in case of buckling restrained braces, and that, on the other hands, no difference is found in case of tension-active brace. In Figure 8 the rule of EV2 increases the fragility due to combined effects from roof and wall. From these results, it might be ascertained that, if based on the rule in Figure 4, the fragility is almost zero for the intensity of $\lambda_E = 1$ and increases sharply up to complete damage at the intensity of $\lambda_E = 4$. Comparison of Figures 8 and 10 reveals a tendency that the dome with slip type brace is more fragile than the buckling restrained brace of bi-linear hysteresis. However the difference will be judged not so clearly large if based on the rule of Table 4. The result of fragility depends on the rule for judging damage, and the results change once a different rule is adopted. At present the rule of Table 4 is assumed presumably for an instant use, accordingly it is necessary to say that more realistic data is required for more realistic and precise evaluation of the fragility.

One important observation in this example is that most of the fragility to roof is occupied by ceilings on the roof irrespective of the brace types, since the vertical and horizontal responses are grown up over 1600cm/s^2 beyond $\lambda_E = 4$. This means, if damage should be reduced, that ceilings should be designed with more resistance against accelerations than those assumed in this study.

Once such fragility is obtained, annual expected total loss will be obtained if seismic activity at the site is connected with the fragility evaluation [5]. This kind of study seems to be urgently required in Japan based on data reflecting real damages and observed functional loss of structures.

6. CONCLUSIONS

The present study proposed just a simple procedure to evaluate the seismic fragility of dome. An example for calculating fragility was presented considering a simple rule for judging damage to each part of building. At present the proposed rule was assumed presumably in this study for an instant use, accordingly it is surely necessary to say that more realistic data is required for more realistic and precise evaluation of the fragility. Once such realistic fragility is possible, this kind of study will surely provide measures for a concept of new and to-be-retrofitted lattice domes, since

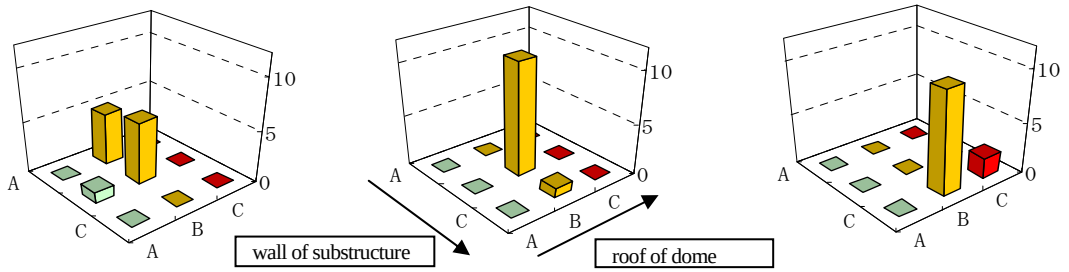

(a) $\lambda_E = 2$ (b) $\lambda_E = 3$ (c) $\lambda_E = 4$

Figure 6 Damage distribution (α_{y0}=0.3, bi-linear)

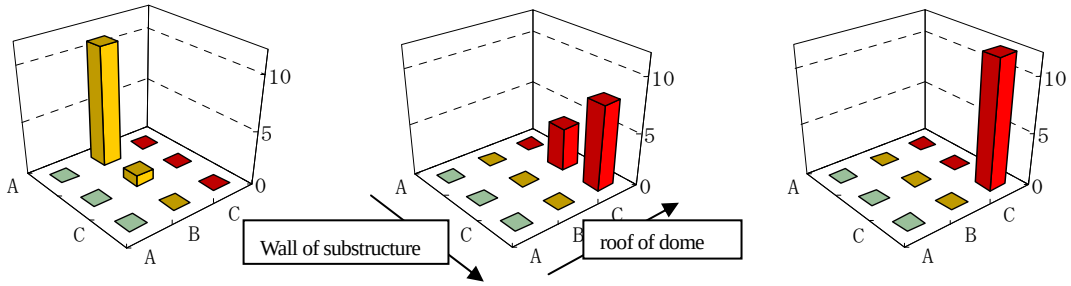

(a) $\lambda_E = 2$ (b) $\lambda_E = 3$ (c) $\lambda_E = 4$

Figure 7 Damage distribution (α_{y0}=0.3, Slip)

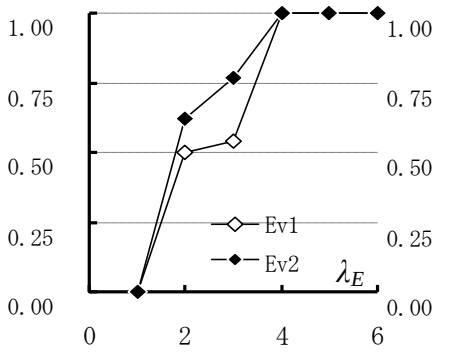

Figure 8 Fragility of dome for (α_{y0}=0.3,bi-linear)

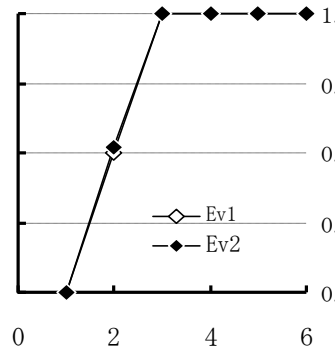

Figure 9 Fragility of dome for (α_{y0}=0.3, Slip)

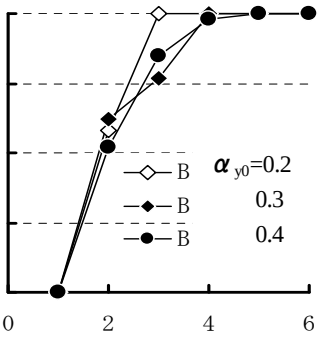

Figure 10 Fragility of dome for (bi-linear): Ev1

nowadays very effective FEM tools for structural dynamics as well as management analysis tools have been developed in direct use.

Acknowledgements:

The first author is grateful for the partial supports as a Grand-in-Aid under grant No.(C)18560546 given by the Ministry of Education, Science, Sports and Culture of Japanese Government as well as the numerical assistance through Grid Computing by Prof. R Shibata.

References:

[1]Shimokita Dome : http://www.taisei.co.jp/giken/report /01_2003_36/B036_008.HTM

[2]Federal Emergency Management Agency : HAZUS99 technical manual, washington, D.C.,NY,1999

[3] Mamoru MIZUTANI: Basic methodology of a seismic risk management procedure, ICOSSAR'97, Vol.3,pp.1581-1588

[4] M. HOSHIYA, T. NAKAMURA, T. MOCHIZUKI: Stochastic asset processing with seismic hazard risk, Journal of Engineering Mechanics, Vol.130, No.7, 2207, pp.780-785

[5] Shoji NAKAZAWA, Shiro KATO, Kenta HIRANO: Methodology to evaluate the effectiveness of retrofit proposal based on the discounted cash flow method, IASS 2007 Symposium, PN368, Venice, Italy, 2007.12

[6] Shiro Kato, Shoji Nakazawa: Dynamic collapse characteristics of single layer reticulated domes with substructure absorbing seismic energy due to strong earthquake motions, J. Struct. Constr. Eng., Architectural institute of Japan, No.548, pp.81-88, Oct., 2001

[7] Ministry of Land, Infrastructure and Transport:Notification No.1457-2000, Technical Standard for Structural Calculation of Response and Limit Strength of Buildings, 2000 (in Japanese)

[8] Shiro Kato, Shoji Nakazawa, Keita Saito: Estimation of Static Seismic Loads for Latticed Domes Supported by Substructure Frames with Braces Deteriorated due to Buckling; Journal of The International Association for Shell and Spatial Structures :IASS, Vol.48 No.2, pp.71-86, 2007.8

Sixth International Conference on Urban Earthquake Engineering
March 3-4, 2009, Tokyo Institute of Technology, Tokyo, Japan

DAMAGE IN EARTHQUAKES AND DYNAMIC CHARACTERISTICS OF HANGING CEILING SYSTEM IN JAPAN

Shojiro Motoyui[1)], Yasuaki Satoh[2)]

1) Associate Professor, Department of Built Environment , Tokyo Institute of Technology, Japan
2) Graduate Student, Department of Built Environment , Tokyo Institute of Technology, Japan
motoyui@enveng.titech.ac.jp, yasuaki.s.aa@m.titech.ac.jp

Abstract: The falling damage of hanging ceilings occurred during the recent earthquakes. The reason why the ceilings fell down has not been clear. In this paper, the serious damage examples are introduced. It is clarified that unique metal parts used at the connection of furring members in the Japanese style of ceiling caused the falling through the observation of the damage condition in the examples and the shaking table test to simulate the falling behavior of a ceiling Next, the mechanical property of the connection parts is clarified experimentally. Finally, we extend the master-slave node model by Crisfield to the contact and detachment behavior of clips and show the validity the present numerical method via the comparison with experimental results.

1. INTRODUCTION

In the recent earthquakes, some serious damage and falling down of ceilings occurred while the measured acceleration was not so great. Actually no damage of building structures was observed. The falling down of ceiling may injure persons or cut off an evacuation route. After the recent earthquakes, the Ministry of Land, Infrastructure, Transport and Tourism (MLIT) announced some technical advices. This is not a standard but only a technical advice. However, if an engineer will not obey the advice and his ceiling will fall down, he may be called to account for the falling. It is noted that the technical advices by the MLIT have not been verified. The reason is that it has not been known why such damage of ceiling occurred during earthquakes. Namely, the mechanism of how the ceiling falls has not been clear. And, mechanical properties of steel members composing ceiling have not been clear. Furthermore the calculation method for the dynamic behavior of ceiling has not been developed. In short, the structural characteristics of this type of ceiling had not been known at all. Then, nobody could judge the validity of the technical advices by MLIT.

In this paper, we describe the detail of falling of ceiling in recent earthquakes in Section 2. The shaking table test by our research team for the falling phenomenon of ceiling will be explained in Section 3. We find out a process for a ceiling to fall during an earthquake through the observation of the shaking table test. Particularly, it becomes obvious that the falling is not accident but inevitable phenomenon and the Japanese style of ceiling involves the possibility of falling during earthquakes. In Section 4 and 5, we will discuss the mechanical characteristics through experimental study for steel members in the Japanese style of ceiling and numerical method for the damage of connection parts in the ceiling.

2. DAMAGE OF CEILING IN JAPAN

2.1 Hanging Ceiling in Japan

In Japan, hanging ceiling style is classified into two types. One is a semi-prefabricated type and it is similar to a ceiling style in the U.S. Another one is a site-built-up type in which unique metal connection parts are used. The latter one is the most popular ceiling type in Japan and is a target in this paper. The ceiling is composed of steel members and plaster boards as shown in Fig.1. The plaster board is attached to a steel member called "M-bar". The M-bar is connected to a steel member which has C-shape cross section and is called "Channel". The Channel is suspended by rods. Each steel member is connected with unique metal parts called "Hanger" and "Clip". See Figure 1.

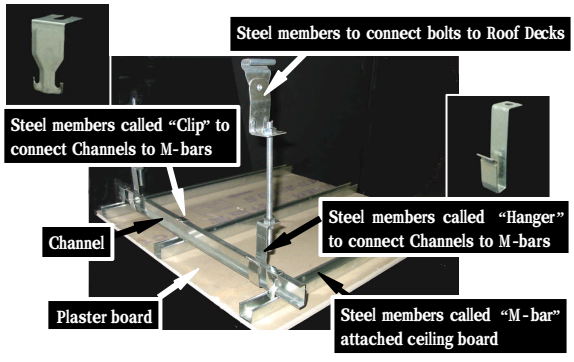

Figure 1 Japanese style of ceiling

. The system has high workability so that it is widely used in Japan. The weight of the ceiling system is about 150N/m^2. Generally speaking, the ceiling system has enough strength to carry self-weight.

After the Geiyo earthquakes 2001, MLIT announced the technical advice. Figure 2 shows the concept of technical advice. The left hand side diagram shows the traditional style of a suspended ceiling and the right hand side diagram shows the recommendation style by MLIT. MLIT recommended that spacing between ceiling and walls surrounding the ceiling should be set and diagonal bracing members should be attached not to swing the ceiling.

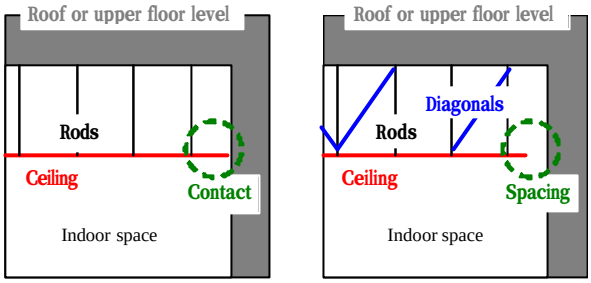

(a) Traditional (b) Recommendation

Figure 2 Traditional and recommendation style by MLIT

2.2 Falling of Ceiling during Earthquake in Japan

These are falling examples of suspended ceiling in recent earthquakes as shown in Table 1. Particularly, Kushiro airport terminal building in 2003 and Sendai indoor swimming pool in 2005, the damage in two cases are serious. The most part of ceiling fell down though measured acceleration values are not so great.

Table 1 Damage of ceiling in recent earthquakes

2001	Geiyo Earthquake	Ceiling boards fell at Gymnasiums and Music halls
2003	Tokachi-oki Earthquake Max.Acc. 200cm/sec^2	Ceiling system fell at Terminal Building and Control Tower of Kushiro Airport
2005	Earthquake with epicenter at Miyagi Prefecture Max.Acc. 260cm/sec^2 in Sendai	Ceiling system fell at Sendai indoor swimming pool
2007	Noto Peninsula Earthquake	Ceiling boards fell at Elementary School's Gymnasium

Figure 3 is the plan of Kushiro airport terminal building. The shadow part shows the area where suspended ceiling fell down. Photographs 1 show the damage at Kushiro Airport Terminal Building. The characteristics of this building and ceiling are as followings:

1. The entrance hall where the ceiling fell down, has the size of 36m x 18m. The area of ceiling is 648m^2. Total weight of ceiling is about 95kN.
2. The roof structure has the curvature in the longer direction. And the ceiling is attached to the roof along the feature of roof.
3. The ceiling has a step in the shorter direction. The steel members to keep the feature of step are arranged at the step.
4. Diagonal bracing members are set according to the technical advice by MLIT in the both direction.

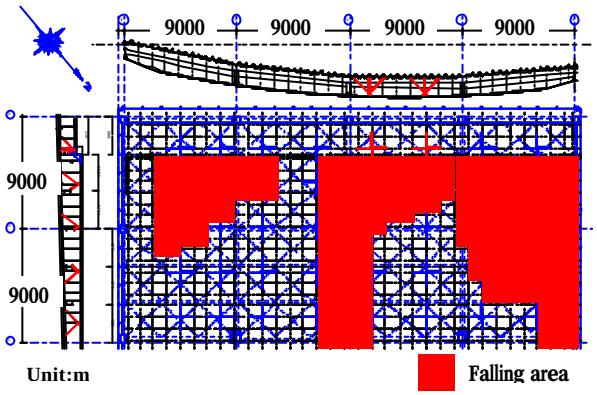

Figure 3 Falling are at Kushiro airport terminal building

In this case, though diagonal bracing members had been set in the ceiling, the half area of ceiling fell down. The

(a) View of the original ceiling level

(b) View of the floor level

Photograph 1 Kushiro airport terminal building

reason why the ceiling fell is the difference between the horizontal rigidity at the upper level of the step and that at the lower level. The unbalance of the rigidity causes that the stress under horizontal load is concentrated on a part of steel furrings near the step in the ceiling. This is the judgment by MLIT after the present falling phenomenon occurred. We also guess the judgment is correct. But the stress concentration is only a trigger of the falling. It is not clear why such a large-scaled falling happened.

Figure 4 shows the plan of the Sendai indoor swimming pool. The Sendai Indoor swimming pool building has the following characteristics:

1. The building has a circular plan of 60meters in diameter. The area of indoor swimming pool is about 1/3 of the total ones.
2. The roof feature is a shallow spherical dome which is composed with curved girders arranged in the radial direction.
3. The ceiling surface is flat. As a result, the length of rods to suspend the ceiling is fairly different at the position in the ceiling area.
4. This ceiling also has a step in the ceiling surface. But any especial members to keep the shape of the step were not arranged.
5. No diagonal bracing members were set.

In this case, the small area shown by shadow area was only remained. Photographs 2 show the damage in the swimming pool. Unfortunately, the falling happened in the summer holiday, so there were many visitors and several persons were injured. The reason why such a large-scaled falling occurred is uncertain while MLIT decided the lack of diagonal bracing caused the falling.

In the two cases of Kushiro airport terminal building and Sendai indoor swimming pool, the pattern of damage is coincident and the direct cause is considered to be the detachment of clips which is a connection metal part between M-bar and Channel since Channels kept the original position as shown in Photographs 1(a) and 2(a) and M-bars fell down together with ceiling boards as shown in Photographs 1(b) and 2(b). However, clips generally has an strength enough to support the weight of ceiling. Some researchers or engineer's opinions on the falling of the ceiling are various. These opinions summarized as

A. The large-scaled falling is not inevitable but accident. At least, the bad construction process caused falling.
B. The great U.D. acceleration acted on the ceiling surface since the shape of roofs was not flat.
C. The ceiling impacted against the wall surrounding ceiling.

3. Shaking Table Tests

3.1 Outline of test

To confirm whether the falling behavior is inevitable or not, we executed a shaking table test. The ceiling test specimen size is 4.5m by 4.5m. It is composed with 5

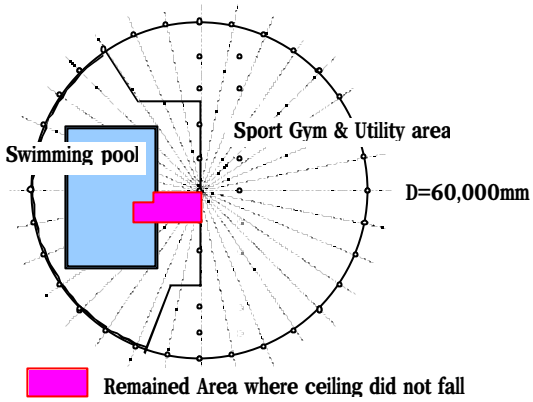

Figure 4 Sendai indoor swimming pool

(a) View of the original ceiling level

(b) View of the floor level
Photograph 2 Sendai indoor swimming pool

channels and 13 M-bars in Figure 5. According to the manual by Architectural Institute of Japan and the technical advice by MLIT, 8 diagonal bracing members are set. The El-Centro NS,EW and UD are simultaneously applied for the input acceleration with maximum acceleration set to be 1.0 G.

3.2 Findings from our experiment.

The experimental result can be summarized as following.

1. The falling behavior can be simulated with a

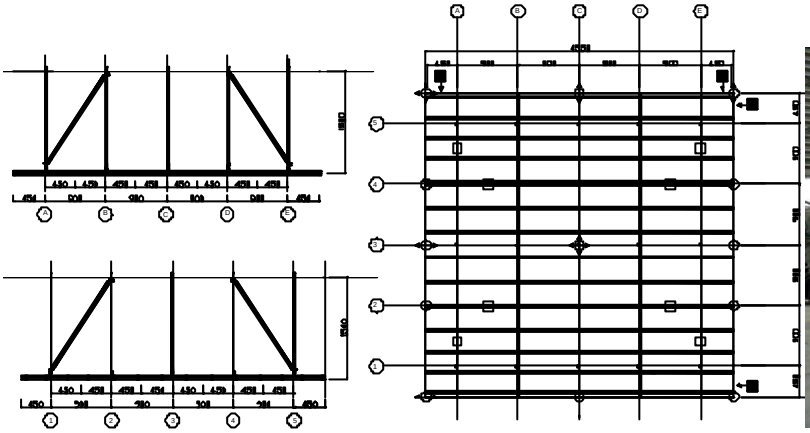

Figure 5 Test specimen for shaking table test

Photograph 3 Test apparatus

experiment. The whole of ceiling fell down during shaking though the present test specimen was built up according the standard erection manual. The matter means that the falling behavior is not accident but it is inevitable. Namely, the present ceiling system contains the possibility of falling down during an earthquake.

2. The falling behavior can be simulated with a experiment. The whole of ceiling fell down during shaking though the present test specimen was built up according the standard erection manual. The matter means that the falling behavior is not accident but it is inevitable. Namely, the present ceiling system contains the possibility of falling down during an earthquake.
3. Next finding is that we have made sure the falling process of ceiling.

< Falling process >

Photographs 4 show the falling process of ceiling during shaking.

Slipping phase

A few Clips near diagonal bracing members begin to slip. A Clip is connection metal parts between M-bar and Channel. In the case of existing bracing members, the horizontal load by shaking is transmitted to the bracing members. As a result, stresses are concentrated at a few clips near the bracing members and the clips slip.

Detachment phase

Then, clips slipping near the diagonal bracing members are detached because the slip behavior is not smooth.

Chain of Detachment phase

If the ceiling state satisfies any condition, which has not been determined, ceiling damage will make progress and reach to the chain of detachment phase.

Falling phase

Then, the whole of ceiling falls in an instance as soon as the condition of ceiling reaches the situation that remained Clips can not support the weight of ceiling.

If the above falling process is correct, Clips should be

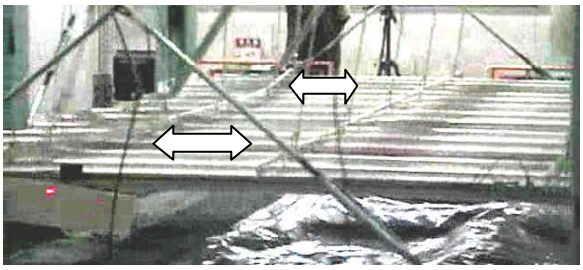

(a) Slipping phase

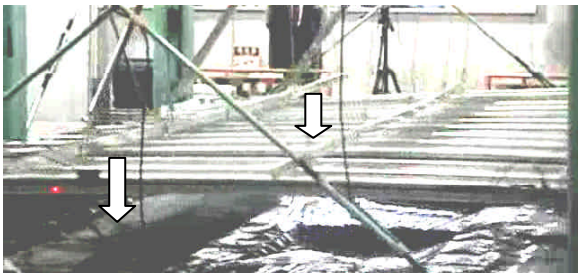

(b) Detachment phase

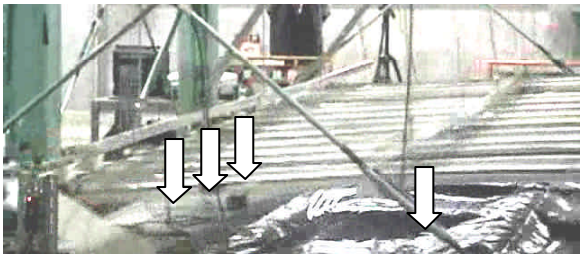

(c) Chain of Detachment phase

(d) Falling phase

Photograph 4 Falling process

detached only in the horizontal force. Furthermore, we should make sure what is the condition for a clip to slip and to be detached. So, we planed the performance tests for the connection by clip between a Channel and M-bar.

4. Mechanical Property of Connection with Unique Metal Parts

Figure 6 is test setting and test specimen for Clip connection. The connection with Clips is two types. One is a front connection type as shown in Photograph 5(a). Another one is a back connection type as shown in Photograph 5(b). The two types of connection are used by turns. Using by turns makes Channels held on tight M-bars. Loading conditions are considered to be two cases of the vertical and horizontal force.

Figure 7(a) is the Load-displacement curve for vertical loading test of the front type of Clip connection. As we mentioned before, the strength of the Clip connection to vertical load is more than enough to suspend ceiling since the vertical load per one clip is only about 40N. The matter means that it is difficult to consider that the UD acceleration in earthquakes caused the falling of the ceiling which is constructed in the regular way. But, the strength to the vertical load depends on the spacing of rods hanging Channels. In this experiment, we assumed that a Channel was suspended with rods by 0.9m. The spacing of 0.9m is the regular one. It is obvious that the strength is smaller as the spacing becomes longer because the Channel may easily deform in the condition of the lateral torsion. Therefore, the spacing is very important to get the strength of supporting the ceiling.

Figure 7(b) is the load-displacement curve for horizontal loading test. The characteristics of a clip become entirely different corresponding to loading direction. For the direction facing a Channel, the clip easily slips. The strength at beginning to slip is 100N. For the opposite direction, the clip does not slip and resist the horizontal load. Finally, the clip is detached at about 260N. The most important finding is that a clip can be detached only by the horizontal load. The phenomenon may cause the ceiling fall.

5. Numerical Simulation of Clip Connection

5.1 Numerical method

Next, we show the numerical simulation of the connection experiment. The slipping and detachment behaviors of a clip are important and should be considered in a numerical simulation of the ceiling damage. We introduced so-called Master-Slave model by Crisfield in order to express slipping and detachment. See Figure 8. In this model, consider relative displacement between the master node and slave node and inner force corresponding to relative displacement. If the inner force is released, the slave node slides in the direction of the released inner force. If all of inner forces are released, the slave node is detached.

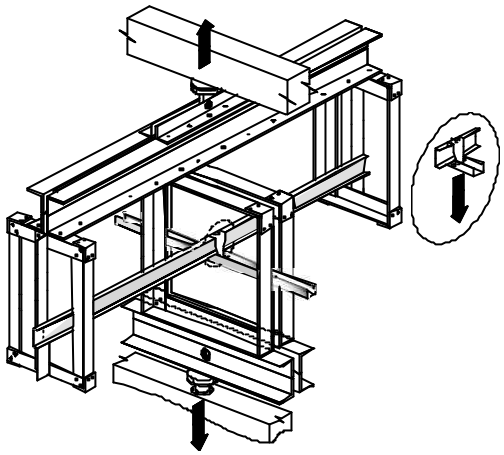

Figure 6 Clip connection Test

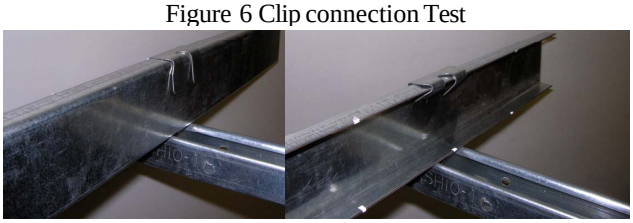

(a) Front connection (b) Back connection
Photograph 5 Clip connection Type

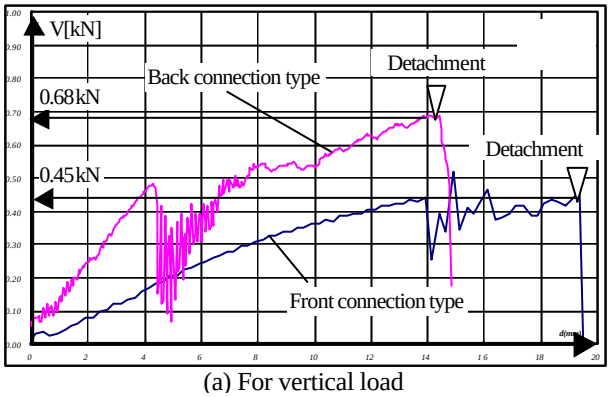

(a) For vertical load

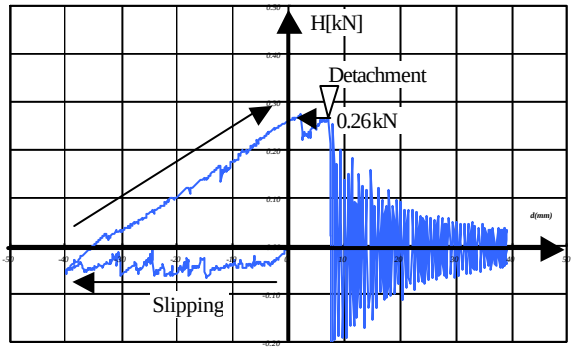

(b) For horizontal load
Figure 7 Load-displacement curve

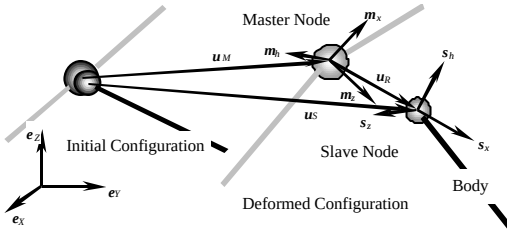

Figure 8 Concept of Master-Slave node

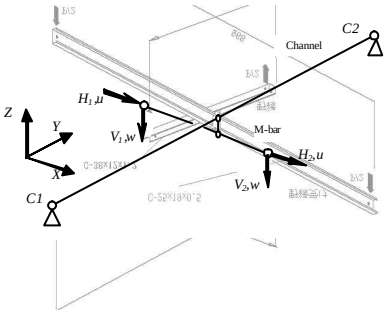

Figure 9 Numerical model

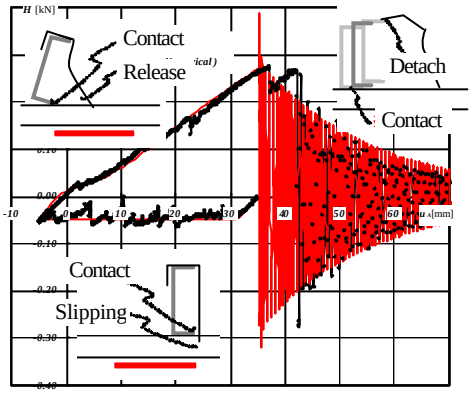

(a) Whole of result

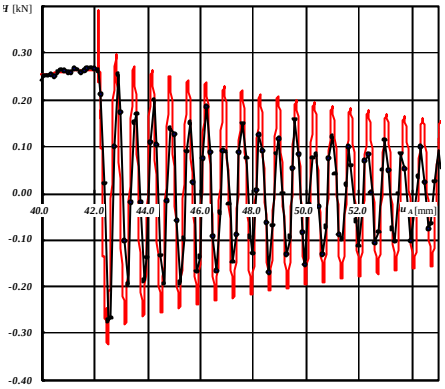

(b) After detachment

Figure 10 Load-displacement curve

The analysis is calculated as a dynamic problem to solve the dynamic behavior after detachment of a Clip though the loading is static at the experiment. The Hilber-Hughes-Taylor α method ($\alpha = -0.05$) is used as a time integral scheme in the present analysis. Time interval is 1.0×10^{-3}sec up to the detachment, 1.0×10^{-6}sec after the detachment.

5.2 Numerical model and result

Figure 9 shows the numerical model macroscopically. The model includes a few dummy elements to represent the contact behavior, slipping and detachment behavior. The round-house type of stress-strain curve is applied for the material property of a Clip to consider the cold metal form process of a Clip.

The numerical result is shown in Figure 10. The bold line is the experimental result and another line is the present solution. The present result agrees with the experimental result in all situation of slipping, resisting and post-detachment. Then, we can simulate the non-linear behavior of a ceiling including the detachment of a Clip numerically.

6. CONCLUSIONS

We showed the damage examples of the Japanese style of ceiling by earthquakes and clarified the falling condition in those examples was similar. For such damage, we verified that the falling behavior is an inevitable phenomenon through our shaking table test. We found out the process to the falling. Next, the mechanical characteristics of a Clip connection between furrings of a ceiling were examined. As a results, the existence of the slipping behavior and detachment behavior at the Clip connection was found out. Consequently, we showed the complicate behavior of a Clip may cause the falling phenomenon.

References:

Crisfield, M.A. (2000), "Non-linear Finite Element Analysis of Solids and Structures Volume 2 Advanced Topics", John Wiley & Sons Inc.

Sixth International Conference on Urban Earthquake Engineering
March 3-4, 2009, Tokyo Institute of Technology, Tokyo, Japan

SEISMIC RESPONSE EVALUATION OF LATTICE ROOFS WITH SUBSTRUCTURES

Toru Takeuchi[1)], Toshiyuki Ogawa[2)], and Tomohiko Kumagai[3)]

1) Associate Professor, Department of Architecture and Building Engineering, Tokyo Institute of Technology, Japan
2) Professor, Department of Architecture and Building Engineering, Tokyo Institute of Technology, Japan
3) Assistant Professor, Department of Architecture and Building Engineering, Tokyo Institute of Technology, Japan
ttoru@arch.titech.ac.jp, togawa@arch.titech.ac.jp, kuma@arch.titech.ac.jp

Abstract: Seismic response of raised lattice shell roofs with substructures is complicated, because these roofs have large numbers of parallel vibration modes, and their amplitude changes drastically along the rise/span ratios and the stiffness ratios between domes and substructures. Under limited condition, however, their response characteristics are considered to become relatively simple. In this paper, simple response evaluation method of domes and cylindrical shell roofs with substructures are proposed using response amplification factors approach. Firstly, the response characteristics of raised roofs with various rise/span ratios and substructure stiffness are numerically discussed with simple arch model. Then response of lattice domes and cylindrical shell roofs are investigated, and simple acceleration response evaluation method using response amplification factors is delivered. The proposed method can be used as equivalent static loads for design, and compared with precise analyses with CQC method.

1. INTRODUCTION

Raised dome or shells under horizontal seismic input are known to cause vertical response together with horizontal response, and applying normal horizontal seismic loads are often dangerous in seismic design. (Figure1). Their characteristics are quite complicated because such roofs normally have large numbers of parallel vibration modes. Such vibration modes are randomly oscillated by their supporting structures, and their amplitudes change drastically along the relationship between the roofs and supporting substructures. To predict these response, large numbers of researches have been carried out. Kato and Nakazawa (2003, 2006) were modeled dome roof structures in parallel mass model, indicated the numbers of oscillated modes are reduced where the out-of-plane stiffness are increased, and proposed the ultimate-state design method using the push-over analyses. For cylindrical shell roofs, S.Yamada et.al. (2006) has analyzed large numbers of cylindrical shells, and proposed equivalent static loads for design using maximum strain-energy concept. Such equivalent static loads are quite useful for practical design. However, the effects of substructures on the equivalent static loads are yet made clear in those studies.

For the effects of substructures on roof response are primarily studied by M.Yamada (2000, 2001) using double degree of mass model. They also proposed the equivalent static loads for arches using parametric time-history analyses, however, effects of rise/span ratio or relationship between substructures were not clearly explained.

In this paper, the basic response characteristics of raised roof are explained using simple arch model. Their maximum responses are expressed by simple equations with parameters of half subtended angle and own-period ratio between the roof and substructures. With these studies, response evaluation method using amplification factors are proposed for spherical domes and cylindrical shells, followed by verification of their accuracies where they are used as equivalent static loads.

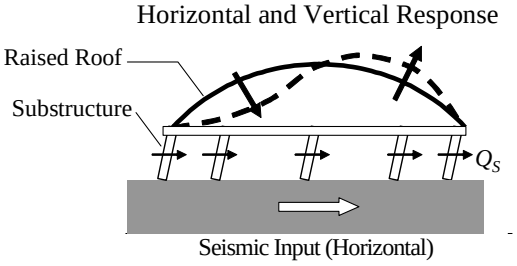

Figure 1 Seismic Response of Raised Roof

2. RESPONSE EVALUATION WITH SIMPLE ARCH MODEL

Firstly, response characteristics of raised roofs are explained theoretically using simple arch model as shown in Figure 2. This model has 3 spring hinges and rigid axial stiffness. From the geometric relationship in Figure 2, the asymmetrical deflection mode vector is expressed as the following.

$$\begin{aligned}\mathbf{u}^T &= [\delta_{1x}, \delta_{1y}, \delta_{2x}, \delta_{2y}, \delta_{3x}, \delta_{3y}] \\ &= u\left[\sin\frac{3}{4}\theta, -\cos\frac{3}{4}\theta, 2\sin\frac{\theta}{4}, 0, \sin\frac{3}{4}\theta, \cos\frac{3}{4}\theta\right]\end{aligned} \quad (1)$$

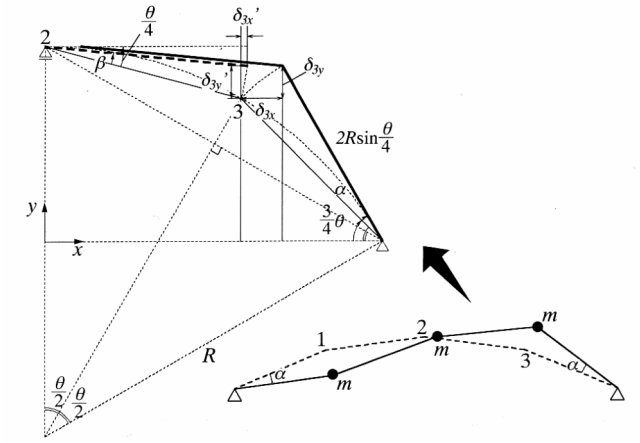

Figure 2 3-hinged Arch Model

Where, $u=2R\alpha\sin(\theta/4)\cdots$(1a). θ is half subtended angel and radian unit should be used in all the following equations. Participation factor for this mode β_{R1}, and effective mass M_{R1} become as follows.

$$\beta_{R1}=\frac{\mathbf{u}^T\mathbf{m}\mathbf{I}_x}{\mathbf{u}^T\mathbf{m}\mathbf{u}}=\frac{2\left(\sin\frac{3}{4}\theta+\sin\frac{\theta}{4}\right)}{u\left(2+4\sin^2\frac{\theta}{4}\right)}=\frac{\sin\frac{3}{4}\theta+\sin\frac{\theta}{4}}{u\left(1+2\sin^2\frac{\theta}{4}\right)} \tag{2}$$

$$M_{R1}=\frac{(\mathbf{u}^T\mathbf{m}\mathbf{I}_x)^2}{\mathbf{u}^T\mathbf{m}\mathbf{u}}=\frac{2m\left(\sin\frac{3}{4}\theta+\sin\frac{\theta}{4}\right)^2}{1+2\sin^2\frac{\theta}{4}} \tag{3}$$

Where, $\mathbf{m}$ is mass matrix whose diagonal elements are $m_{ii}=[m,m,m,m,m,m]$, $\mathbf{I}_X$ is vector whose horizontal elements are 1 and other elements are 0. The rest of effective mass M_{R2} can be calculated by removing M_{R1} from the total mass $M_R=3m$. M_{R2} is given by all other vibration modes with axial deformation, which become identical to the ground motion because the axial stiffness is infinity.

$$M_{R2}=M_R-M_{R1}=3m\left(1-\frac{2m\left(\sin\frac{3}{4}\theta+\sin\frac{\theta}{4}\right)^2}{3\left(1+2\sin^2\frac{\theta}{4}\right)}\right) \tag{4}$$

When θ decreases, M_{R2} increases compared with M_{R1}, and M_{R2} become 100% when θ=0. Maximum response $\boldsymbol{a}_R$ is estimated by calculating SRSS between the vibration mode shown in Figure 2 and ground motion.

$$\begin{aligned}\boldsymbol{a}_R&=[a_{1x},a_{1y},a_{2x},a_{2y},a_{3x},a_{3y}]^T\\&=\sqrt{(S_{AP}\beta_{R1}\mathbf{u})^2+\left(S_{Ag}\mathbf{I}_x\frac{M_{R2}}{M_R}\right)^2}\end{aligned} \tag{5}$$

For understanding the characteristics of response, normalized seismic spectrum is useful for verification. In this paper, artificial seismic spectrum as shown in Figure 3 is defined as BRI-L1 and used for evaluation. In Figure 3, earthquake records normalized their maximum velocity as25cm/sec are also shown. This figure shows the BRI-L1 almost covers

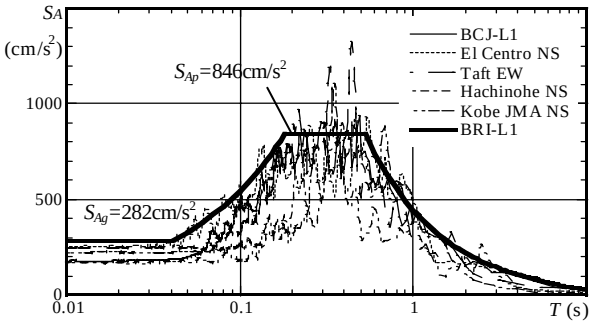

Figure 3 Design Acceleration Spectrum

these earthquake records. BRI-L1 is given in the following equations.

$$S_A(T)=\begin{cases}200D_h & (0\le T<0.04)\\ 200D_h(T/0.04)^{\log 3/\log 4.5} & (0.04\le T<0.18)\\ 600D_h & (0.18\le T<\pi/6)\\ 100\pi D_h/T & (\pi/6\le T<5)\\ 100\sqrt{5}\pi D_h/T^{3/2} & (5\le T<10)\end{cases} \tag{6}$$

$$D_h=\sqrt{(1+97h_0)/(1+97h)}=1.411 \quad (h_0=0.05,\ h=0.02)$$

Eq.(5) is based on the condition that the natural period of asymmetrical vibration mode is placed in the constant-acceleration zone S_{Ap} in Figure 3. Response amplitude factor is estimated as $\boldsymbol{a}_R/S_{Ag}$ as following, with the condition of $S_{Ap}=3S_{Ag}$.

$$\begin{aligned}\frac{\boldsymbol{a}_R}{S_{Ag}}&=\sqrt{\left(\frac{S_{Ap}}{S_{Ag}}\beta_{R1}\mathbf{u}\right)^2+\left(\mathbf{I}_x\frac{M_{R2}}{M_R}\right)^2}\\&=\sqrt{(3\beta_{R1}\mathbf{u})^2+\left(\mathbf{I}_x\frac{M_{R2}}{M_R}\right)^2}\end{aligned} \tag{7}$$

Calculated amplification factors by eq.(7) are shown in Figure 4, compared with M.Yamada's proposal (2000) and results of response spectrum evaluation with CQC method which is confirmed to be consistent with time-history analyses using detailed arch roof models.

Effects of substructures are estimated using SDOF model and equivalent DDOF model as shown in Figure 5(a) and (b), respectively. Maximum acceleration obtained from response spectrum and SDOF model is defined as A_{eq}. Also in DDOF, defining effective mass of the roof and the substructure as $M_{Req}=M_{R1}$, $M_{Seq}=M_S+M_{R2}$ (where, $M_{R1}+M_{R2}=M_R$), maximum response of DDOF is calculated by SRSS of two modes obtained by eigen mode analysis, as follows.

$$\begin{aligned}\boldsymbol{a}_2&=[A_S,A_R]^T\\&=\sqrt{(S_{A1}\beta_1\mathbf{u})^2+(S_{A2}\beta_2\mathbf{u})^2}\end{aligned} \tag{8}$$

Maximum response of upper mass A_R is obtained from Eq.(8). Then S_{Ap} in Eq.(7) is replaced by A_R, and S_{Ag} is replaced by A_{eq}, amplification factor is calculated as follows, divided by A_{eq}.

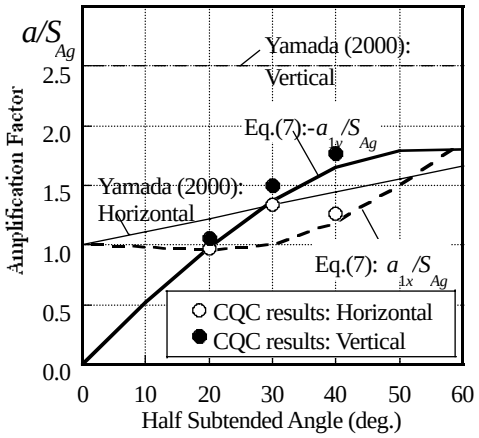

Figure 4 Amplification Ratios for Arch Roof

$$\frac{\boldsymbol{a}_R}{A_{eq}} = \sqrt{\left(\frac{A_R}{A_{eq}}\beta_{R1}\mathbf{u}\right)^2 + \left(\mathbf{I}_x \frac{M_{R2}}{M_R}\right)^2} \qquad (9)$$

Calculated factors are the functions of θ, and natural period ratio between SDOF and the roof $R_T=T_{eq}/T_R$. Horizontal component a_{RH}/A_{eq} and vertical component a_{RV}/A_{eq} in eq.(9) are shown in Figure 5(c) and (d), along R_T. Also the results of CQC method with detailed arch models are shown in marks. The proposed design factors are consistent with CQC results. These amplification factors are also affected by the mass ratio $R_M=M_{eq}/M_R$, as in Figure 6. Where R_M values are large, amplification factors excite around R_T =1, because of resonance between the roof and the substructure.

Using these equations, the maximum acceleration in the raised roofs can be evaluated by the following process, as in Figure 7.

1) Calculate natural period in SDOF model T_{eq} estimating the roof as rigid body, and evaluate A_{eq} with response spectrum.

2) Evaluate the natural period of asymmetric one-wave mode of the roof T_R, and calculate $R_T=T_{eq}/T_R$.

3) Calculate amplification factors ($F_H=A_{Hmax}/A_{eq}$, $F_V=A_{Vmax}/A_{eq}$), and evaluate the acceleration in the roof A_H and A_V, with distribution functions.

4) Evaluate deflections and member forces by estimating A_H and A_V as equivalent static load coefficient.

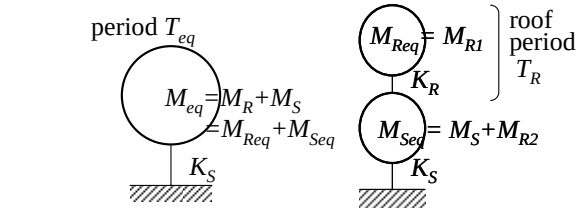

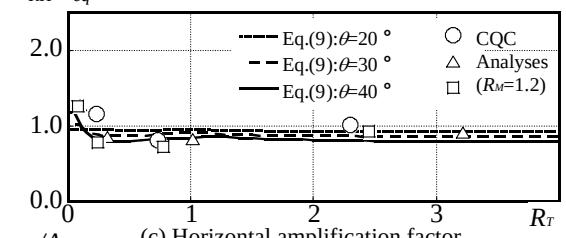

(c) Horizontal amplification factor

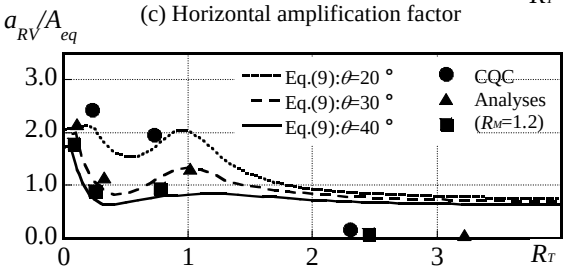

(d) Vertical amplification factor

Figure 5 Amplification Ratios v.s. R_T

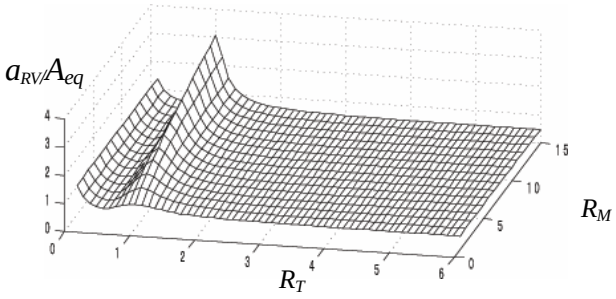

Figure 6 Amplification Ratios v.s. R_M (θ=30 °)

3. RESPONSE OF DOME

The proposed concept is applied to spherical lattice domes and amplification factors are researched. The first analysis models are rigidly jointed lattice domes with substructure as shown in Figure 8. The dome span is 60m and the rises of the domes are varied as the half subtended angle of 20 to 90 degrees, with the pipe elements modeling the truss members with the depth/span ratio of 1/50. The substructure is moment frames, and tension ring is placed at the boundary of the domes.

The first step to estimate the amplification factor is to study the effect of half subtended angle using roof model without substructures. The relationship between the maximum acceleration and half subtended angles are plotted in Figure 9.

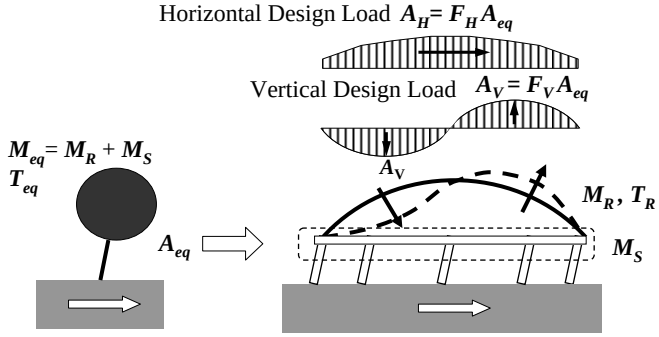

Figure 7 Concept of Equivalent Static-load Evaluation

The maximum values of horizontal and vertical acceleration is roughly expressed as the following equations.

$$F_H = C_H(\theta) = 2.47\sin^2\frac{3}{4}\theta - 1.33\sin\frac{3}{4}\theta + 3.0 \qquad (10)$$

$$F_V/3 = C_V(\theta) = 2.47\sin\frac{3}{4}\theta\cos\frac{3}{4}\theta \qquad (11)$$

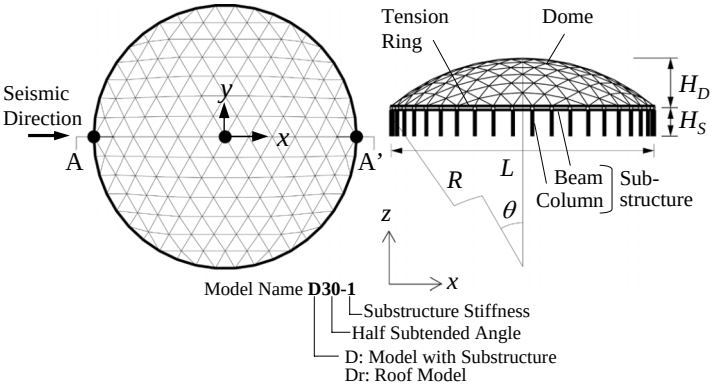

Figure 8 Latticed Dome Roof Model

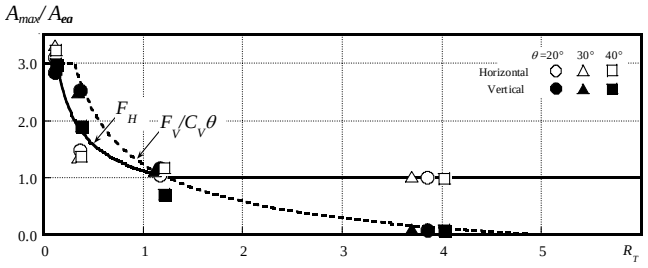

Figure 10 Amplification Factors along R_T for Dome

In the next, amplitude effect by the substructure is evaluated. This effect is considered to be expressed as a function of R_T, and the relationship between $F_H=A_{Hmax}/A_{eq}$, $F_V= A_{Vmax}/A_{eq}$ and $R_T=T_{eq}/T_R$ is plotted in Figure 10. Where A_{Hmax}, A_{Vmax} are maximum acceleration in the roof in horizontal and vertical directions respectively, and A_{eq} is acceleration in SDOF model. To express these effects, horizontal amplitude effect F_H, and vertical amplitude effect F_V is expressed as the following equations, as approximations to cover the parametric study results.

$$F_H = \begin{cases} C_H(\theta) & \left(0 < R_T \le 5/4\left(C_H(\theta)\right)^2\right) \\ \sqrt{5/4R_T} & \left(5/4\left(C_H(\theta)\right)^2 < R_T \le 5/4\right) \\ 1 & \left(5/4 < R_T\right) \end{cases} \quad (12)$$

$$F_V = \begin{cases} 3C_V(\theta) & \left(0 < R_T \le 5/32\theta\right) \\ \left(\sqrt{5/2\theta R_T} - 1\right)C_V(\theta) & \left(5/32\theta < R_T \le 5/2\theta\right) \\ 0 & \left(5/2\theta < R_T\right) \end{cases} \quad (13)$$

In case θ<40 deg., $C_H(\theta)$ can be evaluated as 3.0, and $C_V(\theta)$ can be calculated as 1.85θ.

Comparing these amplification factors with those of simple arch model in Figure 5, magnitudes in lower R_T zones are remarkable. These differences are produced by higher vibration mode amplification in roof models. It is also noted that F_H and F_V should be the function of not only R_T but $R_M=M_{eq}/M_R$, however, Eq.(12)(13) are expressed by R_T only, for lower R_M (=1.2) in these study. From studies, as above, the maximum acceleration distribution can be expressed as the following functions, using the coordinates in the roof.

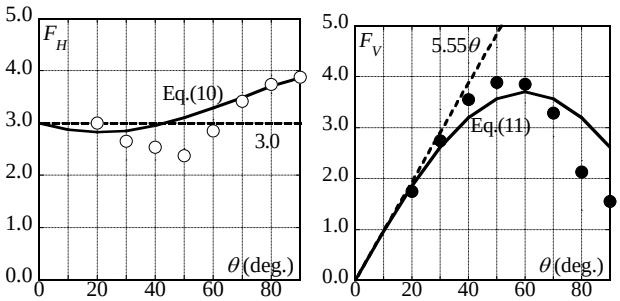

Figure 9 Effect of Half Subtended Angle in Dome

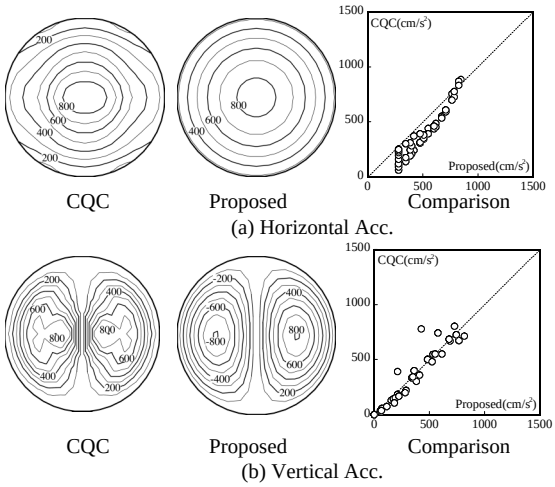

Figure 11 Acceleration Distribution in Dome (θ=30°)

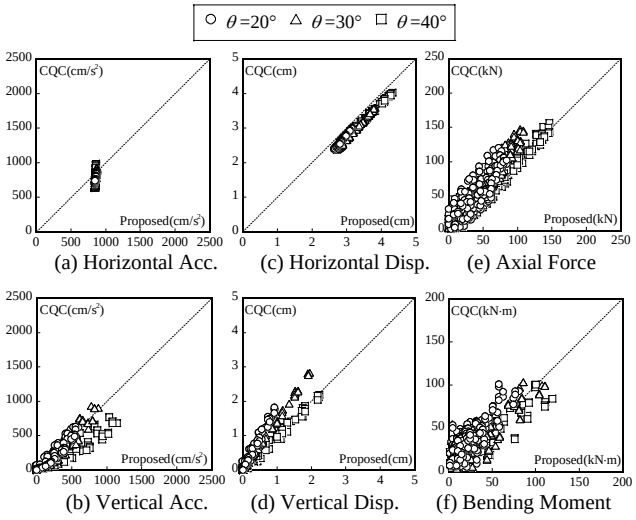

Figure 12 Accuracies of Proposed Static Loads (θ=20°~40°)

Horizontal acceleration:

$$A_H(x,y) = A_{eq}\left\{1 + (F_H - 1)\cos\frac{\pi\sqrt{x^2+y^2}}{L}\right\} \quad (14)$$

Vertical acceleration:

$$A_V(x,y) = A_{eq}F_V\frac{x}{\sqrt{x^2+y^2}}\sin\frac{\pi\sqrt{x^2+y^2}}{L} \quad (15)$$

For high-rise domes with θ>40 deg., Polar coordinate instead of rectangular coordinate should be used (Takeuchi et.al. 2008). The comparison of above factors and CQC results are shown in Figure 11. The equivalent static loads are delivered

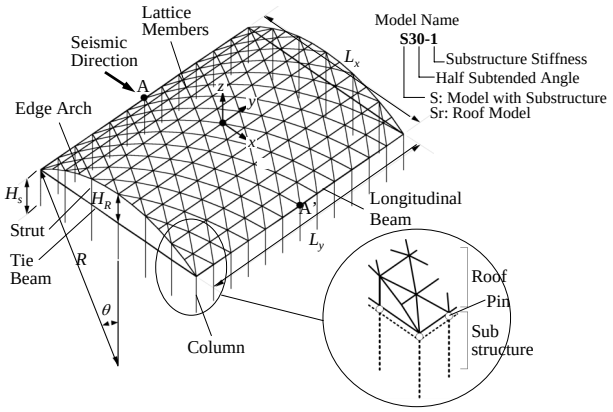

Figure 13 Latticed Cylindrical Shell Roof Model

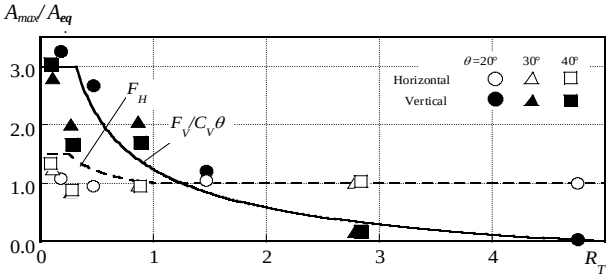

Figure 15 Amplification Factors along R_T for Cylindrical Shells

by multiplying these accelerations with the self-weight distribution of the dome. The displacements and member forces using these equivalent static loads are also compared with CQC results in Figure 12. The results of proposed method seem consistent with those of CQC, and considered to be effective. The accuracies in member forces are relatively worse, which is caused by estimating the equivalent load distributions from the coverage of maximum accelerations, however, the present accuracy is considered to be enough for practical design.

4. RESPONSE OF CYLINDRICAL SHELL

Next, the same concept is applied to cylindrical shell roofs. The analysis models are rigidly jointed lattice shell roofs with substructure as shown in Figure 13. The roof spans are 36m and the rises of the roofs are varied as the half subtended angle of 20, 30 and 40 degrees. The members of the roofs are tubular sections, being designed under the same conditions as the dome models, with the out-of-plane stiffness of the roof members named 10 series or 100 series, which are equal to depth/span ratios of about 1/100 or 1/30 respectively.

Firstly, the effect of half subtended angle is studied using roof model without substructures. The relationship between the maximum acceleration and half subtended angles are plotted in Figure 14. In the shallow rises of $20<\theta<40$ deg., the maximum values of horizontal acceleration shows almost flat values of 1.5 S_{Ag} in Figure 3 spectrum. The maximum values of vertical acceleration are linearly increases along the angle in these zones, and expressed as 4.0 S_{Ag} θ (rad).

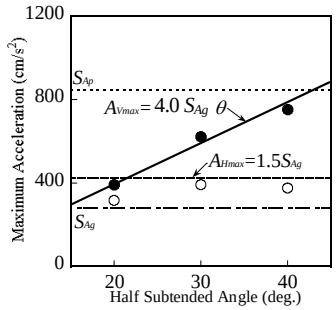

Figure 14 Effect of Half Subtended Angle in Shallow Shell

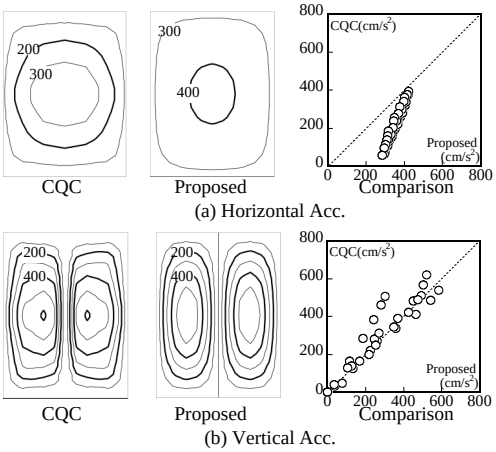

Figure 16 Acceleration Distribution in Cylindrical Shell (θ=30°)

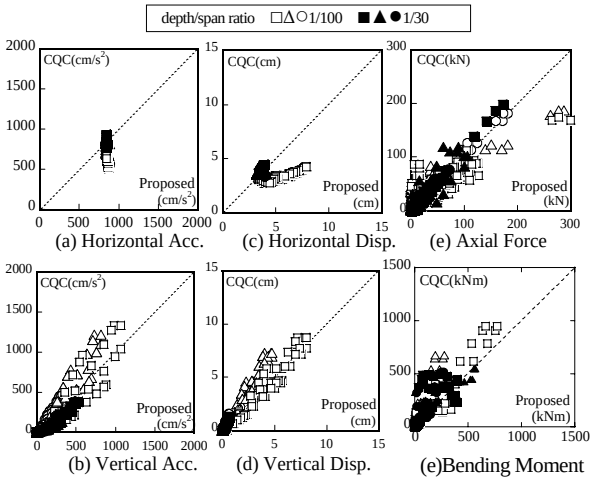

Figure 17 Accuracies of Proposed Static Loads (θ=20°~40°)

Reflecting those, the Eq.(11) is modified as the following.

$$C_{V(\theta)} = 1.77 \sin\frac{3}{4}\theta \cos\frac{3}{4}\theta \qquad (16)$$

From these results, amplitude effect by the substructure is evaluated. The relationship between $F_H = A_{Hmax}/A_{eq}$, $F_V = A_{Vmax}/A_{eq}$ and R_T calculated from each models are plotted in Figure 15. To cover these effects, horizontal amplitude effect F_H, and vertical amplitude effect F_V is expressed as the following equations, which is slightly different from those of domes in F_H.

$$F_H = \begin{cases} C_H(\theta)/2 & (0 < R_T \le 1/(C_H(\theta)-1)^2) \\ \left(\sqrt{1/R_T}+1\right)/2 & (1/(C_H(\theta)-1)^2 < R_T \le 5/4) \\ 1 & (5/4 < R_T) \end{cases} \qquad (17)$$

$$F_V = \begin{cases} 3C_{V(\theta)} & \left(0 < R_T \le 5/32\theta\right) \\ \left(\sqrt{5/2\theta R_T} - 1\right)C_{V(\theta)} & \left(5/32\theta < R_T \le 5/2\theta\right) \\ 0 & \left(5/2\theta < R_T\right) \end{cases} \quad (18)$$

From studies with roof models, the maximum acceleration distribution can be expressed as the following equations.

Horizontal acceleration:

$$A_H(x,y) = A_{eq}\left\{1 + (F_H - 1)\cos\pi\left(\frac{x}{L_x}\right)\cos\pi\left(\frac{y}{L_y}\right)\right\} \quad (19)$$

Vertical acceleration:

$$A_V(x,y) = A_{eq}F_V \sin\pi\left(\frac{2x}{L_x}\right)\cos\pi\left(\frac{y}{L_y}\right) \quad (20)$$

Above distribution is compared with the results of CQC method in Figure 16. The equivalent static loads are delivered by the same process as domes. The displacements and member forces using these equivalent static loads are compared with the results of CQC method in Figure 17. White marks are the results of depth/span ratio of 1/100, and black marks are those of depth/span ratio of 1/30. The results of proposed method are more accurate in roofs with higher out-of-plane stiffness, and considered to be applicable also in cylindrical shells with depth/span ratio over 1/100.

5. EFFECT OF MASS RATIO

Above discussions are under conditions where mass ratio $R_M=M_{eq}/M_R$ is relatively small. However, as indicated in Section 2, excitation of amplification factors around R_T=1 are expected in high R_M cases. In this section, additional indication formulas covering these excitations are discussed.

The similar studies as previous sections are carried out for arches, domes and cylindrical shells with θ=30° with R_M=1.2, 3 and 9. Here, the arch models are defined as removing the end strut from cylindrical shell models, and the results of arches are shown in Figure 18. In this figure, CQC results are indicated as marks, and amplification factors in Eq. (9) are indicated in chained lines, and proposed design equations (Eq.(17), (18)) are indicated in solid lines. When R_M=1.2, the amplification is covered by proposed design formulas, however with increasing R_M factor, the CQC results and Eq.(9) exceeds the solid lines around R_T=1. This condition occurs when the weight of substructures is much higher than the roof, and their natural periods meet each other, as light steel roof sits on multi-story RC buildings, for example. To cover these phenomena, the following equations are proposed.

$$F'_H = \sqrt{F_H^2 + \frac{1}{(1-R_T^2)^2 + (1/R_M)^\theta}} \quad (21)$$

$$F'_V = \sqrt{F_V^2 + \frac{1}{(1-R_T^2)^2 + (1/R_M)}} \quad (22)$$

Where, $R_M=M_{eq}/[M_R\ R_M^{(\theta-\pi/6)/2}]$ should be used for high-rise (θ>40 °) roofs.

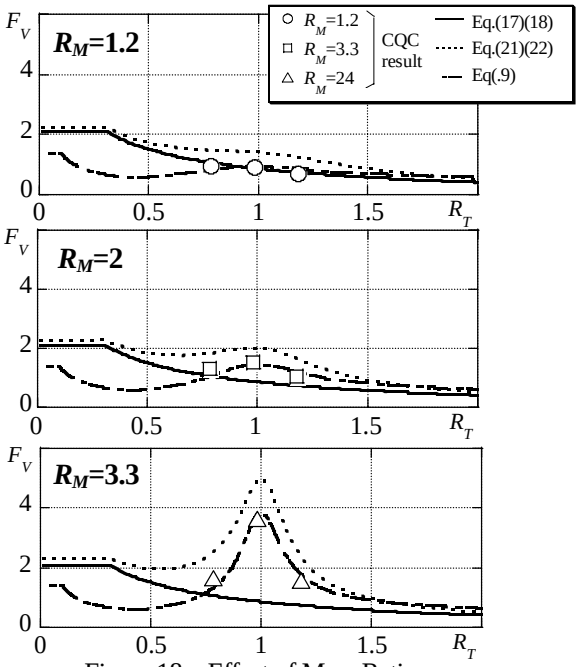

Figure 18 Effect of Mass Ratio

6. CONCLUSIVE REMARKS

The seismic response characteristics of raised roof as domes and cylindrical shell are expressed by simple equations with parameters of half subtended angle, natural period ratio and mass ratio between the roof and substructures, and their validities are studied and discussed. The proposed method delivers roof accelerations from design shear force of each stories and consistent with contemporary multistory seismic-design concepts.

References

Kato, S., Konishi, K., Nakazawa, S. (2003): Push-over analysis and static estimation of seismic responses of large steel space structures, Comparison of static estimation based on push-over analysis with direct dynamic analysis, *IASS-APCS 2003*, Taipei, Taiwan, 54-55.

Kato, S., Nakazawa, S., Saito, K. (2006): Two-mode based estimation of equivalent seismic loads and static estimation of dynamic response of reticular domes supported by ductile substructures, *Journal of IASS*, Vol. 47, n.1, 35-52.

Yamada, S., Matsumoto, Y., Saito, E. (2006).: Static seismic load modeling using continuum shell analogy for single layer latticed cylindrical shell structures, *IASS-APCS 2006*, Beijing, China, 80-81.

Yamada, M. (2001):, A basic study on the effect of substructures for the seismic response of space structures, *Shell and Spatial Structures Seminar, No.10, AIJ symposium*, 2001.11 (in Japanese)

Zheng, Z., Yamada., M. (2000): Seismic response distribution characteristics of arch, *AIJ anural meeting procedure*, B-1, 859-860 (in Japanese)

Takeuchi, T., Kumagai, T., Ogawa, T., (2007): Response Evaluation of Lattice Shell Roofs Using Amplification Factors, *Journal of IASS*, Vol.48, No.3, 197-210

Takeuchi, T., Kumagai, T., Okayama, S., Ogawa, T., (2008): Response Evaluations of High-rise Domes with Supporting Substructures, *J. Struct. Constr. Eng, AIJ*, Vol.73, No.629, 1119-1126 (in Japanese)

Sixth International Conference on Urban Earthquake Engineering
March 3-4, 2009, Tokyo Institute of Technology, Tokyo, Japan

VIBRATION TESTS OF ARCH STRUCTURES SUPPORTED BY SUBSTRUCTURES WITH VARIOUS NATURAL PERIODS AND MASS SUBJECTED TO HORIZONTAL EARTHQUAKE MOTIONS

Tomohiko Kumagai[1)], Toru Takeuchi[2)], and Toshiyuki Ogawa[3)]

1) Assistant Professor, Dept. of Architecture and Building Engineering, Tokyo Institute of Technology, Japan
2) Associate Professor, Dept. of Architecture and Building Engineering, Tokyo Institute of Technology, Japan
3) Professor, Dept. of Architecture and Building Engineering, Tokyo Institute of Technology, Japan
kuma@arch.titech.ac.jp, ttoru@arch.titech.ac.jp, togawa@arch.titech.ac.jp

Abstract: This paper is intended as an investigation of effects of natural periods and mass of substructures on seismic response behavior of arch structures by shaking table tests. In addition, the results of experiments will be compared with the seismic response calculation method proposed by previous papers [1],[2].

The arch structures used for the experiments are made of steel plates with 0.7mm thick. The arch span is 120 cm, the half subtended angles of arches are 20, 30 and 40 degrees. The substructures consist of a linear motion slider, compression or tension springs and weights. The natural periods of substructures are adjusted by varying the spring constants and the weights. The arches are subjected to the horizontal earthquake motions. The responses for structures measure with the accelerometers, the motion capture systems, the strain gauges and the laser displacement sensor.

From the experimental results, the following knowledge is obtained. The response amplification factors increase due to resonance, as the natural periods of substructure and arch structure are equal. The vertical response amplification factors of arches increase following increases of the mass of substructures and the half subtended angles of arches. The seismic responses calculated using the proposed method are in agreement with the experimental results.

1. INTRODUCTION

An arch structure is the basic structural type for a space structure. It is significant to investigate the behavior of this structure for consideration of the mechanical and vibrational behavior of various space structures. Therefore a large number of studies [3]~[5] have been made on the mechanical and vibrational behavior of the arch structures up to the present. However, the arch structures themselves have been an object of most studies, the relationships between vibrational behavior of arch structure and that of substructure have not been made clear sufficiently. This paper is intended as an investigation of effects of natural periods and mass of substructures on seismic response behavior of arch structures by shaking table tests. In addition, the results of experiments will be compared with the seismic response calculation method proposed by previous papers [1],[2].

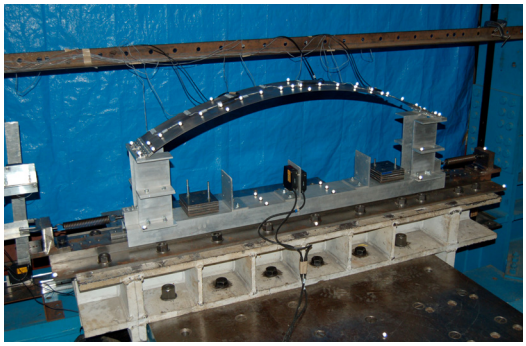

Photograph 1 Experimental Device of Arch Structure (Fa model)

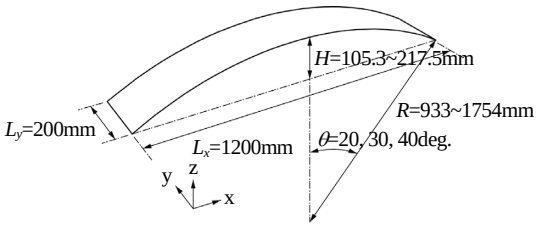

Figure 1 Shape of Arch Structure

2. OUTLINES OF VIBRATION TESTS

2.1. Specimens and Experimental Devices

The experimental models shown in Photograph 1 are the arch roof structures with substructures. The shape and dimensions of arch roofs are shown in Fig.1 and Table 1.

Table 1 Dimensions of Arch Structures

Thickness t (mm)	Span L_x (mm)	Half Subtended Angle θ (deg.)	Rise H (mm)	Mass of Arch M_R (kg)	Total Mass M_{eq} (kg)
0.7	1200	20	105.3	1.32	14.60
		30	160.5	1.35	14.64
		40	217.5	1.41	14.69

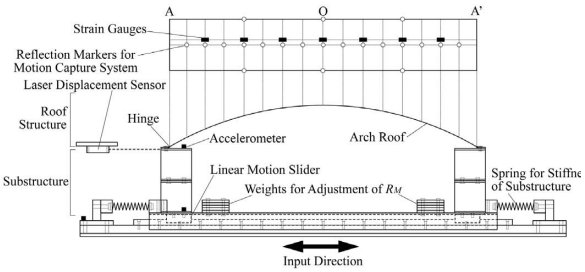

(a) Fa model

(b) Ra model

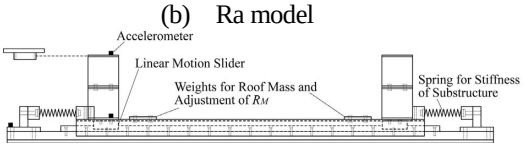

(c) E model

Figure 2 Experimental Devices

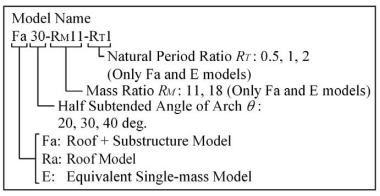

The names of models are shown below Fig.2. The models are the following 3 types shown in Fig.2. Fa model is the model of arch roof with substructure, Ra model is the model of arch roof without substructure and E model is the equivalent single-mass model. The arch roofs are made of cold rolled steel plates (SPCC) 0.7mm thick. The arch span is 1200 mm, the half subtended angles of arches are 20, 30 and 40 degrees. The arch roofs are fixed with hinges, the joints of arch are pin joints. The substructures consist of a linear motion slider, compression or tension springs and weights. The natural periods of substructures are adjusted by varying the spring constants and the weights. The ratios R_T of the natural period of E model to that of Ra model are adjusted to 0.5, 1 and 2. The ratios R_M of the total mass M_{eq} to the mass of arch roof M_R are adjusted to 11 and 18 using the weights.

2.2. Measurement and loading programs

The arches are subjected to the horizontal earthquake motions. The input earthquake motions are BCJ-L1 which is an artificial earthquake motion of the Building Center of Japan, El Centro NS (1940), Taft EW (1952), Hachinohe NS (1968) and JMA Kobe NS (1995). The maximum accelerations of input earthquake motions are standardized to be 100 cm/sec^2. The arches and substructures are in elastic range under these earthquake motions. The shaking table used for the experiments has the capability of 500kN (maximum loading) in the range of 0.5~20Hz.

The responses of arch structures are measured with the accelerometers, the motion capture systems, the strain gauges and the laser displacement sensor. The positions for measurements are shown in Fig.2. The directions of measurement are the horizontal x and vertical z directions. The motion capture system MX40 made by VICON MOTION SYSTEMS Ltd. is used for the measurements of absolute displacements in x and z directions. The accelerations of arch structures are obtained by differentiating these measured displacements twice with respect to time *t*. The accuracies of these accelerations are verified by comparison of the response values by the motion capture systems with those by the accelerometers.

3. VIBRATIONAL CHARACTERISTICS OF ARCH STRUCTURES

In this chapter, the natural periods, mode shapes, effective masses and damping factors of the arch structures are examined as the fundamental vibrational characteristics.

The natural periods are obtained from the predominant periods at Fourier spectra of the responses under sweeping sine waves. Next, the shapes and damping factors of these modes are obtained from the responses under sine waves with the natural periods of each mode. The mode shapes are determined as the distributions of displacements measured with the motion capture systems. The damping factors of each mode are estimated from the damped vibration after the input of sine wave. In the case of Ra (roof) model, the damping factors are obtained by drawing the curve of $\varepsilon = a^* \exp(-hR\omega t)$ to the amplitude of responses. In the case of E (equivalent single-mass) model, the amplitude dependence occur in the relationships between the damping factors and the responses as shown in Fig.3. This behavior is described by means of the friction damping of linear motion slider which is one of the major factors for the damping. The energy consumption by linear motion slider is shown in Fig.4 and Eq.(1).

$$h_{eq} = \frac{1}{4\pi}\left(\frac{\Delta W}{W}\right) = \frac{1}{4\pi}\frac{4u_{\max}\mu mg}{\frac{1}{2}ku_{\max}^2} = \frac{2\mu mg}{\pi k u_{\max}} \quad \propto \frac{1}{u_{\max}} \quad (1)$$

Therefore the damping factors at the maximum value of responses subjected to each seismic wave are applied to the damping factor h_E of E model. The damping factor is calculated using Eq.(2).

$$d = \frac{y_1}{y_2} = e^{2\pi h_E / \sqrt{1-h_E^2}} \quad (2)$$

where d is ratio of amplitude, y_1 is maximum amplitude of seismic responses and y_2 is amplitude 1 period after y_1.

Table 2 shows the vibrational characteristics for Ra model, Fig.5 shows the shapes of 1st and 3rd modes. Table 3 shows those for E model. The natural periods of 1st mode for

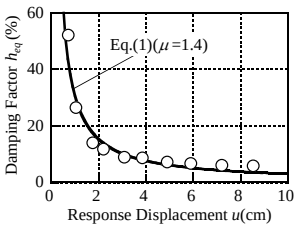

Figure 3 Relationships between Damping Factors and Amplitudes ($E30R_M11R_T1$)

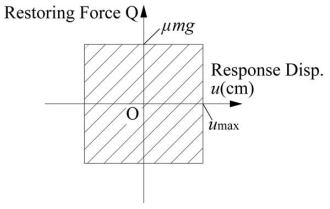

Figure 4 Energy Consumption by Linear Motion Slider

Table 2 Vibrational Characteristics (Ra model)

Model Name	1st Mode			
	Natural Period	Participation Factor	Effective mass Ratio	Damping Factor
	T_{R1}(sec)	β_{R1}	M_{R1}/M_R(%)	h_{R1}(%)
Ra20	0.323	10.9	8.55	12.3
Ra30	0.317	16.9	20.1	6.00
Ra40	0.350	22.0	33.0	8.20
Model Name	3rd Mode			
	Natural Period	Participation Factor	Effective mass Ratio	Damping Factor
	T_{R3}(sec)	β_{R3}	M_{R3}/M_R(%)	h_{R3}(%)
Ra20	0.063	7.59	4.16	3.61
Ra30	0.065	8.51	5.10	1.37
Ra40	0.069	11.7	9.28	4.92

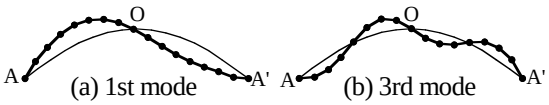

(a) 1st mode (b) 3rd mode

Figure 5 Mode Shapes (Ra30 model)

Table 3 Vibrational Characteristics (E model, BCJ-L1)

Model Name	Natural Period T_E (sec)	Natural Period Ratio R_T	Damping Factor h_E (%)
$E30R_M11R_T0.5$	0.185	0.58	3.58
$E30R_M11R_T1$	0.372	1.17	6.15
$E30R_M11R_T2$	0.735	2.32	8.19
$E30R_M18R_T0.5$	0.181	0.57	2.78
$E30R_M18R_T1$	0.366	1.15	3.61
$E30R_M18R_T2$	0.730	2.30	3.68
$E20R_M11R_T1$	0.372	1.10	6.69
$E20R_M18R_T1$	0.361	1.08	3.84
$E40R_M11R_T1$	0.383	1.15	6.54
$E40R_M18R_T1$	0.376	1.12	3.38

Ra model are about 0.33sec regardless of half subtended angle of arch roof. Those of 3rd mode are about 0.065sec. The 1st mode shape is asymmetrical 1 wave mode. The 3rd mode shape is asymmetrical 2 wave mode. The effective mass ratios tend to increase as the half subtended angle increases. The damping factors for E model increase as the natural period ratio become large.

Next, the values by theoretical formula of natural period of arch roof are estimated, the experimental values are compared with those values. Yamada S. derives the theoretical formula (3) for natural frequency f of partial cylindrical shell [6].

$$f = \frac{\bar{n}}{2\phi}\sqrt{\frac{(p^c - p)}{\rho H}\frac{g}{R}} \qquad (3)$$

where $\bar{n}$ is circumferential half wave number, ϕ is subtended angle ($\phi = 2\theta$), ρ is density of shell, H is shell thickness, p^c is buckling load, p is external pressure, g is gravity acceleration and R is radius of curvature. If the external pressure is the dead load, $\rho H = p$.

The static buckling load q_{cr} [3] is used for p^c in order to apply Eq.(3) to Ra model. The static buckling load q_{cr} is the buckling load of circular arch in a state of deformation with asymmetrical 1 wave mode. The static buckling load q_{cr} is expressed as the following equation.

$$q_{cr} = \frac{EI}{R^3}\left(\frac{\pi^2}{\theta^2} - 1\right) \qquad (4)$$

where EI is flexural rigidity.

The relationships between natural period and half subtended angles for the theoretical formula and the experimental results are shown in Fig.6. The experimental values agree with the theoretical formula in any model.

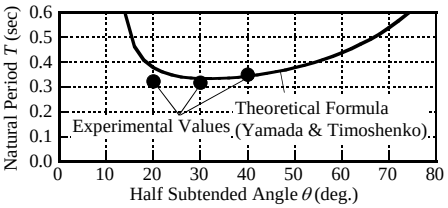

Figure 6 Relationships between Natural Period and Half Subtended Angles (Ra model)

4. SEISMIC RESPONSE BEHAVIOR OF Ra (ARCH ROOF) MODELS

In this chapter, the seismic response behavior of Ra model is examined. Fig.7 shows the distributions of absolute values of maximum response accelerations for Ra model subjected to BCJ-L1 which is an artificial earthquake motion. The experimental results and the calculated values obtained from the modal analysis by response spectrum using square root of sum of squares (SRSS) are shown in figures. This modal analysis using SRSS by 1st mode, 3rd mode and ground motion mode is expressed as the following equations [7].

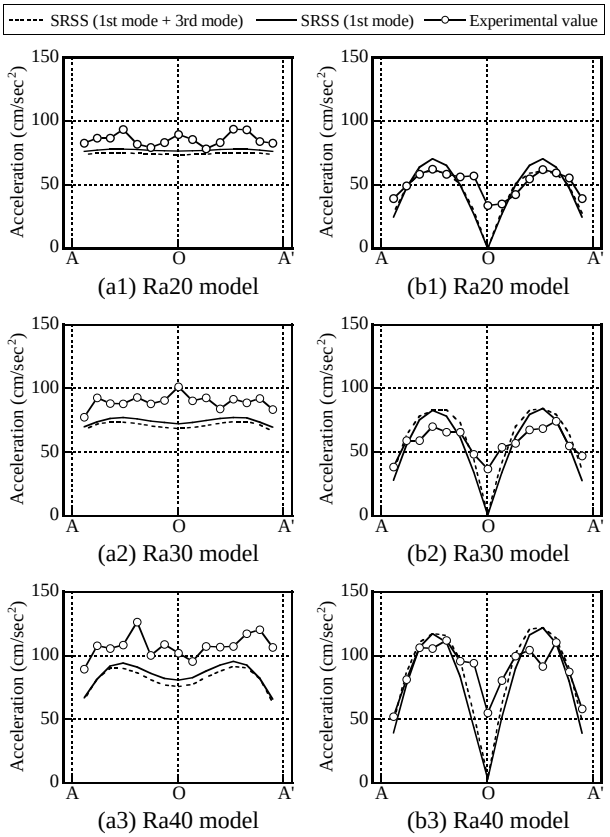

Figure 7 Distributions of Maximum Response Accelerations (Ra model, BCJ-L1)

1st+3rd modes:

$$\mathbf{a}_R = \sqrt{\left(\beta_{R1}\mathbf{u}_{R1}S_A(T_{R1},h_{R1})\right)^2 + \left(\beta_{R3}\mathbf{u}_{R3}S_A(T_{R3},h_{R3})\right)^2 + \left(\frac{M_R - M_{R1} - M_{R3}}{M_R}\mathbf{I}_x S_{Ag}\right)^2} \quad (5)$$

1st mode: $$\mathbf{a}_R = \sqrt{\left(\beta_{R1}\mathbf{u}_{R1}S_A(T_{R1},h_{R1})\right)^2 + \left(\frac{M_R - M_{R1}}{M_R}\mathbf{I}_x S_{Ag}\right)^2} \quad (6)$$

where $\mathbf{u}_{R1}$ and $\mathbf{u}_{R3}$ are eigenmode vectors for 1st mode and 3rd mode respectively, $S_A(T_{R1},h_{R1})$ and $S_A(T_{R3},h_{R3})$ are acceleration response spectrum values for 1st mode and 3rd mode respectively, $\mathbf{I}_x$ is distribution vector of input earthquake acceleration and S_{Ag} is maximum acceleration of input earthquake motion.

In the case of horizontal response accelerations, as the half subtended angle increases, the response accelerations become large, the accelerations at the antinode of 1st mode become larger in comparison with other measured points. The calculated values are slightly smaller than the experimental values. However both values are similar in the distribution shape. In the case of vertical response, the distribution shapes are the shape with asymmetrical 1 wave in any half subtended angle. The vertical response accelerations become large as well as the horizontal responses, as the half subtended angle increases. The acceleration responses at the center point O for calculated values are nearly equal 0. However, the accelerations occur at the center point O on the experiments. The reasons for this are that the modes not considered in Eqs.(5) and (6) apper in the experiments and finite bending deformation of arch roof.

The calculated values by Eq.(6) using only 1st mode are not remarkably different from those by Eq.(5) using 1st and 3rd modes. Therefore the calculated values using only 1st mode are used as calculated values for following examinations.

5. SEISMIC RESPONSE BEHAVIOR OF Fa (ARCH ROOF WITH SUBSTRUCTURE) MODEL

In this chapter, effects of the natural period ratio and mass ratio on the seismic response behavior of Fa model are examined.

The seismic response calculation method [1], [2] for Fa model is explained. First, the E and Fa models are converted into the single-mass and double-mass systems respectively as shown in Fig.8. M_{Req} and M_{Seq} are the effective masses of arch roof and substructure respectively. K_R and K_S are the stiffness of arch roof and substructure respectively, those are obtained from Eqs.(7) and (8).

$$K_R = \frac{M_{Req}}{(T_{R1}/2\pi)^2} \quad (7) \qquad K_S = \frac{M_{eq}}{(T_E/2\pi)^2} \quad (8)$$

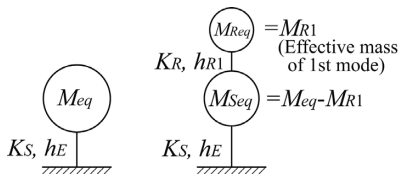

Figure 8 Single-mass System and Double-mass System

Next, the eigenvalue analysis is carried out for this double-mass system. The response accelerations of double-mass system are calculated by the modal analysis using SRSS by obtained 1st and 2nd modes (Eq.(9)).

$$\mathbf{a} = \left[A_S, A_R\right]^T = \sqrt{\left(\beta_{eq1}\mathbf{u}_{eq1}S_A(T_{eq1},h_{eq})\right)^2 + \left(\beta_{eq2}\mathbf{u}_{eq2}S_A(T_{eq2},h_{eq})\right)^2} \quad (9)$$

where β_{eq1} and β_{eq2} are participation factors, $\mathbf{u}_{eq1}$ and $\mathbf{u}_{eq2}$ are eigenmode vectors for 1st and 2nd modes respectively, $S_A(T_{eq1},h_{eq})$ and $S_A(T_{eq2},h_{eq})$ are acceleration response spectrum values at the natural periods T_{eq1} and T_{eq2} for 1st and 2nd modes of double-mass system respectively, h_{eq} is equivalent damping factor obtained by Eq.(10) and A_S and A_R are response accelerations of lower and upper structures respectively.

$$h_{eq} = \frac{h_E W_S + h_{R1} W_R}{W_S + W_R} \quad (10)$$

where W_S and W_R are elastic vibration energies of lower and upper structures respectively. The elastic vibration energies are calculated by using the eigenmode vectors $\mathbf{u}_{eq1}$ and $\mathbf{u}_{eq2}$.

Finally, the theoretical maximum acceleration response amplification factors a_R/A_{eq} of arch structures are calculated by Eq.(11) using the response accelerations of upper structures A_R and the maximum response accelerations of single-mass system A_{eq}.

$$\frac{\mathbf{a}_R}{A_{eq}} = \sqrt{\left(\beta_{R1}\mathbf{u}_{R1}\frac{A_R}{A_{eq}}\right)^2 + \left(\frac{M_R - M_{R1}}{M_R}\mathbf{I}_x\right)^2} \quad (11)$$

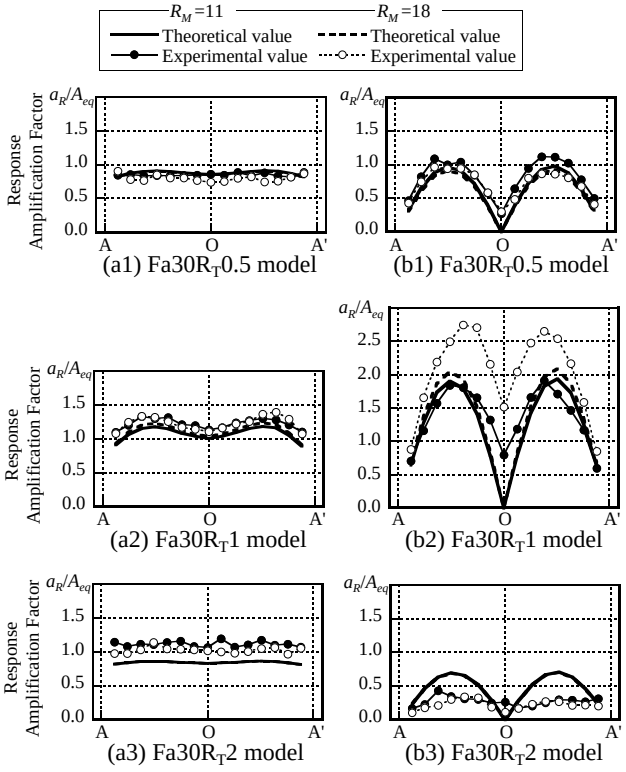

Figure 9 Distributions of Maximum Response Acceleration Amplification Factors (Fa30 model, BCJ-L1)

Fig.9 shows the distributions of absolute values of maximum response acceleration amplification factors for Fa30 model subjected to BCJ-L1. The distribution shapes in vertical direction are the shape with asymmetrical 1 wave except for Fa30R_M11R_T2. In horizontal direction, in the case of Fa30R_T1 model that the natural period of arch roof is equal to that of equivalent single-mass model, the acceleration amplification factors at the antinode of 1st mode are larger in comparison with other models. The acceleration amplification factors of Fa30R_T0.5 and R_T2 models are uniformly distributed on the arch roof. The acceleration amplification factors of R_T1 model amplify due to a resonance in any response direction and mass ratio R_M. In addition, the amplification factors of Fa30R_M18R_T1 model amplify larger than those of Fa30R_M11R_T1 model in vertical direction. On the other hand in the case of R_T2 model, because the natural period of substructure is longer than that of arch roof, the input of earthquake motion to arch roof is reduced. As a result the amplification factors in vertical direction are reduced. The theoretical values for Fa model obtained from Eq.(11) approximately agree with the experimental values.

Fig.10 shows the relationships between maximum acceleration response amplification factors and natural period ratios for Fa model subjected to BCJ-L1. The maximum acceleration response amplification factors are the values at the antinode of 1st mode. The acceleration amplification factors at R_T1 amplify due to a resonance in any response direction and mass ratio R_M as examined in Fig.10. The amplifications by resonance are especially large in vertical responses. However the influence of resonance becomes small as the half subtended angle decreases. In the cases of R_T =1 and vertical response, the amplification factors of R_M18 model amplify larger than those of R_M11 model.

Finally, the accuracy of theoretical values by the seismic response calculation method proposed by previous papers [1], [2] is verified. Fig.11 shows the comparisons between experimental values and theoretical values of maximum acceleration response amplification factor at the antinode of 1st mode for Fa model. The earthquake motions shown in the figures are BCJ-L1, El Centro NS, Taft EW, Hachinohe NS and JMA Kobe NS. The theoretical values are in approximate agreement with the experimental results regardless of the natural period ratio R_T, the mass ratio R_M, the half subtended angle θ of arch roof and the input earthquake motion. Therefore it is possible for the acceleration amplification factor for arch structure to be estimated by using this seismic response calculation method.

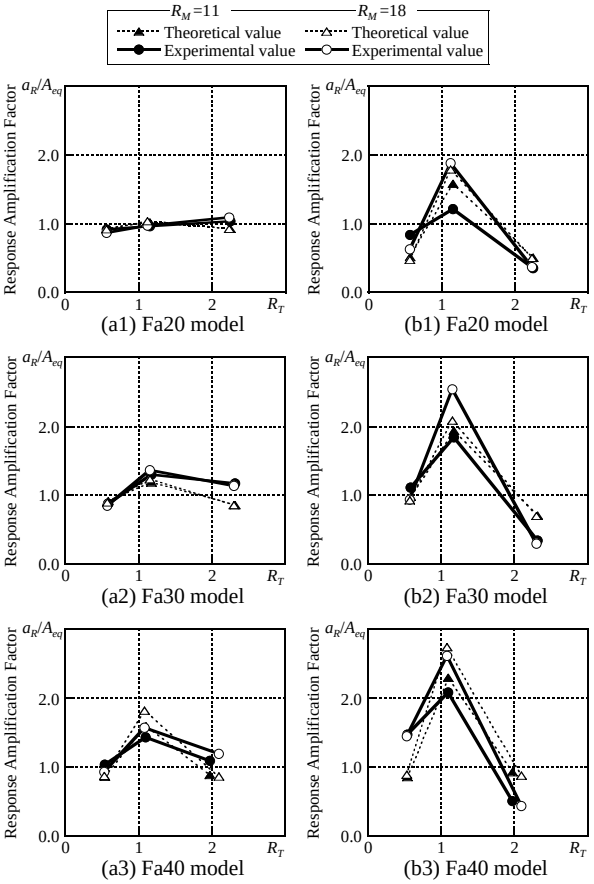

(a) Horizontal Direction (b) Vertical Direction

Figure 10 Relationships between Maximum Acceleration Response Amplification Factors

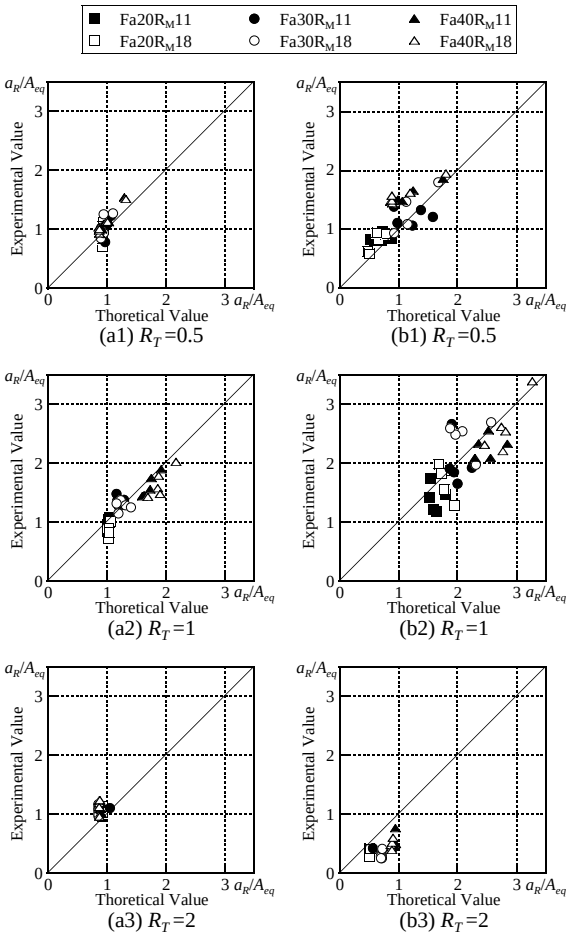

(a) Horizontal Direction (b) Vertical Direction

Figure 11 Comparisons between Experimental Values and Theoretical Values of Maximum Acceleration Response Amplification Factor (Fa model, five seismic waves)

6. CONCLUSIONS

The effects of natural periods and mass of substructures and half subtended angles of arches on seismic response behavior of arch structures are examined by shaking table tests. In addition, the experimental results are compared with the seismic response calculation method proposed by previous papers [1],[2].

It is concluded as follows, from the above results.

(1) On the natural vibrational characteristics of arch roof model, the predominant mode is 1st mode whose shape is asymmetrical 1 wave mode. The natural periods of 1st mode for arch models by experiments agree with the theoretical formula derived in references [3] and [6].

(2) The distributions of maximum seismic response accelerations of arch roof model are the shapes with asymmetrical 1 wave in vertical direction and the shapes with larger accelerations at the antinode of 1st mode in horizontal direction. The maximum vertical response acceleration amplification factors become large as the half subtended angle increases. The calculated values obtained from the modal analysis by response spectrum using square root of sum of squares (SRSS) [7] approximately agree with the experimental results in vertical direction. On the other hand in horizontal direction, those are slightly smaller than the experimental values.

(3) The distribution shapes of maximum vertical response acceleration amplification factors for arch structures with substructure are the shape with asymmetrical 1 wave in any natural period ratio R_T. The acceleration amplification factors of R_T1 model that the natural period of arch roof is equal to that of equivalent single-mass model amplify due to a resonance in any response direction. In the cases of $R_T=1$ and vertical response, the amplification factors of models with mass ratio $R_M=18$ amplify larger than those of R_M11 model. In the case of R_T2 model that the natural period of substructure is longer than that of arch roof, the input of earthquake motion to arch roof is reduced, the amplification factors in vertical direction are reduced.

(4) The theoretical values by the seismic response calculation method proposed by previous papers [1] and [2] are in approximate agreement with the experimental results regardless of the natural period ratio R_T, the mass ratio R_M, the half subtended angle of arch roof and the input earthquake motion.

Acknowledgements:

The present paper was supported in part by a grant from Grant-in-Aid for Young Scientists (B) (Research No.18760414) and Grant-in-Aid for Scientific Research (B) (Research No.19360247) by Japan Society for the Promotion of Science (JSPS) and research-aid fund by the Japan Iron and Steel Federation (JISF). The experiments in this paper are carried out using the facility by JSPS the 21st Century COE Program "Evolution of Urban Earthquake Engineering".

References:

[1] Takeuchi T., Ogawa T., Nakagawa M. and Kumagai T. (2004.9) "Response Evaluation of Medium-Span Lattice Domes with Substructures Using Response Spectrum Analysis", Shell and Spatial Structures from Models to Realization, IASS2004 symposium, Montpellier, TP076 (CD-ROM pp.1-8)

[2] Takeuchi T., Ogawa T., Yamagata C. and Kumagai T. (2005.9) "Seismic Response Evaluation of Cylindrical Lattice Roofs with Substructures Using Amplification Factors", Proceedings of IASS 2005, Bucharest, pp.391-398

[3] Timoshenko Stephen P. and Gere James M. (1961) "Theory of Elastic Stability", McGraw-hill Book Company

[4] Jung C., Shinohara Y. and Yamada M. (2000.9~2002.8) "The Characteristics of the Instantaneous Acceleration Response Distributions of the Arches Subjected to Seismic Motions (Part1~4)", Summaries of Technical Papers of Annual Meeting, Architectural Institute of Japan, Structures I (in Japanese)

[5] Matsui T., Mizuno K., Sugiyama E., Esaka Y. and Hibino T. (2004.8) "Shaking Table Tests on a Seismically-isolated Large-span Arch Supported by Base Structures", Journal of Structural and Construction Engineering, Architectural Institute of Japan, No.582, pp.87-94 (in Japanese)

[6] The Japan Society of Mechanical Engineers (2003) "Vibration and Buckling of Shell Handbook", Gihoudo publication, pp.91-96 (in Japanese)

[7] Guputa K. (1992) "Response Spectrum Method", CRC Press

Sixth International Conference on Urban Earthquake Engineering
March 3-4, 2009, Tokyo Institute of Technology, Tokyo, Japan

EXPERIMENTAL EVALUATION OF STRUCTURAL BEHAVIOR OF SUBASSEMBLIES AFFECTED BY THE PRESENCE OF THE GUSSET-PLATE

Shoichi Kishiki[1)] and Akira Wada[2)]

1) Assistant Professor, Structural Engineering Research Center, Tokyo Institute of Technology, Japan
2) Professor, Structural Engineering Research Center, Tokyo Institute of Technology, Japan
kishiki@serc.titech.ac.jp, wada@serc.titech.ac.jp

Abstract: The majority of these studies have tested isolated braces or simple subassemblies which neglect the influence of the framing components and the gusset-plate on the system performance. In this paper, frame subassemblies with the gusset-plate were subjected to cyclic lateral loading. It was found that effective length of the beam shortened by the presence of the gusset-plate connections. It was indicating that critical section of the beam was moved to the toe of the gusset-plate.

1. INTRODUCTION

In the Northridge and Kobe earthquakes, some buildings lost their structural functions, although many buildings avoided collapse as to save human life. The loss caused the termination of social and industrial activities, and severe economic loss. At the design stage of seismic design in urban areas, it is important to consider restoring structures immediately after an earthquake. Most of high-rise buildings are designed according to Damage-Controlled Design (Wada et al., 1992) seen in Figure 1.

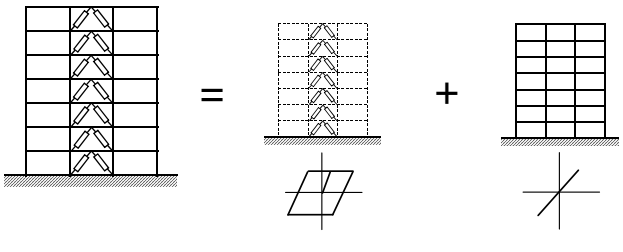

Figure 1 (a) Concept of Damage-Controlled Structures; (b) primary frame; (c) dampers

This system consists of a primary frame and dampers. The primary frame only supports gravity and is able to remain in the elastic range during an earthquake, because dampers absorb the input energy of the earthquake. Therefore, the buildings designed as Damage-Controlled Design can be used continuously by repairing or exchanging dampers after an earthquake. However, the majority of studies on dampers have tested isolated dampers or simple subassemblies which neglect the influence of framing components and gusset-plate on the system performance. Recently, some design-level and beyond design-level cyclic loading tests of frame subassemblies with buckling-restrained braces were carried out. These tests showed good behavior of the braces, and the results indicated a number of important considerations for the design of buckling-restrained braced frames and also of braced frames in general (Mahin et al., 2004). In this paper, four frame subassemblies with the gusset-plate connections were subjected to cyclic loading. The objectives of the tests were to verify structural behavior of the beam affected by the presence of the gusset-plate, removing influences of a brace forces.

2. TEST PLAN

A constant comparison was used for all specimens to investigate structural behaviors of beam-column frame subassemblies affected by the presence of the gusset-plate. Capacity limitations of the testing equipment, as well as constraints on the overall size of the test specimen, dictated that the specimen were approximately half of the actual building bay width and story height. The specimen was cut out from the frame with a bay width of 3.0m and a story height of 2.2m. The tests were cantilever beam, cyclic-load tests with a stiff, strong column as seen in Figure 2. A lateral support was applied to the beam during cyclic loading.

Two pairs of specimen were tested. Each pair consisted of the conventional moment-resisting beam (B) and the beam with the gusset-plate attachment to the beam and column flanges (G). In the first pair, a rectangular hollow section (RHS) was chosen for the column. On the other hand, a wide flange H-shaped section was chosen for the column in the second pair. Overall details are complied in Table 1.

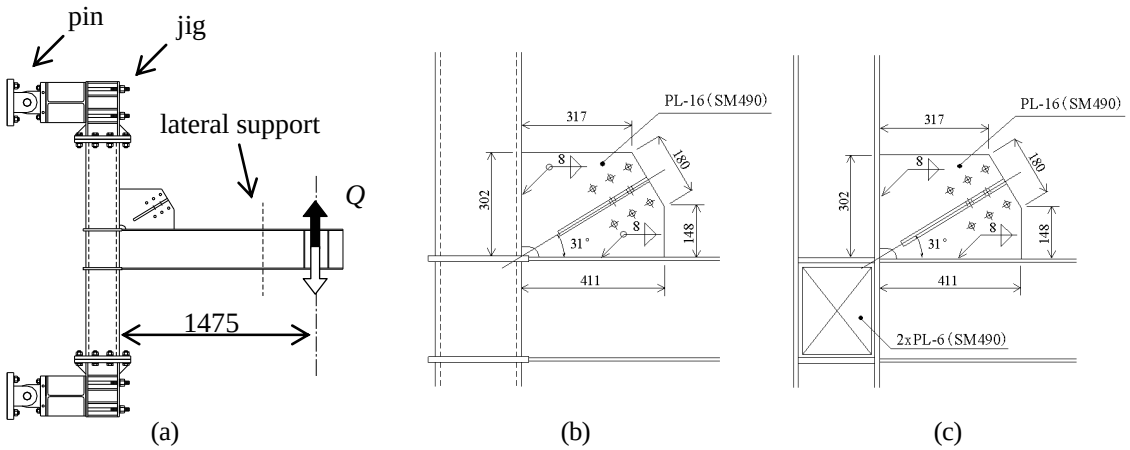

Figure 2 Test set-up and details of beam-column-gusset plate connection: (a) test set-up; (b) specimen Box_G; (c) specimen H_G (unit : mm)

Beam was made of section (depth × flange width × web thickness × flange thickness) of 300×150×6.5×9. Steel grades JIS SS400 were chosen for flange and web of the beam. As shown in Table 2, mechanical properties were obtained from tensile coupon tests according to JIS-1A. Cold-formed RHS columns with 250mm depth, 12mm thickness, and BCR295 steel grade were used for specimen BOX_G and BOX_B. Columns for specimen H_G and H_B were made of section of 250×250×9×14 with JIS SS400 steel grade.

Table 1 List of test specimens

Specimen	Shapes of Columns	Gusset-plate
Box_G	RHS-Roll	Attached
Box_B	RHS-Roll	Nothing (bare)
H_G	Wide Flange	Attached
H_B	Wide Flange	Nothing (bare)

Table 2 Mechanical properties of steel plate used for specimens

Sample plate	Grade	σ_y [MPa]	σ_u [MPa]	ε [%]
Beam-flange	SS400	342	461	29
Beam-web	SS400	406	490	22
Gusset-plate	SM490	400	536	27

A detail of the gusset-plate installed at the beam-column connections is shown in Figure 2. The gusset-plate was attached to the beam and column flange by using shop-welding of filet welds. Gusset-plates are fabricated in many different configurations. The most common configuration in Japan, rectangular non-compact type, was used for the specimen BOX_G and H_G. Steel grades JIS SM490, stronger than the beam and column, were chosen for the gusset-plate.

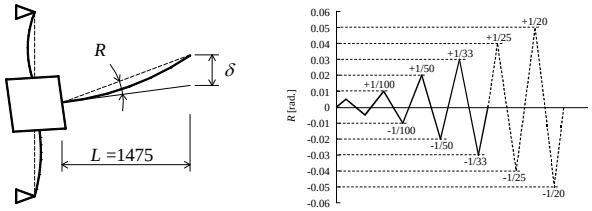

Figure 3 Loading program

Quasi-static loading was carried out following to a simple loading program shown in Figure 3. The loading programs were based on rotation angles of the specimen, which were 1/200, 1/100, 1/50, 1/33, 1/25, and 1/20 radian. The cantilever beams had a length L from the face of the column to the center of the load. The total tip deflection was due to elastic and plastic flexural deformation of the beam and connection. A rotation angle of the specimen can be found out by dividing the total tip deflection by L. Note that length L from the face of the column to the center of the load was used regardless of the presence of the gusset-plate.

3. TEST RESULTS AND CONSIDERATION

3.1 Specimen Performance

A shear force versus a rotation angle of the beam is plotted for all specimens in Figure 4. As observed in Figure 4, all specimens exhibited stable hysteretic behavior during 1/50 radian rotation angle cycles. Locally buckled beam flange led to degrading hysteretic characteristics over 1/50 radian rotation angle cycles. Locally buckled beam flanges grew up shown in Fig. 5. As compared in place of the locally buckled beam flanges, those of test specimen BOX_G and H_G were observed at the toe of the gusset-plate.

"Skelton curves", which are cut out from overall behaviors of the beam, are plotted for all specimens in Figure 6. The gusset-plate attached led to a roughly 35% increase in the yield strength. It was indicating that the

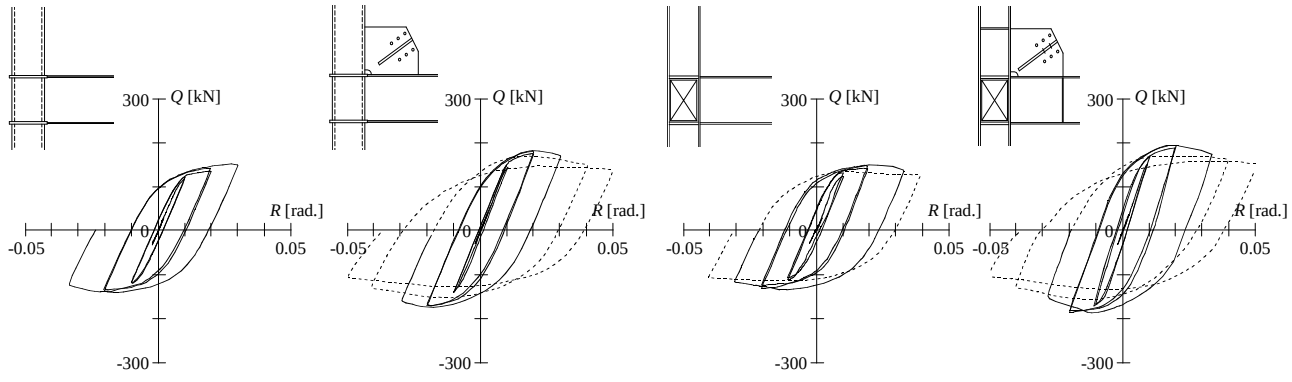

Figure 4 Overall behaviors of the beam with gusset-plate connections:
(a) Box_B; (b) Box_G; (c) H_B; (d) H_G

Figure 5 Photographs of locally buckled beam flange of test specimen
(a) Box_B; (b) Box_G; (c) H_B; (d) H_G

critical section of the beam was moved to the toe of the gusset-plate. And a roughly 25% increase in initial elastic stiffness was caused by the gusset-plate in specimen H_G. On the other hand, initial elastic stiffness in specimen BOX_G was increased by only 5%, indicating that RHS column is hardly affected by the presence of the gusset-plate when a rectangular hollow section (RHS) was used for the column.

3.2 Distribution of the principal stress at the gusset-plate

Distribution of bending moments at the beam and columns at the cycle of ±1/200 radian amplitude is shown in Figure 6. Bending moments were decreased between the toe of the gusset-plate and beam-end by the presence of the gusset-plate. It was indicating that shear forces were transferred between the beam, the column, and the gusset-plate. On the other hand, bending moments were hardly affected by the presence of the gusset-plate when a rectangular hollow section (RHS) was used for the column.

3.3 Distribution of bending moments at the beam and columns

Distribution of bending moments at the beam and columns at the cycle of ±1/200 radian amplitude is shown in Figure 7. Bending moments were decreased between the toe of the gusset-plate and beam-end by the presence of the gusset-plate. It was indicating that shear forces were transferred between the beam, the column, and the gusset-plate. On the other hand, bending moments were hardly affected by the presence of the gusset-plate when a rectangular hollow section (RHS) was used for the column.

4. CONCLUSIONS

This paper presents an experimental study of beam-column frame subassemblies to verify structural behavior of the beam affected by the presence of the gusset-plate, removing influences of a brace forces. It was found that effective length of the beam shortened by the presence of the gusset-plate connections. It was indicating that the critical section of the beam was moved to the toe of the gusset-plate. On the other hand, effective length of the column was hardly affected by the gusset-plate when a rectangular hollow section (RHS) was used for the column.

References:

Wada, A., Conner, J.J., Kawai, H., Iwata, M., and Watanabe, A. (1992), "Damage Tolerant Structure", Proceedings of 5th U.S.-Japan Workshop on the Improvement of Structural Design and Construction Practice, 1-13

Mahin, S., Uriz, P., Aiken, I., Field, C., and Ko, E. (2004), "Seismic Performance of Buckling Restrained Braced Frame Systems", 13th World Conference on Earthquake Engineering, Paper No.1681

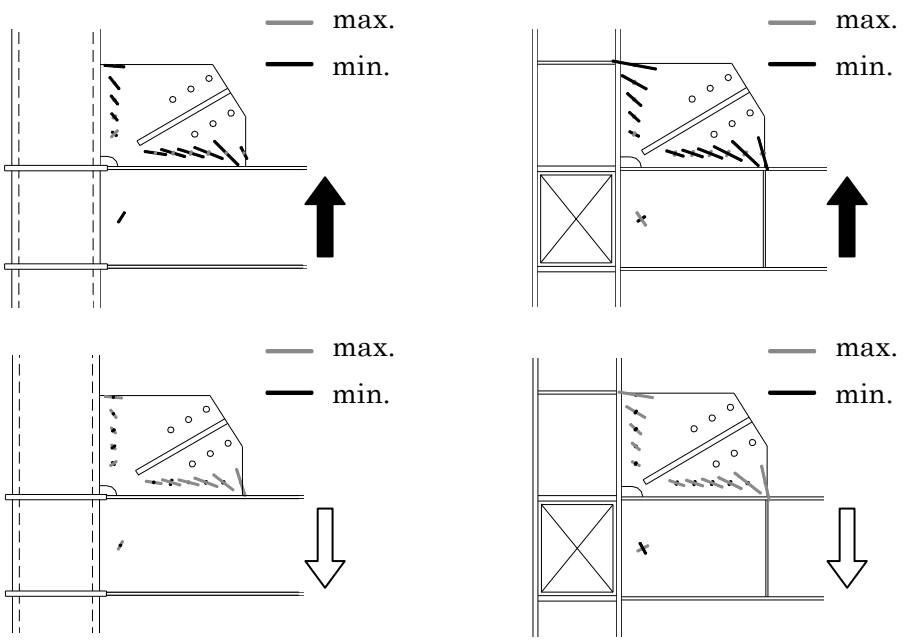

(a) (b)

Figure 6 Distribution of the principal stress at the gusset-plate:
(a) Box_G; (b) H_G

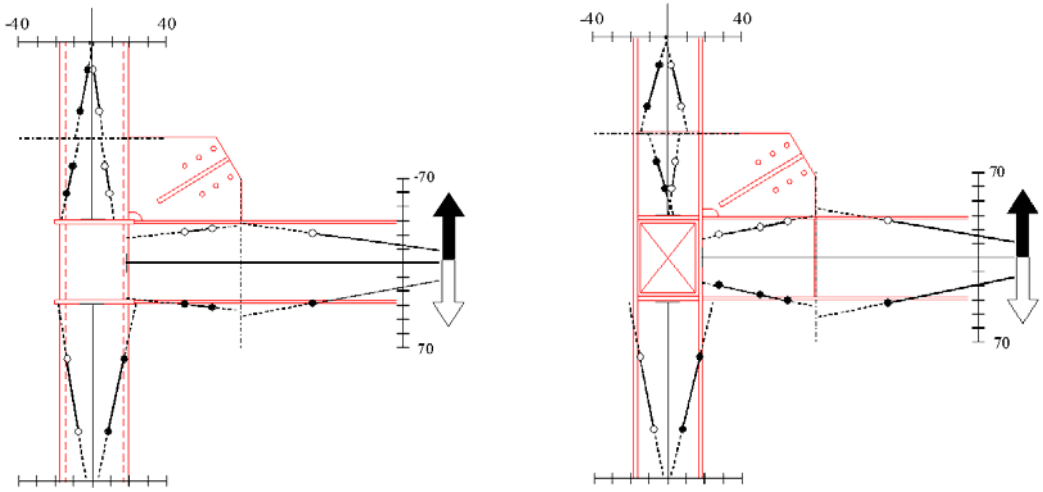

(a) (b)

Figure 7 Distribution of bending moment at the beam and column:
(a) specimen Box_G; (c) specimen H_G (unit:kN-m)

Sixth International Conference on Urban Earthquake Engineering
March 3-4, 2009, Tokyo Institute of Technology, Tokyo, Japan

ELASTO-PLASTIC BEHAVIOR OF PANEL ZONE WITH CONCRETE SLAB

Yuko Shimada[1], Yuichi Matsuoka[2], Satoshi Yamada[3], and Keiichiro Suita[4]

1) Graduate student, Structural Engineering Research Center, Tokyo Institute of Technology, Japan
2) Hyogo Earthquake Research Center, NIED, Japan
3) Assoc. Professor, Structural Engineering Research Center, Tokyo Institute of Technology, Japan
3) Assoc. Professor, Dept., of Architecture and Architectural Eng., Kyoto University, Japan
yuko_shiamda@serc.titech.ac.jp, matsuoka.yuuichi@eng.nsc.co.jp, naniwa@serc.titech.ac.jp, suita@archi.kyoto-u.ac.jp

Abstract: Though a number of studies on the composite effect of the presence of a concrete slab in steel-beam construction have been carried out, studies on the composite effect upon the panel zone are exceptional. Of course, the concrete slab affects not only the beam itself but also the panel zone, since concrete slab of composite beam must transmit compressive force under positive bending. Therefore, the loading point moves up into the slab position from the top flange of the beam, in accordance with the effective depth to which the panel zone extends upward. Although this effect of the presence of a concrete slab on the panel zone has already been noted, insufficient study has been carried out to date. In our study, the structural performance of the panel zone as impacted by this composite effect is investigated via experimental approach. Therefore, a cyclic loading test of a full-scale partial frame was carried out. The specimen consists of a wide-flange sectional beam, a concrete slab, and a square hollow section column. Our experimental results yielded the elasto-plastic hysteretic behavior of the panel zone. This cyclic loading test is a preliminary test of complete collapse test of full-scale steel building at E-Defense in 2007. Obtained data was used to not only prediction of dynamic behavior on building-specimen but also post-test analysis.

1. INTRODUCTION

Generally, steel-frame buildings make use of composite beams that consist of a steel-beam-and-concrete-slab floor construction. Numerous studies over the past four decades have clarified the way in which the composite effect of a concrete slab and steel beam increases the strength and stiffness of a bare steel beam. Likewise, they contribute to our understanding of the failure of steel beams. Some recent studies of beam-to-column connection, such as Nakagomi, T., et. al., (1997), Akiyama, H., et. al., (1998), and a group from The Kinki Branch of The Architectural Institute of Japan (1997), have conducted tests using a bare-steel moment frame. However, studies of beam-to-column connection with the presence of a concrete slab are relatively few: Matsuo, A., et. al., (1998), Tagawa, Y et. al. (1998) and Okada, K. et. al. (2001). Of course, the concrete slab must affect not only the beam itself but also the panel zone. Naka, T., et. al., (1972, 1973, 1979), Kawano, A., et. al., (1993) and Teranishi, K., et. al., (1993) have also studied composite effect for the panel zone. They have pointed out that the loading point moves up toward the slab position from the top flange, in accordance with the effective depth of the panel zone as it extends upward. However, mere experimental research is insufficient. For example, the composite effect in a moment frame consisting of a square hollow section column upon the detailed seismic performance of the panel zone has never been clarified. In our study, seismic performance in the panel zone, yielding earlier than the beam, is clarified by means of a cyclic loading test. Moreover, our test was conducted as one of the preliminary studies to the full-scale complete collapse test at the E-Defense in 2007.

2. CYCLIC LOADING TEST

2.1 Test Specimen

The specimens are three partial frames which contain column-to-beam connection. Each beam and orthogonal beam are RH-400 200 8 13 (SN400B), each column and panel zone are □-300 300 9 (BCR295). All of member is made by same lot steel as the building specimen of the complete collapse test in E-Defense. Figure 1 shows the composition of specimen 2 which has the same detail as complete collapse test. Parameters of the specimen are existence of weld access hole and concrete slab as shown in Table 1. All of specimen used solid weld tab. Specimen 3 is employed the advanced-type weld access hole according to the Japanese Code JASS6 (Architectural Institute of Japan. 1996). Both specimens 2 and 3 have 2,000 mm width concrete slab. Concrete slab is composed of deck-plates and normal strength concrete. Deck plates having 1.2 mm thickness and 175 mm ditch height are set in a parallel with the direction of the beam axis. Deck plates are also used as formwork for concrete and average thickness of concrete is 100 mm. In order to make complete composite beam, stud-bolts with heads whose lengths are 110 mm and

diameters are 19 mm are welded on the beam into two rows at 150～160 mm interval. The welded wire mesh (φ6@150 150) are located in 30mm depth under surface of concrete. Moreover, steel-bars (D10 or D13) for preventing crack on the wire mesh as shown in Figure 1.

Table 2 and Figure 2 are shown the results of steel material based on the coupon test by JIS-1A test piece. The yield strength of column is 10% larger than the standard lower limit value. Otherwise the yield strength of beam flange is roughly 40% larger than the standard lower limit value. Consequently the full-plastic moment of steel beam (*bMp*) is 427 kNm and the full-plastic moment of panel zone (*pMp*) is 386 kNm, which is 90% of *bMp*. The large plastic deformation is predicted to occur in panel zone with concrete slab. It's because that the strength of beam is increased by the effect of concrete slab in positive bending and strain hardening. The concrete characteristics are shown in Table 3.

2.2 Test Procedure

The test setup is shown in Figure 3. Both top and bottom of the column are supported as pins. Cyclic shear force is loaded at the end of the beam. Lateral supports are located near the loading position in or-der to avoid occurring lateral buckling.

The measurement system is shown in Figure 4. The shear force at the end of the beam (Q) is acquired by measured value of the load-cell in the oil-jack. Here, the rotation of oil-jack accompanied deformation of specimen is corrected. The vertical displacement at the loading point is measured by potentiometer-type transducers. The vertical and lateral displacements in the four corners of panel zone are measured by L. V. D. T. located around the panel zone. Figure 5 shows the forces and the displacements operated in speci-men.

Table 1 Parameter of the Test specimen

Specimen	Parameter		notes
	weld access hole	concrete slab	
No.1	×	×	bare steel specimen
No.2	×	○	
No.3	○	○	

Table 2 Steel characteristics

	σ_y [N/mm^2]	σ_u [N/mm^2]
Flange (Beam)	326	454
Web (Beam)	373	482
Column	330	426
Panel Zone		

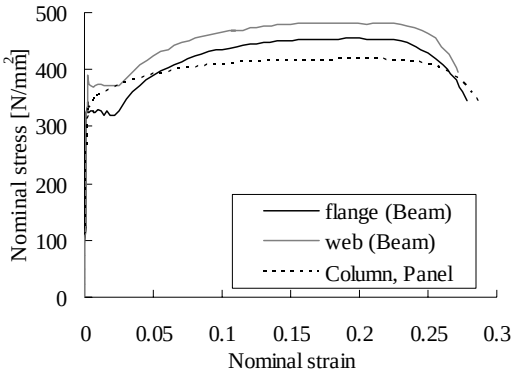

Figure 2 Nominal stress versus nominal strain

Table 3 Concrete characteristics

Age [day]	7	28	33
Compression strength [N/mm^2]	16.7	25.1	25.8
Elastic stiffness [10^4 N/mm]	2.315	2.561	2.584
Tension strength [N/mm^2]	1.08	2.18	2.22

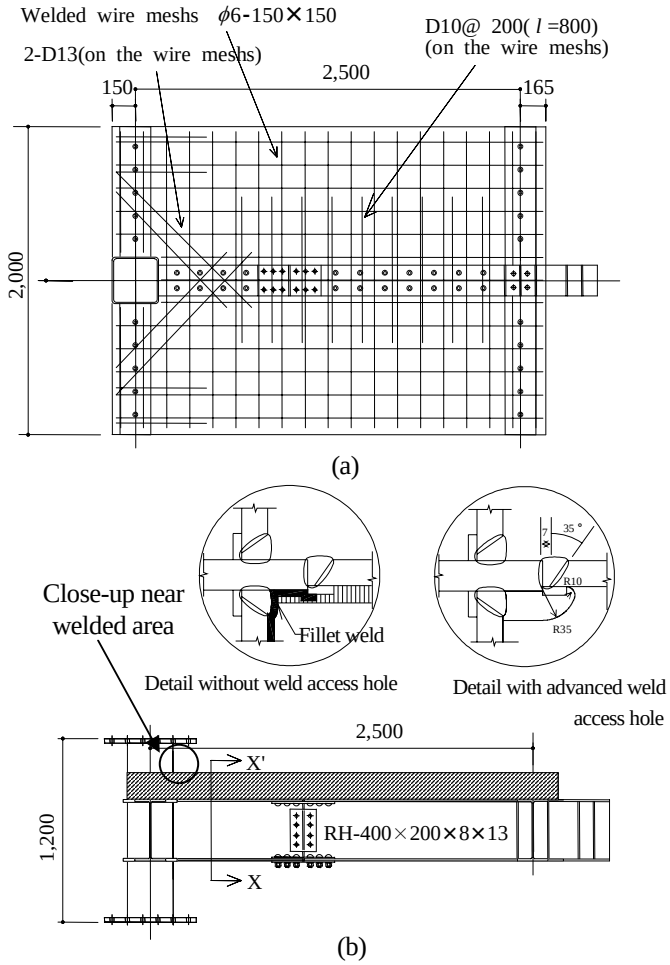

Figure 1 Specimen (No.2): (a) Plan, (b) Elevation, and (c) Section (X-X')

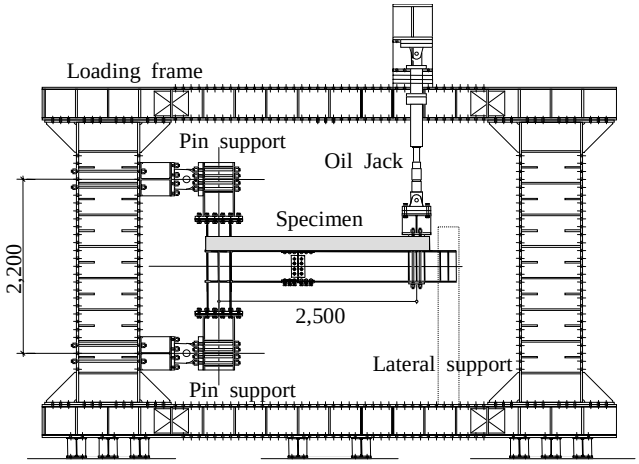

Figure 3 Test setup

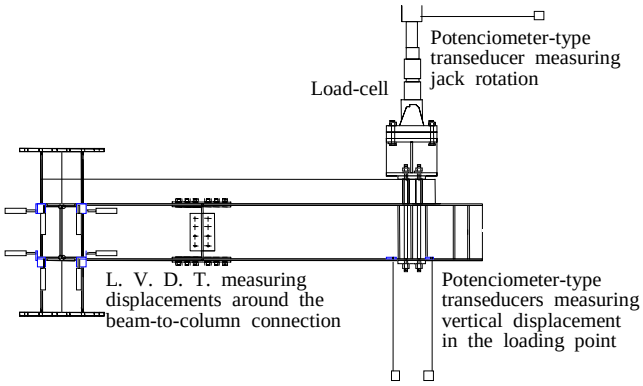

Figure 4 Measurement

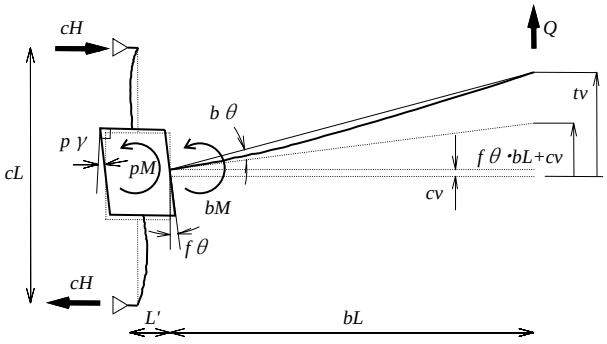

Figure 5 Forces and displacements

where,

Q: shear force operated at the end of beam

bL: bending span length of beam,

bM: moment operated at the end of beam (=*Q*・*bL*),

bθ: rotational angle of beam (=[*tv*- *fθ*・*bL*+ *cv*]/ *bL*)

tv: vertical displacement at the loading point

fθ: rotational angle of column face

cv: vertical displacement of column face

pM: panel moment (=*bM* - *cH*・*bd*)

cH: shear force of column (=- *cH Q*・(*bL*+ *L'*)/ *cL*)

L': horizontal distance between the end of beam and the center of pin

cL: distance between two pins

bd: distance between two centers of gravity in flange of beam

pγ: shear deformation angle of panel zone

The loading patterns of each specimen are shown in Figure 6. Loading is controlled by the rotational angle of beam (*bθ*). The twice of elastic rotational angle of beam (*bθp*) is base unit of loading. The amplitude is increased by 2 *bθp* after every two cycles. Only specimen 1 is loaded against this rule when the panel zone of it deformed significantly in the positive bending side.

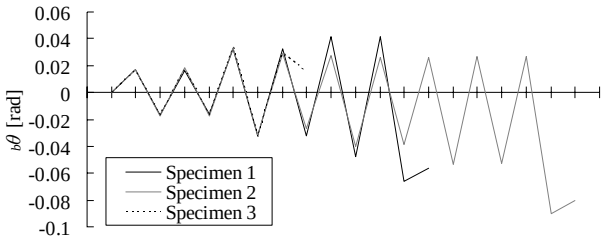

Figure 6 Loading pattern

2.3 Test Results

The relationships between panel moment *pM* and shear deformation angle *pγ* of each specimen are shown in Figure 7, 8, 9. Also, the relationships between beam moment *bM* and rotational angle of beam *bθ* of each specimen are shown in these Figures. Break lines in each graph show the elastic stiffness of bare steel members; *pKe* or *bKe*, and also show the full-plastic moments calculated by *σy* of coupon test; *pMp* or *bMp*.

The panel zone of specimen 1 was occurred large plastic deformation because the strength of beam in-creased by strain hardening. When specimen was under the first negative cycle for 6*bθp*, the beam of this specimen reached the maximum strength by local buckling on the flange occurred near the connection. After that, beam strength deteriorated gradually. The elastic stiffness of panel zone obtained test is generally corresponded to the elastic stiffness of bare steel member (*pKe*). The elastic stiffness of beam is roughly 85% of *bKe*, because its joint efficiency deteriorated.

Both the full-plastic moments of panel zone and beam are corresponded to the calculated values.

Specimen 2 which was without weld access hole was damaged at panel zone when specimen was under the first positive cycle for 4*bθp*. Its panel zone deformed significantly because of increasing its beam strength. Accompanied large deformation of panel zone, the positive stroke of jack was shorter than negative stroke. Therefore, after the first negative cycle for 4*bθp*, this specimen was loaded in positive side till stroke of jack reached its limit. While negative load was as it stands. The beam of specimen 2 reached the maximum strength by local buckling on the flange under the first negative cycle for 4*bθp*. After the maximum strength is observed, beam strength began to

deteriorate and its deterioration grew larger step by step.

Under the first positive cycle, both initial stiffness and unloading stiffness of panel zone are higher than elastic stiffness of bare steel member. Also the full-plastic moment is higher than moment value of bare steel member as shown in the previous studies. Under the first negative cycle, both stiffness and full-plastic moment are corresponded to the each value of bare steel member. Thus, the twist stiffness strength of panel zone are changed. Under positive bending force, strength of panel zone reaches the full-plastic moment of bare steel member. Once it reaches the value, strength of panel zone grows higher gradually observing somewhat slip behavior, after that, it settles down. The reasons the rise of stiffness and strength are that the effective volume of panel zone increases and that concrete slab and orthogonal beam conduct moments to panel zone. Especially slip behavior shows that a position of compressive force operated in the panel moves from upper flange of beam to inside of concrete slab.

Whereas, under negative bending force, stiffness and strength of panel zone after the first cycle are also corresponded to the each value of bare steel member. The initial stiffness of beam in specimen 2 is roughly twice as elastic stiffness of bare steel member under positive bending force. The full-plastic moment of specimen 2 determined

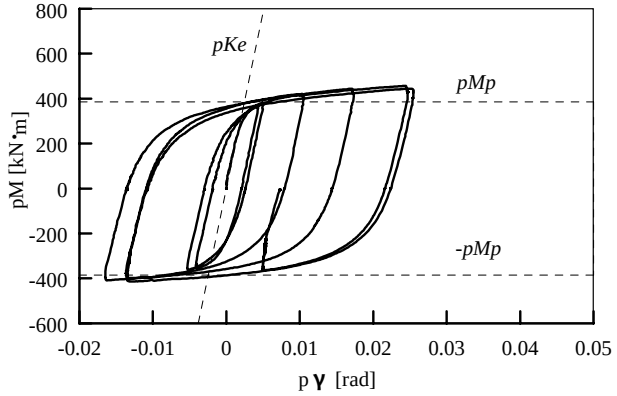

(a) Panel Zone

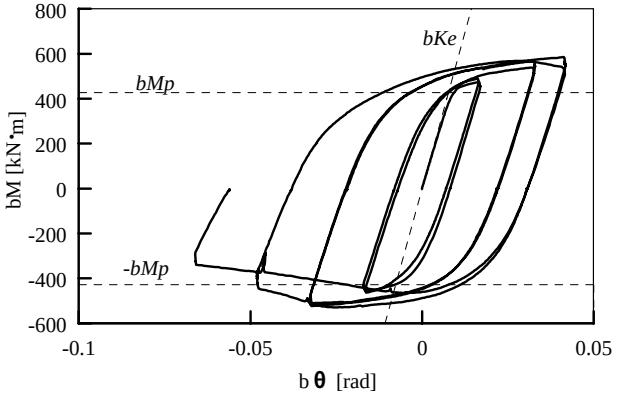

(b) Beam

Figure 7 Moment versus rotation relationship (Specimen 1)

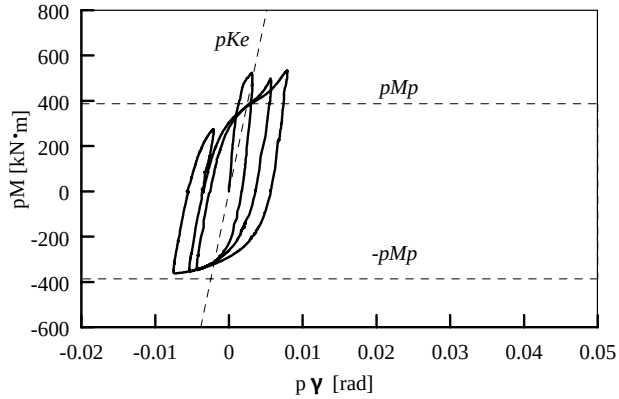

(a) Panel Zone

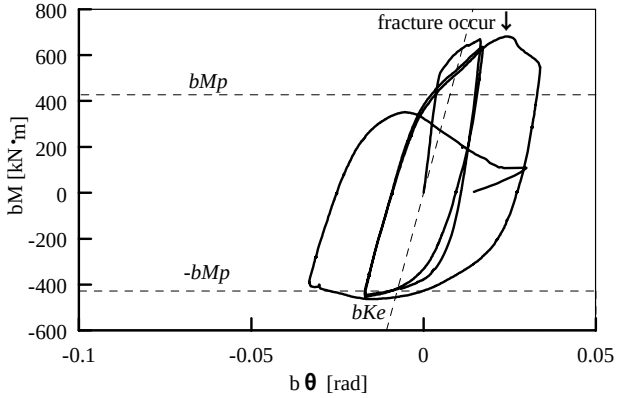

(b) Beam

Figure 8 Moment versus rotation relationship (Specimen 2)

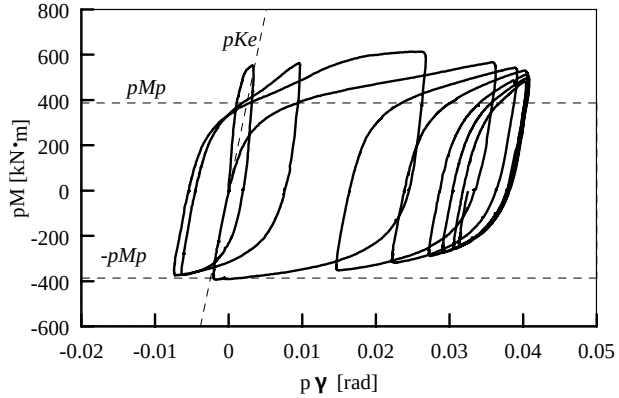

(a) Panel Zone

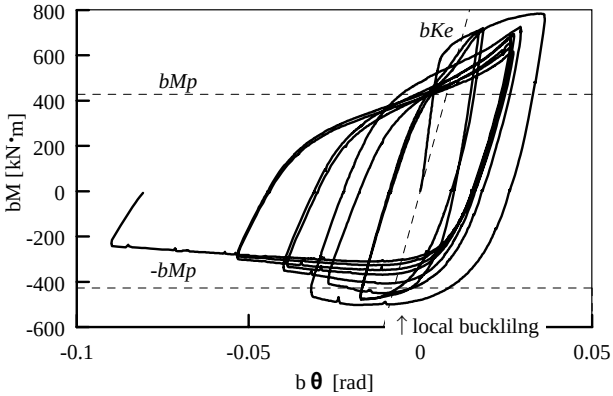

(b) Beam

Figure 9 Moment versus rotation relationship (Specimen 3)

from the relationship between moment and rotational angle [Appendix 2] is 1.4 times higher than the full-plastic moment of bare steel member. Specimen 3 is consisted by weld access holes and composite beam. During the first positive cycle for $4b\theta p$, ductile fracture at beam from the base of scallop proceeded. As soon as fracture occurred, strength of specimen reached the maximum value and began to deteriorate. After that local buck-ling is observed at the end of beam under the first negative cycle for $4b\theta p$, and the lower flange of beam is broken under the next positive cycle. Its panel zone deformed smaller than panel deformation of specimen 2 because of occurring break of beam at the earlier stage.

Both initial stiffness and strength of panel zone are higher than elastic stiffness of bare steel member as same as specimen 2. The initial stiffness of beam is also roughly twice as elastic stiffness of bare steel member under positive bending force. However the full-plastic moment of specimen 3 determined from the relationship between moment and rotational angle is 1.3 times higher than the full-plastic moment of bare steel member. It's because that the partial loss of web area by scallop brings growth of strength less than specimen 2.

The relationship between panel moment versus shear deformation angle of panel zone in specimen 2 and 3 is compared as shown in Figure 8. The behaviors of two specimens are well corresponded each other expect strength of specimen 2 as is rather higher than specimen 3. The stiffness and strength of two specimens under negative bending force are also corresponds, therefore, it is confirmed that the differences about beam-to-column connection details not affect the behaviors of panel zone.

3. CONCLUSIONS

In order to evaluate the seismic performance of a panel zone in composite beam construction, a series of cyclic loading tests in a weak panel-type partial moment frame were conducted. The specimen consists of a composite beam and a square hollow section column. The significant finding here is that panel strength under a positive bending force is greater than the strength of a bare steel member, as also re-ported in previous studies. This is because the con-crete slab contributes to increase beam strength, so that the relationship of panel moment versus the panel shear deformation angle is shown to be slip-shaped under cyclic loading.

Acknowledgements:

This study is a part of 'NEES/E-Defense collaborative re-search program on steel structures' and was occupied by the Building Collapse Simulation Working Group (WG). The Japan team leader for overall program is Kazuhiko Kasai, Tokyo Institute of Technology, and the WG leader is Keiichiro Suita, Kyoto University.

References:

Nakagomi, T., Fujita, T., Minami, K., Lee, K. & Murai, M. 1997. Study on beam-end details for the method of non-scallop on beam-to-column welded joints, Journal of struc-tural and construction engineering. Transactions of AIJ No. 498: 145-151

Committee on Steel Building Structures The Kinki Branch of The Architectural Institute of Japan 1997. Full-Scale Test on Plastic Rotation Capacity of Steel Wide-Flange Beams Connected with Square Tube Steel Columns: Osaka: The Architectural Institute of Japan

Akiyama, H., Yamada, S., Matsumoto, Y., Matsuoka, S., Ogura, K. & Kitamura, H. 1998. Study on fracture of beam-to-column connections by means of full scale shak-ing table test, Journal of structural and construction engi-neering. Transactions of AIJ No. 512: 165-172

Matsuo, A., Nakamura, Y., Takenouchi, T., Mukudai, Y. Ta-kamatsu, T. & Matsui, Y. 1998. A study on deformation capacity of the steel column-to-composite beam welded joint, Part1: Experimental planning & Part2: Experimen-tal result, Summaries of technical papers of Annual Meet-ing Architectural Institute of Japan. C-1, Structures III: 427-430

Tagawa, Y., Yang, I. & Takeshita, K. 1998. A study on the behavior of composite girder under the influence of girder-to-column detail, Part.1 to Part2, Summaries of technical papers of Annual Meeting Architectural Institute of Japan. C-1, Structures III: 431-436

Okada, K., Oh, S., Yamada, S., Imaeda, Y., Yamaguchi, M. & Wada, A. 2001. Experimental study on deformation capac-ity of composite beams with conventional type beam-to-column connections: Evaluation of earthquake resistance of steel moment frames considering deformation capacity of composite beams Part 1, Journal of structural and con-struction engineering. Transactions of AIJ No. 547: 161-168

Naka, T., Umino, S., Nakao, M. & Osano, H. Connection Composed of H-shaped Column and Composite Beams –Report I –, Summaries of technical papers of Annual Meet-ing Architectural Institute of Japan (1972). : 1869-1870, –Report II –, Summaries of technical papers of Annual Meeting Architectural Institute of Japan (1973). : 1259-1260, –Report III –, Summaries of technical papers of An-nual Meeting Architectural Institute of Japan (1979). : 1565-1566

Kawano, A., Asega, H. & Hasebe, H. 1993. An Experimental study on Ductility of Wide-flange Steel Frame with Com-posite Beam including Weak Joint Panel in Different Col-lapse Modes, Journal of structural and construction engi-neering. Transactions of AIJ No. 452: 109-119

Teranishi, K., Mukudai, J., Takamatsu, T. & Matsuo, A. 1993. Experimental Study on Restoring Force Characteristics of Box Column-to-beam Connections under Cyclic Loading : Part 2. Specimens with Composite Beams, Summaries of technical papers of Annual Meeting Architectural Institute of Japan. C, Structures II : 1253-1254

Architectural Institute of Japan, 1996. Japanese architectural standard specification JASS 6 steel work: The Architec-tural Institute of Japan

APPENDIX 1

Our test has been conducted as a preliminary consideration for a four-story and full-scale complete collapse test of steel building. Figure A1 is shown the correspondence of specimens between our test and complete collapse test. As shown previously, our specimen is partial frame of the complete collapse test and is consisting of beam-to-column connection with weak panel and half span of beam from connection. The shown area is not only instability but also twist force in cyclic loading test because

concrete slab is set only one side. In order to avoid them, our specimen is settled orthogonal beam with concrete slab in both side of column. Therefore, stud bolts in our specimen is set into two rows because the force propagated from concrete slab to steel beam at a positive bending load is twice as specimen of complete collapse test.

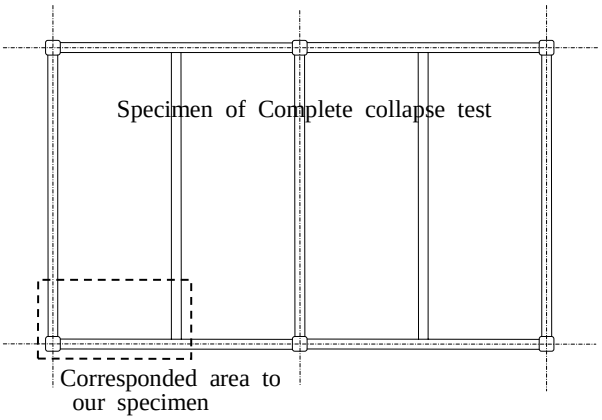

(a)

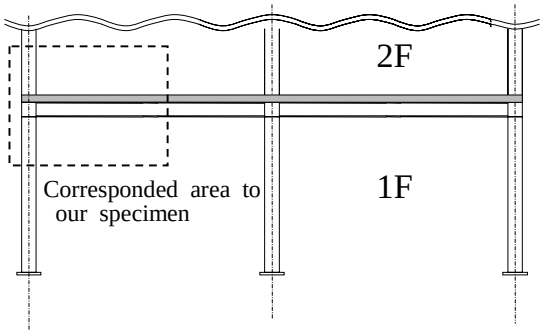

(b)

Figure A1 Close-up of the complete collapse test: (a) Plan, and (b) Elevation

APPENDIX 2

The full-plastic moment of test *Mpe* is decided as shown Figure A2. First, the intersection between the line having the half of initial stiffness in our test and the hysteresis is acquired. Secondary, the tangential line of the hysteresis is drawn from the intersection. Finally, the intersection between the tangential line and initial stiffness line is acquired and obtained moment at the intersection is *Mpe*.

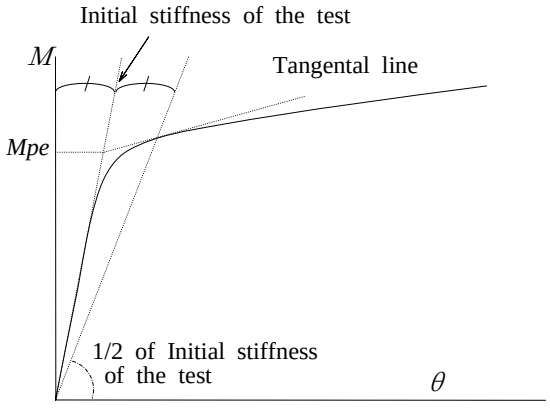

Figure A2 Full-plastic moment in the experiment

Sixth International Conference on Urban Earthquake Engineering
March 3-4, 2009, Tokyo Institute of Technology, Tokyo, Japan

LOCAL BUCKLING FAILURE CONDITIONS FOR BUCKLING RESTRAINED BRACES

Ryota Matsui[1)], Toru Takeuchi[2)], Jerome F. Hajjar[3)]
Kohji Nishimoto[4)] and Ian D. Aiken[5)]

1) Doctoral Student, Dept. of Architecture and Building Engineering, Tokyo Institute of Technology, Tokyo, Japan
2) Associate Professor, Dept. of Architecture and Building Engineering, Tokyo Institute of Technology, Japan
3) Professor, Dept. of Civil and Environmental Engineering, University of Illinois at Urbana Champaign, Illinois, USA
4) Manager, Nippon Steel Engineering, Tokyo, Japan
5) Principal, Seismic Isolation Engineering, California, USA
ttoru@arch.titech.ac.jp, matsui.r.aa@m.titech.ac.jp, jfhajjar@ad.uiuc.edu
nishimoto.kohji1@eng.nsc.co.jp, ida@siecorp.com

Abstract: Buckling Restrained Braces (BRBs) are commonly used as ductile bracing elements in seismic zones. A key limit state governing BRB behavior is overall flexural buckling. However, when the wall thickness of the steel tube restrainer is relatively small compared to the cross section area of the core plate, the restraint conditions against the local buckling of the core plate can be critical for the stability and strength of the BRB. In this study, cyclic loading tests and numerical analyses on BRBs are carried out using various tube restrainer configurations, and local buckling restraint conditions are discussed using these results.

1. INTRODUCTION

Buckling restrained braces (BRB) comprise a steel core plate restrained by a concrete in-filled tube. Developed for practice in the 1980s in Japan, BRBs have been employed in more than three hundred buildings as ductile bracing members or hysteretic dampers. The conditions under which the BRB obtain a stable hysteresis can be classified as follows.

(a) When an axial force is applied to the core plate, the steel tube restrainer must have sufficient stiffness to prevent overall buckling.
(b) Since the core plate section expands when compressed in the plastic range, a certain amount of clearance must be provided between core plate and restrainer to prevent the core plate from prematurely bearing against the restrainer, thus transferring significant axial force to the restrainer through friction and potentially causing overall buckling of the BRB.
(c) When the core plate buckles within the above mentioned clearance, out-of-plane force components are produced at each corner of the buckling wave. Therefore, the walls of the restrainer should possess sufficient stiffness and strength to restrain the core plate.
(d) The connections at the both ends of the BRB must possess sufficient stiffness and strength for the BRB to maintain stable performance under an expected maximum force and deformation.
(e) The effective buckling length for designing BRB should be determined taking into account of the stiffness of its connections.

The condition of the BRB restrainer necessary to prevent overall buckling (a) have been discussed by Fujimoto, Wada et al. (1991), indicating that the core plate yield force needs to be smaller than Euler's buckling force of the restrainer. The appropriate conditions for clearance between the core plate and the restrainer (b) were also discussed by Fujimoto, Wada et al. (1991), for a core plate within a rectangular steel tube, by Takeuchi, Suzuki et al. (2005), for a core tube with an outer tube restrainer. In their study, the condition of core plate local buckling (c) was discussed by using an elastic spring of in-filled mortar, and it was concluded that there are very few possibilities for local buckling failure in an ordinary BRB. The effects of BRB connection stiffness (d) have been researched by Takeuchi, Yamada et al. (2004). K.C.Tsai et al. (2008), and Roeder et al. (2006). The effective buckling length of BRBs was researched by Inoue et al. (2004) by considering the stiffness of the connections (e).

However, for condition (c), it has been reported that there are risks of local buckling failure where the wall thickness of the restrainer and mortar thickness at the edge of the core plate are relatively small compared to the sectional area of the core plate by Iwata et al. (2007). In such a case, the core plate buckles locally about the strong axis, the wall of the restrainer is unable to prevent it, as shown in Fig. 1, and such a failure can lead to overall buckling. In this study, BRBs with rectangular and circular tube restrainers with various thickness ratios are subjected to cyclic loading tests, and the behavior of the local buckling failure of the restrainer is investigated both in these experiments and corroborating finite element method (FEM) analyses. This is followed by a proposal for the criteria preventing this failure mode.

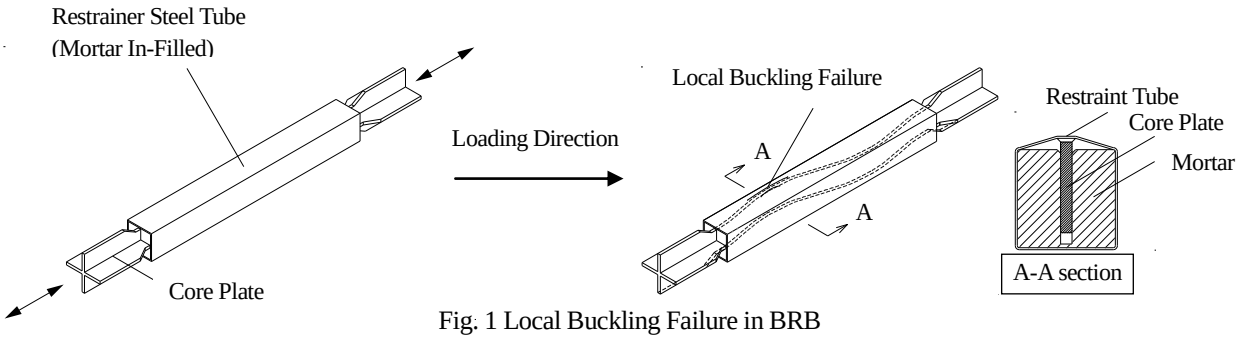

Fig. 1 Local Buckling Failure in BRB

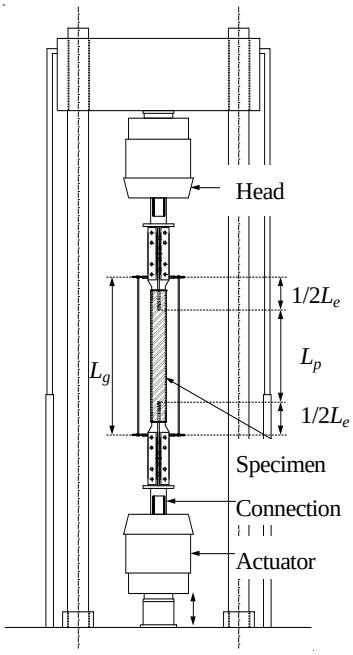

Fig. 2 Setup of Uniaxial Cyclic Tests

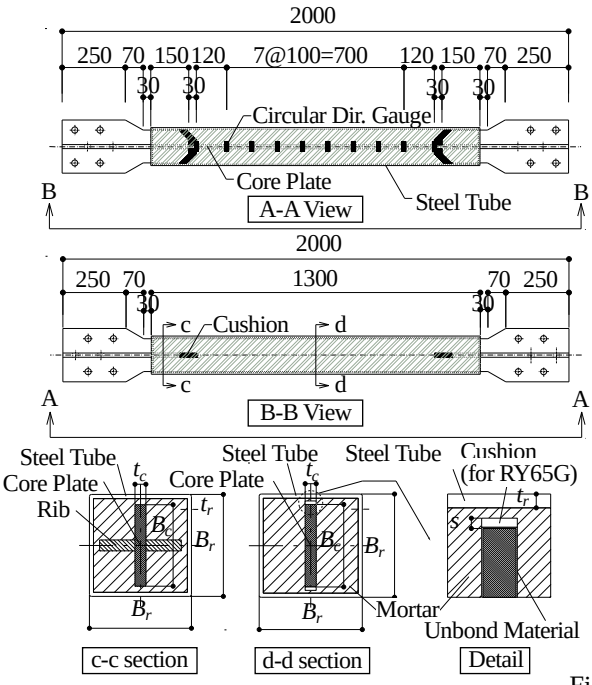

Fig. 3 Uniaxial Cyclic Loading Test Specimen

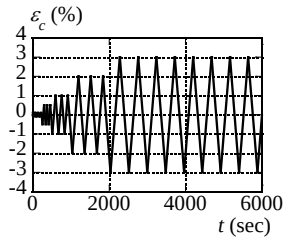

Fig. 4 Test Program of Uniaxial Cyclic Tests

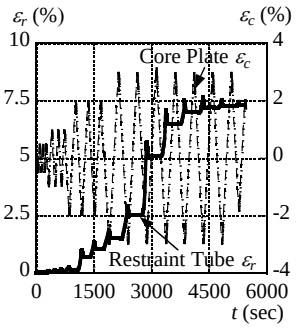

Fig. 5 Restrainer Strain Transition (RY65)

Table 1 Details of the Specimens in Uniaxial Cyclic Loading Tests

Specimen	B_r (mm)	t_r (mm)	Steel Tube	σ_{ry} (N/mm^2)	B_c (mm)	t_c (mm)	Core Plate	σ_{cy} (N/mm^2)	P_{cy}(kN)	s (mm)	Local Buckling Failure
RY25	150	6	STKR400	350.2	130	16	SS400	261.0	542.9	1.0	None
RY65		2.3	SPHC-P	351.2						1.0	Occurred
RY65G										6.0	
CY83	165.2	2		231.2						1.0	None

2. UNIAXIAL CYCLIC LOADING TEST

2.1 Loading Conditions

To confirm the possibility of local buckling failure, cyclic loading tests on BRB were carried out at the University of Illinois at Urbana-Champaign. The setup of the uniaxial cyclic loading test is shown in Fig. 2. Both ends of the BRB are rigidly supported and a cyclic axial force is applied along its axis. The characteristics of the specimens are listed and shown in Table 1 and Fig. 3. The core plate is 16x130, and a cushion piece is added only in RY65G at the edge of the core plate to increase the clearance and to clarify the effect of the clearance on local buckling failure. The loading program of the tests is shown in Fig. 4. The force applied to the BRB is measured by a load cell in the test machine, and axial displacement of the BRB is measured by extensometers installed between both end steel plates. The displacement of the plastic zone of the core plate is defined as δ_c and is estimated by Eq. (1):

$$\delta_c = \delta_g - \frac{P_c}{A_e E_{c0}} L_e \tag{1}$$

where δ_g is the initial extensometer displacement in L_g (the extensometer distance is shown in Fig. 2); P_c is the core plate axial force, A_e is the cross section of the core plate at connections, E_{c0} is the elastic modulus of the core plate, and L_e is the initial length of elastic zone in the connections. From these, the strain of the plastic zone of the core plate ε_c

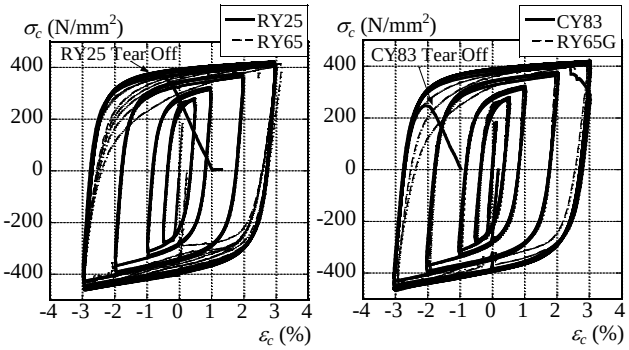

Fig. 6 Hysteretic Stress-Strain Curve of Core Plate (Uniaxial Cyclic Loading Tests)

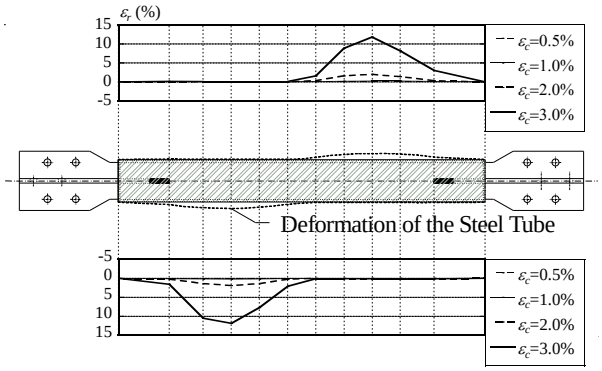

Fig. 7 Strain Distribution of Restraint Tube (RY65)

Photo 1 Local Buckling Failure

is calculated by Eq. (2), where L_p is the initial length of plastic zone:

$$\varepsilon_c = \frac{\delta_c}{L_p} \tag{2}$$

2.2 Results of Cyclic Loading

The surface strain of the buckling restrainer of RY65 along the loading is shown in Fig. 5, and the hysteretic curves of core plate obtained from the test are shown in Fig. 6. RY25 with a thick restrainer wall and CY83 with a circular restrainer showed no local buckling failure, and displayed stable stress-strain curves until the fatigue fracture of the core plates. On the other hand, RY65 and RY65G with a thin restrainer showed local buckling failure at 2% strain amplitude. The local deformation of the restrainer wall grew significantly during the cyclic loading, and the test was stopped when the connection of the BRB became unstable due to the influence of eccentric deformation. As shown in Fig. 5, the initial strain of the restrainer wall was not significant at early stage; however, it increased dramatically along the cyclic loading at amplitude of the strain greater than 2% (Photo 1). As in Fig. 6, the stiffness reduction occurred earlier in RY65G than in RY65. This means that the additional clearance, besides the core plates, influences local buckling failure. The distribution of strain along the restrainer wall is shown in Fig. 7; the figure indicates that the strain increases considerably where out-of-plane deformation of the restrainer is observed.The restrainers were disassembled after the tests and the core plates of RY25 and CY83 showed no local buckling. On the other hand, the core plates of RY65 and RY65G showed significant wave deformation about the strong axis with the mode depicted in Fig. 7.

3. FINITE ELEMENT METHOD ANALYSIS OF LOCAL BUCKLING FAILURE

To clarify the local deformation behavior of the restrainer, FEM analyses were carried out. ABAQUS Ver. 6.5-6 was used for analysis, and various models following previous tests were analyzed as follows. In this case, because the mortar was observed to have very limited contribution to the restraint, the core plates were modeled as directly touching the restrainer walls in the analyses, as in Fig. 8. The deformation of the weak axis and rotation of the core plate are restrained, and initial irregularities are introduced to the core plate within the clearance between the core plate and the mortar. A shell element is used for modeling the core plate and restrainer walls, and each element is divided into an approximately regular hexahedron. The material characteristics are modeled as in Fig. 9 following coupon test results. In Fig. 10, the hysteretic curves obtained from analysis are compared with those of the cyclic loading experiment. Both results generally agree, and these analyses simulate well the behavior of the local buckling failure of the restrainer. Various models changing the thickness of the restrainer wall, the clearance between the core plates and the length of the plastic zone of the core plate were prepared, and a constant cyclic load as shown in Fig. 11 was applied.

The strain transition in each case is shown in Fig. 12. The local deformation increases earlier when the restrainer was thinner, and the clearance between the core plate and the restrainer is larger. On the other hand, the length of the plastic zone of the core plate does not affect local deformation behavior. The half length of the local buckling wave of the core plate was kept around $3.5B_c$~$5B_c$ even when the plastic zone length of the core plate changed, as shown in Fig. 13. The strains of the restrainer walls are compared in Fig. 14 and Fig. 15, where local buckling failure is observed.

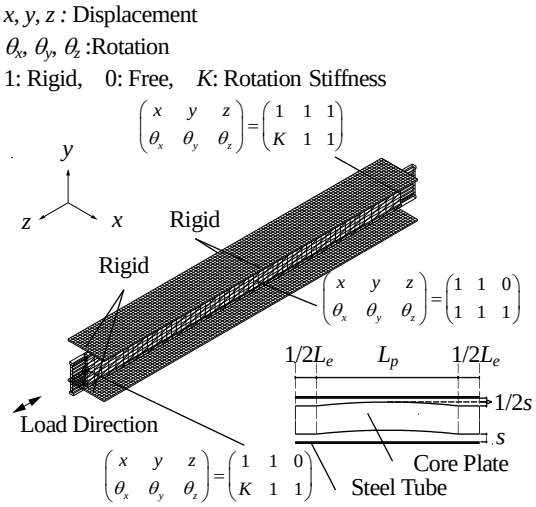

Fig. 8 FEM Analysis Model

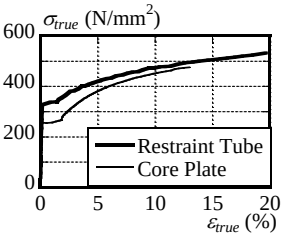

Fig. 9 Material Characteristic

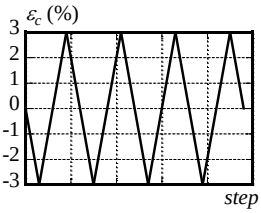

Fig. 11 Input Strain

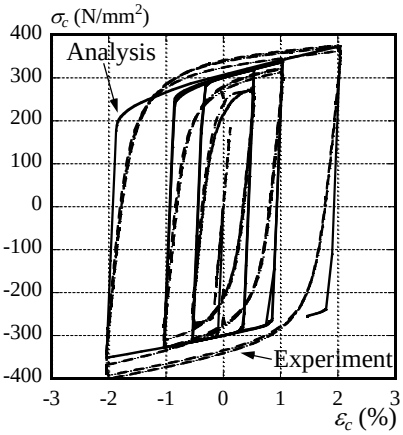

Fig. 10 Stress-Strain Curve of RY65 (FEM versus Experiment)

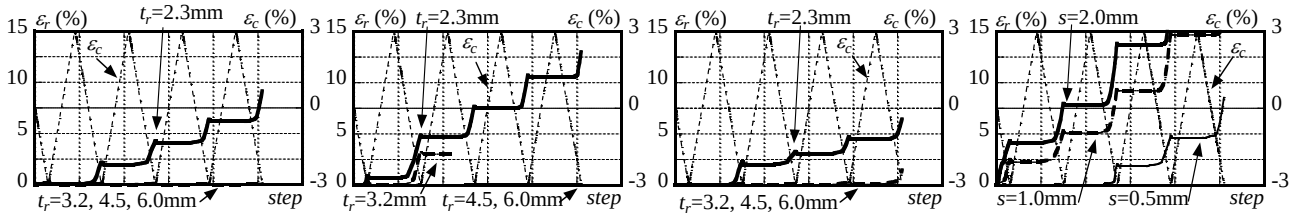

(a) s=0.5mm, L_p=1000mm (b) s=1.5mm, L_p=1000mm (c) s=2.0mm, L_p=1000mm (d) t_r=2.3mm, L_p=1000mm

Fig. 12 FEM Analysis Result of Restraint Tube Strain at Local Buckling Failure

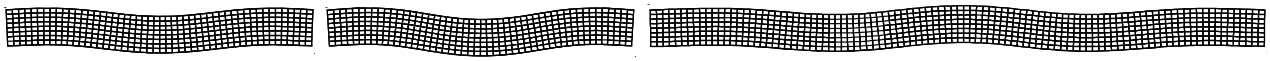

(a) s=0.5mm, L_p=1000mm (b) s=2.0mm, L_p=1000mm (c) s=0.5mm, L_p=2000mm

Fig. 13 Core Plate Deformation (t_r=2.3mm)

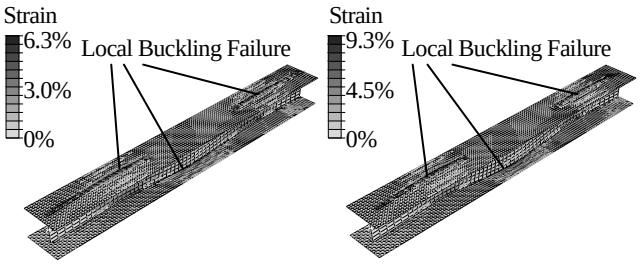

(a) s=0.5mm, L_p=1000mm (b) s=2.0mm, L_p=1000mm

Fig. 14 Strain Distribution Contour (t_r=2.3mm)

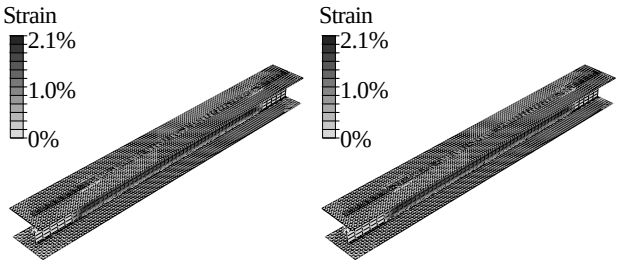

(a) t_r=3.2mm, L_p=1000mm (b) t_r=4.5mm, L_p=1000mm

Fig. 15 Strain Distribution Contour (s=0.5mm)

when the thickness of the restrainer walls is smaller and the clearance between the core plate and the restrainer is larger.

4. DISCUSSION OF LOCAL BUCKLING FAILURE CRITERIA

Based on the results of these experiments and analyses, the length of the local buckling waves of the core plate varies approximately between $3.5B_c$ and $5B_c$. The reason for this behavior is explained as follows. When the core plate buckles within the restrainer as shown in Fig. 16, the number of buckling wave increases with the additional axial force, however, they cease to increase at the point where Euler's buckling forces resulting from the tangent modulus of the core plate reaches the yield strength of the core plate σ_{cy}, as described by Eq. (3):

$$\sigma_{cy} = \frac{P_{cy}}{A_c} = \sigma_{cr} = \frac{\pi^2 E_{tc}}{\bar{\lambda}^2} \tag{3}$$

where A_c is sectional area of the core plate, E_{tc} is tangent modulus of the core plate, and $\lambda = l_p/i_c$ and i_c is radius of moment of inertia of the core plate. The length of the local buckling wave is then determined as Eq. (4):

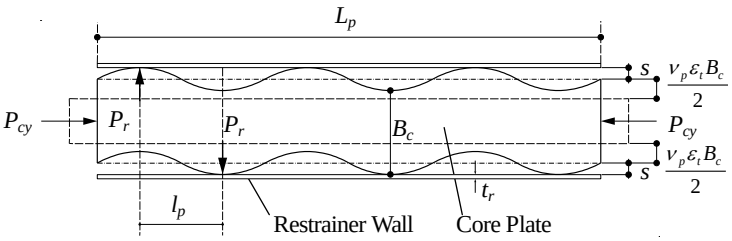

Fig. 16 Local Buckling Failure Model

Fig. 17 Plastic Zone of Restrainer Wall

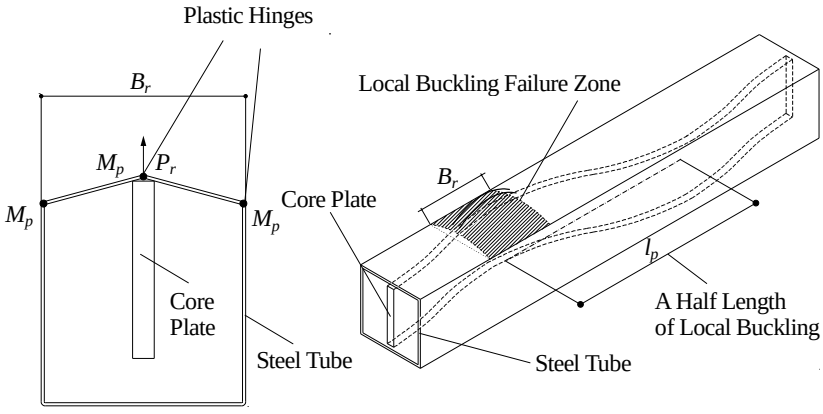

Fig. 18 Local Buckling Failure Mechanism

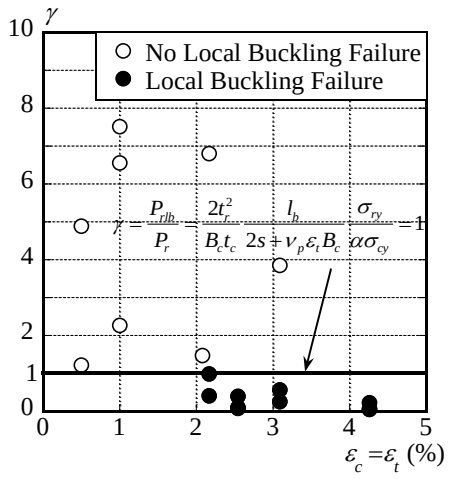

Fig. 19 Condition Confirmation

$$l_p = i_c \bar{\lambda} = \frac{\pi B_c}{2} \sqrt{\frac{E_{tc}}{3\sigma_{cy}}} \tag{4}$$

The length of local buckling wave l_p is determined by the width of core plate and the tangent modulus in the plastic range. Where E/σ_{cy}=832 and the tangent modulus E_{tc}=0.02E, the length of the local buckling wave becomes approximately $l_p = 4B_c$. In the tensile stage, the section of the core plate decreases by $\nu_p \varepsilon_t B_c$, with the plastic Poisson's ratio ν_p=0.5. The clearance between the core plate and the restrainer increases by half of this value. The perpendicular force components working on the restrainer wall can then be calculated by Eq. (5):

$$P_r = \frac{2s + \nu_p \varepsilon_t B_c}{l_p} P_{cy} = \frac{2s + \nu_p \varepsilon_t B_c}{l_p} B_c t_c \sigma_{cy} \tag{5}$$

From the FEM analyses, the length of the zones of the restrainer resisting against this force component is estimated to be approximately equal to the width of the restrainer as shown in Fig. 18. After estimating the collapse mechanism of resistance, the perpendicular force component can be calculated by Eqs. (6) and (7).

$$M_p = \frac{B_r t_r^2}{4} \sigma_{ry} \tag{6}$$

$$P_{rlb} = \frac{8M_p}{B_r} = 2t_r^2 \sigma_{ry} \tag{7}$$

Here σ_y is the yield stress of the restrainer wall. The ratio γ is then defined by Eq. (8) as the ultimate strength of the restrainer wall P_{rlb} divided by the perpendicular force component of the core plate P_r:

$$\gamma = \frac{P_{rlb}}{\alpha P_r} = \frac{2t_r^2}{B_c t_c} \frac{l_p}{2s + \nu_p \varepsilon_t B_c} \frac{\sigma_{ry}}{\alpha \sigma_{cy}} \tag{8}$$

Here ε_t is the maximum tensile strain of the core plate, and α is the increasing ratio of strength after yielding (α=1.2~1.4). The ratio γ represents the safety factor against local buckling failure, and the axial force P_{lb} causing the local buckling failure can be calculated by Eqs. (9) and (10) as follows:

$$P_{lb} = 2t_r^2 \frac{l_p}{2s + \nu_m \varepsilon_t B_c} \sigma_{ry} \tag{9}$$

$$\gamma = \frac{P_{lb}}{\alpha P_{cy}} \tag{10}$$

The γ indexes estimated from previous test specimens are shown in Fig. 19 together with the occurrence of local buckling failure. From this figure, it is observed that all specimens with $\gamma < 1.0$ caused local buckling failure, and the

criteria for the restrainer wall are well explained by this index.

5. CONCLUSIONS

In this study, experiments and numerical analyses were carried out using BRB members with various restrainers, and the phenomenon of local buckling failure encountered in these specimens was investigated. As a result, the following conclusions were obtained:

1) When cyclic loading tests were carried out on BRB specimens with various restrainer thicknesses with thin mortar at the edge of the core plate, local buckling failures were observed in specimens possessing rectangular tubes with a diameter-to-thickness ratio of 65. A significant increase in the strain on the restrainer wall was observed during cyclic loading. On the other hand, specimens containing a rectangular tube with a diameter-to-thickness ratio of 25 and a circular tube with a diameter-to-thickness ratio of 83 did not occasion local buckling failure.
2) From the FEM analyses, the increase of restrainer wall strain is confirmed as becoming more significant with a thinner restrainer wall and a larger clearance between the edge of the core plate and the restrainer. On the other hand, the length of the core plate does not affect local buckling behavior, and local buckling wave lengths are restricted to approximately 4.0 times the core plate width.
3) The local buckling wave length of the core plate can be well explained by the generalized slenderness ratio calculated by employing the tangent modulus. Considering the restrainer wall and the maximum tensile strain of the core plate, a criterion for local buckling restraint failure is established. The condition proposed agrees well with the results of the experiments, and it is considered to be valid for the practical design of BRBs.

Acknowledgements

This material is based upon work supported by Nippon Steel Engineering Co., Ltd. and the University of Illinois at Urbana-Champaign. The authors express thanks to Matthew Eatherton, Grzegorz Banas, and Tim Prunkard for their contributions to this research and experiments. Any opinions, findings, and conclusions or recommendations expressed in this material are those of the authors and do not necessarily reflect the views of either sponsor.

References

Fujimoto, M., Wada, A., Saeki, E., Takeuchi, T., and Watanabe, A. (1991), "Development of a Buckling Restrained Brace," *Quarterly Publication Column*, **115**(9), 91-96 (in Japanese)

Suzuki, K., Takeuchi, T., Marukawa, T., Kimura, Y., Sugiyama, T., Ogawa, T., Kato, S. (2005), "Buckling Behavior of Compressive Tubular Columns with Additional Buckling Restrainer," *International Symposium on Shell and Spatial Structures*, **46**(9), 45-52

Takeuchi, T., Yamada, S., Kitagawa, M., Suzuki, K., and Wada, A. (2004), "Stability of Buckling Restrained Braces Affected by the Out-of-plane Stiffness of the Joint Element," *Journal of Structure and Construction Engineering*, Architectural Institue of Japan, **575**(1), 121-128 (in Japanese)

Tsai, K. C., Hsiao, P. C., Wang, K. C., Weng, Y. T., Lin, M. L., Lin, K. C., Chen, C. H., Lai, J. W., Lin, S. L. (2008), "Pseudo-dynamic Tests of a Full Scale CFT/BRB Frame-Part I :Specimen design, experiment and analysis," *Earthquake Engineering and Structural Dynamics*, **37**, 1081-1098

Charles W. Roeder, Dawn E. Lehman, and A. Christopoulos, "Seismic Performance of Earthquake-Resistant Steel Braced Frames with Buckling Restrained Braces.," Proc., *8th U. S. National Conf. on Earthquake Engineering*, Earthquake Engineering Research Institute, Oakland, Calif., Paper No. 1503

Tembata, H., Koetaka, Y., and Inoue, K. (2004), "Out-of-plane Buckling Load of Buckling Restrained Braces Including Brace Joints," *Journal of Structure and Construction Engineering*, Architectural Institute of Japan, **581**(7), 127-134, (in Japanese)

Iwata, M., Murase, R., Izumita, Y. and Murai, M. (2007), "Experimental Study on Buckling-Restrained Braces Using Steel Mortar Planks – Part3 Buckling Behavior of Core Plate-," *Journal of Structure and Construction Engineering*, Architectural Institute of Japan, **611**(1), 133-139, (in Japanese)

Sixth International Conference on Urban Earthquake Engineering
March 3-4, 2009, Tokyo Institute of Technology, Tokyo, Japan

SHAPE OPTIMIZATION OF UNIDIRECTIONAL FREE SURFACE SHELLS SUBJECTED TO STRONG WIND

Takuzo Yamashita[1], Tomohiko Kumagai[2], Toshiyuki Ogawa[3], Tomoshi Miyamura[4] and Makoto Ohsaki[5]

1) Ph.D. Candidate, Department of Architecture and Building Engineering, Tokyo Institute of Technology, Japan
2) Assistant Professor, Department of Architecture and Building Engineering, Tokyo Institute of Technology, Japan
3) Professor, Department of Architecture and Building Engineering, Tokyo Institute of Technology, Japan
4) Lecturer, Department of Computer Science, Nihon University, Japan
5) Associate Professor, Department of Architecture and Architectural Engineering, Kyoto University, Japan
tyamashi@o.cc.titech.ac.jp kuma@arch.titech.ac.jp togawa@arch.titech.ac.jp miyamura@cs.ce.nihon-u.ac.jp ohsaki@archi.kyoto-u.ac.jp

Abstract: Shape optimization of shell roofs to strong wind is carried out to minimize the maximum vertical displacement. The three dimensional (3D) fluid flow analysis is performed to obtain highly precise dynamic wind load. To reduce the large computational cost of the 3D analysis, the multigrid method (MG method) is employed to solve the pressure Poisson equation. The objective function of the optimization problem is expected to have strong nonlinearity. Employing Response Surface Model (RSM), the objective function is approximated as a smooth function so that computational cost of the optimization is reduced. Analyses for several experimental points are required to generate RSM. As a result, Optimal shapes are obtained in this method, and by using the MG method the computational time become 2.2 times faster.

1. INTRODUCTION

It is important to consider influence of wind action for designing a lightweight space frame structure. In architectural field, wind pressure characteristics of structures has been demonstrated by wind tunnel experiments or computational fluid dynamics simulations.

It is also important to find optimal shape against wind load because influence of wind largely depends on shapes of structure. To date many studies on shape optimization of shell and spatial structures have been presented. However, there are few studies on shape optimization of structures subjected to wind load.

A large-scale three dimensional incompressible viscous fluid flow analysis (herein after referred as 3D fluid flow analysis) using a finite element method is a reliable method to simulate real phenomenon. Huge computational cost is involved in the 3D fluid flow analysis, especially in solving the pressure Poisson equation expressed by the large-scale simultaneous equations. For solving the large-scale simultaneous equations the conjugate gradient method (CG method) is commonly used. Using multigrid method (MG method) as a preconditioning method of the CG method, the computational cost of the pressure Poisson equation can be reduced. The MG method enables the convergence rate of the iterative method to improve using the coarser grid than the original. Miyamura et.al have improved the computational efficiency of 3D fluid flow analyses around shell structures by applying the MG method in which 2D mesh is used as the coarse grid.

It is not easy for multi-peak problem to be optimized based on a sensitivity analysis. The Response Surface Model (RSM) is an effective method for the multi-peak problem because the sensitivity analysis can be easily carried out. The RMS is generated by using the responses from experiments or analyses, and approximates the objective function. The large enough number of data points are required to approximate the objective function accurately. Thus it takes enormous computational time to generate the RSM when carrying out a costly analysis such as 3D fluid flow analysis.

In this paper, our purpose is that using the MG method to the 3D fluid flow analysis the computational time for shape optimization of unidirectional free surface shell subjected to strong wind is reduced and that the method well-applied to this shape optimization problem is realized . The objective function is approximated by the RSM. We see the effect of the MG method on the computational efficiency and give considerations to histories of the optimization and optimal shape.

2. RESPONSE ANALYSIS

2.1 Analytic Model

The Analytic model is shown in Fig. 1. We take unidirectional free surface shell structures as objects of our study . The 3D model is generated by expanding 2D model in *y*-direction and equally dividing it into eight volumes. Bézier curves are utilized to define shapes of analytic

models. Let $\mathbf{q}^0(s) = (q_x^0(s)\ \ q_z^0(s))$ the α-th order Bézier curve on the *x*-*z* plain and expressed by Eq.(1)

$$\mathbf{q}^0(s) = \sum_{i=0}^{\alpha} \mathbf{R}_i B_i^{\alpha}(s) \tag{1}$$

where $\mathbf{R}_i = (R_i^x, R_i^y)$ is a position vector of a control point, $B_i^{\alpha}(i = 0,...,\alpha)$ is an α-th Bernstein base function, and *s* ($0 \le s \le 1$) is a parameter. Roof shape is defined by $\mathbf{q}(s) = (q_x^0(s)\ \ y\ \ q_z^0(s))$. Here, let the order α=5 so as to express a moderate curve shape. The 5th Bézier curve is shown in Fig. 2. It is generated by determining positions of six control points.

The boundary condition is shown in Table 1, where *u*, *v* and *w* are velocities in *x*-,*y*-,*z*- direction, respectively and *p* is pressure. At the inlet boundary, average velocity in *x*-direction is only given a value of V_H whose distribution is uniform. And the turbulent velocity fluctuation is imposed only in *x*-direction, which is stochastically simulated by reflecting characteristic of turbulence in the wind tunnel flow. Non-slip boundary conditions are imposed on the ground and the surface of the structure, and distribution of average velocity in *x*-direction gradually become a gradient flow as the flow goes downstream. Free-slip boundary conditions are imposed on the both sides of analytic domain. The mesh on the *x*-*z* section where *y*=0 is illustrated in Fig. 3.The fluid around the structure is discretized by linear triangular and tetrahedron elements, for 2D and 3D models, respectively. The 3D meshes are generated by dividing each triangle pole generated by pushing out the triangle in *y*-direction into three tetrahedrons. Total non-dimensional time t^* (tV_H/D) is 80. The increment of t^* is 0.01. Parameters of fluid are shown in Table 2. The wind engineering targets the Reynolds number approximately ranging from 7.0×10^4 to 7.0×10^8 . In this study, the value 1.0×10^5 within the semi-critical territory is utilized as Reynolds number .

At the outlet boundary, *p*=0 in order to prevent the pressure Possion equations from being singular. To prevent a reverse current at outlet boundary, viscosity is set higher in the domain between *x*=17.5*D* to 20.0*D*. Model parameters are shown in Table 3. These parameters are determined on the assumption that as a realistic model, 100-meter-span frame-supported membrane roof is subjected to wind whose average velocity at the top of the roof is 50 m/s. Mass parameter C_M and load parameter C_L of the analytic model are determined to correspond to those of realistic model.
C_M and C_L are expressed by Eq. (2) and Eq. (3), respectively.

$$C_M = w/(\rho_{air} D) \tag{2}$$

$$C_L = Q_H D^3/(EI) \tag{3}$$

where Q_H is velocity pressure at the reference point.

2.2 Method of Analysis

Outline of incompressible viscous flow analysis is explained as below. Governing equations in this study are the Navier-Stokes equation and the continuity equation. Discretized in time domain by the Crank-Nicolson method,

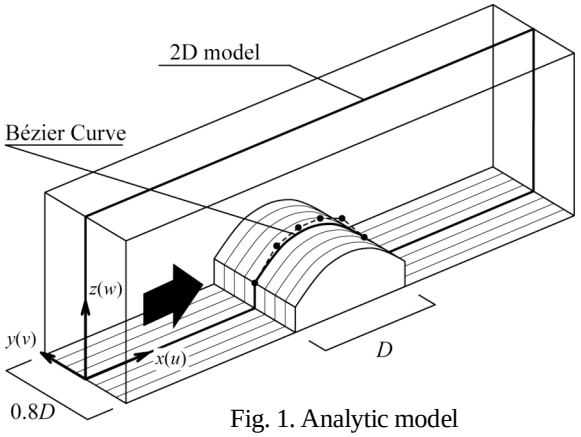

Fig. 1. Analytic model

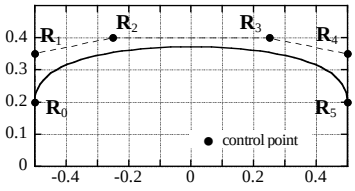

Fig.2. 5th Bézier curve (initial shape)

Table1. Boundary condition

inflow	$u=V_H$, $v=0$,$w=0$
outflow	$p=0$
structure bottom	$u=V_H$, $v=0$,$w=0$
top	$w=0$
side	$v=0$

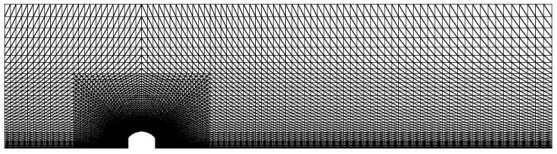

Fig.3. mesh on the *x*-*z* section (*y*=0)

Table 2. Parameter of fluid

Density of air ρ(kg/m^2)	1.25
Viscosity μ(N·s/m^2)	1.81×10^{-5}
Reynolds number	1.0×10^5

Table 3. Model parameter

	Analytic model	Realistic model
Mass per unit area w(kg/m^2)	8.10×10^{-2}	80.0
1st natural frequency (Hz)	3.12×10^2	1.00
Span D (m)	0.10	100
Average velocity at reference point V_H(m/s)	14.5	50.0
Bending stiffness per unit width EI (N·m^2/m)	2.61×10^{-2}	2.65×10^8
Mass parameter C_M	0.65	0.64
Load parameter C_L	5.04	5.90

the Navier-Stokes equation and continuity equation are expressed by Eqs. (4) and (5), respectively

$$\frac{u_i^{n+1} - u_i^n}{\Delta t} + \sum_{j=1}^{d} u_j^n \frac{\partial u_i^{n+1/2}}{\partial x_j} + \frac{\partial p^{n+1/2}}{\partial x_i} - \nu \sum_{j=1}^{d} \frac{\partial}{\partial x_j}\left(\frac{\partial u_i^{n+1/2}}{\partial x_j} + \frac{\partial u_j^{n+1/2}}{\partial x_i} \right) = f_i \tag{4}$$

$$\sum_{j=1}^{d} \frac{\partial u_j^{n+1/2}}{\partial x_j} = 0 \tag{5}$$

where $u_i^{n+1/2} = (u_i^n + u_i^{n+1})/2$. Let the superscript *n* denote the value at the *n*th time-step, Δt denote the time increment and *d* denote the spatial dimension and the value of *d* is 2 or 3. The subscripts of 1, 2 and 3 represent the *x*-, *y*-, *z*-components, respectively. Let *u*, *p* and ν denote a velocity

vector, pressure and coefficient of kinematic viscosity, respectively.

The discretized Navier-Stokes equation and the pressure Poisson equation are introduced by the improved balancing tensor diffusion method and the fractional step method (IBTD + FS method) combined with the finite element method. The Smagolinsky model of LES is employed as a turbulence model. Interaction of fluid and a structure is not considered. As to the response analysis of the structure, the roof is analyzed assuming the wall is rigid. The edge of the roof and the wall are connected with pin-joint. Let the roof 2D model with 49 nodes and 48 linear beam elements on the assumption that the roof unlimitedly expands in *y*-direction. As a solution method of the motion equation, Newtmark-β method (β=0.25) is employed. The damping matrix is introduced using Eq. (6)

$$[C]=([U])^{-1}[\ {}_sC\ ]([U])^{-1} \tag{6}$$

where U is mode matrix and ${}_sC$ is a sth generalized damping coefficient which is determined by a sth damping factor. Let the damping factors of the 1st and 2nd mode 2%, and those of more than 3rd modes 20%. Pressure obtained by the flow analysis every five time steps are utilized as an external force, and the responses at every node are computed. Pressure data of the 3D analysis are utilized by averaging the values on the nodes lining in *y*-direction.

2.3 Application of Multigrid (MG) method

For a 3D fluid flow analysis, a huge computational cost is involved in solving the pressure Poisson equation. In this study, we improve the convergence rate of the solution by preconditioning the conjugate gradient method (CG method) with the MG method. The algorithm of the preconditioned CG method (PCG method) is shown in Fig. 4. The PCG method is employed to solve the pressure Poisson equation **Ax=b**. The MG method is utilized for $\mathbf{e}=\mathbf{M}_{MG}^{-1}\mathbf{d}$ (the subscript i is omitted) . The outline of the MG method is shown in Fig. 5. As a coarse grid 2D mesh is used. This procedure can be divided into three parts. (1) restriction : reflecting the residual **d** of the fine grid on the coarse grid. (2) obtainment of the solution on the coarse grid $\mathbf{e}_{coarse}$ by solving the equation $\mathbf{A}_{coarse}\mathbf{e}_{coarse}=\mathbf{d}_{coarse}$. (3) prolongation : reflecting the solution $\mathbf{e}_{coarse}$ on the fine grid. To be concrete restriction is the way of averaging the residuals of the nodes lining in *y*-direction and giving the value to the corresponding node on coarse grid. And prolongation is the way of distributing the value on the coarse grid to the corresponding nodes on the fine grid lining in *y*-direction.

(*initialization*)

$\mathbf{d}^0=\mathbf{b}-\mathbf{A}\mathbf{x}^0$: *initial residual*

$\mathbf{e}_{MG}^0=\mathbf{M}_{MG}^{-1}\mathbf{d}^0$: *multigrid preconditioning*

$\mathbf{e}_{Diag}^0=\mathbf{M}_{Diag}^{-1}\mathbf{d}^0$: *diagonal scaling preconditioning*

$\mathbf{e}^0=\mathbf{e}_{MG}^0+\mathbf{e}_{Diag}^0$: *preconditioning*

$\mathbf{p}^0=\mathbf{e}^0$: *initial search direction*

(*iteration*)

$\mathbf{q}^i=\mathbf{A}\mathbf{p}^i$

$\alpha=\dfrac{\mathbf{e}^i\cdot\mathbf{d}^i}{\mathbf{p}^i\cdot\mathbf{q}^i}$

$\mathbf{x}^{i+1}=\mathbf{x}^i+\alpha\mathbf{p}^i$: *update solution*

$\mathbf{d}^{i+1}=\mathbf{d}^i-\alpha\mathbf{q}^i$: *update residual*

$\mathbf{e}_{MG}^{i+1}=\mathbf{M}_{MG}^{-1}\mathbf{d}^{i+1}$: *multigrid preconditioning*

$\mathbf{e}_{Diag}^{i+1}=\mathbf{M}_{Diag}^{-1}\mathbf{d}^{i+1}$: *diagonal scaling preconditioning*

$\mathbf{e}^{i+1}=\mathbf{e}_{MG}^{i+1}+\mathbf{e}_{Diag}^{i+1}$: *preconditioning*

$\beta=\dfrac{\mathbf{e}^{i+1}\cdot\mathbf{d}^{i+1}}{\mathbf{e}^i\cdot\mathbf{d}^i}$

$\mathbf{p}^{i+1}=\mathbf{e}^{i+1}+\beta\mathbf{p}^i$: *update search direction*

if $\dfrac{\|\mathbf{d}^{i+1}\|}{\|\mathbf{b}\|}<\varepsilon=1.0\times10^{-6}\Rightarrow$: *stop iteration*

Fig. 4. Algorithm of PCG method

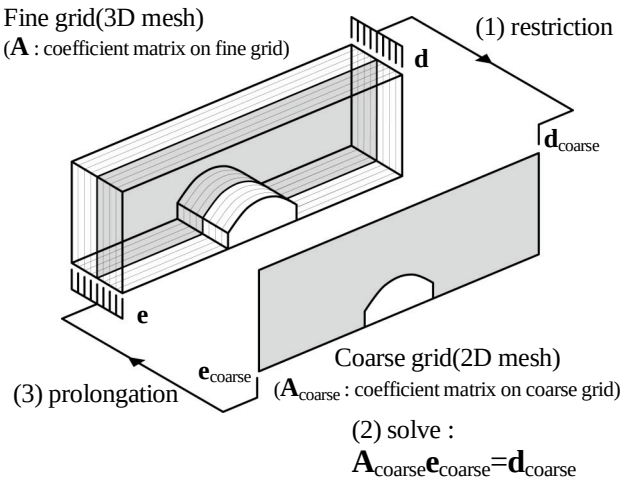

Fig. 5. Outline of MG method

3. SHAPE OPTIMIZATION

In this chapter the outline of the optimization problem in this study is explained

3.1 Formulation

Optimization is applied to roof of the shell structure with the side wall. Stiffness and weight of members are not included in design variable. A shape optimization problem is formulated as below.

$$\textit{Minimize} : f(\mathbf{R})=\max\left\{w^{\max},-w^{\min}\right\} \tag{7}$$

$$\textit{Variable} : \mathbf{R}=\left(R_1^z\ \ R_2^z\ \ R_3^z\ \ R_4^z\right) \tag{8}$$

$$\textit{Subject to} : \left(R_2^z+R_3^z\right)/2\geq 0.4 \tag{9}$$

$$R_i^z\geq 0.2\ (i=1,2,3,4) \tag{10}$$

In the design of buildings maximum response are made to be less than the allowable value. Therefore objective function is set as Eq. (7), where $w^{\max}$ and $-w^{\min}$ are maximum and minimum value of response displacement in *z*-direction of all nodes, respectively. The control point $\mathbf{R}_0$ and $\mathbf{R}_5$ are fixed at the both tops of windward and leeward side walls, respectively. In the other control points *z*-coordinates are the design variables (Eq. (8)). The vector **R** is the design variable vector and the component of **R** of the initial shape shown in Fig. 2 is $(R_1^z\ R_2^z\ R_3^z\ R_4^z)$ = (0.35 0.4

0.4 0.35). Constraints are decided to avoid the roof from being low-rise (Eq. (9) and(10)).

3.2 Optimization Method

Objective function is expanded into RSM so that the sensitivity analysis can be easily carried out. Optimal solution for the RSM is obtained using the optimization software package DOT Ver. 5.0. Sequential quadratic programming is employed as an optimization algorism. The objective function is approximated by complete quadratic function of the vector $\mathbf{r}=\{r_i\}(-1\le r_i\le 1)$ as

$$f \simeq a_0 + \sum_{i=1}^{N} a_i r_i + \sum_{i=1}^{N}\sum_{j=i}^{N} a_{ij} r_i r_j \qquad (11)$$

where N is the number of design variables and Relation of the vector $\mathbf{r}$ and the design variables $\mathbf{R}$ is expressed by Eq. (12)

$$\mathbf{R}(\mathbf{r}) = \mathbf{R}^{(k)} + \Delta R\mathbf{r} \qquad (12)$$

where $\mathbf{R}^{(k)}$ is initial value and optimal solution after kth step of optimization. The initial value where k=0 is design variables at the initial shape and ΔR is move limit. a_0, a_i and a_{ij} are the coefficients that are to be determined from least square method for the responses at the selected data (experiment) points. The number n_c of unknown coefficients a_i, and a_{ij} in Eq. (11) is 15 because n_c= (N+1)(N+2)/2 and N=4 in this study. To obtain accurate results 30 data points are generated by the function 'cordexch' in the statistics toolbox of Matlab that generates 3-level approximation for D-optimality ; i.e., r_i takes one of the values in {–1,0,1}. The origin (0,0,0) is added to obtain 31 data points.

Optimization flow is summarized as

1) Assign initial design variable vector $\mathbf{R}^{(0)}$ and the move limit ΔR .Set k=0
2) Generate data points using $\mathbf{R}^{(k)}$ and ΔR.
3) Compute value of the objective function f in Eq. (7) at each data point.
4) Generate RSM in Eq. (11) using the values of f at 31 data points
5) Find the optimal solution of RSM to obtain $\mathbf{R}^{(k+1)}$
6) Let $k \leftarrow k$+1 and update ΔR . If not converged go to 2)

4. RESULT OF NUMERICAL ANALYSIS

The shape optimization of the unidirectional free surface shell roofs is carried out applying the MG method described in section 2.3 . As a historical data of response a total of 1024 values are sampled every five time steps from 2885th to 8000th step. For calculation TSUBAME Grid Cluster of Tokyo Institute of Technology Global Scientific Information and Computing Center is utilized. There are 8 CPUs and each CPU has 2 cores. Thus the number of cores amounts to 16. The memory is 32 GB.

4.1 Calculation Time

3D analyses at 31 data points are required to carry out one optimization step. And carrying out 3D analyses 31 times occupies almost all time for the optimization. To see the effect of the MG method on the computational efficiency the times are measured for the 3D analysis at $\mathbf{R}^{(0)}$ of the first optimization step both in cases of using and not using the MG method. These measured times are shown in Table 4. From Table 4 it is found that computation using the MG method is approximately 2.2 times faster than not using the MG method.

Table 4. Calculation time for 3D analysis (at $\mathbf{R}^{(0)}$ of first optimization step)

Application of MG method	Calculation time (hour)
yes	5.8
no	12.5

4.2 Result of Optimization

The optimization history is shown in Table 5. The first row in Table 5 indicates the initial design value $\mathbf{R}^{(0)}$ and the objective function f of $\mathbf{R}^{(0)}$. At STEP1 assigning $\mathbf{R}^{(0)}$ as a initial value and setting move limit ΔR=0.05, the optimal solution has been obtained. After STEP1 we assign optimal solution of the former step as a initial value and decrease the value of ΔR in half every two steps. The optimal value of the objective function did not oscillate but decreased in the early stage. Therefore the setting of ΔR was found to be appropriate. f_{RS} is the optimal value of the objective function of RSM. On the other hand, f is the value of the objective function of the optimal shape obtained by carrying out 3D analysis. Comparing f and f_{RS}, the error of RSM is found to be small except STEP5. The final optimal solution $\mathbf{R}^{(6)}$ has been obtained after 6 steps of optimization. The optimal value of the objective function was largely reduced to 11.0% of initial one. To verify the reliability of the optimal solution we check if the RSM can approximate accurately using analysis of variance. An analysis variance is used to linear

Table 5. Optimization history

STEP	Initial value	ΔR	optimal solution	R_1^z	R_2^z	R_3^z	R_4^z	f_{RS}	f
0	---	---	$\mathbf{R}^{(0)}$	0.350	0.400	0.400	0.350	---	8.01×10^{-3}
1	$\mathbf{R}^{(0)}$	5.00×10^{-2}	$\mathbf{R}^{(1)}$	0.300	0.450	0.432	0.300	4.91×10^{-3}	5.35×10^{-3}
2	$\mathbf{R}^{(1)}$	5.00×10^{-2}	$\mathbf{R}^{(2)}$	0.250	0.498	0.466	0.250	1.84×10^{-3}	2.43×10^{-3}
3	$\mathbf{R}^{(2)}$	2.50×10^{-2}	$\mathbf{R}^{(3)}$	0.225	0.473	0.486	0.226	1.75×10^{-3}	1.91×10^{-3}
4	$\mathbf{R}^{(3)}$	2.50×10^{-2}	$\mathbf{R}^{(4)}$	0.200	0.448	0.467	0.201	0.98×10^{-3}	0.90×10^{-3}
5	$\mathbf{R}^{(4)}$	1.25×10^{-2}	$\mathbf{R}^{(5)}$	0.213	0.459	0.470	0.213	0.26×10^{-3}	1.27×10^{-3}
6	$\mathbf{R}^{(5)}$	1.25×10^{-2}	$\mathbf{R}^{(6)}$	0.200	0.447	0.457	0.201	0.95×10^{-3}	0.88×10^{-3}

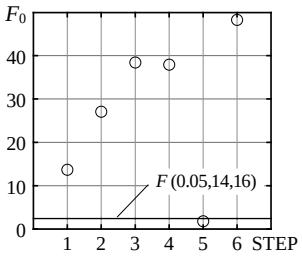

Fig 6. Variance ratio F_0

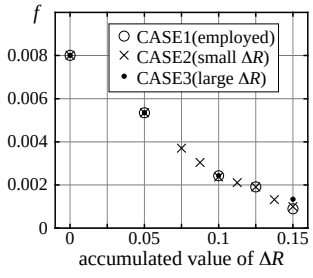

Fig. 7. Change of optimal value of f

regression model. Thus, considering each r_i, $r_i r_j$ ($i \leq j$=1,2,3,4) in Eq. (11) as independent variables, the RSM is treated as a linear multi-regression model. The number of the independent variables amounts to 14. The ratio of variance at each optimization step is shown in Fig. 6. A variance ratio F_0 of the vertical axis is expressed in Eq. (13)

$$F_0 = \frac{S_R / p}{S_E / (n - p - 1)} \tag{13}$$

where S_R is the sum of square of the regression model, S_E is that of the error, n is the number of the data point and p is the number of the independent design variable. This F_0 indicates how accurately the multi-regression model explains the actual data. F(0.05,14,16) is the value of the F-distribution when significance level is 0.05, p=14 and n–p–1=16. If the variant ratio F_0 exceeds F(0.05,14,16), this multi-regression model is statistically significant at 95% level of confidence. In this model the response surface expressed by a complete quadratic equation can explain the real objective function sufficiently except the STEP5 of the optimization, and thus the optimal solution obtained by using this model is reliable

To understand how the optimal solution depends on the way of renewing it with ΔR at each step of optimization, we carry out optimizations in these three cases : CASE1 is using the way employed in Table5, CASE2 is using the way with small ΔR and CASE3 is using the way with large ΔR. The change of optimal value of the objective functions in each case is shown in Fig. 7. These changes are almost same and the optimal solution is found not to be sensitive to ΔR. Therfore ΔR used in this example is appropriate.

4.3 Verification of Optimal Solution

The initial and optimal shape is shown in Fig.8 and these curvatures are shown in Fig.9. x-coordinates and z-coordinates are non-dimensionized dividing by the dome span D. The optimal shape is lower than the initial one in the front and rear parts. In the control points of the optimal shape, $\mathbf{R}_1$ and $\mathbf{R}_4$ are located over and $\mathbf{R}_2$ and $\mathbf{R}_3$ are under the those of initial shape . Distribution of these control points makes the curvature of the optimal shape almost uniform and the optimal roof shape is close to a cylinder. The pressure contours are shown in Fig. 10 when non-dimensional time tV_H/D = 60. Pressure data from Fig. 10 to Fig.12 are averaging values of the data lining in y-direction. The difference of pressure contours of the initial shape and optimal one is that the isobar of the initial shape is denser than that of the optimal shape at the edge of the windward roof surface. And this has been confirmed when the non-dimensional time is 20, 40 and 80.

The mean wind pressure coefficient C_p and fluctuating wind pressure coefficient C_p' on the roof surface are shown in Fig. 11 and Fig.12, respectively. The pressure data from 2000th to 8000th time step are sampled to compute the wind pressure coefficients. The gradient of mean wind pressure coefficient on the optimal shape is gentler than that on the initial shape at the windward edge because the isobars of the optimal shape are sparser than those of the initial shape

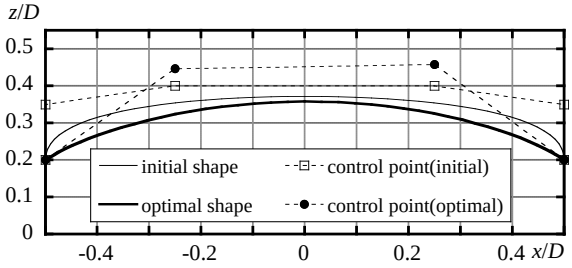

Fig. 8. Initial and optimal shape

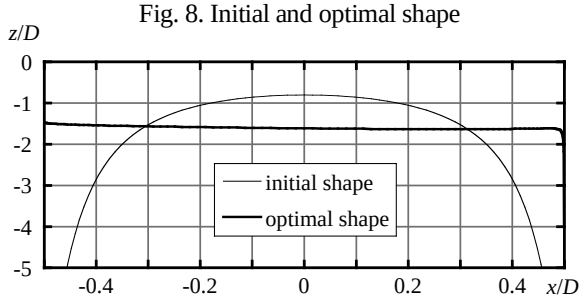

Fig. 9. Curvatures of initial and optimal shape

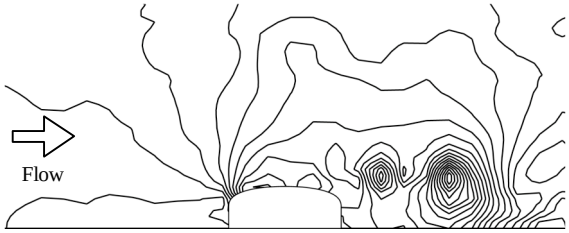

a) initial shape

b) optimal shape

Fig. 10. Pressure contour (tV_H/D=60)

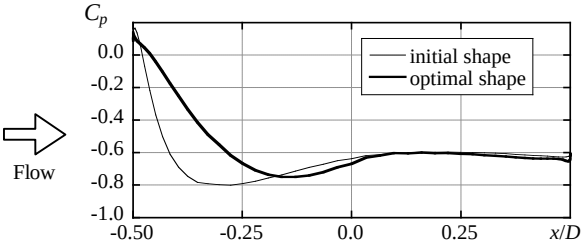

Fig.11. mean wind pressure coefficient C_p

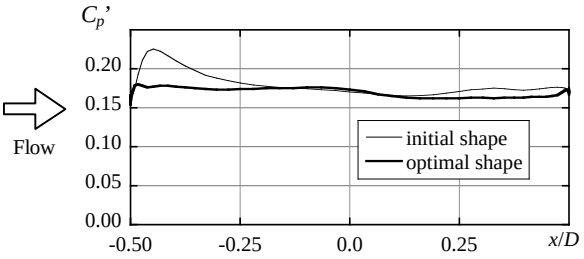

Fig.12. fluctuating wind pressure coefficient C_P'

around the edge. The peak values of C_p on the optimal shape and initial shape are almost same, but the peak value on the optimal shape is located in the more central side of the roof. The fluctuating wind pressure C_p' on the initial shape is larger than that on the optimal shape at the windward edge around which the isobars of the initial shape are denser.

5. CONCLUSIONS

The shape optimization of the unidirectional free surface shell subjected to strong wind is carried out by minimizing the maximum vertical response displacement in all nodes on the roof surface. To improve computational efficiency of the optimization, the multigrid method (MG method) is employed to the three dimensional fluid flow analyses. We see the positive effect of the MG method on the computational efficiency and give considerations to histories of the optimization and optimal shape. The conclusions obtained from this study are shown as follows:

1) Using the MG method computational time become 2.2 times faster.
2) Optimal value of the objective function is approximately 11.0% of initial shape, thus optimization result is significant.
3) The optimal roof shape is found to have uniform curvature; that is, the shape is close to cylinder
4) The gradient of mean wind pressure coefficient C_p on the optimal shape is gentler than the initial shape. The peak value of C_p on the optimal shape is almost equivalent to that on the initial shape, but for the optimal shape the location is more central side of the roof. The peak value of the fluctuating wind pressure coefficient C_p' is seen only on the initial shape at the windward edge of the roof.

References:

Ogawa, T., Nakayama, M., Masuda, K. and Mochizuki, I. (1999), " Numerical Simulation and Experimental Study on Dynamic Behavior of Cylindrical Dome Roofs in Strong Wind," *Proc. IASS 40th Anniversary Congress*, Vol.2, E1.71-E1.80.

Ohsaki, M. and Hayashi, M. (2000), "Fairness Metrics for Shape Optimization of Ribbed Shells," *J. Int. Assoc. Shells and Spatial Struct.*, **41**(1), 31-39.

Ohsaki, M., Ogawa, T. and Tateishi, R. (2004), "Shape Optimization of Curves and Surfaces Considering Fairness Metrics and Elastic Stiffness," *Struct. Multidisc. Optim*., **25**, 250-258.

Barrett, R. et. al. (1994), "Templates for the Solution of Linear Systems : Building Blocks for Iterative Methods," *SIAM*, *http://www.netlib.org/templates/Templates.html*, 91-92.

Trottenberg, U., Oosterlee, C. and Schüller A. (2001), "Multigrid," *Academic Press*.

Roux, W.J., Stander, N. and Haftka, R.T. (1998), "Response Surface Approximations for Structural Optimization," *International Journal for Numerical Methods in Engineering*, **42**(3), 517-534.

Miyamura, T., Kumagai, T., Ogawa, T., Ogata, S., Ohsaki, M. (2007), "Application of Multigrid Method to Three-dimensional Incompressible Viscous Flow Analysis around Shell Roofs," *Journal of structural and construction engineering*, **618**, 135-142 (In Japanese)

Ogawa, T., Ohsaki, M., Miyamura, T. and Kumagai, T. (2005), "Shape Optimization of Shell Roofs Subjected to Strong Wind by Using a Variable Complexity Model," *J. Int. Assoc. Shells and Spatial Struct.*, **46**(2), 108-115.

Sixth International Conference on Urban Earthquake Engineering
March 3-4, 2009, Tokyo Institute of Technology, Tokyo, Japan

NGIBIKAN VILLAGE RECONSTRUCTION: ENHANCING THE SOCIAL STRUCTURE OF THE COMMUNITY

Eko Prawoto[1)]

1) Professor of Architecture, Duta Wacana Christian University, Yogyakarta, Indonesia

Abstract: The social structure is about the interrelationship among the people in the community as well as the values that hold them together. We should be aware about this before making the intervention in a community. In an emergency situation this could be an important and strategic factor for a successful result in assisting the community to be able to overcome the problems. This paper is presenting the direct experience in working together with people in Ngibikan village which was destroyed by the earthquake in May 27,2006 . The village reconstruction was based on appreciating the existing social structure and perceiving it beyond physical matters but in totality for building their lives.

INTRODUCTION

Yogyakarta Earthquake May 27, 2006

Early in the morning, at about 05.53 when people were about to begin their routine activities and some still stayed in their beds when the 5,9 R scale earthquake hit Yogyakarta. It was only 57 seconds that made the areas change their face permanently. More than 140 thousands houses were severely damaged, most of them totally collapsed, and more than 6000 people died . In that days more than 1/3 of the Yogyakarta's inhabitants were staying out side , mostly because they did not have house to stay and the other because of terrified staying inside the damaged house.

Geologically speaking Indonesia is laying on the collided Australian and Asian plates . And those plates are constantly seeking their balance position. Sometime the tension is so big and then it release as a huge amount of energy that appear in the form of earthquake. It happens all the time, and according to geoscientist the big earthquake happens in a certain period of every 75-100 year.

In the north of Yogyakarta there is also an active volcano, mount Merapi which also often creates tremors .

The people actually already familiar with this natural phenomena which is the earth that constantly shakes. The traditional architecture significantly corresponds to this very nature of the earth condition.

The traditional architecture: the wooden construction , was dominated Yogyakarta since long in our history. It is a local wisdom to choose light-weight and elastic structural system. But then along with modernization process the masonry and reinforce concrete structure becoming more and more popular.

Many people want their houses to be look like modern building. The transformation of building style is often not properly followed by the knowledge of construction. People sometimes build their houses just to imitate the modern appearance but using a simple materials and techniques.
In most of the case of the brick work of collapsed buildings used low quality cement or even just mud and then plastered .

Ngibikan village

Ngibikan was one of the villages that severely damaged. It was only 10 km from the earthquake epicenter. The people living there were mostly farmers, building workers , becak drivers ,food and fruit sellers.

It is a typical of Javanese village which still very much living in their traditional culture.

In this neighborhood (RT5&6) there were 65 families approximately 290 people.

The reconstruction process

I visited the Ngibikan village a day after the big earthquake (May 28, 2006). Most of the building in the village were totally destroyed. Mainly because of the low quality building structure, the supporting wall was brick wall with soil mortar without cement. It was not able to resist the strong forces from the earth movement. The wooden roof structure were just went down because the support suddenly collapsed . The roof tiles that covered it mostly were broken. But the doors and windows, which made out of wood were still relatively in a good shape except the broken glasses.

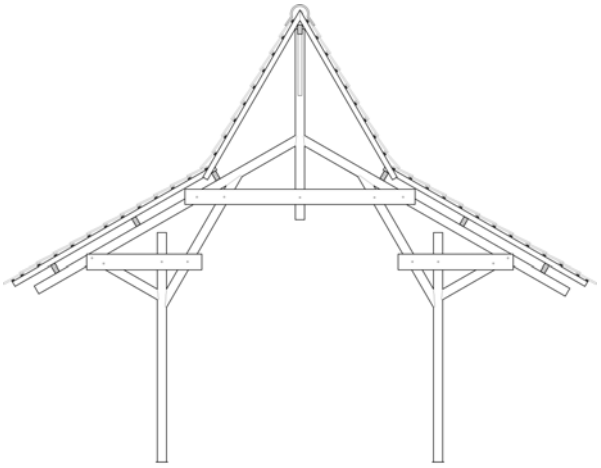

KONSTRUKSI KERANGKA KAYU

People built tents outside their houses. There were 2 big tents use as communal tent accommodating injured people and kids, and also to store some food and medical stuff.

People already started to clean the rubbles using available tools. We brought some tool such as shovels donated from many friends . I was amazed by the fact that their living spirit shining even in the bad condition. (May 31,2006)

Thinking for reconstruction

I met the chief of the village Mr. Maryono. He is my co-worker in most of my building projects. That evening (June 2,2006) we talked and shared about the possibility of re-building the village using available materials. It seemed that there were possibilities to do that. I made a rough sketches about the possible structure using the materials from the ruins. We were thought about a wooden construction house. It is easy and fast to construct and also relatively saver for it's lightweight in comparison to that of brick construction. The next day (June 3,2006) he organized village meeting to share the idea of the house design . The community agreed upon the idea but proposed to use fiber cement roof instead of clay tiles. They thought that the fiber cement roof more appropriate for it is more steady.

The prototype of the structure

The prototype of the structure was made of wood from the ruin (June 4, 2006). It was a wooden truss about 4 m wide span and for the joints fastened by 12mm bolt. Actually this wooden frame had never been tested nor scientifically calculated. But we used this based on the fact that all of our building with similar structure survived in this earthquake.

So we just adopted these for the design of the houses.

The design of the house was very simplistic. It also gave flexibility to make various kind of spatial arrangement .It is a 3-bay rooms 2,4 meter each with 6 meter wide, so in total area were 7,2 meter by 6 m (more than 43 m2).

The wall will be a brick wall but only 1 meter high . On top of it there will be a wooden frame clad with other material such woven bamboo or other light-weight materials.

Room division were decided by the people themselves in accordance to their needs and the existing foundation. They could made it up to 4 bedrooms with a living room.

This house type is an adaptation from the traditional house type called *Limasan*. The roof shape is *kampung* roof type . We made the proportion a bit higher to make the future extension easier.

This high roof were also gave an impression of dignity and spacious I think it is important also to lift up the psychological condition of the people, to give the feeling of living in light and strong structure.

PERSPEKTIF

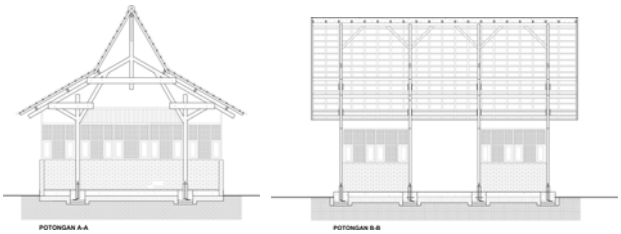

The funding

In the beginning we were just thought how to re use the available materials. There were many people that had a building skill so it might be possible to do reconstruction by themselves .

The other night I got a phone call from the Kompas ,one of the biggest national newspaper company , asking me if I would help them in the humanitarian project concerning with the disaster.

It was quite a coincidence and so I just reply that I will but under a certain condition for the approach or working method.

The condition that I proposed to Kompas :

1. We would respect the socio cultural condition of the people

2. Did not use money to mobilize people . The work should be a participatory project based on *gotong royong* principle.

I was quite aware with this issues in which I had learned from the similar case in Aceh tsunami disaster.

We don't want to destroy their social structure. I believe that what we perceived from outside about this disaster was only half true. The fact that everything was destroyed and gone was only outside appearance . There were many things that still very much in existent and remain not affected with the disaster . Their culture, their values, their skill and knowledge were still there .

So actually we did not build from nothing. We should begin from what was still there.

The funding is very important but not the only one.

Then we realized that the wood from the ruins were only short wood and many of them were broken. So we decided to use new wood which cheaper and easy to find: coconut wood.

The budget for each house that we proposed to Kompas was 10 millions rupiah (approximately 80.000 Y). It was in fact only the price of materials. The community would hand in hand helping each other to reconstruct the village, they were not paid but got meals.

Working together/*gotong royong* and *slametan*

In the beginning we planned to build 65 houses in this village. The aim was to build permanent house directly. We did not want to spend time and money for temporary house. The big work for village reconstruction was started in June 5, 2006.

We had about 50 working force with various skill and ability. They were about 10 people who were real building workers. We hoped they could lead the other people to do many things.

Actually the Javanese people perceive their house not just as a physical private domain but more as a social structure. A house has a broader and larger relationship. It is very important to keep the harmony with the surrounding nature and also relate spiritually with the Devine Power who give and maintain them alive.

There are many ceremonies (*slametan*) indicating important moments of life. Building a house is one of them. In this case we didn't want to perceive this reconstruction project as merely a housing project but as a reconstruction of village life.

So in fact what we built were normal house not a disaster house. And to build that we have to follow and respect their tradition such as doing a *slametan*, a ceremony to ask for blessing from God during their working process.

The *slametan* was held in June 12,2006 at that time the main structures (frames) of 3 houses had already been erected.

Finding an appropriate method

In the first two weeks the working process was not very efficient. Many people were more watching than following the skilled labors doing their jobs. Some people just walked around trying to help the workers but without clear job description.

Finally the chief of the village, Maryono found an interesting work-system, something like 'conveyor belt in an assembling automotive industry'.

Maryono divided the group of workers into 7 specialized working groups, which were (1) clean the site and wood, (2) cut and measure wood, (3) make wooden truss/frame, (4) erect the wooden frame, (5) roofing, (6) wall construction , (7) construct foundation of the house.

Every group only did a specific job . The skill improved and the result got better . Every body also found a perfect job fit with the skill .

With these system he managed to organize the community more efficient, the progress went on very fast

The *gotong royong* started at 8 until 16 o'clock every day. So before 8 and after 16 most of the people did their own house. It was very often that they work quite late at night .

After the earthquake the electricity was cut off.

But we were very fortunate that we got a new generator set from donation , so there were electricity .

The community also showed their creativity and sensitivity in re-using available materials, the door and windows. It made every house looked unique, the need for individual identity naturally found its way.

The community worked harder because they committed that those houses should be standing and ready to be occupied before Ramadhan.

By September 20, 2006 the 65 houses were already standing !.

Reflection

After the handed over ceremony people began to move in their new houses. But the improvement process still continues until the next few months. Finally they also got the money from the government. By that they were able to make extension or other improvement of the houses. Although there were possibility to build another house with that money it seemed that people loved their houses they build themselves .

Now it has been more than 2 years after the reconstruction. Ngibikan village was one of the few villages that used wooden construction. In other villages most of the buildings reconstruction used reinforced concrete structure as the government suggested. With the money given by the government it was not enough to build a $6x6m^2$ house till finished. So there were still many reinforced concrete houses remain unfinished.

In other village some problem still remain unsolved. There were some families still homeless due to the policy that one damaged house got one aid , meant that in one damaged house only one family who got the aid. Before the earthquake it was very common that one house was occupied by many families or kinships.

In other case the house size was too small to accommodate the large number of family members. There were no chance for the people to be involved in the design process. There was no such flexibility in perceiving individual needs.

There was also the most controversy case , the foreign aid just built the houses but neglected the social need and cultural values of the inhabitants there, the Dome Houses. People there still struggle to adjust their lives to fit with the strange design and adapt to a new setting which is strange to their village lifestyle.

The Ngibikan people showed to the world that their strong sense of togetherness and their *gotong royong* spirit were the most important factor in the success of reconstruction of their village.

The participatory approach from the very beginning of the design stage , the construction method they organized, was in the community's hand. It seemed make the whole process went on smoothly. It was more than making a decent house but maintaining the life spirit of the whole community.

References:

1.Geertz, Clifford. "Local Knowledge: Fact and Law in Comparative Perspective," pp. 167-234 in Geertz Local Knowledge: *Further Essays in Interpretive Anthropology*, NY: Basic Books. 1983.

2.Hahn, Robert A. *Anthropology in Public Health: Bridging Differences in Culture and Society* Oxford, UK: Oxford University Press. 1999.

notes:

In a 1983 essay Clifford Geertz points to the importance of *gotong royong* in Indonesian life: An enormous inventory of highly specific and often quite intricate institutions for effecting the cooperation in work, politics, and personal relations alike, vaguely gathered under culturally charged and fairly well indefinable value-images--*rukun* ("mutual adjustment"), *gotong royong* ("joint bearing of burdens"), *tolong-menolong* ("reciprocal assistance")--governs social interaction with a force as sovereign as it is subdued.

Anthropologist Robert A. Hahn writes: Javanese culture is stratified by social class and by level of adherence to Islam. ...Traditional Javanese culture does not emphasize material wealth. ...There is respect for those who contribute to the general village welfare over personal gain. And the spirit of *gotong royong*, or volunteerism, is promoted as a cultural value.

Sixth International Conference on Urban Earthquake Engineering
March 3-4, 2009, Tokyo Institute of Technology, Tokyo, Japan

INDIVIDUALIZED RISK COMMUNICATION FOR SOIL AVALANCHE HAZARD

S. Fujii[1] & A. Taniguchi[2]

1) Professor, Tokyo Institute of Technology, Japan
fujii@plan.cv.titech.ac.jp
1) Lecture, Tsukuba University, Japan
taniguchi@risk.tsukuba.ac.jp

Abstract: It is impossible to perfectly avoid soil avalanche in all the places all over the world by means of hard-ware investment. Therefore, precautionary evacuative behavior of people who live in the areas with the risks of soil avalanche is indispensable in order to avoid human damage due to soil avalanche. In this study, we propose a risk-communication program that is especially to promote precautionary evacuative behavior from soil avalanche.

1. INTRODUCTION

It is impossible to perfectly avoid soil avalanche in all the places all over the world by means of hard-ware investment. Therefore, precautionary evacuative behavior of people who live in the areas with the risks of soil avalanche is indispensable in order to avoid human damage due to soil avalanche. However, the soil avalanche in mountainous area is, of course, frequent hazard. Therefore, many of those live in the area with risks of soil avalanche might ignore the risk. Needless to say, those who ignore the risks, they never tries to precautionary evacuate from the risk. Yet, soil avalanche is quite frequent hazard somewhere in mountainous area, for example, in Japan. Thus human damage due to soil avalanche occurs constantly every year.

In this study, we propose a risk-communication program that is especially to promote precautionary evacuative behavior from soil avalanche. The communication program is proposed while applying basic techniques used in the "travel feedback programs" (TFPs) that were proposed in the area of transportation planning. TFPs are persuasive communication programs to change travel behavior, mainly, from car use into more environmental sustainable travel modes use. In this paper, we will explain about TFPs at the beginning with result to demonstrate the effectiveness of them and then explain about the risk-communication program that we proposed in this study.

2. TRAVEL FEEDBACK PROGRAMS FOR TRAVEL BEHAVIOR CHANGE

We explain a communicative mobility management measure in the workplace, namely a *travel feedback program* (Fujii and Taniguchi, 2005; 2006; Gärling & Fujii, 2006; Taniguchi et al., 2003) , to change employee commuting behavior from car use to other travel modes. Similar programs have been implemented in many countries, including the UK, Australia, Germany, Sweden, and Japan (c.f. Cairns et al., 2004; Gärling & Fujii, 2006). Recently, a travel feedback program requesting recipients to make a behavior plan about how to change their travel behavior was shown to be more effective than programs that did not, as shown experimentally (Fujii & Taniguchi, 2005) and in a meta-analysis of travel feedback programs (Fujii & Taniguchi, 2006). However, no travel feedback program making such a request has been implemented as workplace mobility management. It may be more difficult to change commutes than discretionary trips, such as shopping or leisure trips, because commuters may feel that changing commutes has a greater

subjective cost than changing discretionary trips (c.f. Loukopoulos, et al., 2004; Gärling et al., 2004). Therefore, a travel feedback program may not always be effective at changing commutes. Consequently, one objective of this study was to test whether a travel feedback program asking participants to make a behavior plan can change commute behavior. To assess the effectiveness of the policy intervention, we administered a panel survey before and after a travel feedback program targeted at employee commutes.

2.1 Method

The experiment targeted employees of three organizations in the cities of Kobe, Akashi, and Himeji, along the Sanyo railway line, Japan: Kawasaki Jyuukou and Kikko-man, both industrial plants, and the Akashi city government.

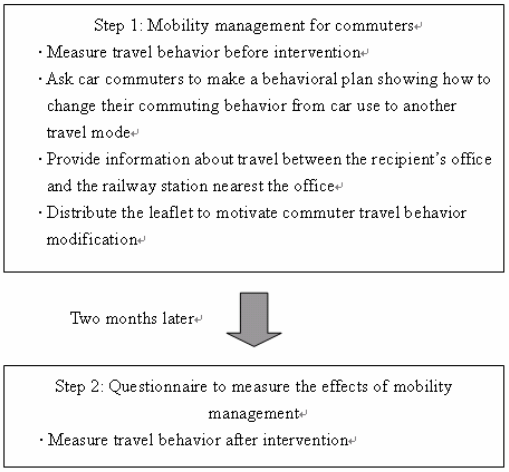

Figure 1. Outline of the mobility management intervention.

The travel feedback program consisted of two steps (Fig. 1). First, we distributed a questionnaire to company employees to measure travel behavior before intervention. A person at each company selected the targets considering the employees' residences. The questionnaire was also used to evaluate commute behavior change. Because only the first step was a communicative intervention involving travel behavior change, this can be called a "*one-shot* travel feedback program."

Respondents who had indicated that they were car commuters were asked to make a behavioral plan about how to change their commuting behavior from car use to another travel mode. This question was included in the questionnaire to give recipients a chance to consider the possibility of using an alternative travel mode (Gollwitzer, 1996; Fujii & Taniguchi, 2005, 2006). To prompt recipients to make a detailed behavioral travel plan, the question on the travel behavioral plan had two components: a request to complete a plan from their office to the nearest railway station, and a request to complete a plan from their home to the nearest railway station from their office (Fig. 2).

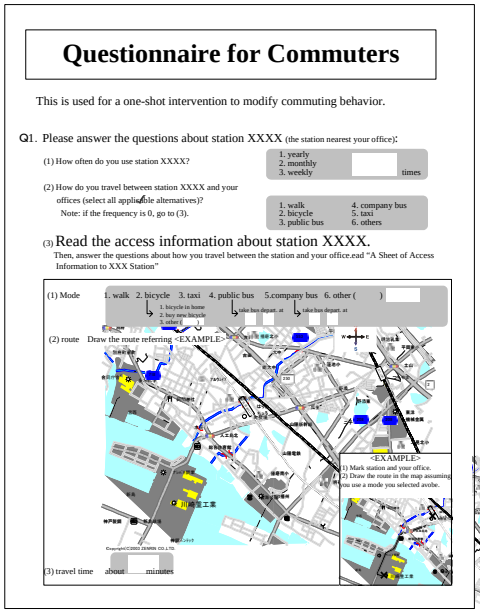

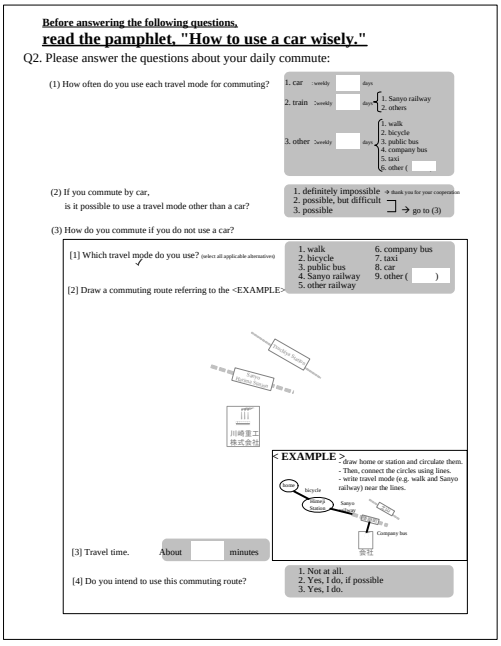

Figure 2. An example of both sides of the questionnaire for the behavioral plan.

Simultaneously, to help recipients complete a plan, they were given information about access trips from the nearest railway station of their office to their office. This information included train and bus timetables, bus lines

Table 1. The mean (M) and standard deviation (SD) for each travel mode, and *t* values for one-way analysis of variance (before vs. after the survey).

		n	Car use					Railway use					Others (bicycle or motorbike)				
			before		after		t	before		after		t	before		after		t
			M	SD	M	SD		M	SD	M	SD		M	SD	M	SD	
Total		99	4.68	(1.14)	4.27	(1.84)	2.63 ***	0.27	(1.04)	0.31	(1.11)	-0.56	0.12	(0.61)	0.54	(1.43)	-3.15 ***
Companies	Kikko-man	31	4.87	(0.43)	4.10	(2.07)	1.99 *	0.00	(0.00)	0.00	(0.00)	-	0.03	(0.18)	0.97	(2.01)	-2.56 **
	Kawasaki-jyuukou	43	4.77	(1.13)	4.67	(1.43)	0.66	0.07	(0.46)	0.05	(0.30)	1.00	0.23	(0.90)	0.42	(1.18)	-1.60
	Akashi city	25	4.28	(1.62)	3.80	(2.08)	1.77 *	0.96	(1.84)	1.16	(1.97)	-0.71	0.04	(0.20)	0.20	(0.71)	-1.44

n: number of samples, M: mean, SD: standard deviation, t: t value, *: $p < 0.1$, **: $p < 0.05$, ***: $p < 0.01$

Table 2. Details of the number of persons who changed travel modes from car use to another mode following mobility management intervention.

		Kikko-Man n = 31	Kawasaki-Jyuukou n = 43	Akashi City n = 25	Total n = 99
Travel modes before mobility management	Car commuters	**6** (19%)	**1** (2%)	**1** (4%)	**8** (8%)
	Commuters using cars and other modes	**0** (0%)	**0** (0%)	**2** (8%)	**2** (2%)
Travel mode changes after mobility management intervention		Bicycle: 5 Motorbike: 1	Bicycle: 1	Railway: 3	Railway: 3 Bicycle: 6 Motorbike: 1

near the office, the location of bicycle parking, the fee for bicycle parking, taxi fairs, and a map showing how to get from the nearest station to the office by walking, cycling, or riding a motorbike. Two months after the first survey, we distributed another questionnaire to the respondents of the first survey to measure the effects of the intervention implemented as workplace mobility management.

The questions in the second questionnaire were the same as in the first questionnaire, but there were no questions on the travel behavioral plan.

2.2 Results

In the first step, 300 of 400 recipients (75%) responded to both questionnaires. Of the 300 respondents, we selected 99 who commuted by car at the time of the first survey and responded without missing data to analyze the effectiveness of the intervention. The data excluded were for those who did not commute by vehicle at all (200 respondents) and for a respondent for whom commuter trips increased from 1 day a week to 7 days a week during the intervention.

For all 99 samples, the average weekly frequency of commuting by car decreased significantly; by train did not change significantly; and by bicycle and motorbike increased significantly (Table 1). There was no significant change in commute behavior for Kawasaki-Jyuukou. For Kikko-Man and Akashi City, there were significant decreases in car use and significant increases in using a bicycle or motorbike.

In addition, 10 of 99 (10%) car commuters at the first survey quit commuting by car completely (Table 2): six changed to bicycle, three to train, and one to motorbike.

Table 2 also shows that 19% of the car commuters at Kikko-Man and 12% of the car commuters at Akashi City changed their commuting mode from car to another mode. In contrast, at Kawasaki-Jyuukou, only one (2%) car commuter changed travel mode. All the commute mode changes from car in Akashi City were to railway, while all the changes at Kikko-Man were to bicycle or motorbike.

These results imply that the one-shot travel feedback program targeting commutes had a significant

Figure 2. Questionnaire distributed in risk communication program in soil avalanche.

effect in reducing car commuters, although the alternative travel modes chosen after intervention differed across companies. This may be due to the difference in the locations of the companies. Kawasaki-Jyuukou is not near a railway station or a residential area, making it difficult to use public transport or bicycles for commuting. The Akashi municipal office is near a railway station and is located in the middle of the city. It takes approximately 10 min to walk through the city center, which may be why all the commuters in Akashi City who changed their commuting trips from car to another mode chose the railway. Finally, Kikko-Man, while near a railway station and residential areas, it takes approximately 15 min to walk to the railway station. In addition, the road from the company to the station may not offer much incentive for pedestrian traffic: there is no sidewalk, and thus people and automobiles share the road, and there are no shops along the road. Therefore, it might not be attractive for commuters to Kikko-Man to change their commute

Figure 2. An information leaflet distributed in risk communication program in soil avalanche.

mode from car to train, but it might be feasible to change to bicycle or motorbike.

The analysis of commuting behavior change using data obtained from 43 respondents who commuted by bicycle or motorbike at the first survey showed that five bicycle or motorbike commuters (12%) became train commuters after the policy intervention. This implies that the intervention of communicative workplace mobility management led to commute changes from both car to public transport and bicycle/motorbike to public transport.

2.3 Discussion

We conducted a survey to verify the effects of

communicative mobility management targeting commuter transport, that is, a one-shot travel feedback program for commuters to companies. The most important finding was that the travel feedback program, which asked recipients to make a behavior plan about how to change their commuting mode from car to another pro-environmental travel mode, was effective. Although such a program has been shown to be more effective at changing discretionary trips than commutes (Fujii & Taniguchi, 2005), no study has yet shown that it is effective at changing commutes for which the subjective cost of the behavior change (c.f. Gärling et al., 2004; Loukopoulos, 2004) might be higher than for other trips, such as discretionary trips. Because our program was a "one-shot" program, the cost of implementing the program was no greater than that of programs with several steps that have been implemented in many cities in different countries (c.f. Gärling & Fujii, 2006). For recipients, the program looked like a "questionnaire survey" that was distributed with complementary information on public transport or bicycle commuting. Those conducting mobility management might expect an aggregate reduction in car use and aggregate increase in more sustainable travel modes with a feasible monetary budget by conducting a one-shot travel feedback program targeting commuting trips.

We also found that the effectiveness of the program differed across companies. This might be due to differences in location. A limited number of car commuters changed their commute mode at a company that had low accessibility to a railway station and residential areas. In contrast, 12% and 19% of the car commuters changed their commute mode at companies that were accessible to railway stations and arterial roads. In addition, commuters at a company that was within walking distance to a railway station tended to use the railway as an alternative commute mode to car, while those at a company that was farther from a railway station tended to use bicycles. Therefore, the type of commute behavior modification caused by the travel feedback program seems to depend on the accessibility of alternative travel modes.

Transportation policy makers may believe that it is difficult to change commute behavior without any economic incentives/disincentives or changes in the level of service of their transportation systems. However, our data clearly indicate that commute behavior can be modified from car use to a sustainable travel mode via a simple communicative intervention that provides information about public transportation, giving people the opportunity to rethink their commute behavior.

3. RISK-COMMUNICATION PROGRAM FOR SOIL AVALANCHE HAZARD

We have developed a risk -communication program for soil avalanche hazard while replicating the abovementioned program for travel behavior communication. The program for soil avalanche hazard is to increase preparedness for escaping from possible soil avalanche in case of extremely heavy rain. Similarly to abovementioned program, the program for soil avalanche is simply to distribute a questionnaire with some information kits, that is, a leaflet and a map. The questionnaire is designed not for investigation of recipient's attitudes and behavior, but for change them. The distributed questionnaire was shown in Figure 3 and an information leaflet distributed with the questionnaire is shown in Figure 4.

In the questionnaires, recipient were asked to read the information leaflet and asked to answer questions regarding the leaflet. Therefore, recipient needed to read the leaflet in order to answer the questions. In the leaflet, it was described that the recipients' residential area was with risks of soil avalanche with statistical information of numbers of actual soil avalanche. In the last page of leaflet, residents in area with risks of soil avalanche need to evaluate from their houses to safer places in case of extremely heavy rain that can be observed quite seldom. After questions for the leaflet, recipients were asked to answer questions regarding a map indicating areas with risks of soil avalanche. The question was, 1) to mark the place of the recipient's house in the map, and 2) to judge whether their house was in the risk of soil avalanche. The recipient who answered that their house was in the risk of soil avalanche were then asked to answer the place to which they evacuate from their house. After this question, all the recipients were asked to answer persons to whom they want to suggest evaluating in case of extremely heavy rains. At the end of the questionnaire, they were asked to write up the place they will evaluate to, and the persons to whom they want to suggest evacuating in case of extremely heavy rains in a card. Then they were eventually asked to put the card somewhere in their house, for example, freezer in the kitchen. Through these

tasks induced by the responding behavior to this questionnaire, increase of risk-awareness regarding soil avalanche and preparedness toward evacuation behavior from the risk were expected.

The questionnaires were distributed to 819 households in Tosa town in Shikoku island, Japan in . September, 2008, and 341 questionnaires were mailed back. The response rate was then 41.6%. The effectiveness of this program in terms of increase of risk-awareness and preparedness regarding soil avalanche will be assessed by the pre-survey that will be conducted in February, 2009. In addition, Similar program was conducted in Satsuma town, in Kyusyu Area, Japan. The results from the evaluation survey will be reported in the presentation.

References:

Cairns, S., Sloman, L., Newson, C., Anable, J., Kikbride, A., and Goodwin, P. (2004) Smarter choices: Changing the way we travel, Department for Transport, UK.

Fujii, S. (2004) Mobility Management. *Transportation and Economics*, 65(3), 21–30 (in Japanese with English abstract).

Fujii, S., and Taniguchi, A. (2006) Determinants of the effectiveness of travel feedback programs—a review of communicative mobility management measures for changing travel behavior in Japan, Transport Policy, 13 (5), pp. 339-348.

Fujii, S., and Taniguchi, A. (2005) Reducing family car use by providing travel advice or requesting behavioral plans: An experimental analysis of travel behavior feedback programs, Transportation Research D, 10(5), 385–393.

Gärling, T., and Fujii, S. (2004) Travel behavior modification: Theories, methods, and programs; *Resource paper for the 11th IATBR conference*, Kyoto, Japan, August 16–20, 2006.

Gärling, T., Jakobsson, C., Loukopoulos, P., and Fujii, S. (2004) Adaptation of private car use in response to travel demand management measures: Potential roles of intelligent transportation system, Intelligent Transportation Systems, 8, 189–194.

Gollwitzer, P. M. (1996). The volitional benefits of planning. In P. M. Gollwitzer & J. A. Bargh (Eds), The Psychology of Action: Linking Cognition and Motivation to Behavior. Guilford Press, New York, pp. 287–312.

Jones, P. (2003) Encouraging behavioural change through marketing and management: What can be achieved? Proceedings of the 10th International Conference on Travel Behavior Research, Lucerne, Switzerland.

Kitamura, R., Fujii, S. and Pas, E. I. (1997) Time-use data, analysis and modeling: toward the next generation of transportation planning methodologies. *Transport Policy* **4**, 225-235.

Loukopoulos, P., Jakobsson, C., Gärling, T., Schneider, C.M., and Fujii, S. (2004) Car-user responses to travel demand management measures: goal setting and choice of adaptation alternatives, Transportation Research D, Transport and Environment, 9, 263–280.

Pas, E. I. (1995) The urban transportation planning process. In *The Geography of Urban Transportation*, ed S. Hanson, pp. 53-77. Elsevier, Amsterdam.

Taniguchi, A. Hara, F., Takano, S., Kagaya S. and Fujii, S. (2003) Psychological and Behavioral Effects of Travel Feedback Program for Travel Behavioral Modification, *Transportation Research Record*, **1839**, 182-190.

Sixth International Conference on Urban Earthquake Engineering
March 3-4, 2009, Tokyo Institute of Technology, Tokyo, Japan

MINING FAILURE RECORDS OF CRITICAL INFRASTRUCTURES TO DISCOVER INTERDEPENDENCY RELATIONSHIPS FOR URBAN DISASTER MITIGATION

Ssu-Min Tseng[1], Ting-Wu Ho[2], and Chien-Cheng Chou[3]

1) Graduate Research Assistant, Department of Civil Engineering, National Central University, Taiwan
2) Graduate Research Assistant, Department of Civil Engineering, National Central University, Taiwan
3) Assistant Professor, Department of Civil Engineering, National Central University, Taiwan
mo_ly_ly@hotmail.com, 973202093@cc.ncu.edu.tw, ccchou@cc.ncu.edu.tw

Abstract: Critical infrastructures (CIs) are important assets for producing or distributing continuous flows of essential goods or services in a country. When one CI shuts down due to a disaster, it can be expected that other CIs that need services or goods provided by the disrupted CI will stop shortly, exacerbating the damage caused by the disaster. Past research has categorized CI interdependency into four relationship types and has proposed several methods to simulate CI interdependency and its effects. However, few researchers focus on CI failure records to build an interdependency model. This paper presents a data mining-based approach that analyzes CI failure records triggered by external events so as to discover interdependency relationships and to predict failure probabilities of other interdependent CIs. City planners can employ the proposed model to mitigate possible dangers due to CI interdependency when a disaster hits certain areas.

1. INTRODUCTION

Critical infrastructures (CIs) are important assets for producing or distributing continuous flows of essential goods or services in a country (Fisher and Peerenboom 2000). These assets include, but are not limited to, facilities for transportation, telecommunication systems, electric power systems, gas and oil storages and pipelines, water supply systems, and wastewater treatment systems. An interdependency relationship of two or more CIs means that one CI explicitly or implicitly needs support from the other CI(s), and vice versa. For instance, a gas pipeline leaks and an explosion occurs, which in turn engenders shutdown of a telecommunication facility. Since the explosion information cannot be transmitted by the telecommunication facility, the leak in the gas pipeline will not be fixed and may cause greater damage. Because the operation of a CI usually requires support from other CIs, these interactions often create complex interdependency relationships that cross system boundaries (Haimes 2005). As the complexity and interconnectedness of a country's CIs evolve, threats and vulnerabilities for the country increase. Investigating how a set of CIs interact thus becomes an important research topic.

Past research has classified myriad CI interdependency relationships into four types: physical, cyber, logical and geographic. Briefly, the physical and cyber types of interdependency relationships represent a bi-directional relationship that the first CI's output is the second CI's input and the second CI's output is the first CI's input. The difference between the two types is that the input and output in the physical relationship type are actual products or services generated or consumed by CIs. For instance, electricity is output of a power plant and serves as input for lighting up the entrance road to the power plant. The input and output in the cyber relationship type are the information generated by or transmitted to CIs. For instance, supervisory control and data acquisition (SCADA) refers to a system that collects data from various sensors in a power network. The data SCADA processes serves as input information to control the power network while the telecommunication system treats it as output of information transmission because it is transmitted in the same way as other types of data. The geographic relationship type means that one CI is actually located near other CIs. When an explosion at the first CI occurs, the nearby CIs usually suffer severely. The final relationship type, logical interdependency, means that two or more CIs have logical connections that cannot be classified as physical, cyber or geographic types of relationships. For example, a company owns two or more types of utility services. The company's finances deeply affect successful operations of these utility services. Obviously, the geographic type of relationships can be identified as long as all infrastructure baseline data are available and accurate and can be integrated. However, comprehensive identification of the other three relationship types for a given set of CIs poses a research challenge because some interdependency relationships are unknown until failures of CIs occur. Additionally, since a CI usually consists of many components that are geographically distributed over certain areas, not only the geographic type

but the other three types of interdependency relationships exist at the component level.

This paper presents a data mining-based approach that analyzes CI failure records directly or indirectly triggered by external events so as to discover interdependency relationships among the CIs. Several researchers have proposed approaches that utilize CI failure records to build CI interdependency model. However, since their focuses are about the system-level interaction, how one component of a CI interacts with another component of a different CI is not the main concern in their research. Our approach aims at investigating component-level interactions among a given set of CIs, based on CI failure records. Theoretically, all of the four interdependency types will be identified if the CI failure records are complete and accurate.

This paper is divided into four sections. The second section introduces fundamental concepts and definitions of CI interdependency. The third section defines a UML-based model to represent essential entities in the CI failure records. The last section presents the main research conclusions.

2. RELATED WORK

2.1 The Disaster Management Process

The disaster management process consists of six disaster-related phases (USFDA 2003): (1) identification; (2) prediction; (3) mitigation; (4) preparation; (5) response; and (6) recovery. The identification phase involves ascertaining any opportunity pertaining to community assets, i.e., critical infrastructure systems, fire trucks, hospital beds, etc., that may be affected by a disaster. The prediction phase consists of scientific analysis tasks, including meteorological, geologic, hydrologic, agricultural, environmental, epidemiologic calculations and simulations. The mitigation phase concerns active reductions of a disaster's impact, whereas the preparation phase includes needed actions to contend with the portion of a disaster's impact that cannot be mitigated. The response phase focuses on real-time actions as a disaster evolves, whereas the recovery phase deals with how to restore community assets affected by a disaster (Pradhan et al. 2007).

Researchers have also analyzed requirements of a DMS covering all six phases of the disaster management process (Pradhan et al. 2007). Briefly, a DMS is designed to significantly lessen the loss of human life and the economic costs of a disaster, and should have three components (Uddin and Engi 2002): (1) a baseline database: which contains the basic information of the community assets affected by a disaster; (2) spatial querying: which can provide disaster management officials with a graphical interface showing designated geographical information of the disaster and community assets, e.g., locating the shortest evacuation path and optimizing the resource distribution; and (3) ubiquitous computing: which means redundant computing resources should be allocated to execute the DMS simultaneously (Pradhan et al. 2007).

Although most of the current DMSs have stored critical infrastructure baseline data for disaster management purposes, CII data have not been rigorously documented and analyzed. The rescue operations after September 11, 2001 were recognized as lack of an integrated data repository that can be used to predict possible subsequent infrastructure failures. CII data can play a major role in establishing the knowledge base for the rescue operations during and after a disaster. Disaster management officials or decision makers need to know not only direct impact on community assets of a disaster but indirect impact on other critical infrastructure systems that may be shut down due to CII. However, since managing the interdependencies of critical infrastructure systems is not their owners' top priority, the only way to collect CII data is for transportation agencies to ask infrastructure owners to upload interdependency data as a part of the rights-of-way permitting process. Some infrastructure owners build very detailed computerized models describing their own facilities, but this kind of information may involve a company's confidential data and cannot be completely shared with the others. Security concerns regarding CII data must be addressed in advance of data collection from different infrastructure owners. A formal model that can describe CIIs and predict a disaster's impact on critical infrastructure systems is highly desired.

2.2 The Time Dimension

Each event during and after a disaster may be associated with a different time scale (Chen et al. 2006). For example, if an accident destroys a power switch facility, the failure due to switching over voltages may ruin other power facilities within milliseconds. Shortage of fuel support as a result of road blockage may take months to fix the problem but might not affect the power generation process immediately. The need of the multi-scale time hierarchy associated with CIIs was reported as one of the most difficult research challenges in this area.

One advanced database technique that has emerged as a main focus of many spatial-temporal information systems such as the digital battlefield in the military is to keep track of object locations over time and to support temporal queries about future locations of the objects (Wolfson 2002, Wolfson et al. 1998). Called moving objects database (MOD), this technique aims to deal with geometries changing over time and to simplify the data update process through use of dynamic attributes (Guting and Schneider 2005), thereby having the potential for eliminating or reducing some of the associated challenges and complications. The way MOD employs to process the time dimension for each moving object may serve as a starting point for CII data modeling.

3. THE CII MODEL

The proposed CII model is shown in Figure 1. Elaboration of each class in the model is described in the following sections. Basically, the model consists of three main parts: (1) infrastructure and management classes; (2) interdependency classes; and (3) infrastructure type classes. The infrastructure and management classes contain information regarding an infrastructure system itself and the owners' organization. The interdependency classes are designed to capture requirements of the three CII types. The infrastructure type classes are the reflection of the need that each type of critical infrastructure systems has its own attributes. The mechanisms of the model are described as follows.

3.1 Infrastructure and Management Classes

Three classes pertain to this part:

- Organization: this class represents the owner of a critical infrastructure system. It includes a person's contact information so that disaster management officials can get in touch with him or her when potential damage of the infrastructure occurs.
- Enterprise: this class represents the concept of the organization's business entity. For example, a city government may be responsible for the water supply system, the wastewater treatment system, and the power distribution system. There must be three engineering divisions in the city government, so "Enterprise" represents the city government whereas "Organization" represents each engineering division. The "Enterprise-Organization" structure can be easily extended to model any infrastructure owners' organizations.
- Infrastructure: this class represents the most important concept in the CII model, i.e., infrastructure. It consists of six fundamental attributes:

1. Name: the name of the infrastructure.
2. Description: notes or other information regarding this infrastructure.
3. Location PolygonZ: the location and shape of the infrastructure, including the vertical dimension. It should be noted that since an infrastructure object may contain a set of other infrastructure objects via composition, the shape and base reference point of the object should be changed accordingly.
4. ServicePeriod T: the expected service period of the infrastructure. Sometimes an infrastructure service may be stopped due to maintenance. The discontinued service may cause a serious problem if a disaster strikes an area where the regular backup infrastructure is working. In the theory of temporal database or MOD, there are two time dimensions associated with each time-sensitive attribute: valid time and transaction time (Tansel et al. 1993, Guting and Schneider 2005). The valid time refers to the time in the real world when an event occurs or a fact is valid. The transaction time refers to the time when a change is recorded in the database. For example, the service period of an infrastructure is defined by a manager as from 2009/1/1 to 2009/5/1. The manager knows the plan on 2008/11/1, but the plan is changed by another manager on 2009/3/1. Hence, the infrastructure will not provide service after 2009/3/2, although the original plan does not say so. Same rules can be applied to the transaction time dimension. Traditional database techniques do not consider such requirements because only the newest status of an object is recorded.
5. Status T: the working status of the infrastructure. This attribute is also time-sensitive. For example, disaster management officials might want to know when the status of an infrastructure is "Working" or "Stopped." They might want to know when the status data is updated. Persisting historical data of the infrastructure status in a database can help decision makers understand past experience.
6. EstimateStatus T: the estimated status of the infrastructure. Because the CII model is designed to predict the interdependencies between critical infrastructure systems, this attribute will be used to record the predicted status of an infrastructure.
7. RecoveryStatus T: the recovery progress of the infrastructure. If an infrastructure is out of order, its recovery plan will be executed. If RecoveryStatus is equal to "Complete," the Status of the infrastructure should be "Working."

3.2 Interdependency Classes

Four classes pertain to this part:

- Relationship: this class represents the concept of a relationship in the CII model. In the one end of the relationship, it is the dependent infrastructure that needs services or resources provided by the supporting infrastructure. For example, the operation of a power plant depends on the entrance road, whereas the traffic control system on the road needs electricity provided by the plant. Two relationship objects should be created for this interdependency. Additionally, the class consists of six attributes:

1. Name: the name of the relationship.
2. Description: notes or other information regarding this relationship.
3. TimeLag: the time span of the relationship that will cause the dependent infrastructure to stop or reduce the service level.
4. MinStatus: the minimum status of the supporting infrastructure that will activate the relationship, i.e., to shut down the dependent infrastructure.
5. ActiveTime T: the time when the relationship is activated. This attribute is time-sensitive and can provide detailed records of how a disaster propagates.
6. ImportantR: the weight or ratio of the relationship with

respect to the dependent infrastructure. For example, two infrastructure systems support the operation of the third infrastructure. The two infrastructure systems may play different roles in supporting the third one. Hence, the weight for each supporting infrastructure is different.

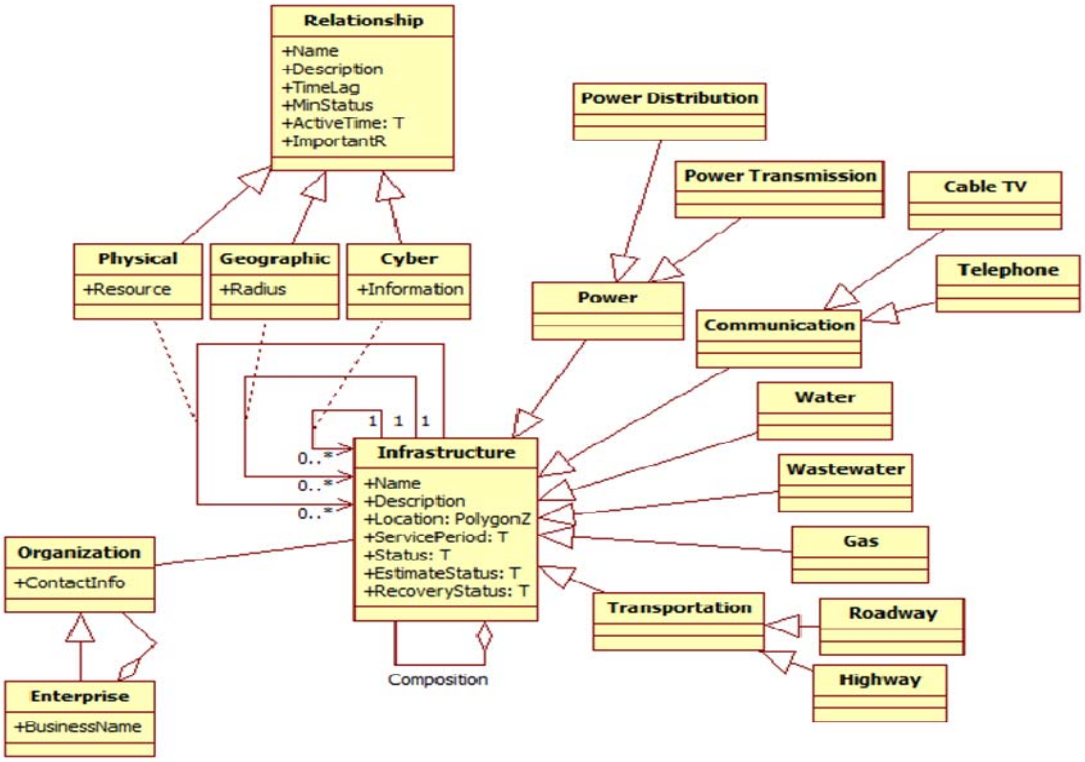

Figure 1 UML Class Diagram of the CII Model

停電日期：97 年 07 月 21 日

停電時段	停　電
自 09 時 00 分 至 11 時 00 分	H38096 表燈增設 中山區敬業一路59號 中山區敬業二路69巷10~12號
自 13 時 30 分 至 16 時 30 分	H38095 表燈增設 南港區重陽路30號前80公尺

Figure 2 Power System Failure Records

中山區江寧里 - 6月28日上午10時至下午2時
停水地點：中山區江寧里
臺北市民權東路3段至敦化北路一帶及民生東路3段至光復北路口一帶等水壓降低。
施工單位：工程總隊
備　　註：

Figure 3 Water System Failure Records

- Physical: this class represents the physical relationship type in the CII model. Relationship attributes can be easily modeled in the class. In the proposed model, the resource that bridges the two infrastructures is recorded here.
- Geographic: this class represents the geographic relationship type in the CII model. In the proposed model, the radius defining the boundary of two infrastructures that may work or stop at the same time is recorded here.
- Cyber: this class represents the cyber relationship type in the CII model. In the proposed model, the information that is consumed by the dependent infrastructure is recorded here.

3.3 Infrastructure Type Classes

This part defines various infrastructure types. Specific attributes pertaining to a certain type of critical infrastructure systems are recorded in respective classes. Additionally, because the structures and functions of a power distribution network is quite different that a power transmission network, two classes are designed to accommodate this requirement.

4. EXPLOITING THE MODEL

Figure 2 shows the failure records of the power system in a certain area in Taipei this year. Figure 3 shows the failure records of the water system in the same area in Taipei. Figure 4 shows the integrated failure records of the two CIs in the same area in Taipei. A simulation tool is currently under development. The tool will use the CII model to simulate events of each critical infrastructure system under an earthquake disaster in a small town in Taiwan. The water supply system, power distribution lines, communication lines, and natural gas pipelines are depicted in the tool. Their baseline and interdependency data are recorded in the database.

With interdependency data in the database, users can find out when the scope of the disaster's impact with respect to the time dimension. A "firewall" concept may be added to an interdependency relationship to have the disaster propagation suspend. Other applications such as querying a certain type of infrastructure failure can be implemented.

	C	D	E	F	G	H	I	J	K	L	M	N
1		區	座標x			座標y			地址	開始	結束	類型
2	台北市	中山	121	31	26.3	25	3	53.9	農安街１７之１號、１７號、１９號、２１號等	2008/10/6 0:00	2008/10/6 06:00	p
3	台北市	大安	121	33	22.9	25	2	22.6	光復南路２８０巷２３號、２５－１號、２５之	2008/10/6 8:30	2008/10/6 10:30	p
4	台北市	信義	121	33	55.1	25	1	47.2	松智路（四號，松智路７５號等	2008/10/6 8:30	2008/10/6 11:00	p
5	台北市	信義	121	34	46.5	25	2	47.5	北市信義區永吉路４４３巷１１弄３３號，北市	2008/10/6 8:30	2008/10/6 11:30	p
6	台北市	大安	121	33	4.5	25	2	5.8	北市大安區安和路一段７８巷１２號，安和路一	2008/10/6 13:30	2008/10/6 17:00	p
7	台北市	大安	121	31	54.2	25	0	57.6	羅斯福路三段２８４巷１０・１２號，羅斯福路	2008/10/6 13:30	2008/10/6 17:00	p
8	台北市	大同	121	30	56.1	25	3	43.9	民權西路１４４巷１０弄２・４號、２號、４號	2008/10/6 14:30	2008/10/6 14:40	p
9	台北市	中山	121	31	59.7	25	2	54	松江路６１號、６３號等	2008/10/6 15:30	2008/10/6 15:40	p
10	台北市	信義	121	34	23.8	25	2	28.3	忠孝東路五段２９７號等	2008/10/7 0:00	2008/10/7 02:00	p
11	台北市	萬華	121	30	7.5	25	2	19.6	康定路１３１號、１３３號、１３５號、１３７	2008/10/7 0:00	2008/10/7 06:00	p
12	台北市	萬華	121	30	6.7	25	2	19	康定路１３９號、１４１號、１４３號、１４５	2008/10/7 0:00	2008/10/7 06:00	p
13	台北市	大安	121	31	58.4	25	2	43.1	北市大安區市民大道三段８號等	2008/10/7 9:30	2008/10/7 09:40	p
14	台北市	中山	121	32	41.9	25	3	51.2	五常街１２９號，五常街１３１巷２，２－１號	2008/10/7 14:30	2008/10/7 15:00	p
15	台北市	大安	121	32	36.2	25	2	4.5	復興南路一段３７２號等	2008/10/8 0:00	2008/10/8 06:00	p
16	台北市	大安	121	31	48.5	25	1	8.4	羅斯福路三段２５１號、２５３號、２５５號、	2008/10/8 0:00	2008/10/8 06:00	p
17	台北市	中山	121	32	25.9	25	3	14	龍江路１５１・１５３號、１５１號、１５３號	2008/10/8 9:30	2008/10/8 10:00	p

Figure 4 Integrated CI Failure Records

5. CONCLUSIONS

With the ever-increasing demand for a streamlined analysis of CII, disaster management officials and decision makers are making substantial efforts to improve the disaster mitigation technology. Because CII data are fundamental to develop a full-fledged DMS and because the management of the time dimension is the most difficult task in modeling CIIs, a rigorous model with time processing capabilities such as the one in this paper can help disaster management officials retrieve relevant information on demand. This research has designed a UML-based model that can describe CIIs with the time-sensitive attributes. Further implementation and evaluation of the CII model proposed is needed in order to demonstrate how such information technology can mitigate a disaster's impact.

References:

Chen, L.C., Wu, J.Y., and Lai, M.J. (2006) "The Evolution of the Natural Disaster Management System in Taiwan." *Journal of the Chinese Institute of Engineers*, 29(4), 633-638.

Chou, C.C., Caldas, C.H., and O'Connor, J.T. (2007) "Decision Support System for Combined Transportation and Utility Construction Strategy." *Transportation Research Record: Journal of the Transportation Research Board*, TRB, 1994, 9-16.

Fisher, R., and Peerenboom, J. (2000) "Interdependencies: A DOE Perspective." *16th Annual Security Technology Symposium & Exhibition*, Office of Critical Infrastructure Protection, June 28, 2000, Williamsburg, Virginia.

Guting R.H., and Schneider, M. (2005) *Moving Objects Databases*, Morgan Kaufmann, San Francisco, CA.

Haimes, Y. (2005) "Infrastructure Interdependencies and Homeland Security." *Journal of Infrastructure Systems*, ASCE, 11(2), 65-66.

Kranc, S.C., Yalcin, A., Tsalatsanis, A., and Collier, N.O. (2007) "The Efficacy of Utility Data Management." *FDOT Research Project BD544-27 Report*, University of South Florida, Tampa, FL.

Kraus, E., Quiroga, C., Brown, R., Stevens, C., and Koncz, N. (2007) "Development of a Utility Conflict Management Tool." *TxDOT Research Project 0-5475 Report*, Texas Transportation Institute, College Station, TX.

Laefer, D., Koss, A., and Pradhan, A. (2006) "The Need for Baseline Data Characteristics for GIS-Based Disaster Management Systems." *Journal of Urban Planning and Development*, ASCE, 132(3), 115-119.

MRA. (2005) *Joint Infrastructure Interdependencies Research Program (JIIRP) Symposium*, the Department of Public Safety and Emergency Preparedness Canada (PSEPC), November 10, 2005, Ottawa, Ontario, Canada.

Peachavanish, R., Karimi, H., Akinci, B., and Boukamp, F. (2006) "An ontological engineering approach for integrating CAD and GIS in support of infrastructure management." *Advanced Engineering Informatics*, Elsevier, 20, 71-88.

Pederson, P., Dudenhoeffer, D., Hartley, S., and Permann, M. (2006) "Critical Infrastructure Interdependency Modeling: A Survey of U.S. and International Research." *INL/EXT-06-11464*, Idaho National Laboratory: Critical Infrastructure Protection Division, Idaho Falls, Idaho.

Pradhan, A., Laefer, D., and Rasdorf, W. (2007) "Infrastructure Management Information System Framework Requirements for Disasters." *Journal of Computing in Civil Engineering*, ASCE, 21(2), 90-101.

Rinaldi, S., Peerenboom, J., and Kelly, T. (2001) "Identifying, Understanding, and Analyzing Critical Infrastructure Independencies." *IEEE Control Systems Magazine*, 21, 11-25.

Tansel, A., Clifford, J., and Gadia, S. (1993) *Temporal Databases: Theory, Design, and Implementation*, Benjamin-Cummings, San Francisco, CA.

Uddin, N., and Engi, D. (2002) "Disaster Management System for Southwestern Indiana." *Natural Hazards Review*, ASCE, 3(1), 19-30.

USFDA. (2003) *Disaster preparedness phases*, U.S. Federal Drug Administration, Rockville MD.

Wolfson, O., Xu, B., Chamberlain, S., and Jiang, L. (1998) "Moving Objects Databases: Issues and Solutions." *Proceedings of the Tenth International Conference on Scientific and Statistical Database Management*, IEEE, Capri, Italy, 111-122.

Wolfson, O. (2002) "Moving Objects Information Management: The Database Challenge." *Lecture Notes in Computer Science*, Springer Berlin / Heidelberg, 2382, 15-26.

Sixth International Conference on Urban Earthquake Engineering
March 3-4, 2009, Tokyo Institute of Technology, Tokyo, Japan

QUANTITATIVE ANALYSIS OF LOT SUBDIVISIONS IN URBAN DISTRICTS

Toshihiro Osaragi[1)]

1) Associate Professor, Department of Mechanical and Environmental Informatics, Tokyo Institute of Technology, Japan
osaragi@mei.titech.ac.jp

Abstract: Recently, a number of subdivisions of building lots have been observed in established urban districts. Such subdivision of standard lots into smaller spatial units could cause serious problems in citywide disasters, such as a strong earthquake, as well as environmental deterioration. It is thus imperative to investigate the mechanism of subdivisions of building lots. In the present study, we construct stochastic models that describe methods of dividing building lots and forming smaller spatial units. Unknown parameters of the models are estimated using the GIS data compiled by a local government ward in Tokyo, and the factors related to the subdivision are examined. Several numerical examples demonstrate that the possibility and probability of lot subdivision is mainly dependent on the condition of the location and properties of the lot.

1. INTRODUCTION

Recent years have seen a steady diminution in plot size with the continuing subdivision of lots, the basic unit of land use in the Tokyo region. Excessively small urban lot sizes have deleterious effects on the living environment, not only as a factor hindering the intensive use of land, but also by increasing the vulnerability of the city to disasters. Because of these effects, urban planners generally seek to discourage division of lots, combine the smallest lots, preserve existing large parcels, and establish new parcels. Thus, it is very useful to have a better understanding of the characteristics of the lots that are subdivided in spite of the above factors.

Numerous reports have addressed lot subdivision. For example, Matsunawa and Komatsu (1986) focused on the individual residential/farming parcel, the basic administrative unit of land, and observed the relationship of division with assembly of parcels and rights transfer. Takamizawa (1977) focused on fine division and rights transfer of existing urban residential plots for the 50-year period 1926-1976 and analyzed the updating process for the affected plots. Osaragi et al. (2003) have employed fixed asset tax records to assemble a database of land and building for lots. This was then used to analyze the land use transition probabilities of lots. Hidaka and Asami (2001) published a leading analysis of the subdivision of lots at the unit level. They then employed the boundary element method to express lot shapes and constructed a genetic algorithm-based system to perform optimized division of lots. Mizuno et al. (2005) examined maps of commercially developed residential projects at three time points and identified time-based changes in land use, lot size, ownership, and other parameters. However, due to the restrictions on availability of data for these research efforts, their scopes were limited to small parts of the regions they attempted to analyze, and their conclusions have only been qualitative. No research can be found that provides quantitative analyses of the characteristics of lot divisions over wide regions.

Nevertheless, a series of reports by Asami and Maniruzzaman (1994) and Maniruzzaman et al. (1994) investigated the shapes of lots and conditions of connecting roadways and examined basic shapes from the viewpoint of their hypothesis (that specific shapes of lots determine the value of the lots). While they did not conduct observations of actual data to confirm their research, their data was collected from the same region (Setagaya Ward, Tokyo, Japan) as the present study, and their studies are important for their findings of the existence of a basic unit for frontage, minimum frontage, and other principles of lot division.

In an attempt to extract fundamental patterns in the division of lots, Osaragi and Watanabe (2001) have analyzed actual data from Mitaka City, Tokyo Prefecture, for fundamental characteristics of lot division. The present report is an extension of that research. Regional GIS data were employed to explain the mechanisms of located subdivision in precise detail. This report begins with an analysis of factors determining the type of lots that are most likely to be divided. It investigates lot characteristics, including area and how it adjoins streets, characteristics of buildings on the lot, land use regulations, walking time to the nearest train or subway station or characteristics of the district to which the lot belongs (properties of location), and how these affect the ease of division of the lot. Next, a model is constructed to describe how lots are divided and then applied in an attempt to analyze how differences in lot characteristics affect lot division.

2. DATABASE FOR EXTRACTING LOT DIVISION

Setagaya Ward of Tokyo (Figure 1; approximately 150,000 lots) was selected for this analysis because it contains many typical densely concentrated districts. The GIS data sets for Setagaya (1991, 1996) indicate lot shapes, and GIS sets from different times were the sources for extracting information about division and assembly of lots. GIS functions were also used to generate other information, including the frontage, depth, orientation(s) of adjoining street(s) and time to the nearest station for each lot. Figure 2 shows the relation between actual assemblies (fraction of lots actually assembled) and actual divisions of properties (fraction of lots divided) in each major administrative town of Setagaya. Towns lying on the 45º line would have shown no change in the number of lots. All of the towns are plotted well below the 45º line, showing that there were a large number of districts where the number of lots had increased considerably.

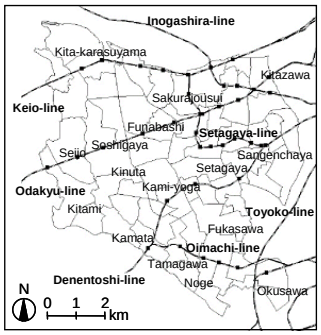

Figure 1 Study Area

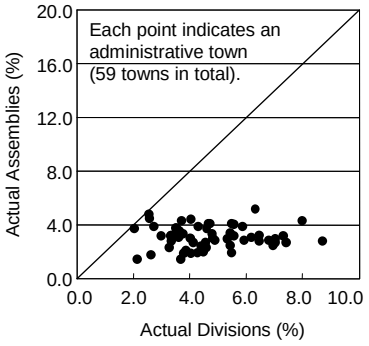

Figure 2 The Relation between Actual Assemblies and Actual Divisions of Properties

3. LOT DIVISION POTENTIAL MODEL

3.1 Creating datasets for the analysis

When considering a model to describe a typical subdivision of lots, it must be considered that only a very small percentage (4.9%) of the total lots surveyed were actually subdivided. If data from all lots were used for analysis, the characteristics of the divided lots would be obscured by the diversity of the lots that were not divided, and it might not be possible to obtain clear indications of all of the important characteristics. Therefore, a number undivided lots equal to that of the divided lots were selected at random for analysis. Undivided lots were extracted so as to maximize the possibility of identifying the district's characteristics found in the divided lots.

3.2 Formulation of model

In the following, a logit model is employed in an attempt to model the potential for a lot to be divided. First, the probability that lot i (i =1,2,..., n) will be divided is P_i, and the utility obtained by division is U_i. Here, there are only two events, that the lot was divided or that it was not, so when a lot was undivided, we can standardize its utility at zero without losing generality. Then, if we assume a Gumbel distribution for the error term for utility, we can state probability of division P_i as follows from the random utility theory:

$$P_i = \frac{1}{1+\exp[-U_i]} \tag{1}$$

Next, let us consider how to formulate the utility U_i. We considered the factors that appear to affect division of lots. In a prior analysis, it was noted that the influences of explanatory variables defined by continuous quantities on utility were not always linear, so here, continuous quantities were divided into multiple ranges and employed as categorical variables (method of classification into categories will be described in the next section). Below, utility U_i is described in the linear model as variables related to lot characteristics and other properties of location.

$$U_i = a_o + \sum_j^m \sum_k^{c_j} a_{jk} d_{jk}(i) \tag{2}$$

where

j: suffix indicting a variable; m: number of variables; c_j: number of categories for variable j; a_{jk}: unknown parameter (influence of category k on variable j); a_0: unknown parameter (constant term); d_{jk} (i): = 1 when category k of variable j applies to lot i; 0 otherwise.

3.3 Estimation of model

The model parameters can be estimated by the maximum likelihood method. The explanatory variables adopted in the model were determined by their statistical significance and how well the estimated parameters could be interpreted.

The categories were classified as follows. (1) First, the lots were classified into as narrow categories as possible. (2) The lots were then cross-tabulated to examine for divisions. (3) New categories were designated by combining categories that showed similar trends. Also, a dummy variable consisting of the product of frontage and lot depth was created to account for the interaction between frontage and depth.

Figure 3 shows the probability of division predicted by the model and the rate of correct predictions (threshold = 0.5). The predictions of whether a particular lot would or

would not be divided were correct 73.8% of the time, which was generally a good prediction.

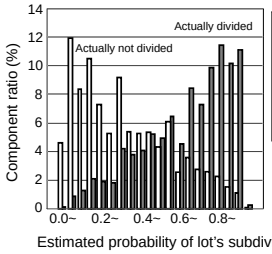

observed \ estimated	divided	not-divided	total	correct ratio
divided	5319	1965	7284	73.0%
not-divided	1852	5432	7284	74.6%
total	7171	7397	14568	73.8%

The predictions of whether a particular lot would or would not be divided were correct 73.8% of the time, in case judgment threshold is 0.5.

Figure 3 Fitness of the Estimated Model.

3.4 Improvement of model by incorporation of regional variables

The original model was good at predicting whether a lot would be divided or not, but the estimates for probability of division of the lots were not always very accurate (left side of Figure 4). Therefore, we examined regional factors affecting lot division in an attempt to improve the model. First, a regional indicator variable was introduced into the explanatory variables. The model was then estimated and a component that could not be described by explanatory variables was extracted. This value (parameter of regional indicator variable) was considered as an index of the local tendency to be divided and designated the "regional lot division coefficient". Next, the relation between the regional lot division coefficient and the variables representing the regional characteristics of lot division were analyzed and the variables with strong relations to lot division were extracted. This provided better accuracy in estimates of the probability of lot division in all districts observed (Figure 4, right panel). The correct predictions for an individual lot of division or non-division were thereby raised to 74.8%.

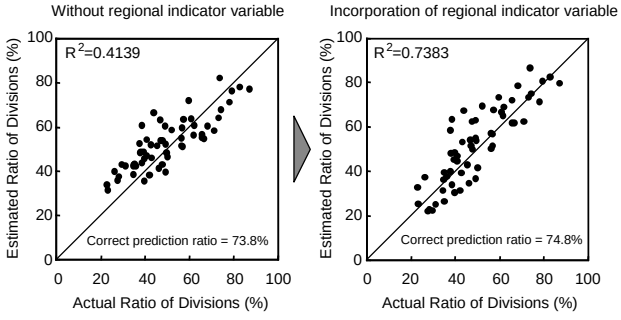

Figure 4 Improvement of Model by Incorporation of Regional Indicator Variable

3.5 Interpretation of parameters

The following results are clear after consideration of the parameter values presented in Tables 1 and 2. (1) The variables of lot area, frontage and depth have considerable effects on the likelihood of division, and the probability of division rises with lot area. Lots also show a higher tendency to be divided when they have larger frontages or depths, although this tendency was weaker for depth. Division was improbable if either frontage or depth was less than 10 m. This is consistent with the suggestions of Maniruzzaman et al. (1994), who mentioned that there seemed to be a lower limit of frontage. (2) The lots containing intact buildings with large floor areas tended to be divided. Lots containing intact wooden or fire-resistant buildings tended not to be divided, but those containing intact fireproof buildings were likely to be divided. This result shows that lot division is likely to occur during the process of demolishing and reconstructing a building. (3) Lots with no direct connection to a street were unlikely to be divided, while those with connections to two or more streets had higher probabilities of division. This is because the new lots are likely to continue to have good connections to streets. Lots with shallow depths, which will continue to have convenient connections to streets, are also more likely to be divided. (4) Lots with low usage rates of their capacities tended to be divided, especially when larger portions of the lot were unused.

Table 1 Estimated parameters relating to lots

Variables	Categories	Parameters	Wald	Variable	Categories	Parameters	Wald
Floor area (m^2)	0-100	-1.212	189.628	Number of connection with the adjoining street	0	-2.495	393.969
	100-150	-0.807	115.183		1	-0.605	168.16
	150-200	-0.332	20.12		2-	0.000	-
	200-	0.000	-	Aspect ratio	0.0-0.5	0.733	59.857
Lot area (m^2)	0-100	-1.551	209.667		0.5-1.0	0.505	63.661
	100-200	-0.621	77.479		1-	0.000	-
	200-300	-0.162	6.854	Mean usage rate of floor area (%)	0-20	0.972	72.891
	300-	0.000	-		20-40	0.867	82.431
Structure of building	Fire resistance	-0.742	59.659		40-60	0.769	71.111
	Semi fire resistance	-0.139	2.88		60-80	0.485	26.129
	Fireproof	0.205	12.711		80-100	0.298	8.205
	Wooden	0.000	-		100-	0.000	-
				Constant		1.253	54.263

Table 2 Estimated parameters relating to frontage and depth of lots

		Frontage		
		-10 m	10-20 m	20 m -
Depth	-10 m	-1.900 (540.301)	-1.436 (595.587)	-1.131 (213.581)
	10-20 m			
	20 m -	-1.225 (78.514)	-0.961 (112.886)	0.000 (-)

The following can be clarified from the parameters of the regional variables in Table 3. (1) Regions with lots with large mean building areas and with low mean usage rates of designated capacity (designated capacity factor) and lots with low mean usage rates of their capacities (capacity factor) tended to be divided. In other words, regions with many lots having capacities allowing division tended to have more divisions as time went by. (2) Regions undergoing urbanization, with high building densities and high commercial usage, saw more lot division, indicating more widespread desire for such division. (3) However, the probability of division was low in residential regions containing dense concentrations of wooden housing.

Table 3 Estimated Parameters of Regional Variables

Variables	Categories	Parameters	Wald	Variable	Categories	Parameters	Wald
Mean building areas	0-100 m^2	-0.540	84.286	Density of wooden structure apartment houses	0-200	0.553	33.829
	100 m^2 -	0.000	-		200-300	0.331	30.893
Mean designated floor area ratio	0-150 %	0.846	74.922		300 -	0.000	-
	150-200 %	0.474	39.799	Density of buildings	0-2000	-0.802	61.967
	200 % -	0.000	-		2000-3000	-0.634	85.305
Mean usage rate of floor area	0-50 %	0.287	20.462		3000-	0.000	-
	50 % -	0.000	-	Ratio of commercial lots	0-10 %	0.000	-
					10 % -	0.417	39.551

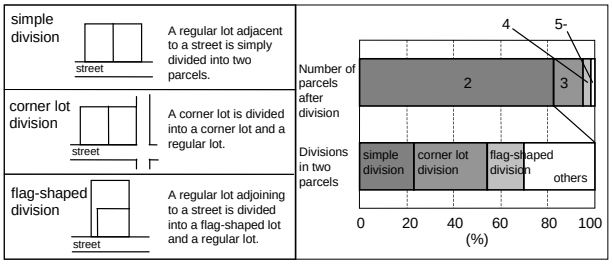

Figure 5 Three Basic Patterns of Division.

3.6 Estimating the probability of division of lots into more than two parcels

The probability of division of a lot into more than two parcels (rate of multiple parcel divisions) was investigated. When a lot is large, it is possible to divide it into a greater number of parcels; the zoning can also affect the probability of multiple-parcel divisions. Therefore, a contingency table analysis based on the Akaike Information Criterion (AIC) (Sakamoto, 1980) was used to examine for variables that could be related to multiple-parcel divisions. Frontage was the variable with the best AIC value, although building area and lot area also showed small AIC values. It was also clear that the lot area was an important factor in how many parcels the lot was divided into, but the frontage was most important.

Table 4 provides an example comparing the rate of multiple-parcel divisions with frontage and lot area. The greater the frontage or the area, the more likely that the lot was divided into more than two parcels.

Table 4 Probability of Multi-division

Frontage (m)	Number of parcels after division				Lot area (m^2)	Number of parcels after division			
	2	3	4	5		2	3	4	5
0-10	0.9299	0.0605	0.0085	0.0012	0-100	0.9654	0.0346	0.0000	0.0000
10-15	0.8931	0.0907	0.0150	0.0013	100-200	0.8802	0.1019	0.0167	0.0013
15-20	0.8385	0.1353	0.0205	0.0058	200-300	0.8596	0.1123	0.0233	0.0048
20-25	0.7868	0.1426	0.0512	0.0194	300-500	0.8199	0.1226	0.0385	0.0190
25-35	0.7500	0.1629	0.0543	0.0328	500-700	0.7576	0.1708	0.0399	0.0317
35-40	0.7500	0.1146	0.0625	0.0729	700-	0.7065	0.1862	0.0607	0.0466
40-	0.6531	0.2089	0.0690	0.0690	Mean	0.8250	0.1264	0.0323	0.0163
Mean	0.8250	0.1264	0.0323	0.0163					

4. LOT DIVISION PATTERN MODEL

4.1 Definition of basic division pattern

Divisions seem very complex at first glance, but the authors found three basic patterns (Figure 5: left panel) among the possible ways in which they can be performed. These are simple division, corner lot division and flag-shaped division, as shown in the figure. Figure 5 (right panel) provides a view of how divisions have proceeded in Setagaya Ward. Divisions resulting in two parcels account for over 80% of these actions; about 70% of these were into the basic patterns mentioned above. The remaining 30% showed more complicated shapes, due to the shapes of the original lots, street connections or other factors.

4.2 Model for distinguishing simple divisions from flag-shaped divisions

The estimated model is shown in Equation (3). If the Z score of the discriminant function was positive, the division was predicted to be simple; if Z was negative, a flag-shaped division was predicted.

$$Z = 0.106x_2 - 0.146x_3 - 0.004x_4 + 0.004x_{12} - 0.550d_1 + 0.466d_2 + 0.312d_3 + 0.945 \quad (3)$$

where

x_2: frontage; x_3: depth; x_4: aspect ratio (ratio of depth to frontage); x_{12}: capacity factor; d_1: through d_3: indicator variables. d_1: 1 if the building was zoned residential, otherwise 0; d_2: 1 if the building was zoned commercial, otherwise 0; d_3: 1 if the building faced north or south on its frontage, otherwise 0.

Table 5 provides the results of this evaluation; division or non-division was correctly predicted in 80.6% of the lots, showing good predictive ability of the model. Table 6 shows the normalized values of the coefficients of the canonical discriminant function and the structure matrix. When examining the structure matrix, it is clear that the aspect ratio has the strongest influence over whether a lot will be divided in a simple way or in a flag-shaped pattern, closely followed by the aspect ratio.

Table 5 Fitting Ratio of Simple Division and Flag-shaped Division

		Predicted		
		Simple division	Flag-shaped division	Total
Observed	Simple division	1110 (81.3 %)	256 (18.7 %)	1366
	Flag-shaped division	153 (20.6 %)	590 (79.4 %)	743
	Total	1263	846	2109

Table 6 Estimated Parameters of Simple Division and Flag-shaped Division

Standardized coefficients of canonical discriminant analysis		Values of structure matrix	
Length of frontage	0.823	Length of depth	-0.637
Length of depth	-0.988	Aspect ratio	-0.420
Aspect ratio	-0.004	Length of frontage	0.345
Actual floor area ratio	0.184	Actual floor area ratio	0.184
Usage of building (residential)	-0.169	Land use regulation (commercial)	0.152
Land use regulation (commercial)	0.138	Usage of building (residential)	-0.115
Direction of connection with street (north or south)	0.156	Direction of connection with street (north or south)	0.073

The following results were clarified from the parameter values. (1) The greater the frontage of a lot, the more likely its division was to be simple, while the greater its depth, the more likely its division was to be flag-shaped. (2) The greater the aspect ratio of a lot, i.e., the greater its depth in relation to its frontage, the more likely it was to be divided in a flag-shaped pattern. (3) Lots with high actual capacity factors tended to be simply divided. This is probably because if they are divided in a flag-shaped pattern, it is difficult to build in the right-of-way to the street (the "flagpole" portion), preventing efficient use of the lot area. (4) Residential-zoned lots are somewhat more likely to be divided in a flag-shaped pattern. This shows that the length of contact with the adjoining street is not as important in residential-zoned lots as in those zoned for other purposes. Conversely, commercial-zoned lots (commercial or neighborhood commercial) tended to be divided in a simple pattern. Most of these were close to a regional train station or adjoining a large street, and the length of the frontage was a critical factor in the lot value. (5) Lots adjoining streets on their north or south side tended to be divided simply. The reason for this was that division in the flag-shaped pattern on a north- or south-facing lot would result in one building being directly north of another, which would raise complaints about blocking of sunlight, especially in residential structures.

4.3 Model of divisions of corner lots

When lots on street corners were divided, most (81.6%) of them were divided across the long dimension. However, although relatively few, some were divided across the short dimension. It was attempted to construct a model to predict whether division would be across the long or short division.

"Good" parcel shapes are more often obtained when a lot is divided across the long dimension. However, in some cases, the commercial interest in keeping frontage along a main street or other priorities such as access to direct sunlight drive the current and future owners to divide property in a different fashion. We considered 18 variables to construct a model for predicting division of a corner lot. A indicator variable was also added to represent the minimum permitted dimension when dividing across the short dimension. The model was estimated, varying the indicator variable value from 4 m to 1 m, to determine which width was the most significant. The numbers of samples were 1484 for divisions across the long dimension and 335 for division across the short dimension. The discriminant function is shown in Equation (4). The prediction was for division across the long dimension when the score Z took a positive value, and across the short dimension when Z was negative.

$$Z = 0.752d_2 - (0.292 + 1.511d_3)\, d_1^{\,6}\, d_5 - 0.718\, d_1^{\,10}\, d_4 d_6 + 1.361x_4 + 0.037x_6 - 2.580 \quad (4)$$

where

x_4: aspect ratio; x_6: walking time to nearest station; d_1 through d_6: indicator variables; $d_1^{\,L}$: 1 if short side length $\geq L$ m, otherwise 0; d_2: 1 if zoning is residential, otherwise 0; d_3: 1 if zoning is commercial, otherwise 0; d_4: 1 if building use is residential, otherwise 0; d_5: 1 if short side faces wide street, otherwise 0; d_6: 1 if short side faces north or south, otherwise 0.

Table 7 shows the results of predictions for this model. The predictions were not as reliable as those for simple or flag-shaped divisions, but were fairly accurate. Table 8 shows the normalized values of the coefficients of the canonical discriminant function and the structure matrix. The structure matrix shows that the aspect ratio has the greatest influence over the direction of division.

Table 7 Fitting Ratio of Corner lot Division

		Predicted		
		Longer dimension	Shorter dimension	Total
Observed	Longer dimension	1092 (73.6 %)	392 (26.4 %)	1484
	Shorter dimension	98 (29.3 %)	237 (70.7 %)	335
	Total	1190	629	1819

Table 8 Estimated Parameters of Corner Lot Model

Standardized coefficients of canonical discriminant analysis		Values of structure matrix	
Aspect ratio	0.710	Aspect ratio	0.716
Walking time to the nearest station	0.151	Shorter dimension is adjoining to wider street and length of shorter dimension is over 6m and land use regulation is commercial	-0.533
Land use regulation is commercial	0.245	Land use regulation is commercial	0.426
Shorter dimension is adjoining to wider street and length of shorter dimension is over 6m	-0.145	Usage of building is residence and direction of shorter dimension is north/south and length of shorter dimension is over 10 m	-0.397
Shorter dimension is adjoining to wider street and length of shorter dimension is over 6m and land use regulation is commercial	-0.341	Shorter dimension is adjoining to wider street and length of shorter dimension is over 6m	-0.253
Usage of building is residence and direction of shorter dimension is north/south and length of shorter dimension is over 10 m	-0.331	Walking time to the nearest station	0.250

The following results were clarified on consideration of the above parameter values. (1) The greater the aspect ratio of a lot (the longer and narrower it was), the more likely it was to be divided across the longer dimension. However, when the two dimensions were nearly the same, the lot was nearly equally likely to be divided across the both dimensions. (2) Residentially zoned lots tended to be divided across the long dimension because shape is a key consideration in designating residential lots. (3) Division across the long dimension becomes more likely with longer walking times to the nearest station. There are two reasons for this: The further from the nearest station, the more undivided large properties there tend to be; and locations far from stations tend to be residential lots. (4) Lots zoned for residential construction, lots whose short dimension is on the north or south side of a street, and lots whose short dimension is at least 10 m are relatively more likely to be divided across the short dimension. This is because access to direct sunlight is an important factor for residential lots. (5) Lots whose short dimension lay along a large street and whose short dimension was at least 6 m tended to be divided across the short dimension; this was particularly true for lots

zoned for commercial use. This is because frontage on main streets is important in commercial regions. Even if lots are long and narrow following such a division, the owners of both lots put priority on frontage on the main street.

The minimum side length of a lot was 6 m for a commercial zone and 10 m for a residential zone. Interestingly, the necessary minimum length varies with the lot use. Maniruzzaman et al. (1994) hypothesized that there is a fundamental unit of frontage length for the long dimension of a lot along a street and showed that the frontage lengths tended to cluster around multiples of this length (the hypothesis of basic shapes). The above results indicate that a similar hypothesis may well hold for corner lots, which contact streets on two of their sides.

4.4 Characteristics of flag-shaped pattern

Lots divided in a flag-shaped pattern were analyzed for the direction of connection with the adjoining street and the location of the new parcel. The orientations of the "flag shapes" were defined as "clockwise" or "counterclockwise" in relation to the adjoining street (see Figure 6). The orientations were examined for relationships with the direction of connection and the results are presented on the left side of Table 9.

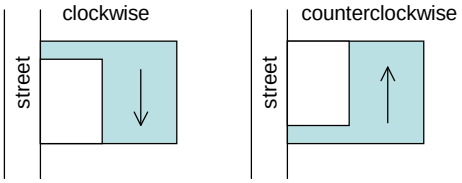

Figure 6 Definition of Direction of Flag-shaped Lot

Table 9 Direction of Flag-shaped Lot According to Direction of Adjoining Street

Setagaya ward					Mitaka city				
rection of ljacent Street	North	East	South	West	Direction of Adjacent Street	North	East	South	West
ockwise	75	111	64	92	Clockwise	7	14	3	5
ounterclockwise	75	88	128	110	Counterclockwise	5	8	2	23

Relatively large fractions of the lots with a clockwise orientation connected to streets on their east borders, and, correspondingly, relatively large fractions of the lots with a counterclockwise orientation connected to streets on their west borders. The reason for this may be that, in a lot of limited area, placing the approach (the "flagpole") along the south side of the old lot allows more access to sunlight. Most of the lots connecting to a street on the south side were of the counterclockwise orientation. This may be intended to avoid the light of the setting sun while obtaining light from the rising sun in the east. The right side of Table 9 shows the results for Mitaka City, Tokyo. Due to the small number of samples, definite results were not obtained for lots connecting to streets on the south side, but there was a tendency for the lots lying on the east and west sides of streets to show the same trends as that in Setagaya Ward.

5. SUMMARY AND CONCLUSIONS

The present paper describes a quantitative analysis of the characteristics of lot divisions in a survey of the entirety of Setagaya Ward, Tokyo, a typical division of Tokyo that includes numerous densely populated districts. The authors began by constructing a model for describing whether or not a lot was likely to be divided (division potential model). The kinds of lot that were most likely to be divided were observed, and it was shown that division depends greatly on the character of the lot, the kinds of building(s) on it, and the features of the surrounding region. A model describing the kind of division occurring in a lot was then constructed (lot division pattern model). It was found that lot conditions, connection(s) to adjoining street(s), convenience of location and other considerations combined to influence the division pattern.

Acknowledgements:

The author would like to give his special thanks to Mr. Takeshi Inoue for computer-based numerical calculations.

References:

Matsunawa T. and Komatsu Y. (1986), "The Study on Subdivision of Lot in Density Built-up Area", *Papers on City Planning*, **21**, 73-78.

Takamizawa K. (1977), "On The Subdivision of Housing Sites and The Changes in Land Ownership", *Journal of Architectural Planning and Engineering*, No.254, 89-96.

Osaragi T., Nishimatsu T. and Yoshikawa T. (2003), "Land Use Conversion Model Based on Transition Probability of Lots", *Journal of Architectural Planning and Engineering*, No.564, 203-209.

Hidaka Y. and Asami T. (2001), "A System for Optimal Division of Lots Based on Genetic Algorithm", *Papers and Proceedings of the Geographic Information Systems Association*, **7**, 275-280.

Mizuno Y., Kadono Y. and Aoki R. (2005), "A Study on The Changing Process in The Suburban Housing Area, Case of Daiwa, Kawanishi City, Part 1", *The Changing of Land Use, Summaries of Technical Papers of Annual Meeting*, Architectural Institute of Japan, 1105-1106.

Asami T. and Maniruzzaman K.M. (1994), "A Statistical Test of the Critical Shape Hypothesis for Residential Lots", *Comprehensive Urban Studies*, **53**, 99-111.

Maniruzzaman, K.M., Asami Y. and Okabe A. (1994), "Land Use and the Geometry of Lots in Setagaya Ward Tokyo", *Theory and Applications of GIS*, **2**, 83-90.

Osaragi T. and Watanabe M. (2001), "Subdivision of Lots in Established Urban Districts", *Papers and Proceedings of the Geographic Information Systems Association*, **10**, 69-72 .

Sakamoto Y. (1980), "Variable Selection in Categorical Data", *The Proceedings of the Institute of Statistical Mathematics*, **28**(1), 135-155.

Inoue T. and Osaragi T. (2005), "Modeling of Lot-subdivision in Established City Area", *Summaries of Technical Papers of Annual Meeting*, Architectural Institute of Japan, **F-1**, 105-106.

Inoue T. and Osaragi T. (2005), "Modeling of Lot-subdivision in Established City Area", *Papers and Proceedings of the Geographic Information Systems Association*, **14**, 49-52.

Osaragi T. and Inoue T. (2005), "Modeling and Analysis of Lots Consolidation in Established City", *Journal of Architectural Planning and Engineering*, No.592, 147-154.

Sixth International Conference on Urban Earthquake Engineering
March 3-4, 2009, Tokyo Institute of Technology, Tokyo, Japan

Requests for Technology and Engineering on Buildings/Facilities From the Viewpoint of Business Continuity

Hiroaki Maruya[1)]

1) Professor, Center for Urban Earthquake Engineering, Tokyo Institute of Technology,
Executive Fellow, Research Institute of Construction and Economy
Maruya-hi16@rice or.jp

Abstract: In the Business Continuity Management (BCM) against earthquakes, necessary information and functions on buildings and facilities to pursuit business continuity are highly diverse and across the sphere of traditional earthquake-proof technology and engineering. This paper presents examples of concrete requests for technology and engineering on building/facilities when the organization pursues continuity of critical operations at the original work place or the substitute place.

1. INTRODUCTION

Business Continuity Management (BCM) is a management strategy by which organizations (including companies, governmental organizations, etc.) secure their critical operations even if they have serious damage by disasters and accident. Recently, importance of BCM has been widely recognized in Japan.

At present, most Japanese companies and organizations seem to choose large-scale earthquakes as a first or main incident type when they start to formulate Business Continuity Plans (BCP). The reason may include that the Cabinet Office (in charge of natural disaster prevention) of Japanese government have promoted BCP by issuing a guideline in order to reduce the spread of economic damage that big earthquakes would cause.

In disaster prevention measures for earthquakes, most important countermeasure is to secure quake resistance of buildings and facilities that an organization is using daily. Researchers and engineers on earthquake disaster prevention have been eager to study technologies on physical risk assessment, tolerability of building and facilities and so on. Of course, these technologies are very useful for organizations to formulate their BCP assuming earthquakes. They are necessary in risk analysis/assessment, which is an important step of BCP formulation in its early stage. In addition, providing quake resistance to buildings and facilities is one of the effective countermeasures, when the organization chooses the strategy of continuing their critical operations at the original place.

However, in actual operation of BCM against earthquakes, necessary information and functions on buildings and facilities to pursuit business continuity are highly diverse and across the scope of traditional physical earthquake-proof technology. This paper will show the outline of various items that BCM assuming earthquakes requests for technology and engineering on buildings and

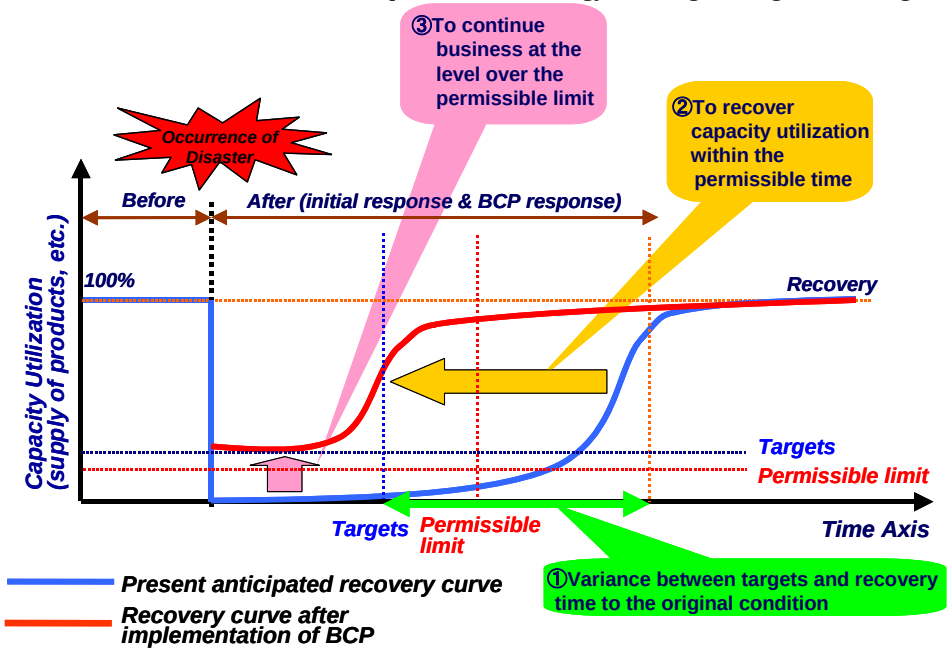

Figure 1 Concept of Business Continuity

facilities.

2. CONCEPT AND PRESENT SITUATION OF BCM/BCP

2.1 Concept of BCM

At the beginning, it may be useful to brief the understanding basic approach of BCM.

Business Continuity is a management strategy for organization to facilitate the rapid recovery and restoration of critical operations and services with minimum interruption in the aftermath of an accident or disaster. This is achieved through BCM, which include development, execution, exercising and review of BCP. Figure 1 shows the concept of Business Continuity.

If a company has no countermeasures to continue its operation, the operation degree of the 'critical operations' turns to be zero % by a disaster or an accident, and then gradually recovers. However, such a late recovery would cause serious problems. Those are :

1) Losing customers (seized by other companies),
2) Decline in market share,
3) Serious social inconvenience,
4) Negative impact on a company's reputation.

Therefore, the company should recognize the 'permissible limit of recovery time', and should recover the operation degree before the limit. The targeted time is called "recovery time objective (RTO)."

Additionally, even shortly after a disaster or an accident, the company should keep the operational degree above the level of permissive limit. This targeted level is called "recovery level objective (RLO)."

2.2 Present Situation of BCP/BCM

Japanese government has been announcing Business Continuity guidelines one after another since 2005, stressing the importance for all companies including small- and medium-scale businesses to introduce BCM. Furthermore, the government positions BCP as a key pillar of corporate disaster policy for national countermeasures in the event of a large-scale earthquake.

In Feb, 2008, the Cabinet Office, Japan conducted a comprehensive questionnaire survey on the diffusion situation of BCP in large and middle scale companies (Figure 2). The main results of the diffusion situation are:

As for large-scale companies,
- Companies already formulated BCP: 18.9 %
- Now formulating BCP: 16.4 %
- Having a plan to formulate BCP: 29.1 %

As for Middle-scale companies,
- Companies already formulated BCP: 12.4 %
- Now formulating BCP: 3.4 %
- Having a plan to formulate BCP: 12.8 %

Even the spread rates above are not so high compared to that of US and UK, it seems that BCP has been gaining the understanding quite fast when one considers that the Japanese government started the policies of BCM diffusion only since 2005. However, share of the companies that do not know BCP is 22.7% for large-scaled companies and 61.2% for middle-scale. This fact is noticeable problem and suggests the necessity of more effort to spread understanding of BCM.

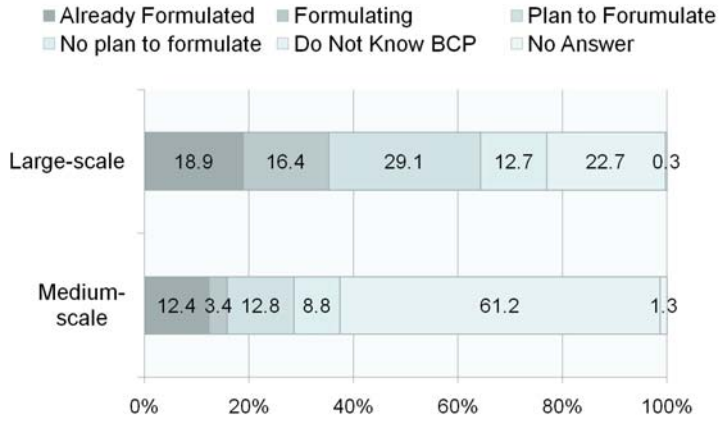

Source: Cabinet Office, Japan, "Survey on Companies' Effort on Business Continuity and Disaster Prevention"

Figure 2 BCP Situation in Japan by Company Scale

3. WHAT NECESSARY FOR BUILDING AND FACILITIES IN VIEW OF BCM

To understand what kind of information and functions on buildings and facilities are necessary for BCM assuming earthquakes, it should be useful to refer the "Guidelines on the Functions of Governmental Buildings for Operational Continuity" issued by Ministry of Land, Infrastructure, Transport and Tourism (MLIT), Japan in March, 2008. The author was a member of the research group to draw up this guideline.

The guideline covers both building structures and facility functions. As a matter of course, it demands government buildings to fulfill quake-resistance standards. It expects building management staffs to check the damage on their building and main facilities when an earthquake occurs.

In addition, the guidelines show clearly the necessity of "functions of basic facilities", "functions of action-support areas" and "functions of working space." The outlines of these functions are as follows;

1) Functions of basic facilities

These functions include those of electric power, information and telecommunication, water supply and drainage, air conditioning, monitor and control, and elevators. These functions secure safety of life and body and prevent secondary disasters. Building users should prepare that these facilities will be able to continue working without major repair when the earthquake occurs. Additionally, building users have to consider the substitute measures for these functions assuming these basic facilities are broken unexpectedly.

《発災時チェックシート》第Ⅱ次／施設管理者用

施設名称：○○○○　　記入担当者：（施設管理者、維持管理受託者、警備受託者）

点検項目	点検内容	判定 はい	判定 いいえ	「はい」の場合の対処・応急対応等	備考・特記事項
Ⅱ．第Ⅱ次					
1．構造体等の二次点検					
1.1．外部点検					
(1) 建物に傾斜や沈下はないか	① 傾いている。沈下している。			建物を退去	ビー玉や下げ振りを利用する。
	② 傾いているように感じる。			要注意 専門家へ詳細診断を要請する。	
	③ ないと感じる			点検継続	
(2) 建物が倒壊による危険はないか	① 大きなX字状のひび割れが多数あり、コンクリートの剥落も著しく、鉄筋がかなり露出している。壁の向こう側が透けて見える。			建物を退去	
	② 斜めやX字形のひび割れがあるが、コンクリートの剥落はわずかである。			要注意 専門家へ詳細診断を要請する。	
	③ ひび割れはあるが、コンクリートの浮きや剥落がない。			点検継続	
(3) 隣接建築物・周辺地盤の破壊による危険はないか	① 隣接建築物や鉄塔等が庁舎の方向に傾いている。周辺地盤が大きく陥没または隆起している。			建物を退去	
	② 隣接建築物の損傷や周辺地盤の地割れがあるが、庁舎への影響はないと考えられる。			要注意 専門家へ詳細診断を要請する。	
	③ 危険はない			点検継続	

・「建物を退去」と判断された項目がある場合は、館内放送等で職員の対処を指示し、職員及び在庁者の全てが退去したことを確認した後、建物を封鎖する。
・「建物を退去」と判断された項目がない場合は、Ⅲ次点検へ移行する。

Source: Guidelines on the Functions of Governmental Buildings for Operational Continuity

Figure 3 Check Sheets for Just after the Earthquake

2) Functions of action-support areas

These functions include those of transfer of workers and goods, preservation of goods and so on, which are necessary to critical operations. For securing the function, building users should prevent the damage caused by fire, water exposure and electric leak.

3) Functions of working space

The purpose of these functions is to assure usable space and working environment. They include brightness, air condition, security checks and so on. For securing the function, building users should prevent the damage caused by fire, water exposure and electric leak.

The guidelines provide 3-level check sheets for emergency use to examine earthquake damages. First level is only one page sheet designed for non-expert officials in charge of government building management to formulate the first report. Second level is 5-page check sheets for the same officials to check building structures and major facilities. The sheets contain check items, contents of check, decision (yes/no) and recommended directions of responses (Figure 3). Third level is 4-page check sheets and designed for technical experts for each facility.

4. REQUESTED FACTORS FOR TECHNOLOGY AND ENGINEERING ON BUILDING/FACILITY

4.1 Urgent Recognition of Obstacles for Business Continuity

When a large earthquake occurs, an organization may suffer from physical and functional damages on their building and important facilities. Additionally, even if the structural or physical damage are not serious, the organization may not be able to continue their critical operation in their work space because of outbreak of fire in the building or neighborhood, disruption of electricity supply, telecommunication network or water supply, difficulty of traffic access and so on.

Therefore, the organization has to check as soon as possible whether they can use their building and important facilities, in view of above mentioned aspects. However, it would be very difficult to secure the necessary number of expert engineers to inspect them. Therefore the measures to examine the damages of building and each important facility should be manageable for non-expert employees to use.

The key point is to examine whether there are any obstacles for business continuity in their work place, regardless whether the building and the facilities was originally quake resistance or not. In addition, the organization has to confirm availability of necessary inputs from outside of the building.

4.2 Business Continuity on the Substitute Place

If the organization cannot continue to use the ordinal place to work, they will decide to continue their critical operation at the substitute place where they have planed in BCP. The substitution strategy is a key strategy of BCM as disaster/accident response method. The organization which has potential substitute work places (for example, plural offices or factories) and has prepared properly as BCP, they have a probability to recover their critical operations at the substitute place before Recovery Time Objective (RTO).

Therefore, for the organization, countermeasures to earthquakes are not limited to increase earthquake resistance of buildings and facilities. Although to secure quake-proof of the original work place are important in views of life safety and preservation of property, preparation of substitute work place should be positively discussed in BCM when it is more advantageous in cost-benefit analysis to use the substitute work place.

Related to the discussion above, we have to recognize clearly that the business continuity measures by the substitute strategy are not only effective for earthquake, but also for wide range of disasters and accidents.

4.3 Importance of Swiftness; Time Is Money

After the earthquake, the organization has to recover the critical operation before the permissible level of time. Recovery of critical operations needs all necessary resources are available. Therefore, checks on buildings and important facilities have to be done very urgently.

As mentioned in 5.2, many organizations have prepared in BCP to continue their critical operations at the substitute work places. If recovery at the original work place seems to

require a long time or a lot of money, they would transfer their place of critical operations to a substitute place. However, starting operations at the substitute work place is not easy; it needs cost and effort including actions such as setting up all substitute equipments, transferring some of employees and other necessary resources from the original place, starting procurement from new suppliers nearby the substitute sight, etc. Thus, the organization needs to examine time and cost for recovery in the original place within the short time. For example, the term may be a day or two in industrial factories, and far shorter in financial companies.

Therefore, quake-proof technology and engineering are requested to shorten the time necessary to examine the capability of recovery in the original place in the aspects of time and cost.

5. Examples of Concrete Requests to Buildings/Facilities in respect of Business Continuity

In the experiences of BCM promotion, the author has recognized following concrete requests to technology and engineering on buildings and facilities.

5.1 Requests for Buildings/Facilities Technology and Engineering

5.1.1 Design and Physical Preparedness

1) Earthquake resistance of buildings

This is most basic request for BCM assuming earthquakes in engineering aspect. Earthquake resistance on buildings and facilities (mentioned in 2)) is expected to increase the probability to recovery on the original place and decrease the necessity of moving to the substitute place. However, it sometimes needs a large amount of cost that may be not payable by the organization for the time being.

2) Earthquake resistance of important facilities

The important facilities include electric power, telecommunication, air conditioning, water supply, gas sewer and monitoring systems.

Fixing or anchoring large equipments and furniture to the floors or walls is also important for the purpose of decreasing the number of injury. Just after earthquake, we have to expect no elevator operation, no ambulance, impossible to drive and clouded hospitals Caring injury would be a burden for business continuity activities.

3) Obstacle caused by non-structural material and interior material

Damage of non-structure material and interior material should not cause the obstacle of evacuation, transfer of employees and goods and business continuity. (Ex.: distortion of doors, fall-down of ceiling.)

4) Space for emergency activity

In the design and management of building, the organization should double evacuation routes, place the disaster headquarters, rooms for top executives, rooms for containing injured people and guests in lower floors. Room for stockpile for emergency should be considered

5) Response to people/crowd who wish to enter the building

The organization should be able to manage separately inner employees and outside people/crowd who wish to enter the building, for crime-prevention and security purpose. This arrangement can be easily executed if the layout in the building is properly considered. Surging crowd may be expected, for example, in mid-winter and mid- summer.

6) Easiness to fix the furniture and equipments

It is desirable that walls and floors are prepared so that non-expert employees are able to fix the furniture and equipments easily and without failure.

5.1.2 Facility preparedness

1) Substitute Systems

Lately, electric power is inevitable in every kind of works. Therefore, many organizations need to equip emergency power systems with enough capacity of generators, enough bulk of oil tank and assured additional oil supply. Additionally, positions of sockets connected to emergency power lines are clearly specified.

Information & communication systems and important data & documents (vital records) should have back-up systems.

2) Consideration on place of main telecommunication equipments

Servers and other main telecommunication equipments are settled in a safe floor and place. Fire-extinguish equipment of this place should use inactive gas instead of water. Water pipes should not be laid on the ceiling to avert water leaking damage. Electric power supply for these equipments should have redundancy.

3) Redundancy of fire alarm and emergency announcement facilities

Fire alarm apparatus, monitoring system, emergency announcement facility and internal phones which are necessary to call for evacuation and other emergency orders should have redundancy on their wires and electric power supply.

4) Elevators

If important business places are laid on upper floors, minimum number of elevators should be able to activate soon after the earthquake to access these important floors.

5.1.3 Operational aspect related to engineering

3) Substitute Systems

Information and communication system and important data and documents (vital records) should have back-up systems.

1) Obtaining accurate drawings or maps of facilities

When examining and evaluating the damage of facilities, accurate drawing or maps that are representing the present state including additional expansion/improvement works are crucial. However, in the author's experience, there is often no correct drawing of electric power wires in old buildings.

2) Secure engineers (in-house & outside) to check

Urgent check on buildings and important facilities is inevitable just after the earthquake, even though the

difficulty to acquire the necessary number of expert engineers. The organization has to make effort to keep them by negotiation with venders and operating contractors. Emergency contact/summons list should include staffs of these companies.

3) Periodic exercise of important facilities

To secure the operation of electrical generators and other emergency equipments, periodical exercises and drills is necessary.

5.2 Requests for Urban Facilities and Community

1) Early recognition of risk spread from neighborhood

Systems or frameworks are required to notice risks to each other spread from neighborhood such as fire, leakage of dangerous materials, collapsed building and so on.

2) Evacuees from building in danger of collapse

There should be frameworks that safety buildings will accept evacuees from those in danger nearby. Additionally buildings of highly earthquake-proof may be given the status as backup business places in the district.

3) People facing difficulty to go home

In big cities, a huge number of people who want to go home but facing difficulty are expected especially near stations and other traffic bases and along main roads. This problem should be widely recognized in each related district.

6. CONCLUSIONS

The organization including companies, public organization and NGOs are the main users of buildings and cities. Therefore, on the basis of user-oriented studies, their business continuity or operational continuity should be important target of architectural and urban earthquake technology and engineering. As shown above, BCM against earthquakes needs many kinds of information and functions related to the buildings and facilities.

Although the examples of concrete requests for the technology and engineering in this paper may not be comprehensive, the author would like to expect urban earthquake experts to think of additional requests and to increase the discussion on how to support BCM practically.

References:

Maruya, H. (2008), "BCP in Japan: Diffusion and Expectation," Fifth International Conference on Urban Earthquake Engineering, Center for Urban Earthquake Engineering, Tokyo Institute of Technology, pp717-720

Maruya, H. (2008), “Significance and Economic Effect of Business Continuity Plan,” Gyousei Inc

Cabinet Office, Japan (2007), “Commentary of Business Continuity Guidelines version 1,” http://www.bousai.go.jp/kigyo-machi/jigyou-keizoku/guideline01_und.pdf

Maruya, H and Sashida, T. (2006), “Commentary and Q&A of Business Continuity Guideline of Central Disaster Prevention Council,” Nikkagiren Inc

Cabinet Office, Japan (2008), “Survey on Companies’ Effort on Business Continuity and Disaster Prevention,” http://www.bousai.go.jp/chousa/h20/080610chousa.pdf

Ministry of Land, Infrastructure, Transport and Tourism, Japan (2007), “Guidelines on the Functions of Governmental Buildings for Operational Continuity,” http://www.mlit.go.jp/gobuild/sesaku/bcp/bcp.htm

Sixth International Conference on Urban Earthquake Engineering
March 3-4, 2009, Tokyo Institute of Technology, Tokyo, Japan

A PRACTICAL STUDY ON RESIDENTIAL ENVIRONMENT OF TEMPORARY HOUSING OF DISASTER

Akihiko Iwasa[1)], Takashi Hasegawa[2)], Shunichi Shinkai[3)] , Masahiko Shinozaki[4)] , Atsuko Yasutake[5)] , Kenichi Kobayashi[6)], Aya Akai[2)] , Tsuyoshi Nakayama[2)] , and Takahiro Kojima[2)]

1) Associate Professor, Department of Architecture, Niigata University, Japan
2) Graduate school of Science and Technology, Niigata University, Japan
3) Associate Professor, Department of Environmental Design, Nagaoka Institute of Design, Japan
4) Associate Professor, Department of Architecture, Toyo University, Japan
5) Lecturer, Department of space Design, Komazawa Women's University, Japan
6) Department of Facility Science, National Institute of Public Health, Japan
iwasa@eng.niigata-u.ac.jp, htwind@hotmail.com, shinkai@s-lab.org, m-shinozaki@toyonet.toyo.ac.jp

Abstract: This study aims to reveal the residential environment of temporary housing after the 7.13 flood and the Chuetsu earthquake. Practical support was provided to residents via a temporary open café. On-site investigations and interviews revealed the following
(1) Knowledge about improving temporary residential units was shared only with certain neighbors.
(2) Community in temporary housing was based on old neighborhoods and common rooms. And the community became exclusive. It seemed to be important to provide a place where residents could escape from the bonds of the community.
(3) Special places of communication and refreshment were born after one and half years' living in temporary site, and
This study conducted a "temporary open café" project to provide practical support to residents of temporary housing.

1. INTRODUCTION

In 2004, the Chuetsu region in central Niigata prefecture in Japan was struck by two disasters, namely, the 7.13 flood and the Chuetsu earthquake (Table 1). These two disasters destroyed or partially destroyed about 126,000 houses. Consequently, 71 temporary sites were developed and 3,860 temporary residential units were built on these sites (Figure 1).

The temporary housing was intended to be in place for only two years[1)]. But these two years contained the important environmental transition that people attempted to recover from the mental and physical damage caused by the disasters. The purpose of this study is to reveal the residential environment of the temporary housing and propose support measures by conducting a "temporary open café" project at temporary sites.

2. METHOD

Through on-site investigations and interviews, this study revealed two aspects of the residential environment of temporary housing:

(1) self-improvement of the temporary housing by residents

(2) community built by residents in the temporary housing.

A temporary open café was established at six temporary sites in order to provide practical support for the residents.

Figure 1 Temporary Housing

Table 1 7.13 Flood And Chuetsu Earthquake

7.13 Flood	
Date	2004.7.13
Death	15
Injured people	3
Housing Damage	
Totally destroyed	70
Half collapse	5,354
Partial damage	94
Flooded house	
up to the floorboards	2,178
above the floorboards	6,117
Temporary Housing	
site	3
residential unit	400

Chuetsu Earthquake	
Date	2004.10.23
Death	51
Injured people	4,795
Housing Damage	
Totally destroyed	3,185
Large scale collapse	2,159
Half collapse	11,566
Partial damage	103,500
Temporary Housing	
site	63
residential unit	3,460

3. OUTLINE OF TEMPORARY HOUSING IN CHUETSU

The temporary house consisted of residential units in linear figure. There were three types of units, namely, 1K, 2DK, and 3DK, all with a separate toilet and bathroom. Regarding to the number of family members, refugee are allowed suitable type of residential unit.

4. SELF-IMPROVEMENT OF TEMPORARY RESIDENTIAL UNIT BY RESIDENTS

In order to have an overview of the residential environment of the temporary housing, 44 temporary sites, each consisting of more than 20 temporary residential units, were examined for factors of self-improvement (Figure 2).

4.1 EXTERIOR ELEMENTS ATTACHED TO THE FACADES OF TEMPORARY RESIDENTIAL UNITS

Temporary residential units were covered with exterior elements such as plants, sunshades, screens, and storage; these activities were carried out by the residents themselves (Figure 3). The temporary sites differed according to the amount of surface area covered with exterior elements (Figure 4). The amount of surface covered was over 40% at 2 temporary sites and under 10% at 1 temporary sites.

4.2 WIND-BREAKING PORCHES

A wind-breaking porch is the space kept in the front of the entrance to prevent wind and snow from entering during the winter. It is a popular facility in cold areas such as Chuetsu, and every temporary residential unit in Chuetsu had one (Figure 1). However, wind-breaking porches provided were unsuitable for weather conditions of the Chuetsu area. As a result, they were improved by the residents (Figure 5).

This survey found that 58% of temporary residential units had wind-breaking porches that were improved by residents. At 8 temporary sites, more than 80% of the wind-breaking porches were improved by residents. Less than 20% were improved at 5 other temporary sites (Figure 6). Thus, differences among temporary sites are found in the number of self-improved wind-breaking porches as well as the added exterior elements.

In every case of improvement, the front panel was attached to the side panel that was set initially when the temporary houses were provided. Some panels had sliding doors and others had swing doors. This survey classifies the wind-breaking poaches into 9 types according to the kind of the front panel attached by residents, as shown in Fig. 7.

The distribution of the 9 types in the 3 sites that are located nearby is analyzed (Figure 8). In every 3 temporary sites, major type is different. Thus, relationship among the near temporary sites is not found in the self-improvement.

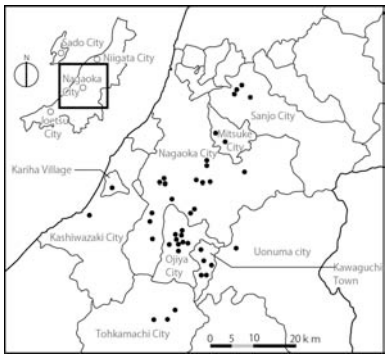

Period
2005.7.28-8.11
Target
41 Temporary sites that have over 20 residential units
Method
1)Outer Observation
-Exterior element
-Wind-breaking porch
2)Interview

Figure 2 Contents of On-site Research

Figure 3 Exterior Elements

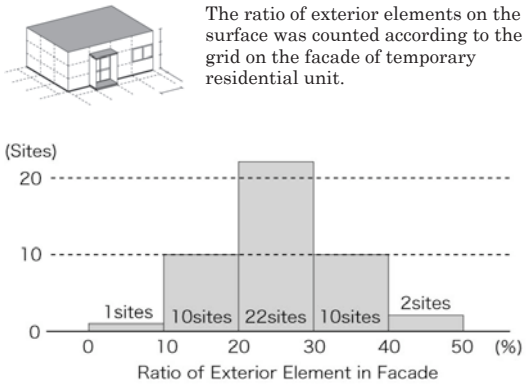

Figure 4 Histgram of Ratio of Exterior Elements

Figure 5 Self-improvement of Wind-breaking Porches

4.3 KNOWLEDGE OF SELF-IMPROVEMENT

According to resident interviews, many people made improvements similar to those of their neighbors. This suggests that neighbors shared their knowledge of how to make improvements. But, as shown in 4.1 and 4.2, the knowledge was shared within small area and was not spread wildly to other temporary sites.

5. PRACTICAL SUPPORT

This study conducted a "temporary open café" project to provide practical support for residents of temporary housing (Figure 9). First, the aim is to provide a space where refreshments could be served and informal interviews could be conducted. Second, basing on the former survey that the knowledge of how to make improvements was spread within closed area by neighbor communication, this project intended to circulate the knowledge around all temporary sites by communicating in an "information space" (Figure 10).

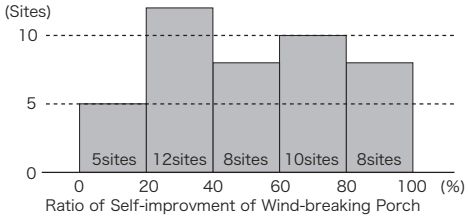

Figure 6 Histgram of Ratio of Self-improvement of Wind-breaking Porch

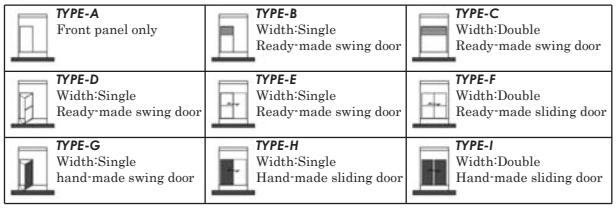

Figure 7 The Kind of the Front Panel Attached by Residents

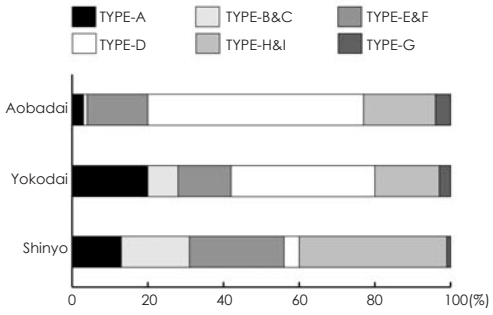

Figure 8 Distribution of the 9 Types in the 3 Temporary sites

A temporary open café was held 9 times at 6 temporary sites where conditions of self-improvement differed. The temporary open café consisted of small tents with stackable boxes. All necessary materials were delivered by cars in order to be independent of the sites' infrastructure and facilities.

The temporary open cafés were set up in open spaces and were open to all residents. Free coffee and tea were served, and the residents could chat with each other. Informal interviews were also conducted.

In addition to coffee service, the temporary open café provided the information space in which all information about how to improve the temporary units was gathered and displayed. New information offered by residents is added one by one in each open café. The information space delivered the knowledge of self-improvement to other temporary site. The free exchange of information enabled all residents to gain knowledge, which gradually spread to other temporary sites. In the process of the exchange, it was important for coordinator to omit illegal and misleading information about self-improvement.

Figure 9 Temporary Open Café (2005)

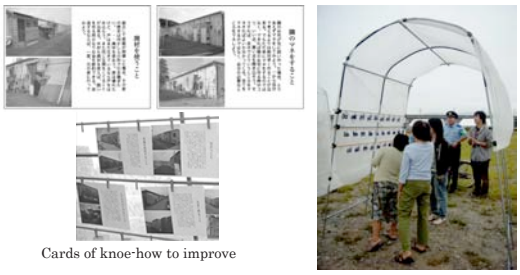

Figure 10 Information Space (2005)

6. ESTABLISHING COMMUNITY

The condition of community in temporary housing was revealed through the open cafés.

After the 1995 Hanshin-Awaji earthquake, some residents were isolated from temporary housing communities. There were 120 cases of "solitary death" where the residents had died alone in their units and were only found a few days later.

In order to avoid similar isolation at these temporary sites, the following two countermeasures were conducted after the Chuetsu earthquake.

(1) People who lived in the same neighborhood before the earthquake were housed on the same temporary site after the earthquake in order to maintain the existing human network.

(2) A common room was built at each temporary site that consisted of more than 50 temporary residential units.

According to resident interviews, the communities formed at the temporary sites were based on former neighborhoods and the common rooms that the residents attended. The countermeasures seemed to be effective. In the case of the Chuetsu earthquake, there was no solitary death for 3 years.

On the down side, because residents live in the small temporary site that is separate from other regional area, there was tendency that the community became too much tight and exclusive. Some residents felt oppressiveness in such community. It is important to maintain a communication among residents in the primary stage of a disaster. Therefore, in the next stage of disaster, it is also important to provide a place where residents can escape the bonds of the community in temporary housing.

The place offered by temporary open café is free from the existing community because the temporary open café is delivered from outside of temporary site. There is a possibility that the temporary open café is effective measure to residential environment of temporary housing in the second step of recovery.

7. PROGRESS OF RESIDENTIAL ENVIRONMENT

In order to grasp a progress of residential environment of temporary housing, this study conducted resident interviews after one and half years of the Chuetsu earthquake.

7.1 SPECIAL SPACES IN TEMPORARY SITE

According to the interviews, it was found that residents had special place in their temporary site. The special places drown from interviews were the following (Figure 11)

- Small farm in vacant space around residential unit
- Bench space in street corner
- Quiet space separated from temporary site
- Viewpoint with beautiful scenery
- Favorite dog of residents
- Friend's units open to residents
- Unique improved unit

Every special place was found or made by residents. And residents could gain the opportunity of communication and refreshment from them. The special places seemed to play important role in daily life of residents.

7.2 PRACTICAL SUPPORT

The temporary open café in 2005 was held 7 times in temporary site, namely, Yokodai, and provided the information space about the special place (Figure 12). In the information space, the large map model of Yokodai temporary site was displayed, on which the special places were pointed by small flags (Figure 13). Residents could add their new information about the special place. Through free exchange of information, the special places intended to be shared with residents.

Figure 11 Special Places

Figure 12 Temporary Open Café (2006)

Figure 13 Information Space (2006)

8. CONCLUSIONS

This study reached the following conclusions:

(1) The knowledge to improve temporary residential unit was shared with neighbors and was not spread over the temporary sites.

(2) This study conducted a “temporary open café” project. This project provided practical support to residents of temporary housing in order to share useful information to all temporary sites. Informal interviews were also conducted at the cafés.

(3) Community in temporary housing was based on former neighborhood communities and the common room attended by the residents in the temporary site. It was efficient that people who used to be neighbors were housed at the same temporary site and a common room was built at each temporary site.

(4) The community in the temporary housing was exclusive. In the second step of recovery, the temporary open cafés seemed to be useful in providing a place where residents could escape the bonds of the community in temporary housing.

(5) After one and half years of the earthquake, the special places providing opportunities of communication and refreshment in temporary site were produced by residents. The temporary open café tried to share the information of the special places with residents.

Acknowledgements:

This study was supported by the Housing Research Foundation for Grant-in-aid for residential research, “Study on Support of Residential Environment in Temporary Housing” from 2005 to 2006.

Note:

1) The term of temporary housing was extended for one year on October 1, 2006.

References:

Hasegawa, T., Iwasa, A., Shinkai, S.,Shinozaki, M., Yasutake, A.,Kobayashi, K., and Miyakoshi, A.(2007),"RESEARCH AND SUPPORT OF TEMPORARY HOUSING OF DISASTER : A practical study by 'Temporary Cafe'", Journal of architecture and planning, Architectural Institute of Japan, No.662, 9-16.

Maki, N., Miura,K., and Kobayashi, M.(1995),"ACTUAL CONDITION AND ISSUES FROM PHYSICAL ASPECT ON TEMPORARY HOUSING : Natural disaster and housing, Part I", Journal of architecture and planning, Architectural Institute of Japan, No.476, 125-133.

Sixth International Conference on Urban Earthquake Engineering
March 3-4, 2009, Tokyo Institute of Technology, Tokyo, Japan

A COMPUTER SIMULATION FRAMEWORK FOR PEDESTRIAN EVACUATION PLANNING

Chih-Yuan James Chu

Assistant Professor, Department of Civil Engineering, National Central University, Jhongli City, Taoyuan County, Taiwan
jameschu@ncu.edu.tw

Abstract: A cellular automation (CA) model of pedestrian movements with 3D visualization is implemented for facility planning. The CA methodology is efficient for large-scale and repeated simulations and describes pedestrian behaviors adequately. Different from the previous studies that attempt to calibrate their models at microscopic level or ignore model calibration completely, this paper calibrates the model with data at macroscopic level (flow, density, and speed). The calibrated pedestrian model is useful for optimal facility design because it reflects the complicated interactions between pedestrians and the facility. After candidate facility designs are evaluated with the pedestrian models, a two-stage procedure is adopted for the statistical selection of the alternatives. The numerical example of a transportation terminal shows that the best design can be selected with a pre-determined probability of correct selection and targeted difference between the best and the second best systems. Moreover, required numbers of repetitions are calculated and conducted to avoid incorrect selection or unnecessary repetitions. Therefore, the procedure proposed is an effective and efficient tool for facility design.

1. INTRODUCTION

New constructions must comply with building codes that regulate specifications such as the minimum number of exits and stairways given the characteristics of a facility (e.g. floor area or purposes). In many countries, the performance measures of hazard mitigation are also required in addition to complying with the building codes (Schadschneider et al., 2008). However, the building codes alone are insufficient to provide information regarding a facility's performance of hazard mitigation. Moreover, the increasing amount of users and complicated layouts of buildings like high rise buildings and transportation terminals create significant interactions between pedestrians and the environment. Thus, a complete procedure for evaluating emergency evacuation of facilities is needed.

To evaluate the design for emergency evacuation, both the facility layout and the characteristics of pedestrians must be considered. The difficulties of capturing pedestrian dynamics are three dimensional movements and highly unpredictable human behaviors. Moreover, the pedestrian behaviors during evacuation are unique because they are relatively irrational and less intelligent. Pedestrian dynamics have been studied through various approaches. The problems encountered by researchers and practitioners are that experiments (i.e. drills) are impractical because they are unrealistic and expensive to repeat and observations from actual events are extremely rare. Since conducting a large number of experiments in order to evaluate facility designs is problematic, it is reasonable to create mathematical models that include facility design as well as pedestrian behaviors and are computationally feasible for the analysis. As a result, computer modeling of pedestrian evacuation has become one of the most promising fields for the hazard mitigation in civil engineering.

The paper reviews the possible methods for developing pedestrian models and proposes an approach to calibrate simulation models for pedestrian movement with actual data using Cellular Automation (CA). After the pedestrian model is validated, it is used in a procedure that supports decision-making for facility design such as gate width, corridor space, and numbers of exits. In this procedure, the minimum numbers of repetitions to achieve a pre-determined probability for correct selections can be used so both accuracy and efficiency are maintained. Finally, the example of evaluating a transportation terminal is conducted to demonstrate the procedure.

2. LITERATURE REVIEW

In this section, related works in pedestrian dynamic, facility design, and system ranking are reviewed.

2.1 Pedestrian Dynamics

As Helbing (2001) stated, regression analysis, queuing models, transition matrix models, stochastic models, gas-kinetic theory, and fluid-dynamic were used for modeling pedestrian. However, for extreme situations and/or irregular spaces, a direct simulation of individual pedestrians is preferable due to its flexibility. The major approaches for pedestrian simulation, which sometimes have common features with each other, include Social (Behavioral) Force Model (SF) (Helbing, 2001), Cellular Automation (CA) (Burstedde et al., 2001), and agent-based models (Batty et al.,

1998; Batty, 2001). In this paper CA model is adopted because it is considered simpler and thus faster than others. The main points of CA model will be explained briefly later and more complete review can be found in Schadschneider et al. (2008).

2.2 Facility Design

The typical guidelines or codes for facility design regulate the number or size of important specifications such as the minimal gate width and number of exits. For the numerical example later in this paper, the building code related to pedestrian evacuation in transportation terminals in Taiwan are summarized as follows:

1. The evacuation floor (ground floor in this case) has at least two exits within 30 meters of each stairway that connects other floors.
2. Any location in the building must have a stairway within 30 meters.
3. The minimum height of the exits is 1.8m and the minimum width is 1.2m.

Since multiple designs will satisfy these regulations, it is highly necessary to have a process that evaluates and selects from these possible plans considering not only the facility layout but also the complex pedestrian dynamics.

2.3 System Ranking

One of the objectives of this paper is to build simulation models for pedestrian and use these models to support facility design. To achieve this goal, individual emergency evacuation designs are evaluated with the simulation model first. Second, candidate designs are compared and the best design is picked from the candidates. To conduct the comparison rigorously, system ranking studied heavily in stochastic simulation will be used.

As Law and Kelton (2000) state, it is naive to evaluate a system, i.e. a facility design, with only a single simulation because the randomness involved in stochastic simulation cannot be ignored. The next question is how many trials are "appropriate" for each system because too many trials are a waste of time and too few trials will lead to incorrect decision. One of the selection scenarios is that the best system is picked from a set of candidate systems. Rinott (1978) proposes a two-stage procedure to determine the necessary numbers of trials to achieve a probability of correct selection that can be determined by the users. The procedure will be described later in the numerical example and the derivations of the procedure can be found in Rinott (1978). It is emphasized that since trials as many as hundreds might be needed to guarantee that the chosen system is the best, the efficiency of the simulation is critical for the study, which is the main reason why CA approach is appropriate for this study.

3. CA MODEL IMPLEMENTATION

In this study, CA is adopted due to its high efficiency and potential for large-scale evacuation simulation. The simulation is written in C++ and the 3-D animation is realized in Microsoft DirectX, which assists the users to understand the system effectively. The following components are used following the definitions of Burstedde et al. (2001):

1. Cell: In CA, the floor is represented by a two-dimensional regular grid of cells. Each cell has its state and all cells are updated every time step based on the same rule. For pedestrian dynamics, an individual moves between cells according to the states of the neighboring cells. Since the moving range is limited to one cell, the range of walking speeds is assumed small; in other words, each individual considers only the adjacent cells when she or he is moving. More importantly, because individuals move based on their locations and do not interact with other people unless they are moving into the same cell, the computations required in the model are greatly simplified and thus CA is beneficial when the number of pedestrians and/or the number of trials are large. In this study, the size of a cell is 40cm × 40cm and the walking speed is 1.5 m/sec, which determine the time interval of the simulation as 0.27(=0.40/1.5) seconds.
2. Static Field: The static field represents the attractiveness of locations; specifically, the field is calculated as the distance to the closest exit(s) in this paper. It follows that the static field of the exits would be zero. In the case of emergency evacuation, the number of destinations such as emergency gates is generally very small and thus the calculations for static field would be limited. The most significant benefit of using static field is that it will be calculated only once when the simulation starts and will not change during the simulation, which reduces the computational work. Examples of static fields will be displayed in the numerical example.
3. Dynamic Field: Another component used in Burstedde et al. (2001) is dynamic field, which represents the records of paths used by the pedestrians. In this study, it is the accumulated number of passing pedestrians of each cell and these values decay overtime. Unlike the static field, the dynamic field updates over time due to the transition of pedestrians in the building.
4. Friction Effect: Kirchner et al. (2003) study the effect that when pedestrians attempt to move into the same location, there is a probability all of the pedestrians give up and stay at their original locations. The phenomenon is called friction effect and it is incorporated in this study. However, the existence of this effect must be tested in the model validation.

The floor field of a cell is the weighted combination of its static field and its dynamic field. As a result, pedestrians will move toward the cells with higher floor field values; equivalently, they will move to the closest stairways or exits and also follow other people's paths. The conflicts between pedestrians are also considered by the friction effect. More detailed algorithm for CA models can be seen in Burstedde et al. (2001) and Kirchner et al. (2003).

The experience of implementing the CA method shows the following benefits. First, in other methods, interaction

between people occurs when two individuals are within a certain distance. In CA, pedestrians only interact with each other when they attempt to move into the same cell. It leads to reduced computation works. Second, the simulation is focused on the update of the floor field whose size is constant and does not change with the number of individuals. As a result, the effect of the number of pedestrians is less significant. Thus, CA method is appropriate for large-scale and repeated simulations.

4. CA MODEL CALIBRATION

As observed in Schadschneider et al. (2008), many of the pedestrian models are constructed based on theories of human behavior, and model calibration with actual data is not conducted because reliable quantitative results are missing for many scenarios. The reasons include that the samples from actual incidents are rare, experiments could not reflect actual human behavior, and they are too expensive to conduct.

Calibration of pedestrian models is not trivial. Although this research constructs the pedestrian model based on observations and theories of human behavior like others, this study calibrates the model by fitting the predictions to the collective behavior of a crowd. In specific, the parameters of the model are estimated with the fundamental relationships of pedestrian movements, that is, flow rate, density, and speed. The advantages of this approach are that quantitative data are used to calibrate the model and the characteristics compared are representative. Indeed, this approach does not examine individual behaviors because of the lack of microscopic observations. It should noted that, even when the data were available, standardized procedures to benchmark a pedestrian model using individual pedestrian data are still absent.

The design of simulation for calibration is a planar corridor that has 6m width. The three fundamental measures, density(D), flow(F), and speed(S), are recorded in a $6\text{m} \times 6\text{m}$ square area. The definitions of the three measures are as follows. The density measure is the total number of pedestrians in the area (people/m^2). The flow measure is the number of pedestrians passing one unit of length of the centerline of the square in a unit of time (people/m/sec). Speed is the average speed over the pedestrians in the square (m/sec). The data for calibration are collected with the process described below. Ten different scenarios of population densities and formations are tested for each model. In each scenario, the simulation time is 200 seconds and the data are recorded every 10 seconds. Thus, 20 data $\times$ 10 scenarios = 200 data are collected.

The parameters of the pedestrian model can be estimated by minimizing the errors between benchmark and the model. The benchmark equations adopted, Equation (1) and (2), are from Nelson and Mowrer (2003), which used for facility design considering pedestrian evacuation. The equations are also plotted in Figure 1. To simplify the calibration, the strength of static field(Js), the strength of dynamic field(Jd), and the probability of friction effect(μ) are estimated only and the rest of the parameters are fixed. The reason is that based on the CA formulation (not described in this paper), it is the ratios between the parameters that have the main effects on the simulation and fixing part of the parameters will make the estimation more efficient.

$$S = 1.400\left(1 - D/3.900\right) \quad (1)$$

$$F = D \cdot S = 1.400D - 0.359D^2 \quad (2)$$

Because of the lack of prior knowledge of the parameters and model characteristics, a brute-force method, grid search algorithm, is adopted to find out the optimal values of these parameters. In the first stage, the simulation uses the following ranges of parameters: $0.1 \le Js \le 9.6$ with the increment of 0.5, $0.1 \le Jd \le 9.6$ with the increment of 0.5, and $0.2 \le \mu \le 0.8$ with the increment of 0.2. μ ranges from 0.0 to 1.0; however, the high and low values (over 0.8 and below 0.2) of μ are discarded because they represent total friction and no friction between people, which are unrealistic. The upper bounds of the other two parameters follow those appeared in the literature (Burstedde et al., 2001; Kirchner et al., 2003). The results from the first stage show that high μ provides better fitting and provide the promising ranges of the parameter values.

In the second stage, the search range and the increments are reduced. The simulation uses $0.6 \le Js \le 1.6$ with the increment of 0.1, $0.6 \le Jd \le 1.6$ with the increment of 0.1, and $0.2 \le \mu \le 0.8$ with the increment of 0.05. The optimal parameters are found to be $Js = 0.9$, $Jd = 0.6$, and $\mu = 0.8$. The comparison of observed and prediction is shown in Figure 1. It can be observed that the model reproduces density up to 2.5 adequately. The most significant differences are that densities over 2.5 are not produced in the simulation and the maximum simulated speed is slightly lower than observed maximum speed (1.4 m/s). Future research will focus on analyzing the causes of these differences.

5. NUMERICAL EXAMPLE

The building codes provide standards and requirements for factors such as gate width and number of gates. However, other factors that affect emergency evacuation such as gate locations are facility-specific and require individual considerations. Computer simulation is a useful tool to provide suggestions and insights for this work.

In this example, the main train station located in Taipei, Taiwan, which started the operation in 1989, is considered. The usage of the station has been significantly changed since the original construction. The second floor has been transformed into one of the most popular locations for restaurants. Currently three rail systems share the station and they include Taiwan High Speed Rail Company, Taiwan

Railways, and Taipei Mass Rapid Transit. The operations of high speed rail and subway system have increased the passengers using the station greatly. In this example, the main focus is the evacuation from B1 floor to the ground floor. The basic layout and the static field of the ground floor are shown in Figure 2(a). The bold line is the boundary of the building. There are ten exits and eight stairways, which are represented by the small rectangles and arrows respectively. Passengers will use the stairways to access the ground floor from the lower level. For the rest of the floor, the lighter color means the higher attraction and vice versa. The ticketing and service centers of Taiwan Railways and High Speed Rail Company are located on the ground floor as well, which are represented by the black blocks. The darkest color means that these locations cannot be passed and have the lowest attraction. The layout and the static field of B1 floor are shown in Figure 2(b). The bold line in the figure is again the boundary of the building and the arrows are the stairways to the ground floor. Since they must be used to reach the exits, they naturally have the highest attraction on the floor.

The regulations for transportation terminals have been described earlier and the current design of the station fulfills all of them. Since eight stairways are constructed in the current design, it is implemented as SYSTEM 8. Other 4 hypothetical designs that also fulfill the regulations are implemented. In SYSTEM 7, one of the two northwest stairways is removed. In SYSTEM 6, one of the southeast stairways is removed from SYSTEM 7. One of the southwest stairways is further removed from SYSTEM 6 as SYSTEM 5. Finally, one of the northeast stairways is removed from SYSTEM 5 for SYSTEM 4. SYSTEM 4-7 might be considered because of, for example, routine maintenance, cost saving, or stairway collapse caused by hazards (e.g. earthquake and fire).

One of the most common pitfalls of computer simulation is to run only a single simulation for each alternative and make decision. When it is done, the stochastic nature of the system is ignored. On the other hand, too many repetitions of simulation are a waste of time and resources. Computer simulation literature has a great collection of studies in comparing and selecting systems. In this study, the goal is to pick the best system, which has the smallest maximum evacuation time with a pre-determined probability, among the alternatives of stairway configurations. The two-stage approach proposed by Rinott (1978) is adopted. In the first stage, a small number of repetitions (n_0) are conducted. Based on the results of the first stage, the necessary number of additional repetitions can be decided and thus minimal work can be done for the remaining simulation.

In the study, 4,000 pedestrians are randomly distributed in the ground floor and B1 floor. The results for the analysis are summarized in Table 1. A relatively small number of initial repetitions (n_0=10) is picked and the first stage mean and variance for all the systems are listed in the second column in the table. It is clear that the evacuation time of SYSTEM 8 is significantly smaller than others and, as expected, the more stairways the lower evacuation time. However, more simulation must be done to conduct statistical selection among the systems. The additional numbers of repetitions are calculated according to Rinott (1978). The general rule is that when the variance from the first stage is large, more repetitions are required for the second stage.

Before second stage comparison is made, the decision-maker must first decide the indifference zone, which indicates the smallest difference that is meaningful to the user. Three comparisons are demonstrated here. In Comparison I, all five systems are candidates and the indifference zone is set to 1 second. Apparently SYSTEM 8 is the best system; strictly speaking, SYSTEM 8 has the smallest maximum evacuation time with the probability 0.90 and the difference between the second best system is at least 1 second. In fact, the confidence interval of this difference is as large as [-28.3, -26.3] seconds.

In Comparison II, only the hypothetical designs are considered. The results show that SYSTEM 7 is the best system with the probability 0.90. However, the difference between the second best system (SYSTEM 6) is [-1.7,0.3] seconds, which contains zero. Therefore, this difference is not statistically significant. If a larger indifference zone, 3 seconds, is picked initially, the best system becomes SYSTEM 6. Note that the required additional repetitions are smaller than those of Comparison II because of the larger indifference zone. Similar to Comparison II, the difference between the best system and the second best system is not statistically significant due to the confidence interval containing zero([-3.3, 2.7] second). Although different systems are picked in Comparison II and III, the results indicate that the maximum evacuation times are identical for these two systems in statistics. Furthermore, if a larger indifference-zone is used initially, the decision can be made with fewer repetitions of simulation. The benefit of this procedure would be that the users can select appropriate indifference zone based on the actual problem and only make repetitions that are necessary, while have confidence in their decisions. In this case that two systems are as good as each other, secondary criteria can be incorporated for facility planning. For example, the decision would select SYSTEM 7 for redundancy and SYSTEM 6 for cost saving.

6. CONCLUSIONS

A system that compares a set of facility evacuation designs and picks the best from them is proposed. The system includes two major parts: a pedestrian model and a selection procedure. First, the cellular automation model that simulates pedestrian movements is implemented. Unlike other studies that do not calibrate their models at all or attempt to calibrate their models at microscopic level, this study calibrates the parameters with macroscopic equations that are widely used in practice. The results show that the pedestrian model reproduces the collective measures (flow,

speed, and density) adequately and the computational effort of the model is relatively low due to its simplicity. Second, to account for the randomness in an emergency evacuation, one of the techniques in system ranking is used to select the best facility design from the candidate designs. The major benefit of the technique is that given the indifference-zone of the users and the desired probability of correct selection, the minimal numbers of repetitions can be determined; therefore, the problems raised by running too many or too few repetitions can be avoided. Further, the difference between the best system and the second best system can be estimated. As shown in the numerical example, it is possible that the difference between the best two systems is not statistically significant, and other considerations can be incorporated to make decisions.

References:

Batty, M. (2001). "Agent-based pedestrian modeling." Environmental and Planning B: Planning and Design, 28.

Batty, M., Jiang, B., and Thurstain-Goodwin, M. (1998). "Local movement: Agent-based models of pedestrian flows." Centre for Advanced Spatial Analysis Working Paper Series 4.

Burstedde, C., Klauck, K., Schadschneider, A., and Zittartz, J. (2001). "Simulation of pedestrian dynamics using two-dimensional cellular automation." Physica A, 295.

Helbing, D. (2001). "Traffic and related self-driven many-particle systems." Reviews of Modern Physics, 73.

Kirchner, A., Nishinari, K., and Schadschneider, A. (2003). "Friction effects and clogging in a cellular automation model for pedestrian dynamics." Physical Review E, 67(056122).

Law, A. M. and Kelton, W. D. (2000). Simulation Modeling and Analysis. The McGraw-Hill Companies, Inc., New York, NY.

Nelson, H. E. and Mowrer, F. W. (2003). "Emergency movement." SFPE Handbook of Fire Protection Engineering, P. J. DiNenno, ed., National Fire Protection Association, Bethesda, MD, 367.

Rinott, Y. (1978). "On two-stage selection procedures and related probability in equalities." Communications in Statistics, A7, 799–811.

Schadschneider, A., Klingsch, W., Kl pfel, H., Kretz, T., Rogsch, C., and Seyfried, A. (2008). "Evacuation dynamics: Empirical results, modeling and applications." Encyclopedia of Complexity and System Science, B. Meyers, ed., Springer, Berlin, Germany.

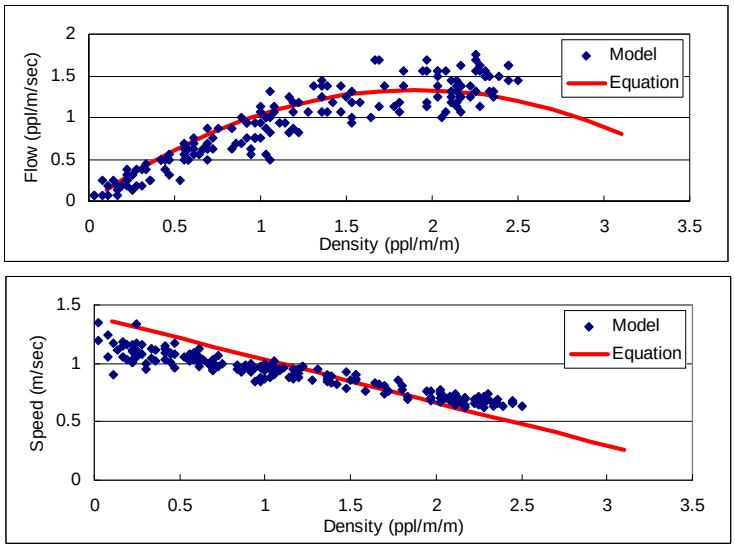

Figure 1. Fundamental Diagrams Fitting for Model Calibration

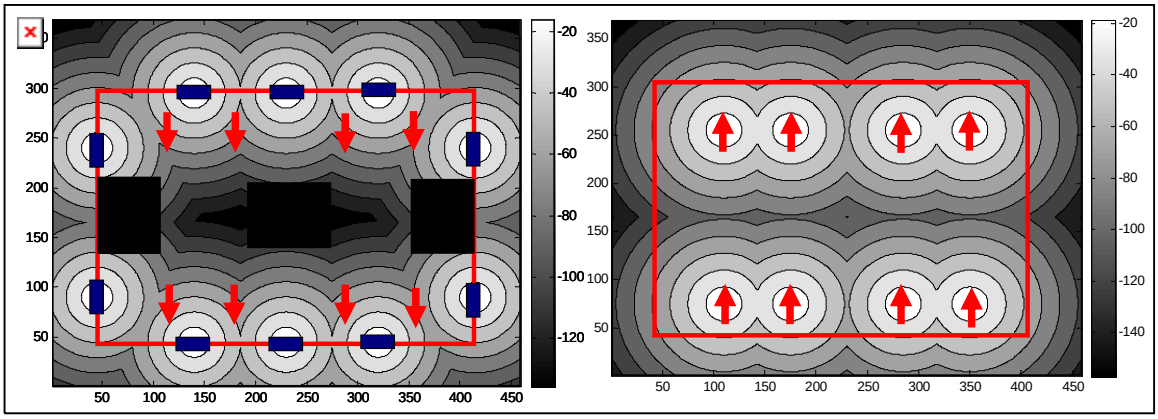

(a) Ground Floor (b) B1 Floor

Figure 2. Illustration of Static Fields

Table 1. System Selection Results

Comparis	-		I		II		III	
Indiffere nce-Zone	-		1		1		3	
System	Stage 1 Mean (sec)	Stage 1 Variance (sec^2	Overall Sample Size	Overall Mean (sec)	Overall Sample Size	Overall Mean (sec)	Overall Sample Size	Overall Mean (sec)
4	146.6	6.3	87	145.9	77	146.1	10	146.6
5	138.6	5.2	71	138.5	63	138.5	10	138.6
6	134.6	16.2	222	134.6	197	134.7	22	**134.6**
7	135.3	9.9	136	134.4	120	**134.4**	14	135.2
8	105.5	2.4	33	**107.1**	-	-	-	-
Candidat e	-		4,5,6,7,8		4,5,6,7		4,5,6,7	
Best System	-		8		7		6	

Sixth International Conference on Urban Earthquake Engineering
March 3-4, 2009, Tokyo Institute of Technology, Tokyo, Japan

DESCRIPTION OF A TSUNAMI SOURCE: POINTS FOR IMPROVEMENT

Mikhail A. Nosov

Professor, Faculty of Physics, M.V.Lomonosov Moscow State University, Russia
nosov@phys.msu.ru

Abstract: Weak points of traditional approach to the description of a tsunami source are revealed. Theoretical background regarding effects of water compressibility in tsunami source is provided. Bottom pressure variations recorded with the aid of JAMSTEC sensors during earthquakes on 25.09.2003 and 11.09.2008 were processed in order to reveal manifestations of water compressibility in tsunami source. It is shown that effects of water compressibility may contribute to tsunami runup heights only by means of non-linear energy transfer from elastic oscillations of water column to long gravitational waves. Improved method of calculation of initial elevation in tsunami source taking into account all three components of the bottom deformation vector in conjunction with bathymetry is suggested.

1. INTRODUCTION

Strong underwater earthquakes are the most prevailing cause for the rise of tsunami waves. As a rule, numerical simulation of tsunami is based on the theory of long waves, which deals with the equations of hydrodynamics, averaged over the vertical coordinate (Titov and Gonzalez 1997, Kowalik et al. 2005, Levin and Nosov 2008, Fujii and Satake, 2008). As for the description of tsunami generation, an earthquake is considered to instantly cause residual deformations of the ocean bottom. Then, the assumption is made that the displacement of the bottom is simultaneously accompanied by formation at the surface of the ocean of a perturbation (initial elevation), the shape of which is fully similar to the vertical residual deformations of the bottom. The initial elevation, thus obtained, is then applied as the initial condition in resolving the problem of tsunami propagation. The initial field of flow velocities is assumed to be zero.

In general, it is obviously not accurate, to set the initial elevation equal to the bottom deformations. In the case of long-lasting deformation of duration $t \sim L/\sqrt{gH}$, where L is the horizontal dimension of the tsunami source, H is the ocean depth, g is the acceleration due to gravity, elevation of the surface will at no particular moment of time coincide with the residual displacements of the bottom. If, on the other hand, the bottom deformation is short $t < \sqrt{H/g} << L/\sqrt{gH}$, then the initial elevation will also differ from the vertical bottom deformation: the elevation will be much smoother. Moreover, in the case of $t < 4H/c$, where c is the velocity of sound in water, water column will certainly behave as a compressible medium, so conception of "initial elevation" will become shaky in a figurative and literal sense.

In past decade, when JAMSTEC (Japan Agency for Marine-Earth Science and Technology) deployed a real-time observatory at the continental slope close to the islands of Japan (Hirata et al. 2002), it became possible to investigate a tsunami formation just at its source. The Tokachi-Oki earthquake of 2003 was the first strong seismic event (Mw=8.3) with its epicenter located in the immediate vicinity of the JAMSTEC sensors (Watanabe et al. 2004). Analysis of the records of bottom pressure variations obtained during this event provided a unique opportunity to reveal manifestations of water compressibility in tsunami source (Nosov et al. 2005, Nosov and Kolesov, 2007). Recently, on September 11, 2008, the second appropriate event (Mw=6.8) was successfully recorded by JAMSTEC sensors.

Above outlined weak points of the traditional approach to the description of a tsunami source are surely the points of improvement. In the present study, first, necessary theoretical background regarding effects of water compressibility in tsunami source is provided. Then, manifestations of effects of water compressibility in bottom pressure records during 2003 and 2008 bottom earthquakes are discussed. After that, non-linear acoustic mechanism of tsunami generation is briefly described. Finally, an improved method of specification of initial conditions in tsunami modeling is suggested.

2. EFFECTS OF WATER COMPRESSIBILITY

2.1 Theoretical Considerations

A liquid can be considered incompressible only when $\Delta\rho << \rho$, where ρ is the density of the liquid. As it is known, the necessary condition for the above to be valid is that the motions of the liquid exhibit small velocities, as compared to the velocity of sound. In the case of stationary motion this condition is sufficient. The problem of tsunami generation is evidently non-stationary, so one more, additional, condition

must be fulfilled. In the problem of tsunami generation both conditions are of the following form (Nosov 2000): 1) $v << c$, 2) $t >> H/c$, where v is the characteristic mass velocity of water. Note that even in those rare cases, when the authors of one or another investigation substantiate application of the theory of incompressible liquids in the tsunami problem, the second condition is always forgotten. The characteristic values of the indicated parameters are the following: v~1 m/s, c~1500 m/s, H~4500 m, τ~1–100 s. The first condition is seen to be well satisfied, while the second can be violated in many cases. Thus, noticeable manifestations are to be expected of the effect of water compressibility in the case of tsunami generation by submarine earthquakes. Additional reasons for it can be found in publications (Nosov 2000, Nosov et al. 2007, Levin and Nosov 2008).

The main difference in behavior between compressible and incompressible ocean consists in the existence of 'fast' oscillations of water column (Nosov 2000). Oscillations take place against the background of the development of a slower gravitational wave. The origin of surface oscillations is due to the excitation of standing acoustic waves in the natural quarter-wave resonator of a 'column of compressible liquid with a free surface on the rigid bottom'. The resonator exhibits a set of frequencies:

$$\nu_n = c(1+2n)/4H\,, \qquad (1)$$

where $n = 0,1,2,3...$

In the case of a basin of variable depth, a most important result consists in the shallow water region turning out to be practically closed to the penetration of elastic waves. The acoustic signal in the shallow water region being suppressed depends on the wave-guide properties of compressible water column. The dispersion relation for normal modes in such a waveguide has the form (Tolstoy and Clay 1987):

$$k_x^{\,n} = \pi\sqrt{4/T^2c^2 - (n+1/2)^2/H^2}\,, \qquad (2)$$

where k_x is the x-component (horizontal) of the wave vector, T is the period of elastic waves and n is the mode number. It is seen that for fixed period T and depth H the horizontal wave number will be real only for a finite number of modes. These modes will be propagating modes. For modes of higher numbers k_x becomes a purely imaginary quantity, consequently, the perturbation in the wave decreases exponentially in the x direction. The situation is possible, when in the deep-water part of the basin there exist several (or one) propagating modes of period T, while in the shallow-water part no mode exists for such a period. Assuming in expression (2) $n = 0$, one can readily find the critical period for the given depth H: $T_c = 4H/c$. The frequency corresponding to the critical period is called the cut-off frequency. Modes of periods inferior to T_c do not propagate in the considered waveguide. Formula (2) also permits to calculate the critical depth H_c for a given period of elastic waves, T. An elastic wave will not penetrate the region, where the depth is smaller than the critical depth, $H < H_c = cT/4$. A displacement of the ocean bottom with residual deformation of duration τ forms elastic waves of period $T \sim \tau$, which are capable of penetrating down to depths $H \sim c\tau/4$.

Note one more interesting effect, related to the shape of the ocean bottom relief. The lowest mode of elastic oscillations ($n = 0$) can be captured by regions of local depressions of the ocean bottom (e.g. deep-water trenches). Indeed, if the lowest mode originates in the region of a local maximum depth, $H_{\max}$, then it exhibits the period $T_{\max} = 4H_{\max}/c$. This mode cannot leave the region, where it originated, since to do so it would have to propagate up the slope.

Assumption an absolutely rigid ocean bottom, considered above, simplifies the problem noticeably and permits to concentrate on manifestations of the compressibility of the water column. A realistic formulation of the problem should, naturally, take into account the finite elasticity of the ocean bottom (Pod'yapol'skiy 1968, Alexeev and Gusyakov 1976, González-González and Sekerzh-Zenkovich 2004). In recent years publications have appeared, in which attempts are made of numerical simulation of the dynamics of a compressible water column with account of the elasticity properties of the ocean bottom (Panza et al. 2000, Ohmachi et al. 2001).

Finiteness of the bottom elasticity does not influence the set of normal frequencies for the water layer; it just leads to a gradual damping of hydroacoustic waves due to their refraction in the bottom. The exponential decay time for energy of hydroacoustic waves (normal incidence) can be estimated as follows (Nosov 2000):

$$\tau_s = \frac{H}{c}\frac{(1+B)^2}{2B}\,, \quad B = \rho_b V_p/\rho c\,, \qquad (3)$$

where ρ_b is density of bottom, ρ_b is density of water, V_p is P-wave velocity ($B \approx 12 - 17$). In reality, due to an arbitrary angle of incidence and coupling between elastic oscillations of water and bottom, the observed decay time should exceed the value given by formula (3). The elastic oscillations of water layer can be observed at least during a few minutes after bottom earthquake (Nosov and Kolesov 2007).

In conclusion, it is worth noting the differences between the T-phase and the oscillations that are considered in this work. T-phase is a series of seismic waves of relatively high frequency (>2 Hz) channeled in the ocean water column by SOFAR (Okal et al. 2003). T-phase propagates for a rather long distance from earthquake epicenter, whereas the low-frequency oscillations remain mostly in the epicenter area gradually losing their energy due to the refraction in bottom.

2.2 Observations

According to the NEIC seismic catalogue, the Tokachi-Oki earthquake of 2003 occurred on September 25 at 19:50:06 UTC. The coordinates of the epicenter were 41.78° N, 143.86° E; the depth of the hypocenter was 27 km; and the magnitude was 8.3Mw. The earthquake

epicenter, location of the Tsunami Sensors off Kushiro-Tokachi (PG1 and PG2) and estimation of the vertical coseismic displacements (Mikada et al. 2006) are shown on Figure 1 a. Both of the Tsunami Sensors turned out to be located just inside the area of coseismic bottom displacement. Thus, a manifestation of the elastic oscillations of water column in bottom pressure records is expected.

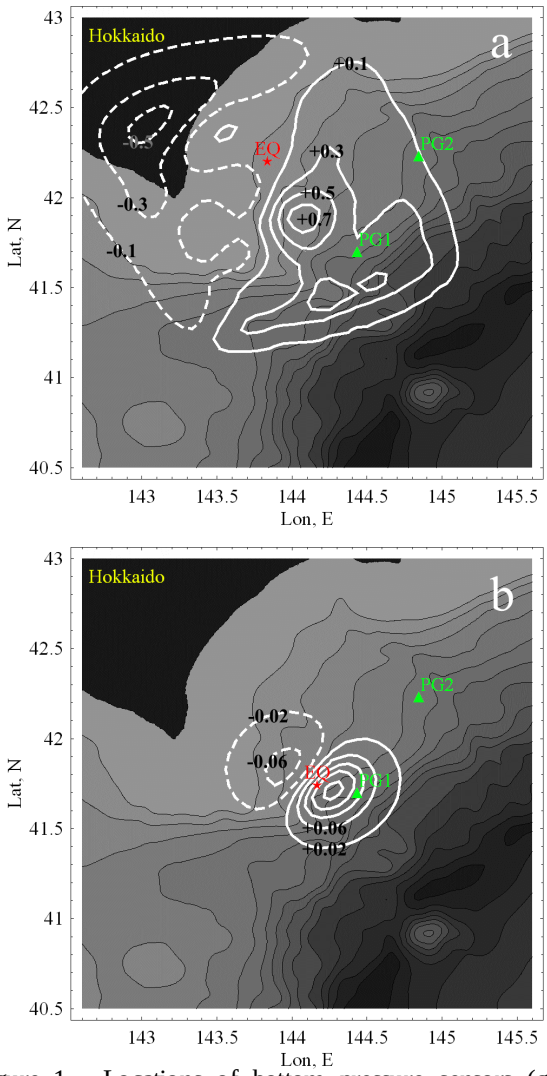

Figure 1. Locations of bottom pressure sensors (green triangles) and earthquake epicenters (red stars): (a) - 25.09.2003, (b) - 11.09.2008. Vertical coseismic bottom deformation is shown by solid (uplift) and dashed (subsidence) white contours at 0.2-m intervals (a) and at 0.04-m intervals (b). Isobaths are shown at 500-m intervals.

As it has been shown in (Nosov et al. 2007), correct theoretical estimation of the value of normal frequency involves not only compressible water column but also elastic sedimentary layer. Indeed, the acoustical basement of the continental slope southeast of Hokkaido is covered with a rather thick sedimentary layer (up to 2 km). Insignificant difference between the acoustic stiffness of water and sediments gives us ground to expect coupled oscillations of water column and sedimentary layer. The set of the normal frequencies γ for such a two-layered system is determined from the following transcendent equation:

$$\mathrm{tg}\left(\frac{2\pi\gamma H}{c}\right)\mathrm{tg}\left(\frac{2\pi\gamma H_s}{c_s}\right)=\frac{\rho_s c_s}{\rho c}, \qquad (4)$$

where H_s is the thickness of the sedimentary layer, c_s is the velocity of elastic longitudinal waves in the sediment, and ρ_s is the density of the sediment. In the case of $H_s = 0$, the set of frequencies described by the equations (1) and (4) naturally coincides.

The 1000 s time series of bottom pressure variations (PG1 and PG2) were used to calculate the spectra. Initial data were reduced to the zero level by means of subtracting the linear trend. We note that only the lowest normal frequency can be observed in the spectra. All other normal frequencies are either quite close to the Nyquist frequency (0.5 Hz) or significantly exceed it.

For calculation theoretical values of the minimum normal frequency γ_0 the following data set was used: depth averaged value of the sound velocity in water for September c=1475 m/s (GDEM-3); depth of ocean at the locations of the pressure sensors H_{PG1}=2237 m and H_{PG2}=2218 m (JODC bathymetry, http://www.jodc.go.jp/); water density $\rho = 1030\,\mathrm{kg/m^3}$; sediment features $c_s = 1740$ m/s and $\rho_s = 1816\,\mathrm{kg/m^3}$ (CRUST2.0, http://mahi.ucsd.edu/Gabi/). We also assume two values for the thickness of the sedimentary layer: 0 m and 1000 m.

The frequency spectra of the pressure variations are shown in Figure 2. Both of the spectra have clearly distinguished main maxima (PG1 – 0.14–0.15 Hz, PG2 – 0.15–0.16 Hz). It should be noted that the location of the maxima on the frequency scale is different. This indicates that the main maxima are associated with the resonance response of the "water-sediments column" at a minimum normal frequency rather than with the spectral characteristics of the seismic source. The result of the theoretical estimation of the minimum normal frequency γ_0 is shown in Figure 2 by vertical dashed lines.

In general, observed main maxima of the spectra and theoretical values of the minimum normal frequency are certainly in a good agreement. Exact coincidence would be observed if we assume thickness of the sedimentary layer $H_s \approx 500\,m$ which is a realistic value for the region under consideration.

The second seismic event occurred on September 11, 2008 at 0:20:56.7 UTC. According to the CMT Catalogue, the coordinates of the epicenter were 41.75° N, 144.17° E; the depth of the hypocenter was 23.9 km; and the magnitude was 6.8Mw. Vertical coseismic bottom displacements shown on Figure 1 b we estimated from CMT source solution applying Okada's formulae (Okada 1985) and empirical relations from (Handbook for Tsunami Forecast 2001). In this case, the PG1 sensor turned out to be located closer to the earthquake epicenter, i.e. within bottom displacement area. The PG2 sensor was surely out of the bottom displacement area. This is why for the seismic event on September 11, 2008 the spectral maximum at the exactly same frequency is observed for PG1 record, whereas, no

relevant maximum exists for PG2 record.

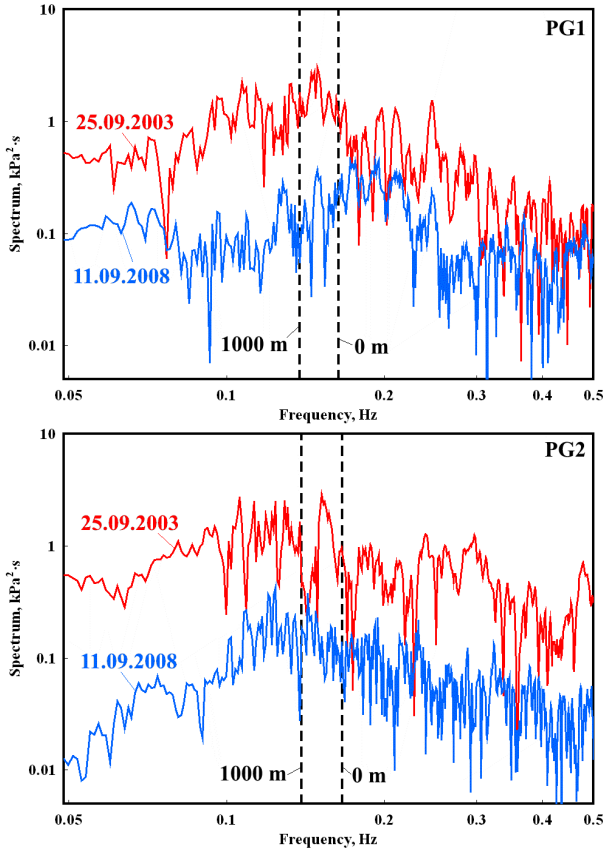

Figure 2. Frequency spectra of bottom pressure variations recorded by JAMSTEC sensors. Dashed lines stand for the positions of normal frequencies calculated for a certain thickness of sediment layer (0 m and 1000 m.)

2.3 Non-linear Mechanism of Tsunami Generation

Due to the cut-off frequency, elastic oscillations of water layer can not provide direct contribution in height of tsunami run-up. Besides, long gravitational waves (tsunamis) and the elastic oscillations exhibit essentially different frequency ranges. Thus, in linear approximation, these two phenomena are not coupled, i.e. one can consider them separately.

In substantiating the application of linear theory in the tsunami generation problem one usually quotes the condition that the amplitude of the ocean bottom deformation be small as compared to the depth of the basin, $h<<H$. Indeed, this condition is quite fulfilled in reality. But even when the amplitude of the ocean bottom displacement is small, the velocity of its movement may turn out to be sufficiently high for the manifestation of non-linear effects. Strong earthquakes may give rise to very intensive elastic oscillations of water column. The non-linear mechanism of tsunami generation related to the non-linear transfer of energy from elastic oscillations to gravitational waves. The usual tsunami generation mechanism, related to residual displacements substituting the water, naturally, remains in force, and in most cases it plays the leading role. However, in some cases non-linear mechanism can provide an additional contribution to a tsunami wave (Novikova and Ostrovsky 1982, Nosov and Kolesov 2005, Nosov et al. 2008, Levin and Nosov 2008).

At present, the non-linear mechanism is still under investigation. This is why further details we prefer to leave out of scope of this paper. Anyway, taking into account water compressibility together with nonlinearity may turn out to be one of the points of improvement in description of tsunami source.

3. IMPROVED METHOD OF INITIAL CONDITION SPECIFICATION

In this section we focus on a practical method of specification of initial conditions in tsunami problem. Due to the reasons described above, in linear approximation, for the sake of calculations of tsunami runup heights, no need to consider effects of water compressibility. As for nonlinear effects, we shall leave them beyond the scope of this paper.

The imperfectness of the traditional approach, within which the initial elevation is set equal to the vertical residual bottom deformation, is due to the following two reasons. *First*, even if the ocean bottom is horizontal, and the bottom deformations are instantaneous, the displacement of the water surface and the vertical residual bottom deformation will not be equal to each other: the displacement of the water surface will be smoother. *Second*, in the case of a sloping (non-horizontal) bottom the horizontal deformation components can also contribute significantly the displacement of the water surface.

Explanations of the first reason are as follows. From analytical solution of the problem of tsunami generation by bottom motions it is known that spatial spectrum of water surface displacement is modulated by function $1/\mathrm{ch}\, kH$, where k is the wave number (Kajiura 1963, Nosov 1998). Thus, "fine spatial structure" of bottom displacement (i.e. wavelength $l < H$) is not manifested on the water surface. It is worth emphasizing, that direct transfer of bottom deformations up to the water surface artificially enriches spectrum of tsunami at the expense of unrealistic short waves. Being a sort of noise, these short waves may lead to artificial resonances in bays, and finally, to incorrect estimation of runup heights or even to instability in numerical calculations. Moreover, the short waves are subject to numerical dispersion. To avoid the numerical dispersion, one should apply fine grids and, therefore, small time steps. In such a way the imperfectness of the traditional approach may also result in a significant increase of the calculating time in numerical simulation of tsunamis.

An attempt at taking "smoothing effect" into account has been done in (Tanioka and Seno 2001) and (Rabinovich et al. 2008).

A logical development of the traditional approach is to calculate the initial elevation from the solution of the 3D problem taking into account all three components of the bottom deformation vector and the distribution of depths in

the vicinity of the source. Let us consider this problem in the framework of classical linear potential wave theory:

$$\Delta F = 0, \tag{5}$$

$$F_{tt} = -gF_z, \quad z = 0, \tag{6}$$

$$\frac{\partial F}{\partial \mathbf{n}} = \left(\frac{\partial \boldsymbol{\eta}}{\partial t}, \mathbf{n}\right), \quad z = -H(x,y), \tag{7}$$

where F is the potential of the flow velocity, $\mathbf{n}$ is the unit vector normal to the bottom surface. The initial elevation is calculated via the potential by the following formula:
$\zeta(x,y,t) = -g^{-1}F_t(x,y,0,t)$.

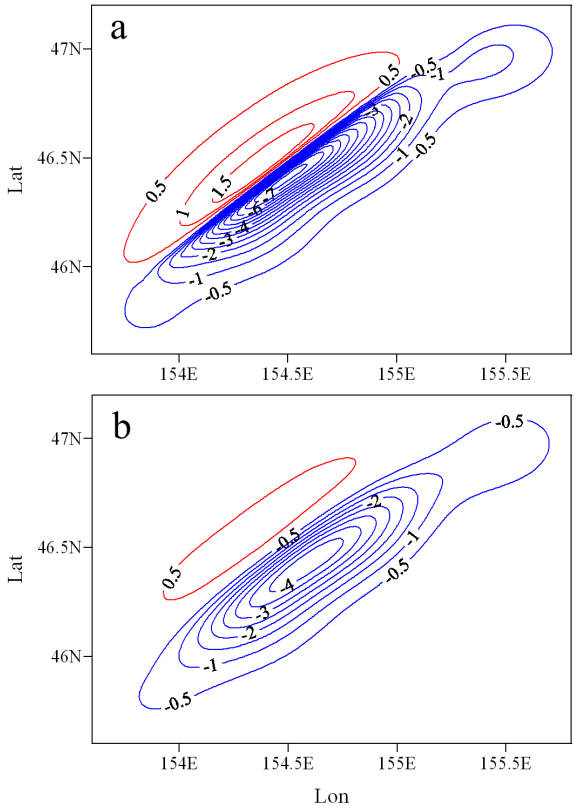

Figure 3. Vertical bottom deformation (a) and initial elevation (b) in the source of Central Kuril Islands tsunami on January 13, 2007.

If the bottom deformation process turns out to be long ($t \sim L/\sqrt{gH}$), then the initial conditions must include, besides the initial elevation, the initial distribution of flow velocities, as well,

$$\mathbf{V}(x,y,t) = \frac{1}{H(x,y)} \int_{-H(x,y)}^{0} dz\, \mathbf{v}F(x,y,z,t). \tag{8}$$

In case of instantaneous deformation, the evolutionary problem (5)–(7) can be reduced to a more simple static problem:

$$\Delta \hat{F} = 0, \tag{9}$$

$$\hat{F} = 0, \quad z = 0, \tag{10}$$

$$\frac{\partial \hat{F}}{\partial \mathbf{n}} = (\boldsymbol{\eta}, \mathbf{n}), \quad z = -H(x,y). \tag{11}$$

The initial elevation is determined from the solution of problem (9)–(11) by the following formula:

$$\zeta(x,y) = \hat{F}_z(x,y,0). \tag{12}$$

In Figure 3 a, the example is presented of vertical bottom deformation calculated for the tsunamigenic Central Kuril Islands earthquake of January 13, 2007. According to USGS NEIC data the moment-magnitude of the earthquake amounted to 8.1Mw. The dip and the strike angles were determined to be 42.36° and 57.88°, respectively. The fault plane dimension was 200 km (along the strike) by 35 km, which was further divided into 175 subfaults (8 km by 5 km). Data on the slip distribution are presented on the site http://earthquake.usgs.gov/regional/world/historical.php.

The bottom deformation, caused by each of these subfaults, is calculated by Okada formulae. Then, the contributions of all elements are summed up. According to calculations, the maximum horizontal bottom deformation amounted to about 3.4 m. The calculated maximum and minimum vertical bottom deformations amounted to 1.9 m and −7.7 m, respectively.

Figure 3 b demonstrates the initial elevation calculated from the numerical solution of the problem (9)-(11). In calculations all three components of the bottom deformation vector are taken into account. It is worth noting that significant bottom deformations were confined to Kuril Trench, i.e. region of large depths and essential slope of the bottom. From Figure 3 it is seen that the initial elevation is much smoother than the bottom deformation. The calculated maximum and minimum initial elevation amounted to 0.8 m and −4.4 m, respectively. These values are nearly two times smaller in comparison with the maximum and minimum of vertical bottom deformation. So traditional approach of specification of the initial conditions may leads to significant overestimation of tsunami amplitude.

Contribution of horizontal displacements of sloping bottom in the in amplitude of initial elevation is relatively small (up to -0.26 m and +0.29 m). However, in terms of displaced volume of water, the contribution of horizontal displacements amounted to 20%.

Complexity of the problem (9)-(11) does not obviously depend on how many components of the bottom deformation vector are taken into account. This is why, in spite of the fact that contribution of the horizontal components is not dominant; it makes sense to consider them all in calculating of initial elevation in tsunami source.

4. CONCLUSIONS

Suggested method of calculation of initial elevation does not violate traditional scheme of tsunami simulation but just improves it. The *first point* of improvement consists in removing from tsunami spectrum of shortwave components which are not peculiar to real tsunami waves. The *second point* of improvement consists in taking into account not

only vertical bottom deformation but all three components of the deformation vector. It is important to note, here, that realization of these two improvements involves rigorous hydrodynamic theory. The *third point* is connected with correct estimation of additional contribution of the non-linear tsunami generation mechanism related to elastic oscillations of water column in tsunami source area.

The first and the second points are ready now for practical use, whereas the third point is still requires additional study.

Acknowledgements:

This work was supported by the Russian Foundation for Basic Research, project 07-05-00414. We are grateful to JAMSTEC for providing the data.

References:

Alexeev, A.S. and Gusyakov, V.K. (1976), "Numerical Modeling of Tsunami and Seismic Surface Waves Generation by Submarine Earthquake," *Tsunami Research Symposium Bulletin Royal Society New Zealand*, 15, 243-251.

Fujii, Y. and Satake, K. (2008), "Tsunami Sources of the November 2006 and January 2007 Great Kuril Earthquakes," *Bulletin of the Seismological Society of America*, **98**(3), 1559–1571.

González-González, R. and Sekerzh-Zenkovich, S. (2004), "Hydroelastic stationary problem on tsunami waves generation," *Computational Mathematics and Mathematical Physics*, **44**(11), 1982-1991.

Kajiura, K. (1963), "The leading wave of a tsunami," *Bulletin of the Earthquake Research Institute, University of Tokyo*, **41**(3), 535–571.

Mikada, H., Mitsuzawa, K., Matsumoto, H., Watanabe, T., Morita, S., Otsuka, R., Sugioka, H., Baba, T., Araki, E., and Suyehiro, K. (2006), "New discoveries in dynamics of an M8 earthquake - Phenomena and their implications from the 2003 Tokachi-oki Earthquake using a long term monitoring cabled observatory," *Tectonophysics*, **426**, 95–105.

Handbook for Tsunami Forecast in the Japan Sea. (2001), Earthquake and Tsunami Observation Division, Seismological and Volcanological Department, Japan Meteorological Agency, 22.

Hirata, K., Aoyagi, M., Mikada, H., Kawaguchi, K., Kaiho, Y., Iwase, R., Morita, S., Fujisawa, I., Sugioka, H., Mitsuzawa, K., Suyehiro, K., Kinoshita, H., and Fujiwara, N. (2002), "Real-time geophysical measurements on the deep seafloor using submarine cable in the southern Kurile subduction zone," *IEEE Journal of Oceanic Engineering*, **27**(2), 170–181.

Kowalik, Z., Knight, W., Logan, T., and Whitmore P. (2005), "Numerical modelling of the global tsunami: Indonesian tsunami of December 26 2004," *Science of Tsunami Hazard*, **23**(1), 40-56.

Levin, B.W. and Nosov, M.A. (2008), "Physics of Tsunamis," Springer.

Nosov, M. A., Kolesov, S. V., and Denisova, A.V. (2008), "Contribution of nonlinearity in tsunami generated by submarine earthquake," *Advances in Geosciences*, **14**, 141-146.

Nosov, M.A. (1998), "On the directivity of dispersive tsunami waves excited by piston-type and traveling-wave sea-floor motion," *Volcanology and Seismology*, **19**(6), 837-844.

Nosov, M.A. and Kolesov, S.V. (2007), "Elastic oscillations of water column in the 2003 Tokachi-oki tsunami source: in-situ measurements and 3-D numerical modeling," *Natural Hazards and Earth System. Sciences*, **7**, 243-249.

Nosov, M. A. and Kolesov, S. V. (2005), "Nonlinear tsunami generation mechanism in compressible ocean," *Vestnik Moskovskogo Universita, Ser. 3 Fizika Astronomiya*, (3), 51–54.

Nosov, M. A., Kolesov, S. V., Ostroukhova, A. V., Alekseev, A.B., and Levin, B. W. (2005), "Elastic oscillations of the water layer in a tsunami source," *Doklady Earth Sciences*, **404**(7), 1097–1100.

Nosov, M. A., Kolesov, S. V., Denisova, A.V., Alekseev, A.B., and Levin, B. W. (2007), "On the near-bottom pressure variations in the region of the 2003 Tokachi-Oki tsunami source," *Oceanology*, **47**(1), 26-32.

Novikova, L. E. and Ostrovsky, L. A. (1982), "On an acoustic mechanism of tsunami wave generation," *Oceanology*, **22**(5), 693–697.

Ohmachi, T., Tsukiyama, H., and Matsumoto, H. (2001), "Simulation of tsunami induced by dynamic displacement of seabed due to seismic faulting," *Bulletin of the Seismological Society of America*, **91**(6), 1898–1909.

Okada, Y. (1985), "Surface deformation due to shear and tensile faults in a half-space," *Bulletin of the Seismological Society of America*, **75**(4) 1135–1154.

Okal, E. A., Alasset, P.J., Hyvernaud, O., and Schindele`, F. (2003), "The deficient T waves of tsunami earthquakes," *Geophysical Journal International*, **152**(2), 416–432.

Panza, F.G., Romanelli, F., and Yanovskaya, T. B. (2000), "Synthetic tsunami mareograms for realistic oceanic models," *Geophysical Journal International*, **141**, 498–508.

Pod'yapol'skiy, G.S. (1968), "Excitation of a long gravitational wave in the ocean from a seismic source in the crust," *Izv. Akad. Nauk SSSR Fiz. Zemli*, (1), 7-24.

Rabinovich, A.B., Lobkovsky, L.I., Fine, I.V., Thomson, R. E., Ivelskaya, T. N., and Kulikov, E. A. (2008), "Near-source observations and modeling of the Kuril Islands tsunamis of 15 November 2006 and 13 January 2007," *Advances in Geosciences*, **14**, 105-116.

Tanioka, Y. and Seno, T. (2001), "Sediment effect on tsunami generation of the 1896 Sanriku tsunami earthquake," *Geophysical Research Letters*, **28**(17), 3389-3392.

Titov, V.V. and Gonzalez, F.I. (1997), "Implementation and testing of the Method of Splitting Tsunami (MOST) model," NOAA Technical Memorandum ERL PMEL-112.

Watanabe, T., Matsumoto, H., Sugioka, H., Mikada, H., Suyehiro, K., and Otsuka, R. (2004), "Offshore monitoring system records recent earthquake off Japan's northernmost island," *Eos*, **85**(2), 14–15.

Sixth International Conference on Urban Earthquake Engineering
March 3-4, 2009, Tokyo Institute of Technology, Tokyo, Japan

FRAGILITY CURVES AND TSUNAMI RISK ASSESSMENT OF REINFORCED CONCRETE BUILDING IN THAILAND

Piyawat Foytong[1] and Anat Ruangrassamee [2]

1) Ph.D candidate, Department of Civil Engineering, Chulalongkorn University, Bangkok, Thailand
2) Assistant Professor, Department of Civil Engineering, Chulalongkorn University, Bangkok, Thailand
fcearr@eng.chula.ac.th

Abstract: This paper presents tsunami risk analysis of Patong Beach, Phuket, Thailand. Fragility curves of reinforced-concrete buildings damaged by the December 26th, 2004 tsunami in Thailand are used to evaluate the damage of reinforced-concrete buildings. The fragility curves are developed by a maximum likelihood function and it describes the damage probability corresponding to a specific damage level for different inundation heights. In this study, four different damage levels are defined ranging from no structural damage to collapse. The fragility curves for reinforced-concrete buildings are classified into two types: one-story buildings and buildings taller than one story. For one-story buildings under the inundation height of 4 m, the probability of exceeding the damage in primary members is 90%. For buildings taller than one story under the same inundation height, the probability of exceeding the damage in primary members is only about 25%. The December 26th, 2004 tsunami generated the inundation height about 3 m. which caused damage to many buildings in Patong Beach, Phuket. The results of evaluated damage of buildings are the highest probability of damage is 73% which is no damage for buildings taller than one story. Most damage for one-story buildings is damaged in primary members and for buildings taller than one story is damage in secondary members only.

1. INTRODUCTION

The December 26th, 2004 Indian Ocean tsunami caused damage to many buildings and killed many people in the South of Thailand. The tsunami risk analysis is useful for estimating residential damage. The residential damage can be estimated from tsunami hazard maps, fragility curve and building inventory. The fragility curves are developed as a function of tsunami inundation height from damaged buildings in the December 26th, 2004 Indian Ocean tsunami. Damage of reinforced-concrete buildings was observed by 8 universities in Thailand (Ruangrassamee et al., 2006). The fragility curves are developed using a maximum likelihood function and it describes the damage probability corresponding to a specific damage level for different inundation heights. The damage levels are classified into 4 damage levels and ranging from no damage to collapse. The fragility curves for reinforced-concrete buildings are classified into two types: one-story buildings and buildings taller than one story. The building data is collected in Patong Beach Phuket Thailand. Finally, tsunami risk analysis is conducted.

2. DATA OF DAMAGED BUILDINGS

Collected information consists of the location of a building, inundation height measured from the ground floor, structural type, column and beam damage and overall damage of a structure. There are 109 reinforced-concrete buildings in database: 73 buildings in Phuket, 25 buildings in Phang-Nga, 8 buildings in Ranong, 2 buildings in Krabi, and 1 building in Trang. Figure 1 shows the percentage of building functions which are hotels, residences, shops and others. Residences share the majority of the buildings observed. The percentage of data classified according to the number of stories is shown in Figure 2. There are 63 one-story buildings and 46 buildings taller than one story.

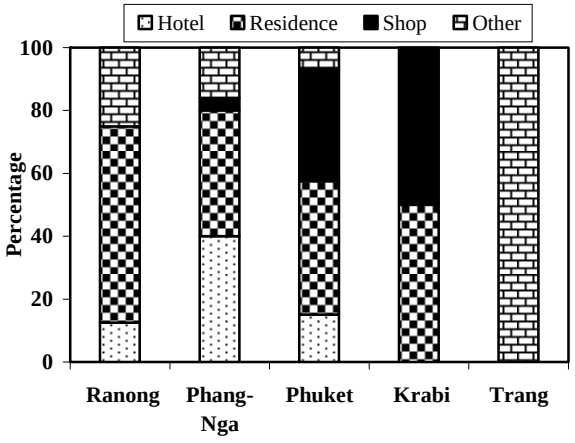

Figure 1 Building functions

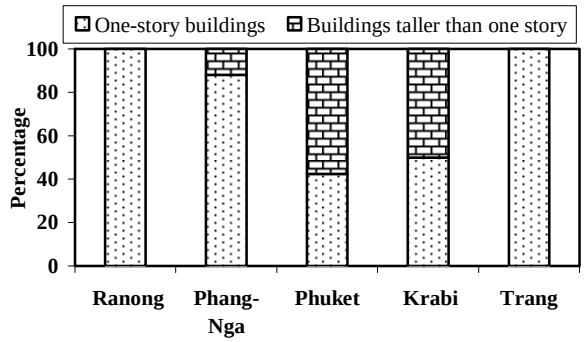

Figure 2 The number of stories

3. DEFINITION OF DAMAGE LEVELS

This study develops fragility curves and evaluates the effect of the numbers of stories. The capacity of buildings and the construction quality are reflected in the number of stories. The buildings taller than one story are usually constructed with better quality and higher capacity than one-story buildings. Hence reinforced-concrete building data are grouped in two types: one-story buildings and buildings taller than one story. Damage levels are defined in terms of the overall damage of buildings and classified into four damage levels 1) no damage, 2) damage in secondary members only, 3) damage in primary members and 4) collapse. The details are explained below.

- No damage (damage level 0): There is no damage in a building.
- Damage in secondary members only (damage level 1): There is damage only in non-structural components, i.e., walls and/or roofs. At this damage level, there are cracks on wall or wall punching, or tiles are wiped out. But there is no damage in a beam or a column.
- Damage in primary members (damage level 2): There is damage in structural components, i.e., a column, a beam, or foundation. At this damage level, there are cracks on a beam or a column, but the building is still reparable.
- Collapse (damage level 3): A building cannot sustain its gravitational load and it is unreparable. At this damage level, a structure may fail at a major joint or absolutely collapse.

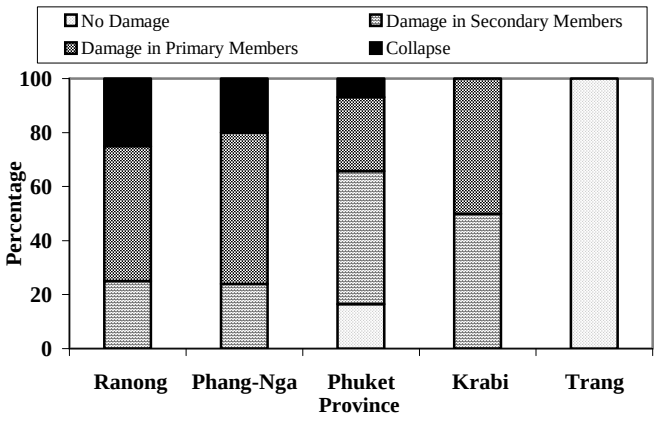

Figure 3 Damage levels of buildings in each province

Figure 3 shows the percentage of damage levels of buildings. In Phuket, the damage of observed buildings ranges from no damage to collapse. Most of buildings suffer damage in secondary members only.

4. FRAGILITY CURVE

Fragility curves are represented as a function of the inundation height, although there are other wave characteristics such as wave velocity. An inundation height can be observed in the field but wave velocity may be obtained from tsunami simulation or image processing of videos. Wave velocity on land may have some uncertainties. For simplicity, an inundation height is used in developing fragility curves. Fragility curves can be expressed in form of two-parameter lognormal distribution functions which are median and lognormal standard deviation. The estimation of these two parameters is done by the maximum likelihood method (Yamazaki and Murao, 2000). The likelihood function can be written as

$$M = \prod_{k=1}^{N} \left[F\left(a_k\right) \right]^{y_k} \left[1 - F\left(a_k\right) \right]^{1-y_k} \qquad (1)$$

The fragility curve can be written by the lognormal function as

$$F\left(a\right) = \Phi\left[\frac{\ln\left(\frac{a}{\alpha}\right)}{\beta} \right] \qquad (2)$$

where

a_k = the inundation height of the k-th damage level

y_k = the variable equal to 1 when the building sustains the specific damage level and equal to 0 when the building cannot sustain the specific damage level under an inundation height equal to a_k

$\Phi\left(.\right)$ = the standardized normal distribution function

N = the total number of buildings

α, β = median and lognormal standard deviation

The parameters α and β are computed in order to maximize $\ln\left(M\right)$ by differentiating $\ln\left(M\right)$ with respect to α and β and equating to zero as

$$\frac{d\ln M}{d\alpha} = \frac{d\ln M}{d\beta} = 0 \qquad (3)$$

Computation is performed numerically using a standard optimization algorithm. The process starts from separating data, depending on whether or not the building sustains a specific damage level. Then, the variable y_k and inundation height are computed. These values are substituted into the likelihood function in Eq. 1 and then a standard optimization algorithm is used to obtain two parameters α and β. Finally, the variable y_k, inundation height and two parameters are used to plot the fragility curve. Inundation heights are arranged from minimum to maximum, and

separated with a 0.5-m interval. After that, the average inundation height and probability is calculated for each interval. Table 1 shows a calculation example of the average probability of damage for buildings taller than one story with an inundation height ranging from 3.5 m to 4 m.

Table 1 A calculation example of the average probability of damage for buildings taller than one story

Location	No. stories	Inundation height (m)	Damage level	y_k of damage level			Average inundation height (m)	Average y_k of damage level		
				1	2	3		1	2	3
Kamala Beach, Phuket	2	3.7	2	1	1	0	3.8	1	0.33	0
Kamala Beach, Phuket	2	3.7	1	1	0	0				
Kamala Beach, Phuket	3	4	1	1	0	0				

Fragility curves of one-story buildings damaged in the 26 December 2004 tsunami are shown in Figure 4. For the damage level 1, it is obvious that damage occurs for inundation higher than 3.5 m. It is seen that the fragility curve agrees well with actual data. Figure 4(d) shows the comparison of fragility curves of each damage level for one-story buildings. The probability reduces for higher damage levels at the same inundation height. To avoid the intersection of the fragility curves of the damage level 1 and the damage level 2, the lognormal standard deviation of the damage level 1 is constrained to be equal to the lognormal standard deviation of the damage level 2. Figure 5 shows the fragility curves for buildings taller than one story. The trend of fragility curves is similar to the fragility curve for one-story buildings, but the probability of damage is less for the same damage level and inundation height. There is no fragility curve of the damage level 3 because there is no data on collapse of buildings taller than one story.

5. BUILDING INVENTORY

Since fragility curves of reinforced-concrete buildings are classified into two types: one-story buildings and buildings taller than one story, building inventory was developed with building information consisting of structural types, the number of stories and building functions. 448 reinforced-concrete buildings were surveyed in the Southern part of Patong Beach, Phuket. Figure 6 shows the distribution of the number of stories. There are 95 one-story buildings and 353 buildings taller than one story. Surveyed buildings are classified into 12 zones for evaluating damage of buildings as shown in Figure 7. Table 2 shows the number of buildings for one-story buildings and buildings taller than one story of each zone. Zone 3 has the largest number of buildings with 72 buildings taller than one story but there is no one-story buildings.

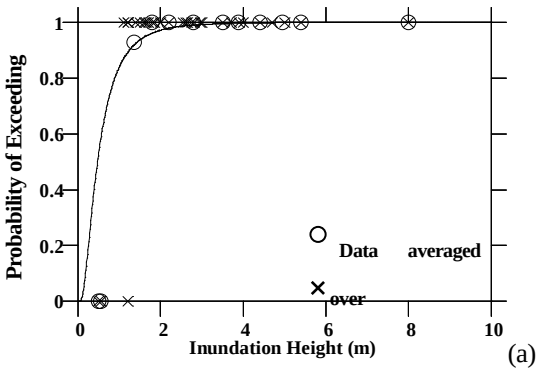

(a) Damage level 1

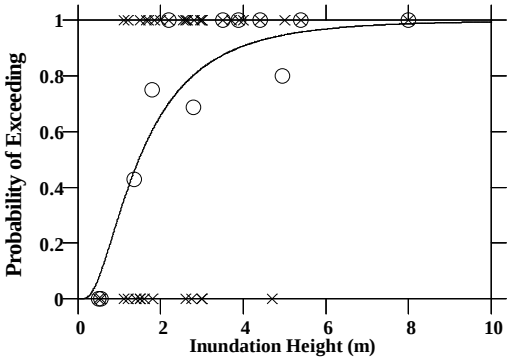

(b) Damage level 2

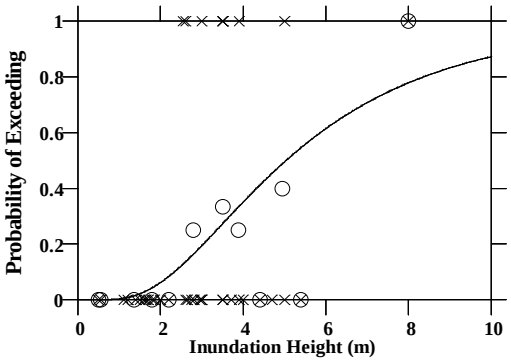

(c) Damage level 3

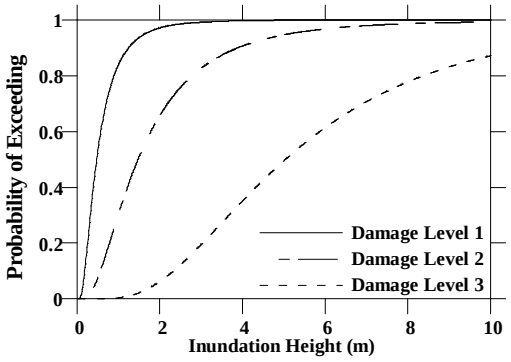

(d) All damage level

Figure 4 Fragility curves for one-story buildings

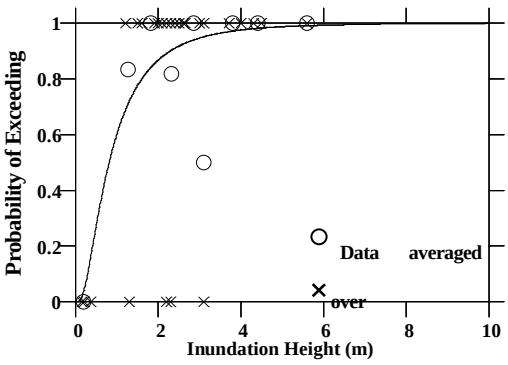

(a) Damage level 1

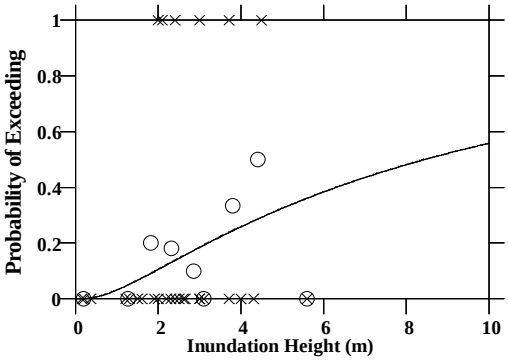

(b) Damage level 2

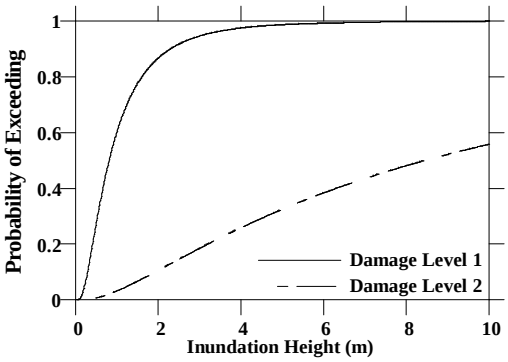

(c) All damage level

Figure 5 Fragility curves of buildings taller than one story

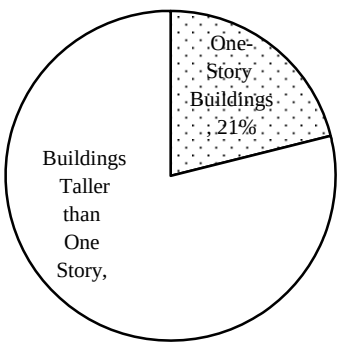

Figure 6 The number of stories

Figure 7 Location of zones

Table 2 The number of one-story buildings and buildings taller than one story in each zone

Zone	The number of one-story buildings	The number of buildings taller than one story
1	8	37
2	13	30
3	0	72
4	2	59
5	3	34
6	3	30
7	4	19
8	1	16
9	1	3
10	25	15
11	1	19
12	34	19

6. EVALUATION OF BUILDING DAMAGE

Tsunami hazard represented by inundation heights is obtained from tsunami simulation of the December 26th, 2004 tsunami. The probability of exceeding each damage level is known from the proposed fragility curves. Then, the probabilities of each damage level are calculated by equation 4. As an example, Figure 8 shows the probabilities of each damage level for one-story buildings at inundation height of 2 m. Probabilities are 0.03, 0.31, 0.60 and 0.06 for damage levels 0, 1, 2 and 3, respectively. The percentage of damaged areas for one-story buildings and buildings taller than one story of each zone are evaluated from the inundation height, probability of damage and area of buildings.

$$P = \frac{\sum_{i}^{n} (p_i \cdot a_i)}{A} \times 100 \qquad (4)$$

where P = the probability of the specified damage level of a zone

p_i = the probability of the specified damage level of a building

a_i = the area of the specified damage level of a building

A = the total area of the specified damage level of a building

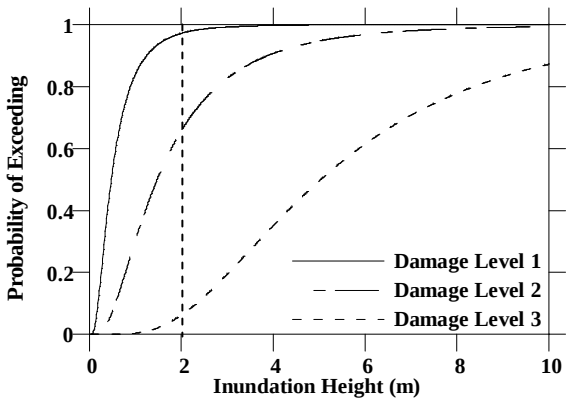

(a) The probability of exceeding damage levels

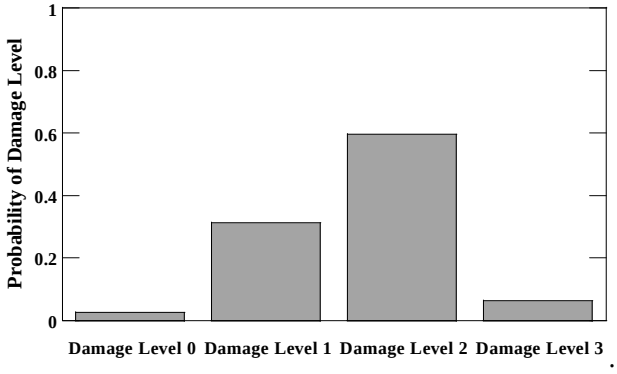

(b) Probability of damage levels

Figure 8 The probability of exceeding damage levels and probability of damage levels of one-story buildings at inundation height of 2 m.

The probabilities damage of buildings taller than one story and one-story buildings are shown in Figures 9 and 10, respectively. Zones along the shoreline have more damage than zones far from the shoreline. It can be seen that zones far from the shoreline have probability of the damage levels 0 and 1 higher than zones along the shoreline. For the damage levels 2 and 3, zones along the shoreline have higher probability than zones far from the shoreline. Most damage for one-story buildings is the damage level 2 and that for buildings taller than one story is the damage level 1.

7. CONCLUSIONS

In this study, damage of buildings in the Southern part of Patong Beach, Phuket is evaluated by tsunami risk analysis using developed fragility curves of reinforced-concrete buildings and building inventory. Findings can be summarized as follows:

1. The fragility curves are obviously dependent on building capacity because the buildings taller than one story are usually constructed with higher capacity than one-story buildings. For one-story buildings under the inundation height of 4 m, the probability of exceeding the damage level 2 is 90%. For buildings taller than one story under the same inundation height, the probability of exceeding the damage level 2 is about 25%.

2. The fragility curve of damage level 3 cannot be developed because in observed data buildings taller than one story did not suffer total collapse in observation.

3. 448 reinforced-concrete buildings were surveyed in the Southern part of Patong Beach, Phuket. There are 95 one-story buildings and 353 buildings taller than one story.

4. The highest probability of damage is 73% which is the damage level 0 for buildings taller than one story. Most damage for one-story buildings is the damage level 2 and that for buildings taller than one story is the damage level 1.

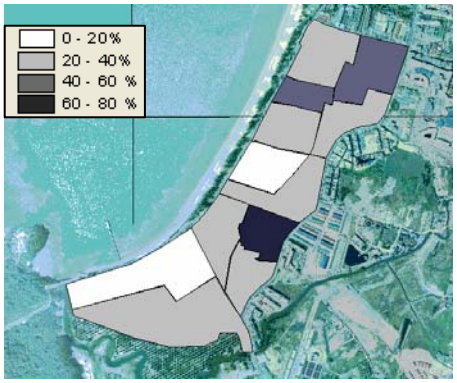

(a) Damage level 0

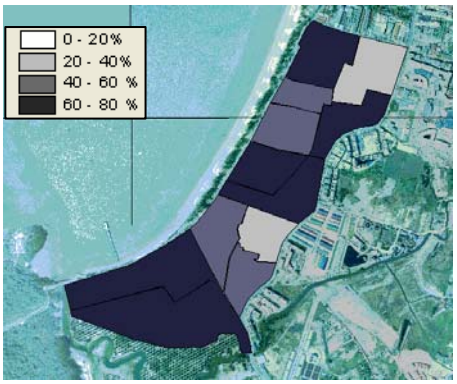

(b) Damage level 1

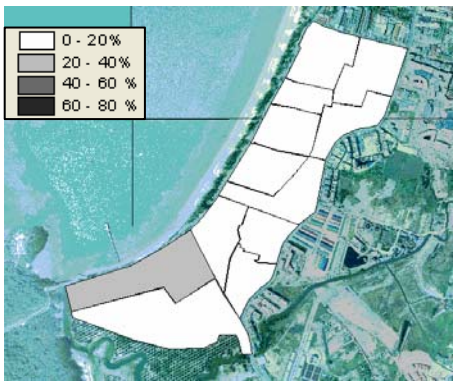

(c) Damage level 2

Figure 9 Probability of damage for buildings taller than one story

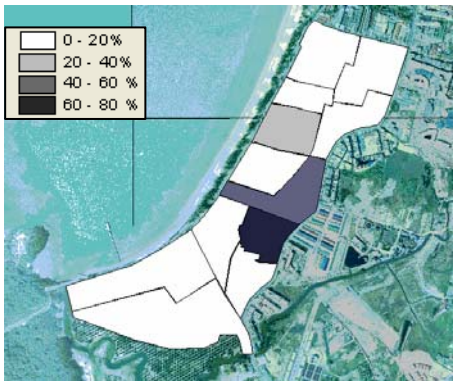

(a) Damage level 0

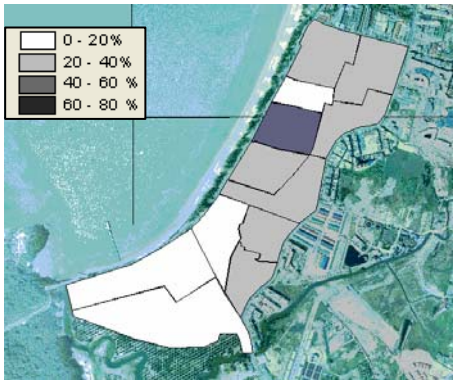

(b) Damage level 1

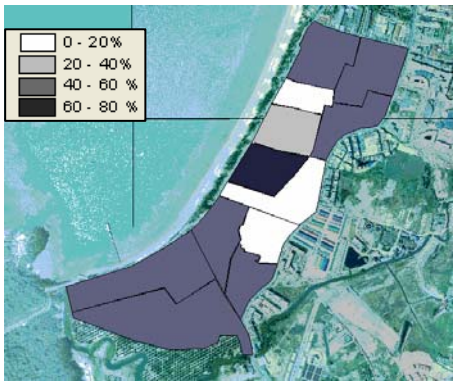

(c) Damage level 2

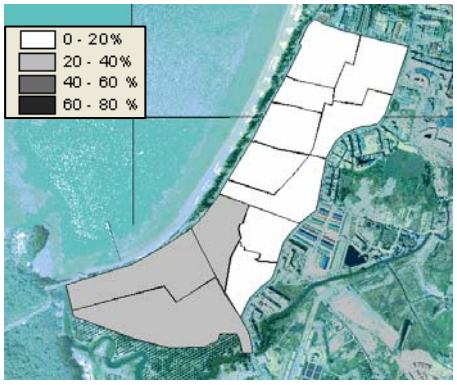

(d) Damage level 3

Figure 10 Probability of damage for one-story buildings

References:

Ruangrassamee, A., Yanagisawa, H., Foytong, P., Lukkunaprasit, P., Koshimura, S., and Imamura, F. (2006) Investigation on Tsunami-Induced Damage and Fragility of Buildings in Thailand, Journal of Earthquake Engineering Research Institute, Earthquake Spectra, Volume 22, Issue S3, pp. S377-S401.

Yamazaki, F. and Murao, O. (2000). Fragility curves for buildings in Japan based on experience from the 1995 Kobe Earthquake, Institute of Industrial Science, University of Tokyo, Tokyo, Japan.

Sergio, M.P., Dominik H.L. and Conrad D.L. (2007). SELANA v2.0: user and technical manual v2.0, NORSAR, Kjeller, Norway.

Sixth International Conference on Urban Earthquake Engineering
March 3-4, 2009, Tokyo Institute of Technology, Tokyo, Japan

TIDE GAUGE RECORDS IN THE INDIAN OCEAN AND ITS USE FOR TSUNAMI STUDY

Hiroyuki Matsumoto[1], Aditya R. Gusman[2], and Yuichiro Tanioka[3]

1) Research Scientist, Japan Agency for Marine-Earth Science and Technology, Japan
2) Doctor Course Student, Institute of Seismology and Volcanology, Hokkaido University, Japan
3) Associated Professor, Institute of Seismology and Volcanology, Hokkaido University, Japan
hmatsumoto@jamstec.go.jp, adit@mail.sci.hokudai.ac.jp, tanioka@mail.sci.hokudai.ac.jp

Abstract: According to the NOAA earthquake database, at least 31 events have been found in the Indian Ocean in terms of tsunami event since 1900, most of which occurred along the Sunda Trench. In this study, we review the history of tide level measurements and their datasets archives in Thailand, Indonesia, India, and Australia. We collected tide gauge paper charts recording historical tsunamis including the 2004 Indian Ocean tsunami in those countries. As a result, systematic collection of historical tsunami records by tide gauges in the Indian Ocean has been difficult, because few tsunamigenic earthquakes occurred in the Indian Ocean during the instrumentally observed period. Additionally, we introduce a result of tsunami computation for the 1977 Sumba earthquake, which caused moderate-to-serious damages to the western Australia in the far-field.

1. INTRODUCTION

The 2004 Indian Ocean tsunami generated by the Sumatra-Andaman earthquake (Mw>9.0) resulted in one of the most devastating damages in history. Causes of such disaster are considered as few records of large tsunamis in the Indian Ocean and no knowledge of tsunami. As a result, the 2004 Indian Ocean tsunami has brought us a cue of establishing an early tsunami warning system in the Indian Ocean. By the way, it is well known that not paleo- but historical tsunamis have occurred in the Indian Ocean. In the meantime, we found that tide level measurements have been carried out since the early 1900s in the Indian Ocean. This study aims to summarize the historical tsunamis occurred in the Indian Ocean, and to systematically collect tsunami records observed by tide gauges including that from the 2004 Sumatra-Andaman earthquake. And we try to reproduce historical tsunamis occurred in the Indian Ocean by using collected tide gauge records.

We focus on four countries, Thailand, Indonesia, India, and Australia among other countries surrounding the Indian Ocean for collection of tide gauge records. In Thailand, two different organizations operate tide gauges, one is Thai Marine Department and the other is Royal Thai Navy. In Indonesia, National Coordinating Agency for Surveys and Mapping (BAKOSURTANAL) deploys and operates tide gauge stations. In India, Survey of India operates a tide gauge network collaborated with National Institute of Oceanography. And in Australia, Department of Planning and Infrastructure operates tide gauges along the western coast of Australia. In this study, history of tide level measurement and their datasets archives in these countries are reviewed. In addition to these tide gauges, Sea Level Center of University of Hawaii also operates the Indian Ocean tide gauge network in Maldives, Sri Lanka, Bangladesh, and Myanmar as a Global Sea Level Observing System (GLOSS) network, and those tide gauges have recorded the 2004 Indian Ocean tsunami (Merrifield et al, 2005).

We realize that the 1977 Sumba earthquake occurred in Indonesia, which is well-known as a tsunamigenic outer-rise earthquake affected the western Australia through our work. In the end, we constrain a slip amount of the seismic fault of the 1977 Sumba earthquake by using the tide gauge records collected in the western Australia.

2. HISTORICAL TSUNAMIS IN THE INDIAN OCEAN

Historical tsunamigenic earthquakes that occurred in the Indian Ocean are extracted from the NOAA earthquake database (NGDC, NOAA website). Search conditions adopted here are as follows; earthquakes 1) that occurred in the Indian Ocean or in the western Pacific Ocean, 2) that occurred from 1900 to the present, and 3) that was registered as tsunami event. As a result, 31 events including aftershocks were extracted from the database (Fig. 1). According to the database, their epicenters in the Indian Ocean focus along the Sunda Trench, where the Indian Plate

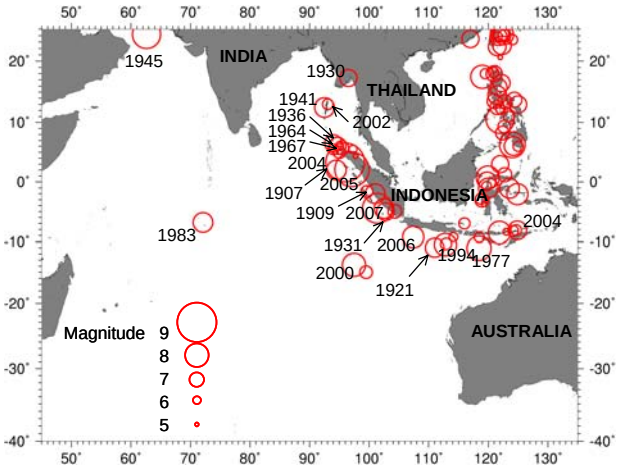

Figure 1 Map showing tsunamigenic earthquakes that occurred in the Indian Ocean and in the western Pacific Ocean since 1900. Data were taken from the NOAA earthquake database.

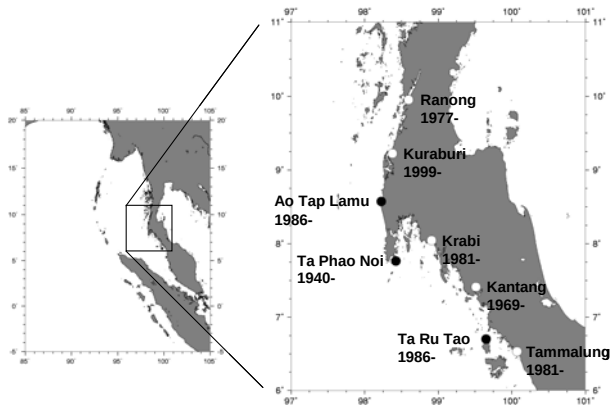

Figure 2 Locations of tide gauge stations along the coast of the Andaman Sea in Thailand. Open and solid circles indicate tide gauges operated by Thai Marine Department and Royal Thai Navy, respectively. Years subscribed to the location name represent the deployed year.

is subducting beneath the Eurasia Plate. A few earthquakes occurred out of the Sunda Trench. An earthquake of M8.3 in 1945 occurred in the Arabian Sea, and another earthquake of M7.7 in 1983 occurred in the central Indian Ocean. Details of the former event is discussed by elsewhere (e.g., Anon., 1945; Beer and Stagg, 1946; Berninghausen, 1966). The latter one triggered a few meters of tsunami near the source region (e.g., SEAN Bulletin, 1983). As mentioned later, sea level measurements in the Indian Ocean have been carried out since 1940 by using permanent tide gauges. Some historical tsunamis, therefore, should have been captured by these tide gauges.

3. TIDE GAUGE RECORDS IN THE INDIAN OCEAN

3.1 Thailand

Two different organizations operate tide gauges along the coast of the Andaman Sea in Thailand, where eight tide gauges are working (Fig. 2). Five of these gauges are operated by Thai Marine Department, and three others are operated by Royal Thai Navy.

All tide gauges use float gauges in stilling wells in harbors or bays, and they are even stand-alone system. Thus tide level is recorded on the paper chart at all tide gauge stations, and then hourly digital datasets are reproduced by reading the original charts. Therefore, both the original paper charts and the digital datasets are available. All paper charts belonging to Thai Marine Department are archived in Hydrology Branch in Bangkok, while those belonging to Royal Thai Navy are archived in Hydrographic Department in Bangkok either. All paper charts and digital datasets are not archived completely for the observation periods (Fig. 3).

The oldest tide gauge station has been established at Ta Phao Noi, in Phuket in 1940, however, tide gauge records in those days have not been found immediately, and hence we

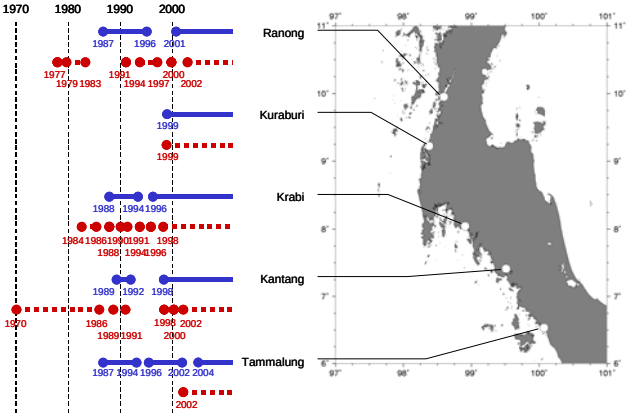

Figure 3 Tide gauge records' archives made by Thai Marine Department. Solid and broken lines respectively represent the paper charts and hourly digital datasets archived completely. Blank period indicate either paper broken, lost, not completely, or not recorded.

could not find tide gauge records during the M7.6 earthquake that took place near the Andaman Islands in 1941. Other tide gauges have been deployed since thelate 1960s.

Another tsunamigenic earthquake of M6.5 occurred in the northern Andaman Islands in 2002 (Fig. 1). However, no tsunami signal was recognized even in the original paper charts archived in Thai Marine Department. As a result, we could not collect tsunami records by the tide gauges in the 1900s. This means that catastrophic tsunami disasters had not been experienced before in Thailand. This might be a reason why tsunami warning system was not established before the 2004 Indian Ocean tsunami.

Seven tide gauges, which excluded Ao Tap Lamu were working during the 2004 Indian Ocean tsunami, and they recorded sea level change successfully as previously reported by Tsuji et al. (2006). We collected seven tide gauge records together with hourly digital datasets of five tide gauges by Thai Marine Department.

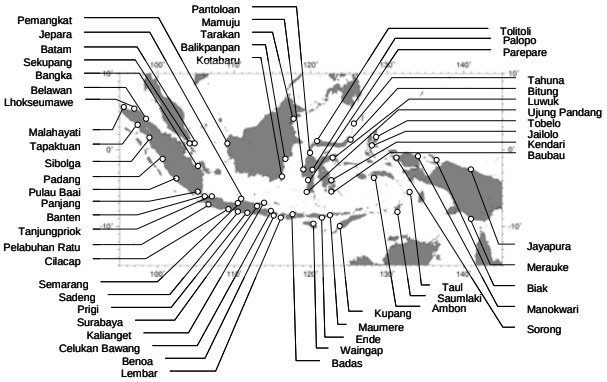

Figure 4 Locations of tide gauge stations in Indonesia. All stations are operated by BAKOSURTANAL. Some analog gauges use digital gauges simultaneously.

3.2 Indonesia

Figure 4 shows the locations of the Indonesian tide gauge stations. The first tide gauge was deployed in Cilacap in 1981. More than 50 tide gauges have been deployed in Indonesia, all of which are operated by the onlyinstitution, i.e., National Coordinating Agency for Surveys and Mapping (BAKOSURTANAL).

Although a dense tide gauge network has been established, most of them have been deployed after 1990. Digital gauges are used for newly deployed tide gauges after 1996, whereas the conventional analog gauges are still used. Digital real-time datasets of tide level are transmitted to BAKOSURTANAL from approximately 30 stations. The sample rate of the digital gauges ranges from 1 to 10 min.

Three tide gauge records at Sibolga, Belawan, and Lembar during the 2004 Indian Ocean tsunami could be collected in this study. Other tide gauge records at Panjang and Prigi are also available as reported elsewhere (Merrifield et al., 2005). More recently, these five tide gauges are re-digitized at 3 min intervals, and Rabinovich and Thomson (2007) compared with the previous records. None of tide gauge records except for Sibolga, Belawan, Lambar, Panjang, and Prigi are reported on the 2004 Indian Ocean tsunami in Indonesia. Additionally, historical tsunami records before the 2004 event could not be collected at all because most tide gauges were deployed in the recent years. Tanioka et al. (2006) used two tide gauge records of Sibolga and Belawan to constrain the rupture velocity of the 2004 Sumatra-Andaman earthquake. Their results suggest that the velocity of the fault rupturing is to be 1.7 km/s.

Although some tide gauges were working during the tsunamigenic earthquakes, their records could not be found even by the 1994 tsunami from the East Java earthquake of M7.8, causing heavy damage on the coast nearby (Tsuji et al., 1995). According to BAKOSURTANAL, tide gauge records obtained after 1996 are easily available. This is probably because the digital datasets are archived better than that by paper charts. Use of historical tsunami records by tide gauges in Indonesia would be somewhat difficult for tsunami study, such as constraining rupture velocities.

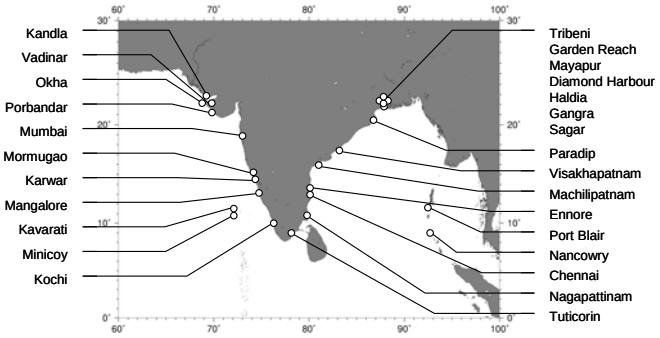

Figure 5 Tide gauge network in India operated by Survey of India, whereas each station is being maintained by National Institute of Oceanography.

3.3 India

Survey of India operates a tide gauge network in India (Fig. 5). Each tide gauge is maintained by National Institute of Oceanography. Tide gauge network consisting of approximately 30 stations covers not only the whole coast of India peninsula but also Andaman and Nicobar Islands. Most tide gauges record sea levels both by analog paper charts and digital datasets, and some tide gauges use pressure sensors at 5 to 6 min intervals in addition to the conventional float type gauges.

The first tide level measurement was carried out in the 1880s by tide gauges. Although not included in Fig. 1, tide gauges located along the Bay of Bengal recorded the tsunami generated in Andaman Islands earthquake (M7.9) in 1881, and they are used to constraint earthquake's source (e.g., Oritz and Bilham, 2003). Tide gauges in those days, however, were not operated continuously. The continuous datasets are archived afterwards, i.e., since 1940 in National Institute of Oceanography. Some historical tsunami records would be accessible in India after 1940.

Digital tide gauge records at Paradip, Visakhapatnam, Chennai, Tuticorin, Kochi, Mormugao, and Okha during the 2004 Indian Ocean tsunami are now available on the website of National Institute of Oceanography. Detailed information of the 2004 Indian Ocean tsunami obtained by tide gauge network of Survey of India is given by Nagarajan et al. (2006). Although those paper charts recorded the 2004 Indian Ocean tsunami, they are not available yet. However, we have confirmed that the first tsunami waveforms recorded in the original paper charts are comparable to the digital datasets on the website of National Institute of Oceanography.

3.4 Australia

Department for Planning and Infrastructure operates tide gauges and some ocean wave buoys along the western coast of Australia. In Australia, tide level measurement has been carried out since the early 1900s. Actually, paper charts of tide level measurement made in those days still exist, in which four times a day by visual tide level measurement were carried out. Tide level has instrumentally observed since the 1960s in order to manage

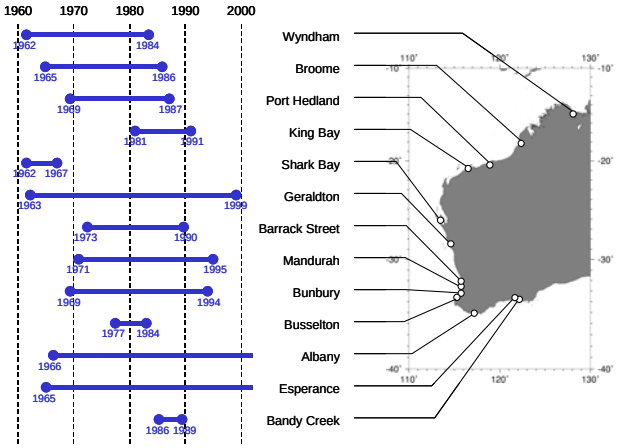

Figure 6 Locations of tide gauge stations in the western Australia, and the periods of their original paper chart archives. Note that currently other 13 tide gauge stations are being operated in addition to above stations.

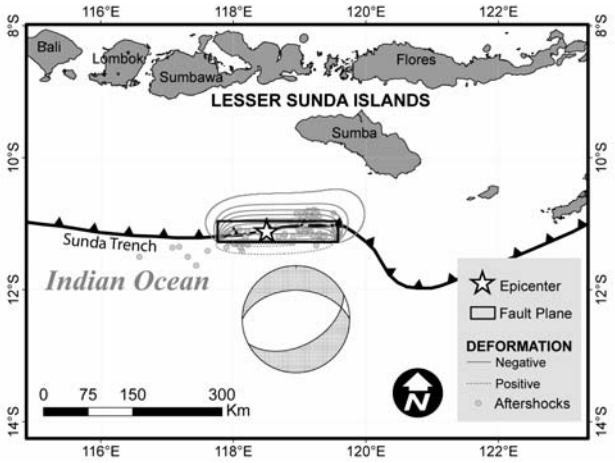

Figure 7 Tectonic setting near the source region of the 1977 Sumba earthquake. Rectangular shows the location of the fault we used for tsunami computation. The circles are aftershocks by USGS.

the ports and the harbors.

Figure 6 shows the location of the tide gauge stations in the western Australia, recorded by paper charts in the past, and their datasets archives. 26 tide gauges including the above 13 tide gauges are now operated in the western Australia. Historical tide gauge records are archived dating back the early 1960s in Department for Planning and Infrastructure (Fig. 6), and we can access them relatively easier than other countries. Hourly digital datasets are reproduced from the paper charts until the 1980s, and datasets of 5 to 15 min sample rates are reproduced in the 1990s. Analog tide gauges have been replaced by digital gauges from the 1980s to the 1990s. Now, all tide gauges use digital gauges, but two tide gauges at Albany and Esperance are still using analog gauges together with the digital gauges. Using digital gauges, tide levels by every 5 min are archived and sent to National Tidal Centre in Adelaide in addition to Department for Planning and Infrastructure in real-time.

As for the 2004 Indian Ocean tsunami, we collected both the paper charts and digital datasets at 5 min intervals at Albany and Esperance. Digital datasets by the other tide gauges along the western coast of Australia are also provided by Department for Planning and Infrastructure.

4. TSUNAMI COMPUTATION FOR THE 1977 SUMBA EARTHQUAKE

In this section, we introduce an example of tsunami computation due to the outer-rise earthquake. According to Fig. 1, the historical tsunamigenic earthquakes occurred near the western Australia in 1921, 1977, 1994, and 2000. Their magnitudes are 7.5, 8.0, 7.8, and 7.9, respectively. The tsunami in 1921 is too old to be instrumentally recorded. Because number of tide gauge records on paper charts is very few after 1990, no tsunami signals are noticed in the paper charts during both the 1994 and the more recent 2000 tsunamis. In the meantime, we have realized that the tsunami due to the 1977 earthquake that occurred off Sumba Island in Indonesia, among the others, affected the western Australia (Fig. 7). It is needless to say that this earthquake caused serious damages in Indonesia (Kato and Tsuji, 1995). Gregson et al. (1979) reported the detailed effects of seismic intensities and tsunami damages to the western Australia, and showed the most catastrophic tsunami disasters in the western Australia since 1900. We collected ten paper charts of tide gauges working during the 1977 earthquake, and found that, among them, tide gauge records further south of Geraldton and further east of Broome have small amplitudes for the tsunami study.

Literature that documented tsunami phenomenon experienced at the port of Dampier together with two tide gauge records at Dampier and Hampton both in King Bay reported by International Tsunami Information Center (1977) have been also found. Gusman et al. (2008) used both the tide gauge records at Dampier, Hampton and Port Hedland, and the eyewitness in order to resolve the seismic moment of the 1977 earthquake. Their result implies that the seismic moment estimated from the tsunamis is slightly smaller than that from the seismic waves. Also, they preliminarily reproduced the inundation area in Lunyuk on Sumba Island in Indonesia using their seismic fault model. Other tsunamis generated in the Indian Ocean are not so important to the western Australia during the era of analog tide gauges.

We introduce a slip amount of the 1977 Sumba earthquake estimated by fitting the observed tsunami records with the computed ones. In general, comparison of the amplitudes can be done by digitized the original marigram and removing the tide from the records. Because of the bad quality of the records as shown in Fig. 8, tsunami waves on the marigram cannot be digitized correctly. Therefore, we use scanned marigram for the comparison and try to fit the waves with adding the tide which calculated from the original marigram on the computed tsunami waves.

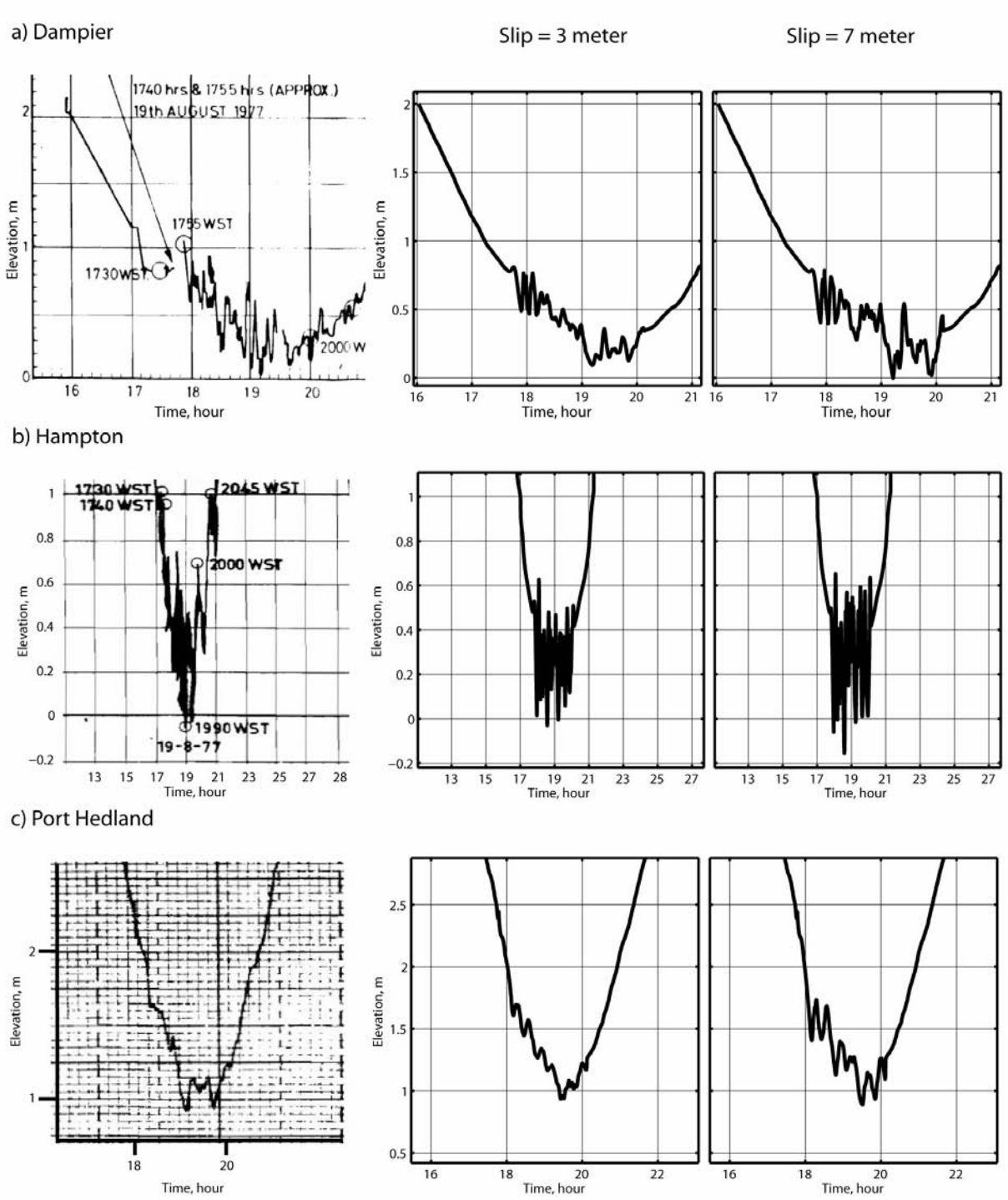

Figure 8 Comparison of recorded (left) with computed tsunamis (center and right) at Dampier, Hampton and Port Hedland for the 1977 Sumba earthquake using the slip amount of 3 m and 7 m on the fault model shown in Fig. 7.

Figure 8 shows the comparison of the observed and computed tsunami waveforms for the 1977 Sumba earthquake. The origin time of the earthquake is 06:08:54.8 UTC (14:08:54.8 WST) on 19 August 1977 (Lynnes and Lay, 1988). Tsunami computation shows that tsunami recorded at Hampton can be explained with slip amounts ranged from 3 to 7 m. Dampier and Hampton are located in a bay with a complex bathymetric feature with islands and shallow bathymetry. The computed tsunami at this location does not change significantly by the slip amounts. The tsunami computation result at Port Hedland which has a simpler bathymetric feature shows that only 3 meter slip amount can generates acceptable tsunami amplitude (Fig. 8c). Gusman et al. (2008) show the tsunami propagates for about 20 minutes before it hits Sumba Island. After the tsunami hits Sumba Island, the tsunami was reflected by the island and propagated to the west and south directions. The reflected tsunami wave which travels to the south may be one of the reasons why tide gauge records at Hampton and Dampier shows a high tsunami on its later phase (Fig. 8).

5. CONCLUSIONS

We reviewed historical tsunamis occurred in the Indian Ocean and tide gauge records' archives in Thailand, Indonesia, India, and Australia. Then, we tried to collect tide gauge's paper charts recording those tsunamis. Most tsunamis in the Indian Ocean were generated along the Sunda Trench. Tide gauges are traditionally designed based on float-type gauges with stilling well. Conventional paper charts are still used in Thailand. In Indonesia, most tide gauges have been deployed after the 1990s. This is the reason why no tsunami records in the near-field are left in Indonesia. In India, continuous tide gauge records have been archived since 1940. In Australia, tide gauge records are archived dating back to the 1960s. All gauges in the western Australia have replaced digital instruments by the end of the 1990s. Systematic collection of historical tsunami records by tide gauges in the Indian Ocean is somewhat difficult. This is partly because few historical tsunami events occurred in the Indian Ocean during instrumentally observation period in the 20th century. Numerous tide gauges have been distributed in the Indian Ocean in recent years. A dense tide level monitoring network possibly contributes to early tsunami warning system in the future.

We also carried out tsunami computation for the 1977 Sumba earthquake, which is well known as a tsunamigenic outer-rise earthquake. We estimated a slip amount of the seismic fault was to be 3 to 7 m in terms of the far-field tide gauge records. Thus, tide gauge records including tsunami signals provide us seismic source information, even full seismic records are not available.

Acknowledgements:

Most part related to tide gauge records' collection has been published elsewhere (Matsumoto et al., 2009), and the associated participants and their contribution to the work are as follows; S. Iwasaki, NIED has made the first contact with those organizations that operate tide gauges in the Indian Ocean. H. Matsumoto and T. Nakasu, NIED have collected tide gauge records in Thailand and Australia. Y. Tsuji, Y. Namegaya, both of Univ. Tokyo and Y. Nishimura, Hokkaido Univ. have summarized tide gauge records in Indonesia. Y. Tanioka and Y. Nishimura have been in charge of those in India. We are grateful to Suriya Tarepakdee, Thai Marine Department, Komsan Klinsukon, Royal Thai Navy, both of Thailand, Parluhutan Maurung, National Coordinating Agency for Survey and Mapping, Indonesia, Satheesh C. Shenoi, National Institute of Oceanography, India, and Tony Lamberto, Department for Planning and Infrastructure, Australia for their support to collect tide gauge records. Some information regarding historical tsunamis in the Indian Ocean are provided by Laura Kong, International Tsunami Information Center. Details of our tsunami computation will be given by Gusman et al. (submitted to *Bull. Sesim. Soc. Am.*) in the near future.

References:

Anonymous (1945), "News and views, Earthquake in the Arabian Sea", *Nature*, **156**, 712-713, 1945.

SEAN Bulletin (1983), *Smithsonian Institute SEAN Bulletin*, **8**, 16-17.

Beer A. and Stagg, J. M. (1946), "Sesmic Sea-Wave of November 27, 1945", *Nature*, **157**, 63.

Berninghausen, W. H. (1966), "Tsunamis and seismic seiches reported from regeions adjacent to the Indian Ocean", *Bull. Seism. Soc. Am.*, **56**, 69-74.

Gregson, P. J., Paull, E. P., and Gaull, B. A. (1979), "The effects in Western Australia of a major earthquake in Indonesia on 19 August 1977", *BMR J. Australian Geology Geophys.*, **4**, 135-140.

Gusman, A., Tanioka, Y., Matsumoto, H., and S. Iwasaki (2008), "Analysis of Tsunami Generated by the Great 1977 Sumba earthquake occurred in Indonesia", *Abst. 5th Ann. Meeting AOGS 2008*, SE81-D5-AM1-102-004.

International Tsunami Information Center (ITIC) (1978), Tsunami Reports, 1977-12.

Kato, K. and Tsuji, Y. (1995), "Tsunami of the Sumba earthquake of August 19, 1977", *J. Natural Disaster Sci.*, **17**, 87-100.

Lynnes C. and Lay, T. (1988), "Source process of the Great Sumba Earthquake". *J. Geophys. Res.*, **93**, 13407-14320.

Merrifield, M. A., Firing, Y. L., Aarup, T., Agricole, W., Brundrit, G., Chang-Seng, D., Farre, R., Kilonsky, B., Knight, W, Kong, L., Magori, C., Manurung, P., McCreery C., Mitchell, W., Pillay, S., Schindele, F., Shillington, F., Testut, L., Wijeratne, E. M. S., Galdwell, P., Jardin, J., Nakahara S., Porter F. Y., and Tuetsky, N. (2005), "Tide gauge observations of the Indian Ocean tsunami, December 26, 2004", *Geophys. Res. Lett.*, **32**, L09603, doi:10.1029/2005GL022610.

Matsumoto H., Tanioka, Y., Nishimura, Y., Tsuji, Y., Namegaya, Y., Nakasu, T., and Iwasaki, S. (2009), Review of tide gauge records in the Indian Ocean, *J. Earthquakes Tsunamis*, in press.

Nagarajan, B, Suresh, I., Sundar, D., Sharma, R., Lal, A. K., Neetu, S., Shenoi, S. C., Shtye, S. R., and Shankar, D. (2006), "The great tsunami of 26 December 2004: A description based on tide-gauge data from the Indian subcontinent and surrounding areas", *Earth Planets Space*, **58**, 211-215.

National Geophysical Data Center (NGDC), NOAA Satellite and Information Service, http://www.ngdc.noaa.gov/ngdc.html

Oritz, M. and Bilham, R. (2003), "Source area and rupture parameters of the 31 December 1881 Mw=7.9 Car Nicobar earthquake estimated form tsunamis recorded in the Bay of Bengal", *J. Geophys. Res.*, **108**, 2215, doi:10.1029/2002JB001941.

Rabinovich, A. B., and Thomson, R. E. (2007), "The 26 December 2004 Sumatra tsunami: Analysis of tide gauge data from the world ocean part 1. Indian Ocean and South Africa", *Pure Appl. Geophys.*, **164**, 261-301.

Tanioka, Y., Yudhicara, Kusunose, T., Kathiroli, S., Nishimura, Y., Iwasaki, S., and Satake, K. (2006), "Rupture process of the 2004 great Sumatra-Andaman earthquake estimated from tsunami waveforms", *Earth Planets Space*, **58**, 203-209.

Tsuji, Y., Imamura, F., Matsutomi, H., Synolakis, C. E., Nanang, P. T., Jumadi, Harada, S., Han, S. S., Arai, K., and Cook, B. (1995), "Field survey of the East Java earthquake and tsunami of June 3, 1994", *Pure Appl. Geophys.*, **144**, 839-854.

Tsuji, Y., Namegaya, Y., Matsumoto, H., Iwasaki, S., Kanbua, W., Sriwichai, M., and Meesuk, V. (2006), "The 2004 Indian tsunami in Thailand: Surveyed runup heights and tide gauge records", *Earth Planets Space*, **58**, 223-232.

Sixth International Conference on Urban Earthquake Engineering
March 3-4, 2009, Tokyo Institute of Technology, Tokyo, Japan

DYNAMIC RESPONSE ANALYSIS OF ROAD BRIDGES STRUCK BY TSUNAMI

KATAOKA Shojiro[1)]

1) Senior Researcher, National Institute for Land and Infrastructure Management, Japan
kataoka-s92rc@nilim.go.jp

Abstract: Though road bridges in Japan are not required to withstand tsunami strike by the design specifications, tsunamis may damage road bridges as seen during the 2004 Indian Ocean tsunami. In this study, dynamic analyses are carried out in order to understand the response of road bridges subjected to tsunami force. The time history waveforms of tsunami force are obtained by filtering and scaling the tsunami force recorded in the wave-channel experiments. The road bridge designed by the current specifications withstands 7m-high tsunami even though the wave is breaking but is washed out by 11m-high tsunami.

1. INTRODUCTION

Bridges may be damaged when tsunami strikes as seen during the 2004 Indian Ocean tsunami. Road bridges in Japan, however, are not required to withstand tsunami strike by the design specifications (Japan Road Association, 2002). Although no modern road bridges in Japan have been damaged by tsunami, we need to understand the tsunami force acts on bridges and their response in order to examine whether we should settle on the design specification for tsunami.

First, we conducted a series of experiment using a wave channel and bridge girder models to investigate wave force acts on a bridge girder struck by tsunami (Kataoka *et al.*, 2006; Kataoka, 2007). Time history waveforms of the observed wave force consist of impulsive force with short duration and drag that slowly decreases. The peak of the impulsive force was found to depend on whether the wave is breaking.

In this study, dynamic response analyses of road bridges are carried out. The time history waveforms of the wave force recorded during the experiment are modified and used as external forces in the analyses.

2. WAVEFORMS OF TSUNAMI FORCE

2.1 Wave Channel Experiment

We conducted a series of experiments using a wave channel and bridge girder models to investigate wave force acting on a bridge girder struck by a tsunami (Kataoka *et al.*, 2006; Kataoka, 2007). The experimental setup of one of the bridge girder models in the wave channel is shown in Figure 1. The wave channel is 140m long, 2m wide, and 5m deep. A fixed bed slope had been constructed and the bridge girder model, which is made of metal, was installed on the slope. As shown in Table 1, 15 combinations of still water level, h, and initial wave height, H_0, of solitary wave were set and the experiment with each combination was executed three times.

Table 1 Still water level, h, set for each initial wave height, H_0.

H_0 [cm]	h [cm]
20	15, 30
30	7.5, 10, 12.5, 15, 30
40	7.5, 10, 12.5, 15, 17.5, 20, 22.5, 30

Photo 1: Solitary wave striking the bridge girder model (H_0 = 40cm, h = 17.5cm).

Photo 1 shows the moment when the horizontal force acting on the bridge girder reached the peak during the experiment with H_0=40[cm] and h=17.5[cm]. The solitary wave was breaking at this moment and hence the peak of both horizontal and vertical forces with this combination of H_0 and h were the largest among all combinations (Figure 2). The time history waveforms of horizontal and vertical wave forces during the experiment with H_0 =40[cm] and h=17.5[cm] are shown in Figure 3.

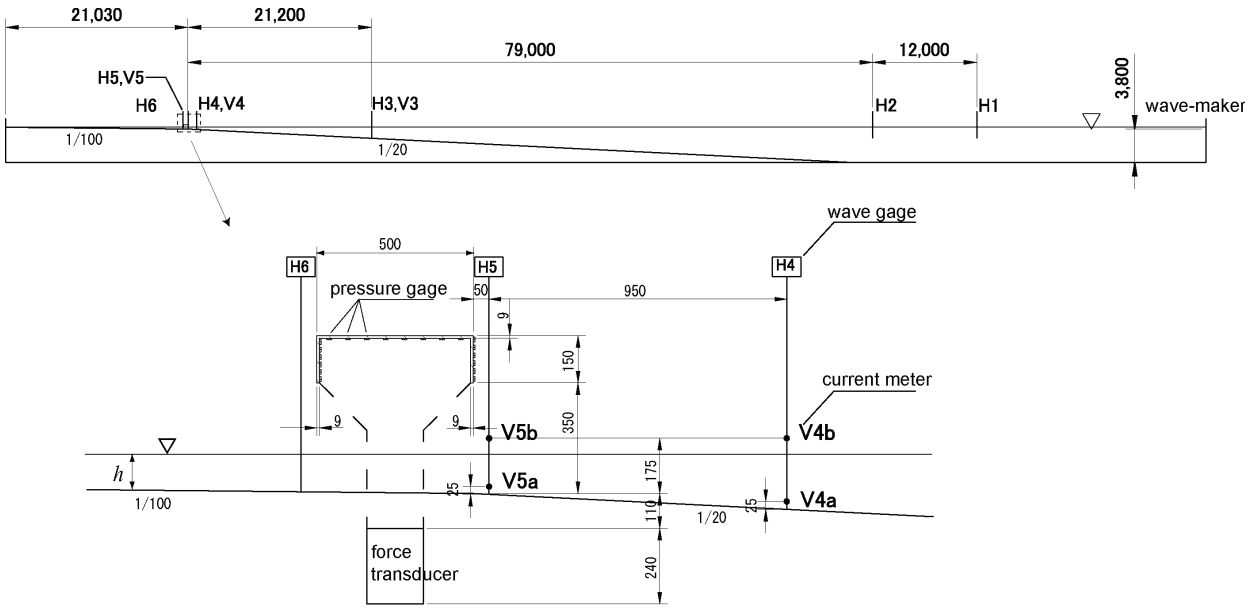

Figure 1: Experimental setup of a bridge girder model in the wave channel (unit: mm).

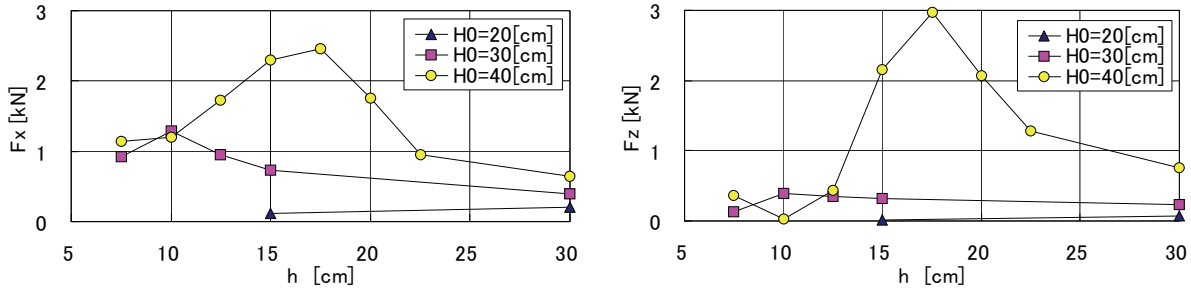

(a) Horizontal force (b) Vertical force

Figure 2 Peak wave forces measured from the experiment using 50cm-wide bridge girder model.

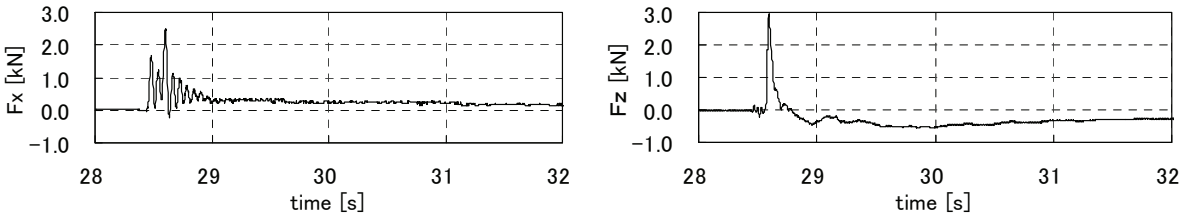

(a) Horizontal force (b) Vertical force

Figure 3: Time history waveforms of wave force on the bridge girder model (H_0 = 40cm, h = 17.5cm).

2.2 Modifying the Waveforms

The waveforms of the horizontal force obtained from the experiments show short period component, such as shown in Figure 3 (a). We checked the time history of wave pressure observed by the pressure gages and found that the solitary wave hit the ocean-side of the girder and then hit the land-side with time interval of 0.14[s]. This gives the predominant frequency of about 7[Hz] to the Fourier amplitude spectrum of the time history waveform of wave force as shown in Figure 4. The predominant frequency of about 16[Hz] is considered to be generated by a free oscillation of the system consists of the bridge model and the force transducer. Thus, a high-cut filter that eliminates the component with 12.5[Hz] or higher frequency was applied to the waveforms.

Since the scale of the experimental model is 1/18, the water pressure and the time of the filtered waveforms are multiplied by 18 and $18^{0.5}$, respectively, in order to convert them into full-size according to the Froude's similarity law. The waveforms of tsunami force used in the dynamic response analyses of a road bridge are thus obtained as shown in Figure 5. Figures (a) and (b) correspond to the tsunamis that strike a bridge while breaking and wave heights are 11[m] and 7[m], respectively.

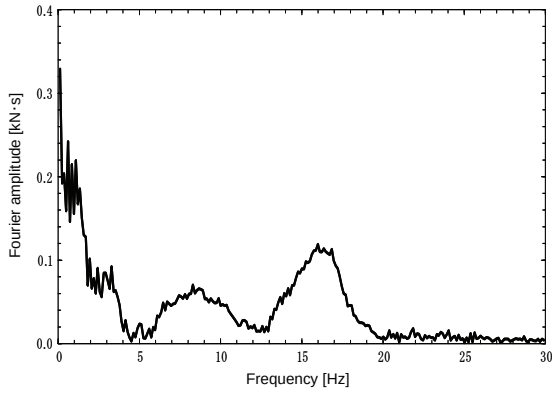

Figure 4 Fourier amplitude spectrum of the time history waveform of wave force shown in Figure 3 (a).

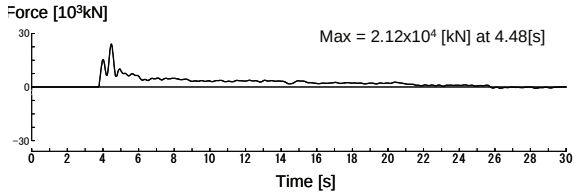

(a) H_0 = 40cm, h = 17.5cm

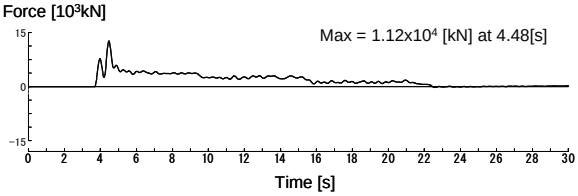

(b) H_0 = 30cm, h = 10cm

Figure 5 Waveforms of tsunami force used in the dynamic response analyses.

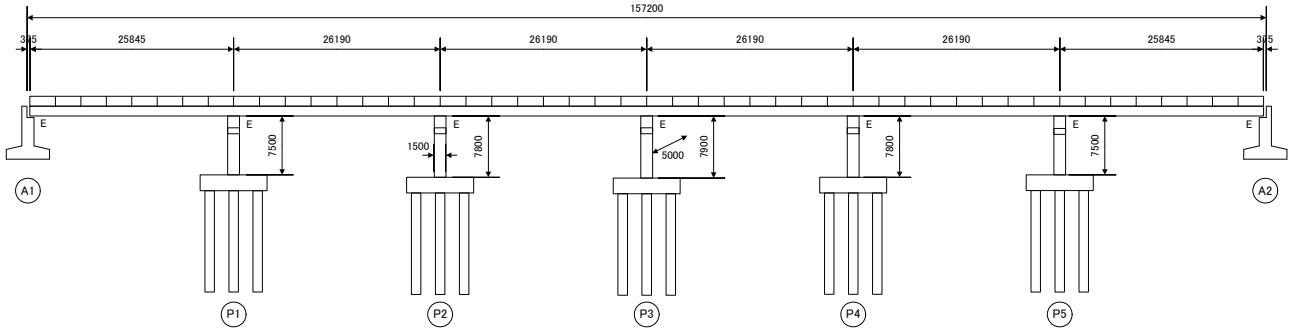

Figure 6 Side view of a road bridge of which section includes P3 is modeled as an SDOF system.

3. DYNAMIC RESPONSE ANALYSES

3.1 Analytical Model

A section includes P3 of the road bridge (Figure 6) is modeled as an SDOF system as shown in Figure 7. The road bridge was designed to satisfy the current specifications (Japan Road Association, 2002). The yield stiffness of P3, I_y=5.70[m^4], was used as the stiffness of the SDOF system because road bridges struck by tsunami are supposed to be subjected to strong ground shaking before tsunami. Tsunami waveforms shown in Figure 5 are directly applied to the mass.

Figure 8 shows P-δ relationships of anchor bars and rubber bearings. The anchor bars are designed for ductility factor μ=3 and the ultimate strength of 20 anchor bars is total of 9,785[kN]. The ultimate strength, which is set to be the strength at 400% strain, of rubber bearings become 25,171[kN]. After the anchor bars and rubber bearings are both broken, only frictional force remains between the pier and the girder. The friction coefficient is assumed 0.6 (Rabbat and Russel, 1985).

3.2 Results

Figure 9 shows the time history of response displacement and acceleration of the mass that models on the girder. Figure (a) shows large response acceleration

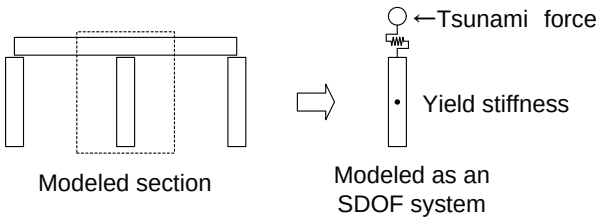

Figure 7 Modeling an SDOF system subjected to the tsunami force.

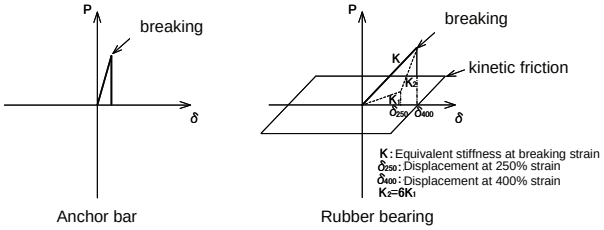

Figure 8 P-δ relationships of anchor bars and rubber bearings.

that reaches almost 5[g]. Both of the anchor bars and the rubber bearings are broken and then the girder is washed out by tsunami. Figure (b) also shows large response acceleration and the anchor bars are broken. But the girder is not washed out because the peak reaction of the rubber

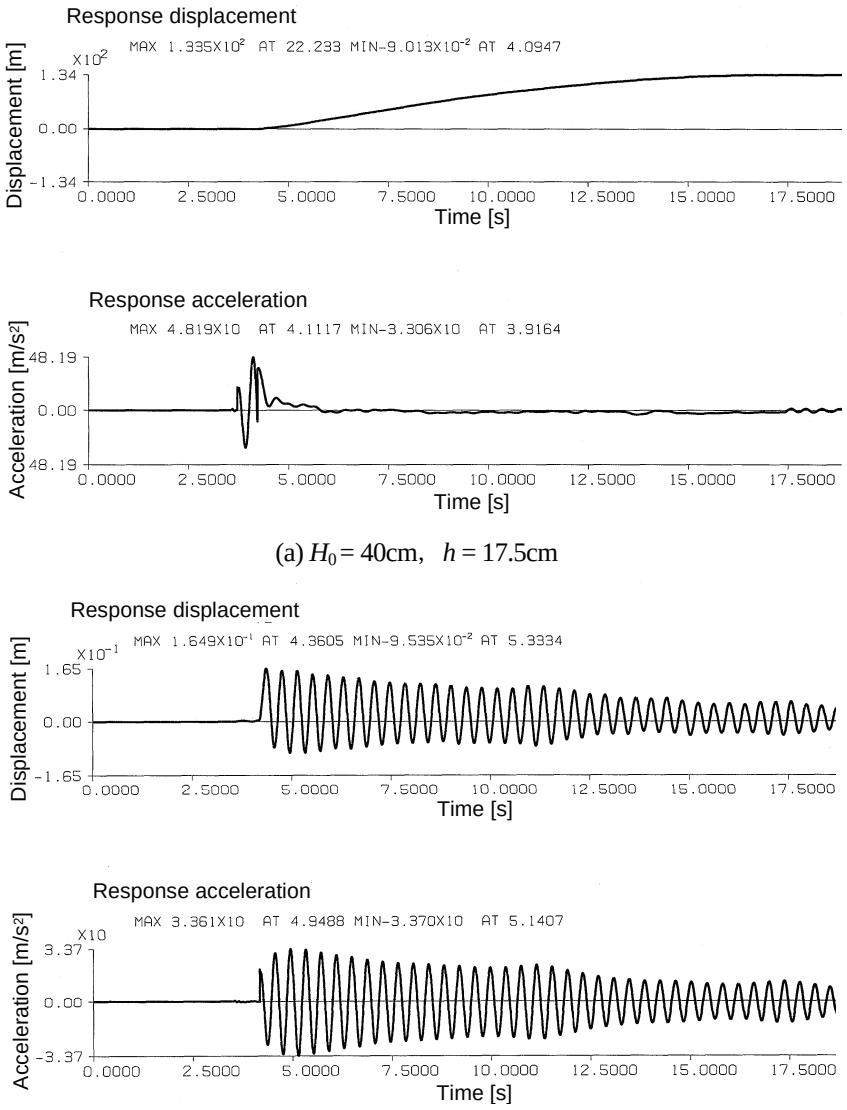

(a) H_0 = 40cm, h = 17.5cm

(b) H_0 = 30cm, h = 10cm

Figure 9 Time history of response displacement and acceleration of the girder obtained from the dynamic response analyses of the SDOF system.

bearings, 20,280[kN], remains smaller than the ultimate strength mentioned above.

4. CONCLUSIONS

Dynamic analyses are carried out in order to understand the response of road bridges subjected to tsunami force. The time history waveforms of tsunami force used in the analyses are obtained by filtering and scaling the tsunami force recorded in the wave-channel experiments. The road bridge designed by the current specifications withstands 7m-high tsunami even though the wave is breaking but is washed out by 11m-high tsunami. Further investigations including the effects of fallen prevention and displacement restriction devices are necessary to examine whether we should settle on the design specification for tsunami.

References:

Japan Road Association (2002), "Specifications for highway bridges", .Maruzen Co. Ltd.

Kataoka, S., Kusakabe, T. and Nagaya, K. (2006), " Wave force acts on a bridge girder struck by tsunami", *12th Japan Earthquake Engineering Symposium*, 154-157.

Kataoka, S. (2007), "A scenario of earthquake-tsunami disaster and a policy of measures for road networks", *4th International Conference on Urban Earthquake Engineering*, 467-474.

Rabbat, B. G. and Russell, H. G. (1985), "Friction coefficient of steel on concrete or grout", *J. Struct. Eng.*, ASCE, **111**(3), 505–515.

Sixth International Conference on Urban Earthquake Engineering
March 3-4, 2009, Tokyo Institute of Technology, Tokyo, Japan

NEAR FIELD TSUNAMI EXCITED BY THE 2003 TOKACHI-OKI EARTHQUAKE

Shusaku Inoue[1], Tatsuo Ohmachi[2], and Tetsuji Imai[3]

1) Research Associate, Department of Built Environment, Tokyo Institute of Technology, Japan
2) Professor, Department of Built Environment, Tokyo Institute of Technology, Japan
3) Graduate Student, Department of Built Environment, Tokyo Institute of Technology, Japan
shusaku@enveng.titech.ac.jp, ohmachi@enveng.titech.ac.jp, imai.t.ab@m.titech.ac.jp

Abstract: The 2003 Tokachi-oki earthquake (M_J 8.0) occurred off the southeastern coast of Tokachi, Japan, and excited a large tsunami which arrived at Tokachi Harbor at 04:56 with a wave height of 4.3 m. Japan Marine Science and Technology Center (JAMSTEC) recorded water pressures and sea-bed accelerations at the bottom of the tsunami source region. The records provide valuable information about characteristics of a near field tsunami and its source. We first introduce these records and results derived from Fourier analysis and band-pass filter analysis of them. Water pressure disturbances last for over 30 minutes and the durations are longer than those of accelerations. One of the predominant periods of the pressures is revealed to be excited by Rayleigh wave. Next, we conduct tsunami simulation to investigate whether our dynamic tsunami simulation technique can represent generation and propagation of Rayleigh wave and tsunami. The result confirmed usefulness of this technique to the near field tsunami.

1. INTRODUCTION

About a decade ago, the dynamic tsunami simulation technique was developed by Ohmachi et al. (2001a) to simulate the generation of tsunamis followed by their propagation, where not only the dynamic displacement of the seabed induced by seismic faulting but also the acoustic effects of the seawater are taken into account. As the dynamic technique assumes weak coupling between the seabed and the seawater, the simulation consists of a two-step analysis. The first step is the dynamic seabed displacement resulting from a seismic faulting, and the second is the seawater disturbance induced by the dynamic seabed displacement. For the first step, the boundary element method (BEM) is used and, for the second step, the finite difference method (FDM) is used to solve the Navier-Stokes equation. A series of dynamic tsunami simulations have demonstrated that in the near-fault area there are some significant features that are water compressibility and short period sea surface disturbances which are mainly excited by Rayleigh waves.

Although most of these findings look quite reasonable, they have to be verified by observed data (Ohmachi et al. 2001b). Hence, in this paper the data obtained by JAMSTEC (Japan Marine Science and Technology Center) for the 2003 Tokachi-oki earthquake and the dynamic tsunami simulation are used in the verification of the findings mentioned above.

2. THE 2003 TOKACHI-OKI EARTHQUAKE AND OFFSHORE MONITORING SYSTEM

The interplate 2003 Tokachi-oki earthquake of JMA magnitude (M_J) 8.0 occurred off the southeastern coast of Tokachi at 04:50 on September 26, 2003. It was reported that the tsunami arrived at Tokachi Harbor at 04:56 with a wave height of 4.3 m, while the Japanese nation-wide coastal wave observation network (NOWPHAS) located on the 23m-deep seabed off Ohtsu Harbor recorded the first tsunami arrival at 04:51 (Nagai and Ogawa 2004). The locations of these harbors and the epicenter of the

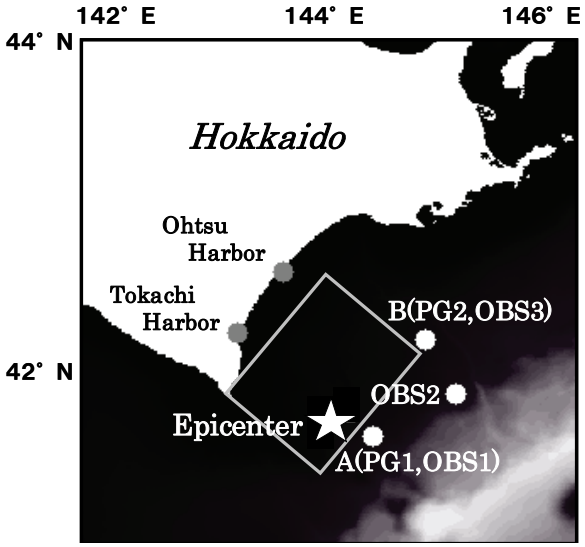

Figure 1 Locations of the JAMSTEC monitoring system equipment and epicenter of the 2003 Tokachi-oki earthquake.

Table 1 The JAMSTEC offshore monitoring system and water depth of equipment.

Equipment of the system		Depth (m)	Recorded data
Cable-end Station (DSO)		2,540	Flow velocity
			Velocity according to layer
			Hydrophone
A	Seismometer (OBS1)	2,329	Ground motion acceleration
			Hydrophone
	Tsunami Sensor (PG1)	2,218	Water-Pressure
Seismometer (OBS2)		3,428	Ground motion acceleration
			Hydrophone
B	Seismometer (OBS3)	2,124	Ground motion acceleration
			Hydrophone
	Tsunami Sensor (PG2)	2,210	Water-Pressure

earthquake are shown in Figure 1, where the location of an offshore monitoring system deployed by JAMSTEC is also shown. The system is equipped with three broadband tri-component seismometers (OBS1-3) and two high-precision pressure gauges (PG1-2). The distances between OBS1 and PG1 and between OBS3 and PG2 are rather short; that is, 4.0 km and 3.4 km, respectively. Thus, as shown in Figure 1, the locations where these pairs of instruments are installed are respectively referred to as St. A and St. B, and the distance between these two stations is about 72 km. In Figure 1, the hypocenter of the main shock and a fault model dipping northwest are shown by a star and a rectangle (Koketsu et al. 2004). Sampling rates of the pressure gauges and seismometers are 1 Hz and 100 Hz, respectively. Table 1 shows details of the offshore monitoring system and seawater depth of each sensor (JAMSTEC 2009).

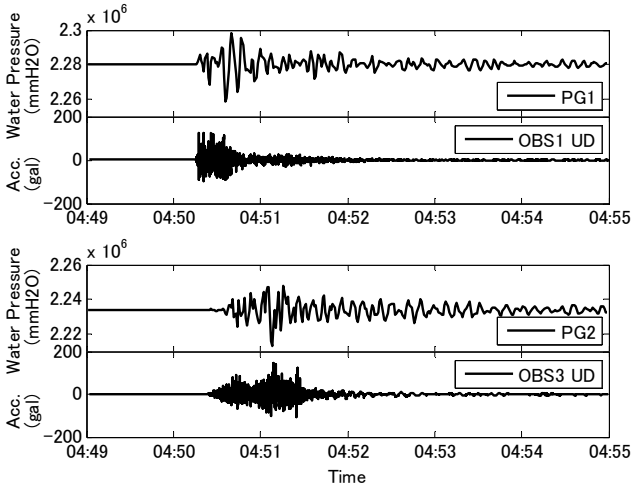

Figure 2 Time histories of water pressure and vertical ground motion acceleration.

3. TSUNAMI GENERATION PROCESS INFERRED FROM OBSERVED DATA

Time histories of water pressure and ground motion acceleration (vertical component) at St. A and St. B are shown in Figure 2. At both stations, the water pressure change lasted longer than the ground motion acceleration.

Fourier spectra of the time histories are shown in Figure 3. Peak periods of 7.0 s at St. A and 6.5 s at St. B are observed for both water pressure and ground motion acceleration, and each period T can be approximated by T=4H/c, where H is the seawater depth (2.2 - 2.3 km) and c is the acoustic wave velocity of water (1.5 km/s). Hence, these periods are thought to correspond to the acoustic waves traveling between the sea bottom and sea surface (Nosov et al.2005).

Time histories of the water pressure change shown in Figure 2 consist of many short period components with amplitudes several times larger than the tsunami-induced water pressure. When the components with period less than 50 s are filtered out, the water pressure time histories are indicated by the gray curves in Figure 4. It is evident from the gray curves that, after the main shock, the base-line of

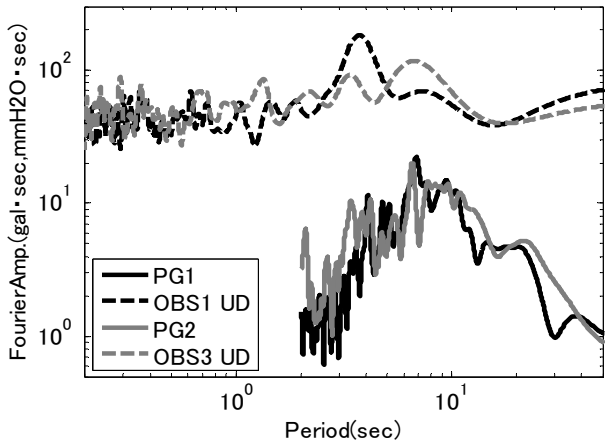

Figure 3 Fourier spectra of time histories shown in Figure 2.

the water pressure shifted by about 40 cm at PG1 and about 10 cm at PG2 in terms of the water depth. These base-line shifts were supposedly caused by the uplift of the seabed resulting from the seismic faulting (Watanabe et al. 2004).

In addition, the gray curves in Figure 4 indicate two important features. First, a generated tsunami was detected

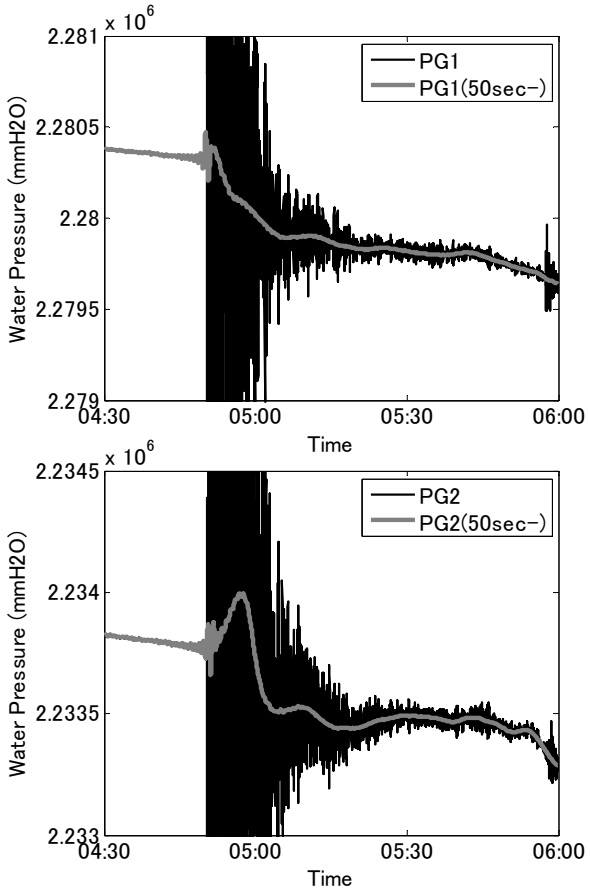

Figure 4 Time histories of water pressure after long-pass filtering of 50 s.

with different shapes. At PG2, the tsunami is clearly observed as a solitary wave with a height of about 20 cm and a period of 15 min. At PG1, the wave height and the period of the recently generated tsunami are not as clear as that of PG2, but only a gentle slope can be observed. The difference in the shape of the tsunami is probably due to the difference in the relative location between the observation stations and the tsunami source. As shown in Figure 1, PG1 is located very close to or just above the seismic fault, while PG2 is located a little apart from the fault and about 72 km away from PG1. Second, another group of water waves preceding the tsunami are seen at the beginning of the short-period water pressure change, and are referred to as preceding waves.

4. WATER WAVES INDUCED BY RAYLEIGH WAVES

Fourier spectra of the 3-component ground motion acceleration and water pressure at St. A and St. B are shown in Figure 5. For both St. A and St. B, the spectrum of the NS component has a similarity with that of the UD component, but not with the ED component. This similarity implies that seismic ground motions in the NS-UD plane are coupled with each other and that the motion has a kind of the so-called directivity or directionality. In addition, according

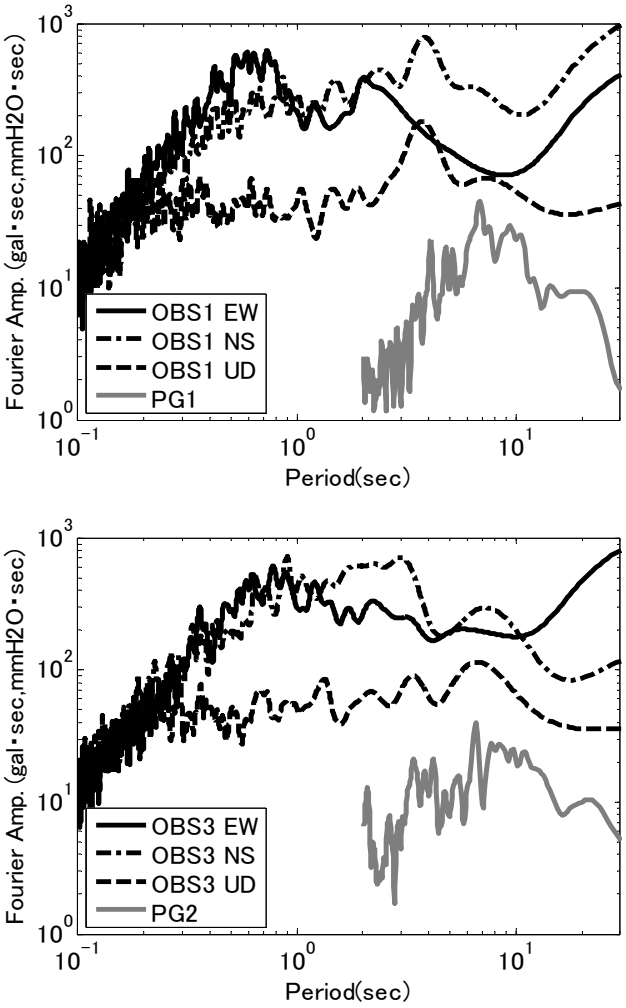

Figure 5 Fourier spectra of three-component ground motion acceleration and water pressure at St. A (top) and at St. B (bottom) .

to Figure 5, for the period ranging from 3 s to 15 s, both ground motion and water pressure are relatively large in amplitude.

A band-pass filtering between 3 s and 15 s is applied to the original time histories of water pressure and vertical ground motion displacement at St. A and St. B and the result is shown in Figure 6. From Figure 6, it can be seen that the water pressure change in this period range shows the largest amplitude at almost the same time or a little later when the seabed displacement shows one or two large amplitudes at an initial state of the earthquake motion. Figure 7 shows the particle orbit of the ground motion displacement plotted in the NS-UD plane during 4:50:20 and 4:50:40. During the 20 s, the particle orbit had an elliptic and retrograde motion in the NS-UD vertical plane.

Figure 8 illustrates ground displacements of UD component at K-net stations, which are calculated by integration of ground acceleration observed. Large amplitude first occurred southeast of Hokkaido at about 20 s after the earthquake occurrence and propagated in northwestern direction. Two crests of the wave can be seen,

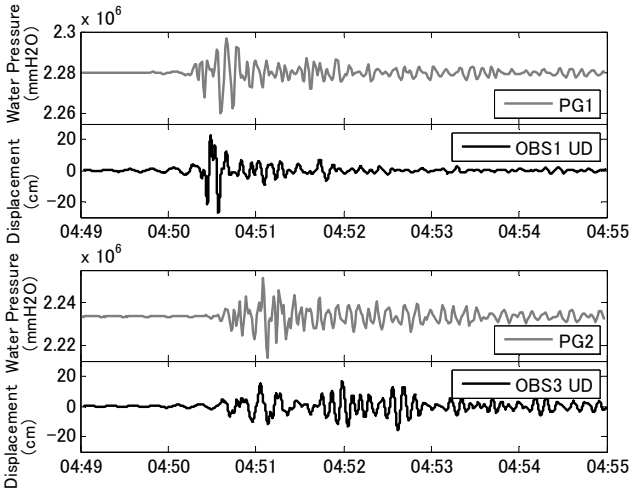

Figure 6 Time histories of water pressure and vertical ground motion displacement after band-pass filtering of 3-15 s

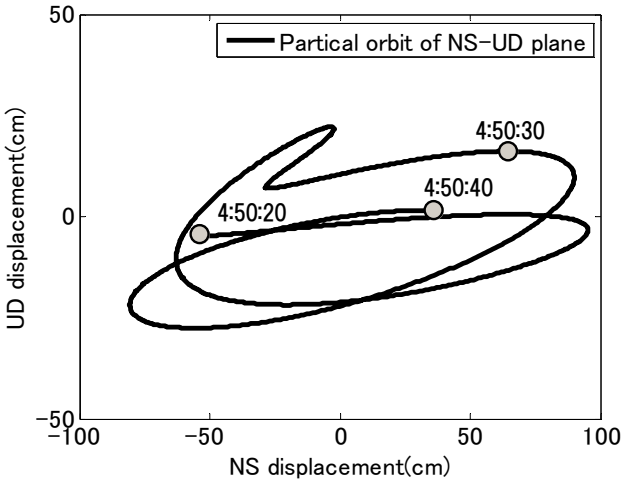

Figure 7 Particle orbit of ground motion displacement at OBS1 during 04:50:20 and 04:50:40.

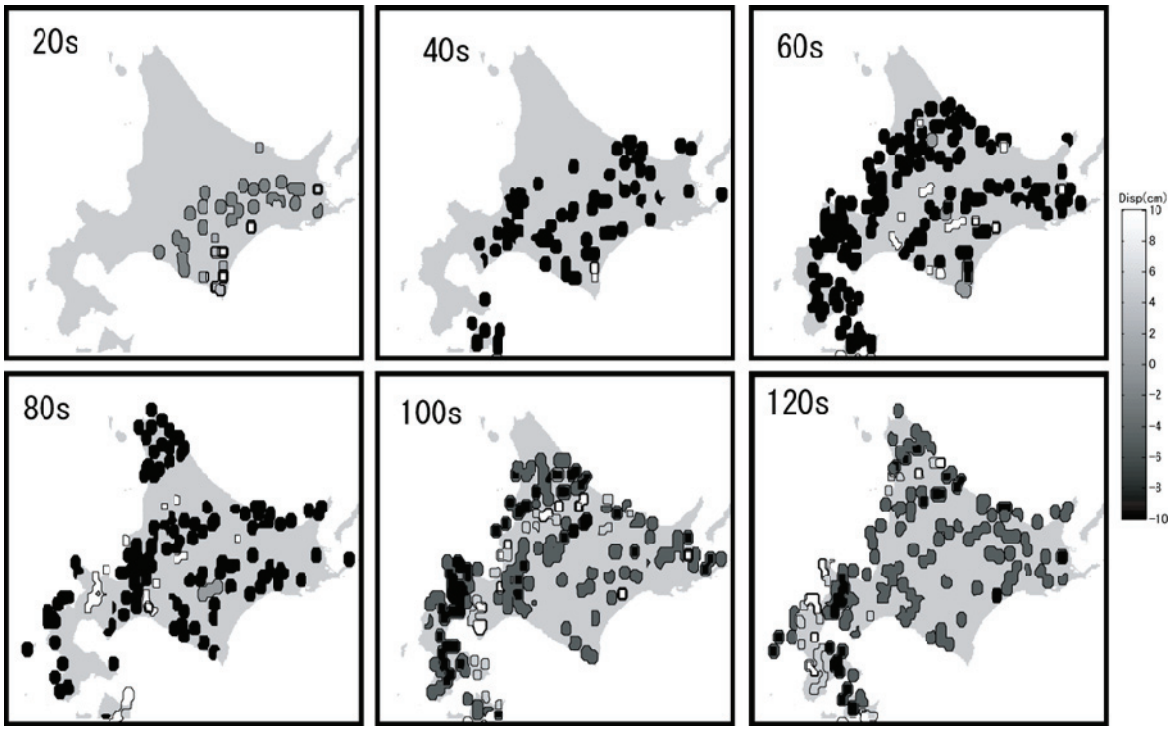

Figure 8 Observed ground displacement of UD-component at K-net.

and these waves can be considered Rayleigh waves propagating from the fault. The distance between the crests is about 100 km. Wave velocity is about 3.5 km/s.

From these features of the earthquake ground motion such as the directivity, an elliptic motion on a vertical plane and the predominant period, it seems reasonable to postulate that the water waves observed in the water pressure preceding the recently generated tsunami was induced by Rayleigh waves, as had been predicted from the dynamic tsunami simulation previously.

6. TSUNAMI SIMULATION

A fault model proposed by Koketsu et el. 2004 which was based on strong dynamic motion and permanent displacement is adopted in this simulation. The fault projection and the calculation area of the ground motion simulation are shown in Figure 9. The area is 250 km long in the NS direction and 350 km wide in the EW directions. The grid size for the seabed and water layer is 5km and 1km, respectively. First rupturing starts at the southeastern edge

and develops in the northwestern direction with velocity of 3km/s. The total duration time of the fault rupturing is about 30sec.

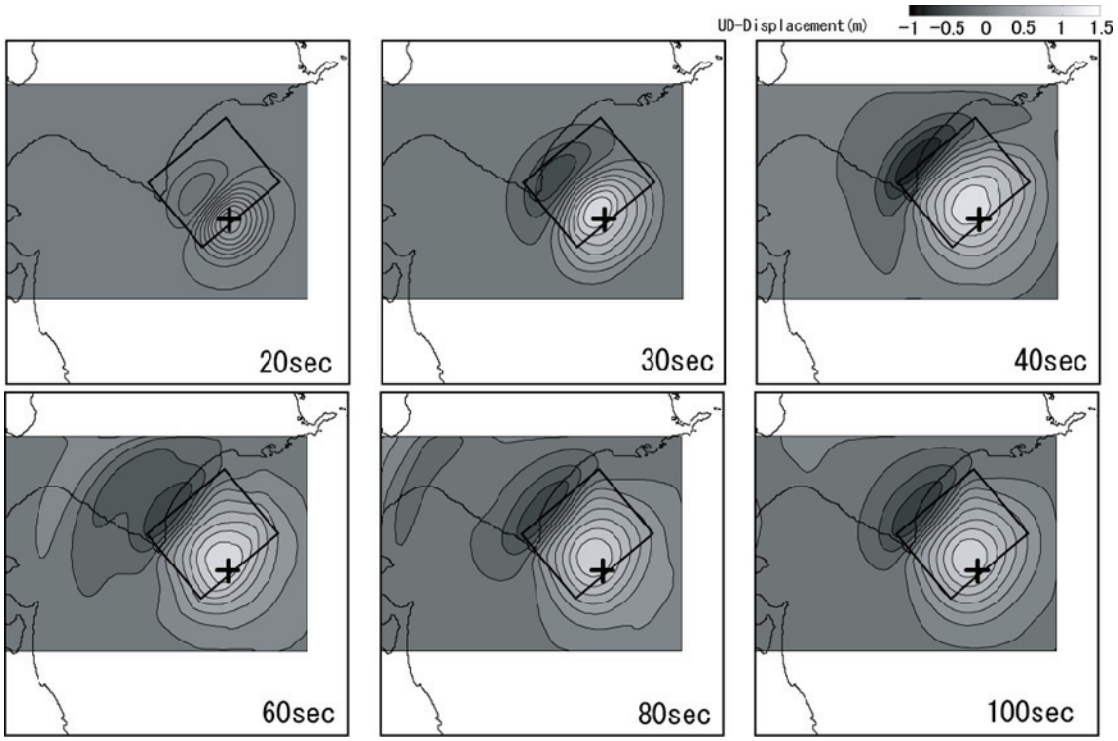

Figure 10 Contour map of simulated vertical displacement of ground and sea-bed.

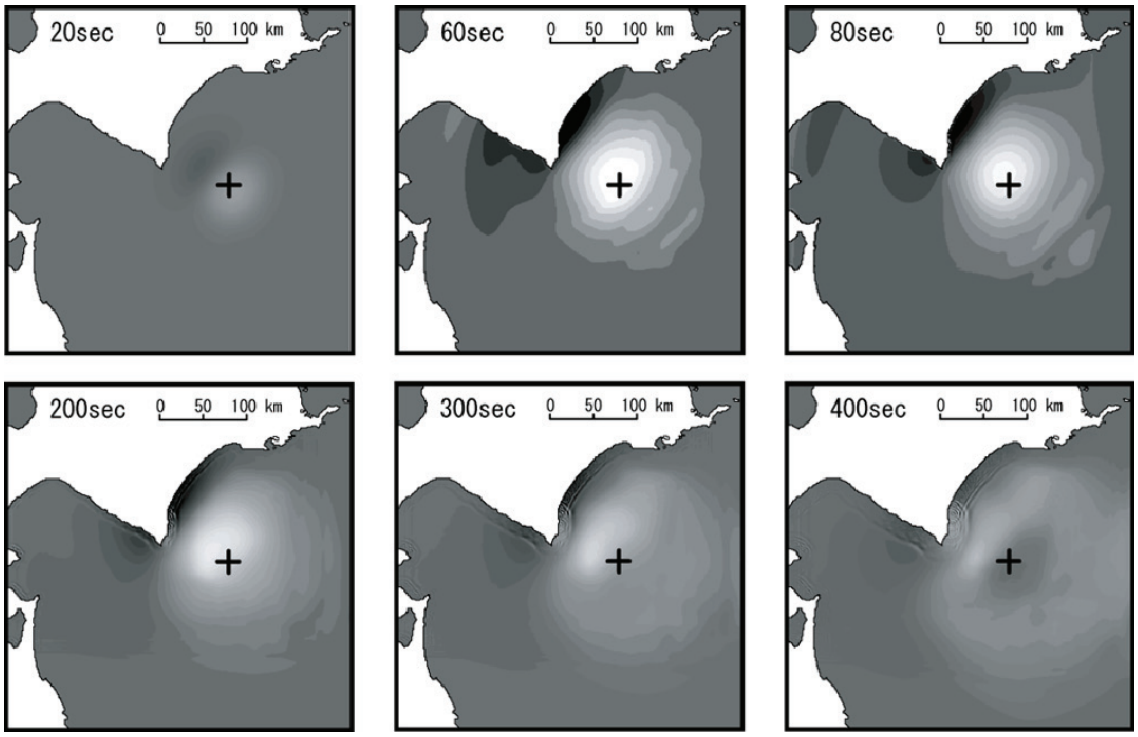

Figure 11 Snapshots of simulated water level.

Snapshots in Figure 10 and 11 show the simulation results of the ground motion at 20, 30, 40, 60, 80 and 100s and tsunami at 20, 60, 80, 200, 300 and 400s after the fault rupturing. At 20s the fault rupturing progresses up to middle of the fault plane. From 60s to 80s, the water wave induced by the Rayleigh wave propagates to the Northwest. At 80s when the fault rupture finishes, static uplift and subsidence

remain in the near-fault area, and the tsunami profile is almost the same as that of the static displacement of the seabed.

The dynamic analysis can demonstrate not only the process of tsunami generation but also water wave induced by the Rayleigh wave. Actually, before arrival of the first tsunami, the sea surface disturbance was observed in actual records shown in previous sections.

5. CONCLUSIONS

Analysis of the JAMSTEC monitoring data have shown that three kinds of water waves were involved in the dynamic tsunami generation process following the 2003 Tokachi-oki earthquake; that is, water pressure waves of short period, a tsunami of long period, and preceding waves of intermediate period.

As for the tsunami of long period, two types of recently generated tsunamis were detected by the water pressure gauges. One was a solitary wave with a height of about 20 cm and a period of 15 min, and the other had a gentle slope and its wave height and period were not as clear as the first type. The first type was detected at a station located a little distant from the seismic fault and the second was detected at a station just above the fault plane. The water waves preceding the tsunami were detected in an early stage of the water pressure change, and seemed to be induced by a large seabed displacement associated with the Rayleigh waves, because the seismic seabed displacement showed the directivity, an elliptical particle orbit, and a predominant period ranging between 3 s and 15 s.

These two waves, which are long wave tsunami and short period wave due to Rayleigh wave, can be calculated by the simulation. Comparison with observed and simulated results including acoustic oscillations of a water column, however, should be examined in detail as a future work.

Acknowledgements:

The authors are grateful to JAMSTEC for providing the monitoring system data used in this study.

References:

JAMSTEC (2009), "Submarine Cable Data Center," http://www.jamstec.go.jp/scdc/

K. Koketsu, K. Hikima, S. Miyazaki and S. Ide (2004), "Joint inversion of strong motion and geodetic data for the source process of the 2003 Tokachi-oki, Hokkaido, earthquake," *Earth Planets Space*, **56(**3), 329-334.

T. Nagai and H. Ogawa (2004), "Characteristic of the 2003 Tokachi-off Earthquake Tsunami Profile," *Technical Note on the Port and Airport Research Institute, No. 1070*.

M. Nosov, S. V. Kolesov, A. V. Ostroukhova, A. B. Alekseev and B. M. Levin (2005), "Elastic oscillations of the water layer in a tsunami source," *Doklady Earth Sciences*, **404**(7), 1097-1100.

T. Ohmachi, H. Tsukiyama and H. Matsumoto (2001a), " Simulation of Tsunami Induced by Dynamic Displacement of Seabed due to Seismic Faulting," *Bull. Seis. Soc. Am.*, **91**(6), 1898-1909.

T. Ohmachi, H. Tsukiyama and H. Matsumoto (2001b), " Sea Water Pressure Induced by Seismic Ground Motions and Tsunamis," *ITS2001*, 595-609 (2001b).

T. Watanabe, H. Matsumoto, H. Sugioka, H. Mikada and K. Suyehiro (2004), " Offshore Monitoring System Records Recent Earthquake Off Japan's Northernmost Island," *Eos Trans. AGU*, **85**(2), doi:10.1029/2004EO020003.

Sixth International Conference on Urban Earthquake Engineering
March 3-4, 2009, Tokyo Institute of Technology, Tokyo, Japan

THE SCENARIO STUDY AND DISPERSION EFFECT ON THE TSUNAMI THREAT FROM SOUTH CHINA SEA TO TAIWAN

Tso-Ren Wu[1], and Dong-Jheng He[2]

1) Professor, Graduate Institute of Hydrological and Oceanic Sciences, National Central University, Taiwan
2) Mr., Graduate Institute of Hydrological and Oceanic Sciences, National Central University, Taiwan
tsoren@ncu.edu.tw, 92602040@cc.ncu.edu.tw

Abstract: Manila Trench, beginning from southern Taiwan, has been identified by USGS as a high-risk earthquake zone. An earthquake of magnitude 9 or higher could be generated (Huang et al., 2008) and followed by gigantic tsunamis. The tsunami arrival time from the Luzon source region to Taiwan ranges from 20 to 40 minutes only. With such a short warning time, a fast and accurate numerical prediction is the key for hazard mitigation. Solving linear or nonlinear shallow water equation (SWE) is one popular method to predict tsunamis. Without high-order partial derivative terms, SWE can be solved explicitly and requires no iterations. However, the effect from dispersion, which is ignored in SWE, might play a role when tsunamis enter the complex shallow water area around Taiwan. Boussinesq model, on the other hand, is able to calculate the dispersion effect, but requires interaction,

In this paper, both SWE and Boussinesq based numerical models, COMCOT and COULWAVE, are performed in the same earthquake-tsunami scenario. Manila Trench is divided into 33 sub-faults (Megawati et al., 2008) for the worst case scenario. An earthquake of magnitude 9.0 is assumed. The comparisons are focused on the wave height, arrival time, and wave period which is analyzed based on Fast Fourier transform. The results show that further the tsunami travels, stronger the dispersion effect becomes. The dispersion has 5% to 10% effect on reducing the leading wave height. Without the dispersion terms, the predicted arrival time is about 2 minutes earlier. After the leading tsunami waves pass by, the dispersion effect becomes strong in terms of wave period and wave height. The detailed analysis is presented in this paper. It is concluded that Non-dispersive SWE model is a suitable choice for tsunami warning, however from the research point of view, an accurate simulation which includes most of the physical phenomena is suggested.

1. INTRODUCTION

The southwest (SW) Taiwan has been considered as a region of tectonic escape because of infrequent intense seismic activities (Lacombe et al., 2001). However, the SW Taiwan is not immune to the attacks of large earthquakes. One piece of the evidence is the Pingtung dual earthquakes on 26 December 2006. Two Mw = 7.0 offshore earthquakes with 8 minutes offset along with the 40 cm tsunami record highlighted the potential tsunami hazard on SW Taiwan coast.

Motivated by the Pingtung dual earthquakes, we wish to understand the potential devastating tsunami event and the hazard to Taiwan. The epicenters of 2006 dual Pingtung earthquakes are located at the north end of Manila (Luzon) trench, where the Eurasian plate is actively subducting eastward underneath the Luzon volcanic arc on the Philippine Sea plate. In the following section, we will present a plausible earthquake rupture model constructed from seismic and geodetic data, together with hydrodynamic simulations of the potential tsunami.

Most of the hydrodynamic models for tsunami studies are based on the shallow water Equation (SWE), which is justified by the fact that the wavelength of typical tsunamis is much larger than water depth. In other words, the frequency dispersion effects are ignored. However, the long waves become intermediate water waves when they approach the continental shelf or interact with complex and shallow bathymetry. The frequency dispersion plays a role in the determination of the leading wave height. Tsunami models based on Boussinesq-type equations are capable of describing frequency dispersive effects accurately from shallow to intermediate water (Nwogu, 1993; Wei and Kirby, 1995; Kirby et al., 1998; Lynett et al., 2002; Hsiao et al., 2005). In this study, the dispersion effect on the tsunami propagation is studied. Both the SWE based model, COMCOT, and the Boussinesq equation based model, COULWAVE are adopted to perform the tsunami simulations. The tsunami characteristics and dispersion effected are presented and discussed.

2. Megathrust and Initial Free-Surface Elevation

The Manila Trench is the 1500-km-long submarine expression of the east-dipping South China Sea subduction zone, which initiated in the early Miocene (22-25 Ma) and remains active to the present day (Fuller et al., 1983; and Yumul 2000; Yumul et al, 2003; Queano et al., 2007). Along this subduction zone, the oceanic crust of the South China

Sea descends eastward beneath the Philippines, southernmost Taiwan and the intervening ocean floor (Figure 1). The broadly convex-westward shape of the Manila Trench is due to the westward migration of Luzon over the subducting oceanic slab, while the southern and northern ends of the trench are pinned at collisions at the latitudes of Palawan Island (~ 12°N, 120°E) and southern Taiwan (~ 23°N, 120°E) (Bautista et al., 2001).

Yu et al. (1999) used 35 GPS stations on Luzon Island and southern Taiwan to calculate the relative motion between Luzon arc and Eurasia. The observation was conducted for two years, from 1996 to 1998. Relative motion is greatest in northern Luzon at 19°N, moving 86 – 90 mm/yr northwestward. The velocities taper gradually towards the north and south as collision regimes pin both ends of the megathrust. The velocity vectors were decomposed into trench-normal and trench-parallel components (Figure 2). This would be analogous to the partitioning of trench-normal and trench-parallel strain across the Sunda megathrust and the strike-slip Sumatran Fault (McCaffrey et al., 2000).

It is significant that since the Spanish colonization of Luzon in the 1560s, no earthquake exceeding magnitude 7.8 has been observed (Repetti, 1946). Conservatively, it can be postulated that very large events on this megathrust have a recurrence interval exceeding 440 years. Taking a trench-normal convergence velocity of 87 mm/yr, strain of ~38 m would have accumulated over this period. Though large, this slip magnitude remains within the range of plausible scenarios. It is comparable to the 1960 Mw 9.5 Chilean earthquake, in which coseismic slip reached 40 m (Barrientos and Ward, 1990), and larger than the 2004 Aceh-Andaman event, which produced 20 m of coseismic slip (Chlieh et al., 2007).

In order to find the vertical seafloor displacement for hydrodynamic modeling, the megathrust interface was discretized into 33 rectangular sub-faults as shown in Figure 3. Alongstrike variation and the dip angle were matched closely to the continuous slip model. Two rows of sub-faults were used, where the first row, starting from sub-fault No. 1 to 18, covers the megathrust interface from the surface up to a depth of 15 km, whereas the second row (sub-fault No. 19 – 33) covers the interface from 15 to 55 km deep. Slip magnitudes were assigned directly such that the value for each rectangular sub-fault conforms to the value at its centroid position on the continuous model. This rupture model would produce an earthquake with Mw 9.0.

The thrust interface was assumed to be fully locked, i.e. the coefficient of coupling was assigned as 1. A source point was placed at the centroid of each sub-fault to simulate dislocation, and the surface deformation with that geometry was computed using an elastic half-space dislocation algorithm (Okada, 1992). The resulting seafloor deformation (Figure 3) was sampled to 2-minute (0.033°) grid resolutions. Large uplifting of up to 9 m occurs along the trench, whereas downgoing movement of up to 4 m occurs about 150 km east of the trench, mostly on Luzon Island.

4. Hydrodynamic Models

The Boussinesq-type equations include the lowest order of frequency dispersion as additions to the simplest non-dispersive long wave theory, and provide a sound and increasingly well-tested basis for the simulation of wave propagation in coastal regions. The standard Boussinesq equations for variable water depth were derived by Peregrine (1967) by using depth-averaged velocity as a dependent variable. Numerical models based on Peregrine's equations or equivalent formulations have been shown to give quite good predictions in comparison with field data (Elgar and Guza, 1985) and laboratory data (Goring, 1978), within their range of validity.

The Boussinesq-type equation model, called Coulwave, was developed by Dr. Lynett (Lynett et al., 2002), allowing for the evolution of fully nonlinear ($\varepsilon = O(1)$) and dispersive waves (up to $kh = 3$) over a variable bathymetry. Implicit finite difference scheme is adopted in this model to solve fully and weakly nonlinear Boussinesq-type equations. This model has been successfully implemented to study lab experiments and field events (Lynett et al., 2002; Hsiao et al., 2005).

In addition to the Boussinesq model, this study solves shallow water equation for comparisons. The well validated open source code, COMCOT (Cornell Multi-grid Coupled Tsunami Model), is chosen to perform the simulation. The COMCOT model has been used to investigate tsunami events, such as the 1992 Flores Islands (Indonesia) tsunami (Liu et al., 1994; Liu et al., 1995), the 2003 Algeria Tsunami (Wang and Liu, 2005), and more recently the 2004 Indian Ocean tsunami (Wang and Liu, 2006). The COMCOT model is capable of solving both linear and nonlinear shallow water equations in the spherical and Cartesian coordinate systems. The nested grid system can provide tsunami simulations in both deep-water and near-shore coastal regions. The COMCOT model also provides the moving boundary algorithm to simulate the tsunami inundation (Wang and Liu 2006). Therefore, we are able to study the near-shore tsunami events in Taiwan by adopting all the functions mentioned above.

Because of the limited pages of this paper, the authors are not intended to express the equations of Boussinesq and SWE model. The readers are referred to the Lynett et al. (2002) and Wang and Liu (2005) for the detailed Boeings model and SWE model, respectively.

3. Results and Discussions

Both Boussinesq and SWE models are performed on the 2-minute grid resolutions over an area within 112°E/124°E/10°N/27°N. Several virtual wave gauges are installed along the Taiwan coast. Based on the physical geometry, the domain is divided into four zones: Northwest (NW), Northeast (NE), Southwest (SW), and Southeast (SE) (Figure 4). Figure 5 shows the simulation comparisons between SWE model (COMCOT) and Boussinesq model

(COULWAVE). The time-history free-surface elevations measured at wave gauge are presented. Good agreement can be seen at Chenggong and Su-ao where water depth is deep. Relatively poor comparison can be observed at Houbihu, Kaohsiung, and Lanyu where water is shallow. Overall speaking, the SWE model is able to perform good simulation on the lead or large waves. However, SWE model has poor performance on predicting the intermediate water waves. This situation is especially observed at Lanyu and Hobihu where high-frequency waves can be simulated by COULWAVE model but absent in COMCOT model.

Figure 6 shows the maximum wave height recorded at each gauge location. The pink bars indicate the simulation results from COMCOT model and the blue bars are the results from COULWAVE model. The data are extracted from the first 3 leading waves to avoid the numerical error accumulated after a long simulation. The comparison shows that both COMCOT and COULWAVE models predict similar maximum wave height. In general, the maximum wave height predicted by COMCOT is slightly higher than the one from COULWAVE, e.g. Kaohsiung, Lanyu, Chenggong, and Su-ao. This is because of the non-dispersive effect in the SWE model.

Figure 7 shows the comparison of nonlinearity obtained from COMCOT and COULWAVE models at time = 45 min. The nonlinearity is defined as wave height divided by water depth. High nonlinearity can be observed in the SW Taiwan. We shall address that nonlinear SWE as well as the moving boundary technique are adopted in COMCOT model. In the COULWAVE model, weakly nonlinear and weakly dispersive Boussinesq model is adopted. In Figure 7, both models predict similar nonlinearity. Nonlinearity smaller than 0.01 dominates the offshore region which indicates linear model is capable of performing the simulation. However, nonlinear effect is significant in the near-coast shallow water area where nonlinear model is suggested.

Figure 8 shows the arrival time predicted by COMCOT and COULWAVE models. Both models predict very similar arrival time in the SW Taiwan water region. However, the difference is greater in the SE region and significant in the NE Taiwan. The tsunami wave takes only 20 minutes for arriving southern Taiwan which leaves little time for the early warning system.

In order to evaluate the threatening from each sub-fault, we perform 33 simulations and inspect the wave height record at Hobihu wave gauge location. Figure 9 shows the wave height at Hobihu caused by 33 sub-faults. The result shows that sub-faults No. 11~14 and 26~27 have the highest initial wave height. However, only sub-fault No. 27 and 16 have significant effect at Hobihu. The reason that Sub-fault No. 16 can generate great wave height is because of the short distance between the tsunami source and the Hobihu, while Sub-fault No. 27 is because of the large initial wave height and the reflecting-wall effect from the north bound of Luzon Island.

Overall speaking, the dispersion effect is significant in the SW region of Taiwan water region in terms of the free-surface elevation, and SE and NE regions in terms of the arrival time. The dispersion effect is insignificant in terms of the maximum wave height and nonlinearity. The SWE model (COMCOT) slightly early predicts the arrival time in the NE and SE regions. COMCOT also over predicts the leading wave height in SW, NE and SE regions. The difference in arrival time is about 5% to 10% in the maximum wave height.

Acknowledgements:

The authors are grateful to Professor Philip L.-F. Liu of Cornell University for providing the latest version of COMCOT and Dr. Xiaoming Wang of Cornell University for providing technical support on using COMCOT and COULWAVE.

This work is founded by the National Science Council, Taiwan. Project No: 95-2116-M-008-006-MY3.

References:

Barrientos, S.E., Ward, S.N. (1990), "The 1960 Chile earthquake - Inversion for slip distribution from surface deformation" *Geophysical Journal International*, **103**, 589-598.

Bellon, H. and Yumul, G.P. (2000), "Mio-Pliocene magmatism in the Baguio Mining District (Luzon, Philippines): age clues to its geodynamic setting," *Comptes Rendus De L Academie Des Sciences Serie II Fascicule A-Sciences De La Terre Et Des Planetes*, **331**, 295-302.

Bautista, C.B., Bautista, M.L.P., Oike, K., Wu, F.T., Punongbayan, R.S. (2001), "A new insight on the geometry of subducting slabs in northern Luzon, Philippines," *Tectonophysics*, **339**, 279-310.

Chlieh, M., Avouac, J.-P., Hjorleifsdottir, V., Song, T.-R. A., Ji, C., Sieh, K., Sladen, A., Hebert, H., Prawirodirdjo, L., Bock, Y., Galetzka, J. (2007), "Coseismic slip and afterslip of the great Mw 9.15 Sumatra-Andaman earthquake of 2004," *Bulletin of the Seismological Society of America*, **97**, S152-S173.

Elgar, S. and Guza, R.T. (1985), "Shoaling gravity waves: comparisons between field observa-tions, linear thoery and a nonlinear model," *J. Fluid Mech*., **158**:47–70.

Fuller, M., McCabe, R., Williams, S., Almasco, J., Encina, R.Y., Zanoria, A.S. (1983), "Paleomagnetism of Luzon, In: Hayes, D.E. (Eds.), "The Tectonic and Geologic Evolution of South East Asian Seas and Islands, Part II," *Geophysics Monogram Series*, **27**, 79– 94, AGU, Washington, D. C.

Megawati, K., Shaw, F., Sieh, K., Huang, Z., Wu, T.-R., Lin, Y., Tan, S.K., and Pan, T.-C. (2009), "Tsunami Hazard from the Subduction Megathrust of the South China Sea: Part I. Source Characterization and the Resulting Tsunami," *Journal of Asian Earth Sciences* (In press).

Huang, Z., Wu, T.-R., Tan, S.K., Megawati, K., Shaw, F., and Liu, X. (2009), "Tsunami Hazard from the Subduction Megathrust of the South China Sea, Part II: Hydrodynamics modeling and possible impact on Singapore," *Journal of Asian Earth Sciences* (In press).

Lacombe, O., Mouthereau, F., Angelier, J., and Deffontaines, B. (2001), "Structural geodetic and seismological evidence for tectonic escape in SW Taiwan," *Tectonophysics*, 333, 323-345.

Liu, P. L.-F., Cho, Y.-S., Briggs, M.J., Kanoglu, U., and Synolakis, C. E. (1995), "Runup of solitary waves on a circular island," *J. Fluid Mech*., **302**, 259-285.

Liu, P. L.-F., Cho, Y.-S., Yoon, S.-B., and Seo, S.-N. (1994), "Numerical simulations of the 1960 Chilean tsunami propagation and inundation at Hilo, Hawaii," *Recent development in tsunami research, M. I. El-Sabh, ed., Kluwer Academic, Dordrecht, The Netherlands*, 99-115.

Nwogu, O. (1993), "Alternative form of Boussinesq equations for nearshore wave propagation," *J. Watry, Port, Coastal, and Ocean Engrg*. (ASCE), **119**:618–638.

Wei, G. and Kirby, J.T. (1995), "A time-dependent numerical code

for extendeded Boussinesq equations," *J. Watry, Port, Coastal, and Ocean Engrg*., (ASCE), **121**:251–261.
Kirby, J.T., Wei, G., Chen, Q., Kennedy, A.B., and Dalrymple, R.A. (1998), "Fully nonlinear boussinesq wave model," *Technical Report CACR-98-06*, Univ. of Delaware.
Lynett, P., Wu, T.-R., and Liu, P.L.-F. (2002), "Modeling wave runup with depth-integrated equations," *Coastal Engineering*, v. **46**(2), p. 89-107.
McCaffrey, R., Zwick, P.C., Bock, Y., Prawirodirdjo, L., Genrich, J.F., Stevens, C.W., Puntodewo, S.S.O., Subarya, C. (2000), "Strain partitioning during oblique plate convergence in northern Sumatra: Geodetic and seismologic constraints and numerical modeling," *Journal of Geophysical Research-Solid Earth*, **105**, 28363-28376.
Hsiao, S.-C., ynett, P., Hwung, H.-H., and Liu, P. L.-F. (2005), "Numerical simulations of non-linear short waves using the multi-layer model," *J. Engrg. Mech.*, **131**(3):231–243.
Okada, Y. (1992), "Internal deformation due to shear and tensile faults in a half-space," *Bulletin of the Seismological Society of America*, **82**, 1018-1040.
Peregrine, D.H. (1967), "Long waves on a beach," *J. Fluid Mech*., **27**:815–827.
Repetti, W.C. (1946), "Catalogue of Philippine Earthquakes, 1589-1899," *Bulletin of the Seismological Society of America*, **36**, 133-322.
Wang, X., and Liu, P. L.-F. (2005), "A numerical investigation of Boumerdes- Zemmouri (Algeria) earthquake and tsunami," *Comput. Model. Eng. Sci.*, **10**(2), 171-184.
Wang, X.., and Liu, P. L.-F. (2006), "An analysis of 2004 Sumatra earthquake fault plane mechanisms and Indian Ocean tsunami," *Journal of Hydraulic research*, **44** (2), 147-154.
Yu, S.B., Kuo, L.C., Punongbayan, R.S., Ramos, E.G. (1999), "GPS observation of crustal deformation in the Taiwan-Luzon region," **Geophysical Research Letters**, **26**, 923-926.
Yumul, G.P., Dimalanta, C.B., Tamayo, R.A., Maury, R.C. (2003.), "Collision, subduction and accretion events in the Philippines: A synthesis," *Island Arc*, **12**, 77-91.

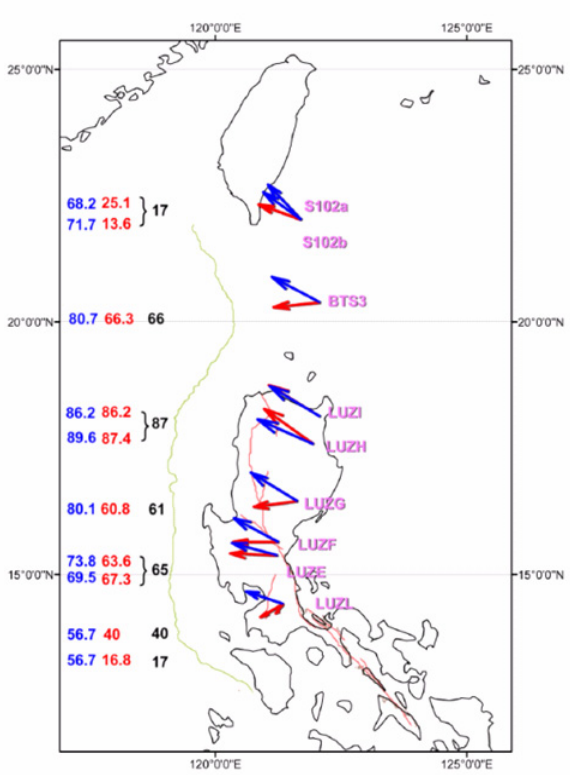

Figure2 GPS data (Yu et al., 1999) indicating motion of the converging Eurasian Plate and the Philippines Sea Plate, where the blue arrows and numbers show raw velocity values (mm/yr) taken from Yu et al. (1999), the red arrow and numbers indicate velocity values (mm/yr) resolved in the direction perpendicular to the trench front, and the black numbers give the rounded values (mm/yr) used for slip estimation..

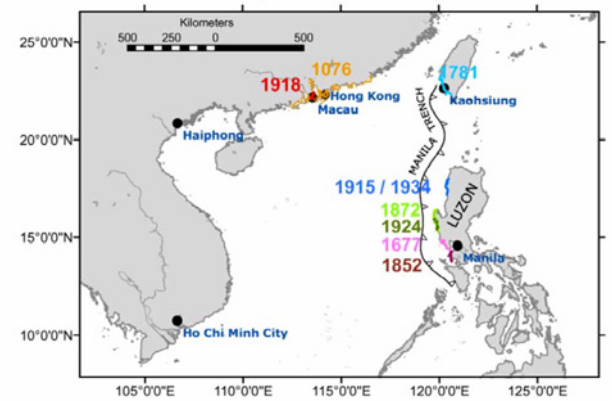

Figure 1 The South China Sea megathrust, together with population centers bordering the sea and areas affected in historical tsunami events.

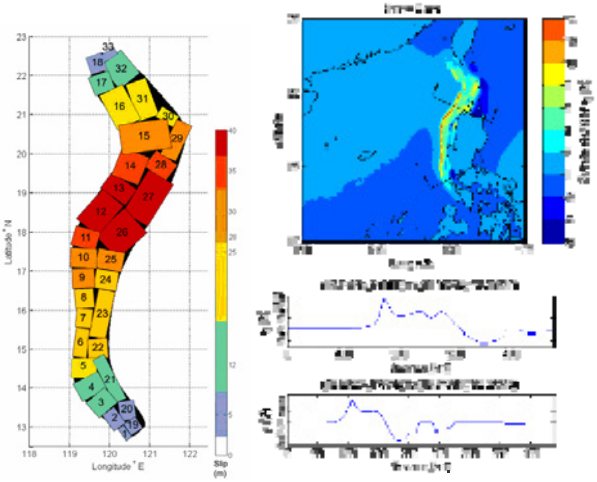

Figure 3. The discretized model for computation of seafloor displacement. (Left). The initial free-surface elevation excited by the seafloor motion (Right).

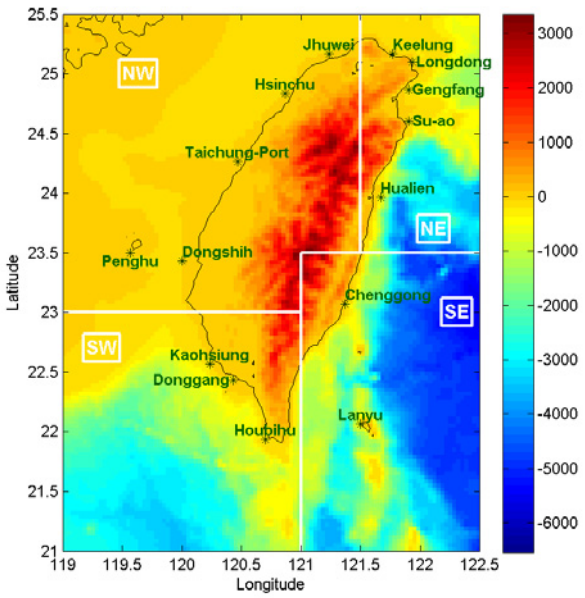

Figure 4. The locations of wave gauges. Colorbar indicates the terrain elevation in meter. Based on the physical geometry, the domain is divided into four zones: Northwest (NW), Northeast (NE), Southwest (SW), and Southeast (SE).

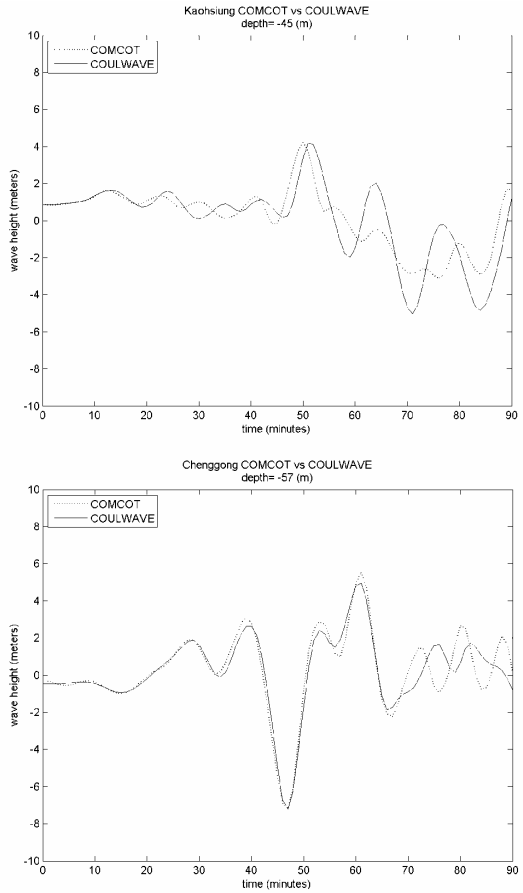

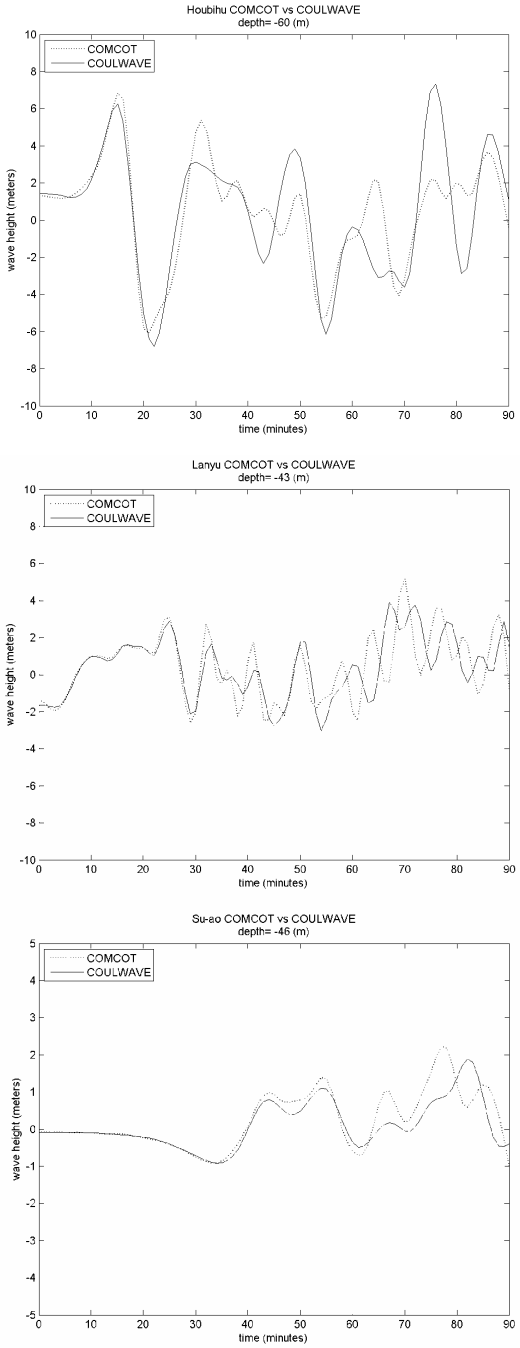

Figure 5. The time-history free-surface elevations at different tidal gauge locations.

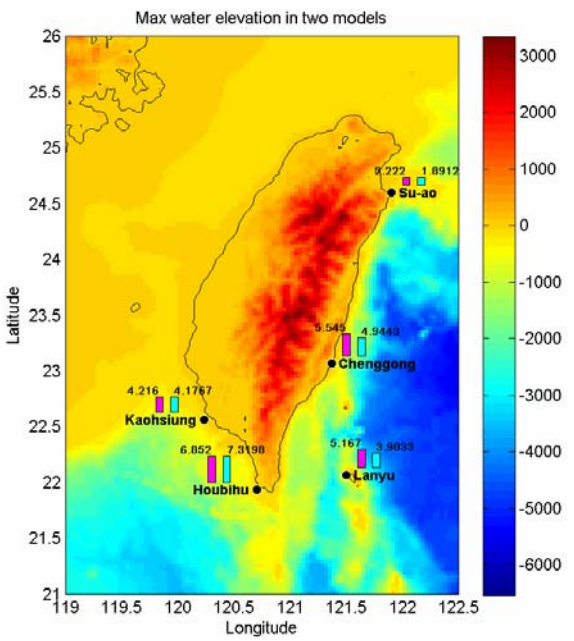

Figure 6. The maximum wave height recorded at different tidal gauge locations.

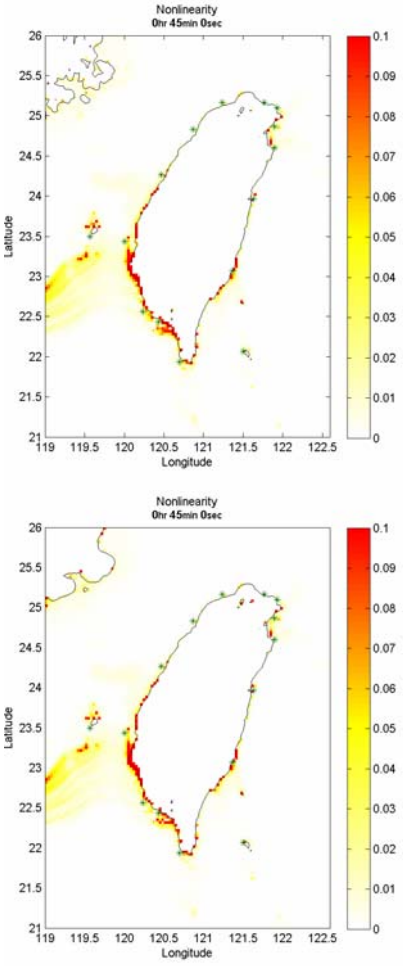

Figure 7. The nonlinearity obtained from COMCOT and COULWAVE.

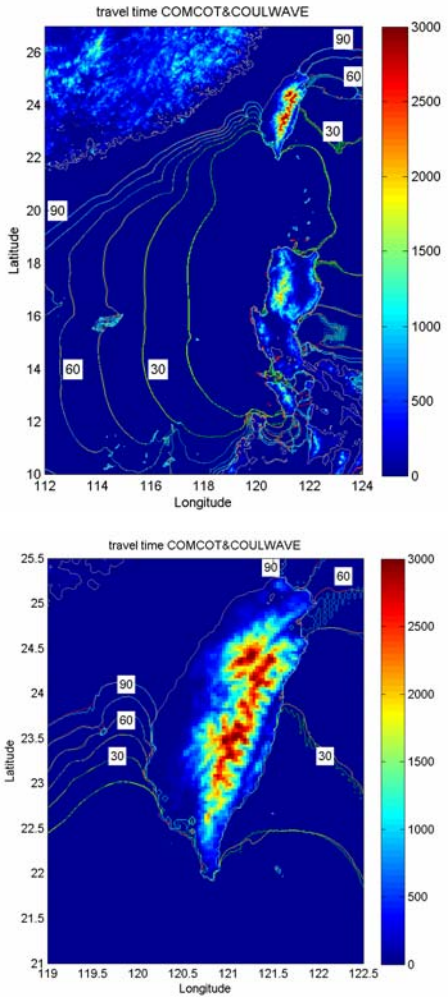

Figure 8. The arrival time predicted by COMCOT (red lines) and COULWAVE (green lines).

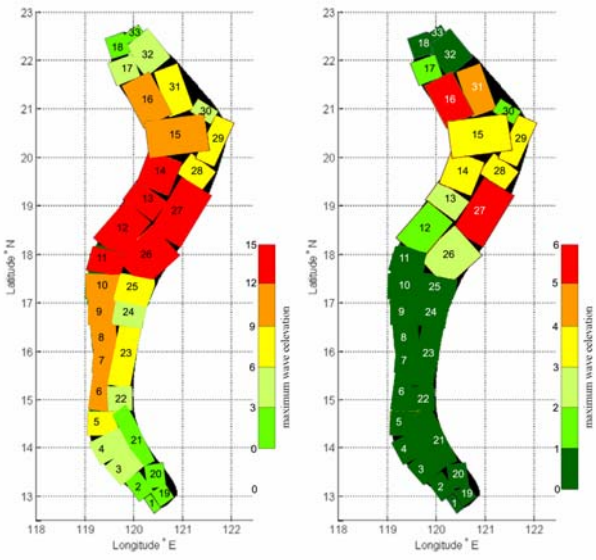

Figure 9. The maximum wave height from each sub-fault recorded at Hobihu wave gauge location. Left: initial free-surface elevation. Right: the wave height recorded at Hobihu.

Sixth International Conference on Urban Earthquake Engineering
March 3-4, 2009, Tokyo Institute of Technology, Tokyo, Japan

NUMERICAL SIMULATION OF TSUNAMI FLOW AROUND I-GIRDER BRIDGE DECKS

Tze Liang Lau[1], Tatsuo Ohmachi[2], and Shusaku Inoue[3]

1) Graduate Student, Department of Built Environment, Tokyo Institute of Technology, Japan
2) Professor, Department of Built Environment, Tokyo Institute of Technology, Japan
3) Research Associate, Department of Built Environment, Tokyo Institute of Technology, Japan
celau@eng.usm.my, ohmachi@enveng.titech.ac.jp, shusaku@enveng.titech.ac.jp

Abstract: Tsunami forces on bridges are not well understood due to the complexity of the flow around the complicated bridge configurations. Physical modeling had been conducted to investigate the forces acting on inland bridges; however, this effort encountered various shortcomings due to the limitations of the instrumentation and the scale effect. To overcome these deficiencies, numerical analysis using an Eulerian hydrodynamics code was implemented to further reinforce the findings from the hydraulic experiments. The wave flume experiment was reproduced in a two-dimensional model at the initial stage and the wave properties were obtained. It was followed by the study on tsunami flow around a three-dimensional bridge model that similar to the one performed in the physical experiment. The numerical results showed good agreement with the measured data from the experiments. The simulation was then extended to the real bridge prototype using the validated bridge model with high confidence. The flow characteristics around the bridge deck were clearly visualized. Wave pressure distributions, horizontal and vertical forces on bridge deck were presented.

1. INTRODUCTION

Tsunami load on bridges has become the interest of scientists and engineers after the devastating 2004 Indian Ocean tsunami. Various extents of damage have been demonstrated on bridges located in near- and far-field regions. The failure of the bridge structure may disrupt the commutation, but the great concern is on the possibility of hampering the emergency relief effort as had been discovered in Banda Aceh (Ghobarah et al., 2006). As a result, numerous studies (Shoji and Mori, 2006; Endoh and Unjoh, 2006; Kataoka et al., 2006; Ikari and Gotoh, 2007; Iemura et al., 2007, Lau et al., 2008a and 2008b; Sugimoto et al., 2008; Araki et al., 2008) were carried out with the purpose to investigate the extreme forces of tsunami on bridges and their failure mechanisms, either adopting the experimental and/or numerical approaches. Both approaches have their advantages and shortcomings. Experimental study may provide a realistic representation and visualization of the physical phenomenon of the wave flow; however, the scale effect, higher cost and time consuming are among the main issues. On the other hand, numerical simulation can overcome the above-mentioned drawbacks of the experimental study but the convincing outcomes from the numerical model, especially for turbulent flow, are always subjected to arguments.

Numerical studies on bridges subject to tsunamis were carried out by Endoh and Unjoh (2006) and Ikari and Gotoh (2007). Both studies used the particle method where the motion of the fluid is described in a Lagrangian coordinate. The former study used the Particle Flow Code to simulate an I-girder bridge in a two-dimensional model. The target bridge was located over a dry bed in Banda Aceh, subject to 30 m height tsunami and a constant velocity of 68 km/h. The latter study used the Moving Particle Semi-implicit (MPS) method to simulate tsunami flow around a simplified rectangular box girder bridge over a wet bed based on the experimental study by Shoji and Mori (2006). Both studies reproduced the failure mechanism of bridges subjected to tsunami attacks; however, comprehensive validation of the numerical model and the formulation of the forces were not addressed.

This paper describes the effort of the authors in conducting the numerical analysis on tsunami flow around an I-girder bridge using an Eulerian approach. The target structure of this study is a girder bridge locates over a dry land that represents an inland highway bridge near to the coastline where prone to tsunami attack from the Indian Ocean. This bridge may function as the lifeline structure during emergency and they are usually not designed to withstand any wave loading due to their location on a dry bed. Moreover, earthquake loading is not taken into consideration in most of the developing countries in the Indian Ocean region with low seismicity. Due to these facts, inland bridges are not well restrained laterally and they are highly vulnerable to tsunami attacks. Even though the target structure is based on a hypothetical bridge prototype in this study, the complete pier-deck model is considered in order to give a rational representation of the bridge structure.

The main objectives of the study are to gain an in-depth

understanding of tsunami flow around bridge decks and to formulate the forces on the bridge decks induced from tsunamis. It has to be stressed that this numerical simulation is the subsequent approach following the experimental modeling in which the details of the experimental study can be found in Lau et al. (2008a and 2008b). Physical study which adopts a 1/100 scaled model has possessed various constraints and in turn defeats the aims of the study. Due to limitation of the instrumentation and relatively small scale model, detailed measurement on the complicated bridge configuration cannot be realized and the uncertainties regarding tsunami forces on bridges remain unresolved.

2. NUMERICAL SIMULATION

2.1 Numerical Modeling

The state-of-the-art computational fluid dynamics (CFD) model, Flow-3D®, was used in this study. In order to understand the flow mechanics of tsunami at bridge decks, the wave flume experiment was reproduced numerically using a two-dimensional (2D) model in the first step. It was then followed by a detailed investigation of the bridge model using a three-dimensional (3D) numerical model. The 3D model was then extended to the prototype scale in order to study the tsunami flow around the actual bridge decks.

2.2 Numerical Methodology

Flow-3D® is a general purpose CFD package that is used to solve transient and three-dimensional flow problems. It was first released in 1985 and it has a comprehensive track record in CFD modeling. Though, the application in modeling tsunami on bridges would be a new attempt. Flow-3D® is developed based on the fractional volume of fluid (VOF) free surface tracking method as discussed in Hirt and Nichols (1981). Under this method, cells are defined with a value between zero and one for empty to fully filled cells with fluid. For partially filled cells, the slope of the free surface is determined by an algorithm that uses the surrounding cells to define a surface angle and a surface location. This method allows the steep fluid slopes to be defined and it would be applicable to describe wave breaking in tsunami run-up zone.

The model constructed in this study is an incompressible and viscous flow model. Flow-3D® employs the finite-volume-finite-difference method to solve the fluid equations of motion of the time dependent Reynolds Averaged Navier-Stokes (RANS) or known as unsteady RANS as below (Flow-3D, 2007):

$$\frac{\partial}{\partial x}(uA_x) + \frac{\partial}{\partial y}(vA_y) + \frac{\partial}{\partial z}(wA_z) = 0 \quad (1)$$

$$\frac{\partial U_i}{\partial t} + \frac{1}{V_F}\left(U_j A_j \frac{\partial U_i}{dx_j}\right) = \frac{1}{\rho}\frac{\partial p}{dx_i} + G_i + f_i \quad (2)$$

where u, v and w are the velocities in the x-, y- and z-directions; V_F is represents the volume fraction of fluid in each cell; A_x, A_y and A_z are the fractional areas open to flow in the x-, y- and z-directions; ρ is the fluid density; p is the pressure; G_i is defined as the body acceleration in the i-direction and f_i is the viscous acceleration for which a turbulence model is required for closure. For cells fully filled of fluid, V_F and A_j equal to 1.

In this study, the computational domain was discretized into an orthogonal and staggered grid of variable-sized hexahedral meshes in a Cartesian coordinates. Due to the complex bridge configuration, multi-block gridding with nested and linked grids were applied in order to reduce the computational cost while maintaining the accuracy of the results. Under this discrete structural grid system, average values of the flow parameters were placed at the center of each cell (for pressure and fractional volume of fluid) and the center of cell faces normal to their associated direction (for velocity). During the simulation, the program automatically adapted the time step to maintain the maximum Courant-Friedrichs-Lewy (CFL) numbers around 0.75; hence, the selection of the appropriate time interval at the initial stage would not be an important factor to the stability of the calculation.

Bridge and other auxiliary structures were constructed as obstacles in the numerical model. The flow obstacle was defined using a porosity technique in rectangular cell meshes called the Fractional Area/Volume Obstacle Representation (FAVOR) method as outlined in Hirt and Sicilian (1985). For cells without obstacle, the grid porosity is one and the fluid dynamics equations are to be hold. In contrast, the grid porosity is zero for cells within obstacle where no flow volume is allowed in the obstacle region. For cells that are partially filled with an obstacle, the grid porosity has a value between zero and one, based on the percent volume that is solid. The surface angle and the surface location are determined based on the same principal of VOF.

2.3 2D Wave Flume Model

Numerical computational domain for a 2D wave flume model was defined to represent the similar setup in the experimental setup as highlighted in Lau et al. (2008a and 2008b). The total length of the flume was 40 m with the height of 1 m (Figure 1). The wave maker which consisted of an elevated water tank was included. The water in the elevated tank was set at 0.9 m for the case discussed in this paper. Without the interaction with the bridge model, the flow in the flume was assumed to be remained in two-dimensional, even though after the wave breaking took place. The model was constructed using three linked blocks and one nested block with the finest mesh density as listed in Table 1. The total number of cells was 536,388. The boundaries at the upstream and the downstream of the flume model were defined as wall and outflow, respectively. The bottom and upper boundaries of the flume were assigned as symmetry. Newtonian viscosity with two equation (k-ε) turbulence model was adopted. With the time interval of 0.05 sec and the running time of 25 sec, the computation was completed in 4 hours and 41.5 minutes, using the Intel® Core™ 2 Duo processor with a 3.16GHz and an 8GB RAM's computer.

2.4 3D Bridge Model

Three-dimensional bridge model (Figure 1) was constructed individually in the latter stage due to the fact that the downscaled bridge model was comparatively small (nearly 1/12 in height and 1/290 in length) as compared to the whole flume model. The calculation of flow at the bridge model using the whole flume model for 3D flow would be too costly in the computation and the flow characteristic at the bridge model would not be easily visualized. Thus, a 3D bridge model in the computational domain of 1.5 m long by 0.25 m high (maximum) by 0.299 m width was used. The calculation was first carried out for the case without bridge model and followed with the bridge model in the flat bed as performed in the experiment. The computational domain contained three linked blocks (Blocks 1, 2 and 3) with a nested block (Block 4) of meshes. The bridge model was located in the middle block where the bridge deck was enclosed in the nested block with higher resolution (Table 2). It had end up with 141,996 cells in total and the required time to complete the running time of 5 sec (at 0.05 sec interval in the same computer capacity as mentioned in the earlier section) was 3 hours and 59 minutes.

For 3D model, six different boundaries of each block were defined. Sidewalls were defined as free slip/symmetry, the bed was no slip/wall; the top was continuative; the upstream and downstream were velocity boundary and the outlet, respectively. The inflow properties were input at the upstream boundary with time-dependent flow velocity and flow depth data, assuming these quantities were uniformly distributed along the width and the height of the flume at each time step. The input data were sourced from the experimental results and improved by the 2D model result in particularly at the initial stage of the wave as discussed in the following section.

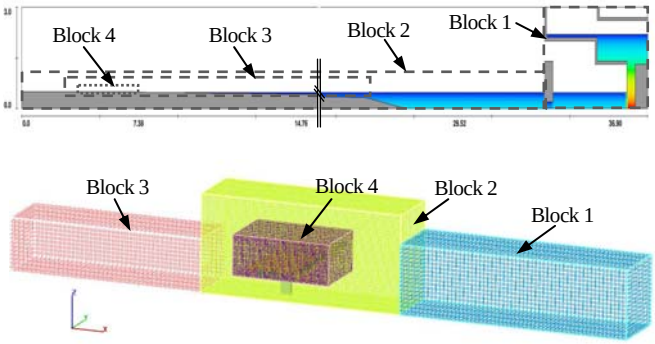

Figure 1 Numerical Models: (top) 2D Wave Flume, and (bottom) 3D Bridge

Table 1 Mesh Property for 2D Wave Flume Model

Block	Type	Total Length (m)			Interval (mm)		
		x	y	z	Δx	Δy	Δz
1	Linked	4.9	0.5	3	50	500	50
2	Linked	31	0.5	0.9	25	500	25
3	Linked	20	0.5	0.4	12.5	500	12.5
4	Nested	2	0.5	0.2	2.5	500	2.5

Table 2 Mesh Property for 3D Bridge Model

Block	Type	Total Length (m)			Interval (mm)		
		x	y	z	Δx	Δy	Δz
1	Linked	0.57	0.156	0.17	10	13	10
2	Linked	0.5	0.156	0.24	5	13	5
3	Linked	0.43	0.156	0.13	10	13	10
4	Nested	0.24	0.156	0.099	3	13	3

3. MODEL VALIDATION

3.1 2D Wave Flume Model

Validation of the numerical model is one of the most crucial steps in the numerical simulation process especially when the model is used as a numerical tool for solving nonlinear and three-dimensional flow. Without proper care in this step, the model may produce the misleading results. Therefore, special considerations on the level of uncertainties associated with the input data, the appropriateness of solution approach and the result interpretation need to be taken into considerations (Ho et al., 2003). Due to the complexity of the problem and the scarcity of the knowledge in the current research focus at this stage, the only available method to ensure the appropriateness of the computational model is to compare the computed results with the independent data measured from the physical modeling. Various flow variables are used in this stage such as the wave profile, flow depth and velocity.

Figure 2 shows the wave forms in the offshore region that are simulated from the calculation model. Solitary-like wave (top figure) is generated from the abrupt release of water from the elevated tank. The wave then breaks (middle figure) when the depth of still-water become finite in a plunging mode (bottom figure). The 2D calculation model predicts these processes well as observed in the experiments though there is slight variation in the location of wave breaking in the order less than one meter.

The measured and calculated flow depths and flow velocity at both offshore and onshore regions are demonstrated in Figure 3. The measurement point in onshore region is at the location of the bridge model. Generally, the results from the calculation are in good agreement with the experimental data in terms of the profile and the magnitude of the flow variables. In terms of the arrival time, except for the velocity record that cannot be accurately traced due to the difficulty in synchronization during the experiment, the calculated wave reaches the location of the model at approximately 0.5 sec earlier. Also observed is the calculated wave form is more uniform than the recorded data. This may due to the simplification of the 2D model in modeling wave breaking process. In addition, the velocity recorded in the experiment shows slightly lower that the calculated value in the first 0.5 sec. This is most likely caused by the inaccuracy of the measurement in the experiment for a very shallow flow of the leading edge of the wave front. Based on these comparisons, it is concluded that this 2D numerical model can represent well the physical wave flume.

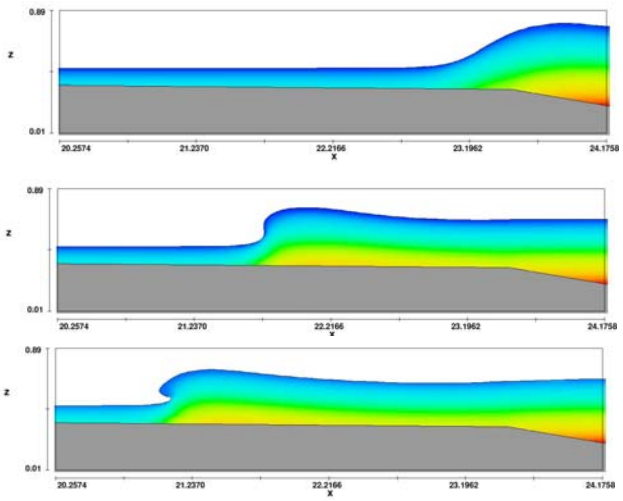

Figure 2 Wave Profiles from the Calculation

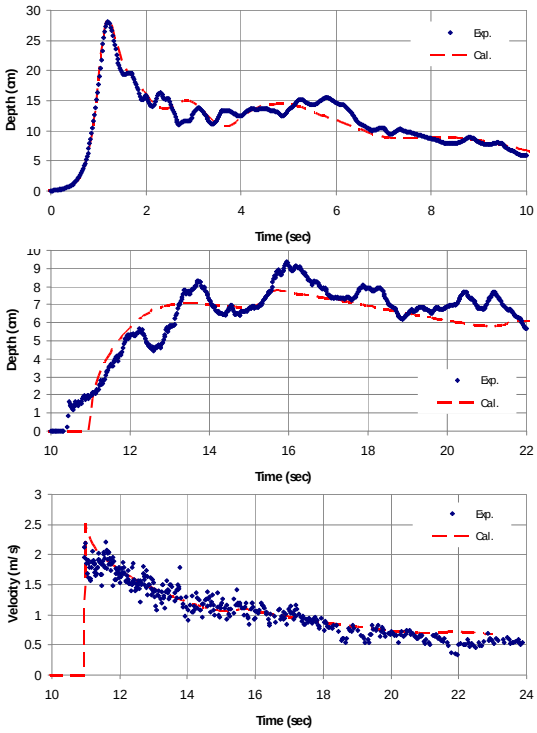

Figure 3 Comparison of Flow Variables: (a) Offshore Depth, (b) Onshore Depth, and (c) Onshore Velocity

3.2 3D Bridge Model

The bridge model was then installed at the location of about 1 m from the designated boundary. The similar wave condition was applied and several important flow parameters were obtained in order to be validated with the experimental data. These data are the pressures act on the pier and girders and the force act on the entire bridge model.

Figure 4 highlights the wave profile when the generated wave strikes the model at different time intervals. In general, the wave impingement phenomena are well simulated by the numerical model as those observed in the experiments (Lau et. al., 2008a). Due to the mesh size used in the calculation model, the fine water particles of splashing wave are hardly shown in the numerical results.

Wave pressures on the bridge model were measured in the front center face of the pier (at 0.5 cm from the bed) and the front and back face of girders (at mid-span of the girder and 6.35 cm from the bed). For validation purpose, the pressure in the front face of the pier (P1,f) and the front and back faces of the front girder (P2,f and P2,b) are discussed. The pressure time histories obtained from the physical and numerical models are compared in Figure 5 while the time histories of the total horizontal force (pressure and viscous drag forces) acts on the entire bridge model are compared in Figure 6. The variations of the calculated and the measured results are not significant. Good agreement of the pressure and the force throughout the considered time domain has evidently justified that this 3D numerical bridge model can reproduce the physical bridge model with high confidence. Consequently, this validated model is used to simulate the bridge prototype onsite as discussed in the following section.

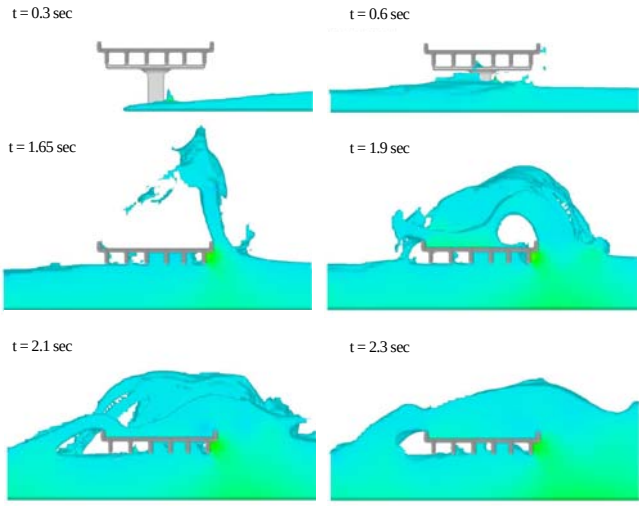

Figure 4 Wave Impingement on Bridge Model at Various Time Steps

4. BRIDGE PROTOTYPE SIMULATION

4.1 Original Bridge Prototype Layout

In the hydraulic experiment, the layout of the bridge pier has been modified in order to accommodate the size of force measuring plate on the bed. The actual distance (center to center) between the piers of 30 cm based on the bridge prototype has been shifted to a shorter distance of about 15 cm as illustrated in Lau et al. (2008a and 2008b). To obtain the realistic flow characteristic, the validated bridge model as discussed in the previous section was changed to its original layout where the piers were located at both ends of the deck span. The model was then scaled up 100 times the dimension in the model and was subjected to the equivalent wave condition as in the model. The simulation was conducted in a computer with the above-mentioned processor. CPU time is 6 hours and 49 minutes.

On top of the horizontal force, the vertical force that is not able to be measured in the physical modeling due to the limitation of the instrumentation can be obtained. Another

difficulty encountered in the hydraulic experiment is the determination of the force impingement on the bridge deck only where the complete pier-deck rigid model is used. Using the numerical model, the force acting at every component can be calculated independently. In addition, the flow at the bridge can be clearly visualized.

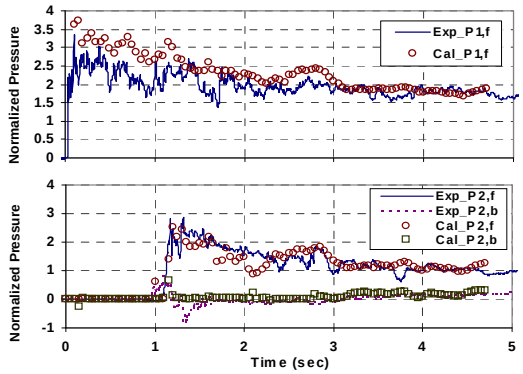

Figure 5 Pressure Time Histories: (top) Front Face of Pier, and (bottom) Front and Back Faces of Front Girder

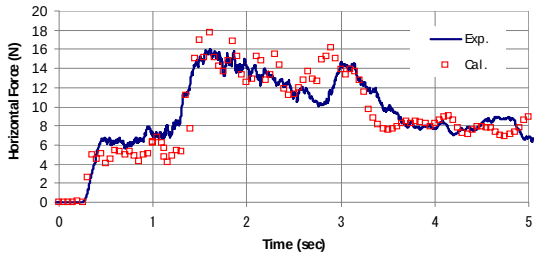

Figure 6 Comparison of the Measured and Calculated Force Time Histories of Entire Bridge Model

4.2 Pressure and Flow Field

Figure 7 displays the pressure and velocity vector at the mid-section of the considered deck in the simulation (at a quarter lengths from the pier in the prototype) during the wave attack on the original bridge layout. It can be seen that the wave impinges on the front face of the front girder with the highest magnitude. In the intermediate girders, the wave hits the front face of the intermediate girders and it circulates in clockwise direction to the back faces of the girders in front of them at different rates. The pressures exerted on the intermediate girders are relatively small except at the initial attack. The wave then splashes vertically upward and this induce certain standing wave pressure on the parapets. The highest pressure (at the stagnation point) is concentrated close to the joint of the protruded slab. At this instant of time, large air entrapment under the deck is observed. After that, the upward splash collapses on the deck and it flows on the deck in all directions. Larger pressure acts on the portion of the back parapets. Generally, the incoming wave that propagates horizontally towards the deck is separated by the deck and merged at some distances behind the deck. A portion of the wave diverts upward and the other portion of the wave flows under the deck. At the confluence point at the back of the deck, the flow reverses and attacks the back face of the deck after some times and causes vortex. The front face experiences the highest pressure. Large amount of the wave overtops the deck and imposes large additional gravity load on it as shown in Figure 8.

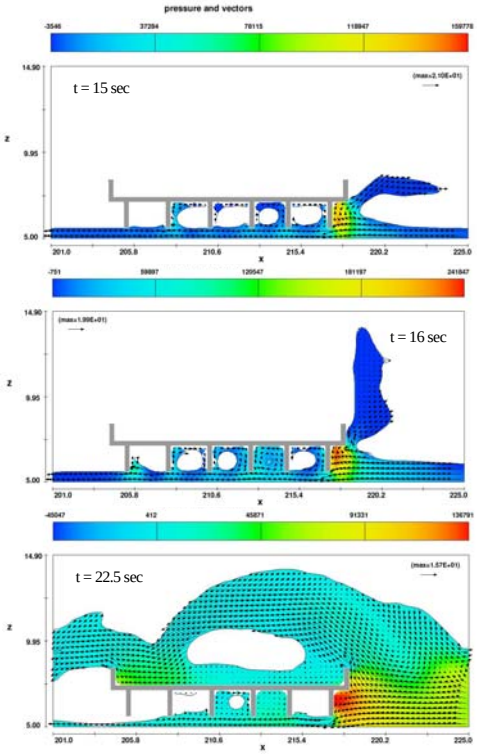

Figure 7 Pressure (Color) and Flow Velocity (Vectors)

4.2 Horizontal and Vertical Forces

Figure 8 shows the calculated results of the total horizontal and vertical forces on the deck. The positive sign in the horizontal force refers to the force in line with the flow direction while the positive and negative signs in vertical force represent the vertical uplift and the additional gravity load, respectively. The horizontal force can be generally characterized into two types, i.e. impulsive and slow-varying forces. Impulsive forces fluctuate in the range of 4 MN to 14 MN with the maximum value of nearly two times the slowly varying forces (approximately 7 MN), which occur after 34 sec from the starting time of the simulation. The vertical uplift is exerted on the deck at the initial wave attack and it is followed by the additional gravity load after second 20, where the water overtops the deck. The maximum vertical uplift and additional gravity forces are 9 MN and 18 MN, respectively.

The results show that both the maximum horizontal and vertical uplift forces happen at the same time, i.e. second 14.5. This indicates that the bridge deck is subjected to an overturning moment about the deck axis at that instant of time. Therefore, the deck may be displaced laterally, floated vertically or overturned due to the action of both forces.

4.3 Pressure Distribution

The pressure distributions along the width and the height of the deck (front face) at various times are plotted in Figure 9. As the unique configuration of the I-beam girder deck where the parapet is protruded from the front girder

plane, the pressure distribution discontinues at the slab level as shown. Due to this fact, the vertical distributions of pressures at parapets and girder are different as presented at the left of Figure 9. It can be seen that the pressure acting on the girder is dominated by hydrodynamics pressure while the pressure on the parapets is dominated by the hydrostatic pressure. The pressures are normalized with the hydrostatic pressure. The maximum normalized pressures are approximately 3 and 1.7 at the girder and parapets, respectively. At the near steady state flow, the discontinuity of the vertical distribution along the deck is much smaller.

At the right of Figure 9, the pressure distribution along the mid-height of the girder and parapets are presented. Due to the symmetrical orientation, only the first half of the distribution with the pier located on the left side is shown. The wave acting on the bridge deck is highly 3D and the pressure fluctuates from one point to another. The maximum pressure occurs at the region near to the pier by the upward splashing. Thereafter, the distribution is non-uniform along the girder until the flow become nearly steady.

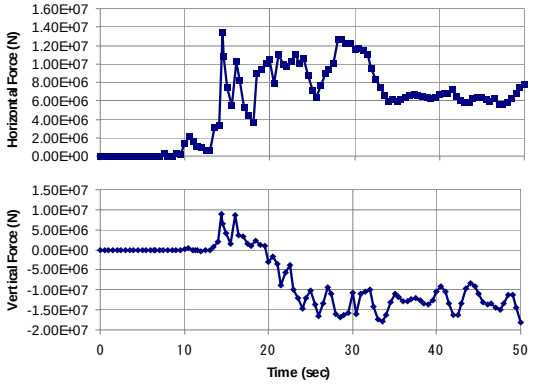

Figure 8 Total Force Time Histories on the Deck Prototype: (top) Horizontal, and (bottom) Vertical

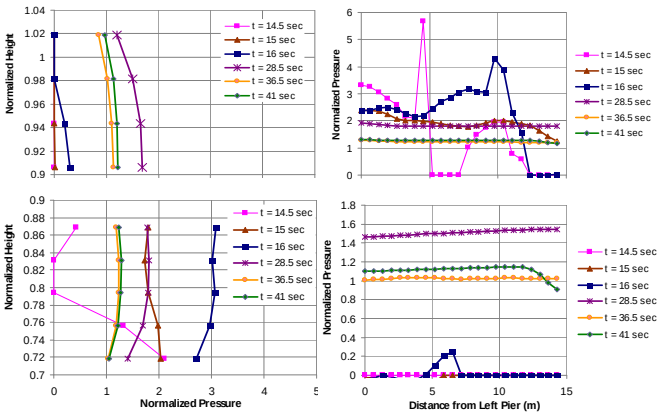

Figure 9 Vertical (left) and Horizontal (right) Pressure Distributions: (top) Parapets, and (bottom) Girder

5. CONCLUSIONS

Numerical simulation can predict well the physical phenomena of the fluid flow around the bridge deck. It is a powerful tool to be used as the alternative approach for physical modeling to obtain detailed flow characteristics. It is important that independent data should be made available for the model validation. The computed results provide beneficial information of tsunami forces on bridges.

Acknowledgements:

The authors would like to express their sincere gratitude to JICA AUN/SEED-Net for providing the financial support to the first author's short term study at Tokyo Institute of Technology, Japan on this research.

References:

Araki, S., Nakajima, Y., Deguchi, I. and Itoh, S. (2008), "Experimental Study on Tsunami Fluid Force Acting on Bridge Beam Near River Mouth," *Journal of Coastal Engineering*, Japan Society of Civil Engineers, **55**(2), 866-870 (in Japanese).

Endoh, K. and Unjoh, S. (2006), "Analitical Study on the Response Characteristics of Bridges against Tsunami," *Proceedings of the 61st JSCE Annual Meeting*, Japan Society of Civil Engineers, 869-870 (in Japanese).

Flow-3D. (2007), "Flow-3D User Manual: Excellence in Flow Modeling Software, v 9.2," Flow Science, Inc., Santa Fe, N.M.

Ghobarah, A., Saatcioglu, M. and Nistor, I. (2006), "The Impact of the 26 December 2004 Earthquake and Tsunami on Structures and Infrastructure," *Engineering Structures*, **28**, 312-326.

Hirt, C.W. and Nichols, B.D. (1981), "Volume of Fluid (VOF) Method for the Dynamics of Free Boundaries," *Journal of Computational Physics*, **39**, 201-225.

Hirt, C.W. and Sicilian, J.M. (1985), "A Porosity Technique for the Definition of Obstacles in Rectangular Cell Meshes, *Proceedings of the 4th International Conference on Ship Hydrodynamics*, National Academy of Science, Washington, D.C., 1-19.

Ho, D.K.H, Donohoo, S.M., Boyes, K.M. and Lock, C.C. (2003), "Numerical Analysis and the Real World: It Looks Pretty but Is It Right?" *Proceedings of the NAFEMS World Congress*, The International Association for the Engineering Analysis Community, Orlando, FL.

Iemura, H., Pradono, M.H., Yasuda, T. and Tada, T. (2007), "Experiments of Tsunami Force Acting on Bridge Models," *Journal of Earthquake Engineering*, Japan Society of Civil Engineers, **29**, 531-536

Ikari, H. and Gotoh, H. (2007), "Numerical Simulation of Washed Process of Girder Bridge by Tsunami Run-up," *Journal of Coastal Engineering*, Japan Society of Civil Engineers, **54**(1), 211-215 (in Japanese).

Kataoka, S., Kusakabe, T. and Nagaya, K. (2006), "Wave Forces Acting on Bridge Girders Struck by Tsunami," *Proceedings of the 12th Japan Earthquake Engineering Symposium*, Japan Association of Earthquake Engineering, 154-157 (in Japanese).

Lau, T.L., Lukkunaprasit, P., Ruangrassamee, A. and Ohmachi, T. (2008a), "Performance of Bridges with Solid and Perforated Parapets in Resisting Tsunami Attacks," *Proceedings of the Symposium on Giant Earthquakes and Tsunamis*, Phuket, 155-160.

Lau, T.L., Lukkunaprasit, P., Ruangrassamee, A. and Ohmachi, T. (2008b), "Physical Modeling: An Estimation of Wave Forces on an Inland Bridge subject to Tsunami Bores," *Proceedings of the 5th International Conference on Urban Earthquake Engineering*, Tokyo Institute of Technology, 441-446.

Shoji, G. and Mori, Y. (2006), "Hydraulic Model Experiment to Simulate the Damage of a Bridge Deck subjected to Tsunamis," *Journal of Coastal Engineering*, Japan Society of Civil Engineers, **53**(2), 801-805 (in Japanese).

Sugimoto, T., Usui, T. and Unjoh, S., (2008), "The Effect of Tsunami and Storm Surge on Bridges in Flume Test," *Civil Engineering Journal*, **50**(11), 24-29 (in Japanese).

Center for Urban Earthquake Engineering (CUEE)
Tokyo Institute of Technology

O-okayama Office
Department of Architecture and Building Engineering
Tokyo Institute of Technology
M1-39 2-12-1 O-okayama, Meguro-ku, Tokyo, Japan 152-8552
Tel: +81-(0)3-5734-3200 Fax: +81-(0)3-5734-3200

Suzukakedai Office
Department of Built Environment
Tokyo Institute of Technology
G3-11 4259 Nagatsuta-cho, Midori-ku, Yokohama, Japan 226-8502
Tel: +81-(0)45-924-5576 Fax: +81-(0)45-924-5199

Email:office@cuee.titech.ac.jp/
URL:http://www.cuee.titech.ac.jp/